Springer

Handbook of Mechanical Engineering

Grote
Hefazi
Editors

2nd Edition

Springer

Springer Handbook of Mechanical Engineering

Springer Handbooks provide a concise compilation of approved key information on methods of research, general principles, and functional relationships in physical and applied sciences. The world's leading experts in the fields of physics and engineering will be assigned by one or several renowned editors to write the chapters comprising each volume. The content is selected by these experts from Springer sources (books, journals, online content) and other systematic and approved recent publications of scientific and technical information.

The volumes are designed to be useful as readable desk book to give a fast and comprehensive overview and easy retrieval of essential reliable key information, including tables, graphs, and bibliographies. References to extensive sources are provided.

Springer Handbook of Mechanical Engineering

Karl-Heinrich Grote, Hamid Hefazi (Eds.)

2nd. Edition
With 1481 Figures and 381 Tables

Springer

Editors
Karl-Heinrich Grote
Otto-von-Guericke-Universität
Magdeburg, Germany
and
University of Western Norway (HVL)
Bergen, Norway

Hamid Hefazi
State University of New York (SUNY)-Korea
Incheon, Republic of Korea

ISBN 978-3-030-47034-0 e-ISBN 978-3-030-47035-7
https://doi.org/10.1007/978-3-030-47035-7

This Springer imprint is published by the registered company Springer Nature Switzerland AG.
The registered company address is: Gewerbestrasse 11, 6330 Cham, Switzerland

Preface

The Springer Handbook series is an essential resource for scientists and practicing engineers, as well as students during all phases of their studies.

The first edition of the *Springer Handbook of Mechanical Engineering* was published in 2008 and was very well received by the mechanical engineering community worldwide. As early as 2015, the publication of an updated second edition of the handbook was discussed with Springer, based on suggestions from authors and readers to include new developments in mechanical engineering. Finalizing the publication took a while, and the mechanical engineering handbook team is now more than happy to present the second edition of the *Springer Handbook of Mechanical Engineering*".

Mechanical engineering is a broad and complex field within the world of engineering and has close relations to many other fields. This handbook provides a broad overview of many areas of the discipline. Springer, however, recommends supplementing this handbook with other editions of Springer Handbooks, such as the Springer Handbook of Robotics, the Springer Handbook of Metrology and Testing, the Springer Handbook of Experimental Solid Mechanics, the Springer Handbook of Experimental Fluid Mechanics, and the Springer Handbook of Materials Data, as well as other specialized literature as references.

Mechanical engineering is also an important economic factor for all industrialized countries, as well as for the global market. Rapid developments in the field allow for a wide range of international competition for products and processes in mechanical engineering. In order to stay on top of the scientific findings and to apply existing knowledge, it is important to renew and continuously update existing information.

We have been privileged to work with approximately 100 authors from all around the world to gather selected and useful information about the discipline. The book can not claim to cover all and every aspect in all areas where mechanical engineers contribute their expertise and knowledge towards solving major societal challenges. However, this handbook will be a valuable guide for all who design, develop, manufacture, operate, and use mechanical artefacts. Compared to the first edition, many chapters, including those about machine elements, electronics, materials in mechanical engineering, and transportation, have been completely rewritten or substantially revised. We also hope to initiate interest in the field of mechanical engineers in others. For example, high-school students can get a first glance and learn about options in engineering and possible career choices.

As with all books of this kind, the individual authors are responsible for their chapters, and questions should be directly addressed to them.

Since Dr Erik Antonsson has entered a new challenging career path, the continuing editor Dr Karl-Heinrich Grote welcomed Dr Hamid Hefazi as coeditor. Furthermore, Dr Werner Skolaut thankfully came out of retirement again to also join the team.

We would like to express our gratitude and thanks to all of the authors of this handbook, who each devoted a considerable amount of time to this project. We would like to thank them for their patience and cooperation during the seemingly ever-lasting preprinting process, and we hope for a long-lasting partnership in this ambitious project. We would also most sincerely like to thank our managers and friends at Springer and le-tex: Dr Judith Hinterberg and others at Springer who were always most cooperative and supportive of this handbook, Petra Möws and the team at le-tex, who did a wonderful job in preparing the diagrams and graphics to meet the high standards of the Springer Handbook series. The printer has done a fantastic job – as always – in printing and binding. We would also like to thank all the people we worked with in the departments, universities, and industry who supported the time and effort spent on this book.

Finally, we know that there is always room for improvement – with this handbook as with engineering products and approaches. We, as well as the other authors, welcome your constructive hints, comments, and criticism. We would also like to draw your attention to what has been accomplished in and with this Springer Handbook of Mechanical Engineering, for the benefit of the engineering world and our society – done by engineers worldwide!

Berlin (Germany),
Incheon (South Korea),
Heidelberg (Germany)
2021

Karl-Heinrich Grote
Hamid Hefazi
Werner Skolaut

About the Editors

Dr Karl-Heinrich Grote German and US citizen, is Full Professor in the Department of Machine Design at the Otto-von-Guericke University in Magdeburg, Germany. He received his "Diploma in Engineering" (Master's of Science in Mechanical Engineering) in 1979 and his "Dr-Ing" in Engineering) in 1984, both from the Technical University in Berlin, Germany. From 1984 to 1986 he was postdoctoral researcher in Long Beach, USA and returned to Germany to become the Technical Chief Manager for Engineering Design at the "Ingenieurgesellschaft für Auto und Verkehr, IAV" in Berlin (Engineering Group for Automotive and Transportation, Berlin). From June 1995 to October 2020, he was Chair and Director of the Department of Machine Design at the Otto-von-Guericke University in Magdeburg, Germany, where he was also Vice President for Academic Affairs from 1989 to 2001. Since 1997 he has been serving as Chair of the Scientific Advisory Board of the Experimental Factory in Magdeburg. From 2002 to 2004 he was Visiting Full Professor of Mechanical Engineering at the California Institute of Technology (Caltech), Pasadena, USA. From 2005 to 2017 Professor Grote was the Dean of the College of Mechanical Engineering at the Otto-von-Guericke University, Magdeburg, Germany. In 2013, he joined the Department of Mechanical and Marine Engineering of HVL, Western Norway University of Applied Science, Bergen, Norway, as Professor II. Dr Grote´s research interests are all mechanical aspects within the practical engineering area and new technologies of creating and manufacturing design solutions for state-of-the-art products and new ideas. Over 330 publications as author/co-author and advising more then 90 dissertations cover his research projects and results in mechanical engineering since 1990.

In 1995, Dr Grote became editor of the "DUBBEL- Taschenbuch für den Maschinenbau" (Handbook of Mechanical Engineering) – the standard handbook for the German-speaking engineering community, with over 1 million copies sold and in 2002 co-author/editor of the book "Pahl/Beitz: Engineering Design" (all books published by Springer). Dr Grote is the 1993 recipient of the Ring of Honor (Young Engineers Award) from the German Society of Professional Engineering (VDI) and the 1993 recipient of the "Thomson-Ramo-Wooldridge (TRW) Excellence Award" in the USA and in 2015 the recipient of an Honorary Doctors Degree (Dr. h.c.) from Kiev Institute of Technology.

Dr Hamid Hefazi is Professor and Chair of the Mechanical Engineering Department at the State University of New York (SUNY) – Korea located in Incheon, Republic of Korea. He received his PhD in Aerospace Engineering from the University of Southern California in 1985. He has extensive teaching and research experience in aerodynamics and the design and optimization of aerospace systems. He has been involved in a broad range of teaching and research topics in fluid mechanics, aeroacoustics, and aerodynamics. His more recent research has been focused on hydrodynamics, advanced multidisciplinary design and optimization (MDO) methods, and their applications to naval engineering. He has authored more than 75 journal publications and 4 book chapters. Dr Hefazi has been the principal investigator for more than 100 externally funded research projects, including projects sponsored by the US National Science Foundation, NASA, the US Office of Naval Research, and the Boeing Company, among others. He has organized several national conferences and taught many short courses for industry. Dr Hefazi has worked extensively as a consultant for wind-energy companies and holds a patent on an innovative vertical axis wind turbine. Dr Hefazi served as the Director of the "Boeing Technology Center", at California State University, Long Beach, for 12 years. The center worked on high priority research and development projects of interest to the aerospace industry. He is the recipient of many awards, including the Boeing Company's Silver Eagle award for innovation and the US Department of Defense's Nunn-Perry Award for 2005 and 2006 for his work with Northrop Grumman Space Technology. He is an associate fellow of the American Institute of Aeronautics and Astronautics.

List of Authors

Gritt Ahrens
EvoBus GmbH
Corporate Quality Daimler Buses
Neu-Ulm, Germany
gritt.ahrens@daimler.com

Daniel Ausling
TUNRA Bulk Solids
The University of Newcastle
Shortland, NSW, Australia
daniel.ausling@newcastle.edu.au

Stanley Baksi
CAE Braking, Active and Passive Safety Systems
ZF Friedrichshafen AG
Koblenz, Germany
stanley.baksi@zf.com

Dirk Bartel
Institute of Machine Design
Otto von Guericke University Magdeburg
Magdeburg, Germany
dirk.bartel@ovgu.de

Asfaw Beyene
Mechanical Engineering
San Diego State University
San Diego, USA
abeyene@sdsu.edu

Thomas Böllinghaus
Department 9 – Component Safety
Bundesanstalt für Materialforschung und -prüfung (BAM)
Berlin, Germany
thomas.boellinghaus@bam.de

Alois Breiing
Institut für mechanische Systeme (IMES), Zentrum für Produkt-Entwicklung (ZPE)
Eidgenössische Technische Hochschule Zürich (ETH)
Zurich, Switzerland
breiing@imes.mavt.ethz.ch

Gerry Byrne
School of Mechanical and Materials Engineering
University College Dublin
Dublin, Ireland
gerald.byrne@ucd.ie

Bin Chen
TUNRA Bulk Solids
Shortland, NSW, Australia
bin.chen@newcastle.edu.au

Wei Chen
School of Engineering, Faculty of Engineering and Built Environment
University of Newcastle
Callaghan, NSW, Australia
w.chen@newcastle.edu.au

Norge I. Coello Machado
Facultad de Ingeniería Mecánica e Industrial
Universidad Central "Marta Abreu" de Las Villas
Santa Clara, Cuba
norgec@uclv.edu.cu

Carl E. Cross
Joining Technology
Federal Institute for Materials Research and Testing (BAM)
Berlin, Germany
carl-edward.cross@bam.de

Frank Dammel
Institute of Technical Thermodynamics
Technical University Darmstadt
Darmstadt, Germany
dammel@ttd.tu-darmstadt.de

Berend Denkena
Produktionstechnisches Zentrum Hannover,
Institut für Fertigungstechnik und Werkzeugmaschinen
Leibniz Universität Hannover
Garbsen, Germany
denkena@ifw.uni-hannover.de

Ludger Deters
Institute of Machine Design
Otto von Guericke University Magdeburg
Magdeburg, Germany
ludger.deters@ovgu.de

Tim Donohue
TUNRA Bulk Solids
University of Newcastle
Shortland, NSW, Australia
timothy.donohue@newcastle.edu.au

Frank Engelmann
Industrial Engineering
Ernst-Abbe-Hochschule Jena University of Applied Science
Jena, Germany
frank.engelmann@eah-jena.de

Thora Falkenreck
Rheinmetall Landsysteme GmbH
Kassel, Germany
thora.falkenreck@rheinmetall.com

David C. Fleming
Dept. of Aerospace, Physics and Space Sciences
Florida Institute of Technology
Melbourne, FL, USA
dfleming@fit.edu

Jens Freudenberger
Department for Metal Physics
Leibniz-Institute for Solid State and Materials Research Dresden
Dresden, Germany
j.freudenberger@ifw-dresden.de

Jon H. van Gerpen
Department of Biological and Agricultural
University of Idaho
Moscow, ID, USA
jonvg@uidaho.edu

Karl-Heinrich Grote
Otto-von-Guericke-Universität
Magdeburg, Germany
karl.grote@ovgu.de

Thomas Guthmann
Industrial Engineering
Ernst-Abbe-Hochschule Jena University of Applied Science
Jena, Germany
thomas.guthmann@eah-jena.de

Timothy Gutowski
Department of Mechanical Engineering
Massachusetts Institute of Technology
Cambridge, MA, USA
gutowski@mit.edu

Takeshi Hatsuzawa
The Laboratory for Future Interdisciplinary Research of Science and Technology (FIRST)
Tokyo Institute of Technology
Yokohama, Japan
hatsuzawa.t.aa@m.titech.ac.jp

Markus Hecht
Institute of Land and Sea Transport Systems,
Department of Rail Vehicles
Berlin University of Technology
Berlin, Germany
markus.hecht@tu-berlin.de

Hamid Hefazi
State University of New York (SUNY)-Korea
Incheon, Korea, Republic of
hamid.hefazi@sunykorea.ac.kr

Martin Heilmaier
Institute for Applied Materials (IAM)
Karlsruhe Institute of Technology (KIT)
Karlsruhe, Germany
martin.heilmaier@kit.edu

Klaus Herfurth
Pulheim, Germany
klaus.herfurth@t-online.de

Detlef von Hofe
Krefeld, Germany
detlef.von.hofe@web.de

Dusan Ilic
School of Engineering, Newcastle Institute for Energy and Resources
University of Newcastle
Callaghan, NSW, Australia
dusan.ilic@newcastle.edu.au

Mark Jones
School of Engineering, Faculty of Engineering and Built Environment
University of Newcastle
Callaghan, NSW, Australia
mark.jones@newcastle.edu.au

Thomas Kannengiesser
Joining Technology
Federal Institute for Materials Research and Testing (BAM)
Berlin, Germany
thomas.kannengiesser@bam.de

Bernhard Karpuschewski
Leibniz Institute for Materials Engineering IWT,
Manufacturing Technologies
University of Bremen
Bremen, Germany
karpu@iwt-bremen.de

André Katterfeld
Institute of Logistics and Material Handling Systems
Otto-von-Guericke-Universität Magdeburg
Magdeburg, Germany
andre.katterfeld@ovgu.de

Brent Keppy
PS/ECW1-NA
Robert Bosch LLC
Waterford, MI, USA
brent.keppy@us.bosch.com

Justin Kern
Powertrain Solutions
Robert Bosch LLC
Farmington Hills, MI, USA
justin.kern@us.bosch.com

Dwarkadas Kothari
School of Electrical Sciences
VIT University
Vellore, India
dkothari@ces.iitd.ac.in

Günter Kunze
Lehrstuhl für Baumaschinen- und Fördertechnik
TU Dresden
Dresden, Germany
guenter.kunze@tu-dresden.de

Ajay Mathur
HSE and Plant Engineering
Indohaan Technologies Pvt Ltd
Faridabad, India
amathur@indohaan.com

Gerhard Mook
Department of Mechanical Engineering Institute of Materials and Joining Technology and Materials Testing
Otto-von-Guericke University
Magdeburg, Germany
gerhard.mook@ovgu.de

Hamidreza Najafi
Department of Mechanical and Civil Engineering
Florida Institute of Technology
Melbourne, FL, USA
hnajafi@fit.edu

Jay M. Ochterbeck
Department of Mechanical Engineering
Clemson University
Clemson, SC, USA
jochter@clemson.edu

João Oliveira
Scenario Automation Ltda
São Carlos, SP, Brazil
oliveirajfg@gmail.com

Hendrik Otto
Institute for Logistics and Material Handling
Otto-von-Guericke Universität Magdeburg
Magdeburg, Germany
hendrik.otto@ovgu.de

Vince Piacenti
Powertrain Solutions
Bosch LLC
Farmington Hills, MI, USA
vince.piacenti@us.bosch.com

Jörg Pieschel
Institute of Materials and Joining Technology
Otto-von-Guericke University
Magdeburg, Germany
pieschel@mb.uni-magdeburg.de

Stefan Pischinger
Institute for Combustion Engines
RWTH Aachen University
Aachen, Germany
pischinger@vka.rwth-aachen.de

Martin Poppe
Electrial Engineering and Computer Science
Muenster University of Applied Sciences
Steinfurt, Germany
poppe@fh-muenster.de

Didier M. Priem
Department of Materials
École Centrale Nantes
Nantes, France
didier.priem@ec-nantes.fr

Michael Rhode
Department 9 – Component Safety
Bundesanstalt für Materialforschung und -prüfung (BAM)
Berlin, Germany
michael.rhode@bam.de

Alan Roberts
TUNRA Bulk Solids Handling Research Associates and Centre for Bulk Solids and Particulate Technologies
University of Newcastle
Callaghan, NSW, Australia
alan.roberts@newcastle.edu.au

Shuichi Sakamoto
Faculty of Engineering
Niigata University
Niigata, Japan
sakamoto@eng.niigata-u.ac.jp

Stefan Scharf
Fraunhofer Institute for Factory Operation and Automation IFF, Institute of Manufacturing Technology and Quality Management IFQ
Otto-von-Guericke-University Magdeburg
Magdeburg, Germany
stefan.scharf@ovgu.de

Markus Schleser
Welding and Joining Institute
RWTH Aachen University
Aachen, Germany
schleser@isf.rwth-aachen.de

Marc Claus Schmitt
Powertrain
BMW Group
Munich, Germany
marc-claus.schmitt@bmw.de

Meinhard T. Schobeiri
Department of Mechanical Engineering
Texas A&M University
College Station,Texas, USA
tschobeiri@tamu.edu

Jan Scholten
Group of Construction Machinery and Materials Handling
Ruhr-Universität Bochum
Bochum, Germany
jan.scholten@bmft.rub.de

Islam Shyha
Mechanical and Construction Engineering
Northumbria University at Newcastle
Newcastle upon Tyne, UK
islam.shyha@northumbria.ac.uk

Aneel A. Singh
Powertrain Solutions
Robert Bosch, LLC
Farmington Hills, MI, USA
aneel.singh@us.bosch.com

Jean-Baptiste R. G. Souppez
Mechanical, Biomedical & Design Department, School of Engineering and Technology, College of Engineering and Physical Sciences
Aston University
Birmingham, UK
j.souppez@aston.ac.uk

Vivek Srivastava
Hindalco Innovation Center
Hindalco Industries Ltd
Taloja, Navi Mumbai, India
vivek.s.srivastava@adityabirla.com

Peter Stephan
Institute of Technical Thermodynamics
Technical University Darmstadt
Darmstadt, Germany
pstephan@ttd.tu-darmstadt.de

Henning Strubelt
Chair of Warehouse Technology, Warehouse Planning, Warehouse Organization
Bremerhaven University of Applied Sciences
Bremerhaven, Germany
hstrubelt@hs-bremerhaven.de

P.M.V. Subbarao
Mechanical Engineering Department
Indian Institute of Technology
New Delhi, India
pmvs@mech.iitd.ac.in

Jens Sumpf
Institute of Materials Handling, Conveying and Plastics Engineering
Chemnitz University of Technology
Chemnitz, Germany
jens.sumpf@mb.tu-chemnitz.de

A. Erman Tekkaya
Institut für Umformtechnik und Leichtbau
Technische Universität Dortmund
Dortmund, Germany
erman.tekkaya@udo.edu

Gnana Bhaskar Tenali
Mathematical Sciences
Florida Institute of Technology
Melbourne, FL, USA
gtenali@fit.edu

Marcel Todtermuschke
Department of Assembling Techniques
Fraunhofer-Institute for Machine Tools and Forming Technology
Chemnitz, Germany
marcel.todtermuschke@saxonia.net

Helmut Tschöke
Institute of Mobile Systems
Otto-von-Guericke University
Magdeburg, Germany
helmut.tschoeke@ovgu.de

Anatoly Vereschaka (deceased)

Nikolaus Wagner
ISF Welding and Joining Institute
RWTH Aachen University
Aachen, Germany
wa@isf.rwth-aachen.de

Ulrich Wendt
Freelance Materials Science Consultant
c/o Otto-von-Guericke University, Department of Materials and Joining Technology
Magdeburg, Germany
wendt@ovgu.de

Steffen Wengler
Institute of Manufacturing Technology and Quality Management
Otto-von-Guericke-University Magdeburg
Magdeburg, Germany
swengler@ovgu.de

Chris Wensrich
School of Engineering, Faculty of Engineering and Built Environment
University of Newcastle
Callaghan, NSW, Australia
christopher.wensrich@newcastle.edu.au

Craig Wheeler
School of Engineering, Faculty of Engineering and Built Environment
University of Newcastle
Callaghan, NSW, Australia
craig.wheeler@newcastle.edu.au

Steven D. White
2466 Sunset Terrace Ln.
West Bloomfield, MI, 48324, USA
steve.white@us.bosch.com

Kenneth Williams
School of Engineering, Newcastle Institute for Energy and Resources
University of Newcastle
Callaghan, NSW, Australia
ken.williams@newcastle.edu.au

Lutz Wisweh
Faculty of Mechanical Engineering
Otto-von-Guericke-University Magdeburg
Magdeburg, Germany
lutz.wisweh@ovgu.de

Johannes Wodara
Schweißtechnik-Consult
Magdeburg, Germany
johanneswodara@hotmail.com

Klaus Woeste
Aachen, Germany
wo@isf.rwth-aachen.de

Hen-Geul Yeh
Department of Mechanical and Aerospace Engineering
California State University Long Beach
Long Beach, CA, USA
henry.yeh@csulb.edu

Hsien-Yang Yeh
Department of Electrical Engineering
California State University
Long Beach, CA, USA
hyyeh@csulb.edu

Shouwen Yu
School of Aerospace
Tsinghua University
Beijing, China
yusw@mail.tsinghua.edu.cn

Contents

List of Abbreviations XXI

Part A Fundamentals

1 **Introduction to Mathematics**
Gnana Bhaskar Tenali 3
1.1 Linear Algebra 4
1.2 Differential Equations 8
1.3 The Laplace Transform 13
1.4 Fourier Analysis 16
1.5 Complex Analysis 19
References 23

2 **Mechanics**
David C. Fleming, Hen-Geul Yeh, Hsien-Yang Yeh, Shouwen Yu 25
2.1 Statics of Rigid Bodies 26
2.2 Dynamics 39
References 59

3 **Thermodynamics**
Peter Stephan, Frank Dammel, Jay M. Ochterbeck 61
3.1 Scope of Thermodynamics and Definitions 61
3.2 Temperatures and Equilibria 63
3.3 First Law of Thermodynamics 66
3.4 Second Law of Thermodynamics 69
3.5 Exergy and Anergy 71
3.6 Thermodynamics of Substances 73
3.7 Changes of State of Gases and Vapors 93
3.8 Thermodynamic Processes 97
3.9 Ideal Gas Mixtures 109
3.10 Heat Transfer 114
References 127

Part B Materials

4 **Atomic Structure and Microstructure Characterization**
Jens Freudenberger, Martin Heilmaier, Ulrich Wendt 131
4.1 Order in Solid State 132
4.2 Microstructure Characterization 152
References 162

5 **Mechanical Properties**
Vivek Srivastava, Martin Heilmaier 165
5.1 Mechanical Properties 165
5.2 Physical Properties 178
References 182

6 **Corrosion and Corrosion Resistance**
Thomas Böllinghaus, Michael Rhode, Thora Falkenreck 185
6.1 Fundamental Aspects 185
6.2 Electrochemical Corrosion 186
6.3 Chemical Corrosion and High-Temperature Corrosion 207
6.4 Corrosion Testing 212
References 212

7 **Nondestructive Inspection (NDI)**
Gerhard Mook, Islam Shyha 215
7.1 Principles of Nondestructive Inspection 216
7.2 Acoustic Methods 217
7.3 Potential Drop Method 219
7.4 Magnetic Methods 220
7.5 Electromagnetic Methods 224
7.6 Thermography 225
7.7 Optical Methods 226
7.8 Radiation Methods 228
7.9 Health Monitoring 229
References 231

8 **Engineering Materials and Their Properties**
Ulrich Wendt 233
8.1 Iron-Based Materials 234
8.2 Aluminum and Its Alloys 258
8.3 Magnesium and Its Alloys 262
8.4 Titanium and Its Alloys 265
8.5 Ni and Its Alloys 269
8.6 Co and Its Alloys 273
8.7 Copper and Its Alloys 275
8.8 Polymers 278
8.9 Glasses and Ceramics 285
8.10 Composite Materials 289
References 290

9 **Tribology**
Ludger Deters, Dirk Bartel 293
9.1 Importance of Tribology 293
9.2 Tribological System (Tribosystem) 294
9.3 Friction 299
9.4 Wear 302
9.5 Fundamentals of Lubrication 306
9.6 Lubricants 311
References 322

Part C Manufacturing

10 **Casting**
Klaus Herfurth, Stefan Scharf 325
10.1 The Foundry Industry 326

10.2 Cast Alloys 328
10.3 Primary Shaping 336
10.4 Shaping of Metals by Casting 339
10.5 Guidelines for Design 350
10.6 Preparatory and Finishing Operations 354
References 355

11 **Metal Forming**
A. Erman Tekkaya 357
11.1 Metallurgical Fundamentals 361
11.2 Theoretical Foundations 364
11.3 Bulk Forming Processes 372
11.4 Sheet Forming Processes 387
11.5 Forming Machines 402
References 407

12 **Machining Processes**
Bernhard Karpuschewski, Gerry Byrne, Berend Denkena, João Oliveira, Anatoly Vereschaka 409
12.1 Cutting 410
12.2 Machining with Geometrically Nondefined Tool Edges 437
12.3 Nonconventional Machining Processes 448
References 456

13 **Precision Machinery Using MEMS Technology**
Takeshi Hatsuzawa 461
13.1 Electrostatic-Driven Optical Display Device 462
13.2 Design of the Device 462
13.3 Evanescent Coupling Switching Device 465
References 467

14 **Measuring and Quality Control**
Steffen Wengler, Lutz Wisweh, Shuichi Sakamoto, Norge I. Coello Machado 469
14.1 Quality Management 469
14.2 Manufacturing Measurement Technology 475
14.3 Further Reading 498
References 498

Part D Machine and Systems Design

15 **Machine Elements**
Frank Engelmann, Karl-Heinrich Grote, Thomas Guthmann 503
15.1 Basic Dimensioning Principles 504
15.2 Fasteners 514
15.3 Axles and Shafts 544
15.4 Shaft–Hub Connections 551
15.5 Rolling Bearings 566
15.6 Plain Bearings 580
15.7 Seals and Gaskets 585
15.8 Gears and Gear Trains 593
15.9 Springs 607

15.10 Pipes 620
References 625

16 **Engineering Design**
Frank Engelmann, Alois Breiing, Timothy Gutowski 629
16.1 Design Theory 629
16.2 Engineering Design Basics 651
16.3 Precisely Defining the Task 651
16.4 Conceptual Design 654
16.5 Design 657
16.6 Design and Manufacturing for the Environment 662
16.7 Failure Mode and Effect Analysis for Capital Goods 671
16.8 Bioindustrial Design: Challenges and Vision 678
References 680

17 **Piston Machines**
Helmut Tschöke, Vince Piacenti, Brent Keppy, Aneel A. Singh, Steven D. White, Justin Kern, Jon H. van Gerpen 683
17.1 Foundations of Piston Machines 683
17.2 Positive Displacement Pumps 697
17.3 Compressors 713
17.4 Internal Combustion Engines 715
References 750

18 **Pressure Vessels and Heat Exchangers**
Ajay Mathur, Hamidreza Najafi 753
18.1 Pressure Vessels – General Design Concepts 753
18.2 Design of Tall Towers 757
18.3 Testing Requirements 758
18.4 Design Codes for Pressure Vessels 759
18.5 Heat Exchangers 763
18.6 Construction Materials 769
References 776

19 **Turbomachinery**
Meinhard T. Schobeiri 777
19.1 Theory of Turbomachinery Stages 777
19.2 Blade Design 790
19.3 Gas Turbine Engines: Design and Dynamic Performance 800
References 827

20 **Conveying and Construction Machinery**
André Katterfeld, Alan Roberts, Craig Wheeler, Kenneth Williams, Chris Wensrich, Jan Scholten, Mark Jones, Günter Kunze, Henning Strubelt, Dusan Ilic, Tim Donohue, Hendrik Otto, Jens Sumpf, Wei Chen, Bin Chen, Daniel Ausling 829
20.1 Background and Fundamentals 830
20.2 Bulk Solid Mechanics and Characterization 837
20.3 Basic Mechanical Elements 848
20.4 Continuous Conveyors 863
20.5 Discontinuous Conveyors 923
20.6 Storage Systems 955
References 981

Part E Transportation – Mobility

21 **Trends and Challenges in Mobility and Transportation**
Marc Claus Schmitt, Stefan Pischinger 995
21.1 Overview 995
21.2 Impact of Safety and Environmental Legislation on Transportation Technologies 997
21.3 Upcoming Changes in Transportation 998
21.4 Automotive Technology 1000
21.5 Aerospace Technology 1005
21.6 Rail Technology 1009
References 1013

22 **Automotive Engineering**
Gritt Ahrens 1015
22.1 Characteristics and Trends of Car Development 1015
22.2 Targets and Challenges for Car Development 1017
22.3 Car Development Processes 1033
22.4 Methods for Car Development 1040
References 1054

23 **Railway Systems–Railway Engineering**
Markus Hecht 1057
23.1 General Interactions of Modules of a Railway System with Surroundings 1057
23.2 Track 1061
23.3 Running Gears 1066
23.4 Superstructures 1074
23.5 Vehicles 1074
23.6 Coupling Systems 1077
23.7 Safety 1080
23.8 Air Conditioning 1081
References 1083

24 **Aerospace Engineering**
Hamid Hefazi 1085
24.1 Aerospace Industry 1086
24.2 Aerospace Technology and Development 1087
24.3 Aircraft 1091
24.4 Spacecraft 1093
24.5 Definitions 1093
24.6 Flight Performance Equations 1102
24.7 Airplane Aerodynamic Characteristics 1102
24.8 Airplane General Configurations 1107
24.9 Weights 1113
24.10 Aircraft Performance 1115
24.11 Stability and Control 1123
24.12 Loads 1129
24.13 Airplane Structure 1132
24.14 Airplane Maintenance Checks 1136
References 1136

25 **Ships and Maritime Transportation**
Jean-Baptiste R. G. Souppez 1139
25.1 Overview 1139
25.2 Ship Geometry and Definitions 1141
25.3 Hydrostatics and Stability 1145
25.4 Resistance and Powering 1152
25.5 Structure 1157
25.6 Additional Considerations 1161
25.7 Summary 1162
References 1163

Part F Related Engineering Fields

26 **Electrical Engineering**
Martin Poppe 1167
26.1 Fundamental Laws 1167
26.2 Capacitors, Resistors, and Inductors 1174
26.3 Semiconductor Devices 1183
26.4 Networks 1194
26.5 Electrical Machines 1205
26.6 Energy Storage 1214
References 1221

27 **Power Generation**
Asfaw Beyene, Dwarkadas Kothari, P.M.V. Subbarao 1223
27.1 Energy Conversion Principles 1224
27.2 Primary Energy 1235
27.3 Boilers and Furnaces 1236
27.4 Combustion 1254
27.5 Nuclear Power Plants 1260
27.6 Renewable Energy 1264
27.7 Energy Storage and Distribution 1268
27.8 Prospects and Conclusion 1269
References 1271

Part G Annex

28 **General Tables**
Stanley Baksi 1275
References 1285

Subject Index 1287

List of Abbreviations

A

A.M.	algebraic multiplicity
ABWR	advanced boiling water reactor
AC	alternating current
ACES	automated, connected, electrified, shared/services
ACI	austempered cast iron
ACM	polyacrylate rubber
ADAS	advanced driver-assistance system
ADI	austempered ductile cast iron
AES	atomic emission spectroscopy
AGR	advanced gas reactor
AGSC	automatic guided straddle carrier
AGV	automated guided vehicle
AI	authorized inspector
AMS	automated miniload system
AND	airplane nose down
ANG	absorbed natural gas
APB	antiphase boundary
APWR	advanced pressurized water reactor
AR	augmented reality
AS/RS	automated storage and retrieval system
ASL	loss due to hot ash or slag
AT	all-terrain
ATC	automatic train control
ATS	air transport system
AVAS	acoustic vehicle alerting system
AVS	angle of vanishing stability
AW	antiwear
AWJ	abrasive waterjet

B

bcc	body-centered cubic
bct	body-centered tetragonal
BD	balanced draft
BDC	bottom dead center
BEV	battery electric vehicle
BiW	body in white
BM	beam machining
BMEP	break mean effective pressure
BOM	bill of materials
BS	British standard
BSE	backscattered electron
BSFC	brake specific fuel consumption
BTL	biomass-to-liquid
BV	Bureau Veritas
BWB	blended wing body
BWR	boiling water reactor

C

CAD	computer-aided design
CAES	compressed air energy storage
CAM	computer-aided manufacturing
CANDU	Canada Deuterium Uranium
CAS	computer-aided styling
CBN	cubic boron nitride
CC	combustion chamber
CCD	charge-coupled device
CCGT	combined cycle gas turbine
CCT	continuous cooling transition
CD	continuous dressing
CDC	crank dead center
CDP	car development process
CF	corrosion fatigue
CFC	chlorofluorocarbon
CFD	computational fluid dynamics
CFRP	carbon fiber reinforced plastic
CGI	compacted graphite iron
CHP	combined heat and power
CI	compression-ignition
CIFI	cylinder-individual fuel injection
Class NK	Nippon Kaiji Kyokai
CMM	coordinate measuring machines
CMOS	complementary metal–oxide–semiconductor
CMP	chemical-mechanical planarization
CN	coordination number
CNC	computer numerical control
CNG	compressed natural gas
CODAP	code français de construction des appareils à pression
CP	critical point
CPI	central-point injection
CPP	controllable pitch propellers
CPT	critical pitting temperature
CPU	central processing unit
CR	chloroprene rubber
CRSS	critical resolved shear stress
CRT	cathode ray tube
CSM	chlorosulphonyl polyethylene rubber
CT	compact tension
CTE	coefficient of thermal expansion
CTEM	conventional transmission electron microscopy
CTL	coal-to-liquid
Cu-DHP	deoxidized copper
CVD	chemical vapor deposition
CVM	comparative vacuum monitoring
CVN	Charpy V-notch

D

DAB	dialkylbenzenes
DBTT	ductile to brittle transition temperature
DC	direct current
DCA	double-circular arc
DCF	duty cycle factor

DEGL	dry exhaust gas losses
DEM	dust extinction moisture
DET	distortion energy theory
DFE	design for the environment
DFM	design for manufacturability
DI	direct injection
DIC	differential interference contrast microscopy
DKD	German calibration service
DLC	dual-load carrier
DME	dimethyl ether
DMIS	dimensional measuring interface specification
DMU	digital mock-up
DPF	diesel particulate filter
DPH	diamond-pyramid hardness number
DRAM	dynamic random-access memory
DSC	differential scanning calorimetry
DWT	deadweight

E

E-GAS	synthetic methane
EAC	environmentally assisted cracking
EAM	European approval of material
EAS	equivalent airspeed
EBM	electron beam machining
EBSD	electron backscatter diffraction
ECDD	evanescent coupling display device
ECDM	electrochemical-discharge machining
ECG	electrochemical grinding
ECM	electronic control module
ECU	electronic control unit
EDG	electro-discharge grinding
EDM	electro-discharge machining
EDX	energy-dispersive x-ray spectrometer
EELS	electron energy-loss spectroscopy
EEOI	energy efficiency operation index
EGR	exhaust gas recirculation
EHD	elastohydrodynamic lubrication
EHL	elastohydrodynamic lubrication
EIS	entry into service
ELI	extralow interstitial
ELID	electrolytic in-process dressing
EMC	electromagnetic compatibility
EN	European Standard
EP	extreme pressure
EPDM	ethylene-propylene diene monomer
EPIWRC	synthetic coated independent wire rope core
EPMA	electron probe microanalysis
ERP	enterprise resource planning
ERS	energy recovery system
ESCA	electron spectroscopy for chemical analysis
ESEM	environmental SEM
ESP	electrostatic precipitator
ESR	essential safety requirement
EYL	effective yield locus

F

F	freshwater
FAME	fatty acid methyl ester
FBC	fluidized-bed combustor
FBR	fast breeder reactor
FC	fiber core
fcc	face-centered cubic
FCEV	fuel cell electric vehicle
FCV	fuel cell vehicle
FD	forced draft
FEA	finite element analysis
FEGT	furnace exit gas temperature
FEM	finite element method
FF	flow function
FFKM	perfluoroelastomer
FFT	fast Fourier transform
FGD	flue gas desulfurization
FIB	focused ion beam
FIFO	first-in first-out
FKM	fluoroelastomer
FLD	forming limit diagram
FMEA	failure mode and effects analysis
FN	ferrite number
FPM	fluorocarbon rubber
FPO	future project office
FRP	fiber-reinforced plastic

G

G.M.	geometric multiplicity
GA	general arrangement
GDI	gasoline direct injection
GDOES	glow-discharge optical emission spectroscopy
GDP	gross domestic product
GHG	greenhouse gas
GIDAS	German In-Depth Accident Study
GMAW	gas metal arc welding
GNC	guidance navigation and control
gt	gross tonnage
GTAW	gas tungsten arc welding
GTL	gas-to-liquid

H

HAC	hydrogen-assisted cracking
HASCC	hydrogen-assisted stress corrosion cracking
HAZ	heat-affected zone
HCFC	hydrochlorofluorocarbon
hcp	hexagonal close-packed
HDC	head dead center
HDPE	high-density polyethylene
HE	heat exchanger
HEDE	hydrogen-enhanced decohesion
HELP	hydrogen-enhanced localized plasticity
HEM	high-efficiency machining
HEV	hybrid electric vehicle

HFID	heated flame ionization detector
HHV	higher heating value
HIL	hardware-in-the-loop
HIP	hot isostatic pressing
HP	high pressure
HPCC	high-pressure combustion chamber
HPDI	high-pressure direct injection
HPT	high-pressure turbine
HRC	hardness Rockwell cone
HRSG	heat recovery steam generator
HSC	high-speed cutting
HSLA	high-strength low-alloy
HSM	high-speed machining
HSS	high-speed steel
HTA	heavier than air
HTHA	high-temperature hydrogen attack
HVACR	heating, ventilation, air-conditioning, and refrigeration

I

I/O	input/output
IAS	indicated airspeed
IBC	international building code
IBM	ion beam machining
IC	integrated circuit
ICL	incomplete combustion loss
ID	induced draft
IDD	interferometric display device
IDI	indirect diesel injection
IE	Erichson index
IFR	instrument flight rules
IGBT	insulated-gate bipolar transistor
IGC	intergranular corrosion testing
IGCC	integrated gasification combined cycle
IISE	ion-induced secondary electron
IoT	Internet of Things
IP	intermediate pressure
ITO	indium tin oxide
IVP	initial value problem
IWRC	independent wire rope core
IYL	instantaneous yield locus

K

KOH	potassium hydroxide

L

LA	lead acid
LAM	laser-assisted machining
LB	laser beam
LBM	laser beam machining
LC	laser cutting
LCA	life cycle analysis
LCB	longitudinal center of buoyancy
LCF	longitudinal centre of flotation
LCG	longitudinal center of gravity
LCI	life cycle inventory
LDPE	low-density polyethylene
LE	leading edge
LED	light-emitting diode
LHV	lower heating value
LIFO	last-in first-out
LMTD	log-mean temperature difference
LNG	liquefied natural gas
LP	low pressure
LPCC	low-pressure combustion chamber
LPG	liquefied petroleum gas
LPT	low-pressure turbine
LRO	long-range order
LTA	lighter than air
LU	loading unit
LYS	lower yield stress

M

m.a.c.	mean aerodynamic chord
MAM	motorized air cycle machine
MAP	main air pipe
MBS	multibody simulation
MC	molecular weight of carbon
MCA	multi-circular arc
MCAL	losses due to moisture in the combustion air
MCD	monocrystalline diamond
MCO	molecular weight of CO
MCTC	moment to change the trim by one centimeter
MDT	mean downtime
MEMS	microelectromechanical system
MEP	mean effective pressure
MHD	magnetohydrodynamic
MIC	microbiologically induced corrosion
MLC	multiload carrier
MLW	maximum landing weight
MMC	metal matrix composites
MOF	metal-organic framework
MOS	metal oxide semiconductor
MP-OVI	multipoint open-valve injection
MPI	magnetic particle inspection
MPS	mean piston speed
MSI	motion sickness incidence
MSS	maximum shear theory
MSW	municipal solid waste
MTBE	methyl *t*-butyl ether
MTBF	mean time between failures
MTOGW	maximum take-off gross weight
MWE	manufacturer's weight empty
MZFW	maximum zero-fuel weight

N

NA	number of atoms
NAND	not and
NBC	national building code
NBR	acrylonitrile butadiene rubber
NC	numerical control
NCAP	new car assessment program
ND	normal direction

NDE	nondestructive evaluation
NDI	nondestructive inspection
NDIR	nondispersive infrared
NDT	nondestructive testing
NEFZ	Neuer Europäischer Fahrzyklus
NFC	natural fiber core
NG	natural gas
NGDI	natural gas direct injection
NMOS	n-channel MOS
NPSH	net positive suction head
NR	natural rubber
NTP	normal temperature and pressure
NVH	noise–vibration–harshness

O

OCP	open-circuit potential
ODE	ordinary differential equation
ODS	oxide-dispersion-strengthened
OEM	original equipment manufacturer
OFA	over fire air
OFW	oblique flying wing
OIM	orientation imaging microscopy
OWE	operating weight empty

P

PA	polyamide
PAM	plasma arc machining
PAO	polyalphaolefines
PBM	plasma beam machining
PCBN	polycrystalline cubic boron nitride
PCC	pneumatic conveying characteristic
PCD	polycrystalline diamond
PCI	peripheral component interconnect
PD	packing density
PDF	powder diffraction file
PDM	product data management
PE	polyethylene
PE-HD	high-density polyethylene
PED	Pressure Equipment Directive
PEMS	portable emissions measurement system
PET	polyethylene terephthalate
PHE	plate heat exchangers
PHEV	plug-in hybrid electric vehicle
PHS	pumped hydro storage
PIB	polyisobutenes
PM	particulate matter
PMA	particular material appraisal
PMMA	polymethylmethacrylate
PMOS	p-channel MOS
PN	particulate number
PP	polypropylene
PPS	polyphenylene sulfide
PQR	procedure qualification record
PREN	pitting resistance equivalent numbers
PS	polystyrene
PSB	persistent slip band
PSD	power spectral density
PTFE	polytetrafluoroethylene
PUR	polyurethane
PVC	polyvinylchloride
PVD	physical vapor deposition
PVDF	polyvinylidene fluoride
PWB	printed wiring board
PWHT	postweld heat treatment
PWR	pressurized water reactor
PWRC	parallel wire rope core

Q

QCC	quality control chart
QFD	quality function deployment
QM	quality management
QMS	quality management system
QPC	quasi-propulsive coefficient
QS	quality management system
QueSST	quiet supersonic transport

R

RA	recuperator air side
RAMS	reliability, availability, maintainability and safety
RAO	response amplitude operator
RC	rate of climb
RD	rolling direction
RDE	real-world driving emission
RG	recuperator gas side
RIE	reactive ion etching
RIT	runaway ignition temperature
rms	root-mean-square
RNG	renewable natural gas
RPV	reactor pressure vessel
RPZ	risk priority number
RT	radiographic testing
RTM	resin transfer molding
RUL	radiation and unaccounted-for losses

S

S	summer saltwater
SAM	scanning Auger electron spectroscopy
SBR	polystyrene-butadiene rubber
SC	supercritical
SCC	stress corrosion cracking
SCI	special crash investigation
SCR	selective catalytic reduction
SDD	silicon drift detector
SDOF	single degree of freedom system
SE	secondary electron
SEDM	spark electro-discharge machining
SEFI	sequential fuel injection
SEM	spark-erosion machining
SFC	synthetic fiber core
SFC	specific fuel consumption
SHM	structural health monitoring
SI	International System
SI	spark ignition

SIMS	secondary-ion mass spectroscopy
SKU	stock keeping unit
SLC	single load carrier
SLCA	streamlined life cycle analysis
SLM	selective laser melting
SLPL	space limit payload
SMAW	shielded metal arc welding
SNCR	selective noncatalytic reduction
SNG	synthetic natural gas
SOF	soluble organic fraction
SOG	speed over the ground
SOLAS	Safety Of Life At Sea
SOP	start of production
SPC	statistical process control
SPV	simple pressure vessel
SQUID	superconducting quantum interference device
SRO	short-range order
SSSF	steady-state steady flow
ST	softening temperature
STEM	scanning transmission electron microscopy
STW	speed through water
SUV	sports utility vehicle
SV	suction valve

T

T	tropical saltwater
TAS	true airspeed
TC	turbocharger
TCG	transverse center of gravity
TD	transversal direction
TDC	top dead center
TE	trailing edge
TEM	transmission electron microscopy
TEU	twenty-foot equivalent unit
TF	tropical freshwater
TGV	train à grande vitesse
TLAR	top-level aircraft requirements
TMAH	tetramethyl ammonium hydroxide
TMC	traffic message channel
TML	transportable moisture limit
TOR	top of rail
TPC	tonnes per centimeter
TQM	total quality management
TRIAC	triode for alternating current
TRIP	transformation induced plasticity
TS	tribological system
TSF	time-strain-to-fracture
TTP	time–temperature–precipitation
TTT	time–temperature transition
TWC	three-way catalyst

U

UAS	unmanned aircraft system
UAV	unmanned aerial vehicle
UBC	uniform building code
UCAV	unmanned combat air vehicle
UCL	unburnt carbon loss
UHC	unburned hydrocarbon
UHCA	ultrahigh-capacity aircraft
UHEGT	ultrahigh-efficiency gas turbine
UNS	unified numbering system
UPS	uninterruptible power supply
UPV	unfired pressure vessel
US	ultrasonic
USC	ultra-supercritical steam
USM	ultrasonic machining
UT	ultrasonic testing
UTS	ultimate tensile strength/stress
UV	ultraviolet
UYS	upper yield stress

V

VCG	vertical center of gravity
VDMOS	vertically double-diffused MOS
VE	vinyl ester resin
VHN	Vickers hardness number
VI	viscosity index
VLCT	very large commercial transport
VNA	very narrow aisle
VOC	volatile organic compound
VOF	volatile organic fraction
VPH	Vickers pyramid hardness
VPP	variable pitch propellers
VPSEM	variable-pressure SEM
VR	virtual reality
VTG	variable turbine geometry
VTOL	vertical take-off and landing

W

W	winter saltwater
WC	wire core
WDX	wavelength-dispersive x-ray spectrometer
WEDM	wire electro-discharge machining
WNA	winter North Atlantic saltwater
WPS	weld procedure specification
WSC	wire strand core
WSP	wheel-slide protection
WWI	World War I
WYL	wall yield locus

X

XPS	x-ray-exited photoelectron spectroscopy
XRD	x-ray diffraction
XRF	x-ray fluorescence spectroscopy

Y

YL	yield locus
YPE	yield point elongation

Part A Fundamentals

1 **Introduction to Mathematics**
Gnana Bhaskar Tenali, Melbourne, FL, USA

2 **Mechanics**
David C. Fleming, Melbourne, FL, USA
Hen-Geul Yeh, Long Beach, CA, USA
Hsien-Yang Yeh, Long Beach, CA, USA
Shouwen Yu, Beijing, China

3 **Thermodynamics**
Peter Stephan, Darmstadt, Germany
Frank Dammel, Darmstadt, Germany
Jay M. Ochterbeck, Clemson, SC, USA

1. Introduction to Mathematics

Gnana Bhaskar Tenali

This chapter presents mathematical concepts and techniques that are fundamental for the study of problems in mechanical engineering. Precisely formulating a mathematical model of the problem at hand, using appropriate methods and techniques to solve the mathematical problem, and, finally, interpreting the solution to the real life problem are some of the important components of the process of solving problems in any engineering field. The topics covered here include linear algebra, differential equations, the Laplace transform, Fourier analysis, and complex analysis. These basic concepts essentially act as tools that facilitate the understanding of many techniques involved in different branches of mechanical engineering.

1.1 **Linear Algebra** 4
1.1.1 Vectors in $\mathbb{R}^n$ 4
1.1.2 Matrix Algebra 4
1.1.3 Eigenvalues and Eigenvectors of a Square Matrix **A** 7
1.2 **Differential Equations** 8
1.2.1 First-Order ODEs 8
1.2.2 Numerical Solution of First-Order ODEs 9
1.2.3 Second-Order Linear ODEs 9
1.2.4 Systems of Linear First-Order ODEs 11
1.3 **The Laplace Transform** 13
1.3.1 The Laplace Transform: Definition and Properties 13
1.3.2 The Inverse Laplace Transform 15
1.4 **Fourier Analysis** 16
1.4.1 Fourier Series 16
1.4.2 The Fourier Transform 18
1.5 **Complex Analysis** 19
1.5.1 Complex Numbers 19
1.5.2 Complex Functions 20
1.5.3 Analytic Functions 21
1.5.4 Complex Integration 22
1.5.5 Conformal Mappings 22
References 23

Mathematical concepts and techniques play an important role in the study of problems in mechanical engineering. Precisely formulating a mathematical model of the problem at hand, using appropriate methods and techniques to solve the mathematical problem, and, finally, interpreting the solution to the real-life problem are some of the important components of the process of solving problems in any engineering field. The topics covered include linear algebra, differential equations, the Laplace transform, Fourier analysis, and complex analysis. Different branches of mechanical engineering employ ideas and techniques from these fundamental topics in mathematics. Linear algebra deals with the study of matrices and linear systems of equations. Ordinary differential equations (ODEs) arise in the study of any phenomena that involve the rate of change with respect to an independent variable. The corresponding models involve ODEs, along with suitable initial or boundary conditions. Analysis of such models requires us to obtain analytical and/or numerical solutions to such problems. Transform techniques are useful in many such settings, where the (real-world) problem may be difficult to solve in its original formulation. So, the problem is recast in a different (more easily solvable) form using a mathematical transformation, and the solution of the modified problem is then transformed using the inverse transform to obtain the solution of the original problem. We discuss the Laplace transform and the Fourier transform among such transform techniques. As a part of Fourier analysis, we also present a brief discussion on Fourier series, a very important and effective tool in representing the solutions of several problems that arise in mechanical engineering, in terms of periodic functions sine and cosine. Complex analysis deals with complex numbers, their properties, and the analysis of functions of a complex variable. This plays an important role in problems arising on potential theory.

K.-H. Grote, H. Hefazi (Eds.), *Springer Handbook of Mechanical Engineering*, Springer Handbooks,
https://doi.org/10.1007/978-3-030-47035-7_1

1.1 Linear Algebra

Linear algebra plays a crucial role in both the analytical and computational aspects of solving various mechanical engineering problems. We start this section with a brief overview of vectors in $\mathbb{R}^n$ and matrix algebra.

1.1.1 Vectors in $\mathbb{R}^n$

Let $\mathbb{R}$ denote the set of all real numbers (scalars). By $\mathbb{R}^n$ we mean the set of all ordered n-tuples of the form $(x_1, x_2, \ldots, x_n)$, where $x_i \in \mathbb{R}$. Each $\boldsymbol{x} = (x_1, x_2, \ldots, x_n)$ is also treated as an n-dimensional *row vector*, and each x_i is called a component of the vector. The zero vector is denoted by $\mathbf{0} = (0, 0, \ldots, 0)$. For $\boldsymbol{x} = (x_1, x_2, \ldots, x_n)$ and $\boldsymbol{y} = (y_1, y_2, \ldots, y_n)$ in $\mathbb{R}^n$, the addition and scalar multiplication are defined as follows

$$\begin{aligned} \boldsymbol{x} + \boldsymbol{y} &= (x_1 + y_1, \ldots, x_n + y_n) \,, \\ k\boldsymbol{x} &= (kx_1, \ldots, kx_n) \,. \end{aligned}$$

The length of a vector $\boldsymbol{x}$ is called the *norm* or *magnitude*, denoted by $\|\boldsymbol{x}\|$ and is given by $\|\boldsymbol{x}\| = \sqrt{x_1^2 + x_2^2 + \cdots + x_n^2}$. The *dot product* of the vectors $\boldsymbol{x}, \boldsymbol{y}$ is given by $\boldsymbol{x} \cdot \boldsymbol{y} = x_1 y_1 + x_2 y_2 + \cdots + x_n y_n$. For nonzero vectors $\boldsymbol{x}$ and $\boldsymbol{y}$ in $\mathbb{R}^2$, and $\mathbb{R}^3$, the angle between these vectors is given by $\cos\theta = \boldsymbol{x} \cdot \boldsymbol{y} / (\|\boldsymbol{x}\| \|\boldsymbol{y}\|)$. Vectors in $\mathbb{R}^n$ may also be represented in *column vector* form

$$\begin{pmatrix} x_1 \\ x_2 \\ \vdots \\ x_n \end{pmatrix} .$$

By a linear combination of the vectors $\boldsymbol{x}_1, \boldsymbol{x}_2, \ldots, \boldsymbol{x}_n$ in $\mathbb{R}^m$ we mean a vector of the form $c_1\boldsymbol{x}_1 + c_1\boldsymbol{x}_1 + \cdots + c_n\boldsymbol{x}_n$, where $c_1, c_2, \ldots, c_n$ are scalars.

1.1.2 Matrix Algebra

A matrix is one of the most powerful mathematical objects that represents data efficiently, and one that includes different perspectives of the data. An $m \times n$ matrix, in the most mundane definition, is simply a rectangular array of mn numbers. More elegantly, it can also be thought of as a collection of m *row vectors* in $\mathbb{R}^n$ or as a collection of n *column vectors* in $\mathbb{R}^m$. An $m \times n$ matrix $\mathbf{A}$ is denoted by $\mathbf{A} = (a_{ij})$, $1 \le i \le m$, $1 \le j \le n$. Here a_{ij} is the entry at the intersection of the i-th row and j-th column. If the number of rows in a matrix $\mathbf{A}$ is same as the number of columns, $\mathbf{A}$ is called a *square* matrix. In a square matrix $\mathbf{A}$, the entries a_{ii} are referred to as *diagonal entries*. Two matrices $\mathbf{A} = (a_{ij})$ and $\mathbf{B} = (b_{ij})$ of size $m \times n$ are said to be *equal* if and only $a_{ij} = b_{ij}$, $1 \le i \le m$, $1 \le j \le n$.

For the $m \times n$ matrices $\mathbf{A} = (a_{ij})$ and $\mathbf{B} = (b_{ij})$ the *sum* $A + B$ is the matrix of same size, whose ij-th entry is $a_{ij} + b_{ij}$. For $k \in \mathbb{R}$ and a matrix $\mathbf{A} = (a_{ij})$, $k\mathbf{A} = (ka_{ij})$.

We denote the row vectors and column vectors of an $m \times n$ matrix $\mathbf{A} = (a_{ij})$ as $\boldsymbol{r}_i$, $1 \le i \le m$, and $\boldsymbol{c}_j$, $1 \le j \le n$, respectively. Given an $n \times 1$ column vector $\boldsymbol{b} = (b_j)$, the product $\mathbf{A}\boldsymbol{b}$ is an $m \times 1$ column vector $\boldsymbol{c} = (c_i)$, where $c_i = \sum_{j=1}^{n} a_{ij} b_j = \boldsymbol{r}_i \cdot \boldsymbol{b}$, $i = 1, \ldots, m$. This column vector can also be realized as the linear combination $b_1\boldsymbol{c}_1 + b_2\boldsymbol{c}_2 + \ldots + b_n\boldsymbol{c}_n$.

If the number of columns of $\mathbf{A}$ does not equal the number of rows of $\mathbf{B}$, the product $\mathbf{AB}$ is not defined. When the product is defined, the ij-th entry of $\mathbf{C}$ is obtained by taking the dot product of the i-th row of $\mathbf{A}$ with the j-th column of $\mathbf{B}$. That is, $c_{ij} = \boldsymbol{r}_i \cdot \boldsymbol{c}_j$, $1 \le i \le m$, $1 \le j \le n$. This is shown schematically in Fig. 1.1.

Example 1.1

Let

$$\mathbf{A} = \begin{pmatrix} 1 & 1 & 1 \\ 1 & 1 & -1 \\ 1 & -1 & -1 \\ -1 & -1 & -1 \end{pmatrix} \quad \text{and} \quad \boldsymbol{b} = \begin{pmatrix} 1 \\ 2 \\ 3 \end{pmatrix} .$$

The product

$$\mathbf{A}\boldsymbol{b} = \begin{pmatrix} \boldsymbol{r}_1 \cdot \boldsymbol{b} \\ \boldsymbol{r}_2 \cdot \boldsymbol{b} \\ \boldsymbol{r}_3 \cdot \boldsymbol{b} \\ \boldsymbol{r}_4 \cdot \boldsymbol{b} \end{pmatrix} = 1 \begin{pmatrix} 1 \\ 1 \\ 1 \\ -1 \end{pmatrix} + 2 \begin{pmatrix} 1 \\ 1 \\ -1 \\ -1 \end{pmatrix} + 3 \begin{pmatrix} 1 \\ -1 \\ -1 \\ -1 \end{pmatrix} = \begin{pmatrix} 6 \\ 0 \\ -4 \\ -6 \end{pmatrix} .$$

For an $m \times n$ matrix $\mathbf{A} = (a_{ij})$ and an $n \times p$ matrix $\mathbf{B} = (b_{ij})$, the product $\mathbf{AB}$ is a $m \times p$ matrix $\mathbf{C} = (c_{ij})$, where

$$c_{ij} = \sum_{k=1}^{n} a_{ik} b_{kj} \,, \quad 1 \le i \le m \,, \quad 1 \le j \le p \,. \tag{1.1}$$

Example 1.2

Let

$$\mathbf{A} = \begin{pmatrix} 1 & 1 & 1 \\ 1 & 1 & -1 \\ 1 & -1 & -1 \\ -1 & -1 & -1 \end{pmatrix} \quad \text{and} \quad \mathbf{B} = \begin{pmatrix} 1 & 0 \\ 2 & -1 \\ 3 & 2 \end{pmatrix} .$$

The product $\mathbf{AB}$ is a 4×2 matrix given by

$$\mathbf{A} = \begin{pmatrix} 6 & 1 \\ 0 & -3 \\ -4 & -1 \\ -6 & -1 \end{pmatrix} .$$

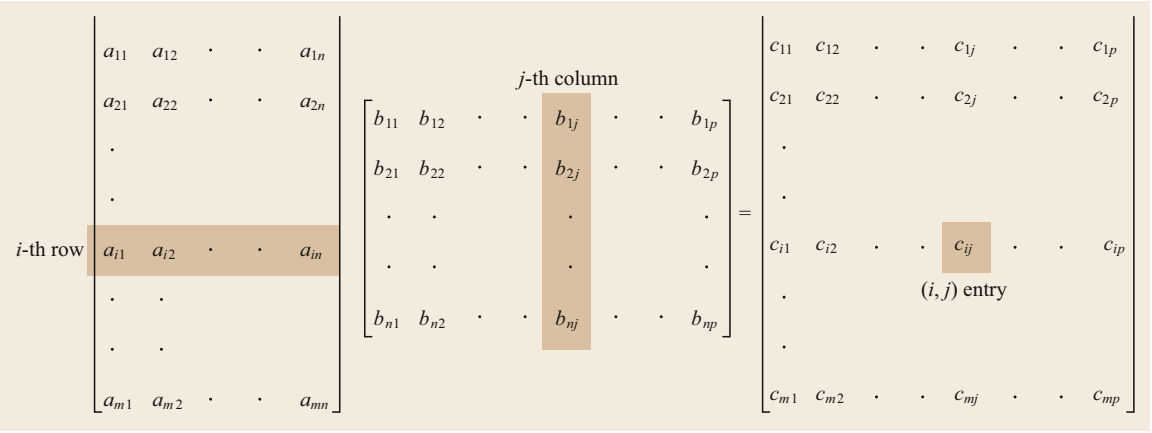

Fig. 1.1 Construction of the matrix product $\mathbf{AB} = \mathbf{C}$

In general, matrix multiplication is not commutative. That is, $\mathbf{AB} \neq \mathbf{BA}$. As can be seen in the example above, the product $\mathbf{BA}$ is not even defined.

For an $m \times n$ matrix $\mathbf{A}$, its transpose $\mathbf{A}^\top$ is obtained by making the rows of $\mathbf{A}$ into columns. That is, the i-th row of $\mathbf{A}$ becomes the i-th column of $\mathbf{A}^\top$. Given that the operations indicated are all valid, we have: $(\mathbf{AB})^\top = \mathbf{B}^\top\mathbf{A}^\top$. We use the notation $\mathbf{A}^k$ to denote the product, $\underbrace{\mathbf{AA}\ldots\mathbf{A}}_{k \text{ times}}$.

Special Matrices

A matrix is said to be *symmetric* if $\mathbf{A}^\top = \mathbf{A}$ and is *skew-symmetric* if $\mathbf{A}^\top = -\mathbf{A}$. A square matrix $\mathbf{A} = (a_{ij})$ is called *upper triangular* (*lower triangular*) if $a_{ij} = 0$ for all $i > j$ ($i < j$), that is, all the entries below (above) the diagonal are zero. The *identity matrix*, $\mathbf{I}_n$ is an $n \times n$ matrix whose diagonal entries are all 1, and the remaining entries are all zero. The *zero matrix*, $\mathbf{0}_{m\times n}$ has all its entries equal to zero.

Determinant

The determinant of a square matrix $\mathbf{A}$ is a real (unique) scalar denoted by $|\mathbf{A}|$ or $\det(\mathbf{A})$. For $n = 1$, $\mathbf{A} = (a_{11})$, and we define $\det(\mathbf{A}) = a_{11}$. For $n \geq 2$, the determinant is defined as (using the i-th row:)

$$|\mathbf{A}| = \sum_{k=1}^{n} a_{ik}(-1)^{i+k} M_{ik}, \quad i = 1, 2, \ldots, n\,. \tag{1.2}$$

or (using the j-th column)

$$|\mathbf{A}| = \sum_{k=1}^{n} a_{kj}(-1)^{k+j} M_{kj}, \quad j = 1, 2, \ldots, n\,. \tag{1.3}$$

Here, M_{ik} is the *minor* of the entry a_{ik}, defined as the determinant of the *submatrix* obtained by deleting the i-th row and the k-th column from $\mathbf{A}$. The quantity $(-1)^{i+k}M_{ik}$ is called the cofactor of a_{ik} and is denoted by C_{ik}. Thus, the determinant of a square matrix can be computed using any row or column of the matrix.

The following properties of determinants are important and useful:

- The determinant of $\mathbf{A}^\top$, the transpose of $\mathbf{A}$, is the same as the determinant of $\mathbf{A}$. That is, $|\mathbf{A}| = |\mathbf{A}^\top|$.
- If a matrix $\mathbf{A}$ has either a row (or a column) of zeros, then $|\mathbf{A}| = 0$.
- If a matrix $\mathbf{A}$ has two identical rows (or columns), then $|\mathbf{A}| = 0$.
- For a square matrix, $\mathbf{A}$ and a scalar k, $|k\mathbf{A}| = k^n\mathbf{A}$.
- For $n \times n$ matrices $\mathbf{A}, \mathbf{B}$, $|\mathbf{AB}| = |\mathbf{A}||\mathbf{B}|$.

Inverse of a Matrix

An $n \times n$ square matrix $\mathbf{A}$ is said be *invertible* if there exists an $n \times n$ matrix $\mathbf{B}$ such that $\mathbf{BA} = \mathbf{AB} = \mathbf{I}_n$. Such an inverse, when it exists, is unique and is denoted by the symbol $\mathbf{A}^{-1}$. If the inverse of $\mathbf{A}$ exists, $\mathbf{A}$ is said to be *nonsingular*, and otherwise it is said to be *singular*.

For an invertible matrix $\mathbf{A}$, the following hold:

- $\mathbf{A}$ is invertible if and only if $|\mathbf{A}| \neq 0$.
- For an $n\times n$ matrix $\mathbf{A} = (a_{ij})$, the matrix $\mathbf{C} = (C_{ij})$ is called the *cofactor matrix* of $\mathbf{A}$, and its transpose $\mathbf{C}^\top$ is called the *adjoint* of $\mathbf{A}$ and is denoted by $\mathrm{adj}(\mathbf{A})$. We have the formula

$$A^{-1} = \frac{\mathrm{adj}(\mathbf{A})}{\det(\mathbf{A})}\,. \tag{1.4}$$

- In particular, for a 2×2 matrix

$$\mathbf{A} = \begin{pmatrix} a_{11} & a_{12} \\ a_{21} & a_{22} \end{pmatrix},$$

we have

$$\mathbf{A}^{-1} = \frac{1}{|\mathbf{A}|}\begin{pmatrix} a_{22} & -a_{12} \\ -a_{21} & a_{11} \end{pmatrix}.$$

- $(\mathbf{A}^{-1})^{-1} = \mathbf{A}$.
- $(\mathbf{A}^{\top})^{-1} = (\mathbf{A}^{-1})^{\top}$.
- For any positive integer k, $(\mathbf{A}^{k})^{-1} = (\mathbf{A}^{-1})^{k}$.
- For invertible $n \times n$ matrices $\mathbf{A}$ and $\mathbf{B}$, we have $(\mathbf{AB})^{-1} = \mathbf{B}^{-1}\mathbf{A}^{-1}$.
- $|\mathbf{A}^{-1}| = 1/|\mathbf{A}|$.

Echelon Form and Systems of Linear Equations

A matrix $\mathbf{U}$ that has the following properties is said to be in *row echelon form*:

1. If a row does not consist entirely of zeros, then the first nonzero entry is called the leading nonzero entry of the row. For two successive rows not consisting entirely of zeros the leading nonzero entry of the lower row occurs to the right of the leading nonzero entry of the row above.
2. If there are any rows consisting of only zero entries, they are grouped together at the bottom of the matrix.

Further, if a matrix $\mathbf{R}$ is in row echelon form and additionally (i) each leading nonzero entry (if any) is 1, (ii) each column containing the leading 1 has zeros everywhere else, R is said to be in *reduced row echelon form*.

Example 1.3

$$\mathbf{U} = \begin{bmatrix} 3 & 5 & 0 & -3 \\ 0 & -1 & 0 & 0 \\ 0 & 0 & 0 & 7 \end{bmatrix};$$

$$\mathbf{R} = \begin{bmatrix} 1 & 0 & 3 & 0 & 4 \\ 0 & 0 & 0 & 1 & 2 \\ 0 & 0 & 0 & 0 & 0 \end{bmatrix}.$$

There are three elementary row operations that can be performed on a matrix:

1. Interchange two rows
2. Multiply an entire row by a nonzero constant
3. Add a nonzero-multiple of a row to another row.

Two matrices $\mathbf{A}, \mathbf{B}$ are said to be *row equivalent* if each can be obtained from the other by means a sequence of elementary row operations. There exists a row echelon matrix $\mathbf{U}$ that is row equivalent to a given matrix $\mathbf{A}$. There exists a unique reduced row echelon matrix $\mathbf{R}$ that is row equivalent to a given matrix $\mathbf{A}$. An $n \times n$ matrix $\mathbf{A}$ is invertible if and only if it is row equivalent to $\mathbf{I}_n$.

The vectors $\boldsymbol{v}_1, \boldsymbol{v}_2, \ldots, \boldsymbol{v}_k$ in $\mathbb{R}^n$ are said to be *linearly independent* if the only scalars $c_1, c_2, \ldots, c_n$ that satisfy the equation

$$c_1\boldsymbol{v}_1 + c_2\boldsymbol{v}_2 + \cdots + c_k\boldsymbol{v}_k = \mathbf{0}$$

are $c_1 = 0, c_2 = 0, \ldots, c_k = 0$. If there are scalars, not all zero, that satisfy this equation, then the vectors are said to be *linearly dependent*.

Given the vectors $\boldsymbol{v}_1, \boldsymbol{v}_2, \ldots, \boldsymbol{v}_k$ in $\mathbb{R}^n$, one way to determine whether they are linearly independent or dependent is to form an $n \times k$ matrix $\mathbf{V}$ with these vectors as the column vectors and determine the associated row echelon form $\mathbf{U}$. If each column in $\mathbf{U}$ contains a leading nonzero entry, then the given vectors are linearly independent. On the other hand, if at least one of the columns in $\mathbf{U}$ does not contain a leading nonzero entry, then the vectors are linearly dependent. The (column) vectors in the matrix $\mathbf{V}$ corresponding to the columns in $\mathbf{U}$ that contain the leading nonzero entries are linearly independent. The maximum number of linearly independent column (or row) vectors in a matrix $\mathbf{A}$ is defined as the *rank* of the matrix $\mathbf{A}$. Clearly, the rank of a matrix $\mathbf{A}$ is the number of columns that contain the leading nonzero entries in its (reduced) row echelon form.

Example 1.4

Let

$$\mathbf{A} = \begin{bmatrix} 2 & 6 & 4 & 8 \\ 4 & 2 & 0 & 0 \\ 3 & 4 & 2 & 5 \end{bmatrix};$$

$$\mathbf{U} = \begin{bmatrix} 1 & 3 & 2 & 4 \\ 0 & 5 & 4 & 7 \\ 0 & 0 & 0 & 0 \end{bmatrix};$$

$\mathbf{A}$ and $\mathbf{U}$ are row equivalent; $\mathbf{U}$ is in row echelon form. The leading nonzero entries of the rows are in the first and the second columns. Columns 3 and 4 do not contain leading nonzero entries. So, the (column) vectors

$$\left\{ \boldsymbol{v}_1 = \begin{pmatrix} 2 \\ 4 \\ 3 \end{pmatrix}, \boldsymbol{v}_2 = \begin{pmatrix} 6 \\ 2 \\ 4 \end{pmatrix}, \boldsymbol{v}_3 = \begin{pmatrix} 4 \\ 0 \\ 2 \end{pmatrix}, \boldsymbol{v}_4 = \begin{pmatrix} 8 \\ 0 \\ 5 \end{pmatrix} \right\}$$

are linearly dependent. Of these four vectors, $\boldsymbol{v}_1, \boldsymbol{v}_2$ that correspond to the columns in $\mathbf{U}$ that contain the leading nonzero entries are linearly independent. Further, $\boldsymbol{v}_3, \boldsymbol{v}_4$ are linearly dependent on the first two vectors. In fact, $(-\frac{2}{5})\boldsymbol{v}_1 + \frac{4}{5}\boldsymbol{v}_2 = \boldsymbol{v}_3$ and $(-\frac{1}{5})\boldsymbol{v}_1 + \frac{7}{5}\boldsymbol{v}_2 = \boldsymbol{v}_4$.

Consider a system of linear equations, $\mathbf{A}\boldsymbol{x} = \boldsymbol{b}$, where $\mathbf{A}$ is an $m \times n$ (coefficient) matrix, $\boldsymbol{x}$ is the (unknown) vector, and $\boldsymbol{b}$ is a given vector. Let $[\mathbf{U}|\tilde{\boldsymbol{b}}]$ be the row echelon form of the augmented matrix $[\mathbf{A}|\boldsymbol{b}]$. The following statements are true:

1. If the augmented matrix $[\mathbf{U}|\tilde{\boldsymbol{b}}]$ has a row of the form $[000\ldots0|a]$, and $a \neq 0$, then the system does not have a solution.
2. If the augmented matrix $[\mathbf{U}|\tilde{\boldsymbol{b}}]$ has a row consisting entirely of zeros, then the system has infinitely many solutions. Further, if $\boldsymbol{b} \equiv \mathbf{0}$, and if r columns of $\mathbf{U}$ have leading nonzero entries, then there are $(n-r)$ number of linearly independent solutions that *span* the set of solutions of the homogeneous system.
3. If $\mathbf{A}$ is an $n \times n$ matrix and is invertible, then there exists a unique solution for $\mathbf{A}\boldsymbol{x} = \boldsymbol{b}$. If in addition, $\boldsymbol{b} \equiv \mathbf{0}$, then $\mathbf{A}\boldsymbol{x} = \mathbf{0}$ has only a trivial solution.
   Solutions to linear systems can be found using Gaussian elimination, or by the Gauss–Jordan elimination method.

1.1.3 Eigenvalues and Eigenvectors of a Square Matrix A

Eigenvalues and eigenvectors of a matrix play an important role in stress analysis and in many other areas of mechanical engineering. Let $\mathbf{A}$ be an $n \times n$ matrix. A scalar λ is called an *eigenvalue* of $\mathbf{A}$ if there is a nonzero $n \times 1$ vector $\boldsymbol{x}$ such that

$$\mathbf{A}\boldsymbol{x} = \lambda\boldsymbol{x}\,. \tag{1.5}$$

All such nonzero vectors $\boldsymbol{x}$ are called eigenvectors of $\mathbf{A}$ corresponding to the eigenvalue λ. The eigenvalues can be determined as roots of the n-th degree *characteristic polynomial*

$$\det(\mathbf{A} - \lambda\mathbf{I}) = 0\,. \tag{1.6}$$

Thus, there are exactly n eigenvalues (counting multiple occurrences). *The eigenvalues may be real or complex numbers.* For each eigenvalue λ, the corresponding eigenvectors are determined as nontrivial solutions of the homogeneous system of equations

$$(\mathbf{A} - \lambda\mathbf{I})\boldsymbol{x} = 0\,. \tag{1.7}$$

For a real matrix $\mathbf{A}$, if an eigenvalue is a complex number, say $\lambda = \alpha + \mathrm{i}\beta$, and $\boldsymbol{v}$ is the corresponding eigenvector, then $\overline{\lambda} = \alpha - \mathrm{i}\beta$ is also an eigenvalue, and the corresponding eigenvector is $\overline{\boldsymbol{v}}$.

Example 1.5

Let

$$\mathbf{A} = \begin{pmatrix} -4 & -1 \\ 2 & -1 \end{pmatrix}.$$

To find the eigenvalues consider $|\mathbf{A} - \lambda\mathbf{I}| = 0$. This results in the characteristic polynomial, $\lambda^2 + 5\lambda + 6 = 0$, and the eigenvalues are $\lambda_1 = -3, \lambda_2 = -2$. The eigenvectors corresponding to $\lambda_1 = -3$ are the solutions of the system: $(\mathbf{A} - (-3)\mathbf{I_2})\ \boldsymbol{v} = 0$. All vectors of the form

$$\begin{pmatrix} t \\ -t \end{pmatrix} \quad \text{for } t \in \mathbb{R}\,,\ t \neq 0\,,$$

are the eigenvectors corresponding to $\lambda_1 = -3$. Similarly, the eigenvectors corresponding to the eigenvalue $\lambda_2 = -2$ are

$$\begin{pmatrix} -t \\ 2t \end{pmatrix} \quad \text{for } t \in \mathbb{R}\,,\ t \neq 0\,.$$

Thus,

$$\boldsymbol{v}_1 = \begin{pmatrix} 1 \\ -1 \end{pmatrix}, \quad \boldsymbol{v}_2 = \begin{pmatrix} -1 \\ 2 \end{pmatrix}$$

are two linearly independent eigenvectors of the matrix $\mathbf{A}$.

The eigenvalues of a symmetric matrix are real, and it has n linearly independent eigenvectors. However, in general, an $n \times n$ matrix may not always have n linearly independent eigenvectors. If an $n \times n$ matrix $\mathbf{A}$ has n linearly independent eigenvectors, $\mathbf{A}$ is said be *diagonalizable*.

Two matrices $\mathbf{A}, \mathbf{B}$ are said to be *similar* if there exists a nonsingular matrix $\mathbf{S}_{n\times n}$, such that $\mathbf{B} = \mathbf{S}^{-1}\mathbf{A}\mathbf{S}$.

Let $\mathbf{P} = [\boldsymbol{v}_1, \boldsymbol{v}_2, \ldots, \boldsymbol{v}_n]$ be the $n \times n$ matrix whose column vectors $\boldsymbol{v}_i$ are the linearly independent eigenvectors of $\mathbf{A}$. Then, we have the relation,

$$\mathbf{P}^{-1}\mathbf{A}\mathbf{P} = \begin{pmatrix} \lambda_1 & & 0 \\ & \ddots & \\ 0 & & \lambda_n \end{pmatrix}.$$

The order of appearance of λ_i along the diagonal is according to the order in which the eigenvectors occur as column vectors in $\mathbf{P}$. That is, $\mathbf{A}$ is similar to a diagonal matrix.

Example 1.6
For the matrix $\mathbf{A}$ in Example 1.5, the matrix

$$\mathbf{P} = \begin{pmatrix} 1 & -1 \\ -1 & 2 \end{pmatrix},$$

and it can be verified that

$$\mathbf{P}^{-1}\mathbf{A}\mathbf{P} = \begin{pmatrix} -3 & 0 \\ 0 & -2 \end{pmatrix} = \begin{pmatrix} \lambda_1 & 0 \\ 0 & \lambda_2 \end{pmatrix}.$$

The *algebraic multiplicity* (A.M.) of an eigenvalue λ_i of an $n \times n$ matrix $\mathbf{A}$ is the number of times λ_i occurs as a root of the characteristic polynomial. Moreover, the number of linearly independent eigenvectors associated with the eigenvalue λ_i is called the *geometric multiplicity* (G.M.) of λ_i. In general, G.M. $\leq$ A.M. So, when, we have G.M. $<$ A.M., for an eigenvalue λ_i, we define the following. A nonzero vector $\boldsymbol{v}$ is called a generalized eigenvector of $\mathbf{A}$ corresponding to λ_i if $(\mathbf{A}-\lambda\mathbf{I})^p\boldsymbol{v} = 0$, where p is the smallest such positive integer. For more details see [1.1].

1.2 Differential Equations

Differential equations play an important role in the modeling of physical engineering systems and help analyze and understand the behavior of these systems. Ordinary differential equations (ODEs) arise when the (unknown) functions under study involve only one independent variable, whereas if there are more than one independent variable, we have partial differential equations. The order of an ODE is the order of the highest-order derivative that occurs in the ODE. So, $yy' + y^2 = 1$ is a first-order equation, whereas $y'' + y^3 = \sin x$ is a second-order ODE. The $'$ here is the derivative with respect to the underlying independent variable. Sometimes, the unknown function y may be a function of x, or in some other applications, y may be a function of t. Further, ODEs are classified as linear and nonlinear ODEs. An ODE is said to be *linear* if it does not involve any products of the dependent variable with itself nor with any of its derivatives, and it does not also contain any products of the derivatives of the dependent variable. An ODE that is not linear is said be a *nonlinear* ODE. An ODE of the form $y'' + (\cos x)y = \sin x$ is a linear ODE, whereas $yy' + y^2 = 1$ is a nonlinear ODE. In this section, we present a few methods of solving a few simple classes of ordinary differential equations that arise in the study of several mechanical engineering problems.

1.2.1 First-Order ODEs

A first-order ODE of the form $F(x, y, y') = 0$ is an *implicit* ODE. We assume that it is possible to solve for y' and obtain an explicit ODE of the form $y' = f(x, y)$ on some interval I. By a solution of such an ODE, we mean a function $y = \phi(x)$:

(i) Defined on an (open) interval $J \subset I$
(ii) With ϕ is differentiable on J
(iii) Satisfies the equation $\phi'(x) = f(x, \phi(x))$ for all $x \in J$.

Such a solution is called an explicit solution. If on the other hand, a relation involving the solution of the form $G(x, y) = 0$ is called an *implicit* solution. In general, there is a one-parameter family of solutions for the first-order ODE.

A first-order initial value problem (IVP) is given by

$$y' = f(x, y)\,, \quad y(x_0) = y_0\,, \tag{1.8}$$

where x_0 is some point in the interval I, and y_0 is a given scalar. Such an initial value is guaranteed to have a unique solution if the function f is continuous on a rectangular region R containing the point (x_0, y_0) and satisfies the *Lipschitz condition*

$$|f(x, y_1) - f(x, y_2)| \leq k|y_1 - y_2| \tag{1.9}$$

for all $(x, y_1), (x, y_2) \in R$.

Separable ODE

A first-order ODE of the form

$$f(y)y' = g(x) \tag{1.10}$$

is separable. Integrating both sides with respect to x, we obtain

$$\int f(y)\,\mathrm{d}y = \int g(x)\,\mathrm{d}x + c\,. \tag{1.11}$$

This (usually) results in an implicit solution of the ODE. The c here is an arbitrary constant.

Example 1.7
Find the solution of the IVP

$$2(y-1)\frac{\mathrm{d}y}{\mathrm{d}x} = 3x^2 + 4x + 2\,, \quad y(0) = -1\,.$$

Separating the variables, integrating, and using the initial condition, we obtain

$$y^2 - 2y = x^3 + 2x^2 + 2x + 3 \,.$$

To obtain an explicit solution, we can solve for y in terms of x. We obtain

$$y = 1 \pm \sqrt{x^3 + 2x^2 + 2x + 4} \,.$$

Only one of these two solutions satisfies the initial condition, and we obtain

$$y = 1 - \sqrt{x^3 + 2x^2 + 2x + 4} \,.$$

This is the (unique) solution of the IVP, existing on the interval $(-2, \infty)$.

A first-order ODE of the form $M(x,y)\,\mathrm{d}x + N(x,y)\,\mathrm{d}y = 0$, is said to be a *homogeneous* ODE if both functions M and N are such that $M(\alpha x, \alpha y) = \alpha^n M(x,y); N(\alpha x, \alpha y) = \alpha^n N(x,y)$ for some real number n. A homogeneous ODE can converted to a separable ODE by the transformation $y = xv(x)$.

Linear First-Order ODEs

A first-order ODE of the form $y' + p(x)y = q(x)$, $x \in I$, where p and q are continuous functions on I, is called a *linear* ODE. If $q(x) \equiv 0$, then this equation is called a *homogeneous* linear ODE, otherwise it is called a *non-homogeneous* linear ODE.

The general solution of the linear (nonhomogeneous) first-order ODE is given by

$$y(x) = \mathrm{e}^{-r(x)} \left[\int \mathrm{e}^{r(x)} q(x)\,\mathrm{d}x + c \right], \tag{1.12}$$

where $r(x) = \int p(x)\,\mathrm{d}x$.

A first-order (nonlinear) ODE of the form $y' + p(x)y = q(x)y^n$, $\in I$, for $n \neq 0, 1$ is called a Bernoulli differential equation. A Bernoulli differential equation can be transformed into a linear ODE by the substitution $v = y^{1-n}$.

Second-Order ODEs of Special Form. Second-order ODEs of the form $y'' = f(x, y')$ can be transformed into a first-order ODE by the substitution $y' = u(x)$, whereas, $y'' = f(y, y')$ can be transformed into a first-order ODE by the substitution $y' = u(y)$.

We discuss one simple example bellow, as an illustration.

Example 1.8

Solve the initial-value problem

$$y'' = y'\mathrm{e}^y \,, \quad y(0) = 0 \,, \quad y'(0) = 1 \,.$$

Let $y' = u(y)$. Then $y'' = u\mathrm{d}u/\mathrm{d}y$, and the ODE becomes $u\mathrm{d}u/\mathrm{d}y = u\mathrm{e}^y$. If $u \neq 0$, we get the separable ODE: $\mathrm{d}u/\mathrm{d}y = \mathrm{e}^y$. Solving this we get, $u(y) = y'(x) = \mathrm{e}^{y(x)} + c$. Using the initial conditions, we get $c = 0$. Thus, $y' = \mathrm{e}^y$, which again is a separable ODE. Solving this ODE, and using the initial conditions again, we get,

$$y(x) = \ln\left(\frac{1}{1-x}\right), \quad x \in (-\infty, 1) \,.$$

1.2.2 Numerical Solution of First-Order ODEs

It is not always possible to obtain the solutions of differential equations in a closed form expression. Numerical (approximate) solutions are obtained using a variety of methods. We present here one such commonly used method called *Runge–Kutta method*.

Consider the first-order ODE

$$y' = f(x,y) \,, \quad y(x_0) = y_0 \,, \quad x_0 \le x \le x_N \,. \tag{1.13}$$

Choosing a step size, $h > 0$, the approximate values for the solution $y(x)$ at the points $x_n = x_0 + nh$, $n = 1, 2, \ldots, N$, are determined using the Runge–Kutta method. The R–K scheme involves a weighted average of values of $f(x,y)$ at different points in $[x_n, x_{n+1}]$. The R–K scheme is given below

$$y_{n+1} = y_n + h\left(\frac{k_{n1} + 2k_{n2} + 2k_{n3} + k_{n4}}{6}\right),$$

where

$$\begin{aligned}
k_{n1} &= f(x_n, y_n) \,, \\
k_{n2} &= f\left(x_n + \frac{1}{2}h, y_n + \frac{1}{2}hk_{n1}\right), \\
k_{n3} &= f\left(x_n + \frac{1}{2}h, y_n + \frac{1}{2}hk_{n2}\right), \\
k_{n4} &= f\left(x_n + \frac{1}{2}h, y_n + \frac{1}{2}hk_{n3}\right).
\end{aligned}$$

1.2.3 Second-Order Linear ODEs

The motion of a mass on a vibrating spring, torsional oscillations of a shaft with a flywheel, and several other physical engineering problems are described using second and higher-order linear ODEs. Nonlinear systems arising in such applications may be treated using numerical methods such as the Runge–Kutta method.

Consider the second-order linear IVP

$$y'' + p(x)y' + q(x)y = f(x)\,, \quad x \in I\,, \tag{1.14a}$$
$$y(x_0) = y_0\,, \quad y'(x_0) = y_1\,. \tag{1.14b}$$

The existence of a unique solution for this IVP on an (open) interval I is guaranteed provided that the functions $p(x)$, $q(x)$ and $f(x)$ are continuous on I.

If $y_(x), y_2(x)$ are any two solutions of the second-order linear (homogeneous) ODE

$$y'' + p(x)y' + q(x)y = 0\,, \tag{1.15}$$

then any linear combination $c_1y_1 + c_2y_2$ is also a solution, where c_1 and c_2 are constants.

A pair of functions f_1 and f_2, defined on an internal I are said to be *linearly independent* on I if the only scalars c_1, c_2 that satisfy the equation

$$c_1f_1(x) + c_2f_2(x) = 0 \quad \text{for all } x \in I$$

are $c_1 = c_2 = 0$. If there are scalars, not both zero, that satisfy the equation, then the functions are said to be *linearly dependent* on I.

In particular, two solutions y_1, y_2 of the linear second-order homogeneous ODE are linearly independent if and only if the *Wronskian*,

$$W(y_1, y_2)(x) = \begin{vmatrix} y_1(x) & y_2(x) \\ y_1'(x) & y_2'(x) \end{vmatrix} \neq 0$$

for some $x = x_0 \in I$.

There exist two linearly independent solutions of (1.15), say $\phi_1(x), \phi_2(x)$. The general solution of $y(x)$ of linear homogeneous ODE (1.15) is given by,

$$y(x) = c_1\phi_1(x) + c_2\phi_2(x)\,,$$

where c_1, c_2 are arbitrary constants.

There are no general methods that can be used to find the general solution of (1.15), when the ODE has variable coefficients. However, it is quite easy to solve ODEs with constant coefficients.

Homogeneous Second-Order ODEs with Constant Coefficients

Consider the second-order linear ODE with constant coefficients

$$y'' + py' + qy = 0 \quad \text{on } (-\infty, \infty) \tag{1.16}$$

where p, q are (real) constants. Seeking solutions of the form $y(x) = e^{mx}$, leads to the auxiliary equation,

$$m^2 + pm + q = 0\,.$$

The following three cases arise:

1. The auxiliary equation has two real roots, say m_1, m_2. Thus, we have two linearly independent solutions $\phi_1(x) = e^{m_1x}$, $\phi_2(x) = e^{m_2x}$. Thus, the general solution of (1.16) is given by $y(x) = c_1e^{m_1x} + c_2e^{m_2x}$.
2. The auxiliary equation has repeated (real) roots. That is, $m_1 = m_2$. In this case, $\phi_1(x) = e^{m_1x}$, $\phi_2(x) = xe^{m_2x}$ are two linearly independent solutions of (1.16), and the general solution is given by $y(x) = c_1e^{m_1x} + c_2xe^{m_2x}$.
3. Complex roots for the auxiliary equation occur in pairs. That is, if $\alpha + i\beta$ is a root, then so is $\alpha - i\beta$. The two (real-valued) solutions of (1.16) are given by $\phi_1(x) = e^{\alpha x}\cos(\beta x)$, $\phi_2(x) = e^{\alpha x}\sin(\beta x)$. The general solution is given by $y(x) = e^{\alpha x}(c_1\cos\beta x + c_2\sin\beta x)$.

Nonhomogeneous Linear Second-Order ODE

The general solution of the nonhomogeneous linear ODE (1.14a) is of the form $y(x) = y_h(x) + y_p(x)$, where $y_h(x)$ is the general solution of the (1.15) homogeneous ODE, and $y_p(x)$ is a particular solution of (1.14a). We could use the *method of undetermined coefficients* in case the (1.14a) has constant coefficients, and the function $f(x)$ is of a special type – polynomial, exponential, sine and/or cosine, or a combination/products of these functions. For details on this method, see [1.2]. We outline a different method, one that applies to a large class of ODEs, including the ones with variable coefficients: the method of variation of parameters.

Given two linearly independent solutions of (1.15), $\phi_1(x), \phi_2(x)$, we know that the Wronskian $W(\phi_1, \phi_2)(x) \neq 0$. By the method of variation of parameters, a particular solution of (1.14a) is obtained in the form, $y_p(x) = c(x)\phi_1(x) + c_2(x)\phi_2(x)$, where

$$c_1(x) = \int \frac{\begin{vmatrix} 0 & \phi_2(x) \\ f(x) & \phi_2'(x) \end{vmatrix}}{W(\phi_1, \phi_2)(x)}\,\mathrm{d}x\,,$$
$$c_2(x) = \int \frac{\begin{vmatrix} \phi_1(x) & 0 \\ \phi_1'(x) & f(x) \end{vmatrix}}{W(\phi_1, \phi_2)(x)}\,\mathrm{d}x\,.$$

The following example illustrates the ideas discussed in the section.

Example 1.9

Solve

$$y'' + y = \sec x\,, \quad y(0) = 1\,,\ y'(0) = -1\,.$$

The auxiliary equation for the associated homogeneous equation $y''+y=0$, $\lambda^2+1=0$. The roots are $\lambda=\pm i$. The general solution $y_h(x)$ is, $y_h(x)=c_1\cos x+c_2\sin x$. Clearly, $W(\cos x,\sin x)\equiv 1$. Using the above formulas, we obtain

$$c_1(x)=-\int \sec x\sin x\,dx=\ln(\cos x)\,,$$
$$c_2(x)=\int \sec x\cos x\,dx=1\,.$$

So the particular solution is

$$y_p(x)=x\sin x+\cos x[\ln(\cos x)]$$

and the general solution of the nonhomogeneous equation is

$$y(x)=c_1\cos x+c_2\sin x + x\sin x+\cos x[\ln(\cos x)]\,.$$

Using the initial conditions, we can determine the constants c_1, c_2 and we get

$$y(x)=\cos x-\sin x+x\sin x+\cos x[\ln(\cos x)]\,.$$

The Cauchy–Euler Equation. A second-order ODE of the form,

$$ax^2y''+bxy'+cy=0 \quad \text{on } (0,\infty)\,, \tag{1.17}$$

is called a Cauchy–Euler equation. We seek a solution of the form $y(x)=x^m$, resulting in the auxiliary equation

$$am(m-1)+bm+c=0\,.$$

Again, we have the three following cases:

1. The auxiliary equation has two real roots, say m_1, m_2. Then, x^{m_1}, x^{m_2} are two linearly independent solutions, and the general solution is given by $y_h(x)=c_1x^{m_1}+c_2x^{m_2}$.
2. The auxiliary equation has repeated roots, say $m_1=m_2$. The two linearly independent solutions are $x^{m_1}, x^{m_1}\ln x$. The general solution is $y_h(x)=c_1x^{m_1}+c_2x^{m_1}\ln x$.
3. The auxiliary equation has (a pair of) complex roots $\alpha\pm i\beta$. Then, $x^\alpha\cos(\beta\ln x)$ and $x^\alpha\sin(\beta\ln x)$ are the two linearly independent solutions resulting in the general solution: $y_h(x)=x^\alpha[c_1\cos(\beta\ln x)+c_2\sin(\beta\ln x)]$.

The principles outlined above extend in a very straightforward manner for higher-order linear ODEs as well. So, in general, for an n-th order linear nonhomogeneous ODE,

$$a_n(x)y^{(n)}+a_{n-1}(x)y^{(n-1)}+\ldots + a_1(x)y'+a_0(x)y=f(x)\,,\quad x\in I\,, \tag{1.18}$$

the general solution is of the form

$$y(x)=c_1\phi_1(x)+\ldots+c_n\phi_n(x)+y_p(x)\,,$$

where $\phi_1(x),\ldots,\phi_n(x)$ are linearly independent solutions of associated n-th order linear homogeneous ODE

$$a_n(x)y^{(n)}+a_{n-1}(x)y^{(n-1)}+\ldots + a_1(x)y'+a_0(x)y=0\,,\quad x\in I\,, \tag{1.19}$$

and $y_p(x)$ is a particular solution of (1.18). For details on the solutions of higher-order ODE, see [1.3].

1.2.4 Systems of Linear First-Order ODEs

Systems of ODEs arise in most physical and engineering applications when there are several (unknown) dependent variables, all depending on the same independent variable. We discuss here only the first-order, linear ODE with constant coefficients

$$\begin{aligned} y_1' &= a_{11}y_1+a_{12}y_2+\cdots+c_{1n}y_n\,,\\ y_2' &= a_{21}y_1+a_{22}y_2+\cdots+c_{2n}y_n\,,\\ &\vdots\\ y_n' &= a_{11}y_1+a_{12}y_2+\cdots+c_{1n}y_n\,. \end{aligned}$$

This system is written in the matrix-vector form: $\boldsymbol{Y}'=\mathbf{A}\boldsymbol{Y}$. It has n linearly independent solution vectors, say $\phi_1(x),\phi_2(x),\ldots,\phi_n(x)$. An $n\times n$ matrix $\Phi(x)$ whose columns are these linearly independent solution vectors is called a *fundamental matrix* of the system. In particular, $\Phi(x)=e^{\mathbf{A}x}$ is the fundamental matrix with $\Phi(0)=I$, $-\infty<x<\infty$:

1. If $\lambda_1,\lambda_2,\ldots,\lambda_n$ are distinct eigenvalues of the matrix $\mathbf{A}$, and $\boldsymbol{v}_1,\boldsymbol{v}_2,\ldots,\boldsymbol{v}_n$ are the corresponding eigenvectors, the solution vectors $\phi_i(x)=e^{\lambda_i x}\boldsymbol{v}_i$, $i=1,2,\ldots,n$ are linearly independent.
2. If $\lambda_1,\lambda_2,\ldots\lambda_k$ are eigenvalues of the matrix $\mathbf{A}$, with respective multiplicities $n_1,n_2,\ldots,n_k$ with $\sum_{j=1}^k n_j=n$. Corresponding to each eigenvalue λ_j of multiplicity n_j consider the system of linear equations

   $$(\mathbf{A}-\lambda_j\mathbf{I})^{n_j}\boldsymbol{x}=0\quad (j=1,2,\ldots,k)\,.$$

   The solutions of each such linear system span a subspace $X_j\subset\mathbb{R}^n$, and for every $\boldsymbol{x}\in\mathbb{R}^n$ there ex-

ist unique vectors $\boldsymbol{x}_j \in X_j$ such that $\boldsymbol{x} = \boldsymbol{x}_1 + \boldsymbol{x}_2 + \cdots + \boldsymbol{x}_k$. Now, the (unique) solution of the initial value problem $\boldsymbol{Y}' = \mathbf{A}\boldsymbol{Y}$, $\boldsymbol{Y}(0) = \boldsymbol{\eta}$ is given by

$$\boldsymbol{\phi}(x) = \sum_{j=1}^{k} \mathrm{e}^{\lambda_j x} \left[\sum_{i=0}^{n_j - 1} \frac{x^i}{i!} (A - \lambda_j I)^i \right] \boldsymbol{v}_j \qquad (-\infty < x < \infty) \,. \tag{1.20}$$

Here, $\boldsymbol{\eta} = \boldsymbol{v}_1 + \boldsymbol{v}_2 + \ldots \boldsymbol{v}_j$, and $\boldsymbol{v}_j$ is a suitable vector in X_j.

Example 1.10

[1.3] Let us find the solution $\phi(x)$ of the IVP

$$\begin{aligned} x_1' &= 3x_1 - x_2 + x_3 \,, \\ x_2' &= 2x_1 + \quad + x_3 \,, \\ x_3' &= x_1 - x_2 + 2x_3 \end{aligned}$$

satisfying the initial condition $\phi(0) = \eta$.

It is easy to find that the eigenvalues of the coefficient matrix $\mathbf{A}$ are $\lambda_1 = 1, \lambda_2 = 2$ with $n_1 = 1, n_2 = 2$. The eigenvectors corresponding to $\lambda_1 = 1$ are

$$\begin{pmatrix} 0 \\ t \\ t \end{pmatrix}, \quad t \in \mathbb{R} \,,\ t \neq 0 \,.$$

Solutions of the system $(\mathbf{A} - \lambda \mathbf{I})^2 \boldsymbol{x} = 0$ are

$$\begin{pmatrix} t \\ t \\ s \end{pmatrix}, \quad t, s \in \mathbb{R} \,,\ t, s \neq 0 \,,$$

simultaneously. Let

$$\eta = \boldsymbol{v}_1 + \boldsymbol{v}_2 = \begin{pmatrix} \eta_1 \\ \eta_2 \\ \eta_3 \end{pmatrix} = \begin{pmatrix} 0 \\ \alpha \\ \alpha \end{pmatrix} + \begin{pmatrix} \beta \\ \beta \\ \gamma \end{pmatrix} .$$

This leads to

$$\boldsymbol{v}_1 = \begin{pmatrix} 0 \\ \eta_2 - \eta_1 \\ \eta_2 - \eta_1 \end{pmatrix}$$

and

$$\boldsymbol{v}_2 = \begin{pmatrix} \eta_1 \\ \eta_1 \\ \eta_3 - \eta_2 + \eta_1 \end{pmatrix} .$$

Substituting these vectors in (1.20), we obtain the solution.

Numerical Solution of First-Order Systems of ODEs

For most (nonlinear) systems of ODE that arise in real-world applications, obtaining numerical solutions is, often, the only choice available. In this section, we discuss two methods that can be used to solve systems of ODE numerically. For more details, see [1.4].

Consider the following initial value problem

$$\boldsymbol{Y}' = \boldsymbol{f}(x, \boldsymbol{Y}), \quad \boldsymbol{Y}(x_0) = \boldsymbol{y}_0 \,. \tag{1.21}$$

We assume that $\boldsymbol{f}$ is such that the problem has a unique solution $\boldsymbol{Y}(x)$ on some open x-interval containing x_0.

The Euler Method. For $x_j = x_0 + jh$ for $j = 1, 2, \ldots$ where h the step size h is a fixed number, define the iterates $\boldsymbol{Y}_n$ (approximate values of the solutions at x_j's) as follows

$$\boldsymbol{Y}_{j+1} = \boldsymbol{Y}_j + h\boldsymbol{f}(x_j, \boldsymbol{Y}_j) \,. \tag{1.22}$$

In terms of the components of $\boldsymbol{Y}_j$ we have, for $i = 1, 2, \ldots, n$, and $j = 1, 2, \ldots$

$$y_{i,j+1} = y_{i,j} + hf_i(x_j, y_{i,j}) \,. \tag{1.23}$$

However, the Euler method is not accurate enough for practical purposes. A more efficient method is the fourth-order Runge–Kutta method. For each step $j = 1, 2, \ldots$, we have the following four auxiliary quantities

$$\begin{aligned} \boldsymbol{k}_1 &= h\boldsymbol{f}(x_j, \boldsymbol{Y}_j) \,, \\ \boldsymbol{k}_2 &= h\boldsymbol{f}\left(x_j + \frac{1}{2}h, \boldsymbol{Y}_j + \frac{1}{2}\boldsymbol{k}_1\right) , \\ \boldsymbol{k}_3 &= h\boldsymbol{f}\left(x_j + \frac{1}{2}h, \boldsymbol{Y}_j + \frac{1}{2}\boldsymbol{k}_2\right) , \\ \boldsymbol{k}_4 &= h\boldsymbol{f}(x_j + h, \boldsymbol{Y}_j + \boldsymbol{k}_3) \,, \end{aligned}$$

and the new value (approximation of the solution $\boldsymbol{y}(x)$ at $x_{j+1} = x_0 + (j+1)h$) is

$$\boldsymbol{Y}_{j+1} = \boldsymbol{Y}_j + \frac{1}{6}(\boldsymbol{k}_1 + 2\boldsymbol{k}_2 + 2\boldsymbol{k}_3 + \boldsymbol{k}_4) \,.$$

These numerical schemes are, of course, applicable for the scalar ODE ($n = 1$) as well.

1.3 The Laplace Transform

Transform techniques are very useful in solving a variety of problems arising in engineering and physical sciences. The basic paradigm is to transform the given problem to a different domain in which the problem is recast in a form that is easier to solve or/and gives an insightful perspective of the underlying problem. Integral transforms such as the Laplace transform and the Fourier transform are the most popular among the integral transforms. Here in this section, we consider the Laplace transform, present its properties, and its use in solving initial value problems for ODE. Using the Laplace transform on such a problem results in an algebraic problem that can be solved easily in the transform domain. To obtain the solution of the original problem, one needs to use the *inverse Laplace transform* and transform the solution obtained in the transform domain back to the original domain.

The schematic diagram given in Fig. 1.2 illustrates the idea of using the Laplace transform to solve initial value problems for ODEs.

1.3.1 The Laplace Transform: Definition and Properties

For a piecewise continuous function $f : [0, \infty) \to \mathbb{R}$, we may define the *Laplace transform* of f as follows. For a suitable transform variable, say s,

$$F(s) = \mathcal{L}\{f(t)\} = \int_0^\infty f(t)\, \mathrm{e}^{-st}\, \mathrm{d}t\,, \tag{1.24}$$

provided that the integral exists. Usually, the Laplace transform of a function $f(t)$ is denoted by the same letter in uppercase as $F(s)$. Such a Laplace transform exists, for example, for a function of *exponential order*. That is, if there exist positive constants M, T, and α such that $|f(t)| \le M\mathrm{e}^{\alpha t}$ for all $t \ge T$. If $F(s)$ is the Laplace transform of a function $f(t)$, then the *inverse Laplace transform* $\mathcal{L}^{-1}\{F(s)\} = f(t)$.

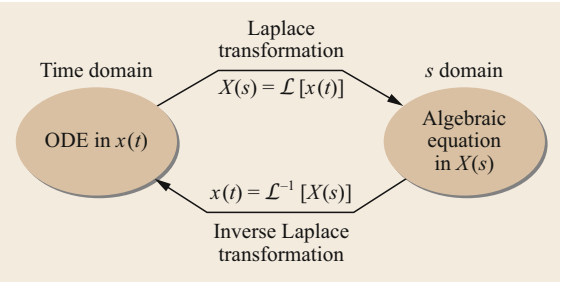

Fig. 1.2 Operations involved in the Laplace transform method

The following properties of the Laplace transform are useful in solving initial value problems:

1. Linearity: $\mathcal{L}\{af(t)+bg(t)\} = a\mathcal{L}\{f(t)\}+b\mathcal{L}\{g(t)\}$. Here a, b are constants.
2. For
$$\mathcal{U}(t-a) = \begin{cases} 1\,, & \text{if } t \ge a\,, \\ 0\,, & \text{if } t < a\,, \end{cases}$$
$$\mathcal{L}\{\mathcal{U}(t-a)\} = \frac{\mathrm{e}^{-as}}{s}\,.$$
3. Translation properties:
(i) $\mathcal{L}\{f(t)\,\mathrm{e}^{at}\} = F(s-a)$
(ii) $\mathcal{L}\{f(t)\,\mathcal{U}(t-a)\} = \mathrm{e}^{-as}\mathcal{L}\{f(t+a)\}$
(iii) $\mathcal{L}\{f(t-a)\,\mathcal{U}(t-a)\} = \mathrm{e}^{-as}F(s)$
4. $\mathcal{L}\{t^n f(t)\} = (-1)^n \mathrm{d}^n/\mathrm{d}s^n F(s)$
5. $\mathcal{L}\{f(t)/t\} = \int_s^\infty F(\sigma)\,\mathrm{d}\sigma$
6. $\mathcal{L}\{\delta(t-t_0)\} = \mathrm{e}^{-st_0}$.
Here, $\delta(t)$ is the Dirac delta function, $t_0 > 0$ is a real number.
7. If $F(s) = \mathcal{L}\{f(t)\}$, then
$$\mathcal{L}\{f'(t)\} = sF(s) - f(0)\,, \tag{1.25}$$
$$\mathcal{L}\{f''(t)\} = s^2F(s) - sf(0) - f'(0)\,. \tag{1.26}$$
In general,
$$\mathcal{L}\{f^{(n)}(t)\} = s^nF(s) - s^{n-1}f(0) - s^{n-2}f'(0) - \cdots - f^{(n-1)}(0)\,. \tag{1.27}$$
8. If $F(s) = \mathcal{L}\{f(t)\}$, then
$$\mathcal{L}\left\{\int_0^t f(\tau)\,\mathrm{d}\tau\right\} = \frac{F(s)}{s}\,. \tag{1.28}$$
9. For piecewise continuous functions f, g on $[0, \infty)$ that are of exponential order, the *convolution* of f and g is defined as
$$(f \star g)(t) = \int_0^t f(\tau)g(t-\tau)\,\mathrm{d}\tau\,. \tag{1.29}$$
We have
$$\mathcal{L}\{(f \star g)(t)\} = F(s)\,G(s)\,, \tag{1.30}$$
where $F(s) = \mathcal{L}\{f(t)\}$ and $G(s) = \mathcal{L}\{g(t)\}$.

10. A piecewise continuous function $f(t)$ is said to be a periodic function with period $T > 0$ if it is defined for all $t > 0$, and $f(t+T) = f(t)$ for all $t > 0$. For such a function,

$$\mathcal{L}\{f(t)\} = F(s) = \frac{1}{1-\mathrm{e}^{-sT}} \int_0^T f(t)\mathrm{e}^{-st}\,\mathrm{d}t\,. \tag{1.31}$$

Table of Laplace Transform Pairs

In Table 1.1, we present the Laplace transforms of several functions. The same table can also be used to find the inverse transforms as well.

Table 1.1 Laplace transform pairs

No.	$f(t)$	$F(s)$
1	Unit impulse $\delta(t)$	1
2	1 , unit step $u_s(t)$	$\frac{1}{s}$
3	t , unit ramp $u_r(t)$	$\frac{1}{s^2}$
4	$\delta(t-a)$	e^{-as}
5	$u(t-a)$	$\frac{\mathrm{e}^{-as}}{s}$
6	t^{n-1} , $n = 1, 2, \ldots$	$\frac{(n-1)!}{s^n}$
7	t^{a-1} , $a > 0$	$\frac{\Gamma(a)}{s^a}$
8	e^{-at}	$\frac{1}{s+a}$
9	$t\mathrm{e}^{-at}$	$\frac{1}{(s+a)^2}$
10	$t^n\mathrm{e}^{-at}$, $n = 1, 2, \ldots$	$\frac{n!}{(s+a)^{n+1}}$
11	$\frac{1}{b-a}(\mathrm{e}^{-at} - \mathrm{e}^{-bt})$, $a \neq b$	$\frac{1}{(s+a)(s+b)}$
12	$\frac{1}{a-b}(a\mathrm{e}^{-at} - b\mathrm{e}^{-bt})$, $a \neq b$	$\frac{s}{(s+a)(s+b)}$
13	$\frac{1}{ab}\left(1 + \frac{1}{a-b}(b\mathrm{e}^{-at} - a\mathrm{e}^{-bt})\right)$	$\frac{1}{s(s+a)(s+b)}$
14	$\frac{1}{a^2}(-1 + at + \mathrm{e}^{-at})$	$\frac{1}{s^2(s+a)}$
15	$\frac{1}{a^2}(1 - \mathrm{e}^{-at} - at\mathrm{e}^{-at})$	$\frac{1}{s(s+a)^2}$
16	$\sin \omega t$	$\frac{\omega}{s^2+\omega^2}$
17	$\cos \omega t$	$\frac{s}{s^2+\omega^2}$
18	$\mathrm{e}^{-\sigma t}\sin \omega t$	$\frac{\omega}{(s+\sigma)^2+\omega^2}$

Table 1.1 (continued)

No.	$f(t)$	$F(s)$
19	$\mathrm{e}^{-\sigma t}\cos \omega t$	$\frac{\omega^2}{s(s^2+\omega^2)}$
20	$1 - \cos \omega t$	$\frac{s+\sigma}{(s+\sigma)^2+\omega^2}$
21	$\omega t - \sin \omega t$	$\frac{\omega^3}{s^2(s^2+\omega^2)}$
22	$t\cos \omega t$	$\frac{s^2-\omega^2}{(s^2+\omega^2)^2}$
23	$\frac{1}{2\omega}t\sin \omega t$	$\frac{s}{(s^2+\omega^2)^2}$
24	$\frac{1}{2\omega^3}(\sin \omega t - \omega t\cos \omega t)$	$\frac{1}{(s^2+\omega^2)^2}$
25	$\frac{1}{2\omega}(\sin \omega t + \omega t\cos \omega t)$	$\frac{s^2}{(s^2+\omega^2)^2}$
26	$\frac{1}{\omega_2^2-\omega_1^2}\left(\frac{1}{\omega_2}\sin \omega_2 t - \frac{1}{\omega_1}\sin \omega_1 t\right)$, $\omega_1^2 \neq \omega_2^2$	$\frac{1}{(s^2+\omega_1^2)(s^2+\omega_2^2)}$
27	$\frac{1}{\omega_2^2-\omega_1^2}(\cos \omega_1 t - \cos \omega_2 t)$, $\omega_1^2 \neq \omega_2^2$	$\frac{s}{(s^2+\omega_1^2)(s^2+\omega_2^2)}$
28	$\sinh at$	$\frac{a}{s^2-a^2}$
29	$\cosh at$	$\frac{s}{s^2-a^2}$
30	$\frac{1}{a^2-b^2}\left(\frac{1}{a}\sinh at - \frac{1}{b}\sinh bt\right)$, $a \neq b$	$\frac{1}{(s^2-a^2)(s^2-b^2)}$
31	$\frac{1}{a^2-b^2}[\cosh at - \cosh bt]$, $a \neq b$	$\frac{s}{(s^2-a^2)(s^2-b^2)}$
32	$\frac{1}{3a^2}\left[\mathrm{e}^{-at} + 2\mathrm{e}^{\frac{1}{2}at}\sin\left(\frac{\sqrt{3}}{2}at - \frac{\pi}{6}\right)\right]$	$\frac{1}{s^3-a^3}$
33	$\frac{1}{3a}\left[-\mathrm{e}^{-at} + 2\mathrm{e}^{\frac{1}{2}at}\sin\left(\frac{\sqrt{3}}{2}at + \frac{\pi}{6}\right)\right]$	$\frac{s}{s^3-a^3}$
34	$\frac{1}{3a^2}\left[\mathrm{e}^{at} - 2\mathrm{e}^{-\frac{1}{2}at}\sin\left(\frac{\sqrt{3}}{2}at + \frac{\pi}{6}\right)\right]$	$\frac{1}{s^3-a^3}$
35	$\frac{1}{3a}\left[\mathrm{e}^{-at} + 2\mathrm{e}^{-\frac{1}{2}at}\sin\left(\frac{\sqrt{3}}{2}at - \frac{\pi}{6}\right)\right]$	$\frac{s}{s^3-a^3}$
36	$\frac{1}{4a^3}(\cosh at \sin at - \sinh at \cos at)$	$\frac{1}{s^4+4a^4}$
37	$\frac{1}{2a^2}\sinh at \sin at$	$\frac{s}{s^4+4a^4}$
38	$\frac{1}{2a^3}(\sinh at - \sin at)$	$\frac{1}{s^4-a^4}$
39	$\frac{1}{2a^2}(\cosh at - \cos at)$	$\frac{s}{s^4-a^4}$

1.3.2 The Inverse Laplace Transform

The inverse Laplace transform plays an important role in solving initial value problems. In general, the process of finding the inverse transform of the solution to the transformed problem to obtain the solution of the original problem often involves the use of algebraic techniques, prior to invoking the properties of Laplace transform. To determine the inverse transform of rational functions of the form,

$$F(s) = \frac{N(s)}{D(s)} = \frac{\text{polynomial of degree } m}{\text{polynomial of degree } n}\,, \quad m < n\,,$$

using the idea of *partial fractions* we can express $F(s)$ as a sum of (simpler) rational functions and find the inverse Laplace transform of each rational function using the table of transforms. There are a few scenarios that depend on the factors of $D(s)$. Factors of $D(s)$ may be linear, repeated linear, irreducible polynomial, or repeated irreducible polynomial.

Case (i): linear factors. That is,

$$D(s) = (s-a_1)(s-a_2)\cdots(s-a_k)\,.$$

Then, we express,

$$F(s) = \frac{N(s)}{D(s)} = \frac{A_1}{(s-a_1)} + \frac{A_2}{(s-a_2)} + \cdots + \frac{A_k}{(s-a_k)}\,.$$

Case (ii): repeated linear factors. If a root of $D(s)$, say, a_i, with multiplicity m, then, $D(s)$ contains the factor $(s-a_i)^m$. This factor is associated with the partial fractions of the form,

$$\frac{A_1}{(s-a_1)} + \frac{A_2}{(s-a_2)^2} + \cdots + \frac{Ak-1}{(s-a_{m-1})^{m-1}} + \frac{A_k}{(s-a_m)^m}\,.$$

Case (iii): irreducible polynomial factor. If $D(s)$ has a pair of complex (conjugate) roots, then $D(s)$ is of the form s^2+as+b. Each irreducible polynomial is associated with a single fraction of the form

$$\frac{Bs+C}{s^2+as+b}\,.$$

This term can be rewritten as

$$\frac{Bs+C}{s^2+as+b} = \frac{BS+C}{(s+\sigma)^2+\omega^2}\,.$$

This, in turn, can be written in terms of rational functions of the form

$$\frac{\omega}{(s+\sigma)^2+\omega^2} \quad \text{and} \quad \frac{s+\omega}{(s+\sigma)^2+\omega^2}\,,$$

and then the inverse Laplace transform can be determined.

Case (iv): repeated irreducible polynomial factor. That is, $D(s)$ has a factor of the form $(s^2+as+b)^m$. In this case, the fractions formed are

$$\frac{B_1s+C_1}{(s^2+as+b)} + \frac{B_2s+C_2}{(s^2+as+b)^2} + \cdots + \frac{B_ms+C_m}{(s^2+as+b)^m}\,.$$

Example 1.11

Let $F(s) = s/(s+16)^2$. Clearly,

$$F(s) = -\frac{1}{2}\frac{\mathrm{d}}{\mathrm{d}s}\left(\frac{1}{(s^2+16)}\right).$$

Invoking property (4) of the Laplace transform listed above, we have $\mathcal{L}^{-1}\{F(s)\} = \frac{1}{8}t\sin t$.

Example: Let

$$F(s) = \frac{6s+3}{s^4+5s^2+4}\,.$$

Using the procedure outlined above in case (iv) for partial fractions, we can show that

$$\frac{6s+3}{s^4+5s^2+4} = \frac{2s}{s^2+1} + \frac{1}{s^2+1} - \frac{2s}{s^2+4} - \frac{\sin 2s}{2}\,.$$

Taking the inverse transform, we obtain $f(t) = 2\cos t + \sin t - 2\cos 2t - \frac{1}{2}\sin 2t$.

Example 1.12

Let us solve the initial value problem: $y'' + y = \sin t$, $y(0) = y'(0) = 0$. Applying the Laplace transform on the nonhomogeneous ODE and using the initial conditions, we obtain

$$Y(s) = \frac{1}{(s^2+1)^2}\,.$$

Invoking property (9) above, we obtain

$$y(t) = \mathcal{L}^{-1}\{Y(s)\} = \mathcal{L}^{-1}\left\{\frac{1}{(s^2+1)}\frac{1}{(s^2+1)}\right\} = \frac{\sin t - t\cos t}{2}\,.$$

Example 1.13
Solve

$$y'' + 4y = \sin t\,\mathcal{U}(t-2\pi)\,, \quad y(0) = 1\,, y'(0) = 0\,.$$

Applying the Laplace transform on the ODE and using the initial conditions, we obtain

$$Y(s) = \frac{s}{s^2+4} + \frac{\mathrm{e}^{-2\pi s}}{(s^2+1)(s^2+4)}\,.$$

It can be easily verified that

$$\mathcal{L}^{-1}\left\{\frac{1}{(s^2+1)(s^2+4)}\right\} = \frac{1}{3}\sin t - \frac{2}{3}\sin 2t\,.$$

Now, using the property (3)(ii) of the Laplace transform, we obtain

$$\mathcal{L}^{-1}\left\{\frac{\mathrm{e}^{-2\pi s}}{(s^2+1)(s^2+4)}\right\} = \frac{1}{3}\sin t\,\mathcal{U}(t-2\pi) - \frac{2}{3}\sin 2t\,\mathcal{U}(t-2\pi)\,.$$

Finally, finding the inverse transform, we obtain

$$y(t) = \begin{cases} \cos 2t\,, & 0 \le t < 2\pi\,, \\ \cos 2t + \dfrac{1}{3}\sin t - \dfrac{2}{3}\sin 2t\,, & t \ge 2\pi\,. \end{cases}$$

1.4 Fourier Analysis

A Fourier series represents a general periodic function in terms of an infinite series of sine and cosine functions, where the coefficients of the series are obtained by using the *orthogonality* properties of the sine and cosine functions on the interval under consideration. Fourier series are widely used in various applications involving ordinary or partial differential equations. On the other hand, the Fourier transform maps a function defined in the time domain to one in the frequency domain. We outline the most basic ideas of this vast and fascinating subject.

1.4.1 Fourier Series

Let $f(x)$ be a piecewise continuous function defined on an interval $(-c, c)$ for $c > 0$. We may extend this function to all of $\mathbb{R}$ as a periodic function of period $p = 2c$. That is, $f(x+p) = f(x)$ for all $x \in \mathbb{R}$. Such functions may be represented by the *Fourier series* of the form

$$\frac{a_0}{2} + \sum_{n=1}^{\infty}\left(a_n \cos\frac{n\pi x}{c} + b_n \sin\frac{n\pi x}{c}\right), \tag{1.32}$$

where the *Fourier coefficients* of $f(x)$ are given by the Euler–Fourier formulas, as

$$a_n = \frac{1}{c}\int_{-c}^{c} f(x)\cos\frac{n\pi x}{c}\,\mathrm{d}x\,, \quad n = 0, 1, \ldots\,, \tag{1.33}$$

$$b_n = \frac{1}{c}\int_{-c}^{c} f(x)\sin\frac{n\pi x}{c}\,\mathrm{d}x\,, \quad n = 1, \ldots \tag{1.34}$$

If the function f is piecewise smooth on $(-c, c)$, that is, both f and f' are piecewise continuous on $(-c, c)$, and $F(x)$ is the $2c$ periodic extension of f, then at each $x \in (-\infty, \infty)$, the Fourier series for f on $(-c, c)$ converges to the average value $(F(x+) + F(x-))/2$.

Each term of the Fourier series above may be written as a *harmonic*, $A\cos(n\pi x/c + \phi)$, where the *amplitude* A is $\sqrt{a^2+b^2}$, the *angular frequency* is $n\pi/c$, and the initial phase ϕ is $\tan^{-1}(b_n/a_n)$. These harmonics describe the variation of f about its average value $\frac{1}{2}a_0$.

If a function f is defined only on $(0, c)$ for $c > 0$, then we can consider the *even* ($f(-x) = f(x)$) and *odd* ($f(-x) = -f(-x)$) extensions of f onto $(-c, c)$. We thus have a *Fourier cosine series* (consisting only of the cosine terms) and a *Fourier sine series* (consisting only of sine terms) for a function f on $(0, c)$. On the other hand, the mapping $s = (2x-b-a)c/(b-a)$ maps the interval $[a, b]$ to the interval $[-c, c]$, and we can write a Fourier series for a function $f(x)$ defined on an interval (a, b) as

$$\frac{a_0}{2} + \sum_{n=1}^{\infty} a_n \cos\frac{n(2x-b-a)c}{(b-a)} + b_n \sin\frac{n(2x-b-a)c}{(b-a)}\,, \tag{1.35}$$

where

$$a_n = \frac{2}{(b-a)}\int_{a}^{b} f(x)\cos\frac{n(2x-b-a)c}{(b-a)}\,\mathrm{d}x\,, \quad n = 0, 1, \ldots\,, \tag{1.36}$$

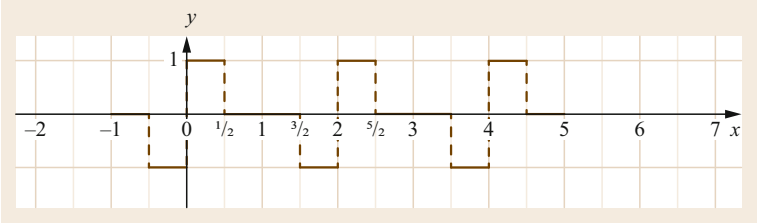

Fig. 1.3 Odd-periodic extension of $f(x)$

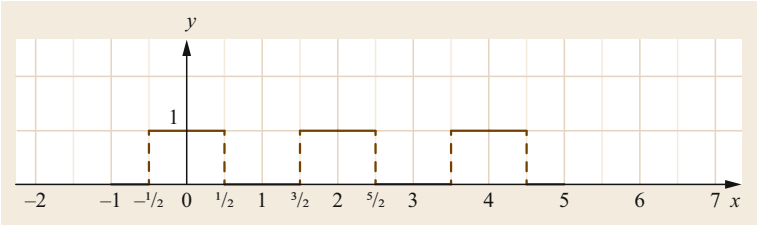

Fig. 1.4 Even-periodic extension of $f(x)$

and

$$b_n = \frac{2}{(b-a)} \int_a^b f(x) \sin \frac{n(2x-b-a)c}{(b-a)} \, \mathrm{d}x \,,$$
$$n = 1, 2, \ldots \qquad (1.37)$$

Example 1.14 gives all the three types of series for a given function.

Example 1.14

Let

$$f(x) = \begin{cases} 1 \,, & 0 < x < \dfrac{1}{2} \,, \\ 0 \,, & \dfrac{1}{2} < x < 1 \,. \end{cases}$$

Find (i) the Fourier sine series, (ii) the Fourier cosine series, and (iii) Fourier series for $f(x)$:

(i) Upon extending the function as an odd function on to $(-1, 1)$ (Fig. 1.3), we have $a_n = 0$ and

$$b_n = 2 \int_0^1 f(x) \sin n\pi x \, \mathrm{d}x$$
$$= \frac{2}{n\pi} \left[1 - \cos\left(\frac{n\pi}{2}\right) \right].$$

So, we have

$$b_1 = \frac{2}{\pi} \,, \quad b_2 = \frac{2}{\pi} \,,$$
$$b_3 = \frac{2}{3\pi} \,, \quad b_4 = 0 \,, \quad \ldots$$

Therefore, the Fourier sine series of f is

$$\frac{2}{\pi} \left(\sin \pi x + \frac{2 \sin 2\pi x}{2} + \frac{\sin 3\pi x}{3} + \sin 5\pi x 5 + \frac{2 \sin 6\pi x}{6} + \ldots \right).$$

(ii) Extending f onto $(-c, c)$ as an even function (Fig. 1.4), we have $b_n = 0$ and

$$a_n = 2 \int_0^1 f(x) \cos n\pi x \, \mathrm{d}x$$
$$= \frac{2}{n\pi} \sin\left(\frac{n\pi}{2}\right).$$

Therefore, the Fourier cosine series of f is

$$\frac{1}{2} + \frac{2}{\pi} \left(\cos \pi x - \frac{\cos 3\pi x}{3} + \frac{\cos 5\pi x}{5} - \ldots \right).$$

(iii) Consider the periodic extension of $f(x)$ of period 1 (Fig. 1.5). Applying the formulas given, we

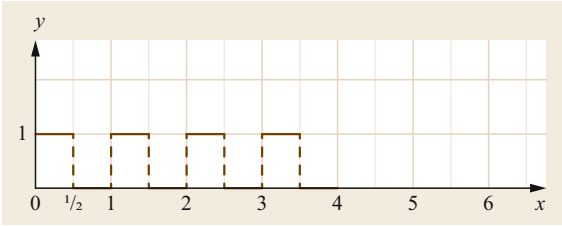

Fig. 1.5 1-periodic extension of $f(x)$

obtain

$$
\begin{aligned}
a_0 &= 1\,,\\
a_n &= 2\int_0^1 f(x)\cos(2x-1)n\pi\,\mathrm{d}x = 0\,,\\
&\qquad n = 1,2,\ldots\,,\\
b_n &= 2\int_0^1 f(x)\sin(2x-1)n\pi\,\mathrm{d}x\\
&= \frac{1}{n\pi}[(-1)^n - 1]\,,\\
f(x) &= \frac{1}{2} + \frac{2}{\pi}\left(\sin 2\pi x + \frac{\sin 6\pi x}{3}\right.\\
&\qquad \left. + \frac{\sin 10\pi x}{5} + \ldots\right).
\end{aligned}
$$

It is a coincidence that in case (iii), the coefficients a_n are all zero. Notice also that while both in case (i) and (iii) we have Fourier sine series, they are different.

1.4.2 The Fourier Transform

Let $f : \mathbb{R} \to \mathbb{C}$ be a piecewise continuous function that is absolutely integrable. That is, $\int_{-\infty}^{\infty} |f(x)|\,\mathrm{d}x < \infty$. The Fourier transform of such an f is defined as

$$
\begin{aligned}
\mathcal{F}(f)(\omega) &= \hat{f}(\omega)\\
&= \frac{1}{\sqrt{2\pi}}\int_{-\infty}^{\infty} f(x)\mathrm{e}^{-\mathrm{i}\omega x}\,\mathrm{d}x\,. \qquad (1.38)
\end{aligned}
$$

The inverse Fourier transform is defined as

$$
f(x) = \frac{1}{\sqrt{2\pi}}\int_{-\infty}^{\infty} \hat{f}(\omega)\mathrm{e}^{\mathrm{i}\omega x}\,\mathrm{d}\omega\,. \qquad (1.39)
$$

In fact, the Fourier transform exists for a more general class of functions, for example, such as square integrable functions on $\mathbb{R}$. That is, $\int_{-\infty}^{\infty} |f(x)|^2\,\mathrm{d}x < \infty$. The following can be easily verified:

1. $$\mathcal{F}(\mathrm{e}^{-|x|}) = \sqrt{\frac{2}{\pi}}\frac{1}{1+\omega^2}\,.$$

2. For $b > 0$,
$$
f(x) = \begin{cases} 1\,, & -b \le x \le b\,,\\ 0\,, & \text{otherwise}\,, \end{cases}
$$
$$\mathcal{F}(f)(\omega) = \frac{\sin\omega b}{\omega\pi} = \mathrm{sinc}(b\omega)\,.$$

3. $$\mathcal{F}(\mathrm{e}^{-x^2}) = \sqrt{\frac{2}{\pi}}\mathrm{e}^{-\frac{\omega^2}{4}}\,.$$

The following properties of the Fourier transform are useful. We assume that the Fourier transform of the functions mentioned in these properties exists:

1. (Linearity) for $a, b \in \mathbb{C}$,
$$\mathcal{F}[af + bg](\omega) = a\mathcal{F}[f](\omega) + b\mathcal{F}[g](\omega).$$

2. $$\mathcal{F}[f](-\omega) = \overline{\mathcal{F}[f](\omega)}\,.$$

3. For $a, b \in \mathbb{C}$, $a \neq 0$, and $g(x) = f(ax + b)$, we have
$$\mathcal{F}[g](\omega) = \frac{1}{|a|}\mathrm{e}^{\frac{\mathrm{i}\omega b}{a}}\mathcal{F}[f]\left(\frac{\omega}{a}\right).$$

4. For $c \in \mathbb{R}$,
$$\mathcal{F}[\mathrm{e}^{\mathrm{i}cx}f(x)](\omega) = \mathcal{F}[f](\omega - c)\,.$$

5. $$\mathcal{F}[f'](\omega) = \mathrm{i}\omega\mathcal{F}[f](\omega)\,.$$

6. $$\mathcal{F}[xf(x)](\omega) = \mathrm{i}\frac{\mathrm{d}}{\mathrm{d}\omega}\mathcal{F}[f](\omega)\,.$$

7. For $(f \star g)(x) = \int_{-\infty}^{\infty} f(x-y)g(y)\,\mathrm{d}y$,
$$\mathcal{F}[f \star g](\omega) = \mathcal{F}[f](\omega)\cdot\mathcal{F}[g](\omega)\,.$$

1.5 Complex Analysis

The study of the functions of a complex variable is very fascinating, and such functions arise in a variety of application areas. We begin this section with a brief introduction to complex number algebra.

1.5.1 Complex Numbers

A complex number z may be represented as $z = x + \mathrm{i}y$, where $\mathrm{i} = \sqrt{-1}$ and $x, y \in \mathbb{R}$ are called the real part and the imaginary part of z, respectively, and are denoted by $x = \mathrm{Re}(z)$ and $y = \mathrm{Im}(z)$. Two complex numbers are said to be equal if and only if their real and imaginary parts are equal. For $z_1 = x_1 + \mathrm{i}y_1$, $z_2 = x_2 + \mathrm{i}y_2$,

$$z_1 + z_2 = (x_1 + x_2) + \mathrm{i}(y_1 + y_2) \tag{1.40}$$

and

$$\begin{aligned} z_1 z_2 &= (x_1 + \mathrm{i}y_1)(x_2 + \mathrm{i}y_2) \\ &= (x_1 x_2 - y_1 y_2) + \mathrm{i}(x_1 y_2 + x_2 y_1) \,. \end{aligned} \tag{1.41}$$

For $z_2 \neq 0$,

$$z = \frac{z_1}{z_2} = \frac{x_1 x_2 + y_1 y_2}{x_2^2 + y_2^2} + \mathrm{i}\,\frac{x_2 y_1 - x_1 y_2}{x_2^2 + y_2^2} \,. \tag{1.42}$$

Complex numbers may be represented as points in a plane, in which the x-axis is called the real axis, and the y-axis is called the imaginary axis. Thus, complex numbers may also be represented as *ordered pairs*. That is, the complex number $x + \mathrm{i}y$ is identified with the (unique) point (x, y) in the complex plane.

The magnitude of a complex number $z = x + \mathrm{i}y$ is defined as

$$|z| = \sqrt{x^2 + y^2} \,. \tag{1.43}$$

The *complex conjugate* $\bar{z}$ of a complex number $z = x + \mathrm{i}y$ is defined by $\bar{z} = x - \mathrm{i}y$. It can be easily verified that $\mathrm{Re}(z) = x = \frac{1}{2}(z + \bar{z})$, $\mathrm{Im}(z) = x = \frac{1}{2\mathrm{i}}(z - \bar{z})$. Geometrically, a complex number and its conjugate are reflections of one another about the real axis (Fig. 1.6).

Polar Representation of Complex Numbers

The polar form of complex numbers, as suggested by its name, uses the polar coordinates to represent complex numbers in the complex plane. We know that $x = r\cos\theta$ and $y = r\sin\theta$, where r is the radial coordinate, and θ is the angular coordinate. Invoking Euler's formula,

$$\mathrm{e}^{\mathrm{i}\theta} = \cos\theta + \mathrm{i}\sin\theta \,,$$

we can represent a complex number

$$z = x + \mathrm{i}y = r\mathrm{e}^{\mathrm{i}\theta} \,.$$

Here, the magnitude of z is $r = |z|$ and the phase (or argument) of z is

$$\theta = \arg z = \tan^{-1}\left(\frac{\mathrm{Im}(z)}{\mathrm{Re}(z)}\right) = \tan^{-1}\left(\frac{y}{x}\right) .$$

The angle θ is measured from the positive real axis and, by convention, is regarded as positive in the counterclockwise direction (Fig. 1.7). It is measured in radians, and the specific value of θ that lies in the interval $(-\pi, \pi]$ is called the principal value of $\arg z$ and is denoted by $\mathrm{Arg}\, z$. The following properties of complex numbers are useful:

1. For complex numbers z_1, z_2, the triangle inequality holds

$$|z_1 + z_2| \leq |z_1| + |z_2| \,.$$

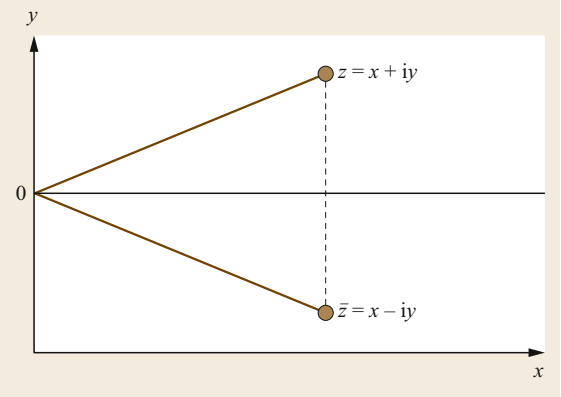

Fig. 1.6 A complex number and its conjugate

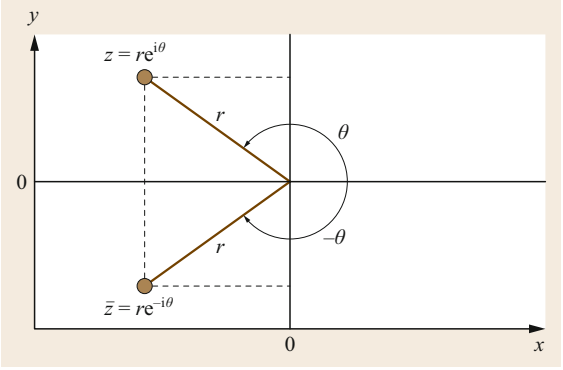

Fig. 1.7 Relation between the rectangular and polar forms of a complex number

2. The product of complex numbers z, and its conjugate, is a positive, real number, equal to the square of its magnitude. That is, $z\bar{z} = |z|^2$.
3. For $z = e^{i\theta}$, $z_1 = r_1 e^{i\theta_1}$ and $z_2 = r_2 e^{i\theta_2}$, we have:

   a) $z_1 z_2 = r_1 r_2 e^{i(\theta_1+\theta_2)}$ and $|z_1 , z_2| = |z_1||z_2|$
   and $\arg(z_1 z_2) = \arg(z_1) + \arg(z_2)$
   (up to a multiple of 2π)
   b) $z_1/z_2 = r_1/r_2 e^{i(\theta_1-\theta_2)}$.
   So, $|z_1/z_2| = |z_1|/|z_2|$,
   and $\arg(z_1/z_2) = \arg(z_1) - \arg(z_2)$
   (up to a multiple of 2π).
   c) $\bar{z} = re^{-i\theta}$.
   d) $z^n = (re^{i\theta})^n = r^n e^{in\theta} = r^n(\cos n\theta + i \sin n\theta)$.

Example 1.15

Let

$$z = \frac{8}{-2+2i} = -2-2i\,.$$

Clearly, z is located in the third quadrant of the complex plane. The phase of z is

$$\theta = \tan^{-1}\left(\frac{-2}{-2}\right) = 45^\circ = \frac{\pi}{4}\,\text{rad}\,.$$

This only tells us that the (smallest) angle between OA and the real axis is 45°. Since z is in the third quadrant, its actual phase is $180^\circ + 45^\circ = 225^\circ$ ($\pi + \pi/4 = 5\pi/4$ rad) in the counterclockwise direction or -135° ($-3\pi/4$) in the clockwise direction. So, the polar form of z can be written as

$$z = -2-2i = \sqrt{8}e^{i(\frac{5\pi}{4})}\,.$$

Thus, the phase of z is $5\pi/4$.

Roots of a Complex Number. For a complex number, $z \neq 0$, and a positive number n, the n-th root of z, denoted by $\sqrt[n]{z}$, is *multivalued*, namely n-valued. The n values of $w = \sqrt[n]{z}$ can be obtained as follows.

For $z = r(\cos\theta + i\sin\theta)$ and $w = R(\cos\phi + \sin\phi)$, we have

$$w^n = R^n(\cos n\phi + \sin n\phi) = z$$
$$= r(\cos\theta + i\sin\theta)\,. \qquad (1.44)$$

Comparing the modulus (which is determined only up to an integer multiple of 2π) and the arguments, we see that $R = \sqrt[n]{r}$ and

$$n\phi = \theta + 2k\pi\,, \quad \text{thus } \phi = \frac{\theta}{n} + \frac{2k\pi}{n}\,,$$

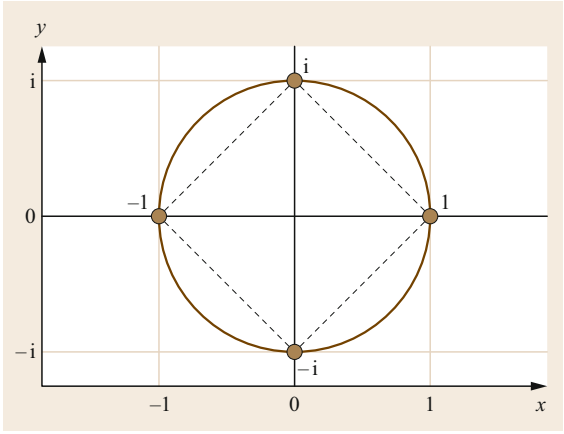

Fig. 1.8 Locations of the fourth roots of unity

where $k = 0, 1, \ldots, n-1$.

Thus, for $k = 0, 1, \ldots, n-1$,

$$\sqrt[n]{z} = \sqrt[n]{r}\left(\cos\frac{\theta+2k\pi}{n} + i\sin\frac{\theta+2k\pi}{n}\right).$$

These n values lie on a circle of radius $\sqrt[n]{r}$ with the center at the origin and constitute the vertices of a regular polygon of n sides.

For $z = 1$, we have $|z| = r = 1$ and $\text{Arg}\, z = 0$. Thus, for $k = 0, 1, \ldots n-1$,

$$\sqrt[n]{1} = \left(\cos\frac{2k\pi}{n} + i\sin\frac{2k\pi}{n}\right). \qquad (1.45)$$

These n values are called the *n-th roots of unity*.

Figure 1.8 shows the fourth roots of unity, namely $1, i, -1$ and $-i$.

1.5.2 Complex Functions

Denoting the set of all complex numbers by $\mathbb{C}$, we consider a subset $S \subset \mathbb{C}$. A function f defined on S is a rule that assigns to every $z \in S$, a $w \in \mathbb{C}$, called the *value* of f at z. We denote this by $f(z) = w$. Here, z varies in S and is called a complex variable. The set S is called the *domain* of f. For example, the domain of the function $w = f(z) = z^2$ is the entire complex plane where as the domain of the function $w = g(z) = z/z-1$ is the set of all complex numbers, except $z = 1$. The set of all values of a function f is called the *range* of f; w is a complex number as well, so we may write $w = u + iv$, and since w depends on $z = x + iy$, we write

$$w = f(z) = u(x, y) + iv(x, y)\,. \qquad (1.46)$$

Unlike the situation for real functions, we are no longer able to draw *graphs* for complex functions. This is because z is in the xy-plane, whereas w is in the uv-plane,

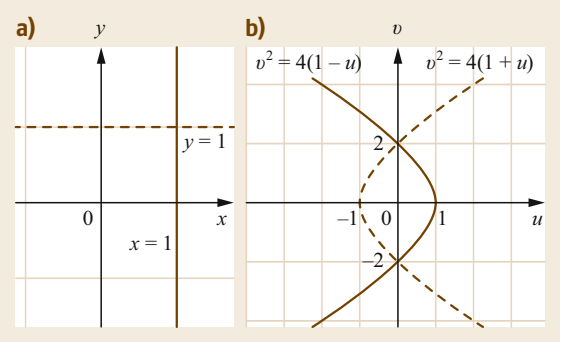

Fig. 1.9a,b The lines $x = 1$ and $y = 1$ **(a)** and their images under the mapping $f(z) = z^2$ **(b)**

and it is not possible to superimpose them onto one diagram. However, we can separately depict the *domain plane* and the *image plane* and think of a complex function f as a transformation that maps points (curves) in the xy-plane onto points (curves) in the uv-plane.

Example 1.16

Consider $f(z) = z^2 = (x + \mathrm{i}y)^2 = (x^2 - y^2) + \mathrm{i}(2xy)$.

Clearly, $u(x, y) = x^2 - y^2$ and $v(x, y) = 2xy$. So, we see that the line $x = 1$ is mapped to $u = 1 - y^2$ and $v = 2y$. Upon eliminating the variable y, we obtain the parabola, $v^2 = 4(1 - u)$, that opens to the left. On the other hand, the horizontal line $y = 2$ is mapped to parabola $v^2 = 4(1 + u)$ that opens to the right. See Fig. 1.9a,b.

Using the polar coordinate representation, we have for $z = re^{\mathrm{i}\theta}$, $w = z^2 = r^2 e^{2\mathrm{i}\theta}$. Thus, we see that circles $r = r_0$ are mapped onto circles $R = r_0^2$, and the ray $\theta = \theta_0$ is mapped onto ray $\phi = 2\theta_0$.

1.5.3 Analytic Functions

By a neighborhood of a point $z_0 \in \mathbb{C}$ we mean an open circular disk of some radius $\epsilon (> 0)$ centered at z_0. That is,

$$N_\epsilon(z_0) = \{z \in \mathbb{C} \,|\, |z - z_0| < \epsilon\} \,.$$

Differentiability at a single point is often of no practical interest. Therefore, the following important notion in defined.

A complex function $f(z)$ is *analytic* (or *holomorphic*) at a point z_0, if it is differentiable throughout some neighborhood of z_0. A function is analytic in a domain if it is analytic at all points of the domain. Analytic functions arise in fluid flows and complex potentials.

Let $f(z) = u(x, y) + \mathrm{i}v(x, y)$ be defined and continuous in some neighborhood of a point $z = x + \mathrm{i}y$ and differentiable at z itself. Then, at that point, the first-order partial derivatives of u and v exist and satisfy the Cauchy–Riemann equations

$$u_x = v_y \,, \quad v_x = -u_y \,. \tag{1.47}$$

Conversely, if two real-valued continuous functions $u(x, y)$, $v(x, y)$ of two real variables x and y have continuous first partial derivatives that satisfy the Cauchy–Riemann equations in some domain D, then the complex function $f(z) = u(x, y) + \mathrm{i}v(x, y)$ is analytic in D.

Example 1.17

Let $f(z) = \mathrm{e}^z = \mathrm{e}^x(\cos y + \mathrm{i} \sin y)$.

Here, $u(x, y) = \mathrm{e}^x \cos y$, $v(x, y) = \mathrm{e}^x \sin y$, and we have

$$u_x = \mathrm{e}^x \cos y \,, \quad v_y = \mathrm{e}^x \cos y \,,$$
$$u_y = -\mathrm{e}^x \sin y \,, \quad v_x = \mathrm{e}^x \sin y \,.$$

We see that the Cauchy–Riemann equations are satisfied. Thus, $f(z)$ is analytic for all z.

If we express a function in polar coordinates, that is, $f(z) = u(r, \theta) + \mathrm{i}v(r, \theta)$, the Cauchy–Riemann equations in polar form are given by

$$u_r = \frac{1}{r} v_\theta \,, \quad v_r = -\frac{1}{r} u_\theta \,. \tag{1.48}$$

If $f(z) = u(x, y) + \mathrm{i}v(x, y)$ is an analytic function on some domain $D \subset \mathbb{C}$, then both u and V satisfy the *Laplace equation*

$$\nabla^2 u = u_{xx} + u_{yy} = 0 \,, \quad \text{and} \quad \nabla^2 v = v_{xx} + v_{yy} = 0$$

in D and have continuous second partial derivatives in D.

Examples of Analytic Functions

1. $f(z) = \mathrm{e}^z$ is analytic on the entire complex plane $\mathbb{C}$; $\mathrm{e}^z = \mathrm{e}^x(\cos y + \mathrm{i} \sin y)$ is, clearly, a periodic function with the complex period $2\pi\mathrm{i}$.
2. The complex trigonometric functions

$$\cos z = \frac{1}{2}(\mathrm{e}^{\mathrm{i}z} + \mathrm{e}^{-\mathrm{i}z}) \quad \text{and} \quad \sin z = \frac{1}{2\mathrm{i}}(\mathrm{e}^{\mathrm{i}z} - \mathrm{e}^{-\mathrm{i}z}) \,.$$

These are analytic, again, in the entire complex plane $\mathbb{C}$. The following properties of these functions are useful:

a) $\cos z = \cos x \cosh y - \mathrm{i} \sin x \sinh y$.
b) $\sin z = \sin x \cosh y + \mathrm{i} \cos x \sinh y$.

c) $|\cos z|^2 = \cos^2 x + \sinh^2 y$
and $|\sin z|^2 = \sin^2 x + \sinh^2 y$.
This tells us that, unlike their real-valued counterparts, these functions are unbounded.

3. For $z \neq 0$, the complex logarithm function, $f(z) = \ln z = \ln r + \mathrm{i}\theta$, where $\theta = \arg z$ is multivalued. However, the *principal complex logarithm*

$$\mathrm{Ln}\, z = \ln |z| + \mathrm{i}\, \mathrm{Arg}\, z \quad (z \neq 0)$$

is single-valued and is analytic on $D = \{z = r\mathrm{e}^{\mathrm{i}\theta} | \ r > 0, -\pi < \theta < \pi\}$.
Note that $\mathrm{Ln}(-1) = \pi\mathrm{i}$ and $\mathrm{Ln}\,\mathrm{i} = \frac{\pi}{2}$.

4. The power function $f(z) = z^c = \mathrm{e}^{c\,\mathrm{Ln}\, z}$ (c complex, $z \neq 0$), is again, multivalued. The particular value $z^c = \mathrm{e}^{c\,\mathrm{Ln}\, z}$ is called the principal value of z^c.

1.5.4 Complex Integration

Curves in the complex plane may be represented parametrically by complex-valued functions of a real variable

$$z(t) = x(t) + \mathrm{i}y(t)\,, \quad a \leq t \leq b\,.$$

The curve C denoted by this function is said to be *oriented* in the increasing direction of t.

The curve C is said to be *smooth* if it can be represented by a function $z(t)$ such that $z'(t) \neq 0$ for all $t \in [a, b]$.

Suppose $C : z(t), a \leq t \leq b$ is a *piecewise smooth* curve (consisting of finitely many smooth curves joined end to end), and f is a continuous function on C. Then, the *line integral* of $f(z)$ over C is computed as follows

$$\int_C f(z)\,\mathrm{d}z = \int_a^b f(z(t))z'(t)\,\mathrm{d}t\,. \tag{1.49}$$

If the initial and terminal points of a curve C coincide, it is called a closed curve; C is *simple* if it does not intersect itself. A domain $D \subset \mathbb{C}$ is called a *simply-connected domain* if every simple closed curve (path) in D encloses only points in D. A domain that is not simply-connected is said to be *multiply-connected*.

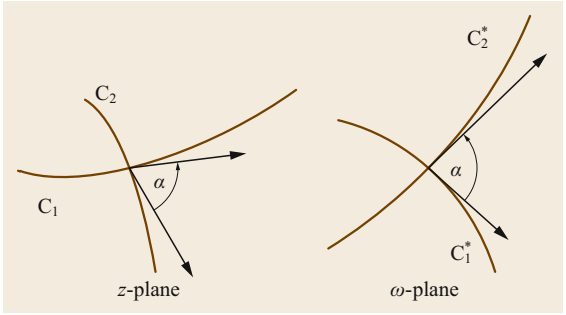

Fig. 1.10 Curves C_1 and C_2 and their respective images C_1^* and C_2^* under a conformal mapping $\omega = f(z)$ (adapted from [1.4])

The Cauchy Integral Theorem

If $f(z)$ is analytic in a simply-connected domain D, then for every simple closed curve C in D, $\oint_C f(z)\,\mathrm{d}z = 0$.

Cauchy Integral Formula

If $f(z)$ is an analytic function in a simply connected domain D, for any point $z_0 \in D$ and any simple closed path C that encloses z_0, we have

$$\oint_C \frac{f(z)}{z - z_0}\,\mathrm{d}z = 2\pi\mathrm{i}f(z_0)\,, \tag{1.50}$$

where the integration is taken in the counterclockwise direction.

1.5.5 Conformal Mappings

A mapping $w = f(z)$ is called a *conformal mapping* if it preserves angles between oriented curves in magnitude as well as in sense. The angle α ($0 \leq \alpha \leq \pi$) between two intersecting curves C_1 and C_2 is defined as the angle between their oriented tangents at the point of intersection of the curves. A mapping f is conformal means that if C_1 and C_2 are two intersecting curves in the domain plane, and C_1^*, C_2^* are their images under f, then the angle of intersection is the same in magnitude and in sense for both pairs of curves (Fig. 1.10).

Conformal mappings play an important role in applications in electrostatics, heat flow, and fluid flow.

If the mapping $w = f(z)$ is analytic, then it is a conformal mapping at all points where $f'(z) \neq 0$.

References

1.1 H. Anton, R.C. Busby: *Contemporary Linear Algebra* (Wiley, New York 2003)

1.2 W.E. Boyce, R.C. DiPrima: *Elementary Differential Equations and Boundary Value Problems*, 8th edn. (Wiley, New York 2005)

1.3 F. Brauer, J.A. Nohel: *The Qualitative Theory of Ordinary Differential Equations, an Introduction* (Dover, New York 1969)

1.4 E. Kreyszig: *Advanced Engineering Mathematics*, 10th edn. (Wiley, New York 2011)

Gnana Bhaskar Tenali

Mathematical Sciences
Florida Institute of Technology
Melbourne, FL, USA
gtenali@fit.edu

Gnana Bhaskar Tenali is Professor of Mathematics at the Department of Mathematical Sciences at Florida Institute of Technology in USA. He received his PhD in Mathematics in 1990. His research interests include linear/nonlinear ordinary and functional differential equations. He has coauthored a research monograph on set differential equations and about 50 research papers in various refereed international journals.

2. Mechanics

David C. Fleming, Hen-Geul Yeh, Hsien-Yang Yeh, Shouwen Yu

Engineering mechanics is the study of forces and their effects on the objects to which they are applied. This chapter presents the fundamentals of the study of mechanics in the two categories of *static mechanics*, (or simply *statics*) and *dynamic mechanics*. The first section deals with statics and addresses stationary objects. Statics is based on a reduction of Newton's second law ($\boldsymbol{F} = m\boldsymbol{a}$) and the equivalent equation describing rotational motion for the special case where the accelerations are zero. This results in the equations of equilibrium, which state that the vector sum of all forces and moments acting on a static body must be zero. Equations of static equilibrium can be used to find, for example, forces generated by supports that constrain a body against externally applied loads. Principles of statics are also used to understand the internal forces in the material comprising a structure under load. Understanding these forces is fundamental to the design of structures to avoid material failure. The second section is devoted to dynamic mechanics which is concerned with the motion of bodies. It is divided into two parts, *kinematics* and *dynamics* (also called *kinetics*). Kinematics is the study of motion without consideration of the forces and moments that produce the motion. Relationships between displacement, velocity, and acceleration are part of the study of kinematics. Dynamics relates the motion of bodies to the action of applied forces and moments, and thus is fundamental to many engineering problems.

2.1 **Statics of Rigid Bodies** 26
2.1.1 Force 26
2.1.2 Addition of Concurrent Forces in Space and Equilibrium of a Particle 28
2.1.3 Moment of a Force and Force Couple 28
2.1.4 Equilibrium Conditions 30
2.1.5 Truss Structures 34
2.1.6 Frames and Machines 35
2.1.7 Internal Resultants in Structural Members 36
2.1.8 Distributed Forces 37
2.1.9 Friction 38
2.1.10 Principle of Virtual Work 39

2.2 **Dynamics** 39
2.2.1 Motion of a Particle 40
2.2.2 Planar Motion, Trajectories 41
2.2.3 Polar Coordinates 42
2.2.4 Motion of Rigid Bodies (Moving Reference Frames) 43
2.2.5 Planar Motion of a Rigid Body 45
2.2.6 General Case of Motion 47
2.2.7 Dynamics 48
2.2.8 Straight-Line Motion of Particles and Rigid Bodies 50
2.2.9 Dynamics of Systems of Particles 51
2.2.10 Momentum Equations 51
2.2.11 D'Alembert's Principle, Constrained Motion 52
2.2.12 Lagrange's Equations 53
2.2.13 Dynamics of Rigid Bodies 54
2.2.14 Planar Motion of a Rigid Body 55
2.2.15 General Case of Planar Motion 56
2.2.16 Rotation About a Fixed Axis 57
2.2.17 Lagrange's Equations of Motion for Linear Systems 58

References 59

Mechanics is the study of the response of matter to forces, and is based on the concepts of time, space, force, energy, and matter. A knowledge of mechanics is needed for the study of all branches of physics, chemistry, biology, and engineering [2.1]. The subject of mechanics is logically divided into two parts: statics, and dynamics. Statics is concerned with the equilibrium of bodies under the action of forces, and hence is unconcerned with motion. Dynamics is concerned with the motion of bodies under the action of applied forces. The principles of mechanics as a science are rigorously expressed by mathematics, which therefore plays an important role in the application of these principles to the solution of practical problems [2.2]. A force is a vector

K.-H. Grote, H. Hefazi (Eds.), *Springer Handbook of Mechanical Engineering*, Springer Handbooks,
https://doi.org/10.1007/978-3-030-47035-7_2

quantity, because its effect depends on the direction as well as on the magnitude of the action. In addition to the tendency to move a body in the direction of its application, a force can also tend to rotate a body about an axis. This rotational tendency is known as the *moment of the force*, or simply the *moment*. Like force, moment can be expressed as a vector quantity. When the resultant force and the resultant moment are both zero the body is in equilibrium and there is no acceleration of the body. This condition is described by satisfying the equations of static equilibrium. If the body is not in equilibrium, it will accelerate and the motion is analyzed using principles of dynamic mechanics.

Problems in mechanics are often defined using free-body diagrams. These are diagrams showing an object, or *body* under study and the forces acting upon it. A large number of problems in mechanics can be approximated by problems concerning the equilibrium or motion of a particle. This is done by choosing a significant particle and creating a free-body diagram showing this particle and all the forces acting on it. Particle models do not consider the effects of moments or rotation of the body; all forces are treated as acting through its center of gravity. For problems where the effects of moments or rotation are significant, the body must be represented as a two-dimensional or three-dimensional object. If deformation of the body due to the applied forces is not significant, the body may be approximated as a rigid-body problem [2.3].

Static equilibrium problems may be used to understand the forces acting on structures or other objects of interest to engineers. Principles of statics can be used to analyze many types of engineering problems including structures, mechanisms, machines, biomechanical systems, and vehicles. Specialized techniques of statics are used to analyze special cases. For example, a truss is a structure composed of (usually straight) members pinned together at their end points and loaded only at the joints. Trusses are commonly seen supporting the roofs of buildings as well as in large railroad and highway bridges [2.4]. Forces in the individual members comprising a truss are found to be either simple tension or compression forces and these forces can be found using specialized application of the principles of statics. Static equilibrium can also be used to help understand the internal forces existing in a body that hold it together.

Dynamic mechanics can be divided into two parts: (1) kinematics, which is the study of a geometry of motion and is used to relate displacement, velocity, acceleration, and time, without taking into account forces and moments as causes of the motion, and (2) dynamics, which is the study of the relation between the forces and moments acting on a body, and the mass and motion of the body; it is used to predict the motion caused by given forces and moments or to determine the forces and moments required to produce a given motion.

Kinematics is the starting point from which the analysis of the basic motion of particles and rigid bodies begins. Dynamics allows the motion of bodies to be related to applied forces and moments. Newton's laws and other principles of dynamics are introduced in this chapter followed by a review of advanced topics, such as the dynamics of systems of particles, momentum equations, Lagrange's equations, energy equations, D'Alembert's principle, and the dynamics of rigid bodies. Lagrange's equations of motion for linear systems are introduced at the end of the chapter, which can be regarded as the beginning of a study of vibration.

2.1 Statics of Rigid Bodies

Statics is a branch of classical mechanics, which is part of the foundation of physics and modern engineering technology. Statics is the study of the equilibrium of rigid bodies under the action of forces and moments. Equilibrium is defined as a condition in which all of the forces and moments applied to an object are in balance, such that the resultant force and moment vectors are zero. According to Newton's laws, if a body is in equilibrium the body must either be at rest or is in uniform motion along a straight line.

Many problems in statics can be analyzed by approximating an object as a rigid body. The size and shape of a rigid body remain constant at all times and under all loading conditions. In other words, rigid bodies are understood in statics as bodies in which the deformations are so small that the points at which force is applied undergo negligible displacement.

2.1.1 Force

A force represents the action of one body on another. Forces may be generated by a variety of phenomena including contact between objects, gravitation, electric or magnetic fields and others. Mathematically, a force is characterized by its magnitude, and direction. Thus, force is a vector quantity. The point of application of a force is also significant in statics problems. Introducing the unit vectors $\boldsymbol{i}, \boldsymbol{j}$, and $\boldsymbol{k}$, directed along the x, y,

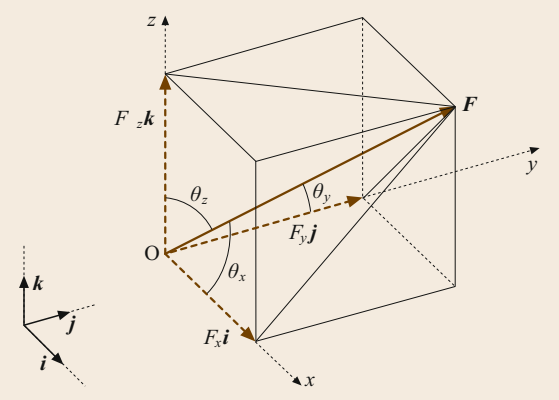

Fig. 2.1 Vector representation of a force $\boldsymbol{F}$

and z axes, respectively, the force $\boldsymbol{F}$ can be expressed in Cartesian vector notation as (Fig. 2.1a,b)

$$\boldsymbol{F} = F_x\boldsymbol{i} + F_y\boldsymbol{j} + F_z\boldsymbol{k}$$
$$\boldsymbol{F} = (F\cos\theta_x)\,\boldsymbol{i} + \big(F\cos\theta_y\big)\boldsymbol{j} + (F\cos\theta_z)\,\boldsymbol{k}\,. \quad (2.1)$$

F_x, F_y and F_z are the scalar components of the vector in the x, y and z coordinate directions, respectively. The magnitude of the force vector relates to these scalar components according to

$$F = |\boldsymbol{F}| = \sqrt{F_x^2 + F_y^2 + F_z^2}\,. \quad (2.2)$$

The orientation of a vector in three-dimensional space is sometimes described in terms of *direction angles*, which are the angles formed between each of the three positive coordinate axes and the force vector. In Fig. 2.1 direction angles are labeled as θ_x, θ_y, θ_z. Cosines of these direction angles are called *direction cosines* and relate to the scalar vector components according to $\cos\theta_x = F_x/F$, $\cos\theta_y = F_y/F$, $\cos\theta_z = F_z/F$. The direction cosines must satisfy $\cos^2\theta_x + \cos^2\theta_y + \cos^2\theta_z = 1$. When solving three-dimensional problems, it is necessary to find the x, y, and z scalar components of a force. In many cases, the direction of a force is not given in terms of direction angles. Often, the direction of a force is described either by defining two points on the line of action of the force (Fig. 2.2a), or by defining angles that orient the line of action of the force using its projection onto coordinate planes (Fig. 2.2b):

1. In Fig. 2.2a the direction of a force $\boldsymbol{F}$ is defined by the coordinates of two points $\mathrm{M}(x_1, y_1, z_1)$ and $\mathrm{N}(x_2, y_2, z_2)$, located on its line of action. Consider the vector $\overrightarrow{\mathrm{MN}}$ joining M and N and in the same direction sense as $\boldsymbol{F}$. Therefore

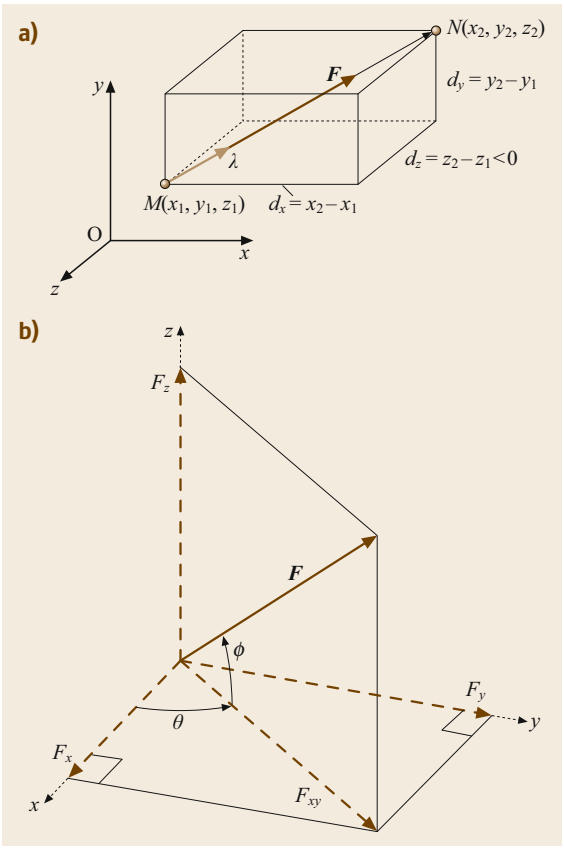

Fig. 2.2a,b Force defined by **(a)** its magnitude and two points on its line of action, or **(b)** by its magnitude and angles describing the projection of the vector onto a coordinate plane

$$\overrightarrow{\mathrm{MN}} = (x_2 - x_1)\,\boldsymbol{i} + (y_2 - y_1)\boldsymbol{j} + (z_2 - z_1)\,\boldsymbol{k}\,. \quad (2.3)$$

The unit vector $\boldsymbol{\lambda}$ along the line of action of $\boldsymbol{F}$ is obtained by dividing the vector $\overrightarrow{\mathrm{MN}}$ by its magnitude MN, thus

$$\boldsymbol{\lambda} = \frac{\overrightarrow{\mathrm{MN}}}{\mathrm{MN}} = \frac{(x_2 - x_1)\,\boldsymbol{i} + (y_2 - y_1)\boldsymbol{j} + (z_2 - z_1)\,\boldsymbol{k}}{\sqrt{(x_2 - x_1)^2 + (y_2 - y_1)^2 + (z_2 - z_1)^2}} = \frac{d_x\boldsymbol{i} + d_y\boldsymbol{j} + d_z\boldsymbol{k}}{d}\,, \quad (2.4)$$

and $\boldsymbol{F} = F\boldsymbol{\lambda}$, where F is the magnitude of the force $\boldsymbol{F}$,

$$d_x = x_2 - x_1\,, \quad d_y = y_2 - y_1\,, \quad d_z = z_2 - z_1$$

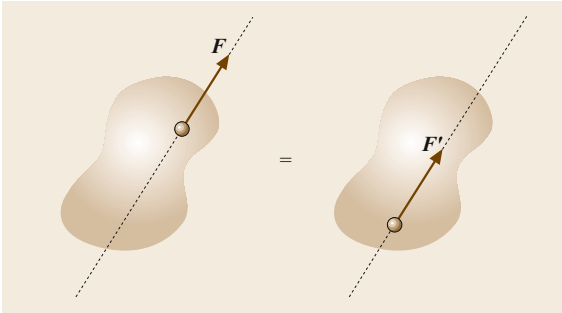

Fig. 2.3 Principle of transmissibility: either $\boldsymbol{F}$ or $\boldsymbol{F}'$ will produce the same effect on the body

and

$$d = \sqrt{(x_2 - x_1)^2 + (y_2 - y_1)^2 + (z_2 - z_1)^2}\,.$$

The angles θ_x, θ_y, and θ_z that $\boldsymbol{F}$ forms with the coordinate axes can be expressed as

$$\cos\theta_x = \frac{d_x}{d}\,, \quad \cos\theta_y = \frac{d_y}{d}\,, \quad \cos\theta_z = \frac{d_z}{d}\,.$$

2. Consider the geometry of Fig. 2.2b, assuming that the angles θ and ϕ are known. F_{xy} represents the projection of $\boldsymbol{F}$ onto the xy plane. First resolve $\boldsymbol{F}$ into its horizontal and vertical components

$$F_{xy} = F\cos\phi\,, \quad F_z = F\sin\phi\,.$$

Then resolve the projection F_{xy} into x- and y-components

$$F_x = F_{xy}\cos\theta = F\cos\phi\cos\theta\,,$$
$$F_y = F_{xy}\sin\theta = F\cos\phi\sin\theta\,.$$

The quantities F_x, F_y, and F_z are the desired scalar components of $\boldsymbol{F}$.

The *line of action* of a force vector is the infinite line passing through the point of application of the force and pointing in the same direction as the force. The *principle of transmissibility* states that the conditions of equilibrium or motion of a rigid body remain unchanged if a force $\boldsymbol{F}$ acting at a given point on the rigid body is replaced by a force $\boldsymbol{F}'$ of the same magnitude and same direction, but acting at a different point on the same line of action (Fig. 2.3); $\boldsymbol{F}$ and $\boldsymbol{F}'$ are known as *equivalent forces*.

2.1.2 Addition of Concurrent Forces in Space and Equilibrium of a Particle

The resultant $\boldsymbol{R}$ of two or more forces in space is usually determined by summing their Cartesian components. Graphical or trigonometric methods are sometimes used to quickly add vectors in two-dimensional problems, but these methods are usually not practical for a systems of many forces or for three-dimensional forces in space, and these methods are not reviewed here [2.2, 3]. If forces are first expressed using Cartesian components, as described above, addition of vectors can be quickly accomplished according to the approach shown in (2.5)–(2.6), where $\boldsymbol{R}$ represents the *resultant* (or sum) of a set of vectors $\boldsymbol{F}$.

$$\boldsymbol{R} = \sum \boldsymbol{F}\,, \tag{2.5}$$

$$\boldsymbol{R} = R_x\boldsymbol{i} + R_y\boldsymbol{j} + R_z\boldsymbol{k} = \left(\sum F_x\right)\boldsymbol{i} + \left(\sum F_y\right)\boldsymbol{j} + \left(\sum F_z\right)\boldsymbol{k} \tag{2.6}$$

From which it follows that

$$R_x = \sum F_x\,, \quad R_y = \sum F_y\,, \quad R_z = \sum F_z\,. \tag{2.7}$$

The magnitude of the resultant and the direction angles of the resultant, θ_x, θ_y, and θ_z are

$$R = \sqrt{R_x^2 + R_y^2 + R_z^2}\,, \tag{2.8}$$

$$\cos\theta_x = \frac{R_x}{R}\,, \quad \cos\theta_y = \frac{R_y}{R}\,, \quad \cos\theta_z = \frac{R_z}{R}\,. \tag{2.9}$$

When a body is in equilibrium, the resultant of all the forces acting on it is zero. Therefore, for equilibrium of a body the following three scalar equilibrium equations apply

$$\sum F_x = 0\,, \quad \sum F_y = 0\,, \quad \sum F_z = 0\,. \tag{2.10}$$

2.1.3 Moment of a Force and Force Couple

In addition to the tendency to move a body in the direction of its application, a force can also tend to rotate a body. This rotational tendency is known as the *moment of the force*, $\boldsymbol{M}$ (Fig. 2.4a). The moment is a vector quantity whose magnitude is the strength of the rotational effect and whose direction describes the axis of rotation. The moment vector depends on the choice of the location O where the axis of rotation is to be considered.

A special case is found by considering the action of two equal, opposite, and non-collinear forces. This combination of two forces is called a *force couple* or, more simply, a *couple* (Fig. 2.4b). The resultant force produced by a couple is zero, and thus a couple will produce no linear acceleration of an object to which it is applied. A couple, however, produces a resultant moment. Thus, imposing a force couple on an object will

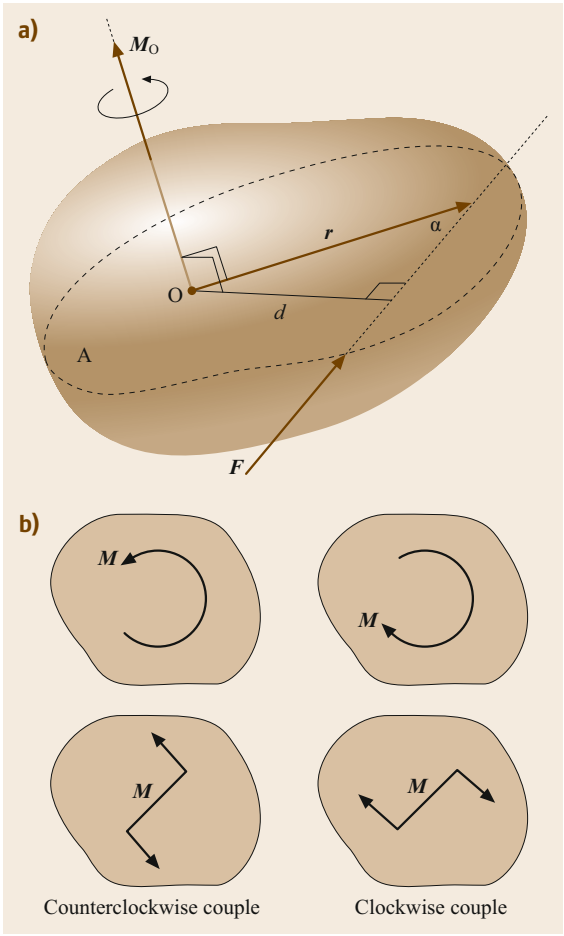

Fig. 2.4 (a) Moment of a force about a point, (b) couple

produce only a tendency toward rotational acceleration. A force couple is therefore commonly represented by showing only the resultant moment vector that the couple provides rather than showing the two force vectors (Fig. 2.4b). An important feature of a force couple is that once the magnitude of the forces comprising the couple and their positions are specified, the resultant moment vector produced by the couple will be the same regardless of where in space one choses to place the axis of rotation, O. This is unlike the moment produced by a single force vector, where the moment is directly dependent on the choice of O.

The moment produced by a single force vector about a chosen point O can be computed as follows. Consider a force $\boldsymbol{F}$ acting on a rigid body as shown in Fig. 2.4a. Define A as the plane containing both point O and the line of action of $\boldsymbol{F}$. The axis of rotation of the moment, and thus the direction of the moment vector $\boldsymbol{M}$ must be perpendicular to plane A. Its direction sense follows a right-hand rule. The moment $\boldsymbol{M}_O$ of $\boldsymbol{F}$ about O has magnitude $M_O = Fd$, where d is the perpendicular distance from O to the line of action of $\boldsymbol{F}$. For simple problems it may be possible to easily determine d and thus compute the moment. For more complex problems, particularly in three-dimensional geometries, direct geometric determination of the plane A and the distance d is difficult. In such cases a vector computation approach is preferred. Let the position vector $\boldsymbol{r}$ be any vector that originates at point O and terminates at any point on the line of action of the force $\boldsymbol{F}$. The moment of $\boldsymbol{F}$ about O can then be computed by taking the cross product between $\boldsymbol{r}$ and $\boldsymbol{F}$

$$\boldsymbol{M}_O = \boldsymbol{r} \times \boldsymbol{F} = \begin{vmatrix} \boldsymbol{i} & \boldsymbol{j} & \boldsymbol{k} \\ r_x & r_y & r_z \\ F_x & F_y & F_z \end{vmatrix} . \tag{2.11a}$$

Expansion of the determinant gives

$$\begin{aligned} \boldsymbol{M}_O = {} & \left(r_y F_z - r_z F_y\right) \boldsymbol{i} + \left(r_z F_x - r_x F_z\right) \boldsymbol{j} \\ & + \left(r_x F_y - r_y F_x\right) \boldsymbol{k} . \end{aligned} \tag{2.11b}$$

For two-dimensional problems, a scalar approach to computing the moments is often used. If the force vector and point O lie in the xy plane as shown in Fig. 2.5, then the moment vector will have only a single nonzero component in the $\boldsymbol{k}$ direction, and it is commonly drawn as in the top of Fig. 2.4b. The direction sense is indicated by the arrowhead. The magnitude of the moment may be computed using $M_O = Fd$ if d is known. Often, it is more convenient to first resolve the vector $\boldsymbol{F}$ into x and y components. The moment M_O is then found as the sum of the moments about O produced by each of the components. This approach is called the *principle of moments*. Using the example shown in Fig. 2.5b, we see that $M_O = F_x d_y - F_y d_x$. Note that the algebraic sign associated with each term has to be carefully considered based on the location of the point of application of $\boldsymbol{F}$ relative to the location of O and the chosen sign convention for M_O.

Sometimes, rather than wanting to know the complete vector moment produced by a force vector about a specified point O, one needs to know only the component of this moment vector about a specified axis direction passing through point O. The moment about such an axis can be found by first computing the moment $\boldsymbol{M}_O$ of that force about O and then using the dot product to find the projection of $\boldsymbol{M}_O$ in the desired axis direction. This process is shown in Fig. 2.6. Let OL be an axis through O. The direction of the OL axis is defined by the unit vector $\boldsymbol{\lambda}$. The moment $\boldsymbol{M}_{OL}$ of $\boldsymbol{F}$ about OL is found as the projection OC of the moment $\boldsymbol{M}_O$ onto the axes using

$$\boldsymbol{M}_{OL} = \boldsymbol{\lambda} \cdot \boldsymbol{M}_O = \boldsymbol{\lambda} \cdot (\boldsymbol{r} \times \boldsymbol{F}) , \tag{2.12a}$$

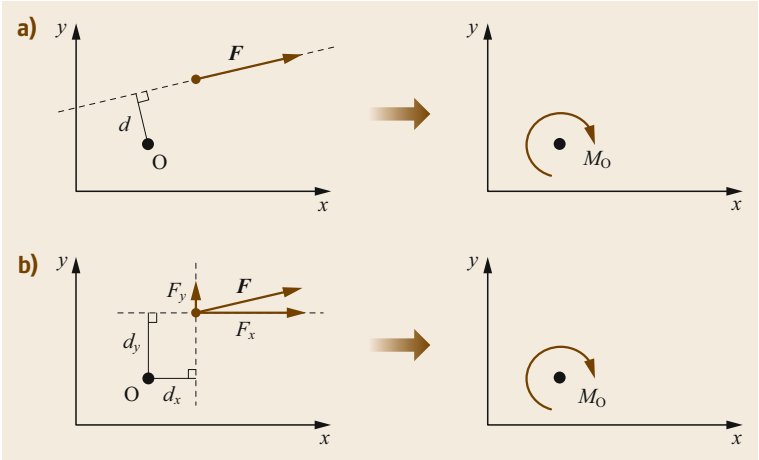

Fig. 2.5 Determination of a moment in two dimensions by scalar computations

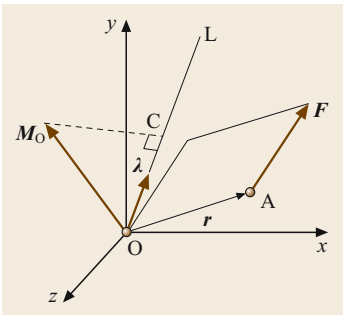

Fig. 2.6 Moment about an arbitrary axis

which shows that the moment $\boldsymbol{M}_{OL}$ of $\boldsymbol{F}$ about the axis OL is the scalar obtained by the scalar triple product of λ, $\boldsymbol{r}$, and $\boldsymbol{F}$.

Expressing $\boldsymbol{M}_{OL}$ in the form of a determinant

$$\boldsymbol{M}_{OL} = \begin{vmatrix} \lambda_x & \lambda_y & \lambda_z \\ r_x & r_y & r_z \\ F_x & F_y & F_z \end{vmatrix}, \qquad (2.12b)$$

where λ_x, λ_y, and λ_z are the direction cosines of the axis OL. x, y, and z are the coordinates of the point of application of $\boldsymbol{F}$, and F_x, F_y, and F_z are the components of the force $\boldsymbol{F}$.

2.1.4 Equilibrium Conditions

When a body is in equilibrium, the resultant effect of all forces acting on it is zero. Thus, the resultant force $\boldsymbol{R}$ and the resultant moment $\boldsymbol{M}$ acting about any point are both zero vectors, and the equilibrium equations result

$$\boldsymbol{R} = \sum \boldsymbol{F} = 0\,, \quad \boldsymbol{M} = \sum \boldsymbol{M} = \sum (\boldsymbol{r} \times \boldsymbol{F}) = 0\,. \qquad (2.13)$$

These requirements are both necessary and sufficient conditions for equilibrium.

Forces can be separated into two groups: (a) external, and (b) internal forces. External forces represent the action of other bodies on the body under consideration. Internal forces are the forces that hold together the particles forming the body. In solving a problem concerning the equilibrium of a rigid body, it is essential to consider all of the external forces acting on the body. Internal forces are typically not included in rigid body equilibrium problems because they are associated with equal and opposite force pairs according to Newton's third law, and therefore cancel each other. Section 2.1.7 describes analytical techniques for studying internal forces.

The first step in the solution of a problem should be to draw a free-body diagram of the rigid body under consideration. The free-body diagram is a diagrammatic representation of the isolated system treated as a single body. The diagram shows all forces applied to the body (Fig. 2.7). Typically, many of these forces result from mechanical contact with other bodies not included in the free-body diagram, which are imagined to be removed. An important category of forces that appear in free-body diagrams are those associated with supports that hold a structure in position. Supports constrain certain displacements or rotations of the structures at locations where the support contacts the structure. The magnitudes of these forces (and sometimes also force couples or *moments*) are typically not known in advance because their size depends on the magnitude of the other external loads applied to the system as well as the structural geometry; these forces develop in reaction to the other loads on the body, and thus are known as *support reactions*. The direction of the support reactions typically is known in advance because they correspond to the direction of the displacement or rotation components that they constrain. Examples of the reactions provided by some basic sup-

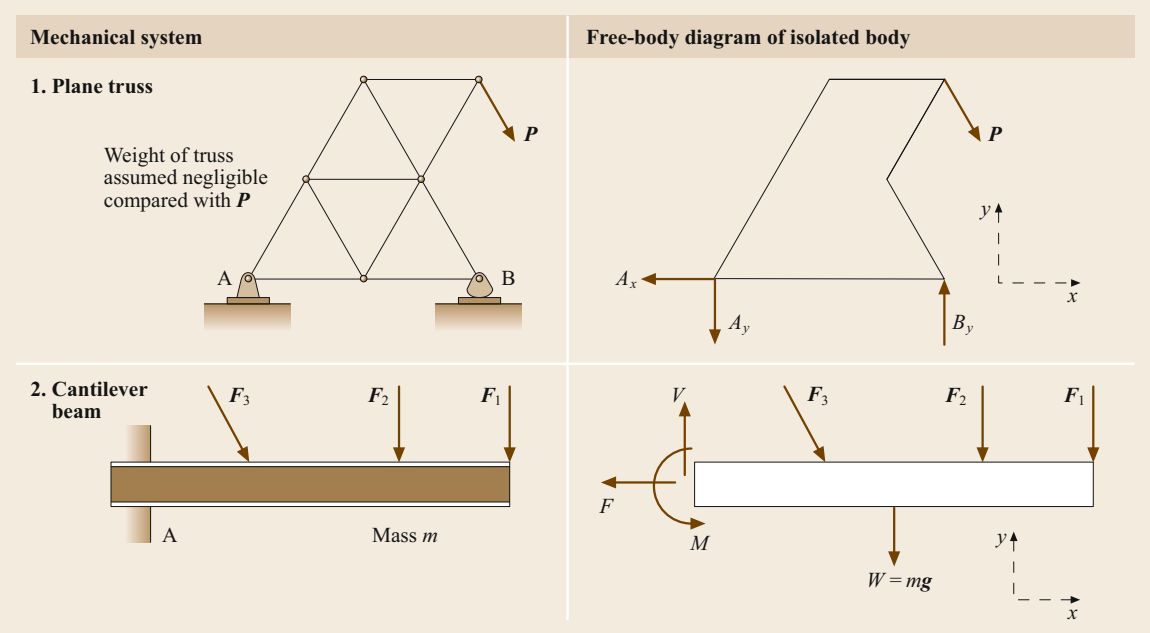

Fig. 2.7 Free-body diagrams (after [2.2]) Note the support reactions identified at points A and B in case 1 and at point A in case 2 and their correspondence to Fig. 2.8

port types is shown in Figs. 2.8 and 2.9. Note that support types that constrain rotation, such as the fixed support, produce reaction moments (force couples) in addition to reaction forces. Often, a statics problem involves determining the magnitude of support reactions as part of the solution process and it is therefore vital that the free-body diagram properly identifies the unknown reactions. Examples of free-body diagrams of simple mechanical systems are shown in Fig. 2.7.

For a two-dimensional rigid-body equilibrium problem in the xy plane, all force vectors have only two nonzero components, and all forces in the xy plane produce only moment components about the z-axis. Therefore, the vector equilibrium equations (2.13) can be reduced to a set of three scalar equations of equilibrium: $\sum F_x = 0$, $\sum F_y = 0$, $\sum M_z = 0$. A solution for unknown forces is possible provided that the number of unknown scalar quantities is three. For example, in case 1 of Fig. 2.7, if the geometry of the truss is specified and the magnitude and direction of the external force $\boldsymbol{P}$ is given then the equations of equilibrium will allow the three unknown reaction force components A_x, A_y and B_y to be determined. Similarly, for the cantilever beam in case 2 of Fig. 2.7 if the three external forces are specified as well as the mass of the beam and the location of its center of gravity then the three support reactions at A (F, V, and M) can be computed. In three dimensional problems, the equations of equilibrium are equivalent to six scalar equations, and solution is typically possible if there are six unknown scalar quantities in the free-body diagrams.

Problems whose solution is possible using only the equations of static equilibrium are called *statically determinate*. Stable bodies supported by the minimum number of constraints necessary to ensure an equilibrium configuration are statically determinate. Not all problems can be solved using static equilibrium alone. For example, if we added an additional rocker support to the plane truss in Fig. 2.7 at the joint midway between support A and support B, then an additional unknown reaction force would be required at that location in the free-body diagram, bringing the number of unknowns to four. We would still have only three equations of equilibrium and thus a solution would not be possible without providing additional information. A rigid body that possesses more external supports or constraints than are necessary to maintain an equilibrium position is called *statically indeterminate*. Supports that can be removed without destroying the equilibrium condition of the body are said to be redundant. The number of redundant supporting elements corresponds to the degree of static indeterminacy and equals the total number of unknown external forces minus the number of available independent equations of equilibrium. The solution of statically indeterminate problems typically involves consideration of the deformations of the structure un-

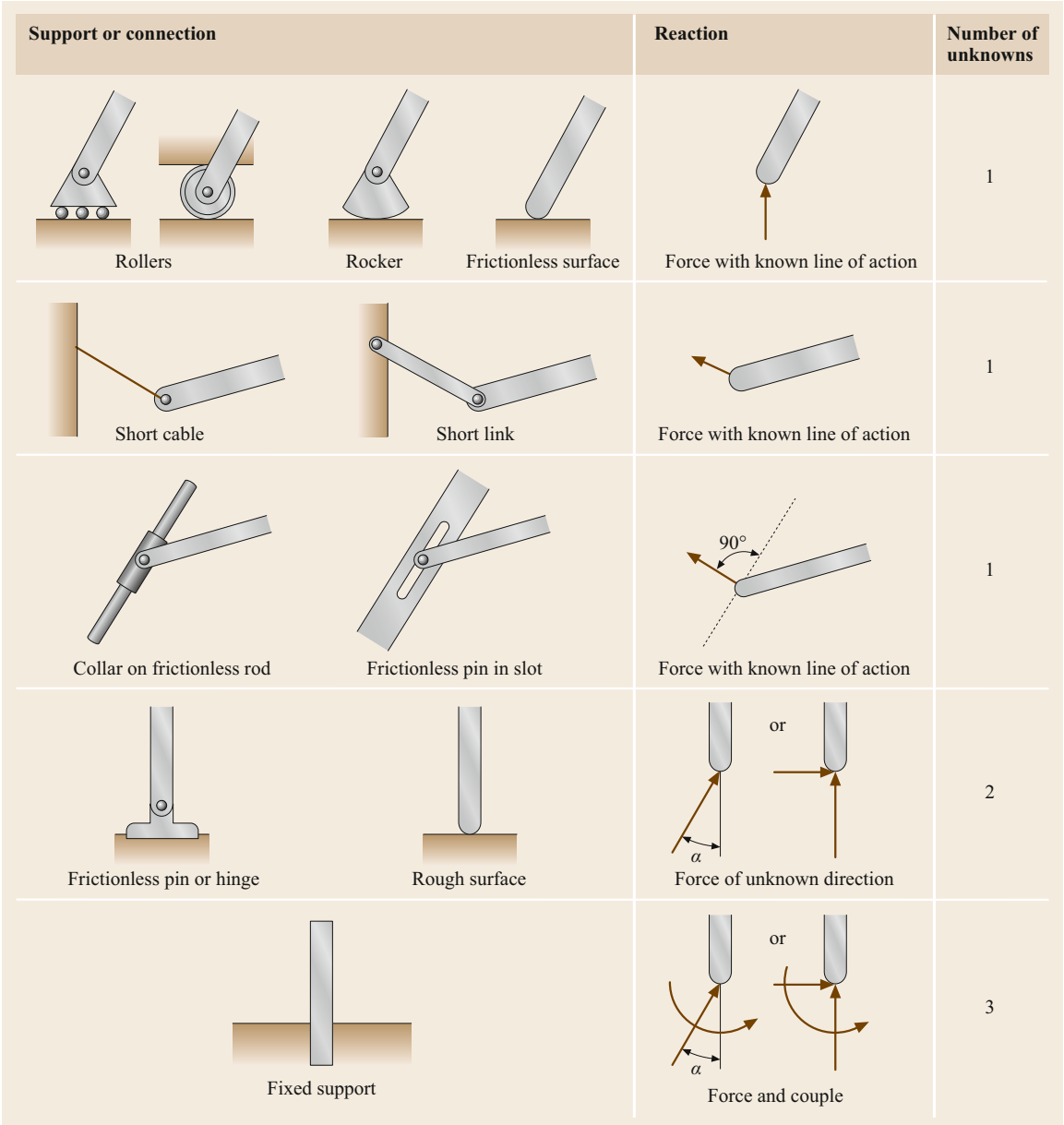

Fig. 2.8 Reactions at supports and connections for a two-dimensional structure (after [2.3])

der load. Solution of statically indeterminate structures problems is studied in detail in [2.5].

Two frequently occurring equilibrium situations permit rapid simplification of equilibrium problems: two- and three-force members. A two-force member is any body under the action of two forces only, as shown in Fig. 2.10. For a two-force member to be in equilibrium, the forces must be equal, opposite and collinear. The shape of the member does not affect this simple requirement.

A three-force member is a body under the action of exactly three forces, as shown in Fig. 2.11. For a three-force member to be in equilibrium, the lines of action of the three forces must be concurrent (or in a special case they may be parallel to each other). The principle of the concurrency of three forces in equilibrium is of considerable use in carrying out a graphical solution of the force equations. If two of the force vectors are specified, the third vector can be quickly determined using a polygon of forces, as shown in Fig. 2.11b.

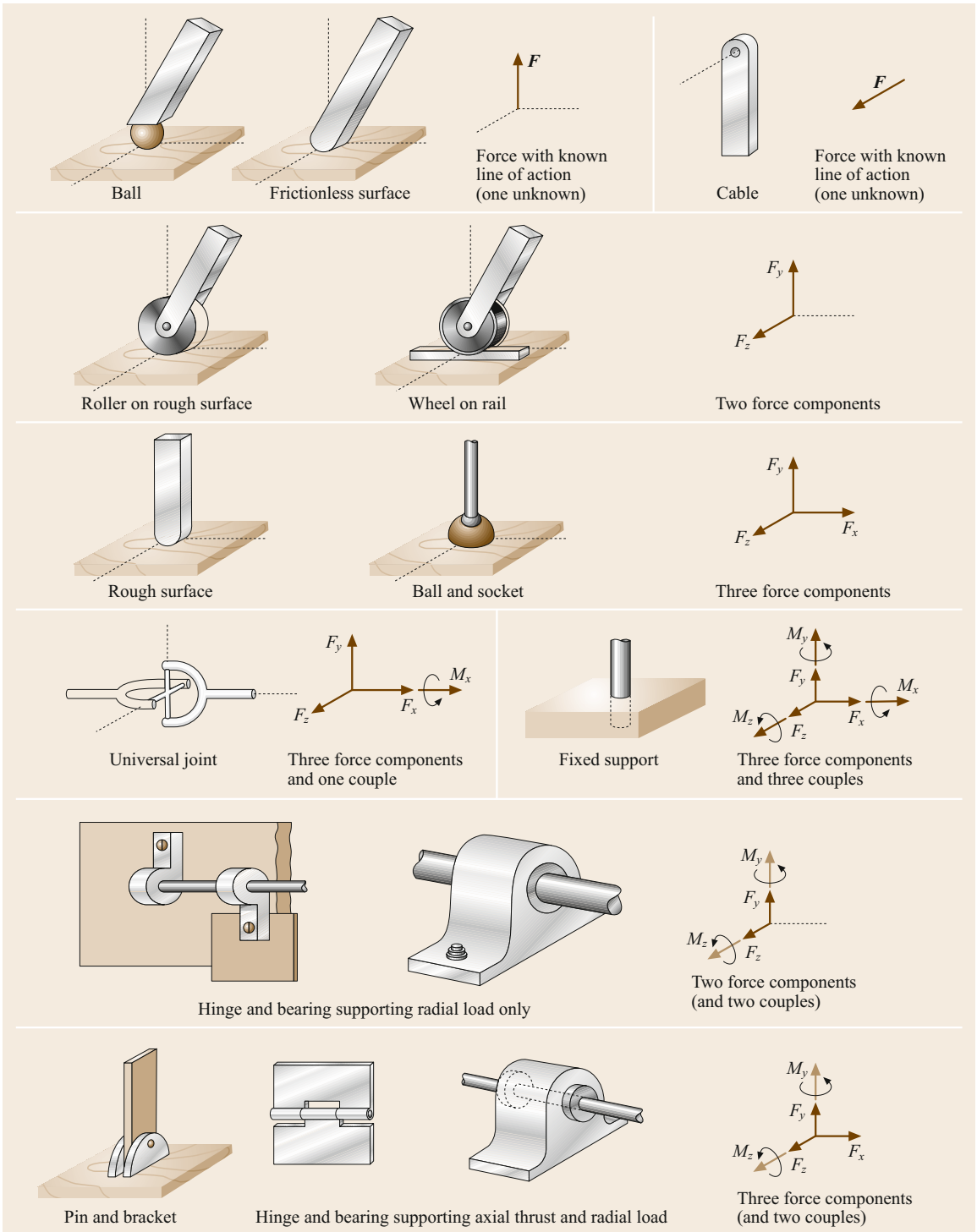

Fig. 2.9 Reactions at supports and connections for a three-dimensional structure (after [2.3])

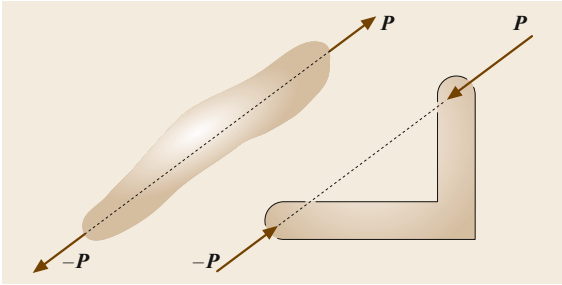

Fig. 2.10 Two-force member

2.1.5 Truss Structures

A framework composed of slender members joined at their ends to form a rigid structure is called a truss. In addition, members in a truss are typically assumed to be straight. When the members of the truss lie essentially in a single plane, the truss is called a *plane truss*. If the truss members are distributed in three-dimensions, the truss is called a *space truss*. The basic element of a plane truss is the triangle (Fig. 2.12a). Three bars joined by pins at their ends constitute a rigid truss and a larger rigid truss can be obtained by adding two new members to the first one and connecting them at a new joint as shown in Fig. 2.12b,c. Trusses obtained by repeating this procedure are called *simple trusses*. If certain simplifying assumptions are made, truss structures can be analyzed by the application of static equilibrium principles. If each member is joined to the rest of the structure at each end by frictionless pins and if we neglect the weight of the member then each member is subject to only two forces: a contact force at each end. Thus, each member in this ideal truss is a two-force member, as described in Sect. 2.1.4. The force within each truss member must be directed along the line joining the two ends of the member. The goal of truss analysis is to determine the magnitude of the force carried by each member and to indicate its directional sense. A truss member subject to loads that tend to lengthen the member are said to be in *tension*, while if the forces tend to shorten the member it is said to be in *compression*. Slender members are typically able to support much larger magnitudes of load in tension than in compression because compressive loads tend to cause a structural instability called buckling. Determining the loads in the truss members is a necessary first step toward designing a truss structure as the necessary size of the parts depends on the magnitude and direction sense of the applied forces.

Internal forces in a truss may be determined using static equilibrium principles provided the truss is statically determinate. In a simple plane truss, the total number of members m is given by $m = 2n-3$, where n is the total number of joints. If the truss is stable, such a simple plane truss is statically determinate, because two equations of equilibrium exist for each joint (providing $2n$ equations). Three unknown reaction forces are necessary to provide equilibrium of the structure, bringing the total number of unknowns, $m+3$ up to $2n$. Thus the number of equations matches the number of unknowns and

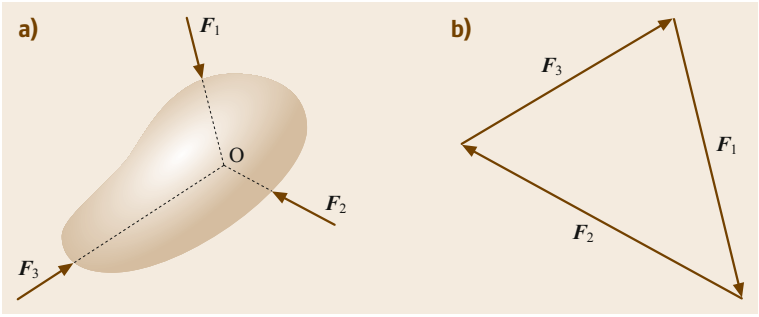

Fig. 2.11a,b Three-force member **(a)**. **(b)** Closed polygon satisfies $\sum \boldsymbol{F} = 0$

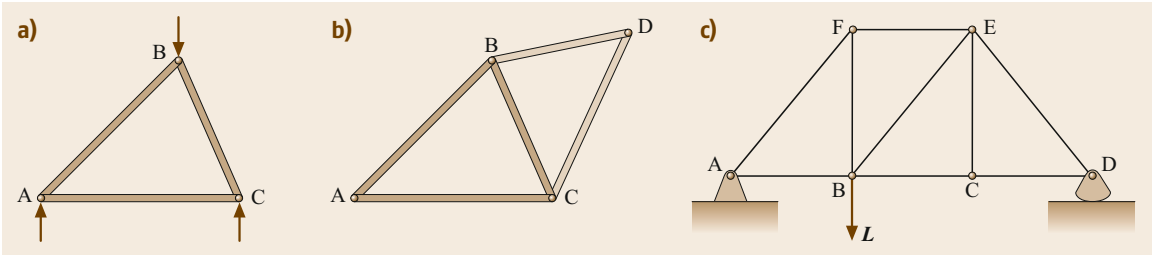

Fig. 2.12a–c Truss structures. **(a)** A basic truss element showing forces applied at the joints. **(b)** A five element truss. **(c)** A truss bridge with supports and an applied load

all unknowns may be determined. A pin-jointed plane truss with $m < 2n - 3$ members is statically indeterminate and kinematically unstable, and a pin-jointed plane truss with $m > 2n - 3$ is internally statically indeterminate, implying that there are redundant members and solutions requires additional consideration of the deformation of the truss beyond static equilibrium principles.

Two methods of analysis are typically used to find the member forces in truss structures, the *method of joints* and the *method of sections*. Before either method is applied, the reactions at the supports can be obtained by considering the entire truss as a free body.

In the method of joints, the free-body diagram of each pin is drawn, showing the forces exerted on the pin by each of the members or supports it connects. Because the members are straight two-force members, the force exerted by a member on the pin is directed along that member and only the magnitude of the force is unknown. It is always possible in the case of a simple plane truss to draw the free-body diagrams of the pins in such an order that only two unknown forces are included in each diagram. For a plane truss, these forces can be determined from the two corresponding equilibrium equations: $\sum F_x = 0$ and $\sum F_y = 0$. If the force exerted by a member on a pin is directed toward that pin, the member is in compression; if it is directed away from the pin, the member is in tension.

The method of sections is usually preferred to the method of joints when the force in only one member or very few members of a truss is desired. For example, to determine the force in member BD of the truss shown in Fig. 2.13, it is better to pass a section through members BD, BE, and CE, remove these members and use the portion ABC of the truss as a free body. Note that the internal forces F_{CE}, F_{BE} and F_{BD} are exposed by this approach because their corresponding equal and opposite reactions act on the part of the structure that is discarded to make the free-body diagram in Fig. 2.13b. If $\boldsymbol{P}_1$ and $\boldsymbol{P}_2$ are specified, equations of equilibrium based on the free-body diagram in Fig. 2.13b permit a solution for the member forces F_{CE}, F_{BE} and F_{BD}.

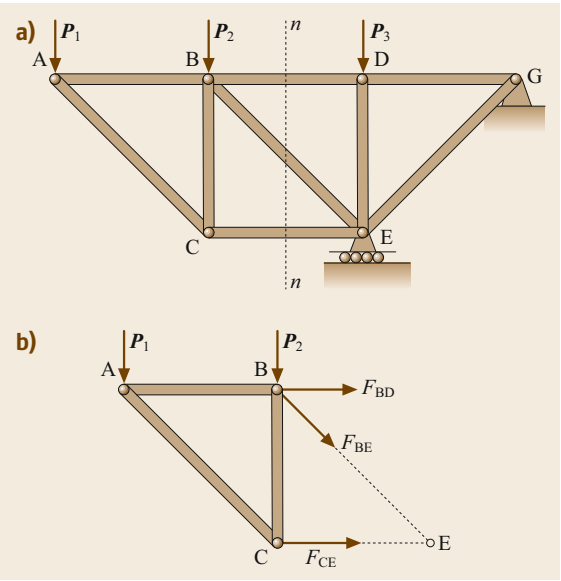

Fig. 2.13a,b Method of sections. **(a)** Complete truss. **(b)** Free body diagram using section *n–n*.

2.1.6 Frames and Machines

Many common structures do not meet the definition of truss structures. *Frames* are defined as static structures that, unlike truss structures, are not comprised solely of two-force members. *Machines* contain moving parts, and likewise are not comprised solely of two-force members. If the motion of a machine is slow enough that inertial effect are not significant, techniques of static equilibrium can be used to analyze the forces in the structure at each geometric configuration of interest. Otherwise, dynamic analysis based on Sect. 2.2 must be considered.

When analyzing frame or machine structures, specialized analysis techniques developed for truss structures, such as the method of joints described in Sect. 2.1.5, must be discarded or modified. Analysis of a frame structure typically involves separating the structure into individual members that are joined by simple connections and then using free-body diagrams and equations of equilibrium to analyze each member. For example, consider the simple frame shown in Fig. 2.14. It is comprised of three members, AB, BC and DE. Assume that joints B, D, and E are frictionless pins, and that there is a fixed support at A. We see that member BC is not a two-force member because it is acted upon by resultant forces at three locations: B, C, and E. Member DE, however, is a two-force member, experiencing only forces at pin D and at pin E. The forces at each end of this member must therefore be equal and opposite and point in the DE direction. The free-body diagram of member BC is shown in Fig. 2.14b. The pinned joint at B acts like a pinned support and thus unknown reaction components in both horizontal and vertical directions are identified at B. Because the force at E results from connection with two-force member DE, the direction of this reaction force is known to be in the DE direction and it is drawn in the free-body diagram as such. By inspection, DE will be loaded in the compression sense and the force that it imposes on member BC will be in the direction shown. Solution for the forces acting on member BC can be found by applying two-dimensional equilibrium equations to the

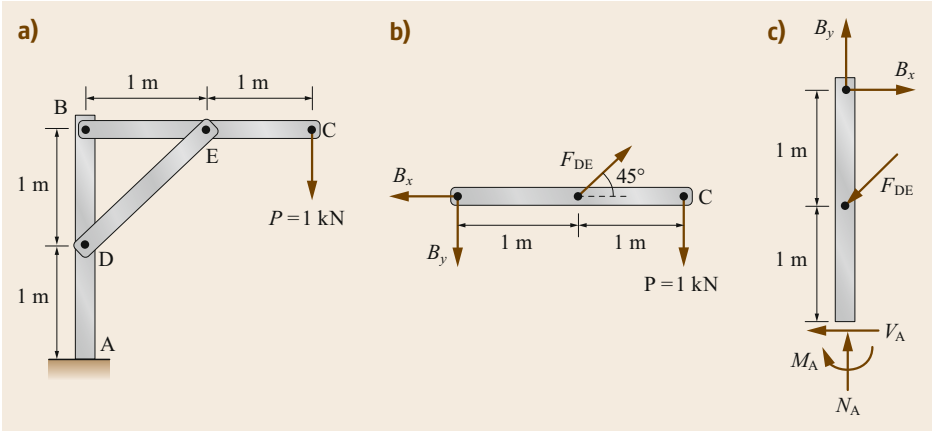

Fig. 2.14a–c Analysis of a simple frame structure. **(a)** Complete frame. **(b)** Free body diagram of member BD. **(c)** Free body diagram of member AB

free-body diagram in Fig. 2.14b as follows

$$\sum F_x = -B_x + F_{DE}\cos 45^\circ = 0\,,$$

$$\sum F_y = -B_y + F_{DE}\sin 45^\circ - 1\,\text{kN} = 0\,,$$

$$\sum M_B = (F_{DE}\sin 45^\circ)\,(1\,\text{m}) - (1\,\text{kN})\,(2\,\text{m}) = 0\,,$$

$$F_{DE} = 2.83\,\text{kN}\,,\ B_x = 2.00\,\text{kN}\,,\ B_y = 1.00\,\text{kN}\,.$$

Next, the forces on member AB can be analyzed using the free-body diagram shown in Fig. 2.14c. Note that the reaction forces at B in this free-body diagram are equal and opposite to those in the free-body diagram of member AB because the forces on member AB at B and the forces on member BC at B form an equal and opposite pair according to Newton's third law. The free-body diagram of member AB can be used with the known values of F_{DE}, B_x and B_y to find the unknown support reactions at A.

2.1.7 Internal Resultants in Structural Members

Principles of static equilibrium can be used to help understand the forces carried internally by structural members. This is a necessary step toward being able to design structural members to carry required loads. Consider the beam shown in Fig. 2.15. Principles of rigid body equilibrium described in Sect. 2.1.4 can be used to determine the reactions at fixed support A. Now, consider analytically *cutting* the beam at location C. A free-body diagram of either of the two portions of the beam can be drawn using the internal resultants shown in Fig. 2.15b. These figures have been rotated to emphasize the internal surfaces exposed by the cut. On each of these internal surfaces there will be a complicated distribution of forces resulting from the attachment of material on that surface to adjoining material on the opposite surface. These forces make equal and opposite reaction pairs according to Newton's third law, and

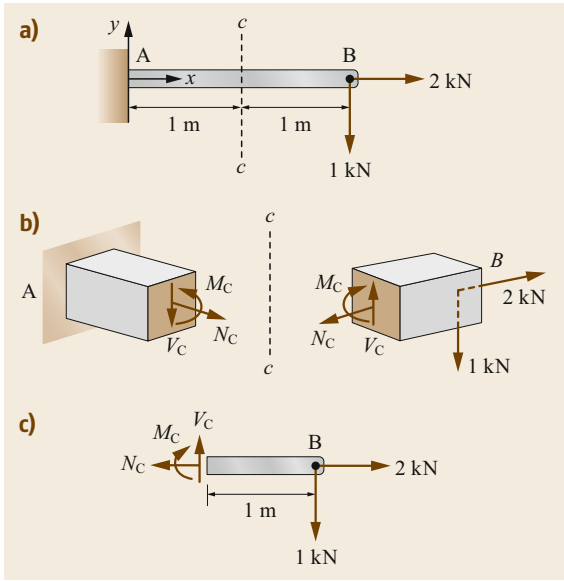

Fig. 2.15a–c Internal resultants in a beam. **(a)** Cantilevered beam AB. **(b)** Internal resultants on section *c–c*. **(c)** Free body diagram of a portion of the beam from section *c–c* to the beam tip

thus the direction of each resultant will be opposite on each of the two exposed surfaces. To simplify the analysis, we consider only the resultants of the forces on each cut surface. These are called the *internal resultants*. In a plane structure, such as in this example, we expect resultant force components in the x and y directions only as well as a resultant moment about the z axis. The force resultants are typically resolved into components perpendicular to the cut surface, called the normal force resultant N and a force component parallel to the surface, called the shear force resultant V. In a three-dimensional structure we expect internal force and moment resultants to have components in all three coordinate directions.

To solve for the internal resultants, one simply chooses one of the two free-body diagrams resulting from the cut and applies the equations of equilibrium. In the case of the example in Fig. 2.15, it is more convenient to choose free-body diagram CB because use of free-body diagram AC would require determination of the reaction forces at support A before finding the internal resultants. Using the free-body diagram for CB shown in Fig. 2.15c, the following equations of equilibrium and solution result.

$$\sum F_x = -N_C + 2\,\text{kN} = 0\,,$$
$$\sum F_y = V_C - 1\,\text{kN} = 0\,,$$
$$\sum M_C = M_C + (1\,\text{kN})(1\,\text{m}) = 0\,,$$
$$N_C = 2\,\text{kN}\,,\ V_C = 1\,\text{kN}\,,\ M_C = -1\,\text{kN m}\,.$$

In general, we expect that each cross-section of a beam will have unique values of internal resultants. These are often presented graphically in the form of shear-moment diagrams [2.6].

2.1.8 Distributed Forces

The mass elements of a body of mass m are affected by the forces of gravity $\mathrm{d}F = \mathrm{d}mg = \mathrm{d}W$, all of which are parallel to one another. The resultant of the gravitational forces acting on all elements is the weight of the body and is given by the integral $W = \int \mathrm{d}W$. To determine the location of the *center of gravity* of any body mathematically, we require that the moment of the resultant gravitational force W about any axis equal to the sum of the moments about the same axis of all the gravitational forces $\mathrm{d}W$ acting on all the particles in the body, be treated as infinitesimal elements. For example, as shown in Fig. 2.16, the moment about the y-axis of the elemental weight is $x\mathrm{d}W$, and the integral of these moments for all elements of the body is $\int x\mathrm{d}W$. This sum of moments must equal $W\overline{x}$, where $\overline{x}$ is the x coordinate of the center of gravity of the body. Therefore, $\overline{x}W = \int x\mathrm{d}W$. With similar expressions for the other two components, the coordinates of the center of gravity G are expressed as

$$\overline{x} = \frac{\int x\mathrm{d}W}{W}\,,\ \overline{y} = \frac{\int y\mathrm{d}W}{W}\,,\ \overline{z} = \frac{\int z\mathrm{d}W}{W}\,. \qquad (2.14)$$

With the substitutions $W = mg$ and $\mathrm{d}W = g\mathrm{d}m$, assuming g is constant within the body the expressions for the coordinates of the center of gravity become

$$\overline{x} = \frac{\int x\mathrm{d}m}{m}\,,\ \overline{y} = \frac{\int y\mathrm{d}m}{m}\,,\ \overline{z} = \frac{\int z\mathrm{d}m}{m}\,. \qquad (2.15)$$

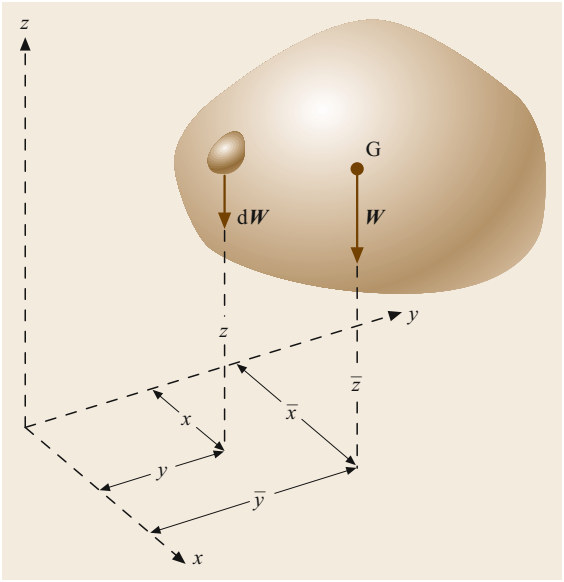

Fig. 2.16 Center of gravity

The density ρ of a body is its mass per unit volume. Therefore, the mass of a differential element of volume $\mathrm{d}V$ becomes $\mathrm{d}m = \rho\mathrm{d}V$, thus, (2.15) can be written as

$$\overline{x} = \frac{\int x\rho\mathrm{d}V}{\int \rho\mathrm{d}V}\,,\ \overline{y} = \frac{\int y\rho\mathrm{d}V}{\int \rho\mathrm{d}V}\,,\ \overline{z} = \frac{\int z\rho\mathrm{d}V}{\int \rho\mathrm{d}V}\,. \qquad (2.16)$$

Since g no longer appears in (2.15) and (2.16), a unique point that is only a function of the distribution of mass is defined in the body. This point is called the *center of mass* and coincides with the center of gravity as long as the gravity field is treated as uniform and parallel.

The *centroid* is defined as the mean position of all the points in a geometric shape. The location of the centroid is the same as the location of the center of mass of an object of the same shape that has uniform density. The concept of the centroid is used in many engineering computations. For example, internal resultant forces on the cross-section of a beam are typically defined with respect to the centroid of the cross-section because a force perpendicular to the cross-section at the centroid produces no bending effect on the beam, simplifying analysis of its behavior. The calculation of centroids is made with consideration of the nature of the geometric shape being considered:

1. Lines: for a slender rod or wire of length L, cross-sectional area A, and density ρ, the coordinates of the centroid C of the line segment may be written

$$\overline{x} = \frac{\int x\mathrm{d}L}{L}\,,\ \overline{y} = \frac{\int y\mathrm{d}L}{L}\,,\ \overline{z} = \frac{\int z\mathrm{d}L}{L}\,. \qquad (2.17)$$

Table 2.1 Properties of plane figures (after [2.2] for full definition of terms)

Figure	Centroid
Arc segment	$\bar{r} = \frac{r \sin \alpha}{\alpha}$
Quarter and semicircular arcs	$\bar{y} = \frac{2r}{\pi}$
Circular area	–
Semicircular area	$\bar{y} = \frac{4r}{3\pi}$
Quarter-circular area	$\bar{x} = \bar{y} = \frac{4r}{3\pi}$
Area of circular sector	$\bar{x} = \frac{2}{3} \frac{r \sin \alpha}{\alpha}$
Rectangular area	–
Triangular area	$\bar{x} = \frac{a+b}{3}, \bar{y} = \frac{h}{3}$
Area of elliptical quadrant	$\bar{x} = \frac{4a}{3\pi}, \bar{y} = \frac{4b}{3\pi}$
Subparabolic area	$\bar{x} = \frac{3a}{4}, \bar{y} = \frac{3b}{10}$
Parabolic area	$\bar{x} = \frac{3a}{8}, \bar{y} = \frac{3b}{5}$

Similarly, for area and volumes, the expressions of centroids are:

2. Areas

$$\bar{x} = \frac{\int x \mathrm{d}A}{A} , \quad \bar{y} = \frac{\int y \mathrm{d}A}{A} , \quad \bar{z} = \frac{\int z \mathrm{d}A}{A} . \qquad (2.18)$$

3. Volumes

$$\bar{x} = \frac{\int x \mathrm{d}V}{V} , \quad \bar{y} = \frac{\int y \mathrm{d}V}{V} , \quad \bar{z} = \frac{\int z \mathrm{d}V}{V} , \qquad (2.19)$$

where A and V represent the area and volume of the body, respectively. Some useful expressions for the centroid of various geometric figures are listed in Table 2.1.

2.1.9 Friction

Consider a solid block resting on an unlubricated horizontal surface, with the application of a horizontal force $\boldsymbol{P}$ that continuously increases from zero to a value sufficient to move the block and give it an appreciable velocity (Fig. 2.17a). Note that the block does not move at first, which shows that a friction force $\boldsymbol{F}$ must have developed to balance $\boldsymbol{P}$. As the magnitude of $\boldsymbol{P}$ increases, the magnitude of $\boldsymbol{F}$ also increases until it reaches a maximum value $F_{\max}$. If $\boldsymbol{P}$ is further increased, the block starts sliding and the magnitude of $\boldsymbol{F}$ drops from $\boldsymbol{F}_{\max}$ to a lower value $\boldsymbol{F}_{\mathrm{k}}$ (Fig. 2.17b). Experimental evidence shows that $\boldsymbol{F}_{\max}$ and $\boldsymbol{F}_{\mathrm{k}}$ are proportional to the normal component $\boldsymbol{N}$ of the reaction of the surface. Thus

$$F_{\max} = \mu_{\mathrm{s}} N , \quad F_{\mathrm{k}} = \mu_{\mathrm{k}} N , \qquad (2.20)$$

where μ_{s} and μ_{k} are called, respectively, the coefficients of static and kinetic friction.

It is sometimes convenient to replace the normal force $\boldsymbol{N}$ and the friction force $\boldsymbol{F}$ by their resultant $\boldsymbol{R}$, as shown in Fig. 2.18. As the friction force increases and reaches its maximum value $F_{\max} = \mu_{\mathrm{s}} N$, the angle ϕ that $\boldsymbol{R}$ forms with the normal to the surface increases and reaches a maximum value ϕ_{s}, called the angle of static friction. If motion actually takes place, the magnitude of $\boldsymbol{F}$ drops to $\boldsymbol{F}_{\mathrm{k}}$, similarly the angle ϕ drops to a lower value ϕ_{k}, called the angle of kinetic friction. Thus

$$\tan \phi_{\mathrm{s}} = \mu_{\mathrm{s}} , \quad \tan \phi_{\mathrm{k}} = \mu_{\mathrm{k}} . \qquad (2.21)$$

It is important to note that a coefficient of friction applies to a given pair of mating surfaces. It is meaningless to speak of a coefficient of friction for a single surface. Also friction coefficients vary considerably, depending on the exact condition of the mating surfaces.

Dry friction plays an important role in a number of engineering applications such as wedges, square-threaded screws, journal bearings, thrust bearings, and

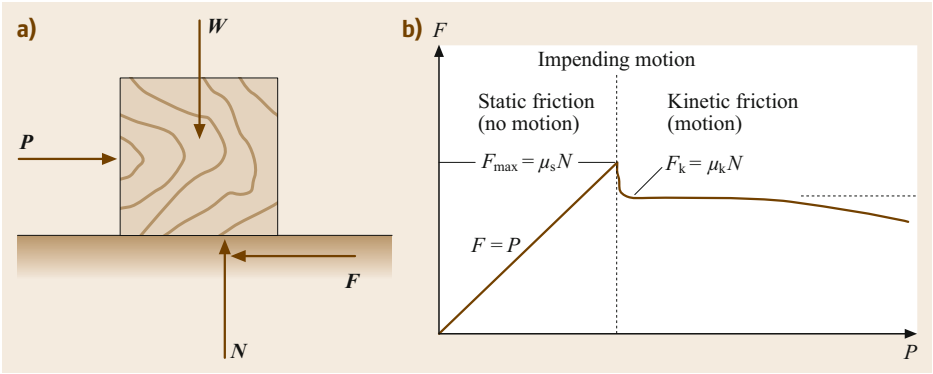

Fig. 2.17a,b Friction on a solid block. **(a)** Dry friction, **(b)** relation of friction

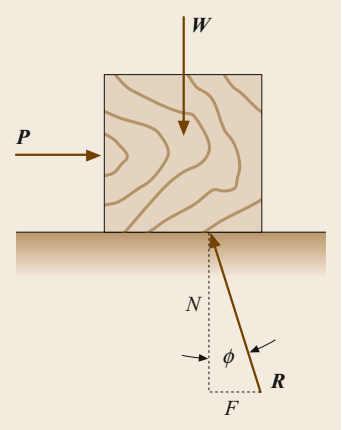

Fig. 2.18 Free-body diagram of a solid block

disk friction. In constructing a free-body diagram when friction is included it is important to draw the direction of the friction force to oppose the direction of motion (or the direction of the tendency toward motion in a purely static case).

2.1.10 Principle of Virtual Work

While static problems are often solved using direct application of Newton's laws, resulting in the equations of static equilibrium (2.13), they may also be approached using work and energy principles. Of these, the most commonly applied to equilibrium problems is the *principle of virtual work*. The principle of virtual work is an analytical technique based on consideration of what would happen to an object if it were somehow to be subject to a hypothetical or *virtual* displacement, $\delta \boldsymbol{r}$. For a rigid body, work would be done by all of the forces as they move in space. As applied to a particle, the principle of virtual work states that *if a particle is in equilibrium, the total virtual work done by the n applied forces during any arbitrary virtual displacement of the particle is zero*. This can easily be verified as follows.

Let the virtual displacement be $\delta \boldsymbol{r}$, then the virtual work done by any force $\boldsymbol{F}_i$ $(i = 1, 2, \ldots, n)$ is the product of the virtual displacement and the component of the force in the direction of the virtual displacement, thus

$$\begin{aligned} \delta U &= \boldsymbol{F}_1 \cdot \delta \boldsymbol{r} + \boldsymbol{F}_2 \cdot \delta \boldsymbol{r} + \cdots + \boldsymbol{F}_n \cdot \delta \boldsymbol{r} \\ &= \left(\sum \boldsymbol{F} \right) \cdot \delta \boldsymbol{r} \,. \end{aligned} \tag{2.22}$$

However, the equilibrium of these static forces requires that the sum of these forces in any direction be zero, hence

$$\delta U = 0 \,.$$

That is, the total virtual work done during any virtual displacement is zero.

In the case of a rigid body, the principle of virtual work states that: *if a rigid body is in equilibrium, the total virtual work of the external forces acting on the rigid body is zero for any virtual displacement of the body*.

The principle of virtual work can be extended to the case of a system of connected rigid bodies. If the system remains connected during a virtual displacement, only the work of the forces external to the system need be considered, since the total work of the internal forces at the various connections is zero. The benefit of the principle of virtual work is that for complex systems, such as mechanisms and machines, a solution may be easier to obtain than when using direct application of equations of equilibrium.

2.2 Dynamics

The study of the motion of a body without regard to the forces and moments causing the motion is known as kinematics. One may think of kinematics as the geometry of motion. Dynamics is the study of the relation between the forces and moments acting on a body, and the mass and motion of the body; it is used to predict the motion caused by given forces and moments or to determine the forces and moments required to produce a given motion. Material presented here is fundamental to the dynamics of systems of particles and rigid bodies.

Dynamic is one of the oldest branches of physics, with its development as a science beginning with Galileo about four centuries ago. His experiments on uniformly accelerated bodies led Newton to formulate his fundamental laws of motion. The study of dynamics of particles and rigid bodies as an engineering subject is not so old, perhaps going back to after World War II as a standard course in engineering curricula. An even later addition to engineering curricula is the study of vibrations, which can be regarded as the part of the dynamics concerned with the motion of elastic systems [2.6–9].

2.2.1 Motion of a Particle

Motion Relative to a Fixed Frame

The position of a particle P in space is defined at any time t by the three Cartesian coordinates $x(t)$, $y(t)$, and $z(t)$. To describe the motion of a particle P along curve C in a three-dimensional space, as depicted in Fig. 2.19, the position vector is expressed as

$$\boldsymbol{r}(t) = x(t)\boldsymbol{i} + y(t)\boldsymbol{j} + z(t)\boldsymbol{k} \,. \tag{2.23}$$

Velocity

The velocity of the particle P in space is defined as the time rate of change of the position. The velocity vector of P is written as

$$\begin{aligned}\boldsymbol{v}(t) = \frac{\mathrm{d}\boldsymbol{r}(t)}{\mathrm{d}t} &= \dot{x}(t)\boldsymbol{i} + \dot{y}(t)\boldsymbol{j} + \dot{z}(t)\boldsymbol{k} \\ &= v_x(t)\boldsymbol{i} + v_y(t)\boldsymbol{j} + v_z(t)\boldsymbol{k} \,,\end{aligned} \tag{2.24}$$

where

$$v_x(t) = \dot{x}(t) \,, \quad v_y(t) = \dot{y}(t) \,, \quad v_z(t) = \dot{z}(t) \tag{2.25}$$

are the Cartesian components of the velocity vector. From Fig. 2.19, the velocity vector is tangent to the curve trajectory C at all time.

Acceleration

The acceleration of the particle P in space is defined as the time rate of change of the velocity. The acceleration vector of P is written as

$$\begin{aligned}\boldsymbol{a}(t) = \frac{\mathrm{d}\boldsymbol{v}(t)}{\mathrm{d}t} &= \dot{v}_x(t)\boldsymbol{i} + \dot{v}_y(t)\boldsymbol{j} + \dot{v}_z(t)\boldsymbol{k} \\ &= a_x(t)\boldsymbol{i} + a_y(t)\boldsymbol{j} + a_z(t)\boldsymbol{k} \,,\end{aligned} \tag{2.26}$$

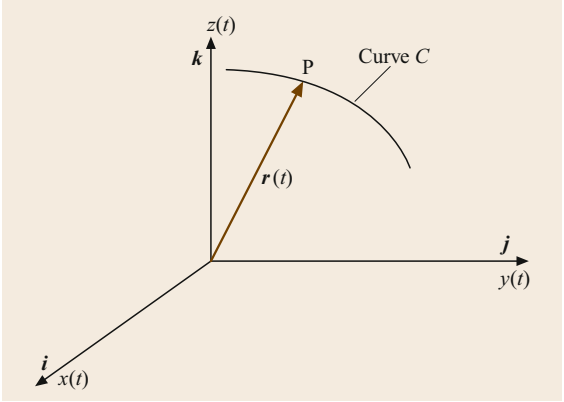

Fig. 2.19 The motion of a particle

where

$$\begin{aligned}&a_x(t) = \dot{v}_x(t) = \ddot{x}(t) \,, \quad a_y(t) = \dot{v}_y(t) = \ddot{y}(t) \,, \\ &a_z(t) = \dot{v}_z(t) = \ddot{z}(t)\end{aligned} \tag{2.27}$$

are the Cartesian components of the acceleration vector.

Rectilinear Motion

Rectilinear motion implies motion along a straight line. Since there is only one component of motion, we may dispense with the vector notation and describe the motion in terms of scalar quantities. Denoting the line along which the motion takes place by s and the distance of the particle P from the fixed origin O by $s(t)$ as depicted in Fig. 2.20, the velocity of P is written as

$$v(t) = \frac{\mathrm{d}s(t)}{\mathrm{d}t} = \dot{s}(t) \,. \tag{2.28}$$

The acceleration of P is written as

$$a(t) = \frac{\mathrm{d}v(t)}{\mathrm{d}t} = \frac{\mathrm{d}^2 s(t)}{\mathrm{d}t^2} = \ddot{s}(t) \,. \tag{2.29}$$

The distance $s(t)$, the velocity $v(t)$, the acceleration $a(t)$ are explicit functions of t. However, one can derive a relation among s, v, and a in which the time t is only implicit. Using the chain rule for differentiation

$$a = \frac{\mathrm{d}v}{\mathrm{d}t} = \frac{\mathrm{d}v}{\mathrm{d}s}\frac{\mathrm{d}s}{\mathrm{d}t} = \frac{\mathrm{d}v}{\mathrm{d}s}v \tag{2.30}$$

or

$$a\mathrm{d}s = v\mathrm{d}v \,. \tag{2.31}$$

Integrating (2.31) between the points $s = s_1$, $v = v_1$ and $s = s_2$, $v = v_2$, we obtain

$$\int_{s_1}^{s_2} a\mathrm{d}s = \int_{v_1}^{v_2} v\mathrm{d}v = \frac{1}{2}\left(v_2^2 - v_1^2\right) . \tag{2.32}$$

Uniform Motion

In this case, $v(t) = v_0 = \text{constant}$. By integration, it follows that

$$s(t) = \int v\mathrm{d}t = v_0 t + C_1 \,. \tag{2.33}$$

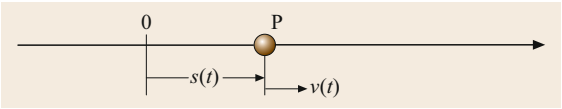

Fig. 2.20 Rectilinear motion

With the initial condition, $s(t=t_1)=s_1$, from this $C_1=s_1-v_0t_1$, therefore,

$$s(t)=v_0\,(t-t_1)+s_1\,. \tag{2.34}$$

Uniform Accelerated Motion

In this case, $a(t)=a_0=$ constant. By integration, it follows that

$$v(t)=\int a\mathrm{d}t=a_0t+C_1 \tag{2.35}$$

or

$$s(t)=\int v\mathrm{d}t=a_0\frac{t^2}{2}+C_1t+C_2\,. \tag{2.36}$$

With the initial condition, $v(t=t_1)=v_1$, and $s(t=t_1)=s_1$, the constants follow: $C_1=v_1-a_0t_1$ and $C_2=s_1-v_1t_1+a_0t_1^2/2$ and therefore

$$s(t)=a_0\frac{(t-t_1)^2}{2}+v_1\,(t-t_1)+s_1\,. \tag{2.37}$$

Example 2.1

A car starting from rest travels with constant acceleration a_0 for 10 s. Determine the value a_0 given that the car has reached a velocity of 108 km/h at the end of the 5 s. What is the distance traveled by the car?

$$v(t)=a_0t$$
$$a_0=\frac{v(t)}{5}|_{t=5}=\frac{108(1000)/3600}{5}=6\,\mathrm{m/s^2}$$
$$s=\frac{1}{2}a_0t^2=\frac{1}{2}6(5)^2=75\,\mathrm{m}$$

Nonuniform Accelerated Motion

In this case, $a(t)=f_0(t)$. By integration, it follows that

$$v(t)=\int a(t)\mathrm{d}t=\int f_0(t)\mathrm{d}t=f_1(t)+C_1 \tag{2.38}$$

or

$$s(t)=\int v(t)\mathrm{d}t=\int[f_1(t)+C_1]\,\mathrm{d}t$$
$$=f_2(t)+C_1t+C_2. \tag{2.39}$$

$f_2(t)=\int f_1(t)\mathrm{d}t$ and the constants C_1 and C_2 are determined from the initial conditions or equivalent conditions.

2.2.2 Planar Motion, Trajectories

Consider a particle with initial velocity v_0 traveling in the xz plane with constant acceleration (gravity) $\ddot{z}=-g$ as shown in Fig. 2.21. Let α be the angle between v_0 and the x-axis. The velocity of the particle at time t in Cartesian components is

$$\boldsymbol{v}=v_0\cos\alpha\boldsymbol{i}+(v_0\sin\alpha-gt)\,\boldsymbol{k}\,. \tag{2.40}$$

The trajectory of the particle at time t in Cartesian components is

$$x=v_0t\cos\alpha\,,\quad z=v_0t\sin\alpha-\frac{1}{2}gt^2\,, \tag{2.41}$$

from which the travel time and trajectory can then be computed as

$$t=\frac{x}{v_0\cos\alpha}\,,\quad z=x\tan\alpha-\frac{1}{2}\frac{gx^2}{v_0^2\cos^2\alpha}\,. \tag{2.42}$$

This trajectory represents a parabola. Its maximum altitude is calculated by locating the point with zero slope

$$\frac{\mathrm{d}z}{\mathrm{d}x}=\tan\alpha-\frac{gx}{v_0^2\cos^2\alpha}=0\,. \tag{2.43}$$

Let x_m be the distance along the x-axis corresponding to the maximum altitude z_m; one obtains

$$x_\mathrm{m}=\frac{v_0^2\sin\alpha\cos\alpha}{g}\,. \tag{2.44}$$

The maximum altitude z_m is

$$z_\mathrm{m}=\frac{v_0^2}{2g}\sin^2\alpha\,. \tag{2.45}$$

The trajectory is symmetrical with respect to the vertical through x_m, as shown in Fig. 2.21. One concludes that the particle hits the ground at $x_\mathrm{f}=2x_\mathrm{m}$. The final velocity $\boldsymbol{v}_\mathrm{f}$ in Cartesian component is

$$v_x=v_0\cos\alpha\,,\quad v_z=-v_0\sin\alpha\,. \tag{2.46}$$

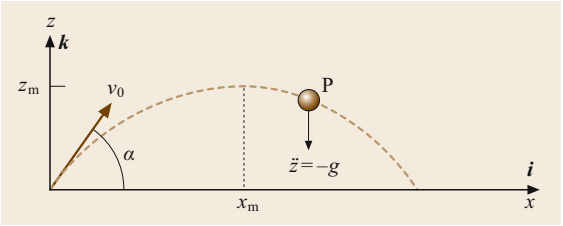

Fig. 2.21 Planar motion

2.2.3 Polar Coordinates

Sometimes it is more convenient to describe the motion of particles using a polar coordinate system. Consider a particle traveling along curve C as shown in Fig. 2.22. In polar coordinates, one defines the radial axis r as the axis coinciding at all times with the direction of the radius vector $\boldsymbol{r}(t)$ from the origin O to the point P. The transverse axis θ is normal to the radial axis as shown in Fig. 2.22. The unit vectors $\boldsymbol{u}_r(t)$ and $\boldsymbol{u}_\theta(t)$, representing the radial and transverse directions, are functions of time. This can be explained by observing that the radius vector $\boldsymbol{r}(t)$ changes directions continuously as the particle moves along the curve C. Because the unit vector $\boldsymbol{u}_r(t)$ is aligned with $\boldsymbol{r}(t)$, $\boldsymbol{u}_r(t)$ also changes direction continuously. Because $\boldsymbol{u}_\theta(t)$ is normal to $\boldsymbol{u}_r(t)$, $\boldsymbol{u}_\theta(t)$ is also a time-dependent unit vector.

The location of the particle P is expressed as

$$\boldsymbol{r}(t) = r(t)\boldsymbol{u}_r(t) \tag{2.47}$$

and the velocity of P is

$$\boldsymbol{v}(t) = \dot{\boldsymbol{r}}(t) = \dot{r}(t)\boldsymbol{u}_r(t) + r(t)\dot{\boldsymbol{u}}_r(t)\,. \tag{2.48}$$

From Fig. 2.23, it follows that

$$\begin{aligned}\dot{\boldsymbol{u}}_r(t) &= \lim_{\Delta t\to 0}\frac{\Delta \boldsymbol{u}_r(t)}{\Delta t} = \lim_{\Delta t\to 0}\frac{\Delta\theta(t)}{\Delta t}\boldsymbol{u}_\theta(t)\\ &= \dot{\theta}(t)\boldsymbol{u}_\theta(t) \qquad (2.49)\\ \dot{\boldsymbol{u}}_\theta(t) &= \lim_{\Delta t\to 0}\frac{\Delta \boldsymbol{u}_\theta(t)}{\Delta t} = \lim_{\Delta t\to 0}\frac{\Delta\theta(t)}{\Delta t}\left[-\boldsymbol{u}_r(t)\right]\\ &= -\dot{\theta}(t)\boldsymbol{u}_r(t)\,. \qquad (2.50)\end{aligned}$$

The velocity of P is rewritten as

$$\begin{aligned}\boldsymbol{v}(t) &= \dot{\boldsymbol{r}}(t) = \dot{r}(t)\boldsymbol{u}_r(t) + r(t)\dot{\boldsymbol{u}}_r(t)\\ &= v_r\boldsymbol{u}_r(t) + v_\theta\boldsymbol{u}_\theta(t)\,,\end{aligned} \tag{2.51}$$

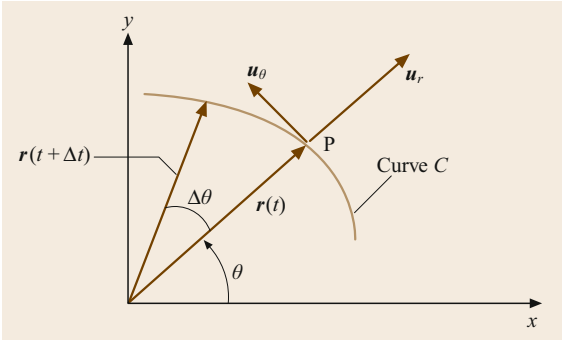

Fig. 2.22 Polar coordinates

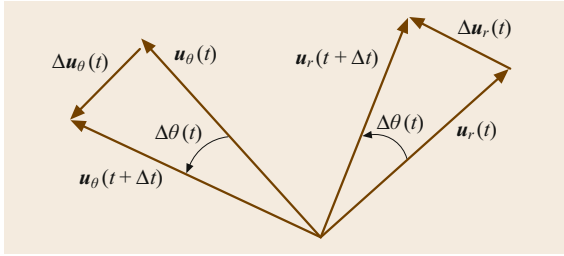

Fig. 2.23 Motion in polar coordinates

where $v_r = \dot{r}$ and $v_\theta = r\dot{\theta}$ are the radial and transverse components of the velocity vector, respectively.

Similarly, the acceleration of point P is

$$\begin{aligned}\boldsymbol{a}(t) &= \dot{\boldsymbol{v}}(t) = \ddot{\boldsymbol{r}}(t)\\ &= \ddot{r}\boldsymbol{u}_r(t) + \dot{r}(t)\dot{\boldsymbol{u}}_r(t) + \dot{r}\dot{\theta}\boldsymbol{u}_\theta + r\ddot{\theta}\boldsymbol{u}_\theta + r\dot{\theta}\dot{\boldsymbol{u}}_\theta\\ &= (\ddot{r} - r\dot{\theta}^2)\boldsymbol{u}_r + (r\ddot{\theta} + 2\dot{r}\dot{\theta})\boldsymbol{u}_\theta\\ &= a_r\boldsymbol{u}_r + a_\theta\boldsymbol{u}_\theta\,,\end{aligned} \tag{2.52a}$$

where

$$a_r = \ddot{r} - r\dot{\theta}^2 \quad \text{and} \quad a_\theta = r\ddot{\theta} + 2\dot{r}\dot{\theta} \tag{2.52b}$$

are the radial and transverse components of the acceleration vector, respectively.

By adding the coordinate z to the polar coordinates r and θ, one obtains the cylindrical coordinates, r, θ, z. The velocity and acceleration vectors can be expressed in terms of cylindrical coordinates as

$$\boldsymbol{v}(t) = v_r\boldsymbol{u}_r + v_\theta\boldsymbol{u}_\theta + v_z\boldsymbol{k}\,, \tag{2.53}$$

where $v_z = \dot{z}$,

$$\boldsymbol{a}(t) = a_r\boldsymbol{u}_r + a_\theta\boldsymbol{u}_\theta + a_z\boldsymbol{k}\,, \tag{2.54}$$

and $a_z = \ddot{z}$.

Example 2.2

A bicycler enters a semicircular track of radius $r = 60\,\mathrm{m}$, as shown in Fig. 2.24, with velocity $v_\mathrm{A} = 18\,\mathrm{m/s}$, and decelerates at a uniform rate, and exits with velocity $v_\mathrm{C} = 12\,\mathrm{m/s}$. Find the circumferential deceleration, the time it takes to complete the semicircle, and the velocity at point B.

Denote the magnitude of the circumferential deceleration as follows

$$a_\theta = r\ddot{\theta}\,. \tag{2.55a}$$

Integrating (2.55a) with respect to time yields

$$v_\theta = r\dot{\theta} = v_\mathrm{A} + a_\theta t\,. \tag{2.55b}$$

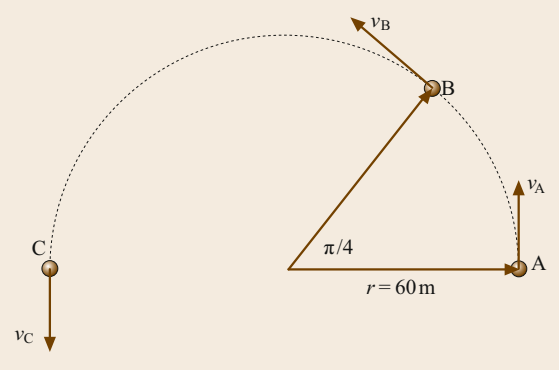

Fig. 2.24 A bicyclist on a semicircular track

Letting $t = t_f$ and $v_\theta = v_C$ in (2.55b), one can write

$$a_\theta t_f = v_C - v_A = 12 - 18 = -6\,\mathrm{m/s}\,. \tag{2.55c}$$

Integrating (2.55b) with respect to time, one obtains

$$r\theta = v_A t + \frac{1}{2} a_\theta t^2\,. \tag{2.55d}$$

Inserting $t = t_f$, $a_\theta t_f = -6$, and $\theta_f = \pi$ in (2.55d) yields

$$t_f = \frac{r\theta_f}{v_A + \frac{1}{2}a_\theta t_f} = \frac{60\pi}{18 + \frac{1}{2}(-6)} = 4\pi\,\mathrm{s} \tag{2.55e}$$

and

$$a_\theta = \frac{-6}{4\pi}\,\mathrm{m/s^2}\,. \tag{2.55f}$$

To obtain v_B, we use

$$a_\theta s_{AB} = \frac{1}{2}\left(v_B^2 - v_A^2\right) \tag{2.55g}$$

so that

$$v_B = \sqrt{v_A^2 + 2a_\theta s_{AB}} = \sqrt{18^2 + 2\left(\frac{-6}{4\pi}\right)\left(\frac{60\pi}{4}\right)}$$
$$= 16.7\,\mathrm{m/s}\,. \tag{2.55h}$$

2.2.4 Motion of Rigid Bodies (Moving Reference Frames)

Consider a reference frame xyz moving relative to the fixed reference frame XYZ as shown in Fig. 2.25. A point P relative to the system XYZ is expressed as

$$\boldsymbol{R} = \boldsymbol{r}_A + \boldsymbol{r}_{AP}\,. \tag{2.56}$$

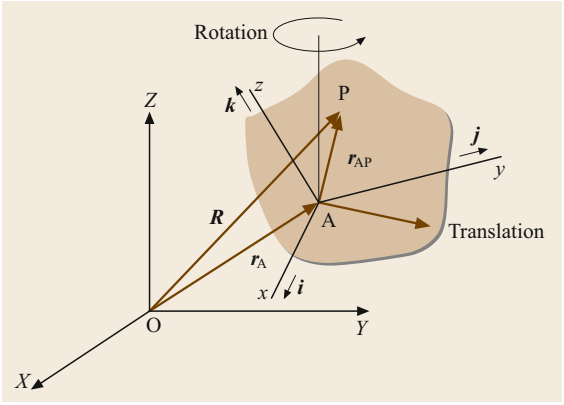

Fig. 2.25 Moving reference frame

The velocity of P relative to an inertial space is

$$\boldsymbol{v} = \dot{\boldsymbol{R}} = \boldsymbol{v}_A + \boldsymbol{v}_{AP}\,, \tag{2.57}$$

where

$$\boldsymbol{v}_A = \dot{\boldsymbol{r}}_A \quad \text{and} \quad \boldsymbol{v}_{AP} = \dot{\boldsymbol{r}}_{AP}\,. \tag{2.58}$$

Similarly, the acceleration of P relative to an inertial space is

$$\boldsymbol{a} = \dot{\boldsymbol{v}} = \ddot{\boldsymbol{R}} = \boldsymbol{a}_A + \boldsymbol{a}_{AP}\,, \tag{2.59}$$

where

$$\boldsymbol{a}_A = \dot{\boldsymbol{v}}_A = \ddot{\boldsymbol{r}}_A \quad \text{and} \quad \boldsymbol{a}_{AP} = \dot{\boldsymbol{v}}_{AP} = \ddot{\boldsymbol{r}}_{AP}\,. \tag{2.60}$$

Rotating Reference Frames

Consider the rigid body shown in Fig. 2.26. Assume that the rigid body is rotating about the axis AB, and consider a point P at a distance $d = |\boldsymbol{d}|$ from point C on axis AB, where C is the intersection between the axis AB and a plane normal to AB that contains the point P. In the time increment Δt the vector $\boldsymbol{d}$ from C to P sweeps an angle $\Delta\theta$ in the plane normal to AB. The vector $\boldsymbol{d}$ rotates in a plane normal to the axis AB with the angular rate $\dot{\theta}$. Because the vector $\boldsymbol{d}$ is embedded in the rigid body, the rigid body and the triad xyz rotate about the axis AB at the same rate $\dot{\theta}$. This angular rate is represented as a vector $\boldsymbol{\omega}$ directed along the axis AB. Note that $\boldsymbol{\omega}$ can be used to represent either the angular velocity of the rigid body, or of the frame xyz

$$\lim_{\Delta t \to 0} \frac{\Delta\theta}{\Delta t} = \dot{\theta} = |\boldsymbol{\omega}|\,. \tag{2.61}$$

Consider the rate of change $\dot{\boldsymbol{d}}$ of the vector $\boldsymbol{d}$ due to the rotation of the body. From Fig. 2.26, we observe that the

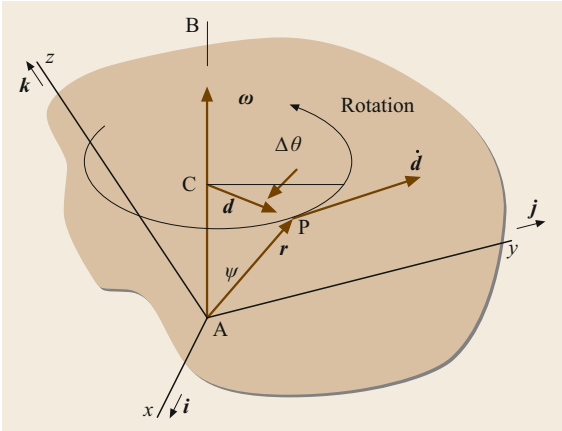

Fig. 2.26 Rotating rigid body

tip P of the vector $\boldsymbol{d}$ describes a circle of radius d, so that $\dot{\boldsymbol{d}}$ is tangent to the circle at P and is normal to the plane defined by the vectors $\boldsymbol{\omega}$ and $\boldsymbol{d}$. In the time increment Δt, the vector $\boldsymbol{d}$ makes the change in magnitude

$$\Delta d = d\Delta\theta \tag{2.62}$$

and

$$\dot{d} = \lim_{\Delta t\to 0}\frac{\Delta d}{\Delta t} = d\dot{\theta}\,. \tag{2.63}$$

In vector notation

$$\dot{\boldsymbol{d}} = \boldsymbol{\omega}\times\boldsymbol{d}\,. \tag{2.64}$$

One can generalize the above equation by observing that

$$d = r\sin\psi\,, \tag{2.65}$$

where r is the magnitude of the vector $\boldsymbol{r}$ and ψ is the angle between AB and $\boldsymbol{r}$. Hence the rate of change of the vector $\boldsymbol{r}$ is

$$\dot{\boldsymbol{r}} = \boldsymbol{\omega}\times\boldsymbol{r}\,. \tag{2.66}$$

The velocity of point P relative to point A is due entirely to the rotation of the frame xyz. Replacing the vector $\boldsymbol{r}$ by the radius vector $\boldsymbol{r}_{\mathrm{AP}}$, yields

$$\boldsymbol{v}_{\mathrm{AP}} = \dot{\boldsymbol{r}}_{\mathrm{AP}} = \boldsymbol{\omega}\times\boldsymbol{r}_{\mathrm{AP}}\,. \tag{2.67}$$

Because point A is at rest, $\boldsymbol{v}_{\mathrm{AP}}$ is also the absolute velocity of P, $\boldsymbol{v} = \boldsymbol{v}_{\mathrm{AP}}$.

The time rate of change of $\boldsymbol{\omega}$ is referred to as the angular acceleration

$$\boldsymbol{\alpha} = \dot{\boldsymbol{\omega}}\,. \tag{2.68}$$

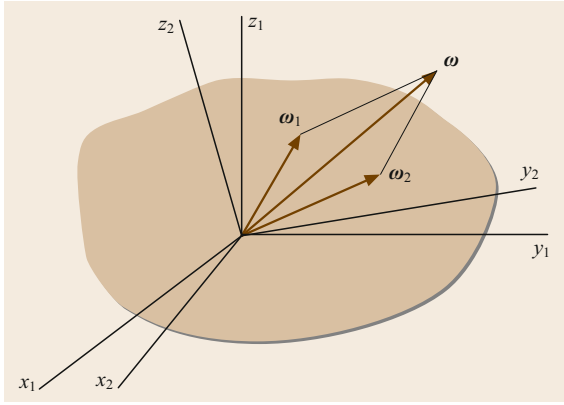

Fig. 2.27 Rotating frame

The acceleration of point P relative to point A is

$$\begin{aligned}\boldsymbol{a}_{\mathrm{AP}} &= \dot{\boldsymbol{v}}_{\mathrm{AP}} = \dot{\boldsymbol{\omega}}\times\boldsymbol{r}_{\mathrm{AP}} + \boldsymbol{\omega}\times\dot{\boldsymbol{r}}_{\mathrm{AP}}\\ &= \boldsymbol{\alpha}\times\boldsymbol{r}_{\mathrm{AP}} + \boldsymbol{\omega}\times(\boldsymbol{\omega}\times\boldsymbol{r}_{\mathrm{AP}})\,.\end{aligned} \tag{2.69}$$

Because point A is at rest, $\boldsymbol{a}_{\mathrm{AP}}$ is also the absolute acceleration of P, $\boldsymbol{a} = \boldsymbol{a}_{\mathrm{AP}}$.

When the origin A of the rotating frame xyz is not fixed, but moves relative to the inertial frame XYZ with the velocity $\boldsymbol{v}_{\mathrm{A}}$ and acceleration $\boldsymbol{a}_{\mathrm{A}}$, then the absolute velocity and acceleration of P are

$$\boldsymbol{v} = \boldsymbol{v}_{\mathrm{A}} + \boldsymbol{v}_{\mathrm{AP}} = \boldsymbol{v}_{\mathrm{A}} + \boldsymbol{\omega}\times\boldsymbol{r}_{\mathrm{AP}}\,, \tag{2.70}$$

$$\boldsymbol{a} = \boldsymbol{a}_{\mathrm{A}} + \boldsymbol{a}_{\mathrm{AP}} = \boldsymbol{a}_{\mathrm{A}} + \boldsymbol{\alpha}\times\boldsymbol{r}_{\mathrm{AP}} + \boldsymbol{\omega}\times(\boldsymbol{\omega}\times\boldsymbol{r}_{\mathrm{AP}})\,. \tag{2.71}$$

Consider the case in which the reference frame $x_1y_1z_1$ rotates with angular velocity $\boldsymbol{\omega}_1$ and the reference frame $x_2y_2z_2$ rotates relative to the frame $x_1y_1z_1$ with angular velocity $\boldsymbol{\omega}_2$, as shown in Fig. 2.27. The angular velocity of the frame $x_2y_2z_2$ is simply

$$\boldsymbol{\omega} = \boldsymbol{\omega}_1 + \boldsymbol{\omega}_2\,. \tag{2.72}$$

Assume that the vector $\boldsymbol{\omega}$ is expressed in terms of components along the frame $x_1y_1z_1$; the angular acceleration then consists of two parts: the first is due to the change in the components of $\boldsymbol{\omega}$ relative to the frame $x_1y_1z_1$ and the second is due to the fact that $\boldsymbol{\omega}$ is expressed in terms of components in a rotating frame. Denoting the first part by $\boldsymbol{\alpha}'$ and noting that the second part can be obtained from (2.66), by replacing $\boldsymbol{r}$ by $\boldsymbol{\omega}$ and $\boldsymbol{\omega}$ by $\boldsymbol{\omega}_1$, yields

$$\boldsymbol{\alpha} = \dot{\boldsymbol{\omega}} = \boldsymbol{\alpha}' + \boldsymbol{\omega}_1\times\boldsymbol{\omega} = \boldsymbol{\alpha}' + \boldsymbol{\omega}_1\times\boldsymbol{\omega}_2\,. \tag{2.73}$$

Example 2.3

A bicycle travels on a circular track of radius R with the circumferential velocity $\boldsymbol{v}_{\mathrm{A}}$ and acceleration $\boldsymbol{a}_{\mathrm{A}}$. Figure 2.28 shows one of the bicycle wheels rotating on

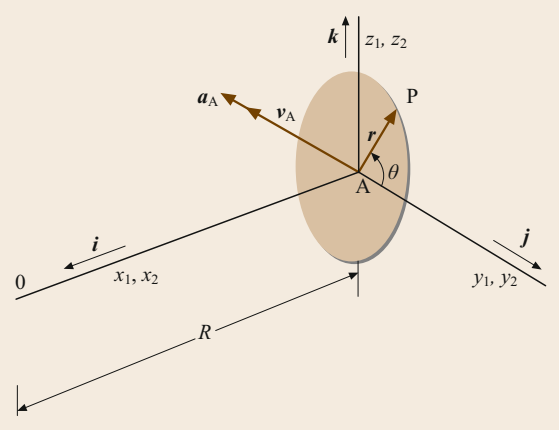

Fig. 2.28 Bicycle wheel

the vertical jk plane. The radius of the wheel is r. Determine the velocity $\boldsymbol{v}$ and acceleration $\boldsymbol{a}$ of a point P on the tire when the radius from the center of the wheel at the point P makes an angle θ with respect to the horizontal plane.

Two reference frames are employed. The frame $x_1y_1z_1$ is attached to the bicycle, and the frame $x_2y_2z_2$ is attached to the wheel. The two frames coincide instantaneously, although the frame $x_2y_2z_2$ rotates relative to the frame $x_1y_1z_1$.

The velocity of the wheel center is

$$\boldsymbol{v}_\mathrm{A} = -v_\mathrm{A}\boldsymbol{j} \tag{2.74a}$$

and the angular velocity of the frame $x_1y_1z_1$ is

$$\boldsymbol{\omega}_1 = \frac{v_\mathrm{A}}{R}\boldsymbol{k}\,. \tag{2.74b}$$

The angular velocity of the frame $x_2y_2z_2$ relative to $x_1y_1z_1$ is

$$\boldsymbol{\omega}_2 = \frac{v_\mathrm{A}}{r}\boldsymbol{i}\,. \tag{2.74c}$$

So, the absolute angular velocity of the frame $x_2y_2z_2$ is

$$\boldsymbol{\omega} = \boldsymbol{\omega}_1 + \boldsymbol{\omega}_2 = \frac{v_\mathrm{A}}{R}\boldsymbol{k} + \frac{v_\mathrm{A}}{r}\boldsymbol{i}\,. \tag{2.74d}$$

The radius vector from A to P is

$$\boldsymbol{r}_\mathrm{AP} = r\,(\cos\theta\boldsymbol{j} + \sin\theta\boldsymbol{k})\,. \tag{2.74e}$$

The velocity of P becomes

$$\begin{aligned}\boldsymbol{v} &= \boldsymbol{v}_\mathrm{A} + \boldsymbol{\omega}\times\boldsymbol{r}_\mathrm{AP}\\ &= -v_\mathrm{A}\boldsymbol{j} + \left(\frac{v_\mathrm{A}}{r}\boldsymbol{i} + \frac{v_\mathrm{A}}{R}\boldsymbol{k}\right)\times r\,(\cos\theta\boldsymbol{j} + \sin\theta\boldsymbol{k})\\ &= -\frac{v_\mathrm{A}r}{R}\cos\theta\boldsymbol{i} - v_\mathrm{A}\,(1+\sin\theta)\boldsymbol{j} + v_\mathrm{A}\cos\theta\boldsymbol{k}\,.\end{aligned} \tag{2.74f}$$

The acceleration of A has two components: a tangential component due to the acceleration of the bicycle along the track and a normal component due to motion along a curvilinear track. Therefore,

$$\begin{aligned}\boldsymbol{a}_\mathrm{A} &= -a_\mathrm{A}\boldsymbol{j} + \boldsymbol{\omega}_1\times(\boldsymbol{\omega}_1\times\boldsymbol{r}_{0\mathrm{A}})\\ &= -a_\mathrm{A}\boldsymbol{j} + \frac{v_\mathrm{A}}{R}\boldsymbol{k}\times\left[\frac{v_\mathrm{A}}{R}\boldsymbol{k}\times(-R)\,\boldsymbol{i}\right]\\ &= \frac{v_\mathrm{A}^2}{R}\boldsymbol{i} - a_\mathrm{A}\boldsymbol{j}\,.\end{aligned} \tag{2.74g}$$

Using (2.73), the angular acceleration of the frame $x_2y_2z_2$ is

$$\begin{aligned}\boldsymbol{\alpha} &= \dot{\boldsymbol{\omega}}_1 + \dot{\boldsymbol{\omega}}_2 + \boldsymbol{\omega}_1\times\boldsymbol{\omega}_2\\ &= \frac{a_\mathrm{A}}{R}\boldsymbol{k} + \frac{a_\mathrm{A}}{r}\boldsymbol{i} + \frac{v_\mathrm{A}}{R}\boldsymbol{k}\times\frac{v_\mathrm{A}}{r}\boldsymbol{i}\\ &= \frac{a_\mathrm{A}}{r}\boldsymbol{i} + \frac{v_\mathrm{A}^2}{rR}\boldsymbol{j} + \frac{a_\mathrm{A}}{R}\boldsymbol{k}\,.\end{aligned} \tag{2.74h}$$

Finally, the acceleration of P is

$$\begin{aligned}\boldsymbol{\alpha} &= \boldsymbol{a}_\mathrm{A} + \alpha\times\boldsymbol{r}_\mathrm{AP} + \boldsymbol{\omega}\times(\boldsymbol{\omega}\times\boldsymbol{r}_\mathrm{AP})\\ &= \frac{v_\mathrm{A}^2}{R}\boldsymbol{i} - a_\mathrm{A}\boldsymbol{j} + \left(\frac{a_\mathrm{A}}{r}\boldsymbol{i} + \frac{v_\mathrm{A}^2}{rR}\boldsymbol{j} + \frac{a_\mathrm{A}}{R}\boldsymbol{k}\right)\\ &\quad\times r\,(\cos\theta j + \sin\theta k) + \left(\frac{v_\mathrm{A}}{r}\boldsymbol{i} + \frac{v_\mathrm{A}}{R}\boldsymbol{k}\right)\\ &\quad\times\left[\left(\frac{v_\mathrm{A}}{r}\boldsymbol{i} + \frac{v_\mathrm{A}}{R}\boldsymbol{k}\right)\times r\,(\cos\theta j + \sin\theta k)\right]\\ &= \left[\frac{v_\mathrm{A}^2}{R}\,(1+2\sin\theta) - \frac{ra_\mathrm{A}}{R}\cos\theta\right]\boldsymbol{i}\\ &\quad - \left[\left(\frac{1}{r} + \frac{r}{R^2}\right)v_\mathrm{A}^2\cos\theta + a_\mathrm{A} + a_\mathrm{A}\sin\theta\right]\boldsymbol{j}\\ &\quad - \left(\frac{v_\mathrm{A}^2}{r}\sin\theta - a_\mathrm{A}\cos\theta\right)\boldsymbol{k}\,.\end{aligned} \tag{2.74i}$$

2.2.5 Planar Motion of a Rigid Body

A body has three degrees of motion in planar motion: two of translation (displacement in the x- and y-directions) and one of rotation (rotation about the z-axis) as shown in Fig. 2.29. The radius vector $\boldsymbol{r}_\mathrm{AP}$ is written as

$$\boldsymbol{r}_\mathrm{AP} = x_\mathrm{AP}\boldsymbol{i} + y_\mathrm{AP}\boldsymbol{j}\,. \tag{2.75}$$

The angular velocity and acceleration of point P are

$$\boldsymbol{\omega} = \omega\boldsymbol{k}\,,\quad \boldsymbol{\alpha} = \alpha\boldsymbol{k}\,, \tag{2.76}$$

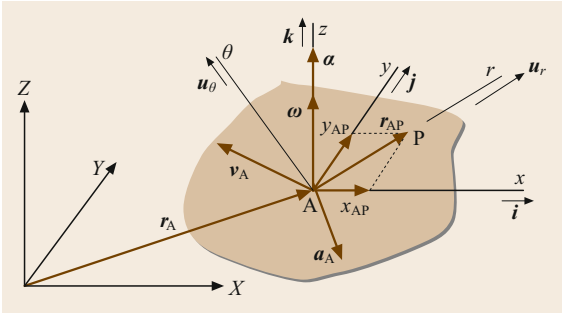

Fig. 2.29 Rigid body motion in a plane

respectively. The velocity of point P is

$$\begin{aligned} \boldsymbol{v} &= \boldsymbol{v}_\mathrm{A} + \boldsymbol{\omega} \times \boldsymbol{r}_\mathrm{AP} = \boldsymbol{v}_\mathrm{A} + \omega \boldsymbol{k} \times (x_\mathrm{AP}\boldsymbol{i} + y_\mathrm{AP}\boldsymbol{j}) \\ &= \boldsymbol{v}_\mathrm{A} - \boldsymbol{\omega} y_\mathrm{AP}\boldsymbol{i} + \boldsymbol{\omega} x_\mathrm{AP}\boldsymbol{j} \,. \end{aligned} \tag{2.77}$$

and the acceleration of point P is

$$\begin{aligned} \boldsymbol{a} &= \boldsymbol{a}_\mathrm{A} + \alpha \times \boldsymbol{r}_\mathrm{AP} + \boldsymbol{\omega} \times (\boldsymbol{\omega} \times \boldsymbol{r}_\mathrm{AP}) \\ &= \boldsymbol{a}_\mathrm{A} + \alpha \boldsymbol{k} \times (x_\mathrm{AP}\boldsymbol{i} + y_\mathrm{AP}\boldsymbol{j}) \\ &\quad + \omega \boldsymbol{k} \times [\omega \boldsymbol{k} \times (x_\mathrm{AP}\boldsymbol{i} + y_\mathrm{AP}\boldsymbol{j})] \\ &= \boldsymbol{a}_\mathrm{A} - \alpha\,(y_\mathrm{AP}\boldsymbol{i} - x_\mathrm{AP}\boldsymbol{j}) - \omega^2 \boldsymbol{r}_\mathrm{AP} \,. \end{aligned} \tag{2.78}$$

The motion can also be expressed in terms of radial and transverse components. The radius vector is

$$\boldsymbol{r}_\mathrm{AP} = r_\mathrm{AP}\boldsymbol{u}_r \,, \tag{2.79}$$

where $\boldsymbol{u}_r$ is the unit vector in the radial direction. The velocity of point P is

$$\boldsymbol{v} = \boldsymbol{v}_\mathrm{A} + \omega r_\mathrm{AP}\boldsymbol{u}_\theta \,, \tag{2.80}$$

where $\boldsymbol{u}_\theta$ is the unit vector in the transverse direction. The acceleration of point P is

$$\begin{aligned} \boldsymbol{a} &= \boldsymbol{a}_\mathrm{A} + \alpha r_\mathrm{AP}\boldsymbol{u}_\theta - \omega^2 \boldsymbol{r}_\mathrm{AP} \\ &= \boldsymbol{a}_\mathrm{A} + \alpha r_\mathrm{AP}\boldsymbol{u}_\theta - \omega^2 r_\mathrm{AP}\boldsymbol{u}_\mathrm{r} \,. \end{aligned} \tag{2.81}$$

Equation (2.77) consists of two parts. The first term represents the velocity of translation of a reference point A. The second part represents the velocity due to rotation about A. If the location of A is specially chosen, the velocity of P can be found to be instantaneously due entirely to rotation. Define this special point as C. It follows that the point C is instantaneously at rest. The point C is called the *instantaneous center of rotation*. Point C may lie inside or outside the body. If both the magnitude and direction of the velocity vector are known, and the angular velocity is also given, then the instantaneous center can be determined by a graphical

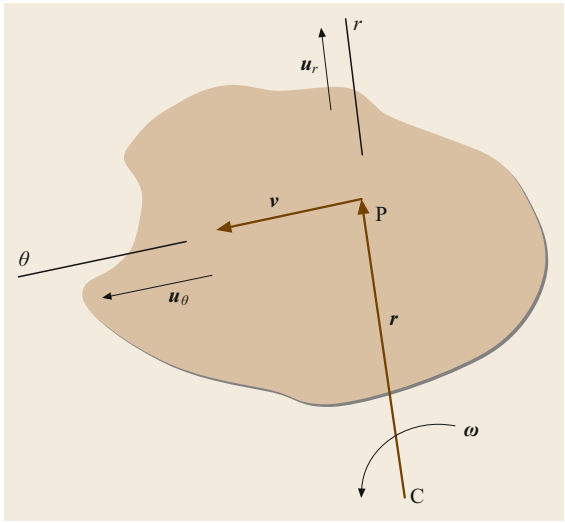

Fig. 2.30 Rigid body and the velocity vector

approach. Figure 2.30 depicts the rigid body and the velocity at point P. The velocity vector can be written

$$\boldsymbol{v} = \boldsymbol{\omega} \times \boldsymbol{r} = \omega \boldsymbol{k} \times r\boldsymbol{u}_r = \omega r \boldsymbol{u}_\theta = v\boldsymbol{u}_\theta \,. \tag{2.82}$$

The radius vector $\boldsymbol{r}$ is normal to the velocity vector $\boldsymbol{v}$, and the angular velocity ω is in the counterclockwise direction as shown in Fig. 2.30. The magnitude of the radius vector is

$$r = \frac{v}{\omega} \,. \tag{2.83}$$

The path taken by the instantaneous center of rotation in relation to a coordinate system fixed in space is called the *space centrode*. The path of the instantaneous center of rotation in relation to a fixed-body coordinate system is called the *body centrode*. During motion, the body centrode rolls on the space centrode.

Example 2.4

A slipping bar of length $L = 20\,\mathrm{m}$ is depicted in Fig. 2.31. The velocity of the point A has magnitude $v_\mathrm{A} = 40\,\mathrm{m/s}$ when the angle between the bar and the wall is $\theta = 30°$; determine the angular velocity of the bar and the velocity of the point B and plot the body and space centrodes.

The instantaneous center of rotation lies at the intersection of the normal to the wall at A and the normal to the floor at the point B. From Fig. 2.31, one has

$$\begin{aligned} r_\mathrm{A} &= L\sin\theta = 10\,\mathrm{m} \,, \\ r_\mathrm{B} &= L\cos\theta = 17.32\,\mathrm{m} \,. \end{aligned} \tag{2.84}$$

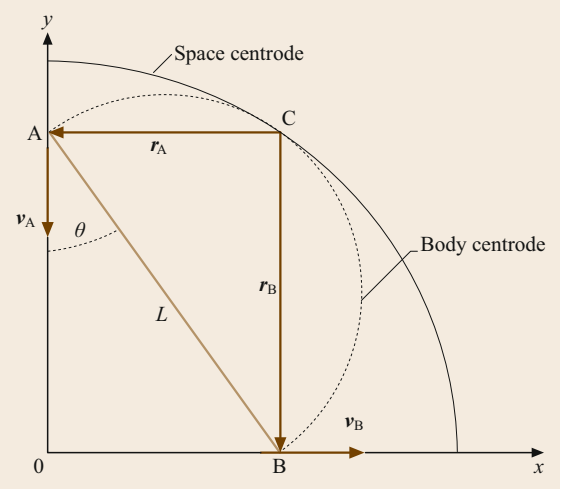

Fig. 2.31 A sliding rod

The velocity vector $\boldsymbol{v}_A$ is in the negative y-direction and the angular velocity in the counterclockwise direction is

$$\omega = \frac{v_A}{r_A} = 4\,\mathrm{rad/s}\,. \tag{2.85}$$

The velocity vector $\boldsymbol{v}_B$ is in the x-direction and its magnitude is

$$v_B = \omega r_B = 69.28\,\mathrm{m/s}\,. \tag{2.86}$$

The points A, O, B, and C are the corners of a rectangular with diagonals equal to L, as shown in Fig. 2.31. Point C is always at a distance L from O. Therefore, the space centrode is one quarter of a circle with radius L and the center at 0, as depicted by the solid line in Fig. 2.31. At the same time, the velocity vectors $\boldsymbol{v}_A$ and $\boldsymbol{v}_B$ make a 90° angle at C. The body centrode is the locus of the point C that is a semicircle as depicted by the dashed line in Fig. 2.31. As the bar slides, the body centrode rolls on the space centrode.

2.2.6 General Case of Motion

Consider the case that the particle P is no longer at rest relative to the moving frame xyz, but can move relative to that frame as depicted in Fig. 2.32. Given an arbitrary vector $\boldsymbol{r}$

$$\boldsymbol{r} = x\boldsymbol{i} + y\boldsymbol{j} + z\boldsymbol{k}\,, \tag{2.87}$$

where x, y, and z are the Cartesian components of the vector and $\boldsymbol{i}$, $\boldsymbol{j}$, and $\boldsymbol{k}$ are the unit vectors along these axes. The unit vectors $\boldsymbol{i}$, $\boldsymbol{j}$, and $\boldsymbol{k}$ rotate with the same

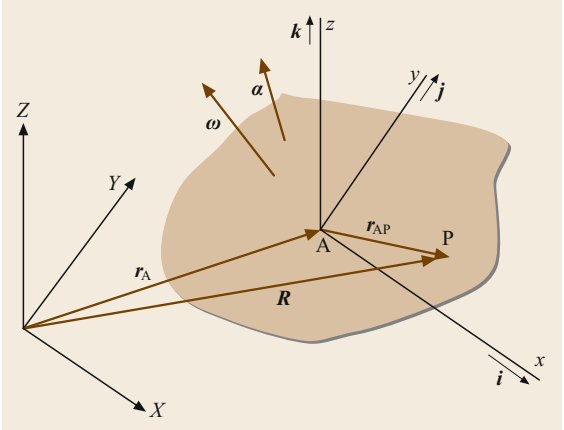

Fig. 2.32 General motion

angular velocity ω as the moving frame. Hence, from (2.66), we have

$$\begin{aligned}\dot{\boldsymbol{r}} &= \dot{x}\boldsymbol{i} + \dot{y}\boldsymbol{j} + \dot{z}\boldsymbol{k} + x\dot{\boldsymbol{i}} + y\dot{\boldsymbol{j}} + z\dot{\boldsymbol{k}} \\ &= \dot{x}\boldsymbol{i} + \dot{y}\boldsymbol{j} + \dot{z}\boldsymbol{k} + \boldsymbol{\omega}\times(x\boldsymbol{i} + y\boldsymbol{j} + z\boldsymbol{k}) \\ &= \dot{\boldsymbol{r}}' + \boldsymbol{\omega}\times\boldsymbol{r}\,,\end{aligned} \tag{2.88}$$

where

$$\dot{\boldsymbol{r}}' = \dot{x}\boldsymbol{i} + \dot{y}\boldsymbol{j} + \dot{z}\boldsymbol{k} \tag{2.89}$$

is the time rate of change of $\boldsymbol{r}$ regarding the reference frame xyz as inertial.

The position vector of point P as depicted in Fig. 2.32 is

$$\boldsymbol{R} = \boldsymbol{r}_A + \boldsymbol{r}_{AP}\,. \tag{2.90}$$

The absolute velocity of P is

$$\boldsymbol{v} = \dot{\boldsymbol{R}} = \dot{\boldsymbol{r}}_A + \dot{\boldsymbol{r}}_{AP} = \boldsymbol{v}_A + \boldsymbol{v}'_{AP} + \boldsymbol{\omega}\times\boldsymbol{r}_{AP}\,, \tag{2.91}$$

where $\boldsymbol{v}_A$ is the velocity of point A relative to the inertial space, and

$$\boldsymbol{v}'_{AP} = \dot{x}_{AP}\boldsymbol{i} + \dot{y}_{AP}\boldsymbol{j} + \dot{z}_{AP}\boldsymbol{k} \tag{2.92}$$

is the velocity of P relative to the moving frame xyz, where x_{AP}, y_{AP}, and z_{AP} are the Cartesian components of $\boldsymbol{r}_{AP}$, and $\boldsymbol{\omega}\times\boldsymbol{r}_{AP}$ is the velocity of P entirely due to the rotation of the frame xyz. Similarly, the absolute acceleration of P is

$$\begin{aligned}\boldsymbol{a} = \dot{\boldsymbol{v}} &= \dot{\boldsymbol{v}}_A + \frac{\mathrm{d}}{\mathrm{d}t}\boldsymbol{v}'_{AP} + \dot{\boldsymbol{\omega}}\times\boldsymbol{r}_{AP} + \boldsymbol{\omega}\times\dot{\boldsymbol{r}}_{AP} \\ &= \boldsymbol{a}_A + \boldsymbol{a}'_{AP} + \boldsymbol{\omega}\times\boldsymbol{v}'_{AP} + \boldsymbol{\alpha}\times\boldsymbol{r}_{AP} + \boldsymbol{\omega}\times\boldsymbol{v}'_{AP} \\ &\quad + \boldsymbol{\omega}\times(\boldsymbol{\omega}\times\boldsymbol{r}_{AP}) \\ &= \boldsymbol{a}_A + \boldsymbol{a}'_{AP} + 2\boldsymbol{\omega}\times\boldsymbol{v}'_{AP} + \boldsymbol{\alpha}\times\boldsymbol{r}_{AP} \\ &\quad + \boldsymbol{\omega}\times(\boldsymbol{\omega}\times\boldsymbol{r}_{AP})\,,\end{aligned} \tag{2.93}$$

where

$$\boldsymbol{a}'_{\mathrm{AP}} = \ddot{x}_{\mathrm{AP}}\boldsymbol{i} + \ddot{y}_{\mathrm{AP}}\boldsymbol{j} + \ddot{z}_{\mathrm{AP}}\boldsymbol{k} \tag{2.94}$$

is the acceleration of P relative to the moving frame xyz, $2\boldsymbol{\omega} \times \boldsymbol{v}'_{\mathrm{AP}}$ is the Coriolis acceleration, and $\boldsymbol{\alpha} \times \boldsymbol{r}_{\mathrm{AP}} + \boldsymbol{\omega} \times (\boldsymbol{\omega} \times \boldsymbol{r}_{\mathrm{AP}})$ is the acceleration of P entirely due to the rotation of the frame xyz, where $\boldsymbol{\alpha} = \dot{\boldsymbol{\omega}}$ is the angular acceleration of the frame xyz.

2.2.7 Dynamics

Particle Dynamics

Dynamics describes the motion of mass particles, mass particle systems, bodies and body systems, in terms of the forces and moments, under the laws of kinematics [2.6–10].

Newton's Laws of Motion

Newton's laws of motion can be applied to systems of particles and rigid bodies. Newton suggested the concept of inertial systems of reference, i.e., systems of reference that are either at rest or moving with uniform velocity relative to a fixed reference frame. The motion of any particle measured relative to such an inertial system is said to be *absolute*. The linear momentum vector $\boldsymbol{p}$ of a particle is defined as the product of the mass m of the particle and its absolute velocity $\boldsymbol{v}$, or $\boldsymbol{p} = m\boldsymbol{v}$. Newton's second law can be expressed as the relationship between a resultant force vector and the time rate of change of momentum as

$$\boldsymbol{F} = \frac{\mathrm{d}\boldsymbol{p}}{\mathrm{d}t} = \frac{\mathrm{d}}{\mathrm{d}t} m\boldsymbol{v} \,. \tag{2.95}$$

In SI units, the unit of mass is the kilogram (kg) and the unit of force is newton (N). If the mass m is constant, then Newton's second law reduces to

$$\boldsymbol{F} = m\frac{\mathrm{d}\boldsymbol{v}}{\mathrm{d}t} = m\boldsymbol{a} \,, \tag{2.96}$$

where $\boldsymbol{a} = \mathrm{d}\boldsymbol{v}/\mathrm{d}t$ is the absolute acceleration of m. Equation (2.96) is the equation of motion of a particle.

Example 2.5

The mass $m = 5\,\mathrm{kg}$ is moved from the position of rest (1) by the force $F_1 = 100\,\mathrm{N}$ with $\beta = 15°$ onto the inclined plane with $\gamma = 25°$ as depicted in Fig. 2.33. The friction coefficient is $\mu = 0.3$. Determine the acceleration, velocity, and time upon arrival at position 2 after traveling $s = 8\,\mathrm{m}$.

$$\begin{aligned} \boldsymbol{F}_{\mathrm{n}} &= mg\cos\gamma + \boldsymbol{F}_1 \sin(\beta+\gamma) = 108.7\,\mathrm{N} \\ ma &= \sum F = \boldsymbol{F}_1 \cos(\beta+\gamma) - \boldsymbol{F}_{\mathrm{g}} \sin\gamma - \mu \boldsymbol{F}_{\mathrm{n}} \\ &= 23.3\,\mathrm{N} \end{aligned} \tag{2.97a}$$

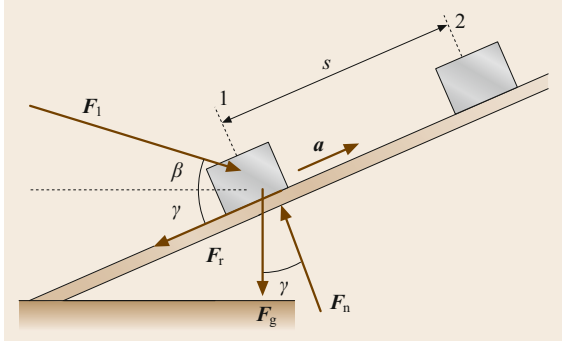

Fig. 2.33 Point mass on an inclined plane

In scalar notation, we have

$$\begin{aligned} a &= \frac{ma}{m} = 4.66\,\mathrm{m/s^2} \,, \quad t = \sqrt{\frac{2s}{a}} = 1.85\,\mathrm{s} \,, \\ v &= \sqrt{2as} = 8.63\,\mathrm{m/s} \,. \end{aligned} \tag{2.97b}$$

Basic Concepts of Energy, Work, and Power

Work. Work is a term used to describe the action of a force moving through a distance. For the simple case of a constant force F moving through a distance d along the line of action of the force, work is simply the product Fd. If the force is not constant, then an integral definition of work must be developed. From Fig. 2.34, the increment of work $\mathrm{d}W$, a scalar, occurring over an infinitesimal vector displacement $\mathrm{d}\boldsymbol{r}$ is defined as the dot product (scalar product) of the force vector and the increment of distance vector

$$\mathrm{d}W = \boldsymbol{F} \cdot \mathrm{d}\boldsymbol{r} = F\cos\beta\,\mathrm{d}r = F_1\,\mathrm{d}r \,. \tag{2.98}$$

The total work is the integral of $\mathrm{d}W$ over the total path length.

From Newton's second law, $\boldsymbol{F} = m\ddot{\boldsymbol{r}}$, and $\mathrm{d}\boldsymbol{r} = \dot{\boldsymbol{r}}\mathrm{d}t$, we obtain

$$\begin{aligned} \mathrm{d}W &= m\ddot{\boldsymbol{r}} \cdot \dot{\boldsymbol{r}}\mathrm{d}t = m\frac{\mathrm{d}\dot{\boldsymbol{r}}}{\mathrm{d}t} \cdot \dot{\boldsymbol{r}}\mathrm{d}t \\ &= m\dot{\boldsymbol{r}} \cdot d\dot{\boldsymbol{r}} = d\left(\frac{1}{2} m\boldsymbol{r} \cdot \boldsymbol{r}\right) . \end{aligned} \tag{2.99}$$

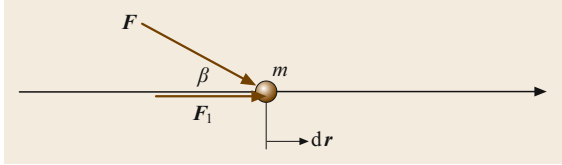

Fig. 2.34 Basic concept of work

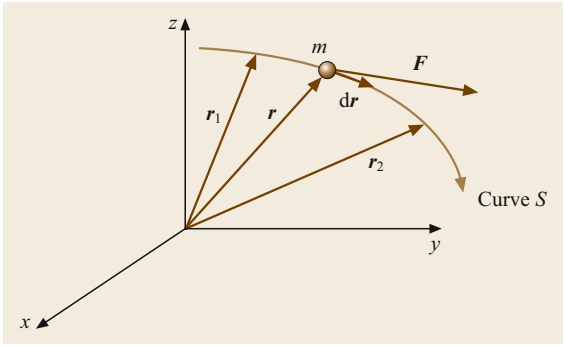

Fig. 2.35 Work of a force

The kinetic energy T, a scalar, is defined as

$$T = \frac{1}{2} m \dot{\boldsymbol{r}} \cdot \dot{\boldsymbol{r}} \,. \tag{2.100}$$

Consider the work performed by force $\boldsymbol{F}$ in moving the particle m from position $\boldsymbol{r}_1$ to position $\boldsymbol{r}_2$ along curve S as depicted in Fig. 2.35, one has

$$W_{1-2} = \int_{r_1}^{r_2} \boldsymbol{F} \cdot d\boldsymbol{r} = \int_{T_1}^{T_2} \mathrm{d}T = T_2 - T_1 \,. \tag{2.101}$$

If forces have a potential as below

$$\boldsymbol{F} = -\mathrm{grad}\, U = -\frac{\partial U}{\partial x}\boldsymbol{i} - \frac{\partial U}{\partial y}\boldsymbol{j} - \frac{\partial U}{\partial z}\boldsymbol{k} \,, \tag{2.102}$$

then it follows that

$$W = -\int_{\mathrm{P}_1}^{\mathrm{P}_2} \left(\frac{\partial U}{\partial x}\mathrm{d}x + \frac{\partial U}{\partial y}\mathrm{d}y + \frac{\partial U}{\partial z}\mathrm{d}z \right)$$

$$= -\int_{\mathrm{P}_1}^{\mathrm{P}_2} \mathrm{d}U = U_1 - U_2 \,. \tag{2.103}$$

In this case, work is independent of the integration distance and is equal to the difference in potential between the initial point P_1 and the final point P_2, as depicted in Fig. 2.36a. Such forces are called conservative forces, and we see from (2.103) that the work done by a conservative force moving from P_1 to P_2 is independent of the path taken between the two points. Examples of conservative forces are the force of gravity and elastic spring forces.

Special Work Examples.

1. Force of gravity. The potential energy $U = F_{\mathrm{g}} z$ and the work is

$$W_{\mathrm{g}} = -\int_{U_1}^{U_2} \mathrm{d}U = U_1 - U_2 = F_{\mathrm{g}}\,(z_1 - z_2) \,. \tag{2.104}$$

2. Spring force (Fig. 2.36b). Potential spring energy $U = cs^2/2$ with spring constant c. The spring force

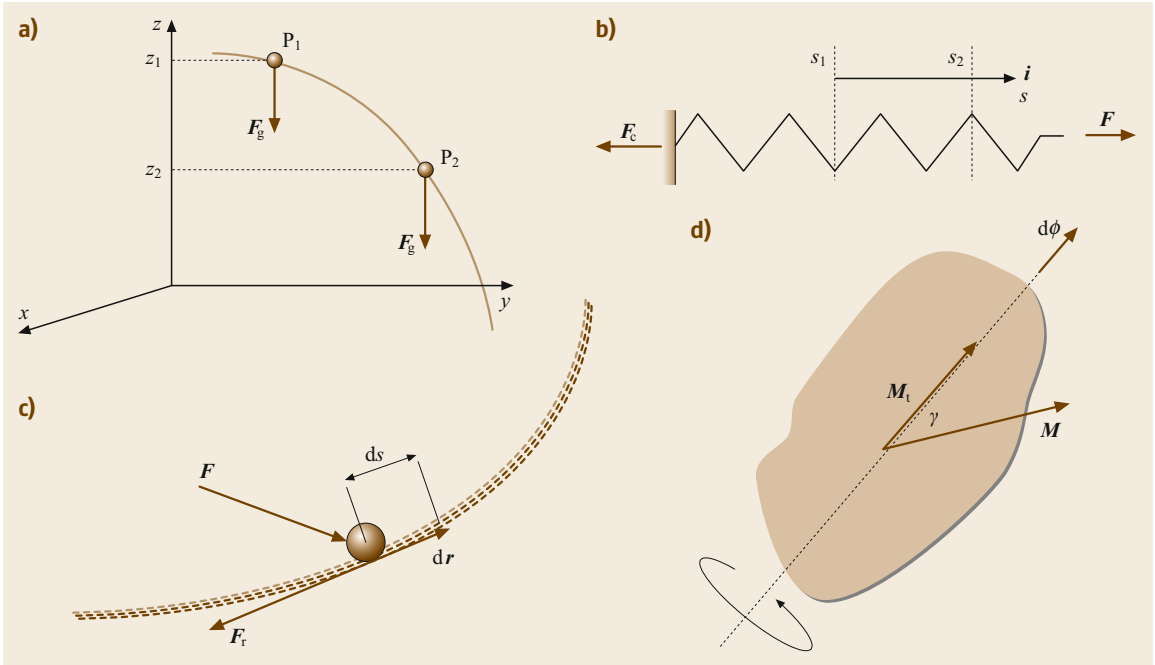

Fig. 2.36a–d Examples of work: **(a)** gravity, **(b)** spring force, **(c)** friction, **(d)** torque

is $\boldsymbol{F}_c = -\nabla U = -\partial U/\partial s\boldsymbol{i} = -cs\boldsymbol{i}$ and the work is

$$W_c = \int_{s_1}^{s_2} cs\mathrm{d}s = \frac{c\left(s_2^2 - s_1^2\right)}{2} . \tag{2.105}$$

3. Frictional force (Fig. 2.36c). This is not a conservative force because work is lost in the form of heat; there is no potential function for this force. For this case we see

$$W_r = \int_{s_1}^{s_2} \boldsymbol{F}_r \cdot \mathrm{d}r = \int_{s_1}^{s_2} F_r \cos\theta \mathrm{d}s$$
$$= -\int_{s_1}^{s_2} F_r \mathrm{d}s . \tag{2.106}$$

4. Torque (Fig. 2.36d). Work is also done by a moment rotating through an angular displacement. Only the moment component parallel to the axis of rotation, M_t, performs work

$$W_M = \int_{\phi_1}^{\phi_2} \boldsymbol{M}(\phi) \cdot d\boldsymbol{\phi} = \int_{\phi_1}^{\phi_2} M(\phi) \cos\gamma \mathrm{d}\phi$$
$$= \int_{\phi_1}^{\phi_2} M_t(\phi)\mathrm{d}\phi . \tag{2.107}$$

Total Work. If several forces and moments are at work on a body simultaneously, then

$$W = \int_{s_1}^{s_2} \sum \boldsymbol{F}_i \cdot \mathrm{d}\boldsymbol{r}_i + \int_{\phi_1}^{\phi_2} \sum \boldsymbol{M}_i \cdot \mathrm{d}\boldsymbol{\phi}_i , \tag{2.108}$$

where the subscript i is an index denoting a specific force or moment.

Power. Power is defined as the rate at which work is done

$$P(t) = \frac{\mathrm{d}W}{\mathrm{d}t} = \sum \boldsymbol{F}_i \cdot \boldsymbol{v}_i + \sum \boldsymbol{M}_i \cdot \boldsymbol{\omega}_i . \tag{2.109}$$

Mean Power. The mean power done over an interval of time relates to the total work done

$$P_m = \frac{\int_{t_1}^{t_2} P(t)\mathrm{d}t}{t_2 - t_1} = \frac{W}{t_2 - t_1} . \tag{2.110}$$

2.2.8 Straight-Line Motion of Particles and Rigid Bodies

Momentum Equation

The time integral of the force is known as the *linear impulse vector* $\boldsymbol{P}$. From (2.95), for constant mass, we have

$$\boldsymbol{P}_{1,2} = \int_{t_1}^{t_2} \boldsymbol{F}\mathrm{d}t = \int_{v_1}^{v_2} m\mathrm{d}\boldsymbol{v} = m\boldsymbol{v}_2 - m\boldsymbol{v}_1 = \boldsymbol{p}_2 - \boldsymbol{p}_1 . \tag{2.111}$$

The linear impulse vector is therefore equal to the change in momentum.

Angular Momentum Equation

Consider a particle of mass m moving under the action of a force $\boldsymbol{F}$. Fig. 2.37 defines the position of m relative to the origin O of the inertial frame xyz as $\boldsymbol{r}$ and the absolute velocity of m is given by $\boldsymbol{v}$. The moment of momentum or angular momentum of m with respect to point O is defined as the moment of the linear momentum $\boldsymbol{p}$ about O and is represented by the cross product of the vectors $\boldsymbol{r}$ and $\boldsymbol{p}$. The angular momentum of m about point O, $\boldsymbol{H}_O$, is

$$\boldsymbol{H}_O = \boldsymbol{r} \times \boldsymbol{p} = \boldsymbol{r} \times m\boldsymbol{v} = \boldsymbol{r} \times m\dot{\boldsymbol{r}} . \tag{2.112}$$

Assuming that m is a constant, the rate of change of angular momentum is

$$\dot{\boldsymbol{H}}_O = \dot{\boldsymbol{r}} \times m\dot{\boldsymbol{r}} + \boldsymbol{r} \times m\ddot{\boldsymbol{r}} = \boldsymbol{r} \times m\ddot{\boldsymbol{r}} = \boldsymbol{r} \times \boldsymbol{F} = \boldsymbol{M}_O . \tag{2.113}$$

Note that $\dot{\boldsymbol{r}} \times m\dot{\boldsymbol{r}} = m(\dot{\boldsymbol{r}} \times \dot{\boldsymbol{r}}) = 0$ and $\boldsymbol{r} \times \boldsymbol{F} = \boldsymbol{M}_O$ is the moment of the force about O. Therefore, the moment of a force about O is equal to the time rate of change of the moment of momentum about O.

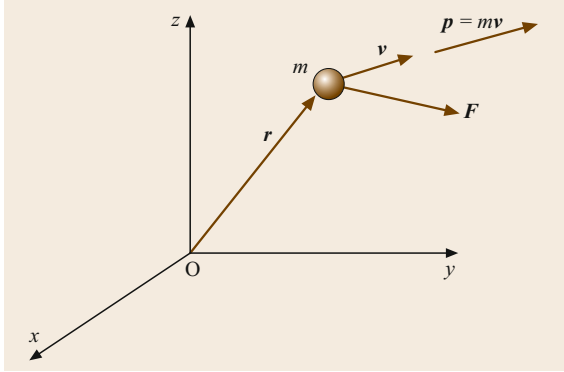

Fig. 2.37 Angular momentum of a particle

The angular impulse vector about O between the times t_1 and t_2 is

$$\hat{\boldsymbol{M}}_{\mathrm{O}} = \int_{t_1}^{t_2} \boldsymbol{M}_{\mathrm{O}} \mathrm{d}t = \int_{t_1}^{t_2} \frac{\mathrm{d}\boldsymbol{H}_{\mathrm{O}}}{\mathrm{d}t} \mathrm{d}t = \boldsymbol{H}_{\mathrm{O}}(t_2) - \boldsymbol{H}_{\mathrm{O}}(t_1)$$
$$= \Delta \boldsymbol{H}_{\mathrm{O}} . \qquad (2.114)$$

Therefore, the angular impulse vector about O between the times t_1 and t_2 is equal to the change in the angular momentum vector about O between the same two instants.

2.2.9 Dynamics of Systems of Particles

A system of particles is a group of n particles as shown in Fig. 2.38. The external and internal forces are denoted by $\boldsymbol{F}_i$ and $\boldsymbol{f}_i$, respectively. The internal force is the resultant of the interaction forces $\boldsymbol{f}_{ij}$ exerted by the particles m_j $(j = 1, 2, \ldots, n, j \neq i)$ on particle m_i $(i = 1, 2, \ldots, n)$. The equation of motion of the system of particles is

$$\sum_{i=1}^{n} \boldsymbol{F}_i + \sum_{j=1}^{n} \sum_{i=1}^{n} \boldsymbol{f}_{ij} = \sum_{i=1}^{n} m_i \ddot{\boldsymbol{r}}_i = \sum_{i=1}^{n} m_i \boldsymbol{a}_i . \qquad (2.115)$$

By Newton's third law, $\boldsymbol{f}_{ij} = -\boldsymbol{f}_{ji}$. Hence

$$\sum_{j=1}^{n} \sum_{i=1}^{n} \boldsymbol{f}_{ij} = 0 .$$

The center of mass C of the system is a point in space representing a weighted average position of the system. The weighting factor is the mass of the particle. We have

$$\boldsymbol{F} = m\boldsymbol{a}_{\mathrm{C}} , \qquad (2.116)$$

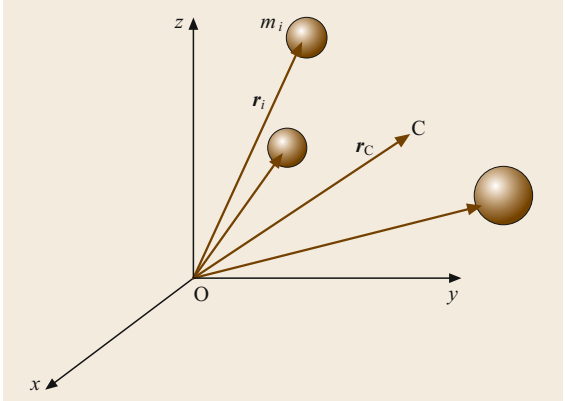

Fig. 2.38 A group of particles

where

$$\boldsymbol{F} = \sum_{i=1}^{n} \boldsymbol{F}_i = \sum_{i=1}^{n} m_i \ddot{\boldsymbol{r}}_i = m\boldsymbol{a}_{\mathrm{C}} . \qquad (2.117)$$

2.2.10 Momentum Equations

From Fig. 2.38, the linear momentum of m_i is

$$\boldsymbol{p}_i = m_i \boldsymbol{v}_i . \qquad (2.118)$$

The linear momentum of the system is

$$\boldsymbol{p} = \sum_{i=1}^{n} \boldsymbol{p}_i = \sum_{i=1}^{n} m_i \boldsymbol{v}_i = m\boldsymbol{v}_{\mathrm{C}} . \qquad (2.119)$$

The resultant of the external forces acting on the system is

$$\boldsymbol{F} = \dot{\boldsymbol{p}} = m\dot{\boldsymbol{v}}_{\mathrm{C}} = m\boldsymbol{a}_{\mathrm{C}} . \qquad (2.120)$$

If $\boldsymbol{F} = 0$, then $\boldsymbol{p} =$ constant. This is the conservation of linear momentum of a system of particles.

The angular momentum of the particle m_i about O is

$$\boldsymbol{H}_{\mathrm{O}i} = \boldsymbol{r}_i \times \boldsymbol{p}_i = \boldsymbol{r}_i \times m_i \boldsymbol{v}_i . \qquad (2.121)$$

The angular momentum of the system about O is

$$\boldsymbol{H}_{\mathrm{O}} = \sum_{i=1}^{n} \boldsymbol{H}_{\mathrm{O}i} = \sum_{i=1}^{n} \boldsymbol{r}_i \times m_i \boldsymbol{v}_i . \qquad (2.122)$$

Hence

$$\dot{\boldsymbol{H}}_{\mathrm{O}} = \sum_{i=1}^{n} \dot{\boldsymbol{r}}_i \times m_i \boldsymbol{v}_i + \sum_{i=1}^{n} \boldsymbol{r}_i \times m_i \dot{\boldsymbol{v}}_i$$
$$= \sum_{i=1}^{n} \boldsymbol{r}_i \times m_i \boldsymbol{a}_i = \sum_{i=1}^{n} \boldsymbol{r}_i \times \boldsymbol{F}_i . \qquad (2.123)$$

Since $\boldsymbol{M}_{\mathrm{O}} = \sum_{i=1}^{n} \boldsymbol{r}_i \times \ddot{\boldsymbol{F}}_i$, we have

$$\boldsymbol{M}_{\mathrm{O}} = \dot{\boldsymbol{H}}_{\mathrm{O}} . \qquad (2.124)$$

If $\boldsymbol{M}_{\mathrm{O}} = 0$, then $\boldsymbol{H}_{\mathrm{O}} =$ constant. This states that, in the absence of external torques about O, the angular momentum of the system about O is a constant. This is the conservation of angular momentum of the system about a fixed point. It can be extended to the conservation of angular momentum about the mass center.

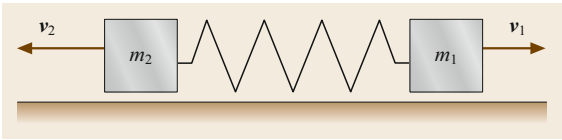

Fig. 2.39 Spring–mass system

Energy Equation

The kinetic energy of particle m_i is

$$T_i = \frac{1}{2} m_i \dot{\boldsymbol{r}}_i \cdot \dot{\boldsymbol{r}}_i \,. \tag{2.125}$$

and the kinetic energy of the system is

$$T = \sum_{i=1}^{n} T_i = \frac{1}{2} \sum_{i=1}^{n} m_i \dot{\boldsymbol{r}}_i \cdot \dot{\boldsymbol{r}}_i \,. \tag{2.126}$$

Example 2.6

A spring with spring constant c, which is compressed by the value s, thrusts the masses m_1 and m_2 apart from rest as depicted in Fig. 2.39. Disregarding the friction forces during the relaxation process of the spring, there is no external force. Determine the maximum velocities of m_1 and m_2.

From the conservation of momentum of a system of particles, we have $m_1 v_1 - m_2 v_2 = 0$.

The energy conservation equation is

$$\frac{1}{2} c s^2 = \frac{1}{2} \left(m_1 v_1^2 + m_2 v_2^2 \right) . \tag{2.127a}$$

It follows that

$$v_1 = \sqrt{\frac{c s^2}{m_1 + m_1^2/m_2}} \,, \quad v_2 = \sqrt{\frac{c s^2}{m_2 + m_2^2/m_1}} \,. \tag{2.127b}$$

Example 2.7

Two masses, connected by an inextensible chain, are drawn out of the position of rest by the constant force $\boldsymbol{F}$ as depicted in Fig. 2.40. Each mass moves along inclined surfaces as shown. Determine the velocity after traveling a distance s_1.

The friction force on masses m_1 and m_2 are $F_{r1} = \mu_1 (F_{g1} \cos\gamma_1 - F \sin\gamma_1)$ and $F_{r2} = \mu_2 F_{g2} \cos\gamma_2$, respectively. As a precondition for the mass m_1 not being lifted, we must have $F \le F_{g1} \cot\gamma_1$.

The energy equation is

$$F \cos\gamma_1 s_1 + F_{g1} h_1 - F_{r1} s_1 - F_{g2} h_2 - F_{r2} s_2 = \frac{1}{2} \left(m_1 v_1^2 + m_2 v_2^2 \right) . \tag{2.128a}$$

Because $s_1 = s_2$, $v_1 = v_2$, $h_1 = s_1 \sin\gamma_1$, and $h_2 = s_2 \sin\gamma_2$, it follows that

$$v_1 = \sqrt{\frac{2 s_1 \left(F \cos\gamma_1 + F_{g1} \sin\gamma_1 - F_{r1} - F_{g2} \sin\gamma_2 - F_{r2} \right)}{m_1 + m_2}} \,. \tag{2.128b}$$

2.2.11 D'Alembert's Principle, Constrained Motion

From Newton's law we know that $\boldsymbol{F} - m\boldsymbol{a} = \boldsymbol{0}$, i.e., the external forces and forces of inertia of a particle form a *state of equilibrium*. In the event of a system of particles m_i $(i = 1, 2, \ldots, n)$, Newton's equations of motion are

$$\boldsymbol{F}_i + \boldsymbol{f}_i - m_i \ddot{\boldsymbol{r}}_i = 0 \,, \quad i = 1, 2, \ldots, n \,, \tag{2.129}$$

where $\boldsymbol{F}_i$ are the applied forces, $\boldsymbol{f}_i$ are the constraint forces, and $-m_i \ddot{\boldsymbol{r}}_i$ are the inertial forces. Equation (2.129) is the dynamic equilibrium of the system of particles. The sum of virtual work for the entire sys-

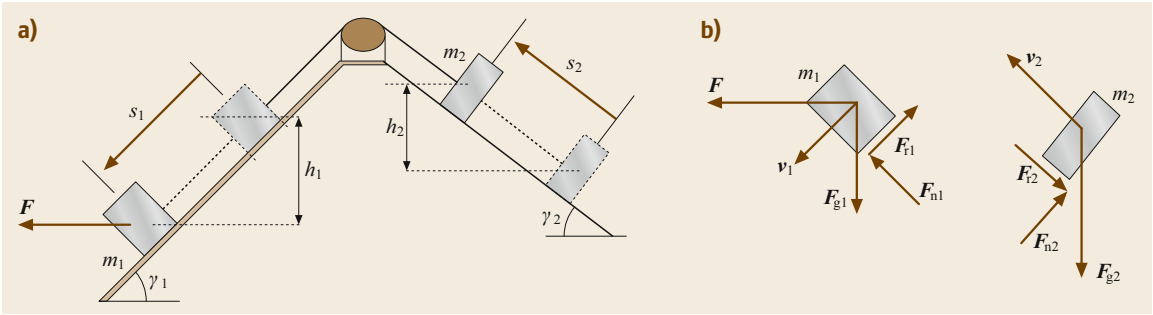

Fig. 2.40 **(a)** Two-mass system, **(b)** forces on each mass

tem is

$$\sum_{i=1}^{n} (\boldsymbol{F}_i + \boldsymbol{f}_i - m_i \ddot{\boldsymbol{r}}_i) \cdot \delta \boldsymbol{r}_i = 0 \,. \tag{2.130}$$

However, the virtual work performed by the constraint forces over virtual displacements is zero. Hence, it follows that

$$\sum_{i=1}^{n} (\boldsymbol{F}_i - m_i \ddot{\boldsymbol{r}}_i) \cdot \delta \boldsymbol{r}_i = 0 \,. \tag{2.131a}$$

Equation (2.131a) is D'Alembert's principle for a system of particles. It can also be applied to a system of rigid bodies. If the motion is planar, D'Alembert's principle for a system of rigid bodies gives

$$\sum_{i=1}^{n} (\boldsymbol{F}_i - m_i \ddot{\boldsymbol{r}}_{Ci}) \cdot \delta \boldsymbol{r}_{Ci} + \left(\boldsymbol{M}_{Ci} - I_{Ci} \ddot{\boldsymbol{\theta}}_i\right) \cdot \delta \boldsymbol{\theta}_i = 0 \,, \tag{2.131b}$$

where r_{Ci} is the position of the mass center of the i-th rigid body, M_{Ci} is the moment of the mass center of the i-th rigid body, and I_{Ci} is the mass moment of inertia about an axis normal to the plane of motion that passes through C.

Example 2.8

Derive the equation of motion of the system shown in Fig. 2.41 by using D'Alembert's principle. Use θ and x as independent coordinates.

There are two rigid bodies in Fig. 2.41. m_1 can be considered as a particle that is subjected to no moments and has no moment of inertia. m_2 is a rigid body with a moment of inertia about C of I_{C2}. Equation (2.130) becomes

$$(\boldsymbol{F}_1 - m_1 \ddot{\boldsymbol{r}}_{C1}) \, \delta \boldsymbol{r}_{C1} + (\boldsymbol{F}_2 - m_2 \ddot{\boldsymbol{r}}_{C2}) \, \delta \boldsymbol{r}_{C2} + \left(\boldsymbol{M}_{C2} - I_{C2} \ddot{\boldsymbol{\theta}}_2\right) \delta \boldsymbol{\theta}_2 = 0 \,. \tag{2.132a}$$

From Fig. 2.41, we have

$$\boldsymbol{F}_1 = -kx\boldsymbol{i} - m_1 g \boldsymbol{j} \,, \quad \boldsymbol{F}_2 = F\boldsymbol{i} - m_2 g \boldsymbol{j} \,,$$
$$\boldsymbol{M}_{C2} = Fa \cos\theta \boldsymbol{k} \,, \quad I_{C2} = \frac{1}{3} m_2 a^2 \,, \tag{2.132b}$$

and

$$\begin{aligned} \boldsymbol{r}_{C1} &= (L + x)\boldsymbol{i} \,, \\ \boldsymbol{r}_{C2} &= (L + x + a \sin\theta)\boldsymbol{i} - a \cos\theta \boldsymbol{j} \,, \\ \delta \boldsymbol{r}_{C1} &= \delta x \boldsymbol{i} \,, \\ \delta \boldsymbol{r}_{C2} &= (\delta x + a \cos\theta \delta\theta)\boldsymbol{i} + a \sin\theta \delta\theta \boldsymbol{j} \,, \end{aligned} \tag{2.132c}$$

where $\theta = \theta_2$, $\delta\theta = \delta\theta_2$, and L is the fixed length of the spring before moving. The accelerations are

$$\begin{aligned} \ddot{\boldsymbol{r}}_{C1} &= \ddot{x}\boldsymbol{i} \,, \\ \ddot{\boldsymbol{r}}_{C2} &= (\ddot{x} + a\ddot{\theta} \cos\theta - a\dot{\theta}^2 \sin\theta)\boldsymbol{i} \\ &\quad + a(\ddot{\theta} \sin\theta + \dot{\theta}^2 \cos\theta)\boldsymbol{j} \,. \end{aligned} \tag{2.132d}$$

Substituting (2.132b)–(2.132d) into (2.132a) and setting each of the coefficients of $\delta\theta$ and δx equal to zero, the equations of motion are

$$\begin{aligned} &(m_1 + m_2)\ddot{x} + m_2 a(\ddot{\theta} \cos\theta - \dot{\theta}^2 \sin\theta) + kx = F \,, \\ &m_2 \cos\theta \ddot{x} + \frac{4}{3} m_2 a \ddot{\theta} + m_2 g \sin\theta = 2F \cos\theta \,. \end{aligned} \tag{2.132e}$$

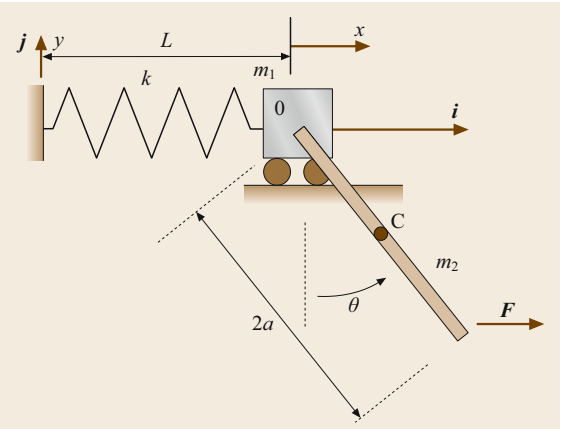

Fig. 2.41 Spring–mass and rod system

2.2.12 Lagrange's Equations

Lagrange provided the equations of motion for a system by a differentiation process related to the dynamic (kinetic and potential) energy. Considering an n-degree-of-freedom system, Lagrange's equations read

$$\frac{\mathrm{d}}{\mathrm{d}t}\left(\frac{\partial L}{\partial \dot{q}_i}\right) - \frac{\partial L}{\partial q_i} = Q_i \quad i = 1, 2, \ldots, n \,, \tag{2.133}$$

where the Lagrangian $L = T - V$, in which T is the kinetic energy, V is the potential energy, q_i are the generalized coordinates of the system, and Q_i are the generalized forces. The Lagrangian approach is very efficient for deriving the equations of motion for both linear and nonlinear systems.

Example 2.9

Derive the equation of motion of the system of Fig. 2.41 using Lagrange's equations.

Suppose $q_1 = x$ and $q_2 = \theta$. First, we need to calculate the virtual work with the nonconservative force $\boldsymbol{F}$. Denoting the point of application of the force by B, the position vector of B is

$$\boldsymbol{r}_\mathrm{B} = (L + x + 2a\sin\theta)\,\boldsymbol{i} - 2a\cos\theta\boldsymbol{j}\,. \tag{2.134a}$$

The virtual displacement of B is

$$\delta\boldsymbol{r}_\mathrm{B} = (\delta x + 2a\cos\theta\delta\theta)\,\boldsymbol{i} + 2a\sin\theta\delta\theta\boldsymbol{j}\,. \tag{2.134b}$$

The force $\boldsymbol{F}$ is

$$\boldsymbol{F} = F\boldsymbol{i}\,. \tag{2.134c}$$

The nonconservative virtual work is

$$\boldsymbol{F}\cdot\delta\boldsymbol{r}_\mathrm{B} = F\,(\delta x + 2a\cos\theta\delta\theta)\,. \tag{2.134d}$$

The coefficients of $\delta\theta$ and δx in (2.134d) are the nonconservative generalized forces

$$X = F\,,\quad \Theta = 2Fa\cos\theta\,. \tag{2.134e}$$

The kinetic energy is

$$\begin{aligned} T &= \frac{1}{2}m_1\boldsymbol{v}_1\cdot\boldsymbol{v}_1 + \frac{1}{2}m_2\boldsymbol{v}_2\cdot\boldsymbol{v}_2 + \frac{1}{2}I_\mathrm{C}\dot\theta^2 \\ &= \frac{1}{2}m_1\dot x^2 + \frac{1}{2}m_2\left[(\dot x + a\dot\theta\cos\theta)^2 + (a\dot\theta\sin\theta)^2\right] \\ &\quad + \frac{1}{2}\frac{1}{12}m_2(2a)^2\dot\theta^2 \\ &= \frac{1}{2}(m_1+m_2)\,\dot x^2 + m_2a\dot x\dot\theta\cos\theta + \frac{2}{3}m_2a^2\dot\theta^2\,. \end{aligned} \tag{2.134f}$$

The potential energy is

$$V = \frac{1}{2}kx^2 + m_2ga\,(1-\cos\theta)\,. \tag{2.134g}$$

Hence,

$$\begin{aligned} L &= T - V \\ \frac{\mathrm{d}}{\mathrm{d}t}\left(\frac{\partial L}{\partial\dot x}\right) &= (m_1+m_2)\,\ddot x + m_2a(\ddot\theta\cos\theta - \dot\theta^2\sin\theta) \\ \frac{\mathrm{d}}{\mathrm{d}t}\left(\frac{\partial L}{\partial\dot\theta}\right) &= m_2a(\ddot x\cos\theta - \dot x\dot\theta\sin\theta) + \frac{4}{3}m_2a^2\ddot\theta \\ \frac{\partial L}{\partial x} &= -kx\,,\ \frac{\partial L}{\partial\theta} = -m_2a\sin\theta(\dot x\dot\theta + g)\,. \end{aligned} \tag{2.134h}$$

From (2.133), the equations of motion are

$$\begin{aligned} &(m_1+m_2)\ddot x + m_2a(\ddot\theta\cos\theta - \dot\theta^2\sin\theta) + kx = F\,, \\ &m_2\ddot x\cos\theta + \frac{4}{3}m_2a\ddot\theta + m_2g\sin\theta = 2F\cos\theta\,. \end{aligned} \tag{2.134i}$$

Note that (2.134i) which were derived using Lagrange's equations agree exactly with (2.132e), derived using D'Alembert's principle.

2.2.13 Dynamics of Rigid Bodies

Rigid bodies can be viewed as a special type of systems of particles, where the distance between any two particles is rigidly constrained to be constant. The relative velocity of between points in a rigid body is due only to the angular velocity of the rigid body.

Linear and Angular Momentum

The angular momentum of a rigid body rotating with angular velocity ω about a fixed point O is defined as

$$H_\mathrm{O} = \int_m \boldsymbol{r}\times\boldsymbol{v}\,\mathrm{d}m\,. \tag{2.135}$$

From Fig. 2.42, because the velocity $\boldsymbol{v}$ of any point in the body is due entirely to the rotation about O, (2.135) becomes

$$\begin{aligned} \boldsymbol{H}_\mathrm{O} &= \int_m \boldsymbol{r}\times(\boldsymbol{\omega}\times\boldsymbol{r})\,\mathrm{d}m \\ &= \int_m ((\boldsymbol{r}\cdot\boldsymbol{r})\,\boldsymbol{\omega} - (\boldsymbol{r}\cdot\boldsymbol{\omega})\,\boldsymbol{r})\,\mathrm{d}m\,, \end{aligned} \tag{2.136}$$

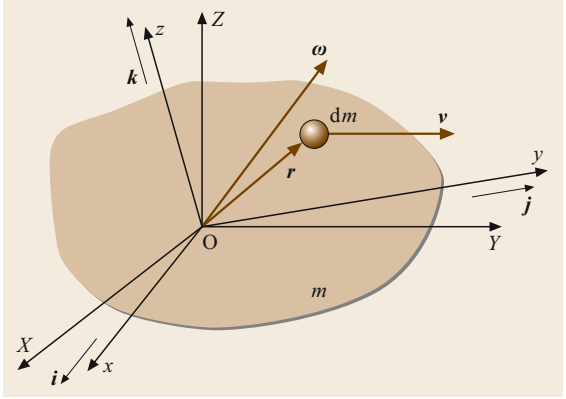

Fig. 2.42 A rotating rigid body

because $\boldsymbol{A}\times(\boldsymbol{B}\times\boldsymbol{C}) = (\boldsymbol{A}\cdot\boldsymbol{C})\boldsymbol{B} - (\boldsymbol{A}\cdot\boldsymbol{B})\boldsymbol{C}$ in vector analysis.

Let

$$\boldsymbol{r} = x\boldsymbol{i} + y\boldsymbol{j} + z\boldsymbol{k} \quad \text{and} \quad \boldsymbol{\omega} = \omega_x\boldsymbol{i} + \omega_y\boldsymbol{j} + \omega_z\boldsymbol{k}\,. \tag{2.137}$$

Substituting (2.137) into (2.135), we have

$$\begin{aligned}\boldsymbol{H}_\mathrm{O} = {} & \left(I_{xx}\omega_x - I_{xy}\omega_y - I_{xz}\omega_z\right)\boldsymbol{i} \\ & + \left(-I_{xy}\omega_x + I_{yy}\omega_y - I_{yz}\omega_z\right)\boldsymbol{j} \\ & + \left(-I_{xz}\omega_x - I_{yz}\omega_y + I_{zz}\omega_z\right)\boldsymbol{k}\,,\end{aligned} \tag{2.138}$$

where

$$I_{xx} = \int_m \left(y^2 + z^2\right)\mathrm{d}m\,, \quad I_{yy} = \int_m \left(x^2 + z^2\right)\mathrm{d}m\,,$$
$$I_{zz} = \int_m \left(x^2 + y^2\right)\mathrm{d}m \tag{2.139}$$

are mass moments of inertia about the body axes xyz, and

$$I_{xy} = I_{yx} = \int_m xy\mathrm{d}m\,, \quad I_{xz} = I_{zx} = \int_m xz\mathrm{d}m\,,$$
$$I_{yz} = I_{zy} = \int_m yz\mathrm{d}m \tag{2.140}$$

are mass products of inertia about the same axes.

Note that the moment of inertia can be represented as the moment of inertia tensor shown below

$$\boldsymbol{I} = \begin{pmatrix} I_{xx} & -I_{xy} & -I_{xz} \\ -I_{yx} & I_{yy} & -I_{yz} \\ -I_{zx} & -I_{zy} & I_{zz} \end{pmatrix}. \tag{2.141}$$

For a pure rotation about a fixed point O, the moment equation of motion is

$$\boldsymbol{M}_\mathrm{O} = \dot{\boldsymbol{H}}_\mathrm{O}\,. \tag{2.142}$$

For any body there are a special set of axes called principal axes which results in each of the products of inertia being zero. If we choose the axes x, y, and z to be the principal axes, $I_{xy} = I_{yz} = I_{zx} = 0$. Then the moment equation of motion becomes

$$\begin{aligned}\boldsymbol{M}_\mathrm{O} &= M_x\boldsymbol{i} + M_y\boldsymbol{j} + M_z\boldsymbol{k}\,, \\ M_x &= I_{xx}\dot{\omega}_x + \left(I_{zz} - I_{yy}\right)\omega_y\omega_z\,, \\ M_y &= I_{yy}\dot{\omega}_y + \left(I_{xx} - I_{zz}\right)\omega_x\omega_z\,, \\ M_z &= I_{zz}\dot{\omega}_z + \left(I_{yy} - I_{xx}\right)\omega_x\omega_y\,,\end{aligned} \tag{2.143}$$

which are called Euler's moment equations.

2.2.14 Planar Motion of a Rigid Body

Assuming that motion takes place in the xy plane, we have $v_z = a_z = 0$, $\omega_x = \dot{\omega}_x = \omega_y = \dot{\omega}_y = 0$, $\omega_z = \omega$. $I_{xz} = I_{yz}$ are approximately 0 if we assume a small dimension of the body in the z-direction compared to the dimensions in the xy plane.

For pure translation, i.e., $\omega = \dot{\omega} = 0$, we have

$$F_x = ma_{\mathrm{C}_x} \quad \text{and} \quad F_y = ma_{\mathrm{C}_y}\,. \tag{2.144}$$

The only moment equation is about the z-axis. The moment equation about the mass center C for pure translation is $M_{\mathrm{C}_z} = 0$.

The kinetic energy is

$$T = \frac{1}{2}m\boldsymbol{v}_\mathrm{C}\cdot\boldsymbol{v}_\mathrm{C} = \frac{1}{2}m\left(v_{\mathrm{C}_x}^2 + v_{\mathrm{C}_y}^2\right), \tag{2.145}$$

where v_{C_x} and v_{C_y} are the Cartesian components of the velocity vector of the mass center.

For pure rotation about a fixed point O, we have the scalar angular momentum and scalar equation of motion as follows

$$H_\mathrm{O} = I_{zz}\omega \quad \text{and} \quad M_\mathrm{O} = I_{zz}\dot{\omega}\,, \tag{2.146}$$

and the kinetic energy is

$$T = \frac{1}{2}I_{zz}\omega^2\,. \tag{2.147}$$

Example 2.10

A uniform horizontal bar with a total mass m is hinged at point O, as depicted in Fig. 2.43. The bar is released from rest. Determine the angular acceleration immediately after release, the reaction force at point O at the same time, and the angular velocity of the bar when it passes through the vertical position.

Consider the counterclockwise moments and angular motion as positive. From (2.113) and (2.146), we have

$$M_\mathrm{O} = I_{zz}\dot{\omega} = -\frac{1}{6}Lmg\,. \tag{2.148a}$$

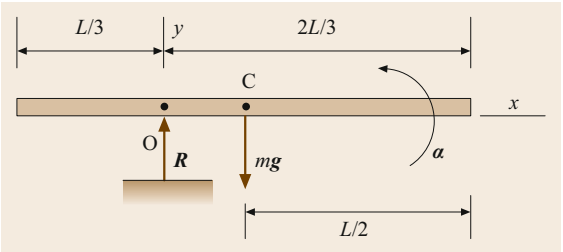

Fig. 2.43 A uniform bar hinged at point O

The mass moment of inertia of the bar about point O is obtained as

$$I_{zz} = \int_m x^2 \mathrm{d}m = \frac{m}{L} \int_{-L/3}^{2L/3} x^2 \mathrm{d}x = \frac{1}{9} L^2 m \,. \tag{2.148b}$$

Hence, the angular acceleration immediately after release is

$$\alpha = \dot{\omega} = -\frac{3g}{2L} \,. \tag{2.148c}$$

From (2.52b) and (2.144), we have the resultant force in the y-axis direction only as follows

$$F_y = R - mg = ma_{C_y} = m\frac{1}{6} L\alpha = \frac{-1}{4} mg \,. \tag{2.148d}$$

The reaction force R at point O is then obtained as

$$R = \frac{3}{4} mg \,. \tag{2.148e}$$

Both the potential and kinetic energy of the bar at horizontal position are zero. At vertical position, the potential energy becomes $V = (-1/6)Lmg$. The kinetic energy becomes $T = (1/2)I_{zz}\omega^2 = (1/18)mL^2\omega^2$. By applying the law of conservation of energy, we have

$$T + V = 0 \quad \text{and} \quad \omega = -\sqrt{\frac{3g}{L}} \,, \tag{2.148f}$$

where the negative sign indicates an angular velocity in the clockwise direction.

2.2.15 General Case of Planar Motion

By using the mass center C, the moment equation has the scalar form $M_C = I_C\alpha$, where I_C is the mass moment of inertia about an axis normal to the plane of motion that passing through C. The kinetic energy consists of the translation of C and rotation about C as follows

$$T = \frac{1}{2} m\left(v_{C_x}^2 + v_{C_y}^2\right) + \frac{1}{2} I_C \omega^2 \,. \tag{2.149}$$

Let us consider the system shown in Fig. 2.44 and write a moment equation about the arbitrary point A as

$$\begin{aligned} \boldsymbol{M}_A &= \int \boldsymbol{\rho}_A \times \mathrm{d}\boldsymbol{F} = \int (\boldsymbol{\rho}_{AC} + \boldsymbol{\rho}) \times \mathrm{d}\boldsymbol{F} \\ &= \boldsymbol{\rho}_{AC} \times \boldsymbol{F} + \boldsymbol{M}_C \,, \end{aligned} \tag{2.150}$$

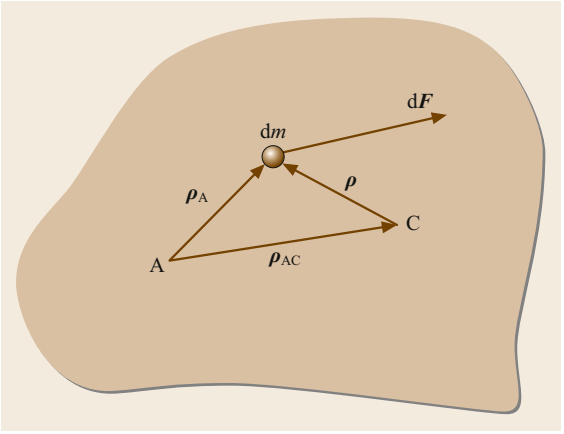

Fig. 2.44 Rigid-body planar motion

or

$$\boldsymbol{M}_A = \boldsymbol{\rho}_{AC} \times m\boldsymbol{a}_C + \boldsymbol{M}_C \quad \text{and} \quad \boldsymbol{M}_C = I_C\boldsymbol{\alpha} \,. \tag{2.151}$$

The acceleration at the mass center C can be written as

$$\boldsymbol{a}_C = \boldsymbol{a}_A + \boldsymbol{a}_{C/A} \,. \tag{2.152}$$

From (2.81), the acceleration reduces to

$$\boldsymbol{a}_C = \boldsymbol{a}_A - \omega^2 \boldsymbol{\rho}_{AC} + \alpha \times \boldsymbol{\rho}_{AC} \,. \tag{2.153}$$

Substituting (2.153) into (2.151) we have

$$\boldsymbol{M}_A = \boldsymbol{\rho}_{AC} \times m\boldsymbol{a}_A + I_A\boldsymbol{\alpha} \,, \tag{2.154}$$

where $I_A = (I_C + m\rho_{AC}^2)$ is the mass moment of inertia of the body about point A.

Example 2.11

A uniform disk of radius R is originally at rest at point 1. It rolls without slipping down to point 2 as depicted in Fig. 2.45. Calculate the velocity at point 2.

The kinetic energy at point 2 is

$$T_2 = \frac{1}{2} m v_2^2 + \frac{1}{2} I_C \omega_2^2 \,. \tag{2.155a}$$

Since $v_2 = -R\omega_2$ and $I_C = mR^2/2$, we have

$$T_2 = \frac{3}{4} m v_2^2 \,. \tag{2.155b}$$

Conservation of energy then yields

$$V_2 + T_2 = -mgh + \frac{3}{4} m v_2^2 = 0 \quad \text{and}$$

$$v_2 = \sqrt{\frac{4gh}{3}} \,. \tag{2.155c}$$

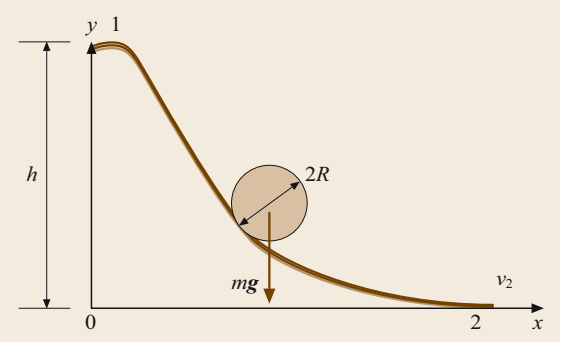

Fig. 2.45 A rolling ball

2.2.16 Rotation About a Fixed Axis

Let us consider the rigid body of Fig. 2.42 and assume that the only motion takes place about the fixed z-axis, i.e., $\omega_x = \dot{\omega}_x = \omega_y = \dot{\omega}_y = 0$, $\omega_z = \omega$. The fixed origin O is also on the fixed axis. The moment equations become

$$M_x = -I_{xz}\dot{\omega} + I_{yz}\omega^2 ,$$
$$M_y = -I_{yz}\dot{\omega} - I_{xz}\omega^2 ,$$
$$M_z = I_{zz}\dot{\omega} . \qquad (2.156)$$

Example 2.12

A thin, uniform disk with radius R and mass m is shown in Fig. 2.46. The normal to the disk makes an angle β with respect to the shaft. The disk rotates with $\omega_z = \omega =$ const. Determine the bearing forces at points A and B.

From Fig. 2.46a, axes XYZ are inertial and axes xyz are body axes, where z is along the shaft and x is embedded in the disk. Fig. 2.46b depicts the body axes xyz, and the principal axes $x'y'z'$. The relationship between these two sets of axes are

$$x = x' , \quad y = y'\cos\beta + z'\sin\beta ,$$
$$z = -y'\sin\beta + z'\cos\beta . \qquad (2.157a)$$

The inertia products I_{xz} and I_{yz} about the axes xyz are

$$I_{xz} = \int_m xz\,dm = \int_m x'\left(-y'\sin\beta + z'\cos\beta\right)dm$$
$$= -\sin\beta I_{x'y'} + \cos\beta I_{x'z'} = 0 \qquad (2.157b)$$

and

$$I_{yz} = \int_m yz\,dm$$
$$= \int_m (y'\cos\beta + z'\sin\beta)$$
$$\times(-y'\sin\beta + z'\cos\beta)dm$$
$$= \sin\beta\cos\beta(I_{y'y'} - I_{z'z'})$$
$$+ (\cos^2\beta - \sin^2\beta)I_{y'z'} . \qquad (2.157c)$$

Note that because $x'y'z'$ are the principal axes, the products of inertia are zero. The moments of inertia of the disk are

$$I_{x'x'} = I_{y'y'} = \frac{1}{4}mR^2 , \quad I_{z'z'} = \frac{1}{2}mR^2 . \qquad (2.157d)$$

Hence,

$$I_{yz} = -\frac{1}{4}mR^2\sin\beta\cos\beta . \qquad (2.157e)$$

Substituting (2.157b) and (2.157e) into (2.156), we obtain

$$M_x = -\frac{1}{4}mR^2\omega^2\sin\beta\cos\beta ,$$
$$M_y = 0 , \quad M_z = 0 . \qquad (2.157f)$$

The moment components along the X- and Y-axes are

$$M_X = M_x\cos\gamma \quad \text{and} \quad M_Y = M_x\sin\gamma . \qquad (2.157g)$$

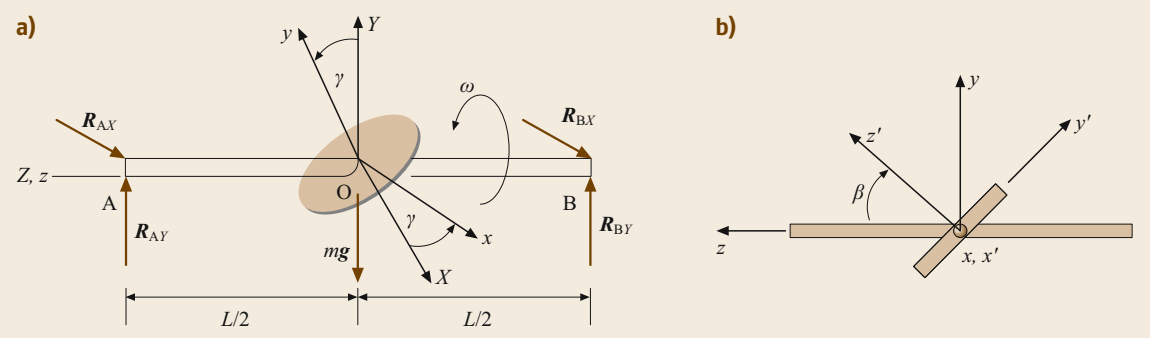

Fig. 2.46a,b A rotating disk: **(a)** the axes XYZ are inertial, **(b)** the axes xyz are body axes

Because the acceleration of the mass center is zero, the force equations along the X- and Y-axes are

$$F_X = R_{A_X} + R_{B_X} = 0 \quad \text{and}$$
$$F_Y = R_{A_Y} + R_{B_Y} - mg = 0 \,. \tag{2.157h}$$

From the reaction forces, the moment equations about 0 yield

$$\begin{aligned} M_X &= \frac{L}{2}\left(R_{B_Y} - R_{A_Y}\right) \\ &= -\frac{1}{4} mR^2\omega^2 \sin\beta \cos\beta \cos\gamma \,, \\ M_Y &= \frac{L}{2}\left(R_{A_X} - R_{B_X}\right) \\ &= -\frac{1}{4} mR^2\omega^2 \sin\beta \cos\beta \sin\gamma \,. \end{aligned} \tag{2.157i}$$

Because $\gamma = \omega t$, (2.157h) and (2.157i) yield

$$\begin{aligned} R_{B_X} &= -R_{A_X} = \frac{1}{4L} mR^2\omega^2 \sin\beta \cos\beta \sin\omega t \,, \\ R_{A_Y} &= \frac{mg}{2} + \frac{1}{4L} mR^2\omega^2 \sin\beta \cos\beta \cos\omega t \,, \\ R_{B_Y} &= \frac{mg}{2} - \frac{1}{4L} mR^2\omega^2 \sin\beta \cos\beta \cos\omega t \,. \end{aligned} \tag{2.157j}$$

Therefore, in addition to the static bearing forces equal to half the weight, there are dynamic bearing forces that vary harmonically with a frequency equal to the spin frequency ω. These dynamic bearing forces will cause the bearings to wear out faster than if the disk were oriented perpendicular to the Z axis.

2.2.17 Lagrange's Equations of Motion for Linear Systems

Lagrange's equations can be applied to the derivation of the equations of motion for a linear n-degree-of-freedom dynamic system. By extending the concept of Sect. 2.2.12, (2.133) can be rewritten as follows

$$\frac{\mathrm{d}}{\mathrm{d}t}\left(\frac{\partial T}{\partial \dot{q}_i}\right) - \frac{\partial T}{\partial q_i} + \frac{\partial D}{\partial \dot{q}_i} + \frac{\partial V}{\partial q_i} = Q_i \,,$$
$$i = 1, 2, \ldots, n \,, \tag{2.158}$$

where D, *the* dissipation function due to the damping force of viscous type, is defined as

$$D = \frac{1}{2}\sum_{i=1}^{n}\sum_{j=1}^{n} c_{ij}\dot{q}_i\dot{q}_j \quad \text{and}$$
$$\frac{\partial D}{\partial \dot{q}_i} = \sum_{j=1}^{n} c_{ij}\dot{q}_j \,, \tag{2.159}$$

where the c_{ij} are known as the damping coefficients.

Equation (2.158) can be rewritten in a compact matrix form as

$$M\ddot{\boldsymbol{q}}(t) + C\dot{\boldsymbol{q}}(t) + K\boldsymbol{q}(t) = \boldsymbol{Q}(t) \,, \tag{2.160}$$

where M is the mass matrix, C is the damping matrix, and K is the stiffness matrix. All three are $n \times n$ symmetric matrices.

$$\boldsymbol{q}(t) = [q_1(t)q_2(t), \ldots, q_n(t)]^\top \quad \text{and}$$
$$\boldsymbol{Q}(t) = [Q_1(t), Q_2(t), \ldots, Q_n(t)]^\top \tag{2.161}$$

Equation (2.161) defines the n-dimensional generalized displacement vector and generalized force vector.

The kinetic energy T, dissipation function D, and the potential energy V can be expressed as

$$\begin{aligned} T &= \frac{1}{2}\dot{\boldsymbol{q}}^\top(t) M \dot{\boldsymbol{q}}(t) \,, \\ D &= \frac{1}{2}\dot{\boldsymbol{q}}^\top(t) C \dot{\boldsymbol{q}}(t) \,, \\ V &= \frac{1}{2}\boldsymbol{q}^\top(t) K \boldsymbol{q}(t) \,. \end{aligned} \tag{2.162}$$

Example 2.13

Derive the equation of motion of the system shown in Fig. 2.47. Use q_1 and q_2 as independent coordinates.

The kinetic energy T, dissipation function D, and the potential energy V are

$$\begin{aligned} T &= \frac{1}{2}\left(m_1\dot{q}_1^2 + m_2\dot{q}_2^2\right) \\ &= \frac{1}{2}\begin{pmatrix}\dot{q}_1 \\ \dot{q}_2\end{pmatrix}^\top \begin{pmatrix} m_1 & 0 \\ 0 & m_2 \end{pmatrix}\begin{pmatrix}\dot{q}_1 \\ \dot{q}_2\end{pmatrix}, \\ D &= \frac{1}{2}\left[c_1\dot{q}_1^2 + c_2\left(\dot{q}_2 - \dot{q}_1\right)^2\right] \\ &= \frac{1}{2}\begin{pmatrix}\dot{q}_1 \\ \dot{q}_2\end{pmatrix}^\top \begin{pmatrix} c_1 + c_2 & -c_2 \\ -c_2 & c_2 \end{pmatrix}\begin{pmatrix}\dot{q}_1 \\ \dot{q}_2\end{pmatrix}, \\ V &= \frac{1}{2}\left[k_1 q_1^2 + k_2\left(q_2 - q_1\right)^2\right] \\ &= \frac{1}{2}\begin{pmatrix}q_1 \\ q_2\end{pmatrix}^\top \begin{pmatrix} k_1 + k_2 & -k_2 \\ -k_2 & k_2 \end{pmatrix}\begin{pmatrix}q_1 \\ q_2\end{pmatrix}. \end{aligned} \tag{2.163}$$

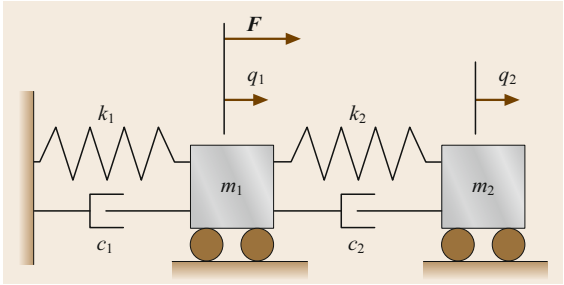

Fig. 2.47 Spring–mass–damping system

The equation of motion of the two-degree-of-freedom dynamic system is obtained as follows

$$\begin{pmatrix} m_1 & 0 \\ 0 & m_2 \end{pmatrix} \begin{pmatrix} \ddot{q}_1 \\ \ddot{q}_2 \end{pmatrix} + \begin{pmatrix} c_1 + c_2 & -c_2 \\ -c_2 & c_2 \end{pmatrix} \begin{pmatrix} \dot{q}_1 \\ \dot{q}_2 \end{pmatrix} + \begin{pmatrix} k_1 + k_2 & -k_2 \\ -k_2 & k_2 \end{pmatrix} \begin{pmatrix} q_1 \\ q_2 \end{pmatrix} = \begin{pmatrix} F \\ 0 \end{pmatrix}. \quad (2.164)$$

This second-order differential equation can be solved and time- and frequency-domain responses can be obtained. Furthermore, this type of problem can be treated as a spring–mass-damping vibration system. Additionally, modern control theory can be introduced to this type of dynamic systems with feedback loops to obtain the desired time- or frequency-domain response.

References

2.1 Y.C. Fung: *A First Course in Continuum Mechanics* (Prentice Hall, Old Tappan 1969) p. 2
2.2 J.L. Meriam, L.G. Kraige: *Statics*, Engineering Mechanics, Vol. 1 (Wiley, New York 2002) p. 4
2.3 F.P. Beer, E.R. Johnston Jr., E.R. Eisenberg: *Vector Mechanics for Engineers – Statics* (McGraw-Hill, New York 2004), pp. 36, 159
2.4 W.F. Riley, L.D. Sturges: *Engineering Mechanics – Statics* (Wiley, Hoboken 1993) p. 263
2.5 F.P. Beer, E.R. Johnston Jr., J.T. DeWolf, D.F. Mazurek: *Mechanics of Materials*, 7th edn. (McGraw-Hill, New York 2015)
2.6 F.P. Beer, E.R. Johnson Jr., J.T. DeWolf: *Vector Mechanics for Engineers: Statics* (McGraw-Hill, New York 2006)
2.7 R.C. Hibbeler: *Engineering Mechanics – Dynamics*, 11th edn. (Prentice Hall, Upper Saddle River 2006)
2.8 J.L. Meriam, L.G. Kraige: *Engineering Mechanics: Dynamics*, 6th edn. (Wiley, New York 2006)
2.9 F.P. Beer: *Vector Mechanics for Engineers: Dynamics* (McGraw-Hill, New York 2005)
2.10 A. Bedford, W. Fowler: *Engineering Mechanics – Statics* (Prentice Hall, Old Tappan 2005) p. 448

David C. Fleming

Dept. of Aerospace, Physics and Space Sciences
Florida Institute of Technology
Melbourne, FL, USA
dfleming@fit.edu

Dr David C. Fleming is associate professor of aerospace engineering and head of the department of aerospace, physics and space sciences at the Florida Institute of Technology. He received a BS in aeronautics and astronautics from MIT and MS and PhD degrees in aerospace engineering from the University of Maryland. His research is in the area of composite structures, with emphasis on the application of composites to crashworthy vehicle design. He is an associate fellow of the American Institute of Aeronautics and Astronautics (AIAA).

Hen-Geul Yeh

Department of Electrical Engineering
California State University
Long Beach, CA, USA
henry.yeh@csulb.edu

Dr Hen-Geul Yeh's research areas are dynamics and adaptive controls, digital signal processing, and digital communication systems. He has been selected twice as the NASA summer faculty fellow, in 1992 and 2003. He was the recipient of four NASA tech brief awards and one NASA new technology award. He was the recipient of the aerospace corporation inventor's award. He was selected as the Boeing A. D. Welliver faculty summer fellow in 2006. He owns several engineering patents.

Hsien-Yang Yeh

Department of Electrical Engineering
California State University
Long Beach, CA, USA
hyyeh@csulb.edu

Dr Hsien-Yang Yeh received his PhD degree from the University of Southern California. His research interests include the mechanics of composite materials, fracture mechanics, structural and machine components failure analysis, and nanotechnology applications.

Shouwen Yu

School of Aerospace
Tsinghua University
Beijing, China
yusw@mail.tsinghua.edu.cn

Dr Shouwen Yu is a professor of engineering mechanics at Tsinghua University, Beijing, China. Yu has served as president (2013-2017) for the International Congress on Fracture (ICF). Yu authored and co-authored six books and has published 440 scientific papers . He was former vice president of the International Federation of Engineering Education Societies (IFEES, 2008-2012) and former vice-president of Tsinghua University. He received the IFEES president's award for "excellence in global engineering education" in 2012 and two national natural science awards in China.

3. Thermodynamics

Peter Stephan, Frank Dammel, Jay M. Ochterbeck

This chapter presents the basic definitions, laws, and relationships concerning the thermodynamic states of substances and thermodynamic processes. It closes with a section describing heat transfer mechanisms.

3.1 **Scope of Thermodynamics and Definitions** 61
3.1.1 Systems, System Boundaries, and Surroundings 61
3.1.2 Description of States, Properties, and Thermodynamic Processes 62

3.2 **Temperatures and Equilibria** 63
3.2.1 Thermal Equilibrium 63
3.2.2 Zeroth Law and Empirical Temperature 63
3.2.3 Temperature Scales 63

3.3 **First Law of Thermodynamics** 66
3.3.1 General Formulation 66
3.3.2 Different Forms of Energy and Energy Transfer 66
3.3.3 Application to Closed Systems 67
3.3.4 Application to Open Systems 67

3.4 **Second Law of Thermodynamics** 69
3.4.1 The Principle of Irreversibility 69
3.4.2 General Formulation 69
3.4.3 Special Formulations 70

3.5 **Exergy and Anergy** 71
3.5.1 Exergy of a Closed System 71
3.5.2 Exergy of an Open System 72
3.5.3 Exergy and Heat Transfer 72
3.5.4 Anergy 72
3.5.5 Exergy Losses 73

3.6 **Thermodynamics of Substances** 73
3.6.1 Thermal Properties of Gases and Vapors 73
3.6.2 Caloric Properties of Gases and Vapors 76
3.6.3 Incompressible Fluids 90
3.6.4 Solid Materials 90
3.6.5 Mixing Temperature and Measurement of Specific Heats 93

3.7 **Changes of State of Gases and Vapors** 93
3.7.1 Changes of State of Gases and Vapors in Closed Systems 93
3.7.2 Changes of State of Flowing Gases and Vapors 95

3.8 **Thermodynamic Processes** 97
3.8.1 Combustion Processes 97
3.8.2 Internal Combustion Cycles 100
3.8.3 Cyclic Processes: Principles 103
3.8.4 Thermal Power Cycles 104
3.8.5 Refrigeration Cycles and Heat Pumps 107
3.8.6 Combined Heat and Power (CHP) 108

3.9 **Ideal Gas Mixtures** 109
3.9.1 Mixtures of Gas and Vapor: Humid Air 109

3.10 **Heat Transfer** 114
3.10.1 Steady-State Heat Conduction 115
3.10.2 Heat Transfer and Heat Transmission 116
3.10.3 Transient Heat Conduction 117
3.10.4 Heat Transfer by Convection 121
3.10.5 Radiative Heat Transfer 126

References 127

3.1 Scope of Thermodynamics and Definitions

Thermodynamics is a subfield of physics that deals with energy and its relationship with the properties of matter. It is concerned with the different forms of energy and their transformation between one another. It provides the general laws that are the basis for energy conversion, transfer, and storage.

3.1.1 Systems, System Boundaries, and Surroundings

A thermodynamic system, or briefly a system, is a quantity of matter or a region in space chosen for a thermodynamic investigation. Some examples of systems are

K.-H. Grote, H. Hefazi (Eds.), *Springer Handbook of Mechanical Engineering*, Springer Handbooks,
https://doi.org/10.1007/978-3-030-47035-7_3

an amount of gas, a liquid and its vapor, a mixture of several liquids, a crystal, or a power plant. The system is separated from its surroundings, the so-called environment, by a boundary (real or imaginary). The boundary is allowed to move during the process under investigation, e.g., during the expansion of a gas, and matter and energy may cross the boundary. Energy can cross a boundary with matter or in the form of heat transfer or work (Sect. 3.3.2). The system with its boundary serves as a region with a barrier in which computations of energy conversion processes take place. The energies that cross the system boundary (in or out), the changes in the stored energy, and the properties of the system are linked by the application of an energy balance relationship (the first law of thermodynamics) to the system. A system is called closed when mass is not allowed to cross the boundary, and open when mass can cross the system boundary. While the mass of a closed system always remains constant, the mass inside an open system may also remain constant when the total mass flows in and out are equal. Changes of the mass stored in an open system will occur when the mass flow into the system over a certain time span is different from the mass flow out. Examples of closed systems are solid bodies, mass elements in mechanics, and a sealed container. Examples of open systems are turbines, turbojet engines, or a fluid (gas or liquid) flowing in a channel. A system is called adiabatic when it is completely thermally isolated from its surrounding and no heat transfer can occur across the boundary. A system that is secluded from all influences from its environment is called isolated. For an isolated system, neither energy in the form of heat transfer or work nor matter are exchanged with the environment.

The distinction between a closed and open system corresponds to the distinction between a Lagrangian and Eulerian reference system in fluid mechanics. In the Lagrangian reference system, which corresponds to a closed system, the fluid motion is examined by dividing the flow into small elements of constant mass and deriving the corresponding equations of motion. In the Eulerian reference system, which corresponds to an open system, a fixed volume element in space is selected and the fluid flow through it examined. Both descriptions are equivalent, and it is often only a question of convenience whether one chooses a closed or open system.

3.1.2 Description of States, Properties, and Thermodynamic Processes

A system is characterized by physical properties, which can be given at any instant, for example, pressure, temperature, density, electrical conductivity, and refractive index. The state of a system is determined by the values of these properties. The transition of a system from one equilibrium state to another is called a change of state.

Example 3.1
A balloon is filled with gas. The gas may then be the thermodynamic system. Measurements show that the mass of the gas is determined by its volume, pressure, and temperature. The properties of the system are thus volume, pressure, and temperature, and the state of the system (the gas) is characterized through a fixed set of values of volume, pressure, and temperature. The transition to another fixed set, e.g., when a certain amount of gas escapes, is called a change of state.

The mathematical relationship between such properties is called an equation of state.

Example 3.2
The volume of gas in the balloon proves to be a function of pressure and temperature. The mathematical relationship between these properties is an equation of state.

Properties can be subdivided into three classes: *intensive properties* are independent of the size of the system and thus keep their values after a division of the system into subsystems.

Example 3.3
If a space filled with a gas at uniform temperature is subdivided into smaller spaces, the temperature remains the same in each subdivided space. Thus, temperature is an intensive property. Pressure would be another example of an intensive property.

Properties that are proportional to the mass of the system (i.e., where the total is equal to the sum of the parts) are called *extensive properties*.

Example 3.4
The volume, the energy, or the mass.

An extensive property X divided by the mass m of the system yields the *specific property* $x = X/m$.

Example 3.5
Take volume as an extensive property of a given gas. The associated specific property is the specific volume $v = V/m$, where m is the mass of the gas. The SI unit for specific volume is m^3/kg. Specific properties all fall into the category of intensive properties.

Changes of state are caused by interactions of the system with the environment, for example, when energy is transferred to or from the system across the system boundary. To describe a change of state, it is sufficient to specify the time history of the properties. The description of a process requires additional specifications of the extent and type of the interactions with the environment. Consequently, a process is a change of state caused by certain external influences. The term *process* is more comprehensive than the term *change of state*; for example, the same change between two states can be induced by different processes.

3.2 Temperatures and Equilibria

3.2.1 Thermal Equilibrium

We often talk about *hot* or *cold* bodies without quantifying such states exactly by a property. When a closed hot system A is exposed to a closed cold system B, energy is transported as heat transfer through the contact area. Thereby, the properties of both systems change until, after a sufficient period of time, new fixed values are reached and the energy transport stops. The two systems are in *thermal equilibrium* in this final state. The speed with which this equilibrium state is approached depends on the type of contact between the two systems and on the thermal properties. If, for example, the two systems are separated by only a thin metal wall, the equilibrium is reached faster than in the case of a thick polystyrene wall. A separating wall that inhibits mass transfer and also mechanical, magnetic, or electric interactions but permits the transport of heat is called diathermal. A diathermal wall is *thermally* conductive. A completely thermally insulating wall such that no thermal interactions occur with the surroundings is called adiabatic.

3.2.2 Zeroth Law and Empirical Temperature

In the case of thermal equilibrium between systems A and C and thermal equilibrium between systems B and C, experience shows that systems A and B must also be in thermal equilibrium. This empirical statement is called the *zeroth law of thermodynamics*. It reads: if two systems are both in thermal equilibrium with a third system, they are also in thermal equilibrium with each other. To determine whether two systems A and B are in thermal equilibrium, they can thus be exposed successively to a system C. The mass of system C may be small compared with those of systems A and B. If so, the changes in state of systems A and B are negligible during equilibrium adjustment. When system C is exposed to system A, certain properties of system C will change, for example, its electrical resistance. These properties then remain unchanged during the subsequent exposure of system C to B, if system A and B were originally in thermal equilibrium. Using C in this way, it is possible to verify whether systems A and B are in thermal equilibrium. It is possible to assign any fixed values to the properties of system C after equilibrium adjustment. These values are called *empirical temperatures*, and the measurement instrument is known as a thermometer.

3.2.3 Temperature Scales

A gas thermometer (Fig. 3.1), which measures the pressure p of a constant volume V of gas, is used for the construction and definition of empirical temperature scales. The gas thermometer is brought into contact with systems of a constant state, e.g., a mixture of ice and water at fixed pressure. After a sufficient period of time, the gas thermometer will reach thermal equilibrium with the system with which it is in contact. The volume of gas is kept constant by changing the height Δz of the mercury column. The pressure exerted by the mercury column and environment is measured, and the

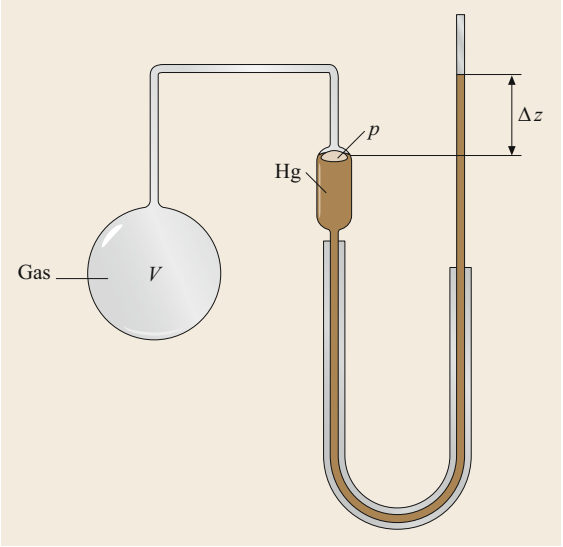

Fig. 3.1 Gas thermometer with gas volume in piston and mercury column

product pV is computed. The extrapolation of measurements at different, sufficiently low pressures leads to a threshold value A for the product pV as pressure approaches zero. This value A, which is determined from the measurements, is assigned to an empirical temperature via the linear relationship

$$T = \text{const}\, A\,. \tag{3.1}$$

After fixing the value *const*, it is only necessary to determine the value of A from the measurements in order to compute the empirical temperature using (3.1). The specification of the empirical temperature scale requires a fixed point. The 10th General Conference of Weights and Measures, held in Paris in 1954, assigned the triple point of water to a temperature $T_{\text{tr}} = 273.16\,\text{kelvin}$ (designated by K). At the triple point of water, vapor, liquid water, and ice coexist in equilibrium at a pressure of $611.657 \pm 0.010\,\text{Pa}$. The temperature scale introduced in this way is named the *Kelvin scale*, and it is identical to the thermodynamic temperature scale. It holds that

$$T = \frac{T_{\text{tr}} A}{A_{\text{tr}}}\,, \tag{3.2}$$

if A_{tr} is the value of A measured using a gas thermometer at the triple point of water.

On the *Celsius scale*, where the unit of temperature t is denoted °C, the ice and steam points are assigned the values of $t_0 = 0\,°\text{C}$ and $t_1 = 100\,°\text{C}$, respectively, at a pressure of 0.101325 MPa. This corresponds quite accurately to absolute temperatures of $T_0 = 273.15\,\text{K}$ and $T_1 = 373.15\,\text{K}$. The temperature $T_{\text{tr}} = 273.16\,\text{K}$ at the triple point of water is roughly 0.01 K higher than the temperature at the ice point. The conversion of temperatures is carried out according to the equation

$$T = t + 273.15\,, \tag{3.3}$$

where t is in °C and T is in K.

Additionally, the Fahrenheit scale is common in some countries, particularly the USA. The corresponding values on this scale are 32°F at the ice point and 212°F at the steam point of water (the pressure in each case being 0.101325 MPa). The conversion of a temperature t_{F} given in °F to a Celsius temperature t in °C is given by

$$t = \frac{5}{9}(t_{\text{F}} - 32)\,. \tag{3.4}$$

The degree increments of the Rankine scale (°R) are the same as Fahrenheit degrees, but the reference 0 is set at absolute zero. It thus holds that

$$T_{\text{R}} = \frac{9}{5} T\,, \tag{3.5}$$

where T_{R} is in °R and T is in K. The ice point of water is thus given as 491.67 °R.

The International Practical Temperature Scale

Since it is difficult and time consuming to measure temperatures precisely using a gas thermometer, the international practical temperature scale was introduced by law. It is arranged by the International Committee for Weights and Measures so that its temperature approaches as close as possible the thermodynamic temperature of certain substances. The international practical temperature scale is fixed by the freezing and boiling points of these substances, which were determined as precisely as possible using a gas thermometer by the scientific national institutes of different countries. Resistance thermometers, thermocouples, and radiation measuring devices are used to interpolate between the fixed points, whereas certain instructions are given for the relationships between the actually measured quantities and temperature. The basic regulations of the international temperature scale are the same in all countries. They read:

1. In the international temperature scale of 1948, the symbol for temperature is t and its unit is "°C" or "°C (Int. 1948)".
2. On the one hand the scale is based on a number of always reproducible equilibrium temperatures (fixed points), which are assigned to certain numerical values, and on the other hand on accurately defined formulas, which establish relationships between the temperature and the indications of the measuring instruments calibrated at the fixed points.
3. The fixed points and the assigned numerical values are summarized in tables (Table 3.1). With the exception of the triple points, the assigned temperatures correspond to equilibrium states at the pressure 0.101325 MPa, which is the standard atmospheric pressure at sea level.
4. Formulas, which also are established by international agreements, are used for interpolation between fixed points. Thus, the indications of the standard instruments with which the temperatures have to be measured are assigned to the numerical values of the international practical temperature.

To simplify temperature measurements,, other additional thermometric fixed points for substances, which can be easily produced in sufficiently pure form, were associated as accurately as possible with this le-

Table 3.1 Fixed points of the international temperature scale of 1990 (ITS-90)

Equilibrium state	Assigned values of the international practical temperature scale	
	T_{90} (K)	t_{90} (°C)
Vapor pressure of helium	3 to 5	−270.15 to −268.15
Triple point of equilibrium hydrogen	13.8033	−259.3467
Vapor pressure of equilibrium hydrogen	≈ 17	≈ −256.15
	≈ 20.3	≈ −252.85
Triple point of neon	24.5561	−248.5939
Triple point of oxygen	54.3584	−218.7916
Triple point of argon	83.8058	−189.3442
Triple point of mercury	234.3156	−38.8344
Triple point of water	273.16	0.01
Melting point of gallium	302.9146	29.7646
Solidification point of indium	429.7485	156.5985
Solidification point of tin	505.078	231.928
Solidification point of zinc	692.677	419.527
Solidification point of aluminum	933.473	660.323
Solidification point of silver	1234.93	961.78
Solidification point of gold	1337.33	1064.18
Solidification point of copper	1357.77	1084.62

All substances except helium may have their natural isotope composition. Hydrogen consists of ortho- and parahydrogen at equilibrium composition

gal temperature scale. The most important ones are summarized in Table 3.2. The platinum resistance thermometer is used as the normal instrument between the triple point of equilibrium hydrogen at 13.8033 K (−259.3467 °C) and the melting point of silver at 1234.93 K (961.78 °C). Between the melting point of silver and the melting point of gold at 1337.33 K (1064.18 °C) a platinum-rhodium (10% rhodium)/platinum thermocouple is used as the normal instrument. Above the melting point of gold, Planck's radiation law defines the international practical temperature

$$\frac{J_t}{J_{\mathrm{Au}}} = \frac{\exp\left(\frac{c_2}{\lambda(t_{\mathrm{Au}}+T_0)}\right)-1}{\exp\left(\frac{c_2}{\lambda(t+T_0)}\right)-1}, \qquad (3.6)$$

where J_t and J_{Au} are the radiation energies emitted by a black body at temperature t and at the gold point t_{Au}, respectively, at a wavelength of λ per unit area, time, and wavelength interval. The value of the constant c_2 is specified as 0.014388 K m (kelvin meters), $T_0 = 273.15$ K is the numerical value of the melting temperature of ice, and λ is the numerical value in m of a wavelength in the visible spectrum. For practical temperature measurements, see [3.1].

Table 3.2 Some thermometric fixed points: E solidification point, Sd boiling point at pressure 101.325 kPa, Tr triple point (after [3.2])

		°C
Normal hydrogen	Tr	−259.198
Normal hydrogen	Sd	−252.762
Nitrogen	Sd	−195.798
Carbon dioxide	Tr	−56.559
Bromobenzene	Tr	−30.726
Water (saturated with air)	E	0
Benzoic acid	Tr	122.34
Indium	Tr	156.593
Bismuth	E	271.346
Cadmium	E	320.995
Lead	E	327.387
Mercury	Sd	356.619
Sulfur	Sd	444.613
Antimony	E	630.63
Palladium	E	1555
Platinum	E	1768
Rhodium	E	1962
Iridium	E	2446
Tungsten	E	3418

3.3 First Law of Thermodynamics

3.3.1 General Formulation

The first law is an empirical statement, which is valid because all conclusions drawn from it are consistent with experience. Generally, it states that energy can be neither destroyed nor created, thus energy is a conserved property. This means that the energy E of a system can be changed only by energy exchange into or out of the system. It is generally agreed that energy transferred into a system is positive while energy transferred out of a system is negative. A fundamental formulation of the first law reads: every system possesses an extensive property called energy, which is constant in an isolated system.

3.3.2 Different Forms of Energy and Energy Transfer

To set up the first law mathematically, it is necessary to distinguish and define the different forms of energy transfer.

Work

In thermodynamics, the basic definition of the term *work* is adopted from mechanics: the work done on a system is equal to the product of the force acting on the system and the displacement from the point of application. The work done by a force F along the distance z between points 1 and 2 is given by

$$W_{12} = \int_1^2 \boldsymbol{F}\,\mathrm{d}z\,. \tag{3.7}$$

The mechanical work $W_{\mathrm{m}12}$ is the result of forces which accelerate a closed system of mass m from velocity w_1 to w_2 and raise it from level z_1 to level z_2 against gravity g. The changes in kinetic energy $mw^2/2$ and potential energy mgz of the system are thus related as

$$W_{\mathrm{m}12} = m\left(\frac{w_2^2}{2} - \frac{w_1^2}{2}\right) + mg(z_2 - z_1)\,. \tag{3.8}$$

Equation (3.8) is known as the energy theorem of mechanics.

Moving boundary work, or simply boundary work, is the work that has to be done to change the volume of a system. In a system of volume V, which possesses the variable pressure p, a differential element $\mathrm{d}A$ of the boundary surface thereby moves the distance $\mathrm{d}z$. The work done is

$$\mathrm{d}W_{\mathrm{v}} = -p\int_A \mathrm{d}\boldsymbol{A}\,\mathrm{d}z = -p\,\mathrm{d}V\,, \tag{3.9}$$

and thus

$$W_{\mathrm{v}12} = -\int_1^2 p\,\mathrm{d}V\,. \tag{3.10}$$

The minus sign is due to the formal sign convention which states that work transferred to the system, which is connected to a volume reduction, is positive. Equation (3.10) is only valid if the pressure p of the system is in each instance of the change of state a continuous function of volume and equal to the pressure exerted by the environment. Then a small excess or negative pressure of the environment causes either a decrease or increase of the system volume. Such changes between states, where even the slightest imbalance is sufficient to drive them in either direction, are called reversible. Accordingly, (3.10) is the moving boundary work for reversible changes of state. In real processes, a finite excess pressure of the environment is necessary to overcome the internal friction of the system. Such changes in state are irreversible, where the added work is increased by the dissipated part $W_{\mathrm{diss}12}$. The moving boundary work for an irreversible change of state is

$$W_{\mathrm{v}12,\mathrm{irr.}} = -\int_1^2 p\mathrm{d}V + W_{\mathrm{diss}12}\,. \tag{3.11}$$

The dissipation work is always positive, increases the system energy, and causes a different path $p(V)$ between the states than in the reversible case. The determination of the integral in (3.11) requires that p be a unique function of V. Equation (3.11) is, for example, not valid for a system area through which a sound wave travels.

Work can be derived as the product of a generalized force F_{k} and a generalized displacement $\mathrm{d}X_{\mathrm{k}}$. In real processes, the dissipated work has to be added

$$\mathrm{d}W = \sum F_{\mathrm{k}}\mathrm{d}X_{\mathrm{k}} + \mathrm{d}W_{\mathrm{diss}}\,. \tag{3.12}$$

This equation shows that, in irreversible processes ($W_{\mathrm{diss}} > 0$), more work has to be done or less work is received than in reversible processes ($W_{\mathrm{diss}} = 0$). Table 3.3 includes different forms of work.

Shaft work is work derived from a mass flow through machines such as compressors, turbines, and jet engines. When a machine increases the pressure of a mass m along the path $\mathrm{d}z$ by $\mathrm{d}p$, the shaft work is

$$\mathrm{d}W_{\mathrm{t}} = mv\mathrm{d}p + \mathrm{d}W_{\mathrm{diss}}\,. \tag{3.13}$$

When the kinetic energy and potential energy of the mass flow are also changed, mechanical work is done

Table 3.3 Different forms of work. SI units are given in parenthesis

Form of work	Generalized force	Generalized displacement	Work done
Linear elastic displacement	Force F (N)	Displacement $\mathrm{d}z$ (m)	$\mathrm{d}W = F\,\mathrm{d}z = \sigma\,\mathrm{d}\varepsilon V$ (N m)
Rotation of a rigid body	Torque M_d (N m)	Torsion angle $\mathrm{d}\alpha$ (–)	$\mathrm{d}W = M_\mathrm{d}\,\mathrm{d}\alpha$ (N m)
Moving boundary work	Pressure p (N/m^2)	Volume $\mathrm{d}V$ (m^3)	$\mathrm{d}W_\mathrm{v} = -p\,\mathrm{d}V$ (N m)
Surface enlargement	Surface tension σ' (N/m)	Area $\mathrm{d}A$ (m^2)	$\mathrm{d}W = \sigma'\,\mathrm{d}A$ (N m)
Electric work	Voltage U_e (V)	Charge Q_e (C)	$\mathrm{d}W = U_\mathrm{e}\,\mathrm{d}Q_\mathrm{e}$ (W s) in a linear conductor with resistance R $\mathrm{d}W = U_\mathrm{e} I\,\mathrm{d}t$ $= RI^2\,\mathrm{d}t$ $= (U^2/R)\,\mathrm{d}t$ (W s)
Magnetic work, in vacuum	Magnetic field strength H_0 (A/m)	Magnetic induction $\mathrm{d}B_0 = \mu_0 H_0$ (Vs/m^2)	$\mathrm{d}W_\mathrm{V} = \mu_0 H_0\,\mathrm{d}H_0$ (W s/m^3)
Magnetization	Magnetic field strength H (A/m)	Magnetic induction $\mathrm{d}B = \mathrm{d}(\mu_0 H + M)$ (Vs/m^2)	$\mathrm{d}W_\mathrm{V} = H\,\mathrm{d}B$ (W s/m^3)
Electrical polarization	Electric field strength E (V/m)	Dielectric displacement $\mathrm{d}D = \mathrm{d}(\varepsilon_0 E + P)$ (As/m^2)	$\mathrm{d}W_\mathrm{V} = E\,\mathrm{d}D$ (W s/m^3)

additionally. The shaft work done along path 1–2 is

$$W_{\mathrm{t}12} = \int_1^2 V\mathrm{d}p + W_{\mathrm{diss}12} + W_{\mathrm{m}12}\,, \tag{3.14}$$

with $W_{\mathrm{m}12}$ given according to (3.8).

Internal Energy

In addition to any kinetic and potential energy, every system possesses energy stored internally as translational, rotational, and vibrational kinetic energy of the elementary particles. This is called the internal energy U of the system and is an extensive property. The total energy E a system of mass m consists of internal energy, kinetic energy E_kin, and potential energy E_pot

$$E = U + E_\mathrm{kin} + E_\mathrm{pot}\,. \tag{3.15}$$

Heat Transfer

The internal energy of a system can be changed by doing work on it or by adding or removing matter. However, it can also be changed by exposing the system to an environment that has a different temperature. As a consequence, energy is transferred across the system boundary as the system tries to reach thermal equilibrium with the environment. This energy transfer is called heat transfer. Thus, heat transfer can generally be defined as the energy that a system exchanges with its environment which does not cross the system boundary as work or by an accompanying mass transfer. The heat transfer from state 1 to 2 is denoted Q_{12}.

3.3.3 Application to Closed Systems

The heat transfer Q_{12} to and work W_{12} done on a closed system during the change of state from 1 to 2 cause a change of the system energy E

$$E_2 - E_1 = Q_{12} + W_{12}\,, \tag{3.16}$$

where W_{12} includes all forms of work done on the system. If no mechanical work is done, only the internal energy changes, and according to (3.15), $E = U$ holds. If it is additionally assumed that only moving boundary work is done on the system, (3.16) reads

$$U_2 - U_1 = Q_{12} - \int_1^2 p\mathrm{d}V + W_{\mathrm{diss}12}\,. \tag{3.17}$$

3.3.4 Application to Open Systems

Steady-State Processes

Very often, work is done by a fluid flowing steadily through a device. If the work per unit time remains constant, such a process is called a *steady flow process*. Figure 3.2 shows a typical example: a flowing fluid (gas or liquid) of pressure p_1 and temperature T_1 may flow with velocity w_1 into system σ. If machine work is done as shaft work, $W_{\mathrm{t}12}$ is supplied at the shaft.

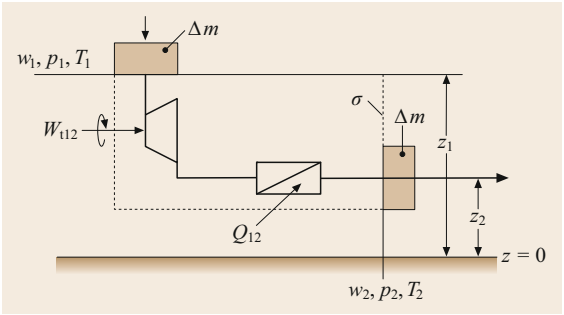

Fig. 3.2 Work for an open system

Then, the fluid flows through a heat exchanger, in which heat transfer Q_{12} occurs with the environment, and the fluid eventually leaves the system σ with pressure p_2, temperature T_2, and velocity w_2. Tracking the path of a constant mass element Δm through the system σ means that a moving observer would consider the mass element Δm as a closed system, thus this corresponds to the Lagrangian description in fluid mechanics. Therefore, the first law for closed systems (3.16) is valid in this case. The work done on Δm consists of $\Delta m p_1 v_1$ to push Δm out of the environment across the system boundary, of the technical work W_{t12}, and of $-\Delta m p_2 v_2$ to bring Δm back into the environment. Thus, the work done on the closed system is

$$W_{12} = W_{t12} + \Delta m(p_1 v_1 - p_2 v_2) \,. \tag{3.18}$$

The term $\Delta m\,(p_1 v_1 - p_2 v_2)$ is referred to as the *flow work*. This flow work is the difference between the shaft work W_{t12} and the work done on the closed system. With this relationship, the first law for closed systems, (3.16), becomes

$$E_2 - E_1 = Q_{12} + W_{t12} + \Delta m(p_1 v_1 - p_2 v_2) \tag{3.19}$$

with E according to (3.15). The property enthalpy is defined as

$$H = U + pV \quad \text{or} \quad h = u + pv \,, \tag{3.20}$$

then (3.19) can be written as

$$0 = Q_{12} + W_{t12} + \Delta m \left(h_1 + \frac{w_1^2}{2} + g z_1 \right) - \Delta m \left(h_2 + \frac{w_2^2}{2} + g z_2 \right) \,. \tag{3.21}$$

The first law is used in this form for steady flow processes in open systems. Equation (3.21) shows that the sum of all the energies entering or leaving the system across the system boundary σ (Fig. 3.2) is zero, because a steady flow process is considered. These energies are in the form of the heat transfer Q_{12}, the shaft work W_{t12}, and the energies $\Delta m(h_1 + w_1^2/2 + g z_1)$ transferred to the system and $\Delta m(h_2 + w_2^2/2 + g z_2)$ transferred from the system with the mass Δm. The differential form of (3.21) reads

$$0 = \mathrm{d}Q + \mathrm{d}W_t + \mathrm{d}m \left(h_1 + \frac{w_1^2}{2} + g z_1 \right) - \mathrm{d}m \left(h_2 + \frac{w_2^2}{2} + g z_2 \right) \,.$$

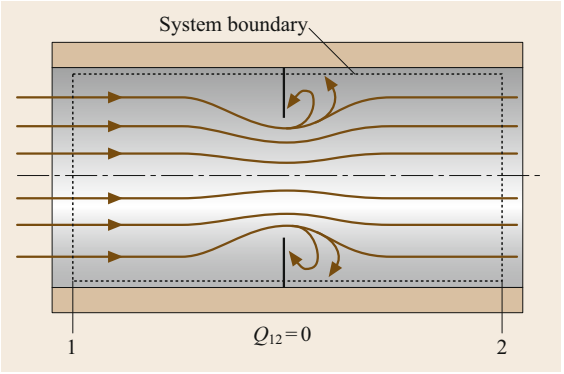

Fig. 3.3 Adiabatic throttling

When a continuous process is considered, it is better to use the following form of the balance equation instead of (3.21),

$$0 = \dot{Q} + P + \dot{m} \left(h_1 + \frac{w_1^2}{2} + g z_1 \right) - \dot{m} \left(h_2 + \frac{w_2^2}{2} + g z_2 \right) \,.$$

In the above equation, $\dot{Q} = \mathrm{d}Q/\mathrm{d}\tau$ is the heat transfer rate, $P = \mathrm{d}W_t/\mathrm{d}\tau$ is the shaft power, and $\dot{m}$ is the mass flow rate. Changes of kinetic and potential energy in these cases are often negligible, such that (3.21) can be simplified to

$$0 = Q_{12} + W_{t12} + H_1 - H_2 \,. \tag{3.22}$$

Special cases of this equation are:

a) Adiabatic changes of state, which typically appear in devices such as compressors, turbines, and jet engines

$$0 = W_{t12} + H_1 - H_2 \,. \tag{3.23}$$

b) Throttling of a flow in an adiabatic tube through a restriction (Fig. 3.3), which causes a pressure reduction. It holds that

$$H_1 = H_2 \tag{3.24}$$

before and after the throttling valve. Thus, the enthalpy remains constant during the throttling, assuming that the changes of kinetic and potential energies are negligible.

Transient Processes

Referring to Fig. 3.2, when the mass Δm_1 transferred to the system over a period of time differs from the

mass Δm_2 transferred from the system during the same period, the result is mass storage (or loss) in the system. This results in a time-variable internal energy of the system and possibly also time-variable kinetic and potential energies. The energy change of a system during a change of state 1–2 is $E_2 - E_1$. Therefore, (3.21) has to be replaced by the following form of the first law,

$$E_2 - E_1 = Q_{12} + W_{t12} + \Delta m_1 \left(h_1 + \frac{w_1^2}{2} + g z_1 \right) - \Delta m_2 \left(h_2 + \frac{w_2^2}{2} + g z_2 \right) . \quad (3.25)$$

If the fluid states 1 at the inlet and 2 at the outlet vary in time, it is appropriate to use the differential notation

$$\mathrm{d}E = \mathrm{d}Q + \mathrm{d}W_t + \mathrm{d}m_1 \left(h_1 + \frac{w_1^2}{2} + g z_1 \right) - \mathrm{d}m_2 \left(h_2 + \frac{w_2^2}{2} + g z_2 \right) . \quad (3.26)$$

When investigating the filling and emptying of containers, it is usually possible to neglect changes in kinetic and potential energies. Furthermore, often no shaft work is done, thus (3.26) reduces to

$$\mathrm{d}U = \mathrm{d}Q + h_1 \mathrm{d}m_1 - h_2 \mathrm{d}m_2 , \quad (3.27)$$

with $U = um$ being the (time-variable) internal energy of the mass stored in the container. It is agreed that $\mathrm{d}m_1$ is mass transferred to and $\mathrm{d}m_2$ mass transferred from the system. If mass is only supplied, $\mathrm{d}m_2$ is equal to zero; if mass is only discharged, $\mathrm{d}m_1$ is equal to zero. For a continuously running process, the following form of the balance equation is more suitable than (3.25),

$$\frac{\mathrm{d}E}{\mathrm{d}\tau} = \dot{Q} + P + \dot{m}_1 \left(h_1 + \frac{w_1^2}{2} + g z_1 \right) - \dot{m}_2 \left(h_2 + \frac{w_2^2}{2} + g z_2 \right) . \quad (3.28)$$

3.4 Second Law of Thermodynamics

3.4.1 The Principle of Irreversibility

When two systems A and B are exposed to each other, energy exchange processes take place and a new equilibrium state is reached after a sufficient period of time. As an example, a system A may be in contact with a system B that has a different temperature. In the final state, both systems will have the same temperature and equilibrium will have been reached. Until equilibrium has been reached, a continuous series of nonequilibrium states will be passed. Common experience shows that this process has a natural direction (e.g., heat transfer from hot to cold) but does not proceed in the reverse direction independently, i.e., without exchange with the environment. Such processes are referred to as being irreversible. Exchange processes, which pass through nonequilibrium states, are in principle irreversible. On the other hand, a process that consists of a continuous series of equilibrium states is reversible. This may be exemplified by the frictionless, adiabatic compression of a gas. It is possible to transfer moving boundary work to the system *gas* by exerting a force, for example, an excess pressure of the environment, on the system boundary. If this force is increased very slowly, the volume of the gas decreases while the temperature increases, whereas the gas is at all times in an equilibrium state. If the force is slowly reduced to zero, the gas returns to its initial state; thus, this process is reversible. Reversible processes are idealized borderline cases of real processes and do not occur in Nature. All natural processes are irreversible, because a finite force is necessary to initiate a process, e.g., a finite force to move a body against friction or a finite temperature difference for heat transfer. These facts known from experience lead to the following formulations of the second law:

- All natural processes are irreversible.
- All processes including friction are irreversible.
- Heat transfer does not independently occur from a body of lower to a body of higher temperature.

Independently in this regard means that it is not possible to carry out the mentioned process without causing effects on Nature. Beside these examples, further formulations valid for other special processes exist.

3.4.2 General Formulation

The mathematical formulation of the second law is realized by introducing the term *entropy* as another property of a system. The practicality of this property can be shown by using the example of heat transfer between a system and its environment. According to the first law, a system can exchange energy by work

and by heat transfer with its environment. The supply of work causes a change of the internal energy such that, for example, the system's volume is changed at the expense of the environment's volume. Consequently, $U = U(V, \ldots)$. The volume is an exchange variable. It is an extensive property, which is *exchanged* between the system and environment. It is also possible to look upon the heat transfer between a system and its environment as an exchange of an extensive property. In this way, only the existence of such a property is postulated. Its introduction is solely justified by the fact that all statements derived from it correspond with experience. This new extensive property is called entropy, and it is denoted S. Consequently, $U = U(V, S, \ldots)$. If only moving boundary work occurs and heat transfer occurs, $U = U(V, S)$. Differentiation leads to the *Gibbs equation*

$$\mathrm{d}U = T\mathrm{d}S - p\mathrm{d}V \tag{3.29}$$

with the thermodynamic temperature

$$T = \left(\frac{\partial U}{\partial S}\right)_V \tag{3.30}$$

and the pressure

$$p = -\left(\frac{\partial U}{\partial V}\right)_S . \tag{3.31}$$

A relationship equivalent to (3.29) can be derived by eliminating U and replacing it by the enthalpy $H = U + pV$, such that

$$\mathrm{d}H = T\mathrm{d}S + V\mathrm{d}p . \tag{3.32}$$

It can be shown that the thermodynamic temperature is identical to the temperature measured by a gas thermometer (Sect. 3.2.3). From examination of the characteristics of entropy, it follows, that in an isolated system which is initially in nonequilibrium (for example, because of a nonuniform temperature distribution) and then approaches equilibrium, the entropy always increases. In the borderline case of equilibrium, a maximum of entropy is reached. The internal entropy increase is denoted by $\mathrm{d}S_{\mathrm{gen}}$. For the considered case of an isolated system, it holds that

$$\mathrm{d}S = \mathrm{d}S_{\mathrm{gen}}$$

with $\mathrm{d}S_{\mathrm{gen}} > 0$. If a system is not isolated, the entropy is also changed by $\mathrm{d}S_{\mathrm{Q}}$ due to heat transfer (with the environment) and by $\mathrm{d}S_{\mathrm{m}}$ because of mass transfer with the environment. However, energy transfer by work with the environment does not change the system entropy. Thus, it holds generally that

$$\mathrm{d}S = \mathrm{d}S_{\mathrm{Q}} + \mathrm{d}S_{\mathrm{m}} + \mathrm{d}S_{\mathrm{gen}} . \tag{3.33}$$

The formulation for the time-variable system entropy $\dot{S} = \mathrm{d}S/\mathrm{d}\tau$ reads

$$\dot{S} = \dot{S}_{\mathrm{Q}} + \dot{S}_m + \dot{S}_{\mathrm{gen}} \tag{3.34}$$

with $\dot{S}_{\mathrm{gen}}$ being the entropy generation rate caused by internal irreversibilities; $\dot{S}_{\mathrm{Q}} + \dot{S}_{\mathrm{m}}$ is called the entropy flow. These values, which are exchanged across the system boundary, are combined thus

$$\dot{S}_{\mathrm{fl}} = \dot{S}_{\mathrm{Q}} + \dot{S}_{\mathrm{m}} . \tag{3.35}$$

The rate of change of the system entropy S therefore consists of the entropy flow $\dot{S}_{\mathrm{fl}}$ and the entropy generation $\dot{S}_{\mathrm{gen}}$:

$$\dot{S} = \dot{S}_{\mathrm{fl}} + \dot{S}_{\mathrm{gen}} . \tag{3.36}$$

For the entropy generation, it holds that

$$\begin{aligned} \dot{S}_{\mathrm{gen}} &= 0 \quad \text{for reversible processes,} \\ \dot{S}_{\mathrm{gen}} &> 0 \quad \text{for irreversible processes,} \\ \dot{S}_{\mathrm{gen}} &< 0 \quad \text{for impossible processes.} \end{aligned} \tag{3.37}$$

3.4.3 Special Formulations

Adiabatic Closed Systems

Since $\dot{S}_{\mathrm{Q}} = 0$ for adiabatic systems and $\dot{S}_{\mathrm{m}} = 0$ for closed systems, it follows that $\dot{S} = \dot{S}_{\mathrm{gen}}$. Thus, the entropy of an adiabatic closed system can never decrease. It can only increase during an irreversible process or remain constant during a reversible process. If an adiabatic closed system consists of α subsystems, then it holds for the sum of entropy changes ΔS^{α} of the subsystems that

$$\sum_{\alpha} \Delta S^{\alpha} \geq 0 . \tag{3.38}$$

With $\mathrm{d}S = \mathrm{d}S_{\mathrm{gen}}$, (3.29) reads for an adiabatic closed system

$$\mathrm{d}U = T\mathrm{d}S_{\mathrm{gen}} - p\mathrm{d}V .$$

On the other hand, it follows from the first law according to (3.17) that

$$\mathrm{d}W_{\mathrm{diss}} = T\mathrm{d}S_{\mathrm{gen}} = \mathrm{d}\Psi \tag{3.39}$$

or

$$W_{\mathrm{diss12}} = TS_{\mathrm{gen12}} = \Psi_{12} , \tag{3.40}$$

where Ψ_{12} is called the dissipated energy during the change in state 1–2. The dissipated energy is always

positive. This statement is true not only for adiabatic systems but also for all general cases, because, by definition, the entropy generation is the fraction of the entropy change that arises when the system is adiabatic and closed, and thus $\dot{S}_{\mathrm{fl}} = 0$ holds.

Systems with Heat Transfer

For closed systems with heat transfer, (3.29) becomes

$$\begin{aligned} \mathrm{d}U &= T\mathrm{d}S_{\mathrm{Q}} + T\mathrm{d}S_{\mathrm{gen}} - p\mathrm{d}V \\ &= T\mathrm{d}S_{\mathrm{Q}} + \mathrm{d}W_{\mathrm{diss}} - p\mathrm{d}V \,. \end{aligned} \tag{3.41}$$

A comparison with the first law, (3.17), results in

$$\mathrm{d}Q = T\mathrm{d}S_{\mathrm{Q}} \,. \tag{3.42}$$

Thus, heat transfer is energy transfer, which together with entropy crosses the system boundary, whereas work is exchanged without entropy exchange. Adding the always positive term $T\mathrm{d}S_{\mathrm{gen}}$ to the right-hand side of (3.42) leads to the *Clausius inequality*

$$\mathrm{d}Q \le T\mathrm{d}S \quad \text{or} \quad \Delta S \ge \int_1^2 \frac{\mathrm{d}Q}{T} \,. \tag{3.43}$$

In irreversible processes, the entropy change is larger than the integral over all $\mathrm{d}Q/T$; the equals sign is only valid for the reversible case. For open systems with heat addition, $\mathrm{d}S_{\mathrm{Q}}$ in (3.41) must be replaced by

$$\mathrm{d}S_{\mathrm{fl}} = \mathrm{d}S_{\mathrm{Q}} + \mathrm{d}S_{\mathrm{m}} \,.$$

3.5 Exergy and Anergy

According to the first law, the energy of an isolated system is constant. As it is possible to transform every nonisolated system into an isolated one by adding the environment, it is always possible to define a system in which the energy remains constant during a thermodynamic process. Thus, a loss of energy is not possible, and energy is only converted in a thermodynamic process. How much of the energy stored in a system is converted depends on the state of the environment. If it is in equilibrium with the system, no energy is converted. The larger the difference from equilibrium, the more energy of the system can be converted and thus the greater the potential to perform work.

Many thermodynamic processes take place in the Earth's atmosphere, which is the environment of most thermodynamic systems. In comparison with much smaller thermodynamic systems, the Earth's atmosphere can be considered as an infinitely large system, in which the intensive properties pressure, temperature, and composition do not change during a process (as long as daily and seasonal variations of the intensive properties are neglected). In many engineering processes, work is obtained by bringing a system with a given initial state into equilibrium with the environment. The maximum work is obtained when all changes of state are reversible.

The maximum work that could be obtained by establishing equilibrium with the environment is called the exergy W_{ex}.

3.5.1 Exergy of a Closed System

To calculate the exergy of a system at state 1, consider a process that brings the system reversibly into thermal and mechanical equilibrium with its environment. Equilibrium exists if the temperature of the system at the final state 2 is equal to the temperature of the environment, i.e., $T_2 = T_{\mathrm{env}}$, and if the pressure of the system in state 2 is equal to the pressure of the environment, i.e., $p_2 = p_{\mathrm{env}}$. Neglecting the kinetic and potential energy of the system, the first law according to (3.16) reads

$$U_2 - U_1 = Q_{12} + W_{12} \,. \tag{3.44}$$

To execute the entire process reversibly, it is necessary to bring the system to the environmental temperature through a reversible, adiabatic change of state. Then, heat transfer has to occur reversibly at the constant temperature T_{env}.

From the second law, (3.42), it follows for the heat transfer that

$$Q_{12} = T_{\mathrm{env}}(S_2 - S_1) \,. \tag{3.45}$$

The work W_{12} done on the system consists of the maximum useful work and the moving boundary work $-p_{\mathrm{env}}(V_2 - V_1)$, which is necessary to overcome the pressure of the environment. The maximum useful work is the exergy W_{ex}, thus it follows that

$$W_{12} = W_{\mathrm{ex}} - p_{\mathrm{env}}(V_2 - V_1) \,. \tag{3.46}$$

Inserting (3.45) and (3.46) into (3.44) gives

$$U_2 - U_1 = T_{\mathrm{env}}(S_2 - S_1) + W_{\mathrm{ex}} - p_{\mathrm{env}}(V_2 - V_1) \,. \tag{3.47}$$

In state 2, the system is in equilibrium with the environment, denoted by the index *env*. Thus, the exergy of

the closed system is

$$-W_{ex} = U_1 - U_{env} - T_{env}(S_1 - S_{env}) + p_{env}(V_1 - V_{env}) \,. \quad (3.48)$$

For a constant-volume system, it holds that $V_1 = V_{env}$ and the last term cancels. If the initial state of the system is already in equilibrium with the environment (state 1 = state env), according to (3.48), no work can be obtained.

Thus, it holds that the internal energy of the environment cannot be transformed into exergy. Consequently, the enormous energies stored in the atmosphere surrounding us cannot be used to power vehicles.

3.5.2 Exergy of an Open System

The maximum shaft work, or the exergy from a mass flow, is obtained when the mass flow is brought reversibly into equilibrium with the environment by performing work and heat transfer with the environment. Neglecting changes of kinetic and potential energies, the first law for steady flow processes in open systems, (3.22), reads

$$-W_{ex} = H_1 - H_{env} - T_{env}(S_1 - S_{env}) \,. \quad (3.49)$$

This means that only a part of the enthalpy, H_1 reduced by $H_{env} + T_{env}(S_1 - S_{env})$, is transformed into shaft work. If the heat transfer from the environment to the mass flow, $T_{env}(S_1 - S_{env})$, is negative, then the exergy exceeds the change in enthalpy by the fraction of this added heat.

3.5.3 Exergy and Heat Transfer

Figure 3.4 shows a device which is used to transform the heat transfer Q_{12} from an energy storage of temperature T into work W_{12}. The heat transfer Q_{env12}, which cannot be transformed into work, is rejected to the environment. The maximum shaft work is obtained if all changes in state are reversible. This maximum shaft work is equal to the exergy of the heat transfer. All changes in state are reversible if

$$\int_1^2 \frac{dQ}{T} + \int_1^2 \frac{dQ_{env}}{T_{env}} = 0$$

with $dQ + dQ_{env} + dW_{ex} = 0$ according to the first law. The resulting exergy of the heat transfer to machines and apparatuses is

$$-W_{ex} = \int_1^2 \left(1 - \frac{T_{env}}{T}\right) dQ \quad (3.50)$$

or in differential notation

$$-dW_{ex} = \left(1 - \frac{T_{env}}{T}\right) dQ \,. \quad (3.51)$$

In a reversible process, only the fraction of the supplied heat transfer multiplied by the so-called Carnot factor $1 - (T_{env}/T)$ can be transformed into work. The fraction $dQ_{env} = -T_{env}(dQ/T)$ has to be transferred to the environment, and it is impossible to obtain it as work. This shows additionally that the heat transfer, which is available at ambient temperature, cannot be transformed into exergy.

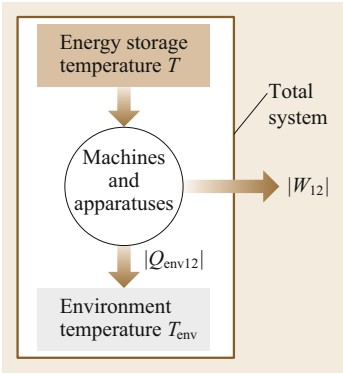

Fig. 3.4 Conversion of heat into work

3.5.4 Anergy

The energy that cannot be converted into exergy W_{ex} is denoted B. Each amount of energy consists of exergy W_{ex} and anergy B, i.e.,

$$E = W_{ex} + B \,. \quad (3.52)$$

Thus, it holds that:

- For a closed system according to (3.48) with $E = U_1$

$$B = U_{env} + T_{env}(S_1 - S_{env}) - p_{env}(V_1 - V_{env}) \quad (3.53)$$

- For an open system according to (3.49) with $E = H_1$

$$B = H_{env} + T_{env}(S_1 - S_{env}) \quad (3.54)$$

- For heat transfer according to (3.51) with $dE = dQ$

$$B = \int_1^2 \frac{T_{env}}{T} dQ \,. \quad (3.55)$$

3.5.5 Exergy Losses

The energy dissipated in a process is not lost completely. It increases the entropy, and because of $U(S, V)$, also the internal energy of a system. It is possible to think of the dissipated energy as heat transfer in a substitutional process, which is transferred from the outside ($\mathrm{d}\Psi = \mathrm{d}Q$) and causes the same entropy increase as in the irreversible process. Since the heat transfer $\mathrm{d}Q$, (3.51), is partly transformable into work, the fraction

$$-\mathrm{d}W_{\mathrm{ex}} = \left(1 - \frac{T_{\mathrm{env}}}{T}\right)\mathrm{d}\Psi \tag{3.56}$$

of the dissipated energy $\mathrm{d}\Psi$ can also be obtained as work (exergy). The remaining fraction $T_{\mathrm{env}}\mathrm{d}\Psi/T$ of the dissipated energy has to be transferred to the environment as heat transfer and is not transformable into work. This exergy loss is equal to the anergy of the dissipated energy and is, according to (3.55), given by

$$W_{\mathrm{loss}12} = \int_1^2 \frac{T_{\mathrm{env}}}{T}\mathrm{d}\Psi = \int_1^2 T_{\mathrm{env}}\mathrm{d}S_i\,. \tag{3.57}$$

For a process in a closed adiabatic system, it holds that $\mathrm{d}S_i = \mathrm{d}S$ and thus

$$W_{\mathrm{loss}12} = \int_1^2 T_{\mathrm{env}}\mathrm{d}S = T_{\mathrm{env}}(S_2 - S_1)\,. \tag{3.58}$$

In contrast to energy, exergy does not follow a conservation equation. The exergy transferred to a system at steady state is equal to the sum of the exergy transferred from the system plus exergy losses. The thermodynamic effect of losses caused by irreversibilities is more unfavorable when the process takes place at lower temperature T; see (3.57).

3.6 Thermodynamics of Substances

In order to utilize the primary laws of thermodynamics, which are generally set up for any arbitrary substance, and to calculate exergies and anergies, it is necessary to determine actual numerical values for the properties U, H, S, p, V, and T. Among these, U, H, and S are typically called caloric, whereas p, V, and T are known as thermal properties. The relationships between these properties depend on the corresponding substance. Equations that specify the relationships between the properties p, V, and T are called *equations of state*.

3.6.1 Thermal Properties of Gases and Vapors

An equation of state for pure substances is of the form

$$F(p, v, T) = 0 \tag{3.59}$$

or $p = p(v, T)$, $v = v(p, T)$, or $T = T(p, v)$. For calculations, equations of state of the form $v = v(p, T)$ are preferred, as the pressure and temperature are typically the independent variables used to describe a system.

Ideal Gases

A particularly simple equation of state is that for ideal gases

$$pV = mRT \quad \text{or} \quad pv = RT, \tag{3.60}$$

which relates the absolute pressure p, the volume V, the specific volume v, the individual gas constant R, and the thermodynamic temperature T. A gas is assumed to behave as an ideal gas only when the pressure is sufficiently low compared with the critical pressure p_{cr} of the substance, i.e., $p/p_{\mathrm{cr}} \to 0$.

Gas Constant and Avogadro's Law

As a measure of the amount of a given system, the *mole* is defined with the unit symbol mol. The amount of a substance is 1 mol when it contains as many identical elementary entities (i.e., molecules, atoms, or elementary particles) as there are atoms in exactly 12 g of pure carbon-12.

The number of particles of the same type contained in a mole is called Avogadro's number (in German literature the number is sometimes referred to as Loschmidt's number). It has the numerical value

$$N_{\mathrm{A}} = 6.02214076 \times 10^{23}\,/\mathrm{kmol}\,. \tag{3.61}$$

The mass of a mole (N_{A} particles of the same type) is a specific quantity for each substance and is referred to as the molar mass (see Table 3.4 for values), which is given by

$$M = \frac{m}{n} \tag{3.62}$$

(SI unit kg/kmol, m mass in kg, n molar amount in kmol). According to Avogadro (1811), ideal gases con-

Table 3.4 Critical data for some substances, ordered according to critical temperature (after [3.3–5])

	Symbol	M (kg/kmol)	P_{cr} (bar)	T_{cr} (K)	v_{cr} (dm³/kg)
Mercury	Hg	200.59	1490	1765	0.213
Aniline	C_6H_7N	93.1283	53.1	698.7	2.941
Water	H_2O	18.0153	220.55	647.13	3.11
Benzene	C_6H_6	78.1136	48.98	562.1	3.311
Ethyl alcohol	C_2H_5OH	46.0690	61.37	513.9	3.623
Diethyl ether	$C_4H_{10}O$	74.1228	36.42	466.7	3.774
Ethyl chloride	C_2H_5Cl	64.5147	52.7	460.4	2.994
Sulfur dioxide	SO_2	64.0588	78.84	430.7	1.901
Methyl chloride	CH_3Cl	50.4878	66.79	416.3	2.755
Ammonia	NH_3	17.0305	113.5	405.5	4.255
Hydrogen chloride	HCl	36.4609	83.1	324.7	2.222
Nitrous oxide	N_2O	44.0128	72.4	309.6	2.212
Acetylene	C_2H_2	26.0379	61.39	308.3	4.329
Ethane	C_2H_6	30.0696	48.72	305.3	4.926
Carbon dioxide	CO_2	44.0098	73.77	304.1	2.139
Ethylene	C_2H_4	28.0528	50.39	282.3	4.651
Methane	CH_4	16.0428	45.95	190.6	6.173
Nitric oxide	NO	30.0061	65	180	1.901
Oxygen	O_2	31.999	50.43	154.6	2.294
Argon	Ar	39.948	48.65	150.7	1.873
Carbon monoxide	CO	28.0104	34.98	132.9	3.322
Air	–	28.953	37.66	132.5	3.195
Nitrogen	N_2	28.0134	33.9	126.2	3.195
Hydrogen	H_2	2.0159	12.97	33.2	32.26
Helium-4	He	4.0026	2.27	5.19	14.29

tain an equal number of molecules at the same pressure and at the same temperature, occupying equal spaces.

After introducing the molar mass into the equation of state for ideal gases, (3.60), it follows that $pV/(nT) = MR$ has a fixed value for all gases

$$MR = R_u \,, \tag{3.63}$$

where R_u is called the universal gas constant, being a fundamental constant with the numerical value

$$R_u = 8.314472 \pm 1.5 \times 10^{-5}\,(\mathrm{kJ/(kmol\,K)}) \,. \tag{3.64}$$

Incorporating R_u, the equation of state for ideal gases reads

$$pV = nR_uT \,. \tag{3.65}$$

Example 3.6

A gas bottle of volume $V_1 = 200\,\mathrm{L}$ contains hydrogen at $p_1 = 120\,\mathrm{bar}$ and $t_1 = 10\,^\circ\mathrm{C}$. What space is occupied by the hydrogen at $p_2 = 1\,\mathrm{bar}$ and $t_2 = 0\,^\circ\mathrm{C}$, if the hydrogen is assumed to behave as an ideal gas? According to (3.65), $p_1V_1 = nRT_1$ and $p_2V_2 = nRT_2$; thus

$$V_2 = \frac{p_1T_2}{p_2T_1}V_1 = \frac{120\,\mathrm{bar} \times 273.15\,\mathrm{K}}{1\,\mathrm{bar} \times 283.15\,\mathrm{K}}0.2\,\mathrm{m}^3 = 23.15\,\mathrm{m}^3 \,. \tag{3.66}$$

Real Gases

The ideal gas equation of state is valid for real gases and vapors only as a limiting law at sufficiently low pressures. The deviation of the behavior of gaseous water from the ideal gas equation of state is shown in Fig. 3.5, in which $pv/(RT)$ is displayed against t for different pressures. The real gas factor Z, where $Z = pv/(RT)$, is equal to 1 for ideal gases, but deviates from this value for real gases. For air between 0 and 200 °C, and for hydrogen between −15 and 200 °C, the deviations of Z from ideal gas behavior are approximately 1% at a pressure of 20 bar. At atmospheric pressure, the deviations from the ideal gas law are negligible for nearly all gases. For cases where significant deviation is found from ideal gas behavior, different equations of state are established to describe the behavior of real gases. In one of the simplest forms, a series of additive correc-

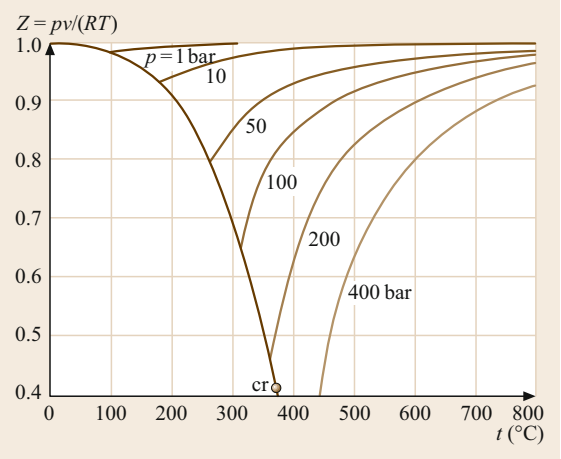

Fig. 3.5 The real gas factor of water vapor

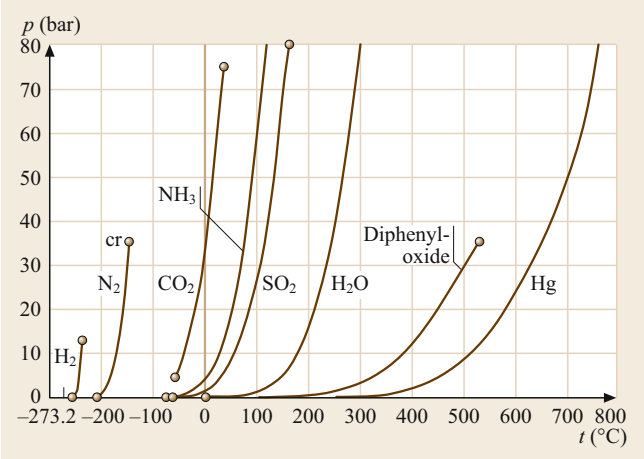

Fig. 3.6 Liquid–vapor saturation curves of some substances

tion terms are used to modify the real gas factor Z from the value of unity for the ideal gas case:

$$Z = \frac{pv}{RT} = 1 + \frac{B(T)}{v} + \frac{C(T)}{v^2} + \frac{D(T)}{v^3} , \qquad (3.67)$$

where B is called the second, C the third, and D the fourth virial coefficients. A compilation of second virial coefficients for many gases is provided by reference charts [3.6, 7]. The virial equation with two or three virial coefficients is only valid at moderate pressures. A balanced compromise between computational effort and achievable accuracy is given by the equation of state of Benedict–Webb–Rubin [3.8] for denser gases, which reads

$$Z = 1 + \frac{B(T)}{v} + \frac{C(T)}{v^2} + \frac{a\alpha}{v^5 RT} + \frac{c}{v^3 RT^2}\left(1 + \frac{\gamma}{v^2}\right)\exp\left(-\frac{\gamma}{v^2}\right) , \qquad (3.68)$$

with

$$B(T) = B_0 - \frac{A_0}{RT} - \frac{C_0}{RT^3} \quad \text{and} \quad C(T) = b - \frac{a}{RT} .$$

The equation contains eight constants A_0, B_0, C_0, a, b, c, α, and γ, which are available for many substances [3.8]. Highly exact equations of state are needed for the working substances water [3.9], air [3.10], and refrigerants [3.11] used in heat engines and refrigerators. The equations for these substances are more elaborate and contain more constants, and computer software is typically needed to utilize them.

Vapors

Vapors are gases which are close to saturation conditions and to condensation. A vapor is called *saturated* if the slightest temperature reduction leads to condensation, and *superheated* if a finite temperature reduction is necessary to obtain condensation. If heat is transferred to a liquid at constant pressure, the temperature of the liquid rises. When a certain temperature is reached, vapor at the same temperature begins to be generated, where the vapor and liquid are in equilibrium. This state is called the saturation state. It is characterized by corresponding values for *saturation temperature* and *saturation pressure*. Their interdependence is described by the *liquid–vapor saturation curve* in Fig. 3.6. It starts at the triple point and ends at the critical point (cr) of a substance. Above the critical state p_{cr}, T_{cr}, vapor and liquid are no longer separated by a clear boundary but merge continuously (Table 3.4). As with the triple point, at which the vapor, liquid, and solid phases of a substance are in equilibrium, every substance also has a characteristic critical point.

The vapor pressure of many substances is well approximated between the triple point and the boiling point at atmospheric pressure by the Antoine equation

$$\ln p = A - \frac{B}{C + T} , \qquad (3.69)$$

in which A, B, and C are the *Antoine coefficients* that vary from substance to substance (Table 3.5). If superheated vapor is compressed at constant temperature by reducing the volume, the pressure increases similar to an ideal gas almost like a hyperbola; e.g., see the 300 °C isotherm in Fig. 3.7. Condensation starts as soon as the saturation pressure is reached, and the volume is reduced without a pressure increase until all vapor is condensed. Any further volume reduction causes a considerable pressure increase. The band of curves in Fig. 3.7 is, as a graphical description of an

Table 3.5 Antoine equation ($\log_{10} p = A - \frac{B}{C+t}$, p in hPa, t in °C), constants for some substances (after [3.12])

Substance	*A*	*B*	*C*
Methane	6.82051	405.42	267.777
Ethane	6.95942	663.70	256.470
Propane	6.92888	803.81	246.99
Butane	6.93386	935.86	238.73
Isobutene	7.03538	946.35	246.68
Pentane	7.00122	1075.78	233.205
Isopentane	6.95805	1040.73	235.445
Neopentane	6.72917	883.42	227.780
Hexane	6.99514	1168.72	224.210
Heptane	7.01875	1264.37	216.636
Octane	7.03430	1349.82	209.385
Cyclopentane	7.01166	1124.162	231.361
Methylcyclopentane	6.98773	1186.059	226.042
Cyclohexane	6.96620	1201.531	222.647
Methylcyclohexane	6.94790	1270.763	221.416
Ethylene	6.87246	585.00	255.00
Propylene	6.94450	785.00	247.00
1-Butylene	6.96780	926.10	240.00
cis-2-Butylene	6.99416	960.100	237.000
trans-2-Butylene	6.99442	960.80	240.00
Isobutylene	6.96624	923.200	240.000
1-Pentylene	6.97140	1044.895	233.516
1-Hexylene	6.99063	1152.971	225.849
Propadiene	5.8386	458.06	196.07
1,3-Butadiene	6.97489	930.546	238.854
2-Methylbutadiene	7.01054	1071.578	233.513
Benzene	7.03055	1211.033	220.790
Toluene	7.07954	1344.800	219.482
Ethylbenzene	7.08209	1424.255	213.206
m-Xylene	7.13398	1462.266	215.105
p-Xylene	7.11542	1453.430	215.307
Isopropylbenzene	7.06156	1460.793	207.777
Water (90–100 °C)	8.0732991	1656.390	226.86

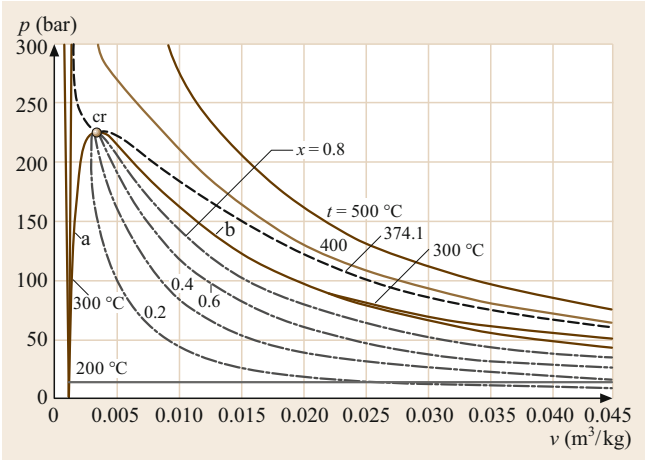

Fig. 3.7 p–V diagram of water

equation of state, characteristic for many substances. Connecting the specific volumes of the liquid at saturation temperature before evaporation and of the saturated vapor, v' and v'', results in two curves a and b, called the *saturated liquid line* and the *saturated vapor line*, which meet at the critical point. With the steam quality x, defined as the mass of the saturated vapor m'' related to the total mass of saturated vapor m'' and saturated liquid m', and the specific volumes v' of the saturated liquid and v'' of the saturated vapor, it holds for wet steam that

$$v = xv'' + (1-x)v' \,. \tag{3.70}$$

Lines of constant x are shown in Fig. 3.7.

Example 3.7

Consider 1000 kg of saturated wet steam at 121 bar in a vessel of 2 m^3 volume. How is the total mass distributed between liquid and vapor? An interpolation of the values in the saturated water table (Table 3.6) leads to the specific volumes $v' = 0.001530\,\mathrm{m^3/kg}$ of saturated liquid and $v'' = 0.01410\,\mathrm{m^3/kg}$ of saturated vapor at 121 bar. The average specific volume $v = V/m$ is $v = 2\,\mathrm{m^3}/1000\,\mathrm{kg} = 0.002\,\mathrm{m^3/kg}$. Equation (3.70) gives

$$\begin{aligned} x &= \frac{v - v'}{v'' - v'} \\ &= \frac{0.002 - 0.001530}{0.01410 - 0.001530} \\ &= 0.03739 \\ &= \frac{m''}{m} \,, \end{aligned}$$

and thus

$$\begin{aligned} m'' &= 1000 \times 0.03739\,\mathrm{kg} = 37.39\,\mathrm{kg} \,, \\ m' &= (1000 - 37.39)\,\mathrm{kg} = 962.61\,\mathrm{kg} \,. \end{aligned}$$

It is also possible to display the equation of state as a surface in space with coordinates p, v, and t (Fig. 3.8).

The two-dimensional diagrams in Figs. 3.6 and 3.7 are projections of this three-dimensional surface onto the respective planes.

3.6.2 Caloric Properties of Gases and Vapors

Ideal Gases

The internal energy of ideal gases depends only on temperature, $u = u(T)$, and thus also the enthalpy $h = u + pv = u + RT$ is solely a function of temperature, $h = h(T)$. The derivatives of u and h with respect to

Table 3.6 Saturated water temperature table (after [3.9])

t (°C)	p (bar)	v' (m^3/kg)	v'' (m^3/kg)	h' (kJ/kg)	h'' (kJ/kg)	Δh_v (kJ/kg)	s' (kJ/(kg K))	s'' (kJ/(kg K))
0.01	0.006117	0.001000	205.998	0.00	2500.91	2500.91	0.0000	9.1555
2	0.007060	0.001000	179.764	8.39	2504.57	2496.17	0.0306	9.1027
4	0.008135	0.001000	157.121	16.81	2508.24	2491.42	0.0611	9.0506
6	0.009354	0.001000	137.638	25.22	2511.91	2486.68	0.0913	8.9994
8	0.010730	0.001000	120.834	33.63	2515.57	2481.94	0.1213	8.9492
10	0.012282	0.001000	106.309	42.02	2519.23	2477.21	0.1511	8.8998
12	0.014028	0.001001	93.724	50.41	2522.89	2472.48	0.1806	8.8514
14	0.015989	0.001001	82.798	58.79	2526.54	2467.75	0.2099	8.8038
16	0.018188	0.001001	73.292	67.17	2530.19	2463.01	0.2390	8.7571
18	0.020647	0.001001	65.003	75.55	2533.83	2458.28	0.2678	8.7112
20	0.023392	0.001002	57.762	83.92	2537.47	2453.55	0.2965	8.6661
22	0.026452	0.001002	51.422	92.29	2541.10	2448.81	0.3250	8.6218
24	0.029856	0.001003	45.863	100.66	2544.73	2444.08	0.3532	8.5783
26	0.033637	0.001003	40.977	109.02	2548.35	2439.33	0.3813	8.5355
28	0.037828	0.001004	36.675	117.38	2551.97	2434.59	0.4091	8.4934
30	0.042467	0.001004	32.882	125.75	2555.58	2429.84	0.4368	8.4521
32	0.047593	0.001005	29.529	134.11	2559.19	2425.08	0.4643	8.4115
34	0.053247	0.001006	26.562	142.47	2562.79	2420.32	0.4916	8.3715
36	0.059475	0.001006	23.932	150.82	2566.38	2415.56	0.5187	8.3323
38	0.066324	0.001007	21.595	159.18	2569.96	2410.78	0.5457	8.2936
40	0.073844	0.001008	19.517	167.54	2573.54	2406.00	0.5724	8.2557
42	0.082090	0.001009	17.665	175.90	2577.11	2401.21	0.5990	8.2183
44	0.091118	0.001009	16.013	184.26	2580.67	2396.42	0.6255	8.1816
46	0.10099	0.001010	14.535	192.62	2584.23	2391.61	0.6517	8.1454
48	0.11176	0.001011	13.213	200.98	2587.77	2386.80	0.6778	8.1099
50	0.12351	0.001012	12.028	209.34	2591.31	2381.97	0.7038	8.0749
52	0.13631	0.001013	10.964	217.70	2594.84	2377.14	0.7296	8.0405
54	0.15022	0.001014	10.007	226.06	2598.35	2372.30	0.7552	8.0066
56	0.16532	0.001015	9.145	234.42	2601.86	2367.44	0.7807	7.9733
58	0.18171	0.001016	8.369	242.79	2605.36	2362.57	0.8060	7.9405
60	0.19946	0.001017	7.668	251.15	2608.85	2357.69	0.8312	7.9082
62	0.21866	0.001018	7.034	259.52	2612.32	2352.80	0.8563	7.8764
64	0.23942	0.001019	6.460	267.89	2615.78	2347.89	0.8811	7.8451
66	0.26183	0.001020	5.940	276.27	2619.23	2342.97	0.9059	7.8142
68	0.28599	0.001022	5.468	284.64	2622.67	2338.03	0.9305	7.7839
70	0.31201	0.001023	5.040	293.02	2626.10	2333.08	0.9550	7.7540
72	0.34000	0.001024	4.650	301.40	2629.51	2328.11	0.9793	7.7245
74	0.37009	0.001025	4.295	309.78	2632.91	2323.13	1.0035	7.6955
76	0.40239	0.001026	3.971	318.17	2636.29	2318.13	1.0276	7.6669
78	0.43703	0.001028	3.675	326.56	2639.66	2313.11	1.0516	7.6388
80	0.47415	0.001029	3.405	334.95	2643.01	2308.07	1.0754	7.6110
82	0.51387	0.001030	3.158	343.34	2646.35	2303.01	1.0991	7.5837
84	0.55636	0.001032	2.932	351.74	2649.67	2297.93	1.1227	7.5567
86	0.60174	0.001033	2.724	360.15	2652.98	2292.83	1.1461	7.5301
88	0.65017	0.001035	2.534	368.56	2656.26	2287.70	1.1694	7.5039
90	0.70182	0.001036	2.359	376.97	2659.53	2282.56	1.1927	7.4781
92	0.75685	0.001037	2.198	385.38	2662.78	2277.39	1.2158	7.4526
94	0.81542	0.001039	2.050	393.81	2666.01	2272.20	1.2387	7.4275
96	0.87771	0.001040	1.914	402.23	2669.22	2266.98	1.2616	7.4027
98	0.94390	0.001042	1.788	410.66	2672.40	2261.74	1.2844	7.3782
100	1.0142	0.001043	1.672	419.10	2675.57	2256.47	1.3070	7.3541
105	1.2090	0.001047	1.418	440.21	2683.39	2243.18	1.3632	7.2951
110	1.4338	0.001052	1.209	461.36	2691.07	2229.70	1.4187	7.2380

Table 3.6 (continued)

t (°C)	p (bar)	v' (m^3/kg)	v'' (m^3/kg)	h' (kJ/kg)	h'' (kJ/kg)	Δh_v (kJ/kg)	s' (kJ/(kg K))	s'' (kJ/(kg K))
115	1.6918	0.001056	1.036	482.55	2698.58	2216.03	1.4735	7.1827
120	1.9867	0.001060	0.8913	503.78	2705.93	2202.15	1.5278	7.1291
125	2.3222	0.001065	0.7701	525.06	2713.11	2188.04	1.5815	7.0770
130	2.7026	0.001070	0.6681	546.39	2720.09	2173.70	1.6346	7.0264
135	3.1320	0.001075	0.5818	567.77	2726.87	2159.10	1.6872	6.9772
140	3.6150	0.001080	0.5085	589.20	2733.44	2144.24	1.7393	6.9293
145	4.1564	0.001085	0.4460	610.69	2739.80	2129.10	1.7909	6.8826
150	4.7610	0.001091	0.3925	632.25	2745.92	2113.67	1.8420	6.8370
155	5.4342	0.001096	0.3465	653.88	2751.80	2097.92	1.8926	6.7926
160	6.1814	0.001102	0.3068	675.57	2757.43	2081.86	1.9428	6.7491
165	7.0082	0.001108	0.2725	697.35	2762.80	2065.45	1.9926	6.7066
170	7.9205	0.001114	0.2426	719.21	2767.89	2048.69	2.0419	6.6649
175	8.9245	0.001121	0.2166	741.15	2772.70	2031.55	2.0909	6.6241
180	10.026	0.001127	0.1939	763.19	2777.22	2014.03	2.1395	6.5841
185	11.233	0.001134	0.1739	785.32	2781.43	1996.10	2.1878	6.5447
190	12.550	0.001141	0.1564	807.57	2785.31	1977.75	2.2358	6.5060
195	13.986	0.001149	0.1409	829.92	2788.86	1958.94	2.2834	6.4679
200	15.547	0.001157	0.1272	852.39	2792.06	1939.67	2.3308	6.4303
205	17.240	0.001164	0.1151	874.99	2794.90	1919.90	2.3779	6.3932
210	19.074	0.001173	0.1043	897.73	2797.35	1899.62	2.4248	6.3565
215	21.056	0.001181	0.09469	920.61	2799.41	1878.80	2.4714	6.3202
220	23.193	0.001190	0.08610	943.64	2801.05	1857.41	2.5178	6.2842
225	25.494	0.001199	0.07841	966.84	2802.26	1835.42	2.5641	6.2485
230	27.968	0.001209	0.07151	990.21	2803.01	1812.80	2.6102	6.2131
235	30.622	0.001219	0.06530	1013.77	2803.28	1789.52	2.6561	6.1777
240	33.467	0.001229	0.05971	1037.52	2803.06	1765.54	2.7019	6.1425
245	36.509	0.001240	0.05466	1061.49	2802.31	1740.82	2.7477	6.1074
250	39.759	0.001252	0.05009	1085.69	2801.01	1715.33	2.7934	6.0722
255	43.227	0.001264	0.04594	1110.13	2799.13	1689.01	2.8391	6.0370
260	46.921	0.001276	0.04218	1134.83	2796.64	1661.82	2.8847	6.0017
265	50.851	0.001289	0.03875	1159.81	2793.51	1633.70	2.9304	5.9662
270	55.028	0.001303	0.03562	1185.09	2789.69	1604.60	2.9762	5.9304
275	59.463	0.001318	0.03277	1210.70	2785.14	1574.44	3.0221	5.8943
280	64.165	0.001333	0.03015	1236.67	2779.82	1543.15	3.0681	5.8578
285	69.145	0.001349	0.02776	1263.02	2773.67	1510.65	3.1143	5.8208
290	74.416	0.001366	0.02556	1289.80	2766.63	1476.84	3.1608	5.7832
295	79.990	0.001385	0.02353	1317.03	2758.63	1441.60	3.2076	5.7449
300	85.877	0.001404	0.02166	1344.77	2749.57	1404.80	3.2547	5.7058
305	92.092	0.001425	0.01994	1373.07	2739.38	1366.30	3.3024	5.6656
310	98.647	0.001448	0.01834	1402.00	2727.92	1325.92	3.3506	5.6243
315	105.56	0.001472	0.01686	1431.63	2715.08	1283.45	3.3994	5.5816
320	112.84	0.001499	0.01548	1462.05	2700.67	1238.62	3.4491	5.5373
325	120.51	0.001528	0.01419	1493.37	2684.48	1191.11	3.4997	5.4911
330	128.58	0.001561	0.01298	1525.74	2666.25	1140.51	3.5516	5.4425
335	137.07	0.001597	0.01185	1559.34	2645.60	1086.26	3.6048	5.3910
340	146.00	0.001638	0.01078	1594.45	2622.07	1027.62	3.6599	5.3359
345	155.40	0.001685	0.009770	1631.44	2595.01	963.57	3.7175	5.2763
350	165.29	0.001740	0.008801	1670.86	2563.59	892.73	3.7783	5.2109
355	175.70	0.001808	0.007866	1713.71	2526.45	812.74	3.8438	5.1377
360	186.66	0.001895	0.006945	1761.49	2480.99	719.50	3.9164	5.0527
365	198.22	0.002016	0.006004	1817.59	2422.00	604.41	4.0010	4.9482
370	210.43	0.002222	0.004946	1892.64	2333.50	440.86	4.1142	4.7996
373.946	220.64	0.003106	0.003106	2087.55	2087.55	0.00	4.4120	4.4120

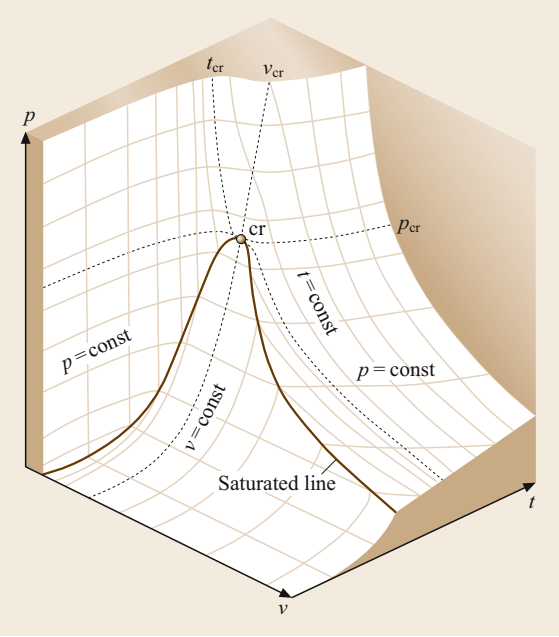

Fig. 3.8 Area of states for water

temperature are called *specific heats*. The specific heats are also functions of temperature (Table 3.7 for values of air).

$$\frac{\mathrm{d}u}{\mathrm{d}T} = c_v \tag{3.71}$$

is the specific heat at constant volume and

$$\frac{\mathrm{d}h}{\mathrm{d}T} = c_p \tag{3.72}$$

is the specific heat at constant pressure. The derivative of $h - u = RT$ is

$$c_p - c_v = R\,. \tag{3.73}$$

The difference between the molar specific heats $\overline{C}_p = Mc_p$ and $\overline{C}_v = Mc_v$ is equal to the universal gas constant

$$\overline{C}_p - \overline{C}_v = R_\mathrm{u}\,.$$

The specific heat ratio $\varkappa = c_p/c_v$ plays an important role in reversible adiabatic changes of state and is hence also called an *adiabatic exponent*.

Fairly accurately, the specific heat ratio is $\varkappa = 1.66$ for monatomic gases, $\varkappa = 1.40$ for diatomic gases, and $\varkappa = 1.30$ for triatomic gases. The average specific heat is the integral mean value defined by

$$\left[c_p\right]_{t_1}^{t_2} = \frac{1}{t_2 - t_1}\int_{t_1}^{t_2} c_p \mathrm{d}t\,,$$

$$\left[c_v\right]_{t_1}^{t_2} = \frac{1}{t_2 - t_1}\int_{t_1}^{t_2} c_v \mathrm{d}t\,. \tag{3.74}$$

From (3.71) and (3.72), it follows for the change of internal energy and enthalpy that

$$u_2 - u_1 = \left[c_v\right]_{t_1}^{t_2}(t_2 - t_1) = \left[c_v\right]_0^{t_2} t_2 - \left[c_v\right]_0^{t_1} t_1 \tag{3.75}$$

and

$$h_2 - h_1 = \left[c_p\right]_{t_1}^{t_2}(t_2 - t_1) = \left[c_p\right]_0^{t_2} t_2 - \left[c_p\right]_0^{t_1} t_1\,. \tag{3.76}$$

Numerical values for $\left[c_p\right]_0^t$ and $\left[c_v\right]_0^t$ can be determined from the average molar specific heats given in Table 3.8.

Taking into account (3.71) and (3.60), the specific entropy arises from (3.29) as

$$\mathrm{d}s = \frac{\mathrm{d}u + p\mathrm{d}v}{T} = c_v\frac{\mathrm{d}T}{T} + R\frac{\mathrm{d}v}{v}\,, \tag{3.77}$$

or after integration with $c_v = \text{const}$ as

$$s_2 - s_1 = c_v \ln\frac{T_2}{T_1} + R\ln\frac{v_2}{v_1}\,. \tag{3.78}$$

The integration of (3.32) with constant c_p leads to the equivalent equation

$$s_2 - s_1 = c_p \ln\frac{T_2}{T_1} + R\ln\frac{p_2}{p_1}\,. \tag{3.79}$$

Real Gases and Vapors

The caloric properties of real gases and vapors are usually determined by measurements, but it is also possible to derive them, apart from an initial value, from equations of state. They are displayed in tables and diagrams

Table 3.7 Specific heats of air at different pressures calculated with the equation of state (after [3.10])

p (bar)		1	25	50	100	150	200	300	
$t = 0\,°C$	$c_p =$	1.0065	1.0579	1.1116	1.2156	1.3022	1.3612	1.4087	kJ/(kg K)
$t = 50\,°C$	$c_p =$	1.0080	1.0395	1.0720	1.1335	1.1866	1.2288	1.2816	kJ/(kg K)
$t = 100\,°C$	$c_p =$	1.0117	1.0330	1.0549	1.0959	1.1316	1.1614	1.2045	kJ/(kg K)

Table 3.8 Mean molar specific heats $[\bar{C}_p]_0^t$ of ideal gases in kJ/(kmol K) between 0 and t °C. The mean molar specific heat $[\bar{C}_v]_0^t$ is determined by subtracting the value of the universal gas constant 8.3143 kJ/(kmol K) from the numerical values given in the table. For the conversion to 1 kg, the numerical values have to be divided by the molar weights given in the last line

t (°C)	$[\bar{C}_p]_0^t$ (kJ/(kmol K))							
	H_2	N_2	O_2	CO	H_2O	CO_2	Air	NH_3
0	28.6202	29.0899	29.2642	29.1063	33.4708	35.9176	29.0825	34.99
100	28.9427	29.1151	29.5266	29.1595	33.7121	38.1699	29.1547	36.37
200	29.0717	29.1992	29.9232	29.2882	34.0831	40.1275	29.3033	38.13
300	29.1362	29.3504	30.3871	29.4982	34.5388	41.8299	29.5207	40.02
400	29.1886	29.5632	30.8669	29.7697	35.0485	43.3299	29.7914	41.98
500	29.2470	29.8209	31.3244	30.0805	35.5888	44.6584	30.0927	44.04
600	29.3176	30.1066	31.7499	30.4080	36.1544	45.8462	30.4065	46.09
700	29.4083	30.4006	32.1401	30.7356	36.7415	46.9063	30.7203	48.01
800	29.5171	30.6947	32.4920	31.0519	37.3413	47.8609	31.0265	49.85
900	29.6461	30.9804	32.8151	31.3571	37.9482	48.7231	31.3205	51.53
1000	29.7892	31.2548	33.1094	31.6454	38.5570	49.5017	31.5999	53.08
1100	29.9485	31.5181	33.3781	31.9198	39.1621	50.2055	31.8638	54.50
1200	30.1158	31.7673	33.6245	32.1717	39.7583	50.8522	32.1123	55.84
1300	30.2891	31.9998	33.8548	32.4097	40.3418	51.4373	32.3458	57.06
1400	30.4705	32.2182	34.0723	32.6308	40.9127	51.9783	32.5651	58.14
1500	30.6540	32.4255	34.2771	32.8380	41.4675	52.4710	32.7713	59.19
1600	30.8394	32.6187	34.4690	33.0312	42.0042	52.9285	32.9653	60.20
1700	31.0248	32.7979	34.6513	33.2103	42.5229	53.3508	33.1482	61.12
1800	31.2103	32.9688	34.8305	33.3811	43.0254	53.7423	33.3209	61.95
1900	31.3937	33.1284	35.0000	33.5379	43.5081	54.1030	33.4843	62.75
2000	31.5751	33.2797	35.1664	33.6890	43.9745	54.4418	33.6392	63.46
M (kg/kmol)	2.01588	28.01340	31.999	28.01040	18.01528	44.00980	28.953	17.03052

as $u = u(v,T)$, $h = h(p,T)$, $s = s(p,T)$, $c_v = c_v(v,T)$, and $c_p = c_p(p,T)$. Often, computer software is necessary to analyze equations of state.

For vapors, it holds that the enthalpy h'' of the saturated vapor differs from the enthalpy h' of the saturated boiling liquid at p, T = const by the enthalpy of vaporization

$$\Delta h_v = h'' - h' \,, \tag{3.80}$$

which decreases with increasing temperature and reaches zero at the critical point, where $h'' = h'$. The enthalpy of wet vapor is

$$h = (1-x)h' + xh'' = h' + x\Delta h_v \,. \tag{3.81}$$

Accordingly, the internal energy is

$$u = (1-x)u' + xu'' = u' + x(u'' - u') \tag{3.82}$$

and the entropy

$$s = (1-x)s' + xs'' = \frac{s' + x\Delta h_v}{T} \,, \tag{3.83}$$

because the enthalpy of vaporization and the entropy of vaporization $s'' - s'$ are related through

$$\Delta h_v = T(s'' - s') \,. \tag{3.84}$$

According to the Clausius–Clapeyron relation, the enthalpy of vaporization with gradient $\mathrm{d}p/\mathrm{d}T$ is connected to the liquid–vapor saturation curve $p(T)$ via

$$\Delta h_v = T(v'' - v')\frac{\mathrm{d}p}{\mathrm{d}T} \,, \tag{3.85}$$

with T being the saturation temperature at pressure p. This relationship can be used to calculate the remaining quantity when two out of the three quantities Δh_v, $v'' - v'$, and $\mathrm{d}p/\mathrm{d}T$ are known.

If properties do not have to be calculated continuously or if powerful computers are not available, saturated water tables, in which the results of theoretical and experimental investigations are collected, are used for practical calculations. Such tables are collected in Tables 3.6–3.12 for working fluids important in engineering. Diagrams are advantageous to determine reference values and to display changes of state, e.g., a t–s diagram as shown in Fig. 3.9. Most com-

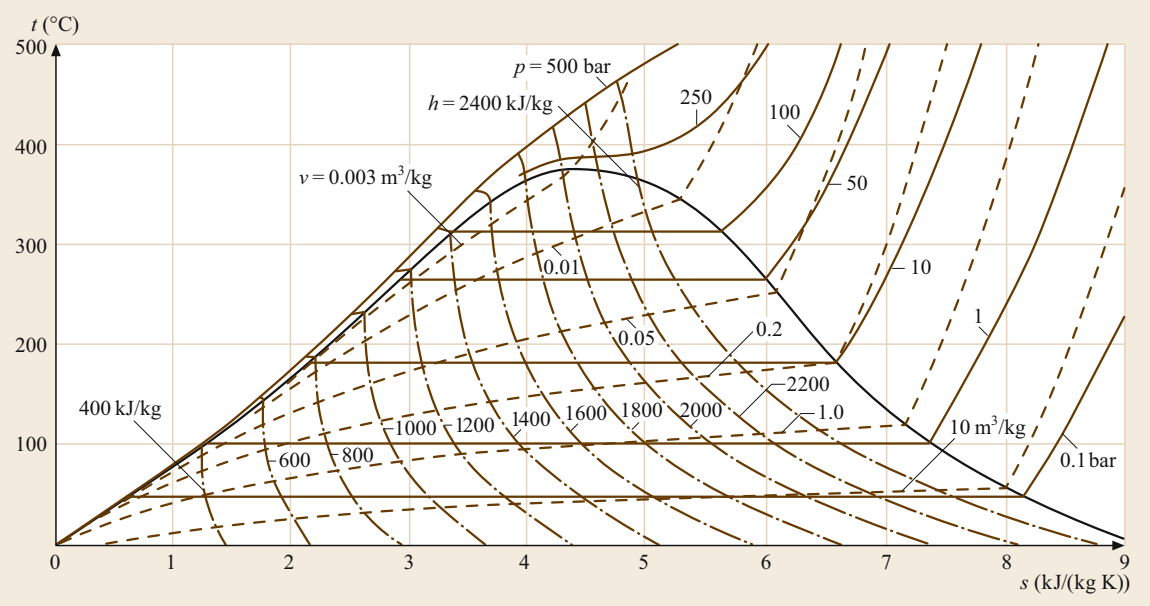

Fig. 3.9 *t–s* diagram of water with curves $p = \text{const}$ (*solid lines*), $v = \text{const}$ (*dashed lines*), and $h = \text{const}$ (*dash-dotted lines*)

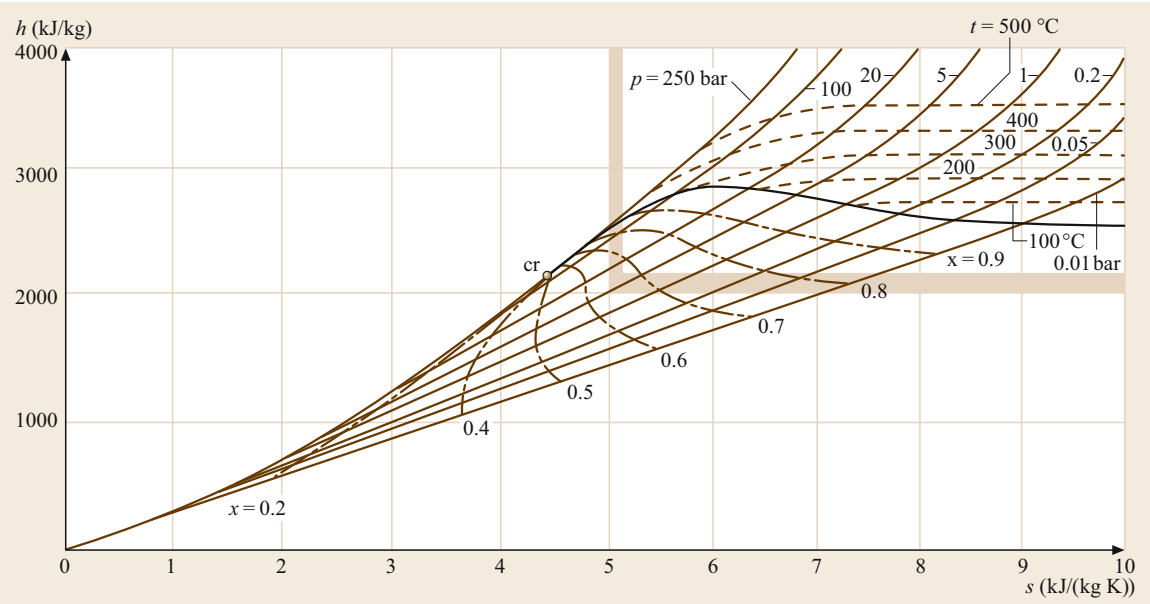

Fig. 3.10 *h–s* diagram of water with curves $p = \text{const}$ (*solid lines*), $t = \text{const}$ (*dashed lines*), and $x = \text{const}$ (*dot* and *dash lines*). The area of interest for the purpose of vapor technology is marked by the *hatched boundary*

monly used in practice are Mollier diagrams, which include the enthalpy as one of the coordinates, see Fig. 3.10.

The specific heat $c_p = (\partial h/\partial T)_p$ of vapor depends, as well as on temperature, also considerably on pressure. In the same way, $c_v = (\partial u/\partial T)_v$ depends, besides on temperature, also on the specific volume. Approaching the saturated vapor line, the c_p of the superheated vapor increases considerably with decreasing temperature and tends toward infinity at the critical point. While $c_p - c_v$ is a constant for ideal gases, this is not true for vapors.

Table 3.9 Properties of water and superheated water vapor (after [3.9])

$p \rightarrow$	1 bar t_s = 99.61 °C			5 bar t_s = 151.884 °C			10 bar t_s = 179.89 °C			15 bar t_s = 198.330 °C		
	v''	h''	s''	v''	h''	s''	v''	h''	s''	v''	h''	s''
	1.69402	2674.9	7.3588	0.37480	2748.1	6.8206	0.19435	2777.1	6.5850	0.13170	2791.0	6.4431
t	v	h	s	v	h	s	v	h	s	v	h	s
(°C)	(m^3/kg)	(kJ/kg)	(kJ/(kg K))	(m^3/kg)	(kJ/kg)	(kJ/(kg K))	(m^3/kg)	(kJ/kg)	(kJ/(kg K))	(m^3/kg)	(kJ/kg)	(kJ/(kg K))
0	0.001000	0.06	−0.0001	0.001000	0.47	−0.0001	0.001000	0.98	−0.0001	0.000999	1.48	−0.0001
10	0.001000	42.12	0.1511	0.001000	42.51	0.1510	0.001000	42.99	0.1510	0.001000	43.48	0.1510
20	0.001002	84.01	0.2965	0.001002	84.39	0.2964	0.001001	84.86	0.2963	0.001001	85.33	0.2962
40	0.001008	167.62	0.5724	0.001008	167.98	0.5722	0.001007	168.42	0.5720	0.001007	168.86	0.5719
60	0.001017	251.22	0.8312	0.001017	251.56	0.8310	0.001017	251.98	0.8307	0.001016	252.40	0.8304
80	0.001029	334.99	1.0754	0.001029	335.31	1.0751	0.001029	335.71	1.0748	0.001028	336.10	1.0744
100	1.695959	2675.77	7.3610	0.001043	419.40	1.3067	0.001043	419.77	1.3063	0.001043	420.15	1.3059
120	1.793238	2716.61	7.4676	0.001060	504.00	1.5275	0.001060	504.35	1.5271	0.001060	504.70	1.5266
140	1.889133	2756.70	7.5671	0.001080	589.29	1.7391	0.001079	589.61	1.7386	0.001079	589.94	1.7381
160	1.984139	2796.42	7.6610	0.383660	2767.38	6.8655	0.001102	675.80	1.9423	0.001101	676.09	1.9417
180	2.078533	2835.97	7.7503	0.404655	2812.45	6.9672	0.194418	2777.43	6.5857	0.001127	763.44	2.1389
200	2.172495	2875.48	7.8356	0.425034	2855.90	7.0611	0.206004	2828.27	6.6955	0.132441	2796.02	6.4537
220	2.266142	2915.02	7.9174	0.445001	2898.40	7.1491	0.216966	2875.55	6.7934	0.140630	2850.19	6.5658
240	2.359555	2954.66	7.9962	0.464676	2940.31	7.2324	0.227551	2920.98	6.8837	0.148295	2900.00	6.6649
260	2.452789	2994.45	8.0723	0.484135	2981.88	7.3119	0.237871	2965.23	6.9683	0.155637	2947.45	6.7556
280	2.545883	3034.40	8.1458	0.503432	3023.28	7.3881	0.247998	3008.71	7.0484	0.162752	2993.37	6.8402
300	2.638868	3074.54	8.2171	0.522603	3064.60	7.4614	0.257979	3051.70	7.1247	0.169699	3038.27	6.9199
320	2.731763	3114.89	8.2863	0.541675	3105.93	7.5323	0.267848	3094.40	7.1979	0.176521	3082.48	6.9957
340	2.824585	3155.45	8.3536	0.560667	3147.32	7.6010	0.277629	3136.93	7.2685	0.183245	3126.25	7.0683
360	2.917346	3196.24	8.4190	0.579594	3188.83	7.6676	0.287339	3179.39	7.3366	0.189893	3169.75	7.1381
380	3.010056	3237.27	8.4828	0.598467	3230.48	7.7323	0.296991	3221.86	7.4026	0.196478	3213.09	7.2055
400	3.102722	3278.54	8.5451	0.617294	3272.29	7.7954	0.306595	3264.39	7.4668	0.203012	3256.37	7.2708
420	3.195351	3320.06	8.6059	0.636083	3314.29	7.8569	0.316158	3307.01	7.5292	0.209504	3299.64	7.3341
440	3.287948	3361.83	8.6653	0.654838	3356.49	7.9169	0.325687	3349.76	7.5900	0.215960	3342.96	7.3957
460	3.380516	3403.86	8.7234	0.673565	3398.90	7.9756	0.335186	3392.66	7.6493	0.222385	3386.37	7.4558
480	3.473061	3446.15	8.7803	0.692267	3441.54	8.0329	0.344659	3435.74	7.7073	0.228784	3429.90	7.5143
500	3.565583	3488.71	8.8361	0.710947	3484.41	8.0891	0.354110	3479.00	7.7640	0.235160	3473.57	7.5716
520	3.658087	3531.53	8.8907	0.729607	3527.52	8.1442	0.363541	3522.47	7.8195	0.241515	3517.40	7.6275
540	3.750573	3574.63	8.9444	0.748250	3570.87	8.1981	0.372955	3566.15	7.8739	0.247854	3561.41	7.6823
560	3.843045	3618.00	8.9971	0.766878	3614.48	8.2511	0.382354	3610.05	7.9272	0.254176	3605.61	7.7360
580	3.935503	3661.65	9.0489	0.785493	3658.34	8.3031	0.391738	3654.19	7.9795	0.260485	3650.02	7.7887

Table 3.9 (continued)

$p \rightarrow$	1 bar t_s = 99.61 °C			5 bar t_s = 151.884 °C			10 bar t_s = 179.89 °C			15 bar t_s = 198.330 °C		
	v''	h''	s''	v''	h''	s''	v''	h''	s''	v''	h''	s''
	1.69402	2674.9	7.3588	0.37480	2748.1	6.8206	0.19435	2777.1	6.5850	0.13170	2791.0	6.4431
t (°C)	v (m^3/kg)	h (kJ/kg)	s (kJ/(kg K))	v (m^3/kg)	h (kJ/kg)	s (kJ/(kg K))	v (m^3/kg)	h (kJ/kg)	s (kJ/(kg K))	v (m^3/kg)	h (kJ/kg)	s (kJ/(kg K))
600	4.027949	3705.57	9.0998	0.804095	3702.46	8.3543	0.401111	3698.56	8.0309	0.266781	3694.64	7.8404
620	4.120384	3749.77	9.1498	0.822687	3746.84	8.4045	0.410472	3743.17	8.0815	0.273066	3739.48	7.8912
640	4.212810	3794.26	9.1991	0.841269	3791.49	8.4539	0.419824	3788.03	8.1311	0.279341	3784.55	7.9411
660	4.305227	3839.02	9.2476	0.859842	3836.41	8.5026	0.429167	3833.14	8.1800	0.285608	3829.86	7.9902
680	4.397636	3884.06	9.2953	0.878406	3881.59	8.5505	0.438502	3878.50	8.2281	0.291866	3875.40	8.0384
700	4.490037	3929.38	9.3424	0.896964	3927.05	8.5977	0.447829	3924.12	8.2755	0.298117	3921.18	8.0860
720	4.582433	3974.99	9.3888	0.915516	3972.77	8.6442	0.457150	3970.00	8.3221	0.304361	3967.22	8.1328
740	4.674822	4020.87	9.4345	0.934061	4018.77	8.6901	0.466465	4016.14	8.3681	0.310600	4013.50	8.1789
760	4.767206	4067.04	9.4796	0.952601	4065.04	8.7353	0.475775	4062.54	8.4135	0.316833	4060.03	8.2244
780	4.859585	4113.48	9.5241	0.971136	4111.58	8.7799	0.485080	4109.21	8.4582	0.323061	4106.82	8.2693
800	4.951960	4160.21	9.5681	0.989667	4158.40	8.8240	0.494380	4156.14	8.5024	0.329284	4153.87	8.3135

Table 3.9 (continued)

$p \rightarrow$	20 bar t_s = 212.38 °C			25 bar t_s = 223.96 °C			50 bar t_s = 263.94 °C			100 bar t_s = 311.0 °C		
	v''	h''	s''	v''	h''	s''	v''	h''	s''	v''	h''	s''
	0.09958	2798.4	6.3392	0.07995	2802.0	6.2560	0.03945	2794.2	5.9737	0.01803	2725.5	5.6159
t (°C)	v (m^3/kg)	h (kJ/kg)	s (kJ/(kg K))	v (m^3/kg)	h (kJ/kg)	s (kJ/(kg K))	v (m^3/kg)	h (kJ/kg)	s (kJ/(kg K))	v (m^3/kg)	h (kJ/kg)	s (kJ/(kg K))
0	0.000999	1.99	0.0000	0.000999	2.50	0.0000	0.000998	5.03	0.0001	0.000995	10.07	0.0003
10	0.000999	43.97	0.1509	0.000999	44.45	0.1509	0.000998	46.88	0.1506	0.000996	51.72	0.1501
20	0.001001	85.80	0.2961	0.001001	86.27	0.2960	0.001000	88.61	0.2955	0.000997	93.29	0.2944
40	0.001007	169.31	0.5717	0.001007	169.75	0.5715	0.001006	171.96	0.5705	0.001004	176.37	0.5685
60	0.001016	252.82	0.8302	0.001016	253.24	0.8299	0.001015	255.33	0.8286	0.001013	259.53	0.8259
80	0.001028	336.50	1.0741	0.001028	336.90	1.0738	0.001027	338.89	1.0721	0.001024	342.87	1.0689
100	0.001042	420.53	1.3055	0.001042	420.90	1.3051	0.001041	422.78	1.3032	0.001039	426.55	1.2994
120	0.001059	505.05	1.5262	0.001059	505.40	1.5257	0.001058	507.17	1.5235	0.001055	510.70	1.5190
140	0.001079	590.26	1.7376	0.001078	590.59	1.7371	0.001077	592.22	1.7345	0.001074	595.49	1.7294
160	0.001101	676.38	1.9411	0.001101	676.67	1.9405	0.001099	678.14	1.9376	0.001095	681.11	1.9318
180	0.001127	763.69	2.1382	0.001126	763.94	2.1375	0.001124	765.22	2.1341	0.001120	767.81	2.1274
200	0.001156	852.57	2.3301	0.001156	852.77	2.3293	0.001153	853.80	2.3254	0.001148	855.92	2.3177

Table 3.9 (continued)

$p \rightarrow$	20 bar t_s = 212.38 °C			25 bar t_s = 223.96 °C			50 bar t_s = 263.94 °C			100 bar t_s = 311.0 °C		
	v''	h''	s''	v''	h''	s''	v''	h''	s''	v''	h''	s''
	0.09958	2798.4	6.3392	0.07995	2802.0	6.2560	0.03945	2794.2	5.9737	0.01803	2725.5	5.6159
t	v	h	s	v	h	s	v	h	s	v	h	s
(°C)	(m^3/kg)	(kJ/kg)	(kJ/(kg K))	(m^3/kg)	(kJ/kg)	(kJ/(kg K))	(m^3/kg)	(kJ/kg)	(kJ/(kg K))	(m^3/kg)	(kJ/kg)	(kJ/(kg K))
220	0.102167	2821.67	6.3868	0.001190	943.69	2.5175	0.001187	944.38	2.5129	0.001181	945.87	2.5039
240	0.108488	2877.21	6.4972	0.084437	2852.28	6.3555	0.001227	1037.68	2.6983	0.001219	1038.30	2.6876
260	0.114400	2928.47	6.5952	0.089553	2908.19	6.4624	0.001275	1134.77	2.8839	0.001265	1134.13	2.8708
280	0.120046	2977.21	6.6850	0.094351	2960.16	6.5581	0.042275	2858.08	6.0909	0.001323	1234.82	3.0561
300	0.125501	3024.25	6.7685	0.098932	3009.63	6.6460	0.045347	2925.64	6.2109	0.001398	1343.10	3.2484
320	0.130816	3070.16	6.8472	0.103357	3057.40	6.7279	0.048130	2986.18	6.3148	0.019272	2782.66	5.7131
340	0.136023	3115.28	6.9221	0.107664	3104.01	6.8052	0.050726	3042.36	6.4080	0.021490	2882.06	5.8780
360	0.141147	3159.89	6.9937	0.111881	3149.81	6.8787	0.053188	3095.62	6.4934	0.023327	2962.61	6.0073
380	0.146205	3204.16	7.0625	0.116026	3195.07	6.9491	0.055552	3146.83	6.5731	0.024952	3033.11	6.1170
400	0.151208	3248.23	7.1290	0.120115	3239.96	7.0168	0.057840	3196.59	6.6481	0.026439	3097.38	6.2139
420	0.156167	3292.18	7.1933	0.124156	3284.63	7.0822	0.060068	3245.31	6.7194	0.027829	3157.45	6.3019
440	0.161088	3336.09	7.2558	0.128159	3329.15	7.1455	0.062249	3293.27	6.7877	0.029148	3214.57	6.3831
460	0.165978	3380.02	7.3165	0.132129	3373.62	7.2070	0.064391	3340.68	6.8532	0.030410	3269.53	6.4591
480	0.170841	3424.01	7.3757	0.136072	3418.08	7.2668	0.066501	3387.71	6.9165	0.031629	3322.89	6.5310
500	0.175680	3468.09	7.4335	0.139990	3462.59	7.3251	0.068583	3434.48	6.9778	0.032813	3375.06	6.5993
520	0.180499	3512.30	7.4899	0.143887	3507.17	7.3821	0.070642	3481.06	7.0373	0.033968	3426.31	6.6648
540	0.185300	3556.64	7.5451	0.147766	3551.85	7.4377	0.072681	3527.54	7.0952	0.035098	3476.87	6.7277
560	0.190085	3601.15	7.5992	0.151629	3596.67	7.4922	0.074703	3573.96	7.1516	0.036208	3526.90	6.7885
580	0.194856	3645.84	7.6522	0.155477	3641.64	7.5455	0.076710	3620.38	7.2066	0.037300	3576.52	6.8474
600	0.199614	3690.71	7.7042	0.159313	3686.76	7.5978	0.078703	3666.83	7.2604	0.038377	3625.84	6.9045
620	0.204362	3735.78	7.7552	0.163138	3732.07	7.6491	0.080684	3713.34	7.3131	0.039442	3674.95	6.9601
640	0.209099	3781.07	7.8054	0.166953	3777.57	7.6995	0.082655	3759.94	7.3647	0.040494	3723.89	7.0143
660	0.213827	3826.57	7.8547	0.170758	3823.27	7.7490	0.084616	3806.65	7.4153	0.041536	3772.73	7.0672
680	0.218547	3872.29	7.9032	0.174556	3869.17	7.7976	0.086569	3853.48	7.4650	0.042569	3821.51	7.1189
700	0.223260	3918.24	7.9509	0.178346	3915.30	7.8455	0.088515	3900.45	7.5137	0.043594	3870.27	7.1696
720	0.227966	3964.43	7.9978	0.182129	3961.64	7.8927	0.090453	3947.58	7.5617	0.044612	3919.04	7.2192
740	0.232667	4010.86	8.0441	0.185907	4008.21	7.9391	0.092385	3994.88	7.6088	0.045623	3967.85	7.2678
760	0.237361	4057.52	8.0897	0.189679	4055.01	7.9848	0.094312	4042.35	7.6552	0.046629	4016.72	7.3156
780	0.242051	4104.43	8.1347	0.193446	4102.04	8.0299	0.096234	4090.02	7.7009	0.047629	4065.68	7.3625
800	0.246737	4151.59	8.1791	0.197208	4149.32	8.0744	0.098151	4137.87	7.7459	0.048624	4114.73	7.4087

Table 3.9 (continued)

$p \rightarrow$	150 bar t_s = 342.16 °C			200 bar t_s = 365.765 °C			250 bar			300 bar		
	v''	h''	s''	v''	h''	s''						
	0.01034	2610.9	5.3108	0.00586	2411.4	4.9299						
t	v	h	s	v	h	s	v	h	s	v	h	s
(°C)	(m^3/kg)	(kJ/kg)	(kJ/(kg K))	(m^3/kg)	(kJ/kg)	(kJ/(kg K))	(m^3/kg)	(kJ/kg)	(kJ/(kg K))	(m^3/kg)	(kJ/kg)	(kJ/(kg K))
0	0.000993	15.07	0.0004	0.000990	20.03	0.0005	0.000988	24.96	0.0004	0.000986	29.86	0.0003
10	0.000993	56.52	0.1495	0.000991	61.30	0.1489	0.000989	66.06	0.1482	0.000987	70.79	0.1474
20	0.000995	97.94	0.2932	0.000993	102.57	0.2921	0.000991	107.18	0.2909	0.000989	111.78	0.2897
40	0.001001	180.78	0.5666	0.000999	185.17	0.5646	0.000997	189.54	0.5627	0.000995	193.91	0.5607
60	0.001011	263.71	0.8233	0.001008	267.89	0.8207	0.001006	272.07	0.8181	0.001004	276.24	0.8156
80	0.001022	346.85	1.0657	0.001020	350.83	1.0625	0.001018	354.82	1.0593	0.001016	358.80	1.0562
100	0.001036	430.32	1.2956	0.001034	434.10	1.2918	0.001031	437.88	1.2881	0.001029	441.67	1.2845
120	0.001052	514.25	1.5147	0.001050	517.81	1.5104	0.001047	521.38	1.5061	0.001045	524.97	1.5019
140	0.001071	598.79	1.7244	0.001068	602.11	1.7195	0.001065	605.45	1.7147	0.001062	608.80	1.7099
160	0.001092	684.12	1.9261	0.001089	687.15	1.9205	0.001085	690.22	1.9150	0.001082	693.31	1.9097
180	0.001116	770.46	2.1209	0.001112	773.16	2.1146	0.001108	775.90	2.1084	0.001105	778.68	2.1023
200	0.001144	858.12	2.3102	0.001139	860.39	2.3030	0.001135	862.73	2.2959	0.001130	865.14	2.2890
220	0.001175	947.49	2.4952	0.001170	949.22	2.4868	0.001164	951.06	2.4787	0.001159	952.99	2.4709
240	0.001212	1039.13	2.6774	0.001205	1040.14	2.6675	0.001199	1041.31	2.6581	0.001193	1042.62	2.6490
260	0.001256	1133.83	2.8584	0.001247	1133.83	2.8466	0.001239	1134.08	2.8355	0.001231	1134.57	2.8248
280	0.001310	1232.79	3.0406	0.001298	1231.29	3.0261	0.001287	1230.24	3.0125	0.001277	1229.56	2.9997
300	0.001378	1338.06	3.2275	0.001361	1334.14	3.2087	0.001346	1331.06	3.1915	0.001332	1328.66	3.1756
320	0.001473	1453.85	3.4260	0.001445	1445.30	3.3993	0.001421	1438.72	3.3761	0.001401	1433.51	3.3554
340	0.001631	1592.27	3.6553	0.001569	1571.52	3.6085	0.001526	1557.48	3.5729	0.001493	1547.07	3.5437
360	0.012582	2769.56	5.5654	0.001825	1740.13	3.8787	0.001697	1698.63	3.7993	0.001628	1675.57	3.7498
380	0.014289	2884.61	5.7445	0.008258	2659.19	5.3144	0.002218	1935.67	4.1670	0.001873	1838.26	4.0026
400	0.015671	2975.55	5.8817	0.009950	2816.84	5.5525	0.006005	2578.59	5.1399	0.002796	2152.37	4.4750
420	0.016875	3053.94	5.9965	0.011199	2928.51	5.7160	0.007579	2769.45	5.4196	0.004921	2552.87	5.0625
440	0.017965	3124.58	6.0970	0.012246	3020.26	5.8466	0.008697	2897.06	5.6013	0.006228	2748.86	5.3416
460	0.018974	3190.02	6.1875	0.013170	3100.57	5.9577	0.009617	2999.20	5.7426	0.007193	2883.84	5.5284
480	0.019924	3251.76	6.2706	0.014011	3173.45	6.0558	0.010418	3087.11	5.8609	0.007992	2991.99	5.6740
500	0.020828	3310.79	6.3479	0.014793	3241.19	6.1445	0.011142	3165.92	5.9642	0.008690	3084.79	5.7956
520	0.021696	3367.79	6.4207	0.015530	3305.21	6.2263	0.011810	3238.48	6.0569	0.009320	3167.67	5.9015

Table 3.9 (continued)

$p \rightarrow$	150 bar t_s = 342.16 °C			200 bar t_s = 365.765 °C			250 bar			300 bar		
	v''	h''	s''	v''	h''	s''						
	0.01034	2610.9	5.3108	0.00586	2411.4	4.9299						
t	v	h	s	v	h	s	v	h	s	v	h	s
(°C)	(m^3/kg)	(kJ/kg)	(kJ/(kg K))	(m^3/kg)	(kJ/kg)	(kJ/(kg K))	(m^3/kg)	(kJ/kg)	(kJ/(kg K))	(m^3/kg)	(kJ/kg)	(kJ/(kg K))
540	0.022535	3423.22	6.4897	0.016231	3366.45	6.3026	0.012435	3306.55	6.1416	0.009899	3243.71	5.9962
560	0.023350	3477.46	6.5556	0.016904	3425.57	6.3744	0.013028	3371.29	6.2203	0.010442	3314.82	6.0826
580	0.024144	3530.75	6.6188	0.017554	3483.05	6.4426	0.013595	3433.49	6.2941	0.010955	3382.25	6.1626
600	0.024921	3583.31	6.6797	0.018184	3539.23	6.5077	0.014140	3493.69	6.3638	0.011444	3446.87	6.2374
620	0.025683	3635.28	6.7386	0.018799	3594.37	6.5701	0.014667	3552.32	6.4302	0.011914	3509.28	6.3081
640	0.026432	3686.79	6.7956	0.019399	3648.69	6.6303	0.015179	3609.69	6.4937	0.012368	3569.91	6.3752
660	0.027171	3737.95	6.8510	0.019987	3702.35	6.6884	0.015678	3666.03	6.5548	0.012808	3629.12	6.4394
680	0.027899	3788.82	6.9050	0.020564	3755.46	6.7447	0.016165	3721.54	6.6136	0.013236	3687.16	6.5009
700	0.028619	3839.48	6.9576	0.021133	3808.15	6.7994	0.016643	3776.37	6.6706	0.013654	3744.24	6.5602
720	0.029332	3889.99	7.0090	0.021693	3860.50	6.8527	0.017113	3830.64	6.7258	0.014063	3800.53	6.6175
740	0.030037	3940.39	7.0592	0.022246	3912.57	6.9046	0.017575	3884.47	6.7794	0.014464	3856.17	6.6729
760	0.030736	3990.72	7.1084	0.022792	3964.43	6.9553	0.018030	3937.92	6.8317	0.014858	3911.27	6.7268
780	0.031430	4041.03	7.1566	0.023333	4016.13	7.0048	0.018479	3991.08	6.8826	0.015246	3965.93	6.7792
800	0.032118	4091.33	7.2039	0.023869	4067.73	7.0534	0.018922	4044.00	6.9324	0.015629	4020.23	6.8303

Table 3.9 (continued)

$p \rightarrow$	350 bar			400 bar			500 bar			
t	v	h	s	v	h	s	v	h	s	
(°C)	(m^3/kg)	(kJ/kg)	(kJ/(kg K))	(m^3/kg)	(kJ/kg)	(kJ/(kg K))	(m^3/kg)	(kJ/kg)	(kJ/(kg K))	
0	0.000983	34.72	0.0001	0.000981	39.56	−0.0002	0.000977	49.13	−0.0010	
10	0.000984	75.49	0.1466	0.000982	80.17	0.1458	0.000978	89.46	0.1440	
20	0.000987	116.35	0.2884	0.000985	120.90	0.2872	0.000980	129.96	0.2845	
40	0.000993	198.27	0.5588	0.000991	202.61	0.5568	0.000987	211.27	0.5528	
60	0.001002	280.40	0.8130	0.001000	284.56	0.8105	0.000996	292.86	0.8054	
80	0.001013	362.78	1.0531	0.001011	366.76	1.0501	0.001007	374.71	1.0440	
100	0.001027	445.47	1.2809	0.001024	449.26	1.2773	0.001020	456.87	1.2703	
120	0.001042	528.56	1.4978	0.001040	532.17	1.4937	0.001035	539.41	1.4858	
140	0.001060	612.18	1.7052	0.001057	615.57	1.7006	0.001052	622.40	1.6917	
160	0.001079	696.44	1.9044	0.001076	699.59	1.8992	0.001070	705.95	1.8891	
180	0.001101	781.51	2.0964	0.001098	784.37	2.0906	0.001091	790.20	2.0793	
200	0.001126	867.60	2.2823	0.001122	870.12	2.2758	0.001115	875.31	2.2631	

Table 3.9 (continued)

$p \rightarrow$	350 bar			400 bar			500 bar			
t (°C)	v (m^3/kg)	h (kJ/kg)	s (kJ/(kg K))	v (m^3/kg)	h (kJ/kg)	s (kJ/(kg K))	v (m^3/kg)	h (kJ/kg)	s (kJ/(kg K))	
220	0.001155	955.00	2.4632	0.001150	957.10	2.4558	0.001141	961.50	2.4415	
240	0.001187	1044.06	2.6402	0.001181	1045.62	2.6317	0.001171	1049.05	2.6155	
260	0.001224	1135.25	2.8145	0.001217	1136.11	2.8047	0.001204	1138.29	2.7861	
280	0.001268	1229.20	2.9875	0.001259	1229.13	2.9760	0.001243	1229.67	2.9543	
300	0.001320	1326.81	3.1608	0.001308	1325.41	3.1469	0.001288	1323.74	3.1214	
320	0.001384	1429.36	3.3367	0.001368	1426.02	3.3195	0.001341	1421.22	3.2885	
340	0.001466	1538.97	3.5184	0.001443	1532.52	3.4960	0.001405	1523.05	3.4574	
360	0.001579	1659.61	3.7119	0.001542	1647.62	3.6807	0.001485	1630.63	3.6300	
380	0.001755	1800.51	3.9309	0.001682	1776.72	3.8814	0.001588	1746.51	3.8101	
400	0.002106	1988.43	4.2140	0.001911	1931.13	4.1141	0.001731	1874.31	4.0028	
420	0.003082	2291.32	4.6570	0.002361	2136.30	4.4142	0.001940	2020.07	4.2161	
440	0.004413	2571.64	5.0561	0.003210	2394.03	4.7807	0.002266	2190.53	4.4585	
460	0.005436	2753.55	5.3079	0.004149	2613.32	5.0842	0.002745	2380.52	4.7212	
480	0.006246	2888.06	5.4890	0.004950	2777.18	5.3048	0.003319	2563.86	4.9680	
500	0.006933	2998.02	5.6331	0.005625	2906.69	5.4746	0.003889	2722.52	5.1759	
420	0.007540	3093.08	5.7546	0.006213	3015.42	5.6135	0.004417	2857.36	5.3482	
540	0.008089	3178.24	5.8606	0.006740	3110.69	5.7322	0.004896	2973.16	5.4924	
560	0.008597	3256.46	5.9557	0.007221	3196.67	5.8366	0.005332	3075.37	5.6166	
580	0.009073	3329.64	6.0425	0.007669	3276.01	5.9308	0.005734	3167.66	5.7261	
600	0.009523	3399.02	6.1229	0.008089	3350.43	6.0170	0.006109	3252.61	5.8245	
620	0.009953	3465.45	6.1981	0.008488	3421.10	6.0970	0.006461	3332.05	5.9145	
640	0.010365	3529.55	6.2691	0.008869	3488.82	6.1720	0.006796	3407.21	5.9977	
660	0.010763	3591.77	6.3365	0.009235	3554.17	6.2428	0.007115	3478.99	6.0755	
680	0.011149	3652.46	6.4008	0.009589	3617.59	6.3100	0.007422	3548.00	6.1487	
700	0.011524	3711.88	6.4625	0.009931	3679.42	6.3743	0.007718	3614.76	6.2180	
720	0.011889	3770.27	6.5219	0.010264	3739.95	6.4358	0.008004	3679.64	6.2840	
740	0.012247	3827.78	6.5793	0.010589	3799.38	6.4951	0.008281	3742.97	6.3471	
760	0.012598	3884.58	6.6348	0.010906	3857.91	6.5523	0.008552	3804.99	6.4078	
780	0.012942	3940.78	6.6887	0.011217	3915.68	6.6077	0.008816	3865.93	6.4662	
800	0.013280	3996.48	6.7411	0.011523	3972.81	6.6614	0.009074	3925.96	6.5226	

Table 3.10 Properties of ammonia (NH_3) at saturation (after [3.13])

Temperature	Pressure	Specific volume		Enthalpy		Enthalpy vaporization	Entropy	
		liquid	vapor	liquid	vapor		liquid	vapor
t (°C)	p (bar)	v' (dm^3/kg)	v'' (dm^3/kg)	h' (kJ/kg)	h'' (kJ/kg)	$\Delta h_v = h'' - h'$ (kJ/kg)	s' (kJ/(kg K))	s'' (kJ/(kg K))
−70	0.10941	1.3798	9007.9	−110.81	1355.6	1466.4	−0.30939	6.9088
−60	0.21893	1.4013	4705.7	−68.062	1373.7	1441.8	−0.10405	6.6602
−50	0.40836	1.4243	2627.8	−24.727	1391.2	1415.9	0.09450	6.4396
−40	0.71692	1.4490	1553.3	19.170	1407.8	1388.6	0.28673	6.2425
−30	1.1943	1.4753	963.96	63.603	1423.3	1359.7	0.47303	6.0651
−20	1.9008	1.5035	623.73	108.55	1437.7	1329.1	0.65376	5.9041
−10	2.9071	1.5336	418.30	154.01	1450.7	1296.7	0.82928	5.7569
0	4.2938	1.5660	289.30	200.00	1462.2	1262.2	1.0000	5.6210
10	6.1505	1.6009	205.43	246.57	1472.1	1225.5	1.1664	5.4946
20	8.5748	1.6388	149.20	293.78	1480.2	1186.4	1.3289	5.3759
30	11.672	1.6802	110.46	341.76	1486.2	1144.4	1.4881	5.2631
40	15.554	1.7258	83.101	390.64	1489.9	1099.3	1.6446	5.1549
50	20.340	1.7766	63.350	440.62	1491.1	1050.5	1.7990	5.0497
60	26.156	1.8340	48.797	491.97	1489.3	997.30	1.9523	4.9458
70	33.135	1.9000	37.868	545.04	1483.9	938.90	2.1054	4.8415
80	41.420	1.9776	29.509	600.34	1474.3	873.97	2.2596	4.7344
90	51.167	2.0714	22.997	658.61	1459.2	800.58	2.4168	4.6213
100	62.553	2.1899	17.820	721.00	1436.6	715.63	2.5797	4.4975
110	75.783	2.3496	13.596	789.68	1403.1	613.39	2.7533	4.3543
120	91.125	2.5941	9.9932	869.92	1350.2	480.31	2.9502	4.1719
130	108.98	3.2021	6.3790	992.02	1239.3	247.30	3.2437	3.8571

At the reference state $t = 0\,°C$, saturated liquid possesses enthalpy $h' = 200.0\,kJ/kg$ and specific entropy $s' = 1.0\,kJ/(kg\,K)$

Table 3.11 Properties of carbon dioxide (CO_2) at saturation (after [3.14])

Temperature	Pressure	Specific volume		Enthalpy		Enthalpy vaporization	Entropy	
		liquid	vapor	liquid	vapor		liquid	vapor
t (°C)	p (bar)	v' (dm^3/kg)	v'' (dm^3/kg)	h' (kJ/kg)	h'' (kJ/kg)	$\Delta h_v = h'' - h'$ (kJ/kg)	s' (kJ/(kg K))	s'' (kJ/(kg K))
−55	5.540	0.8526	68.15	83.02	431.0	348.0	0.5349	2.130
−50	6.824	0.8661	55.78	92.93	432.7	339.8	0.5793	2.102
−45	8.319	0.8804	46.04	102.9	434.1	331.2	0.6629	2.075
−40	10.05	0.8957	38.28	112.9	435.3	322.4	0.6658	2.048
−35	12.02	0.9120	32.03	123.1	436.2	313.1	0.7081	2.023
−30	14.28	0.9296	26.95	133.4	436.8	303.4	0.7500	1.998
−25	16.83	0.9486	22.79	143.8	437.0	293.2	0.7915	1.973
−20	19.70	0.9693	19.34	154.5	436.9	282.4	0.8329	1.949
−15	22.91	0.9921	16.47	165.4	436.3	270.9	0.8743	1.924
−10	26.49	1.017	14.05	176.5	435.1	258.6	0.9157	1.898
−5	30.46	1.046	12.00	188.0	433.4	245.3	0.9576	1.872
0	34.85	1.078	10.24	200.0	430.9	230.9	1.000	1.845
5	39.69	1.116	8.724	212.5	427.5	215.0	1.043	1.816
10	45.02	1.161	7.399	225.7	422.9	197.1	1.088	1.785
15	50.87	1.218	6.222	240.0	416.6	176.7	1.136	1.749
20	57.29	1.293	5.150	255.8	407.9	152.0	1.188	1.706
25	64.34	1.408	4.121	274.8	394.5	119.7	1.249	1.650
30	72.14	1.686	2.896	304.6	365.0	60.50	1.343	1.543

Reference points: see footnote of Table 3.10

Table 3.12 Properties of tetrafluoroethane ($C_2H_2F_4$ (R134a)) at saturation (after [3.15, 16])

Temperature	Pressure	Specific volume		Enthalpy		Enthalpy	Entropy	
		liquid	vapor	liquid	vapor	vaporization	liquid	vapor
t	p	v'	v''	h'	h''	$\Delta h_v = h'' - h'$	s'	s''
(°C)	(bar)	(dm^3/kg)	(dm^3/kg)	(kJ/kg)	(kJ/kg)	(kJ/kg)	(kJ/(kg K))	(kJ/(kg K))
−100	0.0055940	0.63195	25 193	75.362	336.85	261.49	0.43540	1.9456
−95	0.0093899	0.63729	15 435	81.288	339.78	258.50	0.46913	1.9201
−90	0.015241	0.64274	9769.8	87.226	342.76	255.53	0.50201	1.8972
−85	0.023990	0.64831	6370.7	93.182	345.77	252.59	0.53409	1.8766
−80	0.036719	0.65401	4268.2	99.161	348.83	249.67	0.56544	1.8580
−75	0.054777	0.65985	2931.2	105.17	351.91	246.74	0.59613	1.8414
−70	0.079814	0.66583	2059.0	111.20	355.02	243.82	0.62619	1.8264
−65	0.11380	0.67197	1476.5	117.26	358.16	240.89	0.65568	1.8130
−60	0.15906	0.67827	1079.0	123.36	361.31	237.95	0.68462	1.8010
−55	0.21828	0.68475	802.36	129.50	364.48	234.98	0.71305	1.7902
−50	0.29451	0.69142	606.20	135.67	367.65	231.98	0.74101	1.7806
−45	0.39117	0.69828	464.73	141.89	370.83	228.94	0.76852	1.7720
−40	0.51209	0.70537	361.08	148.14	374.00	225.86	0.79561	1.7643
−35	0.66144	0.71268	284.02	154.44	377.17	222.72	0.82230	1.7575
−30	0.84378	0.72025	225.94	160.79	380.32	219.53	0.84863	1.7515
−25	1.0640	0.72809	181.62	167.19	383.45	216.26	0.87460	1.7461
−20	1.3273	0.73623	147.39	173.64	386.55	212.92	0.90025	1.7413
−15	1.6394	0.74469	120.67	180.14	389.63	209.49	0.92559	1.7371
−10	2.0060	0.75351	99.590	186.70	392.66	205.97	0.95065	1.7334
−5	2.4334	0.76271	82.801	193.32	395.66	202.34	0.97544	1.7300
0	2.9280	0.77233	69.309	200.00	398.60	198.60	1.0000	1.7271
5	3.4966	0.78243	58.374	206.75	401.49	194.74	1.0243	1.7245
10	4.1461	0.79305	49.442	213.58	404.32	190.74	1.0485	1.7221
15	4.8837	0.80425	42.090	220.48	407.07	186.59	1.0724	1.7200
20	5.7171	0.81610	35.997	227.47	409.75	182.28	1.0962	1.7180
25	6.6538	0.82870	30.912	234.55	412.33	177.79	1.1199	1.7162
30	7.7020	0.84213	26.642	241.72	414.82	173.10	1.1435	1.7145
35	8.8698	0.85653	23.033	249.01	417.19	168.18	1.1670	1.7128
40	10.166	0.87204	19.966	256.41	419.43	163.02	1.1905	1.7111
45	11.599	0.88885	17.344	263.94	421.52	157.58	1.2139	1.7092
50	13.179	0.90719	15.089	271.62	423.44	151.81	1.2375	1.7072
55	14.915	0.92737	13.140	279.47	425.15	145.68	1.2611	1.7050
60	16.818	0.94979	11.444	287.50	426.63	139.12	1.2848	1.7024
65	18.898	0.97500	9.9604	295.76	427.82	132.06	1.3088	1.6993
70	21.168	1.0038	8.6527	304.28	428.65	124.37	1.3332	1.6956
75	23.641	1.0372	7.4910	313.13	429.03	115.90	1.3580	1.6909
80	26.332	1.0773	6.4483	322.39	428.81	106.42	1.3836	1.6850
85	29.258	1.1272	5.4990	332.22	427.76	95.536	1.4104	1.6771
90	32.442	1.1936	4.6134	342.93	425.42	82.487	1.4390	1.6662
95	35.912	1.2942	3.7434	355.25	420.67	65.423	1.4715	1.6492
100	39.724	1.5357	2.6809	373.30	407.68	34.385	1.5188	1.6109

Reference points: see footnote of Table 3.10

3.6.3 Incompressible Fluids

An incompressible fluid is a fluid whose specific volume depends on neither temperature nor pressure, such that the equation of state is given by $v = \text{const}$. As a good approximation, liquids and solids can generally be considered as incompressible. The specific heats c_p and c_v do not differ for incompressible fluids, $c_p = c_v = c$. Thus, the caloric equations of state are

$$\mathrm{d}u = c\mathrm{d}T \tag{3.86}$$

and

$$\mathrm{d}h = c\mathrm{d}T + v\mathrm{d}p\,, \tag{3.87}$$

as well as

$$\mathrm{d}s = c\frac{\mathrm{d}T}{T}\,. \tag{3.88}$$

3.6.4 Solid Materials

Thermal Expansion

Similar to liquids, the influence of pressure on volume in equations of state $V = V(p, T)$ for solids is mostly negligibly small. Nearly all solids expand like liquids with increasing temperature and shrink with decreasing temperature. An exception is water, which has its highest density at 4 °C and expands at temperatures both higher and lower than 4 °C. A Taylor-series expansion with respect to temperature of the equation of state, truncated after the linear term, leads to the volumetric expansion with the cubic volumetric expansion coefficient γ_V (SI unit 1/K)

$$V = V_0\left[1 + \gamma_\mathrm{V}(t - t_0)\right]\,.$$

Accordingly, the area expansion is

$$A = A_0\left[1 + \gamma_\mathrm{A}(t - t_0)\right]$$

and the length expansion

$$l = l_0\left[1 + \gamma_\mathrm{L}(t - t_0)\right],$$

where $\gamma_\mathrm{A} = (2/3)\gamma_\mathrm{V}$ and $\gamma_\mathrm{L} = (1/3)\gamma_\mathrm{V}$. Average values for γ_L in the temperature interval between 0 °C and t °C can be derived for some solids from the values in Table 3.13 by dividing the given length change $(l - l_0)/l_0$ by the temperature interval $t - 0\,°C$.

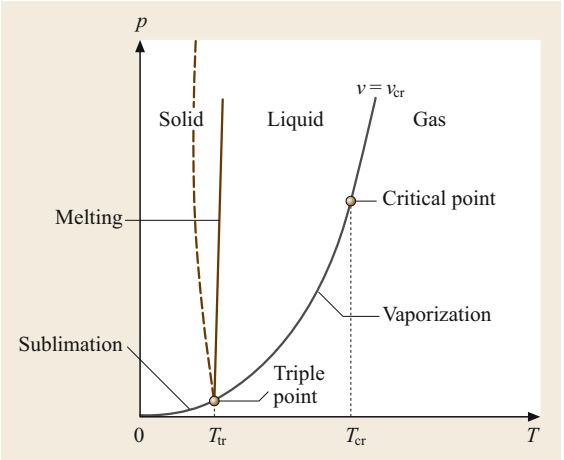

Fig. 3.11 p–T diagram with the three boundary lines of the phases. (The gradient of the melting line of water is negative, *dashed line*)

Melting and Sublimation Curves

Within certain limits, each pressure of a liquid corresponds to a temperature at which the liquid is in equilibrium with its solid. This relationship $p(T)$ is determined by the melting curve (Fig. 3.11), whereas the sublimation curve displays the equilibrium between gas and solid. Figure 3.11 includes additionally the liquid–vapor saturation curve. All three curves meet at the triple point, at which the solid, the liquid, and the gaseous phase of a substance are in equilibrium with each other. The triple point of water is 273.16 K by definition, which corresponds to a pressure at the triple point of 611.657 Pa.

Caloric Properties

During the freezing of a liquid, the latent heat of fusion Δh_f is released (Table 3.14). At the same time, the liquid entropy is reduced by $\Delta s_\mathrm{f} = \Delta h_\mathrm{f}/T_\mathrm{f}$, with T_f being the melting or freezing temperature. According to the Dulong–Petit law, the molar specific heat divided by the number of atoms in the molecule is, above ambient temperature, about 25.9 kJ/(kmol K). If absolute zero is approached, this approximate rule is no longer valid. Therefore, for all solids, the molar specific heat at constant volume is

$$\overline{C} = a\left(\frac{T}{\Theta}\right)^3\,, \quad \text{for} \quad \frac{T}{\Theta} < 0.1$$

with $a = 4782.5\,\mathrm{J/(mol\,K)}$ and where Θ is the Debye temperature (Table 3.15).

Table 3.13 Thermal extension $(l - l_0)/l_0$ of some solids in mm/m in the temperature interval between 0 and t °C; l_0 is the length at 0 °C

Substance	0 to −190 °C	0 to 100 °C	0 to 200 °C	0 to 300 °C	0 to 400 °C	0 to 500 °C	0 to 600 °C	0 to 700 °C	0 to 800 °C	0 to 900 °C	0 to 1000 °C
Aluminum	−3.43	2.38	4.90	7.65	10.60	13.70	17.00	–	–	–	–
Lead	−5.08	2.90	5.93	9.33	–	–	–	–	–	–	–
Al-Cu-Mg (0.95 Al; 0.04 Cu + Mg, Mn, St., Fe)	–	2.35	4.90	7.80	10.70	13.65	–	–	–	–	–
Iron-nickel alloy (0.64 Fe; 0.36 Ni)	–	0.15	0.75	1.60	3.10	4.70	6.50	8.5	10.5	12.55	–
Iron-nickel alloy (0.77 Fe; 0.23 Ni)	–	–	–	2.80	4.00	5.25	6.50	7.80	9.25	10.50	11.85
Glass: Jena, 16 III	−1.13	0.81	1.67	2.60	3.59	4.63	–	–	–	–	–
Glass: Jena, 1565 III	–	0.345	0.72	1.12	1.56	2.02	–	–	–	–	–
Gold	−2.48	1.42	2.92	4.44	6.01	7.62	9.35	11.15	13.00	14.90	–
Gray cast iron	−1.59	1.04	2.21	3.49	4.90	6.44	8.09	9.87	11.76	–	–
Constantan (0.60 Cu; 0.40 Ni)	−2.26	1.52	3.12	4.81	6.57	8.41	–	–	–	–	–
Copper	−2.65	1.65	3.38	5.15	7.07	9.04	11.09	–	–	–	–
Sintered magnesia	–	–	2.45	3.60	4.90	6.30	7.75	9.30	10.80	12.35	13.90
Magnesium	−4.01	2.60	5.41	8.36	11.53	14.88	–	–	–	–	–
Manganese bronze (0.85 Cu; 0.09 Mn; 0.06 Sn)	−2.84	1.75	3.58	5.50	7.51	9.61	–	–	–	–	–
Manganin (0.84 Cu; 0.12 Mn; 0.04 Ni)	–	1.75	3.65	5.60	7.55	9.70	11.90	14.3	16.80	–	–
Brass (0.62 Cu; 0.38 Zn)	−3.11	1.84	3.85	6.03	8.39	–	–	–	–	–	–
Molybdenum	−0.79	0.52	1.07	1.64	2.24	–	–	–	–	–	–
Nickel	−1.89	1.30	2.75	4.30	5.95	7.60	9.27	11.05	12.89	14.80	16.80
Palladium	−1.93	1.19	2.42	3.70	5.02	6.38	7.79	9.24	10.74	12.27	13.86
Platinum	−1.51	0.90	1.83	2.78	3.76	4.77	5.80	6.86	7.94	9.05	10.19
Platinum-iridium alloy (0.80 Pt; 0.20 Ir)	−1.43	0.83	1.70	2.59	3.51	4.45	5.43	6.43	7.47	8.53	9.62
Quartz glass	+0.03	0.05	0.12	0.19	0.25	0.31	0.36	0.40	0.45	0.50	0.54
Silver	−3.22	1.95	4.00	6.08	8.23	10.43	12.70	15.15	17.65	–	–
Sintered corundum	–	–	1.30	2.00	2.75	3.60	4.45	5.30	6.25	7.15	8.15
Steel, soft	−1.67	1.20	2.51	3.92	5.44	7.06	8.79	10.63	–	–	–
Steel, hard	−1.64	1.17	2.45	3.83	5.31	6.91	8.60	10.40	–	–	–
Zinc	−1.85	1.65	–	–	–	–	–	–	–	–	–
Tin	−4.24	2.67	–	–	–	–	–	–	–	–	–
Tungsten	−0.73	0.45	0.90	1.40	1.90	2.25	2.70	3.15	3.60	4.05	4.60

Table 3.14 Thermal engineering properties: density ρ, specific heat c_p for 0–100 °C, melting temperature t_f, latent heat of fusion Δh_f, boiling temperature t_s, and enthalpy of vaporization Δh_v

	ρ (kg/dm^3)	c_p (kJ/(kg K))	t_f (°C)	Δh_f (kJ/kg)	t_s (°C)	Δh_v (kJ/kg)
Solids (metals and sulfur) at 1.0132 bar						
Aluminum	2.70	0.921	660	355.9	2270	11 723
Antimony	6.69	0.209	630.5	167.5	1635	1256
Lead	11.34	0.130	327.3	23.9	1730	921
Chrome	7.19	0.506	1890	293.1	2642	6155
Iron (pure)	7.87	0.465	1530	272.1	2500	6364
Gold	19.32	0.130	1063	67.0	2700	1758
Iridium	22.42	0.134	2454	117.2	2454	3894
Copper	8.96	0.385	1083	209.3	2330	4647
Magnesium	1.74	1.034	650	209.3	1100	5652
Manganese	7.3	0.507	1250	251.2	2100	4187
Molybdenum	10.2	0.271	2625	–	3560	7118
Nickel	8.90	0.444	1455	293.1	3000	6197
Platinum	21.45	0.134	1773	113.0	3804	2512
Mercury	13.55	0.138	−38.9	11.7	357	301
Silver	10.45	0.234	960.8	104.7	1950	2177
Titanium	4.54	0.471	1800	–	3000	–
Bismuth	9.80	0.126	271	54.4	1560	837
Tungsten	19.3	0.134	3380	251.2	6000	4815
Zinc	7.14	0.385	419.4	112.2	907	1800
Tin	7.28	0.226	231.9	58.6	2300	2596
Sulfur (rhombic)	2.07	0.720	112.8	39.4	444.6	293
Liquids at 1.0132 bar						
Ethyl alcohol	0.79	2.470	−114.5	104.7	78.3	841.6
Ethyl ether	0.71	2.328	−116.3	100.5	34.5	360.1
Acetone	0.79	2.160	−94.3	96.3	56.1	523.4
Benzene	0.88	1.738	5.5	127.3	80.1	395.7
Glycerin [a]	1.26	2.428	18.0	200.5	290.0	854.1
Saline solution (saturated)	1.19	3.266	−18.0	–	108.0	–
Sea water (3.5% salt content)	1.03	–	−2.0	–	100.5	–
Methyl alcohol	0.79	2.470	−98.0	100.5	64.5	1101.1
n-Heptane	0.68	2.219	−90.6	141.5	98.4	318.2
n-Hexane	0.66	1.884	−95.3	146.5	68.7	330.8
Spirits of turpentine	0.87	1.800	−10.0	116.0	160.0	293.1
Water	1.00	4.183	0.0	333.5	100.0	2257.1
Gases at 1.0132 bar and 0 °C						
Ammonia	0.771	2.060	−77.7	332.0	−33.4	1371
Argon	1.784	0.523	−189.4	29.3	−185.9	163
Ethylene	1.261	1.465	−169.5	104.3	−103.9	523
Helium	0.178	5.234	–	37.7	−268.9	21
Carbon dioxide	1.977	0.825	−56.6	180.9	−78.5 [b]	574
Carbon monoxide	1250	1.051	−205.1	30.1	−191.5	216
Air	1.293	1.001	–	–	−194.0	197
Methane	0.717	2.177	−182.5	58.6	−161.5	548
Oxygen	1.429	0.913	−218.8	13.8	−183.0	214
Sulfur dioxide	2.926	0.632	−75.5	115.6	−10.2	390
Nitrogen	1.250	1.043	−210.0	25.5	−195.8	198
Hydrogen	0.09	14.235	−259.2	58.2	−252.8	454

[a] Solidification point at 0 °C. Melting and solidification point do not always coincide
[b] CO_2 does not boil, but sublimates at 1.0132 bar

Table 3.15 Debye temperatures of some substances

Metal	Θ (K)
Pb	88
Hg	97
Cd	168
Na	172
Ag	215
Ca	226
Zn	235
Cu	315
Al	398
Fe	453
Other substances	Θ (K)
KBr	177
KCl	230
NaCl	281
C	1860

3.6.5 Mixing Temperature and Measurement of Specific Heats

If several substances with different masses m_i, temperatures t_i, and specific heats c_{pi} ($i = 1, 2, \ldots$) are mixed at constant pressure without external heat supply, a mixing temperature t_m arises after a sufficient period of time. It is

$$t_\mathrm{m} = \frac{\sum m_i c_{pi} t_i}{\sum m_i c_{pi}}$$

with c_{pi} being the mean specific heats between 0 °C and t °C. It is possible to calculate an unknown specific heat from the measured temperature t_m, if all the other specific heats are known.

Example 3.8

A mass of $m_\mathrm{a} = 0.2\,\mathrm{kg}$ of aluminum at $t_\mathrm{a} = 100\,^\circ\mathrm{C}$ is inserted into a thermally perfectly isolated calorimeter, which is filled with 0.8 kg water ($c_p = 4.186\,\mathrm{kJ/(kg\,K)}$) at 15 °C and which consists of 0.25 kg of silver ($c_{ps} = 0.234\,\mathrm{kJ/(kg\,K)}$). After reaching equilibrium, a mixing temperature of 19.24 °C is measured. What is the specific heat of aluminum? We proceed thus:

$$t_\mathrm{m} = \frac{(mc_p + m_\mathrm{s}c_{ps})t + m_\mathrm{a}c_{pa}t_\mathrm{a}}{mc_p + m_\mathrm{s}c_{ps} + m_\mathrm{a}c_{pa}} ,$$

which resolves to

$$c_{pa} = \frac{(mc_p + m_\mathrm{s}c_{ps})(t - t_\mathrm{m})}{m_\mathrm{a}(t_\mathrm{m} - t_\mathrm{a})} ,$$

$$c_{pa} = \left(0.8\,\mathrm{kg} \times 4.186 \frac{\mathrm{kJ}}{\mathrm{kg\,K}} + 0.25\,\mathrm{kg} \times 0.234 \frac{\mathrm{kJ}}{\mathrm{kg\,K}}\right) \times \frac{15\,^\circ\mathrm{C} - 19.24\,^\circ\mathrm{C}}{0.2\,\mathrm{kg}(19.24\,^\circ\mathrm{C} - 100\,^\circ\mathrm{C})} ,$$

$$c_{pa} = 0.894\,\mathrm{kJ/(kg\,K)} .$$

3.7 Changes of State of Gases and Vapors

3.7.1 Changes of State of Gases and Vapors in Closed Systems

A closed thermodynamic system has a fixed mass Δm. The following changes of state (constant volume, constant pressure, and constant temperature) are idealized limiting cases of real changes of state. The gas volume remains unchanged during changes of state at *constant volume* or *isochoric* changes of state, e.g., when a gas volume is in a container with solid, rigid walls. No work is done, and the supplied heat transfer causes only a change of internal energy. During a change of state at *constant pressure* or an *isobaric* change of state, the gas volume has to increase if heat transfer is supplied. The supplied heat transfer increases the enthalpy during reversible changes of state. Changes of state at constant temperature are also called isothermal changes of state. Apart from a very few exceptions, heat has to be transferred to the gas during expansion and transferred from the gas during compression in order for the temperature to remain constant. For an ideal gas at constant temperature, the internal energy does not change, as $U(T) = \mathrm{const}$, thus the supplied heat transfer is equal to the work done by the system. The isotherm of an ideal gas ($pV = mRT = \mathrm{const}$) is a hyperbola in the p–V diagram.

During adiabatic changes of state, there is no heat exchange between the system and its environment. This case is approximately realized in compressors and expansion machines, because there the compression or expansion takes place in a very short period of time such that little heat transfer is exchanged with the environment during the change of state. According to the second law (see Sect. 3.4.3) the entire entropy change is caused by internal irreversibilities of the system, $\dot{S} = \dot{S}_\mathrm{gen}$. A reversible adiabatic process proceeds at constant entropy $\dot{S} = 0$, where such a change of state is called isentropic. Thus, a reversible adiabatic process is at the same time also an isentropic process. However, an isentropic process is not necessarily also an adiabatic

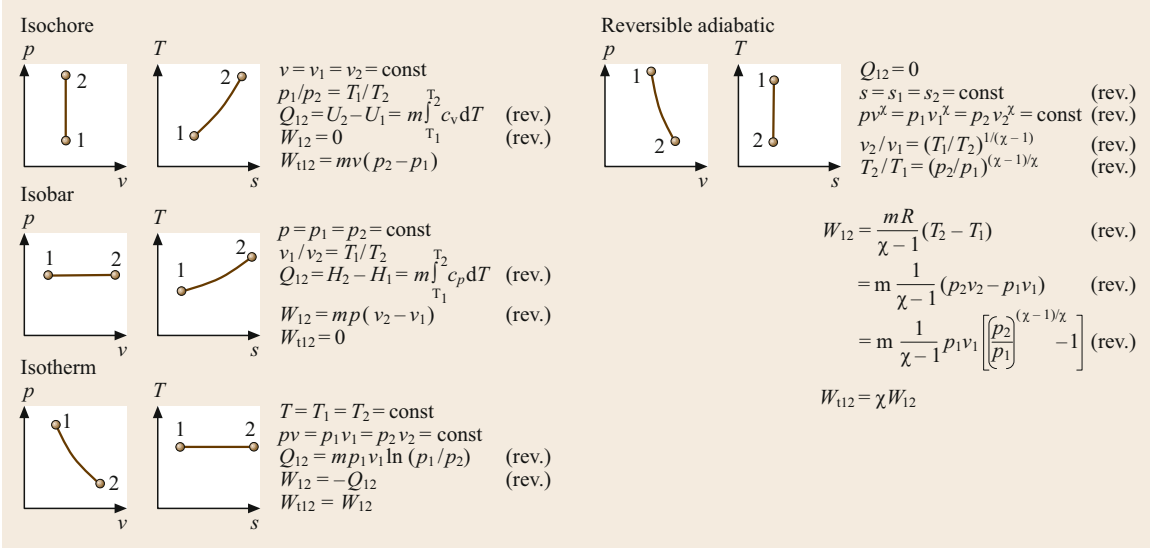

Fig. 3.12 Changes of state of ideal gases. The (rev.) denotes that the change of state is reversible

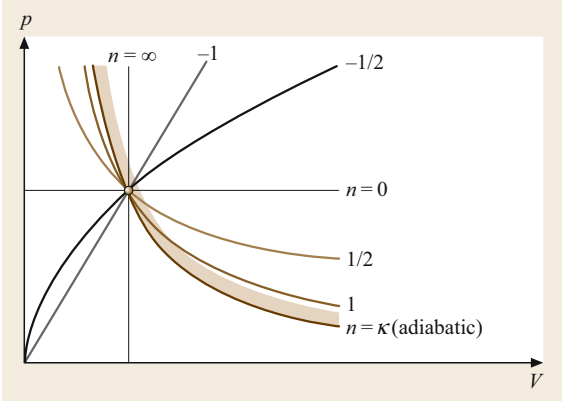

Fig. 3.13 Polytropic processes with different exponents

process, because from $\dot{S} = \dot{S}_Q + \dot{S}_{gen} = 0$ it does not always follow that $\dot{S}_Q = 0$.

Figure 3.12 shows the different changes of state in p–V and T–S diagrams. Additionally, the most important relationships for the properties of ideal gases are given.

An isothermal change of state requires perfect heat exchange, whereas no heat exchange at all with the environment must take place during an adiabatic change of state. Both cannot be achieved completely in reality. Therefore, a *polytropic* change of state is introduced via

$$pV^n = \text{const}\,, \tag{3.89}$$

where in practice n is usually between 1 and $\varkappa$. Isochore, isobar, isotherm, and reversible adiabate are special cases of a polytrope with the following exponents (Fig. 3.13): isochore ($n = \infty$), isotherm ($n = 1$), and reversible adiabate ($n = \varkappa$). It holds further that

$$\frac{v_2}{v_1} = \left(\frac{p_1}{p_2}\right)^{1/n} = \left(\frac{T_1}{T_2}\right)^{1/(n-1)}\,,$$

$$\begin{aligned} W_{12} &= \frac{mR(T_2 - T_1)}{n-1} \\ &= \frac{p_2V_2 - p_1V_1}{n-1} \\ &= \frac{p_1V_1\left[\left(\frac{p_2}{p_1}\right)^{(n-1)/n} - 1\right]}{n-1} \end{aligned} \tag{3.90}$$

and

$$W_{t12} = nW_{12}\,. \tag{3.91}$$

The heat exchanged is

$$Q_{12} = mc_v(n - \varkappa)\frac{T_2 - T_1}{n-1}\,. \tag{3.92}$$

Example 3.9

A compressed air system should deliver 1000 m_n^3 compressed air of 15 bar/h (note: 1 m_n^3 = 1 standard cubic meter for a gas volume at 0 °C and 1.01325 bar). The air inlet is at a pressure of $p_1 = 1$ bar and a temperature of $t_1 = 20$ °C. The adiabatic exponent of air is $\varkappa = 1.4$. How much power is required, if the compression is polytropic with $n = 1.3$? What heat transfer rate has to be exchanged for this process?

The inlet air volume flow is, as given in the requirements, 1000 m³ at 0 °C and 1.01325 bar,

$$\begin{aligned}\dot{V}_1 &= \frac{p_0 T_1}{p_1 T_0}\dot{V}_0 \\ &= \frac{1.01325 \times 293.15}{1 \times 273.15} 1000 \frac{\mathrm{m}^3}{\mathrm{h}} \\ &= 1087.44 \frac{\mathrm{m}^3}{\mathrm{h}} .\end{aligned}$$

For polytropic changes of state, (3.91) and (3.90) yield

$$\begin{aligned}P = \dot{W}_\mathrm{t} &= \frac{n p_1 \dot{V}_1}{n-1}\left[\left(\frac{p_2}{p_1}\right)^{\frac{n-1}{n}} - 1\right] \\ &= \frac{1.3 \times 10^5 \frac{\mathrm{N}}{\mathrm{m}^2} 1087.44 \frac{\mathrm{m}^3}{\mathrm{h}}}{1.3-1}\left(15^{\frac{1.3-1}{1.3}} - 1\right) \\ &= 113.6\,\mathrm{kW} .\end{aligned}$$

According to (3.91) and (3.92),

$$\frac{Q_{12}}{W_{\mathrm{t}12}} = \frac{\dot{Q}}{P} = c_v \frac{n-\varkappa}{nR}$$

or, since $R = c_p - c_v$ and $\varkappa = c_p/c_v$,

$$\frac{\dot{Q}}{P} = \frac{1}{n}\frac{n-\varkappa}{\varkappa-1} .$$

Thus,

$$\dot{Q} = \frac{1}{1.3}\frac{1.3-1.4}{1.4-1} 113.6\,\mathrm{kW} = -21.85\,\mathrm{kW} .$$

3.7.2 Changes of State of Flowing Gases and Vapors

To describe the flow of a fluid mass Δm, in addition to the thermodynamic properties, the size and direction of the velocity everywhere in the field are also required. The following discussion is limited to steady flows in channels with constant, diverging, or converging cross sections.

In addition to the first and second laws, the conservation of mass law holds

$$\dot{m} = A w \varrho = \text{const} . \tag{3.93}$$

For a flow that does no work on the environment, the first law, (3.21), reduces to

$$\begin{aligned}&\Delta m(h_2 - h_1) + \Delta m\left(\frac{w_2^2}{2} - \frac{w_1^2}{2}\right) + \Delta m g(z_2 - z_1) \\ &= Q_{12} ,\end{aligned} \tag{3.94}$$

regardless of whether the flow is reversible or irreversible. Neglecting changes in potential energy, it holds that, for an adiabatic flow,

$$h_2 - h_1 + \frac{w_2^2}{2} - \frac{w_1^2}{2} = 0 . \tag{3.95}$$

Thus, the increase in kinetic energy is equal to the decrease in enthalpy of the fluid. For an adiabatic throttle process, it follows from (3.93), provided A and $\varrho = \text{const}$, that $w = \text{const}$ and thus from (3.95) that $h_1 = h_2 = \text{const}$. The pressure reduction in an adiabatic throttle process is accompanied by an entropy increase, since the process is irreversible. According to (3.32), the enthalpy change in a reversible adiabatic flow is caused by a change in pressure, $\mathrm{d}h = v\,\mathrm{d}p$.

Flow of Ideal Gases

Applying (3.95) to an ideal gas exiting a vessel (Fig. 3.14), in which the gas in the vessel possesses the constant state p_0, v_0, T_0 with $w_0 = 0$, and where $h_\mathrm{e} - h_0 = c_p(T_\mathrm{e} - T_0)$, $w_0 = 0$, leads to

$$\begin{aligned}\frac{w_\mathrm{e}^2}{2} &= c_p(T_0 - T_\mathrm{e}) \\ &= c_p T_0\left(1 - \frac{T_\mathrm{e}}{T_0}\right) .\end{aligned}$$

For a reversible adiabatic change of state, according to (3.90), $T_\mathrm{e}/T_0 = (p_\mathrm{e}/p_0)^{(\varkappa-1)/\varkappa}$. Additionally, it holds that $T_0 = p_0 v_0/R$ according to (3.60) and $c_p/R = \varkappa/(\varkappa-1)$ according to (3.73). Thus, the exit velocity is given by

$$w_\mathrm{e} = \sqrt{2\frac{\varkappa}{\varkappa-1} p_0 v_0\left[1 - \left(\frac{p_\mathrm{e}}{p_0}\right)^{\frac{\varkappa-1}{\varkappa}}\right]} . \tag{3.96}$$

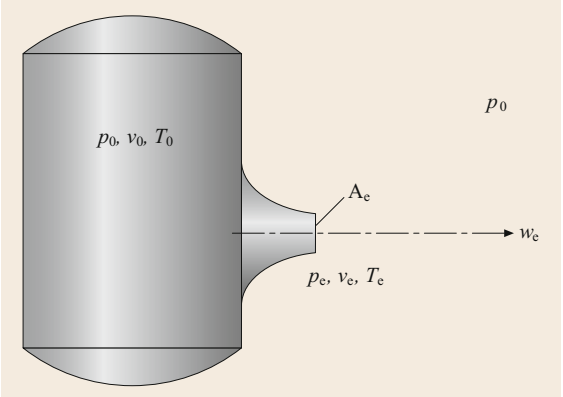

Fig. 3.14 Flow out of a pressure vessel

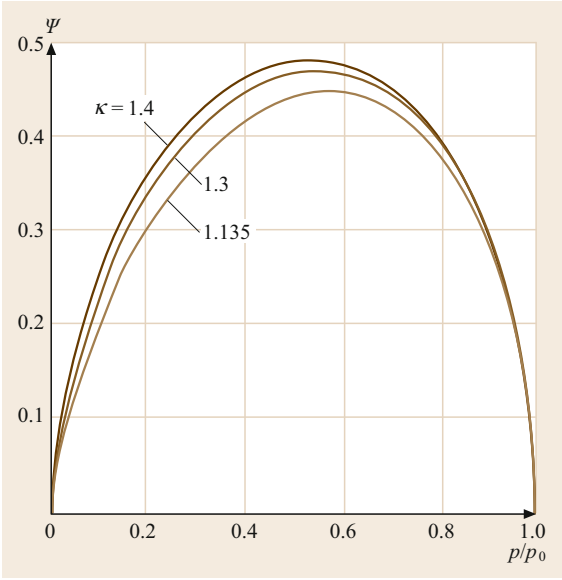

Fig. 3.15 Outlet function Ψ

Taking into account $p_0 v_0^{\varkappa} = p_e v_e^{\varkappa}$, the out-flowing mass $\dot{m} = A_e w_e / v_e$ is

$$\dot{m} = A\Psi \sqrt{\frac{2p_0}{v_0}} \tag{3.97}$$

with the outlet function

$$\Psi = \sqrt{\frac{\varkappa}{\varkappa - 1}} \sqrt{\left(\frac{p}{p_0}\right)^{\frac{2}{\varkappa}} - \left(\frac{p}{p_0}\right)^{\frac{\varkappa+1}{\varkappa}}} \,. \tag{3.98}$$

The result is a function of the adiabatic exponent $\varkappa$ and of the pressure ratio p/p_0 (Fig. 3.15) and has a maximum Ψ_{max}, which can be determined from evaluating $d\Psi/d(p/p_0) = 0$. This maximum corresponds to a specific pressure ratio that is called the *Laval pressure ratio*

$$\frac{p_s}{p_0} = \left(\frac{2}{\varkappa + 1}\right)^{\frac{\varkappa}{\varkappa - 1}} \,. \tag{3.99}$$

At this pressure ratio

$$\Psi_{max} = \left(\frac{2}{\varkappa + 1}\right)^{\frac{1}{\varkappa - 1}} \sqrt{\frac{\varkappa}{\varkappa + 1}} \,. \tag{3.100}$$

Corresponding to this pressure ratio, according to (3.96) with $p_e/p_0 = p_s/p_0$ and a velocity $w_e = w_s$, is the relation

$$w_s = \sqrt{2\frac{\varkappa}{\varkappa + 1} p_0 v_0} = \sqrt{\varkappa p_s v_s} = \sqrt{\varkappa R T_s} \,. \tag{3.101}$$

This is equal to the sonic velocity in the state p_s, v_s. Generally, the sonic velocity is the velocity at which pressure and density fluctuations are transmitted. For reversible adiabatic changes of state, it is given by

$$w_s = \sqrt{\left(\frac{\partial p}{\partial \varrho}\right)_s} \,.$$

Thus, for ideal gases, it takes on the value $w_s = \sqrt{\varkappa R T}$, where the sonic velocity is a property.

Example 3.10

A steam boiler produces 10 t of saturated vapor at $p_0 = 15$ bar. The vapor may be treated as an ideal gas ($\varkappa = 1.3$). How large must the cross section of the safety relief valve be in order to be able to discharge the entire vapor mass flow?

Since the out-flowing mass $\dot{m}$ is constant in every cross section, it follows from (3.97) that $A\Psi =$ const as well. As the discharge flow area is decreased, A decreases, and Ψ increases, reaching at most the value Ψ_{max}. Then the back pressure is less than or equal to the Laval pressure. In the present case the back pressure of the atmosphere, $p = 1$ bar, is less than the Laval pressure, which is calculated with (3.99) to be 8.186 bar. With this result, the required cross section follows from (3.97), if $\Psi = \Psi_{max} = 0.472$ according to (3.100) is inserted. With $\dot{m} = 10 \times 10^3 \times (1/3600)\,\mathrm{kg/s} = 2.7778\,\mathrm{kg/s}$ and $v_0 = v'' = 0.1317\,\mathrm{m^3/kg}$ (according to Table 3.9 at $p_0 = 15$ bar), it follows from (3.97) that $A = 12.33\,\mathrm{cm^2}$. Because of the jet's contraction, where the size depends on the design of the valve, an increase should be added.

Jet and Diffusion Flow

As shown in Fig. 3.16, for a given adiabatic exponent $\varkappa$, a certain pressure ratio p/p_0 corresponds to a spe-

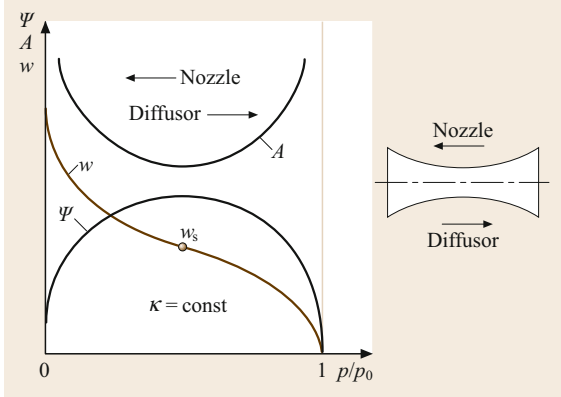

Fig. 3.16 Nozzle and diffusor flow

cific value of the outlet function Ψ. Since the mass flow $\dot{m}$ is constant in each cross section, it follows from (3.97) that also $A\Psi = \text{const}$. Thus, it is possible to assign to each pressure ratio a certain cross section A; see Fig. 3.16. Two cases have to be distinguished:

a) The pressure decreases in the flow direction. The curves Ψ, A, and w in Fig. 3.16 are passed through from right to left. At first the cross section A decreases, then it increases again. The velocity increases and goes from subsonic to supersonic. The kinetic energy of the flow increases. Such an apparatus is called a nozzle. In a nozzle that operates only in the subsonic regime the cross section decreases continuously, whereas it increases in the supersonic regime. In a nozzle narrowing in the flow direction the pressure at the outlet cross section cannot decrease below the Laval pressure, even if the outside pressure is arbitrarily small. This follows from $A\Psi = \text{const}$. Since A decreases in the flow direction, Ψ can only increase, reaching at most the value $\Psi_{\max}$ to which the Laval pressure ratio corresponds.
If the pressure at the outlet cross section of a nozzle is reduced below the pressure value corresponding to the outlet cross section, the jet expands after leaving the nozzle. If the back pressure is increased above the correct value, the pressure increase moves upstream, where in this case the gas exits with subsonic velocity. If the gas exits with sonic, or in a diverging nozzle with supersonic velocity, a shock occurs at the nozzle outlet and the pressure increases to the pressure of the environment.
b) The pressure increases in the flow direction. The curves Ψ, A, and w in Fig. 3.16 are passed through from left to right. At first the cross section decreases, then increases again. The velocity decreases from supersonic to subsonic, and the kinetic energy decreases while the pressure increases. Such an apparatus is called a diffuser. In a diffuser that works only in the subsonic regime the cross section increases continuously, whereas it decreases in the supersonic regime.

3.8 Thermodynamic Processes

3.8.1 Combustion Processes

Heat transfer for technical processes is still mostly obtained through combustion. Combustion is a chemical reaction during which a substance, e.g., carbon, hydrogen, or hydrocarbons, is oxidized, which is strongly exothermic; i.e., a large quantity of heat is released. Fuels can be solid, liquid, or gaseous (Tab. 3.16). The required oxygen is mostly provided by atmospheric air. To start a combustion process, the fuel must be brought above its ignition temperature, which, in turn, varies according to the type of fuel being used. The main components of all important technical fuels are carbon (C) and hydrogen (H). In addition, oxygen (O), and with the exception of natural gas a certain amount of sulfur, are also present. Sulfur reacts during a combustion process to produce the unwanted compound sulfur dioxide SO_2.

Reaction Equations

The elements H, C, and S, which are contained in fuels as mentioned above, are burned to CO_2, H_2O, and SO_2, if complete combustion takes place. The reaction equations determine the amount of oxygen required and the resulting amount of each product in the exhaust gas. For combustion of carbon C, it holds that

$$\begin{aligned} \mathrm{C} + \mathrm{O_2} &= \mathrm{CO_2}\,, \\ 1\,\mathrm{kmol\,C} + 1\,\mathrm{kmol\,O_2} &= 1\,\mathrm{kmol\,CO_2}\,, \\ 12\,\mathrm{kg\,C} + 32\,\mathrm{kg\,O_2} &= 44\,\mathrm{kg\,CO_2}\,. \end{aligned}$$

From this, it follows that the minimum oxygen demand for complete combustion is

$$o_{\min} = \frac{1}{12}\,\frac{\mathrm{kmol\,O_2}}{\mathrm{kg\,C}}$$

Table 3.16 Composition and calorific values of solid fuels

Fuel	Ash (mass%)	Water (mass%)	Composition of ash-free dry substance (mass%)					Gross calorific value (MJ/kg)	Net calorific value (MJ/kg)
			C	H	S	O	N		
Wood, air-dried	< 0.5	10–20	50	6	0.0	43.9	0.1	15.91–18.0	14.65–16.75
Peat, air-dried	< 15	15–35	50–60	4.5–6	0.3–2.5	30–40	1–4	13.82–16.33	11.72–15.07
Raw soft coal	2–8	50–60	65–75	5–8	0.5–4	15–26	0.5–2	10.47–12.98	8.37–11.30
Soft coal briquette	3–10	12–18	65–75	5–8	0.5–4	15–26	0.5–2	20.93–21.35	19.68–20.10
Hard coal	3–12	0–10	80–90	4–9	0.7–1.4	4–12	0.6–2	29.31–35.17	27.31–34.12
Anthracite	2–6	0–5	90–94	3–4	0.7–1	0.5–4	1–1.5	33.49–34.75	32.66–33.91

or

$$O_{\min} = 1\,\frac{\text{kmol O}_2}{\text{kmol C}}\,.$$

The minimum air demand for complete combustion is called the *theoretical air* and results from the oxygen fraction of 21 mol% in air

$$l_{\min} = \left(\frac{o_{\min}}{0.21}\right)\,\text{kmol air/kg C}$$

or

$$L_{\min} = \left(\frac{O_{\min}}{0.21}\right)\,\text{kmol air/kmol C}\,.$$

The amount of CO_2 in the exhaust gas is $(1/12)$ kmol/kg C. Similarly, the reaction equations for the combustion of hydrogen H_2 and sulfur S are

$$\begin{aligned}
\text{H}_2 + \tfrac{1}{2}\,\text{O}_2 &= \text{H}_2\text{O}\,,\\
1\,\text{kmol H}_2 + \tfrac{1}{2}\,\text{kmol O}_2 &= 1\,\text{kmol H}_2\text{O}\,,\\
2\,\text{kg H}_2 + 16\,\text{kg O}_2 &= 18\,\text{kg H}_2\text{O}\,,
\end{aligned}$$

$$\begin{aligned}
\text{S} + \text{O}_2 &= \text{SO}_2\,,\\
1\,\text{kmol S} + 1\,\text{kmol O}_2 &= 1\,\text{kmol SO}_2\,,\\
32\,\text{kg S} + 32\,\text{kg O}_2 &= 64\,\text{kg SO}_2\,.
\end{aligned}$$

Denoting the carbon, hydrogen, sulfur, and oxygen fractions by c, h, s, and o in kg per kg fuel, according to the above calculations, the minimum oxygen demand becomes

$$o_{\min} = \left(\frac{c}{12} + \frac{h}{4} + \frac{s}{32} - \frac{o}{32}\right)\,\text{kmol/kg}\,, \qquad (3.102)$$

or for short

$$o_{\min}\,\frac{1}{12}c\sigma\,\text{kmol/kg}\,, \qquad (3.103)$$

where σ is a characteristic of the fuel (O_2 demand in kmol related to the kmol C in the fuel). The actual air demand (related to 1 kg fuel) is

$$l = \lambda l_{\min} = \left(\frac{\lambda o_{\min}}{0.21}\right)\,\text{kmol air/kg}\,, \qquad (3.104)$$

where λ is the excess air number. In addition to the combustion products CO_2, H_2O, and SO_2, the exhaust gases also ordinarily contain water with a content of $w/18$ (SI units of kmol per kg fuel), and the supplied combustion air l less the spent oxygen $o_{\min}$. The supplied combustion air is therefore assumed to be dry, or it is assumed that the water vapor content is negligibly small. The corresponding exhaust amounts, related to 1 kg of fuel, are given by

$$\begin{aligned}
n_{\text{CO}_2} &= \frac{c}{12}\,,\\
n_{\text{H}_2\text{O}} &= \frac{h}{2} + \frac{w}{18}\,,\\
n_{\text{SO}_2} &= \frac{s}{32}\,,\\
n_{\text{O}_2} &= (\lambda - 1)o_{\min}\,,\\
n_{\text{N}_2} &= 0.791\,.
\end{aligned}$$

The sum is the total exhaust amount

$$n_{\text{exh}} = \left[\frac{c}{12} + \frac{h}{2} + \frac{w}{18} + \frac{s}{32} + (\lambda - 1)o_{\min} + 0.791\right]\,\text{kmol/kg}.$$

This can be simplified by using (3.102) and (3.104) to yield

$$n_{\text{exh}} = \left[l + \frac{1}{12}\left(3h + \frac{3}{8}o + \frac{2}{3}w\right)\right]\,\text{kmol/kg}\,. \qquad (3.105)$$

Example 3.11

Consider 500 kg coal with composition $c = 0.78$, $h = 0.05$, $o = 0.08$, $s = 0.01$, and $w = 0.02$ and ash content $a = 0.06$ which is completely burned per hour in a furnace with excess air number $\lambda = 1.4$. How much air is necessary, how much exhaust arises, and what is its composition?

The minimum oxygen demand is determined according to (3.102)

$$\begin{aligned}
o_{\min} &= \left(\frac{0.78}{12} + \frac{0.05}{4} + \frac{0.01}{32} - \frac{0.08}{32}\right)\,\text{kmol/kg}\\
&= 0.0753\,\text{kmol/kg}\,.
\end{aligned}$$

The minimum air demand is

$$l_{\min} = \frac{o_{\min}}{0.21} = 0.3586\,\text{kmol/kg}\,.$$

The amount of air that has to be supplied is

$$l = \lambda l_{\min} = 1.4 \times 0.3586 = 0.502\,\text{kmol/kg}\,.$$

Thus $0.502\,\text{kmol/kg} \times 500\,\text{kg/h} = 251\,\text{kmol/h}$. With the molar mass of air $M = 28.953\,\text{kg/kmol}$, the air demand becomes $0.502 \times 28.953\,\text{kg/kg} = 14.54\,\text{kg/kg}$.

Thus, $14.54\,\mathrm{kg/kg} \times 500\,\mathrm{kg/h} = 7270\,\mathrm{kg/h}$. The exhaust amount is determined according to (3.105)

$$n_{\mathrm{exh}} = \left(0.502 + \frac{1}{12}\left(3 \times 0.05 + \frac{3}{8} \times 0.08 + \frac{2}{3} \times 0.02\right)\right) \mathrm{kmol/kg} = 0.518\,\mathrm{kmol/kg}\,.$$

Thus, $0.581\,\mathrm{kmol/kg} \times 500\,\mathrm{kg/h} = 259\,\mathrm{kmol/h}$ with $0.065\,\mathrm{kmol\,CO_2/kg}$, $0.0261\,\mathrm{kmol\,H_2O/kg}$, $0.0003\,\mathrm{kmol\,SO_2/kg}$, $0.3966\,\mathrm{kmol\,N_2/kg}$ and $0.0301\,\mathrm{kmol\,O_2/kg}$.

Net Calorific Value and Gross Calorific Value

The net calorific value is the energy released during combustion, if the exhaust gases are cooled down to the temperature at which the fuel and air are supplied. Water is included in the exhaust gases as vapor. If the water vapor is condensed, the released heat is called the gross calorific value. Net and gross calorific values are specified, according to DIN 51900, for combustion at atmospheric pressure, if all involved substances are at a temperature of 25 °C before and after combustion. Net and gross calorific values (Tables 3.17–3.19) are independent of the amount of excess air and are only a characteristic of the fuel. The gross calorific value Δh_{gcv} exceeds the net calorific value Δh_{ncv} by the enthalpy of vaporization Δh_{v} of the water included in the exhaust gas

$$\Delta h_{\mathrm{gcv}} = \Delta h_{\mathrm{ncv}} + (8.937h + w)\,\Delta h_{\mathrm{v}}\,.$$

Because the water leaves technical furnaces mostly as vapor, often only the net calorific value can be utilized. The net calorific value of heating oil can be expressed quite well, as experience shows [3.17], by the equation

$$\Delta h_{\mathrm{ncv}} = (54.04 - 13.29\varrho - 29.31s)\,\mathrm{MJ/kg}\,, \tag{3.106}$$

where the density ϱ of the heating oil in $\mathrm{kg/dm^3}$ is at 15 °C and the sulfur content s is in kg/kg.

Table 3.17 Net calorific values of the simplest fuels at 25 °C and 1.01325 bar

	C	CO	H_2 (gross calorific value)	H_2 (net calorific value)	S
kJ/kmol	393 510	282 989	285 840	241 840	296 900
kJ/kg	32 762	10 103	141 800	119 972	9260

Table 3.18 Combustion of liquid fuels

Fuel	Molar weight (kg/kmol)	Content (mass%) C	H	Characteristic σ	Calorific value (kJ/kg) Gross	Net
Ethyl alcohol C_2H_5OH	46.069	52	13	1.50	29 730	26 960
Spirit 95%	–	–	–	1.50	28 220	25 290
90%	–	–	–	1.50	26 750	23 860
85%	–	–	–	1.50	25 250	22 360
Benzene (pure) C_6H_6	78.113	92.2	7.8	1.25	41 870	40 150
Toluene (pure) C_7H_8	92.146	91.2	8.8	1.285	42 750	40 820
Xylene (pure) C_8H_{10}	106.167	90.5	9.5	1.313	43 000	40 780
Benzene I on sale [a]	–	92.1	7.9	1.26	41 870	40 190
Benzene II on sale [b]	–	91.6	8.4	1.30	42 290	40 400
Naphthalene (pure) $C_{10}H_8$ (melting temp. 80 °C)	128.19	93.7	6.3	1.20	40 360	38 940
Tetralin $C_{10}H_{12}$	132.21	90.8	9.2	1.30	42 870	40 820
Pentane C_5H_{12}	72.150	83.2	16.8	1.60	49 190	45 430
Hexane C_6H_{14}	86.177	83.6	16.4	1.584	48 360	44 670
Heptane C_7H_{16}	100.103	83.9	16.1	1.571	47 980	44 380
Octane C_8H_{18}	114.230	84.1	15.9	1.562	48 150	44 590
Benzine (mean values)	–	85	15	1.53	46 050	42 700

[a] 0.84 benzene, 0.31 toluene, 0.03 xylene (mass fractions)
[b] 0.43 benzene, 0.46 toluene, 0.11 xylene (mass fractions)

Table 3.19 Combustion of some simple gases at 25 °C and 1.01325 bar

Gas	Molar mass [a] (kg/kmol)	Density (kg/m³)	Characteristic σ	Calorific value (MJ/kg) Gross	Net
Hydrogen H_2	2.0158	0.082	∞	141.80	119.97
Carbon monoxide CO	28.0104	1.14	0.50	10.10	10.10
Methane CH_4	16.043	0.656	2.00	55.50	50.01
Ethane C_2H_6	30.069	1.24	1.75	51.88	47.49
Propane C_3H_8	44.09	1.80	1.67	50.35	46.35
Butane C_4H_{10}	58.123	2.37	1.625	49.55	45.72
Ethylene C_2H_4	28.054	1.15	1.50	50.28	47.15
Propylene C_3H_6	42.086	1.72	1.50	48.92	45.78
Butylene C_4H_8	56.107	2.90	1.50	48.43	45.29
Acetylene C_2H_2	26.038	1.07	1.25	49.91	48.22

[a] According to DIN 51850: gross and net calorific values of gaseous fuels, April 1980

Example 3.12

What is the net calorific value of a light heating oil with a density of $\varrho = 0.86\,\mathrm{kg/dm^3}$ and a sulfur content of $s = 0.8$ mass%? According to (3.106)

$$\begin{aligned}\Delta h_{\mathrm{ncv}} &= (54.04 - 13.29 \times 0.86 \\ &\quad - 29.31 \times 0.8 \times 10^{-2})\,\mathrm{MJ/kg} \\ &= 42.38\,\mathrm{MJ/kg}\,.\end{aligned}$$

Combustion Temperature

The theoretical combustion temperature is the temperature of the exhaust gas at complete isobar–adiabatic combustion if no dissociation takes place. The heat released during combustion increases the internal energy and thus the temperature of the gas, which provides the basis for doing flow work. The theoretical combustion temperature is calculated under the condition that the enthalpy of all substances transferred to the combustion chamber must be equal to the enthalpy of the discharged exhaust gas.

$$\begin{aligned}&\Delta h_{\mathrm{ncv}}\,[c_{\mathrm{fuel}}]_{25\,^\circ\mathrm{C}}^{t_{\mathrm{fuel}}}\,(t_{\mathrm{fuel}} - 25\,^\circ\mathrm{C}) \\ &\quad + l\,\left[\overline{C}_{p\,\mathrm{air}}\right]_{25\,^\circ\mathrm{C}}^{t_{\mathrm{air}}}\,(t_{\mathrm{air}} - 25\,^\circ\mathrm{C}) \\ &= n_{\mathrm{exh}}\,\left[\overline{C}_{p\,\mathrm{exh}}\right]_{25\,^\circ\mathrm{C}}^{t}\,(t - 25\,^\circ\mathrm{C})\,. \qquad (3.107)\end{aligned}$$

This equation includes the temperatures t_{fuel} of the fuel and t_{air} of the air, the theoretical combustion temperature t, the mean specific heat $[c]_{25\,^\circ\mathrm{C}}^{t_{\mathrm{fuel}}}$ of the fuel, and the mean specific heats $\left[\overline{C}_{p\,\mathrm{air}}\right]_{25\,^\circ\mathrm{C}}^{t_{\mathrm{air}}}$ of the air and $\left[\overline{C}_{p\,\mathrm{exh}}\right]_{25\,^\circ\mathrm{C}}^{t}$ of the exhaust gas. The latter consists of the mean molar specific heats of the single components

$$\begin{aligned}&n_{\mathrm{exh}}\,\left[\overline{C}_{p\,\mathrm{exh}}\right]_{25\,^\circ\mathrm{C}}^{t} \\ &= \frac{c}{12}\,\left[\overline{C}_{p\mathrm{CO_2}}\right]_{25\,^\circ\mathrm{C}}^{t} + \left(\frac{h}{2} + \frac{w}{18}\right)\,\left[\overline{C}_{p\mathrm{H_2O}}\right]_{25\,^\circ\mathrm{C}}^{t} \\ &\quad + \frac{s}{32}\,\left[\overline{C}_{p\mathrm{SO_2}}\right]_{25\,^\circ\mathrm{C}}^{t} + (\lambda - 1)\,o_{\mathrm{min}}\,\left[\overline{C}_{p\mathrm{O_2}}\right]_{25\,^\circ\mathrm{C}}^{t} \\ &\quad + 0.79 l\,\left[\overline{C}_{p\mathrm{N_2}}\right]_{25\,^\circ\mathrm{C}}^{t}\,. \qquad (3.108)\end{aligned}$$

The theoretical combustion temperature must be determined iteratively from (3.107) and (3.108). The actual combustion temperature is, even with complete combustion of the fuel, lower than the theoretical combustion temperature due to heat transfer to the environment, mainly by radiation. Another effect that lowers the combustion temperature is the break-up of molecules (dissociation) starting above 1500 °C and the considerable dissociation above 2000 °C. The dissociation heat is released again when the temperature decreases below the dissociation temperature.

3.8.2 Internal Combustion Cycles

In internal combustion cycles, the combustion gas serves as a working fluid. It does not operate through a closed process but is discharged as exhaust gas to the environment after performing work in a turbine or a piston engine. Open, gas turbine cycles and internal combustion engines (Otto and Diesel), as well as fuel cells, are internal combustion cycles. The quality of the energy transformation is assessed by the total energy efficiency

$$\eta = -\frac{P}{\dot{m}_{\mathrm{fuel}}\,\Delta h_{\mathrm{ncv}}}\,,$$

where P is the power output of the cycle, $\dot{m}$ is the mass flow rate of the supplied fuel, and Δh_{ncv} is its net calorific value. The total exergetic efficiency $\xi = -P/(\dot{m}_{\mathrm{fuel}}\,w_{\mathrm{ex,fuel}})$ specifies the fraction of the exergy flow coming with the fuel that is transformed into power output. Generally, w_{ex} is only slightly larger than the net calorific value, and η and ξ thus hardly differ in their numerical values. The typical total efficiency is approximately 45% for large engines (Diesel), 30% for automotive engines, and 30% for open gas turbine cycles.

Open Gas Turbine Cycle

In an open gas turbine plant, the inlet air is brought to a high pressure through a compressor, then preheated

and heated in a combustion chamber via the combustion of the injected fuel. The combustion gases pass through a turbine, in which they do work (against the blades). The gas exiting the turbine is used to preheat the combustion air in a heat exchanger, and is then discharged into the environment. The compressor and turbine are placed on the same shaft. The power output is transformed into electric energy by a generator, which is connected to the shaft.

Otto Engine

Figure 3.17 shows the cycle of an Otto engine on p–V and T–S diagrams. At the end of the intake stroke, the cylinder is filled with a combustible fresh air–fuel mixture of state 1 at the environmental temperature and atmospheric pressure. The mixture is compressed along the adiabate 1–2 from the initial volume $V_c + V_d$ to the compression volume V_c, where V_d is the displacement volume. At the top dead center 2, combustion is initiated by electric spark ignition, whereby the pressure rises from state 2 to state 3. This change of state takes place so quickly that it can be assumed to be isochoric. In Fig. 3.17 (simplifying), it is assumed that the gas is not changed and that the heat released during combustion $Q_{23} = Q$ is supplied from the outside. The gas expands along the adiabatic 3–4–4″–4′ and forces the piston to return. The exhaust beginning in state 4 is substituted by the removal of energy by heat transfer $|Q_0|$ at constant volume, whereas the pressure decreases from state 4 to state 1. In state 1, the combustion gases have to be replaced by a new mixture. In order to do so, twin-stroke operation (not shown) is necessary in a four-stroke Otto engine.

The heat transfer to the gas is

$$Q = Q_{23} = mc_v(T_3 - T_2)\,, \tag{3.109}$$

while that from the gas is

$$|Q_0| = |Q_{41}| = mc_v(T_4 - T_1)\,. \tag{3.110}$$

The work is

$$|W_t| = Q - |Q_0|\,, \tag{3.111}$$

and the thermal efficiency is given by

$$\eta = \frac{|W_t|}{Q} = 1 - \frac{T_4 - T_1}{T_3 - T_2} = 1 - \frac{T_1}{T_2}$$
$$= 1 - \left(\frac{p_1}{p_2}\right)^{\frac{\varkappa-1}{\varkappa}} = 1 - \frac{1}{\varepsilon^{\varkappa-1}}\,. \tag{3.112}$$

The compression ratio $\varepsilon = V_1/V_2 = (V_c + V_d)/V_c$ specifies the degree of adiabatic compression of the mixture.

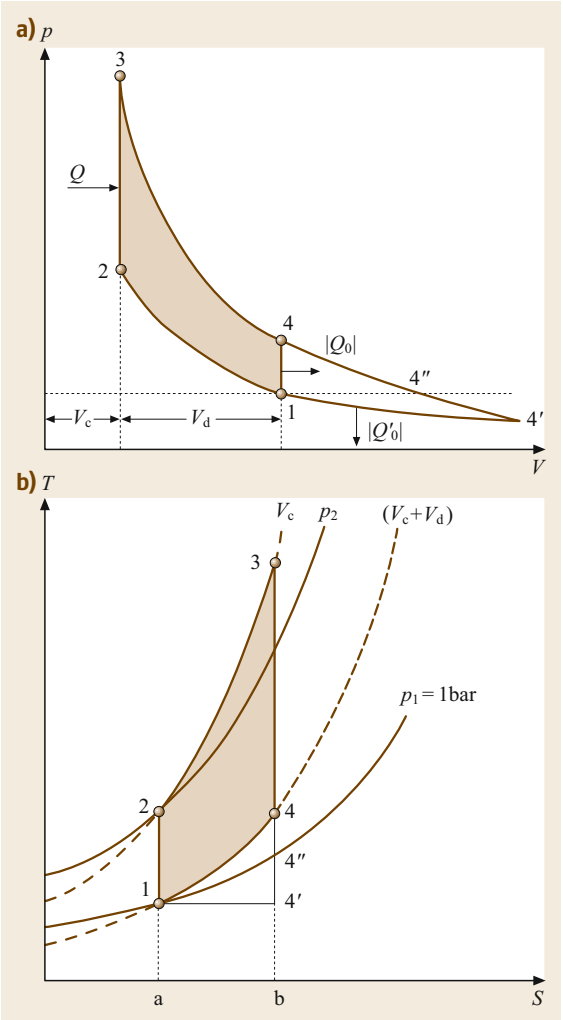

Fig. 3.17a,b Theoretical process of the Otto engine on **(a)** p–V and **(b)** T–S diagrams

Thus, the thermal efficiency depends, except for the adiabatic exponent, only on the pressure ratio p_2/p_1 or the compression ratio ε but not on the amount of energy supplied by heat transfer. The compression ratio is limited by the self-ignition temperature of the fuel–air mixture.

Diesel Engine

The limitation to moderate compression ratios and pressures does not apply for the Diesel engine, in which the high compression heats the combustion air above the self-ignition temperature of the fuel that is injected into the hot air. Figure 3.18 shows the simplified process of the Diesel engine. It consists of the adiabatic compression 1–2 of the combustion air, isobaric combustion 2–3′ after the injection of the fuel into the hot,

compressed combustion air, adiabatic relaxation 3′–4, and ejection 4–1 of the exhaust gases, which is replaced in Fig. 3.18 by an isochore with heat removal. The supplied heat transfer is

$$Q_{23'} = Q = mc_p(T_{3'} - T_2)\,, \tag{3.113}$$

and the removed heat transfer is

$$|Q_{41}| = |Q_0| = mc_v(T_4 - T_1) \tag{3.114}$$

during the imaginary isochore 4–1. The work is given by

$$|W_t| = Q - |Q_0|\,,$$

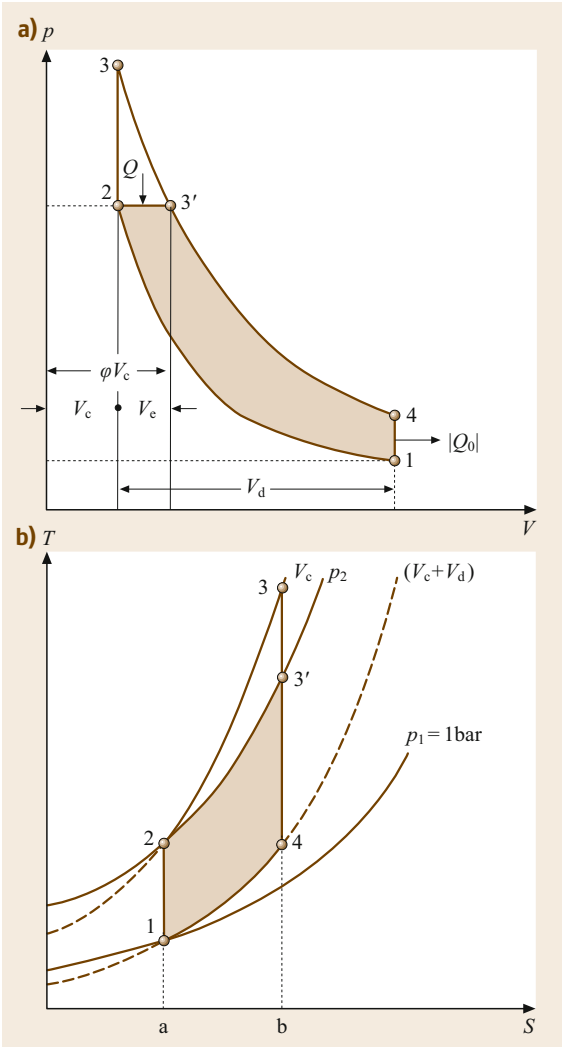

Fig. 3.18a,b Theoretical process of the Diesel engine on **(a)** p–V and **(b)** T–S diagrams

and the thermal efficiency by

$$\eta = \frac{|W_t|}{Q} = 1 - \frac{1}{\varkappa}\frac{T_4 - T_1}{T_{3'} - T_2} = 1 - \frac{1}{\varkappa}\frac{\frac{T_4}{T_3}\frac{T_3}{T_2} - \frac{T_1}{T_2}}{\frac{T_{3'}}{T_2} - 1}\,. \tag{3.115}$$

With the compression ratio $\varepsilon = V_1/V_2 = (V_c + V_d)/V_c$ and the cutoff ratio $\varphi = (V_c + V_e)/V_c$, the following equation for the thermal efficiency results:

$$\eta = 1 - \frac{1}{\varkappa\,\varepsilon^{\varkappa-1}}\frac{\varphi^{\varkappa} - 1}{\varphi - 1}\,. \tag{3.116}$$

The thermal efficiency of the Diesel cycle depends, except for the adiabatic exponent, only on the compression ratio ε and on the cutoff ratio φ, which increases with increasing load.

Fuel Cells

In a fuel cell, hydrogen reacts electrochemically with oxygen to produce water

$$H_2 + \frac{1}{2}O_2 \rightarrow H_2O\,.$$

In this so-called cold combustion, the chemical bond energy is transformed directly into electrical energy. Figure 3.19 shows, as an example, a fuel cell with a proton-conductive electrolyte, where hydrogen is supplied at the anode side. With the help of a catalyst, it is decomposed into two protons (H^+) and two electrons (e^-). The electrons move through a load, e.g., a motor, to the cathode. The protons move through the electrolyte to the cathode, where they, supported by a catalyst, react with the supplied oxygen, O_2, and the electrons to produce water, H_2O. There is a voltage U

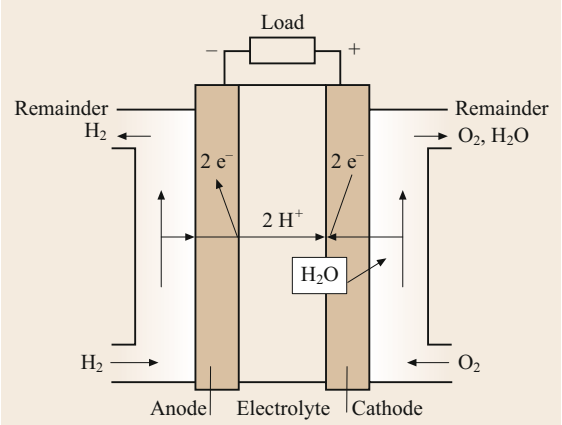

Fig. 3.19 Scheme of a fuel cell with a proton-conductive electrolyte

between the anode and cathode, and an electric current $I = F\dot{n}_{el}$ with $\dot{n}_{el} = 2\dot{n}_{H_2}$ flows. F is the Faraday constant $F = 96\,485.3\,\mathrm{As/mol}$, and $\dot{n}_{el}$ is the flow rate of electrons (SI units mol/s). The actual terminal voltage is smaller than the reversible one because of losses due to energy dissipation in the cell. The electric power of the cell is calculated from

$$\dot{Q} + P = \dot{n}_{H_2} \Delta H^{R}_{H_2}$$

with the flow rate $\dot{n}_{H_2}$ of the supplied hydrogen and its molar reaction enthalpy $\Delta H^{R}_{H_2}$ (SI unit J/mol), which is equal to the negative molar net calorific value $\Delta H_{m\,ncv} = M_{H_2} \Delta h_{ncv}$ (Sect. 3.8.1). Analogous to the efficiency of other combustion plants, the efficiency of a fuel cell is defined as

$$\eta_{fc} = \frac{-P}{\dot{n}_{H_2}\, \Delta H_{m\,ncv}} ,$$

with fuel cells generally being about 50% efficient.

3.8.3 Cyclic Processes: Principles

A process that brings a system back to its initial state is called a cyclic process. After the system has passed through such a cycle, all the properties of the system such as pressure, temperature, volume, internal energy, and enthalpy return to their initial values and thus produce

$$\sum Q_{ik} + \sum W_{ik} = 0 . \qquad (3.117)$$

The total work done is $-W = -\sum W_{ik} = \sum Q_{ik}$.

Machines in which a fluid is undergoing a cyclic process serve to transform heat transfer into work or to transfer thermal energy from a low to a high-temperature level while work is supplied. According to the second law of thermodynamics, it is not possible to transform all the supplied heat transfer into work. If the amount of heat supplied is larger than the amount of heat discharged, the process works as a power cycle or a thermal power plant whose purpose is to deliver work. If the amount of heat discharged is smaller than the amount of heat supplied, work must be supplied. Such a process can be used for heat transfer from a medium at a lower temperature to a medium at a higher temperature, e.g., ambient temperature. The required work is also discharged as heat at the higher temperature. Such a process works as a refrigeration cycle. In a heat pump process, heat is absorbed from the environment and is discharged together with the supplied work at a higher temperature.

Carnot Cycle

The cyclic process introduced in 1824 by Carnot is shown in Figs. 3.20 and 3.21. Even though not very important in practice, the Carnot cycle played a decisive roll in the historical development of heat transfer theory. It consists of the following changes of state (here, the clockwise process of a power cycle):

1–2 Isothermal expansion at temperature T with heat addition Q
2–3 Reversible adiabatic expansion from pressure p_2 to pressure p_3
3–4 Isothermal compression at temperature T_0 with heat removal $|Q_0|$
4–1 Reversible adiabatic compression from pressure p_4 to pressure p_1.

The heat supplied is

$$Q = mRT \ln \frac{V_2}{V_1} = T(S_2 - S_1) , \qquad (3.118)$$

and the heat removed is

$$|Q_0| = mRT_0 \ln \frac{V_3}{V_4} = T_0(S_3 - S_4) = T_0(S_2 - S_1) . \qquad (3.119)$$

The technical work done is $-W_t = Q - |Q_0|$, and the thermal efficiency is

$$\eta = \frac{|W_t|}{Q} = 1 - \left(\frac{T_0}{T}\right) . \qquad (3.120)$$

With the inverse sequence 4–3–2–1 of changes of state, the heat absorbed Q_0 is from a body at a lower temperature and, with the supply of the technical work W_t, the heat discharged Q is at the higher temperature T. Such a counterclockwise Carnot cycle results in heat removal Q_0 from a chilled system at the low temperature T_0, thus working as a refrigerator, and can discharge the

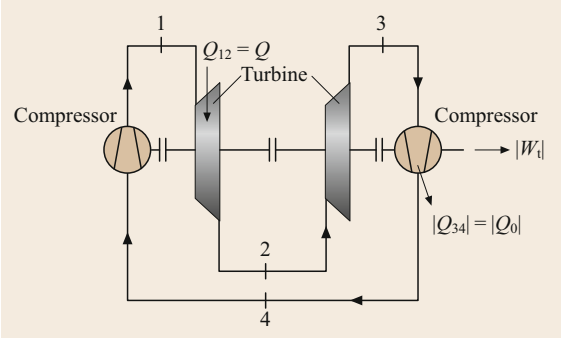

Fig. 3.20 Scheme of a Carnot power cycle

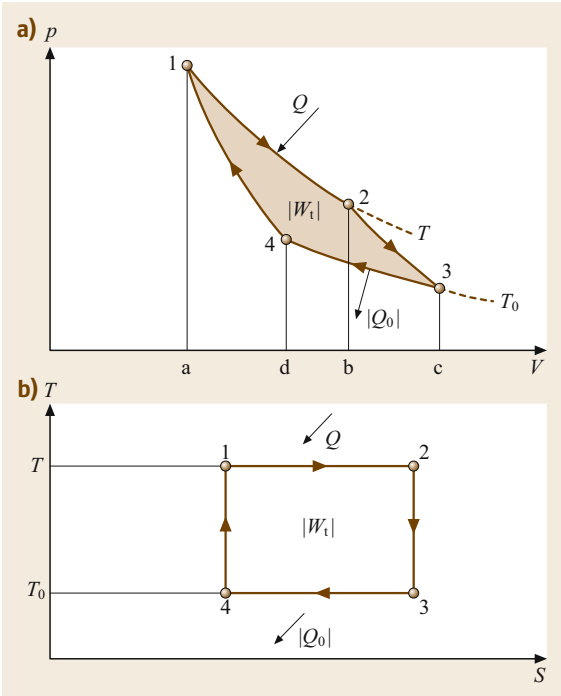

Fig. 3.21a,b The Carnot cycle on **(a)** p–V and **(b)** T–S diagrams

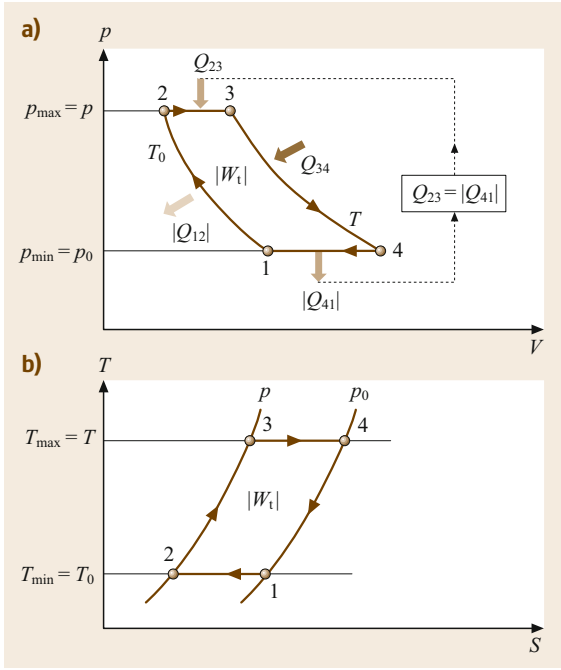

Fig. 3.22a,b The Ackeret–Keller process on **(a)** p–V and **(b)** T–S diagrams

heat $|Q| = W_t + Q_0$ at the higher temperature T to the environment. If the purpose of the process is the heat release $|Q|$ at the higher temperature T for heating, the process works as a heat pump. The heat transfer Q_0 is then removed from the environment at the lower temperature T_0. Carnot cycles have not achieved practical importance, however, because their power relative to the volume of the corresponding machine is very small. However, as an ideal, i.e., reversible, process the Carnot cycle is often used for comparison in order to assess other cyclic processes.

3.8.4 Thermal Power Cycles

In thermal power plants, energy in the form of heat transfer is transformed from the combustion gases in the working fluid, which undergoes a cyclic process. The Ackeret–Keller process consists of the following changes of state as shown in Fig. 3.22 in a p–V and T–S diagram:

1–2 Isothermal compression from pressure p_0 to pressure p at temperature T_0
2–3 Isobaric heat supply at pressure p
3–4 Isothermal expansion from pressure p to pressure p_0 at temperature T
4–1 Isobaric heat removal at pressure p_0.

Because this process can be traced back to a proposal by the Swedish engineer J. Ericsson (1803–1899), it is also called the Ericsson cycle. It was first used in 1941, however, by Ackeret and Keller as a comparison process for gas turbine plants. The heat transfer required for the isobaric heating 2–3 of the compressed working fluid is provided by the isobaric cooling 4–1 of the expanded working fluid, $Q_{23} = |Q_{41}|$.

The thermal efficiency is equal to the efficiency of the Carnot cycle, because

$$-W_t = Q_{34} - |Q_{21}| \tag{3.121}$$

and

$$\eta = 1 - \frac{|Q_{21}|}{Q_{34}} = 1 - \frac{T_0}{T} \,. \tag{3.122}$$

However, the technical realization of this process is difficult because isothermal compression and relaxation are hardly achievable due to the fact that they can only be approximated by multistage adiabatic compression with intermediate cooling. The Ackeret–Keller process serves mainly as a comparison process for the gas turbine process with multistage compression and relaxation. In a closed gas turbine plant (Fig. 3.23), a gas is compressed in the compressor, heated to a high temperature in the heat exchanger and the gas heater, then

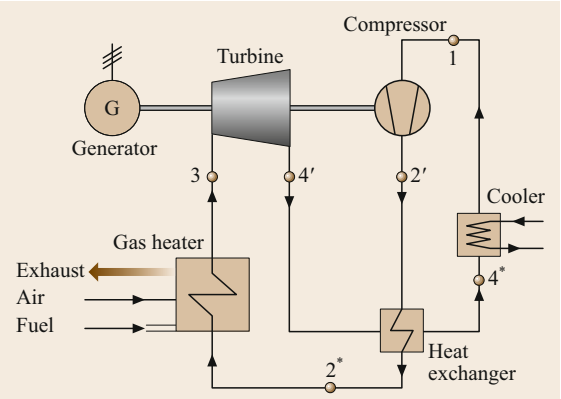

Fig. 3.23 Gas turbine process with a closed cycle

expanded in a turbine, where work is done, and cooled again to the initial temperature in the heat exchanger and the adjacent cooler. Then, the gas is drawn in by the compressor once again. Often air is used as the working fluid, but other gases such as helium or nitrogen are also sometimes used. The closed gas turbine plant is easily adjustable, and fouling of the turbine blades can be prevented by using suitable gases. A drawback in comparison with open plants is the higher energy costs, because a cooler is required and high-quality steels are needed for the heater. Figure 3.24 shows the process on p–V and T–S diagrams.

The reversible cyclic process consisting of two isobars and two isentropes is called the Joule process (states 1, 2, 3, 4). The supplied heat transfer is

$$\dot{Q} = \dot{m} c_p \, (T_3 - T_2) \ , \tag{3.123}$$

and the discharged heat transfer is

$$\left|\dot{Q}_0\right| = \dot{m} \, c_p \, (T_4 - T_1) \ . \tag{3.124}$$

The power is

$$\begin{aligned} -P &= -\dot{m} w_t = \dot{Q} - \left|\dot{Q}_0\right| \\ &= \dot{m} \, c_p (T_3 - T_2) \left(1 - \frac{T_4 - T_1}{T_3 - T_2}\right) \ , \end{aligned} \tag{3.125}$$

and the thermal efficiency is

$$\eta = \frac{|P|}{\dot{Q}} = \left(1 - \frac{T_4 - T_1}{T_3 - T_2}\right) \ . \tag{3.126}$$

Because of the isentropic equation,

$$\left(\frac{p_0}{p}\right)^{\frac{\varkappa-1}{\varkappa}} = \frac{T_1}{T_2} = \frac{T_4}{T_3} \tag{3.127}$$

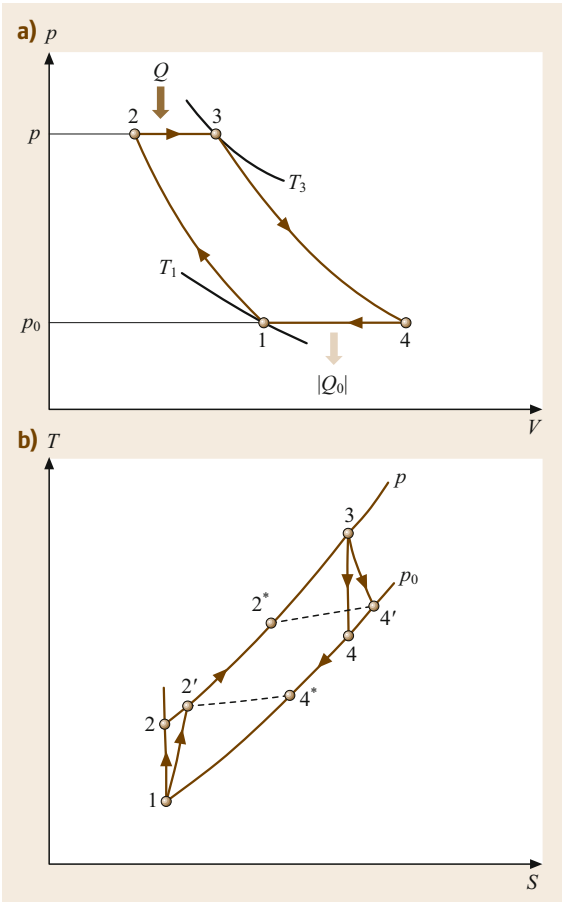

Fig. 3.24a,b The gas turbine process on **(a)** p–V and **(b)** T–S diagram. The p–V diagram shows only the reversible process (Joule process) 1, 2, 3, 4

so

$$\frac{T_4 - T_1}{T_3 - T_2} = \frac{T_1}{T_2} = \left(\frac{p_0}{p}\right)^{\frac{\varkappa-1}{\varkappa}} \ , \tag{3.128}$$

and the thermal efficiency is

$$\eta = \frac{|P|}{\dot{Q}} = 1 - \left(\frac{p_0}{p}\right)^{\frac{\varkappa-1}{\varkappa}} \ , \tag{3.129}$$

which depends only on the pressure ratio p/p_0 or on the temperature ratio T_2/T_1 of the compression. The compressor power increases faster with the pressure ratio than does the turbine power, so the received power output according to (3.125), taking into account (3.128), becomes

$$-P = \dot{m} c_p T_1 \left[\frac{T_3}{T_1} - \left(\frac{p}{p_0}\right)^{\frac{\varkappa-1}{\varkappa}}\right]\left[1 - \left(\frac{p_0}{p}\right)^{\frac{\varkappa-1}{\varkappa}}\right] \ , \tag{3.130}$$

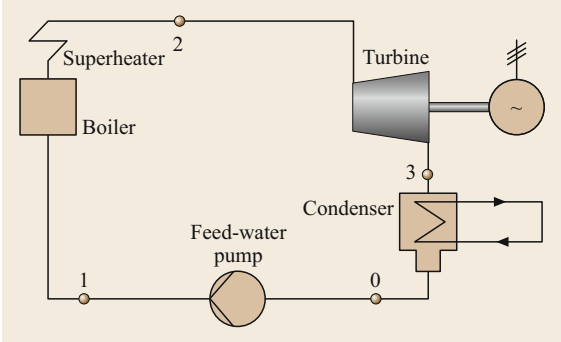

Fig. 3.25 Vapor power plant

which reaches a maximum at a certain pressure ratio for given values of the highest temperature T_3 and the lowest temperature T_1. This optimal pressure ratio follows from (3.130) through differentiation as

$$\left(\frac{p}{p_0}\right)^{\frac{\varkappa-1}{\varkappa}}_{\text{opt}} = \sqrt{\frac{T_3}{T_1}}\,, \tag{3.131}$$

which is, because of (3.128), equivalent to $T_4 = T_2$. Considering the efficiencies η_T of the turbine and η_C of the compressor, and the mechanical efficiency η_m for the energy transformation between the turbine and compressor, the optimal pressure ratio results as

$$\left(\frac{p}{p_0}\right)^{\frac{\varkappa-1}{\varkappa}}_{\text{opt}} = \sqrt{\eta_\text{m}\eta_\text{T}\eta_\text{C}\left(\frac{T_3}{T_1}\right)}\,. \tag{3.132}$$

More than half of the turbine power of a gas turbine plant is required to drive the compressor. The completely installed power is thus four to six times the power output.

The working fluid of vapor power plants, usually water, evaporates and condenses during the process. Most electric energy is generated with such plants. The simplest form of the cyclic process (Fig. 3.25) is as follows:

In the boiler, the working fluid is heated isobarically at a high pressure to the boiling point, evaporated, then superheated in the superheater. The vapor is then expanded adiabatically in the turbine, where work is done, and condensed with heat removal in the condenser. The liquid is pressurized in the feed-water pump to the pressure of the boiler and again discharged into the boiler. The reversible cyclic process 0–1′–2–3′–0 (Fig. 3.26), consisting of two isobars and two isentropes, is called the Clausius–Rankine process. The real cycle consists of the changes of state 0–1–2–3–0 in Fig. 3.26. The heat absorption in the steam generator is

$$\dot{Q}_\text{in} = \dot{m}(h_2 - h_1)\,, \tag{3.133}$$

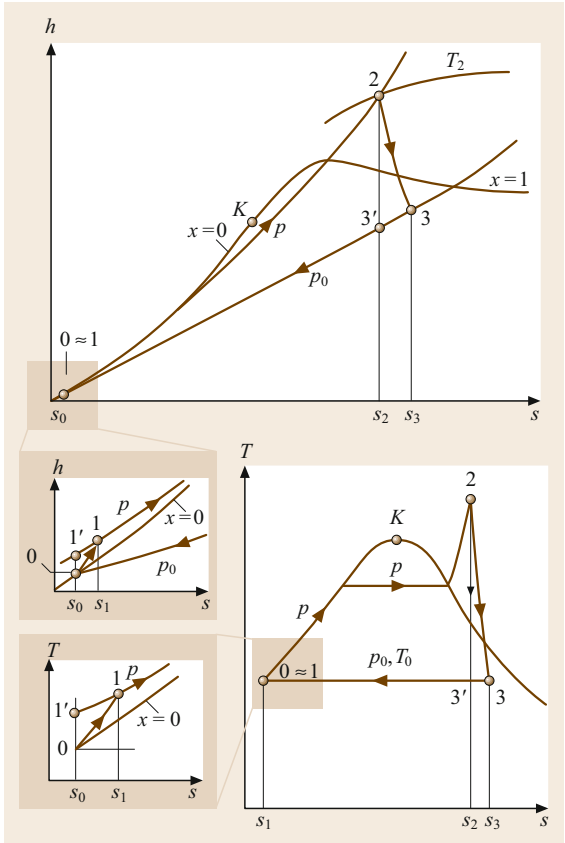

Fig. 3.26 Changes of state of the water in the cycle of a basic vapor power plant on T–S and h–s diagrams

and the power of the adiabatic turbine is

$$|P_\text{T}| = |\dot{m}w_{\text{t}23}| = \dot{m}(h_2 - h_3) = \dot{m}\eta_\text{T}(h_2 - h_3')\,, \tag{3.134}$$

with the isentropic turbine efficiency η_T. The heat transfer discharged in the condenser is

$$-\dot{Q}_\text{out} = \dot{m}(h_3 - h_0)\,. \tag{3.135}$$

The power output of the cyclic process is

$$-P = -\dot{m}w_\text{t} = -P_\text{T} - P_\text{P}\,, \tag{3.136}$$

with the pump power

$$P_\text{P} = \dot{m}(h_1 - h_0) = \dot{m}\frac{1}{\eta_\text{C}}(h_{1'} - h_0)\,, \tag{3.137}$$

where η_C is the efficiency of the feed-water pump. The power output differs only slightly from the power output of the turbine. The thermal efficiency is

$$\eta = -\frac{\dot{m}w_\text{t}}{\dot{Q}_\text{in}} = \frac{(h_2 - h_3) - (h_1 - h_0)}{h_2 - h_1}\,. \tag{3.138}$$

At a counterpressure of $p_0 = 0.05$ bar, a main steam pressure of 150 bar, and a vapor temperature of 500 °C, the thermal efficiency achieves values of $\eta \approx 0.42$. Considerably higher thermal efficiencies of (presently) up to $\eta \approx 0.58$ can be achieved in combined gas–vapor power plants, in which the combustion gas at first does work in a gas turbine, where it is expanded, then is supplied to a vapor power plant in order to generate steam.

3.8.5 Refrigeration Cycles and Heat Pumps

Compression Refrigeration Cycle

In refrigerating machines, as well as in power plants, gases or vapors are used as working fluids. These gases/vapors are called refrigerants. A refrigeration machine is used to remove heat from a chilled system. For this purpose, it is necessary to do work, which is then transferred as heat together with the heat removed from the chilled system to the environment. For cooling with temperatures to about −100 °C, compression refrigeration machines are primarily used.

Figure 3.27 shows a schematic diagram of a compression refrigeration machine. The compressor, which is usually a piston compressor for small powers and a turbo compressor for large powers, draws in vapor from the evaporator at the pressure p_0 and the corresponding saturation temperature T_0 and compresses it along adiabate 1–2 (Fig. 3.28) to pressure p. The vapor is then liquefied at pressure p in the condenser. The liquid refrigerant is expanded in the throttle valve and returns to the evaporator, where it is supplied with heat. The refrigeration machine removes from the chilled system the heat transfer q_0, which is transferred to the evaporator. In the condenser, the heat transfer $|q| = q_0 + w_t$ is transferred to the environment.

Since water freezes at 0 °C, and water vapor has an inconveniently large specific volume, other fluids such as ammonia NH_3, carbon dioxide CO_2, propane C_3H_8, butane C_4H_{10}, and tetrafluoroethane $C_2H_2F_4$ are used as refrigerants. Saturated refrigerant properties are given in Tables 3.10–3.12. For mass flow $\dot{m}$ of the circulating refrigerant, the refrigeration capacity is

$$\dot{Q}_0 = \dot{m} q_0 = \dot{m}(h_1 - h_4) = \dot{m}\left[h''(p_0) - h'(p)\right] , \tag{3.139}$$

since $h_4 = h_3 = h'(p)$. The required power for the compressor is

$$P_C = \dot{m} w_{t12} = \dot{m}(h_2 - h_1) = \dot{m}\frac{1}{\eta_C}\left[h_{2'} - h''(p_0)\right] , \tag{3.140}$$

where η_C is the isentropic efficiency of the compressor. The heat transfer from the condenser is given by

$$|\dot{q}| = \dot{m}\,|q| = \dot{m}(h_2 - h_3) = \dot{m}\left[h_2 - h'(p)\right] . \tag{3.141}$$

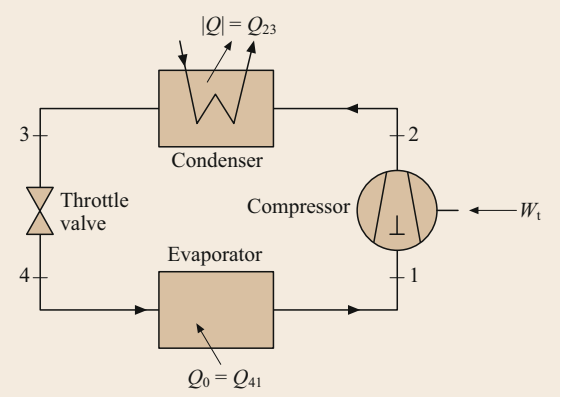

Fig. 3.27 Scheme of a vapor refrigeration plant (see text for explanation)

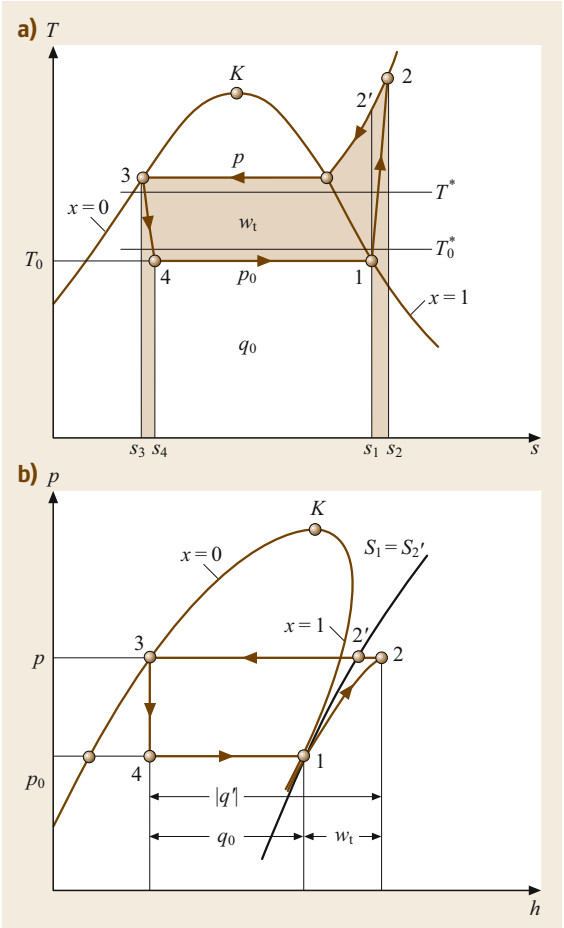

Fig. 3.28a,b Cycle of the refrigerant in a vapor refrigeration plant on **(a)** the T–S and **(b)** the p–h (Mollier) diagrams

The coefficient of performance of a refrigeration machine is defined as the ratio of the refrigeration capacity $\dot{q}_0$ to the required power P of the compressor

$$\varepsilon_R = \frac{\dot{q}_0}{P_C} = \frac{q_0}{w_{t12}} = \eta_C \frac{h''(p_0) - h'(p)}{h_{2'} - h''(p_0)} , \qquad (3.142)$$

which depends, besides on the isentropic compressor efficiency, only on the two pressures p and p_0.

Compression Heat Pump

A compression heat pump works according to the same process as the compression refrigeration system shown in Figs. 3.27 and 3.28, but its purpose, however, is for heating. To provide heating, then, the heat transfer q_0 (anergy) is from the environment and is, together with the done work, w_t (the exergy), supplied as a heat transfer $|q| = q_0 + w_t$ to the heated system. The coefficient of performance of a heat pump is defined as the ratio of the heating output $|\dot{q}|$ to the required power P of the compressor

$$\varepsilon_{hp} = \frac{|\dot{q}|}{P} = \frac{|q|}{w_t} = \eta_V \frac{h_2 - h'(p)}{h_{2'} - h''(p_0)} . \qquad (3.143)$$

As shown in the T–S diagram in Fig. 3.28, the area representing w_t becomes smaller at a high ambient temperature T_0^* and at a low heating temperature T^* because less power is required for the compressor and the coefficient of performance increases. To run heat pumps economically for the heating of housing spaces, the heating temperature must be kept low, e.g., by using floor heating at $t^* \lessapprox 29\,^\circ\mathrm{C}$. Additionally, heat pumps become uneconomic when the environment temperature is too low. If the coefficient of performance decreases below about 2.3, no primary energy is saved when compared with conventional heating, because the mean efficiencies for the transformation of primary energy P_{Pr} into electrical energy P in a power plant in order to run the heat pump $\eta_{el} = P/P_{Pr}$ are typically about 0.4. In that case, the heating coefficient $\xi = |\dot{q}|/P_{Pr}$ of 0.92 corresponds to the efficiency of conventional heating. Today's electrically driven heat pumps rarely achieve heating coefficients of 2.3 in the annual mean, unless the heat pump is switched off at ambient temperatures lower than approximately 3 °C and the housing space is heated conventionally. Motor-driven heat pumps with waste heat recovery and sorption heat pumps exploit the primary energy better than electrically driven heat pumps.

3.8.6 Combined Heat and Power (CHP)

The generation of thermal energy and electrical energy in heating power plants is called combined heat and power generation. A large amount of a power plant's waste heat, which arises in the process, is used for heating. Since the heat required for heating consists mainly—more than 90%—of anergy, less primary energy, which consists mainly of exergy, is transformed into thermal energy than in conventional heating. Low-pressure vapor is discharged from the vapor turbine; it contains, in addition to the anergy, so much exergy that the heating energy and the exergy losses in the heat distribution—normally in a long-distance heating network—are covered. Even though, compared with a simple power plant, operation work is lost due to the vapor withdrawal, the primary energy consumption for the simultaneous generation of work and thermal energy is smaller than the separate generation of work in a power plant and of thermal energy in a conventional heating system. A simplified circuit is shown in Fig. 3.29. Depending on the kind of circuit used, heating coefficients, $\xi = |\dot{q}|/P_{Pr}$, up to about 2.2 are accessible [3.18], whereas P_{Pr} is only the fraction of the primary energy that accounts for the heating. The heating coefficients are considerably above those of most heating pump systems.

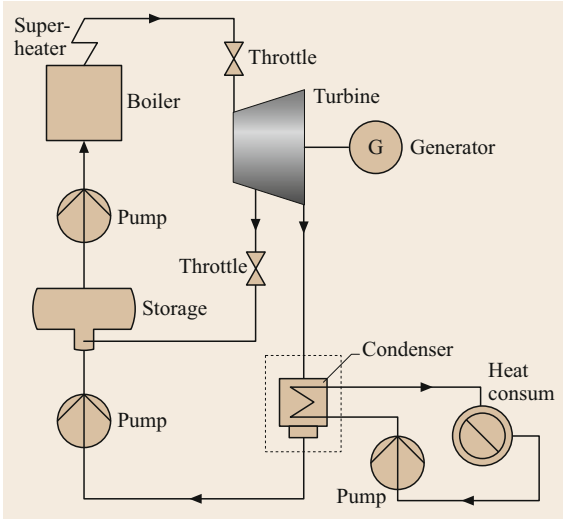

Fig. 3.29 Scheme of combined heat and power generation in extraction back-pressure operation

3.9 Ideal Gas Mixtures

A mixture of ideal gases that do not react chemically with each other also behaves as an ideal gas. The following equation of state holds:

$$pV = nR_u T \,. \tag{3.144}$$

Each single gas, called a component, spreads over the entire space V as though the other gases were not present. Thus, the following equation holds for each component:

$$p_i V = n_i R_u T \,, \tag{3.145}$$

where p_i is the pressure exerted by each gas individually, which is referred to as the partial pressure. The sum of all the *partial pressures* leads to $\sum p_i V = \sum n_i R_u T$ or $V \sum p_i = R_u T \sum n_i$. Comparison with (3.144) shows that

$$p = \sum p_i \tag{3.146}$$

holds. In other words, the total pressure p of the gas mixture is equal to the sum of the partial pressures of the single gases, if each gas occupies the volume V of the mixture at temperature T (Dalton's law). The thermal equation of state of an ideal gas mixture can also be written as

$$pV = mRT \,, \tag{3.147}$$

with the gas constant R of the mixture

$$R = \sum R_i \frac{m_i}{m} \,. \tag{3.148}$$

Specific (related to the mass in kg) caloric properties of a mixture at pressure p and temperature T result from adding the caloric properties at the same values p and T of the single gases according to their mass fractions, or

$$\begin{aligned} c_v &= \frac{1}{m} \sum m_i c_{vi} \,, & c_p &= \frac{1}{m} \sum m_i c_{pi} \,, \\ u &= \frac{1}{m} \sum m_i u_i \,, & h &= \frac{1}{m} \sum m_i h_i \,. \end{aligned} \tag{3.149}$$

An exception to this general rule is entropy. During the mixing of single gases in state p, T to a mixture of the same state, an entropy increase takes place. This process is described by the following relation:

$$s = \frac{1}{m} \left(\sum m_i s_i - \sum m_i R_i \ln \frac{n_i}{n} \right) \,, \tag{3.150}$$

where n_i is the number of moles of the single gases and n is the number of moles of the mixture. Consequently, $n_i = m_i / M_i$ and $n = \sum n_i$, with the mass m_i and the molar mass M_i of the single gases. Mixtures of real gases and liquids deviate from the above relations, in particular at higher pressures.

3.9.1 Mixtures of Gas and Vapor: Humid Air

Mixtures of gases and easily condensable vapors occur often in physics and in technology. Atmospheric air consists mostly of dry air and water vapor. Drying and climatization processes are governed by the laws of vapor–air mixtures. This holds true in the same way for the formation of fuel and vapor–air mixtures in a combustion engine. The following discussion is limited to the examination of atmospheric air. Dry air consists of 78.04 mol% nitrogen, 21.00 mol% oxygen, 0.93 mol% argon, and 0.03 mol% carbon dioxide. Atmospheric air can be considered as a binary mixture of dry air and water, which can be present as vapor, liquid, or solid. This mixture is also called humid air. Dry air is considered a uniform substance. Since the total pressure during changes of state is almost always close to atmospheric pressure, it is possible to consider humid air, consisting of dry air and water vapor, as a mixture of ideal gases. The following relation then holds for dry air and water vapor:

$$p_{air} V = m_{air} R_{air} T \quad \text{and} \quad p_v V = m_v R_v T \,. \tag{3.151}$$

These equations, together with $p = p_{air} + p_v$, allow the determination of the mass of water vapor which is added to 1 kg dry air.

$$x_v = \frac{m_v}{m_{air}} = \frac{R_{air} p_v}{R_v (p - p_v)} \,. \tag{3.152}$$

The quantity $x_v = m_v / m_{air}$ is called the absolute or specific humidity. This quantity must not be confused with the quality x for mixtures of vapors and liquid. If water in the air is not only present as vapor, but also as liquid or solid, the water content x must be distinguished from the specific humidity x_v. The water content is defined as

$$x = \frac{m_w}{m_{air}} = \frac{m_v + m_\ell + m_{ice}}{m_{air}} = x_v + x_\ell + x_{ice} \,, \tag{3.153}$$

where m_v denotes the vapor mass, m_ℓ denotes the liquid mass, and m_{ice} denotes the ice mass in the dry air of mass m_{air}. The value x_v is the specific humidity (vapor content), x_ℓ is the liquid content, and x_{ice}

is the ice content. The water content can lie between 0 (dry air) and ∞ (pure water). If humid air at temperature T is saturated with water vapor, the partial pressure of the water vapor is equal to the saturation pressure $p = p_{vs}$ at temperature T, and the specific humidity becomes

$$x_s = \frac{R_{air} p_{vs}}{R_v (p - p_{vs})} \,. \tag{3.154}$$

Example 3.13

What is the specific humidity of saturated humid air at a temperature of 20 °C and a total pressure of 1000 mbar?

The gas constants are $R_{air} = 0.2872\,\mathrm{kJ/(kg\,K)}$ and $R_v = 0.4615\,\mathrm{kJ/(kg\,K)}$. The saturated water temperature (Table 3.6) includes the vapor pressure, which is $p_{vs}(20\,°C) = 23.39\,\mathrm{mbar}$. It follows then that

$$x_s = \frac{0.2872 \times 23.39}{0.4615\,(1000 - 23.39)} \times 10^3 \,\frac{\mathrm{g}}{\mathrm{kg}} = 14.905 \,\frac{\mathrm{g}}{\mathrm{kg}} \,.$$

Other values of x_s are given in Table 3.20.

Table 3.20 Partial pressure p_{vs}, specific humidity x_s, and enthalpy h_{1+x} of saturated humid air at temperature t related to 1 kg dry air at total pressure of 1000 mbar

t (°C)	p_{vs} (mbar)	x_s (g/kg)	h_{1+x} (kJ/kg)
−20	1.032	0.64290	−18.5164
−19	1.136	0.70776	−17.3503
−18	1.249	0.77825	−16.1700
−17	1.372	0.85499	−14.9741
−16	1.506	0.93862	−13.7609
−15	1.652	1.02977	−12.5288
−14	1.811	1.12906	−11.2762
−13	1.984	1.23713	−10.0015
−12	2.172	1.35462	−8.7030
−11	2.377	1.48277	−7.3777
−10	2.598	1.62099	−6.0269
−9	2.838	1.77117	−4.6459
−8	3.099	1.93456	−3.2314
−7	3.381	2.11120	−1.7834
−6	3.686	2.30235	−0.2987
−5	4.017	2.50993	1.2277
−4	4.374	2.73398	2.7960
−3	4.760	2.97640	4.4109
−2	5.177	3.23851	6.0758
−1	5.626	3.52097	7.7926
0	6.117	3.8303	9.5778
1	6.572	4.1167	11.3064
2	7.061	4.4251	13.0915
3	7.581	4.7540	14.9290
4	8.136	5.1046	16.8222
5	8.726	5.4781	18.7741
6	9.354	5.8759	20.7884
7	10.021	6.2993	22.8684
8	10.730	6.7497	25.0181
9	11.483	7.2288	27.2416
10	12.281	7.7377	29.5421
11	13.129	8.2791	31.9263
12	14.027	8.8534	34.3956
13	14.979	9.4635	36.9572
14	15.988	10.111	39.6166
15	17.056	10.798	42.3778
16	18.185	11.526	45.2449
17	19.380	12.299	48.2272
18	20.644	13.118	51.3306
19	21.979	13.985	54.5595
20	23.388	14.903	57.9202
21	24.877	15.876	61.4240
22	26.447	16.906	65.0741
23	28.104	17.995	68.8823
24	29.850	19.148	72.8537
25	31.691	20.367	77.0006
26	33.629	21.656	81.3286
27	35.670	23.019	85.8505
28	37.818	24.460	90.5757
29	40.078	25.983	95.5160
31	44.953	29.292	106.088
32	47.578	31.088	111.745
33	50.335	32.985	117.668
34	53.229	34.988	123.869
35	56.267	37.104	130.368
36	59.454	39.338	137.179
37	62.795	41.697	144.317
38	66.298	44.188	151.805
39	69.969	46.819	159.662
40	73.814	49.597	167.907
41	77.840	52.530	176.563
42	82.054	55.628	185.654
43	86.464	58.901	195.208
44	91.076	62.358	205.248
45	95.898	66.009	215.806
46	100.94	69.868	226.912
47	106.21	73.947	238.603
48	111.71	78.259	250.913
49	117.45	82.817	263.878
50	123.44	87.637	277.536
51	129.70	92.743	291.958
52	136.23	98.149	307.175
53	143.03	103.87	323.221
54	150.12	109.92	340.176
55	157.52	116.36	358.126
56	165.22	123.17	377.094
57	173.24	130.40	397.178
58	181.59	138.08	418.457

Table 3.20 (continued)

t (°C)	p_{vs} (mbar)	x_s (g/kg)	h_{1+x} (kJ/kg)
59	190.28	146.24	441.020
60	199.32	154.92	464.964
61	208.73	164.16	490.418
62	218.51	174.00	517.474
63	228.68	184.50	546.288
64	239.25	195.71	577.001
65	250.22	207.68	609.745
66	261.63	220.51	644.782
67	273.47	234.24	682.254
68	285.76	248.98	722.413
69	298.52	264.83	765.546
70	311.76	281.90	811.941
71	325.49	300.30	861.924
72	339.72	320.19	915.870
73	358.00	347.02	988.219
74	369.78	365.14	1037.670
75	385.63	390.62	1106.609
76	402.05	418.43	1181.826
77	419.05	448.89	1264.123
78	436.65	482.36	1354.501
79	454.87	519.28	1454.151
80	473.73	560.19	1564.509
81	493.24	605.71	1687.252
82	513.42	656.65	1824.503
83	534.28	713.93	1978.817
84	555.85	778.83	2153.558
85	578.15	852.89	2352.928
86	601.19	938.12	2582.259
87	624.99	1037.15	2848.667
88	649.58	1153.60	3161.844
89	674.96	1292.27	3534.691
90	701.17	1460.20	3986.110
91	728.23	1667.55	4543.419
92	756.14	1929.63	5247.698
93	784.95	2271.51	6166.305
94	814.65	2735.21	7412.089
95	845.29	3400.16	9198.391
96	876.88	4432.25	11 970.735
97	909.45	6250.33	16 854.112
98	943.01	10 297.46	27 724.303
99	977.59	27 147.34	72 980.326
100	1013.20	–	–

Degree of Saturation and Relative Humidity

The degree of saturation is defined as $\Psi = x_v/x_s$, which is a relative measure of the vapor content. In meteorology, however, the relative humidity $\varphi = p_v(t)/p_{vs}(t)$ is often used. Close to saturation, the two values differ only slightly because

$$\frac{x_v}{x_s} = \frac{p_v(p-p_{vs})}{p_{vs}(p-p_v)} \quad \text{or} \quad \Psi = \varphi\frac{(p-p_{vs})}{(p-p_v)} .$$

At saturation, $\Psi = \varphi = 1$. If the pressure of saturated humid air is increased or if the temperature is decreased, the excess water vapor condenses. The condensed vapor drops out as fog or precipitation (rain); at temperatures below 0 °C, ice crystals (snow) arise. In this case, the water content is larger than the vapor content: $x > x_v = x_s$. The relative humidity can be determined with directly displaying instruments (e.g., a hair hygrometer) or with the help of an aspiration psychrometer.

Enthalpy of Humid Air

Since the amount of dry air remains constant during changes of state of humid air, and only the added amount of water varies as a result of thawing or evaporation, all properties are related to 1 kg dry air. The dry air contains $x = m_w/m_{air}$ kg water per kg dry air, of which $x_v = m_v/m_{air}$ is vaporous. For the enthalpy h_{1+x} of the unsaturated ($x = x_v < x_s$) mixture of 1 kg dry air and x vapor, it holds that

$$h_{1+x} = c_{p\,air}t + x_v(c_{p\,v}t + \Delta h_v) , \qquad (3.155)$$

with the constant-pressure specific heats $c_{p\,air} = 1.005\,\text{kJ/(kg K)}$ of air and $c_{p\,v} = 1.86\,\text{kJ/(kg K)}$ of water vapor, and the enthalpy of vaporization $\Delta h_v = 2500.5\,\text{kJ/kg}$ of water at 0 °C. In the temperature range of interest between −60 and 100 °C, constant values of c_p can be assumed. At saturation, $x_v = x_s$ and $h_{1+x} = (h_{1+x})_s$. If the water content x is larger than the saturation content x_s at temperatures $t > 0\,°\text{C}$, the water fraction $x - x_s = x_\ell$ drops out of the mixture as fog or as precipitate, and it holds that

$$h_{1+x} = (h_{1+x})_s + (x-x_s)c_w t . \qquad (3.156)$$

At temperatures $t < 0\,°\text{C}$, the water fraction $x - x_s = x_{ice}$ drops out as snow or ice, then

$$h_{1+x} = (h_{1+x})_s - (x-x_s)(\Delta h_f - c_{ice}t) . \qquad (3.157)$$

The specific heat of water is $c_w = 4.19\,\text{kJ/(kg K)}$, the specific heat of ice is $c_{ice} = 2.04\,\text{kJ/(kg K)}$, and the latent heat of fusion of ice is $\Delta h_f = 333.5\,\text{kJ/kg}$. Saturation pressures, specific humidities, and enthalpies of saturated humid air at temperatures between −20 and +100 °C for a total pressure of 1000 mbar are given in Table 3.20. At $t = 0\,°\text{C}$, water can be present simultaneously in all three states of aggregation. The following relation then holds for the enthalpy h_{1+x} of the mixture:

$$h_{1+x} = x_s\Delta h_v - x_{ice}\Delta h_f . \qquad (3.158)$$

Mollier Diagram of Humid Air

Figure 3.30a shows the h_{1+x}–x diagram introduced by Mollier for the graphical depiction of changes of state of humid air. The enthalpy h_{1+x} of $(1+x)$ kg humid air is plotted in an oblique coordinate system against the water content. The axis $h = 0$ corresponding to humid air at 0 °C is inclined right downward in such a way that the 0 °C isotherm of unsaturated humid air is horizontal. Figure 3.30b shows the construction of isotherms according to (3.155) and (3.156). Lines of constant x are vertical, while lines of constant h are straight lines parallel to the axis $h_{1+x} = 0$. Figure 3.30a includes the saturation curve $\varphi = 1$ for a total pressure of 1000 mbar. It divides the region of unsaturated mixtures (top) from the fog region (bottom), in which the humidity is contained in the mixture partly as vapor, partly as liquid (fog, precipitate) or solid (ice, fog, snow). Isotherms in the unsaturated region are, according to (3.155), towards the right, slightly ascending straight lines, which deviate at the saturation curve downward and in the fog region are nearly parallel to the straight lines of constant enthalpy, according to (3.156). The vapor content of a state in the fog region with temperature t and water content x is determined by following isotherm t until it intersects with the saturation curve $\varphi = 1$. The fraction x_s read off at the intersection point is as vapor, thus the fraction $x - x_s$ is as liquid and/or ice contained in the mixture. The inclined, beam-like pieces of straight lines $\Delta h_{1+x}/\Delta x$ determine, together with the zero point, the direction of a change of state starting from an arbitrary state in the diagram, when water or vapor with an enthalpy in kJ/kg corresponding to the values at the boundary beams is added to the mixture. In order to find the direction of the change of state, a straight line parallel to the line determined by the origin ($h = 0$, $x = 0$) and the boundary beam must be drawn through the point of the initial state.

Changes of State of Humid Air

Heating or Cooling. If a given mixture is heated, the change of state is vertically upwards (1–2 in Fig. 3.31a). If a given mixture is cooled, the change of state is vertically downwards (2–1). As long as states 1 and 2 are in the unsaturated region, the exchanged heat related to 1 kg dry air corresponds to the vertical distance of two state points measured on the enthalpy scale.

$$Q_{12} = m_{\text{air}}(c_{\text{p air}} + c_{\text{p v}}x)(t_2 - t_1)\ , \tag{3.159}$$

where $c_{\text{p air}} = 1.005\,\text{kJ/(kg K)}$ and $c_{\text{p v}} = 1.852\,\text{kJ/(kg K)}$. When humid air is cooled below the dew point of water (1–2 in Fig. 3.31b), precipitation drops out. The discharged heat is

$$Q_{12} = m_{\text{air}}\left[(h_{1+x})_2 - (h_{1+x})_1\right]\ , \tag{3.160}$$

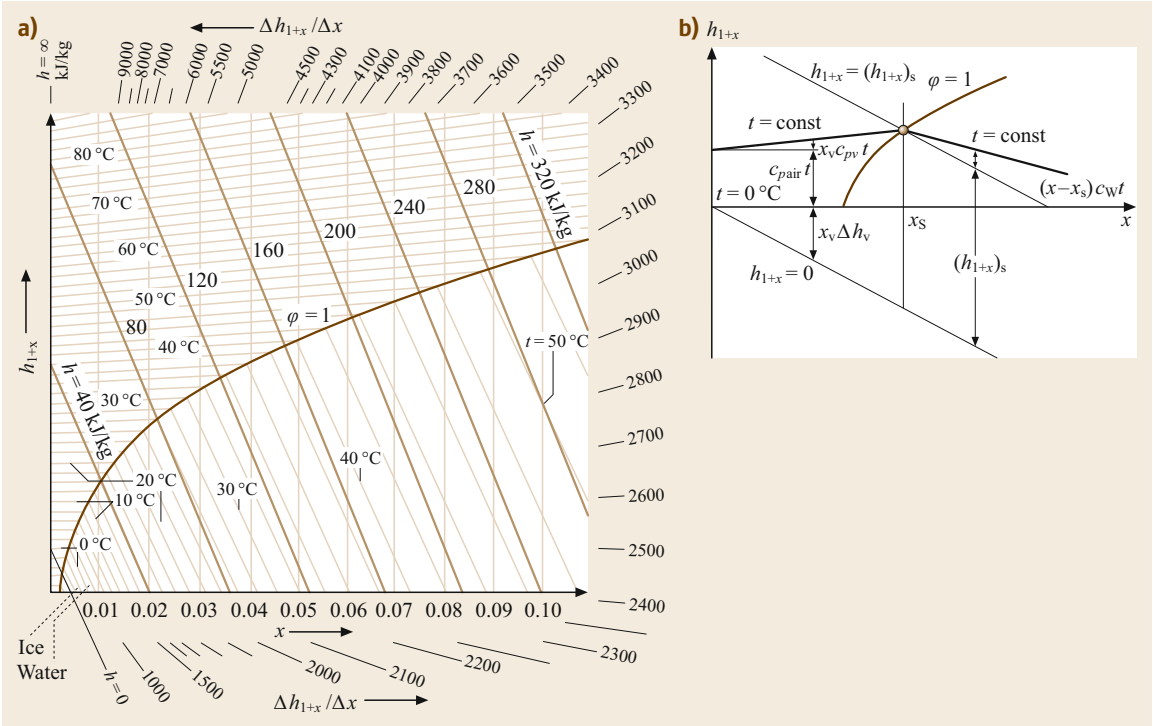

Fig. 3.30a,b h_{1+x}–x diagram of humid air according to Mollier

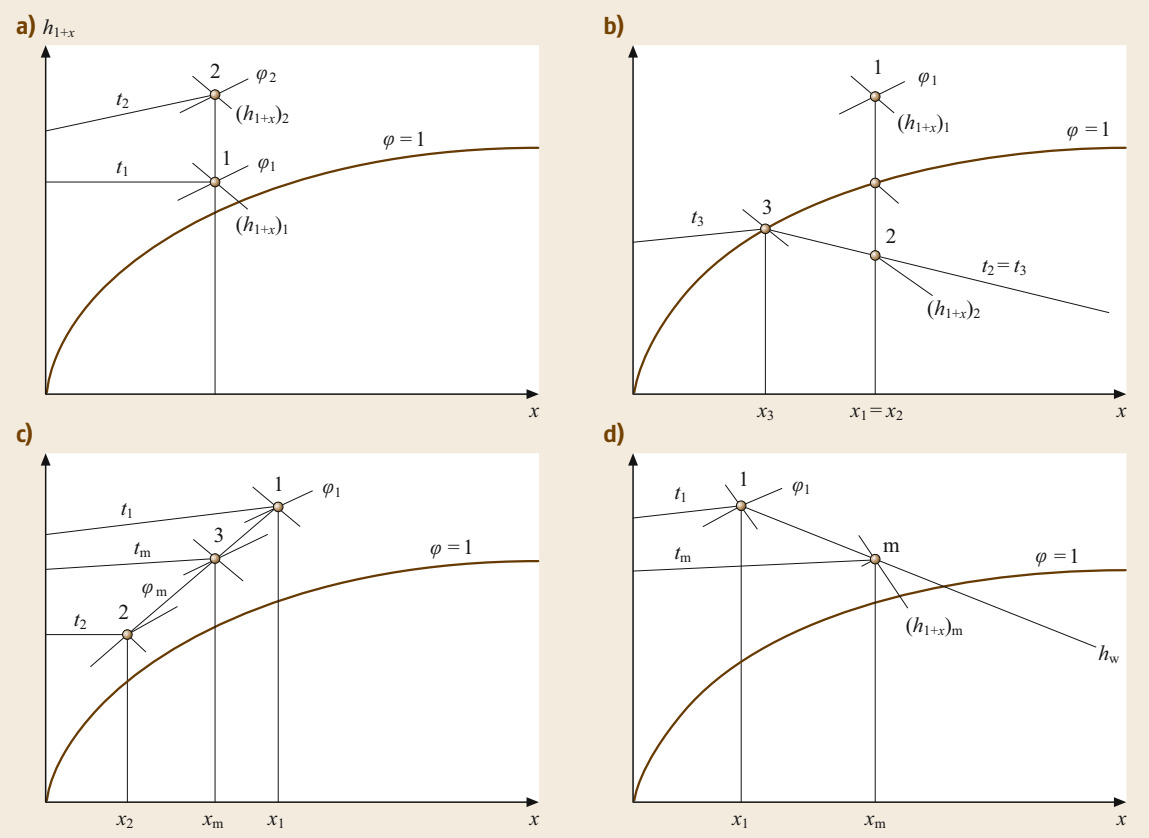

Fig. 3.31a–d Changes of state of humid air: **(a)** heating and cooling **(b)** cooling below dew point **(c)** mixture **(d)** addition of water or vapor

where $(h_{1+x})_1$ is given by (3.155) and $(h_{1+x})_2$ by (3.156). An amount of water specified by

$$m_w = m_{air}(x_1 - x_3) \tag{3.161}$$

is removed.

Example 3.14

Consider 1000 kg of humid air at $t_1 = 30\,°C$, $\varphi_1 = 0.6$, and $p = 1000$ mbar that is cooled to 15 °C. How much precipitation falls out?

The specific humidity results from (3.152) with $p_v = \varphi_1 p_{vs}$. According to Table 3.20, $p_{vs}\,(30\,°C) = 42.46$ mbar, thus

$$x_1 = \frac{R_{air}\,(\varphi_1\,p_{vs})}{R_v\,(p - \varphi_1\,p_{vs})} = \frac{0.2872 \times 0.6 \times 42.46}{0.4615\,(1000 - 0.6 \times 42.46)} = 16.25 \times 10^{-3}\,\text{kg/kg} = 16.25\,\text{g/kg}\,.$$

The 1000 kg of humid air consists of $1000/(1+x_1) = 1000/1.01625\,\text{kg} = 984.01\,\text{kg}$ dry air and $(1000 - 984.01)\,\text{kg} = 15.99\,\text{kg}$ water vapor. The water content at point 3, $x_3 = x_s$, follows from Table 3.20 at $t_3 = 15\,°C$ to $x_3 = 10.79\,\text{g/kg}$, thus

$$m_\ell = 984.01 \times (16.25 - 10.80) \times 10^{-3}\,\text{kg} = 5.36\,\text{kg}\,.$$

Mixture of Two Amounts of Air. If two amounts of humid air at states 1 and 2 are mixed adiabatically (i.e., without heat exchange with the environment), state m after the mixture (point 3 in Fig. 3.31c) is located on the straight line connecting states 1 and 2. Point m is determined by subdividing the straight connecting line 1–2 equivalent to the ratio of the dry air masses m_{air2}/m_{air1}. It is then

$$x_m = \frac{m_{air1}x_1 + m_{air2}x_2}{m_{air1} + m_{air2}}\,. \tag{3.162}$$

Mixing two amounts of saturated air at different temperatures always leads to the formation of fog, as the water amount $x_m - x_s$ drops out, where x_s is the specific humidity at saturation on the isotherm passing through the mixture point in the fog region.

Example 3.15

Consider 1000 kg of humid air at $t_1 = 30\,^\circ\text{C}$ and $\varphi_1 = 0.6$ mixed at 1000 mbar with 1500 kg of saturated humid air at $t_2 = 10\,^\circ\text{C}$. What is the temperature of the mixture?

As calculated in the previous example, $x_1 = 16.25\,\text{g/kg}$. The specific humidity at saturation for $t_2 = 10\,^\circ\text{C}$ given in Table 3.20 is $x_{2s} = 7.7377\,\text{g/kg}$. The dry air masses are

$$m_{air1} = \frac{1000}{1+x_1}\,\text{kg} = \frac{1000}{1+16.25\times10^{-3}}\,\text{kg} = 984.01\,\text{kg}\,,$$

and

$$m_{air2} = \frac{1500}{1+x_{2s}}\,\text{kg} = \frac{1500}{1+7.7377\times10^{-3}}\,\text{kg} = 1488.5\,\text{kg}\,.$$

The water content after mixing therefore becomes

$$x_m = \frac{984.01\times16.25 + 1488.5\times7.7377}{984.01+1488.5}\,\text{g/kg} = 11.12\,\text{g/kg}\,.$$

The enthalpies, calculated according to (3.155), are

$$(h_{1+x})_1 = \left[1.005\times30 + 16.25\times10^{-3}\times(1.86\times30+2500.5)\right]\text{kJ/kg} = 71.69\,\text{kJ/kg}\,,$$

$$(h_{1+x})_2 = \left[1.005\times10 + 7.7377\times10^{-3}\times(1.86\times10+2500.5)\right]\text{kJ/kg} = 29.54\,\text{kJ/kg}\,.$$

The enthalpy of the mixture is

$$(h_{1+x})_m = \frac{m_{air1}(h_{1+x})_1 + m_{air2}(h_{1+x})_2}{m_{air1}+m_{air2}} = \frac{984.01\times71.69 + 1488.5\times29.54}{984.01+1488.5}\,\text{kJ/kg} = 46.31\,\text{kJ/kg}\,.$$

On the other hand, according to (3.155), the following also holds:

$$(h_{1+x})_m = \left[1.005\,t_m + 11.12\times10^{-3}\times(1.86\,t_m + 2500.5)\right]\text{kJ/kg}\,.$$

From this, it follows that $t_m = 18\,^\circ\text{C}$.

Addition of Water or Vapor. If humid air is mixed with m_w kg of water or water vapor, the water content after mixing is $x_m = (m_{air1}x_1 + m_w)/m_{air1}$. The enthalpy is

$$(h_{1+x})_m = \frac{m_{air\,1}(h_{1+x})_1 + m_w h_w}{m_{air1}}\,. \qquad (3.163)$$

The final state after mixing is located in the Mollier diagram for humid air (Fig. 3.31d) on a straight line passing through the origin with the gradient h_w, where $h_w = \Delta h_{1+x}/\Delta x$ is given by the pieces of straight lines on the boundary scale.

Wet-Bulb Temperature. When unsaturated humid air of state t_1, x_1 passes over a water or ice surface, water evaporates or ice sublimates, causing the specific humidity of the humid air to increase. During this increase in specific humidity, the temperature of the water or of the ice decreases and adopts, after a sufficiently long time, a final value, which is called the wet-bulb temperature. The wet-bulb temperature t_{wb} can be determined in the Mollier diagram by looking for the isotherm t_{wb} in the fog region whose extension passes through state 1.

3.10 Heat Transfer

If temperature differences exist between bodies that are not isolated from each other or within different areas of the same body, energy flows from the region of higher temperature to the region of lower temperature. This process is called heat transfer and will continue until the temperatures are balanced. Three modes of heat transfer are distinguished:

- Heat transfer by conduction in solids, motionless liquids, or motionless gases. Kinetic energy is hereby transferred from a molecule or an elementary particle to its neighbor.
- Heat transfer by convection in liquids or gases with bulk fluid motion.
- Heat transfer by radiation takes place in the form of electromagnetic waves and without the presence of an intervening medium.

In engineering, all three modes of heat transfer are often present at the same time.

3.10.1 Steady-State Heat Conduction

Steady-State Heat Conduction Through a Plane Wall

If different temperatures are prescribed on two surfaces of a plane wall with thickness δ, according to Fourier's law, the heat transfer

$$Q = \lambda A \frac{T_1 - T_2}{\delta} \tau$$

flows through the area A over time τ. Here, λ is a material property (SI unit W/(K m)) that is called the thermal conductivity (Table 3.21). The rate of heat transfer is given by $Q/\tau = \dot{Q}$ (SI unit W), and $Q/(\tau A) = \dot{q}$ is referred to as the heat flux (SI unit W/m^2). It holds, then

$$\dot{Q} = \lambda A \frac{T_1 - T_2}{\delta} \quad \text{and} \quad \dot{q} = \lambda \frac{T_1 - T_2}{\delta} . \qquad (3.164)$$

Table 3.21 Thermal conductivities λ (W/(K m))

Solids at 20 °C	
Silver	458
Copper, pure	393
Copper, commercial	350–370
Gold, pure	314
Aluminum (99.5%)	221
Magnesium	171
Brass	80–120
Platinum, pure	71
Nickel	58.5
Iron	67
Gray cast iron	42–63
Steel, 0.2% C	50
Steel, 0.6% C	46
Constantan, 55% Cu, 45% Ni	40
V2A, 18% Cr, 8% Ni	21
Monel metal 67% Ni, 28% Cu, 5% Fe + Mn + Si + C	25
Manganin	22.5
Graphite, increasing with density and purity	12–175
Hard coal, natural	0.25–0.28
Stone, different kinds	1–5
Quartz glass	1.4–1.9
Concrete, ferroconcrete	0.3–1.5
Fire-resistant stones	0.5–1.7
Glass (2500) [a]	0.81
Ice, at 0 °C	2.2
Soil, clayey damp	2.33
Soil, dry	0.53
Quartz sand, dry	0.3
Brickwork, dry	0.25–0.55
Brickwork, damp	0.4–1.6

Similar to electric conduction, where a current I flows only when a voltage U exists to overcome the resistance R ($I = U/R$), heat transfer occurs only when a temperature difference $\Delta T = T_2 - T_1$ exists

$$\dot{Q} = \frac{\lambda A}{s} \Delta T .$$

Analogous to Ohm's law, $R_{th} = \delta/(\lambda A)$ is called the thermal resistance (SI unit K/W).

Fourier's Law

Considering a layer perpendicular to the heat transfer of thickness dx instead of the wall with the finite thickness δ leads to Fourier's law in the differential form

$$\dot{Q} = -\lambda A \frac{\mathrm{d}T}{\mathrm{d}x} \quad \text{and} \quad \dot{q} = -\lambda \frac{\mathrm{d}T}{\mathrm{d}x} , \qquad (3.165)$$

where the minus sign results from the fact that heat transfer occurs in the direction of decreasing temperature. Here, $\dot{Q}$ is the heat transfer in the direction of the x-axis, as is the same for $\dot{q}$. The heat flux in the direction of the three coordinates x, y, and z is given in vector

Table 3.21 (continued)

Insulating material at 20 °C	
Alfol	0.03
Asbestos	0.08
Asbestos plates	0.12–0.16
Glass wool	0.04
Cork plates (150) [a]	0.05
Diatomite, fired	0.08–0.13
Slag wool, rockwool matte (120) [a]	0.035
Slag wool, dense (?)	0.045
Synthetic resins – foams (15) [a]	0.035
Silk (100) [a]	0.055
Peat plates, air dry	0.04–0.09
Wool	0.04
Liquids	
Water [b] of 1 bar at 0 °C	0.562
Water [b] of 1 bar at 20 °C	0.5996
Water [b] of 1 bar at 50 °C	0.6405
Water [b] of 1 bar at 80 °C	0.6668
At saturation: 99.63 °C	0.6773
Carbon dioxide at 0 °C	0.109
Carbon dioxide at 20 °C	0.086
Lubricating oils	0.12–0.18
Gases at 1 bar and temperature t in 20 °C	
Hydrogen, $-100\,°C \le \theta \le 1000\,°C$	$0.171(1 + 0.00349\theta)$
Air, $0\,°C \le \theta \le 1000\,°C$	$0.0245(1 + 0.00225\theta)$
Carbon dioxide, $0\,°C \le \theta \le 1000\,°C$	$0.01464(1 + 0.005\theta)$

[a] In parenthesis, density in kg/m^3
[b] According to [3.19]

form by

$$\dot{q} = -\lambda \left(\frac{\partial T}{\partial x} \boldsymbol{e}_x + \frac{\partial T}{\partial y} \boldsymbol{e}_y + \frac{\partial T}{\partial z} \boldsymbol{e}_z \right) \tag{3.166}$$

with the unit vectors $\boldsymbol{e}_x$, $\boldsymbol{e}_y$, and $\boldsymbol{e}_z$. At the same time, (3.166) is the general form of Fourier's law. In this form, Fourier's law holds for isotropic materials, i.e., materials with equal thermal conductivities in the direction of the three coordinate axes.

Steady-State Heat Conduction Through a Tube Wall

According to Fourier's law, the heat transfer rate through a cylindrical area of radius r and length l is $\dot{Q} = -\lambda\, 2\pi r l (\mathrm{d}T/\mathrm{d}r)$. Under steady-state conditions, the heat transfer rate is the same for all radii and thus $\dot{Q} = \text{const}$. It is therefore possible to separate the variables T and r and to integrate from the inner surface of the cylinder, $r = r_\mathrm{i}$ with $T = T_\mathrm{i}$, to an arbitrary location r with temperature T. The temperature profile in a tube wall of thickness $r - r_\mathrm{i}$ becomes

$$T_\mathrm{i} - T = \frac{\dot{Q}}{\lambda\, 2\pi l} \ln \frac{r}{r_\mathrm{i}} \,.$$

With temperature T_o at the outer surface at radius r_o, the heat transfer rate through a tube of thickness $r_\mathrm{o} - r_\mathrm{i}$ and length l becomes

$$\dot{Q} = \lambda\, 2\pi l \frac{T_\mathrm{i} - T_\mathrm{o}}{\ln \frac{r_\mathrm{o}}{r_\mathrm{i}}} \,. \tag{3.167}$$

In order to obtain formal agreement with (3.164), it is also possible to write

$$\dot{Q} = \lambda A_\mathrm{m} \frac{T_\mathrm{i} - T_\mathrm{o}}{\delta} \,, \tag{3.168}$$

where $\delta = r_\mathrm{o} - r_\mathrm{i}$ and $A_\mathrm{m} = (A_\mathrm{o} - A_\mathrm{i})/\ln(A_\mathrm{o}/A_\mathrm{i})$, if $A_\mathrm{o} = 2\pi r_\mathrm{o} l$ is the outer and $A_\mathrm{i} = 2\pi r_\mathrm{i} l$ is the inner surface of the tube. A_m is the logarithmic mean of the outer and inner tube surfaces. The thermal resistance of the tube $R_\mathrm{th} = \delta/(\lambda A_\mathrm{m})$ (SI unit K/W) must be overcome by the temperature difference so that heat transfer occurs.

3.10.2 Heat Transfer and Heat Transmission

If heat is transferred from a fluid to a wall, conducted through the wall and, on the other side, transferred to a second fluid, this process is called heat transmission. In this case, two heat transfer processes and a heat conduction process are connected in series. There exists a steep temperature drop in a layer directly at the wall (Fig. 3.32), while the temperature changes only slightly farther away from the wall. Due to the no-slip condition

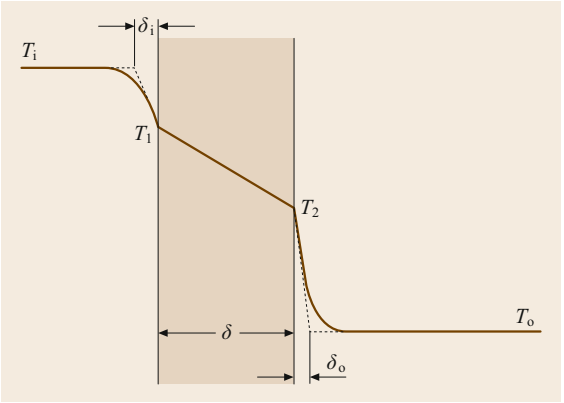

Fig. 3.32 Heat transmission through a flat wall

for the fluid at the wall surface, it can simplistically be assumed that a thin fluid boundary layer at rest, of thickness δ_i and δ_o, respectively, adheres to the wall while the fluid outside balances the temperature differences. In the thin fluid layer, heat transfer is by conduction and, according to Fourier's law, the heat flow transfer rate at the left wall side is given by

$$\dot{Q} = \lambda A \frac{T_\mathrm{i} - T_1}{\delta_\mathrm{i}} \,,$$

where λ is the thermal conductivity of the fluid. The film thickness depends on many parameters such as the velocity of the fluid along the wall and the form and surface conditions of the wall. It has been proven suitable to use the quotient $\lambda/\delta_\mathrm{i} = \alpha$ instead of the film thickness δ_i. This leads to the Newtonian formulation for the heat transfer rate from a fluid to a solid surface

$$\dot{Q} = \alpha A (T_\mathrm{f} - T_0) \,, \tag{3.169}$$

where T_f is the fluid temperature and T_0 is the surface temperature. The quantity α is defined as the heat transfer coefficient (SI unit $\mathrm{W/(m^2K)}$). Orders of magnitude for heat transfer coefficients are given in Table 3.22.

Table 3.22 Heat transfer coefficients α

Natural convection in	α ($\mathrm{W/(m^2K)}$)
Gases	3–20
Water	100–600
Boiling water	1000–20 000
Forced convection in	**α ($\mathrm{W/(m^2K)}$)**
Gases	10–100
Liquids	50–500
Water	500–10 000
Condensing vapor	1000–100 000

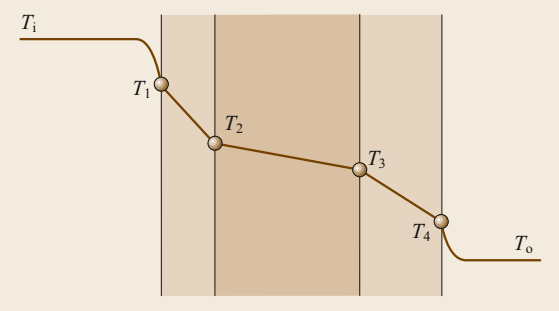

Fig. 3.33 Heat transmission through a plane, multilayered wall

The basics needed for the calculation of α are contained in Sect. 3.10.4. Following Ohm's law $I = (1/R) \times U$, the quantity $1/(\alpha A) = R_{th}$ is also called the convective heat transfer resistance (SI units K/W). It must be overcome by the temperature difference $\Delta T = T_f - T_0$ to enable the heat transfer $\dot{Q}$. In Fig. 3.32, the heat transfer must overcome three single resistances in series, which sum to the total resistance.

Heat Transmission Through a Plane Wall

The heat transfer passing through a plane wall (Fig. 3.32) is given by

$$\dot{Q} = kA(T_i - T_o) \,, \tag{3.170}$$

where $1/(kA)$ is the total heat resistance, which is, again, the sum of the individual resistances

$$\frac{1}{kA} = \frac{1}{\alpha_i A} + \frac{\delta}{\lambda A} + \frac{1}{\alpha_o A} \,. \tag{3.171}$$

The quantity k, defined by (3.170), is called the heat transmission coefficient (SI units $W/(m^2K)$). If the wall consists of several homogeneous layers (Fig. 3.33) with thicknesses $\delta_1, \delta_2, \ldots$ and thermal conductivities $\lambda_1, \lambda_2, \ldots$, (3.170) holds likewise with the total resistance

$$\frac{1}{kA} = \frac{1}{\alpha_i A} + \sum \frac{\delta_j}{\lambda_j A} + \frac{1}{\alpha_o A} \,. \tag{3.172}$$

Example 3.16

The wall of a cold store consists of a 5-cm-thick, internal concrete layer ($\lambda = 1\,W/(K\,m)$), a 10-cm-thick cork stone insulation ($\lambda = 0.04\,W/(K\,m)$), and a 50-cm-thick external brick wall. The inner heat transfer coefficient is $\alpha_i = 7\,W/(m^2\,K)$, and the outer coefficient is $\alpha_o = 20\,W/(m^2\,K)$. What is the heat transfer rate through $1\,m^2$ of the wall if the temperatures inside and outside are -5 and $25\,^\circ C$, respectively?

According to (3.172) the heat transmission resistance is

$$\frac{1}{kA} = \left(\frac{1}{7 \times 1} + \frac{0.05}{1 \times 1} + \frac{0.1}{0.04 \times 1} + \frac{0.5}{0.75 \times 1} + \frac{1}{20 \times 1} \right) \frac{K}{W} = 3.41 \frac{K}{W} \,.$$

The heat transfer rate is $\dot{Q} = (1/3.41)\,(-5 - 25)\,W$, $|\dot{Q}| = 8.8\,W$.

Heat Transmission Through Tubes

For heat transmission through tubes, (3.170) again holds, where the thermal resistance is the sum of the single resistances

$$\frac{1}{kA} = \frac{1}{\alpha_i A_i} + \frac{\delta}{\lambda A_m} + \frac{1}{\alpha_o A_o} \,.$$

The heat transmission coefficient k is usually related to the outer tube surface $A = A_o$, which is often easier to determine. The following equation therefore holds:

$$\frac{1}{kA_o} = \frac{1}{\alpha_i A_i} + \frac{\delta}{\lambda A_m} + \frac{1}{\alpha_o A_o} \,, \tag{3.173}$$

where $A_m = (A_o - A_i)/\ln(A_o/A_i)$. If the tube consists of several homogeneous layers with thicknesses $\delta_1, \delta_2, \ldots$ and thermal conductivities $\lambda_1, \lambda_2, \ldots$, (3.170) likewise holds for the total resistance

$$\frac{1}{kA_o} = \frac{1}{\alpha_i A_i} + \sum \frac{\delta_j}{\lambda_j A_{mj}} + \frac{1}{\alpha_o A_o} \,, \tag{3.174}$$

where the total resistance must be summed from the single layers j with their respective mean logarithmic areas

$$A_{mj} = (A_{oj} - A_{ij}) \ln\left(\frac{A_{oj}}{A_{ij}}\right) .$$

3.10.3 Transient Heat Conduction

During transient heat conduction, the temperatures vary with respect to time. In a plane wall with prescribed surface temperatures, the temperature profile is no longer linear as the heat transfer into the wall differs from the heat transfer out. The difference between the transfer in and the heat transfer out increases (or decreases) the internal energy of the wall, thus its temperature is a function of time. For plane walls with heat transfer

in the direction of the x-axis, Fourier's heat conduction equation holds

$$\frac{\partial T}{\partial \tau} = a\frac{\partial^2 T}{\partial x^2} \,. \tag{3.175}$$

Multidimensional heat conduction is represented by the following relation:

$$\frac{\partial T}{\partial \tau} = a\left(\frac{\partial^2 T}{\partial x^2} + \frac{\partial^2 T}{\partial y^2} + \frac{\partial^2 T}{\partial z^2}\right) \,. \tag{3.176}$$

In this form, both equations assume constant thermal conductivity λ (isotropic). The quantity $a = \lambda/(\varrho\, c)$ is defined as the thermal diffusivity (SI units m^2/s), numerical values for which are given in Table 3.23.

For the solution of Fourier's equation, it is suitable to introduce—as in other heat transfer problems—dimensionless quantities, which reduce the number of variables. Equation (3.175) is considered to demonstrate the basic procedure. The dimensionless temperature is set to $\Theta = (T - T_c)/(T_0 - T_c)$, where T_c is a characteristic constant temperature and T_0 is the initial temperature. If the cooling of a plate with an initial temperature T_0 in a cold environment is considered, T_c could be, for example, the ambient temperature T_{env}. All lengths are related to a characteristic length X, e.g., half of the plate thickness. Furthermore, it is suitable to introduce the dimensionless time, which is called the *Fourier number*, as $\mathrm{Fo} = a\tau/X^2$. The solution of the heat conduction equation then has the form

$$\Theta = f\frac{x}{X, \mathrm{Fo}} \,.$$

In many problems, the heat transfer from the surface of a body occurs by convection to the surrounding fluid at temperature T_{env}. The energy balance then holds at the surface (index w = wall)

$$-\lambda\left(\frac{\partial T}{\partial x}\right)_w = \alpha(T_w - T_{env})$$

or

$$\frac{1}{\Theta_w}\left(\frac{\partial \Theta}{\partial \xi}\right)_w = -\frac{\alpha X}{\lambda} \,,$$

where $\xi = x/X$, $\Theta = (T - T_{env})/(T_0 - T_{env})$, and $\Theta_w = (T_w - T_{env})/(T_0 - T_{env})$. The solution is also a function of the dimensionless quantity $\alpha X/\lambda$, which is defined as the Biot number Bi, where the thermal conductivity λ of the body is assumed to be constant, and α is the heat transfer coefficient between the body and the surrounding fluid. Solutions of (3.175) have the form

$$\Theta = f\frac{x}{X}, \mathrm{Fo}, \mathrm{Bi} \,. \tag{3.177}$$

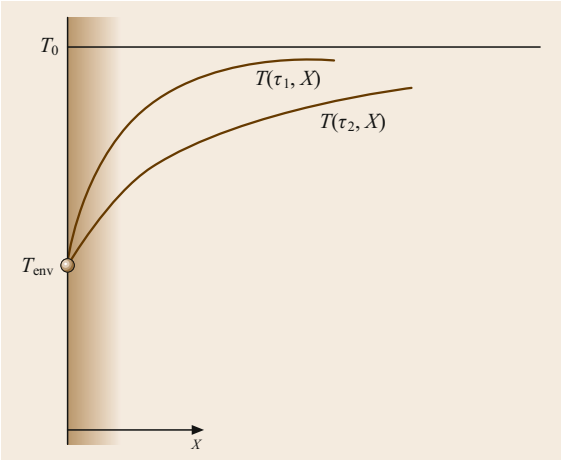

Fig. 3.34 Semiinfinite body

Semiinfinite Body

Temperature changes may also take place in a region that is thin in comparison with the overall dimensions of the body. Such a body is called semiinfinite. In this case, a semiinfinite plane wall (Fig. 3.34) with a constant initial temperature T_0 is considered. At time $\tau = 0$, the surface temperature of the wall is reduced to $T(x = 0) = T_{env}$ and then remains constant. The temperature profiles at different times $\tau_1, \tau_2 \ldots$ are given by

$$\frac{T - T_{env}}{T_0 - T_{env}} = f\left(\frac{x}{2\sqrt{a\tau}}\right) \tag{3.178}$$

with the Gaussian error function $f(x/(2\sqrt{a\tau}))$; see Fig. 3.35. The heat flux at the surface results from the differentiation $\dot{q} = -\lambda(\partial T/\partial x)_{x=0}$, which yields

$$\dot{q} = \frac{b}{\sqrt{\pi\tau}}(T_{env} - T_0) \,. \tag{3.179}$$

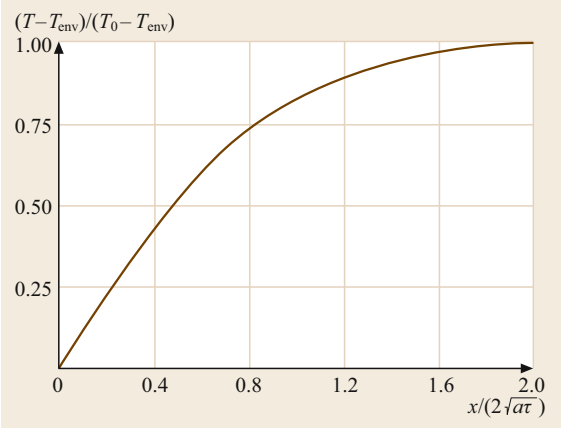

Fig. 3.35 Temperature course in a semiinfinite body

Table 3.23 Material properties of liquids, gases, and solids

	t (°C)	ρ (kg/m^3)	c_p (J/kg)	λ (W/(K m))	$a \times 10^6$ (m^2/s)	$\eta \times 10^6$ (Pa s)	Pr
Mercury	20	13 600	139	8000	4.2	1550	0.027
Sodium	100	927	1390	8600	67	710	0.0114
Lead	400	10 600	147	15 100	9.7	2100	0.02
Water	0	999.8	4217	0.562	0.133	1791.8	13.44
	5	1000	4202	0.572	0.136	519.6	11.16
	20	998.3	4183	0.5996	0.144	1002.6	6.99
	99.3	958.4	4215	0.6773	0.168	283.3	1.76
Thermal oil	20	887	1000	0.133	0.0833	426	576
	80	835	2100	0.128	0.073	26.7	43.9
	150	822	2160	0.126	0.071	18.08	31
Air	−20	1.3765	1006	0.02301	16.6	16.15	0.71
	0	1.2754	1006	0.02454	17.1	19.1	0.7
	20	1.1881	1007	0.02603	21.8	17.98	0.7
	100	0.9329	1012	0.03181	33.7	21.6	0.69
	200	0.7256	1026	0.03891	51.6	25.7	0.68
	300	0.6072	1046	0.04591	72.3	29.2	0.67
	400	0.5170	1069	0.05257	95.1	32.55	0.66
Water vapor	100	0.5895	2032	0.02478	20.7	12.28	1.01
	300	0.379	2011	0.04349	57.1	20.29	0.938
	500	0.6846	1158	0.05336	67.29	34.13	0.741
Aluminum 99.99%	20	2700	945	238	93.4	–	–
V2A steel, hardened and tempered	20	8000	477	15	3.93	–	–
Lead	20	11 340	131	35.3	23.8	–	–
Chrome	20	6900	457	69.1	21.9	–	–
Gold, pure	20	19 290	128	295	119	–	–
Uranium dioxide	600	11 000	313	4.18	1.21	–	–
	1000	10 960	326	3.05	0.854	–	–
	1400	10 900	339	2.3	0.622	–	–
Gravel concrete	20	2200	879	1.28	0.662	–	–
Plaster	20	1690	800	0.79	0.58	–	–
Fir, radial	20	410	2700	0.14	0.13	–	–
Cork plates	30	190	1880	0.041	0.11	–	–
Glass wool	0	200	660	0.037	0.28	–	–
Soil	20	2040	1840	0.59	0.16	–	–
Quartz	20	2300	780	1.4	0.78	–	–
Marble	20	2600	810	2.8	1.35	–	–
Chamotte	20	1850	840	0.85	0.52	–	–
Wool	20	100	1720	0.036	0.21	–	–
Hard coal	20	1350	1260	0.26	0.16	–	–
Snow (compact)	0	560	2100	0.46	0.39	–	–
Ice	0	917	2040	2.25	1.2	–	–
Sugar	0	1600	1250	0.58	0.29	–	–
Graphite	20	2250	610	155	1.14	–	–

The heat penetration coefficient $b = \sqrt{\lambda \varrho c}$ (SI units W s$^{1/2}$/(m^2 K)) (Table 3.24) is a measure for the heat transfer that would penetrate into the body at a given time, if the surface temperature were suddenly increased by the amount $T_{\text{env}} - T_0$ as compared with the initial temperature T_0.

Example 3.17

A sudden change in weather causes the temperature at the Earth's surface to drop from +5 to −5 °C. How much does the temperature decrease at a depth of 1 m after 20 days? The thermal diffusivity of the soil is $a = 6.94 \times 10^{-7}$ m^2/s. According to (3.178), the decrease

Table 3.24 Heat penetration coefficients $b = \sqrt{\lambda \varrho c}$

	b ($\mathrm{W\,s^{1/2}/(m^2\,K)}$)
Copper	36 000
Iron	15 000
Concrete	1600
Water	1400
Sand	1200
Wood	400
Foam	40
Gases	6

is

$$\frac{T-(-5)}{5-(-5)} = f\left(\frac{1}{2(6.94\times10^{-7}\times20\times24\times3600)^{1/2}}\right) = f(0.456)\,.$$

Figure 3.35 gives $f(0.456) = 0.48$, thus $T = -0.2\,^{\circ}\mathrm{C}$.

Finite Heat Transfer at the Surface. According to Fig. 3.34, heat transfer is by convection from the surface of a body to the environment. At the surface, the relation $\dot{q} = -\lambda(\partial T/\partial x) = \alpha(T_\mathrm{w} - T_\mathrm{env})$ holds, with the ambient temperature T_env and the time-variable wall temperature $T_\mathrm{w} = T(x=0)$. In this case, (3.178) no longer holds. Instead, the heat transfer rate is given by

$$\dot{q} = \frac{b}{\sqrt{\pi\tau}}(T_\mathrm{env} - T_0)\Phi(z)\,, \qquad (3.180)$$

where

$$\Phi(z) = 1 - \frac{1}{2z^2} + \frac{1\times3}{2^2z^4} - \ldots + (-1)^{n-1}\left(\frac{1\times3\times\ldots\times(2n-3)}{2^{n-1}z^{2n-2}}\right) \quad \text{and}$$

$$z = \alpha\frac{\sqrt{a\tau}}{\lambda}\,.$$

Two Semiinfinite Bodies in Thermal Contact

Two semiinfinite bodies at different, but initially constant, temperatures T_1 and T_2 with the thermal properties λ_1, a_1 and λ_2, a_2 are suddenly brought into contact at time $t = 0$ (Fig. 3.36). After a very short time at both sides of the contact area, a temperature T_m is present and remains constant. This temperature is given by

$$\frac{T_\mathrm{m} - T_1}{T_2 - T_1} = \frac{b_2}{b_1 + b_2}\,.$$

The contact temperature T_m is closer to the temperature of the body with the higher heat penetration coefficient b. One of the values b can be determined by measuring T_m, if the other value is known.

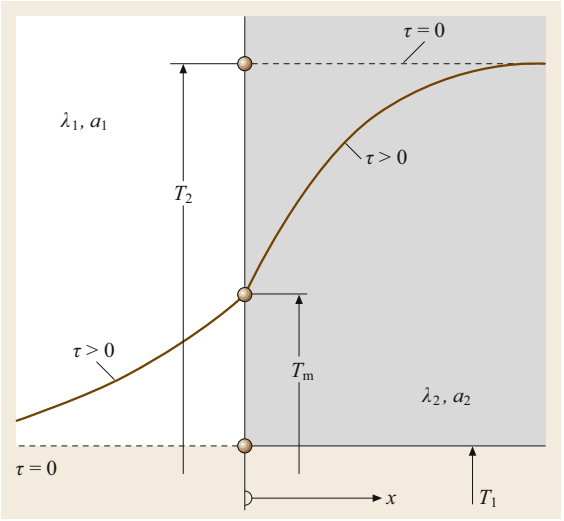

Fig. 3.36 Contact temperature T_m between two semiinfinite bodies

Temperature Equalization in Simple Bodies

A simple body such as a plate, a cylinder, or a sphere may have a uniform temperature T_0 at time $\tau = 0$. Afterwards, however, it is cooled or heated due to heat transfer between the body and a surrounding fluid of temperature T_env given by the boundary condition $-\lambda(\partial T/\partial n)_\mathrm{w} = \alpha(T_\mathrm{w} - T_\mathrm{env})$, where n is the coordinate perpendicular to the body surface.

Plane Plate. The temperature profile shown in Fig. 3.37 is described by an infinite series. However, for $a\tau/X^2 \geq 0.24$ (where $a = \lambda/(\varrho c)$ is the thermal diffusivity), the following relation provides a good approximation:

$$\frac{T - T_\mathrm{env}}{T_0 - T_\mathrm{env}} = C\exp\left(-\delta^2\frac{a\tau}{X^2}\right)\cos\left(\delta\frac{x}{X}\right) \qquad (3.181)$$

with less than a 1% error in temperature. The constants C and δ depend, according to Table 3.25, on the Biot number $\mathrm{Bi} = \alpha X/\lambda$. When $x = X$, (3.181) leads to the surface temperature T_w at the wall. The heat transfer rate follows from $\dot{Q} = -\lambda A(\partial T/\partial x)_{x=X}$.

Cylinder. The radial coordinate r replaces the coordinate x in Fig. 3.37, and the radius of the cylinder is R. Again, the temperature profile is described by an infinite series, which can be approximated for $a\tau/R^2 \geq 0.21$ by

$$\frac{T - T_\mathrm{env}}{T_0 - T_\mathrm{env}} = C\exp\left(-\delta^2\frac{a\tau}{R^2}\right)I_0\left(\delta\frac{r}{R}\right) \qquad (3.182)$$

Table 3.25 Constants C and δ in (3.181)

Bi	∞	10	5	2	1	0.5	0.2	0.1	0.01
C	1.2732	1.2620	1.2402	1.1784	1.1191	1.0701	1.0311	1.0161	1.0017
δ	1.5708	1.4289	1.3138	1.0769	0.8603	0.6533	0.4328	0.3111	0.0998

Table 3.26 Constants C and δ in (3.182)

Bi	∞	10	5	2	1	0.5	0.2	0.1	0.01
C	1.6020	1.5678	1.5029	1.3386	1.2068	1.1141	1.0482	1.0245	1.0025
δ	2.4048	2.1795	1.9898	1.5994	1.2558	0.9408	0.6170	0.4417	0.1412

Table 3.27 Constants C and δ in (3.183)

Bi	∞	10	5	2	1	0.5	0.2	0.1	0.01
C	2.0000	1.9249	1.7870	1.4793	1.2732	1.1441	1.0592	1.0298	1.0030
δ	3.1416	2.8363	2.5704	2.0288	1.5708	1.1656	0.7593	0.5423	0.1730

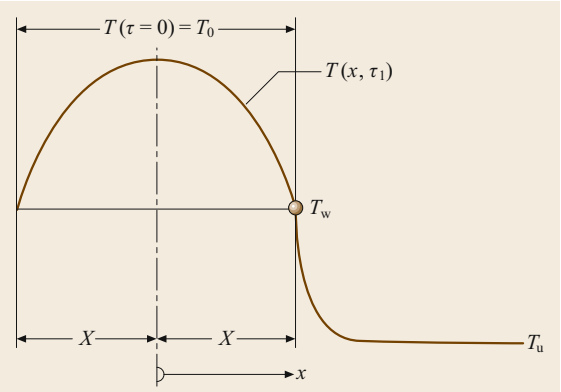

Fig. 3.37 Cooling of a flat plate

with less than 1% error. The term I_0 is a Bessel function of zeroth order. Its values are presented in tables [3.20]. The constants C and δ depend, according to Table 3.26, on the Biot number. When $r = R$, the surface temperature at the wall results from (3.182) and the heat transfer rate from $\dot{Q} = -\lambda A(\partial T/\partial r)_{r=R}$, where the first derivative of the Bessel function $I_0' = I_1$ appears. The Bessel function of first order I_1 is also given in [3.21].

Sphere. The cooling or heating of a sphere of radius R is also described by an infinite series. For $a\tau/R^2 \geq 0.18$, the temperature profile can be approximated by

$$\frac{T - T_{\text{env}}}{T_0 - T_{\text{env}}} = C \exp\left(-\delta^2 \frac{a\tau}{R^2}\right) \frac{\sin\left(\delta \frac{\mathrm{r}}{R}\right)}{\delta \frac{\mathrm{r}}{R}} \qquad (3.183)$$

with less than 2% error. The constants C and δ depend, according to Table 3.27, on the Biot number.

3.10.4 Heat Transfer by Convection

If heat transfer in fluids with bulk fluid motion is considered, in addition to (molecular) heat conduction, energy transport by convection must be taken into account. Each volume element of the fluid possesses internal energy, which is transported by the flow and, in the case considered here, is transferred by convection to a solid body.

Dimensionless Characteristic Numbers

The basis for the description of processes of convective transport is the use of similarity mechanics. These descriptions allow for a considerable reduction of the number of influencing parameters and for the expression of the general heat transfer laws for geometrically similar bodies and different substances. The following dimensionless characteristic numbers are of importance:

- Nusselt number

$$\mathrm{Nu} = \frac{\alpha l}{\lambda} ,$$

- Reynolds number

$$\mathrm{Re} = \frac{wl}{\nu} ,$$

- Prandtl number

$$\mathrm{Pr} = \frac{\nu}{a} ,$$

- Péclet number

$$\mathrm{Pe} = \frac{wl}{a} = \mathrm{Re}\,\mathrm{Pr} ,$$

- Grashof number

$$\mathrm{Gr} = l^3 g \beta \Delta \frac{T}{\nu^2} ,$$

- Stanton number

$$\mathrm{St} = \frac{\alpha}{\varrho\, w c_\mathrm{p}} = \frac{\mathrm{Nu}}{\mathrm{Re\,Pr}} ,$$

- Geometric characteristic numbers

$$\frac{l_n}{l} , \quad n = 1, 2, \ldots$$

The variables signify the following:

λ thermal conductivity of the fluid
l a characteristic length of the flow domain $l_1, l_2, \ldots$
ν the kinematic viscosity of the fluid
ϱ density
a $= \lambda/(\varrho\, c_p)$ thermal diffusivity
c_p constant-pressure specific heat of the fluid
g gravitational acceleration
ΔT $= T_\mathrm{w} - T_\mathrm{f}$ difference between the wall temperature T_w of a cooled or heated body and the mean temperature T_f of the fluid along the body
β thermal volume expansivity at the wall temperature with $\beta = 1/T_\mathrm{w}$ for ideal gases.

The Prandtl number is a fluid property (Table 3.23).

Forced and natural convection are distinguished as follows: In forced convection, the fluid motion is caused by external forces, e.g., by the pressure increase in a pump. In natural convection, the fluid motion is caused by density differences in the fluid and the corresponding buoyancy effects in a gravitational field. These density differences usually arise due to temperature differences, rarely due to pressure differences. In mixtures, density differences are also caused by concentration differences. The heat transfer in forced convection is described by equations of the form

$$\mathrm{Nu} = f_1 \left(\mathrm{Re}, \mathrm{Pr}, \frac{l_n}{l} \right) , \tag{3.184}$$

and in natural convection by

$$\mathrm{Nu} = f_2 \left(\mathrm{Gr}, \mathrm{Pr}, \frac{l_n}{l} \right) . \tag{3.185}$$

The desired heat transfer coefficient is obtained from the Nusselt number by $\alpha = \mathrm{Nu}\lambda/l$. The functions f_1 and f_2 can be determined theoretically only for special cases. In general, they must be determined through experimentation and depend on the shape of the cooling or heating areas (even, vaulted, smooth, rough, or finned), the flow structure and, usually to a minor extent, on the direction of the heat transfer (heating or cooling).

Heat Transfer Without Change of Phase

Forced Convection.

Laminar Flow Along a Flat Plate. According to *Pohlhausen* [3.22], for the mean Nusselt number of a plate of length l, the following relation holds:

$$\mathrm{Nu} = 0.664\, \mathrm{Re}^{1/2} \mathrm{Pr}^{1/3} , \tag{3.186}$$

where $\mathrm{Nu} = \alpha l/\lambda$, $\mathrm{Re} = wl/\nu < 10^5$, and $0.6 \le \mathrm{Pr} \le 2000$. The material properties must be evaluated at the mean fluid temperature $T_\mathrm{m} = (T_\mathrm{w} - T_\infty)/2$, where T_w is the wall temperature and T_∞ is the free-stream temperature far beyond the wall surface.

Turbulent Flow Along a Flat Plate. From about $\mathrm{Re} = 5 \times 10^5$, the boundary layer becomes turbulent. The mean Nusselt number of a plate of length l in this case is

$$\mathrm{Nu} = \frac{0.037\, \mathrm{Re}^{0.8} \mathrm{Pr}}{1 + 2.443\, \mathrm{Re}^{-0.1} (\mathrm{Pr}^{2/3} - 1)} , \tag{3.187}$$

where $\mathrm{Nu} = \alpha l/\lambda$, $\mathrm{Re} = wl/\nu$, $5 \times 10^5 < \mathrm{Re} < 10^7$, and $0.6 \le \mathrm{Pr} \le 2000$. The material properties must be evaluated at the mean fluid temperature $T_\mathrm{m} = (T_\mathrm{w} - T_\infty)/2$. T_w is the wall temperature and, T_∞ is the free-stream temperature far beyond the wall surface.

Flow Through Pipes in General. Below a Reynolds number of $\mathrm{Re} = 2300$ ($\mathrm{Re} = wd/\nu$, where w is the mean cross-sectional velocity and d is the pipe diameter), the flow is laminar, while above $\mathrm{Re} = 10^4$, the flow is turbulent. In the range $2300 < \mathrm{Re} < 10^4$, whether the flow is laminar or turbulent depends on the roughness of the pipe, the means of inflow, and the shape of the pipe in the inflow section. The mean heat transfer coefficient α over the pipe length l is defined by $\dot{q} = \alpha \Delta\vartheta$, with the mean logarithmic temperature difference described by

$$\Delta\vartheta = \frac{(T_\mathrm{w} - T_\mathrm{in}) - (T_\mathrm{w} - T_\mathrm{out})}{\ln \frac{T_\mathrm{w} - T_\mathrm{in}}{T_\mathrm{w} - T_\mathrm{out}}} , \tag{3.188}$$

where T_w is the wall temperature, T_in is the temperature at the inlet, and T_out is the temperature at the outlet cross-section.

Laminar Flow Through Pipes. A flow is termed hydrodynamically developed if the velocity profile no longer changes in the flow direction. In a laminar flow of a highly viscous fluid, the velocity profile adopts the shape of a Poiseuillean parabola after only a short distance from the inlet. The mean Nusselt number at constant wall temperature can be calculated exactly via an infinite series (the Graetz solution), which, however,

converges poorly. According to *Stephan* [3.23], as an approximate solution for the hydrodynamically developed laminar flow, the following equation holds:

$$\mathrm{Nu}_0 = \frac{3.657}{\tanh(2.264X^{1/3} + 1.7X^{2/3})} + \frac{0.0499}{X}\tanh X\,, \qquad (3.189)$$

where $\mathrm{Nu}_0 = \alpha d/\lambda$, $X = l/(d\mathrm{Re}\,\mathrm{Pr})$, $\mathrm{Re} = wd/\nu$, and $\mathrm{Pr} = \nu/a$. This equation is valid for laminar flow ($\mathrm{Re} \leq 2300$) in the entire range $0 \leq X \leq \infty$ and the maximum deviation from the exact values of the Nusselt number is 1%. The fluid properties must be evaluated at the mean fluid temperature $T_\mathrm{m} = (T_\mathrm{w} + T_\mathrm{B})/2$, where $T_\mathrm{B} = (T_\mathrm{in} + T_\mathrm{out})/2$.

If a fluid enters a pipe at an approximately constant velocity, the velocity profile changes along the flow path until it reaches the Poiseuillean parabola after a distance described by the equation $l/(d\mathrm{Re}) = 5.75 \times 10^{-2}$. According to *Stephan* [3.23], for this case, that of a hydrodynamically developed laminar flow, the following equation holds for the range $0.1 \leq \mathrm{Pr} \leq \infty$:

$$\frac{\mathrm{Nu}}{\mathrm{Nu}_0} = \frac{1}{\tanh(2.43\,\mathrm{Pr}^{1/6}X^{1/6})}\,, \qquad (3.190)$$

where $\mathrm{Nu} = \alpha d/\lambda$ and the quantities are defined as above. The error is less than 5% for $1 \leq \mathrm{Pr} \leq \infty$ but is up to 10% for $0.1 \leq \mathrm{Pr} < 1$. The fluid properties must be evaluated at the mean fluid temperature $T_\mathrm{m} = (T_\mathrm{w} + T_\mathrm{B})/2$, where $T_\mathrm{B} = (T_\mathrm{in} + T_\mathrm{out})/2$.

Heat Transfer for Turbulent Flow Through Pipes. For a hydrodynamically developed flow ($l/d \geq 60$), the McAdam equation holds in the range $10^4 \leq \mathrm{Re} \leq 10^5$ and $0.5 < \mathrm{Pr} < 100$:

$$\mathrm{Nu} = 0.024\,\mathrm{Re}^{0.8}\mathrm{Pr}^{1/3}\,. \qquad (3.191)$$

The fluid properties have to be evaluated at the mean temperature $T_\mathrm{m} = (T_\mathrm{w} + T_\mathrm{B})/2$ with $T_\mathrm{B} = (T_\mathrm{in} + T_\mathrm{out})/2$.

For hydrodynamically undeveloped flow and for developed flow, Petukhov's equation (modified by Gnielinski) holds in the range $10^4 \leq \mathrm{Re} \leq 10^6$ and $0.6 \leq \mathrm{Pr} \leq 1000$:

$$\mathrm{Nu} = \frac{\mathrm{Re}\,\mathrm{Pr}\zeta/8}{1 + 12.7\sqrt{\zeta/8}(\mathrm{Pr}^{2/3} - 1)}\left[1 + \left(\frac{d}{l}\right)^{2/3}\right], \qquad (3.192)$$

where the friction factor $\zeta = (0.78\ln\mathrm{Re} - 1.5)^{-2}$, $\mathrm{Nu} = \alpha d/\lambda$, and $\mathrm{Re} = wd/\nu$. The fluid properties must be evaluated at the mean temperature $T_\mathrm{m} = (T_\mathrm{w} + T_\mathrm{B})/2$. Under otherwise similar conditions, the heat transfer coefficients are larger in pipe bends than in straight pipes with the same cross section. For a pipe bend with a bend diameter D, the following equation holds, according to Hausen, for turbulent flow:

$$\alpha = \alpha_\mathrm{straight}\left[1 + (21\,\mathrm{Re}^{0.14})\left(\frac{d}{D}\right)\right]. \qquad (3.193)$$

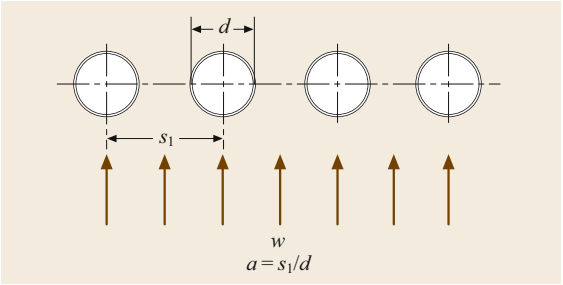

Fig. 3.38 A row of pipes placed transversely in a flow

A Single Pipe Placed Transversely in a Flow. The heat transfer coefficient for a pipe placed transversely in a flow can be determined from Gnielinski's equation:

$$\mathrm{Nu} = 0.3 + \left(\mathrm{Nu}_\ell^2 + \mathrm{Nu}_\mathrm{t}^2\right)^{1/2}\,, \qquad (3.194)$$

where the Nusselt number Nu_ℓ of the laminar plate flow is described according to (3.186), Nu_t of the turbulent plate flow is described according to (3.187), and $\mathrm{Nu} = \alpha l/\lambda$, $1 < \mathrm{Re} = wl/\nu < 10^7$, and $0.6 < \mathrm{Pr} < 1000$. For length l, the overflowed length $l = d\pi/2$ must be inserted. The fluid properties must be evaluated at the mean temperature $T_\mathrm{m} = (T_\mathrm{in} + T_\mathrm{out})/2$. This equation holds for mean turbulence intensities of 6–10%, which can be expected in technical applications.

A Row of Pipes Placed Transversely in a Flow. Mean heat transfer coefficients for a single row of pipes placed transversely in a flow (Fig. 3.38) can also be determined using (3.194). Now, however, the Reynolds number must be calculated with the mean velocity w_m in the pipe row placed transversely in the flow. The Reynolds number is described by the equation: $\mathrm{Re} = w_\mathrm{m}l/\nu$, where $w_\mathrm{m} = w/\psi$, w is the far-field velocity and $\psi = 1 - \pi/(4a)$ is the void space fraction, where $a = s_1/d$ (Fig. 3.38).

A Pipe Bundle. If the pipes are placed in straight lines (Fig. 3.39a), the axes of all the pipes are consecutively in the flow direction. If the arrangement is staggered (Fig. 3.39b), the axes of a pipe row are shifted in comparison with the axes of the row in front. The

heat transfer depends additionally on the crosswise and longwise division of the pipes, $a = s_1/d$ and $b = s_2/d$. The determination of the heat transfer coefficient starts with the calculation of the Nusselt number for a single pipe placed transversely in the flow, according to (3.194), in which the Reynolds number contains the mean velocity w_m in the pipe bundle: $\mathrm{Re} = w_m l/\nu$, where $w_m = w/\psi$, w is the far-field velocity of the pipe row, and ψ is the void space fraction $\psi = 1 - \pi/(4a)$ for $b > 1$ and $\psi = 1 - \pi/(4ab)$ for $b < 1$. The Nusselt number determined in this way must be multiplied by an arrangement factor f_A. This leads to the Nusselt number $\mathrm{Nu_B} = \alpha_B l/\lambda$ (where $l = d\pi/2$) of the bundle

$$\mathrm{Nu_B} = f_A \mathrm{Nu} \,. \tag{3.195}$$

For a straight arrangement, the following holds:

$$f_A = 1 + 0.7 \frac{\frac{b}{a} - 0.3}{\psi^{3/2}\left(\frac{b}{a} + 0.7\right)^2} \,, \tag{3.196}$$

and for a staggered arrangement

$$f_A = 1 + \frac{2}{3b} \,. \tag{3.197}$$

The heat flux is $\dot{q} = \alpha \Delta\vartheta$ with $\Delta\vartheta$ according to (3.188). Equations (3.196) and (3.197) hold for pipe bundles consisting of ten or more pipe rows. For heat exchangers with fewer pipe rows, the heat transfer coefficient (3.195) must be multiplied by a factor $(1 + (n - 1) f_A/n)$, where n is the number of pipe rows.

Natural Convection. The heat transfer coefficient for a vertical wall can be calculated by using the equation of Churchill and Chu:

$$\mathrm{Nu} = \left(0.825 + \frac{0.387\,\mathrm{Ra}^{1/6}}{[1 + (0.492/\mathrm{Pr})^{9/16}]^{8/27}}\right)^2 \,, \tag{3.198}$$

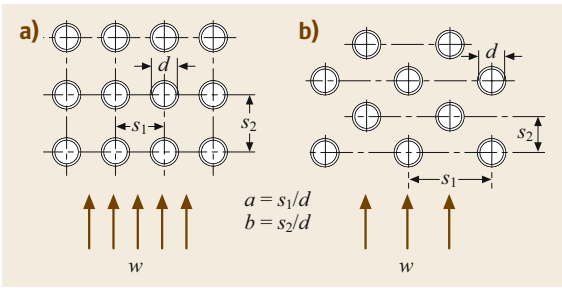

Fig. 3.39a,b Arrangement of pipes in pipe bundles: **(a)** in straight lines and **(b)** staggered

in which the mean Nusselt number $\mathrm{Nu} = \alpha l/\lambda$ is formed with the wall height l, and the Rayleigh number is defined as $\mathrm{Ra} = \mathrm{GrPr}$, where the Grashof number is described as

$$\mathrm{Gr} = \frac{g l^3}{\nu^2} \frac{\varrho_\infty - \varrho_w}{\varrho_w}$$

and the Prandtl number as $\mathrm{Pr} = \nu/a$.

If natural convection is caused solely by temperature differences, the Grashof number can be written as

$$\mathrm{Gr} = \frac{g l^3}{\nu^2} \beta (T_w - T_\infty) \,,$$

where the volume expansivity is denoted by β, where $\beta = 1/T_w$ for ideal gases. Equation (3.198) holds in the range $0 < \mathrm{Pr} < \infty$ and $0 < \mathrm{Ra} < 10^{12}$. The fluid properties must be evaluated at the mean temperature $T_m = (T_w - T_\infty)$. A similar equation holds according to Churchill and Chu also for natural convection in a horizontal cylinder:

$$\mathrm{Nu} = \left(0.60 + \frac{0.387\,\mathrm{Ra}^{1/6}}{[1 + (0.559/\mathrm{Pr})^{9/16}]^{8/27}}\right)^2 \,. \tag{3.199}$$

The same definitions used in (3.198) hold over the range of validity $0 < \mathrm{Pr} < \infty$ and $10^{-5} \le \mathrm{Ra} \le 10^{12}$, and the characteristic length is the diameter d. For *horizontal rectangular plates*, the following holds for $0 < \mathrm{Pr} < \infty$:

$$\mathrm{Nu} = 0.766(\mathrm{Ra} f_2)^{1/5} \quad \text{if} \quad \mathrm{Ra} f_2 < 7 \times 10^4 \tag{3.200}$$

and

$$\mathrm{Nu} = 0.15(\mathrm{Ra} f_2)^{1/3} \quad \text{if} \quad \mathrm{Ra} f_2 > 7 \times 10^4 \,, \tag{3.201}$$

where

$$f_2 = \left[1 + \left(\frac{0.322}{\mathrm{Pr}}\right)^{11/20}\right]^{-20/11} \,,$$

where $\mathrm{Nu} = \alpha l/\lambda$, if l is the shorter side of the rectangle.

Heat Transfer in Condensation and in Boiling

Condensation. If the temperature of a wall surface is lower than the saturation temperature of adjacent vapor, the vapor condenses at the wall surface. Depending on the wetting characteristics, the condensate forms drops or a continuous liquid film. The heat transfer coefficients are usually larger for dropwise condensation than for film condensation. However, in order to maintain dropwise condensation for a certain amount of time, particular measures such as the application of dewetting agents are necessary. Dropwise condensation therefore appears rather seldom.

Film Condensation. If the condensate flows as a laminar film on a vertical wall of height l, the mean heat transfer coefficient α is

$$\alpha = 0.943 \left(\frac{\varrho g r \lambda^3}{\nu (T_s - T_w)} \frac{1}{l} \right)^{1/4} . \tag{3.202}$$

For condensation on horizontal single pipes with an outer diameter d, the following relation holds:

$$\alpha = 0.728 \left(\frac{\varrho g r \lambda^3}{\nu (T_s - T_w)} \frac{1}{l} \right)^{1/4} . \tag{3.203}$$

These equations require that no noticeable shear stress be exerted by the vapor on the condensate film. At Reynolds number $\mathrm{Re}_\delta = w_m \delta / \nu$ (where w_m is the velocity of the condensate, δ the film thickness, and ν the kinematic viscosity) between 75 and 1200 the transition to turbulent flow in the condensate film gradually takes place. In the transition range, the following relation holds:

$$\alpha = 0.22 \frac{\lambda}{\left(\frac{\nu^2}{g} \right)^{1/3}} , \tag{3.204}$$

whereas for turbulent film flow ($\mathrm{Re}_\delta > 1200$), the following relation according to Grigull holds:

$$\alpha = 0.003 \left(\frac{\lambda^3 g \, (T_s - T_w)}{\varrho \nu^3 r} l \right)^{1/2} . \tag{3.205}$$

Equations (3.204) and (3.205) are valid also for vertical pipes and plates but not for horizontal pipes.

Evaporation. If a liquid in a container is heated, evaporation starts after the boiling temperature T_s is exceeded. For small excess wall temperatures $T_w - T_s$, the liquid evaporates only on its free surface (silent boiling). Heat is transported by the buoyancy flow from the heating surface to the free surface of the liquid. For higher excess wall temperatures, vapor bubbles are formed at the heating surface (nucleate boiling) and rise. They increase the movement of the liquid and thus the heat transfer. With increasing excess wall temperature, the bubbles merge more and more into a continuous vapor film, whereby the heat transfer is decreased (transition boiling). Figure 3.40 shows the different heat transfer ranges. The heat transfer coefficient α is defined as

$$\alpha = \frac{\dot{q}}{T_w - T_s} ,$$

where the heat flux is $\dot{q}$ in $\mathrm{W/m^2}$.

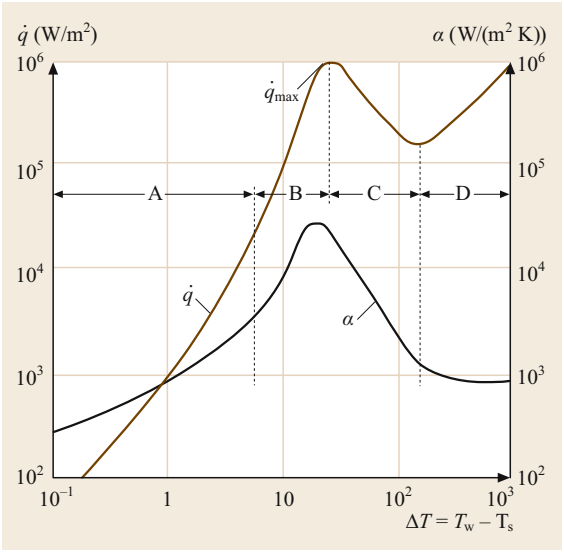

Fig. 3.40 Boiling ranges for water of 1 bar. A: natural convection (silent boiling), B nucleate boiling, C transition boiling, D film boiling

Industrial evaporators work in the range of silent boiling or, more often, in the nucleate boiling range. In the silent boiling range, the laws for heat transfer in natural convection hold, (i.e., (3.198) and (3.199)). In the nucleate boiling region,

$$\alpha = c \dot{q}^n F(p) \quad \text{with } 0.5 < n < 0.8 .$$

For water at boiling pressures between 0.5 and 20 bar, according to *Fritz* [3.24], the following relation holds:

$$\alpha = 1.95 \dot{q}^{0.72} p^{0.24} \tag{3.206}$$

with α in $\mathrm{W/(m^2\,K)}$, $\dot{q}$ in $\mathrm{W/m^2}$, and p in bar. According to Stephan and Preußer, for arbitrary liquids the following relation is valid for nucleate boiling close to ambient pressure:

$$\mathrm{Nu} = 0.0871 \left(\frac{\dot{q} d}{\lambda' T_s} \right)^{0.674} \left(\frac{\varrho''}{\varrho'} \right)^{0.156} \times \left(\frac{r d^2}{a'^2} \right)^{0.371} \left(\frac{a'^2 \varrho'}{\sigma d} \right)^{0.350} (\mathrm{Pr}')^{-0.162} . \tag{3.207}$$

$\mathrm{Nu} = \alpha d / \lambda'$ is formed with the detachment diameter of the vapor bubbles $d = 0.851 \beta_0 [2\sigma / g(\varrho' - \varrho'')]^{1/2}$, where the contact angle is $\beta_0 = 45°$ for water, 1° for low-boiling and 35° for other liquids. Quantities denoted with a single prime relate to the boiling liquid, while those with a double prime relate to the saturated vapor. The equations above are not valid for boiling in forced flow.

Table 3.28 Emissivity ε at temperature t

Substance	Surface	t (°C)	ε
Roofing paper		21	0.91
Oak wood	Planed	21	0.89
Enamel varnish	Snow white	24	0.91
Glass	Smooth	22	0.94
Lime mortar	Rough, white	21–83	0.93
Marble	Light grey, polished	22	0.93
Porcelain	Glazed	22	0.92
Soot	Smooth	–	0.93
Chamotte slab	Glazed	1000	0.75
Spirit varnish	Black, shiny	25	0.82
Brick	Red, rough	22	0.93–0.95
Water	Vertical radiation	–	0.96
Oil	Thick layer	–	0.82
Oil coating		–	0.78
Aluminum	Rough	26	0.071–0.087
Aluminum	Polished	230	0.038
Lead	Polished	130	0.057
Gray cast iron	Lathe-turned	22	0.44
Gray cast iron	Liquid	1330	0.28
Gold	Polished	630	0.035
Copper	Polished	23	0.049
Copper	Rolled	–	0.16
Brass	Polished	19	0.05
Brass	Polished	300	0.031
Brass	Dead	56–338	0.22
Nickel	Polished	230	0.071
Nickel	Polished	380	0.087
Silver	Polished	230	0.021
Steel	Polished	–	0.29
Zinc	Zinc-coated iron sheet	28	0.23
Zinc	Polished	230	0.045
Zinc	Shiny, tinned sheet	24	0.057–0.087
Oxidized metals			
Iron	Red, slightly rusted	20	0.61
Iron	Totally rusted	20	0.69
Iron	Smooth or rough cast skin	23	0.81
Copper	Black	25	0.78
Copper	Oxidized	600	0.56–0.7
Nickel	Oxidized	330	0.40
Nickel	Oxidized	1330	0.74
Steel	Matt oxidized	26–356	0.96

3.10.5 Radiative Heat Transfer

In addition to direct contact modes, heat can also be transferred by radiation. Thermal radiation (heat radiation) consists of a spectrum of electromagnetic waves in the wavelength range between 0.1 and 1000 µm. Visible light, as a reference, has a wavelength range between 0.4 and 0.76 µm. If a body is supplied with a heat transfer $\dot{Q}$ by radiation, the fraction $r\dot{Q}$ is reflected, the fraction $a\dot{Q}$ is absorbed, and the fraction $d\dot{Q}$ passes through (where $r + d + a = 1$). A body that reflects radiation completely ($r = 1$, $d = a = 0$) is called an ideal mirror, while a body that absorbs radiation completely ($a = 1$, $r = d = 0$) is called a black body. A body is called diathermal ($d = 1$, $r = a = 0$) if radiation passes completely through, where examples for this are gases such as O_2, N_2, etc.

Stefan–Boltzmann Law

Every body emits radiation corresponding to its surface temperature. The maximum radiation possible is emitted by a black body. It can be experimentally ap-

proximated by a blackened surface (e.g., with soot) or by a hollow space, whose walls have the same temperature everywhere and that has a small opening to let radiation out. The total radiation emitted by a black body per unit area is

$$\dot{e}_\mathrm{s} = \sigma T^4 \,, \tag{3.208}$$

where $\dot{e}_\mathrm{s}$ is called the emission ($\mathrm{W/m^2}$) of the black radiator, and $\sigma = 5.67 \times 10^{-8}\,\mathrm{W/(m^2\,K^4)}$ is the *radiation coefficient*, also called the Stefan–Boltzmann constant. The emission $\dot{e}_\mathrm{s}$ is an energy flux and thus equal to the heat flux $\dot{q}_\mathrm{s} = \mathrm{d}\dot{Q}/\mathrm{d}A$ a black radiator emits. With the emission $\dot{e}_\mathrm{n}$ in a normal direction and $\dot{e}_\varphi$ in the direction of angle φ to the normal, *Lambert's cosine law* $\dot{e}_\varphi = \dot{e}_\mathrm{n} \cos\varphi$ for black radiators holds true. Often the radiation of real bodies differs from this general law, however.

Kirchhoff's Law

Real bodies emit less than black radiators, where the energy emitted from real surfaces is

$$\dot{e} = \varepsilon \dot{e}_\mathrm{s} = \varepsilon \sigma T^4 \tag{3.209}$$

with the emissivity being in the range $0 < \varepsilon < 1$ and in general depending on temperature (Table 3.28). In limited temperature ranges, many engineering surfaces (with the exception of shiny metal) can be interpreted as grey radiators. The energy radiated by them is distributed over wavelength in the same way as it is for black radiators, but reduced by a factor $\varepsilon < 1$. Strictly speaking, $\varepsilon = \varepsilon(T)$ holds true for grey radiators. For small temperature ranges, however, it is admissible to assume ε as constant. Assuming a body emits energy per unit area $\dot{e}$, and this energy flux strikes another body, this second body absorbs the energy or rather the heat transfer

$$\mathrm{d}\dot{Q} = a\dot{e}\,\mathrm{d}A \,. \tag{3.210}$$

The absorptivity defined by this equation depends on the temperature T of the origin of the incident radiation and on the temperature T' of the receiving surface. For black bodies, this value is $a = 1$, as all radiation striking the surface is absorbed. For surfaces which are not black, this value is $a < 1$. For grey radiators, the absorptivity is $a = \varepsilon$. According to Kirchhoff's law, the emissivity is equal to the absorptivity, $\varepsilon = a$, for each surface which is in thermal equilibrium with its environment so that the temperature of the surface does not change in time.

Heat Exchange by Radiation

Between two parallel black surfaces with temperatures T_1 and T_2 and area A, which is very large in comparison with their separation, the heat transfer

$$\dot{Q}_{12} = \sigma A \left(T_1^4 - T_2^4\right) \tag{3.211}$$

is exchanged by radiation. Between grey radiators with emissivities ε_1 and ε_2, the heat transfer is

$$\dot{Q}_{12} = C_{12} A \left(T_1^4 - T_2^4\right) \tag{3.212}$$

with the *radiation exchange number*

$$C_{12} = \frac{\sigma}{\frac{1}{\varepsilon_1} + \frac{1}{\varepsilon_2} - 1} \,. \tag{3.213}$$

Between an internal pipe with outer surface A_1 and an external pipe with inner surface A_2, which are both grey radiators with emissivities ε_1 and ε_2, respectively, the heat transfer rate is given according to (3.212), but with

$$C_{12} = \frac{\sigma}{\frac{1}{\varepsilon_1} + \frac{A_1}{A_2}\left(\frac{1}{\varepsilon_2} - 1\right)} \,. \tag{3.214}$$

If $A_1 \ll A_2$, e.g., for a pipe in a large room, it holds that $C_{12} = \sigma\varepsilon_1$.

Gas Radiation

Most gases are transparent to thermal radiation and neither emit nor absorb radiation. Exceptions are carbon dioxide, carbon monoxide, hydrocarbons, water vapor, sulfur dioxide, ammonia, hydrochloric acid, and alcohols. They emit and absorb radiation only in certain wavelength regions. The emissivity and absorptivity of these gases depend not only on temperature, but also on the geometric shape of the gas body.

References

3.1 VDI/VDE (Ed.): *Temperature Measurement in Industry—Principles and Special Methods of Temperature Measurement*, VDI/VDE, Vol. 3511 (VDI/VDE-Gesellschaft Mess- und Automatisierungstechnik, Berlin 1996)

3.2 F. Pavese, G.F. Molinar: *Modern Gas-Based Temperature and Pressure Measurements* (Plenum, New York 1992)

3.3 D. Rathmann, J. Bauer, P.A. Thompson: *A Table of Miscellaneous Thermodynamic Properties for Various Sustances, with Emphasis on the Critical Proper-*

ties, Ber., Vol. 6 (Max-Planck-Inst. Strömungsforsch., Göttingen 1978)
3.4 N.E. Holden, R.L. Martin: Atomic weights of elements 1981, Pure Appl. Chem. **55**, 1102–1118 (1983)
3.5 D. Ambrose: *Vapour-Liquid Critical Properties* (Nat. Phys. Lab., Teddington 1980)
3.6 K. Schäfer, G. Beggerow (Eds.): *Mechanical-Thermal Properties of State*, Landolt-Börnstein Ser., Vol. II/1, 6th edn. (Springer, Heidelberg, Berlin 1971) pp. 245–297
3.7 J.R. Dymond, E.B. Smith: *The Virial Coefficients of Pure Gases and Mixtures* (Clarendon, Oxford 1980)
3.8 R.C. Reid, J.M. Prausnitz, B.E. Poling: *The Properties of Gases and Liquids*, 4th edn. (McGraw-Hill, New York 1986)
3.9 W. Wagner, A. Kruse: *Properties of Water and Steam. Zustandsgrößen von Wasser und Wasserdampf* (Springer, Heidelberg, Berlin 1998)
3.10 H.D. Baehr, K. Schwier: *Die thermodynamischen Eigenschaften der Luft* (Springer, Heidelberg, Berlin 1961), in German
3.11 R. Span, W. Wagner: Equations of state for technical applications, III. Results for polar fluids, Int. J. Thermophys. **24**, 111–162 (2003)
3.12 R.C. Wilhoit, B.J. Zwolinski: *Handbook of Vapor Pressures and Heats of Vaporization of Hydrocarbons and Related Compounds*, Thermodyn. Res. Center Dept. Chem. Texas A&M Univ. Ser., Vol. 101 (American Petroleum Institute Research, Texas 1971), Proj. 44
3.13 R. Tillner-Roth, F. Harms-Watzenberg, H.D. Baehr: Eine neue Fundamentalgleichung für Ammoniak, DKV-Tagungsbericht **20**(II/1), 167–181 (1993)
3.14 R. Span, W. Wagner: A new equation of state for carbon dioxide covering the fluid region from the triple-point temperature to 1100 K at pressures up to 800 MPa, J. Phys. Chem. Ref. Data **25**, 1509–1596 (1996)
3.15 R. Tillner-Roth: *Die thermodynamischen Eigenschaften von R134a, R152a und ihren Gemischen – Messungen und Fundamentalgleichungen*, Forschungsberichte des Deutschen Kälte- und Klimatechnischen Vereins, Vol. 41 (DKV, Stuttgart 1993)
3.16 R. Tillner-Roth, H.D. Baehr: An international standard formulation for the thermodynamic properties of 1,1,1,2-tetrafluorethane (HFC-134a) for temperatures from 170 K to 455 K and pressures up to 70 MPa, J. Phys. Chem. Ref. Data **23**, 657–729 (1994)
3.17 F. Brandt: *Brennstoffe und Verbrennungsrechnung*, 3rd edn. (Vulkan, Essen 1999), in German
3.18 H.D. Baehr: Zur Thermodynamik des Heizens, Part I, Brennst. Wärme Kraft **32**, 9–15 (1980), in German
3.19 E. Schmidt: *Properties of Water and Steam in SI Units*, 3rd edn. (Springer, Heidelberg, Berlin 1982)
3.20 I.N. Bronstein: *Taschenbuch der Mathematik*, 5th edn. (Deutsch, Frankfurt/Main 2000), in German
3.21 I.N. Bronstein, K.A. Semendyayev, G. Musiol, H. Mühlig: *Handbook of Mathematics*, 5th edn. (Springer, Heidelberg, Berlin 2007)
3.22 E. Pohlhausen: Der Wärmeaustausch zwischen festen Körpern und Flüssigkeiten mit kleiner Reibung und kleiner Wärmeleitung, Z. Angew. Math. Mech. **1**, 115–121 (1921)
3.23 H.D. Baehr, K. Stephan: *Heat and Mass Transfer* (Springer, Heidelberg, Berlin 2006)
3.24 W. Fritz, W. Wanninger: Blasenverdampfung im Sättigungszustand der Flüssigkeit an einfachen Heizflächen. In: *VDI-Wärmeatlas* (VDI, Düsseldorf 1963), Sect. Hb2

Peter Stephan

Institute of Technical Thermodynamics
Technical University Darmstadt
Darmstadt, Germany
pstephan@ttd.tu-darmstadt.de

Peter Stephan is a Professor at the Technische Universität Darmstadt and Director of the Institute of Technical Thermodynamics in the Department of Mechanical Engineering since 1997. He is also director of the university's cross-departmental Profile Area Thermo-Fluids and Interfaces. His main fields of research are two-phase heat transfer, microscale heat and mass transfer, interfacial phenomena, and thermal system analysis.

Frank Dammel

Institute of Technical Thermodynamics
Technical University Darmstadt
Darmstadt, Germany
dammel@ttd.tu-darmstadt.de

Frank Dammel is a senior scientist (Akad. Direktor) at the Institute of Technical Thermodynamics at the Technische Universität Darmstadt. He is head of the research group "Analysis of Thermal Energy Systems." His main fields of research are thermal energy supply of districts, low-temperature district heating networks, and thermal energy storage.

Jay M. Ochterbeck

Department of Mechanical Engineering
Clemson University
Clemson, SC, USA
jochter@clemson.edu

Jay M. Ochterbeck has been a Professor of Mechanical Engineering at Clemson University since 1994. His main fields of research are multiphase flows and heat transfer, capillary-driven loops, heat pipe science and technology, and thermal contact conductance. He is an Associate Fellow of the AIAA and is a member of several professional societies and international committees in thermal sciences.

Part B Materials

Part B Materials

4 **Atomic Structure and Microstructure Characterization**
Jens Freudenberger, Dresden, Germany
Martin Heilmaier, Karlsruhe, Germany
Ulrich Wendt, Magdeburg, Germany

5 **Mechanical Properties**
Vivek Srivastava, Taloja, Navi Mumbai, India
Martin Heilmaier, Karlsruhe, Germany

6 **Corrosion and Corrosion Resistance**
Thomas Böllinghaus, Berlin, Germany
Michael Rhode, Berlin, Germany
Thora Falkenreck, Kassel, Germany

7 **Nondestructive Inspection (NDI)**
Gerhard Mook, Magdeburg, Germany
Islam Shyha, Newcastle upon Tyne, UK

8 **Engineering Materials and Their Properties**
Ulrich Wendt, Magdeburg, Germany

9 **Tribology**
Ludger Deters, Magdeburg, Germany
Dirk Bartel, Magdeburg, Germany

4. Atomic Structure and Microstructure Characterization

Jens Freudenberger, Martin Heilmaier, Ulrich Wendt

This chapter is structured into two main parts. Part 1 describes the fundamentals of the atomic (ideal) structure and (real) microstructure arrangement of solid matter. The way in which (metallic) materials are generated from the melt and the resulting phase diagrams for common binary systems are elucidated in the first part of this chapter (Sect. 4.1). In order to understand materials properties, microstructural characterization has to be carried out on various length scales. Therefore, in the second part (Sect. 4.2), the most common preparation steps for microscopy methods used in materialography are given. Next, basic micromethods for the investigation of the local chemical composition and local crystalline structure are outlined. This includes methodologies for the quantification of the complex microstructures in engineering materials.

4.1 **Order in Solid State** 132
4.1.1 Principal Arrangements in Solids 132
4.1.2 Microstructure 136
4.1.3 Atomic Movement in Materials 142
4.1.4 Transformation into Solid State 144
4.1.5 Binary Phase Diagrams 147
4.2 **Microstructure Characterization** 152
4.2.1 Basics 152
4.2.2 Crystal Structure Analysis by X-ray Diffraction 152
4.2.3 Materialography 154
References 162

This chapter covers the structure of *engineering materials*, ranging from the atomistic level to the microstructural scale on which their properties are based. As the chemical composition determines the formation of phases and the arrangement of matter (atoms, ions, and molecules) in the solid state, the creation of (metallic) solid-state materials from the melt is discussed, including nucleation theory, and the thermodynamics and kinetics of phase transformation. The nature of phase equilibria is discussed upon principle binary phase diagrams, which also include the non-variant reactions.

The real crystal structure (i.e., microstructure), which includes all the lattice defects within crystalline solids, has a strong influence on their structural and functional properties, which is why *engineering materials* can be tuned to create a wide property portfolio to fulfill the demands of various application ranges. The fundamental underlying principle with respect to mechanical properties is exemplified by the mechanism of the movement of dislocations within the crystal lattice. The paramount influence of two- and three-dimensional lattice defects such as grain boundaries, precipitates, and dispersoids on those movements is discussed.

To gain an understanding of the performance of materials, thorough characterization of their microstructure on various length scales must be carried out. Therefore, an overview of the preparation steps used in materialography is given first. Second, the basic micromethods used to investigate the local chemical composition and local crystalline structure are outlined in this chapter too. Third, common methodologies for the quantification of the microstructure with respect to the volume fraction as well as geometrical arrangements (size, size distribution, shape, grain and crystal orientation, etc.) of grains, phases, precipitates, dispersoids, other reinforcements, filler, etc. are discussed.

K.-H. Grote, H. Hefazi (Eds.), *Springer Handbook of Mechanical Engineering*, Springer Handbooks,
https://doi.org/10.1007/978-3-030-47035-7_4

4.1 Order in Solid State

While many physical and/or chemical problems should be considered at the atomic level, it may be satisfactory for mechanical engineers to remain on the microstructural level. Therefore, we discuss in this section the different possibilities for the (ideal) arrangement of matter (atoms, ions, and molecules) in the solid state, then introduce the so-called *lattice defects* in the subsequent section. Then, three main categories of atomic arrangement can be distinguished (Fig. 4.1):

- No order (or disordered state), which is the case for gases (Fig. 4.1a), where the interaction between the single atoms is essentially limited to random collisions. Since we focus on materials in the solid state, gases will be disregarded in the following.
- Short-range order (SRO), where only a few atoms or building blocks are regularly arranged e.g., in polymers and glasses; e.g., silica is built of chains of tetrahedrons with a (central) Si atom surrounded by four oxygen atoms (Fig. 4.1c). These materials are thus called *amorphous solids* or, in view of their similarity to liquids, *undercooled liquids*.
- Long-range order (LRO), which requires the atoms to be arranged on a periodic *crystal lattice* (*crystallos* is Greek for *ice*) with—in principle—infinite extension in three-dimensional space, where the atoms sit at certain lattice points in such a way that the next-neighbor situation is the same for each atom under consideration. An example of a *primitive cubic lattice* is shown in Fig. 4.1d. Such an ideal atomic arrangement is also called a *single crystal*. Then, the smallest possible three-dimensional geometrical unit representing the lattice structure is called the *unit cell* of the corresponding crystal structure, with the three unit vectors defining the *lattice constants* of the crystal structure. This equilibrium distance of adjacent atoms can then be considered to result from a superposition of the attractive and repulsive forces between them.

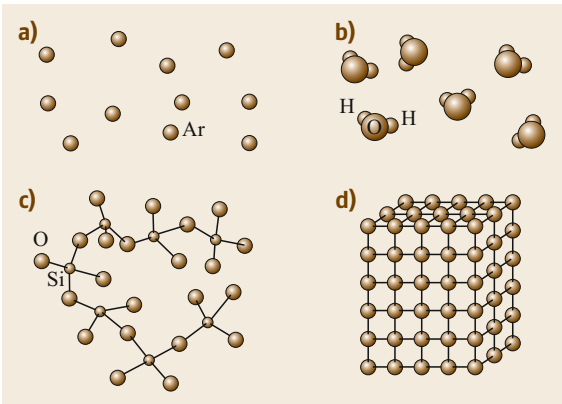

Fig. 4.1a–d Categories of atomic arrangement in materials: **(a)** inert gases with no order, **(b)** and **(c)** polar liquids and amorphous solids with short-range order, and **(d)** crystalline materials with long-range order (of infinite extension)

4.1.1 Principal Arrangements in Solids

Amorphous Structures

As pointed out before, two important classes of materials, namely glasses and many polymers, exist in the solid state but without possessing a long-range periodic crystallographic lattice structure: these are amorphous solids. Figure 4.2 elucidates how these structures may form upon cooling from the melt: usually, a liquid starts to form a crystalline solid when it is cooled below the melting point T_m of the material due to crystal nucleation and growth (see Sect. 4.2.3 for details). The crystallization event is accompanied by an abrupt jump in density. If, however, the kinetics for this transition to solid state is too sluggish or the cooling rate is too high,

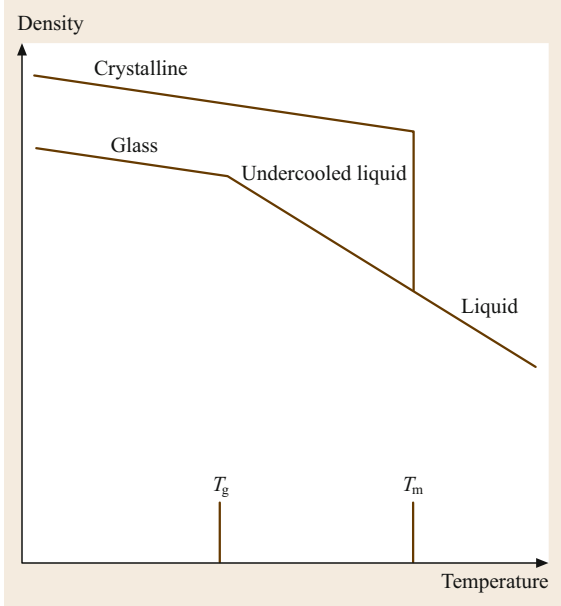

Fig. 4.2 Cooling of a silica melt: crystallization at T_m leads to an abrupt increase in density; if crystallization is suppressed, however, the undercooled melt transforms into a glassy state at T_g and the density–temperature curve shows a bend

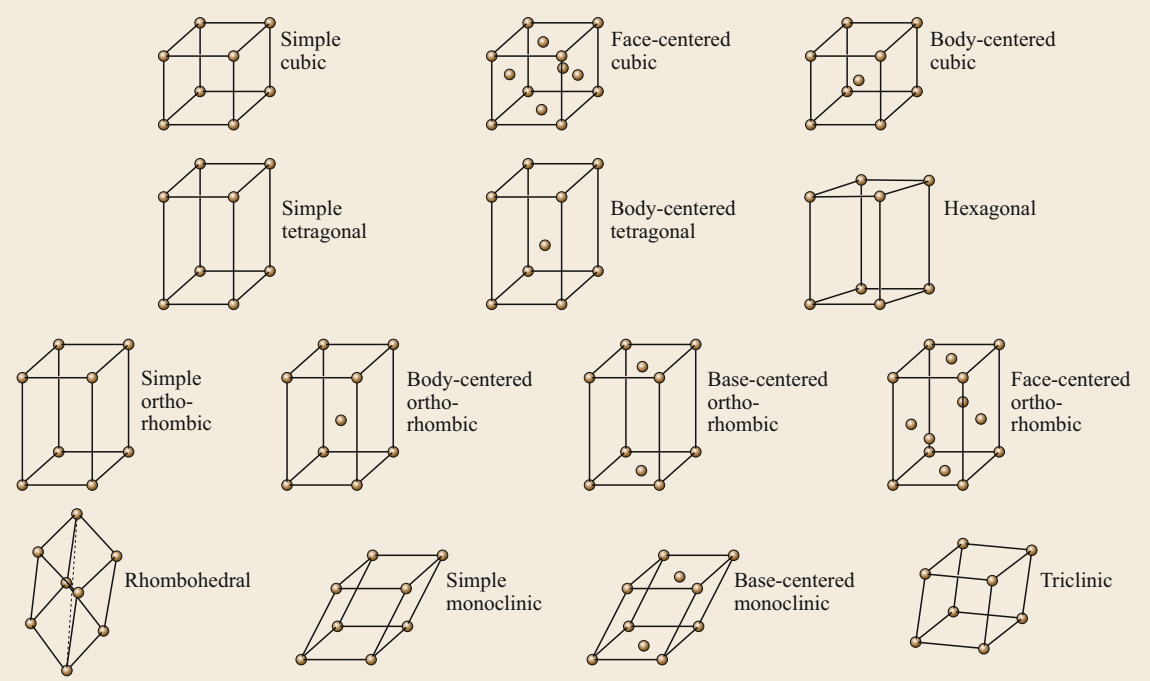

Fig. 4.3 The 7 crystal systems and 14 types of unit cell (Bravais lattices)

crystallization may be completely suppressed and an undercooled liquid be formed, which eventually transforms below the glass-transition temperature T_g into a glassy state. Note that the transition from the undercooled liquid into a glassy state (with both structures being *amorphous*) is a second-order thermodynamic reaction. This is manifested in Fig. 4.2 as a bend of the curve such that both the crystalline and glassy states show an identical temperature dependence of density below the glass transition.

An important conclusion can be drawn from Fig. 4.2. Since the glassy state exhibits the lower density, it is in a thermodynamically metastable state (with higher free energy G, Sect. 4.2.3) and will eventually transform into the crystalline structure, i.e., into the thermodynamically stable state (with minimal free energy G_{min}).

Like glasses and polymers, some metals can also be solidified into an amorphous structure. However, while simple binary and ternary systems can be produced only in the form of thin metallic ribbons via rapid solidification (requiring cooling rates of up to $10^6\,K\,s^{-1}$; see [4.1] for a review), multicomponent metallic glassy alloys in bulk form produced by slow cooling from the melt have attracted widespread interest, ranging from scientific curiosity about their structure and resulting properties to technological aspects of their preparation and potential applications. Readers interested in the outstanding properties of this new emerging class of advanced metallic materials may refer to relevant literature [4.2–5].

Crystal Structures

As early as the 19th century, the French scientist *Bravais* demonstrated that, in three-dimensional space, the seven major crystallographic unit cells can be better classified into 14 *Bravais lattices* (Fig. 4.3). The resulting geometric relations between the crystal axes are presented in Table 4.1. However, of those listed, most metallic materials used in mechanical engineering crystallize in hexagonal or cubic form, i.e., in crystal lattice structures with high symmetry and close packed crystal structures.

The most important characteristics of these crystal structures are summarized in Table 4.2. In essence, they can be distinguished by the number of atoms per unit cell (NA), the coordination number (i.e., the number of nearest neighbors, CN), and the packing density (PD). The latter is defined as $PD = NA/V_{uc}$ (with V_{uc} being the volume of the unit cell) and ranges between 0 and 1.

The comparison of the different crystal structures in Table 4.2 yields that:

1. For the cubic systems, both the coordination number and packing density increase with increasing number of atoms in the unit cell.

Table 4.1 Characteristic relations between crystallographic axes (lattice constants) and angles in the seven crystal systems

Structure	Lattice constants	Angles between axes
Cubic	$a = b = c$	All angles equal 90°
Tetragonal	$a = b \neq c$	All angles equal 90°
Orthorhombic	$a \neq b \neq c$	All angles equal 90°
Hexagonal	$a = b \neq c$	Two angles equal 90°, one angle equals 120°
Rhombohedral	$a = b = c$	All angles are equal and none equals 90°
Monoclinic	$a \neq b \neq c$	Two angles equal 90°, one angle (β) is not equal to 90°
Triclinic	$a \neq b \neq c$	All angles are different and none equals 90°

Table 4.2 Characteristics of cubic and hexagonal unit cells unit cells (bcc: body-centered cubic, fcc: face-centered cubic)

Structure	NA	CN	PD
Simple cubic	1	6	0.52
bcc	2	8	0.68
fcc	4	12	0.74
Hexagonal	6	12	0.74 (if $c/a = 1.633$)

2. CN and PD are identical for fcc and hexagonal crystals if the ratio of the *c*- and *a*-axis in the hexagonal system is 1.633 (which is nearly the case for the metallic elements Ti, Mg, and Co).

These systems are then called *hexagonally close-packed* (hcp) and can be distinguished from fcc structures only by the different stacking sequence, which is *ABAB*... along the *c*-axis for hcp and *ABCABC*... along the space diagonal ⟨111⟩ for fcc (in crystallography it is convenient to use Miller indices to describe lattice vectors and planes; in cubic systems, the space diagonal is the ⟨111⟩ direction [4.6]).

It is obvious from the comparison in Table 4.2 that even the close-packed crystal structures with space filling of 74% are still far from being fully dense. The open spaces left between the regular lattice sites are called *interstitial sites*. They may be filled by atomic species that are significantly smaller than the matrix atoms which build the regular crystal lattice. For cubic systems, three different interstitial sites can be distinguished depending on the crystal structure and the ratio of the radii of the (foreign) interstitial atom r_{ia} and matrix atom r_m, respectively (Fig. 4.4). For relatively large interstitial atoms and $r_{ia}/r_m = 0.732$–1, these interstitials will likely occupy *cubic interstitial lattice sites* with CN = 8. *Octahedral interstitial sites* with CN = 6 may be filled when $r_{ia}/r_m = 0.414$–0.732. *Tetrahedral interstitial sites* with CN = 4 provide the least free space, hence $r_{ia}/r_m = 0.225$–0.414. This is technically most relevant since the interstitial carbon atom in the Fe–C alloy system (i.e., *steel*) obeys these empirical rules and favors octahedral sites (largest holes) in the fcc structure, whereas it occupies tetrahedral sites in the bcc structure. The incorporation of carbon atoms at interstitial sites leads to significant elastic lattice distortion and, thus, readily explains the increased strength of steels as compared with pure iron.

Polymorphism

If materials of identical chemical composition exist in more than one crystal structure depending on temperature and/or pressure, they are called *polymorphic*. A more specific term applicable for pure elements is *allotropy*. Two prominent representative metallic materials show polymorphism:

1. Iron and low carbon steels transform from the low-*T ferritic* bcc structure into a higher-temperature *austenitic* fcc structure and back to a bcc structure called δ-*ferrite* close to the melting point.
2. Titanium undergoes a transformation from α-hcp structure at low *T* to a β-bcc structure at high *T*.

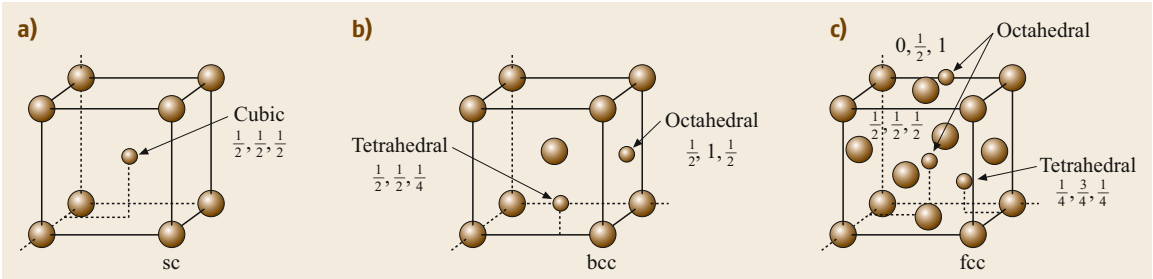

Fig. 4.4a–c Location of interstitial sites within cubic unit cells: (**a**) simple cubic, (**b**) body-centered cubic (bcc), (**c**) face-centered cubic. The numbers denote the lattice positions of the interstitial sites

Both transformation reactions form the basis for the heat treatment of steels and titanium alloys and, thus, the potential for widely adjusting the properties of these alloy systems; see Part B, Chaps. 5 and 8, respectively. A further example of polymorphism is the covalently bonded element carbon, which exists in a hexagonal structure of two-dimensional layers called *graphite*, or *diamond* with the open diamond cubic crystal structure (with a PD of only 0.34).

Crystal Structures with More than One Chemical Element/Component

In most cases, technically relevant materials consist of more than one chemical element. Depending on how the different elements are mixed with each other, one can classify them into:

1. *Solid solutions*, where the different atomic elements are randomly mixed and placed at the lattice points of the crystal structure. Two subcases can be distinguished:
   - Substitutional solid solutions, where the atomic species occupy regular lattice points in a random manner (see also Fig. 4.6c,d). According to Hume-Rothery [4.6, 7] this occurs when the elements (e.g., A and B) have comparable atomic radii ($\delta = (r_B - r_A)/r_A < 15\%$) and crystallize in the same structure. A prominent example is the binary alloy system Ag-Au, which exhibits unlimited mutual solubility.
   - Interstitial solid solution, where the smaller atomic species occupies interstitial sites because of too large a difference in atomic radius between them and the matrix atoms ($\delta > 15\%$) (Fig. 4.6b). The most prominent example is again C in Fe, but this can be generalized to impurities such as H, O, and N in metals. In contrast to the former case, the maximum solubility is much smaller, typically < 1 at.%, which means that, in the case of a bcc lattice, only about every 50th unit cell hosts one interstitially solved atom:
2. Stoichiometric compositions, where the ratio between the atomic species is fixed to small integer numbers. This is called *stoichiometry*. Two categories can be distinguished here, depending on how these structures are formed:
   - An ordered *superlattice structure* with the same basic crystal structure type may form upon cooling a disordered solid solution. The following example elucidates this scenario: a Cu alloy containing 25 at.% Au has a simple fcc crystal structure in the solid state at elevated temperatures. Upon further cooling, it transforms into an ordered fcc $L1_2$ crystal structure of type Cu_3Au, where the gold atoms occupy the corner lattice points of the unit cell while the copper atoms sit on the faces of the cube.
   - An intermetallic compound made up of two or more elements, producing a new phase with its own composition, crystal structure, and properties substantially different from those of its constituents, namely higher hardness, strength, and melting point but almost always at the expense of a lack of ductility. A recent, technically relevant example are the titanium aluminides (Fig. 4.5), which are being considered for a variety of high-temperature applications, such as automotive valves and turbocharger wheels, and turbine blades and vanes in aerospace engines, as structural materials, mainly because of their attractive combination of high melting point and strength together with low density.

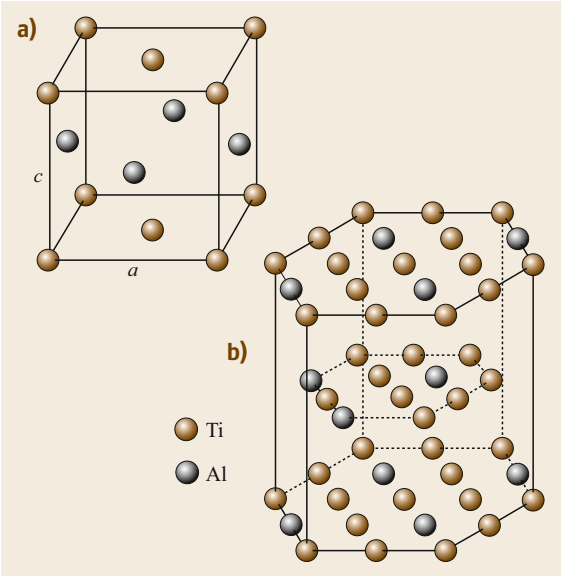

Fig. 4.5a,b Some unit cells of technically relevant intermetallic phases within the binary Ti-Al system: **(a)** γ-TiAl with (tetragonally distorted) $L1_0$ crystal structure, **(b)** α_2-Ti_3Al with hexagonal $D0_{19}$ crystal structure (Pearson symbols [4.8])

A final point should be noted here: many superlattice structures and intermetallic compounds have a range of compositions (*stoichiometry range*) in which they appear with the same crystal structure as compared with the fixed stoichiometric composition. This is, e.g., the case for both of the TiAl-based inter-

metallic compounds shown in Fig. 4.5, making alloy property improvement and fine-tuning through addition of further alloying elements more feasible. This *nonstoichiometry* can lead to partial disordering of the atomic arrangement within the unit cell.

4.1.2 Microstructure

The crystal structure introduced in the previous section describes the ideal arrangement of atoms within a crystalline material and, hence, determines several *intrinsic* material properties (e.g., elastic stiffness and compliance constants). However, lattice imperfections, which destroy the infinite extension of the periodic atomic structure, are decisive for many *extrinsic* properties (e.g., the mechanical properties discussed in Sect. 4.2.1). As a result, a real structure containing crystalline areas and a variety of lattice imperfections is called a *microstructure*. Lattice imperfections are created and can be controlled during the processing and manufacturing of materials. They can be classified based on their dimensionality as follows.

Point Defects

Figure 4.6 provides an overview of the various types of point defects (of zero dimensionality) in materials. Foreign atoms, solved either substitutionally at regular lattice sites (Fig. 4.6c,d) or interstitially (Fig. 4.6b), have already been treated in the previous section. If a lattice site lacks an atom, a *vacancy* is formed in the lattice (Fig. 4.6a). From thermodynamics calculations, it is known that a certain (small) number of vacancies will exist in thermal equilibrium. A more detailed treatment [4.9] yields

$$c_{\mathrm{V}}^{\mathrm{e}} = \exp\frac{-\Delta G_{\mathrm{V}}}{RT} = \exp\frac{-(\Delta H_{\mathrm{V}} - T\Delta S_{\mathrm{V}})}{RT}\,, \qquad (4.1)$$

where $c_{\mathrm{V}}^{\mathrm{e}}$ is the equilibrium concentration of vacancies, which follows an Arrhenius-type increase with increasing temperature. At the melting point of the material, $c_{\mathrm{V}}^{\mathrm{e}} = 10^{-4}{-}10^{-3}$; meanwhile, at absolute zero, i.e., 0 K, then $c_{\mathrm{V}}^{\mathrm{e}} \equiv 0$. From the above, it becomes obvious that vacancies will very likely be introduced into materials upon solidification from the melt. Figure 4.6b–d represents the various types of alloying elements in solid solution, which were already treated in the previous section. Two special types of point defect are displayed in Fig. 4.6e,f: *Frenkel defects*, consisting of a vacancy-interstitial atom pair, can be created upon neutron irradiation (Fig. 4.6e), while *Schottky defects* exist only in ionic crystals as pairs of vacancies formed in the cationic and anionic partial lattice, respectively (Fig. 4.6f).

Solid-Solution Strengthening. It has long been well known that the introduction of alloying elements into a pure metal increases its hardness. When the difference in size and electronegativity of the alloying element is less than a critical value, the alloying element forms a solution with the matrix. The alloy atoms occupy either lattice sites, leading to a *substitutional solid solution*, or interstitial voids in the lattice, i.e., *interstitial solid solutions*. Carbon, nitrogen, oxygen, hydrogen, and boron are elements that commonly occupy interstitial sites. Solute atoms interact with dislocations (see next paragraph) in a number of ways.

- *Parelastic interaction* due to the overlapping strain energy of the solute atom and dislocation core. The interaction energy is directly proportional to the size difference between the solute and matrix atoms.
- *Modulus interaction* due to a local change of modulus, thereby affecting the elastic energy of the dislocation. This is also called the *dielastic interac-*

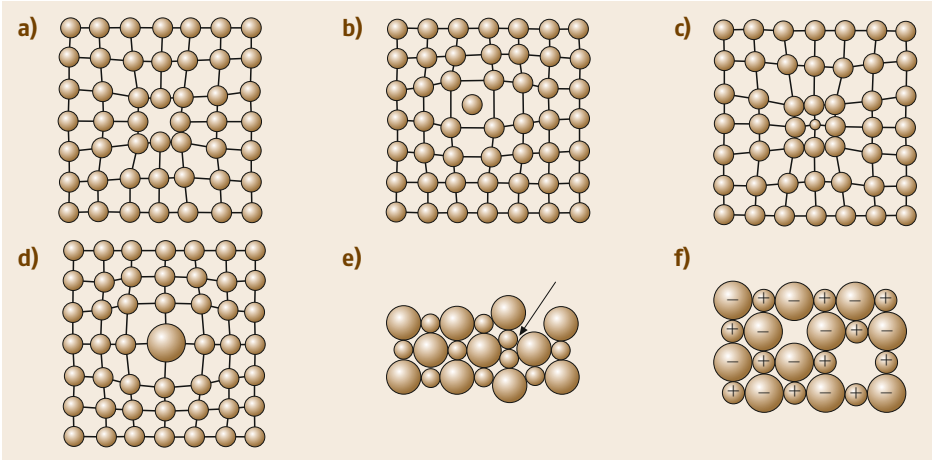

Fig. 4.6a–f Overview of the various types of point defect: **(a)** vacancy, **(b)** interstitial atom, **(c)** smaller and **(d)** larger substitutional atom, **(e)** Frenkel defect, and **(f)** Schottky defect

tion in the literature [4.7]. The interaction energy is directly proportional to the difference in shear modulus between the solute and matrix atoms.

- *Stacking-fault interaction* or *Suzuki hardening* due to preferential segregation of solutes to the stacking fault of extended dislocations.
- *Electrical interactions* due to localization of the electron cloud, leading to interaction with dislocations with electrical dipoles. This effect is smaller than the above mechanisms.

All these interactions require extra energy to be expended to overcome the solute atom, requiring higher stresses for dislocation motion and, hence, giving rise to *solid-solution hardening*. It may be pointed out that the presence of vacancies, introduced due to rapid quenching or high-energy radiation, also leads to considerable strengthening via some of the above mechanisms. For further details see [4.7].

Dislocations

Independently from each other, Orowan, Polanyi, and Taylor introduced the term "dislocations" in 1934 to explain the observed strength values and plastic deformability of materials on a theoretical basis. It should be emphasized here that the existence of these one-dimensional lattice imperfections was proven experimentally more than a decade later with the advent of the first transmission electron microscopes in materials science. To motivate why dislocations are essential in explaining the deformation behavior of materials, first consider the theoretical (shear) strength of materials shown in Fig. 4.7, in which A and B represent sites of stable equilibrium for the atoms within the hexagonal plane. Then, a is the displacement required to shift any atom to another stable position, thus the potential connected with a displacement z of any atom is

$$U(z) = U_0 \left(1 - \cos \frac{2\pi z}{a}\right) . \tag{4.2}$$

From (4.2), one can obtain the necessary force by differentiating with respect to z

$$F(z) = \frac{\partial U(z)}{\partial z} = U_0 \frac{2\pi}{a} \sin \frac{2\pi z}{a} . \tag{4.3}$$

The shear stress is simply $\tau = F(z)/A$. For $z \ll a$ and since the sin function is point-symmetric about the origin, one gets from (4.3) that

$$\tau \approx \tau_{\max} \frac{2\pi z}{a} . \tag{4.4}$$

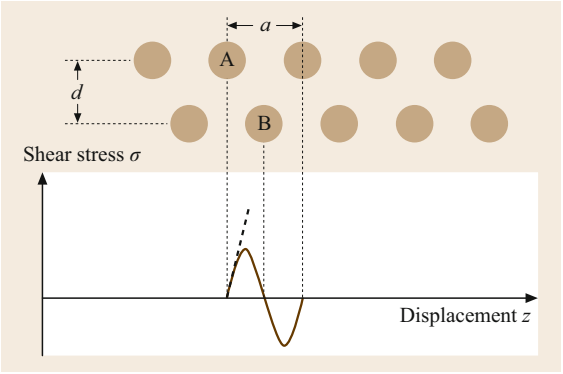

Fig. 4.7 The theoretical strength of crystalline materials: the shear displacement z between two neighboring lattice planes of interplanar spacing d causes a sinusoidal shear stress fluctuation σ. A and B are regular lattice sites, respectively, and a is the lattice constant within the hexagonal plane

On the other hand, Hooke's law for simple shear is

$$\tau = G\gamma = G\frac{z}{d} . \tag{4.5}$$

Setting (4.4) and (4.5) equal, one obtains for the maximum shear stress

$$\tau_{\max} = \frac{Ga}{2\pi d} \approx \frac{G}{6} . \tag{4.6}$$

Thus, the theoretical shear strength $\tau_{\max}$ is only dependent on the elastic properties of a material, i.e., the shear modulus G. As an example, for pure copper with $G \approx 45\,\text{GPa}$, one gets $\tau_{\max} = 7500\,\text{MPa}$. However, in experiments one observes for pure copper single crystals that plastic shearing occurs already at shear stresses below 10 MPa [4.7] (Fig. 4.11). This obvious discrepancy by about three orders of magnitude can be rationalized only by assuming the existence of dislocations that enable plastic shearing by moving in a direction $\boldsymbol{r}$ perpendicular to its line (the dislocation line represented by the vector $\boldsymbol{s}$) through the lattice.

We can identify two basic types of dislocations:

1. *Screw dislocations*, which can be illustrated by cutting halfway through a perfect crystal (Fig. 4.8a) and subsequently skewing the crystal by one atomic spacing (Fig. 4.8b,c). If one follows a crystallographic plane one revolution around the axis on which the crystal was skewed, starting at point x and moving an equal number of atomic spacings in each of the four planar directions, one ends up one lattice site below the starting point (point y). The vector required to close the loop is called the *Burgers vector* $\boldsymbol{b}$ and represents the unit of plastic shearing of the crystal through the movement of the dislocation line

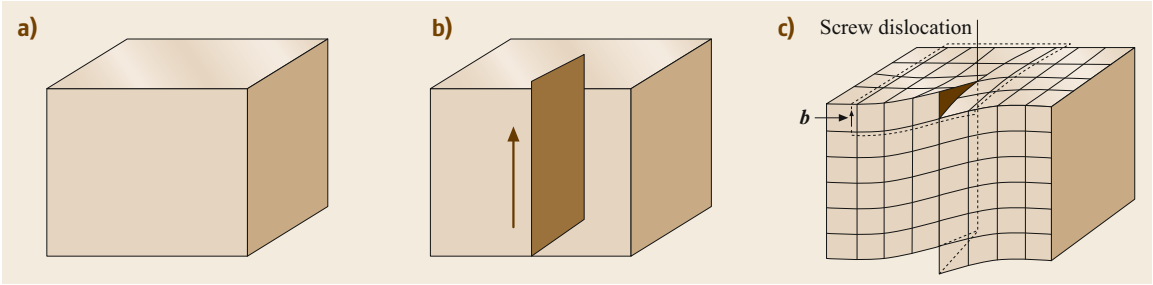

Fig. 4.8a–c A perfect crystal (a) is cut and (b) and (c) sheared by one atomic spacing. The line along which shearing is carried out is a screw dislocation with its Burgers vector $\boldsymbol{b}$ closing a loop of equal atomic spacings around itself

(from the front to the back in Fig. 4.8c). Hence, in screw dislocations, $\boldsymbol{b} \parallel \boldsymbol{s} \perp \boldsymbol{r}$.

2. *Edge dislocations*, which can be illustrated by slicing halfway through a perfect crystal (Fig. 4.9a), tearing the crystal apart, and inserting an extra (half) plane of atoms into the cut (Fig. 4.9b). The bottom edge of this inserted plane represents the edge dislocation (Fig. 4.9c). A clockwise loop, starting at point x and going an equal number of lattice sites into each direction within the plane, finishes at point y, hence leaving the required Burgers vector $\boldsymbol{b}$ to close the loop in Fig. 4.9c. For edge dislocations, $\boldsymbol{r} \parallel \boldsymbol{b} \perp \boldsymbol{s}$.

The more general case of a dislocation with *mixed* character when $\boldsymbol{b}$ is neither parallel nor perpendicular to $\boldsymbol{s}$ is plotted in Fig. 4.10. Likewise, note from Fig. 4.10 that pure screw or edge configurations can be considered as the extremal cases of the general mixed configuration for either $\boldsymbol{b} \parallel \boldsymbol{s}$ or $\boldsymbol{b} \perp \boldsymbol{s}$.

From the above, the following important conclusions can be drawn:

- The dislocation line is the border between the undeformed and slipped area of the crystal plane.
- Dislocations cannot end within a crystal: they have to either form a loop or penetrate an internal (e.g., grain or phase boundaries, see below) or external surface.
- Dislocations exhibit a long-range three-dimensional stress field within the crystal lattice, allowing them to interact with all kinds of other lattice imperfections. This feature is the basis for the various approaches for strengthening materials in metallurgy.
- Dislocations are the carriers of plastic (i.e., irreversible) deformation in crystalline materials.
- The slip system of a dislocation in crystalline materials is composed of: 1. A close-packed slip plane and 2. A short slip direction which is identical to $\boldsymbol{b}$.
- The Burgers vector must be contained within the slip plane. Both the slip plane and slip direction depend on the lattice structure of the material.

Similarly as for the grain boundaries explained below, dislocations are created in crystals during solidification due to thermal stresses arising from the density mismatch between the liquid and solid phases. Hence, the creation of a dislocation within a crystal increases the (total) free energy of the system. A satisfactory approximation for the dislocation line energy E is

$$E = \frac{1}{2} G b^2 \,. \tag{4.7}$$

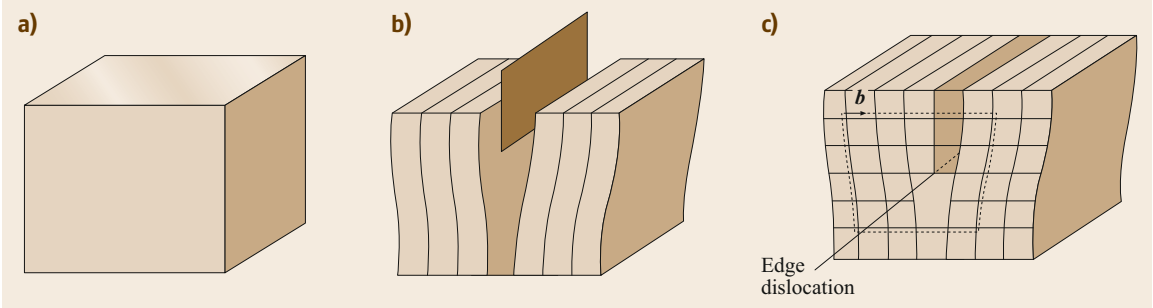

Fig. 4.9a–c A perfect crystal (a) is cut and an extra half-plane of atoms is inserted (b). The bottom edge of the extra plane is an edge dislocation with its Burgers vector $\boldsymbol{b}$ closing a loop of equal atomic spacings around itself

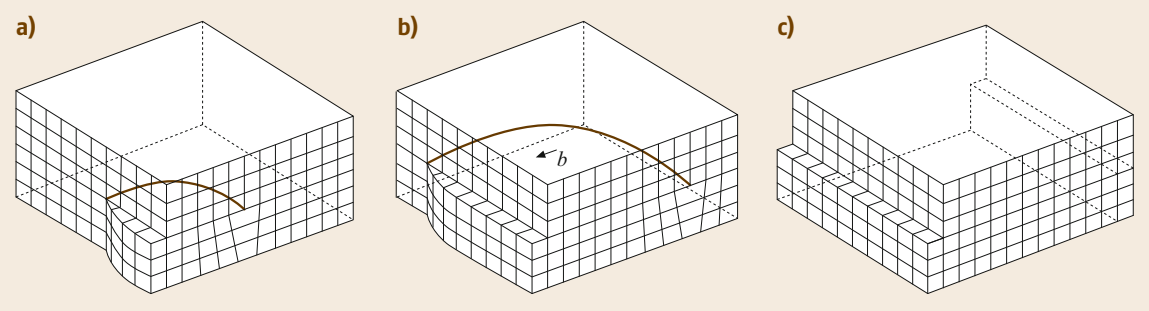

Fig. 4.10a–c Movement of a mixed dislocation through a simple cubic lattice: **(a)** and **(b)** the dislocation character is purely screw type *on the left-hand side* and purely edge type *on the right-hand side* of the crystal; **(c)** after completion of the movement, the dislocation has disappeared, leaving a slip step of height b

Equation (4.7) reveals that the dislocation line energy is an *intrinsic* materials property, depending only on crystal lattice parameters. Experimentally, dislocations can be detected either via optical microscopy as *etch pits* stemming from the penetration points of the dislocation lines through the crystal surface or via transmission electron microscopy (TEM), where the slight lattice distortions caused by the dislocations gives rise to a visible contrast; see [4.10] for details. To explain the strength and deformability of materials, it is useful to introduce the dislocation density as the number of dislocations per unit volume

$$\rho = \frac{\text{dislocation line length}}{\text{unit volume}} = \frac{\text{number of dislocations}}{\text{unit area}} \,. \tag{4.8}$$

As an example, for well-annealed metals, $\rho = 10^9 - 10^{11}\,\mathrm{m}^{-2}$; meanwhile, for ceramics and semiconductors, $\rho = 10^4 - 10^{10}\,\mathrm{m}^{-2}$.

Strain Hardening. Strain hardening is caused by the interaction of dislocations with each other. During plastic deformation, e.g., cold working, the number of dislocations increases with increasing strain to values of $\rho = 10^{14} - 10^{16}\,\mathrm{m}^{-2}$. Similarly, an increase of the dislocation density is connected with tensile straining. An example for the stress–strain behavior of Cu single crystals with different crystallographic orientations with respect to the loading axis is depicted in Fig. 4.11. The *flow curve* comprises three stages:

1. Stage I or *easy glide*
2. Stage II or *dislocation pile-ups*
3. Stage III or *dynamic recovery*.

Stage I is observed only in well-annealed crystals oriented such that only one slip system is operative (cf.

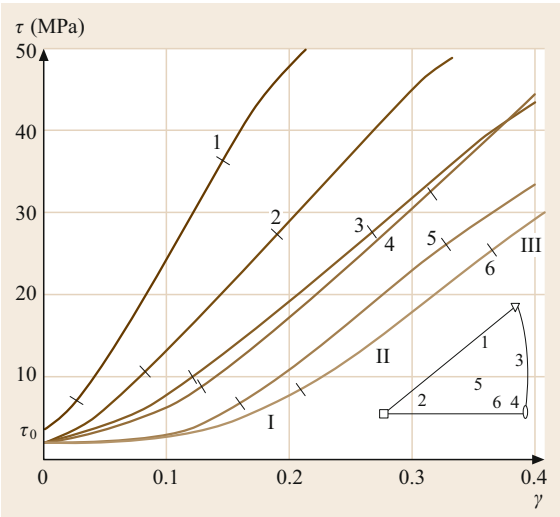

Fig. 4.11 Shear stress τ versus shear strain γ curves for differently oriented copper single crystals at room temperature. Samples 1–6 are oriented within the standard orientation triangle as depicted

curves 5 and 6 in Fig. 4.11). Stage II dominates the flow curve of most engineering polycrystalline alloys, and measurements over a wide range show that

$$\sigma_\rho = \sigma_\mathrm{i} + \alpha \mathrm{G} \mathrm{b} \sqrt{\rho} \,, \tag{4.9}$$

where α is a numeric constant (typically ≈ 0.3). Equation (4.9) is also referred to as Taylor's relation and originates from the interaction of the stress fields of dislocations (long-range interaction) or from dislocations cutting due to intersecting slip systems. The strain hardening rate during stage II is fairly insensitive to temperature and/or impurities. On the other hand, the region of dominance of stage III, *dynamic recovery*, is strongly temperature dependent. For further details see, e.g., [4.11].

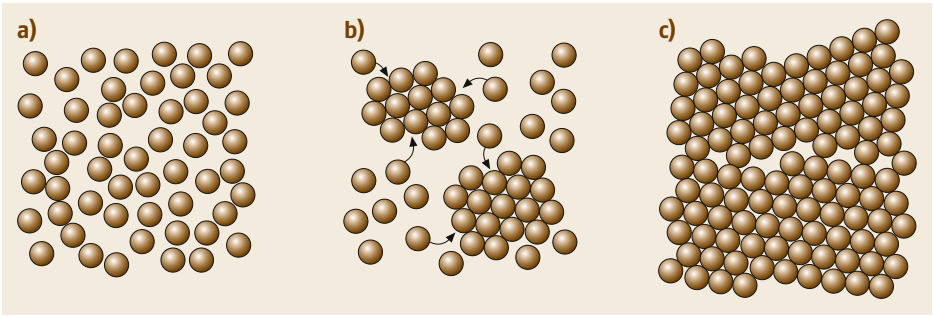

Fig. 4.12a–c The development of grains and grain boundaries upon solidification from the melt: **(a)** amorphous melt, **(b)** two crystals begin to nucleate within the liquid melt, **(c)** a grain boundary has been created between two crystallites of different crystallographic orientation

Grain Boundaries

Grain boundaries are two-dimensional lattice faults. Like vacancies and dislocations, they are created during the manufacture of materials, as can be exemplified by metallic materials upon solidification from the amorphous (or disordered) melt (Fig. 4.12a). When decreasing the temperature of the melt below the liquidus temperature (Sect. 4.1.2), nuclei that have the crystal structure of the solid are formed within the liquid and grow with continuing time and cooling (Fig. 4.12b). When T falls below the solidus temperature, the material has solidified completely and adjacent grains with the same crystal lattice but different crystallographic orientation (Fig. 4.12c) do not fit perfectly to each other. The narrow zone where the atoms are not properly spaced, but lie in a more or less disordered state, is called a *grain boundary*. Typically, $d_{gb} = 0.5$ nm is a good estimate for the grain boundary thickness.

Fine-Grain Strengthening. One important method for controlling the properties of a material is to adjust the grain size. By reducing the grain size, the number of grains and hence the fraction of grain boundaries is increased. As far as the mechanical properties are concerned, any dislocation that moves within a grain is stopped when it encounters a grain boundary. The mean free path of dislocations is, thus, limited by the grain size or the grain boundary density (Sect. 4.2.3, *Quantification of Microstructure/Quantitative Stereology*), and the strength of the metal is increased. The famous Hall–Petch relation relates the grain size to the yield strength at room temperature [4.12, 13],

$$\sigma_y = \sigma_0 + K_y d_{gb}^{-1/2} , \qquad (4.10)$$

where σ_y is the yield strength (Sect. 4.2.1), $d_{gb}^{-1/2}$ is the inverse square root of the grain size, preferentially measured as the mean intercept length (4.44) in Sect. 4.2.3, and σ_0 and K_y are material constants (σ_0 is often related to the *Peierls stress* in crystallographic slip [4.7]). Figure 4.13 shows the relationship according to (4.10) for some steels.

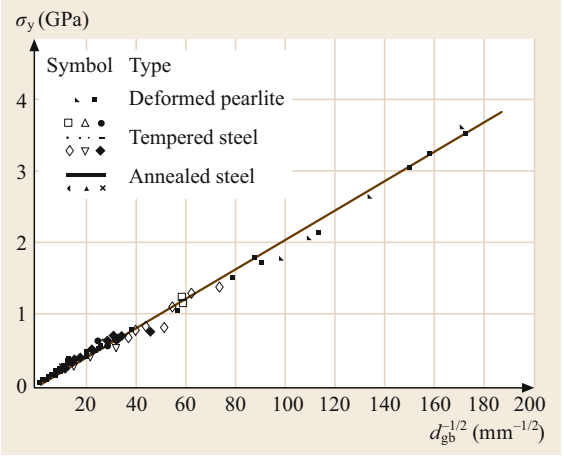

Fig. 4.13 Dependence of yield strength σ_y on inverse root of grain size, $d_{gb}^{-1/2}$, for steel (after [4.14])

Optical or scanning electron microscopy (SEM) can be used to reveal microstructural features such as grain boundaries (Sect. 4.2.3) and to assess the grain size of materials quantitatively.

Dispersoids and Precipitates

When the solubility of a material is exceeded for any alloying element, a second phase forms in the volume and a two-phase alloy is produced. Hence, second-phase particles such as *dispersoids* or *precipitates* are classified as three-dimensional lattice imperfections. The continuous phase that surrounds the particles and is usually present in a larger fraction is called the *matrix*. The boundary between the two phases is an internal surface or *interface*, at which, as for the grain boundaries in the previous section, the atomic arrangement is not perfect. Again, this boundary impedes the slip of dislocations and, thus, strengthens the material.

Dispersion and Precipitation Strengthening. Two types of second-phase particles can be distinguished. In *dispersion strengthening*, particles are introduced into the matrix using powder metallurgical techniques or

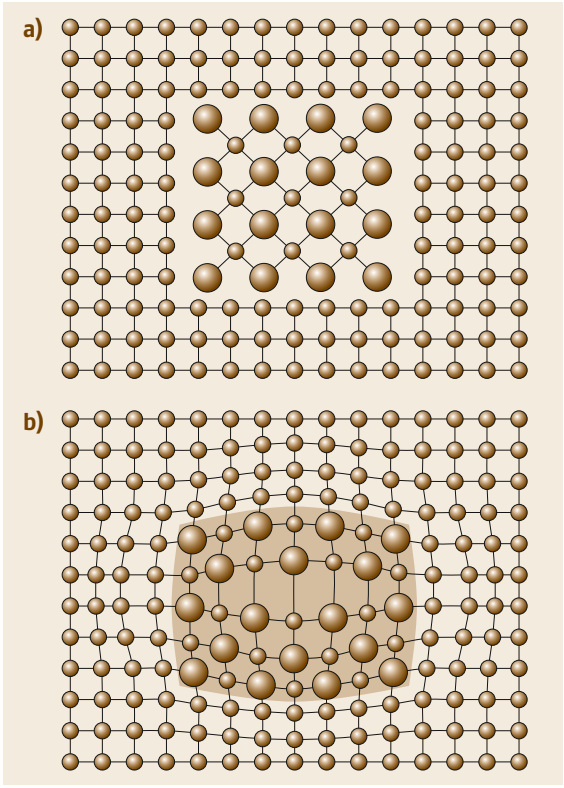

Fig. 4.14 **(a)** An incoherent second-phase particle has no crystallographic relationship with the structure of the surrounding matrix; **(b)** coherent precipitates show a definite crystallographic relationship with the matrix

through solid reactions. These particles are in essence insoluble in and *incoherent* (Fig. 4.14a) with the matrix. *Precipitation strengthening* or *age hardening* is produced through a series of heat treatments that exploit the decrease in solubility of a given solute with decreasing temperature. This requirement for elevated-temperature solubility places a limitation on the number of useful precipitate-strengthened alloy systems. Due to their insolubility within the metallic matrix, dispersion-hardened alloys are stable up to temperatures relatively close to the melting point of the matrix, in contrast to precipitate-strengthened alloys, which are degraded upon prolonged exposure to high temperature due to *precipitate coarsening*, i.e., *Ostwald ripening*. Nevertheless, precipitation hardening due to very small *coherent* particles (2–10 nm, Fig. 4.14b) is a very efficient strengthening mechanism. Fine particles can act as barriers to dislocation motion, either by requiring the dislocations to shear them or by acting as strong impenetrable particles, forcing dislocations to bypass them. When the particles are small and/or soft, they get sheared and the following mechanisms contribute to the strength increment:

- *Coherency strain*, arising from the strain field resulting from the mismatch between the particle and matrix.
- *Stacking fault energy* variation between the matrix and particles, which leads to local variation in the stacking fault width.
- If the precipitates have an *ordered structure*, as in many Ni-based superalloys (Sect. 8.5.2), motion of dislocation through them introduces antiphase boundaries (APB).
- A difference in the *local modulus* between the particle and matrix alters the energy of a dislocation passing through the particle. Likewise, counterintuitively, voids can contribute significantly to the strength via this mechanism.
- As dislocations pass through a precipitate, a step that is one Burgers vector high is produced. This raises the particle–matrix *interfacial energy*, contributing to strengthening.
- Finally, there is a strengthening contribution due to the difference in lattice friction stress or Peierls stress between the particle and matrix.

For larger precipitates or dispersoids, Orowan proposed a mechanism for particle overcoming, as illustrated in Fig. 4.15. In essence, the strength increase is related to the increase of the dislocation line length when the dislocation deposits a loop around the particle after bypassing it (Fig. 4.15d). The critical situation for bypassing is reached when the dislocation line possesses its maximum curvature around the particle, i.e., the half-circle. According to Fig. 4.16, one obtains for the critical configuration for dislocation bypassing

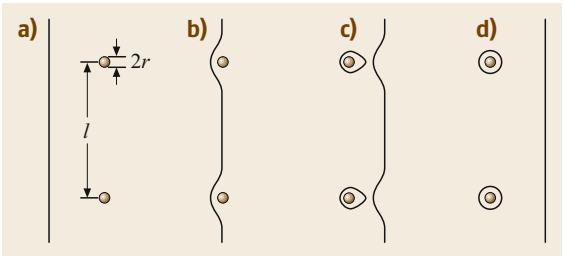

Fig. 4.15a–d Schematic of dislocation bypassing fine nonshearable particles by Orowan bowing: driven by shear stress τ, a dislocation approaches an array of (two) particles with radius r separated by a distance l **(a)**. It bows out between the particles **(b)**, until it deposits loops around them **(c)**. After bypassing, the dislocation line remains unchanged **(d)**

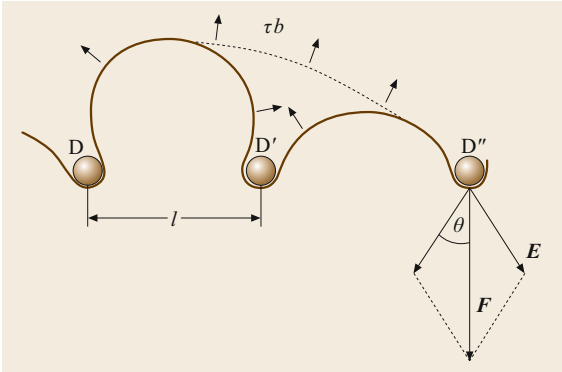

Fig. 4.16 Bowing out of a dislocation line between an array of impenetrable incoherent particles (designated D, D′, D″) with spacing l due to a shear force (per unit length of dislocation) τb. The obstacle force acting against bypassing is F

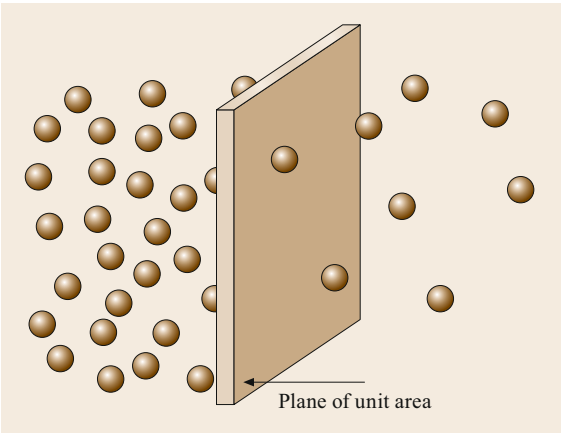

Fig. 4.17 The flux j_D during diffusion is defined as the number of atoms passing through a plane of unit area per unit time

$(\theta \to 0°)$

$$F = \tau b l = 2E \cos \Theta = Gb^2 \,. \tag{4.11}$$

Solving (4.11) for τ and assuming maximum force for $\theta = 0$, one obtains the strength increase due to Orowan bypassing as

$$\tau_{Or} = \frac{Gb}{l} \,. \tag{4.12}$$

Since the particle spacing l is not directly extractable from microstructure analysis (Sect. 4.2), the following more useful expression has been established for the strength increment from Orowan bypassing which also takes into account the conversion of the shear stress τ into a normal stress σ via the Taylor factor $M = \sigma/\tau$

$$\sigma_{Or} = 0.8MGb\frac{\sqrt{f}}{r} \,, \tag{4.13}$$

where f is the volume fraction of particles present in the material and r is the (directly measurable) particle radius within the slip plane. For a detailed review on the various types of particle strengthening sketched above, see [4.15].

4.1.3 Atomic Movement in Materials

The movement of atoms (or molecules) within materials (or liquids) is called *diffusion*. It is emphasized here that diffusion can take place without a superimposed mechanical stress just by random movement of atoms, provided that sufficient thermal energy is introduced into the system. Vice versa, as for the concentration of vacancies, (4.1) in Sect. 4.1.2, atoms in crystalline solids are at rest only at absolute zero. The driving force behind this movement is usually a gradient in concentration of atoms according to

$$j_D = -D \,\mathrm{grad}\, c = -D\frac{\partial c}{\partial y} \,, \tag{4.14}$$

where the latter fraction is the *concentration gradient* in the simplified case for one-dimensional atom movement. Equation (4.14) is called *Fick's first law* and is visualized in Fig. 4.17. j_D is the flux of atoms through a plane of unit area per unit time, and D is the *diffusion coefficient* ($m^2\,s^{-1}$).

Consider now a sheet of nickel and copper bonded to each other (Fig. 4.18a). The steep concentration gradient at the contact surface will cause continuous mutual diffusion of both atomic species to either side (Fig. 4.18b) until eventually an equilibrium concentration is attained (Fig. 4.18c). The kinetics, i.e., the velocity of this interdiffusion process, is triggered by the absolute temperature T according to an Arrhenius law

$$D = D_0 \exp\left(-\frac{Q}{RT}\right) . \tag{4.15}$$

D_0 is a constant prefactor and—in essence—an intrinsic material parameter, $R = 8.314\,J\,mol^{-1}\,K^{-1}$ is the gas constant, and Q is the activation energy required for an atom to carry out a single jump event. In crystalline solids, as pointed out in Sect. 4.1.2, two mechanisms of atom movement are conceivable depending on the size ratio δ of the solute and matrix atom (Sect. 4.1.1):

- $\delta < 0.15$: This is the case for self-diffusion and diffusion of substitutionally solved atoms and requires the presence of a vacancy next to the lattice site of the moving atom (see the upper part of Fig. 4.19).

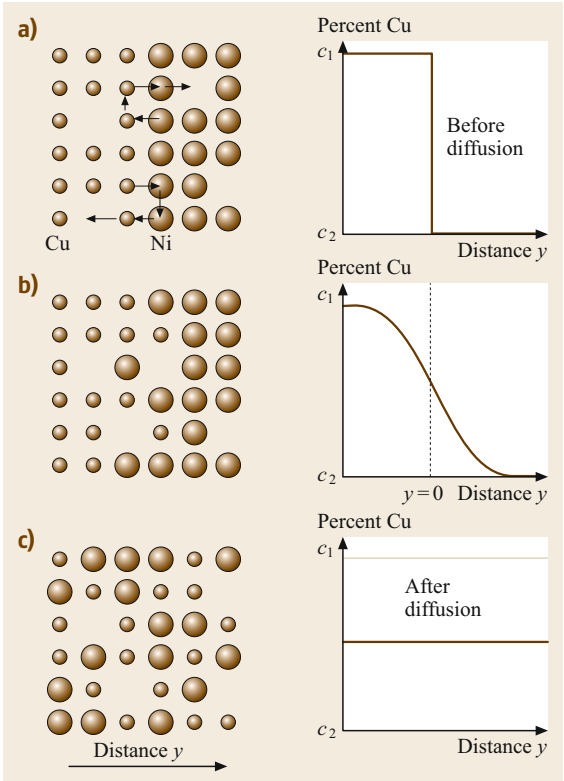

Fig. 4.18a–c Mutual diffusion of Cu and Ni atoms into each other through a vacancy mechanism: **(a)** $t = 0$, **(b)** $t > 0$, intermediate time, **(c)** $t \to \infty$

After the jump, the atom has created a new vacancy at the original lattice site, hence one observes counterflows of atoms and vacancies. Consequently, this mechanism is also called *vacancy diffusion*. Since this diffusion mechanism requires the presence of vacancies, its activation energy Q_v is composed of two terms, namely one for the formation of vacancies, Q_f, and one for their migration, Q_m, hence $Q_v = Q_f + Q_m$ replaces Q in (4.15) for self-diffusion or vacancy diffusion.

- $\delta > 0.15$: This is the case for (small) interstitial atoms moving from one interstitial site to another. No vacancies are required for this mechanism, and the activation energy for *interstitial diffusion*, Q_i, accounts for the migration of interstitials and is therefore smaller than its counterpart for vacancy diffusion Q_v (Fig. 4.19). For interstitial diffusion, Q_i substitutes for Q in (4.15).

Examples of the temperature dependence of the diffusion coefficient according to (4.15) are given in Fig. 4.20 in the form of an Arrhenius-type plot of $\ln D$ versus reciprocal temperature $1/T$. One notes the following characteristic features:

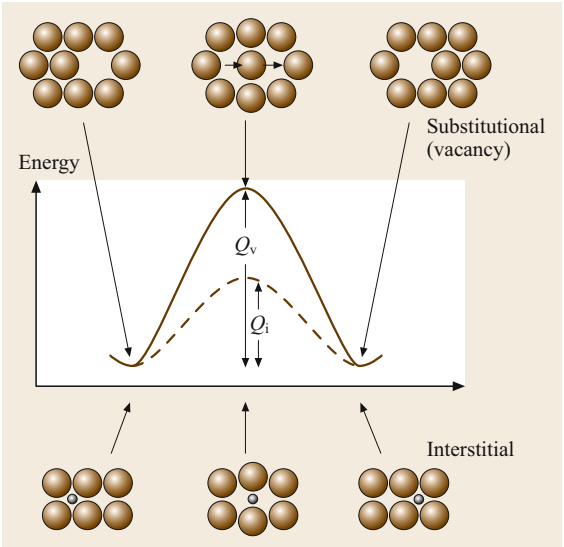

Fig. 4.19 Visualization of diffusion mechanisms in crystalline solids. *Top*: vacancy diffusion with activation energy Q_v, *bottom*: interstitial diffusion with activation energy Q_i

1. The slope of the curves is a measure of the activation energy Q, with a steeper slope indicating a higher value of Q.
2. As anticipated from Fig. 4.19, interstitial diffusion is considerably faster than vacancy diffusion (cf. the curves for Fe self-diffusion with those of carbon and hydrogen diffusion in iron).
3. The lower PD of the bcc crystal structure as compared with the fcc or hcp structure (Table 4.2) gives rise to a higher diffusivity D.

This holds for Fe as well as for Ti, which undergoes an allotropic transformation from hcp α-Ti to bcc β-Ti at 882 °C.

The scenario depicted in Fig. 4.18 is typical for many engineering applications of diffusional processes such as the heat treatment of materials for equilibrating concentration inhomogeneities stemming from alloy solidification or joining operations. Figure 4.18 can be considered as an exemplification of diffusional bonding or the consolidation of metallic and/or ceramic powder particles by solid-state sintering (*powder metallurgy*). Fick's first law (4.14) is unable to describe the local and temporal distribution of atoms during different time stages of diffusion, e.g., the concentration profile shown in Fig. 4.18b. However, as the number of atomic species

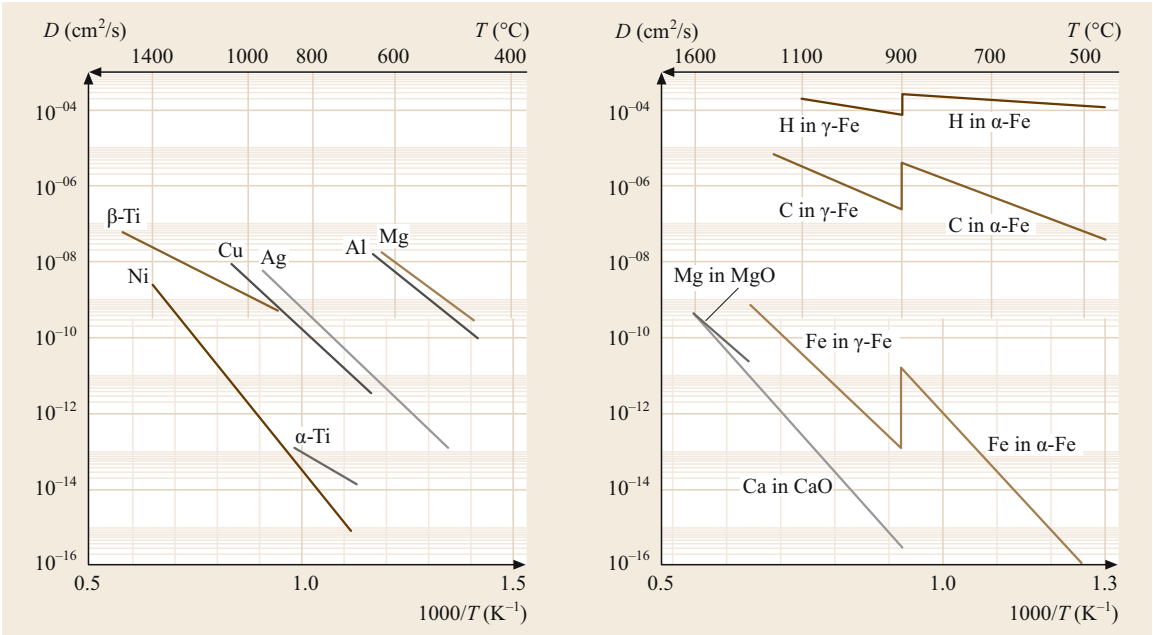

Fig. 4.20 Temperature dependence of diffusion coefficient D in various metals and oxide ceramics. The slope of the ln D versus $1/T$ plot represents the activation energy for diffusion Q

in the system remains constant

$$\frac{\partial c}{\partial t} + \nabla j_{\mathrm{D}} = 0 \qquad (4.16)$$

and with (4.14) one obtains finally after some manipulations (see [4.9] for a detailed derivation) Fick's second law (in its one-dimensional form)

$$\frac{\partial c}{\partial t} = D\frac{\partial^2 c}{\partial y^2}\,, \qquad (4.17)$$

whose solution depends on the specific boundary conditions of the diffusion problem. For the scenario depicted in Fig. 4.18 (*diffusion bonding* of two semiinfinite rods of different metals), one obtains

$$\frac{c(y,t) - c_1}{c_2 - c_1} = \frac{1}{2}\left[1 + \mathrm{erf}\left(\frac{y}{2\sqrt{Dt}}\right)\right], \qquad (4.18)$$

with erf(ξ) being the *error function* (also called the *Gaussian probability integral*), which can only be solved numerically. Note that the error function is point-symmetric with respect to the origin and $-1 \le \mathrm{erf}(\xi) \le 1$ for $-\infty \le \xi \le \infty$. Equation (4.18) reveals that, to obtain a certain given concentration c_0 at depth y_0, both the temperature (via D) and time t can be varied independently to design an optimum heat treatment in view of the availability of appropriate furnaces as well as the cost of the operation. The most prominent application of diffusional problems is carburization of steels, for which solutions similar to (4.18) are available in literature [4.9].

4.1.4 Transformation into Solid State

In Sect. 4.1.2, we already noted that the solidification process of materials critically influences their microstructure in general, and the amount of dislocations and grain boundaries in particular. While physical vapor deposition (PVD) and chemical vapor deposition (CVD) techniques on (cold) surfaces have become increasingly important for thin-film technologies, the main and most important phase transformation in metallic materials, semiconductors, and glasses in terms of both mass production and annual turnover is still by far solidification from the melt (*cast metallurgy*). This phase transformation can be quantitatively treated by applying the principles of thermodynamics. Hence, in this section, we introduce the basic thermodynamic concepts, focusing on the behavior of pure materials, in other words a single-component *system*, a material that can exist as a mixture of one or more phases. A *phase* can then be defined as a portion of the system with the same structure. The *components* are the different (chemical) elements which make up a system, and the composition of a phase or the system can be described by giving the relative amounts of each component.

Consequently, the subsequent sections show how solidification occurs in alloys and multiple-*phase* systems, and the main species of binary phase diagrams are derived.

The reason why a transformation occurs at all is because the initial state of the material is unstable relative to the final state. This scenario can be expressed by thermodynamics principles (at constant temperature T and pressure p) through the Gibbs free energy G of the system

$$G = U + pV - TS = H - TS\,, \tag{4.19}$$

where U is the intrinsic energy, H is the enthalpy, i.e., the heat content arising (to a good approximation for condensed matter) from the total kinetic and potential energies of the atoms, and S is the entropy, i.e., a measure of the randomness of the system.

A system is in *equilibrium* when it is in its most stable state. This translates (4.19) for a closed system (with fixed mass and composition) at constant T and p into

$$\mathrm{d}G = 0\,. \tag{4.20}$$

From (4.19) and (4.20), one can intuitively conclude that the state with the highest stability will be the one with the best compromise between a low value of H and a high entropy. Thus, at low temperatures, solid phases are most stable, since they have the strongest atomic binding and hence lowest enthalpy. At higher temperatures, however, the $-TS$ term in (4.19) will dominate over H, and phases with increasingly greater degrees of atom movement become stable: first liquids, then gases. This is elucidated in Fig. 4.21, where the intersection of the curves with the ordinate is a measure of the enthalpy of the respective phases and the slope of the curves represents the entropy.

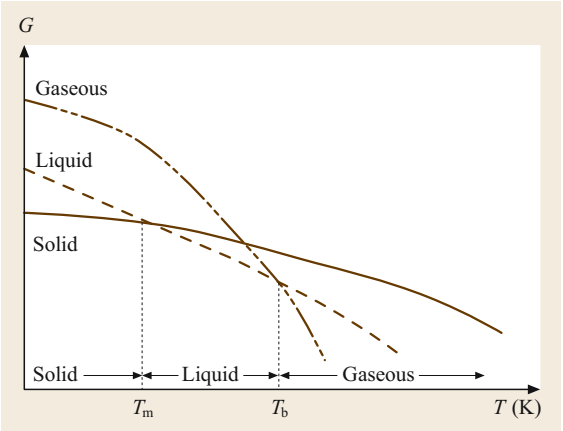

Fig. 4.21 Differences in molar free energy ΔG between solids, liquids, and gases in a single-component system (pure material). T_m and T_b denote the melting and boiling point, respectively

Homogeneous Nucleation

Undercooling a liquid below its equilibrium temperature T_m yields a driving force for solidification $\Delta G = (G_{Solid} - G_{Liquid}) < 0$, so one might expect the melt to solidify spontaneously. However, this is not the case, and liquids can be supercooled by more than a hundred kelvin below T_m without crystallization [4.2–5], as a nucleus of solid matter has to be formed within the homogeneous liquid. The change in free energy of the system ΔG_{cryst} when producing a solid sphere of radius r within the liquid for a given undercooling ΔT consists of two terms

$$\Delta G_{cryst} = -\frac{4}{3} r^3 \pi \Delta G_V + 4 r^2 \pi \gamma_{SL}\,, \tag{4.21}$$

of which the first, ΔG_V, is the gain in energy due to the formation of a spherical volume of crystalline solid, while the second, ΔG_S, is the expenditure energy due to the formation of the interface with specific interfacial energy γ_{SL} between the liquid and solid phases. The individual terms ΔG_V and ΔG_S are plotted together with the sum curve ΔG_{cryst} as a function of the crystal radius r in Fig. 4.22.

The critical radius r^* of a stable nucleus of crystalline solid is reached when further growth of the nucleus leads to a gain in ΔG_{cryst}. Mathematically, this is obtained from the first derivative of ΔG_{cryst} in (4.21)

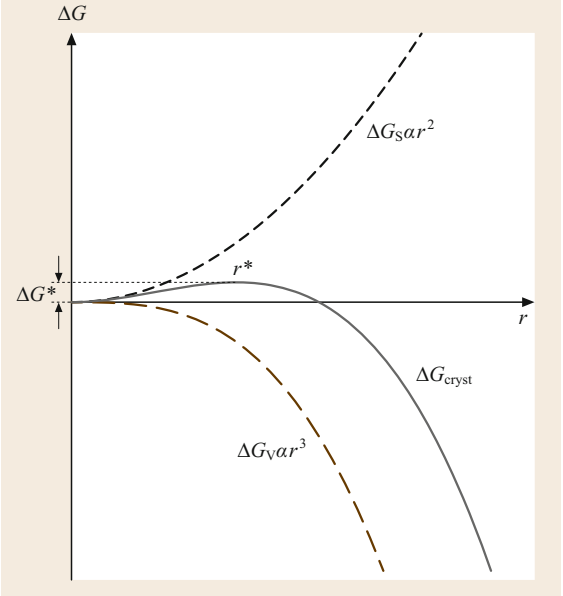

Fig. 4.22 Free energy change associated with homogeneous nucleation of a sphere of radius r

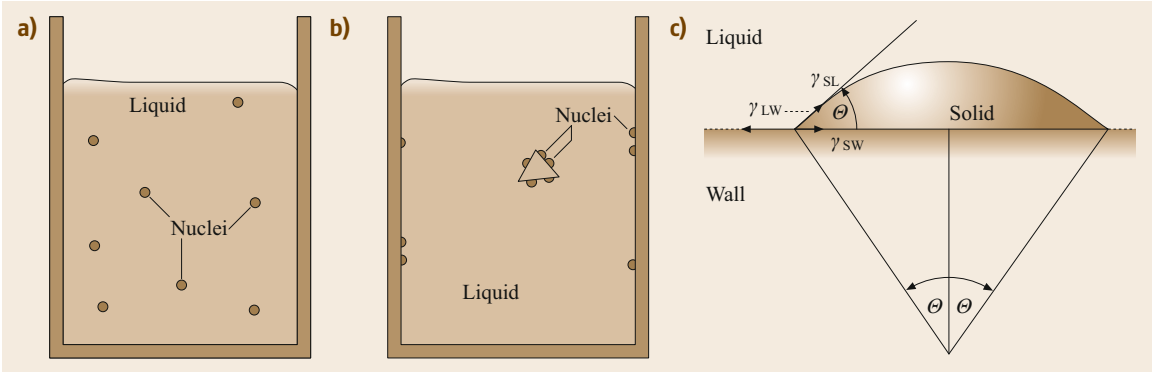

Fig. 4.23a–c Homogeneous (a) versus heterogeneous nucleation (b,c): a spherical cap of a solid needs fewer atoms to become a stable nucleus than a sphere, see text

with respect to r

$$\frac{\partial \Delta G_{\text{cryst}}}{\partial r} = 0 = -4r^{*2}\pi\Delta G_{\text{V}} + 8r^{*}\pi\gamma_{\text{SL}} \,. \qquad (4.22)$$

Solving (4.22) yields the critical radius as

$$r^{*} = \frac{2\gamma_{\text{SL}}}{\Delta G_{\text{V}}} \,, \qquad (4.23)$$

and for the excess free energy

$$\Delta G^{*} = \frac{16\pi\gamma_{\text{SL}}^{3}}{3(\Delta G_{\text{V}})^{2}} \,. \qquad (4.24)$$

Since ΔG is proportional to the undercooling ΔT, (4.23) and (4.24) straightforwardly demonstrate that small undercoolings require a large amount of ΔG^{*} and the formation of a large cluster of atoms to create a stable nucleus. Vice versa, for large undercoolings, nuclei with a small critical radius are already stable within the melt and can grow.

Heterogeneous Nucleation

From (4.24) for ΔG^{*}, it is obvious that nucleation can become easier if the interfacial energy term is reduced. This is effectively achieved if the nuclei form in contact with the mold wall (or likewise, impurities within the melt). Consider a solid embryo in contact with a perfectly flat mold wall (Fig. 4.25b,c). For a given volume of solid, the total interfacial energy of the system can be minimized if the condition

$$\gamma_{\text{LW}} = \gamma_{\text{SW}} + \gamma_{\text{SL}}\cos\Theta \qquad (4.25)$$

is fulfilled in the plane of the mold wall. The embryo has the shape of a spherical cap with radius r and wetting angle Θ. *Porter* and *Easterling* [4.9] compared this situation with that of a sphere with the same radius r which undergoes homogeneous nucleation (Fig. 4.23a) and derived the following relation for the energy barrier for heterogeneous nucleation

$$\Delta G^{*}_{\text{het}} = \frac{16\pi\gamma_{\text{SL}}^{3}}{3(\Delta G_{\text{V}})^{2}} S(\Theta) \,, \qquad (4.26)$$

where

$$S(\Theta) = \frac{(2+\cos\Theta)(1-\cos\Theta)^{2}}{4} \,. \qquad (4.27)$$

Except for the shape factor $S(\Theta)$, (4.26) is the same as the relation obtained for homogeneous nucleation in (4.24). Since $S(\Theta) \leq 1$ and the critical radius r^{*} is unaffected, heterogeneous nucleation is always energetically favored over homogeneous nucleation, thus also the rate of heterogeneous nucleation becomes faster [4.9]. If, for example, $\Theta = 10°$, then $S(\Theta) \approx 10^{-4}$ and the energy barrier for heterogeneous nucleation becomes dramatically smaller than that for homogeneous nucleation. Even for the upper limit $\Theta = 90°$ (half sphere), $S(\Theta) = 0.5$.

Heat Flow and Interface Stability

Neglecting the effect of alloying, solidification is controlled by the rate at which the heat of crystallization is conducted away from the solid–liquid interface. Two options are conceivable:

1. If the solid grows with a planar interface into a superheated liquid (Fig. 4.24a), the heat flow away from the interface through the solid must balance that from the liquid plus the heat of crystallization generated at the interface. Then, a small branch of solid protruding into the liquid will arrive in a region of increased temperature. Consequently, more heat will be conducted into the protruding solid and less heat will be transported away, such that

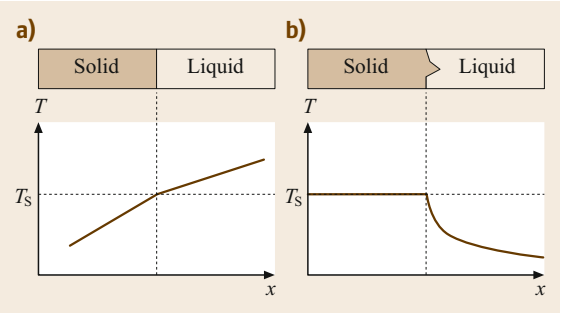

Fig. 4.24a,b Temperature distribution for solidification and the form of the solid–liquid interface when the heat is conducted through **(a)** the solid and **(b)** the liquid

the growth rate will slow down below that of the surrounding planar region and the protrusion will eventually disappear and the solid–liquid interface remains planar. Heat conduction through the solid, as depicted in Fig. 4.24a, can be promoted when solidification takes place from the cooler walls of the mold. This effect is applied technically by using a cold plate or a zone melter to apply a temperature gradient for producing microstructures consisting of coarse and elongated grains or even single crystals. An example for the Ni-20Cr alloy is shown in Fig. 4.25: starting from the left side with coarse but equiaxed grains, the temperature gradient causes a single dominant grain to grow preferentially towards the right of the sample.

2. If the solid grows into a supercooled liquid (Fig. 4.24b), an eventual protrusion of the solid into the liquid is forced to grow more rapidly by the negative temperature gradient in the liquid because the heat is removed more efficiently from the tip of the protrusion than from the surrounding regions. Thus, a solid–liquid interface advancing into a supercooled liquid is inherently unstable.

In alloys, the formation of dendrites is connected with compositional changes (or constitutional effects) between the solid and liquid phase, so dendrite formation is known to be caused by *constitutional supercooling*. An example of a dendritic microstructure in a cast Al alloy is shown in Fig. 4.26. For further details and a more quantitative treatment of these issues see [4.9].

4.1.5 Binary Phase Diagrams

In single-component systems, all phases have the same composition, and equilibrium involves temperature T and pressure p as variables. Obviously, in alloys, the composition is also variable and understanding phase transformations requires an appreciation of how the Gibbs free energy of the respective phases involved depends on all these parameters. However, pressure p can be ruled out and treated as being constant in what follows, since we consider only the liquid–solid transformation with both phases being essentially incompressible. Besides, to keep the physical model simple, we restrict ourselves in the following to binary alloys, i.e., two-component systems.

Gibbs Free Energy of Binary Solutions

Assume that two components A and B can be mixed in any proportions (because they have the same crystal structure; an example of this scenario would be the alloy system Ag-Au). Then the Gibbs free energy of a homogeneous solid solution can be calculated in two steps: first, we bring together x_A moles of pure A and

Fig. 4.25 Microstructure of Ni-20Cr alloy produced by zone melting, a single (*light grey*) grain evolves on the right half of the micrograph due to the horizontal temperature gradient

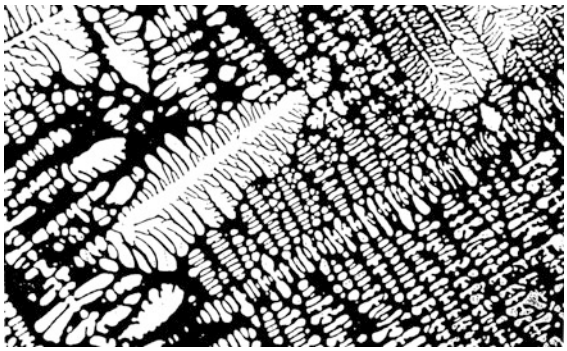

Fig. 4.26 Dendritic microstructure in die-cast Al-Zn10-Si8-Mg alloy

x_B moles of pure B, so the free energy of the system is simply the arithmetic mean

$$\overline{G}(x) = G_A x_A + G_B x_B \,, \tag{4.28}$$

with $x_A + x_B = 1$ for binary systems. Please note that in this section (Sect. 4.1.5) x is used as parameter for the molar concentration (in contrast to the concentration c used in Sect. 4.1.3). For all alloy compositions, $\overline{G}(x)$ lies on a straight line between G_A and G_B. The second step is now to let A and B mix in a random fashion. The free energy of the system will not remain constant during mixing, and

$$G(x) = \overline{G} + \Delta G_M \,, \tag{4.29}$$

where $\Delta G_M = \Delta H_M - T\Delta S_M$ is the change in the Gibbs free energy due to mixing. The simplest case of mixing is the *ideal solution*, in which one assumes that no preferences can be found for the different types of interatomic bonds between neighboring atoms. If preferred bondings are found, however, this situation is called a *regular solution* and describes more realistic scenarios of alloying; this case will not be treated here for simplicity. For ideal solutions, $\Delta H_M = 0$ and $\Delta G_M = -T\Delta S_M$. From statistical thermodynamics [4.6, 16] we know that entropy is quantitatively related to randomness by Boltzmann's equation and one obtains

$$\Delta G_M = -T\Delta S_M = RT\,(x_A \ln x_A + x_B \ln x_B)\,. \tag{4.30}$$

Since $\Delta S_M > 0$, i.e., there is an increase in entropy on mixing, ΔG_M is negative and the course of $G(x)$ according to (4.29) is shown schematically in Fig. 4.27. Note that, as the temperature increases, G_A and G_B decrease and the free energy curve $G(x)$ assumes a greater curvature due to the increasing degree of randomness.

For any given mole fraction x_B, the extrapolation of the tangent to G to both sides of the molar free energy

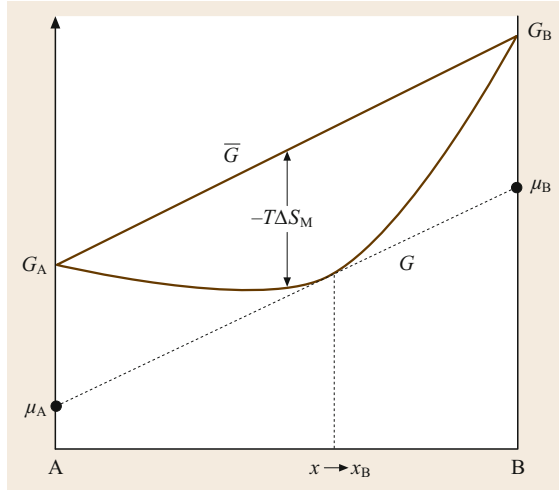

Fig. 4.27 Molar free energy of a system consisting of two components A and B before mixing ($\overline{G}$) and for an ideal solution (G)

diagram (Fig. 4.27) yields the chemical potentials μ_A and μ_B of the components A and B, respectively, which describe how the free energy changes when an infinitesimally small quantity of the atomic species i is added to the system (at constant T and p). Consequently,

$$\mu_i = \left(\frac{\partial G}{\partial x_i}\right). \tag{4.31}$$

Equilibrium in Heterogeneous Systems

Assume now that the components A and B do not form a homogeneous solid solution in the whole concentration range, but form two different phases appearing next to the two components with a limited extension towards the other component. In this case, two free energy curves G_α and G_β have to be sketched, as shown in Fig. 4.28, and the stable forms of both structures are those with the lower free energy; thus, in thermodynamic equilibrium, a homogeneous α solid solution is found for A-rich compositions while β is the stable phase for B-rich compositions. For alloy compositions near the crossover in the $G(x)$ curves (see, e.g., the composition x_0 in Fig. 4.28), a minimal total free energy can be achieved by forming a mixture of two phases α and β with equilibrium compositions x_α and x_β, respectively. From Fig. 4.28, it can be concluded that heterogeneous equilibrium between the two phases requires that the tangents to each G curve at x_α and x_β lie on a common line (the *common tangent rule*). In other words, each component must have the same chemical potential in the two phases and

$$\mu_A^\alpha = \mu_A^\beta \,, \quad \mu_B^\alpha = \mu_B^\beta \,. \tag{4.32}$$

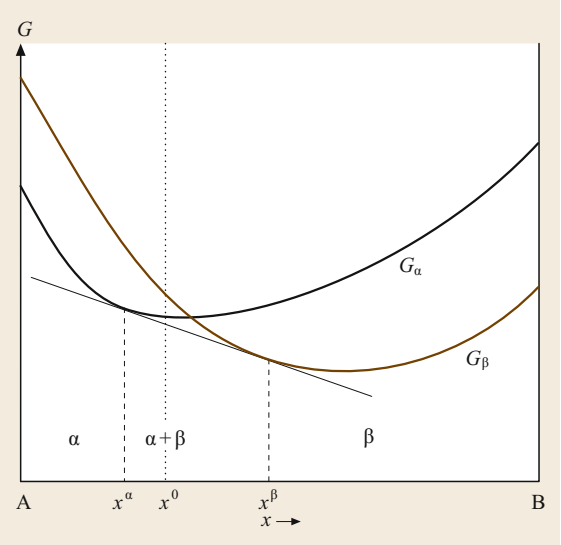

Fig. 4.28 Molar free energy curves for two phases α and β. At equilibrium, alloy x_0 has a minimum free energy when it is composed of a mixture of x_α and x_β

Binary Phase Diagram with Complete Miscibility

The simplest case conceivable is when the two components A and B are completely miscible in both the liquid and solid states and both are ideal solutions. Then, the free energy curves for the liquid and solid phases vary with temperature according to Fig. 4.29. At T_1, the liquid phase is thermodynamically stable over the whole composition range (Fig. 4.29a), thus $G_\alpha > G_L$. With decreasing temperature, one approaches the melting points T_2 and T_4 of pure A and B (see Fig. 4.29b,d, respectively), where the $G(x)$ curves meet in a single point on either side of the diagram. These points are plotted on the temperature axes for pure A and B, respectively, in the *equilibrium phase diagram* (Fig. 4.29f). With a further decrease in temperature (T_5), the solid phase is stable for all compositions (Fig. 4.29e), and $G_\alpha < G_L$. In the temperature interval between T_2 and T_4, the common tangent rule indicates a two-phase region with coexisting solid and liquid phase (see the two vertical dashed lines at T_3 in Fig. 4.29c). These points are transferred into the equilibrium phase diagram at T_3.

Lever Arm Rule

Figure 4.30 shows an enlarged view of the binary phase diagram with complete miscibility derived in Fig. 4.29. The region where the two phases coexist is limited by the two curved lines, the upper of which separates this region from the liquid phase. Consequently, this line is called the *liquidus line*. The lower line separates the two-phase region from the solid phase and is thus called the *solidus line*. For any given temperature T_3 and overall composition x_0 within the two-phase region, it may now be interesting to know the amount of liquid and

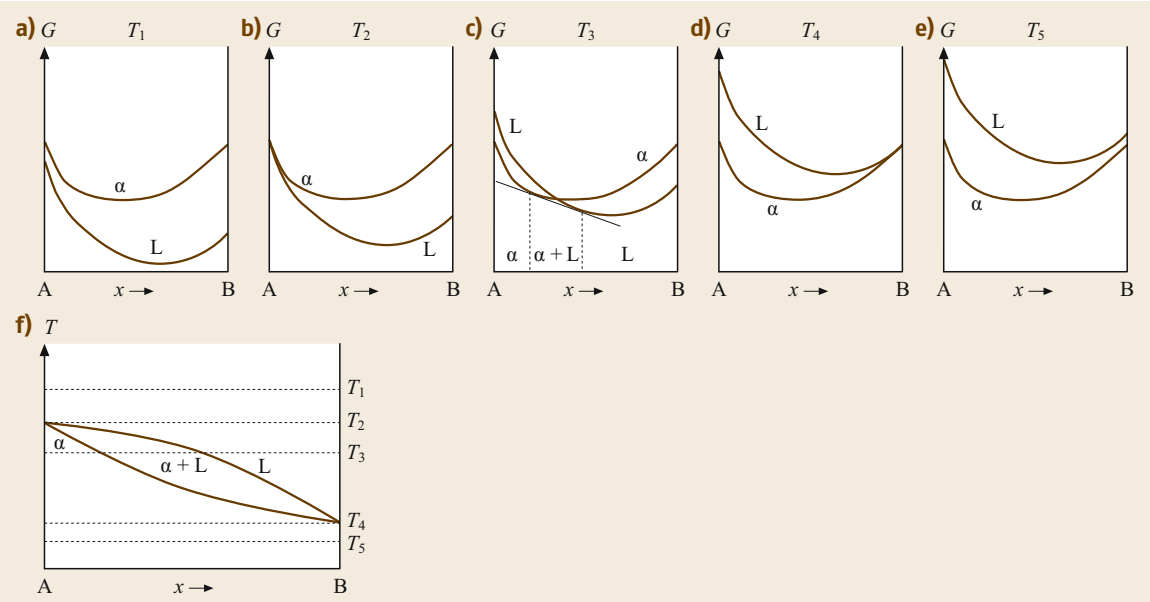

Fig. 4.29a–f Derivation of a phase diagram with complete miscibility in the liquid (L) and solid (α) state **(f)**: **(a)** at T_1, all compositions are liquid, **(b)** T_2 represents the melting point of element A, **(c)** at T_3, a two-phase region of α and L exists, **(d)** T_4 is the melting point of element B, **(e)** all compositions are solid at T_5

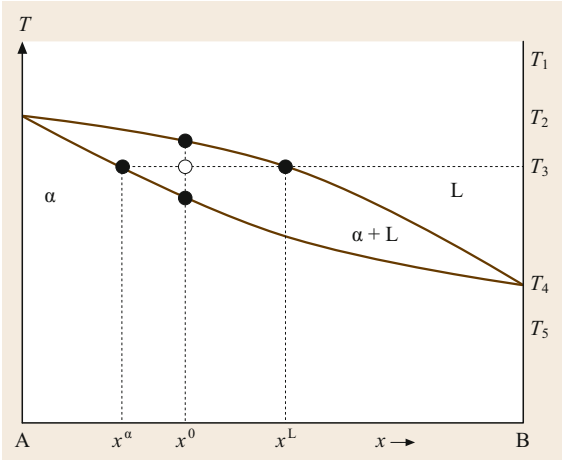

Fig. 4.30 Lever arm rule for estimating the molar fraction of solid and liquid phase in a two-phase region

solid phase, respectively, as well as their concentration (or, more precisely, their molar fractions). Drawing a horizontal straight line at T_3, the intersection with the liquidus and solidus line yields the concentration x_L and x_α of the liquid and the solid phase, respectively, within the two-phase region. The amount of α-phase f_α can be determined graphically utilizing the lever arm rule

$$f_\alpha = \frac{x_L - x_0}{x_L - x_\alpha} \,. \tag{4.33}$$

Analogously, one obtains for the amount of liquid phase f_L

$$f_L = \frac{x_0 - x_\alpha}{x_L - x_\alpha} \,, \tag{4.34}$$

and finally for the ratio between the solid and liquid phase

$$\frac{f_\alpha}{f_L} = \frac{x_L - x_0}{x_0 - x_\alpha} \,. \tag{4.35}$$

Equations (4.33)–(4.35) hold in general for all two-phase regions in binary phase. The application of this law to the eutectoid pearlite grains (0.8% carbon) (Sect. 8.1.1) shows that they contain 88% ferrite and 12% cementite, what can be confirmed by quantitative stereology (Sect. 4.2.3, *Quantification of Microstructure/Quantitative Stereology*).

Eutectic Systems

Figure 4.31 exemplifies the situation where the liquid phase is approximately ideal but the solid phase α is composed of two solid solutions α_1 and α_2; i.e., the atoms A and B *dislike* each other. Rather, preferred A–A- and B–B-type bondings can be found and ΔH_M in (4.31) becomes positive (regular solution). Therefore, at low temperatures T_5, the (combined) free energy

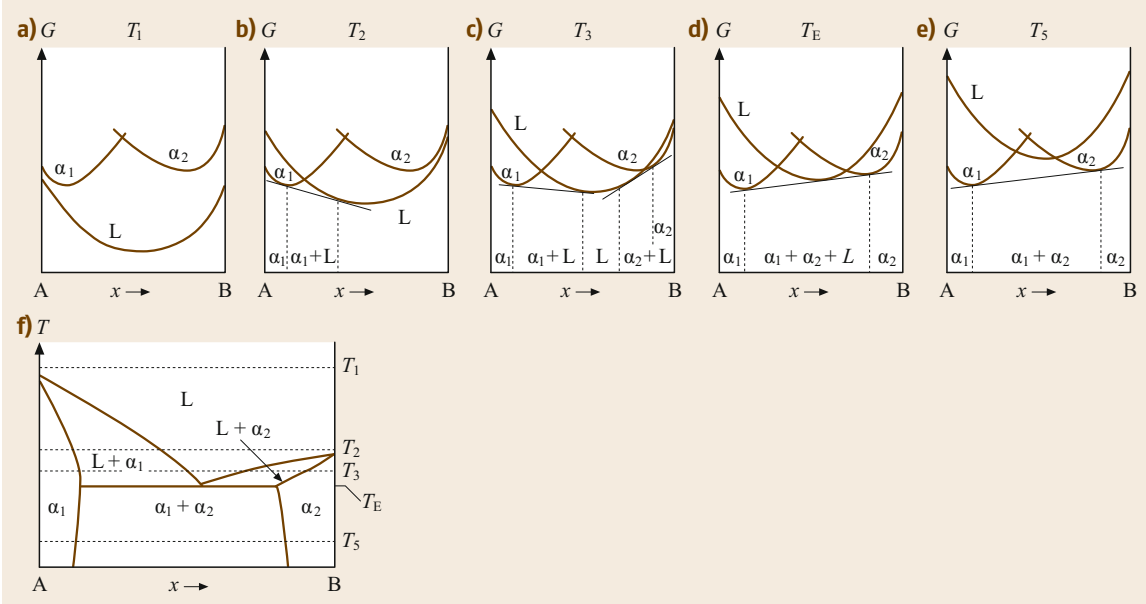

Fig. 4.31a–f Derivation of a eutectic phase diagram with a limited solubility for the A-rich solid solution α_1 and the B-rich solid solution α_2 **(f)**: **(a–e)** G–x curves of the solid phases α_1 and α_2, respectively, and the liquid phase L at temperatures T_1–T_3, T_E, and T_5. For further details see text

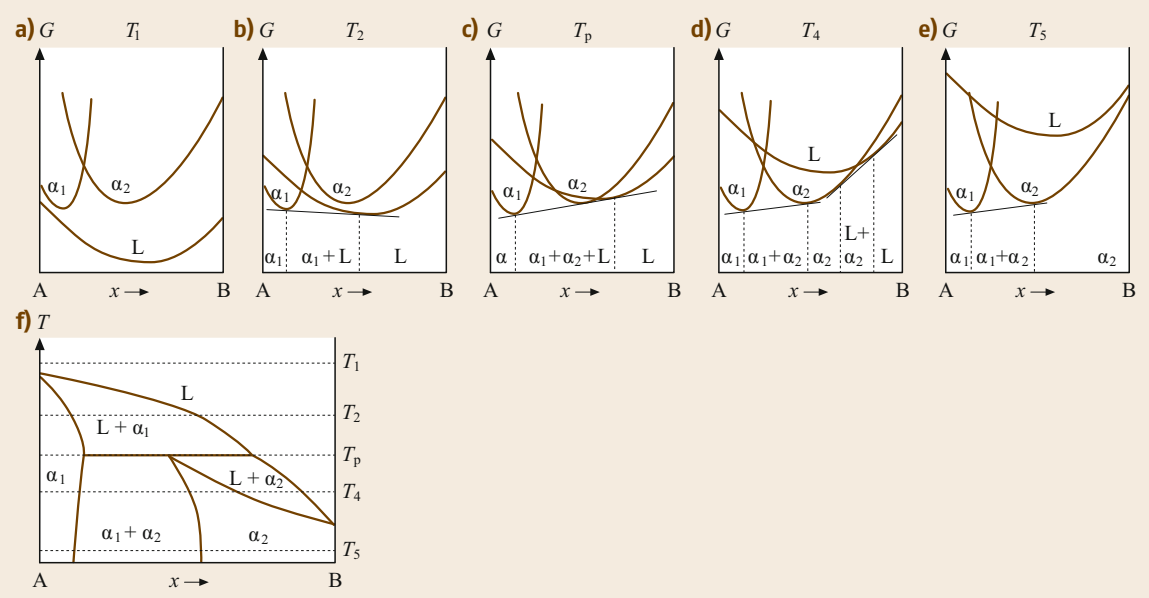

Fig. 4.32a–f Derivation of a peritectic phase diagram with a limited solubility for the A-rich solid solution α_1 and the B-rich solid solution α_2 **(f)**: **(a–e)** G–x curves of the solid phases α_1 and α_2, respectively, and the liquid phase L at temperatures T_1, T_2, T_p, T_4, and T_5. For further details see text

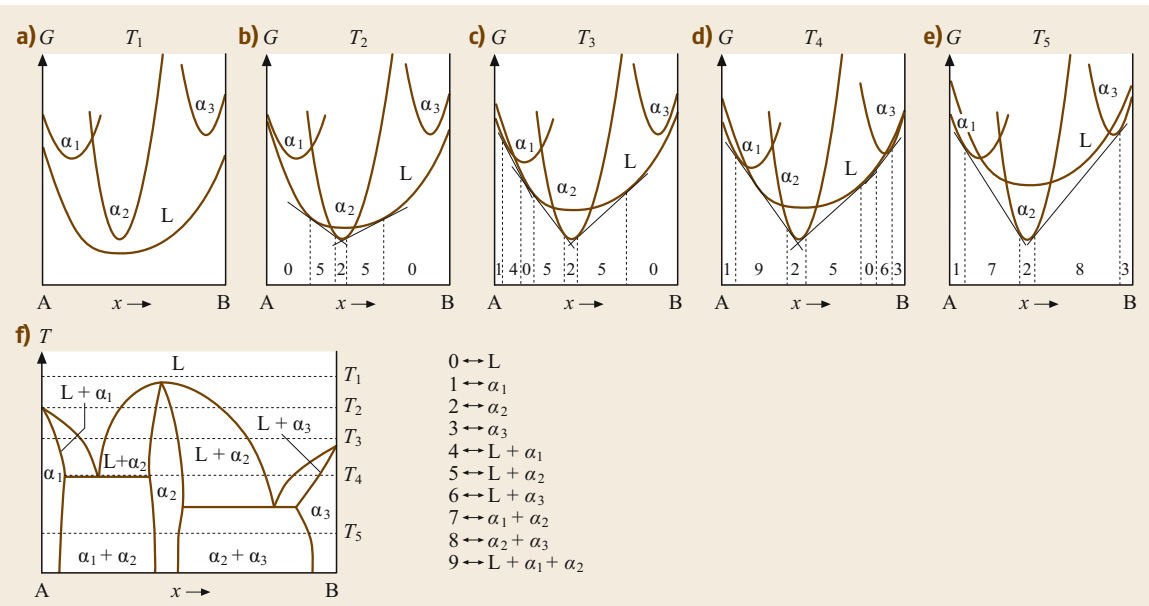

Fig. 4.33a–f Derivation of a complex system with an intermetallic phase α_2 **(f)**: **(a–e)** G–x curves of the solid phases α_1 to α_3 and the liquid phase L at temperatures T_1–T_5

curves of α_1 and α_2 in Fig. 4.31 assume a negative curvature in the middle and the solid solution is most stable as a mixture of the two phases α_1 and α_2. In this region eutectic decomposition occurs, and the lever arm rules (4.33)–(4.35) apply. The second effect of $\Delta H_M > 0$ becomes obvious at the *eutectic temperature* T_E, where one common tangent line can be applied to the $G(x)$ curves of all three phases: as a consequence, the *eutectic* composition has the lowest melting point within the system. For a *eutectic*

reaction,

$$L \rightarrow \alpha_1 + \alpha_2 \,. \tag{4.36}$$

Peritectic Systems

Figure 4.32 illustrates how a *peritectic* phase transformation is related to the free energy curves. Again, $\Delta H_M > 0$, but in contrast to the eutectic system, the $G(x)$ curves for the two solid solutions α_1 and α_2 are shifted to one side of the composition relative to the liquid phase L. As for the eutectic system, one common tangent line can be applied to the $G(x)$ curves of all three phases at T_P and the *peritectic reaction* is

$$\alpha_1 \rightarrow L + \alpha_2 \,, \tag{4.37}$$

which quite naturally explains why peritectic systems likely emerge when two components with substantially different melting points are alloyed.

Systems with Intermetallic Phases

The opposite type of effect arises when $\Delta H_M < 0$ and the atoms *like* each other within a certain composition range. In such systems (Fig. 4.33), melting will be more difficult in the α_2 phase because of its very deep $G(x)$ curve and a maximum melting point may appear. If the attraction between the unlike atoms is very strong and the α_2 phase extends as far as the liquid, it may be called an *intermetallic* phase.

4.2 Microstructure Characterization

4.2.1 Basics

The primary characteristic of a material is its integral and percentual chemical composition, that is, e.g., for metals the chemical elements, for polymer materials the types of polymers and possible reinforcements, and for ceramics the oxides, nitrides, or carbides. For the analysis of the chemical composition, for example, to monitor metallurgical processes or identify materials in warehouses, mostly *atomic emission spectroscopy (AES/OES)*, based on light emission, and *x-ray fluorescence spectroscopy (XRF)*, based on x-ray emission, are used. For chemical depth profiling of coatings, for example, methods based on step-by-step ablation of the material are necessary during the analysis process, e.g., *glow-discharge optical emission spectroscopy (GDOES)*. Starting with the chemical composition, a specific microstructure [4.17] will be generated during the solidification of a melt, the mixing of polymeric components, heat treatment, the manufacturing process (rolling, milling, deep drawing, and welding), or during usage (aging and corrosion).

The (usually three-dimensional) microstructure of materials can consist of several constituents, for example, grains (or crystallites) with different chemical compositions or crystallographic orientations (separated from each other by grain boundaries, Fig. 4.25) or precipitates, dispersoids, impurities (slags, oxides, and sulfides), pores, reinforcement particles, fibers, and others.

The constituents of a microstructure can be visualized using material-specific preparation and imaging methods. However, for complete characterization of a microstructure (materialography, or more specifically metallography, plastography, and ceramography), more methods than microscopic imaging are often necessary. For the interpretation and understanding of a microstructure, knowledge on the presence and nature of the crystallinity of the constituent phases is essential. This information can be obtained by x-ray diffraction analysis, which is a nonmicroscopic integral method. Meanwhile, information on the local chemical composition, local crystal structure, and characteristic geometric parameters of the constituents can be obtained using microscopic methods, which differ in their generated signals, optical resolution, and contrast mechanism.

4.2.2 Crystal Structure Analysis by X-ray Diffraction

The first goal of microstructure characterization is to learn which crystalline phases are present in a material. This is achieved mainly by x-ray diffraction (XRD) analysis [4.18, 19], which provides information on the crystal structure of the constituents of a microstructure. This is possible based on their crystallographic parameters such as type of crystal lattice, crystal symmetry, and unit cell dimension (Sect. 4.1). Moreover, information on the perfection of the crystal lattice (or number of dislocations), and thereby the degree of plastic deformation, and on the external and residual stresses acting on the lattice is also obtainable.

The theory of x-ray diffraction is based on Bragg's law, which describes how electromagnetic waves of a certain wavelength λ interfere with a regular lattice. At certain angles of incidence (θ) with regard to a set of parallel crystal planes, which are therefore called reflectors, constructive interaction takes place according to

$$n\lambda = 2d_{hkl} \sin\theta \,, \tag{4.38}$$

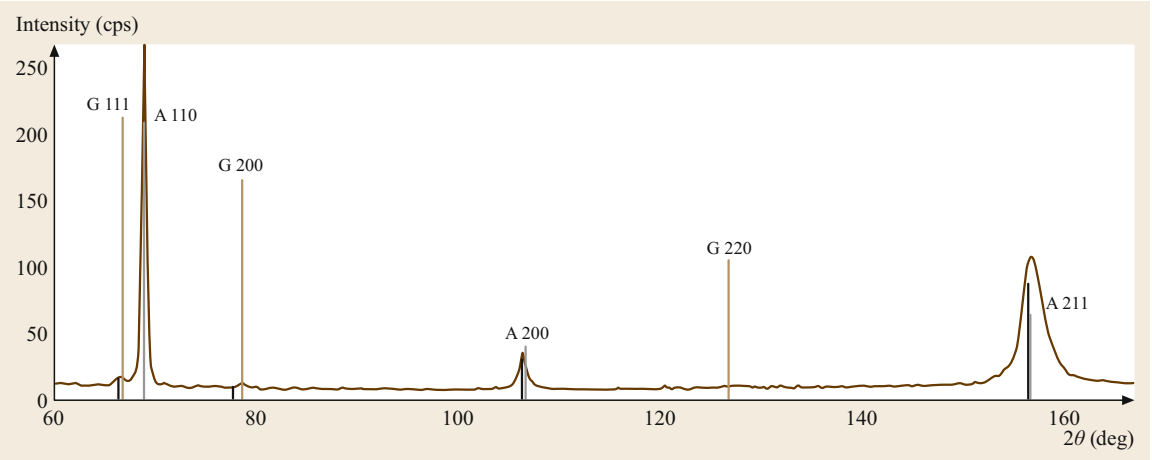

Fig. 4.34 X-ray diffraction pattern of a quenched and tempered hot-working steel 56NiCrMoV7, with metastable austenite (8%); the small peaks marked with a G represent the austenite phase, whereas the large peaks marked with an A show the ferrite matrix. G and A can be attributed to γ-Fe and α-Fe, respectively

where n is a positive integer and d_{hkl} is the interplanar spacing between the crystal planes that cause constructive interaction; λ is the known wavelength of the incident x-ray beam.

In XRD analysis, the specimen is irradiated using a monochromatic x-ray beam, e.g., Cu-K_α or Cr-K_α, which is generated by an x-ray tube with a metallic film for monochromatization. The diffracted x-ray beam is detected by, e.g., a scintillation counter at an angle of 2θ from the incident beam, and the signal is stored in a computer. Both the x-ray source and detector rotate on a circle around the sample in the center. The measuring spot typically has an area of several mm^2—in special cases of a few μm^2. Measurements are possible on bulk specimens, powders, and films. In materials science, XRD analysis applied to polycrystalline bulk materials is also called the *powder* diffraction method. Sample preparation is relatively easily accomplished by grinding or polishing, although destruction of the crystal structure by severe plastic deformation must be avoided. X-ray diffraction can be treated as an integral method for measuring the crystal structure, because the exposed area is usually composed of a number of crystallites. However, single-crystal measurements are also possible. The information depth of a few tens of μm depends on the angle of incidence, atomic number of the sample, and x-ray energy used.

From the x-ray diffraction profile, which is commonly plotted as the x-ray intensity versus 2θ (Fig. 4.34), the following information can be obtained [4.19, 20]: From the angle θ of the Bragg peaks, the lattice constants of the unit cell of the crystal can be calculated by applying (4.38). From the combination of these values, the type of crystal and its symmetry can also be deduced. Because a set of d values and the relative intensities of their corresponding x-ray peaks are characteristic of a certain crystalline material, they can be used for phase identification by comparing the measured diffraction pattern with those contained in databases. The most commonly used database is the powder diffraction file (PDF), maintained and distributed by the International Centre for Diffraction Data (ICDD).

In the case of a material consisting of multiple phases, the weight ratio of the crystalline phases can be calculated from the relative peak intensities. Quantification without a standard sample is based on such comparison of the peak intensities. However, a better way to obtain such ratios is to use a standard substance.

The width of the peaks provides information on the perfection of the arrangement of the atoms within the crystal lattice and on the number of dislocations resulting from plastic deformation. External and residual stresses applied to a crystal lead to dilatation or compression of the atomic distances and therefore to a shift of the diffraction peaks to greater or smaller angle. Practically, the strain in a sample is measured by recording the angular shift of a given reflector as a function of the angle of incidence. The measured strain is then used to calculate the stress with the help of the elastic modulus [4.21].

A preferred orientation of the crystallites in polycrystalline materials with respect to the sample coordinate system is called (crystallographic) texture. The orientation distribution can be determined by x-ray diffraction (XRD)-based texture analysis [4.22]. In this technique, pole figures are measured by recording the intensity distribution of a single reflection by tilting and rotating the sample while radiating it with an x-ray beam. In this way, the orientation distribution of a single

reflection, and thus for a single lattice plane, is determined [4.23].

4.2.3 Materialography

Materialography is the investigation of the microstructure of materials [4.24]. It includes specimen preparation and imaging of the microstructure, the quantification of the constituents (volume fraction, arrangement, size, shape, and grain orientation), as well as the local chemical and crystallographic characterization of the constituents, if necessary.

Specimen Preparation

The three-dimensional microstructure of a material is usually deduced from two-dimensional images, which are obtained by sectioning the sample. The resulting specimen is either in bulk form or thin and transparent, depending on the type of material and the goal of the investigation. The whole process of specimen preparation, starting with cutting small parts from larger pieces, has to be performed without disturbing the microstructure by mechanical or thermal effects. Small specimens (wire, or cross sections of sheet metal) are mounted in resin using pans which can be easily handled and have the right size for grinding machines. Bulk samples are prepared by grinding and polishing using metallographic machines with rotating disks fit with grinding paper or diamond pads, for example. A large number of material-specific abrasives and lubricants are available [4.25]. The selection of the most suitable ones is based on the material's composition and the mechanical properties of its constituents. Mechanical polishing is performed using a rotating wheel covered with cloth and small particle abrasives (for final polishing steps with grain size $< 1\,\mu m$), such as powders of diamond or aluminum oxide, or colloidal silicon dioxide. For further smoothing of the surface, electrolytic polishing can be applied, especially for homogeneous, i.e., single-phase, materials.

A prerequisite for microscopic imaging is a sufficient optical contrast, meaning that neighboring regions must show a certain difference of brightness or color. The contrast (C) is defined as the ratio of intensities I, which can be the intensity of white light (gray values) or colors (red, green, and blue)

$$C = \frac{I_1 - I_2}{I_1}\,, \tag{4.39}$$

where $I_2 < I_1$. Contrast can already be present after polishing the samples, e.g., if black graphite is present in a bright matrix of gray cast iron, colored grains in copper alloys and mineralic materials, and contours due to different abrasion of constituents. In most cases, however, the contrast has to be developed by means of chemical or physical etching [4.26]. Chemical etchants are water-based acidic or basic solutions or complex solutions of salts, sometimes containing organic substances. Grain boundary etching is usually applied to microstructures consisting of only one constituent (Fig. 4.35), where the etching agent reacts preferentially with the more reactive grain boundaries. Large differences in the etching rate of the constituents of a microstructure generate slopes at the grain boundaries between different constituents, which also gives a grain boundary contrast. For some etching agents, the ablation depends on the crystallographic orientation of the grains, so topographies with different light-scattering capability are developed. If a grain consists of two phases, such as pearlite (consisting of ferrite and cementite), one of them can be selectively etched, leaving a light-scattering topography of pearlite grains, which are dark under the microscope as compared with the brighter ferrite grains in a carbon steel (Fig. 4.36, compare also Fig. 4.38).

Fig. 4.35 Grain-boundary etching of an austenitic CrNi steel; the large number of twins is due to severe plastic deformation; light optical micrograph

Physical etching methods are based on selective ablation of constituents by a plasma generated in a glow-discharge apparatus or by ion-beam bombardment, for example, in a focused ion beam (FIB) instrument (see below).

For light and electron microscopy [4.27] of polymer materials, transparent specimens are prepared by cutting lamellae using a microtome with a glass or dia-

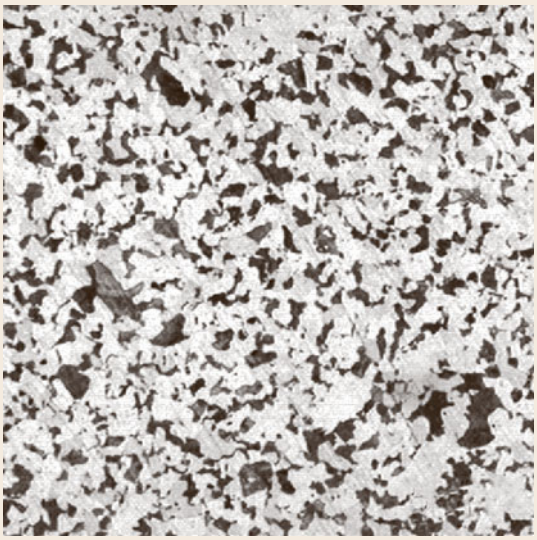

Fig. 4.36 Microstructure of a carbon steel (0.35% C), etched with 3% HNO_3; light microscopy of a polished and etched metallographic cross-section

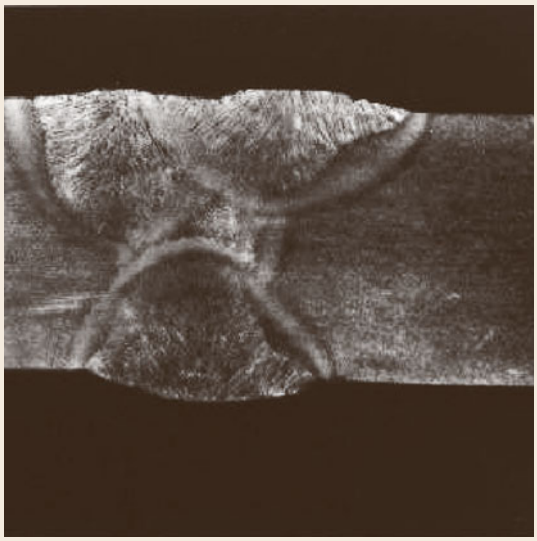

Fig. 4.37 Microstructure of a weld; macroscopy of an etched specimen

mond knife from the sample. The specimens are some micrometers thick and are positioned between a glass microscope slide and a cover glass by adding a drop of immersion oil to exclude air bubbles and increase the refractive index of the interspace. Easily plastically deformable polymers, such as polyethylene, are cut at low temperature (at −70 °C or lower) using a cryomicrotome or a ultra-cryomicrotome (at −175 °C). From polymer matrix composites, thin transparent specimens are obtained by grinding and polishing small pieces which are glued to a glass strip.

Microscopy of Microstructure

For some metallographic samples, it is sufficient to image the specimen with no or little magnification. This *macrometallography* is used, e.g., for the inspection of the microstructure of welds (Fig. 4.37).

In most cases, however, microscopy is necessary to visualize the microstructure, with magnification ranging from 20- to about 1000-fold. The most commonly used method is reflection light microscopy of bulk specimens. The contrast, as mentioned above, is based on the different reflection capability or color intensities of the constituents. If sufficient contrast cannot be obtained by specimen preparation, other imaging modes can be used, such as light microscopy with polarized light for aluminum and magnesium alloys, or differential interference contrast microscopy (DIC) for refractory metals (Mo, W, and V).

Inverted microscopes are used for bulk metallographic samples, because they allow easy positioning of the specimen on the microscope stage with the viewed surface exactly perpendicular to the optical axis. This is a basic requirement to have all parts of the viewed area in focus. Images are captured using a digital microscope camera with a charge-coupled device (CCD) or complementary metal–oxide–semiconductor (CMOS) sensor and a computer; easy-to-handle software is useful, which should allow calibration, the setting of scale markers (micrometer bar), and some interactive distance measurements. Microscope calibration standard patterns are imaged to calibrate the magnification of a selected microscope configuration. As a calibration value, the pixel size, viz. the micrometers per edge length of the square pixels, is stored with the image. A micrometer bar can then be burned permanently into the image if necessary, although one then has to be careful if the micrograph is to be used for automatic image analysis afterwards.

In some cases, dark-field microscopy, in which the diffuse reflected light is detected instead of the directly reflected light, gives better visibility of small objects. The lateral resolution of light microscopy is 0.25 µm at best (due to the wavelength of visible light). The best values are obtained when a substance with a high refractive index (immersion oil) is placed between the specimen and the objective.

For higher resolutions (and magnifications) than are possible with optical methods, *electron microscopy* is

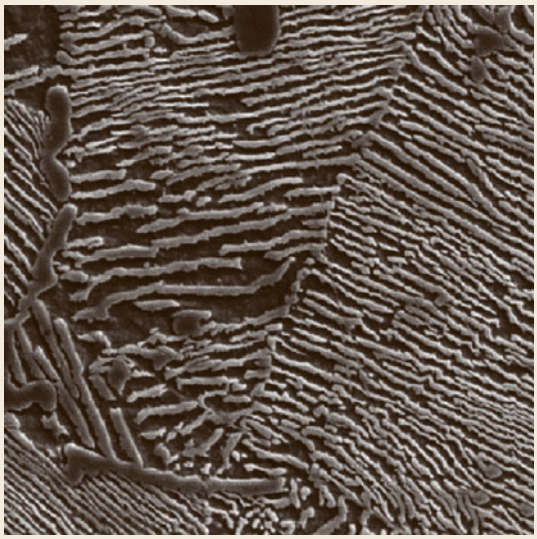

Fig. 4.38 Scanning electron microscopy (SEM) image of pearlite in plain carbon steel; secondary-electron (SE) image

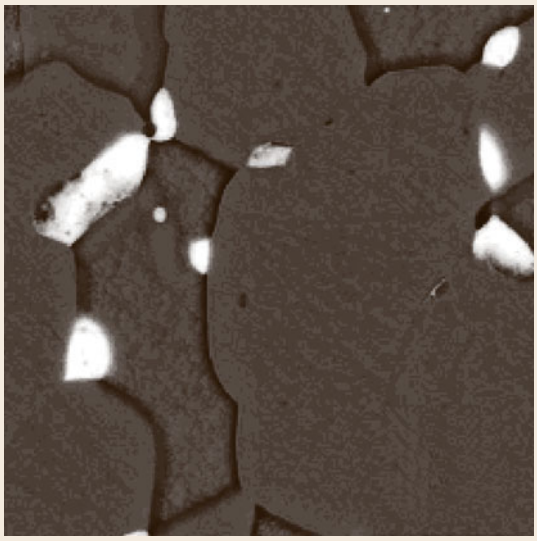

Fig. 4.39 Atomic number contrast in a SEM BSE image of brass; Pb particles are *bright* due to their higher atomic number as compared with Cu and Zn

a method that is widely applied in metallography. In addition, it can provide complementary information on the local chemical composition and the crystal structure. *Scanning electron microscopy* (SEM) is used for imaging metallographically prepared surfaces of bulk samples, and *transmission electron microscopy* (TEM) is used for imaging thin foils which are transparent to electrons. With both techniques, electrons are emitted from an electron gun, accelerated in an electric field (0.5–25 kV in SEM, and 80–400 kV—in some cases over 1 MV—in TEM) towards the anode, and then formed into a narrow beam (with a diameter of a few nanometer) by means of an electron optical system. High vacuum is necessary all along the electron path to prevent collisions of the electrons with gas molecules.

In an SEM [4.28, 29], the specimen, mounted on a multiaxis stage in the specimen chamber, is scanned with a focused electron beam. The emitted secondary electrons (SE) and backscattered electrons (BSE) are registered by detectors mounted above the specimen, and the signal intensities are stored as digital grayscale images. The SE detector is a scintillator–photomultiplier system, while for BSE a scintillator or semiconductor detector can be used.

The best resolution is achievable with the SE signal, and can be as good as 1 nm for suitable instrument parameters and specimen constitution. The information depth is a few tens of nanometers in the SE mode. For imaging of very small particles or thin layers, especially if they consist of low-atomic-number elements, the emission depth can be decreased by applying a lower accelerating voltage, down to some hundred volts. With SE, a topography contrast is generated, which is based on the dependence of the SE intensity on the angle of incidence between the electron beam and the imaged surface area (Fig. 4.38).

With BSE, a composition contrast image can be obtained, because the intensity of the BSE emission is related to the atomic number of the material. Regions containing higher-atomic-number elements are brighter than those composed of lower-atomic-number elements (Fig. 4.39). Even atomic number differences smaller then unity can result in a contrast which is in many cases good enough for imaging the microstructure of polished, but unetched, specimens.

SEM samples must be stable under high-vacuum conditions. This is not the case if they contain water or other liquids which can evaporate. Therefore, in some SEMs, fit with special vacuum devices and detectors, imaging at a pressure of up to about 25 mbar is possible by the injection of water vapor into the specimen chamber; this is known as variable-pressure SEM (VPSEM) or environmental SEM (ESEM). The resulting water partial pressure prevents the evaporation of water from the specimen and the resulting alteration of its structure. Cooling the specimen with the aid of a cooling stage to a temperature just above the freezing point supports this effect. Imaging electrically nonconductive materi-

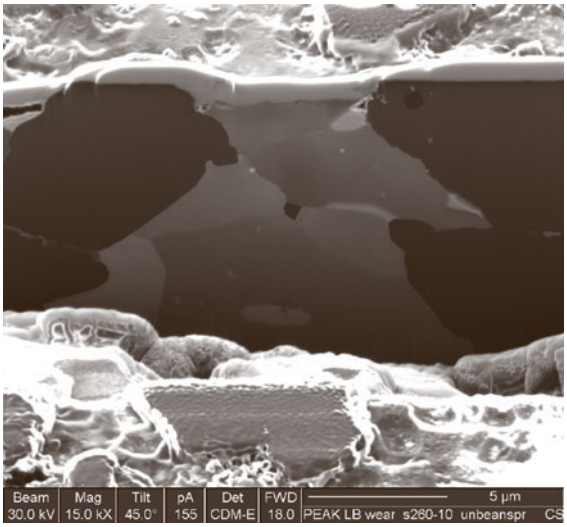

Fig. 4.40 Cross-section prepared using a focused ion beam (FIB); Al alloy, edge protected by a Pt strip, IISE image

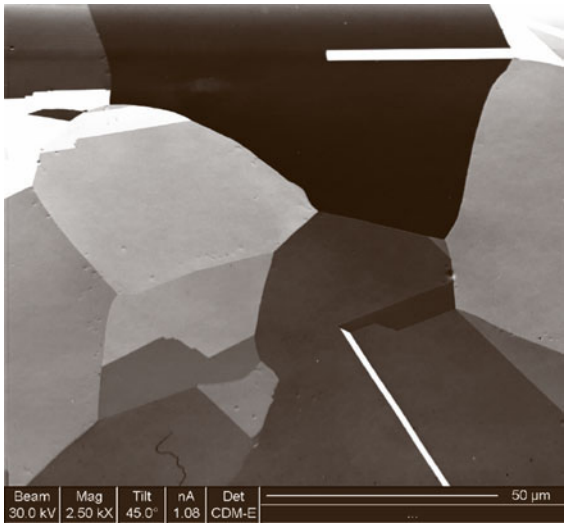

Fig. 4.41 Crystal orientation contrast due to ion channeling effect in Cu; FIB IISE image

als, such as polymers, ceramics, oxides, and mounting resins, is possible in different ways. Either they are coated with a conductive layer (Au, C, Pt, or Cr) by sputtering or evaporation, or a low accelerating voltage is applied (< 2 kV), or imaging is performed under low-vacuum conditions (at least 1 mbar), whereby ions generated by the collisions of electrons with gas atoms prevent the specimen surface from becoming charged.

Cross sections are commonly prepared for microstructural investigation of subsurface regions and of thin surface layers. The edge of the specimen must be preserved to prevent its rounding and the ablation of thin layers during grinding and polishing. Often, resins filled with hard particles are used, or a metal is plated on the sample surface before mounting; chemical deposition of Ni is preferred. A good alternative for the inspection of subsurface regions is cross sectioning with ion beams. Larger areas (with edge length of up to some millimeters) are cut with broad beams of Ar [4.30]. Target cross sections can be prepared using focused ion beam (FIB) instruments [4.31], in which a Ga^+ ion beam (0.5–30 kV accelerating voltage, 7 nm diameter) is scanned over the specimen. The ion bombardment results in a milling effect. Preparation is possible in any region of interest on the specimen surface by milling a stair-shaped trench, typically 20 µm wide and deep. The cross section is imaged after the specimen is tilted (Fig. 4.40). The edge of the trench is protected by a Pt strip, which is deposited before milling by ion-induced decomposition of a metalorganic Pt compound that is fed into the specimen chamber through a small tube. Imaging is possible in a FIB by means of secondary ions (SI) or ion-induced secondary electrons (IISE). The latter give both topographical and compositional contrast. Some crystalline materials show good orientation contrast due to the channeling effect [4.32], and the microstructure is visible without etching (Fig. 4.41).

Modern instruments combine the SEM and FIB functions. The SEM mode is used for conventional imaging with electrons, even during ion-milling steps, and for charge neutralization. An *energy-dispersive* (EDX) and a *wavelength-dispersive* (WDX) x-ray spectrometer and a digital camera for electron backscatter diffraction (EBSD) imaging (see below) can additionally be fit into such an instrument. Thus, the real three-dimensional chemical composition, crystal structure, and microstructure of a sample can be obtained by slice-milling the wall of a cross section in small steps (50 nm to a few µm) and subsequent reconstruction of the microstructure from the resulting EDX and EBSD image series.

TEM [4.33] is used to investigate microstructural constituents smaller than about 50 nm in the conventional (CTEM) or scanning mode (STEM), whereby a resolution of 0.1 nm can be achieved with dedicated instruments. The specimen must be electron transparent, with a thickness of 20–1000 nm, depending on the electron energy and specimen composition. Areal ion beam milling, electrolytic thinning, and ultramicrotomy are common methods applied for specimen preparation. Usually, the specimen is mounted on a 3-mm-diameter Cu grit, which is fixed to the TEM specimen holder. Target preparation, starting with a bulk specimen, is possible by means of FIB milling. One approach is to mill a trench on either side of the region of interest,

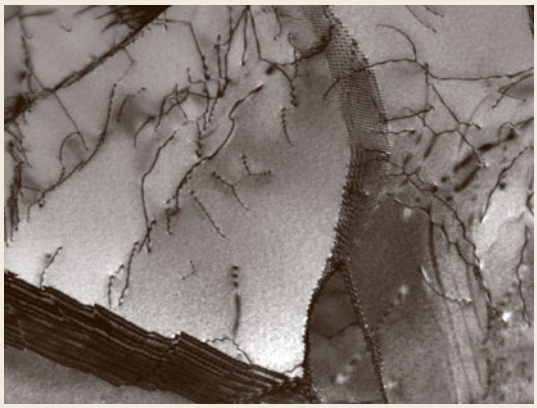

Fig. 4.42 Single dislocations within grains and dislocations forming subgrain boundaries; Mo alloy; multibeam TEM image of a 180-nm-thick specimen; 200 kV accelerating voltage

followed by cutting free the resulting lamella and its transfer to a TEM grid with the help of a nanomanipulator. In some cases, STEM can be carried out in a SEM equipped with a FIB and a STEM detector.

The contrast in TEM imaging depends on different materials properties and the imaging conditions. Mass–thickness contrast is based on differences in elemental composition and in the thickness of the corresponding transmitting region. Diffraction contrast appears if the crystal planes are oriented such that they give rise to Bragg diffraction as described by (4.38) (Fig. 4.42). Analysis of the local chemistry of a sample is possible in TEM by means of EDX and *electron energy-loss spectroscopy* (EELS) [4.34] with a resolution of a few nanometers.

Local Chemical Analysis

Local chemical analysis is a mandatory tool to identify microstructural features such as grains, precipitates, particles, and corrosion products, or to record concentration profiles. For this purpose, spectroscopy of x-rays emitted as a result of electron bombardment can be performed in a SEM or TEM (*electron probe microanalysis*, EPMA) [4.35]. In most cases, *energy-dispersive x-ray spectroscopy* (EDX) is used with a silicon drift detector (SDD) or semiconductor (Si-Li) detector connected to a multichannel analyzer. The resulting x-ray spectrum (Fig. 4.43) provides information on the presence of chemical elements represented by element-characteristic x-ray energies. The quantitative composition can be calculated from the intensities of the peaks by taking various correction parameters into account [4.36]. The x-ray spectrum can

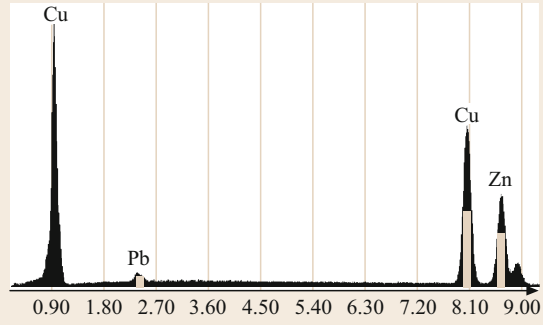

Fig. 4.43 Energy-dispersive x-ray spectrum (EDX) of brass: element-specific peaks and energy windows for element mapping

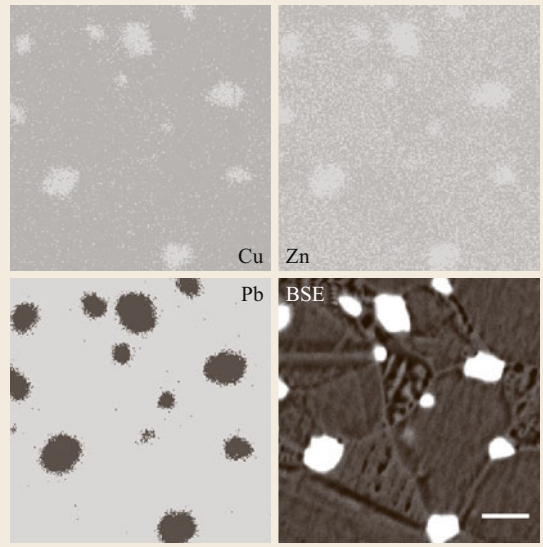

Fig. 4.44 EDX element map showing presence of Cu, Zn, and Pb as well as BSE image of the microstructure of brass

represent the average elemental composition of a larger scanned area (up to 1×1 mm) or of a spot as small as about 0.5 µm in diameter, which is the lateral resolution of EDX measurements. With a line scan, the intensity of an element-specific peak (energy window) is recorded and used to determine the concentration of this chemical element along a preselected line, across a grain border, for example. Extending this method to an area of interest enables so-called element mapping (Fig. 4.44).

Typically, EDX measurements in a SEM have a lateral and depth resolution of 0.5 µm for high-atomic-number elements, and up to 10 µm for low-atomic-number elements (graphite, polymers), and relative errors of 3–8%. Better resolution can be obtained if

the analysis is performed on thin specimens (≈ 100 nm thick) in a SEM or a TEM. Elements can be analyzed qualitatively starting with the atomic number of ^{5}B, whereas quantitative results can be obtained for elements starting from ^{11}Na. *Wavelength-dispersive x-ray spectroscopy* (WDX), using one or more crystal spectrometers attached to a SEM, allows the quantification of low-atomic-number elements (B, C, N, and O) and the analysis of trace elements. Because WDX cannot be used in a TEM, EELS is the alternative method of interest here.

Chemical Analysis of Thin Layers

Methods which are suitable for the chemical analysis of thin layers (in the nanometer thickness range), for measuring the concentration profile perpendicular to the surface within such layers, and for interface layers must possess a very small information depth. Layers of interest are, e.g., galvanic, sputtered or plasma-assisted coatings, corrosion layers, tribological reaction layers, and grain boundaries. The methods most widely used for the analysis of engineering materials are *scanning Auger electron spectroscopy* (SAM), *x-ray-exited photoelectron spectroscopy* (XPS)/electron spectroscopy for chemical analysis (ESCA), and *secondary-ion mass spectroscopy* (SIMS) [4.35]. Their lateral resolution ranges from a few nm (SAM, SIMS) to a few µm (XPS). Concentration–depth profiles with a resolution of a few nanometers can be obtained during spectroscopy by simultaneous sputtering of the specimen with accelerated ions (O^+, Ar^+, Ga^+, etc.). A method for depth profiling without local resolution is GDOES (Sect. 4.2.1).

Local Measurement of the Crystal Structure

Knowing the crystal structure locally in a microstructure, for example, of a single grain or a specific precipitate, is of interest for the following reasons:

1. In cases when EDX analysis cannot discriminate between chemically similar phases, determining the crystal structure may support phase identification.
2. Crystallographic orientation of single grains with respect to the specimen coordinates, for example, with respect to the rolling direction of sheet metal, can influence many properties significantly, such as the deformation behavior, corrosion, electrical conductivity, magnetic permeability, etc. of electrical steel.

The local crystal structure is obtained by electron diffraction with different resolutions in a TEM (< 1 nm) or SEM (> 20 nm) by applying Bragg's law (4.38). In a TEM, electron diffraction of a single grain gives rise to a point pattern (Fig. 4.45), from which the relevant crystal parameters (crystal structure, symmetry, and unit cell dimensions) can be deduced. It is noteworthy here that, when using TEM, only a few grains or particles can be investigated and the sample preparation may become a difficult and tedious task.

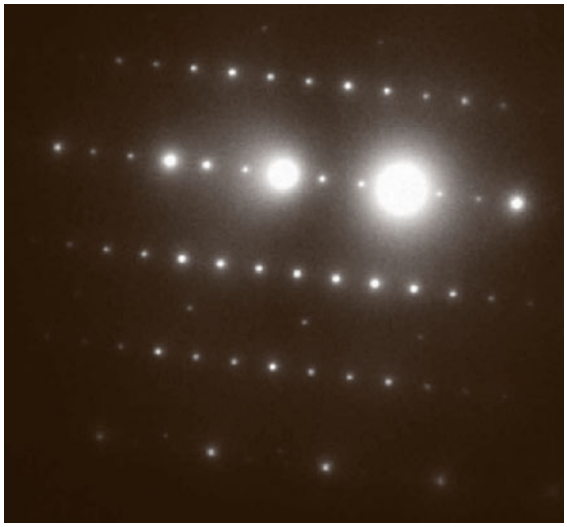

Fig. 4.45 Electron diffraction pattern of a Ni alloy obtained in a TEM at 200 kV; the *small spots* are superlattice peaks stemming from coherent and ordered precipitates embedded in a disordered fcc matrix

In an SEM, *electron backscatter diffraction* (EBSD) [4.37, 38] patterns can be recorded by using a combination of a phosphor screen and a digital camera fit to the specimen chamber. In the pattern (Fig. 4.46), each of the so-called Kikuchi bands represents a pair of lattice planes, with their width corresponding to the lattice plane spacing. The EBSD technique utilizes the knowledge of the crystal structure to visualize symmetry, and crystallographic orientation of a single grain by using commercial software. This method is also known as orientation imaging microscopy (OIM) [4.38]. Note, that the image quality (sharpness) deteriorates as the number of dislocations within a grain increases, in other words with the degree of plastic deformation. Since the information depth of EBSD is about 50 nm, the investigated surfaces have to be prepared very carefully by mechanical and occasionally electrochemical polishing, without disturbing the microstructure through the generation of dislocations due to plastic deformation [4.39, 40]. Milling the surface in a FIB or with a broad-beam ion miller is an elegant alternative preparation procedure.

For phase identification [4.41], the different crystal structures visualized by EBSD and the chemical composition simultaneously acquired by EDX analysis can

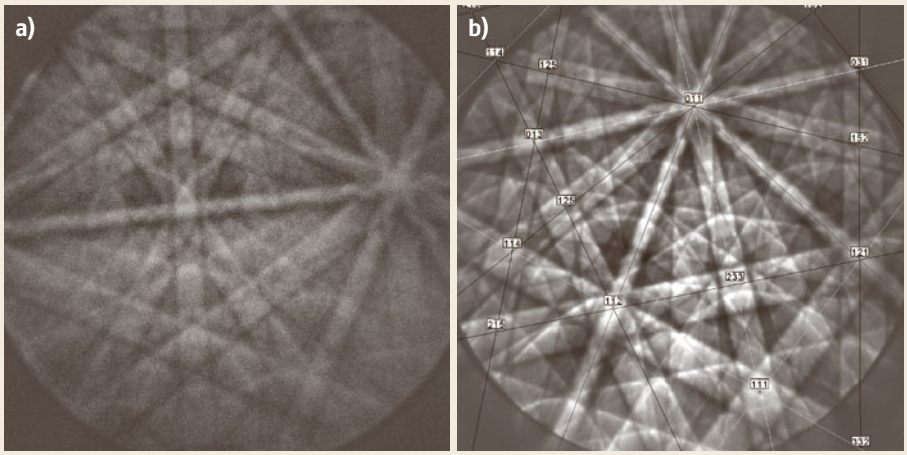

Fig. 4.46a,b Electron backscatter diffraction pattern (EBSD) of austenitic steel **(a)** and obtained from a grain in Ni with displayed zone axis directions **(b)**

be compared with data for known phases in a database such as the ICDD database (Sect. 4.2.2).

The crystallographic orientation, defined as the orientation of the coordinate system of a crystallite with respect to the coordinate system of the sample and represented by the Euler angles, can be calculated from the orientation of the diffraction pattern in an EBSD image. For engineering materials, the coordinate system of the sample is often defined by the rolling direction (RD), transversal direction (TD), and normal direction (ND). To obtain an orientation map, selected areas of the specimen (up to several hundred µm in edge length) are scanned with step sizes between 20 and 2000 nm, depending on the grain size, and the orientation at each measuring point is calculated [4.42]. The results are usually presented as an inverse pole figure, in which the orientation is color coded (Fig. 4.47). Specifically, in Fig. 4.47, the red-colored grains have an orientation in which the crystallographic direction [001] is parallel to the normal direction of the sample while the main axes of the cubic unit cell are parallel to RD, TD, and ND.

The different crystallographic orientations of neighboring grains can be used to generate an image of the microstructure. For this purpose, the difference in the crystallographic orientation between adjacent measuring points is used; for example, a difference of $> 15°$ can be chosen as a criterion for discriminating between high-angle grain boundaries. The result is a colored grain map (Fig. 4.48), from which a quantitative determination of grain sizes is possible.

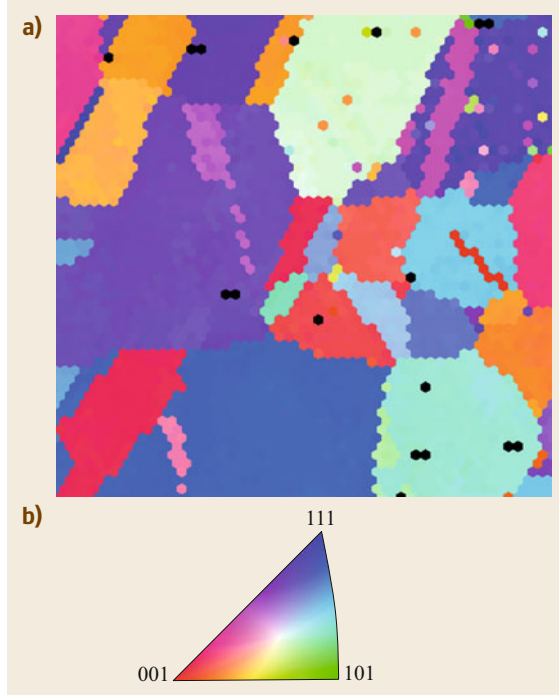

Fig. 4.47a,b Crystallographic orientation of grains in a polished section of pure Cu; inverse pole figure map **(a)** and corresponding legend **(b)**

Quantification of Microstructure/Quantitative Stereology

In many cases, a quantitative analysis of the microstructure is desired, e.g., to detect small differences between microstructures for quality control purposes, or to obtain numbers for modeling the material behavior. One example is the correlation of the grain size with the strength of a material, as described by the Hall–Petch equation (4.10) (Sect. 4.1.2).

Microstructure quantification can be performed by image comparison using standard charts, by manual measurement or counting, and with the help of digital image analysis software. Standards for microstructure

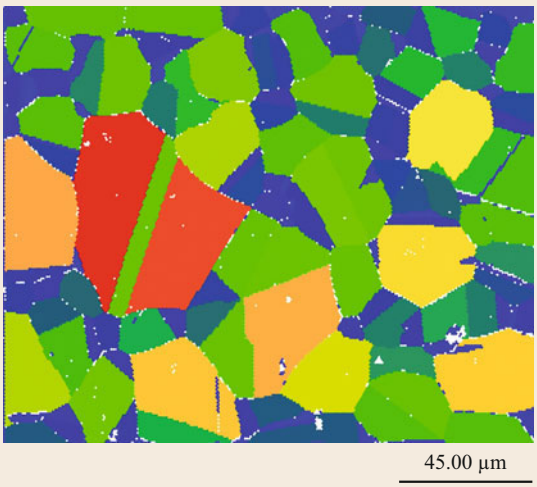

Fig. 4.48 Microstructure of an austenitic Cr-Ni steel based on EBSD measurements; different grains are defined as areas with misorientation > 15°

quantification describe the specimen preparation as well as the measuring procedure, the necessary equipment, and the form of the test report.

The study of the three-dimensional microstructure using images of two-dimensional sections through the structure is known as stereology [4.43, 44]. A basic stereological parameter [4.45, 46] is the volume fraction $V_V(\alpha)$ of a constituent (α), expressed as the ratio of the constituent volume $V(\alpha)$ and the testing volume V_t

$$V_V(\alpha) = \frac{V(\alpha)}{V_t} \,. \tag{4.40}$$

The volume fraction equals that fraction which can be obtained from the corresponding equilibrium phase diagram (Sect. 4.1.5, *Lever Arm Rule*), where the volume fraction has to be calculated from the weight fraction using the densities of the constituents. The volume fraction can be estimated using the fundamental stereological equation

$$V_V(\alpha) = A_A(\alpha) = L_L(\alpha) = P_P(\alpha) \tag{4.41}$$

from the areal fraction $A_A(\alpha)$ or line fraction $L_L(\alpha)$ determined by digital image analysis, by measuring the sum of the length of all the segments $L(\alpha)$ of the test lines L_t which lie within the grains of the constituent (α), or from the point fraction $P_P(\alpha)$. The latter is estimated by a manual point-counting procedure, in which a point grid is placed on the micrograph and the total number of points in the testing area P_t and the number of points hitting the constituent of interest $P(\alpha)$ are counted. This method has been standardized for steel [4.47] and duplex steel [4.48]. Rules for the use of automatic image analysis to determine the volume fraction of constituents are also described [4.49].

Another important stereological parameter is the surface density as an equivalent to the grain size (Sect. 4.1.2). It is calculated as the sum of the surfaces (boundaries) of all grains $S(\alpha)$ of a constituent (α) in a given test volume V_t

$$S_V(\alpha) = \frac{S(\alpha)}{V_t} \quad (\mathrm{m}^{-1}) \,. \tag{4.42}$$

$S_V(\alpha)$ is obtained by counting the number of intersections of test lines of total length L_t with grain boundaries P

$$S_V(\alpha) = \frac{2P}{L_t} = 2P_L \quad (\mathrm{m}^{-1}) \,. \tag{4.43}$$

Several parameters can be applied for the quantification of grains, for example, size, shape, orientation, and arrangement. A simple procedure for determining the average grain size is accomplished by comparing micrographs of the sample at a given magnification against a standard chart of grains, as standardized for graphite in gray cast iron [4.50] and for copper and its alloys [4.51], or by measuring the mean intercept length $\overline{L}_S$ (intercept method). The latter has been standardized for ferritic and austenitic steel [4.52, 53]. It is estimated by laying test lines of total length L_t over the micrograph and measuring the mean length of the segments $\overline{L}_S$ within the grains, or the number P of intersections of the test lines L_t with grain boundaries P_L in order to calculate $\overline{L}_S$ as

$$\overline{L}_S = \frac{L_t}{P} \,. \tag{4.44}$$

The surface density is then related to the mean intercept length by

$$S_V = \frac{2}{\overline{L}_S} = 2P_L \,. \tag{4.45}$$

A relatively simple and quick procedure to describe the grain size, particularly applied for ferritic and austenitic steel, is to use the grain size number G [4.53]. This is obtained by image comparison or by estimating the number of grains m in a unit area of 1 mm^2 of the specimen. In this procedure, a circle is drawn on the micrograph and the number of grains within the circle n_1 and those touching the perimeter n_2 are counted. With the microscopic magnification g and the circle radius r, the number of grains per mm^2 of the specimen surface can then be calculated as

$$m = \frac{\left(n_1 + \frac{n_2}{2}\right) g^2}{r^2 \pi} \,. \tag{4.46}$$

The grain size index G is calculated from [4.52]

$$m = 8 \times 2^G \,, \tag{4.47}$$

and is related to the mean intercept length $\overline{L}_S$ and the surface density S_V through

$$\begin{aligned} G &= 16.64 - 6.64 \log\left(\overline{L}_S\right) \\ &= 16.64 - 6.64 \log\left(2/S_V\right) \\ &= 16.64 - 6.64 \log\left(P_L\right) . \end{aligned} \tag{4.48}$$

The shape of single grains and particles can be estimated by image comparison or digital image analysis. With the latter method, geometric parameters for each particle such as the area A, perimeter P, and greatest and smallest extent d_{max} and d_{min} are measured. Shape factors are calculated by expressing the deviation from a circular shape (circular form factor $f_c = 4\pi A/P^2$) and the aspect ratio $f_a = d_{max}/d_{min}$. These form factors are needed to verify the results of heat treatment, where grains are rounded, or rolling and deep drawing processes, where grains may be elongated.

References

4.1 R.W. Cahn, P. Haasen, E.J. Kramer: Materials science and technology. In: *Glasses and Amorphous Materials*, Vol. 9, ed. by J. Zarzycki (Wiley-VCH, Weinheim 2005)

4.2 A. Inoue, T. Zhang, T. Masumoto: Production of amorphous cylinder and sheet of $La_{55}Al_{25}Ni_{20}$ alloy by a metallic mold casting method, Mater. Trans. **31**, 425–428 (1990)

4.3 A. Peker, W.L. Johnson: A highly processable metallic glass: $Zr_{41.2}Ti_{13.8}Cu_{12.5}Ni_{10.0}Be_{22.5}$, Appl. Phys. Lett. **63**, 2342 (1993)

4.4 A. Leonhard, L.Q. Xing, M. Heilmaier, A. Gebert, J. Eckert, L. Schultz: Effect of crystalline precipitations on the mechanical behavior of bulk glass forming Zr-based alloys, Nanostruct. Mater. **10**, 805–817 (1998)

4.5 A. Inoue: Stabilization of metallic supercooled liquid and bulk amorphous alloys, Acta Mater **48**, 279–306 (2000)

4.6 C. Kittel: *Introduction to Solid State Physics*, 8th edn. (Wiley, Chichester 2004)

4.7 R.W. Cahn, P. Haasen: *Physical Metallurgy*, 4th edn. (North Holland, Amsterdam 1996)

4.8 R. Tilley: *Crystals and Crystal Structures* (Wiley, Chichester 2006)

4.9 D.A. Porter, K.E. Easterling: *Phase Transformations in Metals and Alloys*, 2nd edn. (Chapman Hall, London 1997)

4.10 D.B. Williams, C.B. Carter: *Transmission Electron Microscopy* (Plenum, New York 1996)

4.11 G.E. Dieter: *Mechanical Metallurgy, SI Metric Edition* (McGraw-Hill, London 1988)

4.12 E.O. Hall: The deformation and aging of mild steel: III Discussion of results, Proc. R. Soc. B **64**, 747–752 (1951)

4.13 N.J. Petch: The cleavage strength of polycrystals, J. Iron Steel Inst. **174**, 25 (1953)

4.14 J. Gurland: Correlation between yield strength and microstructure of some carbon steels. In: *Stereology and Quantitative Metallography*, ed. by G. Pellissier, S. Purdy (ASTM International, West Conshohocken 1972) pp. 108–118

4.15 B. Reppich: Particle strengthening. In: *Plastic Deformation and Fracture of Materials*, Materials Science and Technology, Vol. 6, ed. by R.W. Cahn, P. Haasen, E.J. Kramer (Wiley-VCH, Weinheim 1993) pp. 312–357

4.16 R.J. Silbey, R.A. Alberty, M.G. Bawendi: *Physical Chemistry*, 4th edn. (Wiley, Hoboken 2005)

4.17 H.E. Exner, M. Rettenmayr, C. Müller: Komplexe Grenzflächengeometrien bei Phasenumwandlungen, Prakt. Metallogr. **41**, 443–458 (2004)

4.18 V.K. Pecharsky, P. Zavalij: *Fundamentals of Powder Diffraction and Structural Characterization of Materials* (Kluwer, Dordrecht 2003)

4.19 D.J. Dyson: *X-ray and Electron Diffraction Studies in Materials Science* (Maney, London 2004)

4.20 F.H. Chung, D.K. Smith: *Industrial Applications of X-ray Diffraction* (Dekker, New York 1999)

4.21 M. Howes, T. Inoue, G.E. Totten: *Handbook of Residual Stress and Deformation of Steel* (ASM International, Materials Park 2002)

4.22 V. Randle, O. Engler: *Introduction to Texture Analysis* (Gordon Breach, Amsterdam 2000)

4.23 H.J. Bunge: *Texture Analysis in Materials Science, Mathematical Methods* (Butterworth-Heinemann, London 1982)

4.24 G.F. Vander Voort: *ASM Handbook: Metallography and Microstructures* (ASM International, Materials Park 2004)

4.25 B. Bousfield: *Surface Preparation and Microscopy of Materials* (Wiley, Chichester 1992)

4.26 G. Petzow, V. Carle: *Metallographic Etching* (ASM International, Materials Park 1999)

4.27 H.G. Michler: *Electron Microscopy of Polymers* (Springer, Berlin, Heidelberg 2008)

4.28 L. Reimer: *Scanning Electron Microscopy. Physics of Image Formation and Microanalysis* (Springer, Berlin 1998)

4.29 J.I. Goldstein, D.E. Newbury, P. Echlin, D.C. Joy, C. Fiori, E. Lifshin: *Scanning Electron Microscopy and X-ray Microanalysis* (Plenum, New York 1992)

4.30 W. Hauffe: Production of microstructures by ion beam sputtering. In: *Sputtering by Particle Bombardment III*, Topics in Applied Physics, Vol. 64, ed. by R. Behrisch, K. Wittmaack (Springer, Berlin, Heidelberg 1991) pp. 305–338

4.31 L.A. Giannuzzi, F.A. Stevie: *Introduction to Focused Ion Beams* (Springer, New York 2004)

4.32 B.W. Kempshall, S.M. Schwarz, B.I. Prenitzer, L.A. Giannuzzi, R.B. Irwin, F.A. Stevie: Ion channeling effects on the focused ion beam milling of Cu, J. Vac. Sci. Technol. B **19**, 749–754 (2001)

4.33 L. Reimer: *Transmission Electron Microscopy. Physics of Image Formation and Microanalysis* (Springer, Berlin 2006)

4.34 C.C. Ahn, M.M. Disko, B. Fultz: *Transmission Electron Energy Loss Spectrometry in Materials Science and the EELS Atlas* (Wiley-VCH, Weinheim 2004)

4.35 J.P. Eberhart: *Structural and Chemical Analysis of Materials* (Wiley, Chichester 1991)

4.36 V.D. Scott, G. Love, S.J.B. Reed: *Quantitative Electron Probe Microanalysis* (Ellis Horwood, New York 1995)

4.37 A.J. Schwartz, M. Kumar, B.L. Adams: *Electron Backscatter Diffraction in Materials Science* (Kluwer, New York 2000)

4.38 D.J. Dingley, K.Z. Baba-Kishi, V. Randle: *Atlas of Backscattering Kikuchi Diffraction Patterns* (IOP, Bristol 1995)

4.39 D. Katrakova, F. Mücklich: Specimen preparation for electron backscatter diffraction. Part I: Metals, Prakt. Metallogr. **38**, 547–565 (2001)

4.40 D. Katrakova, F. Mücklich: Specimen preparation for electron backscatter diffraction. Part II: Ceramics, Prakt. Metallogr. **39**, 644–662 (2002)

4.41 R.P. Goehner, J.R. Michael: Phase identification in a scanning electron microscope using backscattered electron Kikuchi patterns, J. Res. Natl. Inst. Stand. Technol. **101**, 301–308 (1996)

4.42 R.A. Schwarzer, A. Huot: The study of microstructure on a mesoscale by ACOM, Cryst. Res. Technol. **35**, 851–862 (2000)

4.43 E.E. Underwood: *Quantitative Stereology* (Addison-Wesley, Reading 1970)

4.44 J. Ohser, F. Mücklich: *Statistical Analysis of Microstructures in Materials Science* (Wiley, Chichester 2000)

4.45 H.E. Exner: Quantitative description of microstructures by image analysis. In: *Characterization of Materials (Part II)*, Materials Science and Technology, Vol. 2B, ed. by R.W. Cahn, P. Haasen, E.J. Kramer (VCH, Weinheim 1994) pp. 281–350

4.46 E.E. Underwood: Quantitative metallography. In: *Metallography and Microstructures*, 9th edn., Metals Handbook, Vol. 9, ed. by K. Mills (ASM, Materials Park 1985) pp. 123–134

4.47 ISO: *ISO 9042:1988: Steel – Manual Point Counting Method for Statistically Estimating the Volume Fraction of a Constituent with a Point Grid* (ISO, Geneva 1988)

4.48 ISO: *ISO 14250:2000 Steel – Metallographic Characterization of Duplex Grain Size and Distributions* (ISO, Geneva 2000)

4.49 ASTM: *ASTM E1245-03: Standard Practice for Determining the Inclusion or Second-Phase Constituent Content of Metals by Automatic Image Analysis* (ASTM International, West Conshohocken 2003)

4.50 ISO: *ISO 945:1975: Cast Iron – Designation of Microstructure of Graphite* (ISO, Geneva 1975)

4.51 ISO: *ISO 2624:1990: Copper and Copper Alloys – Estimation of Average Grain Size* (ISO, Geneva 1990)

4.52 ASTM: *ASTM E112-96(2004): Standard Test Methods for Determining Average Grain Size* (ASTM International, West Conshohocken 2004)

4.53 ISO: *ISO 643-2003: Steels – Micrographic Determination of the Apparent Grain Size* (ISO, Geneva 2003)

Jens Freudenberger

Department for Metal Physics
Leibniz-Institute for Solid State and Materials Research Dresden
Dresden, Germany
j.freudenberger@ifw-dresden.de

Jens Freudenberger is Head of the Department for Metal Physics at the Leibniz-Institute for Solid State and Materials Research Dresden and Professor of Physics of metallurgy of non-ferrous metals at the University of Mining and Technology Freiberg. He graduated in Physics from the Johann Wolfgang Goethe University Frankfurt/Main and has a doctoral degree in Physics from the University of Technology Dresden, where he earned his Habilitation in Materials Science. His research is dedicated to the synthesis, processing and characterization of metals with a strong focus on their plasticity.

Martin Heilmaier

Institute for Applied Materials (IAM)
Karlsruhe Institute of Technology (KIT)
Karlsruhe, Germany
martin.heilmaier@kit.edu

Martin Heilmaier graduated in materials science from the University of Erlangen-Nuremberg. From 2002 he was Professor for Materials Testing at Otto-von-Guericke University. Since November 2011 he holds the chair for Materials Science & Technology at Karlsruhe Institute ofTechnology. His research is dedicated to the synthesis and properties of structural materials such as refractory metal silicide alloys and intermetallic alloys for high-temperature applications.

Ulrich Wendt

Freelance Materials Science Consultant
c/o Otto-von-Guericke University,
Department of Materials and Joining Technology
Magdeburg, Germany
wendt@ovgu.de

Professor Ulrich Wendt studied chemistry and earned a diploma degree with a thesis on organic synthesis, a doctoral degree RNDr on heterogeneous catalysis, and a habil. degree on polymer melt crystallization. For more than 30 years he headed the Microscopy and Stereology Laboratory at the Department of Materials and Joining Technology, University Magdeburg. He lectured on microscopic and spectroscopic characterization, image analysis, topometry, and failure analysis of materials. He is now a freelance Materials Science consultant.

5. Mechanical Properties

Vivek Srivastava, Martin Heilmaier

This chapter is structured into two main parts. Section 5.1 provides an overview of the most common methods for mechanical testing of materials. In this section, the different available and standardized methods are further subdivided into quasistatic and dynamic testing methods. The former include, e.g., tensile and hardness testing, while the latter focus on impact and cyclic testing, including linear elastic fracture mechanics. Section 5.2 introduces the most common electrical (Sect. 5.2.1) and thermal (Sect. 5.2.2) physical properties for all material classes relevant for mechanical engineering applications.

5.1 **Mechanical Properties** 165
5.1.1 Framework 165
5.1.2 Quasistatic Mechanical Properties 165
5.1.3 Dynamic Mechanical Properties 174
5.2 **Physical Properties** 178
5.2.1 Electrical Properties 178
5.2.2 Thermal Properties 180
References 182

5.1 Mechanical Properties

5.1.1 Framework

Measurements regarding elastic properties, fracture toughness, fatigue, plastic flow, creep, etc. all belong to the framework of *mechanical properties*. Engineers and scientists working in fields related to engineering materials require a fundamental understanding of mechanical properties. Engineers are primarily concerned with the *strength* of a material, which is a measure of the external force required to overcome the internal forces of attraction between its fundamental building blocks. In most engineering applications, only very small deformation of a component under a given loading condition is tolerable, and the strength often governs the choice of an acceptable material. Meanwhile, for a production engineer, the ease of inducing permanent deformation at the expense of as little energy as possible (i.e., *malleability* and *ductility*) is the critical mechanical property for a material under consideration. Given the importance of mechanical properties, it is essential to have a range of tests to *quantify* these mechanical properties. Additionally, standardized and inexpensive tests are needed for *quality assurance*. Scientists and alloy designers routinely use mechanical tests to assess the *performance* of a new material as compared with available materials.

5.1.2 Quasistatic Mechanical Properties

Tensile Testing

In this section, we address the response of a material to the application of an external applied static (or quasistatic) force. In its simplest form, the basic description of a material is obtained by a *tension* (or pull) test. Standard procedures for sample preparation and conducting such tests are described in ASTM (American Society for Testing of Materials) standard E8M-16ae1. Accordingly, the test specimen may be in plate, sheet, round, wire, or pipe form (Fig. 5.1) but must conform to certain guidelines in terms of its dimensions. Different gripping mechanisms, such as wedge grips, threads, pins, or shoulders, may be considered during specimen design. It is important to emphasize that, during specimen preparation, special care must be directed towards ensuring that the reduced section of the sample is free of defects, both microstructural and due to machining, and that the specimen is representative of the bulk material.

A typical tensile testing machine (Fig. 5.2) comprises a stiff frame, a specimen gripping device, a force measuring device (or load cells), an elongation measuring device (extensometer), and a data-recording device (X–Y plotter or computer). After careful measurement

K.-H. Grote, H. Hefazi (Eds.), *Springer Handbook of Mechanical Engineering*, Springer Handbooks,
https://doi.org/10.1007/978-3-030-47035-7_5

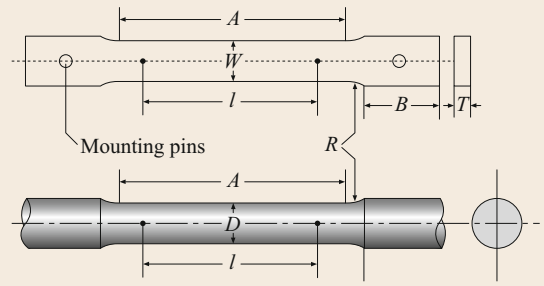

Fig. 5.1 Schematics of flat and cylindrical tensile test samples with critical sample dimensions (after [5.1])

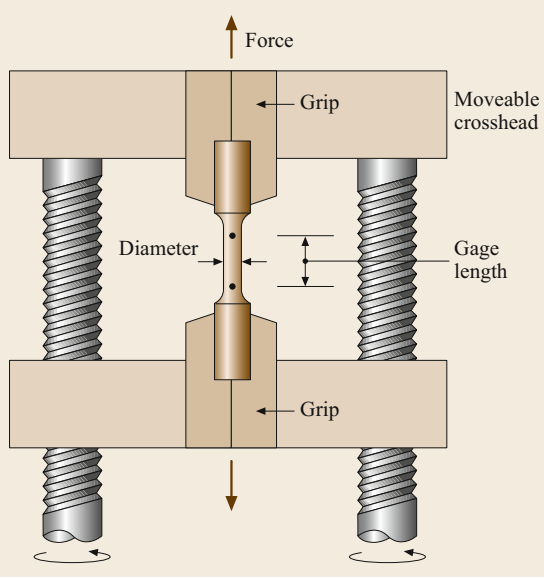

Fig. 5.2 Schematic representation of the components of a tensile testing machine (after [5.2])

of the relevant specimen dimensions, a tensile test may be run at a constant displacement, stress or strain rate. The load required to produce a given elongation is recorded as the specimen is pulled and is then plotted on a load–elongation chart. To obtain a more fundamental description of the material properties, it is essential to normalize the load–elongation data for the used specimen geometry. To achieve this, the load and elongation are converted to engineering stress and engineering strain, respectively.

The engineering stress (σ) is defined as

$$\sigma = \frac{P}{A_0}\,, \tag{5.1}$$

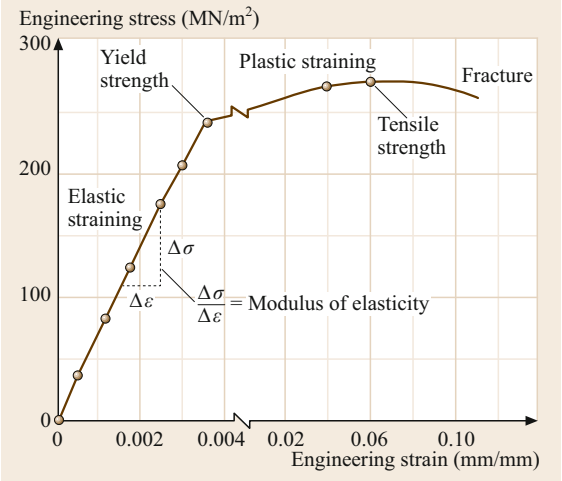

Fig. 5.3 A typical engineering stress–strain curve for a ductile material showing key mechanical properties (after [5.2])

where P is the applied load in MN and A_0 is the original cross-sectional area of the test specimen in square meter. The engineering strain (ε) is defined as

$$\varepsilon = \frac{l - l_0}{l_0} = \frac{\Delta l}{l_0}\,, \tag{5.2}$$

where l and l_0 are the gage length (see Fig. 5.1 for definition) under load and the original gage length, respectively.

Figure 5.3 shows a schematic engineering stress–strain diagram obtained from a tension test. The diagram is divided into two distinct regions:

1. Exclusively elastic deformation, i.e., linear and fully recoverable upon removal of load
2. (Elastic and) plastic deformation, where the latter is the nonlinear and nonrecoverable portion of the total deformation.

From this curve, certain key material properties can be evaluated, as described below:

- The *Young's modulus* E is the ratio of the axial stress to the corresponding strain in the elastic region. In some materials (typically polymers), the elastic region of the curve is not perfectly linear and a chord method is applied to estimate the elastic modulus (Fig. 5.4).
- The *yield strength* σ_y is the stress at which it is considered that plastic elongation of the material has commenced. This stress may be specified according to one of the following definitions:

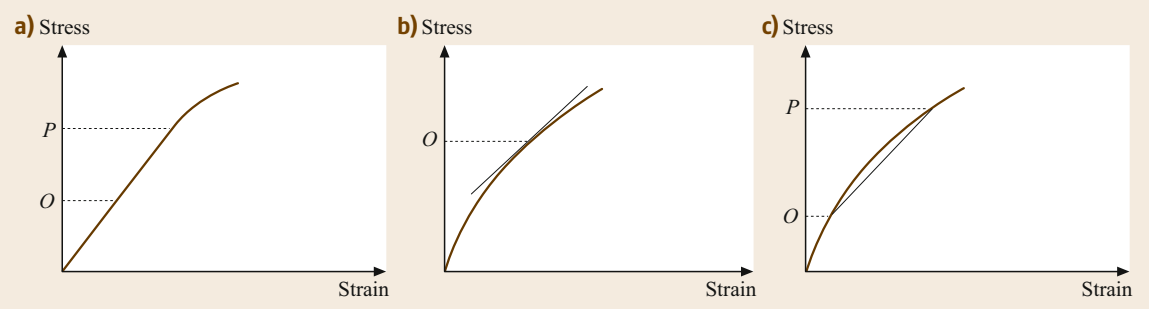

Fig. 5.4a–c Different methods to calculate the Young's modulus: **(a)** from the slope of the curve between *O* and *P* below the proportional limit, **(b)** from the tangent at a given stress *O*, and **(c)** from the slope of the chord between the stress *O* and *P* (after [5.3])

  - A specified deviation from a linear stress–strain relationship, i.e., the proof stress
  - A specified total extension attained
  - The maximum and minimum engineering stresses measured during discontinuous yielding, i.e., the upper and lower yield point, respectively (Fig. 5.5).
- The yield stress of a material may be engineered by several mechanisms including altering the grain size or adding alloying elements and/or second phases.
- The *ultimate tensile strength (UTS)*: is the maximum stress recorded during the tensile test. After this stress level has been reached, the specimen starts to show localized deformation called *necking*. Beyond this point, the engineering stress is seen to fall due to the fact that the engineering stress is defined according to the original specimen dimensions. However, the true stress ($\sigma = P/A$, where A is the actual cross-sectional area) continues to rise until fracture.
- The *ductility/elongation* is the ability of a material to deform before fracture under tensile load. Ductility, using this test method, is frequently quantified as the percentage elongation at failure, i.e., $\varepsilon_{\text{fracture}}$ ($\times 100$), where $\varepsilon_{\text{fracture}}$ is the plastic strain at the point of fracture.
- The *resilience and toughness* is the ability of a material to absorb energy when deformed elastically/plastically. It is defined as the area under the stress–strain curve in the elastic and plastic region, respectively.

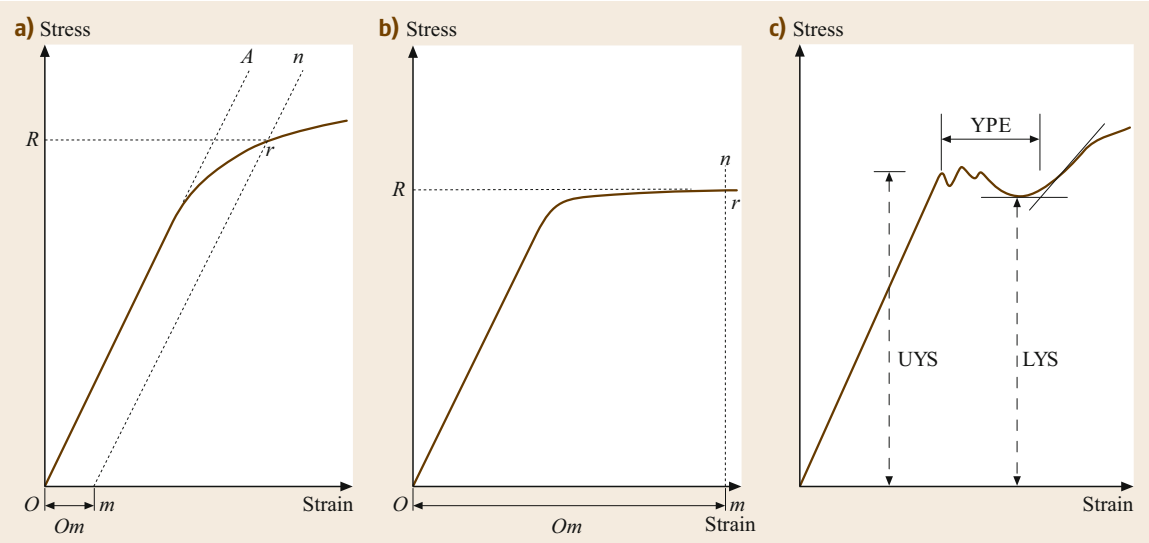

Fig. 5.5a–c Calculation of the yield stress according to **(a)** a prespecified plastic offset (*Om* = specified offset), **(b)** a prespecified total strain (*Om* = specified extension under load), **(c)** the upper and lower yield point (upper yield stress (UYS), lower yield stress (LYS), yield point elongation (YPE)) (after [5.3])

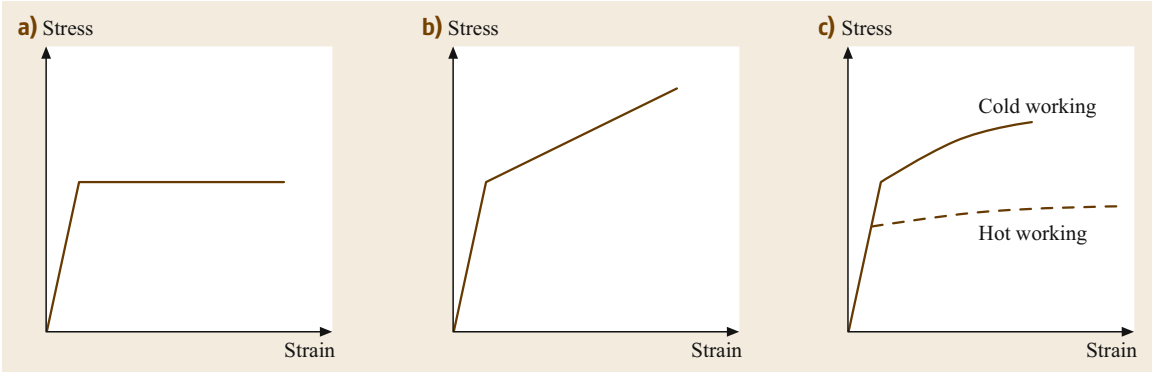

Fig. 5.6a–c Schematic representation of strain hardening in ductile metals: **(a)** elastic–ideal plastic, **(b)** elastic–plastic, and **(c)** flow curve during cold working showing strain hardening and hot working without significant strain hardening (after [5.4])

To differentiate between the elastic and plastic regions of the stress–strain curve, it is appropriate to look at the origin of strain. During elastic deformation, it is the stretching of interatomic bonds that leads to the observed macroscopic strain, which is (to a good approximation) linear due to the nature of the interatomic forces. On the other hand, the fundamental mechanism of plastic deformation is distortion and re-formation of atomic bonds. During this process, the total volume of the material is however conserved. During plastic deformation of crystalline solids (note that this does not apply for glassy materials and most polymers), *dislocations* within the material become operative and *slip* due to the shear stresses acting on them. For an ideal plastic material, the stress required for dislocations to continue slipping is a material constant and does not depend on the prior strain (Fig. 5.6a). However, in real materials, as the deformation proceeds, more dislocations are generated within the material and an additional driving force/stress is required for slip to proceed. This phenomenon is called *strain hardening* and is beneficially exploited during *cold working* to raise the yield strength of the resultant material. Strain hardening may be overcome by *hot working*, since dislocations start to become annihilated at higher temperatures ($T > 0.5T_{\mathrm{m}}$, where T is the hot working temperature and T_m is the absolute melting temperature in kelvin; Fig. 5.6). Furthermore, mechanical properties such as the elastic modulus and tensile strength are strongly temperature dependent and decrease with increasing temperature. Ductility though is generally found to increase with increasing temperature.

The plastic region of the true stress–true strain curve is also referred to as the *flow curve*, as it is the locus of stress required to cause the metal to *flow* plastically to any given strain. The expression most commonly used to describe the flow curve empirically takes the form

$$\sigma = K\varepsilon^n \,, \tag{5.3}$$

where K is the stress at $\varepsilon = 1$ and n is the strain hardening exponent, viz. the slope of a log–log plot of the flow curve. It can be shown mathematically that $n = \varepsilon_{\mathrm{fracture}}$, thus it is a measure of the ductility of the material.

The appearance of the surface of the specimen after fracture provides clues to the mode of fracture. Brittle fracture is accompanied by a flat (and *grainy, often shiny*) surface (Fig. 5.7a), while ductile fracture after considerable plastic deformation results in a *cup-and-cone* fracture surface (Fig. 5.7b).

Compression Testing

Mechanical properties such as the yield strength, yield point, elastic modulus, and stress–strain curve may also be determined from compressive tests. This test procedure offers the possibility to test brittle and nonductile metals that fracture at low strains and avoids the complications arising out of necking. On the other hand, for certain metallic materials, *buckling* and *barreling* complicate such testing (Fig. 5.8) but can be minimized by designing the samples as per specifications and using proper lubricants. Solid round/rectangular cylindrical samples (aspect ratio 0.8–10) may be used. Surface flatness and parallelism are important considerations during sample machining. After marking the gauge length and measuring the specimen dimensions, the specimen is placed in the test fixture and should be aligned carefully to ensure concentric loading. The specimen is then subjected to an increasing axial compressive load; both load and strain may be monitored either continuously or in finite increments. Relevant mechanical properties may be determined as

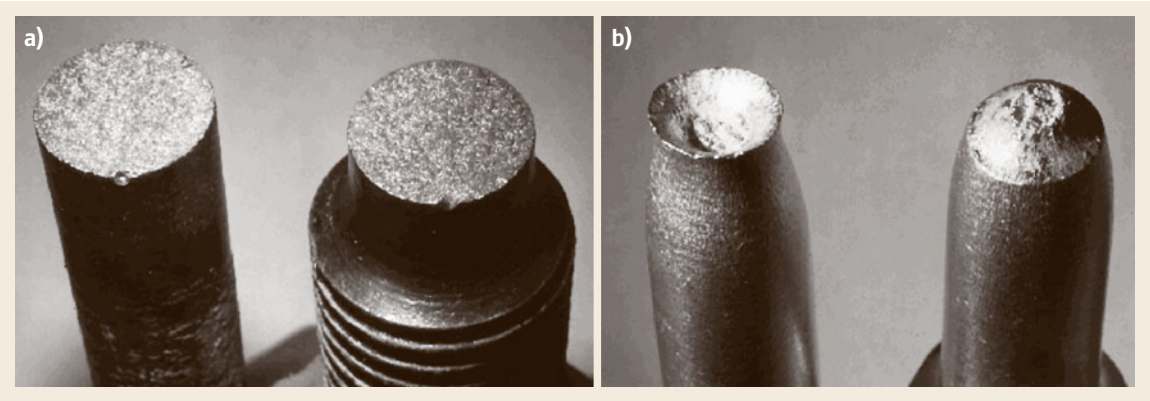

Fig. 5.7a,b Appearance of fracture surfaces after tensile testing. **(a)** Brittle fracture leads to a relatively flat surface, whereas **(b)** ductile fracture shows considerable deformation prior to fracture, leading to a classical cup-and-cone arrangement

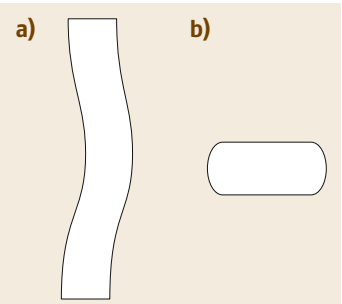

Fig. 5.8a,b Schematic representation of **(a)** buckling and **(b)** barreling during compressive testing (after [5.3])

described in Sect. 5.1.1. Compression testing is usually easier to conduct than tension testing and is used more commonly at elevated temperatures in plasticity or formability studies, since it simulates compressive stress as is expected under rolling, forging, or extrusion operations.

Hardness

In general, the hardness of a material refers to its resistance to plastic deformation, although it is a loosely defined term. However, it is an easily measurable quantity and frequently employed in quality assurance and inspection. Standard hardness test procedures involve slowly applying an indentation to the surface of the material and measuring the relevant dimensions of the depression. Depending on the shape of the indenter and method of calculation, the following hardness tests are commonly employed:

Brinell hardness: An indenter made of a hardened steel or tungsten carbide *ball* with diameter D (1−10 mm) is forced into the surface of a test piece, and the diameter of the indentation, d, left in the surface after removal of the test force F (100−3000 kgf) is measured. The Brinell hardness (BHS or BHW) is then obtained by dividing the test force by the curved surface area of the indentation as

$$\text{BHS} \quad \text{or} \quad \text{HBW} = \frac{2F}{\pi D\left(D - \sqrt{D^2 - d^2}\right)} \,. \tag{5.4}$$

Later, Meyer suggested a more rational definition of hardness based on the projected area, but it did not gain acceptance despite its more fundamental nature. The Meyer hardness is given as $4F/\pi d^2$ in kgf/mm^2.

The *Vickers hardness* test uses a *square-based diamond pyramid* as the indenter with the included angle between the opposite faces being 136°. Due to the shape of the indenter, the Vickers hardness number (VHN) or Vickers pyramid hardness (VPH) is also frequently referred to as the diamond-pyramid hardness number (DPH) and is defined as the load divided by the surface areas of the indentation according to the equation

$$\text{DPH} = \frac{2F\sin(\theta/2)}{L^2} = \frac{1.854F}{L^2} \,, \tag{5.5}$$

where L is the average length of the diameters in mm and θ is the angle between opposite faces of the diamond (= 136°). The advantage of the Vickers hardness is that it provides a continuous scale of hardness, from very soft to very hard materials. However, the VHN is fairly sensitive to surface finish and human error.

The *Rockwell hardness* test is the most widely used in industry due to its speed, freedom from human error, and ability to distinguish small hardness differences in hardened steels. This test utilizes the depth of indentation, under constant load, as a measure of hardness. A minor load of 10 kg is first applied to seat the specimen, followed by the major load for the required dwell time. The depth of indentation is automatically recorded

electronically or using a dial indicator in terms of an arbitrary scale without units. The Rockwell hardness indenter is either a 120° diamond *spheroconical* or steel *ball* $\frac{1}{16} - \frac{1}{2}$ inches in diameter. Major loads of 60, 100, and 150 kg are used. Different combinations of load and indenter are used for materials with different hardnesses, and it is necessary to specify the combination employed when reporting Rockwell hardness values. This is done by prefixing the hardness number with a letter that indicates the particular combination. Hardened stress is tested on the *C* scale using the diamond indenter and a major load of 150 kg.

Hardness testing is a very useful and reproducible method to measure and compare the mechanical strength of a material, provided that sufficient precautions are taken during testing. Hardness tests are carried out on the surface of the specimen, so it is very important that the surface be flat, free of defects, and representative of the bulk material. Additionally, there are empirical correlations available to estimate the tensile strength from the hardness value and to convert a result from one type of hardness test to that of a different type. However, it is important to verify these correlations for the specific class of material under consideration, although some standard conversion tables are available for commercial carbon and alloy steels and aluminum alloys. Micro- and nanohardness testing procedures are available for measuring hardness over smaller areas, while hot hardness testers are used to measure hardness at elevated temperatures.

Bend or Flexure Testing

Bend tests are used primarily to obtain values of proof stress and modulus of elasticity in bending (E_b) as well as the ductility of relatively flexible materials such as polymers and their composites. Bend testing also provides a convenient method for characterizing the strength of the miniature components and specimens that are typical of those found in microelectronics applications.

There are two test types (Fig. 5.9): three-point flex and four-point flex. In a three-point test, the area of uniform stress is quite small and concentrated under the central loading point. In a four-point test, the area of uniform stress extends between the inner span loading points (typically half the outer span length).

A flexure test produces tensile stress on the convex side of the specimen but compressive stress on the concave side, resulting in an area of shear stress along the midline. To ensure that the primary failure comes from tensile or compressive stress, the shear stress must be minimized; This is done by controlling the span (S) to depth (h) ratio, the length of the outer span divided by the height (depth) of the specimen. For most materials,

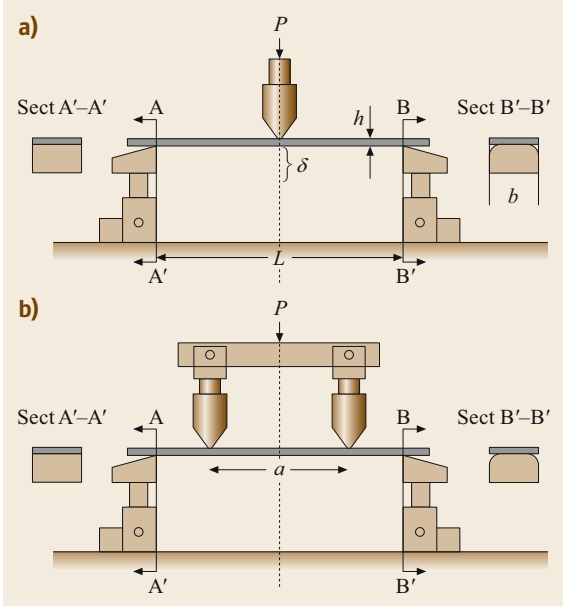

Fig. 5.9a,b Schematic representation of **(a)** three- and **(b)** four-point bend tests (after [5.3])

$S/h = 16$ is acceptable. However, some materials require $S/h = 32-64$ to keep the shear stress low enough. Usually, a specimen with a rectangular cross-section is used. E_b varies as the third power of the beam thickness, thus the uniformity of the thickness is of paramount importance.

The test apparatus consists of two adjustable supports and means for measuring the deflection and applying the load. The supports are generally knife-edge or convex. The load applicator is a rounded knife-edge with an included angle of 60°, applied either at the midspan (for three-point testing) or symmetrically spaced from the supports (for four-point testing). The elastic deflection δ is measured at the midspan, as shown in Fig. 5.9. The stress and E_b are related to the applied load and deflection as

$$\sigma_p = \frac{3PL}{2bh^2}\,; \qquad E_b = \frac{PL^3}{4bh^3\delta}$$

for three-point bend testing (5.6)

and

$$\sigma_p = \frac{3Pa}{bh^2}\,; \qquad E_b = \frac{Pa\left(3L^2 - 4a^2\right)}{4bh^3\delta}$$

for four-point bend testing. (5.7)

Torsion Testing

Torsion tests have not met with the same wide acceptance and use as tensile testing. However, in many

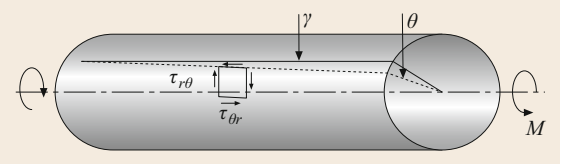

Fig. 5.10 Idealized schematic of a tubular pipe under torsion showing the shear stress and strain (after [5.4])

engineering applications and theoretical studies, they are of considerable importance. Torsion tests are used to determine properties such as the modulus of elasticity in shear (G), torsional yield strength, and modulus of rupture. During a torsion test, measurements are made of the twisting moment, M_T and the angle of twist θ. From linear elastic mechanics (Fig. 5.10), the shear stress τ and shear strain γ can then be calculated according to the relation

$$\tau_{max} = G\gamma = \frac{M_T r}{J}, \qquad \gamma = \frac{r\theta}{L}, \tag{5.8}$$

where r and L are the radius and length of the test specimen, respectively, and J is the polar moment of inertia of the area with respect to the axis of the specimen. For a solid cylindrical specimen, $J = \pi r^4/2$. Because of the stress gradient across the diameter of a solid bar, it is preferable to use a tubular specimen for the determination of the shearing yield strength and elastic modulus. However, care must to be taken to avoid buckling in this case.

Beyond the torsional yield strength, the shear stress is no longer a linear function of distance from the axis and the analysis becomes slightly more complicated; in this case, the maximum shear at the surface is given as

$$\tau_{max} = \frac{1}{2\pi r^3}\left(\theta\frac{dM_T}{d\theta} + 3M_T\right). \tag{5.9}$$

It is possible to convert the shear stress–strain curve into a tensile stress–strain curve using the following relations

$$\sigma = \sqrt{3}\tau_{max}, \qquad \varepsilon = \frac{\gamma}{\sqrt{3}}. \tag{5.10}$$

A major advantage of torsion tests over tensile tests is that the fracture is delayed and it is possible to extend the flow curve to larger strains. This is of significance for the study of the plastic flow behavior of ductile materials. Torsion tests are regarded as complicated due to the considerable labor involved in converting torque–twist data to stress–strain data. However, the computational resources available today considerably ease this restraint. Torsion testing provides a more fundamental description of the plasticity of metals and avoids complications such as the necking and barreling associated with tension and compression tests.

As mentioned above, the specimen design and fabrication are rather important for obtaining reliable mechanical properties from torsion tests. Specimens in the form of solid cylinders should be straight and of uniform diameter, with a length equal to the gauge length plus two to four diameters. In the case of tubes, the total specimen length should be the gauge length plus at least four outer diameters. The prescribed ratio of the gauge length to diameter is at least four to ten. For tubular samples, the ratio of the outer diameter to the wall thickness should lie between eight and ten. During testing, the twist angle is generally applied by mechanical, optical, or electrical means using rings fastened to the sample. A torsiometer, fastened to the sample and the base of the machine, is used to measure the angle of twist in radians in both the elastic and plastic regions.

Creep Testing

A metal subjected to a constant load at elevated temperature ($> 0.5T_m$, where T_m is the absolute melting temperature) undergoes time-dependent (anelastic) deformation called creep. At these temperatures, the mobility of vacancies increases significantly according to Fick's laws and diffusion-controlled processes have a significant effect on the mechanical properties (Chap. 4). The rate of dislocation climb, the concentration and mobility of vacancies, activation of new slip systems, and grain-boundary sliding are all temperature and diffusion controlled and affect the mechanical behavior of materials at high temperatures. In addition, corrosion or oxidation mechanisms, which also are diffusion rate dependent, will have an effect on the lifetime of materials at high temperatures.

Conceptually, a creep test is rather simple: a force is applied to a test specimen exposed to a relatively high temperature, and the dimensional change over time is measured. If a creep test is continued to its conclusion (that is, the fracture of the test specimen), often without precise measurement of the dimensional change, then it is called a stress rupture test. Although conceptually quite simple, creep tests are more complicated in practice. Temperature control is critical (the absolute temperature must be met within a few degrees and the fluctuation must be kept to $< 0.5\,^{\circ}C$). The resolution and stability of the extensometer are important concerns (for low-creep materials, the displacement resolution must be on the order of 0.5 μm). Environmental effects can complicate creep tests by causing premature failure unrelated to elongation and thus must either mimic the actual service conditions or be controlled to limit the failure to creep mechanisms. The uniformity of the applied stress is critical if creep tests are to be

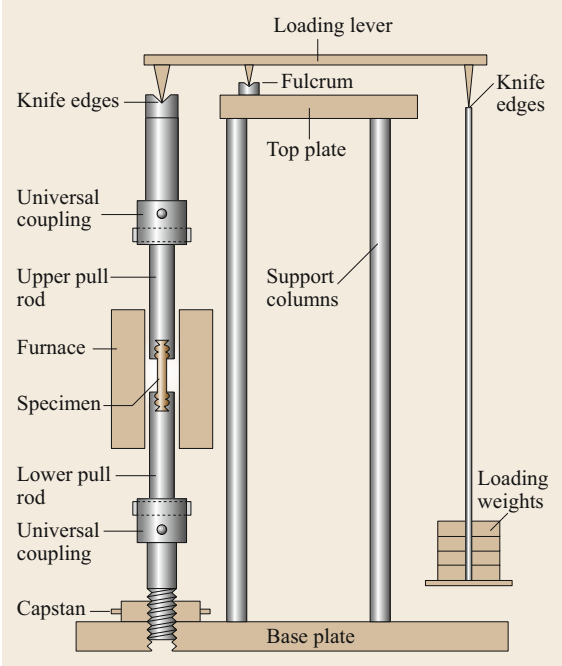

Fig. 5.11 Schematic of a constant-load creep testing setup

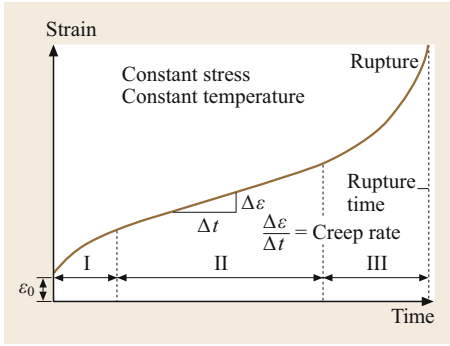

Fig. 5.12 An idealized creep curve showing the three stages during creep (ε_0 = elastic strain) (after [5.2])

interpreted properly. Figure 5.11 shows a typical creep testing setup.

The curve in Fig. 5.12 illustrates the idealized shape of a creep (strain–time) curve. The slope of this curve ($\Delta\varepsilon/\Delta t$ or $\dot{\varepsilon}$) is referred to as the creep rate. The initial strain $\varepsilon_i = \sigma_i/E$ is simply the elastic response to the applied load. The strain itself is usually calculated as the engineering strain, $\varepsilon = \Delta l/l_0$, see (5.2). The primary region (I) is characterized by transient creep, with a decreasing creep rate due to the increase in the creep resistance of the material by virtue of material deformation. The secondary region (II) is characterized by steady-state creep (where the creep strain rate $\dot{\varepsilon}_{min} = \dot{\varepsilon}_{ss}$ is constant), in which competing mechanisms of strain hardening and recovery may occur. The tertiary region (III) is characterized by an increasing creep strain rate, in which necking under constant load or consolidation of the failure mechanism occur prior to failure of the test piece. The relative significance of the three creep stages depends on the temperature, creep stress, and material.

Traditionally, a creep curve is described by the following empirical relation, due to *Andrade* [5.2]:

$$\varepsilon = \left(1 + \beta t^{1/3}\right) \exp(\kappa t) \,, \tag{5.11}$$

where β and κ are empirically determined constants related to the primary and steady stages of the creep curve, respectively. However, for engineering applications, it is the steady-state creep rate that is of major concern; for example, what is the permissible stress needed to produce a minimum strain rate of 10^{-6}/h (i.e., a strain of 0.01 in 10 000 h)? The *Mukherjee–Bird–Dorn* equation is often used as a scaling relation

$$\frac{\dot{\varepsilon} k T}{D_0 G \boldsymbol{b}} = A_0 \left(\frac{\sigma}{\mu}\right)^n \left(\frac{d}{\boldsymbol{b}}\right)^p \exp\left(-\frac{Q_c}{\mathrm{RT}}\right) \,, \tag{5.12}$$

where $\boldsymbol{b}$ is the Burgers vector, d is the grain size, D_0 is the self-diffusion coefficient, μ is the shear modulus, k is Boltzmann's constant, σ is the applied stress, Q_c is the activation energy for creep, R is the universal gas constant, T is the absolute temperature, and A, p, and n are dimensionless constants. Various creep mechanisms have been identified (both theoretically and experimentally) and can be classified as

1. Diffusion creep
2. Dislocation creep
3. Dower-law breakdown.

In diffusion creep processes, atomic vacancies generated close to grain boundaries normal to the applied stress migrate to grain boundaries parallel to the applied stress, where they are absorbed. This process leads to a shape change, but it does not involve dislocation flow (as the higher-stress processes do). This diffusive transport of vacancies at higher temperatures occurs through the bulk of the grain (Nabarro–Herring creep), whilst at lower temperatures it dominates along the grain boundaries (Coble creep). Creep rates are reported to be inversely proportional to the square of the grain size for Nabarro–Herring creep ($p = -2$ in (5.12)) but inversely proportional to the cube of the grain size for Coble creep ($p = -3$). When creep is controlled by diffusion alone, $n = 1$ in (5.12).

At higher stresses, steady-state creep occurs by dislocation glide plus climb and values of n are typically 3–5; this is called the power-law regime. The upper boundary of the power-law creep regime is defined by

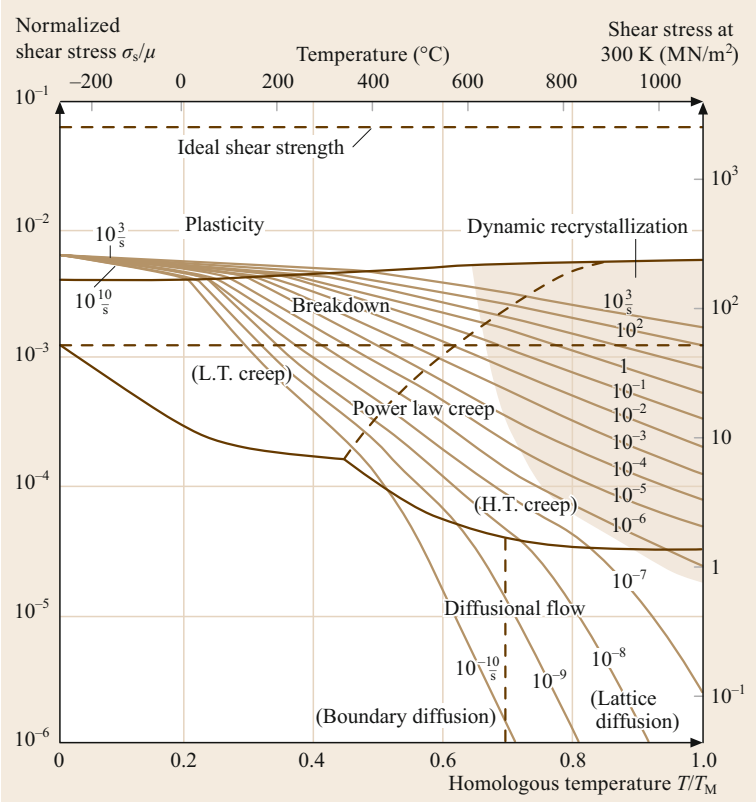

Fig. 5.13 Deformation mechanism map for pure copper with grain size of 100 μm showing different creep mechanisms operating in a given temperature–stress region (after [5.5])

the ratio of the applied shear stress to the elastic shear modulus that corresponds to the onset of general plasticity. For face-centered cubic (fcc) metals, this ratio is given as 1.26×10^{-3} and deformation at stresses exceeding this value is said to be in the power-law breakdown regime, where the Dorn equation is no longer valid. In the power-law and power-law breakdown regime, the steady-state creep rate is independent of grain size, i.e., $p = 0$. By solving the equations for diffusional flow, power-law creep, and general plasticity, it is possible to prepare deformation mechanism diagrams for a given material. The diagram for pure copper with a 100 μm grain size is reproduced in Fig. 5.13.

Two important phenomena related to creep are *superplasticity* and *stress relaxation*. Superplasticity is the ability of a material to undergo large elongation without failure; see [5.6] for an overview. Stress jump tests are carried out to assess the superplasticity of a material quickly at a given temperature by measuring the flow stress at different loading rates while keeping the temperature constant. The strain-rate exponent, m $(= 1/n)$, can then be evaluated and should be close to 0.5 for superplastic behavior to be observed. To determine the stress relaxation of a material, the specimen is deformed by a given amount, and the decrease in stress is recorded over a prolonged period of exposure at a constant, elevated temperature. The stress-relaxation rate is then the slope of the curve at any point.

The goal in engineering design for creep is to predict the performance over the long term. To this end, one of three approaches is applied:

- Stress-rupture tests. A large number of tests are run at various stresses and temperatures to develop plots of applied stress versus time to failure. While it is relatively easy to use these plots to provide estimates of stress rupture life, it is very expensive and time consuming to develop these plots. Additionally, extrapolation of the data can be problematic.
- Minimum strain rate versus time to failure. This type of relation is based on the observation that strain is the macroscopic manifestation of cumulative creep damage. A critical level of damage, independent of stress and/or temperature, is then defined as the failure criterion as follows

$$\dot{\varepsilon}_{\min} t_f = C \propto \varepsilon_f \,. \tag{5.13}$$

A log–log plot of $\dot{\varepsilon}_{\min}$ versus t_f or Monkman–Grant chart can then be constructed from relatively few

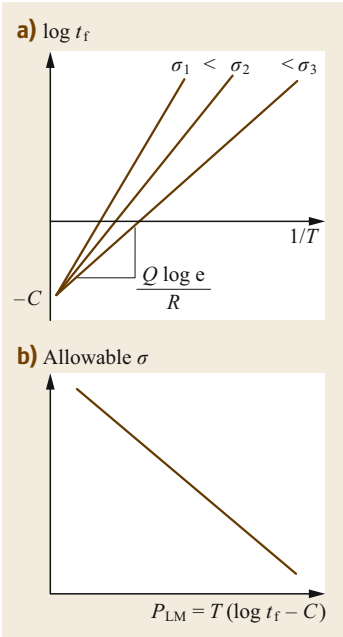

Fig. 5.14a,b Summary of the Larson–Miller method for creep life prediction. **(a)** Experimental results, **(b)** *universal* Larson–Miller relation

creep tests to determine the value of the empirical constant C and be used to predict the creep life.

- Temperature-compensated time. In these methods, a higher temperature is used at the same stress so as to cause a shorter time to failure, such that temperature is traded for time. In this form of accelerated testing, it is assumed that the failure mechanism does not change and hence is not a function of temperature or time. In the most commonly used method, the Larson–Miller parameter P_{LM} at a given stress is expressed as

$$P_{LM} = 2.303\frac{Q_c}{R} = T(C + \log t_f)\,, \qquad (5.14)$$

where C is the Larson–Miller constant, typically ranging between 25 and 60. Experimental data in terms of $\log t_f$ and $1/T$ at a given stress are plotted to estimate Q_c and C_1 as shown in Fig. 5.14.

5.1.3 Dynamic Mechanical Properties

In structural applications, members are often subjected to varying load/stress over time, in the form of either vibrations or high-energy impacts. It is important to have an understanding of the effect of such forces on their structural integrity to avoid catastrophic failure due to fractures.

Impact Testing

Toughness is a qualitative measure of a material's ability to absorb impact energy by undergoing plastic deformation. Notched-bar impact tests are generally used to detect the tendency of a material to fail in a brittle manner. Two classes of notched specimens are commonly used for this class of tests, namely the *Charpy* notched bar and the *Izod* specimen (Fig. 5.15). The specimen may have a square or circular cross-section, and a V notch is machined either at the center (Charpy) or towards one end (Izod) of the specimen. The impact load is then applied by a heavy swinging hammer as indicated in Fig. 5.15 by the arrows. The presence of the notch results in a triaxial stress state on the fracture plane. The response of the sample is usually measured by the energy absorbed in fracturing the specimen and can be estimated from the loss in kinetic energy before and after the impact.

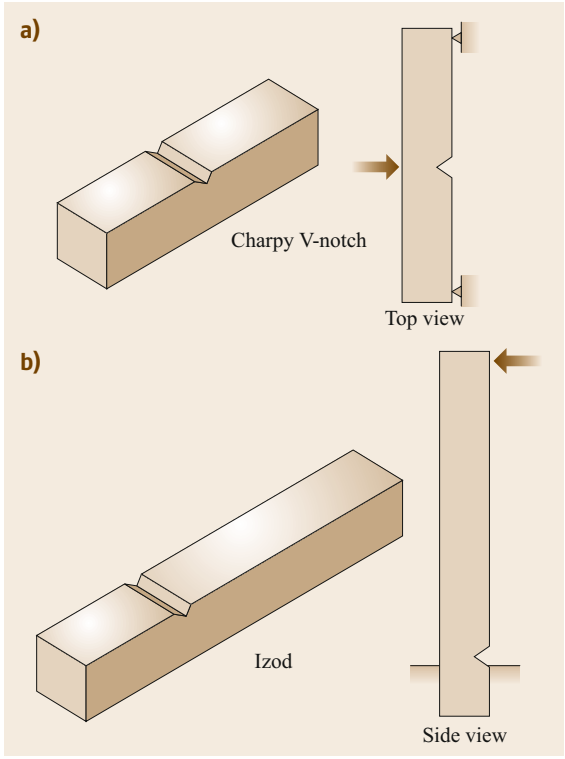

Fig. 5.15a,b Specimen geometry and test procedure for **(a)** Charpy V-notch test and **(b)** Izod impact test (after [5.4])

The notched-bar impact test is most meaningful when conducted over a range of temperatures. Most metallic materials undergo a transition from a ductile to brittle mode of fracture with decreasing temperature. This transition temperature is called the ductile to brittle transition temperature (DBTT) and is an important design parameter. Figure 5.16 shows the typical variation of the absorbed impact energy as a function of temperature for two steels, a ferritic one with body-centered

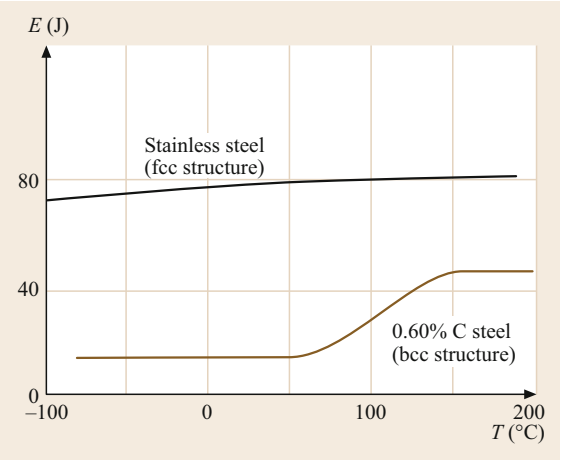

Fig. 5.16 Variation of absorbed energy as a function of temperature showing ductile to brittle transition (DBTT) in a plain carbon steel (after [5.4])

cubic (bcc) structure and an austenitic one with fcc structure. The material with the lowest DBTT should be preferred in structural applications at low temperatures to avoid catastrophic failure, hence austenitic stainless steels are recommended.

Cyclic Testing

It is well known that a component subjected to a load well below its yield stress can still fail due to fatigue, i.e., a fluctuating load over a period of time (Fig. 5.17). Fatigue failure usually occurs without any obvious warning and is usually accompanied by fracture. A periodic stress cycle of the kind shown in Fig. 5.18a,b comprises a mean stress, σ_m $(= (\sigma_{max} + \sigma_{min})/2)$, and an alternating stress amplitude σ_a $(= (\sigma_{max} - \sigma_{min})/2)$. The stress ratio R is then defined as

$$R = \frac{\sigma_{min}}{\sigma_{max}} , \qquad (5.15)$$

where σ_{max} and σ_{min} are the maximum and minimum stress, respectively. The basic method of presenting engineering fatigue data is by means of the S–N curve, which represents the dependence of the cycles to failure N on the maximum applied stress σ_{max}. Most investigations of fatigue properties are carried out by means of a rotating beam machine, where $\sigma_m = 0$ and $R = -1$. Figure 5.18 shows a schematic of the test apparatus and a typical S–N curve for this type of test. For most ferrous alloys, the S–N curve becomes horizontal at a certain limiting stress called the endurance or fatigue limit. Most nonferrous metals have S–N curves that do not show a true endurance limit, and in such cases, it is customary to define the endurance limit as the maximum stress that does not cause failure after 5×10^8 cycles. It must be noted that considerable scatter is observed during fatigue testing and it is standard to test three or four samples at a given stress level.

Application of a cyclic load, i.e., σ_a, leads to a cyclical strain response $\Delta\varepsilon_a$, which comprises elastic $\Delta\varepsilon_e$ and plastic $\Delta\varepsilon_p$ components. Figure 5.19 shows the variation of the elastic, plastic, and total strain amplitude as a function of the number of cycles to failure. Based on this figure, it is easy to visualize that, below a particular *transition life* ($N_{f,t}$), plastic deformation controls the cycles to failure, while above the transition life, elastic strain is the major source of fatigue damage. The two regions are termed low- or high-cycle fatigue, respectively, and the transition life is usually close to 10^4 cycles.

The fatigue process of a material can be divided into the following stages:

- *Crack initiation*, including the early state of fatigue damage due to localization of slip at persistent slip bands (PSB) or embryonic cracks.
- *Slip-band crack growth*, which involves the deepening of the initial crack on planes of high shear stress. This is frequently called stage I crack growth.
- *Crack growth on planes of high tensile stress*, which involves the growth of well-defined cracks in a direction normal to the maximum tensile stress. This is usually called stage II crack growth.

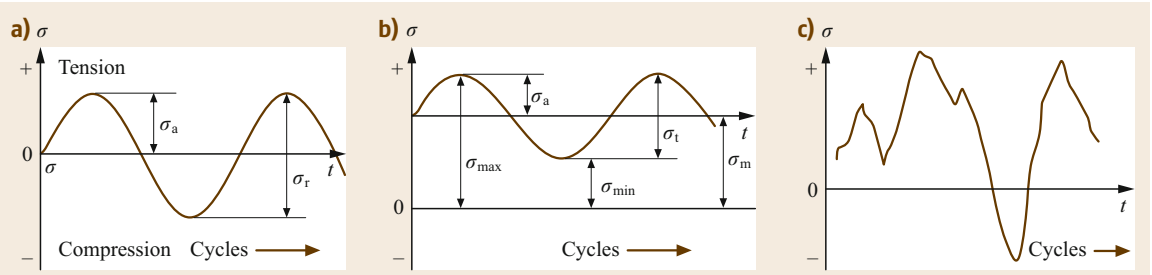

Fig. 5.17 (a,b) Definition of different stress parameters during cyclic stress testing of materials. (c) A typical stress variation curve for an airfoil in service (after [5.4])

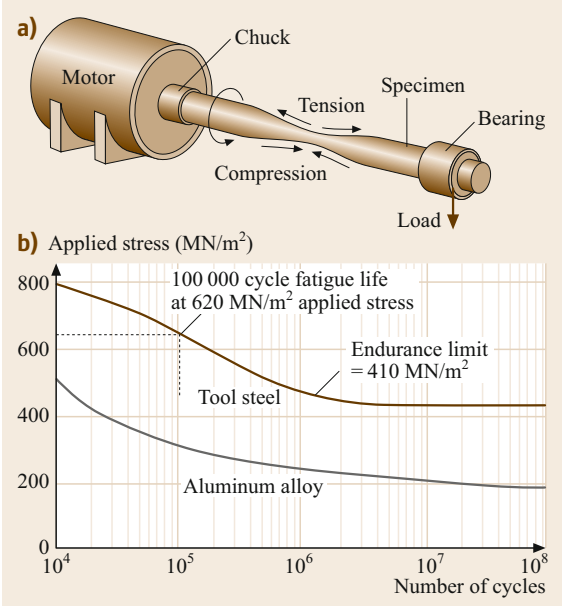

Fig. 5.18 (a) Schematic of rotation bending fatigue testing equipment and (b) typical stress–number of cycles (S–N) curve for a ferrous and nonferrous alloy (after [5.2])

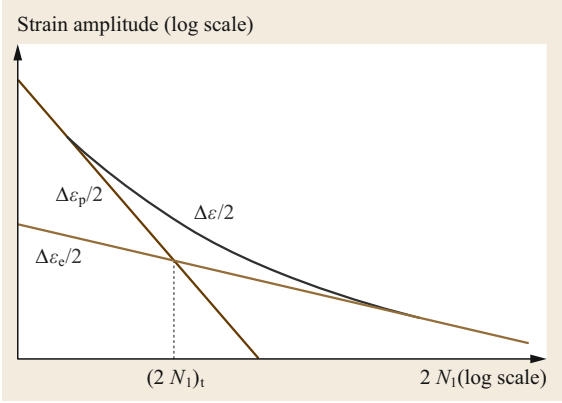

Fig. 5.19 Definition of a transition life between low- and high-cycle fatigue (after [5.7])

- *Ultimate ductile failure*, which occurs when the crack reaches a sufficient length that the remaining cross section cannot support the applied load.

In general, larger proportions of the total cycles to failure are involved with the propagation of stage II cracks in low-cycle fatigue than in high-cycle fatigue, while stage I crack growth accounts for the largest segment during low-stress high-cycle fatigue. If the tensile stress is high, as in the fatigue of specimens with preexisting surface flaws or notches, stage I crack growth may not be observed at all. Specialized crack growth-

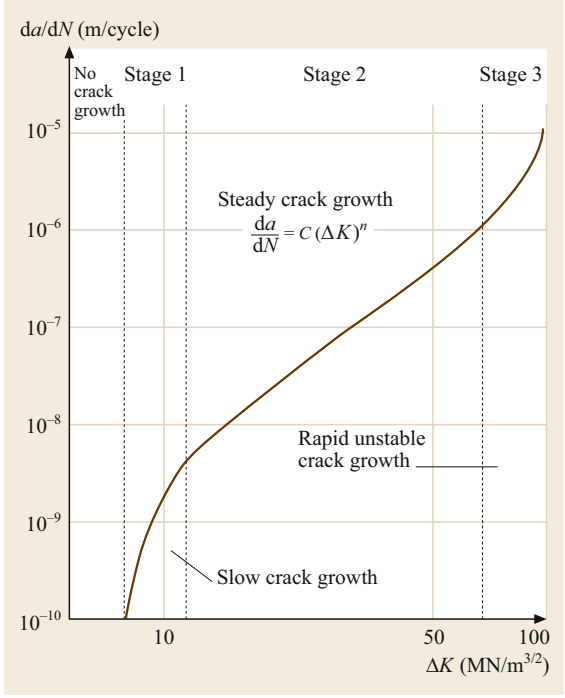

Fig. 5.20 A schematic fatigue crack-growth curve showing the three regimes of crack growth, in the steady state regime the so-called Paris law is observed (after [5.2])

rate tests using specimens which have been precracked in fatigue (see below) are employed to establish material selection criteria and establish the effect of the following factors that are known to have a significant influence on fatigue life:

1. Stress or strain range
2. Mean stress
3. Surface finish and quality
4. Surface treatments
5. Load sequence and overload.

Typical test results from these crack growth studies are shown in Fig. 5.20. Additional factors such as environmental conditions, elevated temperatures, and corrosive media also drastically affect the fatigue life and can accelerate failure.

Fracture Mechanics

New nondestructive testing techniques allow designers to adopt a more *damage-tolerant* approach to structural design. Accordingly, material with defects is no longer considered as failed but can be further used in service provided it is safe against *fast fracture*. The criterion for continued safe operation is that the strain energy release rate (called G for brittle materials and J for duc-

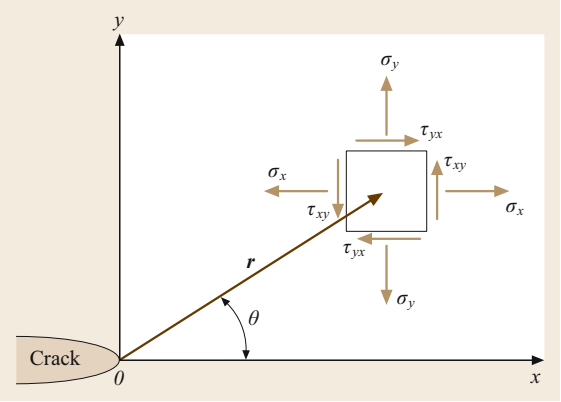

Fig. 5.21 Stress distribution at a point (r, θ) in the material stressed under a far-field tensile stress (mode 1) away from an elliptical crack (after [5.7])

tile materials) should be less than a critical value. The strain energy release rate is the amount of energy per unit length along the crack edge that is supplied by the elastic and plastic energy in the body and by the applied force in creating the new fracture surface area.

From linear elastic theory, the stress field around a crack (Fig. 5.21) can be expressed as

$$\lim_{r\to 0}\sigma_{ij}^{\mathrm{M}} = \frac{K_{\mathrm{M}}}{\sqrt{2\pi r}} f_{ij}^{\mathrm{M}}(\theta)\,, \tag{5.16}$$

where the superscript and subscript "M" denote the mode of load application (Fig. 5.22), f_{ij} is a function of location, and K is the stress intensity factor, expressed as

$$K = Y\sigma\sqrt{\pi a}\,, \tag{5.17}$$

where Y is a dimensionless factor dependent on the sample geometry and a is the crack half-length. K can be related to G according to the following relations:

$$G = \begin{cases} \frac{K^2}{E} & \text{(plane stress)} \\ \frac{K^2}{E}\left(1-\nu^2\right) & \text{(plane strain)} \end{cases}. \tag{5.18}$$

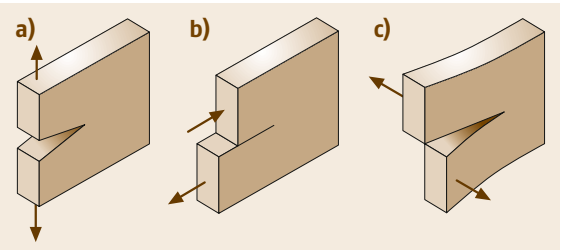

Fig. 5.22a–c Schematic representation of the three crack opening modes: **(a)** tensile (mode 1), **(b)** shear (mode 2), and **(c)** bending (mode 3) (after [5.3])

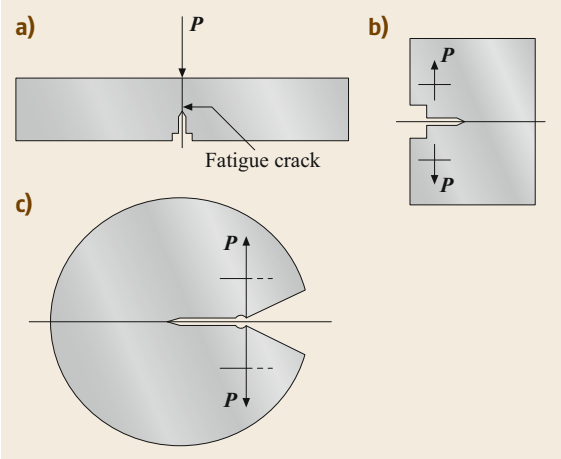

Fig. 5.23a–c Standard samples for fracture toughness (K or J) measurement: **(a)** single-edge bend, **(b)** compact tension (CT), and **(c)** cylindrical disc; ***P*** denotes the loading vector (after [5.3])

For ductile materials, the equivalent of the energy release rate G is the J-integral, which is defined as

$$J = \int_{\Gamma}\left(W\mathrm{d}y - \overline{T}\frac{\partial\overline{u}}{\partial x}\mathrm{d}s\right)\,, \tag{5.19}$$

where W is the load per unit volume, Γ is the path of the line integral that encloses the crack tip, ds is the increment of the contour path, and $\overline{\boldsymbol{T}}$ and $\overline{\boldsymbol{u}}$ are the outward traction and normal vectors, respectively, on ds. The first term corresponds to the elastic component, while the second term corresponds to the plastic energy due to the crack.

As mentioned above, the stress intensity factor K should be less than a critical value (K_{c}) as a design criterion. The critical stress intensity factor in the tension mode, K_{Ic}, is a material property and can be interpreted as the inherent resistance of a material to failure. Hence, it is frequently called the *fracture toughness* of a material. Like other mechanical properties, it is determined experimentally as described below. The same test procedure applies to the determination of the J-integral, although the test data are treated differently. The test specimen may be a single-edge notched beam, compact tension specimen, or cylindrical disc (Fig. 5.23). The load line displacement is recorded as a function of the applied load. A fatigue precracked test specimen is loaded in tension or bending to induce either:

1. Unstable crack extension (or *fracture instability*) or
2. Stable crack extension (or *stable tearing*).

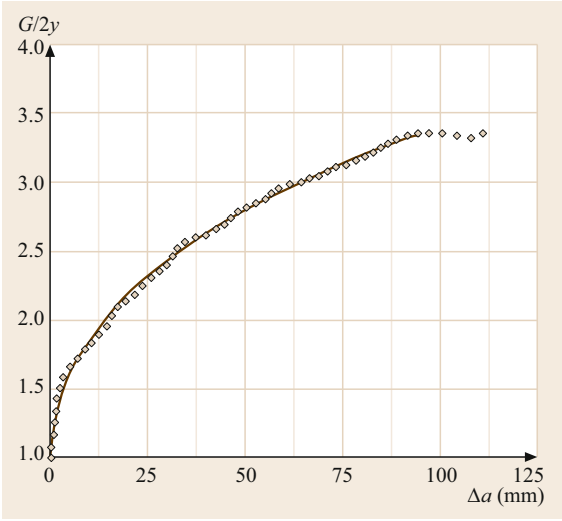

Fig. 5.24 A typical *R*-curve for a ferrous alloy showing the resistance to unstable crack extension (after [5.3])

The first method is used to determine the value of the fracture toughness at the point of instability, while the second method results in a continuous relationship for the fracture toughness versus the crack extension (called the *R*-curve, Fig. 5.24). For *R*-curve determination, the crack extension is also recorded simultaneously by optical or electrical means. The recorded data are then used to evaluate K_{Ic}, J_{Ic} or the *J*–*R* curve using standard relations. K_{Ic} is independent of the specimen geometry only under plane-strain conditions, and this criterion should be assessed carefully. Similar crack growth tests may also be used to evaluate the performance of a material under creep and/or fatigue.

Table 5.1 summarizes standards for mechanical testing of materials according to ASTM [5.8].

Table 5.1 Standards for mechanical testing of materials [5.8]

Test type	Standard
Methods of mechanical testing	ASTM E6-15e3
Tensile test of metallic materials	ASTM E8-15ae1
Elevated-temperature tension tests for metallic materials	ASTM E21-17e1
Young's modulus, tangent modulus, and chord modulus	ASTM E111-17
Brinell hardness of metallic materials	ASTM E10-18
Vickers hardness of metallic materials	ASTM E92-17
Rockwell hardness and Rockwell superficial hardness of metallic materials	ASTM E18-20
Hardness conversion tables for metals	ASTM E140-12b
Microhardness of materials	ASTM E384-17
Compression testing of metallic materials at room temperature	ASTM E9-19
Compression tests of metallic materials at elevated temperatures with conventional or rapid heating and strain rates	ASTM E209-18
Bend testing of mechanical flat materials for spring applications	ASTM E855-08
Shear modulus at room temperature	ASTM E143-13
Conducting creep, creep-rupture, and stress-rupture tests of metallic materials	ASTM E139-11
Stress relaxation for materials and structures	ASTM E328-13
Notched-bar impact testing of metallic materials	ASTM E23-18
Conducting force-controlled constant-amplitude axial fatigue tests of metallic materials	ASTM E466-15
Constant-amplitude low-cycle fatigue testing	ASTM E606-19e1
Measurement of fatigue crack growth rates	ASTM E647-15e1
Measurement of fracture toughness	ASTM E1820-20a

5.2 Physical Properties

While the prime design criteria in most applications in mechanical engineering relate to mechanical properties (Sect. 5.1), physical properties are instead decisive for most applications of functional materials. As some of these materials are of paramount importance in fields related to mechanical engineering, such as microelectronics, mechatronics, and the production, conversion, and distribution of electric power, we briefly discuss in this section selected properties such as electrical and thermal conductivity with respect to materials in mechanical engineering, i.e., metals, ceramics, glasses, and polymers, as described in more detail in Chap. 4. In particular, a discussion of the broad and still-emerging fields of *magnetism and superconductivity* and *semiconducting materials* must be omitted here. For in-depth information, the interested reader is referred to the recent version of [5.9] and to the *Springer Handbook of Materials Data* [5.10].

5.2.1 Electrical Properties

Ohm's Law and Electrical Conductivity

The relation between the voltage *U* (in V) and the current *I* (in A) in an electric conductor (often in the form

of a wire) is given by (the macroscopic) form of *Ohm's law* as

$$R = \frac{U}{I} , \tag{5.20}$$

where R is the resistance (in Ω) of the material to the current flow and depends critically on the geometry and (intrinsic) properties of the material, therefore

$$R = \rho\frac{l}{A} = \frac{l}{\sigma A} , \tag{5.21}$$

where l is the length and A is the cross-section of the conductor; ρ (Ω^{-1} m) and σ (Ω^{-1} m^{-1}) are the *electrical resistivity* and *electrical conductivity*, respectively, being specific to the material under consideration. Combining (5.20) and (5.21) yields

$$j = \frac{I}{A} = \sigma\frac{V}{l} = \sigma E , \tag{5.22}$$

with the current density j (A/m^2) and the electric field strength E (V/m). Alternatively, j is given by the product of the number of charge carriers n, the charge of each carrier q, and the average *drift velocity* v of the carriers, thus

$$j = nqv . \tag{5.23}$$

Setting (5.22) and (5.23) equal yields the microscopic form of Ohm's law, which is more relevant for materials engineers

$$\sigma = nq\frac{v}{E} = nq\mu . \tag{5.24}$$

The term v/E is called the *mobility* μ (m^2 V^{-1} s^{-1}) of the charge carriers. While the charge q of the carriers of the electric current is a constant, one may readily recall from (5.24) that the electrical conductivity of materials can be controlled essentially by two factors, namely:

1. The number of charge carriers n
2. Their mobility μ.

While electrons are the charge carriers in conductors (metals), semiconductors, and many insulators, ions carry the charge in ionic compounds. Therefore, in pure materials, the mobility μ depends critically on the bonding strength and—in addition in ionic compounds—on diffusion rates, which in turn gives rise to the tremendous variation of electrical conductivity over more than 20 decades (Table 5.2).

Table 5.2 Electrical conductivity σ at RT for selected (pure) materials [5.2, 10]

Material	Electric conductivity σ (Ω^{-1} m^{-1})
Al	3.77×10^7
Ag	6.80×10^7
Au	4.26×10^7
Cu	5.98×10^7
Fe	1.00×10^7
Mg	2.257×10^7
Ni	1.46×10^7
Pb	5.21×10^6
Ti	2.56×10^6
W	1.82×10^7
Zn	1.84×10^7
Si	5×10^{-4}
Polyethylene	10^{-13}
Polystyrene	10^{-15}–10^{-17}
Al_2O_3	10^{-12}
Diamond	$< 10^{-16}$
SiC	1–10
SiO_2 (silica)	10^{-15}

Effect of Temperature on the Electrical Conductivity of Metallic Materials

When heat is applied to metallic materials, the atoms gain thermal energy and vibrate at a particular amplitude and frequency. Thus, increasing the temperature increases the probability of scattering electrons within the crystal, which ultimately leads to a reduction of the mobility of electrons; the resistivity ρ_T (of a pure material) at a particular temperature changes according to

$$\rho_T = \rho_{RT}[1 + a(T - RT)] , \tag{5.25}$$

where a is the *temperature resistivity coefficient* and "RT" indicates room temperature. The relationship between resistivity and temperature is linear over a wide temperature range; values of a for metals are positive and are tabulated in [5.10].

Effect of Lattice Defects on the Electrical Conductivity of Metallic Materials

An additional contribution to electron scattering stems from all kinds of lattice imperfections, as described in Chap. 4. As a representative, the increase in resistivity due to atoms in solid solution can be described as

$$\rho_d = C(1 - x)x , \tag{5.26}$$

where ρ_d is the increase in resistivity due to the lattice defects present in the material and x is defined as the molar fraction of these defects (Sect. 4.1.2); C is the defect resistivity coefficient. Thus, the overall resistivity is

$$\rho = \rho_T + \rho_d . \tag{5.27}$$

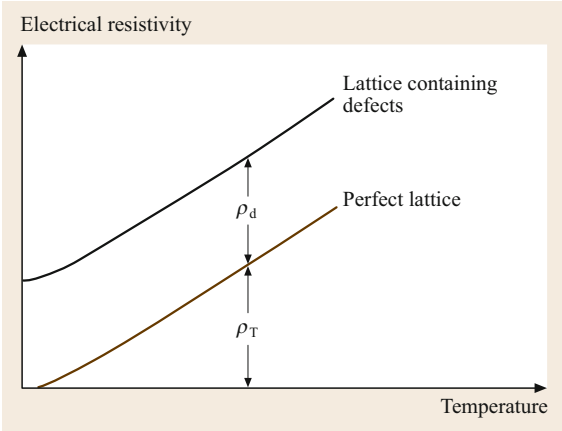

Fig. 5.25 Dependence of electrical resistivity of metallic materials on temperature; see text for further explanation

Note that the effect of defects is virtually independent of temperature (Fig. 5.25).

5.2.2 Thermal Properties

As outlined in Sect. 4.1.2, the atoms in a material have a minimum free energy at absolute zero. However, as mentioned in the previous subsection, the supply of thermal energy causes the atoms to vibrate at a particular amplitude and frequency. This gives rise to a number of physical effects and related quantities such as the *heat capacity* or *specific heat*, *thermal expansion*, and *thermal conductivity*, which will be discussed briefly in the following subsections.

Heat Capacity and Specific Heat

Since vibrations of atoms are transferred through the whole crystal as elastic waves, heating up or cooling down a material is realized by accepting or losing *phonons* of energy

$$E = \frac{hc}{\lambda} = h\nu \,. \tag{5.28}$$

Then, the *heat capacity* is the energy required to raise the temperature of *one mole* of a given material by 1 K. It can be determined by various methods either at constant pressure C_p or at constant volume C_V. As depicted in Fig. 5.26, the heat capacity approaches a nearly constant value of $C_p = 3R \approx 25\,\mathrm{J\,mol^{-1}\,K^{-1}}$ at sufficiently high temperatures for most metallic (above $\approx$ RT) and ceramic (> 800 K) materials. An exception to this rule is the (toxic) element Be, which has a mere $C_p \approx 16\,\mathrm{J\,mol^{-1}K^{-1}}$ [5.10].

By contrast, the *specific heat* c is the energy required to raise the temperature of a particular weight

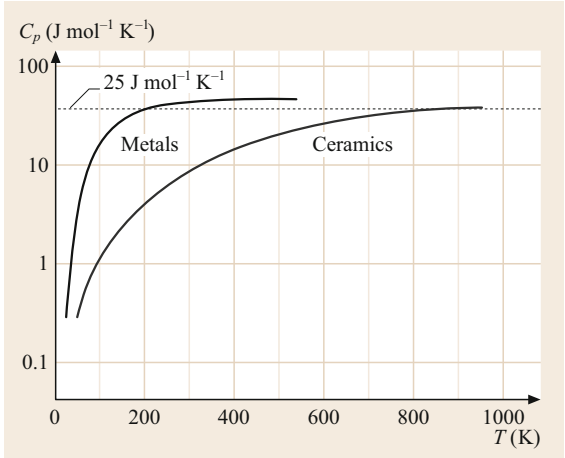

Fig. 5.26 Heat capacity as a function of temperature for metals and ceramics

Table 5.3 Specific heat c of selected materials at RT [5.2, 10]

Material (metals)	c ($\mathrm{J\,kg^{-1}\,K^{-1}}$)	Material (others)	c ($\mathrm{J\,kg^{-1}\,K^{-1}}$)
Al	900	Al_2O_3	837
Cu	385	Diamond	519
Fe	444	SiC	1047
Mg	1017	Si_3N_4	712
Ni	444	SiO_2 (silica)	1109
Pb	159	Polyamide	1674
Ti	523	Polystyrene	1172
W	134	Water	4186
Zn	389	Nitrogen	1042

or mass of a material by 1 K. The relationship between the heat capacity and specific heat is simply given by $c = C_p/M$, where M is the atomic mass (see Periodic Table). For engineering applications, the specific heat is more appropriate to use than the heat capacity. A compilation of specific heat values of typical materials is presented in Table 5.3. Data on water (liquid) and nitrogen (gas) are given also for comparison, with H_2O having the highest value of specific heat. Note that neither the specific heat nor the heat capacity depend significantly on microstructure.

Thermal Expansion

As pointed out in Sect. 5.1.1, the lattice constant of a material is a measure of the strength of atomic bonding, which is in turn the result of the force equilibrium between an attractive and repulsive potential. If a material gains thermal energy, however, this equilibrium separation increases, since the material is lifted from its energy minimum into a higher-energy state. The change in the dimensions of the material is usually measured by

Table 5.4 Linear coefficient of thermal expansion α at RT for selected materials [5.2, 10]

Material	α (10^{-6} K^{-1})
Al	23.03
Cu	16.5
Fe	12.3
Mg	26.1
Ni	13.3
Pb	29.1
Ti	8.35
W	4.31
Zn	25.0
0.2% C steel	12.0
304 stainless steel	17.3
Invar alloy (Fe-36%Ni)	1.54
Polyamide	80
Polystyrene	70
Al_2O_3	6.7
Diamond	1.06
SiC	4.3
Si_3N_4	3.3
SiO_2 (silica)	0.55

dilatometry as

$$\alpha = \frac{l_f - l_0}{l_0\,(T_f - T_0)} = \frac{\Delta l}{l_0 \Delta T}\,, \tag{5.29}$$

where the indices "f" and "0" denote the final and initial values of the length l and temperature T. Linear coefficients of thermal expansion α at RT for selected materials are listed in Table 5.4.

Two conclusions can be drawn from the compilation in Table 5.4, namely that materials possessing strong atomic bonds, in particular covalently bonded materials such as many ceramics, have:

1. Low α values and
2. High melting points T_m

The latter relationship is shown for metals in Fig. 5.27.

A particular behavior must be noted for the Invar alloy Fe-36%Ni, which reveals that the interaction with magnetic domains may suppress the thermal expansion nearly completely until the Curie temperature is reached. This makes Invar attractive for bimetallic applications.

Thermal Conductivity

In essence, *thermal energy* is transferred in solid materials by two mechanisms:

1. Transfer of free (valence) electrons
2. Lattice vibrations (phonons)

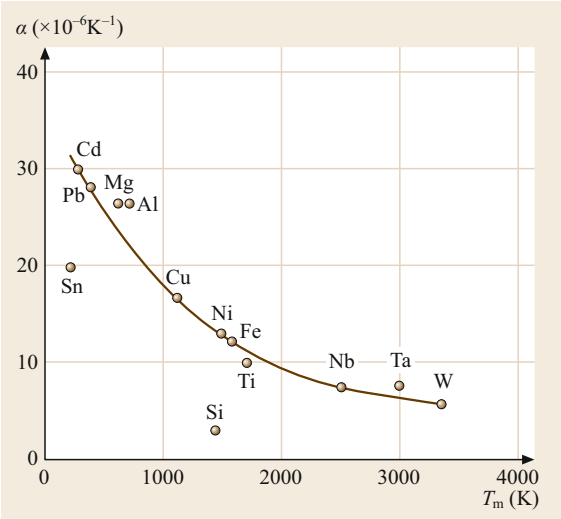

Fig. 5.27 Relationship between the linear coefficient of thermal expansion (at RT) and the melting point in metals

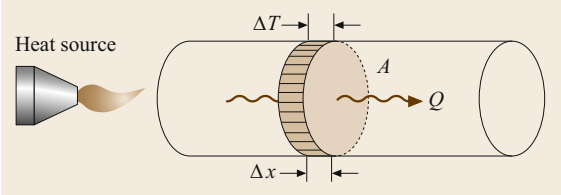

Fig. 5.28 Schematic of method for measuring the thermal conductivity k according to (5.27)

of which the latter is closely related to the phenomenon of storing thermal energy, i.e., the *heat capacity* (see above).

Hence, the *thermal conductivity* k is a measure of the rate at which heat is transferred through the material and follows the relationship

$$\frac{Q}{A} = k\frac{\Delta T}{\Delta x}\,, \tag{5.30}$$

where Q is the heat transferred through a cross-section A induced by a temperature gradient $\Delta T/\Delta x$. Note the striking similarity between k and the diffusion coefficient D in mass transfer, where the *heat flux* Q/A is analogous to the flux of atoms j_D. A schematic experimental setup for measuring k is shown in Fig. 5.28, where heat is introduced on one side of a bar- or disc-shaped sample through a heat source and the change of temperature on the other side is measured as a function of time. The commonly employed technique is called the *laser flash method*.

Values for the thermal conductivity k of selected materials are listed in Table 5.5. A comparison reveals that the k values of metals and alloys are usually much

larger than those of ceramics, glasses, and polymers. This is due to the fact that, in metals and alloys, thermal energy is transferred through the movement of (loosely bonded) valence electrons, which can be excited with little thermal energy into the conduction band. This leads to a relationship between the thermal and electrical conductivity of many metals of the form

$$\frac{k}{\sigma T} = L = 2.3 \times 10^{-8}\,\mathrm{W\,\Omega\,K^{-2}}\,, \tag{5.31}$$

where L is the Lorenz constant.

In contrast, the prime energy transfer mechanism in ceramics, glasses, and polymers is vibration of lattices and (silicate or molecular polymeric) chains, respectively. Since the electronic contribution is absent, the thermal conductivity in these material classes is usually much lower than that in metals and alloys. An exception to this rule is *carbon* in its covalently bonded form as *diamond*, which has the highest k value and therefore commonly serves as a *heat sink* material.

The situation is reversed when the temperature of the materials is increased: the greater lattice and chain vibrations usually lead to an increase of the thermal conductivity in ceramics, glasses, and polymers. In metals and alloys the same mechanism applies in principle, however, the electronic contribution will be lowered, even though the number of carriers is increased, as their mobility is more strongly reduced due to increasing scattering effects. Therefore, the thermal conductivity of metals and alloys usually decreases with increasing temperature. Like the electrical conductivity, the thermal conductivity of metals and alloys also decreases with increasing number of lattice defects of various dimensionality, introduced into the microstructure due to the increased electron scattering.

Table 5.5 Thermal conductivity k of selected materials at RT [5.2, 10]

Material (metals/alloys)	k ($\mathrm{W\,m^{-1}\,K^{-1}}$)	Material (others)	k ($\mathrm{W\,m^{-1}\,K^{-1}}$)
Al	238	Al_2O_3	16
Cu	1401	Diamond	2320
Fe	80	Graphite	335
Mg	100	SiC	88
Ni	444	Si_3N_4	15
Pb	35	SiO_2 (silica)	1.34
Ti	22	ZrO_2	5.0
W	172	Polyamide	0.25
Zn	117	Polyethylene	0.33
0.2% C steel	100	Polyimide	0.21
304 stainless steel	30		
Grey cast iron	80		
Cu-30% Ni	50		

References

5.1 American Society for Testing and Materials: *Practice E1245-03: Standard Practice for Determining the Inclusion or Second-Phase Constituent Content of Metals by Automatic Image Analysis* (ASTM, Philadelphia 2003)

5.2 D.R. Askeland: *The Science and Engineering of Materials, S.I*, 3rd edn. (Wiley-VCH, Weinheim 1996)

5.3 ISO: *ISO 643-2003: Steels—Micrographic Determination of the Apparent Grain Size* (ISO, Geneva 2003)

5.4 G.E. Dieter: *Mechanical Metallurgy* (McGraw-Hill, London 1988), SI Metric Edition

5.5 H.J. Frost, M.F. Ashby: *Deformation Mechanism Maps* (Oxford Univ. Press, Oxford 1982)

5.6 O.D. Sherby, J. Wadsworth: Superplasticity—recent advances and future directions, Prog. Mater. Sci. **33**, 169 (1989)

5.7 S. Suresh: *Fatigue of Materials* (Cambridge Univ. Press, Cambridge 1998)

5.8 American Society for Testing and Materials: *Annual Book of ASTM Standards*, Vol. 03.01 (ASTM, Philadelphia 1998)

5.9 J. Buschow: *Concise Encyclopedia of Magnetic and Superconducting Materials*, 2nd edn. (Elsevier, Amsterdam 2006)

5.10 W. Martienssen, H. Warlimont (Eds.): *Springer Handbook of Materials Data* (Springer, Berlin, Heidelberg 2005)

Srivastava Vivek

Hindalco Innovation Center
Hindalco Industries Ltd
Taloja, Navi Mumbai, India
vivek.s.srivastava@adityabirla.com

Vivek Srivastava completed the PhD degree at University of Sheffield on high temperature creep of metals and alloys. Since 2007, he has worked at Aditya Birla Group in various positions. His research interest include aluminum metallurgy, rolling and extrusion processes, aluminum alloys and applications.

Martin Heilmaier

Institute for Applied Materials (IAM)
Karlsruhe Institute of Technology (KIT)
Karlsruhe, Germany
martin.heilmaier@kit.edu

Martin Heilmaier graduated in materials science from the University of Erlangen-Nuremberg. From 2002 he was Professor for Materials Testing at Otto-von-Guericke University. Since November 2011 he holds the chair for Materials Science & Technology at Karlsruhe Institute ofTechnology. His research is dedicated to the synthesis and properties of structural materials such as refractory metal silicide alloys and intermetallic alloys for high-temperature applications.

6. Corrosion and Corrosion Resistance

Thomas Böllinghaus, Michael Rhode, Thora Falkenreck

The chapter starts with a brief introduction about corrosion, which is defined as the interdependency between a metal, a corrosive environment, and the respective component design. The second section introduces the most important forms of aqueous electrochemical corrosion (uniform corrosion, galvanic corrosion, selective and intergranular corrosion, and finally pitting and crevice corrosion in the case of passive layer forming metals). In addition, electrochemical corrosion under applied mechanical load is introduced (stress corrosion cracking, hydrogen-assisted cracking, corrosion fatigue), as well as special forms of corrosion (erosion, fretting, and microbiologically induced corrosion). The third section of this chapter introduces (mostly dry) chemical corrosion and high-temperature corrosion (oxidation, carburization, high-temperature hydrogen attack, sulfurization, nitriding, halogenation). As in the case of electrochemical corrosion, chemical corrosion can also be superimposed by mechanical loads. Finally, general facts on the testing of corrosion are introduced.

6.1 **Fundamental Aspects** 185
6.2 **Electrochemical Corrosion** 186
6.2.1 Uniform Corrosion 190
6.2.2 Galvanic Corrosion 192
6.2.3 Selective and Intergranular Corrosion ... 193
6.2.4 Passivation, Pitting, and Crevice Corrosion 196
6.2.5 Stress Corrosion Cracking 200
6.2.6 Erosion and Cavitation Corrosion 204
6.2.7 Fretting Corrosion 206
6.2.8 Microbiologically Induced Corrosion 206
6.3 **Chemical Corrosion and High-Temperature Corrosion** 207
6.3.1 High-Temperature Corrosion Without Mechanical Load 207
6.3.2 High-Temperature Corrosion with Superimposed Mechanical Loads .. 211
6.4 **Corrosion Testing** 212
References 212

6.1 Fundamental Aspects

The corrosion of metals is the physicochemical interdependency between a metal and its environment, which may result in a change of material properties. This can cause serious impairments of the material performance, the environment, or of the entire technical system, of which both material and environment are part [6.1]. Thus, corrosion resistance is a property of a component member or of the entire component in a technical system. Corrosion resistance defines the ability of a material, considering the component design, to withstand a corrosive environment to keep the function of the technical system (Fig. 6.1). The corrosive load is a result of the environmental conditions from both corrosive environments and constructional design aspects. If the corrosive load exceeds the corrosion resistance of a material that is used in a component, then corrosion damage may occur. Hence, damage is not necessarily existent in the presence of corrosion itself. Only in the case of impaired functional capability of the technical system is this, then, called corrosion damage. Additionally, corrosion damage of a component does not necessarily mean that failure occurs, i.e., there is not necessarily a total loss of function of the entire system. The term corrosion is mostly related to metallic materials. Nonetheless, this term is also used for the corrosive effect in glasses, ceramics, and organic nonmetallic materials. However, these phenomena are not considered below.

Basically, the corrosion of metals is separated into the following:

1. Electrochemical corrosion (for example, atmospheric corrosion of steels, which is commonly expressed as "rusting")

K.-H. Grote, H. Hefazi (Eds.), *Springer Handbook of Mechanical Engineering*, Springer Handbooks,
https://doi.org/10.1007/978-3-030-47035-7_6

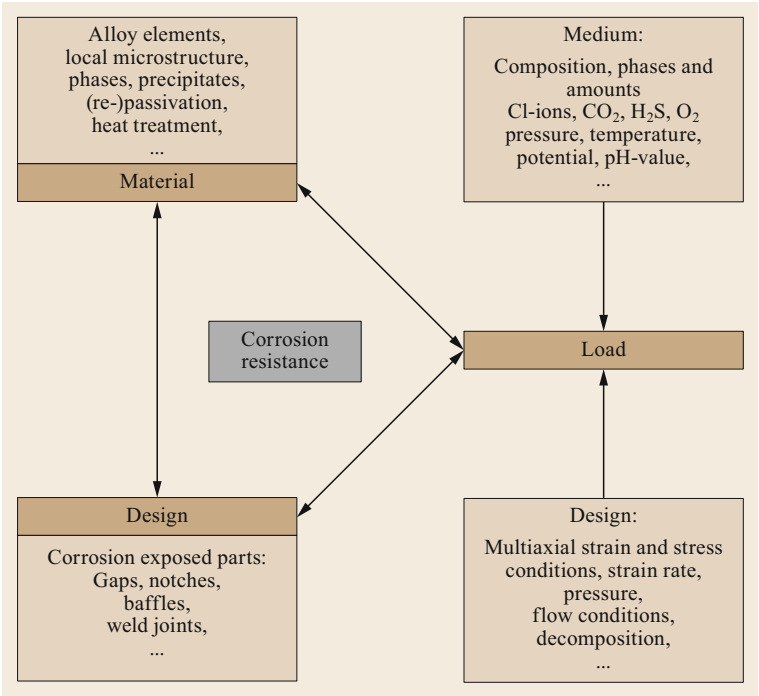

Fig. 6.1 Corrosion resistance as a part of component properties

2. Chemical corrosion (which encompasses mostly high-temperature corrosion processes).

In contrast to many other fields of technology, it is very often impossible to describe the behavior of components and facilities in equations, tables, or standards. The main reason is that corrosion is more complex than the interdependencies between the three mentioned facts: material, design, and load (Fig. 6.1). Furthermore, very different physical processes and chemical reactions take place in the three local areas of influence: the medium, the material, and the interface between both. To summarize, these processes and reactions are the actual corrosive load (Fig. 6.2).

Both process and reaction are time-dependent. Hence, the corrosive load always has a thermodynamic part and a kinetic part. The corrosive load may be superimposed by an additional load type in the three areas of influence at the same time. For example, corrosion cracking occurs if corrosive and mechanical loads are coupled. If friction and corrosive loads are coupled, it is called fretting. Respectively, erosion corrosion is the coupled effect of erosion and corrosion [6.2].

Due to the local and temporal variation of the manifold influences, the reasons for corrosion damage are often quite different, even in cases of frequently similar damage symptoms. To understand and assess the individual cases of corrosion as well as to recommend preemptive actions, it is necessary to be familiar with the different influencing factors (Fig. 6.1) and the local physical processes and chemical reactions (Fig. 6.2).

6.2 Electrochemical Corrosion

In most cases, the interaction between the metal and its environment consists of electrochemical reactions and their physical processes, e.g., diffusion processes. The thermodynamic driving force of electrochemical reactions is for the material to attain a lower energy state. Electrochemical corrosion is, therefore, the pursuit of a metallic material to reach a favorable energy state by electron donation (oxidation). In an electrically conductive environment (electrolyte), the electron donation commonly causes the dissolution of a metal.

If a metallic surface comes into contact with an electrolyte, the process of metal dissolution begins spontaneously. During this process, the metal dissolves as an ion (Me^{z+}) and, depending upon its valence (z), one or more electrons ($z\,e^-$) are released and remain within the metal. The location of this process is referred

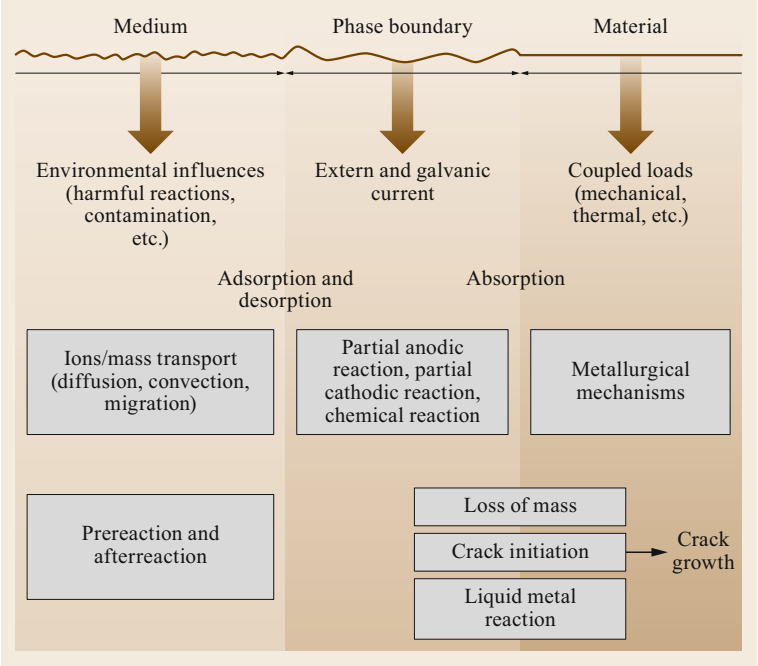

Fig. 6.2 Corrosion processes at the interface of material and medium

to as an anode. The metal ions undergo dissolution and are returned to the metallic state (6.1).

$$\mathrm{Me} \rightarrow \mathrm{Me}^{z+} + z\,\mathrm{e}^- \qquad (6.1)$$

The dissolution process can be described electrically by means of Faraday's law (6.2).

$$\Delta m = \frac{MIt}{zF} \quad (\mathrm{g}) \qquad (6.2)$$

In (6.2), Δm is the loss of mass, M is the molarity, I is the flow of electrons (current amplitude) as a result of metal dissolution, t is time, and $F = 96\,485\,\mathrm{C\,mol^{-1}}$ is Faraday's constant.

The originally neutral metal becomes negatively charged via the electrons left behind during this process. If the electrons are not consumed, charge separation rapidly leads to an increase in electrostatic forces, which then prevents further metal dissolution.

Thus, a so-called dynamic equilibrium is attained, in which the same number of metal ions undergo dissolution as are returned to the metallic state. This only applies to homogeneous, pure metals with contact to an electrolyte.

In practice, however, metals represent technical materials that are anything but homogeneous. The presence of impurities and/or alloying elements (either in solution or as precipitates), the existence of different heat treatment states, levels of deformation, different protective or adsorbed layers, crystallographic anisotropy, and various lattice defects all lead to the creation of locations with different (usually higher) energy states. The tendency of the metal to return to an energetically lower state is, thus, particularly high at such locations.

Furthermore, the equilibrium of the electrostatic forces between free electrons and metal ions on the material surface is often disturbed.

Since electron neutrality must prevail both for the electrolyte and for the metallic material, electrons are absorbed at another site on the inhomogeneous metal surface, i.e., they are absorbed by a reaction partner from the electrolyte. Due to this process of electron acceptance (referred to as reduction), which takes place at the cathode, dissolution at the anode is enabled. The following four different types of corrosion can take place as a cathodic reaction:

1. Reduction of hydrogen in oxygen-free/oxygen-reduced neutral or alkaline electrolytes

$$2\,\mathrm{H_2O} + 2\,\mathrm{e}^- \rightarrow \mathrm{H_2} + 2\,\mathrm{OH}^- \qquad (6.3a)$$

Moreover, in oxygen-free/oxygen-reduced sour electrolytes (e.g., local corrosion, corrosion in acid)

$$2\,\mathrm{H}^+ + 2\,\mathrm{e}^- \rightarrow \mathrm{H_2} \qquad (6.3b)$$

(more exactly: $2\,\mathrm{H_3O}^+ + 2\,\mathrm{e}^- \rightarrow 2\,\mathrm{H_2O} + \mathrm{H_2}$)

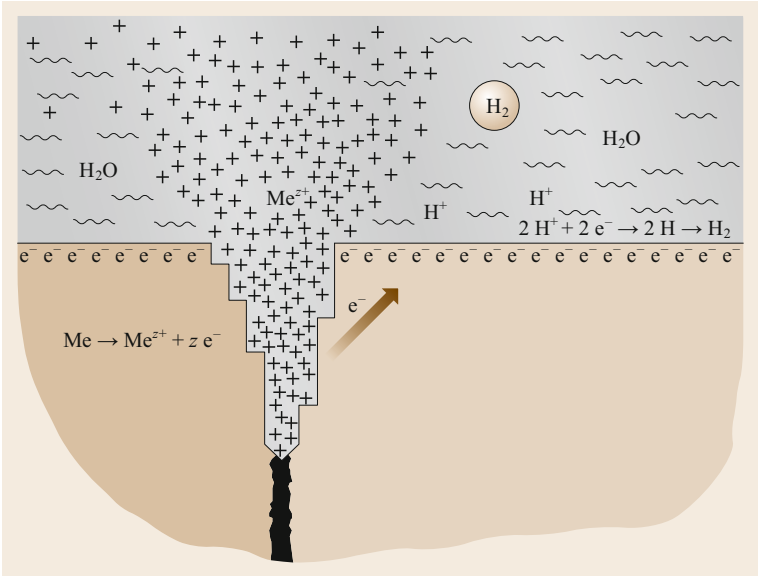

Fig. 6.3 Corrosion at a grain boundary

2. Reduction of oxygen dissolved in the water (atmospheric corrosion leading to formation of rust via subsequent reactions)

$$O_2 + 2\,H_2O + 4\,e^- \rightarrow 4\,OH^- \qquad (6.4a)$$

and in sour electrolytes with contact of the ambient atmosphere (corrosion in acid)

$$O_2 + 4\,H^+ + 4\,e^- \rightarrow 2\,H_2O \qquad (6.4b)$$

(more precisely: $O_2 + 4\,H_3O^+ + 4\,e^- \rightarrow 6\,H_2O$)

3. Deposition of more noble metallic ions (corrosion through use of mixed metals)

$$Cu^{2+} + 2\,e^- \rightarrow Cu \qquad (6.5)$$

4. Applied current (e.g., corrosion through stray currents in soil near tram lines).

Figure 6.3 shows a local inhomogeneity where dissolution of metal and electron acceptance can take place. The dissolution of a polycrystalline metallic material in acid at a grain boundary is shown schematically. When anodes and cathodes are of limited size and spread homogeneously on the metal surface, this is referred to as mixed electrodes. This applies to corroding low-alloyed steel surfaces in liquid electrolytes. Due to the high mobility of the electrons in the electron cloud of the metal, the electron acceptance can take place far away from the location of the dissolution of metal. So, the electron transfer—the reaction of the acid—takes place at the grain and not at the location of the dissolution of the metal. The distance between dissolution at the anode and electron acceptance at the cathode can be quite far. This can be seen in liquid electrolytes of materials with phases of different alloy content (e.g., austenitic-ferritic duplex steels) or components consisting of different materials which are in contact (e.g., galvanic corrosion or bimetallic corrosion of two metals with different alloy content in a weld).

Electrochemically, the cathode and the anode form a corrosion cell together with the electrolyte. Corrosion reactions occur spontaneously when metal atoms can attain a condition of lower energy. Much like in a battery, the corrosion cell is doing work ($W_{el} = EQ$). Therefore, the Gibbs free energy ΔG has to adopt a negative value. The excess heat available is released as work energy. For one mole of mass, the representative amount of charge is $Q = zF$. Therefore, the energy released is

$$\Delta G = -zF\Delta E\,. \qquad (6.6)$$

In this equation, E represents the electromotive force EMF. It can be regarded as voltage ΔU and measured like in a battery; ΔG results from the activities or approximations of the concentration C of the reactant at the cathode (reduction) and anode (oxidation) according to the law of mass action.

$$\Delta G = \Delta G^0 + RT\ln(K) = RT\ln\frac{C_{Red}}{C_{Ox}}$$
$$= RT\,2.303\lg\frac{C_{Red}}{C_{Ox}} \qquad (6.7)$$

Table 6.1 Standard potentials (electrochemical series) and closed-circuit potentials in simulated sea water (practical electrochemical series) in comparison to a standard hydrogen electrode (N/A: not available)

Element/material → partial reactions	Standard potential ΔE^0 (V)	Closed-circuit potentials in simulated sea water [6.3] (V)
$H_2 \rightarrow 2\,H^+ + 2\,e^-$	0.00 (Reference)	N/A
$Mg \rightarrow Mg^{2+} + 2\,e^-$	−2.36	−1.40
$Al \rightarrow Al^{3+} + 3\,e^-$	−1.66	−0.67 (Al99.5)
$Ti \rightarrow Ti^{2+} + 2\,e^-$	−1.77	−0.11
$Zn \rightarrow Zn^{2+} + 2\,e^-$	−0.76	−0.80 (Zinc coating on steel)
$Cr \rightarrow Cr^{3+} + 3\,e^-$	−0.71	−0.29
$Fe \rightarrow Fe^{2+} + 2\,e^-$	−0.44	−0.35 (Quenched and tempered steel), −0.05 (X5CrNi18.8)
$Sn \rightarrow Sn^{2+} + 2\,e^-$	−0.14	−0.19
$Cu \rightarrow Cu^{2+} + 2\,e^-$	+0.34	+0.01
$Ag \rightarrow Ag^{+} + e^-$	+0.80	+0.15
$Pt \rightarrow Pt^{2+} + 2\,e^-$	+1.20	N/A

The combination of (6.6) and (6.7) results in the important Nernst equation

$$\Delta G = \Delta G^0 + RT\ln(K) = RT\ln\frac{C_{\mathrm{Red}}}{C_{\mathrm{Ox}}} = RT\,2.303\,\lg\frac{C_{\mathrm{Red}}}{C_{\mathrm{Ox}}}\,. \tag{6.8}$$

In the electrochemical corrosion of metallic materials however, the anodic and cathodic partial reactions are not as strict as in a battery. In order to have a thermodynamic measure of the severity of an electrochemical corrosion reaction, the standard conditions are defined as room temperature 298 K, a normal pressure of 0.1 MPa, and the concentration of reactants 1 mol L^{-1}. Due to the neutrality of the complete corrosion cell, the anodic and cathodic partial reactions cannot be measured individually. As a substitute, the overall reaction ((6.1) and (6.3b)) is used to define the standard electromotive force ΔE^0, where the EMF as a standard potential of the individual reactions explains the metal dissolution.

$$z\,H_3O^+ + M \rightarrow M^{z+} + z\,H_2O + \tfrac{z}{2}\,H_2 \tag{6.9}$$

This also means that the standard potential of the hydrogen deposition is equal to zero, which also considers the high binding energy of the hydrogen molecule H_2 (approximately 436 kJ mol^{-1}) in corrosive reactions. Table 6.1 shows the single reactions and standard potentials of the most important alloying elements of technical materials in comparison to the standard hydrogen electrode, which allows estimating the dissolution in liquid electrolyte. Metals and materials that are lower in the galvanic series (electropotential series) compared to the standard hydrogen electrode are referred to as less noble, while elements with higher electrode potential are referred to as noble. However, the disadvantage is that these standard potentials usually do not reflect the technical application. Additionally, Table 6.1 contains a list of closed circuit potentials that depend on the medium (e.g., simulated sea water, pH7.5) [6.3]. These lists are referred to as practical electrochemical series.

The thermodynamics of the electrochemical corrosion reactions which are mentioned above are superimposed by kinetic influences. These are caused by the resistance and the inhomogeneity in the electrolyte and on the metal surface. Inhomogeneous electrolytes are formed by depletion processes (e.g., locally high consumption of oxygen), enrichment processes (e.g., alkalization by formation of OH^- ions) and diffusion processes (e.g., transport processes at the surface and in the electrolyte). In the electrolyte, the mobility of the reaction partners and ions is significantly lower than the electrons in the metal and those which are on the metal surface. If chlorides are present in aqueous electrolytes, the conductivity increases as compared to pure water and also, the solubility of metal ions in the water is increased which accelerates the metal dissolution. Especially at locations where positively charged ions in the electrolyte (cations) are neutralized by electrons, the charge exchange strongly depends on the diffusion velocity in the direction of the metal surface. In other words, this causes an electron congestion on the metal surface and causes a negative polarization. In the same way, locations where metal atoms are dissolving have a higher anodic potential. At the cathode, such diffusion boundary layers can significantly impede the charge exchange. These are the explanations for the decrease of ion mobility in an electrolyte because of the interference of cations at high salt concentrations. The corrosion at the metal surface proceeds slower than at lower salt concentrations. If hydrogen is neutralized at the cathode (6.3b) and the hydrogen solubility of the

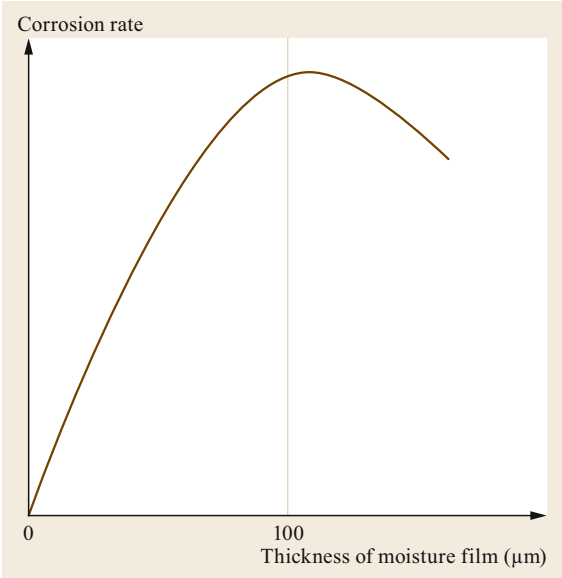

Fig. 6.4 Influence of the thickness of a moisture film on the rate of atmospheric corrosion [6.3, 4]

metal is comparatively low, a so-called hydrogen over voltage is produced. The resulting molecular gaseous hydrogen covers the cathode and impedes further cathodic reactions. Therefore, the anodic partial reaction of the metal solution can also be blocked. Figure 6.4 shows these effects using the example of the moisture film thickness on the corrosion under atmospheric conditions. It shows that as the water supply increases, the consumption of electrons is faster and the metal dissolves more easily. However, starting from a certain film thickness (100 μm), the corrosion rate decreases because of the larger diffusion path of the oxygen from the atmosphere. Consequently, no more electrons can be consumed. In practice, this means that thin films of Cl containing condensates or dew on metal surfaces are more corrosive than large quantities of liquid electrolyte or rain. Inhomogeneous metal surfaces are caused by hindered charge transitions through adsorption layers and secondary corrosion products (rust). Oxide layers on the surface of technical materials, so-called passive layers, have a particularly large kinetic influence. These are layers with very large electrical resistances, which are poorly soluble by an electrolyte. The kinetics of the anodic reaction of the metal dissolution is influenced primarily by how these passive layers are formed again after destruction (repassivation of metal surface). Due to a very low diffusivity of hydrogen atoms or protons compared to the subjacent metal, these layers also influence the kinetics of the cathodic hydrogen reaction. As a result, the hydrogen absorption at the cathode is extremely reduced, more molecular hydrogen is formed on the metal surface, and the adsorption of further hydrogen protons is hindered. Metals like chromium, aluminum, and titanium form these oxide/passive layers.

Seldom, a result of these kinetic processes is that the closed-circuit potentials at real metal surfaces correspond to the electromotive force of dissolution at a standard hydrogen electrode (Table 6.1). Based on practical electrochemical series in realistic electrolytes, the corrosion behavior of material pairings, especially for bimetallic corrosion, can be assessed much better.

While the scientific consideration of corrosion is based essentially on the investigation of electrochemical reactions and kinetics, a classification according to the type of corrosion is suitable for technical consideration. Out of 56 types of corrosion, listed in [6.1], the most important for mechanical engineering are shown in Fig. 6.5; they will be dealt with in more detail in the following sections.

6.2.1 Uniform Corrosion

Uniform corrosion (Fig. 6.5) is predominantly homogeneous on the entire metal surface and is referred to as uniform corrosion [6.1]. The best example is corrosion of low-alloyed steels in a humid atmosphere or neutral water. Oxygen and water are necessary for oxidation of the iron, and corrosion occurs as the sum of the partial reactions (6.1) and (6.4a).

$$2\,\mathrm{Fe} + \mathrm{O_2} + 2\,\mathrm{H_2O} \rightarrow 2\,\mathrm{Fe(OH)_2} \qquad (6.10)$$

A sufficient amount of oxygen is available from the atmosphere. Water mostly condenses from the ambient air as an electrolyte film on the steel surface, preferably on particles. No noteworthy corrosion occurs below a relative humidity of 70%. In very clean air no noticeable corrosion takes place even at 100% relative humidity.

During uniform corrosion, the entire material surface is removed by alternating anodic and cathodic partial regions. These local reactions can be simplified by the illustration of the corrosion of iron underneath a water drop (Fig. 6.6). At the edge of the droplet, the diffusion path of the oxygen is shortest. This is where the cathodic and electron-accepting process takes place with the formation of OH ions. The anodic partial reaction of the iron dissolution takes place in the center of the droplet. At first, iron(II) hydroxide is formed, which is not rust in the classical meaning. In the presence of dissolved oxygen, it transforms due to secondary reactions (shown in (6.11)–(6.15)) to different rust minerals. Cl ions are mainly responsible for iron dissolution due to the increased solubility in water and the formation of unstable hydroxyl complexes. These keep the anodic

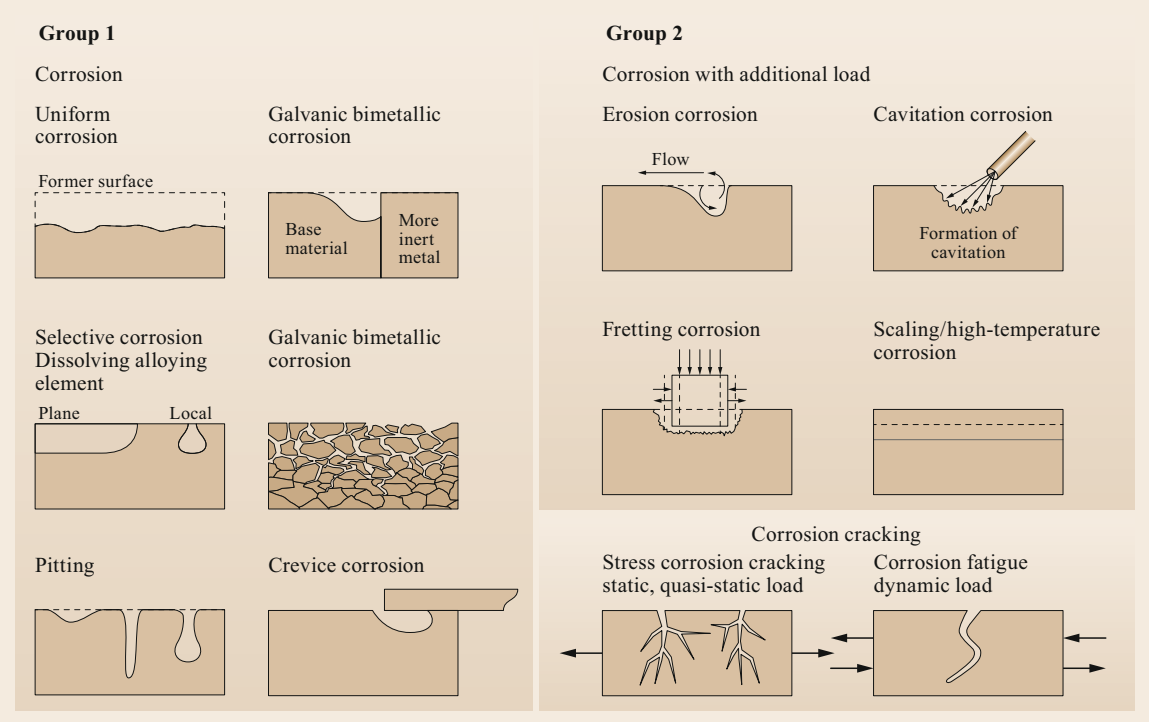

Fig. 6.5 Forms of corrosion at metal

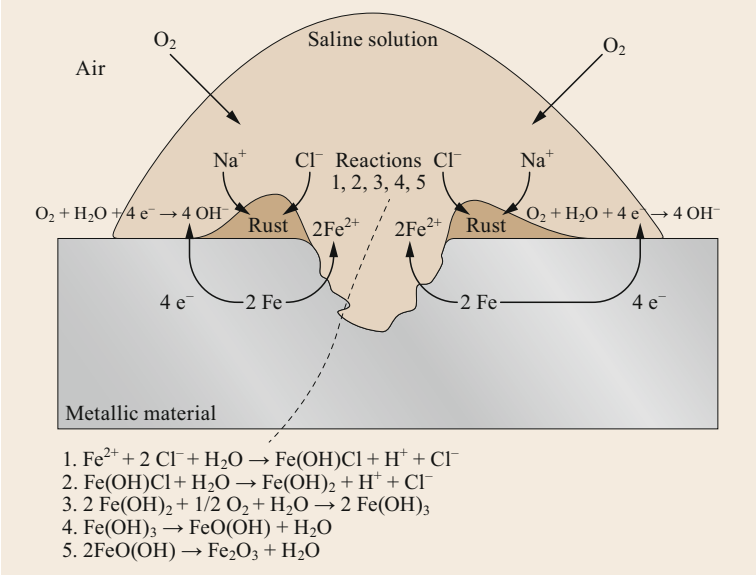

Fig. 6.6 Corrosion underneath a drop of water [6.5]

metal dissolution in motion (Fig. 6.6).

$$Fe^{2+} + 2\,Cl^- + H_2O \rightarrow Fe(OH)Cl + H^+ + Cl^- \quad (6.11)$$

$$Fe(OH)Cl + H_2O \rightarrow Fe(OH)_2 + H^+ + Cl^- \quad (6.12)$$

$$2\,Fe(OH)_2 + \tfrac{1}{2}\,O_2 + H_2O \rightarrow 2\,Fe(OH)_3 \quad (6.13)$$

$$Fe(OH)_3 \rightarrow FeO(OH) + H_2O \quad (6.14)$$

$$2\,FeO(OH) \rightarrow Fe_2O_3 + H_2O \quad (6.15)$$

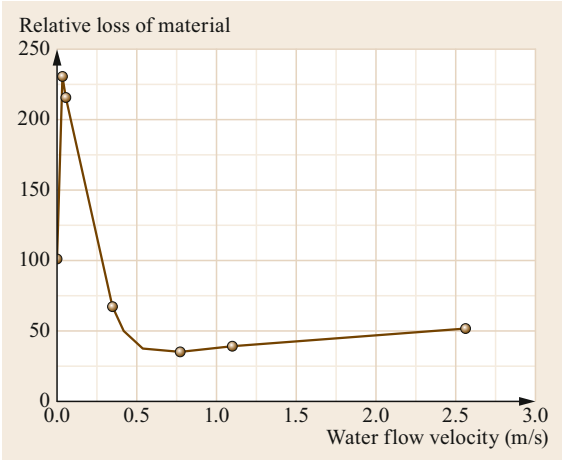

Fig. 6.7 Dependence of corrosion on flow velocity in drinking pipes [6.6]

The volume of the rust is, depending on the composition, six to eight times greater than the amount of absent (corroded) iron. The conversion of rust products depends very much on climate conditions and the resulting weather cycles. Rust products do not form a cohesive top layer but can significantly reduce the corrosion rate. Depending on the chemical composition of the steel and the surrounding medium, the corrosion rates can be reduced from 0.1 to 0.01 mm/a. The flow velocity of the ambient medium is also important, for example in fresh water pipes. Initially, corrosion increases with higher flow rates because more oxygen collects on the surface. At medium speed, corrosion products deposit on the surface that are removed at higher flow speeds (Fig. 6.7). Permissible flow velocities have been specified, for example, by *Mörbe* et al. [6.6] and are summarized in Table 6.2.

6.2.2 Galvanic Corrosion

When two materials or regions of materials that differ in their electrochemical behavior are connected to conduct electrons, they are referred to as galvanic elements.

Table 6.2 Permissible flow velocities according to *Mörbe* et al. [6.6]

Material	v_{min} (m/s)	v_{max} (m/s)
Unalloyed steel	0.5	2.0
Hot-dip galvanized steel	0.5	2.0
Polymer-coated steel	0.5	6.0
Chromium-nickel steel	0.5	5.0
Copper DR-Cu 99,7	0.7	1.2
Brass CuZn30	1.0	2.0
Special brass CuZn20Al2	1.0	2.5

Galvanic corrosion, sometimes also referred as to contact corrosion or bimetallic corrosion, describes that as a result of the conductive contact, the metal dissolution is accelerated at the less noble material (anode), and the electron acceptance process proceeds preferentially at the more noble region (cathode). If both materials are metals, this process is referred to as bimetallic corrosion. Depending on the contact geometry, bimetallic corrosion can be distinguished as uneven, often ditch-shaped dissolution of the less noble material at the immediate contact area. Simultaneously, the more noble material shows reduced corrosion. Bimetallic corrosion can cause decreased strength of the joined materials or their perforation. Furthermore, it can accelerate the formation of corrosion products and change the optical appearance.

However, it is difficult to evaluate the galvanic corrosion resistance of material pairings based on standard potential differences of both materials (Table 3.8). Out of practical experience, materials can be summarized as groups with a reduced risk of pronounced galvanic corrosion within one group:

Group 1. Highly electronegative, nonnoble metals: magnesium, and its alloys
Group 2. Nonnoble metals: aluminum, cadmium, zinc, and their alloys
Group 3. Moderate nonnoble metals: lead, tin, iron, and their alloys (except for high-alloyed chromium and chromium-nickel steels)
Group 4. Precious metals: copper, silver, gold, platinum, and their alloys
Group 5. Strongly passivating metals: titanium, chromium, nickel, cobalt, and their alloys, as well as highly alloyed chromium and chromium-nickel steels
Group 6. Nonmetallic cathodes: graphite, CFK, well-conductive carbides, oxides, and borides.

This simplified consideration cannot eliminate the possibility of galvanic corrosion. Especially if one or even several group boundaries are exceeded, the corrosive behavior of the material pairing needs to be evaluated.

The kinetics of the anodic and cathodic partial reaction on both materials and the characteristics of the partial flow density potential curves are essential for the overall corrosive behavior. The joint potential of the electrically short-circuited elements differs from the equilibrium state of a single material during corrosion (open corrosion potential). The less noble partner produces an increased anodic corrosion current in addition to self-corrosion. This enhances metal dissolution, and the cathodic partial reaction is shifted proportionally to

the more noble partner. In an acid solution, this is often accompanied by an increased amount of hydrogen gas at the more noble cathodic metal than would be the case if it would be sporadically dipped into the solution. If, in such a case, additional mechanical stresses are present, bimetallic corrosion could lead to hydrogen-assisted cracking of the more noble metal. This danger especially exists when the electrolyte contains promoters. These substances prevent recombination to molecular hydrogen (recombination poisons), such as, e.g., H_2S, cyanide, and arsenic compounds.

Attention should be paid to the area ratio between anode and cathode. According to the condition that the magnitude of the anodic and cathodic partial currents in the equilibrium state must be equal, the dissolution current density ($i = I/F$) at the anode increases proportionally to the area ratio F_A/F_K,

$$I_A = |I_K|^+ \quad (A)\,, \tag{6.16}$$

$$i_A = \left(\frac{F_K}{F_A}\right)|i_K|^+ \quad (A\,mm^{-2})\,. \tag{6.17}$$

To avoid highly localized corrosion of the anode ($i_A \gg i_K$), it is recommended that the noble anode be as large, and the cathode as small, as possible. An example of this is when aluminum sheets (large anode) are joined with rivets made of Monel (about 70% Ni and 30% Cu) to homogenize bimetallic corrosion as far as possible. In the case of high-alloyed chromium and chromium-nickel steel welds, a higher-alloy filler material is used for the smaller surface area, which then acts as a cathode.

In practice, the formation of contacting materials as a cathode or anode is less dependent on the galvanic series, but rather on the ability to repassivate. The ability to repassivate influences the kinetics of the anodic and cathodic partial reactions. The formation as a cathode or anode also relies on the electrical transitional resistances between the connected metals and the conductivity of the electrolyte solution.

The following list provides solutions to avoid galvanic corrosion, which has consequences on the design of components, especially in multimaterial applications under light-weight aspects:

- Materials that are corrosion resistant in a solution can be incompatible in a conductive connection, e.g., due to accelerated corrosion of the less noble material.
- The combination of approved standard assembly groups in complex systems needs to be questioned, e.g., the connection of copper pipes with Al-heat exchangers in cooling circuits. Also, traces of incompatible metals (such as the deposit of dissolved Cu-ions on aluminum) or conductive materials (graphite in lubricants) can also form galvanic elements.
- Passive and cover layers can make incompatible pairs possible by inhibiting rate-determining partial reactions, such as contact between aluminum and Cr-Ni steel parts at mild atmospheric conditions or dense carbonate-containing deposits on copper water pipes.
- An increase of transition resistances (up to isolation) between materials reduces or prevents bimetallic corrosion.
- The extent of the galvanic element is directly proportional to the conductivity of the solution. Reduced conductivity can limit damage at the immediate contact area, e.g., by formation of thin adsorbed films during atmospheric corrosion.

There are also applications in mechanical engineering where bimetallic corrosion is deliberately generated to extend the lifetime of components and systems. This is achieved by applying a less noble contact partner, e.g., by galvanizing of nonalloy steels in automobile construction or by so-called sacrificial anodes, made of aluminum or magnesium, in maritime technology. In principle, cathodic protection of high-strength, low-alloyed steels needs to be weighed against the risk of hydrogen absorption, especially in slightly acidic electrolytes. In the case of less noble coatings, a so-called long-distance protection effect is achieved by dissolving the less noble regions adjacent to defects, which allows a greater robustness when the coating is damaged. Coating of low-alloyed steels with more noble metals, e.g., during nickel-plating or chromium-plating, must be produced without errors to prevent galvanic corrosion of the base material.

6.2.3 Selective and Intergranular Corrosion

In contrast to galvanic corrosion, selective corrosion occurs at material pairings that are identical or at least similar. Only certain parts of the microstructure, such as areas near grain boundaries or alloying parts, corrode [6.3, 5, 7]. The preferred corrosion of certain parts of the microstructure requires a heterogeneous formation of the material structure. During selective corrosion, the less noble phase forms the anode, and the more noble phase becomes the cathode. During this process, microscopic contact elements are formed. Welded joints are the preferred areas of attack, since the weld metal and the heat-affected zone (HAZ) often differ in microstructure and alloy composition. Reasons for these differences are the

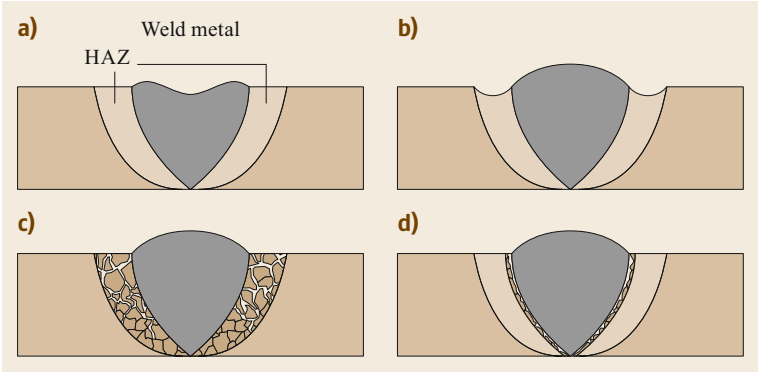

Fig. 6.8a–d Types of selective corrosion in welded joints [6.5]. **(a)** Selective corrosion of weld metal, **(b)** selective corrosion of HAZ, **(c)** intergranular corrosion, **(d)** knife-line corrosion

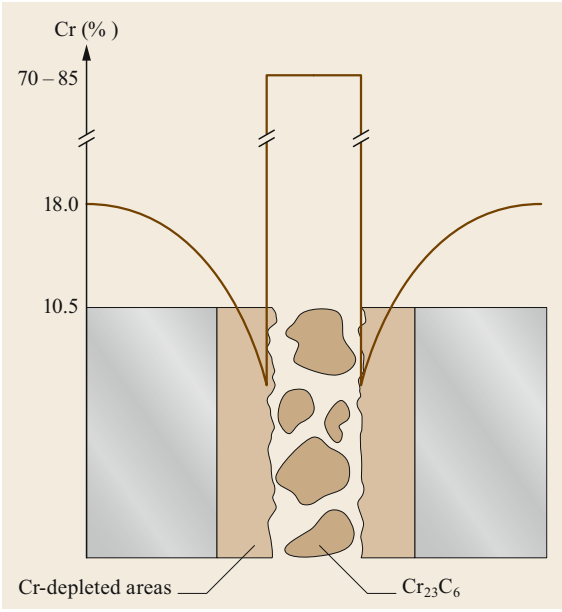

Fig. 6.9 Chromium distribution at a grain boundary of Cr-Ni steel with 18% chromium

combustion of alloying elements during welding, segregation, and precipitation. Depending on which welding region is less noble, it can be distinguished between selective corrosion of weld metal or HAZ. Intergranular corrosion and its special type, the so-called knife-line attack, frequently occur in welded joints.

Intergranular corrosion takes place when metallic materials are subject to less corrosion-resistant phases at grain boundaries, and these form a coherent network. This can cause localized dissolution along grain boundaries and complete decomposition of the material into individual crystallites (grain decay). This can occur in aluminum-magnesium alloys as a result of the Al_3Mg_2-phase and, in the case of brass, due to the β-phase. During welding and heat treatment of high-alloyed chromium and chromium-nickel steels, precipitation of chromium carbides ($Cr_{23}C_6$) at grain boundaries is a major cause of intergranular corrosion. The formation and growth of phases up to 85% chromium at temperatures between 425 and 815 °C (depending on alloying and microstructure) can result in chromium depletion in the immediate surroundings (Fig. 6.9). This process is called sensitization and is often caused by improper heat treatment, operating temperatures, or temperature control during welding. If the chromium content drops below a critical limit of 10.5% Cr and the conditions in the media are disadvantageous, a stable passive layer is no longer formed, and the dissolution speed increases. A 10^6 times higher corrosion rate can occur along such precipitate-rich grain boundaries compared to the grain surface (Fig. 6.10).

It is important that the sensitization and subsequent intergranular corrosion are caused by the growth of the chromium carbides and not by the segregation or their presence per se (Fig. 6.11). The microstructure of the material, in combination with the chromium and carbon contents, is relevant for the susceptibility to sensitization and intergranular corrosion. An example of this is that high-alloyed ferritic chromium steels are much more susceptible to intergranular corrosion than austenitic chromium-nickel steels with the same chromium and carbon contents, due to their lower solubility in carbon.

Both groups of materials are, however, prone to intergranular corrosion because they segregate chromium carbides solely at the grain boundaries and not in the grain interior. On the other hand, high-alloyed martensitic steels with about 13% chromium can be alloyed with more than four times higher carbon contents (> 0.2%) without an increased susceptibility to intergranular corrosion after welding or heat treatment. This is due to the fact that these steels precipitate chromium carbides predominantly within the former austenite grains along the martensite plate. Therefore,

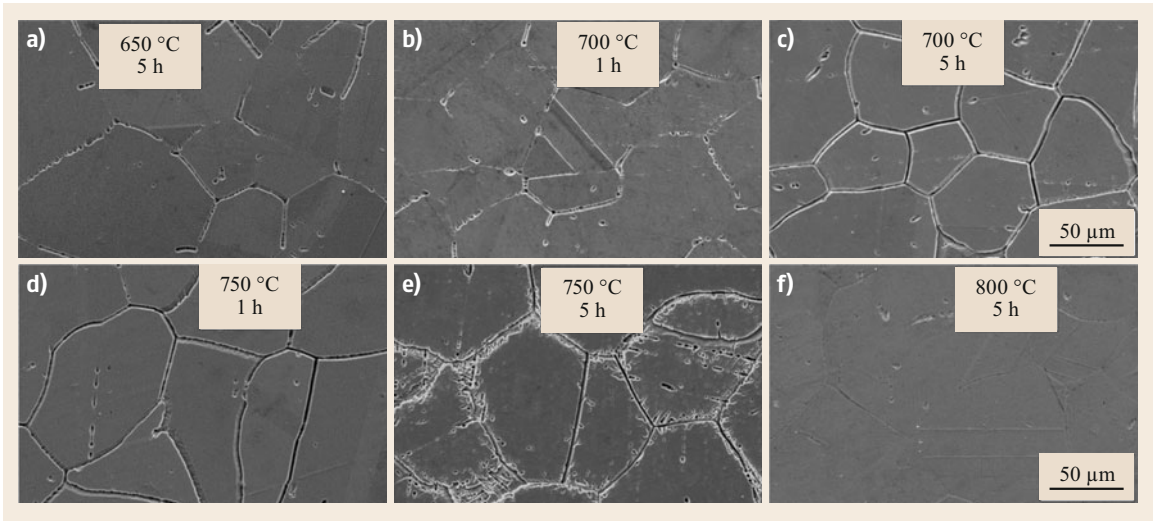

Fig. 6.10a–f Different states of sensitization for intergranular corrosion depending on the heat treatment condition (temperature and time) of 316L-based corrosion resistant steel tested with 10% oxalic acid solution [6.8]

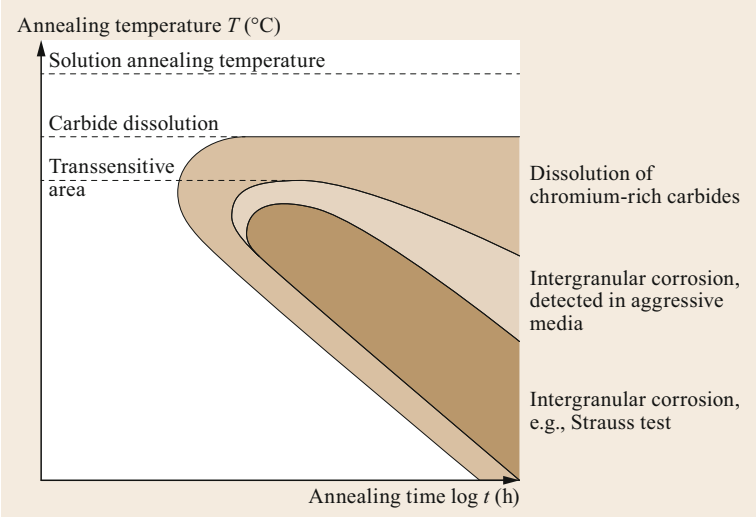

Fig. 6.11 Time–temperature–precipitation

chromium depletion takes place over the whole surface area and is not preferred only along the former austenite grain boundaries. To roughly estimate the susceptibility of a material for intergranular corrosion, time–temperature–precipitation (TTP) diagrams, which characterize the area of chromium carbide precipitation, can be used (Fig. 6.11). The real sensitization is illustrated in so-called grain decomposition diagrams, which are often determined by a Strauss test (Fig. 6.12). However, realistic quantitative evidence of sensitization due to chromium depletion along the grain boundaries can only be achieved by analytical methods such as energy dispersive x-ray spectroscopy (EDX).

Since the formation of a passive layer is strongly influenced by the corrosion potential, while the pH value has a great influence on the potential, a paradoxical behavior occurs at steels that can passivate. An example of this is when strong intergranular corrosion can occur on sensitized steel in a low-acid medium (e.g., beer, wine, shampoo), and no corrosion occurs in a substantially acidic medium by a shift of the potential in the positive direction. In oxidizing acids with even higher positive potential, the chromium carbides may dissolve and, therefore, lead to intergranular corrosion.

High-alloyed austenitic chromium-nickel steels can be stabilized against intergranular corrosion by alloy-

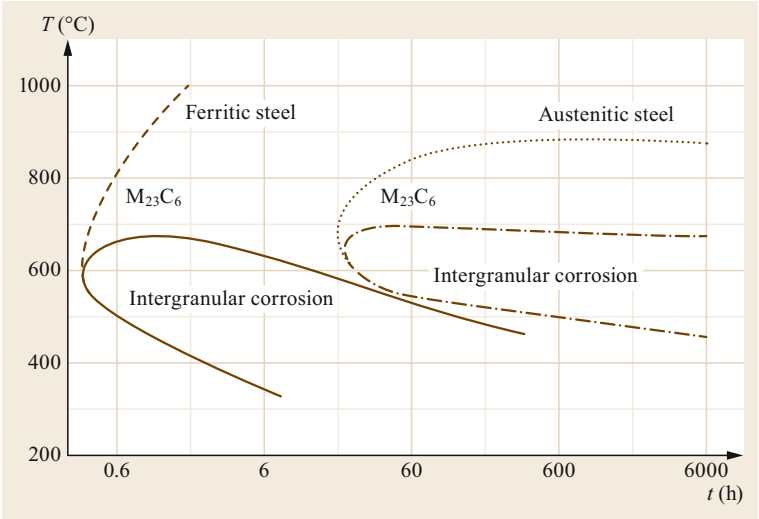

Fig. 6.12 Grain decomposition diagram for high-alloyed, ferritic Cr steels and austenitic Cr-Ni steels

ing with titanium. This causes the formation of titanium carbides instead of chromium carbides, which cause chromium depletion at the grain boundaries.

However, welding of these stabilized high-alloyed austenitic chromium-nickel steels can lead to knife-line corrosion as a particular form of intergranular corrosion. The stabilizing (titanium) carbides are being dissolved in a very narrow region of the HAZ, usually parallel to the fusion line. This area is characterized by the high temperature, which is only slightly below the melting temperature of the steel. The new formation of carbides is suppressed as a result of the rapid cooling. The welding of the following layers causes the precipitation of both titanium and chromium carbides in this narrow zone because of the heat input. This sensitization of the base material results in intergranular corrosion in a very narrow area next to the fusion line.

6.2.4 Passivation, Pitting, and Crevice Corrosion

Reactive metals, such as aluminum, titanium, zirconium, zinc, chromium, tantalum, cobalt, and nickel, form an oxide-like layer, the so-called passive layer, on the surface of the material. Passive layers are naturally grown, do not have a uniform chemical structure and, therefore, do not have the properties of a technical coating. It cannot be detected by conventional means because the layer is substantially smaller than the wavelength of visible light. High mechanical stresses and high potential gradients (about 1 MV/cm) are usually present in the layer. Iron and nickel alloys are usually alloyed with chromium to achieve a protective passive layer.

These materials form a stable passive layer of 10 nm (about 50 atomic layers, pure chromium only 5 atomic layers) at an alloy content of 10.5% chromium. The passive layer is more amorphous towards the metal and has a crystalline structure on the side of the medium. These layers, which are predominantly composed of chromium oxide, have a significantly lower ductility than the base material underneath. These are more likely to crack when subjected to mechanical loads.

The thermodynamics of electrochemical corrosion reactions are superimposed by kinetic influences due to the formation of such semiconducting, partially insulating passive layers. The kinetic property of the self-healing of passive layers after destruction or tearing, e.g., due to mechanical or tribological stress, is a great advantage. This property significantly differentiates passive coatings from technical coatings, which, after exposure of the base material, can no longer provide adequate barrier effects.

The passive layer is not a rigid cover layer but a dynamic system. Submicroscopic activation and repassivation processes take place on the surface, which can be measured as small potential and current impulses. These pulses are referred to as electrochemical noise. They depend on the type of metal and its state, temperature, and pH value, and also on the type and concentration of ions dissolved in the medium. These pulses provide valuable information about the condition of the passive layer and thus possible corrosive processes. Figure 6.13 shows a typical current pulse, which occurs as a result of metal dissolution in a locally destroyed passive layer.

At this small active location, a new passive layer is formed within a short time. This process is called repassivation.

Fresh metal surfaces have a large transient during the start of passive layer formation (dashed line

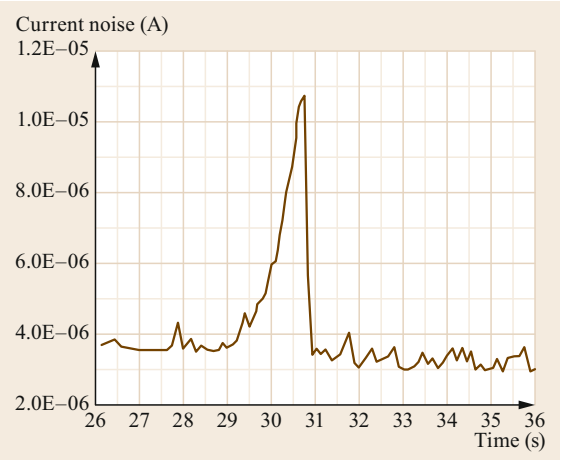

Fig. 6.13 Individual transient on a fresh surface of high-alloyed steel (X5CrNi18-10/SS304L) in a chloride-ion containing environment [6.9]. The amount of charge can be used to calculate the number of metall ions released to the electrolyte and corresponds further to a cubic metal defect

in Fig. 6.14). Over time, these events become less frequent, and the amplitudes decrease. A solution containing chloride ions has a significant noise behavior (solid line in Fig. 6.14). Multiple large current pulses are detectable, which only decay slightly after long periods. Chloride ions are not the initiator of local defects, but they interfere with the process of repassivation by increasing the solubility of metal ions in the local electrolyte significantly. In the case of larger amounts of chloride and material impurities, the repassivation can be severely affected. The electrochemically active sites grow and become a starting point for visible local corrosion.

This means that, for example, containers made of high-alloyed chromium-nickel steels should not be filled with chloride-containing media until the passive layer is built up and the activities of the passive layer are decayed. This can take hours or days, depending on the microstructure and alloy content of the material, as well as the ambient conditions. It must be considered that chloride ions are present as small concentrations in many neutral electrolytes. The low concentrations can accumulate, for example, due to evaporation processes on the material surface.

For the manufacture, processing, and operation of materials that form passive layers, it has to be considered that good corrosion properties are based on an extremely sensitive surface. The passive layer is only effective if the conditions for a constant, new formation are present. All deposits and impurities on the surface, whether visible or invisible (for example, in high-alloyed steels: sweat, dust, tool abrasion, rust particles, etc.) make the formation of the passive layer difficult and can result in local corrosion. However, a change in the metal itself due to high heat input, local work hardening, tensile stresses, etc., has an effect on the formation of the passive layer and, therefore, on local corrosion. Local corrosion can be divided into pitting and crevice corrosion.

Intentionally controlled corrosion is also used to form a homogeneous passive layer and to remove im-

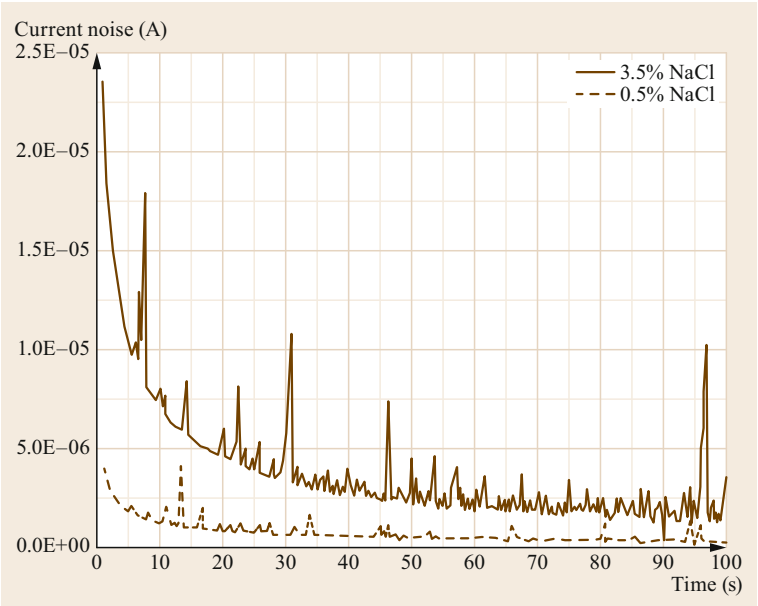

Fig. 6.14 Current noise of X5CrNi18-10/SS304L in different chloride-ion containing electrolytes: 0.5% NaCl (*dashed line*) and 3.5 NaCl (*solid line*) in accordance with [6.9]

purities. One example is the pickling of high-alloyed chromium-nickel steels in nitric acid to reduce the probability of types of local corrosion. The unavoidable priming colors after welding of high-alloyed corrosion resistant steels need to be removed mechanically or by chemical pickling. This region has locally different chemical compositions at the surface, and this causes a heterogeneous passive layer.

Pitting Corrosion

Pitting corrosion can occur in all technical systems that are made of materials that form passive layers. These are especially high-alloyed chromium-nickel steels, titanium and aluminum alloys, as well as nickel based-alloys. Pitting corrosion occurs mainly in the following steps:

1. Local destruction of the protective passive layer, for example, by mechanical, abrasive, erosive, or tribological stress.
2. Formation of a pit: the chemical composition of the surrounding medium reduces the rate of healing due to an increased solubility of metals in liquids with a higher halide ion concentration (especially chlorides and bromides) or sulfur concentration.
3. Metastable pit formation due to ongoing metal dissolution in the depth of the pit: simultaneous formation of a porous layer at the pit opening traps the electrolyte inside the pit with no connection to the ambient medium. This causes oxygen deficiency approximately 100 µm below the porous layer, and the electrolyte composition differs from the ambient medium outside the pit.
4. Stable growth of pit and hydrogen absorption due to local acidification: Chloride ions can enter the electrolyte of the pit through the porous layer. These cause increased solubility of metal ions in the pit electrolyte and disturb the repassivation in the case of an existing oxygen deficiency. The oxidation and formation of a passive layer is replaced by hydrolysis of the metals and the reactivity of the chromium acts as a reinforcing agent. As a result, the pit electrolyte is so strongly acidified (pH < 1) that the repassivation stops, and the pit corrosion can accelerate into the depth of the material. The hydrolysis causes the release of a great amount of hydrogen ions in the pit electrolyte. Only a small fraction of hydrogen recombines to molecular hydrogen, which, however, can hardly transfer through the porous layer. Larger quantities of gas would cover the metal surface in a way that the partial anodic reaction of the metal dissolution in the pit ground would also come to a stop. For this reason, it can be assumed that most of the hydrogen ions that are created in the base of the pit by hydrolysis are directly absorbed by the material (Fig. 6.15).

Two separate cathodic reactions are carried out during pitting corrosion, as well as during crevice corrosion. In addition to the partial cathodic hydrogen reaction, the anodic partial reaction in the pit electrolyte is additionally accelerated by the electron acceptance of the cathodic oxygen reaction (6.4a) even in a neutral ambient electrolyte. Pitting corrosion spreads rapidly into the material depth when only a few pit nuclei are formed.

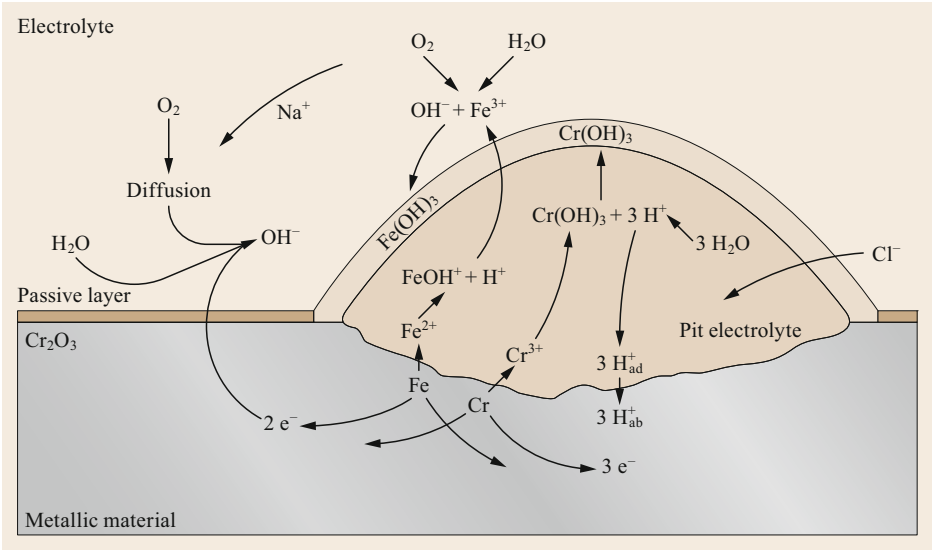

Fig. 6.15 Individual reactions and separation of the cathodic partial reaction during pitting corrosion of high-alloyed chromium-containing steels

The ability of a material to repassivate, and, therefore, the resistance to pitting corrosion, is predominantly determined by its alloying elements. Chromium and molybdenum are particularly important. To evaluate the influence of the alloying elements, the concentrations are provided with factors and summed up. For this purpose, various so-called pitting resistance equivalent numbers (PREN) were determined. However, there are several approaches that weigh the main alloying elements such as chromium, nickel, and molybdenum (and in many cases nitrogen) differently.

The critical pitting temperature (CPT) is a common, easily determinable parameter. It is determined in a 10% $FeCl_3$ solution, and the temperature is increased by 2.5 °C every 24 h until pitting corrosion becomes visible. A faster procedure is the determination of CPT by electrochemical noise. It is, however, more important to quantify the behavior of repassivation. This is evaluated by the so-called repassivation potential or repassivation temperature.

Crevice Corrosion

At first, crevice corrosion is similar to pitting corrosion. For components made of high-alloyed steels, the following four stages of crevice corrosion, which occur in a similar manner also in the electrolyte solution in the crack, can be distinguished (Fig. 6.16):

1. Oxygen consumption in the crevice.
   At first, uniform corrosion with the formation of metal hydroxide occurs in the crevice. The typical passive layer is formed on the surface of high-alloyed steels and nickel alloys. The anodic metal dissolution and cathodic oxygen reduction run parallel inside and outside the crevice. As a result of passive layer formation, the oxygen consumption increases inside the crevice. Depending on the crevice width, oxygen can no longer diffuse from the ambient electrolyte into deeper regions exceeding 100 µm. The time until total consumption of oxygen in the crevice can be calculated by Faraday's law. In combination with Fick's first law, the critical depth of the crevice can be determined. Within the critical depth, there is still a sufficient oxygen supply, and no crevice corrosion occurs.
2. Hydrolysis and drop of pH, as well as drop of electrochemical potential.
   As a result of oxygen deficiency, hydrolysis of chromium takes place, which precipitates as $Cr(OH)_3$. This often closes the crevice opening with a porous layer and prevents the further supply of relatively large oxygen molecules. Reasons for the preferential hydrolysis of chromium are its reactivity, the increased solubility of chromium due to diffusing chloride ions, and the higher solubility of other hydroxides. Hydrolysis causes the release of a large amount of hydrogen ions. This results in drops in pH and electrochemical potential with increasing hydrolysis. Cracks in metals cause similar corrosion mechanisms as crevices, and the pH at the tip of progressive cracks is significantly lower than in stationary cracks. The pH value in crevices and cracks of high-alloyed steels in a maritime environment is typically $0 \leq pH \leq 3$. The tendency of crevice corrosion increases with an increasing chromium content of above 15% due to the anodic current density and Cr concentration in the crevice increasing with decreasing pH.
3. Destruction of the passive layer and accelerated corrosion.
   As the hydrogen ions in the crevice increase, chloride ions diffuse from the ambient medium

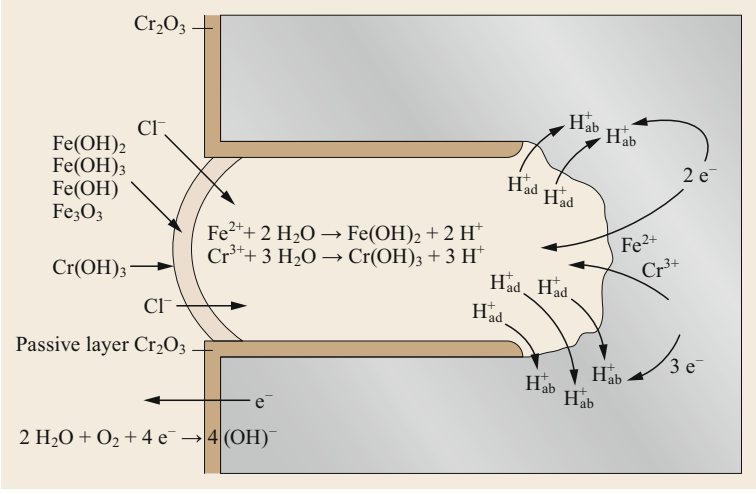

Fig. 6.16 Individual reactions and the separation of the cathodic partial reactions during crevice corrosion of high-alloyed chromium-containing steels

through the porous layer into the crevice to restore charge equalization. This increases the solubility of chromium in the gap and the formation of hydroxyl complexes [6.2, 4]. The hydrolysis of the chromium comes to a standstill and no passive layer can be formed. The crevice is activated, and the anodic current density in the crevice increases. The activation of the crevice can be registered as a drop in the open circuit potential.

4. Repassivation and hydrogen absorption.
In natural and artificial crevices or cracks, most of the hydrogen formed by metal hydrolysis is absorbed by the nonpassivated crevice ends or crack ends. Only a small amount recombines to form molecular hydrogen, which cannot effuse from deep crevices or cracks. If more gaseous hydrogen is produced in the gap, it would cover the metal surface in the crevice, and crevice corrosion would stop. The absorbed hydrogen causes material degradation, particularly at the end of the crevice or crack. Crevice and pitting corrosion can also cause hydrogen-induced cracking if an additional mechanical stress perpendicular to the crevice or crack is applied. If fresh metal surfaces are provided at the crack tip, further corrosion depends on the oxygen deficiency and crack length, as well as the repassivation behavior of the metal.

Crevice corrosion and its effects can be avoided by

- High purity and adaption of the alloying contents of material
- Low vertical mechanical stresses
- Avoiding crevices and the access of Cl-ions containing aqueous electrolytes into the crevice.

6.2.5 Stress Corrosion Cracking

Significant for all cracking phenomena coupled with corrosion is that the actual corrosive load due to an aggressive corrosive environment is superimposed by a mechanical load (stresses), mostly perpendicular to the crack propagation direction (Fig. 6.17). Hence, the mechanical load is regarded as the main cause for crack initiation, and the corrosion reactions, as a result of the surrounding medium, only assist the cracking process. This process is called environmentally assisted cracking (EAC). Frequently, the environmental conditions influence both mechanical and corrosive loads. Ambient temperature and pressure load the material mechanically but also have a particular influence on the simultaneous corrosion reactions. Crack initiation mostly occurs at already prematurely damaged surfaces. From the phenomenological point of view, it is necessary to distinguish between mere corrosion cracking and superimposed corrosion cracking with previous local corrosion (for example, pitting or crevice corrosion).

Basically, cracking in corrosive environments occurs with the interaction of three areas of influence: the material (mostly with a susceptible microstructure), coupled corrosion and mechanical loads (simultaneously), and design aspects (for example, gaps or unfavorable cross sections versus the load direction). In the case of a superimposed static mechanical load, this is commonly called stress corrosion cracking (SCC). Nonetheless, even straining of the material as the result of static tensile stresses can be the cause of SCC. In the case of mere cyclic mechanical load, it is called corrosion fatigue (CF).

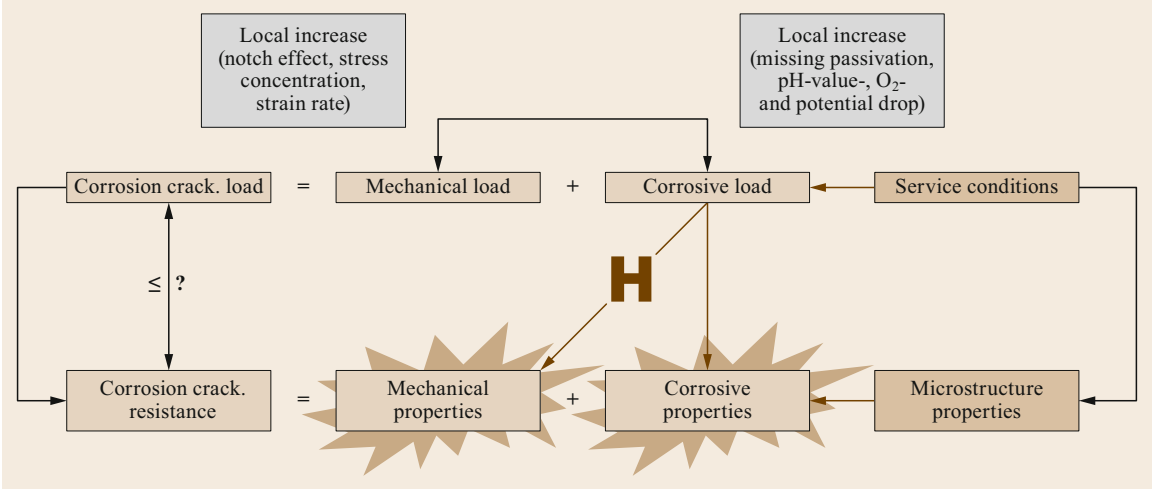

Fig. 6.17 Coupled loads for initiation of corrosion cracking

Stress Corrosion Cracking Under an Open-Circuit Potential

In the case of an open-circuit potential (OCP), in most cases, SCC starts from already existing corrosion types or from other respective defects at the material's surface. Especially in the case of pitting or crevice corrosion, an aggressive medium can be generated at the bottom of the pit or the gap within a depth of ca. 100 mm due to the decreased oxygen content and the potential drop. Under these circumstances, crack initiation is not only a consequence of the anodic dissolution of the metal. In fact, the separation of the cathodic partial reaction is responsible for the highly-increased hydrogen absorption in the material. This locally accumulated hydrogen may result in a distinct degradation of the mechanical properties (ductility) of the material and assists crack initiation because of the additional high strains and stresses at the bottom of the pit or gap. Components made from materials that form passive or cover layers and where pitting or crevice corrosion can take place, are generally susceptible to an SCC failure. Gaps, undercuts, a lack of penetration, and temper colors located at welded components (made from materials forming the passive layer) are quite often locations for initiation of SCC.

After crack initiation, the velocity of further crack propagation can increase rapidly under the coupled effect of the mechanical load and the corrosive environment. The corrosion reactions inside the crack are similar to those during crevice corrosion. Two different and separate cathodic reactions are involved, local and global reaction. Supported by the sharp decrease in oxygen content, the pH value and potential drop in the sharp and narrow crack, the generating electrolyte in the crack becomes more aggressive (compared to crevice corrosion). Hence, the crack propagation is a result of the accompanying hydrolysis due to the missing oxygen. Most of the generated hydrogen is absorbed at the fresh metal surface directly at the crack tip. However, partial pressure of the generated gaseous hydrogen can suppress further recombination. Nonetheless, even small amounts of promoters (like H_2S, arsenate, or cyanide compounds) in the electrolyte may suppress the hydrogen absorption totally at the freshly formed and not yet passivated metal surface at the crack tip. Hence, crack propagation depends on how fast the material is locally strained at the crack tip (Fig. 6.18). This is important for the necessary passivation to hinder further anodic dissolution of the metal and subsequent hydrogen absorption.

Hence, under the OCP condition, crack initiation with previous pitting or crevice corrosion and the corresponding crack propagation are not solely initiated by the anodic partial reaction at the bottom of the pit or the end of the crevice. In that connection, the former term anodic dissolution seems to be outdated.

SCC under the OCP condition takes place mostly in aqueous, especially Cl-ion-containing, electrolytes. This reaction is always accompanied by hydrogen absorption due to the local cathodic partial reaction. The partial cathodic reaction itself is mostly unaffected by the surrounding electrolyte (pH value, oxygen content, and composition of the electrolyte). The level of the locally absorbed and accumulated hydrogen concentration versus hydrogen-dependent material properties, decides if and how fast this type of SCC generates. Hence, this type

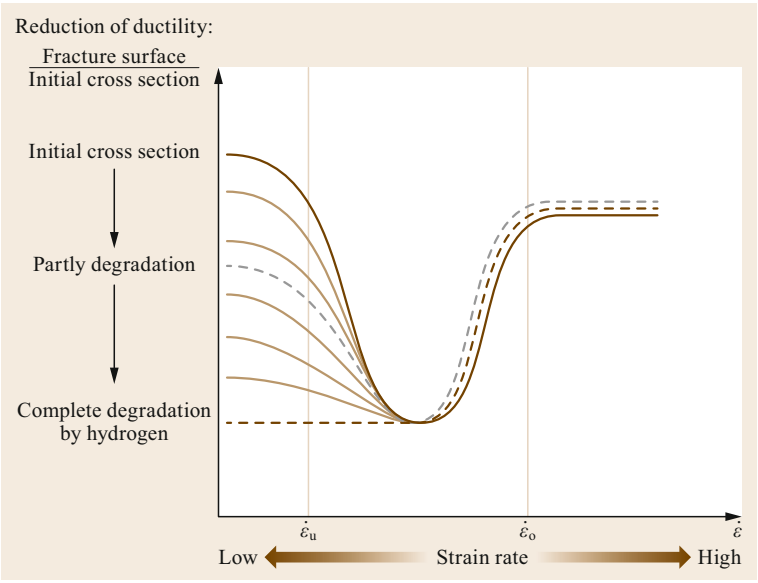

Fig. 6.18 HASCC susceptibility versus strain rate dependency

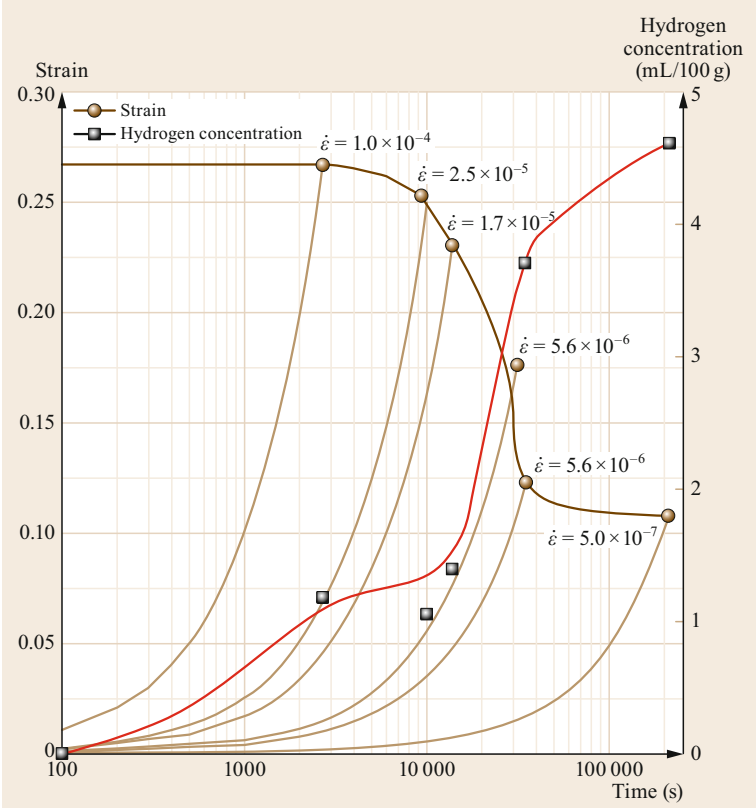

Fig. 6.19 Time-strain-to-fracture (TSF) diagram of Ni-Mo alloyed 13% Cr martensitic steel, tested in 10% NaCl H_2S-saturated solution

of corrosion is called hydrogen-assisted stress corrosion cracking (HASCC), as shown in Figs. 6.18 and 6.19.

In specific environments, SCC under the OCP condition can appear without previously visible pitting or crevice corrosion. This is the case if aqueous media contains high amounts of promoters (or recombination poison) so that crack initiation can occur directly at the metal surface. These substances suppress the cathodic oxygen reaction as well as the cathodic hydrogen recombination at the metal surface. The use of high-alloyed materials in neutral Cl-containing media, which contain pH value reducing H_2S, is called *sour service* internationally. During sour service, hydrogen protons can enter the material unaffectedly and are absorbed in very high concentrations at a large area. As a consequence of the significant reduction of ductility, the crack grows very fast and results in sudden component failure without any prior visible change of the metal surface. The avoidance of this SCC sequence is, therefore, of high importance. International standards for the construction of components in the oil and gas industry demand operators of such facilities to communicate with the respective manufacturers and to disclose possible sour service conditions.

In oxygen-free conditions, as well as at elevated temperatures and pressure, hydrogen can be generated from the so-called Schikkor reaction [6.3], for example, in high-temperature water or steam. Practically, this reaction is intentionally used in thermal power plants. At first, the Fe surface of the components undergoes electrochemical corrosion. Subsequently, the generated $Fe(OH)_2$ decomposes to magnetite (Fe_3O_4), water (H_2O), and molecular hydrogen (H_2).

$$3\,Fe(OH)_2 \rightarrow Fe_3O_4 + H_2O + H_2 \qquad (6.18)$$

The aim is to form a stable cover layer of magnetite in pipes made of heat and creep-resistant steels, for example in boiler components. This layer protects the metal surface from further electrochemical corrosion.

Stress Corrosion Cracking at a Defined Corrosion Potential

A whole component or specific area, e.g., in a welded joint, can be exposed to a solely cathodic partial reaction during galvanic or selective corrosion. The same applies to the intended cathodic protection by sacrificial anodes or artificial current supply. In the worst case, the

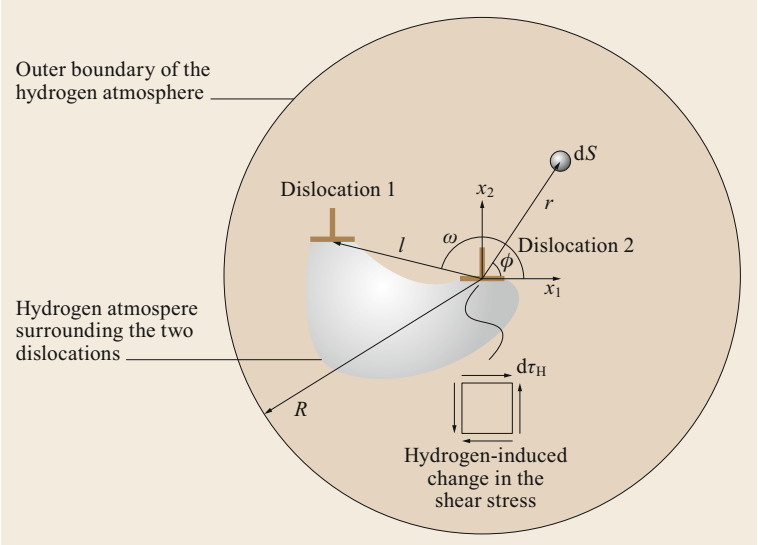

Fig. 6.20 The HELP mechanism by *Hirth* [6.10] and *Brinbaum* et al. [6.11] The effect of hydrogen on interacting dislocations is considered as a change in the shear stresses $d\tau_H$ (dS is the considered area in the material at the coordinates r and ϕ; the coordinates l, ω describe the position of two dislocations towards each other)

cathodic potential is in the range of the cathodic hydrogen reaction. This could cause hydrogen absorption and, therefore, rapidly progressing hydrogen-induced cracking, especially if additional promoters are present in the electrolyte. These cases are commonly referred to as cathodic stress corrosion cracking.

In the opposite case, a positive/anodic potential is applied to the component or specific area. It has to be distinguished whether or not the material is able to form a passive layer. Materials without this ability and simultaneously applied mechanical stress will not fail due to the combination of mechanical stresses and corrosion. The reduction of the cross section because of other highly abrasive corrosion forms, such as shallow pits or groove corrosion, will cause failure. If, in a rarer case, a material that can form passive layers is exposed to an anodic potential, the above-mentioned pitting or crevice corrosion takes place with a separate cathodic partial reaction. The speed of the crack start and crack propagation depends on the local strain rate, hydrogen absorption rate, diffusion capacity, and the rate of repassivation.

Crack Mechanisms

The mechanical properties of most metallic materials can be deteriorated by hydrogen. This affects, the deformability in particular and to a lesser extent, the strength. An outdated term for this is hydrogen embrittlement, which is replaced by the concept of degradation of material properties by hydrogen. In order to describe the metallurgical process of hydrogen-assisted cracking (HAC) microscopically, two metallurgical mechanisms are combined [6.10–13]. On the one hand, this is the interaction of hydrogen with dislocations. The absorbed hydrogen emits new dislocations locally, which then begin to migrate (hydrogen-enhanced localized plasticity, HELP) (Fig. 6.20) [6.11]. In this case, ductility-reducing effects due to hydrogen trapped at dislocations can also occur in the form of blockages, stacking errors, accumulation at grain boundaries, etc. On the other hand, the dissolved hydrogen at the interstitials decreases the cohesion of the metal lattice (hydrogen-enhanced decohesion, HEDE) (Fig. 6.21) [6.11].

It should be noted that in addition to the hydrogen, which is dissolved in the lattice, hydrogen that is bound to defects (dislocations, etc.) also has an effect. Furthermore, it must be noted that mechanical stress and strain are primarily the cause of crack formation (material separation). This results in the terminology of HAC and, instead of cathodic stress corrosion cracking, it is referred to as hydrogen-assisted stress corrosion cracking (HASCC). Cracking occurs if the mechanical stress exceeds the deformability of the material. This depends on the degradation of properties due to hydrogen concentration. The following aspects are important for the occurrence of HASCC: how much hydrogen is absorbed at the crack tip; how much is absorbed in the strain field; and the concentration of hydrogen that decreases the deformability. These criteria are increasingly used in numerical models to avoid HASCC in components [6.12].

Corrosion Fatigue

As in the case of corrosion cracking, conjoint corrosion and cyclic mechanical loading may also result in sudden component failure. In a similar manner, this type of corrosion cracking (corrosion fatigue) is separated

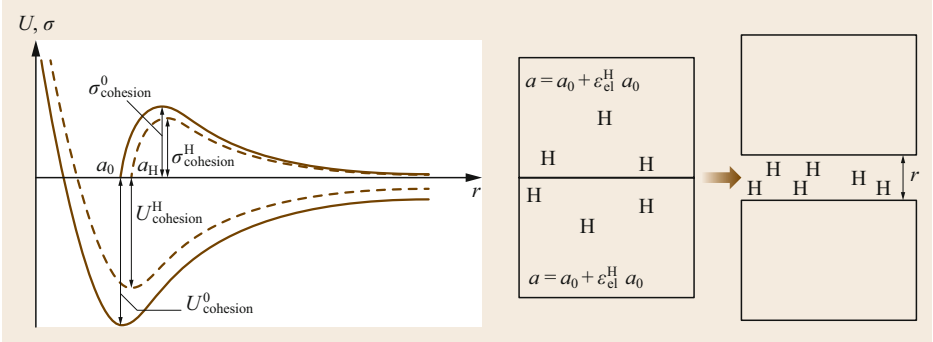

Fig. 6.21 The HEDE mechanism by *Schatt* et al. [6.14]. The effect of hydrogen is understood as a reduction of the cohesive energy U^0_{cohesion} (the cohesive stress $\sigma^0_{\text{cohesion}}$) on $U^{\text{H}}_{\text{cohesion}}$ ($\sigma^{\text{H}}_{\text{cohesion}}$); $\varepsilon^{\text{H}}_{\text{el}}$ is the elastic strain induced by H, and a_0 is the lattice constant

into incubation of crack, crack propagation, and overload fracture. The crack initiation is typically located at already damaged surface areas, as a consequence of pitting or crevice corrosion, or at a grain boundary.

Nonetheless, a crack can be initiated only by cyclic mechanical loads. For example moving edge dislocations can be transferred to the material surface by plastic straining and act as nuclei for corrosion. Under the OCP condition, the crack initiation and propagation are like those of SCC, i.e., it depends on oxygen content and the related decrease of pH value and the potential drop. In addition, the cathodic partial reactions are separated, and locally high amounts of hydrogen may be absorbed in the material. Then, the hydrogen can degrade the mechanical properties and influences crack propagation and the crack path. Hence, crack initiation and propagation of CF are not only influenced by the anodic partial reaction, neither for OCP nor for defined corrosion potentials in electrolytes.

Similarly to the strain rate influence during SCC, the frequency and amplitude of the load cycles during CF have great influence on crack initiation, the crack path, and its growth velocity. As a consequence of the alternating mechanical load, pump effects may occur in the electrolyte in an existing crack. These pump effects are responsible for the exchange of oxygen with the surrounding electrolyte and permanently change the passivation behavior. Thus, the independency of anodic and cathodic partial reaction is much more influenced in the case of CF compared to SCC.

CF occurs within a limited frequency range (i.e., the number of load cycles per time increment). This range is characterized by a very high crack growth rate. Hence, testing of CF should always be conducted with a varied frequency of the load cycles. The effect of the coupled cyclic mechanical and corrosive load (decreased cycle number) is demonstrated in Fig. 6.22 in the respective Wöhler diagrams (S/N curve).

Generally, it can be stated that the very high frequency of the load cycles mostly results in mechanical effects. During the single cycles, there is insufficient time to generate corresponding corrosion reactions at the freshly formed metal surfaces. In that case, crack propagation is merely mechanically based without any visible corrosion effect at the surface.

In the case of low frequency, the effect of corrosion is predominantly due to the extended corrosive load. Here, the crack path is characterized by a typical corrosion effect. Contrary to mechanical fatigue cracking, typical features like streaking cannot be seen immediately. This becomes more complicated due to very frequent intergranular and transgranular hydrogen-assisted cracks.

6.2.6 Erosion and Cavitation Corrosion

The combination of corrosive fluids with high flow velocity can result in erosion corrosion [6.2]. Often, a different kind or no corrosion occurs in the same media in the stationary or slow flowing state. The surface of passivated materials is especially susceptible to erosion corrosion at high flow velocities due to the small thickness of the protective oxide layer (or the passive layer). If this layer is removed by erosion, material is exposed to aggressive media and is activated. In many water or steam-bearing facilities, erosion corrosion can appear if the medium has a high flow velocity and contains solid-state particles, which additionally load the metal surface due to their mechanical impact. However, the relative share of the mechanical and electrochemical parts of corrosion can be different. Hence, erosion corrosion ranges from pure erosion loads to pure corrosive loads. The appearance of erosion corrosion is typically flow-oriented and dependent on the ability of the material to generate a protective coating layer. For example, copper alloys generally form light and loose

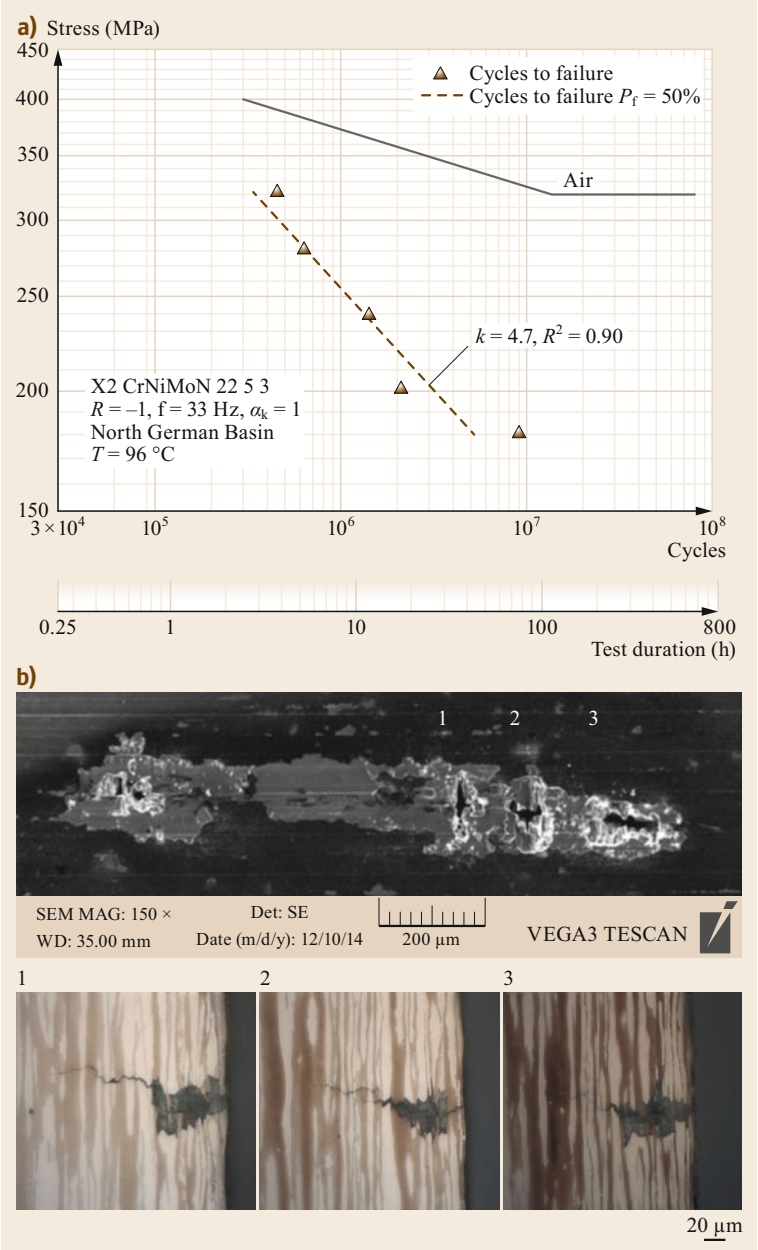

Fig. 6.22a,b CF exemplified by austenitic-ferritic duplex steel in 96 °C hot salt solution versus air. **(a)** Decrease of stress amplitudes in the case of CF, **(b)** pitting corrosion coupled with starting CF at the surface. (Reprinted from [6.15], with permission from Elsevier)

layers, which can be easily destroyed and removed. In practice, erosion corrosion is a well-known problem in heat exchangers [6.5].

Cavitation is the process of formation and collapse of steam and gas-filled bubbles in fluids, caused by a temporary decreased static pressure below the vapor pressure. This can be initiated by flow instabilities (flow cavitation) or waves of low pressure (oscillation cavitation). As a result of the implosion of the bubbles, the material surface can be locally destroyed. This prematurely damaged surface is indicated by increased reactivity. If corrosion superimposes the cavitation process, then it is called cavitation corrosion. Repeated bubble implosions in the same position prevent the material from renewing the protective covering layer, and the existent layer is destroyed followed by crater-like corrosion pits. In addition, the bubble implosions increase the local temperature, whereby the corrosion rate increases. Cavitation corrosion typically occurs in technical components, where the material surface has to

withstand a high relative movement within (corrosive) surrounding media, for example in centrifugal pumps, turbines, propellers, or stirring devices. To avoid cavitation corrosion, the geometry of the components should be optimized, media pressure increased, and the flow velocity decreased. From the material point of view, hardened materials or coatings can be used [6.5].

6.2.7 Fretting Corrosion

Fretting is a special type of erosion corrosion in gaseous media [6.2]. Basically, this process involves the coupled effect of an environmental (corrosive) medium and a tribological load in terms of friction. Vibrations are very often the main cause. Both corrosion and tribological loads result in wear. In this case, the material is in contact with another solid-state body via relative movement. These small movements, like vibrations or slipping, lead to the abrasion of oxide layers on the contact surfaces of frictional connections. Subsequently, the freshly formed metal surface can undergo accelerated anodic dissolution. The generation of metallic particles by wear is the primary cause for fretting. These particles react instantaneously with the surrounding medium. They are ground, sintered, chemically changed, or compacted further because of the simultaneous tribological load. During fretting, the formation of dimples can frequently be superimposed by additional oscillating mechanical loads so that subsequent corrosion fatigue occurs.

6.2.8 Microbiologically Induced Corrosion

Microbiologically induced corrosion (MIC) is a synonym for all types of corrosion that are initiated, intensified, or perpetuated by microbial activities [6.5, 16]. Microbiologically affected corrosion encompasses multiple partial reactions (Fig. 6.23) and is not fully understood still today. However, it can occur on almost all plant and building materials and estimates are that at least 20% of all corrosion damage is microbiologically influenced. Microorganisms that initiate this type of corrosion are a wide range of fungi, algae, and lichens. These can colonize on material surface in nearly all environments. So-called biofilms require liquid surrounding media, solid-state material, and microorganisms. Their formation can be divided into three stages:

1. Incubation: primary adhesion of the biofilm, which is mostly without effects for technical systems.
2. Irreversible absorption of macromolecules (polysaccharides, lipopolysaccharides, humic substances, proteins, and so on) and related growth of primary colonizers on the material surface.
3. Plateau-stage: the biofilm thickness depends on the growth rate of colonizers and is in biodynamic equilibrium.

Inside such biofilms, anaerobic conditions are generated with an increasing thickness of the biofilm due to the decreasing partial pressure of missing oxygen.

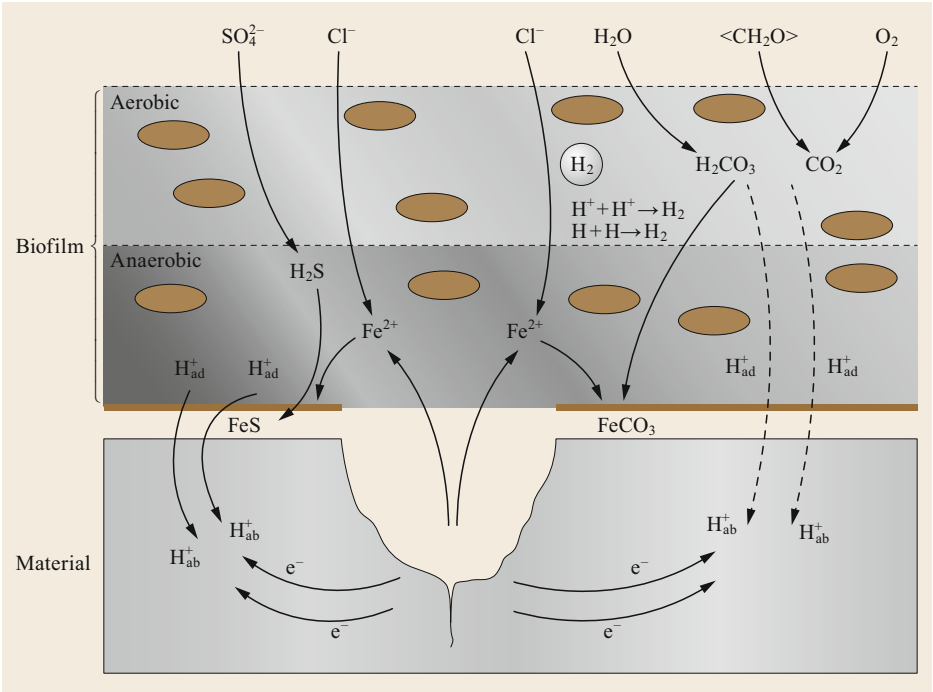

Fig. 6.23 Reactions of microbiologically affected corrosion, simplified in accordance with *Enning* and *Garrelfs* [6.16]

In the outer area, the organic substances are oxidized under aerobic conditions. They are then released into the surrounding media. In between, there is a layer of anaerobic bacteria that forms decomposition products in terms of water and organic acids via fermentation. Directly at the material surface (the inner area of the biofilm), anaerobic sulfate-reducing bacteria transform hydrogen, organic acids, and SO_4^{2-} ions to sulfides and water (Fig. 6.23).

Thus, amongst others, H_2S is produced, which acts as a promoter for hydrogen absorption in the material beneath the biofilm. In the case of a simultaneous mechanical load, hydrogen-assisted stress corrosion cracking can occur. Additional surface corrosion, as a result of firmly adhering biofilms, is pitting and crevice corrosion. Special attention is paid to microbiologically affected corrosion in the petrochemical branch of the offshore industry. In this industrial branch, H_2S is produced mostly as a result of subsoil oil or gas reservoirs being flushed with seawater to increase output. In that case, microorganisms are enriched in anaerobic conditions.

6.3 Chemical Corrosion and High-Temperature Corrosion

Chemical corrosion is characterized by the instantaneous reaction of the material and the corrosive environment. The resulting corrosion products determine any further reactions. As in the case of conventional corrosion, the generation of protective layers that impede the diffusion of elements and, hence, disable or delay further corrosion reactions is desired. In contrast to electrochemical corrosion, chemical corrosion implies that partial reactions occur at the same local position. The result of the corrosion can be determined by gravimetric or metallographic analysis.

If the instantaneous chemical reaction of a material occurs in the corrosive environment at elevated temperatures (mostly accompanied by elevated pressure) and in the absence of aqueous electrolytes, this process is called high-temperature corrosion. High-temperature levels create a reactive layer at the atmosphere–solid boundary layer. The adsorption and absorption of molecules from the gas phase at the material surface and the diffusion of absorbed molecules (or ions) through the reactive layer determine the chemical reaction kinetics, as well as the diffusion of elements from the bulk material to the surface. If the material is permanently dissolving or decomposing, catastrophic corrosion is existent.

6.3.1 High-Temperature Corrosion Without Mechanical Load

Different types of high-temperature corrosion exist (Fig. 6.24) and occur mostly in different combinations in technical utilization [6.18]. The reaction product formed at the material surface in a gaseous atmosphere is called scale. In general, this term is used for corrosion processes in oxidizing (oxygen-containing) or reducing (sulfur-containing) atmospheres. A special type

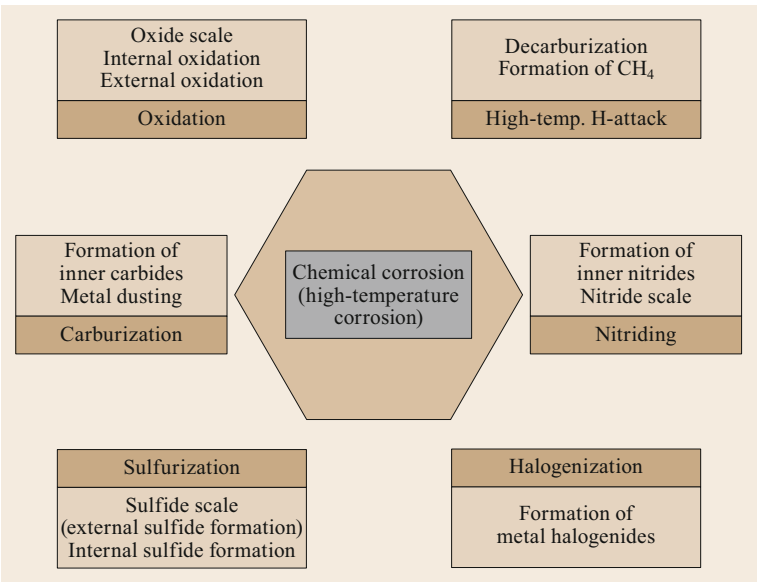

Fig. 6.24 Types of high-temperature corrosion

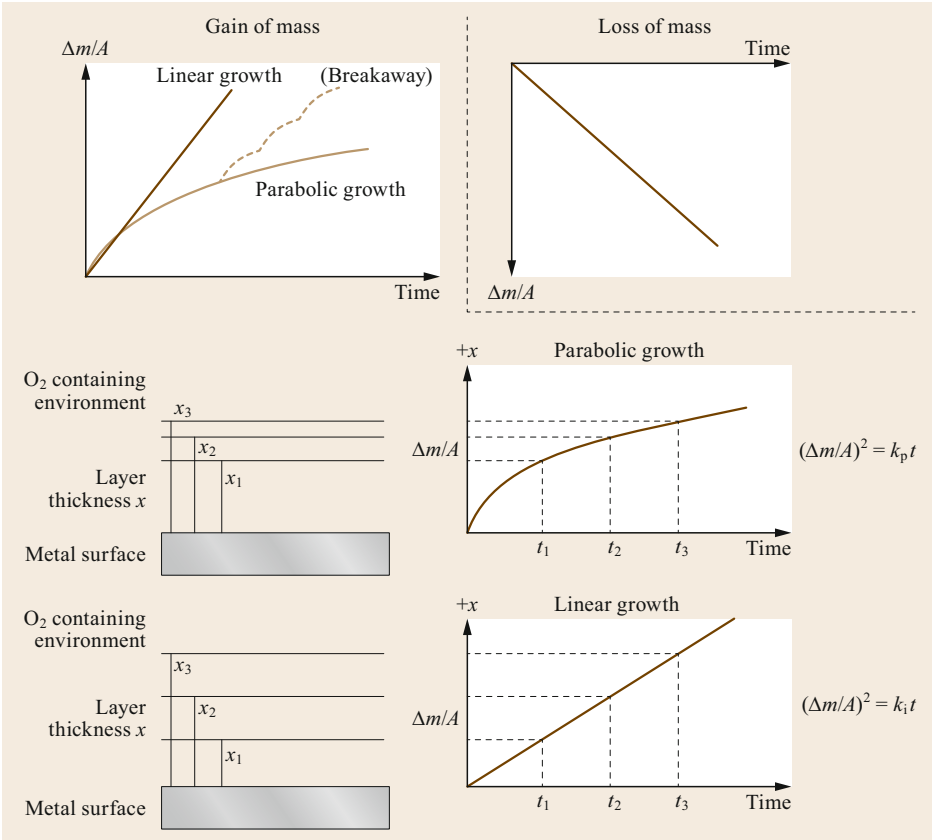

Fig. 6.25 Evolution of mass change during high-temperature corrosion: assumption of linear or parabolic scale growth and linear loss of mass (catastrophic oxidation, in accordance with *Schütze* [6.17])

of high-temperature corrosion is hot corrosion, which occurs with the participation of molten salts. Thus, sulfurization, nitriding, and oxidation (Fig. 6.24) are significantly accelerated. In a few technical processes, e.g., glass-making, molten salts can be directly present. However, in most technical processes, the corrosion promoting molten salts condense from the surrounding atmosphere on the hot component surface, e.g., in the case of combustion of fossil fuels (coal, petroleum, or natural gas). Hot corrosion is mostly more complicated to handle due to the nonprotective and porous nature of the scales generated. These scales cannot protect the material from decomposition in corrosive environments. Susceptible materials are, for instance, Ni- or Co-based alloys and high-alloyed ferritic steels.

A simplified assessment of the corrosion resistance of metals in gaseous atmospheres is the use of the Ellingham–Richardson diagrams. These diagrams show the stability of the scale formers versus the partial pressure of the corrosive gas. Thus, the corrosive reaction of the base material can be observed [6.19]. The reaction kinetics can be determined by the scale growth by gravimetric analysis due to the loss of mass, Δm. An increase in mass (scale growth) or loss in mass (flaking or evaporating of the corrosive scale) depends on the material, temperature, partial pressure, and dissociation kinetics of the gas at the corrosion scale and many more. The scale growth (e.g., in the case of oxidation) can be described by parabolic, linear or logarithmic law and is in all cases related to a certain material surface area A (Fig. 6.25). The proportionality constant k_p describes the corrosion resistance of different materials in the case of parabolic scale growth. This law represents the common case for most technical materials. The typical range of k_p for steels with 12–14% Cr content is about 10^{-8}–10^{-9} kg^2 m^{-4} s^{-1} (corrosion in air). However, the opposing effect by loss of mass is existent in the case of flaking of the oxide scales at very high temperatures or increased mass loss by evaporating reaction products (breakaway corrosion). This is also called catastrophic oxidation and is indicated by a linear loss of mass.

To avoid or reduce high-temperature corrosion protective scales must be generated (as in the case of electrochemical corrosion), for example, stable oxides like Cr_2O_3 or Al_2O_3. Alloys that form one or both mentioned

covering scales are called chromium or aluminum oxide formers. Al-oxide forming materials can be used up to 1300 °C. The temperature limit of the technical usage of a material is also dependent on a simultaneous mechanical load. Dense oxide scales also protect against carburization, nitriding, and sulfurization.

Oxidation

Pure high-temperature corrosion in terms of oxidation is the formation of scales (for example, during milling) on steel surfaces. The surface of Fe-rich alloys reacts with scale formation at 570 °C in oxygen-rich gases. The sequence of the scales is Fe-FeO-Fe_3O_4-Fe_2O_3-O_2. The wüstite (FeO) formed covers nearly 90%, magnetite (Fe_3O_4) has a share of 7–10%, and hematite (Fe_2O_3) only has a share of 1–3%. In the case of slow cooling (below 570 °C), wüstite decomposes to pure Fe and magnetite. Due to the different density and decreased ductility of magnetite, the scales generated are brittle and contain microcracks. By rapid cooling, for example, in the case of hot rolling of sheet metal, this transformation can be suppressed, and the scale remains on the material surface. In that connection, the oxidation rate of steels can be reduced by alloying of Cr, Al, or Si. Typically, low-alloyed heat-resistant steels are sufficiently resistant to scale formation.

Furthermore, special scale-resistant high-alloyed steels are used as commercial alloys. These steels can be pure ferritic or martensitic, or may have a ferritic-martensitic microstructure. They are typically used in steam boilers and tubes or in industrial furnaces. Austenitic scale-resistant steels are mostly used in flue-gas treatment facilities or in components of the chemical or petrochemical industries [6.14]. Depending on the Al, Si and Cr content, the scale resistance is sufficient up to 800 °C (for example, X10CrAl7) or 1200 °C (X10CrAl24 and X15CrNiSi25-20). Alternatively, low-alloyed steels can be protected by coatings during steel-making. This is exemplified by the Al-Si or Al-Zn coatings used in the automotive industry. These are used to protect 22MnB5 steel during press-hardening (austenitization and quenching during drop forging) against scale (or oxide scale) formation. Otherwise, these scales would later complicate painting of the car body parts [6.20].

Carburization (Metal Dusting)

A representative example of carburization of materials is the carbide formation in corrosion-resistant Cr-Ni alloys in a carbon-dispensing gas atmosphere. Subsequently, carbides are also formed in the bulk material. The inner carbide formation occurs from 800 to 1200 °C (formation of Cr, Ni, or Fe-rich carbides of type $M_{23}C_6$, which decompose to type M_7C_3). This kind of corrosion reaction causes deterioration of the mechanical properties (ductility and toughness at low temperatures), the thermal properties (conductivity), as well as the oxidation resistance. Especially the weldability of a material can be influenced (an increase of carbon equivalent).

A catastrophic carburization can occur in an intermediate temperature range (400 to 800 °C) and is called metal dusting [6.21]. Nonetheless, this temperature range can vary (350 to 900 °C) depending on the material and its service conditions. Metal dusting is characterized by the decomposition of the material into a dust of pure metal and carbon. In contrast to conventional carburization, metal dusting demands a carbon-supersaturated gaseous atmosphere. The process of metal dusting starts with fast supersaturation of the material with carbon of both surface areas and grain boundaries. This is followed by the formation of unstable carbides like Me_3C (Me = Fe, Ni) and the final decomposition into the metal and pure carbon.

$$Me_3C \rightarrow 3\,Me + C \tag{6.19}$$

The fine metal particles generated additionally accelerate the carbon absorption due to the catalytic effect of the enlarged surface of particles compared to the solid-state material. The result is voluminous segregation of carbon at the metal surface. In the case of insufficient adherence of the particles (for example, by removal due to flowing gases), indentations that are similar to electrochemical pits occur.

High-Temperature Hydrogen Attacks

In contrast to carburization, steel components in the chemical or petrochemical industries (for example, synthesis gas production, ammonia, and so on) can suffer from decarburization. This loss of carbon is mostly a result of pressurized hydrogen. This phenomenon is called a high-temperature hydrogen attack (HTHA). Typically, service conditions of 200 °C and 200 bar pressure are necessary for atomic hydrogen to be generated by thermal dissociation from the surrounding corrosive environment (pressurized pure molecular hydrogen or synthesis gases). The degradation of the component itself occurs due to the adsorption of atomic hydrogen into the material. Subsequently, the hydrogen reduces the cementite (Fe_3C) of the steel by removing the carbon and further forms methane (CH_4) and pure iron.

$$4\,H_{(Fe)} + Fe_3C \rightarrow CH_4 + 3\,Fe \tag{6.20}$$

Due to its size, the methane molecule cannot diffuse and is trapped in the microstructure. The result is an ag-

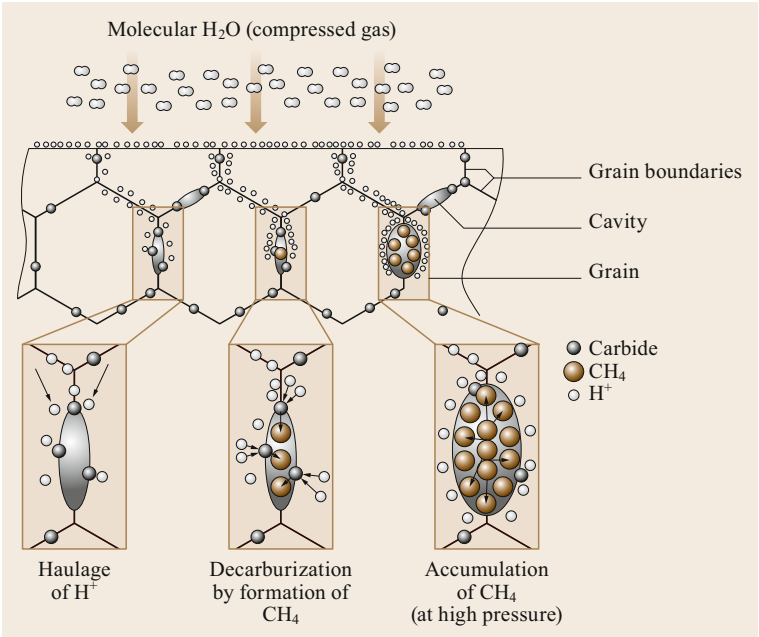

Fig. 6.26 HTHA in low-alloyed steels

glomeration of methane molecules under high pressure in the material. In addition to the detrimental formation of gas bubbles in the material there is the degradation of the mechanical properties of the steel by dissolution of the carbides (reduction of precipitation strengthening effect). In the case of already present microcracks at inclusions (preferably at grain boundaries), HTHA results in brittle fractures, which perhaps result in unexpected component failure. The mechanism of degradation by HTHA is exemplified in Fig. 6.26. The most susceptible steels are unalloyed carbon steels, Cr-Mo alloy steels show a much higher HTHA resistance. However, this resistance is also strongly related to the service conditions of the material (pressure, temperature, corrosive environment).

To avoid decarburization service the pressure and temperature of the components should be strictly monitored. The maximum boundaries for service conditions (pressurized hydrogen) can be found in the latest version of the Nelson diagram, for example, in API RP (American Petroleum Institute Recommended Practice) 941 (2016). The chemical and petrochemical industries operate components under high pressure and elevated temperatures for the processing of pure hydrogen or ammonia. Nowadays, 2.25% Cr-1% Mo-0.25% V-alloy steels are state-of-the-art and have replaced the conventional Cr-Mo steels. The alloying of V results in very small and very finely dispersed carbides (VC, V_4C, V_4C_3) in the microstructure. These precipitates have two positive effects: (1) they improve the necessary creep resistance of the material at higher temperatures, and (2) stabilize the carbides due to the higher affinity of V to carbon compared to hydrogen. Metallurgically optimized steels may also contain carbide stabilizers like Nb or Ti. The result is a higher strength of the material accompanied by an increased possible operational temperature and pressure.

Sulfurization

The ingress of sulfur into the microstructure leads to soft or brittle metal sulfides (Me_xS_2, Me_xS_3, Me_xS_4), or metal sulfates (Me_xSO_4) on the steel surface. These can also be molten at elevated temperatures. Typically, they are formed in combustion chambers as a part of the flue gas as a result of combustion of S-rich fuels (such as lignite coal or crude oil). Nonetheless, sulfurization occurs in waste incineration plants or biogas plants due to the complex composition of the flue-gas mixture.

Corrosion by sulfurization is called catastrophic in the case of the formation of eutectic phases with a low melting point, such as NiS ($T_m = 995\,°C$) or Ni/Ni_3S_2 ($T_m = 637\,°C$). For example, sulfur forms together with alkaline metals (Na, K), chloride, and oxygen aggressive molten salts. Additional reactions with Ni, Co, or Fe result in complex molten salts with a very low melting point compared to the surrounding atmosphere, e.g., $Na_3Fe(SO_4)_3$ ($T_m = 620\,°C$), $Na_3Fe(SO_4)_3/K_3Fe(SO_4)_3$ ($T_m = 555\,°C$), $CoSO_4$ ($T_m = 565\,°C$), and $NiSO_4$ ($T_m = 671\,°C$). These molten salts can result in very fast corrosion that perhaps finally leads to component failure. In contrast

to carburization, sulfurization is more dangerous. The reason is the increased rate of material degradation. In oxygen-rich atmospheres, a high content of SO_2 is the reason for sulfurization of the material and its further accelerated corrosion. As mentioned, the chemical corrosion of a material is mostly the result of a complex interaction of several corrosion mechanisms like oxidation and sulfurization.

Nitriding

Nitriding is a side effect of the service of components in N_2-containing atmospheres at high temperatures. Examples are materials operated in the flue-gas environment or for ammonia synthesis (Haber–Bosch process). Nitrogen is adsorbed on the material surface and forms corrosion scales. For example, at 300 °C high-alloyed Cr steels already show the formation of covering scales that consist of chromium nitrides. The scales are very brittle and have low thermal expansion coefficients. These are not stable and flake off each time in the case of mechanical or thermal loads. Hence, they are permanently formed and cause a high amount of removed parent material.

Compared to the formation of nitride covering scales, inner nitriding is more common. In this case, nitrogen diffuses into the bulk material and causes microstructural changes. In general, phases are formed that are hard and brittle (Me_2N or Me_3N) but increase the hardness of the material. This effect is intentionally used in the case of surface hardening to increase the wear resistance of a component. However, this technique is limited, e.g., in the case of high-Cr steels. In this case, Cr could diffuse from the bulk material to the surface in the nitrided scale. The hardened surface would be accompanied by decreased corrosion resistance.

Halogenation

Besides oxygen, carbon, sulfur, and nitrogen a few more dry corrosive environments like halogens can result in high-temperature corrosion. The most important halides are Cl, F, or Br. A halogen-containing atmosphere is the basis for very aggressive hydrogen halides (HF, HCl, HBr), and their acids are responsible for very high corrosion rates. For example, HCl can react with oxygen to form pure chlorine accompanied by water generation. This purified Cl can react with Cr-oxides (for example from the passive layer of corrosion-resistant Cr-Ni steels). This finally results in the formation of metal chlorides, for example (in accordance to [6.21]).

$$2\,Cr_2O_3 + 6\,Cl_2 \rightarrow 4\,CrCl_3 + 3\,O_2 \qquad (6.21)$$

These chlorides influence the protective oxide scale of the stainless steel. In addition, the metal chlorides show high vapor pressure at higher temperatures. This results in instantaneous evaporation of the unprotected material surface accompanied by highly increased corrosion rates. This effect should be considered in waste incineration plants or biogas plants due to the complex composition of the flue gas. Waste products may contain halogens. Sources for chlorine can be polymers like PVC and fluorine maybe from halogenated hydrocarbons like PTFE (in general known as *teflon*). Nonetheless, halogenation is intentionally used in coating processes like CVD (chemical vapor deposition) to deposit Cr, Al, or Si.

6.3.2 High-Temperature Corrosion with Superimposed Mechanical Loads

High-temperature corrosion as well as an additional superimposed mechanical load have a synergistic effect: a reduced lifetime of the component. On the one hand, it should be considered that a cross section can already be damaged due to an oxidation-related decrease of the material thickness. In addition, high-temperature corrosion can change the chemical composition and microstructure of the material, even in deeper sections. Thus, the tensile and ductile properties may vary significantly from the as-delivered condition. On the other hand, the protective oxide scales mostly have a decreased ductility compared to the parent material. Hence, these scales can crack and flake off very easily because of mechanical tensile loads. For example, due to unwanted nitriding, scales of chromium nitrides are very brittle. In addition, thermally induced stresses and distortions or temperature gradients between material and the covering scale (accompanied by internal growth stresses in the scale) can lead to early failure of the covering scale. All these facts increase the corrosion rates and accelerate the material degradation.

A practical example for high-temperature corrosion with a superimposed mechanical load is the increased number of shutdowns in fossil-fired power plants (due to the increasing peak power of renewable green energy—wind, water, solar—that has to be compensated in the power grid). The power-on and shutdown cycles causes high-temperature gradients and mechanical stresses in the steam tubes accompanied by a weakening of the inner magnetite layer. Additional creep load and alternating mechanical loads (short-term tensile/compression) always result in accelerated crack initiation and propagation [6.18]. Based on these facts, the monitoring of high-temperature loaded components is necessary.

6.4 Corrosion Testing

For corrosion resistance testing of a component, it is necessary to investigate the material behavior in a way that considers the design aspects of the component as well as realistic mechanical (mostly multiaxle) loads. Hence, no uniform corrosion test is available. To have realistic conditions, a corrosion test must be close to the loads that occur. To keep the time and cost frame within the necessities, the aims of the corrosion test must be defined in advance. These can be, for example:

- Determination of the best material (fitness for purpose)
- Determination of the service duration/lifetime of the technical product
- Investigation of new alloys or technical processes
- Development of new materials with increased corrosion resistance
- Investigation of the effect of different corrosive environments
- Determination of the most economic corrosion protection system
- Research studies to reveal corrosion mechanisms.

To achieve these aims, and in terms of product-oriented testing, several combinations of corrosion tests exist. These can be categorized with respect to their rate of abstraction compared to the real system (Fig. 6.27):

- Online monitoring and in-field experiments at real sites
- Full-scale tests with realistic modeling of the entire corrosion system for identification of type, location, and time of corrosion damage
- Product-oriented testing of component-like specimens with prior identification of relevant loads considering their value, location, and direction
- Small-scale tests with standardized mechanical loads
- Basic experiments to identify and examine corrosion mechanisms and time-dependent appearance of corrosion under laboratory conditions.

Nowadays, modern corrosion tests are accompanied by modeling and simulation techniques within the entire range from laboratory specimens to full-scale specimens. The choice of corrosion tests is very important and tailored for a defined aim and corrosion system. Corrosion testing demands highly skilled and trained staff and should be conducted by designated corrosion experts.

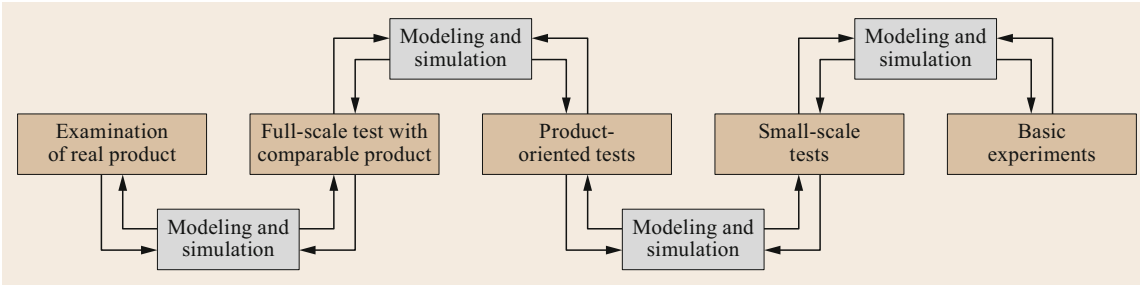

Fig. 6.27 Combination of different corrosion test procedures

References

6.1 DIN EN ISO 8044: *Korrosion von Metallen – Grundbegriffe* (Beuth, Berlin 2015)

6.2 D.A. Jones: *Principles and Prevention of Corrosion*, 2nd edn. (Prentice Hall, Upper Saddle River 1996)

6.3 H. Kaesche: *Die Korrosion der Metalle*, 3rd edn. (Springer, Berlin 1991)

6.4 K.A. van Oeteren: *Korrosionsschutz durch Beschichtungsstoffe* (Hanser, München 1980)

6.5 E. Wendler-Kalsch, H. Gräfen: *Korrosionsschadenkunde* (Springer, Berlin 1998)

6.6 K. Mörbe, W. Morenz, H.-W. Pohlmann, H. Werner: *Korrosionsschutz wasserführender Anlagen* (Springer, Berlin 1998)

6.7 R.W. Revie: *Uhlig´s Corrosion Handbook*, 2nd edn. (Wiley, New York 2000)

6.8 M. Sun, Y.Y. Yang, M. Luo, L.Z. Jiang, Y.-M. Jiang, J. Li: Investigation of susceptibility to intergranular corrosion of tin-added austentitic stainless steel, Acta Metall. Sin. (Engl. Lett.) **28**(9), 1183–1189 (2015)

6.9 M.S. Bihade, A.P. Patil, N.K. Khobragade: Analysis of electrochemical current noise from metastable pitting of SS304L in NaCl solutions, Trans. Indian Inst. Met. **66**(2), 155–161 (2013)

6.10 H.K. Birnbaum, I.M. Robertson, P. Sofronis, D. Teter: Mechanisms of hydrogen related fracture—A Review. In: *2nd Int. Conf. Corros.-Deform. Interact., EFC*, ed.

by T. Magnin (The Institute of Materials, London 1997) pp. 172–195
6.11 I.M. Robertson, P. Sofronis, A. Nagao, M.L. Martin, S. Wang, D.W. Gross, K.E. Nygren: Hydrogen embrittlement understood, Metall. Mater. Trans. B **46**, 1085–1103 (2015)
6.12 T. Boellinghaus, T. Mente, P. Wongpanya, E. Viyanit, E. Steppan: Numerical modelling of hydrogen assisted cracking in steel welds. In: *Cracking Phenomena in Welds IV*, ed. by T. Boellinghaus, J.C. Lippold, C.E. Cross (Springer, Cham 2016) pp. 383–439
6.13 J.P. Hirth: Effects of hydrogen on the properties of iron and steel, Metall. Trans. A **11**(6), 861–890 (1980)
6.14 W. Schatt, E. Simmchen, G. Zouhar: *Konstruktionswerkstoffe des Maschinen- und Anlagenbaues* (Wiley-VCH, Weinheim 2009)
6.15 M. Wolf, R. Afanasiev, T. Böllinghaus, A. Pfennig: Investigation of corrosion fatigue of duplex steel X2CrNiMoN22-5-3 exposed to a geothermal environment under different electrochemical conditions and load types, Energy Procedia **114**, 5337–5345 (2017)
6.16 D. Enning, J. Garrelfs: Corrosion of iron by sulfate-reducing bacteria: New views of an old problem, Appl. Environ. Microbiol. **80**, 1226–1236 (2014)
6.17 M. Schütze: High-temperature corrosion. In: *Corrosion Mechanisms in Theory and Practice*, 3rd edn., ed. by P. Marcus (CRC, Boca Raton 2011)
6.18 M. Schütze: *Protective Scales and Their Breakdown* (Wiley, New York 1997)
6.19 F. Pawlek: *Metallhüttenkunde* (De Gruyter, Berlin 1983)
6.20 C. Allely, L. Dostat, O. Clauzeau, K. Ogle, P. Volovitch: Anticorrosion mechanisms of aluminized steel for hot stamping, Surf. Coat. Technol. **238**, 188–196 (2014)
6.21 H. Grabke, M. Schütze: *Corrosion by Carbon and Nitrogen – Metal Dusting, Carburisation and Nitridation*, European Federation of Corrosion Publications, Vol. 41 (Woodhead, Cambridge 2007)

Thomas Böllinghaus

Department 9 – Component Safety
Bundesanstalt für Materialforschung und -prüfung (BAM)
Berlin, Germany
thomas.boellinghaus@bam.de

Professor Thomas Böllinghaus received his Dr-Ing. degree from Helmut-Schmidt University, Hamburg (1995) and became Professor for Materials Science and Welding Technology in 1999. He is Head of Department 9 "Component Safety" at Bundesanstalt für Materialforschung und -prüfung (BAM), Berlin. His research interests focus on hydrogen-assisted cracking of structural metallic materials, numerical simulation of hydrogen transport and cracking, hot-cracking phenomena in welds, and failure analysis and life cycle evaluations of joined components.

Michael Rhode

Department 9 – Component Safety
Bundesanstalt für Materialforschung und -prüfung (BAM)
Berlin, Germany
michael.rhode@bam.de

Michael Rhode is Assistant Professor for welding of creep-resistant steels at Otto-von-Guericke University Magdeburg and the leader of the corresponding research group at Bundesanstalt für Materialforschung und -prüfung (BAM) Berlin. He has a doctoral degree in mechanical engineering. His multidisciplinary research interests are the interaction of metallurgy and cracking susceptibility of welded joints. A special focus is stress relief cracking during post weld heat treatment and environmentally (hydrogen) assisted cracking.

Thora E. Falkenreck

Rheinmetall Landsysteme GmbH
Kassel, Germany
thora.falkenreck@bam.de

Thora E. Falkenreck studied industrial engineering at Kassel University (Germany) within the scope of a dual study scholarship. Afterwards, she was at the Bundesanstalt für Materialforschung und -prüfung (BAM) in Berlin to accomplish her doctoral degree in mechanical engineering. The main topic of her research is arc welding of high-strength steels at high strain rates. Since 2018, she has been applying her knowledge at Rheinmetall Landsysteme GmbH (Kassel).

7. Nondestructive Inspection (NDI)

Gerhard Mook, Islam Shyha

This chapter discusses various nondestructive inspection (NDI) methods. Nondestructive inspection includes all methods to characterize a material without indenting, extracting samples, reducing its service capabilities or destroying it. The following chapter describes principles of NDI. Subsequently, NDI methods will be classified into seven categories namely, acoustic, potential drop, magnetic, electromagnetic, thermography, optical, and radiation methods. Each category may involve several methods where all will be discussed. For each method presented in this chapter, principles, setup and probes, nondestructive testing (NDT), nondestructive evaluation (NDE) and current scope are discussed. Last but not least, the chapter presents NDI methods that rely on integrated sensors in the inspected structure itself, known as structural health monitoring (SHM).

7.1 **Principles of Nondestructive Inspection** 216
7.2 **Acoustic Methods** 217
7.2.1 Ultrasonic Methods 217
7.2.2 Resonance Methods 218
7.2.3 Acoustic Emission Analysis 219
7.3 **Potential Drop Method** 219
7.3.1 Principles 219
7.3.2 Probes 219
7.3.3 NDT 220
7.3.4 NDE 220
7.3.5 Current Scope 220
7.4 **Magnetic Methods** 220
7.4.1 Stray Flux and Magnetic Particle Inspection 220
7.4.2 Flux Method 221
7.4.3 Residual-Field Method 222
7.4.4 Barkhausen Noise Analysis 223
7.5 **Electromagnetic Methods** 224
7.5.1 Eddy-Current Method 224
7.5.2 Microwave Method 224
7.6 **Thermography** 225
7.6.1 Principles 225
7.6.2 Setup and Probes 225
7.6.3 NDT 225
7.6.4 NDE 226
7.6.5 Current Scope 226
7.7 **Optical Methods** 226
7.7.1 Visual Methods 226
7.7.2 Penetration Methods 226
7.7.3 Speckle Interferometry 227
7.8 **Radiation Methods** 228
7.8.1 X-ray Method 228
7.8.2 Gamma-Ray Method 229
7.9 **Health Monitoring** 229
References 231

NDI includes defect detection and quantification, called nondestructive testing (NDT), and the assessment of material properties, called nondestructive evaluation (NDE). NDI is an integral part of the design, manufacturing, maintenance, and recycling of components.

More components are now designed following the rule of fitness-for-service. This concept assumes the presence of a maximum undetectable-by-NDI defect. The designer has to make sure that this defect does not become critical during a well-defined service period. To maintain the safety coefficient at a predefined level, the component will be larger or heavier than it should be without the defect. With the increasing capabilities of NDI, the scale of this maximum undetectable defect is reduced, allowing the designer to reduce component weight without lowering the safety coefficient.

In manufacturing, NDI enables the inspection of the whole output, while destructive methods rely on a more or less satisfactory number of samples, which are more or less representative for the current production. Besides questions of its suitability, the speed of inspection is the deciding criterion for NDI application.

In maintenance, there is no alternative to NDI. According to considerations of fracture mechanics, the concept of damage tolerance requires the detection and characterization of all defects starting from

K.-H. Grote, H. Hefazi (Eds.), *Springer Handbook of Mechanical Engineering*, Springer Handbooks,
https://doi.org/10.1007/978-3-030-47035-7_7

an individually defined level. Depending on the findings of NDI, the next service period may be shorter or longer. The typical requirement for inspection is a high probability of defect detection accompanied by a tolerable rate of false indications. Modern maintenance concepts include the online monitoring of components or the structural health of the entire component.

All industrial sectors use NDI, the best known of which is the manufacturing of flying structures. However, pipelines, heat exchangers, vessels, bridges, and car components are also inspected nondestructively. This chapter focuses on the most important and widely used methods in mechanical engineering but also touches on the promising field of structural health monitoring (SHM).

7.1 Principles of Nondestructive Inspection

The basic principles of NDI are shown in Fig. 7.1. The goal is either to detect relevant defects or to estimate quality parameters such as hardness or the thickness of the heat treatment or coating layers. This goal cannot easily be achieved using nondestructive methods. The only possible way is to measure physical properties such as thermal or electric conductivity, sound propagation or magnetic behavior. Both quality parameters and physical properties are defined by the material's structure. The challenge is to find a correlation between them. Research is needed to fully understand the relationship between the quality parameters to be inspected and the physical properties which can be recorded nondestructively.

A wide variety of NDI sensors and transducers are able to record physical properties locally or integrally. The relevant signals are processed in an instrument and displayed in different forms. Some physical properties may be recorded by matrix sensors, immediately providing an image, while other properties have to be measured by point-like sensors that are hand-guided by an operator or mechanically guided by a scanner.

The result will be either an image, a vector or a scalar value. In most applications a threshold is used to separate acceptable from nonacceptable quality. For this purpose, differential measurements are most suitable. The current measurement is compared with the measurement of a master piece or of a neighboring area of the same object. If the difference is below the threshold, the object passes; otherwise it fails. If quantitative assessment is required, calibration curves are typically considered based on well-known samples with a gradual variation of the parameter to be evaluated. Here, the increasing effectiveness of numerical modeling provides valuable help. In some cases of NDI, absolute values of a physical property are expected, which can be provided using dedicated instruments.

How reliable is NDI? To date no method is known to detect defects with a probability of 100%. On the other hand, all methods may produce false indications, such as indicating a defect in a material/component when none is actually present. All NDI applications have to be optimized regarding both probabilities.

The following sections present a selection of approved methods and show directions for future development. Comprehensive fundamentals of NDI are presented elsewhere [7.1–5]. Further references on individual methods will provide detailed information, but it is recommended that users should seek advice from experienced specialists. International standards and rules of application are also described for all methods.

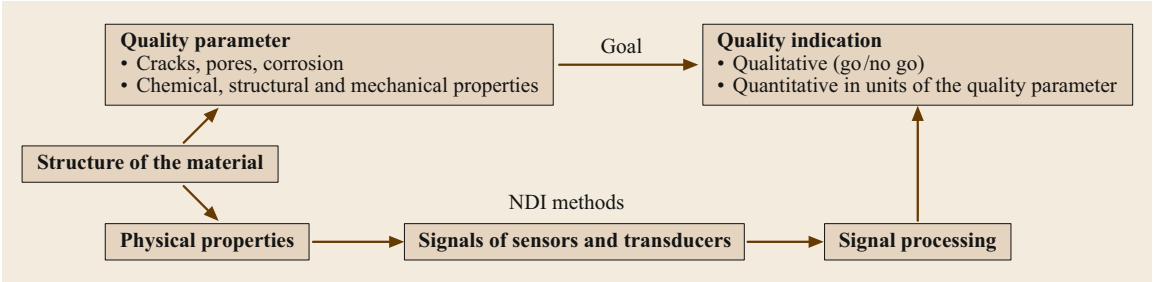

Fig. 7.1 Principles of nondestructive inspection

7.2 Acoustic Methods

Acoustic methods rely on the propagation of sound waves though the material. These waves may be excited by external or internal sources. In solids, longitudinal (compressional) and transverse (shear) waves may spread and are partially reflected and their modes converted at boundaries. Additional wave modes may exist at the material's surface and in thin plates (Rayleigh and Lamb waves). While propagating through the material, the waves are attenuated depending on the material's properties and the wave's frequency.

7.2.1 Ultrasonic Methods

Principles

The basic idea is to transmit a short elastomechanical wave packet into the material. If its wavelength is short enough, it will interact with defects starting from ≈ 0.5 mm in diameter. Therefore, exiting frequencies from 0.5 to 15 MHz (ultrasonic frequencies) are required. Depending on the material's attenuation, the wave packet can travel over long distances through the material. In the transmission technique, the pulse is received at the opposite side of the object whereas in the pulse-echo technique the reflected waves are recorded at the same side as where they are fed. Nearly all metals, ceramics, concrete, low-damping plastics and composites may be inspected using ultrasonic methods [7.6, 7].

Probes (Transducers)

For perpendicular wave propagation, perpendicular-incidence probes are attached to the surface. For non-perpendicular wave propagation angle-beam probes are required which commonly generate longitudinal waves diffracted into a longitudinal and a transverse wave at different angles at the material's surface. The acoustic waves must be coupled to the material using a couplant such as water or grease. Figure 7.2 shows a perpendicular-incidence probe consisting of a piezoelectric ceramic disc emitting and receiving the ultrasonic waves. A resin damping block absorbs the waves emitted in the reverse direction. The ultrasonic waves are passed through a protecting layer and the couplant into the material. After entering the material, the sound field is characterized by local maxima and minima due to the interference of waves emitted from different parts of the piezoelectric disc. This initial area of the sound field is called the near field, where no inspection is possible. The near field becomes taller and ends in a final maximum sound pressure. From this point onwards, the sound field diverges and the sound pressure gradually decreases. This area is best suited for NDI.

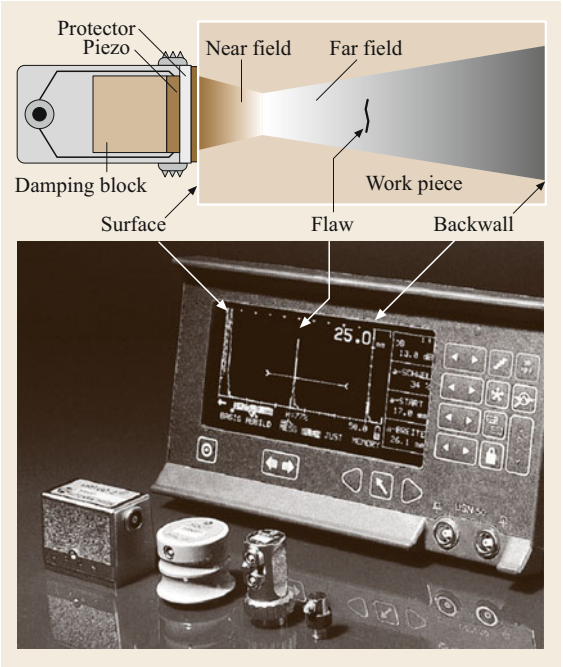

Fig. 7.2 Principles of ultrasonic inspection, instrument, transducers, and signal representation

NDT

Defects may be detected if they interact with the ultrasonic waves. The best detection performance is available for defects oriented perpendicularly to the sound field axis. Both transmission and pulse-echo techniques are suitable. With decreasing wavelength (increasing frequency) smaller defects may be detected, but reflections from grain boundaries are also superimposed onto the signal. In Fig. 7.2, the screen of an ultrasonic instrument displays the A-scan formed by the rectified and amplified echo sequence. At the entrance, a significant part of the sound energy is directly reflected back to the probe, producing the large entrance echo. At the back wall nearly all the sound energy is reflected. A properly oriented planar or volumetric defect produces an intermediate echo between the entrance and back wall echo. This echo may be analyzed to evaluate the defect's position and dimensions. In weld inspection, angle beam probes are generally used due to the nonsmooth surface of the weld and the orientation of possible defects.

NDE

Sound velocity and attenuation carry information about the structural and geometrical parameters of the material. The time-of-flight method is used in measuring the

dynamic Young's modulus and to evaluate the structure of cast iron with spherical graphite, stress and strain assessment in steel, and the thickness of metal or nonmetal walls. Grain boundary reflections are used to estimate grain size or surface hardening depth. Sound attenuation measurement is also applied for structural characterization such as grain sizing and deformation-induced alterations.

Current Scope

Instead of single transducers, one- or two-dimensional arrays are used to incline and shape the ultrasonic beam. Electronic movement enables fast imaging techniques. To avoid liquid couplants, current research focuses on air-coupled techniques and thermally induced sound waves and interferometric readout.

7.2.2 Resonance Methods

Principles

The object is excited by a mechanical pulse or a continuous wave in a defined audible or ultrasonic range. It starts vibrating on its eigenmodes and the eigenfrequencies are recorded. The signal is analyzed in the time and frequency domains, comparing the signals to those of one or more master pieces with well-known properties. Nearly all metals, ceramics, plastics, and composites, and often the adhesive bonding between them, may be inspected according to the *go/no go* principle.

Setup and Probes

The object is positioned on a low-damping fixture and is excited by defined mechanical pulses using impact hammers, piezoactuators or electromechanical shakers. In the low-frequency range the acoustic response

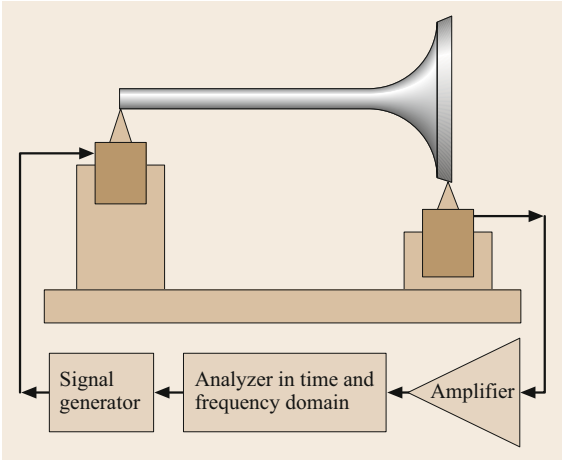

Fig. 7.3 Schematic view of valve inspection using resonance method (after [7.8])

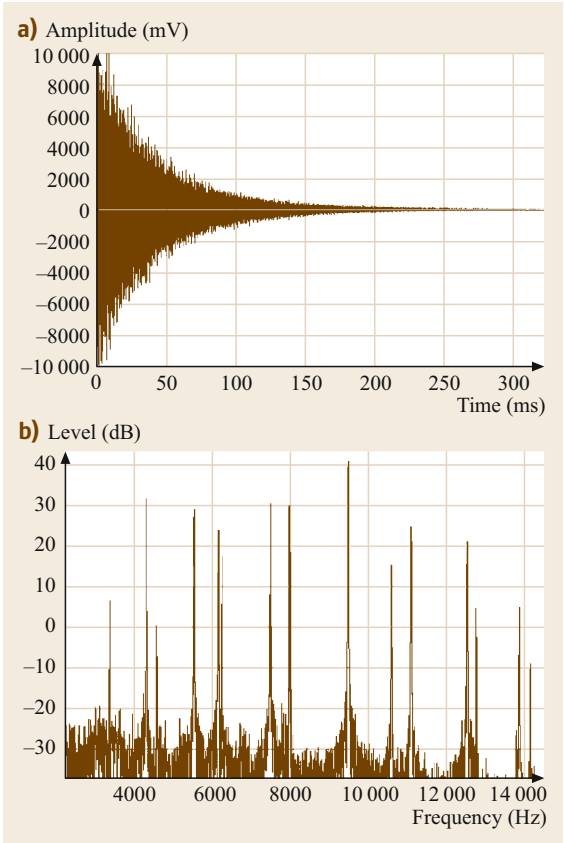

Fig. 7.4a,b Resonance analysis of valve: **(a)** signal in the time domain, **(b)** signal in the frequency domain (after [7.9])

can be heard or is picked up by microphones via air coupling. At higher frequencies and lower amplitudes piezoelectric sensors are attached to the object or optical interferometers record the oscillation at one or more positions. Figure 7.3 shows the setup for valve inspection. Figure 7.4 presents the signals in the time and frequency domains.

NDT

Complex-shaped objects such as gears and cast housings are inspected for missing components, imperfect shape, cracks, and cavities. The frequency content of the response signal is usually analyzed. In a first step, a representative amount of sound and flawed objects are analyzed in a broad frequency band. Comparing the response spectra, the most sensitive narrow bands are selected for defect detection.

NDE

The resonance method allows the estimation of structural damping, the comparison of elastic properties

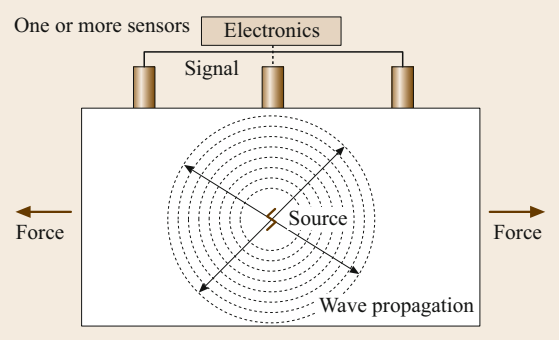

Fig. 7.5 Acoustic emission generated by a discontinuously growing crack

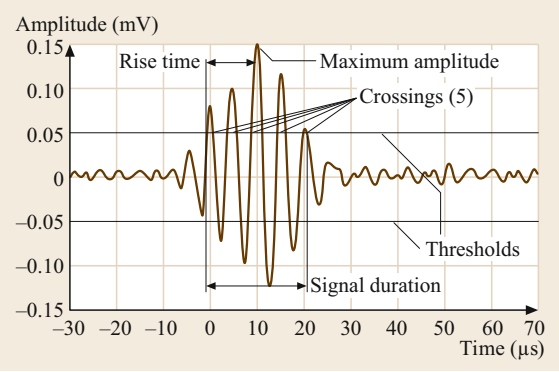

Fig. 7.6 Burst signal recorded by attached sensors

between identically shaped samples, and even the measurement of the dynamic Young's modulus with simply shaped specimens.

Current Scope

With increasing sensitivity, smaller defects become detectable. Extensive signal processing allows the suppression of disturbing signals from the environment.

7.2.3 Acoustic Emission Analysis

Principles

When an object is loaded, defects grow and discontinuously radiate elastic wave bursts (Figs. 7.5 and 7.6). These bursts are picked up and analyzed according to their spectral content, signal energy, and other specific parameters. Defect location becomes possible using time-of-flight differences to different sensors [7.10]. For leakage detection, the continuous acoustic radiation arising at the leak point is recorded. For leakage location, signals from two or more separated sensors are correlated to determine the time-of-flight difference.

Setup and Probes

For loading, the object may be heated or stressed by different means. Piezoelectric probes with internal or closely attached external preamplifiers pick up the emission. More than one sensor is usually required to cover the whole object or to locate defects.

NDT

Growing cracks, hydrogen embrittlement, stress corrosion, and creep can generate acoustic emissions. The advantage of analyzing these is that they enable information about the whole object to be gathered at the same time. Inspection is commonly performed before running the object and during inspection breaks. Generally, acoustic emissions may be recorded online, thus enabling structural health monitoring (see Sect. 7.9). No information about defect dimensions is available.

Current Scope

With increasing knowledge of signal generation, signal conversion, and nonresonant sensors, more detailed information can be obtained by characterizing the source of radiation, thus making acoustic emission analysis more reliable.

7.3 Potential Drop Method

7.3.1 Principles

Once found, a surface crack's depth should often be estimated. For this, an electric current is passed perpendicularly across the crack. The current will be deflected by the crack depending on its depth and length [7.11]. Two electrodes are placed in contact on both sides of the crack to measure the potential drop. Assuming that the crack is much longer than its depth, the voltage primarily depends on the crack depth. Figure 7.7 shows the reason for increasing potential drop with crack depth.

7.3.2 Probes

Modern probes combine current supply and potential drop electrodes in one probe. Figure 7.8 presents such a four-point probe. The outer electrodes feed the current and the inner ones measure the voltage. For the online

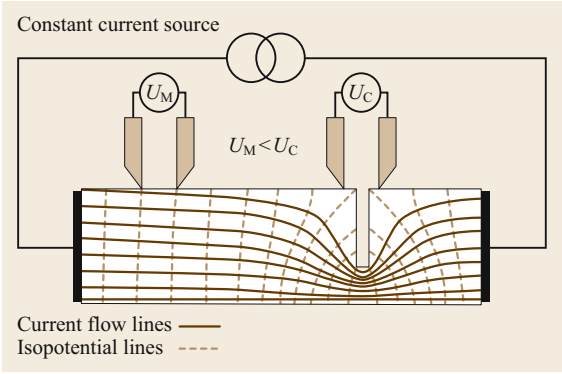

Fig. 7.7 Potential drop measurement of crack depth

observation of crack growth, electrodes may be permanently fixed to the object.

7.3.3 NDT

For crack depth assessment in ferrous steels, alternating current is advantageous due to the skin effect. This effect causes a current concentration at the near-surface regions while direct current spreads out at much deeper levels. That is why the crack's influence on lengthening the current path is more pronounced with alternating than with direct current. After careful calibration, the crack depth can be estimated with an accuracy of some tenths of a millimeter, taking into account the fact that the first electric bridge between the crack faces defines the measured crack depth. To estimate crack inclination, an additional electrode fixed at a greater distance from the crack is necessary.

Fig. 7.8 Potential probes able to measure crack depth and inclination

7.3.4 NDE

Potential drop measurement can be used to measure the conductivity of metals. The advantage over the eddy-current method (Sect. 7.5) is its suitability for ferrous steels, while eddy-current conductivity measurement may only be applied with nonferromagnetic materials. The disadvantage is the unavoidable direct contact with the metal, requiring at least local stripping of paint and corrosion products.

7.3.5 Current Scope

Calibration curves of most common materials are stored in the instrument. Combined inductive feed and contact gauging is a subject of current research.

7.4 Magnetic Methods

Magnetic methods use the ferromagnetism of ferritic steels. A magnetic flux passing through the material orients the magnetic domains of the material, thus increasing the flux density. This orientation process is nonlinear and follows a hysteresis loop. When all domains are oriented according to the exciting field, the material is magnetically saturated. For NDI, a number of physical properties may be used such as saturation induction, remanence, coercive force, and magnetic permeability [7.12].

7.4.1 Stray Flux and Magnetic Particle Inspection

Principles

If the magnetic flux passing through the ferromagnetic material faces a boundary to a less permeable area such as air in a crack, it is refracted into this area nearly perpendicularly to the boundary. Figure 7.9 details this situation where a part of the flux spreads over the boundaries of the workpiece. This stray or leakage flux is much wider than the crack. The remaining flux lines pass below the crack or across it. They are not accessible for NDI. The estimation of crack depth is not possible.

Setup and Probes

The magnetic flux must be oriented perpendicularly to the crack. This flux may be excited, whether by permanent magnets, electric current or electromagnetic coils. For stationary equipment, combined electric and electromagnetic excitation is preferred to produce a circular magnetic field. The objects are placed in the gap of a yoke that carries the magnetic flux as well as the electric current. Mobile excitation is possible us-

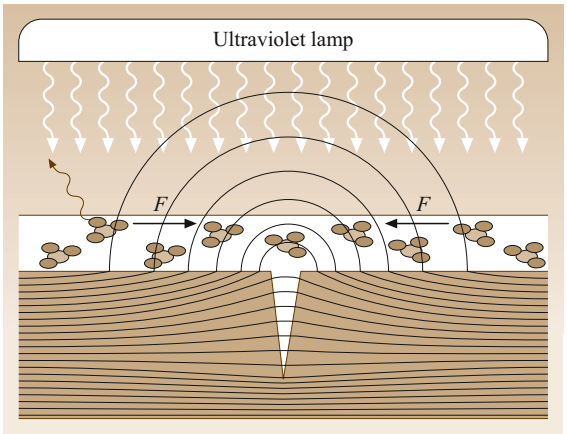

Fig. 7.9 Magnetic stray flux generates the force F attracting the magnetic particles

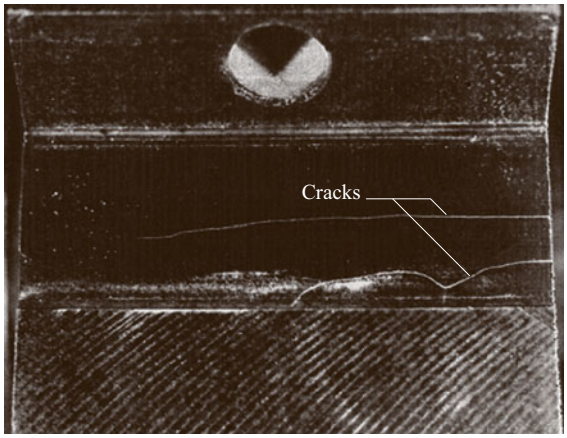

Fig. 7.10 Magnetic particle indication of cracks in a switch shaft

ing electromagnetic hand yokes and current electrodes. The stray flux can be detected by magnetic sensors such as flux gates, magnetoresistors, Hall sensors or moving coils, or even visualized according to magnetic particles (magnetic particle inspection, MPI). After inspection, the object has to be demagnetized.

NDT by Flux Sensors

In automatic inspection lines, objects such as pipes, rods or sheets are moved through a magnetizing yoke. Between the poles, sensors or sensor arrays are guided over the surface to detect and quantify the stray flux.

NDT by MPI

A suspension of high-permeability fluorescent powder in a low-viscosity carrier liquid is flushed over the surface. The magnetic particles are attracted by the stray flux, dragging the fluorescent particles with them. In a darkroom under ultraviolet illumination, these particles become visible, indicating the crack (Fig. 7.10) [7.13]. For documentation, photographs can be taken. In difficult conditions such as underwater inspection, the suspension is contained in a double-wall package. After exposing the package to the stray flux, the suspension can be cured by a second component to fix the particles at their positions and to analyze the image later.

Current Scope

To increase the reliability of MPI, attempts are being made to record MPI images using video cameras and to process the image automatically. Instead of magnetic particles, magneto-optical flux sensors are being investigated in order to enable the direct visualization of stray flux.

7.4.2 Flux Method

Principles

The object becomes a part of a magnetic circuit. The flux in this circuit is generated by a permanent magnet or an electromagnet. The measured flux magnitude depends on the object's cross-section and its magnetic permeability.

Probes

The flux in the circuit is measured directly by flux gates, magnetoresistors, Hall sensors or mechanical forces caused by the flux.

NDT

To detect and quantify corrosion damage that reduces the cross-section of ferritic steel components, magnetic yokes are guided over the surface. Assuming that the permeability of the material is constant, the flux only depends on the cross-section of the object. To locate corrosion, the flux magnitude should be mapped.

NDE

Under the assumption of constant permeability, the wall thickness or cross-section of ferritic steel components such as sheets, pipes or cables may be assessed. The measurement of magnetic permeability becomes possible with components of sufficient thickness and lateral dimensions starting from a few square centimeters. The sensors pick up the degree of flux deflection caused by the ferromagnetic object. The same principles may be used to measure the thickness of nonferromagnetic walls. An additional ferromagnetic body (usually a steel ball) placed on the back side deflects the magnetic field [7.14].

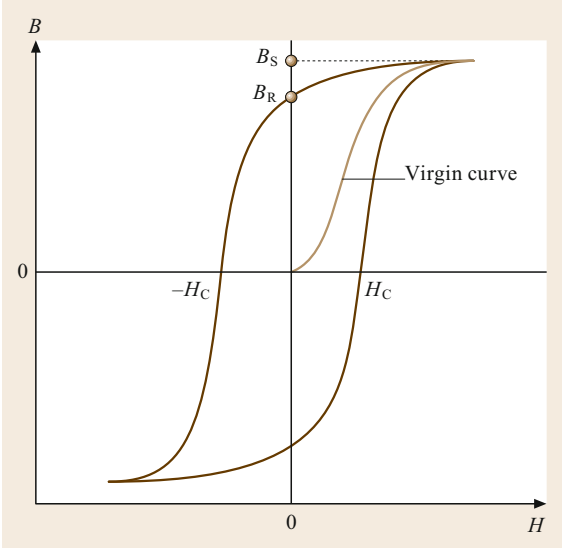

Fig. 7.11 Ferromagnetic hysteresis loop. B_S – saturation induction, B_R – remanent induction remaining on the part after removing the exciting magnetic field H, H_C – coercivity

Current Scope

For the assessment of more distant ferromagnetic objects, high-sensitivity superconducting quantum interference devices (SQUIDs) are used.

7.4.3 Residual-Field Method

Principles

The ferromagnetic object or a part of it is firstly magnetized by a strong direct field as close as possible to its saturation. In the second step, the residual field (Fig. 7.11, remanent induction, remanence) is measured, carrying information about the presence of the object, its microstructure, dimensions, and orientation.

Setup and Probes

The object can be magnetized by a yoke, a permanent magnet or an electromagnet. The magnetization can include the whole object or can be limited to a small area of a few square millimeters. The residual field is measured by flux gates, magnetoresistors, Hall sensors, or SQUIDs.

NDT

This method is suitable for the detection and characterization of ferromagnetic particles in nonferromagnetic surroundings, such as splinters of cutting tools in nonferromagnetic pieces [7.15].

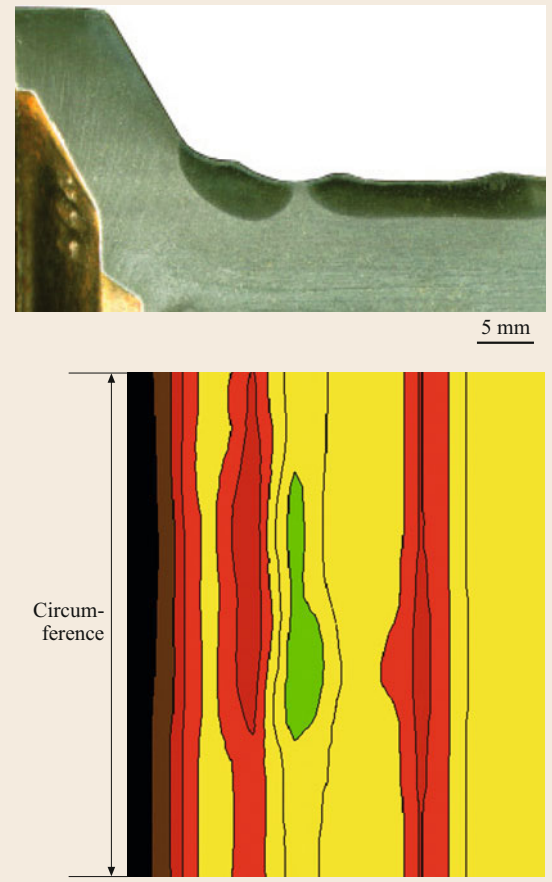

Fig. 7.12 Imperfectly hardened surface layer and residual field distribution along the circumference (after [7.16])

NDE

The residual induction strongly depends on the microstructure of ferromagnetic steels or cast iron due to its correlation with the mobility of magnetic domain walls. The evaluation of residual induction allows the assessment of heat treatment, toughness, hardness, surface hardening (Fig. 7.12, [7.16]) or even carbon content. Calibration is the most important feature for the success of this method and should be accomplished according to appropriate guidelines. The method allows fast automatic inspection using the conveyer movement of the objects through a magnetization tunnel and along a sensor station. Usually the object must be demagnetized afterwards.

Current Scope

In order to mitigate the influence of the dimensions of the object, on the results of NDE, the coercive force

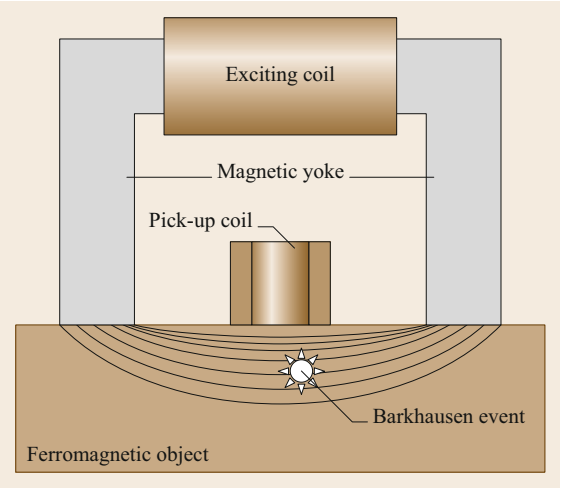

Fig. 7.13 Barkhausen noise excitation and measurement

may be evaluated. For this, after magnetization, the object is demagnetized by a contrary field, and the strength of the demagnetizing field when the residual field vanishes is recorded.

7.4.4 Barkhausen Noise Analysis

Principles

The excitation of ferromagnetic material by a magnetic field that varies with time changes the spatial dimensions of the magnetic domains. The Bloch walls separating the domains from each other move discontinuously through the grain, emitting electromagnetic pulses. The superposition of these pulses produces a noise-like signal called magnetic Barkhausen noise [7.17]. The amplitude and rate of these pulses are discontinuously distributed over a complete magnetization cycle. They reach their maximum when close to coercivity.

Setup and Probes

Excitation is accomplished by a magnetic yoke placed on the object. The driving coil is fed by an alternating current of a frequency ranging from a few tenths of a hertz to a few hundred hertz. Figure 7.13 displays a yoke and a sensing coil between the yoke limbs to receive the emitted pulses.

NDE

The amplitude and pulse rate of Barkhausen noise depend on the Bloch wall mobility at different field

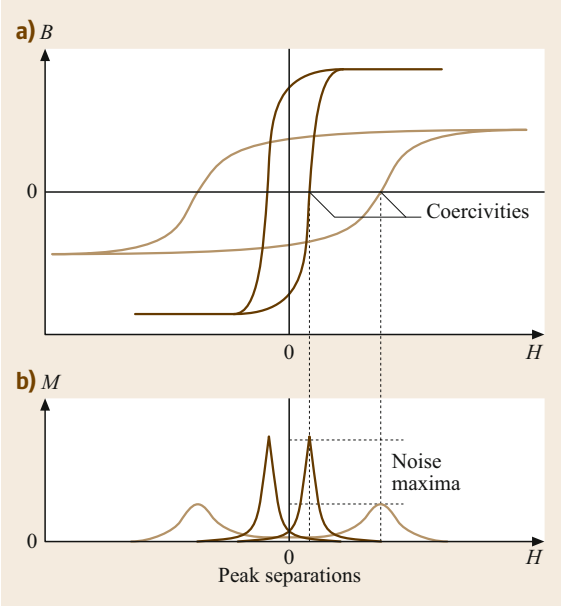

Fig. 7.14a,b Assessment of surface hardening depth of ferromagnetic steel. **(a)** Hysteresis loops, **(b)** Barkhausen noise (after [7.18])

strengths. This mobility is influenced by load and residual stress, grain and phase boundaries, grain orientation, and microstructural defects such as vacancies, dislocations, precipitates, segregations, and inclusions. The method is used to estimate hardness obtained by lattice defects, laser- and case-hardening depth, and stress state.

Figure 7.14 shows the principle of the thickness assessment of surface-hardened layers in ferromagnetic steel. The wide hysteresis loop describes the magnetic properties of the surface layer, while the narrow loop results from the bulk material. During cyclic magnetization, different maxima of the amplitude of Barkhausen noise may be observed [7.18]. At lower field strength, the bulk material provides the first maximum followed by the maximum of the surface layer. The ratio of these maxima correlates with the depth of the hardened layer [7.19].

Current Scope

A frequency analysis of the noise signal yields the source depth of the pulses. In combination with other micromagnetic parameters such as incremental permeability, local remanence or tangential field strength, the method will find a wide field of applications.

7.5 Electromagnetic Methods

Electromagnetic methods rely not only on magnetic properties but also on the behavior of the material in an alternating electric field. For conductive materials such as metals, even low-frequency electromagnetic fields induce an electric current. For nonconductive materials such as most ceramics and plastics, higher frequencies (> 10 MHz) are necessary to generate a so-called dislocation current caused by various polarization mechanisms in the atoms or molecules.

7.5.1 Eddy-Current Method

Principles

An alternating magnetic field between 10 Hz and 10 MHz is applied to a conductive material. This field induces a circular voltage that drives a circular current with alternating direction almost parallel to the surface. As Fig. 7.15 shows, this so-called eddy current builds up its own magnetic field that counteracts the source. The sensor evaluates the resulting field, which contains information about magnetic permeability, conductivity, and geometric parameters [7.14].

Probes

The probe consists of a transmitter generating the alternating magnetic field and a receiver to pick up the resultant magnetic field. The transmitter is commonly a coil; the receiver may be a coil or another magnetic field sensor such as a magnetoresistor, a flux gate, or even a SQUID for very low frequencies. Most simple sensors combine the transmitter and receiver in a single coil. For the direct visualization of eddy currents in flat surfaces, their magnetic fields can be picked up by magneto-optic sensors such as garnet films.

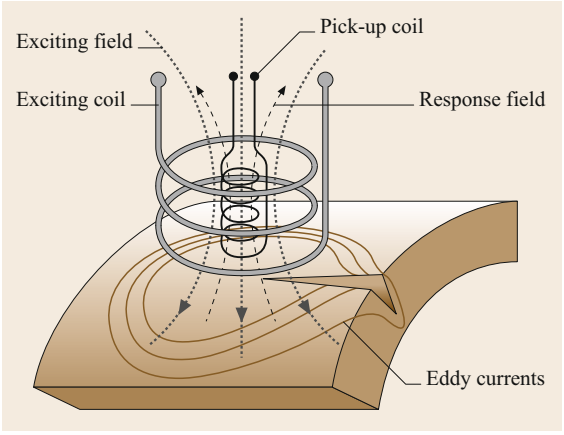

Fig. 7.15 An eddy-current surface probe detects cracks due to the deflection of eddy-current lines

NDT

Surface crack detection in all metals, even below nonconducting coatings, is the most common field of application [7.20]. The detection and quantification of hidden defects such as pores, corrosion, and cracks is also possible in nonferromagnetic materials up to a few millimeters below the surface. Figure 7.16 shows an example of eddy-current turbine blade inspection.

NDE

The eddy-current method is best suited for the measurement of conductivity in nonferromagnetic materials and heat treatment characterization of pure metals and alloys. Material sorting can be accomplished as well as the thickness assessment of nonconducting layers or conducting bulk or wall thickness assessment of nonferromagnetic sheets or pipes. In conducting composites such as carbon fiber reinforced plastic (CFRP), fiber orientation can be evaluated using the anisotropy of conductivity.

Current Scope

Array sensors provide a fast and convenient opportunity to visualize eddy-current behavior. Highly sensitive and resolving sensors make smaller defects visible at greater material depth.

7.5.2 Microwave Method

Principles

Electromagnetic fields excited at frequencies from a few to a few hundred gigahertz provide wavelengths in

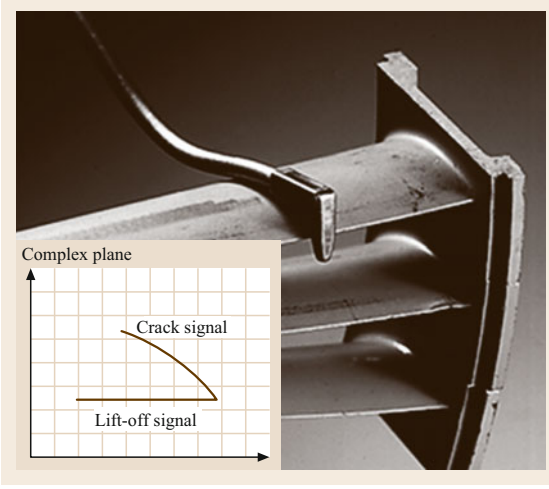

Fig. 7.16 Eddy-current inspection of the trailing edge of a turbine blade

the centimeter and subcentimeter range; so-called microwaves. These waves are reflected at the surface of metals but can penetrate many nonmetals, such as plastics, ceramics, and composites. Various polarization mechanisms of the material components change the amplitude, phase, and polarization of the microwaves.

Setup and Probes

Horn aerials are generally used to transmit and receive microwaves. Single- or double-sided aerials allow reflection and transmission measurements. For near-field applications, an aperture may shape the field transmitted from the antenna. Directional couplers, phase shifters, and modulators complete the equipment [7.21].

NDT

Flaws in metals may be detected and characterized if they break through the surface. At very high frequencies, wave propagation in open cracks may be used for crack depth estimation. In dielectric material, internal flaws such as pores and delaminations may be detected due to the scattering of energy.

NDE

Nonconductive materials can be inspected for material composition, structure, density, porosity, homogeneity, the orientation of reinforcing fibers, state of cure, and moisture content. The reinforcing components in concrete in buildings may be visualized. For metals, only the thickness measurement of plates becomes possible using a double-sided reflection technique [7.22].

Current Scope

Smaller electronic devices enable the integration of increasing numbers of components into one instrument, so that handling problems are decreasing. With the use of higher frequencies, smaller defects will become detectable.

7.6 Thermography

7.6.1 Principles

Heat storage and transport capabilities depend on the heat capacity and thermal conductivity of the material as well as the local geometry of the object. Stimulated heat transport is used to evaluate the material for homogeneity, isotropy, and defects. For noncontact assessment, the temperature distribution in the object is recorded using the thermally induced electromagnetic radiation of the object, which starts from wavelengths of about 10 μm at room temperature and can be visualized using infrared sensors.

7.6.2 Setup and Probes

Figure 7.17 shows that a dynamic heat flow can be generated by periodically activated external (or internal) sources. External sources such as lamps, electric heaters, fans, and liquids heat the object from the front or back side. Internal sources may be stimulated by vibration or electric current. The temperature of the surface is recorded by infrared cameras based on scanning point, line or matrix sensors [7.23, 24].

7.6.3 NDT

Lock-in thermography is based on the harmonic excitation of the heat source. The surface temperature of the object is analyzed according to its amplitude and phase. The phase signal is free of disturbances resulting from the emissivity of the surface. Another approach is the pulsed heating of the object and the time-dependent analysis of surface temperature. Both methods are able to detect and characterize inner flaws like delaminations in composites, impact damage and the debonding of joints. Figure 7.18 presents an application for turbine blades.

Defect selection may be achieved by activating cracks as heat sources. To do this, powerful acoustic waves are fed into the object. A local temperature in-

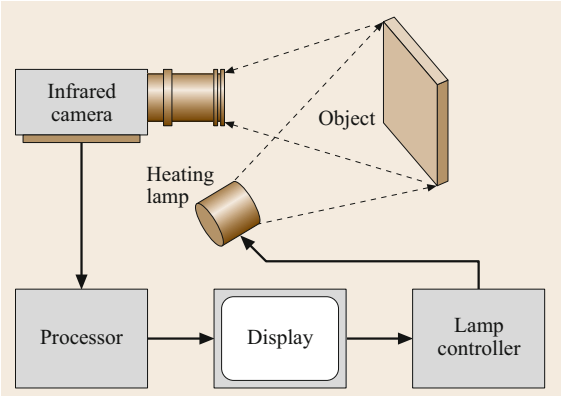

Fig. 7.17 An infrared camera picks up the temperature profile of the surface. The object can be heated by lamps (after [7.23])

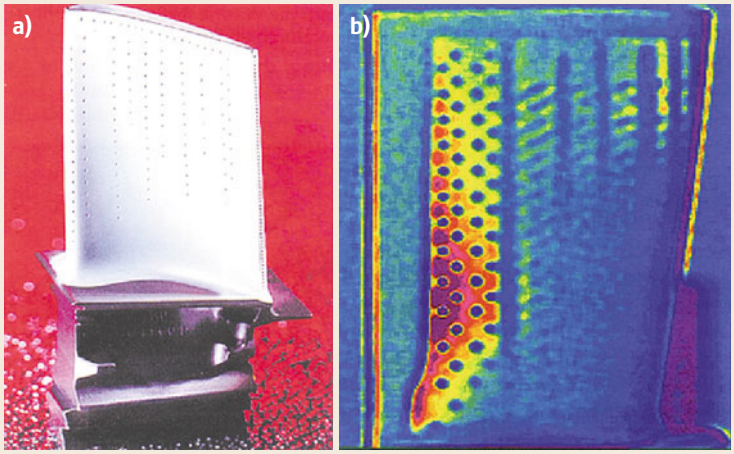

Fig. 7.18 (a) Turbine blades with heat protection layer and cooling channels. (b) Thermography highlights clogged channels

crease due to face friction indicates the presence of a crack.

7.6.4 NDE

The thickness of surface layers in conducting and nonconducting bulk material can be measured as well as the orientation of carbon fibers in CFRP.

7.6.5 Current Scope

Current investigations focus on defect-selective thermography, the assessment of the quality of adhesive joints, and composite materials. The increasing efficiency of infrared sensors means that infrared cameras are increasingly affordable and convenient.

7.7 Optical Methods

This section summarizes methods based on visible light that is reflected from the object's surface. Most attention has been paid to the illumination and the visual abilities of operators. Clear instructions and master pieces of what to look for are required.

7.7.1 Visual Methods

Principles

The object surface is cleaned and systematically searched for defined patterns corresponding to cracks, corrosion, microstructure change or other features.

Probes

Many tasks are solved using the naked human eye. If necessary, lenses, microscopes, endoscopes, and appropriate recording instruments are used. The incidence, intensity, and color of the illumination have to be optimized for a specific inspection task.

NDT

Without optical enlargement, only large surface-breaking defects may be detected. For the maintenance of engines, gearboxes, and other nearly closed hollow objects, endoscopes combining illumination, sensors, and sensor controllers are used [7.25]. Despite the distorted aspect ratio of the recorded picture, it is possible to measure the dimensions of the visual pattern.

NDE

For the analysis of structural features, the object has to be carefully prepared, including mechanical surface treatment such as grinding, polishing and, if necessary, etching. Patterns can be interpreted under defined illumination, but this requires long experience.

Current Scope

Tube-based endoscopes are being replaced by fiber and video endoscopes. Additionally, endoscopes may carry sensors for other NDI methods such as eddy-current probes. Some endoscopes allow the use of mechanical tools to treat any defects found.

7.7.2 Penetration Methods

Principles

Figure 7.19 illustrates the operation of this method. The cleaned surface of the object is coated with a penetrant

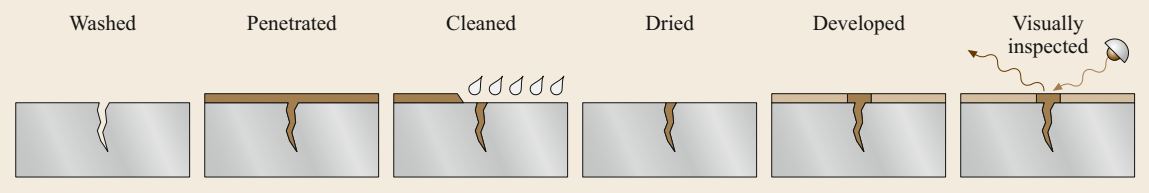

Fig. 7.19 For penetration inspection the object is first washed, then penetrated, cleaned, dried, developed, and visually inspected

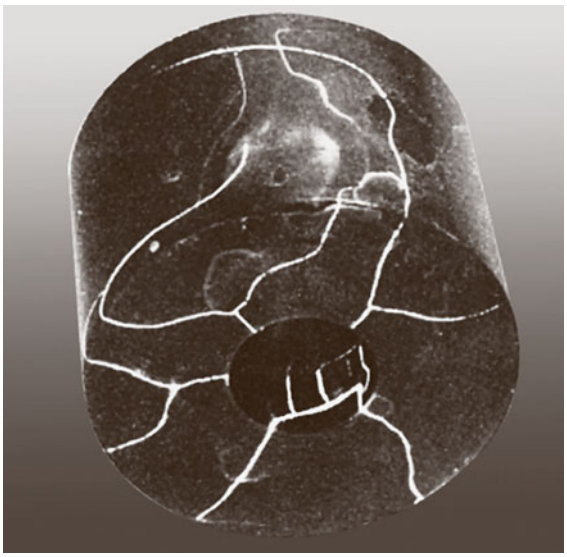

Fig. 7.20 Result of penetrant inspection for cracks in a roller

in which a visible or fluorescent dye is dissolved or suspended. The penetrant is pulled into surface cracks by capillary action. After cleaning the surface of excess penetrant, a developer is sprayed or dusted over the object, partially lifting the penetrant out of the crack. Under defined illumination, the penetrant provides an enlarged crack pattern with high contrast [7.26]. A roller with surface cracks is shown in Fig. 7.20.

Equipment and Inspection Agents

For manual inspection, spray cans with the penetrant and the developer are used. In modern inspection lines, all objects are washed, penetrated, cleaned, and developed automatically at defined agent temperatures and action times in immersion tanks. Visual inspection for defect indication is performed by human operators under either visible or ultraviolet illumination.

NDT

Crack indication varies with developing time. Reference master pieces with known defects and exact instructions enhance the reliability of this method. No information about defect depth can be obtained. Post-emulsifiable penetrants keep viscosity at low levels over time.

Current Scope

To date the interaction of an operator is needed to distinguish between real defects and pseudo-indications. Much effort is focused on replacing inspectors with an automatic vision system.

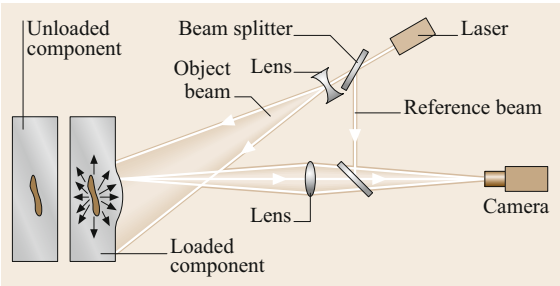

Fig. 7.21 Electronic speckle interferometer (after [7.23])

7.7.3 Speckle Interferometry

Principles

Speckle interferometry uses the interference phenomena of laser light. Figure 7.21 shows that the object is entirely illuminated with laser light, producing a speckle pattern on the object surface. This pattern is superimposed by reference light and the resulting image is recorded using a video camera. For NDI, this method is used to detect and quantify surface dislocation at loading.

Setup and Probes

Laser illumination is performed by a defocused laser so that the entire surface is illuminated at once. No scanning is necessary. To smooth the illumination, the laser light may reach the surface via several paths. A beam splitter directs a small portion of the light as a reference to the camera for interference with the reflected light from the object. The camera records the images and passes them to data storage.

NDT

The speckle pattern of the object is recorded twice. The correlation of the images of the unloaded and loaded object highlights discontinuities or displacements penetrating the surface and allows local debonding, delaminations, and cavities to be recognized as fringes. An example is shown in Fig. 7.22.

Current Scope

The differential speckle interferometry method, known as shearography, highlights differences in the surface dislocation at points at a certain distance from each other. The method is less sensitive to disturbances and is best suited for in-field inspection [7.27].

Fig. 7.22 Speckle fringes caused by discontinuities of off-plane surface displacements

7.8 Radiation Methods

High-energy radiation is able to penetrate solid bodies and to interact with their atoms. The transmitted intensity depends on the atomic number of the material and its density and thickness. The object is illuminated entirely and imaging can be performed by filming or electronic matrix imagers [7.28, 29].

7.8.1 X-ray Method

Principles

An x-ray tube generates radiation with energy up to a few hundred keV. The radiation is directed to the object positioned a certain distance from the tube. A radiographic film or conversion screen close behind the object records the transmitted radiation intensity as a grey scale image.

Equipment

An x-ray source is shown in Fig. 7.23. It consists of an evacuated tube in which a cathode emits electrons that are accelerated towards the anode. The electrons strike the anode and emit bremsstrahlung, which is x-ray radiation with a continuous range of energies. This energy can by controlled by the voltage between the cathode and anode. The radiation leaves the tube via a beryllium window and radiates the object. Increasingly, conversion screens and storage foils are used for imaging.

NDT

Defect detection is based on the alteration of the attenuation of x-rays by the defect. Depending on the defect material, this attenuation may be smaller or greater than in its absence, so that either increased or decreased x-ray intensity can be detected. While the detection of volume defects such as pores starting from a defined extension is very reliable, crack detection requires their correct orientation in the x-ray beam. Figure 7.24 shows the equipment involved and an x-ray image of a weld. For defect detection in steel, x-ray energy of up to 500 keV is required to penetrate walls of 100 mm thickness.

NDE

X-rays are used to gauge the wall thickness of pipes and sheets. With a multi-energy technique it is possible to detect the atomic order of the material, which is used for material identification.

Current Scope

To reduce blurring in x-ray images, microfocus tubes are used. For cross-sectional imaging computer tomo-

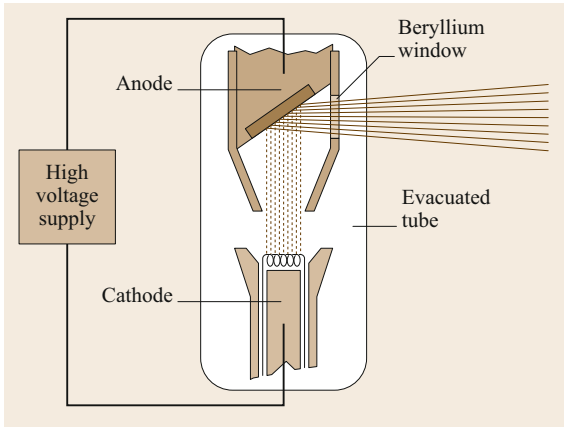

Fig. 7.23 Scheme of an x-ray tube (for explanation see text)

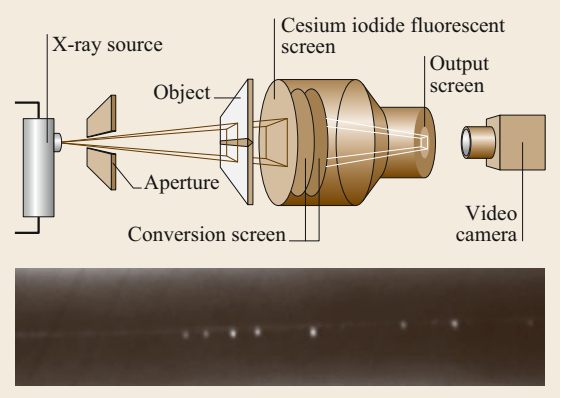

Fig. 7.24 Radioscopic equipment and x-ray image of a weld with pores

graphs are used, turning the object in the x-ray beam. Tubes with turning anodes are needed to increase x-ray intensity with increased electron current in the tube.

7.8.2 Gamma-Ray Method

Principles

The radioactive decay of some elements produces high-energy gamma rays that are able to penetrate metals to a thickness of a few centimeters. Small pellets measuring a few millimeters are activated in a nuclear reactor and then stored in highly damping containers. These continuously radiating pieces are called sources. The decrease in their activity with time is described by the half-life constant, which depends strongly on the source material.

Equipment

The source is loaded into a mobile source holder made from a dense material such as tungsten, uranium or lead. Via remote control, this holder is opened and the source is moved out to radiate the object through a beam collimator. The transmitted radiation is recorded using a radiographic film.

NDT

For very thick steel components, cobalt-60, which radiates with an energy of more than 1 MeV, is used. For steel less than 50 mm thick, softer sources such as iridium-192 are sufficient. The safety requirements for X- and gamma-ray exploitation are very restrictive due to their harmful interaction with biological tissues.

Current Scope

Selenium-75 is best suited for steel walls up to 30 mm and has a significantly longer half-life. This source is able to replace x-ray equipment.

7.9 Health Monitoring

Structural health monitoring (SHM) refers to nondestructive inspection methods that rely on integrated sensors in the inspected structure itself. The sensor signals may be monitored online at the loaded structure or recorded for offline analysis. Various NDI techniques are being investigated for SHM applications in aircraft [7.30, 31], buildings [7.32], and power stations. Active sensors can transmit and receive signals while passive sensors receive signals generated by the damage process or damage growth.

Acoustic emissions (see Sect. 7.2.3) can be recorded by embedded or attached piezoelectric sensors. As shown in Fig. 7.25, the source of an emission can be an impact, the growth of cracks, fiber or matrix breakage, delamination, and other damage processes. To localize these sources, signals from different sensors are correlated, yielding differences in time-of-flight for use in triangulation algorithms.

Acousto-ultrasonic interrogation is a single-sided nondestructive inspection technique employing separate sending and receiving transducers (Fig. 7.26). The method is used in assessing microstructural conditions and distributed damage states in the material between the transducers [7.11].

Impedance spectroscopy uses either a single piezoelectric element or a transmitter–receiver combination (Fig. 7.27). The excitation oscillates in a predefined frequency band and either the impedance or the complex voltage at the receiver is measured. The frequency-dependent behavior of the measurement indicates defects on or close to the piezoelectric element [7.34]. Both acousto-ultrasonic and impedance spectroscopy can be used to inspect polymer, metal, ceramic matrix composites, and even monolithic metallic materials.

Eddy-current foil sensors are an alternative technology to the classical eddy-current technique (see Sect. 7.5) for the detection of surface or hidden cracks. In this method, a copper winding is printed onto a plastic substrate, just like an electronic track. Due to their thin geometry, these sensors can be mounted onto the interfaces between structural parts, around bolts, in corners, and in other hardly accessible regions. Periodic

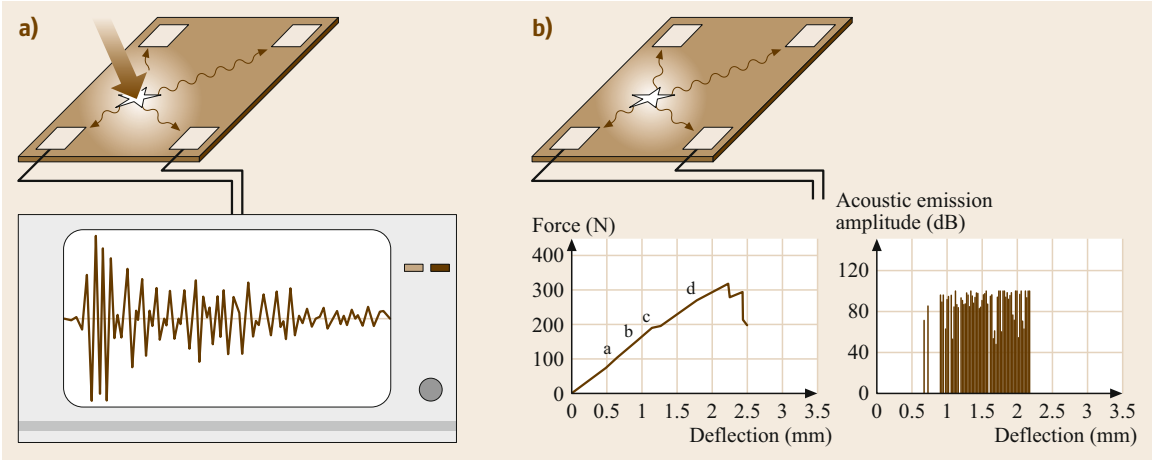

Fig. 7.25a,b Damage processes can be detected by their acoustic emission. Impact damage **(a)** or crack growth **(b)** can be detected and localized (after [7.33])

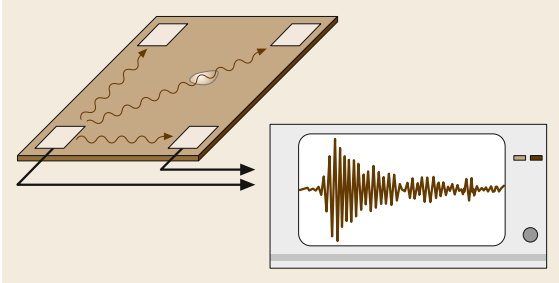

Fig. 7.26 Acousto-ultrasonic measurements (*left*) reveal defects between transmitter and receiver

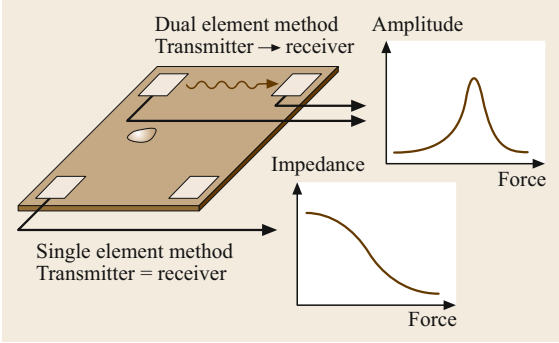

Fig. 7.27 Impedance spectroscopy allows the detection of defects on or close to the piezoelectric element (after [7.34])

reading of the coils can provide information on structural health.

Comparative vacuum monitoring offers an effective method for the in situ real-time monitoring of crack initiation and/or propagation. This method measures the

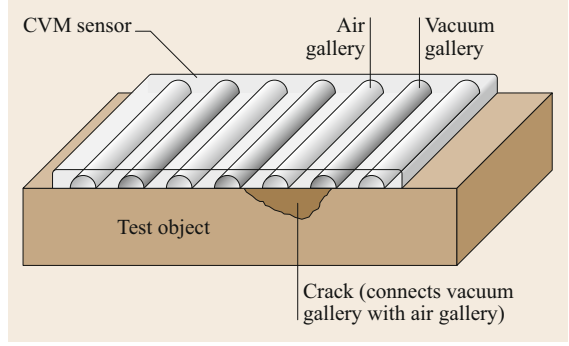

Fig. 7.28 Comparative vacuum monitoring (CVM) detects defects due to varying differential pressure (after [7.35])

differential pressure between fine galleries containing a low vacuum alternating with galleries at atmosphere in a simple manifold (Fig. 7.28). Comparative vacuum monitoring enables the monitoring of the external surfaces of materials for crack initiation, propagation, and corrosion. The galleries can also be embedded between components or within compound materials such as composite fiber.

Fiber Bragg gratings measure either the tensile or compressive strain applied along the grating length of an optical fiber (Fig. 7.29). The grating consists of a periodic variation of the index of refraction and provides a linear relationship between the change in wavelength of the reflected light and the strain in the fiber caused by externally applied loads or thermal expansion. To operate multiple sensors along a single optical fiber, the various Bragg gratings should have different Bragg wavelengths in order to differentiate between them.

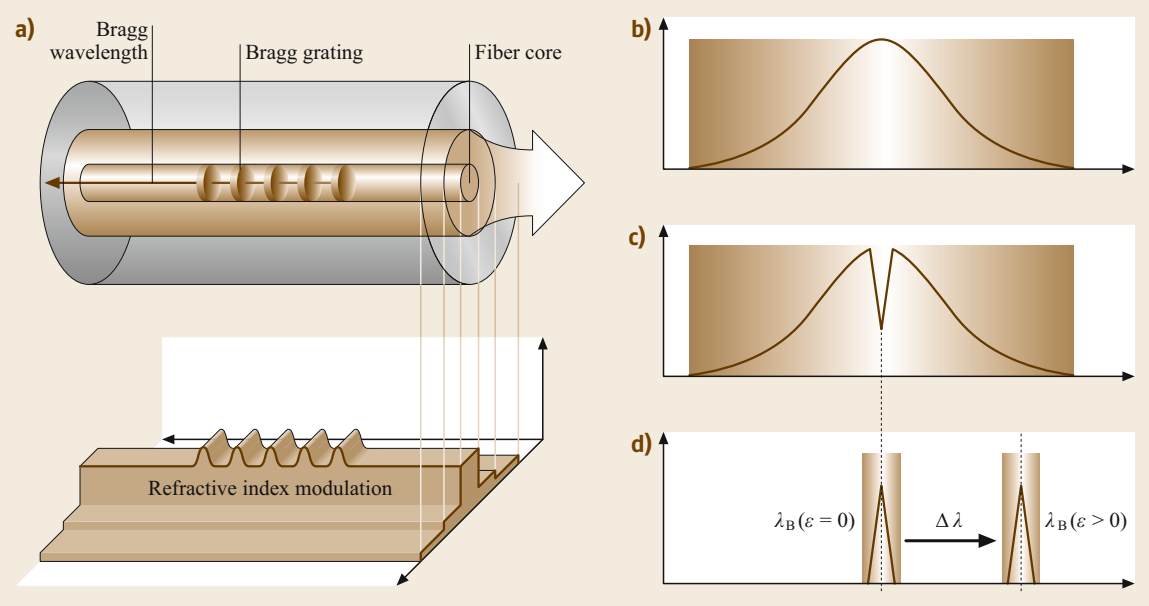

Fig. 7.29a–d Fiber Bragg grating. **(a)** Sensor principle; **(b)** emitted, **(c)** transmitted, **(d)** reflected spectrum (after [7.35])

References

7.1 S. Ness, C.N. Sherlock, P.O. Moore, P. McIntire: *Overview*, NDT Handbook, Vol. 10, 2nd edn. (ASNT, Columbus 1996)

7.2 H. Blumenauer: *Werkstoffprüfung* (Deutscher Verlag für Grundstoffindustrie, Leipzig, Stuttgart 1994)

7.3 W. Grellmann, S. Seidler: *Kunststoffprüfung* (Carl Hanser, München, Wien 2005)

7.4 K. Nitsche: *Schichtmeßtechnik* (Vogel, Würzburg 1997)

7.5 S. Steeb: *Zerstörungsfreie Werkstoff- und Werkstückprüfung* (Expert, Ehningen 2004)

7.6 J. Krautkrämer, H. Krautkrämer: *Ultrasonic Testing of Materials* (Springer, Berlin, Heidelberg 1990)

7.7 A.S. Birks, R.E. Green Jr., P. McIntire: *Ultrasonic Testing*, NDT Handbook, Vol. 7, 2nd edn. (ASNT, Columbus 1991)

7.8 U. Netzelmann, H. Reiter, Y. Shi, J. Wang, M. Maisl: Ceramic automotive valves – Chances and limitations of nondestructive testing, e-J. NDT **2**(7), (1997) https://www.ndt.net/article/dresd97/netzel/netzel.htm

7.9 I. Hertlin, T. Herkel: Riss- und Gefügeprüfung mit akustischer Resonanzanalyse im Schall- und Ultraschallbereich für Kfz-Sicherheitsteile. In: *Annu. Conf. DGZfP, Mainz* (2003), V18

7.10 R.K. Miller, E.V.K. Hill, P.O. Moore: *Acoustic Emission Testing*, NDT Handbook, Vol. 6, 3rd edn. (ASNT, Columbus 2005)

7.11 S. Roderick, P.O. Moore, P. McIntire: *Special Nondestructive Methods*, NDT Handbook, Vol. 9, 2nd edn. (ASNT, Columbus 1995)

7.12 B.G. Livschitz: *Physikalische Eigenschaften der Metalle und Legierungen* (Deutscher Verlag für Grundstoffindustrie, Leipzig 1989)

7.13 J.T. Schmidt, K. Skeie, P. McIntire: *Magnetic Particle Testing*, NDT Handbook, Vol. 6, 2nd edn. (ASNT, Columbus 1989)

7.14 H. Heptner, H. Stroppe: *Magnetische und magnetinduktive Werkstoffprüfung* (Deutscher Verlag für Grundstoffindustrie, Leipzig 1972)

7.15 W.D. Feist, G. Mook, J.H. Hinken, J. Simonin, H. Wrobel: Electromagnetic detection and characterization of tungsten carbide inclusions in non-ferromagnetic alloys, Adv. Eng. Mater. **7**(9), 841–846 (2005)

7.16 W. Morgner, F. Michel: Some new results in nondestructive case depth measurement. In: *9th Eur. Conf. NDT, Berlin* (2006), Paper 118

7.17 W. Willmann, G. Wollmann: Der Barkhausen-Effekt und seine technische Nutzung, Exp. Techn. Phys. **31**, 533–543 (1983)

7.18 G. Dobmann: Nondestructive testing of laser processing of material. In: *Workshop Laser Tech.* (2003)

7.19 I. Altpeter, J. Bender, J. Hoffmann, D. Rouget: Barkhausen-effect and eddy-current testing for the characterization of the microstructure and residual stress states with local resolution. In: *EURO MAT '97 Charact. Prod. Design*, Vol. 4 (Society for Materials Science, Zwijndrecht 1997) pp. 123–128

7.20 S. Udpa, P.O. Moore: *Electromagnetic Testing*, NDT Handbook, Vol. 5, 3rd edn. (ASNT, Columbus 2004)

7.21 R. Zoughi: *Microwave Nondestructive Testing and Evaluation—A Graduate Textbook* (Kluwer Academic, Dordrecht 2000)

7.22 A.J. Bahr: *Microwave Nondestructive Testing Methods* (Gordon Breach, New York 1982)
7.23 G. Busse: Zerstörungsfreie Kunststoffprüfung. In: *Kunststoffprüfung*, ed. by W. Grellmann, S. Seidler (Carl Hanser, München, Wien 2005)
7.24 X.V.P. Maldague, P.O. Moore: *Infrared and Thermal Testing*, NDT Handbook, Vol. 3, 3rd edn. (ASNT, Columbus 2001)
7.25 S.R. Lampman, T.B. Zorc, H.J. Frissell, G.M. Crankovic, A.W. Ronke: *Nondestructive Evaluation and Quality Control*, ASM Handbook, Vol. 17 (ASM International, Materials Park 1989)
7.26 N. Tracy, P.O. Moore: *Liquid Penetrant Testing*, NDT Handbook, Vol. 2, 3rd edn. (ASNT, Columbus 1999)
7.27 W.J. Bisle, D. Scherling, M.K. Kalms, W. Osten: Improved shearography for use on optical non cooperating surfaces under daylight conditions, AIP Conf. Proc. **557**(1), 1928–1935 (2001)
7.28 R.H. Bossi, F.A. Iddings, G.C. Wheeler, P.O. Moore: *Radiographic Testing*, NDT Handbook, Vol. 4, 3rd edn. (ASNT, Columbus 2002)
7.29 R. Glocker: *Materialprüfung mit Röntgenstrahlen* (Springer, Berlin, Heidelberg 1985)
7.30 A.K. Mukherjee, J.E. Bird, J.E. Dorn: Experimental correlations for high-temperature creep, Trans. Am. Soc. Met. **62**, 155 (1969)
7.31 W.J. Staszewski, C. Boller, G.R. Tomlinson: *Health Monitoring of Aerospace Structures: Smart Sensor Technologies and Signal Processing* (Wiley, New York 2003)
7.32 F.-K. Chang (Ed.): *Structural Health Monitoring. The Demands and Challenges* (CRC, Boca Raton 2002)
7.33 G. Mook, J. Pohl, F. Michel: Non-destructive characterization of smart CFRP structures, Smart Mater. Struct. **12**, 997–1004 (2003)
7.34 J. Pohl, S. Herold, G. Mook, F. Michel: Damage detection in smart CFRP composites using impedance spectroscopy, Smart Mater. Struct. B **10**, 834–842 (2001)
7.35 H. Speckmann, R. Henrich: Structural health monitoring (SHM)—overview on airbus activities. In: *16th World Conf. NDT, Montreal* (2004), paper 536

Gerhard Mook

Department of Mechanical Engineering
Institute of Materials and Joining Technology and Materials Testing
Otto-von-Guericke University
Magdeburg, Germany
gerhard.mook@ovgu.de

Professor Mook's main area of research is nondestructive testing and evaluation as well as structural health monitoring. His work is focused on high-resolution imaging systems suitable for in-field application in aerospace and ground transportation systems. He is the chairman of the Board of University Teachers of the German Society for Nondestructive Testing (DGZfP).

Islam Shyha

Mechanical and Construction Engineering
Northumbria University at Newcastle
Newcastle upon Tyne, UK
islam.shyha@northumbria.ac.uk

Dr Shyha received his PhD from The University of Birmingham in 2010. He is now an Associate Professor in Mechanical Engineering and Director of Postgraduate Research in the Faculty of Engineering and Environment at Northumbria University, UK. He teaches mechanical and manufacturing courses and supervises PhD projects in the field of advanced manufacturing and materials.

8. Engineering Materials and Their Properties

Ulrich Wendt

Because engineering materials must cover a wide range of very different properties, a great number of such materials are necessary to address all technical applications. The main classes of engineering materials are dealt with in this chapter: metals and their alloys, polymeric materials, ceramics, glasses, and composites. The specific composition, the manufacturing processes leading to specific constituents/phases and structures, and the resulting properties are outlined for iron and its alloys, for some light metals, and for alloys based on nickel, cobalt, and copper. Great space is dedicated to iron alloys, because they offer the widest range of properties and thus applications in mechanical engineering based on one metal, such as construction steel, automobile sheet steel, cutting tools, and silverware, to name but a few examples. The fine-tuning of properties using heat and mechanical treatments is outlined. A special field of modification is the chemical alteration of surfaces to increase the carbon concentration, leading to different properties of the core and surface of parts.

Polymeric materials with carbon as the main component can be distinguished into thermoplastics, elastomers, and duromers, depending on their mechanical and thermal properties. The most widely used polymers are described. Special attention is paid to the interaction of polymeric materials with solvents and mineral oils. Glasses and ceramics are included as examples of nonmetallic inorganic materials. Composites combine the properties of two or more materials, opening important applications based on their mechanical properties and density.

8.1 **Iron-Based Materials** 234
8.1.1 The Iron-Carbon Phase Diagram and Relevant Microstructures 234
8.1.2 Heat Treatments 236
8.1.3 Steel Grades 242
8.1.4 Steel Castings and Cast Iron 254

8.2 **Aluminum and Its Alloys** 258
8.2.1 General Properties 258
8.2.2 Pure Aluminum 258
8.2.3 Aluminum Alloys 259

8.3 **Magnesium and Its Alloys** 262
8.3.1 General Properties 262
8.3.2 Magnesium Alloys 263

8.4 **Titanium and Its Alloys** 265
8.4.1 General Properties 265
8.4.2 Commercially Pure and Low-Alloy Grades of Titanium 265
8.4.3 Titanium Alloys 266
8.4.4 Two-Phase Intermetallic Ti-Al Alloys 268
8.4.5 Ti-Ni Shape-Memory Alloys 268

8.5 **Ni and Its Alloys** 269
8.5.1 General Properties 269
8.5.2 Corrosion-Resistant Alloys 269
8.5.3 Ni-Based Superalloys 269

8.6 **Co and Its Alloys** 273
8.6.1 General Properties 273
8.6.2 Co-Based Hard-Facing Alloys 273
8.6.3 Co-Based Superalloys 273
8.6.4 Cemented Carbides 273

8.7 **Copper and Its Alloys** 275
8.7.1 Pure Copper 275
8.7.2 Copper Alloys 275

8.8 **Polymers** 278
8.8.1 Chemical Composition and Molecular Structure 278
8.8.2 Microstructure of Polymer Materials 280
8.8.3 Thermal Properties 281
8.8.4 Mechanical Properties of Polymer Materials 282
8.8.5 Polymer Interaction with Solvents 283
8.8.6 Aging and Corrosion 285

8.9 **Glasses and Ceramics** 285
8.9.1 Glasses 285
8.9.2 Glass Ceramics 285
8.9.3 Silicate Ceramics 286
8.9.4 Refractory Ceramics 286
8.9.5 Oxide Ceramics 286
8.9.6 Nonoxide Ceramics 289

8.10 **Composite Materials** 289

References 290

K.-H. Grote, H. Hefazi (Eds.), *Springer Handbook of Mechanical Engineering*, Springer Handbooks,
https://doi.org/10.1007/978-3-030-47035-7_8

Table 8.1 Properties of some widely used metallic materials, carbon fiber, and high-density polyethylene (HDPE): Meltung point T_m, density ρ, yield strength YS, specific yield strength SYS, Young's modulus E, and cost. Note that some of the values given in this table are prone to variation (data compiled from different sources [8.1–3])

Material	T_m of base metal (°C)	ρ (g/cm^3)	YS (MPa)	SYS (MPa cm^3/g)	E (GPa)	Cost (US $/t)
High-carbon steels	1536	7.8	350–1600	45–205	210	700
Stainless steels	1536	7.8	150–500	19–64	193	2500
Cast irons	1147 (eutectic)	7.4	50–400	7–54	150	160
Aluminum 2000 series	660	2.8	200–500	71–179	70	1700[a]
Titanium alloys	1668	4.5	400–1100	89–244	100	6020
Copper alloys	1083	8.9	75–520	8–58	135	5800[b]
Superalloys	1453	7.9	800	101	180	6500
Magnesium alloys	650	1.75	300	171	45	2800
Carbon fiber	3650	1.75	3500–5500	2000–3140	230–400	30 000
HDPE	≈ 250	0.95	26–33	27–35	0.7	1000

[a] Al/2019, [b] Cu/2019

Engineering materials, in principle, can be divided into four main classes:

1. Metals
2. Carbon-based polymeric materials
3. Ceramics and glasses
4. Composites.

Materials in each classes exhibit comparable properties, processing routes, and most often applications as well. The criteria for material selection are rather complex and depend on the intended application purpose. The main design criteria are based on strength, stiffness, fracture toughness, formability, joinability, corrosion resistance, thermal expansion, cost, density, and last but not least recyclability. For structural applications in mechanical engineering, metallic materials [8.4, 5] are still the most widely used group of materials; their order of importance is Fe, Al, Cu, Ni, then Ti. While the physical properties of materials belonging to different classes are described in Chap. 5, Table 8.1 presents a comparison of the mechanical properties of some important metals and alloys, carbon fiber, and a polymer.

8.1 Iron-Based Materials

Iron-based materials are the most widely used metallic materials in terms of number of applications and tonnage, mainly because of their relatively inexpensive manufacturing and enormous flexibility. Accordingly, the properties of Fe-based materials can be varied to a great extent, allowing precise adaptation to specific application requirements ranging from high-strength, high-temperature, and wear-resistant alloys for tools to soft or hard ferromagnetic alloys for applications in electrical industries.

Pure iron, however, is only of minor importance in structural applications, since its mechanical properties are simply inadequate. Alloying with carbon leads to the most important groups of constructional alloys, namely:

1. Steels with carbon content of up to about 2.06% carbon (unless otherwise stated, all compositions are giving in wt%)
2. Cast iron, which practically contains 2.5–5% carbon.

These Fe-C alloys exhibit outstanding properties, including widely variable mechanical properties: yield strengths ranging from 200 MPa to values exceeding 2000 MPa, hot and cold rolling ability, weldability, chip-removing workability, high toughness, high wear resistance, high corrosion resistance, heat resistance, high-temperature resistance, high Young's modulus, nearly 100% recyclability, and many more.

In the following sections, the characteristic phases, microstructures, compositions, and applications of iron-carbon alloys are treated, with an emphasis on the fundamental background. For further reading, references such as [8.6–11] and the online database [8.12] are recommended.

8.1.1 The Iron-Carbon Phase Diagram and Relevant Microstructures

Fe-C-based materials, in general, can be classified into two main categories:

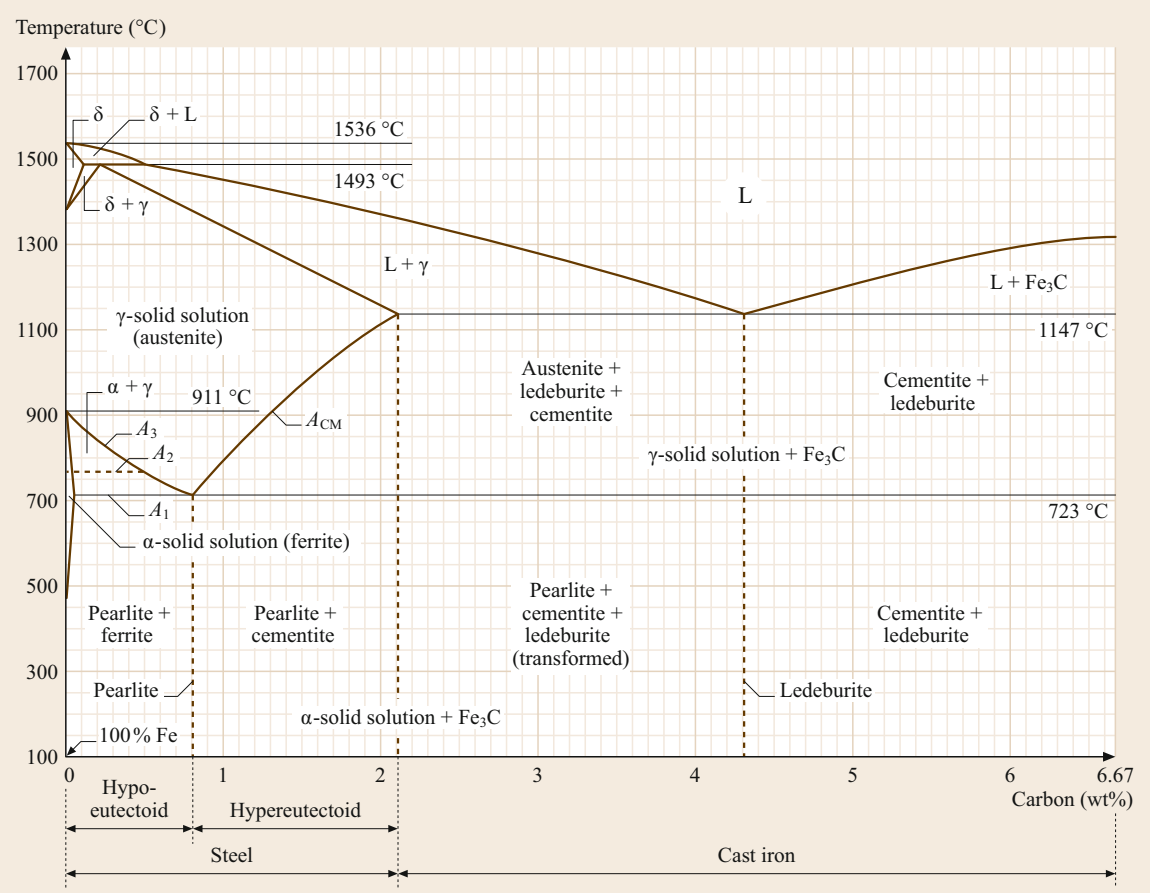

Fig. 8.1 The metastable Fe-Fe_3C (6.67% C) diagram

1. Steels or steel castings, which are forgeable iron-carbon alloys with up to about 2.06% C
2. Gray iron or pig iron with more then 2.06% C (in practice 2.5–5%), which cannot be forged and can be brought into the final form only by casting.

These two groups of Fe-C alloys divide the iron-carbon diagram (Fig. 8.1) into two parts, namely a eutectoid (steel) part and a eutectic (cast iron) part. In the thermally stable condition, carbon prevails in the form of graphite. Although graphite, or more precisely its shape and proportion, plays a major role in adjusting the properties of cast irons, this equilibrium phase is usually not obtained in common steels. Instead, carbon in steels emerges in the form of metastable iron carbide (Fe_3C cementite). Therefore, the metastable equilibrium (Fig. 8.1) between iron and iron carbide is relevant to the behavior of most steels in practice. A closer look at the Fe-Fe_3C phase diagram reveals the three fundamental ideal diagrams introduced in Sect. 4.1.5, namely a peritectic and a eutectoid system in the steel part and a eutectic system in the cast-iron part of the diagram.

Pure iron appears in three different allotropic forms, for which the following notations are used:

- α-Fe with body-centered cubic (bcc) structure, which is stable at temperatures below 911 °C; note that, from 769 °C (A_2 line) to lower temperatures, α-Fe is ferromagnetic without a lattice transformation;
- γ-Fe with face-centered cubic (fcc) structure, which is stable between 911 and 1392 °C;
- δ-Fe with bcc structure, which exists from 1392 °C to the melting point at 1536 °C.

With its significantly smaller atomic radius, carbon occupies interstitial lattice sites (see Sect. 4.1.5) in the iron phases. Its solubility, however, depends on the size of the lattice gap and therefore on the lattice type of the specific Fe phase (Fig. 8.1). These differences in the maximum solubility of carbon are the basis for the

Table 8.2 Phases and phase mixtures of the Fe-Fe_3C diagram. Carbon content means maximum carbon content for single-phase regions or percentage of particular phase for phase mixtures (SS: solid solution)

Phase and phase mixture	Carbon content	Designation
α-Fe	0.02% (at 723 °C)	Ferrite
γ-Fe	2.06% (at 1147 °C) 0.8% (at 723 °C)	Austenite
δ-Fe	0.1% (at 1493 °C)	δ-Ferrite
Fe_3C	6.67%	Cementite
(α-Fe + Fe_3C)	88% α-SS + 12% Fe_3C	Pearlite (eutectoid)
(γ-Fe + Fe_3C)	51.4% γ-SS + 48.6% Fe_3C	Ledeburite I (eutectic)
(α-Fe + Fe_3C)	35.5% α-SS + 64.5% Fe_3C	Ledeburite II

enormous variability of the mechanical properties of steels. In Table 8.2, the phases and phase mixtures of the Fe-Fe_3C system, their corresponding (maximum) carbon content at different temperatures, and their microstructural nomenclature are summarized.

The intermetallic compound Fe_3C (*cementite*), or more accurately its microstructural appearance, plays a crucial role in the adjustment of the mechanical properties of steels. Cementite with 6.67% carbon is based on an orthogonal lattice where dislocation glide at low temperatures is nearly impossible. It therefore exhibits very high hardness (1400 HV) and brittleness. However, in the form of finely distributed particles or lamellae in the grain interiors, it can hinder dislocations from glide very effectively. At the carbon content of about 0.8% at which the eutectoid reaction occurs, a phase mixture of 88% α-Fe and 12% Fe_3C (eutectoid) is formed from γ-Fe(C) solid solution (Table 8.2). The typical arrangement of the eutectoid in contiguous lamellae (Fig. 8.2) is the result of fast decomposition, and the designation "pearlite" is used for this microstructure.

Likewise, the eutectic microstructure at about 4.3 wt% C, i.e., a phase mixture of 51.4% γ-Fe and 48.6% Fe_3C, is called "ledeburite". At carbon concentrations that differ from the exact eutectoid or eutectic composition, the microstructure contains more than one component. This is shown in Fig. 8.3 for *hypo-* and *hypereutectoid* steels.

On slow cooling of hypoeutectoid compositions, i.e., of alloys containing less than 0.8% C, the austenite partly transforms to ferrite in the temperature range of 911–723 °C. Since the solubility of carbon in α-Fe is significantly lower than in γ-Fe, the residual austenite simultaneously enriches in carbon along the A_3 line, until at 723 °C the remaining austenite, now exactly at the eutectoid composition, transforms to pearlite as a second microstructural component (Fig. 8.3). Hypereutectoid alloys with 0.80–2.06% carbon first form cementite at γ-Fe grain boundaries on cooling in the temperature interval from 1147 to 723 °C, while the austenite depletes in carbon. The carbon concentration of the austenite reaches in turn 0.8% at 723 °C, and it transforms to pearlite on further cooling. The microstructural composition of Fe-C alloys in the thermodynamic equilibrium can easily be derived from microstructure diagrams such as that shown in Fig. 8.4.

8.1.2 Heat Treatments

Since modification of the atomic configuration requires diffusion (Sect. 4.1.3) of the atoms to occupy appropriate lattice sites, phase transitions in the solid state are typically time dependent. Therefore, the equilibrium phases of the Fe-C phase diagram only appear upon slow cooling or after sufficiently long heat treatments.

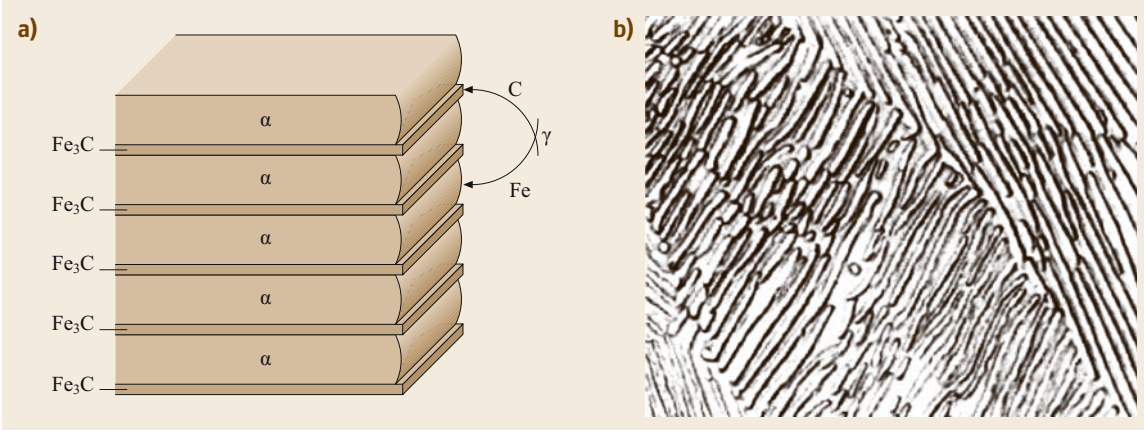

Fig. 8.2a,b Transformation of austenite to pearlite below 723 °C. **(a)** Decomposition of γ-Fe into lamellae of two different phases (α-Fe and Fe_3C). **(b)** Microstructure of pearlite lamellae (after [8.13])

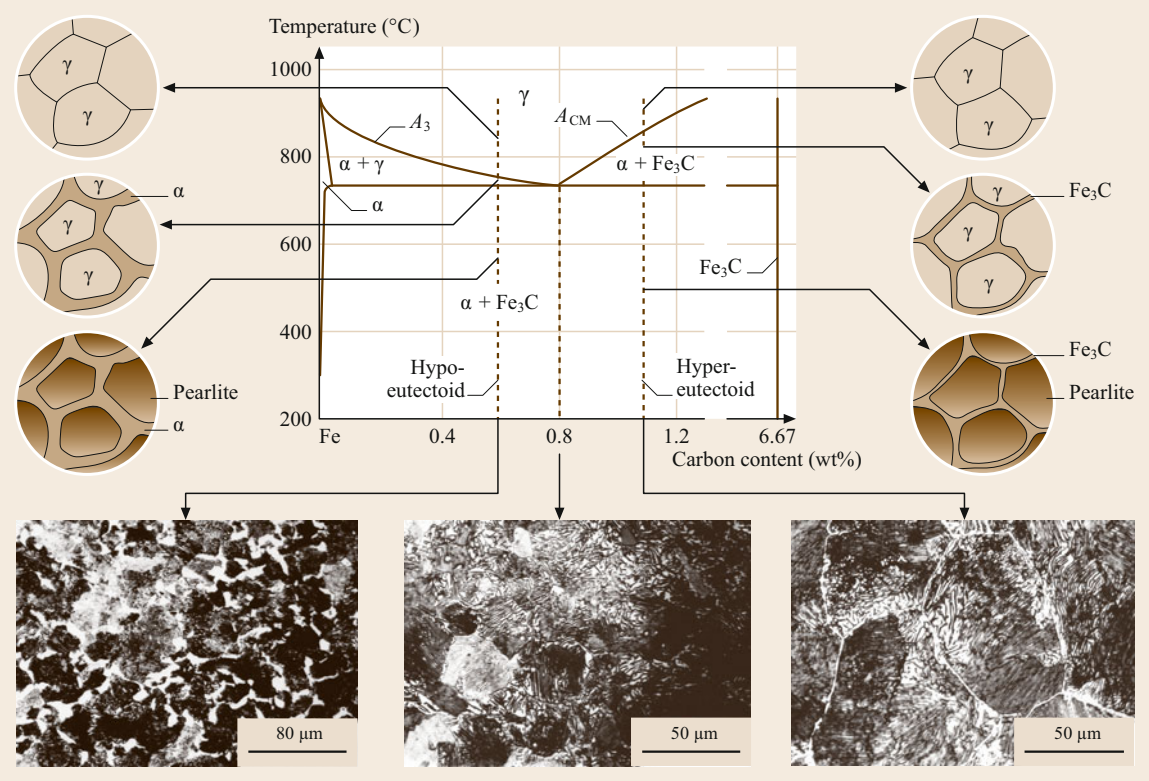

Fig. 8.3 Microstructural evolution of hypo- and hypereutectoid steels upon cooling from the austenitic region of the Fe-C diagram (after [8.13])

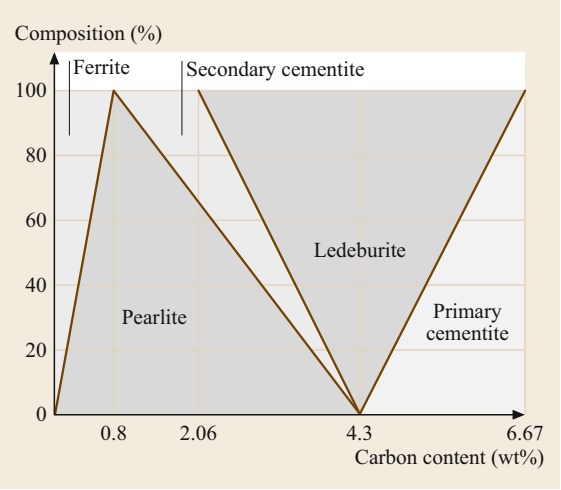

Fig. 8.4 Composition of Fe-C alloys depending on carbon content

The microstructures shown in Fig. 8.3, on the other hand, arise only under specific cooling conditions. By altering the time–temperature path, metastable phases as well as totally different microstructures can be formed. Heat treatment procedures differ with regard to the following parameters:

- Heating method
- Holding temperature
- Holding time
- Cooling method (for example, in air, oil, water, or a furnace).

According to the cooling method applied, the following principle division of heat treatment procedures is widely used:

1. Annealing treatments (slow cooling close to equilibrium)
2. Hardening treatments (fast cooling).

In the following, the main parameters and objectives of frequently used heat treatment procedures for steels are summarized using the above scheme.

Annealing Treatments

In Fig. 8.5, the temperatures and main parameters of frequently used annealing treatments of steels are shown [8.8].

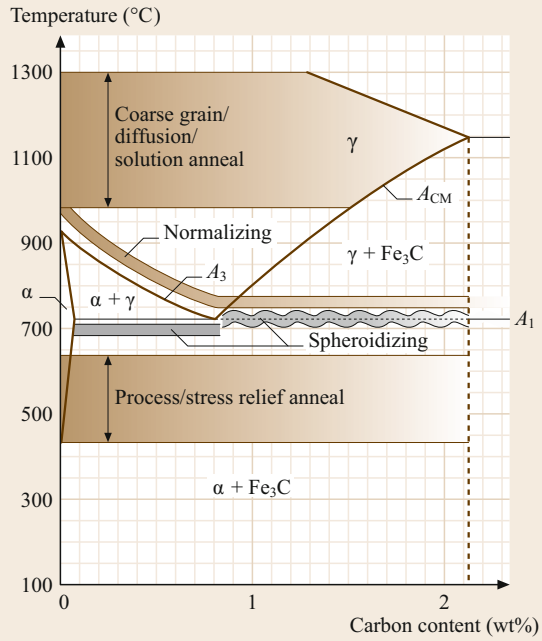

Annealing treatments:

- Normalizing:
  30–50 K above A_3
  for 20–60 min
  cooling in air
- Spheroidizing:
  below/around A_1
  for up to 5 h
  slow cooling in furnace
- Stress relief anneal:
  450–650 °C
  for 2–4 h
  slow cooling in furnace

Hardening:

- Solution annealing:
  30–50 K above A_3
  for 20–60 min
- Quenching to room temperature:
  media: oil, water, ice water or salt solutions

Tempering:

- Heat treatment between 100 and 650 °C, outdiffusion of carbon

Fig. 8.5 Annealing treatments of steels

Normalizing. Due to the heat flow during cooling of castings, in the heat-affected zone of welding joints as well as after cold or warm rolling, the microstructure of steels can be extremely inhomogeneous. Normalizing, therefore, first of all serves to homogenize the steel and should result in a fine-grained microstructure (grain size $< 100\,\mu m$). To do so, the workpiece is austenitized by heating to temperatures 30–50 K above the A_3 line, i.e., into the region of the γ-Fe solid solution, or above the A_1 line in case of hypereutectoid steels. Subsequent cooling in air leads to complete new formation of fine-grained pearlitic-ferritic or pearlitic-cementitic microstructures (Fig. 8.6a) with high strength and high toughness. The strength and toughness of steels in the normalized condition strongly depend on the carbon content. As shown in Fig. 8.7, the strength reaches its maximum at about 1.0% carbon. Toughness, as characterized by the impact energy in Charpy tests, gives the steel a brittle behavior at carbon concentrations as low as 0.8%.

Spheroidizing. The cold workability of normalized steels is normally insufficient to achieve the desired degree of deformation. However, since the lamellar arrangement of α-Fe and Fe_3C in pearlite is energetically unstable, on heat treatment slightly below the A_1 transformation temperature (or in the case of hypereutectoid steels by oscillating around A_1 to accelerate spheroidization of the cementite network), the cementite lamellae rearrange to form stable spherical particles (Fig. 8.6b). Dislocation movement, which is restricted in pearlite to the region within the small α-Fe lamellae, is now possible in the whole grain interior, thus the steel can be deformed more severely. After annealing, the workpiece is cooled slowly (in the furnace) to prevent heat stresses from arising.

Process Annealing. Cold deformation as well as hot deformation to a high degree result in the formation of a dense dislocation network, which hinders dislocation movement and therefore further material deformation. A high dislocation density, on the other hand, stores high levels of energy, which encourages the formation of a completely new grain structure (recrystallization) upon annealing at temperatures exceeding $T_p = 0.4T_m$ (T_p = recrystallization temperature, T_m = melting temperature). As a consequence the strength and toughness of the recrystallized state reach levels which are close to the undeformed condition, and the material can therefore be further deformed.

Coarse-Grain Annealing. Coarse grains are beneficial when the material is machined by chip-removal methods, because short fragile shear chips are formed. Such a microstructure is the result of heat treatment at temperatures between 950 and 1200 °C, i.e., in the austenitic region well above the A_3 line. On subsequent cooling in a furnace, the coarse-grained γ-Fe solid solution transforms into a coarse-grained ferritic-pearlitic microstructure. Since the accompanying decrease in toughness deteriorates the properties of the steel, a final heat treatment (hardening, tempering, etc.) must be applied to retransform the microstructure to a fine-grained state.

Stress-Relief Annealing. Stress-relief annealing serves to relieve stresses in the workpiece which are caused by cold deformation, microstructural transformations, thermal loading, or chip-removal working. Stress-relief annealing is usually carried out at temperatures between 450 and 650 °C for several hours,

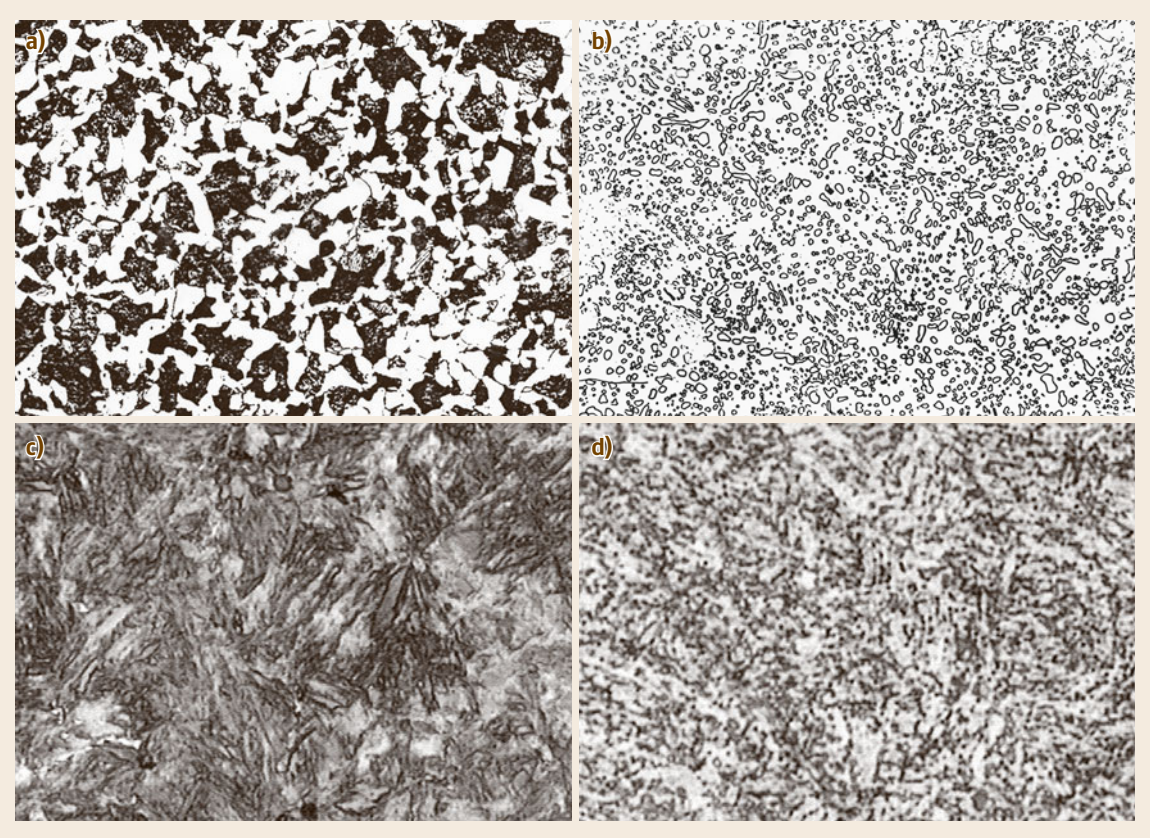

Fig. 8.6a–d Microstructures of steel after different heat treatments: **(a)** C45: normalized, **(b)** C60: spheroidized, **(c)** C45: hardened, and **(d)** C45: hardened and tempered at 550 °C

followed by slow cooling. It does not lead to apparent changes in the microstructure, nor does it change the mechanical properties significantly.

Diffusion Annealing. Diffusion annealing is applied when segregation (local variations of the chemical composition) must be compensated; it requires temperatures as high as 1000–1300 °C and annealing times as long as 50 h. Since this treatment is very expensive, segregation should be prevented by optimizing the cooling conditions after casting.

Solution Annealing. Solution annealing is predominantly applied for austenitic steels and serves to solve (large) precipitates in steels. Annealing at temperatures between 950 and 1200 °C and fast cooling results in a supersaturated solid solution at room temperature. Subsequent aging leads to the formation of small precipitates which lead to a significant strength increase at moderate toughness values.

While the annealing treatments introduced above lead to phase compositions which are close to equilibrium with increasing cooling rate, the transformation behavior of austenite can be completely different. Since the formation and growth of nuclei are diffusion-controlled processes, fast cooling from the γ-Fe phase region may suppress the formation of the temperature-equivalent equilibrium phases. At increasing cooling rates, the transformation temperatures A_1 and A_3 decrease until they coincide at the point of the lower critical cooling rate (Fig. 8.8). At even faster cooling rates, *bainite* (consisting of aggregates of plates of ferrite, so-called sheaves, separated by untransformed austenite), *martensite* (see below), or cementite is formed; for a more comprehensive review of bainite, see [8.15]. Due to the high cooling rate, the diffusivity of Fe is reduced so strongly that the formation of cementite only occurs by diffusion of carbon, while iron transforms from fcc to bcc via a diffusionless shear process. When the cooling rate reaches the upper critical limit, the diffusivity of carbon is completely suppressed as well. Due to the supersaturated solution of carbon in α-ferrite, a distorted body-centered tetragonal (bct) lattice, so-called martensite, is now formed as the product

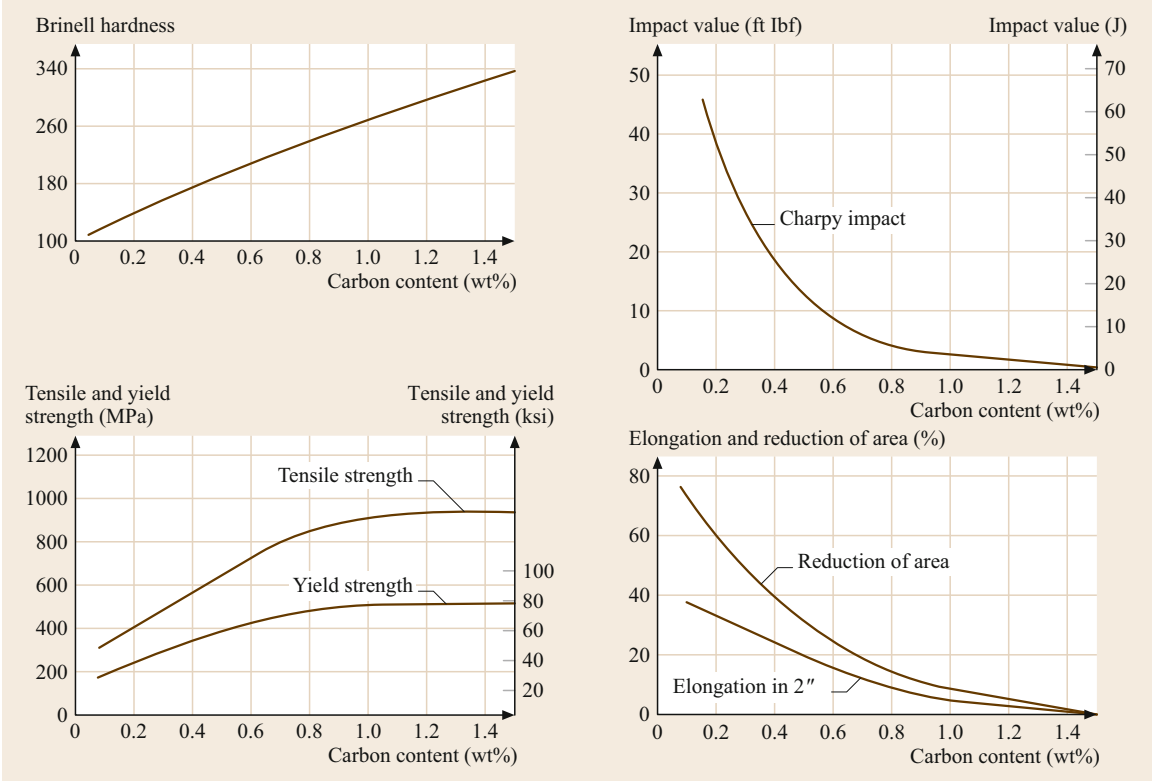

Fig. 8.7 Mechanical properties of Fe-C alloys depending on carbon content (after [8.14])

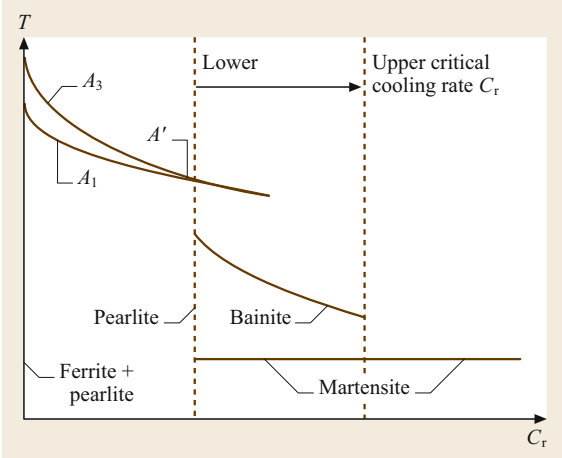

Fig. 8.8 Transition temperatures and products in steels as functions of cooling rate (C_r)

of a phase transition from the fcc γ-lattice. This results in a steel with very high strength, but at the expense of low ductility.

The kinetics of the phase transitions from the γ-Fe phase region can be visualized in time–temperature transition (TTT) diagrams obtained under isothermal holding conditions, or in continuous cooling transition (CCT) diagrams for varying (but fixed) cooling rates. One example for steels is given in Fig. 8.9, which shows the CCT diagram of 42MnV7. Depending on the cooling rate, the transition of γ-Fe leads to the formation of martensite, bainite, pearlite, or a mixture thereof at room temperature. The transformation quantity after crossing a transformation region is given in Fig. 8.9, as well as the hardness values of the resulting microstructure at room temperature.

Hardening

The basis of hardening is the mechanism of martensitic transformation, which results in a massive increase in hardness. In the case of hypoeutectic steels, austenitization is done above the A_3 line in the Fe-Fe_3C diagram; in the case of hypereutectic alloys, annealing in the two-phase region γ-Fe + Fe_3C is usually sufficient. The distortion caused by the supersaturation of carbon in the α-ferrite increases with increasing carbon content. On the other hand, at least about 0.3% C is necessary to yield a significant increase in strength. The temperature to which the material has to be cooled from the austenite region (without any other nucleus formation to apply during cooling) to form martensite M_s

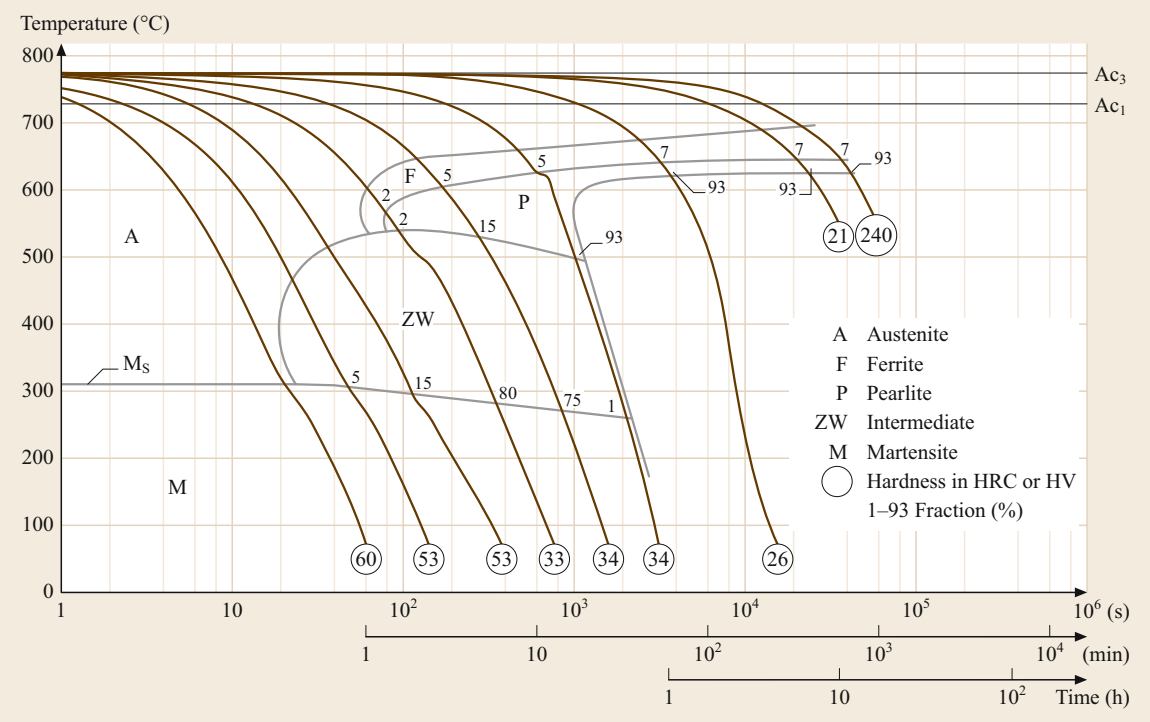

Fig. 8.9 Continuous cooling transition (CCT) diagram of 42MnV7: austenite-forming temperature 1050 °C (holding period 8 min) heat-up in 2 min

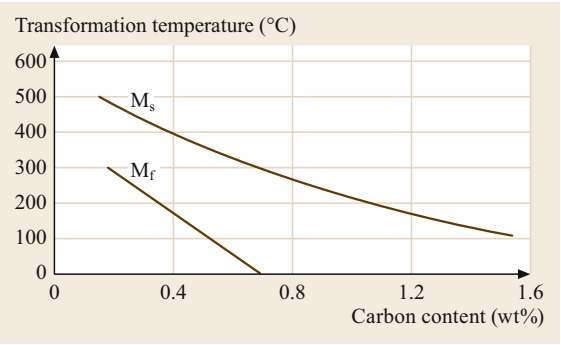

Fig. 8.10 Dependence of martensite transformation temperatures on carbon content (after [8.6])

(the *martensite start*) as well as the temperature where the whole microstructure consists of martensite M_f (the *martensite finish*) decrease with increasing carbon content (Fig. 8.10).

Therefore, hardening through the whole cross section of a workpiece with higher carbon content is possible only for low dimensions, and the hardening depth can be increased by accelerated cooling or by alloying. The cooling media commonly used are oil, water, ice-water, or salt solutions. Alloying with Mn, Cr, Mo, and Ni in the concentration range of 1–3% can improve the through-hardening capability of the steel. Thermal stresses caused by high temperature gradients superimpose onto transformation-induced stresses and can lead to hardening cracks. The crack sensibility can be reduced by warm-bath hardening, in which a temperature-balancing step above the M_s temperature is done before final quenching to martensite.

Tempering. To achieve technically relevant properties, especially suitable toughness values, a final heat treatment after the hardening process step is required. This tempering step is done below the A_1 line and serves to reduce the brittleness of martensite by means of outdiffusion of carbon from the distorted ferrite lattice. In the temperature range up to about 300 °C, diffusion of carbon leads to a decrease of the lattice distortion, which reduces the brittleness but does not lead to a significant change of the strength. This is ensured by the formation of small metastable ϵ-carbides and the disintegration of residual austenite. Tempering above 300 °C leads to disintegration of the remaining martensite to form ferrite with finely distributed spherical cementite, while the ϵ-carbide transforms to cementite as well. Consequently, the strength is lowered significantly while the toughness increases considerably. Tempering above 450 °C yields a homogeneous, fine-grained

microstructure with high toughness and strength, as desired for many structural parts.

In the case of alloyed steels containing Mo, W, and/or V, i.e., tool steels or heat-resistant steels, tempering at temperatures between 450 and 600 °C leads to the formation of small, homogeneously distributed carbide precipitates which counteract the strength decrease during annealing (so-called secondary hardening).

Surface Hardening. In many practical applications such as crankshafts, spigots, rolls, or gears, high hardness and wear resistance may be required at the surface, and there only in some regions, but at the same time, high fracture toughness of the bulk part is required in order not to trade off fatigue strength. Therefore, for these applications, hardening is done only in the near-surface areas of the workpiece. Steels that are suitable for this treatment are plain carbon steels and low-alloy steels with carbon content of 0.3–0.7%. The following treatments are commonly used for direct hardening:

1. Flame hardening, in which the surface of the workpiece is heated to the austenitization temperature using a gaseous oxygen flame
2. Induction heating, in which a high-frequency coil is used to heat the material surface via the skin effect
3. Beam hardening (electron and laser beam), by which small areas of the workpiece can be treated selectively
4. Dip hardening, which is especially suitable for pieces with curved surfaces for which other treatments would be too costly.

In the case of steels with less than about 0.25% C, the surface has to be enriched in carbon prior to hardening and the workpiece is heated to temperatures between 850 and 950 °C in a carbon-rich atmosphere (e.g., methane). It has to be kept in mind that the enriched (up to 0.9% C) surface shows a lower transition temperature then the core with a lower carbon content. Therefore, hardening can be done from the transition temperature of either the core or the surface. If only the surface region is austenitized, the core is not completely transformed to γ-Fe. This can lead to significant grain growth, and lower toughness values are expected. If, however, the core is fully austenitized, a fine-grained core with significantly higher toughness results after hardening. After surface hardening, a tempering treatment at 150–250 °C is usually done.

Nitriding. Nitriding is a thermochemical treatment of steels. The surface area of steels is enriched in nitrogen (usually in an ammonia atmosphere). Nitriding is carried out at relatively low temperatures (495–565 °C), and no quenching is required after the process. Hence, this process leads to relatively little distortion but produces, on the other hand, a relatively shallow (0.2–0.3 mm) casing. In contrast to carbon-enriched surface layers, nitride layers provide significantly higher temperature resistance (up to 500 °C).

8.1.3 Steel Grades

Effect of Alloying Elements

Besides carbon as the main alloying element, steels generally contain further alloying additions [8.16]. A semantic distinction can be made between:

1. Residual elements, which are not intentionally added to the steel but result from raw materials and steel-making practices
2. Alloying elements, which are added to cause changes in the properties of steels.

To the residual elements in group (1) belong predominantly phosphorus, sulfur, oxygen, hydrogen, manganese, and silicon. Phosphorus, sulfur, oxygen, and hydrogen are usually undesired, because they reduce ductility and toughness. Their content has to be reduced to a harmless level by secondary metallurgy. The only exception is the group of free-machining steels, where sulfur or phosphorus may be added deliberately to improve machinability. The effect of alloying elements of group (2) can be separated into four different fundamental mechanisms:

1. Change of the phase equilibria in the Fe-C phase diagram
2. Solid-solution hardening by elements such as Mn, Si, Ni, Co, Cu, and Al in Fe
3. Formation of carbides
4. Influencing the composition of oxides at the surface.

Alloying elements can influence the equilibrium diagram in two principal ways:

- By expanding (or opening) the γ-phase field, thereby facilitating the formation of austenite over a wider compositional range. These elements are referred to as γ-stabilizers (Fig. 8.11a,b).
- By contracting (or closing) the γ-phase field, which encourages formation of ferrite over a wider compositional range; these elements are termed α-stabilizers (Fig. 8.11c,d).

Consequently, elements such as Mn and Ni, which open the γ-phase field, lead to a decrease of the eutectoid temperature, which facilitates hardening; others

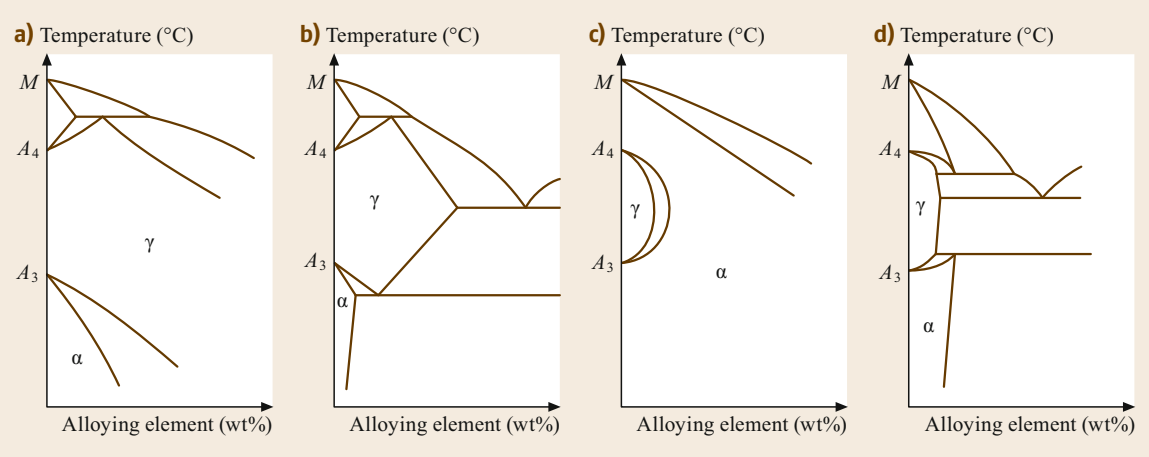

Fig. 8.11a–d Classification of iron alloy phase diagrams: **(a)** opened γ-phase field, **(b)** expanded γ-phase field, **(c)** closed γ-phase field, and **(d)** contracted γ-phase field (after [8.7])

such as Ti and Mo lead to an increase of the eutectoid temperature (Fig. 8.12). However, most of the alloying elements in steels have in common that they help to decrease the carbon concentration in the eutectoid, which provides better hardenability for low-carbon steel grades.

Alloying elements can be separated according to their impact on the iron-carbon phase diagram into four groups [8.7]:

- *Class 1*: These elements open the γ-phase field. To this group belong the most important alloying additions in steels: *manganese* and *nickel*. Cobalt and the inert metals ruthenium, rhodium, palladium, osmium, iridium, and platinum show a similar behavior. With a sufficient amount of nickel or manganese, the formation of α-Fe under normal cooling conditions can be suppressed down to room temperature, allowing the formation of austenitic steels. At least 0.3% *manganese* is present in all commercial steel grades. It serves primarily to deoxidize the melt and counteracts the harmful influence of iron sulfide via the formation of manganese sulfide stringers. Excess content of manganese can partly dissolve in the iron lattice, leading to the mentioned solid-solution hardening effect and partly form Mn_3C. Through the opening of the γ-phase field, the critical cooling rate is considerably decreased, allowing better hardenability of the steel. With increasing Mn content, the amount of C in the steel can be reduced while retaining a constant strength level, which finally leads to improved ductility. The hot working capability is improved at Mn contents up to 2%, since it reduces the susceptibility to hot shortness. However, if the manganese content is increased above 1.8%, the steel tends to become air-hardened, with resulting impairment of the ductility. With 5–12% Mn, the steel becomes martensitic even after slow cooling. At Mn contents

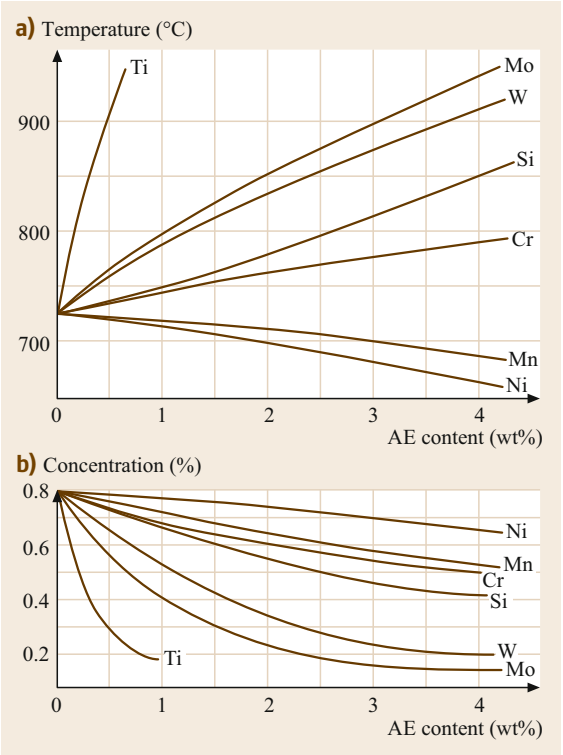

Fig. 8.12a,b Effect of alloying additions (AE content: content of alloying element) on **(a)** eutectoid temperature and **(b)** carbon concentration of eutectoid in steels (after [8.16])

above 12% and high C contents, the austenite phase is retained down to room temperature. Under impact loading, such steels can be strongly cold worked at the surface while the core remains ductile. In contrast to manganese, *nickel* does not form any carbon compounds in steel. Up to content of about 0.5%, it is primarily an efficient ferrite strengthener. This is additionally intensified by a refinement of the pearlite lamellae. As in the case of manganese, with increasing Ni content and hence decreasing transition temperature, the hardenability is improved (Fig. 8.13). The sudden drop in the Ar_1 temperature at 8–10% nickel encourages the formation of martensite, while above 24% Ni this transformation is depressed below room temperature. As shown in the lower part of Fig. 8.13, the mechanical properties behave accordingly: while steels with more than 10% nickel have high tensile strength, the elongation drops from about 20% at nickel contents below 8% to about 10% in the martensitic region. Above 24% Ni and thus stabilization of austenite at room temperature, the tensile strength decreases and the material becomes ductile, tough, and workable. The effect of increasing the Ni and C contents on the microstructure is shown in the *Guillet* diagram for a constant cooling rate in Fig. 8.13. Steels with high nickel content also show a low coefficient of thermal expansion (CTE). The so-called *Invar* alloy, containing 36% Ni, 0.2% C, and 0.5% Mn, has a coefficient of thermal expansion which is nearly zero over the temperature range 0–100 °C. These alloys are therefore used in clocks, tapes, and wire measurements.

- *Class 2*: These elements expand the γ-phase field. The most important elements belonging to this group are carbon and nitrogen. Copper, zinc, and gold show a similar effect. Cu in amounts exceeding 0.2% enhances the atmospheric corrosion resistance of carbon and low-alloy steels. Those steels are referred to as weathering steels and are used in the building industry. Furthermore, copper increases the yield strength, and at content above 0.3%, age hardening is possible. However, copper exaggerates surface defects (grain boundaries), leading to high surface sensitivity during hot rolling. It is therefore sometimes regarded as a *steel pester*.
- *Class 3*: These elements close the γ-phase field. Elements which restrict the formation of γ-Fe to a small area appearing like a loop include silicon, aluminum, beryllium, and phosphorus as well as the carbide"0forming elements titanium, vanadium, molybdenum, tungsten, and chromium. In other words, there are more elements which encourage the formation of bcc iron. Note that the normal heat treatment processes which are based on a γ–α transformation are no longer available. When adding *chromium* to steel, most often its capability to increase the resistance to corrosion and oxidation is considered. However, chromium also improves the hardenability by decreasing the critical hardening rate. Furthermore, it raises the high-temperature strength and improves the abrasion resistance of high-carbon compositions through carbide formation. Since carbides are stable at high temperatures, the solution annealing temperature has to be increased. In combination with nickel, chromium stabilizes austenite, resulting in a steel that superimposes the positive properties of chromium, i.e., high hardness and resistance to wear, and those of nickel, i.e., high strength, ductility, and toughness. The effect of tempering nickel-chromium steel on the room"0temperature mechanical properties is shown in Fig. 8.14. Note that there is a distinct minimum in the Izod impact curve in the temperature range of 250–450 °C, which is known as embattlement. This is caused by the enrichment of grain boundaries with alloying elements such as Mn and Cr during austenitization, which leads to enhanced segregation of em-

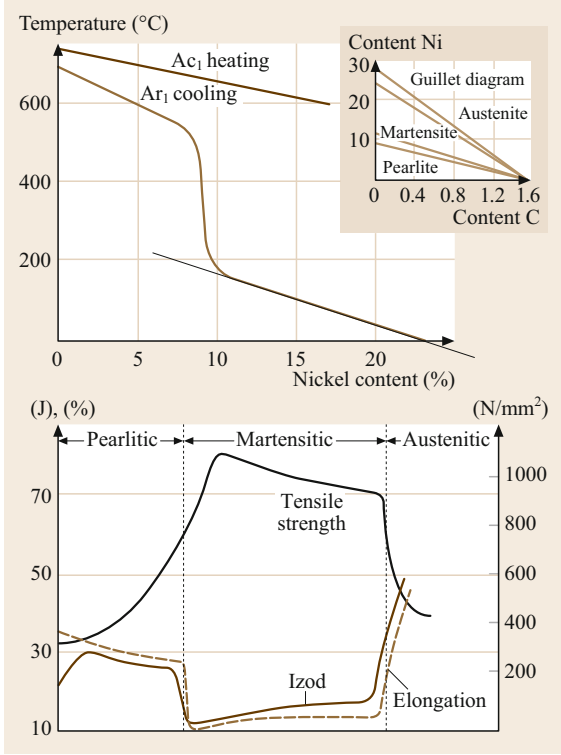

Fig. 8.13 Effect of nickel on transition temperatures (*inset*: Guillet diagram) and mechanical properties of 0.2% carbon steels cooled at constant rate (after [8.12])

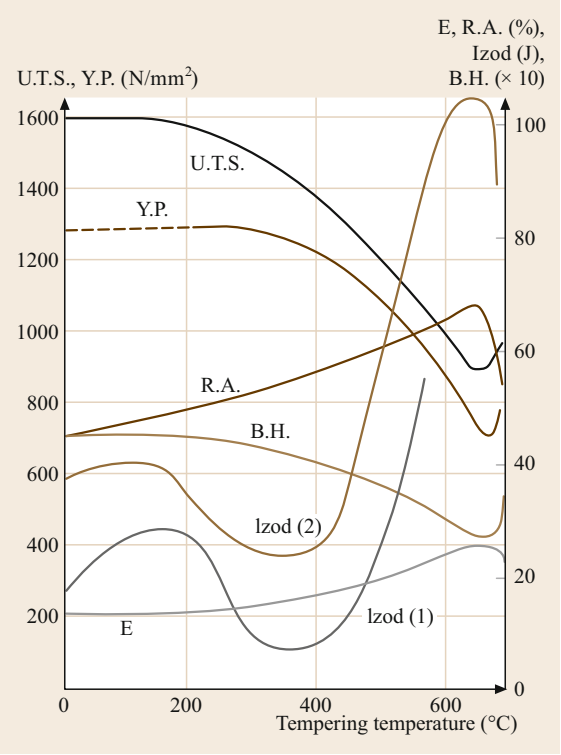

Fig. 8.14 Effect of tempering on mechanical properties of nickel-chromium steel (0.26% C, 3% Ni, 1.2% Cr), 29 mm-diameter bars hardened in oil from 830 °C. Izod (2) for steel with 0.25% Mo added (U.T.S.: ultimate tensile strength; Y.P.: yield point; E.: elongation; R.A. reduction in area; B.H.: Brinell hardness) (after [8.12])

battling elements such as P, Sn, Sb, and As on slow cooling from 600 °C. This can be prevented by increasing the cooling rate during hardening. However, as shown in Fig. 8.14, Izod (2) addition of *molybdenum* significantly reduces the tempering embrittlement at intermediate temperatures and increases the high-temperature tensile and creep strength of the steel. Ni-Cr-Mo steels are therefore widely used for ordnance and turbine rotors. Aluminum, silicon, and titanium are commonly used as deoxidizers. Furthermore, aluminum and titanium can limit grain growth when added to steel in specific amounts. This is critical for preventing grain coarsening during solution annealing prior to hardening. Titanium is, however, one of the strongest carbide formers (Fig. 8.15), and since its carbides are quite stable, they may not dissolve in austenite and can therefore have adverse effects on the hardenability. It is used as a stabilizer in corrosion-resistant steels.

- *Class 4*: These elements contract the γ-phase field. This is observed when carbide-forming elements

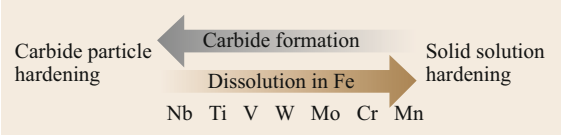

Fig. 8.15 Tendency of alloying elements to form carbides in steels, and vice versa dissolution in Fe lattice

such as tantalum, niobium, and zirconium are present. Boron also belongs to this class of alloying additions. Zirconium is primary used in so-called high-strength low-alloy (HSLA) steels to improve their hot-rolling properties.

Classification and Designations

A variety of steel classification systems are in use; they subdivide, for example, with regard to chemical composition, application area, required strength level, microstructure, manufacturing methods, finishing method, or the product form (a comprehensive comparison of steel standards is given in [8.17, 18]). Chemical composition is, however, by far the most widely used basis for classification and/or designation of steels. The most commonly used system of designation is that of the American Iron and Steel Institute (AISI) and Society of Automotive Engineers (SAE), which is based upon a four- or five-digit number, where the first two digits refer to the main alloying elements and the latter two or three digits give the carbon content in wt%.

The designation 1020 according to the SEA-AISI classification is used, for example, for a carbon steel with nominally 0.2 wt% C, while the steel 10120 according to SEA-AISI contains 1.2 wt% C. The various grades of carbon and alloy steels are presented in Table 8.3.

The unified numbering system (UNS) for metals and alloys is being used with increasing frequency. It was developed by ASTM and SAE and other technical societies, trade associations, individual users and producers of metals and alloys, and US government agencies. The system helps to avoid confusion, preventing the use of more than one identification number for the same metal or alloy. Each UNS designation consists of a single-letter prefix followed by five digits. The prefix usually indicates the family class of metals: for example, "T" for tool steel, "S" for stainless steel, or "F" for cast irons, while "G" is used for carbon and alloy steels. Existing designation systems, such as the AISI-SAE system, were incorporated into the UNS system wherever feasible. More information on the UNS system and an in-depth description can be found in SAE J1086 and ASTM E 527. Table 8.4 presents an overview of the main groups of UNS designations for iron-based materials.

Table 8.3 SAE-AISI system of designation for carbon and alloy steels [8.12]

Numerals and digits	Type of steel and nominal alloy content (%)
Carbon steels	
10xx[a]	Plain carbon
11xx	Resulfurized
12xx	Resulfurized and rephosphorized
15xx	Plain carbon (max. Mn 1.00–1.65)
Manganese steels	
13xx	Mn 1.75
Nickel steels	
23xx	Ni 3.50
25xx	Ni 5.00
Nickel-chromium steels	
31xx	Ni 1.25; Cr 0.65 and 0.80
32xx	Ni 1.75; Cr 1.07
33xx	Ni 3.50; Cr 1.50 and 1.57
34xx	Ni 3.00; Cr 0.77
Molybdenum steels	
40xx	Mo 0.20 and 0.25
44xx	Mo 0.40 and 0.52
Chromium-molybdenum steels	
41xx	Cr 0.50, 0.80, and 0.95; Mo 0.12, 0.20, 0.25, and 0.30
Nickel-chromium-molybdenum steels	
43xx	Ni 1.82; Cr 0.50 and 0.80; Mo 0.25
43BVxx	Ni 1.82; Cr 0.50; Mo 0.12 and 0.25; V 0.03 (min)
47xx	Ni 1.05; Cr 0.45; Mo 0.20 and 0.35
81xx	Ni 0.30; Cr 0.40; Mo 0.120
86xx	Ni 0.55; Cr 0.50; Mo 0.20
87xx	Ni 0.55; Cr 0.50; Mo 0.25
88xx	Ni 0.55; Cr 0.50; Mo 0.35
93xx	Ni 3.25; Cr 1.20; Mo 0.12
94xx	Ni 0.45; Cr 0.40; Mo 0.12
97xx	Ni 0.55; Cr 0.20; Mo 0.20
98xx	Ni 1.00; Cr 0.80; Mo 0.25
Nickel-molybdenum steels	
46xx	Ni 0.85 and 1.82; Mo 0.20 and 0.25
48xx	Ni 3.50; Mo 0.25
Chromium steels	
50xx	Cr 0.27, 0.40, 0.50, and 0.65
51xx	Cr 0.80, 0.87, 0.92, 0.95, 1.00, and 1.05
50xx	Cr 0.50; C 1.00 (min)
51xx	Cr 1.02; C 1.00 (min)
52xx	Cr 1.45; C 1.00 (min)
Chomium-vanadium steels	
61xx	Cr 0.60, 0.80, and 0.95; V 0.10 and 0.15 (min)
Tungsten-chromium steels	
72xx	W 1.75; Cr 0.75
Silicon-manganese steels	
92xx	Si 1.40 and 2.00; Mn 0.65, 0.82, and 0.85; Cr 0 and 0.65
Boron steels	
xxBxx	B denotes boron steel
Leaded steels	
xxLxx	L denotes leaded steel
Vanadium steels	
xxVxx	V denotes vanadium steel

[a] The last two digits "xx" of these designations indicate the carbon content (in hundredths of a percent)

Table 8.4 Main groups of UNS designations for iron-based materials

D00001–D99999	Steels with specified mechanical properties
F00001–F99999	Cast irons
G00001–G99999	AISI and SAE carbon and alloy steels (except tool steels)
H00001–H99999	AISI and SAE H-steels
J00001–J99999	Cast steels (except tool steels)
K00001–K99999	Miscellaneous steels and ferrous alloys
S00001–S99999	Heat- and corrosion-resistant (stainless) steels, valve steels, iron-based *superalloys*
T00001–T99999	Tool steels, wrought and cast

The American Society for Testing and Materials (ASTM) standard contains full specifications of specific products, such as A 574 for alloy steel socket-head cap screws, and is oriented towards the performance of the fabricated end product. These commonly used steels are not initially included in the SAE-AISI designations.

From a user's viewpoint, steels can generally be divided into two main categories, namely *standard steels* and *tool steels*. It is useful to further subdivide *standard steels* according to their chemical composition into three major groups:

1. Carbon steels
2. Alloy steels
3. Stainless steels.

Carbon Steels. Carbon steels contain less than 1.65% Mn, 0.6% Si, and 0.6% Cu. According to the SAE standard J142 *General Characteristics and Heat Treatments of Steels*, plain carbon steels of the 10xx and 15xx series in Table 8.3 can be divided into four groups [8.14]:

- Group I steels with carbon content below 0.15%, providing enhanced cold formability and drawability. These steels are therefore used as cold-rolled sheets in automobile panels and appliances and are suitable for welding and brazing. Note, however, that these alloys are susceptible to grain growth upon annealing after cold working and, as a consequence, exhibit a tendency to embrittlement (strain-age embrittlement).
- Group II steels with carbon content of 0.15–0.3%, which show increased strength and hardness and are less suitable for cold forming. These steels are applicable for carburizing or case hardening. As shown above, increasing the manganese content enhances the hardenability of the core and case, and intermediate manganese levels (0.6–1.0%) are preferred for machining. Carburized plain carbon steels are used for parts which require a hard wear-resistant surface but a *soft* core, for example, small shafts, plungers, and lightly loaded gears.
- Group III steels with medium carbon content of 0.3% to nearly 0.55%, which can be directly hardened by induction or flame hardening or by cold working. These steels are found in automotive applications and can be used for forgings and for parts which are machined from bar stock.
- Group IV steels with high carbon levels of 0.55% to nearly 1.0%, which offer improved wear characteristics and high yield strength and are generally heat treated before use. Since cold-forming methods are not practical for this group of alloys, application parts such as flat stampings and springs are coiled from small-diameter wire. Considering their good wear properties, typical applications are found in the farm implement industry as plow beams, plow shares, scraper blades, discs, mower knives, and harrow teeth.

The so-called *free-machining grades* are either resulferized (group 11xx steels) or resulferized and rephosphorized carbon steels (group 12xx). These additives enhance their machining characteristics and lower machining costs.

The chemical compositions as well as mechanical properties of some carbon steels are presented in Table 8.5.

Alloy Steels. Alloy steels constitute a category of ferrous metals that exceed the element limits for carbon steels. They contain elements not found in carbon steels such as nickel, molybdenum, chromium (up to 3.99%), cobalt, etc. The primary function of these alloying elements is to increase the hardenability and optimize the mechanical properties such as toughness after the final heat treatment. Table 8.6 summarizes the mechanical properties of selected alloy steels in the normalized, annealed, and quenched-and-tempered condition. In the following, alloy steels are divided into five major groups according to their application area [8.14].

According to the SAE-AISI system, structural steels include carburized, through-hardening, and nitriding grades.

Carburizing grades with low alloying combinations such as SAE-AISI 4023 or 4118 have better core properties than plain carbon steels and are hardenable in oil in small cross-sections, resulting in less distortion compared with water-quenched alloys. These alloys are applied as cam shafts, wrist pins, clutch fingers, and other automotive parts. For applications requiring higher core and case hardness such as automotive gears, universal joints, small hand tools, piston pins, bear-

Table 8.5 Chemical composition and mechanical properties in as-rolled, normalized, annealed, and quenched-and-tempered condition of some carbon steels [8.14]

SAE-AISI number	Cast or heat chemical ranges and limits (wt%)				Treatment	Austenitizing/tempering temperature (°C)	Tensile strength (MPa)	Yield strength (MPa)	Elongation (%)
	C	Mn	P_{max}	S_{max}					
1020	0.17–0.23	0.3–0.6	0.04	0.05	As rolled	–	448.2	330.9	36.0
					Normalized	870	441.3	346.5	35.8
					Annealed	870	394.7	294.8	36.5
1040	0.36–0.44	0.6–0.9	0.04	0.05	As rolled	–	620.5	413.7	25.0
					Normalized	900	589.5	374.0	28.0
					Annealed	790	518.8	353.4	30.2
					Quenched	205	779	593	19
					+ Tempered	650	634	434	29
1095	0.9–1.04	0.3–0.5	0.04	0.05	As rolled	–	965.3	572.3	9.0
					Normalized	900	1013.5	499.9	9.5
					Annealed	790	656.7	379.2	13.0
					Quenched	205	1289	827	10
					+ Tempered	650	896	552	21
1137	0.32–0.39	1.35–1.65	0.04	0.08–0.13	As rolled	–	627.4	379.2	28.0
					Normalized	900	668.8	396.4	22.5
					Annealed	790	584.7	344.7	26.8
					Quenched	205	1082	938	5
					+ Tempered	650	655	483	28

Table 8.6 Mechanical properties of selected alloy steels in normalized, annealed, and quenched-and-tempered condition [8.14]

SAE-AISI number	Treatment	Austenitizing temperature (°C)	Tempering temperature (°C)	Tensile strength (MPa)	Yield strength (MPa)	Elongation (%)
1340	Normalized	870	–	836	558	22
	Annealed	800	–	703	436	26
	Quenched	–	205	1806	1593	11
	+ Tempered	–	650	800	621	22
3140	Normalized	870	–	892	600	20
	Annealed	815	–	690	423	24
	Quenched	–	–	–	–	–
	+ Tempered	–	–	–	–	–
4130 (w)	Normalized	870	–	669	436	26
	Annealed	865	–	560	361	28
	Quenched	–	205	1627	1462	10
	+ Tempered	–	650	814	703	22
4140	Normalized	870	–	1020	655	18
	Annealed	815	–	655	417	26
	Quenched	–	205	1772	1641	8
	+ Tempered	–	650	758	655	22
4150	Normalized	870	–	1155	734	12
	Annealed	815	–	730	379	20
	Quenched	–	205	1931	1724	10
	+ Tempered	–	650	958	841	19
4320	Normalized	895	–	793	464	21
	Annealed	850	–	579	610	29
	Quenched	–	–	–	–	–
	+ Tempered	–	–	–	–	–
4340	Normalized	870	–	1279	862	12
	Annealed	810	–	745	472	22
	Quenched	–	205	1875	1675	10
	+ Tempered	–	650	965	855	19

Table 8.6 (continued)

SAE-AISI number	Treatment	Austenitizing temperature (°C)	Tempering temperature (°C)	Tensile strength (MPa)	Yield strength (MPa)	Elongation (%)
4620	Normalized	900	–	574	366	29
	Annealed	855	–	512	372	31
	Quenched	–	–	–	–	–
	+ Tempered	–	–	–	–	–
4820	Normalized	860	–	750	485	24
	Annealed	815	–	681	464	22
	Quenched	–	–	–	–	–
	+ Tempered	–	–	–	–	–
5046	Normalized	–	–	–	–	–
	Annealed	–	–	–	–	–
	Quenched	–	205	1744	1407	9
	+ Tempered	–	650	786	655	24
5140	Normalized	870	–	793	472	22.7
	Annealed	830	–	572	293	29
	Quenched	–	205	1793	1641	9
	+ Tempered	–	650	758	662	25
5160	Normalized	855	–	957	531	18
	Annealed	815	–	723	276	17
	Quenched	–	205	2220	1793	4
	+ Tempered	–	650	896	800	20
6150	Normalized	870	–	940	616	22
	Annealed	815	–	667	412	23
	Quenched	–	205	1931	1689	8
	+ Tempered	–	650	945	841	17
8630	Normalized	870	–	650	430	24
	Annealed	845	–	564	372	29.0
	Quenched	–	205	1641	1503	9
	+ Tempered	–	650	772	689	23
8740	Normalized	870	–	929	607	16
	Annealed	815	–	695	416	22
	Quenched	–	205	1999	1655	10
	+ Tempered	–	650	986	903	20
9255	Normalized	900	–	933	579	20
	Annealed	845	–	774	486	22
	Quenched	–	205	2103	2048	1
	+ Tempered	–	650	993	814	20
9310	Normalized	890	–	907	571	19
	Annealed	845	–	820	440	17
	Quenched	–	–	–	–	–
	+ Tempered	–	–	–	–	–

ings, etc., higher-alloy carburizing steels such as Ni-Mo (SAE-AISI 4620), plain Cr (SAE-AISI 5120), or Ni-Cr-Mo (SAE-AISI 8620) steels are used. Aircraft engine parts, truck transmissions and differentials, rotary rock-bit cutters, and large antifriction bearings are made from high-alloy steels as SAE-AISI 4820 and 9310.

Through-hardening grades in principle contain higher carbon levels than carburized grades. In this group, the lower-alloy steels are used for applications in small sections or in larger sections that may not have optimal properties but allow weight savings due to the higher strength of the alloys. Typical examples are manganese steels (SAE-AISI 1330–1345), which are used for high-strength bolts, molybdenum steels (SAE-AISI 4037–4047) and chromium steels (SAE-AISI 5130–5150), which are used for automotive steering parts, and low-Ni-Cr-Mo steels (SAE-AISI 8630–8650), which are used for small machinery axles and shafts. Heavy aircraft or truck parts or ordnance materials require higher-alloy structural steels, such as SAE-AISI 3430 or 86B45. There are several constructional alloy steels which are used for specialized applications; for exam-

ple, SAE-AISI 52100 steels are used almost exclusively for ball-bearing applications, and the chromium steels SAE-AISI 5150 and 5160 were developed for spring steel applications.

Steels that belong to the *nitriding grades* are in most cases either medium-carbon and chromium-containing low-alloy steels, which are covered by the SAE-AISI (for example, the 4100, 4300, 5100, 6100, 8600, 9300, and 9800 groups), or Al-containing (up to 1%) low-alloy steels, which are not described by SAE-AISI designations but have simple names such as "Nitralloy." Typical applications for nitride grades include gears designed for low contact stresses, spindles, seal rings, and pins.

Low-carbon quenched-and-tempered steels typically contain less than 0.25% C and less than 5% alloy additions. Economics has driven the development of these steels and the choice of alloying additions accordingly. With their low carbon content, these steels exhibit high ductility and notch toughness and are suitable for welding while still offering high yield strength (approximately 340–900 MPa). In addition, they show two to six times higher corrosion resistance compared with plain carbon steels. Depending on the final treatment, these steels can be either martensitic, bainitic, and, for some compositions, ferritic. These steels are not covered by SAE-AISI designations, although most of them can be found in ASTM specifications such as A514, A517, and A543. Thanks to their high strength and toughness values, these steels can be applied at lower final costs than plain carbon steels, which leads to a wide variety of applications. They are used as major members of large steel constructions, pressure valves, and in earth-moving and mining equipment.

Ultrahigh-strength steels are a group of alloy steels with yield strength in excess of 1300 MPa; some have plain-strain fracture toughness levels exceeding 100 MPa $\sqrt{\text{m}}$. Some of these steels are included in the SAE-AISI designation system and have medium carbon contents with low-alloy additions. Examples are steels in the SAE-AISI 4130 series, the higher-strength 4140, and the deeper hardening higher-strength 4340 steels. Starting from the 4340 alloy series, numerous modifications have been developed. Addition of silicon, for example, reduces the sensitivity to embrittlement on tempering at low temperatures (required to retain high strength levels). Addition of vanadium leads to grain refinement, which improves the strength and toughness of the material. Medium-carbon alloys can be welded in annealed or normalized condition, requiring a further heat treatment to recover the desired strength. If high fracture toughness as well as high strength is specifically desired, as for aircraft structural components, pressure vessels, rotor shafts for metal-forming equipment, drop hammer rods, and high-strength shock-absorbing automotive parts, high nickel (7–10.5%) and Co (4.25–14.50%) contents are used as primary alloying elements. While offering plane-strain fracture toughness of 100 MPa $\sqrt{\text{m}}$, HP-9-4-30 steel can exhibit tensile strength as high as 1650 MPa. Furthermore, this steel can be hardened to martensite in sections up to 150 mm thick. AF 1410 steel (developed by the US Air Force) has an ultimate tensile strength (UTS) of 1615 MPa and a K_{IC} value of 154 MPa $\sqrt{\text{m}}$.

The group of *alloy steels for elevated- or low-temperature applications* includes two different alloying systems. For high-temperature applications, chromium-molybdenum steels offer a good combination of oxidation and corrosion resistance (provided by the chromium content of up to 9%) on the one hand and high strength at elevated temperatures (provided by the molybdenum content of 0.5–1.0%) on the other. These steels can be applied at temperatures up to 650 °C for pressure vessels and piping in the oil and gas industries and in fossil-fuel and nuclear power plants. In low-temperature service applications such as storage tanks for liquid hydrocarbon gases and structures and machinery design for use in cold regions, ferritic steels with high nickel content (approximately 2–9%) are typically used.

Another important category of alloy steels are the *high-strength low-alloy steels* (HSLA). HSLA steels, or microalloyed steels, are designed to achieve specific mechanical properties rather than a chemical composition. So, the chemical composition can vary for different end-product thicknesses while still retaining specific mechanical properties. The low carbon content (0.05–0.25%) of these steels allows good formability and excellent weldability. Further alloying elements are added to meet the application requirements (Table 8.7), resulting in a division into six categories, as follows:

- Weathering steels, where small amounts of copper and phosphorus are added to improve the atmospheric corrosion resistance;
- Microalloyed ferritic-pearlitic steels, with small amounts (< 0.1%) of carbide-forming elements such as niobium, vanadium, or titanium, which enable precipitation strengthening and grain refinement;
- As-rolled pearlitic steels, with high strength, toughness, formability, and weldability, which have carbon, manganese, and further additions;
- Acicular ferrite (low-carbon bainite) steels (< 0.08%), which offer an excellent combination of high yield strength, weldability, formability, and good toughness;

Table 8.7 Characteristics and uses of HSLA steels according to ASTM standards [8.14]

ASTM specification[a]	Title	Alloying elements[b]	Available mill forms	Special characteristics	Intended uses
A 242	High-strength low-alloy structural steel	Cr, Cu, N, Ni, Si, Ti, V, Zr	Plate, bar, and shapes ≤ 100 mm in thickness	Atmospheric corrosion resistance four times that of carbon steel	Structural members in welted, bolted, or riveted construction
A 572	High-strength low-alloy niobium-vanadium steels of structural quality	Nb, V, N	Plate, bar, and sheet piling ≤ 150 mm in thickness	Yield strength of 290–450 MPa in six grades	Welded, bolted, or riveted structures, including many bolted or riveted bridges and buildings
A 588	High-strength low-alloy structural steel with 345 MPa minimum yield point ≤ 100 mm in thickness	Nb, V, Cr, Ni, Mo, Cu, Si, Ti, Zr	Plate, bar, and shapes ≤ 200 mm in thickness	Atmospheric corrosion resistance four times that of carbon steel; nine grades of similar strength	Welded, bolted, or riveted structures, but primarily welded bridges and buildings in which weight savings or added durability is important
A 606	Steel sheet and strip hot-rolled steel and cold-rolled, high-strength low-alloy steel with improved corrosion resistance	Not specified	Hot-rolled and cold-rolled sheet and strip	Atmospheric corrosion twice that of carbon steel (type 2) or four times that of carbon steel (type 4)	Structural and miscellaneous purposes for which weight savings or added durability is important
A 607	Steel sheet and strip hot-rolled steel and cold-rolled, high-strength low-alloy niobium and/or vanadium	Nb, V, N, Cu	Hot-rolled and cold-rolled sheet and strip	Atmospheric corrosion twice that of carbon steel, but only when copper content is specified; yield strength of 310–485 MPa in six grades	Structural and miscellaneous purposes for which greater strength or weight savings are important
A 618	Hot-formed welded and seamless high-strength low-alloy structural tubing	Nb, V, Si, Cu	Square, rectangular, round, and special-shape structural welded or seamless tubing	Three grades of similar yield strength; may be purchased with atmospheric corrosion resistance twice that of carbon steel	General structural purposes include welded, bolted, or riveted bridges and buildings
A 633	Normalized high-strength low-alloy structural steel	Nb, V, Cr, Ni, Mo, Cu, N, Si	Plate, bar, and shapes ≤ 150 mm in thickness	Enhanced notch toughness; yield strength of 290–415 MPa in five grades	Welded, bolted or riveted structures for service at temperatures at or above −45 °C
A 656	High-strength low-alloy, hot rolled structural vanadium-aluminum-nitrogen and titanium-aluminum steels	V, Al, N, Ti, Si	Plate, normally ≤ 16 mm in thickness	Yield strength of 552 MPa	Truck frames, brackets, crane booms, mill cars, and other applications where weight savings are important
A 690	High-strength low-alloy steel H-piles and sheet piling	Ni, Cu, Si	Structural-quality H-pills and sheet piling	Corrosion resistance two to three times greater than that of carbon steel in the splash zone of marine structures	Dock walls, sea walls, bulkheads, excavations, and similar structures exposed to seawater
A 709, grade 50 and 50 W	Structural steel	V, Nb, N, Cr, Ni, Mo	All structural shape groups and plate ≤ 100 mm thickness	Minimum yield strength of 345 MPa; grade 50 W is a weathering steel	Bridges

Table 8.7 (continued)

ASTM specification[a]	Title	Alloying elements[b]	Available mill forms	Special characteristics	Intended uses
A 714	High-strength low-alloy welded and seamless steel pipe	V, Ni, Cr, Mo, Cu, Nb	Pipe with nominal diameter of 13–660 mm	Minimum yield strength of ≤ 345 MPa and corrosion resistance two or four times that of carbon steel	Piping
A 715	Steel sheet and strip hot-rolled, high-strength low alloy with improved formability	Nb, V, Cr, Mo, N, Ti, Zr, B	Hot-rolled sheet and strip	Improved formability[c] compared with A 606 and A 607; yield strength of 345–550 MPa in four grades	Structural and miscellaneous applications for which high strength, weight savings, improved formability, and good weldability are important
A 808	High-strength low-alloy steel with improved notch toughness	V, Nb	Hot-rolled plate ≤ 65 mm in thickness	Charpy V-notch impact energies of 40–60 J (40–60 ft lfb) at −45 °C	Railway tank cars
A 812	High-strength low-alloy steel	V, Nb	Steel sheet in coil form	Yield strength of 450–550 MPa	Welded layered pressure vessels
A 841	Plate produced by thermomechanical controlled processes	V, Nb, Cr, Mo, Ni	Plates ≤ 100 mm in thickness	Yield strength of 310–345 MPa	Welded pressure vessels
A 847	Cold-formed, welded, and seamless high-strength low-alloy structural rubbing with improved atmospheric corrosion resistance	Cu, Cr, Ni, Si, V, Ti, Zr, Nb	Welded rubbing with maximum periphery of 1625 mm and wall thickness of 16 mm, or seamless tubing with maximum periphery of 810 mm and wall thickness of 13 mm	Minimum yield strength ≤ 345 MPa with atmospheric corrosion twice that of carbon steel	Round, square, or specially shaped structural tubing for welded, riveted, or bolted bridges and buildings
A 860	High-strength butt-welding fittings of wrought high-strength low-alloy steel	Cu, Cr, Ni, Mo, V, Nb, Ti	Normalized or quenched-and-tempered wrought fittings	Minimum yield strength ≤ 485 MPa	High-pressure gas and oil transmission lines
A 871	High-strength low-alloy steel with atmospheric corrosion resistance	V, Nb, Ti, Cu, Mo, Cr	As-rolled plate ≤ 35 mm thickness	Atmospheric corrosion resistance four times that of carbon structural steel	Tubular structures and poles

[a] For grades and mechanical properties
[b] In addition to C, Mn, P, and S. A given grade may contain one or more of the listed elements but not necessarily all of them; for specified compositional limits
[c] Obtained by producing killed steel, made to fine-grain practice, and with microalloying elements such as niobium, vanadium, titanium, and zirconium in the composition

Table 8.8 Compositions and properties of some widely used stainless steels [8.19]

AISI-SAE grade	Nominal composition (wt%) C	Cr	Ni	Others	Condition	Yield strength (MPa)	Tensile strength (MPa)	Elongation (%)
Austenitic grades								
201	0.15	17	5	Mn 6.5	Annealed	310	650	40
304	0.08	19	10		Annealed	205	520	30
					Cold-worked	965	1275	9
304L	0.03	19	10		Annealed	205	520	30
316	0.08	17	12	Mo 2.5	Annealed	205	520	30
321	0.08	18	10	Ti 0.4	Annealed	240	585	55
347	0.08	18	11	Nb 0.8	Annealed	240	620	50
Ferritic grades								
430	0.12	17			Annealed	205	450	22
442	0.12	20			Annealed	275	520	20
Martensitic grades								
416	0.15	13		Mo 0.6	Quenched and tempered	965	1240	18
431	0.2	16	2		Quenched and tempered	1035	1380	16
440C	1.1	17		Mo 0.7	Quenched and tempered	1895	1965	2
Nonstandard (precipitation-hardened) grades								
17–4	0.07	17	4	Nb 0.4	Age-hardened	1170	1310	10
17–7	0.09	17	7	Al 1.0	Age-hardened	1585	1650	6

- Dual-phase steels, with martensitic portions finely dispersed in a ferritic matrix. These steels have high tensile strength and sufficient toughness;
- Inclusion-shape-controlled steels, in which the shape of sulfide is changed from elongated stringers to small, dispersed, near-spherical globules to improve ductility and toughness; elements which are suitable are, e.g., Ca, Zr, and Ti.

The allocation to a specific group is not rigorous; many of these steels have properties which would also allow their allocation to other groups mentioned.

Stainless Steels. Stainless steels in general contain at least 12% Cr, which forms a thin protective layer at the surface (Cr-Fe oxide) when exposed to air [8.19]. As shown above, chromium stabilizes the ferrite to remain stable up to the melting point, presuming, however, a low carbon content. Stainless steels can be differentiated depending on their crystal structure or the strengthening mechanisms according to Table 8.8. Ferritic stainless steels are relatively inexpensive and contain as much as 30% chromium but typically less than 0.12% C. They show good strength and intermediate ductility. Martensitic stainless steels typically contain less than 17% chromium to contract the austenitic region not too strongly but have higher C content of up to 1.0%. These alloys are used for high-quality knifes, ball bearings, or fittings.

Austenitic stainless steels are formed by the addition of nickel, offer high ductility, and are intrinsically not ferromagnetic. These alloys are well suited for high-temperature applications because of their high creep resistance and, thanks to their high toughness at low temperatures, for cryogenic service as well.

Precipitation-strengthened stainless steels contain additions such as Al, Nb, or Ta, which form precipitates such as Ni_3Al during heat treatment and can have very high strength levels.

Stainless steels with duplex microstructure consist of about 50% ferrite and austenite each. They show an ideal combination of strength, toughness, corrosion resistance, formability, and weldability, which no other stainless steel can supply.

Tool Steels. *Tool steels* are made to meet special quality requirements, primarily due to their use in manufacturing processes as well as for machining metals, woods, and plastics [8.20]. Some examples are cutting tools, dies for casting or forming, and gages for dimensional tolerance measurements. Tool steels are very clean ingot-cast wrought products with medium (minimum 0.35%) to high carbon content and high alloy (up to 25%) contents, making them extremely expensive. They must withstand temperatures up to 600 °C and should in addition have the following properties:

- Generally a high hardness to resist deformation.
- Resistance to wear for economical tool life, which depends directly on hardness; this can be increased by alloying with carbide-forming elements such as W and Cr.
- Dimensional stability. Dimensional changes of tools can be caused by microstructural alteration, by

exceeding the elastic limit, by transformation of the remaining austenite, and by changes of the grain dimensions. The highest dimensional stability is exhibited by ledeburitic cut steels with 12% chromium, which are used for precise cutting and punch tools.

- Working capability. To guarantee fault-free operation, tools must have a certain working capability, meaning that they should be able to collect elastic distortion energy to a certain degree. Therefore, steels with high toughness and at the same time high yield strength are required.
- Through hardening. The through-hardening capability can be improved by alloying with carbide formers such as Cr, Mo, and Mn, which additionally increase wear resistance.

Tool steels can be categorized into five principal groups; compositions and application examples are given in Table 8.9:

1. Cold-work tool steels, which include the oil-hardening O alloys, the water-hardening W alloys, the high-chromium class D (stainless steel), and the medium-alloy air-hardening class A alloys. Water-hardening grades have high resistance to surface wear but are not suited for high-temperature applications.
2. Shock-resistant tool steels in the S group of alloys, which are the toughest of the tool steels due to the presence of only 0.5% C and low-alloying additions.
3. Hot-work tool steels are class H alloys and include chromium, tungsten, and molybdenum alloying elements.
4. High-speed steels are either tungsten (T class) or molybdenum (M class) alloys. They have high hardness of 62–67 HRC and maintain this hardness at service temperatures as high as 550 °C.
5. Special-purpose tool steels are low-alloy (L) or mold tool steels (P).

From the compositions given in Table 8.9, it is obvious that the main alloying elements in tool steels are:

1. Chromium to increase hardenability, which if alloyed in excess forms $Cr_{23}C_6$ for high wear resistance.
2. Molybdenum and tungsten, which are strong hard carbide formers $(Mo,W)_6C$ that can be dissolved in austenite, and precipitate as fine particles in martensite upon annealing (secondary hardening, Fig. 8.16). Furthermore, they resist growth at low red heat.

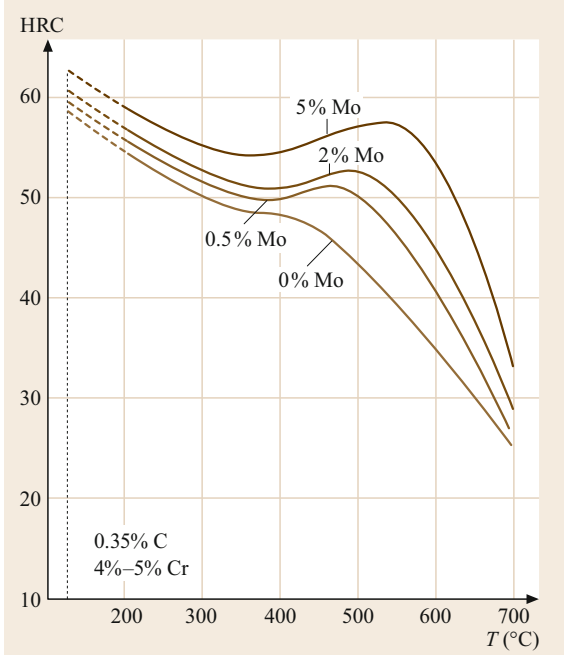

Fig. 8.16 Influence of molybdenum content on occurrence of a secondary hardening maximum during tempering (after [8.21])

3. Vanadium, which forms the hardest carbide V_4C_3, resists solution in austenite, and remains unchanged through heat treatment cycles .

8.1.4 Steel Castings and Cast Iron

Steel castings and cast iron are preferable for the manufacture of complex geometries at relatively low cost because expensive reworking steps are not necessary or only a few processing steps are required to obtain the final product [8.23]. Against this advantage there are two important restrictions, namely:

1. The appearance of cast defects and, in conjunction
2. Inferior mechanical properties compared with components prepared by deformation.

Iron-carbon cast materials can be roughly divided according to their carbon content into: 1. Steel castings (C < 2%) and 2. Cast iron (C > 2%).

Steel castings have a better combination of high strength and ductility compared with cast iron. However, because of their high melting point and strong shrinkage (about 2%) upon cooling, the castability of steel castings is poor and their affinity for cavity formation more pronounced. Therefore, steel castings are only used when high strength and toughness are

Table 8.9 Chemical composition and usage of selected tool steels [8.19]

Designation		Composition in % (with emphasis to show differences between steels belonging to each group)								Typical uses
AISI-SAE	UNS No.	C	Mn	Si	Cr	V	W	Mo	Co	
Water-hardening grades										
W1	T72301	0.7–1.5				0.1 max				Cold-heading dies, wood-working tools, etc.
W2	T72302	0.85–1.5				0.15–0.35				
Shock-resisting tool steels										
S1	T41901	0.4–0.55	0.1–0.4	0.15–1.2	1.00–1.80		1.50–3.00	0.5 max		Chisels, hammers, rivet sets, etc.
S2	T41902	0.4–0.55	0.3–0.5	0.9–1.2				0.30–0.60		
Oil-hardening cold-work tool steels										
O1	T31501	0.85–1.00	1.0–1.4		0.4–0.6		0.4–0.6			Short-run cold-forming dies, cutting tools
O2	T31502	0.85–0.95	1.4–1.8		0.5 max					
Air-hardening medium-alloy cold-work tool steels										
A2	T30102	0.95–1.05	1.00 max		4.75–5.5		0.9–1.4			Thread rolling and slitting dies, intricate die shapes
A6	T30106	0.65–0.75	1.8–2.5		0.9–1.2		0.9–1.4			
High-carbon high-chromium cold-work steels										
D2	T30402	1.40–1.60			11–13	1.1 max		0.7–1.2		Uses under 482 °C, gages, long-run forming and blanking dies
D3	T30403	2.00–2.35			11–13	1.0 max				
D4	T30404	2.05–2.40			11–13	1.0 max		0.7–1.2		
Chromium hot-work steels										
H12	T20812	0.30–0.45		0.8–1.2	4.75–5.5	0.5 max	1.0–1.7	1.25–1.75		Al or Mg extrusion dies, die-casting dies, mandrels, hot shears, forging dies
H13	T20813	0.32–0.45		0.8–1.2	4.75–5.5	0.8–1.2		1.1–1.75		
H19	T20819	0.32–0.45		0.2–0.5	4.0–4.75	1.75–2.2	4.0–5.25	0.3–0.55	4.0–4.5	
Tungsten high-speed steels										
H21	T20821	0.26–0.36		0.15–0.5	3.0–3.75	0.3–0.6	8.5–10.0			Hot extrusion dies for brass, nickel, and steel, hot-forging dies
H23	T20823	0.25–0.45		0.15–0.4	11.0–12.75	0.75–1.25	11–12.75			
Tungsten high-speed steels										
T1	T12001	0.65–0.8			3.75–4.5	0.9–1.3	17.25–18.75			Original high-speed cutting steel, most wear-resistant grade
T15	T12015	1.5–1.6			3.75–5	4.5–5.25	11.75–13.0	1.0 max	4.75–5.25	
Molybdenum high-speed steels										
M1	T11301	0.78–0.88			3.5–4.0	1–1.35	1.4–2.1	8.2–9.2		Lower cost than T-type tools
M2	T11302	0.78–0.88			3.75–4.5	1.75–2.2	5.5–6.75	4.5–5.5		
M3	T11313	1.0–1.1			3.75–4.5	2.25–2.75	5.5–6.75	4.75–6.5		
M10	T11310	0.84–0.94			3.75–4.5	1.8–2.2				

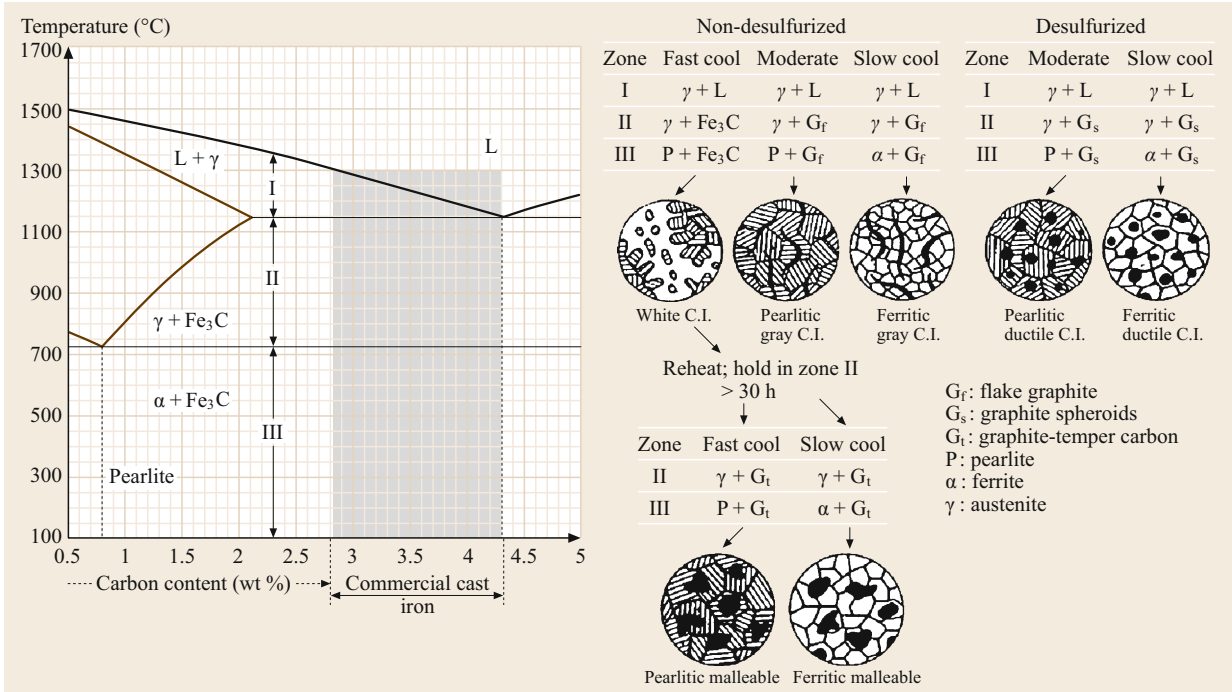

Fig. 8.17 Influence of casting conditions on resulting microstructure of cast irons (after [8.22])

a must, as in the case of permanent magnet castings and manganese hard castings. A far broader spectrum of applications exists for cast irons, based of the advantage that they are also very cost-efficient construction materials. The precipitation of carbon (as graphite) during solidification counteracts the normal shrinkage of the solidified metal.

Classification of Cast Irons

Cast irons solidify by the eutectic reaction and are generally ternary alloys of Fe with 2–4% C and 0.5–3% Si. With increasing contents of C and Si and decreasing cooling rate, the formation of stable graphite instead of unstable cementite is favored. Furthermore, their high carbon and silicon contents give cast irons excellent castability with melting points appreciably lower than those of steel. Pattern-making is no longer a necessary step in manufacturing cast-iron parts. Many gray, ductile, and alloy-iron components can be machined directly from bars that are continuously cast to near-net shape. Not only does this *parts without patterns* method save the time and expense of pattern-making, but continuous-cast iron also provides a uniformly dense, fine-grained structure, essentially free from porosity, sand, or other inclusions. Cast irons are usually not classified according to their chemical composition. The microstructure of the final product depends strongly upon foundry practice and the shape and size of the castings, which influence the cooling rate; so several entirely different types of iron may be produced starting with the same nominal composition. Thus, cast irons are usually specified by their mechanical properties. A principal classification can be made concerning their microstructure, which depends on the casting conditions:

1. Gray cast iron
2. Ductile cast iron
3. White cast iron
4. Compacted graphite iron
5. Malleable cast iron
6. High-alloy cast irons.

Gray cast iron is formed when excess carbon graphitizes during solidification to form separate graphite flakes. The resulting microstructure depends on the cooling rate from the eutectoid temperature downwards (region II in Fig. 8.17). If cooling is fast, pearlite (α-Fe + Fe_3C) is formed from the γ-Fe. If the cooling rate is slow, ferrite is formed during transformation and the material has lower strength compared with pearlitic gray cast iron. Depending on the cooling rate, a mixture of ferrite (surrounding the graphite flakes) and pearlite may be formed as well. The flake-type shape of the graphite in gray cast iron leads to generally brittle behavior. Furthermore, the impact strength of gray cast iron is low, and it does not exhibit a distinct yield

point. On the other hand, excellent damping against vibrations, excellent wear resistance, and acceptable fatigue resistance are desirable properties of gray cast iron. Typical applications are engine blocks, gears, flywheels, brake discs and drums, and machine bases.

In *ductile iron*, the form of the graphite is nodular or spheroidal instead of flake type. This is achieved by the addition of trace amounts Mg and/or Ce, which react with sulfur and oxygen. However, in ductile iron, the impurity level has to be controlled more precisely than in gray cast iron, since it affects nodule formation. Ductile cast iron exhibits improved stiffness and shock resistance. It exhibits good machinability and fatigue strength as well as high modulus of elasticity, yield strength, wear resistance, and ductility. Its damping capacity and thermal conductivity are lower than those of gray iron. By weight, ductile gray iron castings are more expensive than gray iron. Ductile iron is used in applications such as valve and pump bodies, crankshafts, heavy-duty gears or automobile door hinges, and nowadays with increasing frequency also as engine blocks.

Austempered ductile cast iron (ADI) is a subgroup of the ductile iron family but could be treated as a separate class of engineering materials. In contrast to the former, the matrix of this spheroidal graphite cast iron is bainitic (not pearlitic). This microstructure is obtained by isothermal transformation of austenite at temperatures below that at which pearlite forms. In terms of properties, the bainitic matrix has almost twice the strength of pearlitic ductile iron while retaining high elongation and toughness. While exhibiting superior wear resistance and fatigue strength, the castability of ADI is not very different from that of other ductile irons, but heat treatment is a critical issue to fully exploit its beneficial properties; For example, the yield strength of ADI is more than three times that of the best cast or forged aluminum. In addition ADI castings weigh only 2.4 times more than Al alloys and are 2.3 times stiffer. ADI is also 10% less dense than steel. Furthermore, for a typical component, ADI costs 20% less per unit weight than steel and half that of Al. A comparison of forged steel, pearlitic ductile iron, and ADI is presented in Table 8.10.

White cast irons are formed trough fast cooling and consist of Fe_3C and pearlite. The origin of this designation is the white-appearing crystalline fracture surface. While exhibiting excellent wear resistance and high compressive strength, the principal disadvantage of white cast iron is its catastrophic brittleness. Therefore, in most applications, white cast iron is only formed on the surface of cast parts, while the core consists of either gray cast iron or ductile iron. Examples of the application of white cast iron are mill liners and shot-blasting nozzles, as well as railroad brake shoes, rolling-mill rolls, and clay-mixing and brick-making equipment, crushers, and pulverizers.

Table 8.10 Mechanical properties of forged steel, pearlitic ductile iron, and ADI [8.23]

Mechanical property	Forged steel	Pearlitic ductile iron	Grade 150/100/7 ADI
Tensile strength (MPa)	790	690	1100
Yield strength (MPa)	520	480	830
Elongation (%)	10	3	10
Brinell hardness	262	262	286
Impact strength (ft-lb)	130	40	120

Compacted graphite iron (CGI), also known as vermicular iron, can be considered to be an intermediate between gray and ductile iron, possessing many of the favorable properties of each. CGI is difficult to produce successfully on a commercial scale because the alloy additions must be kept within very tight limits. The advantages of CGI compared with gray cast iron are its higher fatigue resistance and ductility, which are at the same levels as those of ductile iron. Its machinability, however, is superior to that of ductile iron, and its damping capacity almost as good as that of gray iron. This combination and the high thermal conductivity of CGI suggest applications in engine blocks, brake drums, and exhaust manifolds of vehicles.

Malleable iron is white iron that has been converted by a two-stage heat treatment to a condition in which most of its carbon content is in the form of irregularly shaped nodules of graphite, called temper carbon. In contrast to white iron, it is malleable and easily machined. The matrix of malleable cast iron may be ferritic, pearlitic, or martensitic. Ferritic grades are more machinable and ductile, whereas pearlitic grades are stronger and harder. Malleable iron castings are often used for heavy-duty bearing surfaces in automobiles, trucks, railroad rolling stock, and farm and construction machinery. Their applications are, however, limited to relatively thin-sectioned castings because of the high shrinkage rate and the need for rapid cooling to produce white iron.

High-alloy irons are ductile, gray, or white irons that contain 3% to more than 30% alloy content. The properties achieved by specialized foundries are significantly different from those of unalloyed irons. These irons are usually specified by chemical composition as well as by various mechanical properties. White high-alloy irons containing nickel and chromium develop a microstructure with a martensitic matrix around primary chromium carbides. This structure provides high hardness with extreme wear and abrasion resistance. High-chromium irons (typically, about 16%) combine

wear and oxidation resistance with toughness. Irons containing 14–24% nickel are austenitic; they provide excellent corrosion resistance for nonmagnetic applications. The 35% nickel irons have an extremely low coefficient of thermal expansion and are also nonmagnetic and corrosion resistant.

8.2 Aluminum and Its Alloys

8.2.1 General Properties

Despite the ten times higher cost of preparation of primary aluminum compared with pig iron, aluminum-based materials are today the second most widely used metallic materials. For structural applications in mechanical engineering, their most important advantage is an excellent combination of intrinsically good corrosion and oxidation resistance and high specific strength (strength-to-density ratio; Table 8.1) compared with stainless steels. However, with strength values as low as 45 MPa (1199-O), technically pure aluminum is very soft and requires the addition of alloying elements for most applications. In doing so, the strength can be increased considerably to almost 700 MPa (alloy 7055-T77). Because the specific stiffness (stiffness-to-density ratio) of aluminum alloys ($E \approx 70$ GPa) is comparable to that of steels ($E \approx 210$ GPa), components must have significantly larger dimensions (volume) in order to achieve a stiffness equal to that of their steel counterparts. However, various constructive arrangements, such as tabular or box-shaped hollow sections, locally strengthened rips, flanges welts, and coils, are known and can be used as an alternative to larger components. In contrast to steels, Al does not exhibit an endurance limit in fatigue. Moreover, the low hardness of aluminum leads to generally poor wear resistance.

Further important properties, which contribute to the still-growing applications of aluminum and its alloys, are their high electrical and thermal conductivity as well as good formability. Furthermore, the high chemical affinity of aluminum to oxygen leads to very acceptable corrosion and oxidation resistance but causes at the same time the high production costs mentioned. To manufacture primary aluminum based on aluminum oxide, a costly reduction (mostly smelting electrolytic reduction) is necessary. Bauxite with hydrated forms of aluminum oxide serves as the primary mineralogical source of alumina, since its reduction is economically most efficient amongst the different types of aluminum ore.

Al alloys can be very well machined by chip removal, and additions of Pb can prevent the formation of long chips in the case of pure aluminum or soft Al alloys. Joining of Al-based components can be done by all common procedures. Fusion welding is predominantly done by inert gas welding. Adhesion joints are also gaining in importance. Aluminum and its alloys do not show a sharp ductile-to-brittle transition temperature; rather they remain ductile even at very low temperatures. Comprehensive treatments of Al-based materials are given in [8.24–26].

8.2.2 Pure Aluminum

Commercial-purity aluminum, mainly manufactured by modified Hall–Héroult electrolysis, usually reaches a purity of 99.5–99.8%. On further electrolytic refinement (the three-layer method [8.24]) of commercially pure aluminum or secondary aluminum, superpurity aluminum (99.95–99.99%) can be prepared. Finally, for special purposes, aluminum can be further purified by zone melting to obtain aluminum with extreme purity of up to 99.999 95%. A classification of pure aluminum is presented in Table 8.11 from [8.24].

In the annealed condition, aluminum possesses only low strength at room temperature. By cold deformation, however, it is possible to improve its strength significantly, whereas the elongation is reduced considerably (Fig. 8.18).

Traditionally, pure aluminum is used in wrought condition for electrical conductors (EC aluminum).

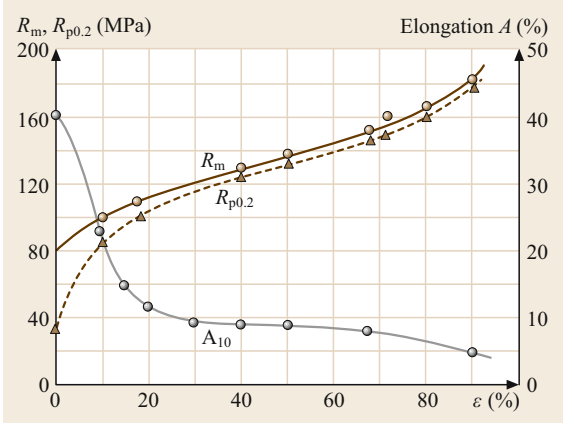

Fig. 8.18 Hardening of Al 99.5 strip (0.15 wt% Si, 0.28 wt% Fe) after recrystallization annealing and subsequent cold rolling. R_m – tensile strenght, $R_{p0.2}$ – 0.2% proof stress, A – elongation, ε – degree of cold work (after [8.6])

Table 8.11 The various degrees of purity of pure aluminum [8.24] as mentioned by the International Organization for Standardization (ISO), and the Aluminum Association (AA)

Aluminum (%)	Examples (ISO)	Examples (AA)	Designation
99.5000–99.7900	A 199.5–A 199.8	1050–1080, 1145	Commercial purity
99.8000–99.9490	A 199.8–A 199.95R	1080–1090, 1185	High purity
99.9500–99.9959	A 199.95R–A 199.99R	1098, 1199	Superpurity
99.9960–99.9990	A 199.99R	–	Extreme purity
> 99.9990	–	–	Ultra purity

Further important applications of aluminum are as foils for the food processing industries and in packaging practice (alloy 1145), as case components, boxes in tool-building, in the building industry as well as claddings, and to improve resistance to corrosion with heat-treatable Al alloys.

8.2.3 Aluminum Alloys

The major alloying elements of aluminum are copper, manganese, magnesium, silicon, and zinc. Depending on the production route to its final form, aluminum alloys may in principle be divided into wrought alloys and cast alloys. The wrought alloys can be classified into two main groups: 1. Age-hardenable alloys and 2. Non-age-hardenable alloys.

The nomenclature used for wrought alloys consists of four digits in the form 2xxx–8xxx, where the last two digits are the alloy identifier (Table 8.12). The second digit indicates certain alloy modifications (0 stands for the original alloy). A second designation is usually used, and describes the final temper treatment (Table 8.13).

Aluminum responds readily to strengthening mechanisms (Sect. 4.1) such as age hardening, solution hardening, and strain hardening, resulting in 2–30 times higher strength compared with pure aluminum (Table 8.14). Age hardening is the most effective hardening mechanism. It is based on the fact that the solubility of certain elements increases with increasing temperature. In the case of Cu as the alloying element, the maximum solubility is reached at about 550 °C (Fig. 8.19). For age hardening, the material is solution annealed in the single-phase region, quenched to room or low temperature, and finally age-hardened at higher temperatures (100–200 °C) to facilitate the formation of small precipitates. On further age hardening, the precipitates continue to grow, resulting in overaging (Fig. 8.19), which is accompanied by a loss in material strength.

The strength increase $\Delta\sigma$ is inversely proportional to the separation distance l of the precipitates and is giving in the peak-aged condition (Fig. 8.20) by $\Delta\sigma \approx 2Gb/l$, where G is the shear modulus and $\boldsymbol{b}$ is the Burgers vector.

Table 8.12 Constitution of aluminum alloys

Wrought alloys	
1xxx Commercially pure Al (> 99% Al)	Not aged
2xxx Al-Cu	Age hardenable
3xxx Al-Mn	Not aged
4xxx Al-Si and Al-Mg-Si	Age hardenable if Mg is present
5xxx Al-Mg	Not aged
6xxx Al-Mg-Zn	Age hardenable
7xxx Al-Mg-Zn	Age hardenable
8xxx Other elements (for example Al-Li)	Depends on additions
Casting alloys	
1xx.x Commercially pure Al	Not aged
2xx.x Al-Cu	Age hardenable
3xx.x Al-Si-Cu or Al-Mg-Si	Some are age hardenable
4xx.x Al-Si	Not aged
5xx.x Al-Mg	Not aged
7xx.x Al-Mg-Zn	Age hardenable
8xx.x Al-Sn	Age hardenable
9xx.x (Other elements)	Depends on additions

However, on further annealing, the precipitates can grow by Ostwald ripening; i.e., small precipitates are consumed while larger particles grow continuously at their expense. This process results in a severe strength decrease when the material is exposed to high temperatures during service (Fig. 8.21).

Depending on the alloying additions, different strengthening mechanisms are activated:

- 2xxx: Precipitation of Cu-rich phases allows the formation of high-strength alloys at the expense of weldability. Precipitation from the α-solid solution appears in the following order: $\alpha_{ss} \rightarrow \alpha +$ GP-I $\rightarrow \alpha +$ GP-II $\rightarrow \alpha + \theta' \rightarrow \alpha + \theta$ with GP = Guinier–Preston zone. As shown in Fig. 8.22, the highest strength is reached when coherent GP-II zones have been formed, where Orowan bypassing and precipitation cutting require almost the same amount of energy.
- 3xxx: These alloys are single-phase alloys except for the presence of inclusions or intermetallic compounds. Their strength is achieved by a solid solu-

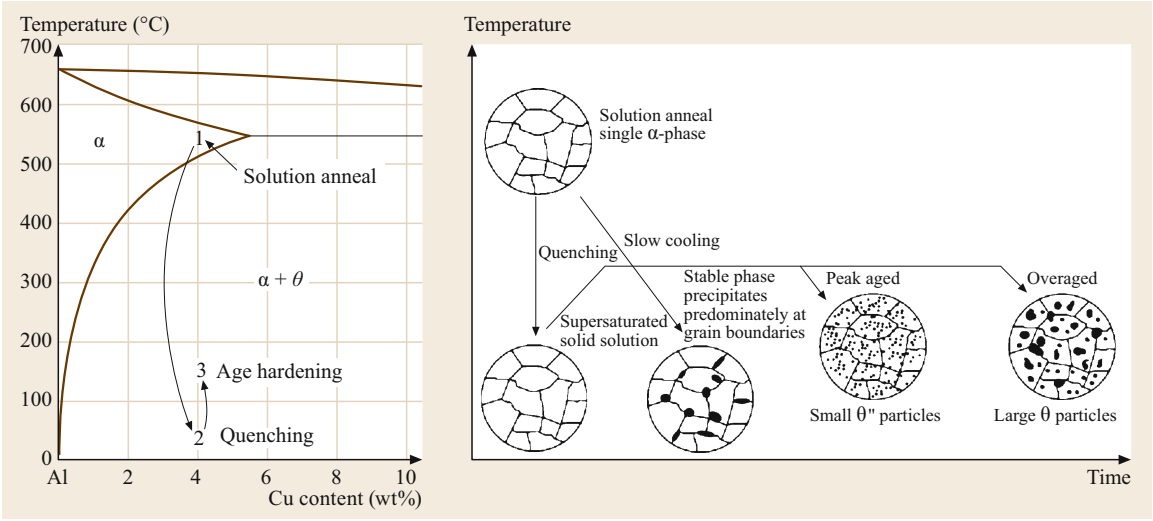

Fig. 8.19 Principle of age hardening in Al-based alloys

Table 8.13 Heat treatments of aluminum alloys

F	As-fabricated (hot worked, forged, cast, etc.)	
O	Annealed (in the softest possible condition)	
H	Cold worked	
	H1x	cold worked only ("x" refers to the amount of cold work and strengthening)
	H-12	cold work that gives a tensile strength midway between the O and H14 tempers
	H-14	cold work that gives a tensile strength midway between the O and H18 tempers
	H-16	cold work that gives a tensile strength midway between the H14 and H18 tempers
	H-18	cold work that gives about 75% reduction
	H-19	cold work that gives a tensile strength greater than 2000 psi of that obtained by the H18 temper
	H2x	cold worked and partly annealed
	H3x	cold worked and stabilized at low temperature to prevent age hardening of the structure
W	Solution treated	
T	Age hardened	
	T1	cooled from the fabrication temperature and naturally aged
	T2	cooled from the fabrication temperature, cold worked, and naturally aged
	T3	solution treated, cold worked, and naturally aged
	T4	solution treated and naturally aged
	T5	cooled from the fabrication temperature and artificially aged
	T6	solution treated and artificially aged
	T7	solution treated and stabilized by overaging
	T8	solution treated, cold worked, and artificially aged
	T9	solution treated, artificially aged, and cold worked
	T10	cooled from the fabrication temperature, cold worked, and artificially aged

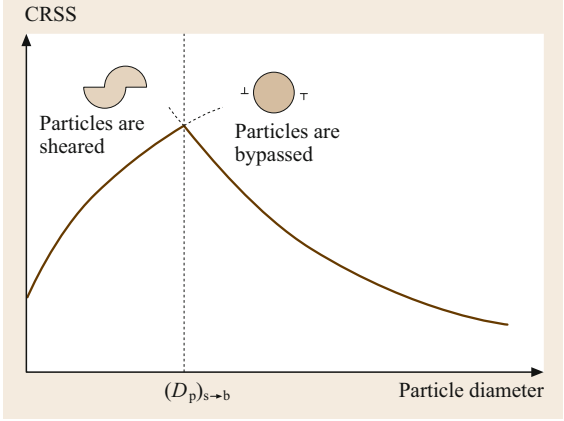

Fig. 8.20 Change in critical resolved shear stress (CRSS – at which dislocations glide freely in single crystals) as a function of particle (precipitate) size. Maximum strength is obtained when the dislocation interaction changes from shearing to Orowan bypassing. In the peak-aged condition, the average particle size corresponds to D_p and the particle size variation should be marginal (after [8.24])

tion of Mn and is not as high as for 2xxx alloys, but they exhibit excellent corrosion and oxidation resistance and are weldable.

- 4xxx: The high strength of this group of wrought alloys is achieved via a solid solution of Mg and in the case of the presence of Si by the formation of finely dispersed Mg_2Si particles as well.
- 5xxx: These alloys are strengthened by a solid solution of Mg and contain a second phase: Mg_2Al_3 particles, a hard and brittle intermetallic compound.

Table 8.14 Effect of strengthening mechanisms on mechanical properties of aluminum alloys (after data in [8.26])

Material	Tensile strength (MPa)	Yield strength (MPa)	Elongation (%)	Yield strength (alloy) / Yield strength (pure)
Pure annealed Al (99.999% Al)	45	17	60	
Commercially pure Al (annealed, 99% Al)	90	34	45	2.0
Solid-solution strengthened (1.2% Mn)	110	41	35	2.4
75% cold-worked pure Al	165	152	15	8.8
Dispersion strengthened (5% Mg)	290	152	35	8.8
Age hardened (5.6% Zn, 2.5% Mg)	570	503	11	29.2

Table 8.15 Mechanical properties and applications of selected aluminum alloys (after [8.26])

Alloy	Chemical composition	Condition	Tensile strength (MPa)	Yield strength (MPa)	Elongation (%)	Typical applications
3003	1.2 Mn	Annealed (-O) Half-hard (-H14)	110 150	40 145	30 8	Pressure vessels, builders' hardware, sheet metal work
5052	2.5 Mg, 0.25 Cr	Annealed (-O) Half-hard (-H32)	195 230	90 195	25 12	Sheet metal work, hydraulic tubes, appliances
2024	4.4 Cu, 1.5 Mg, 0.6 Mn	Annealed (-O) Heat-treated (-T6)	220 442	97 345	12 5	Truck wheels, screw machine product, aircraft structures
6061	1.0 Mg, 0.6 Si, 0.27 Cu, 0.2 Cr	Annealed (-O) Heat-treated (-T6)	125 310	55 275	25 12	Heavy-duty structures requiring good corrosion resistance, pipelines
7075	5.6 Zn, 2.5 Mg, 1.6 Cu, 0.23 Cr	Annealed (-O) Heat-treated (-T6)	230 570	105 505	17 11	Aircraft and other structures

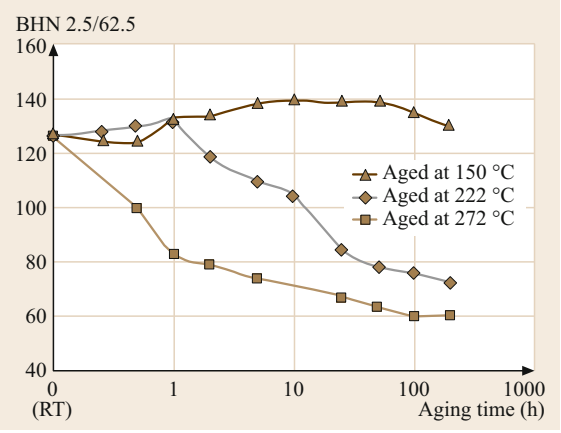

Fig. 8.21 Room-temperature hardness (BHN 2.5/62.5) of T6 age-hardened Al_6Si_4Cu (A319) after static annealing at different temperatures for up to 200 h (after [8.27])

The corrosion resistance of these alloys is almost comparable to that of pure Al.

- 6xxx: Alloys belonging to this group show a good balance of properties. They are moderately heat treatable and show moderate corrosion resistance and weldability.
- 7xxx: The highest strength levels of commercial aluminum alloys are attained by the members of this group, which are strengthened by addition of Mg and Zn. These alloys are age hardenable by the

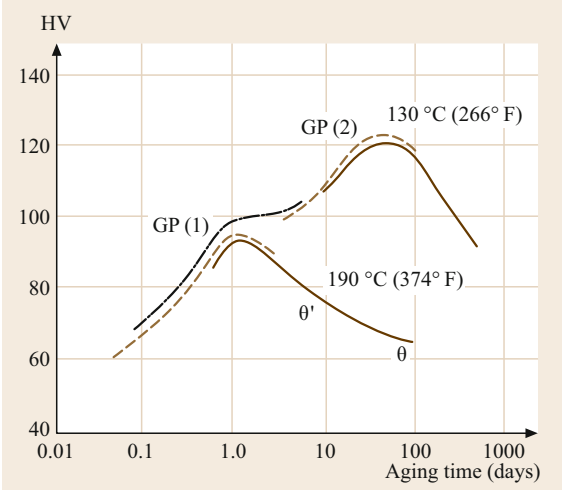

The general sequence of precipitation in binary Al-Cu alloys can be represented by

Super saturated solid solution
GP (1) zones
GP (2) zones (θ" phase)
θ'
θ ($CuAl_2$)

Fig. 8.22 Room-temperature (Vickers) hardness of 2000 series alloy after static annealing at different temperatures

Table 8.16 Selected cast aluminum alloys and their mechanical properties (after data in [8.28], see also [8.26])

Alloy	Chemical composition	Tensile strength (MPa)	Yield strength (MPa)	Elongation (%)	Casting process
201-T6	4.5% Cu	483	434	7	Sand
319-F	6% Si, 3.5% Cu	186	124	2	Sand
		234	131	2.5	Permanent mold
356-T6	7% Si, 0.3% Mg	228	165	3.5	Sand
		262	186	5	Permanent mold
380-F	8.5% Si, 3.5% Cu	317	156	3.5	Permanent mold
384-F	11.2% Si, 4.5% Cu, 0.6% Mg	331	165	2.5	Permanent mold
390-F	17% Si, 4.5% Cu, 0.6% Mg	283	241	1	Die casting
443-F	5.2% Si	131	55	8	Sand
		159	62	10	Permanent mold
		228	110	9	Die casting
413-F	12% Si	296	145	2.5	Die casting
518-F	8% Mg	310	193	7	Sand
713-T5	7.5% Zn, 0.7% Cu, 0.35% Mg	207	152	4	Sand
850-T5	6.2% Sn, 1% Ni, 1% Cu	159	76	10	Sand

formation of $MgZn_2$ particles in the followingsequence: $\alpha_{ss} \rightarrow \alpha + \text{GP zones} \rightarrow \alpha + \eta\,(MgZn_2) \rightarrow \alpha + \eta\,(MgZn_2)$. Most alloys of this group are not weldable. An exemption is the alloy 7005, which is used as a standard alloy for bike frames.

Mechanical properties and some typical applications of selected aluminum alloys are presented in Table 8.15.

Cast aluminum alloys are developed to have good fluidity and feeding ability during casting. Their designation (Table 8.12) is based on three major digits of the form 2xx–9xx, giving the alloy group, and a further digit following a dot, which indicates the material form (casting/ingot). The most widely used casting alloys belong to the 300 series (319 and 356), where hardening is done by Cu or Mg_2Si precipitates. Examples of casting alloys are presented in Table 8.16.

8.3 Magnesium and Its Alloys

8.3.1 General Properties

Magnesium is the lightest structural metal, with a density close to that of polymers (plastics). It is therefore not surprising that Mg alloys are especially found in applications where the weight of a workpiece is of paramount importance, as is generally the case in the transportation industry. In recent years, magnesium cast alloys have particularly becoming increasingly important and have partly replaced well-established Al-based alloys. The main reason is the excellent die-filling characteristics of magnesium, which allow large, thin-walled, and unusually complex castings to be produced economically. Magnesium can be cast with thinner walls (1−1.5 mm) than plastics (2−3 mm) or aluminum (2−2.5 mm) and, by designing appropriately located ribs, the stiffness disadvantage of magnesium versus aluminum can be compensated without increasing the wall thickness of the overall magnesium part.

Further positive properties to be noted are the excellent machinability, high thermal conductivity (Chap. 5), and good weldability. However, Mg alloys suffer from poor corrosion resistance, and their manufacturing costs are comparatively high. With its hexagonal close-packed crystal structure, the room-temperature deformation behavior of Mg alloys is moderate, resulting in poor cold workability. Thus, all current applications are manufactured through casting. Furthermore, Mg is a very reactive metal and readily oxidizes when exposed to air. Since pure Mg is only of minor importance for structural applications, it appears almost always in

Table 8.17 Designation of Mg alloys

1.	Two letters which indicate the major alloying additions (A for Al; Z for Zn; M for Mn; K for Zr; T for Sn; Q for Ag; C for Cu; W for Y; E for rare earths)
2.	Two or three numbers which indicate the nominal amounts of alloying elements (rounded off to the nearest percent)
3.	A letter which describes the variation from the normal alloy
4.	If needed, the temper treatment according to Table 8.18

Table 8.18 Temper designations (after [8.6])

General designations	
F	As fabricated
O	Annealed, recrystallized (wrought products only)
H	Strain-hardened
T	Thermally treated to produce stable tempers other than F, O, or H
W	Solution heat-treated (unstable temper)
Subdivisions of H	
H1, Plus one or more digits	Strain-hardened only
H2, Plus one or more digits	Strain-hardened and then partially annealed
H3, Plus one or more digits	Strain-hardened and then stabilized
Subdivisions of T	
T2	Annealed (cast products only)
T3	Solution heat-treated and cold worked
T4	Solution heat-treated
T5	Artificially aged only
T6	Solution heat-treated and artificially aged
T7	Solution heat-treated and stabilized
T8	Solution heat-treated, cold worked, and artificially aged
T9	Solution heat-treated, artificially aged, and cold worked
T10	Artificially aged and cold worked

alloyed condition with additions such as Al and Zn. A comprehensive treatment of Mg and its alloys is given in [8.29].

8.3.2 Magnesium Alloys

Major alloying elements of Mg are Al, Zn, and Mn, while elements such as Sn, Zr, Ce, Th, and B are occasionally of importance. Impurities in Mg alloys are commonly Cu, Fe, and Ni. Mg alloys are designated based on the main alloying elements (such as AZ for aluminum and zinc) followed by the amount of additives and a letter that indicates the variation with respect to the normal alloy (Table 8.17). When referring to mechanical properties, it is useful to indicate the temper treatment as well (Table 8.18). The alloy AZ91A, for example, is a Mg-based alloy with nominally about 9% Al and 1% Zn, while the letter A indicates that only minor changes to the normal alloy were carried out.

An overview of the general effect of certain alloying additions is presented in Table 8.19 [8.6, 29–31]. The addition of up to 10% aluminum (Mg-Al alloys) increases the strength (age hardenable), castability, and corrosion resistance. During precipitation heat treatment, the intermetallic phase $Mg_{17}Al_{12}$ is formed and is usually not finely distributed enough to lead to a strong strengthening effect. The supplementary addition of zinc (Mg-Al-Zn alloys) improves the strength of Mg-Al alloys by refining the precipitates and by solid-solution strengthening. The frequently used alloy AZ91, for example, offers yield strength and ductility levels that are comparable to those of its aluminum counterpart

Table 8.19 General effects of alloying elements in magnesium materials (after [8.6], see also [8.29–31])

Series	Alloying elements	Melting and casting behavior	Mechanical and technological properties
AZ	Al, Zn	Improve castability; tendency to microporosity; increase fluidity of the melt; refine weak grains	Solid-solution hardener; precipitation hardening at low temperatures (< 120 °C); improve strength at ambient temperatures; tendency to brittleness and hot shortness unless Zr is refined
QE	Ag, rare earths	Improve castability; reduce microporosity	Solid-solution and precipitation hardening at ambient and elevated temperatures; improve elevated-temperature tensile and creep properties in presence of rare-earth metals
AM	Al, Mn	Improve castability; tendency to microporosity; control of Fe content by precipitating Fe-Mn compound; refinement of precipitates	Solid-solution hardener; precipitation hardening at low temperatures (< 120 °C); increase creep resistivity
AE	Al, rare earth	Improve castability; reduce microporosity	Solid-solution and precipitation hardening at ambient and elevated temperatures; improve elevated-temperature tensile and creep properties; increase creep resistivity
AS	Al, Si	Tendency to microporosity; decreased castability; formation of stable silicide alloying elements; compatible with Al, Zn, and Ag; refine weak grains	Solid-solution hardener, precipitation hardening at low temperatures (< 120 °C); improves creep properties
WE	Y, rare earths	Grain refining effect; reduce microporosity	Improve elevated-temperature tensile and creep properties; solid-solution and precipitation hardening at ambient and elevated temperatures

Table 8.20 Typical tensile properties and characteristics of selected cast Mg alloys (after [8.6], see also [8.29–31])

ASTM designation	Condition	Tensile properties			Characteristics
		0.2% proof stress (MPa)	Tensile strength (MPa)	Elongation to fracture (%)	
AZ63	As-sand cast	75	180	4	Good room-temperature strength and ductility
	T6	110	230	3	
AZ81	As-sand cast	80	140	3	Tough, leak-tight casting with 0.0015 Be, used for pressure die casting
	T4	80	220	5	
AZ91	As-sand cast	95	135	2	General-purpose alloy used for sand and die casting
	T4	80	230	4	
	T6	120	200	3	
	As-chill cast	100	170	2	
	T4	80	215	5	
	T6	120	215	2	
AM50	As-die cast	125	200	7	High-pressure die casting
AM20	As-die cast	105	135	10	Good ductility and impact strength
AS41	As-die cast	135	225	4.5	Good creep properties up to 150 °C
AS21	As-die cast	110	170	4	Good creep properties up to 150 °C
ZK51	T5	140	253	5	Sand casting, good room-temperature strength and ductility
ZK61	T5	175	275	5	As for ZK51
ZE41	T5	135	180	2	Sand casting, good room-temperature strength, improved castability
ZC63	T6	145	240	5	Pressure-tight casting, good elevated-temperature strength, weldable
EZ33	Sand cast T5	95	140	3	Good castability, pressure-tight, weldable, creep resistant up to 250 °C
	Chill cast T5	100	155	3	
HK31	Sand cast T6	90	185	4	Sand casting, good castability, weldable, creep resistant up to 350 °C
HZ32	Sand or chill cast T5	90	185	4	As for HK31
QE22	Sand or chill cast T6	185	240	2	Pressure-tight and weldable, high proof stress up to 250 °C
QH21	As-sand cast T6	185	240	2	Pressure-tight, weldable, good creep resistance and stress-proof to 300 °C
WE54	T6	200	285	4	High strength at room and elevated temperatures, good corrosion resistance
WE43	T6	190	250	7	Weldable

A380. However, in terms of high-temperature creep resistance (applications limited to about 125 °C), fatigue strength, and corrosion resistance, the alloy AZ91 is inferior to Al alloys. Its application is therefore restricted to nonstructural components such as brackets, covers, cases, and housings. With the development of the low-impurity AZ91D alloy (Fe < 0.005%; Ni < 0.001%, Cu < 0.015%), the corrosion resistance has been dramatically improved. For structural applications where crashworthiness is important, such as instrument panels, steering systems, and seating structures, magnesium die-cast alloys with small amounts of manganese (Mg-Al-Mn alloys) such as AM50 or AM60 are used, as they offer higher ductility (expensive to failure 10–15%). These alloys are less expensive than Al alloys. The poor high-temperature creep resistance of Mg alloys is the reason why these alloys are rarely found in automotive powertrains. The high operating temperatures (transmission cases: 175 °C, engine blocks: > 200 °C) are already a challenge for aluminum alloys, which have higher creep resistance. For this application, Mg alloys containing rare-earth elements are under development to improve the creep resistance by precipitation strengthening (some examples such as QE22 and WE43 are given in Tables 8.20, 8.21 [8.6, 29–31]).

Table 8.21 Typical tensile properties and characteristics of selected wrought Mg alloys (after [8.6], see also [8.29–31])

ASTM designation	Condition	Tensile properties			Characteristics
		0.2% proof stress (MPa)	Tensile strength (MPa)	Elongation to fracture (%)	
M1	Sheet, plate F	70	200	4	Low- to medium-strength alloy, weldable, corrosion resistant
	Extrusion F	130	230	4	
	Forgings F	105	200	4	
AZ31	Sheet, plate O	120	240	11	Medium-strength alloy, weldable, good formability
	H24	160	250	6	
	Extrusion F	130	230	4	
	Forging F	105	200	4	
AZ61	Extrusion F	105	260	7	High-strength alloy, weldable
	Forging F	160	275	7	
AZ80	Forging T6	200	290	6	High-strength alloy
ZM21	Sheet, plate O	120	240	11	Medium-strength alloy, good formability, good damping capacity
	H24	165	250	6	
	Extrusions	155	235	8	
	Forgings	125	200	9	
ZMC711	Extrusions T6	300	325	3	High-strength alloy
LA141	Sheet, plate T7	95	115	10	Ultra-lightweight (S.G. 1.35)
ZK61	Extrusion F	210	185	6	High-strength alloy
	T5	240	305	4	
	Forging T5	160	275	7	
HK31	Sheet, plate H24	170	230	4	High-creep resistance to 350 °C, weldable
	Extrusion T5	180	255	4	
HM21	Sheet, plate T8	135	215	6	High-creep resistance to 350 °C, weldable after short-time exposure to 425 °C
	T81	180	255	4	
	Forging T5	175	225	3	
HZ11	Extrusion F	120	215	7	Creep resistance to 350 °C, weldable

8.4 Titanium and Its Alloys

8.4.1 General Properties

With a density below 5 g/cm^3 (Table 8.1), titanium, like aluminum and magnesium, belongs to the light structural materials. However, in contrast to Al and Mg, it also offers a high melting point of $T_m = 1670\,°C$, which is even higher than that of pure iron. Furthermore, amongst the materials which are under consideration for light structural constructions, Ti-based alloys have the highest specific strength (Table 8.1) and excellent corrosion resistance in oxidizing acids, chloride media, and most neutral environments. Titanium is well known for its biocompatibility, low thermal conductivity ($\kappa = 21\,W\,m^{-1}\,K^{-1}$), and low coefficient of thermal expansion ($\lambda = 8.9 \times 10^{-6}\,K^{-1}$). Beside a slightly lower specific stiffness compared with iron-based materials, the most annoying disadvantage of Ti and its alloys is the high manufacturing cost, which is about six times that of aluminum and ten times that of stainless steels. Therefore, Ti alloys are primary used in areas where strength-to-weight ratio and elevated-temperature properties are of prime importance, i.e., in aerospace applications (Fig. 8.23 [8.26]).

As an allotropic material, Ti undergoes a structural phase transformation at 883 °C from an (almost) closed-packed hexagonal structure (α) to a body-centered cubic high-temperature phase (β). By alloying additions and applying appropriate heat treatments, titanium alloys can be age hardened to form a two-phase (α + β) alloy. The solubility of interstitials such as O, N, C, and H is very high, on the one hand allowing the strength to be increased by solid-solution hardening, but on the other hand leading to a severe reduction of toughness when the material is penetrated by gases. Comprehensive treatments on Ti and its alloys can be found in [8.30, 32, 33].

8.4.2 Commercially Pure and Low-Alloy Grades of Titanium

Commercially pure grades of titanium in the purity range of 99.0–99.5% can actually be considered to be

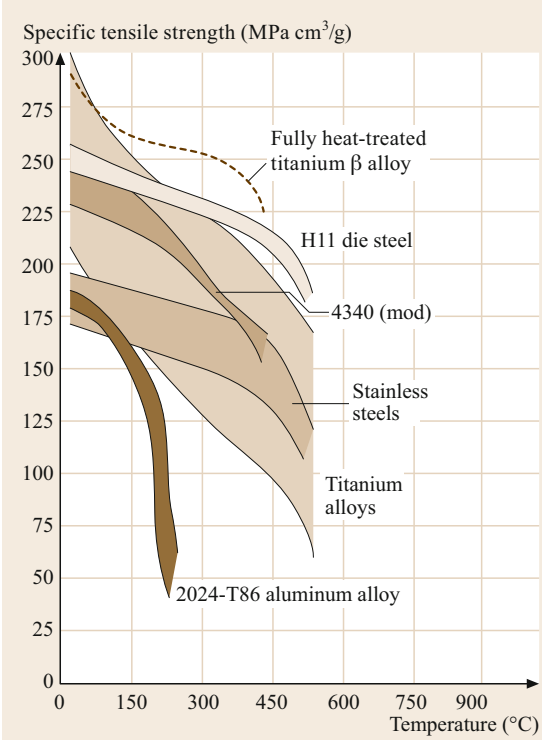

Fig. 8.23 High-temperature properties of Ti alloys compared with those of steels and aluminum alloys (after [8.26])

α-phase alloys, since they contain certain levels of O, N, C, and Fe, resulting from the manufacturing process. Furthermore, oxygen may be added deliberately for solid-solution strengthening. Interstitials in titanium are very effective strengtheners; a 0.1% oxygen equivalent (% O equivalent = % O + 2% N + 0.67% C) in pure titanium increases the strength by about 120 MPa. However, interstitials counteract the fracture toughness; some applications, especially at low temperatures, may therefore require titanium grades with extralow interstitials (ELI). Despite its hcp structure, Ti exhibits surprisingly high room-temperature ductility and can be cold-rolled to > 90% without crack formation. This behavior is attributed to the relative ease of activating slip systems and the availability of twinning planes in the crystal lattice. The chemical composition and mechanical properties of commercially pure and low-alloy grades of titanium are presented in Table 8.22.

8.4.3 Titanium Alloys

Alloying additions, which are usually added to improve the mechanical properties of Ti, influence the phase stability in different manners. The low-temperature hexagonal α-phase is stabilized by the impurities O, N, and C as well as by Al and Sn (Table 8.23), whereas elements such as V, Mo, and Cr expand the β-phase stability region (the Ti-rich part of the Ti-Al and the Ti-Mo phase diagram are shown in Fig. 8.24 [8.34]).

By varying the alloying content, pure α- or β-phase alloys can be stabilized at room temperature, as well as a mixture of both phases. α-Phase Ti alloys have high solid solubility at room temperature and are weldable. The most widely used α-Ti alloy is Ti-5Al-2.5Sn (Table 8.24). While offering the highest strength levels

Table 8.23 Alloying elements in Ti alloys [8.26, 30, 32]

Alloying element	Range (approx.) (wt%)	Effect on structure
Carbon, oxygen, nitrogen	–	α stabilizer
Aluminum	2–7	α stabilizer
Tin	2–6	α stabilizer
Vanadium	2–20	β stabilizer
Molybdenum	2–20	β stabilizer
Chromium	2–12	β stabilizer
Copper	2–6	β stabilizer
Zirconium	2–8	α and β strengthener
Silicon	0.05–1	Improves creep resistance

Table 8.22 Chemical composition and mechanical properties of commercially pure and low-alloy grades of titanium (from [8.6])

O content (wt%)	R_m (MPa)	$R_{p0.2}$ (MPa)	A_{10} (%)	Standard grade[a] (cp)	Standard grade[a] (low alloyed)
0.12	290–410	> 180	> 30	Grade 1	Pd: grade 11
0.18	390–540	> 250	> 22	Grade 2	Pd: grade 7 Ru: grade 27
0.25	460–590	> 320	> 18	Grade 3	Ru: grade 26
0.35	540–740	> 390	> 16	Grade 4	
0.25	> 480	> 345	> 18		Ni + Mo: grade 12

[a] ASTM B265, ed. 2001; N_{max}: 0.03 wt%; C_{max}: 0.08 wt%; H_{max}: 0.015 wt%

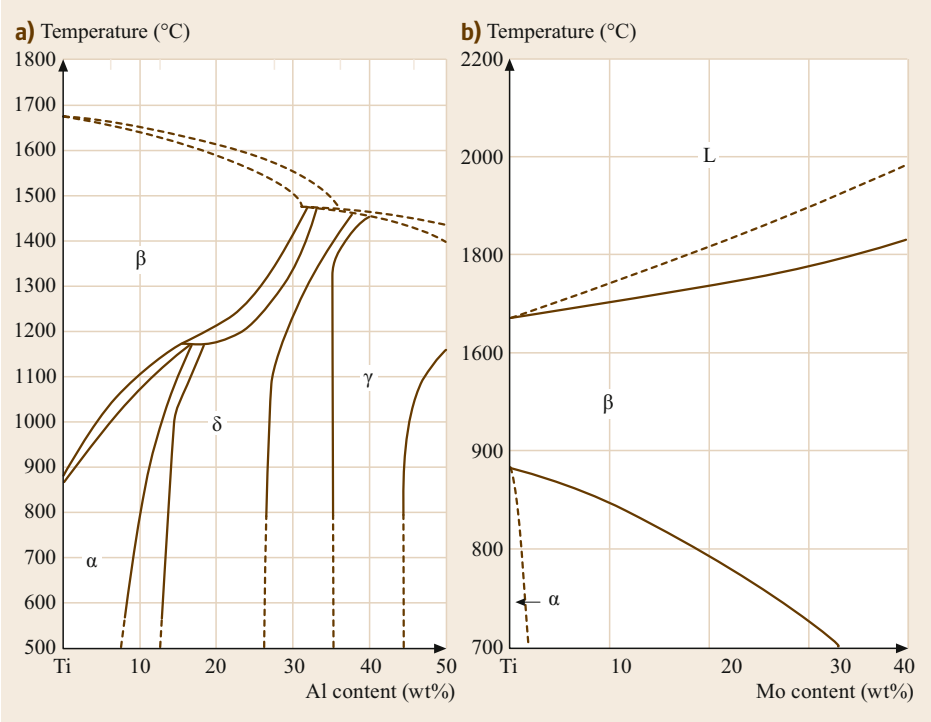

Fig. 8.24a,b Ti-rich part of the **(a)** Ti-Al and **(b)** Ti-Mo phase diagrams, showing the effect of Al as α-phase and Mo as β-phase stabilizer, respectively (after [8.34])

among the Ti alloys and the ability for cold working, the usage of β-phase alloys is rather limited compared with pure α- or α + β-alloys. Besides costs, the reasons for this include the higher density, caused by the addition of V or Mo, the low ductility in the high-strength condition, and the poor fatigue performance in thick sections, which is caused by segregations at grain boundaries. The most widely used group (about 60%) of Ti alloys are two-phase α + β-alloys, with Ti-6Al-4V being the most prominent representative. These alloys are heat treatable and allow large variations of the microstructure by altering the cooling and heat-treatment conditions. Some typical applications of α + β-alloys and the conditions of their usage are presented in Table 8.25.

Table 8.24 Chemical composition and mechanical properties (minimal values) of Ti-based alloys at room temperature (after [8.6])

Alloy composition[a]	Alloy types	R_m (MPa)	$R_{p0.2}$ (MPa)	ρ (g/cm^3)	E (GPa)	Main property	Standard grade[b]
Ti5Al2.5Sn	α	830	780	4.48	110	High strength	
Ti6Al2Sn4Zr2MoSi	near α	900	830	4.54	114	High-temperature strength	3.7145
Ti6Al5Zr0.5MoSi	near α	950	880	4.45	125	High-temperature strength	3.7155
Ti5.8Al4Sn3.5Zr0.7-Nb0.5Mo0.2Si0.05C	near α	1030	910	4.55	120	High-temperature strength	
Ti6Al4V	α + β	900	830	4.43	114	High strength	
Ti4Al4Mo2Sn	α + β	1100	960	4.60	114	High strength	3.7185
Ti6Al6V2Sn	α + β	1030	970	4.54	116	High strength	3.7185
Ti10V2Fe3Al	near β	1250	1100	4.65	103	High strength	
Ti5V3Cr3Sn3Al	β	1000	965	4.76	103	High strength; cold formability	
Ti3Al8V6Cr4Zr4Mo	β	1170	1100	4.82	103	High corrosion; resistance	
Ti15Mo3Nb3AlSi	β	1030	965	4.94	96	High corrosion; resistance	

[a] Figure before chemical symbol denotes nominal wt%
[b] According to DIN 17851, ASTM B 265 ed. 2001

Table 8.25 Typical applications of two-phase α + β-alloys (after [8.26])

Alloy composition	Condition	Typical applications
6% Al, 4% V	Annealed; solution + age	Rocket motor cases; blades and disks for aircraft turbines and compressors; structural forgings and fasteners; pressure vessels; gas and chemical pumps; cryogenic parts; ordnance equipment; marine components; steam-turbine blades
6% Al, 4% V, low: O_2, Sn	Annealed	High-pressure cryogenic vessels operating down to −196 °C
6% Al, 6% V, 2% Sn	Annealed; solution + age	Rocket motor cases; ordnance components; structural aircraft parts and landing gears; responds well to heat treatments; good hardenability
7% Al, 4% Mo	Solution + age	Airframes and jet engine parts for operation at up to 427 °C; missile forgings; ordnance equipment
6% Al, 2% Sn, 4% Zr, 6% Mo	Solution + age	Components for advanced jet engines
6% Al, 2% Sn, 2% Zr, 2% Mo, 2% Cr, 0.25% Si	Solution + age	Strength, fracture toughness in heavy sections; landing-gear wheels
10% V, 2% Fe, 3% Al	Solution + age	Heavy airframe structural components requiring toughness at high strengths
8% Mo	Annealed	Aircraft sheet components, structural sections and skins; good formability, moderate strength
3% Al, 2.5% V	Annealed	Aircraft hydraulic tubing, foil, combines strength, weldability, and formability

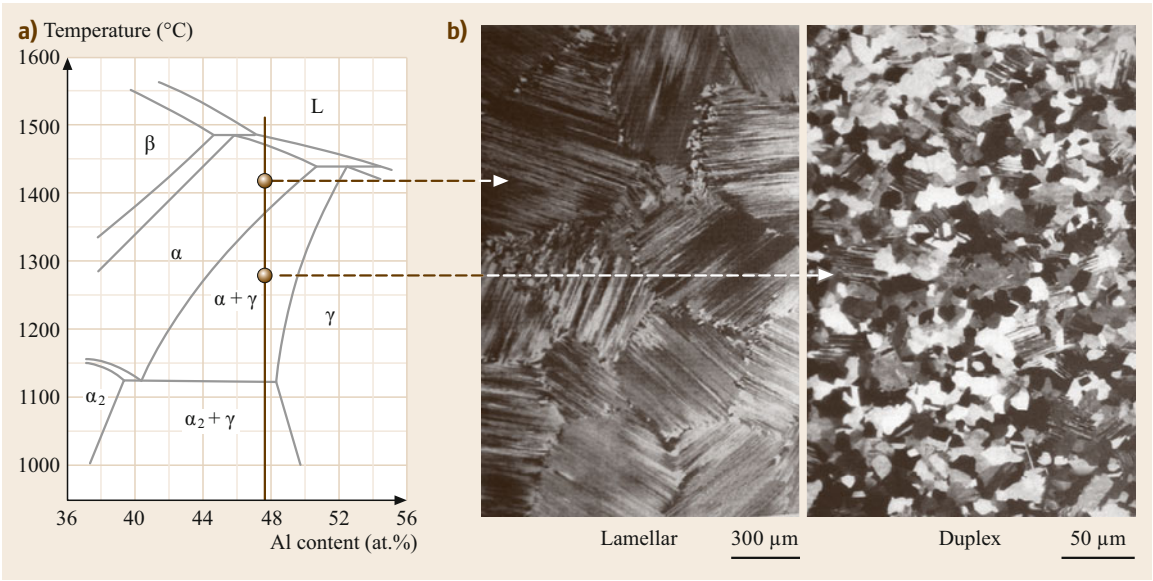

Fig. 8.25 **(a)** Partial Ti-Al phase diagram near the stoichiometric TiAl composition. The marks indicate the heat treatment temperature; **(b)** resulting microstructures after heat treatment and cooling to room temperature (solid-state transitions) (after [8.35])

8.4.4 Two-Phase Intermetallic Ti-Al Alloys

With density as low as 3.5 g/cm^3 and specific stiffness as high as 45 GPa cm^3/g (steel: 27 GPa cm^3/g), intermetallic compounds in the Ti-Al system are attractive candidates for use in high-temperature applications [8.36], mainly because of their unique combination of very low density and high melting point (> 1350 °C). The most promising alloys are Ti-rich two-phase (γ-TiAl and α_2-Ti_3Al) Ti-Al alloys with lamellar or duplex microstructures, which can be adjusted by adequate heat treatments (Fig. 8.25). Additions such as Cr and Nb lead to further enhancement of the mechanical properties and allow elongations of up to about 3%, while the room-temperature toughness values of 10–35 MPa $\sqrt{m}$ underline their principal suitability as constructional materials.

8.4.5 Ti-Ni Shape-Memory Alloys

Ti-Ni alloys are the most prominent representatives of shape-memory alloys [8.37]. The shape-memory effect, allowing the return of a highly deformed material to its starting shape, is based on a reversible martensitic trans-

formation. In the case of Ti-Ni, this effect is provided by a transition of the cubic, high-temperature B2 structure to the monoclinic low-temperature B19 structure upon cooling or by deformation. The transformation start (M_s) temperature can be varied between −200 and 110 °C by altering the Ni content. Therefore, the transformation can be reversed either on heating or on releasing the stress isothermally. For further reading, see [8.6, 37].

8.5 Ni and Its Alloys

8.5.1 General Properties

Due to its similarity to Fe with respect to the most relevant physical (and chemical) properties such as density, Young's modulus, melting point, thermal conductivity, and CTE (Chap. 5), it is straightforward to conclude that nickel is one of the major alloying elements in Fe-based alloys. Since Ni possesses an fcc crystal structure, it stabilizes the austenite in Fe-based alloys at higher concentrations. In fact, over 60% of the annual Ni consumption is devoted to alloying of stainless steels and a further 10% is used in (ferritic) alloy steels.

Nickel forms extensive solid solutions with many other elements: complete solid solutions with Fe and Cu (such as those exemplified by the phase diagrams in Figs. 3.30 and 3.31) and limited solid solutions with 35 wt% Cr, 20 wt% Mo, 10 wt% Al, Ti, to mention only the most important. Based on the fcc crystal structure, Ni and its solid solutions show high ductility, fracture toughness, and formability.

Ni-Fe alloys exhibit ferromagnetism over a wide range of compositions which, in combination with their other intrinsic properties, gives rise to alloys with soft magnetic [8.38] and controlled thermal expansion properties (*Invar alloy*, Sect. 8.1.3, *Effect of Alloying Elements*). Ti-Ni shape-memory alloys are briefly discussed in Sect. 8.4.5. Finally, nickel plating is widely used for decorative applications. Most frequently, electroless deposition of either Ni-P or Ni-B binary solutions is carried out by autocatalytic reduction of Ni ions from aqueous solutions. For more details, see [8.39].

Besides these functional applications, structural applications of nickel and its alloys can be essentially grouped into two categories, namely: 1. Corrosion-resistant alloys and 2. High-temperature alloys.

These are briefly described in the following two subsections. A survey on commonly used alloying additions in nickel and their effects on its properties and applications is shown in Fig. 8.26.

8.5.2 Corrosion-Resistant Alloys

The main application of commercially pure nickel is to combine corrosion resistance with outstanding formability. The 200 alloy series typically contains minor amounts of less than 0.5 wt% Cu, Fe, Mn, C, and Si. According to Fig. 8.23, the intrinsically good corrosion resistance of nickel 200 can be substantially improved by high alloying in solid solution with:

- Cu for increased resistance against seawater and reducing acids, leading to the Monel alloys (e.g., 400, K-500)
- Mo for increased resistance against reducing acids and halogens, leading to the Hastelloy alloys (B2, B3)
- Cr for increased high-temperature strength and resistance to oxidizing media, leading to alloy 600 (which also contains about 8 wt% Fe, mainly for economic reasons).

Alloy 600 can be considered to be the base alloy for a series of further high-alloyed Ni-base alloys for use in various applications in aggressive environments, as displayed in Fig. 8.26. An extensive compilation of chemical compositions and mechanical properties can be found in [8.6], while some typical examples of Ni alloys are presented in Table 8.26 together with their corresponding fields of application.

8.5.3 Ni-Based Superalloys

The term "superalloy" is generally used for metallic alloy systems which can operate under structural loading conditions at *elevated temperatures* above 1200 °F (or around 650 °C correspondingly). Note that this is synonymous with operating under creep conditions since $T_{app} > 0.5T_m$ (Chap. 5). As displayed in Fig. 8.27, superalloys can be grouped into three main subcategories according to the strengthening mechanism (Sect. 4.1.2) employed. One distinguishes:

1. Solid-solution-strengthened Fe, Ni and Co alloys
2. Carbide-strengthened Co alloys (see next section) and most prominently
3. Precipitation-strengthened Ni and Ni-Fe alloys.

The paramount importance of the latter group regarding high-temperature creep strength stems from alloying with Al and Ti, which leads to the formation

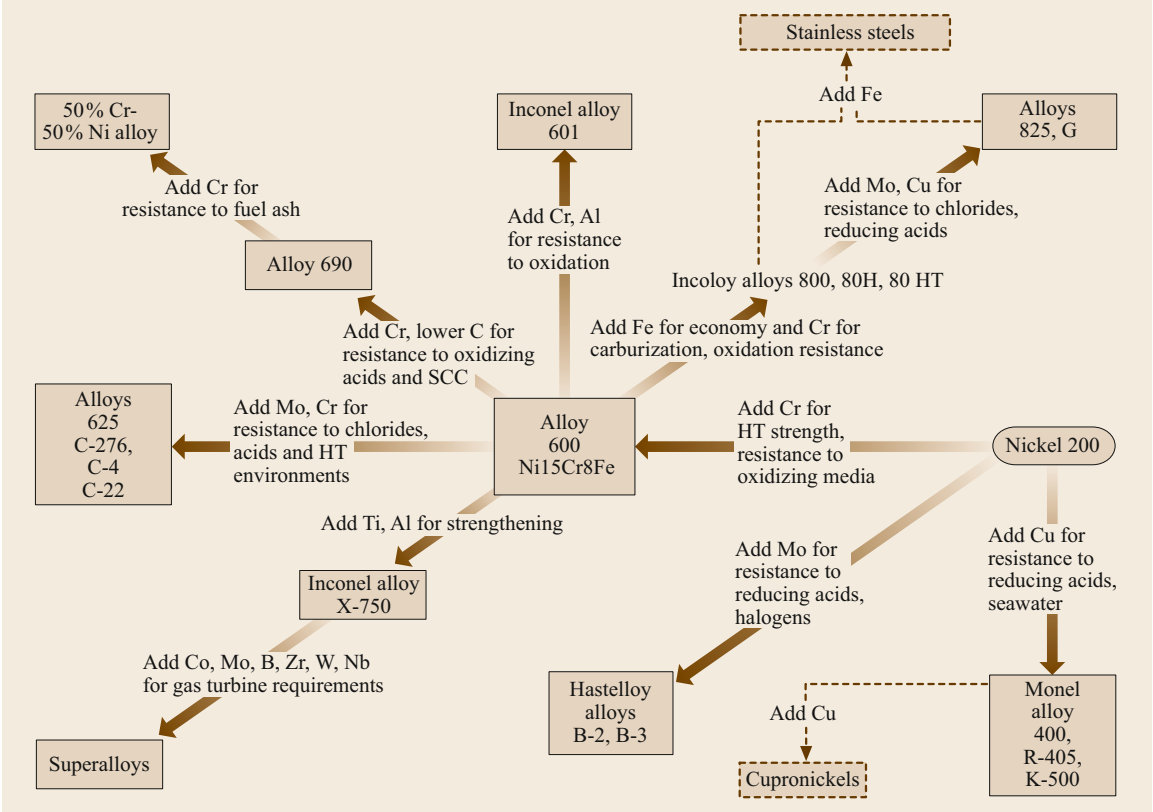

Fig. 8.26 Effects of alloying additions on corrosion resistance of nickel alloys (HT denotes high temperature, SCC denotes stress corrosion cracking) (after [8.6])

Table 8.26 Typical applications and properties of Ni-based alloys and superalloys

Material	Tensile strength (MN/m^2)	Yield strength (MN/m^2)	Elongation (%)	Strengthening mechanism	Application
Pure Ni (99.9% Ni)	345	110	45	Annealed	Corrosion resistance
	655	620	4	Cold-worked	Corrosion resistance
Ni-Cu alloys					
Monel 400 (Ni-31.5% Cu)	540	270	37	Annealed	Valves, pumps, heat exchangers
Monel K-500 (Ni-29.5% Cu-2.7% Al-0.6% Ti)	1030	760	30	Aged	Shafts, springs, impellers
Ni superalloys					
Inconel 600 (Ni-15.6% Cr-8% Fe)	620	200	49	Carbides	Heat-treatment equipment
Hastelloy B-2 (Ni-28% Mo)	900	415	61	Carbides	Corrosion resistance
DS-Ni (Ni-2% ThO_2)	490	330	14	Dispersion	Gas turbines
Fe-Ni superalloys					
Incoloy 800 (Ni-46% Fe-21% Cr)	615	258	37	Carbides	Heat exchangers
Co superalloys					
Stellite 6B (60% Co-30% Cr-4.5% W)	1220	710	4	Carbides	Abrasive wear resistance

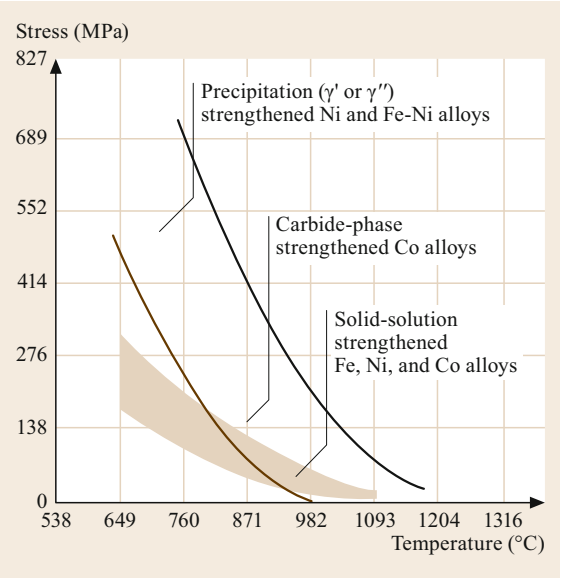

Fig. 8.27 Temperature dependence of 100-h stress-rupture characteristics of wrought superalloys (after [8.6])

of a coherent ordered intermetallic γ′-Ni_3(Al,Ti) phase. This $L1_2$ crystal structure has a superlattice structure with regard to the disordered fcc structure of the γ phase. The binary Al-Ni phase diagram (Fig. 8.28) clearly demonstrates that the γ′ phase is stable up to its melting point close to 1400 °C. Since the γ phase exhibits a decreasing solubility for Al with decreasing temperature, precipitation strengthening by age hardening can be carried out in analogy to the Al-Cu system (Fig. 8.18). The maximum fractions of γ′-phase exceed 60% by volume in single-crystal cast alloys such as CMSX 4 (Fig. 8.29). The pronounced hardening effect of the precipitate phase is mainly due to the γ/γ′ lattice mismatch, which causes dislocation reactions at the interphase and an anomalous temperature dependence of the strength of the γ′ phase [8.40]. This strength anomaly is also the reason why forming and machining operations on wrought superalloys require special attention and tools and restrict γ′ volume fractions to below 50%.

Another major alloying element is carbon, which forms carbides (of type MC, M_7C_3, $M_{23}C_6$, and M_6C) with Ti, Cr, Nb, Mo, and W in order to stabilize the microstructure (grain structure) against creep deformation. The latter *heavy* elements are added also for γ matrix solid-solution strengthening, since they segregate preferentially there. This effect has been further accentuated recently with noble elements such as rhenium and ruthenium (Fig. 8.29). Finally, Cr is deliberately

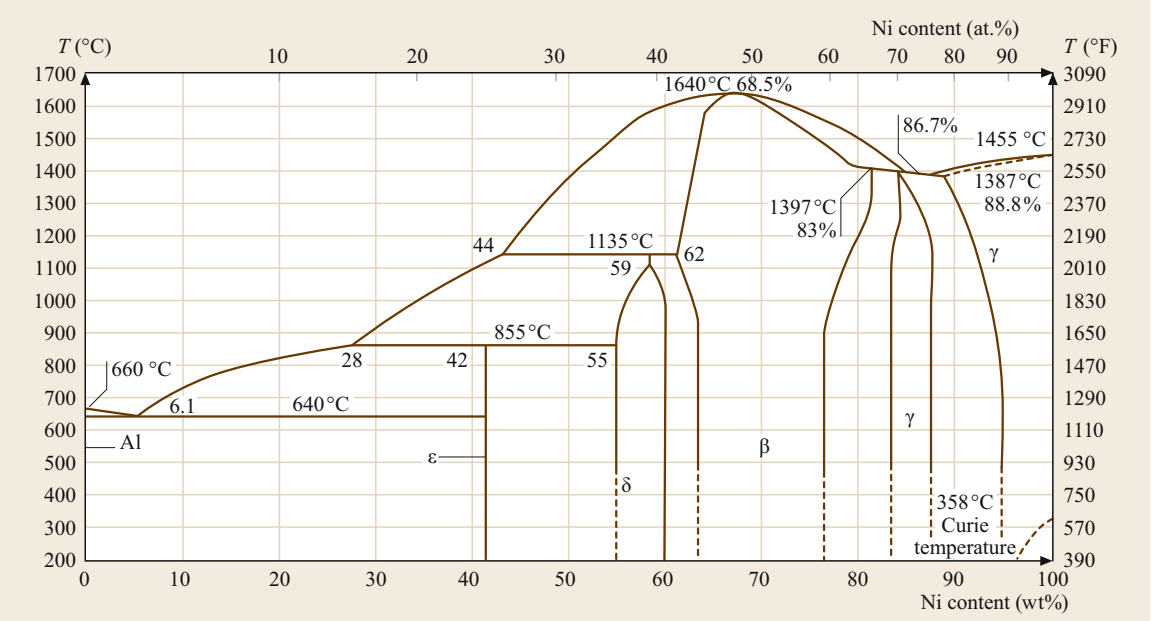

Fig. 8.28 Al-Ni phase diagram, the phases of interest are the Ni solid solution γ and the $L1_2$ ordered coherent Ni_3Al γ phase. Considerable interest has also been given to the B2 ordered NiAl β phase as a high-temperature structural material due to its very high melting point (after [8.6])

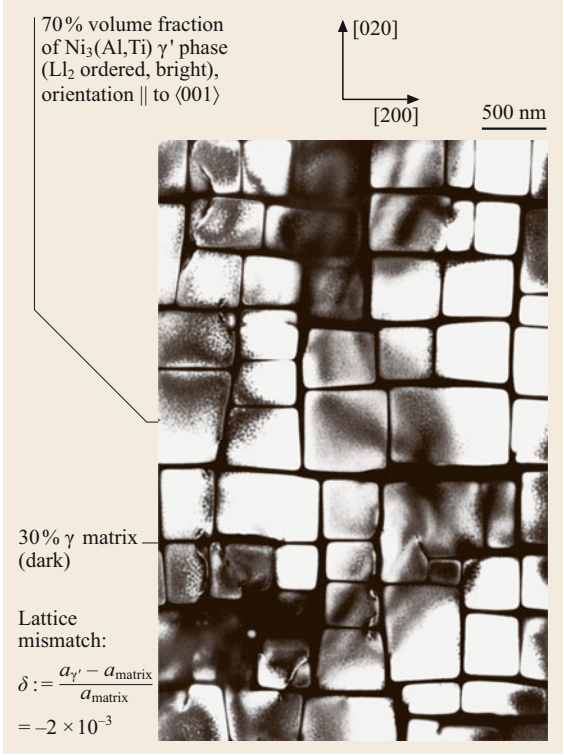

Fig. 8.29 Transmission electron microscopy (TEM) micrograph of a second-generation Ni-based single-crystalline superalloy CMSX 4 (courtesy of U. Glatzel, University of Bayreuth, Germany) ►

added in large concentrations of > 10 wt%, typically around 20 wt%, for chromia scale formation and protection against oxidation up to about 1000 °C.

A compilation of the most commonly employed wrought and cast Ni-based superalloys and their chemical composition can be found in [8.6]. Data for mechanical properties as a function of temperature are also extensively tabulated in [8.6]; some characteristic examples for superalloys and their fields of application are also presented in Table 8.26. Figure 8.30 illustrates some typical results of long-term stress-rupture tests, demonstrating the suitability of Ni-based superalloys for application in gas turbines and related power-generation applications.

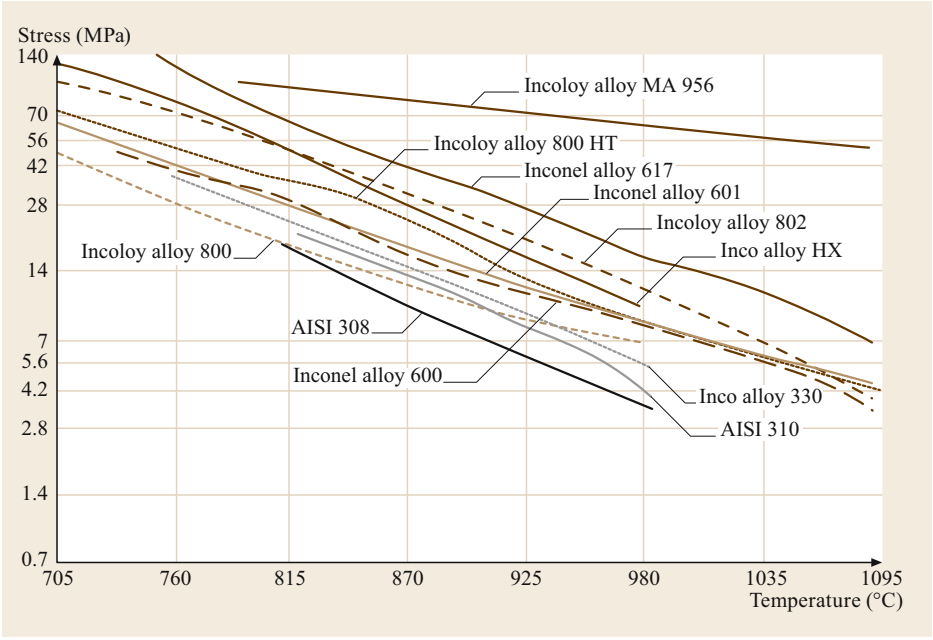

Fig. 8.30 Rupture strength (10 000 h) of Ni-based superalloys in comparison with selected stainless steels (after [8.6])

8.6 Co and Its Alloys

8.6.1 General Properties

Due to their proximity in the Periodic Table, there are many analogies between Co and Ni. Like Ni, cobalt also possesses physical properties that are similar to those of Fe [8.6]. However, at room temperature, it exhibits a hcp crystal structure like Mg, which undergoes an allotropic transformation into an fcc crystal structure above approximately 660 K. Therefore, wrought deformation requires elevated temperatures, and structural applications rely on the intrinsically high hardness of Co alloys, mainly manufactured via casting or powder-metallurgical technologies. Besides its use as an alloying element in steel, Co is frequently used as a component for many inorganic compounds such as a colorizer for glass and ceramics or in battery applications. While applications as surgical implant alloys and corrosion-resistant alloys are not treated further here, Co-based alloys may be grouped according to their field of application into the following three main categories:

8.6.2 Co-Based Hard-Facing Alloys

Co-based alloys with carbon content in the range of 1–3 wt% C are widely used as wear-resistant hard-facing materials and weld overlays. In analogy to Ni-base alloys, carbides of the type $M_{23}C_6$, M_6C, and MC are formed depending on the composition and heat treatment, and *heavy* elements such as Mo, Ta, and W are deliberately added for solid-solution strengthening. Finally, a high Cr content of typically > 15 wt% provides oxidation and hot corrosion resistance by chromia scale formation. To provide the necessary wear resistance under abrasive conditions, the microstructure of hard-facing Co-based alloys consists of a rather coarse dispersion of hard carbide phases embedded in a tough Co-rich metallic matrix. Due to the high C content of up to 3 wt%, the carbide volume fraction can exceed 50%. As a consequence, hot hardness values can exceed 500 HV at 650 °C (1200 °F) and compressive strength can approach 2000 MPa, albeit trading off for tensile ductility (< 1%) and UTS (around 800 MPa). Among some others, the most commonly known family of hard-facing Co-based alloys is designated *stellites*. For further details, see [8.6] and Chap. 9 on tribology.

8.6.3 Co-Based Superalloys

Both wrought and cast Co-based superalloys differ significantly in chemical composition from their hard-facing counterparts as follows: First, they are based on the high-temperature fcc crystal structure, which is stabilized between room temperature (RT) and the melting point by alloying with > 10 wt% Ni. Second, to enable wrought deformation, the carbon content is reduced to below 0.5 wt%, which forms fine and homogeneously distributed carbides for dispersion strengthening. Finally, like for many Ni-based superalloys, in some Co-based superalloys, addition of Al and Ti serves to form the coherent ordered $Co_3(Al,Ti)$ phase, thus leading to precipitation strengthening by age hardening. These (often investment-cast) alloys are used in the very hot parts of gas turbines because of their excellent oxidation resistance. By contrast, they are inferior to Ni-based superalloys regarding creep strength (Fig. 8.27). A survey of the temperature dependence of the 1000-h rupture stress of typical Co-based superalloys is shown in Fig. 8.31.

8.6.4 Cemented Carbides

Cemented carbides, also called *hardmetals*, can be considered to be powder-metallurgically manufactured composite materials consisting of (rather coarse) carbide particulates embedded in a metallic Co-based matrix (*binder*). Most commonly, tungsten carbide (WC)

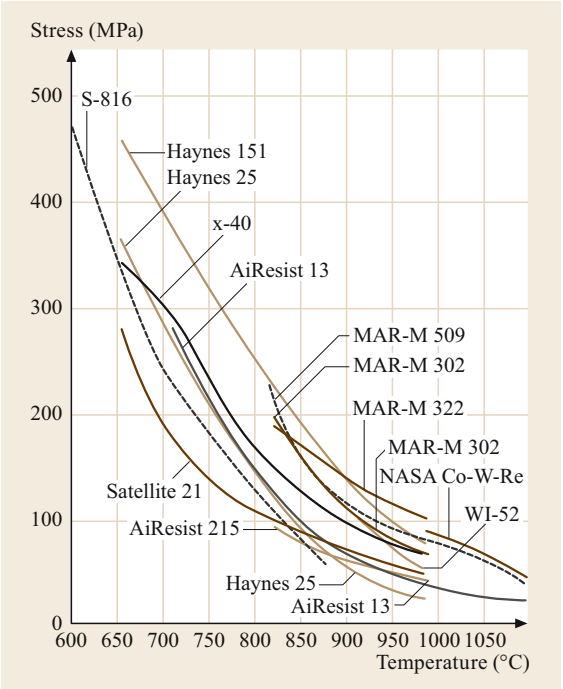

Fig. 8.31 Temperature dependence of 1000-h rupture stress of cast Co-based superalloys (after [8.6])

Table 8.27 Composition, microstructure, and properties of representative Co-bonded cemented carbides (after [8.6, p. 279])

Nominal composition	Grain size	Hardness	Density		Transverse strength		Compressive strength		Modulus of elasticity		Relative abrasion resistance[a]	Coefficient of thermal expansion ($\mu m\,m^{-1}\,K^{-1}$)		Thermal conductivity ($W\,m^{-1}\,K^{-1}$)
		(HRA)	($g\,cm^{-3}$)	($oz\,in^{-3}$)	(MPa)	(ksi)	(MPa)	(ksi)	(GPa)	($\times 10^6$ psi)		at 200 °C	at 1000 °C	
97WC-3Co	Medium	92.5–93.2	15.3	8.85	1590	230	5860	850	641	93	100	4.0	–	121
94WC-6Co	Fine	92.5–93.1	15.0	8.67	1790	260	5930	860	614	89	100	4.3	5.9	–
	Medium	91.7–92.2	15.0	8.67	2000	290	5450	790	648	94	58	4.3	5.4	100
	Coarse	90.5–91.5	15.0	8.67	2210	320	5170	750	641	93	25	4.3	5.6	121
90WC-10Co	Fine	90.7–91.3	14.6	8.44	3100	450	5170	750	620	90	22	–	–	–
	Coarse	87.4–88.2	14.5	8.38	2760	400	4000	580	552	80	7	5.2	–	1.12
84WC-16Co	Fine	89	13.9	8.04	3380	490	4070	590	524	76	5	–	–	–
	Coarse	86.0–87.5	13.9	8.04	2900	420	3860	560	524	76	5	5.8	7.0	88
75WC-25Co	Medium	83–85	13.0	7.52	2550	370	3100	450	483	70	3	6.3	–	71
71WC-12.5TiC-12TaC-4.5Co	Medium	92.1–92.8	12.0	6.94	1380	200	5790	840	565	82	11	5.2	6.5	35
72WC-8TiC-11.5TaC-8.5Co	Medium	90.7–91.5	12.6	7.29	1720	250	5170	750	558	81	13	5.8	6.8	50

[a] Based on a value of 100 for the most abrasion-resistant material

is used for the particulates, while the elements Ta, Nb, and Ti are deliberately added for economic reasons and to form complex multigrade cemented carbides. Then, the term "cermets" is used occasionally. Cobalt is the element of choice for the binder, since it wets the carbides particularly well. Usually, Ni is added to the binder phase to increase the corrosion and oxidation resistance. The main field of application is as grinding and turning tools for *difficult-to-machine* materials. Table 8.27 lists selected relevant hardmetals and their main properties.

8.7 Copper and Its Alloys

The most striking evidence of the presence of copper in constructions is in rooftops, where it is distinctively marked (after 10–15 years) by a green-colored layer of copper acetate, which prevents further corrosion (the statue of liberty is referred to as a prominent example). Copper and copper alloys have been in use for about 11 000 years, with Cu-Sn (bronze) probably being the first alloy of all. They generally show good corrosion resistance with excellent electrical and thermal conductivity, and their fabrication is easy due to their excellent formability (ductility). This favorable combination of electrical, mechanical, and corrosion properties aided the establishment of Cu as a structural material. On the other hand, Cu is susceptible to hydrogen embrittlement and stress corrosion cracking and has a relatively low strength-to-weight ratio. Comprehensive treatments and data of copper and copper alloys are given in [8.41–43]. The designation system of Cu alloys is presented in Table 8.28.

Table 8.28 Designation of Cu and its alloys (according to UNS)

Wrought alloys	
C100xx–C159xx	Commercially pure Cu
C160xx–C199xx	Nearly pure Cu, age hardenable
C2xxxx	Cu-Zn (classical brass)
C3xxxx	Cu-Zn-Pb (leaded brass)
C4xxxx	Cu-Zn-Sn (tin bronze)
C5xxxx	Cu-Sn (classical bronze) and Cu-Sn-Pb (phosphor bronze)
C6xxxx	Cu-Al (aluminum bronze), Cu-Si (silicon bronze), Cu-Zn-Mn (manganese bronze)
C7xxxx	Cu-Ni (cupronickel), Cu-Ni-Zn (nickel silver)
Cast alloys	
C800xx–C811xx	Commercially pure Cu
C813xx–C828xx	95–99% Cu
C833xx–C899xx	Cu-Zn alloys containing Sn, Pb, Mn, or Si
C9xxxx	Other Cu alloys, including tin bronze, aluminum bronze, cupronickel, and nickel silver

8.7.1 Pure Copper

Due to its high electrical conductivity, pure copper is primarily used for cables, wires, electrical contacts, and other electrical devices. A conductivity of 100% International Annealed Copper Standard (IACS) corresponds to a resistivity of 1.724 38 μΩ cm. However, the properties of Cu are subject to dramatic changes with varying alloy content; i.e., the conductivity decreases substantially with increasing impurity content. Small oxygen additions of up to about 0.04% (electrolytic tough pitch copper) can bind metallic impurities to form oxides, thus leading to an increase of the conductivity (Table 8.29), on the one hand. On the other hand, the presence of oxygen in Cu diminishes its weldability, since hydrogen diffuses into the metal and interacts with oxide to form steam, which leads to cracking. For torch welding and brazing, copper must be deoxidized, for example, by addition of a small amount of phosphorus; this lowers the electrical conductivity substantially but allows the material to be used in plumbing devices.

8.7.2 Copper Alloys

Elements which are solid-solution strengtheners in copper include Zn, Sn, Al, and Si, whereas Be, Cd, Zr, and Cr are suitable for age hardening. *Age-hardenable*

Table 8.29 Composition and properties (yield stress, ultimate tensile strength, fracture strain, thermal conductivity, and electrical resistivity) of characteristic unalloyed coppers (after [8.6])

Material	UNS No.	Composition (wt%)	$R_{p0.2}$ (MPa)	R_m (MPa)	A_f (%)	κ (W m^{-1} K^{-1})	ρ (μΩ cm)
Pure Cu (oxygen-free electronic)	C10100	99.00Cu	69–365	221–455	4–55	392	1.741
Pure Cu (oxygen free)	C10200	99.95Cu	69–365	221–455	4–55	397	1.741
Electrolytic tough pitch Cu	C11000	99.90Cu-0.04O	69–365	224–455	4–55	397	1.707
Oxygen-free low phosphorus Cu	C10800	99.95Cu-0.009P	69–345	221–379	4–50	397	2.028
Phosphorus deoxidized arsenical Cu	C14200	99.68Cu-0.35As-0.02P	69–345	221–379	8–45	397	3.831

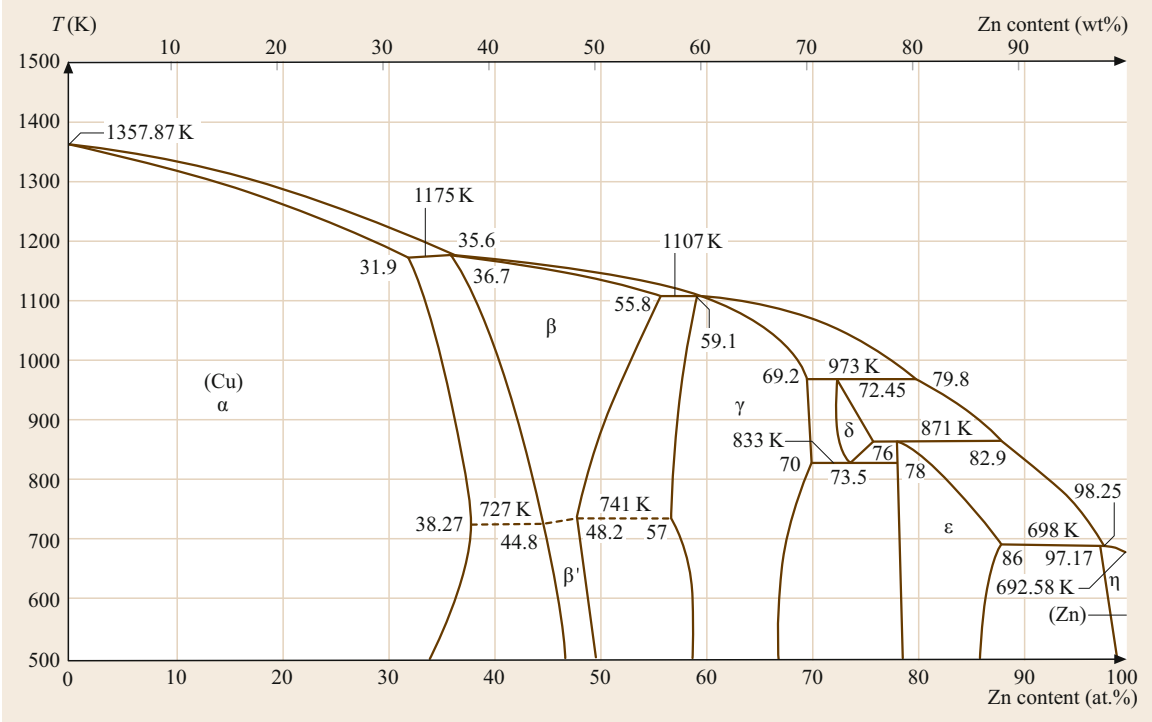

Fig. 8.32 Cu-Zn phase diagram (after [8.6])

alloys with small amounts of alloying additions (up to about 3%) can reach very high strength levels (yield stress $R_{p0.2} > 1300$ MPa at RT in the case of copper beryllium), offer high stiffness, and are nonsparking.

The term "brass" has been established for binary Cu-Zn alloys (Fig. 8.32) but is nowadays used for alloys containing additional components such as Pb, Fe, Ni, Al, and Si as well. Brasses are less expensive than pure Cu and can have different microstructures which depend on the Zn content. Pure α-(Cu) solid solutions (up to about 38% Zn) are cold-working alloys. As the Zn content is increased, the natural color of brass changes from copper-like red (5% Zn) to yellow-gold (40% Zn) (Table 8.30). *Muntz metal brass* is a binary α + β alloy with high strength and still reasonable ductility.

The most important properties of selected commonly used brasses are summarized in Table 8.31.

Wrought products of brasses and bronzes are used in automobile radiators, heat exchangers, and home heating systems, as pipes, valves, and fittings for carrying potable water, and as springs, fasteners, hardware, small gears, and cams, to give a few examples. Cast leaded red and semired brasses find applications as lower-pressure-rating valves, fittings, and pump components, as well as commercial plumbing fixtures, cocks, faucets, and certain lower-pressure valves.

Table 8.30 Designation, composition, and natural color of some brasses

Brass designation	Zn content (%)	Color
Gilding metal	5	Copper red
Commercial bronze	10	Golden
Red brass	15	Red gold
Yellow brass	35	Yellow
Muntz metal (α + β)	40	Yellow gold

General hardware, ornamental parts, parts in contact with hydrocarbon fuels, and plumbing fixtures are made from yellow leaded brass, while high-strength (manganese-containing) yellow brass is suitable for structural, heavy-duty bearings, hold-down nuts, gears, valve stems, and some marine fittings.

Bronzes are Cu-Sn- (Fig. 8.33), Cu-Al-, and Cu-Si-based alloys. Tin and aluminum are the most effective solid-solution strengtheners in copper. Cast products of tin bronzes are used as high-quality valves, fittings, and pressure vessel for applications at temperatures of up to 290 °C, special bearings, pump parts, gears, and steam fittings. Aluminum and silicon bronzes have very good strength, excellent formability, and good toughness. They are used as gears, slides, gibs, cams, bushings, bearings, molds, forming dies, combustion engine components, valve stems, spark-resistant tools,

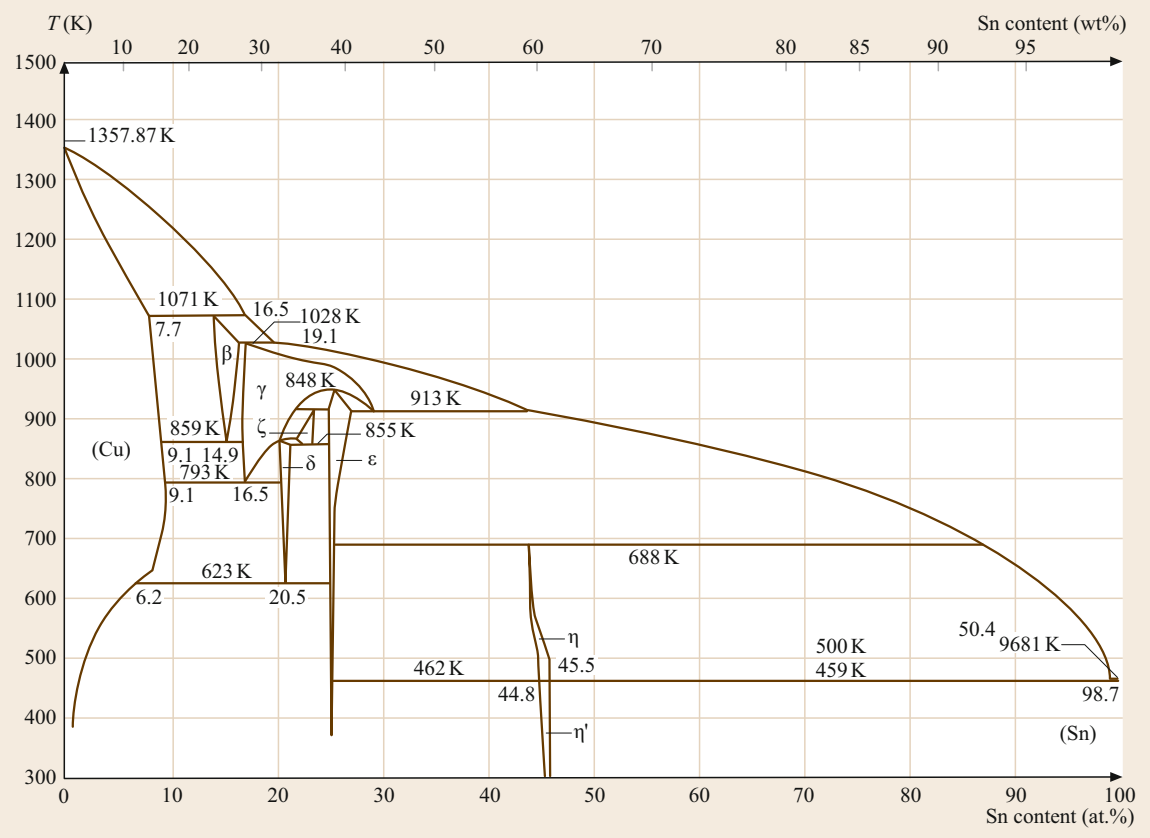

Fig. 8.33 Cu-Sn phase diagram (after [8.6])

Table 8.31 Composition and properties of characteristic brasses, bronzes, and Cu-Ni and Cu-Ni-Zn alloys (after [8.6])

Material	UNS No.	Composition	Yield strength (MPa)	Tensile strength (MPa)	Elongation (%)	Thermal conductivity ($W\,m^{-1}\,K^{-1}$)	Electrical resistivity ($\mu\Omega$ cm)
Gilding metal (cap copper)	C21000	95Cu-5Zn	69–400	234–441	8–45	234	3.079
Red brass	C23000	85Cu-15Zn	69–434	269–724	3–55	159	3.918
Yellow brass	C26800	65Cu-35Zn	97–427	317–883	3–65	121	6.631
Muntz metal	C28000	60Cu-40Zn	145–379	372–510	10–52	126	6.157
Free-cutting brass	C36000	61.5Cu-35.5Zn-3Pb	124–310	338–469	18–53	109	6.631
High-tensile brass (architecture bronze)	C38500	57Cu-40Zn-3Pb	138	414	30	88–109	8.620
Aluminum bronze	C60800	95Cu-5Al	186	414	55	85	9.741
Aluminum bronze	C63000	Cu-9.5Al-4Fe-5Ni-1Mn	345–517	621–814	15–20	62	13.26
Phosphor bronze D	C52400	90Cu-10Sn	193	455–1014	3–70	63	12.32
Silicon bronze A	C65500	97Cu-3Si	145–483	386–1000	3–63	50	21.29
Copper nickel	C71500	67Cu-31Ni-0.7Fe-0.5Be	138–483	372–517	15–45	21	38.31
Nickel silver 10%	C74500	65Cu-25Zn-10Ni	124–524	338–896	1–50	37	20.75

and in marine applications such as propellers, impellers, and hydrofoils. The properties of some widely used bronzes are given in Table 8.31.

Copper-nickel alloys show excellent corrosion resistance against seawater. Accordingly, they are used in shipboard components, power plants in coastal areas, and saline-water conversion installations. Since Ni in Cu leads to a drastic decrease in its electrical and thermal conductivity, Cu-Ni alloys are also suitable for cryogenic applications.

8.8 Polymers

Polymers (polymer materials, polymeric materials, solid polymers, or macromolecular materials) consist of very large molecules (chain molecules and macromolecules) which are synthesized from small molecules (monomers or monomer units) by a chemical reaction called polymerization (e.g., polyethylene, polyvinylchloride, polyurethane, and polyamide) or are modified natural products (modified silk and regenerated cellulose) [8.44, 45]. In this section, only polymers with carbon as the main component within the molecule chain are considered (organic polymers).

Polymerization reactions can be classified into four groups [8.46]. *Chain polymerization* proceeds by the reaction of a monomer unit with the reactive site at the end of a polymer chain. These are mostly reactions via a radical mechanism [8.47]. Terminus *condensation chain polymerization* is used in cases where a low-molar-mass byproduct is formed during polymerization. In *polycondensation*, pregenerated polymer chains react with each other or with a monomer unit to generate a low-molar-mass byproduct, for example, the reaction of an −OH (alcohol) group with a −COOH (organic acid) group, resulting in an ester group with water as the byproduct. During *polyaddition*, the growth of the polymer chains proceeds by an addition reaction between molecules of all degrees of polymerization or monomer units.

The annual world production of polymer materials is about 150–200 Mt. Some polymer materials are produced in amounts of > 1 Mt/year (polypropylene ≈ 14 Mt/year, which is about the same amount as for cotton), whereas others are polymer materials for special purposes with only small production volumes. Beside the use of bulk polymers as engineering materials, a great amount of polymers is fabricated in the shape of fibers for manufacturing fabric, packaging films, paintings, thermal isolation materials (foam), and, for example, artificial leather.

8.8.1 Chemical Composition and Molecular Structure

In the presentation of a polymer molecule, the monomer unit is enclosed in brackets with an index n showing that a certain number of monomer units react to form the backbone of the polymer molecule. The polymerization of ethylene to polyethylene, for example, is written as $n\,CH_2{=}CH_2 \rightarrow [-CH_2-CH_2-]_n$, where the last part represents the whole molecule $CH_3-CH_2-CH_2\cdots CH_2-CH_2-CH_3$, with n being between some hundreds and some millions.

Most polymers that are used as engineering materials are organic polymers with backbones (main chains) consisting of C–C bonds, or they contain bondings between C and other chemical elements (Table 8.32). Polymers with a backbone containing noncarbon atoms are called inorganic polymers. For most polymers, common abbreviations are used and trademarks exist (Table 8.32).

Polymer materials can be classified, e.g., by their specific molecular structure and the resulting mechanical properties at different temperatures into *thermoplastics*, *elastomers*, and *duromers* [8.48].

Table 8.32 Examples of widely used polymer materials and their abbreviations, characteristic backbone units, element groups within the backbone, and trademarks

Polymer	Backbone unit	Backbone	Trademarks
Organic polymers			
Polyethylene (PE)	$-CH_2-CH_2-$	–C–C–C–C–	Polythen, Lupolen, Hostalen
Polypropylene (PP)	$-CH_2-(CH_3)-CH_2-$	–C–C–C–C–	Hostalen, PPH, Luparen
Polyvinylchloride (PVC)	$-CH_2-CHCl-$	–C–C–C–C–	Hostalit, Vinidur, Vinylite
Polystyrene (PS)	$-CH_2-CH(C_6H_5)-$	–C–C–C–C–	Styroflex, Vestyron, Styropor (foam)
Polytetrafluoroethylene (PTFE)	$-CF_2-CF_2-$	–C–C–C–C–	Teflon, Hostaflon
Polyamide (PA)	$-(CH_2)_6-NH-CO-(CH_2)_6-$	–C–N–C–C–	Nylon, Perlon
Polyethylene terephthalate (PET)	$-O-CO-C_6H_4-CO-O-CH_2-CH_2-$	–C–O–C–C–C–	Trevira (fiber), Diolen, Mylar (foil)
Polyurethane (PUR)	–NH–CO–O–	–C–C–N–C–O–C–C	
Polycarbonate (PC)	–O–CO–O–R	–C–O–C–C–	
Polyphenylene sulfide (PPS)	$-C_6H_4-S-$	–C–S–C–	Noxon, Ryton, Sulfar (fiber)
Inorganic polymers			
Polyphosphazene	$-N{=}PCl_2-$	–N=P–	
Polysiloxane (polydimethylsiloxane)	$-Si(CH_3)_2-O-$	–Si–O–Si–O–	
Polysilane		–Si–Si–Si–Si–	

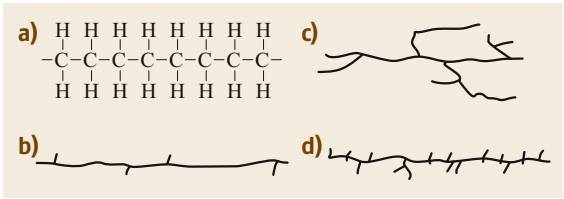

Fig. 8.34a–d Examples of linear polymer molecules: **(a)** theoretical backbone with carbon–carbon bonds and no side chains, **(b)** backbone with only a few small side chains (≈ 10 side chains/1000 C atoms, for example, high-density PE), **(c)** backbone with longer side chains/branches (for example, low-density PE), and **(d)** a great number of side chains attached to the backbone (for example, very low-density PE)

Thermoplastics

Thermoplastics show good strength and high Young's modulus at RT, and they are plastically deformable at elevated temperatures, in most cases above 100 °C. They consist in their simplest molecule structure of linear molecules with no branches (Fig. 8.34). In technical products, small (e.g., $-CH_3$ groups) or larger side chains (short −C−C− chains) are attached to the main chain, forming a branched polymer. The degree of branching determines the density of solid polymers, because with increasing branching the possibility of a dense arrangement of macromolecules decreases.

A typical example is polyethylene, with a density of 0.91–0.94 g/cm^3 for the strongly branched low-density PE (LDPE) and a density of 0.94–0.97 g/cm^3 for the weakly branched high-density PE (HDPE). In thermoplastics, very strong intramolecular covalent bonds (with a bonding energy of 348 kJ/mol for the −C−C bond) exist within the chain molecules, whereas only weak intermolecular bonds with small bonding energies (0.5–5 kJ/mol for van der Waals bonds, ≈ 7 kJ/mol for hydrogen bonds) are present between neighboring molecule chains. The chain molecules can therefore, already at around room temperature (rubber-like polymers, elastomers) or at elevated temperatures (thermoplastics), move with respect to one another, and such polymer solids can be deformed elastically or plastically. The molecular structure of thermoplastics can be distinguished by the kind of atoms forming the backbone or the kind of atoms or chemical groups attached to the backbone (Table 8.33). The side groups determine the polymer properties to a large extent, because they influence the strength of the intermolecular bonding.

Other significant parameters that determine the properties of polymer solids are based on the mean size of the macromolecules (degree of polymerization, mean chain length, or mean molar mass) and, because the polymer molecules show no unit length, the deviation of the molecule size, which depends on the production parameters.

Table 8.33 Examples of chemical groups/atoms on the backbone of linear polymers

X	Y	Polymer
H	H	Polyethylene
CH_3	H	Polypropylene
Cl	H	Polyvinylchloride
C_6H_5	H	Polystyrene
CH_3	$COOCH_3$	Polymethylmethacrylate (PMMA)

Elastomers

Elastomers (rubber-like polymers) consist, similarly to thermoplastics, of linear molecules, but the molecule chains are bridged by small-molecule segments via covalent bondings. The molecules can thus undergo strong elastic deformation at *room temperature*. This effect is due to the stretching of the molecules out of the disordered state if a load is applied, followed by a redeformation into a random tangle of molecules due to the increased entropy after the load is released.

Duromers

Duromers consist of a three-dimensional molecule network, bridged by covalent bondings. Even at elevated temperatures, they undergo no plastic deformation and can, in most cases, be heated up to their decomposition temperature without any elastic or plastic deformation. Most duromers are thermosets (phenolics, unsaturated polyesters, epoxy resins, and polyurethanes) which solidify by an exothermal chemical reaction (curing). Thermosets are obtained by molding a thermoplastic material into the desired shape, which is then cross-linked. The curing reaction can be initiated at RT by mixing the components, or it starts at an elevated temperature, or irradiation by energetic radiation (ultraviolet light, laser beam, or electron beam) is applied.

Most polymers are formed by chain polymerization from one type of monomer (e.g., PE, PP, PVC, and PS); For example, PE is obtained by polymerization of ethylene: $n\,[CH_2{=}CH_2] \rightarrow [-CH_2{-}CH_2-]_n$. Another possibility is that two different monomers containing different types of chemical groups react with each other (e.g., PA, PC, PET, and polyurethane), thus forming a polymer unit built by two molecules; for example, PET is obtained by polycondensation of ethylene glycol with terephthalic acid with water generated as a byproduct, as exemplified in Fig. 8.35.

In copolymers, the polymer chain is composed of two or more types of monomer. The monomers can be arranged randomly, alternating, or as blocks (short molecule chains, consisting of the same monomer

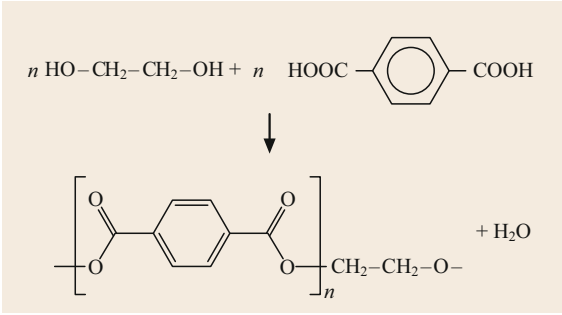

Fig. 8.35 PET formation by polycondensation of ethylene glycol with terephthalic acid

units). Another variant is where blocks built from one type of monomer are fixed as side chains onto a backbone built from another monomer type. Common copolymers are polystyrene-butadiene rubber (SBR) and acrylonitrile-butadiene-styrene (ABS).

The properties of polymeric materials can be further tailored by mixing or blending two or more polymers [8.49]. One goal of such blending is to obtain materials with greater impact toughness than the pure polymers, whereby one component functions as a toughener for the other. In high-impact polystyrene, the high modulus of polystyrene is combined with the high impact strength of rubber particles (polybutadiene). Other example blends are PP-PC, PVC-ABS, and PE-PTFE.

The toughness of otherwise stiff polymers and the glass-transition temperature (see below) can be increased by mixing low-molar-mass substances (plasticizers) into them. The most common case is dioctyl phthalate as a plasticizer for PVC. A similar effect results if up to 3% water is incorporated into polyamide, when in contact with water or high humidity.

In a process known as cross-linking, molecules are linked to one another to increase the temperature resistance, long-time creep strength, and insensitivity to stress cracks. Cross-linking can be achieved very precisely by irradiating plastics with high-energy electron beams or gamma rays. This optimization can be applied even to pure and widely used plastics, such as PE and PVC. Another approach is to add special compounds which are cross-linkable by irradiation, thus fixing two polymer chains to each other. The advantages of the cross-linking technique are that the properties are modified after the components have been formed into parts and that the process takes place at room temperature and normal pressure.

Fig. 8.36 Amorphous and crystalline regions in the morphology of a semicrystalline polymer

8.8.2 Microstructure of Polymer Materials

Linear polymers can have a disordered state (amorphous) or a semicrystalline arrangement of the molecules (Fig. 8.36).

The amorphous state is characterized by a random tangle of molecules. In semicrystalline polymers, some parts of the polymer molecules are ordered in the shape of folded-chain lamellae, which are eventually arranged to form blocks. The degree of crystallinity can be estimated by density measurements, thermal analysis/differential scanning calorimetry (DSC), or x-ray diffraction (XRD) analysis. It depends on the number and length of the side chains on the molecule backbone (degree of branching) and determines the density and elastic moduli of the polymer material. For polyethylene, the degree of crystallinity varies from 45% for LDPE to 95% for HDPE (Table 8.34).

In some semicrystalline polymers, the folded-chain lamellae grow, starting at a nucleus, outwards, yielding globules/spherulites [8.50]. The size of the spherulites can be modified by the addition of nucleants. The toughness and light transparency decrease with increasing spherulite size. Spherulites are visible under polarized-light microscopy of microtome sections (about 25 μm thick) (Fig. 8.37).

Table 8.34 Degree of crystallinity of common polymer materials

Polymer	Degree of crystallinity (%)
LDPE	45–75
HDPE	65–95
PP fiber	55–60
PET fiber	20–60

Fig. 8.37 Spherulites in polypropylene; transmission light microscopy of a microtome section; polarized light

Polymer molecules can be strongly oriented parallel to the flow direction during production processes such as injection molding due to the high viscosity of the melt. This occurs especially if metallic parts are used as inserts, by which the melt flow is divided and then reunited after the flow around the insert [8.51, 52]. As a result, regions that show strongly anisotropic mechanical properties can be found within normally isotropic polymer solids [8.53]. The aligned molecules can result in substantial residual stresses and give rise to crack initiation even when a low external load is applied. This molecular alignment effect can be reduced by relaxation at elevated temperatures, whereby changes of the shape can occur. This effect has to be taken into account if parts made from polymer materials are to be heated during further manufacturing or while in use. One application of this relaxation effect is the use of polymer films for shrink packaging, where an article is wrapped at room temperature and the film shrinks upon heating.

8.8.3 Thermal Properties

The strength of duroplastic materials does not change much with increasing temperature. They do not melt at all due to the three-dimensional molecule network, but rather start to decompose. During heating of thermoplastic and elastomeric polymers, temperature ranges with different polymer properties are observed: strong, hard, and brittle at low temperatures, but ductile and deformable at increased temperatures, finally changing

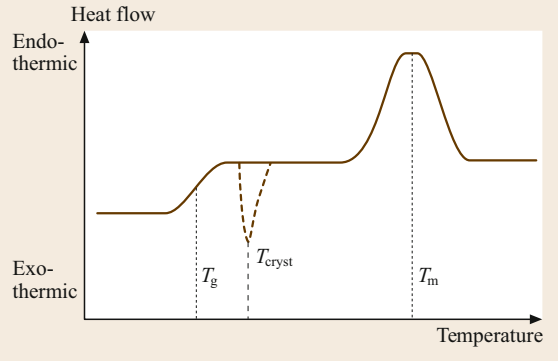

Fig. 8.38 DSC results for a partially crystalline polymer; schematic heating curve with characteristic transition points: glass transition T_g, crystallization temperature T_{cryst}, and melting point T_m

from a solid to the state of a viscous melt. The transitions between the different states, which are due to the arrangement and mobility of the molecules, can be investigated by differential scanning calorimetry (DSC) [8.54], whereby the exothermic and endothermic heat flux is registered (Fig. 8.38).

At a material-specific temperature, an endothermic hump appears, extending over a certain temperature range. This is the transition into the glassy state due to the increased mobility of the molecule segments in the amorphous parts of the microstructure and is accompanied by an enormous decrease of viscosity and, thus, strength. The glass-transition temperature (T_g), which can be defined as the temperature at the first inflection point of the graph, is heating rate dependent and specific to each material (Table 8.35). The high level of heat flux is maintained because the specific heat of the glassy polymer is greater than that of the solid polymer.

In very few cases and at very low temperatures, partial crystallization of the polymer can follow the transition into the glassy state, connected with an exothermic heat flow (dashed line in Fig. 8.38). With increasing

Table 8.35 Typical glass-transition temperatures and melting temperatures of polymers

Polymer	T_g (°C)	T_m (°C)
PE	−120	130
PP	−15	170
PS	90	200
PVC (amorphous)	80	–
PVC (partially crystalline)	80	210
PTFE	−115	330
PMMA	45	160
PA6 (polyamide 6)	75	230
PET	75	280

temperature, the crystalline regions of semicrystalline polymers will melt, which is indicated by another endothermic event, which represents the melting temperature (T_m) (Table 8.35). The large peak width, as compared with metals, is related to the nonuniformity of the polymer molecules and the high degree of imperfection of the polymer crystals. After that temperature range, the polymer behaves like a high-viscosity melt.

Usually, technical applications of polymer materials are restricted to temperatures below the glass transition (PS, PMMA, and PET). However, in some cases, polymers are also used above that temperature (polyisoprene, polybutadiene, and polyethylene); then some polymers exhibit rubber-like properties.

Polymeric materials start to decompose or to be oxidized in air if heated above a certain temperature. In some cases (PE, PP, and PS), they burn with a characteristic flame color. The decomposition is a process of thermal cracking of the material and/or an oxidation, whereby sometimes a fume with a characteristic smell occurs when the flame is blown out (PE: like burning candle or wax; PA: like burned hair or horn; PVC: stinging, acidic; PS: fruity). In some cases, chemicals which are dangerous to humans or can alter other materials are released. Burning PUR generates toxic hydrocyanic acid. Overheating or burning of PVC yields hydrochloric acid (HCl) vapor, which leads to the corrosion of parts made from Cu or other metals and is toxic to humans.

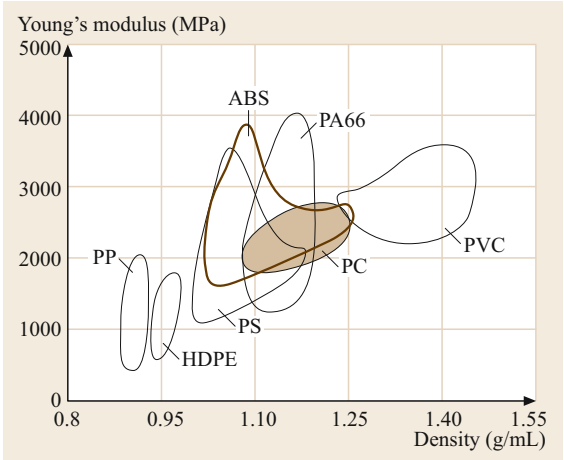

Fig. 8.39 Young's modulus versus density for selected thermoplastic polymers (after [8.56])

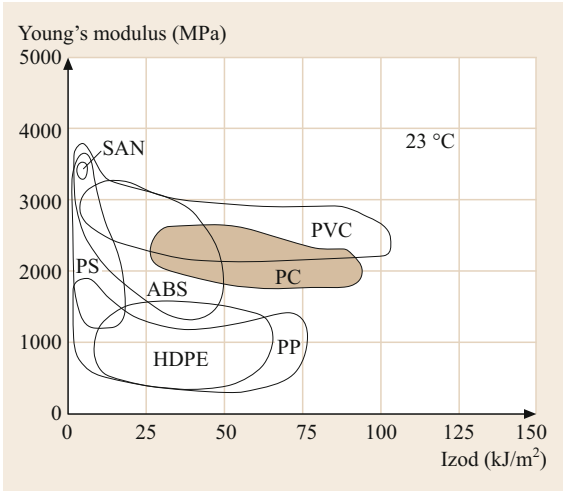

Fig. 8.40 Young's modulus versus notch impact strength (Izod) for thermoplastics (after [8.56])

8.8.4 Mechanical Properties of Polymer Materials

As stated above, the three basic types of polymer – thermoplastics, elastics, and duromers – show very different properties with different temperature dependences, which can be a reason for selecting a certain polymer. The choice of a polymeric material for a specific application [8.55] can be based on the difference in mechanical properties, such as tensile strength, impact, and elastic behavior, but also often other properties have to be considered, such as density, corrosion resistance, or formability. The ratio of the density to the Young's modulus (Fig. 8.39) can be a potential criterion for selecting a polymer material for a certain application. Alternatively, the ratio of the Young's modulus to the impact strength of a polymer material may be taken into account (Fig. 8.40).

Standardized mechanical testing methods for polymer materials (Table 8.36) in most cases differ from those applied to other materials (Chap. 5.). This is especially true for the size and shape of the specimens and the applied load [8.57].

Tensile stress–strain curves can be very different for polymer materials (Fig. 8.41) and are strongly dependent on the testing temperature (Fig. 8.42). No linear region of the stress–strain curve of polymer materials exists from which the Young's modulus could be obtained. Therefore, a *secant modulus* is calculated based on the slope of the stress–strain curve within a certain range of elongation, e.g., between 0.05% and 0.25% elongation

$$E_t = \frac{\sigma_{0.05} - \sigma_{0.25}}{\varepsilon_{0.05} - \varepsilon_{0.25}} \,. \tag{8.1}$$

In general, the values of the mechanical properties of polymer materials are inferior to those of metallic materials (Table 8.38).

The tensile strength generated by stretching the polymer chains during the manufacturing process can yield values of the ultimate tensile strength which

Table 8.36 Selected standard mechanical testing methods for polymer materials

Standard	Testing method
ISO 178:2001	Plastics – Determination of flexural properties
ISO 179-1:2000	Plastics – Determination of Charpy impact properties; Part 1: Noninstrumented impact test
ISO 179-2:1997	Plastics – Determination of Charpy impact properties; Part 2: Instrumented impact test
ISO 180:2000	Plastics – Determination of Izod impact strength
ISO 527-1:1993	Plastics – Determination of tensile properties; Part 1: General principles
ISO 527-2:1993	Plastics – Determination of tensile properties; Part 2: Test conditions for molding and extrusion plastics
ISO 527-3:1995	Plastics – Determination of tensile properties; Part 3: Test conditions for films and sheets
ISO 6721-1:2001	Plastics – Determination of dynamic mechanical properties; Part 1: General principles
ISO 6721-2:1994	Plastics – Determination of dynamic mechanical properties; Part 2: Torsion-pendulum method
ISO 899-1:2003	Plastics – Determination of creep behavior; Part 1: Tensile creep
ISO 899-2:2003	Plastics – Determination of creep behavior; Part 2: Flexural creep by three-point loading
ISO 8256:2004	Plastics – Determination of tensile-impact strength
ISO 2039-1:2001	Plastics – Determination of hardness; Part 1: Ball indentation method
ISO 868:2003	Plastics and ebonite – Determination of indentation hardness by means of a durometer (Shore hardness)

Table 8.37 Properties of common polymer materials

Material	Density (g/cm^3)	Young's modulus (GPa)	Ball indentation hardness	Izod A[a] (kJ/m^2)
LDPE	0.92	0.2	50[b]	2–35
HDPE	0.95	1	50[c]	2–35
PP	0.9	1.5	70	3–10
PA 6,6	1.1	3	160	5–90
PVC	1.4	3	110	4; 40–70[c]
PS	1.05	3.2	150	2–15
PC	1.2	2.5	110	80
ABS	1.05	3	95	10–35
PMMA	1.19	3.3	200	3
PTFE	2.1	0.75		16

[a] At room temperature, [b] Shore D, [c] with plasticizer

Table 8.38 Comparison of specific ultimate tensile strength (tensile strength/density) with steel: value for Aramid set to 100

Material	Relative specific UTS
Aramid/KEVLAR	100
Glasfiber E	46
PA/nylon fiber	45
Low-carbon steel	19

Table 8.39 Solubility parameter for solvents and polymers [8.59]

Solvent	δ $(MPa)^{1/2}$	Polymer	δ $(MPa)^{1/2}$
n-Hexane	14.9	Polyethylene	12.7
Benzene	18.8	Polystyrene	18.4

are greater than those known for steel (for example, $\approx 400\,N/mm^2$ for steel S355) (Table 8.39). An outstanding high tensile strength is exhibited by Aramid (polyparaphenylene terephthalamide; Kevlar), which is used as a fiber.

The orientation of segments of the molecule chains as generated by the shaping process [8.60] (see above) has a significant influence on the mechanical properties (Fig. 8.43). For the determination of the dynamic mechanical properties of polymers, a torsion pendulum is used [8.61, 62]. As a result, the elastic shear modulus G and $\tan\delta$ are obtained. The shear modulus is strongly dependent on temperature (Fig. 8.44).

The mechanical properties of polymer materials can be further improved by fiber reinforcement ([8.63, 64], Sect. 8.10).

8.8.5 Polymer Interaction with Solvents

The dissolution of solid polymers in organic solvents or water starts with swelling, whereby the macromolecules are not degraded, which means that the chain length is not changed [8.65]. Only in some polymers are the chain molecules shortened by a chemical reac-

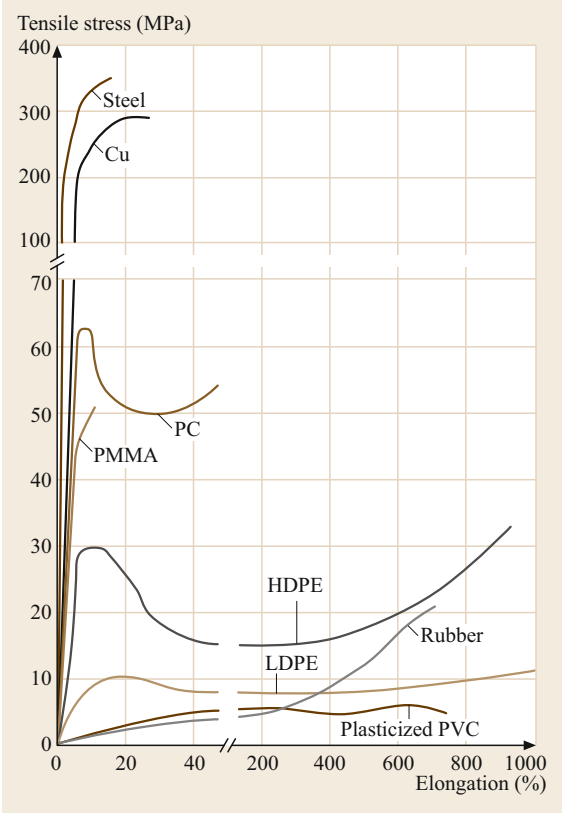

Fig. 8.41 Tensile stress–strain curves for polymers in comparison with copper and steel (after [8.56])

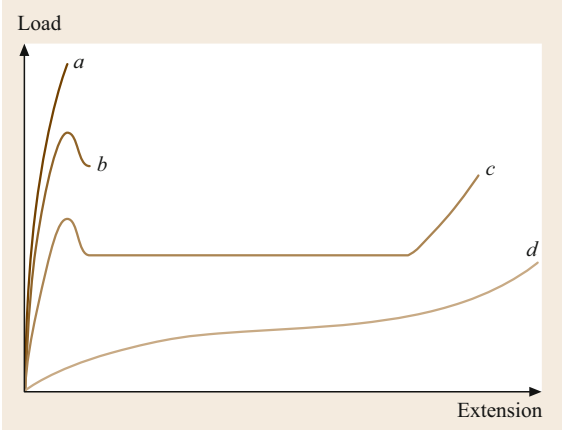

Fig. 8.42 Temperature dependence of load–extension curve for a polymer; with increasing temperature: *Curve a* brittle ductile, *curve b* homogeneous deformation, *curve c* necking and cold-drawing, *curve d* quasi-rubber-like behavior (after [8.58])

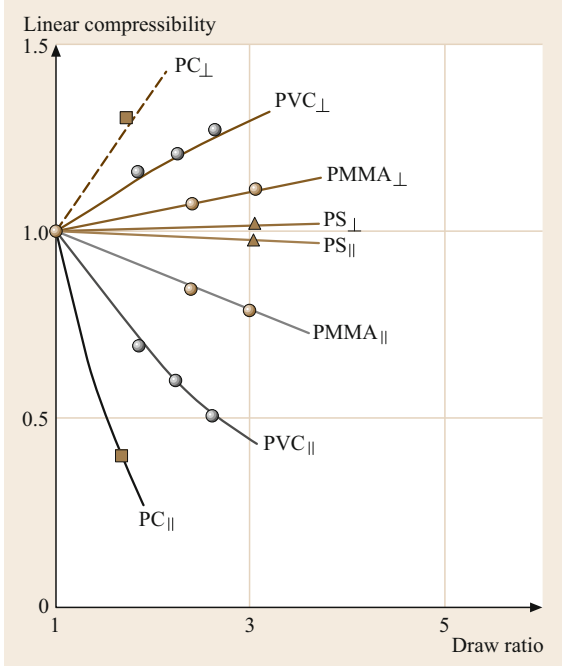

Fig. 8.43 Influence of drawing ratio on linear compressibility, γ/γ_0 parallel and perpendicular to drawing direction (after [8.56])

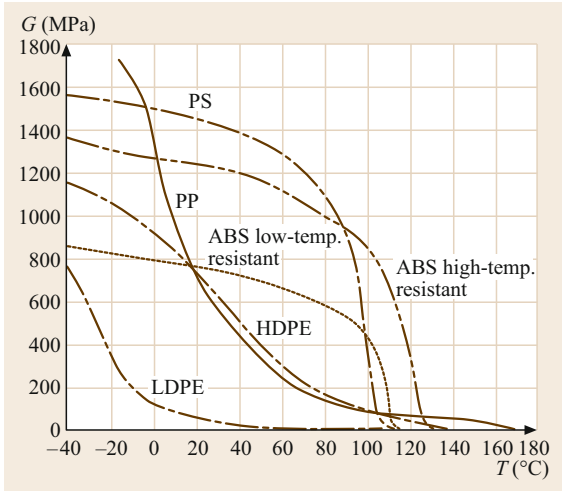

Fig. 8.44 Shear modulus versus temperature for several common polymer materials (after [8.56])

tion with a chemical substance contained in a solvent; For example, the amide groups in polyamides undergo hydrolysis under basic conditions (saponification), resulting in the generation of chain molecule fragments of different lengths. The swelling and subsequent dissolution are due to competition between the intermolecular bonding forces between the chains of the polymer versus the bonding forces between the macromolecules and the small solvent molecules, respectively. As a re-

sult, increasing numbers of solvent molecules penetrate the tangled polymer chain arrangement and lead to an increase of the volume of the polymer solid. This is accompanied by a lowering of the interaction forces between adjacent macromolecule segments and an increase of the mobility of the molecules with respect to each other, with a loss of strength. The swelling and dissolution process may take up to several days or weeks at ambient temperature. For the same reason, the contact of many polymers with mineral oils must be avoided. Swelling often results in a sticky substance before true dissolution occurs. In some cases, polymer solutions can be used as glue which will have the strength of the starting polymer after the solvent has evaporated.

Some polymers can only incorporate a limited fraction of solvent into the solid. The interaction between a polymer and a selected solvent and therefore the solubility of the polymer can be predicted using the solubility parameter δ (Table 8.39), which is based on the cohesion forces, beside other factors [8.59]. As a rule, a substance can be regarded as a solvent if the difference of δ values is < 2.

8.8.6 Aging and Corrosion

Aging of polymers is mainly due to chemical changes of the structure of the macromolecules accompanied by a shortening of the chain molecules, branching, crosslinking, and the generation of new chemical groups. A prerequisite for aging is the influence of light, especially ultraviolet (UV) light, and eventually oxygen from the air. As a result, the polymer becomes brittle, cracks are generated, the quality of the surface is changed, and a loss of electrical insulation behavior will appear. Loss of plasticizer by diffusion also lowers the elasticity and ductility, especially at lower temperatures. An especially dangerous situation is the interaction of a solvent or a solution and the mechanical stress of a polymer part, leading to stress-corrosion failure.

8.9 Glasses and Ceramics

Glass and ceramic materials are complex compounds and solid solutions containing metallic and nonmetallic elements, being composed of either ionic or covalent bonds. Typical properties of glasses and ceramics include high hardness, high compressive strength, high brittleness, high melting point, and low electrical and thermal conductivity. There are several ways in which ceramics can be classified, such as by chemical composition, properties, or applications. In Fig. 8.45, this classification is made on the basis of chemical composition [8.6].

In the following, we take a closer look at some of the ceramic materials listed in Fig. 8.45. Detailed treatments of ceramics are given in [8.66, 67].

8.9.1 Glasses

Glasses are solid materials which have become rigid without crystallization (Sect. 4.1.1). The microstructure is based on SiO_4 tetrahedral units which possess short-range order and are connected to each other by bridging oxygen, resulting in a three-dimensional framework of strong Si–O–Si bonds. The main advantages of glasses are their optical transparency, pronounced chemical resistance, high mechanical strength, and relatively low fabrication costs. Glasses usually contain other oxides, notably CaO, Na_2O, K_2O, and Al_2O_3, which influence the glass properties. Besides about 70% SiO_2, soda-lime glasses, which are used for windows and containers, additionally consist of Na_2O (soda) and CaO (lime). Further applications of glasses are as lenses (optical glasses), fiberglass, industrial and laboratory ware, and for metal-to-glass sealing and soldering. The compositions of some commercial glass materials are described in Table 8.40 [8.68].

8.9.2 Glass Ceramics

Glass ceramics contain small amounts of nucleating agents (such as TiO_2 and ZrO_2) which induce crys-

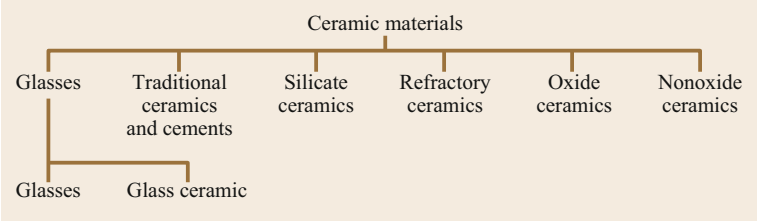

Fig. 8.45 Classification of ceramic materials based on chemical composition (after [8.6])

Table 8.40 Compositions and characteristics of some common commercial glasses (after [8.68])

Glas type	Composition (wt%)						Characteristics and applications
	SiO_2	Na_2O	CaO	Al_2O_3	B_2O_3	Other	
Fused silica	> 99.5						High melting temperature, very low coefficient of expansion (shock resistant)
96% Silica (Vycor)	96				4		Thermal shock and chemically resistant (laboratory ware)
Borosilicate (Pyrex)	81	3.5		2.5	13		Thermal shock and chemically resistant (ovenware)
Container (soda lime)	74	16	5	1		4MgO	Low melting temperature, easily worked, also durable
Fiberglass	55		16	15	10	4MgO	Easily drawn into fibers (glass–resin composites)
Optical flint	54	1				37PbO, $8K_2O$	High density and high index of refraction (optical lenses)
Glass-ceramic (Pyroceram)	43.5	14		30	5.5	$6.5TiO_2$, $0.5As_2O_3$	Easily fabricated; strong; resists thermal shock (ovenware)

tallization of glasses when exposed to high temperatures. After melting and shaping of the glassy material, it is partly crystallized using a specific heat treatment at temperatures between 800 and 1200 °C. The residual glass phase occupies 5–50% of the volume, and the crystalline phase has a grain size of 0.05–5 μm. In contrast to conventional ceramics, e.g., prepared by powder processing routes, glass ceramics are fully dense and pore free, resulting in relatively high mechanical strength. Glass ceramics of the system Li_2O-Al_2O_3-SiO_2 show near-zero linear thermal expansion, so such glass ceramic ware will not experience thermal shock. These materials also have a relatively high thermal conductivity and show exceptionally high dimensional and shape stability, even when subjected to considerable temperature variations. Glass ceramics are used in astronomical telescopes, as mirror spacers in lasers, as ovenware and tableware, as electrical insulators, for architectural cladding, and in heat exchangers and regenerators.

8.9.3 Silicate Ceramics

Silicates are the most important constituents of the Earth's crust. Their structure, which is based on SiO_4 tetrahedrons (glasses are a derivative of silicates), depends on the actual composition. A three-dimensional network (quartz) is only stable when the ratio of O/Si is exactly 2. The addition of alkali or alkali-metal oxides to silica increases the overall O/Si ratio of the silicate and results in the progressive breakdown of the silicate structure into smaller units. The relationship between the O/Si ratio and the silicate structure is presented in Table 8.41. Silicates are particularly useful for electrotechnical, electronic, and high-temperature applications as well as in the processing of materials.

8.9.4 Refractory Ceramics

Refractory ceramics are another important group of ceramics that are utilized in large tonnages. These materials must withstand high stresses at high temperatures without melting or decomposing and must remain nonreactive and inert when exposed to severe environments. Refractory ceramics are composed of coarse oxide particles bonded by a finer refractory material. The finer material usually melts during firing and bonds the remaining material. Refractory ceramics generally contain 20–25% porosity as an important microstructural variable that must be well controlled during manufacturing. They are used for various applications ranging from low- to intermediate-temperature building bricks to high-temperature applications, where magnesite, silicon carbide, and stabilized zirconia (also used as thermal barrier coatings on nickel-based turbine components) are suitable. Typical applications include furnace linings for metal refining, glass manufacturing, metallurgical heat treatment, and power generation. Depending on their chemical composition and reaction, oxide refractories can be classified into acidic, basic, and neutral refractories. Fireclays are acidic refractories and are formable with the addition of water (castable and cements). Very high melting points are provided by chromite and chromite-magnesite ceramics, which are neutral refractories. Examples of commercial refractories are presented in Table 8.42.

8.9.5 Oxide Ceramics

Oxide ceramics are treated as a separate group of ceramics in [8.6] since they are the most common constituents of ceramics. The properties and applications of some important members are summarized in Table 8.43. For further reading, the extensive treatment in [8.69] is recommended.

Table 8.41 Relationship between silicate structure and O/Si ratio

Structure	O/Si ratio	O atoms per Si atom		Structure and examples
		Bridging	Nonbridging	
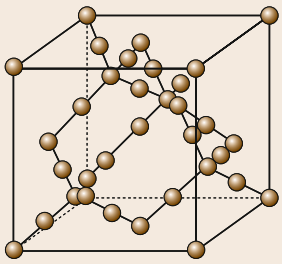	2.00	4.0	0	Three-dimensional network quartz, tridymite, and cristobalite are all polymorphs of silica
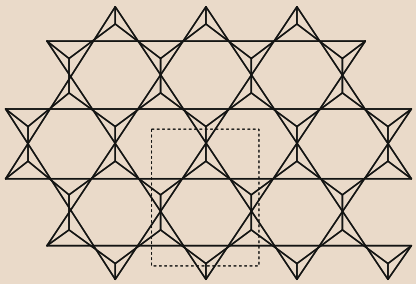 Repeat unit $(Si_4O_{10})^{4-}$	2.50	3.0	1.0	Infinite sheets $Na_2Si_2O_5$, clays (kaolinite)
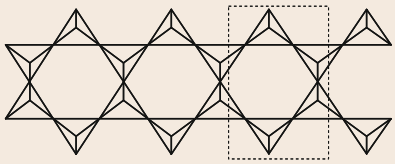 Repeat unit $(Si_4O_{11})^{6-}$	2.75	2.5	1.5	Double chains, e.g., asbestos
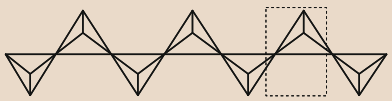 Repeat unit $(SiO_3)^{2-}$	3.00	2.0	2.0	Chains $(SiO_3)_n^{2n-}$, Na_2SiO_3, $MgSiO_3$
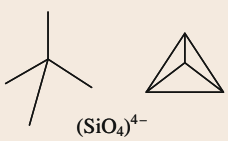 $(SiO_4)^{4-}$	4.00	0	4.0	Isolated $(SiO_4)^{4-}$, tetrahedra Mg_2SiO_4 olivine, Li_4SiO_4

The simplest way to determine the number of nonbridging O atoms per Si atom is to divide the charge on the repeat unit by the number of Si atoms in the repeat unit

Table 8.42 Properties of fired refractory brick materials (after [8.6])

Brick (major chemical components)	ρ (kg/m^3)	T_m (°C)	κ (W/(m K))
Building brick	1842	1600	0.72
Chrome-magnesite brick (52 wt% MgO, 23 wt% Cr_2O_3)	3100	3045	3.5
Fireclay brick (54 wt% SiO_2, 40 wt% Al_2O_3)	2146–2243	1740	0.3–1.0
High-alumina brick (90–99 wt% Al_2O_3)	2810–2970	1760–2030	3.12
Silica brick (95–99 wt% SiO_2)	1842	1765	1.5
Silicon carbide brick (80–90 wt% SiC)	2595	2305	20.5
Zirconia (stabilized) brick	3925	2650	2.0

Table 8.43 Properties of commercial oxides according to DIN EN 60672: density, Young's modulus, bending strenght, coefficient of thermal expansion (at room temperatur), thermal conductivity (at room temperatur) [8.6]

Oxide	ρ ($g\,cm^{-3}$)	E (GPa)	σ (MPa)	α ($10^{-6}\,K^{-1}$)	κ ($W\,m^{-1}\,K^{-1}$)	Application examples
MgO (C 820; 30% porosity)	2.5	90	50	11–13	6–10	For insulation in sheathed thermocouples; in resistive heating elements
Al_2O_3 (> 99.9)	3.97–3.99	366–410	550–600	6.5–8.9	38.9	In insulators; in electrotechnical equipment; as wear-resistant machine parts; in medical implants
TiO_2 (C 310)	3.5	–	70	6–8	3–4	In powder form as a pigment and filler material; in optical and catalytic applications
BeO (C 810)	2.8	300	150	7–8.5	150–220	In heat sinks for electronic components
ZrO_2 (partially stabilized)	5–6	200–210	500–1000	10–12.5	1.5–3	As thermal barrier coating of turbine blades

Table 8.44 Properties and applications of advanced ceramics

Property	Application examples
Thermal	
Insulation	High-temperature furnace linings for insulation (oxide fibers such as silica, alumina, and zirconia)
Refractoriness	High-temperature furnace linings for insulation and containment of molten metals and slags
Thermal conductivity	Heat sinks for electronic packages (AlN)
Electrical and dielectric	
Conductivity	Heat elements for furnaces (SiC, ZrO_2, $MoSi_2$)
Ferroelectricity	Capacitors (Ba-titanate-based materials)
Low-voltage insulators	Ceramic insulation (porcelain, steatite, forsterite)
Insulators in electronic applications	Substrate for electronic packaging and electrical insulators in general (Al_2O_3, AlN)
Insulators in hostile environments	Spark plugs (Al_2O_3)
Ion-conducting	Sensors, fuel cells, and solid electrolytes (ZrO_2, β-alumina, etc.)
Semiconducting	Thermistors and heating elements (oxides of Fe, Co, and Mn)
Nonlinear I–V characteristics	Current surge protectors (Bi-doped ZnO, SiC)
Gas-sensitive conductivity	Gas sensors (SnO_2, ZnO)
Magnetic and superconductive	
Hard magnets	Ferrite magnets [$(Ba,Sr)O \times 6Fe_2O_3$]
Soft magnets	Transformer cores [$(Zn,M)Fe_2O_3$, with M = Mn, Co, Mg]; magnetic tapes (rare-earth garnets)
Superconductivity	Wires and SQUID magnetometers ($YBa_2Cu_3O_7$)
Optical	
Transparency	Windows (soda-lime glasses), cables for optical communication (ultrapure silica)
Translucency and chemical inertness	Heat- and corrosion-resistant materials, usually for Na lamps (Al_2O_3, MgO)
Nonlinearity	Switching devices for optical computing ($LiNbO_3$)
Infrared transparency	Infrared laser windows (CaF_2, SrF_2, NaCl)
Nuclear applications	
Fission	Nuclear fuel (UO_3, UC), fuel cladding (C, SiC), and neutron moderators (C, BeO)
Fusion	Tritium breeder materials (zirconates and silicates of Li, Li_2O); fusion reactor lining (C, SiC, Si_3N_4, B_4C)
Chemical	
Catalysis	Filters (zeolites); carrier for catalytic active components, purification of exhaust gases
Anticorrosion properties	Heat exchangers (SiC), chemical equipment in corrosive environment
Biocompatibility	Artificial joint prostheses (Al_2O_3)
Mechanical	
Hardness	Cutting tools (SiC whisker-reinforced Al_2O_3, Si_3N_4)
High-temperature strength retention	Stators and turbine blades, ceramic engines (Si_3N_4)
Wear resistance	Bearings (Si_3N_4)

8.9.6 Nonoxide Ceramics

The *nonoxide ceramics* include essentially borides, carbides, nitrides, and silicides. A comprehensive overview of these materials is given in [8.6, 66, 67]. A few application examples will be given in the following. In recent years, some effort has been made in the construction of ceramic automobile engine parts such as engine blocks, valves, cylinder liners, rotors for turbochargers, etc. Ceramics under consideration for use in ceramic turbine engines include silicon nitride Si_3N_4, and silicon carbide SiC, which possess high thermal conductivity and thus excellent thermal shock resistance. Boron carbide (B_4C), silicon carbide (SiC), and titanium diboride (TiB_2) are also being considered for armor systems to protect military personnel and vehicles from ballistic projectiles. The low density of ceramics makes them very attractive in this field. High-purity ceramics with simple crystal structures such as boron nitride (BN), silicon carbide (SiC), and aluminum nitride (AlN) may be used as substrates for integrated circuits (ICs), since they have better thermal conductivity and thermal expansion coefficients which are closer to those of silicon IC chips compared with the presently used alumina. Further applications of nonoxide ceramics as well as advanced oxide ceramics are given in Table 8.44.

8.10 Composite Materials

Composite materials are formed when two materials which belong to different material classes are combined to obtain properties which are not provided by the original materials. Possible combinations are:

- Metal-ceramic
- Metal-polymer
- Ceramic-polymer
- Polymer-glass fiber
- Polymer-carbon fiber.

Either the second phase can be introduced into the matrix material in the form of homogeneously distributed particles or fibers, or the materials form a laminate structure (Fig. 8.46).

In *dispersion-strengthened* alloys, a small amount (usually $< 10\%$ volume fraction) of second-phase particles (metallic oxide or ceramic) is homogeneously distributed into the matrix material, commonly by mechanical alloying techniques [8.70]. These dispersoids are generally not coherent and, thus, effectively inhibit dislocation motion (Orowan circumvention at room temperature or by lowering dislocation line energy at higher temperatures [8.40]) when their distance is typically about 100 nm. The most important advantage over age-hardened alloys is the excellent elevated-temperature stability. Due to their insolubility in the metallic matrix, no significant coarsening of the dispersoids is observed even after long-term exposure at temperatures close to the melting point of the matrix. Prominent examples are the oxide-dispersion-strengthened (ODS) nickel- and iron-based superalloys [8.71]. When the particles are large so that they do not interact significantly with moving dislocations, the rule of mixtures can be applied for property determination; i.e., the properties can be directly determined by adding the percentage contribution of each phase. Hence, the term "particulate-reinforced material" is more appropriate, and the volume fraction of the reinforcement phase can exceed 50%. Applications are, e.g., cemented carbides in a Co matrix for wear and cutting tools (Sect. 8.6), abrasives such as Al_2O_3, SiC, and BN, which are added to grinding and cutting wheels, and electrical contacts such as tungsten or oxide particle-reinforced silver.

The fibers in *fiber-reinforced* composites can be continuously (as in Fig. 8.46), orthogonally, or randomly distributed. The properties of the fiber, i.e., strength, stiffness, etc., the aspect ratio l/d, where l is the fiber length and d is the diameter, and the volume fraction of the fibers play a decisive role in the final performance

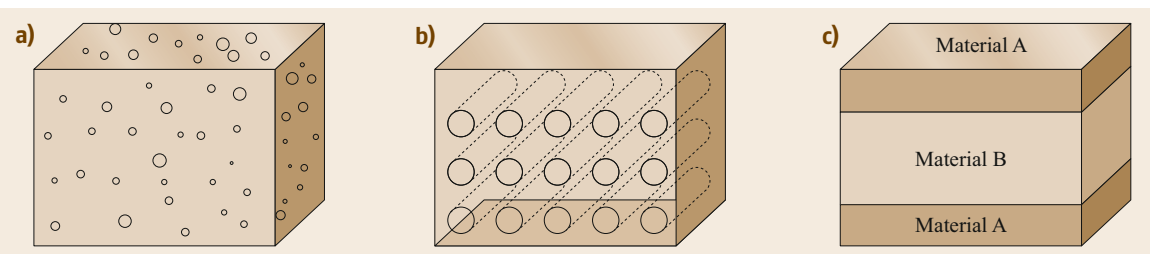

Fig. 8.46a–c Types of composites (schematic): **(a)** particulate, **(b)** fiber, and **(c)** laminated

Table 8.45 Typical longitudinal and transverse tensile strengths for three unidirectionally fiber-reinforced composites. The fiber content in each is ≈ 50 vol.% (after [8.72])

Material	Longitudinal tensile strength (MPa)	Transverse tensile strength (MPa)
Glass-polyester	700	20
Carbon (high modulus)-epoxy	1000	35
Kevlar-epoxy	1200	20

of the reinforced composite. In the longitudinal direction (along the fiber axis), the strength is much higher than in the transverse direction (Table 8.45).

The matrix of fiber-reinforced materials should be tough enough to support the fibers and prevent cracks in broken fibers from propagating, and one has to be aware of chemical reactions when the matrix is a metallic material. If the fibers are to be exposed to high temperatures, the coefficient of thermal expansion should not differ substantially from that of the matrix. Fiber composites may be used as fan blades in gas turbine engines and other aircraft and aerospace components, in lightweight automotive applications such as fiber-reinforced Al-matrix pistons, sporting goods (such as tennis rackets, golf club shafts, and fishing rods), and as corrosion-resistant components, to name some of the possible applications.

Laminar compositions could be very thin coatings such as thermal barrier coatings to protect Ni-based superalloys in high-temperature turbine applications (Sect. 8.5), thicker protective layers, or two-dimensional sheets or panels that have a preferred high-strength direction. The layers are stacked and joined using organic adhesives. Examples of laminar structures are adjacent wood sheets in plywood, capacitors composed of alternating layers of aluminum and mica, printed circuit boards, and insulation for motors, to mention a few.

References

8.1 M.F. Ashby, D.R.H. Jones: *Engineering Materials 2: An Introduction to Microstructures, Processing and Design* (Butterworth-Heinemann, Burlington 1998)
8.2 A.M. Howatson, P.G. Lund, J.D. Todd: *Engineering Tables and Data*, 2nd edn. (Chapman Hall, London 1991)
8.3 D.K. Roylance: Material Properties (Module), http://web.mit.edu/course/3/3.11/www/modules/props.pdf (2000), MIT-Textbook approach based on D.K. Roylance: *Mechanics of Materials* (Wiley, New York 1995)
8.4 R.B. Ross: *Metallic Materials Specification Handbook*, 4th edn. (Chapman Hall, London 1992)
8.5 A. Nayar: *The Metals Databook* (McGraw-Hill, New York 1997)
8.6 W. Martienssen, H. Warlimont (Eds.): *Springer Handbook of Condensed Matter and Materials Data* (Springer, Berlin, Heidelberg 2005)
8.7 R.W.K. Honeycombe, H.K.D.H. Bhadeshia: *Steels – Microstructure and Properties*, 2nd edn. (Edward Arnold, London, New York, Sydney, Auckland 1995)
8.8 G. Krauss: *Steel – Heat Treatment and Processing Principles* (ASM Int, Materials Park 1989)
8.9 W.C. Leslie: *The Physical Metallurgy of Steels* (McGraw-Hill, New York 1981)
8.10 A.K. Sinha: *Ferrous Physical Metallurgy* (Butterworths, London 1989)
8.11 D.T. Llewellyn, R.C. Hudd: *Steels, Metallurgy and Applications* (Butterworth-Heinemann, Oxford 1998)
8.12 M. Wegst, C. Wegst: *Stahlschlüssel – Key to Steel*, 25th edn. (Stahlschlüssel, Marbach a.N. 2019)
8.13 D.R. Askeland: *The Science and Engineering of Materials, S.I.* 3rd edn. (Wiley-VCH, Weinheim 1996)
8.14 J.R. Davis (Ed.): *Carbon and Alloy Steels*, ASM Speciality Handbook (ASM Int, Metals Park 1996)
8.15 H.K.D.H. Bhadeshia: *Bainite in Steels, Transformation, Microstructure and Properties* (IOM, London 2001)
8.16 E.C. Bain, H.W. Paxton: *Alloying Elements in Steel* (ASM, Metals Park 1966)
8.17 P.M. Unterweiser: *Worldwide Guide to Equivalent Irons and Steels* (ASM, Materials Park 1996)
8.18 J.E. Bringes: *Handbook of Comparative World Steel Standards* (ASTM, West Conshohocken 2001)
8.19 J.R. Davis (Ed.): *Stainless Steels*, ASM Speciality Handbook (ASM, Metals Park 1994)
8.20 J.R. Davis (Ed.): *Tool Materials*, ASM Speciality Handbook (ASM, Metals Park 1995)
8.21 H.E. McGannon: *The Making, Shaping and Treatment of Steel* (United States Steel Corporation, Pittsburgh 1971)
8.22 W.G. Moffatt, G.W. Pearsall, J. Wulff: *The Structure and Properties of Materials*, Vol. 1 (Wiley, New York 1964) p. 195
8.23 J.R. Davis (Ed.): *Cast Irons*, ASM Speciality Handbook (ASM, Metals Park 1996)
8.24 G.E. Totten, D.S. MacKenzie: *Handbook of Aluminum. Vol. 1: Physical Metallurgy and Processes* (Dekker, New York 2003)
8.25 C. Kammer: *Aluminium Taschenbuch 1: Grundlagen und Werkstoffe*, 16th edn. (Aluminium-Verlag, Düsseldorf 2002), in German
8.26 J.R. Davis (Ed.): *Aluminum and Aluminum Alloys*, ASM Specialty Handbook (ASM, Metals Park 1993)
8.27 A. Dehler, S. Knirsch, V. Srivastava, H. Saage, M. Heilmaier: Assessment of creep behaviour of the die-

cast cylinder-head alloy AlSi6Cu4-T6, Int. J. Mater. Res. Adv. Tech. **97**, 1679–1686 (2006)
8.28 H. Baker, B. David, K.W. Craig: *Metals Handbook*, Vol. 2 (ASM, Metal Parks 1979)
8.29 M.M. Avdesian, H. Baker: *Magnesium and Magnesium Alloys*, ASM Specialty Handbook (ASM, Metals Park 1999)
8.30 I.J. Polmear: *Light Alloys, Metallurgy of the Light Metals* (Wiley, New York 1995)
8.31 G. Neite: Magnesium-based alloys. In: *Structure and Properties of Nonferrous Alloys*, Materials Science and Technology, Vol. 8, ed. by K.H. Matucha (VCH, Weinheim 1996) pp. 113–212
8.32 R. Boyer, G. Welsch, E.W. Collings: *Materials Properties Handbook: Titanium Alloys* (ASM, Materials Park 1994)
8.33 K.H. Matchuta: *Structure and Properties of Nonferrous Alloys*, Materials Science and Technology, Vol. 8 (VCH, Weinheim 1996)
8.34 W.F. Hosford: *Physical Metallurgy* (Taylor Francis, New York 2005)
8.35 M. Dietrich (Ed.): *Titan-Aluminid-Legierungen – Eine Werkstoffgruppe mit Zukunft* (Forschungszentrum Jülich (PTJ-NMT), Jülich 2003), in German
8.36 S.C. Huang, J.C. Chessnut: Gamma-TiAl and its alloys. In: *Intermetallic Compounds. Vol. 2: Principles and Practice*, ed. by J.H. Westbrook, R.L. Fleischer (Wiley, Chichester 1994) pp. 73–90
8.37 K. Otsuka, C.M. Wayman: *Shape Memory Materials* (Cambridge Univ. Press, Cambridge 1998)
8.38 J. Buschow: *Concise Encyclopedia of Magnetic and Superconducting Materials*, 2nd edn. (Elsevier, Amsterdam 2006)
8.39 J.R. Davies (Ed.): *Heat-Resistant Materials*, ASM Specialty Handbook (ASM Int., Metals Park 1997)
8.40 B. Reppich: Particle strengthening. In: *Materials Science and Technology, Vol. 6* (Wiley-VCH, Weinheim 2005) pp. 312–357
8.41 G. Joseph, K.J.A. Kundig: *Copper, Its Trade, Manufacture, Use, and Environment Status* (ASM Int, Materials Park 1998)
8.42 J.R. Davis (Ed.): *Copper and Copper Alloys*, ASM Specialty Handbook (ASM, Metals Park 2001)
8.43 H. Lipowsky, E. Arpaci: *Copper in the Automotive Industry* (Wiley-VCH, Weinheim 2006)
8.44 J. Brandrup, E.H. Immergut, E.A. Grulke: *Polymer Handbook* (Wiley, New York 2004)
8.45 H.-G. Elias: *An Introduction to Polymer Science* (Wiley-VCH, Weinheim 1999)
8.46 I. Mita, R.F.T. Stepto, U.W. Suter: Basic classification and definitions of polymerization reactions, Pure Appl. Chem. **66**, 2483–2486 (1994)
8.47 K. Matyjaszewski, T.P. Davis: *Handbook of Radical Polymerization* (Wiley, New York 2002)
8.48 G.W. Ehrenstein, R.P. Theriault: *Polymeric Materials: Structure, Properties, Applications* (Hanser Gardner, Munich 2000)
8.49 G.H. Michler, F.J. Baltá-Calleja: *Mechanical Properties of Polymers Based on Nano-structure and Morphology* (CRC, Boca Raton 2005)
8.50 A.E. Woodward: *Atlas of Polymer Morphology* (Hanser Gardner, Munich 1988)
8.51 E.A. Campo: *The Complete Part Design Handbook for Injection Moulding of Thermoplastics* (Hanser, Munich 2006)
8.52 D.V. Rosato, A.V. Rosato, D.P. DiMattia: *Blow Molding Handbook*, 2nd edn. (Hanser, Munich 2003)
8.53 L.C.E. Struik: *Internal Stresses, Dimensional Instabilities and Molecular Orientations in Plastics* (Wiley, New York 1990)
8.54 ISO: *ISO 1135 parts 1–7:1997: Plastics – Differential Scanning Calorimetry (DSC) – Part 1: General Principles* (ISO, Geneva 1997)
8.55 P.C. Powell: *Engineering with Polymers* (CRC, Boca Raton 1998)
8.56 T.A. Osswald, G. Menges: *Materials Science of Polymers for Engineers* (Hanser, Munich 1995)
8.57 H. Czidios, T. Saito, L. Smith (Eds.): *Springer Handbook of Materials Measurement Methods* (Springer, Berlin, Heidelberg 2006) pp. 283–397
8.58 I.M. Ward, D.W. Hadley: *An Introduction to the Mechanical Properties of Solid Polymers* (Wiley, Chichester 1993)
8.59 E.A. Grulke: Solubility parameter values. In: *Polymer Handbook*, 3rd edn., ed. by J. Brandrup, E.H. Immergut (Wiley, New York 1989) pp. 519–559
8.60 I.M. Ward: *Structure and Properties of Oriented Polymers* (Chapman Hall, London 1997)
8.61 ISO: *ISO 6721-1:2001 Plastics – Determination of Dynamic Mechanical Properties – Part 1: General Principles* (ISO, Geneva 2001)
8.62 ISO: *ISO 6721-2: 1994 Plastics – Determination of Dynamic Mechanical Properties – Part 2: Torsion-Pendulum Method* (ISO, Geneva 1994)
8.63 G.W. Ehrenstein: *Faserverbund-Kunststoffe, Werkstoffe – Verarbeitung – Eigenschaften* (Hanser, Munich 2006)
8.64 L.H. Sperling: *Polymeric Multicomponent Materials* (Wiley, New York 1997)
8.65 C.M. Hansen: *Solubility Parameters: A User's Handbook* (CRC, Boca Raton 1999)
8.66 R. Freer: *The Physics and Chemistry of Carbides, Nitrides and Borides* (Kluwer, Boston 1989)
8.67 M.V. Swain: *Structure and Properties of Ceramics*, Materials Science and Technology, Vol. 11 (VCH, Weinheim 1994)
8.68 W.D. Callister Jr.: *Fundamentals of Materials Science and Engineering* (Wiley, New York 2001)
8.69 G.V. Samson: *The Oxides Handbook* (Plenum, New York 1974)
8.70 J.S. Benjamin: Dispersion strengthened superalloys by mechanical alloying, Metall. Trans. **1**, 2943–2951 (1970)
8.71 Y. Estrin, S. Arndt, M. Heilmaier, Y. Bréchet: Deformation beahviour of particle strengthened alloys: A Voronoi mesh approach, Acta Mater. **47**, 595–606 (1999)
8.72 D. Hull, T.W. Clyne: *An Introduction to Composite Materials*, 2nd edn. (Cambridge Univ. Press, Cambridge 1996)

Ulrich Wendt

Freelance Materials Science Consultant
c/o Otto-von-Guericke University,
Department of Materials and Joining Technology
Magdeburg, Germany
wendt@ovgu.de

Professor Ulrich Wendt studied chemistry and earned a diploma degree with a thesis on organic synthesis, a doctoral degree RNDr on heterogeneous catalysis, and a habil. degree on polymer melt crystallization. For more than 30 years he headed the Microscopy and Stereology Laboratory at the Department of Materials and Joining Technology, University Magdeburg. He lectured on microscopic and spectroscopic characterization, image analysis, topometry, and failure analysis of materials. He is now a freelance Materials Science consultant.

9. Tribology

Ludger Deters, Dirk Bartel

The main subjects of this chapter are the tribological system, friction, wear and lubrication. Regarding the tribological system essential information on structure, real contact geometry, tribological loads, operating and loss variables are provided. Concerning friction, the different friction types, states and mechanisms are discussed. In the sections on wear a lot of details on types and mechanisms of wear, wear profiles and the determination of wear and the average lifetime are introduced. The sections on lubrication contain relevant expositions on the lubrication states, like hydrodynamic, elastohydrodynamic, hydrostatic, mixed and boundary lubrication and lubrication with solid lubricants. Lubricants like mineral, synthetic and biodegradable oils and additives, lubricating greases and solid lubricants are also considered, as are the properties of lubricants, like the dependence of oil viscosity on temperature, pressure and shear rate, and the consistency of lubricating greases.

9.1 **Importance of Tribology** 293
9.2 **Tribological System (Tribosystem)** 294
9.2.1 Structure 294
9.2.2 Contact Geometry 295
9.2.3 Tribological Loads and Interactions 297
9.2.4 Operating Variables (Input Variables) 298
9.2.5 Output Variables (Useful Variables) 299
9.2.6 Loss Variables 299
9.3 **Friction** 299
9.3.1 Types of Friction 299
9.3.2 Friction States 300
9.3.3 Friction Mechanisms 300
9.3.4 Coefficient of Friction 301
9.4 **Wear** 302
9.4.1 Types and Mechanisms of Wear 302
9.4.2 Wear Profiles and Measurable Variables 303
9.4.3 Determination of Wear and Lifetime 304
9.5 **Fundamentals of Lubrication** 306
9.5.1 Fluid Film Lubrication 306
9.5.2 Hydrodynamic Lubrication 306
9.5.3 Boundary Lubrication 309
9.5.4 Mixed or Partial Lubrication 311
9.5.5 Lubrication with Solid Lubricants and Surface Coatings 311
9.6 **Lubricants** 311
9.6.1 Lubricating Oils 312
9.6.2 Lubricants (Lubricating Greases) 316
9.6.3 Solid Lubricants 316
9.6.4 Properties of Lubricants 318
9.6.5 Dependence of Viscosity on Temperature and Pressure 319
9.6.6 Dependence of Viscosity on Shear Rate 321
References 322

9.1 Importance of Tribology

Tribology is the science and technology of interacting surfaces in relative motion. Tribology includes boundary-layer interactions both between solids and between solids and liquids and/or gases. Tribology encompasses the entire field of friction and wear, including lubrication [9.1].

Tribology aims to optimize friction and wear for a particular application case. Apart from fulfilling the required function, this means assuring high efficiency and sufficient reliability at the lowest possible manufacturing, assembly, and maintenance costs.

Friction and wear are frequently undesirable. While friction impairs the efficiency of machine elements, machines, and plants and thus increases the energy demand, wear diminishes the value of components and assemblies and can lead to the failure of machines and plants. On the other hand, many technical applications strive for high friction, e.g., brakes, clutches, wheels/

K.-H. Grote, H. Hefazi (Eds.), *Springer Handbook of Mechanical Engineering*, Springer Handbooks,
https://doi.org/10.1007/978-3-030-47035-7_9

rails, car tires/road, friction gears, belt drives, bolted joints, and press fits. To a limited extent, wear can also be advantageous in special cases, e.g., in breaking-in processes.

Friction and wear are not properties specific to the geometry or substance of only one of the elements involved in friction and wear, e.g., external dimensions, surface roughnesses, thermal conductivity, hardness, yield point, density or structure, but rather are properties of a system. The system's friction and/or wear behavior can already change seriously when one influencing variable of the tribological system is marginally modified.

Lubrication is employed to lessen friction and minimize wear or to prevent them entirely. In the case of circulatory lubrication, the lubricant can additionally remove wear particles and heat from the friction contact. Other important tasks of lubrication are preventing corrosion (rusting) and, in the case of grease lubrication, sealing the friction points.

9.2 Tribological System (Tribosystem)

Friction and wear occur within a tribological system (TS). To delimit a TS, a system envelope is appropriately placed around the components and materials directly involved in friction and wear, thus virtually isolating these from the remaining components. The materials and components involved in friction and wear are the elements of the TS and are characterized by their material and shape properties. A tribological system is described by the function to be fulfilled, the input variables (operating variables), the output variables, the loss variables, and the structure (Fig. 9.1).

Apart from desired *input variables*, undesired input variables, so-called *disturbance variables*, also arise. Together with the structure, they influence the *output* and *loss variables* of the TS.

The function of a TS is to use the system structure to convert input variables (e.g., input torque, input speed, input type of motion, and sequence of motions) into technically utilizable output variables (e.g., output torque, output speed, output motion) (Fig. 9.1).

9.2.1 Structure

The elements involved, their properties, and the interactions between the elements describe the structure of a TS. The basic structure of every TS consists of four elements: the base body, counterbody, interfacial medium, and ambient medium (Fig. 9.1). Table 9.1 displays some TS with different elements. While the base body and counterbody are found in every TS, the interfacial medium and, in a vacuum, even the ambient medium can be absent.

In transport and machining processes, the base body is constantly stressed by new material zones of the counterbody. Such systems are called an *open* TS. By contrast, the stressed zones of the base body and counter-

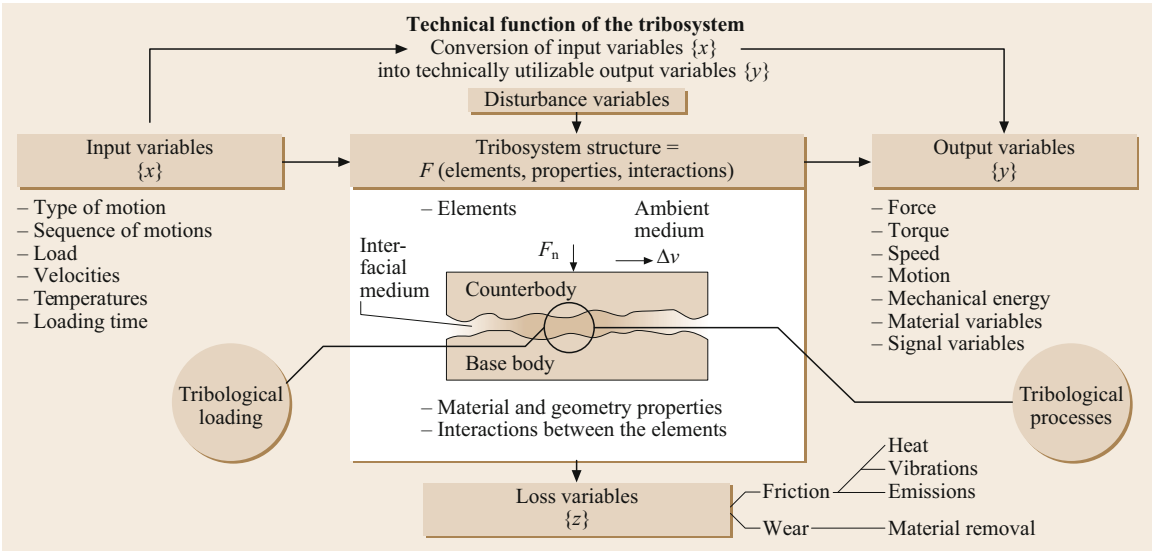

Fig. 9.1 Expanded representation of a tribological system (after [9.2])

Table 9.1 Examples of elements of tribological systems

TS	Base body	Counterbody	Interfacial medium	Ambient medium	System type
Press and shrink joints	Shaft	Hub	–	Air	Closed
Sliding bearing	Journal	Bearing bush	Oil	Air	Closed
Mechanical face seal	Seal head	Seat	Liquid or gas	Air	Closed
Gear train	Pinion	Wheel	Gear oil	Air	Closed
Wheel/rail	Wheel	Rail	Moisture, dust, grease	Air	Open
Excavator bucket/ excavated material	Bucket	Excavated material	–	Air	Open
Turning tool	Cutting edge	Workpiece	Cutting lubricant	Air	Open

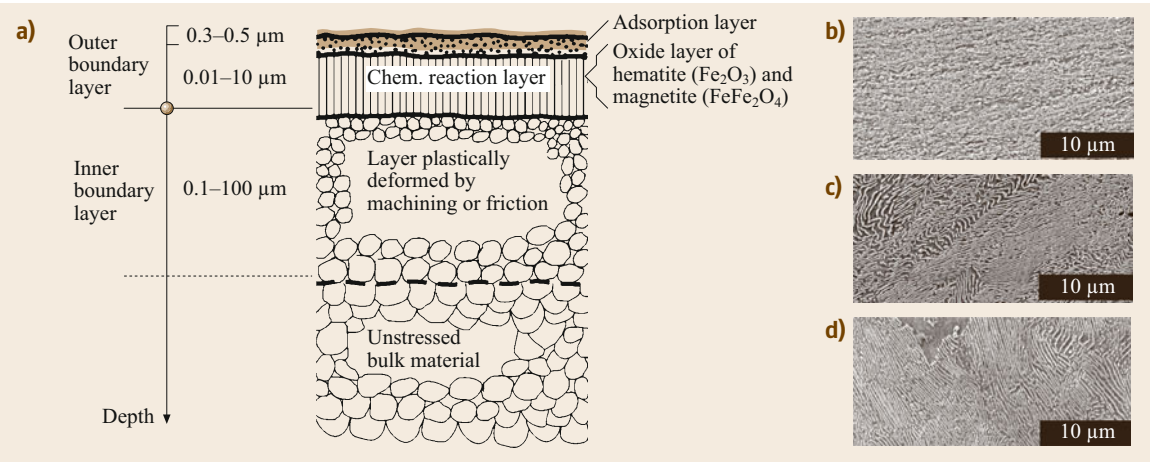

Fig. 9.2a–d Boundary-layer composition in metallic materials using a tribologically loaded steel rail: (a) cross-section diagram; (b) depth approximately 50 µm; (c) transition zone; (d) bulk material (after [9.3])

body in a *closed* TS are repeatedly in contact. Examples of open and closed systems can also be found in Table 9.1. The function in open systems mainly depends on the wear of the base body. The counterbody generates the load; as a rule, the wear on it is not of interest. By comparison, when systems are closed, the ability to operate depends on the wear of both friction bodies. The elements of the TS are characterized by a large number of *properties*, largely listed in Table 9.2.

A difference is made principally between geometric and material properties in the base body and counterbody, which are supplemented by physical variables. The interfacial medium and ambient medium can appear in different aggregate states, on which other important tribological properties depend. A difference in the material properties of the base body and counterbody is made between bulk material and the near-surface zone. The properties of the near-surface zone, e.g., structural composition, hardness, and chemical composition, are particularly important for the tribological processes. In addition, the surface roughness's play an important role.

Figure 9.2 shows a diagram of the possible composition of *boundary layers* in metallic materials. The undisturbed *basic structure* generally has attached to it a hardened composition of machined or deformed layers endowed with a structure that is fine-grained compared with the basic structure. A reaction layer and an adsorption layer lie on top of this. Taken together they are also called the *outer boundary layer*. Wear is generally acceptable as long as it occurs in the outer boundary layer.

As a rule, not only the near-surface zone's material structure but also its chemical composition differs from those of the bulk material. This is apparent in Fig. 9.3. The material beneath the surface already changes during manufacturing in terms of the concentration of elements present compared with the bulk material. Other considerable changes undergone by the near-surface zone's element concentrations are caused by breaking-in or occur after a short running time.

9.2.2 Contact Geometry

It is not only the input variables, the material properties and the physical variables of the base body and counterbody, the interfacial medium, and the ambient medium but also the contact areas that greatly influence friction

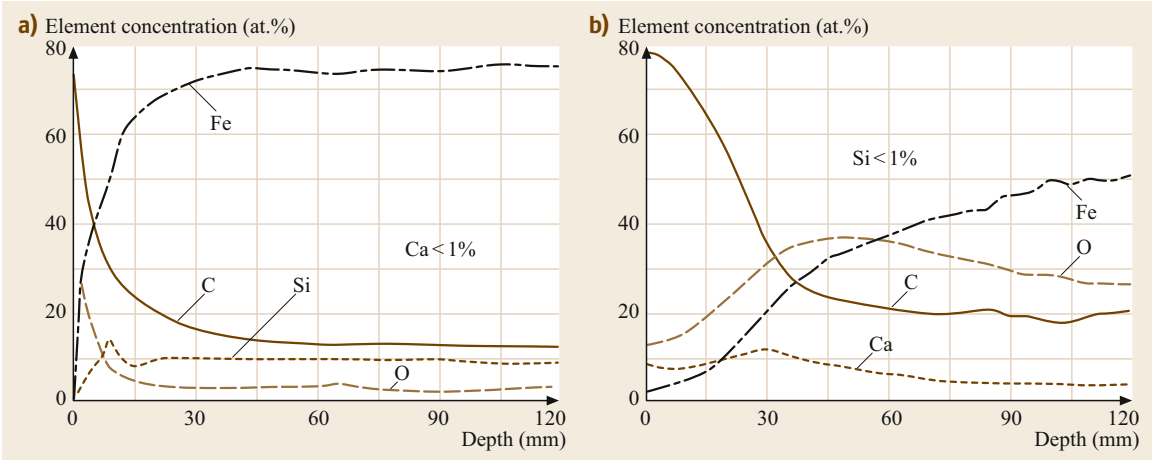

Fig. 9.3a,b Auger electron spectroscopy depth profiles as element concentration in the cylinder wall at top dead center in a diesel engine **(a)** before running in and **(b)** after 15 h running time (oil: SAE 15W-40) [9.4]

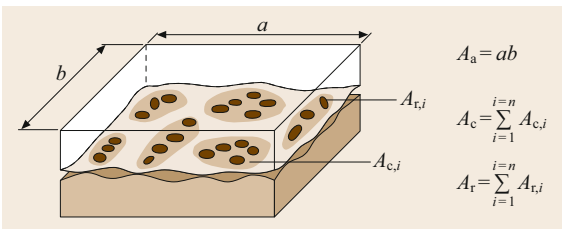

Fig. 9.4 Various types of contact areas

and wear of the base body and counterbody and the tribological system's lubrication state.

In turn, the contact areas appearing during operation depend on the form of contact (Table 9.3), the input variables, the geometric properties of the base body and counterbody (Table 9.1), and the other system properties.

In the contact areas, a difference is made between the *nominal or apparent contact area* and the *real contact area* (Fig. 9.4).

The nominal or apparent contact area A_a corresponds to the macroscopic contact area of the bodies in contact, e.g., of the contact area ab of a cuboid on one plane or the Hertzian contact area between a cylinder and a plane. Not only the apparent contact area but also the real contact areas $A_{r,i}$ play a key role when the asperities of the friction bodies meet in the apparent contact area.

The real contact areas result from the asperity contacts, which occur when the friction bodies are not completely separated by a lubricating film or in the cases of application in which no lubricant is used (dry friction). Not only the roughness but also the waviness on the friction body surfaces have to be taken into account when analyzing the real contact areas. The waviness causes so-called *contour areas* $A_{c,i}$ to form as well as the real contact areas on the asperity contacts within the contour areas.

As a rule, the sum of the real contact areas A_r, which is dependent on the roughness distributions and the separation of the two friction body surfaces, is substantially smaller than the apparent contact area ($A_r \approx 10^{-1}$–$10^{-4} A_a$). Hence the real contact pressures in the asperity contacts are substantially higher than the nominal pressure. While the nominal pressure displays elastic macromaterial behavior, plastic deformation may already have begun for a majority of the microcontacts (real contact areas). Results of calculations have yielded that the sum of the real contact areas is nearly proportional to the normal force F_n [9.5]. In addition, as the normal force increases, the number of real individual contacts increases, while the real individual contact area $A_{r,i}$ remains roughly constant.

Apart from the real contact area, the *overlap ratio* ε also plays an important role as well. It represents the ratio of the apparent contact area A_a to a friction body's friction area A_f. Thus, for example, the nonrotating bush of a sliding bearing with bearing clearance has an overlap ratio of $\varepsilon = 1$, since the apparent contact area A_a for the bearing bush corresponds to the friction area A_f. For the rotating shaft however, the friction area $A_f = \pi db$, with shaft diameter d and bearing bush width b, is larger than the apparent contact area $A_a = db\gamma/2$, with contact angle γ, so that the overlap ratio is $\varepsilon < 1$. For a constantly loaded friction body, an overlap ratio $\varepsilon = 1$ means permanent contact, no cyclical mechanical loads (macroscopic), permanent frictional heat absorption, and limited microchemical reaction with the ambient medium. For the friction body concerned, an overlap ratio of $\varepsilon < 1$ leads to an intermittent contact, to cyclical mechanical loading, to intermittent frictional heat absorption, and to

Table 9.2 Tribologically relevant properties of elements of the tribological system (Fig. 9.1)

1. Base body and counterpart
1.1 *Geometric properties*
● External dimensions
● Shape and position tolerances
● Waviness
● Surface roughnesses
1.2 *Material properties*
1.2.1 *Bulk material*
● Strength
● Hardness (macro, micro, and Martens hardness)
● Structure, texture, microstructure phases (distribution, size, number type)
● Young's modulus, Poisson's ratio
● Residual stress
● Chemical composition
1.2.2 *Near-surface zone*
● Hardness (macro, micro, and Martens hardness)
● Surface energy
● Metallurgical structures, texture, microstructure phases (distribution, size, number type)
● Chemical composition
● Young's modulus, Poisson's ratio
● Residual stress
● Boundary-layer thickness and structure
1.3 *Physical variables*
● Density
● Heat conductivity
● Coefficient of thermal expansion
● Melting point
● Specific thermal capacity
● Hygroscopic properties
2. Interfacial medium (lubricant)
● Aggregate state (solid, liquid, gaseous)
● For *solid* interfacial medium
– Hardness
– Grain size distribution
– Grain shape
– Grain quantity, grain number
– Number of components, mixing ratio
– Chemical composition
● For *liquid* interfacial medium
– Viscosity depending on temperature, pressure and shear rate
– Consistency
– Wettability
– Lubricant quantity and pressure
– Chemical composition
– Mixing ratio of components
3. Ambient medium
● Aggregate state (solid, liquid, gaseous)
● Heat conductivity
● Chemical composition
● Moisture
● Ambient pressure

tribochemical reactions with the ambient medium in the range A_f–A_a. When both friction bodies (the base body and counterbody) have an overlap ratio of $\varepsilon \approx 1$, the wear particles can remain in the contact area and hence adversely influence the further wear profile.

9.2.3 Tribological Loads and Interactions

Tribological loads in a TS are generated by the input and disturbance variables' action on the system structure. They chiefly include contact, kinematic, and thermal processes [9.2]. According to [9.1], the tribological load represents "the loading of the surface of a solid caused by contact and relative motion of a solid, liquid or gaseous counterbody." It is introduced via the real contact areas. Plastic deformation and wear can cause the real contact areas to change during TS operation.

When mechanical energy is converted by friction, energy dissipates, which makes itself noticeable by changing the thermal situation. Since the thermal behavior also continuously adapts to the new conditions as a result of wear, changes to the contact geometry, and resulting changes in the friction, dynamic rather than static influencing variables determine the tribological loading in a real contact.

The contact geometry, the processes occurring in the contact, and the thermal behavior of a TS are influenced by, among other things, the load, the motion conditions, the element properties, and the friction state.

While the apparent contact area alone is decisive in fluid lubrication, according to [9.6], in mixed lubrication, i.e., when the dimensionless film thickness parameter

$$\Lambda = \frac{h_{\min}}{\left(R_{q1}^2 + R_{q2}^2\right)^{1/2}}\,, \tag{9.1}$$

with the minimum lubrication film thickness $h_{\min}$ and the root-mean-square (rms) surface roughnesses R_{q1} and R_{q2} of the base body and counterbody, is in the range $\Lambda < 3$, in boundary lubrication with $\Lambda < 1$ and for dry friction, both the apparent contact area and the real contact areas must be considered and allowed for (Fig. 9.4).

When there are contacts between the friction bodies, *interactions* occur in the real contact areas and in the near-surface zones. *Atomic/molecular* interactions occur on the one hand and *mechanical* interactions on the other. Whereas the former cause adhesion on solid–solid boundary layers or are extremely important technically in the form of physisorption and chemisorption on solid–fluid boundary layers, the latter lead to elastic and plastic contact deformations and to the development of the real contact areas.

Table 9.3 Contact geometry (form of contact) of tribological systems

Form of contact	Base body	Counterbody	Sketch	Example application
Conformal				
Areal	Plane	Plane	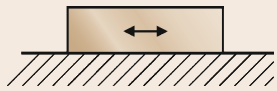	Thrust bearings
	Hollow cylinder	Solid cylinder	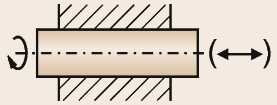	Sliding bearings, round fittings, cylinder races
Nonconformal				
Line contact	Plane	Cylinder	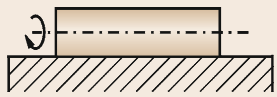	Thrust roller bearings
	Cylinder	Cylinder	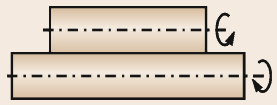	Roller, roller bearings
	Pinion tooth	Gear tooth		Gears
Point contact	Plane	Ball	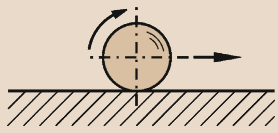	Thrust ball bearings
	Inner ring (circumferential direction)	Ball	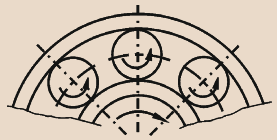	Ball bearings

The type of interaction that primarily occurs depends greatly on the friction state. Thus, when a lubricant is present the atomic/molecular interaction can be disregarded more often than the mechanical.

Friction and wear in a given TS ultimately depend on the interactions between the elements. The friction state, the effective mechanisms of friction and wear, and the contact state can be used to describe the interactions.

The tribological loads occurring in the real contact areas produce *tribological processes*. These subsume the dynamic physical and chemical mechanisms of friction and wear and boundary-layer processes that can be attributed to friction and wear.

9.2.4 Operating Variables (Input Variables)

According to [9.1], the operating variables are: the type of motion, the time sequence of motions of the elements contained in the system structure, and a number of technical-physical load parameters, which act on the system structure when the function is executed. The operating variables originate from:

- Type of motion and time sequence of motions
- Load
- Velocities
- Temperatures
- Loading time.

The type of motion can frequently be attributed to one of the basic types of motion *sliding*, *rolling*, *spin*, *impact* or *flowing* or can be composed from these. The time sequence of motions can occur regularly, irregularly, back and forth, or intermittently. The sequence of motions frequently also consists of different components. As a rule, the normal force F_n is decisive for the load.

Both the relative velocity between the friction bodies and the entraining velocity of the lubricant in the

contact and the slippage as a ratio of the relative velocity to the average circumferential velocity play a role for the velocities. The friction body temperatures and the effective contact temperature produced in operation are critically important for the temperature variables. It is normally not possible to measure the contact temperatures. Apart from these desired input variables, which as a rule are specified by a technical function, *disturbance variables* such as vibrations or dust particles must be considered under certain circumstances.

9.2.5 Output Variables (Useful Variables)

The TS provides output variables for subsequent utilization. These useful variables reflect the performance of a function of the TS. The useful variables can differ over extremely wide ranges depending on the main task of the TS. In an energy-determined system, for example, the following output variables may be desired:

- Force
- Torque
- Velocity
- Motion
- Mechanical energy.

Particular material or signal variables could be interesting as useful variables in a material- or signal-determined TS.

9.2.6 Loss Variables

The loss variables of a TS are essentially represented by friction and wear. While friction leads to losses of force, torque or energy, wear means a progressive loss of material.

The energy losses produced when there is friction are converted into heat for the most part. This process is irreversible and is called energy dissipation. Along with the conversion of friction into heat and the generation of wear particles, the tribological process generates other tribologically induced loss variables such as vibrations that frequently become apparent through sound waves, photon emission (triboluminescence), electron, ion emission, etc.

9.3 Friction

Friction can be ascribed to the interactions between bodies' material zones that are in contact or moving relative to one another; it counteracts relative motion. External and internal friction are differentiated. When friction is external, the different friction bodies' material zones are in contact; when friction is internal, material zones that are in contact belong to one friction body or the interfacial medium.

A number of parameters can characterize friction. Thus, depending on the application, friction is characterized by the friction force F_f, the friction torque M_f or the coefficient of friction f. Instead of f the symbol μ is also frequently used for the coefficient of friction. The coefficient of friction f is formed from the ratio of the friction force F_f to the normal force F_n

$$f = \frac{F_f}{F_n} . \tag{9.2}$$

The work of friction or friction energy W_f is used to calculate the frictional heat or the amount of deformation of the friction force in solid friction. It is calculated as

$$W_f = F_f s_f , \tag{9.3}$$

with the friction distance s_f. The friction power P_f is of interest for an energy balance or efficiency calculation. The friction power is a power loss and, disregarding signs, the following applies

$$P_f = F_f \Delta v , \tag{9.4}$$

with the relative velocity Δv. (The power loss is frequently defined negatively.)

9.3.1 Types of Friction

Friction can be classified according to various features. Types of friction are distinguished depending on the type of relative motion between the friction bodies. Figure 9.5 presents the most important types of friction with sample applications. There are three main types of friction:

- Sliding friction
- Rolling friction
- Spin friction.

Apart from these three kinematically defined types of friction, there can be overlaps (mixed forms), namely:

- Sliding-rolling friction (rolling friction)
- Sliding-spin friction
- Rolling-spin friction.

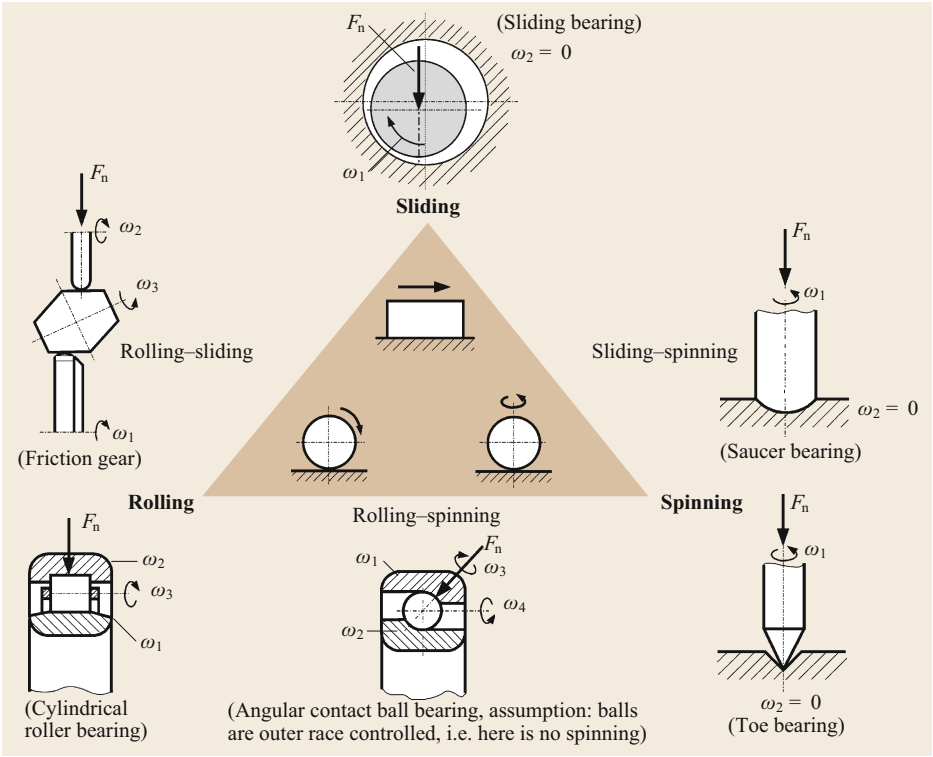

Fig. 9.5 Types of dynamic friction

Along with the types of friction shown in Fig. 9.5, another type of friction is impact friction, which applies when a body strikes another body perpendicular or oblique to the contact surface and possibly withdraws again. The angular contact ball bearing is a machine element in which sliding and rolling and spin friction appear.

9.3.2 Friction States

Various friction states can be defined if friction is classified as a function of the aggregate state of the material zones involved. To illustrate this, Fig. 9.6 presents different states of friction based on the Stribeck curve using a radial sliding bearing as an example. Generally, the following friction states are differentiated:

- Solid friction
- Fluid friction
- Gas friction
- Mixed friction.

In *solid friction* the friction acts between material zones that exhibit solid properties and are in direct contact. If the friction occurs between solid boundary layers with modified properties compared with the bulk material, e.g., between reaction layers, then this is *boundary-layer friction*. If the boundary layers on the contact surfaces each consist of a molecular film coming from a lubricant, then this is called *boundary friction*. In boundary friction, the lubricant's hydrodynamic effect can be disregarded because the velocity is very low and/or only a very small quantity of lubricant, insufficient to fill the lubrication gap, is present.

Fluid friction is internal friction in a lubricating film with fluid properties and is present in a hydrodynamically, elastohydrodynamically or hydrostatically produced lubricating film.

Gas friction is internal friction in a lubricating film with gas properties and is present in an aerodynamically or aerostatically produced lubricating film.

Mixed friction is any mixed form of the friction states. The term is primarily used in the simultaneous presence of boundary and liquid friction.

9.3.3 Friction Mechanisms

Solid friction can be ascribed to interactions between the elements. As already addressed before, there are essentially two different types of interaction, i.e., atomic/molecular and mechanical. *Kragelski* [9.7] speaks of friction's "dual nature". Hence, the friction mechanisms can be divided into two groups. Generally a difference can initially be made between the following four fric-

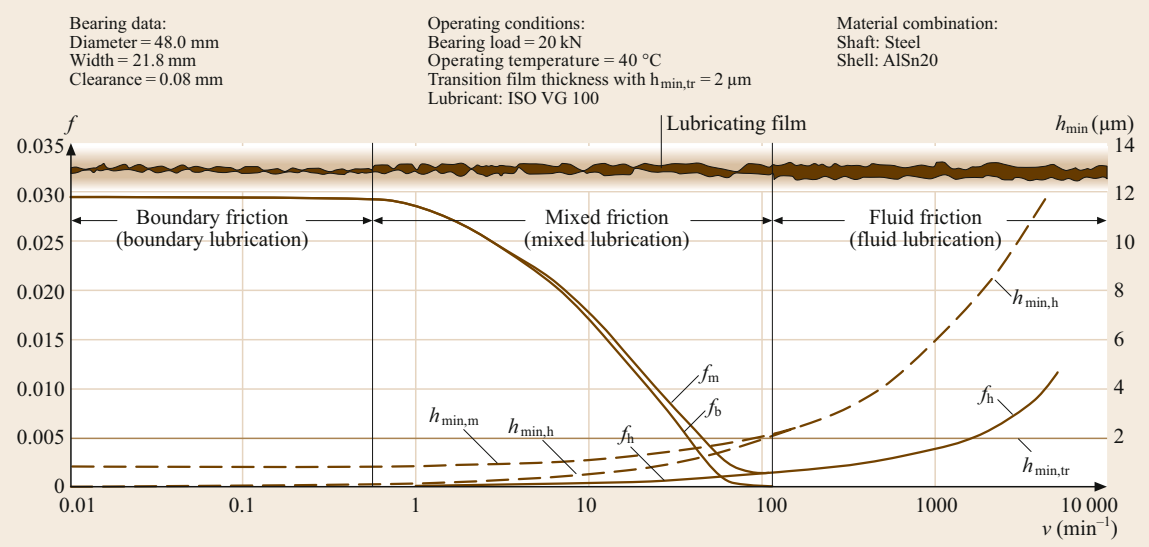

Fig. 9.6 Stribeck curve, minimum lubrication film thickness, and friction states in a radial sliding bearing (f_m friction coefficient in mixed friction, f_b friction coefficient in boundary friction, f_h friction coefficient in fluid friction, $h_{min,tr}$ minimum lubrication film thickness during the transition from fluid to mixed friction, $h_{min,h}$ minimum lubrication film thickness during fluid friction, $h_{min,m}$ minimum lubrication film thickness during mixed friction)

tion mechanisms, compiled schematically in Fig. 9.7:

- Adhesive bond shearing
- Plastic deformation
- Abrasion
- Hysteresis losses in elastic deformation.

Adhesion is an atomically/molecularly based friction mechanism. Its frictional effect is based on the bonds formed atomically or molecularly in the real contact areas that separate again when relative motion occurs, as a result of which energy loss occurs.

Deformation, abrasion, and hysteresis can be classified as mechanically based friction mechanisms. The action of friction in deformation and abrasion can above all be ascribed to the displacement of overlaps of asperities. Hysteresis is based on internal friction and has a damping effect. Different friction mechanisms frequently appear at the same time. The friction mechanisms that are principally acting depends on the state of friction.

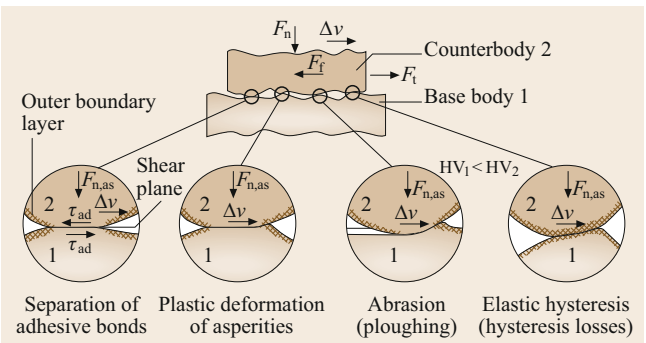

Fig. 9.7 Basic friction mechanisms viewed microscopically (F_n normal force on apparent contact area, F_f friction force between base body and counterbody, F_t tangential force, $F_{n,as}$ normal force on asperity contact, Δv relative velocity, τ_{ad} shear stress for shearing an adhesive bond, HV Vickers hardness)

9.3.4 Coefficient of Friction

Table 9.4 reproduces ranges of friction coefficients in various types and states of friction [9.8]. It should however be recalled that friction does not represent a constant property of a material or a combination of material properties but rather depends on the operating variables and the system structure, i.e., on the load and the elements involved in the friction process with their properties and interactions.

Table 9.4 Coefficients of friction for different types and states of friction

Type of friction	Friction state	Coefficient of friction f
Sliding friction	Solid friction	0.1–1
	Boundary friction	0.1–0.2
	Mixed friction	0.01–0.1
	Fluid friction	0.001–0.01
	Gas friction	0.0001
Rolling friction	(Grease lubrication)	0.001–0.005

9.4 Wear

As soon as the base body and counterbody come into contact, i.e., when the lubrication film thickness becomes too small or lubricant is unavailable, wear occurs. Wear is a progressive loss of material from the surface of a solid, brought about by mechanical causes, i.e., by contact and relative motion of a solid, fluid or gaseous counterbody [9.1]. Signs of wear are small detached wear particles, material removal from one friction body to the other, and material and shape changes of the tribologically loaded material zone of one or both friction partners.

9.4.1 Types and Mechanisms of Wear

Wear processes can be classified into different types according to the type of tribological load and the materials involved, e.g., sliding wear, fretting wear, abrasive wear, and material cavitation. Wear is caused by a number of mechanisms, the following four being especially important:

- Surface fatigue
- Abrasion
- Adhesion
- Tribochemical reaction.

Table 9.5 provides a breakdown of wear according to types of wear and wear mechanisms based on [9.1].

Figure 9.8 presents a chart of the effective wear mechanisms. The wear mechanisms can occur individually, successively or concomitantly.

Surface fatigue manifests itself through cracking, crack growth, and detachment of wear particles, brought about by alternating loads in near-surface zones of the base body and counterbody.

In *abrasion* microcuttings, fatigue due to repeated ploughing, and fracture of the base body caused by the

Table 9.5 Types and mechanisms of wear (after [9.1])

System structure	Tribological load (types of motion and simplified symbols)	Type of wear	Effective wear mechanism			
			Surface fatigue	Abrasion	Adhesion	Tribochemical reactions
Solid ● Interfacial medium (complete solid separation) ● Solid	Sliding Rolling Bouncing Impacting 	–	×			×
Solid ● Solid (solid friction, boundary lubrication, mixed lubrication)	Sliding 	Sliding wear	×	×	×	×
	Rolling Revolving 	Rolling wear	×	×	×	×
	Oscillating 	Fretting wear	×	×	×	×
Solid ● Solid and particles	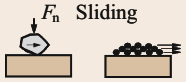 Sliding	Sliding abrasion (three-body abrasion)		×		×
	Sliding 	Sliding abrasion (three-body abrasion)	×	×		×
	Rolling 	Rolling abrasion (three-body abrasion)	×	×		×
Solid ● Fluid	Flowing Vibrating 	Material cavitation (cavitation erosion)	×			×
Solid ● Fluid and particles	Flowing 	Particle erosion (erosion wear)	×	×		×

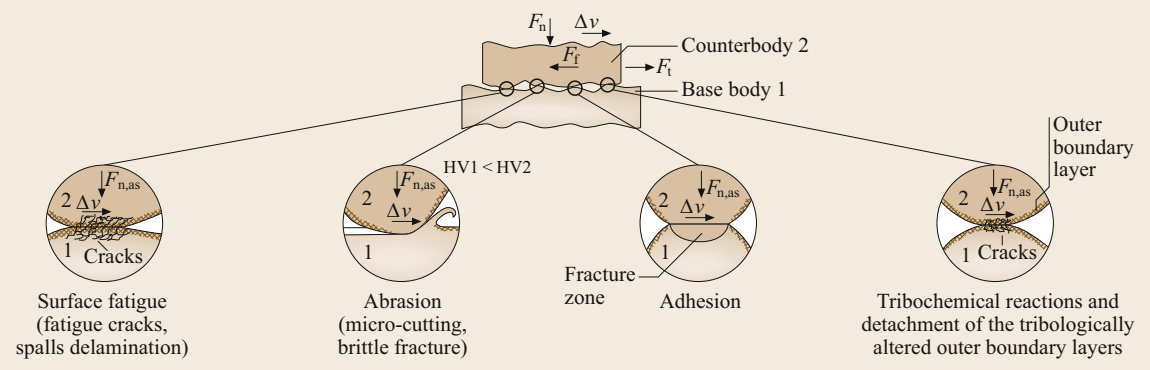

Fig. 9.8 Basic wear mechanisms viewed microscopically (F_n normal force on apparent contact surface, F_f friction force between base body and counterbody, $F_{n,as}$ normal force on asperity contact, Δv relative velocity, HV Vickers hardness)

Table 9.6 Typical wear phenomena caused by the main wear mechanisms (after [9.1])

Wear mechanism	Wear phenomenon
Adhesion	Scuffing or galling areas, holes, plastic shearings, material transfer
Abrasion	Scratches, grooves, ripples
Surface fatigue	Cracks, pitting
Tribochemical reactions	Reaction products (layers, particles)

counterbody's hard asperities or by hard particles in the interfacial medium lead to wear.

In *adhesion*, after possibly extant protective surface layers have been broken through, atomic bonds (microwelds) form above all on the plastically deformed microcontacts between the base body and counterbody. If the strength of the adhesive bonds is greater than that of the softer friction partner, material eventually detaches from the deformed surface of the softer friction partner and is transferred to the harder one. The transferred material can either remain on the harder friction partner or detach, or even return.

In *tribochemical reactions*, friction-induced activation of loaded near-surface zones causes elements of the base body and/or counterbody to react chemically with elements of the lubricant or ambient medium. Compared with the base body and counterbody, the reaction products exhibit changed properties and, after reaching a certain thickness, can be subject to brittle chipping or even exhibit properties reducing friction and/or wear.

Apart from the types and mechanisms of wear, *wear phenomena* are also extremely interesting for interpreting the result of wear (Table 9.6). These mean the changes of a body's surface layer resulting from wear and the type and shape of the wear particles accumulating. Light or scanning electron microscope images can present this extremely clearly.

9.4.2 Wear Profiles and Measurable Variables

Estimating the service life of components necessitates knowing the wear profile over the loading time and/or the rate of wear (amount of wear per loading time). According to [9.1, 8], different wear profiles are frequently generated depending on the effective wear mechanism (Fig. 9.9).

Three phases are distinguished: break-in, steady state, and failure. During breaking-in, increased wear, so-called break-in wear, with a degressive profile can occur and, for example, switch over into a long-lasting state with a constant increase of the amount of wear (constant rate of wear) until failure is announced by a progressive increase of wear (Fig. 9.9a).

If surface fatigue takes effect as the primary mechanism of wear, then measurable wear after break-in frequently only becomes noticeable after a certain incubation period during which microstructural changes, cracking, and crack growth commence. Wear particles only detach after the incubation period (Fig. 9.9b). A negative amount of wear is even occasionally measured at the beginning of the wear process. This is caused by material transfer from the wear partner (Fig. 9.9c).

In principle, the profile of the amount of wear W over the loading time t can be progressive, linear or digressive (Fig. 9.9d).

A difference is made between directly measurable wear variables, such as linear, planimetric, volumetric and mass amount of wear, and related measurable wear variables (wear rates), such as rate of wear, wear–distance ratio, and wear–throughput ratio. As a rule, the amount of wear can be measured. It is advisable to use specific or relative amounts of wear in comparative wear tests whenever the operating variables or the

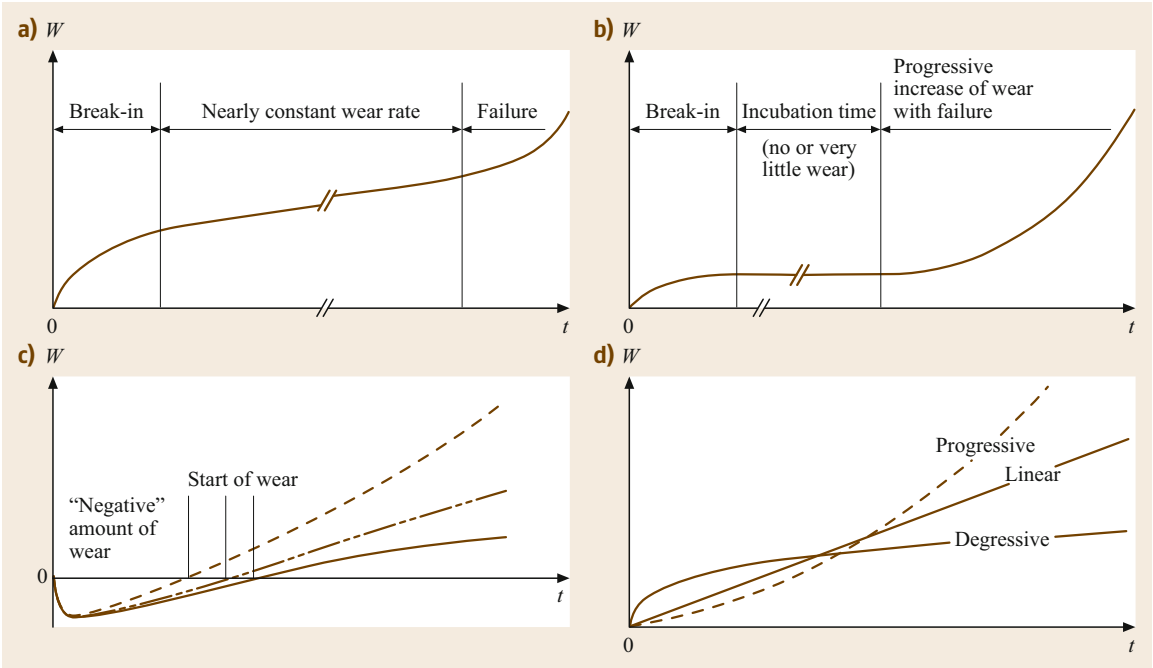

Fig. 9.9a–d Amount of wear as a function of loading time: **(a)** typical wear profile with a nearly constant wear rate; **(b)** wear profile with an incubation time; **(c)** wear profile with negative amount of wear; **(d)** different wear profiles

properties of the elements involved in the wear cannot be kept constant or are intentionally changed.

9.4.3 Determination of Wear and Lifetime

In unlubricated tribological systems and in systems operated in the boundary or mixed lubrication range, practically usable information about friction and wear can frequently only be found through experimentation since the physical and chemical mechanisms occurring here frequently cannot be described sufficiently exactly theoretically so that a precise calculation of friction and wear is often impossible.

However, mathematical equations for an approximate preliminary determination of friction and wear provide the energy balance of the friction process. If friction is approached as an energetic problem, the energy balance forms the basis for determining the friction and wear [9.9]. The friction force F_f and the friction coefficient f can be determined from the friction energy W_f

$$W_f = W_{el,hys} + W_{pl} + W_{abr} + W_{ad} = fF_n s_f = fF_n \Delta v t \,, \quad (9.5)$$

where $W_{el,hys}$ is the proportion of the work of friction from the hysteresis during elastic deformation, W_{pl} is the work of friction from plastic deformation, W_{abr} is the work of friction caused by abrasion, W_{ad} is the work of friction caused by separation of adhesive bonds, f is the friction coefficient, F_n is the normal force, s_f is the friction distance, Δv is the relative velocity between the friction bodies, and t is the friction time [9.9].

The action time of a friction pair usually depends on the wear. The anticipated lifetime L_h under specific operating conditions is frequently determined by calculation. A function-based maximum allowable wear is assumed. Thus, the lifetime L_h corresponds to the action time for which the friction pair can be safely operated.

Wear properties as a function of the friction time are presented in Fig. 9.10. The development of wear with its scatter as a function of the friction time is shown for various operating conditions. The wear height h_w serves as the gauge of wear. The function-based wear limit is characterized by the maximum allowable wear height $h_{w,al}$. As a rule, a wear profile exists, which is composed of a break-in process and a steady state (Fig. 9.10, cases 2 and 3). In addition, Fig. 9.10 also shows the distribution densities $f(t)$ for the lifetimes L_h defined by $h_{w,al}$.

Despite a large allowable wear height, case 1 is not practicable since the friction pair here fails early and

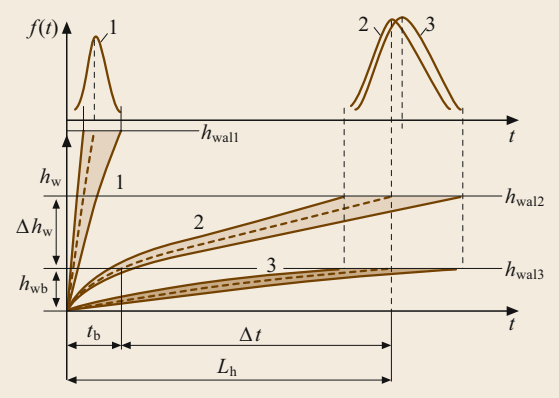

Fig. 9.10 Courses of wear height h_w and distribution density $f(t)$ as a function of the friction time t when allowable wear height values have been reached for different high stresses and different frictional states (after [9.10])

does not reach a steady state. Case 2 shows a normal progression in pure solid friction. More favorable conditions exist in case 3 (e.g., mixed friction), but the allowable wear height is small.

The average lifetime (action time) for the median of the distribution density results from the expression

$$L_h = t_b + \Delta t = t_b + \frac{h_{w,al} - h_{w,b}}{I_h \Delta v} , \qquad (9.6)$$

with the linear wear intensity I_h formed from the ratio of the wear height h_w to the friction distance s_f ($I_h = \Delta h_w / \Delta s_f$), the break-in time t_b, and the break-in wear height $h_{w,b}$. If it is assumed that the wear volume V_w and the work of friction W_f are proportional ($W_f \propto V_w$), and the value e_w as a proportionality factor is introduced as the wear energy density, as a result of which the basic wear equation becomes $W_f = e_w V_w$, and if the probabilistic nature of real operation is allowed for (through the introduction of $L(\gamma)_h$ as γ percentage lifetime, x as the quantile (random variable) of the standardized normal distribution, and v as an empirical coefficient of variation that represents a measure of the scatter of the wear rate), then the following expression can be set up for the lifetime [9.10]

$$L(\gamma)_{h1,2} = t_{b1,2} + \frac{(h_{w,al1,2} - h_{w,b1,2})\, e_{w1,2}}{\alpha_{f1,2} \tau_f \Delta v\, (1 - x v_{1,2})} , \qquad (9.7)$$

with the friction shear stress $\tau_f = f F_n / A_a$, where A_a stands for the apparent contact area, and the energy proportion factor $\alpha_{f1,2}$ is used to quantify the share of the work of friction induced in friction body 1 or 2.

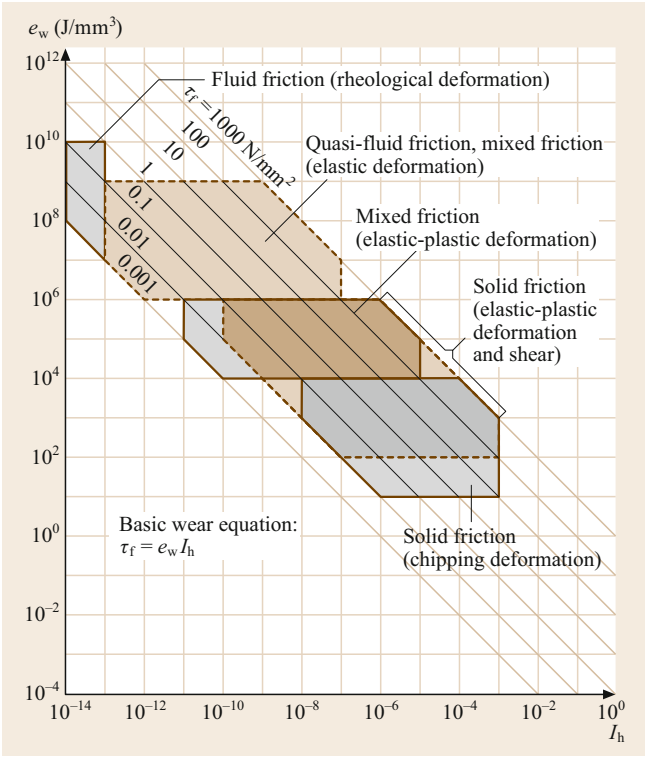

Fig. 9.11 Wear energy density e_w as a function of the linear intensity of wear I_h and the friction shear stress τ_f (after [9.9])

For a survival probability of $\gamma = 50\%$, when there is a standardized normal distribution, the quantile is $x = 0$, whereas $x = -1.28$ applies for $\gamma = 90\%$. The coefficient of variation depends on the operating conditions (common values based on [9.11] are $v = 0.2$–0.8; when there is fatigue wear, $v = 0.2$–0.4).

Determining the lifetime by using (9.7) not only requires knowledge of the break-in time t_b, the allowable wear height $h_{w,al}$, the break-in wear height $h_{w,b}$, the energy proportion factor α_f, the normal force F_n, the apparent contact surface A_a, the relative velocity Δv, and the statistical variables quantile x and coefficient of variation v but above all also information about the friction coefficient f and the wear energy density e_w appearing in the contact.

The friction coefficient can be determined experimentally or estimated through calculations [9.3, 12]. Values for the wear energy density e_w are either determined in tests or taken out of [9.9–11]. Figure 9.11 presents the nomogram of the basic wear equation $W_f = e_w V_w$, with ranges for typical friction and wear states for evaluating and classifying the tribological behavior of friction pairs.

9.5 Fundamentals of Lubrication

Lubrication completely or partially separates the surfaces of the friction bodies by selectively introducing an interfacial medium (lubricant) that minimizes friction and wear. Most lubricants are fluids (mineral oils, synthetic oils, water, etc.), yet they can also be solid, e.g., for use in dry sliding bearings (polytetrafluoroethylene (PTFE), graphite, molybdenum disulfide (MoS_2), etc.). Greases are also applied, e.g., in ball bearings and sliding bearings and occasionally in gears too. Gases (air) are also employed, e.g., in gas-lubricated bearings. Figure 9.12 reproduces the areas of application of different lubricants. Powders, lubricating varnishes, and pastes can be classified as solid lubricants [9.13].

Similar to friction states, different lubrication states can also be defined (Table 9.7), to be precise: fluid film lubrication, mixed lubrication, boundary lubrication, and solid lubrication (lubrication with solid lubricants and surface coatings).

9.5.1 Fluid Film Lubrication

Fluid film lubrication, i.e., the complete separation of the frictional surfaces by a lubricating film, can be achieved by hydrodynamic, elastohydrodynamic or hydrostatic lubrication (Table 9.8). A load-dependent pressure is developed in the lubricating film, as a result of which the load can be carried.

9.5.2 Hydrodynamic Lubrication

The following conditions must be met to produce hydrodynamic lubrication. A viscous lubricant that adheres to both the moving and the fixed friction body must be used (adhesive effect of the lubricant). Furthermore, the friction body surfaces must be converging and the lubricant must be dragged into the converging gap. The entraining velocity depends on the velocity at which the lubricant is dragged into the contact and is frequently confused with the relative velocity. The latter is decisive for friction, while the entraining velocity is essential for load-carrying capacity.

The lubricant adhering to the surface is dragged into the lubrication gap by the friction bodies moving relative to the minimum lubrication film thickness. Since the gap converges in the direction of motion, the quantity of oil dragged by the friction bodies accumulates in front of the narrowest gap cross section and cannot be completely transported by the moving friction bodies' drag effect alone through the minimal cross section.

Thus, overpressure is inevitably produced in the converging zone in between the sliding surfaces, which grows to be just large enough that the difference between the quantities supplied and discharged by the drag flow are squeezed out of the lubricant gap as a result of compressive flows (satisfaction of the condition of continuity). The overpressure produces the friction contact's load-carrying capacity in equilibrium with the external load.

Figure 9.13 presents examples of velocity distributions at various points in the lubrication gap and the pressure distribution for an inclined plane bearing pad. The level of the average pressure developed (normally < 7 MPa) is usually not high enough to cause significant elastic deformation of the surfaces. The

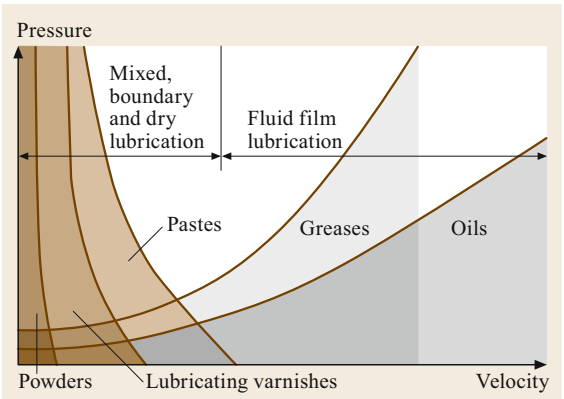

Fig. 9.12 Areas of lubricant application (after [9.13])

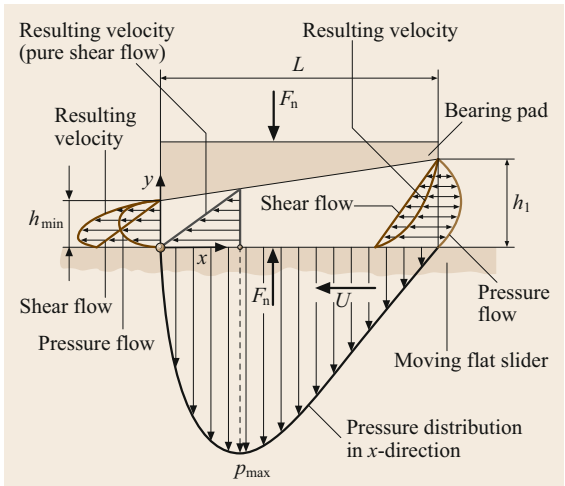

Fig. 9.13 Velocity distributions and pressure distribution in a bearing pad

Table 9.7 Friction and lubrication states

	Friction/lubrication states
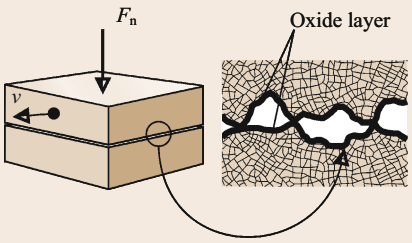	1. Solid friction/no lubrication ● Direct contact of friction partners ● Formation of oxide reaction layers and adsorption of gases ● High wear rates probable, risk of seizing ● Friction coefficients (reference values): $f \approx 0.35$ to > 1 ● Special cases *Boundary-layer friction* Friction between solid boundary layers with modified properties compared with the bulk material (e.g., oxide layers) *Friction of pure metallic surface* Direct contact of pure metallic surfaces (e.g., in machine or scuffing processes)
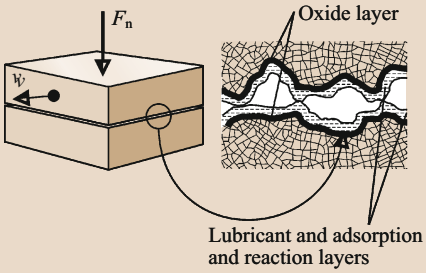	2. Boundary friction/boundary lubrication ● Surfaces of the friction partners covered with a thin friction minimizing lubrication film ● Physisorption, chemisorption, and tribochemical reaction with additives from the lubricant form friction-minimizing, lightly shearing layers on the surfaces ● Lower wear rates than for solid friction ● Friction coefficients (reference values): $f \approx 6 \times 10^{-2}$–$2 \times 10^{-1}$
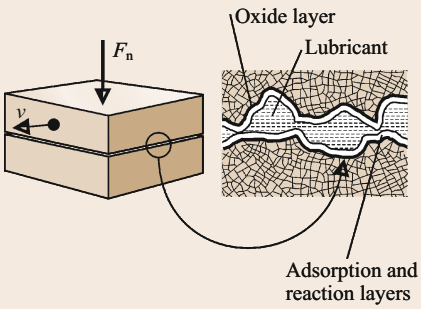	3. Mixed friction/mixed lubrication ● Lubrication film not thick enough to separate surfaces from each other completely; consequence: roughness contacts ● Load is partially carried by lubricating film through hydrodynamic effect and partly by the roughness contacts ● As in boundary friction, use of additives in lubricant is also important to generate friction-minimizing absorption and reaction layers on the surfaces ● Wear rates are smaller, the larger the hydrodynamic part of the load-carrying capacity ● Friction coefficients (reference values): $f \approx 10^{-3}$–10^{-1}
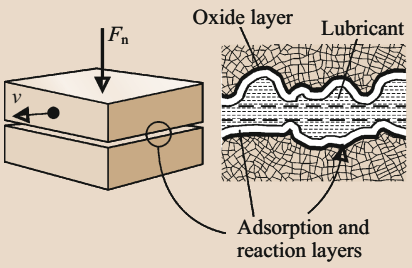	4. Fluid friction/fluid film lubrication ● Friction partners are completely separated from each other by a fluid film that can be generated, hydrodynamically or hydrostatically ● Virtually wear-free operation ● Friction coefficients (reference values): $f \approx 6 \times 10^{-4}$–$5 \times 10^{-3}$

hydrodynamic pressure is dependent on the friction bodies' geometry, the inclination of the surfaces to each other, the viscosity of the lubricant, the load, and the velocity of the lubricant dragged into the converging lubrication gap.

Table 9.8 specifies the correlation between the minimum lubrication film thickness h_{min} and the entraining velocity, the viscosity of the lubricant, and the load. It is evident that the minimum lubrication film thickness increases as the entraining velocity increases and the viscosity becomes greater, and that it decreases as the load grows, although only with an exponent of 0.5 in each case. The minimum lubrication film thickness is normally greater than 1 μm.

Above all, it is the lubricant's viscosity that determines the lubricating effect in hydrodynamic lubri-

Table 9.8 Different types of fluid film lubrication

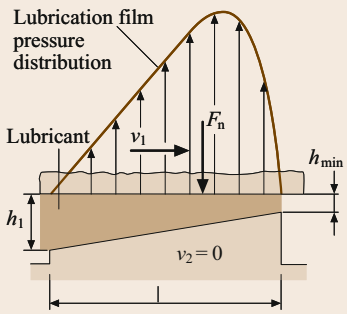	**Hydrodynamic** [9.14] For a given geometry $h_{min} \approx \sqrt{\frac{\overline{v}\eta}{F_n}} = (\overline{v}\eta)^{0.5} F_n^{-0.5}$, $\overline{v} = \frac{v_1+v_2}{2}$ entraining velocity, η average viscosity of the lubricant in the lubricating film, F_n load
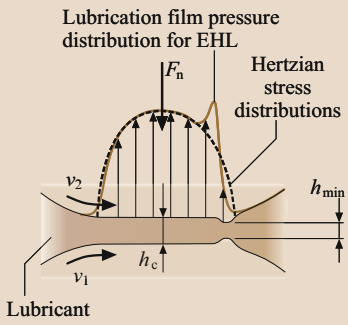	**Elastohydrodynamics** [9.6] a) *Hard material surfaces (hard EHL)* Elliptical contact surfaces, given geometry $h_{min} \approx (\overline{v}\eta_0)^{0.68} \alpha^{0.49} E^{*-0.117} F_n^{-0.073}$, $\frac{h_{min}}{h_c} \approx 0.56$ $\overline{v} = \frac{v_1+v_2}{2}$ entraining velocity, η_0 viscosity of the lubricant at gap entry at $p = 0$, α viscosity–pressure coefficient, $\frac{1}{E^*} = \frac{1}{2}\left(\frac{1-\upsilon_1^2}{E_1} + \frac{1-\upsilon_2^2}{E_2}\right)$ reduced modulus of elasticity, E_1 and E_2 Young's modulus of friction bodies 1 and 2, υ_1 and υ_2 Poisson's ratio of friction bodies 1 and 2, F_n load b) *Soft material surfaces (soft EHL)* Elliptical contact surfaces, given geometry $h_{min} \approx (\overline{v}\eta_0)^{0.65} E^{*-0.44} F_n^{-0.21}$; $\frac{h_{min}}{h_c} \approx 0.77$
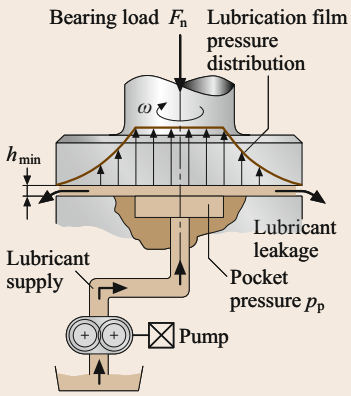	**Hydrostatic** [9.14] For a given geometry and constant lubricant volumetric flow ($\dot{V} = \text{const.}$) $h_{min} \approx \sqrt[3]{\frac{\eta}{F_n}} = \eta^{0.33} F_n^{-0.33}$, F_n load, η average viscosity of the lubricant in the lubricant cap

cation. Friction is only generated by the shear of the viscous lubricant. Apart from the viscosity, the relative velocity between the moving bodies' lubrication gap surfaces and the lubrication gap height are decisive for friction. If both surfaces slide with the same sliding velocity, the relative velocity is $\Delta v = 0$, i.e., friction does not occur. However, when the sliding conditions are identical, the entraining velocity in the lubrication gap can be high (e.g., in the case of radial sliding bearings, in which the shaft and bushing rotate with the same speed in the same direction) so that the tribological system then has a high load-carrying capacity and a friction force of zero.

Elastohydrodynamic Lubrication

Elastohydrodynamic lubrication (EHL) is a form of hydrodynamic lubrication in which elastic deformations of the lubricated surfaces become significant. The essential prerequisites for hydrodynamic lubrication, such as a converging lubricating film, the lubricant entraining

velocity in the converging gap, and a viscous lubricant between the surfaces, are also important in EHL. Elastohydrodynamic lubrication is normally connected with nonconformal surfaces (Table 9.3). There are two different forms of EHL: for hard surfaces (hard EHL) and soft surfaces (soft EHL).

Hard EHL. Elastohydrodynamic lubrication for hard surfaces (hard EHL) refers to materials with high moduli of elasticity, e.g., metals. Both the elastic deformations and the viscosity's pressure dependence are equally important in this type of lubrication. The maximum occurring lubricating film pressure is typically between 0.5 and 4 GPa. The minimum lubrication film thickness normally exceeds 0.1 μm. When the loads are those normally occurring in nonconformal contacts of machine elements, the elastic deformations in hard EHL exhibit values several magnitudes greater than the minimum lubrication film thicknesses. Furthermore, the lubricant viscosity in the lubrication film can change by a magnitude of 3–4 or more, depending on the lubricant, pressure, and temperature.

The minimum lubrication film thickness h_{min} is a function of the same parameters as in hydrodynamic lubrication, but these must be augmented by the effective Young's modulus E^* and the lubricant's viscosity–pressure coefficients α. Table 9.8 indicates that, in the relationship for the minimum lubrication film thickness, the exponent for the normal load in hard EHL is approximately seven times smaller than it is in hydrodynamic lubrication. This means that, in contrast to hydrodynamic lubrication, the load only marginally influences the lubrication film thickness in hard EHL. The reasons are to be found in the increase of the contact area as the load increases in hard EHL, as a result of which a larger lubrication area is provided to bear the load. The exponent for the lubricant entraining velocity in hard EHL is greater than in hydrodynamic lubrication. Typical applications for hard EHL are toothed gears, rolling element bearings, and cam–follower pairs.

Soft EHL. Elastohydrodynamics for soft surfaces (soft EHL) refers to materials with low moduli of elasticity, e.g., rubber. In soft EHL, sizeable elastic deformations occur even at low loads. The maximum occurring pressures in soft EHL are typically 1 MPa, in contrast to 1 GPa for hard EHL. This low lubricating film pressure only negligibly influences the viscosity during the flow through the lubrication gap. The minimum lubrication film thickness is a function of the same parameters as in hydrodynamic lubrication with the addition of the effective modulus of elasticity E^*. The minimum lubricating film thickness in soft EHL is typically 1 μm. Applications for soft EHL are seals, artificial human joints, tires and nonconformal contacts in which rubber is used.

A common feature that hard and soft EHL exhibit is the generation of coherent lubricating films as a result of local elastic deformations of the friction bodies and thus the prevention of interactions between asperities. Hence, only the lubricant's shear generates frictional resistance to motion.

Hydrostatic Lubrication

In hydrostatic lubrication of friction bodies, a pocket or recess is incorporated in one friction body's loaded surface into which a fluid is forced from outside at constant pressure. A pump outside the bearing generates the lubricant pressure. Hence, the lubricant pump and the lubricating pocket into which the lubricant is fed under pressure are the most important features of hydrostatic lubrication. The lubricating pocket is normally positioned opposite the external load. The load-carrying capacity of a contact with hydrostatic lubrication is also assured when surfaces are not moving. When the volumetric flow of lubricant into the lubricating pocket is constant, the minimum lubrication film thickness is proportional to the cube root of the ratio of the average lubricant viscosity in the lubrication gap and the load, i.e., the minimum lubrication film thickness is less dependent on the viscosity and the load than is the case in hydrodynamic lubrication.

Hydrostatic lubrication is mainly used: where the friction partners' surfaces do not have any metallic contact, i.e., wear may not occur, not even when ramping up and ramping down a machine or at low speed; where as low a friction coefficient as possible must be produced at low speeds; and where, as a result of less effective lubricant entraining velocities in the lubrication gap, the wedge effect cannot produce any bearing lubricating film hydrodynamically.

9.5.3 Boundary Lubrication

In *boundary lubrication*, the friction bodies are not separated by a lubricant, the hydrodynamic lubricating film effects are negligible, and there are extensive asperity contacts. The physical and chemical properties of thin surface films of molecular thickness control the lubricating mechanisms in the contact. The base lubricant's properties are of little importance. The coefficient of friction is on the whole independent of the lubricant's viscosity. The frictional characteristic is determined by the properties of the solids involved in the

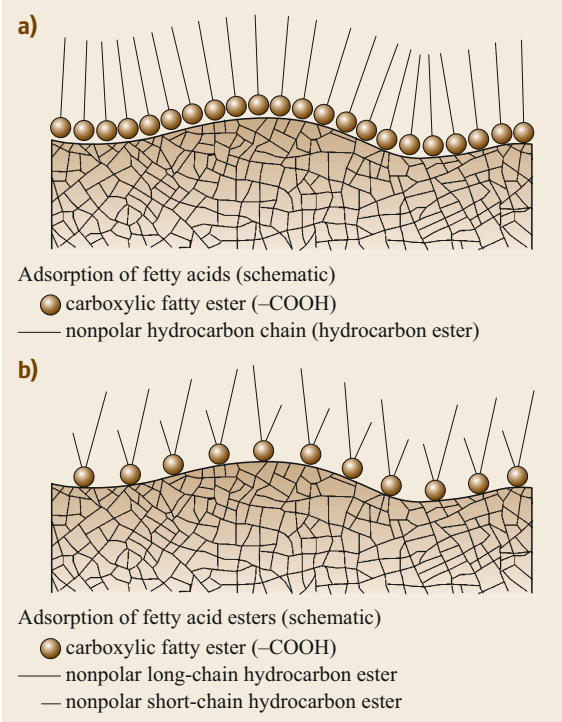

Fig. 9.14 Adsorption on metal surfaces (after [9.15])

friction process and the boundary layers forming on the material surfaces, which primarily depend on the lubricant's properties, particularly the lubricant additives, as well as the material surfaces' properties. These boundary layers are formed by physisorption, chemisorption, and/or tribochemical reaction. The thickness of the surface boundary layer varies between 1 and 10 nm, depending on the molecule size.

In *physisorption*, additives contained in the lubricant (e.g., antiwear (AW) additives) such as saturated and unsaturated fatty acids, natural and synthetic fatty acid esters, and primary and secondary alcohols are adsorbed on the tribologically loaded surfaces. Such materials have in common a high dipole moment because of at least one polar group in the molecule (Fig. 9.14).

The coverage of the surfaces follows the laws of adsorption and is dependent on temperature and concentration. A prerequisite for the adsorption of polar groups is that the material surface exhibits a polar character so that van der Waals bonds can form. This is usually attained for metallic materials by oxide films forming on the surfaces. Problems can arise for ceramic materials however. While, for example, adsorption of fatty acids with polar end groups occurs easily on aluminum oxide with ionic bonding so that friction is diminished from a certain chain length onward, adsorption apparently does not occur on silicon carbide with covalent bonds so that the friction coefficient is not influenced [9.2].

In *chemisorption*, molecules are bonded to the surface. Substantially more-stable boundary layers develop because chemical bonds with greater bonding force are formed on the surface (e.g., the reaction of stearic acid with iron oxide when water is present, as a result of which metallic soap forms as iron stearate). Chemisorbed layers have excellent lubricating properties up to their melting point. At medium loads, temperatures, and velocities, they produce a sustained reduction of friction.

Tribochemical reactions between elements of the lubricant and the metallic material surface form reaction layers that generally have more thermal and mechanical load-carrying capacity than layers formed by physisorption or chemisorption. For this, chlorine, phosphorous or sulfur compounds are added to the lubricants as additives (extreme-pressure (EP) additives). The effectiveness of such EP additives depends on the speed of reaction layer formation, which is influenced by the reaction's activation energy, the surface temperature, and the concentration of the additive. EP active ingredients themselves, or their thermal cleavage products, react with the surface metallic oxide in very short time (10^{-6}–10^{-7} s), forming a reaction layer that adheres well and shears easily (Fig. 9.15).

While only very little or no wear appears in hydrodynamic and elastohydrodynamic lubrication because there are no asperity contacts, the number of asperity contacts grows in boundary lubrication and thus so does the rate of wear as the load increases. However, compared with unlubricated conditions, the rates of wear in boundary lubrication are substantially lower.

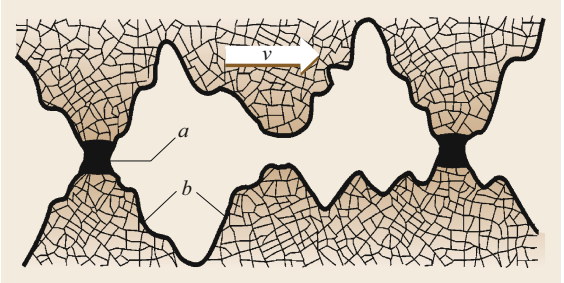

Fig. 9.15 Formation of a protective layer by EP active ingredients of sulfur compounds. *a*: metal-sulfide compound; *b*: metal surface (after [9.15])

9.5.4 Mixed or Partial Lubrication

If the load in hydrodynamically or elastohydrodynamically lubricated machine elements grows too large or the lubricant entraining velocity in the lubrication gap is too small, the lubricating film becomes too thin so that asperity contacts appear at some points. This is mixed friction, in which the states of boundary friction and fluid friction coexist. The lubricating film is no longer coherent because individual surface asperities of the paired parts penetrate it and cause direct contact of the sliding surfaces. In partial or mixed lubrication, the normal load is partly carried by hydrodynamic film pressures and partly by contact of the frictional surfaces at the asperity contacts. The transition from hydrodynamic or elastohydrodynamic lubrication to partial lubrication does not happen suddenly when the load is increased but rather the share of the load carried by the hydrodynamic pressure buildup decreases gradually, while the share carried by the asperities grows in equal measure.

9.5.5 Lubrication with Solid Lubricants and Surface Coatings

In lubrication with solid lubricants and in coatings, the most important measures for improving friction, preventing scuffing or seizing, and minimizing wear are applying metallic (e.g., indium) or nonmetallic layers (e.g., synthetic resin coatings), forming reactionlayers through chemical transformation (e.g., phosphatizing),

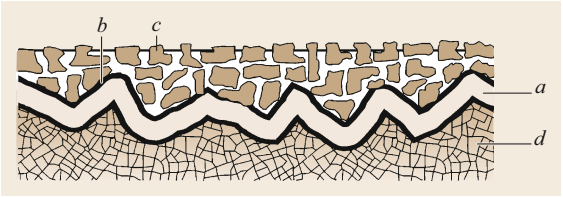

Fig. 9.16 Solid lubrication made of lubricating varnish: *a*: phosphate layer (3 µm); *b*: binder; *c*: solid lubricant; *d*: base metal (after [9.15])

and using solid lubricants. Nonmetallic layers also include layers obtained by physical vapor deposition (PVD) or chemical vapor deposition (CVD) from the gas phase; the layer has a thickness in the micrometer range and can be made of, for example, titanium nitride (TiN), titanium aluminum nitride (TiAlN), chromium nitride (CrN) or tungsten carbide/carbon (WC/C).

Among the solid lubricants, crystalline solids with layer lattices (lamina structure) appear particularly suitable. Their structure is characterized by lamellae that can be displaced slightly with respect to each other along glide planes. Typical representatives are graphite (C) and molybdenum disulfide (MoS_2). Certain plastics such as PTFE are also used as solid lubricants.

Apart from these, coating layers on metals, which are adhesive, act as lubricants, and are firm to the touch, so-called lubricating varnishes, also play a role (Fig. 9.16). They have a large proportion of solid lubricants and can be used as dry films over a wide range of temperatures.

9.6 Lubricants

Gaseous, fluid, consistent or solid lubricants are used in mechanical engineering. Gaseous lubricants are utilized, for example, in high-speed, lightly loaded machines (e.g., ultracentrifuges, gas pumps for nuclear power plants) or in equipment technology. The most important group of substances for fluid lubricants are the mineral oils, as well as synthetic, animal, and vegetable oils and even water in special applications. Greases and adhesive lubricants are consistent lubricants. Greases consist of mineral or synthesis oils that are thickened with, for instance, soaps. There are bitumen-based adhesive lubricants as well as bitumen-free adhesive spray lubricants. These are principally used to lubricate larger, open-toothed gears. Solid lubricants are frequently introduced into fluid or consistent carrier substances. Solid lubricants are used in pure form only under special operating conditions. Among others substances, solid lubricants include graphite, molybdenum disulfide, PTFE, etc.

During operation, pressure and shear stresses, among others, act on a lubricant at different temperatures. The lubricant comes into contact with gases (e.g., air), liquids (e.g., water), and solids (e.g., metals, sealing materials, wear particles). In addition, contact with human skin cannot be ruled out. This results in a number of requirements that a good lubricant should have. For a particular application, it should have an appropriate viscosity–temperature and viscosity–pressure behavior, a low pour point, and preferably not be volatile, exhibit high-temperature, shear, and oxidation stability, and be hydrolysis and radiation resistant in special cases. Beyond this, a good lubricant should be compatible with the constructional materials used and be nontoxic and not cause any disposal problems.

9.6.1 Lubricating Oils

Among the fluid lubricants, a difference is made between mineral oils and synthetic oils.

Mineral Oils

Mineral oils are obtained from naturally deposited crude oil with the aid of distillation and refining. Crude oils chiefly consist of hydrocarbons and organic oxygen, sulfur, and nitrogen compounds. The exact composition of a crude oil depends on its origin (provenance). When mineral oils are manufactured, systematic selection of the base oil and control of the manufacturing process can produce particular compositions and thus influence desired properties. Mineral oils are mixtures of hydrocarbons, which can be subdivided as a function of their structure into open-chain hydrocarbons (paraffins) and cyclic hydrocarbons (naphthalenes, aromatics), which can each be saturated or unsaturated.

Mineral oils' performance characteristics change as their working life increases. A primary reason for diminished performance is gradual oxidization of hydrocarbon chains, with aromatics reacting more than naphthenes and naphthenes more than paraffins. As a result, sludge-like deposits can form, which impede the oil supply by clogging oil feed lines and filters. Moreover, the formation of organic acids can be boosted, which can cause corrosion of machine parts. This can be prevented in part by admixing additives (e.g., antioxidants, detergent, and dispersant agents). More information on their effect and the use of additives can be found in Sect. 9.6.1, *Additives*.

Synthetic Oils

Synthetic-base lubricating oils are produced by chemical synthesis from chemically defined structural elements (e.g., ethylene). Their development has made it possible to systematically satisfy even extreme requirements (e.g., lubricant temperature > 150 °C). According to their chemical composition, synthetic lubricants are subdivided into synthetic hydrocarbons, which only contain carbon and hydrogen (e.g., polyalphaolefines (PAO), dialkylbenzenes (DAB), polyisobutenes (PIB)), and synthetic fluids (e.g., polyglycols, carboxylic acid esters, phosphoric acid esters, silicon oils, polyphenyl ethers, fluorine-chlorine-carbon oils). Typical characteristics of synthetic oils are provided in Table 9.9 and a comparison of the properties of synthesis oils with those of mineral oil is presented in Table 9.10.

Synthetic oils have a number of advantages over mineral oils. They have better resistance to aging (thermal and oxidative stability) and thus their useful life is three to five times longer. They exhibit a more favorable viscosity–temperature behavior (with a significantly lower dependence of viscosity on temperature), display better flow properties at low temperatures and lower volatility at high temperatures, can cover applications operating at a substantially expanded range of temperature, and are radiation and flame resistant. Moreover, synthetic lubricants can be used to obtain

Table 9.9 Characteristics of various synthetic oils (after [9.16])

Property	Mineral oil	PAO	Polyglycol (water insoluble)	Ester	Silicon oil	Alcoxifluorine oil
Viscosity at 40 °C (mm^3/s)	2–4500	15–1200	20–2000	7–4000	4–100 000	20–650
Use for oil-sump temperature (°C)	100	150	100–150	150	150–200	150–220
Use for oil-sump temperature (°C)	150	200	150–200	200	250	240
Pour point (°C)	−20[a]	−40[a]	−40	−60[a]	−60[a]	−30[a]
Flash point (°C)	220	230–260[a]	200–260	220–260	300[a]	–
Evaporation losses[b]	○	+	○ to −	+	+[a]	++[a]
Water resistance[c]	+	+	+[a,d]	+ to ○	+	+
η–T behavior[c]	○	+ to ○	+	+	++	+ to ○
Pressure–viscosity coefficient (10^8 m^2/N)[e]	1.1–3.5	1.5–2.2	1.2–3.2	1.5–4.5	1.0–3.0	2.5–4.4
Suitable for high temperatures (≈ 150 °C)[c]	○	+	+ to ○[a]	+[a]	++	++
Suitable for high load[c]	++[f]	++[f]	++[f]	+	−[a]	+
Compatibility with elastomers[c]	+	+[a]	○[g]	○ to −	++	+
Price ratios	1	6	4–10	4–10	40–100	200–800

[a] dependent on type of oil;
[b] very low, ++; low, +; moderate, ○; moderate to high, ○ to −;
[c] excellent, ++; good, +; moderate to good, + to ○; moderate, ○; moderate to poor ○ to −; poor, −;
[d] difficult to separate since density is identical;
[e] measured up to 2000 bar, amount is dependent on type of oil and the viscosity;
[f] with EP additives;
[g] inspect when coating

Table 9.10 Comparison of the properties of natural and synthetic base oils for lubricants (after [9.15])

Property	A	B	C	D	E	F	G	H	I	J	K
Viscosity–temperature behavior (viscosity index, VI)	−	+	○	+	+	○	−−	−−	++	++	−
Low-temperature performance (pour point)	−−	○	++	++	+	○	−−	−	++	+	○
Oxidation stability (aging test)	−	−−	+	○	+	−−	+	○	+	+	++
Thermal stability (heating under absence of oxygen)	−	−	−	○	+	○	++	−	+	○	+
Volatility (evaporating loss)	−	○	○	++	++	○	○	+	+	○	○
Finish compatibility (effect on coatings)	++	−	++	−	−	−	−	−−	○	−	○
Water resistance (hydrolysis test)	++	−−	++	−	−	○	++	−	○	−	+
Antirust properties (corrosion test)	++	++	++	−	−	○	−	−	○	−−	+
Seal compatibility (swelling behavior)	○	−	++	−	−	○	○	−−	○	○	−
Flame resistance (ignition temperature)	−−	−−	−−	−	−	−	−	++	○	−	++
Additive solubility (dissolving of larger concentrations)	++	○	+	−−	○	−	+	○	−−	○	−
Lubricity (load-carrying ability)	○	++	○	+	+	○	++	++	−−	−	++
Biodegradability (degradability test)	−	++	○	++	++	++	−−	+	−−	−	−−
Toxicity	○	++	++	○	○	+	○	−−	++	−	+
Miscibility (formation of a homogeneous phase)	++	++	++	+	+	−−	○	−	−−	−	−−
Price ratio to mineral oil	1	3	4	7	8	8	350	7	65	25	350

Weighting: 1: ++; 2: +; 3: ○; 4: −; 5: −−
A – Mineral oil (solvent neutral);
B – Rape oil;
C – Polyalphaolefin;
D – Carboxylic acid ester;
E – Neopentyl polyol esters;
F – Polyalkylenglycol (polyglycol);
G – Polyphenyl ether;
H – Phosphoric acid ester;
I – Silicon oil;
J – Silicate ester;
K – Fluorine-chlorine-carbon oil (chlorotrifluoroethylene)

specific frictional properties, e.g., lower friction coefficients to minimize power loss in ball bearings or gears, or higher friction coefficients to increase the transmittable torque in friction gears.

On the other hand, synthetic lubricants often cannot be used as universally as mineral oils since they have been developed for specific properties. In addition, they are more strongly hydroscopic (water attracting), display only slight air release characteristics (risk of foaming), mix poorly or not at all with mineral oils, are toxic to a large extent, and are characterized by poor compatibility with other materials (risk of chemical reaction with seals, paints, and nonferrous metals) and by poor solubility for additives. They are not always available, most notably in certain viscosity classes, and they frequently cost substantially more. Table 9.11 details examples of typical areas of application of synthetic oils.

Biodegradable Oils

Environmentally compatible lubricating oils are increasingly being used, for example, in motor vehicles and equipment in water protection areas and in hydraulic engineering, in vehicles for agriculture and forestry, and in openly running gears with loss lubrication (excavators, mills). They are readily and rapidly degradable, have a low water hazard class, and are toxicologically harmless. Their base substances have to be degraded in a degradability test (e.g., CEC L-33-T-82) by a defined amount within a specified time and the additives used (up to a maximum of 5%) should be potentially degradable. Native oils and native base synthetic esters as well as fully synthetic esters and polyglycols are used. Native oils (e.g., rape oil and natural esters) are unsuitable for high temperatures (>70 °C) and additionally have low thermal stability and resistance to aging. The synthetic oils suitable for continuous high temperatures are often used as hydraulic oils in agricultural and forestry machines. Polyglycols are used, for example, as readily biodegradable oils in water engineering.

Additives

Additives are substances that either give new characteristics to mineral, synthesis or vegetable oils or enhance already existing positive properties. The quantity of ad-

Table 9.11 Examples of use of the most important synthetic lubricants (after [9.17])

Product group	Examples of use
PAO (synthetic hydrocarbons)	● High-performance oils for diesel engines ● Multigrade engine oils ● Gear lubrication at high thermal stress ● Compressor oils
Carboxylic acid esters	● Aircraft engine oils ● Fuel economy oils (low-friction engine oils) ● Base oil for high- and low-temperature greases ● Applications requiring good and fast biodegradability
Neopentyl polyol esters	● Applications similar to those for carboxylic acid esters but especially wherever oxidation stability and better additive solubility are required
Polyalkylglycols (polyglycols)	● Metalworking fluids ● Gear oils (worm gears) ● Hydraulic fluids (flame resistant) ● Lubricant for compressors and pumps
Polyphenyl ethers	● High-temperature lubricants (up to 400 °C) ● Applications requiring resistance to ionizing radiation (γ rays and thermal neutrons)
Phosphoric acid esters	● Plasticizers ● Flame-resistant hydraulic oils ● Safety lubricants for air and gas compressors ● EP additives
Silicone oils	● Special lubricants for high temperatures ● Base oil for lifetime lubricating greases (e.g., for clutch release bearings for motor vehicle clutches, starters, brakes, and axle components)
Silicate esters	● Hydraulic oils for lower temperatures ● Heat exchange fluids
Fluorine-chlorine-carbon oils	● Lubricants for oxygen compressors and for pumps for aggressive fluids

ditive used differs greatly. Thus, circulating or hydraulic oils may only contain 0.1%, whereas special engine and gear oils may contain up to 30% additives.

All properties of lubricants cannot be changed by additives. However, by using additives a clear improvement in lubrication can be obtained by modifying some properties. Thus, for example, heat dissipation, viscosity–density properties, and temperature resistance cannot be influenced by additives. Improvements brought about by additives are obtained for low-temperature performance, aging stability, viscosity–temperature properties, and corrosion protection. Only additives can attain good cleaning performance, favorable dispersion behavior, antiseizing properties, and foam inhibition.

Additives have to be matched to the base oil in terms of quantity and composition and the presence of other additives since they respond differently to the base oil and are not mutually compatible in every case. For example, there are antagonistic effects between viscosity index improves and antifoam additives, between detergent/dispersant additives and antiwear, antiseizing, and antifoam additives, and between corrosion inhibitors and antiwear and antiseizing additives [9.15].

A difference can be made between additives that form surface layers and those that change the properties of the lubricant itself. Additives forming surface layers act as a lubricating film above all when there is insufficient lubrication, as a result of which friction is reduced and the load-carrying capacity of sliding–rolling pairs is improved. Among others, this group of additives includes antiwear (AW) additives, extreme pressure (EP) additives, and friction modifiers. Adding additives that form surface layers also has drawbacks though. Thus, lubricants with additives oxidize faster than normal mineral oils and corrosive acids and insoluble residues frequently form. Hence these additives should only be used when necessitated by the operating conditions. Additives that modify lubricants influence, for example, foaming behavior, corrosion behavior, sludging, and pour point. Table 9.12 provides an overview of the most important types of additives and their applications.

During operation, the effectiveness of some additives can decrease (exhaustion) since reaction with the

Table 9.12 Additives, typical types of additives, applications, and active mechanisms (after [9.18])

Additive	Types of additive	Application	Active mechanisms
AW additive	Zinc dialcyldithiophosphates, tricresylphosphates	Decrease of inordinate wear metal surfaces	Reaction with metal surfaces produces layers that are plastically deformed and improves the contact pattern
EP additives	Sulfurized greases and olefines, chlorohydrocarbons, lead salts of organic acids, aminophosphates	Prevention of microwelding between metal surfaces at high pressures and temperatures	Reaction with metal surfaces produces new bonds with lower shear resistance than the base metal. There is constant shearing off and reformation
Friction modifiers	Fatty acids, fat amines, solid lubricants	Reduction of friction between metal surfaces	Highly polar molecules are absorbed on metal surfaces and separate the surfaces, solid lubricants form friction-reducing surface film
Viscosity index improvers	Polyisobutylenes, polymethylacrylates, polyacrylates, ethylenepropylene, styrene maleic acid esters, copolymers, hydrogenated styrene-butadiene-copolymers	Reduction of dependence of viscosity on temperature	Polymer molecules are strongly balled in cold oil (poor solvent) and take on greater volume in warm oil (good solvent) by unballing. This produces a relative thickening in oil
Pour point depressants	Paraffin-alkylated naphthalenes and phenols, polymethylacrylates	Decrease of pour point of the oil	Encasing prevents the agglomeration of paraffin crystals
Detergent additives	Normal or alkaline calcium, barium or magnesium-sulfinates, phenates or phosphonates	Reduction or prevention of deposits in engines at high operating temperatures	Reaction with the oxidation products controls the formation of coating and sludge. Products are produced that are oil soluble or suspended in oil
Dispersant additives	Polymers such as nitrogenous polymethylacrylates, alkyl succunimides and succinate esters, high molecular weight amines and amides	Prevention or delay of the development and deposition of sludge at low operation temperatures	Dispersants have a pronounced affinity for impurities and encase these with oil soluble molecules that suppress the agglomeration and deposition of sludge in the engine
Oxidation inhibitors	Inhibited phenols, amines, organic sulfides, zinc dithiophosphates	Minimization of the formation of resin, coating, sludge, acid, and polymer-like compounds	Reducing the organic peroxides ends the oxidation chain reaction. reduced oxygen intake by the oil decreases the acid formation. Catalytic reactions are prevented
Corrosion inhibitors	Zinc dithiophosphates, sulfurized terpenes, phosphorized, sulfurized olefines	Protection of bearing and other metal surfaces against corrosion	Acts as an anticatalyst; film forms on metal surfaces as protection against attacks from acids and peroxides
Rust inhibitors	Amine phosphates, sodium, calcium, and magnesium sulfates, alkyl succinic acid, fatty acids	Protection of ferrous surfaces against rust	Metal surfaces prefer to adsorb polar molecules and they serve as a barrier against water neutralization by acids
Metal deactivators	Triarylphosphate, sulfur compounds, diamines, dimercaptothiadiazop deriviatives	Suppression of the catalytic influence on oxidation and corrosion	A protective film is adsorbed an metal surfaces, which inhibits the contact between the bases metal and the corrosive substance
Foam inhibitors	Silicon polymers, tributylphosphates	Protection of the development of stable foam	Attacking the oil film surrounding every air bubble reduces the boundary surface stress. As a result smaller bubbles coalesce into larger bubbles that rise to the surface
Adhesion improvers	Soaps, polyisobutylenes and polyacrylate polymers	Increase of the oils's adhesive ability	Viscosity is increased. Additives are viscous and sticky
Emulsifier	Sodium salts of sulfonic acids and other organic acids, fat amine salts	Emulsification of oil in water	Adsorbing the emulsifier in the oil/water boundary surface reduces boundary surface stress, as a result of which one fluid disperses into another
Demulsifier	Anionic sulfon acid compounds (dinonylnaphthalinsulfonate)	Demulsification of water	A boundary layer develops between water and oil form substances active in the boundary surface
Bactericide	Phenols, chlorine compounds, formaldehyde derivatives	Increase of the emulsion's working life, prevention of unpleasant odors	The growth of microorganisms is prevented or delayed

materials or atmospheric oxygen causes their concentration to drop. Once the concentration of the additive falls below a certain value, an oil change is necessary.

9.6.2 Lubricants (Lubricating Greases)

Consistent lubricants have a flow limit. No movement occurs below a shear stress that is specific to the lubricant. Only when this flow limit has been exceeded does the viscosity drop from a virtually infinitely high to a measurable value.

Lubricating greases consist of three components: a base oil (75–96 wt%), a thickener (4–20 wt%), and additives (0–5 wt%). Suitable thickeners can be dispersed both in mineral oils and in synthetic or vegetable oils so that consistent lubricants are produced. By far, most greases are manufactured using soaps (metallic salts from fatty acids) as thickeners. Thus, fatty acids are dissolved in the base oil at relatively high temperatures and a suitable metal hydroxide (e.g., hydroxides of sodium, lithium, and calcium or to a lesser extent barium and aluminum) is added subsequently. Long-chain fatty acids come from vegetable or animal oils and can be hydrogenated. Occasionally, not only long-chain fatty acids but also short-chain acids such as acetic, propionic, benzoic acid, etc. are used. Then so-called complex soaps are produced [9.15]. Most soap compounds form a fibrous matrix of interlocking particles, which retains the base oil (Fig. 9.17).

By contrast, aluminum soaps contain a spherical gel structure. The grease's lubricating action is based on the base oil being dispensed slowly and sufficiently in operation under load. The delivery of the base oil depends strongly on the temperature. The lubricating grease releases less and less oil as the temperature drops and the grease becomes stiffer and stiffer (consistency). Beyond a certain temperature limit, this eventually leads to insufficient lubrication in the friction contact. As the temperature increases, more and more oil is released. Simultaneously, the grease ages and oxidizes faster and the deterioration products produced have an adverse effect on the lubrication. A standard value is to cut the grease's working life and thus the relubrication interval in half for every 15 °C rise in temperature above approximately 70 °C. Below 70 °C, the grease's working life and consequently the relubrication interval can be extended unless the temperature drops below the lower limit. The type of base oil, its viscosity, and the additives it contains are decisive for the lubricating properties.

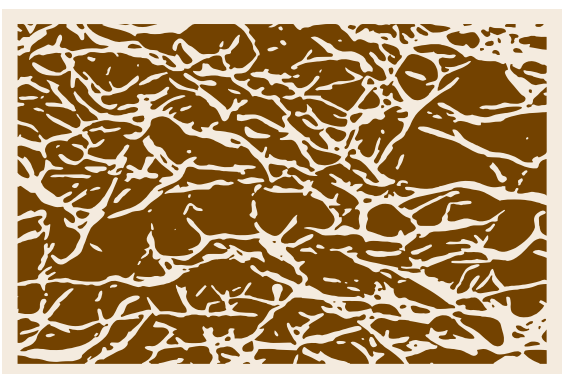

Fig. 9.17 Fiber structure of a grease with soap thickener [9.19]

Lubricating greases are predominantly used at low speeds since the lubricant results in lower frictional heat transportation than oil lubrication. The relevant temperature ranges are generally from −70 to +350 °C. Lubricating greases also frequently have the job of protecting lubricating points from the infiltration of water and dirt and keeping out small quantities of dirt without disrupting the function. Tables 9.13 and 9.14 present performance the characteristics and applications of different lubricating greases.

Additives mainly serve to improve particular performance characteristics of the base oils. They must be uniformly distributed and be dissolved. Additives can improve the following properties of greases in particular: oxidation stability, corrosion protection, water resistance, adhesiveness, and antiwear properties.

The greatest care is necessary when mixing different types of lubricating greases since not all types of lubricating greases are mutually compatible (Table 9.15). Thus, for example, sodium soap grease is incompatible with nearly all other lubricating greases with the exception of barium complex soap grease. Lithium soap grease is incompatible with sodium soap grease, aluminum complex soap grease, and bentonite grease. In turn, bentonite grease is incompatible with all other types of grease.

9.6.3 Solid Lubricants

Solid lubricants are used especially whenever fluid and consistent lubricants cannot provide the lubricating action required. This is frequently the case under the following operating conditions: low sliding speeds, oscillating motions, high specific loads, high or low operating temperatures, extremely low ambient pressures (vacuum), and aggressive ambient atmospheres. Solid lubricants are also used to improve particular properties of fluid and consistent lubricants, i.e., as additives, for example, to minimize friction and wear and to guar-

Table 9.13 Performance characteristics of mineral-oil-based lubricating greases [9.15]

Characteristic		Sodium	Lithium	Calcium	Calcium complex	Bentonite
Thickener form		Fiber	Fiber	Fiber	Fiber	Platelets
Fiber length (μm)		100	25	1	1	0.5
Fiber diameter (μm)		1	0.2	0.1	0.1	0.1
Short description		Long fibered	Medium fibered	Short fibered	Short fibered	Short fibered
Properties						
Drop point (°C)		150–200	170–220	80–100	250–300	≈ 300
Operating temperature	Upper (°C)	+100	+130	+50	+130	+150
	Lower (°C)	−20	−20	−20	−20	−20
Water resistance		Not stable	Good	Very good	Very good	Good
Mechanical stability[a] (0.1 mm)		60–100	30–60	30–60	< 30	30–60
Corrosion protection[b]		Good	Very poor	Poor	Poor	Good
Use						
Suitability for ball bearings		Good	Very good	Variable	Variable	Very good
Suitability for sliding bearings		Good	Good	Variable	–	–
Primary use		Low-viscosity gear grease	Multipurpose grease	–	Multipurpose grease	High-temperature grease
Price		Medium	High	Low	Very high	Very high

[a] Difference in penetration after 60 and 100 000 double strokes
[b] Can be noticeably improved by additives

Table 9.14 Areas of application of synthetic lubricating greases [9.15]

	Mineral oil (benchmark)	PAO	Ester oils	Silicon oils	Alkoxyfluorine oils
Upper limit of application (°C)	150	200	200	250	250
Lower limit of application (°C)	−40	−70	−70	−75	−30
Lubrication of metals	++	++	+++	−−−	–
Lubrication of plastics	○	++	○	+++	+++
Hydrolysis resistance	++	++	○	+++	+++
Chemical resistance	+	+	−−	++	+++
Elastomer compatibility	○	+	○	+++	+++
Toxicity	–	+	+	+++	+++
Flammability	−−−	−−−	+	++	+++
Radiation resistance	−−	−−	–	+	++

+++ excellent; ++ very good; + good; ○ moderate; – adequate; −− limited; −−− poor

Table 9.15 Compatibility of types of lubricating grease [9.15]

Grease type	Na	Li	Ca	Ca complex	Ba complex	Al complex	Bentonite
Na grease		–	–	–	+	–	–
Li grease	–		+	+	+	–	–
Ca grease	–	+		–	+	–	–
Ca complex	–	+	+		+	–	–
Ba complex	+	+	+	+		+	–
Al complex	–	–	–	–	+		–
Bentonite	–	–	–	–	–	–	

+ compatible; – incompatible

antee antiseizure performance. Solid lubricants in the form of powders, pastes or lubricating varnishes contribute directly to the build up of the lubricating film on the one hand or improve the lubricating properties in oils, greases or bearing materials on the other hand.

Substances with a layer lattice structure (graphite, the sulfides MoS_2 and WS_2), selenides (WSe_2), organic substances (PTFE, amides, imides), soft nonmetals (lead sulfide, iron sulfide, lead oxide, and silver iodide), soft nonferrous metals (gold, silver, lead, copper, and indium), and reaction layers on the surface (oxide, sulfide, nitride, and phosphate layers) are used as solid lubricants. Graphite needs water to adhere and to reduce shear strength (low friction) and hence is unsuitable for use in a dry atmosphere or vacuum. Molybdenum disulfide adheres well to all metal surfaces with the exception of aluminum and titanium. It is a highly suitable solid lubricant for temperatures up to 350 °C but costs more than graphite. Polytetrafluoroethylene (PTFE or Teflon) exhibits a low friction factor at low speeds and high loads and is suitable for temperatures from −250 to +250 °C.

Their high proportion of solid lubricants (graphite, molybdenum disulfide or PTFE) distinguishes lubricating varnishes from decorative industrial varnishes. They can be used as a dry film at temperatures between −180 and +450 °C. Lubricating varnishes with oil-resistant binders can also be used in oily systems and are suitable, for example, for bypassing the critical break-in phase without damage or for shortening the break-in time.

9.6.4 Properties of Lubricants

The properties of fluid and consistent lubricants are specified by data predominantly determined with standardized test procedures. It should be noted that not all results from laboratory tests are meaningful for lubrication applications. Along with viscosity, other properties of lubricants are density, specific heat, thermal conductivity, pour point, flashpoint, fire point, foaming behavior, compatibility with sealing materials, and consistency in the case of lubricating grease. Furthermore, aging resistance is vital since it characterizes the abatement of the lubricity and thus the useful life of lubricating oils and determines the oil change interval (Fig. 9.18).

Viscosity

One of a lubricant's most important rheological properties is its viscosity. A fluid's dynamic (or absolute) viscosity η is a measure of the amount it resists a relative motion. The dynamic viscosity η is defined as the shear force F required to realize the relative movement between two planes, acting in the direction of the lubricant flow between the two planes and related to the friction area A and the velocity gradient $\mathrm{d}v/\mathrm{d}y$ between the planes (Fig. 9.19).

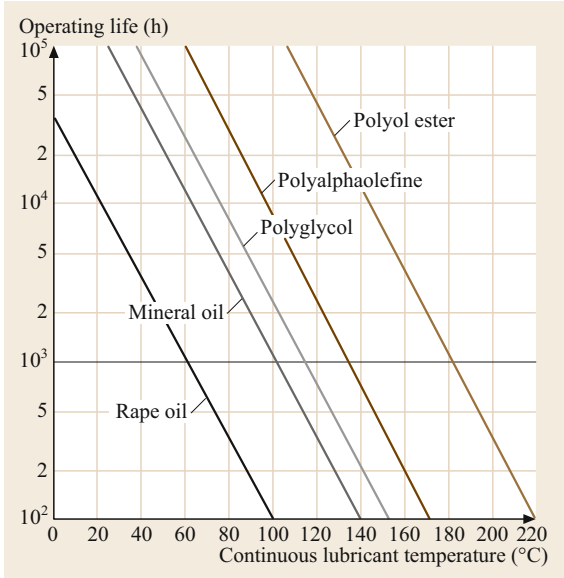

Fig. 9.18 Influence of the lubricant continuous temperature on the approximate useful life of mineral-oil-based and synthetic lubricants (after [9.17])

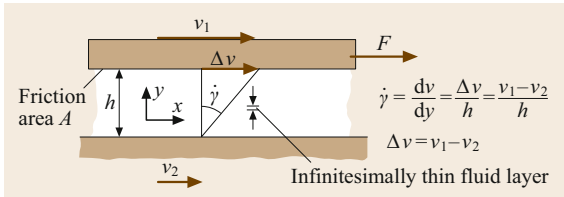

Fig. 9.19 Gap flow and velocity gradient for a Newtonian fluid

Since the shear force per friction area corresponds to the shear stress τ and the velocity gradient to the local shear strain rate $\dot{\gamma}$ (also called shear rate), the following relationship applies

$$\eta = \frac{F/A}{\mathrm{d}v/\mathrm{d}y} = \frac{\tau}{\dot{\gamma}}\,, \tag{9.8}$$

with $\dot{\gamma} = \mathrm{d}v/\mathrm{d}y = \Delta v/h$, where Δv stands for the relative velocity between the two friction bodies and h is the lubrication gap height. The absolute value of the shear force F equals that of the frictional force F_f.

Fluids that can be characterized with (9.8) at constant temperatures and pressures are also called *Newtonian fluids*. Many common fluids, especially those with relatively simple molecular structures, fall into this group (e.g., undoped mineral oils, synthetic fluids, vegetable oils, water, and gases). The unit for dynamic viscosity η is $\mathrm{N\,s/m^2} = \mathrm{Pa\,s}$. Engineering gen-

erally uses mPa s however, which corresponds to cP (centipoise), which was common earlier.

The viscosity is measured with commercially available viscometers, which are standardized as rotation, capillary, falling ball, and falling rod viscometers. Rotation and falling ball viscometers determine the dynamic viscosity η, while the capillary viscometer used most determines the ratio of the dynamic viscosity η and the density ρ. This ratio is known as the kinematic viscosity ν, so that the following applies

$$\nu = \frac{\eta}{\rho} . \tag{9.9}$$

The kinematic viscosity ν is a mathematical value, i.e., it is not a material property. Its units are m^2/s. Usually however mm^2/s is used, corresponding to cSt (centistokes), which was used earlier. The kinematic viscosity is the basic of the standardization of oils. Table 9.16 shows the 20 ISO viscosity groups (ISO VG) by ISO 3448. The basic of the viscosity groups is the middle kinematic viscosity ν_m at 40 °C. Oils of a viscosity group can vary ± 10% around the middle viscosity.

The viscosity of substances that do not behave like a Newtonian liquid is dependent on the temperature, pressure, shear rate, and mean molecular weight. In addition, shear strains are dependent not only on the instantaneous shear rate but also on the past shear history (the lubricant's *memory properties*).

Table 9.16 Viscosity groups by ISO 3448

ISO VG	Middle kinematic viscosity at 40 °C (mm^2/s)	Minimum kinematic viscosity at 40 °C (mm^2/s)	Maximum kinematic viscosity at 40 °C (mm^2/s)
2	2.2	1.98	2.42
3	3.2	2.88	3.52
5	4.6	4.14	5.06
7	6.8	6.12	7.48
10	10	9.00	11.0
15	15	13.5	16.5
22	22	19.8	24.2
32	32	28.8	35.2
46	46	41.4	50.6
68	68	61.2	74.8
100	100	90.0	110
150	150	135	165
220	220	198	242
320	320	288	352
460	460	414	506
680	680	612	748
1000	1000	900	1100
1500	1500	1350	1650
2200	2200	1980	2420
3200	3200	2880	3520

9.6.5 Dependence of Viscosity on Temperature and Pressure

The viscosity of lubricating oils greatly depends on the operating temperature. As the temperature increases, the viscosity of the lubricating oil decreases considerably.

To design lubricated tribological contacts it is important to know the viscosity at the operating temperature since this decisively influences the lubrication film thickness between the surfaces to be separated. The lubricant's viscosity–temperature behavior (η–T behavior) is determined metrologically with viscometers and is frequently specified by simple power and exponential equations. The following equation from Vogel has proven to be valuable for lubricating oils used in the field

$$\eta(T) = A \exp\left(\frac{B}{C+T}\right) . \tag{9.10}$$

In this equation, η stands for the dynamic viscosity in Pa s, A, B, and C are values specific to lubricants that have to be determined for every lubricant, and T is the operating temperature in °C.

Figure 9.20 shows an example for the viscosity–temperature behavior for liquid industrial lubricants in accordance with ISO 3448. The selection of a logarithmic scale on the ordinate axis and a hyperbolic scale on the abscissa gives the viscosity curves a straight gradient. This makes it possible to determine the η–T behavior with only two measurements.

The viscosity index (VI) is also frequently used in practice to specify viscosity–temperature behavior. The viscosity index is a measure of the slope of the *straight lines* of viscosity–temperature compared with a reference lubricant. The higher the VI, the more favorable the η–T behavior. A high VI is characterized by a relatively mild change of viscosity as temperature changes and a low VI by a relatively intense change. Oils that hardly tend to thicken at low temperatures and that do not become low viscosity too fast at high temperatures, i.e., oils with a high VI, should be preferred when machine parts to be lubricated have to operate over a wide range of temperatures. Common paraffin basic oils exhibit a VI of 90−100, synthetic lubricants have a VI of approximately 200 and above.

The viscosity of lubricating oils increases as the pressure rises. The viscosity's pressure dependence only really becomes noticeable at high pressure though. The influence of the pressure decreases as the temperature increases. The viscosity of mineral oil increases more strongly as the pressure increases as the viscosity–temperature curve becomes steeper. The viscosity–pressure behavior can be approximated by

$$\eta(p) = \eta_0(T) \exp\left[\alpha\,(p - p_u)\right] . \tag{9.11}$$

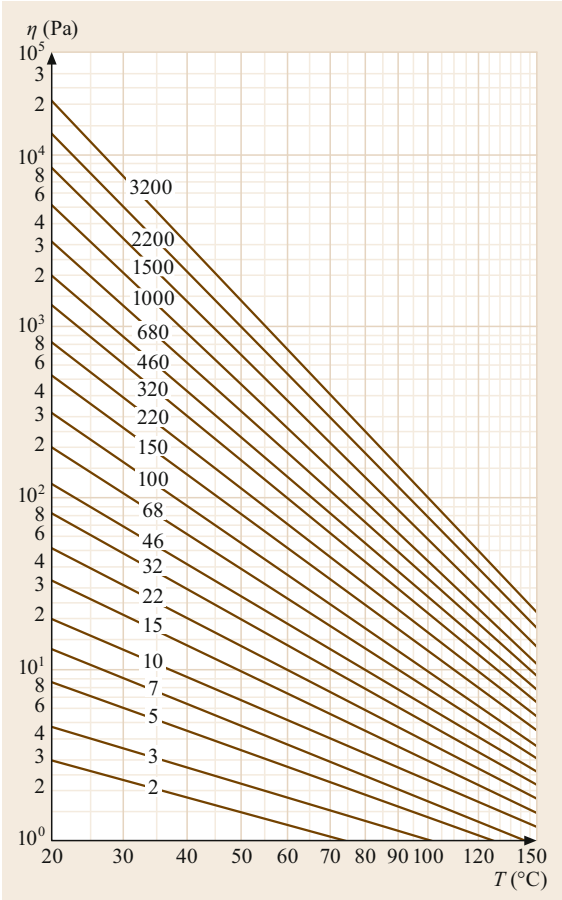

Fig. 9.20 Dependence of the dynamic viscosity η on the temperature T for the ISO VGs (Table 9.16) at density $\rho = 900\,\mathrm{kg/m^3}$ and VI = 95 in accordance with ISO 3448

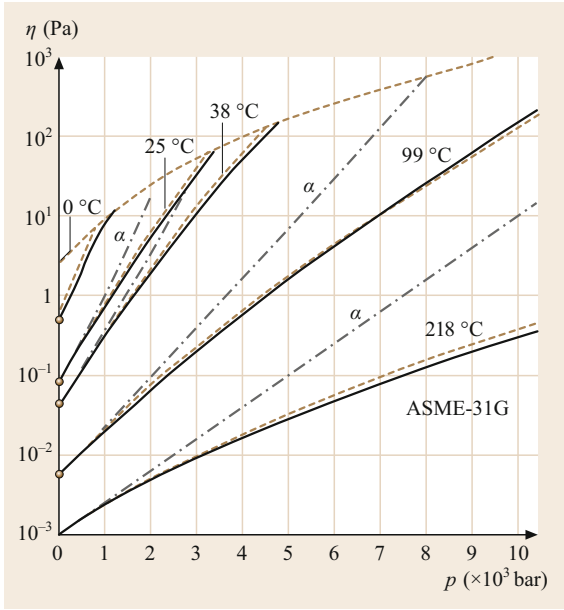

Fig. 9.21 Viscosity of the lubricating oil ASME-31G as a function of pressure and temperature [9.21] (ASME-31G is roughly equivalent to a lubricating oil ISO VG 46). *Dash-dotted lines*: calculations based on (9.11), *dashed lines*: calculations based on (9.12), *continuous lines*: ASME measurements

In the equation, $\eta_0(T)$ is the viscosity at 1 bar and the corresponding operating temperature, α is the viscosity–pressure coefficient, and p_u is the ambient pressure; α is dependent on the base oil (mineral or synthetic) and the additives (Tables 9.12 and 9.17).

Reference [9.1] provides an expression that simultaneously reproduces the dependence of the dynamic viscosity η on the state variables pressure p and temperature T

$$\eta(T,p) = A \exp\left[\frac{B}{C+T}\left(\frac{p-p_u}{2000}+1\right)^{\left(D+E\frac{B}{C+T}\right)}\right]. \tag{9.12}$$

The dependence of the dynamic viscosity on the temperature is represented by the coefficients A, B, and C (Vogel equation) and the dependence on the pressure is described by the coefficients D and E. Tests are employed to determine the coefficients A–E. Figure 9.21 presents the viscosity of a lubricating oil as a function of pressure and temperature.

Table 9.17 Viscosity–pressure coefficient α and examples of increasing viscosity for different lubricants [9.20]

Type of oil	$\alpha_{25\,°C}$ ($\times 10^8\,m^2/N$)	$\frac{\eta_{2000\,bar}}{\eta_0}$ at 25 °C	$\frac{\eta_{2000\,bar}}{\eta_0}$ at 80 °C
Paraffin basic mineral oils	1.5–2.4	15–100	10–30
Naphthene basic mineral oils	2.5–3.5	150–800	40–70
Aromatic solvent extracts	4.0–8.0	1000–200 000	100–1000
Polyolefines	1.3–2.0	10–50	8–20
Ester oils (diester, dendritic)	1.5–2.0	20–50	12–20
Polyether oils (aliph.)	1.1–1.7	9–30	7–13
Silicon oils (aliph. subst.)	1.2–1.4	9–16	7–9
Silicon oils (arom. subst.)	2.0–2.7	300	–
Chlorinated paraffin (depending on level of halogenation)	0.7–5.0	5–20 000	–

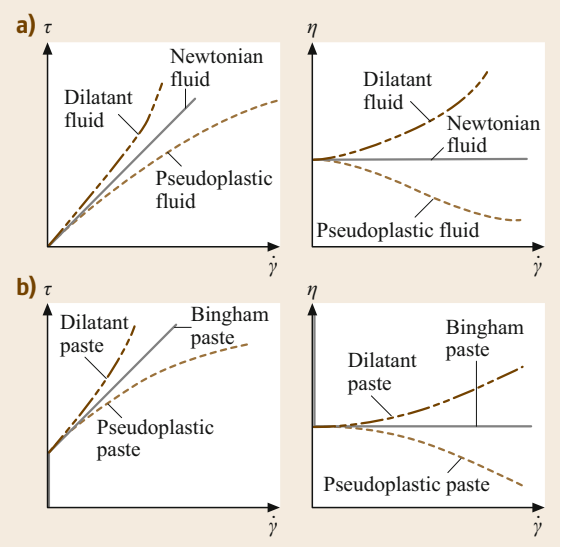

Fig. 9.22a,b Typical flow curves of different lubricants. **(a)** Newtonian, dilatant and pseudoplastic fluid; **(b)** Bingham paste, dilatant and pseudoplastic paste

9.6.6 Dependence of Viscosity on Shear Rate

When the rheological properties are independent of time, the flow properties of viscous lubricants can be easily described. Then the shear stress τ in the lubricant is a simple function of the local shear rate $\dot{\gamma}$, i.e., $\tau = f(\dot{\gamma})$. If this function is linear so that the shear stress is proportional to the shear rate, then a Newtonian fluid exists and the proportionality coefficient is the dynamic viscosity, which also remains constant when shear rates vary (Fig. 9.22a). Pure mineral oils generally exhibit Newtonian properties up to relatively high shear rates of 10^5–$10^6\ s^{-1}$. At higher shear rates, which occur relatively often in tribological contacts such as toothed gears, ball bearing, cam-follower pairs, etc., the viscosity's constancy frequently disappears and the viscosity decreases as the shear rate increases. The lubricant begins to behave like a non-Newtonian fluid, i.e., the viscosity now depends on the shear rate.

Pseudoplastic behavior, also known as shear thinning, is characterized by a decrease of viscosity as the shear rate increases (Fig. 9.22a). Dilatant fluids manifest the opposite of pseudoplastic behavior, i.e., thickening of the lubricant as the shear rate increases (Fig. 9.22a). Dilatant fluids are normally suspensions with a high solid content.

The flow properties of greases can be compared with those of a Bingham substance. In order to generate a flow, a threshold shear stress must first be overcome (Fig. 9.22b). This means that grease behaves like a solid at first. Once the threshold shear stress τ_0 is exceeded, the lubricating grease then flows, for example, with constant viscosity like a Newtonian fluid or even pseudoplastically or dilatantly.

Consistency of Lubricating Greases

The behavior of a lubricating grease is frequently described by its consistency (plasticity). Penetration according to ASTM D-217 and ASTM D-1403 is used as a characteristic. To determine the penetration, the penetration depth of a standard cone with predetermined dimensions into the surface of a lubricating grease is measured in a penetrometer after a penetration time of 5 s at a temperature of 25 °C (in units of 0.1 mm). A difference is made between unworked and worked penetration. Unworked penetration is measured in the unused lubricating grease, whereas worked penetration in measured in already sheared grease that has been worked under standardized conditions in a standard lubricating grease mixer. The higher the worked penetration, the softer the grease. Table 9.18 shows the relationship between penetration and consistency class.

Table 9.18 NLGI consistency classes and applications of lubricating greases (after [9.2]) (NLGI – National Lubricating Grease Institute)

NLGI class	Penetration (0.1 mm)	Consistency	Sliding bearings	Ball bearings	Centralized lubricating systems	Gears	Water pumps	Block greases
000	445–475	Almost fluid			+	+		
00	400–430	Semifluid			+	+		
0	355–385	Extra soft			+	+		
1	310–340	Very soft			+	+		
2	265–295	Soft	+	+				
3	220–250	Medium	+	+				
4	175–205	Relatively firm		+			+	
5	130–160	Firm					+	
6	85–115	Very firm						+

+ Primary fields of application

References

9.1 Gesellschaft für Tribologie: *Tribologie – Verschleiß, Reibung, Definitionen, Begriffe, Prüfung*, GfT Arbeitsblatt, Vol. 7 (GfT, Moers 2002)

9.2 H. Czichos, K.-H. Habig: *Tribologie-Handbuch; Reibung und Verschleiß*, 3rd edn. (Vieweg, Wiesbaden 2003)

9.3 S. Engel: *Reibungs- und Ermüdungsverhalten des Rad-Schiene-Systems mit und ohne Schmierung*, Dissertation (Universität Magdeburg, Magdeburg 2002)

9.4 A. Gervé, H. Oechsner, B. Kehrwald, M. Kopnarski: *Tribomutation von Werkstoffoberflächen im Motorenbau am Beispiel des Zylinderzwickels*, FVV-Heft, Vol. R497 (FVV, Frankfurt am Main 1998)

9.5 J.A. Greenwood, J.B.P. Williamson: The contact of nominally flat surfaces, Proc. R. Soc. A **295**, 300–319 (1966)

9.6 B.J. Hamrock: *Fundamentals of Fluid Film Lubrication* (McGraw-Hill, New York 1994)

9.7 J.W. Kragelski: *Reibung und Verschleiß* (VEB Technik, Berlin 1971)

9.8 K.-H. Habig: Tribologie. In: *Dubbel – Taschenbuch für den Maschinenbau*, 24th edn., ed. by K.-H. Grote, J. Feldhusen (Springer, Berlin, Heidelberg 2014)

9.9 G. Fleischer, H. Gröger, H. Thum: *Verschleiß und Zuverlässigkeit* (Verlag Technik, Berlin 1980)

9.10 K. Wächter: *Konstruktionslehre für Maschineningenieure* (Verlag Technik, Berlin 1989)

9.11 H. Thum: *Verschleißteile* (Verlag Technik, Berlin 1992)

9.12 D. Bartel: *Simulation von Tribosystemen – Grundlagen und Anwendungen*, 1st edn. (Vieweg, Wiesbaden 2010)

9.13 P. Deyber: Möglichkeiten zur Einschränkung von Schwingungsverschleiß. In: *Reibung und Verschleiß von Werkstoffen, Bauteilen und Konstruktionen*, ed. by H. Czichos (Expert-Verlag, Grafenau 1982) p. 149

9.14 O.R. Lang, W. Steinhilper: *Gleitlager* (Springer, Berlin, Heidelberg 1978)

9.15 U.J. Möller, J. Nassar: *Schmierstoffe im Betrieb*, 2nd edn. (Springer, Berlin, Heidelberg 2002)

9.16 G. Poll: Wälzlager. In: *Dubbel – Taschenbuch für den Maschinenbau*, 24th edn., ed. by K.-H. Grote, J. Feldhusen (Springer, Berlin, Heidelberg 2014) pp. 516–531

9.17 G. Niemann, H. Winter, B.-R. Höhn: *Maschinenelemente Band 1; Konstruktion und Berechnung von Verbindungen, Lagern, Wellen*, 4th edn. (Springer, Berlin, Heidelberg 2005)

9.18 W.J. Bartz: Additive – Einführung in die Problematik. In: *Additive für Schmierstoffe*, ed. by W.J. Bartz (Expert, Renningen-Malmsheim 1994)

9.19 G.W. Stachowiak, A.W. Batchelor: *Engineering Tribology*, 2nd edn. (Butterworth-Heinemann, Boston 2001)

9.20 D. Klamann: *Schmierstoffe und verwandte Produkte. Herstellung-Eigenschaften-Anwendung* (VCH, Weinheim 1982)

9.21 Gesellschaft für Tribologie: *Zahnradschmierung*, GfT-Arbeitsblatt, Vol. 5 (GfT, Moers 2002)

Ludger Deters

Institute of Machine Design
Otto von Guericke University Magdeburg
Magdeburg, Germany
ludger.deters@ovgu.de

Ludger Deters was Professor of machine elements and tribology at the Otto von Guericke University Magdeburg for almost 23 years. He retired at end of September 2016. Prof. Deters received his PHD degree from the mechanical engineering department of the University of Clausthal in 1983. From 1983 to 1994 he worked in executive positions in different development and design departments of the machine-building industry. His main research activities at the University of Magdeburg include tribology, lubrication, slider and rolling bearings, wheel/rail contacts, and friction and wear of combustion engine parts.

Dirk Bartel

Institute of Machine Design
Otto von Guericke University Magdeburg
Magdeburg, Germany
dirk.bartel@ovgu.de

Dirk Bartel is Professor at the Otto von Guericke University Magdeburg. In 2000 he completed his PhD and in 2009 his habilitation. Since 2016 he is the head of the institute of competence in mobility (IKAM) and the chair of machine elements and tribology and since 2018 managing director of the Tribo Technologies GmbH. Scientifically, he and his team deal with the development of models for the simulation of lubricated and unlubricated tribosystems and the experimental study of these at the model, component and assembly level.

Part C Manufacturing

Part C Manufacturing

10 **Casting**
Klaus Herfurth, Pulheim, Germany
Stefan Scharf, Magdeburg, Germany

11 **Metal Forming**
A. Erman Tekkaya, Dortmund, Germany

12 **Machining Processes**
Bernhard Karpuschewski, Bremen, Germany
Gerry Byrne, Dublin, Ireland
Berend Denkena, Garbsen, Germany
João Oliveira, São Carlos, SP, Brazil
Anatoly Vereschaka,

13 **Precision Machinery Using MEMS Technology**
Takeshi Hatsuzawa, Yokohama, Japan

14 **Measuring and Quality Control**
Steffen Wengler, Magdeburg, Germany
Lutz Wisweh, Magdeburg, Germany
Shuichi Sakamoto, Niigata, Japan
Norge I. Coello Machado, Santa Clara, Cuba

10. Casting

Casting

Klaus Herfurth, Stefan Scharf

Primary shaping, by definition the production of a solid body from formless material while creating a material cohesion, forms one of the six main groups of production technology according to DIN 8580. It is upstream of all other production processes and creates the precondition for their application. In addition to state-of-the-art manufacturing technologies, such as additive manufacturing, classical casting is still the main application of primary shaping processes. In particular, the casting of metals has a long history of development that goes back to the beginnings of human metallurgical activity. Over time, castings often have been and continue to be decisive for the cultural, technological and economic progress of mankind. Although it has been used for more than 5000 years, the casting process, which has been continuously developed through continuous innovation, is still of central importance within the most modern production processes. Last but not least, a wide variety of casting processes as well as casting materials offer unique conditions for manufacturing high-quality components in a very economical manner. The extraordinary range of applications for cast components extends from one-off production in the arts and crafts sector to highly stressed components for the aerospace industry and up to millionfold mass production in the automotive industry. The following chapter gives an overview of common casting materials and the special features of individual variants of these fascinating manufacturing processes.

10.1 **The Foundry Industry** 326
10.1.1 Advantages of Casting Production 326
10.1.2 Properties of Castings 326
10.1.3 The Development of Casting Processes . 327

10.2 **Cast Alloys** 328
10.2.1 Cast Iron Alloys 328
10.2.2 Cast Steel 333
10.2.3 Cast Nonferrous Alloys 334

10.3 **Primary Shaping** 336
10.3.1 Process Principle in Primary Shaping ... 337
10.3.2 Material State Ready for Primary Shaping 337
10.3.3 Primary Shaping Tools 338
10.3.4 Filling the Primary Shaping Tools 338
10.3.5 Change of State Ready for Primary Shaping 338

10.4 **Shaping of Metals by Casting** 339
10.4.1 Manufacturing of Semifinished Products 339
10.4.2 Manufacturing of Cast Parts 340

10.5 **Guidelines for Design** 350
10.5.1 Manufacture-Orientated Design 351
10.5.2 Stress-Orientated Design 352
10.5.3 Near-Net-Shape Manufacturing and Integral Castings 353

10.6 **Preparatory and Finishing Operations** 354
10.6.1 Melting of Materials for Casting 354
10.6.2 Cleaning of Castings 354
10.6.3 Heat Treatment 354
10.6.4 Inspection and Testing Methods 354

References 355

Manufacturing is the production of workpieces of a geometrically defined shape. Unlike other production technologies, manufacturing technology produces products distinguished by material and geometric characteristics.

According to DIN 8580 [10.1] today's and tomorrow's many and varied manufacturing processes can be classified into six main groups (Fig. 10.1) according to the criteria *changing of material cohesion* (creation, preservation, increase, and reduction). These main groups are: primary shaping, forming, cutting, joining, coating, and changing of material properties. The main groups are subdivided into groups. Within these groups, the manufacturing processes themselves are distinguished by subgroups.

K.-H. Grote, H. Hefazi (Eds.), *Springer Handbook of Mechanical Engineering*, Springer Handbooks,
https://doi.org/10.1007/978-3-030-47035-7_10

Create cohesion	Preserve cohesion	Reduce cohesion	Increase cohesion	
	Shape changing			
1. Primary shaping	2. Metal forming	3. Cutting	4. Joining	5. Coating
	6. Changing of material properties			
	Rearrangement of material particles	Elimination of material particles	Addition of material particles	

Fig. 10.1 Classification of manufacturing processes (DIN 8580) ◄

Casting is an important group of the main group *primary shaping*. The products of casting are so-called castings from metallic materials, so-called cast alloys. The foundry industry produces the castings.

10.1 The Foundry Industry

The foundry industry produces castings from metallic materials. Castings in various shapes and materials are to be found in all branches of engineering, such as in road and rail vehicles, machinery, the aerospace industry, electric power engineering, shipbuilding, pumps and fittings, electrical engineering, fine mechanics, architecture, electronics, medicine and optics, as well as office machines and cast art. Most technical products are not conceivable without castings.

10.1.1 Advantages of Casting Production

The following outlines the economical advantages resulting from the use of castings. It is based on two fundamental aspects. Firstly, the overall consideration from melting to recycling, [10.1]. The advantages are the following:

- Exceptional freedom in the choice of shape
- Castability of all technically important metals
- Mechanical properties of cast materials that are no longer governed by those of the wrought materials
- Optimal components through the combination of material properties and shape
- Near net shape castings, i.e., reduced machining costs
- Integral castings, i.e., reduced assembly costs
- Tailored castings
- A high recycling rate, no down-cycling
- Material savings through the use of castings
- Ecological benefits
- When considered in overall terms, a lower specific use of energy on the whole.

Production from the shapeless condition, i.e., the melt, and solidification in the prescribed cavity, i.e., sand or a permanent mold, naturally enables great freedom in the choice of shape. It is possible to produce castings weighing less than 1 g and as much as 200 t, the weight only being restricted by handling and transport facilities.

There are very few restrictions with regard to the geometry of castings. All that can be drawn is also castable, but it is sometimes difficult to draw what is easy to cast.

High quality casting designs increasingly result from the incorporation of numerical simulation of mold filling and solidification, rapid prototyping, and simultaneous engineering. This takes place through close cooperation between foundrymen and designers. In the future it is expected that bionic and biological designing will provide new impulses for shaping. This will enable a large amount of freedom in the choice, thereby leading to full utilization of modern computer technology in the foundry industry.

10.1.2 Properties of Castings

Castings are produced from the following material groups: Iron alloys (cast steel, cast iron), aluminum, magnesium, titanium, copper, zinc, tin, nickel, and cobalt alloys. All of these are cast alloys.

Independent of the type of production process, in the manufacture of metallic components by casting, differentiation is always to be made between the material properties and the properties of the casting itself. In order to achieve a prescribed component characteristic the material and the geometry determine and complement each other in the properties of the component. These properties depend on the following:

- The geometry of the part
- The chemical composition of the cast material
- The treatment of the melted material (inoculation, modification, desulfurization, deoxidation, magnesium treatment, grain refinement, etc.)

- The type of molding and casting process
- The rate of cooling from casting to the ambient temperature
- The subsequent heat treatment
- The subsequent treatment of the outer layer (chemical-thermal process, surface deformation, surface alloying, surface remelting, etc.)
- Changes in the surface layer through machining
- The type of coating (painting, galvanizing, enameling etc.)

During the past decades the properties of cast alloys have also been further developed and considerably improved. For example, whereas in the 1950s only steel casting was able to achieve tensile strengths of more than $400\,N/mm^2$, today the designer has the choice of three higher strength groups of ferrous materials, i.e., spheroidal graphite cast iron, malleable cast iron, and cast steels. In many cases, this has enabled the highly economical substitution of forged and rolled steels.

There have also been further developments in nonferrous metal cast alloys, especially in the fields of aluminum and magnesium materials, which increasingly enable the use of these alloys in automotive manufacturing.

Consequently, the last decade has seen substantial rates of growth in the production of spheroidal graphite cast iron, as well as in aluminum and magnesium alloy castings. This is directly associated with the efforts towards light construction but also towards the reduction of total production costs.

The trend towards light construction is not only being realized with less dense cast materials, e.g., aluminum, but is also being achieved with higher density materials, e.g., spheroidal graphite cast iron. This is the result of the combined effect of material and shape as well as further development of casting technology.

In the selling of castings the material properties were traditionally (and often still are) taken as a basis for the contract, i.e., such material characteristics as yield strength, tensile strength, elongation at fracture, fatigue strength etc., which were determined from separately quasi simple geometrical samples. However, these samples only partially reflect the capabilities of the cast materials. Cast components are increasingly being designed on the basis of fracture mechanics. This shows that cast components are frequently unbeatable.

10.1.3 The Development of Casting Processes

The development of molding and casting processes over recent decades has led to the fact that the casting more closely approaches the shape of the finished part. The best results have been achieved with investment casting (lost wax molding process) and high pressure die casting, which can produce almost finished parts. These often require only minimum machining, e.g., fine machining of operating surfaces. Additionally, the development of weldable aluminum pressure die castings has enabled further possibilities of use.

Mechanical machining requires a relatively high amount of energy, the generation of 1 t of chips requiring the same amount of energy as that for the melting of 1 t of material.

The chips produced in machining the casting to the complete product, which can often result in a material utilization of less than 50%, should now be a thing of the past. The future lies in the production of near net shape castings with the resultant large savings in energy.

In many cases, groups of parts were and are being assembled from numerous individual components (turned, milled, and sheet metal components) by means of welding, riveting, bolting, etc. This type of assembly not only necessitates expensive manufacture of individual parts but also gives rise to considerable assembly costs.

The casting of integral components (one-piece-castings), through which the numerous previously necessary individual parts are combined in one casting, is an ideal way towards a new generation of parts. These integral castings can additionally better incorporate specific functional elements, resulting in considerable savings in material and energy.

Recycling is understood to be the return of material into the production process. In doing so, the aim is not to leave industrial production open-ended but, as with nature, to close the circuit, where material flows.

Recycling is in no way a new term for metallic materials but is rather a thousands of years old practice of returning metallic waste into the production process. Recycling of cast steel, cast iron, and cast nonferrous metals is a worldwide normal practice. Recycling of metallic materials leads to the saving of energy, preservation of our raw materials reserves, and thus to relief of our environment.

Development of the properties of the cast materials and the improvement of the molding and casting processes in the foundry industry have not only led to higher productivity but also material saving through:

- The reduction of wall thicknesses as a result of better pouring possibilities
- The use of higher strength materials
- Optimal casting design with, for example, ribbing or realization of hollow structures
- The reduction of machining allowances

- Material substitution, e.g., spheroidal graphite cast iron instead of forged steel and aluminum alloys instead of cast iron

These savings in materials reduce the weight of the components as well as the amount of machining. They also result in energy savings and thus preservation of the environment.

Overall consideration of component manufacture from the raw material to the finished part and taking account of recycling of metallic materials, i.e., an economic balance, illustrated that, by comparison with the other main production processes, the manufacture and use of castings results in substantial energy savings and thus ecological advantages, e.g., the reduction of CO_2.

From case studies, it is a well-known fact that, by comparison with other process variants, near net shape castings are clearly advantageous with regard to specific energy requirements for the finished components, especially with respect to machining from solid semiproducts. Component manufacture by casting is also clearly preferential when considering ecological aspects such as CO_2 emission.

Foundries pursue objective environmental management and confront public option with declarations of their achievements.

10.2 Cast Alloys

Cast alloys are metallic materials manufactured by primary shaping in a foundry. Cast alloys can be classified into two main groups: Cast ferrous materials (cast irons and cast steels) and cast nonferrous materials (cast aluminum, cast magnesium, cast copper, and cast zinc alloys).

10.2.1 Cast Iron Alloys

Cast iron alloys can be classified into seven groups:

- Gray cast iron
- Spheroidal graphite cast iron
- *Solid solution strengthened cast iron*
- Ausferrite spheroidal graphite cast iron
- Compacted graphite cast iron
- Malleable cast iron
- Austenitic cast iron
- Abrasion resisting alloyed cast iron
- *Continuous cast iron*.

Cast Iron

The term *cast iron* designates an entire family of metallic materials with a wide variety of properties. It is a generic term like steel, which also designates a family of metallic materials. Steels and cast irons are both primarily iron with carbon as the main alloying element. Steels contain less than 2%, while all cast irons contain more than 2% carbon. About 2% is the maximum carbon content at which iron can solidify as a single phase alloy with all of the carbon in solution in austenite. Thus, the cast irons by definition solidify as heterogeneous alloys and always have more than one constituent in their microstructure.

In addition to carbon, cast irons also must contain appreciable silicon, usually from 1 to 3%, and thus they are actually iron-carbon-silicon alloys. The high carbon content and the silicon in cast irons make them excellent casting alloys. Their melting temperatures are appreciably lower than those of steel. Molten cast irons are more fluid than molten steel and less reactive with molding materials. Formation of lower density graphite in cast iron during solidification reduces the change in volume of the metal from liquid to solid and makes production of more complex castings possible.

The various types of unalloyed cast irons cannot be designated by chemical composition because of similarities between the types. Unalloyed cast irons are designated by their mechanical properties. High-alloy cast irons are designated by their chemical composition and mechanical properties. These have a wide range in chemical composition and also contain major quantities of other elements.

The presence of certain minor elements is also vital for the successful production of each type of cast iron. For example, nucleating agents, called inoculants, are used in the production of gray cast iron to control the graphite type and size. Trace amounts of bismuth and tellurium in the production of malleable cast iron, and the presence of a few hundredth of a percent of magnesium causes the formation of spheroidal graphite cast iron.

In addition, the composition of a cast iron must be adjusted to suit particular castings. Small castings and large castings of the same grade of cast iron cannot be made from the same composition of alloy. For this reason, most cast iron castings are purchased on the basis of mechanical properties rather than composition. The common exception is for castings that require special properties such as corrosion resistance or elevated temperature strength.

The various types of cast iron can be classified according to their microstructure. This classification is based on the form and shape in which the major portion

of carbon occurs in the cast irons. This system provides for five basic types of gray cast iron, spheroidal graphite cast iron, malleable cast iron, compacted graphite cast iron, and white cast iron. Each of these types may be moderately alloyed or heat treated without changing its basic classification. The high-alloyed cast irons, generally containing over 3% of added alloying element, can also be individually classified as gray or spheroidal graphite cast iron or white cast iron, but the high-alloyed cast irons are classified as a separate group.

Gray Cast Iron. When the composition of a molten cast iron and its cooling rate are appropriate, the carbon in the cast iron separates during solidification and forms separate graphite flakes that are interconnected within each eutectic cell (EN 1561). The graphite grows edgewise into the liquid and forms the characteristic flake shape. When gray cast iron is broken, most of the fracture occurs along the graphite, thereby accounting for the characteristic gray color of the fractured surface.

Because the large majority of iron castings produced are of gray cast iron, the generic term is often improperly used to mean gray cast iron specifically.

The properties of gray cast iron are influenced by the size, amount, and distribution of the graphite flakes, and by the relative hardness of the matrix metal around the graphite. These factors are controlled mainly by the carbon and silicon contents of the metal and the cooling rate of the casting. Slower cooling and higher carbon and silicon contents tend to produce more and larger graphite flakes, a softer matrix structure, and lower strength. The flake graphite provides gray cast iron with unique properties such as excellent machinability at hardness levels that produce superior wear-resisting characteristics, the ability to resist galling, and excellent vibration damping.

The amount of graphite present, as well as its size and distribution, are important to the properties of the cast iron. Wherever possible, it is preferable to specify the desired properties rather than the factors that influence them.

Microscopically, all gray cast irons contain flake graphite dispersed in an iron-silicon matrix. How much graphite is present, the length of the flakes, and how they are distributed in the matrix directly influence the properties of the cast iron.

The basic strength and hardness of the cast iron is provided by the metallic matrix in which the graphite occurs. The properties of the metallic matrix can range from those of a soft, low-carbon steel to those of hardened, high-carbon steel. The matrix can be entirely ferritic for maximum machinability, but the cast iron will have reduced wear resistance and strength. An entirely pearlitic matrix is characteristic of high-strength gray cast iron, and many castings are produced with a matrix microstructure of both ferrite and pearlite to obtain intermediate hardness and strength. Alloying element additions and/or heat treatment can be used to produce gray cast iron with very fine pearlite or with an acicular matrix structure.

Graphite has little strength or hardness, so it decreases these properties of the metallic matrix. However, graphite provides several valuable characteristics to gray cast iron: the ability to produce sound castings economically in complex shapes, good machinability, even at wear-resisting hardness levels and without burring, dimensional stability under different heating, high vibration damping, and borderline lubrication retention.

The properties of gray cast iron primarily depend on its chemical composition. The lower strength grades of gray cast iron can be produced consistently by simply selecting the proper melting stock. Grey cast iron castings in the higher strength grades require close control of their processing and chemical composition.

The majority of the carbon in gray cast iron is present as graphite. Increased amounts of graphite result from an increased total carbon content in the gray cast iron. This decreases the strength and hardness of the gray cast iron, but increases other desirable characteristics.

An appreciable silicon content is necessary in gray cast iron because this element causes the precipitation of the graphite in the material. The silicon also contributes to the distinctive properties of the gray cast iron. It maintains a moderate hardness level, even in the fully annealed condition, and thus assures excellent machinability. Also, silicon imparts corrosion resistance at elevated temperature and oxidation resistance in gray cast iron.

Gray cast iron can be alloyed to increase its strength and hardness as-cast or its response to hardening by heat treatment.

A very important influence on gray cast iron properties is the effective section thickness in which it is cast. The thicker the wall and the more compact the casting, the lower the temperature at which liquid metal will solidify and cool in the mold. As with all metals, slower solidification causes a larger grain size to form during solidification. In gray cast iron, slower solidification produces a larger graphite flake size.

Gray cast iron is commonly classified by its minimum tensile strength or by hardness (Table 10.1). The mechanical properties of gray cast iron are determined by the combined effect of its chemical composition, processing technique in the foundry, and the solidification and cooling rates. Thus, the mechanical properties

Table 10.1 Mechanical properties of gray cast iron

Tensile strength (N/mm^2)	100–350
Brinell hardness	155–265

of the gray cast iron in a casting will depend on its shape, size and wall thickness as well as on the gray cast iron that is used to pour it. Five grades of gray cast iron are classified by their tensile strength in EN 1561. The grades of gray cast iron also can be specified by Brinell hardness only. The chemical composition and heat treatment, unless specified by the purchaser, shall be left to the direction of the manufacturer, who shall ensure that the casting and heat treatment process is carried out with the same process parameters.

Spheroidal Graphite Cast Iron. Spheroidal graphite cast iron or ductile iron (EN 1563) is characterized by the fact that all of its graphite occurs in microscopic spherolites. Although this graphite constitutes about 10% by volume of this material, its compact spheroidal shape minimizes the effect on mechanical properties.

The difference between the various grades of spheroidal graphite cast irons is in the microstructure of the material around the graphite, which is called the matrix. This microstructure varies with the chemical composition and the cooling rate of the casting. It can be slowly cooled in the sand mold for a minimum hardness as-cast condition or, if the casting has sufficiently uniform sections, it can be shaken out of the mold while still at a temperature above the critical and normalized.

The matrix microstructure and hardness can also be changed by heat treatment. The high ductility grades are usually annealed so that the matrix structure's ferrite is entirely free of carbon. The intermediate grades are often used in the as-cast condition without heat treatment and have a matrix structure of ferrite and pearlite. The ferrite occurs as rings around the graphite spheroids. Because of this, it is called bull-eye ferrite. The high-strength grades are usually given a normalizing heat treatment to make the matrix all pearlite, or they are quenched and tempered to form a matrix of tempered martensite. However, spheroidal graphite cast iron can be moderately alloyed to have an entirely pearlitic matrix as-cast condition.

The chemical composition of spheroidal graphite cast iron and the cooling rate of the casting directly affect its tensile properties by influencing the type of matrix structure that is formed. All of the regular grades of the spheroidal graphite cast iron can be made from the same cast iron provided that the chemical composition is appropriate so that the desired matrix microstructure can be obtained by controlling the cooling rate of the casting after it is poured or by subsequent heat treatment. For most casting requirements, the chemical composition of the spheroidal graphite cast iron is primarily a matter of facilitating production.

Table 10.2 Mechanical properties of spheroidal graphite cast iron

Tensile strength (N/mm^2)	350–900
Yield strength (N/mm^2)	220–600
Elongation (%)	6–22
Brinell hardness	130–330

The common grades of spheroidal graphite cast iron differ primarily in the matrix structure that obtains the spheroidal graphite. These differences are the result of differences in the chemical composition, in the cooling rate of the casting, or the result of heat treatment.

Solid Solution Strengthened Cast Iron. Solid solution strengthened ferritic spheroidal graphite cast iron [10.2] has a matrix of predominantly ferrite with a maximum pearlite of 5%. The amount of free cementite should not exceed 1%. In order to fulfil the requirements for the mechanical properties, a ferritic structure solid solution strengthened by silicon is recommended. The silicon content is for tensile strength of $450\,N/mm^2$ approx. 3.20%, for tensile strength of $500\,N/mm^2$ approx. 3.80% and for tensile strength of $600\,N/mm^2$ approx. 4.30%. These solid solution strengthened ferritic spheroidal graphite iron grades are used for applications where good machinability, high ductility and high proof strength are required. The solid solution strengthened cast iron grades were included in EN 1563.

All in all 16 grades of spheroidal graphite cast iron are classified by their tensile properties or hardness in EN 1563 (Table 10.2). The common grades of spheroidal graphite cast iron also can be specified only by Brinell hardness. The method of producing spheroidal graphite, the chemical composition and heat treatment will be specified by the purchaser.

Ausferrite Spheroidal Graphite Cast Iron. This group of spheroidal graphite cast iron (EN 1564) is well known as ACI (austempered cast iron), and recently as ausferrite spheroidal graphite cast iron. The development of ausferrite spheroidal graphite cast iron has given the design engineer a new group of cast ferrous materials that offer the exceptional combination of mechanical properties (Table 10.3) equivalent to cast and forged steels, and production costs similar to those of conventional spheroidal graphite cast iron.

Ausferrite spheroidal graphite cast iron provides a wide range of properties, all produced by varying

Table 10.3 Mechanical properties of ausferrite spheroidal graphite cast iron

Tensile strength (N/mm^2)	800–1400
Yield strength (N/mm^2)	500–1100
Elongation (%)	1–10
Brinell hardness	250–480
Abrasion resistant spheroidal graphite ausferritic cast irons	
Tensile strength (N/mm^2)	1400–1600
Yield strength (N/mm^2)	1100–1300
Elongation (%)	0–1
Vickers hardness	400–500

Table 10.5 Mechanical properties of malleable cast iron

White malleable cast iron	
Tensile strength (N/mm^2)	350–500
Yield strength (N/mm^2)	170–350
Elongation (%)	3–16
Brinell hardness	200–250
Black malleable cast iron	
Tensile strength (N/mm^2)	300–800
Yield strength (N/mm^2)	200–600
Elongation (%)	1–10
Brinell hardness	150–320

the heat treatment (austempering) of the same castings. Austempering is a special heat treatment process, which consists of three steps:

- Austenitize in the temperature range of 840–950 °C for a time sufficient to produce a fully austenitic matrix that is saturated with carbon.
- Rapidly cool the entire part to an austempering temperature in the range of 230–400 °C without forming pearlite or allowing the formation of ausferrite to begin.
- Isothermally treat at the austempering temperature to produce ausferrite with an austenite carbon content in the range of 1.8–2.2%.

After heat treatment (austempering) the matrix consists of acicular ferrite and residual austenite without carbides.

Six grades of ausferrite spheroidal graphite cast iron are classified by their tensile properties in ISO/WD 17804 and two abrasion resistant grades are classified by Vickers hardness.

Compacted Graphite Cast Iron. Compacted graphite cast iron (vermicular graphite cast iron, EN 16079) is a recent addition to the family of commercially produced cast irons (Table 10.4). Its characteristics are between that of the gray cast iron and spheroidal graphite cast iron. The graphite in compacted graphite cast iron is in the form of interconnected flakes. The short span and blunted edges of graphite in this material provide improved strength, some ductility and a better machined finish than gray cast iron. The interconnected compacted graphite cast iron provides slightly higher thermal conductivity, more damping capacity, and better machinability than those obtained with spheroidal graphite cast iron.

Compacted graphite cast iron provides similar tensile and yield strengths to ferritic spheroidal graphite cast iron and malleable cast iron, although the ductility is less.

Table 10.4 Mechanical properties of compacted graphite cast iron

Tensile strength (N/mm^2)	300–500
Yield strength (N/mm^2)	220–380
Elongation (%)	0.5–1.5
Brinell hardness	140–260

Malleable Cast Iron. The starting point is a cast iron in which the carbon and silicon contents are arranged so that the casting is graphite-free after solidification, the entire carbon content being bonded to the iron carbide (cementite). If the casting is then heat-treated (tempered), the cementite decomposes without residue.

Two kinds of malleable cast iron are distinguished (Table 10.5):

- White malleable cast iron, which is decarbonized during heat treatment; and
- black malleable cast iron, which is not decarbonized during heat treatment.

White malleable cast iron (EN 1562) is produced by heating for 50–80 h at about 1050 °C in a decarburizing atmosphere (CO, CO_2, H_2, H_2O). In this process carbon is removed from the casting, so that after cooling a purely ferritic microstructure is in the casting. White malleable cast iron with small cross sections welds easily.

Black malleable cast iron is produced by heating in a neutral atmosphere, first for about 30 h at 950 °C. In this process the cementite of the ledeburite decomposes into austenite and graphite (temper carbon), which is precipitated in fluky clusters. In a second step of the heat treatment the austenite is converted during slow cooling from 800 to 700 °C into ferrite and temper carbon or transformed during quick cooling into pearlite and temper carbon.

In EN 1562 five grades of white malleable cast iron and nine grades of black malleable cast iron are classified by tensile strength.

Table 10.6 Mechanical properties of austenitic cast iron

With flake graphite	
Tensile strength (N/mm^2)	140–220
Elongation (%)	2
Brinell hardness	120–150
With spheroidal graphite	
Tensile strength (N/mm^2)	370–500
Yield strength (N/mm^2)	210–290
Elongation (%)	1–45
Brinell hardness	120–255

Austenitic Cast Iron. High-alloy cast iron is used to produce components that require resistance to corrosives in the operating environment such as seawater, sour well oils, commercial organic and inorganic acids, and alkalis. The ability to easily cast it into complex shapes and the ease of machining some types of this material, make high-alloy cast iron an attractive material for the production of components for chemical processing plants, petroleum refining, food handling, and marine service. Two types dominate high alloy corrosion resistant cast iron: nickel-alloyed cast iron (austenitic cast iron, EN 13835) and high-Si cast iron.

Nickel-alloyed cast iron owes its excellent corrosion resistance to the presence of nickel in concentrations of 12.0–36.0%, a chromium content of 1.0–5.5% and, in one type, s copper content of 5.5–7.5%. These cast irons have an austenitic matrix.

Ten grades of austenitic cast iron with spheroidal graphite and two grades of austenitic cast iron with flake graphite are classified in EN 13835 by chemical composition and mechanical properties, like austenitic steels.

The mechanical properties of austenitic cast iron with spheroidal graphite and with flake graphite are shown in Table 10.6.

Abrasion Resisting Alloyed Cast Iron. High-alloy white cast iron (EN 12513) is specially qualified for abrasion-resistant applications. The predominant carbides in its microstructure provide the high hardness necessary for crushing and grinding other materials without degradation. The supporting matrix structure may be adjusted by alloy content and/or heat treatment to develop the most cost-effective balance between resistance to abrasive wear and the toughness required to withstand repeated impact loading. High-alloy white cast iron is easily cast into shapes required for crushing and grinding or the handling of abrasive materials.

Abrasion resistance concerns the conditions under which a metal or alloy is used. The ability of a part to resist a weight loss due to abrasion depends upon its microstructure, the actual mechanical operations of the part, and the kind and size of material being moved, crushed or ground.

Most of the white cast iron designated for abrasion-resistant applications falls within the high-alloy cast iron category, but unalloyed white cast iron is common and provides satisfactory service where the abrading material is not fine or where replacement is not frequent or expensive. All alloyed cast iron contains chromium to prevent the formation of graphite and to ensure the stability of the carbides in the microstructure. Alloy white cast iron also may contain nickel, molybdenum, copper, or a combination of these alloying elements to prevent or minimize the formation of pearlite in the microstructure.

Unalloyed white cast iron castings develop hardnesses in the range 350–550 BHN. Their microstructures consist of primary iron carbides with a microhardness of 900–1200 VHN in a pearlitic matrix with a microhardness of 220–300 VHN. Alloyed martensitic white cast iron, however, develops Brinell hardnesses in the 500–700 range. The carbide hardness remains 900–1200 VHN, but martensitic, always associated with some retained austenite, exhibits a microhardness of 600–700 VHN. For many abrasion-resistant applications; the more costly alloyed white cast iron with martensitic matrix structures provide the most economical service.

EN 12513 covers the composition and hardness of abrasion-resistant white cast iron. Martensitic white cast iron falls into two major groups:

- The low-chromium group with 1–4% chromium and 3–5% nickel
- The high-chromium white cast iron containing 14–28% chromium with 1–3% of molybdenum, often alloyed further with additions of nickel and copper

A third but minor category comprise the straight 25–28% chromium white cast iron.

Continuous Cast Iron. In the manufacture of continuous cast iron (EN 16482) solidification begins in a water-cooled, open-ended die. Because the thermal conditions are different from those for sand casting, solidification is faster. Depending on the process, the results in properties that differ from those obtained by sand casting and a particularly close-grained, dense material structure. Very high pressure tightness in respect of liquids and gases is a feature of continuous cast iron. Continuous cast grey and spherolitic graphite iron is manufactured using the horizontal continuous casting method. The mechanical properties of grey iron and spherolitical graphite cast iron are described in

EN 16482 [10.3]. It gives four grades of grey cast irons and 14 grades of spherolitic graphite cast iron. Continuous cast irons are semifinished cast products. The products of continuous cast irons are round, quadratic, rectangular or half round bars.

10.2.2 Cast Steel

Cast steels can be classified into four groups:

- Cast carbon and cast low-alloy steel
- Cast high-alloy steel
- Cast stainless steel
- Cast heat-resisting steel.

Cast Carbon and Cast Low-Alloy Steel

This group of cast steels consists of many subgroups: steel castings for general purposes (DIN 1681, EN 10293 steel casting for general engineering uses), steel casting for pressure purposes (partially EN 10213), steel castings with improved weldability and toughness for general purposes (DIN 17182, EN 10293 steel castings for general engineering uses, draft), quenched and tempered steel castings for general purposes (DIN 17205, EN 10293 steel castings for general engineering uses, draft), steel castings for use at room temperature and elevated temperatures (EN 10213-2), and steel castings for use at low temperatures (EN 10293-3).

Carbon steel is considered to be steel in which carbon is the principal alloying element. Other elements that are present and that, in general, must be reported are manganese, silicon, phosphorus, and sulfur. In a sense, all of these elements are *residuals* from the raw materials (coke, iron ore) used in the manufacture of the steel, although the addition of manganese is often made during the steel making process to counter the deleterious effect of sulfur.

Low-alloy cast steels are considered to be those steels to which elements (other than carbon) are added deliberately to improve mechanical properties.

For all cast carbon and cast low-alloy steels, the mechanical properties are controlled by the chemical composition, the heat treatment and the microstructure of these cast steels. Among the exceptions are the effect of carbon on increasing hardness, the effect of nickel on increasing toughness, and the effect of combinations of chromium, molybdenum, vanadium, and tungsten on increasing elevated temperature strength. The major reason for using alloying elements in low-alloy cast steels is to make the role of heat treatment on increasing strength effective over a wide range of material thickness by quenching and tempering. This effectiveness is termed *hardenability*.

Table 10.7 Mechanical properties of steel castings for general engineering uses

Tensile strength (N/mm^2)	380–1250
Yield strength (N/mm^2)	200–1000
Elongation (%)	7–25

Table 10.8 Mechanical properties of cast stainless steels

Tensile strength (N/mm^2)	430–1100
Yield strength (N/mm^2)	175–1000
Elongation (%)	5–30

Thirty grades of steel castings for general engineering uses (five grades of carbon cast steels, 20 grades of low alloy cast steels, and five grades of high alloy cast steels) are classified by their chemical composition, heat treatment processes (austenitizing, air cooling/austenitizing, quenching, tempering), and mechanical properties in EN 10293 (Table 10.7).

EN 10213 consists of steel castings for pressure purposes, in specially cast steel grades for use at room temperature and elevated temperatures (carbon cast steels, low alloy cast steels, high alloy cast steels), cast steel grades for use at low temperatures (low alloy cast steels, high alloy cast steel), and cast austenitic and austenitic-ferritic steel grades (high alloy cast steel grades).

High-Alloy Cast Steel

There are two main groups of high-alloy cast steels: Cast stainless steels and cast heat-resisting steels.

Corrosion Resistant Cast Steel. Cast stainless steels (EN 10213, EN 10283, SEW 410) are distinguished by their special resistance to chemically corrosive substances; in general, they have a chromium content of at least 12 wt %. The cast stainless steels in EN 10213, EN 10283, and SEW 410 are subdivided into martensitic, ferritic-carbidic, ferritic-austenitic, austenitic, and full austenitic steels. Cast stainless steels are suitable for welding. Their resistance to intercrystalline corrosion in mill finishing is an important property of cast stainless steels (Table 10.8).

A special kind of cast stainless steels are the duplex-steels (dual phase steels) with about 50% austenite and 50% soft martensite, in which the two phases fulfil different functions: The austenite guarantees corrosion protection, e.g., seawater resistance in this case, and the soft martensite guarantees component strength.

In EN 10213, EN 10283, and SEW 410 44 grades of cast stainless steels are classified by chemical composition and mechanical properties. The main alloying elements are chromium, nickel, and molybdenum.

Table 10.9 Mechanical properties of heat-resistant cast steel at room temperature

Tensile strength (N/mm^2)	400–440
Yield strength (N/mm^2)	220–230
Elongation (%)	5–15

Heat-Resisting Cast Steel. The chief requirement for heat-resisting cast steels (EN 10295, SEW 471, SEW 595) is not especially good high-temperature strength but sufficient resistance to hot gas corrosion in the temperature range above 550 °C. The highest temperature at which a heat-resisting steel can be used depends on operational conditions. Recommended temperatures for air and hydrogen atmospheres are up to 1150 °C depending on the chemical composition.

The scaling limit temperatures for the heat-resisting steels is defined as the temperature at which the material loss in clean air is 0.5 mg cm^{-2} h^{-1}.

The scale resistance of heat-resisting cast steels is based on the formation of dense, adhesive surface layers of oxides of the alloying elements chromium, silicon, and aluminum (Table 10.9). The protective effect starts when the chromium content is 3–5%, but chromium contents up to 30% can be alloyed. The protective effect of these layers is limited by the corrosive low-melting-point eutectics and by carburizing. To increase the heat resistance the alloying element nickel is added in addition to chromium (Cr + Ni = 25–35%).

In EN 10295, SEW 471, and SEW 595, 25 grades of heat-resistant cast steels are classified by the chemical composition and the mechanical properties. The main alloying elements are chromium, silicon, and nickel.

The creep behavior with the creep rupture strength and the creep limit in the temperature range of 600 up to 1100 °C is the most important property.

10.2.3 Cast Nonferrous Alloys

The cast nonferrous alloys are classified into four main groups:

- Cast aluminum alloys
- Cast magnesium alloys
- Cast copper alloys
- Cast zinc alloys.

There are other groups, for example cast titanium alloys, cast tin alloys, cast lead alloys, cast nickel alloys, cast cobalt alloys, etc.

Cast Aluminum Alloys

The specification of a cast aluminum alloy (EN 1706) for a cast component is based upon the mechanical properties it can achieve. These properties are obtained from one particular combination of cast alloy, melt treatment (grain refining, modification) foundry practice, and thermal treatment. In all cast aluminum alloys the percentage of alloying elements and impurities must be carefully controlled.

The main alloying elements of the cast aluminum alloys are copper, silicon, magnesium, and zinc. Grain refiners, which are usually materials that liberate titanium, boron, or carbon, are generally added in the form of a master-alloy to the melt. In casting alloy this is a well-proven method to influence the nucleation conditions in a melt, so that it solidifies with as fine-grained and dense a structure as possible. Hypereutectic aluminum-silicon alloys can be grain-refined with additions that release phosphorus, which promotes the nucleation of primary silicon. Modifying aluminum-silicon alloys of eutectic and hypereutectic composition means treating the melt to binder primary silicon from precipitating to form coarse, irregularly shaped particles. The melt can be modified by adding capsules of metallic sodium or compounds that release sodium. Alternatively, the addition of strontium has proved successful in castings. In contrast to sodium, which burns off and is lost fairly quickly, strontium lasts longer.

Industrial casting processes consist of traditional sand casting, low-pressure sand casting, investment casting, lost-foam casting, permanent mold casting, high pressure die casting, low-pressure permanent mold casting, back-pressure die casting, vacuum die casting, squeeze casting, and thixocasting.

Sand and permanent mold castings may be heat treated to improve mechanical and physical properties. The following thermal treatments are used in industry:

- Stress relief or annealing
- Solution heat treatment and quenching, artificial aging
- Solution heat treatment, quenching and natural aging and
- Solution heat treatment, quenching, and artificial overaging (for the groups 1, 2 and 4 in Table 10.10).

In EN 1706 37 grades of cast aluminum alloys are classified by their chemical composition and mechanical properties (Table 10.10). The mechanical properties depend on the chemical composition of the cast aluminum alloys, the casting technology, and the heat treatment process.

Cast Magnesium Alloys

Magnesium combines a density two-thirds that of aluminum and only slightly higher than that of fiber-

Table 10.10 Mechanical properties of aluminum cast alloys (sand molding—1, permanent mold casting—2, high pressure die casting—3, investment casting—4)

Tensile strength (N/mm^2)	140–300	150–330	200–240	150–300
Yield strength (N/mm^2)	70–210	70–280	120–140	80–240
Elongation (%)	1–5	1–8	1–2	1–5
Brinell hardness	40–100	45–100	55–80	50–90

reinforced plastics with excellent mechanical and physical properties as well as processability and recyclability.

Cast magnesium alloys (EN 1753) can be divided into two groups: the sand-casting alloys that have a fine grain structure due to a melt treatment with small additions of zirconium, and the die casting alloys, in which aluminum is the principal alloying element. The alloys can also be classified as general purpose (Table 10.11), high ductility, and high temperature alloys. Most of the alloys are produced as high-purity versions to reduce potential corrosion problems associated with higher levels of iron, nickel, and copper.

Aluminum improves the mechanical strength, corrosion properties, and castability of the castings. Ductility and fracture toughness are gradually reduced with increasing aluminum content.

Manganese is added to control the iron content of the alloys. The level of manganese additions varies from one alloy to the next, depending on the mutual solubilities of iron and manganese in the presence of other alloying elements. A basic requirement of high-purity alloys is that the iron content of diecast parts is limited to a maximum of 0.005 wt%. Other impurities like nickel and copper also must be strictly controlled. Other alloying elements are zinc, manganese, silicon, copper, zirconium, and rare earth elements.

Following are some of the advantages magnesium alloys offer casting designers:

- *Light weight*—The lightest of all structural alloys, magnesium alloys preserves the light weight of a design without sacrificing strength and rigidity.
- *High stiffness to weight ratio*—This characteristic is important where resistance to deflection is desired in a light-weight component.
- *Damping capacity*—Magnesium is unique among metals because of its ability to absorb energy inelastically. This property yields the vibration absorption capacity to ensure quieter operation of equipment.

Table 10.11 Mechanical properties of cast magnesium alloys

Tensile strength (N/mm^2)	140–250	160–250	150–260
Yield strength (N/mm^2)	90–175	90–175	80–160
Elongation (%)	2–8	2–8	1–18
Brinell hardness	50–90	50–90	50–85

- *Dimensional stability*—Annealing, artificial aging or stress-relieving treatments normally are not necessary to achieve stable final dimensions.
- *Impact and dent resistance*—The elastic energy absorption characteristics of magnesium alloys result in a good impact and dent resistance and energy management.
- *Anti-galling*—Magnesium alloys possess a low galling tendency and can be used as a bearing surface in conjunction with shaft hardness above 400 HB.
- *High conductivity*—Magnesium alloys have a high thermal conductivity and a good electrical conductivity.
- *Wall thickness*—Magnesium alloy die castings are commonly produced with a wall thickness from 0.15 to 0.4 cm.

Magnesium alloys can be cast by a variety of methods, including high-pressure die casting, low pressure permanent mold casting, sand casting, plaster/investment casting, and thixocasting and squeeze casting.

Different alloys may be specified for the different processes. In cases where the same alloy is used with different casting processes, it is important to note that the properties of the finished castings will depend on the casting method. The most prevalent casting method for magnesium alloys is die casting. In this process, thin-walled parts are produced at high production rates with reduced tool wear compared to aluminum alloys, due to the lower heat content per volume of molten metal. Both hot chamber and cold camber machines are currently used for magnesium alloys. Thixocasting is another casting method that has shown progress with magnesium alloys.

There are seven cast magnesium alloys in EN 1753.

Cast Copper Alloys

Cast copper alloys (EN 1982) are known for their versatility. They are used in a wide range of applications because they are easily cast, have a long history of successful use, are readily available from a multitude of sources, can achieve a range of physical and mechanical properties, and are easily machined, brazed, soldered, polished, or plated.

Table 10.12 Mechanical properties of cast copper alloys

Tensile strength (N/mm^2)	150–750
Yield strength (N/mm^2)	40–480
Elongation (%)	5–25
Brinell hardness	40–190

Table 10.13 Mechanical properties of cast zinc alloys

Tensile strength (N/mm^2)	220–425
Yield strength (N/mm^2)	200–370
Elongation (%)	2.5–10
Brinell hardness	83–120

The following lists the physical and mechanical properties common to cast copper alloys:

- Good corrosion resistance, which contributes to the durability and long-term cost-effectiveness.
- Favorable mechanical properties ranging from pure copper, which is soft and ductile, to manganese-bronze, which rivals the mechanical properties of quenched and tempered steel. In addition, all cast copper alloys retain their mechanical properties, including impact toughness at low temperatures.
- High thermal and electrical conductivity, which is greater than any metal except silver. Although the conductivity of copper drops when alloyed, cast copper alloys with low conductivity still conduct both heat and electricity better than other corrosion-resistant materials.
- Bio-fouling resistance, as copper inhibits marine organism growth. Although this property (unique to copper) decreases upon alloying, it is retained at a useful level in many alloys, such as copper-nickel.
- Low friction and wear rates, such as with the high-leaded tin-bronzes, which are cast into sleeve bearings and exhibit lower wear rates than steel; good castability, as all cast copper alloys can be sand cast and many can be centrifugally, continuously, and permanent mold cast, as well as diecast.
- Good machinability, as the leaded copper alloys are free-cutting at high machining speeds, and many unleaded alloys such as nickel-aluminum bronze are readily machinable at recommended feeds and speeds with proper tooling.
- Ease of post-casting processing, as good surface finish and high tolerance control is readily achieved. In addition, many cast copper alloys are polished to high luster, and platting, soldering, and welding also are routinely performed.
- Large alloy choice, since several alloys may be suitable candidates for any given application depending upon design loads and corrosivity of the environment.
- Comparable costs to other metals due to their high yield, low machining costs, and little requirement for surface coatings such as paint.

In EN 1982 the cast copper alloys are divided into cast copper, cast copper-chromium, cast copper-zinc, cast copper-tin, cast copper-tin-lead, cast copper-aluminum, cast copper-manganese-aluminum, and cast copper-nickel alloys.

Thirty five grades of cast copper alloys are classified by their chemical composition and mechanical properties in EN 1982.

Cast Zinc Alloys

Cast zinc alloys (EN 1774 and EN 12844) are assigned to three alloy groups. The first group of alloys have 4% aluminum as the primary alloying element with 0.099% or less magnesium to control intergranular corrosion. Another alloying element is copper. The alloys with the highest copper content have the highest hardness. The mechanical properties can be improved with 0.005–0.2% nickel as the alloying element. The second group has higher aluminum contents (8–27%) These alloys have superior hardness, wear and creep resistance that increase with the aluminum content. The third group is a cast zinc alloy that has copper as the primary alloying element. Castings of the cast zinc alloys are manufactured by the high pressure die casting.

In EN 12844 8 grades of cast zinc alloys are classified by their chemical composition and mechanical properties.

10.3 Primary Shaping

According to DIN 8580 [10.4], primary shaping is the manufacturing of a solid body from a shapeless material by creating cohesion. Thus primary shaping serves to give a component made from a material in shapeless condition an initial form. Shapeless materials are gases, liquids, powders, fibers, chips, granules, solutions, melts, and the like. Primary shaping may be divided into two groups with regard to the form of the products and their further processing:

- Products produced by primary shaping, which will be further processed by forming, severing, cutting,

and joining. The final product no longer resembles the original product of primary shaping in form and dimensions, i.e., a further material change in shape and dimensions is accomplished by means of other main groups of manufacturing processes.

- Products produced by primary shaping, which essentially have the form and dimensions of finished components (e.g., machine parts) or end-products, i.e., their shape essentially corresponds to the purpose of the product. The attainment of the desired final form and dimensions usually requires only operations that fall into the main process group *cutting* (machining).

Most powders are produced by primary shaping, whereby the powders are atomized out of the melt, and rapid solidification is followed. From powder, sintering parts are produced as a result of powder metallurgical manufacturing.

The production of cast parts from metallic materials in the foundry industry (castings), from metallic materials in powder metallurgy (sintered parts), and from high-polymer materials in the plastics processing industry has major advantages for economic efficiency.

The production of cast parts is the shortest route from the raw material to the finished part. It bypasses the process of forming and all the associated expense. The final form of a finished component with a mass ranging from a few grams to several hundred tonnes is practically achieved in one direct operation.

The production of cast parts by primary shaping from the liquid state allows the greatest freedom of design. This cannot be achieved by any other manufacturing process.

Primary shaping also enables processing of materials that cannot be achieved by means of other manufacturing methods. The direct route from the raw material to the preform or the end-product results in a favorable material and energy balance.

The continual further development of primary shaping processes increasingly permits the production of components and end-products with enhanced practical characteristics, i.e., cast parts with lower wall thicknesses, lower machining allowances, narrower dimensional tolerances, and improved surface quality.

In the following, primary shaping of metallic materials from the liquid state in foundry technology, of metallic materials from the solid state in powder metallurgy, and of high-polymer materials (plastics) from the plasticized state or from solutions is discussed on a common basis with regard to the fundamental technological principles. The discussion is restricted to subjects relevant to mechanical engineering.

For a better appreciation of the relevant principle of action, many detailed technological operations are omitted, which although vital to the specific manufacturing technology, are of minor importance. Furthermore, when discussing the specific primary shaping processes, only products with a simple form are referred to, because the diversity of the possible geometric forms cannot be described here.

Only the most important primary shaping processes are selected, as the large number of technological processes and process variables means that it is impossible to provide anything like a complete description. The processes are selected first according to their technical importance and second according to the principle of action.

Materials technology problems will only be mentioned briefly, although they are vital in order to understand the technological processes, their applicability and efficiency, and the changes in material properties brought about by the technological processes.

10.3.1 Process Principle in Primary Shaping

In the processes of primary shaping, the technological manufacturing process essentially comprises the following steps:

- Supply or production of the raw material as an amorphous substance
- Preparation of a material state ready for primary shaping
- Filling of a primary shaping tool with the material in a state ready for primary shaping
- Solidification of the material in the primary shaping tool
- Removal of the product of primary shaping from the primary shaping tool.

These individual steps are discussed in the following section.

10.3.2 Material State Ready for Primary Shaping

In primary shaping of metallic materials from the liquid state, the raw materials (pig-iron, scrap, ferroalloys and the like) are melted in a metallurgical melting furnace by means of thermal energy. The melting furnaces are usually physically separated from the primary shaping tool. The molten metal is carried by means of transfer vessels (ladles) to the primary shaping tools, termed molds in the foundry industry, and cast there.

In primary shaping of high-polymer materials from the plasticized state, bulk raw materials (granules, pow-

der) are fed after proportioning into a preparation device, which is usually integral with the primary shaping tool. There, thorough mixing, homogenizing and plasticizing of the material to be processed are accomplished under the action of heat and pressure. When solutions are used, these are produced in a mixing unit and then poured into the primary shaping tool. In primary shaping of metallic and also high-polymer materials from the solid state, the bulk raw materials (metal powder, plastic powder, or plastic granules) are poured straight into the primary shaping tool, where they sinter, or first become plastic and then solidify under the action of pressure and thermal energy.

10.3.3 Primary Shaping Tools

The primary shaping tool contains a hollow space which, with the allowance for contraction, usually corresponds to the form of the product (unmachined part) to be manufactured, but may be smaller or larger than the resulting unmachined part. Furthermore, primary shaping tools often contain systems of channels (runners) for feeding the material in the state ready for primary shaping. The allowance for contraction corresponds to the dimensional changes that occur in the material to be processed from the moment of solidification to its cooling to room temperature.

In the production of cast parts, a distinction is made between primary shaping tools for once-only use and those for repeated use. Primary shaping tools for once-only use are only used for primary shaping of metallic materials from the liquid state in foundry technology. They are termed expendable or *dead* molds. Only one product (casting) can be manufactured, as the mold is subsequently destroyed. However, primary shaping tools for repeated use (permanent molds) are also used in foundry technology. A larger quantity of cast parts can be produced. The primary shaping technologies for processing of high-polymer materials and powder metallurgy use only primary shaping tools for repeated use. Primary shaping tools for repeated use are usually made of metallic, and more rarely of nonmetallic, materials. Primary shaping tools for once-only use (dead molds) are made with the aid of patterns.

10.3.4 Filling the Primary Shaping Tools

Filling of the primary shaping tools with the material ready for primary shaping may be accomplished by means of the following principles of action: under the influence of gravity, elevated pressure or centrifugal force and by displacement. The material to be processed can be put into the primary shaping tools in solid, pourable form (e.g., powder), as molten metal in the case of metallic materials, or in a plasticized condition, as a solution or as a paste in the case of high-polymer materials.

10.3.5 Change of State Ready for Primary Shaping

Shaping into the Solid State of Aggregation

Liquid metallic materials (molten metals) change by crystallization to the solid state of aggregation on cooling owing to the removal of heat.

Thermoplastics are cooled in the primary shaping tool after forming. As a result of temperature reduction, which is accomplished either by heat removal in cooled tools or in downstream equipment (cooling baths), the plastic mass passes through the following states: plastic–rubber like–elastic–solid. In setting by cooling, secondary valency bonds are restored. This process is repeatable; therefore thermoplastics cart be restored to the plastic state by reheating.

Thermosetting plastics or thermosets (cross-linkable plastics) are cured after forming by a hardening process. Primary valency bonds form, and the plasticized mass solidifies directly under the effect of heat and/or pressure. The curing is an irreversible chemical process: thermosets disintegrate on reheating without needing to pass through a plastic state. Fundamental chemical reactions during solidification are polymerization, polycondensation, and polyaddition.

In primary shaping of high-polymer materials, if solutions are used then the transformation to the solid state may be accomplished by the physical process of solvent evaporation.

In primary shaping by sintering, a process of shrinkage of the internal and external surface area of a body formed from powder by pressure takes place. Powder particles that are in contact are joined by the formation or reinforcement of bonds (material bridges) and/or by reducing the pore volume; at least one of the material constituents involved remains solid throughout the process. The bonding of the porous pressed body of powder takes place mainly through diffusion mechanisms.

The description of the technological aspects of primary shaping and details of the processes are not described here but can be found in the relevant literature.

10.4 Shaping of Metals by Casting

10.4.1 Manufacturing of Semifinished Products

This group of primary shaping processes involves the production of initial and intermediate products, which are further processed by, for instance, metal forming (plastic deformation).

The Ingot Casting Process

Here, ingots, slabs, wirebars, etc. are produced in permanent molds made of metal (usually cast iron). These products are converted by metal forming (rolling, forging, pressing, wire drawing, etc.) into a semifinished product (sheet, plate, section, wire) that no longer resembles the original ingot in form and dimensions. In ingot casting a distinction is made between top pouring (downhill casting, Fig. 10.2a), where the mold is filled by directly pouring the molten metal in from above, and bottom pouring (uphill casting, Fig. 10.2b), where one mold or several molds simultaneously (group casting) are filled from below by means of a distribution system (pouring gate and runner bricks).

Procedure: The prepared molds are set up into the teeming box as illustrated. They are filled with the liquid metal, which solidifies in them. The molds are stripped from the ingots, which are taken away.

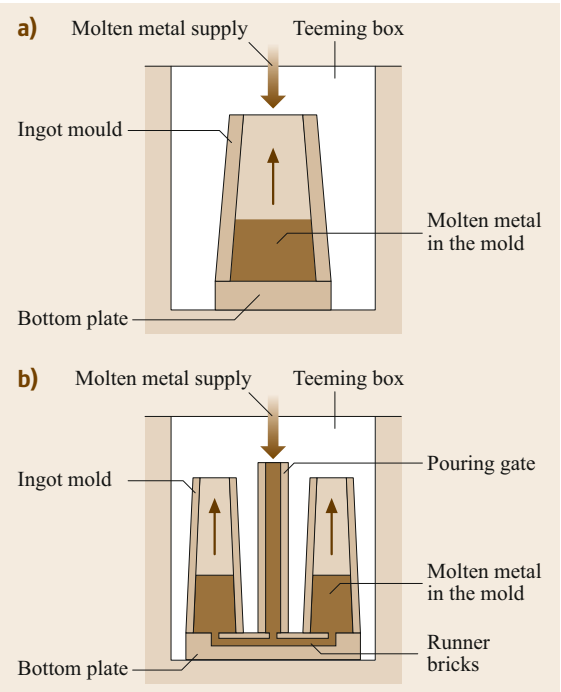

Fig. 10.2a,b Ingot casting methods: **(a)** top pouring, **(b)** bottom pouring [10.1]

Continuous Casting Processes

In these processes, which are used to produce either intermediate products for metal forming or semifinished products, the primary shaping tool (continuous mold, casting roller, casting belt, casting wheel) is always smaller than the product of primary shaping.

Casting with Stationary Molds. Continuous casting with a stationary mold. In this casting process, a bath of molten metal is fed into a stationary continuous mold, where the solidification begins.

Depending on the design, a distinction is made between batch or continuous vertical (Fig. 10.2a) and horizontal continuous casting systems (Fig. 10.2b). On leaving the continuous mold the resulting continuous casting (solid or hollow section) is cooled until it solidifies completely. The continuous casting is usually cut into defined lengths at intervals. Like ingots from ingot casting, these are further processed by metal forming.

Traveling Primary Shaping Tools. In this continuous casting process, metal-forming equipment for rolling or drawing is installed directly following the casting plant, thus dispensing with the manufacturing stages of metal forming. In this case, there is usually no cutting of the continuous castings into sections.

Continuous Casting with Moving Molds. The continuous casting with moving molds is realized with strip and wire rod casting plants.

In vertical uphill casting between two casting rollers (Fig. 10.3a) the molten metal is fed from below between two casting rollers. Solidification takes place between these two rollers, and the finished continuous casting (a strip) emerges vertically upward from these rollers.

In horizontal casting (Fig. 10.3b), both the feeding of the molten metal and the discharge of the solidified continuous casting (strip) take place horizontally. In casting between a casting roller or a casting wheel having the profile of the desired strip or rod and an endless casting belt (Fig. 10.4a, b), the molten metal solidifies between the casting roller/wheel and the casting belt and emerges into the open air. In casting in belt molds (two endless, rotating casting belts), solidification is accomplished with the aid of further rotating equipment to restrict the product laterally between these casting belts (Fig. 10.5a–c); the solidified

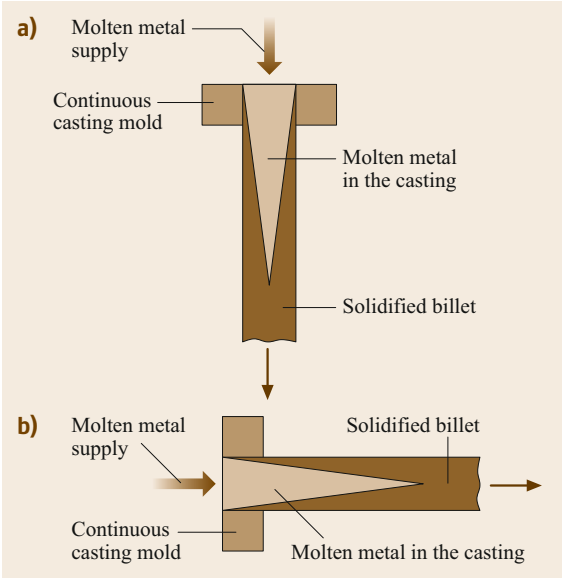

Fig. 10.3a,b Continuous casting: (a) vertical, (b) horizontal continuous casting [10.1]

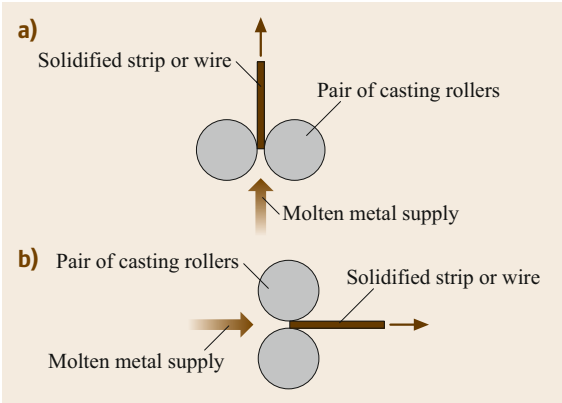

Fig. 10.4a,b Strip casting: (a) vertically uphill, (b) horizontally [10.1]

continuous casting then emerges into the open air as a strip.

10.4.2 Manufacturing of Cast Parts

Manufacturing of cast parts is accomplished with primary shaping processes by means of which a practically finished component, e.g., a machine part or an end-product, is produced without metal forming. The product's shape and dimensions do not undergo any further significant change. However, primary shaping is followed by other manufacturing processes, e.g., cutting (turning, planing, milling, drilling), to obtain a component ready for fitting. The intention is to perfect and

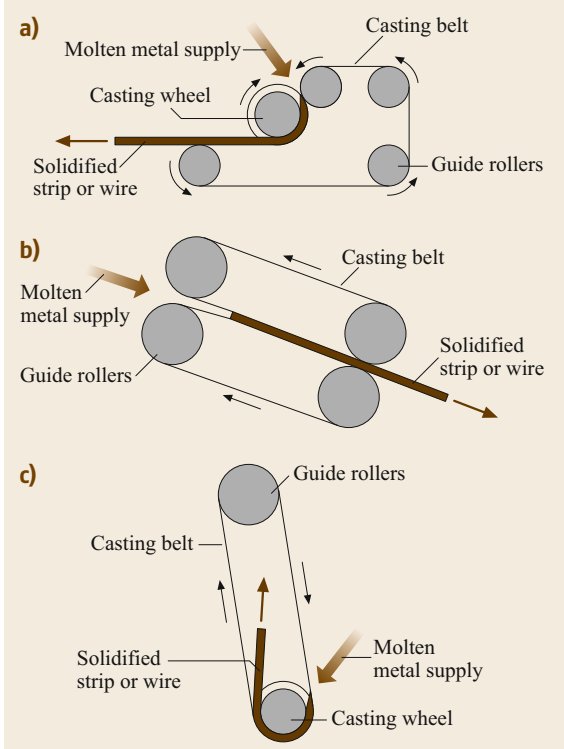

Fig. 10.5a–c Casting machines: (a) strip casting machine (rotary process), (b) strip casting machine (Hezelett process), (c) wire rod casting machine [10.1]

further develop the primary shaping techniques in order to, for instance, reduce the amount of machining work to a minimum. A good view of the manufacturing of cast parts—cast alloys, manufacturing processes and applications of cast parts—is given in [10.1, 5].

Use of Lost Primary Shaping Tools (Lost Molds)

This technique, which is only used in primary shaping of metallic materials from the liquid state in foundry technology, uses a pattern to produce the expendable primary shaping tool. Depending on the type of pattern used, a distinction is made between processes using a permanent pattern and those using an expendable pattern. A permanent pattern can be used to make many expendable molds, but an expendable pattern can only be used for one expendable mold. Expendable patterns are also made in an appropriate primary shaping tool.

The patterns are similar in shape to the case part to be manufactured, but are larger by the allowance for contraction of the material to be cast. They also incorporate the machining allowances, which will subsequently be eliminated by machining of the casting with the aim of achieving accuracy in dimensions, shape and position, as well as tapers to enable the pat-

tern to be removed from the mold. Most patterns have a pattern joint, i.e., they consist of at least two parts (pattern halves). In addition, for castings with hollow spaces the pattern has care marks for insertion of the cores in the mold.

In the case of permanent patterns for making an expendable mold for casting, these patterns or their sections made from metals, high polymers or wood are used to make the molds by the sand molding, template molding, or shell molding process.

Hand Molding. The mold is expendable (i.e., used only once). The medium used may be natural or synthetic sand with bentonite; other molds used sand with a resin binder. It is worked by hand.

Pattern. Patterns for repeated use, and patterns and core boxes, are made of wood or plastics.

Process Characteristics. Hand molding denotes the production of a sand mold without using a molding machine. The mold consists of the external parts for the external profile and the internal parts for the internal profile. Hollow spaces in the casting are formed by cores placed in the mold.

The principle of molding is illustrated in Fig. 10.6. First of all the bottom half of the two-part pattern is molded. After turning the molding box over, the top half of the pattern and the pouring gate and risers are placed in position and the top mold is made. The top box is lifted off, the pattern halves are removed from the mold, and the core is inserted. The halves of the mold are joined and the casting is made.

Casting Materials. All metals and alloys that are castable with the current technology.

Weight of Castings. The maximum transportable weight and the melting capacity determine the maximum weight.

Number of Castings. Single items, small production runs.

Tolerances. From about 2.5 to 5%.

Machine Molding. The mold is expendable (used only once). Natural sand, artificial sand, sand with synthetic resin binders, CO, sand. Preparation on molding and core molding machines. Used in semiautomatic and fully automatic production lines.

Pattern. Patterns and core boxes are made of metal or plastic.

Process Characteristics. Mechanical molding is characterized by a semiautomatic or fully automatic manufacturing operation for efficient production of ready-to-cast sand molds (Fig. 10.7). The casting process is often

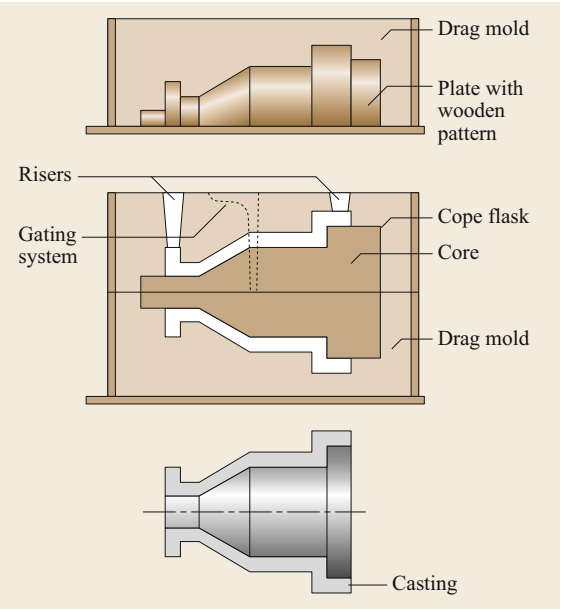

Fig. 10.6 Hand molding [10.1, 6]

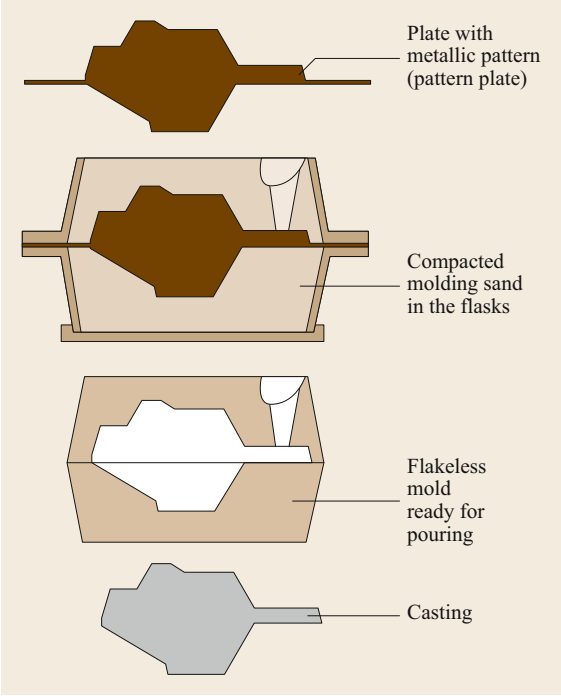

Fig. 10.7 Machine molding [10.1, 6]

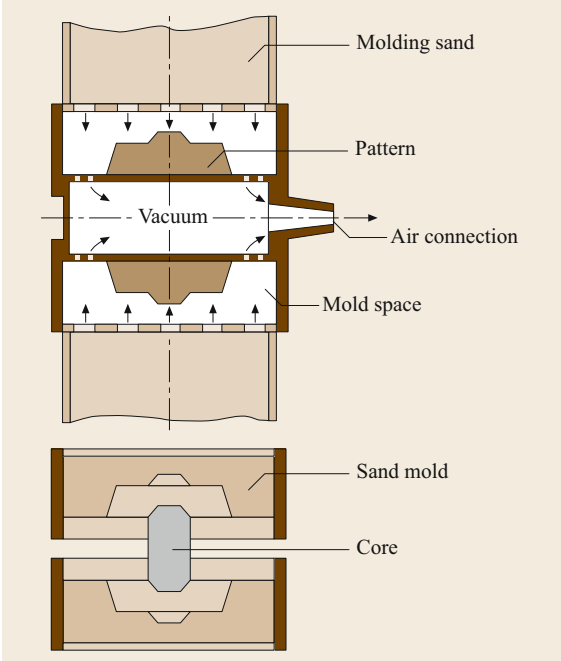

Fig. 10.8 Suction molding [10.1, 6]

incorporated into the production line. The main stages are: Molding station, core insertion section, casting section and cooling section. The emptying station releases the cast molds. The molding station may consist of one automatic molding machine for complete molds or of two or more for making separate top and bottom boxes. There are also boxless molding units, where the molds are made using only a frame, which is withdrawn after compacting the sand.

Casting Materials. All metals and alloys that are castable with the current technology.

Weight of Castings. Limited by the size of the molding machines: up to ≈500 kg.

Number of Castings. Owing to the mechanical preparation, mechanical molding is suitable for series and mass production of quantities of 1000 and multiples thereof.

Tolerances. From about 1.5 to 3%.

Suction Molding. The mold is expendable (used once only), made from wet artificial casting sand (Fig. 10.8).

Pattern. Wood, plastic, metal.

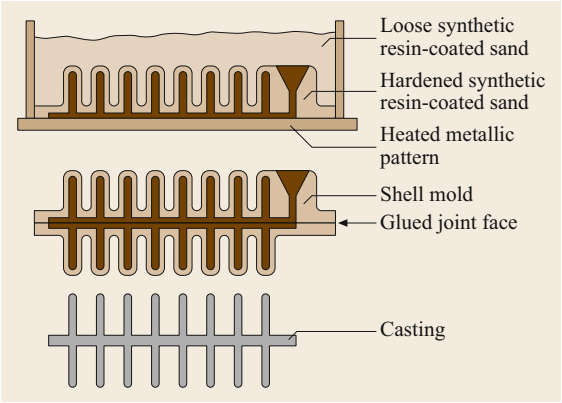

Fig. 10.9 Shell molding [10.1, 6]

Process Characteristics. The process is characterized by the formation of a vacuum by withdrawing air from the mold space and the incoming molding sand. This accelerates the sand, which spreads over the wall of the pattern. The sand can be subsequently pressed against the pattern. Advantages of the process are optimum mold, compaction around the pattern, no shadow effect with plane surfaces, decreasing hardness of compacted sand from the inside to the outside, high surface quality, dimensionally stable castings, reduced cleaning. This process should not be confused with vacuum molding.

Casting Materials. Iron, steel, aluminum.

Weights of Castings. From about 0.1 to 120 kg.

Number of Castings. Small, medium, and large production runs.

Tolerances. Conventional to DIN 1683; maximum offset of compacted sand 0.3 mm.

Shell Molding. The mold is expendable (used only once). Resin-coated sands or sand/resin mixtures (Fig. 10.9).

Pattern. Patterns for repeated use, heatable metal patterns, and metal core boxes.

Process Characteristics. These molds are shell molds with walls only a few mm thick. The mold material is poured onto the heated metal pattern. This cures the synthetic resins in the mold material, solidifying the mold. The result is a self-supporting, stable shell mold. Shell molds are often molded in one piece and then di-

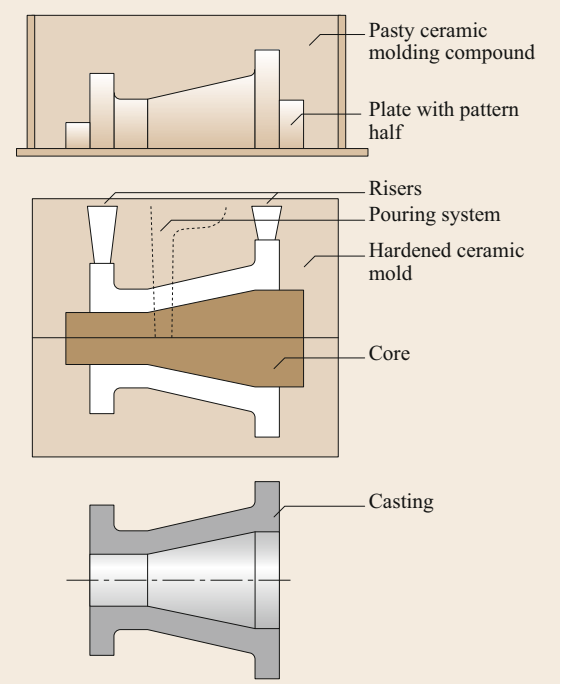

Fig. 10.10 Ceramic molding [10.1, 6]

vided. After putting in the cores, the two halves of the mold are glued together. The shell molding process is used in various stages of mechanization and automation. This process is used not only for making molds for shell casting, but also for producing hollow shell cores for sand and chill casting. These cores are produced on special core molding machines. Shell casting offers high dimensional accuracy with excellent surface quality.

Casting Materials. All metals and alloys that are castable with the current technology.

Weight of Castings. Up to 150 kg.

Number of Castings. Medium to large production runs.

Tolerances. From about 1 to 2%.

Ceramic Molding. The mold is expendable (used only once). This mold is made of highly refractory ceramic similar in kind to mold materials for investment casting (Fig. 10.10).

Pattern. Reusable, made of metal, plastic, or specially varnished wood.

Process Characteristics. A slip consisting of highly refractory substances is poured around the pattern; these substances then harden by chemical reaction. Often only one layer is poured, which is then back-filled with *normal* molding sand. After removing the pattern, the ceramic is fired or skin-dried (Shaw process). To keep ceramic molding, which is relatively expensive, to a minimum, it is usually only the parts of the mold that are made from special ceramic that will be cast in finished or near-finished shape. Castings from ceramic molds have no casting skin in the conventional sense and are among the precision casting processes that, as the technology develops, are becoming more and more widely used owing to their efficiency.

Casting Materials. All metals and alloys that are castable with the current technology, especially iron-based materials.

Weight of Castings. From about 0.1 to 25 kg, depending on the production equipment.

Number of Castings. Single items, small and medium runs, also larger runs in the case of fluid flow machines.

Tolerances. Up to about 100 mm ± 0.2%, over 100 mm ± 0.3–0.8% of nominal dimensions.

Vacuum Molding (V-Process). The mold is expendable (used only once). A plastic foil is vacuum-molded to the contours of the pattern, back-filled with fine-grained, binder-free quartz sand and sealed with a covering foil. Dimensional stability is preserved by means of a vacuum of 0.3–0.6 bar.

Pattern. Permanent patterns, not subject to significant wear. Patterns are made of wood or metal. Core boxes according to the core manufacturing method.

Process Characteristics. (Fig. 10.11). The process is characterized by the use of a vacuum for both deep drawing the pattern sheet over a pattern with nozzle holes and maintaining the stability of the mold. A molding box equipped with suction systems is connected by a pipe to the vacuum grid. The fine, binder-free sand with which the mold box is filled is compacted by vibration. After applying a cover sheet, the air is evacuated from the sand and the mold thus becomes rigid. The mold is constantly connected to the vacuum grid before, during, and after casting. To empty the mold, the vacuum is switched off and the sand and cast parts drop out of the mold box without additional force. The advantages of the process are: high, reproducible di-

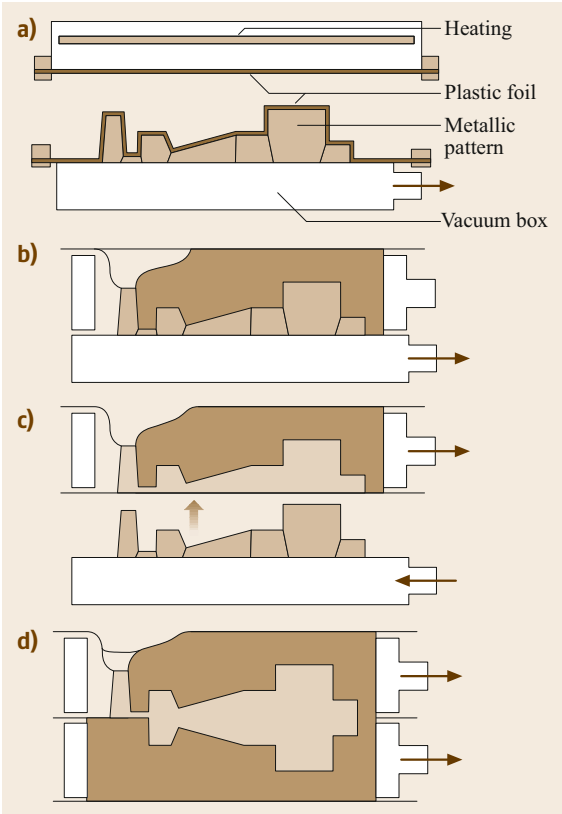

Fig. 10.11a–d Vacuum molding: **(a)** The plastic foil is softened by means of a foil-type heating element and drawn tightly against the pattern by vacuum through holes. **(b)** The mold box is placed on top, filled with binderless sand, precompacted, and the top of the box is covered with plastic foil. **(c)** Vacuum is applied to the mold box, compacting the sand. By switching off the vacuum, the mold box can easily be lifted off the pattern. **(d)** The top and bottom halves of the box are joined. The vacuum is maintained during pouring [10.1, 6]

mensional accuracy with outstanding surface quality; the mold seam at the joins and core marks is very small; tapers can be entirely dispensed with in certain areas of the casting.

Casting Materials. All metals and alloys that are castable with the current technology.

Weight of Castings. Restricted by the equipment available, not by the process.

Tolerances. 0.3–0.6%.

Casting Under Vacuum. The mold is expendable (used once only), shell molds (for investment casting) and precision casting molds made of special mold materials.

Pattern. Wax for investment casting, also of metal, plastic or the like, depending on the type of mold.

Process Characteristics. Titanium and zirconium are among the reactive metals that have high affinities with oxygen, nitrogen, and hydrogen in the molten state. This is even the case when present as alloying constituents in appropriate percentages in, e.g., molten nickel. All these alloys must therefore be produced and cast under defined conditions, normally under high vacuum.

The new mold ceramics, e.g., those made of yttrium and zirconium oxides, resist attack by reactive metals and melts. However, these special ceramics are not (yet) required for nickel-base alloys that are only alloyed with titanium, aluminum, etc.

To optimize quality and structure, the castings are usually isostatically pressed at high temperature by means of the hot isostatic pressing (HIP) process.

Casting Materials. Alloys based on (in order of importance) nickel, titanium, cobalt, iron, and zirconium.

Weight of Castings. Approximately 0.01–100 kg and more, depending on the manufacturing equipment.

Number of Castings. Small series to fairly large production runs.

Tolerances. From 0.3 to ±0.8% of nominal size, depending on the molding process.

Investment Casting (Lost Wax Process). The mold is expendable (used once only), made of highly refractory ceramic, single or group pattern with runners, combined to form casting units (*clusters* or *trees*) (Fig. 10.12)

Pattern. Made by injection molding from special waxes or the like, thermoplastics or mixtures thereof.

Process Characteristics. The distinguishing features are the expendable patterns, the one-piece molds and the casting in hot molds (900 °C for steel). A casting skin in the conventional sense does not form. The patterns are inject ion-molded in single or multiple tools made of aluminum, steel or soft metal, for which an original pattern is required. The most suitable injection molding tool in each particular case is chosen according to the planned total quantity, the form of the casting, and the nature of the pattern material. The formation of certain undercut contours may require the use of water-

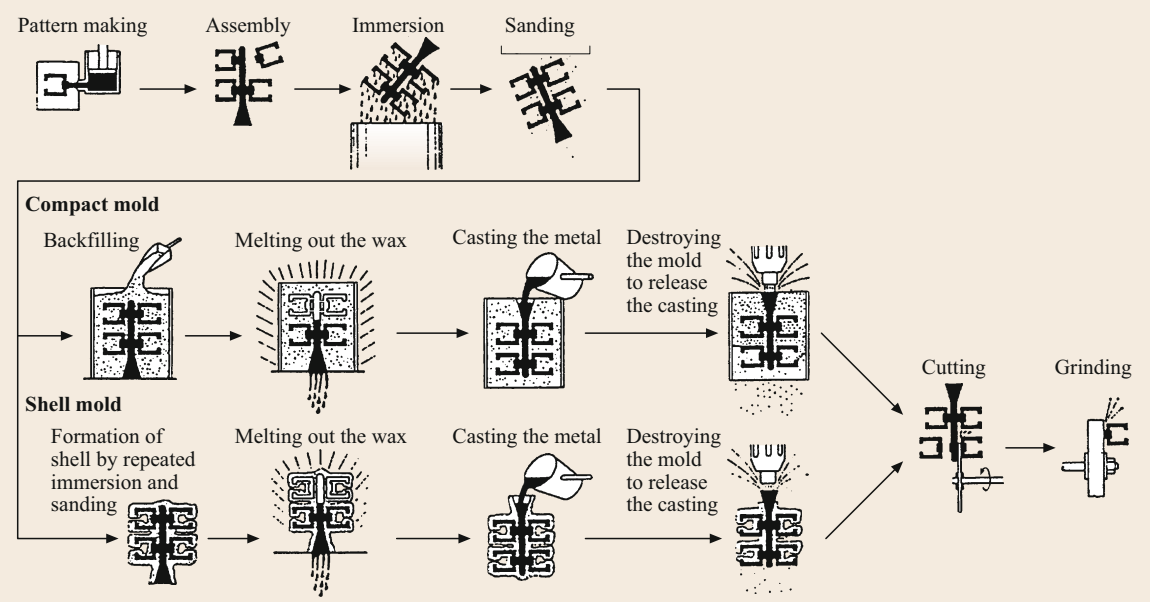

Fig. 10.12 Schematic of manufacturing stages in investment casting [10.1, 6]

soluble or ceramic cores, for which a supplementary tool is used. The patterns are assembled into clusters by means of casting systems, usually again employing injection molding. The method of this assembly is crucial for the quality of the castings and for efficiency. Viscous ceramic coatings which cure by chemical reaction are then applied to these clusters. For aluminum, special plasters are also used. After melting out (lost wax process) or dissolving away the pattern material, the resulting one-piece molds are fired. Casting takes place in molds that are usually still hot from firing, so that narrow cross-sections and fine profiles *turn out* cleanly. Precision casting, with its tight tolerances and high surface quality, is the casting technology that offers the greatest freedom of design coupled with high quality.

Casting Materials (in Order of Importance). Steels and alloys based on iron, aluminum, nickel, cobalt, titanium, copper, magnesium, or zirconium, including aerospace, materials, produced at atmospheric pressure or under vacuum.

Weight of Castings. 0.001 to 0.001–50 kg, also up to 150 kg and over depending on manufacturing equipment.

Number of Castings. Small series to large production runs, depending on the complexity and/or machinability of the workpiece concerned.

Tolerances. From ±0.4 to ±0.7% of nominal dimensions.

Full Mold Casting (Evaporative Pattern Casting, Lost Foam Casting). The mold is lost (used only once), mold material is usually self-curing.

Pattern. Expendable, foam material.

Process Characteristics. (Fig. 10.13). One-piece pattern made of foam material (polystyrene). Shape and dimensions match the part to be cast (taking into account allowance for contraction). The pattern need not be removed from the mold after mold-making. The heat of the molten metal flowing into the full mold vaporizes the pattern, which is continuously replaced by cast metal. Mold joints and cores are usually unnecessary. Bolts, sleeves, lubrication lines, etc. can be integrally cast in. The absence of mold tapers reduces the weight of the casting. The time and cost of manufacture are only a fraction of those encountered with a wooden pattern.

Casting Materials. All metals and alloys that are castable with the current technology, especially those with high casting temperatures.

Weight of Castings. From ≈50 kg up to maximum transportable weight; especially suitable for large components.

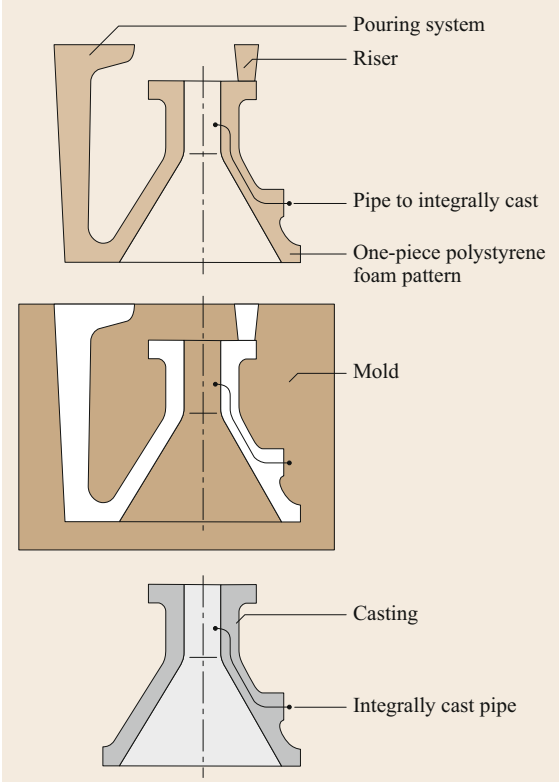

Fig. 10.13 Full mold casting [10.1, 6]

Number of Castings. Single pieces, small production turns.

Tolerances. From about 3 to 5%.

Magnet Molding. The mold is expendable (used once only), iron granules.

Pattern. Expendable, foam material.

Process Characteristics. Magnetic molding is a type of full mold casting. The casting units, prefabricated from foam material (patterns with pouring gates and runner), are coated with a refractory ceramic (similar to shell molds for precision casting). They are then back-filled with pourable iron granules in a mold box. By applying (or switching on) a DC magnetic field, the iron powder becomes rigid and thus supports the casting unit. After casting and solidification of the die metal, the magnetic field is switched off, causing the iron granules to become pourable again. Then the casting is removed. The iron granules can be reused.

Casting Materials. All metals and alloys that are castable with the current technology. As the thermal conductivity of the magnetizable mold material is higher than that of quartz sand, the cooling rate of the castings is higher and leads to a finer metallographic structure. The properties in use are especially improved in the case of steel castings.

Number of Castings. Single items, small production runs.

Tolerances. From about less than 3 to 5%.

Use of Permanent Molds

Permanent Mold Casting (Gravity Die Casting). The mold is a permanent mold from cast iron or steel, cores made of steel.

Pattern. None required.

Process Characteristics. (Fig. 10.14). Casting takes place by gravity in permanent metal molds. These molds are made in two or more parts for removal of the finished casting. The higher thermal conductivity of the metal mold compared with molding sand brings about faster cooling of the solidifying molten metal. The result is a relatively fine-grained, dense structure with better mechanical properties than parts made by sand casting. High dimensional accuracy, excellent surface quality, and good reproduction of contours characterize chill casting. This process fully meets the specifications for gas- and liquid-tight valves, owing to the production of a dense structure. A rapid, efficient casting sequence, with machining generally being unnecessary

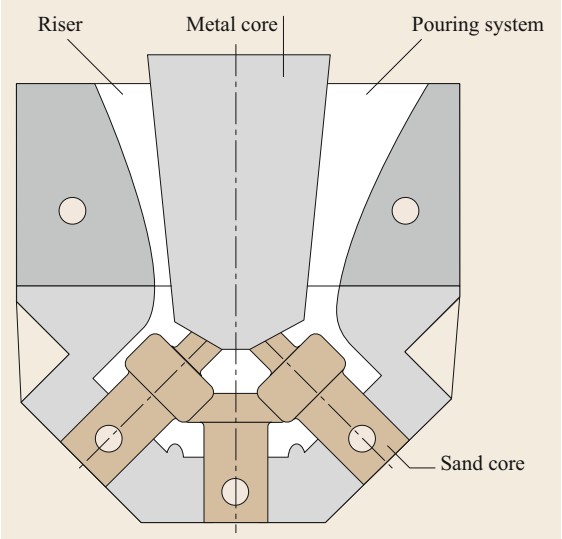

Fig. 10.14 Permanent mold casting (composite mold with metallic and sand cores, the latter for undercuts) [10.1, 6]

or requiring only small machining allowances, are further features of this process.

Casting Material. Copper-zinc alloys, copper-aluminum alloys, aluminum alloys, magnesium alloys, high-grade zinc alloys, also copper, copper-chromium alloys, super-eutectic aluminum-silicon alloys, lamellar and nodular graphite cast iron.

Weight of Castings. Nonferrous metals and cast iron up to ≈100 kg, more depending on equipment. Cast iron for certain purposes up to ≈20 t (=20 000 kg).

Number of Castings. From about 1000 and multiples thereof, depending on the material being cast (e.g., Al ≈ 100 000 castings).

Tolerances. From about 0.3 to 0.6%.

Low-Pressure Permanent Mold Casting. The mold is a permanent mold from cast iron or steel.

Pattern. No pattern required.

Process Characteristics. (Fig. 10.15). Casting is carried out under pressure (usually with compressed air) in permanent metal molds. These molds are made in two or more parts for removal of the finished casting. The higher thermal conductivity of the metal mold compared with molding sand brings about faster cooling of the solidifying molten metal. The result is a relatively fine-grained, dense structure with better mechanical properties than parts made by sand casting. The distinguishing feature is the application of pressure, which dispenses with the need for risers on the casting. High dimensional accuracy, excellent surface quality, and good contour reproduction together with a rapid, efficient casting sequence and considerable machining economies are further features of this process. Gas-tight and liquid-tight valves can be efficiently manufactured owing to the dense structure of the casting.

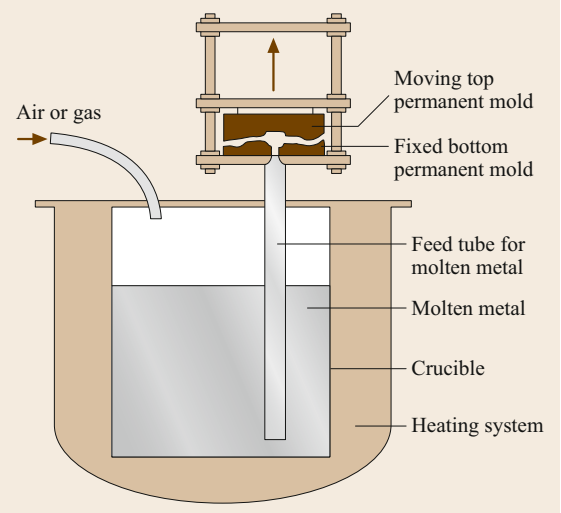

Fig. 10.15 Low-pressure permanent mold casting [10.1, 6]

Casting Materials. Light metal, especially aluminum alloys.

Weight of Castings. Up to 70 kg.

Number of Castings. From about 1000 and multiples thereof.

Tolerances. From about 0.3 to 0.6%.

High-Pressure Die Casting (Die Casting). The mold is a permanent mold, usually from high-tensile hot forming tool steel or special metals.

Pattern. No pattern required.

Process Characteristics. (Fig. 10.16). The distinguishing feature of this process is that the molten metal is forced into the two-part permanent mold at high pressure and relatively high speed in pressure die casting machines. Two types of process are distinguished, namely:

- The hot-chamber process. Here the die casting machine and the holding furnace for the molten metal form a unit. The casting assembly is immersed in the molten metal. In each casting operation, a precisely predetermined volume of molten metal is forced into the mold. The hot-chamber die casting process is especially suitable for lead, magnesium, zinc, and tin. The output of components manufactured by this process is considerable, but varies according to the size of the component and the casting material.
- The cold-chamber process. In this process the die casting machine and the holding furnace for the molten metal are separate. After being taken from the furnace, the molten metal is poured into the cold pressure chamber and forced into the mold. The pressure chamber is mounted directly on the runner-side mold block. This process is chiefly suitable for aluminum-based and copper-based alloys, as these would attack the steel casting assembly when molten if the hot-chamber process were employed. Cold-chamber die casting machines do not achieve the rates of output of hot-chamber ma-

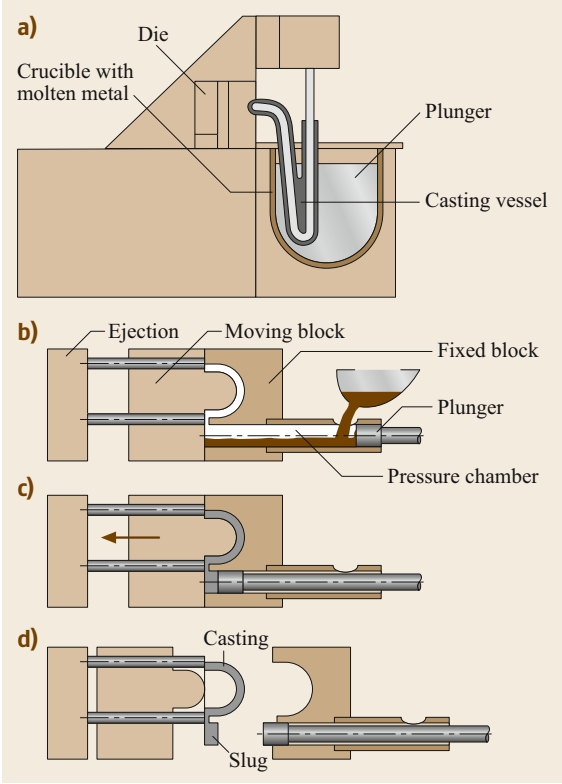

Fig. 10.16a–d High pressure die casting: **(a)** hot chamber process, **(b–d)** cold-chamber process, **(b)** filling of casting chamber, **(c)** plunger for molten metal into die, **(d)** ejection of casting [10.1, 6]

chines, owing to the nature of the process. Pressure die casting is today one of the most efficient casting processes around. The machines are mostly semi-automatic or fully automatic. Pressure die-cast parts have smooth, clean surfaces and edges. They are extremely dimensionally accurate. Therefore, only the fitting and bearing surfaces, at most, require machining. Very low machining allowances result in short machining times.

Special cases of high pressure die casting are squeeze-casting and thixocasting.

Squeeze-Casting and Thixocasting. In the direct squeeze casting, the die is filled with a defined amount of liquid metal via a trough. The die, which has two or more parts, is closed above by hydraulic pressure, forcing the metal to conform to the die surfaces. The pressure is maintained during solidification. Unlike direct squeeze-casting, the indirect version has proved itself in production and has obtained a foothold in foundries producing castings for special applications. The principle of operation differs from the direct process in that the melt is not poured directly into the die, but into a casting chamber situated below it. The bottom of the chamber is sealed by a piston whose actuating cylinder is fixed to a pivot. After filling, the chamber is swung into position under the die and the piston is raised to fill the die.

Thixocasting takes advantage of the thixotropic properties of metal alloys in the partly solidified state (semisolid state). Thixotropic behavior means that the material behaves as a solid when at rest but flows like a liquid when rapidly deformed, its viscosity falling as the stress increases. To bring this about, the alloy has to be heated to a point in its freezing range between solidus and liquidus temperatures. This point is chosen so that, for example, 40% of the volume is liquid, with the rest remaining solid. Aluminum alloys having a long freezing range are suitable for thixocasting. To attain a good thixotropic state, the crystals in the solid solution must be equiaxed in order to ensure the liquid and solid phases flow uniformly and do not separate. Such a structure can be created by so-called *rheocasting*, whereby the melt is mechanically or electromagnetically stirred during solidification at continuous casting. This breaks off or melts off the dendrite arms, which condense to globular shapes when held just above the solidus temperature, resulting in indigenous growth of free-floating crystals with the desired equiaxed structure.

Current practice in thixocasting is as follows: The rheocasted bar is first cut off in pieces having sufficient weight for the part to be casted. The pieces are then preheated to a predetermined temperature in their melting range. This is done automatically using temperature sensors to attain a definite proportion of liquid metal, often between 35 and 50%. It is placed in the casting chamber of the casting machine and is injected into the mold cavity by the casting piston.

Casting Materials. Materials suitable for pressure die casting are copper-zinc alloys, copper-aluminum alloys, aluminum alloys, magnesium alloys, lead alloys, tin alloys, high-grade zinc alloys. For the hot-chamber process: Lead, magnesium, zinc, and tin alloys. For the cold-chamber process: Particularly for aluminum- and copper-based materials.

Weight of Castings. Up to 45 kg for light alloys, up to 20 kg for other materials, depending on the material being cast and the working dimensions of the die casting machines.

Number of Castings. Varies widely depending on the material being cast (e.g., Zn alloys $\approx$ 500 000 castings).

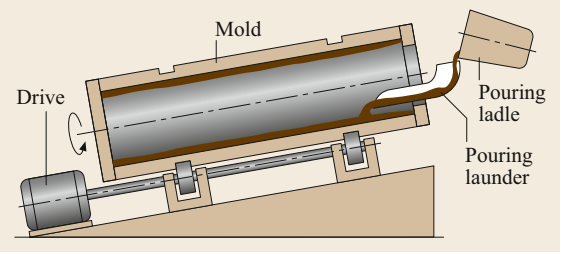

Fig. 10.17 Centrifugal casting (after [10.1, 6])

Tolerances. From about 0.1 to 0.4%.

Centrifugal Casting. The mold is a permanent, water-cooled cast iron or steel mold.

Pattern. None required.

Process Characteristics. (Fig. 10.17). The centrifugal casting process is used to manufacture hollow products having a rotationally symmetrical hollow space and an axis coinciding with the axis of rotation of the centrifugal casting machine. The external form of the casting is determined by the shape of the mold. The internal form is determined by the effect of the centrifugal force of the rotating mold. The wall thickness of the casting depends on the quantity of molten metal supplied. A variant of the process is centrifugal mold casting, which produces finished hollow or even massive castings using rotating molds. Composite centrifugal casting is also possible, as is centrifugal casting with a flange. The condition on delivery of centrifugal cast Fe, Ni and Co-based alloys is normally (at least) preturned.

Casting Materials. Especially cast iron, cast steel, heavy and light metals.

Weight of Castings. Up to about 5000 kg.

Number of Castings. From about 5000 to over 100 000, depending on the mold material and the casting material. In special cases, e.g., castings of stainless steel and the like, also for single pieces and small production runs (from ≈104 mm internal diameter upwards).

Tolerances. About 1%.

Composite Casting (Compound Casting)

The mold is a lost or permanent mold. Metal mold. e.g., for centrifugal composite casting.

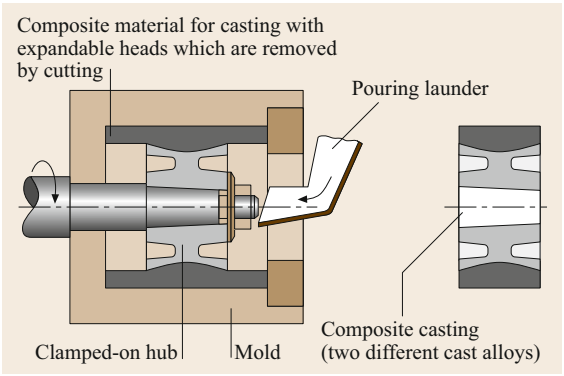

Fig. 10.18 Composite casting [10.1, 6]

Pattern. None.

Process Characteristics. (Fig. 10.18). These types of process are used to cast structural parts from two or more different metallic materials that are firmly joined together. At least one material is poured in the molten state into a mold, which may also be part of a product to be manufactured. For composite casting of various metals and/or alloys in a molten or semisolid condition, e.g., in centrifugal casting and for casting in, casting round and lining solid components, which may be made not only of metal but also of ceramic. The bonding may be formed by shrinkage, diffusion, or both.

Casting Materials. All metals and alloys that are castable with the current technology.

Weight of Castings. Up to about 50 kg and over, depending on the manufacturing equipment.

Number of Castings. Medium and large production runs.

Tolerances. From about 0.1 to 0.6%, depending on the process.

Additive Manufacturing Processes

The basics of these additive manufacturing processes are powders of the materials and a selective acting heat source. The process is a layer manufacturing process that generating complex 3-D parts by consolidating successive layers of powder material in selected areas using a heat source. Each layer is scanned according to its corresponding cross section as calculated from a CAD/CAM model. In the foundry industry selective laser melting, selective laser sintering, selected hardening of polymer and selected clogging of polymer are being used.

Selected Laser Melting. The new innovative selective laser melting technique (SLM-process) is a primary shaping technology. The SLM (selective laser melting) fabrication process is described: A focused laser beam driven by a CAD/CAM-model transmits the contour information of a desired part slice-by-slice into a bed of metallic powder, which locally melts and consolidates. This allows the fabrication of complex-shaped parts with predefined 3-D architecture and near full dense and mechanical properties comparable to those of bulk materials. SLM is reserved for metallic materials. Up until now it has manufactured parts from aluminum-, chromium-, copper-, nickel-, titanium- and precious metal alloys.

Selected Laser Sintering. This sintering method is used for manufacturing of complex inserts from metallic or ceramic powders e.g., helical cooling coil for in dies of high pressure die casting process.

Selected Hardening of Polymers. This method is used for manufacturing of sand molds or sand cores from quartz sand or olivin sand powders with furan or phenolic resin binders. The binder is spread on the molding or core sand corresponding to the CAD/CAM-model. These areas are cold hardened.

Selected Clogging of Polymer. The cores for investment casting process are PMMAs (poly(methyl methacrylate)) are made from PMMA-granulat with an adhesive material (Polypor).

These four techniques were used to successfully manufacture metal parts in the field of rapid prototyping.

10.5 Guidelines for Design

Forming by casting enables design ideas to be turned into reality to a particularly high degree, owing to the extensive freedom of design that it offers. A design appropriate for manufacturing, which contributes decisively to the efficient production of a casting, can generally be achieved only by close collaboration between the design engineer and the founder. Forming by casting differs from other forming processes in that the material only receives its shape, material structure, and quality after cooling; with shrinkage—which may sometimes be considerable—in the liquid state and during solidification, and appreciable contraction in the solid state (Fig. 10.19, Table 10.14). The contraction in the solid state should be accounted for by means of a suitable allowance (allowance for contraction). The alloying specifications often suffer considerable deviations, owing to obstruction of contraction by ribs, projections, more or less flexible cores, and mold parts (Table 10.15). Provided that they fall within the acceptable dimensional variations or are compensated for by machining allowances, as is usually the case with small castings, they do not present a problem. With large castings, though, empirical values for the deviations due to contraction have to be taken into account when making the pattern. If there is a one-sided obstruction of contraction, e.g., due to the mold or even the shape, especially in the case of longer castings (different cross-sections along their length and consequently

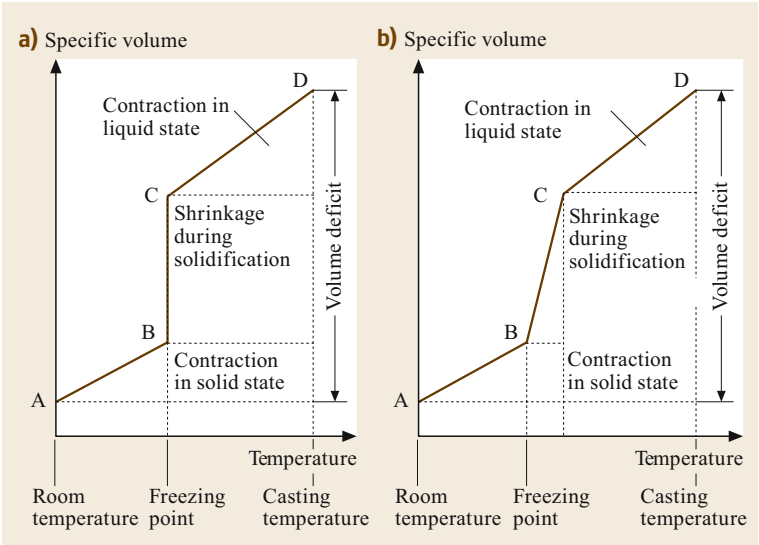

Fig. 10.19a,b Schematic of contraction of metallic materials during cooling from the molten state: **(a)** for pure metals and eutectic alloys, **(b)** for noneutectic alloys [10.7]

Table 10.14 Contraction of various casting materials (approximate values)

Lamellar graphite cast iron	3	1
Nodular graphite cast iron	5	2
Cast steel	6	3
Malleable cast iron	5.5	2
Copper alloys	4	2
Aluminum alloys	5	1.25

Table 10.15 Guide values for linear contraction and possible deviations

Lamellar graphite cast iron	1.0	0.5–1.3
Nodular graphite cast iron, unannealed	1.2	0.8–2.0
Nodular graphite cast iron, annealed	0.5	0.0–0.8
Cast steel	2.0	1.5–2.5
Austenitic manganese steel	2.3	2.3–2.8
White malleable cast iron	1.6	1.0–2.0
Black malleable cast iron	0.5	0.0–1.5
Aluminum casting alloys	1.2	0.8–1.5
Magnesium casting alloys	1.2	1.0–1.5
Casting copper (electrolytic)	1.9	1.5–2.1
CuSn casting alloys (cast bronzes)	1.5	0.8–2.0
CuSn-Zn casting alloys (gunmetal)	1.3	0.8–1.6
CuZn casting alloys (cast brass)	1.2	0.8–1.8
CuZn (Mn, Fe, Al) casting alloys (special cast brasses)	2.0	1.8–2.3
CuAl (Ni, Fe, Mn) casting alloys (cast aluminum bronzes and cast multicomponent aluminum bronzes)	2.1	1.9–2.3
Zinc casting alloys	1.3	1.1–1.5
Babbitt (Pb, Sn)	0.5	0.4–0.6

different cooling rates and thermal stresses), the castings would distort unless the pattern is curved in the opposite direction. Large wheel centers, for instance, are not infrequently split, e.g., to prevent unacceptable out-of-roundness. Thermal stresses that are not reduced by plastic deformation may, besides distortion, also result in undesirable *relief by cracking*. Therefore, if insufficient attention is paid to contraction of the material being cast at the design stage, taking into account the possibilities afforded by gating of molds and risering, pipes (shrinkage cavities), shrinkage voids, sinks, hot (pipe) cracks, distortion, and stress cracks may form.

10.5.1 Manufacture-Orientated Design

The correct design of changes in wall thickness with a view to shrinkage during solidification and contraction in the solid state is outlined below:

- Wall thickness graduations should permit directional solidification.

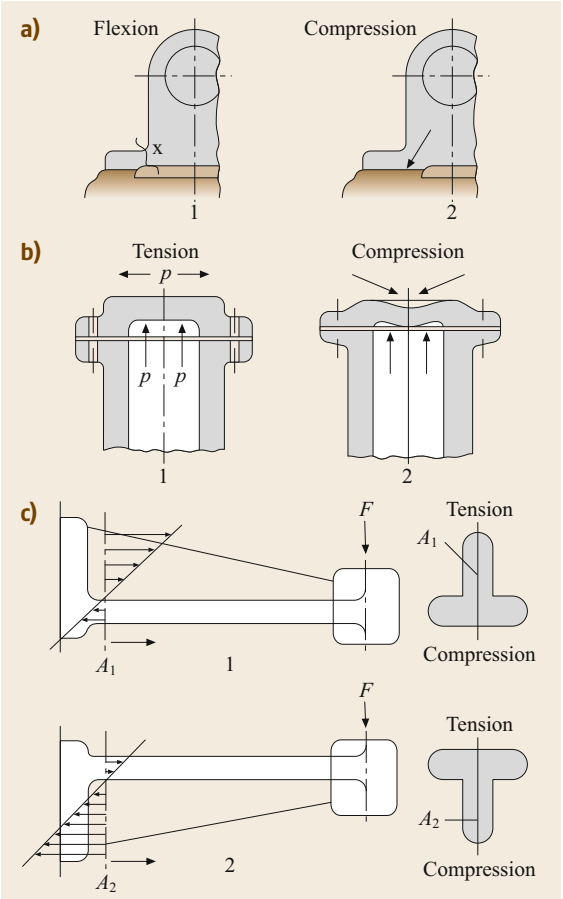

Fig. 10.20a–c Examples for stress-orientated casting design for a material having more compression stress strength than tensile strength according to [10.7]: **(a)** Pedestal (1 flexurally stressed—inadequate bearing surface, 2 compressively stressed—bearing surface widened); **(b)** cylinder cover (1 tensionally stressed—poor design, 2 compressively stressed—bearing surface—good design); **(c)** wall bracket arm (1 poor cross-sectional arrangement, 2 stress-absorbing cross-sectional arrangement) [10.8]

- Junctions formed by the meeting of two or more walls. They should be separated as far as possible, or designed for efficient casting by narrowing the cross-section. Concentrations of material, especially at locations that are inaccessible to feeding, lead to piping.
- Sudden changes in wall thickness should be avoided, as they produce high thermal stresses due to different cooling rates. In addition, there is often increased obstruction of contraction by the mold. The risk of formation of hot cracks (*pipe cracks* between liquidus and solidus temperatures) and stress cracks (during further cooling in the solid state) is

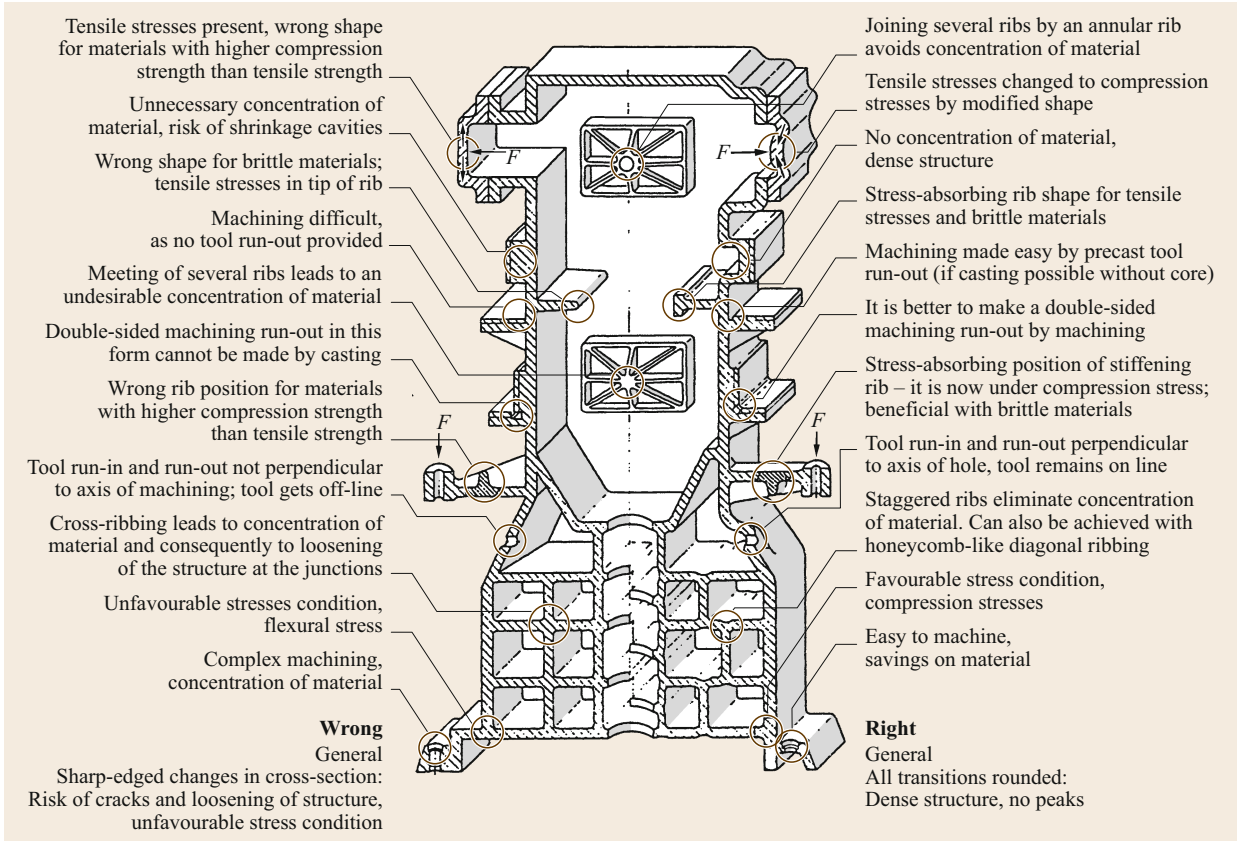

Fig. 10.21 Illustration of important design guidelines [10.9]

therefore high. Locations prone to cracking can be protected by ribs.

- Sharp corners additionally cause a heat build-up (hot sand effect) and, accordingly, not only hot cracks but also porosity due to contraction as well as drawholes.

For a summary of design recommendations see Fig. 10.21.

10.5.2 Stress-Orientated Design

When designing castings, the main stresses occurring during manufacture have to be taken as a basis. Here, the freedom of design offers excellent adaptation to the technical requirements. Forming by casting permits the efficient manufacture of parts of the most complicated kind with high strength in relation to shape. The stress condition of the design can often be made more favorable by suitable ribbing or slight modification (Figs. 10.20 and 10.21).

It is important to know the load-bearing capacity of the materials to be cast. For approximate values for lamellar graphite cast iron see Fig. 10.22.

Examples

A casting made from EN-GJL-150 gray cast iron (top horizontal gray bar) with a wall thickness of 10 mm or a test bar diameter of 20 mm (vertical line) has a tensile strength of $\approx 220\,N/mm^2$, a hardness of ≈ 220 HB, and a modulus of elasticity of $10\,000\,dN/mm^2$. For a wall thickness of 45 mm, on the other hand, the tensile strength is $\approx 100\,N/mm^2$, the hardness is ≈ 130 HB, and the modulus of elasticity almost $8000\,dN/mm^2$.

If however, the tensile strength of this 45 mm thick wall is $220\,N/mm^2$, a hardness ≈ 180 HB and an modulus of elasticity of $\approx 11\,500\,dN/mm^2$ should be expected. The material grade EN-GJL-30 should be selected. For a wall thickness of 10 mm, this cast iron has a tensile strength of $\approx 350\,N/mm^2$, a hardness of ≈ 260 HB, and a modulus of elasticity of $\approx 13\,000\,dN/mm^2$.

10.5.3 Near-Net-Shape Manufacturing and Integral Castings

The main advantage of shaping by casting is the realization of near-net-shape production of castings, thereby minimizing cutting processing and drastically shortening the process chains due to fewer process stages. The process chain is dominated up to the finished part by chip-arm shaping. The calculations of cumulative energy demands were carried out on the basis of the VDI Guideline 4600 [10.11].

Development in shaping by casting is focused on two directions. First, the components become increasingly closer to the finished parts. Second, many single parts are aggregated to one casting (integral casting, one-piece-casting). Both directions of development are realized in all variants of casting technology.

For evaluation, the manufacturing examples in Figs. 10.23 and 10.24 were considered from melting up to a commensurable part.

Fig. 10.23 shows a technical drawing of a flat part that had previously been produced by cutting starting from a bar, that is now made as a casting (malleable cast iron) using the sand-molding principle. In cutting from a semifinished material, material is utilized at only 25.5%. As a result of shaping by casting, utilization of material was increased to 40%. The effects of shaping by casting become evident in the energy balance (primary energy, cumulative energy demand). For cutting the flat part from a semifinished product, 49 362 GJ/t

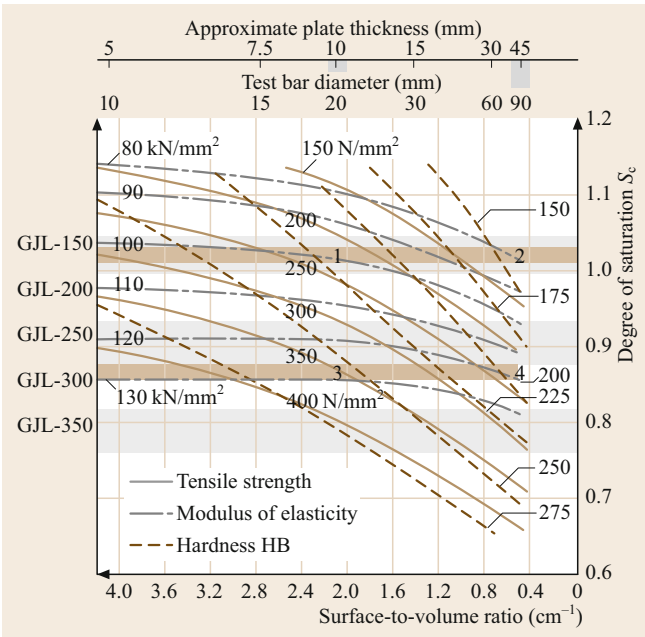

Fig. 10.22 Chart illustrating the mechanical properties of gray cast iron. The relationship between chemical composition, rate of cooling, and mechanical properties (tensile strength, hardness, modulus of elasticity) in the casting (wall thickness) and the separately cast test bar is detailed in[10.10]. Each point on the diagram signifies a specific combination of mechanical properties for a specific material. It also determines the material grade to be selected

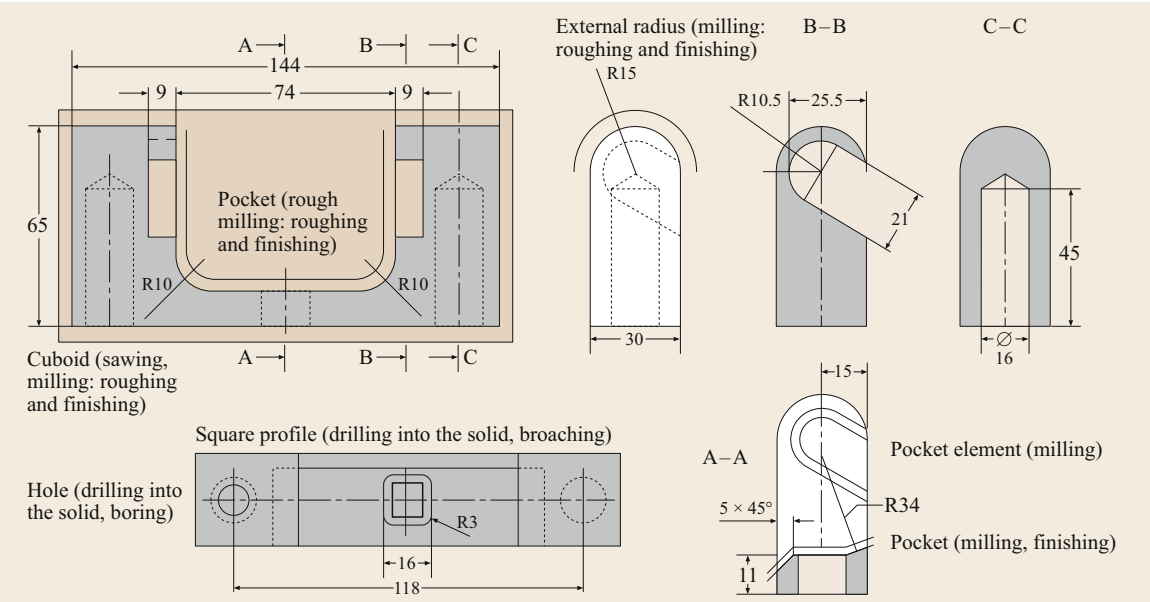

Fig. 10.23 Example: Flat part [10.12]

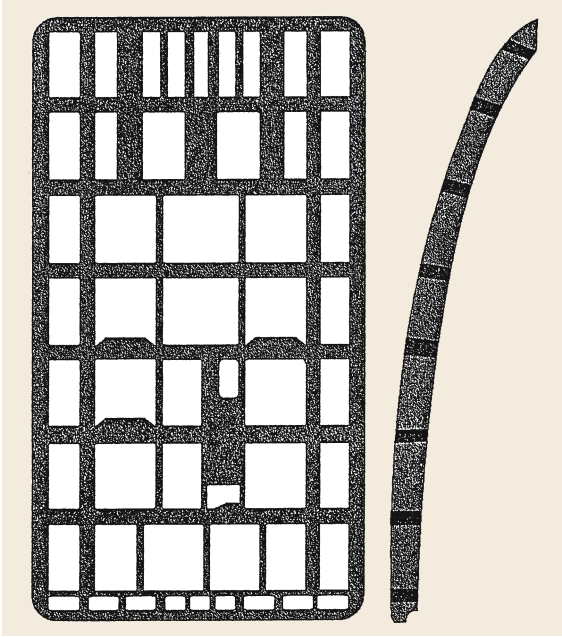

Fig. 10.24 Example: Airbus doorway [10.12]

parts are required. For shaping by casting, 17 462 GJ/t parts are required. Consequently, 64.6% of the energy can be saved. Compared to cutting of semifinished steel material, for part manufacturing about a third as much primary energy is required.

The doorway structure of an Airbus passenger door (height about 2100 mm; width about 1200 mm) is illustrated in Fig. 10.24.

The conventional manufacturing of the doorway structure as practiced until now, apart from the standard parts such as rivets, rings, and pegs, involved 64 milling parts cut from semifinished aluminum materials with very low material utilization. Afterwards, those parts were joined by about 500 rivets.

As an alternative technological variant, it is proposed that the doorway structure be made of three cast segments. Assuming almost the same mass, in production from semifinished materials, the ratio of chips amounted to about 63 kg, whereas in casting, this can be reduced to about 0.7 kg. Thus, in casting, the chip ratio amounts to only 1% in comparison to the present manufacturing strategy. In the method starting from the semifinished material, about 175 kg of material have to be molten; however, in shaping by casting, this value is about 78 kg—that is 44.6%. As a result of the energy balance (primary energy, cumulative energy demand), about 34 483 MJ are required for manufacturing the doorway from the semifinished material. However, in shaping by casting, 15 002 MJ are needed—that is about 46%. The result of having drastically diminished the cutting volume due to near-net shaping can be clearly proven in the energy balance: in the variant starting from the semifinished material, 173 MJ were consumed for cutting, while in casting it was less than 2 MJ.

In contrast to the studies mentioned before, today, the Airbus door constructions that have been cast as one part only are used. 64 parts are aggregated to one casting (integral casting).

10.6 Preparatory and Finishing Operations

10.6.1 Melting of Materials for Casting

For transforming the metal to be cast and the additives into the molten state, a wide variety of melting equipment—e.g., shaft (cupola), crucible, and hearth-type furnaces—is available. These furnaces are heated with coke, gas, oil, or electricity. The most important types of melting equipment are: for cast iron, including malleable cast iron: cupola (shaft) furnaces, induction furnaces, rotary kilns (oil-fired); cast steel: electric arc furnaces, induction furnaces; nonferrous metal castings: Induction furnaces, electrically, gas-heated or oil-heated crucible furnaces.

10.6.2 Cleaning of Castings

The molds are emptied by means of emptying jiggers. The sand adhering to the casting is generally removed by means of abrasive blasting equipment employing, without exception, steel shot or steel grit made from wire.

10.6.3 Heat Treatment

Many materials only obtain the physical and technological characteristics required in use from heat treatment. This treatment requires the use of electrically heated or gas- or oil-fired furnaces in continuous or batch operation. Their size is matched to the size and quantity of the castings and their mode of operation to the wide variety of heat treatment processes.

10.6.4 Inspection and Testing Methods

The diverse demands made on the casting, which become greater with advances in technology, and the trend

towards lightweight construction and thus more efficient use of materials inevitably lead to stringent requirements with regard to casting quality, with particular emphasis on consistency. Inspections of the process and the castings begin with checking of the metallic and nonmetallic feed stocks and end with the final inspection of the castings. Materials and workpieces are mainly tested by means of nondestructive testing methods [10.1] such as radiographic (EN 12681 [10.13]), ultrasonic (EN 12680, part 1, 2 and 3 [10.14–16]), magnetic powder (EN 1369 [10.17]), and liquid penetrant (EN 1371 part 1 and 2 [10.18, 19]) testing. Destructive tests, e.g., tensile, notched-bar impact and bending, are usually carried out with specimens cast either separately or as an appendage to the casting; in exceptional cases, specimens taken from the casting itself may be used.

In the last 20 years the certification of quality management systems on the basis of ISO 9000 etc. and QS (quality management system) 9000 has risen appreciably in the foundry industry.

References

10.1 K. Herfurth, N. Ketscher, M. Köhler: *Gießereitechnik kompakt, Werkstoffe, Verfahren, Anwendungen* (Gießerei, Düsseldorf 2003)

10.2 K. Herfuth, R. Gorski, K. Beute, M. Hering: GOPAG C 500 F – Gusswerkstoff mit höherer Festigkeit und Bruchdehnung bei sehr homogener Härteverteilung, Giesserei **98**(6), 68–79 (2011)

10.3 R. Gorski, A. Gädke, M. Hering, K. Herfurth: Die Europäische Norm für Gusseisen-Strangguss EN 16482, Giesserei **10**(11), 78–83 (2014)

10.4 DIN: *DIN 8580: Fertigungsverfahren – Begriffe, Einteilung* (Beuth, Berlin 2003)

10.5 W. Hilgenfeld, K. Herfurth: *Tabellenbuch Gusswerkstoffe* (VEB Deutscher Verlag für Grundstoffindustrie, Leipzig 1983)

10.6 R. Roller, V. Buck, J. Ludwig, H. Polzin, M. Pröm, H. Rödter, M. Schlotterbeck, D. Trauzeddel, R. Wintgens: *Fachkunde Gießereitechnik, Technologie des Formens und Gießens*, 8th edn. (EUROPA-Lehrmittel, Haan-Gruiten 2016)

10.7 G. Pahl, W. Beitz: *Konstruktionslehre – Handbuch für Studium und Praxis*, 7th edn. (Springer, Berlin, Heidelberg 2007)

10.8 VDI: *VDI-Richtlinie 3237: Fertigungsgerechte Gestaltung von Gusskonstruktionen* (VDI, Düsseldorf 1976)

10.9 ZGV: *Leitfaden für Gusskonstruktionen* (ZGV, Düsseldorf 1966)

10.10 A. Collaud: Strukturelle Anisotropie, mechanisches Verhalten und Normung von Grauguß, Giesserei **14**, 709–726 (1954), techn.-wiss. Beih.

10.11 N. Ketscher, K. Herfurth, R. Kademann: Kumulierter Energieaufwand der Gussteilfertigung-Variantenvergleich zum Spanen von Halbzeug, Giesserei Rundsch. **45**(5/6), 5–13 (1998)

10.12 N. Ketscher, K. Herfurth, A. Huppertz: Analyse des Energieverbrauchs in Gießereien und Realisierung von Material- und Energieeinsparungen durch Gussteile, Giesserei **88**(1), 21–27 (2001)

10.13 EN: *EN 12681: Founding—Radiographic Inspection* (Beuth, Berlin 1998)

10.14 EN: *EN 12680-1: Founding—Ultrasonic Inspection—Part 1: Steel Castings for General Purposes* (Beuth, Berlin 2003)

10.15 EN: *EN 12680-2: Founding—Ultrasonic Inspection—Part 2: Steel Castings for Turbine Components* (Beuth, Berlin 2003)

10.16 EN: *EN 12680-3: Founding—Ultrasonic Inspection—Part 3: Spheroidal Graphite Cast Iron Castings* (Beuth, Berlin 2003)

10.17 EN: *EN 1369: Founding—Magnetic Particle Inspection* (Beuth, Berlin 1997)

10.18 EN: *EN 1371-1: Founding—Liquid Penetrant Inspection Part 1: Sand, Gravity Die and Low Pressure Die Castings* (Beuth, Berlin 1997)

10.19 EN: *EN 1371-2: Founding—Liquid Penetrant Inspection Part 2: Investment Castings* (Beuth, Berlin 1998)

Klaus Herfurth

Pulheim, Germany
klaus.herfurth@t-online.de

Professor Dr.-Ing. habil. Klaus Herfurth is an expert on the foundry industry. He earned the Dr.-Ing. degree from Technische Universitat Bergakademie Freiberg, Germany in 1963, and his Habilitation in 1979. He is the author of 148 technical papers and book and handbook chapters. He was a Teacher at the Technische Universitat Chemnitz from 1968 to 2002 in foundry technology and materials science. From 1987 to 2001 he was manager of the iron and steel casting technical group and the standardization technical group of the German Foundrymen's Association in Düsseldorf. He also worked in R&D at this time in the field of analysis of energy demand in foundries and realization of material and energy savings through castings.

Stefan Scharf

Fraunhofer Institute for Factory Operation and Automation IFF, Institute of Manufacturing Technology and Quality Management IFQ
Otto-von-Guericke-University Magdeburg
Magdeburg, Germany
stefan.scharf@ovgu.de

After studying industrial/mechanical engineering and graduating with a diploma, Stefan Scharf started working at the Otto-von-Guericke University of Magdeburg, Germany, where he developed hybrid compound-material-solutions for the automotive industry. After obtaining his doctorate in 2014, he worked as a project manager at the Institute of Manufacturing Technology and Quality Management at the University of Magdeburg, focusing his research on the development of sustainable and energy-efficient production solutions. In 2015, he completed a research semester at the LMAS of the University of California, Berkeley, as a visiting scientist. Since September 2018 Stefan Scharf has been working at the Fraunhofer Institute for Factory Operation and Automation IFF, Magdeburg, where he is responsible for business development.

11. Metal Forming

A. Erman Tekkaya

Metal forming processes do not only shape workpieces but also set their properties over the whole volume including the surface. They improve the physical properties such as mechanical, electrical, acoustical, etc. of workpieces and hence increase their capabilities in service. Besides the hardness, ductility, residual stresses also the ductile damage level of the formed components can be controlled during forming. Formed metallic components have low imbedded energy per mass thanks the minimal or even none scrap. Hence, metal forming is among the most environmentally friendly manufacturing processes. This chapter starts with an overview of various processes of metal forming. There are over 250 different forming processes and every year new ones are invented showing the vitality of the technology. The metallurgical fundamentals relevant for metal forming processes are described next covering the mechanisms of plastic deformation, strain hardening and heat treatment. The basic concepts of elementary plasticity including the true stress, true strain, flow stress, flow condition and flow rules are followed by simple analytical methods necessary to understand the process mechanics effectively. The technological processes are covered in two groups: Bulk and sheet forming processes. Upsetting, forging, cold extrusion, rolling and shear forming is discussed in detail as bulk forming representatives. Emphasis is placed on the process description, process windows, stress states in the forming region and force displacement curves. Where necessary, tools are included as well. An introduction to sheet metal forming is given through the analytical models (such as membrane theory) and the material characterization for formability. Bending as a basic sheet forming process is studied in detail. This is followed by stretch- and deep drawing processes including hydroforming. The chapter concludes with a summary of typical forming machines including energy-, force- and displacement-controlled machines.

11.1 **Metallurgical Fundamentals** 361
11.1.1 Mechanisms of Plastic Deformation 361
11.1.2 Reverting Strain Hardening 362

11.2 **Theoretical Foundations** 364
11.2.1 Basic Concepts 364
11.2.2 Flow Condition 365
11.2.3 The Flow Rule 367
11.2.4 Equivalent Plastic Strain and the Flow Curve 367
11.2.5 Temperature Increase During Forming 367
11.2.6 Analytical Methods 368
11.2.7 Empirical Methods 370
11.2.8 Numerical Methods 370

11.3 **Bulk Forming Processes** 372
11.3.1 Upsetting 372
11.3.2 Forging 374
11.3.3 Extrusion 376
11.3.4 Drawing 382
11.3.5 Rolling 384

11.4 **Sheet Forming Processes** 387
11.4.1 Membrane Theory 387
11.4.2 Plastic Anisotropy 389
11.4.3 Formability 390
11.4.4 Bending 393
11.4.5 Stretch Forming and Deep Drawing 396
11.4.6 Hydroforming 399

11.5 **Forming Machines** 402
11.5.1 Parameters of Forming Presses 402
11.5.2 Energy-Controlled Presses 404
11.5.3 Stroke-Controlled Presses 405
11.5.4 Force-Controlled Presses 407

References 407

Metal forming is the manufacturing through plastic (permanent) change of the form of a solid body while preserving both its mass and cohesion. The term "forming" should be used for controlled plastic straining with a predefined target shape, whereas the term "deforming" should be used for unwanted or uncontrolled plas-

K.-H. Grote, H. Hefazi (Eds.), *Springer Handbook of Mechanical Engineering*, Springer Handbooks,
https://doi.org/10.1007/978-3-030-47035-7_11

tic straining. The basic advantages of metal-forming processes as compared with alternative processes such as casting and machining are [11.1, 2]:

- High material utilization and hence high energy conservation
- High productivity with short production times
- High dimensional and shape accuracy within certain tolerances
- Superior mechanical material properties of the product (especially for dynamic loadings).

On the other hand, these processes can suffer from the following disadvantages:

- Due to the high loads required for plastic forming, the tools and machines are expensive, requiring minimum batch sizes for economic production.
- The limited formability of metals restricts the range of product geometries.
- The process usually requires a high level of engineering, including analytical modeling, numerical analysis (process simulation), and also extended experience.

Metal-forming processes can be classified according to various criteria. An academic classification is done according to the dominant stress state existing in the deformation zone. Accordingly, forming processes can be classified into compressive, tensile, tensile–compressive, bending, and shearing processes. A more practical classification is according to the type of product, according to which two classes of processes can be identified: bulk forming and sheet forming processes. In bulk forming processes, the workpieces have spatial geometries (i.e., their geometries are more or less balanced in all spatial directions). During forming, large changes in the cross-sections and thickness of the products occur. The material flows in all directions. Generally, multiaxial compressive stress states exist in the deformation zone. Larger relative forming forces are needed. Bulk forming can be done with workpieces at either room temperature (cold forming) or an elevated temperature (warm or hot forming). Where hot forming is done with workpieces heated above their recrystallization temperature, warm forming is performed with workpieces between the room and recrystallization temperature or slightly above the recrystallization temperature. Examples of typical bulk forming processes are given in the following.

Figure 11.1 shows the primary forming process of flat rolling, in which an initial blank is reduced in thickness by means of two rolls. Usually, the width of the workpiece remains approximately constant. The product is then used as the initial workpiece for other basically sheet forming processes. After rolling, the casting microstructure is also changed to a more homogeneous, defect-free microstructure.

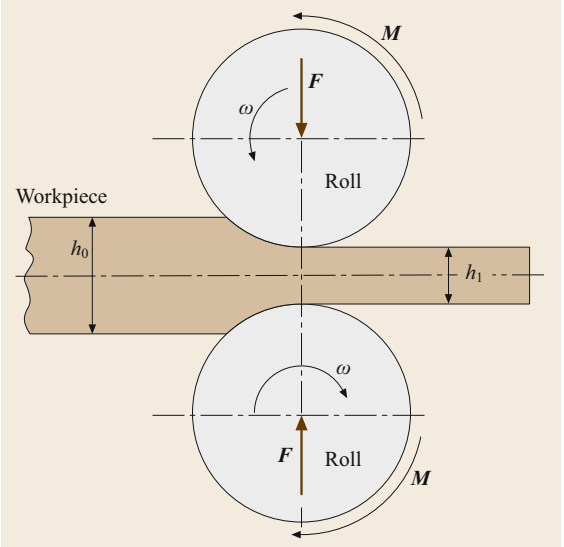

Fig. 11.1 Flat rolling

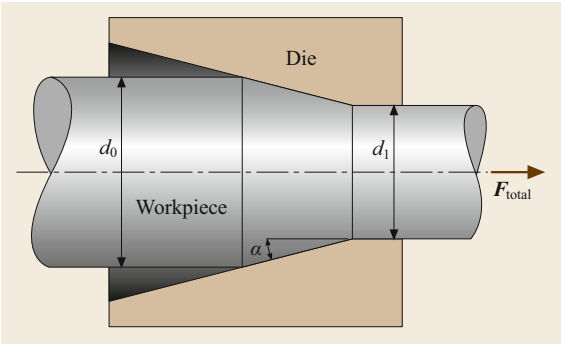

Fig. 11.2 Wire drawing

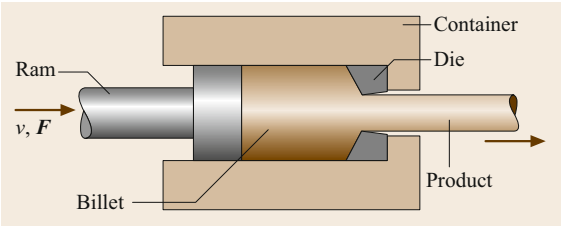

Fig. 11.3 Extrusion

Figure 11.2 shows the basic process of wire drawing, in which an initial rod or wire is forced through a conical die to reduce its diameter. Due to the application of a drawing force, the area reduction is limited to about 20%.

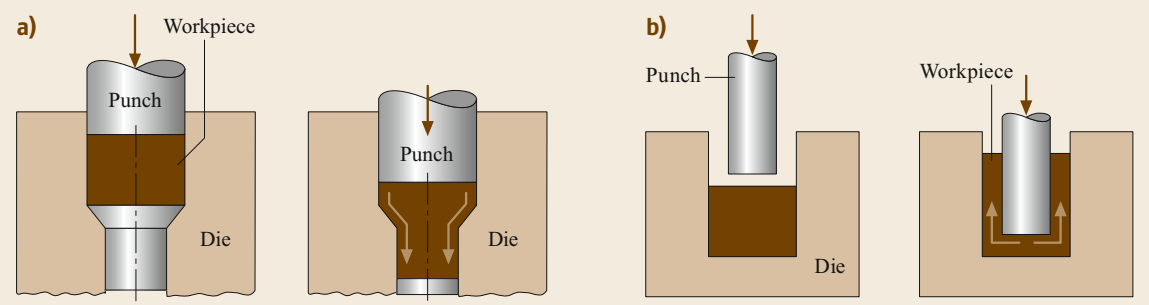

Fig. 11.4a,b Impact extrusion: (a) forward rod extrusion, (b) backward can extrusion

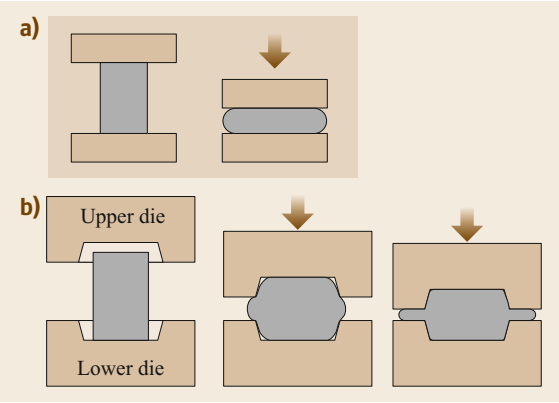

Fig. 11.5a,b Forging: (a) upsetting, (b) impression forging

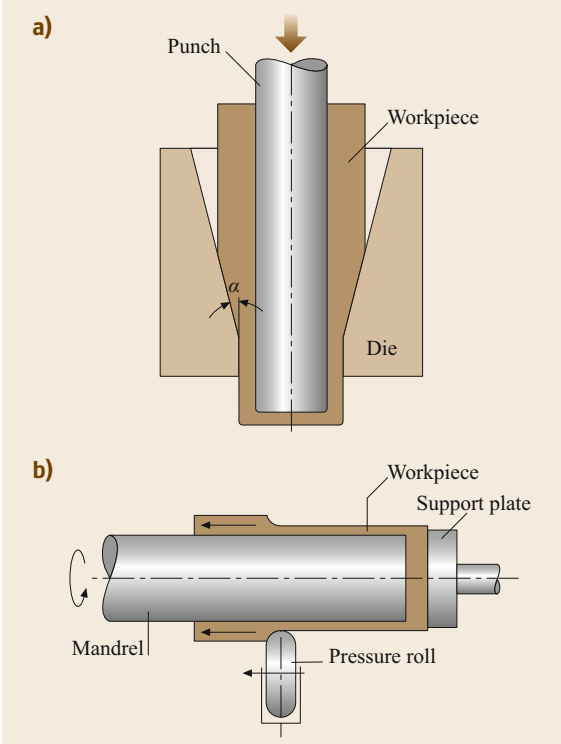

Fig. 11.6 (a) Ironing and (b) flow turning

Extrusion is demonstrated in Fig. 11.3. Similar to wire drawing, the cross-section of a rod is reduced by forcing it through a die opening. However, this time, the workpiece is pushed into instead of pulled through the die. The extrusion process shown in this figure produces continuous profiles with various cross-sections. The resulting semifinished products are then usually processed further in subsequent processes. Whereas the extrusion process in Fig. 11.4, also called impact extrusion or cold forging, aims to produce discrete parts, here net-shaped or near-net-shaped parts, i.e., parts that need no or only minor machining or similar shaping operations, are formed.

Figure 11.5 shows typical forging processes, in which an initial – usually heated – workpiece is formed between two dies. If the dies are flat, this process is called upsetting or open-die forging (Fig. 11.5a). However, if the part is formed between shaped dies and during forging the excess material flows to form a flash, this process is called impression die forging (Fig. 11.5b). Closed die forging is a forging process in which no flash is produced. This is also called trapped-die forging.

Two further bulk forming processes to create sheet-like products are shown in Fig. 11.6. Ironing (Fig. 11.6a) is a process in which the wall thickness of a cup is reduced. This is considered to be a bulk forming process, since the thickness is reduced and the stress state resembles that in a typical bulk forming process. Figure 11.6b shows the flow turning process, where the thickness of a hollow workpiece is again reduced and the stress state is typical of bulk forming.

Sheet forming processes, on the other hand, operate on planar workpieces (sheets, plates) and aim to produce hollow pieces with almost constant wall thickness. Here, a change of the wall thickness is not intended. Generally, two axial stress states exist, viz. tensile–compressive or tensile–tensile, while the third stress component normal to the sheet plane is zero or nearly zero. Sheet forming

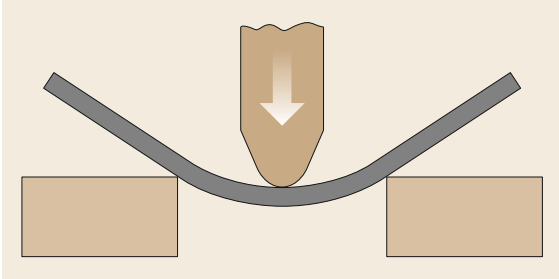

Fig. 11.7 Bending

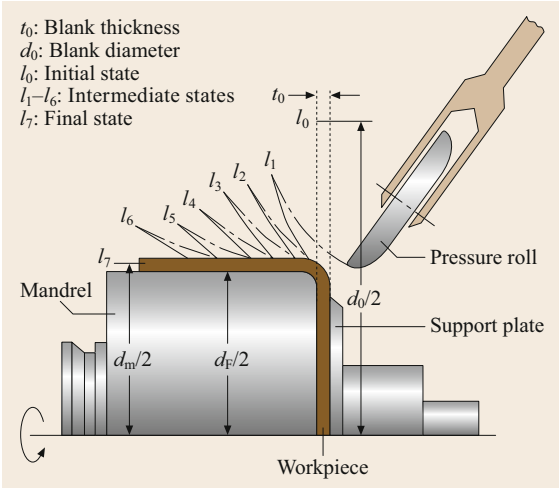

Fig. 11.8 Spinning

processes are usually conducted on workpieces that are not heated. Figures 11.7–11.9 show some examples of typical sheet forming processes. Figure 11.7 describes the bending of sheets. The mechanics of deformation during bending depends greatly on the ratio of the sheet thickness to the bending radius. Mostly, the thickness of the sheet varies only slightly during bending. In the figure, the free bending process is shown. Bending can also be conducted in dies.

The process of stretching (Fig. 11.79) consists of applying tensile forces in the plane of the sheet. The thickness of the sheet is reduced considerably during stretching. Figure 11.80 shows the basic process of deep drawing. During this process, an originally mainly flat sheet is drawn by means of a punch into a die, producing a hollow cup. The basic deformation occurs in the flange of the workpiece, and the stress state here consists of a tensile and a compressive component. The sheet is thickening at the outer rim. In this process, bending at the die radius and stretching in the cup walls also occur.

Figure 11.8 illustrates the process of spinning. Spinning is a typical incremental process in which an

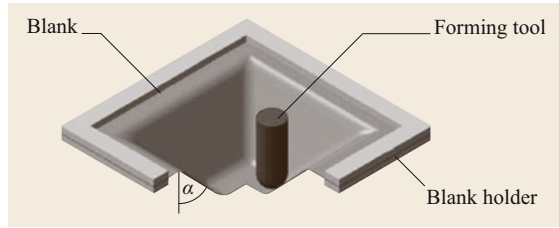

Fig. 11.9 Incremental sheet forming

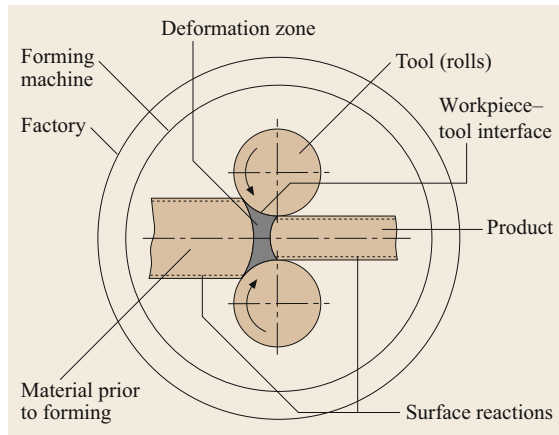

Fig. 11.10 Metal forming system (after [11.1, 2])

originally flat sheet is formed by moving a roll towards a mandrel on which the sheet is rotating while the roll also performs translatory motion.

Another recent incremental sheet formingprocess is sketched in Fig. 11.9. In this process, a punch controllable on three to five axes is used to shape an originally flat sheet incrementally. The process is much slower than the classical deep-drawing or stretching process but offers the advantage of flexibility. Besides solid tools, pressure media can also be used in sheet forming operations (Figs. 11.89–11.91). Hydroforming, aquadrawing, and tube hydroforming are variants in this process family.

Metal forming processes can be analyzed most effectively using a systems approach. The basic items of a metal forming system are shown in Fig. 11.10, for the flat rolling process. The first item is the material prior to forming. The deformation zone is the second item. The material properties of the plastically formed workpiece, the product, constitute the third item. The tools (here the rolls) make up another item. The interface between the workpiece and tools is the fifth item. The surface reactions of the workpiece before and after deformation constitute the sixth item of the metal forming system. The two final items are the forming machine and the factory. All these items influence each other and must, therefore, be considered together.

11.1 Metallurgical Fundamentals

11.1.1 Mechanisms of Plastic Deformation

If a metal crystal is exposed to shear stresses, first the lattice will deform elastically, as shown in Fig. 11.11a. After removal of the shear stress, the lattice will recover its original form. If the shear stress is increased, the crystal will deform elastically and plastically, such that, upon removal of the stresses, the crystal will not recover its original shape completely (Fig. 11.11b). Plastic deformations occur via the movement of atomic layers. Such movement occurs on so-called slip planes along slip directions [11.3].

The theoretical shear stress necessary to move one part of the lattice along a slip plane with respect to the other part can be estimated as

$$\tau_{\text{theoretical}} = \frac{G}{30} \quad \text{to} \quad \frac{G}{2\pi}\,, \tag{11.1}$$

where G is the shear modulus of the metal. For typical metallic materials, the theoretical shear strength calculated using (11.1) is presented in Table 11.1.

A second mechanism for plastic deformation is twinning (Fig. 11.12). During twinning, atoms on one side of the twinning plane are almost instantaneously moved to a mirror position on the other side of the plane. Twinning is a preferred mechanism of plastic deformation in hexagonal closed-packed (hcp) metals such as titanium, magnesium, and zinc alloys. Also, for other metals, twinning is preferred if the strain rates are very high, since plastic deformation by twinning needs much less time than that occurring by sliding.

The actual shear strengths of metals are up to several orders of magnitude less than their theoretical values (Table 11.1). Real metals show crystal defects called dislocations that facilitate another mechanism of slip that requires much less shear stress than the slip in a defect-free crystalline structure. Figure 11.13 shows that this dislocation shear occurs only incrementally over the shear plane and hence requires much lower shear stress values. Dislocations are present in virtually any metal, being introduced during solidifica-

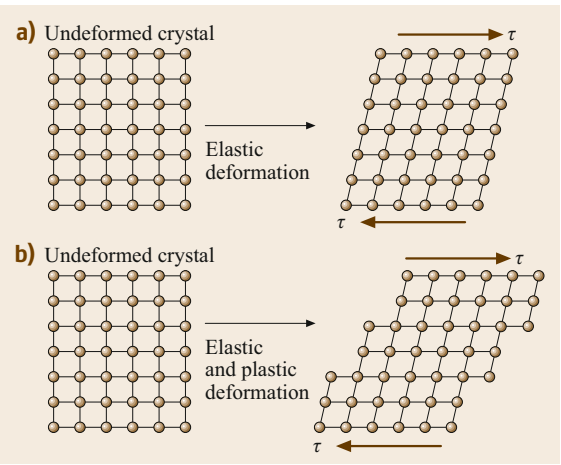

Fig. 11.11a,b Elastic and plastic deformations of the lattice structure

Table 11.1 Theoretical and actual shear strength for typical metallic materials

Material	Shear modulus (MPa)	Theoretical shear strength (MPa)	Actual shear strength (MPa)
Steel	75 800	2527–12 063	150–750
Aluminum alloys	27 500	917–4377	50–150
Copper alloys	41 400	1380–6589	100–250
Titanium alloys	44 800	1493–7130	350–800

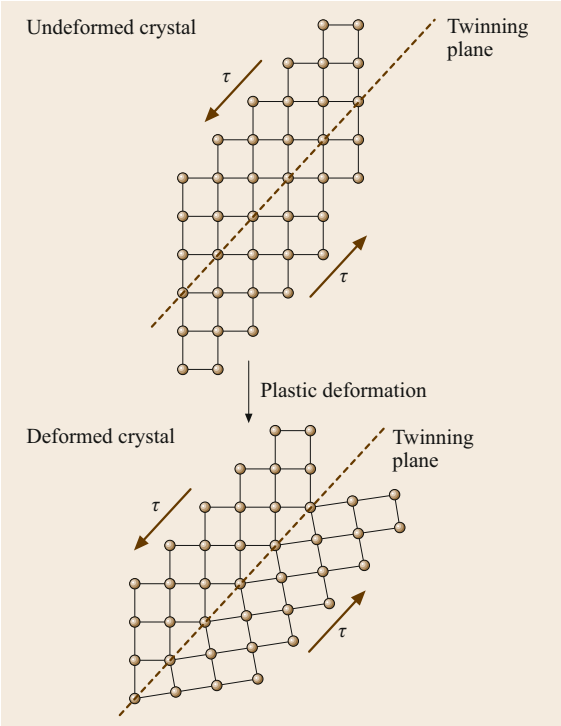

Fig. 11.12 Twinning mechanism for plastic deformation

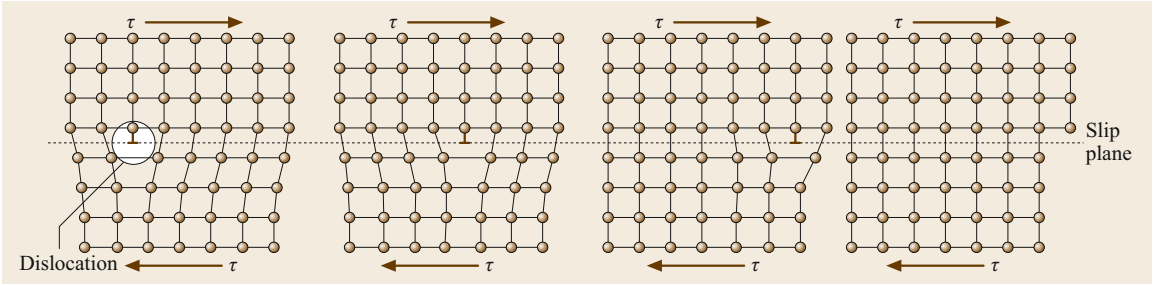

Fig. 11.13 Plastic deformation by dislocation motion

tion. In annealed metals, the length of dislocation lines is $\approx 10^4$–10^8 cm/cm^3 of metal. As plastic deformation proceeds, new dislocations are generated through various mechanisms such as the Frank–Read mechanism. As the number of dislocations increases, they start to hinder each other's motion, so that an increased shear stress is necessary to move them. This increase in yield strength is called strain hardening. In cold-worked metals, the density of dislocations increases to 10^{10}–10^{12} cm/cm^3 of metal. During plastic deformation, about 85–90% of the deformation energy is dissipated as heat. Recent measurements have indicated that this ratio varies with the amount of plastic strain. The rest of the energy is stored in the lattice as strain energy and is directly related to the dislocations.

Other mechanisms that increase the yield strength include solid-solution hardening, particle (dispersion) hardening, and grain-size hardening. These mechanisms can be superposed to obtain an analytical relation for the yield strength as

$$Y = Y_0 + \Delta Y_\mathrm{s} + \Delta Y_\mathrm{d} + \Delta Y_\mathrm{p} \,, \tag{11.2}$$

where Y_0 is the yield stress of the pure single-crystal metal with some dislocations, ΔY_s is the increase in yield strength due to solid-solution hardening, ΔY_d is the increase due to dispersion hardening, and ΔY_p is the increase due to phase boundaries. For ferritic steel, for instance, Y_0 is about 30 MPa, and

$$\Delta Y_\mathrm{s} = \sum_i k_i x_i \,, \tag{11.3}$$

where x_i is the weight percentage of each alloying element and k_i is a weight factor, given in Table 11.2.

Meanwhile, the yield strength increase due to grain refinement is given by the Hall–Petch relationship

$$\Delta Y_\mathrm{p} = \frac{k_y}{\sqrt{d}} \,, \tag{11.4}$$

Table 11.2 Weight factors for solid-solution hardening (after [11.4])

Element	Si	Mn	P	Ni	Mo	Cu	Sn	Al	N
k_i	81	18	590	8	15	40	130	24	2300

where d is the grain size and the constant k_y ranges from 15 to 24 MPa mm$^{1/2}$ for common steels. This relationship reflects the fact that grain boundaries impose geometrical constraints on dislocation motion and hence increase the shear stress that is necessary to move them. The value of ΔY_d depends on the form and morphology of the carbides generated in ferrite.

11.1.2 Reverting Strain Hardening

If a polycrystalline metal is plastically deformed at temperatures below one-third of its melting temperature T_m (in K), the grain shapes change (leading to texturing) and the dislocation density increases (leading to strain hardening). Strain hardening is naturally accompanied by a reduction of the ductility (Fig. 11.14). Although the strain-hardened state of the material is mechanically stable, it is thermodynamically unstable. Hence, at elevated temperatures, this state of the plastically deformed material can be altered.

Recovery

Heating a deformed metal in the range of $0.3T_\mathrm{m}$–$0.5T_\mathrm{m}$ will activate diffusion of atoms. This diffusion of atoms enables the motion of some dislocations, which will cancel each other or restructure themselves. Stored energy is relieved. Residual stresses will be removed, the yield stress will be reduced slightly, while the ductility will increase. Electrical and thermal properties will be recovered as well.

Recrystallization

If a deformed metal is heated at $T > 0.5T_\mathrm{m}$, diffusion processes continue such that similar dislocations start to

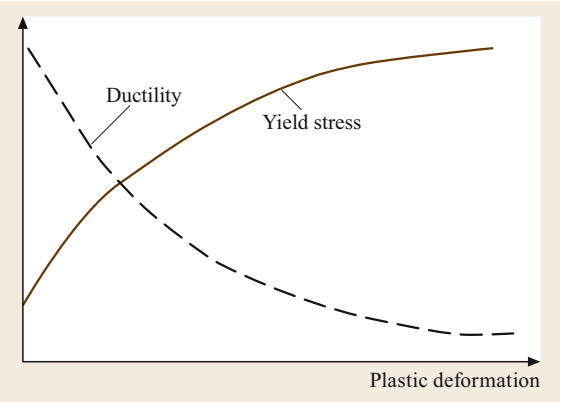

Fig. 11.14 Decrease of ductility and increase of yield stress for $T_m < 0.3$ (in K)

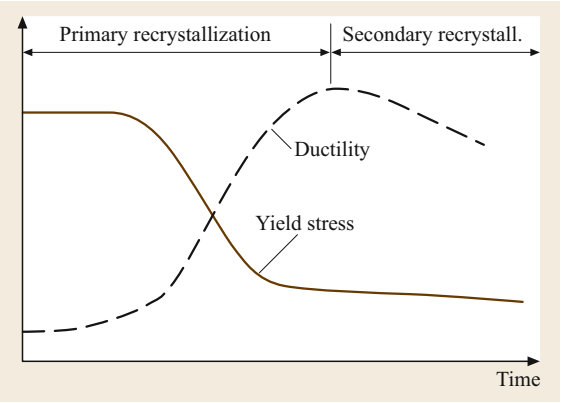

Fig. 11.15 Recrystallization of cold-formed metal ($T > 0.5T_m$)

align in certain regions to form low-angle grain boundaries. If the number of aligned dislocations increases, they can build large-angle grain boundaries via a process called recrystallization. The movable collocated dislocations are the recrystallization nuclei. During recrystallization, a refined grain structure forms and the yield stress of the metal drops to its original value, while the ductility also increases back to its preworked value (Fig. 11.15).

After recrystallization, the new grains show a preferred orientation that is related to both the deformation texture and the character of the grain boundaries. The temperature at which the whole structure is completely recrystallized within 1 h is called the recrystallization temperature of that metal (Table 11.3). Heat treatment that results in recrystallization is called annealing. Recrystallization can only occur after a minimum amount of plastic deformation, since a minimum number of dislocations must be mobilized to form large-angle grain boundaries. The greater the plastic deformation that a metal has experienced, the lower its recrystallization temperature. Time and temperature or prior plastic deformation play interchangeable roles (Fig. 11.16). At high temperatures and following large prior cold plastic deformation, grains can continue to grow after recrystallization has completed, such that larger grains form than before recrystallization. This process is called secondary recrystallization and results in a material with less superior properties than after primary recrystallization (such as lower ductility, or the orange peel effect in deep drawing and bending).

Table 11.3 Recrystallization temperatures for typical metals

Material	T_{rc} (°C)	Material	T_{rc} (°C)
C steel	550	Sn	0–40
Pure Al	290–300	Zn	50–100
Duralumin	360–400	Mo	870
Cu	200	W	900–1000
Pb	−50 to 50	Ni	400–600

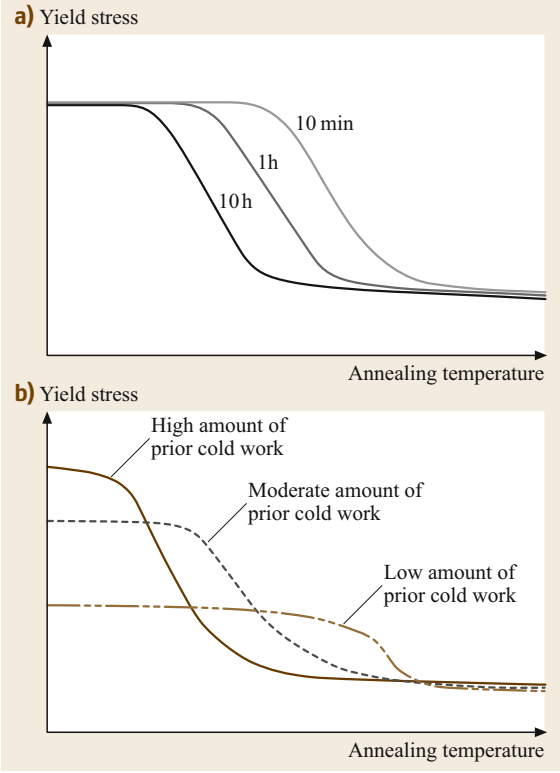

Fig. 11.16a,b Effect of time (**a**) and cold forming (**b**) on recrystallization

11.2 Theoretical Foundations

The theoretical framework for plastic deformation [11.5, 6] is based on four phenomenological foundations: the basic concepts of strain and stress, the flow condition, the flow rule, and the flow curve. Based on these, in conjunction with the equilibrium equations, analytical and numerical methods can be established. Physical simulations also make use of these fundamentals.

11.2.1 Basic Concepts

The Concept of Strain

The intensity of plastic deformation in metal forming is measured by the true strain increment $d\varepsilon$. Considering the uniaxial tension test (Fig. 11.17) in which a uniform rod with current length ℓ and current cross-sectional area A is exposed to an axial force F, the instantaneous strain increment in the axial direction is defined as

$$d\varepsilon = \frac{d\ell}{\ell} \,. \tag{11.5}$$

Assuming uniform straining, the total strain at any point in the rod experienced from the original length ℓ_0 to the final length ℓ_1 is given by

$$\varepsilon = \int_{\ell_0}^{\ell_1} \frac{d\ell}{\ell} = \ln\left(\frac{\ell_1}{\ell_0}\right) . \tag{11.6}$$

Due to the logarithmic nature of this expression, this strain is also called the logarithmic or natural strain. In contrast to the engineering strain, the true strain describes finite deformations correctly, is additive between different straining steps, and supplies the same strain values for the same amount of elongation or compression.

The total strain given in (11.6) is the sum of the elastic (recoverable) and plastic (permanent) strains.

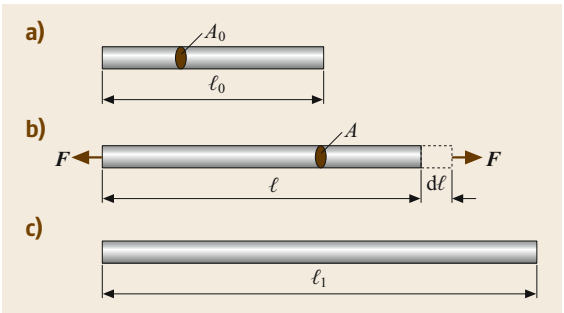

Fig. 11.17a–c Uniaxial tension of a rod: initial **(a)**, intermediate **(b)**, and final configuration **(c)**

However, in metal forming processes, the elastic strains are several orders of magnitude smaller than the plastic strains and can thus be neglected

$$\varepsilon = \varepsilon^{\text{elastic}} + \varepsilon^{\text{plastic}} \approx \varepsilon^{\text{plastic}} \,. \tag{11.7}$$

Therefore, in the forthcoming sections, the superscripts will be omitted.

Strain Rates

If the elongation $d\ell$ takes place in time dt, the strain rate can be defined as

$$\dot{\varepsilon} = \frac{d\varepsilon}{dt} = \frac{d\ell/\ell}{dt} = \frac{d\ell/dt}{d\ell} = \frac{v_{\text{tool}}}{\ell} \,, \tag{11.8}$$

where v_{tool} is the velocity of extension of the rod as imposed by the tool. The concept of strain rate can be extended to three-dimensional general deformations by introducing the velocity field for each particle in three Cartesian directions (v_x, v_y, v_z). The components of the resulting strain rate tensor are then defined by

$$\dot{\varepsilon}_{ij} \equiv \begin{pmatrix} \dot{\varepsilon}_{xx} & \dot{\varepsilon}_{xy} & \dot{\varepsilon}_{xz} \\ \dot{\varepsilon}_{yx} & \dot{\varepsilon}_{yy} & \dot{\varepsilon}_{yz} \\ \dot{\varepsilon}_{zx} & \dot{\varepsilon}_{zy} & \dot{\varepsilon}_{zz} \end{pmatrix}$$

$$= \begin{pmatrix} \dfrac{\partial v_x}{\partial x} & \dfrac{1}{2}\left(\dfrac{\partial v_x}{\partial y} + \dfrac{\partial v_y}{\partial x}\right) & \dfrac{1}{2}\left(\dfrac{\partial v_x}{\partial z} + \dfrac{\partial v_z}{\partial x}\right) \\ & \dfrac{\partial v_y}{\partial y} & \dfrac{1}{2}\left(\dfrac{\partial v_y}{\partial z} + \dfrac{\partial v_z}{\partial y}\right) \\ \text{symm.} & & \dfrac{\partial v_z}{\partial z} \end{pmatrix} . \tag{11.9}$$

Total Strains

For the three-dimensional general deformation state, the strain rates can be integrated over time if and only if all the shear strain rates are zero and the straining path, that is, the ratio of the normal strains, is constant over the respective time increment. In this case, the normal strains are also the principal strains. The total strains can then be determined for the deformation depicted in Fig. 11.18 as

$$\begin{aligned} \varepsilon_1 &= \ln\left(\frac{a_1}{a_0}\right) , \\ \varepsilon_2 &= \ln\left(\frac{b_1}{b_0}\right) , \\ \varepsilon_3 &= \ln\left(\frac{c_1}{c_0}\right) . \end{aligned} \tag{11.10}$$

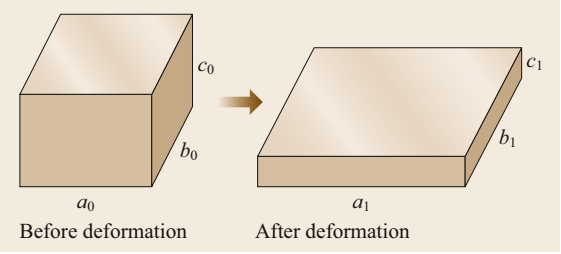

Fig. 11.18 Principal strains

Obviously, total strains can only be used in idealized cases. Here, the Arabic indices denote the principal directions.

Principle of Volume Constancy

Experimental observations have shown that the volume during plastic deformations remains approximately constant. Referring to Fig. 11.18, this means

$$V = \underbrace{a_0 \times b_0 \times c_0}_{\text{initial}} = \underbrace{a_1 \times b_1 \times c_1}_{\text{final}} = \text{const.}\,, \tag{11.11}$$

or in terms of strain rates and strains

$$\begin{aligned} &\dot{\varepsilon}_1 + \dot{\varepsilon}_2 + \dot{\varepsilon}_3 = 0 \quad \text{or} \\ &\varepsilon_1 + \varepsilon_2 + \varepsilon_3 = 0 \quad \text{or} \\ &\varepsilon_x + \varepsilon_y + \varepsilon_z = 0\,. \end{aligned} \tag{11.12}$$

The Concept of Stress

Referring to Fig. 11.17, the true stress (also called the Cauchy stress) in the axial direction is defined by

$$\sigma = \frac{F}{A}\,, \tag{11.13}$$

where A is the current area of the rod. This stress must be carefully distinguished from the engineering stress, which refers to the original cross-sectional area.

The three-dimensional generalization of the internal forces according to (11.13) leads to the stress tensor at a point

$$\boldsymbol{\sigma}_{ij} = \begin{pmatrix} \sigma_{xx} & \tau_{xy} & \tau_{xz} \\ \tau_{yx} & \sigma_{yy} & \tau_{yz} \\ \tau_{zx} & \tau_{zy} & \sigma_{zz} \end{pmatrix}. \tag{11.14}$$

This tensor is also symmetric like the strain rate tensor. Two important special cases of the general stress tensor are the uniaxial stress state (with only the σ_{xx}-component being nonzero) and the plane stress state (in which all components with a z-index are zero).

The three independent stress invariants are defined as

$$\begin{aligned} I_1 &= \sigma_{xx} + \sigma_{yy} + \sigma_{zz} = \sigma_1 + \sigma_2 + \sigma_3\,, \\ I_2 &= \tau_{xy}^2 + \tau_{yz}^2 + \tau_{zx}^2 - \sigma_{xx}\sigma_{yy} - \sigma_{yy}\sigma_{zz} - \sigma_{zz}\sigma_{xx} \\ &= -(\sigma_1\sigma_2 + \sigma_2\sigma_3 + \sigma_3\sigma_1)\,, \\ I_3 &= \sigma_{xx}\sigma_{yy}\sigma_{zz} + 2\tau_{xy}\tau_{yz}\tau_{zx} \\ &\quad - \sigma_{xx}\tau_{yz}^2 - \sigma_{yy}\tau_{zx}^2 - \sigma_{zz}\tau_{xy}^2 \\ &= \sigma_1\sigma_2\sigma_3\,, \end{aligned} \tag{11.15}$$

where σ_1, σ_2, and σ_3 are the principal stresses.

Hydrostatic and Deviatoric Stresses

The hydrostatic stress (a stress invariant) is defined as

$$\sigma_\mathrm{h} = \frac{\sigma_{xx} + \sigma_{yy} + \sigma_{zz}}{3}\,. \tag{11.16}$$

The respective hydrostatic stress tensor is hence

$$\boldsymbol{\sigma}_{ij}^\mathrm{h} = \begin{pmatrix} \sigma_\mathrm{h} & 0 & 0 \\ 0 & \sigma_\mathrm{h} & 0 \\ 0 & 0 & \sigma_\mathrm{h} \end{pmatrix} = \sigma_\mathrm{h} \begin{pmatrix} 1 & 0 & 0 \\ 0 & 1 & 0 \\ 0 & 0 & 1 \end{pmatrix}. \tag{11.17}$$

It is an experimental observation that hydrostatic stress does not initiate any plastic deformation. However, the ultimate amount of plastic deformation that a metal can withstand increases with increasing compressive hydrostatic stress. Plastic deformation is induced by the deviatoric stress tensor, obtained as

$$\begin{aligned} \boldsymbol{\sigma}'_{ij} &= \boldsymbol{\sigma}_{ij} - \boldsymbol{\sigma}_{ij}^\mathrm{h} \\ &= \begin{pmatrix} (\sigma_{xx} - \sigma_\mathrm{h}) & \tau_{xy} & \tau_{xz} \\ \tau_{yx} & (\sigma_{yy} - \sigma_\mathrm{h}) & \tau_{yz} \\ \tau_{zx} & \tau_{zy} & (\sigma_{zz} - \sigma_\mathrm{h}) \end{pmatrix}. \end{aligned} \tag{11.18}$$

11.2.2 Flow Condition

The flow condition (also called the yield condition) is a hypothesis describing the condition that must be fulfilled for plastic flow to start or continue. Most flow conditions are expressed in terms of components of the stress tensor. Any flow condition must fulfill the trivial case of the uniaxial stress state, for which plastic flow starts if the axial stress is equal to the yield stress. In metal forming, instead of the yield stress, the term "flow stress" is preferred. Referring to Fig. 11.19, the elastic region is terminated by the initial yield stress or the initial flow stress $\sigma_{\mathrm{f}0}$. Increasing the tension force further will also increase the axial stress, but with a much

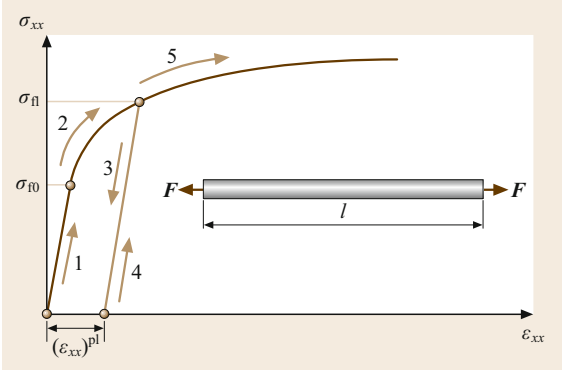

Fig. 11.19 Flow stress in simple tension test (numbers give the sequence)

lower gradient than in the elastic region. If loading is terminated at a flow stress of σ_{fl} and the specimen is unloaded and then reloaded, plastification will this time start at a higher flow stress of σ_{fl}. This phenomenon is called strain or work hardening. Under certain circumstances, the flow stress σ_{fl} may be equal to the initial flow stress σ_{f0}. Such kinds of materials are called nonhardening or perfectly plastic materials. If the flow stress after plastification decreases, the material is strain softening.

The two flow conditions used extensively in metal forming for general three-dimensional stress cases are the Tresca flow condition and the von Mises flow condition.

The Tresca Flow Condition

The Tresca flow condition states that plastic flow will start or continue if the maximum shear stress τ_{max} is equal to a material constant that can be found as $\sigma_f/2$ after tuning this criterion by the simple tension test

$$\tau_{max} = \frac{\sigma_f}{2} , \tag{11.19}$$

or in terms of principal normal stresses

$$\sigma_{max} - \sigma_{min} = \sigma_f , \tag{11.20}$$

where σ_{max} and σ_{min} are the largest and smallest principal normal stresses. Figure 11.20 shows the flow locus for plane stress states according to Tresca. The table in the figure depicts the various forms that the Tresca flow criterion takes in terms of the spatial plane stress components σ_I and σ_{III}.

The von Mises Flow Condition

In contrast to the Tresca flow condition, the von Mises flow condition considers all the principal shear stresses.

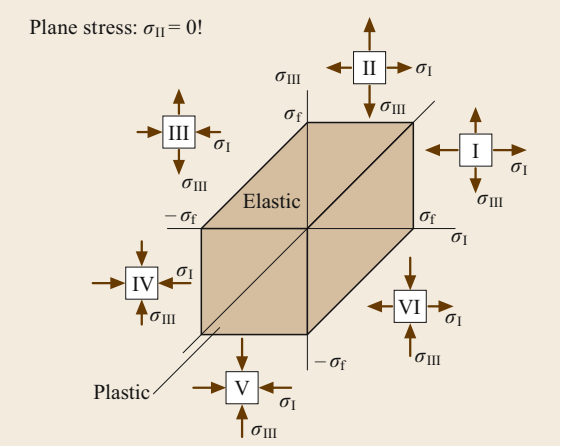

Region		
I	$\sigma_I > \sigma_{III} > 0$	$\sigma_f = \sigma_I$
II	$\sigma_{III} > \sigma_I > 0$	$\sigma_f = \sigma_{III}$
III	$\sigma_{III} > 0 > \sigma_I$	$\sigma_f = \sigma_{III} - \sigma_I$
IV	$0 > \sigma_{III} > \sigma_I$	$\sigma_f = -\sigma_I$
V	$0 > \sigma_I > \sigma_{III}$	$\sigma_f = -\sigma_{III}$
VI	$\sigma_I > 0 > \sigma_{III}$	$\sigma_f = \sigma_I - \sigma_{III}$

Fig. 11.20 Tresca flow hexagon

Accordingly, plastic flow starts or continues if

$$c' = \sqrt{\frac{1}{3}\left[\left(\tau^1_{max}\right)^2 + \left(\tau^2_{max}\right)^2 + \left(\tau^3_{max}\right)^2\right]} , \tag{11.21}$$

where c' is a material constant. Again tuning this equation by the simple tension test gives

$$\sigma_f = \sqrt{\frac{1}{2}\left[\begin{array}{l}(\sigma_{xx} - \sigma_{yy})^2 + (\sigma_{yy} - \sigma_{zz})^2 \\ \quad + (\sigma_{zz} - \sigma_{xx})^2 + 6\left(\tau^2_{xy} + \tau^2_{yz} + \tau^2_{zx}\right)\end{array}\right]} . \tag{11.22}$$

Figure 11.21 shows the flow locus for plane stress states. In this case, (11.22) reduces to

$$\sigma_f = \sqrt{\sigma_I^2 + \sigma_I \sigma_{III} + \sigma_{III}^2} . \tag{11.23}$$

A comparison of the von Mises flow criterion with the Tresca criterion reveals that, for plane stress states, the maximum deviation between the two criteria is 15.5%. Each criterion finds a different shear stress in pure shear for the initiation of plastic flow k

$$k = \begin{cases} \frac{1}{2}\sigma_f & \text{by Tresca} \\ \frac{1}{\sqrt{3}}\sigma_f & \text{by von Mises} . \end{cases} \tag{11.24}$$

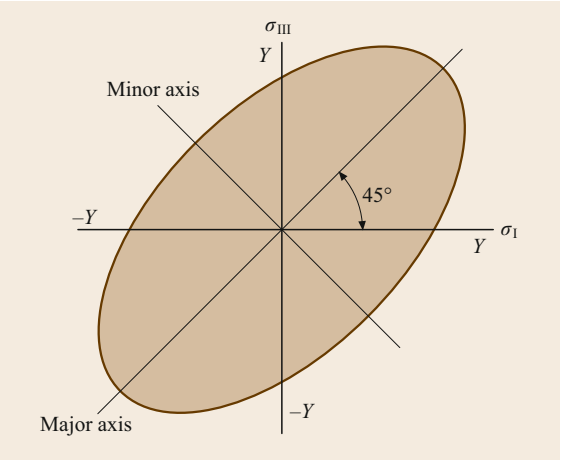

Fig. 11.21 von Mises flow ellipse

Both criteria assume that plastic flow is independent of the hydrostatic stress and of the sense of the stresses. Violation of the latter is also called the Bauschinger effect or kinematic hardening.

11.2.3 The Flow Rule

The relationship between plastic strains and stresses is expressed by the Levy–Mises flow rule. Unlike in Hooke's law for elastic deformations, in plasticity true strain rates are related to deviatoric stresses

$$\dot{\boldsymbol{\varepsilon}}_{ij} = \lambda \boldsymbol{\sigma}'_{ij} \,, \tag{11.25}$$

where λ is a nonnegative real number. By inserting (11.25) into (11.22), the nonnegative parameter can be eliminated, yielding

$$\dot{\boldsymbol{\varepsilon}}_{ij} = \frac{\sqrt{3I_2^{\dot{\varepsilon}_{ij}}}}{\sigma_\mathrm{f}} \boldsymbol{\sigma}'_{ij} \,, \tag{11.26}$$

where $I_2^{\dot{\varepsilon}_{ij}}$ is the second invariant of the strain rate tensor.

11.2.4 Equivalent Plastic Strain and the Flow Curve

The plastic power per unit volume due to the stresses during plastic deformation can be expressed as

$$p = \sum_i^3 \sum_j^3 \sigma_{ij} \dot{\varepsilon}_{ij} = \sum_i^3 \sum_j^3 \sigma'_{ij} \dot{\varepsilon}_{ij} \,. \tag{11.27}$$

Equating this power to the power done by the respective flow stress and a fictitious strain rate leads to the definition of the equivalent plastic strain rate $\dot{\bar{\varepsilon}}$ as

$$p = \sum_i^3 \sum_j^3 \sigma'_{ij} \dot{\varepsilon}_{ij} = \sigma_\mathrm{f} \dot{\bar{\varepsilon}} \,. \tag{11.28}$$

Together with (11.26), this yields

$$\begin{aligned} \dot{\bar{\varepsilon}} &= \sqrt{\frac{4}{3} I_2^{\dot{\varepsilon}_{ij}}} = \sqrt{\frac{2}{3} \left(\sum_i^3 \sum_j^3 \dot{\varepsilon}_{ij} \dot{\varepsilon}_{ij} \right)} \\ &= \sqrt{\frac{2}{3} \left[\left(\dot{\varepsilon}_{xx}^2 + \dot{\varepsilon}_{yy}^2 + \dot{\varepsilon}_{zz}^2 \right) + 2 \left(\dot{\varepsilon}_{xy}^2 + \dot{\varepsilon}_{yz}^2 + \dot{\varepsilon}_{xz}^2 \right) \right]} \,. \end{aligned} \tag{11.29}$$

The total equivalent plastic strain is the time integral of (11.29)

$$\bar{\varepsilon} = \int_t \dot{\bar{\varepsilon}} \, \mathrm{d}t \,, \tag{11.30}$$

or in terms of total strain components

$$\bar{\varepsilon} = \sqrt{\frac{2}{3} \left(\dot{\varepsilon}_1^2 + \dot{\varepsilon}_2^2 + \dot{\varepsilon}_3^2 \right)} \,. \tag{11.31}$$

The equivalent plastic strain is a measure of the increase of the dislocation density and the mutual hindrance of dislocations; i.e., it measures the increase of the flow stress. The change of the flow stress with the equivalent plastic strain is a material property called the flow curve

$$\sigma_\mathrm{f} = \sigma_\mathrm{f}(\bar{\varepsilon}) \,. \tag{11.32}$$

Typical flow curves for various temperatures and strain rates are shown in Fig. 11.22 for the typical cold-forming steel C15. Usually, the flow stress at a given equivalent strain decreases with temperature but increases with strain rate. The flow curve can be determined basically in simple tension, compression, and torsion tests. All theses tests have their limitations regarding the attainable strain values and stress states [11.7].

11.2.5 Temperature Increase During Forming

During plastic deformation, about 85–90% of the plastic work is dissipated as heat. For a homogeneous adiabatic deformation, the average temperature increase can be computed as

$$\Delta T = \frac{(0.85 - 0.95)\, \bar{\sigma}_{\mathrm{f,mean}} \bar{\varepsilon}}{\rho c} \,, \tag{11.33}$$

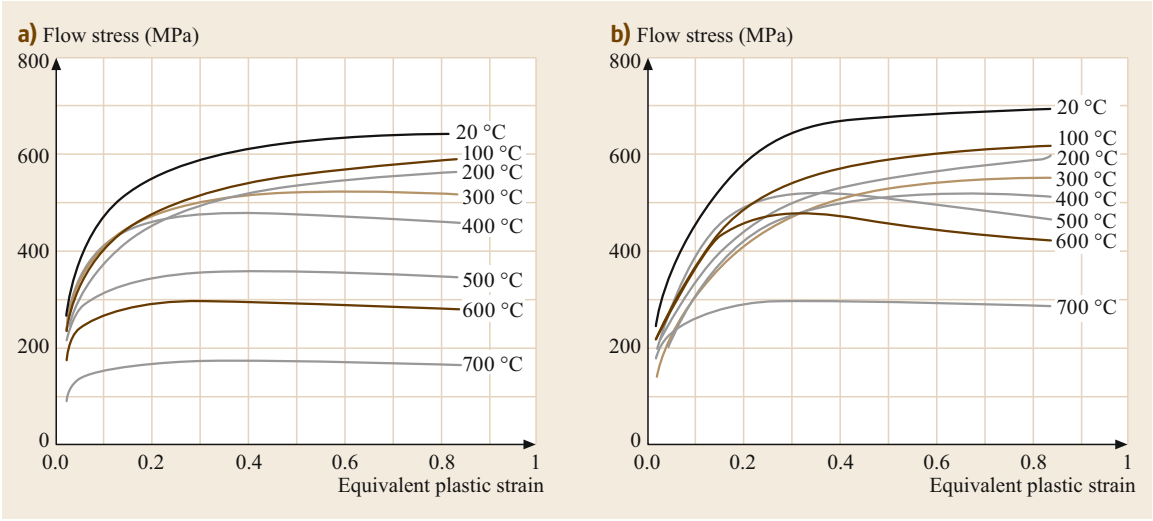

Fig. 11.22a,b Flow curve of a low-carbon steel (C15 steel) at various temperatures and strain rates: **(a)** strain rate: 0.1 s^{-1}, **(b)** strain rate: 10 s^{-1} (after [11.8])

Table 11.4 Average temperature increase during homogeneous metal forming with average plastic strain of unity (after [11.9])

Material	ρ (kg/dm^3)	c (J/(kg K))	$\sigma_{f,mean}$ (N/mm^2)	ΔT (K)
Steel	≈ 7.8	≈ 500	400–1200	100–300
Al alloys	≈ 2.7	≈ 1000	100–300	35–100
Cu alloys	≈ 8.7	≈ 400	200–400	50–100
Ti alloys	≈ 4.5	≈ 600	750–1500	250–500

where $\bar{\sigma}_{f,mean}$ is the mean flow stress during deformation, $\bar{\varepsilon}$ is the mean equivalent plastic strain, c is the specific heat capacity, and ρ is the density of the material. Table 11.4 presents the average temperature increase for a moderate equivalent plastic strain of unity for various materials.

11.2.6 Analytical Methods

All the methods discussed in this section assume rigid plastic behavior and quasistatic loading [11.10–12].

Elementary Plasticity and Friction Models

Here, only equilibrium methods are discussed, being based on the static equilibrium of simple, elementary, standard free bodies (semiinfinitesimal slabs) for which the strain rate state can be easily determined. Basically, three types of elementary free bodies are considered, viz. rectangular (Fig. 11.23a), circular (Fig. 11.23b), and tubular slabs (Fig. 11.23c). The basic assumptions are:

1. The strain rate state in each semiinfinitesimal slab is homogeneous.
2. Plane sections remain plane.
3. The stresses along the characteristic directions of the slabs are principal stresses.
4. Friction at the contact interfaces can be described by either the Coulomb friction model or the constant shear model.

The Coulomb friction model states that the frictional shear stress at a surface element at the interface

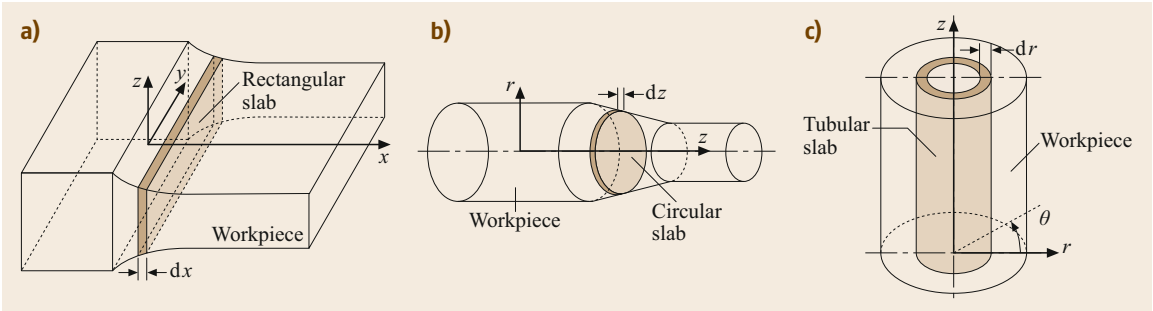

Fig. 11.23a–c Various slab elements: **(a)** rectangular slab, **(b)** circular slab, **(c)** tubular slab

Table 11.5 Typical values of the coefficient of friction and friction factor

Process	Coefficient of friction μ	Friction factor m
Cold forging (steel, stainless steel, Cu alloys, brass)	0.05–0.10 (lower values for phosphated workpieces)	0.05–0.10
Cold forging (Al, Mg alloys)	0.05	0.05–0.10
Wire drawing (steel, stainless steel, Cu alloys, brass)	0.05–0.10	–
Wire drawing (Al, Mg alloys)	0.03–0.10	–
Hot forging	Use not recommended	0.20–0.40
Forging of Ti and Ni alloys	Use not recommended	0.10–0.30 (glass lubrication)
Hot rolling	Use not recommended	0.70–1.00 (no lubrication)
Deep drawing (steel)	0.05–0.10	Use not recommended
Deep drawing (stainless steel)	0.10	Use not recommended
Deep drawing (Cu alloys, brass)	0.05–0.10	Use not recommended
Deep drawing (Al, Mg alloys)	0.05	Use not recommended
Ironing (steel)	0.05–0.10	Use not recommended
Ironing (stainless steel)	0.05	Use not recommended
Ironing (Cu alloys, brass)	0.10	Use not recommended
Ironing (Al and Mg alloys)	0.05	Use not recommended

is proportional to the normal stress

$$\tau_{\text{friction}} = \mu\sigma_{\text{normal}} \,. \tag{11.34}$$

The proportionality factor μ is called the coefficient of friction. In metal forming, the range for μ is given as

$$0 \le \mu \le 0.577 \,. \tag{11.35}$$

The constant shear friction model states that the frictional stress is proportional to the flow stress in shear k

$$\tau_{\text{friction}} = mk \,. \tag{11.36}$$

The proportionality factor m is called the friction factor. The range of m is given by

$$0 \le m \le 1 \,. \tag{11.37}$$

Both models only approximately describe reality. Recent friction models are a combination of both elementary models. Typical values for the coefficient of friction and the friction factor are presented in Table 11.5.

The unknown stresses can be solved using the equilibrium equations and the flow condition. The flow rule is not used. The accuracy of this approach decreases as the friction or the inclination of the free surfaces increases.

Upper- and Lower-Bound Methods

The upper-bound method is based on the first law of thermodynamics. For a kinematically admissible velocity field that satisfies volume constancy and all the velocity boundary conditions for a plastically deforming body, an upper bound for the forming force is given by [11.13]

$$(F_{\text{tool}})^{\text{upper-bound}} = \frac{1}{v_{\text{tool}}}\left(\int_V \sigma_{\text{f}}\dot{\bar{\varepsilon}}\,\mathrm{d}V + \int_{A_{\text{s}}} \text{mk}v_{\text{shear}}\,\mathrm{d}A - \int_{A_{\text{f}}} \boldsymbol{p}\boldsymbol{v}\,\mathrm{d}A\right), \tag{11.38}$$

where v_{tool} is the tool velocity, $\boldsymbol{p}$ is the known pressure vector acting on the workpiece, v_{shear} is the shearing velocity at shear surfaces, v is the velocity vector of points on the workpiece surface, A_{s} is the workpiece area on which friction is specified, and A_{f} is the workpiece area on which forces are specified. To apply the upper-bound method, the plastic region has to be estimated, the constant flow stress has to be estimated in the plastic region, friction stresses must be constant and hence described by the constant shear model, and finally, a kinematically admissible velocity field or appropriate shear planes have to be assumed.

Lower-bound methods lead to forces that are always lower than the actual forces. Here, a statically admissible stress field that fulfills the equilibrium equations and the stress boundary conditions must be guessed. Ideally, for an analysis, the force can be limited between an upper and lower bound. However, the application of the lower-bound method is much more difficult, since the guess of an admissible stress field is not straightforward. Furthermore, in practical applications, an upper bound for the forming forces is sufficient. The *upper-bound* property for the forming force is given if and only if the material's flow stress is correct and the friction stresses are correct. Otherwise, the computed *upper bound* may also be *lower* than the actual physical forces.

The Slip Line Field Solution

The slip line field solution also assumes rigid, perfectly plastic material behavior. Furthermore, the plane strain state is assumed. Moreover, the processes have to be frictionless. If these assumptions are fulfilled, then the theory supplies an exact solution. The slip line field solution is based on the governing equations including the flow condition, the volume constancy equation, the flow rule, and the equilibrium equations for the plane strain state. These equations build up a hyperbolic system of partial differential equations that can be solved by the method of characteristics. If the stresses are expressed in terms of the hydrostatic stress and the orientation of the stress element in the maximum shear stress direction, the two characteristic lines are orthogonal to each other (α and β-slip lines) and correspond to the directions of maximum shear stress; therefore they are called slip lines. The governing equations can be written as ordinary differential equations along each slip line. These equations can be summarized as the Hencky equations for the stresses

$$\begin{aligned}\sigma_\mathrm{h} - 2k\phi &= \text{constant along the } \alpha\text{-slip line}\,,\\ \sigma_\mathrm{h} + 2k\phi &= \text{constant along the } \beta\text{-slip line}\,,\end{aligned} \tag{11.39}$$

and the Geiringer equations in terms of the particle velocities

$$\begin{aligned}\frac{\mathrm{d}v_\alpha}{\mathrm{d}s} &= v_\beta \frac{\mathrm{d}\phi}{\mathrm{d}s} \qquad \text{along } \alpha\text{-slip line}\,,\\ \frac{\mathrm{d}v_\beta}{\mathrm{d}s} &= v_\alpha \frac{\mathrm{d}\phi}{\mathrm{d}s} \qquad \text{along } \beta\text{-slip line}\,,\end{aligned} \tag{11.40}$$

where ϕ is the inclination of the slip line and s is the distance along the slip line. Constructing the slip line field from known boundary conditions, the use of (11.39) and (11.40) supplies the stress and velocity (and hence strain rates) at any point in the deformation zone.

11.2.7 Empirical Methods

The Visioplasticity Method

The visioplasticity method consists of splitting the workpiece before deformation into two parts and marking a grid on one side, then closing these two parts and forming the workpiece. The grids are deformed after forming, then measured in order to determine the particle velocities and displacements. From these data, the strain rates and thus stresses can be computed. Figure 11.41 shows a typical visioplasticity specimen used in forward rod extrusion. The basic assumption is that the initial plane on which the grid is produced remains planar during plastic deformation. The grids can be marked on the specimens by mechanical methods, photomechanical methods, electrochemical methods, or photolithographic methods.

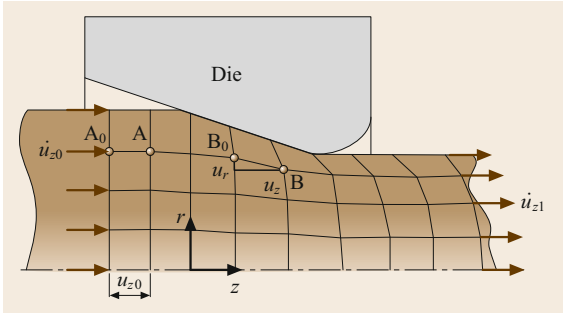

Fig. 11.24 Visioplasticity analysis (after [11.9])

In the case of steady-state processes, the velocities can be determined (Fig. 11.24) by first computing a time increment

$$\Delta t = \frac{u_{z0}}{\dot{u}_{z0}} = \frac{u_z}{\dot{u}_z(\bar{r}_\mathrm{B}, \bar{z}_\mathrm{B})} = \frac{u_r}{\dot{u}_r(\bar{r}_\mathrm{B}, \bar{z}_\mathrm{B})}\,, \tag{11.41}$$

where $\bar{r}_\mathrm{B}$ and $\bar{z}_\mathrm{B}$ are the mean coordinates of point B. Hence, the velocity components of point B can be found as

$$\begin{aligned}\dot{u}_z(\bar{r}_\mathrm{B}, \bar{z}_\mathrm{B}) &= \frac{u_z}{\Delta t} = \frac{u_z}{u_{z0}}\dot{u}_{z0}\,,\\ \dot{u}_r(\bar{r}_\mathrm{B}, \bar{z}_\mathrm{B}) &= \frac{u_r}{\Delta t} = \frac{u_r}{u_{z0}}\dot{u}_{z0}\,.\end{aligned} \tag{11.42}$$

Using these components, the strain rate components can be found. The deviatoric stress components are given by the flow rule in (11.26). The hydrostatic stress found from the stress boundary conditions and the previously found deviatoric stresses are then used to determine the total stress components finally.

Physical Simulation

Using modeling materials such as wax or plastiline, the flow pattern can be visualized and observed through transparent dies, for instance [11.14]. The key idea here is the fact that two materials behave similarly from the viewpoint of plasticity if they have the same strain-hardening exponent n. It is possible to add additives such as kaolin, Indramic, and Filia to wax and plastiline to change the n value and even the strain-rate sensitivity value m. Also, the ductility and strength level can be manipulated by additives. Hence, the basic difference from the forming process of metals is the much lower stress level.

11.2.8 Numerical Methods

The equations governing plasticity cannot be solved in closed form except for a very few simple applications.

An approximate solution of the differential equations can be obtained numerically using various methods. Among these methods, the finite element approach has found the most extended application because of its generality and efficiency.

Rigid–Plastic Finite Element Formulations

The elastic part of the strain is neglected, and the whole body is assumed to deform rigid plastically. The solutions obtained by these formulations cannot describe residual stresses, springback, or similar elastic-strain-dependent variables. Furthermore, since the formulation assumes a pseudoelastic behavior in the rigid parts of the workpiece, friction in these parts may be modeled incorrectly [11.15].

The rigid-plastic formulation is based on Markov's variational principle, which holds only for rigid-plastically deforming bodies

$$\Pi(v) = \int_V \sigma_f \dot{\bar{\varepsilon}}\, \mathrm{d}V + \int_V \frac{S}{2}\dot{\varepsilon}_V^2\, \mathrm{d}V - \int_{A_t} \boldsymbol{t}\boldsymbol{v}\, \mathrm{d}A$$
$$\Rightarrow \text{stationary}\,, \tag{11.43}$$

where Π is the functional, $\boldsymbol{v}$ is the velocity vector of material particles, $\dot{\varepsilon}_V$ is the volumetric strain rate, $\boldsymbol{t}$ is the specified traction acting over the surface A_t of the body, and S is a constant called the penalty factor. The penalty factor term is necessary to impose the volume constancy constraint approximately. Alternatively, the volume constancy constraint can be imposed exactly by using a Lagrange multiplier λ.

It can be shown that the hydrostatic stress is given in both cases by

$$\sigma_H = S\dot{\varepsilon}_V\,,$$
$$\sigma_H = \lambda\,. \tag{11.44}$$

These functionals can be easily discretized by assuming shape functions for the velocities over the element domain.

After the standard discretization procedure, the resulting finite element equations read

$$\left(\mathbf{K}_D^e + \mathbf{K}_H^e\right)\boldsymbol{v}^e = \boldsymbol{f}^e\,, \tag{11.45}$$

where $\boldsymbol{f}^e$ is the nodal force vector of the element compatible with the nodal velocity vector $\boldsymbol{v}^e$. The nonlinear deviatoric stiffness matrix is given by $\mathbf{K}_D^e$, and the linear hydrostatic stiffness matrix by $\mathbf{K}_H^e$. The resulting nonlinear (w.r.t. nodal velocities) equations (11.45) can be solved by using standard numerical methods. The common ones applied are the direct iteration and Newton–Raphson methods. Both methods are iterative and are applied in increments. The time integration is performed explicitly in most commercial software.

Implicit Static Elastoplastic Finite Element Formulations

These formulations usually assume an additive composition of the elastic and plastic strain rate tensors

$$\dot{\boldsymbol{\varepsilon}}_{ij} \approx \dot{\boldsymbol{\varepsilon}}_{ij}^{\mathrm{el}} + \dot{\boldsymbol{\varepsilon}}_{ij}^{\mathrm{pl}}\,. \tag{11.46}$$

This is based on so-called hypoelastic models. Models based on hyperelasticity are also used, leading to a multiplicative split of the elastic and plastic deformations. The generalized Hooke law is used for the elastic strain rates, and the Levy–Mises equations for the plastic strain rates. These then lead to the modified Prandtl–Reuss equations between the objective (frame-invariant) rate of the stress tensor and the strain rates

$$\hat{\boldsymbol{\sigma}}_{ij} = \mathbf{C}_{ijmn}\dot{\boldsymbol{\varepsilon}}_{mn}\,. \tag{11.47}$$

Various types of objective rates can be used, such as the Jaumann rate, the Truesdell rate, or generally any Lie derivative of the true stress tensor. The constitutive fourth-order tensor contains the elastic constants and the plastic properties such as the normal of the flow surface and the slope of the flow curve. For consistent linearization, (11.47) has to be modified slightly.

The elastoplastic field equations are derived from the principle of virtual work, giving (neglecting inertial forces)

$$\int_V \boldsymbol{\sigma}_{ij}\,\delta\left(\frac{\partial u_j}{\partial x_i}\right)\mathrm{d}V - \int_A t_i \delta u_i\,\mathrm{d}A = 0\,. \tag{11.48}$$

Equation (11.48) must be fulfilled in the unknown current configuration. Linearization of this equation about the last known state and space discretization yield the nonlinear finite element equations. Time integration is performed primarily implicitly.

Explicit Dynamic Elastoplastic Finite Element Formulations

The explicit dynamic finite element formulations are based on the virtual work principle, to which an inertia term is added

$$\int_V \boldsymbol{\sigma}_{ij}\,\delta\left(\frac{\partial u_j}{\partial x_i}\right)\mathrm{d}V - \int_A t_i\delta u_i\,\mathrm{d}A + \int_V \rho\ddot{\boldsymbol{u}}_i\delta u_i\,\mathrm{d}V = 0\,, \tag{11.49}$$

where $\ddot{\boldsymbol{u}}_i$ is the acceleration vector and ρ is the density. Discretization of (11.49) leads to

$$\mathbf{M}\ddot{\boldsymbol{u}} = \boldsymbol{F} - \boldsymbol{I}\,, \tag{11.50}$$

where $\mathbf{M}$ is the mass matrix, $\boldsymbol{F}$ is the external force vector, and $\boldsymbol{I}$ is the internal force vector at the current time. Time discretization using a central difference scheme and the addition of a damping term C gives the fundamental equations for the formulation

$$\left[\frac{1}{(\Delta t)^2}\mathbf{M}\right]\boldsymbol{u}^{t+\Delta t} = \boldsymbol{F}^t - \boldsymbol{I}^t + \left(\frac{\mathbf{M}}{2\Delta t} - C\right)\left(\frac{\boldsymbol{u}^t - \boldsymbol{u}^{t-\Delta t}}{\Delta t}\right), \quad (11.51)$$

where Δt is the time increment for the computation, which must satisfy the stability condition

$$\Delta t \leq \frac{L}{c_\mathrm{d}}, \quad (11.52)$$

where c_d is the current dilatational wave speed (the speed of sound) in the material and L is the characteristic element dimension, which can be taken as the minimum distance between any two nodes of an element. The elastic wave speed can be found from

$$c_\mathrm{d} = \sqrt{\frac{2G(1-\nu)}{(1-2\nu)\rho}}. \quad (11.53)$$

11.3 Bulk Forming Processes

This section describes the basic bulk forming processes.

11.3.1 Upsetting

A workpiece with initial diameter d_0 and initial height h_0 is reduced between two flat dies to a specimen with final diameter d_1 and final height h_1 (Fig. 11.25). This process is also called open die forging or free forming.

Due to the friction between the dies and the workpiece, the workpiece bulges. The upsetting process is used as a material characterization process and as a production process in various forms. The basic parameters characterizing the process are the ideal equivalent plastic strain

$$\bar{\varepsilon} = \ln\left(\frac{h_0}{h_1}\right), \quad (11.54)$$

the upsetting ratio

$$s = \frac{h_0}{d_0}, \quad (11.55)$$

the relative height reduction

$$e = \frac{\Delta h}{h_0} = \frac{h_0 - h_1}{h_0}, \quad (11.56)$$

and finally the ideal equivalent plastic strain rate

$$\dot{\bar{\varepsilon}} = \frac{\mathrm{d}\bar{\varepsilon}}{\mathrm{d}t} = \frac{v_\mathrm{tool}}{h}, \quad (11.57)$$

where v_tool is the tool velocity (precisely the velocity difference between the upper and lower dies).

Utilizing elementary plasticity theory (slab method), the axial, radial, and tangential stresses can be found for Coulomb friction as

$$\sigma_z(r) = -\sigma_\mathrm{f} \mathrm{e}^{\frac{2\mu}{h}\left(\frac{D}{2}-r\right)} \approx \underbrace{-\sigma_\mathrm{f}\left[1 + \frac{2\mu}{h}\left(\frac{D}{2}-r\right)\right]}_{\text{after a Taylor's series expansion}},$$

$$\sigma_r(r) = \sigma_\theta(r) = \sigma_z(r) + \sigma_\mathrm{f} \approx \underbrace{-\sigma_\mathrm{f}\left[\frac{2\mu}{h}\left(\frac{D}{2}-r\right)\right]}_{\text{after a Taylor's series expansion}}, \quad (11.58)$$

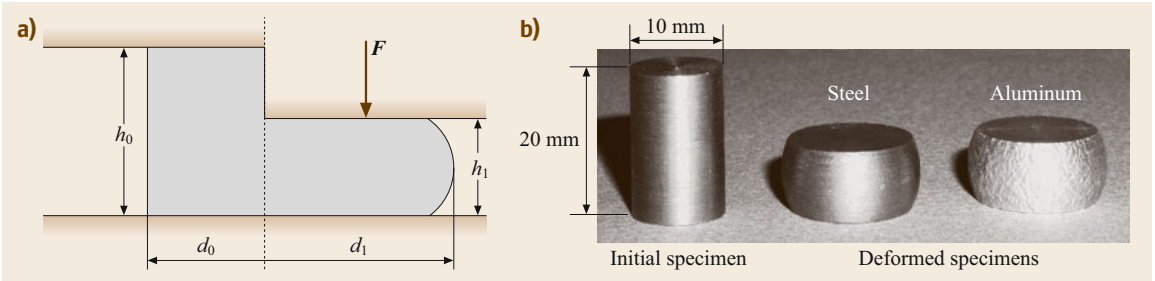

Fig. 11.25 (a) Principle of upsetting process, (b) application examples

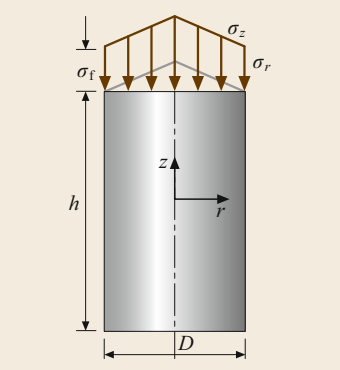

Fig. 11.26 Stresses in upsetting

and for the constant shear friction model

$$\sigma_z(r) = -\sigma_f\left[1 + \frac{m}{\sqrt{3}}\frac{D}{h}\left(1 - \frac{r}{D/2}\right)\right],$$
$$\sigma_r(r) = \sigma_\theta(r) = -\sigma_f\frac{m}{\sqrt{3}}\frac{D}{h}\left(1 - \frac{r}{D/2}\right). \quad (11.59)$$

The stress distribution is shown in Fig. 11.26 for the linearized Coulomb friction model. The upsetting force at a given height is

$$|F_z| = -\int_A \sigma_z \, dA \approx \frac{\pi}{4}D^2\sigma_f\left(1 + \frac{1}{3}\mu\frac{D}{h}\right). \quad (11.60)$$

Figure 11.27 shows a typical force–displacement curve for upsetting. The steep increase of the force towards smaller specimen heights is characteristic of upsetting.

Cold upsetting has the process limits shown in Fig. 11.28. These limits consist of the formability of the workpiece material characterized by a maximum height reduction of 80%, the buckling limit given by the maximum upsetting ratio of 2.3, and finally the tool load limit. The buckling limit can be increased by

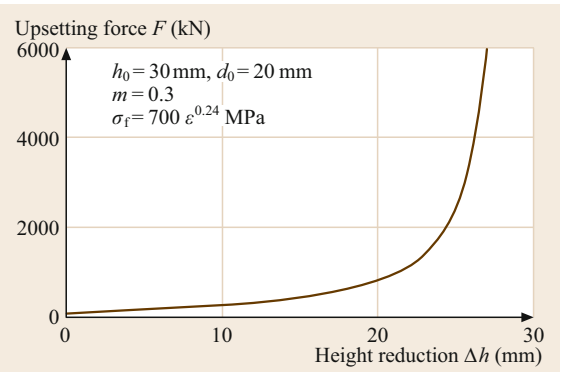

Fig. 11.27 Force–displacement curve in upsetting

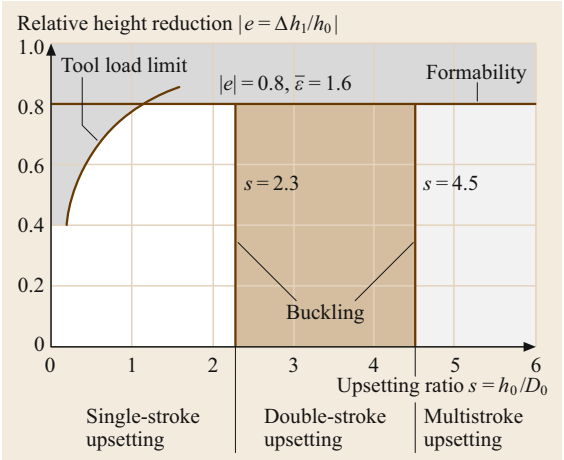

Fig. 11.28 Process limits of cold upsetting (after [11.1, 16])

upsetting in multiple strokes. So, for a two-stroke process, the upsetting ratio can be increased to 4.5, for instance. Formability limits are characterized by two types of cracks: shear cracks in the upset part and longitudinal cracks (basically due to initial faults in the workpiece).

For heading, i.e., the upsetting of one end instead of all of the workpiece, Fig. 11.29 shows the three-step process necessitated by the buckling forming limit. Note that the last step is no longer an open die process.

The design rules for the preforms during head upsetting are given in Fig. 11.30.

The accuracy achieved during cold upsetting depends on the conditions of the forming tools and machines. Wear of the tools is hereby an important issue. Table 11.6 presents some typical accuracy values for a reasonable number of parts formed.

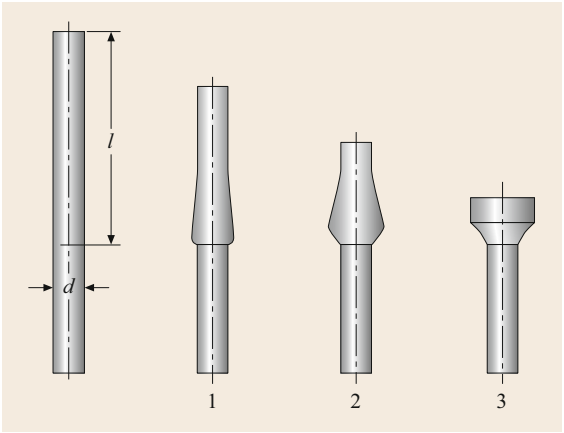

Fig. 11.29 Heading in three steps, upsetting ratio $s = l/d = 7$ (after [11.16])

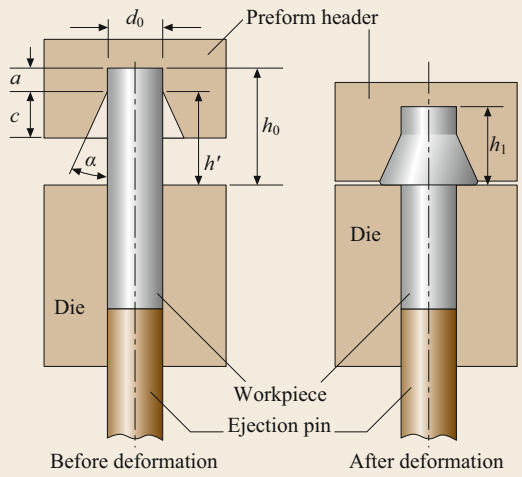

Pre-upsetting design

Upsetting ratio $s = h_0/d_0$	Cone angle 2α (°)	Guide length a (mm)	Conical portion c (mm)
2.5	15	0.6 d_0	1.37 d_0
3.3	15	1.0 d_0	1.56 d_0
3.9	15	1.4 d_0	1.66 d_0
4.3	20	1.7 d_0	1.56 d_0
4.5	25	1.9 d_0	1.45 d_0

Fig. 11.30 Preform design (after [11.17])

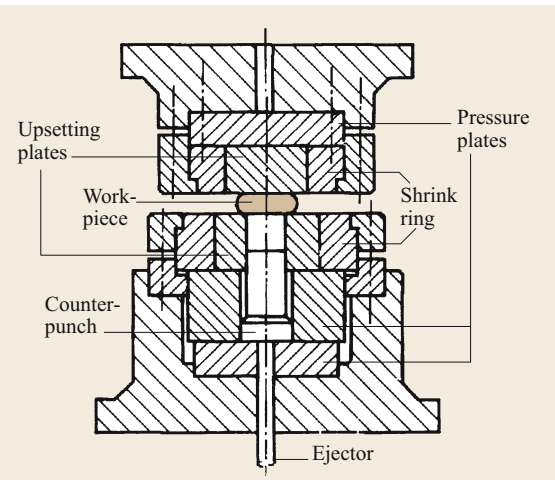

Fig. 11.31 Sketch of a typical upsetting tool (after [11.16])

A typical tool construction is shown in Fig. 11.31. The die is usually supported by a shrink ring to increase its load-carrying capacity. The basic tool materials are presented in Table 11.7, together with their hardness values.

11.3.2 Forging

Forging processes can classified be basically into two groups: open-die forging and closed-die forging (Fig. 11.32). In open-die forging, the dies have simple geometries (usually flat) and the process is conducted hot. This process primarily serves to produce preforms for subsequent forming processes by reducing or increasing the cross-section of the workpiece. Upsetting is a fundamental process of open-die forging.

The basic closed-die forging process is impression forging, in which a flash is produced and must be separated from the workpiece after forging [11.19]. The processes of fullering and gathering are used as preform processes before impression die forging. A typical impression-forged product is shown in Fig. 11.33.

A typical closed die for forging (Fig. 11.34) consists of upper and lower die parts. These parts form the forging cavity and the flash cavity, separated by the parting line. A gutter is placed at the end of the flash land to collect the excess material. The forging cavity consists of webs and ribs. The flash is an important element in forging and controls the filling of the die. Furthermore, it serves as a means to compensate excess material. On the other hand, it is also a source of waste material in forging and should be kept as small as possible.

The force–displacement characteristics during closed-die forging exhibit three regions (Fig. 11.35): Until point P_1, the workpiece in the cavity is upset and then widens. At point P_1, the flash starts to form and hence the resistance to material flow increases, leading to the rising of the material, during which the form of the die cavity is filled. At P_2, the die cavity fills and additional load is applied to close the dies finally. The necessary forming work is the shaded area under the load–displacement curve. This work has to be supplied as the forming energy by the forming machine.

The effect of the flash dimensions is twofold (Fig. 11.36): Increasing the flash–land length-to-thickness ratio (b/s) will increase the braking effect of the flash and hence the stress $\sigma_{z,\max}$ in the die–workpiece contact zone, so that the forging force $\boldsymbol{F}$ will increase. However, at the same time, the excess mass Δm flowing into the die or gutter decreases the required forming energy W. In the given example, for a flash–land ratio of 4.5, there is nearly no change in the excess material, so the minimum forging energy is obtained for a die-to-land ratio of 4–5.

Table 11.6 Typical accuracy during mass production by upsetting (after [11.18])

Nominal dimension (mm)	5	10	20	30	40	50	100
Head height accuracy (mm)	0.18	0.22	0.28	0.33	0.38	0.42	0.50
Head diameter accuracy (mm)	0.12	0.15	0.18	0.20	0.22	0.25	0.30

Table 11.7 Some typical tool materials for cold upsetting and heading (after [11.16, 18])

Tool part	Material description by DIN	Material number	Hardness (HRC)
Dies	S6-5-2	1.3343	59–63
	X165CrMoV12	1.2601	60–62
	100V1	1.2833	58–61
	55NiCr10	1.2718	54–58
Shrink rings	56NiCrMoV7	1.2714	40–50
	X40CrMoV51	1.2344	40–50
	X2NiCoMo1885	1.6359	50–53
Preform punches (bulk)	100V1	1.2833	57–60
	145V33	1.2838	57–60
Preform punches (shrunk)	S6-5-2	1.3343	60–63
	X165CrMoV12	1.2601	60–63
End-form punches (bulk)	100V1	1.2833	58–61
	145V33	1.2838	58–61
End-form punches (shrunk)	S6-5-2	1.3343	60–63
	X165CrMoV12	1.2601	60–63
Ejector	X40CrMoV51	1.2344	55–58
	60WCrV7	1.2550	55–58

The stress distribution for axisymmetric forgings given by elementary plasticity theory resembles the stress distribution in upsetting (Fig. 11.37). The maximum stress occurs at the center of the part and is higher for wider flash–land ratios.

The maximum forging force can be estimated, for instance, by the upsetting equations as

$$\boldsymbol{F}^{\max} = -\sigma_{\mathrm{f}} \left(1 + 2\mu \frac{b}{s}\right) A_{\mathrm{p}} \,, \tag{11.61}$$

where σ_{f} is the flow stress (Table 11.8, see also [11.22]), μ is the Coulomb friction coefficient (for steel at 1000–1100 °C, $\mu = 0.12$ for lubricated and $\mu = 0.35$ for unlubricated cases), b/s (Table 11.9) is the flash–land ratio, and A_{p} is the total projected area including the flash. The flow stress can be approximated using the temperature and strain rate at the beginning of the process, although the maximum force occurs towards the end. Hence, the strain rate is found as

$$\dot{\varepsilon} = \frac{v}{h_0} \,, \tag{11.62}$$

where h_0 is the initial height of the billet and v is the striking speed of the tool (11.5). Note that, in Table 11.9, the b/s ratio is given for the three basic types of material flow in forging: upsetting, spreading (with large relative motions along the die surface), and rising (filling of the die cavities).

Typical failures in forged products are as follows:

1. Surface defects: These are surface scratches and cracks that are basically due to defects on the sheared surfaces of the billets or flash formation during preforming, as well as imprints of cracks on the die surfaces.
2. Incomplete filling: Due to insufficient initial workpiece mass, inappropriate preforms, inaccurate workpiece positioning, incorrect flash–land ratios, or too high gas pressures of the lubricant, causing the die cavities to not fill completely.
3. Microstructural failures: The basic failure type is insufficient grain flow.

Some of these failures can be removed by subsequent machining operations on the forged products, so such workpieces need not be scrapped.

Basic die failures in forging are shown in Fig. 11.38. Dies are exposed to high temperatures, pressures, and sliding of workpiece materials along their surfaces. Local pressures can reach as high as 1000 MPa or even higher, and they vary with time. The wear is caused by sliding of workpiece materials with relative speeds of up to 50 m/s. The temperature increases from 100–200 to 700–800 °C in extremely short times, with temperatures gradients of 1000–3000 °C/s. These effects lead to failure of dies through wear, thermal fatigue, mechanical fatigue, and plastic deformation.

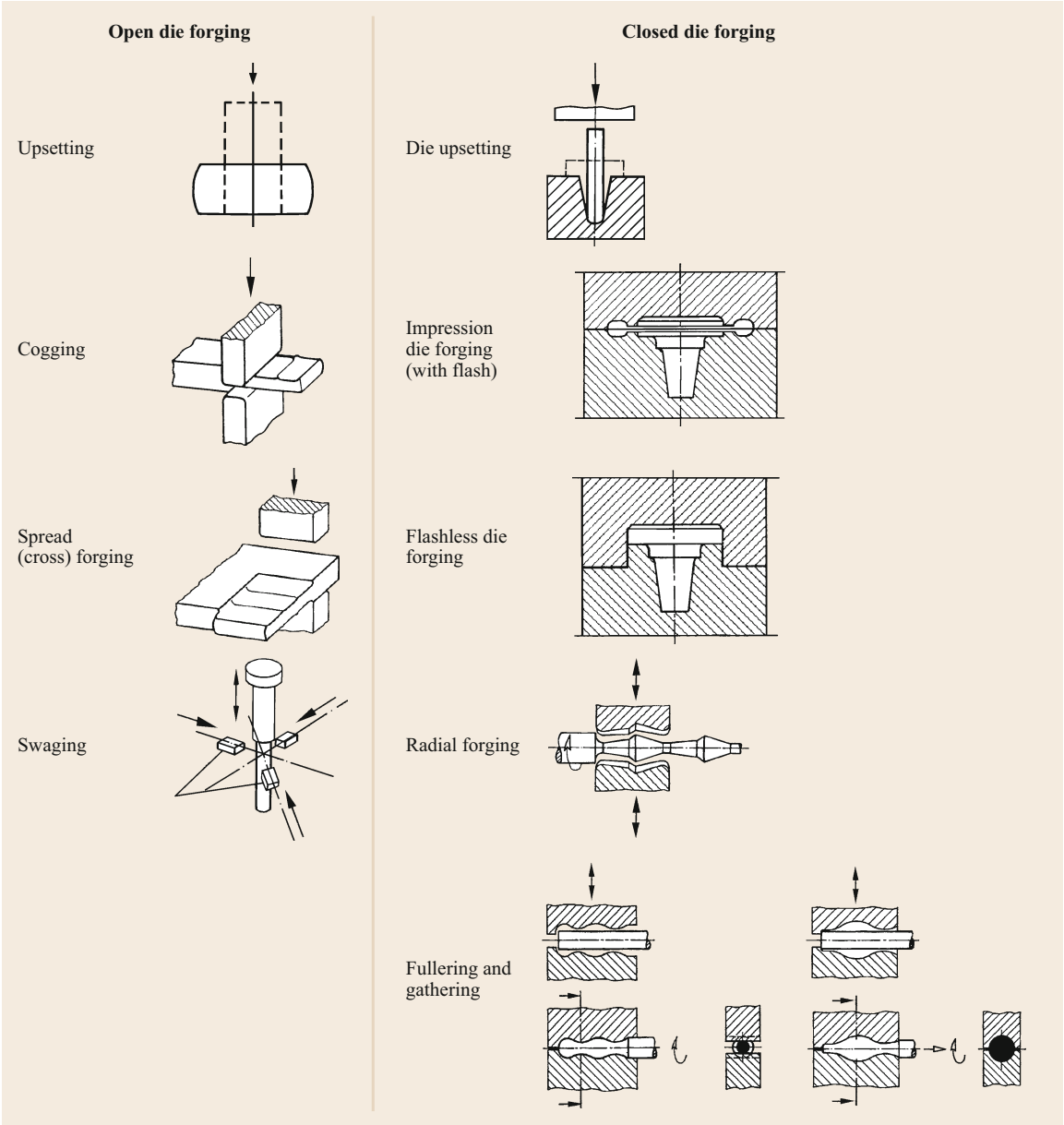

Fig. 11.32 Classification of forging processes

11.3.3 Extrusion

Extrusion processes can be classified according to their technological differences into extrusion, impact extrusion, and reducing (open-die) extrusion. The basic differences between extrusion and impact extrusion are that extrusion aims to produce profiles (semifinished products) whereas impact extrusion aims to produce single parts which are finished products. Furthermore, extrusion is usually performed hot (especially for steel materials almost always), whereas impact extrusion is usually performed cold (therefore also named cold forging). Reducing is extrusion with area reductions less than 25–30%. In this case, there is no deformation of the material in the container. Further classifications can be made according to the workpiece geometry and the relative motion between the tools and workpiece during forming.

Figure 11.39 provides an overview of the principles of various extrusion processes.

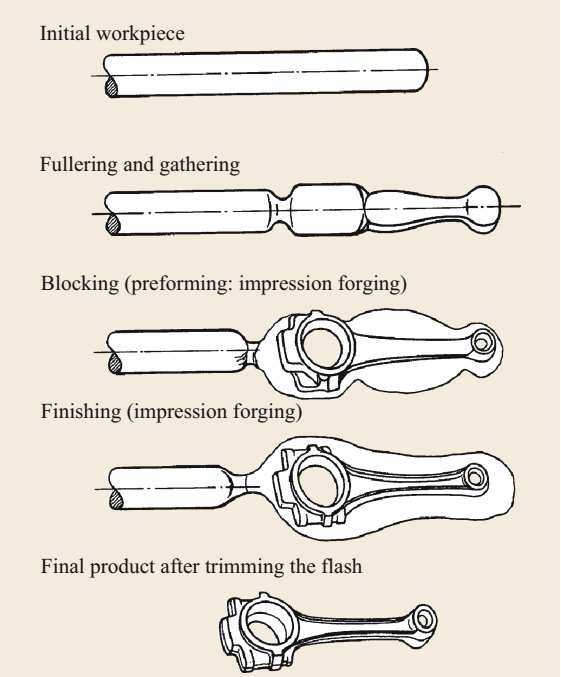

Fig. 11.33 Typical forging sequence (after [11.20])

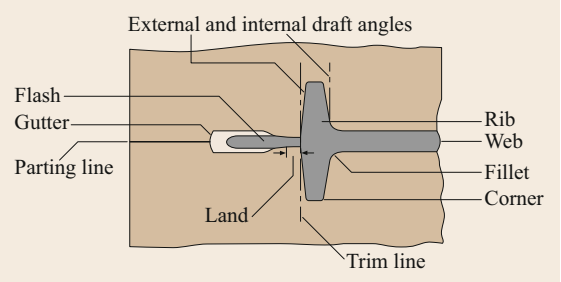

Fig. 11.34 Typical closed forging die (after [11.20]) ◀

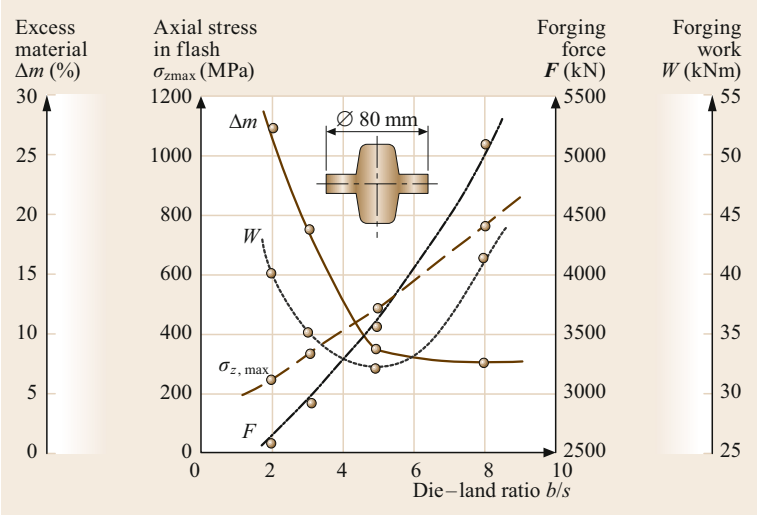

Fig. 11.36 Effect of flash dimensions on forging force and excess material (after [11.16])

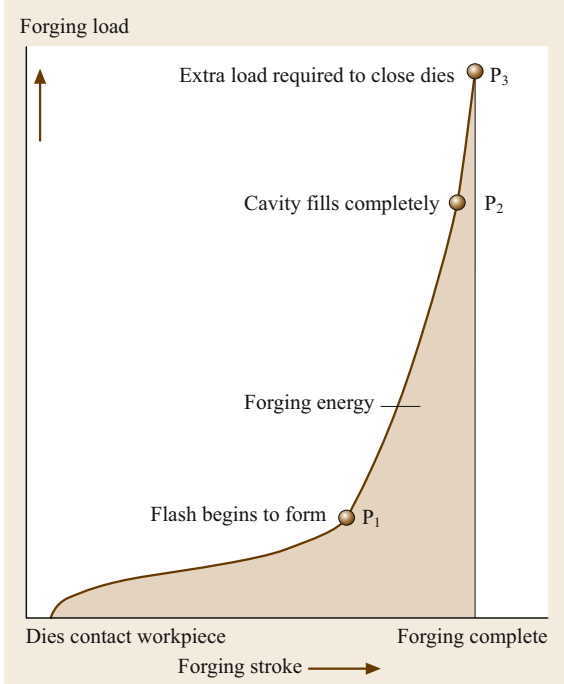

Fig. 11.35 Force–displacement characteristics during impression forging (after [11.21])

In Fig. 11.40, the stress states as estimated by elementary plasticity theory for forward rod extrusion are given. Plastic deformation only occurs in the die-shoulder region, and all stress components are compressive. The workpiece within the container remains basically elastic, as does the extruded rod after exiting the die.

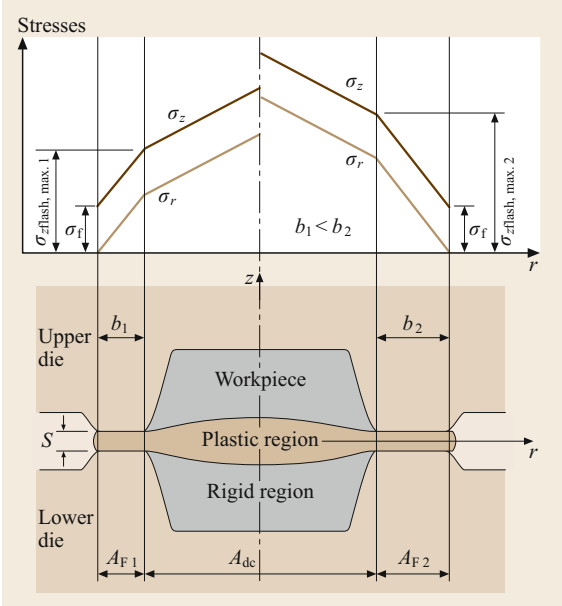

Fig. 11.37 Stress distribution in forging (after [11.16])

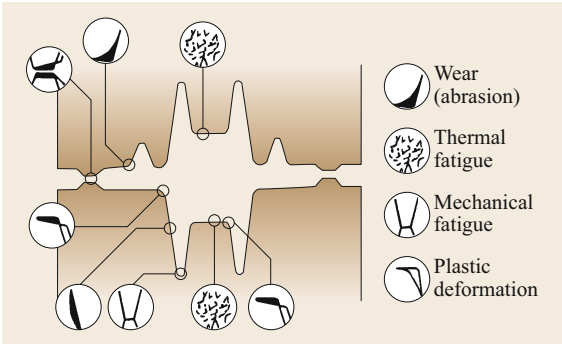

Fig. 11.38 Basic die failures in forging (after [11.16])

The fundamental parameters of the process are defined as the area reduction

$$e = \frac{A_0 - A}{A_0}\,, \tag{11.63}$$

where A_0 and A_1 are the initial and final cross-sectional areas of the workpiece, and the ideal equivalent plastic strain φ

$$\varphi = \ln\left(\frac{A_0}{A} = 2\right) \ln\left(\frac{d_0}{d_1}\right). \tag{11.64}$$

The latter is the plastic equivalent strain at the axis of the extrudate. This strain is the minimum strain across the cross section of the steady-state region of the extruded shaft (Fig. 11.41).

A typical force–displacement curve for the extrusion process is shown in Fig. 11.42. After the process starts at point A, there is a steep increase in force due to the elastic deformation of the billet, followed by its plastification and filling of the die. In many processes, a discontinuity in the curve between A and B can be observed, which is due to the upsetting of the billet in the container (billets are slightly smaller in diameter – by about 0.1–0.2 mm – than the container). The die is filled until point C. There is a local maximum due to the contact between the unlubricated sheared surfaces of the specimens and the die. After point D, the deformation zone in the die shoulder remains steady, so there is only a decrease in the force due to the decrease in the friction forces in the die chamber.

Table 11.8 Flow stress data for various hot-forming metals (after [11.18])

Material	*m*	*K* (MPa)	*T* (°C)
C15	0.154	99/84	1100/1200
C35	0.144	89/72	1100/1200
C45	0.163	90/70	1100/1200
C60	0.167	85/68	1100/1200
X10Cr13	0.091	105/88	1100/1250
X5CrNi189	0.094	137/116	1100/1250
X5CrNiTi189	0.176	100/74	1100/1250
E-Cu	0.127	56	800
CuZn28	0.212	51	800
CuZn37	0.201	44	750
CuZn40Pb2	0.218	35	650
CuZn20Al	0.180	70	800
CuZn28Sn	0.162	68	800
CuAl5	0.163	102	800
Al99.5	0.159	24	450
AlMn	0.135	36	480
AlCuMg1	0.122	72	450
AlCuMg2	0.131	77	450
AlMgSi1	0.108	48	450
AlMgMn	0.194	70	480
AlMg3	0.091	80	450
AlMg5	0.110	102	450
AlZnMgCu1.5	0.134	81	450

$$\sigma_f(T, \dot{\varepsilon}) = K(T)\dot{\varepsilon}^{m(T)}$$

Table 11.9 Recommended flash–land ratios (after [11.18])

Projected area of workpiece excluding the flash area (mm^2)	Flash–land ratio *b/s*		
	Mainly upsetting	Mainly spreading	Mainly rising
Up to 2000	8	10	13
2001–5000	7	8	10
5001–10 000	5.5	6	7
10 001–25 000	4	4.5	5.5
26 000–70 000	3	3.5	4.5
71 000–150 000	2	2.5	3.5

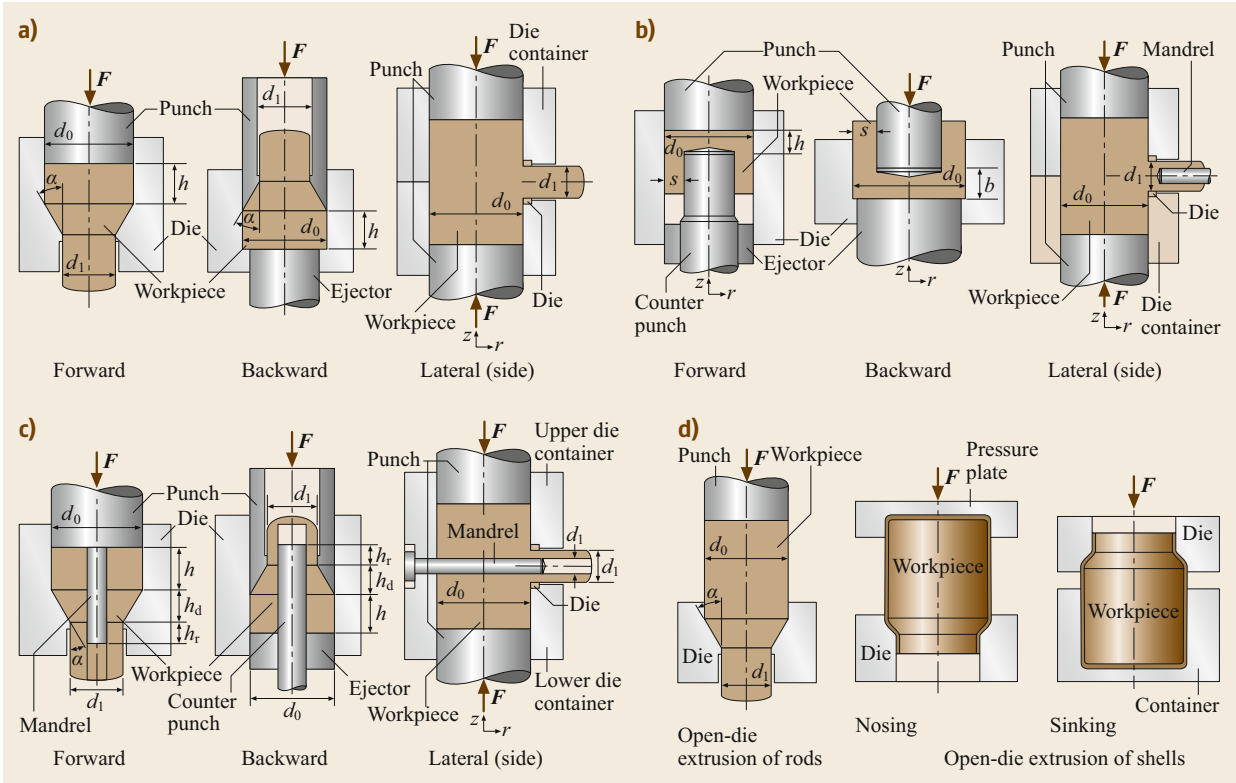

Fig. 11.39a–d Principles of typical extrusion processes: **(a)** rod extrusion, **(b)** can extrusion, **(c)** tube extrusion, and **(d)** open-die extrusion

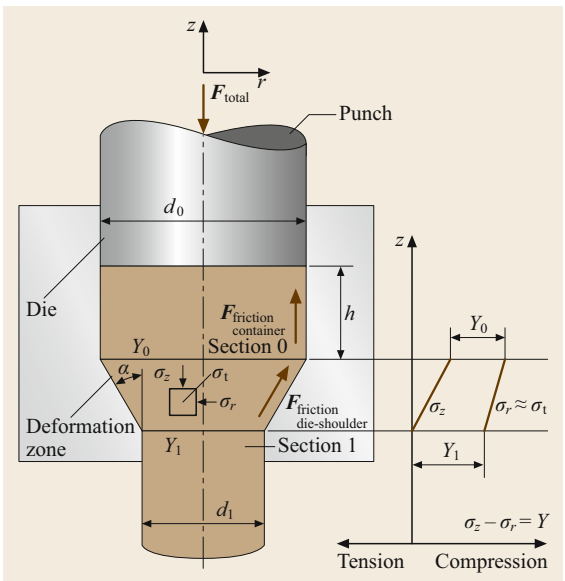

Fig. 11.40 Schematic of forward (impact) extrusion of rods and stress states during extrusion (after [11.16])

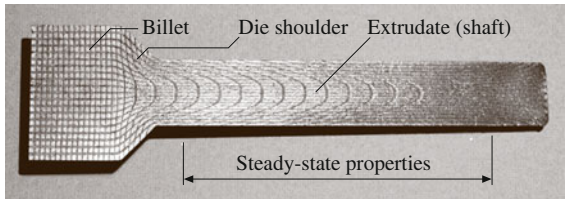

Fig. 11.41 Cross-section of a typical forward rod extrusion product with a deformation grid

The forming forces in extrusion of rods and tubes can be determined by using a model suggested by Siebel. The total extrusion force consists in this case of the following parts

$$F_{total} = F_{ideal} + F_{shear} + F_{friction\ container} + F_{friction\ die\text{-}shoulder} + F_{friction\ mandrel} + F_{friction\ mandrel\text{-}land} \,. \quad (11.65)$$

The force components are described in Table 11.10. Here, σ_{fm} is the mean flow stress in the deformation

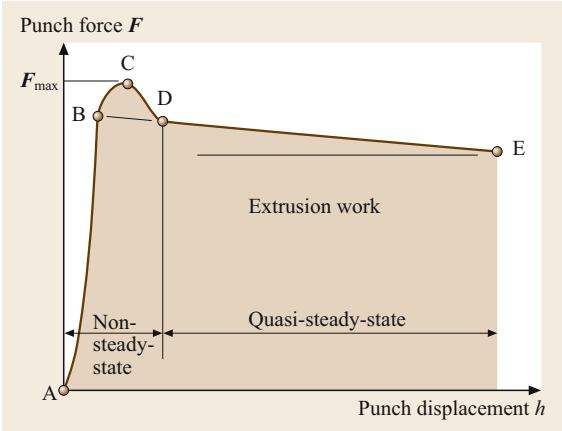

Fig. 11.42 A typical force–displacement curve for forward rod extrusion

zone, given by

$$\sigma_{\mathrm{fm}} = \frac{1}{\varphi_1 - \varphi_0} \int_{\varphi_0}^{\varphi_1} \sigma_{\mathrm{f}}(\varphi)\mathrm{d}\varphi \,. \tag{11.66}$$

μ is the friction coefficient (0.04–0.08 for forward rod extrusion, 0.1–0.125 for tube extrusion), h is the billet length in the container, h_{r} is the length of the die exit land, and p_{r} is the pressure acting between the workpiece and the die (10–12 N/mm^2). For backward extrusion and the open-die container, the friction is zero. For extrusion of profiles, the cone angle 2α is usually 180°. In this case, a dead zone of workpiece material builds up in the die, so that the effective cone angle is $2\alpha = 90°$. This effective angle must be used in all force terms, and the coefficient of Coulomb friction must be taken as 0.5 for the die-shoulder.

The effect of the die cone angle on various force components is shown in Fig. 11.43. The ideal force and the container friction are independent of the cone angle. The shear force increases with the cone angle, whereas the die-shoulder friction is minimum at $2\alpha = 90°$. Hence, the total force assumes a minimum value for the given process parameters at around $2\alpha = 40°$.

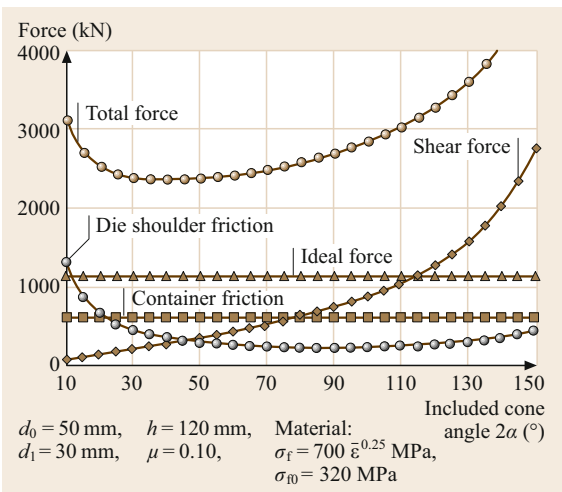

Fig. 11.43 Effect of various parameters on extrusion force

The force for backward can extrusion can be computed using the equation of Dipper (Fig. 11.39)

$$F_{\mathrm{punch}} = A_i\sigma_{\mathrm{f1}}\left(1 + \frac{1}{3}\mu\frac{d_i}{b}\right) + \sigma_{\mathrm{f2}}\left(1 + \frac{\mu + 0.5}{2}\frac{b}{s}\right), \tag{11.67}$$

where A_i is the punch cross-sectional area, μ is the coefficient of friction (0.04–0.08), and the flow stresses

$$\sigma_{\mathrm{f1}} = \sigma_{\mathrm{f}}\left[\varphi = \ln\left(\frac{h_0}{b}\right)\right],$$
$$\sigma_{\mathrm{f2}} = \sigma_{\mathrm{f}}\left[\varphi = \ln\left(\frac{h_0}{b}\right)\left(1 + \frac{d_i}{8s}\right)\right], \tag{11.68}$$

where h_0 is the initial height of the billet.

A simpler but effective equation for the punch load during backward can extrusion was given by Hoogenboom for ideal plastic materials

$$\frac{p}{\sigma_{\mathrm{f}}} = \frac{2+\sqrt{3}}{\sqrt{3}} + \frac{1}{3}\sqrt{\frac{6s + d_i}{s}} \quad \text{early stage},$$
$$\frac{p}{\sigma_{\mathrm{f}}} = \frac{2+\sqrt{3}}{\sqrt{3}} + \frac{1}{2\sqrt{3}}\sqrt{\frac{s}{b} + \frac{b}{s}} \quad \text{late stage}, \tag{11.69}$$

where p is the punch pressure and σ_{f} is the constant flow stress. The early stage is the quasi-steady-state process, whereas the late stage corresponds to the transient de-

Table 11.10 Force computations for rod and tube extrusion (after [11.16])

Process	F_{ideal}	F_{shear}	F_{friction} (container)	F_{friction} (die-shoulder)	F_{friction} (mandrel-die)	F_{friction} (mandrel-land)
Rod extrusion	$A_0\sigma_{\mathrm{fm}}\varphi$	$2/3\ \tan\alpha\sigma_{\mathrm{fm}}A_0$	$\pi d_0 h\sigma_{\mathrm{f0}}\mu$	$2\sigma_{\mathrm{fm}}\varphi\mu A_0/\sin 2\alpha$	0	0
Tube extrusion	$A_0\sigma_{\mathrm{fm}}\varphi$	$1/2\ \tan\alpha\sigma_{\mathrm{fm}}A_0$	$\pi d_0 h\sigma_{\mathrm{f0}}\mu$	$2\sigma_{\mathrm{fm}}\varphi\mu A_0/\sin 2\alpha$	$\sigma_{\mathrm{fm}}\varphi\mu A_1/\tan\alpha$	$\pi d_2 h_{\mathrm{r}} p_{\mathrm{r}}\mu$

a) Forward rod extrusion

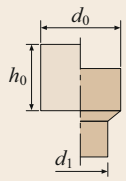

	$d_{0,\max}$ [a] (mm)	$\left(\frac{A_0}{A_1}\right)_{\max}$	$\varepsilon_{A,\max}$	$\left(\frac{h_0}{d_0}\right)_{\max}$ [a]
Aluminum (Al99.5), lead, zinc	500–300	50	0.98	[c]
Copper (E-Cu)	350–200	5	0.80	[c]
Brass (Ms 63 to Ms 72)	300–150	4	0.75	[c]
Easily deformable steel (C10, C15, …)	250–125	3.3	0.70	8–3
Less easily deform. steel (Ck35, 16MnCr5)	220–110	2.2	0.55	6–2.5
Difficult to deform. steel (C45, 34Cr04)	200–100	2.0	0.50	4–2

b) Forward tube extrusion

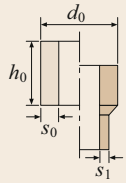

	$d_{0,\max}$ [a] (mm)	$\left(\frac{A_0}{A_1}\right)_{\max}$	$\varepsilon_{A,\max}$	$\left(\frac{s_0}{s_1}\right)$	$\left(\frac{h_0}{d_0}\right)_{\max}$ [a]
Aluminum (Al99.5), lead, zinc	500–300	50	0.98	⩾0.05	[c]
Copper (E-Cu)	350–200	5	0.80	⩾0.15	[c]
Brass (Ms 63 to Ms 72)	300–150	4	0.75	⩾0.20	[c]
Easily deformable steel (C10, C15, …)	250–125	3.3	0.70	⩾0.20	8–3
Less easily deform. steel (Ck35, 16MnCr5)	220–110	2.2	0.55	⩾0.30	6–2.5
Difficult to deform. steel (C45, 34Cr04)	200–100	2.0	0.50	⩾0.40	4–2

c) Backward can extrusion

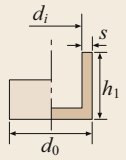

	$d_{0,\max}$ [b] (mm)	$\left(\frac{A_0}{A_1}\right)_{\max}$	$\varepsilon_{A,\max}$	$\frac{s_{\min}}{d_0}$	$\frac{s_{\max}}{d_0}$	$\left(\frac{h_1}{d_1}\right)_{\max}$
Aluminum (Al99.5), lead, zinc	500–300	50	0.98	⩾0.01	⩽0.40	5
Copper (E-Cu)	350–200	5	0.75	⩾0.03	⩽0.35	3.5
Brass (Ms 63 to Ms 72)	300–150	3.3	0.70	⩾0.05	⩽0.30	2.5
Easily deformable steel (C10, C15, …)	250–125	2.9	0.65	⩾0.04	⩽0.30	2.5–3
Less easily deform. steel (Ck35, 16MnCr5)	220–110	2.5	0.60	⩾0.07	⩽0.25	2
Difficult to deform. steel (C45, 34Cr04)	200–100	2.2	0.55	⩾0.09	⩽0.22	1.5

[a] From the smallest ideal equivalent strain ($\zeta = 0.4$) to the largest strain. The basis for the value of d_0 is a 25 MN force.
[b] From $s/d_0 = 0.15$ to $s_{\min}/d_0$ [c] Values unknown

Fig. 11.44a–c Process limits for impact extrusion: **(a)** forward rod extrusion, **(b)** forward tube extrusion, and **(c)** backward can extrusion (after [11.16])

formation for a can bottom of

$$\frac{b}{s} < 5.5\frac{A_i}{A_e}\,, \tag{11.70}$$

where A_e is the cross-sectional area of the billet. Other useful equations are given in [11.13].

For workpieces with non-axisymmetric cross sections such as bolts and nuts, the above equations can be applied but replacing the diameters by equivalent diameters corresponding to the cross section of the products.

Typical limits for the various extrusion processes are given in Fig. 11.44. The basic reason for limiting the process is the capacity of the forming presses and the tools. Another limiting factor is the formability of the material.

Typical failures in cold-forged parts are internal and surface ductile cracks as well as galling. Examples of internal cracks are so-called chevron cracks in extrusion (Fig. 11.45). Galling is a type of adhesive wear. Adhesive wear occurs when the tools slide against the workpiece under high pressure after the breakdown of the lubricant. The heat generated due to friction causes microwelds to form between the sliding surfaces. The surface of both the tools and the workpiece may then be damaged.

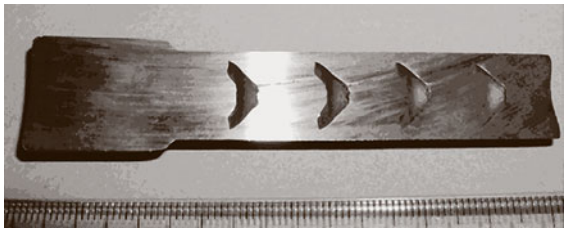

Fig. 11.45 Chevron cracks in cold-extruded rods (material: 100Cr6 (not annealed), $2\alpha = 100°$, $\varphi = 0.25$)

Figure 11.46 shows a typical sequence of processes for cold backward can extrusion. First, a slug is sheared off from a rod. Then, these pieces are phosphated to carry the lubricant under high pressures. The lubricant in this case is soap. An upsetting process is performed to remove the irregular shear surface and act as a centering

Fig. 11.46 Typical process sequences for backward can extrusion

Table 11.11 Typical lubrication procedures (after [11.23])

Process	Deformation	Lubrication
Upsetting	Light	None
		Mi + EP + FA
	Severe	Ph + SP
Ironing and open-die extrusion	Light	Ph + Mi + EP + FA
	Severe	Ph + SP
Extrusion	Light	Ph + Mi + EP + FA
		Ph + SP
		Ph + MoS_2
		Ph + MoS_2 + SP

Mi = mineral oil, SP = soap, EP = extreme pressure additive, Ph = phosphate coating, FA = fatty additives

aid for the main extrusion process. Besides soap, various other lubricants can be possible (Table 11.11). Depending on the degree of deformation, soap or MoS_2 or both with various pressures and fatty additives must be used.

A standard cold-forging tool setup is shown in Fig. 11.47. It consists of reusable parts such as the base plates, pressure plates, intermediate plate, and guides, as well as product-dependent interchangeable parts such as the punch, die insert, and shrink ring. The dies are exposed to radial, tangential, and equivalent stresses, as shown in Fig. 11.48. With no precautions, the maximum internal pressure can be

$$p_i \leq \frac{\text{yield strength of die material}}{2} . \qquad (11.71)$$

By imposing on the die a ring that has a smaller internal diameter than the outer diameter of the inner die, the sustainable internal pressure can be increased to

$$p_i \leq \text{yield strength of die material} . \qquad (11.72)$$

11.3.4 Drawing

Drawing processes can be broadly classified into drawing of solid parts such as rods, wires, or slabs and drawing of hollow parts such as tubes or cans [11.24]. Figure 11.49a,b shows typical wire drawing processes with the associated stress state in the deformation zone.

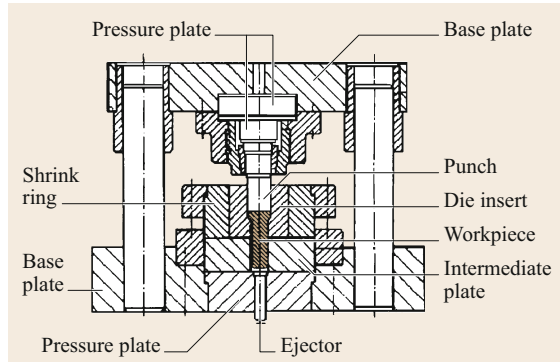

Fig. 11.47 Typical tool setup for cold forward rod extrusion (after [11.23])

Principally, the mechanics of deformation in drawing and extrusion are similar. The only difference is that, in drawing, the external force is applied on the exit side of the die as a tension force, in contrast to extrusion, where this force is applied on the entry side of the die and is compressive. Hence, the axial stresses in drawing processes are basically tensile, in contrast to the compressive ones in extrusion. However, both the radial and circumferential stresses are compressive as in extrusion. In the case of the drawing of tubes, basically two broad categories are recognized: drawing with a mandrel, or drawing without a mandrel. If a mandrel is used, this can be fixed or freely moving, or may have guided movement. One distinct type of tube drawing process is ironing. This is often considered to be a sheet metal forming process, since basically the workpiece is a can obtained by deep drawing. However, in terms of the mechanics of deformation, this process is a typical bulk forming process in which the wall thickness of the can is reduced by drawing it through a die (Fig. 11.49b).

The drawing force can be determined by Siebel's equation

$$F_{\text{total}} = F_{\text{ideal}} + F_{\text{shear}} + F_{\text{friction die-shoulder}} + F_{\text{friction mandrel}} , \qquad (11.73)$$

where the force components are presented in Table 11.12. In the case of ironing, the punch force is

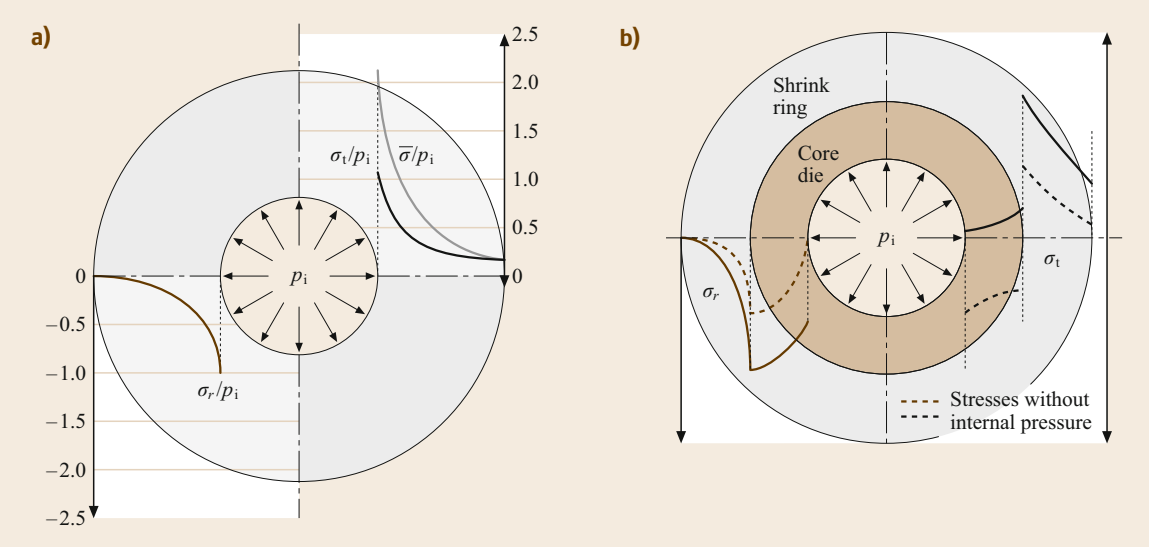

Fig. 11.48a,b Stresses in a die as a function of the internal forming pressure: **(a)** without and **(b)** with a shrink ring

given only by the first three components. However, if the force to be transmitted by the base of the can must be determined, the force due to friction at the mandrel must be taken as negative.

The operating window of the tube drawing process is shown in Fig. 11.50. There are basically three types of failure mode:

1. Rupture of the tube: The basic limitation of the process is that the tensile force must be applied through the formed tube portion. To prevent plastification leading to rupture

$$\sigma_z \leq \sigma_{f1} \,, \tag{11.74}$$

where σ_z is the uniform axial stress at the exit side and σ_{f1} is the mean flow stress at the same side. To ensure the stability of the process, usually the axial stress is taken to be less than 75% of the mean flow stress.
2. Chatter marks: Due to stick–slip effects, the surface of the product shows marks that lower its quality. This defect can be avoided by increasing the stiffness of the workpiece–tool system.
3. Wrinkling: This failure type results from the compressive circumferential stresses in the tubes.

The maximum area reduction for various wire materials during multiple die drawing is presented in Table 11.13.

Wire drawing is basically a cold forming process. Residual stresses in the product are important both for service loading as well as for subsequent processing of the material. Basically, harmful, large tensile resi-

Table 11.12 Force computations for wire and tube drawing (after [11.16])

Process	F_{ideal}	F_{shear}	$F_{friction}$ (die-shoulder)	$F_{friction}$ (mandrel-die)
Wire and bar drawing	$A_1\sigma_{fm}\varphi$	$2/3\tan\alpha\sigma_{fm}A_1$	$2\sigma_{fm}\varphi\mu A_1/\sin 2\alpha$	0
Ironing and tube drawing over fixed mandrel	$A_1\sigma_{fm}\varphi$	$1/2\tan\alpha\sigma_{fm}A_1$	$2\sigma_{fm}\varphi\mu_s A_1/\sin 2\alpha$	$\pm\sigma_{fm}\varphi\mu_M A_1/\tan\alpha$

Table 11.13 Allowable area reduction for wire drawing (after [11.18])

Material	Ultimate strength (MPa)	Initial wire diameter (mm)	Strain φ in each die	Total strain	Number of draws
Steel	400	4–12	0.18–0.22	2.80–4.00	8–21
	1200	4–12	0.18–0.22	3.80–4.00	
	1200	0.5–2.5	0.12–0.15	1.20–1.50	
Cu alloys	Cu (soft)	8–10	0.40–0.50	3.50–4.00	5–13
	250	1–3.5	0.18–0.20	2.00–2.00	
Al alloys	Al (soft)	12–16	0.20–0.25	2.50–3.00	5–13
	80	1–3.5	0.15–0.20	1.50–2.00	

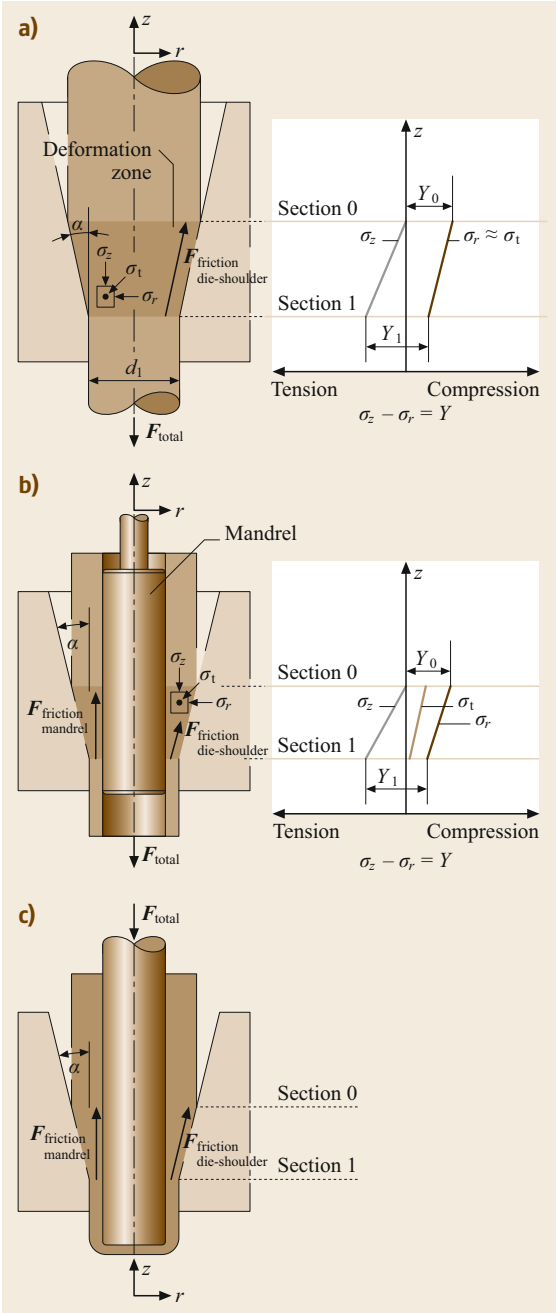

Fig. 11.49a–c Principles of typical drawing processes: **(a)** wire drawing, **(b)** tube drawing, **(c)** ironing

dual stresses are left at the surface of the tube or rod after forming. Therefore, various precautions are suggested to reduce these high tensile residual stresses. One methodology is to use a double-die design in which the second die has a very low area reduction. Figure 11.51 shows the effect of the afterreduction.

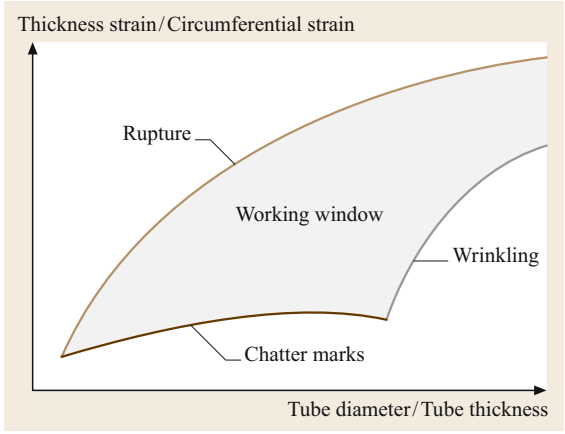

Fig. 11.50 Operating window for tube drawing process (after [11.16])

Through a second low-strain drawing die, the high tensile stresses are reduced from about 550 to 250 MPa.

If the second area reduction is too small, the plastification in the second die will be so low that the residual stress state will not change considerably; if, however, the area reduction is too large, this may cause a high plastic strain that may generate its own residual stress state that may also not be beneficial. Hence, there is an optimum amount of area reduction and also a minimum distance between the two drawing dies.

11.3.5 Rolling

The forming process of passing a workpiece between rotating rolls is called rolling [11.9, 10]. According to the kinematics of the rolls and the workpiece motion, rolling can be classified into three process families (Fig. 11.52). Based on the die geometry, flat rolling (Fig. 11.53a) and profile rolling (Fig. 11.53b) processes can be categorized. The process of reducing the thickness of a slab to produce a thinner and longer but only slightly wider product is referred to as flat rolling, whereas forming by shaped rolls is known as profile rolling. Besides producing continuous products such as slabs, rolling is also used to form discrete parts such as bolts (Fig. 11.54) and rings.

Flat rolling is the basic forming process used to produce plates and sheets. In the initial stages, it is conducted hot. For precision sheets, the final passes are done cold. In both cases, the rolling process generates a typical texture in the products that is the source of anisotropic behavior of sheet products.

The variables of the rolling process are shown in Fig. 11.55. It can be assumed that the width b of the workpiece is large enough such that, during rolling, no widening occurs. At a position s_n, a neutral plane ex-

ists. Before this neutral plane, the workpiece material is slower than the rolls, whereas afterwards, it is faster. To ensure initial grasping of the workpiece by the rolls, the contact angle α must fulfill

$$\alpha \leq \mu \,, \tag{11.75}$$

where μ is the coefficient of Coulomb friction. The mean equivalent strain over the deformation zone is given by

$$\varphi = \ln\left(\frac{h_0}{h_1}\right), \tag{11.76}$$

whereas the mean equivalent strain rate is

$$\dot{\varphi} = \varphi\omega\sqrt{\frac{R}{h_0 - h_1}} \,, \tag{11.77}$$

where ω is the rotational speed of the rolls in rad/s and R is the roll radius.

The vertical component of the pressure on the rolls can be approximated as [11.9]

$$\sigma(x) = \sigma_{\mathrm{fm}}\left(1 + \frac{x^2/R + 2\mu x}{h_1 + x^2/R}\right) \quad \text{for } 0 \leq x \leq s_{\mathrm{n}} \,,$$

$$\sigma(x) = \sigma_{\mathrm{fm}}\left(1 + \frac{2\mu R\,(s-x) - \left(s^2 - x^2\right)}{h_1 R + x^2}\right) \quad \text{for } s_{\mathrm{n}} \leq x \leq s \,. \tag{11.78}$$

The location of the neutral plane is given by

$$s_{\mathrm{n}} = \frac{s}{2}\left(1 - \frac{s}{2\mu R}\right), \tag{11.79}$$

with

$$s = \sqrt{R\,(h_0 - h_1)} \,.$$

The mean flow stress is given in hot rolling for the mean equivalent strain rate and in cold rolling for the mean equivalent strain. The pressure on the rolls assumes a maximum value at the neutral plane (*friction hill*).

The rolling force F is found as

$$F = b\int_0^s \sigma(x)\mathrm{d}x \,. \tag{11.80}$$

The rolling moment M of a single roll is given by

$$M = Fr \,, \tag{11.81}$$

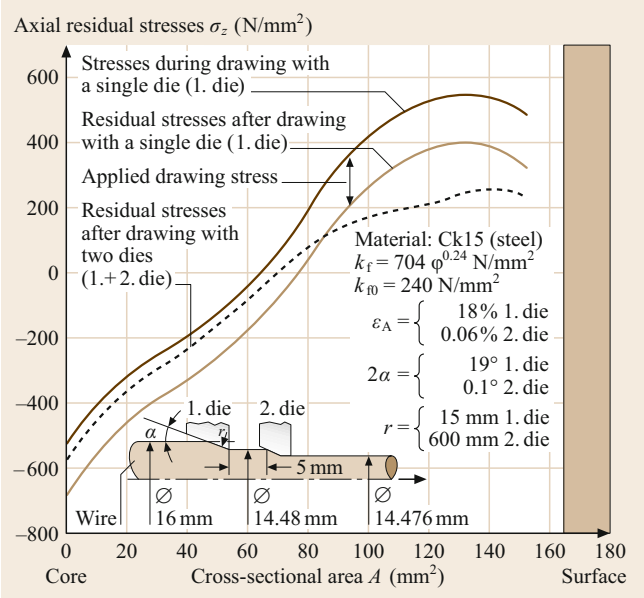

Fig. 11.51 Effect of second drawing die on residual stresses (after [11.25])

where r is the moment arm given by [11.26]

$$r = 0.385s \quad \text{for } \frac{R}{h_1} > 25 \,,$$

$$r = \left[0.78 + 0.017\left(\frac{R}{h_1} - 0.163\sqrt{\frac{R}{h_1}}\right)\right]s \quad \text{for } s \leq 25 \,. \tag{11.82}$$

The power necessary for the rolling process is

$$P = 2M\omega \,. \tag{11.83}$$

The rolls are exposed to a rather uniformly distributed forming load along their axis and hence behave like simply supported beams, bending with a maximum deflection at the center of the roll. To counter this deflection, which may lead to a rolled sheet with varying thickness, rolls are usually cambered, i.e., profiled rather than cylindrical. If the camber is insufficient, the thinner edges elongate plastically more than the center. Hence, in the rolled product, compressive residual stresses are built up at the edges and tensile residual stresses in the center parts (Fig. 11.56). This may also lead to centerline cracking, warping, or edge wrinkling. On the other hand, if the camber is too great, the edge regions are elongated less plastically, leading to tensile residual stresses at the edge region, with edge cracking, centerline wrinkling, and splitting (Fig. 11.57). Roll bending can also be reduced by one or several backup rolls.

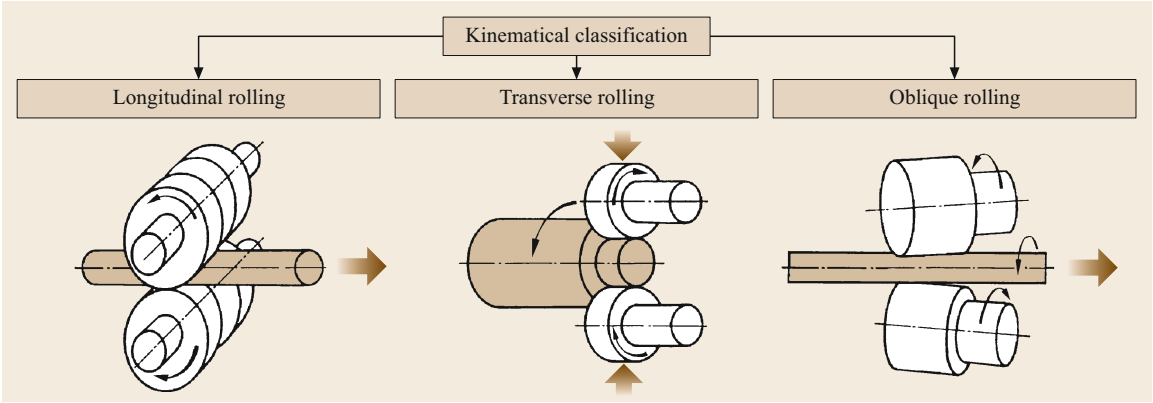

Fig. 11.52 Kinematic classification of rolling processes

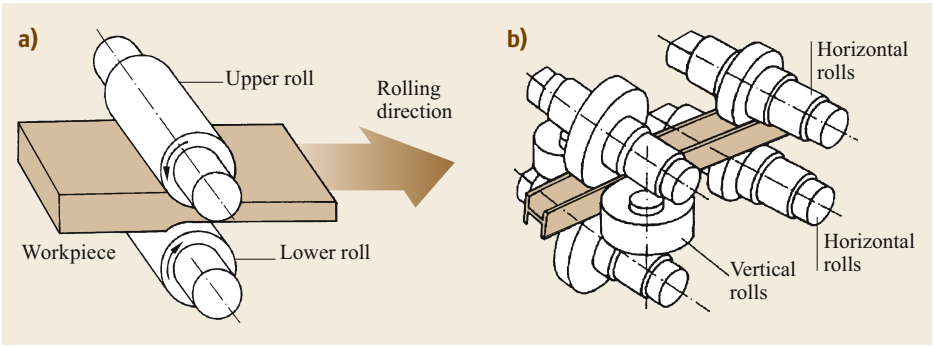

Fig. 11.53a,b Classification of rolling processes by die geometry: **(a)** flat rolling, **(b)** profile rolling

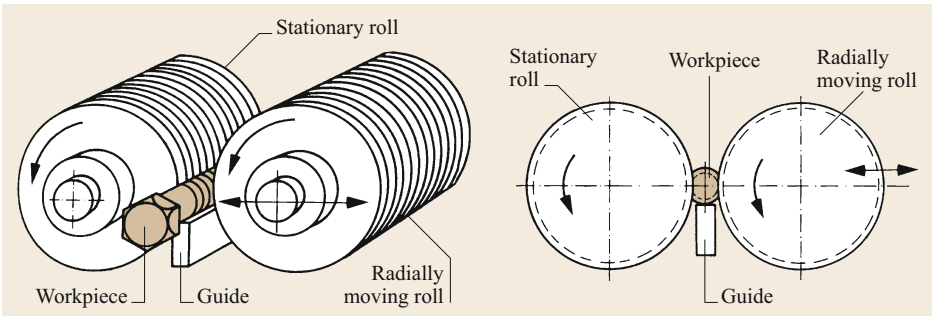

Fig. 11.54 Thread rolling of bolts

Roll flatting is another limiting phenomenon of flat rolling. Due to the elastic deformation of the rolls, there is a minimum thickness of the end product [11.10]

$$(h_1)_{\min} = \frac{C\mu R}{E/(1-\nu^2)}(\sigma_{\mathrm{fm}} - \sigma_{\mathrm{t}}) \,, \qquad (11.84)$$

where C is a factor between 7 and 8, E is the Young's modulus of the roll material, ν is Poisson's ratio, σ_{fm} is the mean flow stress for the deformation zone, and σ_{t} is the front or back tension applied to the rolled sheet. Hence, the minimum thickness that can be rolled can be decreased by decreasing the friction, decreasing the roll diameter, increasing the stiffness of the rolls, decreasing the flow stress, or increasing the back and/or front tension.

Another rolling process is the flow (shear) forming (turning) process (Fig. 11.58). In this process, a flat sheet is formed over a mandrel by means of a shear forming roll that reduces its thickness while keeping its diameter constant. This process should not be mixed with sheet forming process spinning, in which the sheet thickness is more or less constant but the diameter of the initial workpiece is reduced (Fig. 11.10). The final thickness of the workpiece is given by

$$s_1 = s_0 \sin\alpha \,. \qquad (11.85)$$

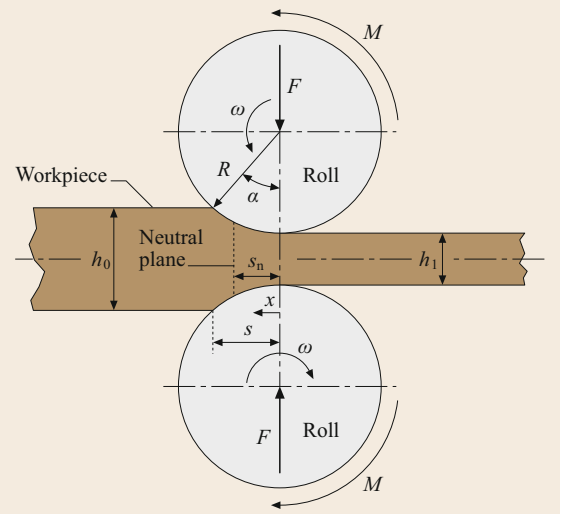

Fig. 11.55 Parameters of flat rolling

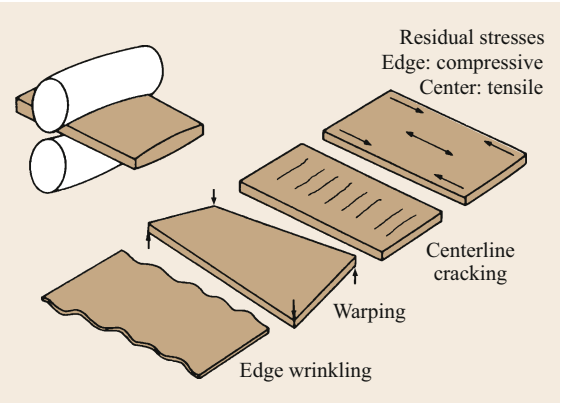

Fig. 11.56 Effects of insufficient camber of rolls (after [11.10])

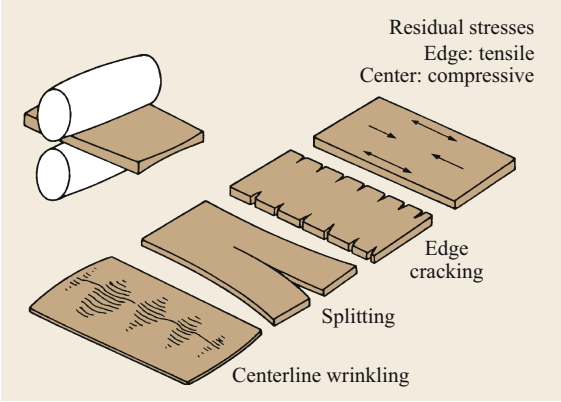

Fig. 11.57 Effects of excessive camber of rolls (after [11.10])

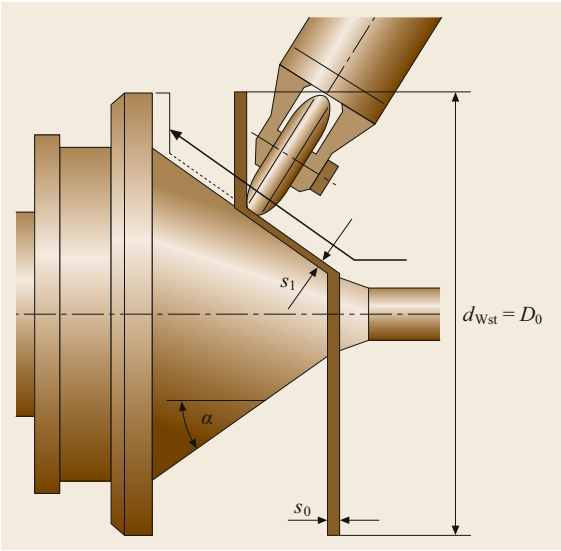

Fig. 11.58 Principle of shear forming

If the final thickness is selected correctly, the plastic deformation is confined only to the roll region, so that the rest of the workpiece remains stress free. The key parameter in this process is the mandrel angle α. This angle must be less than 80° for localized plastic shear deformation and can be at least 12°–18°. Using a second pass, this minimum angle can be reduced to even 8°.

The process of producing cylindrical parts is usually called flow forming, whereas the forming of tapered parts is called shear forming.

11.4 Sheet Forming Processes

11.4.1 Membrane Theory

Approximate analysis of sheet forming processes can be performed using membrane theory [11.27]. Consider an axisymmetrical shell as shown in Fig. 11.59. The principal radii of curvature are in the hoop plane and in the meridian plane.

For thin, plastically deforming shells, the bending moments are negligible, and because of axial symmetry, the hoop (σ_θ) and tangential (σ_ϕ) stresses are principal stresses (Fig. 11.60). The stress normal to the surface can be neglected, so that the resulting stress state is one of plane stress. Friction forces are neglected. Only uniform pressure loads normal to the surface (although

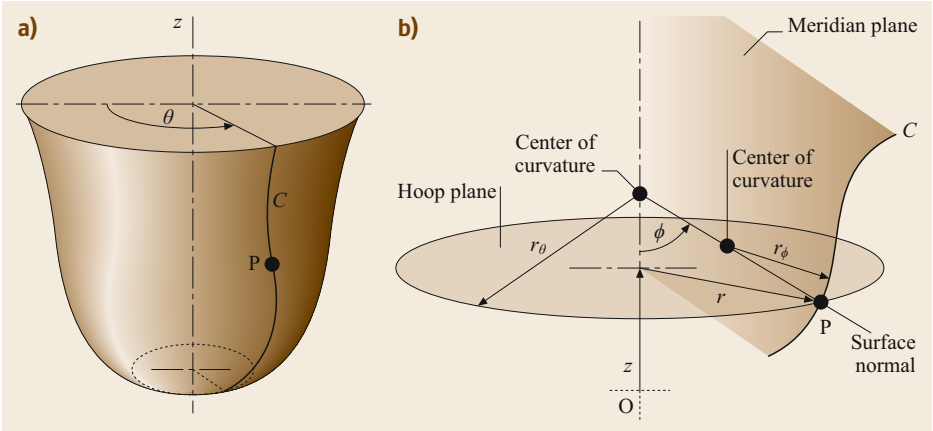

Fig. 11.59 **(a)** Axisymmetrical shell, **(b)** radii of curvature r_θ and r_ϕ

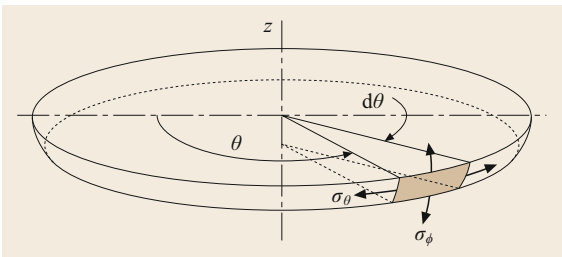

Fig. 11.60 Stress components in a shell

small enough with respect to the flow stress) and uniform edge tensions tangential to the surface are allowed.

It is furthermore assumed that work hardening is compensated by thinning of the sheet, so that the product of flow stress times current thickness is constant

$$\sigma_f t = T_f = \text{const.}\,, \tag{11.86}$$

where T_f is the so-called force resultant.

Finally, the Tresca flow criterion is assumed to be valid, as given in Fig. 11.61.

The static equilibrium of forces acting on a typical infinitesimal shell element (Fig. 11.62) supplies in the normal direction to the shell

$$p = \frac{T_\theta}{r_\theta} + \frac{T_\phi}{r_\phi} \tag{11.87}$$

and in the circumferential direction

$$\frac{dT_\phi}{dr} - \frac{T_\theta - T_\phi}{r} = 0\,. \tag{11.88}$$

Equations (11.87) and (11.88) together with the Tresca flow criterion (Fig. 11.61) constitute the framework of the membrane model used to analyze sheet forming processes.

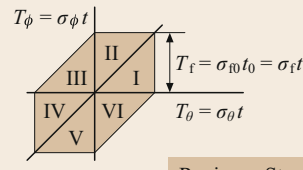

Region	Stress state	Flow condition
I	$T_\theta > T_\phi > 0$	$T_\theta = T_f$
II	$T_\phi > T_\theta > 0$	$T_\phi = T_f$
III	$T_\phi > 0 > T_\theta$	$T_\phi - T_\theta = T_f$
IV	$0 > T_\phi > T_\theta$	$T_\theta = -T_f$
V	$0 > T_\theta > T_\phi$	$T_\phi = -T_f$
VI	$T_\theta > 0 > T_\phi$	$T_\theta - T_\phi = T_f$

Fig. 11.61 Tresca flow criterion in terms of the force resultants

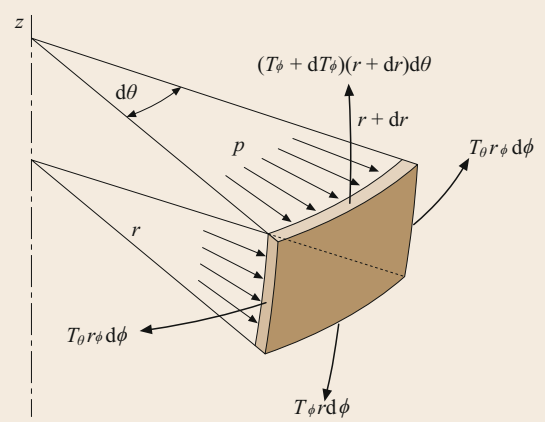

Fig. 11.62 Free body diagram of a typical shell element

11.4.2 Plastic Anisotropy

Characterization of Anisotropy

Grains tend to assume preferred orientations during plastic deformation, since this deformation is achieved by slip or twinning. Such preferred grain orientation will induce a direction-dependent behavior of metals called anisotropy. The most obvious effect of anisotropy is observed in forming of sheets that are produced by rolling. Anisotropy of sheets results in earing at the rim of a deep-drawn product (Fig. 11.84c).

Anisotropy in sheets is characterized by the Lankford parameter or anisotropy coefficient r. It is measured in the simple tension test (Fig. 11.63)

$$r = \frac{\varepsilon_b}{\varepsilon_t} = \frac{\ln(b_1/b_0)}{\ln(t_1/t_0)} , \tag{11.89}$$

where ε_b and ε_t are the true strains in the width and thickness directions. For most metals, the value of r changes with the longitudinal strain, and by convention a longitudinal elongation of 20% is used for comparison purposes.

More importantly, the r-value changes with the orientation of the specimen with respect to the rolling direction. This variation is determined by three r-values obtained from specimens in the rolling direction, transverse to the rolling direction, and at 45° to it. The average r-value, also called the normal anisotropy r_n, is defined as

$$r_n = \frac{r_{0°} + 2r_{45°} + r_{90°}}{4} . \tag{11.90}$$

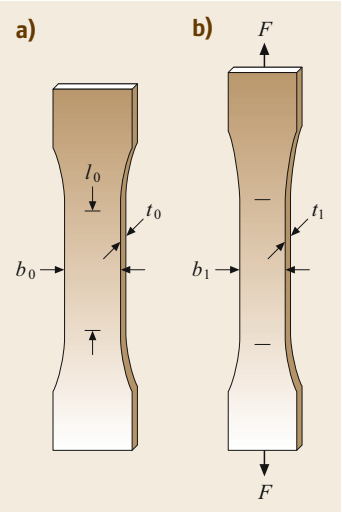

Fig. 11.63a,b Simple tension test of sheet metal: **(a)** undeformed, **(b)** deformed states

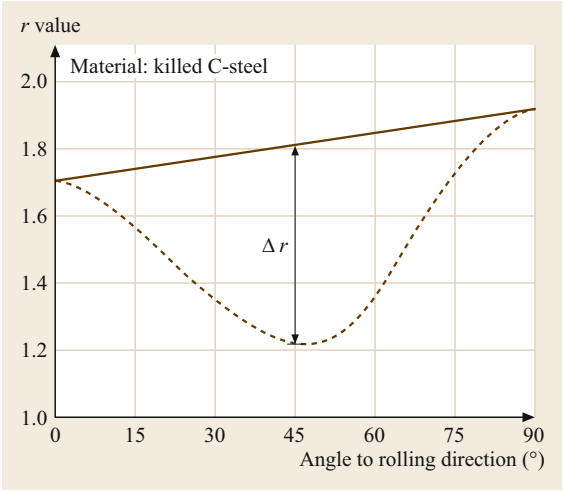

Fig. 11.64 Geometrical interpretation of the planar anisotropy coefficient

Table 11.14 Anisotropy values for various materials

Material	r_n value	Δr
Deep-drawing steels (DC01–DC07; cold rolled)	1.30–2.00	up to 0.70
Stainless steel	0.70–1.10	−0.25 to 0.20
TRIP[a] steels	0.9	about −0.03
Aluminum alloys	0.60–0.80	−0.60 to −0.15
Copper	0.60–0.80	–
Brass	0.80–1.00	–
Zinc alloys	0.20–0.6	–
Titanium alloys	2.00–8.00	up to 4.00

[a] TRIP (transformation induced plasticity) steels

The variation of the r-value over the plane of the sheet is described by Δr, the planar anisotropy coefficient

$$\Delta r = \frac{r_{0°} + r_{90°} - 2r_{45°}}{2} . \tag{11.91}$$

The geometric interpretation of the planar anisotropy coefficient is given in Fig. 11.64.

Typical anisotropy values for various materials are presented in Table 11.14.

The Anisotropic Flow Condition

The first anisotropic flow condition was proposed by *Hill* [11.5]. Neglecting planar anisotropy and assuming plane stress states (which is usually justified for sheet forming processes), the criterion reads in the principal stress configuration as

$$\sigma_1^2 - \frac{2r}{r+1}\sigma_1\sigma_2 + \sigma_2^2 = \sigma_f^2 , \tag{11.92}$$

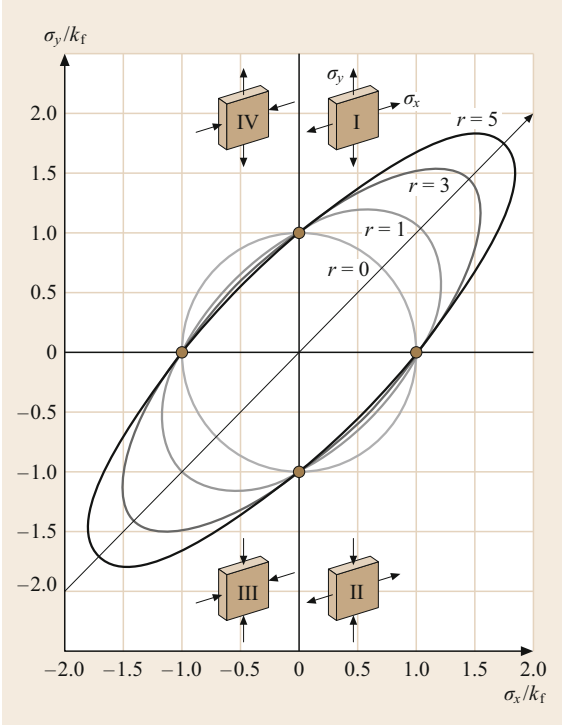

Fig. 11.65 Effect of r value on flow locus

where σ_1 and σ_2 are the in-plane principal stresses and σ_f is the flow stress. The effect of the normal anisotropy value r on the flow locus is shown in Fig. 11.65. For $r = 1$, the standard von Mises ellipse is obtained. For r values larger than 1, the ellipse elongates along the major axis but shrinks along the minor axis. Hence, in the case of biaxial tension or biaxial compression, larger relative stresses are necessary to initiate plastic flow. In the second and fourth quadrants, plastic flow will occur for slightly lower relative stresses than in the isotropic case.

Hill's criterion has proven to be successful for steel, but it fails for aluminum in particular. Also, it can only predict two or four ears in deep drawing, although a different number of ears is also observed for certain materials. Several criteria, also called nonquadratic flow criteria, have been introduced for these reasons. Table 11.15 depicts a few of these. Most of them have been developed basically to model forming of aluminum sheets.

11.4.3 Formability

Basic Failure Modes

Sheet parts can fail under various modes (Fig. 11.66) There are three basic failure types:

1. Wrinkling caused by compressive stresses
2. Rupture/tearing caused by exceeding the capability of the material, usually preceded by necking
3. Surface defects.

Most of the tests used to evaluate the formability of sheet metals in sheet forming operations, and particularly in deep drawing and stretch forming, focus on the fracture failure mode. Fracture usually follows necking, i.e., localized thinning of the metal. Therefore, necking is usually accepted as a failure mode as well.

Necking

Sheets neck under simple tension in two stages: diffuse necking and localized necking (Fig. 11.67); bulk specimens only exhibit diffuse necking. If the material's flow curve is represented by the Ludwik flow curve $\sigma_f = C \times \bar{\varepsilon}^n$, then it can be shown that

$$\text{for diffuse necking:} \quad \varepsilon_1^{\text{necking}} = n\,,$$
$$\text{for localized necking:} \quad \varepsilon_1^{\text{necking}} = 2n\,. \qquad (11.93)$$

Table 11.15 Various nonquadratic anisotropic flow criteria (flow planar isotropy) (after [11.15])

Flow criterion	Equation	Suggested parameter values
Hill 1979	$\lvert\sigma_1+\sigma_2\rvert^m + (2r+1)\lvert\sigma_1-\sigma_2\rvert^m = 2(r+1)\sigma_f^m$	$1.3 \le m \le 2.2$ (for $m = 2$, this criterion reduces to Hill 1948)
Hosford	$\sigma_1^a + r(\sigma_1-\sigma_2)^a + \sigma_2^a = (r+1)\sigma_f^a$	$a = 6$ for fcc metals $a = 8$ for bcc metals
Barlat 1989	$a\lvert k_1+k_2\rvert^M + a\lvert k_1-k_2\rvert^M + (2-a)\lvert 2k_2\rvert^M = 2\sigma_f^M$ $k_1 = \frac{\sigma_x+h\sigma_y}{2},\ k_2 = \left[\left(\frac{\sigma_x-h\sigma_y}{2}\right)^2 + p^2\tau_{xy}^2\right]^{1/2}$	a, h, p, and M are material parameters
Banabic–Barlat 2000	$(m\sigma_1+n\sigma_2)^{2k} + (p\sigma_1+q\sigma_2)^{2k} + (r\sigma_1+s\sigma_2)^{2k} = 2\sigma_f^{2k}$ $m = \frac{-(\sigma_f/\sigma_b)+4}{3},\ n = \frac{(\sigma_f/\sigma_b)-4}{3},\ p = 2\frac{(\sigma_f/\sigma_b)-1}{3},$ $q = \frac{(\sigma_f/\sigma_b)+2}{3},\ r = \frac{-(\sigma_f/\sigma_b)-2}{3},\ s = 2\frac{(\sigma_f/\sigma_b)+1}{3}$	σ_f is the uniaxial flow stress and σ_b is the biaxial flow stress

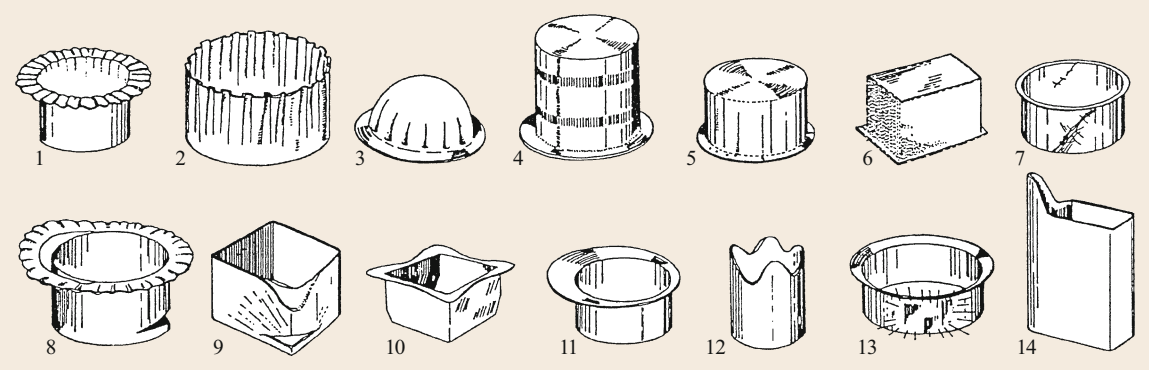

Fig. 11.66 Various failure modes in deep-drawing: 1 – flange wrinkling; 2 – wall wrinkling; 3 – part wrinkling; 4 – ring prints; 5 – traces; 6 – orange skin; 7 – Lüders strips; 8 – bottom fracture; 9 – corner fracture; 10–12 – folding; 13, 14 – corner folding (after [11.15])

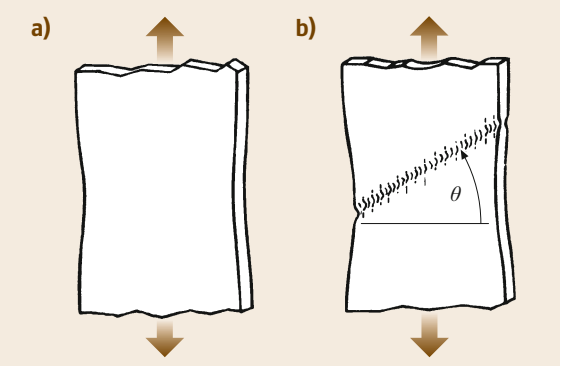

Fig. 11.67a,b Necking of sheet specimens under uniaxial tension: **(a)** diffuse necking, **(b)** localized necking (after [11.10])

If the stress state is not uniaxial, as is the usual case in most sheet forming processes, then the localized necking strain for an isotropic material is given as [11.10, 27]

$$\varepsilon_1^{\text{necking}} = \frac{n}{1 + (\varepsilon_2/\varepsilon_1)} \,. \tag{11.94}$$

The localized necking angle with the tension axis is estimated as

$$\tan\theta = \frac{1}{\sqrt{-(\varepsilon_2/\varepsilon_1)}} \,, \tag{11.95}$$

yielding an angle of 54° for simple tension of an isotropic specimen. For positive ratios of the two principal in-plane strains, no localized necking is possible and only diffuse necking occurs.

Simulative Formability Tests

The Olsen or Erichsen test (Fig. 11.68) was the first test used to evaluate the formability of sheet metals. These

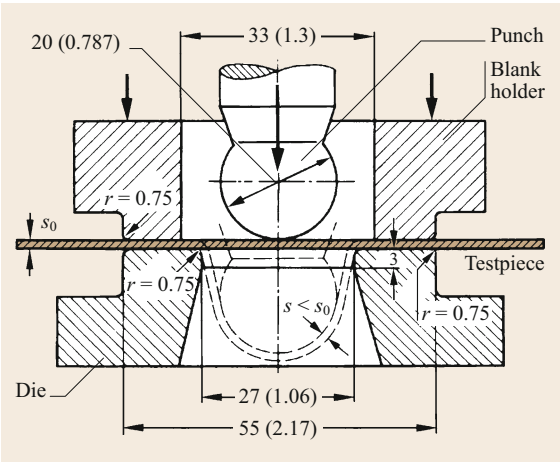

Fig. 11.68 Erichsen test. Dimensions given in mm (inches in parentheses)

two tests only differ slightly in the size of the tools. The principle is to stretch a sheet of metal using a hemispherical punch until fracture is observed. The punch depth in millimeters corresponds to the Erichson index (IE).

Another common test is the limiting dome height test by *Hecker* [11.28] (Fig. 11.69). Hecker's test is an improved Erichson test with larger tools and draw beads to increase the measurement accuracy.

Other tests such as Swift's cup test, the stretch–bend test, the wedge drawing test, the biaxial stretch test, the plane torsion test, hole expansion test etc. have been introduced in practice.

Forming Limit Diagrams

The forming limit diagram (FLD) consists of a curve in the principal in-plane strain space at which either necking starts or fracture is observed. It is basically a material property. Necking is localized in the tension–

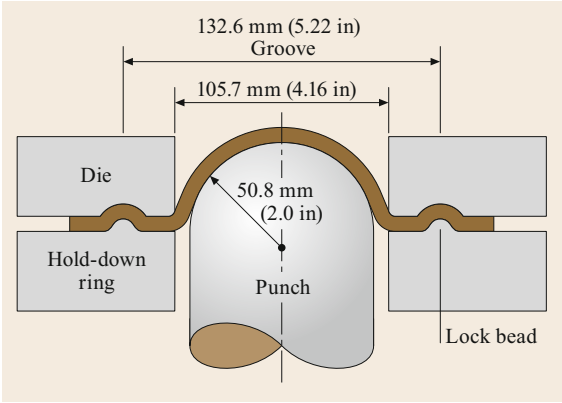

Fig. 11.69 Limiting dome height test by Hecker

compression part and is expected to be diffuse in the tension–tension part (Fig. 11.70). The loading line on the left (dashed line) corresponds to pure shear deformation, the central vertical line to plane strain tension, and the left dashed line to equibiaxial tension. Uniaxial simple tension is seen as a loading line between the left dashed and middle vertical lines.

The FLD provides an efficient and practical method to assess the formability of a sheet product. It is applied in two different manners. *Experimentally*, a circular grid pattern is imposed on the sheet either mechanically, photochemically, or electrochemically. During forming, the circles are deformed into ellipses. The principal strains are assumed to be along the major and minor axes of the ellipses. These minor and major radii of the ellipse are measured either manually or automatically

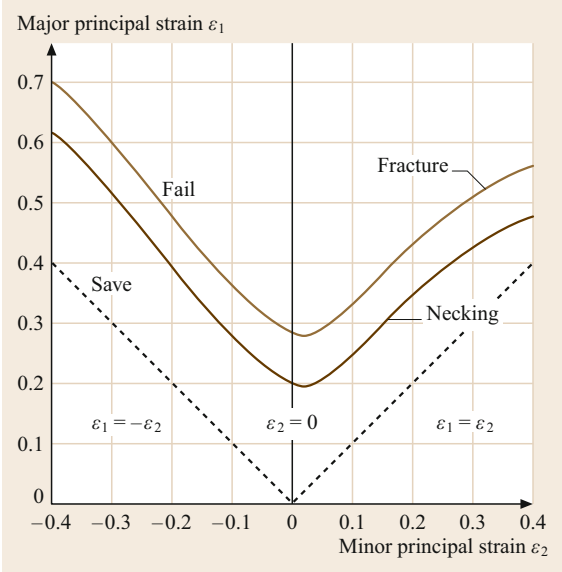

Fig. 11.70 Forming limit diagram for plane stress

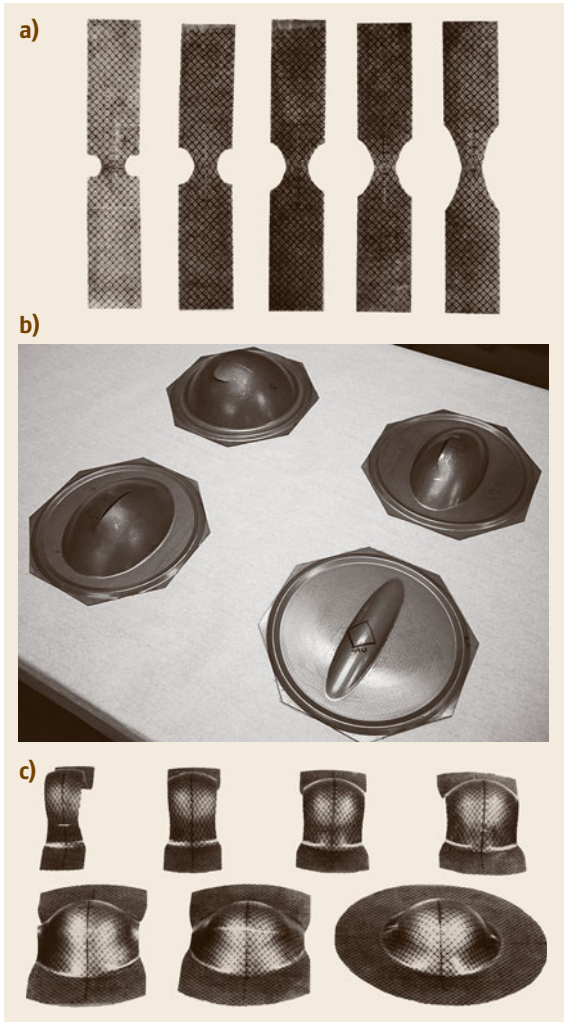

Fig. 11.71a–c Various methods of determining FLD: **(a)** uniaxial tensile test (courtesy V. Hasek), **(b)** hydraulic bulging test (courtesy N. Bay, DTU), **(c)** punch stretching test (courtesy V. Hasek)

by a digital camera. By comparing the measured local strains with the FLD, the range of safety for deep drawing, the critical zones where necking and/or fracture are most likely to occur, the strain level, and the favorable working conditions (blank-holder pressure, lubrication, placement of draw beads, etc.) can be determined, and hence the deep-drawing process can be improved. In this context, a *severity index* ranging from 0 to 10 is introduced, indicating the distance of the measured strain state from the FLD curve. *Numerically*, the analysis of the sheet forming process can be done, for instance, by finite element models before the actual pressing, and the computed strains can be compared with the respective FLD to assess the forming process.

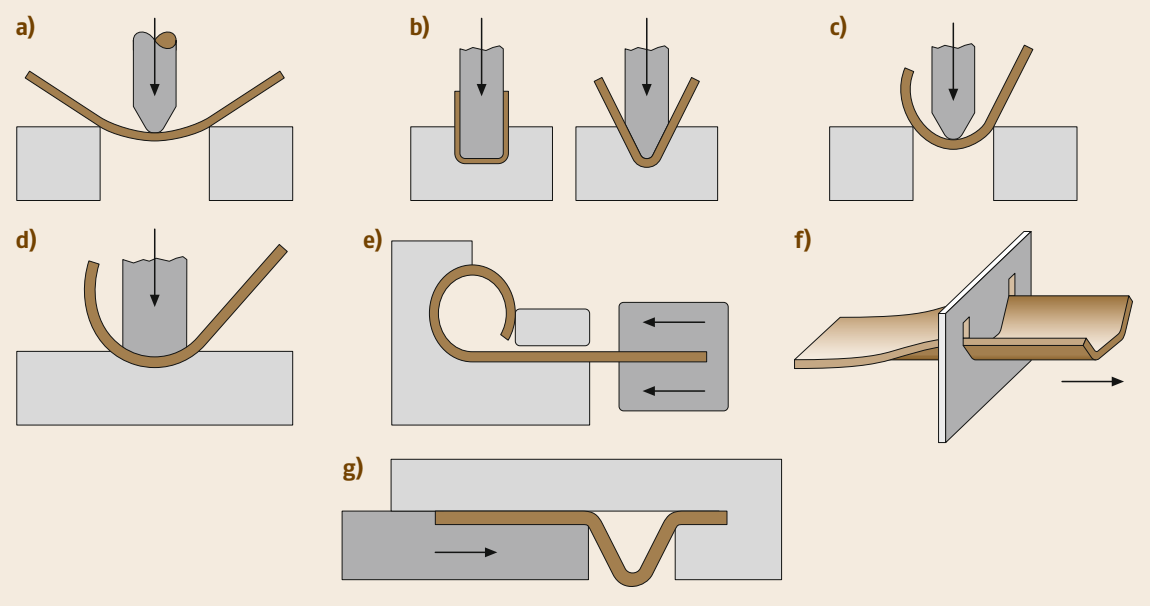

Fig. 11.72a–g Bending with linear tool motion: **(a)** free (air) bending, **(b)** die bending, **(c)** free round bending, **(d)** round bending in a die, **(e)** curling, **(f)** draw bending, and **(g)** bending by buckling

This latter application is basic industrial practice today.

FLDs can be measured using various methods such as the uniaxial tensile test on specimens having various dimensions with and without notches (Fig. 11.71a), the hydraulic bulge test using elliptical dies (Fig. 11.71b), the punch stretching test using strips with various widths (Fig. 11.71c), the Nakazima test (which is similar to the punch stretching test with the difference that the sheet is drawn instead of being stretched), the Hasek test (where circular specimens with various recesses are used), the Marciniak test with hollow punches, etc. Common to all tests is that numerous specimens or die geometries have to be used to simulate various principal strain ratios corresponding to various points on the FLD curve.

Experimentally measured FLDs are not completely material properties; They depend on various other factors. It is known that the FLD curve rises with increasing sheet thickness. Furthermore, it has been noticed experimentally that the failure shows some strain path dependence. Hence, if a tensile load path (meaning a strain path with positive slope in Fig. 11.70) is followed by a compressive load path (negative slope), the failure strain is lower than that predicted by the FLD. On the other hand, if a compressive load path is followed by a tensile one, the failure strain is larger than the FLD strain. Also, the grid size used in the experiments affects the measurements.

11.4.4 Bending

Bending Processes

Basic bending processes can be classified into two broad groups [11.29]: bending by linear tool motion (Fig. 11.72) and bending by rotary tool motion (Fig. 11.73).

In free bending [11.30], there is no contact between the workpiece and the die surface, whereas in die bending the sheet is bent between male and female dies. Free round bending is a continuous free bending process conducted in steps along the bending legs. In curling ,the workpiece is continuously bent by pushing it into a curved die. Bending by buckling is obtained by causing the workpiece to buckle normal to the applied force. The deformation region is limited by either local heating of the workpiece or clamping of the portion of the workpiece not to be deformed. In draw bending, the sheet is shaped by being pulled through a die opening.

Roll bending is achieved by moving the workpiece through the gap created by three adjustable rolls. In roll forming, the sheet is formed into a section between rolls with the form of the section. Folding is bending with a folding wing that folds the workpiece around the bending edge, whereas wiper bending or wiping is bending that creates a full plastic section between a roll and a tool. The section is forced to conform to the roll as the tool is dragged around the roll. In roll straightening, the roll axes can be normal or inclined to the bending

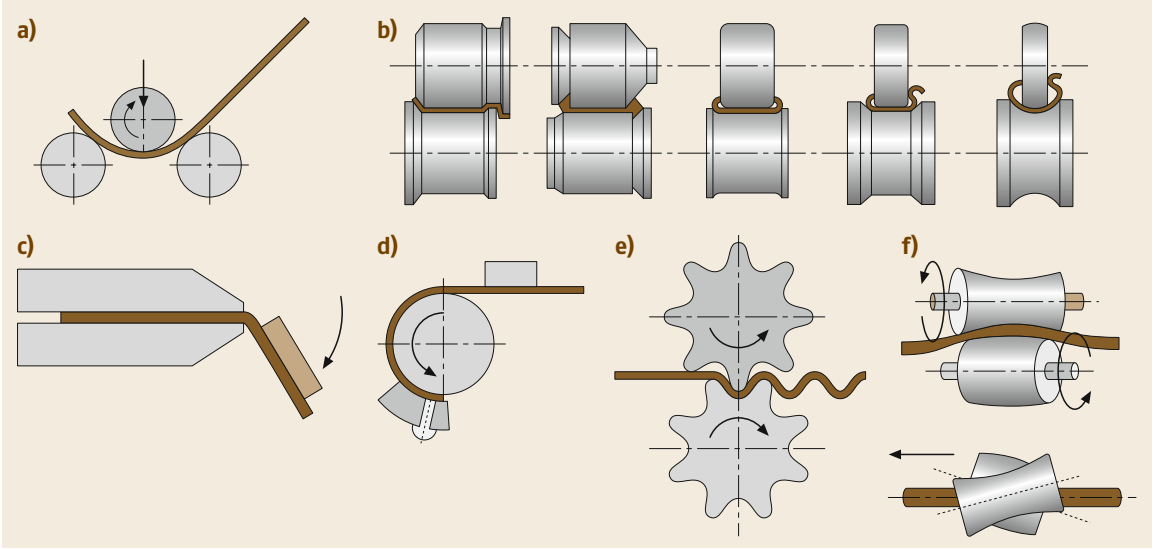

Fig. 11.73a–f Bending with rotary tool motion: **(a)** roll bending (round bending with rolls), **(b)** roll forming, **(c)** folding, **(d)** wiper bending, **(e)** corrugating, and **(f)** roller straightening

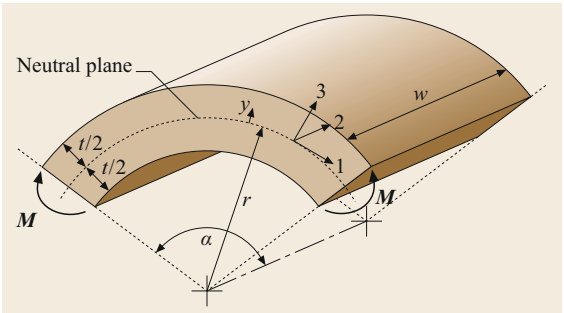

Fig. 11.74 Bending of a strip by pure moments

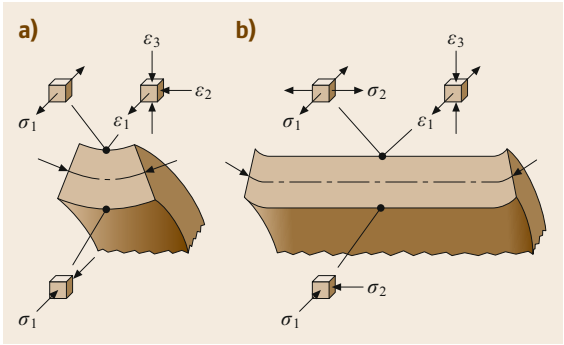

Fig. 11.75a,b Stress and strain states for bending of **(a)** narrow and **(b)** wide strips (after [11.31])

plane. The workpiece is roll bent by corrugated rolls in the corrugating process.

The Mechanics of Bending

If a strip of width w and thickness t is bent by pure moments M at both ends, the strip assumes a curvature with radius r at its neutral axis (Fig. 11.74). The directions 1–3 are assumed as shown in the figure.

The bending strain for any axial fiber is given by

$$\varepsilon_1 = \ln\left(1 + \frac{y}{r}\right), \tag{11.96}$$

where y is the distance of the fiber from the neutral axis having a radius of curvature r. This strain is positive at the upper fibers and negative at the lower fibers.

There are two extreme bending cases [11.31]: If the width of the bent strip w is small compared with its thickness t (Fig. 11.75a), then only bending (axial) stress will develop, hence the stress state will be uniaxial with tensile stresses at the larger-radius side and compressive stresses at the smaller-radius side. The corresponding strain state is therefore

$$\varepsilon_1 = \varepsilon_2 = -\frac{1}{2}\varepsilon_1 . \tag{11.97}$$

Hence, the width of the tension side of the strip will decrease while the width of the compressive side will increase. On the other hand, if the width of the bent strip is much larger than its thickness, then in the middle regions of the strip a plane strain state will develop (Fig. 11.75b) with $\varepsilon_2 = 0$. If furthermore the plane stress state is assumed to have $\sigma_3 = 0$, it can be shown using the flow rule that $\sigma_2 = \sigma_1/2$. For this case of the plastic state, the flow stress and the equivalent strain are related to the axial components by

$$\varepsilon_1 = \sqrt{\frac{3}{2}}\bar{\varepsilon}\,, \quad \sigma_1 = \frac{2}{\sqrt{3}}\sigma_\mathrm{f}\,. \tag{11.98}$$

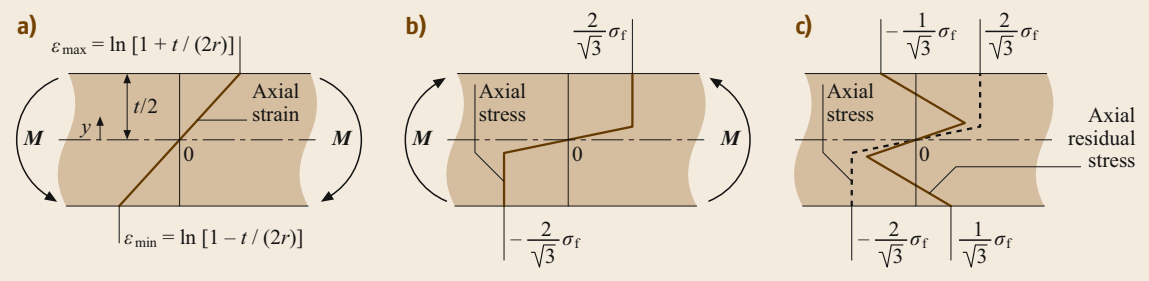

Fig. 11.76 (a) Strains, (b) loading stresses, and (c) residual stresses for a perfectly plastic material during plane strain bending

Even for a wide strip, an uniaxial stress state exists at the ends, leading to a transverse curvature at both ends.

The elastic stress–strain relationship for the plane strain case is given by the generalized Hooke's law as

$$\sigma_1 = \frac{E}{1-\nu^2}\varepsilon_1 \,, \tag{11.99}$$

where E is the Young's modulus and ν is the Poisson's ratio. Introducing the plane strain Young's modulus E', the elastic stress–strain relation becomes

$$\sigma_1 = E'\varepsilon_1 \quad \text{with } E' = \frac{E}{1-\nu^2} \,. \tag{11.100}$$

Figure 11.76a shows the axial strain distribution through the thickness of a strip. The true strain distribution is nearly linear. If the strains are large enough, the material will plastify in the outer regions. Assuming that the material is perfectly plastic and that the strip is wide, in the plastic regions the axial stress will be equal to the flow stress for plane strain as given by (11.98) (Fig. 11.76b). Assuming that the whole cross-section plastifies, the bending moment is given by

$$M = \frac{1}{2\sqrt{3}} W t^2 \sigma_f \,. \tag{11.101}$$

After the moment is removed, the bent part will spring back due to the elastic energy stored during bending (Fig. 11.77). The new radius of curvature will now be

$$r' = \left(\frac{1}{r} - \frac{2\sqrt{3}}{t} \frac{\sigma_f}{E'} \right)^{-1} \,. \tag{11.102}$$

The residual stresses after unloading are given for the plastified region by (Fig. 11.76c)

$$\sigma_1^{\text{residual}} = \frac{2}{\sqrt{3}}\sigma_f \left(1 - \frac{3y}{t}\right) . \tag{11.103}$$

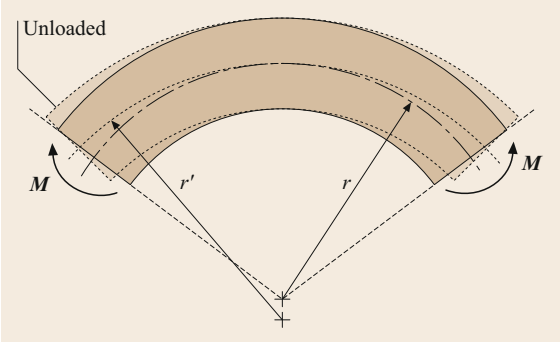

Fig. 11.77 Springback after unloading

The springback factor K_s is defined by

$$\text{springback factor} \equiv \frac{r}{r'} \tag{11.104}$$

and is presented for various materials and two relative bending radii in Table 11.16.

The basic failure mode in bending is fracture at the tensile side of the sheet. The smallest radius to which a sheet can be bent without failure is considered to be

Table 11.16 Springback factor (after [11.32])

Material	Springback factor	
	$r'/t = 1$	$r'/t = 10$
St 0-24, St 1-24	0.990	0.970
St 2-24, St 12	0.990	0.970
St 3-24, St 13	0.985	0.970
St 4-24, St 14	0.985	0.960
Stainless austenitic steels	0.960	0.920
High-temperature ferritic steels	0.990	0.970
High-temperature austenitic steels	0.990	0.970
Nickel w	0.990	0.960
Al99.5F7	0.990	0.980
AlMg1F13	0.980	0.900
AlMgMnF18	0.985	0.935
AlCuMg2F43	0.910	0.650
AlZnMgCu1.5F49	0.935	0.850

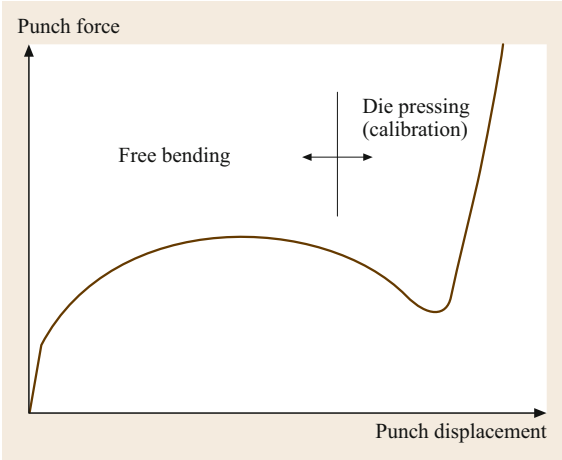

Fig. 11.78 Force–displacement curve in die bending

its bendability. The bendability is highest if the bending axis is transverse to the rolling direction.

A typical force–displacement curve for die bending (Fig. 11.72) is shown in Fig. 11.78. The force increases during free bending then starts to drop as the sheet overbends. The steep increase at the end of process occurs when the bent sheet is pressed towards the die by the punch to calibrate the part.

11.4.5 Stretch Forming and Deep Drawing

Industrial sheet forming processes such as the manufacturing of automobile panels involve both stretch forming as well as deep-drawing processes. Stretch forming and deep drawing are similar processes in the sense that they shape a sheet using a rigid punch and a rigid die. On the other hand, they differ fundamentally in the sense that, in stretching, the sheet is fixed at its circumference, and hence the whole in-plane deformation is achieved by thinning of the sheet, whereas in deep drawing the sheet is allowed to be drawn at its circumference so that the shape change of the sheet is achieved under rather unchanged sheet thickness.

Stretch Forming

A circular sheet blank with diameter $2a$ being clamped firmly at its rim is stretched by a spherical punch with radius ρ_p (Fig. 11.79).

Using the membrane equation (11.87), it can be shown that the pressure between the punch and the sheet is

$$p_\mathrm{c} = 2\frac{T_\mathrm{f}}{\rho_\mathrm{p}}\,, \tag{11.105}$$

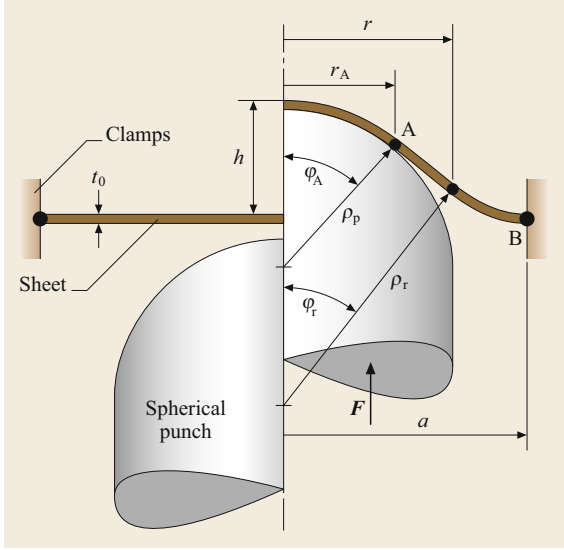

Fig. 11.79 Stretch forming with a spherical punch (after [11.31])

and the punch force for a given contact angle ϕ_A is found as

$$F = T_\mathrm{f}\left(2\pi\rho_\mathrm{p}\right)\sin^2\phi_\mathrm{A}\,. \tag{11.106}$$

Recall that the force resultant T_f is assumed constant and is therefore given as

$$T_\mathrm{f} = \sigma_{\mathrm{f}0}t_0 = \text{const.}\,, \tag{11.107}$$

where t_0 is the initial sheet thickness and $\sigma_{\mathrm{f}0}$ is the initial flow stress.

The shape of the stretched sheet is given by the variable radius of curvature of the unsupported sheet region

$$\rho_\mathrm{r} = \frac{r^2}{r_\mathrm{A}\sin\phi_\mathrm{A}}\,. \tag{11.108}$$

Deep Drawing

In the deep-drawing process, an initially flat sheet (the blank) is formed by a rigid punch into a die cavity (Fig. 11.80). To prevent wrinkling of the blank, a blank holder is usually used. Since the material in the blank is drawn in, the circumferential stresses are compressive here. The strain state at the rim is given by

$$\begin{aligned}
\varepsilon_\theta &= \ln\left(\frac{r_0'}{r_0}\right) \quad \text{(circumferential strain)}\,,\\
\varepsilon_\mathrm{t} &= -\frac{1}{2}\varepsilon_\theta \quad \text{(thickness strain)}\,,\\
\varepsilon_\mathrm{r} &= -\frac{1}{2}\varepsilon_\theta \quad \text{(radial strain)}\,.
\end{aligned} \tag{11.109}$$

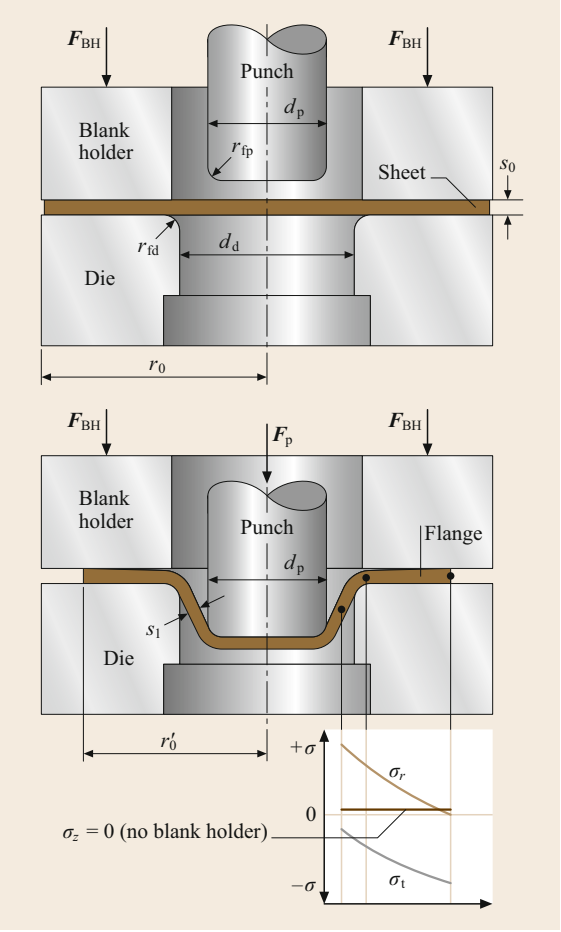

Fig. 11.80 Principle of deep drawing

The wall thicknesses of the drawn cup are given in Fig. 11.81. Assuming that the mean thickness of the cup wall is equal to the initial sheet thickness, the drawn cup height is given as

$$h \approx \frac{r_0^2 - r_m^2}{2r_m} \qquad (11.110)$$

with an error of ±5%.

The limiting drawing ratio β_{max} is an indicator of the drawability of a material and is defined as

$$\beta_{max} = \frac{d_{0,max}}{d_m}\,, \qquad (11.111)$$

where $d_{0,max}$ is the largest blank diameter that can be drawn into a cup with mean diameter of d_m without failure. According to membrane theory, the ideal limiting drawing ratio is

$$\beta_{max} \leq e \approx 2.72\,. \qquad (11.112)$$

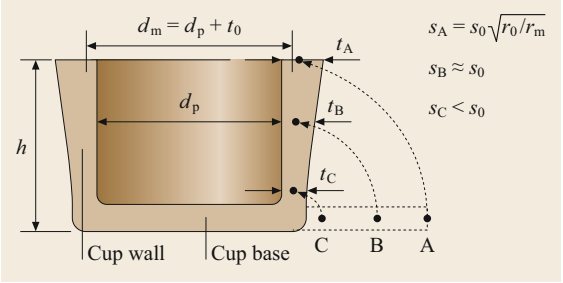

Fig. 11.81 Deep-drawn cup (after [11.29])

In reality, the limiting drawing ratios are 1.8–2.0 for aluminum sheets and 1.9–2.2 for steel sheets (for d_0 =100 mm). This is because various process parameters are not considered in the simplifying membrane theory. One such factor is the dimension of the blank or equivalently the punch. As the relative punch diameter increases, the limiting drawing ratio decreases (Fig. 11.82). Furthermore, as the normal anisotropy r_n increases, the limiting drawing ratio increases; however, as the planar anisotropy Δr increases, β_{max} decreases. Similarly, as the hardening exponent n increases β_{max} increases, but as the friction between the blank and die increases, β_{max} decreases.

To increase the drawing ratio, cups can be drawn successively. This can be achieved by direct redrawing or reverse redrawing (Fig. 11.83). In direct redrawing, the outer surface of the initially drawn cup remains the outer

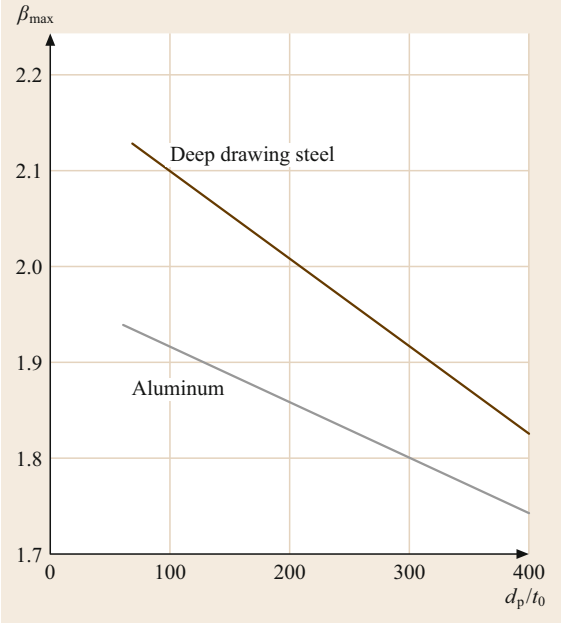

Fig. 11.82 Effect of relative punch diameter on limiting drawing ratio

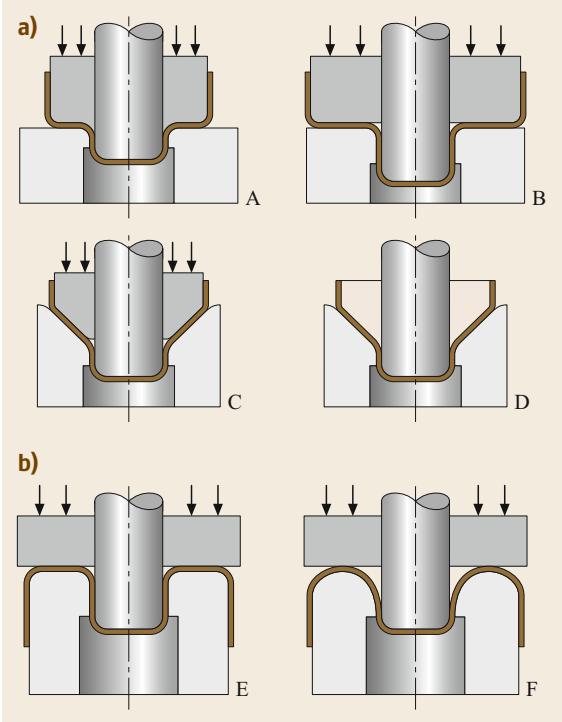

Fig. 11.83a,b Redrawing process to increase the overall drawing ratio: **(a)** direct redrawing, **(b)** inverse redrawing

surface in the redrawn cup, whereas the same surface becomes the inner surface in a reversely redrawn cup. Redrawing can be done either with or without annealing between the draws. Using the redrawing technique, the total drawing ratio achieved without annealing between draws is up to 6.5 for deep-drawing steel. Hereby, the first draw is conducted at a drawing ratio of 2.0 and all the following draws at a drawing ratio of 1.3.

The height of a drawn cup can be increased by reducing the wall thickness of the drawn cup by ironing (Fig. 11.49c). This process is also used to make the wall thickness of the cup uniform. This is virtually a drawing process and must be considered bulk forming.

Typical failure modes in deep drawing are given in Fig. 11.84. Tearing occurs if the drawing force cannot be transmitted by the cup bottom; this is the failure type controlling the limiting drawing ratio. The limiting drawing force is

$$F \leq a\mathrm{UTS}\pi d_\mathrm{p} t_0 \,, \tag{11.113}$$

where a is a correction factor (1.05–1.55 for steel, 0.99–1.22 for aluminum, and 0.92–1.27 for brass) and UTS is the ultimate tensile strength of the sheet material. Wrinkling is caused by compressive stresses that occur in the flange of the workpiece. If the clearance between the punch and die is large, wrinkles can also occur in the cup wall. If the sheet thickness is large enough ($d_0/t_0 <$ 25–40), the sheet has sufficient buckling resistance. For thinner sheets, wrinkles in the flange are prevented by a blank holder. It is suggested to use a blank-holder pressure of 1–2% of the flow stress of the workpiece material.

The working window for the deep-drawing process is sketched in Fig. 11.85. The working window can be enlarged by reducing the flow stress of the workpiece in the flange region, by reducing friction in the flange and at the die radius, by increasing the strength of the material at the cup base–wall transition, and by increasing the friction at the cup base region.

The drawing force during deep drawing (Fig. 11.86) can be estimated as

$$F = 2\pi r_\mathrm{m}\left\{\left[\underbrace{\sigma_{\mathrm{fm,flange}} t_0 \ln\left(\frac{r'_0}{r_\mathrm{m}}\right)}_{\text{ideal force}} + \underbrace{\frac{\mu F_\mathrm{BH}}{\pi r'_0}}_{\text{flange friction}} + \underbrace{\frac{\sigma_{\mathrm{fm,die\text{-}ring}} t_0^2}{2r_\mathrm{fd} + t_0}}_{\text{bending/unbending}}\right] \underbrace{\mathrm{e}^{\mu\phi}}_{\text{die-ring friction}}\right\} \sin\alpha \,. \tag{11.114}$$

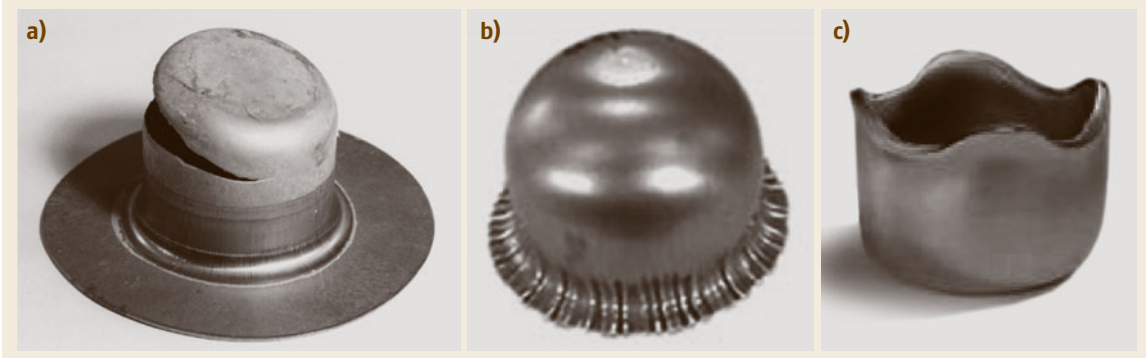

Fig. 11.84a–c Typical failure modes in deep drawing: **(a)** tearing, **(b)** wrinkling (courtesy T. Altan, ERC), and **(c)** earing (courtesy Hydro Aluminium Deutschland GmbH)

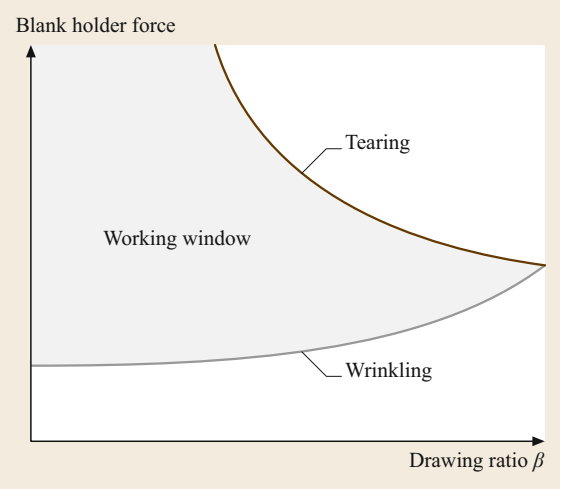

Fig. 11.85 Working window in deep drawing (after [11.31])

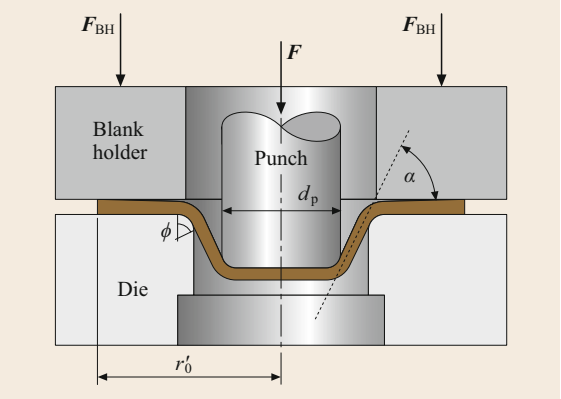

Fig. 11.86 Deep-drawing parameters

The typical force–displacement curve in deep drawing shows a maximum when the blank radius is reduced to around 77% of the initial value (Fig. 11.87). This is the result of the decreasing flange volume and the increasing flow stress in the flange as the punch advances. If the clearance between the punch and the die ring is smaller than the increased sheet thickness towards the rim of the cup, there will be an additional increase in the force due to ironing after the force maximum is reached.

Forming of complex three-dimensional sheets is a combination of stretch forming and deep drawing. The critical issue is to control the material flow within the sheet part during forming. This is achieved basically by four methods:

1. Designing the blank geometry appropriately.
2. Using draw beads or lock beads (Fig. 11.88) that partially or completely prevent the draw-in of the material.

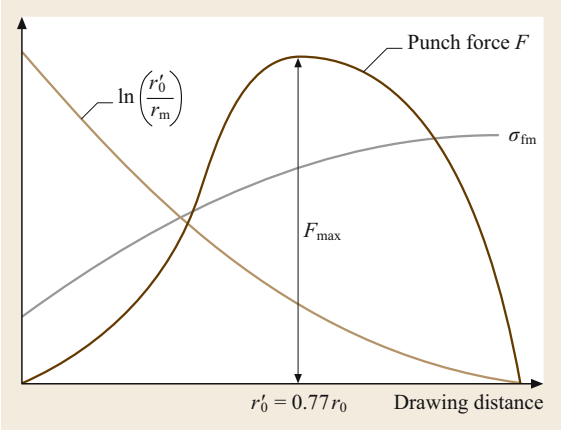

Fig. 11.87 Typical force–displacement curve for deep drawing

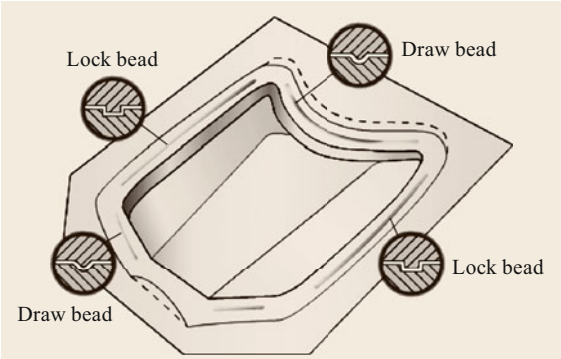

Fig. 11.88 Deep drawing of complex parts using draw beads and lock beads

3. Regulating the blank-holder force. Advanced deep-drawing dies have segmented blank holders to adjust the blank-holder force locally.
4. Regulating the type, amount, and distribution of lubricant during sheet forming.

11.4.6 Hydroforming

Hydroforming is characterized by the replacement of a rigid tool with a pressure medium such as water or oil. There are two broad groups of these processes: Sheet hydroforming and tube hydroforming. Sheet hydroforming processes are basically of two types: processes in which the die is replaced by a pressurized fluid (called hydromechanical deep drawing, the hydromech process, the aquadraw process, hydraulic counterpressure deep drawing, or just hydroform) and processes in which the punch is replaced by a pressurized fluid (called high-pressure sheet forming or just fluid forming).

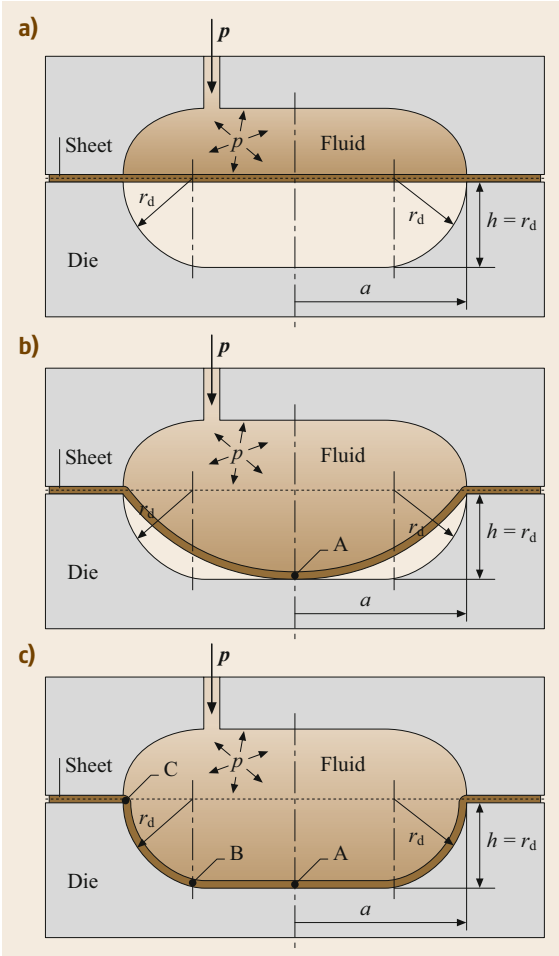

Fig. 11.89a–c Principle of high-pressure sheet forming: **(a)** beginning of process, **(b)** end of free bulging, **(c)** end of cavity filling (after [11.31])

High-Pressure Sheet Forming (Fluid Forming)

The high-pressure sheet forming process consists of two stages (Fig. 11.89): the free bulging stage and the cavity filling stage. Compared with conventionally deep-drawn parts, hydroformed parts have better tolerances and repeatability. Moreover, parts made from blanks of different thickness and materials (tailored blanks) can be produced using the same tools. Another advantage is the low springback and low residual stress levels in the product. On the other hand, due to the free bulging, the depths of the parts are limited. Also, the cycle time is relatively slow, and dies cannot be changed as quickly as conventional dies.

For the typical process shown in Fig. 11.89, the internal pressure at the end of the free bulging state can be estimated using membrane theory as

$$p \approx 4\sigma_{f0} t_0 \frac{r_d}{a^2 + r_d^2} \,. \tag{11.115}$$

The maximum height for the free bulging stage is given by

$$h_{max} = \frac{a}{\sqrt{5}} \approx 0.447a \,. \tag{11.116}$$

The pressure to fill the cavities is approximately

$$p = \sigma_{f0} t_0 \left(\frac{1}{a} + \frac{1}{r_d} \right) . \tag{11.117}$$

The contact pressure at the interface of the sheet and the rigid die between point B and C can be estimated as

$$p_{contact} \approx \frac{\sigma_{f0} t_0}{a} \,. \tag{11.118}$$

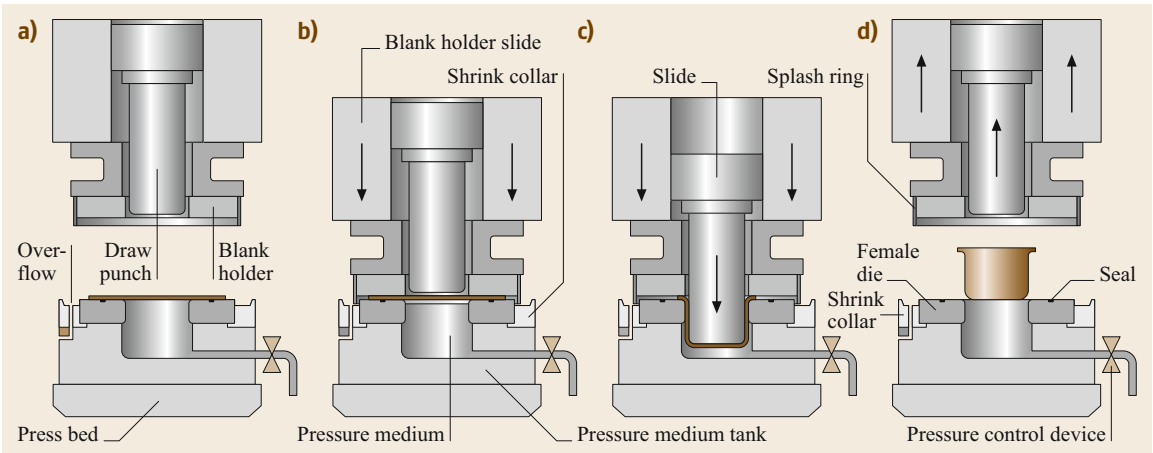

Fig. 11.90a–d Principle of hydromechanical deep drawing. **(a)** Before forming, **(b)** dies closed, **(c)** forming, **(d)** after forming (after [11.32])

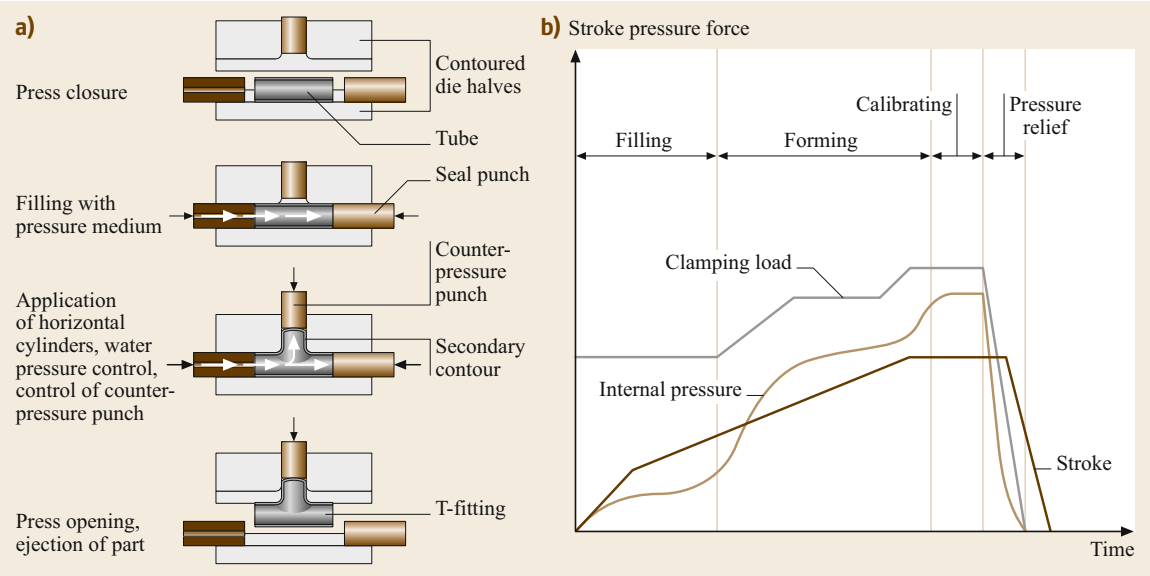

Fig. 11.91 (a) Principle of tube hydroforming and (b) process control (after [11.32])

Hydromechanical Deep Drawing

The working principle of hydromechanical deep drawing is shown in Fig. 11.90 [11.32]. First, the press is opened and the water container is filled in the home position. After the insertion of the blank, the press closes, and the blank holder grips the blank. The blank-holder pressure, set at the press, seals the pressure chamber, and the actual forming process is initiated. The medium pressure builds up as a result of penetration of the draw punch into the water container. During deformation, the sheet metal is pressed against the draw punch. During the forming phase, the control system, which is linked to the pressure chamber, controls the application of the hydraulic pressure as a function of the draw depth.

After reaching the mechanically limited draw depth, the pressure in the chamber is released and the press travels back to its home position.

The advantages of hydromechanical deep drawing are the higher limiting drawing ratio (β_{max} = 2.7) as compared with mechanical deep drawing (β_{max} = 2.0), the better surface quality, and the lower springback of the product. Pressures for various materials during hydromechanical deep drawing are presented in Table 11.17.

Table 11.17 Pressures during hydromechanical deep drawing

Material	Pressure (bar)
Aluminum	50–200
Steel	200–600
Stainless steel	300–1000

Tube Hydroforming

Tube hydroforming is a cold-forming process in which a tube is pressurized internally and simultaneously compressed axially and/or radially [11.32]. The tube is thereby expanded and pressed against a die. The process steps can be illustrated by the manufacturing of a T-fitting (Fig. 11.91a): A special hydraulic press is equipped with a two-part multiple-purpose die. Depending on the workpiece, the dies have two seal punches (horizontal cylinders) positioned axially relative to the tube ends and a counterpressure punch. The tubular preform is placed in the bottom die, and the die is closed. The ends of the tube are sealed by the axial punches, and the tube is filled with pressure medium.

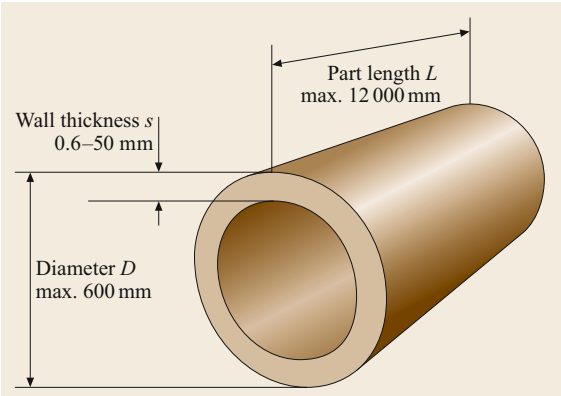

Fig. 11.92 Current limits on workpiece geometry for tube hydroforming (after [11.32])

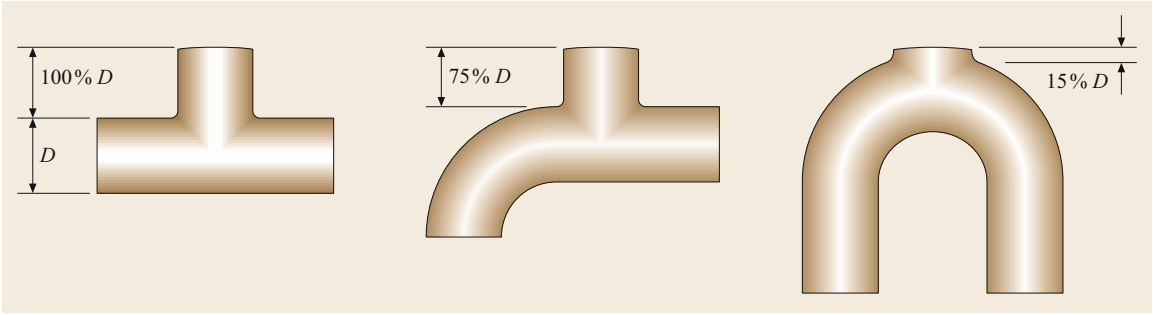

Fig. 11.93 Product geometries producible by tube hydroforming (after [11.32])

In the actual forming process, the punches compress the tube, while the pressure medium is fed to inflate the part until the part wall rests against the die contour. Pressures can reach values up to 4000 bar. The counterpressure punch additionally controls the material flow. The calibration pressure forms the workpiece in such a way that its contour corresponds to that of the die accurately and reproducibly. The die is finally opened, and the formed component is ejected.

Currently, tubes with the maximum dimensions shown in Fig. 11.92 can be formed by tube hydroforming. Typical achievable product dimensions are given in Fig. 11.93.

Tube hydroforming is limited by three failure modes (Fig. 11.94): buckling, wrinkling, and bursting.

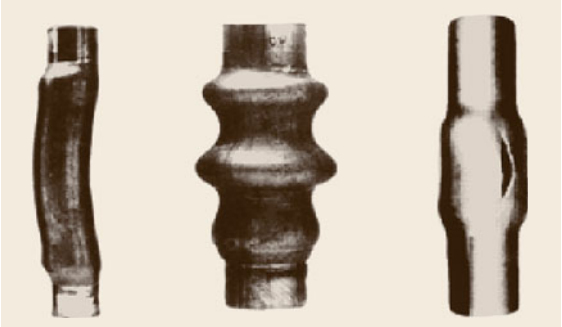

Fig. 11.94 Failure modes in tube hydroforming (after [11.33])

11.5 Forming Machines

Metals are plastically formed by usually at least two tools. These tools have to be moved with certain kinematics and with certain forces. This is achieved by a forming machine. Since various metal forming processes need various load–stroke characteristics, the forming machines used have to be selected accordingly. Besides satisfying the mechanical requirements, forming machines must also provide a long uptime, i.e., the time they are used for forming, and should ensure long tool lives. The latter depends, for instance, on the precision of the guidance of the slides.

The largest group of forming machines is presses. These are machines with linear relative motion between the two tools. Other forming machines include rolling machines, wire or tube drawing machines, and magnetic or explosive forming machines. Here only presses will be discussed.

11.5.1 Parameters of Forming Presses

The various requirements of the forming process such as necessary force, moment, energy, etc. must be matched with the capabilities of the forming press. This can be achieved by comparing characteristic parameters of the forming press with those of the forming process. Basically, four groups of parameters can be identified [11.1, 2]: energy and force parameters, transient parameters, accuracy parameters, and other parameters.

Energy and Force Parameters

For a feasible forming process, the nominal ram force provided by the machine F_{nom} must be larger than or equal to the necessary maximum forming force F_{form} and the available energy of the forming machine E_{nom} must be larger than or equal to the necessary process work W_{proc}. Practically, however, equality makes no sense due to the inherent fluctuations of the forming loads; on the other hand, for economic utilization of the usually expensive forming machines, F_{nom} and E_{nom} should be as close as possible to F_{form} and W_{proc}, respectively. The necessary process work is given by

$$W_{\mathrm{proc}} = W_{\mathrm{form}} + W_{\mathrm{el}} + W_{\mathrm{fr}} + W_{\mathrm{aux}} \,, \qquad (11.119)$$

where W_{form} is the work necessary to plastically deform the metal (including the frictional work at the tool/workpiece interface), W_{el} is the work to elastically deform the press frame and the tools, W_{fr} is the frictional work consumed in the various guides and bearings, and finally W_{aux} is the work consumed by auxiliary equipment such as blank holders, ejectors, etc.

The elastic work absorbed by the press frame and the tools is given by

$$W_{el} = \frac{1}{2}\frac{F_{form}^2}{C}\,, \qquad (11.120)$$

where C is the stiffness of the forming press including the tools. As long as $C > dF_{form}/ds$ (where s is the ram stroke), the elastic energy spent until the maximum forming load is reached can be recovered afterwards. The unrecovered elastic energy leads to vibrations in the drives and in the machine frame. Hence, the higher C is, the higher the chance that the elastic energy can be recovered and the vibrations reduced.

According to the basic physical parameter controlling their action, presses can be classified into stroke-controlled, force-controlled, or energy-controlled presses (Fig. 11.95): *Energy-controlled forming machines* provide a certain amount of energy (E_{nom}) for the process. If this energy is consumed, the press stops. If the energy required for the process is greater than that available, multiple strokes can be executed (Fig. 11.95a). Hence, the basic characteristic parameter of energy-controlled presses is the nominal energy E_{nom}. Hammers and screw presses are two typical representatives of this group. In contrast to hammers, screw presses have drives and frame elements under load, so that for these, in addition to the nominal energy, a nominal force also has to be specified for the design of these machine elements. *Force-controlled presses* provide (independently of the stroke) a given force, obtained as the hydraulic pressure p multiplied by the cylinder cross-sectional area A (Fig. 11.95b). The basic parameter for these presses is therefore the maximum allowable force F_{nom}. The typical representative of this group is the hydraulic press. Finally, *stroke-controlled presses* (Fig. 11.95c) provide a ram force for each ram position depending on the kinematics of the mechanical drive. The characteristic parameters, therefore, are the ram force as a function of the stroke and the maximum ram force F_{nom}. Typical representatives are crank and toggle presses.

Transient Parameters

The basic time-dependent parameters are the effective stroke rate, the contact time of the tools with the workpiece under the forming load, and finally the speed of the

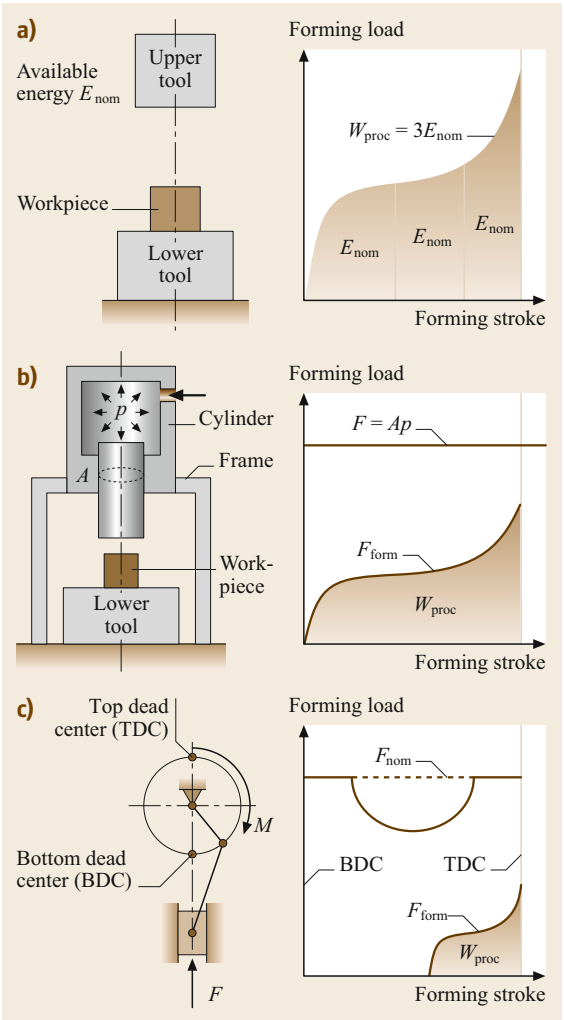

Fig. 11.95a–c Basic types of forming presses: **(a)** energy-controlled forming presses, **(b)** load-controlled forming presses, **(c)** stroke-controlled forming presses

press. The effective stroke rate determines the economic efficiency of the press. This parameter is related to the falling height in case of hammers, to the speed during the load free stroke in case of hydraulic presses, and to the speed and total stroke in case of crank presses. The contact time under pressure is especially important for warm and hot forming processes, since it determines the amount of workpiece cooling required. Typical contact times for various machines are presented in Table 11.18. For stroke-controlled presses, the contact time under pressure is larger the softer the frame and tool system are (i.e., the lower C is). Another important parameter is the speed of the ram of the press. This directly influences the strain rates during forming. Especially in warm and hot forming, the higher the strain rate, the higher

Table 11.18 Order of magnitude of contact times for various press types (after [11.1, 2])

Press type	Contact time under pressure (s)
Hammers	10^{-3}–10^{-2}
Screw presses (with flywheel)	10^{-2}–10^{-1}
Stroke-controlled presses	10^{-1}–5×10^{-1}
Hydraulic presses	10^{-1}–1

the flow stress and hence the higher the forming load. In hammers, the speed is given during the forming process by the power balance, whereas for stroke-driven presses, the ram speed is a function of the ram position. For the latter, note that the true ram speed depends on the stiffness of the frame–tool system.

Accuracy Parameters

The accuracy parameters of presses are related to geometric errors of the workpiece, such as position errors during impact, eccentricity of the product, dimensional errors in product height, the angle of twist of the product, etc. These errors are caused either by inaccuracies of the presses in the idle state, such as excessive clearance of the guides or skewness of the lower die and upper die leading to position errors during impact, or by inaccuracies of the press under load, such as elastic deformations leading to height errors in the tool. The latter errors are strongly dependent on the stiffness of the press, so that this characteristic parameter is the key parameter for the press specification. In presses, generally the frame, the upper tool, the lower tool, and the drive system deflect elastically. In the case of hammers, only the lower tool deflects elastically.

Other Parameters

Finally, parameters such as stroke length, tooling space, space requirements of the press, weight of the press, and necessary power supply can be listed as other characteristic parameters.

11.5.2 Energy-Controlled Presses

Energy-controlled presses provide a certain predetermined amount of energy for the forming process. Force as well as displacement is not controlled directly. There are basically two types of energy-controlled presses: hammers and screw presses.

Hammers

There are basically three types of hammers (Fig. 11.96): Drop hammers provide the energy by a freely falling ram including the upper die. In double-acting hammers, the ram is accelerated by a fluid such as steam, air, or hydraulic oil acting through a cylinder and piston. Finally, in counter-blow hammers, the upper and lower dies are accelerated towards each other. The first two types transmit the forging force to the ground, whereas for the counterblow hammer, the ground remains practically unaffected by the forming load.

The properties of these hammers are presented in Table 11.19. Hammers are basically used in hot forging operations, so that the impact speeds are important for determining the strain rates for the forming process. Furthermore, the contact time of the dies with the workpiece is important to determine the cooling of the workpiece. The contact time for hammers is 10^{-3}–10^{-2} s, being the shortest contact time among all press types. The maximum nominal energy of the hammer cannot be entirely used for forming due to energy losses such as friction at the slides and elastic deformations of the dies. For small loads and large displacements, about 80–90% of the nominal energy can be used, whereas for high loads and small displacements, only 20–50% of the nominal blow energy is available for the forming process.

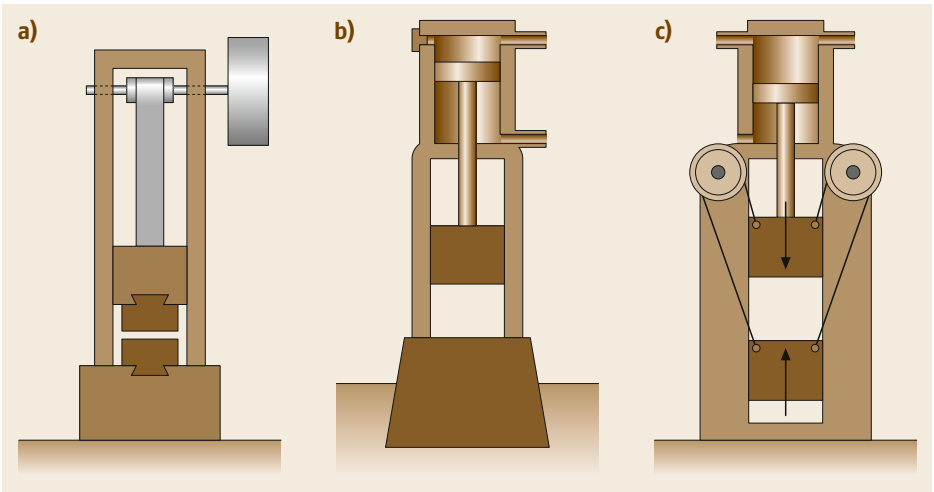

Fig. 11.96a–c Basic types of hammers: **(a)** drop hammer, **(b)** double-acting hammer, **(c)** counterblow hammer

Table 11.19 Properties of various hammers (after [11.18])

Property	Drop hammers	Double-acting hammers	Counterblow hammers
Maximum drop height (m)	1.3–2	about 1.3	–
Acceleration of ram	$< g$	$> g$	$> g$
Impact speed of ram (m/s)	3–5	3–9	5–14
Maximum nominal energy E_N (kN m)	80–160	200	1000
Blow energy equation	mgh	$mgh + pAh$	$\frac{1}{2}(m_1 + m_2)v^2$

Parameters: m: mass of ram, g: gravitational acceleration, h: drop height, p: pressure in cylinder, A: cross-sectional area of cylinder, m_1: mass of upper ram, m_2: mass of lower ram, v: speed of each ram

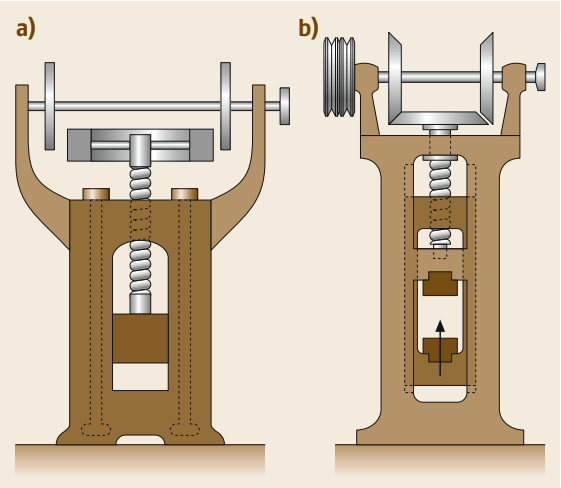

Fig. 11.97a,b Basic types of screw presses: **(a)** friction screw press, **(b)** Vincent friction screw press

Screw Presses

Screw presses are of two basic types (Fig. 11.97): presses with axially moving screw drives and presses with stationary screw drives (also called Vincent presses). The angular kinetic energy of the flywheel is transferred to the screw, which either moves the upper ram (Fig. 11.97a) or the lower die (Fig. 11.97b). In the case of Vincent presses, the frame of the press is not under load during forming. The available energy can be expressed using the rotational speed ω (in rad/s) of the flywheel and its moment of inertia I as

$$E = \frac{1}{2} I\omega^2 \,. \tag{11.121}$$

This energy is used for forming, for overcoming friction in the slides, and for elastically deforming the frame of the press.

The contact time of the dies with the workpiece is longer for screw presses than for hammers and is between 10^{-2} and 10^{-1} s. The impact speed of the dies on the workpiece ranges between 0.7 and 1 m/s. The maximum nominal energy ranges from 800 to 7500 kN m, and the maximum nominal press loads from 20 000 to 140 000 kN, depending on the drive used to accelerate the flywheel (friction, gear, electrical, or hydraulic drives). Impact loads are between 40 000 and 300 000 kN.

Compared with hammers, screw presses have a lower noise level. Because of the lower hitting speed, the strain rates are lower, yet the cooling time of the workpiece under pressure is longer. Also, for the same energy, screw presses have a flywheel mass that is about one-sixth that of the upper die of a hammer. Furthermore, the accuracy of screw presses is higher than that of hammers. A disadvantage of screw presses is, however, that their stroke rate is lower than that of hammers. Screw presses are, therefore, also used in cold calibration operations and coining in addition to hot forging.

11.5.3 Stroke-Controlled Presses

Stroke-controlled presses are also simply called mechanical presses. They all utilize a flywheel to store the necessary forming energy. Figure 11.98 shows a typical eccentric press. A slider crank mechanism is used to transfer the energy of the flywheel through the

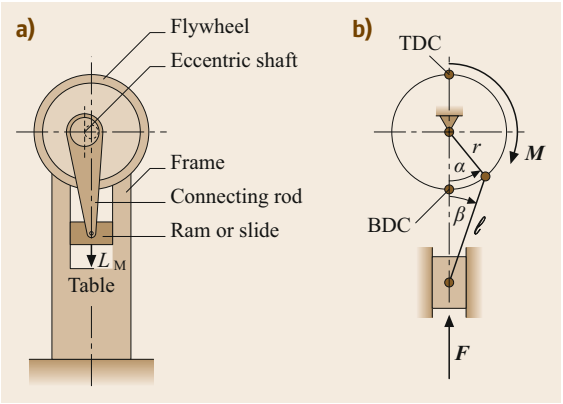

Fig. 11.98a,b A typical eccentric press **(a)** and its mechanism **(b)**

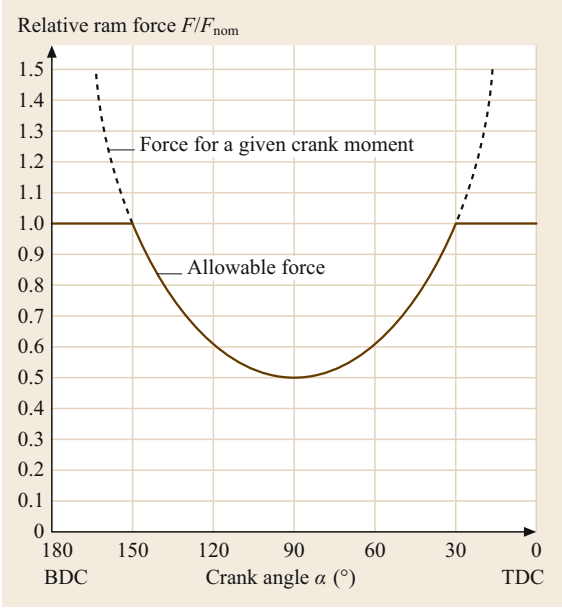

Fig. 11.99 Allowable press force as a function of crank position

crank, the connecting rod, and finally the slide to the workpiece. A slight variation on the eccentric press is the crank press, where a crank link is used instead of an eccentric shaft. These presses are sometimes differentiated by the fact that the total stroke of the crank press cannot be changed whereas the total stroke of the eccentric press is adjustable [11.21].

For crank presses, the ratio of the crank length to coupler length r/ℓ takes values between 1/15 and 1/4, so that the included angle between the coupler link and the press axis β is less than 6°. For this case, the axial ram force acting on the slider is given by

$$F(\alpha) \approx \frac{M}{r \sin \alpha} , \qquad (11.122)$$

where M is the torque supplied by the crank and r is the crank radius. The nominal force of a mechanical press is given for a crank position at 30° to its bottom dead center

$$F_{nom} = F(\alpha = 30°) . \qquad (11.123)$$

This is the highest allowable forming force for the given press. All the mechanical elements of the press are designed for this load. For various crank angles, the current allowable force and the theoretical available force are shown in Fig. 11.99. The crank angle dependence can be converted to the stroke of the press s as measured from bottom dead center using

$$s = r\left[(1 - \cos \alpha) + \frac{1}{2}\left(\frac{r}{\ell}\right) \sin^2 \alpha\right] . \qquad (11.124)$$

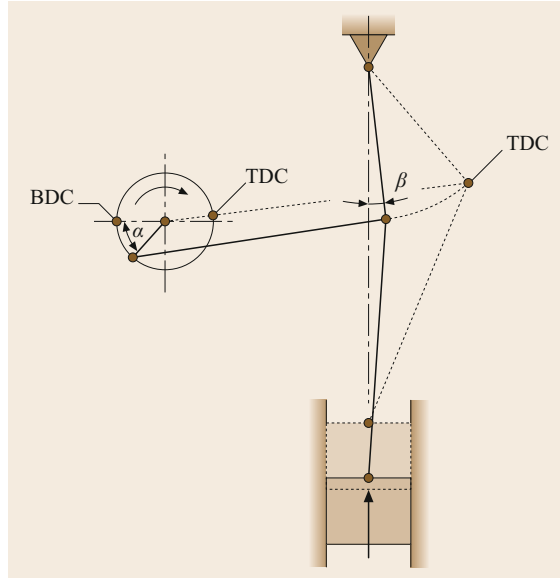

Fig. 11.100 Mechanism of a knuckle-joint press

Table 11.20 Properties of mechanical presses (after [11.18])

Property	Eccentric or crank press	Knuckle-joint press
Stroke (mm)	10–300	3–12
Nominal load (kN)	1000–16 000	1000–16 000
Stroke rate (strokes/min)	10–100	20–200

If the total stroke of the press is denoted by S (= $2r$), then the stroke for which the nominal force is available corresponds to 7.3% of S for r/ℓ = 0.1. Beyond this rather small stroke, the available ram force decreases rapidly.

Another force–stroke characteristic is found for knuckle-joint (toggle) presses (Fig. 11.100). The six-link mechanism employed in this press provides the nominal force over a much smaller stroke than in crank presses, so that they are suitable basically for processes with force maximums toward the end of the stroke, requiring also short strokes. Despite this disadvantage, the velocity characteristic of toggle presses is superior to crank presses, since they are faster over a long stroke but slower towards the dead centers, i.e., in the forming regime, than crank presses (Table 11.20).

A recent development in press technology is the servomotor press [11.21]. One or multiple servomotors are used to drive a crank or toggle mechanism. The obvious advantage of the servomotor press is the almost limitless control of the press. Current limitations are the available motor torques and hence forming forces, since the forming energy must be supplied instantaneously. Despite this disadvantage, 1000-t presses are expected to be available in the near future.

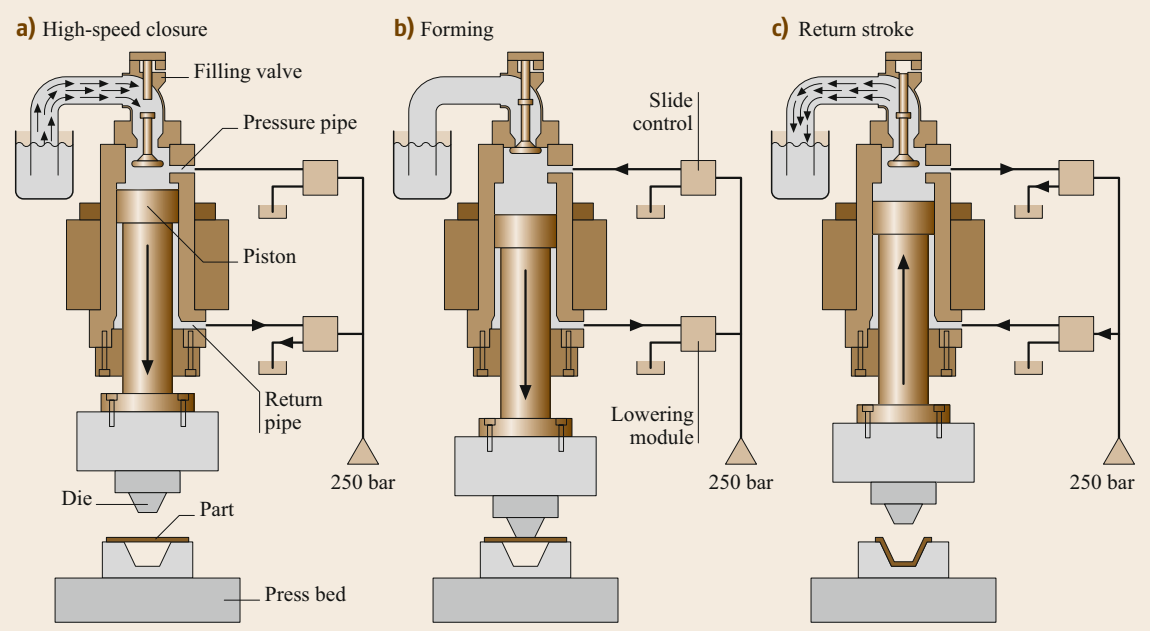

Fig. 11.101a–c Working principle of a hydraulic press: **(a)** high-speed closure, **(b)** forming, **(c)** return stroke (after [11.32])

11.5.4 Force-Controlled Presses

Hydraulic presses supply the nominal forming force independently of the stroke. Figure 11.101 shows the basic working principle of a hydraulic press: A pump converts electrical energy into hydraulic energy, which is finally converted into mechanical energy. A cylinder in the die closure phase is pressurized by hydraulic fluid from a reservoir with high flow rates. This fluid is usually oil. This oil is compressible such that a 0.7–0.8% volume change occurs per 100 bar pressure. After the dies are closed, control of the cylinder is passed to the slide control for the forming action. The cylinder is returned by reversing the fluid flow into the lowering cylinder. Hydraulic presses have the advantage that the whole cycle of die closure/forming/punch reversal can be programmed efficiently and individually. Therefore, these press types are appropriate for many forming processes, such as sheet forming, cold forging, and especially hot forging and hot extrusion.

The basic characteristic parameter of a hydraulic press is the nominal forming force, which can be found from the hydraulic pressure p and the cross-sectional area of the cylinder A as

$$F_{\text{nom}} = pA \,. \tag{11.125}$$

The hydrostatic pressure is up to 320 bar. In contrast to mechanical presses, there is no energy reservoir, so the energy necessary for forming must be supplied instantaneously by the pump. This pump power P is given by

$$P = \frac{1}{\eta_{\text{total}}} p\dot{V} \,, \tag{11.126}$$

where $\dot{V}$ is the volumetric flow rate of the fluid and η_{total} is the total efficiency of the hydraulic system including mechanical and electrical losses. The maximum flow rates are $\approx 185\,\text{L/min}$.

References

11.1 K. Lange (Ed.): *Handbook of Metal Forming* (McGraw-Hill, New York 1985)

11.2 K. Lange (Ed.): *Umformtechnik, Band 1: Grundlagen*, 2nd edn. (Springer, Berlin 1984), in German

11.3 W.D. Callister Jr.: *Materials Science and Engineering* (Wiley, New York 1990)

11.4 ICFG: *ICFG Document No. 11/01: Steels for Cold Forging* (Meisenbach, Bamberg 2001)

11.5 R. Hill: *The Mathematical Theory of Plasticity* (Oxford Univ. Press, Oxford 1950)

11.6 L.E. Malvern: *Introduction to the Mechanics of a Continuous Media* (Prentice-Hall, Englewood Cliffs 1969)

11.7 K. Pöhlandt: *Materials Testing for the Metal Forming Industry* (Springer, Berlin 1989)

11.8 E. Doege, H. Meyer-Nolkemper, I. Saeed: *Fliesskurvenatlas metallischer Werkstoffe* (Hanser, München 1986), in German

11.9 R. Kopp, H. Wiegels: *Einführung in die Umformtechnik* (Augustinus, Aachen 1998), in German

11.10 W.F. Hosford, R.M. Caddell: *Metal Forming. Mechanics and Metallurgy*, 2nd edn. (Prentice-Hall, Englewood Cliffs 1993)

11.11 H. Ismar, O. Mahrenholtz: *Technische Plastomechanik* (Vieweg, Braunschweig 1979), in German

11.12 W. Johnson, P.B. Mellor: *Engineering Plasticity* (Van Nostrand Reinhold, Berkshire 1973)

11.13 B. Avitzur: *Metal Forming Processes and Analysis* (McGraw-Hill, New York 1968)

11.14 T. Wanheim: Physikalische Prozeßanalyse und -simulation mit nichtmetallischen Modellwerkstoffen. In: *Umformtechnik, Band 4: Sonderverfahren, Prozeßsimulation, Werkzeugtechnik, Produktion*, 2nd edn., ed. by K. Lange (Springer, Berlin 1993), in German

11.15 D. Banabic, H.-J. Bunge, K. Pöhlandt, A.E. Tekkaya: *Formability of Metallic Materials* (Springer, Berlin 2000)

11.16 K. Lange (Ed.): *Umformtechnik, Band 2: Massivumformung*, 2nd edn. (Springer, Berlin 1988), in German

11.17 VDI: *VDI 3171 Kaltmassivumformen, Stauchen, Formpressen* (VDI, Düsseldorf 1958), in German

11.18 H. Tschätsch: *Praxiswissen Umformtechnik* (Vieweg, Braunschweig 1997), in German

11.19 K. Lange, H. Meyer-Nolkemper: *Gesenkschmieden* (Springer, Berlin 1977), in German

11.20 S. Kalpakjian, S.R. Schmid: *Manufacturing Engineering and Technology* (Prentice-Hall, New Jersey 2001)

11.21 T. Altan, G. Ngaile, G. Shen: *Cold and Hot Forging. Fundamentals and Applications* (ASM Int., Materials Park 2004)

11.22 T. Altan, S. Oh, H. Gegel: *Metal Forming. Fundamentals and Applications* (ASM Int., Materials Park 1983)

11.23 ICFG: ICFG Document No. 4/82: General aspects of tool design and tool materials for cold and warm forging. In: *ICFG 1967–1992: Objectives, History, Published Documents* (Meisenbach, Bamberg 1992)

11.24 B. Avitzur: *Handbook of Metal Forming Processes* (Wiley, New York 1983)

11.25 A.E. Tekkaya: *Ermittlung von Eigenspannungen in der Kaltmassivumformung* (Springer, Berlin 1986), in German

11.26 G. Spur, T. Stöferle: *Handbuch der Fertigungstechnik. Band 2/1 Umformen* (Hanser, München 1983), in German

11.27 Z. Marciniak, J.L. Duncan, S.J. Hu: *Mechanics of Sheet Metal Forming* (Butterworth-Heinemann, Oxford 2002)

11.28 S.S. Hecker: A cup test for assessing stretchability, Met. Eng. Q. **14**, 30–36 (1974)

11.29 K. Lange (Ed.): *Umformtechnik, Band 3: Blechbearbeitung*, 2nd edn. (Springer, Berlin 1990), in German

11.30 CIRP: *Dictionary of Production Engineering. Metal Forming 1* (Springer, Berlin 1997)

11.31 Z. Marciniak, J.L. Duncan: *Mechanics of Sheet Metal Forming* (Arnold, London 1992)

11.32 Schuler GmbH: *Metal Forming Handbook* (Springer, Berlin 1998)

11.33 F. Dohmann, C. Hartl: Hydroforming – A method to manufacture light-weight parts, J. Mater. Process. Technol. **60**, 669–676 (1996)

A. Erman Tekkaya

Institut für Umformtechnik und Leichtbau
Technische Universität Dortmund
Dortmund, Germany
erman.tekkaya@udo.edu

Professor Tekkaya completed his doctoral thesis at the University of Stuttgart in 1985. Until 2005 he was Professor at the METU, Ankara. From 2005 he was the Chairman of the Department of Manufacturing at ATILIM University in Ankara, Turkey. From 2007 he was Director of the Institute of Forming Technology and Lightweight Components at the TU Dortmund University. His current research is on numerical simulation of sheet/bulk metal forming processes and material characterization. He is a fellow of CIRP and member of the International Cold Forging Group (ICFG).

12. Machining Processes

Bernhard Karpuschewski, Gerry Byrne, Berend Denkena, João Oliveira, Anatoly Vereschaka

In this handbook, machining processes are seen in the first place as material removal processes. Any surplus material is removed from a solid object (workpiece) either in the form of small pieces (e.g., chips) or by chipless processes based on e.g., evaporation. To achieve this kind of material removal different tools are mandatory, thus generating surfaces by relative motions between the workpiece and tool provided by the respective machine tool. The following chapter is structured in three major subgroups:

Cutting with geometrically well-defined tool edges
These processes are widely used for material removal in any kind of industrial application. The most prominent processes are turning, drilling, and milling, but also less prominent processes like planning and shaping, broaching, and sawing will be discussed.

Cutting with geometrically undefined tool edges
The tools of this group of processes cannot be described with simple geometrical quantities, because they consist of thousands of small abrasive grains in a bonded structure or as loose grains, but they still generate chips during material removal. The most prominent processes are grinding, honing, lapping, and jet-based applications.

Nonconventional machining (chipless) processes
In chipless machining material, particles are removed from a solid object by nonmechanical means, i.e., by electrical discharges, electrochemical machining, or high-energy beams (laser or electron beams).

12.1 **Cutting** 410
12.1.1 Fundamentals 410
12.1.2 Turning 413
12.1.3 Drilling and Reaming 417
12.1.4 Milling 421
12.1.5 Other Processes: Planing and Shaping, Broaching, Sawing 427
12.1.6 Cutting Tool Materials 429
12.1.7 Tooling 433
12.1.8 Microcutting 433
12.1.9 High-Speed Cutting 435
12.1.10 Hard Machining 436

12.2 **Machining with Geometrically Nondefined Tool Edges** 437
12.2.1 Fundamentals 437
12.2.2 Grinding with Rotating Tools 439
12.2.3 Belt Grinding 443
12.2.4 Honing, Superfinishing 445
12.2.5 Other Processes: Inside Diameter Cut-Off Grinding, Lapping, and Abrasive Waterjet Cutting 446

12.3 **Nonconventional Machining Processes** 448
12.3.1 Electro-Discharge Machining (EDM) 448
12.3.2 Electrochemical Machining 450
12.3.3 Ultrasonic Machining 451
12.3.4 Beam Machining 451
12.3.5 Combined Methods of Machining 455

References 456

In material removal processes, surplus material is removed from a solid object (workpiece) in the form of small pieces (e.g., chips) by means of tools, thus generating surfaces by relative motions between the workpiece and tool provided by the machine tool.

The material removal processes that will be discussed in this section can be divided into three subgroups:

- Cutting with geometrically well-defined tool edges
- Cutting with geometrically undefined tool edges
- Nonconventional machining (chipless) processes.

Cutting is accomplished with the mechanical action of a tool on a workpiece. In chipless machining, material particles are removed from a solid object by nonmechanical means.

K.-H. Grote, H. Hefazi (Eds.), *Springer Handbook of Mechanical Engineering*, Springer Handbooks,
https://doi.org/10.1007/978-3-030-47035-7_12

12.1 Cutting

12.1.1 Fundamentals

During a cutting process particles of material are mechanically removed as chips from a blank or a workpiece by the cutting action of a tool. In machining with geometrically well-defined tool edges, the number of cutting edges, the geometry of the tool, and the position of the cutting edges in relation to the workpiece are known and describable (as opposed to cutting with geometrically undefined tool edges, e.g., grinding).

Figure 12.1 [12.1] illustrates the important processes of this group. The processes differ according to the cutting motion (cutting speed v_c), the feed motion (feed speed v_f), and the resulting effective motion (effective cutting speed v_e). Feed and cutting direction vectors span the working plane. The angle between these two vectors is called the feed motion angle φ, while the angle between the effective direction and the cutting direction is called the effective cutting speed angle η. The following equation applies for all processes

$$\tan\eta = \frac{\sin\varphi}{\frac{v_c}{v_f} + \cos\varphi} \,. \tag{12.1}$$

The mechanical process of separation of material parts from the workpiece, i.e., chip formation, can be described by the example of an orthogonal process (two-dimensional deformation). The wedge is described by the rake angle γ, the clearance angle α, and the edge radius r_B. The wedge penetrates into the working material, which is plastically deformed. Figure 12.2 [12.2] shows the zones of plastic deformation in continuous chip formation. Five effective zones can be distinguished.

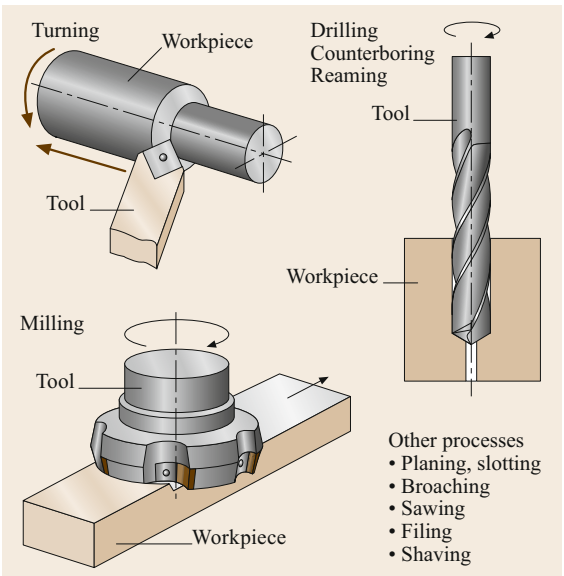

Fig. 12.1 Cutting processes (machining with geometrically well-defined tool edges) [12.1]

The primary shear zone comprises the actual area of chip formation by shearing. In the secondary shear zones in front of the rake and flank face, friction forces act between the tool and the workpiece, causing plastic deformation of these material layers. In the zone in front of the deformation area, chip formation results in stresses that lead to plastic and elastic deformations. In the pressure and cutting zone, the material is deformed and separated under high compressive stresses.

In the course of these processes, the undeformed chip thickness h gives way to the chip thickness h' with the resultant chip compression ratio being $\lambda_h = h'/h$. The shear plane comprises the shear angle ϕ with the cutting speed vector. The deformation angle χ characterizes the shearing of a small part that has passed through the shear plane.

The following chip types can be distinguished: in continuous chip formation the chip slides off over the rake face at a constant speed in a stationary flow. Periodical changes in the intensity of the deformation may occur, mainly at higher cutting speeds. Lamellae are formed in the chip that can reach as far as material separation and the formation of chip segments.

Segmented chip formation is the discontinuous formation of a still continuous chip that, however, shows recognizable differences in the degree of deformation along the direction of flow. Especially negative tool-orthogonal rake angles, but also greater undeformed chip thicknesses, as well as very slow and very fast cutting speeds can result in segmented chip formation. The chip formation is uneven.

Discontinuous chip formation occurs in working materials that possess only a small ability to deform, such as cast iron with graphite lamellae. The parting surface between the chip and the workpiece proceeds irregularly.

Built-up edges can form in ductile, work-hardening materials at low cutting speeds and sufficiently continuous chip formation. Parts of the working material that have been strongly deformed and cold-hardened in the area of the compression zone weld under high pressure at the rounded cutting edge to the chip surface, thus becoming a part of the cutting tip.

The forces acting on the tool in orthogonal cutting can be represented by *Ernst* and *Merchant*'s force cir-

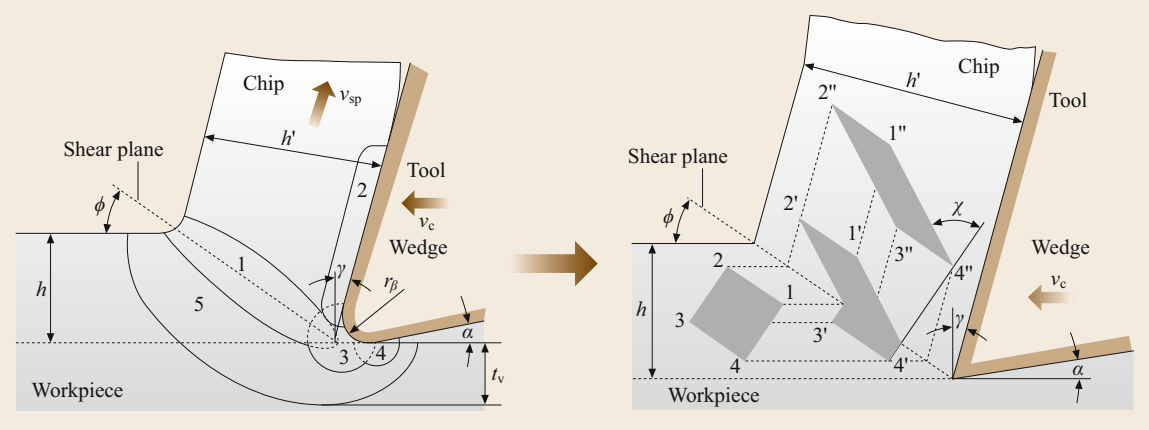

Fig. 12.2 Effective zones in chip formation (*left*) and derived model of deformation (*right*) in the shear plane. 1: Primary shear zone, 2: secondary shear zone at the rake face, 3: secondary shear zone at the cutting edge, 4: secondary shear zone at the flank face, 5: deformation advance zone, χ: deformation angle $\tan\chi = \tan(\phi-\gamma)+1/\tan\phi$, ϕ: shear angle $\tan\phi = \cos\gamma/(\lambda_h - \sin\gamma)\lambda_h = h'/h$, γ: rake angle, α: clearance angle, t_v: deformation depth

cle as shown in Fig. 12.3 [12.3]. The resultant force F_z has two components, F_c and F_p. The cutting force F_c in the direction of the tool path determines the amount of work done in cutting. The thrust force F_p, together with F_c, produces deflections of the tool. The resultant force has two components on the shear plane: $F_{T\varphi}$ is the force required to shear the metal along the shear plane, and $F_{N\varphi}$ is the normal force on this plane. Two other force components on the face of the tool are also represented: the friction force $F_{T\gamma}$ and the normal force $F_{N\gamma}$. From the geometries within the circle, the following relationships can be derived.

The frictional force on the tool rake face

$$F_{T\gamma} = F_p\cos\gamma + F_c\sin\gamma\,. \tag{12.2}$$

The coefficient of friction at the tool–chip interface

$$\mu = \frac{F_p + F_c\tan\gamma}{F_c - F_p\tan\gamma}\,. \tag{12.3}$$

The shear stress in the shear plane, where $A_0 = hw$ is the undeformed chip cross section, and w is the width of the cut

$$\tau = \frac{F_c\sin\varphi\cos\varphi - F_p\sin^2\varphi}{A_0}\,. \tag{12.4}$$

In the chip formation zone, the cutting energy applied, E_c, is completely converted. It can be calculated from

$$E_c = F_c l_c\,, \tag{12.5}$$

where F_c is the cutting force, and l_c is the travel length in the cutting direction.

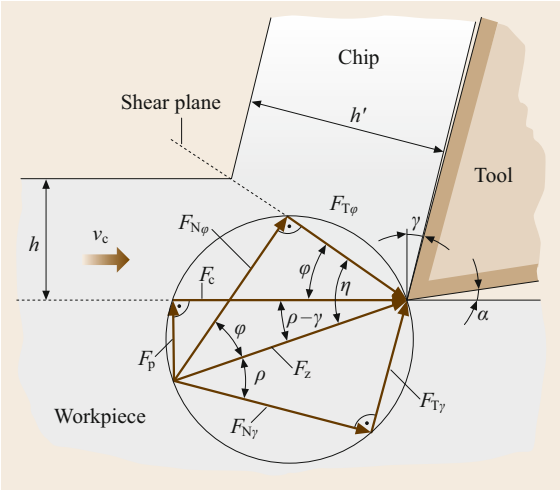

Fig. 12.3 Ernst and Merchant's force circle

The cutting energy is composed of deformation and shear energy E_φ, friction energy at the rake face E_γ, friction energy at the flank face E_α, surface energy for the formation of new surfaces E_τ, and kinetic energy due to chip deflection E_M.

The energy converted during machining one unit of volume is

$$e_c = \frac{E_c}{V_w}\,, \tag{12.6}$$

where e_c is the specific energy, and V_w is the volume of material removed. Like E_c, itself, its individual components can be expressed in relation to V_w.

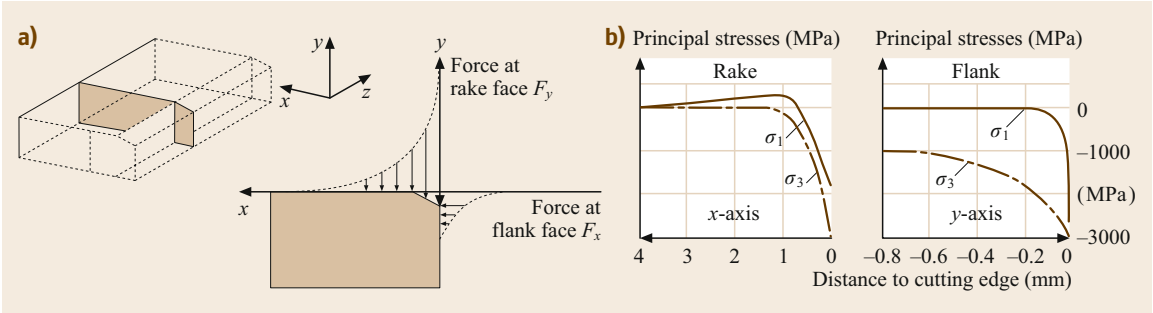

Fig. 12.4a,b Load distribution due to mechanical stress perpendicular to the major cutting edge. **(a)** Surface forces beneath the rake and flank face surfaces; **(b)** principal stresses at rake and flank face

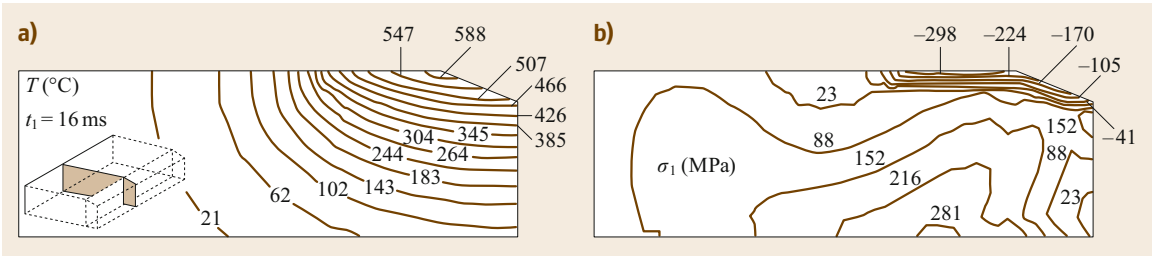

Fig. 12.5a,b Temperature **(a)** and stress distribution **(b)** during constant heat flow to the ceramic cutting tool

From the specific energy e_c the specific cutting force k_c can be derived as a characteristic value for calculating the cutting force

$$k_c = \frac{F_c}{A} = \frac{F_c}{hb}\,, \tag{12.7}$$

where A is the undeformed chip cross section, b is the undeformed chip width, and h is the undeformed chip thickness

$$e_c = \frac{E_c}{V_w} = \frac{P_c}{Q_w} = \frac{F_c v_c}{A v_c} = k_c\,, \tag{12.8}$$

where P_c is the cutting power, Q_w is the material removal rate, and F_c is the cutting force.

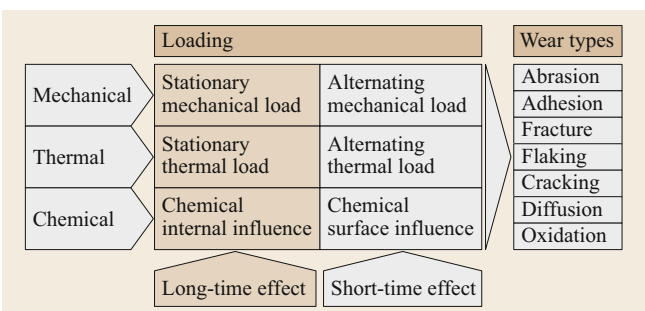

Fig. 12.6 Loading and wear types of cutting tools

Estimation shows that the largest amount of cutting energy is converted into deformation and frictional energy. Thus, the specific cutting force k_c can be seen as an energy-related variable (the application and determination of k_c will be dealt with in more detail in Sect. 12.1.2). The energy introduced into the chip formation zone is almost entirely converted into heat, the minor amount being transformed into residual stress in the chip and in the workpiece (spring energy). Due to this process high temperatures in the cutting edge arise, introducing mechanical and thermal load into this area. Surface forces beneath the rake and flank face surfaces and the principal stresses that can be calculated thereby are shown in Fig. 12.4 [12.2].

Figure 12.5 [12.2] represents the temperature distribution on a highly-loaded ceramic indexable insert and the resulting thermally-induced tensile stresses. These tensile stresses are particularly critical for high-temperature ceramic cutting materials. Mechanical and thermal loads supported by chemical reactions may cause significant wear.

The characteristics of worn cutting tools can be described by different types of wear (Fig. 12.6; [12.2]):

- Fractures and cracks arise in the area of the cutting edge because of mechanical or thermal overload.

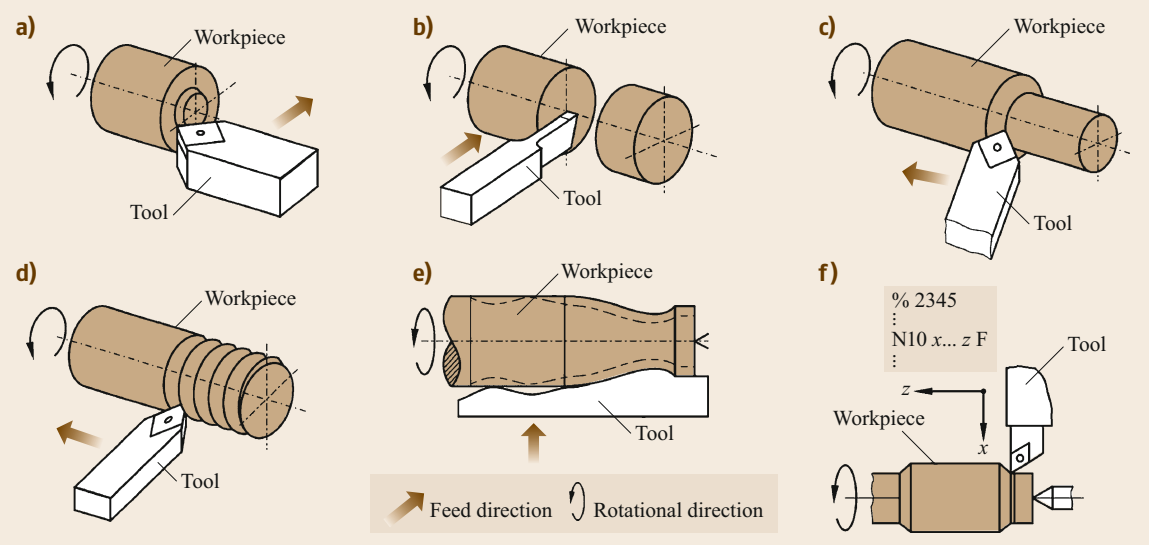

Fig. 12.7a–f Turning processes: **(a)** facing, **(b)** parting-off, **(c)** longitudinal turning, **(d)** thread turning, **(e)** profile turning (tool contour is duplicated in workpiece), **(f)** form turning [12.4]

- Mechanical abrasion (frictional wear) is mainly caused by hard inclusions such as carbides and oxides in the working material.
- Plastic deformation occurs if the cutting material offers inadequate resistance to deformation but provides sufficient toughness.
- Adhesion is the shearing off of pressure-welding areas between the working material and the chip, whereby the point of shearing is located in the cutting material.
- Diffusion occurs at high cutting speeds and mutual solubility of the cutting material and the working material. The cutting material is weakened by chemical reactions, dissolves, and is removed.
- Oxidation also occurs only at high cutting speeds. By contact with oxygen in the air the cutting material oxidizes, and the structure is weakened.

The machinability of a workpiece is determined by the composition of the workpiece material, its structural configuration in the machined area, its previous casting or forging process, and its heat treatment. Machinability is evaluated considering the following criteria:

- Tool wear
- Surface quality of the workpiece
- Machining forces
- Chip form.

For the evaluation of an individual criterion, the machining task must be considered.

12.1.2 Turning

Turning is defined as machining with a continuous (usually circular) cutting motion and any desired feed motion in a plane perpendicular to the cutting direction. The turning axis of the cutting motion keeps its position relative to the workpiece independently of the feed motion. Figure 12.7 [12.4] shows some important turning processes.

In the following, longitudinal cylindrical turning is taken as an example of a turning process. Terminology, names, and designations for geometrical descriptions of the cutting processes can be found in ISO 3002/1 [12.5]. Figure 12.8 [12.2] shows the surfaces and cutting edges defined for the cutting tip.

The angles represented in Fig. 12.9 [12.6] serve to determine the position and shape of the tool in three dimensions. The tool cutting edge angle κ is the angle between the primary cutting edge plane and the working plane. The tool included or edge angle ε is the angle between the primary and secondary cutting edge planes and is given by the cutting edge geometry. The tool cutting edge inclination λ is the angle between the cutting edge and the reference plane and is apparent when looking down onto the primary cutting edge. The clearance angle α, wedge angle β, and rake angle γ can be measured in the tool-orthogonal plane and make up 90° in sum. The values of the relevant tool angles are determined from approximate value tables in relation to the workpiece and cutting materials and the machining process. The tool cutting edge angle κ influences the shape

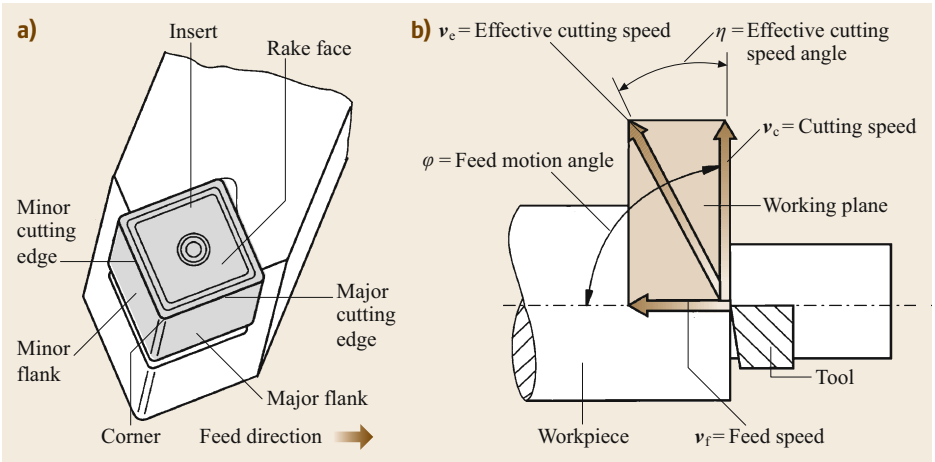

Fig. 12.8a,b Terminology at cutting tip and directions of motion of tool (ISO 3002/1). **(a)** Surfaces; **(b)** motion vectors

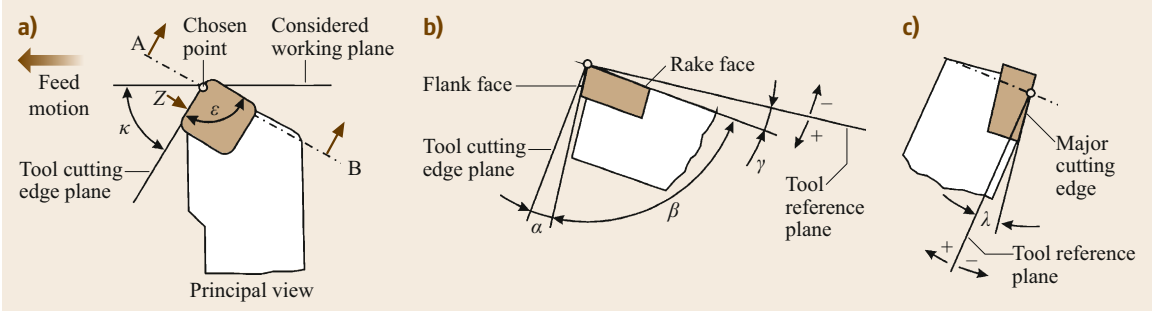

Fig. 12.9a–c Single-point cutting tool angles [12.6]. **(a)** Principal view; **(b)** A–B (tool-orthogonal plane); **(c)** view *Z* (on tool cutting edge plane)

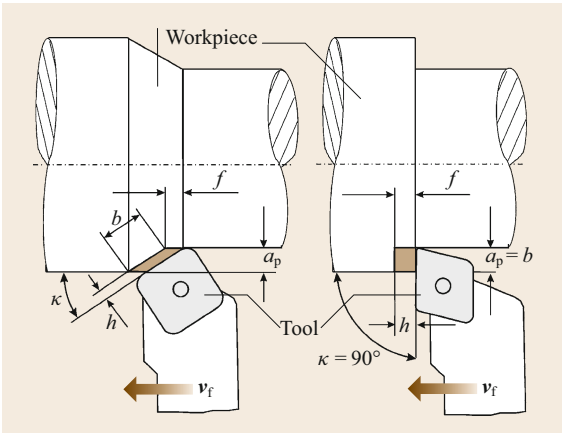

Fig. 12.10 Cut and chip variables in turning; $A = a_p f = bh$, $h = f \sin\kappa$, $b = a_p / \sin\kappa$, $a_e = f$, with A = chip cross section, a_p = depth of cut, f = feed, b = chip width, h = chip thickness, v_f = feed speed, κ = tool cutting edge angle, a_e = width of cut

of the undeformed chip cross section to be removed and, thus, the power required for the machining process (Fig. 12.10; [12.2]).

The bulk volume Q' of the chips flowing over the rake face of the tool varies depending on chip type and form. The characteristic parameter is the chip volume ratio RZ specifying the relationship between the removed chip volume in a given time Q' (bulk chip volume) and the material removal rate Q_w. In this case,

$$RZ = \frac{Q'}{Q_w} , \tag{12.9}$$

$$Q_w = a_p F_c = a_p f D \pi n . \tag{12.10}$$

The chip volume ratio RZ characterizes the *bulkiness* of the chips. It serves to determine the machine tool working spaces, the chip conveying devices, and chip spaces in the cutting tools. The chip volume ratio can amount to very different values according to the chip form (Table 12.1; [12.7]). The more brittle the material,

Table 12.1 Chip shapes, their related chip volume ratio ($RZ = Q'/Q_w$), and rating

Chips	Chip shape	*RZ*	Rating
Ribbon chips	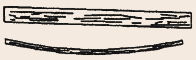	≥ 90	Not positive
Snarled chips	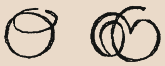	≥ 90	Not positive
Flat helical chips	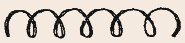	≥ 50	Not positive
Cylindrical chips		≥ 50	Not positive
Helical chip segments		≥ 25	Good
Spiral chips		≥ 8	Good
Spiral chip segments		≥ 8	Acceptable
Discontinuous chips		≥ 3	Acceptable

the lower this value. Brittleness can be influenced via the composition of the material. For steel, higher sulfur contents (more than 0.04%, free cutting steel with 0.2% S) have a beneficial effect. However, this may impair the toughness of the material in the transverse direction, depending on the form of the dispersed sulfides. Chip breakers ground into the chip surface, sintered in, or attached with the clamping system of inserts cause additional chip deformation, i.e., an additional material load in the chip. The chip is bent by contact with the cut surface of the workpiece or the flank face of the tool and breaks (secondary chip breaking in contrast to segmented or discontinuous chip formation, where the chips leave the chip formation zone as small fragments). Favorable chip forms can also be achieved by selecting the appropriate machine setting data such as feed rate and depth of cut [12.8].

Each material provides resistance towards the penetration of the tool during chip removal. This has to be overcome by means of a force, the resultant force F_z. This force is analyzed by resolving it into its three components (Fig. 12.11; [12.9]). The active force F_a is formed by the cutting force F_c in the direction of the cutting motion together with the feed force F_f. The passive force F_p does not contribute to power conversion, because no motion between the tool and the workpiece takes place in its direction. Thus,

$$F_z = F_a + F_p = F_c + F_f + F_p \,. \tag{12.11}$$

The cutting force related to the area of the undeformed chip is defined as the specific cutting force k_c

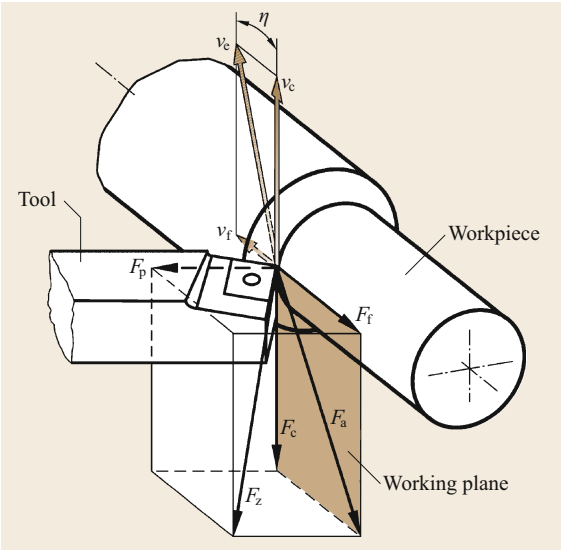

Fig. 12.11 Components of the cutting force (after [12.9])

and depends on a variety of factors

$$k_c = \frac{F_c}{hb} = \frac{F_c}{a_p f} \,. \tag{12.12}$$

It is known from experiments that the specific cutting force k_c is a function of the undeformed chip thickness h. From the logarithmic representation (Fig. 12.12; [12.2]), it can be seen that

$$k_c = k_{c1.1} \left(\frac{h}{h_0} \right)^{-m_c} \,. \tag{12.13}$$

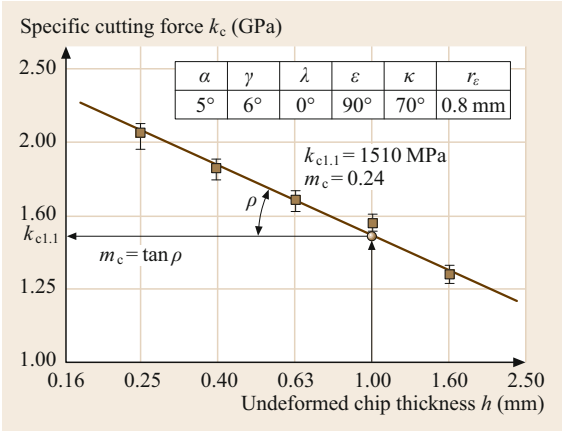

Fig. 12.12 Specific cutting force as a function of undeformed chip thickness. Workpiece material: 20 MnCr5 BG, (1.7147 BG); cutting speed: $v_c = 100\,\mathrm{m/min}$; depth of cut: $\alpha_p = 3\,\mathrm{mm}$; cutting material: HM P10

Here, $k_{c1.1}$ is the unit specific cutting force, i.e., k_c at $h = 1\,\mathrm{mm}$ (indices 1.1 due to $k_{c1.1} = F_c/1.1$ at $b = h = 1\,\mathrm{mm}$). The quantity m_c indicates the increase and is the exponent of the specific cutting force. This equation is named *Kienzle*'s cutting force formula in honor of the initial researcher [12.10] and can also be written as

$$F_c = k_{c1.1} b h^{1-m_c}\,; \tag{12.14}$$

$k_{c1.1}$ and $1 - m_c$ are listed for various ferrous materials in Table 12.2. A direct comparison of the $k_{c1.1}$ values of different materials to indicate the machinability or the energy required for machining is not acceptable, as the exponent m_c can vary significantly. From $m_c < 1$, it follows that at a given cross-sectional area the cutting force and power requirements increase with decreasing undeformed chip thickness. This can be explained physically by the higher share of friction at decreasing undeformed chip thicknesses (Sect.12.1.1).

In addition to the working material and the undeformed chip thickness, k_c depends on further factors as well. Therefore, additional influencing factors will be specified. The correction factors considering the cutting speed K_v, the rake angle K_γ, the cutting material K_{CM}, the tool wear K_{TW}, the cooling lubricant K_{CL}, and the workpiece shape K_{WS} are given in Table 12.3.

The passive force F_p (Fig. 12.11; [12.9]), which is not relevant for the power balance due to its perpendicular orientation, is of importance for the size and form accuracy of the system—machine/workpiece/tool/fixture. Passive force F_p and feed force F_f can be merged to a thrust force F_D. For thin undeformed chip cross sections (bh), the resultant cutting force is perpendicular to the primary cutting edge. From this it follows that

$$\frac{F_f}{F_p} = \tan\kappa\,. \tag{12.15}$$

For normal values of h and b it can be approximated that

$$F_D \approx (0.65 - 0.75) F_c\,, \tag{12.16}$$

wherein F_f and F_p have to be determined.

The exponential functions corresponding to the cutting force formula can be used for a more exact determination. Exponents and the unit-specific cutting force are given in Table 12.2.

The surface finish is determined by the profile of the cutting edge that is creating the workpiece surface and by the feed. From the shaping of the cutting edge corner radius r_ε, the theoretical maximum roughness Rz, th according to EN ISO 4287 [12.11] can be geometrically determined as

$$Rz,\mathrm{th} = \frac{f^2}{8 r_\varepsilon}\,. \tag{12.17}$$

This value should be regarded as a minimum for the surface roughness, which increases due to vibrations, especially at higher rotational and cutting speeds, on the formation of built-up edges (Sect. 12.1.1), and with the progressive wear of the cutting edge.

The tool is subject to mechanical stress due to the machining force, thermal stress due to heating, and chemical attack due to the interaction of the cutting material, the workpiece material, and the surrounding medium. This results in wear on the cutting tool (Sect. 12.1.1). Typical forms of wear are illustrated in Fig. 12.13 [12.12]. In addition, cutting edge wear, rounding of the cutting edge, and scoring may occur on the secondary cutting edge. The type of wear that determines the end of tool life (tool-life criterion) is determined by the respective use. Weakening of the cutting edge by crater wear or an increase in the share of friction in the resultant force due to flank wear are critical in roughing. Cutting edge wear leads to changes in workpiece dimensions, and flank wear or scoring impair surface quality and determine the end of tool life in finishing. Often the lifetime end is set at $V_B = 0.4\,\mathrm{mm}$ or $KT = 0.1\,\mathrm{mm}$. The flank is divided into three zones for more precise identification of the wear.

For a specific cutting material–workpiece-material combination and a given tool-life criterion, the tool life depends mainly on the cutting speed according to an exponential function (Taylor's equation shown on a straight line on a log–log graph) [12.13]

$$\frac{T}{T_0} = \frac{v_c^k}{C}\,. \tag{12.18}$$

Table 12.2 Values for Kienzle's cutting force formula for ferrous materials $k_{c1.1}$ and $1-m_c$

Cutting conditions		**Cutting edge geometry**						
			α (°)	γ (°)	λ (°)	ε (°)	κ (°)	r_ε (mm)
Cutting speed	$v_c = 100$ m/min	Steel	5	6	0	90	70	0.8
Depth of cut	$a_p = 3.0$ mm	Cast iron	5	2	0	90	70	0.8
Cutting material	Cemented carbide P10							
Material	**Material number**	R_m (N/mm^2)	**Specific machining forces** $k_{i_{1.1}}$					
			$k_{c1.1}$	$1-m_c$	$k_{f1.1}$	$1-m_f$	$k_{p1.1}$	$1-m_p$
St 50-2	1.0050	559	1499	0.71	351	0.30	274	0.51
St 70-2	1.0070	824	1595	0.68	228	–0.07	152	0.10
Ck45N	1.1191 N	657	1659	0.79	521	0.51	309	0.60
Ck45V	1.1191 V	765	1584	0.74	364	0.27	282	0.57
40Mn4V	1.1157 V	755	1691	0.78	350	0.31	244	0.55
37MnSi5V	1.5122 V	892	1656	0.79	239	0.31	249	0.67
18CrNi8BG	1.5920 BG	618	1511	0.80	318	0.27	242	0.46
34CrNiMo6V	1.6582 V	1010	1686	0.82	291	0.37	284	0.72
41Cr4V	1.7035 V	961	1596	0.77	291	0.27	215	0.52
16MnCr5N	1.7131 N	500	1411	0.70	406	0.37	312	0.50
20MnCr5N	1.7147 N	588	1464	0.74	356	0.24	300	0.58
42CrMo4V	1.7225 V	1138	1773	0.83	354	0.43	252	0.49
55NiCrMoV6V	1.2713 V	1141	1595	0.71	269	0.21	198	0.34
100Cr6	1.2067	624	1726	0.72	318	0.14	362	0.47
GG30	JL1050	HB = 206	899	0.59	170	0.09	164	0.30

Table 12.3 Correction factors for cutting force calculation

Cutting speed correction factor	$K_v = \frac{2.023}{v_c^{0.153}}$ for $v_c < 100$ m/min $K_v = \frac{1.380}{v_c^{0.07}}$ for $v_c > 100$ m/min
Rake angle correction factor	$K_\gamma = 1.09 - 0.015\,\gamma$ (steel) $K_\gamma = 1.03 - 0.015\,\gamma$ (cast iron)
Cutting material correction factor	$K_{CM} = 1.05$ (HSS) $K_{CM} = 1.0$ (cemented carbide) $K_{CM} = 0.9$–0.95 (ceramic)
Tool wear correction factor	$K_{TW} = 1.3$–1.5 $K_{TW} = 1.0$ for sharp cutting edge
Cutting fluid correction factor	$K_{CL} = 1.0$ (dry) $K_{CL} = 0.85$ (nonwater-soluble coolant) $K_{CL} = 0.9$ (emulsion-type coolant)
Workpiece shape correction factor	$K_{WS} = 1.0$ (outer diameter turning) $K_{WS} = 1.2$ (inner diameter turning)

Here, T_0 and v_c are reference values; T_0 is normally set at $T_0 = 1$ min, and C is the cutting speed for an operating period of $T_0 = 1$ min.

The Taylor straight line is plotted on the basis of a wear/tool-life turning test according to [12.12]. With these tests, suitable settings for high-speed steel, hard metals of all machining application categories, and ceramic inserts have been determined. It is usually sufficient to determine the width of the flank wear land VB and/or the crater depth KT, as well as the distance from the crater center to the point of the cutting tip. Table 12.4 shows normal values of the gradient exponent k and the cutting speed C for a tool life of $T = 1$ min and a width of wear land of $VB = 0.4$ mm for various materials.

For metal cutting machines, the optimum cutting speed must be established to meet economical criteria (Fig. 12.14; [12.2]). The optimum cutting speed in relation to time is expressed by

$$v_{c,opt} = C(-k-1)t_{CT}^{1/k}\,. \tag{12.19}$$

Optimization of the cutting speed to minimize unit costs takes into account not only the tool changing time t_{CT} but also the tool costs per cutting edge K_{CT} and the hourly machine tool rate K_M

$$v_{c,opt} = C(-k-1)\left(t_{CT}, +, \frac{K_{CT}}{K_M}\right)^{\frac{1}{k}}\,. \tag{12.20}$$

12.1.3 Drilling and Reaming

Drilling is a metal-cutting process with a rotary cutting motion (primary motion). The tool, i.e., the drill, performs the feed motion in the direction of the rotational axis. Figure 12.15 [12.1] shows common drilling processes. With drilling into solid metal either through holes or blind holes can be produced. The tool is usually a twist drill. Drilled holes are either enlarged with twist drills or with countersinks or counterbores having two or more cutting edges. Step drills produce stepped holes. They usually have multiple cutting edges; for

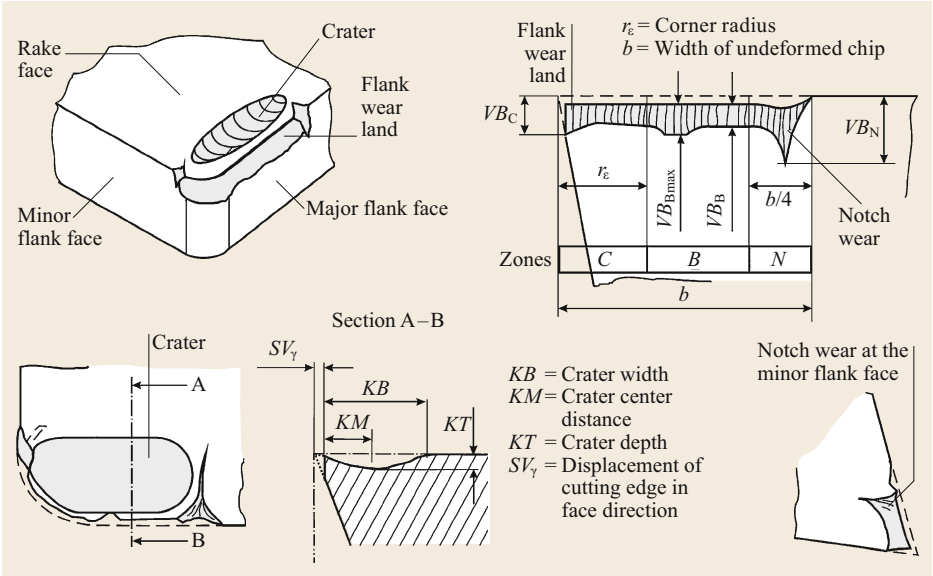

Fig. 12.13 Forms of wear in turning [12.12]

Table 12.4 Coefficients of Taylor tool-life equations. Taylor function $v_c = CT^{1/k}$. Table values are valid for $a_p = 1$ mm, $f = 1$ mm, $VB = 0.4$ mm

Material	Material number	Tungsten carbide uncoated				Oxide ceramic (St) nitride ceramic (GG) coated	
		C (m/min)	k	C (m/min)	k	C (m/min)	k
St 50-2	1.0050	299	−3.85	385	−4.55	1210	−2.27
ST 70-2	1.0070	226	−4.55	306	−5.26	1040	−2.27
Ck45N	1.1191N	299	−3.85	385	−4.55	1210	−2.27
16MnCrS5BG	1.7131BG	478	−3.13	588	−3.57	1780	−2.13
20MnCr5BG	1.7147BG	478	−3.13	588	−3.57	1780	−2.13
42CrMoS4V	1.7225V	177	−5.26	234	−6.25	830	−2.44
X155CrVMo12-1	1.2379	110	−7.69	163	−8.33	570	−2.63
X40CrMoV5-1G	1.2344	177	−5.26	234	−6.25	830	−2.44
GG-30	GJL-300	97	−6.25	184	−6.25	2120	−2.50
GG-40	GJL-400	53	−10.00	102	−10.00	1275	−2.78

St: steel materials; GG: cast iron

manufacturing reasons, not every cutting edge has to support all parts of the contour (e.g., one cutting edge may break the edge of a step, while the adjacent one produces a planar surface). Center drills are special profile drills with a thinner spigot and a short, stiff drill section in order to attain a good centering effect. Trepanning cutters produce an annular cut into solid material with the coincidental formation of a solid cylinder or plug. Taps are used to cut internal threads. Reaming is a hole-enlarging process with a small undeformed chip thickness, for producing holes of precise size and shape with a high-quality surface.

For drilling holes with diameters of 1−20 mm and with drilling depths up to five times the diameter, the twist drill is the tool most commonly used (Fig. 12.16; [12.1]). The twist drill consists of the shank and the cutting section. The shank is used to locate and clamp the drill in the machine tool. It is straight or tapered. If a high cutting torque is to be transmitted, tangential flat surfaces transmit the force. The cutting section has a complex geometry, which can be modified to adapt the drill to the respective machining task. Essential parameters are the profile and the web thickness, the flute geometry, and the helix angle, i.e., the pitch of the flutes, the ground drill point, and the drill-point angle. Especially the ground drill point and the drill-point angle can be determined by the user. The profile of the twist drill is designed in such a way that the flutes provide the maximum space for chip removals while ensuring that the drill is capable of adequately

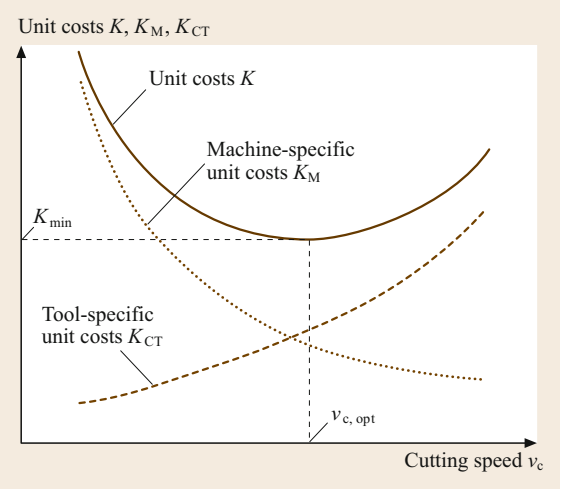

Fig. 12.14 Manufacturing cost as a function of cutting speed v_c

withstanding torsional stresses. These are the two main requirements. A further demand on the drill may be the production of favorable chip forms. This has led to a diversity of special profiles and allows the adaption of the drilling process to particular constraints. Working material also has to be removed from the area in front of the core of the twist drill, with the special boundary condition that the cutting speed v_c in the center is zero. This is achieved by the chisel edge, which connects the major cutting edges.

Along the major and minor cutting edges, the rake angle γ as an important factor influencing the drilling process is not constant but already decreases in front of the major cutting edge from the outside towards the inside. In Fig. 12.17 [12.2], the rake angles at three positions on the major cutting edge and chisel edge, respectively, are shown.

At the outer diameter the rake angle is almost identical to the helix angle δ and decreases in direct proportion to the diameter. Close to the chisel edge, the rake angles on the major cutting edge are already strongly negative. Here, the workpiece material has to be displaced in radial direction. As shown on the left-hand side of Fig. 12.17 all rake angles on the chisel edge are negative. These negative rake angles and the material displacement effect generate high pressures in the area of the chisel edge. To diminish this effect, twist drills are pointed. The center of the drill is tapered by profile grinding in the direction of the flute and towards the drill tip on a conical or similar surface. This way, the rake angle at the chisel edge is increased, and/or the chisel edge is shortened.

The most important type of wear concerning the twist drill is flank wear at the corners. This wear, which is mainly caused by abrasion, generates an increase in the torsional load on the drill, as higher machining forces are present in the corner area. This torsional load may cause the drill to break. Worn twist drills are, therefore, reground until the damaged area of the secondary cutting edge is removed.

Cutting Forces

The forces and moments in drilling are calculated on the basis of *Kienzle*'s approach [12.10, 14]. Figure 12.18 [12.2] illustrates the cutting geometry and the forces implied in drilling processes. The forces arising per cutting edge, which are assumed to act in the middle of the cutting edge, are divided into their components F_c, F_p, and F_f. The cutting forces F_{c1} and F_{c2} generate the cutting moment via the lever arm r_c and the cutting moment M_c

$$M_c = (F_{c1} + F_{c2}) r_c \,, \tag{12.21}$$

$$F_{c1} = F_{c2} = F_{cZ} \,, \tag{12.22}$$

$$M_c = F_{cZ} 2 r_c \,. \tag{12.23}$$

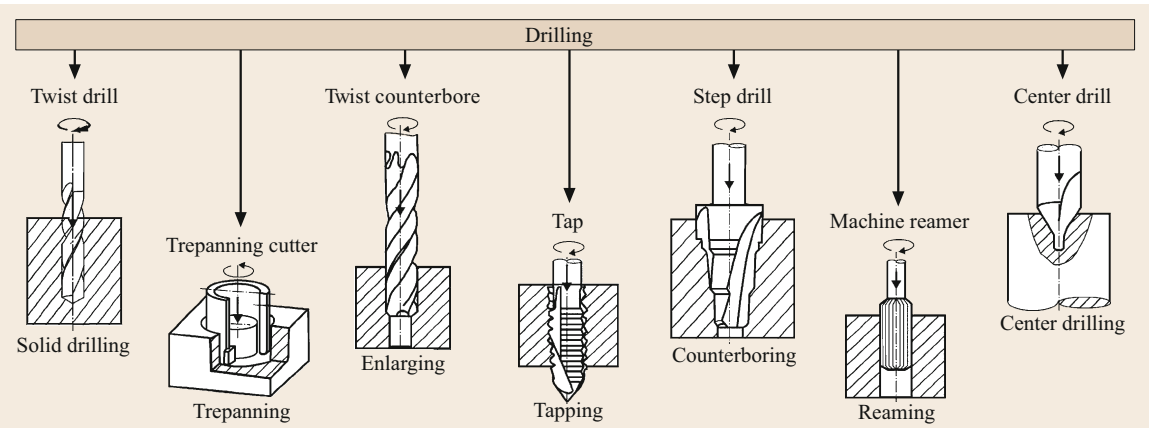

Fig. 12.15 Drilling processes [12.1]

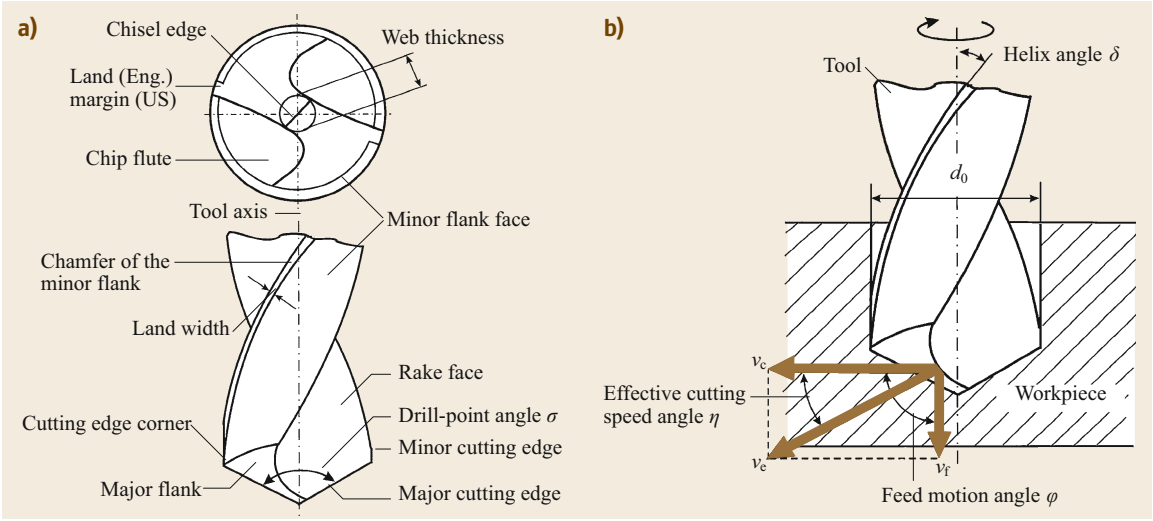

Fig. 12.16a,b Terminology (a) and mode of operation (b) of twist drills [12.1]

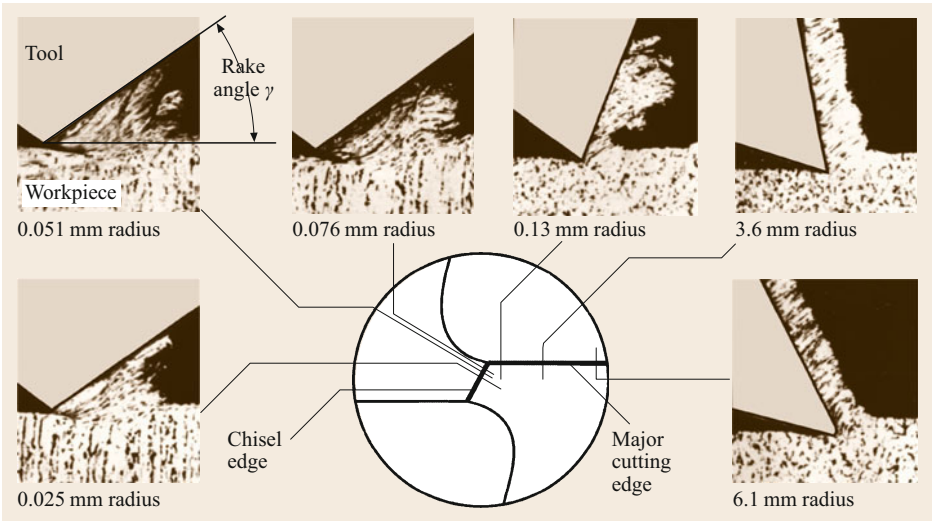

Fig. 12.17 Rake angles at different positions on a drill tip

The sum of the feed forces F_{f1} and F_{f2} is F_f,

$$F_f = F_{f1} + F_{f2} \,, \tag{12.24}$$

$$F_{f1} = F_{f2} = F_{fZ} \,, \tag{12.25}$$

$$F_f = 2F_{fZ} \,. \tag{12.26}$$

In the ideal case, i.e., with a symmetrical drill, the passive forces F_{p1} and F_{p2} cancel each other out. If there are symmetry deviations, F_{p1} and F_{p2} generate interference forces, which impair the quality of the hole. The cutting force per cutting edge results in

$$F_{cZ} = bh^{(1-m_c)}k_{c1.1} \,, \tag{12.27}$$

$$h = F_z \sin\kappa \,, \tag{12.28}$$

$$b = \frac{d_0 - d_i}{2\sin\kappa} \,. \tag{12.29}$$

By analogy, the feed force is

$$F_f = bh^{(1-m_c)}k_{f1.1} \,. \tag{12.30}$$

Values are given in Table 12.5. The feed forces are strongly dependent on the shape of the chisel edge. They can be lowered significantly by web thinning [12.2]. Wear causes them to reach twice their original value or more.

Surface quality in drilling with twist drills corresponds to roughing with $Rz = 10–20\,\mu m$. The surface

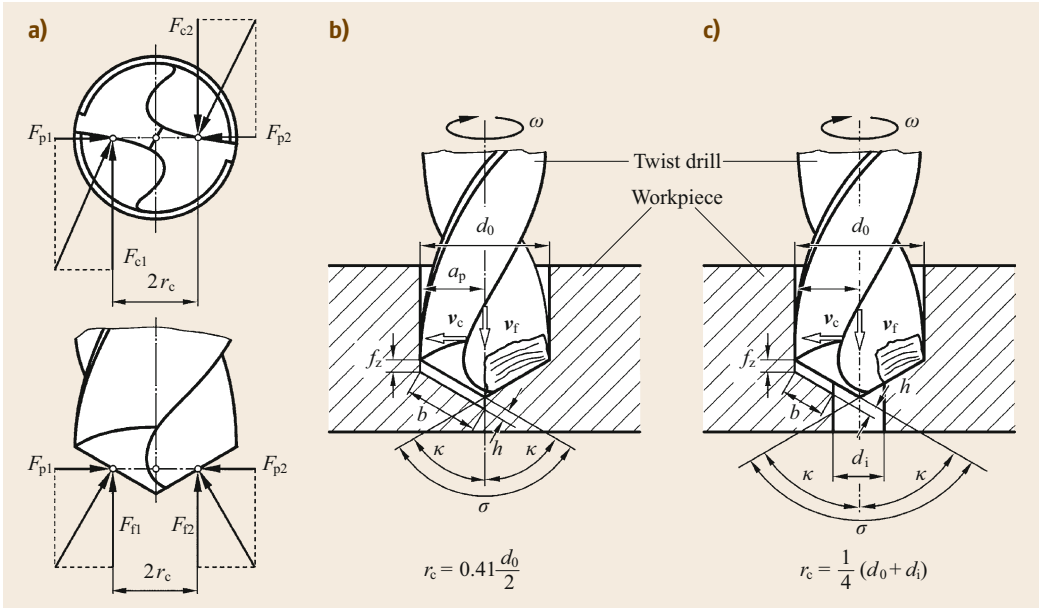

Fig. 12.18a–c Cutting geometry and machining forces in drilling. **(a)** Forces; **(b)** solid drilling; **(c)** enlarging

Table 12.5 Cutting force components for drilling

Material	Mat. No.	R_m (N/mm^2)	$1-m_c$	$k_{c1.1}$ (N/mm^2)	$1-m_f$	$k_{f1.1}$ (N/mm^2)
18CrNi8	1.5920	600	0.82 ± 0.04	2690 ± 230	0.55 ± 0.06	1240 ± 160
42CrMo4	1.7225	1080	0.86 ± 0.06	2720 ± 420	0.71 ± 0.04	2370 ± 230
100Cr6	1.2076	710	0.76 ± 0.03	2780 ± 220	0.56 ± 0.07	1630 ± 300
46MnSi4	1.5121	650	0.85 ± 0.04	2390 ± 250	0.62 ± 0.02	1360 ± 100
Ck60	1.1221	850	0.87 ± 0.03	2200 ± 200	0.57 ± 0.03	1170 ± 100
St50	1.0531	560	0.82 ± 0.03	1960 ± 160	0.71 ± 0.02	1250 ± 70
16MnCr5	1.7131	560	0.83 ± 0.03	2020 ± 200	0.64 ± 0.03	1220 ± 120
34CrMo4	1.7220	610	0.80 ± 0.03	1840 ± 150	0.64 ± 0.03	1460 ± 140
Gray cast iron						
Up to G-22	–	–	0.51	504	0.56	356
Over G-22	–	–	0.48	535	0.53	381

roughness can be reduced by reaming with increased dimensional accuracy. The application of solid cemented carbide drills provides another solution. When drilling solid metal, surface qualities, dimensional accuracy, and accuracy of shape like those obtained with reaming are achieved. Most of the drilling tools are further improved by suitable coatings.

Short-Hole Drilling

Short-hole drilling with drilling depths of $L < 2D$ covers a large proportion of bolt-hole drilling, through hole drilling and tapping. For this, short-hole drills with indexable inserts may be used for diameters from 10 to over 120 mm. Their advantage compared to twist drills is the absence of a chisel edge and the increase in cutting speed and feed rate achieved with indexable cemented carbide or ceramic inserts. Due to the asymmetrical machining forces, the use of short-hole drills requires rigid tool spindles similar to those found on common machining centers and milling machines. The higher rigidity of the tool enables pilot drilling of inclined or curved surfaces with an accuracy of IT7.

12.1.4 Milling

Classification of Milling Processes

In milling, the necessary relative motion between the tool and the workpiece is achieved by means of a circular cutting motion of the tool and a feed motion perpendicular to or at an angle to the axis of rotation of the tool. The cutting edge is not continuously in engagement with the workpiece. Therefore, it is subject to alternating thermal and mechanical stresses. The

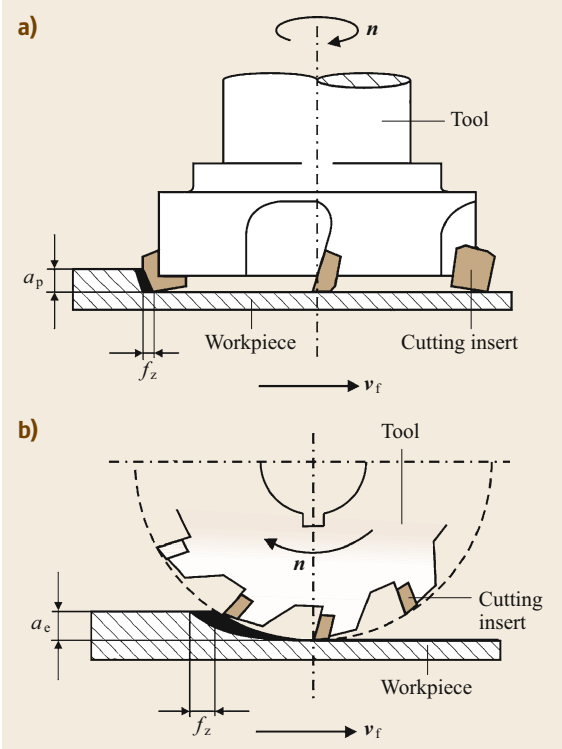

Fig. 12.19a,b Comparison of face milling and peripheral milling. **(a)** Face milling: workpiece surface generated by minor cutting edge. **(b)** Peripheral milling: workpiece surface generated by major cutting edge

complete machine-tool–workpiece-fixture system is dynamically stressed by the interrupted cutting action.

Milling processes are classified according to [12.1] on the basis of the following:

- The nature of the resulting workpiece surface
- The kinematics of the cutting operation
- The profile of the milling cutter.

Milling can be used to produce a practically infinite variety of workpiece surfaces. A distinguishing feature of a process is the cutting edge (major or minor) that produces the workpiece surface (Fig. 12.19): in face milling the minor cutting edge is located at the face of the milling cutter, while in peripheral milling, the major cutting edge is located on the circumference of the milling cutter.

A distinction can be made on the basis of the feed-direction angle φ (Fig. 12.20): in down-milling, the feed direction angle φ is $> 90°$, thus the cutting edge of the milling cutter, enters the workpiece at the maximum undeformed chip thickness, while in up-milling, the feed direction angle φ is $< 90°$; thus the cutting edge enters at the theoretical undeformed chip thickness $h = 0$. This initially results in pinching and rubbing.

A milling operation may include both up-milling and down-milling. The principal milling processes are summarized in Fig. 12.21.

Plain Face Milling with End-Milling Cutters

The kinematics of cutting and the relationship of the cutting forces during milling will be discussed with reference to plain face milling with an end-milling cutter.

Kinematics of Cutting in Milling

To describe the process, it is necessary to distinguish between the tool–workpiece engagement variables and the cutting variables. The engagement variables, which are expressed in relation to the working plane, describe the interaction of the cutting edge and the workpiece. The working plane is described by the cutting speed vector v_c and the feed velocity vector v_f. In milling, the engagement variables are (Fig. 12.22): depth of cut a_p, measured at a right angle to the working plane, cutting engagement a_e, measured in the working plane at right angles to the feed direction, and feed of the cutting edge f_z, measured in the feed direction.

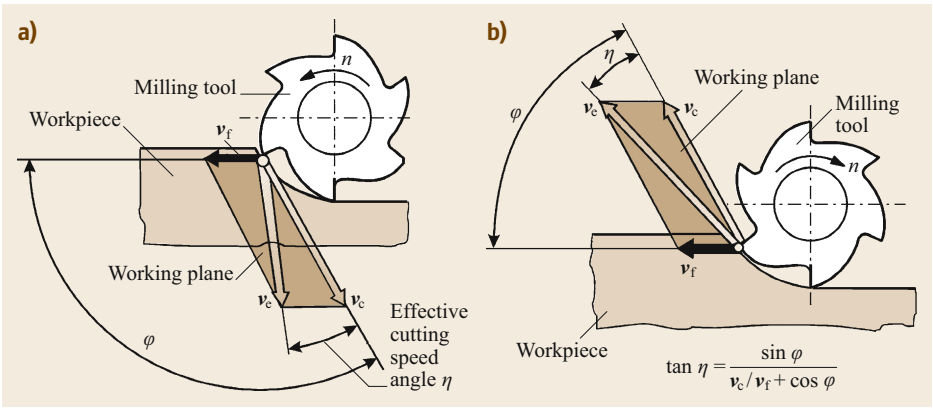

Fig. 12.20a,b Comparison of down and up-milling (DIN 6580) [12.15]. **(a)** Down-milling: feed direction angle $90° \leq \varphi \leq 180°$; **(b)** up-milling: feed direction angle $0° \leq \varphi \leq 90°$

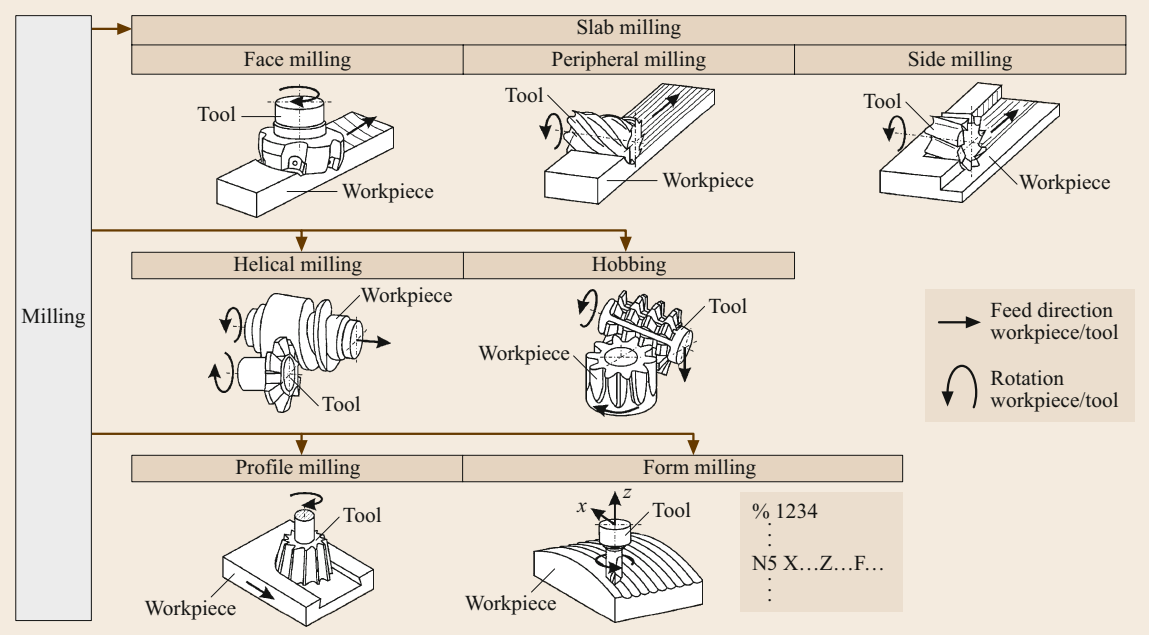

Fig. 12.21 Milling processes [12.1]

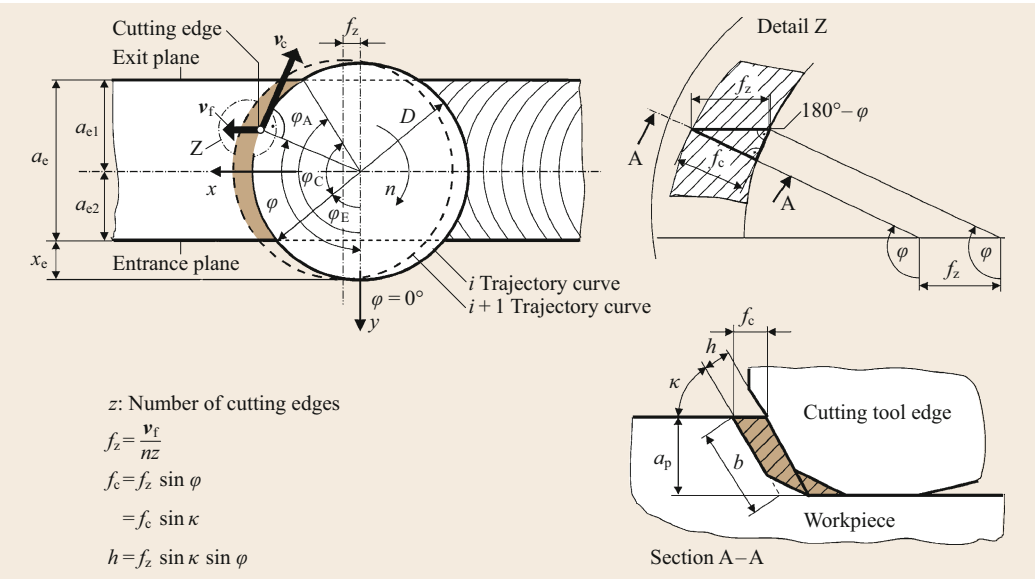

Fig. 12.22 Tool–workpiece engagement variables in plain face milling

For a full description of the kinematics of cutting, the following data are required: milling cutter diameter D, number of teeth z, tool excess x_e, and the cutting edge geometry (side-rake angle γ_f, back-rake angle γ_p, side-clearance angle α_f, back-clearance angle α_p, entry angle κ_r, angle of inclination λ_s, cutting edge radius r, and chamfer).

Due to the interrupted cut, the entry and exit conditions of the cutting edge, and the types of contact, are especially important for milling processes. The types of contact describe the nature of the first and last contacts of the cutting edge with the workpiece. They can be determined from the entry angle φ_E, the exit angle φ_A, and the tool geometry. Generating the first point of contact with the cutting edge tip should be avoided.

From the engagement variables the cutting variables can be derived, which indicate the dimensions of the layer of material to be removed from the workpiece.

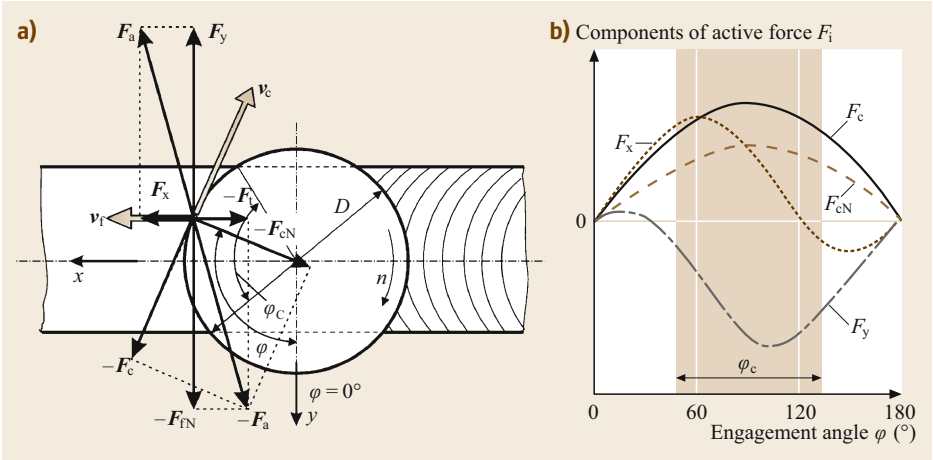

Fig. 12.23a,b Components of cutting force in plain face milling. **(a)** Force vectors in the working plane; **(b)** course of forces versus engagement angle; tool specific forces: F_c, F_{cN}; workpiece-specific forces: F_x, F_y

The cutting variables are not identical to the chip variables, which describe the dimensions of the resulting chips. The cutting edges describe cycloids in relation to the workpiece. As the cutting speed is significantly higher than the feed velocity, they can be approximated by circular paths. Taking this into account, the undeformed chip thickness is (Fig. 12.22)

$$h(\varphi) = f_z \sin\kappa \sin\varphi \,. \tag{12.31}$$

With the undeformed chip width $b = a_p/\sin\kappa$, the undeformed chip cross section is

$$A(\varphi) = bh(\varphi) = a_p f_z \sin\varphi \,. \tag{12.32}$$

The time-related chip volume is $Q = a_c a_p v_f$. The undeformed chip thickness is a function of the entry angle φ and is, thus, not constant as in turning. The evaluation of the milling process is based on the mean undeformed chip thickness

$$\begin{aligned} h_m &= \frac{1}{\varphi_c}\int_{\varphi_E}^{\varphi_A} h(\varphi)\,\mathrm{d}\varphi \\ &= \frac{1}{\varphi_c} f_z \sin\kappa\,(\cos\varphi_E - \cos\varphi_A)\,. \end{aligned} \tag{12.33}$$

Cutting Force Components

The machining force required for chip formation has to be absorbed by the cutting edge and the workpiece. According to [12.9], the machining force F can be resolved into an active force F_a, which lies in the working plane, and a passive force F_p, which is perpendicular to the working plane. The direction of the active force F_a changes with the entry angle φ. The components of the active force can be expressed in relation to the following directions (Fig. 12.23):

- Direction of the cutting speed v_c: the components cutting force F_c and perpendicular cutting force F_{cN} relate to a corotating system of coordinates (tool-specific components of the active force).
- Direction of rate of feed v_f: the components feed force F_f and perpendicular feed force F_{fN} relate to a fixed system of coordinates (workpiece-specific components of the active force).

For converting the active force from the fixed system of coordinates into a corotating system, the following equations apply

$$F_c(\varphi) = F_f(\varphi)\cos\varphi + F_{fN}(\varphi)\sin\varphi \,, \tag{12.34}$$

$$F_{cN}(\varphi) = F_f(\varphi)\cos\varphi + F_{fN}(\varphi)\cos\varphi \,, \tag{12.35}$$

$$F_x(\varphi) = F_f(\varphi) \,, \tag{12.36}$$

$$F_y(\varphi) = F_{fN}(\varphi) \,. \tag{12.37}$$

This transformation is important if, for instance, the cutting force F_c is to be measured with a three-component force-measuring dynamometer that holds the workpiece. Figure 12.23 shows the pattern of the components of the active force in the tool and workpiece-specific systems of coordinates for plain face milling with an end-milling cutter.

Prediction of Cutting-Force Components

Kienzle's machining force equation [12.10] can also be applied to milling. For the machining force components, cutting force F_c, perpendicular cutting force F_{cN}, and passive force F_p, the calculation is

$$F_i = Ak_i \,, \tag{12.38}$$

where $i = c, cN, p$; A is the undeformed chip cross section, and k_i is the specific machining force. Owing to the

Table 12.6 Cutting force components for plain face milling

Cutting edge geometry										
	γ_f (°)	γ_p (°)	α_f (°)	α_p (°)	λ_s (°)	κ_r (°)	κ_F (°)	ε (°)	Chamfer	
Neg.	−4	−7	6	23	−6	75	60/30/0	90	1.4/0.8/1.4	
Pos.	0	8	9	29	8	75	45/0	90	0.8/1.4	
Material	**Material number**	**Cutting material**	**v_c (m/min)**	**Cutting edge geometry**	**Main and incremental values for spec. machining force in axial face milling**					
					$k_{c1.1}$ (N/mm²)	m_c	$K_{cN1.1}$ (N/mm²)	m_{cN}	$k_{p1.1}$ (N/mm²)	m_p
St 52-3 N	1.0570 N	HM P25	120	Neg.	1831	0.29	809	0.54	705	0.41
				Pos.	1469	0.25	447	0.57	174	0.56
Ck45N	1.1191 N	HM P25	190	Neg.	1506	0.45	708	0.62	653	0.52
X22CrMoV12-1	1.4923	HM P40	120	Pos.	1533	0.29	497	0.70	164	0.77

wide range of undeformed chip thicknesses that is covered by milling (the undeformed chip thickness depends on the engagement angle φ), Kienzle's relationship only applies to certain areas. The undeformed chip thickness range of 0.001 mm < h < 1.0 mm is divided into three sections (Fig. 12.24). For each section, a straight line can be determined, depending on, the unit-specific cutting force k_i and its exponent m_i. For the specific cutting force, the following equations apply

$$k_i = k_{i1.0,01} h^{-m_{i0,01}} \quad \text{for } 0.001\text{ mm} < h < 0.01\text{ mm}\,, \tag{12.39}$$

$$k_i = k_{i1.0,1} h^{-m_{i0,1}} \quad \text{for } 0.01\text{ mm} < h < 0.1\text{ mm}\,, \tag{12.40}$$

$$k_i = k_{i1.1} h^{-m_i} \quad \text{for } 0.1\text{ mm} < h < 1\text{ mm}\,, \tag{12.41}$$

where i = c, cN, p.

Thus, the cutting force for milling with an end-milling cutter is

$$F_i = b k_{i1.1} h^{1-m_i}\,, \tag{12.42}$$

where i = c, cN, p.

The corresponding component of the cutting force can be calculated for milling if the unit-specific cutting force k_i and its exponent m_i for the workpiece/cutting material combination and the cutting conditions are available. The machining indices for axial-plane face milling with a milling head are given in Table 12.6 for a number of workpiece materials and cutting conditions [12.10]. Often, though, to estimate the cutting force during milling, values obtained from turning will have to be used.

The milling machine capacity is designed on the basis of the average machining force

$$F_i = b k_{i1.1} h_m^{1-m_i} K_{pro} K_\gamma K_v K_{TW} K_{CM}\,, \tag{12.43}$$

where i = c, cN, p.

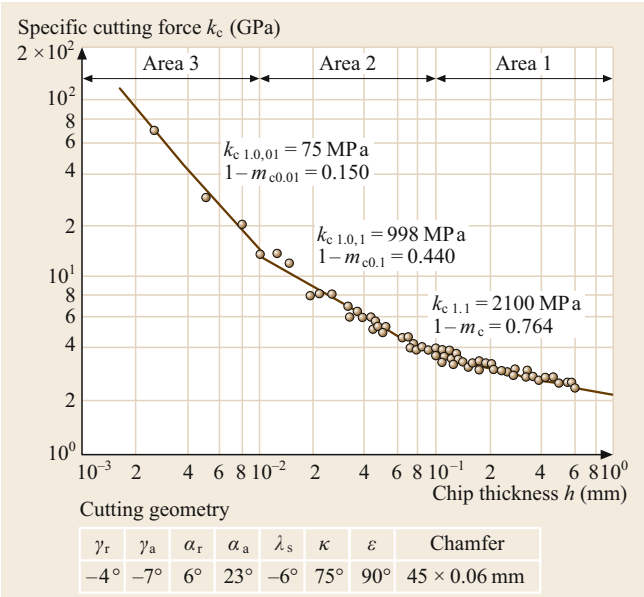

Fig. 12.24 Specific cutting force in plain face milling. Material: Ck45N; material-no.: 1.1191N; cutting tool: HM P 25; cutting conditions: v_c = 190 m/min

In (12.43), h_m is the mean undeformed chip thickness, K_{pro} = 1.2−1.4 is the correction factor for the manufacturing process (the factor takes into account the fact that the machining indices were obtained from turning tests), K_γ is the correction factor for the rake angle (Sect. 12.1.2), K_v is the correction factor for the cutting speed, K_{TW} is the correction factor for tool wear, and K_{CM} is the correction factor for the cutting material. Experimental research on plain face milling has proven that the influence of wear on the machining force components cannot be ignored.

Vibrations

Depending upon the elasticity frequency response of the complete machine-milling cutter–workpiece-fixture

system, the metal cutting forces generate vibrations that may affect surface quality and tool life. According to their origin, these vibrations are divided into separately excited and self-excited vibrations [12.16, 17].

In the case of separate excitation, the complete system vibrates at the frequency of the exciting external forces. Due to the intermittent cutting action of milling, the cutting edges are not constantly in engagement. With a multiple-edged milling cutter, the number of cutting edges in engagement at any time should be taken into account. Depending on the ratio a_c/D, z_{iE} cutting edges are in engagement, the following relationship being valid

$$z_{iE} = \frac{\varphi_c}{2\pi} z, \quad \text{where} \quad \frac{\varphi_c}{2} = \frac{a_c}{D} . \tag{12.44}$$

The mean cutting force acting on the milling cutter and, thus, on the spindle of the milling machine is

$$F_{cm} = z_{iE} F_{cmz} , \tag{12.45}$$

where F_{cmz} is the mean cutting force of a single cutting edge. Superimposed on the mean cutting force is a dynamic-force element. The larger the value of z_{iE}, the smaller the force amplitude; if z_{iE} is an integer, the cutting-force amplitude is at a minimum. The dynamic-force element leads to separately excited vibrations between the workpiece and the milling cutter.

In the case of self-excitation, the complete machining system vibrates at one or more eigenfrequencies, without an external interference force affecting the system. Special importance is attached to self-excited vibrations that arise because of the regenerative effect which are also referred to as *regenerative chatter*. The chatter is caused by variations in cutting force due to changes in undeformed chip thickness [12.16]. Chatter can be influenced by varying the cutting speed, depth of cut, feed rate, and cutting edge geometry.

Tool Wear in Milling

Due to the intermittent cutting action in milling, the cutting material is subject to alternating thermal and mechanical stresses. As a consequence, not only face and flank wear but also cracking in the cutting tip may determine tool life. Figure 12.25 depicts the tool-life travel per tooth based on the flank wear of the primary cutting edge of a ball-nose end-mill cutter for different cutting tool materials [12.2]. As shown especially with the development of cubic boron nitride (CBN), the wear behavior of milling tools could be significantly improved, thus allowing finish-machining of hardened materials by milling [12.18–20]. Suitable data for cutting parameters are accessible via catalogues

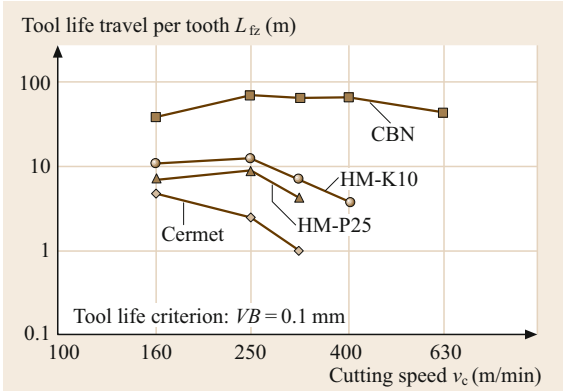

Fig. 12.25 Milling tool wear depending on cutting tool material and speed (after [12.2]). Material: X32CrMoV33; material-no.: 1.2365; $R_m = 1900\,N/mm^2$; ball-nose end mill: $\varnothing = 16$ mm ($z = 2$), $l_w = 37$ mm; cutting conditions: $a_e = 0.8$ mm, $a_p = 0.5$ mm, $f_z = 0.1$ mm, $\beta_f = -40°$

of all major milling tool manufacturers. Depending on the cutting conditions, surface roughness values comparable to those obtained in grinding are achieved. In grinding, the accuracy of shape is achieved by spark-out. As there has to be a minimum undeformed chip thickness in milling, shape defects occur, which can be attributed to the following influencing variables: environment, operating behavior of the milling machine, inhomogeneity in material hardness, heat absorption of the workpiece due to metal cutting, and a change of residual stresses in the edge zone of the workpiece.

Form Milling

Hollow-mold tools such as deep-drawing tools are manufactured by both chip removal and chipless machining processes. Milling plays a dominant role as a controlled material-removal process. The essential characteristic in form milling is the number of actively controlled axes, a distinction accordingly being made between three-axis milling and five-axis milling (Fig. 12.26). In five-axis milling, not only the tip but also the axial direction of the milling cutter is continuously and simultaneously controlled relative to the workpiece coordinate system. The profile of the milled grooves determines the productivity and quality of the process (small final finishing with a small profile depth being desired). It is formed by machining a curved surface in parallel lines and depends on the milling cutter geometry, the workpiece geometry, and the method of work. For a given groove depth t_R, five-axis milling with an end-milling cutter produces significantly larger groove widths b_R than three-axis milling with a convex ball-nose end-mill cutter.

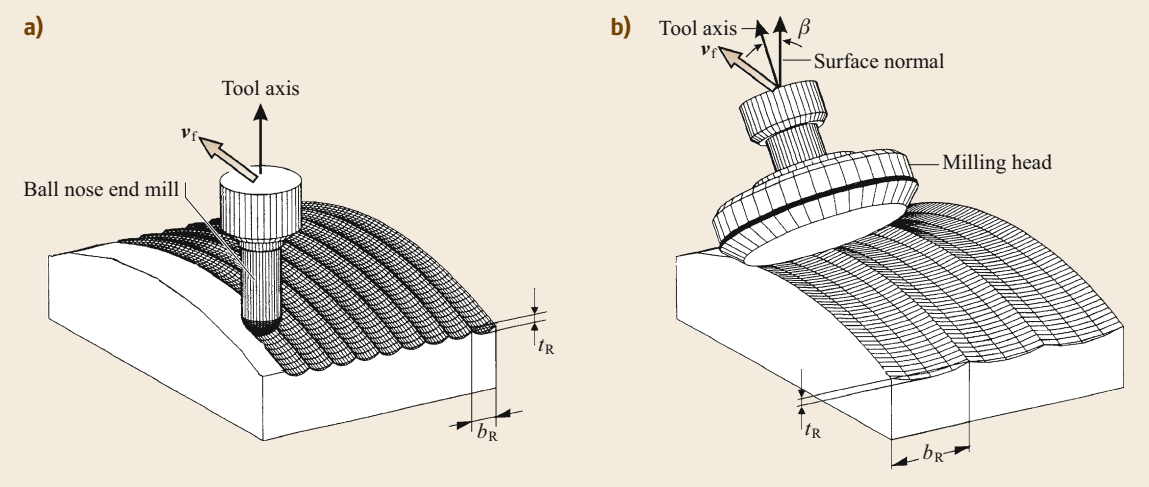

Fig. 12.26a,b Form milling by three-axis milling **(a)** and five-axis milling **(b)**

12.1.5 Other Processes: Planing and Shaping, Broaching, Sawing

Planing and Shaping

According to a German standard, a distinction can be made between planing and shaping. Chip removal is accomplished during the working stroke with a single-point cutting tool. The following return stroke resets the tool to its original position. The feed is performed intermittently, usually at the end of a return stroke.

In planing, the workpiece performs the cutting motion with the cutting speed v_c and the return motion with v_r. Feed f and depth of cut a_p are accomplished by the tool (Fig. 12.27a). In shaping, the tool performs the cutting and return motion, while feed and engagement are accomplished by the workpiece or the tool.

The reciprocating motion of the workpiece (in planing) or the tool (in shaping) produces high inertial forces and limits the cutting speed. As a guideline for the cutting speed, for machining steels, the ranges $v_c = 60–80\,\mathrm{m/min}$ (roughing) and $v_c = 70–100\,\mathrm{m/min}$ (finishing) are well established for cemented carbide tools. Frequently-used special methods are manufacturing by planing or shaping (Fig. 12.27b) to produce involute gears [12.21].

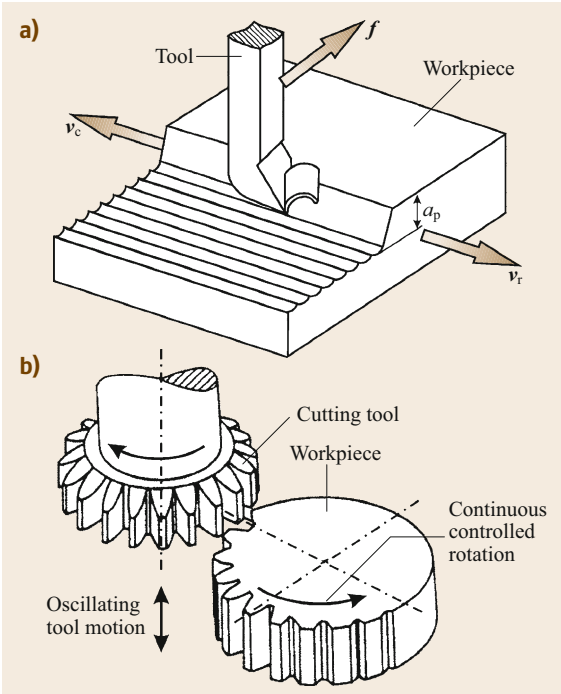

Fig. 12.27 **(a)** Planing and **(b)** gear shaping

Broaching

In broaching, material is removed using a multiple-pointed tool, the teeth of which are one behind the other and are successively stepped by one layer of the material to be removed. Thus, no feed motion is required, as it is *built into* the tool. The cutting motion is usually linear or, under certain circumstances, helical or circular.

The advantages of the process are the high productivity and the possibility of finishing workpieces with a single tool because high-surface finish and dimensional accuracies with tolerances up to IT7 can be achieved. Due to the high cost of the tools, the main areas of use are series and mass production; a new tool is required for each workpiece shape.

A basic distinction is made between internal broaching and external broaching. In internal broaching, the broach is pushed or pulled through a hole, while in external broaching, the tool moves along the surface.

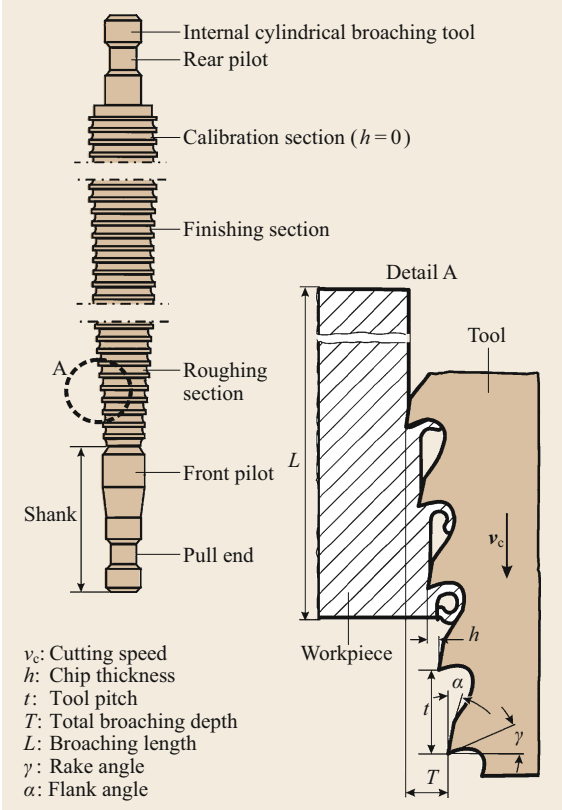

Fig. 12.28 Internal cylindrical broaching tool and process characteristics

Broaches are divided into roughing, finishing, and calibrating teeth sections (Fig. 12.28). Normal undeformed chip thicknesses in flat broaching of steels are $h_z = 0.01–0.15$ mm for roughing and $h_z = 0.003–0.023$ mm for finishing. Broaching of cast materials is carried out up to a thickness of $h_z = 0.02–0.2$ mm in the roughing section and $h_z = 0.01–0.04$ mm in the finishing section.

Cutting speeds are restricted by the hardness of the chosen cutting material at high temperature and by the efficiency of the machine. The cutting material most commonly used, high-speed steel (HSS), permits only low cutting speeds owing to its hot hardness of approximately 600 °C. Cutting speeds of $v_c = 1–30$ m/min are used, with speeds of up to 70 m/min in exceptional cases. The capacity of the process can be increased by using coated HSS or cemented carbide. Due to these developments broaching of case-hardened steel workpieces with cemented carbide tools has also become possible [12.22]. High cutting speeds require high drive-power outputs to accelerate and decelerate the tool and the broach slide, causing a disproportionate increase in equipment costs. Vibration problems might also occur, especially with thin internal broaches.

In broaching, mainly mineral oils are used as cutting fluid for lubricating and cooling in the contact zone, but above all to prevent the formation of built-up edges and to carry away the chips. They usually contain EP (extreme pressure) additives, which are nowadays mostly chlorine free.

Besides the above-mentioned internal and external broaching operations, also special process configurations like gear scraping or turn broaching are used in industry [12.21].

Sawing

Sawing is metal cutting with a multiple-pointed tool with a small width of cut for severing or slitting workpieces. The rotational or linear principal motion is performed by the tool. The teeth of the tool are offset in alternate directions. Thus, the kerf is widened in relation to the saw blade, thus reducing friction between tool and workpiece (Fig. 12.29).

Band sawing is sawing with a continuous, usually straight, cutting motion of a rotating endless band. The motions and cutting parameters are shown in Fig. 12.29a.

The normal cutting speeds for high-speed steels lie within the range of $v_c = 6–45$ m/min, with feed rates per tooth of $F_z = 0.1–0.4$ mm. If bands with inserted cemented carbide teeth are used, the cutting speed can be increased to 200 m/min for steels and up to 2000 m/min for light metals.

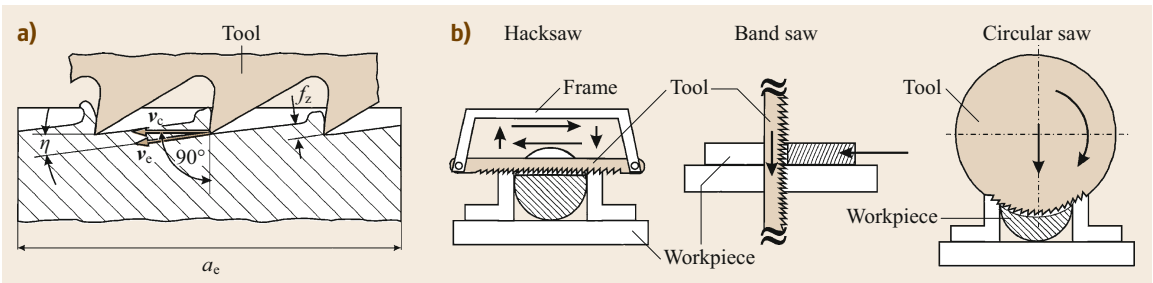

Fig. 12.29a,b Process kinematics of band sawing **(a)** and different sawing variants **(b)**

In reciprocating sawing (hack sawing), a tool of finite length clamped in a holding frame is used. The feed motion is carried out intermittently only as the tool advances or at a constant perpendicular force.

Circular sawing is sawing with a continuous cutting motion using a circular saw blade. In terms of kinematics and metal cutting technique, circular sawing resembles peripheral milling.

12.1.6 Cutting Tool Materials

Cutting tools consist of the cutting tip, the holder, and the shank. Holders and shanks are designed according to constructional and organizational requirements, such as mating dimensions of the machine, the nature and extent of tool storage and tool changing, or the geometry of the workpiece. The cutting tip is responsible for chip removal. It is subject to mechanical and thermal stresses and chemical attack. The tip consequently wears.

A basic dualism applies to all cutting materials. Harder and more wear-resistant materials are typically less tough and stable under periodically changing loads, as well as under unstable cutting conditions and in intermittent cutting. Materials that cope better with variable mechanical or thermal stresses, are often less resistant to wear. The perfect cutting material combining both features is yet to be developed (Fig. 12.30).

To overcome this restricting dualism, various cutting materials are manufactured as composite materials. Coating with hard-wearing carbides or oxides produces a separation of functions; the physically (PVD—physical vapor deposition) or chemically (CVD—chemical vapor deposition) vapor-deposited layers provide wear protection and enhanced tribological performance. The tougher substrate performs the supporting function, even under dynamic load conditions. Examples of these coatings include TiN and TiAlN. The latter is applied in dry-machining applications due to its higher hardness and enhanced thermal stability compared to TiN [12.23]. Multilayer coatings are also increasingly employed due to their superior tribological performance compared to single-layer coatings [12.24].

The primary cutting tool materials include: alloy steels, high-speed steels (HSS), cemented carbides, ceramics, and superhard cutting materials (e.g., diamond and cubic boron nitride).

High-Speed Steels

High-speed steels are usually used for drilling, milling, broaching, sawing, and turning tools. Their hot hardness (up to approximately 600 °C) is far superior to that of tool steels (Fig. 12.31). Their hardness results from their basic martensitic structure and from interspersed carbides: tungsten carbides, tungsten-molybdenum carbides, chromium carbides, and vanadium carbides.

The through-hardenability of tools with large cross sections is increased with molybdenum and/or by alloying with chromium. Tungsten increases the wear resistance and tempered strength, vanadium increases the wear resistance (but is difficult to grind when hard),

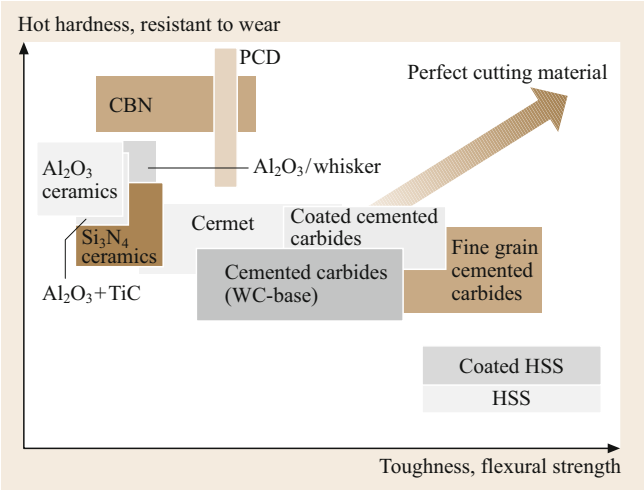

Fig. 12.30 Cutting tool materials (after [12.21])

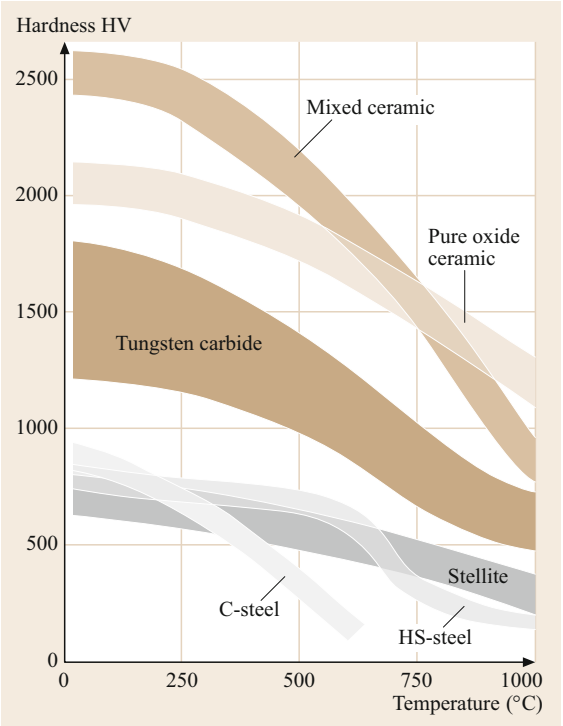

Fig. 12.31 Hot hardness of cutting materials

Table 12.7 Properties of some coatings of HSS tools

Properties	Coating materials				
	TiN	TiCN	CrN	TiCrN[a]	TiAlN[a]
Hardness (HV)	2200–2600	3200–3300	2450–2900	3000–3200	3000–3300
Critical load before coating failure (N)	70–80	65–75	40–50	60–70	50–60
Maximum coating thickness (μm)	10	10	50	20	10
Deposition speed (μm/h)	6–8	6–7	2–4	4–5	4–6
Stability against oxidation (°C)[b]	550	550	700	650–700	800
Friction coefficient (against steel 100Cr6)	0.67	–	0.57	–	0.67–0.75

[a] For composition: 50% Ti-50% Cr; 50% Ti-50% Al;
[b] Heating in air for 1 h

and cobalt increases the high-temperature hardness. High-speed steels are traditionally manufactured by casting but can also be manufactured by powder metallurgy (PM). PM steels provide enhanced edge strength and cutting edge durability. They are used for thread-cutting and reaming tools. PM high-speed steels with high vanadium contents are easier to grind than their cast high-speed steel counterparts. Their acceptance is only limited because of their higher cost.

Coated HSS

High-speed steels are usually coated with PVD, which is reactive ion plating performed at low temperatures in order to stay below the tempering temperature during the process. Simple shapes, such as indexable inserts, can be treated by CVD followed by rehardening. Coated tools (drills, taps, hobs, form turning tools) can have a significantly increased tool life compared to uncoated tools.

A coating of single layers or multilayers deposited on the cutting tools improves its performance. The most frequently used coating materials are titanium carbide (TiC), titanium nitride (TiN), titanium-aluminum nitride (TiAlN), and titanium carbonitride (TiCN).

Coated HSS provides increased hot hardness and wear resistance combined with a high ductility and bending strength of the tool. Tool life can be increased up to 2–2.5 times at increased cutting speed by 20–40%. The most important physical-mechanical properties and parameters obtained by PVD processes are shown in Table 12.7.

The application areas of coatings for cutting tools strongly depend on their properties. TiN has high thermodynamic stability; it is chemically passive to ferrous materials. It combines high hardness and sufficient plasticity. TiN-coated HSS tools are mainly used for operations in continuous cutting, e.g., turning, drilling, etc., with the application of cutting fluid.

TiCN provides higher hardness than TiN, and it shows high resistance against oxidation at increased temperatures. TiCN coating is mostly used for milling at increased cutting speeds.

TiAlN has high hardness and increased resistance against oxidation. This material is recommended for high-speed machining combined with flood type application of cutting fluid.

CrN and TiCrN possess high hardness at a rather high level of plasticity. They have high resistance against corrosion and oxidation. HSS tools coated with CrN and TiCrN are recommend for finishing and semifinishing operations at milling with the application of cutting fluid.

Cemented Carbides

Cemented carbides are two-phase or multiphase alloys manufactured by powder metallurgy with a metallic binder. The materials used are tungsten carbide (WC: α-phase), titanium carbide, and tantalum carbide (TiC, TaC: γ-phase). The binder is cobalt (Co; β-phase) with a content of 5–15%. Nickel and molybdenum binders (Ni, Mo) are also used in so-called *cermets* (also cemented carbides). A higher β-phase content increases toughness, while a higher α-phase content increases wear resistance, and a higher γ-phase content enhances wear resistance at high temperatures. Cermets have high edge strength and cutting edge durability. They are suitable for finishing under stable cutting conditions. The manufacturing of cemented carbides by powder metallurgy permits considerable freedom in the choice of constituents (in contrast to casting).

Cemented carbides retain their hardness up to over 1000 °C (Fig. 12.31). They can, therefore, be used at higher speeds (by a factor of 3 or more) than high-speed steels. According to standards (DIN 4990/ISO 513), [12.25, 26] cemented carbides are classified into the metal cutting application groups P (for long-chipping, ductile ferrous materials), K (for short-chipping ferrous materials), M (for ductile cast iron and for ferritic and austenitic steels), N (for nonferrous metals such as aluminum and copper alloys), S (for superalloys and titanium alloys), and H (for hardened materials, such as steels and cast irons). Each group is subdivided due to toughness and wear-resistance grades by adding a num-

Table 12.8 Classification of cemented carbides according to ISO 513:2004-07

Groups of cutting carbide materials			Subgroups of application		Hardness, wear resistance, cutting speed	Toughness, bending strength, feed speed
Designation	Color	Material machined				
P	Dark blue	Steel: all steel, cast steels, except stainless steels	P01 P10 P20 P30 P40 P50	P05 P15 P25 P35	↑	↓
M	Yellow	Stainless steels: austenitic stainless, austenitic-ferritic steels, cast steels	M01 M10 M20 M30 M40	M05 M15 M25 M35	↑	↓
K	Red	Cast irons: cast irons with lamellar graphite, cast irons with spherical graphite	K01 K10 K20 K30 K40	K15 K25 K35	↑	↓
N	Green	Nonferrous metals: aluminum and other nonferrous metals, nonmetal containing materials	N01 N10 N20 N30	N05 N15 N25	↑	↓
S	Brown	Special alloys and titanium: heat resistant special alloys, ferrous – nickel-cobalt, titanium and titanium alloys	S01 S10 S20 S30	S05 S15 S25	↑	↓
H	Gray	Hard materials: tempered steel, high-strength pig iron, chilled cast pig iron	H01 H10 H20 H30	H05 H15 H25	↑	↓

ber. For example, P02 stands for very hard-wearing cemented carbide and P40 stands for tough cemented carbide. The metal cutting application groups do not correspond to grades of cutting tool material, but to the application areas of the finished cutting tools.

Most cemented-carbide cutting tools are coated with titanium carbide (TiC), titanium nitride (TiN), aluminum oxide (Al_2O_3), or chemical or physical combinations of these substances. The coatings are applied by CVD or PVD techniques. They are used to achieve longer tool lives or higher cutting speeds. They broaden the range of use of a grade. Coated cemented carbides should not be used for nonferrous metals, high-nickel ferrous materials, or, because of the edge rounding caused by the coating process, for precision or ultra-precision machining (cermets are better suited for this purpose). Intermittent cutting and milling requires coatings of especially high bonding strength, which can be influenced by process control during coating.

The application areas of carbides fall into six groups, as shown in Table 12.8. The classification is based on the properties of each grade and the machining conditions, type of material being machined, and chip formation.

Ceramics

Ceramic cutting tool materials are single-phase or multiphase sintered, hard materials based on metal oxides, carbides, or nitrides. In contrast to cemented carbides, no metallic binders are needed, and the material provides high hardness even at temperatures above 1200 °C. Ceramic inserts are generally suitable for machining at high cutting speeds, usually exceeding 500 m/min.

The use of aluminum oxide ceramic is restricted by its lower bending strength and fracture toughness compared to cemented carbide. In intermittent cutting with alternating mechanical and thermal stresses,

Table 12.9 Properties of oxide ceramics

Properties	Al_2O_3	Al_2O_3-ZrO_2	Al_2O_3-TiC	Al_2O_3 with SiC whiskers
Hardness (30 HV)	2000	2000	2200	2400
Young's modulus (GPa)	390	380	400	390
Bending strength σ_B (MPa)	350	600	600	600–800
Fracture toughness K_{1C} (MPa $m^{1/2}$)	4.5	5.8	5.4	6–8
Coefficient of thermal expansion α (10^{-6} K^{-1})	7.5	7.4	7.0	–
Thermal conductivity λ (W/(m K))	30	28	35	35

Table 12.10 Application of and cutting parameters for PCB and PCD tools

Work material	Cutting speed (m/min)	
	Turning	Milling
PCB		
Structural and tool steels (without thermal treatment) (< 30 HRC)	–	400–900
Hardened steels (35–55 HRC)	50–200	200–400
Hardened steels (55–70 HRC)	40–120	80–300
Gray iron, high strength cast iron (150–300 HB)	300–1000	600–3000
White cast iron and hardened cast iron (400–650 HB)	40–200	150–800
PCD		
Aluminum and aluminum alloys	600–3000	600–6000
Al-Si-alloys (Si < 20%)	500–1500	500–2500
Copper and copper alloys	300–1000	300–2000
Composed nonmetallic materials and plastics	200–1000	200–2000
Wood	–	2000–4000
WC-Co carbides	15–30	15–45

microcracking, crack growth with microchipping, or total fracture can occur. This effect greatly depends on the nature and composition of the ceramic. The change from single-phase materials (Al_2O_3) to multiphase materials has improved toughness considerably: today, Al_2O_3 containing 10–15% ZrO_2 (transformation toughening), Al_2O_3 with TiC (dispersion strengthening), or Al_2O_3 reinforced with SiC whiskers (high toughness) are used. The main field of application is the turning of flake graphite cast iron at high cutting speeds, though the turning of steel is also feasible. Additions of up to 40% TiC to the Al_2O_3 ceramic (black mixed ceramic) increase toughness and edge strength. These are used for hard machining and the finishing of cast iron.

Silicon nitride (Si_3N_4) exhibits many excellent cutting material qualities (high strength, hardness, oxidation resistance, thermal conductivity, and resistance to thermal shock) owing to strong covalent bonding of the elements. Here, fracture toughness is not a primary limiting factor in selecting application areas. Sintered Si_3N_4 ($\rho = 3.1\,g/cm^3$, $R_m = 650\,MPa$), hot-pressed Si_3N_4 ($\rho = 3.2\,g/cm^3$, $R_m = 700\,MPa$), and the material system Y-Si-Al-O-N are all used as cutting tool materials. The manufacture and use of Si_3N_4 is currently limited by the sintering auxiliaries (e.g., magnesium oxide, yttrium oxide), which determine the glassy phases in the cutting material. When machining steel or ductile cast iron, failure occurs due to severe wear; Si_3N_4 is suitable for turning and milling of gray cast iron, for highly intermittent cutting actions, and for the turning of high-nickel content materials. The properties of some oxide ceramic materials are given in Table 12.9.

Superhard Cutting Tool Materials

Superhard cutting tool materials include polycrystalline diamond (PCD), polycrystalline cubic boron nitride (PCBN), monocrystalline diamond (MCD), and various forms of chemical vapor deposition diamonds (both thin-film coatings and self-supporting thick films). The polycrystalline diamond is typically manufactured as a *backed* 0.5–2.0 mm layer of superhard composite on a cemented carbide substrate. PCD is used to machine nonferrous metals, including metal matrix composites (MMC), wood, composites, stone, and certain cast irons. Due to a well-defined maximum operating temperature of between 700–800 °C, it cannot be used for machining of steels. PCBN is manufactured either as a carbide-backed or solid material. Different grades of PCBN are used for the machining of gray, white, and high-alloy cast irons, and hardened steels. Coatings on PCBN tools are becoming increasingly popular as with cemented carbides. Monocrystalline diamond tools are used for high-precision and ultraprecision machining of aluminum, copper, electroless nickel, glass, plastic, and silicon where, for example; surface finish require-

Table 12.11 Tool clamping devices for advanced applications (after [12.28])

Shank-type tool clamping devices	Precision collet chuck	Hydraulic expansion chuck	Heat shrink chuck
			
rmp	< 20 000	< 30 000	< 30 000
Torque	Average	High	Very high
Accuracy	< 3 µm	< 3 µm	< 2 µm
Damping	Good	Very good	Very good
Stiffness	High	Very high	Very high
Handling	Average	Very simple	Complex

ments of several nm and form errors of less than 0.1 µm are common [12.27]. Because it is a single-crystal material, it is possible to produce an extremely sharp cutting edge, within the range of 10–100 nm. Thick-film CVD diamond is generally considered as lying between monocrystalline and polycrystalline diamond, in terms of properties and behavior in application.

In Table 12.10, conditions of cutting parameters and application areas of PCB and PCD tools are shown.

12.1.7 Tooling

The design of tools has to take all possible impacts into account, which can occur during the specific process, comprising mechanical, thermal and chemical loads, as well as flexibility, changeability, maintenance, and costs. Therefore, solid tools, tools with brazed tips, and tools with indexable inserts are in use.

In turning, the toolholders have to be mounted to the different types of turrets on a lathe, taking into account tool changing time and collision contours. In the case of driven tools, like milling, shank-type cutters have to be clamped in specific toolholders, which are used as an interface between the actual cutting tool and the main spindle of the milling machine (Table 12.11). The stiffness of the cutters and the toolholders is important for the required surface quality and has a strong influence on the probability of chatter in milling.

In the case of high performance or high-speed cutting conditions, significant attention has to be paid to the quality of the machine–tool-interface regarding unbalance, stiffness, and damping [12.28, 29]. The machine facing side of these toolholders is standardized. Most often, short tapers, steep-angle tapers, or hollow shank tapers are used. The toolholders are fixed in the main spindle by mechanical or hydraulic power.

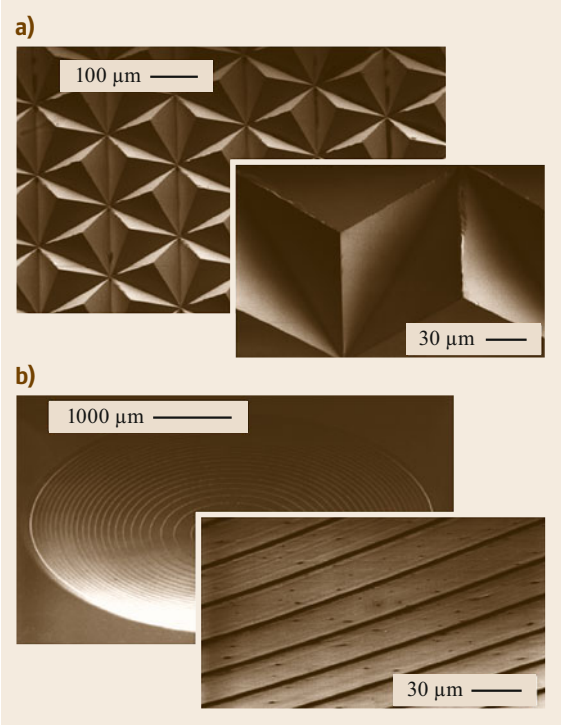

Fig. 12.32a,b Features produced by diamond microcutting (source: LFM, Bremen; after [12.33]). **(a)** Mold for reflection foils with microprisms, material: $AlMg_3$, cutting process: diamond fly cutting; **(b)** injection mold for Fresnel lenses, material: electroless nickel coating on powder metallurgical steel, cutting process: diamond turning

A number of different toolholder systems are available on the market. This system, the machine tool, and the tool changer determine the possible chip-to-chip time in the case of a change of the tool [12.30].

12.1.8 Microcutting

Micromanufacturing is defined as the production of components with feature sizes in the range of 1–500 µm. Microcutting is, therefore, a process used for the production of components of micron dimensions with submicron-form accuracy and surface roughness to within a few tens of nanometers [12.31, 32], achieved by the mechanical removal of material using defined edge tools. Common microcutting operations include microturning, microdrilling, and micromilling. Examples of features produced by microcutting are shown in Fig. 12.32, while microcutting tools are shown in Fig. 12.33.

The scale of the tool cutting edge geometry, often simplified as a single radius of curvature, is generally similar to the scale of the undeformed chip thickness

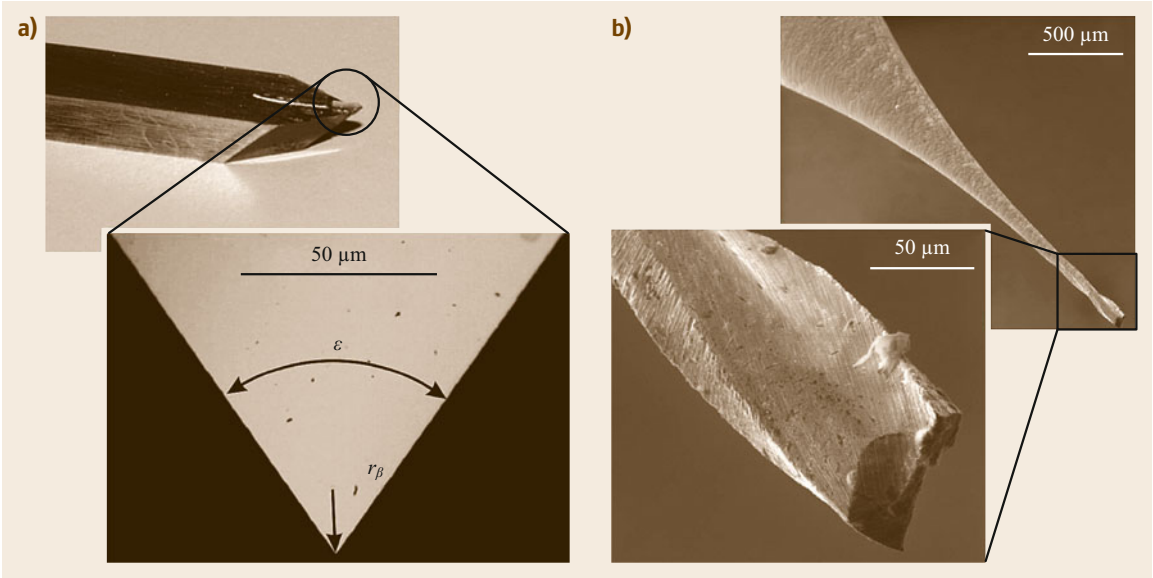

Fig. 12.33a,b Microcutting tools for turning (source: LFM, Bremen) and milling (source: IPK, Berlin; after [12.27, 34]). **(a)** Monocrystalline pointed diamond tool, nose angle ε: 70°30′, cutting edge radius γ_β: < 50 mm; **(b)** micro end mill $D = 0.1$ mm, cemented carbide substrate, coating: TiAlN

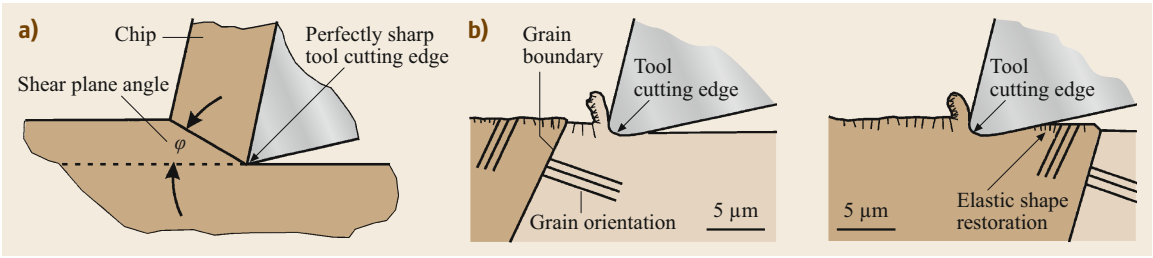

Fig. 12.34 **(a)** Conventional orthogonal cutting and **(b)** microcutting showing finite tool cutting edge geometry and workpiece anisotropy

(as indicated in Fig. 12.34b). The result is a *size effect* due to a more negative *effective rake angle* as the undeformed chip thickness is reduced. There is also an increase in friction, elastic and ploughing energies, relative to the energy expended in material removal, and, therefore, an increase in the specific cutting energy. The increasing negative rake produces hydrostatic stresses in the near surface, enabling ductile mode machining of brittle materials (optical glasses, ceramics, etc.) [12.35]. An isotropic material size effect also pertains, whereby the material strength approaches the theoretical value due to the reduction in dislocation density in the cutting zone as the undeformed chip thickness decreases.

The work material microstructure may also affect the performance of the microcutting process. For example, the grain size and anisotropy of polycrystalline (PC) metals and alloys can affect the surface finish. Figure 12.34b shows a simplified model of this mechanism. The modulus of elasticity E of a PC material varies in different atomic lattice directions. After the cutting tool has passed, as shown, the grains return to equilibrium positions (the *springback effect*) but to different surface levels due to the differences in the crystal orientations and modules of elasticity.

Tool materials for microcutting must be of high hardness. Diamond tools are generally used for cutting nonferrous metals, ceramics, semiconductors, and glasses. Tungsten carbide is used for ferrous-based metals where diamond tools are limited due to their wear conditions (graphitization, oxidation, diffusion, and carbide formation). Single-crystal diamond cutting tools are preferred for microcutting, as they can have cutting edge *radii* in the order of 10 nm. With polycrystalline tools, such as tungsten carbide-based tools, the edge sharpness achievable is limited by the grain size. Ferrous alloys were recently machined with

single-crystal diamond tools using ultrasonic elliptical vibration cutting to lower cutting temperatures [12.36].

The mechanics of tool and machine-tool design must be considered in microcutting. Tools with a small diameter for microdrilling and micromilling require very high spindle speeds. Furthermore, the precision of a machine tool has to be increased in order to maintain a given relative dimensional tolerance. As a component and associated load are reduced in scale, the structural stiffness will decrease, and the natural frequency and internal stresses will increase. Finally, the ratio of the total surface area to the workpiece (feature) volume is increased in microcomponents, making the surface integrity of the component more significant in comparison with bulk properties.

12.1.9 High-Speed Cutting

The development of high-efficiency machine tools and new cutting tool materials facilitated the application of high-speed cutting (HSC) in metal working.

The main objective of HSC application is to the reduce machining time and increase the removal rate. High cutting speeds lead to lower cutting forces, higher machining accuracy, and improved surface quality compared to traditional cutting [12.37].

The high-speed machining (HSM) concept was initially developed for the aerospace industry, especially for machining titanium alloys, but it was soon adapted by other industrial branches using different materials. At present, a range of materials are being machined with HSM, including nickel-based alloys, titanium, steel, cast iron, aluminum, and reinforced plastics. Industries using HSM include the aerospace, automotive, and tool/die industries, just to mention the most important users, primarily for manufacturing parts made from aluminum, titanium, and steel alloys. There are a number of extremely important challenges affecting high-speed machining, namely the need for hard machining, environmentally-friendly hard machining, and the machining of free-form (sculptured) surfaces, high material removal rates, and increased productivity and quality.

In aerospace, the wing spar and stringer components are made from high-grade aerospace aluminum materials. Typically, at least 85% of the aluminum billet is turned into chips, which requires excellent off-line work preparation to eliminate machine tool loading time waste, powerful chip management, and cutting fluid management systems. It is extremely important in the aerospace industry that the HSM technology does not induce residual stresses into the machined component, thus it drastically reduces the problem otherwise caused by fatigue. It is also important that thin walls can be machined easily without deformation.

There are a number of major automotive industries in the world that also use HSM for making their strategic components in combination with hard cutting to replace the very expensive grinding technology.

In the tool/die industry, tools and dies are normally made of difficult-to-machine alloys, which have to be heat treated for high production performance. This represents an extremely great challenge for high-speed machining, including machine tools, cutting tools, and technology alike.

In HSM, the maximum cutting speed depends upon the workpiece material, the type of cutting operation, and the cutting tool used.

Salomon proposed to use high cutting speeds when machining various materials [12.38]. This idea was based on the hypothesis that when the cutting speed increases to a critical value, the cutting temperature decreases. Some research has been carried out with cutting speeds within the range of $v_c = 47\,000–132\,000\,\mathrm{m/min}$. The most general definition of HSM is the economical utilization of resources and functions to remove the greatest amount of material in the shortest time span by mechanical means.

The achievable maximum cutting speed largely depends on the available high-speed spindle technology and tool technology, including the tool diameter. The high-speed range lies between 800 and 10 000 m/min, depending on the cutting material, productivity, and accuracy [12.39].

In principle, the higher the cutting speed, the more energy is required to remove material [12.40]. The heat generated causes a softening of the material, thus the energy requirement is reduced. During high-speed machining, friction and the length of the contact area between the chip and the rake face of the tool reduce contact time. This results in corresponding heat distribution in the cutting system and decreased intensity of heat flow to the tool and workpiece.

The increased productivity of processes using HSC is attributed to the improved material removal rate. Reduction of cutting forces, the thermal emission level at the cutting area, and the thermal-mechanical effect on the machined surface, as well as its elastic form recovery allows considerable improvement of quality and accuracy of machined parts.

HSC has a number of competitive advantages over traditional machining:

- A substantially increased material removal rate.
- An excellent surface finish with superb surface integrity.

Table 12.12 Examples of high-speed cutting technologies

Material	Cutting tool	Machining operation	Cutting speed (m/min)
Al-alloys	Coated carbides, PCD	Milling	1000–7000
Mg-alloys			
High-temperature steel, graphite, copper	Coated carbides, cutting ceramics, PCB	Milling	350–2000
Reinforced plastics, nonferrous metals	Coated cermets	Drilling	100–300

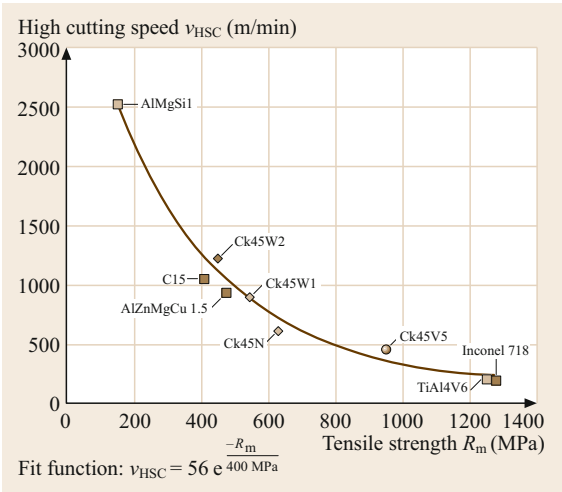

Fig. 12.35 Material dependence definition of HSC (after [12.41])

- Low cutting forces, which allow for the machining of thin-walled sections.
- A high-frequency system that does not cause any vibration during machining. .
- *Cold* machining, whereby the chips take away most of the heat generated in the process.
- An increased accuracy of machining.

Table 12.12 shows some high-speed cutting applications.

The efficiency of high-speed cutting becomes apparent when cutting hardened steels with hardness above 45 HRC. HSC of hardened steels and refractory materials is only possible at a small depth of cut and with small wear land of the cutting tool. Machine tools for high-speed cutting should have high rigidity and be equipped with a high-pressure or minimum-quantity lubrication system.

In any case, the definition of a high cutting speed is material dependent. In Fig. 12.35, an attempt is presented to deduce the area of the high cutting speed v_{HSC} from material properties. Extensive research has led to the conclusion that the tensile strength of the workpiece material is suitable for a definition of v_{HSC} by means of an empirical equation [12.41].

High-Efficiency Machining (HEM)

High-efficiency machining means cutting a part in the least amount of time, which is the real target function in machining. High-efficiency machining can be achieved by a variation in the feed rate. Typically, high-speed machining is accomplished with very small axial cut depths in order to achieve good surface finish and avoid damage to the cutter, workpiece, or spindle. Feed-rate optimization software can be employed to achieve better cutting efficiency with greater axial depths at high feed rates similar to those of HSM and to protect the cutter in those few places where the chip load momentarily increases. Constant chip load tool paths allow optimum use of the cutter's strength and the machine's speed and power. The software detects conditions under which the chip load would be too high and adjusts the feed rate to a more reasonable level. It returns to the higher feed rate when it is suitable [12.42].

Thin-walled components are widely used in the aerospace industry. However, thin-walled components deflect very easily under the cutting forces during the cutting process, which results in compromised machining precision and efficiency. Some solutions have been proposed for the control of machining deflection, such as the NC compensation approach by a tilting tool.

Using this method, the machining deflections are analyzed by FEM. Then, the feed rate is adjusted to the degree of deflection by CNC (computerized numerical control) compensation in order to cut off the excessive material due to the deflection. Thus, the thin-walled component can be machined with high precision and high efficiency on a five-axis CNC machining center.

12.1.10 Hard Machining

Machining of steels of hardness beyond 45 HRC (hardness Rockwell cone) is often required in metal cutting; this is called hard machining. Therefore, hard machining, turning, milling, and drilling, are viable alternatives to grinding.

Hard machining is characterized by a low friction coefficient in the cutting area, the application of a relatively high cutting speed, low feed and depth of cut, which result in reduced chip–tool contact length. Due to the redistribution of the heat generated that causes

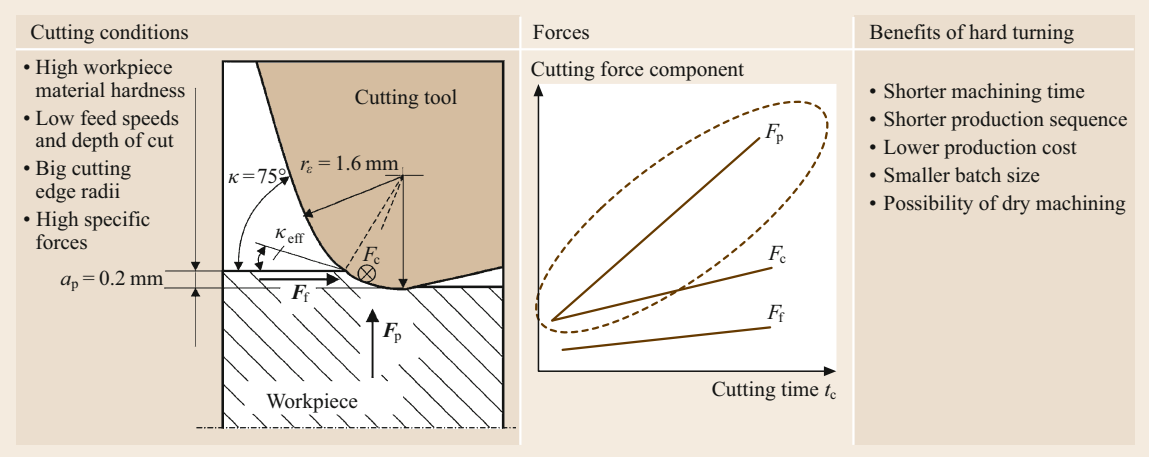

Fig. 12.36 Principle and benefits of hard turning (after [12.43])

a softening of the material and to the high compression load on the workpiece material, machining efficiency increases. The major breakthrough of this technology was connected with the introduction of suitable cutting tool materials such as ceramics and CBN for turning and coated tungsten carbides for milling and drilling. These developments made hard machining a serious competitor for grinding and electro-discharge machining. As an example of successful application of hard machining, the conditions and benefits of hard turning are presented in Fig. 12.36. It is important to mention that this is the fast-rising and dominating passive or back force F_p, which needs an excellent lathe with superior stiffness to compete with grinding. Also the possibility to apply dry machining is a major benefit, allowing all costs and problems related to cutting fluids to be avoided.

12.2 Machining with Geometrically Nondefined Tool Edges

12.2.1 Fundamentals

Machining with geometrically nondefined tool edges is cutting by the mechanical action of cutting edges on the material. The cutting edges are formed by grains of hard material that are randomly shaped and arranged. They are either bonded together into a tool (grinding, honing) or are used loose (lapping, abrasive blasting). The cutting edge geometry is not described with reference to a single grain. The individual cutting edge is geometrically nondefined. The processes are divided into the following subgroups:

- Grinding with rotating tools
- Belt grinding
- Honing
- Lapping
- Free abrasive grinding/abrasive tumbling
- Machining by abrasive blasting.

The common factor in these processes is that the grains of hard material generally form several cutting edges. The important cutting edge angles for chip formation, the clearance angle α, the rake angle γ, and the wedge angle β are only indicated by means of statistical parameters such as mean values or distributions. On average, sharply negative rake angles and large contact and friction zones are formed between the grain and the workpiece. The cutting edges penetrate only a few micrometers into the material. The undeformed chip thickness distribution depends on the positioning of the cutting edges in the mixture of grains (microtopography of the cutting zone) and the geometry of the machined workpiece surface. Not only chip removal but also elastic and plastic deformations without chip removal take place.

High normal forces result between tool and workpiece at the predominantly negative rake angles of the cutting edges. They lead to elastic deformations in the machine (stretching of the frame and deflection of the spindle), the tool, and the workpiece. The amplitude of deformations may be comparable to the normal small feed motions. Therefore, a distinction should be made between the theoretical and the actual feed motion (Fig. 12.37).

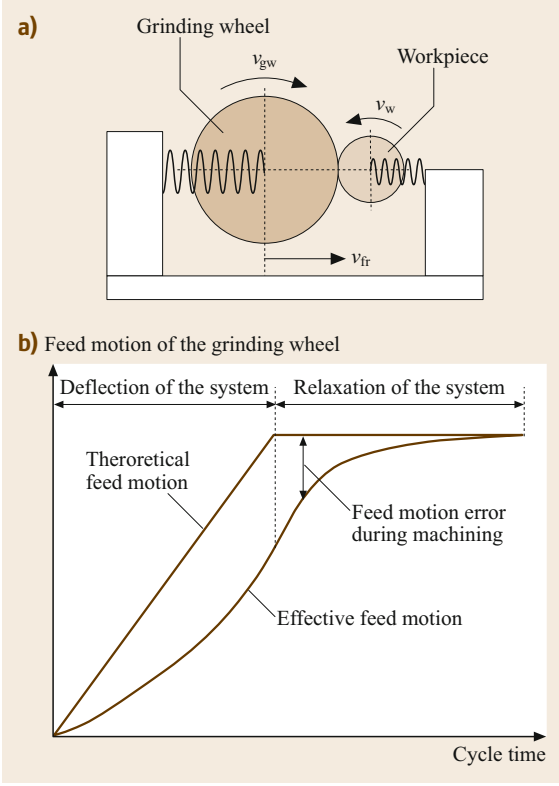

Fig. 12.37a,b Feed motion errors in grinding due to elastic deformations in the machine tool–workpiece system. **(a)** Elastic model of the tool–workpiece system. **(b)** Theoretical versus effective feed motion

Machining processes with geometrically nondefined tool edges are frequently used as final machining processes for workpieces subject to exacting quality requirements. Figure 12.38 shows a comparison of various precision machining processes with regard to operational results and efficiency. It can be seen that the grinding processes achieve high rates of material removal, while honing and lapping are able to produce the best surface qualities.

The chip formation mechanism when using geometrically nondefined tool edges differs from that of machining with geometrically well-defined tool edges (Fig. 12.39). In phase 1, the often sharply negative rake angle of the individual grains causes elastic deformation of the material. In phase 2, plastic deformation occurs, while in phase 3, the actual chip removal takes place. A large amount of friction occurs between the individual grains and the workpiece.

The mechanical energy supplied is almost exclusively converted into heat. Figure 12.40 shows a qualitative distribution of the heat flows around an individual grain. Most of the heat generated flows into the workpiece, while a small part finds its way into the grain, the bond, and the surroundings (cooling lubricant, atmosphere). Temperature increases in the workpiece may harm its surface integrity. This is manifested in thermally-induced residual stresses, structure changes, or cracks, which influence the subsequent behavior of the workpiece in service. The use of abrasive materials (CBN, diamond) and bonds with superior thermal conductivity reduces the proportion of heat that penetrates into the workpiece [12.44, 45].

In machining with geometrically nondefined tool edges, the use of cooling lubricants is important for the end result. The cooling and lubricating effect can reduce tool wear. Furthermore, the temperature of the workpiece is reduced, and the danger of thermal damage to its surface is decreased. The lubricants used are nonwater-miscible (oils) and water-miscible (emulsions, solutions) cooling lubricants, the effect of which can be

	Grinding	Honing	Lapping
Accuracy of shape	+	0	++
Dimensional accuracy	+	++	++
Positional accuracy	+	–	–
Surface quality	0	+	++
Positive influence on surface integrity	0	+	+
Material removal rate	++	0	–
Manufacturing costs	–	+	++

– Minor influence + Major influence
0 Moderate influence ++ Superior influence

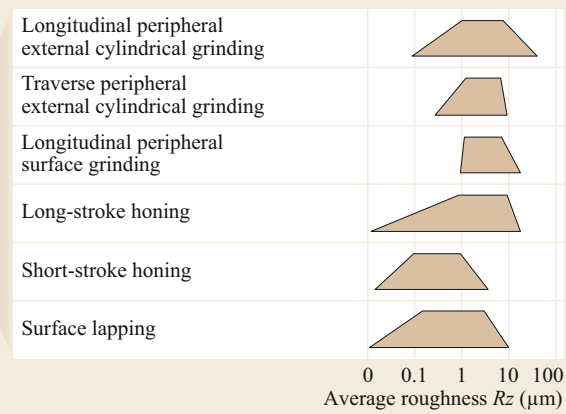

Fig. 12.38 Economic and technological comparison of various precision machining processes

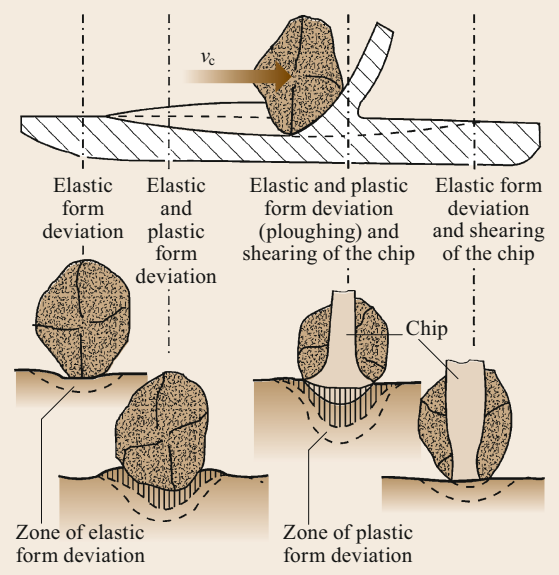

Fig. 12.39 Phases of chip formation during grinding

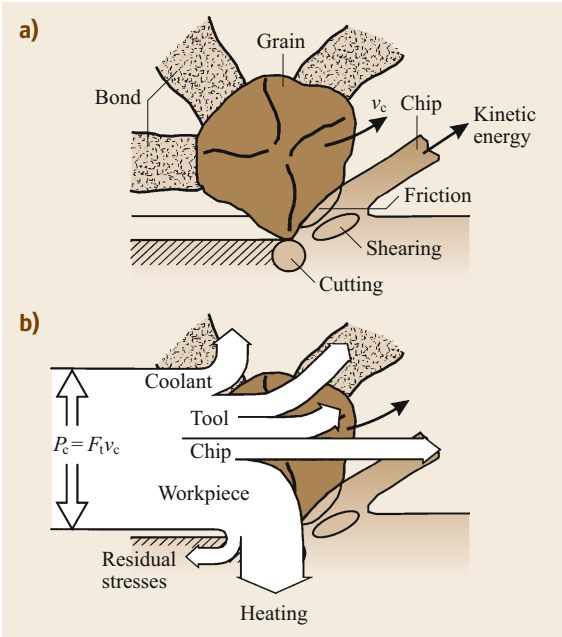

Fig. 12.40a,b Energy conversion: **(a)** effects of energy conversion; **(b)** energy flows

further improved with additives (polar and EP additives to improve the lubricating effect, antifoaming agents, biocides, and rust inhibitors). The cooling effect depends on physical parameters: the specific heat capacity c in kJ/(kg K), the heat transmission coefficient α in W/(m^2 K), the thermal conductivity λ in W/(m K), the heat of evaporation I_d in kJ/kg, and the surface tension σ in N/m. The lubricating effect is described by the tribological parameters of the cooling lubricant.

A comprehensive study on the main effects of coolant type, composition, and application in grinding is presented in [12.46]. The correct selection and use of grinding fluids normally results in enhanced process performance, better workpiece quality, and longer tool life. Lower volumetric wear of the wheel and improved surface finishing are achieved when neat oil is used instead of water-based fluids. On the other hand, water-based fluids can reduce workpiece temperature, pose less risk of fire, and are generally better suited for the working environment and the machine tool operator.

12.2.2 Grinding with Rotating Tools

Processes

Grinding can be performed in a large variety of motions. The six main classifications are related to the shape of the surfaces produced, namely surface, peripheral, thread, gear, profile, and form grinding. Figure 12.41 shows examples of various motion classifications and tool shapes.

Chip Formation

Material is removed by the penetration of abrasive grains into the workpiece material along a defined path. Owing to the generally unfavorable shape of the cutting edge, the actual chip formation is accompanied by friction and displacement processes. The process is evaluated by calculating statistical averages. Figure 12.42 shows, in simplified terms, how a comma-shaped chip is formed by the successive action of two cutting edges. While grain 1 has traveled the path AB, the center of the grinding wheel has moved from P_0 to P_1. The next grain 2 will travel the path CD. In this process, the thickness of an average chip increases from 0 up to h_{max}. A simple relationship for the average undeformed chip thickness $\overline{h}$ is obtained by applying the continuity relationship

$$v_{ft} a_e a_p = v_c C V_{sp} a_p \,, \tag{12.46}$$

$$\overline{h} = \frac{v_{ft}}{v_c} \frac{1}{\overline{b} C} \sqrt{\frac{a_e}{d_{eq}}} \,, \tag{12.47}$$

with $\overline{l} = \sqrt{a_e d_{eq}}$, $V_{sp} = \overline{l}\,\overline{b}\overline{h}$ and $d_{eq} = (d_w d_s)/(d_w \pm d_s)$ (+ external cylindrical grinding, − internal cylindrical grinding) or

$$\overline{h} = \sqrt{\frac{v_{ft}}{v_c} \frac{1}{rC} \sqrt{\frac{a_e}{d_{eq}}}} \quad \text{with} \quad r = \frac{\overline{b}}{\overline{h}} \,. \tag{12.48}$$

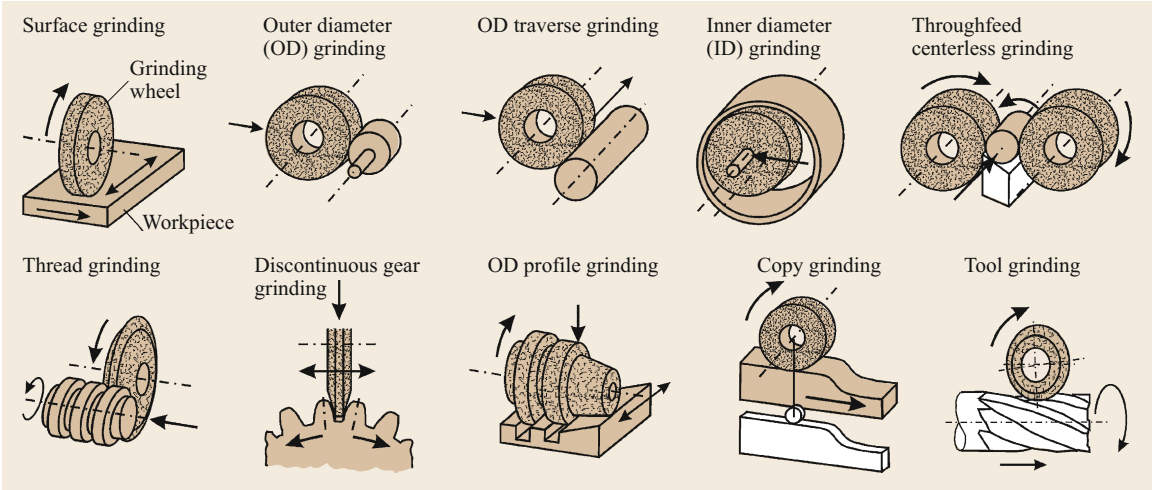

Fig. 12.41 Various grinding processes

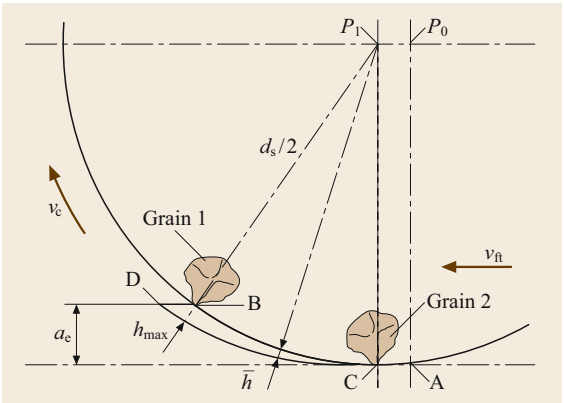

Fig. 12.42 Chip formation in surface grinding

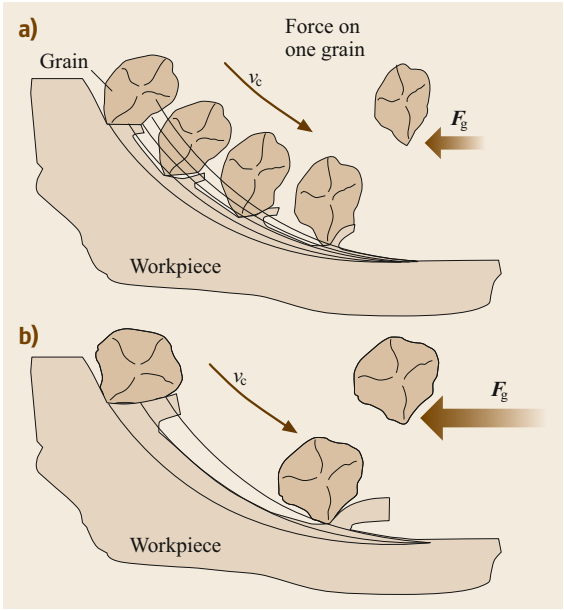

Fig. 12.43a,b Influence of grain concentration on the chip formation mechanism. **(a)** High grain density; **(b)** low grain density

The symbols are as follows: $\overline{h}$ is the average (undeformed) chip thickness, $\overline{l}$ is the average (undeformed) chip length, $\overline{b}$ is the average (undeformed) chip width, v_{ft} is the feed speed of the workpiece, v_c is the cutting speed, a_e is the depth of cut, a_p is the width of engagement (width of grinding), d_{eq} is the equivalent grinding wheel diameter, d_s is the grinding wheel diameter, d_w is the workpiece diameter ($\rightarrow \infty$ in surface grinding), C is the number of active cutting edges per unit of surface area of the grinding wheel, and r is the ratio of the average chip thickness to the average chip width. The maximum chip thickness h_{max} is twice the average chip thickness $\overline{h}$.

The chip thickness is highly dependent on the concentration of abrasives on the grinding wheel surface C (Fig. 12.43). Higher grain density leads to thinner chips and, consequently, lower forces per grain. The grain density decreases with increasing grain size. The correction of these parameters can influence the wear mechanisms on a grinding wheel. Owing to technical difficulties in measuring the number and distribution of grains, the equivalent chip thickness h_{eq} is often used as a parameter for evaluating the grinding process [12.47]. This parameter is directly related to the grinding forces and surface finishing

$$h_{eq} = a_e \left(\frac{v_{ft}}{v_c} \right) . \qquad (12.49)$$

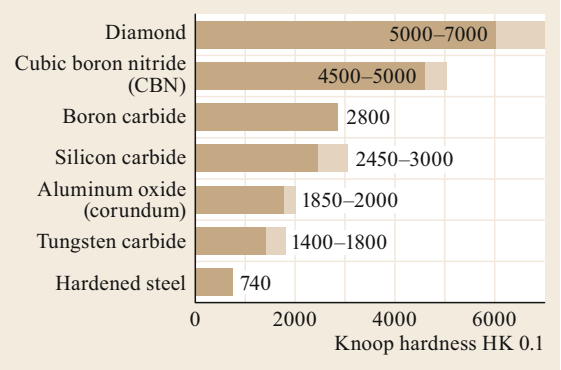

Fig. 12.44 Knoop hardness of various materials

Composition of Grinding Wheels

A grinding wheel consists of grains, bonding material (bond), and pores. The abrasive materials used are hard-brittle ones such as zirconium-corundum (ZrO_2 with Al_2O_3), corundum (Al_2O_3), silicon carbide (SiC), cubic boron nitride (CBN), and diamond (C); their hardness values are presented in Fig. 12.44. However, diamond is unsuitable for machining steel, as there is a high chemical affinity between diamond with its carbon-based cubic lattice structure and iron, which leads to rapid tool wear.

Sorting of the grains according to size is accomplished by screening. The basis of all standards is the mesh of the screens through which the abrasive grains pass. The average grain size is determined by the shape (angularity) of the individual grains. Below a certain grain size, sorting can be carried out by settlement out of a slurried suspension of water and grains. For conventional abrasives (e.g., SiC, Al_2O_3), the grain size is usually given in a mesh number; thus, high numbers represent small grain sizes in the grinding wheel specification. The grain size for superabrasive wheels (only CBN and diamond) follows the FEPA specification related to the grit diameter.

The bonding material (bond) is chosen according to the requirements of the machining process and of the grain material. Inorganic (ceramic, silicate, magnesite), organic (rubber, synthetic resin, glue) and metallic bonds (bronze, steel, cemented carbide) are used; the most popular bonds are those made of ceramic or synthetic resin. In manufacturing a tool, its structure can be influenced to a certain extent by varying the proportions of grains, bond, and pore volume [12.48].

Superabrasive wheels exhibit a particular construction. They consist of a core to which the grinding layer is applied. Usual layer thicknesses are 2–5 mm for resin or vitrified bonds. The core material can be made of metals or fiber-reinforced plastics. Superabrasive

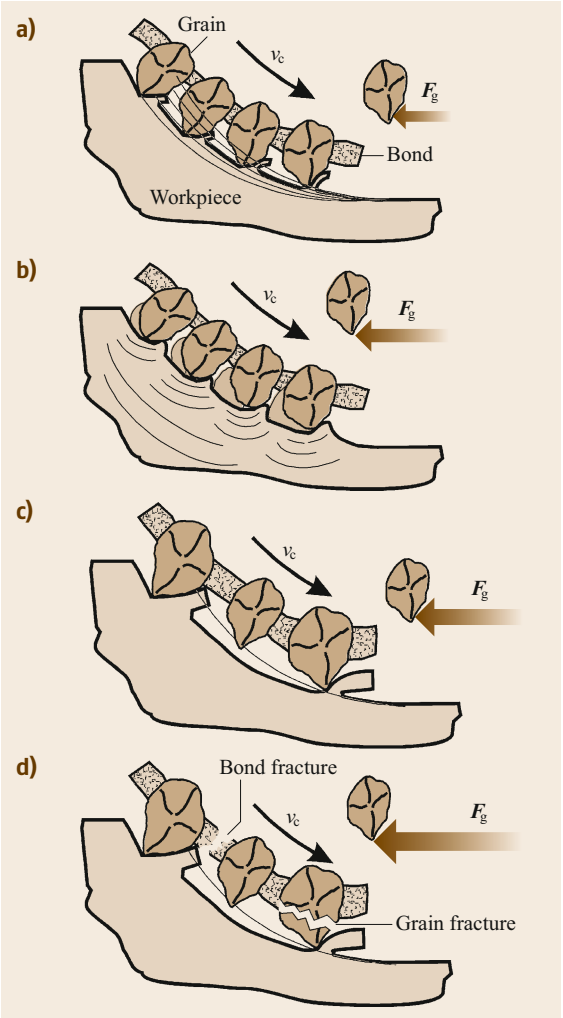

Fig. 12.45a–d Grinding wheel wear mechanisms: **(a)** sharp wheel with low load per grain, **(b)** dulling and loading, **(c)** sharp wheel with high load per grain, **(d)** grain and bond fracture due to very high load

wheels can grind at higher speeds due to the resistance of the core and the higher hardness of the grains. In the grinding wheel specification for superabrasives, the average grain size is usually directly given in µm.

Electroplated bonds are mostly used in superabrasive wheels. They are very thin since they hold only one layer of abrasives. This kind of bond is used for grinding at high speeds due to its high wear and stress resistance. Electroplated wheels are recommended for rough and semifinish grinding. The final surface finish can be obtained with vitrified or resin bonds. The specification of a grinding wheel is standardized in DIN 69100 (for conventional wheels) and ISO 6104 (for CBN and diamond wheels) [12.49, 50].

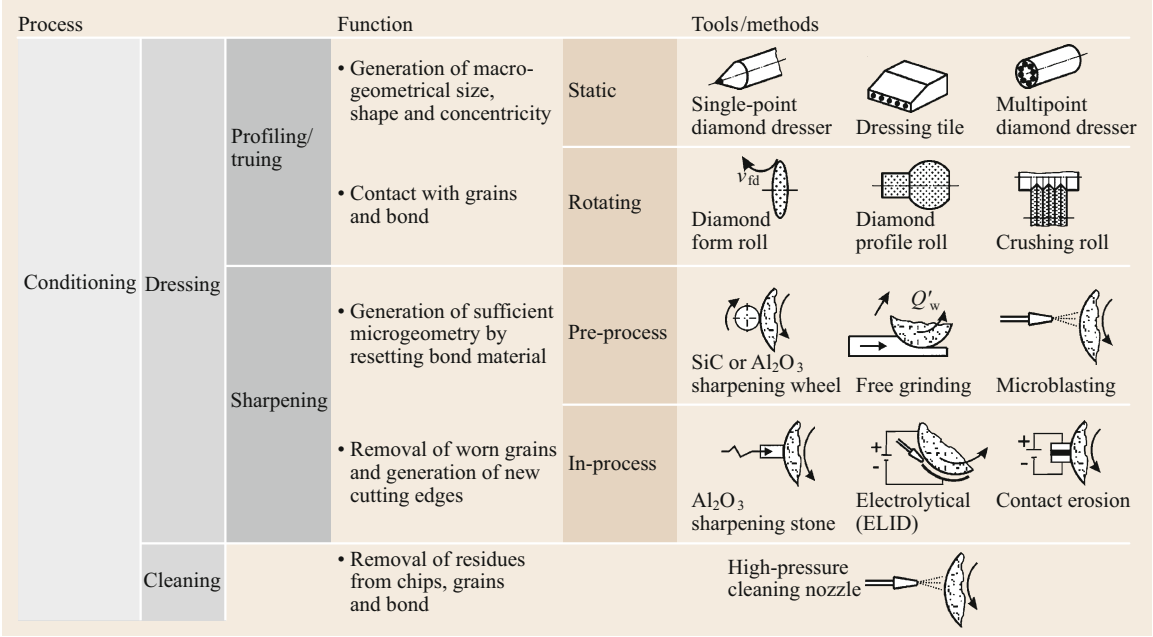

Fig. 12.46 Classification system for grinding wheel conditioning

Tool Wear

Grinding wheel wear may take place in the grains and the bond. The wear phenomena can be related to dulling or grain/bond breakage (Fig. 12.45). In dulling, wear flat areas are formed on the edges. They lead to increasing grinding forces and temperature. This normally happens when the abrasives are submitted to gentle grinding conditions. When the abrasive grains are under higher loads, the grain/bond breakage mechanisms will lead to higher volumetric wear resulting in constant grinding forces and temperature. The quality of the surface finish may deteriorate, and form errors may increase.

Grinding Wheel Conditioning

The purpose of conditioning is to give the grinding wheel the required profile and concentricity (profiling or truing) to produce the necessary grinding wheel topography with sharp grains (sharpening) and to clean the grinding wheel surface [12.51]. The first two operations are summed up under the term dressing and are generally performed simultaneously by passing a dressing tool over the surface of the grinding wheel (Fig. 12.46). In some applications, a separate sharpening step is necessary, which can be performed preprocess or in-process. It is often performed with special equipment with electrolyte supply (ELID = electrolytic in-process dressing) [12.52] or with contact erosion [12.53]. The main components of dressing tools are metallic bonds mixed with diamond particles; however, there are also single-point diamonds, diamond-free steel, and ceramic tools. They reach the end of their life when the diamond layer or the tool geometry is worn out.

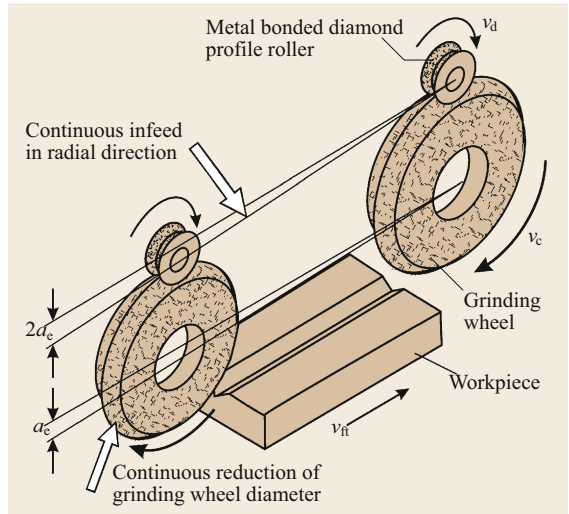

Fig. 12.47 Principle of grinding with continuous dressing (CD grinding)

A special variant of a rotating diamond form roll is called grinding with continuous dressing (CD grinding) (Fig. 12.47). Here, the dressing tool is in engagement during grinding and is continuously advanced radially to the grinding wheel. As a constant grinding wheel

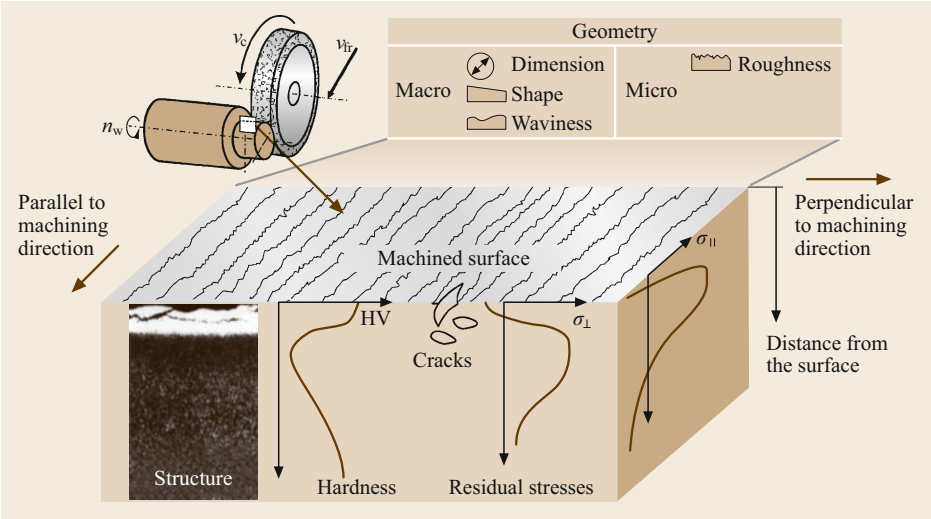

Fig. 12.48
Geometrical and physical quality characteristics after grinding

profile and a uniform grinding wheel topography with sharp cutting edges are permanently ensured, the material removal rate can be increased considerably [12.54]. With the aid of the machine control system, the dressing tool and the grinding wheel have to be advanced in relation to the workpiece in such a way that the decrease in the diameter of the grinding wheel is compensated. This technique is often used for profile grinding of difficult-to-machine materials like the nickel-based alloys used for turbine blades.

Limits of the Grinding Process

Restrictions on the process arise if the original data, e.g., dimensional accuracy, accuracy of shape, surface quality, or condition of the surface integrity of the workpiece do not lie within the required limits. The interaction of the various influencing variables, such as workpiece, machine-setting data, tool, cutting fluid, etc., may be extremely diverse. Mechanical and/or thermal overstressing of the material in the grinding process may adversely affect the characteristics of a ground component [12.55]. Typical grinding defects due to poor process control are visible marks on the surface as a result of regenerative chatter [12.56], hardness and structure changes, tensile residual stresses, and probably even cracks in the workpiece ([12.57], Fig. 12.48). The latter defects can be summarized by the term grinding burn.

Development Trends in Grinding

Grinding has been continuously developed from a traditional precision machining process to improve dimensions, shape, and surface quality into a very versatile and efficient manufacturing process. Creep-feed grinding, high-speed grinding, grinding with continuous dressing (CD grinding), the growing use of superhard abrasives combined with CNC and sensor technologies have been extensively applied in industry [12.58–60]. With the development of advanced open CNC systems, the control of grinding processes nowadays includes intelligent routines. Sensors allow the detection of contact between grinding wheel and workpiece, collisions, and wheel topographic conditions where necessary conditioning/dressing can be automatically activated [12.61]. Gear and other complex profile grinding processes have also been improved with the help of high-performance interpolation routines able to increase productivity and quality with high process flexibility [12.62]. Even the fact that grinding might generate a high amount of heat is turned into a benefit by using this energy for process-integrated hardening while grinding [12.63].

Ultrasonically (US) assisted grinding has reached industrial maturity especially for brittle materials like glass or ceramics. While in the first applications, the US-vibration was generated in a complex spindle system or from the workpiece clamping side, in latest developments the US-excitation is realized with wireless induction transmission in the tool–spindle interface, allowing the tools to be mounted to the actuating tool holder (Fig. 12.49; [12.64]).

12.2.3 Belt Grinding

Belt grinding is grinding with bonded abrasives on a supporting flexible bed. Belt grinding can also be classified according to the surfaces machined, e.g., surface, cylindrical, profile or form-belt grinding. Surface belt grinding predominates in industrial applications (Fig. 12.50). Belt grinding is normally performed at a constant perpendicular force F_n (pressing force).

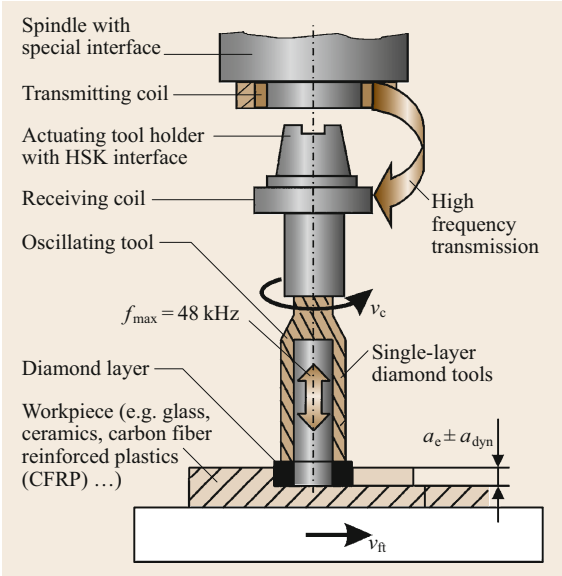

Fig. 12.49 Ultrasonically assisted grinding

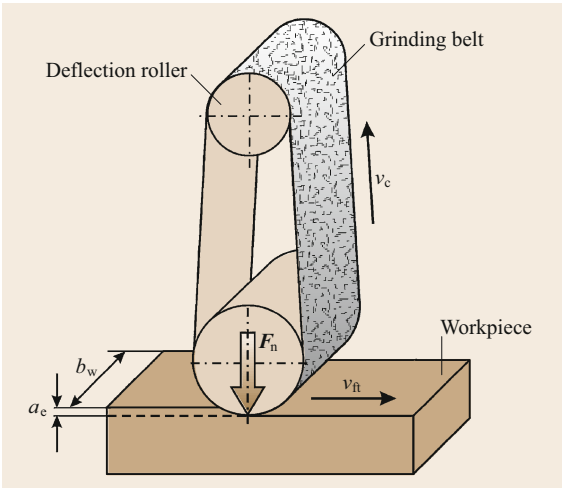

Fig. 12.50 Schematic representation of surface belt grinding

Thus, consistent surface qualities can be produced. The material removal rate is determined by the sharpness of the belt (of the active cutting edges). In belt grinding with constant working engagement a_e, a constant material removal rate is achieved. Surface quality depends on the condition of the cutting edges. This process is especially suitable for removing large volumes of material with high efficiency [12.65].

The adjustment of the process variables during belt grinding derives from the changes of the cutting edges during working. In contrast to grinding wheels, grinding belts generally consist of a single layer of

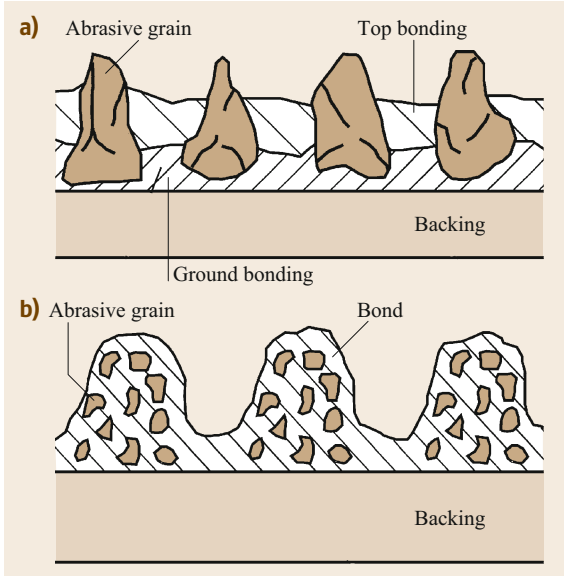

Fig. 12.51a,b Schematic setup of grinding belts. **(a)** Single-layer grinding belt; **(b)** multilayer grinding belt

abrasives. Therefore, the cutting edge zone changes over the period of use, owing to progressive abrasive and bond wear.

Grinding belts consist of four elements: backing (paper, fabric), ground bonding and top bonding materials (phenol resins), and abrasive grains (corundum, zirconium-corundum, silicon carbide). Scattering of the grains on the first coat of bonding material is carried out in an electrostatic field. This ensures that the abrasive grains are aligned perpendicularly (Fig. 12.51). An even grain distribution in belt manufacture compared with conventional gravity scattering can be achieved [12.66].

For higher material-removal rates, multilayer grinding belts are available, where several abrasive grains are held in a bond and mounted to the backing (Fig. 12.51b).

The grinding belt is supported in the working zone by contact elements. A contact disc is used in peripheral grinding, while a contact shoe or beam is used in side grinding. Hard contact rolls made of aluminum or steel are particularly suitable for roughing with coarse grinding belts because they transmit the relatively high grinding forces. Soft, rubber-coated contact rolls are used in finishing with fine grinding belts [12.67]. They absorb the shocks that occur during the process. Conventional applications of belt grinding are grinding of individual sheets and sheet coils, deflashing and deburring, and grinding down of excess metal in welded joints. Heavy-duty belt grinding might even work as a substitute for turning and milling of components made of gray cast iron or aluminum alloys [12.65, 66].

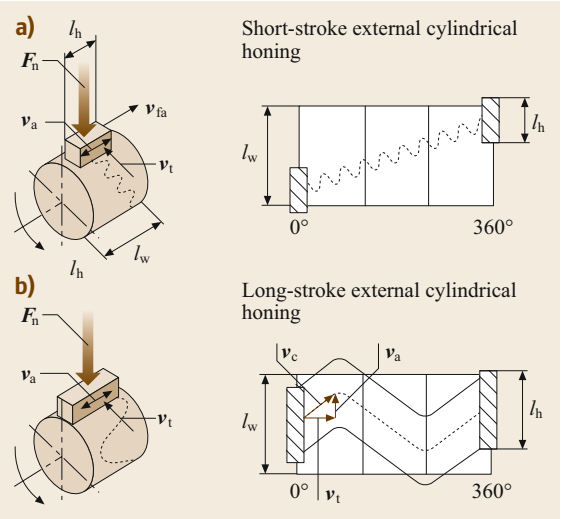

Fig. 12.52a,b Geometry and kinematics in short (**a**) and long-stroke (**b**) superfinishing

12.2.4 Honing, Superfinishing

Honing is performed with a multiple-point cutting tool consisting of bonded abrasive grains using a cutting motion with two components of which at least one is oscillating. The most common honing processes are external cylindrical honing, internal cylindrical honing, and surface honing. The external honing variant is often called superfinishing. According to the oscillation amplitude, a further distinction can be made between two main groups: long-stroke honing and short-stroke honing (Fig. 12.52; [12.68]).

Long-stroke honing employs large oscillation amplitudes at a low frequency; in short-stroke honing, the oscillating motion is performed at low amplitudes and a correspondingly high frequency. The path curves in Fig. 12.52 depict the motion of a honing strip over a developed workpiece surface.

Owing to the superimposed motion during honing, the workpiece surface exhibits intersecting tracks of the cutting grains, the two tracks enclosing an overlap angle α (Fig. 12.53). The magnitude of the overlap angle α is determined by the selection of the ratio of the axial (v_a) and tangential (v_t) cutting speed components. For workpieces without longitudinal and transverse grooves, the angle α is generally 45°. The cutting speed v_c can be calculated by means of the aforementioned speed components according to $v_c = (v_a^2 + v_t^2)^{1/2}$. Usually, the cutting speed does not exceed $v_c = 1.5\,\mathrm{m/s}$ [12.68, 69].

During the cutting motion the honing stones are pressed against the workpiece surface that is to be machined with a perpendicular honing force F_n, which may be generated by means of various feed systems (Fig. 12.54). In force-dependent feeding, a defined hydraulic pressure p_{oil} is set on the machine. The resulting advancing force F_z is transmitted to the honing stones via an advancing pin and cones. In path-dependent feeding, defined feed paths are generated e.g., with a stepping motor, which produces the perpendicular force F_n on the honing stones.

Important variables influencing the result of honing are the type of abrasive, grain size, type of bond, hardness, and impregnation of the honing stones. The types of abrasive can be classified into conventional abrasive materials, such as corundum and silicon carbide, and the superhard abrasive materials diamond and cubic boron nitride (CBN). The grain size influ-

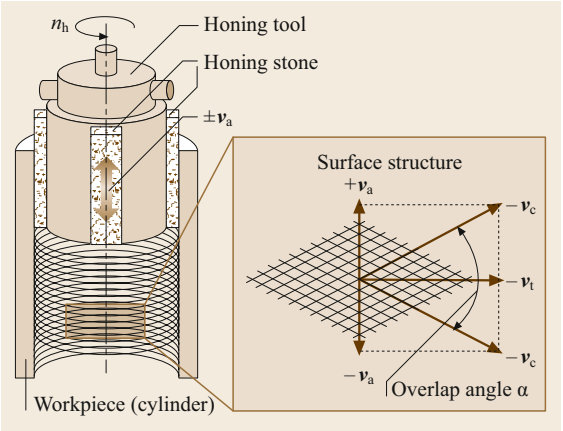

Fig. 12.53 Principle of internal long-stroke honing and the resulting surface structure

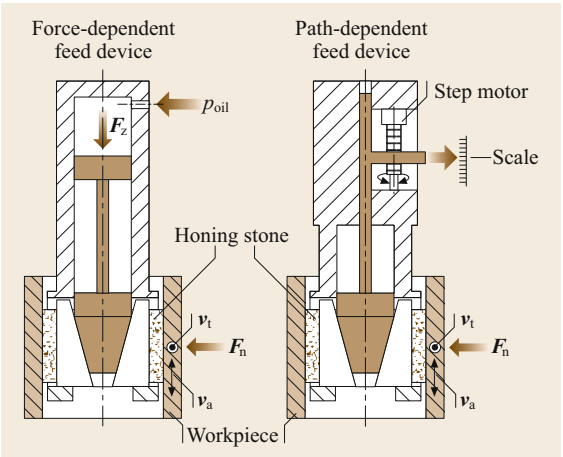

Fig. 12.54 Force and path-dependent feed devices for honing

ences the material removal rate and the surface quality. The achievable surface roughness values are $Rz = 1\,\mu m$ for long-stroke honing and $Rz = 0.1\,\mu m$ for short-stroke honing. Dimensional accuracies and accuracies of shape of the machined workpieces of $1-3\,\mu m$ are achieved [12.70]. Unlike in grinding, the grains bonded in the honing stone are stressed on more than one axis owing to the oscillating motion. Honing tools are, therefore, self-sharpening.

Cutting fluids are used in honing as well as in grinding. Due to the low cutting speed, however, heating is minimal, so the cooling effect plays a minor role. However, the surface contact between the honing stone and the workpiece requires instead a friction-reducing lubrication. For this purpose, pure oil, with additives if required, is generally used.

The applications of honing can also be categorized according to whether long-stroke or short-stroke honing is used. Long-stroke honing is generally used for bores, e.g., cylinders in internal combustion engines. Short-stroke honing is mainly used for machining small cylindrical components, e.g., running surfaces of inner and outer rings and rollers of rolling contact bearings. Furthermore, the application of gear honing should be mentioned. With the coupled motion of a gear-shaped abrasive tool and the workpiece counterpart, a high surface quality for gears can be achieved, thus qualifying honing as an attractive gear finishing technique [12.71].

12.2.5 Other Processes: Inside Diameter Cut-Off Grinding, Lapping, and Abrasive Waterjet Cutting

Inside-Diameter Cut-Off Grinding

Inside-diameter (ID) cut-off grinding is a high-precision finishing-machining process for hard-brittle materials. It is used to cut rod-shaped materials into thin slices (Fig. 12.55). Besides its applications to optical materials (glasses, glass ceramics), magnetic materials (samarium-cobalt, neodymium-iron-boron), and ceramics and crystals for solid-state-type lasers, this process is also used for semiconductor materials. Single-crystal silicon rods are cut into thin slices called wafers.

Compared to conventional abrasive cutting processes, the loss of material in the cutting gap can be reduced by approximately 80% by means of a narrow width of cut. This is a decisive advantage, especially for expensive, high-grade materials.

To achieve the narrow widths of cut that are typical of this process, a comparatively unconventional tool is used for ID cut-off grinding. The basic body of the tool consists of a cold-rolled ring of high-tensile stainless steel with a thickness of $100-170\,\mu m$.

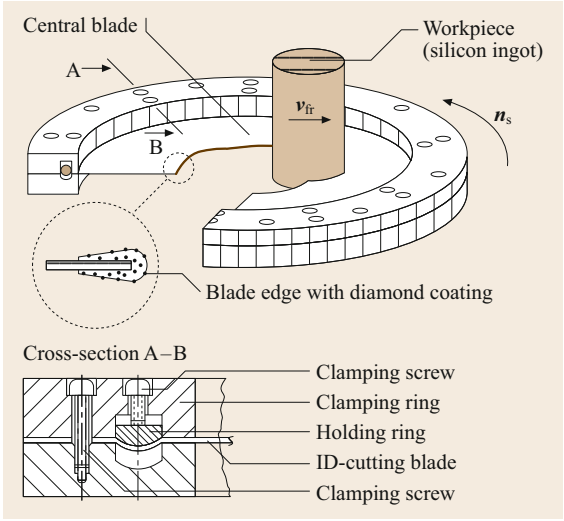

Fig. 12.55 Principle of ID cut-off grinding

The inside edge of the cutting blade is coated by electrodeposition with a diamond layer in a nickel-based bond; this layer forms the droplet-shaped cutting edge. Grain sizes commonly range from 45 to $130\,\mu m$. The width of the cut extends between 0.25 and 0.7 mm. Natural diamond is generally used as the cutting material. CBN may also be used for special applications. Workpieces with a diameter of up to 200 mm can be cut. Due to this diameter limitation, this process has lost its pole position for wafer manufacturing because of the constantly rising diameters of silicon ingots for wafer production in the semiconductor industry.

To achieve the stiffness at the cutting edge that is necessary for cutting, the cutting blade, which can be compared to an eardrum, is clamped at its outside edge with a special clamping device. This widens the ID cutting blade radially until the tangential stresses at the inside edge reach around $1800\,N/mm^2$. In cut-off grinding, the workpiece performs a radial feed motion relative to the rotating tool [12.72, 73].

Lapping

Lapping is defined in a German standard [12.1] as metal cutting with loose grains of abrasive material distributed in a paste or a liquid, the lapping mixture, which is carried on a generally shape-imparting counterpart (lap), and the individual grains following cutting paths, which are random. Lapping processes are divided into surface lapping, cylindrical lapping, hole lapping, and ultrasonically assisted lapping (Fig. 12.56).

Surface lapping or plane-parallel lapping is carried out on single-disc or twin-disc lapping machines. The lapping discs act as the holder for the lapping abrasive. They are frequently made of perlitic cast materials

or hardened steel alloys. The workpieces are usually driven in specific carrier discs, for larger diameter lapping discs often use the planetary gear principle to achieve cycloid motion. A special variant of plane-parallel lapping is based on the use of special slurry as the liquid to carry the abrasives and to improve the material removal process by chemical activation. This process is called chemical-mechanical planarization (CMP) and is widely used in the semiconductor industry to machine wafers made of silicon or other suitable materials [12.74].

The abrasive consists of lapping powder and fluid in a ratio of 1:2−1:6. Particles of silicon carbide, corundum, boron carbide, or diamond are used as the lapping powder. The type of grain for a particular application is determined by the material to be machined. Grain sizes ranging between 5 and 40 µm are generally used. Besides high-viscosity oils or similar fluids, water with suitable additives has been more and more frequently used as a transport medium for the abrasive in recent years. The main purpose of lapping fluids is to cool the workpiece and ensure chip removal from the effective zone.

Lapping is a precision or ultraprecision machining process for the production of functional surfaces of optimum surface quality. Surface roughness values down to $Rt = 0.03\,\mu m$, flatness, and plane parallelisms of $0.2\,\mu m$ are achieved. Besides the semiconductor application, other typical fields of lapping are the machining of precision-cemented carbide tools, calliper gauges, or hydraulic rams.

A special category is ultrasonically (US) assisted lapping, which is particularly suitable for machining hard-brittle materials, e.g., fully-sintered ceramic components [12.75, 76]. The process is carried out by moving a complex-shaped tool called sonotrode downwards into the workpiece while hammering the loose abrasive particles, which are supplied via a liquid to the contact zone, into the workpiece surface for material removal. If rotational symmetric shapes are to be produced, nowadays US-grinding substitutes for this lapping process due to its higher efficiency (Fig. 12.49).

Due to the above-mentioned increase of silicon ingot diameters for wafer production a special variant of lapping has been developed, called multiwire slicing by lapping (Fig. 12.57). In this process, a silicon ingot is glued to a steel support and radially fed downwards to a multiwire field. Comparable to an egg cutter, hundreds of wafers are separated at the same time, because on the specially developed high-strength wire a spray of silicon carbide abrasives in special slurry is applied. This process is capable of significantly increasing the productivity compared to ID cut-off grinding and currently works for diameters up to 300 mm. Parallel research is being done to develop an abrasive coated wire instead of loose lapping grains, thus reintroducing grinding for wafer manufacturing.

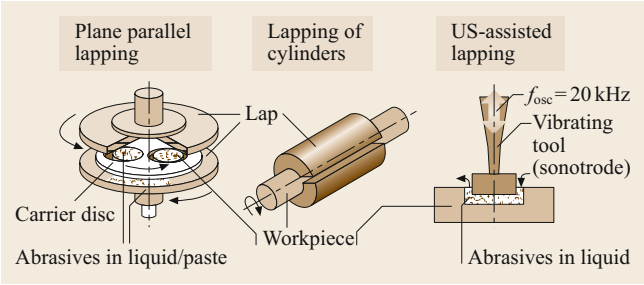

Fig. 12.56 Lapping processes

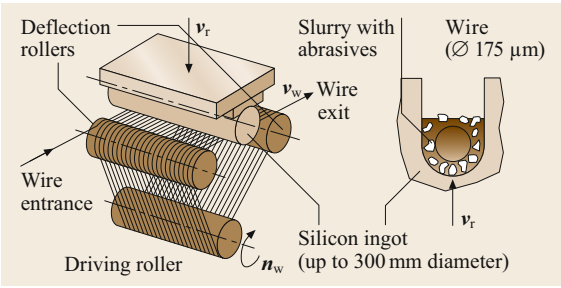

Fig. 12.57 Multiwire slicing

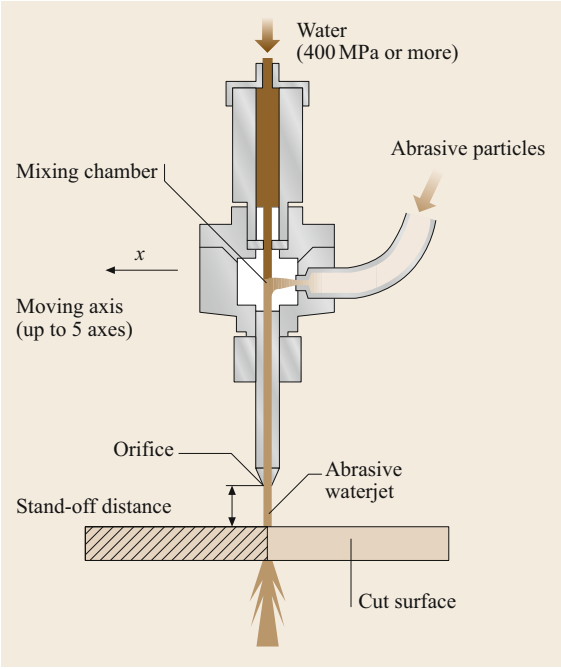

Fig. 12.58 Basic concept of abrasive waterjet cutting

Abrasive Waterjet Machining

Abrasive waterjet (AWJ) machining is a material removal process with a high-velocity slurry jet. The slurry is formed by the injection of abrasive particles into a waterjet by an orifice (Fig. 12.58; [12.77]). The abrasive waterjet head is controlled in two to five axes by a CNC system or by a robot arm. The process is mainly used for cutting a large variety of materials. The main advantages are the versatility regarding complex shapes and the ability to cut both ductile and brittle materials at very low process temperatures.

Abrasive waterjet machining is usually performed at jet pressures up to 400 MPa. The applicability and the advantages of the cutting process beyond 400 MPa pressure have been investigated [12.78]. The success of this process at increased levels of pressure depends on the endurance of the system components subjected to high alternating stresses, the avoidance of solidification of water at ultrahigh pressures, and the good coherence of the jet.

The quality obtained in waterjet cut is higher than that achieved by conventional cutting processes, mainly in the edges. The dimensional and form quality will depend on the CNC system and the coherence of the jet. A cutting thickness of 200 mm and dimensional tolerances of about 0.1 mm can be achieved with this process. The main quality disturbances are related to the jet distortion or turbulence during cutting. Shape distortions occur when cutting corners, thick parts, or at high feed speeds.

The equipment for AWJ can be very simple and relatively inexpensive. A stationary waterjet is usually used in the aerospace industry to trim composites similarly to a band saw. However, abrasive waterjet cutting can also be performed in CNC machines and robots allowing the cutting of complex shapes. In any case, the waterjet has to be caught in a suitable catching system after cutting through the workpiece material to avoid danger to the operator or the environment. Furthermore, noise protection measures are recommended.

12.3 Nonconventional Machining Processes

Nonconventional machining processes can be classified according to the type of energy employed: mechanical, thermoelectric, electrochemical, mechanical, and combinations thereof. The way of material removal varies, and so do the transfer media.

Mechanical energy is used in the abrasive jet and waterjet applications, which were already covered in Sect. 12.2.

Thermoelectric energy is used in electro-discharge machining (EDM) for making cavities, mostly in difficult-to-machine materials. Metal removal is accomplished through the controlled vaporization of the workpiece material by suitably applied electric sparks. A very important variant of EDM applies thin wires to generate small gaps in the workpiece. This is called spark electro-discharge machining (SEDM), spark erosion machining (SEM), or wire-EDM.

The principle of electron beam machining (EBM) is the transformation of the kinetic energy of high-speed electrons into thermal energy as they strike the workpiece. Laser beam machining is based on the transformation of light energy into thermal energy. Plasma arc machining (PAM) and ion beam machining (IBM) utilize ionized plasma for energy transfer. These beam machining processes are used in hole-making and slicing operations and in welding metals and alloys.

Electrochemical energy is harnessed in electrochemical machining (ECM) and in combination with grinding in electrochemical grinding (ECG). Another application is the combination of ECM with EDM, in the form of electrochemical-discharge machining (ECDM). The beam machining group also applies electrical energy in various forms.

Common in all nonconventional electrophysical-chemical machining is the application of high-energy density in the range of 10^3–10^8 W/cm^2. High energy concentration is achieved by space and time localization of the emitted energy [12.79, 80].

12.3.1 Electro-Discharge Machining (EDM)

In the EDM process, material is removed by a series of discrete electrical discharges (sparks) in the machining gap between the electrode and the workpiece, as illustrated in Fig. 12.59. The dielectric fluid creates a path for the discharge as the fluid becomes ionized between the nearest opposing points. The initiation of discharge takes place to cause ionization, and current starts to flow. As conduction continues, the size of the discharge column increases, and so does the current. The discharge temperature is far beyond the melting point of the work materials, including exotic materials.

However, the machinability of metals and alloys depends on their thermal-physical properties and the electric parameters of the process. Material removal is not affected by the mechanical properties of workpiece materials.

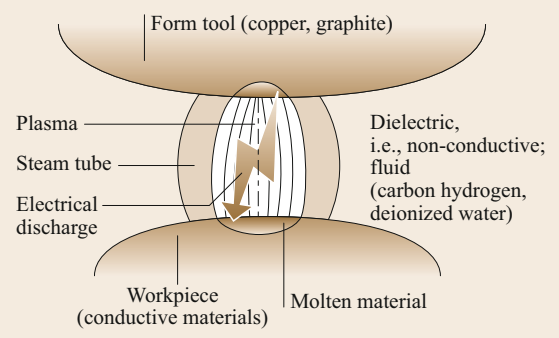

Fig. 12.59 Electro-discharge machining (EDM)

Electric-spark machining is characterized by the use of electric discharge with an on–off time ratio, where the current amplitude to pulse duration is high. The tool electrode is of direct polarity (cathode), applying powers between a few watts and several kilowatts. Application areas include cutting components of complex form by wire electrodes, broaching, and die sinking of precision components from refractory alloys, sintered carbides, and nonferrous metals with surface sizes up to 3–5 cm^2.

In electric pulse machining, the use of electric discharge with a small on–off time ratio with reduced current amplitude to pulses is common. The tool electrode is of reverse polarity (anode). Application areas include the generation of complex surfaces with an area of up to hundreds of thousands mm^2.

The dielectric fluid is an important variable in the EDM process. The methods of its application are shown in Fig. 12.60. It has three main functions: it works as an insulator between tool and workpiece, it acts as coolant, and it acts as a flushing medium to remove chips [12.81]. It also affects electrode wear, material removal rate, and other EDM characteristics. The dielectric fluid normally used is hydrocarbon based, but other fluids like triethylene glycol and tetraethylene glycol are also used to improve the material removal rate. For wire erosion, it is common to use deionized water in constant supply to the working zone.

Tool electrodes are made of graphite and copper, but other materials can also be used. The machined surface shows no direction of marks; on the contrary, the surface is formed from a number of craters and might show areas of molten material with accompanying surface integrity changes, as can be seen in Fig. 12.61 for very progressive parameters [12.82]. This drastic surface modification can be reduced by adapted EDM-process conditions. The application areas of EDM are shown in Fig. 12.62.

Electro-discharge machining provides machining accuracies of up to 0.005–0.02 mm in the case of through holes and up to 0.01–0.1 mm when machining cavities [12.83].

Surface roughness when machining through holes is in the region of $Ra = 0.4–1\ \mu m$ and $Ra = 1–2.5\ \mu m$ for machining cavities.

The material removal rate depends on the volume of material removed by individual sparks and by the dis-

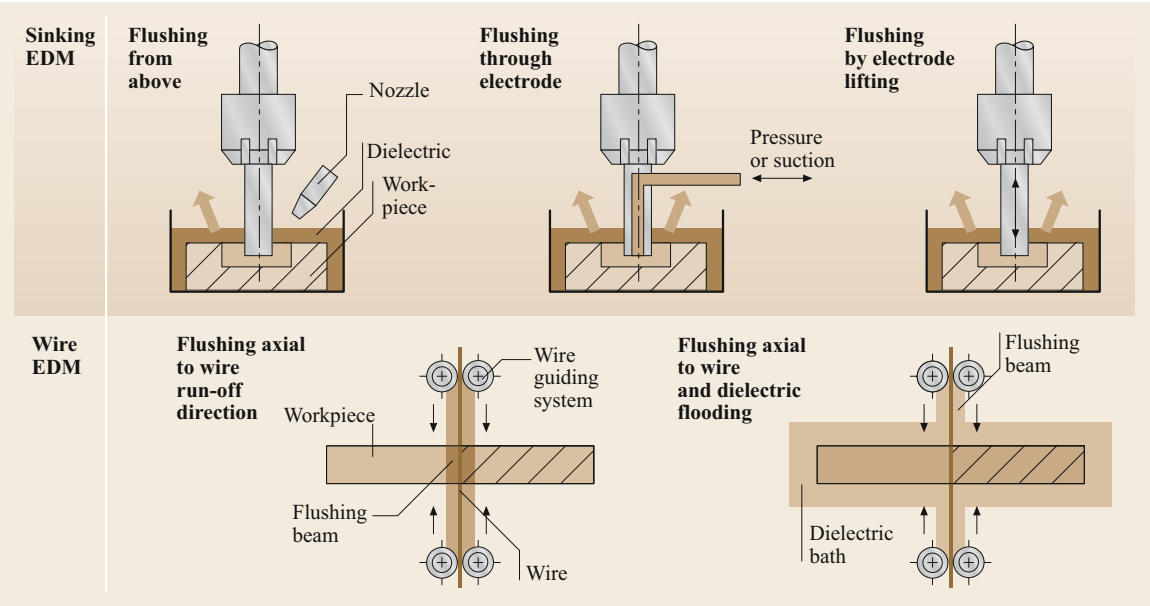

Fig. 12.60 Application of dielectric fluid in EDM (after [12.79])

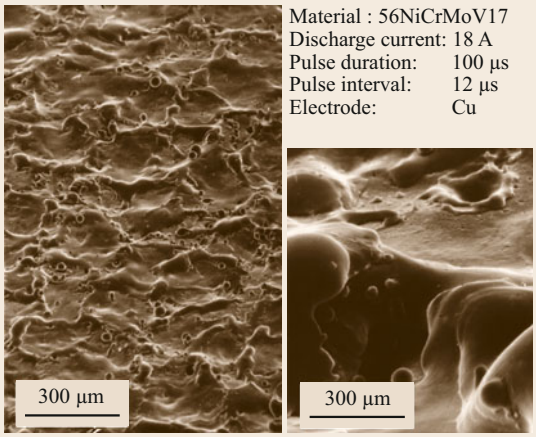

Fig. 12.61 Electro-discharge machined surface

charge frequency. The volume of material is a function of the discharge energy, which increases with the current. The typical removal rate when machining steels lies in the region of $10-12\times10^3\,\mathrm{mm^3/min}$.

Typical output parameters of wire electro-discharge machining (WEDM) are: dimensional accuracy 0.005–0.03 mm, surface roughness $Ra = 0.4-2\,\mu\mathrm{m}$, the surface division rate for steels up to $300\,\mathrm{mm^2/min}$, and for carbides up to $120\,\mathrm{mm^2/min}$.

The given parameters of electro-discharge machining allow these processes to be applied in tool manufacturing and in the production of components made from hard-to-machine materials with complex shapes.

12.3.2 Electrochemical Machining

The operating principles of electrochemical machining (ECM) have been known for a long time. Its two conductive poles are placed in an electrolyte bath and energized by direct current; metal may be removed from the positive pole (anode), the negative pole (cathode) is also metallic.

ECM requires a cathode tool with an appropriate mirror image of the cavity to be made; a workpiece and locating/holding fixture in close proximity to the tool, a suitable electrolyte supply and removal to/from the gap, and a DC (direct current) electrical source with sufficient power to provide high current density between the tool and workpiece [12.84, 85]. The metal is removed rapidly from the workpiece, and, therefore, provision has to be made to feed the tool to maintain the gap at a constant value.

Metal removal is governed by Faraday's and Ohm's laws. The material removal is proportional to the current flow through the gap and the elapsed time, while the current is proportional to the applied voltage and inversely proportional to the gap's electrical resistance.

ECM is carried out as anodic dissolution of metal, and the product is removed from the working zone (gap) by an electrolyte flowing at speeds of about 5–50 m/s. A DC generator supplies the current at a working voltage of 3–24 V governed by the material and technology requirements. A working gap between the two electrodes is maintained accurately by a process-monitoring system between 0.02–0.5 mm. The tool electrodes are typically made of stainless steel, brass, and graphite. A typical ECM arrangement is shown schematically in Fig. 12.63.

Many process parameters affect the output parameters, including tolerances of the product. These can be electrical, chemical, and mechanical parameters, which have to be monitored and controlled all the time.

The applications of ECM include turning, die sinking, hole drilling/multiple-hole drilling, trepanning, broaching, milling, and deburring. In ECM, sinking and broaching the shape of the tool electrode is copied into

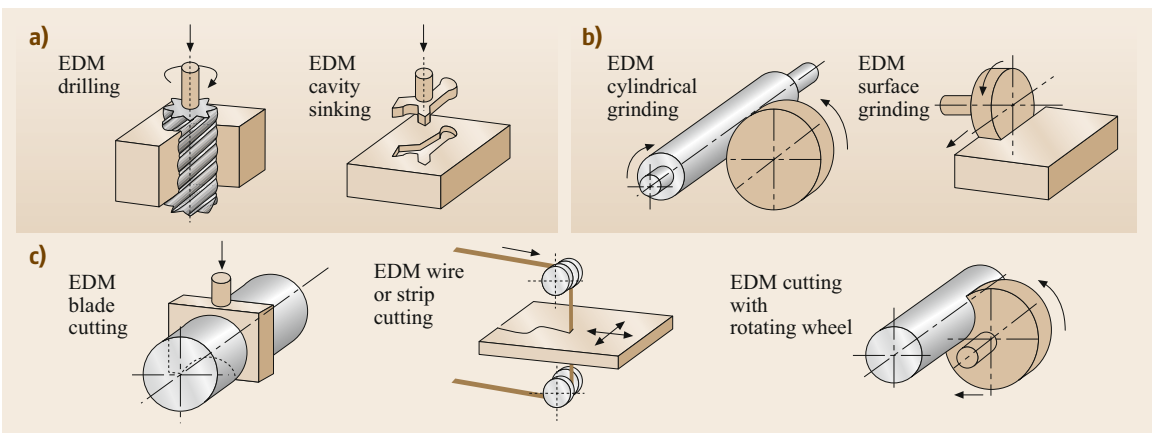

Fig. 12.62a–c Examples of electro-discharge machining. **(a)** EDM shrinking; **(b)** EDM grinding; **(c)** EDM cutting

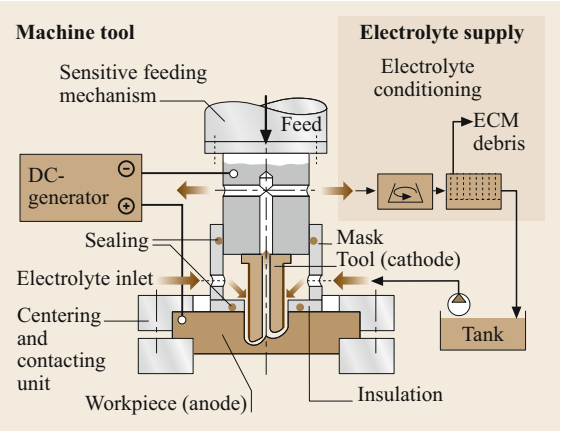

Fig. 12.63 Principle of electrochemical machining (ECM) (after [12.79])

the component. This is used to make cavities for dies, forging stamps, compression molds, casting forms, etc. The roughness of the machined surface is within the range of $Ra = 0.25$ up to $Rz = 20\,\mu\text{m}$. Feed rates of 0.03–0.5 mm/min can be selected.

Electrochemical milling, using rotary cathodes, can be used for the production of profile, flat, and round external surfaces by the cathode wheel at a removal rate of 150–200 mm^3/min in the case of stainless steels and 60–80 mm^3/min when machining carbides. This process can be used to produce thread-cutting dies, various form tools, and thread-rolling dies with a surface roughness of about $Ra = 0.63\,\mu\text{m}$ to $Rz = 20\,\mu\text{m}$. The process can also be used for machining magnetic materials (permanent magnets).

Electrochemical deburring is particularly suited for the deburring of holes, gears, and components of hydraulic equipment, mainly in mass production.

12.3.3 Ultrasonic Machining

Ultrasonic machining (USM) utilizes a tool that oscillates at high frequency beyond the audible limit (hence, the name of the process), i.e., beyond 20 000 Hz. In the case of ultrasonically assisted lapping with loose abrasives, the tool has the same shape as the required cavity in the workpiece (Sect. 12.2.5). The high-speed alternating motion of the tool drives the abrasive grains across a small working gap against the workpiece. The impact energy is responsible for the material removal. Although this process is not restricted to brittle materials, and ductile failure works in machining tough materials as well, it is usually used to machine hard and fragile materials, such as glass, ceramics, silicon, ferrite, ruby, sintered carbide, diamond and the like [12.86]. Besides the oscillation from the tool side, ultrasonic movement of the workpiece is also possible [12.87].

It is accepted that material removal results from the combined effects of hammering (impacting) abrasive particles in the work surface, the impact of free abrasive particles on the surface, cavitations, erosion, and the chemical action of the fluid employed.

The most important process input parameters controlling the material removal rate, surface roughness, and accuracy are the frequency and amplitude of oscillation, abrasive particle size, and, by implication, the impact force. During machining abrasive grains enter the machining zone as abrasive suspension.

Mechanical vibrations of the tool with ultrasonic frequency are achieved by a suitable electromechanical converter. Usually, the converter will consist of magneto-resistive elements with the ability to change their linear size in a variable magnetic field. In some cases, piezoelectric converters are employed in a variable electric field.

Tools for USM are made of structural steels, whilst carbides, CBN, silicon, and diamond are used as grits with grain sizes up to 3–10 µm [12.88].

The abrasive slurry moves into the machining zone either freely or under pressure and is removed by suction through the tool or workpiece, which substantially increases machining productivity. Mass concentration of grits in the abrasive slurry at free feed is in the region of 30–40% and 20–25% when it is supplied under pressure.

When machining sintered carbides, USM can be combined with electrochemical anodic dissolution. Processes of rough and finishing ultrasonic operations can be carried out on one machine tool.

USM can provide a removal speed of up to 5500 m^3/min when machining glass and up to 500 m^3/min when machining carbides; the corresponding surface finish is $Ra = 0.32$–$0.16\,\mu\text{m}$.

In recent ultrasonic developments, the loose abrasive setup is replaced by a tool with bonded abrasives (Sect. 12.2.2). Regarding the kinematics it is an ultrasonically assisted grinding process, but in some cases, it is referred to as ultrasonic milling. Besides milling and drilling also ultrasonically assisted turning has gained attention due to the improved wear behavior of the chosen tools [12.89, 90].

12.3.4 Beam Machining

Thermoelectric processes utilize concentrated thermal energy to remove material and electrical energy, in some ways, to generate thermal energy. The main characteristics of these processes are high temperatures and

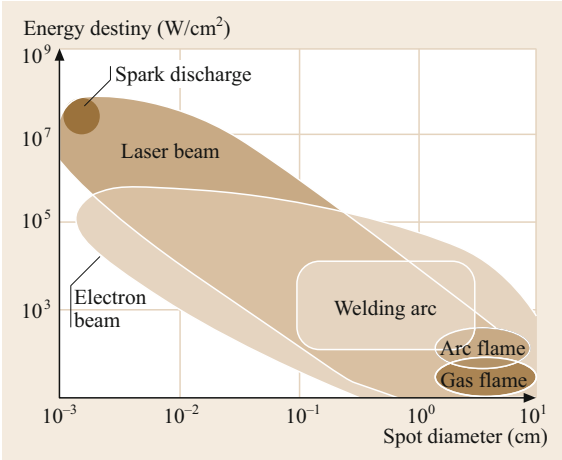

Fig. 12.64 Energy density of various thermal sources (after [12.91])

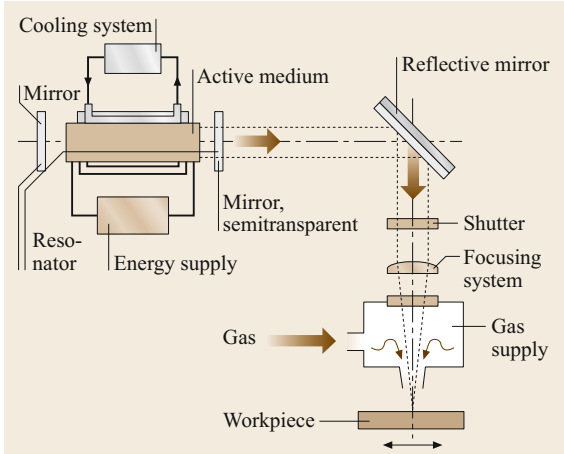

Fig. 12.65 Laser beam cutting

high thermal energy densities that can be achieved for material removal up to 10^9 W/cm^2. The main beam machining processes are: laser beam machining (LBM), electron beam machining (EBM), and plasma beam machining (PBM). Beam machining (BM) can be used for machining both electrically conductive and nonconductive materials.

The energy concentration of beam sources and that of comparative technologies are illustrated in Fig. 12.64. Of the beam-based technologies laser and electron beams provide the greatest intensity of energy in the region of 10^8–10^9 W/cm^2. The main characteristics of high-density beam thermal sources are given in Table 12.13.

Laser Beam Machining

The technical term *laser* is the acronym of light amplification by stimulated emission of radiation. Laser cutting (LC) is based on the use of the monochromatic electromagnetic radiation generated by the laser. The laser beam is formed by means of an optical system and is focused on the machined surface, causing heating, fusion, evaporation, or explosive destruction of the workpiece material (Fig. 12.65).

In the radiation zone, the form and diameter of a light spot changes over a wide range, from several up to hundreds of micrometers. Depending on the temperature and energy concentration on the machined surface, various laser machining processes can be applied, e.g., drilling, cutting, marking, welding, heat treatment, and others. The application of laser beam (LB)-based manufacturing processes is summarized in Fig. 12.66. Meanwhile, the application of laser technology has become state-of-the-art in every area of manufacturing processes.

Laser cutting can be carried out in air, vacuum, or the required gas media. The type of LB-radiation is determined by duration, frequency of following and peak capacity, and also in a kind of continuous or quasicontinuous radiation with the set average capacity modulated with a frequency of 5–50 kHz.

Laser cutting of metallic materials requires intensities of $>10^6$ W/cm, which are achieved by focusing the laser beam with the aid of lenses or mirrors. The ther-

Table 12.13 Characteristics and application of thermal sources (after [12.91, 92])

Thermal source	Limiting concentration of energy (W/cm^2)	Energy source	Application
Gas flame	8×10^2	Jet of the heated gas $T \approx 3500$ K	Cutting off, accompanying heating, maximum thickness up to 3 mm
Arc plasma	6×10^3	Gas and the metal steam ionized by electric discharge	Cutting off up to 3 mm, welding, heat treatment, welding
Electron beam	10^5	Electron beam in vacuum	Cutting off, welding (up to 20 mm/pass), heat treatment, welding
CW-type laser beam	10^9	Beam of photons in a gas	Welding (up to 10 mm/pass), heat treatment, welding on, evaporation of layers
Pulsed laser beam	10^{10}	Beam of photons in a gas	Evaporation of layers, drilling of apertures, surfaces amorphous, shock hardening

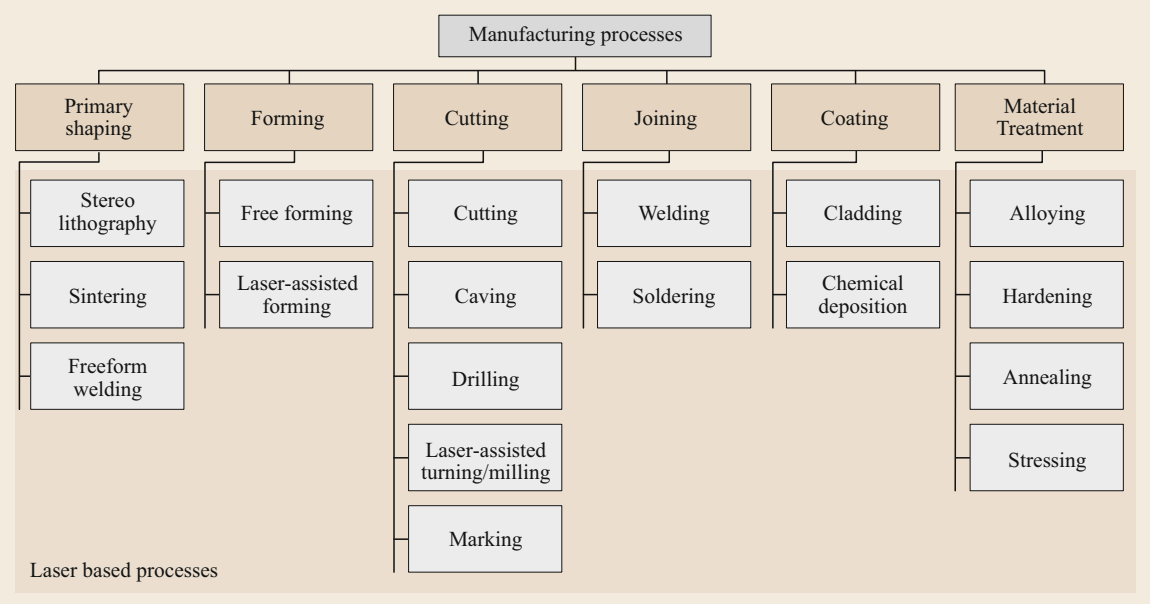

Fig. 12.66 Application of laser beam-based manufacturing processes

mal material removal process, which is directed into the depths of the material, produces a kerf in the material when the feed motion is applied [12.93, 94].

The material is melted (laser fusion cutting), burnt (laser flame cutting), or vaporized (laser sublimation cutting) at the focal point of the laser beam, depending on the intensity and the length of interaction. It is expelled from the kerf by a stream of gas emitted from a nozzle coaxially to the optical axis (Fig. 12.65). The cutting gas also serves to protect the sensitive focusing optics from spattered material.

In laser flame cutting, oxygen or oxygen-rich gas is used as the cutting gas at higher cutting speeds. However, this leads to oxidation of the cut surfaces owing to the introduction of additional exothermic energy. In contrast to the other laser cutting processes mentioned above, inert gases (e.g., argon, nitrogen) are used as cutting gases, which results in a slower cutting speed. However, they produce an oxide-free cut.

The relative motion between the laser beam that produces a continuous kerf and the workpiece is achieved in various ways. For laser cutting of small, easily handled components, the latter are generally moved underneath the stationary laser beam. e.g., with the aid of an X–Y coordinate table. For laser machining of larger workpieces, the laser unit, including the cutting tip, is either moved across the stationary workpiece, or a movable system of mirrors is guided together with the cutting tip (*flying optics*) between the fixed laser unit and the workpiece. For Nd:YAG lasers alone, flexible optical fibers may be used to guide the beam.

The cutting speeds for other metallic and nonmetallic materials for a CO_2 laser with a power of 500 W are summarized in Table 12.14.

High-powered lasers of the type mentioned above generally belong to laser (protection) class 4, which has the highest hazard level (except for laser machining systems with dosed working chambers, which are equipped with additional safety facilities such as interlock systems and radiation-absorbing protective windows). Allocation to this safety class means that even diffusely reflected laser radiation is a hazard to the skin and the human eye.

Technological laser systems mainly use the following types (active media) of laser radiation: excimer lasers (gas); CO_2 lasers (gas); Nd:YAG lasers (solid-state). The special characteristics of each laser system define its optimal field of application. The characteristics of the laser sources are shown in Fig. 12.67, and the main parameters are summarized in Table 12.15.

Basic elements of the equipment for laser machining are the generation source, beam guidance, forming and focusing system, and fixation and control of the workpiece moving system (Fig. 12.68).

The laser equipment based on solid-state lasers is generally used for precision machining in various materials (ceramics, polycrystalline glass, ferrite, ruby) and applications like e.g., apertures for input of a wire electrode, apertures in thin foils and films, apertures in watches, stone billets, diamond marking, atomizers, etc., or precision cutting out and marking.

Table 12.14 Machining parameters for laser cutting of various materials (after [12.95])

Material	Thickness (mm)	Cutting gas/pressure (MPa)	Cutting speed (m/min)
PMMA	4	Air/0.06	3.5
Rubber	3	N_2/0.3	1.8
Asbestos	4	Air/0.3	1.6
Plywood	3	N_2/0.15	5.5
Cement asbestos	4	Air/0.3	0.8
AlTi ceramic	8	N_2/0.5	0.07
Aluminum	1.5	O_2/0.2	0.4
Titanium	3	Air/0.5	2
CrNi steel	2	O_2/0.45	1.9
Electrical sheet	0.35	O_2/0.6	7
Gray cast iron	3	N_2/1	0.9
Laser CO_2/500 W; focal length $f = 127$ mm			

Table 12.15 Parameters and application area for various laser systems (after [12.92])

Parameters and application	CO_2 laser	Nd:YAG laser	Excimer laser
Average power (W)	Up to 10^4	Up to 300 (pulse type)	< 0.3
		Up to1000 (continuous type)	
Wave length (nm)	10 600	1064	193, 248
		532 (double frequency)	308, 351
Pulses duration (s)	10^{-5}–10^{-2}	$(4–20) \times 10^{-8}$	$(3–30) \times 10^{-9}$
Pulse energy (mJ)	–	Up to 18	Up to 15000
Pulse frequency (kHz)	Up to 20	Up to 50	Up to 1
Pumping source	Gas discharge	Lamps/diodes	Gas discharge
Machinable workpiece materials	Glass, Al_2O_3-ceramics	Si_3N_4/AlN-ceramics, various metals	Polymers, plastics, ceramics, glass
Application	Cutting out, welding, heat treatment, drilling	Cutting out, welding, heat treatment, drilling, marking	Heat treatment, marking, surface modification

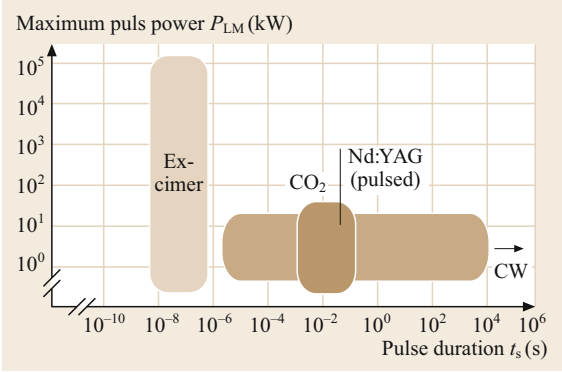

Fig. 12.67 Characteristics of different laser sources (source: LZH)

The fast development of laser sources and the large variety of beam forming systems open a wide field of applications, as shown in Fig. 12.66. Especially in the fields of micromachining and medical applications, laser systems have become an essential driver for innovation and improvement [12.32, 96].

Electron Beam Machining

Electron beam machining (EBM) is based on acceleration and focusing of electrons in a narrow bunch (beam), radiating from the cathode in deep vacuum with the help of a powerful electric field, to hit the machinable workpiece surface (anode). The physical essence of the EBM process is the transformation of electron kinetic energy into thermal energy. The electrons are emitted from a hot cathode and accelerated towards a ring-shaped anode with a round opening (Fig. 12.69). The acceleration voltage is around 25–200 kV. The electrons reach the workpiece surface and release their high kinetic energy. The energy density of an electron beam is up to 10^5–10^7 W/cm^2, which is comparable to laser beams. Due to the fact that electrons, unlike photons, have a mass ($m_e = 9.108 \times 10^{-31}$ kg) and an electric charge ($e = 1.602 \times 10^{-19}$ A s), the energy transfer and effect on the workpiece surface is different compared to laser processes. To prevent electron collisions with gas molecules, the system is highly evacuated. The focusing of the electron beam is done with magnetic fields, which are generated by so-called mag-

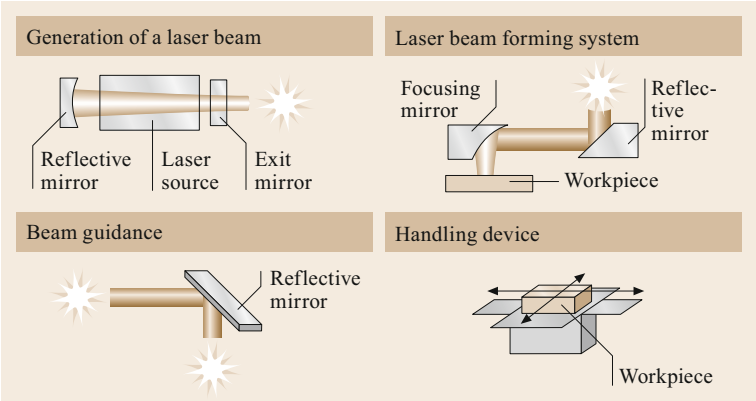

Fig. 12.68 Components of a laser manufacturing system

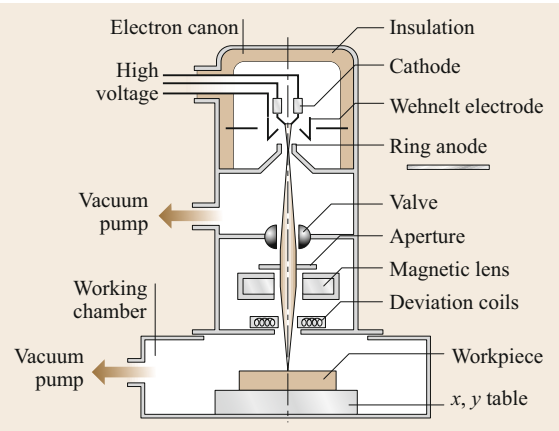

Fig. 12.69 Schematic setup of electron beam machining

netic lenses. The electrons can penetrate much more deeply into the workpiece material than laser beams. They transfer their energy via collisions with enveloping electrons.

EBM systems are more complex compared to regular laser systems. Due to the limitation of the working chamber, this process is dedicated to special applications, where the benefits of a high penetration depth, a high impulse frequency, and fast beam deflection can be used [12.97]. Thus, drilling is a perfect process to elaborate the potential of EBM, e.g., small bores (diameters down to few μm) can be made in thin foils at a rate of up to 10 000 bores/s without moving the target.

Typical application fields are combustion-chambers of aircraft turbines (difficult to machine cobalt-based material, several thousand holes) or spinning heads for glass fiber production (6000 holes of 0.8 mm diameter in 5 mm-thick material [12.98]). A disadvantage of the technology is related to the fact that x-rays are generated above an acceleration voltage of 80 kV, which makes a severe shielding of the system necessary.

Plasma Beam Machining

Plasma beam machining is based on the use of low-temperature open plasma, which is applied to increase the operational properties of machined components, such as wear resistance, corrosion stability, thermal stability, etc. Such an amelioration is carried out in order to attain the formation of functional coatings from corresponding materials, generated by a plasma jet, plasma welding, and plasma depositing. Furthermore, plasma is used in some combined plasma-mechanical processes, in particular in plasma-mechanical machining.

Plasma coating is characterized by a great concentration of the thermal stream and high speed of the plasma jet. For coating, fine-grained powders are used (40–100 μm). The thickness of the deposited layer is around 0.3–0.5 mm and higher; the deposition productivity is 2–4 kg/h.

Plasma cutting is characterized by local removal of metal along a cut line by a plasma jet using quality plasma-forming gases like argon, nitrogen, hydrogen, air, etc. It is applied for cut-off stainless steels with thicknesses up to 60–80 mm and low-carbon and low-alloying steels with thicknesses up to 30–500 mm. After plasma cutting, the surface roughness may reach $Rz = 80–160\,\mu m$.

12.3.5 Combined Methods of Machining

For further development of manufacturing technologies, a combination of energy sources is possible. With a complex joint use of mechanical, thermal, chemical, or electrical energy, an enhanced material removal, better surface quality, or improved tool life can be achieved. Examples of these process combinations are, e.g., electrochemical grinding, electro-discharge grinding, ultrasonic-electrochemical, electro-discharge-chemical, anodic-mechanical, plasma-mechanical, and laser-mechanical processes.

Electrochemical Grinding

Electrochemical grinding (ECG) is carried out by overlapping material removal by microabrasive grains (diamond, CBN) with anodic (electrochemical) dissolution. Anodic dissolution of metallic workpiece materials reduces the microchip thickness and the area of mechanical contact between workpiece and the grinding wheel [12.99]. Furthermore, ECG reduces the material resistance against mechanical penetration by means of reduction of the strength of the superficial microlayer.

ECG processes work at a voltage of up to $U_p = 5-10\,V$ (at machining with an independent electrode $U_p = 24\,V$) and a current density of up to $15-150\,A/cm^2$. Nitrate/nitrite solutions are often used as working media (dielectric fluid). They contain various passivation additives (soda, glycerin, triethylamine, etc.) for reduction of the corrosion activity.

ECG processing is applied on surface ground components of hard, magnetic, heat resisting steels and alloys; surface and cylindrical grinding of thin-walled, nonrigid components; profile grinding; grinding of viscous materials, etc.

Electro-Discharge Grinding

During electro-discharge grinding (EDG), metal removal is carried out by microcutting of bonded abrasive grains, while the grinding wheel working surface is continuously influenced by electroerosion. Electric discharges provide an opening of the grinding wheel topography, allowing new abrasive grains to come into contact, and the removal of adhering chips from the wheel surface to prevent loading. Also just-cut chip segments might be directly evaporated in the zone of contact. Discharges occur between the workpiece and the wheel or between the tool and a specially adapted additional electrode [12.100, 101]. EDG processes can be actively controlled, and their intensity can be adjusted to provide substantial increase and stabilization in the lifetime and cutting ability of the grinding wheel.

For EDG processes, either a standard cutting fluid or 3% water–soda solution is used as the working medium. Current-conducting metal bonded abrasive wheels (or wheels with diamond or CBN grains) are connected to the positive pole, and the workpiece is connected to the negative pole of a pulse voltage source. EDG is applied in tool grinding, surface grinding, and cylindrical internal and external grinding machine tools.

Laser-Assisted Machining

Laser-assisted machining (LAM) has found rising acceptance due to its potential to significantly increase machining efficiency, in particular, in processes of punching and cutting complex-shaped workpieces. Laser radiation is employed for two reasons. Firstly, the laser source is used for heating (thus, annealing or hardness reduction) of the workpiece material surface layer directly in front of the cutting tool. This way, tool life is extended, and the productivity is drastically increased. It even opens the possibility of applying cutting technologies to materials that were not machinable this way before, like laser-assisted turning of ceramics [12.102]. Secondly, the laser can be used for final surface formation (for example, a groove after milling by an end mill). Applied in this combination, LAM processes increase the accuracy and quality of the machined parts.

References

12.1 DIN: *DIN 8589: Manufacturing Processes Chip Removal* (Beuth, Berlin 2003)

12.2 H.K. Tönshoff, B. Denkena: *Spanen* (Springer, Berlin 2011)

12.3 H.J. Ernst, M.E. Merchant: Chip formation, friction and finish, Trans. Am. Soc. Mech. Eng. **29**, 299–378 (1941)

12.4 DIN: *DIN 8589-1 Manufacturing Processes Chip Removal–Part 1: Turning; Classification, Subdivision, Terms and Definitions* (Beuth, Berlin 2003)

12.5 ISO: *ISO 3002-1: Basic Quantities in Cutting and Grinding; Part 1: Geometry of the Active Part of Cutting Tools* (ISO, Geneva 1982)

12.6 DIN: *DIN 6581: Terminology of Chip Removing; Reference Systems and Angles on the Cutting Part of the Tool* (Beuth, Berlin 1985)

12.7 Verein Deutscher Eisenhüttenleute: *Stahl-Eisen-Prüfblatt 1178-69* (Stahlinstitut VDEh, Düsseldorf 1969)

12.8 I.S. Jawahir, C.A. van Lutterfeld: Recent developments in chip control research and applications, CIRP Annals **42**(2), 659–693 (1993)

12.9 DIN: *DIN 6584: Terminology of Chip Removing; Forces, Energy, Work, Power* (Beuth, Berlin 1982)

12.10 O. Kienzle, H. Victor: Die Bestimmung von Kräften und Leistungen an spanenden Werkzeugmaschinen, VDI-Zeitschrift **94**, 299–305 (1952)

12.11 ISO: *EN ISO 4287: Geometrical Product Specifications (GPS) – Surface Texture: Profile Method – Terms, Definitions and Surface Texture Parameters* (ISO, Geneva 2010)

12.12 ISO: *ISO 3685: Tool-Life Testing with Single-Point Turning Tools* (Beuth, Berlin 1993)

12.13 F.W. Taylor: On the art of cutting metals, Trans. Am. Soc. Mech. Eng. **28**, 30–351 (1907)

12.14 G. Spur: *Beitrag zur Schnittkraftmessung beim Bohren mit Spiralbohrern unter Berücksichtigung*

der Radialkräfte, Dissertation (TU Braunschweig, Braunschweig 1961)
12.15 DIN: *DIN 6580: Terminology of Chip Removing; Movements and Geometry of the Chip Removing Process* (DIN, Berlin 1985)
12.16 Y. Altintas, M. Weck: Chatter stability of metal cutting and grinding, CIRP Annals **53**(2), 619–642 (2004)
12.17 J. Tlusty: *Manufacturing Processes and Equipment* (Prentice Hall, Eglewood Cliffs 2000)
12.18 F. Klocke, E. Brinksmeier, K. Weinert: Capability profile of hard cutting and grinding, CIRP Annals **54**(2), 557–580 (2005)
12.19 H.K. Tönshoff, C. Arendt, R. Ben Amor: Cutting of hardened steel, CIRP Annals **49**(2), 547–566 (2000)
12.20 H.K. Tönshoff, B. Karpuschewski, C. Borbe: Hard machining–state of research. In: *Proc. Int. CIRP/VDI Conf. High Perform. Tools, Düsseldorf* (1998) pp. 253–277
12.21 W. König, F. Klocke: *Fertigungsverfahren: Drehen, Fräsen, Bohren* (Springer, Heidelberg, Berlin 2008)
12.22 M. Klinger: *Räumen einsatzgehärteter Werkstücke*, Dissertation (RWTH Aachen, Aachen 1993)
12.23 G.S. Fox-Rabinovich, G.C. Weatherly, A.I. Dodonov, A.I. Kovalev, L.S. Shuster, S.C. Veldhuis, G.K. Dosbaeva, D.L. Wainstein, M.S. Migranov: Nano-crystalline filtered arc deposited (FAD) TiAlN PVD coatings for high-speed machining applications, Surf. Coat. Technol. **177/178**, 800–811 (2004)
12.24 C. Mendibide, P. Steyer, C. Esnouf, P. Goudeau, D. Thiaudière, M. Gailhanou, J. Fontaine: X-ray diffraction analysis of the residual stress state in PVD TiN/CrN multilayer coatings deposited on tool steel, Surf. Coat. Technol. **200**, 165–169 (2005)
12.25 DIN: *DIN 4990: Designation of Main Groups of Chip Removed and Application Groups of Hardmetals* (DIN, Berlin 1942), in German
12.26 ISO: *ISO 513: Classification and Application of Hard Cutting Materials for Metal Removal with Defined Cutting Edges* (ISO, Geneva 2014)
12.27 E. Brinksmeier, L. Autschbach: Development of ultraprecise milling techniques for the manufacture of optical quality molds with continuous and microstructured surfaces. In: *Proc. 4th Euspen Int. Conf., Aachen* (2003) pp. 193–197
12.28 P. Andrae: *Hochleistungszerspanung von Aluminiumknetlegierungen*, Dissertation (Univ. Hannover, Hannover 2002)
12.29 J. Fleischer, B. Denkena, B. Winfough, M. Mori: Workpiece and tool handling in metal cutting machines, CIRP Annals **55**(2), 817–840 (2006)
12.30 M. Weck: *Werkzeugmaschinen – Maschinenarten und Anwendungsbereiche* (Springer, Heidelberg, Berlin 2005)
12.31 N. Ikawa, R.R. Donaldson, R. Komanduric, W. König, P.A. McKeown, T. Moriwaki, I.F. Stowers: Ultraprecision metal cutting–the past, the present and the future, CIRP Annals **40**(2), 587–594 (1991)
12.32 T. Masuzawa: State of the art of micromachining, CIRP Annals **49**(2), 473–487 (2000)
12.33 E. Brinksmeier, O. Riemer, R. Stern: Machining of precision parts and microstructures. In: *Proc. 10th Int. Conf. Precis. Eng. (ICPE), Yokohama* (2001) pp. 3–11
12.34 E. Uhlmann, K. Schauer: Dynamic load and strain analysis for the optimization of micro end mills, CIRP Annals **54**(1), 75–78 (2005)
12.35 D. Dornfeld, S. Min, Y. Takeuchi: Recent advances in mechanical micromachining, CIRP Annals **55**(2), 745–768 (2006)
12.36 E. Shamoto, T. Moriwaki: Ultraprecision diamond cutting of hardened steel by applying elliptical vibration cutting, CIRP Annals **48**(1), 441–444 (1999)
12.37 G. Warnecke, S. Siems: Machining of different steel types at high cutting speeds, Ann. Ger. Acad. Soc. Prod. Eng. **8**(1), 1–4 (2001)
12.38 C. Salomon: German Patent 523594 (1931)
12.39 H. Schulz: *High Speed Machining* (Hanser, München 1996)
12.40 H. Schulz, T. Moriwaki: High speed machining, CIRP Annals **41**(2), 636–645 (1992)
12.41 R. Ben Amor: *Thermomechanische Wirkmechanismen und Spanbildung bei der Hochgeschwindigkeitszerspanung*, Dissertation (Univ. Hannover, Hannover 2003)
12.42 A. Kaldos, A. Boyle, I. Dagiloke: Computer aided cutting process parameter selection for high-speed milling, J. Mater. Process. Technol. **61**, 219–224 (1996)
12.43 D. Brandt: *Randzonenbeeinflussung beim Hartdrehen*, Dissertation (Univ. Hannover, Hannover 1995)
12.44 S. Malkin: *Grinding Technology: Theory and Applications of Machining with Abrasives* (Ellis Horwood, Chichester 1989)
12.45 H.K. Tönshoff, I. Inasaki, B. Karpuschewski, T. Mandrysch: Grinding process achievements and their consequences on machine tools–challenges and opportunities, CIRP Annals **47**(2), 651–668 (1998)
12.46 E. Brinksmeier, C. Heinzel, M. Wittmann: Friction, cooling and lubrication in grinding, CIRP Annals **48**(2), 581–598 (1999)
12.47 R. Snoeys: The mean undeformed chip thickness as a basic parameter in grinding, CIRP Annals **20**, 183–186 (1971)
12.48 J. Webster, M. Tricard: Innovations in abrasive products for precision grinding, CIRP Annals **53**(2), 597–642 (2004)
12.49 DIN: *DIN 69100: Bonded Abrasive Products; Designation, Types, Dimensional Letters, Materials* (DIN, Berlin 1988), in German
12.50 ISO: *ISO 6104: Abrasive Products; Diamond or Cubic Boron Nitride Grinding Wheels and Saws; General Survey, Designation and Multilingual Nomenclature* (ISO, Geneva 1979)
12.51 K. Wegener, H.-W. Hoffmeister, B. Karpuschewski, F. Kuster, W.-C. Hahmann, M. Rabiey: Conditioning and Monitoring of Grinding Wheels, CIRP Annals **60**(2), 603–626 (2011)
12.52 H. Ohmori, T. Nakagawa: Surface grinding of silicon wafers electrolytic in-process dressing, CIRP Annals **39**(1), 329–332 (1990)
12.53 H.K. Tönshoff, T. Friemuth: Electro contact discharge dressing of diamond wheels for tool

grinding. In: *Proc. ICPE Int. Conf. Precis. Eng., Taipei* (1997) pp. 565–570
12.54 E. Westkämper, H.K. Tönshoff: CBN or CD grinding of profiles, CIRP Annals **42**(1), 371–374 (1993)
12.55 B. Karpuschewski: Sensors for physical properties. In: *Sensors in Manufacturing*, ed. by H.K. Tönshoff, I. Inasaki (Wiley, Weinheim 2001) pp. 123–142
12.56 I. Inasaki, B. Karpuschewski, H.S. Lee: Grinding chatter—origin and suppression, CIRP Annals **50**(2), 515–534 (2001)
12.57 W.B. Rowe, J.A. Pettit: Avoidance of thermal damage in grinding and prediction of the damage threshold, CIRP Annals **37**(1), 327–330 (1988)
12.58 C. Guo, M. Campomanes, D. McIntosh, C. Becze, T. Green, S. Malkin: Optimization of continuous dress creep-feed form grinding process, CIRP Annals **52**(1), 259–262 (2003)
12.59 F. Klocke, E. Brinksmeier, C.J. Evans, I. Inasaki, T. Howes, H.K. Tönshoff, J.A. Webster, D. Stuff: High-speed grinding—fundamentals and state of the art in Europe, Japan and the USA, CIRP Annals **46**(2), 715–724 (1997)
12.60 B. Karpuschewski, I. Inasaki: Monitoring systems for grinding processes. In: *Condition Monitoring and Control for Intelligent Manufacturing*, ed. by L. Wang, R.X. Gao (Springer, Heidelberg, Berlin 2006) pp. 83–107
12.61 J.F.G. de Oliveira, D.A. Dornfeld: Application of AE contact sensing in reliable grinding monitoring, CIRP Annals **50**(1), 217–220 (2001)
12.62 H.K. Tönshoff, B. Karpuschewski, A. Türich: Tooth profile grinding of precision forged gears. In: *4th World Congr. Gearing Power Transm. Vol. 2, Paris* (1999) pp. 1697–1708
12.63 T. Brockhoff, E. Brinksmeier: Grind-hardening: a comprehensive view, CIRP Annals **48**(1), 255–259 (1999)
12.64 M. Lewis: Blasting through today's hard material—ultrasonic cutting matures into a viable machining process, Am. Mach. **146**(6), 42 (2002)
12.65 P. Dennis: *Hochleistungsbandschleifen*, Dissertation (Univ. Hannover, Hannover 1989)
12.66 W. König, H.K. Tönshoff, J. Fromlowitz, P. Dennis: Belt grinding, CIRP Annals **35**, 487–494 (1986)
12.67 E. Brinksmeier, V. Gehring: Automated finishing of dies and molds by belt grinding. In: *2nd Int. Conf. Die Mold Technol., Singapore* (1992) pp. 78–91
12.68 H. Mushardt: *Modellbetrachtungen und Grundlagen zum Innenrundhonen*, Dissertation (TU Braunschweig, Braunschweig 1986)
12.69 U.-P. Weigmann: *Honen keramischer Werkstoffe*, Dissertation (TU Berlin, Berlin 1997)
12.70 E. Saljé, M. von See: Process-optimization in honing of automotive cylinders, CIRP Annals **36**(1), 235–238 (1987)
12.71 H.K. Tönshoff, C. Marzenell: Properties of tooth surfaces due to gear honing with electroplated tools. In: *4th World Congr. Gearing Power Transm., Paris* (1999) pp. 1711–1724
12.72 M. Hartmann: *Stabstirn-Trennschleifen von einkristallinem Silizium*, Dissertation (Univ. Hannover, Hannover 1997)
12.73 H.K. Tönshoff, H.-G. Wobker, M. Klein, C. Menz: Precision grinding and slicing of Si-wafers. In: *7th Int. Precis. Eng. Semin., Kobe* (1993)
12.74 C.J. Evans, E. Paul, D. Dornfeld, D.A. Lucca, G. Byrne, M. Tricard, F. Klocke, O. Dambon, B.A. Mullany: Material removal mechanisms in lapping and polishing, CIRP Annals **52**(2), 611–634 (2003)
12.75 G. Spur, D. Simpfendörfer: Neue Erkenntnisse und Entwicklungstendenzen beim Planläppen. In: *Jahrbuch Schleifen, Honen, Läppen und Polieren*, 55th edn., ed. by E. Saljé (Vulkan, Essen 1988) pp. 469–480
12.76 H.-H. Nölke: *Spanende Bearbeitung von Siliziumnitrid-Werkstoffen durch Ultraschall-Schwingläppen*, Dissertation (Univ. Hannover, Hannover 1980)
12.77 D.A. Axinte, B. Karpuschewski, M. Kong, A.T. Beaucamp, S. Anwar, D. Miller, M. Petzel: High Energy Fluid Jet Machining (HEFJet-Mach)—from scientific and technological advances to niche industrial applications, CIRP Annals **63**(2), 751–771 (2014)
12.78 A.M. Hoogstrate, T. Susuzlu, B. Karpuschewski: High performance cutting with abrasive waterjets beyond 400 MPa, CIRP Annals **55**(1), 339–342 (2006)
12.79 W. König, F. Klocke: *Fertigungsverfahren: Abtragen, Generieren und Lasermaterialbearbeitung* (Springer, Heidelberg, Berlin 2007)
12.80 J. Meijer, A. Du, A. Gillner, D. Hoffmann, V.S. Kovalenko, T. Masuzawa, A. Ostendorf, R. Poprawe, W. Schulz: Laser machining by short und ultrashort pulses, state of the art and new opportunities in the age of the photons, CIRP Annals **51**(2), 531–550 (2002)
12.81 P.M. Lonardo, A.A. Bruzzone: Effect of flushing and electrode material on die sinking EDM, CIRP Annals **48**(1), 123–127 (1999)
12.82 J.P. Kruth, L. Steven, L. Froyen, B. Lauwers: Study of the white layer of a surface machined by die sinking electro discharge machining, CIRP Annals **44**(1), 169–172 (1995)
12.83 T. Kawakami, M. Kunieda: Study on factors determining limits of minimum machinable size in micro EDM, CIRP Annals **54**(1), 167–170 (2005)
12.84 T. Masuzawa, M. Kimura: Electrochemical surface finishing of tungsten carbide alloy, CIRP Annals **40**(1), 199–202 (1991)
12.85 A. de Silva, H. Altena, J. McGeough: Influence of electrolyte concentration on copying accuracy of precision ECM, CIRP Annals **52**(1), 165–168 (2003)
12.86 T. Moriwaki, E. Shamoto, K. Inoue: Ultraprecision ductile cutting of glass by applying ultrasonic vibration, CIRP Annals **41**(1), 141–144 (1992)
12.87 K. Egashira, T. Masuzawa: Micro-ultrasonic machining by the application of workpiece vibration, CIRP Annals **48**(1), 131–134 (1999)
12.88 M. Lucas, J.N. Petzing, A. Cardoni, L.J. Smith: Design and characterisation of ultrasonic cutting tools, CIRP Annals **50**(1), 149–152 (2001)
12.89 K.L. Kuo: Experimental investigation of brittle material milling using rotary ultrasonic machin-

ing. In: *Proc. 35th Int. MATADOR Conf.* (Springer, Heidelberg, Berlin 2007) pp. 195–198
12.90 Z.W. Zhong, G. Lin: Ultrasonic assisted turning of an aluminum-based metal matrix composite reinforced with SiC particles, Int. J. Adv. Manuf. Technol. **27**(11/12), 1077–1081 (2006)
12.91 V.O. Bushma, V.M. Borovik, R.V. Rodiakina: *Physical Bases of Generating Concentrated Energy Streams* (MEI, Moscow 1999) p. 104
12.92 V.C. Golubev, F.V. Lebedev: *Physical Bases of Technological Lasers* (Vicshya Shkola, Moscow 1987) p. 192
12.93 N. Rykalin, A. Uglov: *Laser Machining and Welding* (Elsevier, Amsterdam 1980)
12.94 W.M. Steen, K. Watkins: *Laser Material Processing* (Springer, Heidelberg, Berlin 2003)
12.95 K.H. Grote, J. Feldhusen: *Dubbel Taschenbuch für den Maschinenbau* (Springer, Heidelberg, Berlin 2007)
12.96 J.J. Ramsden, D.M. Allen, D.J. Stephenson, J.R. Alcock, G.N. Peggs, G. Fuller, G. Goch: The design and manufacture of biomedical surfaces, CIRP Annals **56**(2), 687–711 (2007)
12.97 G. Smolka, W. Gillner, L. Bosse, R. Lützeler: Micro electron beam welding and laser machining—potentials of beam welding methods in the microsystem technology, Microsyst. Technol. **10**(3), 187–192 (2004)
12.98 G. Spur, T. Stöferle: *Handbuch der Fertigungstechnik – Abtragen, Beschichten* (Fachbuchverlag, Leipzig 1998)
12.99 J.R. Duncan: Electrochemical grinding of a stainless steel felt, J. Appl. Electrochem. **6**(3), 275–277 (1976)
12.100 E. Uhlmann, S. Piltz, U. Doll: Electrical discharge grinding (EDG) using microstructured disk electrodes, Ann. Ger. Acad. Soc. Prod. Eng. **8**(1), 25–31 (2001)
12.101 T. Masuzawa, M. Fujino, K. Kobayashi: Wire-electro-discharge grinding for micro-machining, CIRP Annals **34**(1), 431–434 (1985)
12.102 B. Lauwers, F. Klocke, A. Klink, E. Tekkaya, R. Neugebauer, D. Mcintosh: Hybrid Processes in Manufacturing, CIRP Annals **63**(2), 561–583 (2014)

Bernhard Karpuschewski

Leibniz Institute for Materials Engineering
IWT, Manufacturing Technologies
University of Bremen
Bremen, Germany
karpu@iwt-bremen.de

After receiving his PhD and holding the Chief Engineer position at the University of Hannover, Germany, Bernhard Karpuschewski worked for 1.5 years as Associate Professor at Keio University, Japan, and for 4.5 years as Full Professor for Production Technology at TU Delft, The Netherlands. He has been Full Professor at the University of Bremen and Director of the Leibniz Institute for Materials Engineering IWT Bremen since 2017.

Gerry Byrne

School of Mechanical and Materials Engineering
University College Dublin
Dublin, Ireland
gerald.byrne@ucd.ie

Gerry Byrne FREng is the Professor of Mechanical Engineering and the former Director of the Advanced Manufacturing Science Research Centre at University College Dublin (UCD), Ireland. He has over 30 years of experience with high-precision manufacturing processes, surface engineering, and aspects of surface microstructuring. He is an expert in the field of cutting processes and has published extensively. He is a senior advisor to the President of the Fraunhofer-Gesellschaft.

Berend Denkena

Produktionstechnisches Zentrum Hannover, Institut für Fertigungstechnik und Werkzeugmaschinen
Leibniz Universität Hannover
Garbsen, Germany
denkena@ifw.uni-hannover.de

Professor Berend Denkena is Head of the Institute of Production Engineering and Machine Tools at the Leibniz Universität Hannover. He is Professor of Production Engineering and Machine Tools and Director of the Institute of Production Engineering and Machine Tools at the University of Hannover. His primary areas of research are geometry and functionalizing manufacturing processes, machine tools for cutting and grinding, production planning and control, and simulation of manufacturing processes.

João Oliveira

Scenario Automation Ltda
São Carlos, SP, Brazil
oliveirajfg@gmail.com

Dr Oliveira is Professor of Production Engineering at the University of São Paulo, Brazil. His area of research is abrasive machining processes and their automation. He has published over 220 papers and 6 patents. He is a member of the Brazilian National Science Council Board, Vice President of the Brazilian Academy of Sciences, and a member of the International Academy for Production Engineering.

Anatoly Vereschaka (deceased)

Anatoly Vereschaka received his PhD from Moscow State University (1986). He was Professor of Engineering Technology, Material Cutting Technology, and Surface Engineering Technology in the Department of Mechanical Engineering Technology of Moscow State University of Technology (STANKIN), Russia. His research fields were the physics of metal cutting processes, design theory and methodology of wear resistance, and functional coating for cutting tools. He passed away in 2016.

13. Precision Machinery Using MEMS Technology

Takeshi Hatsuzawa

Some examples of optical microelectromechanical systems MEMS are presented with their fabrication processes. The MEMS-specific driving and display principles and experimental evaluations are also shown. Two types of electrostatic-driven optical MEMS devices: An interferometric display device and an evanescent coupling switching device are shown, in which no liquid crystal or organic electroluminescence materials are required except for a silicon dioxide film with conductive layers.

The interferometric display device consists of a Si reflection mirror at the bottom of an etch pit. On the pit, a SiO_2 film with a metal layer is suspended by two folded leaf springs at both sides, which works as both a half mirror of an interferometer and electrode for positioning. Applying a high voltage between the pit and the half mirror, an electrostatic force acts on two electrodes generating an attractive force to the half mirror. Therefore, the half mirror is drawn to the bottom balancing the repellent force from the leaf springs, which means the distance between the half mirror and the bottom can be controlled by the voltage. Thus, various colors can be generated at the micropit of the interferometer, enabling a microcolor display device. The fabrication process based on the conventional MEMS technology is also described, in which anisotropic etching of the Si is the key technology for forming the flat etch pit of the interferometer.

Another device is based on the evanescent switching between two SiO_2 films. A cantilever, working as a display pixel and an optical pickup from the substrate, is fabricated on an optical waveguide sheet with a separator. The cantilever has a transparent electrode film and it can be attracted and touch down on the substrate when a high voltage is applied between the substrate and the cantilever. Because of the surface roughness of the substrate and cantilever, the two cannot contact perfectly; however, fairly close contact within optical wavelengths can be realized. Therefore, the evanescent light generated by the waveguide sheet can be transferred to the cantilever, resulting in light emission on the cantilever surface as long as it has a high enough roughness for light scattering. The fabrication process using MEMS technology and evaluation of the device are described.

13.1 **Electrostatic-Driven Optical Display Device** 462
13.1.1 Principle of the Interferometric Display Device 462
13.2 **Design of the Device** 462
13.2.1 Fabrication of the Device 463
13.2.2 Performance of Prototype IDD 463
13.2.3 Improvement of the IDD 464
13.3 **Evanescent Coupling Switching Device** 465
13.3.1 Principle of the Evanescent Coupling Display Device 465
13.3.2 Fabrication Process of the ECDD 465
13.3.3 Evaluation of the ECDD 466
References 467

MEMS (microelectromechanical systems) is one of the new approaches to producing or assembling precision machinery with electronics. Originally, MEMS emerged from the silicon process, which is a combination of techniques such as chemical vapor deposition (CVD), reactive ion etching (RIE), photo or electron beam lithography systems, etc.; it is a concept of creating small mixtures of machines and electronics regardless of the fabrication technology.

K.-H. Grote, H. Hefazi (Eds.), *Springer Handbook of Mechanical Engineering*, Springer Handbooks,
https://doi.org/10.1007/978-3-030-47035-7_13

13.1 Electrostatic-Driven Optical Display Device

Various types of optical switching devices have been proposed and developed. Most of them are intended for switchboard purposes – typically optical-fiber communication [13.1]. For display purposes, the digital micromirror device developed by TI [13.2] is a good example of a commercial application of MEMS. In the micromirror, an application of mechanical action for display purposes is one of the promising potential capabilities of MEMS. In particular, the frequency response of such mechanisms is shown to reach more than hundreds of kilohertz due to their small mass.

Two examples of optical switches are shown: An interferometric display device (IDD) is composed of a small set of interferometers to control contrast and color [13.3, 4]. An evanescent coupling display device (ECDD) is an application of near-field optics for switching light perpendicularly. The basic principle of the device, its manufacturing process, and experimental results are shown.

13.1.1 Principle of the Interferometric Display Device

Figure 13.1 shows the schematic construction of the IDD. An SiO_2 half mirror suspended by leaf springs forms a capacitor to the base plate with a gap of $(n + 1/4)\lambda$ to construct a Fizeau interferometer. When a DC voltage is applied to the capacitor, the half mirror is attracted to the base plate balancing the leaf springs, and the reflection beam from the base plate interferes with the beam reflected from the half mirror. When a monochromatic light source illuminates the device, the contrast is changed periodically according to the displacement of every $\lambda/4$. In the case of a white light source, color variation is realized with a fine half mirror positioning control. Integrating this device like a dot matrix, a reflection-type display can be constructed. The device has the potential to triple the pixel density compared to RGB space separation displays. Also, static driving consumes little energy, and the mirrors have a fast response because of their light mass of tens of micrograms.

13.2 Design of the Device

The displacement of the mirror z is a balance of the leaf spring force and the electrostatic force F. It can be expressed as

$$F = \frac{1}{2}\epsilon S\left(\frac{V}{d-z}\right)^2 = kz\,, \tag{13.1}$$

where ϵ is the dielectric constant, S is the area of the half mirror, V is the applied voltage, d is the gap length without voltage, and k is the spring constant of the leaf spring. The resonant frequency of the mirror f_n is calculated by

$$f_n = \frac{1}{2\pi}\sqrt{\frac{ml^3}{192EI}}\,, \tag{13.2}$$

where m is the mass of the leaf spring, l is the length of the leaf spring, E is the Young modulus of the spring material, and I is the moment of inertia of the leaf spring. This predicts that the relationship between voltage and displacement is nonlinear.

The maximum contrast of the device is obtained when the intensity of the beam reflected by the half mirror and that reflected from the bottom is equal. Suppose the following: half mirror reflectance R_h, transmittance T_h ($\simeq 1 - R_h$), and reflectance of the bottom mirror R_b. The relationship is expressed as

$$R_h = T_h^2 R_b\,. \tag{13.3}$$

This is the optical requirement for the device to obtain the maximum contrast.

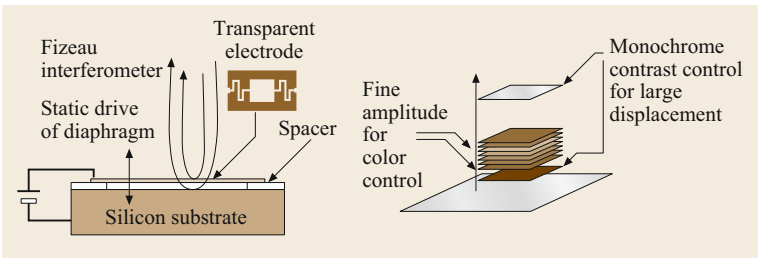

Fig. 13.1 Principle of the interferometric display device

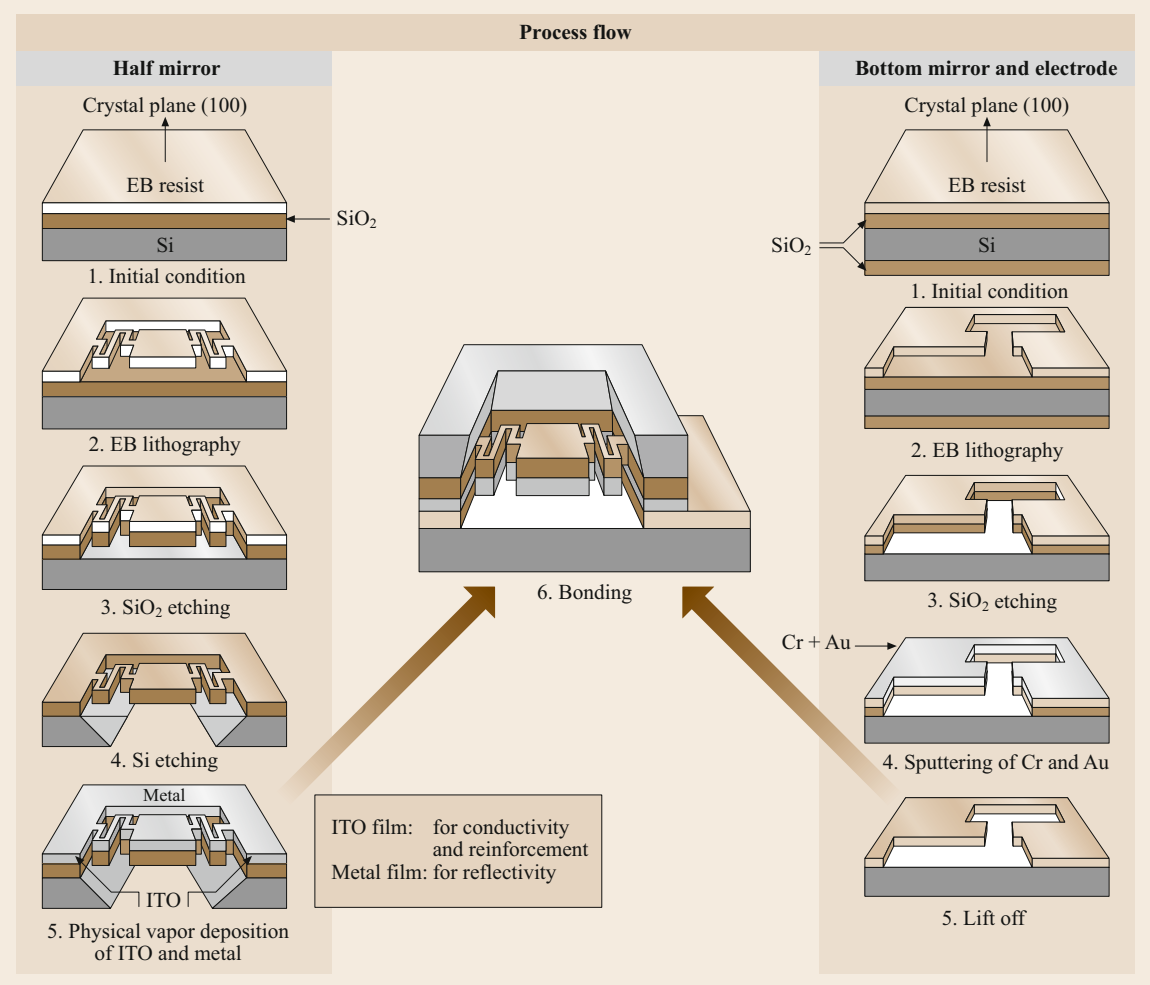

Fig. 13.2 Fabrication process of the IDD

13.2.1 Fabrication of the Device

The half mirror is the key element of this device and it should have a fine parallel movement to the base plate. A double leaf spring suspended mirror is used for this purpose. A 100 μm square mirror is fabricated from a thermally oxidized silicon film of thickness 1 μm, with a spring length of 400 μm, which is folded for a wider pixel aperture. A theoretical resonant frequency of 27 kHz is calculated for the film thickness, a beam width of 5 μm, and an applied voltage of 45 V. Thus, a displacement of the mirror more than a quarter of the wavelength can be obtained by the application of a low driving voltage to the mirror gap.

Figure 13.2 is the process flow for manufacturing the IDD. A wafer bonding technique has been employed to adjust the mirror gap easily. The half mirror and the bottom mirror electrode are fabricated separately. Then the gap is controlled by the film thickness of the SiO_2 as the spacer.

13.2.2 Performance of Prototype IDD

Figure 13.3 is a fabricated example of the IDD. For this prototype, a half mirror dimension of 100 μm, a leaf spring width of 10 μm, and a mirror gap of 5 μm are realized. A driving DC voltage of 15 V and a resonant frequency of 5.3 kHz have been obtained. When the device is illuminated by a halogen lamp, interferometric fringes are observed on the half mirror, instead of uniform contrast change. This originates from the deformation of the half mirror, because of its thin thickness and short leaf spring length compared to the width, and should be improved by increases the film thickness as well as structural modification.

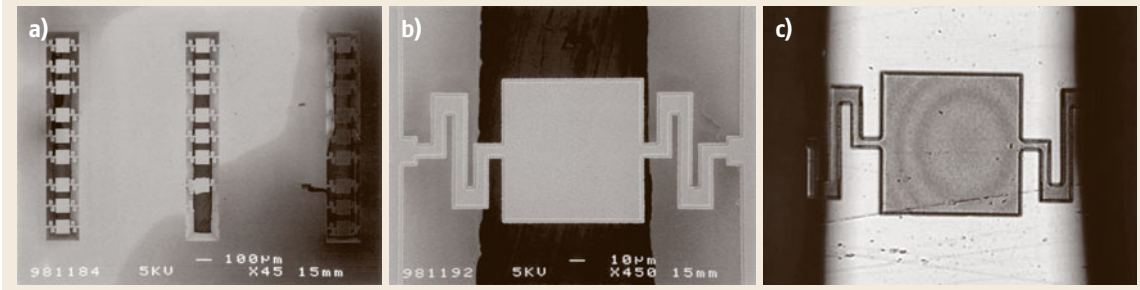

Fig. 13.3a–c Example of the (a) IDD array, (b) IDD pixel and (c) interferometric fringes

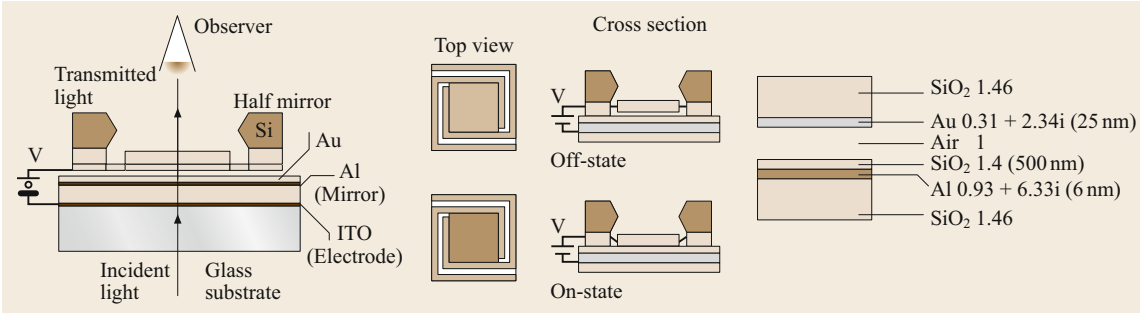

Fig. 13.4 Improved construction of the IDD based on Fabry–Pérot interferometer

13.2.3 Improvement of the IDD

The principle of the device is alternated from the Fizeau interferometer to Fabry–Pérot interferometer, shown in Fig. 13.4, for easier optical adjustment for high contrast and illumination. By experimental optimization, a combination of gold and aluminum film in Fig. 13.4 was found to be the best for satisfying (13.3). Also, to achieve smaller deformation of the half mirror, a spiral structure, shown in Fig. 13.5, is adopted to realize longer leaf spring length so that the deformation may be concentrated only on the leaf spring. With a twofold film thickness of 2 μm surrounding the half mirror, the deformation of the mirror itself was improved to 0.2 μm, which is comparable to a quarter of the wavelength.

By a CCD video capture system, the RGB contrast of the IDD is evaluated. In Fig. 13.6, RGB contrast is obtained for the halogen illumination. Although the pixel image still has a distribution in both color and contrast, no interferometric fringe is observed for this construction thanks to smaller film deformation.

The average contrast of a pixel for each color $C_{R,G,B}$ is calculated as

$$C_{R,G,B} = \frac{I_{max} - I_{min}}{I_{max} + I_{min}} , \qquad (13.4)$$

where I_{max} is the maximum and I_{min} is the minimum intensity of the pixel. The obtained contrasts for Fig. 13.6 were $C_R = 0.18$, $C_G = 0.03$, and $C_B = 0.08$. The con-

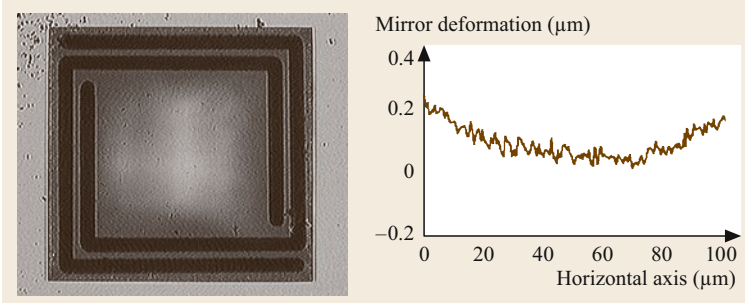

Fig. 13.5 A spiral leaf spring structure and cross sectional deformation

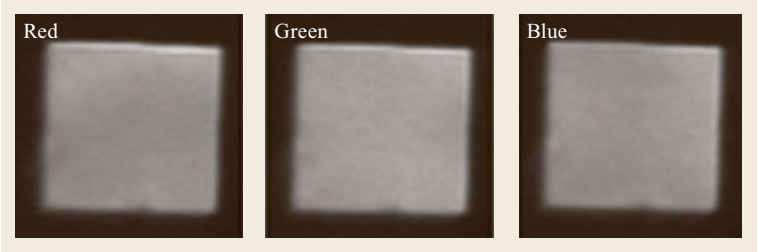

Fig. 13.6 RGB pixel image

trast dependence on color may be attributed to the interferometric layer, which is designed to be fit for only one wavelength.

Frequency response was examined by a function generator and high-voltage power source. Up to 100 Hz, the device follows the input voltage, and for higher driving frequency, it has a phase delay because of the squeeze damping effect of the air. For a driving frequency of 2 Hz and a voltage of 10 V, a maximum contrast of 0.3 was obtained.

13.3 Evanescent Coupling Switching Device

Fabrication for this device is very difficult because of various process problems such as deformation of the half mirror, adhesion of the mirror to the substrate, etc. An alternative is the evanescent coupling display device (ECDD), which uses microfabricated cantilevers for optical switching and is free from mirror deformation [13.5–7]. The principle of the device, its fabrication process, and evaluation are presented in this section.

13.3.1 Principle of the Evanescent Coupling Display Device

The ECDD is fabricated on a glass substrate together with cantilevers as micro-optical switches (Fig. 13.7). The substrate works as a waveguide sheet propagating light horizontally, and the cantilevers are driven electrostatically by DC voltage to engage in or disengage from the switching action. When the cantilevers are attracted to the substrate making mechanical contact, light energy in the waveguide sheet transfers to the optical cantilevers by the evanescent coupling, even if there is a small gap within the wavelength. The transferred light also propagates in the cantilevers horizontally; however, it is scattered from the top surface of the cantilevers because of the rough surface. Then, the cantilevers emit the light perpendicularly, enabling the brightness change of the device. By the on–off switching of the driving voltage, the cantilevers work as a pixel of the optical display.

13.3.2 Fabrication Process of the ECDD

As shown in Fig. 13.8, multicantilevers are fabricated from a silicon substrate with a 2 mm-thick thermal oxide layer. The multicantilevers on the substrate are patterned by photolithography and RIE etching, using a Cr layer as a mask for SiO_2 etching. The silicon substrate under the cantilevers is etched in a solution of 15 wt% tetramethyl ammonium hydroxide (TMAH) solution at 90 °C. Next, the indium tin oxide (ITO) layer as a transparent electrode is sputtered on the cantilevers. A micrograph of the fabricated cantilevers is also shown in Fig. 13.8, nesting eight cantilevers from both sides of the substrate to increase the effective pixel area. The length and width of the cantilevers are 490 and 20 μm, respectively. Due to residual stress of the ITO layer, the fabricated cantilevers are curved toward the silicon substrate with a displacement of 10 μm. Because of the

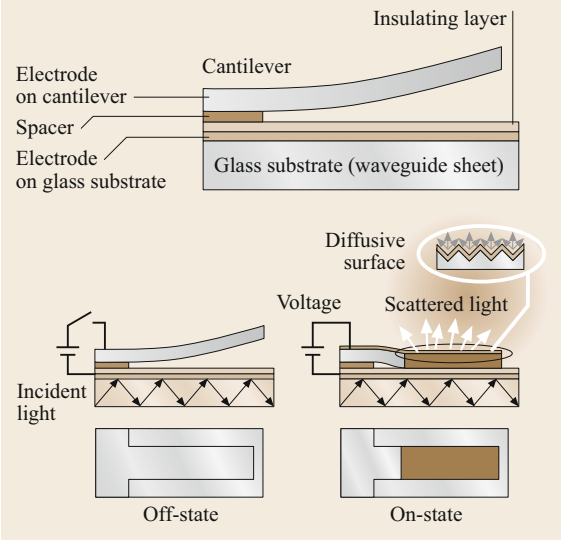

Fig. 13.7 Principle of the evanescent coupling switching device

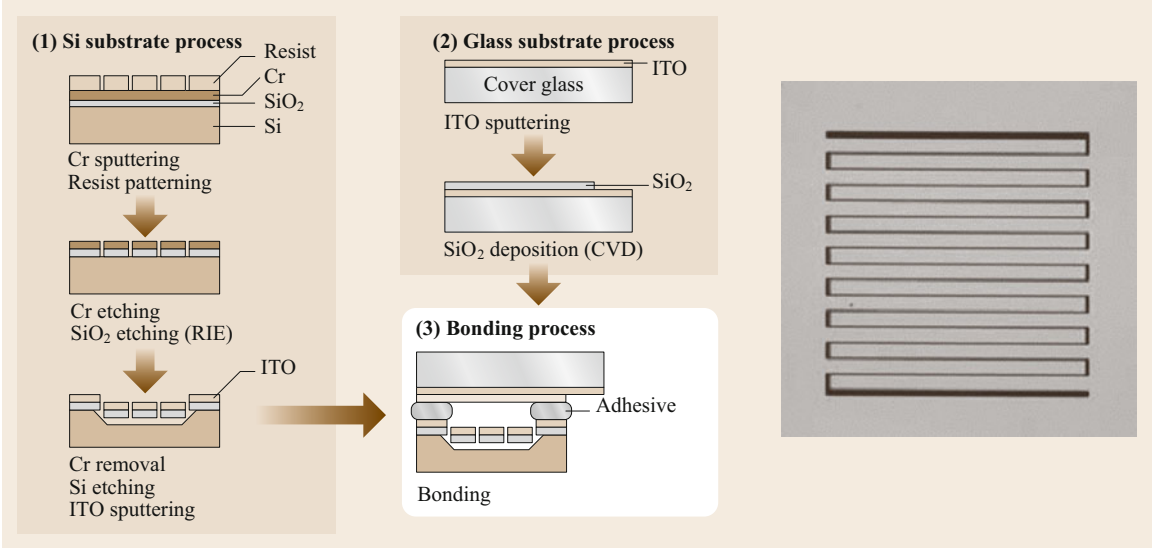

Fig. 13.8 Fabrication process of the ECDD

residual stress, the sticking problem between the cantilevers and the substrate is cleared up even after voltage application.

13.3.3 Evaluation of the ECDD

The characteristics of the ECDD were evaluated by the same system as the IDD. A result of the driving evaluation is shown in Fig. 13.9. Although unnecessary scattering appeared in the off-state, a clear brightness is observed in the on-state of the pixel. A maximum contrast of 0.9, defined by (13.4), was obtained at a driving voltage of 170 V. Hysteresis of the contrast was observed in a slow driving test; however, it does not cause the switching speed to deteriorate.

For frequency response, a square voltage of 170 V and a frequency of 1 kHz can drive the multicantilevers. From this performance, the device has a sufficient response for display application. However, for higher response speed, reduction of the sheet resistance of ITO layers, as well as the size and cantilevers, must be optimized.

A dot matrix-type device, shown in Fig. 13.10, is fabricated to confirm the function as a display. An 8×8 pixel matrix is constructed in $6 \times 6\,\mathrm{mm}^2$ square, with a pixel size of 500 µm. Using an external voltage driver with a laser incident beam to the glass substrate, the device shows the ability of an individual pixel drive as well as row and column driving.

This type of device can display images on transparent media and can be seen from both sides, when every part is made of transparent material.

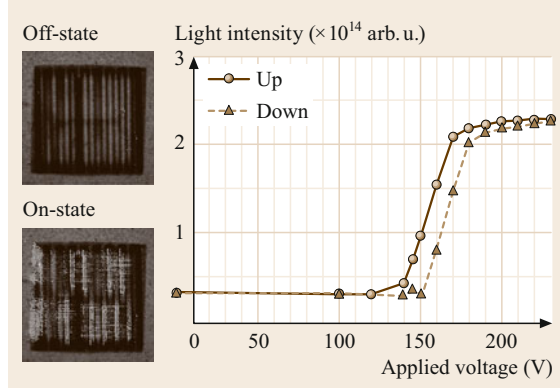

Fig. 13.9 On–off characteristics of the ECDD

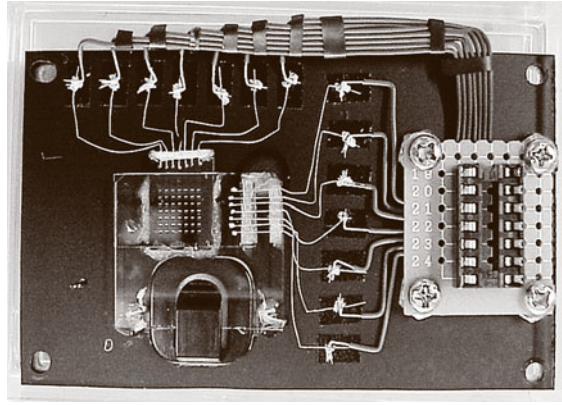

Fig. 13.10 8×8 dot matrix-type ECDD

References

13.1 K.W. Goosen, J.A. Walker, S.C. Arney: Silicon modulator based on mechanically-active antireflection layer with 1 Mb/s capability or fiber-in-the-loop applications, IEEE Photonics Technol. Lett. **6**, 1119–1121 (1994)

13.2 J.B. Sampell: Digital micromirror device and its application to projection displays, J. Vac. Soc. Technol. B **12**, 3242–3246 (1994)

13.3 T. Hatsuzawa, T. Oguchi: Application of micromachined SiO_2 film for display devices. In: *Digest of Technical Papers. 10th Int. Conf. Solid-State Sens. Actuators* (1999) pp. 804–807

13.4 T. Oguchi, M. Hayase, T. Hatsuzawa: Driving performance improvement of the interferometric display device (IDD). In: *IEEE/LEOS Int. Conf. Opt. MEMS* (2001) pp. 107–108

13.5 T. Hatsuzawa, T. Oguchi, M. Hayase: An electrostatic-driven optical switching structure for display device. In: *IEEE/LEOS Int. Conf. Opt. MEMS* (2001) pp. 149–150

13.6 T. Oguchi, H. Masanori, T. Hatsuzawa: Electrostatically driven micro-optical switching device based on interference of light and evanescent coupling, Proc. SPIE **4902**, 213–220 (2002)

13.7 T. Oguchi, M. Hayase, T. Hatsuzawa: Electrostatically driven display device using evanescent coupling between sheet waveguide and multicantilevers, Proc. SPIE **5264**, 134–141 (2003)

Takeshi Hatsuzawa

The Laboratory for Future Interdisciplinary Research of Science and Technology (FIRST)
Tokyo Institute of Technology
Yokohama, Japan
hatsuzawa.t.aa@m.titech.ac.jp

Takeshi Hatsuzawa received the Dr Eng degree from Tokyo Institute of Technology in 1993. After 12 years at the National Research Laboratory of Metrology, he became Associate Professor in the Tokyo Institute of Technology in 1995, and full professor in 2002. His current research is focused on MEMS and NEMS applications in biochemistry using biotechnology.

14. Measuring and Quality Control

Steffen Wengler, Lutz Wisweh, Shuichi Sakamoto, Norge I. Coello Machado

Considering the incessantly increasing requirements on the quality of products and processes, it is necessary to ensure a quality-orientated management in all departments of any type of company and the advantageous application of manufacturing measurement equipment.

In addition to diverse technical requirements, the requirements of national, international, and company-specific norms must also be considered. Companies must not only fulfill the requirements of quality but also those pertaining to safety, the environment, and the economy.

In the following, some aspects of manufacturing measurement technology and quality management and their integration into a manufacturing process will be introduced.

Starting with manufacturing geometrical conditions and statements on drawings (nominal state and geometrical limits) the use of measurement equipment and gages to the evaluation of geometric elements will be described. Basic knowledge of measurement standards, measurement uncertainties as well as calibration and testing of measuring instruments are presented. Based on the physical principles, the equipment and methods for the registration of measurement values, form and position deviations, and surface characteristics will be introduced.

14.1 **Quality Management** 469
14.1.1 Quality Management Methods 469
14.1.2 Quality Management Systems 474
14.1.3 CE Marking 474
14.2 **Manufacturing Measurement Technology** 475
14.2.1 Arrangement in the Manufacturing Process 475
14.2.2 Specifications on the Drawing 476
14.2.3 Gauging 478
14.2.4 Application of Measuring Devices 479
14.2.5 Coordinate Measurements 482
14.2.6 Surface Metrology 487
14.2.7 Form and Position Measuring 490
14.2.8 Laser Measuring Technology 493
14.2.9 Measuring Uncertainty and Traceability 496
14.2.10 Inspection Planning 497
14.3 **Further Reading** 498
References 498

14.1 Quality Management

Nowadays, the quality of products, assemblies, and services not only includes the fulfilment of functional requirements by maintaining tolerances. It also includes the fulfilment of numerous requirements such as shown in part in Fig. 14.1. In this section, some fundamentals of quality management will be described from the multitude of requirements. In Sect. 14.2, some aspects of the requirements of manufacturing measurement technology for the qualification of the geometrical quality of products will be shown.

Among the requirements for organizations involved in quality control, the key concepts of quality management (QM) and total quality management (TQM) include planning, monitoring, and improvement of quality, such as the consideration of representatives and departments relevant to quality, as shown in Fig. 14.2.

14.1.1 Quality Management Methods

To conform to the requirements of modern quality management, nowadays numerous procedures and methods, with many different applications, are available [14.1]. Figure 14.3 presents a selection of relevant methods used in the area of mechanical engineering.

K.-H. Grote, H. Hefazi (Eds.), *Springer Handbook of Mechanical Engineering*, Springer Handbooks,
https://doi.org/10.1007/978-3-030-47035-7_14

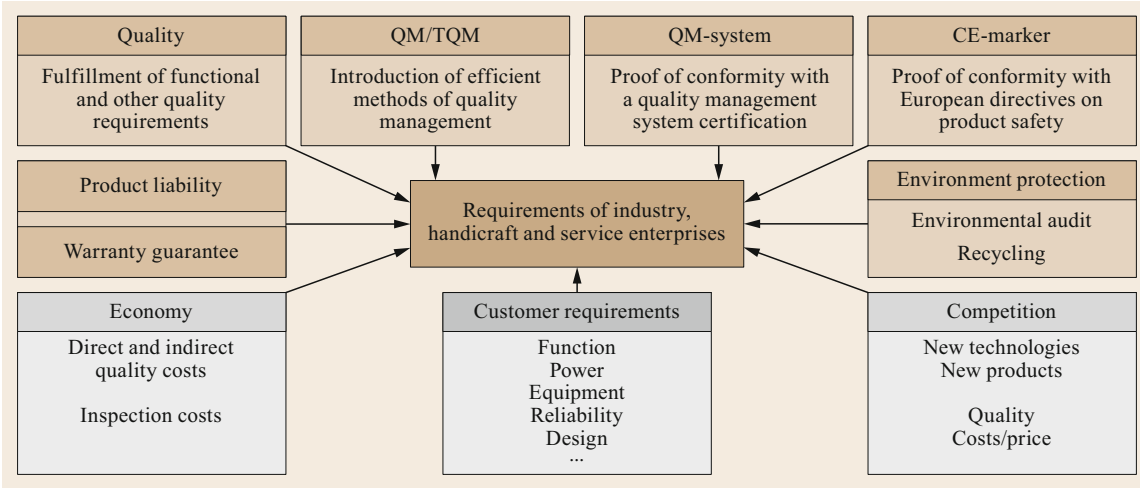

Fig. 14.1 Requirements for industry, craft, and service enterprises

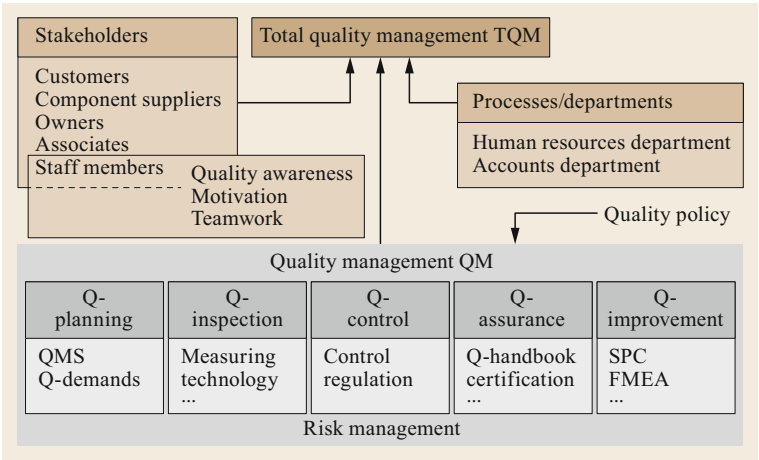

Fig. 14.2 Elements of quality management

The different methods can be associated to two essential groups: *problem-resolving techniques* and *preventive techniques*. The problem-resolving techniques can also be divided into the two other categories: those that find causes of existing quality problems and those that help the engineer develop definite aims in a systematical manner (management methods).

The prime conditions for quality analysis are the collection and preparation of quality data with respect to measured data. *Tally lists* enable a visualization of the accumulation of certain failures or various kinds of mistakes. *Histograms* demonstrate the probability of the occurrence of a certain event within intervals of the measurement range. *Pareto analyses*, also called *ABC analyses*, enable a weighting of the dominant influencing parameters. In combination with the corresponding costs, they are known as Lorenz–Pareto analyses.

Referring to a definite problem, a comprehensive structuring of clustered influences or causes can be presented as a *cause–effect diagram*, also known as a *fishbone diagram* or *Ishikawa diagram*, which can be used to solve possible problems.

The determination of pairs of values in an x–y coordinate system is especially applicable in the experimental causal research of measurement (e.g., quality characteristics). These *scatter diagrams* can be described with the help of statistical calculations, such as regression and correlation analyses, in which the identified regression function describes the kind of functional connection, while the correlation describes the intensity of that connection through the correlation coefficient.

Nowadays, *analysis and evaluation of the quality capability* of procedures and processes takes place

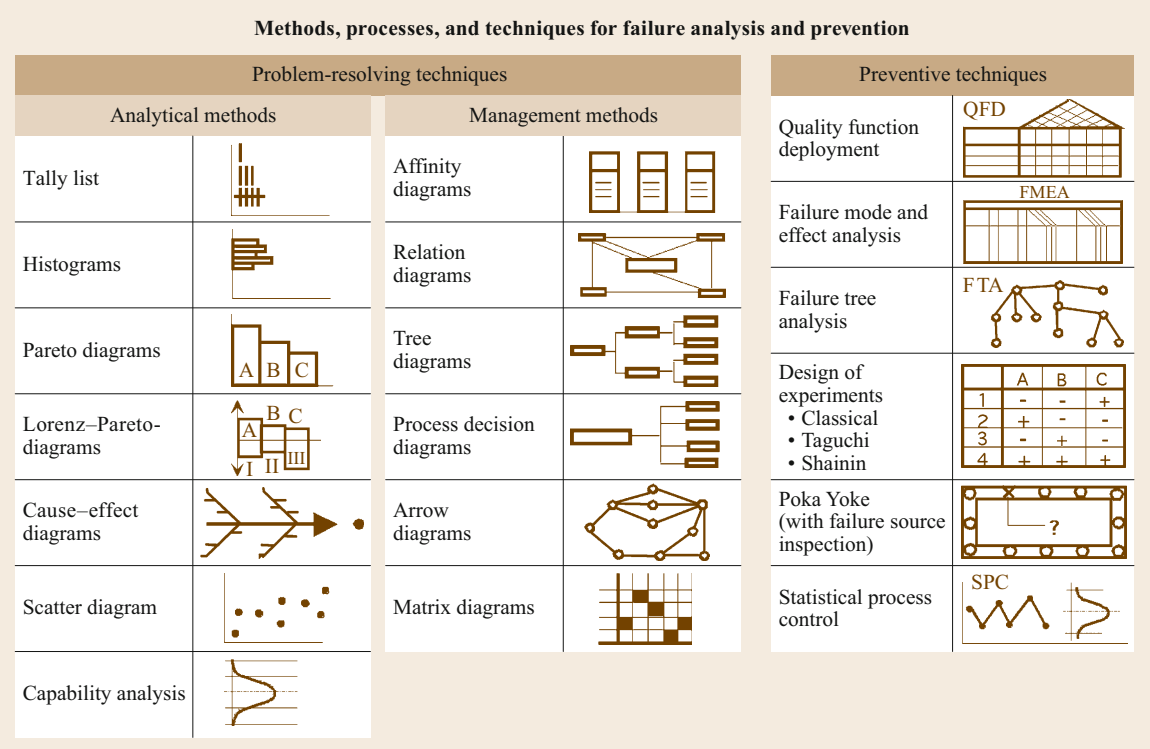

Fig. 14.3 Problem-resolving and preventive techniques

in many areas of mechanical engineering by a comprehensive statistical evaluation in terms of capability coefficients, which express the relation of process spread (6σ) to the tolerance and the position of the arithmetic mean of the tolerance borders. This way, it is possible to compare the quality level of different processes.

Management methods support the solution of problems by a targeted systematic procedure. *Affinity diagrams* allow a structured systematization of ideas in order to point out the correlation between these ideas.

Relation diagrams enable the development of cause–effect relations by visualizing networked structures. *Tree diagrams* specifically subdivide aims until directly realizable activities are practicable.

Firstly, *process–decision diagrams* start by arranging possible problems by

- Urgency
- Probability of occurrence
- Difficulty of prevention.

With the aim of detecting potential problems already in the planning phase and to elaborate corresponding countermeasures.

Arrow diagrams or *net plans* are important resources for project planning for the investigation of *critical paths*, which determine the total permanence of a project. In this method, the determination of a process sequence is made using series and parallel paths to develop a detailed explanation of the working steps required to achieve the project aim, followed by the assignment of the corresponding process durations.

If a lot of information quantities for certain circumstances are available, *matrix diagrams* are suitable for detection of latent structures. By using data evaluation in pairs with the help of matrices for different characteristics, this method enables, for instance, manufacturing and market analysis.

Nowadays, in the field of preventive techniques for failure prevention in technological processes, the schematically compounded methods shown in Fig. 14.3 are mostly applied.

In current quality management, product-related customer wishes are the source of motivation for development from the designing process through the manufacturing process up to the delivery of the products.

With the help of *quality function deployment (QFD)* the *voice of the company* can be developed from the *voice of the customers*. The QFD method systematizes

this process under the application of matrices based on the following four steps:

- Customer wishes in terms of product characteristics
- Product characteristics in terms of part characteristics
- Part characteristics in terms of manufacturing regulations
- Manufacturing regulations in terms of production instructions.

Every phase can be described by matrices in the form of a so-called *house of quality*.

This method offers the possibility of affecting the production aim in the conception phase and at the same time obtaining information about the critical product and process characteristics for the fulfilment of customer expectations. Besides the implementation of marketing information in the product, target conflicts between the individual product characteristics may also become visible.

For the detection of potential failure modes during product development, the introduction of new manufacturing methods and the modification of manufacturing technologies' *failure mode and effect analysis* (FMEA) is used. FMEA is especially used in the case of cost-intensive and risk-products and processes. FMEA has universal application and is not connected with a special field. At the base of a standardized procedure, which can be supported by corresponding blank forms, the main steps of a FMEA can be divided into risk analysis, risk assessment, the determination of measures, and the evaluation of effectiveness. The risk evaluation results from evaluation of the probability of occurrence, its importance (for the customer), and the probability of detection of the corresponding failure before delivery to the customer. The advantages of FMEA are above all a decreased number of failures in the early phases of product manufacturing and in product planning.

The systematic search for imaginable reasons for a failure, called an unwanted event, is possible with the method of *failure-tree analysis*. This method, which originated in the field of safety engineering, enables an evaluation of fixed correlations by the determination of the quantitative probability of the appearance of failures.

For this purpose, the function of single components (devices) is described under different conditions using a so-called *components tree*. A subsequent system analysis aims to holistically describe their organization and the behavior of the technical system. The contribution of the individual components to the protection of the overall function of the system, the evaluation of the consequences of the environmental influences of the overall system, and the description of the reaction of the overall system to failures within the system, of resources and by faulty operations, can be described by a failure-tree analysis and calculated or simulated by various evaluation methods.

The methods of *statistical research planning* have the general aim of adjusting the relevant product and process parameters using a systematically procedure in such a way that the quality-relevant characteristics closely approach the ideal value with as few experiments as possible.

The weighting of the influencing factors and the quantification of their effect can be achieved based on classical statistical research planning using mathematical models (such as factorial research plans); if there are a very large number of influencing factors, this can be solved with the help of the empirical procedures developed by Taguchi or Shainin.

The *Poka Yoke* method (from the Japanese: the avoidance of unintentional errors) is dedicated to preventive avoidance of failures in manual manufacturing and assembling processes through the development of precautions (design measures that eliminate incorrect handling) and facilities for failure avoidance for immediate failure detection in the manufacturing process. This can be realized by a comprehensive implementation of applicable rules for product and process design or by the use of simple ancillary equipment.

The *statistical evaluation and control of the quality of processes* (statistical process control (SPC)) is not only a main goal of modern quality management systems but is also required for cost-efficient production processes.

The aim of the use of statistical methods in quality management also exists in the classical detection of faulty products in the manufacturing process and is increasingly widespread in the qualitative monitoring, control, and improvement of the manufacturing and assembling process.

According to algorithms such as that shown in Fig. 14.4 some basic decisions can be made.

Quality control of processes can be performed using continuous, 100% inspection or on the basis of periodically chosen samples in the form of statistical process control (SPC). Statistical methods can also be used to achieve the aim of monitoring and improving product and process quality. Therefore, it is a direct component

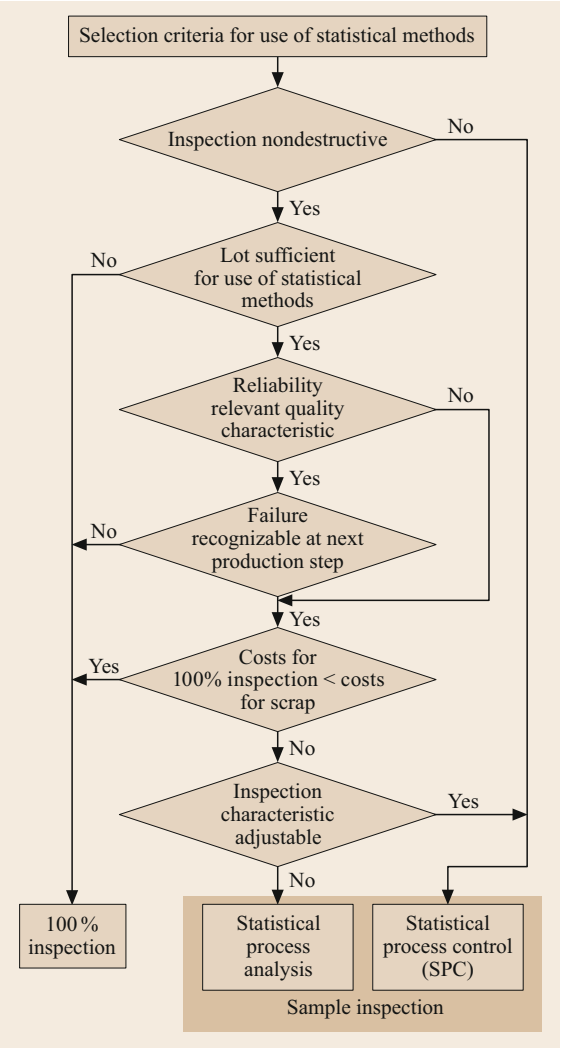

Fig. 14.4 Selection criteria for the use of statistical methods

of the quality control circle. The most important methods in this regard are (Fig. 14.5):

- Measuring controls with statistical control algorithms
- quality control charts
- Capability analyses and evaluations
- Sample inspection by statistical sample plans.

Processes in practice, especially newly-introduced processes, are influenced by numerous systematic and

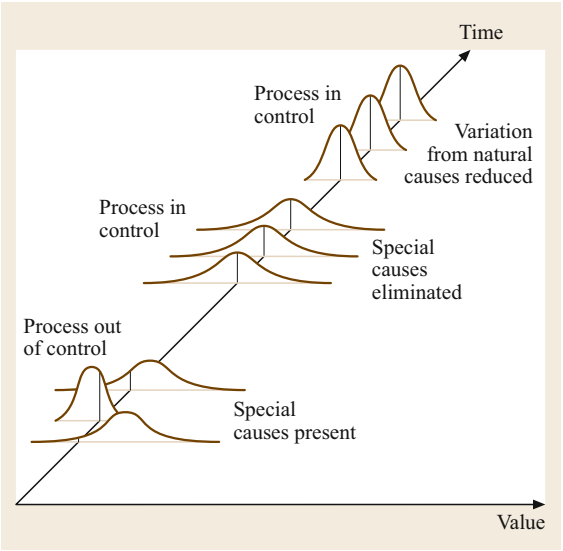

Fig. 14.5 Overview of the use of statistical methods for the evaluation and control of processes

random influences, which make the use of statistical methods difficult.

Many statistical methods require the prerequisite of a normal distribution (e.g., double-sided tolerances or limited quality characteristics) or a logarithmic normal distribution (e.g., one-sided tolerance quality characteristics), which are free of systematical influences.

In such cases, we also speak about the requirement of stable or stationary processes or of so-called *processes in or under statistical control* (Fig. 14.6).

If stable processes are available, they can be further inspected using quality control charts. A quality control chart (QCC) is a graphical representation of a process calculated from the measured results from a small sample or chronological characteristics. The target of quality control charts is to capture quantitative changes in a process that exceed statistically derived control limits (Fig. 14.7).

The recorded results can then be the basis for subsequent statistical evaluations or characterizations in the form of capability coefficients. These coefficients can also be used for the evaluation of machines and processes.

If a product-orientated decision about the acceptance or rejection of a product series or lot takes place, sample plans can be used. The producer (supplier) may also use these in the form of a final inspection, as may the customer in the form of an inspection on receipt.

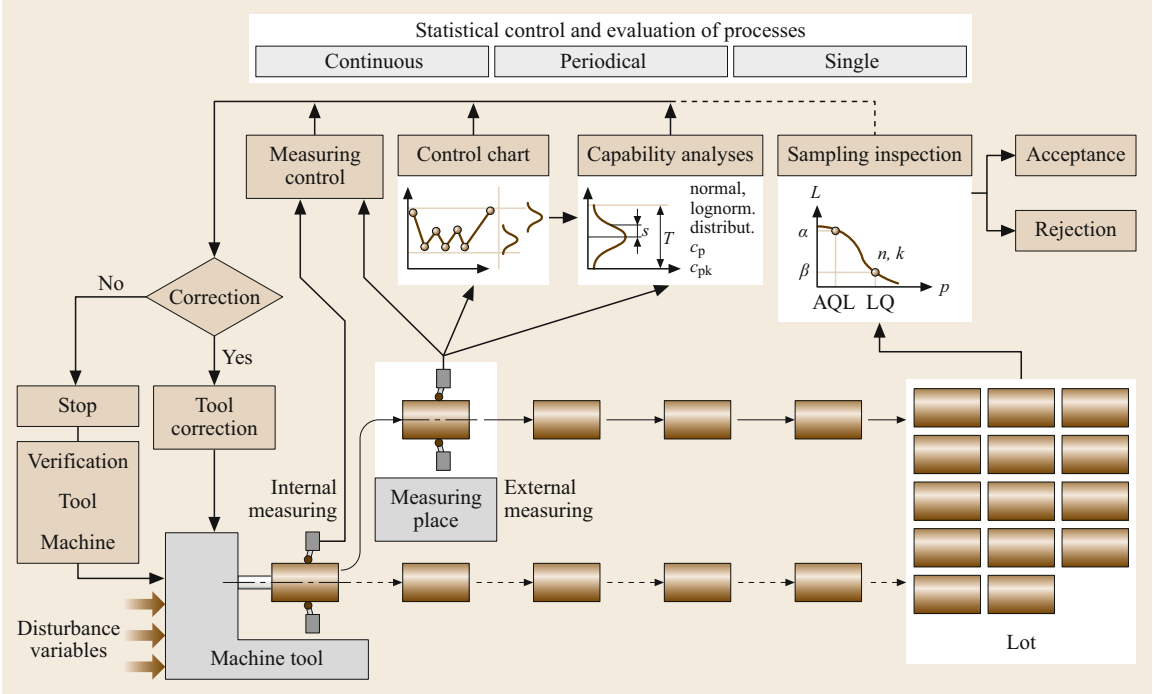

Fig. 14.6 Stabilization of processes through the reduction of systematic and random processes disturbing variables

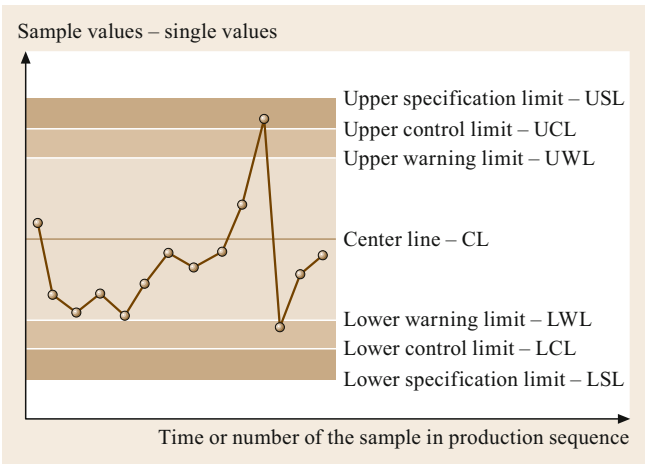

Fig. 14.7 Process monitoring with quality control charts

Statistical analysis results have a wide variety of uses in quality monitoring, evaluation, control, and management, as is shown in Fig. 14.8.

14.1.2 Quality Management Systems

The organizational realization of the concept of quality in all departments of enterprise and in all phases of product realization can be supported by *quality management systems* (QMS), as is shown in Fig. 14.1. In addition to this, the organizational structure and the processes organization of all quality-relevant departments and operations can be evaluated and compared to standardized regulations. The successful introduction and realization of a QMS can be evaluated and validated by an accredited certification body.

As the basis for this, the independent ISO 9000 series of standards can be used [14.2–5]. Based on this, for the worldwide automotive industry, comprehensive additional requirements exist, which are fixed in company-dependent standards. Efforts for the integration of the different requirements of the automotive industry to date are contained in the standard IATF 16949 [14.6].

14.1.3 CE Marking

Within the single market of the European Union, a requirement for the commencement of operation and the placing on the market of products is the fulfilment of harmonized safety requirements. To obtain a conformity certificate for these European Community (EC) requirements, a CE marking is required. This is also valid for products that are produced outside of the European Union if they are also distributed within it.

Examples of EC directives include those for machines, toys, electromagnetic compatibility (EMC), detonating devices, and medical products, etc.

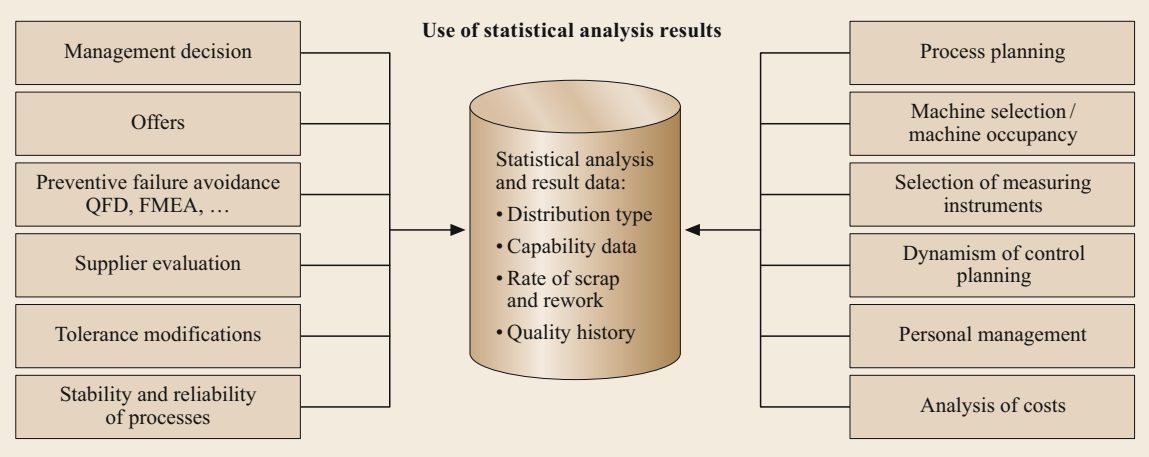

Fig. 14.8 Use of statistical results

14.2 Manufacturing Measurement Technology

Measurement is the determination of the value of a physical quantity (measured quantity) by comparison with a reference value.

Manufacturing measurement technology is part of the field of measurement technology. It deals with the methods, equipment, and strategies for measurement in the realm of mechanical production processes. Manufacturing measurement technology is utilized in various locations, such as rooms with special, controlled environmental conditions, as well as directly integrated into the assembly line. The aims of manufacturing measurement technology are:

- Evaluation of the product
- Evaluation of processes and machines
- Quality-orientated process control.

Here we confine the discussion to the description of the relevant geometrical features and/or technical aspects of obtaining such objects from workpieces. These features include lengths, angles, distances, and surface structures. Most of the principles and definitions described also apply to nongeometrical parameters. The relevant SI unit used to describe these geometrical features is meter. Angles are described in degrees or radians.

The physical measurement that comes from the measuring process is called the measure. The object from which this quantity was measured is called the measuring object. The value of the measure, which actually exists but is currently unknown, is the true value. The aim of the measuring process is to determine this true value. A variable that does not change with time (for example, a diameter) is measured by a static measurement. Dynamic measurement is the measuring of a variable that changes with time (for example, a vibration) or the measurement of a variable, whose variation arises from the time-dependent behavior of another variable (for example, for a roughness measurement, the dependence of the measured value on the scanned measuring length).

In order to determine whether an object fulfils a particular requirement, it is inspected. As subjective inspection should not be considered, one can differentiate objective inspection into measuring and gauging. The inspection means that are employed can be divided into indicating measuring devices, measurement standards, gauges, and additional measuring devices. Figure 14.9 shows a digital dial indicator and a measuring block, as the most important measurement standard of dimensional measuring technology. Measuring blocks are quadrilateral metal or ceramic gauges, whose parallel end faces have a known width and minimal deviation. A gauge and a stand, an example of additional measuring equipment, are represented on the figure too.

14.2.1 Arrangement in the Manufacturing Process

Measuring technology has become an essential ingredient in manufacturing processes. Figure 14.10 shows the multitude of integration possibilities and the corresponding relationships between the production process and measuring technology as well as different possibilities for analyzing the measured data and its feedback into the process.

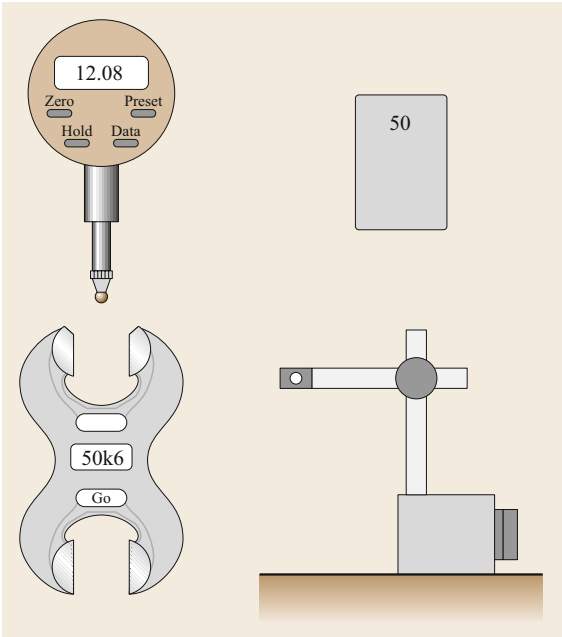

Fig. 14.9 Inspection devices

Inside every tooling machine integrated measuring devices are used to collect parameters (the position of the axes, temperature, force, voltage, current, etc.). These values can be directly used by the machine operator or the machine itself to control future operations. In reference to the collection of data from finished products and in consideration of the drawing specifications, these finished product parameters can be evaluated, classified, and documented. Furthermore, parameters can be derived from the measured values through continued analysis, or more specifically, these parameters that can regulate or control the machining or production of the product. Using an adjustment, the measured value (the controlled variable), which has an instantaneous value, is continuously measured and corrected with a controller with respect to a known value (the set value). It is then possible to eliminate disturbance factors from outside the process. The constant, targeted influencing of a process on the basis of a previously defined model without feedback is what is meant by open-loop control.

Starting from the process analysis, the machining process and/or the processing machines themselves can be evaluated (for example, for machine and process capabilities) and documented. The result of the machine evaluation is, for example, a quality-orientated machine selection. Should the machine not be in a position to produce the desired tolerances, selective inspection and correction of the machine systems may be necessary, or a complete overhaul or a new revision of the machine may even be necessary. Through the additional use of measuring technology for preventive monitoring of a machine, it is possible to implement maintenance procedures or schedules to avoid losses or stops in production.

14.2.2 Specifications on the Drawing

The drawing is the defined input to the manufacturing process based on the required functions outlined by the designer, and is, therefore, the basis for the manufacturing measuring process. The complete, integrated product drawings, as well as single-product element drawings, are used to clarify the permitted allowances and, thereby, the tolerances for manufacturing. The geometrical specifications can be separated into measuring

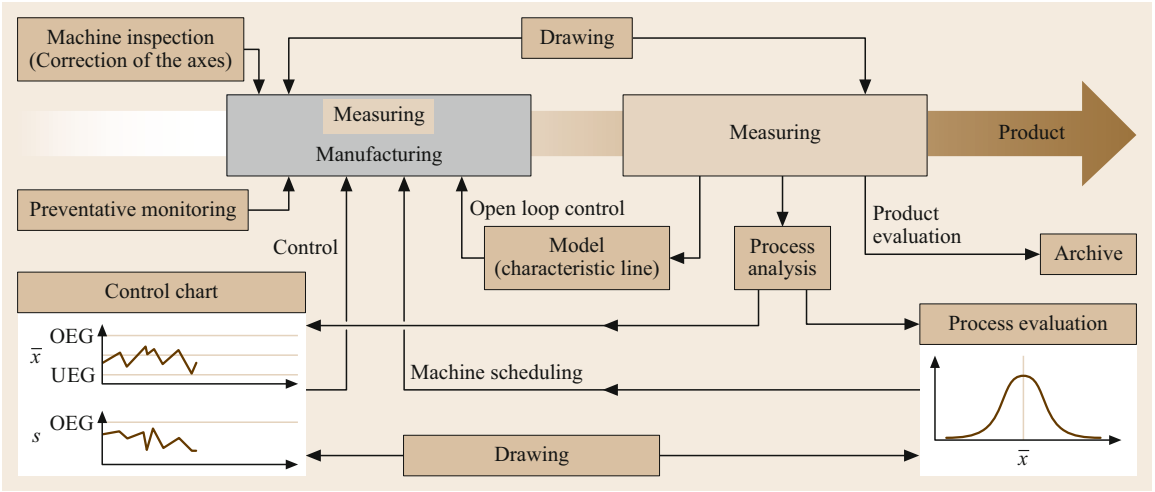

Fig. 14.10 Measuring technology and measuring value analysis in manufacturing processes

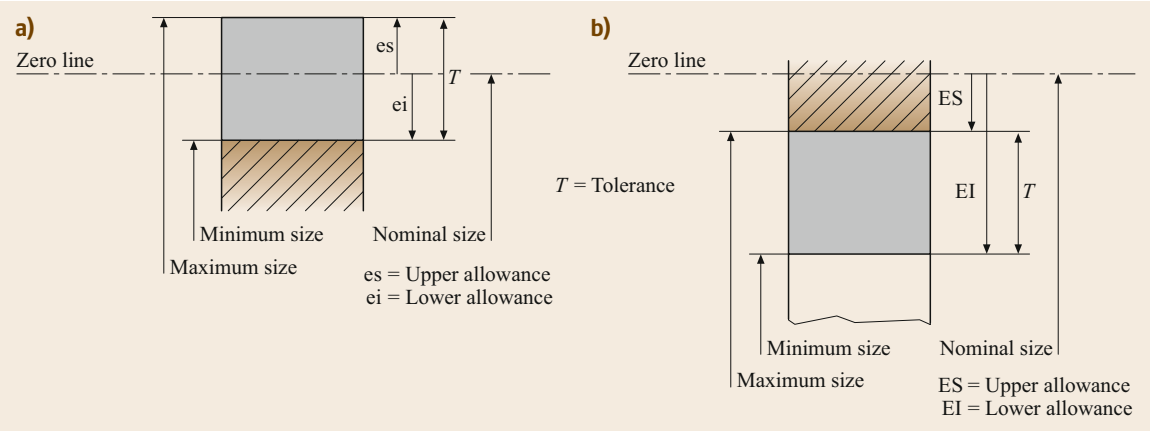

Fig. 14.11a,b Tolerance specifications for lengths: **(a)** shaft, **(b)** hole

tolerances and shape tolerances. Shape tolerances include not only form and position tolerances, but also surface finish tolerances, which can be divided into roughness and waviness.

Tolerance specifications for lengths consist of the nominal size and defined permissible upper and lower allowances (Fig. 14.11). The nominal size plus the upper allowance is the largest acceptable measure, and the nominal size plus the lower allowance is the smallest acceptable measure. The difference between the upper and lower allowances is the tolerance. The definition on the drawing is shown through the specification of a nominal size supplemented either directly by a coded specification of the allowance or through a letter and a number combination (ISO 286 [14.7, 8]). The letter describes the position of the tolerance field with respect to the zero line, and the number represents the magnitude of the tolerance. The specification $36^{-0.025}_{-0.050}$ corresponds to the drawing specification, 36f7, which, in manufacturing terms, means that the largest acceptable measurement is 35.975 mm, and the smallest acceptable measurement is 35.950 mm. Whenever the nominal sizes are the only values displayed on the drawing, free size tolerances according to ISO 2768 can be specified [14.9, 10].

The position of the tolerance with respect to the zero line (which corresponds to the nominal size) and the size of the tolerance determine the function of the proposed piece. The size of the tolerance is, furthermore, decisive for the cost of the manufacturing process.

The form and location tolerances in each case define zones, into which the corresponding element must fit in, when it is within the tolerance. Form tolerances, which are defined in ISO 1101 [14.11], are shown in Table 14.1. Single elements, such as lines, rectangles, circles, cylinders, and profiles are specified as form tolerances. Position tolerances are divided into direction, place, and run tolerances, as summarized in Table 14.2. In each case, position tolerances refer to an individual element of the workpiece. On the drawing, the necessary specifications are represented in a tolerance frame (Fig. 14.12). The tolerance frame contains a symbol that describes the type of tolerance that is being signified and a tolerance value, possibly with a reference length. The indication arrow connects the tolerance frame with the associated element, or rather the associated lines of

Table 14.1 Form tolerances

Form tolerances	Single elements
Straightness	—
Flatness	▱
Roundness	○
Cylindricity	⌭
Profile	⌒

Table 14.2 Position tolerances

Position tolerances		Related elements
Direction	Parallelism	//
	Perpendicularity	⊥
	Angle	∠
Place	Alignment	⌖
	Concentricity	◎
	Symmetry	⌯
Run	Runout	↗
	Total runout	⌰

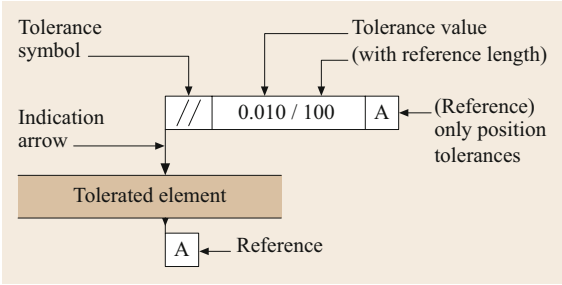

Fig. 14.12 The tolerance frame as a drawing entry

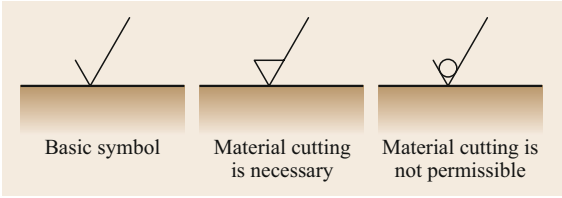

Fig. 14.13 Symbols for surface conditions

measurement or symmetry on the drawing. Whenever the type of tolerance requires it, the reference element is indicated at the end of the tolerance frame through the specification of a letter, which repeats the necessary reference basis. In a few cases, more reference elements are possible.

The tolerance specification for surface finish is shown on the drawing by a basic symbol and supplemented by additional specifications. Whether material cutting machining is *necessary* or *not permissible* is also indicated, as is shown in Fig. 14.13. Additional specifications include tolerances for the roughness value (most of the time, the arithmetic average surface finish (Ra)), and when necessary, amongst others, specifications for the manufacturing process, tolerances for further roughness or waviness parameters, and the grooving direction.

14.2.3 Gauging

Gauges are inspecting devices that represent the dimension and/or form of the workpiece that is to be tested. There are three types of gauges: limit gauges, receiving gauges, and so-called *go and no-go* limit gauges. The procedure is always the same: to try to mate the workpiece elements with the correct gauges. A simple yes or no decision is the result of this process. With limit gauges, one can determine whether the value of a test object is larger or smaller than the value of the gauge (for example, with a pin gauge). With receiving gauges (for example, radius or screw pitch gauges), a comparison is made with the workpiece's form and the form of the gauge, and the best-fitting pieces can then be separated out.

Go and no-go limit gauges are the most important for the inspection of manufacturing tolerance elements. Figure 14.9 shows an example of an external caliper gauge, which is suitable for the inspection of shafts. Limit gauges consist of a *go* side and a *no-go* side, which correspond, respectively, to the largest and smallest measurement possible; the *go* and *no-go* sides are verified one after the other to check for mating. The inspection result is *good* when the workpiece fits comfortably into the *go* side and not into the *no-go* side. The Taylor principle states that, on the *go* side, all the

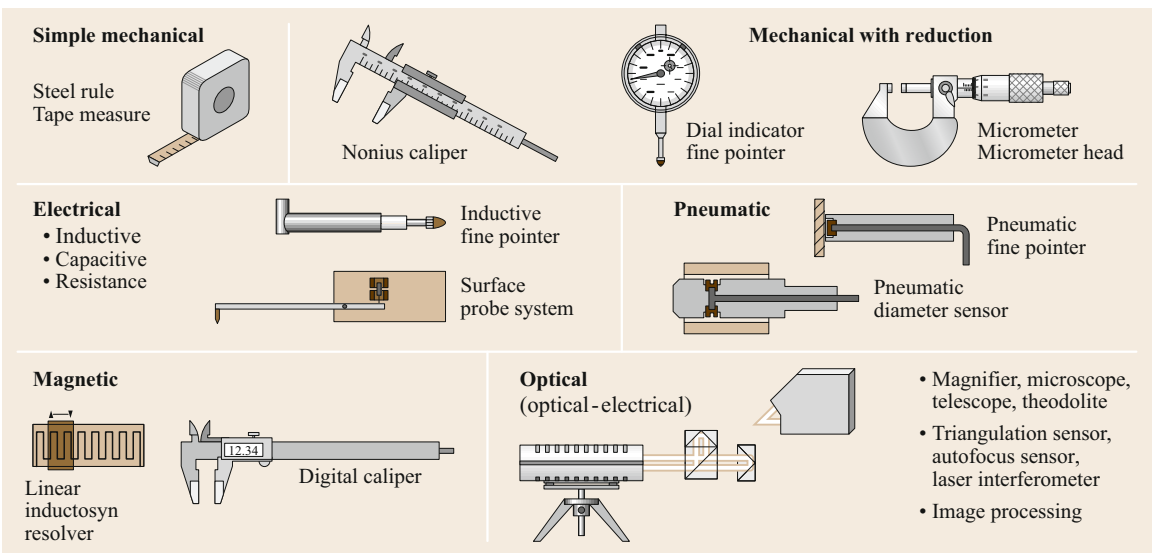

Fig. 14.14 Physical principles of measurement-value collection and example instruments

measurements or control measurements are tested at the same time, but on the *no-go* side, every measurement or control measurement is tested in isolation.

14.2.4 Application of Measuring Devices

Measuring devices work on very different physical principles. Simple mechanical measuring devices include the steel rule or measuring tapes. Measuring devices with mechanical reduction include nonius calipers, dial indicators, and micrometers. Pneumatic systems have long been used because of their noncontact scanning. At present, electrical, magnetic, and optical (more specifically, optical-electrical) principles have emerged in the field of measurements. Their common essential property is that the value measured can be directly transformed into an output signal or onto recording media. A few examples of such equipment are shown in Fig. 14.14.

Essential for a secure measuring value collection is the construction of a measuring chain that is as short as possible and stiff. The measuring chain in Fig. 14.15 is composed of a measuring device, the supports of a stand, a base plate, and the object measured. In the measuring device, starting from the input value (in this case, the displacement of the probe by the measuring object) the output (in this case, the measuring value 8.02 mm) is obtained through the measuring sensor, an amplifier, and an analog-to-digital converter. Depending on which measuring devices are used, their internal parts may be quite different. The output value can then be transferred to a storage device or a processing machine (for example, a personal computer).

The following explains several essential properties of measuring devices. These properties determine the applicability of the equipment. The achievable *information content* of a measurement is an essential distinction criteria. Also, the *accessibility* of the measuring value to the workpiece reduces the possible selection of measuring devices. The *type of probe* (contact and noncontact) is also relevant. Spheres, planes, or cutting edges are the fundamental probe shapes.

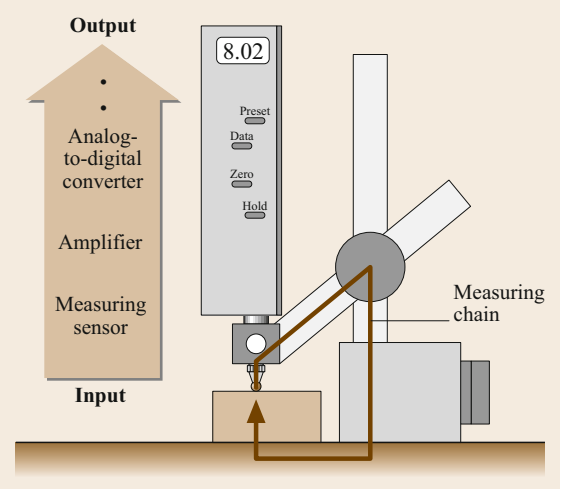

Fig. 14.15 The measuring chain

The *indicating range* of a measuring device is the range of values over which the device can indicate (smallest to largest indicated measuring value). The *measuring range* can deviate from the indicating range and corresponds to the section of the indicating range over which the measuring deviations remain within defined boundaries. The *scale division value* is the change in the measuring value that leads to the movement of the pointer from one to the next dash on a line scale (on digit scales to a digit step). When the measuring devices are clamped (for example, by a support, Fig. 14.15), the range of adjustment of the support and the measuring range of the measuring devices constitute the *range of application*. The relationship between the value of the input and the corresponding output value is the *transfer function*. A linear transfer function is usually aimed for. The *threshold limit* is the smallest possible change in the input that leads to a recognizable change in the output. The effect whereby the same value of the input produces two different results depending on the direction in which the value is approached, is called the *hysteresis*. A slow, time-varying change of the output without a change in the input value is called *drift*. The *response time* is the time between a step change of the input and the time when the output value remains constant within a prescribed range.

Additionally, the *measuring uncertainty* should be highlighted as an essential characteristic of measuring devices. A measuring device is qualified for a designated measuring task only when the uncertainty does not exceed a ratio with the tolerance of $U/T = 0.1$–0.2. Because the exact uncertainty of a chosen measuring device is often not known, one can make do with the *limit of error*. The limit of error is the largest measuring deviation of a measuring device and is usually defined for a group of measuring devices through a standard or by the manufacturer.

The *direct collection of measuring values* (for example, with calipers or micrometers) is the easiest type of measuring implementation. The measuring range of the measuring devices must overlap with the measuring object. In Fig. 14.16, the measurement of a length by means of a micrometer is shown. The range of measurement of the displaced micrometer is shown as being 25 mm. Objects with lengths ranging from 0 to 25 mm can be measured. The measuring uncertainty for such a micrometer can be expected to be in the range of 10–20 µm.

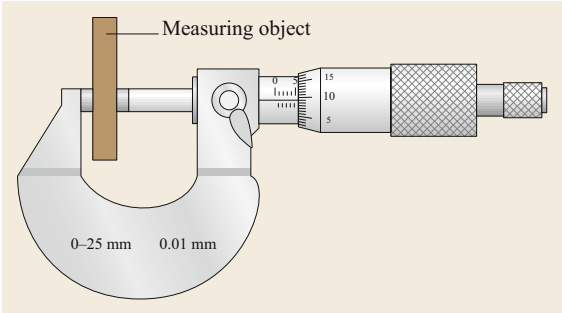

Fig. 14.16 Direct measurement

If the tolerance of the measuring value is so small that the required ratio between the measuring uncertainty and tolerance can no longer be met, one must choose a measuring device with a smaller measuring uncertainty. Smaller measuring uncertainties are often accompanied by smaller measuring ranges. Whenever a measuring device whose range of measurement is smaller than the measuring value must be used, for example because of the requirements of the measuring uncertainty, one can employ *difference measurement* (Fig. 14.17). One chooses a measurement standard, which is shown as a combination of block gauges in Fig. 14.17, whose value differs from the measuring value by no more than the measuring range of the measuring device. The measuring device is used so that the readout both by probing the measurement standard and the measuring object is possible. The length of the measuring object is the sum of the length of the precision gauge block, and the difference between the readout for the measurement standard and the measured object.

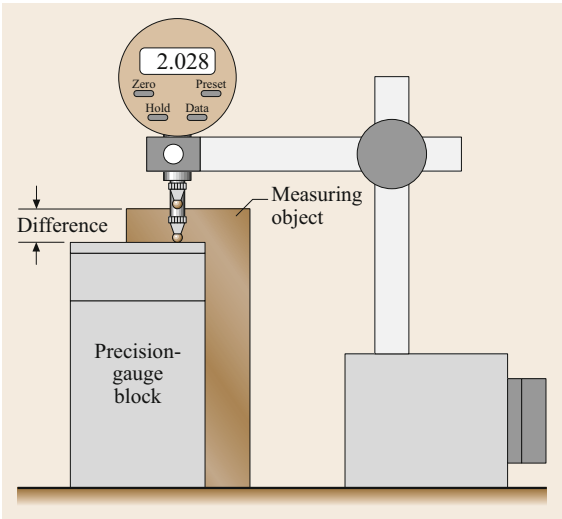

Fig. 14.17 Difference measurement

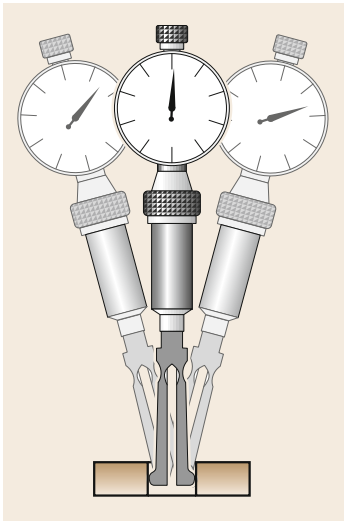

Fig. 14.18 Inversion point

Another important application option is the search for an inversion point. Figure 14.18 shows an example of the measurement of an inside diameter with a two-point measuring instrument (two probing points on the cylinder's interior). Through the measuring force and supported by special structures, the instrument aligns itself so that the cylinder axis intersects the connecting line between the two probe points. The instrument can be pivoted from the left in Fig. 14.18, through the middle, to the right position. One can see that the displayed measuring value becomes smaller at first but, after the middle position, becomes larger. The smallest displayed value, the inversion point of the needle, corresponds to the shortest connection of the probed cylinder surface line and, thus, the diameter.

When measuring workpieces, different influences have a negative impact on the measuring result. For example, inclination between the measuring instrument and measured object, bending, deformation on account of the measuring force, and environmental conditions can lead to deviations of the measurement. Some of these effects can be avoided or notably reduced through the operation of the proper equipment.

Through the adherence to a fundamental measuring technology principle, the Abbe comparator principle, one can reduce the influence of tilting errors. According to this principle, the measured object and the measuring rule are to be aligned flush. Figure 14.19 shows the universal length gauge as one of the essential instruments using this principle. The measured object and the integrated measuring system, which is inside the movable quill, are consecutively aligned flush. Brackets for interior measurement are attached. After removing the brackets the instrument can collect of external measurements. As measuring systems, glass measuring scales

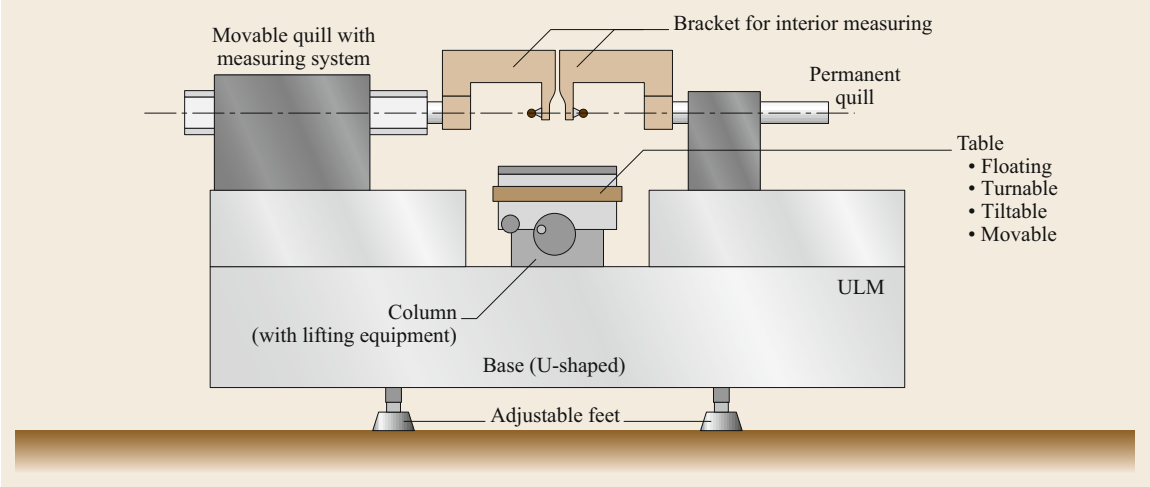

Fig. 14.19 Universal length gauge

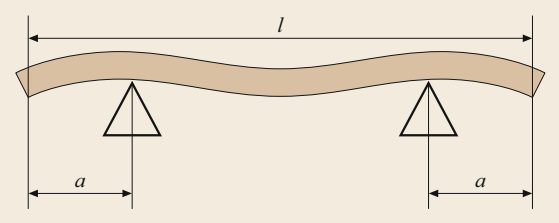

Fig. 14.20 Bessel points

Table 14.3 Linear expansion coefficients

Material	Linear expansion coefficient (µm/(m K))
Steel	13
Copper	16
Aluminum	23
Magnesium	26
Polyvinyl chloride	80

and laser measuring systems are utilized. Such measuring instruments are suitable for the monitoring of gauges and measuring means.

The deflection of workpieces due to their own weight also has a considerable impact on their length. On a bar-type component, one obtains the smallest shortening of the whole length whenever the piece is supported on the so-called Bessel points (Fig. 14.20). These support points are located at a distance $a = 0.220l$ from the ends. Similar effects lead to deformations on account of the measuring force. Deformations of the material are mostly only problematic for soft materials (plastics) and nonmassive workpieces. Here, the workpiece can bend itself whenever the measuring force presses against thin-walled positions. This effect can be reduced using proper fixtures.

Environmental conditions are generally specified by the room where the measurement takes place. Measuring rooms are classified into five classes. Precision measuring rooms (class 1) serve the calibration of reference standards. Fine measuring rooms (class 2) serve for the calibration of the standards used and for acceptance inspection of precision parts. In standard measuring rooms (class 3), measuring tasks for the monitoring of a process, measuring of fixtures and tools, as well as the control of inspection equipment (factory standards) and first prototype inspections are conducted. The production-related measuring room (class 4) serves for monitoring production, machine settings, and instruments. Production-related measuring takes place on the manufacturing measuring site (class 5). The spectrum is supplemented by the special measuring room, for example, for the measuring of semiconductor wafers. Properties whose limit values in every measuring room class are predefined include temperature (basic temperature, time and local temperature variation), vibrations, air quality (fine dust, suspended matter), air humidity, and lighting.

A substantial influential parameter for geometrical data acquisition is temperature. The reference temperature for measurement is 20 °C. The reference temperature is the temperature at which workpieces have their true measurement value and at which the inspection equipment detects it. These specifications apply to all pieces in the measuring chain. Table 14.3 shows the linear expansion coefficients of different materials. For example, for a temperature increase of 1 K, a 1 m-long piece of steel will become about 13 µm longer. The alternative measuring of the existing temperature and consequent correction of the measuring

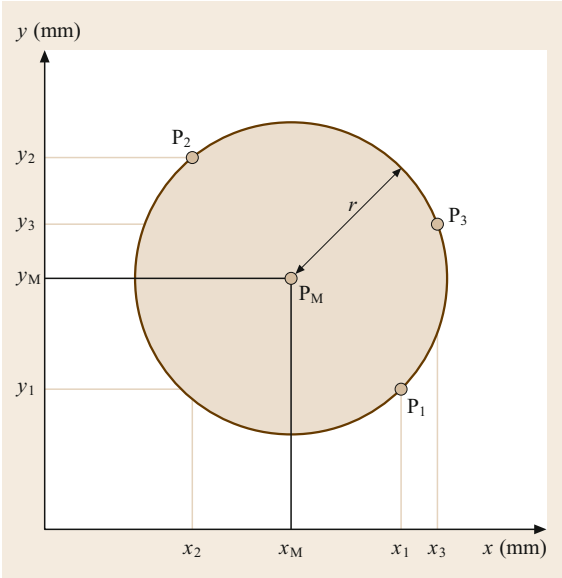

Fig. 14.21 Measuring points on a circle

value is particularly problematic for geometrically and compositionally inhomogeneous inspection equipment or workpieces and with temporally and spatially varying temperatures.

14.2.5 Coordinate Measurements

Coordinate measuring machines are universal, flexibly applicable equipment for the recording of workpiece geometry. As well as measurements of parameter (e.g., diameter and length) position and form (e.g., roundness and concentricity), special (e.g., cylindrical or bevel gears) and free-formed surfaces (castings) can be measured [14.12].

In contrast to conventional measuring techniques, the desired measurements are not measured directly. The principle is the acquisition of single data points from geometrical elements. These elements include circles, planes, cylinders, spheres, and cones. Furthermore, these elements can be combined together to identify distances, angles, or position deviations. The acquired measuring points, which are on the boundary of standard elements, are mostly described by a Cartesian coordinate system (Fig. 14.21, x, y, z). However, it should be noted that cylindrical and spherical coordinate systems are also possible. The described size of these geometrical elements will then be calculated from these measured points. The following example shows the strategy for identifying the radius r and the middle point coordinates x_M, y_M of a circle. For simplification, this example will be confined to a circle in the x–y plane.

The equation for a circle whose center point does not lie at the origin is as follows

$$r^2 = (x - x_M)^2 + (y - y_M)^2 .$$

The variables r, x_M and y_M are unknown. One appoints a measuring point on the circumference of the circle for the variables x and y. Now, because there are three unknowns, and we need a clear description of the circle, we need three equations, which means three data points (the smallest number of data points for determining a circle is three). This yields the following system of equations

$$\begin{aligned}
&\text{For } P_1 \text{ with } [x_1, y_1]\text{: } r^2 = (x_1 - x_M)^2 + (y_1 - y_M)^2 ,\\
&\text{For } P_2 \text{ with } [x_2, y_2]\text{: } r^2 = (x_2 - x_M)^2 + (y_2 - y_M)^2 ,\\
&\text{For } P_3 \text{ with } [x_3, y_3]\text{: } r^2 = (x_3 - x_M)^2 + (y_3 - y_M)^2 .
\end{aligned}$$

Since we are dealing with elements of measured, real-world objects, whose bordering areas deviate from geometrical standards, the collection of a larger number of data points is essential for the determination of the element parameters. An overdetermined (no longer explicitly solvable) system of equations results from a higher number of measured points. This system has the following form

$$\begin{aligned}
&\text{For } P_1 \text{ with } [x_1, y_1]\text{: } f_1 = (x_1 - x_M)^2 + (y_1 - y_M)^2 - r^2 ,\\
&\text{For } P_2 \text{ with } [x_2, y_2]\text{: } f_2 = (x_2 - x_M)^2 + (y_2 - y_M)^2 - r^2 ,\\
&\qquad\vdots\\
&\text{For } P_n \text{ with } [x_n, y_n]\text{: } f_n = (x_n - x_M)^2 + (y_n - y_M)^2 - r^2 ,
\end{aligned}$$

where f_i represents the deviation of the corresponding data point from an ideal circle. One can employ a compensation method to solve this system of equations. A widely used method is the regression equation by Gauss. The sums of the squared deviations are minimized with this method

$$\sum_{i=1}^{n} f_i^2 \rightarrow \min .$$

This least-squares method ensures that all measuring points are included in the calculation. Problems especially arise when one wishes to verify mating. In this case, the inscribed circle gives the description for holes, while the circumscribed circle gives the description for shafts. (The *inscribed circle* is the largest possible circle that has all of the measuring points outside, while the *circumscribed circle* is the smallest possible circle that contains all of the measuring points; Fig. 14.22.) In certain cases, an outlier test may be necessary.

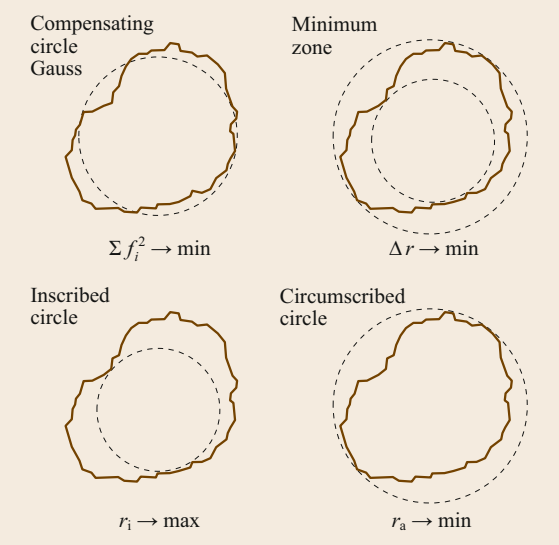

Fig. 14.22 Compensation methods

Equipment, Sensor Technology, and Software

One can subdivide coordinate measuring machines on the basis of their construction into portal, bridge, and standing measuring machines. In Fig. 14.23, the basic configuration of a portal measuring machine is represented. The mechanically embodied axes (in the example shown, portal and quill) are arranged on the measuring table at right angles to each other. Additionally, the axes of rotation can be integrated for the realization of rotary movement. The instantaneous positions of the axes are logged through the measuring system and forwarded to the connected computer. Glass measuring scales are mostly used in measuring systems.

The probe system is attached to the quill. In addition to the frequently utilized mechanical probe systems, there are contactless options such as edge recognition, optical methods, and/or laser probes. One speaks of a multisensor coordinate measuring machine when various probing systems are arranged inside (Fig. 14.24).

Figures 14.25 and 14.26 illustrate various mechanic probing systems. One can distinguish between measuring and switching mechanical probing systems. In both cases, the workpiece is touched with the probe element, which is fixed onto the probing system. The probe element consists mostly of a shaft and an almost ideally round, wear-resistant sphere (in most cases, made of ruby). In a switching measuring system (Fig. 14.25), the contact between the probe sphere and workpiece releases an impulse. At the moment of this signal, the x, y, and z-coordinates of the current position from the table, portal, and pinhole are transferred to the computer and stored there for further processing as required.

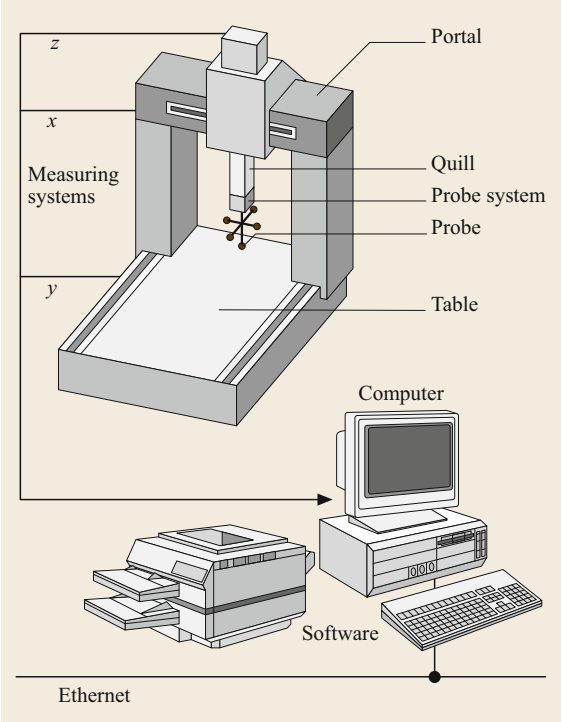

Fig. 14.23 Basic configuration

Contact between the probe and workpiece leads to deflections of the probe head in all three coordinates in a measuring probe system (in Fig. 14.26, the deflection is only represented in one direction). These deflections are measured and combined with the associated coordinates of the inherent positions of the table, portal, and quill. The measuring point coordinates obtained in this way are passed to the computer. However, care must be taken to note that the measuring point coordinates acquired always refer to the middle point of the probe sphere of the reference probe, not to the contact point between actual probe and workpiece.

Very flat outlines or color transitions are not mechanically probable. In these cases, optical acquisition is an option. For this purpose, the measuring object is illuminated, according to the target measurement (using through light, light-field, or dark-field illumination) and imaged through optics. The optics used may work with changed or zoom objectives in order to obtain different magnifications between the measured object and the image. In the simplest case, only the contours to be measured are scanned, using an edge finder. In the next most sophisticated system, based on image processing, the measured object is displayed on a charge-coupled device (CCD) matrix. As with a mechanical measuring probe system, the measuring point coordinates results

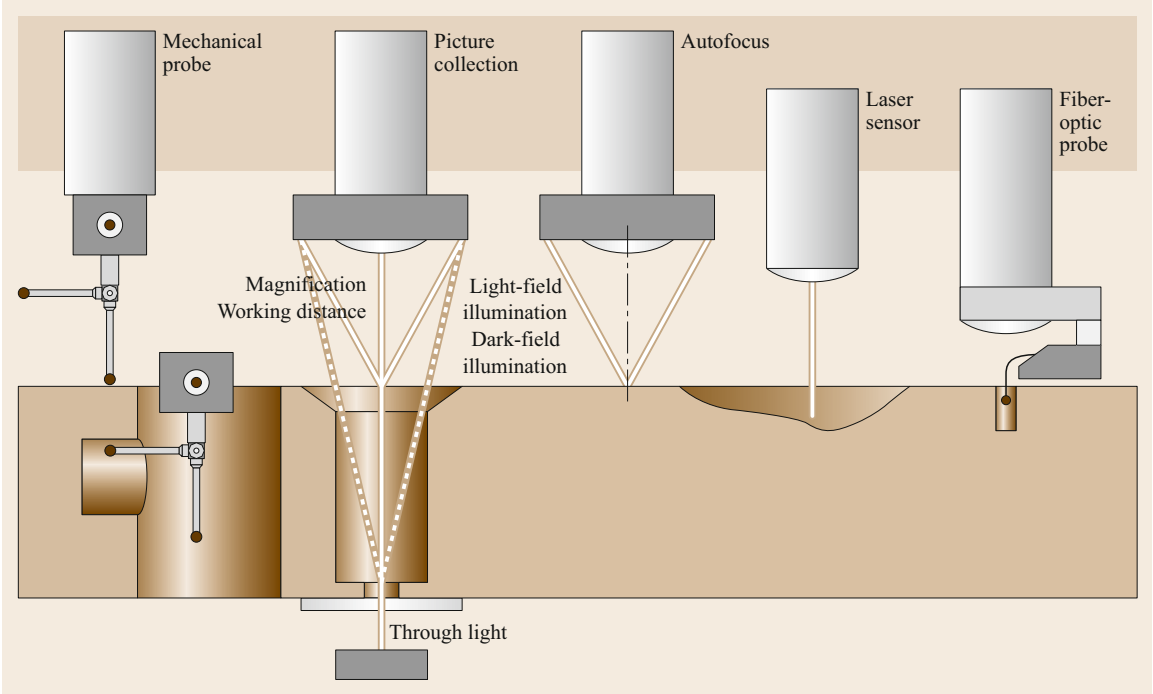

Fig. 14.24 Multisensor technology

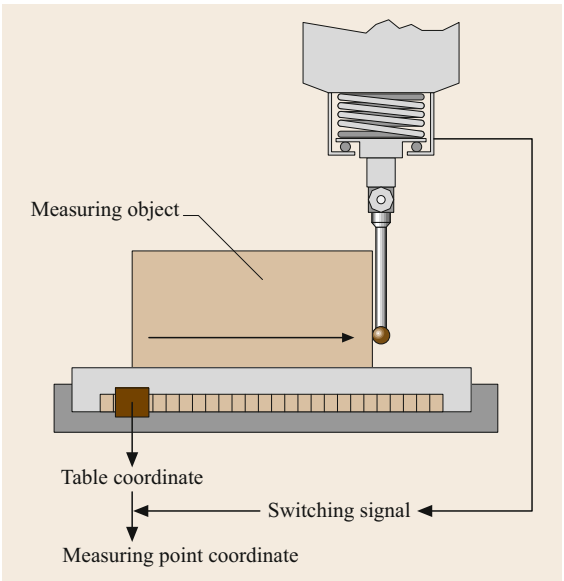

Fig. 14.25 Switching probe system

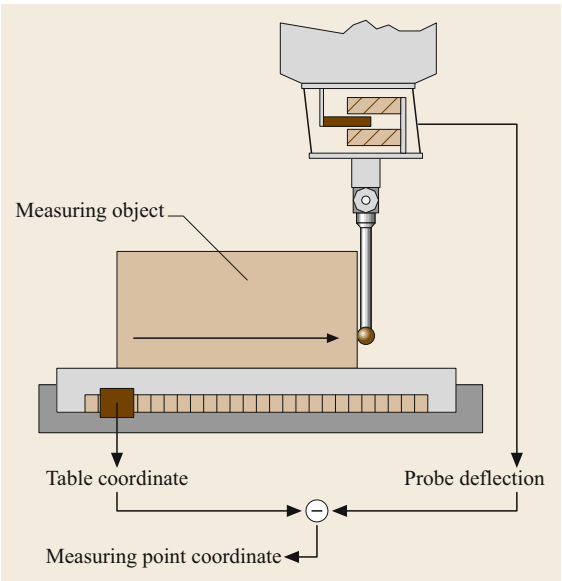

Fig. 14.26 Measuring probe system

as a combination of the pixel coordinates and the inherent positions of the table, portal, and quill.

While the optical variants described so far operate in the x–y plane, the focusing of an optical system can also capture the z-coordinate. The focusing can be automated by means of a laser or contrast evaluation in the image-processing system. The sensor controls the shift of the quill in the z-direction. The respective z-value supplements the x–y coordinates of the associated position to actual measured three-dimensional (3-D) values. Instead of autofocusing options, one can also use a direct laser measuring system for the addition of

the third coordinate, for example, a triangulation sensor. This method forms a laser point on the surface of the workpiece. Using observational optics arranged at a defined angle with respect to the sensor, a difference in the height of the surface of the workpiece is recorded directly. When the measuring range of the triangulation sensor is not sufficient, one can extend its application range by shifting with the quill. The measured z-value can then be calculated from the z-axis of the measuring system and the measured value from the triangulation sensor.

One very new and interesting sensor variation is the fiber-optic sensor patented by Werth Messtechnik (Fig. 14.24). It consists of an extremely small glass sphere, which is suspended by a glass fiber. Over this light pipe, the sphere can be directly illuminated. To capture the measuring points, the glass sphere is placed on the workpiece to be measured. The image-capturing system (CCD matrix) can detect this probe either in transmitted light or through its self-lighting. The center of the sphere describes the coordinate of the measuring point, just as for normal mechanical probes.

The *software* in the attached computer essentially has the following tasks:

- Capture of the measuring points
- Corrections, for example, perpendicularity and guideway deviations of the measuring machine components, probe radius and middle point, probe bending, temperature influences
- Coordinate transformations, for example turntable and workpiece coordinate systems
- The calculation of ideally geometric substitution elements from the measuring points
- The combination of single elements
- Conversions, projections, etc.
- Evaluation (nominal-actual comparison), protocol, statistics.

Device control (point or path-control, scanning) comes with the computer numerical controlled (CNC) coordinate measuring machines.

For the archiving of results or for further processing, data transfer by means of a network is possible.

Proceeding with the Measurement

The completion of a measuring task by means of coordinate measuring machines is explained in the following. Three phases will be differentiated.

Phase 1: Planning. The planning phase can be done remotely from the measuring machine, but requires knowledge of the technical possibilities, the available probes and clamping elements as well as extensive experience. Especially this phase is decisive for a metrologically safe and economically justifiable execution of the measuring task. The test task, which is generally fixed on the drawing, forms the basis for the planning of the measurement. Differences in the path arise, whenever the aims of the measurement (evaluation of the part), quality-orientated production control, or check for assembling possibility are changing. In this case, knowledge about the production of the piece (for example, the machining base) or its later application (subsequent machining and assembly) is useful. The test task is divided into its single elements and combinations. A sequence from easiest to most complicated is then sought.

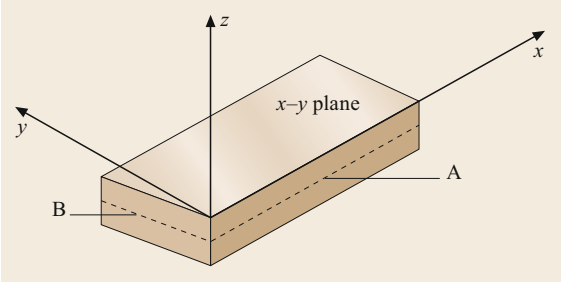

Fig. 14.27 The workpiece coordinate system

It is advantageous to specify a coordinate system on the workpiece not only for the measurement, but also for the evaluation of the results. This workpiece coordinate system must be clearly described mathematically. To do this, the following steps are required:

1. Space adjustment: description of a coordinate axis (mainly z) as the main direction of important form elements (for example, the direction normal to a surface, the axle of a cylinder). The z-axis is described in the example picture (Fig. 14.27) by the normal to the upper workpiece plane.
2. Plane adjustment: hindering the rotation of a coordinate system around these under point 1 defined axes (for example, by fixing to an edge or the straight line connecting the middle of two holes). The direction of the x-axis in the example picture (Fig. 14.27) is defined in the x–y plane by the corresponding direction of the long rectangular surface (dashed line A). This fixes also the direction of the y-axis, which must be orientated at a right angle to the x-axis.
3. Point adjustment: definition of the origin for x, y, and z. The origin of the z-axis through the measured x–y plane and the origin for the x- and y-axes through the intersection of lines A and B are described in Fig. 14.27.

The probe element must be chosen so that all of the elements to be measured are reachable. For this reason, more probing elements may be necessary, as shown

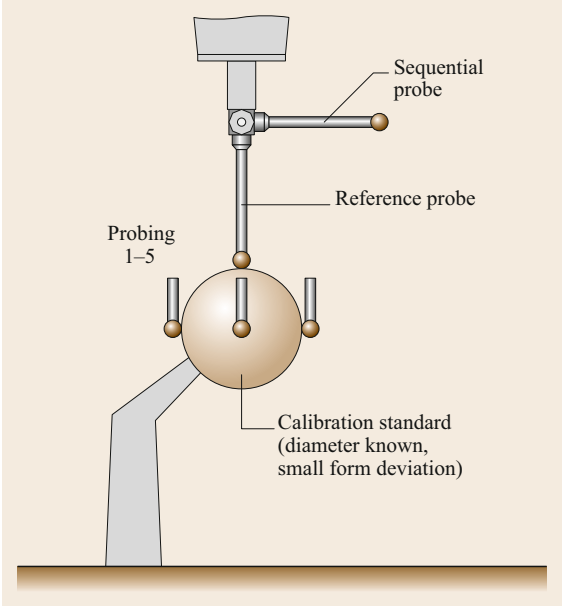

Fig. 14.28 Probe setup and calibration

in Fig. 14.28. One calls the connection of more than one probe element a probe combination or a probe tree. It can also occur that different sensors are needed for a particular measuring task. In the preparation for the calibration, a probe element is specified as a reference probe element. With multiple probe combinations or sensors, there is only one reference probe. Whenever more probe combinations are necessary, the work is implified by an automatic probe-changing mechanism.

The workpiece is set or clamped onto the measuring machine table, so that it lies as firmly and clearly as possible. Easy clamping elements, clamping element component systems, or special clamping devices are available. All of the form elements to be measured must be reachable with the chosen probe configuration. It is not allowed to come into contact with gripping or clamping elements.

The specification of the sequence of probing essentially occurs from an economical point of view (shortest routes between the elements). The type of probing (for example, mechanical or optical, point-to-point or scanning, auto-centering) is substantially limited by the technical capabilities of the measuring machine. Remark: scanning is the independent tracing of a workpiece contour by the measuring machine. One must give a starting point, an end point, the direction, and a scanning plane. The path results from the cut of the scanning plane with the workpiece surface. The scanning speed and point density must be provided by the operator. The minimum measuring point count follows from the type of geometrical elements. The aim of measurement (parameter or form deviation) forms the basis for the definition of the real measuring point count used. With increasing numbers of measuring points, the determination of the individual form elements becomes more certain. In any case, more measuring points than the minimum should be utilized. Around two to three times the minimum point count for the recording of a measurement and its deviation is sound from a measuring technology and economic viewpoint. For form deviation, one needs substantially more points. Here, the number depends on the size of the smallest geometric portions to be recorded. The measuring points should, if possible, be evenly distributed on the measured element and, in addition, must be able to represent these form elements with the desired deviations.

Phase 2: Preparation and Measuring. The probe combination is assembled as defined and then calibrated. Figure 14.28 shows the calibration of one probe of a two-probe combination. Through measurement of a calibration standard (a sphere with a known diameter and a very small spherical deviation) with both probes, the actual diameter of the probe tips and the distance of the middle of the sequential probe sphere to the middle of the reference probe sphere in the x, y, and z-directions are determined. After clamping the workpiece the machine parameters (e.g., velocity, measuring force) are defined.

The degree of automation of the measuring machine is of deciding importance for the probing of the measuring points. For manually controlled machines, the entire course (measuring point probing and manoeuvres in space between the machine elements and gripping devices) at every single point is realized by the operator. CNC-controlled machines allow the programming of a course of motion and have an automatic drive to adopt the required positions. One distinguishes between three possible programming methods:

- By teach-in, the machine learns the course of the measuring directly from the handling of the operator, i.e., his motion. He executes the course to the points to be measured as on a manually controlled machine. This way, all of the measuring point coordinates and all necessary points for collision-free manoeuvring between the machine parts and gripping mechanisms can be recorded. Afterwards, the control system can reproduce this course independently.
- The generation of the target coordinates can take place far from the machine. In this method, all measuring coordinates and position coordinates are derived from the figures or drawing data. This procedure requires great spatial imagination from the programmer. This approach is used mostly in conjunction with teach-in portions.

- Computer-aided design (CAD) systems that have a measuring module at their disposal can directly provide measuring machine programs (compare with the next section).

Phase 3: Evaluation. The description parameters for the associated geometric elements are determined from the measuring points through compensating calculations (for example: Gauss, inscribed circle, circumscribed circle). Take note that either the measuring points or the description parameters are to correct by the calibration data (probe sphere diameter, distance to the reference probe). On the foundations of the description parameters, elements can be mathematically linked or joined with each other. So, new characteristics that describe the geometry of the entire workpiece can be developed. The parameters of the individual elements (diameter, length) and the resulting parameters from the links (distance, angle) can be compared with the nominal and tolerance data. Afterwards, the results can be represented graphically or numerically.

Integration into CAD and CAM

Coordinate measuring machines (CMM) are suitable for integration into CAD/CAM environments (Fig. 14.29). This integration is possible under two criteria.

In CAD systems, the geometric data for a new workpiece is created. With that, outstanding conditions exist for the derivation of the measuring program on the basis of this data. In addition to the data describing the workpiece, a measuring module implemented in the CAD system needs data for the possible elements of the probe combination and the gripping system. *The complete measuring program can be produced in a simulated measuring run*. It is important for later functions that the coordinate system for the description in the CAD system agrees with that for the measured workpiece on the measuring machine. The measuring program can be written in a specialized programming language for the measuring equipment manufacturer or in the manufacturer-independent universal language dimensional measuring interface specification (DMIS), depending on the measuring modules available. For integration into the measuring machine program, a special interpreter is then necessary. After successful measuring, the possibility exists for the acquired deviations to be transferred back to the CAD system, to be processed or represented. Of course, an external process through best-fit and distance determination of the CAD data is possible.

The second possibility for the integration of a coordinate measuring machine is the *digitalization of an unknown workpiece geometry*. Here, a manufactured sample forms the basis (prototype). This sample is touched in a previously-defined grid. The measuring point coordinates acquired are handed over to the CAD system. There, a surface feedback or reproduction of the data model takes place. This can then be transferred to a manufacturing machine that makes a copy of the prototype.

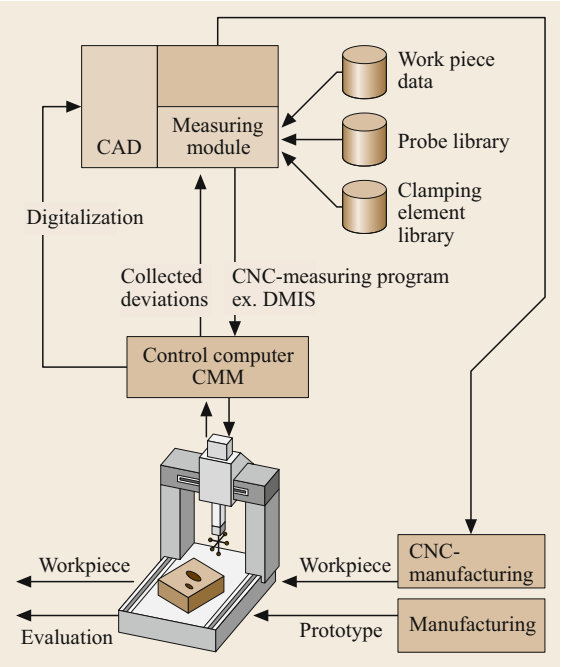

Fig. 14.29 Connection CMM–CAD

14.2.6 Surface Metrology

Instrument Technology

The surfaces of geometric objects continuously provide an informative testing object. Considerations include appearance, evaluation of the expected functional behavior, and manufacturing and wear conditions. The application of modern measuring devices in conjunction with sophisticated computer technology facilitates detailed evaluations and conclusions, which were unthinkable only a few years ago. With the equipment available and the demands of the user, these approaches are being widely applied.

Small, independent, portable instruments with skid pick-up systems are easily implemented to directly monitor tooling processes. In addition, stationary laboratory instruments with free probing systems, with correspondingly large measuring ranges and higher resolutions, have become established. Figure 14.30 shows the basic construction of a stationary surface metrology instrument. It consists of a base and pillar. The

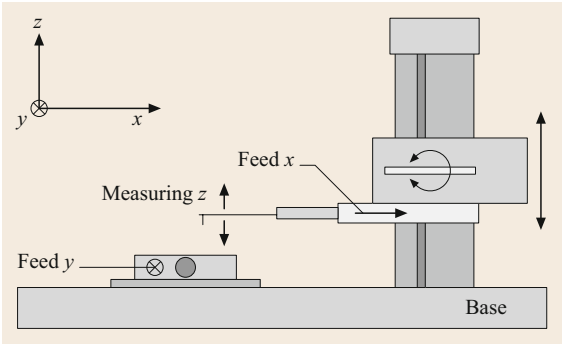

Fig. 14.30 Stationary surface metrology instrument

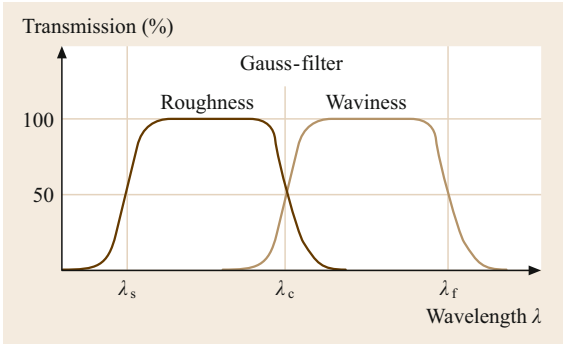

Fig. 14.31 Roughness and waviness profiles

feed unit, attached to the pillar, can be positioned aloft and be pivoted opposite the base. The probing system is positioned with high precision on the feed unit. This positioning constitutes the measuring basis for the probing of a measuring object. If required, the system can be supplemented with an additional y-table. This y-table facilitates the step-by-step movement of the workpiece perpendicular to the feeder movement, enabling three-dimensional scanning.

Instruments constructed as component systems allow a surface probing system to be used as a contour probing system (larger measuring range, many different types of possible probes) and, therefore, to expand the application range of the instrument considerably. It is also possible to implement, instead of a mechanical probing system, a noncontact probing system if the surfaces are sensitive to mechanical probing. One option is to use autofocusing laser sensors (Sect. 14.2.8).

Developments in electronics over the last few years have made it possible to digitize large quantities of data with a higher decimal precision (a higher number of levels) with sufficient speed. This has enabled the collection of many measuring points (with a smaller distance between measuring points at an acceptable collection speed) over larger measuring ranges with greater resolution (small Δz). The accessories for roughness measuring instruments range from stylus stop attachments to a large selection of speciality probing elements and various skids. The instrument can be tailored to the measuring task with these specialized accessories. As well as instrument equipment, the environmental conditions are also an important aspect to consider. The implementation in the laboratory setting, in contrast to the factory floor, brings with it a significant improvement in environmental conditions. This facilitates tasks with greater demands for precision.

ISO Standards and Consequent Requirements

The relevant ISO standards give not only the definition of characteristics but also requirements on the measuring instruments (e.g., the probe-tip radius, the distance between measuring points) and software (e.g., a phase-correction Gauss filter). The profile, which is obtained by means of the section probing method, is called, after the application of the filter for short wavelengths λ_s, the primary profile (P-profile). The roughness profile (R-profile) is obtained through the deletion of the long-wavelength profile features (threshold wavelength λ_c) from the primary profile. The waviness profile (W-profile) is made by filtering the primary profile by means of λ_c and λ_f, as is depicted in Fig. 14.31.

The cut-off wavelengths λ_c and λ_s required for this filtering can be seen in Fig. 14.32 according to the profile classification between periodic and aperiodic. Currently, no concrete definition exists for the threshold wavelength λ_f, only the recommendation of $\lambda_f = 10(5)\lambda_c$. Besides the threshold wavelengths for the separation of profile elements, definitions of the maximum probe element radii and the distances between measuring points are being established. However, there are severe restrictions for the use of instruments in this way.

Characteristics can be calculated from all profile types (P, R, W). Figure 14.33 shows the arrangement of surface characteristics based on the example of the roughness profile. Fundamentally, horizontal, vertical, and hybrid characteristics can be differentiated. These are supplemented by characteristic curves from which parameters can be derived.

Because the explanation of the single characteristic definitions would be too lengthy, the corresponding standards (ISO 4287 [14.15]) is referred to instead.

Analysis of a Surface

Whereas the previously explained, easy-to-handle instruments with skid pick-up systems can only collect and evaluate roughness, instruments with reference-surface probing systems produce data that, with proper software, can measure not only roughness and waviness characteristics but also size, form, and positional deviations. Also, a description of surface alterations by

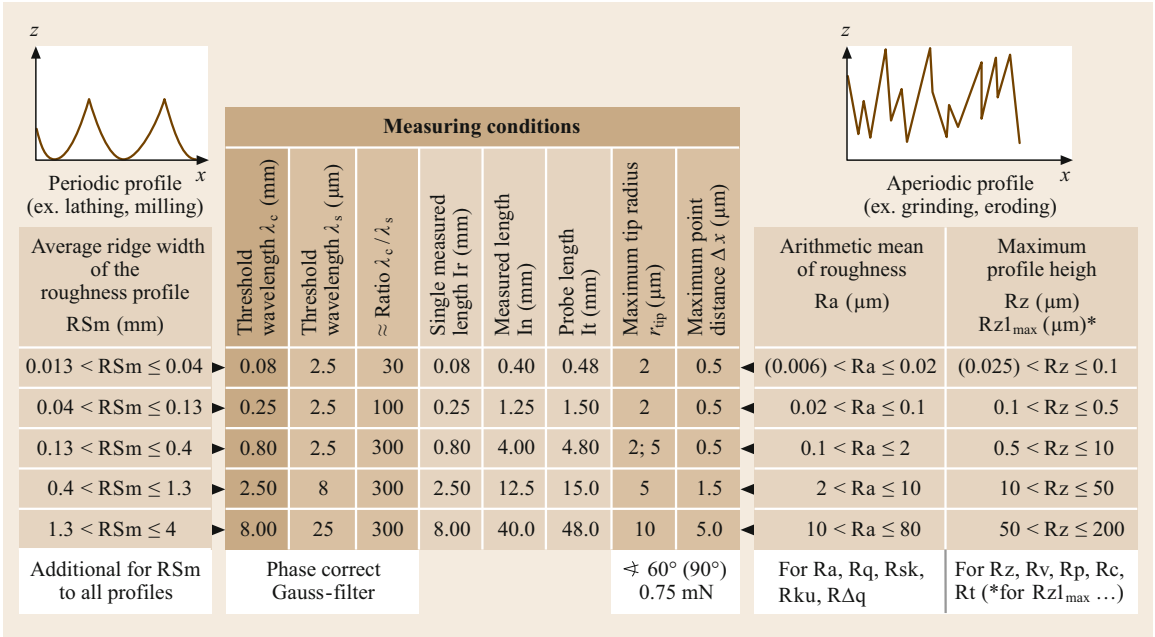

Average ridge width of the roughness profile RSm (mm)	Measuring conditions: Threshold wavelength λ_c (mm)	Threshold wavelength λ_s (µm)	≈ Ratio λ_c / λ_s	Single measured length lr (mm)	Measured length ln (mm)	Probe length lt (mm)	Maximum tip radius r_{tip} (µm)	Maximum point distance Δx (µm)	Arithmetic mean of roughness Ra (µm)	Maximum profile heigh Rz (µm) Rzl_{max} (µm)*
0.013 < RSm ≤ 0.04	0.08	2.5	30	0.08	0.40	0.48	2	0.5	(0.006) < Ra ≤ 0.02	(0.025) < Rz ≤ 0.1
0.04 < RSm ≤ 0.13	0.25	2.5	100	0.25	1.25	1.50	2	0.5	0.02 < Ra ≤ 0.1	0.1 < Rz ≤ 0.5
0.13 < RSm ≤ 0.4	0.80	2.5	300	0.80	4.00	4.80	2; 5	0.5	0.1 < Ra ≤ 2	0.5 < Rz ≤ 10
0.4 < RSm ≤ 1.3	2.50	8	300	2.50	12.5	15.0	5	1.5	2 < Ra ≤ 10	10 < Rz ≤ 50
1.3 < RSm ≤ 4	8.00	25	300	8.00	40.0	48.0	10	5.0	10 < Ra ≤ 80	50 < Rz ≤ 200
Additional for RSm to all profiles	Phase correct Gauss-filter						∢ 60° (90°) 0.75 mN		For Ra, Rq, Rsk, Rku, RΔq	For Rz, Rv, Rp, Rc, Rt (*for Rzl_{max} …)

Fig. 14.32 Measuring conditions (ISO 3274 [14.13] and ISO 4288 [14.14])

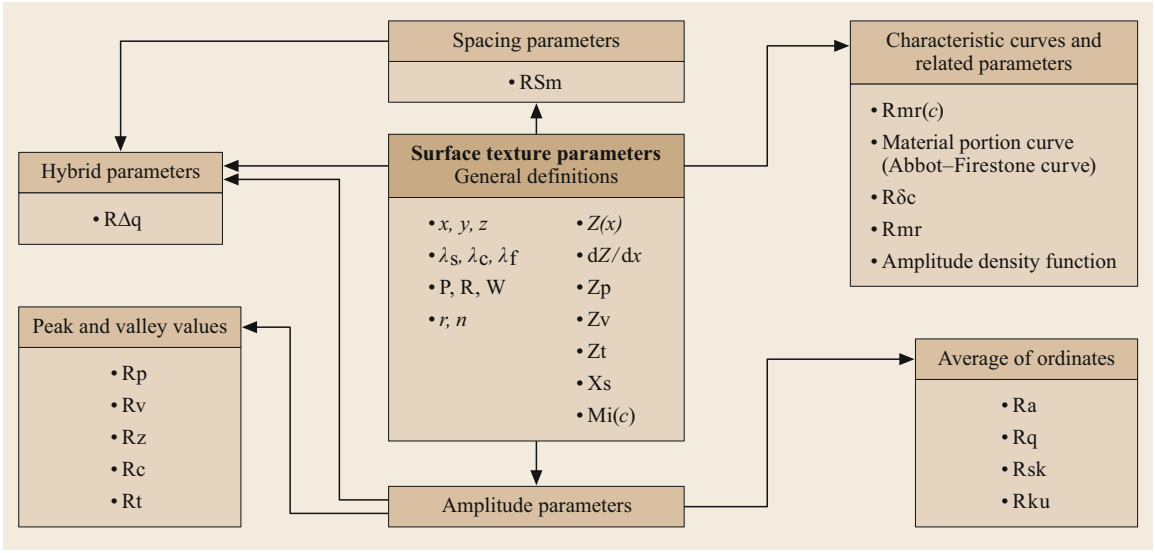

Fig. 14.33 Surface texture parameters (ISO 4287 [14.15])

abrasion and coating, amongst other effects, is possible with these systems.

The difference in the information content of the data is immediately recognizable in Fig. 14.34. Whereas the skid pick-up system only captures the roughness portion approximately, a slant and curvature can be recognized in the data collected from the reference-surface probe system. The skid pick-up system manages with essentially small measuring ranges and poor guidance, which makes these instruments much more affordable. However, one should pay attention to the fact that the mechanical filtering of the signal, by means of the skid, cannot be removed during the follow-up evaluation.

The larger information content collected with a reference-surface probe system is accompanied by substantial disadvantages related to the instrument technology. The disadvantages are the relatively large measuring range of the probing system, which is required

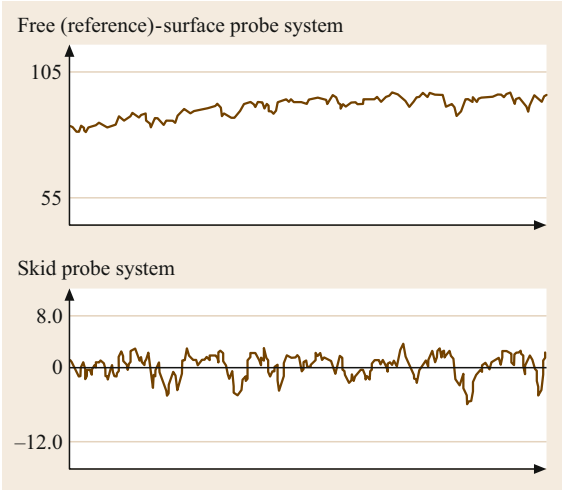

Fig. 14.34 Primary profile

in order to obtain the primary signal within a justifiable adjustment effort, and the fact that the straightness of the feed unit movement must be very good, as it contributes to the measuring signal. Both effects lead to relatively high instrument costs.

Figure 14.35 shows the example of the implementation of surface metrology equipment with a reference-surface probing system. At the top, data collected from a partially coated workpiece is shown. The implementation of a probe element with a comparatively large radius ($r = 500\,\mu m$) leads to the low-pass mechanical filtering. For the compensating calculation, only data that represents the uncoated material is used. After this calculation, the course of the layer thickness between the measured profile and the extended compensation profile is clearly recognizable in the coated section. Similar approaches are also suitable for wear measurement whenever unworn workpiece sections are still available. On the lower part of Fig. 14.35, production progress is shown by a double profile. The basic result is a turning surface profile, which is then smoothed in a second processing step. Clearly, the varying manufacturing results achieved by changing the machining parameters (low or optimal pressing force on the tool) can be noted.

The additional assembly of a *y*-shift table perpendicular to the actual feed direction (Fig. 14.30) allows the collection of data from flat, three-dimensional structures. With the use of an appropriate software package, one can derive three-dimensional surface characteristics from this data, or rather a visual impression of the surface for the benefit of the user. This allows conclusions on properties of the surface, which one cannot easily derive from a single profile. Figure 14.36 shows the three-dimensional measured structure of a workpiece

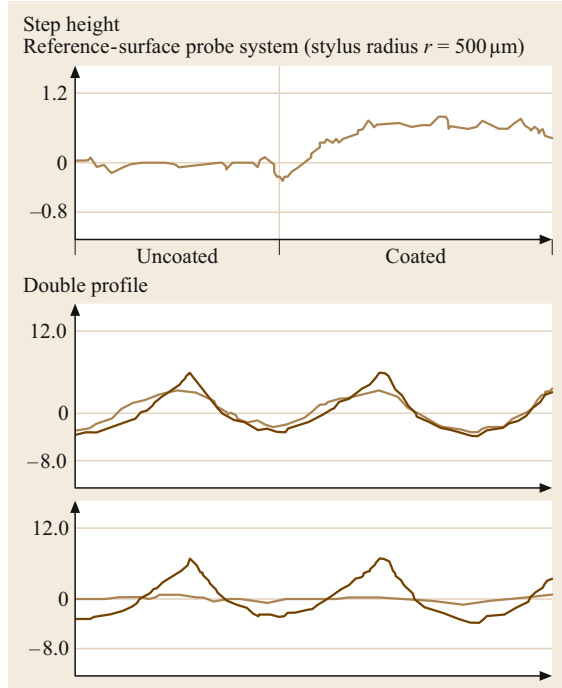

Fig. 14.35 Application for the manufacturing measurement technology

that was milled with a spherical-headed milling tool. In the left-hand side of the figure, a detail from the actual surface is shown. The differences in altitude are represented by different brightness. There is also the choice of an isoline representation (connected lines of equal height). The curvature left behind by the spherical cutter is clearly recognizable. Under this relatively strong curvature, the detailed structure remains hidden.

The right-hand side of Fig. 14.36 shows the same section. In order to make the details clearer, the dominating curvature in the left part of Fig. 14.36 is removed with the use of a compensating calculation (a three-dimensional, second-order polynomial fit). Now the milling feed is clearly recognizable. The unclear structure in the middle of the illustration emerges because there are no definite cutting properties in the domain of the center of the cutting tool.

14.2.7 Form and Position Measuring

Instrument Technology

Form inspection equipment in most cases consists of a base and a column. A turntable is integrated into the base. An arm that carries the measuring system is located on the column. Even after construction of the instrument, the turntable, the column, and/or the arm can be arranged as a measuring base. In most cases,

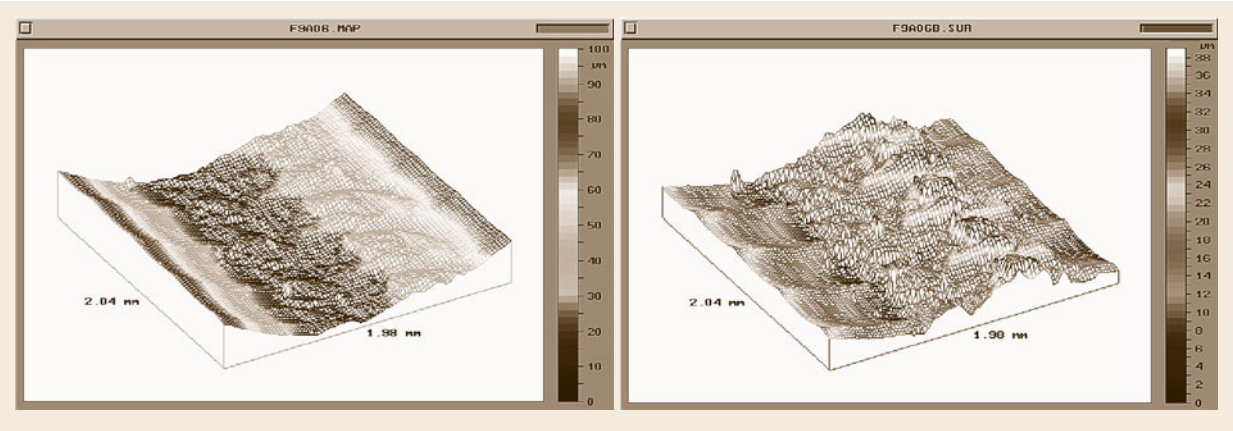

Fig. 14.36 3-D surface structure

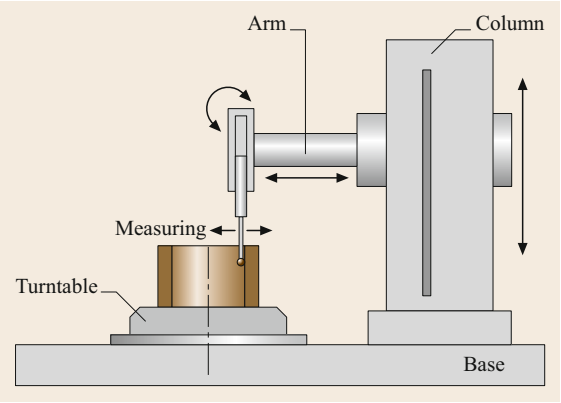

Fig. 14.37 Form inspection instrument

the measuring system is inductive. Probing is carried out with a spherical probe element. In order to keep abrasion to a minimum, ruby probing elements, as used in coordinate measuring machines, are utilized. The measuring system is inclinable so that the direction of the measuring force can be reversed. Therefore, almost all necessary measuring points can be reached. Figure 14.37 shows a vertically arranged probe system, by which the measuring force from the workpiece acts radially outwards. Subject to the measuring task, one or more feed axes can be implemented.

Measuring Execution

Figure 14.38 shows, in the upper left-hand corner, a roundness inspection. After positioning the piece on the turntable, the piece is orientated to the rotating axis so that the measuring system remains in the measuring range during the course of inspection. With a large measuring range, visual judgement suffices for orientation. The large measuring range leads to a bad resolution. A more accurate orientation of the piece is demanded

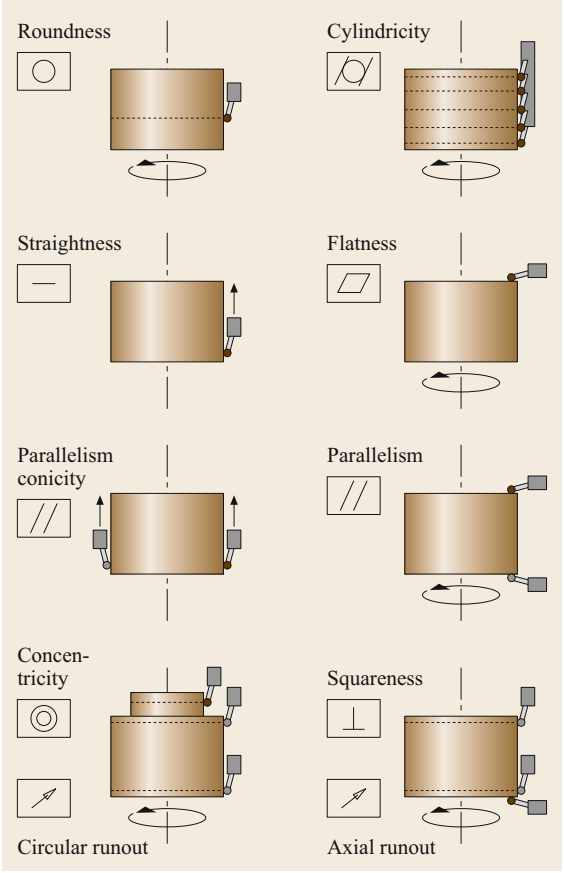

Fig. 14.38 Measuring execution

for a smaller measuring range, which directly leads to a better resolution.

After the probe is brought into contact with the desired position on the object, the measuring object is rotated 360° by the turntable, and, while the object is

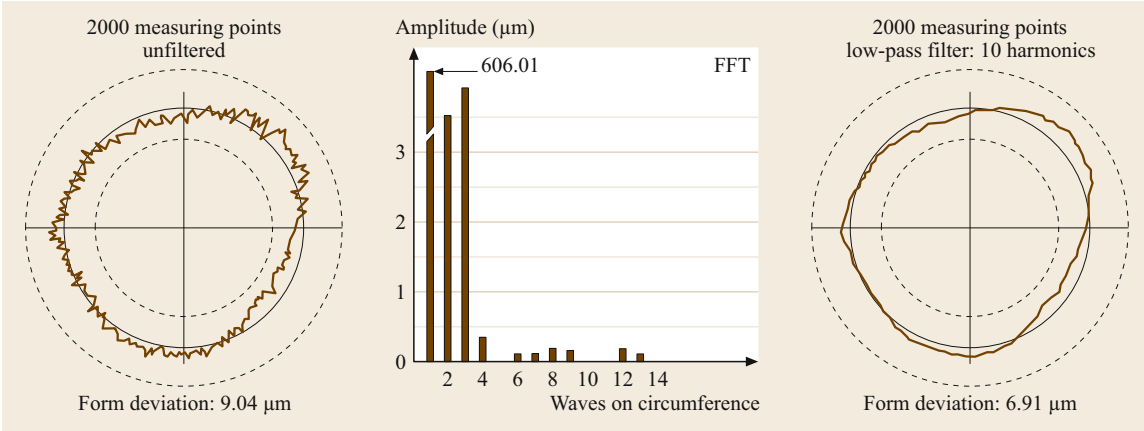

Fig. 14.39 Roundness deviation

turning, the measuring points are scanned. An ideal circle is calculated from the measuring points. For this, depending on the aims of the inspection, compensating methods (e.g., Gauss, circumscribed circle, inscribed circle, see Sect. 14.2.5) can be chosen. In reference to the compensating circle, the range between the lowest point and the highest point is the roundness deviation. For the investigation of causes of deviations, one can filter the desired frequency domains or use a frequency analysis, e.g., a fast Fourier transform (FFT) (Fig. 14.39).

On the left-hand side of Fig. 14.39, the unfiltered circular form deviation is depicted for evaluation of the workpiece. The frequency analysis in the graph next to it shows that waves, especially with a period of two and three harmonics, dominate the result. The right-hand side of Fig. 14.39 shows the measuring result after running the data through a low-pass filter (limit wavelength of 10 harmonics). Here, it is easier to recognize causes of deviations and to implement corresponding quality-orientated corrective action into the manufacturing process.

Figure 14.40 shows the collection of cylinder form deviation. Here, in addition to a high-precision rotating axis, a column axis with a correspondingly small straightness deviation is used in order to facilitate vertical movement. When positioning, movement of the arm should be avoided. All of the measuring points collected, located on circles, are put through a compensating calculation together. From the distances between the single measuring points and the compensating cylinder, the cylinder form-deviation is derived.

Just as the number of points on a circle is important for the determination of the circular form deviation, the number of measured circles for the cylinder-form deviation is not to be neglected. In Fig. 14.40, a picture that used three circles is shown on the left, and a picture that

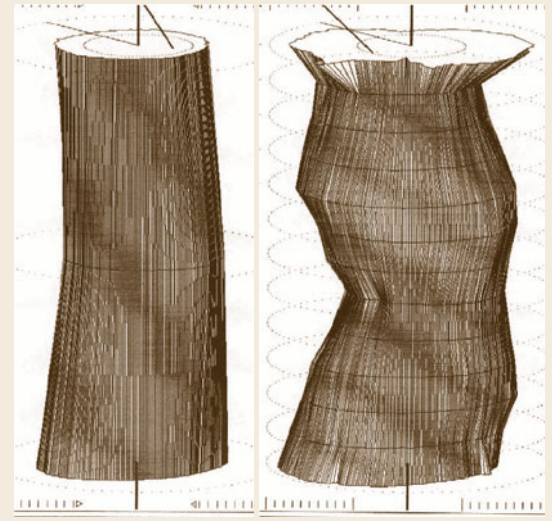

Fig. 14.40 Cylinder form deviation

used 13 circles to calculate the cylinder form deviation is shown on the right-hand side. Clearly, there is a noticeable difference in information content between the two.

To detect referenced elements, like for example, the concentricity depicted in Fig. 14.38, one uses methods already known from coordinate measuring technology. First, both of the circles on the lower cylinder are probed. The circles should have the largest possible distance from each other in order to reduce the measuring uncertainty. Compensating circles are calculated from the corresponding measuring points. The line that connects both midpoints of the circles serves as the reference axis. After the inspection of the circle on the smaller cylinder and the corresponding determina-

tion of the parameters of the compensating circle, the eccentricity is calculated as the distance between the midpoint of the circle and the reference axis. The tolerance zone for the concentricity describes a circle around the reference axis.

14.2.8 Laser Measuring Technology

Due to its properties, laser measuring technology has gained a strong position in the field of integrated measuring technology inside the manufacturing processes. In this section, a few examples are explained and the advantages and disadvantages highlighted. The application profiles of laser measuring systems are as different as their parameters and range from simple dimensional completeness checks to high-precision measuring systems that determine surface roughness or even the acceleration of tooling machine components. From the many possible implementation variations, only a few are considered, those that use the various properties of light. After the time-of-flight method, which is not commonly implemented in mechanical engineering applications, come uses of such properties include linear propagation, reflection, or interference. The selection of the best sensor for the specific application and the arrangement of the sensor to the measuring object is based on criteria such as:

- Operating distance
- Measuring range
- Resolution (scale value)
- Measurement uncertainty
- Measuring spot diameter
- Light color and intensity.

Of course, the price of the complete system which consists of sensor, evaluation electronics and possibly components for moving the measuring object, is also relevant.

In addition to the technical and scientific considerations, protection against accidents is also an issue that should not be ignored. Because most laser measuring systems are equipped with low-power lasers (hazard category 1–3), skin burns are rather improbable. However, the eyes must be well protected. Reflected radiation from metallic surfaces is also problematic. The mandatory guidelines, for instance in Germany, demand labeling for hazard category 3B and above, the application of opaque enclosures, laser protection eyewear, and special warning and emergency facilities.

Laser Applications in Measuring Technology

The *linear propagation* of a laser beam is used by a whole range of measuring devices. To clarify this application, two examples are presented. The first is a laser scanner (Fig. 14.41), which amongst other applications is used here for the quick scanning of the diameter of shafts.

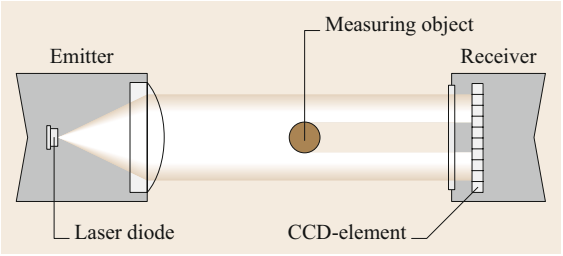

Fig. 14.41 Laser scanner

The laser beam, created by a diode, is expanded into a fan shape and aligned so that the beam is parallel. As shown in Fig. 14.41, this alignment is done by optical components. There are also laser scanners in which the beam expansion occurs by means of a spinning polygonal mirror. The laser beam is directed toward the measuring object. Behind the measuring object, a receiver is arranged where the laser beam strikes a light-sensitive CCD line array. Because the laser beam is broken by the measuring object, in this case the shaft, the size of the shadow on the receiver can determine the diameter of the object. The emitter and receiver can be adjusted axially to the shaft very quickly, so that in a short time, the diameters of various shaft sections can be determined.

A second application of linear laser expansion is shown in Fig. 14.42. The emitter, which emits a laser beam with a narrow diameter, is arranged on the fixed part of a tooling machine base. The receiver is assembled on the sliding bed and consists of a CCD matrix sensor field (in the middle of the figure). Different manufacturers also use four quadrant diodes at this location as a receiver.

Now, the sliding bed of the tooling machine is steered to its home position. The point at which the laser beam strikes the sensor field is registered (y_1, z_1 at $x_1 = 0\,\text{mm}$). On the way to the end position, it is stopped at defined points, and for each stop, the laser point is registered on the sensor field (y_2, z_2 at x_2, and so on). From the points obtained, the straightness deviation of the sliding bed movement is shown divided into the x–y and x–z planes.

A laser beam reflected by the measuring object is generally used by laser distance sensors. These are employed for the contactless measurement of deformable, very rough, sensitive, hot, or moving surfaces. A laser autofocusing sensor and a laser triangulation sensor are given as application examples. Figure 14.43 shows schematically the construction of an autofocus sensor

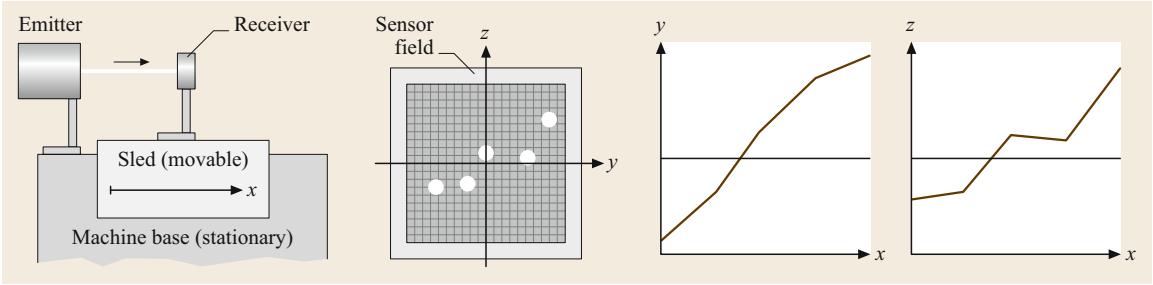

Fig. 14.42 Alignment measuring system

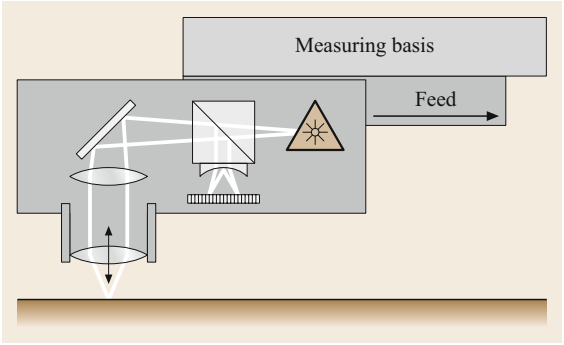

Fig. 14.43 Autofocus sensor

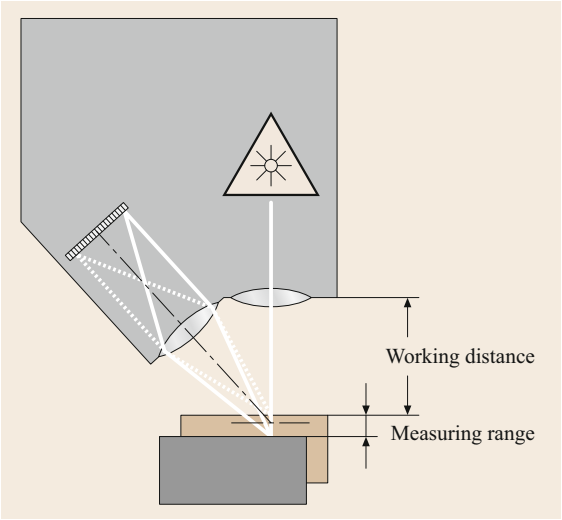

Fig. 14.44 Triangulation sensor

(Mikrofokus from UBM). The laser beam is projected onto the surface of the measuring object, and the laser beam is reflected from this surface. Specialized electronics monitor the focusing and, when necessary, readjust the lens system. The displacement of the lenses is recorded as the measuring value. The previously-mentioned sensor example has a working distance of about 5 mm and a measuring range of 1 mm. The laser spot focused on the surface of the measuring object has a diameter of 1–5 µm, while the beam has an angular aperture of 30°. The electronics used in the example allow the measuring signal to be broken up into steps of 16 nm. With these parameters, the sensor is well suited for contactless surface inspection. The advantages of noncontact probing are also accompanied with disadvantages. Problems especially arise due to locally strong reflective materials (for example, single grains on grinding wheels) and also by nonreflective materials, as well as by steeply inclined surfaces (over 30°). In these cases, the reflected beam cannot be collected for evaluation. The reaction of the system to such problems is variable (measuring value setting, holding or searching) and must be taken into consideration by evaluation of the signal.

Triangulation sensors (Fig. 14.44) likewise project a light point onto the surface of the object measured. This light point is observed from a defined angle. By changing the distance between the sensor and measuring object, the reflected point wanders across a CCD row. This way, the change of the distance is collected directly. In addition, some sensors project one or many laser lines onto the surface inspected. These lines can then be evaluated in terms of the contour of the measuring object by means of a CCD matrix.

The example sensor chosen has an average working distance of 105 mm, a measuring range of ±25 mm, a projected laser spot diameter of 0.1 mm, and a triangulation angle of 18°. With these parameters, these sensors can be applied, for example, to:

- Size or form inspection
- The collection of runout and position deviation
- The collection of thickness
- The collection of deformations
- Completeness or integrity control.

As Fig. 14.45 shows, single or combined sensors are necessary for these applications. The measuring signal collects the surface of the measuring object in the range of the entire measuring spot diameter. So, a low-pass

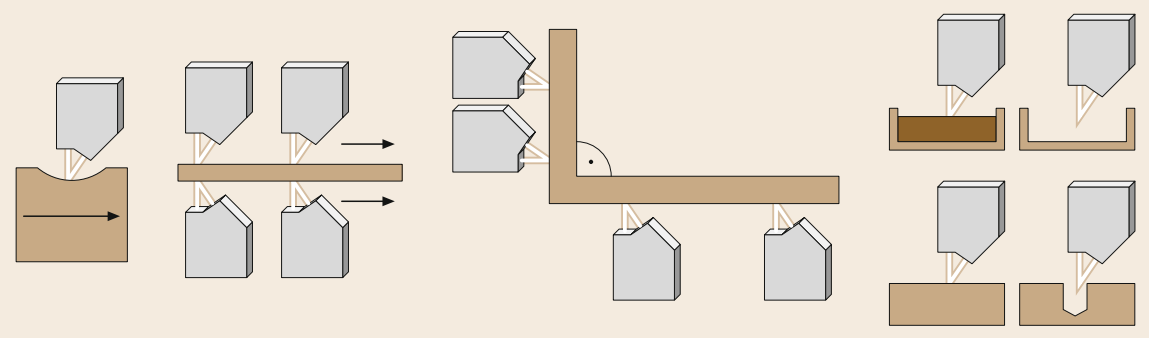

Fig. 14.45 Examples of applications using triangulation sensors

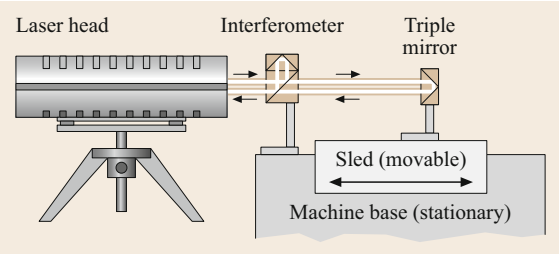

Fig. 14.46 Interferometer for the determination of position

filter processes and determines the mean distance in this area. The plane in which the beam is sent and reflected is arranged parallel to the surface structure to guarantee a reflection.

In laser interferometers, the laser beam is separated into two beams (reference and measuring beam) by means of a semireflecting mirror. While the reference beam always follows the same path inside the interferometer, the measuring beam is reflected off a triple mirror on the object to be measured, as shown in Fig. 14.46. When the two beams come together, interference occurs (Fig. 14.47). When the peaks of the waves meet (phase shift 0°), the light is amplified. When the peak of one wave meets the valley of the other (phase shift 180°), the waves cancel. The distance between the interferometer and the triple mirror changes when the sled moves. The phase between the reference and measuring beam shifts. This resulting change in the interference is interpreted as the measuring value.

This type of measuring system is used for applications with large lengths (10–20 m) and with a high resolution (5 nm). In each case, it only collects the changes from an initial state. A disadvantage is that the optical components must be mounted on the object that is to be measured and that the frequency of the light, and therefore the measuring result, is strongly influenced by environmental conditions such as air temperature, humidity, and pressure. Corrections can be made by collecting these environmental conditions and carrying out a subsequent adjustment of the data, or more specifically, through the application of a refractometer (an instrument in which the effects of the environmental conditions can be directly compared with the light properties in a vacuum).

Figure 14.46 shows an example combination that determines the position of a machine component with

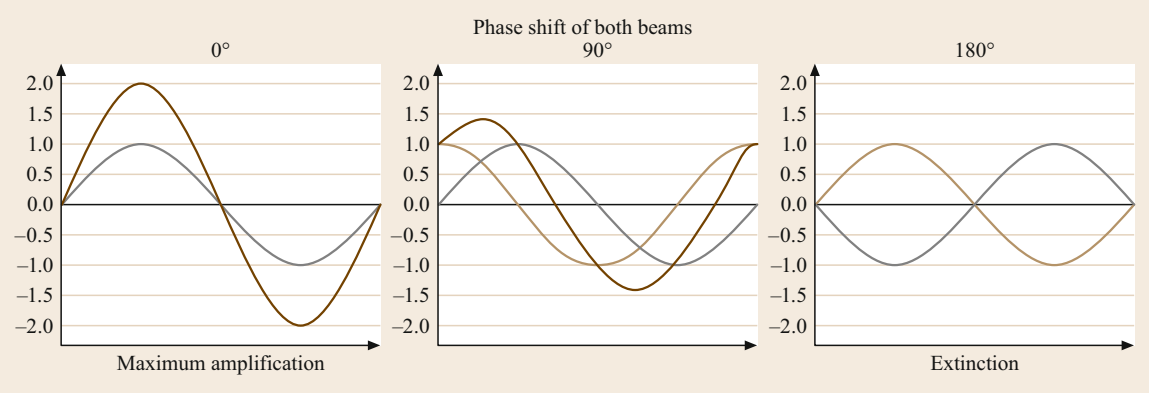

Fig. 14.47 Phase shift and interference

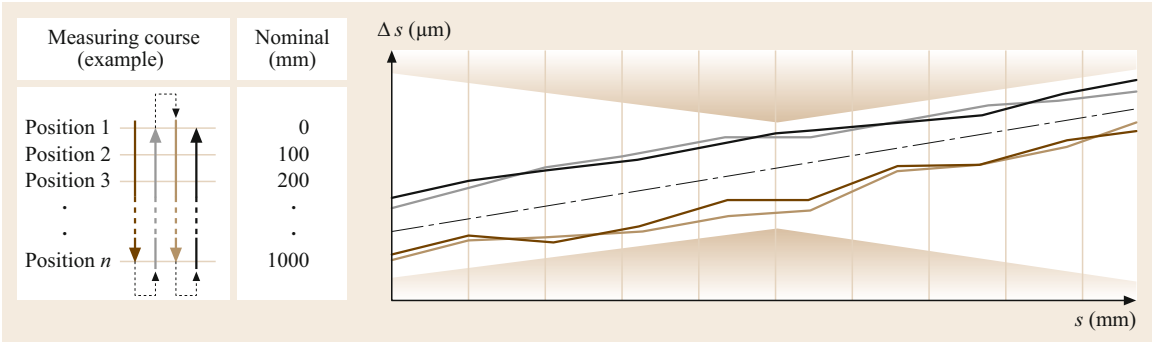

Fig. 14.48 Position deviation, measuring course, and results

respect to another, or rather to a chosen fixed point. This setup is used as an independent measuring system (for example, with coordinate measuring machines) but also as a measuring system for the collection of position deviations. Figure 14.48 shows the procedure for the collection of position deviations of a tooling machine. While the machine, controlled by its measuring system, follows the defined positions labeled 1 to n, the position deviations are determined by means of a laser interferometer. The measuring course, which is executed step by step over the entire range of the positions to be measured, is completed multiply in both directions (increasing and decreasing values). The deviances collected in this way are shown on the right-hand side of Fig. 14.48. From the depicted course of measuring values, a linear trend and span superimposed with random sections can be read. The limits shown in the diagram depict usual tolerance ranges for tooling machine position deviations. The systematic parts are compensated for, when necessary, through mechanical aligning of machine components, or afterwards by means of a correction table or correction function.

Similar arrangements allow the collection of tilt and rotation angles, as well as the determination of straightness deviations. When the measuring value transmission frequency can be chosen to be sufficiently large, a dynamic series (for example, the reaching of a desired position) can be collected with the layout shown.

14.2.9 Measuring Uncertainty and Traceability

The result of measuring is the measurement value. This measurement includes the true value and also systematic and random deviations of the measurement (Fig. 14.49). It is possible to estimate the expected value of the measurement by calculating the arithmetic mean of several independent measurements. The more single values that are processed, the more the random parts of the measuring deviation are reduced.

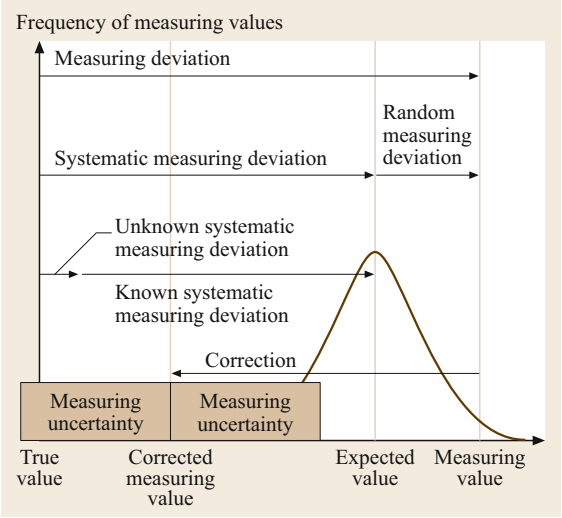

Fig. 14.49 Summary of measuring values

The systematic part of the measuring deviation can be determined by measuring an object with a known value. Such objects, measurement standards, are measuring blocks for lengths. Angles can be represented with angle gauges, precision polygons, or with sine bars used in conjunction with measuring blocks. The known value of the measurement standard (whose small deviation from the true value is negligible for the purpose of comparison), is called the correct value. The systematic measurement deviations can be calculated from the difference between the measured value of the measurement standard and its correct value. Afterwards, one can correct all measuring values by use of the known systematic deviation. The nonmeasurable or not measured (for instance, because it is too expensive) elements of the systematic measuring deviation are combined with random measuring deviations to constitute the measuring uncertainty. So, the measuring uncertainty is a parameter obtained from the measurement. It describes the region around the cor-

rected measuring value where the true value must be found. The complete result of measuring is given as the corrected measuring value plus/minus the measuring uncertainty [14.16].

In order to guarantee the correctness of measuring results, measuring devices must be affiliated to the national standard of the respective measurement. In Germany for instance, this is the National Physical Technical Institute (PTB), located in Braunschweig, which is responsible for the representation and propagation of physical units. Through the PTB, calibrating laboratories are accredited, so that their measuring devices and measuring standards coincide with the national standards (the units), according to the defined and accepted techniques. These are the laboratories of Germany's national accreditation body (DAkkS), former German Calibration Service (DKD).

All in-company measuring devices, or rather standards, should be consistently traceable back to the national standard of the PTB (Fig. 14.50). In order to verify this, the instruments are calibrated by a DAkkS laboratory or the PTB themselves. *Calibration* is defined as the inspection of measuring devices and measurement standards with reference to the accepted national standard. Successful calibration is generally documented through a protocol, the calibration certificate. On the calibration certificate, all of the calibration results, the reference standards, and additional measuring equipment (used during the calibration), the environmental conditions, and the calculated measuring uncertainty are documented.

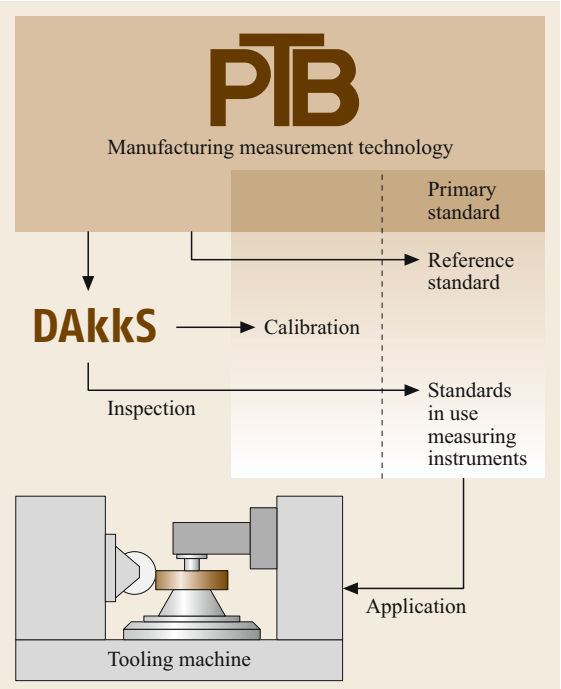

Fig. 14.50 Traceability

One should use certified instruments, standards, and methods in order to achieve cost-effective, in-company control of inspection instruments. Otherwise, a traceability certificate is not possible.

The setting-up and balancing of a measuring instrument, by which known systematic deviations of the measuring result are eliminated, is called *adjusting*.

14.2.10 Inspection Planning

Inspection planning means the planning of quality inspection in the entire production process, from the arrival of raw products to the delivery of the final product. For this, inspection tasks and procedures are specified with inspection feature, inspection location (close to production, measuring room), frequency of inspection, point of time within the production process, inspection methods, inspection equipment, and operators. One should consider both technical and economic aspects. The inspection planner must consider knowledge of the function and application of the piece or the components, safety hazards, the production process, technical documentation (drawings, standards, stipulations), and the inspection equipment. It should be consistently checked that the data is complete, current, and inspected (approved by the operating department).

For the selection of the test methods a systematic search in the drawing(s), in the work plan, in the documentation, in delivery instructions and in contractual agreements, is required. When searching in drawings it is possible to search according to the type of parameter (dimension, shape and positional tolerance, surface tolerance, etc.), according to the drawing view and/or according to grid squares (e.g. starting at the top left, clockwise).

The definition of the inspection frequency (number of samples, sample size) occurs on the basis of mathematical statistical facts. The time point in the production process allows company organizational and economical considerations. The late recognition of inadmissible errors can bring about several disadvantages.

The definition of inspection methods and inspection equipment are related, and, thus, should each be chosen with the other in mind. The choice of measuring device begins with a consideration of the required information content of the measuring result. This way, the aim of the inspection (evaluation of workpiece or process, manufacturing control) and the impact of the measuring instrument itself can be taken into account. Geometrical

limitations, such as the accessibility of the piece, the geometry of the probing element, the range of measurement (direct measurement, difference measurement) of the instrument, and especially for soft materials, the measuring force, have been previously decided upon. Finalized statements for the usability of a measuring instrument can be made after inspection of the scale division value and the measuring uncertainty. The measuring uncertainty must adhere to the ratio of the inspected tolerance by the relation $U/T = 0.1–0.2$. Alternatively, it is possible to obtain measuring capability coefficients and check the adherence of these characteristics to previously defined limits [14.17]. Supplemental criteria are, for example, the surfaces available for the measurement and transfer for processing, protocol, and archiving.

The required measuring time (capability of the measurement to be automated) in conjunction with the number of pieces to be tested is the essential criterion for the cost effectiveness of the application of a measuring device. Included in the inspection costs are also the equipment costs, equipment observation, calibration, and personnel costs (work time, education).

To guarantee the comparability of the measuring result and low uncertainty of the acquired characteristics the following conditions should be taken into account when specifying measurement methods:

- Explicit guidelines for the measuring procedure, including the parameters required for an appropriate measurement. Specification of the reference basis for the measuring procedure, the accuracy of the applied measuring instruments and measurement standards, gripping elements employed, and additional measuring equipment.
- Details of the measuring strategy, for example, the definition of the measurement location on the piece, or the number and arrangement of single measurements as a basis for a good average value.
- Details of the measuring value collection method for selective inspection and of the further steps of measured value processing, or guidelines for the application of analyzing software (for example, the selection of a compensating method).
- Legal warranty of adequate qualification of the personnel conducting the measurement.

The result of inspection planning is the inspection plan.

14.3 Further Reading

- T.M. Bosch, M. Lescure: *Laser Distance Measurements* (Atlantic, London 1995)
- H. Czichos, T. Saito, L. Smith (eds.): *Springer Handbook of Materials Measurement Methods* (Springer, Berlin, Heidelberg 2006)
- P.F. Dunn: *Measurement and Data Analysis for Engineering and Science* (Taylor Francis, London 2014)
- H. Pham (ed.): *Springer Handbook of Engineering Statistics* (Springer, Berlin, Heidelberg 2006)
- J.A. Bosch: *Coordinate Measuring Machines and Systems*, 2nd edn. (CRC, Boca Raton 2011)
- S. Vardeman, J.M. Jobe: *Statistical Quality Assurance Methods for Engineers* (Wiley, New York 1999)
- G.T. Smith: *Industrial Metrology: Surfaces and Roundness* (Springer, Berlin, Heidelberg 2013)
- W.N. Sharpe, Jr. (ed.): *Springer Handbook of Experimental Solid Mechanics* (Springer, Berlin, Heidelberg 2008)

References

14.1 E. Dietrich, A. Schulze: *Statistical Procedures for Machine and Process Qualification* (Hanser, München 2010)

14.2 ISO 9000: 2015-09 Quality management systems – Fundamentals and vocabulary (Beuth, Berlin 2015)

14.3 ISO 9001: 2015-09 Quality management systems – Requirements (Beuth, Berlin 2015)

14.4 ISO/TS 9002: 2016-11 Quality management systems – Guidelines for the application of ISO 9001:2015 (Beuth, Berlin 2016)

14.5 ISO 9004: 2018-04 Quality management – Quality of an organization – Guidance to achieve sustained success (Beuth, Berlin 2018)

14.6 IATF 16949: 2016-10 Quality management system requirements for automotive production and relevant service parts organisations (Beuth, Berlin 2016)

14.7 ISO 286-1: 2010-04 Geometrical product specifications (GPS) – ISO code system for tolerances on linear sizes – Part 1: Basis of tolerances, deviations and fits (Beuth, Berlin 2010)

14.8 ISO 286-2: 2010-06 Geometrical product specifications (GPS) – ISO code system for tolerances on linear sizes – Part 2: Tables of standard tolerance classes and limit deviations for holes and shafts (Beuth, Berlin 2010)
14.9 ISO 2768-1: 1989-11 General tolerances; part 1: tolerances for linear and angular dimensions without individual tolerance indications (Beuth, Berlin 1989)
14.10 ISO 2768-2: 1989-11 General tolerances; part 2: geometrical tolerances for features without individual tolerance indications (Beuth, Berlin 1989)
14.11 ISO 1101: 2017-02 Geometrical product specifications (GPS) – Geometrical tolerancing – Tolerances of form, orientation, location and run-out (Beuth, Berlin 2017)
14.12 H. Linke, J. Börner, R. Heß: *Cylindrical Gears: Calculation – Materials – Manufacturing* (Hanser, München 2016), Chap. 8: Assuring the accuracy of cylindrical gears
14.13 ISO 3274: 1996-12 Geometrical Product Specifications (GPS) – Surface texture: Profile method – Nominal characteristics of contact (stylus) instruments (Beuth, Berlin 1996)
14.14 ISO 4288: 1996-08 Geometrical Product Specifications (GPS) – Surface texture: Profile method – Rules and procedures for the assessment of surface texture (Beuth, Berlin 1996)
14.15 ISO 4287: 1997-04 Geometrical Product Specification (GPS) – Surface texture: Profile method – Terms, definitions and surface texture parameters (Beuth, Berlin 1997)
14.16 L. Wisweh, M. Sandau, R. Ichimiya, S. Sakamoto: *Determination of measuring uncertainty and its use for quality assessment and quality control*, Research report Faculty of Engineering, Vol. 47 (Niigata University, Japan 1998)
14.17 E. Dietrich, A. Schulze: *Measurement Process Qualification* (Hanser, München 2011)

Steffen Wengler

Institute of Manufacturing Technology
and Quality Management
Otto-von-Guericke-University Magdeburg
Magdeburg, Germany
swengler@ovgu.de

Steffen Wengler obtained his Dr-Ing in Mechanical Engineering 1989 from Otto-von-Guericke-University of Magdeburg, Germany. His special fields of interest include manufacturing measurement technology and gear metrology (mainly cylindrical involute gears and gear pairs). Since 1990 he has been Head of the Laboratory for Measurement Technology at the Institute of Manufacturing Technology and Quality Management at Otto-von-Guericke-University of Magdeburg, Germany.

Lutz Wisweh

Faculty of Mechanical Engineering
Otto-von-Guericke-University Magdeburg
Magdeburg, Germany
lutz.wisweh@ovgu.de

Lutz Wisweh received his Dr-Ing degree from the University of Magdeburg. In 1999, he was Professor at Niigata University, Japan. In 1999, he was Visiting Professor at the Universidad Central de Las Villas, Cuba. Until his retirement in 2015 he was Extracurricular Professor at the University of Magdeburg. His research interests lie mainly in the use of statistical methods in quality management and measurement uncertainty in manufacturing measurement technology.

Shuichi Sakamoto

Faculty of Engineering
Niigata University
Niigata, Japan
sakamoto@eng.niigata-u.ac.jp

Shuichi Sakamoto worked as Research Associate (DC) of JSPS in 1989 and 1990. He received his PhD from Niigata University in 1991 and joined Niigata University in 1991 as Research Associate. He became Associate Professor there in 1998. His research interests are developments of new measuring or detecting methods using of acoustics, characteristics of airborne sound absorbing material, noise control, and the area of ultrasonics.

Norge I. Coello Machado

Facultad de Ingeniería Mecánica e
Industrial
Universidad Central "Marta Abreu" de Las
Villas
Santa Clara, Cuba
norgec@uclv.edu.cu

Norge Isaías Coello Machado received his Dr-Ing degree from the University of Magdeburg in 1989. From 2003, he was temporary Professor at the University of Magdeburg, Germany, for 3 years. In 2012, he was awarded the Dr hc title by the Slovak University of Technology, Slovakia. His research interests lie mainly in the application of statistical methods in quality management, quality engineering, and measurement technology.

Machine Part D

Part D Machine and Systems Design

15 **Machine Elements**
Frank Engelmann, Jena, Germany
Karl-Heinrich Grote, Magdeburg, Germany
Thomas Guthmann, Jena, Germany

16 **Engineering Design**
Frank Engelmann, Jena, Germany
Alois Breiing,
Timothy Gutowski, Cambridge, MA, USA

17 **Piston Machines**
Helmut Tschöke, Magdeburg, Germany
Vince Piacenti, Farmington Hills, MI, USA
Brent Keppy, Waterford, MI, USA
Aneel A. Singh, Farmington Hills, MI, USA
Steven D. White, West Bloomfield, MI, USA
Justin Kern, Farmington Hills, MI, USA
Jon H. van Gerpen, Moscow, ID, USA

18 **Pressure Vessels and Heat Exchangers**
Ajay Mathur, Faridabad, India
Hamidreza Najafi, Melbourne, FL, USA

19 **Turbomachinery**
Meinhard T. Schobeiri, College Station,Texas, USA

20 **Conveying and Construction Machinery**
André Katterfeld, Magdeburg, Germany
Alan Roberts, Callaghan, NSW, Australia
Craig Wheeler, Callaghan, NSW, Australia
Kenneth Williams, Callaghan, NSW, Australia
Chris Wensrich, Callaghan, NSW, Australia
Jan Scholten, Bochum, Germany
Mark Jones, Callaghan, NSW, Australia
Günter Kunze, Dresden, Germany
Henning Strubelt, Bremerhaven, Germany
Dusan Ilic, Callaghan, NSW, Australia
Tim Donohue, Shortland, NSW, Australia
Hendrik Otto, Magdeburg, Germany
Jens Sumpf, Chemnitz, Germany
Wei Chen, Callaghan, NSW, Australia
Bin Chen, Shortland, NSW, Australia
Daniel Ausling, Shortland, NSW, Australia

15. Machine Elements

Frank Engelmann, Karl-Heinrich Grote, Thomas Guthmann

Machine elements are components with the same or similar form that are very frequently found in machines, plants, and apparatus. They can be simple elements, such as washers or keys, or more complex components such as shafts, rolling bearings, or gears. The essential functional properties of the elements are mostly defined in corresponding standards. In general, guidelines and calculation regulations are available for the design and dimensioning of machine elements.

The machine elements most frequently used in practice, such as fasteners, connectors, axles/shafts, shaft-hub joints, bearings, seals and gaskets, sprockets, springs, and pipes are introduced and discussed in this chapter. It focuses on choosing suitable elements for a specific problem and proper design/dimensioning of these elements. The chapter is aimed both at engineers in practice and students in training.

15.1 **Basic Dimensioning Principles** 504
15.1.1 Types of Load and Effects 504
15.1.2 Complex Stress 506
15.1.3 Static and Dynamic Effects 507
15.1.4 Strength Characteristics 508
15.1.5 Strength-Reducing Effects 510
15.1.6 Practical Strength Calculation 512
15.1.7 Further Reading 514

15.2 **Fasteners** 514
15.2.1 Modes of Action 514
15.2.2 Form-Closure Joints 515
15.2.3 Force-Closure Joints 523
15.2.4 Material-Bonded Joints 538
15.2.5 Further Reading 543

15.3 **Axles and Shafts** 544
15.3.1 Standard Types 544
15.3.2 Special Types 544
15.3.3 Materials for Axles and Shafts 545
15.3.4 Design Calculation 545
15.3.5 Check Calculations 548
15.3.6 Further Reading 551

15.4 **Shaft–Hub Connections** 551
15.4.1 Form-Closure Shaft–Hub Connections 551
15.4.2 Frictional Shaft–Hub Connection 555
15.4.3 Press-Fit Connection Through Hydrojoining 561
15.4.4 Further Reading 566

15.5 **Rolling Bearings** 566
15.5.1 Structure and Properties 566
15.5.2 Types, Properties, and Use 568
15.5.3 Load Capacity and Life of the Rolling Bearings 568
15.5.4 Design 574
15.5.5 Lubrication of the Rolling Bearings 574
15.5.6 Sealing of Rolling Bearings 576
15.5.7 Rolling Bearing Damage 576
15.5.8 Further Reading 578

15.6 **Plain Bearings** 580
15.6.1 Hydrostatic Plain Bearings 580
15.6.2 Hydrodynamic Plain Bearings 581
15.6.3 Hydrostatic Starting Aids 581
15.6.4 Maintenance-Free Plain Bearings 581
15.6.5 Bearing Materials 581
15.6.6 Bearing Types 582
15.6.7 Design 584
15.6.8 Further Reading 585

15.7 **Seals and Gaskets** 585
15.7.1 Contacting Seals and Gaskets 585
15.7.2 Noncontact Seals 590
15.7.3 Further Reading 593

15.8 **Gears and Gear Trains** 593
15.8.1 Classification of Gears and Gear Trains 593
15.8.2 Gear Geometry of the Spur Gear System 595
15.8.3 Forces on the Spur Gear Pair and Transferred Power 604
15.8.4 Design of Spur Gear Systems 605
15.8.5 Further Reading 607

15.9 **Springs** 607
15.9.1 Properties 608
15.9.2 Oscillatory Behavior 609
15.9.3 Spring Systems 609
15.9.4 Spring Materials 611

K.-H. Grote, H. Hefazi (Eds.), *Springer Handbook of Mechanical Engineering*, Springer Handbooks,
https://doi.org/10.1007/978-3-030-47035-7_15

15.9.5 Springs Subjected to Tensile and Compressive Loading 612
15.9.6 Springs Subjected to Bending 613
15.9.7 Torsionally Loaded Springs 616
15.9.8 Elastomeric Springs 619
15.9.9 Further Reading 620
15.10 **Pipes** 620
15.10.1 Materials, Types, and Dimensions 620
15.10.2 Calculation 621
15.10.3 Further Reading 624
References 625

15.1 Basic Dimensioning Principles

Components must be dimensioned so that they can absorb the forces acting on them with sufficient safety and without becoming unacceptably damaged. Possible damage/failure modes include:

- Unacceptable deformation
- Fracture (fast/forced or creep rupture/fatigue fracture)
- Kinking or buckling
- Unacceptable wear
- Unacceptable heating

If several failure modes can occur, each individual mode must be assessed. The most unfavorable (worst case) conditions are decisive.

The mechanical stresses that occur in the cross section must be smaller than allowable stresses.

The level of the allowable stresses is influenced by:

- The strength of the material
- The type of load/effect (e.g., stress)
- The geometrical shape of the component
- Other influences (temperature, internal or residual stresses in the component, material defects, etc.)

15.1.1 Types of Load and Effects

Load and Effect

The terms load and strain are often inadequately differentiated in practice. In this text, the terms are used as follows.

If external forces and moments act on a component, the component is loaded by a load and this results in component strain.

Strain is subdivided into intentional and unintentional strain:

- Intentional strain: results from the function of the component and its ability to absorb and/or transfer loads; mostly known or can be recorded reliably
- Unintentional strain: results from unwanted effects that are mostly difficult to record, for example, from impacts or shocks, vibrations, and thermal stresses

The internal force effects caused by the strain produce mechanical stresses depending on the component cross section.

Even without the effect of external loads, production, deformation, jointing, and heat-treatment processes can cause stresses to occur in the components in the form of so-called residual stresses. These are often difficult to record. They can be mitigated or minimized through stress relieving.

Loading Modes

Possible loading modes are shown in Fig. 15.1.

The moments of inertia necessary to calculate the bending or torsional stress are listed in Table 15.1.

Special Forms of Compressive Loading. Possible special forms resulting from compressive loading (compression) are:

- Surface pressure
- Hertzian contact pressure
- Buckling (instability)

Surface Pressure. Surface pressure p acts on the contact surface A of two parts pressed together by an external force F. In this case, the average surface pressure equals the specific surface pressure $\overline{p}$ (Fig. 15.2a) and is determined from

$$\overline{p} = \frac{F}{A} = \frac{F}{ab} \,. \tag{15.1}$$

If the contact surfaces are curved, surface pressure only occurs if both surfaces have exactly the same curvature, e.g., in pairs of round objects with zero clearance according to Fig. 15.2b,c.

The pressure in zero clearance pairs of round objects is then uniformly distributed if the bore (housing, eye) is pliable, i.e., yielding.

Then, according to Fig. 15.2b,

$$\overline{p} = \frac{F}{A} = \frac{F}{db} \,. \tag{15.2}$$

Hertzian Contact Pressure. If the bodies have different curvatures, very small contact surfaces result in the

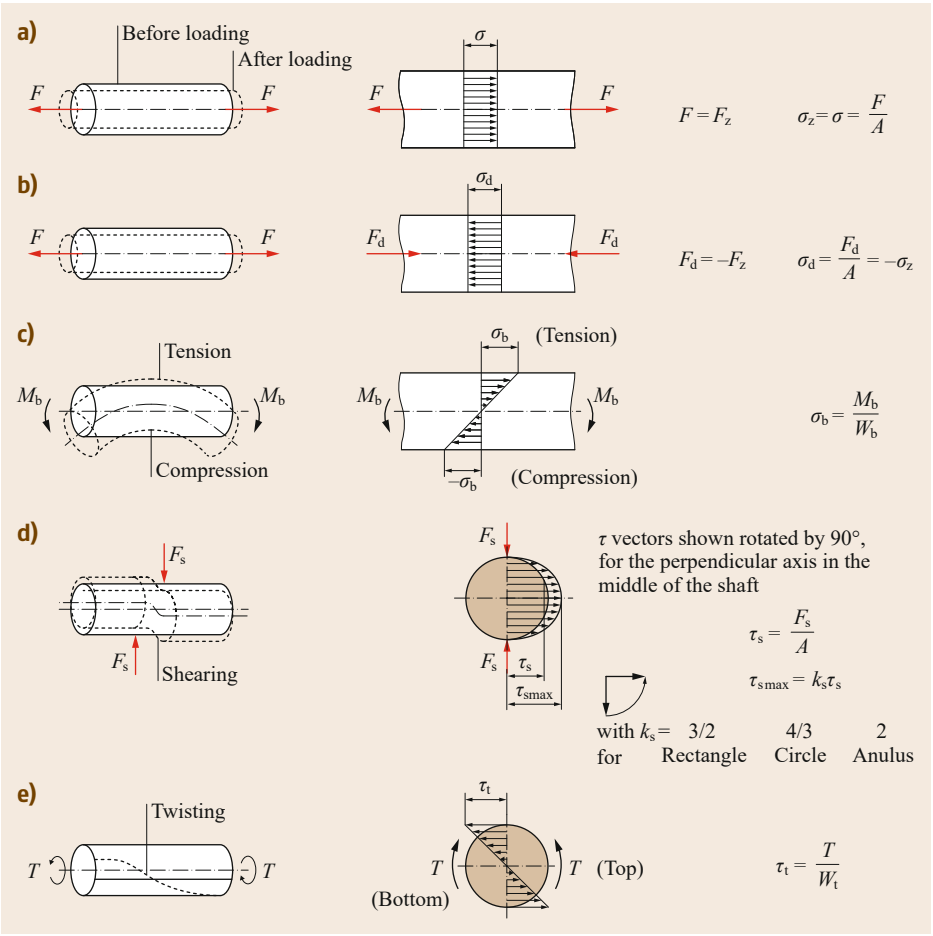

Fig. 15.1a–e Overview of types of loading. Direct stresses **(a,b)** with bending **(c)**; tangential stresses: shear **(d)** and torsion **(e)**

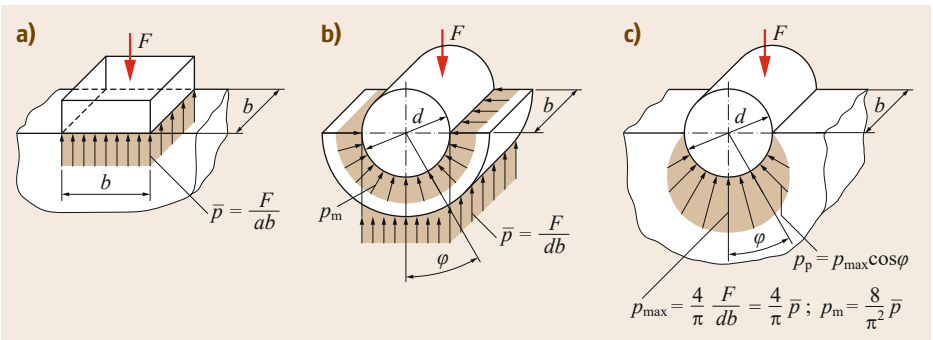

Fig. 15.2a–c Surface pressure on flat **(a)** and curved surfaces in which the bore is yielding **(b)** or stiff **(c)**

contact zone as a result of deformation. In the case of punctiform contact, these are (theoretically) circular or ellipsoidal, and in the case of linear contact they are rectangular.

The normal forces F acting on the objects cause compressive stresses/pressures called Hertzian contact pressures in the small contact surfaces.

Buckling. If slender components (e.g., bars, rods, pipes, columns, spindles) are loaded by a compressive force in the longitudinal direction, their straight condition is stable only up to a certain critical load. Above this load, buckling is expected.

Exceeding of the critical compressive load on thin, flat components leads to outward bulging.

Table 15.1 Axial second moments of area and bending resistance moments

Cross-sectional shape	Bending and buckling Second moment of area I	Axial section modulus W	Twisting (torsion) Polar section modulus W_p
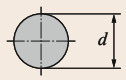	$I = \frac{\pi d^4}{64}$	$W = \frac{\pi d^3}{32}$	$W_p = \frac{\pi d^3}{16}$
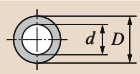	$I = \frac{\pi\left(D^4 - d^4\right)}{64}$	$W = \frac{\pi\left(D^4 - d^4\right)}{32D}$	$W_p = \frac{\pi\left(D^4 - d^4\right)}{16D}$
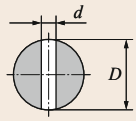	$I = 0.05D^4 - 0.083dD^3$	$W = 0.1D^3 - 0.17dD^2$	$W_p = 0.2D^3 - 0.34dD^2$
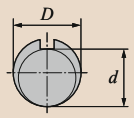	$I = 0.003\,(D + d)^4$	$W = 0.012\,(D + d)^3$	$W_p = 0.2d^3$
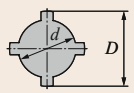	$I = 0.003\,(D + d)^4$	$W = 0.012\,(D + d)^3$	$W_p = 0.024\,(D + d)^3$
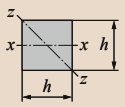	$I_x = I_z = \frac{h^4}{12}$	$W_x = \frac{h^3}{6}$ $W_z = \frac{\sqrt{2}h^3}{12}$	$W_p = 0.208h^3$
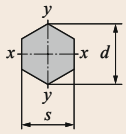	$I_x = I_y = \frac{5\sqrt{3}s^4}{144}$ $I_x = I_y = \frac{5\sqrt{3}d^4}{256}$	$W_x = \frac{5s^3}{48} = \frac{5\sqrt{3}d^3}{128}$ $W_y = \frac{5s^3}{24\sqrt{3}} = \frac{5d^3}{64}$	$W_p = 0.188s^3$ $W_p = 0.123d^3$
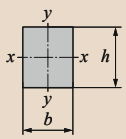	$I_x = \frac{bh^3}{12}$ $I_y = \frac{hb^3}{12}$	$W_x = \frac{bh^2}{6}$ $W_y = \frac{hb^2}{6}$	$W_p = \eta b^2 h$ See table below for values
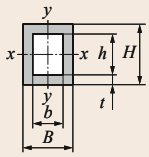	$I_x = \frac{BH^3 - bh^3}{12}$ $I_y = \frac{HB^3 - hb^3}{12}$	$W_x = \frac{BH^3 - bh^3}{6H}$ $W_y = \frac{HB^3 - hb^3}{6B}$	$W_p = \frac{t\,(H + h)\,(B + b)}{2}$

Reference values for the polar section moduli of rectangular cross sections								
h/b	1	1.5	2	3	4	6	8	10	∞
	0.208	0.231	0.246	0.267	0.282	0.299	0.307	0.313	0.333

15.1.2 Complex Stress

In a loaded component, in general a normal (perpendicular) stress and two tangential stresses can act in each of the six bounding surfaces of an (imaginary) cubic solid element (Fig. 15.3).

If all surfaces of the cube are stressed, this is called a (spatial) triaxial stress state.

If all stresses on two opposite surfaces of the cube equal zero, as is frequently assumed for flat components, this is called a (plane/2-D) biaxial stress state. In such a case, only the stresses σ_x, σ_y, and $\tau_{xy} = \tau_{yx}$ (due to the moment equilibrium about the z-axis) exist, and all other stresses on the element are zero.

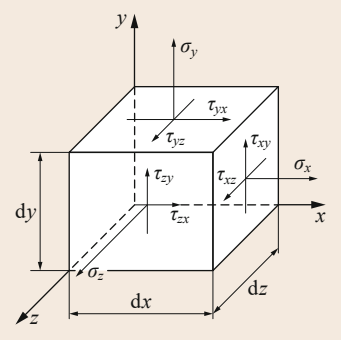

Fig. 15.3 Spatial (3-D) stress state

If only one direct stress (also known as normal stress) acts on the cubic element, that is to say all other stresses equal zero, this is called a uniaxial stress state.

Strength values of materials are (usually) determined in a tensile test, in which only direct stresses occur (uniaxial stress state).

However, in real components, normal and tangential stresses frequently occur simultaneously in different directions. In such a case, the equivalent stress must be formed from the individual stresses [15.1, 2]. The equivalent stress σ_v represents a (notional) direct stress, which brings about the same effect in the component as the direct stresses and tangential stresses that exist.

Various strength hypotheses are used to calculate this equivalent stress, depending on the strength properties of the material (Table 15.2).

The Von Mises distortion energy theory (DET) criterion is used for tough (ductile) materials (e.g., structural steel, quenched, and tempered steel with $\sigma_{lim} \approx \sqrt{3}\tau_{lim}$). In this hypothesis it is assumed that the component fails if the maximum shear strain energy exceeds a (material dependent) limit value.

The maximum principal stress (MPS) criterion (Rankine's maximum principal stress fracture criterion) is used for brittle materials (e.g., gray cast iron and tempered steel with $\sigma_{limit} \approx \tau_{limit}$). Here it is assumed that the component fails as a result of the largest direct stress on exceeding the fracture strength (R_m, σ_B) without prior plastic deformation.

The maximum shear theory, or Tresca maximum shear stress (MSS) criterion, is used for particularly tough materials (tough steel with $\sigma_{limit} \approx 2\tau_{limit}$) with a distinct yield point and Hertzian contacts. The cause of the failure is the largest difference in the principal stresses $\sigma_{max} - \sigma_{min}$.

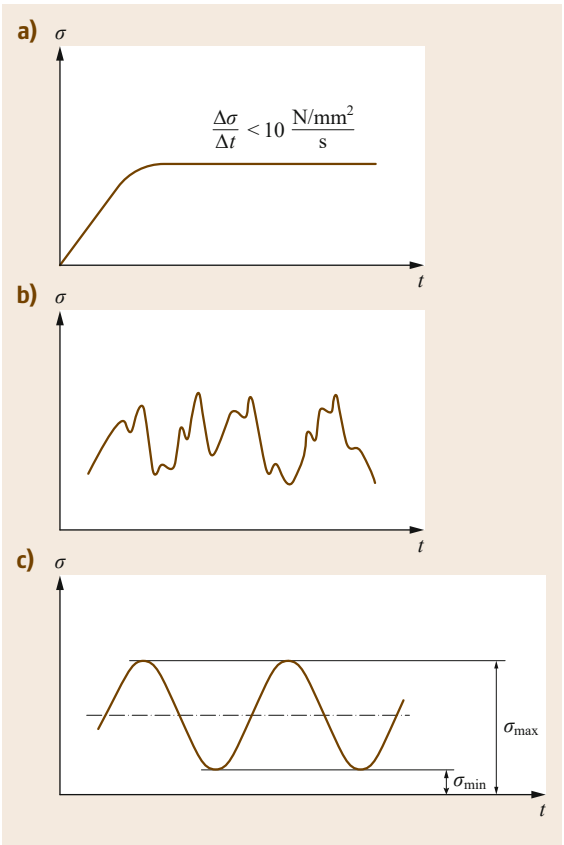

Fig. 15.4a–c Stress–time curves: **(a)** static, **(b)** dynamic (general arbitrarily oscillating), and **(c)** dynamic (idealized, uniformly oscillating)

If the stresses that occur are of the same type, they can be added together to form a resultant stress

$$\sigma_{res} = \sigma_{z;d} + \sigma_b\,; \quad \tau_{res} = \tau_s + \tau_t\,. \tag{15.3}$$

15.1.3 Static and Dynamic Effects

The loads (actions) acting on a component are frequently not constant over time. For this reason, not only is the maximum load significant for the dimensioning of components, but also the load change over time (load–time profile).

Therefore, for the calculation, a differentiation must be made between static and dynamic effects of loading (stress states):

Table 15.2 Equivalent stresses of established failure theories for the plane stress state

DET	MPS	MSS
$\sigma_V = \sqrt{\sigma_x^2 + \sigma_y^2 - \sigma_x\sigma_y + 3\tau_{xy}^2}$	$\sigma_V = \frac{\sigma_x+\sigma_y}{2} + \sqrt{\left(\frac{\sigma_x+\sigma_y}{2}\right)^2 + \tau_{xy}^2}$	$\sigma_V = \sqrt{(\sigma_x - \sigma_y)^2 + 4\tau_{xy}^2}$

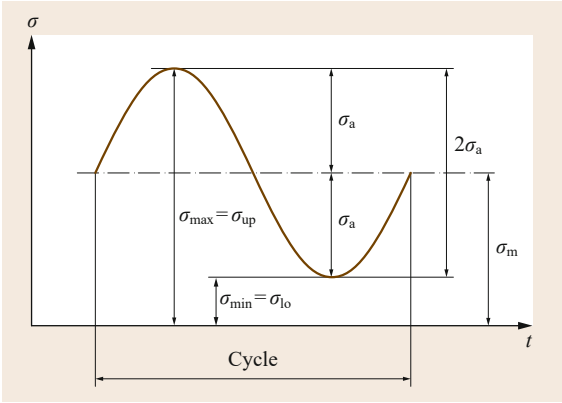

Fig. 15.5 Characteristics of a stress cycle

- Static stresses are constant over time (Fig. 15.4a).
- Dynamic stresses are (arbitrarily) changeable over time (Fig. 15.4b). Periodic oscillation is a frequently occurring special case (Fig. 15.4c).

In practice, the real change over time of an arbitrary dynamic load can frequently be idealized by a simply applied mathematical function (e.g., sine function) (Fig. 15.4c).

The characteristics of a cycle are used to describe stress–time profiles (Fig. 15.5).

Distinctive characteristics are:

- The mean stress σ_m
- The stress amplitude σ_a
- The upper stress σ_{up} (= maximum stress σ_{max})
- The lower stress σ_{lo} (= minimum stress σ_{min})
- The (limit) stress ratio $\kappa = \sigma_{lo}/\sigma_{up}$

The position of the mean stress σ_m relative to the zero stress line ($\sigma = 0$) is also important for the loading, or rather stress, of a component (Table 15.3). A differentiation is made between:

- The static stress (as a special case of stress in general)
- The repeated stress (cyclic stress, pulsating stress), which only change in the positive (compression) or in the negative (tension) area

Table 15.3 Stress cases and their representation

Stress types		
Static Load case I	Dynamic, cyclic Load case II	Dynamic, alternating Load case III
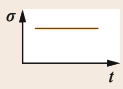	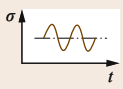	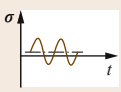

- The alternating stress (alternating cyclic stress, reversing stress), in which the stress profiles intersect the zero line (constant change between tensile and compressive stress)

If different types of load act on a component simultaneously, the load cases can differ. For rough calculations, the correction factor α_0 can be used to convert the shear stress to the respective direct stress load case and can then be used in the modified equation for the equivalent stresses ((15.4)–(15.6)). Rough values for the correction factor are given in Table 15.4.

Maximum principal stress criterion:

$$\sigma_V = 0.5\left[\sigma_b + \sqrt{\sigma_b^2 + 4\,(\alpha_0\tau_t)^2}\right] \qquad (15.4)$$

Maximum shear stress criterion:

$$\sigma_V = \sqrt{\sigma_b^2 + 4\,(\alpha_0\tau_t)^2} \qquad (15.5)$$

Maximum shear strain energy criterion:

$$\sigma_V = \sqrt{\sigma_b^2 + 3\,(\alpha_0\tau_t)^2} \qquad (15.6)$$

Load peaks can occur while dynamically loaded components are in service that exceed the nominal force (nominal load) or the nominal torque (rated torque) significantly. As these are very difficult to record by measurement in practice, they are taken into account in calculations by the application and service factor K_A (15.7). Values for the application and service factor can be found in Table 15.5.

$$F = K_A F_{nom} \quad \text{and} \quad T = K_A T_{nom} \qquad (15.7)$$

15.1.4 Strength Characteristics

In principle, a distinction is made between static and dynamic strength.

Static Strength

The static strength is generally determined by tensile testing and is represented in the stress–strain diagram (Fig. 15.6).

Depending on the failure criterion, the dimensioning of the components is based on the elastic limit R_e or

Table 15.4 Rough correction factors for steel (after *Decker* [15.3])

	Load cases with τ stress			
Load cases with σ stress	α_0	τ_I	τ_{II}	τ_{III}
	σ_I	1	1.5	2
	σ_{II}	0.7	1	1.35
	σ_{III}	0.5	0.75	1

Table 15.5 Application and service factors K_A (based on ISO 6336-1 [15.4])

Working characteristics of the driving machine	Working characteristics of the driven machine			
	Uniform	Light shocks	Moderate shocks	Heavy shocks
Uniform	1.00	1.25	1.5	1.75
Light shocks	1.10	1.35	1.60	1.85
Moderate shocks	1.25	1.50	1.75	2.00
Heavy shocks	1.50	1.75	2.00	≥ 2.25

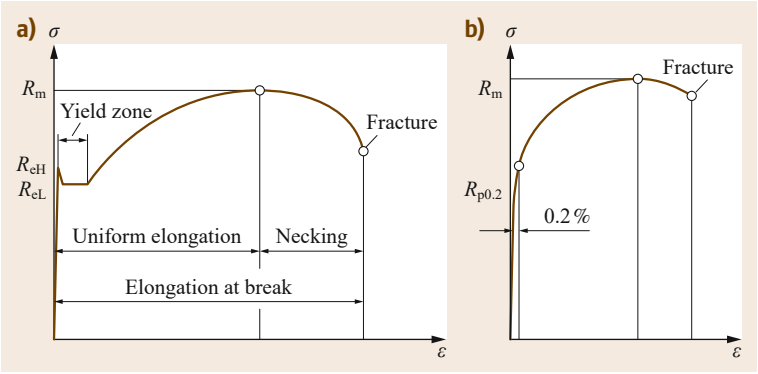

Fig. 15.6a,b Stress–strain diagram for steel (schematic) **(a)** with and **(b)** without a distinct yield point

the ultimate strength R_m (fracture limit). Instead of R_e, the 0.2% proof strength $R_{p0.2}$ (yield strength) is used for brittle materials without a distinct yield point.

Depending on the loading mode (type of stress), the underlying material strengths result in the strength characteristics for steel materials at room temperature according to Table 15.6.

Dynamic Strength

The stress fluctuations that occur due to dynamic loading can intensify at outer (geometric) and/or inner (metallurgical) notches and lead to damage to the material. Local exceeding of the ultimate strength can cause microcracks to form, which gradually grow into the component and ultimately lead to fatigue fracture.

A fatigue fracture is mostly characterized by smooth, bright fracture surfaces with arrest lines (also known as a clamshell pattern or beach marks) and a fast fracture (forced fracture) in the remaining cross section (fracture zone) (Fig. 15.7).

The sustainable load intensity depends on the number of load changes (cycles). If a test piece is loaded by a defined repeated load (alternating or cyclic) just under R_m, it can withstand N_D cycles before failure occurs. Different numbers of sustainable load cycles result depending on the level of the repeated load.

If the repeated load is sufficiently small, the test piece does not fail. The value of the load equals the fatigue strength and the corresponding number of cycles is the fatigue life N_{FS}. The fatigue strength of steel exists if the sustainable number of load cycles is $N_{FS} > 10^7$. The graphic representation of the maximum possible repeated load above the corresponding number of cycles produces the so-called Wöhler curve (also known as a stress-cycle (S–N) curve) (Fig. 15.8).

A component can be designed for a finite life or for infinite life. A component has a finite life if the stresses that occur exceed the value of the fatigue strength σ_{FS} (Fig. 15.9a). If the stresses that occur are smaller than σ_{FS}, the component is considered to have an infinite life (Fig. 15.9b).

Table 15.6 Loading and corresponding static material characteristics for steel at room temperature (based on [15.2, 5])

Loading	Failure criterion	Underlying strength value	Symbol
Tension	Deformation	$= R_e$; $R_{p0.2}$	σ_{zF}
	Fracture	$= R_m$	σ_{zB}
Compression	Deformation	$= R_e$; $R_{p0.2}$	σ_{dF}
	Fracture	$= R_m$	σ_{dB}
Bending[a]	Deformation	$\approx R_e$	σ_{bF}
	Fracture	$\approx R_m$	σ_{bB}
Torsion[a]	Deformation	$\approx 0.58 R_e$	τ_{tF}
	Fracture	$\approx R_m$	τ_{tB}
Shearing	Deformation	$\approx 0.58 R_e$	τ_{sF}
	Fracture	$\approx 0.58 R_m$	τ_{sB}

[a] The strength characteristics in bending and torsion are dependent on the stress gradient. The supporting effect of partial plasticization results in higher strength characteristics

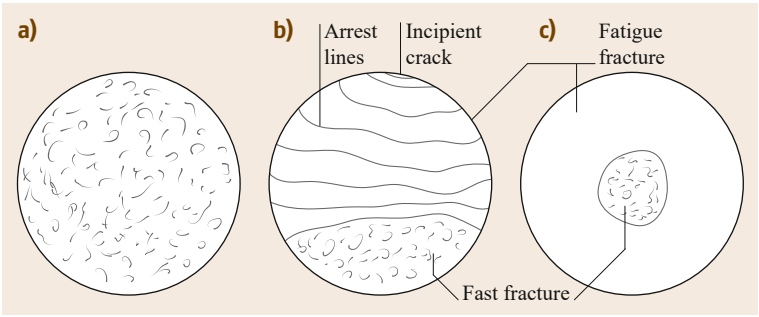

Fig. 15.7a–c Fast fracture (**a**), fatigue fracture under one-sided loading (**b**), and fatigue fracture under rotating bending load (**c**)

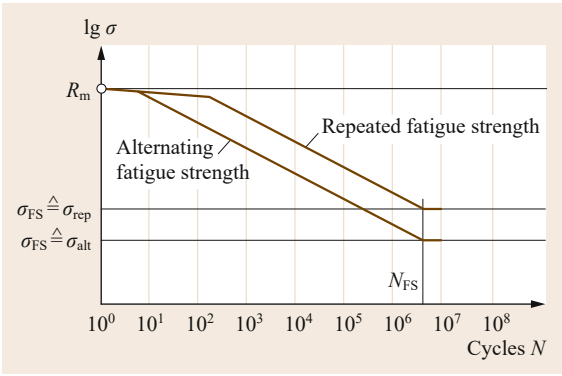

Fig. 15.8 Wöhler curve for steel (schematic)

15.1.5 Strength-Reducing Effects

Strictly speaking, the strength characteristics described in the literature apply only to the standardized test piece with which they were determined. As the real components differ substantially from the test bars with regard to their size, shape, and surface properties, the material strengths determined by testing must be converted into the corresponding component strengths or component design strengths τ_G; σ_G. To do this, all strength-changing influencing factors (e.g., notch effect) must be taken into consideration.

Notch Effect

In a component without cross-sectional change, the force lines and nominal stresses are undisturbed. If the force line pattern or path is disturbed by cross-sectional changes (e.g., notches), force line compression (stress concentration) can occur in this area. This leads to nonuniform stress distribution with local stress peaks (Fig. 15.10a,b), which reduces the load-bearing capacity of the component.

The level of the stress peaks depends on the geometry of the discontinuity, also known as the stress raiser (notch). The more sharp-edged or acute-angled the notches are, the larger the stress peaks that occur at them (Fig. 15.10c). The ratio of the stress peak σ_{max} and the calculated nominal stress $\sigma_N = F/A$ is called the theoretical stress concentration factor $\alpha_{ki} \geq 1$:

$$\alpha_{k\sigma} = \frac{\sigma_{max}}{\sigma_N} \quad \text{and} \quad \alpha_{k\tau} = \frac{\tau_{max}}{\tau_N} \,. \tag{15.8}$$

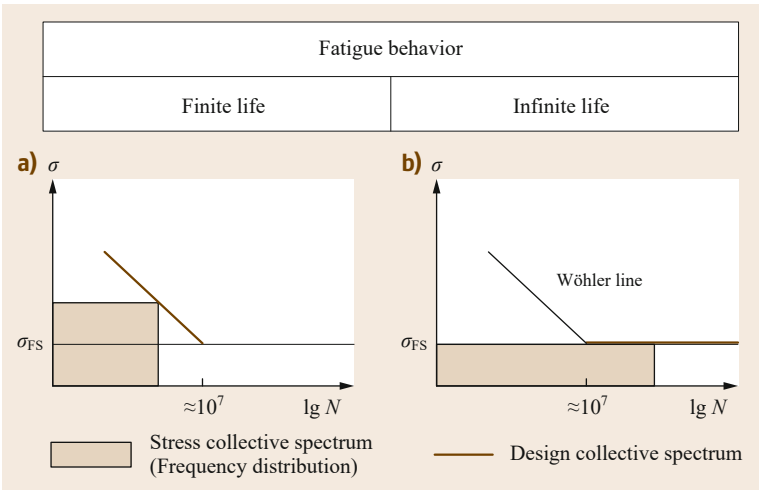

Fig. 15.9a,b Types of repeated stress and fatigue strength: (**a**) high cycle fatigue and (**b**) very high cycle fatigue

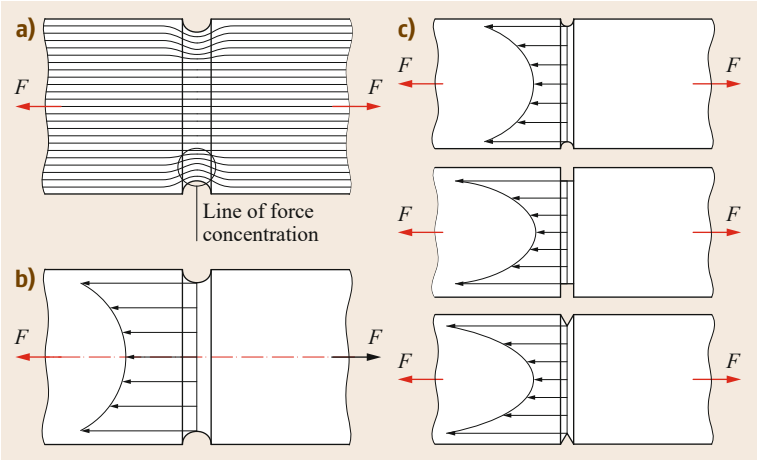

Fig. 15.10a–c Stress distribution in notched components with the same stress cross sections: **(a)** force line profile in a tension bar, **(b)** stress distribution in the tension bar, and **(c)** influence of the notch shape on the stress peaks

When the local stress peak σ_{max} is below the material yield point R_e, the value of the theoretical stress concentration factor α_{ki} of the notch depends only on the notch geometry and the loading mode. If the local stress peak lies above the material yield point, the effect of the notch increases with increasing material brittleness.

Ductile materials can partly minimize stress peaks that occur through locally limited yield. As a result, areas originally subjected to low stress become more highly loaded. The area immediately surrounding the notch is relieved, so that the notch effect is reduced compared to brittle materials with the same notch geometry. In this way, the areas further away from the notch have a support function for the near-notch areas.

The fatigue strength of a component is also changed by notches:

- The static strength (yield point) increases as a result of the support function from R_e to R_{ek}.
- The dynamic strength (alternating fatigue strength or amplitude fatigue strength) drops from σ_W and σ_A to σ_{GW} and σ_{GA}, respectively.

The ratio of the alternating fatigue strength of the smooth test bar σ_W and the alternating fatigue strength of the notched test bar σ_{GW} under the same conditions is defined as the fatigue notch factor β_k (for dynamic loading, by analogy for tangential stress):

$$\beta_k = \frac{\sigma_W}{\sigma_{GW}} = \frac{\sigma_A}{\sigma_{GA}} , \qquad (15.9)$$

where $1 \le \beta_k \le \alpha_k$. For (brittle) materials completely sensitive to notches, β_k takes the value of the theoretical stress concentration factor of the notch α_k.

Values for the fatigue notch factor can be determined experimentally or can be taken from the appropriate literature (for example, [15.6–8]).

Relief notches can reduce the notch effect at design-related main notches through a more uniform stress profile (Fig. 15.11).

Other Influences

In addition to notches, the following factors also affect component strength:

- The surface roughness. Roughnesses act like small notches.
- The size effect. The higher strength of the boundary zone (e.g., through quenching and tempering) or geometrical size dependency of the stress gradients reduce the component strength with increasing component cross section, especially in bending and torsion.
- Surface hardening. Residual compressive stresses due to production-related surface hardening can increase the fatigue strength.
- The shape of the loaded cross section (rectangle, circle, etc.). This is taken into consideration in the stress concentration factor.
- The temperature. Higher temperatures reduce the strength, while lower temperatures increase the risk of brittle failure.
- The load frequency. Very high and very low frequencies reduce the alternating fatigue strength.
- The ambient medium. Aggressive media (e.g., saltwater) reduce the alternating fatigue strength.
- The support effect (i.e., higher strength values) is more favorable in terms of tension than in compression in gray cast iron.

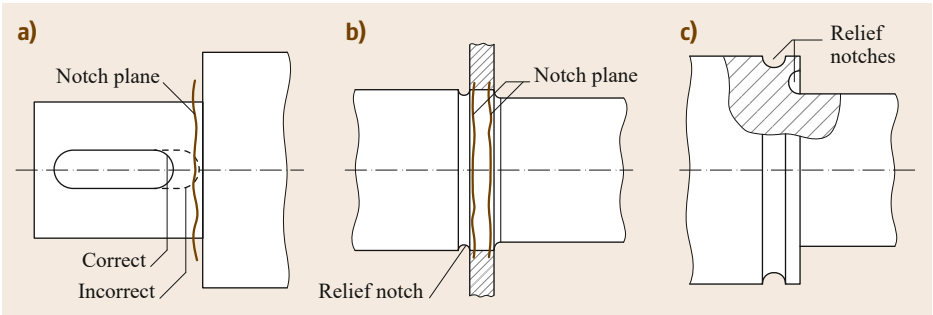

Fig. 15.11a–c Notch form and notch effect: **(a)** superimposition of notch planes, **(b)** relief notch in seized hub, and **(c)** relief notch on shaft shoulder

The effect of the individual influences on the component strength is taken into consideration by corresponding influence factors, which are given in the relevant literature [15.2–10].

15.1.6 Practical Strength Calculation

The objective of component dimensioning is to specify the component dimensions, taking into consideration defined boundary conditions. These boundary conditions result from:

- Allowable stresses
- Allowable deformations
- Allowable heating
- Allowable speeds
- Allowable noise emissions
- Necessary life

This requires all influence factors acting on the component (e.g., forces, climatic conditions, and vibrations) to be known or identifiable.

Components that are mainly loaded mechanically are dimensioned on the basis of the allowable stresses, with consideration of the required safety factors. The strength values necessary for this are generally only available from static tensile tests. For rough estimate calculations, they can be used to approximately deduce the sustainable stresses for other static loads and stresses according to Table 15.7.

The following relationship exists between the sustainable stresses and the allowable stresses:

$$\text{allowable stress} = \frac{\text{sustainable stress}}{\text{factor of safety}} .$$

The durability of a component is considered to be assured, if

$$\text{sustainable stress} \leq \text{allowable stress} .$$

For statically or mainly statically loaded components made of tough materials, the yield strength (yield point) R_e is decisive (or rather σ_{bF} or τ_{tF}) and for brittle materials the fracture strength R_m is decisive, from which

$$\sigma \leq \sigma_{all} = \frac{R_e}{S_Y} , \tag{15.10}$$

or rather

$$\sigma \leq \sigma_{all} = \frac{R_m}{S_F} , \tag{15.11}$$

where S_Y is the factor of safety against yielding in tough materials and S_F is the factor of safety against fracture in brittle materials.

For dynamically loaded components, for which the notch effect, size, and surface properties are initially unknown, the relevant fatigue strength is assumed initially

$$\sigma \leq \sigma_{all} = \frac{\sigma_D}{S_D} \quad \text{or} \quad \tau \leq \tau_{all} = \frac{\tau_D}{S_D} , \tag{15.12}$$

Table 15.7 Standard static strength characteristics for rough estimate calculations (approximate values, after [15.2])

	Material					
	Ductile (tough)			**Brittle**		
Loading mode	Steel, Cast steel, Cu alloy	Al wrought alloy	Al cast alloy	Ductile iron	Malleable cast iron	Gray iron
Tension	R_e ($R_{p0.2}$)			R_m		
Compression	R_e	R_e	$1.5R_e$	$1.3R_m$	$1.5R_m$	$2.5R_m$
Bending	$1.1R_e$	R_e	R_e	R_m	R_m	R_m
Torsion	$0.65R_e$	$0.6R_e$	–	–	–	–
Shear	$0.6R_e$	$0.6R_e$	$0.75R_e$	$0.65R_m$	$0.75R_m$	$0.85R_m$

Table 15.8 Standard safety values [15.2]

			Rolled and forged steel		Ductile cast iron materials			
			Consequences of damage		Untested consequences of damage		Nondestructive tested consequences of damage	
			High	Low	High	Low	High	Low
S_Y (S_F)	Likelihood of occurrence of the largest stresses or the most unfavorable stress combination	High	1.5 (2.0)	1.3 (1.75)	2.1 (2.8)	1.8 (2.45)	1.9 (2.5)	1.65 (2.2)
		Low	1.35 (1.8)	1.2 (1.6)	1.9 (2.55)	1.65 (2.2)	1.7 (2.25)	1.5 (2.0)
S_D	Regular inspection	No	1.5	1.3	2.1	1.8	1.9	1.65
		Yes	1.35	1.2	1.9	1.7	1.7	1.5

where S_D is a factor of safety against fatigue fracture. The allowable stresses (σ_{all}, τ_{all}) relate to the cross sections weakened by notches and/or grooves or the smaller cross sections in places with cross-sectional change.

The safety factors reduce the sustainable material strengths in calculation terms, as a result of which they allow for uncertainties and inaccuracies in the calculation operation (e.g., calculation with average values and simplifications in the calculation approach), the load assumption (e.g., load fluctuations that are difficult to record), and the material properties (e.g., scatter in the determination of strength values):

- The value of the safety factors to be used is essentially based on experience and is only partly defined in standards and guidelines.

The following aspects play a role when specifying the values:

- Smaller safety if the external loads can be reliably identified and recorded and failure does not have any disastrous consequences
- Larger safety if the external forces cannot be precisely identified or recorded and if failure can have disastrous consequences (e.g., risk to life and serious operational disruptions)

The effects must be carefully analyzed. A safety factor that is too high can also be fatal (apart from the economic viability or unviability). For example, in the case of components that heat up in service, it must be noted that the thermal stresses increase with increasing wall thickness and that the force effects induced by thermal expansion between fixed points become larger the stronger or sturdier the design. Table 15.8 gives an overview of standard, commonly used safety values.

The (actual) available component safety can only be determined for components that have already been designed, as only then can all influences (size, notch effect, surface quality) be approximately recorded.

For a component subjected to static and dynamic loading, after it has been designed (dimensioning and form), the appropriate strength verifications (stress analyses) can be used to ensure that it satisfies the planned static and dynamic loading.

The general algorithm for performing strength verifications is illustrated graphically in Fig. 15.12.

Notes on Component Dimensioning and Design

The following steps must be worked through systematically when dimensioning and designing a component:

- Definition/determination of the external forces and moments (loads) acting on the component
- Rough calculation (and choice) of the dimensions based on allowable stresses, design, and functional requirements
- Design (including the details) of the component
- Calculation of the stresses occurring at the relevant parts of the component (stresses)
- Calculation of the static and dynamic component strengths (design strengths) for the relevant places on the component
- Determination of the existing safety and comparison with the required safety (static and dynamic strength verification (stress analysis))

If the existing safety is inadequate, the component must be modified (e.g., changing its dimensions, detailed design, and material as well as possibly its load and application points) so that the required safety is achieved. Repeated calculations are frequently necessary.

If an existing safety is disproportionately high, it is necessary to examine how improved utilization of the strength can be achieved. It may be possible to

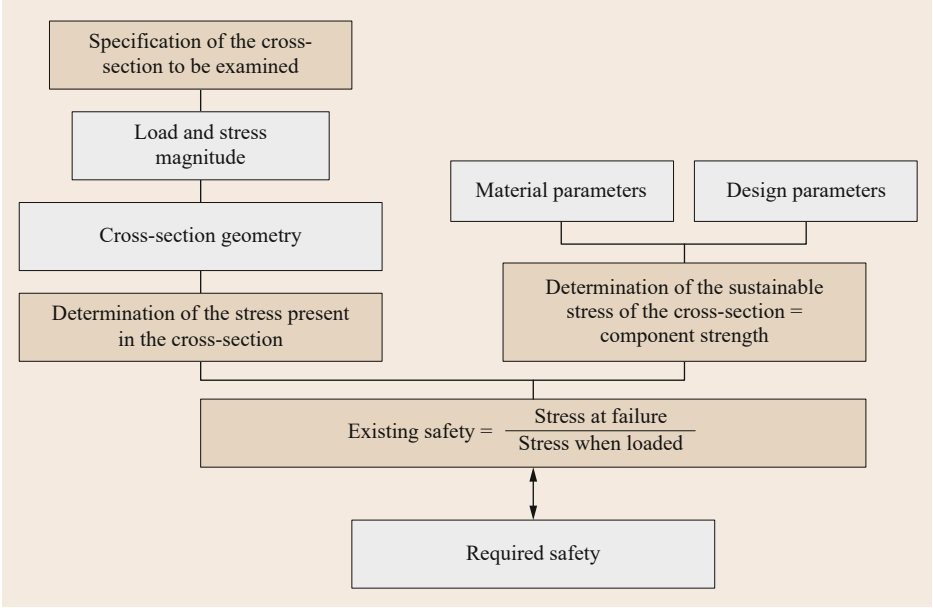

Fig. 15.12 General algorithm for strength verification

build smaller and more lightweight or to use more cost-effective materials with a lower strength. This frequently leads to solutions that are more favorable economically.

It should be noted that the required safety must be achieved at the critical places of the component, while for design reasons, other places can be overdimensioned with regard to strength (even with disproportionately high safety).

Other dimensioning criteria (deformation, heating, and wear) may also have to be considered in the assessment accordingly.

The specified allowable strength values must never be exceeded.

If use of a component requires compliance with several dimensioning criteria, all these criteria must be examined. The design must then be performed according to the failure criterion (failure limit) to be achieved first. Compliance with the remaining required criteria must be demonstrated.

15.1.7 Further Reading

Hibbeler [15.1], *Young* et al. [15.11] and *Issler* et al. [15.12] provide deeper insight into the mechanics of materials and the strength of materials.

Further information on service strength is provided by *Lee* et al. [15.13], *Haibach* [15.14], *Bannantine* et al. [15.15] and *Manson* and *Halford* [15.16]. In their book, *Fatigue Assessment of Welded Joints by Local Approaches* [15.17], *Radaj* et al. discuss in particular the service strength of welded joints.

Guidelines for the calculated verification of component strength are given in the FKM Guidelines [15.5].

15.2 Fasteners

Fasteners (connecting elements) are used to joint components and/or to define their position relative to each other. They are used to transfer forces. The mode of action of the connection (joint) can be based on form closure (also known as positive locking), force closure (also known as force locking), or material bonding (Table 15.9).

15.2.1 Modes of Action

In several jointing methods (e.g., riveted joints, keyed connections, and fitting bolts), several modes of action apply simultaneously so that clear separation between the modes of action is not possible.

Table 15.9 Modes of action of the fasteners and connectors

Modes of action	Form closure	Force closure	Material bonding
Joint	Through engagement or interlocking of the components or through drivers or fasteners/connectors engaging with the components	(Including friction), achieved by pressing together the adjoining faces (contact surfaces) of components	Achieved by means of an additional material that permanently bonds with the components
Example	Bolts, pins, keys, etc. 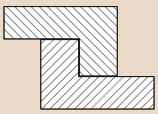	In screw and press-fit connections or joints, friction couplings, stopping breaks, etc. 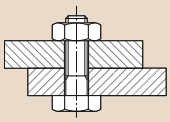	Welding, soldering, adhesive bonding 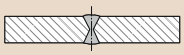

15.2.2 Form-Closure Joints

General Information

Form-closure fasteners, such as bolts, pins, keys, woodruff keys, wedges, profiled shafts, and rivets, are all standardized and are available as standard components. They are characterized by the fact that, unlike force closure and material bonding, the components permanently or immovably connect together or continue to be able to move, e.g., the possibility for bolts to turn or sliding keys to be pushed. In addition, form-closure joints can normally be nondestructively undone, whereby the rivet constitutes an exception.

Form-closure fasteners are generally mainly subjected to surface pressure, shearing, and possibly bending and must be dimensioned according to these loading modes.

The calculation approaches listed in the following give an overview of the dimensioning of the individual fasteners. Here it must be noted that the calculation principles may need to be adapted to the specific calculation case.

Pinned Joints

Pinned joints are used:

- To form a fixed connection between wheel and lever hubs and axles or shafts
- To secure the position/centering machine parts
- As pins for fixing tabs, link plates, springs, etc.
- As overload protection (shear pins)

Application examples are shown in Fig. 15.13.

Depending on their shape, a differentiation is made between parallel pins, tapered pins, grooved pins, and spring-type straight pins (Fig. 15.14).

Parallel pins are primarily used for the fixed (tolerance grade m6) or loose (tolerance grade h8 or h11) connection of components. The holes in the components to be connected must be reamed to the required size limit according to the requirements, which results in high production costs.

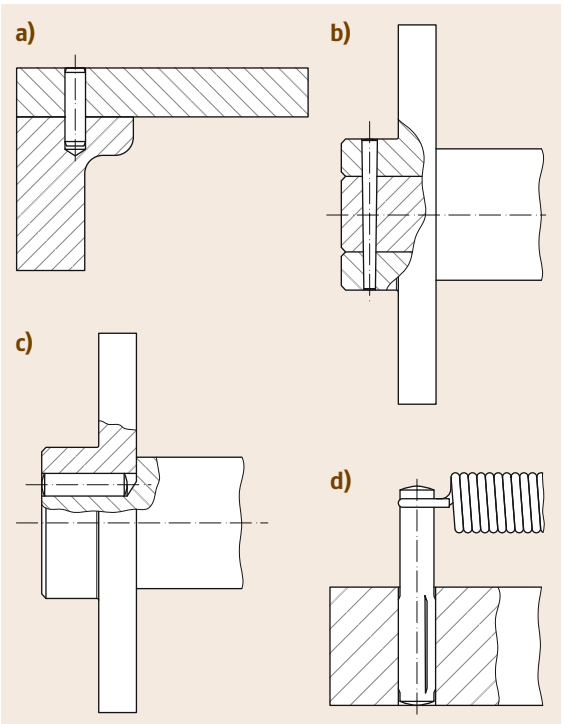

Fig. 15.13a–d Pinned joints (examples): **(a)** position fixing using parallel pins, **(b)** transverse pin jointing using tapered pin, **(c)** longitudinal pin with cylindrical grooved pin, and **(d)** cylindrical grooved pins (with neck) as pins

Tapered pins are used in a similar way to parallel pins. Due to the tapered hole (expensive) the contact surfaces only briefly rub together on removing the pin, which results in low wear. Above all, they are suitable for precise positioning of components/devices that must be frequently undone or detached.

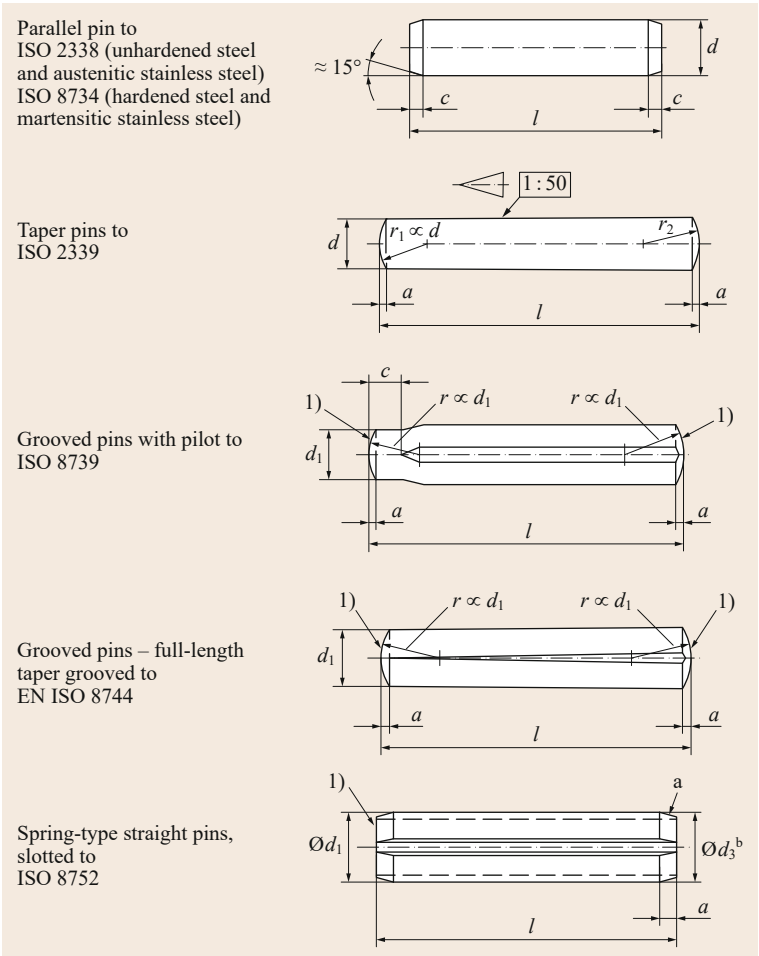

Fig. 15.14 Standardized pin types (selection) (after [15.18–22])

Grooved pins have several swaged grooves on their circumference with a raised portion on the side of each groove; these raised portions are deformed when knocked into the hole and produce a tight, interference fit on the hole. Due to the raised portions, tight hole tolerances are not necessary.

Axially slotted spring-type straight pins are an alternative to grooved pins. They are made of spring steel and have a large oversize (interference) of 0.2–0.5 mm. Due to their directional transverse load elasticity compared to parallel, tapered, and grooved pins, they tend to displace the pinned parts.

As a result of the applied forces and moments, pins are subjected to surface pressure and shear; shear pins are also subjected to bending (Fig. 15.15).

Transverse Pinned Joints. Transverse pin joints, which are for transferring a nominal torque T_{nom}, as in a lever hub (Fig. 15.15a), must be checked for surface pressure and shearing in the case of larger forces.

With the symbols from Fig. 15.15 and the application and service factor K_A according to Table 15.5:

- The mean surface pressure p_N in the hub is

$$p_N = K_A \frac{F_{\text{nom}}}{ds} = K_A \frac{T_{\text{nom}}}{ds(d_W + s)} \leq p_{\text{all}} , \quad (15.13)$$

where:
d pin diameter
D external diameter of the hub
d_W shaft diameter
s pin width in the hub; $s = D - d_w/2$

- The maximum value of the mean surface pressure p_W in the shaft is

$$p_W = 4K_A \frac{F_{W\,\text{nom}}}{dd_w} = 2K_A \frac{3T_{\text{nom}}}{2d_W dd_W/2}$$
$$= K_A \frac{6T_{\text{nom}}}{dd_W^2} \leq p_{\text{all}} . \quad (15.14)$$

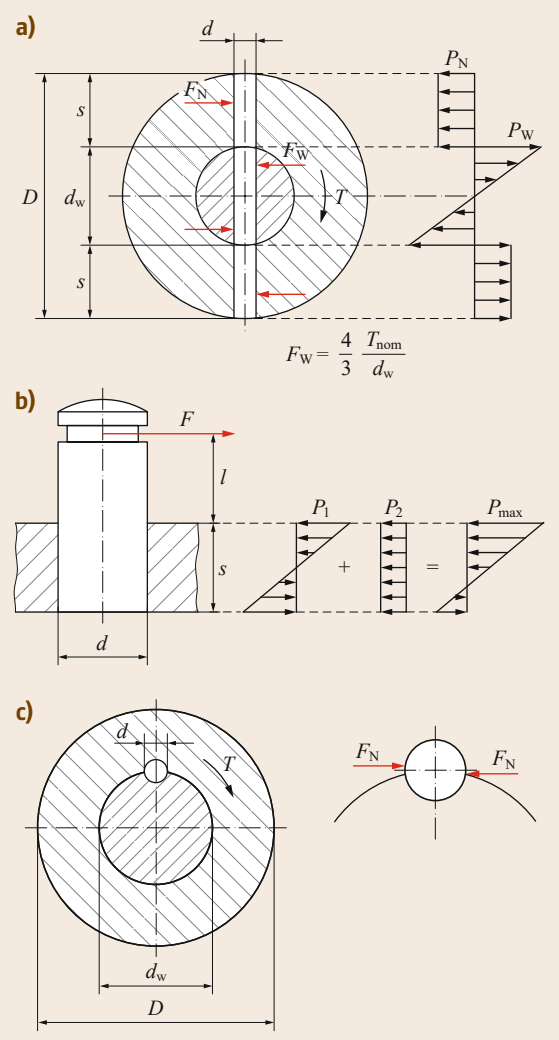

Fig. 15.15a–c Forces on pinned joints: **(a)** transverse pin, **(b)** push-fit pin, and **(c)** longitudinal pin

- For the mean shear stress τ_S in the pin

$$\tau_S = K_A \frac{F_{W\,nom}}{A_S} = K_A \frac{4T_{nom}}{d_W \pi d^2} \le \tau_{s\,all}\,, \qquad (15.15)$$

where:

p_{all} see Table 15.10 (multiply values by 0.7 for slotted straight pins)

$\tau_{s\,all}$ see Table 15.10 (multiply values by 0.8 for slotted straight pins)

From experience, for the design a pin diameter $d = (0.2–0.3)d_W$ and hub wall thicknesses $s = (0.25–0.5)d_W$ are chosen for steel hubs and $s = 0.75d_W$ for gray cast iron hubs.

Longitudinal Pinned Joints. Under the force F_N on the longitudinal pin (also round key) (Fig. 15.15c), the mean surface pressure p is twice the magnitude of the shear stress τ_s.

Therefore, it is not necessary to calculate the shear stress in solid pins. The relevant mean surface pressure in both parts (shaft and hub) is calculated from

$$p = K_A \frac{F_{nom}}{A} = K_A \frac{4T_{nom}}{d_W dl} \le p_{all}\,, \qquad (15.16)$$

where Table 15.10 lists p_{all} values (multiply values by 0.7 for slotted straight pins.)

From experience, pin diameters $d = (0.15–0.2)d_W$ and load-bearing pin lengths $l = (1–1.5)d_W$ are chosen.

In the case of large torques, several pins can be arranged on the circumference.

Clevis Pin Joints. Clevis pins (Fig. 15.15b) must be calculated for bending and for surface pressure. The transverse force (shear) can be ignored.

The bending stress σ_b must be verified with bending moment $M_b = Fl$:

$$\sigma_b = K_A \frac{M_b}{W_b} \approx K_A \frac{M_b}{0.1d^3} \le \sigma_{b\,all}\,, \qquad (15.17)$$

where:

$\sigma_{b\,all}$ see Table 15.10 (multiply values by 0.7 for slotted straight pins)

W_b see Table 15.1

The surface pressure is made up of the component changeable along the hole $p_1 = F(l + s/2)/(ds^2/6)$ (corresponds to $p_1 = M_b/W_b$, where $M_b = F(l + s/2)$ and $W_b = d^2/6$ due to the bending stress profile as in a slab or plate) resulting from the overturning effect on the pin and the component constant along the hole $p_2 = F/(ds)$ resulting from the shearing effect of F.

The maximum mean surface pressure is then

$$p_{max} = p_1 + p_2 = K_A \frac{F_{nom}}{ds^2}(6l + 4s) \le p_{all}\,, \qquad (15.18)$$

where Table 15.10 lists p_{all} values (multiply values by 0.7 for slotted straight pins).

Bolted Joints

Bolts are used to make preferably free-to-rotate joints (Fig. 15.16).

Taking into account their type of use, bolted joints are adapted according to the required fit tolerances and properties of the mating material. Thus, diameter

Table 15.10 Guide values for allowable stresses for bolted and pinned joints under approximately static load [15.23, 24]

Material	Type of bolt, pin, component	Allowable stress (N/mm²)			
		p_{all}	$\sigma_{b\,all}$	$\tau_{s\,all}$ Static	Sliding
S235JR...E295	Tapers, parallel pins, bolts, shafts	160	140	90	15
E335; E360	Bolts, grooved pins, shafts	240	200	140	
Cast steel	Hubs	120	–	–	8
Cast iron	Hubs	90	–	–	5

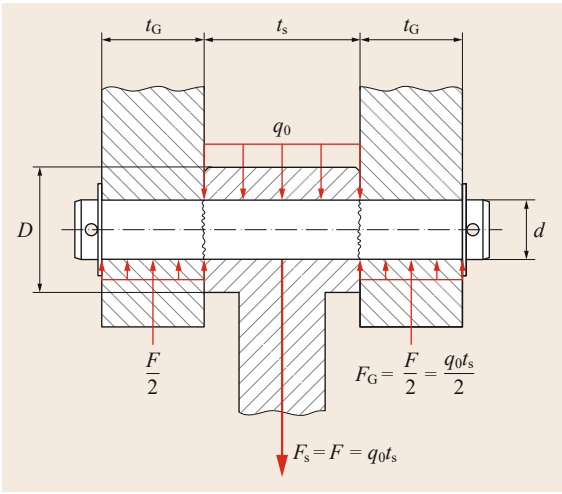

Fig. 15.16 Basic design and loading of a bolted joint with related dimensions

tolerances h11 or h8 with appropriate choice of hole tolerance enable clearance or interference fit for different use cases. Movable bolted joints are subjected to wear at the contact points that slide on each other. This can be reduced by lubrication, suitable selection of the material combination or by using bearing bushes. The force transfer within the bolted joints loads the fasteners with bending, shear, and surface pressure, whereby in general for joints at rest, the bending load is decisive and for moving joints the surface pressure is decisive. Standard bolt forms for different applications are shown in Fig. 15.17.

Depending on the type of fit between the bolt and bar or between the bolt and fork, three different installation cases are possible, which lead to different types of bending moment profiles and thus to different stresses in the bolt. The possible installation cases and equations required for the calculation are shown in Table 15.11.

Guide values for the allowable stresses are shown in Table 15.10.

If sliding movement occurs in the bolted joint, this must be taken into account in the material selection. If necessary, the sliding surfaces must be lubricated and a significantly lower allowable surface pressure must be used.

In highly loaded hinged joints, in addition to the bolt and bar cross section, the strength of the cross sections at the bar head and the fork most at risk must also be checked.

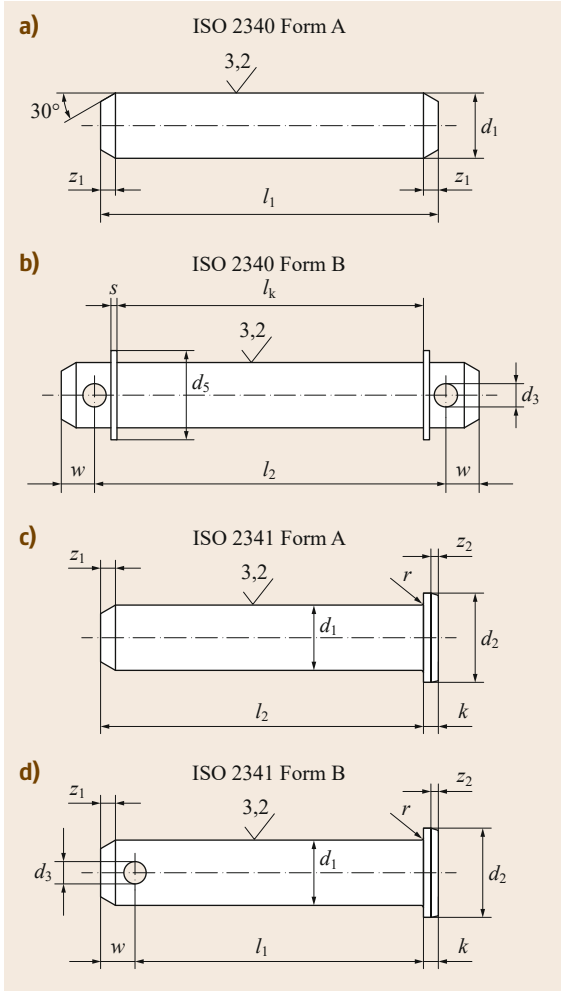

Fig. 15.17a–d Bolt forms: **(a)** without head, **(b)** without head with split pin holes and washers, **(c)** with head, and **(d)** with head and split pin hole (after [15.25, 26])

Table 15.11 Possible installation cases with the corresponding calculation equations

	Installation case 1	Installation case 2	Installation case 3
Fork fit	Clearance fit	Interference fit	Clearance fit
Rod fit	Clearance fit	Clearance fit	Interference fit
Moment profiles (bending moment diagrams)	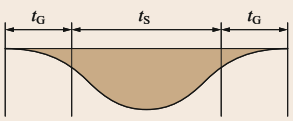	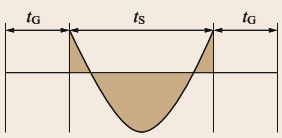	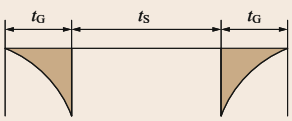
Maximum bending stress	$\sigma_{b\,max} = \frac{8F(t_G + t_S)}{\pi d^3}$	$\sigma_{b\,max} = \frac{8Ft_S}{3\pi d^3}$	$\sigma_{b\,max} = \frac{8Ft_G}{\pi d^3}$
Shear stress	$\tau_S = \frac{2F}{\pi d^2}$		
Fork surface pressure	$p = \frac{F}{2dt_S}$		
Rod surface pressure	$p = \frac{F}{dt_G}$		

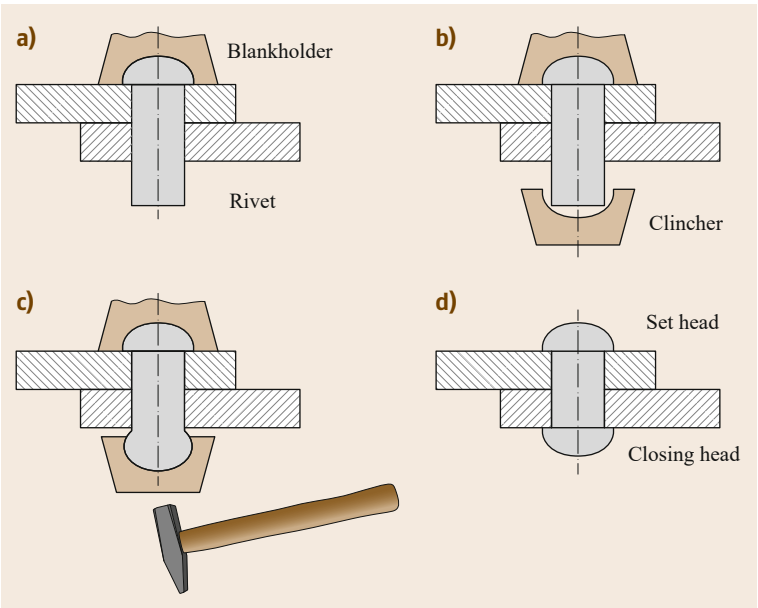

Fig. 15.18a–d Classic riveting. **(a)** Position of the rivet and blankholder, **(b)** position of the clincher, **(c)** plastic forming of the head, **(d)** finished riveted joint

Other Form-Closure Joints

Riveted Joints. Rivets are primarily used to join two or more overlapping components. Unlike welding procedures, dissimilar materials can be joined when cold, so that effects such as distortion, hardening, or (micro) structural changes are avoided. To make the classic rivet joint, a rivet is placed in an existing hole or hole to be made (exception: punch riveting with a semitubular rivet), fixed and is then plastically deformed from the opposite side, so that a rivet head forms (Fig. 15.18). Here a differentiation is made between hot and cold riveting.

Hot riveting is primarily used for steel rivets with diameters of 10 mm and larger. The rivet, inserted when heated (approximately 1000 °C), contracts due to cooling, resulting in the overlapping components being pressed together (force-closure joint).

With cold riveting, the radial widening of the rivet forms a primarily form-closure joint.

If the rear of the joint is not accessible, blind rivets (pop rivets) can be used (Fig. 15.19). These are an economically favorable solution for many fastening tasks. Compared to conventional riveted joints, they can be made by one person.

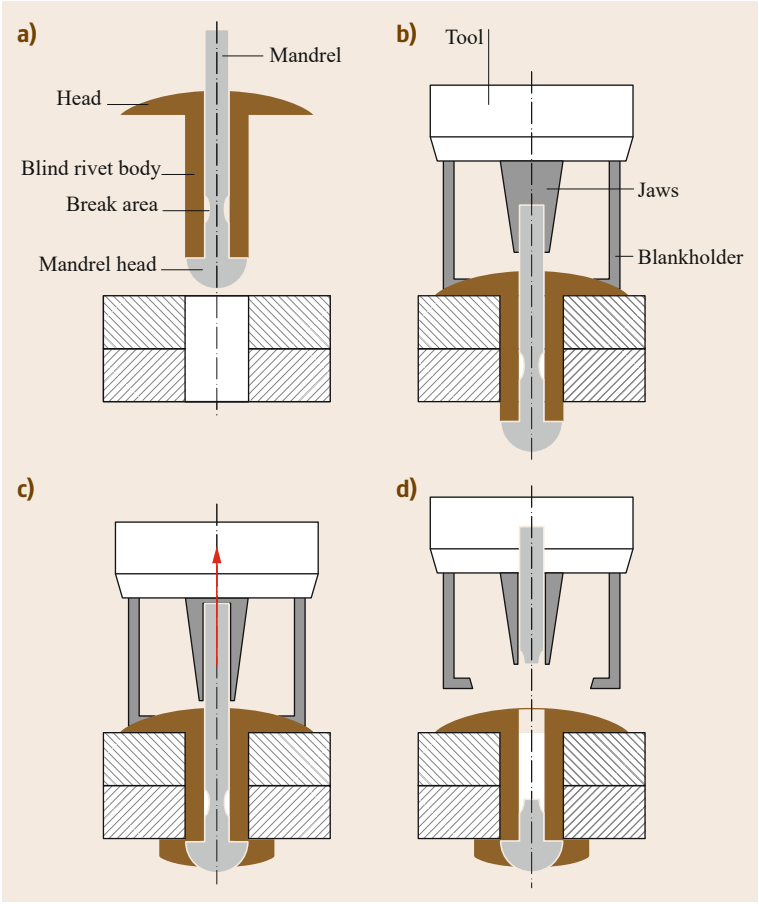

Fig. 15.19a–d Blind riveting process

With punch riveting, unlike the classic riveting process, making the hole before the actual riveting is omitted. With self-piercing riveting with solid rivets, the actual rivet simultaneously functions as a cutting punch and perforates the parts to be joined. The bottom sheet is then pressed by an appropriately shaped die into an all-round groove of the rivet (plastically deformed), which results in a form-closure joint (Fig. 15.20a). With self-piercing riveting with semitubular rivets, the rivet also acts as a cutting punch; however, it does not completely penetrate the components to be jointed, and as a result a gas- and liquid-tight joint is formed (Fig. 15.20b).

Riveted joints are generally not nondestructively separable. They can only be undone by removing the rivet (or rather drilling out or cutting off the rivet head).

Other standard riveting processes are listed in Table 15.12.

The advantages and disadvantages of riveting methods are shown in Table 15.13.

Reference is made to the relevant literature for the calculation of riveted joints (design and strength verification), for example [15.2, 24].

Form-Closure Retaining Elements. Form-closure retaining elements, for example, retaining rings, cotter pins (split pins), setting rings, and axle holders (axle stays) are frequently used for axial fixing and locating (keeping in position) shafts and bearings.

Figure 15.21 shows different retaining rings for various application cases for installation in corresponding annular grooves in round bodies (e.g., axles, shafts, bolts, and pins) or in holes.

When axial forces act on retaining rings they cause surface pressure on the load-bearing shoulders between the ring and groove, which must not exceed allowable values. In cases of doubt, these should be checked by calculation.

Axially mounted retaining rings according to DIN 471 [15.29] for metric round bodies (Fig. 15.21a) and according to DIN 472 [15.30] for metric bores (Fig. 15.21b) are most frequently used. Retaining rings for inch-measure round bodies and holes are also available. The dimensions for the retaining rings and corresponding groove are given in the manufacturers' catalogs.

Table 15.12 Riveting processes according to DIN 8593-5 [15.27]

Process	Figure	Description
Riveting	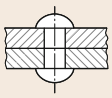	Setting (squeezing) a bolt-shaped rivet
Semitubular riveting	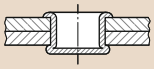	Turning over of protruding parts of a hollow rivet (bifurcated rivets)
Peg riveting	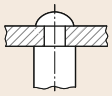	Setting a peg-shaped end on one of the two parts to be joined
Tubular peg riveting	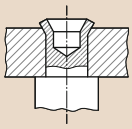	Turning over of protruding parts of the tubular peg-shaped end on one of the two parts to be joined
Intermediate peg riveting	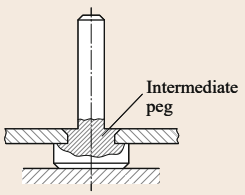	Setting an intermediate peg on one of the two parts to be joined

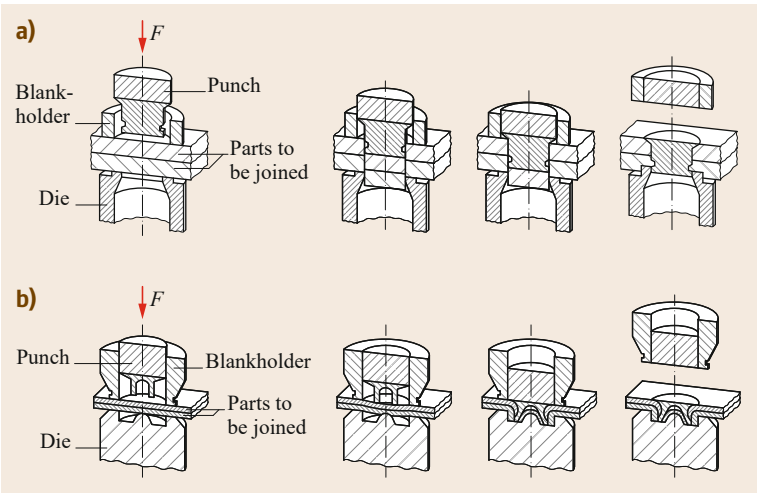

Fig. 15.20a,b Punch (self-piercing) rivets: **(a)** solid rivet process and **(b)** semitubular rivet process (after [15.27])

If the load-bearing surfaces are too small due to large chamfers or rounding on the annular grooves, or if axial clearances have to be levelled out, additional shim washers or supporting rings according to DIN 988 [15.31] are used in conjunction with the retaining rings according to DIN 471 and DIN 472 (Fig. 15.21c).

The locating surfaces can also be enlarged using rings according to DIN 983 [15.32] and DIN 984 [15.33] (Fig. 15.21d,e).

Radial mountable retaining washers according to DIN 6799 [15.34] (Fig. 15.21f) (E-clips) are used for small shaft diameters. They surround the groove bottom, are radially resilient with segments, and form a relatively high shoulder.

Round wire snap rings according to DIN 9925 [15.35] and DIN 9926 [15.36] (Fig. 15.21g) (external snap rings) for bores and shafts are used for axial position fixing for secondary purposes with small axial forces. They are often difficult to remove from holes.

Table 15.13 Advantages and disadvantages of rivet joints

Advantages	Disadvantages
Unlike materials can be joined together	Butt joints not possible
No distortion of the components	Components are weakened by rivet holes
No material change (hardening, transformations), unlike welding	No smooth walls due to necessary overlapping (lap joints) or cover plates
On construction sites, frequently more cost effective than other joints	Unfavorable force flow
They do not fail suddenly, because they can absorb high deformation energy	More cost intensive than welded joints
Easier to check (visual inspection, impact control)	

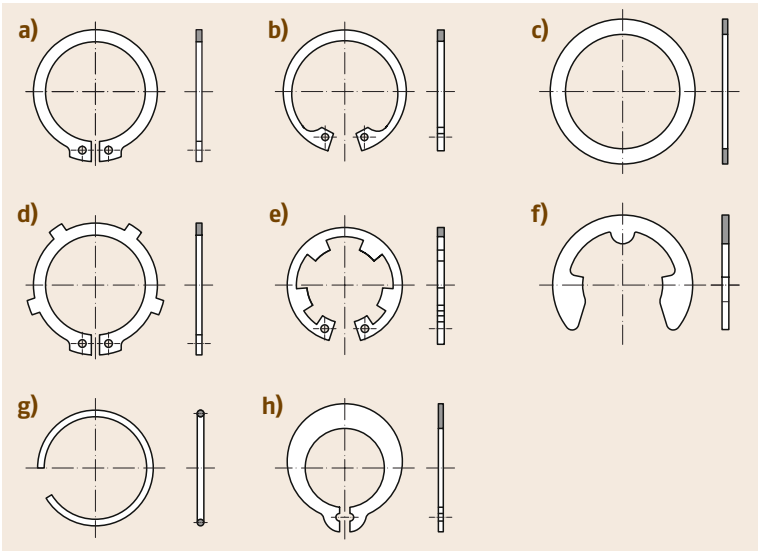

Fig. 15.21a–h Types of retaining rings (selection). **(a)** Circlips for axles or shafts, **(b)** circlips for bores, **(c)** shim washer, **(d)** circlips for axles or shafts with enlarged locating surface, **(e)** circlips for bores with enlarged locating surface, **(f)** E-clips, **(g)** round wire snap ring, and **(h)** grip rings

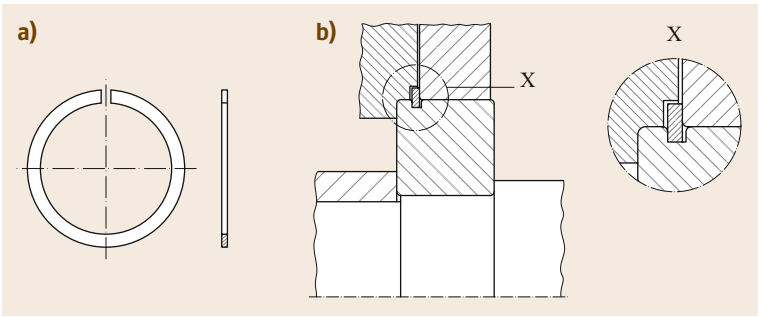

Fig. 15.22a,b Snap ring: **(a)** according to DIN 5417 and **(b)** installation example (after [15.28])

Self-locking grip rings for shafts without a groove (Fig. 15.21h) have a force-closure effect. They can be used to adjust axial clearances under small axial forces.

Snap rings for rolling bearings according to DIN 5417 [15.28] (Fig. 15.22) can be used to fasten radial bearings with an annular groove according to DIN 616 [15.37].

Laminar rings (Fig. 15.23) are an alternative to retaining rings according to DIN 471 and DIN 472. They can be mounted without special pliers and require less installation space due to their lack of eyes.

The fact that in many cases, depending on the existing requirements, the use of retaining rings can achieve substantial design simplifications and thus save costs, is shown by the rolling bearing design in Fig. 15.24. Figure 15.24b requires fewer parts, less production work (smooth continuous housing hole, no thread), and is also more compact.

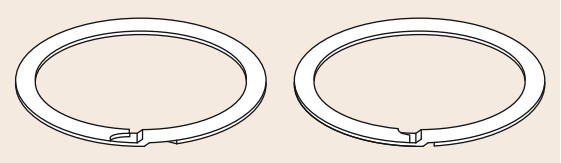

Fig. 15.23 Spiral rings for holes (*left*) and shafts (*right*)

Split pins (Fig. 15.25a) are mainly used for loose, articulated pin joints and for bolted joints (castellated nuts). In general, they may only be used once and cannot be used for force transfer.

Spring cotters are used for bolted joints, which have to be undone often. Spring cotters are frequently captively connected to the assembly to be secured, for example, by a chain (Fig. 15.25b).

15.2.3 Force-Closure Joints

Force-closure joints transfer forces from one component to another by friction between the components.

Modes of Action

The contact forces necessary in a force-closure joint can be generated by special clamping elements (e.g., screws, wedges, and clamping collars) or as contact forces, which arise between the components due to jointing with interference fit.

If additional clamping elements are used, the contact forces are produced by tensioning these elements with the components to be joined.

Threaded Fasteners

Screws and bolts are the elements used most to connect components. They are all standardized and can be nondestructively undone and reused.

Apart from fastening and connecting, screws and bolts are also used to set and adjust, to measure, to tension, and as leadscrews for translating rotational movements into longitudinal movements.

The advantages of bolted assemblies are shown in Table 15.14.

Mode of Action, Variants, and Descriptive Sizes. The screw or bolt thread can be thought of as being a cylinder with a helix-shaped notch. The notch usually runs rising clockwise (Fig. 15.26). The mating thread (nut or threaded hole) corresponds to the negative image of the screw or bolt thread.

The thread pitch P is the relative axial displacement between the screw (external thread) and nut (internal thread) in one screw turn. The pitch angle φ follows from the thread pitch P and the (mean) pitch diameter d_2 and is calculated as

$$\tan\phi = \frac{P}{\pi d_2}\,; \quad \phi = \arctan\frac{P}{\pi d_2}\,. \tag{15.19}$$

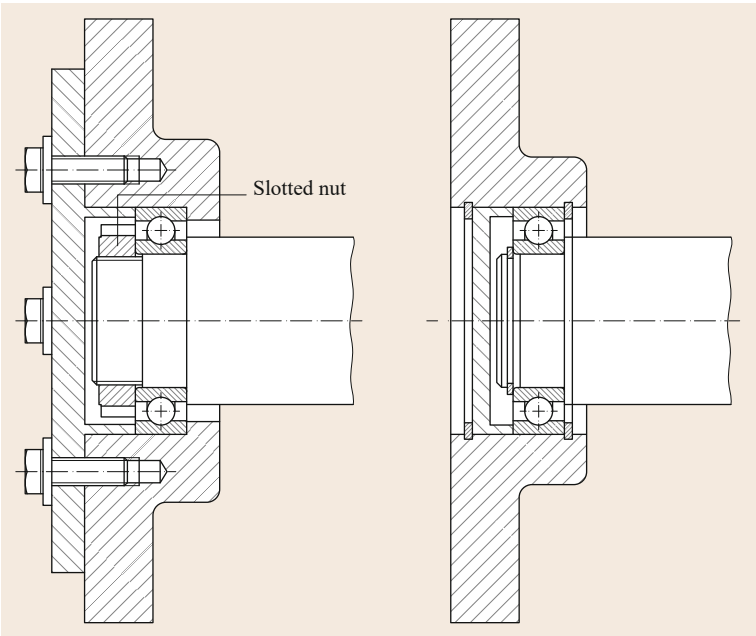

Fig. 15.24 Installation options for a rolling bearing as fixed bearing

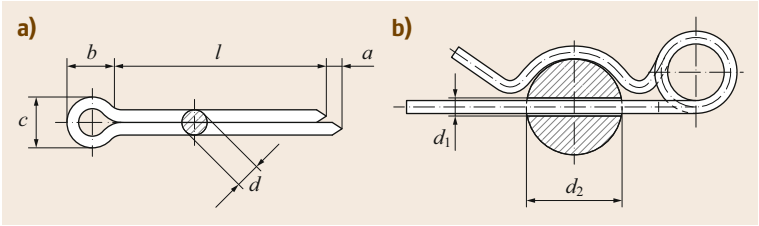

Fig. 15.25a,b Split pins according to ISO 1234 [15.38] **(a)** and spring cotters according to DIN 11024 [15.39] **(b)** in their mounted condition

Table 15.14 Advantages and disadvantages of screwed joints

Advantages	Disadvantages
Easy assembly and dismantling	Necessary holes disturb force path
Can be nondestructively undone	High costs compared to riveted, adhesive bonding and welded joints
Generally reusable	Susceptible to crevice corrosion
Different materials can be joined	
Good temperature resistance	

Depending on the intended use and underlying standard, the dimensions vary in detail within the thread form, so that in general there is no exchangeability between the individual thread types. Table 15.15 shows standard international thread forms with their corresponding designation.

Coarse thread (for example metric ISO thread according to DIN 13-1 or UNC thread to ANSI B1.1) is used for fixing screws and bolts (and corresponding nuts) of all kinds.

The fine pitch thread (for example according to DIN 13-2, DIN 13-11, or UNF according to ANSI B1.1) is used for large dimensions, loads, and stresses, in thin-walled parts and for micrometers and adjustment screws.

Trapezoidal thread (for example according to DIN 103 or ANSI B1.5) is preferably used as a translation or power transmission thread on spindles, for example, in machine tools, presses, valves, and vices.

Buttress threads (for example, according to DIN 513 or ANSI B1.9) have a higher load capability compared to the trapezoidal thread due to the larger rounded thread roots and due to the larger thread engagement depth and their radial *jump-out effect* in the nut thread remains lower than in other thread forms. Buttress threads are used as single or multistart translation or power transmission threads for high one-sided loads, for example, in jackscrews and pressing spindles.

Round threads (for example, according to DIN 405) display almost no notch effect, however have only a small thread engagement depth. Due to their large root and thread clearance they are suitable as translation or power transmission threads in severe soiling conditions, for example, as coupling rods in railway carriage couplings.

In addition to the above-mentioned thread forms or thread types, there are other variants for special applications, some of which are standardized.

The thread and screw/bolt dimensions required for the calculation of threaded fasteners (fixing screws and bolts) are shown for metric ISO thread (coarse thread) in Table 15.16 and for inch-measure UNC threads in Table 15.17. Reference is made to relevant books of tables and standards for other thread forms.

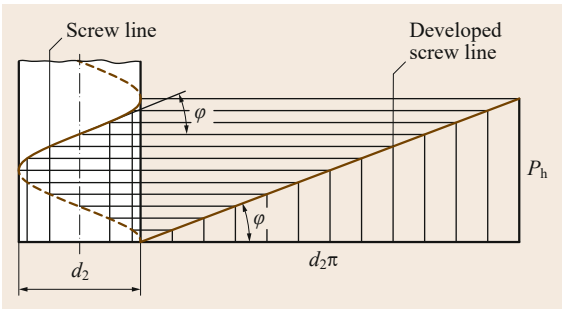

Fig. 15.26 Creation of the screw line

Calculation of Bolted Joints. The calculation method presented in the following for fixing screws and bolts is mainly based on the VDI Guideline 2230 *Systematic calculation of highly stressed bolted joints–Joints with one cylindrical bolt* [15.40, 41].

Bolted joints are generally loaded by:

- Transverse forces F_Q at right angles to the bolt axis (Fig. 15.28) and/or
- By tensile forces (bolt loads or forces) F_S along the bolt axis,

whereby the joint must be designed so that bending moments and shear forces in the bolt or screw are avoided as much as possible and it is loaded under tension only.

Table 15.15 Overview of the most common types of thread

Shape	Use	Designation	Abbreviation	Standard		Abbreviation
V-thread						
Metric ISO thread						
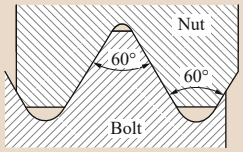	General	Coarse thread (single and multiple start)	M	ISO 1502	DIN 14 0.3–0.9 mm DIN 13 1–68 mm	M 0.8 M 12
	General (fine pitch thread)	Fine pitch thread			DIN 13 1000 mm	M 12 × 1.5
Unified screw thread						
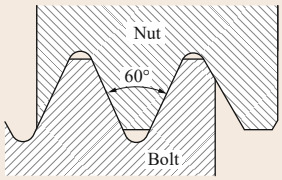	General	Unified coarse thread (coarse thread)	UNC	ANSI B 1.1		1/4-20 UNC
		Unified fine thread	UNF			1/4-28 UNF
	Precision engineering	Unified extrafine thread	UNEF			1/4-32 UNEF
Pipe thread						
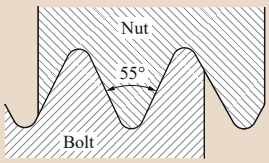	Pipes and pipe joints (nonsealing in the thread)	Cylindrical pipe thread (internal and external)	G	EN ISO 228-1 1/8–6 in		G 1 1/2
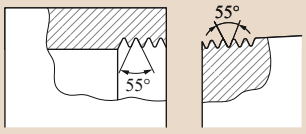	Metal-to-metal sealing thread for threaded pipes and fittings	Internal cylindrical pipe thread	Rp	EN 10226-1 1/16–6 in		Rp 3/4
		Taper external thread (taper ratio 1/16)	R			R 3/4
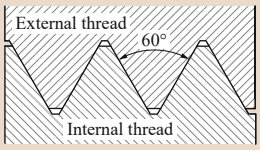	For mechanical joints, pipes without internal pressure, hose connections	Cylindrical pipe thread	NPSM/ NPSL/ NPSH	ANSI B1.20.1 1/8–6 in		1/2-14 NPSM
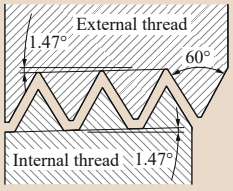	Sealing pipe joints for threaded pipes and flanges	National American standard taper pipe thread, sealed with sealant (taper ratio 1/16)	NPT	ANSI B1.20.1		3/4 in 18 NPT
		National pipe tapered fuel, dry sealing (taper ratio 1/16)	NPTF			1/2 in 14 NPTF dryseal
Trapezoidal thread						
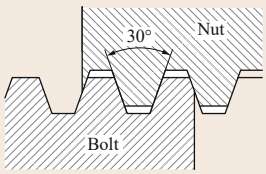	General (translational thread)	Metric ISO trapezoidal thread	Tr	ISO 2901	DIN 103 8–300 mm	Tr 40 × 7
	Filler necks/nozzles and adapters	American trapezoidal thread	ACME	ANSI B1.5		1 3/4 in 4 ACME

Table 15.15 (Continued)

Shape	Use	Designation	Abbreviation	Standard	Abbreviation
Buttress thread					
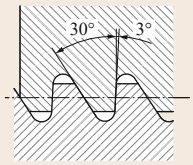	For withstanding forces acting in one direction	Metric buttress thread	S	DIN 513 10–640 mm	S 48 × 8
Round thread					
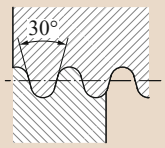	General (round thread)	Cylindrical round thread (single and multiple start)	Rd	DIN 405 8–200 mm	Rd 40 × 4
Steel conduit thread (Panzer Gewinde)					
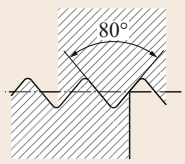	Electrical engineering	Steel conduit thread (Steel Panzer Gewinde)	Pg	DIN 40430 7–48 mm	Pg 21
Others					
	Tapping screws	Tapping screw thread	ST	EN ISO 1478 1.5–9.5 mm	2.9
	Wood screws	Wood screw thread	–	DIN 7998 1.6–20 mm	3.5

Table 15.16 Metric ISO thread (coarse thread) according to DIN 13-1 (selection). Dimensions as defined in Fig. 15.27

Thread designation	Nominal diameter $d = D$ (mm)	Pitch P (mm)	Core diameter d_3 (mm)	D_1 (mm)	Pitch diameter $d_2 = D_2$ (mm)	Pitch angle φ (°)
M 1	1	0.25	0.693	0.729	0.838	5.43
M 1.2	1.2	0.25	0.893	0.929	1.038	4.38
M 1.6	1.6	0.35	1.170	1.221	1.373	4.64
M 2	2	0.4	1.569	1.567	1.740	4.19
M 2.5	2.5	0.45	1.948	2.013	2.208	3.71
M 3	3	0.5	2.387	2.459	2.675	3.41
M 4	4	0.7	3.141	3.242	3.545	3.60
M 5	5	0.8	4.019	4.134	4.480	3.25
M 6	6	1	4.773	4.917	5.350	3.41
M 8	8	1.25	6.446	6.647	7.188	3.17
M 10	10	1.5	8.160	8.376	9.026	3.03
M 12	12	1.75	9.853	10.106	10.863	2.94
M 16	16	2	13.546	13.835	14.701	2.48
M 20	20	2.5	16.933	17.294	18.376	2.48
M 24	24	3	20.319	20.752	22.051	2.48
M 30	30	3.5	25.706	26.211	27.727	2.30
M 36	36	4	31.093	31.670	33.407	2.19
M 42	42	4.5	36.477	37.129	39.077	2.10
M 48	48	5	41.866	42.387	44.752	2.04
M 56	56	5.5	49.252	50.046	52.428	1.91
M 64	64	6	56.639	57.505	60.103	1.82

Table 15.17 Unified national coarse (UNC) thread to ANSI B1.1 (inch measure) (selection). Dimensions as defined in Fig. 15.27

Thread designation	Nominal diameter $d = D$		Pitch P	Core diameter d_3	D_1	Pitch diameter $d_2 = D_2$	Threads per inch
	(mm)	(in)	(mm)	(mm)	(mm)	(mm)	
N 1 - 64 UNC	1.854	–	0.397	1.50	1.58	1.61	64
N 2 - 56 UNC	2.184	–	0.453	1.78	1.87	1.91	56
N 3 - 48 UNC	2.515	–	0.529	2.05	2.14	2.19	48
N 4 - 40 UNC	2.845	–	0.653	2.27	2.38	2.44	40
N 5 - 40 UNC	3.175	–	0.653	2.59	2.70	2.77	40
N 6 - 32 UNC	3.505	–	0.794	2.77	2.90	3.02	32
N 8 - 32 UNC	4.166	–	0.794	3.42	3.53	3.68	32
N 10 - 24 UNC	4.826	–	1.058	3.82	3.95	4.18	24
N 12 - 24 UNC	5.486	–	1.058	4.47	4.59	4.84	24
1/4 - 20 UNC	6.350	1/4	1.270	5.11	5.25	5.57	20
5/16 - 18 UNC	7.938	5/16	1.411	6.55	6.68	7.07	18
3/8 - 16 UNC	9.525	3/8	1.587	7.95	8.08	8.55	16
7/16 - 14 UNC	11.112	7/16	1.814	9.30	9.44	10.00	14
1/2 - 13 UNC	12.700	1/2	1.954	10.73	10.88	11.50	13
9/16 - 12 UNC	14.288	9/16	2.117	12.15	12.30	12.99	12
5/8 - 11 UNC	15.875	5/8	2.309	13.53	13.69	14.46	11
3/4 - 10 UNC	19.050	3/4	2.540	16.46	16.62	17.49	10
7/8 - 9 UNC	22.225	7/8	2.822	19.34	19.52	20.49	9
1 - 8 UNC	25.400	1	3.175	22.15	22.34	23.45	8
1 1/8 - 7 UNC	28.575	1 1/8	3.628	24.87	25.08	26.35	7
1 1/4 - 7 UNC	31.750	1 1/4	3.628	28.04	28.26	29.52	7
1 3/8 - 6 UNC	34.925	1 3/8	4.233	30.60	30.85	32.33	6
1 1/2 - 6 UNC	38.100	1 1/2	4.233	33.70	34.03	35.50	6
1 3/4 - 5 UNC	44.450	1 3/4	5.080	39.26	39.56	41.33	5
2 - 4 1/2 UNC	50.800	2	5.644	45.03	45.37	47.34	5
2 1/4 - 4 1/2 UNC	57.150	2 1/4	5.644	51.38	51.72	53.69	5
2 1/2 - 4 UNC	63.500	2 1/2	6.350	57.00	57.39	59.60	4
2 3/4 - 4 UNC	69.850	2 3/4	6.350	63.36	63.74	65.95	4
3 - 4 UNC	76.200	3	6.350	69.71	70.09	72.30	4
3 1/4 - 4 UNC	82.550	3 1/4	6.350	76.06	76.44	78.65	4
3 1/2 - 4 UNC	88.900	3 1/2	6.350	82.41	82.79	85.00	4
3 3/4 - 4 UNC	95.250	3 3/4	6.350	88.76	89.14	91.35	4
4 - 4 UNC	101.600	4	6.350	95.11	95.48	97.70	4

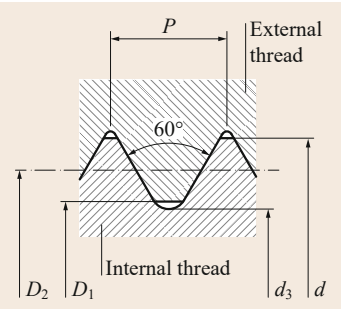

Fig. 15.27 Thread sizes

This does not include preloaded fit bolts, which are calculated like bolts for shear and surface pressure (hole friction).

If transverse forces F_Q occur, the bolts must be preloaded so that the friction force $F_R > F_Q$ necessary for the required force closure is generated, i.e.,

$$F_R = F_{V\,min}\,\mu n i_R \geq F_Q S_H \quad \text{or}$$

$$F_{V\,min} \geq \frac{F_Q S_H}{\mu n i_R}\,, \tag{15.20}$$

where:

F_Q transverse force on the bolted joint
$F_{V\,min}$ minimum preload in the bolt
μ coefficient of friction in the interface (separating joint) between the components to be connected (e.g., $\mu = 0.1$–0.15 for dry steel–steel pairings)

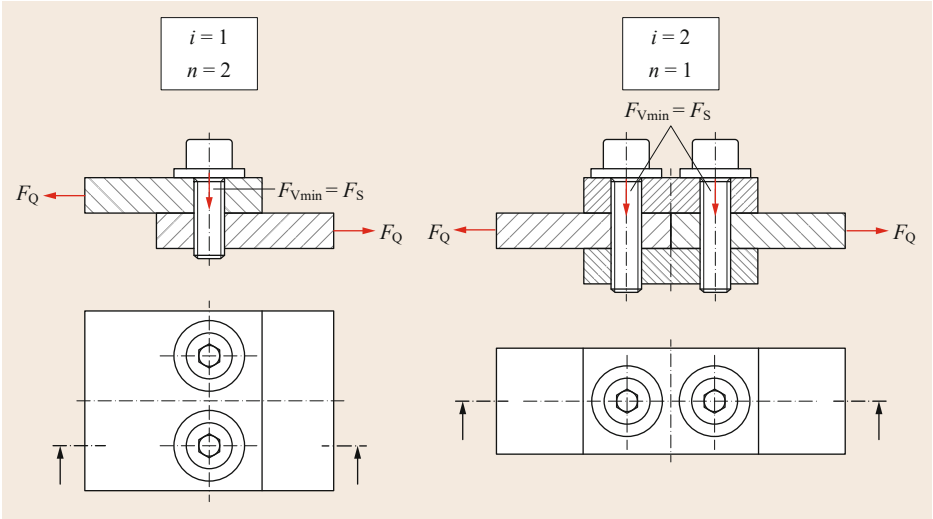

Fig. 15.28 Diagram showing the relevant number of bolts n and the friction pairings i_R in transversely loaded bolted joints

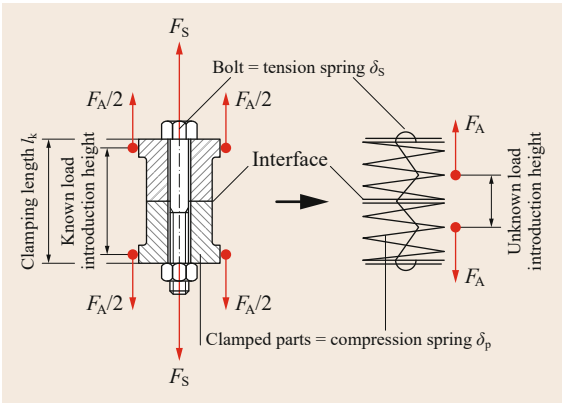

Fig. 15.29 Centrically clamped bolted joint and corresponding spring model according to VDI 2230 (after [15.40])

n relevant number of bolts in the joint (Fig. 15.28)
i_R number of effective friction couples (friction pairing) (Fig. 15.28)
S_H adhesion safety factor: $S_H \approx 1.3$ under static and $S_H \approx 1.5$ under dynamic loading

Due to the elasticity of the bolt and the clamped parts, the bolted joint behaves like springs connected in parallel (Fig. 15.29), where the bolt acts as a tensile spring and the clamped parts act as compression springs.

The elongation of the bolt f_S is more or less proportional to the acting force F_S and can be calculated using (15.21):

$$f_S = c_S F_S = \frac{1}{\delta_S} F_S \,, \tag{15.21}$$

where c_S is the spring stiffness of the bolt and δ_S is the resilience of the bolt.

The compression of the clamped parts f_P is calculated from

$$f_P = c_P F_P = \frac{1}{\delta_P} F_P \,, \tag{15.22}$$

where c_P is the clamped length and δ_P is the modulus of elasticity of the clamped parts.

According to (15.23), the total resilience δ_S of the bolt is made up of the resiliences of the partial areas:

$$\delta_S = \delta_{SK} + \delta_{Gew} + \delta_{GM} + \sum_1^n \delta_i \,, \tag{15.23}$$

where:

δ_{SK} resilience of the bolt head
δ_{Gew} resilience of the exposed (protruding) thread
δ_{GM} resilience of the screwed-in thread
δ_i resilience of the cylindrical shank section i

The resilience of the bolt head of hexagon and hexagon socket head bolts can be calculated using

$$\delta_{SK} = \frac{4 l_{SK}}{E_S \pi d} \,. \tag{15.24}$$

where:

l_{SK} height of the bolt head (Fig. 15.30); for hexagon head bolts $l_{SK} = 0.5d$ and for hexagon socket head cap screws (bolts), $l_{SK} = 0.4d$

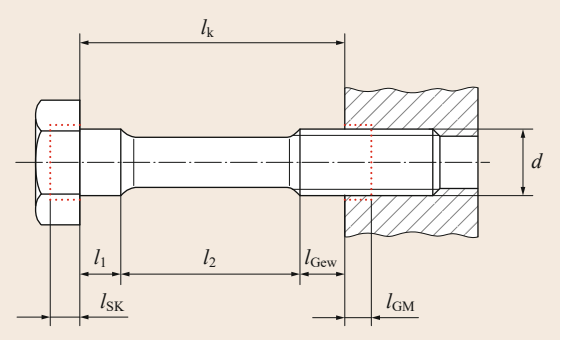

Fig. 15.30 Individual deformation areas of the bolt (after [15.40])

E_S modulus of elasticity of the bolt material
d nominal diameter of the thread (Fig. 15.30)

The resilience of the protruding thread, not screwed in, is calculated from

$$\delta_{Gew} = \frac{4 l_{Gew}}{E_S \pi d_3} , \tag{15.25}$$

where:

l_{Gew} length of the protruding thread (Fig. 15.30)
d_3 core diameter of the thread (Fig. 15.30).

In the area of the screwed-in thread, the total resilience is made up of the resilience of the nut δ_M and of the thread δ_G as given by

$$\delta_{GM} = \delta_G + \delta_M , \tag{15.26}$$

where

$$\delta_G = \frac{4 l_G}{E_S \pi d_3} , \tag{15.27}$$

and

$$\delta_M = \frac{4 l_M}{E_M \pi d} , \tag{15.28}$$

where:

l_G length of thread engagement; as a rule $l_G = 0.5d$
l_M height of the nut; for screw-in thread $l_M = 0.33d$ and for through-bolted joints $l_M = 0.4d$
E_M modulus of elasticity of the nut

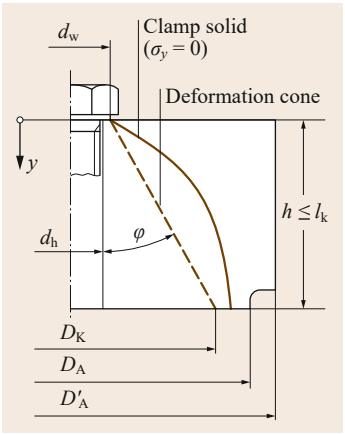

Fig. 15.31 Clamped body and derived deformation cone (after [15.40])

The resiliences of the individual shank areas can be calculated using (15.29):

$$\delta_i = \frac{4 l_i}{E_S \pi d_i} , \tag{15.29}$$

where l_i is the shank length i and d_i is the shank diameter i.

Calculating the resilience of the clamped parts is significantly more difficult due to the more complex stress curve. Below the bolt head, a rotational paraboloid clamped body (solid) forms, at whose boundaries $\sigma_y = 0$ (Fig. 15.31). The spring stiffness or rather the resilience in this area is defined by:

$$\delta_P = \int_{y=0}^{l_K} \frac{dy}{E(y)\, A(y)} . \tag{15.30}$$

In practical calculations, this deformation body is approximated by a deformation cone.

The complete distribution of an equivalent deformation cone in a cylindrical screw-in joint is shown in Fig. 15.32a. If the deformation cone cannot form radially in full due to the limited component width, the cone is replaced by a sleeve in the relevant area (Fig. 15.32b). In the special case in which the bolt head or nut bearing surface is larger than the external diameter of the clamped parts, only a deformation sleeve exists and not a deformation cone.

Complete formation of the deformation cone exists if

$$D_A \ge D_{A,Gr} = d_W + w l_K \tan\varphi , \tag{15.31}$$

where:

D_A external diameter of the clamped parts
$D_{A,Gr}$ limiting diameter of the deformation cone

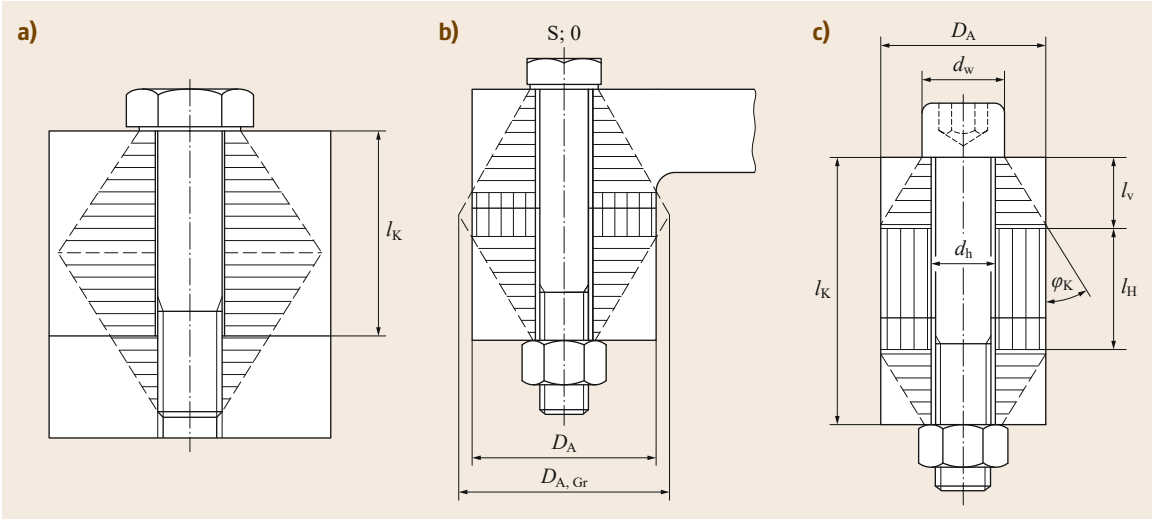

Fig. 15.32a–c Completely formed equivalent deformation cone of a screw-in joint **(a)** and through-bolted joint with deformation cone and sleeve **(b,c)** according to VDI 2230 (after [15.40])

d_w bearing diameter of the bolt head; the nut
w joint coefficient:
$w = 2$ for screw-in joints
$w = 1$ for through-bolted joints
l_K clamped length (Fig. 15.32a)
φ_K cone taper angle of the joint (15.32)

If (15.31) is not fulfilled, a deformation sleeve must be considered in addition to the deformation cone.

The angle of the deformation cone is calculated for screw-in joints as

$$\tan\varphi_{KE} = 0.348 + 0.013\ln\beta_L + 0.193\ln y$$

and for through-bolted joints as

$$\tan\varphi_{KD} = 0.362 + 0.032\ln\left(\frac{\beta_L}{2}\right) + 0.153\ln y\,, \tag{15.32}$$

where: $\beta_L = l_K/d_w$

$$y = \frac{D'_A}{d_w}$$

D'_A equivalent external diameter of the basic solid (Fig. 15.31)

The resilience of the individual deformation cone can be calculated using

$$\delta_P^V = \frac{\ln\left(\frac{(d_w+d_h)(d_w+2l_V\tan\varphi_K-d_h)}{(d_w-d_h)(d_w+2l_V\tan\varphi_K+d_h)}\right)}{E_P d_h \pi\tan\varphi_K}\,, \tag{15.33}$$

where d_h is hole diameter (Fig. 15.31) and the height of the deformation cone is

$$l_V = \frac{D_A - d_w}{2\tan\varphi_K} \le \frac{w l_K}{2}\,. \tag{15.34}$$

The resilience of the sleeve is calculated from

$$\delta_P^H = \frac{4l_H}{E_P\pi\left(D_A^2 - d_h^2\right)}\,, \tag{15.35}$$

where the height of the sleeve is

$$l_H = l_K - \frac{2l_V}{w}\,. \tag{15.36}$$

From these equations, the total resilience is

$$\delta_P = \frac{2}{w}\delta_P^V + \delta_P^H\,. \tag{15.37}$$

If several components with different moduli of elasticity are bolted together, the deformation bodies (cone and sleeve) must be broken down into corresponding partial areas $j; m$ with the same modulus of elasticity and the resilience calculated bit by bit.

In the area of the deformation cone, instead of the bolt head bearing diameter d_w, the end diameter of the adjacent cone $d_{w,i}$ is used in (15.33), where

$$d_{w,i} = d_w + 2\tan\varphi\sum_{i=1}^{j} l_{i-1}\,. \tag{15.38}$$

Furthermore, in (15.33) and (15.35) the height of the deformation body, l_V or rather l_H, is replaced by the height

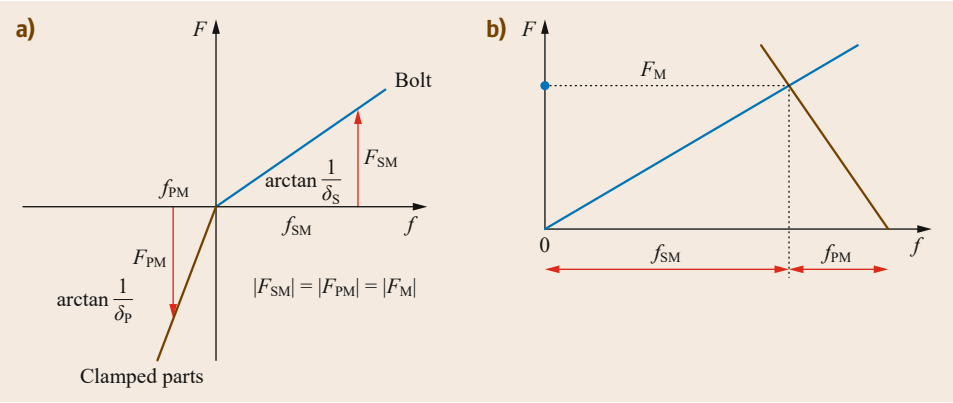

Fig. 15.33a,b Deformation characteristics of the bolt and the clamped parts (**a**) and the resulting joint diagram (**b**)

l_i of the subsegment and the modulus of elasticity E_P is replaced by E_{Pi}.

The total resilience of the clamped parts is thus

$$\delta_P = \sum_{i=1}^{j} \delta_{Pi}^{V} + \sum_{i=j+1}^{m} \delta_{Pi}^{H} . \qquad (15.39)$$

Strictly speaking, the equations given only apply to cylindrical components with centrally inserted bolts. Rectangular flanges or multiple bolt joints are assumed to be approximately cylindrical, whereby the external diameter corresponds to twice the average edge distance in the interface.

For details of how to calculate eccentric bolted joints or multiple bolt joints, reference is made to the relevant literature, for example, VDI 2230-2 [15.41].

The resilience of the bolt and of the clamped parts can be used to construct the joint diagram of the joint. First the deformations of the parts are drawn on a diagram with the correct sign (+/–) (Fig. 15.33a).

The deformation characteristic of the clamped parts is then mirrored about the abscissa (x-axis) and is moved to the right in the first quadrant, until $|F_{PM}| = |F_{SM}| = |F_M|$. The result is the joint diagram shown in Fig. 15.33b with the assembly force F_M and the resulting deformation of the bolt f_{SM}, or rather the clamped parts f_{PM}.

The relatively small bearing surfaces in the threads, underneath the bolt head, or rather of the nut in conjunction with the surface roughness in the contact zones of the joint partners leads to high surface pressures in these areas, as a result of which creep and thus relaxation of the joint occurs. The amount of relaxation is called the embedding (set) f_Z and the resulting loss of force is called the loss of preload F_Z, where

$$F_Z = \frac{f_Z}{(\delta_S + \delta_P)} . \qquad (15.40)$$

Guide values for the embedding are given in Table 15.18.

As a result of the loss of preload, the assembly force $F_{M\,min}$ of the bolt must be larger than the minimum preload required according to (15.20), so that

$$F_{M\,min} = F_{V\,min} + F_Z . \qquad (15.41)$$

The maximum assembly force $F_{M\,max}$ allows for fluctuations in the assembly force due to imprecise tightening methods or errors in the determination of the coefficients of friction. It is obtained from

$$F_{M\,max} = \alpha_A F_{M\,min} . \qquad (15.42)$$

Values for the tightening factor α_A are given in Table 15.19.

Table 15.18 Guide values for embedments of uncoated steel bolts and compact clamped parts made of steel depending on surface roughness [15.40]

Mean roughness depth R_z (µm) according to ISO 4287	Load	Guide values for embedments (µm)		
		In the thread	Per head or nut bearing	Per internal interface
< 10	Tension/compression	3	2.5	1.5
	Shear	3	3	2
10–40	Tension/compression	3	3	2
	Shear	3	4.5	2.5
40–160	Tension/compression	3	4	3
	Shear	3	6.5	3.5

Table 15.19 Guide values for tightening factor α_A

α_A	Use
1.1–1.2	With the most precise tightening method (e.g., checking the change in bolt length)
1.25–1.8	Tightening with torque wrench
1.8–2	Tightening with controlled impact wrench
2.5–4	Tightening by hand or with impact wrench

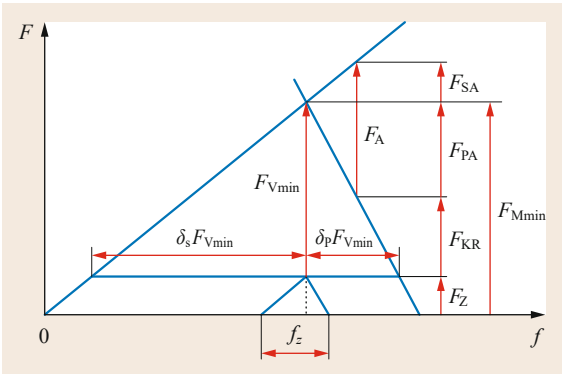

Fig. 15.34 Joint diagram showing the main dimensional variables acting

If a preloaded bolted joint is additionally loaded by an axial working load F_A directly underneath the bolt head, or rather the nut is tensioned, the bolt extends further by the amount f_{SA}, which causes the upsetting (compressive strain) of the clamped components to reduce by the same amount f_{PA} (Fig. 15.34).

The increase in axial bolt force due to the working load is called the additional bolt load F_{SA}:

$$F_{SA} = \frac{\delta_P}{\delta_S + \delta_P} F_A = \Phi F_A \,, \tag{15.43}$$

where the term Φ is the simplified dimensionless force ratio and

$$\Phi = \frac{\delta_P}{\delta_S + \delta_P} \,. \tag{15.44}$$

While the bolt is subjected to additional loading due to the working load, the clamped parts are relieved by F_{PA}:

$$F_{PA} = F_A - F_{SA} = (1 - \Phi)\, F_A \,. \tag{15.45}$$

As a result of the relieving of the clamped parts, the clamping force between them also reduces. The remaining residual clamp load is given by

$$F_{KR} = F_V - F_{PA} = F_V - (1 - \Phi)\, F_A \,. \tag{15.46}$$

The maximum bolt load (before embedding) is given by

$$\begin{aligned} F_{S\,max} &= \alpha_A\,(F_V + F_Z) + F_{SA} \\ &= F_{M\,max} + F_{SA} \,. \end{aligned} \tag{15.47}$$

In practice, the working load does not generally act directly underneath the bolt head or rather the nut, as shown in Fig. 15.35a. In most cases the load application point is in the area of the clamped parts, so that these are only partly relieved, while the compressive load increases in the remaining part (Fig. 15.35b,c). As a result of the load application point shifted from the ideal point, the resilience of the bolt appears to be larger, while the resilience of the clamped parts is smaller.

The type of load introduction is taken into account in the calculation by the dimensionless load introduction factor n, such that

$$\Phi = n\Phi_K \,, \tag{15.48}$$

where Φ_K is the simplified force ratio (15.44).

For the special case of load introduction directly underneath the bolt head, $n = 1$, so $\Phi = \Phi_K$. The force introduction factors for clamping cases deviating from this are given in Table 15.20, whereby the following points apply:

- The plates must have the same modulus of elasticity.
- The joint must be able to be classified as a joint type in Fig. 15.36 with regard to the position of the interface and load introduction point.

For rough bolt dimensioning of transversely loaded bolts, $n = 1$ can be assumed, as the resulting bolt load is highest in this case.

The assembly force required for the joint is generated by tightening the bolt with an appropriate *tightening torque* (wrench torque) M_A.

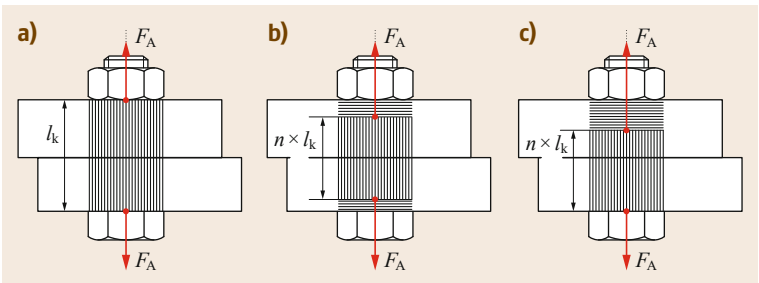

Fig. 15.35a–c Load introduction in the clamped parts: **(a)** simplified case, **(b,c)** general cases

Table 15.20 Guide values for load introduction factor n depending on the joint type SV and the dimensions of the bolted joint according to VDI 2230 [15.40]. For an explanation, see Fig. 15.36

I_A/h	0				0.1				0.2				≥ 0.30			
a_k/h	0.00	0.10	0.30	≥ 0.50	0.00	0.10	0.30	≥ 0.50	0.00	0.10	0.30	≥ 0.50	0.00	0.10	0.30	≥ 0.50
SV1	0.70	0.55	0.30	0.13	0.52	0.41	0.22	0.10	0.34	0.28	0.16	0.07	0.16	0.14	0.12	0.04
SV2	0.57	0.46	0.30	0.13	0.44	0.36	0.21	0.10	0.30	0.25	0.16	0.07	0.16	0.14	0.12	0.04
SV3	0.44	0.37	0.26	0.12	0.35	0.30	0.20	0.09	0.26	0.23	0.15	0.07	0.16	0.14	0.12	0.04
SV4	0.42	0.34	0.25	0.12	0.33	0.27	0.16	0.08	0.23	0.19	0.12	0.06	0.14	0.13	0.10	0.03
SV5	0.30	0.25	0.22	0.10	0.24	0.21	0.15	0.07	0.19	0.17	0.12	0.06	0.14	0.13	0.10	0.03
SV6	0.15	0.14	0.14	0.07	0.13	0.12	0.10	0.06	0.11	0.11	0.09	0.06	0.10	0.10	0.08	0.03

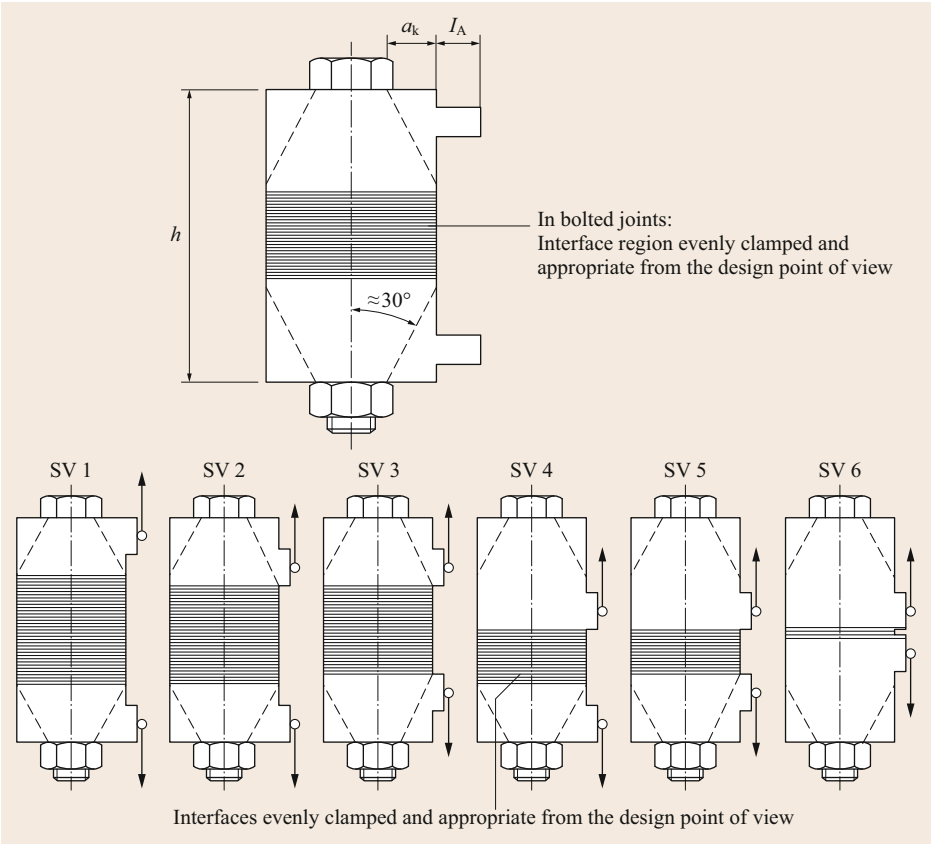

Fig. 15.36 Joint type and parameters for determining the load introduction factor according to VDI 2230 (after [15.40])

The tightening torque M_A is made up of

$$M_A = M_G M_K \,, \tag{15.49}$$

where:

M_G friction moment (friction torque) in the screwed-in thread
M_K bearing friction moment (torque) in the contact area between the bolt head, or rather the nut, and the parts to be bolted

The friction torque in the thread is given by

$$M_G = F_{M\max} \frac{d_2}{2} \tan\left(\phi \pm \rho'\right) , \tag{15.50}$$

where:

d_2 pitch diameter of the thread
φ pitch angle (helix angle) of the thread (15.19)
ρ' friction angle of the thread

The plus sign in (15.50) applies to the tightening and the minus sign to the undoing of the bolt.

Table 15.21 Thread coefficients of friction μ_G after *Schlecht* [15.42]

Thread					External (bolt)								
Thread	Material				Steel								
	Material	Surface			Black tempered or phosphated				Electrolytically galvanized		Electrolytically cadmium plated		Adhesive
		Surface	Production		Rolled			Cut	Rolled and cut				
			Production	Lubrication	Dry	Oiled	MoS_2	Oiled	Dry	Oiled	Dry	Oiled	Dry
Internal (nut)	Steel	Blank	Cut	Dry	0.12 – 0.18	0.10 – 0.16	0.08 – 0.12	0.10 – 0.16	–	0.10 – 0.18	–	0.08 – 0.14	0.16 – 0.25
		Electrolytically galvanized			0.10 – 0.16	–	–	–	0.12 – 0.20	0.10 – 0.18	–	–	0.14 – 0.25
		Electrolytically cadmium plated			0.08 – 0.14	–	–	–	–	–	0.12 – 0.16	0.12 – 0.14	–
	Grey-/-malleable iron	Blank			–	0.10 – 0.18	–	0.10 – 0.18	–	0.10 – 0.16	–	0.08 – 0.16	–
	Al/Mg	Blank			–	0.08 – 0.20	–	–	–	–	–	–	–

The friction angle of the thread is a notional variable and results from the coefficient of friction in the thread μ_G (Table 15.21) and the flank angle of the thread α.

$$\tan \rho' = \mu'_G = \frac{\mu_G}{\cos\left(\frac{\alpha}{2}\right)} \tag{15.51}$$

Threaded fasteners must be self-locking so that they do not undo themselves. The thread is self-locking if the pitch angle φ of the thread is smaller than the thread friction angle ρ', i.e., $\varphi < \rho'$.

For a metric ISO thread with flank angle 60°, $\mu'_G \approx 1.155\mu_G$. Thus (15.50) can be rearranged to

$$M_G = F_{M\,max}\,(0.16P + 0.58 d_2 \mu_{G\,min})\,, \tag{15.52}$$

where P is the thread pitch (15.19) and $\mu_{G\,min}$ is the smallest coefficient of friction in the thread.

The bearing friction torque M_K is calculated from the assembly force $F_{M\,max}$ on tightening the bolt:

$$M_K = F_{M\,max}\frac{(d_W + D_{Ki})}{4} = F_{M\,max}\frac{D_{Km}}{2}\mu_K\,, \tag{15.53}$$

where

d_W external diameter of the bolt head or nut bearing ($d_W \approx 1.4d$)
D_{Ki} internal diameter of the flat (planar) head bearing
D_{Km} mean bearing diameter at the nut or at the bolt head ($D_{Km} \approx 1.3d$ for metric hexagon head and head cap bolts and screws)

μ_K coefficient of friction ($\mu_K \approx 0.12$ for the normal case or similar to μ_G according to Table 15.21)

The thread torque M_G and the bearing friction torque M_K can be used to calculate the tightening torque (bolt torque):

$$M_A = M_G + M_K \tag{15.54}$$
$$= F_{M\,max}\left(\frac{d_2}{2}\right)\tan\left(\phi \pm \rho'\right) + F_{M\,max}\,\mu_K\frac{D_{Km}}{2},$$

$$M_A = F_{M\,max}\left(0.16P + 0.58d_2\,\mu_{G\,min} + \frac{D_{Km}}{2}\mu_K\right). \tag{15.55}$$

Due to the scatter of the coefficients of friction (Table 15.21), when calculating tightening torques or when tightening screws and bolts, it should be borne in mind that with low coefficients of friction the same tightening torques can produce substantially larger preloads (bolt stresses) and with high coefficients of friction small preloads can result.

The assembly preload $F_{M\,max}$ causes a tensile stress $\sigma_M = F_{M\,max}/A_0$ in the loaded stress cross section (or shank cross section) $A_0 = A_{min}$.

As a result of the thread torque M_G according to (15.55), a torsional stress $\tau_t = M_G/W_t$, where $W_t \approx \pi d_{min}^3/16$ is introduced into the bolt cross section.

According to the maximum shear strain energy hypothesis, this leads to an equivalent stress $\sigma_V = \sigma_{red}$:

$$\sigma_v = \sigma_{red} = \sqrt{\sigma_M^2 + 3\tau_t^2}\,. \tag{15.56}$$

In general, on tightening the bolted joint the maximum strength of the bolt is not utilized and this prevents exceeding the yield point in the service case. Usually, 90% of the yield point is used as the limit value, so that

$$\sigma_{red} \le 0.9R_{p0.2}\,, \tag{15.57}$$

where $R_{p0.2}$ is the elasticity limit of the bolt material (Tables 15.24 and 15.25).

Furthermore, it must also be checked that the increase in bolt load as a result of the working load does not lead to plastic deformation:

$$F_{AS} = n\Phi_K F_A \le 0.1R_{p0.2}A_0\,. \tag{15.58}$$

In addition to the allowable stresses in the bolt, the surface pressure on the bearing surfaces of the bolt head, or rather the nut, and the clamped parts must also be checked. In the assembled state this is done by calculating

$$p_{M\,max} = \frac{F_{M\,max}}{A_{p\,min}} \le p_G\,. \tag{15.59}$$

Table 15.22 Allowable limit surface pressures (interface pressures) (after *Wittel* et al. [15.2])

Material of the compressed parts	Tensile strength R_m (N/mm²)	Interface pressure p_G (N/mm²)
S235	370	260
E295	500	420
C45	800	700
42CrMo4	1000	850
30CrNiMo8	1200	750
X5CrNiMo18 10	500–700	210
X10CrNiMo18 9	500–750	220
Rust-free, precipitation hardening materials	1200–1500	1000–1250
C15 case-hardened (Eht 0.6)	–	1400
16MnCR5 case-hardened (Eht 1)	–	1800
Titanium, unalloyed	390–540	300
TiA16V4	1100	1000
EN-GJL-150	150	600
EN-GJL-250	250	800
EN-GJL-350	350	900
EN-GJS-350-LT	350	480
EN-GJMB-450-G	450	500
GD-MgA19	300 (200)	220 (140)
GK-MgA19	200 (300)	140 (220)
GK-AlSi6Cu4	–	200
AlZnMgCu0.5	450	370
Al99	160	140
GRP composite	–	120
CRP composite	–	140

And in the service state

$$p_{B\,max} = \frac{(F_{V\,max} + F_{SA\,max})}{A_{p\,min}} \le p_G\,, \tag{15.60}$$

where $p_{M\,max}$ is the maximum surface pressure immediately after installation of the bolt, $p_{B\,max}$ is the maximum surface pressure under service load, $A_{p\,min}$ is the minimum contact area, p_G is the allowable surface pressure on the boundary surfaces (interfaces) (VDI = limit surface pressure) (Table 15.22), $F_{V\,max}$ is the maximum preload of the joint, and $F_{SA\,max}$ is the maximum additional bolt load.

The nominal diameter of bolts and screws depending on the strength class is estimated according to Table 15.23, in conjunction with the Fig. 15.37.

First, using the axial and/or transverse forces (loads) acting on the bolt $F_{A,Q}$, the next highest load is looked for in the first column of Table 15.23. Depending on the load case and assembly method, the choice must then be shifted a certain number of rows down. The sum of the

Table 15.23 Preselection of screws and bolts according to VDI 2230-1 (after [15.40])

1 Force $F_{A,Q}$ (N)	2 Nominal diameter (mm) Strength class 12.9	3 10.9	4 8.8
250			
400			
630			
100			
1600	3	3	3
2500	3	3	4
4000	4	4	5
6300	4	5	5
10 000	5	6	8
16 000	6	8	8
25 000	8	10	10
40 000	10	12	14
63 000	12	14	16
100 000	16	16	20
160 000	20	20	24
250 000	24	27	30
400 000	30	36	
630 000	36		

rows to be moved down can be determined using the flow chart in Fig. 15.37. The necessary bolt diameter, depending on the bolt's strength class, is found in the corresponding row, in columns 2–4.

Example 15.1

A bolted joint tightened with a torque wrench must withstand an eccentric, static axial load of 10 000 N and an additional transverse force of 5000 N. The screw has strength class 10.9.

Solution 15.1

According to Table 15.23, the next highest load is 10 000 N (row 9).

$$\frac{F_{Q\max}}{\mu} = \frac{5000\,\mathrm{N}}{0.15} = 3333.3\,\mathrm{N} < F_A = 10\,000\,\mathrm{N}$$

From the flow chart, for this load case (static and eccentrically acting axial load), one row must be skipped.

In addition, due to the assembly using a torque wrench, the row selection must be moved downwards by an additional row.

Thus, the selection (row 9) must be moved downwards by an additional two rows, which gives row 11.

Thus, the necessary bolt diameter for the selected strength class (10.9) is 10 mm.

Bolts, screws, and nuts made of steel are classified in strength classes depending on the material strength. The strength classes for bolts and screws made of steel and alloyed steel with metric thread according to ISO 68-1 [15.44] are defined in EN ISO 898-1 [15.43] (Table 15.24).

The strength class of hexagon head screws and bolts and hexagon socket head cap screws and bolts is marked by two numbers separated by a dot on the top of the screw or bolt head. The first number indicates one hundredth of the minimum tensile strength R_m in N/mm^2. The second number stands for 10 times the ratio R_e/R_m, or rather $R_{p0.2}/R_m$.

Table 15.24 Strength classes, materials, and mechanical properties of screws, bolts, and studs according to EN ISO 898-1 (excerpt) [15.43]

Mechanical or physical property		Strength class 4.6	4.8	5.6	5.8	6.8	8.8 $d \le 16$ mm[a]	8.8 $d > 16$ mm[b]	9.8 $d \le 16$ mm	10.9	12.9
Tensile strength R_m (N/mm^2)	Nom.	400		500		600	800		900	1000	1200
	Min.	400	420	500	520	600	800	830	900	1040	1220
Lower yield point R_{eL} (Mpa)	Nom.	240	–	300	–	–	–	–	–	–	–
	Min.	240	–	300	–	–	–	–	–	–	–
0.2% proof strength $R_{p0.2}$ (Mpa)	Nom.	–	–	–	–	–	640	640	720	900	1080
	Min.	–	–	–	–	–	640	660	720	940	1100
Percentage elongation at break of a machined test piece A (%)	Min.	22	–	30	–	–	12	12	10	9	8
Percentage reduction of area after fracture of a machined test piece Z (%)	Min.	–					52		48	48	44
Elongation after fracture of a full-size bolt, screw, or stud A_f	Min.	–	0.24	–	0.22	0.20	–	–	–	–	–

[a] Values do not apply to steel construction screws
[b] For steel construction screws $d \ge M12$

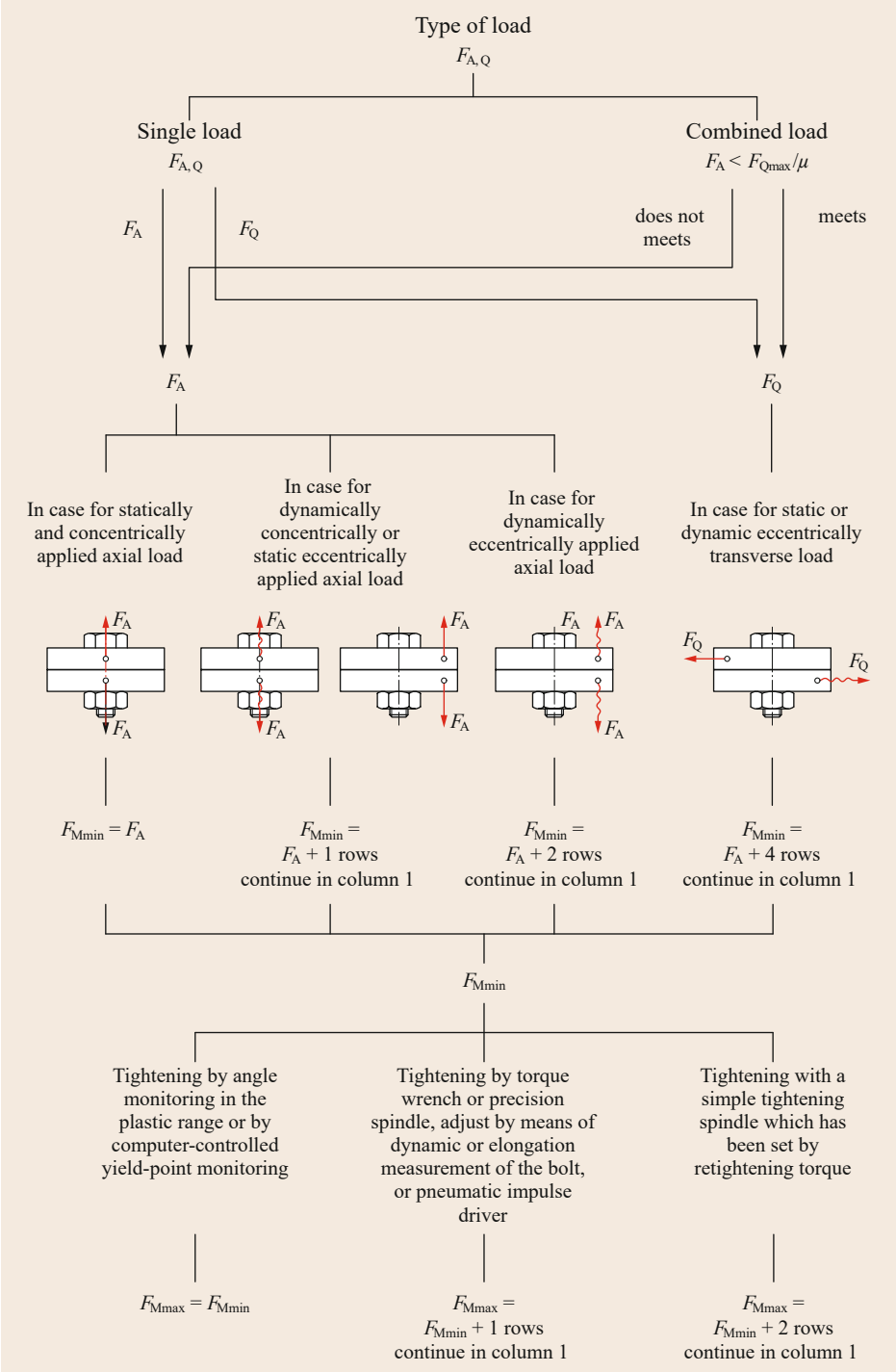

Fig. 15.37 Flow chart for rough screw/bolt selection according to VDI 2230-1 (after [15.40])

Example 15.2

An example of the strength class

Strength class 5.6:

$$R_m = 5 \times 100 = 500\,\mathrm{N/mm^2}$$

$$R_{e;p0.2} = 0.6R_m = 0.6 \times 500\,\frac{\mathrm{N}}{\mathrm{mm^2}} = 300\,\frac{\mathrm{N}}{\mathrm{mm^2}}\,.$$

Several different specifications, some of which are similar, exist in parallel for imperial and inch-measure screws and bolts. The individual strength classes are marked on the screw or bolt head by a marking system, whereby the corresponding strength values are given in the relevant tables (Table 15.25).

Design Guidelines for Bolted Joints. A small selection of examples of unfavorable and favorable designs of bolted joints is shown in Table 15.26.

Screw-/Bolt-Locking and Accessories. Dynamically loaded bolted joints must be locked to prevent them from loosening themselves. This can be done by using form closure, force closure or material-bonding screw or bolt locking.

Force-closure locking elements are spring-loaded components, whose spring load provides additional axial clamping force in the bolted joint and as a result increases the force closure (e.g., split washers, spring lock washers, and lock nuts) (Fig. 15.38a–c). Force-closure bolt locking is also achieved by *locking* (clamping against each other) two nuts.

Form-closure locking elements immobilize the nut or bolt head through their shape or deformation (Fig. 15.38d,e).

Material-bonding locking is achieved by adhesive bonding of the bolt thread with the help of special adhesives (threadlockers) or by coating the bolt with special plastics in the factory.

These coloaded elements are partly standardized as accessory components for bolted joints.

If the material of the bolted parts is very soft, the pressure on the bearing surfaces of the components can be reduced by using (plain) *washers*.

15.2.4 Material-Bonded Joints

Material-bonded joints include, for example, adhesive bonding, welding and, soldering joining methods. What they have in common is that the parts to be joined (components) are permanently bonded together, either directly or by means of an additional substance. In general, undoing such joints involves damaging or destroying the components or rather the additional material.

Table 15.25 Strength classes for inch-measure screws and bolts according to SAE [15.45] and ASTM [15.46] (excerpt)

Grade identification marking/head marking										
									307A	307B
Product specification/ standard	SAE J-429 Grade 1	SAE J-429 Grade 2	SAE J-429 Grade 5	SAE J-429 Grade 5.2	SAE J-429 Grade 7	SAE J-429 Grade 8	SAE J-429 Grade 8.2	ASTM A307 Grade A	ASTM A307 Grade B
Nominal size range	1/4–1 1/2	1/4–3/4 (> 3/4–1 1/2)	1/4–1 (> 1–1 1/2)	1/4–1	1/4–1 1/2	1/4–1 1/2	1/2–1 1/2	1/4–4	1/4–4
Material	Low- or medium-carbon steel	Low- or medium carbon steel	Medium-carbon steel, heat treated	Low-carbon martensitic steel, quenched and tempered	Medium-carbon alloy steel, quenched and tempered	Medium-carbon steel heat treated	Low-carbon boron steel quenched & tempered	Low- or medium-carbon steel	Low- or medium-carbon steel
Tensile strength in psi, minimum	60 000	74 000 (60 000)	120 000 (105 000)	120 000	133 000	150 000	150 000	60 000	100 000 (60 000)
Minimum yield strength (stress) in psi	36 000	57 000 (36 000)	91 000 (81 000)	92 000	115 000	130 000	130 000	–	–
Proof (test) load in psi	33 000	55 000 (33 000)	85 000 (74 000)	85 000	105 000	120 000	120 000	–	–
Hardness **Min.**	B70	B80	C25		C24	C33	C33	B69	B69
Max.	B100	B100	C34		C38	C39	C39	B100	B95

Table 15.26 Design examples for bolted joints

No.	Unfavorable	Favorable	Comments
1	a) 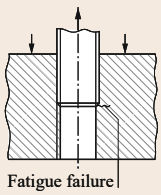 	b) 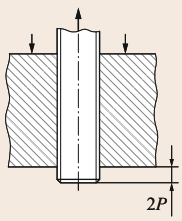 c) 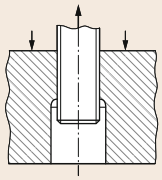 d) 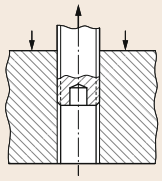	In the case of blind-hole threaded fasteners, the highest stress concentration for the nut thread is at the end of the threaded bolt. There is thus a risk of fatigue failure of the nut thread under dynamic loading. The stress peaks in the nut thread can be dissipated by various measures: b) Protruding bolt thread, overhang $\geq 2P$ c) Rounded cylindrical counterbore and protruding bolt thread d) Reboring/drilling out of the threaded bolt
2	a) 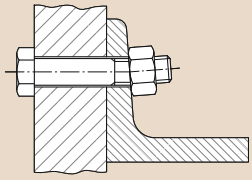 b) 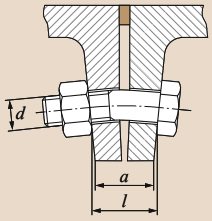 	c) 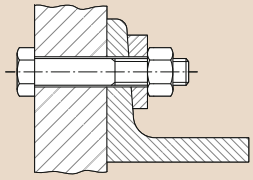 d) 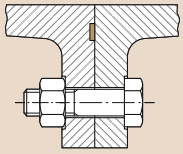	The nuts and bolt heads should have a bearing surface perpendicular to the bolt axis, as otherwise additional bending stresses occur in the bolt shank: $\sigma_b = adE/(2l)$ If a skewed head bearing is unavoidable, e.g., due to component deformation (b), flexible bolts (d small, l large) are favorable. The flange inclination of sections can be levelled out by square washers, e.g., by using tapered washers for U-sections according to DIN 434 or tapered washers for I-sections according to DIN 435 (c). In the case of cast parts, counterbores according to DIN 974 or machine cut eyes are to be provided (d).
3	a) 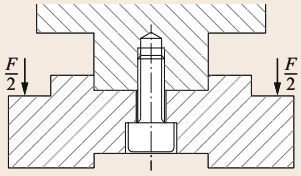 	b) 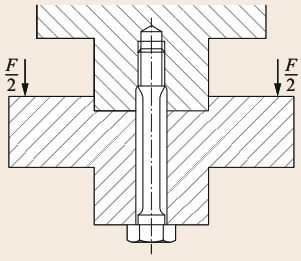 	In the case of high stresses the fatigue life can be improved by the following measures: – Greater elastic resilience of the bolt (δ_s large) – Moving the working load application point towards the interface (n small)

Table 15.26 (continued)

No.	Unfavorable	Favorable	Comments
4	a) 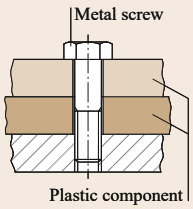 	b) 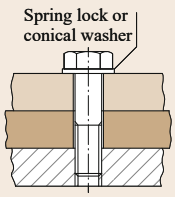 c) 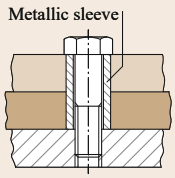 	If clamped with metal screws or bolts, plastic components creep under gradual loss of the preload or the bolt or screw cracks as a result of the large thermal elongation of the plastic. The following measures can be taken: b) By using coloaded spring lock washers or conical spring washers the preload is largely maintained, even after creep has occurred and in changing temperatures. c) Metallic support sleeves transfer the preload.
5	a) 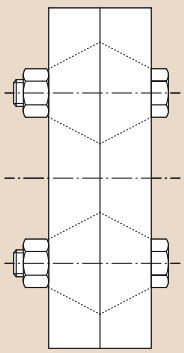	b) 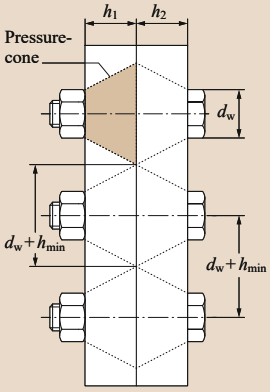 	Due to the overlapping of the pressure cone that forms in the component under prestress, a continuous force flow results in the interface. This leads to low additional bolt loads, good sealing, and prevention of fretting corrosion (frictional corrosion). The bolt spacing should roughly equal the component height: $\approx d_W + h_{min}$

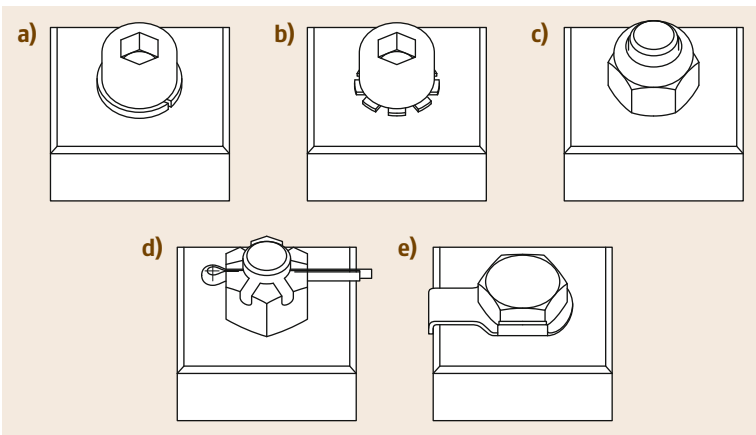

Fig. 15.38a–e Locking elements: **(a)** bolt with split washer, **(b)** bolt with toothed lock washer, **(c)** nut with clamping part, **(d)** castellated nut with split pin, and **(e)** tab washer with long tab

Table 15.27 Advantages and disadvantages of adhesive joints

Advantages	Disadvantages
Different materials can be joined	Joint not nondestructively separable
Faces of very thin components can be joined	Low thermal endurance
Joining of heat-sensitive components is possible	Low peeling strength
High stiffness due to continuous, uniformly distributed load transfer via joined surfaces	The surface often requires pretreating before bonding
Joint has vibration damping effect	Only limited resistance to environmental effects and chemicals
If executed properly, no internal (residual) stresses in the joined components	Volume reduction when liquid adhesives set or harden
Uniform stress distribution when loaded (Fig. 15.39)	Adhesives or rather their solvents can be harmful
Joint is gas- and/or liquid-tight	
Very good gap bridgeability (rough tolerancing possible)	
Depending on the adhesive selection, the joint can be electrically insulating or conductive	
In general, cost effective and easily automatable	

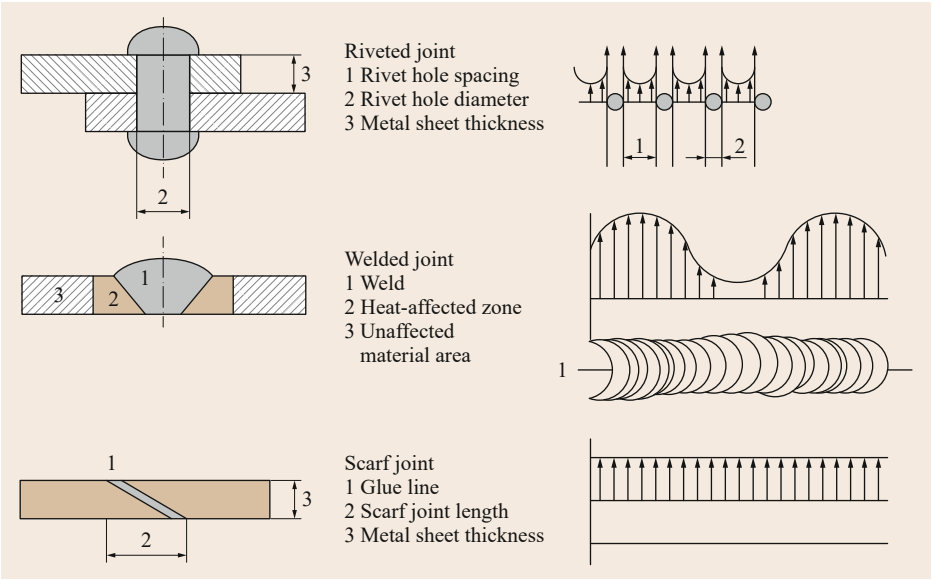

Fig. 15.39 Comparison of the stress distribution in riveting, welding, and adhesive bonding

Adhesive Bonding

In the case of adhesive bonding, components (mostly flat) are joined with the help of an adhesive, with the objective of transferring forces (loads) and/or achieving a sealing effect.

According to EN 923 [15.47], an adhesive is a "non-metallic substance capable of joining materials by surface bonding (adhesion), and the bond possessing adequate internal strength (cohesion)."

Adhesive bonding is one of the oldest jointing methods. Even in the Stone Age, people used natural adhesives such as tree gum or pitch to join together materials. The advantages (Table 15.27) of adhesive bonding, particularly the possibility of quickly and reliably bonding together different materials (composite construction), the easy automatability, and the development of special high-strength and aging-resistant adhesives mean that adhesive joints are still a modern jointing method and are used industrially to an ever-increasing extent.

Adhesive joints are now used on a large scale, among other things, to produce packaging in the consumer goods industry, in the wood-processing industry, and also to an increasing extent in vehicle manufacturing.

The adhesives used industrially nowadays are generally made of synthetically produced polymers. They can be divided into physically setting adhesives and chemically reacting adhesives, depending on their type of solidification mechanism.

Table 15.28 Areas of application of standard adhesives (excerpt)

Adhesive type	Hardening/curing	Use/special features	Chemical resistance	Service temperature (°C)	Tensile shear strength (N/mm^2)
Anaerobic adhesive	Hardens in absence of air (oxygen) in the presence of metal irons	Adhesive bonding of metallic components (e.g., shaft–hub connection, threadlocker) An activator may have to be used for passive metal surfaces (chrome or stainless steel) or plastics	Good	−55…200	Up to 30
Cyanoacrylate (superglue)	Hardens due to humidity or surface moisture Very fast hardening	Frequently used instant adhesive Metals, plastics (e.g., PMMA, POM, ABS, H-PVC, PS, NBR, EPDM) Conditionally suitable for bonding glass Adhesive joint is very brittle and can only withstand low mechanical load	Poor	−30…100	Up to 20
Silicone adhesive	Interlinking due to humidity or through the addition of hardener	Above all as sealants and as adhesive for glass Very good gap bridging Permanently elastic		−55…180	< 1
Epoxy resin (1-component)	Hardening takes place by application of heat	For bonding load-bearing structures made of metal, plastic or ceramic	Very good	−50…200	Up to 29
Epoxy resin (2-component)	Curing achieved by adding a curing agent (hardener)	Good bridging of gaps	Good	−50…130	Up to 40
Polyurethane adhesive (2-component)	Curing achieved by adding a curing agent (hardener)	Suitable for adhesive bonding of metal, wood, and plastic Good gap bridgeability Suitable for large area bonding	Medium	−40…100	Up to 25
Radiation curing plastics	By UV radiation	Suitable for metals, plastics, ceramics, and glass	Good	−40…100	Up to 25

Physically setting adhesives solidify by:

- Volatilization of solvent/dispersant (solvent-borne adhesive/dispersion adhesive)
- Melting and subsequent solidifying of the polymer (hot-melt adhesive)
- Gelling of a mixture of powdered thermoplastic polymers and liquid plasticizers through the addition of heat (plastisols)

Chemically reacting adhesives solidify due to a reaction of mostly one- or two-component systems at room temperature or at increased temperatures.

The technical properties and thus the possible uses of modern adhesives are vary widely. They are often especially adapted to the application case. A rough overview of industrially used adhesives is given in Table 15.28, whereby it should be noted that depending on the composition, the properties can vary within a wide framework. For this reason, refer to the corresponding data sheets of the manufacturers for precise information.

The strength of the adhesive joint decisively depends on the adhesive forces between the adhesive and the components to be joined. Although adhesives are now available that can be applied directly onto oily metal sheets, in general the surfaces must be cleaned and pretreated before joining. The adhesive forces can be increased, for example, by roughening or pickling the bond planes.

The wettability of plastic surfaces can be problematic due to their low surface energy. The wettability of plastics can be improved by treating them with reactive gases (for example ozone or fluorine), plasmas, or by flame treatment.

The special properties of adhesive bonds must be taken into consideration in their design. For example, adhesive bonds respond very sensitively to peel loading. Table 15.29 shows examples of appropriate, process-compatible designs of the adhesive joints.

Welding

In welding, the parts to be joined and the optional filler material made of similar materials are melted. They form a joint melt and solidify together during subsequent cooling, as a result of which a permanent bond is formed. The welding process can be assisted by using

Table 15.29 Design examples for adhesive joints

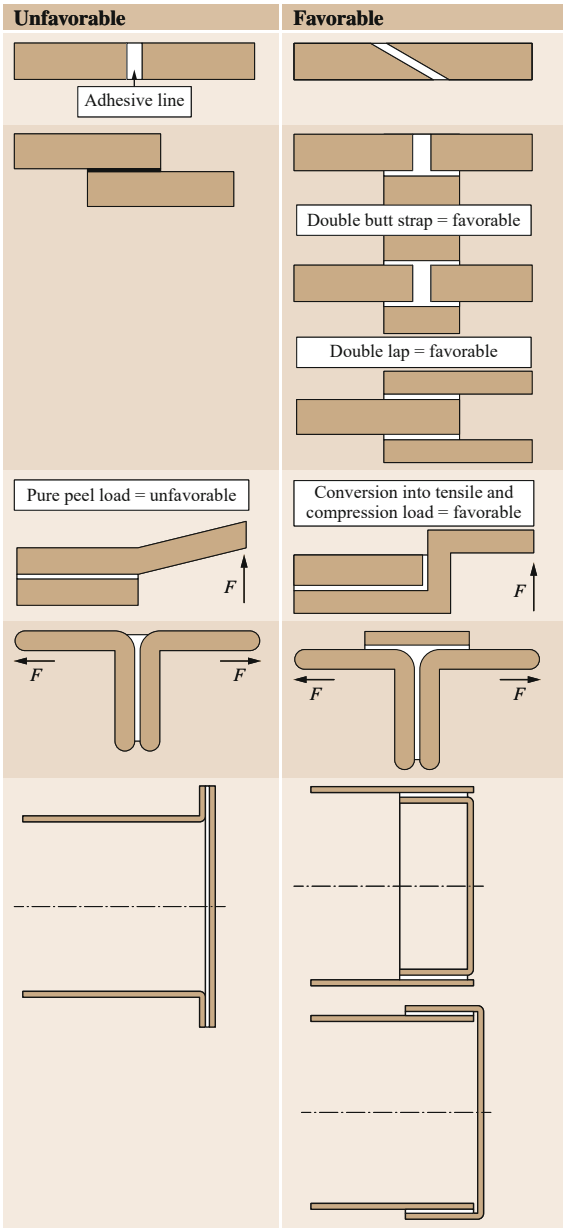

welding auxiliaries (e.g., powder, pastes, or gases). The energy (heat) required for melting the materials can be provided directly by using gas flames, arcs, or radiation or indirectly by, for example, electrical current or friction heat.

Both metallic and nonmetallic materials (e.g., plastics and glass) can be bonded together.

Soldering

Soldering is a process characterized by the fact that a metallic filler material (solder) with a melting point significantly lower than that of the materials to be joined is used to join metallic components and the joint can form by adhesion and diffusion mechanisms.

Soldered joints can be undone under certain circumstances by melting the filler metal.

Apart from the different soldering methods, soldering is also divided into hard soldering and soft soldering.

In *hard soldering (brazing)* (at operating temperatures up to 1100 °C) joints must be achieved that satisfy certain strength requirements.

In *soft soldering* (at operating temperatures below 450 °C) the focus is on the sealing and/or electric conducting properties of the soldered joint. The strength requirements of the joint are secondary. It can be undone by melting the solder.

15.2.5 Further Reading

Further details on the calculation of fasteners and jointing compounds are given, for example, by *Spotts* et al. [15.48], *Wittel* et al. [15.2], *Niemann* et al. [15.24] and *Schlecht* [15.42]. VDI guidelines 2230-1 [15.40] and 2230-2 [15.41] are the standard works for the calculation of fixing screws and bolts.

Information on individual welding procedures is given in *Matthes* and *Schneider* [15.49]. Details of the design of welded joints in structural steelwork are given in the Eurocode EN 1993-1-8 [15.50].

The adhesive bonding manual by *Rasche* [15.51] describes further literature on the topic.

15.3 Axles and Shafts

The primary task of axles and shafts is the storage of rotating machine elements such as rollers, wheels, or joints.

15.3.1 Standard Types

Axles

Axles are used to hold and support stationary, rotating, and swinging machine parts, for example, wheels or pulleys. By definition, they do not transfer torque. They are mainly loaded by transverse forces and bending moments. Longitudinal forces rarely occur.

A differentiation is made between fixed and rotating axles. In the case of fixed axles, mounted components rotate loosely on the fixed axle. Therefore, the loading and stresses are generally only caused at rest or repeated (cyclic, pulsating) by shear from the transverse forces and by bending. Rotating axles are defined by the fixed components, which turn with the bearing-mounted axle. The loading and stresses result from alternating and rotating bending. As a result of this, rotating axles with the same shape and material have less load-bearing capacity than a fixed axle.

Shafts

Shafts are rotating components used to transfer torque. The loads are caused by torsion, transverse forces, and bending moments. Additional longitudinal forces can occur in certain transmission elements, such as bevel gears or helical spur gears.

Journals

A journal is the name given to stepped axle and shaft ends, which are used for support and bearing. These elements can be cylindrical, conical, and spherical.

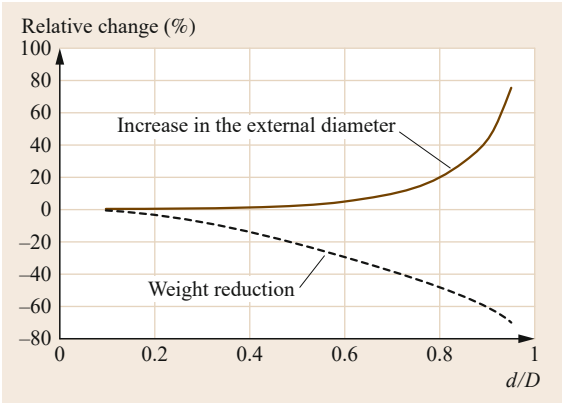

Fig. 15.40 Comparison of solid shaft and hollow shaft

15.3.2 Special Types

Hollow Shafts and Axles

Axles and shafts with a through-hole are called hollow axles or hollow shafts, respectively.

The load-bearing capability of shafts under bending and torsion increases with the cube of the diameter. Due to the nonuniform distribution of the bending and torsion stress, the internal area of the shaft volume of a solid shaft is hardly used for the load-bearing capacity, however it increases the component weight noticeably. From this it follows that hollow shafts with the same load-bearing capacity have a lower weight than solid shafts. In this special type, if the strength remains constant, as the ratio d/D increases the increase in the external diameter is far smaller than the reduction in weight (Fig. 15.40). For example, for the ratio $d/D = 0.6$; the weight G of the hollow shaft is 30% less than the solid shaft. However, the diameter D increases by only approximately 5%. One disadvantage

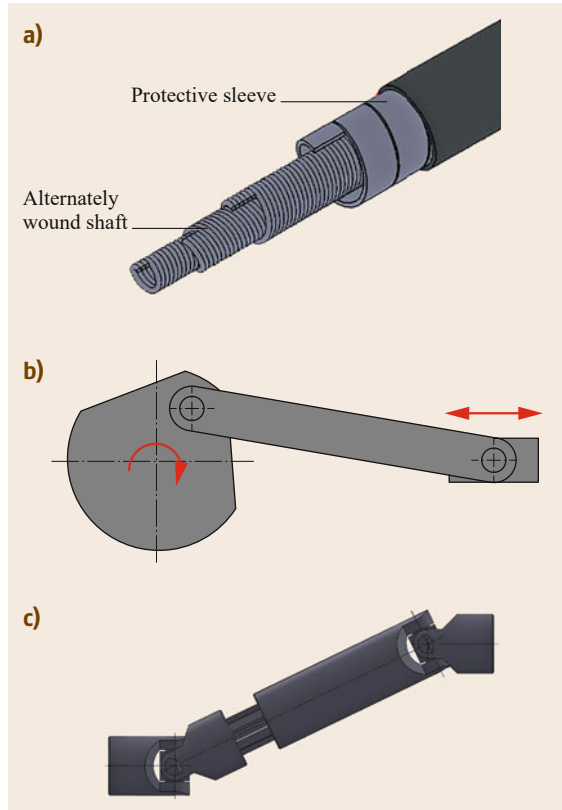

Fig. 15.41a–c Special types of shafts: **(a)** flexible shaft, **(b)** crankshaft, and **(c)** cardan shafts

Table 15.30 Materials for axles and shafts (standard materials) [15.2, 52, 53]

Use								
Standard-loaded axles and shafts			**High-load axles and shafts**			**Applications with increased wear**		
Examples								
Simple gears/transmissions, lifting gear, machine tools			**Combustion engines, motor vehicles, heavy-duty machine tools**			**Plain bearings or pinion shafts in gear trains**		
Structural (mild) steels, e.g.,			**Quenched and tempered steel, e.g.,**			**Case-hardened steel, e.g.,**		
Europe *EN 10025*	USA *ASTM*	Russia *GOST*	Europe *EN 10083*	USA *ASTM/AISI*	Russia *GOST*	Europe *EN 10084*	USA *ASTM*	Russia *GOST*
S235	1015	St2ps St2sp St3ps St3sp	C22	SAE 1020	20	C10	1011 M1010	10
S275	A529	St4ps St4sp	C25	–	25	C15	1015 (SAE); 1017 (SAE)	–
E295	–	S285 St5ps St5sp	C30	SAE1030	30	16MnCr5	SAE 5115	18KHG
E335	–	St5ps St5sp St6ps St6sp	C35	SAE 1035 SAE 1040	35 40	20MnCr5	SAE 5120	18KHG
E360		S375	C40	1038 1040	40	15CrNi6	4320 (SAE); 4320 H (SAE); 4320 RH (SAE)	–
			C50	1049 1050	50	1042 1045 Gr.1043	45	15KH
			C55	1055	50 55		–	–
			C60	1060	60 60G			
			28Mn6	1527 Gr.1330	30G 30G2			
			42CrMo4	4140 4142	35KHM 38KHM			
			34CrNiMo6	4340	36KH2N2MFA 38KH2N2MA 40KHN2MA			
			51CrV4	6150	50KHGFA			

of the hollow shaft compared to the solid version is the amount of production work, cost, and disadvantageous stress distribution in force-closure shaft–hub connections.

Other Special Types of Shafts

Flexible shafts are used to drive movable tools with fixed drives and low torques. Crankshafts are used to convert translational movement into rotational movement. Cardan shafts are used to transfer torques at nonaligned shaft ends. The different special types of shafts are shown in Fig. 15.41.

15.3.3 Materials for Axles and Shafts

In addition to strength, the choice of material is influenced by other factors such as wear and corrosion resistance as well as high-temperature strength. Table 15.30 shows the standard materials used in practice for different application cases.

15.3.4 Design Calculation

The main load on axles occurs as a result of bending. The rotational bending must be considered for rotating

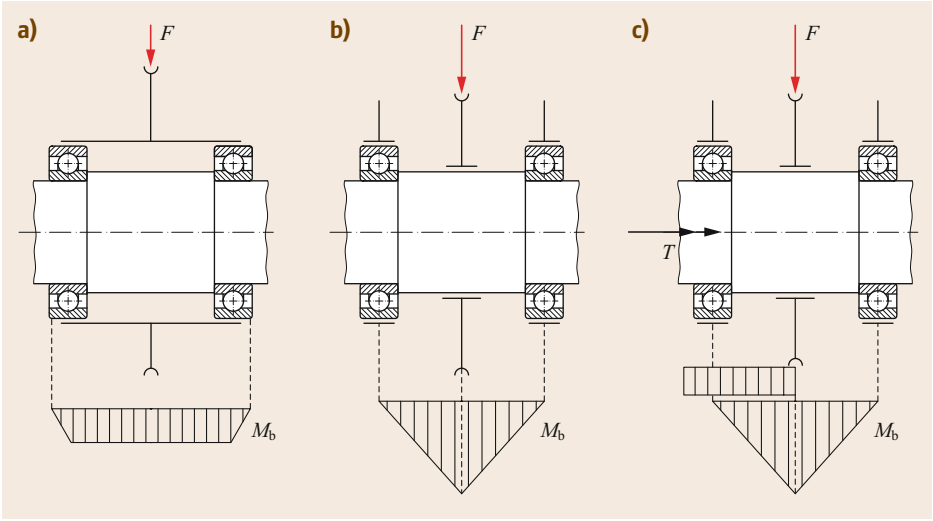

Fig. 15.42a–c Different loading of axles and shafts. **(a)** Rope pulley with stationary axle (static bending), **(b)** rope pulley with rotating axle (rotating bending), and **(c)** belt pulley with drive shaft (torsion and bending)

axles. Shear can be the priority loading of very short axles. In general, the main loading of shafts is caused by torsion (Fig. 15.42).

Careful analysis of the loading conditions is generally indispensable, as the application of torsional moments and transverse forces can vary greatly.

Frequent causes of loading:

- Driving power (torque)
- Vibrations:
  - Inertia forces
  - Imbalances
- Preloading and circumferential forces of belts and chains (radial forces)
- Service factors:
  - Acceleration and braking
  - Drive and load characteristics
- Foundation vibrations
- Temperature effect

A differentiation is made between two cases for the calculation of the given torque:

a) If the installation space for the shaft is predefined by the overall design, the bearing spacing is known and thus the bending moment can be determined.
b) If the installation space is unknown, the bearing spacing is determined by the shaft to be designed and the bending forces are initially unknown.

In case b) the diameter can thus only be determined temporarily in a rough calculation. The precise calculation is performed after the details have been defined (e.g., bearing spacing).

Determination of the Torques and Bending Moments

The nominal torque of a shaft to be transferred is formed as the quotient of the power to be transferred P and the angular velocity $\omega = 2\pi n$:

$$T_{\text{nom}} = \frac{P}{\omega} \,. \tag{15.61}$$

Equation (15.61) can be expressed as a numerical value equation with T_{nom} in Nm, P in kW, and n in min^{-1} as follows:

$$T_{\text{nom}} \approx 9550 \frac{P}{n} \,. \tag{15.62}$$

The action forces (belt and tooth forces) must be determined based on the maximum torsional moment. The reaction forces (bearing forces) must be determined for all cases. The following simplifications are to be taken into consideration:

- External forces are applied as point loads.
- In the case of long hubs, the load is assumed to be uniformly distributed.

In Fig. 15.43 the forces and moment diagrams of a shaft with straight-cut spur gears are shown highly simplified (all forces lie within one plane and only tangential forces act on the teeth).

If the action forces do not lie within one plane they must be resolved vectorially. If additional axial forces act (e.g., on helical gears), as a result of the *tilting effect*, these produce an additional radial tilting moment with a corresponding radial bearing force, which must also be considered.

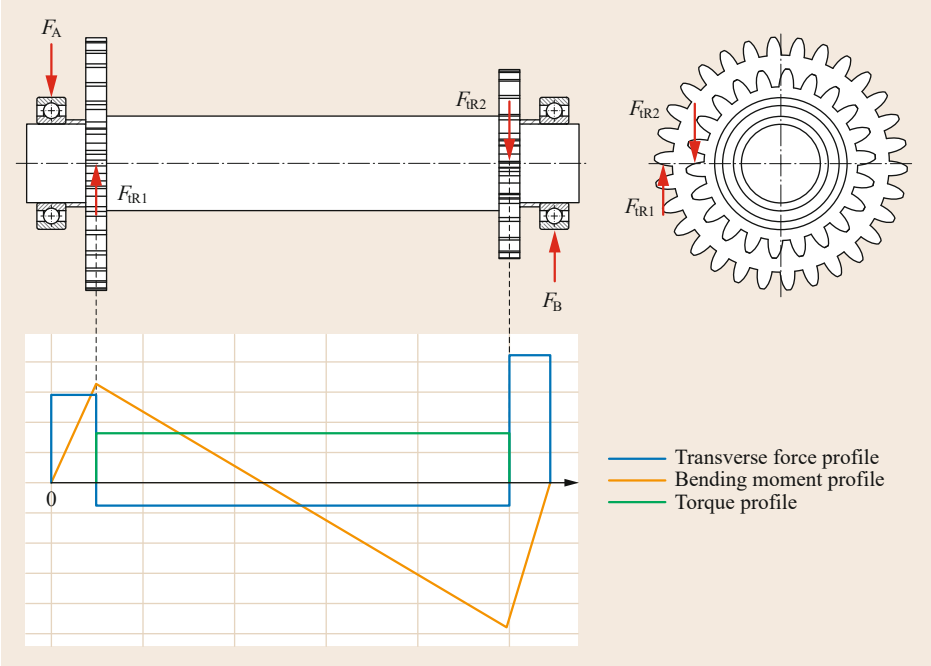

Fig. 15.43 Forces and moment diagrams of a shaft with straight-cut spur gears (simplified representation)

Determination of the Diameter

The allowable and actual loads and stresses are decisive for the dimensioning of the diameter of axles and shafts. However, under certain circumstances the deformations (twist angle or deflections) or the speeds (Sect. 15.3.5, *Critical Speed*) can be decisive for the definition of the diameter and require an adjustment. These aspects must be considered especially if higher requirements are set for the running accuracy and for longer shafts.

Determination of the Diameter from Bending (Axles). The maximum bending stress in cylindrical axles is calculated from the maximum bending moment $M_{b\,max}$ and the section modulus W_b under pure bending (mostly assumed, as longitudinal forces generally have only a small influence):

$$\sigma_{b\,max} = \frac{M_{b\,max}}{W_b} \le \sigma_{b\,all} \,. \tag{15.63}$$

The minimum diameter d required for the cylindrical axle is calculated with the help of the axial section modulus $W_b = \pi d^3/32$ from

$$d \ge \sqrt[3]{\frac{32M_b}{\pi\sigma_{b\,all}}} \approx 2.17\sqrt[3]{\frac{M_b}{\sigma_{b\,all}}} \,. \tag{15.64}$$

The allowable bending stress $\sigma_{b\,all}$ is determined as a rough estimate depending on the type of loading and the existing influencing variables (e.g., notch effects).

Table 15.31 Indicative values for allowable bending stress (after *Niemann* et al. [15.24])

Stationary axles	$\sigma_{b\,all} = \sigma_W/(1.2\ldots2)^a$
Rotating axles	$\sigma_{b\,all} = \sigma_W/(1.8\ldots4)^a$

[a] Smaller values apply to light service; larger values apply to heavy-duty service

Indicative values for the allowable bending stress are shown in Table 15.31.

To save material and weight for heavy-duty axles and shafts that are mainly subjected to bending, in accordance with (15.65), they can also be executed as a beam with the same strength.

$$d \ge \sqrt[3]{\frac{32M_{bx}}{\pi\sigma_{b\,all}}} \approx 2.17\sqrt[3]{\frac{F_A x}{\sigma_{b\,all}}} \tag{15.65}$$

If (15.65) is applied throughout, a body of revolution results, which is bound by a cubic parabola (Fig. 15.44).

The surface pressure in the bearing points must be handled in the same way as in a bolted joint (Sect. 15.2.2).

Determination of the Diameter from the Torsional Load (Shafts). Pure torsional loading of shafts is rare, as additional bending is often present. The maximum torsional stress in solid cylindrical shafts is calculated from the torsional moment T and the polar section mod-

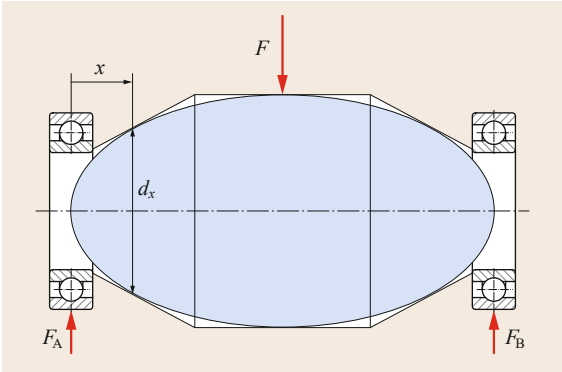

Fig. 15.44 Beam with the same strength

ulus W_p:

$$\tau_{t\,max} = \frac{T}{W_p} \le \tau_{t\,all} \,. \tag{15.66}$$

If $W_p = \pi d^3/16$, the requirement minimum diameter of the shaft is

$$d \ge \sqrt[3]{\frac{6T}{\pi \tau_{t\,all}}} \approx 1.72 \sqrt[3]{\frac{T}{\tau_{t\,all}}} \,. \tag{15.67}$$

The allowable torsional stress $\tau_{t\,all}$ is determined as an estimate value depending on the type of load and the influencing variables that exist (e.g., notch effects). Indicative values for the allowable torsional stress result after *Niemann* et al. [15.24] from

$$\tau_{t\,all} = \frac{\sigma_W}{(3 \ldots 6)} . \tag{15.68}$$

When using (15.68), it must be taken into account that smaller safety values are used for light service and larger safety values for heavy-duty service.

Determination of the Diameter from Torsion and Bending. In practice, a combination of torsion and bending usually occurs in shafts, which produces a multiaxial stress state. An equivalent stress hypothesis can be used to transform the individual superimposed bending and torsional stresses into a single-axis stress state corresponding to pure tension or pure bending, which allows an equivalent stress to be calculated. In most cases, the equivalent stress for the calculation of shafts subjected to torsion and bending is formed on the basis of the Von Mises criterion (Sect. 15.1.2 or rather Sect. 15.1.3):

$$\sigma_V = \sqrt{\sigma_b^2 + 3\,(\alpha_0 \tau_t)^2} \le \sigma_{all} = \sigma_{b\,all} \,. \tag{15.69}$$

The equivalent moment M_V (equivalent bending moment with the same effect as the bending and torsional moment together) with $\sigma_b = M_b/W_b$ and $\tau_t = T/\left(W_p\right) = T/\left(2W_b\right)$ is calculated from

$$M_v = \sqrt{M_b^2 + 0.75\,(\alpha_0 T)^2} \,. \tag{15.70}$$

With the condition $\sigma_V = M_V/W_b \le \sigma_{b\,all}$, the required shaft diameter is

$$d \ge \sqrt[3]{\frac{32 M_v b'}{\pi \sigma_{b\,all}}} \approx 2.17 \sqrt[3]{\frac{M_v b'}{\sigma_{b\,all}}} \,. \tag{15.71}$$

The factor b' for a solid or hollow shaft is:

$$\text{Solid shaft:} \quad b' = 1 \tag{15.72}$$

$$\text{Hollow shaft:} \quad b' = \frac{1}{1 - (d_i/d)^4} \tag{15.73}$$

Depending on the type of load and the existing influencing variables (e.g., not effects), the allowable bending stress $\sigma_{b\,all}$ is initially determined as an estimate value (Table 15.31).

For the initial design, the minimum shaft diameters determined above form the basic size and stand for the calculated required cross section. For the final definition, however, grooves, holes and other features must be considered. However, the executed core diameter d_c should not be less than the determined diameter d' (Fig. 15.45).

15.3.5 Check Calculations

Following the design of the axle or shaft, taking into account the determined minimum diameter, the strength of the component must be verified. In particular, this verification should be performed for areas in which cross-sectional weaknesses exist, such as thread undercuts, grooves, or shaft shoulders.

Strength Verification

The strength verification basically includes three calculation steps. In the first calculation step, the equivalent stress σ_V produced in the component by all applied forces and moments is calculated. The procedure for this is explained in Sect. 15.1.2. The fatigue strength σ_G of the component is determined in the second calculation step. This results from the material strength, taking into consideration all strength-reducing effects (Sects. 15.1.4 and 15.1.5). The strength verification is performed in the third step. It demonstrates

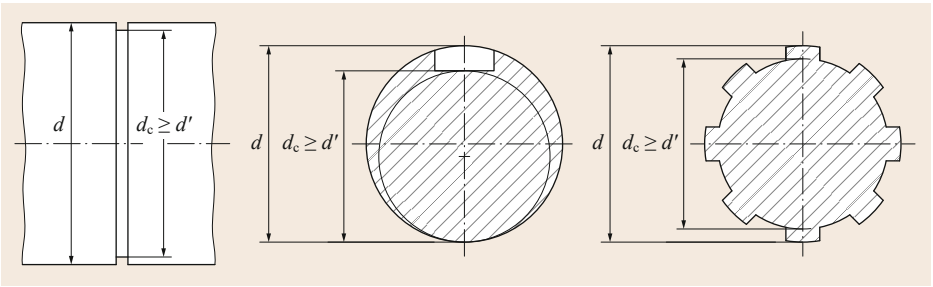

Fig. 15.45 Estimated and final shaft diameter

Table 15.32 Indicative values for allowable deflection (after *Niemann* et al. [15.24])

General shafts	$f_{all}/l^a = 0.3 \times 10^{-3}$
Shafts without guide functions	$f_{all}/l = 0.5 \times 10^{-3}$
Shafts in machine tools	$f_{all}/l = 0.2 \times 10^{-3}$
Shafts in electric motors	$f_{all} = (0.2 \ldots 0.5) \times$ air gap

[a] l = distance between the bearings

Table 15.33 Indicative values for allowable inclination angle (after *Niemann* et al. [15.24])

Roller bearings	$\beta_{all} = 0.3 \times 10^{-4}$
Deep-groove ball bearings	$\beta_{all} = (0.6 \ldots 3) \times 10^{-3}$
Plain bearings with movement shells	$\beta_{all} = 3 \times 10^{-4}$
Plain bearings with adjustable shells	$\beta_{all} = 1 \times 10^{-3}$
Gear train	$\beta_{all} = (4 \ldots 15) \times 10^{-4}$

that the safety S is greater or equal to the agreed safety S_{agr}

$$S = \frac{\sigma_G}{\sigma_V} \leq S_{agr} \,. \tag{15.74}$$

The safety required depends on the application case and potential damage. For rough calculations, from practical experience: $S_{agr} = 1.2 \ldots 2.0$.

A detailed strength verification procedure is described in the DIN 743 [15.9] standard and in the FKM guidelines [15.5].

Deformation Due to Bending Forces

For deformation due to bending forces, the deflection f of the axle or shaft and the inclination angle β of the elastic curve must be checked. These are decisively influenced by the acting forces and the elasticity of the material used. Increased deflection and inclination, especially in shafts with gears, leads to meshing faults on the teeth, which in turn results in noise generation and premature wear. In bearing positions, excessive inclination also results in increased bearing wear.

The deflection and inclination angle of the bending line can be determined both graphically using Mohr's method and analytically via the elastic bending line or Castigliano's theorem. In complex axle/shaft geometries or load conditions the deformation can be calculated with the help of numerical methods such as the finite element method.

Guide values for the allowable deflection are given in Table 15.32 and for the inclination angle in Table 15.33.

Deformation Due to Torsional Moments

For the dimensioning of longer shafts, for example, slewing gear shafts of slewing cranes or power take-off drive shafts in utility vehicles, the twist is decisive due to torques (Fig. 15.46). Together with torque fluctuations, these deformations can lead to vibrations. Furthermore, low torsional stiffness requires a large twist angle and consequently gives rise to a low critical speed.

As a result of the described effects, the actual twist angle φ must be below the allowable twist angle φ_{all} ($\varphi \leq \varphi_{all}$). Equation (15.75) can be used as indicative values for the allowable twist angle:

$$\varphi_{all} = (0.25 \ldots 0.5) \, \frac{^\circ}{m} \, l \,. \tag{15.75}$$

Critical Speed

Vibration and Resonance. If a body is deformed elastically by a force F or rather by a torque T, it can be made

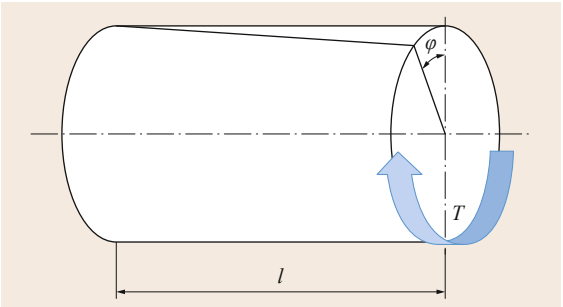

Fig. 15.46 Elastic deformation under torsion

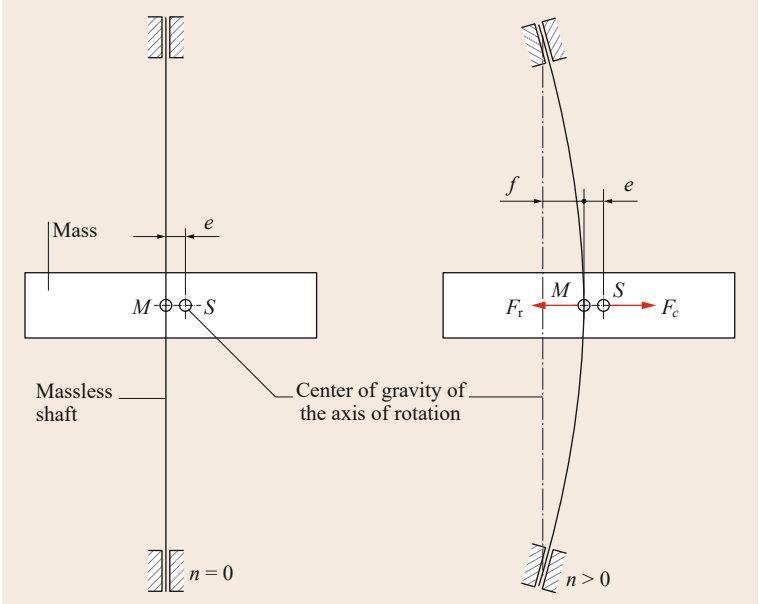

Fig. 15.47 Deformation of the shaft by centrifugal force

to vibrate flexurally (bending) or torsionally (rotation) by the restoring force acting in the opposite direction after sudden withdrawal of the force (unloading).

With increasing stiffness (spring constant) and decreasing mass of the component, the vibration frequency increases. This is independent of the size of the exciting force, which only determines the vibrational amplitude. Consequently, all bodies have a certain constant natural frequency. Multibody systems with $i = 1 \ldots n$ masses and $i = 1 \ldots n$ springs, have $n = 1 \ldots n$ natural frequencies.

If a body is made to vibrate by an excitation frequency that equals the natural frequency (or an integral multiple of it), the excitation frequency superimposes the natural frequency and resonance occurs. The vibration amplitude increases as a result, which can cause the axle or shaft to fracture.

Together with the coupled machine parts, rotating shafts and axles form vibratory systems. In general it must be considered that flexural and torsional vibrations are also caused by rotational frequencies induced as excitation and periodically varying forces and moments.

Critical Bending Speed. Due to nonrotationally symmetrical design elements (for example, parallel key connections) or production inaccuracies, the center of gravity of shafts and axles does not generally coincide with the center of rotation (Fig. 15.47).

If the shaft or axle rotates with angular velocity ω, the unbalance produces the centrifugal force F_C:

$$F_C = mr\omega^2 = m\,(f + e)\,\omega^2\,. \tag{15.76}$$

At the same time, a restoring force F_r dependent on the spring bending stiffness of c_b counteracts the centrifugal force:

$$F_r = c_b f\,. \tag{15.77}$$

In force equilibrium,

$$\begin{aligned} 0 &= F_r - F_C \\ &= m\,(f + e)\,\omega^2 - c_b f\,. \end{aligned} \tag{15.78}$$

Rearranging to obtain the deflection f we get

$$y = \frac{e}{\left(\frac{c_b}{m\omega^2} - 1\right)}\,. \tag{15.79}$$

From (15.79) it can be seen that in the case where $\omega^2 = c_b/m$, deflection tends to infinity, so that the critical angular velocity ω_C is

$$\omega_C = \sqrt{\frac{c_b}{m}}\,. \tag{15.80}$$

Accordingly, the critical bending speed is

$$n_k = \frac{30}{\pi}\sqrt{\frac{c_b}{m}} \quad \text{in} \quad \frac{1}{\text{min}}\,. \tag{15.81}$$

Multisupport shafts with n masses also have n critical speeds, whereby in most cases the lowest critical speed is significant in practice. Due to the complexity of such a multimass system, the critical speed is mostly determined approximately using special calculation programs or is determined experimentally.

Torsional Critical Speed. A system of shafts with components fixed on it can also be characterized as a torsion rod. Torque impulses, for example, due to a pulsating drive torque in combustion engines, a critical torsional vibration can be caused with the natural frequency of the shaft system. Torsional vibration resonances occur, which can damage the shaft.

The torsional critical speed n_C of a single degree of freedom system (SDOF) (e.g., torsion pendulum) is calculated from

$$n_C = \frac{30}{\pi}\sqrt{\frac{R_t}{I_m}}\,, \tag{15.82}$$

where:

R_t torsion spring rate of the shaft in Nm
I_m moment of inertia in kg m^2

For a shaft with two masses,

$$I_m = \frac{I_{m1} I_{m2}}{I_{m1} + I_{m2}}\,. \tag{15.83}$$

Conclusions for the Design of Shafts and Axles. Determining the deformation in multiple shouldered shafts and calculating the moments of inertia are difficult. For this reason, an exact calculated determination of the critical speeds with a reasonable calculation time is often only possible with very large effort. Furthermore, the influence of the environment and the shaft length on the system cannot be ignored. As a result of this, the natural frequency is often determined experimentally. For safe operation of the shaft, the excitation frequency (mostly the speed) should be at least 20% above or below the natural frequency.

When dimensioning, the following design measures must be considered to prevent resonance phenomena:

- The bearings must be positioned as closely as possible to the rotating discs. This achieves smaller deflection.
- Through careful balancing of shafts with rotating parts, smaller centrifugal forces occur.
- On the material side, the critical speeds can only be influenced by the modulus of elasticity or the shear modulus.

15.3.6 Further Reading

A deeper insight into the dimensioning of axles and shafts is given, among others, by *Wittel* et al. [15.2] and the DIN 743 Part 1–4 series of standards [15.7, 9, 10].

In their book *Maschinendynamik* [15.54] (machine dynamics), *Dresig* and *Holzweißig* provide a standard reference on vibration analysis of machine parts.

15.4 Shaft–Hub Connections

Shaft–hub connections are standardized connections for fastening components, such as wheels, gears, pulleys, levers, etc., on shafts, axles, and journals. They are primarily used to transfer torques and rotary movements. In certain applications, however, bending moments (e.g., in the case of inclined shaft positions) or axial forces (e.g., in the case of helical gears) must also be transferred.

Depending on the type of force transfer, shaft–hub connections are divided into:

- Form-closure shaft–hub connections: The connection is made by a specific shape design (e.g., by spline profiles, serrations, or polygonal splines) or through additional elements (e.g., by parallel keys, Woodruff keys, or transverse pins/cross pins).
- Frictional shaft–hub connections: The connection is achieved by frictional clamping or pressing of the hub onto the shaft or axle (e.g., via interference fit assemblies/press fit, taper seats, or clamping elements).
- Preloaded form-closure shaft–hub connections: Combination of frictional and form-closure connections (primarily achieved through different types of wedges and compression connections secured by parallel keys).
- Material-bonding shaft–hub connections: The connection is made by material bonding (e.g., by adhesive bonding, soldering, or welding). In many cases the connection can only be undone by destroying it.

A selection aid for specifying a suitable shaft–hub connection is given in Table 15.34.

15.4.1 Form-Closure Shaft–Hub Connections

Form-closure shaft–hub connections are simple and inexpensive in their structure and assembly. The form closure is achieved by appropriate shaping of the shaft and/or hub (e.g., serrated or polygonal connection) or by using additional components (e.g., parallel keys and pins). The torques to be transferred are resolved

Table 15.34 Notes on the selection of shaft–hub connections (after *Niemann* et al. [15.24])

Suitable for	Form closure	Friction	Preloaded form-closure	Material bonding
Smaller torques	Transverse pin, Woodruff key	Force fit (clamped seat), hollow key (saddle key), tolerance ring	–	Adhesive bonded sliding seat, soldered joint
Mean one-sided torques	Transverse pin, parallel key	Press fit, force fit (clamped seat)	–	Shrink-adhesive bonded fit
Mean alternating torques	Parallel key (with limitations)	Hollow key (saddle key), tolerance ring	–	
Large alternating or pulsating, intermittent torques, e.g., flywheel fixing	–	Transverse press fit (shrink fit seat, compressed oil connection)	Multispline and polygonal spline with press fit, tangential key	Welded joint
Short hub with large torque	Multispline, serrated and polygonal spline	Shrink fits with carborundum powder	–	Welded joint (direct connection of the wheel discs with the shaft), shrink-adhesive bonded fit
Sliding hub and shaft	Sliding key, multiple spline	–	–	–
Easily separable hub	Parallel key, multispline, serrated and polygonal spline	Force fit (clamped seat), taper seat, taper bush, pressurized oil assembly, Ringfeder clamping element, clamp rings	Gib head taper key, thread with longitudinal positioning of the hub on the shaft shoulder and tapered thread for one rotational direction	Adhesive bonded, sliding and shrink fit seat (heating)
Hub to be subsequently attached to smooth shaft	–	Hollow key (saddle key), force fit (clamped seat), taper bush, Ringfeder clamping element	–	–
Hub adjustable in rotational direction	Serrated profile	Hollow key (saddle key), force fit (clamped seat), taper seat, taper bush, clamp rings	–	–
Thin-walled hub	Serrated profile	Clamp rings	Thread with longitudinal positioning of the hub on the shaft seat with one-sided torque	Adhesive bonded, sliding and shrink fit seat

into tangential forces or surface pressure at the contact points of the parts to be joined. Axial forces can generally only be transferred in conjunction with additional axial fixing (for example, stops or shaft retaining rings).

Parallel Key Connection

Parallel key connections are the most frequently used form-closure shaft–hub connection for a torque acting on one side, for example, for belt pulleys, gears, and couplings.

They can be easily mounted, dismantled, and reused.

Frequently used forms according to DIN 6885-1 [15.55] (Fig. 15.48) are:

- Form A: high form with round end faces
- Form B: high form with straight end faces

For hubs that move longitudinally, for example, sliding gears in gear units, the parallel key with corresponding tolerances becomes a sliding key.

In conjunction with force fit (clamped seat) or taper seats, they are used as a so-called preloaded form-closure connection for position fixing.

The circumferential force F_u resulting from the torque is transferred via the side faces (flanks) of the parallel key. This results in loading of the side faces with surface pressure and shear in the interface between the shaft and hub. With standard parallel keys the surface pressure on the side faces is exceeded before the allowable shear stress is exceeded. For this reason, parallel keys must be dimensioned for surface pressure.

Surface pressure in the hub:

$$p = \frac{F_u}{(h - t_1)\, l_t i \varphi} = \frac{2T}{d\,(h - t_1)\, l_t i \varphi} \leq p_{all} \qquad (15.84)$$

Surface pressure in the shaft:

$$p = \frac{F_u}{t_1 l_t i \varphi} = \frac{2T}{d t_1 l_t i \varphi} \leq p_{all} \qquad (15.85)$$

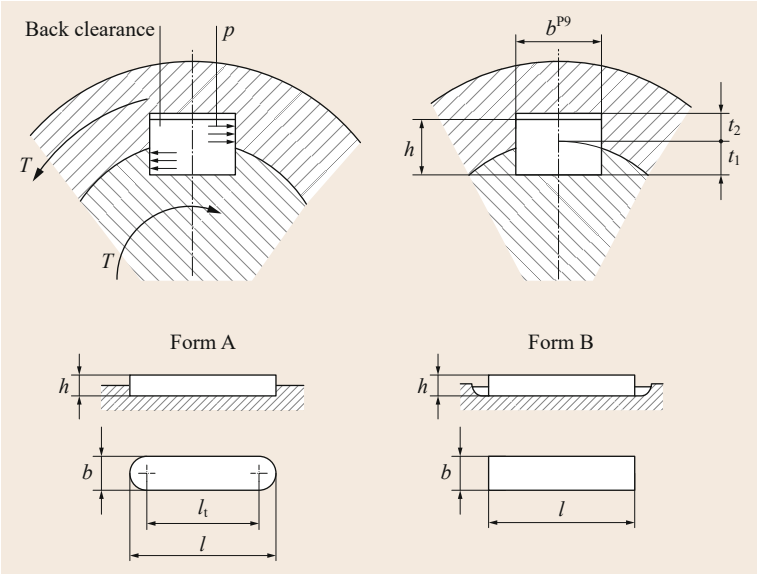

Fig. 15.48 Parallel key connection. Mode of action and forms (selection) according to DIN 6885-1 [15.55]

Table 15.35 Allowable pressures for parallel keys made of steel in N/mm^2

	For light shocks		For strong shocks	
	One-sided	Alternating	One-sided	Alternating
Cast iron hubs	65	45	40	20
Cast steel or steel hubs	120	80	80	35

where

F_u circumferential force $F_u = 2T/d$
h parallel key height (Fig. 15.48)
t_1 shaft groove depth (Fig. 15.48)
l_t effective length of the parallel key
T torsional moment
d shaft diameter
i number of parallel keys
φ bearing factor $\varphi = 1$ if $i = 1$; $\varphi = 0.75$ if $i > 1$
p_{all} allowable pressures (Table 15.35)

For parallel keys with round end faces (feather keys) (Fig. 15.48), the load-bearing length (effective length) l_t is determined by deducing the width of the parallel key b from the total length l ($l_t = l - b$).

If more than one parallel key is used, the bearing factor φ allows for nonuniform load bearing of the individual parallel keys.

Dimensions and tolerances of the parallel keys for a given shaft diameter are given in the relevant standards/reference tables (DIN 6885-1 [15.55] for metric parallel keys and ANSI B17.1 [15.56] for inch-measure parallel keys).

Table 15.36 Empirical values for hub lengths l_N and hub external diameters d_N depending on the shaft diameter d

	Cast iron	Steel/cast steel
Hub diameter d_N	$1.8 \ldots 2.0d$	$1.6 \ldots 1.8d$
Hub length l_N	$1.8 \ldots 2.0d$	$1.6 \ldots 1.8d$

Indicative values for allowable surface pressures p_{all} are given in Table 15.35. The dimensions of the hub depends on the joining diameter (Table 15.36).

Woodruff Key Joint

Woodruff keys are frequently used in small machine tools and in vehicle construction to transfer smaller torques (Fig. 15.49). Compared to a normal parallel key connection, it is easier to produce and thus less expensive. However, at the same time, due to the deeper shaft groove, it leads to greater weakening of the shaft.

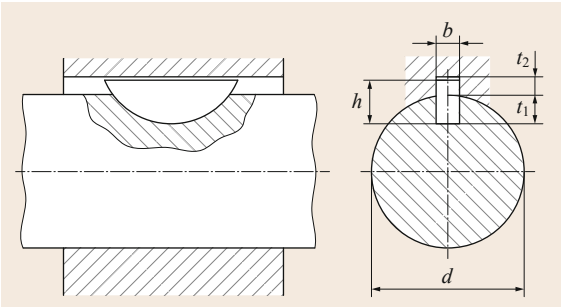

Fig. 15.49 Woodruff keys according to ISO 3912/ANSI B17.2

Table 15.37 Standard profile shaft connections

Straight-sided spline connections	Splined-shaft connections		Polygonal connections
	Involute spline profile	Serrated spline profile	
Transfer surfaces are parallel with each other	Transfer surfaces are involute surfaces	Transfer surfaces are triangular	Transfer surfaces are out-of-round (not circular) (generally triangular and rectangular profiles)
Light- and medium-duty series according to DIN ISO 14 Heavy-duty series according to DIN 5464	According to ISO 4156 (metric); ANSI B92.1 (inch)	According to DIN 5481, NF E22-151	Triangle (P3G) according to DIN 32711 Rectangle (P4C) according to DIN 32712
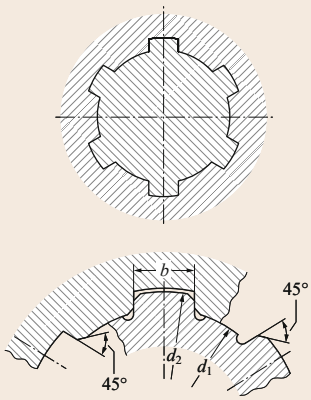	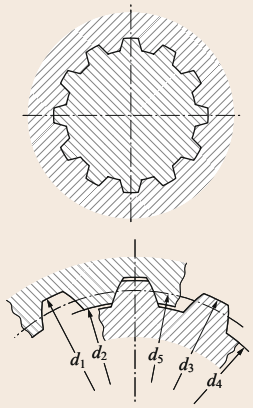	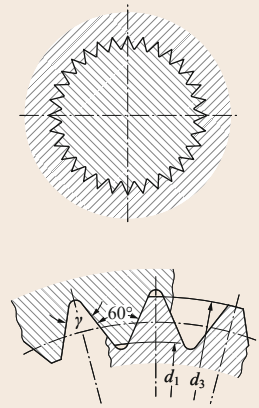	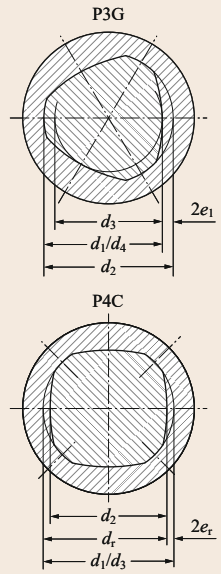

The dimensions of woodruff keys are defined in the ISO 3912 standard [15.57] and in the American code ANSI B17.2 [15.58].

The calculation is performed similarly to that for a parallel key connection, whereby in most cases the surface pressure in the hub groove is the limiting factor.

Profile Shaft Connections

Profile shaft connections transfer the torques (in the form of tangential forces) via several effective areas. They are suitable for higher, intermittent (shock-like) torques (including alternate torques). They have a very good centering effect, which results in low unbalance and uniform distribution of the circumferential load. They can also be designed as sliding hubs by choosing an appropriate fit.

Standard profile shaft connections are shown in Table 15.37.

Straight-Sided Spline Connections

The even number of *male splines* arranged on the circumference act like parallel keys. They are relatively inexpensive to produce and are used, for example, in gear units in combination with sliding hubs (gear wheel or clutch sleeve). A differentiation is made, depending on the type of centering effect, between:

- Internal centering: very precise centering; used in machine tools
- Flank centering: difficult to produce; advantageous for shock and alternate loading

Splined-Shaft Connections

Due to their large number of teeth, splined-shaft connections can absorb particularly large and intermittent (shock-like) forces. At the same time, the large number of teeth enables fine adjustment from tooth to tooth, as a result of which the angular position of actuating elements can be easily varied. The small tooth height leads to narrow hubs. Their cost-effective production and good adjustability makes them especially suitable for actuating elements. A differentiation is made between involute and serrated spline connections, depending on the shape of the teeth.

Polygonal Connections

These are used as separable connections in sliding or press-fit seats for the transfer of shock-like, intermittent torques. However, due to micromovements between the parts to be joined there is a risk of vibration fretting.

Tight or interference fit is possible, depending on the clearance chosen. Clearance fits are to be avoided due to the associated micromovements.

Triangular and rectangular profiles P3G and P4C (Table 15.37) are primarily used.

Compared to the P3G profile, the P4C profile is particularly suitable for connections that are intended to be longitudinally slidable under load (torque).

The profile geometries are usually turned on a profile lathe (shaft) or are broached using a broaching machine (hub).

Calculation of Profile Shaft Connections

Profile shaft connections are designed for surface pressure on the respective effective surfaces. For straight-sided spline and splined-shaft connections

$$p = \frac{2T}{d_m h l_t i \varphi} \leq p_{all} \,, \tag{15.86}$$

where:

T torsional moment
d_m average profile diameter
h load-bearing tooth height
l_t effective length of the connection
i number of teeth
φ bearing factor:
splined shaft with internal centering: $\varphi = 0.75$
splined shaft with external centering: $\varphi = 0.9$
splined shaft with serrated toothing: $\varphi = 0.5$
splined shaft with involute toothing: $\varphi = 0.75$
p_{all} see Table 15.35

For P3G polygonal connections, the surface pressure must be checked using

$$p \approx \frac{T}{l_t \left(0.75 \pi e_1 d_1 + 0.05 d_1^2\right)} \leq p_{all} \,, \tag{15.87}$$

where e_1; d_1 is the geometrical profile size (Table 15.37).

For the P4C profile, the surface pressure is approximately

$$p \approx \frac{T}{l_t \left(\pi e_r d_r + 0.05 d_r^2\right)} \leq p_{all} \,, \tag{15.88}$$

where e_r; d_r is the geometrical profile size (Table 15.37)

The allowable surface pressures are given in Table 15.35.

15.4.2 Frictional Shaft–Hub Connection

Frictional connections generate the forces necessary for force and moment transfer solely through friction at the interfaces between the shaft and hub.

According to Coulomb's friction law,

$$F_\mu = \mu_i F_n \,. \tag{15.89}$$

The friction coefficient μ_i used to calculate the friction forces is either the sliding coefficient of friction μ or the static coefficient of friction μ_0, depending of the form of friction present.

In frictional connections, the frictional force must always be larger than the forces to be transferred, so that for slip-free transfer of axial forces F_a and torques $T = F_u D_F / 2$:

Axial force:

$$F_a \leq F_{\mu a} = \frac{\mu_0 F_n}{S_r} = \frac{\mu_0 \pi D_F l_F p_F}{S_r} \tag{15.90}$$

Torque:

$$T \leq T_\mu = \mu_0 F_n \frac{D_F}{2 S_r} = \frac{\mu_0 \pi D_F^2 l_F p_F}{2 S_r} \,, \tag{15.91}$$

where:

μ_0 static coefficient of friction (Table 15.38)
D_F nominal diameter of the joint
p_F surface pressure in the joint gap (joint compression, interference of the joint)
l_F specified factor of safety against plastic elongation (1–1.3)
S_r factor of safety against slipping (1.5–2)

Table 15.38 Guide values for coefficients of friction of longitudinal press-fit connections with quick loading according to DIN 7190-1 [15.59]

Material pairing (shaft/hub)	Friction values Dry		Lubricated	
	μ_0	μ	μ_0	μ
Steel/cast steel	0.10–0.11	0.08–0.09	0.07–0.08	0.06–0.07
Steel/cast iron	0.10–0.12	0.09–0.11	0.06	0.05
Steel/aluminum	0.07	0.06	0.05	0.04

Table 15.39 Coefficients of friction of transverse press-fit assemblies in longitudinal and circumferential direction on slipping according to DIN 7190-1 [15.59]

Material pairing, lubrication, joining	Friction values μ
Steel-steel pairing	
Pressurized oil assemblies normally joined with mineral oil	0.12
Pressurized oil assemblies with degreased pressure contact surfaces joined together with glycerine	0.18
Shrink-fit assembly, normal, after heating the external part up to 300 °C in the electric furnace	0.14
Shrink-fit assembly with degreased pressure contact surfaces after heating in the electric furnace up to 300 °C	0.20
Steel-cast iron pairing	
Pressurized oil assemblies normally joined with mineral oil	0.10
Pressurized oil assemblies with degreased pressure contact surfaces	0.16
Steel-MgAl pairing, dry	0.10–0.15
Steel-CuZn pairing, dry	0.17–0.25

The ability of a connection or joint to transfer forces and moments essentially depends on the coefficient of friction and the normal (perpendicular) force F_n.

While the coefficient of friction is highly dependent on the type of paired materials, the surface finish, the lubricated condition, and relative speed of the paired components (guide values in Tables 15.38 and 15.39), F_n is limited by the allowable surface pressure $p_{F\,all}$.

Table 15.40 Advantages and disadvantages of frictional shaft–hub connections

Advantages	Disadvantages
Simple structure	Assembly and dismantling difficult at times (press-fit connection)
Low unbalances (high speeds possible)	A minimum preload is required for force transfer
Withstands high dynamic loads	Risk of fretting in the case of alternating (cyclic) stress or loading
No cross-sectional weakening of the shaft	
Simultaneous transfer of axial and tangential forces	
Very suitable for alternating (cyclical) loads	

Frictional connections can basically be divided into (Fig. 15.50):

- Connections with and without intermediate parts
- Connections with cylindrical and tapered fit joints

When selecting friction connections, in addition to the force closure, other properties such as self-centering, setting and adjustability, production and assembly costs, the necessary production tolerances, and the separability or reusability must also be considered.

Advantages and disadvantages of frictional shaft–hub connections are given in Table 15.40; execution examples are given in Fig. 15.51.

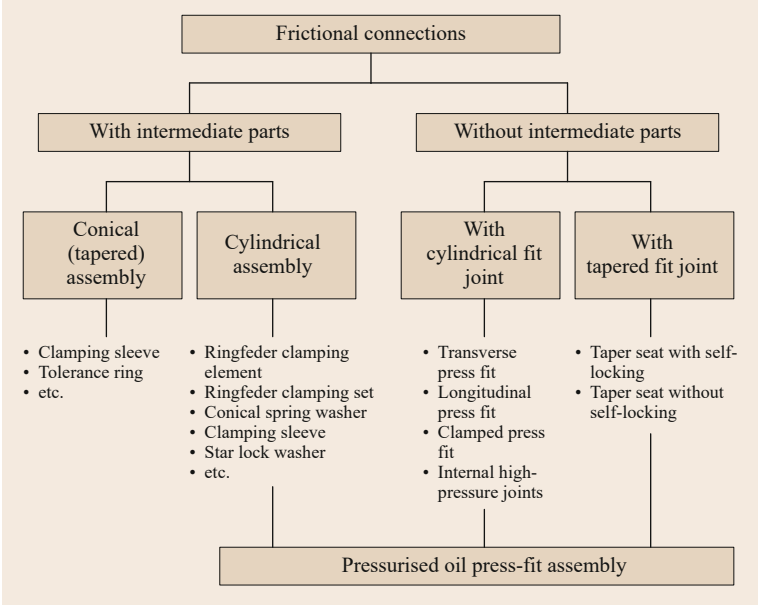

Fig. 15.50 Classification of frictional shaft–hub connections

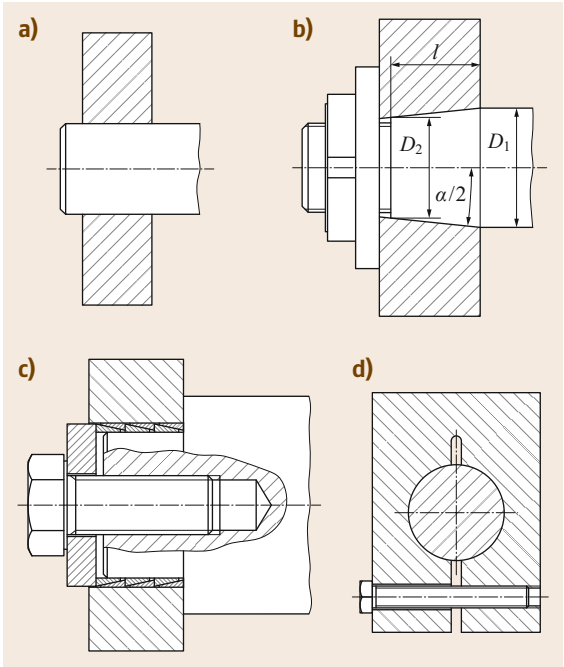

Fig. 15.51a–d Examples of frictional connections. **(a)** Cylindrical press-fit assembly, **(b)** conical press-fit assembly, **(c)** press-fit connection with intermediate parts (tapered clamping elements), and **(d)** compression connection

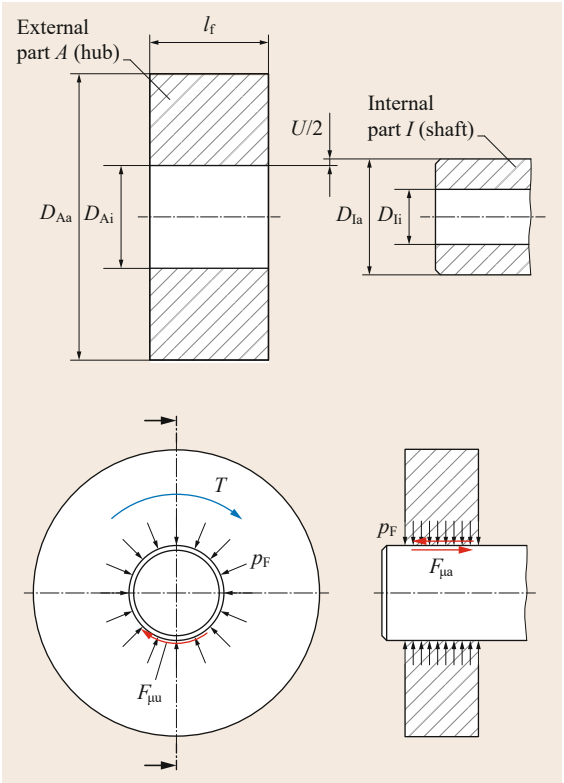

Fig. 15.52 Mode of action of a press-fit connection and force (load) distribution. Index i = internal; index a = external

Cylindrical Compression (Press-Fit) Connections

The internal diameter of the external part D_{Ai} and the external diameter of the internal part D_{Ia} are chosen so that an oversize (interference) U results (Fig. 15.52). If the external part is joined with the internal part, the oversize causes surface pressure p_F, also called joint compression, in the joint gap. Combined with the existing coefficient of friction in the joint gap, a friction force results that enables the frictional transfer of axial or rather circumferential forces.

Due to the elasticity of the clamped parts, they are permanently joined together, which makes correction of the hub position very difficult.

Cylindrical press-fit connections are mainly used for permanent connections, such as flywheels, belt pulleys, gears, plain bearing bushes in housings, and rolling bearing rings.

After the type of joining has been chosen, a differentiation is made between longitudinal press-fit connections, transverse press-fit connections, and press-fit connections to be mounted or dismantled with pressurized oil methods (Fig. 15.53).

Longitudinal press-fit connections are mostly joined at room temperature by pressing the shaft into the hub. A slight taper at the end of the shaft makes it easier to insert the shaft. The longitudinal displacement causes smoothing of the surface, as a result of which the adhesive force is less than in a transverse force joint. Lubricants reduce the sliding coefficient of friction and thus make it easier to press in the shaft. After joining, they are slowly displaced from the joint gap so that the full adhesive force is not reached until after a longer adhesion time (approximately 48 h).

In the case of transverse press-fit connections the oversize necessary for the force transfer is cancelled out by heating the hub and/or cooling the shaft, so that a clearance fit results. In this condition, the components can be joined without force. After the temperature has equalized, the press fit required for the force transfer results.

Similar to transverse press-fit connections, oil injection press-fit connections can be joined almost force-free. In this case, during assembly or dismantling, oil is

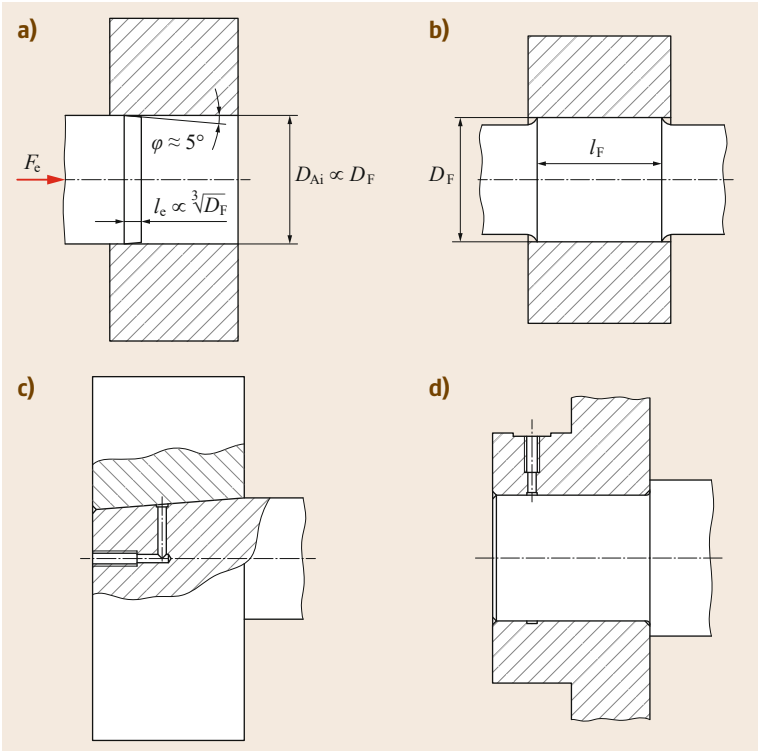

Fig. 15.53a–d Press-fit connections. **(a)** Longitudinal press-fit connection, **(b)** transverse press-fit connection, **(c)** conical press-fit connection joined with pressurized oil method, and **(d)** cylindrical press-fit connection to be dismantled with pressurized oil method

injected from the outside under high pressure through a slightly tapered fitting joint, which causes the hub to widen slightly and a thin film of oil results between the shaft and hub, which separates the contact surfaces from each other. Thus, when the parts are pushed together only fluid friction acts. Cylindrically shaped press-fit connections cannot be joined by this method; however, it can be used to undo them. After joining, a waiting time of approximately 2 h is required before loading the joint. The advantages and disadvantages of cylindrical press-fit connections are listed in Table 15.41.

Practical Calculation of Cylindrical Press-Fit Connections. The press-fit connection is calculated based on the standard DIN 7190-1 [15.59], whereby the calculation sequence has been modified. In calculation terms, the smallest required oversize U_{min} and the largest allowable oversize U_{max} must be determined based on the minimum surface pressure required in the joint gap $p_{F\,min}$ and the maximum allowable surface pressure in the joint gap p_{Fall}.

Calculation of the required and allowable oversizes requires knowledge of all other geometrical variables of the press-fit connection.

According to Table 15.42, the hub dimensions can be roughly defined depending on the joint diameter.

Table 15.41 Advantages and disadvantages of cylindrical press-fit connections

Advantages	Disadvantages
Transfer of large, alternating, and/or intermittent, shock-like axial forces and torques	Tight tolerancing required
Precise centering of the hub on the shaft	Difficult or rather permanent (except oil injection press-fit connections)
Minor unbalances	Correction of the hub position not possible
No weakening of the shaft due to grooves (keys)	
Simple, inexpensive production	

Table 15.42 Rough, estimated values for hub dimensions of press-fit connections

	Cast iron	Steel/cast steel
Hub diameter D_{Aa}	$2.2 \ldots 2.6 D_F$	$2.0 \ldots 2.5 D_F$
Hub length l	$1.2 \ldots 1.5 D_F$	$0.8 \ldots 1.0 D_F$

The stated calculation requires pure elastic deformation of the internal and external parts; in practice, certain proportions of plastic deformation are allowed. The DIN 7190-1 standard gives a simple calculation

method for elastic-plastic loaded press-fit assemblies (interference fits) for limited application, which is not discussed any further here.

Smallest Required and Largest Allowable Joint Compression. For a given torsional moment T, or rather a given axial force F_a, (15.90) and (15.91) can be rearranged to determine the minimum joint compression $p_{F\min}$ necessary for safe and reliable transfer:

Pure torque:

$$p_{F\min} = \frac{2TS_r}{\mu_0 \pi D_F^2 l_F} \tag{15.92}$$

Pure axial force:

$$p_{F\min} = \frac{F_a S_r}{\mu_0 \pi D_F l_F} \tag{15.93}$$

Simultaneous axial force and torque:

$$p_{F\min} = \frac{\sqrt{{F_a}^2 + \left(\frac{2T}{D_F}\right)^2}\, S_r}{\mu_0 \pi D_F l_F} \tag{15.94}$$

The maximum allowable joint compression $p_{F\max}$ is limited by the allowable material strength in the hub, or rather in the shaft.

External part:

$$p_{F\max A} = \frac{1 - Q_A^2}{\sqrt{3} S_{PA}} R_{elA} \tag{15.95}$$

Internal part (hollow shaft):

$$p_{F\max I} = \frac{1 - Q_i^2}{\sqrt{3} S_{PI}} R_{elI} \tag{15.96}$$

Internal part (solid shaft):

$$p_{F\max I} = \frac{2R_{elI}}{\sqrt{3} S_{PI}} \tag{15.97}$$

where:

Q_A; Q_I diameter ratios $Q_A = D_F/D_{Aa}$; $Q_I = D_{Ii}/D_F$ (Fig. 15.53a)
S_{PA}; S_{PI} specified factor of safety of the hub, or rather the shaft against plasticization (1−1.3)
R_{elA}; R_{elI} lower elasticity limit of the hub, or rather the shaft

For further calculation, the smallest value of the minimum allowable surface pressure according to (15.95)–(15.97) must be used.

Smallest Required and Largest Allowable Oversize. From the smallest required and largest allowable joint compression $p_{F\min}$ and $p_{F\max}$, with joint diameter D_F and the auxiliary variable K according to (15.99), the smallest required and largest allowable adhesion $Z_{\min}$ and $Z_{\max}$ can be calculated as follows:

Smallest required adhesion:

$$Z_{\min} = \frac{p_{F\min} D_F}{E_A}$$

Largest allowable adhesion:

$$Z_{\max} = \frac{p_{F\max} D_F}{E_A} \tag{15.98}$$

with

$$K = \frac{E_A}{E_I}\left(\frac{1 + Q_I^2}{1 - Q_I^2} - \upsilon_I\right) + \frac{1 + Q_A^2}{1 - Q_A^2} + \upsilon_A\,, \tag{15.99}$$

where:

E_A; E_I modulus of elasticity of the hub, or rather of the shaft, respectively
υ_A, υ_I Poisson's ratio of the hub, or rather of the shaft, respectively

On joining the components, smoothing (plastic deformation) of the surface roughnesses causes a loss in oversize ΔU (Fig. 15.54). With smoothing amounts of the surfaces $G_{Ai} \approx 0.2R_{zAi}$ and $G_{Ia} \approx 0.2R_{zIa}$, the total loss in oversize is:

$$\Delta U = 2G_{Ai} + 2G_{Ia} = 0.4\,(R_{zAi} + R_{zIa})\,. \tag{15.100}$$

The smallest required or largest allowable oversizes to be set in before joining are made up of the adhesions

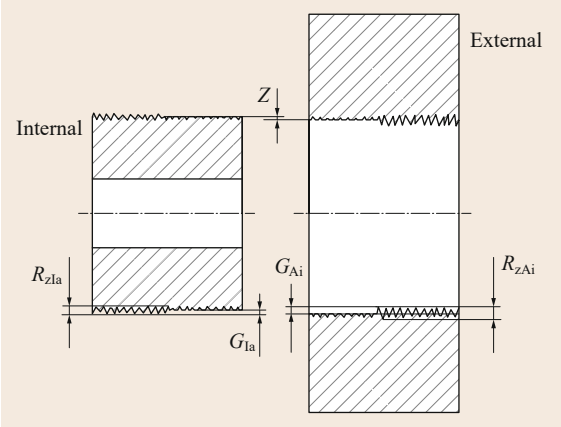

Fig. 15.54 Surface smoothing in the longitudinal joints of the components

according to (15.98) and the loss of oversize according to (15.100) as follows:

$$\begin{aligned} &\text{Smallest required oversize:} \quad U_{\min} = Z_{\min} + \Delta U \\ &\text{Largest allowable oversize:} \quad U_{\max} = Z_{\max} + \Delta U \end{aligned} \tag{15.101}$$

The maximum allowable dimensional fluctuation of the components, the fit tolerance P_T, is defined by the oversizes $U_{\min}$ and $U_{\max}$:

$$P_T = U_{\max} - U_{\min} \,. \tag{15.102}$$

The fit tolerance P_T must be divided between the tolerance zones of the hole T_A and the shaft T_I:

$$P_T = T_A + T_I \,. \tag{15.103}$$

Notes:

- In the case of very fast rotating press-fit connections, the centrifugal forces that occur can reduce the fitting joint pressure. For this reason, the effect of the speed on fast rotating connections must be checked (DIN 7190-1 [15.59]).
- If the press-fit assembly is loaded dynamically, the fatigue strength of the shaft must be verified using a suitable method (FKM guidelines [15.5] or DIN 743 [15.9]).

Joining Temperatures for Transverse Press Fits. The clearance fit S_e required for unforced joining must be established by heating the hub and/or cooling the shaft. For the necessary clearance, depending on the joint diameter D_F or the maximum oversize $U'_{\max}$ measured at ambient temperature, the following conditions apply: $S_e/D_F \approx 10^{-3}$, or rather $S_e/U'_{\max} \approx 0.5$.

The joining temperature of the external part ϑ_A at known joining temperature of the internal part ϑ_I with ambient temperature ϑ, the coefficients of thermal expansion of the external and internal part α_A and α_I (Table 15.43) and the joint diameter D_F is approximately calculated as

$$\vartheta_A \approx \vartheta + \frac{U'_{\max} + S_e}{\alpha_A D_F} + \frac{\alpha_I}{\alpha_A} (\vartheta_I - \vartheta) \,. \tag{15.104}$$

The maximum possible heating of the hub is limited by its temperature resistance. Above this temperature limit, material strength losses are to be expected due to structural changes in the material. Guide values for the maximum joining temperature are given in Table 15.44.

Table 15.43 Coefficients of thermal expansion according to DIN 7190-1 [15.59]

Material	α_A (heating) (1/K)	α_I (undercooling) (1/K)
Steel and cast steel	11×10^{-6}	-8.5×10^{-6}
Cast iron	10×10^{-6}	-8×10^{-6}
Lightweight metal alloys (Al alloys)	23×10^{-6}	-18×10^{-6}
Copper alloys		
Red brass	17×10^{-6}	-15×10^{-6}
Brass	18×10^{-6}	-16×10^{-6}

Table 15.44 Maximum joining temperatures [15.59]

Hub material	Maximum joining temperature (°C)
Low-strength structural steel Cast steel Nodular cast iron	350
Steel or cast steel, quenched and tempered	300
Steel, boundary-hardened	250
Steel, case-hardened or high-strength quenched and tempered structural steel	200

Pressing-In and Pressing-Out Forces in Longitudinal Press-Fit Connections. The jointing force necessary to join the longitudinal press-fit connection is calculated from

$$F_{in} = \pi D_F l_F p'_{F\max} \mu \,, \tag{15.105}$$

where:

D_F joint diameter
l_F hub length
$p'_{F\max}$ largest joint compression ((15.106))
μ coefficient of friction on pressing in (Table 15.38)

The largest joint compression $p'_{F\max}$ present describes the joint compression that sets in under the stated largest oversize $U'_{\max}$:

$$p'_{F\max} = \frac{(U'_{\max} - \Delta U)\, p_{F\max}}{Z_{\max}} \,, \tag{15.106}$$

where:

$U'_{\max}$ available interference
ΔU interference loss (−100)
$z_{\max}$ largest allowable adhesion (15.98)
$p_{F\max}$ maximum allowable joint compression ((15.95)–(15.97))

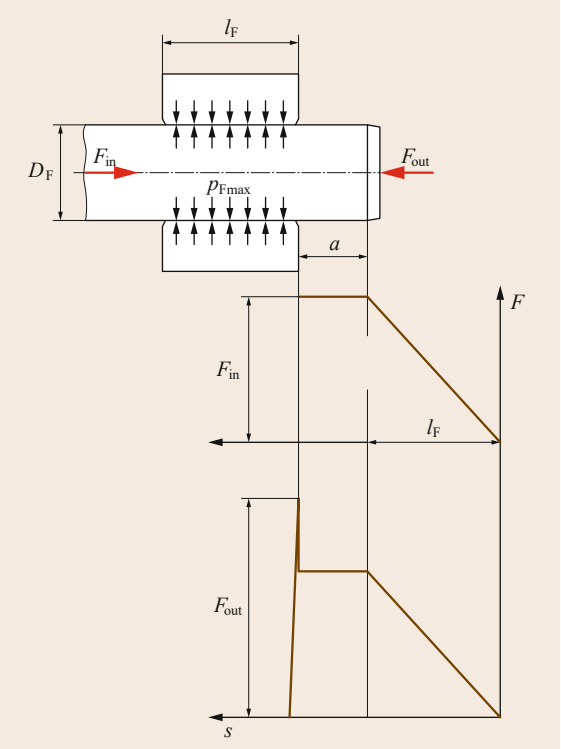

Fig. 15.55 Pressing-in and pressing-out forces in longitudinal press-fit connection

Due to the static friction, a larger force is required for the pressing out, so that: $F_{out} > F_{in}$ (Fig. 15.55). By inserting the static coefficient of friction μ_0 (Table 15.38) for μ in (15.105), the pressing-in force is specified on the safe side.

The empirical value $F_{in}/D_F = 4–7\,\text{kN/mm}$ is used for orientation.

15.4.3 Press-Fit Connection Through Hydrojoining

Unlike the classic longitudinal or rather transverse press-fit connection, with this type of connection a joint clearance exists between the hub and the hollow shaft before the joining. To produce the necessary joint compression for the force transfer, a pressure (joining pressure) is applied to the hollow shaft underneath the hub, which causes it to widen (Fig. 15.56). The parts to be joined and the process parameters (joint gap, joining pressure) are matched with each other so that the shaft undergoes plastic deformation and the hub undergoes elastic deformation. As a result, even after the joining pressure is removed, a permanent surface pressure occurs between the parts to be joined, which enables frictional force transfer.

Table 15.45 Advantages and disadvantages of hydrojoined press-fit connections

Advantages	Disadvantages
Generous tolerancing of the joint gap possible	Connection cannot be separated nondestructively
No additional unbalances	Shaft must be hollow underneath the hub
Less susceptible to fretting corrosion due to the favorable surface pressure curve	Joining probe requires an appropriate surface quality on the inside of the shaft due to the attached seal
Hub can be very easily positioned on the shaft	Calculation very difficult/time consuming

The advantages and disadvantages of hydrojoined press-fit connections are shown in Table 15.45.

Conical Press-Fit Connections

In conical (tapered) press-fit connections the conical hub is pressed axially onto a (mainly attached to the end of the shaft) rotationally symmetrical cone (Fig. 15.51b). They are used to transfer dynamic forces and moments, for example, in wheel, disc and clutch hubs or in machine tools for holding the tools. Their advantages and disadvantages are clearly shown in Table 15.46.

The internal and external part have the same cone taper angle or inclination angle $\alpha/2$:

$$\tan\left(\frac{\alpha}{2}\right) = \frac{D_1 - D_2}{2l}\,. \tag{15.107}$$

The cone inclination can also be given by the rate of taper:

$$C = \frac{D_1 - D_2}{l}\,. \tag{15.108}$$

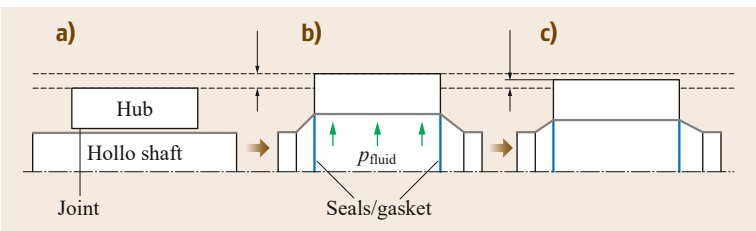

Fig. 15.56a–c Production process for hydrojoining. **(a)** Clearance fit before joining, **(b)** maximum widening during the joining process, and **(c)** permanent widening after joining process

Table 15.46 Advantages and disadvantages of conical press-fit connections

Advantages	Disadvantages
Easy assembly and dismantling	More expensive production than cylindrical press-fit connections
No weakening of the shaft and hub due to grooves (keys)	In the case of large alternating, intermittent loads, small relative movements can occur, which in turn can cause fretting (vibration wear)
Low unbalances due to a rotationally symmetrical contact surface	
High running accuracy and smooth and quiet running due to the very good centering effect	
Backlash-free joining possible	
Axial force is adjustable	

The following rates of taper are suggested in DIN 254 [15.60]:

Easily separable connection: $C = 1:5$
Difficult to separate connection: $C = 1:10$
Toolholders: $C = 1:20$, $C = 1:30$, $C = 1:50$
Morse taper: $C = 1:19.002$ to $1:20.047$

Self-locking exists in the conical press-fit connection if the angle of friction $\rho = \arctan(\mu_0)$ is larger than the taper angle $\alpha/2$.

The conical press-fit connection can be calculated as described in the DIN 7190-2 [15.61] standard.

Clamping-Element Connections

In this type of connection, the load is transferred via an additional component, the clamping element. Clamping-element connections are a special type of conical connections. Axial clamping causes conical clamping elements to be elongated elastically in the tangential direction (external part) and compressed (internal part), which produces a surface pressure between the shaft surface and the clamping element, or rather between the clamping element and the hub hole. The advantages and disadvantages are shown in Table 15.47.

Tapered Clamping Elements. The mode of action of tapered clamping elements is similar to that of conical press-fit connections. They mostly consist of two rings pushed inside each other (clamping set), which are conical on their joint contact surface (Fig. 15.57). The clamping set is cylindrical on the inside and outside, and is dimensioned so that it can be pushed into the hub or onto the shaft with clearance.

Table 15.47 Advantages and disadvantages of clamping-element connections

Advantages	Disadvantages
Easy assembly and dismantling	Clamping element is an additional component
Fixing of hubs, wheels, etc. onto smooth shafts	In most cases, separate centering of the hub on the shaft is required
Axially and tangentially freely settable and adjustable	Increased space requirement compared to press fit
Generally reusable	
Clearance-/backlash-free connection	
Suitable for transferring intermittent, shock-like or alternating torsional moments (torques)	

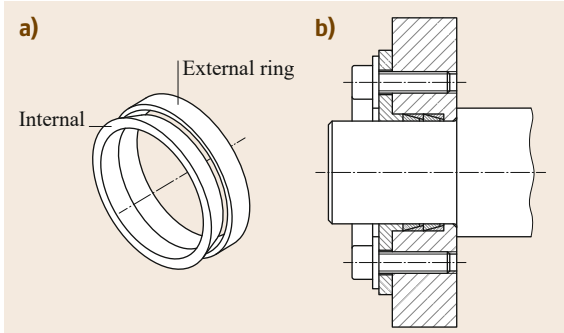

Fig. 15.57a,b Tapered clamping elements, individually **(a)** and assembled **(b)**

If the two rings are pushed inside each other by an axial force (mostly generated by screws or bolts) (Fig. 15.57), the external ring widens elastically, while the internal ring is compressed elastically. This radial deformation causes friction forces between the hub and clamping set and the shaft and clamping set, and these enable force transfer.

Several tapered clamping elements can be connected successively to transfer higher forces/torques. In this case, it must be noted that due to friction losses, the axial force acting on the individual elements reduces from element to element (Fig. 15.58).

Refer to the manufacturers' information for notes on dimensioning and calculation. The advantages and disadvantages of tapered clamping element are listed in Table 15.48.

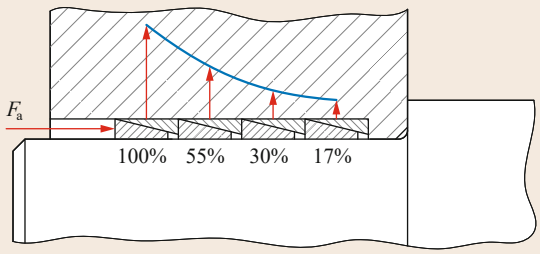

Fig. 15.58 Force distribution of the contact forces in several successive tapered clamping elements

Table 15.48 Advantages and disadvantages of tapered clamping elements

Advantages	Disadvantages
Easy assembly and dismantling	Force transfer less than with normal press-fit connection
Larger production tolerances possible for shaft and hub	Additional centering of the hub on the shaft required
Clamping set is available as a finished, ready-to-use component	Increased space requirement due to clamping elements
No additional axial fixing necessary	

Ringfeder Clamping Sets. The mode of action of Ringfeder (brand name) clamping elements is the same as that of tapered clamping elements. They differ in that the elements for clamping (bolts) are already integrated in the clamping set (Fig. 15.59).

The advantages and disadvantages of Ringfeder clamping sets are described in Table 15.49.

In addition to Ringfeder clamping sets, other special clamping sets are available with the same mode of action. They differ in their number of conical friction surfaces and the way in which the contact force is produced (Fig. 15.60).

Table 15.49 Advantages and disadvantages of Ringfeder clamping sets

Advantages	Disadvantages
Easy assembly and dismantling	Large hub dimensions due to large space requirement
Suitable for heavy-duty designs for transferring high static and/or dynamic moments	
No threaded holes	
No additional axial fixing necessary	

Table 15.50 Advantages and disadvantages of Taper Lock® connections

Advantages	Disadvantages
Easy assembly and dismantling	Large installation space
No additional axial fixing necessary	High production cost due to conical (tapered) hub hole and threaded hole for studs
Standardized hub geometries can be adapted to different shaft sizes with the help of various taper bushes	

Taper Lock® Connection. Taper Lock® connections are an alternative to the fixing of standardized belt pulleys and sprockets with classic parallel key connection. In these connections, an external conical taper bush is pressed, with the help of studs, into a hub with a corresponding mating shape (Fig. 15.61). They have a parallel keyway for additional security against twisting. Due to its longitudinal slot, the taper bush has very high elasticity. The press-fit connection can be undone with the help of specially threaded dismantling holes.

The advantages and disadvantages of Taper Lock® connections are shown in Table 15.50.

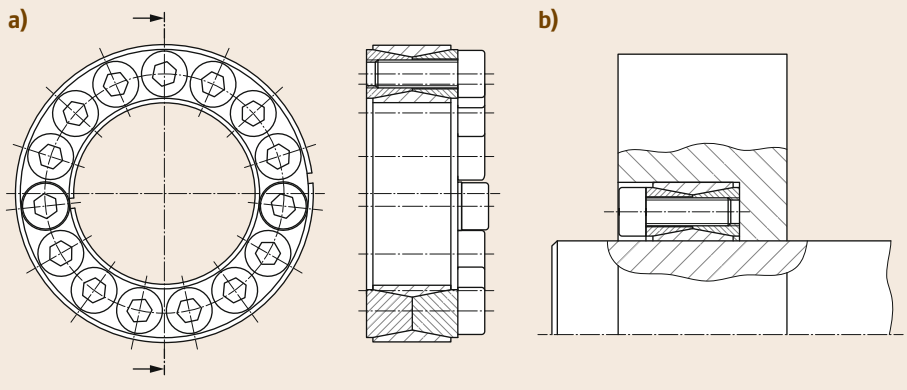

Fig. 15.59a,b Ringfeder clamping set **(a)** and assembled clamping set **(b)**

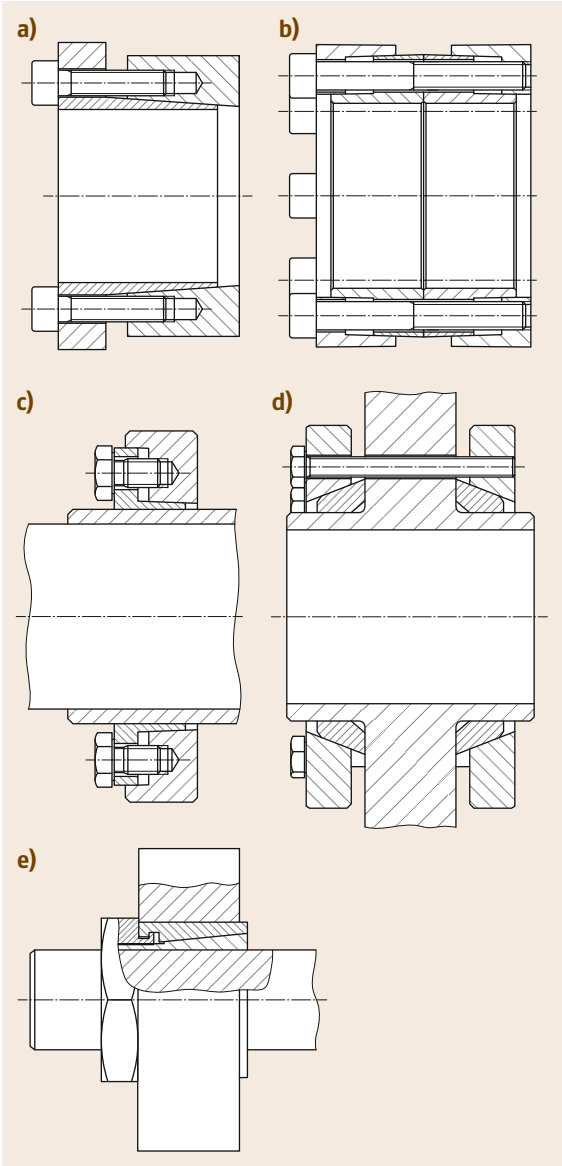

Fig. 15.60a–e Other clamping sets (selection): **(a)** self-centering internal clamping set (make: Klempex), **(b)** internal clamping set for transferring large torques (make: Stüwe), **(c)** clamp ring (make: Stüwe), **(d)** two-piece clamp ring (make: Stüwe), and **(e)** clamping set with hexagon nut

Compression Connections

Compression connections are mainly used to fix belt pulleys and levers. The clamping forces necessary for the force transfer are applied by screws/bolts or tilting forces. Parallel keys or tangential keys are also frequently installed for position fixing in the case of larger loads.

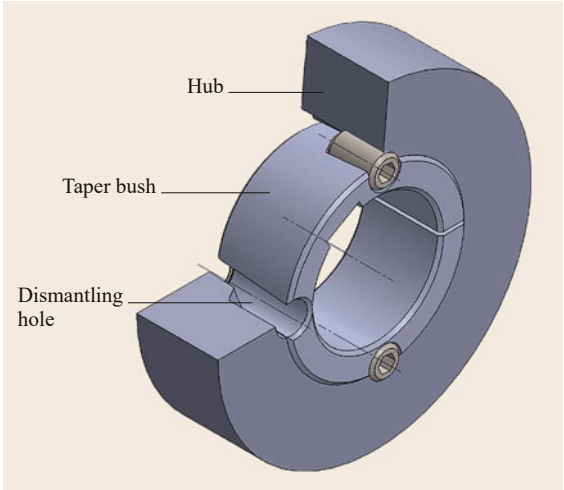

Fig. 15.61 Connection with taper bush

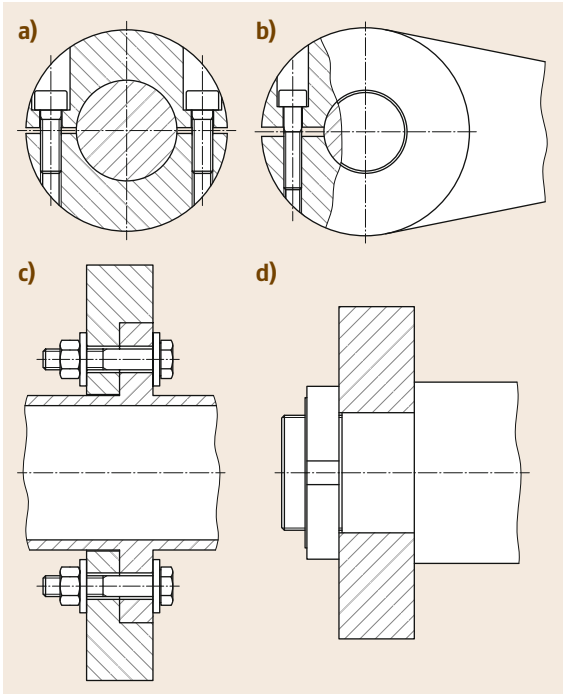

Fig. 15.62a–d Radial and axial compression connections. **(a)** Radially clamped with divided hub, **(b)** radially clamped with slotted hub, **(c)** axially clamped by circumferential bolts, and **(d)** axially clamped by central bolt

Table 15.51 Rough, estimated values for hub dimensions of compression connections

Materials	Cast iron	Steel/cast steel
Hub diameter	$(2.0 \ldots 2.2)d$	$(1.8 \ldots 2.0)d$
Hub length	$(1.6 \ldots 2.0)d$	$(1.2 \ldots 1.5)d$

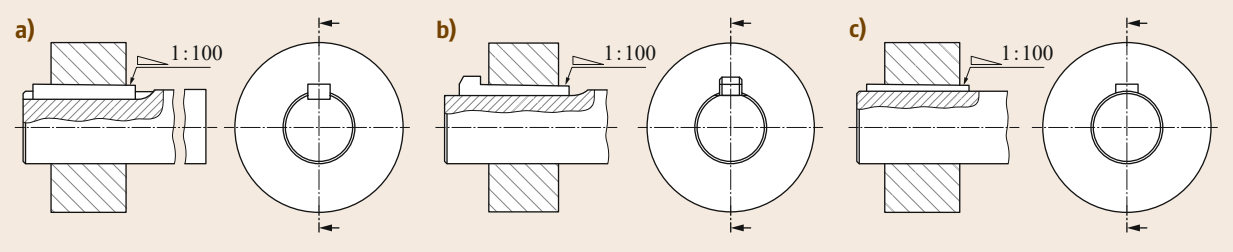

Fig. 15.63a–c Longitudinal key connection with keyway **(a)**, flat gib-head key **(b)**, and hollow (saddle) key connection **(c)**

Guide values for the selection of the hub dimensions depend on the shaft diameter d according to Table 15.51.

Depending on the direction of the clamping forces, the connections can be divided into axial and radial compression connections. In the case of axial compression connections, the hub or the flange is pressed onto the shaft by one or several bolts, which produces a force-closure connection (Fig. 15.62a,b). Radial compression connections can be achieved by hubs that are clamped with the help of bolts and that are slotted on one side or divided (Fig. 15.62c,d).

Keyed Joints

Keyed joints are preferably used for rough service and alternating, intermittent shock-like torques and low precision requirements, for example, for the fixed connection of heavy-duty discs, wheels, or clutches in large machines, excavators, cranes, agricultural machines, or heavy-duty machine tools.

Driving-in forces produce surface pressures and thus friction forces on the keys, which results in the superimposition of frictional and form-closure connections.

A differentiation is made between longitudinal key connections, which produce a frictional connection in normal service and cottered connections with a preloaded form-closure connection. The advantages and disadvantages of keyed connections are shown in Table 15.52.

Table 15.52 Advantages and disadvantages of keyed connections

Advantages	Disadvantages
Secure and fixed fit of the hub without additional axial securing	Difficult dismantling (especially gib-head keys)
Insensitive to dirt	Excessive force applied for driving in can cause the hub to crack or tear (especially gray cast iron hubs)
	One-sided driving in of the key can cause canting and off-center fit of the hub
	High speeds not possible

Longitudinal Key Connections. In normal service, the force transfer is by means of force closure (clamping of the shaft and hub by means of longitudinally inserted key) (Fig. 15.63). If the forces/moments to be transferred exceed the friction forces present, form-closure force transfer also occurs (except for hollow saddle key connections).

Longitudinal key connections are frequently used due to the ease with which they can be tightened and reclamped, and due to their reusability.

Cottered Joints. Cottered joints are used to connect parts that are mainly loaded in the longitudinal direction or as fixing and adjusting keys, for example, to secure tool tapers and as a clamping element in jig construction.

The disadvantages of this connection are the relatively high production costs, the unfavorable stress distribution, and the difficulty in controlling the driving-in force. A bolted connection can be a useful alternative.

The basic structure of a cottered connection is shown in Fig. 15.64.

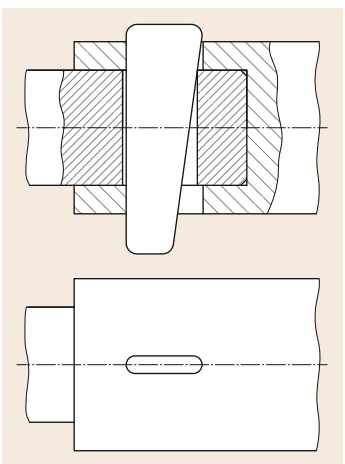

Fig. 15.64 Cottered joints

To be on the safe side, keyed connections are frequently dimensioned in the same way as parallel key connections, as the size of the driving-in force and thus the friction force are often difficult to determine.

15.4.4 Further Reading

More information on shaft–hub connections is provided in the reference book of the same name by *Kollmann* [15.62].

15.5 Rolling Bearings

The main tasks of bearings are to guide components that move relative to each other as well as absorb and transfer the acting forces or loads. They should enable movements (rotation and translation) in the required degrees of freedom and inhibit them in unwanted degrees of freedom.

They can basically be divided into rolling bearings and plain bearings. The movement or force transfer in rolling bearings takes place via rolling elements, which are arranged between rings or discs. Rolling friction dominates, so energy losses are low. In the case of plain bearings (sometimes called sliding bearings), the surfaces moving relative to each other rub each other directly (Fig. 15.65).

Rolling bearings, as maintenance-free or low-maintenance bearings, are preferably used under normal requirements, for example, in gear units, machine tools, conveyor systems, or all kinds of vehicles. They are also used in spindle guides and cradles/turrets, as they operate with low friction from a standstill and at low speeds and withstand large loads. Their advantages and disadvantages are given in Table 15.53.

Table 15.53 Advantages and disadvantages of rolling bearings

Advantages	Disadvantages
Cost effective in mass production and can be produced with high degree of accuracy	More expensive than simple plain bearings
Replaceability possible within wide limits due to international standardization	Noisy running
Less frictional losses than comparable plain bearings at low speeds	Speed limited due to centrifugal force effect on rolling elements
No distinct running-in characteristic	Sensitive to dirt (sealing required)
Low maintenance cost and lubricant requirement	Sensitive to large temperature differences
	Sensitive to vibrations and shocks (especially when at a standstill and at low speeds)
	Lubrication required (except for special plastic bearings)
	Higher wear than hydrodynamic plain bearings

15.5.1 Structure and Properties

Structure

A differentiation is made between *radial rolling bearings* (Fig. 15.66a) and *thrust rolling bearings* (Fig. 15.66b) depending on the type of position fixing.

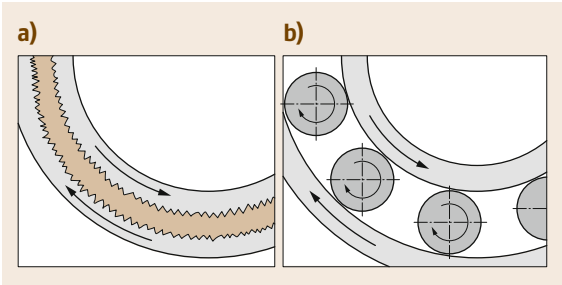

Fig. 15.65a,b Plain (a) and rolling (b) bearings

Depending on their type, radial rolling bearings can absorb axial forces in addition to radial forces, while rolling thrust bearings are generally only suitable for axial loads.

Rolling bearings are further subdivided depending on their rolling element geometry (Fig. 15.66c) into:

- Ball bearings
- Cylindrical roller bearings
- Needle roller bearings
- Tapered roller bearings
- Barrel roller bearings

The basic structure of rolling bearings is shown in Fig. 15.67:

- Radial bearings: outer ring, inner ring, rolling element, cage
- Thrust bearings: shaft washer, housing washer, rolling element, cage

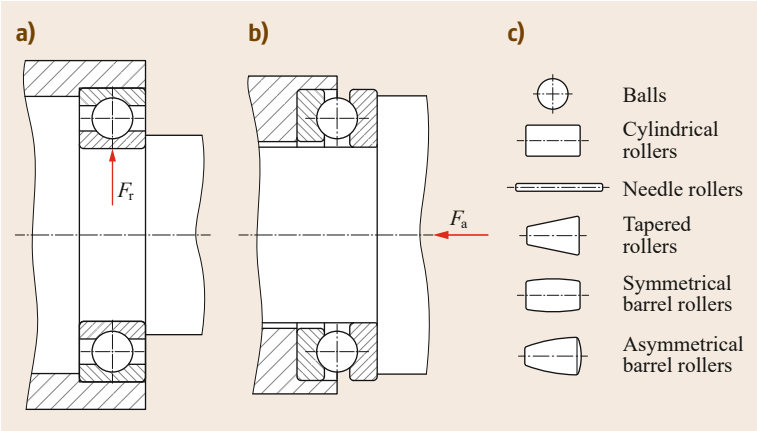

Fig. 15.66a–c Radial and thrust bearings (selection with installation examples). **(a)** Radial deep-groove ball bearings; **(b)** deep-groove thrust ball bearings, and **(c)** rolling element shapes

The inner and outer ring, or rather shaft and housing washer, of the roller bearings, via corresponding tolerances, are in direct contact with the surroundings of the bearing position.

During service, with the help of the lubricant, an elastohydrodynamic lubricant film (EHD contact) builds up between the rolling elements and the raceways of the bearing rings or washers. A ring-shaped cage secures the position of the rolling elements (Fig. 15.67).

Bearing Dimensions and Designation

The external dimensions for metric bearings (inside and outside diameter, width, height, chamfer dimensions) are internationally standardized in ISO 15 [15.63] (radial bearings), ISO 355 [15.64], DIN 720 [15.65] (tapered roller bearings), and ISO 104 [15.66] (thrust bearings). Rolling bearings with inch-size or imperial dimensions are available (for example, ANSI/ABMA 12.2 [15.67], ANSI/ABMA 19.2 [15.68]), but should no longer be used for new designs.

Bearing designation based on the DIN 623-1 [15.69] standard is widely used internationally. Here, the bearing designation is made up of a prefix, a basic designation, a suffix, and additional designations (characters or numbers).

Prefixes. Prefixes are used if applicable to identify certain individual rolling bearing parts or special bearing materials, for example:

K: Cage with rolling elements
L: Free ring of a separable bearing
R: Bearing ring with roller and cage or needle roller and cage assembly
S: Stainless steel

Basic Designation. The basic designation contains the bearing type in a coded form, the dimension series (width series for bearing width B and diameter series for the outer diameter D), and the bore diameter (bore ID number for the bore diameter d) (Fig. 15.68).

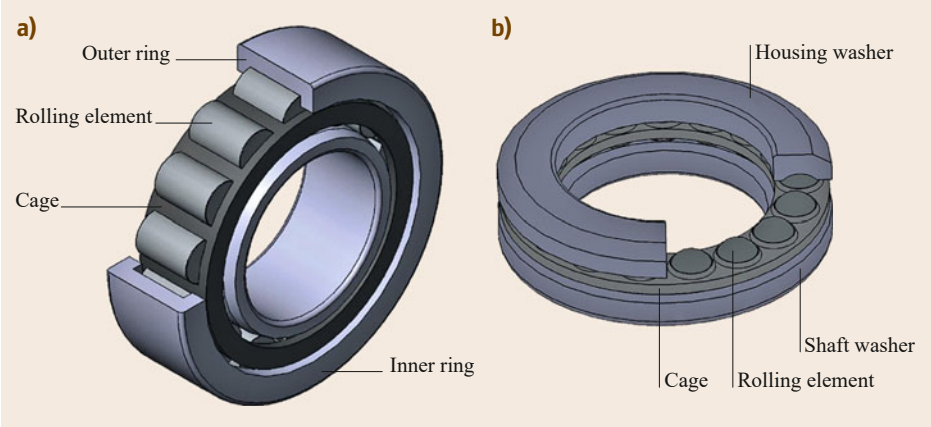

Fig. 15.67a,b Basic structure of a rolling bearing according to ISO 5593. **(a)** Radial bearing and **(b)** thrust bearing

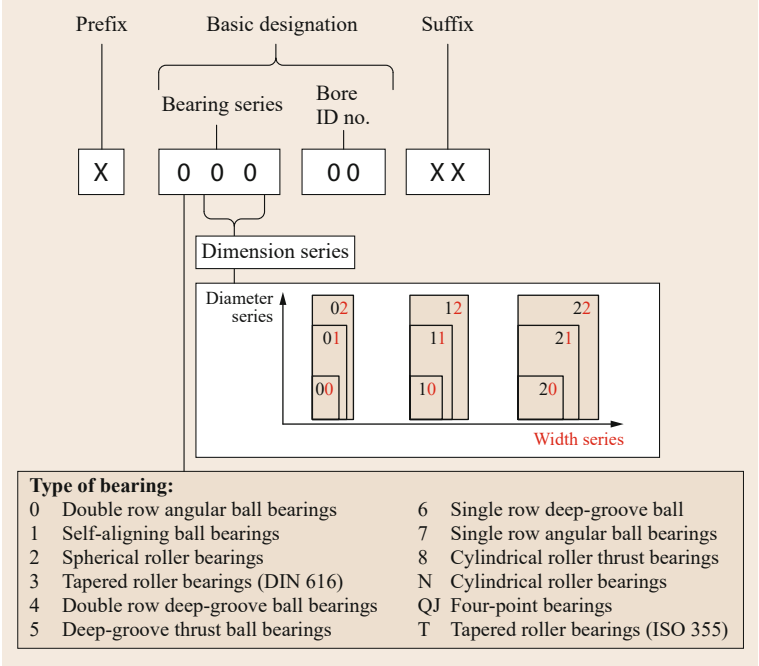

Fig. 15.68 Bearing designation according to DIN 623-1 (after [15.69])

Suffixes. Deviations from the standard version are to be given by suffixes.

As there are a large number of different suffixes, reference is made here to the bearing catalogs of the bearing manufacturers.

Additional Designation. Can contain additional information from the manufacturer.

15.5.2 Types, Properties, and Use

Table 15.54 gives an overview of the most commonly used types of rolling bearings.

Depending on the axial loadability and the installation situation, the following application cases result for radial bearings:

- As guide or fixed bearings (axial forces possible in both directions)
- As support bearings (axial forces possible in one direction)
- As a loose bearing (no absorption of axial forces)

Rolling bearings in which the external force is always divided into an axial and radial component, regardless of the load angle, are called angular contact bearings.

Standard Types

Many different types of rolling bearings are available. Table 15.55 gives a brief overview of the most commonly used types of rolling bearings.

Bearing Selection. For frequently occurring service cases and certain requirements, the bearing can be selected using Fig. 15.69. As deep-groove ball bearings are suitable for radial and for axial loads, have high running accuracy, have a small installation space, and are also readily available, their usability should be checked first.

15.5.3 Load Capacity and Life of the Rolling Bearings

Static Load Capacity According to ISO 76

In relation to rolling bearings, static loading is assumed if the bearing is loaded when it is at a standstill, at very low speeds ($n < 10\,\mathrm{min}^{-1}$), or during slow oscillatory movements. The forces acting on the bearing can be changeable over time (dynamic).

The static load capability is limited by the occurrence of plastic deformations in the contact point between the rolling elements and their raceway.

A rolling bearing is deemed to be statically operable if, at the contact point subject to the highest loading, the

Table 15.54 Overview of types of rolling bearings

Rolling bearings			Ball bearings	Roller bearings	
	Rotational movements	Mainly radial loading	Deep-groove ball bearings	Cylindrical roller bearings with cage	
			Aligning deep-groove ball bearings	Cylindrical roller bearings, full complement	
			Self-aligning ball bearings	Spherical roller bearings	
			Magneto ball bearings	Barrel roller bearings	
			Angular roller bearings	Needle roller bearings	
			Angular ball bearings, single row	Needle roller and cage assemblies	
			Angular ball bearings, double-row	Drawn cups with one closed end	
		Combined radial and axial loading	Magneto ball bearings (in pairs)	Tapered roller bearings (in pairs)	
			Angular ball bearings, single row	Cylindrical roller bearings (with ribs)	
			Angular ball bearings, double-row	Crossed roller bearings	
			Four-point bearings	Roller slewing ring bearings	
			Ball slewing ring bearings		
		Mainly axial loading	Deep-groove thrust ball bearings	Cylindrical roller thrust bearings	
			Angular roller thrust bearings	Spherical-roller thrust bearings	
				Needle roller thrust bearings	
	Linear movements		Flat ball cages	Flat roller cages	Linear guide systems
			Recirculating ball shoe bearings	Flat cage guides	
			Linear ball bearings	Recirculating roller shoe bearings	
			Recirculating ball guides	Recirculating roller units	
			Track rollers	Track rollers	

size of the total permanent deformation of the rolling element and raceway does not exceed 0.01% of the rolling element diameter.

The safety of a rolling bearing compared to the static loading is calculated from the ratio of the static load rating C_0 to the equivalent static load P_0 and is given in the form of the static safety factor S_0 as follows:

$$\text{For radial bearings:} \quad S_0 = \frac{C_{0r}}{P_{0r}}$$

$$\text{For thrust bearings:} \quad S_0 = \frac{C_{0a}}{P_{0a}} \qquad (15.109)$$

Guide values for the static safety factor are given in Table 15.56.

The static load rating C_0 of a rolling bearing equals the load at which a calculated stress of 4000–4600 MPa (depending on the bearing type) occurs at the contact points between the rolling elements and the raceways.

Values for C_0 are given in the corresponding catalogs of the relevant manufacturers or must be calculated with the help of the equations given in ISO 76 [15.70].

As the static load rating corresponds to pure radial loading for radial bearings and pure axial loading for thrust bearings, simultaneously occurring radial and axial forces F_r and F_a with radial and axial factors X_0 and Y_0 are to be summarized as an equivalent static load P_0.

Table 15.55 Overview of the most commonly used standard rolling bearings

Bearing type	Loadability		Features
	Radial	Axial	
Deep-groove ball bearings 	High	Medium	– Balls run between the inner and outer ring – Diverse uses – Very common and particularly economical – Suitable for high speeds – Design is not separable, i.e., is not easily separable – Only small shaft displacement tolerable – Bearings also available sealed
Single-row angular roller bearings 	High	One-sided depending on the contact angle	– Bearing rings each with a low and a high shoulder – Intended for pair-wise installation in face-to-face, back-to-back, or tandem arrangement – Design is not separable – Only small shaft displacement tolerable – Sealed bearings available
Self-aligning ball bearings 	High	Low	– Double row type with spherical raceway in outer ring – Design is not separable – For levelling out shaft displacement and shaft deflection (up to 4°) – Sealed bearings available
Cylindrical roller bearings 	Very high	Not loadable	– In the standard version, two fixed ribs on one ring (inside or outside ring) and no rib on the other ring – Maximum speed lower compared to ball bearings – Enable very stiff and precise shaft bearing – Standard version is separable
Spherical roller bearings 	Very high	Low	– Double-row type with spherical raceway in the outer ring – Rolling element barrel-shaped – Enable levelling out of shaft displacement and shaft deflection up to 4°
Tapered roller bearings 	High	High on one side	– Tapered raceways, whose extended generatrices intersect at a point – Removable outer ring makes assembly easier – Internal clearance settable by axial displacement of the bearing rings – Installation often in pairs with face-to-face, back-to-back, or tandem arrangement (Sect. 15.5.4, *Bearing Arrangements*)
Needle roller bearings 	Very high	Not loadable	– Special type of the cylindrical roller bearing – Combines the smallest installation dimensions with large radial stiffness – Insensitive to shocks – Separable – Version with or without inside and outside ring

Table 15.55 (Continued)

Bearing type	Loadability		Features
	Radial	Axial	
Deep-groove thrust ball bearings 	Not loadable	High on one side	– Thrust bearing acting on one side – Ball and cage assembly runs between two housing washers – Bearing is separable
Spherical-roller thrust bearings 	Low	High on one side	– Thrust bearing acting on one side – Rolling elements are asymmetrical barrel rollers – For levelling out shaft displacement up to 3°

Rolling bearing types and their usability	Requirement									
	Radial load	Axial load	Levelling out alignment errors	Readjusting the bearing clearance	Separable bearing	Version with increased accuracy	High speeds	High loadability	Low-noise running	Fixing with sleeve
a	+	+	○	–	–	+	+	○	+	○
b	+	+	–	+	–	+	+	○	+	–
c	○	+	–	–	–	○	○	○	–	–
d	+	+	–	–	–	–	○	+	–	–
e	+	○	+	–	–	–	–	○	–	+
f	+	○	–	–	+	+	○	+	+	○
g	+	+	○	+	+	+	○	+	–	–
h	+	○	+	–	–	–	–	+	–	+
i	+	+	+	–	–	–	–	+	–	+
j	+	–	–	–	+	○	○	○	+	–
k	–	+	–	+	+	+	–	+	–	–
l	–	+	–	+	+	–	–	+	–	–
m	○	+	+	+	+	–	–	+	–	–
n	+	+	–	–	–	+	+	+	○	–

+ Unconditionally usable ○ Conditionally usable – Not usable

a Deep-groove ball bearings
b Angular ball bearings, single row
c Four-point bearings
d Angular ball bearings, double-row
e Self-aligning ball bearings
f Cylindrical roller bearings
g Tapered ball bearings
h Barrel roller bearings
i Sopherical roller bearings
j Needle roller bearings
k Deep-groove thrust ball bearings, single direction
l Deep-groove thrust ball bearings, double-direction
m Spherical-roller thrust bearings
n UKF ball bearings

Fig. 15.69 Selection of rolling bearings

Table 15.56 Guide values for the required static safety factor according to ISO 76 [15.70] (excerpt)

Type of service	S_0 min. for ball bearings	S_0 min. for roller bearings
Application cases with low-noise running: Smooth, quiet running, vibration free, high rotational accuracy	2	3
Application cases with normal running: Smooth, quiet running, vibration free, normal rotational accuracy	1	1.5
Application cases with shock, intermittent loading: Distinct shock loading	1.5	3

For spherical roller thrust bearings, a minimum value of 4 is recommended for S_0 in all operating modes, and a minimum value of 3 for case-hardened cups with one closed end or both ends open

Table 15.57 Values for the factors X_0 and Y_0 according to ISO 76 (excerpt)

Type of bearing		Single row bearings[a]		Double row bearings	
		X_0	Y_0	X_0	Y_0
Radial ball bearings		0.6	0.5	0.6	0.5
Angular ball bearings, $\alpha =$	5°	0.5	0.52	1	1.04
	15°	0.5	0.46	1	0.92
	25°	0.5	0.38	1	0.76
	35°	0.5	0.29	1	0.58
	45°	0.5	0.22	1	0.44
Self-aligning ball bearings, $\alpha \neq 0°$		0.5	$0.22 \cot \alpha$	1	$0.44 \cot \alpha$
Radial roller bearings, $\alpha \neq 0°$		0.5	$0.22 \cot \alpha$	1	$0.44 \cot \alpha$

[a] The allowable maximum value of F_a/C_{0r} depends on the bearing design
α is the nominal contact angle in degrees

The equation for the static equivalent radial load is

$$P_{0r} = X_0 F_r + Y_0 F_a$$
$$\text{if } F_a = 0 \quad \text{then } P_{0r} = F_r \,. \tag{15.110}$$

Values for X_0 and Y_0 are given in Table 15.57 and the relevant information of the bearing manufacturers.

The static equivalent axial load can be calculated using

$$\text{If } \alpha \neq 90° \quad \text{then: } P_{0a} = 2.3 F_r \tan \alpha + F_a \,;$$
$$\text{if } \alpha = 90° \quad \text{then: } P_{0a} = F_a \,. \tag{15.111}$$

Equation (15.111) applies to double-direction bearings for all ratios of radial to axial loads.

It applies to single-direction bearings under the following condition: $F_r/F_a \leq 0.44 \cot \alpha$.

For spherical-roller thrust bearings simultaneously subjected to radial and axial loads:

$$P_0 = F_a + 2.5 \ldots 2.9 F_r \,. \tag{15.112}$$

Dynamic Load Capability

During their service, rolling bearings are subject to wear, which limits their life. According to ISO 281, the life of a rolling bearing is defined as the number of revolutions completed by a bearing ring (or a bearing washer) in relation to the other bearing ring (other bearing washer), before the first indication of material fatigue becomes visible on one of the two rings (or washers) or on rolling elements [15.71].

Statements on the life of rolling bearings are of a statistical character, which means that the given/calculated values are subject to a certain scatter.

When calculating the life, a differentiation is made between the basic and the modified rating life.

Basic Rating Life. According to ISO 281, the basic rating life L_{10} is the rating life associated with 90% reliability for bearings manufactured with commonly used high-quality material, of good manufacturing quality, and operating under conventional operating conditions [15.71]. From a statistical point of view, 10% of the bearings used can thus fail before reaching the basic rating life.

Table 15.58 Values for radial factors X and axial factors Y for selected types of bearings according to ISO 281 [15.71] (excerpt)

Type of bearing		X	Y
Radial deep-groove ball bearings	$\frac{F_A}{F_R} \le e^a$	1	0
	$\frac{F_A}{F_R} > e^a$	0.56	See Fig. 15.70
Single direction radial deep-groove ball bearings, separable (magneto ball bearings)	$\frac{F_A}{F_R} \le 0.2$	1	0
	$\frac{F_A}{F_R} > 0.2$	0.5	2.5

[a] For values of e see Fig. 15.70.

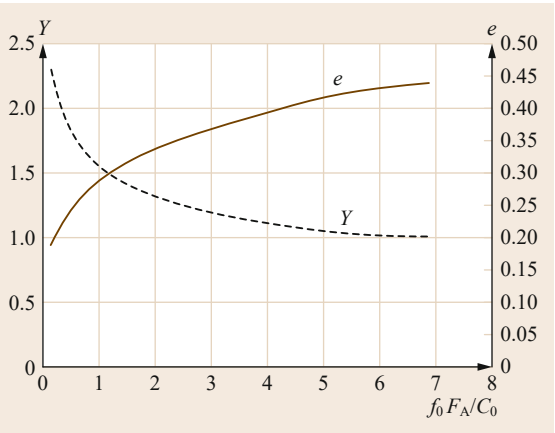

Fig. 15.70 Axial factor Y and limit value for applicability e. Indicative values for f_0 (after *Niemann* et al. [15.24]): deep-groove and angular ball bearings $f_0 \approx 14$, roller bearings $f_0 \approx 35$, and self-aligning and magneto ball bearings $f_0 \approx 2.5$; for precise values, see ISO 76 (after [15.70])

The basic rating of a bearing can be determined with the help of

For radial bearings

$$L_{10} = \left(\frac{C_r}{P_r}\right)^p 10^6 \; revolutions \; ;$$

for thrust bearings

$$L_{10} = \left(\frac{C_a}{P_{r,a}}\right)^p 10^6 \; revolutions \; , \qquad (15.113)$$

where:

$C_{r,a}$ dynamic load rating of the radial/thrust bearing
$P_{r,a}$ equivalent bearing load of the radial/thrust bearing (15.114)
p life exponent for ball bearings: $p = 3$; for roller bearings $p = 10/3$

The dynamic load rating C is the bearing load at which the bearing can statistically complete 10^6 revolutions with a failure probability of 10%. It is given in the respective information of the rolling bearing manufacturers.

The life calculation using (15.113) applies to pure radial and axial loads. If radial and axial loads occur simultaneously, they must be converted into a dynamic equivalent load $P_{r;a}$, which has the same effect on the bearing as the pure radial or axial load such that,

$$P_{r;a} = XF_r + YF_a \; , \qquad (15.114)$$

where:

F_r actual radial load
F_a actual axial load
X radial factor
Y axial factor

The radial and axial factors for several selected bearing types are shown in Table 15.58.

For spherical roller thrust ball bearings simultaneously subjected to radial and axial load, under the condition $F_r \le 0.55F_a$,

$$P_{r;a} = F_a + 1.2F_r \; . \qquad (15.115)$$

The life of a bearing is usually given in operating hours. With the given speed n in 1/min, (15.113) thus becomes

for radial bearings:

$$L_{10h} = \left(\frac{C_r}{P_r}\right)^p \frac{10^6}{60n} \quad \text{in h} \; ,$$

and for thrust bearings:

$$L_{10h} = \left(\frac{C_a}{P_a}\right)^p \frac{10^6}{60n} \quad \text{in h} \; . \qquad (15.116)$$

A selection of guide values for the required basic rating lives in operating hours is given in Table 15.59.

Table 15.59 Guide values for the required basic rating lives L_{10h} of ball bearings and roller bearings (selection) (according to *Schaeffler* [15.72])

Machine type	L_{10h} in operating hours	
	Ball bearings	Roller bearings
Car drives	500–1100	500–1200
Heavy trucks	4000–8800	5000–12 000
Gear boxes/transmissions of rail vehicles	14 000–46 000	20 000–75 000
Agricultural machines	500–4000	500–5000
Electric motors for household appliances	1700–4000	–
Electric motors for industrial applications	21 000–32 000	35 000–50 000
Lathe and milling-cutter spindles of machine tools	14 000–46 000	20 000–75 000

Modified Life. The basic rating life calculated with the help of the equations above applies to normal material qualities under standard operating conditions.

The actual life of the rolling bearings, however, is highly influenced by other criteria:

- Lubrication of the bearing (type and viscosity of the lubricant, contained additives)
- Material properties (purity, hardness, fatigue limit, surface quality, temperature resistance)
- Internal stresses (due to production or assembly)
- Ambient conditions (dirt, moisture)

With the help of the modified rating life, compared to the basic rating life, more precise values can be determined for the durability of the bearings under the specific use conditions.

Detailed calculation steps are given in the ISO 281 standard [15.71] or the calculation regulations of the individual manufacturers.

Minimum Bearing Load

A minimum force (axial or radial, depending on the bearing type) is required to ensure correct rolling of the rolling elements on the contact surfaces.

As a rough guide value, the bearing load for ball bearings and for roller bearings should not fall below 1 and 2%, respectively, of the dynamic load capability.

When in doubt, follow the regulations of the individual bearing manufacturers.

15.5.4 Design

In addition to suitable bearing selection, the design of the bearings must also consider the bearing arrangement, the installation tolerances, and the lubricant supply with the corresponding seals.

Bearing Arrangements

Bearings must basically be arranged so that the components can be guided both axially and radially. Depending on the amount and direction of the actual loads, running accuracy requirements, and assembly and dismantling options, a suitable arrangement must be chosen for the rolling bearings. A differentiation is made between fixed-loose bearings, spring-loaded or preloaded bearings, and floating bearings (support bearings). The features and examples for the individual bearings are shown in Table 15.60.

Installation Guidelines

The design of the bearing seat on the shaft or in the housing essentially depends on the task (fixed or loose bearings) and the type of load (point or circumferential load).

The bearings must be fixed onto the shaft or in the housing in both the radial and in the axial direction (except loose bearings). The radial fixing is achieved via appropriately designed fits. Oversize fit is necessary if a circumferential load acts on the bearing ring (inner or outer ring). If the load direction relative to the bearing ring does not change (point load), a transition fit or slight clearance fit is allowed.

In the axial direction, the fixing is mostly achieved by one-sided ridge and steps/shoulders, whereby moving in the opposite direction is prevented by retaining rings, threaded fasteners, or the housing cover (Figs. 15.71 and 15.72).

15.5.5 Lubrication of the Rolling Bearings

The life of rolling bearings depends to a decisive degree on their lubrication. During the rolling operation, a thin film of lubricant should form between the parts moving relative to each other in the bearing (rolling element, raceways, and cage); this film separates the contact surfaces from each other and thus reduces wear significantly. In addition, the lubricant should protect the bearing against corrosion, remove any friction heat that occurs, dampen vibrations, remove abraded material (circulating oil lubrication), or bind abraded material (permanent lubrication). To a limited extent, bearings with a grease fill also have a sealing effect.

Table 15.60 Features and examples of different bearings

Fixed-loose bearings	Spring-loaded bearing	Floating bearings
• Combination of fixed bearing and loose bearing • Fixed bearing absorbs radial and axial forces • Loose bearings can only absorb radial forces and have axial clearance; for levelling out production tolerances and thermal expansion • Standard bearing combination for multi-support shafts	• Tapered roller bearings or angular ball bearings are clamped with a mirror image • Depending on the pressure line curve, a differentiation is made between a face-to-face and back-to-back arrangement • Heating of a face-to-face arrangement leads to an increase in the bearing preload, it is reduced in a back-to-back arrangement • Face-to-face arrangement for load application between bearings • Back-to-back arrangement for load application outside of the bearing	• Combination of two bearings with axial clearance for levelling out production tolerances and thermal expansion • Shaft can move axially within the range of the axial clearance • Only possible with nonseparable bearings • Simple and cost-effective variant if axial forces only act in one direction and axial clearance is allowed
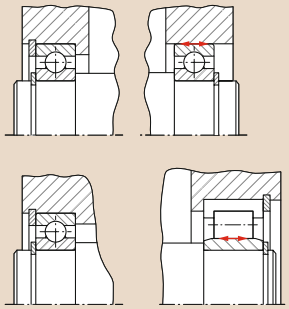	Face-to-face arrangement 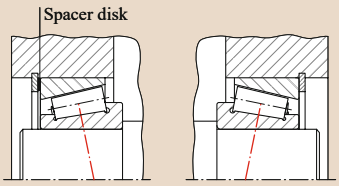 Back-to-back arrangement 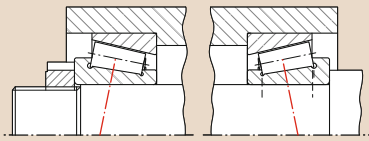	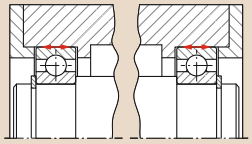

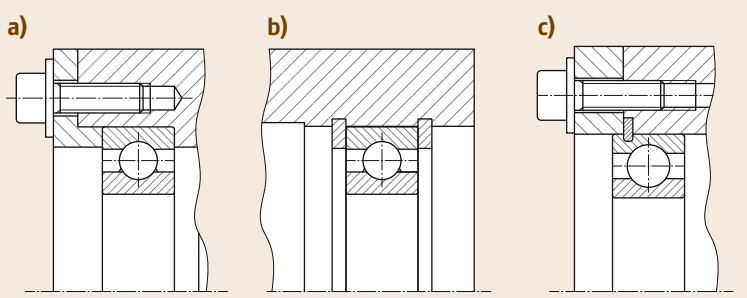

Fig. 15.71a–c Axial fixing of rolling bearings in the housing: **(a)** through cover and rib, **(b)** through retaining rings, and **(c)** through bearing with groove and snap ring

Selection of the Lubrication Method

Choice of the correct lubrication method and the corresponding lubricant should take place at the beginning of the bearing design. The choice of suitable lubrication method depends, among other things, on:

- The size and type of bearing
- The operating conditions
- The running quietness/smooth running requirements
- The connection design

Depending on the lubricant used, a differentiation is basically made between grease, oil, and solid lubrication, although solid lubrication is only seldom used.

The advantages and disadvantages of grease and oil lubrication are listed in Table 15.61.

In practice, approximately 90% of all rolling bearings are lubricated with grease. As the lubricants age due to thermal and mechanical loading and also become contaminated due to abraded material and dirt input, their life is limited. If replacement of the lubricant (relubrication) is not possible, as for example with two-sided sealed bearings, the service life of the lubricant can, under certain circumstances, constitute the limiting factor in the bearing life consideration.

Table 15.61 Advantages and disadvantages of grease and oil lubrication

	Grease lubrication	Oil lubrication
Advantages	• Low design cost (time and effort) • Additional sealing effect • Low maintenance cost (lifetime lubrication under certain circumstances) • Low friction moment	• Good lubricant distribution • Heat removal possible (important especially for high speeds) • Wear particles and dirt are flushed out • Precise metering possible (drip, oil-mist lubrication)
Disadvantages	• No heat removal by lubricant • No transporting away of wear particles and dirt or contamination	• More expensive/complicated design (supply and sealing) • Very low friction losses with minimum lubrication

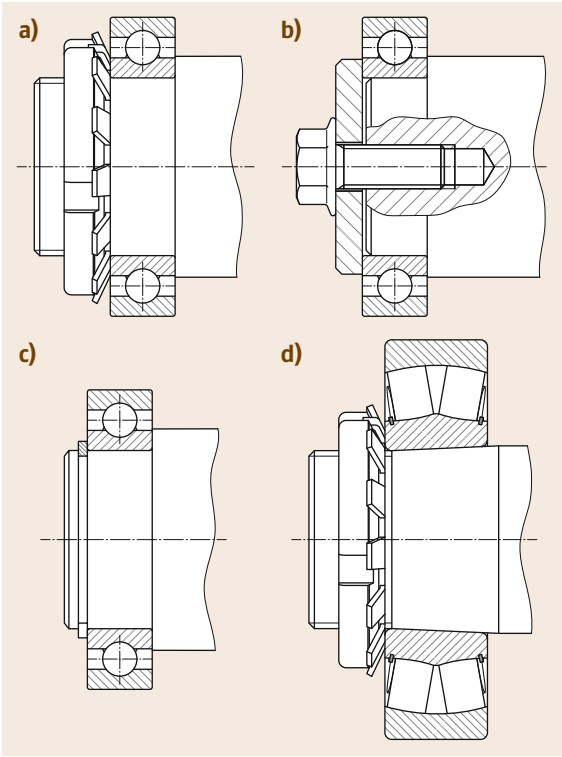

Fig. 15.72a–d Axial fixing of rolling bearings on the shaft: **(a)** with slotted nut, **(b)** with end washer, **(c)** with retaining ring, and **(d)** taper seat with slotted nut

15.5.6 Sealing of Rolling Bearings

The sealing of rolling bearings should essentially fulfill two functions:

1. Sealing the bearing against gaseous, liquid, and/or solid substances/contamination
2. Prevent the escape of lubricant

To achieve this, the bearings themselves can have a seal (for example RS bearings or Z bearings) or the surroundings of the bearing must be sealed accordingly. More detailed information on the possible sealing systems is given in Sect. 15.7.

15.5.7 Rolling Bearing Damage

If installed correctly and operated as intended, rolling bearings are very reliable and are generally largely maintenance free.

Statistically, only 0.335% of all rolling bearings fail prematurely as a result of production or material errors [15.73].

Premature failure of a bearing significantly before the rated life L_{10h}, is generally viewed as being bearing damage.

The most frequent causes of bearing damage are shown graphically in Fig. 15.73.

The bearing damage that occurs can be divided into six different categories according to ISO 15243 [15.76] (Fig. 15.74).

Bearing Damage Due to Fatigue

Fatigue is the term used to describe the flaking or spalling of surface layers as a result of cyclical loading of the contact surfaces.

Depending on the origin of the damage, a differentiation is also made between subsurface-initiated fatigue (fatigue beginning under the surface) and surface-initiated fatigue (fatigue beginning on the surface).

Subsurface-initiated fatigue in the form of microcracks under the surface is caused by continuous rolling over the contact surfaces with high loads. These microcracks propagate up to the surface where they cause flaking/spalling, pitting, and peeling.

Surface-initiated fatigue is caused, among other things, by surface fatigue wear as a result of microcracks on roughness peaks, microchips/spalling on roughness peaks, and zones with microchips.

Indentations due to dirt particles or incorrect handling/assembly can also result in fatigue phenomena on the surface.

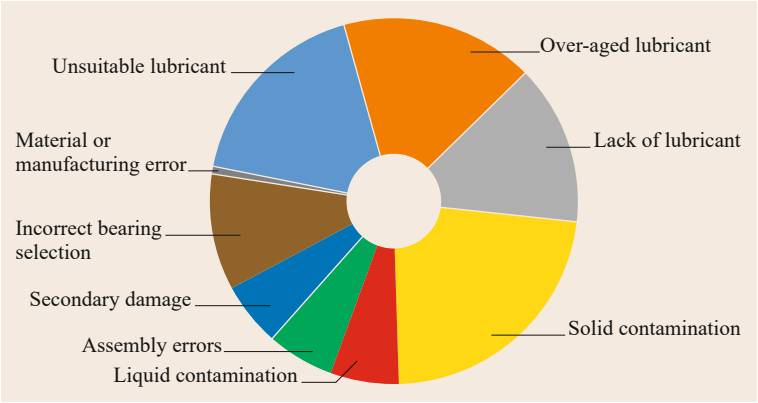

Fig. 15.73 Causes of bearing damage (after [15.74, 75])

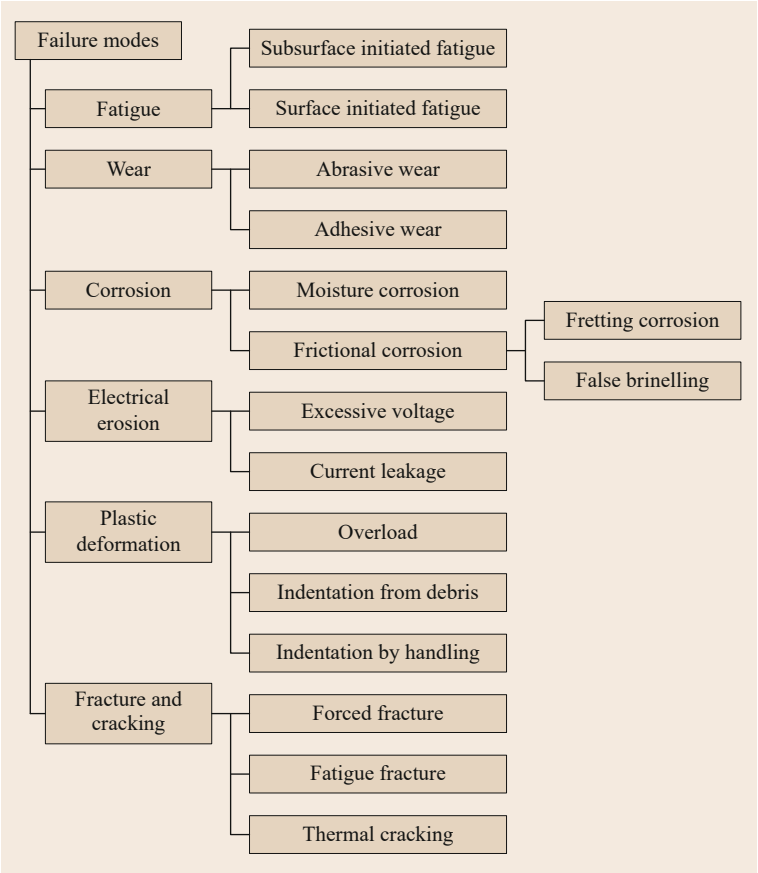

Fig. 15.74 Types of damage to rolling bearings according to ISO 15243 (after [15.76])

Bearing Damage Due to Wear

The removal of material at the contact surface between the rolling elements and the contact surfaces is called wear. While rolling bearings are always subject to normal wear, increased wear leads to premature failure of the bearing.

Abrasive wear is caused by the abrasive effect of very small particles between the contact surfaces. These particles form marks (indentations) in the contact surfaces or the rolling elements when rolled over and this in turn causes damage to the surfaces and elements. The abrasion produced accelerates the wear so that a chain reaction occurs, which reduces the life of the bearing severely.

Unwanted sliding movements between the rolling elements and the contact surfaces can, among other

things, initiate material transfer from one contact partner to the other which causes adhesive wear. This is mostly caused by inadequate lubrication or excessive speeds.

Bearing Damage Due to Corrosion

Moisture corrosion is initiated by the effect of water or aggressive liquids on the bearing and can irreparably damage the bearing within a very short time.

Microsliding movements between the two loaded surfaces can cause the formation of fretting corrosion. The bearing seats in the housing or on the shaft are mainly affected by this type of corrosion. Due to the increase in volume caused by the formation of iron oxide in the joint gab, considerable stresses are produced in the bearing rings, which can ultimately lead to fracture.

Microsliding movements between the rolling elements and the contact surfaces can also initiate a type of friction corrosion (fretting). This is called *false brinelling*. This mainly applies to bearings at a standstill, which are primarily exposed to vibrations.

Bearing Damage Due to Electrical Erosion

If the flow of electrical current through the bearing is too large due to excessive voltage, microscopic light arcs can be triggered in the contact area between the rolling elements. These light arcs generate very high temperatures locally, which extend up to the melting range of the bearing material. The high temperatures also lead to thermal decomposition of the bearing lubricant, which causes it to lose its lubricity.

Compared to excessive voltage, leakage currents generate lower temperatures in the contact area, which primarily lead to a loss of hardness in the contact zone. Electrical installations with frequency converters are particularly susceptible to this type of electrical erosion.

Bearing Damage Due to Plastic Deformation

Caused if the bearing material is loaded above its yield strength.

Overloading of the allowable surface pressures cause indentations of the rolling elements on the contact surfaces, which reduce the life as well as the smooth and quiet operation severely.

Foreign bodies (debris) in the bearings can leave behind plastic deformation (indentations) on the contact partner rolling over it.

Indentations due to improper handling are caused by incorrect assembly (pressure on the wrong bearing ring) or handling errors (dropping the bearings).

Fracture and Cracking

Fractures or cracks occur in the bearing components (the bearing rings of the bearing cage) if the tensile strength of the respective bearing material is exceeded.

Large shocks, impacts with a hardened chisel, or excessive pressure on the bearing seat can cause forced fracture during assembly or startup of the bearing.

Exceeding the fatigue strength under cyclical loading causes a fatigue fracture. Small cracks are formed, which increasingly propagate. If the tensile strength is exceeded in the remaining cross section, a forced fracture also occurs.

High dynamic (sliding) friction between the contact partners can result in thermal cracking caused by the friction heat.

Table 15.62 shows the relationship between the bearing damage that occurs and its cause in the form of a matrix.

It is advisable to comply with the following points to avoid bearing damage:

- Ensure precise analysis of the bearing loads that occur (forces, speeds, temperatures).
- Use and design the bearing according to the manufacturer's information.
- Pay attention to tolerancing of the connection dimensions (fit tolerances, shaft offset/deflection).
- Prevent the flow of electrical current through the bearing.
- Ensure adequate protection of the bearing from moisture/dirt.
- Select a lubricant suitable for the operating situation.
- Lubricate the bearing adequately.
- Use suitable tools/jigs for the assembly and installation.
- Ensure cleanliness during assembly.

15.5.8 Further Reading

In addition to the standard machine element references, principles for the selection and design of rolling bearings are also provided, for example, in [15.77].

Details on bearing calculations are given in the ISO 76 [15.70] and ISO 281 [15.71] standards.

Information on the bearing construction, its dimensions, load capabilities, and examples of the connection geometry design are provided in the manufacturers' catalogs, for example, [15.78, 79].

Typical rolling bearing damage and its causes are described in [15.73, 80].

Table 15.62 Matrix of the bearing damage according to ISO 15243 [15.76]

Possible causes		Characteristic features of defects																				
		Wear								Fatigue		Corrosion			Fractures			Deformation			Cracks		
		Increased wear	Tracks	Scores	Seizing marks, smearing	Scratches, scuffing marks	Fluting, washboarding	Chatter marks	Hot running	Pitting	Flaking, spalling	General corrosion (rust)	Fretting corrosion (rust)	Electrical craters, fluting	Through crack, fracture	Cage fractures	Local spalling, chipping	Deformation	Indentations	Marking	Thermal cracks	Heat-treatment cracks	Grinding cracks
Lubricant	Insufficent lubricant	•			•	•			•	•	•					•					•		
	Excessive lubricant								•														
	Incorrect viscosity	•			•	•			•	•	•					•					•		
	Inadequate quality	•			•	•			•	•	•	•									•		
	Contamination	•	•	•						•	•	•							•				
Operating condition	Excessive speed	•			•	•			•	•	•					•		•					
	Excessive load	•			•				•	•	•				•			•	•		•		
	Frequently fluctuating loads	•		•	•	•				•	•					•							
	Vibration	•			•	•		•		•	•		•		•	•							
	Passage of electrical current						•			•	•			•									
Mounting	Faulty electrical insulation						•		•	•	•			•									
	Incorrect mounting					•				•	•												
	Incorrect heating	•																•			•		
	Misalignment	•				•				•	•							•					
	Undesirable preloading	•	•						•	•	•				•	•		•			•		
	Impact	•	•													•		•					
	Inadequate fixing	•	•		•					•	•				•		•	•			•		
	Uneven seating surface	•	•							•	•		•		•			•					
	Incorrect seating fit	•	•						•	•	•		•				•	•			•		
Design	Incorrect bearing selectors				•	•			•				•		•	•	•						
	Unsuitable adjacent components				•	•			•				•		•	•	•						
Handling	Incorrect storage											•											
	Vibration during transportation					•		•					•						•	•			
Manu-facture	Incorrect heat treatment	•							•	•	•											•	
	Incorrect grinding																						•
	Inadequate surface finish	•	•							•	•												
	Inaccurate application component	•	•						•	•	•				•		•						
Material	Structural defects									•	•				•								
	Combination of incompatible materials	•			•	•			•									•					

15.6 Plain Bearings

Plain bearings are used to store the components. In this type of bearing, the parts moving relative to each other slide off each other, whereby the sliding surfaces can touch or can be separated by an intermediate medium (mostly oil or grease). The advantages and disadvantages of plain bearings are listed in Table 15.63.

Depending on the bearing type and lubrication condition, dry friction, surface layer friction, mixed friction, and liquid friction occur [15.73].

Dry friction (Fig. 15.75a) is technologically of hardly any significance, as under atmospheric conditions, surface reaction layers form on all technical surfaces, or rather gas or liquid modules adhere, which generally reduce the frictional resistance.

Surface layer friction occurs on unlubricated technical surfaces under atmospheric conditions (Fig. 15.75b). The sliding process here is favored by the constant shearing off and reformation of the surface layers with low shear strength.

Dry lubrication exists if the friction process is helped by applying solid lubricants such as graphite, molybdenum(IV)-sulfide, very fine ceramic particles, or plastics (PTFE, PA, POM). Solid lubricants act in two different ways. The contact surfaces are separated by the solid particles and can slide/roll off of them. At the same time, they fill uneven irregularities, which improves the load-bearing behavior of the surfaces.

In the case of fluid or pasty lubricants, the type of friction depends on the friction speed (relative speed between mating parts) (Fig. 15.76).

At low friction speeds, the touching of the contact surfaces causes solid friction, also called boundary friction. The lubricant is displaced from the contact point by the very high local surface pressures. With increasing relative speed, the lubricant begins to separate the contact partners, so that mixed friction exists, whereby the coefficient of friction reduces with increasing speed. With complete separation of the contact surfaces the mixed friction becomes liquid friction.

The relationships between the prevailing form of friction and the friction speed in lubricated plain bearings are shown graphically in the so-called Stribeck curve (Fig. 15.76).

According to ISO 4378-1 [15.81], among other things, plain bearings can be subdivided according to the type of load (static or dynamic), the load direction (radial or thrust bearings), and the type of lubrication (for example, hydrostatic, hydrodynamic, and maintenance-free plain bearings).

Table 15.63 General advantages and disadvantages of plain bearings

Advantages	Disadvantages
Low noise	Increased wear in start-stop operation
Insensitive to impacts/shocks	Increased friction moment on starting up
Low unit volume	Increased thermal load compared to rolling bearings
High load-bearing capacity	Rolling bearings, as a standardized component in mass production, are mostly less expensive
Very large speed range	Sensitive to canting
Very easy assembly and installation due to separate half-bearings	Risk of seizure
Long life	
Separable bearings easy to implement	

15.6.1 Hydrostatic Plain Bearings

In the case of hydrostatic plain bearings, liquid or gaseous lubricant is pressed into the bearing gap under high pressure with the help of an external pressure

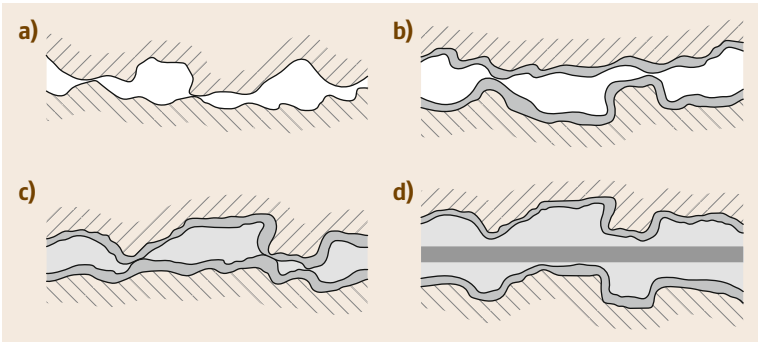

Fig. 15.75a–d Friction states between the contact surfaces: (a) dry friction, (b) surface layer friction, (c) mixed friction, and (d) liquid (viscous) friction

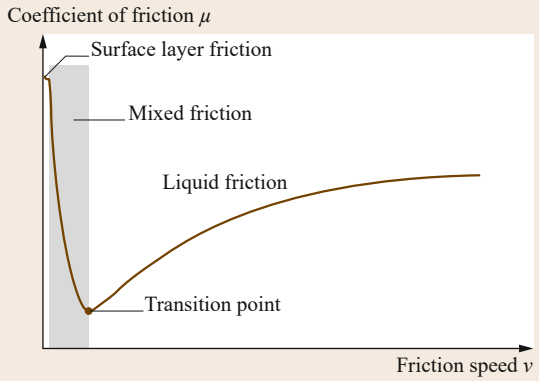

Fig. 15.76 Stribeck curve (schematic)

Table 15.64 Advantages and disadvantages of hydrostatic plain bearings

Advantages	Disadvantages
No minimum speed required	External pressure supply is required
No stick-slip effect on starting up (high accuracy)	Large space requirement
Movement is seemingly wear-free	
Very good damping properties	

source; this causes the contact surfaces to be separated, so that liquid friction exists even if the contact surfaces are at a standstill. As a result, these bearings operate as if wear-free. The advantages and disadvantages of this type of bearing are listed in Table 15.64.

15.6.2 Hydrodynamic Plain Bearings

Unlike hydrostatic plain bearings, in hydrodynamic plain bearings the contact surfaces are separated by the dynamic build-up of pressure in the bearing itself. This requires the contact surfaces to move relative to each other with an appropriately high speed (Fig. 15.76), a viscous lubricant, and a constricting lubrication gap. The lubricant is pressed into the constricting gap by adhesive forces, which causes a pressure to form that separates the contact surfaces.

The constricting lubrication gap in radial bearings is formed by the eccentricity e of the shaft in the bearing and in thrust bearings, for example, by key beds (wedge-shaped surfaces) (Fig. 15.77).

The eccentricity e and the attitude angle β in plain radial bearings depend on the bearing force, the bearing geometry, the viscosity, and the speed ratios such that the integral of the pressure distribution over the bearing surface is in equilibrium with the external bearing force.

Table 15.65 Advantages and disadvantages of hydrodynamic plain bearings compared to hydrostatic plain bearings

Advantages	Disadvantages
Compact design	Increased friction and wear on starting
Simple structure	Requires a minimum speed for complete separation of the contact surfaces
Easier lubricant supply	Radial displacement of the shaft
	Susceptible to vibration at high speeds

Table 15.65 lists the advantages and disadvantages of hydrodynamic plain bearings.

15.6.3 Hydrostatic Starting Aids

If frequent starting under high starting load, idling with low speeds, or very long run-down times occur in hydrodynamic plain bearings, using hydrostatic starting aids (boosters) can be advisable.

To do this, one or two oil pockets in the bottom half-bearing are introduced in the contact area with the shaft, which are supplied with a pressurized lubricant by an external pump with a pump pressure of max. 200 bar on lifting and of approximately 100 bar for holding the shaft.

15.6.4 Maintenance-Free Plain Bearings

Plain bearings without a separate lubricant supply are called maintenance-free plain bearings. With these bearings, increased wear at the start of use is accepted, whereby the softer bearing material and/or integrated solid lubricants (for example, PTFE, molybdenum(IV) sulfide, or graphite) are rubbed off and fill up the roughness valleys on the mating surface. In the ideal case, the roughness valleys are completely clogged with the abraded material (acts as solid lubricant), which results in favorable load-bearing behavior. Compared to hydrodynamic plain bearings, maintenance-free plain bearings have a significantly higher load-bearing capacity at lower friction speeds.

15.6.5 Bearing Materials

The material of the plain bearing must be matched with the material of the shaft/axle. In general, a softer material is chosen for the bearing than for the shaft, so that wear occurs in the bearing first (because it is easier and less expensive to replace).

In addition to adequate strength, the bearing material should have good corrosion resistance and be

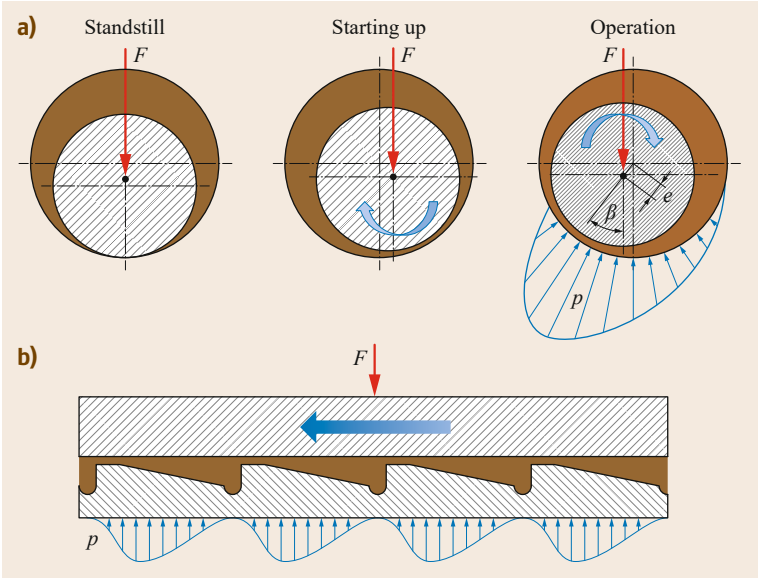

Fig. 15.77a,b Schematic diagram of the function of a hydrodynamic radial bearing **(a)** and a thrust bearing **(b)**

insensitive to the lubricants used, or rather the additives they contain.

Due to the good wetting ability of the sliding surfaces, the lubricant can also penetrate narrow gaps and separate the contact surfaces from each other.

This is significant, especially in the mixed friction area on starting up and running out the bearing, if there is only little lubricant in the contact zone.

Bearings with good emergency running properties (resistance to galling) handle short-term failure of the lubrication without major damage. The emergency running properties are primarily determined by the bearing materials. Metals with a low hardness, low melting temperature, and that do not tend to bond with the contact partner due to adhesive forces are particularly suitable.

Plain bearing materials with good running-in characteristics, adapt to the geometry of the shaft/axle through local wear and deformation, without noticeably impairing the function of the bearing.

The introduction of hard foreign bodies (dirt and/or wear particles) into the sliding surface of the bearing is called embedment. This should largely cancel the harmful effect of the foreign bodies. However, even in bearings with good embedment properties, attention must be paid to the cleanliness of the lubricant used.

High wear resistance ensures a long bearing life. In practice, plain bearings are only subjected to noteworthy wear if they are operated within the area of boundary or mixed friction. In the case of hydrodynamic plain bearings, this is the case above all during starting up and runout.

Generally valid statements about wear resistance cannot be reliably made, as in addition to the operating conditions, the properties of the mating parts and lubricant have a large effect on the wear resistance of the bearing.

Metallic bearing materials are, for example, lead, tin, copper, and aluminum alloys.

For certain application cases (water lubrication, dry running, chemically aggressive media), nonmetallic materials, such as rubber, plastics, and ceramic materials are used.

Table 15.66 shows the general properties of some of the most important bearing materials.

Steel with a defined surface roughness is mostly used for the shafts/axles. If the surface roughness is too low, the stick-slip effect can occur; wear increases if the shaft surfaces are too rough. Galvanic (electroplated) surface coatings are only conditionally possible due to wear. The shaft surfaces are hardened in the case of higher requirements.

15.6.6 Bearing Types

It is possible to basically differentiate between solid and composite (multilayer) bearings and between thick- and thin-walled bearings.

Small solid bearings are made of pipe material; large ones are made in the centrifugal casting method as bushes (linings) and are pressed into housing bores.

Composite (multilayer) bearings combine the advantages of a mechanically stable half-bearing with the

Table 15.66 General properties of plain bearing materials [15.82]

Properties	Materials								
	White (babbit) metals on		Bronze on			Aluminum alloys	Porous sintered bearing	Plastics	Artificial carbon
	Lead based	Tin based	Lead based	Tin based	Aluminum based				
Antifriction (sliding) property	++	+	0 +[a]	0	0	+…0 +[a]	0…−	−	−
Embeddability	++	+	0 +[a]	0	0	+…0 +[a]	0	−	−−
Resistance to galling/ antiseizing property	++	+	+ ++[a]	0	+	+ ++[a]	++	++	++
Loadability	−	0	+	+	+	+	0	−	−−
Thermal conduction/ thermal expansion	−	−	0	0	0	+	−	−−	−−
Corrosion resistance	−−	0	−	0	+	+	+…−− depending on structure	0	+
Incomplete or solid lubrication (tribological coating)	+	0	− 0[a]	−−	−	0	++	++	++

++ very good; + good, 0 adequate, − moderate, −− poor
[a] with additional tertiary overlay

positive properties of the softer sliding layer applied on it. In simple two-layer bearings, the soft bearing metal is applied with layers 0.3–0.5-mm thick onto a backing made of steel by means of a belt casting or roll cladding process.

Multilayer bearings can be used for particularly high loads and stresses (Fig. 15.78). In the process, a soft plain bearing running-in layer is applied to the bearing material layer (bronze or aluminum) with a thin intermediate layer and is finally covered with a corrosion-inhibiting layer.

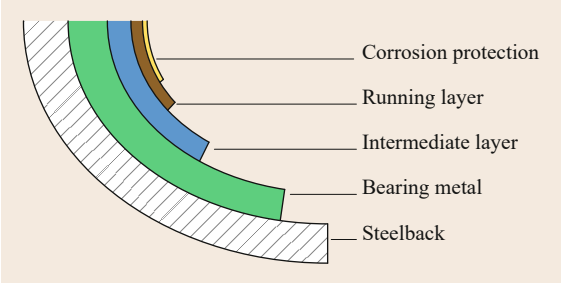

Fig. 15.78 Structure of a multilayer plain bearing

Bearing Lubrication

Plain bearings must be lubricated to reduce the friction between the contact surfaces. According to ISO 4378-3 [15.83], the lubrication methods can be divided, among other things, into:

- Recirculating lubrication
- Lifetime lubrication
- Once-through lubrication (loss lubrication)

In recirculating lubrication, the lubricant, generally a liquid, is in a closed circuit. This can be achieved, for example, by a bearing running in an oil bath, centrifugally cast metal sheets, ring lubrication with fixed or loose oil rings (Fig. 15.79), or recirculating lubrication with filter and pump (Fig. 15.80).

Loose oil rings can be used up to shaft circumferential speeds of 20 m/s and fixed oil rings up to 10 m/s. Above this circumferential speed the oil is spun off by the centrifugal forces and foams (aerates). Loose oil rings reach delivery rates of 1–4 L/h and fixed oil rings up to 24 L/h [15.85].

Recirculating lubrication is necessary for discharges above 30 L/h (Fig. 15.80). Recirculating lubrication systems pump the oil out of an oil reservoir (for example the housing) with the help of a pump and pass it through a filter to the relevant bearings (in most cases one pump supplies several bearings at the same time). The oil is additionally cooled in the case of high thermal loads.

The discharge pressure is within the range of 0.2–5 bar. In general, the lubricant supply must be de-

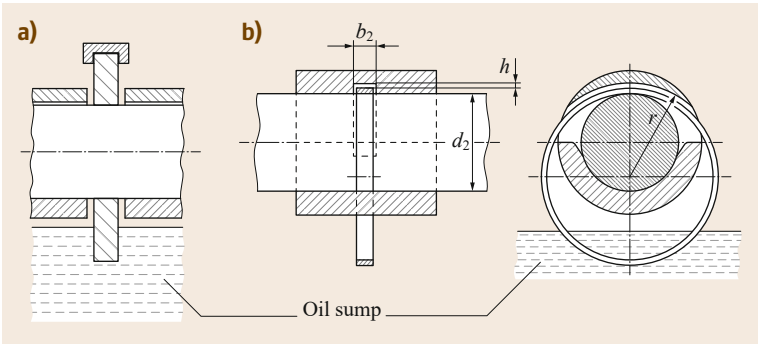

Fig. 15.79a,b Ring lubrication: **(a)** fixed oil ring with wiper for oil discharge on both sides and **(b)** loose oil ring, projection (after [15.84])

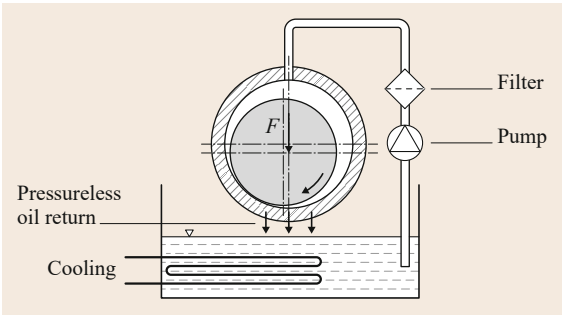

Fig. 15.80 Circulating oil lubrication with cooling (schematic)

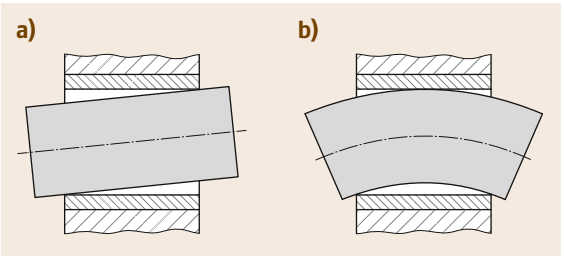

Fig. 15.81a,b Edge wear in rigid bearing bodies: **(a)** shaft misalignment in an end bearing and **(b)** shaft curvature in a center bearing

signed so that it takes place in an unloaded area of the bearing (area of the diverging gap), whereby appropriate holes, grooves, or pockets can be made for distribution of the lubricant in the bearing clearance. Dimensions and types are given in ISO 12128 [15.86].

In the case of plain thrust bearings for vertically arranged shafts, it must be ensured that even under the effect of the centrifugal force, the inner areas of the sliding surfaces are adequately supplied with lubricant.

Lifetime lubrication for plain bearings is only possible for low loads and speeds. The main lubricants used are dry lubricants such as graphite or molybdenum(IV) sulfide. Under certain circumstances, lubricant-impregnated sintered bearings or plastic bearings can be designed to be maintenance-free, which in the broader sense corresponds to lifetime lubrication.

If the effect of the lubricant is limited in time and cannot be supplied to the lubrication gap again in a closed circuit, this is called once-through lubrication system (also known as loss lubrication). These are mainly used for bearings with low thermal loads and low lubricant requirements. Grease-lubricated bearings with equipment for relubricating (for example, lubricating nipples or Stauffer lubricator (grease cup)) are always once-through lubrication systems, as the used grease is displaced from the lubrication gap by new grease. Other types of once-through lubrication systems are, for example, drop-feed lubricators and compressed-air bearings.

15.6.7 Design

The load acting on the shaft/axle deforms it, which causes the lubrication gap in axial directions to no longer be parallel. Edge wear (edge loading wear), shown in Fig. 15.81 is particularly problematic; it occurs most where the diameter to width ratio $B/D > 0.3$ or in end bearings.

Edge wear can be avoided by using bearings with a narrow width or by adapting the bearing to the deformed condition of the shaft/axle.

Shaft misalignment, which mostly occurs at the end bearings, can be avoided, for example, by adjusting the elastic resilience of the bearing body (Fig. 15.82a) or by a movable tilting arrangement (Fig. 15.82b).

In the case of center bearings, in which shaft curvature frequently causes problems, the edge wear can be reduced by slightly tapered widening of the ends of the bearing bores (Fig. 15.82c) or, if the half-bearing is not supported, in the bearing body over its entire length (Fig. 15.82d,e).

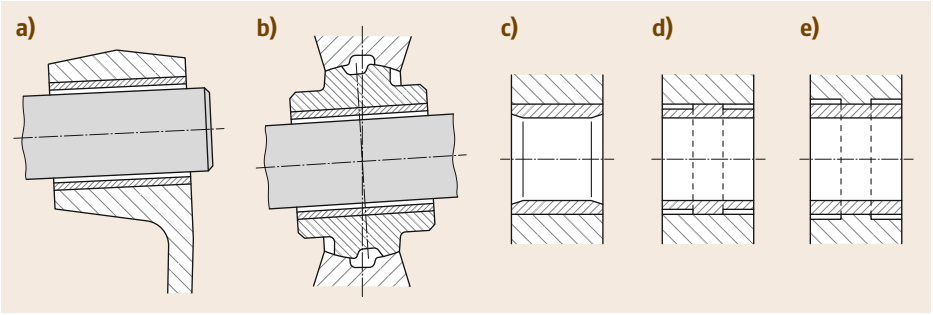

Fig. 15.82a–e Design measures to reduce edge wear: **(a)** elastic resilience, **(b)** tilting movability of the bearing body, **(c)** tapered widening of the ends of the bearing bores, **(d,e)** elastic deformation of the bearing bush with reduced support width in the bearing body

15.6.8 Further Reading

A comprehensive compilation on the topic of plain bearings is provided, for example, by [15.87, 88].

Details of the calculation of hydrodynamic plain bearings are given in the VDI Guidelines 2204 Parts 1 to 4 [15.89].

In his book, *Perovic* [15.90] provides information on the design and calculation of hydrostatic plain bearings.

Friction and wear principles are found in *Czichos* and *Habig* [15.91].

Further literature on the analysis of damage to lubricated machine elements is provided by *Bartz* [15.73].

15.7 Seals and Gaskets

Seals and gaskets are components or designed elements for achieving spatial separation of fixed, solid, or gaseous media with the objective of preventing the exchange of materials, or rather to reduce it to an acceptable level (allowable loss due to leakage). Absolute tightness in the physical sense (complete prevention of exchange of materials) cannot be achieved technologically, as diffusion processes cannot be prevented.

In addition to the blocking effect, seals and gaskets often fulfill other functions, for example, heat conduction/insulation, electrical insulation, vibration damping, force or load transfer, and guide function/bearing.

A basic differentiation can be made between static and dynamic seals, which are in turn further divided into contacting and noncontacting seals and gaskets (Fig. 15.83).

In the case of static seals (gaskets) the spaces to be sealed from each other, or rather the seal faces, are not slidable, i.e., they are stationary. Contacting seals are primarily used; noncontacting seals have only secondary significance.

If the seal faces are slidable relative to each other or are pivoted they are called dynamic seals. These can be contacting or noncontacting.

Absolute tightness in a technical sense can only be achieved through elastic or elastic-plastic deformations of the contacting seal faces or by material-bonding joints.

15.7.1 Contacting Seals and Gaskets

Material-Bonding Seals

Material-bonding joints are generally permanent. Material-bonding joints include welded, soldered, adhesive bonding, and press-fit connections or joints. Apart from the task of transferring force, the above types of connections or joints are often used to seal at the same time.

In the broadest sense, sealing compounds can also be included in nonmaterial-boding seals and gaskets.

Flat-Face and Molded Gaskets

Flat-face and molded gaskets are used as static seals.

A differentiation is made between flat and molded seals, depending on the shape of the contact surface or seal face:

- In the case of flat-face gaskets, the seal face is formed by the flat surfaces of the seal, or rather the sealing element (Fig. 15.84); the sealing face does not change due to assembly or installation.
- In the case of molded seals, the sealing face does not form until assembly/installation, as a result of elastic or elastic-plastic deformation of the sealing element, caused by internal and/or external forces.

For correct function of flat and molded seals and gaskets, the seal faces must be continuously pressed together during operation by a defined contact force.

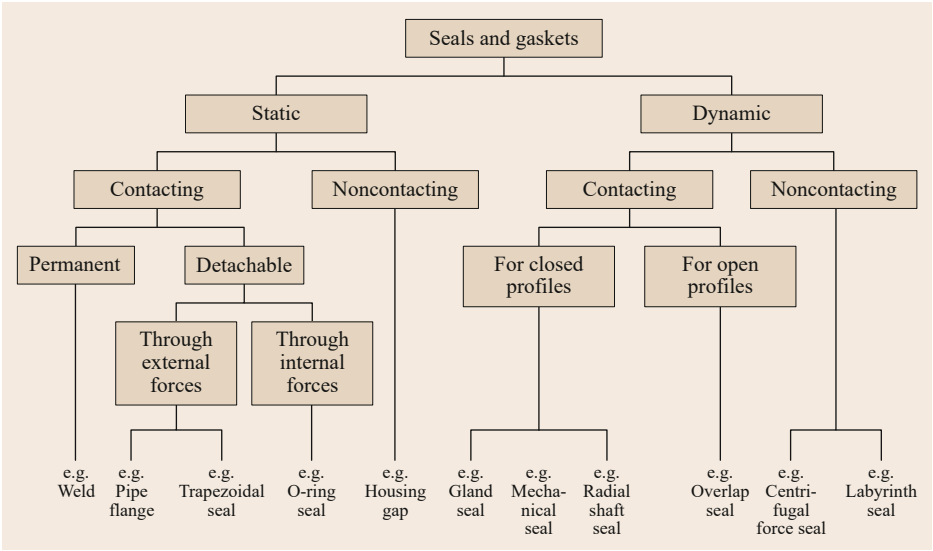

Fig. 15.83 Classification of seals and gaskets according to type of load

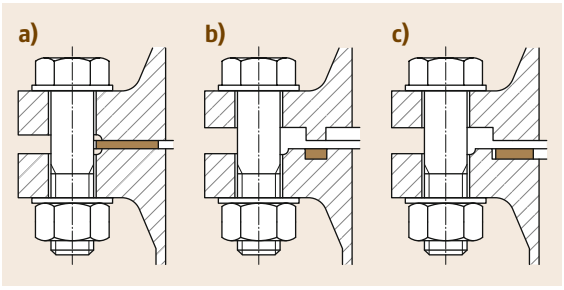

Fig. 15.84a–c Flat gaskets according to EN 1514-1 [15.92]: **(a)** for flanges with flat face, **(b)** with tongue and groove, and **(c)** with raised and recessed face (male and female face)

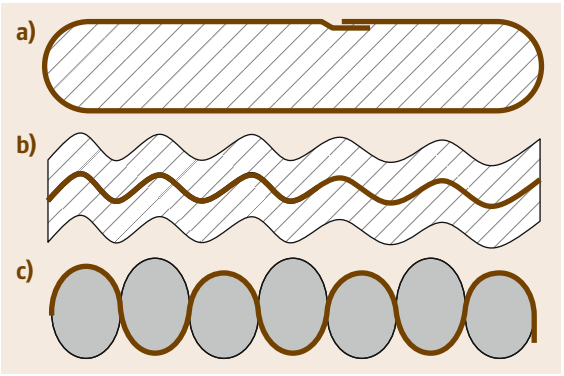

Fig. 15.85a–c Composite material seals: **(a)** metal jacketed with overlapped joint, **(b)** corrugated seal ring with metal core, and **(c)** corrugated seal ring with asbestos rope support

Sealing Materials for Flat Gaskets. Soft material seals in the form of paper/cardboard, cork, rubber, or plastics, or hard material seals or gaskets in the form of copper, brass, aluminum, soft iron, or steel are used, depending on the quality of the surface and the magnitude of the forces to be absorbed. Composite material seals are available for complex application cases (Fig. 15.85) that combine the properties of soft and hard material seals.

Toroidal Rings

Toroidal rings (also known as O-rings) are also made of rubber-elastic materials (elastomer) and are used both as a static seal (gasket) for pressures up to 400 bar, and as a dynamic seal at low relative speeds for valves, or as hydraulic/pneumatic components (Fig. 15.86).

The sealing effect is achieved by elastic material deformation of the cross section when the components to be sealed are assembled. A continuously acting preload is necessary. The pressure applied causes self-reinforcing of the sealing effect (Fig. 15.87).

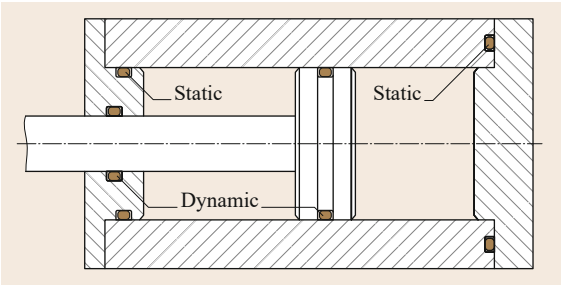

Fig. 15.86 O-ring as static or dynamic sealing element

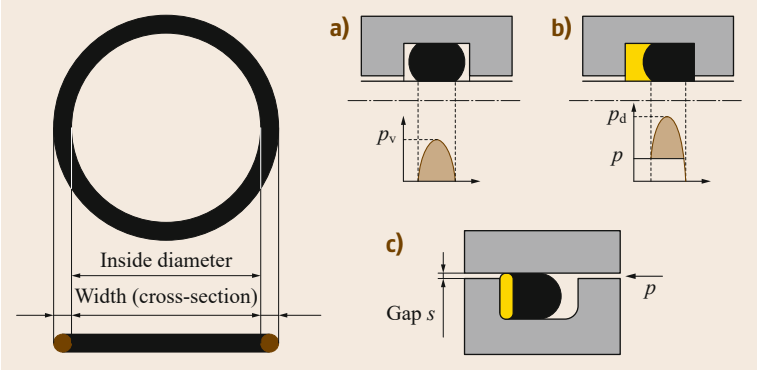

Fig. 15.87a–c Toroidal ring (*left*) and installation example: **(a)** in the preloaded condition, **(b)** with self-reinforcing effect due to operating pressure without backup ring, and **(c)** with self-reinforcing effect due to operating pressure with backup ring

The temperature resistance is limited by the elastomer element and lies between −55 and +240 °C.

Dimensions for O-rings and the corresponding installation space are given in the relevant standards (for example ISO 3601 [15.93, 94], AS 568A [15.95]), or the manufacturers' information.

Where toroidal rings are used as dynamic seals, it should be ensured that the toroidal ring does not have a guide function, otherwise very large wear is expected.

Materials. The choice of material for the O-ring is primarily determined by the media compatibility and use temperatures. Table 15.67 lists standard materials with their corresponding areas of use. As the properties of the materials are very highly dependent on the composition or rather production, the relevant manufacturers' information must be noted when making the choice.

Rotary Shaft Lip-Type Seals

Rotary shaft lip-type seals, also known as rotary shaft seals or radial shaft seals, are the most frequently used dynamic seal for sealing rotating shafts or axles under relatively small pressure differences. They can also be used as a static sealing element. Rotary shaft lip-type seals are standardized internationally by ISO 6194-1 [15.96].

The basic structure of a rotary shaft lip-type seal is shown in Fig. 15.88.

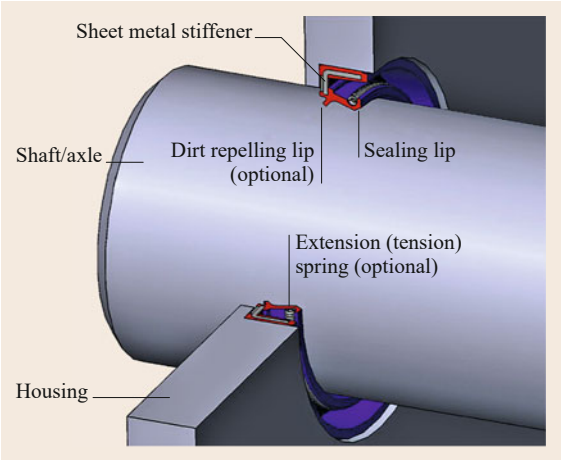

Fig. 15.88 Rotary shaft lip-type seals with dirt repelling lip

Mode of Action. If the shafts/axles are at rest, the sealing effect is achieved by the radial contact forces of the elastically deformed sealing lip on the surface of the shaft/axle. In most cases the contact force of the sealing lip is strengthened by an extension (tension) spring.

In the case of rotating shafts/axles, a thin film of the medium to be sealed forms between the twist-free ground shaft surface and the sealing lip. Due to the asymmetrical distribution of the contact pressure, in conjunction with the relative movement between

Table 15.67 Typical materials for O-rings and their typical areas of use

Designation	Area of use	Temperature range (°C)
Acrylonitrile butadiene rubber (NBR)	Standard material for normal applications (mineral oils, mineral oil-based pressurized liquids, vegetable, and animal greases)	−35 to +110
Fluoroelastomer (FKM)	For mineral oils and greases at high temperatures	−25 to +200
Perfluoroelastomer (FFKM)	For chemically aggressive media and high temperatures	−25 to +240
Ethylene-propylene diene monomer (EPDM)	For glycol-based pressurized liquids, brake fluid, solvents, organic and inorganic acids, hot water applications	−55 to +130

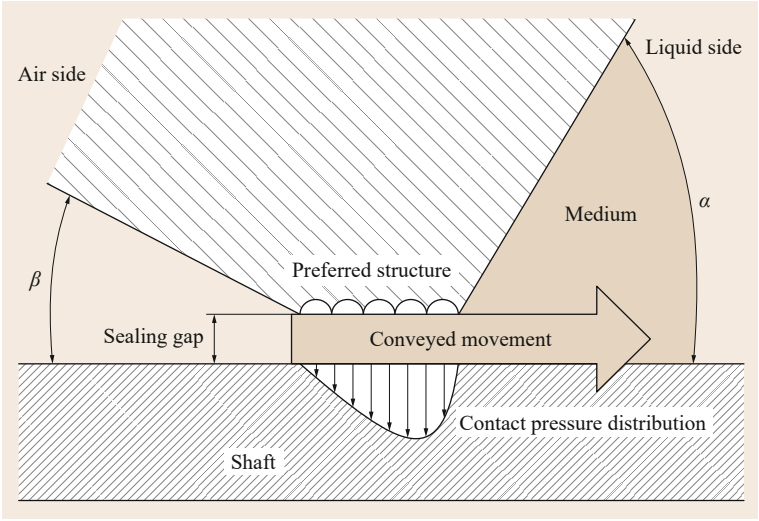

Fig. 15.89 Contact pressure distribution of a rotary shaft lip-type seal (radial shaft seal ring)

the contact surfaces, a conveying effect results in the direction of the media side (Fig. 15.89). If contamination (dirt, dust or liquids) is expected on the atmosphere side, radial shaft rings with a dirt-repelling lip must be used, as otherwise the conveying effect can cause dirt to be input into the medium to be sealed. Dry running of the seal ring must always be prevented.

Depending on the shaft/axle speed, standard radial shaft seals can be used up to pressure differences of approximately 0.3 bar. Higher pressures (up to 10 bar) are possible with reinforced sealing lips.

Materials for Radial Shaft Seals.

Standard materials for radial shaft seals with their areas of application are given in Table 15.68.

Axial Shaft Seal

Axial shaft seals are used for dynamic sealing of the flat faces of rotating shafts/axles. Unlike radial shaft seals, axial shaft seals can only be used without pressure. For this reason, they are usually used for secondary sealing tasks or in combination with radial shaft seals in the case of greater contamination. Widely used types are the V-ring or the gamma ring (Fig. 15.90).

Table 15.68 Materials for radial shaft seals [15.97]

	Rubber type					
	Nitrile	**Polyacrylate**	**Viton**	**Silicone**	**Polytetrafluorethylene**	**Leather**
Properties	High wear resistance Good running properties for general use	Better heat, oil, and chemical resistance than NBR; recommended for use in oil that contains load-bearing additives such as EP gear oils	High level of chemical resistance; high temperature resistance	Wide temperature range; commonly used in low temperature applications; very prone to mechanical damage during fitting	Chemical resistant; low coefficient of friction; poor elastic properties; not wear resistant if used by dynamic applications	Recommended for abrasive applications; good running properties due to the impregnated seal lip; can be used on shafts that have a surface roughness outside the range for rubber seals; not suitable for water
Material code ISO 1629	NBR	ACM	FPM	MVQ	PTFE	
Heat resistance (°C)	−35 to +100	−20 to +130	−30 to +180	−50 to +150	−80 to +200	−40 to +90

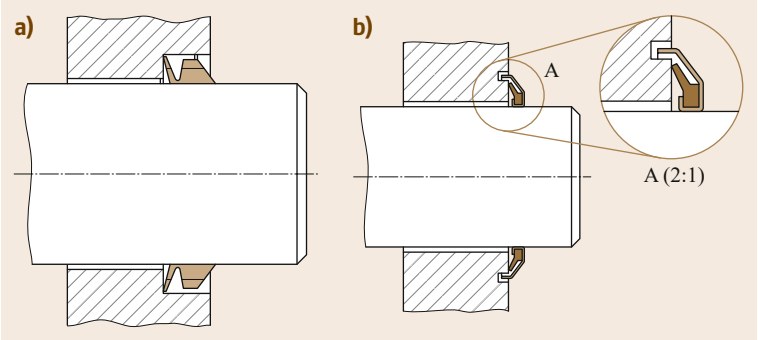

Fig. 15.90a,b Axial shaft seals: V-ring **(a)** and gamma ring **(b)**

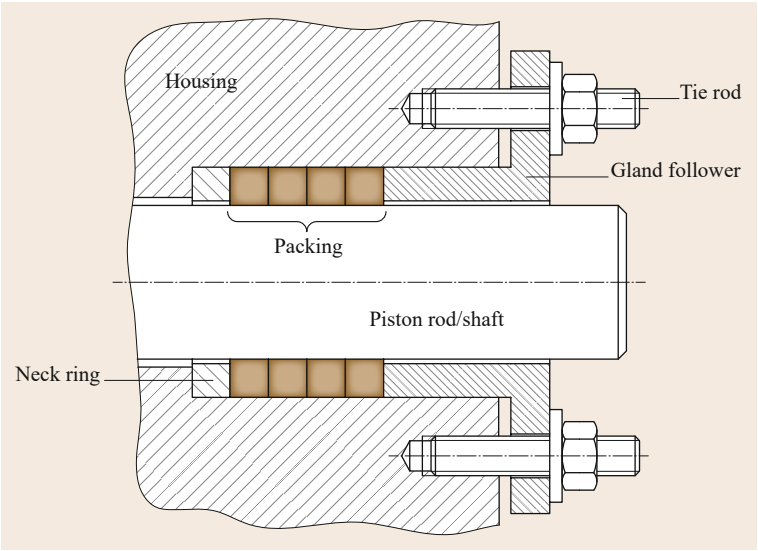

Fig. 15.91 Structure of a gland packing

Gland Packings

Gland packings are used for dynamic sealing of rotating shafts or axially moved piston rods. An exemplary structure is shown in Fig. 15.91.

The radial sealing pressure in the sealing gap between the shaft or piston rod and the gland packings is generated by elastic or elastic-plastic deformation of the packings as a result of axial force applied by clamping the gland using the tie rod, which in turn leads to axial shrinking and transverse expansion of the gland seals.

Gland seals are used, due to their relatively low price, for the economical sealing of pumps, agitators, and control valves. Due to the compression, a high friction force or rather a high friction moment acts between the packing and the moved component. Gland packings must also be readjusted regularly during service.

Their area of use is limited with regard to pressure and sliding speed (Fig. 15.92).

The leakage that inevitably occurs is used to cool and lubricate the sealing faces.

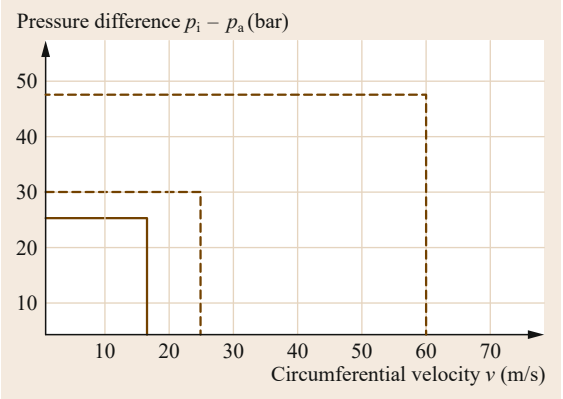

Fig. 15.92 Area of use of gland packings

Braided natural fibers such as hemp, cotton, or ramie, or synthetic braided fibers such as PTFE, PA, graphite fibers, or carbon fibers are used as materials for gland packings.

Table 15.69 Advantages and disadvantages of mechanical seals

Advantages	Disadvantages
Defined sealing gap	Expensive
Readjustment not required	Sensitive to dirt
Low friction	

Mechanical Seals

Are used for (mainly axial) sealing of rotating machine parts in lead-throughs, for example in pumps, agitators, centrifuges, and turbines. Here the rotating seal ring together with the stationary mating ring form a defined sealing gap, which limits the leakage to a very small, allowable size. The surrounding medium forms a gaseous or liquid lubricating film in the sealing gap. The advantages and disadvantages of mechanical seals are listed in Table 15.69.

Basic Structure, Types and Use Limits. Figures 15.93 and 15.94 show the principle of a single-action and double-action mechanical seal, respectively.

Double-action mechanical seals are mainly used if gaseous, contaminated, or dirty media have to be sealed. The space between the two alternately arranged mechanical seals are filled with a barrier fluid (usually oil or water).

The following application applies to mechanical seals in standard cases:

Shaft diameter (of one-piece type): 5...500 mm
Pressure range: 10^{-5} to 450 bar
Temperature range: −200 to 450 °C
Circumferential speeds: up to 150 m/s

Materials. The choice of material for the seal ring, or for the mating ring depends on the application case (e.g., medium and degree of contamination) and the operating parameters (e.g., temperature, pressure, and sliding speed).

According to EN 12756 [15.100], the following material groups are available:

- Synthetic carbons
- Metals (coated and uncoated)
- Carbides (tungsten carbides, silicon carbides)
- Metal oxides
- Plastics

Diaphragms and Bellows

Diaphragms and bellows are very flexible elements that allow a large clearance for movement. They can be used to seal or protect against dirt/damage.

While diaphragms are mainly used for stroke or lifting movements (repeated linear movements) (Fig. 15.95) bellows allow significantly greater movement clearance (Fig. 15.96).

Depending on the material and shape, bellows can also deform rotationally to a limited extent.

Due to their low weight and high degree of flexibility, diaphragms are suitable as fast reacting switching elements (some also automatic) in pneumatic or hydraulic systems or for the separation of variable volumes (for example in diaphragm accumulators). Bellows (frequently corrugated or concertinaed) are frequently used to protect piston rods, Bowden cables, and gearshift linkages against dirt (Fig. 15.97).

15.7.2 Noncontact Seals

Noncontact seals account for the majority of dynamic seals and are mainly used if the surfaces to be sealed move with high speed relative to each other, require long running times, or if maintenance is very difficult. The advantages and disadvantages are shown in Table 15.70.

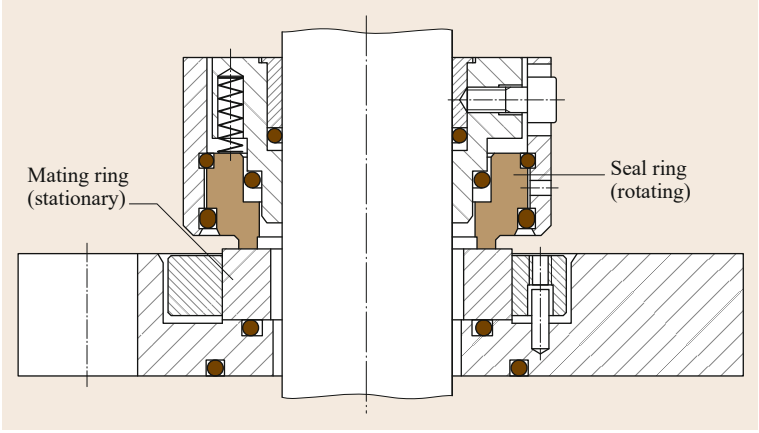

Fig. 15.93 Single mechanical seal made by *EagleBurgmann* (Type: SeccoMix 1) (after [15.98])

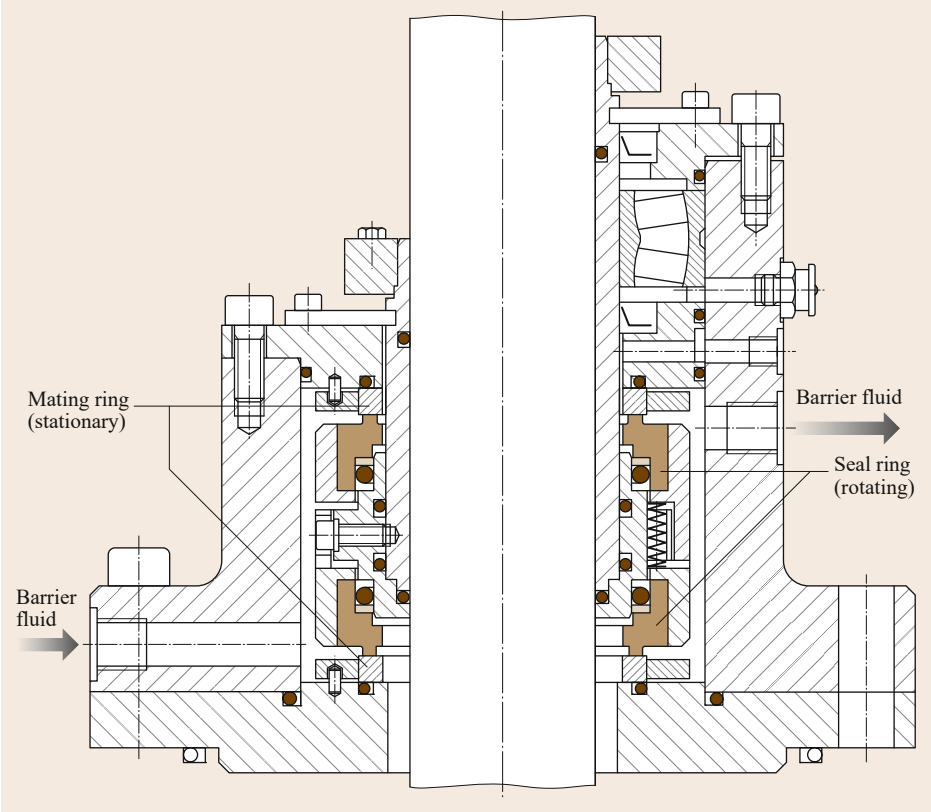

Fig. 15.94 Dual (tandem) mechanical seal with sealing medium made by *EagleBurgmann* (Type HSH-D) (after [15.99])

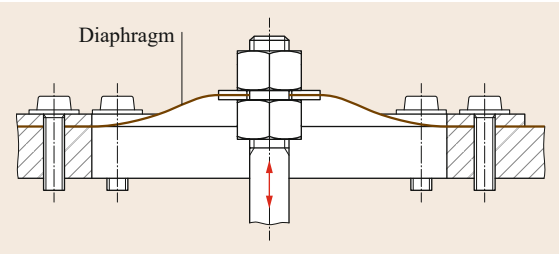

Fig. 15.95 Rubber diaphragm for small strokes

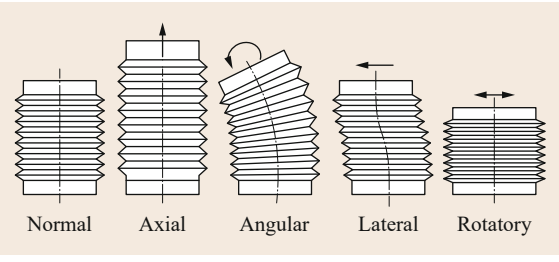

Fig. 15.96 Metal bellows with possible deformations

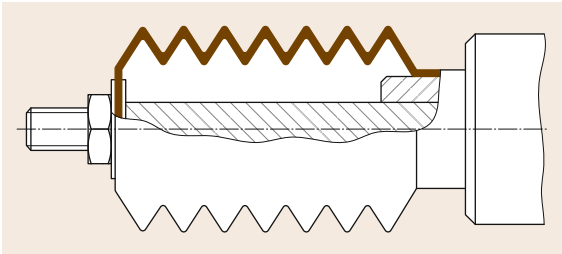

Fig. 15.97 Bellows for protecting a piston rod

Table 15.70 Advantages and disadvantages of noncontact seals

Advantages	Disadvantages
Very low friction (liquid or gas friction)	Complete leaktightness can only be achieved with barrier fluid (sealing, confining fluid)
Wear-free	Seal gap requires high-precision production
No readjustment required	
Thermally and electrically insulating	

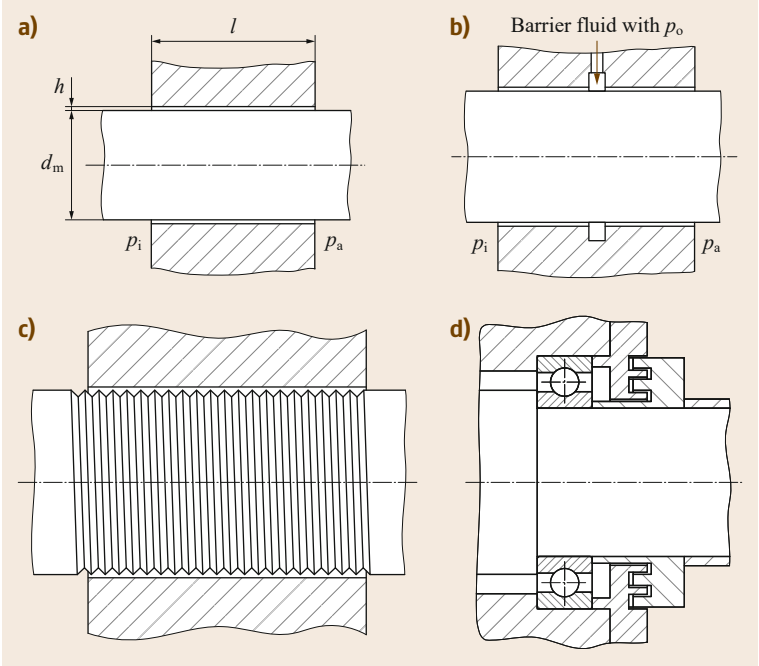

Fig. 15.98a–d Gap seals: **(a)** annular gap seal, **(b)** annular gap seal with barrier fluid, **(c)** threaded shaft seal, and **(d)** labyrinth seal

Gap Seals

The simplest type of noncontact seal is the gap seal (sealing ring) (Fig. 15.98a). The seal prevents escape of the medium to be sealed through a narrow gap, or rather to limit the escape to an acceptable amount. For an incompressible medium, the leak flowing through the annular gap can be calculated approximately using

$$\dot{V}_L = \frac{h^3}{12\eta}\frac{\Delta p}{l} d_m \pi \,, \qquad (15.117)$$

where:

$\dot{V}_L$ leakage flow rate
h gap height
η dynamic viscosity of the operating liquid
Δp pressure difference across the gap ($p_i - p_a$)
l gap length
d_m mean bore diameter

From (15.117), it is clear that the flow rate depends on the cubed gap height h and only linearly on the gap length l. For this reason, particular attention should be paid to the tolerancing of the gap height.

Gas-tight gap seals can be achieved by using barrier fluids (usually liquids) (Fig. 15.98b).

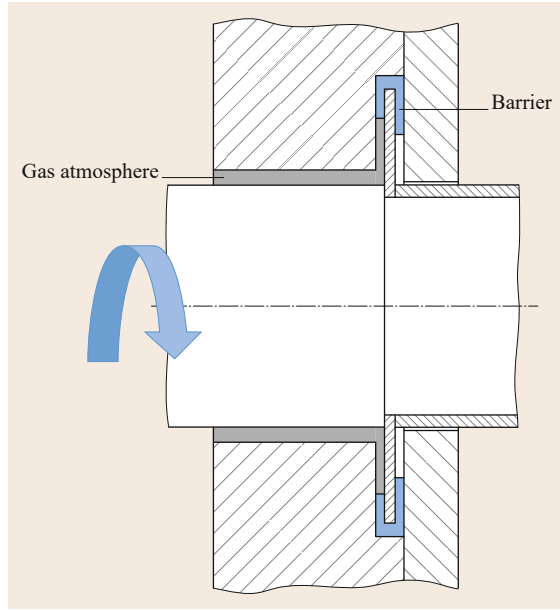

Fig. 15.99 Spinning disc with barrier fluid for sealing gases

In the case of rotating gap geometries, attaching a thread-like structure (threaded shaft seal) improves the gap sealing effect through directed conveying of the media (Fig. 15.98c).

A labyrinth seal is a further development of the gap seal. In this case, the fluid flow is limited by several consecutive restrictions (Fig. 15.98d).

Centrifugal Seals

The centrifugal forces caused by rotating shafts or axles can also be used for sealing. Special spinning discs, for example, keep liquid media away from the actual place to be sealed. Used in conjunction with a barrier fluid, gastight designs can also be achieved (Fig. 15.99).

15.7.3 Further Reading

Further information on seal technology can be found, among other things, in *Müller* and *Nau* [15.101] and *Tietze* and *Riedl* [15.102].

15.8 Gears and Gear Trains

Gears are used in pairs for form-closure and thus slip-free transfer of moments (gears) and forces (gear racks). The gears touch the flanks of the teeth.

Combinations of one or several gear pairs is called a gear train. They can be used not only to change the movement direction, speed, and torque, but also to adjust the center-to-center distance and the angular position.

The advantages and disadvantages of gear trains are listed in Table 15.71.

15.8.1 Classification of Gears and Gear Trains

Among other things, gears can be differentiated according to their geometry (e.g., cylindrical gears, bevel gears, helical gears, racks), the tooth profile (e.g., involute toothing, hypoid toothing), the angle of the tooth flanks relative to the axis of rotation (e.g., straight toothing, helical toothing, spiral toothing), and position of the toothing relative to the wheel body (external toothing, internal toothing).

Gear trains are differentiated on the basis of the gears used (Table 15.72). In addition, they can also be classified on the basis of the following features:

- The kinematics of the rolling movement, e.g., rolling contact gears, screw mechanism (gears operating on crossed axes), crossed rolling contact gear
- The number of stages, e.g., single stage, multistage
- The gear ratio shiftability, e.g., shiftable (manual car gearbox) or nonshiftable (fixed) gear ratio
- The position of the input and output shafts, e.g., parallel, crossing, intersecting
- The intended purpose, e.g., auxiliary/transfer gear, speed reduction gear

Fundamental Law of Gearing

Two profiles are suitable for toothing if, during their common meshing, the common normal to the tooth profiles at their point of contact B passes through a fixed point C on the line of centers (Fig. 15.100). This point, the pitch point, divides the distance between the two centers r of the pitch circles with a ratio equal to the ratio of the two angular velocities ω:

$$\frac{\omega_2}{\omega_1} = \frac{r_1}{r_2} \,. \tag{15.118}$$

The general law of toothing defines how the tooth profiles have to be designed in order for the transmission of motion to be constant.

Due to the fundamental law of gearing, the mating profile for a given tooth profile and rolling circle (generating pitch circle) is clearly defined and can be designed or rather built.

Of the theoretically infinite number of tooth profiles (flank profiles), only a very few are usable in practice (Sect. 15.8.2).

Gear Ratios

The speed ratio i results from the ratio of the angular velocity of the input gear ω_1 (driver) or speed of the input gear n_1 to the angular velocity of the output gear ω_2 (driven) or speed of the output gear n_2:

$$i = \frac{\omega_1}{\omega_2} = \frac{n_1}{n_2} \,. \tag{15.119}$$

Table 15.71 Advantages and disadvantages of gear trains

Advantages	Disadvantages
Slip-free movement	Complicated geometry of the toothing is time-consuming in production
Relatively small size	Noise is produced by the rolling of the teeth
Small mass-output ratio with high efficiency	Helical teeth (helical gearing) leads to axial forces
High load-bearing capability	
Alternating rotational directions possible	

Table 15.72 Gear train

Transmission (gear) type	Type		Position of the axles
Rolling contact gear			
Cylindrical gear	Straight cut	Helical	Parallel Shaft angle = 0° Center-to-center distance > 0
	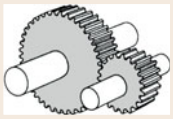	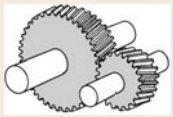	
			Parallel Shaft angle = 0° Center-to-center distance < 0
Bevel gear (rolling contact gear)	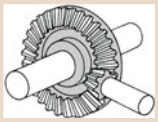	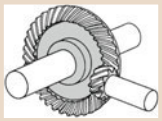	Intersecting Shaft angle > 0° Center-to-center distance = 0
Rack and pinion gear	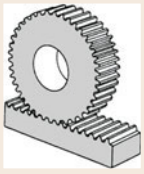	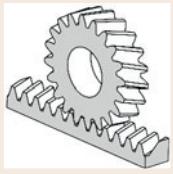	Crossing Shaft angle > 0° Center-to-center distance > 0
Crossed rolling contact gears			
Pair of crossed helical gears/spiral gears	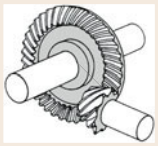		Crossing Shaft angle > 0° Center-to-center distance > 0
Crossed gears/screw mechanism			
Worm gears	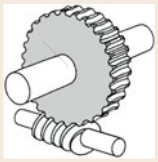		Crossing Shaft angle = 90° Center-to-center distance > 0

The circumferential velocities of the gears $v_i = \omega_i r_i$ at the point of contact B can be resolved into a tangential component v_{it} and a normal component v_{in}. For the tooth profiles to touch constantly during the movement, the normal velocity of the two profiles must be the same, thus

$$v_{1n} = v_{2n} = v_n = \omega_1 r_1 = \omega_2 r_2 \,. \tag{15.120}$$

If the point of contact B coincides with the pitch point C, in addition to the normal velocity, the tangential velocity of the gears is also equal $v_{1t} = v_{2t} = v_t$, which means that at this point a pure rolling motion (generating motion) takes place momentarily.

From (15.119) and (15.120) we get the following equation for the transmission ratio:

$$i = \frac{\omega_1}{\omega_2} = \frac{r_2}{r_1} \,. \tag{15.121}$$

The teeth ratio u is defined as the quotient of the number of teeth of the large wheel z_{max} and the number of teeth of the small wheel z_{min}:

$$u = \frac{z_{max}}{z_{min}} \geq 1 \,. \tag{15.122}$$

Because the pitch diameter of a gear d and the number of teeth z ($d \sim z$, Sect. 15.8.2, *Geometry of the Toothing*) are directly proportional, the ratio of the number of

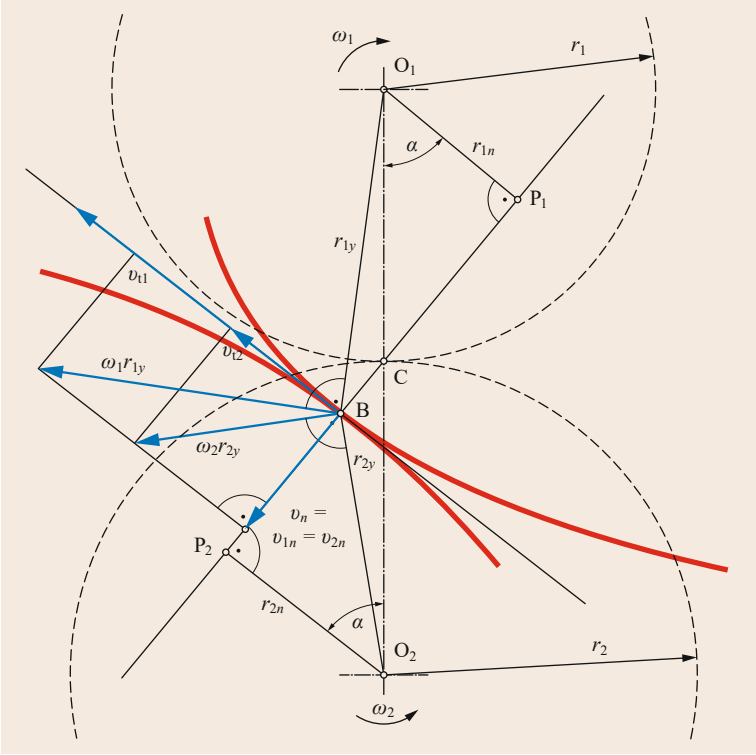

Fig. 15.100 Velocity vectors at tooth engagement

teeth u equals the transmission ratio i, so that

$$i = \frac{\omega_1}{\omega_2} = \frac{z_2}{z_1} \,. \tag{15.123}$$

The overall transmission ratio of a multistage gear train i_{all} is the product of the individual transmission stages (gear ratios):

$$i_{all} = i_1 i_2 i_3 \ldots i_n \,. \tag{15.124}$$

15.8.2 Gear Geometry of the Spur Gear System

By applying the law of gearing, the mating profile can be designed on the basis of a predefined gear tooth profile. It corresponds to the geometry that the predefined tooth profile would leave behind on rolling off a plastic material.

Gear racks (A_0 and B_0 in Fig. 15.101) can also be considered to be gears with an infinitely large rolling circle diameter and are generally called basic rack tooth profiles.

The gears shown in Fig. 15.101 can be paired with each other, as they have matching basic profiles A_0

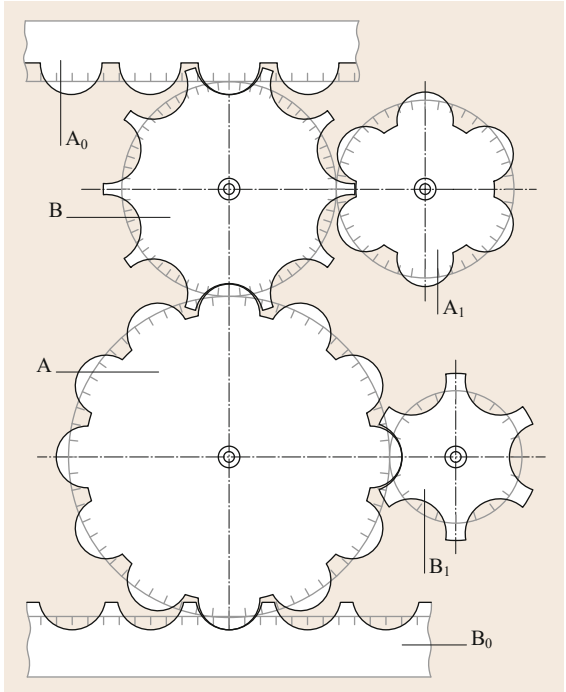

Fig. 15.101 Mating gears and basic profile (after [15.103])

Table 15.73 Advantages and disadvantages of involute toothing

Advantages	Disadvantages
Simple straight-sided gear cutting tools	Undercut (cutter interference) in the case of small numbers of teeth
Insensitive to center-to-center deviations	Unfavorable pressure conditions for external teeth, due to convex–convex contact
Gear set property	
Constant gear force direction (line of action)	
Tooth profile shift (profile modification, addendum correction) possible	

and B_0. They are said to be a paired mating gear teeth and two different tools are required for their production.

For simplification of the production, in most cases the same basic profiles are used for the individual gears, as this only requires one tool. In this case they are called sets of gear teeth.

Economically and technologically advantageous tooth systems, in addition to the gear set properties, should fulfill the following properties:

- Uniform tooth pitch
- Simple tooth shape for production of the teeth
- High load-bearing capability
- Not sensitive to production and assembly inaccuracies
- Low noise development

The tooth profiles used in practice are involute toothing, cycloidal profile toothing, and circular arc toothing (also known as Wildhaber–Novikov tooth system).

In mechanical engineering, involute toothing dominates due to its positive properties (Table 15.73).

Cycloid profile toothing and circular arc toothing are generally only used for special applications such as in the clock and watch industry (cycloidal profile toothing) or increased edge load-bearing capacity (circular arc toothing).

Involute Toothing

An involute is created when a straight line rolls without slipping on a circle, the base circle. Each point on the straight line describes an involute (construction shown in Fig. 15.102). At point 0, the tangent t is positioned at right angles to the line segment. Each involute begins on the base circle and ends in infinity.

Due to the slip-free rolling off, the section $\overline{04}$ shown as an example in Fig. 15.102a is equal to the arc length $\widehat{0'4'}$.

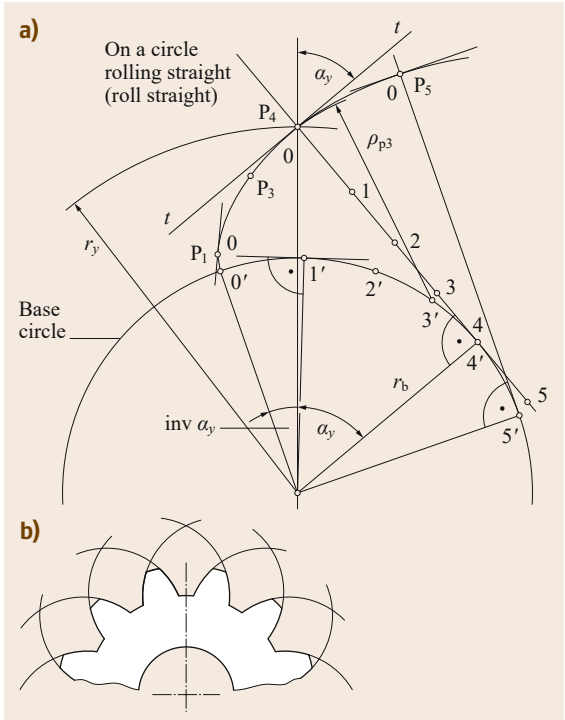

Fig. 15.102 **(a)** Involute of a circle and **(b)** involutes on a spur gear

With base circle radius r_b and according to Fig. 15.102a, the following geometrical relationship applies:

$$\widehat{0'4'} = \overline{04} = r_b \tan\alpha_y = r_b\left(\widehat{\alpha_y} + \text{inv}\,\alpha_y\right). \quad (15.125)$$

Rearranged to obtain $\text{inv}\,\alpha_y$ the equation is

$$\text{inv}\,\alpha_y = \tan\alpha_y - \widehat{\alpha_y}\,. \quad (15.126)$$

The involute function $\text{inv}\,\alpha_y$ (i.e., involute α_y) plays a fundamental role in the gear toothing calculation.

Geometry of the Toothing

The geometrical features of involute gears (gear toothing) are standardized internationally by ISO 21771 [15.104]. The corresponding basic profiles are defined in ISO 53 [15.105].

A basic differentiation is made between gear toothing with spur toothing and helical toothing. In the case of spur toothing, the flanks of the teeth are arranged parallel to the wheel axis; in helical gearing they are inclined by the helix angle β (Fig. 15.103). The helix angle usually lies within the following ranges:

- For single- or double-helical gearing: $\beta \approx 8$– $20°$
- for herringbone gearing: $\beta \approx 30$–$45°$

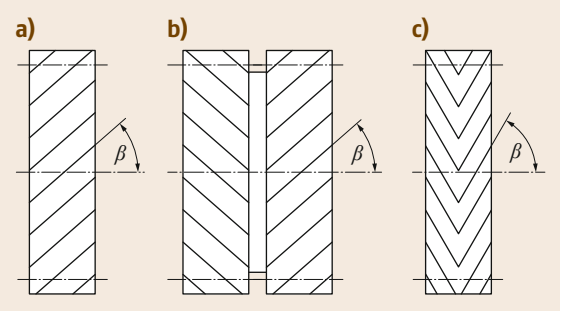

Fig. 15.103a–c Helical spur gears: **(a)** single helical gearing, **(b)** double helical gearing with recess for tool runout, and **(c)** herringbone gearing

Table 15.74 Advantages and disadvantages of helical gearing compared to straight gearing

Advantages	Disadvantages
Smoother and quieter running due to gradual tooth engagement	Due to the inclination of the toothing an axial force component occurs, which acts on the shaft, or rather the bearing (exception: double helical and herringbone toothing, Fig. 15.103b,c)
Larger degree of overlap, i.e., more teeth engaged (meshed) at the same time	Greater production effort (time and cost)
Loading capacity somewhat higher	Risk of tooth corner fracture

Spur gearing can also be taken both mathematically and geometrically as a special case of helical gearing with helix angle $\beta = 0$.

The advantages and disadvantages of helical gearing compared to spur gearing are listed in Table 15.74.

Definition of the Reference Surfaces in the Gear Tooth Geometry. In the case of helical gearing, ISO 21771 differentiates between the cutting planes of the normal section N–N (cut at right angles to the flank lines) and the transverse section S–S (cut at right angles to the gear axis) (Fig. 15.104).

The normal profile shows pure involutes; the transverse profile shows only an approximate involute as a result of distortion, such that:

- Subscript n: variables relate to the normal section N–N
- Subscript t: variables relate to the transverse section S–S

Table 15.75 Geometrical relationships of basic rack tooth profiles according to ISO 53 (Fig. 15.105)

Symbol	Types of basic rack tooth profile			
	A	B	C	D
α_P	20°			
h_{aP}	$1m$			
c_P	$0.25m$			$0.4m$
h_{fP}	$1.25m$			$1.4m$
ρ_{fP}	$0.38m$	$0.3m$	$0.25m$	$0.39m$

Rack and Basic Rack Tooth Profile. As already explained, racks can be interpreted as being gears with infinitely large diameters. The flank profile of the tooth thus becomes a straight line.

Basic rack tooth profiles according to ISO 53 are used for involute toothing.

The geometrical relationships shown in Table 15.75 apply to the basic profiles standardized to ISO 53.

Geometrical Variables.

Number of Teeth z and Corresponding Sign. The number of teeth z equals the number of teeth on the gear circumference. The number of teeth of gears with external teeth has a positive sign, and that of gears with internal teeth has a negative sign.

Pitch Diameter d. The diameter of the pitch cylinder d acts as a reference surface for the cylindrical gear

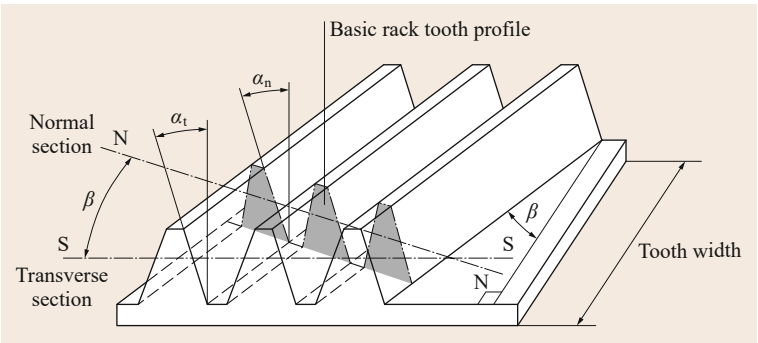

Fig. 15.104 Relationship between the variables in the transverse section S–S and normal section N–N for helical x-zero gears (zero profile shift) (after [15.105])

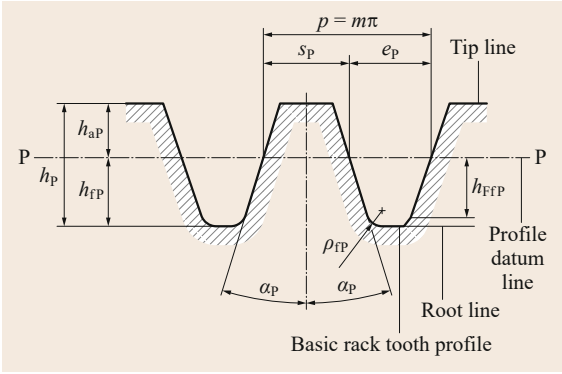

Fig. 15.105 Basic rack tooth profile of involute toothing according to ISO 53 (after [15.105])

toothing. The pitch of the spur gear, i.e., the distance between two adjacent teeth, is defined on the reference surface.

Condition: The pitch diameter d is directly proportional to the number of teeth z:

$$d \sim |z| \,. \tag{15.127}$$

With the introduction of the normal module m_n as a proportionality factor, the pitch diameter can be calculated as follows in the same way as for straight gearing:

$$d = m_n\,|z| \,. \tag{15.128}$$

For helical gearing, the helix angle β must be taken into consideration in order to determine the pitch diameter:

$$d = \frac{m_n\,|z|}{\cos\beta} \,. \tag{15.129}$$

Normal Module m_n, Tangential Module, and Diametral Pitch P_d. The normal module equals the module of the basic rack profile and thus the module in normal section N–N (Fig. 15.104). Values for the module are standardized to ISO 54 (Table 15.76).

The module in the transverse section S–S is called the transverse module and results from

$$m_t = \frac{m_n}{\cos\beta} \,. \tag{15.130}$$

For straight gearing with a helical angle $\beta = 0°$ the following equation applies to the modules

$$m_t = m_n = m \,. \tag{15.131}$$

In the USA, the diametral pitch is generally given instead of the module. The diametral pitch P_d is the ratio of the number of teeth and the pitch diameter d (usually given in inches)

$$P_d = \frac{n}{d} \quad \left(\frac{1}{\text{in}}\right) \,. \tag{15.132}$$

The diametral pitch can be converted into the normal module using the following equation:

$$m_n = \frac{25.4}{P_d} \quad \text{(mm)} \,. \tag{15.133}$$

In the following text, only the module is used as a calculable value. If necessary, it can be converted into the diametral pitch with the help of (15.133).

Normal Pitch p_n and Transverse Pitch p_t. The normal pitch p_n represents the distance between two adjacent teeth on the pitch circle in the normal section N–N (Fig. 15.104) and is calculated from the circumference of the pitch circle $u = \pi d = \pi m_n|z|/\cos\beta$ as

$$p_n = \frac{u}{|z|} = \pi m_n = \pi m_t \cos\beta \,. \tag{15.134}$$

At right angles to the gear axis, the distance between two adjacent tooth flanks equals the transverse pitch p_t:

$$p_t = \frac{\pi d}{|z|} = \pi m_t \,. \tag{15.135}$$

Table 15.76 Preferred values for the module and the diametral pitch according to ISO 54 [15.106] (selection)

m	**1**	**1.058**	**1.25**	**1.27**	**1.411**	**1.5**	**1.587**	**1.814**	**2**	**2.116**	**2.5**	**2.54**	**3**	**3.175**	**4**
P_d	25.40	**24**	20.32	**10**	**18**	16.93	**16**	**14**	12.70	**12**	10.16	**10**	8.466	**8**	6.350
m	**4.233**	**5**	**5.08**	**6**	**6.350**	**8**	**8.466**	**10**	**10.16**	**12**	**12.7**	**16**	**16.93**	**20**	**25.40**
P_d	**6**	5.080	**5**	4.233	**4**	3.175	**3**	2.540	**2.5**	2.116	**2**	1.587	**1.5**	1.277	**1**

Module m in mm
Diametral pitch P_d in 1/in

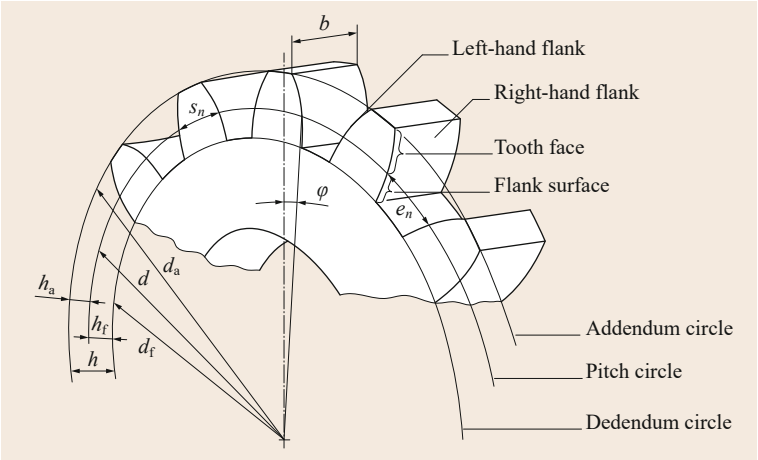

Fig. 15.106 Naming of the straight-toothed spur gear

Normal Profile Angle α_{yn}, Profile Angle α_P, Normal Pressure Angle α_n, Transverse Pressure Angle α_t. The normal profile angle α_{yn} equals the tangential gradient of the involute of a circle at any point on the involute path in the normal section N–N and depends on the distance from the base circle (Fig. 15.102). On the pitch diameter, this corresponds to the profile angle of the basic tooth profile α_P (Fig. 15.105). For gears without profile shift the profile angle α_P equals the normal pressure angle α_n.

The profile angle defined in ISO 53 of $\alpha_P = 20°$ is generally considered to be favorable. However, in some cases this value is deviated from in practice, for example, in precision engineering pressure angles of up to 5° can be found. For smooth and quiet running, vehicle transmissions have a profile angle of 17.5°.

The relationship between the normal pressure angle α_n and the transverse pressure angle α_t is

$$\alpha_t = \arctan \frac{\tan \alpha_n}{\cos \beta} = \frac{d_b}{d} , \qquad (15.136)$$

where

d_b base circle diameter (15.137).

In general, both the right- and the left-hand flank have the same pressure angle (Fig. 15.106). If the pressure angles of the two tooth flank sides differ, the toothing or gearing is asymmetrical.

Base Circle Diameter d_b. Construction of the involute (Fig. 15.111) begins on the base circle, so that the size of the base circle determines the curvature of the involute. It is positioned coaxially to the gear axis.

The base circle diameter is calculated from the pitch diameter d and the normal pressure angle α_n as

$$d_b = \frac{d}{\sqrt{\tan^2 \alpha_n + \cos^2 \beta}} = \frac{|z|\, m_n}{\sqrt{\tan^2 \alpha_n + \cos^2 \beta}} . \qquad (15.137)$$

For the straight toothing, (15.137) is simplified to

$$d_b = d \cos \alpha_n = |z|\, m_n \cos \alpha_n . \qquad (15.138)$$

Tooth Height h, Tooth Tip Height h_a, and Tooth Root Depth h_f. The tooth height h is made up of the addendum h_a (height of the tooth above the pitch circle diameter) and the dedendum h_f (depth of the tooth below the pitch circle diameter) (Fig. 15.106).

The addendum h_a is calculated from the module m and, for a spur gear with profile shift, the profile shift factor x and the addendum modification factor k (Sect. 15.8.2, *Profile Shift*) as

$$h_a = h_{aP} + x m_n + k m_n , \qquad (15.139)$$

where:

h_{aP} addendum of the spur gear reference profile (Table 15.75)
x profile shift factor
k addendum modification factor (15.150)

The dedendum h_f is calculated from the dedendum of the reference profile h_{fP} (Table 15.75), whereby in the case of profile shift, this must be taken into account with the profile shift factor x:

$$h_f = h_{fP} - x m_n . \qquad (15.140)$$

Table 15.77 Size ratio of the addendum and dedendum cycle diameter for external and internal toothing (gearing)

	External teeth	Internal teeth
d_a	$d_a > d$	$d_a < d$
d_f	$d_f < d$	$d_f > d$

The addendum h is calculated from the sum of the addendum and the dedundum h_a and h_f as

$$h = h_a + h_f = h_{aP} + km_n + h_{fp} \,. \tag{15.141}$$

For standard gearing according to ISO 53, the tooth height with tip clearance c (Table 15.75) is thus

$$h = m_n\,(2 + k) + c \,. \tag{15.142}$$

Addendum Circle Diameter d_a and Dedendum Circle Diameter d_f. The pitch diameter d, enlarged by twice the addendum $2h_a$ or reduced by twice the dedendum $2h_f$, gives the addendum and dedendum circle diameter d_a and d_f, respectively, as

$$d_a = d + 2\frac{z}{|z|}\,(xm_n + h_{aP} + km_n)\,, \tag{15.143}$$

$$d_f = d - 2\frac{z}{|z|}\,(h_{fP} - xm_n)\,. \tag{15.144}$$

Depending on the type of toothing or rather gearing, the size ratios shown in Table 15.77 result for the respective diameters.

Tooth Thickness s and Tooth Space Width e on the Pitch Diameter. The tooth thickness and the tooth space width equal the length of the arc between the corresponding involute flanges on the pitch diameter (Fig. 15.106). For tooth thickness s_t and space width e_t at right angles to the gear axis:

$$s_t = \frac{m_n}{\cos\beta}\left(\frac{\pi}{2} + 2x\tan\alpha_n\right), \tag{15.145}$$

$$e_t = \frac{m_n}{\cos\beta}\left(\frac{\pi}{2} - 2x\tan\alpha_n\right). \tag{15.146}$$

For the normal section N–N:

$$s_n = s_t\cos\beta = m_n\left(\frac{\pi}{2} + 2x\tan\alpha_n\right), \tag{15.147}$$

$$e_n = e_t\cos\beta = m_n\left(\frac{\pi}{2} - 2x\tan\alpha_n\right). \tag{15.148}$$

Profile Shift

Profile shifts are primarily used to influence the geometry of the tooth flank (to prevent undercut) or to adjust the gears to the center-to-center distance specified by the design while retaining the standardized modules.

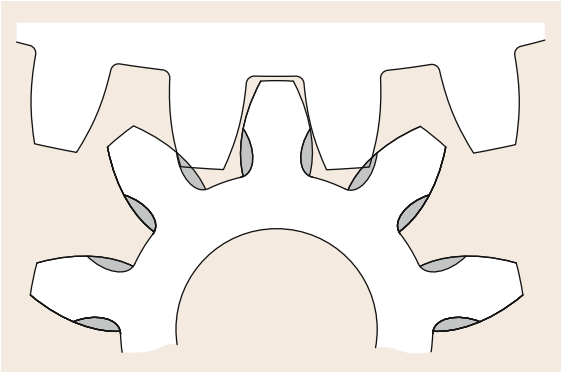

Fig. 15.107 Undercut at the tooth root (*gray area*)

Table 15.78 Theoretical and practical limit number of teeth for standardized gearing with $\alpha_n = 20°$, depending on the helix angle β [15.107]

β	0	10	20	30
z_g	17	16	14	11
z'_g	14	13	12	9

Undercut. If gears are made by hobbing or generating planing and if the number of teeth is too small, so-called undercut can occur. This means that the tool cuts away part of the root of the tooth. As a result the root is weakened and the rolling of the mating gear is disrupted (Fig. 15.107).

The number of teeth from which undercut can occur is called the limit number of teeth z_g. However, in practice it has been found that undercut is only significant from a smaller number of teeth, the practical limit number of teeth z'_g. Due to their inclined position, helical teeth allow a smaller limit number teeth, which is especially important for very small gears. The theoretical and practical limit number of teeth for normal gearing is shown in Table 15.78.

Generating Profile Shift. The profile shift is achieved by moving the tool used to make the toothing more (negative profile shift) or less (positive profile shift) radially (Fig. 15.108).

The geometrical amount of profile shift is calculated by multiplying the profile shift factor x including sign (+/−) and the module m (Fig. 15.108).

Figure 15.109 shows graphically the relationship between the tooth form, the number of teeth, and the applied profile shift with constant module.

Profile shift in the positive direction is limited by the tooth tip width (top land width) $s_a \geq (0.2\text{–}0.4)\,m$ [15.107]. In the negative direction, undercut occurs if the profile shift is too large.

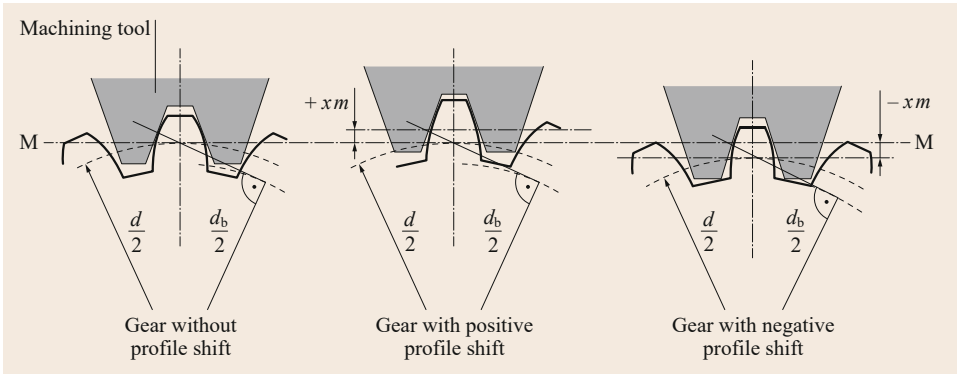

Fig. 15.108 Profile shift by changing the radial tool position

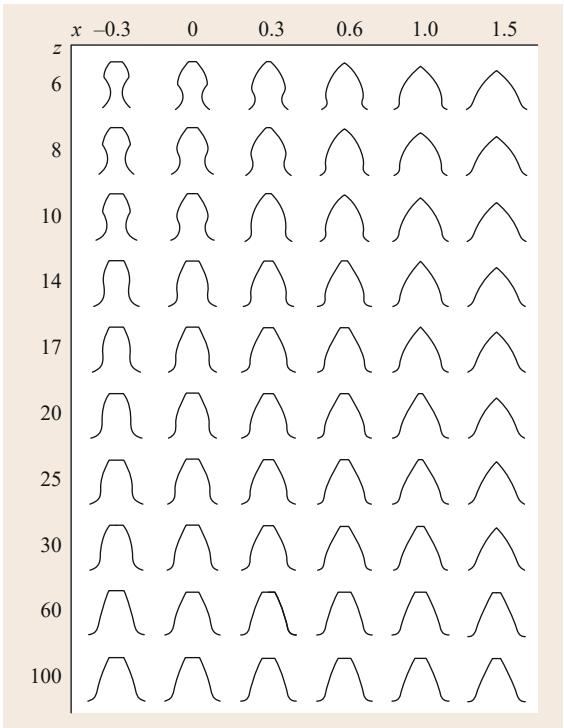

Fig. 15.109 Profile shift by changing the radial tool position depending on the number of teeth z and the profile shift factor x (after [15.103])

Profile shift influences the following properties of the gears, or rather gear combinations [15.103]:

- Tooth thickness and tooth form
- Radii of curvature of the tooth flank/root circle transition curve
- Profile overlapping or rather position of the engagement contact points
- Operating pressure angle
- Sliding speed, slip, and toothing losses
- Load-bearing capacity

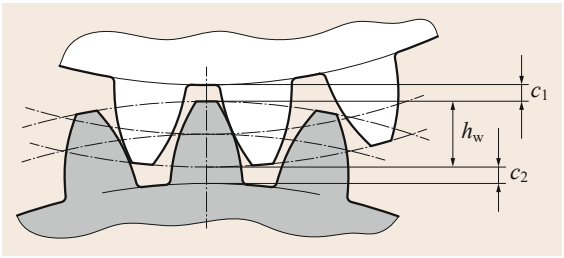

Fig. 15.110 Tip clearance c for gear combinations (after [15.104])

To avoid teeth that are too pointed or to adjust the tip clearance c (Fig. 15.110) for gear mating, under certain circumstances it may be necessary to adjust the addendum accordingly. The addendum change Δh_a is calculated from the addendum change factor k and the module m:

$$\Delta h_a = k m_n \,, \tag{15.149}$$

where

$$k = \frac{a - a_d}{m_n} - (x_1 + x_2) \,, \tag{15.150}$$

where:

a center-to-center distance of the gears used
a_d reference center distance (15.154)
$x_1; x_2$ profile shift factors (Fig. 15.108).

The following designations apply, depending on the profile shift applied:

- X-zero gears: Gears without profile shift
- V_{Plus} gears: Gears with positive profile shift
- V_{Minus} gears: Gears with negative profile shift

Table 15.79 Suffix used for gear mating

Suffix	External gear mating	Internal gear mating
1	Smaller gear (pinion)	External gear (external teeth)
2	Larger gear	Internal gear (internal teeth)

Geometry of the Spur Gear Mating

For gears to mate, they must have a uniform basic tooth profile. In the case of helical gears, the gears must also have the same basic helix angle and in the case of external gear mating, they must have alternate helixes (right-hand and left-hand helical gearing).

The designations in Table 15.79 apply to the gear mating in the following text.

The point of contact between the gears is called the engagement contact point. During rolling, the contact point moves on the tooth flanks, whereby the contact point moves along the straight line $\overline{AE}$ (Fig. 15.111). This straight line is called the length of path of contact. Point A on the straight line marks the start of the engagement and Point E the end of the engagement. For gear mating without profile shift, the length of engagement touches the base circles d_{bi} of the corresponding gears tangentially.

Pressure Angle, Center-To-Center Distance, and Profile Shift Factors. The length of engagement is inclined by angle α (pressure angle) with the right angles of the connecting line of the two gear centers.

In the case of helical gearing a differentiation is made between the normal pressure angle (pressure angle in normal section N–N) α_n and the transverse pressure angle α_t (pressure angle at right angles to the gear axis). The following relationship applies:

$$\tan\alpha_n = \tan\alpha_t \cos\beta \,, \tag{15.151}$$

with

$$\cos\alpha_t = \frac{d_{bi}}{d_i} \,. \tag{15.152}$$

For straight-cut gears with $\beta = 0$,

$$\alpha_n = \alpha_t = \alpha \quad \text{and} \quad \alpha_{yn} = \alpha_{yt} \,. \tag{15.153}$$

The center-to-center distance a_d of gear trains with profile shift (reference center distance) is calculated from

$$a_d = \frac{(d_1 + d_2)}{2} = \frac{d_{b1}}{2\cos\alpha_t} + \frac{d_{b2}}{2\cos\alpha_t} \,. \tag{15.154}$$

If gears with profile shift are combined with each other, depending on the profile shift factors applied, the following combinations are possible:

- $x_1 = x_2 = 0 \rightarrow$ zero gear
- $x_1 + x_2 = 0 \rightarrow$ V-zero gear
- $x_1 + x_2 > 0 \rightarrow V_{Plus}$ gear
- $x_1 + x_2 < 0 \rightarrow V_{Minus}$ gear

Due to the adjustment of the center-to-center distance a made in the case of V_{Plus} and V_{Minus} gears, the rolling (generating pitch) circle diameter $d_W \neq d$ and thus the pressure angle α move towards the operating pressure angle α_W, while the pitch diameter d and the base circle diameter d_b remain the same (Fig. 15.112).

For a predefined center-to-center distance a, the necessary operating pressure angle (in transverse section S–S) can be determined using

$$\alpha_{wt} = \arccos\left[|z_1 + z_2|\left(\frac{m_n\cos\alpha_t}{2a\cos\beta}\right)\right] . \tag{15.155}$$

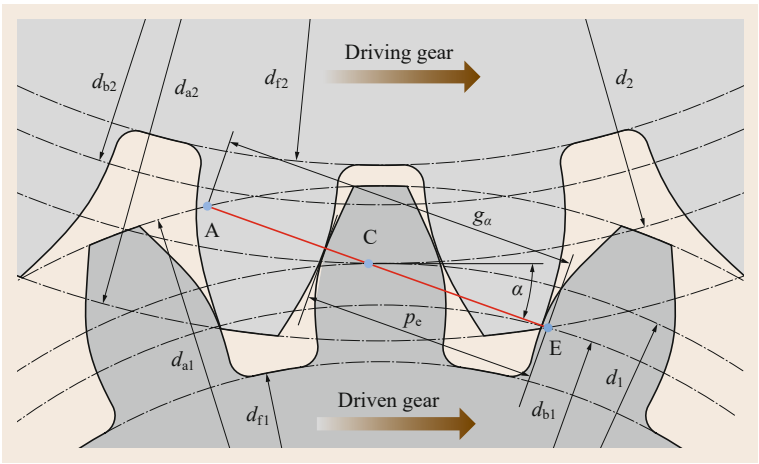

Fig. 15.111 Length of path of contact

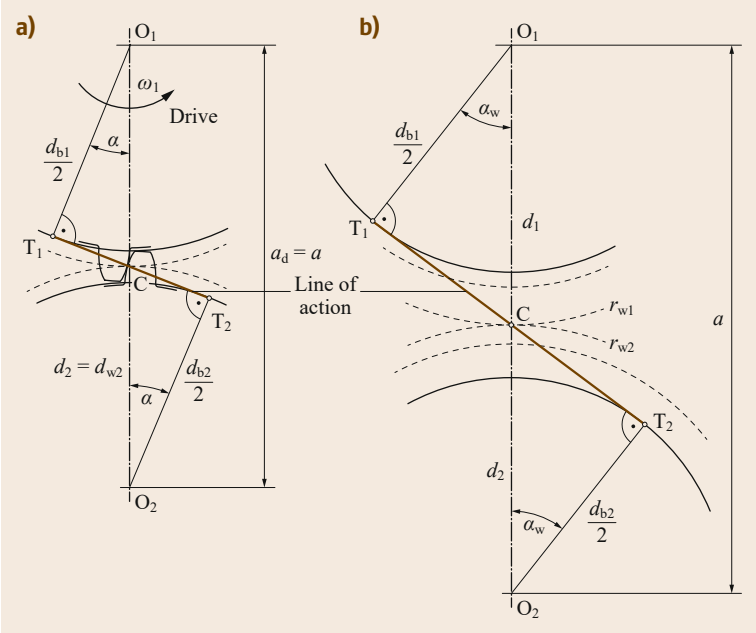

Fig. 15.112a,b Line of action and operating pressure angle α_w with center-to-center distance change: **(a)** zero gear pair (no profile shift) $a = a_d$ and **(b)** gear pair with profile shift $a \neq a_d$

The profile shift factors necessary to achieve the required center-to-center spacing is calculated from

$$\sum x = x_1 + x_2 = \frac{(z_1 + z_2)\,(\operatorname{inv}\alpha_{wt} - \operatorname{inv}\alpha_t)}{2\tan\alpha_n} \,. \qquad (15.156)$$

The sum of the profile shift factors (15.156) is sensibly divided between the two engaging (meshing) gears. Recommendations for favorable division of the profile shift factors are given, for example, in standard DIN 3992 [15.108].

Rolling (Generating Pitch) Circle Diameter d_w. The rolling circles with diameters d_{w1} and d_{w2} touch at the pitch point C and roll without slipping (15.121).

If the fundamental law of gearing applies, the ratio of the rolling circle diameters d_{w2}/d_{w1} must equal the transmission ratio i (gear ratio) (Section 15.8.1 *Fundamental Law of Gearing*):

$$i = \frac{\omega_1}{\omega_2} = \frac{z_2}{z_1} = \frac{d_2}{d_1} = \frac{d_{w2}}{d_{w1}} \,. \qquad (15.157)$$

The sum of the rolling circle radii $r_{w1} = d_{w1}/2$ and $r_{w2} = d_{w2}/2$ equals the center-to-center distance a (Fig. 15.112b):

$$a = r_{w1} + r_{w2} = \frac{d_{w1}}{2} + \frac{d_{w2}}{2} \,. \qquad (15.158)$$

From (15.157) and (15.158) we can calculate:

$$d_{w1} = 2a\frac{1}{1+i} \qquad (15.159)$$

$$d_{w2} = d_{w1} i = 2a\frac{i}{1+i} \,. \qquad (15.160)$$

For zero gear pairs ($a = a_d$), the rolling diameters equal the pitch diameters (reference diameters) ($d_{w1} = d_1$ and $d_{w2} = d_2$) (Fig. 15.112a).

Profile Overlapping ε. For the movement from one gear to the other gear (or gear rack) to take place uniformly and without jolting, at least one pair of teeth along the length of engagement $\overline{AE}$ must be continuously engaged (meshed) (Fig. 15.111). This is guaranteed if the length of engagement is longer than the distance between two tooth flanks of the same type along this length (corresponds to the normal base pitch p_e in Fig. 15.111). For the profile overlap ε_α in gear pairs without rounded tips, the following thus applies:

$$\varepsilon_\alpha = \frac{\overline{AE}}{p_{et}} = \frac{\sqrt{{d_{a1}}^2 - {d_{b1}}^2} + \frac{z_2}{|z_2|}\sqrt{{d_{a2}}^2 - {d_{b2}}^2} - 2a\sin\alpha_{wt}}{2\pi m_t \cos\alpha_t} \geq 1 \,, \qquad (15.161)$$

where:

d_{ai} addendum circle diameter (15.143)
d_{bi} base circle diameter (15.137)
m_t transverse module (15.130)
α_t transverse pressure angle (15.136)

In the case of helical spur gear combinations, as a result of the inclined position of the tooth flanks at the start of the tooth engagement (meshing), only part of the tooth width is load bearing, not the whole tooth width. At the end of the tooth engagement, part of the contact surface separates while the remaining part remains in contact, which results in further overlap, called the overlap ratio (face contact ratio). The degree of overlap ratio (face contact) ε_β is

$$\varepsilon_\beta = \frac{b \sin\beta}{\pi m_n} , \tag{15.162}$$

where:

b gear width (Fig. 15.106)
β helix angle
m_n normal module

To reduce vibration and noise, it is best to choose values for ε_β that are high integer values ($\varepsilon_\beta = 1, 2, 3, \ldots$).

The total degree of overlap ratio ε_γ of a helical gear is calculated from

$$\varepsilon_\gamma = \varepsilon_\alpha + \varepsilon_\beta . \tag{15.163}$$

A total degree of overlap ratio of $\varepsilon_\gamma = 2.5$ is favorable in vibration terms.

15.8.3 Forces on the Spur Gear Pair and Transferred Power

To determine the forces, for reasons of simplification, it is assumed that only one pair of teeth is engaged, that it touches at the pitch point C and the forces are applied in the middle of the tooth width b (Fig. 15.113). The force (load) transfer between the wheels occurs through the normal force F_{bn} perpendicular to the tooth flanks (normal tooth force). By vectorially resolving this normal tooth force we obtain the tangential force F_t, the axial force F_a and the radial force F_r.

The tangential force is calculated from the transferred torque T and the rolling circle diameters d_w as

$$F_t = \frac{2T_1}{d_1} = \frac{2T_2}{d_2} . \tag{15.164}$$

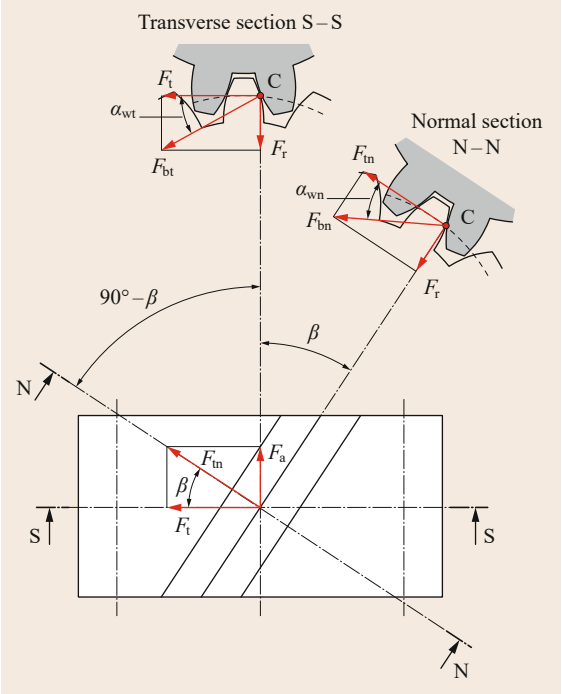

Fig. 15.113 Forces on the driving gear 1 of a helical spur gear in the transverse section S–S and in the normal section N–N

The tangential forces can then be used to determine the radial and the axial forces:

$$\text{Radial forces:} \quad F_r = \frac{F_t \tan\alpha_n}{\cos\beta} \tag{15.165}$$

$$\text{Axial forces:} \quad F_a = F_t \cos\beta \tag{15.166}$$

From (15.166) it is clear that no axial forces occur in straight-cut gears (with $\beta = 0°$).

The functional relationship between the power P, the torque T, and the angular velocity ω is

$$P = T\omega = \frac{F_t d\omega}{2} . \tag{15.167}$$

As a result of friction losses, the power on the driven gear and thus the corresponding tangential force on it is slightly lower than on the driving gear.

The efficiency η gives the loss in driving power (input power) within the gear system and is defined as an absolute amount equal to the ratio of the output power P_{out} and the input power P_{in}:

$$\eta = \left| \frac{P_{out}}{P_{in}} \right| = \left| \frac{T_{out}\omega_{out}}{T_{in}\omega_{in}} \right| . \tag{15.168}$$

Table 15.80 Efficiency η of different types of gears (for one stage) (after *Linke* [15.103])

Transmission (gear) type	η	Comment
Spur gear system	0.97–0.99	0.97 for imprecise toothing
Planetary spur gear train	0.98–0.995	For favorable type
Bevel gear	0.97–0.99	
Worm gear	0.2–0.97	Falls with increasing i
Crossed helical gear train	(0.6)–0.96	Falls with increasing crossing angle
Chain gear	0.97–0.98	
Flat belt	0.96–0.98	Larger than for V-belts
V-belt	0.93–0.94	Smaller than for flat belts
Friction gear	0.90–0.98	
Hydrodynamic gear train (converter)	By 0.85–0.9	Maximum value of the parabolic profile

The efficiencies of typical gearbox designs are shown in Table 15.80. The overall efficiency η_{all} is calculated from the product of the individual efficiencies of the consecutive gears or gear stages (reduction stage/step down):

$$\eta_{all} = \eta_1 \eta_2 \ldots \eta_{k-1} \eta_k \,. \tag{15.169}$$

Strength Verification

The surface pressure at the gear contact points and the maximum root stress are decisive for the strength verification.

The load-bearing capacity of the toothing can be checked by calculation according to ISO 6336 [15.109] or the American standard ANSI/AGMA 2001-D04 [15.110], whereby the results differ depending on the calculation method used.

15.8.4 Design of Spur Gear Systems

The main dimensions of a spur gear pair (ratio of number of teeth, pitch diameter, module, tooth width, etc.) are chosen from empirical values at the start of the calculation or are roughly calculated.

The design calculation is based on a requirements specification containing the following information:

- Gear train type
- Connection conditions of the motor, gear train, and machine
- Input and output speeds
- Size
- Performance data
- Other operating and production data

Definition of the Gear Stages and Gear Transmission Ratios

Large overall transmission ratios must be divided between several stages, as these cannot be implemented economically and reliably with only one stage.

The type of division/distribution influences the installation volume, mass, and cost of the gear train.

Standard versions according to [15.24]:

1 stage: total transmission ratio $i \leq 6$
(possibly ≤ 8, extreme ≤ 18)
2 stages: total transmission ratio $i \leq 35$
(possibly ≤ 45, extreme ≤ 60)
3 stages: overall transmission ratio $i \leq 150$
(possibly ≤ 200, extreme ≤ 300)

Figure 15.114 summarizes empirical values for the distribution of an overall transmission ratio i into ratios of numbers of teeth u_I and u_{II} for two- and three-stage, volume-optimized spur gear trains.

Pitch Diameter of the Pinion d_1

With the help of the empirical characteristic K^* after Table 15.81, the torque on the pinion T_1 and the ratio of the number of teeth u and a ratio of tooth width and pitch diameter b/d_1 to be defined from empirical values (Table 15.82), the pitch diameter of the pinion d_1 can be roughly calculated as follows:

$$d_1 \geq \sqrt[3]{\frac{2T_1}{K^*\left(\frac{b}{d_1}\right)} \frac{u+1}{u}} \,. \tag{15.170}$$

Table 15.82 summarizes empirical values for the width ratios b/d_1 of fixed spur gear trains.

When defining the tooth width, it must be noted that flank line corrections are required for larger tooth widths to level out elastic deformations and that the tooth width influences the overlap ratio of helical spur gears.

Number of Teeth and Module

The usual numbers of teeth depending on the transmission ratio and the gear material used or heat-treatment process are given in Table 15.83.

Table 15.81 Values for K^* for steel gears [15.111]

Use Input/output	K^* factor (N/mm^2)
Turbines/generators	0.8–2.8
Electric motor/industrial gears (24 h operation)	1.2–4.4
Electric motor/large gear train	0.6–1.0
Electric motor/small gear train	0.35–0.53
Electric motor/machine tools	3.0–9.0
Milling/cutting machines (headstock)	0.7

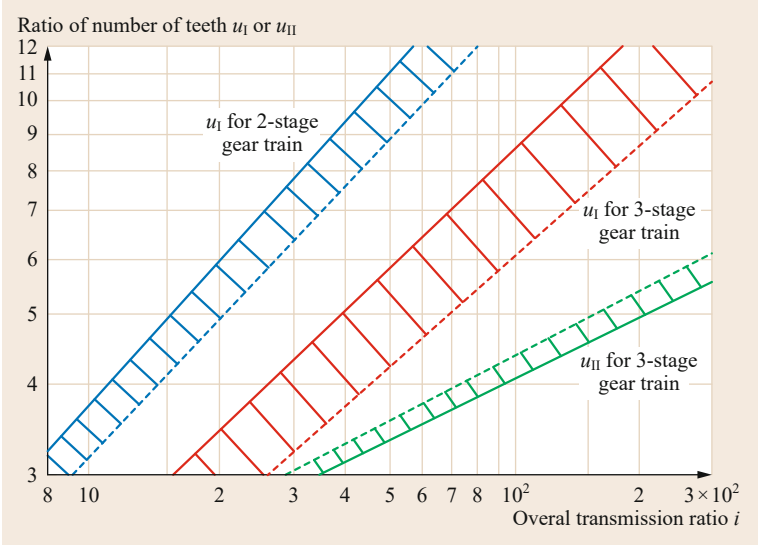

Fig. 15.114 Empirical values for the distribution of an overall transmission ratio for two- and three-stage spur gear trains (after [15.24])

The limit numbers of teeth according to Table 15.78 must be noted when defining the numbers of teeth.

For strength reasons, the number of teeth of the gears of a spur gear pair should be defined so that they do not have any common integer divisors.

The module should be chosen according to the module series specified in ISO 54 (Table 15.76).

After determining the module, it is necessary to check whether versions with pushed-on pinions have a sufficiently wide rim under the tooth root. The guide value for the pitch diameter of the pinion d_1 depends on the shaft diameter d_{shaft} and the module m:

$$d_1 > d_{shaft} + 3m \,. \qquad (15.171)$$

Lubrication of Gear Trains

Lubrication systems are used:

- To reduce friction and wear on flanks that slide on each other
- To build up a separating lubricating film
- To dampen vibrations and shocks
- As anticorrosion protection
- To cool the gear train

Table 15.84 gives an overview of the standard lubrication methods and their areas of use.

Table 15.82 Maximum values for the width ratio b/d_1 of fixed spur gear trains with rigid foundation [15.24]

Straight and helical toothing with bearing symmetrical on both sides	
Normalized (HB ≤ 180)	$b/d_1 \leq 1.6$
Quenched and tempered (HB ≥ 200)	$b/d_1 \leq 1.4$
Case-hardened or boundary-hardened	$b/d_1 \leq 1.1$
Nitrated	$b/d_1 \leq 0.8$
Double helical gearing	Up to 180% of the above values
Straight and helical toothing with bearing asymmetrical on both sides	Up to 80% of the above values
Straight and helical toothing with same size pinions and gears	Up to 120% of the above values
Straight and helical toothing with cantilever mounting of the bearings	Up to 50% of the above values

Table 15.83 Standard numbers of teeth for the pinion z_1; lower range for speeds: $n < 1000\,\text{min}^{-1}$, upper range for speeds: $n > 3000\,\text{min}^{-1}$ [15.24]

Transmission ratio *i*	**1**	**2**	**4**	**8**
Quenched and tempered up to 230 HB	32–60	29–55	25–50	22–45
Over 300 HB (and hard/quenched and tempered)	30–50	27–45	23–40	20–35
Cast iron GGG	26–45	23–40	21–35	18–30
Nitrated	24–40	21–35	19–31	16–26
Case-hardened or surface-hardened	21–32	19–29	16–25	14–22

Table 15.84 Selection of lubricant and lubrication methods of gear trains (after [15.111])

Circumferential velocity v_t in (m/s)	Lubricant	Lubrication method	Gear train type	Special features
≤ 2.5	Adhesive lubricant	Apply with brush, spatula [a,b]	Not specified	Provide cover where possible
≤ 4 (possibly ≤ 6)	Low-viscosity gears	Spray lubrication		
≤ 8 (possibly ≤ 10)		Splash lubrication or injection lubrication for large gear trains (> 400 kW), gear trains with plain bearings, vertical gear trains	Closed	
≤ 15	Oil			
≤25 (possibly ≤30)				Splash lubrication with sheet metal sump, cooling fins
> 25 (possibly > 30)		Injection lubrication		
≤ 40		Mist lubrication		For low loads, intermittent operation

[a] for lowest consistency class (NLGI 000-0) possible from splash lubrication
[b] for example, cement mills, rotary furnaces, excavators, river weirs; provide cover where possible

Gear trains for transferring high powers often require active cooling of the lubricant due to the thermal loading caused by friction losses.

15.8.5 Further Reading

A good overview of spur gears and spur gear trains is given by *Linke* [15.103] and *Niemann* and *Winter* [15.112]. Further information on crossed helical, bevel, and worm gear trains is also given by *Niemann* and *Winter* [15.113].

Calculation equations for strength verifications for spur gear toothing are given in ISO 6336 [15.109] and the American standard ANSI/AGMA 2001-D04 [15.110].

Damage to spur gears and its causes are discussed in detail in *Barz* [15.73] and the standard DIN 3979 [15.114].

15.9 Springs

Springs are elastic elements for connecting components in which particular use is made of the material's elasticity through appropriate design.

Springs are used to:

- Return a component to its initial position (e.g., valve springs and return springs of operating elements)
- Store potential energy (e.g., clock drives, spring motors in toy cars, and spring energy stores in hydraulic systems)
- Dampen shocks and vibrations by absorbing the shock energy along longer distances
- Maintain an almost constant force in the case of small displacement changes (e.g., spring washers for locking screws and springs on contact elements)
- Distribute forces (e.g., sprung mattresses)
- Generate the normal force for force-closure joints (e.g., friction clutches and slip clutches)
- Measure forces or moments (e.g., spring balances (spring scales) and torque wrenches)
- Influence the vibrating behavior of machines (e.g., vibrating conveyors)

Springs can be differentiated by their shape (for example, disc springs, spiral springs, and leaf springs), the type of load (for example, extension (tension) springs, torsion springs, and flexible (bending) springs), and the spring material (for example, metal springs and rubber springs) (Fig. 15.115).

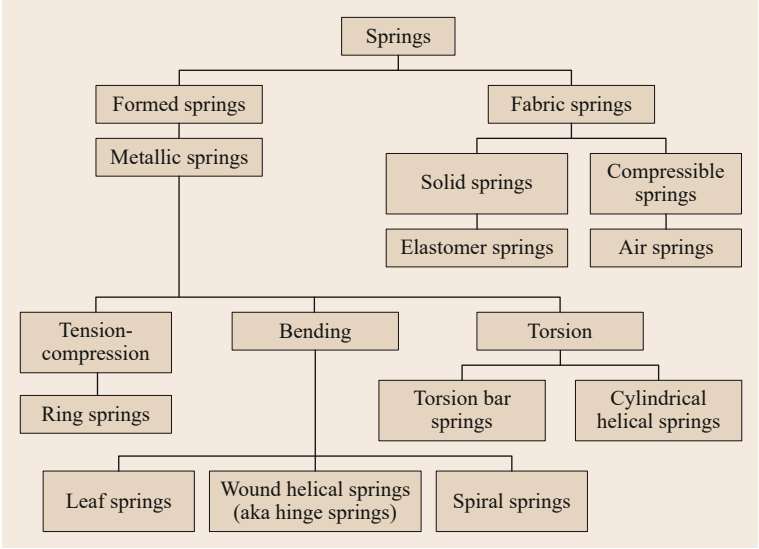

Fig. 15.115 Overview of types of elastic springs

15.9.1 Properties

The spring characteristic gives the relationship between the deformation of the spring and the force (load) acting on it. A basic differentiation is made between a progressive, a linear, and a degressive spring characteristic (Fig. 15.116).

Spring Rate

The spring rate c is the slope of the characteristic curve. Depending on the type of deformation, the following relationships apply:

$$\text{Translational:} \quad c_\mathrm{T} = \frac{\mathrm{d}F}{\mathrm{d}s} \tag{15.172}$$

$$\text{Rotational:} \quad c_\mathrm{R} = \frac{\mathrm{d}T}{\mathrm{d}\varphi} \tag{15.173}$$

The inverse (reciprocal) of the spring rate is the spring compliance δ:

$$\delta = \frac{1}{c}\,. \tag{15.174}$$

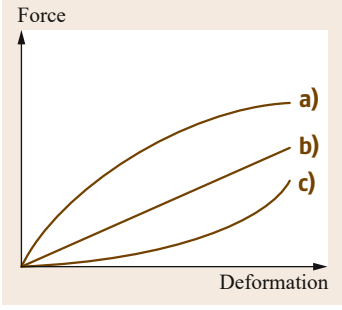

Fig. 15.116a–c Characteristic types: *a* degressive (decreasing curved), *b* linear (straight), and *c* progressive (increasing curved)

Springs with a steep spring characteristic (high spring rate) are called stiff or hard. Springs with a flat spring characteristic are called soft.

Linear springs have a constant spring rate. Their deformation characteristic corresponds to Hooke's law and is a straight line (Fig. 15.116). On the other hand, in the case of progressive springs, the spring rate increases with increasing deformation and the spring becomes *harder* with increasing deformation. The spring characteristic of degressive springs falls with increasing spring deflection.

Spring Work

The area under the spring characteristic equals the integral

$$\mathrm{d}W_\mathrm{el} = \int_0^s F\mathrm{d}s\,, \tag{15.175}$$

which is the elastic deformation energy stored by the spring, the spring work.

Accordingly, the maximum stored work capacity of a spring is

$$\mathrm{d}W_\mathrm{el} = \int_0^{s_\mathrm{max}} F\mathrm{d}s\,. \tag{15.176}$$

For springs with a linear spring characteristic, the maximum work capacity is:

Translational:

$$W_\mathrm{elT} = \frac{F_\mathrm{max}s_\mathrm{max}}{2} = c_\mathrm{T}\frac{s_\mathrm{max}^2}{2} = \frac{F_\mathrm{max}^2}{2c_\mathrm{T}} \tag{15.177}$$

Rotational:

$$W_{elR} = \frac{T_{max}\varphi_{max}}{2} = c_R\frac{\varphi_{max}^2}{2} = \frac{T_{max}^2}{2c_R} \qquad (15.178)$$

Damping Work W_D, Damping Coefficient ψ

Due to external and internal friction, when the spring is relaxed there is less work output than was input on loading the spring (Fig. 15.117). The difference is called the damping work W_D.

The quotient of the damping work and spring work is the damping coefficient ψ:

$$\psi = \frac{W_D}{W_{el}} . \qquad (15.179)$$

The efficiency of a spring η_F is the ratio of the spring work that is output and the absorbed spring work where

$$\eta_F = \frac{W_{el} - W_D}{W_{el}} . \qquad (15.180)$$

From the work absorption capacity W of a spring and the work absorption capacity W_{th} of an ideal equivalent spring, assuming Hooke's law of deformation (linear spring characteristic) and uniform stress distribution, the degree of utilization η_A of the spring due to its type (*type efficiency*) can be determined (Fig. 15.118):

For pure normal stress:

$$\eta_A = \frac{W}{W_{th}} = \frac{W2E}{V\sigma_{max}^2} \qquad (15.181)$$

For pure shear/torsional stress:

$$\eta_A = \frac{W}{W_{th}} = \frac{W2G}{V\tau_{max}^2} \qquad (15.182)$$

The degree of utilization for different types of springs are shown in Fig. 15.117. In addition to the *type efficiency*, the *volume efficiency* η_V (evaluation of the required volume V) and the *weight efficiency* η_Q (evaluation of the spring weight Q) also play a role in the assessment of a spring:

$$\eta_V = \frac{W}{V} = \eta_A\frac{\sigma_{max}^2}{2E} , \qquad (15.183)$$

$$\eta_Q = \frac{W}{Q} = \eta_A\frac{\sigma_{max}^2}{2\rho E} . \qquad (15.184)$$

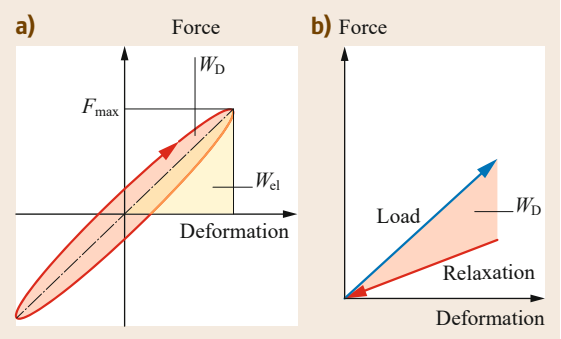

Fig. 15.117a,b Spring characteristic with damping under vibrating loading **(a)** and under one-off loading **(b)**

15.9.2 Oscillatory Behavior

In conjunction with a mass, a spring forms a vibratory system. The natural frequency of the system is:

$$\text{Translational:} \quad f_{eT} = \frac{1}{2\pi}\sqrt{\frac{c_T}{m}} \qquad (15.185)$$

$$\text{Rotational:} \quad f_{eR} = \frac{1}{2\pi}\sqrt{\frac{c_R}{J}} \qquad (15.186)$$

where:

m mass of the oscillating body (without spring mass)
J mass moment of inertia of the oscillating/vibrating body

Under dynamic loading, it must be ensured that the excitation frequency does not lie within the natural frequency of the spring.

However, applications exist in which resonance phenomena are wanted and deliberate, and the springs are excited with their natural frequency, for example, in vibrating screens, vibrating conveyors, and concrete vibrators.

15.9.3 Spring Systems

Individual springs can be combined with each other in design terms in different ways. A differentiation is then made between connection in series, connection in parallel, and combined connections (Fig. 15.119).

Connection in Parallel

The external load F is divided between the individual springs with spring rate c_i. The deformation (spring deflections) s_i of the individual springs is equally large. Thus, by way of example, for the arrangement shown in Fig. 15.119a:

Total spring force:

$$F = \sum_1^n F_i = F_1 + F_2 + F_3 + \ldots \qquad (15.187)$$

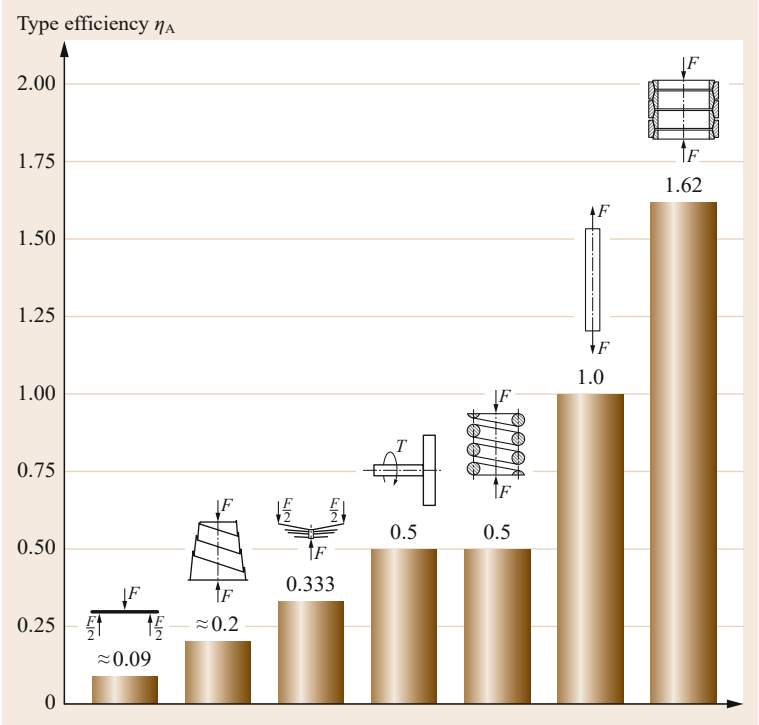

Fig. 15.118 Type efficiency η_A of different types of springs (after [15.115])

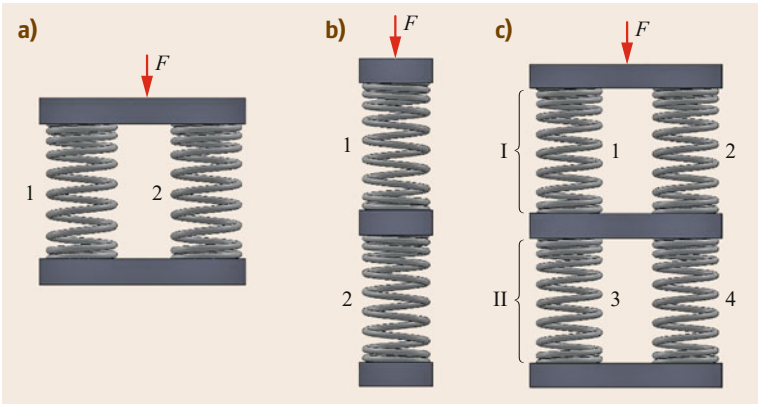

Fig. 15.119a–c Connection of springs: **(a)** connection in parallel, **(b)** connection in series, and **(c)** combined connection

Total spring deflection:

$$s = s_1 = s_2 = s_3 = \ldots \tag{15.188}$$

Total spring rate:

$$c = \sum_1^n c_i = c_1 + c_2 + c_3 + \ldots \tag{15.189}$$

Connection in Series

If springs are connected in series, the force F acts equally on all springs. The individual springs deform differently, depending on their spring stiffness. Thus, for the example of the combination of three springs shown in Fig. 15.119b:

Total spring force:

$$F = F_1 = F_2 = F_3 = \ldots \tag{15.190}$$

Total spring deflection:

$$s = \sum_1^n s_i = s_1 + s_2 + s_3 + \ldots \tag{15.191}$$

Total spring rate:

$$c = \frac{1}{\frac{1}{c_1} + \frac{1}{c_2} + \frac{1}{c_3} + \ldots} \tag{15.192}$$

Table 15.85 Spring materials with the relevant standards [15.116]

Standard	Designation	Use
Hot-rolled steels for quenched and tempered springs according to EN 10089	38Si7	Spring washers
	54SiCr6	Leaf springs for rail vehicles
	60SiCr7	Vehicle leaf springs, disc springs
	55Cr3	Heavy-duty vehicle springs
	50CrV4	Highly stressed leaf and helical springs, disc springs
	51CrMoV4	Highly stressed leaf, coil, and torsion bar strings with large dimensions
Cold-rolled narrow strip steel as quality steel according to EN 10132	C55 C60 C67 C75 55Si7	All kinds of different springs and spring-loaded parts
Cold-rolled narrow strip steel as stainless steel according to EN 10132	Ck55, Ck60, Ck67, Ck75, Ck85, Ck101, 71Si7, 67SiCr5, 50CrV4	Heavy-duty tension springs
Patented cold-drawn unalloyed spring steel wire according to EN 10270-1	Wire grade SL	Springs with low static loading
	Wire grade SM	Springs with medium static and low dynamic loading
	Wide grade DM	Springs with medium dynamic loading
	Wire grade SH	Springs with high static and low dynamic loading
	Wire grade DH	Springs with high static and medium dynamic loading
Hardened and tempered spring steel wire according to EN 10270-2	Wire grade FDC	Springs with static loading
	Wire grade TDC	Springs with medium dynamic loading
	Wire grade VDC	Springs with high dynamic loading
Stainless steel according to EN 10151	X12CrNi 17 7 X7CrNiAl 17 7 X5CrNiMo 18 10	Springs under corroding influences
Spring wires made of copper alloys according to EN 12166	CuZn36F70	All types of springs
	CuSn6F95	Current-conducting springs
	CuNi18Zn20F83	Relay springs
	CuBe2, CuCoBe	All types of springs

Combined Connection

If springs are connected in parallel and in series, this is called a combined or hybrid connection. To calculate the total deformation and total spring rate, the overall system is divided into individual areas of springs connected in parallel or in series; these are then calculated separately and then combined. Thus, for the combined connection shown in Fig. 15.119c:

Total spring force:

$$F = F_{\mathrm{I}} = F_{\mathrm{II}} = F_1 + F_2 = F_3 + F_4 \tag{15.193}$$

Total spring deflection:

$$s = s_{\mathrm{I}} + s_{\mathrm{II}} \tag{15.194}$$

Total spring rate:

$$c = \frac{1}{\frac{1}{c_{\mathrm{I}}} + \frac{1}{c_{\mathrm{II}}}} = \frac{1}{\frac{1}{c_1+c_2} + \frac{1}{c_3+c_4}} \tag{15.195}$$

15.9.4 Spring Materials

Metallic Materials

Metallic materials are used to make formed springs due to their high stiffness and elasticity. Use of carbon steels and alloyed steels is predominant. Nonferrous metals are used for particular requirements (for example, electrical conductivity and corrosion resistance) or as nonmagnetic spring materials. Table 15.85 lists standard metallic spring materials with the corresponding standards.

Nonmetallic Materials

In addition to metallic materials, nonmetallic materials are also used for springs. These can be of both natural origin (e.g., natural rubber or wood) or be made synthetically.

Elastomers are used for vibration dampers due to their high elasticity and good damping properties (Table 15.86).

Table 15.86 Selection of standard elastomer materials for rubber springs [15.111]

Material name, abbreviation according to ISO 1629	Shore A hardness (DIN 53505)	Elongation at break (DIN 53504)	Temperature range (°C)	Resistance to hydrocarbons	Damping
Natural rubber (NR)	20...100	100...800	−55...90	Low	Moderate
Styrene butadiene rubber (SBR)	30...100	100...800	−50...100	Low	Good
Ethylene propylene rubber (EPDM)	40...85	150...500	−50...130	Moderate	Good
Butyl rubber (BIIR, CIIR)	40...85	400...800	−40...120	Low	Very good
Chloroprene rubber (CR)	20...90	100...800	−40...100	Moderate	Good
Chlorosulphonyl polyethylene rubber (CSM)	50...85	200...250	−20...120	Moderate to good	Very good
Nitrile butadiene rubber (NBR)	40...100	100...700	−40...100	Good	Very good
Polyacrylate rubber (ACM)	55...90	100...350	−60...200	Good	Very good
Fluorocarbon rubber (FPM)	65...90	100...300	−20...200	Excellent	Highly temperature dependent

In addition to the solid spring materials described, gaseous materials (e.g., nitrogen or air) are also used as a spring-loaded element in gas storage due to their compressibility.

15.9.5 Springs Subjected to Tensile and Compressive Loading

Extension (Tension) Springs Made of Wire

Tension wires have a linear spring characteristic (Fig. 15.120). They are rarely used, as a large spring length L_0 is required to achieve noteworthy spring deflections. Due to uniform stress distribution in the spring cross section, the load factor (degree of utilization) is $\eta_A = 1$.

Calculation.

Load capacity:

$$F_{max} \le A\sigma_{all} \tag{15.196}$$

Spring deflection:

$$s = L_0\varepsilon = \frac{L_0\sigma}{E} = \frac{L_0 F}{EA} \tag{15.197}$$

Spring work:

$$W = \frac{Fs}{2} = \frac{V\sigma^2}{2E} \tag{15.198}$$

Spring rate:

$$c = \frac{F}{s} = \frac{EA}{L_0} \tag{15.199}$$

Type efficiency:

$$\eta_A = 1 \tag{15.200}$$

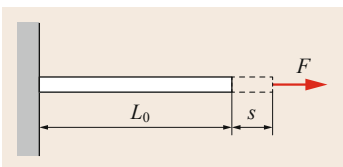

Fig. 15.120 Extension (tension) springs made of wire

Ring Springs

Ring springs are rings alternately stacked on top of each other with tapered contact surfaces (Fig. 15.121). The axially applied force acts on the contact surfaces between the internal and external ring at right angles to the contact surfaces. This causes the external ring to expand and the internal ring to compress, which enables the rings to slide in each other. As a result of the friction on the tapered contact surfaces, the springs have a very high damping effect.

The spring deflection is limited by the axial distance t of the external or rather internal rings to limit the maximum tensile stress (external ring), or rather the compressive stress (internal ring).

The taper angle α on the contact surfaces is generally approximately 12−14°, which prevents blocking of the springs as a result of self-locking in the deflected state.

As single stacks of rings have very steep spring characteristics, in practice, several stacks of rings are

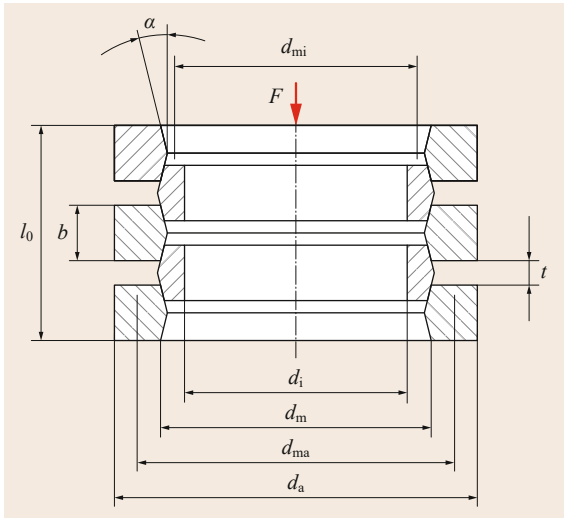

Fig. 15.121 Stack of ring springs

combined to achieve gentler characteristics and in some cases individual internal rings are slotted.

Ring springs are used as buffer springs on wagons or to protect against overload in presses.

Calculation.

Spring force on loading:

$$F\uparrow = F_C \frac{\tan(\alpha + \varrho)}{\tan\alpha} \approx (1.5 \ldots 1.6)\, F_C \qquad (15.201)$$

Spring force on unloading:

$$F\downarrow = F_C \frac{\tan(\alpha - \varrho)}{\tan\alpha} \qquad (15.202)$$

Spring deflection:

$$s = \frac{n}{2}\left(\frac{d_{ma}\sigma_z + d_{mi}\sigma_d}{E\tan\alpha}\right) \qquad (15.203)$$

Spring work on loading:

$$W\uparrow = \frac{F\uparrow s}{2} \qquad (15.204)$$

Spring work on unloading:

$$W\downarrow = \frac{F\downarrow s}{2} \qquad (15.205)$$

Type efficiency:

$$\eta_A = \frac{\tan(\alpha - \varrho)}{\tan(\alpha + \varrho)} \qquad (15.206)$$

where:

α taper angle of the contact surfaces (Fig. 15.121)
ϱ friction angle: finely machined rings $\varrho \approx 7°$; unmachined or die-forged ring $\varrho \approx 9°$
F_C spring force without consideration friction (Fig. 15.121)
n number of rings (including the two half end rings)
σ_z tensile stress in the external ring
σ_d compressive stress in the internal ring
d_{ma} average diameter of the external part (Fig. 15.121)
d_{mi} average diameter of the internal part (Fig. 15.121)

15.9.6 Springs Subjected to Bending

Springs subjected to bending are used, among other things, as contact springs in relays and switches, as press-on springs, or as clips in plug-in connections. The deformation (deflection) in the x-direction of the spring is a function of the bending moment acting on the spring:

$$w_x = \int\left(\int \frac{M_{by}(x)}{EI_y(x)}\mathrm{d}x\right)\mathrm{d}x\,, \qquad (15.207)$$

where:

$M_{by}(x)$ bending moment
$I_y(x)$ second moment of area

Calculation

Flexible bending springs are calculated based on the middle of a flexible beam fixed at one end. For a beam with linearly changeable width and a constant height (Fig. 15.122), the spring parameters are calculated using

Load capacity: $$F_{max} \le \frac{b_0 t^2}{6}\frac{\sigma_{all}}{l} \qquad (15.208)$$

Spring deflection: $$s = \psi\frac{4Fl^3}{b_0 tE} \qquad (15.209)$$

Spring work: $$W = \psi\frac{b_0 tl\sigma_b^2}{18E} \qquad (15.210)$$

Spring stiffness: $$c = \frac{b_0 t^3 E}{\psi 4l^3} \qquad (15.211)$$

Type efficiency: $$\eta_A = \frac{2\psi}{9(1+\beta)} \qquad (15.212)$$

where:

b_0 spring width at the clamped point
t spring height
l spring length
ψ form factor in accordance with Table 15.87
β width ratio $\beta = b_1/b_0$.

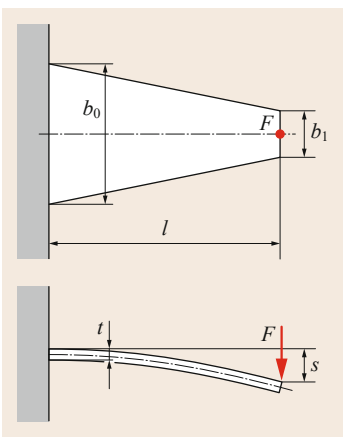

Fig. 15.122 Leaf spring with linearly changeable width

Table 15.87 Form factor and width ratio for calculating leaf springs

$\beta = \frac{b_1}{b_0}$	0	0.1	0.2	0.3	0.4	0.5	0.6	0.7	0.8	0.9	1
ψ	1.5	1.39	1.315	1.25	1.202	1.16	1.121	1.085	1.054	1.025	1

The equations above for the trapezoidal spring also apply to rectangular springs ($\beta = b_1/b_0 = 1$), triangular springs ($\beta = b_1/b_0 = 0$), and double-sided springs (notionally fixed in the middle of the spring).

Laminated Leaf Springs

Laminated leaf springs are made by layering several spring layers on top of each other. They can be roughly calculated by arranging the individual spring layers next to each other, so that they form a single spring element as a trapezoidal or triangular spring (Fig. 15.123).

However, the friction between the individual spring layers is not considered here. In practice, however, it results in a slightly increased load-bearing capacity (up to 12%) and limited damping. At the same time, however, laminated leaf springs are susceptible to fretting.

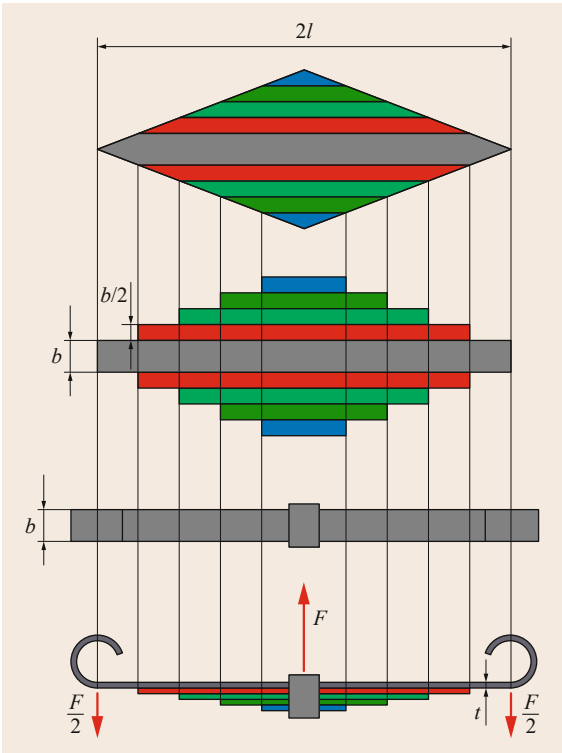

Fig. 15.123 Laminated leaf springs with computational model as triangular spring

Wound Helical Springs

Wound helical springs are used, for example, as restoring springs in actuating elements or in door hinges. The load should be applied in the coil direction, whereby it should be noted that the internal diameter of the spring is reduced by the load. The spring must be mounted on a guide pin to guide the spring, or the spring ends must be fixed.

Calculation. A rough calculation for flexible helical springs is based on EN 13906-3 [15.117]:

Load-bearing capacity:

$$F_{\max} \leq \frac{\pi d^3 \sigma_{\text{all}}}{32r} \tag{15.213}$$

Angle of rotation:

$$\alpha = \frac{3667 D_{\text{m}} F r n}{E d^4} \tag{15.214}$$

Spring work:

$$W = \frac{F r \alpha \pi}{360} \tag{15.215}$$

Spring rate:

$$c_{\text{R}} = \frac{dT}{d\alpha} = \frac{d^4 E}{3667 D_{\text{m}} n} \tag{15.216}$$

where:

d wire diameter
r effective lever arm (Fig. 15.124)
σ_{all} allowable bending stress $\sigma_{\text{all}} \approx 0.7 R_{\text{m}}$
D average diameter of the spring (Fig. 15.124)
n number of coils

Disc Springs

Disc springs, as shown in Fig. 15.125, are circular ring layers (discs) mostly with rectangular (in rare cases trapezoidal) cross sections, loaded in the direction of their axis, which are turned up or shielded in a tapered or disc shape in the axial direction by height h_0.

They are mainly used if a special spring characteristic profile, large forces with small spring deflections,

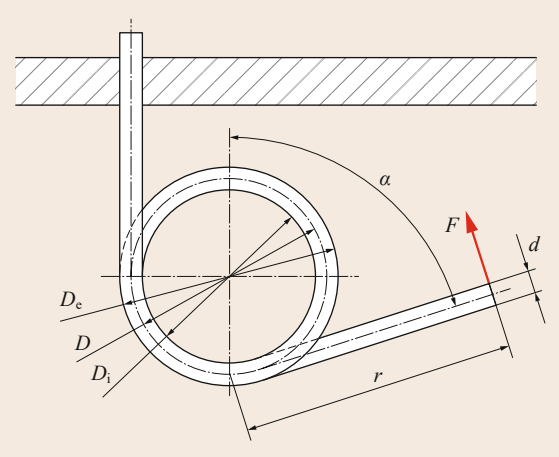

Fig. 15.124 Wound helical springs

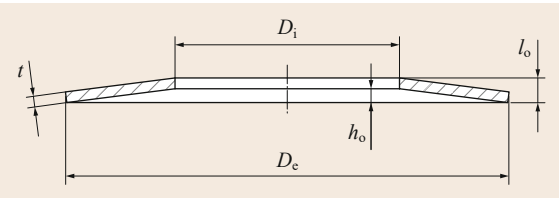

Fig. 15.125 Disc springs

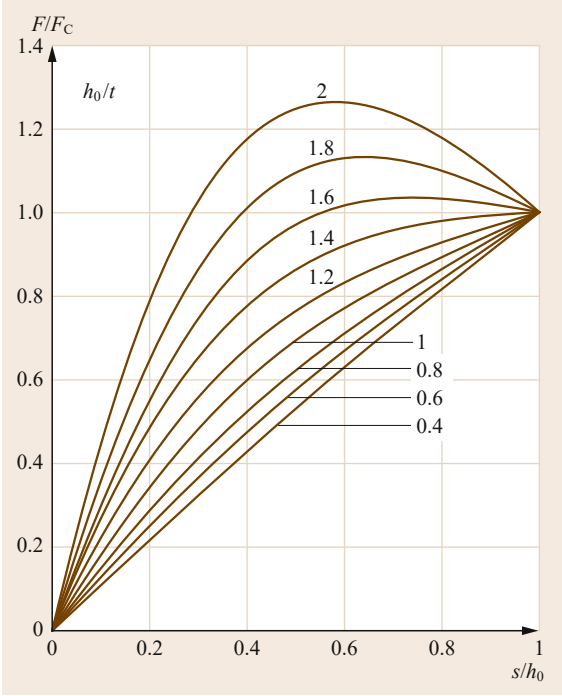

Fig. 15.126 Characteristic curves of individual discs up to the flat position $s = h_0$ (after [15.118])

or a small axial space requirement is required, for example, in clutches, as a clamping element, or to compensate for clearance in ball bearings.

The spring characteristic is largely dependent on the ratio h_0/t (Fig. 15.126).

As the force application points move with increasing deflection, smaller lever arms result for the elastic deformation, as a result of which the spring load increases compared to the calculation. For this reason, the spring parameters given in the EN 16983 [15.119] standard relate to a spring deflection $s \approx 0.75 h_0$.

In general, several disc springs are combined to form a stack of springs. The effect of the spring arrangement on the characteristic curve of the spring stack is shown in Fig. 15.127.

Progressive characteristic curves can be achieved by combined disc springs with different stiffnesses (Fig. 15.128).

Calculation. The calculations given are based on EN 16984:

Load-bearing capacity (flat position):

$$F\,(s = h_0) = \frac{4E}{1-\mu^2}\,\frac{t^3 h_0}{K_1 D_e^2}\,K_4^2 \qquad (15.217)$$

Spring work:

$$W = \frac{2E}{1-\mu^2}\,\frac{t^5}{K_1 D_e^2}\,K_4^2\left(\frac{s}{t}\right)^2\left[K_4^2\left(\frac{h_0}{t}-\frac{s}{2t}\right)^2+1\right] \qquad (15.218)$$

Spring rate:

$$W = c = \frac{4E}{1-\mu^2}\,\frac{t^3}{K_1 D_e^2}\,K_4^2 \times\left\{K_4^2\left[\left(\frac{h_0}{t}\right)^2-3\frac{h_0}{t}\,\frac{s}{t}+\frac{3}{2}\left(\frac{s}{t}\right)^2\right]+1\right\} \qquad (15.219)$$

where:

μ Poisson's ratio
t thickness of the disc spring
h_0 calculated spring deflection up to flat position of the disc spring
s spring deflection
$K_1; K_4$ parameters for calculation:

$$K_1 = \frac{1}{\pi}\,\frac{[(\delta-1)/\delta]^2}{(\delta+1)/(\delta-1)-2/\ln\delta} \qquad (15.220)$$

$$K_4 = \frac{3}{\pi}\,\frac{\delta-1}{\ln\delta} \qquad (15.221)$$

where:
δ diameter ratio $\delta = D_e/D_i$ (Fig. 15.125).

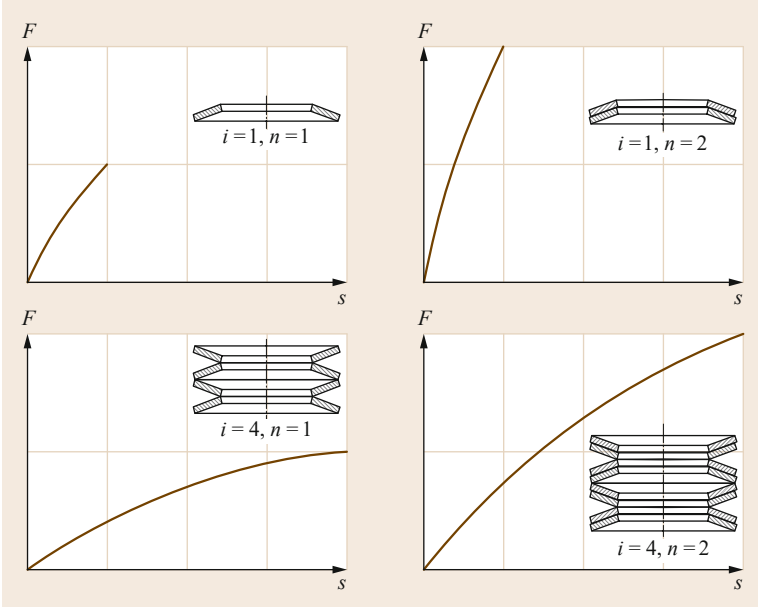

Fig. 15.127 Characteristic curves of spring stacks depending on the spring arrangement (after [15.118])

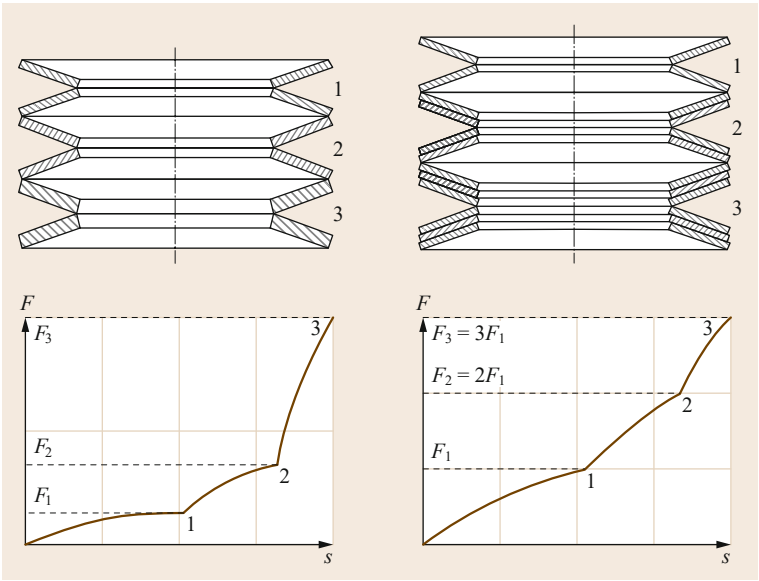

Fig. 15.128 Progressive characteristics of spring stacks achieved by combining disc springs with different stiffness (after [15.118])

15.9.7 Torsionally Loaded Springs

Torsion Bar Springs

Torsion bar springs are straight bars with round or rectangular cross sections that are twisted by an external force. Bundles of torsion bar springs (as a bar or plate bundle) enable shorter construction methods compared to individual solid bars with the same load-bearing capacity.

Torsion bar springs are used, among other things, as suspensions or spring mountings for cars and utility vehicles or as torque shafts, for example, in torque wrenches.

The basic structure of a torsion bar spring is shown in Fig. 15.129.

The torsional moment T is caused by a force F acting at distance r from the pivot point. The twist angle is proportional to the torsional moment (linear spring characteristic).

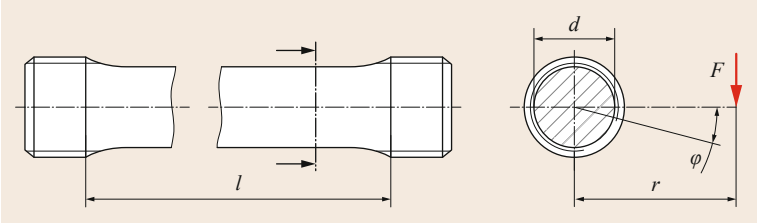

Fig. 15.129 Torsion bar spring with interlocking gripping heads

Calculation. The calculation equations given apply to simple torsion bar springs with round cross sections.

Load-bearing capacity: $$T_{max} \leq \frac{\pi d^3 \tau_{all}}{16} \quad (15.222)$$

Twist angle: $$\varphi = \frac{180^\circ}{\pi} \frac{Tl32}{G\pi d^4} \quad (15.223)$$

Spring work: $$W = \frac{16lT^2}{G\pi d^4} \quad (15.224)$$

Spring rate: $$c_T = \frac{\pi d^4 G}{32l} \quad (15.225)$$

Type efficiency: $$\eta_A = \frac{1}{2} \quad (15.226)$$

Cylindrical Helical Springs with Constant Cross Section

Helical springs are the most frequently used type of spring. They are made of a wire with a constant cross section wound in a (mostly round) screw shape (helix).

The deformation behavior of helical springs corresponds to that of a coiled torsion bar spring.

The springs can be cold formed up to a wire diameter of 17 mm. Larger springs are hot-wound and are then subjected to heat treatment.

In the case of dynamically loaded springs, the fatigue strength can be improved by shot peening.

A differentiation is made between tensile and compressive helical springs, depending on the type of loading.

Helical Compression Springs. The winding ratio $w = D/d$ of helical compression springs according to EN 13906-1 [15.120] is usually within the range $5 \leq w \leq 9$. If the winding ratios are too small ($w \leq 4$) production is difficult; if the winding ratios are too large ($15 \leq w$) there is a risk of the spring wire becoming tangled.

The spring ends are mostly ground flat and closed (Fig. 15.130). To achieve a centrally acting force it is favorable to arrange the spring ends offset by 180°.

Highly loaded springs are sometimes compressed until the spring coils sit on top of each other before installation, which causes the yield point of the spring material to be exceeded. The resulting plastic deformation leads to a permanent change in length, the set amount (also known as embedding). During production the spring length is increased by the set amount so that the required spring length sets in after setting.

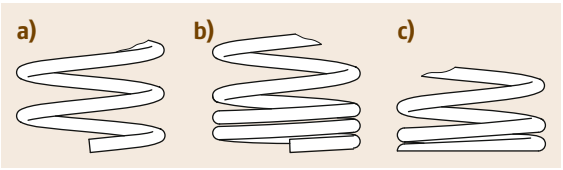

Fig. 15.130a–c Standard spring ends of helical compression springs: **(a)** unmachined, **(b)** closed and unmachined, and **(c)** closed and ground

Calculation. The number of active coils necessary n, depending on the compressive force F acting on the spring, and the required spring deflection s, is calculated using

$$n = \frac{Gd^4 s}{8D^3 F}, \quad (15.227)$$

where:

G modulus of rigidity
D average coil diameter (Fig. 15.131)
d wire diameter (Fig. 15.131).

Depending on the manufacturing method, the total number of coils n_t is:

Cold-coiled springs $$n_t = n + 2 \quad (15.228)$$

Hot-coiled springs $$n_t = n + 1.5 \quad (15.229)$$

The maximum spring deflection is limited by the solid length L_c of the spring (coils of the spring pressed together):

Cold-coiled spring with closed, machined spring ends $$L_C \leq n_t d \quad (15.230)$$

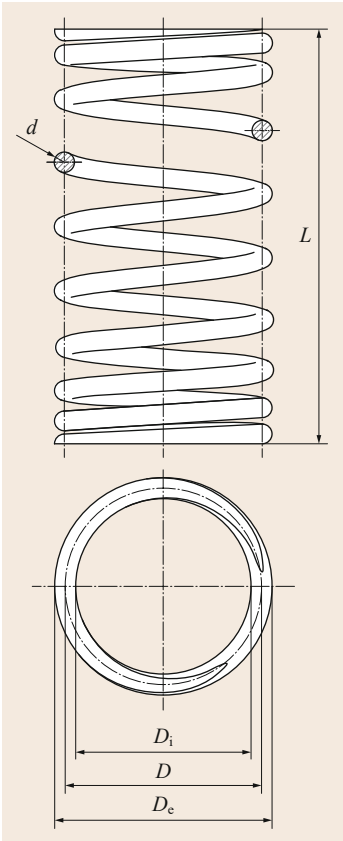

Fig. 15.131 Helical compression spring with ground spring ends

Cold-coiled spring with closed, unmachined spring ends $L_C \leq (n_t + 1.5)\, d$ (15.231)

Hot-coiled spring with closed, machined spring ends $L_C \leq (n_t - 0.3)\, d$ (15.232)

Cold-coiled spring with closed, unmachined spring ends $L_C \leq (n_t + 1.1)\, d$ (15.233)

A minimum spacing should be maintained between the individual coils in service. According to EN 13906-1, the sum of the minimum spacings s_a is calculated from:

Cold-coiled springs $s_a = n\left(0.0015\,\frac{D^2}{d} + 0.1d\right)$ (15.234)

Hot-coiled springs $s_a = 0.02n\,(D + d)$ (15.235)

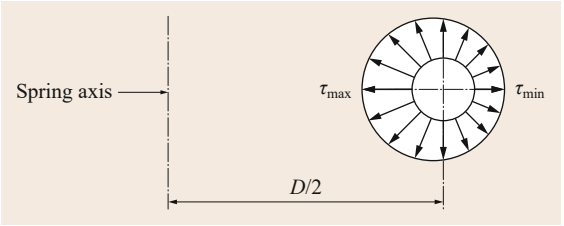

Fig. 15.132 Distribution of the torsional stress in the wire cross section (after [15.120])

For dynamic loading, the minimum spacing must be doubled (cold-formed springs), or rather increased 1.5 times (hot-formed springs).

The smallest allowable spring length L_n is the sum of the block length and the minimum spacings according to (15.234), or rather (15.235):

$$L_n = L_c + s_a\,. \tag{15.236}$$

Similar to a torsion bar spring, a helical spring is mainly loaded in torsion as a result of the twisting. Nonuniform distribution of the torsional stress occurs as a result of the wire curvature, with the maximum at the edge of the cross section inside the spring (Fig. 15.132).

While the nonuniform stress distribution can be ignored when dimensioning statically or quasistatically loaded springs, the corrected stress must be used in the calculations for dynamically loaded springs.

From the mean shear stress in the wire cross section,

$$\tau = \frac{8DF}{\pi d^3} \tag{15.237}$$

and the corrected shear stress is

$$\tau_k = k\tau\,, \tag{15.238}$$

with

$$k = \frac{w + 0.5}{w - 0.75}\,. \tag{15.239}$$

The spring parameters are calculated using

Load-bearing capacity: $F_{max} \leq \frac{\pi d^3 \tau_{all}}{8D}$ (15.240)

Spring deflection: $s = \frac{8D^3 nF}{Gd^4}$ (15.241)

Spring work: $W = \frac{Fs}{2} = \frac{4D^3 nF^2}{Gd^4}$ (15.242)

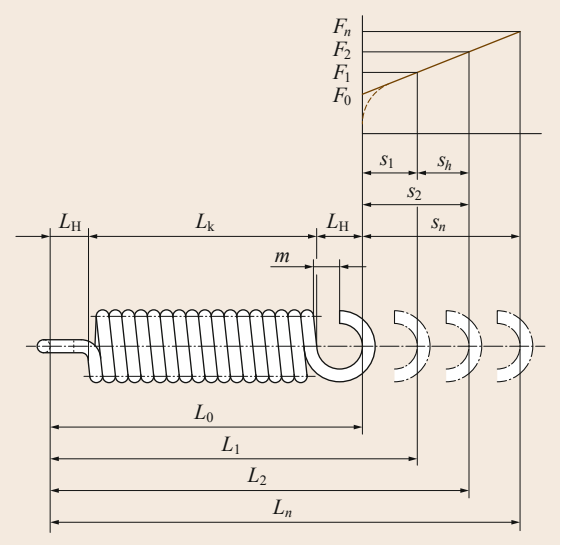

Fig. 15.133 Extension springs according to EN 13906-2 (after [15.121])

Spring rate: $$c = \frac{d^4 G}{8 D^3 n} \quad (15.243)$$

Type efficiency: $$\eta_A = \frac{1}{2} \quad (15.244)$$

where:

τ_{all} allowable material strength (see also EN 13906-1 [15.120])

Long springs or unfavorable clamping can cause the springs to kink. When in doubt, this must be checked according to EN 13906-1.

Helical Extension Springs. Cold-wound helical extension springs according to EN 13906-2 [15.121] are made so that when unloaded, the individual spring coils sit on top of each other, which produces an initial tension force.

In the case of the far more rarely used hot-formed extension springs, the coils do not lie on top of each other in the unloaded condition (free from initial tension).

The spring ends can have different shapes. Standard versions are shown in Fig. 15.134.

Calculation. Extension springs are calculated in a similar way to the calculation of compression springs, whereby the initial tension must be taken into account in the calculations for cold-wound springs:

$$F = F_0 + F_z \,, \quad (15.245)$$

where:

F_0 initial tension in unloaded condition
F_z tensile force acting on spring

15.9.8 Elastomeric Springs

Elastomeric springs are elastic elements made of natural or synthetic rubber and other macromolecular materials (Table 15.86).

Compared to steel springs, they have less spring stiffness with very high elasticity. In addition, elastomeric springs have good to very good damping properties, however, these depend on temperature.

The very low electrical and thermal conductivity must also be highlighted.

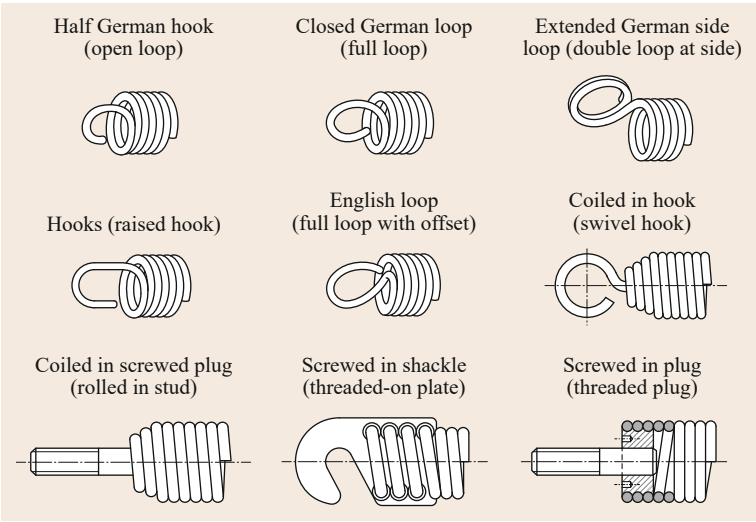

Fig. 15.134 Design of extension spring ends according to DIN 13906-2 (after [15.121])

The limited aging or rather media resistance and, in some cases, distinct creep tendency of the elastomers are disadvantageous factors.

Elastomeric springs are used for:

- Cushioning machines, vehicles, and equipment
- Damping vibrations, shocks, and noises
- Torsionally stiff self-aligning couplings and maintenance-free joints with small angular travel (e.g., vehicle wheel suspension)

Calculation and Design

Hardly any generally valid calculation equations exist for elastomeric springs due to their very different properties, the different influencing variables, and spring variations.

The springs are frequently purchased from the manufacturer as a ready-to-install machine element, in which case the manufacturer also supplies the appropriate characteristic data. The springs should always be installed so that the spring material is mainly loaded in shear or bending. Tensile loading is only acceptable for secondary purposes.

15.9.9 Further Reading

Further reading on the topic of metal springs can be found, for example, in *Meissner* et al. [15.122] or in the design guides of the Spring Research Association [15.123, 124].

Elastomeric springs are discussed, among others, by *Göbel* [15.125].

Information on the design of springs and the materials used is given in the corresponding standards, for example:

- Disc springs: EN 16984 [15.118]
- Spiral springs: EN 13906-3 [15.117]
- Leaf springs: DIN 2094 [15.126]
- Torsion bar springs: DIN 2091 [15.127]
- Helical compression springs: EN 13906-1 [15.117]
- Helical extension springs: EN 13906-2 [15.119]

15.10 Pipes

Pipes are used extensively to route and transport fluids or flowable solids. Rigid lines are called pipes; flexible lines are called hoses. Pipes and hoses are used in practically all areas in which flowable materials are used, from water installations in households to complex pipe systems in the chemical industry or oil refineries.

The order of size ranges from simple plastic hoses or capillary tubes with diameters significantly smaller than 1 mm through to pipelines with a diameter significantly larger than 1 m.

The medium to be transported moves due to the pressure differences in the pipe system that are caused, for example, by pumps, fans, or height differences (hydrostatic pressure). The absolute pressure in the pipe system is essentially limited by the strength of the pipe and the capacity of the pressure generator and lies within a range from around 300 mbar through to several thousand bar.

Flowable solids, such as sand, grain or granulate, can only be transported against gravity with the help of an additional transfer fluid (mostly gaseous).

In addition to the pipes, a pipe system also includes pipe fittings (for example, branches, angle bends, and reducer adapters), valves for adjusting and controlling the flow, connectors (for example, flanges, sockets, and fittings), elements for levelling out deformations, and fasteners.

15.10.1 Materials, Types, and Dimensions

Metallic materials are frequently used for pipes due to their high strength. Steel pipes hold a dominant position due to their high strength, good malleability, high elasticity, and their weldability. Depending on the area of application, the materials used include unalloyed quality steel (e.g., E355, P235TR2, and S355J2H), unalloyed stainless steel (e.g., C35E and C45E), alloyed stainless steel (e.g., 16Mo3 and 13CrMo4-5) and, where high corrosion resistance requirements exist, stainless steel (e.g., X5CrNi18-10 and X5CrNiMo17-12-2).

Quality steel with low carbon content (e.g., E195, E235, and P235TR2) is used for welded steel pipes, as it is more weldable.

Ductile cast iron is used for pipes with push-in socket or flange joints, especially for drinking water and wastewater piping. To increase the anticorrosion properties and protect against mechanical abrasion, the pipes often have an internal and external protective coating. In addition to epoxy resin coatings, among other things, protective cement mortar coatings are used.

Seamlessly drawn copper pipes are primarily used for installations in utility, refrigeration, and air-conditioning technology or as pressure pipes for gases. The pipes are generally made of deoxidized copper (Cu-DHP) with purity greater than 99.9%.

Table 15.88 Preferred nominal sizes for pipes [15.128]

DN 10	DN 250	DN 1500
DN 15	DN 300	DN 1600
DN 20	DN 350	DN 1800
DN 25	DN 400	DN 2000
DN 32	DN 450	DN 2200
DN 40	DN 500	DN 2400
DN 50	DN 600	DN 2600
DN 60	DN 700	DN 2800
DN 65	DN 800	DN 3000
DN 80	DN 900	DN 3200
DN 100	DN 1000	DN 3400
DN 125	DN 1100	DN 3600
DN 150	DN 1200	DN 3800
DN 200	DN 1400	DN 4000

Aluminum pipes are mostly seamlessly extruded. As a pipe element for routing fluids, they are used for example in oil hydraulics, the food industry, in vehicle manufacturing, and as pipes in heat exchangers. Weldable wrought alloys (e.g., AW-AlMgSi and AW-Al Si1MgMn) are mainly used as an alloy.

Plastic pipes are increasingly being used due to their positive properties (good corrosion resistance, easy workability, and low weight). The materials used include not only thermoplastics but also duroplastics.

Standard thermoplastic materials for all types of pipes are polyvinylchloride (PVC-U), polypropylene (PP), high-density polyethylene (PE-HD), and the more rarely used polyvinylidene fluoride (PVDF).

Duroplastics are mainly used as matrix material (e.g., vinyl ester resin (VE)) in fiber-reinforced plastic pipes.

Plastic pipes with a metallic core (mostly made of aluminum) are called multilayer pipes. They are mainly found in heating, sanitary, and gas installations. Compared to pure plastic pipes, they are easier to work (bend) and have a significantly better diffusion resistance (higher gastightness).

Hoses are mostly made of elastomers such as rubber, ethylene propylene diene rubber (EPDM), fluorinated rubber (FKM), silicone, or similar elastic materials. Metallic hoses obtain their (limited) flexibility through the wavy structuring of the pipe material.

Plastic hoses with reinforced fabrics made of natural/synthetic fibers or metallic wire are used for applications with higher pressures. Suction hoses must also be protected against contracting by spiral-shaped wire rings made of plastic or metal.

According to EN ISO 6708 [15.128], pipe nominal sizes (Table 15.88) are to be used. Depending on the pipe variant, the nominal size can stand not only for the external diameter, but also the internal diameter of the pipe.

Table 15.89 Linear coefficient of expansion α of selected materials at 20 °C

Material	α (10^{-6}/K)
Nonalloy steel	11.7
Stainless steel	16
Ductile cast iron	10
Copper	16.5
Aluminum	22.8
PP	100–200
PE-HD	120–200
PVC-U	50–80

Components for making pipe bends, branches, connections, maintenance openings, and special joints or rather built-in parts are grouped together under the term fittings. They are often available as a standardized component for the relevant type of pipe.

The connection between two pipe segments is made using so-called pipe connectors (Fig. 15.135). A differentiation can be made between pipe connections that can be disassembled (mechanical joints) and those that cannot be disassembled. The pipe connections (joints) that can be disassembled include:

- Pipe couplings (for example as a fitting or compression joint)
- Flange joints
- Socket joints

Pipe connections that cannot be disassembled are made, for example, by welding, soldering, adhesive bonding, or press-fit connections (press ends).

Expansion joints are used to compensate for thermal or load-dependent length changes in a rigid pipe system. The free length change of a pipe as a result of an increase in temperature can be determined using

$$\Delta L = L_0 \alpha \Delta T \,, \tag{15.246}$$

where:

L_0 initial length
α linear coefficient of expansion (Table 15.89)
ΔT temperature change

According to EN 736-1 [15.129], valves are piping components that influence fluid flow by opening, closing, or partially obstructing (Fig. 15.136). They can be used to control, divert, or mix the fluid flow.

15.10.2 Calculation

The essential equations for dimensioning piping are given here.

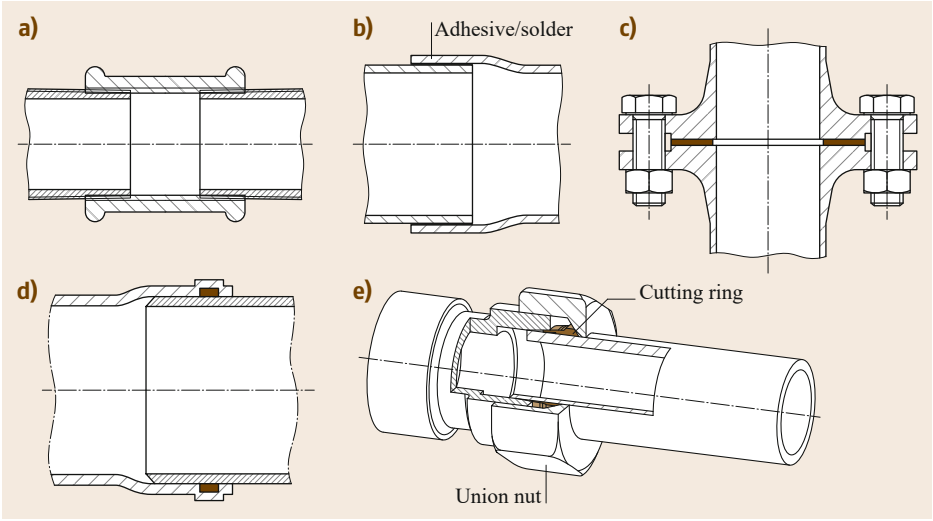

Fig. 15.135a–e Overview of pipe connections: **(a)** threaded socket, **(b)** soldered or rather adhesive joint, **(c)** flange joint, **(d)** push-in joint with sealing ring, and **(e)** compression joint (also known as bite-type fitting joint)

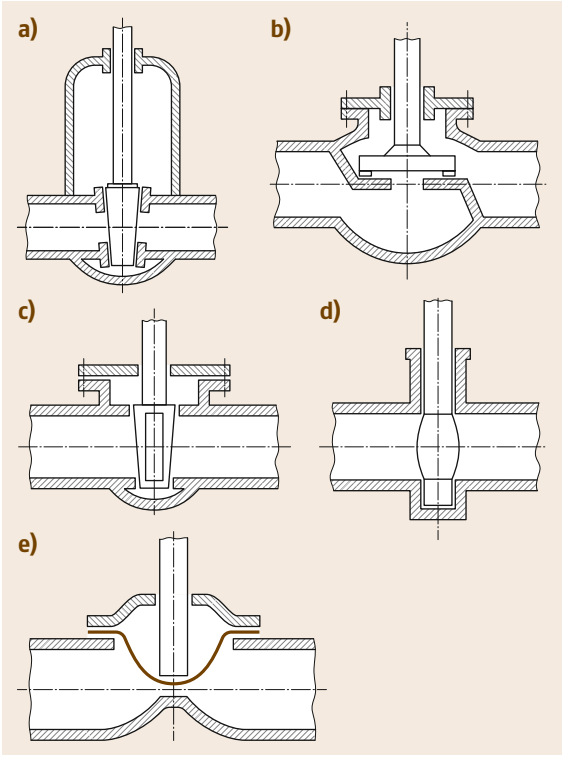

Fig. 15.136a–e Basic types of valves: **(a)** gate valve; **(b)** globe valve, **(c)** plug and ball valves, **(d)** butterfly valve, and **(e)** diaphragm valve (after [15.129])

Flow Velocity

The flow velocity inside a pipe can be calculated from

$$v = \frac{\dot{V}}{A} = \frac{4\dot{V}}{\pi d^2} , \qquad (15.247)$$

where:

$\dot{V}$ flow rate
A free cross section inside the pipe
d internal diameter of the pipe

Guide values for economical (efficient) flow velocities are listed in Table 15.90.

Pressure Loss

As a fluid flows through the pipe or pipe valves and fittings, friction on the boundary surfaces (interfaces) and inside the fluid cause energy losses that lead to a drop in pressure.

The level of the pressure drop depends on the type of flow (laminar or turbulent), surface roughness, and shape of the flow cross section. The general equation for the pressure loss inside a pipe through which incompressible fluid flow occurs is:

$$\Delta p = \lambda \frac{L}{d} \frac{\rho v^2}{2} , \qquad (15.248)$$

Table 15.90 Economical flow velocities in pipes in m/s [15.2]

Water pipes (pressure pipes)	0.5–3
Water pipes (suction pipes)	0.5–1
Compressed air pipes	2–10
Gas pipes	3–15
Steam pipes (superheated steam)	30–60
Steam pipes (saturated steam)	15–25
Oil pipes, general	0.5–1
Suction pipes of oil hydraulics	0.6–1.3
Pressure pipes of oil hydraulics	3–6

Table 15.91 Kinematic viscosity ν of selected substances in mm^2/s at 1.013 bar (unless stated otherwise)

Water (20 °C)	0.658
Hydraulic oil (HLP 46 at 40 °C)	41.4–50.6
Kerosene (Jet A-1, 20 °C)	2.5
Diesel according to EN 590 (40 °C)	2–4.5
Methanol (20 °C)	0.759
Glycerine with 50% water (20 °C)	5.29
Ethylene glycol with 50% water (20 °C)	3.9
Dry air (20 °C and 1 bar abs.)	15.3×10^{-6}
Dry air (20 °C and 9 bar abs.)	1.71×10^{-6}

where:

λ pipe coefficient of friction
L length of pipe section under consideration
d internal diameter of the pipe
ρ density of the fluid
v flow velocity

The coefficient of friction of the pipe is dependent on the Reynolds number and roughness of the pipe wall. The Reynolds number is a dimensionless similarity parameter from flow theory (fluid mechanics). For pipe flows, it is defined by

$$\mathrm{Re} = \frac{d\overline{v}}{\nu}\,, \tag{15.249}$$

where:

d hydraulic pipe diameter
$\overline{v}$ mean flow velocity
ν kinematic viscosity of the fluid (Table 15.91).

If the Reynolds number exceeds a critical value ($\mathrm{Re_{crit}}$), laminar pipe flow can be expected to change into turbulent pipe flow, as a result of which the friction losses increase sharply. For internal pipe flows, $\mathrm{Re_{crit}} \approx 2300$.

The pipe coefficient of friction for laminar pipe flows ($\mathrm{Re} < 2300$) can be calculated from (15.250). In this type of flow, the friction inside the fluid dominates, so that the roughness of the pipe walls can be ignored.

$$\lambda = \frac{64}{\mathrm{Re}} \tag{15.250}$$

In the case of turbulent flows, the friction inside the fluid increases significantly due to the larger velocity gradients. In addition, the flow velocity increases in the immediate vicinity of the wall, so that the effect of wall roughness on the pressure loss has to be taken into account. If the roughness of the surface is very small compared to the height of the viscous sublayer h_v (Fig. 15.137a), the pipe is called a hydraulically smooth pipe and the pipe coefficient of friction is calculated from

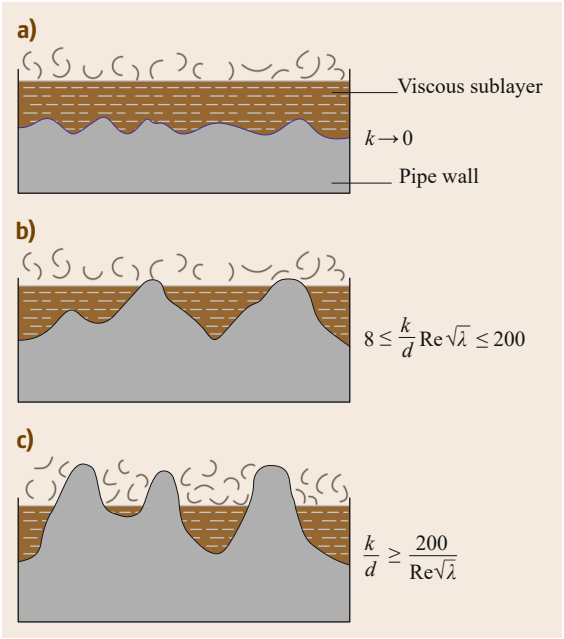

Fig. 15.137a–c Relationships between pipe roughness and viscous sublayer. **(a)** Hydraulical, **(b)** transition zone, and **(c)** rough wall

$$\lambda = \frac{1}{(1.82\log_{10}\mathrm{Re} - 1.64)^2}\,. \tag{15.251}$$

If the pipe wall is fully rough, the roughness peaks largely protrude out of the viscous sublayer (Fig. 15.137c). In this case, the friction of the pipe wall is decisive for the level of pressure loss and

$$\lambda = 0.0055 + 0.15\left(\frac{k}{d}\right)^{1/3}\,. \tag{15.252}$$

In the transition zone between a hydraulically smooth and a fully rough wall (Fig. 15.137b) the pipe coefficient of friction is calculated as

$$\lambda = 0.0055\left[1 + \left(20\,000\frac{k}{d} + \frac{10^6}{\mathrm{Re}}\right)^{1/3}\right]. \tag{15.253}$$

In the calculation of the pipe coefficient of friction it must be noted that the roughness k does not equal the technical roughnesses Ra and Rz. Standard values for k are shown in Table 15.92.

For pipe elements (for example, valves and fittings), for which the geometric ratio L/d used in (15.248) cannot be determined precisely, the pressure loss coef-

Table 15.92 Average roughness k of different types of pipes [15.2]

Pipes made of aluminum, copper, brass	New drawn or pressed pipes	0.001–0.002
Seamless steel pipes	New, with mill scale	0.02–0.06
	Pickled	0.03–0.04
	Moderate rust and slightly incrusted (scale)	0.15–0.4
	Severe incrustation	2–4
Welded steel pipes	New, with mill scale	0.04–0.10
Cast iron pipes	New, with casting skin	0.2–0.6
	New, bitumen coated	0.1
	Used, slightly rusty	1–1.5
	Incrusted	1.5–4
Steel pipes after many years' service	–	0.2–1.2

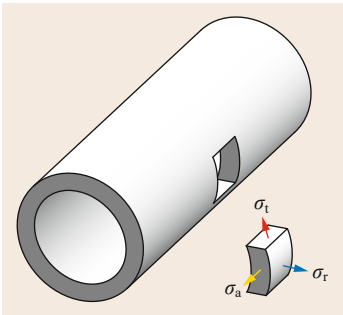

Fig. 15.138 Stresses in a pipe bend

ficient $\zeta = \lambda L/d$ is preferably determined, from which (15.248) follows:

$$\Delta p = \zeta \frac{\rho v^2}{2} \,. \tag{15.254}$$

Values for the pressure loss coefficients of different pipe elements are given in the manufacturers' information or the relevant literature ([15.130–132]).

Mechanical Stress in the Pipe Wall

As a result of the internal force acting on the pipe wall, a tangential stress σ_t, axial stress σ_a, and radial stress σ_r result (Fig. 15.138). For thin-walled pipes, where $d_a/d_i \leq 1.2$, the mean stresses are calculated from

$$\sigma_t = \frac{p d_i}{2\,s} \,, \tag{15.255}$$

$$\sigma_a = \frac{p d_i}{4\,s} \,, \text{ and} \tag{15.256}$$

$$\sigma_r = -\frac{p}{2} \,, \tag{15.257}$$

where:

p internal pressure
d_i internal diameter of the pipe
s pipe wall thickness

From (15.255) to (15.257) it can be seen that the tangential stress has the largest value and the radial stress has the smallest value. For this reason, pipes burst longitudinally in the event of overload.

An equivalent stress must be formed as a result of the multiaxial stress state. The maximum shear stress theory, also known as Tresca theory (Sect. 15.1.2), is useful for this due to its simple structure.

By inserting (15.255) and (15.257) in the equation for the maximum shear stress theory we get

$$\sigma_V = \sigma_{max} - \sigma_{min} = \frac{p d_i}{2s} + \frac{p}{2}$$
$$= \frac{p}{2}\left(\frac{d_i}{s} + 1\right) \leq \sigma_{all} \,. \tag{15.258}$$

This is also known as the *boiler equation*. After rearranging to obtain s, the value for the minimum necessary wall thickness is

$$s_{min} = \frac{d_i p}{2\sigma_{all} - p} \,. \tag{15.259}$$

Production tolerances, corrosion, or rather wear and strength losses, lead to weakening of the pipe and must be taken into account using appropriate correction values when dimensioning the pipe (DIN 2413 [15.133] or AD-2000 [15.134]).

15.10.3 Further Reading

Further literature on the topic of pipes is given, among other things, in *Wagner* [15.135] and *Wossog* [15.136]. Requirements for pressure equipment with an internal pressure above 0.5 bar, as defined in the Pressure Equipment Directive 2014/68/EU, are given in the AD 2000 standard [15.134]. More detailed calculation models and methods for determining pipe flow are given in *Wagner* [15.131].

References

15.1 R.C. Hibbeler: *Mechanics of Materials*, 10th edn. (Prentice Hall, Boston 2016)

15.2 H. Wittel, D. Muhs, D. Jannasch, J. Voßiek: *Roloff/Matek Maschinenelemente, Normung, Berechnung, Gestaltung – Lehrbuch und Tabellenbuch*, 23rd edn. (Springer, Berlin, Heidelberg 2017)

15.3 K.-H. Decker: *Decker Maschinenelemente: Funktionen, Gestaltung und Berechnung*, 19th edn. (Hanser, München 2014)

15.4 ISO 6336-1: Calculation of load capacity of spur and helical gears – Part 1: Basic principles, introduction and general influence factors (Beuth Berlin 2006)

15.5 R. Rennert: *Rechnerischer Festigkeitsnachweis für Maschinenbauteile aus Stahl, Eisenguss- und Aluminiumwerkstoffen*, FKM-Richtlinie, 6th edn. (VDMA, Frankfurt a. M. 2012)

15.6 H. Neubert: *Kerbspannungslehre, Theorie der Spannungskonzentration, Genaue Berechnung der Festigkeit*, 4th edn. (Springer, Berlin, Heidelberg 2001)

15.7 DIN 743-2: Calculation of load capacity of shafts and axles – Part 2: Theoretical stress concentration factors and fatigue notch factors (Beuth, Berlin 2012)

15.8 W.D. Pilkey, B.F. Pilkey: *Peterson's Stress Concentration Factors*, 3rd edn. (Wiley, Hoboken 2008)

15.9 DIN 743-1: Calculation of load capacity of shafts and axles – Part 1: General (Beuth, Berlin 2012)

15.10 DIN 743-3: Calculation of load capacity of shafts and axles – Part 3: Strength of materials (Beuth, Berlin 2012)

15.11 W.C. Young, R.G. Budynas, A.M. Sadegh: *Roark's Formulas for Stress and Strain*, 8th edn. (McGraw-Hill, New York 2012)

15.12 L. Issler, H. Ruoß, P. Häfele: *Festigkeitslehre – Grundlagen*, 2nd edn. (Springer, Berlin, Heidelberg 2006)

15.13 Y.-L. Lee, M.E. Barkey, H.-T. Kang: *Metal Fatigue Analysis Handbook: Practical Problem-Solving Techniques for Computer-aided Engineering* (Elsevier, Amsterdam 2012)

15.14 E. Haibach: *Betriebsfestigkeit Verfahren und Daten zur Bauteilberechnung*, 3rd edn. (Springer, Berlin, Heidelberg 2006)

15.15 J.A. Bannantine, J.J. Comer, J.L. Handrock: *Fundamentals of Metal Fatigue Analysis* (Prentice Hall, Englewood Cliffs 1990)

15.16 S.S. Manson, G.R. Halford: *Fatigue and Durability of Structural Materials* (ASM International, Materials Park 2006)

15.17 D. Radaj, C.M. Sonsino, W. Fricke: *Fatigue Assessment of Welded Joints by Local Approaches*, 2nd edn. (Woodhead, Cambridge 2006)

15.18 ISO 8734 Parallel pins of hardened and martensitic stainless steel (Dowel pins) (Beuth, Berlin 1997)

15.19 ISO 2339:1986 Taper pins, unhardened (Beuth, Berlin 1986)

15.20 ISO 8739 Grooved pins – Full-length parallel grooved, with pilot (Beuth, Berlin 1997)

15.21 ISO 8744 Grooved pins – Full-length taper grooved (Beuth, Berlin 1997)

15.22 ISO 8752 Spring-type straight pins – Slotted, heavy duty (Beuth, Berlin 2009)

15.23 A. Böge, W. Böge (Eds.): *Handbuch Maschinenbau: Grundlagen und Anwendungen der Maschinenbautechnik*, 23rd edn. (Springer, Wiesbaden 2017)

15.24 G. Niemann, H. Winter, B.-R. Höhn: *Maschinenelemente, Band 1: Konstruktion und Berechnung von Verbindungen, Lagern, Wellen*, 3rd edn. (Springer, Berlin, Heidelberg 2013)

15.25 ISO 2340: Clevis pins without head (Beuth, Berlin 1986)

15.26 ISO 2341: Clevis pins with head (Beuth, Berlin 1986)

15.27 DIN 8593-5: Fertigungsverfahren Fügen – Teil 5: Fügen durch Umformen; Einordnung, Unterteilung, Begriffe (Beuth, Berlin 2003)

15.28 DIN 5417: Securing parts for rolling bearings – Snap rings for bearings with ring groove (Beuth, Berlin 2011)

15.29 DIN 471: Retaining rings for shafts – Normal type and heavy type (Beuth, Berlin 2011)

15.30 DIN 472: Retaining rings for bores – Normal type and heavy type (Beuth, Berlin 2011)

15.31 DIN 988: Shim rings and supporting rings (Beuth, Berlin 1990)

15.32 DIN 983: Retaining rings with lugs for shafts (Beuth, Berlin 2011)

15.33 DIN 984: Retaining rings with lugs (internal circlips) for use in bores (Beuth, Berlin 2013)

15.34 DIN 6799: Retaining washers for shafts (Beuth, Berlin 2011)

15.35 DIN 9925: Round wire snap rings for shafts (Beuth, Berlin 2016)

15.36 DIN 9926: Round wire snap rings for bores (Beuth, Berlin 2016)

15.37 DIN 616: Rolling bearings – Dimensions – General plan (Beuth, Berlin 2000)

15.38 ISO 1234: Split pins (Beuth, Berlin 1997)

15.39 DIN 11024: Spring Cotters (Beuth, Berlin 1973)

15.40 VDI 2230 Part 1: Systematic Calculation of Highly Stressed Bolted Joints—Joints with one Cylindrical Bolt (Beuth, Berlin 2015)

15.41 VDI 2230 Part 2: Systematic Calculation of Highly Stressed Bolted Joints—Multi Bolted Joints (Beuth, Berlin 2014)

15.42 B. Schlecht: *Festigkeit, Wellen, Verbindungen, Federn, Kupplungen*, Maschinenelemente, Vol. 1 (Pearson, Boston 2007)

15.43 ISO 898-1: Mechanical properties of fasteners made of carbon steel and alloy steel – Part 1: Bolts, screws and studs with specified property classes – Coarse thread and fine pitch thread (Beuth, Berlin 2013)

15.44 ISO 68-1: ISO general purpose screw threads – Basic profile – Part 1: Metric screw threads (Beuth, Berlin 1998)

15.45 SAE J429: Mechanical and Material Requirements for Externally Threaded Fasteners (SAE, Warrendale 2014)

15.46 ASTM A307: Standard Specification for Carbon Steel Bolts, Studs, and Threaded Rod 60000 PSI Tensile Strength, ASTM International: West Conshohocken 2014

15.47 EN 923: Adhesives – Terms and definitions (Beuth, Berlin 2016)

15.48 M. Spotts, T. Shoup, L. Hornberger: *Design of Machine Elements*, 8th edn. (Prentice Hall, Englewood Cliffs 2004)

15.49 K.-J. Matthes, W. Schneider: *Schweißtechnik: Schweißen von metallischen Konstruktionswerkstoffen*, 5th edn. (Hanser, München 2012)

15.50 EN 1993-1-8: Eurocode 3: Design of steel structures – Part 1–8: Design of joints (Beuth, Berlin 2010)

15.51 M. Rasche: *Handbuch Klebtechnik* (Hanser, München 2012)

15.52 American Welding Society: Standards Comparison, https://app.aws.org/mwf/attachments/56/63556/Standards_Comparison.pdf (2017)

15.53 D. Breslavsky: Steel and Cast Iron Standards, http://www.steelnumber.com/en/standard_eu.php, last accessed 11 Nov (2019)

15.54 H. Dresig, F. Holzweißig: *Maschinendynamik*, 12th edn. (Springer, Berlin, Heidelberg 2016)

15.55 DIN 6885-1: Drive Type Fastenings without Taper Action; Parallel Keys, Keyways, Deep Pattern (Beuth, Berlin 1968)

15.56 ANSI B17.1: Keys and Keyseats (ANSI, New York 1967)

15.57 ISO 6912: Woodruff keys and keyways (Beuth, Berlin 1977)

15.58 ANSI B17.2: Woodruff keys and keyseats (ANSI, New York 1967)

15.59 DIN 7190-1: Interference fits – Part 1: Calculation and design rules for cylindrical self-locking pressfits (Beuth, Berlin 2017)

15.60 DIN 253: Geometrical product specifications (GPS) – Series of conical tapers and taper angles; Values for setting taper angles and setting heights (Beuth, Berlin 2003)

15.61 DIN 7190-2: Interference Fits—Part 2: Calculation and Design Rules for Conical Self-locking Pressfits (Beuth, Berlin 2017)

15.62 F.G. Kollmann: *Welle-Nabe-Verbindungen* (Springer, Berlin, Heidelberg 1984)

15.63 ISO 15: Rolling bearings – Radial bearings – Boundary dimensions, general plan (Beuth, Berlin 2011)

15.64 ISO 355: Rolling bearings – Tapered roller bearings – Boundary dimensions and series designations (Beuth, Berlin 2007)

15.65 DIN 720: Rolling Bearings – Tapered roller bearings (Beuth, Berlin 2007)

15.66 ISO 104: Rolling bearings – Thrust bearings – Boundary dimensions, general plan (Beuth, Berlin 2015)

15.67 American Bearing Manufacturers Association: *ANSI/ABMA 12.2: Instrument Ball Bearing-Inch Design* (ABMA, Washington 2010)

15.68 American Bearing Manufacturers Association: *ANSI/ABMA 19.2: Taperes Roller Bearings-Radial-Inch Design* (ABMA, Washington 2014)

15.69 DIN 623-1: Rolling bearings; fundamental principles; designation, marking (Beuth, Berlin 1993)

15.70 ISO 76: Rolling bearings – Static load ratings (Beuth, Berlin 2006)

15.71 ISO 281: Rolling bearings – Dynamic load ratings and rating life (Beuth, Berlin 2007)

15.72 Schaeffler Technologies: Tragfähigkeit und Lebensdauer, http://medias.schaeffler.de/medias/de!hp.tg.cat/tg_hr*ST4_102027403 (2017)

15.73 W.J. Barz (Ed.): *Schäden an geschmierten Maschinenelementen: Gleitlager, Wälzlager, Zahnräder*, 3rd edn. (Expert, Renningen-Malmsheim 1999)

15.74 L. Engel, H. Winter: Wälzlagerschäden, Antriebstechnik **18**(3), 71–74 (1979)

15.75 Schaeffler Technologies AG: *Rolling Bearing Damage, Rolling Bearing Damage Recognition of Damage and Bearing Inspection* (Schaeffler Technologies, Herzogenaurach 2010)

15.76 ISO 15243: Rolling bearings – Damage and failures – Terms, characteristics and causes (Beuth, Berlin 2004)

15.77 H. Dahlke: *Handbuch Wälzlagertechnik: Bauarten-Gestaltung-Betrieb* (Vieweg, Braunschweig 1994)

15.78 Schaeffler Technologie: *Katalog Wälzlager, Kugellager Rollenlager, Nadellager, Laufrollen, Lager für Gewindetriebe, Spannlager, Gehäuseeinheiten Lagergehäuse Zubehör* (Schaeffler Technologies, Schweinfurt 2014)

15.79 SKF Group: *Rolling Bearings* (SKF, Göteborg 2016)

15.80 Schaeffler Technologies: *Rolling Bearing Damage Recognition of Damage and Bearing Inspection* (Schaeffler Technologies, Schweinfurt 2010)

15.81 ISO 4378-1: Plain bearings – Terms, definitions, classification and symbols – Part 1: Design, bearing materials and their properties (Beuth, Berlin 2009)

15.82 B. Sauer (Ed.): *Konstruktionselemente des Maschinenbaus*, Vol. 2, 8th edn. (Springer, Berlin, Heidelberg 2018)

15.83 ISO 4378-3: Plain bearings – Terms, definitions, classification and symbols – Part 3: Lubrication (Beuth, Berlin 2009)

15.84 DIN 322: Gleitlager; Lose Schmierringe für allgemeine Anwendung (Beuth, Berlin 1983)

15.85 VDI 2204-Blatt 1: Auslegung von Gleitlagerungen; Grundlagen (Beuth, Berlin 1992)

15.86 ISO 12128: Plain bearings – Lubrication holes, grooves and pockets – Dimensions, types, designation and their application to bearing bushes (Beuth, Berlin 2001)

15.87 W. Bartz (Ed.): *Auslegung, Konstruktion, Werkstoffwahl und Schmierung*, Gleitlagertechnik, Vol. 1 (Expert, Grafenau 1981)

15.88 W. Bartz (Ed.): *Auslegung, Konstruktion, Werkstoffwahl und Schmierung*, Gleitlagertechnik, Vol. 2 (Expert, Sindelfingen 1986)

15.89 VDI 2204 1-4: Design of plain bearings (Beuth, Berlin 1992)

15.90 B. Perovic: *Hydrostatische Führungen und Lager* (Springer, Berlin, Heidelberg 2012)

15.91 H. Czichos, K.-H. Habig (Eds.): *Tribologie-Handbuch – Tribometrie, Tribomaterialien, Tribotechnik*, 4th edn. (Springer, Berlin, Heidelberg 2015)

15.92 EN 1514-1: Flanges and their joints – Dimensions of gaskets for PN-designated flanges – Part 1: Non-metallic flat gaskets with or without inserts (Beuth, Berlin 1997)

15.93 ISO 3601-1: Fluid power systems – O-rings – Part 1: Inside diameters, cross-sections, tolerances and designation codes (Beuth, Berlin 2012)

15.94 ISO 3601-2: Fluid power systems – O-rings – Part 2: Housing dimensions for general applications (Beuth, Berlin 2016)

15.95 SAE AS 568D: Aerospace Size Standard for O-rings (SAE, Warrendale 2014)

15.96 ISO 6194-1: Rotary shaft lip-type seals incorporating elastomeric sealing elements – Part 1: Nominal dimensions and tolerances (Beuth, Berlin 2007)

15.97 Eriks bv: Eriks Oil Seals, http://eriks.nl/documentatie/afdichtingen/asafdichtingen/oilseals.pdf (2017)

15.98 EagleBurgmann: SeccoMix 1, https://www.eagleburgmann.com/en/products/mechanical-seals/agitator-seals/dry-running-seals/seccomix-1 (2017)

15.99 EagleBurgmann: HSH-D, https://www.eagleburgmann.com/en/products/mechanical-seals/agitator-seals/liquid-lubricated-seals/hsh-d?set_language=en (2017)

15.100 EN 12756: Mechanical Seals—Principal Dimensions, Designation and Material Codes (Beuth, Berlin 2000)

15.101 H. Müller, B. Nau: *Fluid Sealing Technology: Principles and Applications* (Marcel Decker, New York, Basel 1998)

15.102 W. Tietze, A. Riedl (Eds.): *Taschenbuch Dichtungstechnik*, 3rd edn. (Vulkan, Essen 2011)

15.103 H. Linke (Ed.): *Stirnradverzahnung Berechnung-Werkstoffe-Fertigung*, 2nd edn. (Hanser, München 2010)

15.104 ISO 21771: Gears – Cylindrical involute gears and gear pairs – Concepts and geometry (Beuth, Berlin 2007)

15.105 ISO 53: Cylindrical gears for general and heavy engineering – Standard basic rack tooth profile (Beuth, Berlin 1998)

15.106 ISO 54: Cylindrical gears for general engineering and for heavy engineering – Modules (Beuth, Berlin 1996)

15.107 W. Skolaut (Ed.): *Maschinenbau. Ein Lehrbuch für das ganze Bachelor-Studium* (Springer, Berlin, Heidelberg 2014)

15.108 DIN 3992: Addendum modification of external spur and helical gears (Beuth, Berlin 1964)

15.109 ISO 6336-1;2;3;5;6: Calculation of load capacity of spur and helical gears (Beuth, Berlin 2006–2017)

15.110 ANSI/AGMA 2001-D04: Fundamental Rating Factors and Calculation Methods for Involute Spur and Helical Gear Teeth (AGMA, Alexandria 2004)

15.111 K.-H. Grote, J. Feldhusen (Eds.): *Dubbel, Handbuch Maschinenbau*, 21st edn. (Springer, Berlin, Heidelberg 2014)

15.112 G. Niemann, H. Winter: *Getriebe allgemein, Zahnradgetriebe – Grundlagen, Stirnradgetriebe*, Maschinenelemente, Vol. 2, 2nd edn. (Springer, Berlin, Heidelberg 2003)

15.113 G. Niemann, H. Winter: *Schraubrad-, Kegelrad-, Schnecken-, Ketten-, Riemen-, Reibradgetriebe, Kupplungen, Bremsen, Freiläufe*, Maschinenelemente, Vol. 3, 2nd edn. (Springer, Berlin, Heidelberg 1983)

15.114 DIN 3979: Tooth Damage on Gear Trains; Designation, Characteristics, Causes (Beuth, Berlin 1979)

15.115 B. Sauer (Ed.): *Konstruktionselemente des Maschinenbaus*, Vol. 1, 9th edn. (Springer, Berlin, Heidelberg 2016)

15.116 H. Habenhauer, F. Bodenstein: *Maschinenelemente: Gestaltung, Berechnung, Anwendung*, 17th edn. (Springer, Berlin, Heidelberg 2014)

15.117 DIN-EN 13906-3: Cylindrical Helical Springs Made From Round Wire and Bar—Calculation and Design—Part 3: Torsion Springs (Beuth, Berlin 2014)

15.118 DIN-EN 16984: Disc Springs—Calculation (Beuth, Berlin 2016)

15.119 BSI: BS-EN 16983: Disc Springs—Quality Specifications—Dimensions (Beuth, Berlin 2016)

15.120 DIN-EN 13906-1: Cylindrical Helical Springs Made from Round Wire and Bar—Calculation and Design—Part 1: Compression Springs (Beuth, Berlin 2013)

15.121 DIN-EN 13906-2: Cylindrical Helical Springs Made from Round Wire and Bar—Calculation and Design—Part 2: Extension Springs (Beuth, Berlin 2013)

15.122 M. Meissner, H.-J. Schorcht, U. Kletzin: *Metallfedern Grundlagen, Werkstoffe, Berechnung, Gestaltung und Rechnereinsatz*, 3rd edn. (Springer, Berlin, Heidelberg 2014)

15.123 A.A.D. Brown: *Mechanical Springs*, Engineering Design Guides, Vol. 42 (Oxford Univ. Press, London 1981)

15.124 Spring Research Association: *Helical springs*, Engineering Design Guides, Vol. 8 (Oxford Univ. Press, Oxford 1974)

15.125 S. Göbel: *Gummifedern. Berechnung und Gestaltung*, 3rd edn. (Springer, Berlin, Heidelberg 1967)

15.126 DIN 2094: Road vehicles leaf springs – Requirements, testing (Beuth, Berlin 2006)

15.127 DIN 2091: Circular section torsion bar springs; Calculation and design Beuth, Berlin 1981)

15.128 DIN-EN ISO 6708: Pipework Components—Definition and Selection of DN (Nominal Size) (Beuth, Berlin 1995)

15.129 BSI: BS-EN 736-1: Valves—Terminology—Part 1: Definition of Types of Valves (Beuth, Berlin 1995)

15.130 I.E. Idelchik: *Handbook of Hydraulic Resistance*, 4th edn. (Begell House, Redding 2007)

15.131 W. Wagner: *Strömung und Druckverlust*, 7th edn. (Vogel, Würzburg 2012)

15.132 A. Schweizer: Zeta Werte, http://www.schweizer-fn.de/zeta/start_zeta.php, last accessed 11 Nov (2019)
15.133 DIN 2413: Seamless steel tubes for oil- and water-hydraulic systems – Calculation rules for pipes and elbows for dynamic loads (Beuth, Berlin 2011)
15.134 Verband der Technischen Überwachungs-Vereine e. V.: *AD-2000-Regelwerk – Taschenbuch 2016*, 10th edn. (Beuth, Berlin 2017)
15.135 W. Wagner: *Rohrleitungstechnik*, 11th edn. (Vogel, Würzburg 2012)
15.136 G. Wossog (Ed.): *Planung – Herstellung – Einrichtung*, Handbuch Rohrleitungsbau, Vol. 1, 4th edn. (Vulkan, Essen 2016)

Frank Engelmann

Industrial Engineering
Ernst-Abbe-Hochschule Jena University of Applied Science
Jena, Germany
frank.engelmann@eah-jena.de

Frank Engelmann studied mechanical engineering at the Engineering Department of the University of Magdeburg. He then obtained a PhD at the same institution while working as the managing Director of a production business. His research activities focus on secondary explosion protection and biomedical technology. In October 2007, Frank Engelmann joined the University of Applied Sciences in Jena, Germany, as a full professor.

Karl-Heinrich Grote

Otto-von-Guericke-Universität
Magdeburg, Germany
karl.grote@ovgu.de

1973 to 1984: Studies at TU-Berlin and Dissertation; 1984 to 1986: Postdoc in the USA then Head of the Engineering Design Department at "IAV-Company" in Berlin; 1995 to 2020: Univ.-Professor for Engineering Design and Department Chair at Otto-von-Guericke University Magdeburg (OvGU), and Editor of the DUBBEL – Taschenbuch für den Maschinenbau, Springer-Verlag, Edition 19 to 25; 2002–2004: Visiting Full Professor at the California Institute of Technology (Caltech), Pasadena, USA; 2003 to 2013: Editor of Pahl/Beitz: Engineering Design, Springer-Verlag, Edition 5 to 8; since 2008: Editor of Handbook of Mechanical Engineering, Edition 1 and 2; 2005–2016: Dean of the College of Engineering at OvGU; since 2012: Professor II at the Bergen University College, Norway; 1993: VDI Young Engineers Award ("Ehrenring"); 2015: Honorary Doctors Degree (Dr. h.c.) from Kiev Institute of Technology (KPI); over 330 mostly peer-review publications and advisor of more than 90 dissertations reflect the research projects of 30+ years.

Thomas Guthmann

Industrial Engineering
Ernst-Abbe-Hochschule Jena University of Applied Science
Jena, Germany
thomas.guthmann@eah-jena.de

Thomas Guthmann is a section leader at the University of Applied Sciences Jena (Ernst-Abbe-Hochschule Jena). After studying general mechanical engineering, he received his doctorate in 2018 at the Otto von Guericke University Magdeburg with a thesis on the subject of construction methods. His current research focus is primarily in the field of dimensioning explosion protection components.

16. Engineering Design

Frank Engelmann, Alois Breiing, Timothy Gutowski

The development and design of engineering systems using a methodical approach based on guidelines in the literature [16.1–6] has been found to be a very useful approach. Such design methodology guidelines have also been applied to interdisciplinary development projects of this nature using aids such as requirements lists, functional structures, and the morphological box, to name just a few. During the design phase of the product development process, it is important to comply with the basic design rules: *simple*, *clear*, and *safe* [16.3]. Several examples that clearly show the realization of these three criteria are included in this chapter.

16.1 **Design Theory** 629
16.1.1 Product Planning Phase 629
16.1.2 The Development of Technical Products 633
16.1.3 Construction Methods 638
16.2 **Engineering Design Basics** 651
16.3 **Precisely Defining the Task** 651
16.3.1 The Task 651
16.3.2 Functional Description 652
16.3.3 Requirements List 653
16.4 **Conceptual Design** 654
16.5 **Design** 657
16.5.1 Identification of Requirements that Determine the Design and Clarification of the Spatial Conditions 657
16.5.2 Structuring and Rough Design of the Main Functional Elements and Selection of Suitable Designs 658
16.5.3 Detailed Design of the Main and Secondary Functional Elements 658
16.5.4 Evaluation According to Technical and Economic Criteria and Specification of the Preliminary Overall Design 659
16.5.5 Subsequent Consideration, Error Analysis, and Improvement 661
16.6 **Design and Manufacturing for the Environment** 662
16.6.1 Life Cycle Format for Product Evaluation 663
16.6.2 Life Cycle Stages for a Product 664
16.6.3 Product Example: Passive House 667
16.6.4 Design for the Environment (DFE) 669
16.6.5 System-Level Observations 670
16.7 **Failure Mode and Effect Analysis for Capital Goods** 671
16.7.1 General Innovations for the Application of FMEA 671
16.7.2 General Rules for Carrying Out FMEA 672
16.7.3 Procedure 673
16.7.4 Description of the Project 673
16.7.5 Further Use of FMEA Results 678
16.8 **Bioindustrial Design: Challenges and Vision** 678
References 680

16.1 Design Theory

16.1.1 Product Planning Phase

It is possible to define the individual life stages of a technical product. These stages are often the basis for work done by the product manufacturer and the product user. Examples include schedules for the development of a product and maintenance plans.

Figure 16.1 shows the essential life stages of a product during its production and application. It is also possible to subdivide the individual product life stages into steps, which helps the product engineer to precisely categorize the activities involved in each stage.

Product Life Cycle Stages and the Technical Life Cycle

The life cycle of a technical product is closely linked to the general *material cycle* (Fig. 16.1). The cycle starts with an idea for a product, arising from a market or

K.-H. Grote, H. Hefazi (Eds.), *Springer Handbook of Mechanical Engineering*, Springer Handbooks,
https://doi.org/10.1007/978-3-030-47035-7_16

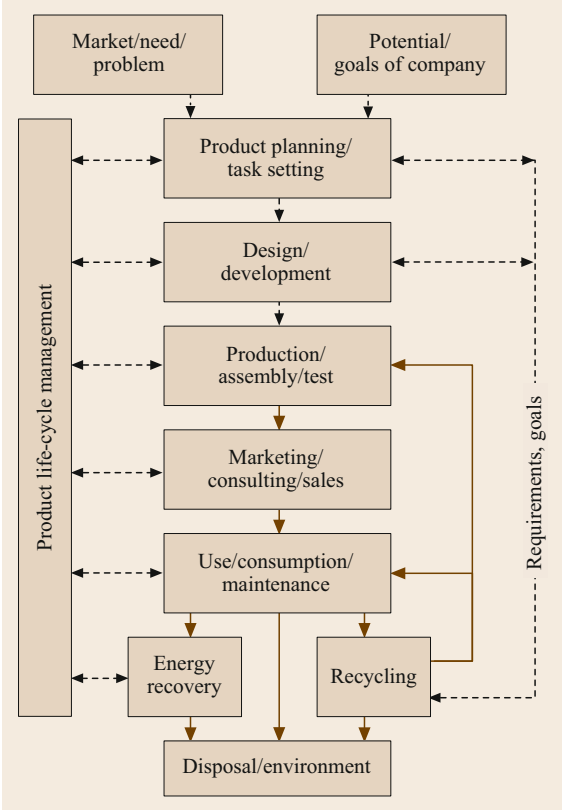

Fig. 16.1 Life cycle of a product (after [16.7])

customer need. This is concretized in the first phase of product life: product planning. The result is that a task is set, which provides the basis for the second phase of product life: development and construction. At this stage, the implementation of the idea and/or resolution of the task to obtain a viable product takes place in individual steps. The life cycle then continues with the manufacturing process, in which parts are manufactured and the product is assembled and quality tested.

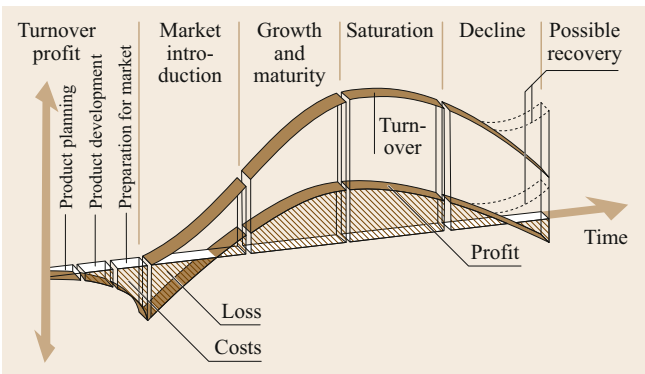

Fig. 16.2 Life cycle of a product (after [16.3])

This phase in the life cycle of the product ends when the manufacturer passes the product on to the distribution department.

This life-cycle stage is the interface to the application (i.e., the usage or consumption) of the product. Intermediate maintenance steps can help to extend its useful life. After the primary use of the product, it may be utilized again for the same purpose or for a different purpose (reuse/further use), or it may be converted into a secondary material that is used to create new products that are employed for the same purpose as the primary product (recycling) or for a different purpose (further utilization). Nonrecyclable components end up in a landfill site or are burnt to produce thermal energy.

Except for the recycling or landfill stages, this life cycle applies to physical products such as machinery, equipment, and devices, as well as to software products. It is usual for companies to employ such structuring techniques for product tracking.

Economic Life Cycle

As well as a succession of product life stages and/or concrete manufacturing and application steps, the life cycle of a product can be viewed in terms of economic data relating to the various stages of the product's life cycle. Figure 16.2 shows the relationship of each product stage to turnover, profit, and loss. It can be seen that before any turnover can be attained, the company must investment in implementation costs. The size of this investment is heavily dependent on the product. The company must recover this investment (i.e., it must break even) before it can begin to realize its ultimate goal: to make profits.

The profit zone is characterized by a growth phase and a market saturation phase before decline sets in through reductions in turnover and profit. At that point, sales and profits can be revived (e.g., through special sales and promotional activities), but usually only for a short period, so it is better to periodically establish rising life curves through the development of new products than to offset declining life curves of old products.

Product Planning

Importance. The first two phases of product life—product planning and product development—are among the most important tasks in industry. The continuous generation of marketable products provides the foundation for the economic success of a company. Because of the inevitable downturn phases for existing products or product groups (Sect. 16.1.1), the systematic planning of new products (i.e., an innovative product policy) must be implemented [16.4]. Strategies for product planning should not present a barrier to creative com-

panies and their engineers; instead, they should play a supporting role as methodological aids.

Fundamentals. Product planning is performed based on the relationships in the market, in the business environment of the company, and in the company itself. These relationships can be defined as either external or internal influences on the company, particularly its product planning process. *External influences* include:

- The global economy (e.g., exchange rates)
- The domestic economy (e.g., inflation rate, labor market situation)
- Legislative and administrative acts (e.g., environmental protection)
- The buying market (e.g., the suppliers' market and commodity market)
- Research (e.g., government-funded research priorities)
- Technology (e.g., developments in microelectronics or laser technology)
- The market.

As such, the conditions of the market are crucial. A distinction can be made between a buyer's market and a seller's market. In the former, supply is larger than demand; in the latter, demand is larger than supply. In a seller's market, production is the bottleneck; in a buyer's market, products face strong competition from products produced by other companies, so the products must be designed and developed with this in mind.

Further criteria for market identification encompass:

- Economic areas (domestic market, export markets)
- New factors for the company (current market, new markets)
- Market position (market share, strategic free rein of the company, the technical value of its products).

Internal factors include:

- The organization of the company (e.g., product-oriented vertical or task-oriented horizontal organization)
- The staff (e.g., availability of qualified development and manufacturing staff)
- Financial strength (e.g., investment opportunities)
- The size of the company (e.g., in terms of turnover that can be sustained)
- The production fleet (e.g., with regard to certain manufacturing technologies)
- The product program (e.g., with regard to components that can be adopted and predevelopment)
- Expertise (e.g., development, marketing, and production experience)
- The management (e.g., project management).

The influences listed are also termed the potential of the company.

Product Development

General Approach. The second phase of product life is development and construction. This is also often referred to simply as product development. To further structure this phase of product life, it is usual to break the stages down into individual steps. This procedural approach to handling construction tasks is based on general solution methods and/or working method approaches as well as the general relationships involved in building technical products. It is not a rigidly prescribed approach, but it is an essential tool for the engineer during product development. The individual working steps form the basis for other activities, such as the preparation of schedules or the planning of product development costs. They also help the engineer to orient him- or herself during the development process. A possible structure is depicted in Fig. 16.3.

Despite the wide range of possible product development phases, it is possible to derive a sector-independent flowchart with working steps that must be modified to the special conditions in setting the task. The first step in this flowchart is to clarify and specify the task, which is an especially important step for a new design task. The basis for this is setting tasks for individual requirements derived from product planning tasks. The design engineer must identify the essential problems to solve from among the myriad of specified requirements and formulate these problems in the language of his/her field of design. The result is a requirements list, which is also known as a specification sheet. This is both the technical and the legal basis for all other activities.

In the next step, a *solution-neutral* definition of the task is obtained (i.e., based on the assumption that the solution is not predetermined). This is realized by defining functions whose links lead to functional structures.

The functional structures that are generated during this working step collectively represent an abstract form of the solution concept, and these structures are then gradually implemented (Sect. 16.1.2).

The next step is to search for solution principles for the key subfunctions. For mechanical products, these are based on physical effects and are realized through the appropriate use of geometric and material characteristics (Sect. 16.1.2).

The individual solution principles are represented by a *morphological box*. For each key subfunction,

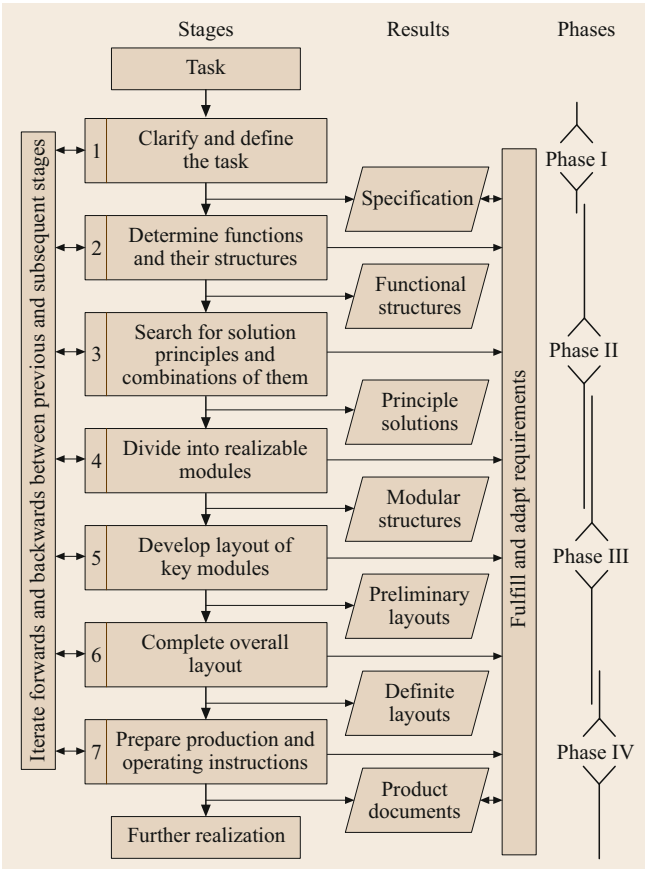

Fig. 16.3 General approach to product design (after [16.3])

a maximum of three to four solution principles should be derived simultaneously. With the help of the morphological box (Table 16.5), the individual solution principles are linked together to give effective structures. Generally speaking, no more than three effective structures are determined. The effective structures (also known as *principle solutions* or concepts) generated in this way are compared through appropriate evaluation mechanisms (Sect. 16.1.3). Thus, based on this work, it is possible to green light a principle solution for further treatment. This principle solution is then divided into realizable modules that can be translated into structures, allowing functional design or design priorities to to be addressed before the labor-intensive concretization stage. Furthermore, it is necessary to consider the possibility of realizing a structure that is production-like, easy to assemble, easy to maintain and recycle, and/or *building block-like* for use in subsequent work steps. The result is known as the *modular structure*.

Relevant structural modules are designed in the subsequent working step; e.g., the assemblies, components, and necessary connections are specified for mechanical systems. Essentially, this step includes the following activities: procedural calculations, stress and deformation analyses, arrangement and design considerations, and manufacturing and assembly examinations. As a rule, these procedures are not performed to generate production-related and materials engineering-related detail specifications; they are carried out to specify key characteristics of the design structure that can be optimized based on technical and economic considerations. The results of this step are the draft concepts.

The next working step involves designing other (usually dependent) functional elements (i.e., the micro design of all subassemblies and components) and establishing how they are combined in the overall design. A variety of calculation and selection methods, materials catalogs, machine parts, norm parts, and purchased parts are used in this step, and costing procedures are employed to determine costs. The result of this step is the overall design.

The last working step involves tasks related to execution and usage: the development of full diagrammatic documents, including parts lists for manufacturing and assembly, as well as the development of operating manuals and maintenance specifications. This step yields the complete product documentation.

In practice, several working steps in the development and construction phases are often combined (e.g., for organizational or work-related reasons). Thus, in mechanical engineering, the first three steps are viewed as a *concept* phase, the next three steps as a *draft* phase, and the final step as a *preparation* phase.

Product Specification. The general approach must be modified for tasks and/or products in which several specialist units are involved.

The goal is to carry out the corresponding technical tasks largely independently, but in a coordinated way. Such relationships apply, for example, to biomedical products, where medicine, biology, mechanical engineering, electrical engineering, and computer science are all involved. Precision engineering is another example; in this case, the design of the mechanical component, the development of the electrical and electronic circuits and control parts, and the development of the necessary software take place largely independently.

Whilst the requirement specifications and the functional structure of the overall product are prepared, the other working steps are split into parallel development paths that involve close coordination with the various specialist areas. To facilitate this, after major concretization targets have been attained (e.g., after

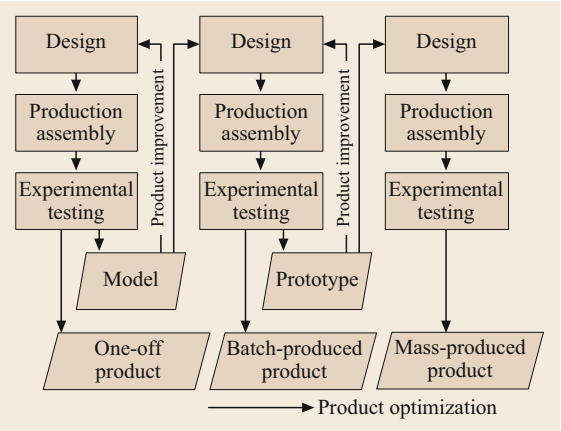

Fig. 16.4 Stepwise development of a mass-produced product (after [16.7])

defining the modular structure and presenting the individual working drafts), it is helpful to document the overall results of the work (system structure, system draft) in order to detect missing coordination and to obtain a homogeneous product. Documentation is created for the overall product. Whilst all working steps must be implemented for *new developments*, steps 2 and 3 are often dispensed with in *further developments* (Fig. 16.3). Similarly, steps 4 and 5 are dispensed with in *adaptation constructions*.

In many cases it has proven advantageous to control and/or reconstruct development steps allowing for comparison with the current state of knowledge. This kind of development process is intended for *products made individually*, usually only once. In the case of unsatisfactory results, individual working steps are performed again. For *mass production* products, like motor vehicles or household appliances, such process iterations are associated with high economic risk. According to Fig. 16.4, it is usual for such products to pass through the development and manufacturing cycle several times in order to identify vulnerable areas in the production process. This is initially done for functional and laboratory samples, but can also involve (where necessary) additional prototypes and/or pilot runs during the intermediate trial and testing phases. These are then optimized in a redesign and manufacturing process.

16.1.2 The Development of Technical Products

The construction of technical products is characterized by several general relationships that also determine the different levels of specific product development.

Function Relationships

The term function describes the general relationship between the input and output of a system that performs a task (Fig. 16.7).

For technical products or systems, the input and output variables are *energy variables*, *material variables*, and/or *signal variables* (Fig. 16.5). As a signal is a physical realization of information transmission, *information* is often also selected an as input and output signal variable.

Target functions set tasks in an abstract, solution-neutral, and clear manner. They are used to develop new products from requirement schedules.

Based on Fig. 16.6, we can distinguish between:

- The overall function, which describes the overall task of a product and/or system that must be solved.
- Subfunctions, which arise when the overall function is divided into simpler functions to make it easier to solve the overall task. The optimal degree of subdivision is dependent on the novelty of the task set, the complexity of the product to be developed, and the knowledge of solutions that can fulfill the required functions.

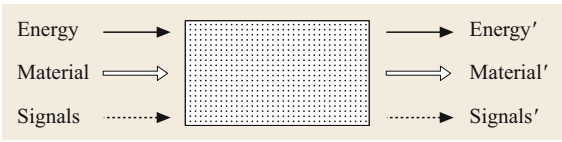

Fig. 16.5 Conversion of energy, material, and signals. The solution is not yet known; the task or function is described on the basis of inputs and outputs (after [16.3])

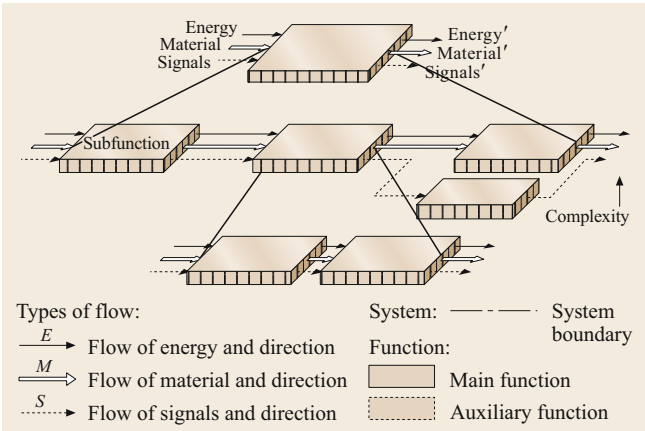

Fig. 16.6 Establishing a function structure by splitting an overall function into subfunctions (after [16.3])

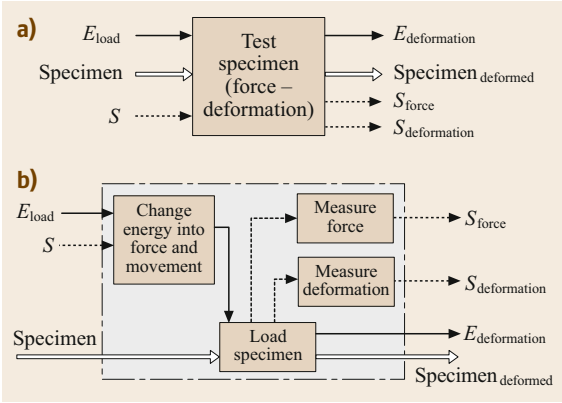

Fig. 16.7a,b Overall function **(a)** and subfunctions (main functions) **(b)** of a tensile testing machine (after [16.8])

Subfunctions are linked together in a *function structure*, where the linkages are determined by logical and/or physical compatibilities.

As an example, Figs. 16.7 and 16.8 show the function structure of a testing machine [16.8]. The overall function (overall task) of the machine is to define the stress applied to a test specimen and measure its deformity. The transfer from the input to the output of the function structure and/or the processing of energy, material, and signal variables can be thought of as energy, material, and signal flows or volumes. The various flows or volumes typically occur simultaneously, but one or several flows or volumes dominate and therefore determine the product. The latter are termed the *main flows* or *main volumes*. They fulfill the function of the product. As such, we can imagine a conveyor system in which the material volume is the product-determining main volume, the energy volume is the driving function, and the signal volume is the control function.

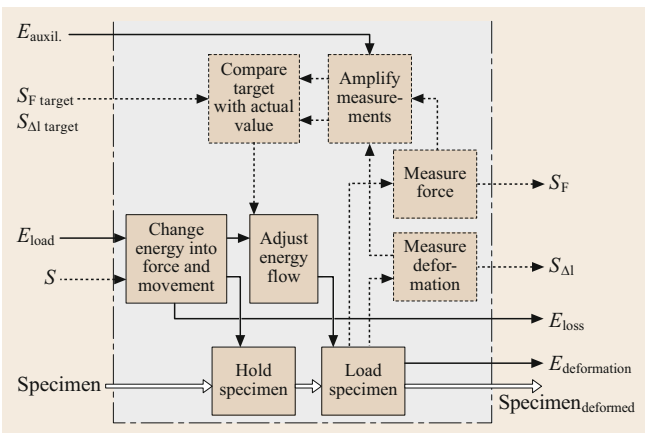

Fig. 16.8 Complete function structure for the overall function shown in Fig. 16.7 (after [16.8])

Volumes and/or flows that accompany the main volumes are supportive and only indirectly related to the functional performance of the product because they are not directly derived from the nominal functions (main functions) associated with the overall task. The generated solutions for the main functions always provide the basis for the accompanying flows. Accordingly, they are also referred to as *tributaries*, while the participating subfunctions are known as *side functions*. In the function structure illustrated in Fig. 16.7, all of the listed subfunctions resulting from the overall function (overall task) are main features. The subfunctions that result from the measurement principles (*amplify measurements* and *compare target with actual value*) are, on the other hand, side functions (Fig. 16.8).

In summary, there is no material or signal flow without an accompanying flow of energy, even if the energy required is very small and can easily be provided. It is, however, possible to have a signal volume without an accompanying material volume, (e.g., in measuring devices). Even the energy volume (e.g., in production of electrical energy) is connected to the material volume (e.g., fuel) where the accompanying signal flow is utilized for controlling.

Specific Functions.

Logical Function. Bivalent or *binary* role variables are often used to describe conditions (fulfilled–not fulfilled), statements (true–false), and switch positions (on–off) when designing and describing technical systems. System design aimed at realizing the required dependencies between binary variables is known as logical design. It uses mathematical statement logic in the form of Boolean algebra with the fundamental linkages AND and OR and negation [16.8].

Using Boolean combination elements, it is possible to build complex circuits that can, for instance, increase the safety of control and reporting systems.

As an example, Fig. 16.9 shows the scheme used to monitor an oil supply system for bearings. In this scheme, the nominal and actual values are linked by an AND function, as are the pressure monitor and the flow monitor, while the output signals from the pressure and flow monitors are connected by an OR function. All of the bearings are linked to an AND link, i.e., all bearings must be sufficiently oiled before the monitoring scheme will allow them to be used.

Generally Valid Functions. These functions are becoming increasingly common in technical products, as they can serve as sort keys for solution catalogs, as the basis for functional structure variations, and as abstraction aids in the analysis of existing products, depending on their functional relationships.

Table 16.1 shows five generally valid functions derived from the input and output of a function in terms of type, variable, number, place, and time with the help of a cluster variation. For other suggestions concerning generally valid functions, refer to [16.8]. It must be noted that such an approach and task structure is very abstract. For this reason, these functions are usually only used for new construction designs.

Cause–Effect Relationships

The subfunctions and the function structure of a technical functional relationship must be fulfilled by a cause–effect relationship. Accordingly, this arises from *active principles* to fulfill the subfunctions and from an *active structure* to fulfill the function structure. The active structure results from the interconnection of several active principles. An active principle is determined by a physical, chemical, or biological effect, by a combination of several effects, as well as through their principal realization using geometric and material characteristics (active structural characteristics). In engineering, physical effects usually predominate. Examples can be seen in Table 16.2.

Physical, Chemical, and Biological Effects. For material products produced by systems, machinery, equipment, and manufacturing, the solution is based on effects—in particular physical effects, but also chemical and/or biological effects. Effects are described by laws that assign particular variables to them, even quantitatively. For example, in the clutch shown in Table 16.3, the subfunction *change switching force* F_S *into normal force* F_N is realized by the effect of physical leverage, and the subfunction *generate tangential force* F_U is realized by the effect of friction. In particular, *Rodenacker* [16.5], *Koller* [16.6], and *Roth* [16.2] have all described physical effects on structures. The fulfillment of a subfunction can often only be achieved by linking multiple established effects, e.g., the impact of a bimetal is fulfilled through the effects of thermal expansion and Hooke's law (stress–strain relationship). A screw connection can be cited as another example: apart from Hooke's law, the interconnection is between the friction effect, the wedge effect, and the leverage effect.

In general, a subfunction can be fulfilled by various effects, such as the hydraulic/pneumatic effect listed in Table 16.3 or a *force change function* that arises through the leverage effect, the wedge effect, or the electromagnetic effect. Thus, various solutions are generated after a task is set, and these solutions lead to different products with different characteristics.

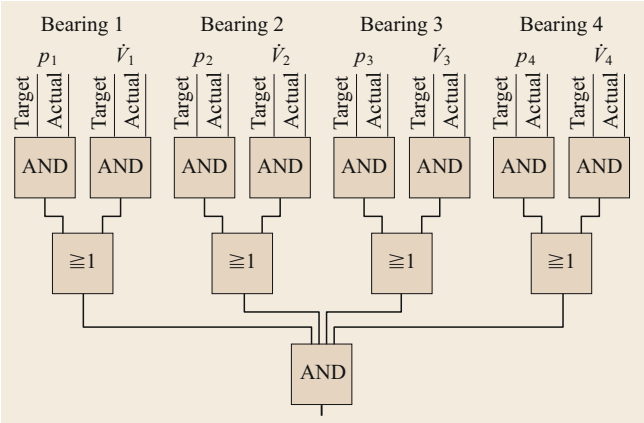

Fig. 16.9 Logical functions used to monitor a bearing lubrication system. A positive signal for every bearing (oil present) permits the utilization of the bearings. Monitor pressure p; monitor oil flow $\dot{V}$ (after [16.8])

Table 16.1 Generally valid functions derived from five characteristics (type, magnitude, number, place, and time) for the conversion of energy, materials, and signals (after [16.8])

Characteristic input (I)/output (O)	Generally valid function	Symbols	Explanations
Type	Chance		Type and outward form of I and O differ
Magnitude	Vary		I < O I > O
Number	Connect		Number of I > O Number of I < O
Place	Channel		Place of I ≠ O Place of I = O
Time	Store		Time of I ≠ O

Table 16.2 Fulfilling subfunctions using working principles built up from physical effects and geometric and material characteristics (after [16.3])

Subfunction	Physical effect (independent of solution)	Working principle for the subfunction (physical effect and geometric and material characteristics)
T_1 → Transfer torque → T_1	Friction $F_R = \mu F_N$	H7/r6
F_A → Amplify muscular force → F_B	Lever $aF_A = bF_B$	
I, ϑ → Send signal when $\vartheta \geq \vartheta_A$ → I	Expansion $\Delta l = \alpha l \Delta\vartheta$	Hg Bimetallic strip

Geometric and Material Characteristics. The place at which an effect or a combination of effects become(s) effective (active) is known as the *effective location*. Here, the fulfillment of the function is forced by applying the respective effect through an *effective geometry*, i.e., an arrangement of effective surfaces or active areas and selected working motions (in the case of moving systems). The effective material properties must be established before the effective relationship in the effective geometry can be identified. The combination of effects and geometric/material characteristics (effective geometry, working motion, and materials) comprise the solution principle. This relationship is referred to as the *active principle*. The combination of several active principles leads to an (effective structure) solution (also known as the *solution principle*). For example, in Table 16.3, the participating effective surfaces take the form of clutch discs (friction discs), and the rotational working motion of the lever produces contact pressure. Examples of the various effective surfaces used in clutches, e.g., a friction clutch, are shown in Table 16.3 [16.9].

Structural Relationships

The design-related concretization of the effective relationship leads to the *structure*. This materializes an effective structure through the utilization of individual components, units, and connections (Table 16.3) that are defined according to the needs of design, manufacturing, assembly, and transportation based on scientific principles, including the laws of material strength, materials engineering, thermodynamics, fluid mechanics, and manufacturing (among others). Good machine elements are also important fundamentals [16.10].

System Relationships

Technical products are components of superior systems that can include persons, other technical systems, and the surroundings (Table 16.3). At the same time, a *system* is determined by system elements and subsystems within a system boundary. These are linked to each other and to the surroundings by energy, materials, and/or signal variables. A system and/or product is initially characterized by its own *system structure*. Figure 16.10 shows such a system structure for the clutch in Table 16.3 used in combination with a rotationally elastic coupling. In a higher order system, this forms the purposeful effect (target function). Added to this are disturbing (effects) from the surroundings, side effects on the outside world and within the system, as well as the effects of humans and retroactive effects on humans (Fig. 16.11). All effects must be viewed in relation to one another (system context, Table 16.3).

General Objectives of Technical Products

Objectives for and restrictions on technical products are first received as requirements, requests, and conditions in the requirement list (i.e., when setting the task). This

Table 16.3 Interrelationships in technical systems (after [16.3])

Interrelationships	Elements	Structures	Examples
Functional interrelationship	Functions	Function structure	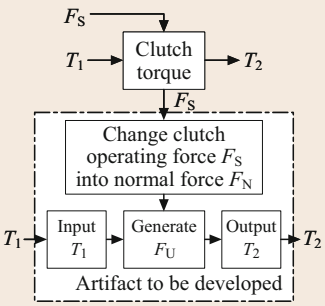
Working interrelationship	Physical effects and geometric and material characteristics ↓ Working principles	Working structure	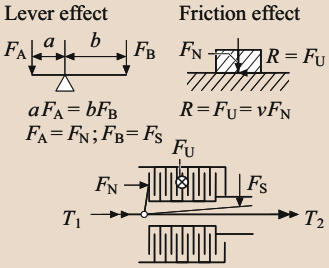
Constructional interrelationship	Components Joints Assemblies	Construction structure	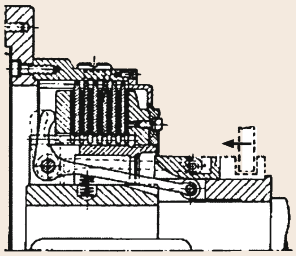
System interrelationship	Artifacts Human beings Environment	System structure	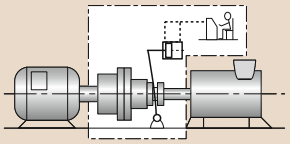

is a fundamental step in specific product development. However, beyond this, there are general objectives that have different weights in different instances but are still generally valid. Such goals serve as a guideline for setting up requirement lists and for choosing solutions during the various concretization stages of the construction process.

Table 16.4 contains a list of the general objectives for a tangible product and indicates how they are correlated with the life stages of the product (Fig. 16.1).

Applications

The general relationships that determine the construction of a technical product are important foundations for several applications.

In product development, they enable a gradual approach in which principle solutions are initially sought for the required set of functions. These solutions are then concretized in design and material specifications. At each practical level, a variety of solutions can be compared as a basis for solution optimization across the different characteristics of the respective relationship.

Another important area of application is the analysis of existing technical products with the aim of improving, developing, or adapting specific conditions [16.11]. Such system analyses require procedural steps and characteristics derived from the general relationships. An important example is value analysis, which attempts to minimize the functional cost of a technical product [16.12]. Distinctive product features, also called

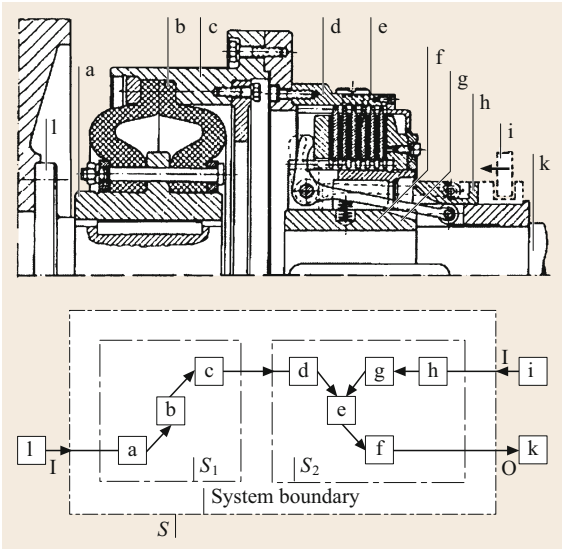

Fig. 16.10 System coupling: *a–h* system elements, *i–l* connecting elements, *S* overall system, S_1 flexible coupling subsystem, S_2 clutch subsystem, *I* inputs, *O* outputs (after [16.3])

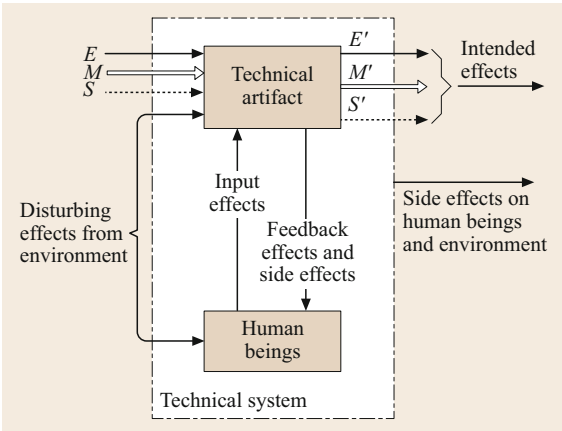

Fig. 16.11 Interrelationships in a technical system that includes human beings (after [16.3])

component parameters [16.13], are used to populate construction catalogs and databases providing useful assistance when searching for particular solutions in data and storage media [16.14]. General relationships and general objectives are also utilized in the derivation of *component parameters* [16.15].

16.1.3 Construction Methods

General Solution Methods

Regardless of the specific degree of concretization performed while searching for a solution, several general techniques are applied as a working methodology [16.16–18]. The requirements for such a methodical approach are:

Table 16.4 General objectives for technical products (after [16.3])

Fulfill *function*
Guarantee *safety*
Take into account *ergonomics*
Simplify *manufacturing*
Make *assembly* easier, ensure *quality*
Enable *transportation*
Improve *use*
Support *maintenance*
Aim to *recycle*, minimize *costs*

- Defining goals
- Identifying conditions
- Resolving prejudices
- Searching for variations
- Passing judgments
- Making decisions.

The General Solution Process. The task solution process consists of an analysis and a subsequent synthesis. This involves alternating working and decision steps. At the same time, progress is usually made from quantitative to qualitative steps or from abstract to concrete steps. Breaking down the process into working and decision steps ensures that the required uniformity of objectives, planning, implementation, and control is maintained.

Figure 16.12 shows the basic pattern of the general solution process [16.19, 20]. Task setting initially prompts a confrontation with an *unknown*. This unknown can be resolved to some degree by obtaining additional information. Subsequently defining the key

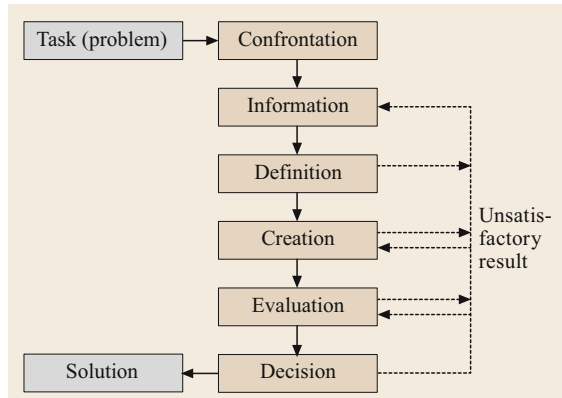

Fig. 16.12 The general problem solving process (after [16.7])

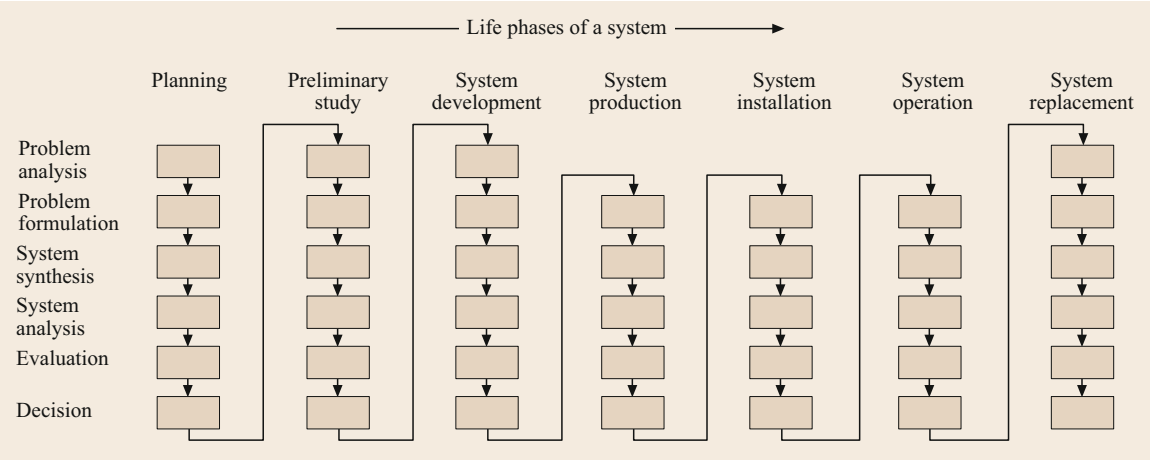

Fig. 16.13 Model of the systems approach (after [16.7])

problems to be solved specifies the task without predetermining the solution, thus leaving the door open to various possible solutions. The creative phase that follows the definition phase involves identifying solutions. When there are several appropriate ways of solving the task, they must all be evaluated so that the best solution can be discerned. When a working step delivers unsatisfactory results, it (or multiple working steps) must be repeated. Repeating the working process should lead to even better results, as the process will be guided by more or better information when it is repeated. In other words, this iterative process is a learning process.

Systematic Approach. System technology—an interdisciplinary science—has well-developed methods for analyzing, planning, selecting, and optimizing the design of complex systems [16.21]. Upon defining a system, a process model is introduced that is subsequently used for the different life stages of the system (Fig. 16.1). Figure 16.13 shows that the working steps involved in this model are practically identical to those in Fig. 16.12, and that the time continuum for the system runs from the abstract to the concrete.

Problem and System Structure. Complex new tasks are usually easier to solve if the overall problem is initially divided into subproblems or individual problems. This allows subsolutions or individual solutions to be found [16.7].

The methodological basis for this approach is the structuring of systems into subsystems and system elements to facilitate the identification of relationships and effects within the system and its surroundings. The extent to which a system is broken down is determined by utilitarian considerations and depends on the novelty of the problem and the knowledge of the engineer/scientist.

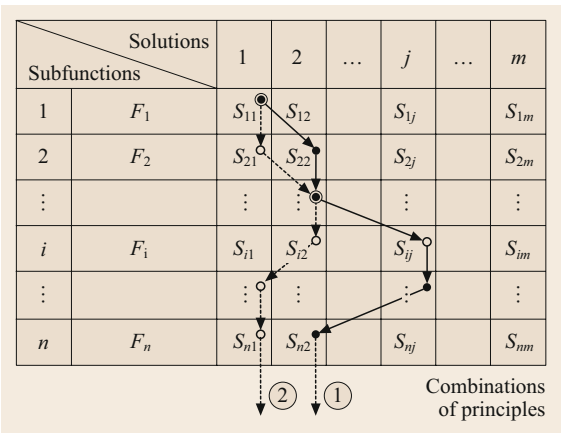

Fig. 16.14 Combining solution principles into combinations of principles. Combination 1: $S_{11} + S_{22} + \ldots + S_{n2}$; combination 2: $S_{11} + S_{21} + \ldots + S_{n1}$

Structuring a system in this manner also encourages the adoption of known and proven subsolutions, the derivation of alternative solutions, the systematization of solution catalogs and databases, the identification of integrated relationships, and the introduction of rational working divisions.

While splitting problems into individual problems makes solutions easier to find, the subsequent combination process (i.e., the process of linking the subsolutions to the overall solution) leads to problems with subsolution compatibility. Combination schemes such as the morphological box (Fig. 16.14) devised by *Zwicky* [16.22] have proven to be important tools, as they allow subsolutions to be assigned to subfunctions in a two-dimensionally ordered scheme.

There are also tasks for which it is not helpful to break down the problem at the beginning of the

solution process; these require an initial integrated approach. Examples include products for which *industrial design* is especially important, e.g., cars and household appliances. Here, the overall appearance, including ergonomic features, is prioritized over construction details [16.23]. However, industrial design and methodological problem solving are not incompatible; in the products mentioned above, tasks are broken down methodologically and solutions are identified only after adopting a draft for the overall appearance of the product.

General Aids. *Literature research* focusing on books, journals, patents, and company documents is performed to obtain a summary of the state of the art in the market of interest and the company's competitors. It can be a source of new ideas for designers searching for optimal solutions.

Nature can provide the creative spark for designers [16.24–27]. In an *analysis of natural systems* (bionics and biomechanics), new ideas for technical solutions are drawn from natural forms, structures, organisms, and processes.

An *analysis of known technical systems* makes it possible to transfer trusted solutions (from the company performing the analysis or from its competitors) to new tasks and thus to identify fruitful further developments or alternative solutions [16.3].

A problem can also be solved or a system identified by referring to an analogous system or a previously solved problem or identified system. This can aid in the investigation or assessment of a system's characteristics and facilitate simulation or modeling [16.3].

When attempting to identify new solution characteristics and carry out further development step by step, *measurements* of working systems and *model experiments* that involve similar mechanics are among the main sources of information for designers. *Heuristic operations* increase creativity in the search for solutions, primarily in conventional approaches carried out by people. These operations are also known as creativity technology and are considered a tool for methodological solving and a pathway to thinking and working in an orderly and effective manner. They also repeatedly appear alongside special solution and approach methods [16.18].

Conception Methods

The following methods can be used to identify principle solutions when conceiving a fundamental solution principle or a solution concept for a set task (function) (Sect. 16.1.3). Each method can also be used for more concrete design tasks.

Intuitive Methods. Intuition-based methods exploit group dynamics by stimulating intuition through mutual associations. In this context, intuition is considered to be an imagination-based reflexive reaction that produces ideas for solutions from the conscious or unconscious—a process that is termed *primary creativity* [16.28].

In the *dialog method*, two equal partners discuss the solution to a problem, and a first solution approach is adopted.

In *brainstorming*, an interdisciplinary group meeting without aids is implemented. Ideas are expressed without criticism and evaluation in the meeting (a *quantity before quality* approach is adopted). *Synectics* is similar to brainstorming, but additional analogies from nontechnical areas or semitechnical areas are used to generate ideas during the meeting.

Method 635 is a brainwriting method in which six participants each express three problem-solving ideas in written form. This is repeated for five rounds. The proposals of the previous round are known to the participants and the level of information is constantly increased with each new round.

The *gallery method* combines individual work with group work such that each individual in a group meeting proposes solution sketches that are hung up in a kind of gallery.

Through the discussion of these suggestions with appropriate commentary, new solutions or improvements are conceived to be worked on individually by the group members.

The intuition-based methods described above are detailed in [16.3].

Discursive Methods. Discussion based methods consciously seek solutions through gradual, influenceable, and documentable procedures (*secondary creativity* [16.28]).

In the *systematic study of physical events* derived from a known physical relationship with several variables (i.e., a physical effect) different solutions are modelled to analyze the relationship between dependent and independent variables with all other variables held constant.

Another approach is to break down physical events into their component effects and ascertain their root causes [16.5].

A *systematic search with the help of order schemata* assumes that an order scheme (for example, a two-dimensional table) stimulates the identification of novel solution paths without identifying key solution characteristics along with their corresponding relationships. Possible starting points are one or more known solu-

Table 16.5 Working principles that implement the *store energy* function using different forms of energy (after [16.3])

Working principle	Type of energy Mechanical	Hydraulic	Electrical	Thermal
1	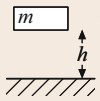 Potential energy	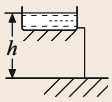 Liquid reservoir (potential energy)	Battery 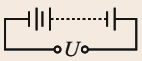	Mass 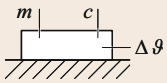
2	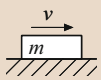 Moving mass (translation)	Flowing liquid	Capacitor (electr. field) 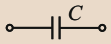	Heated liquid
3	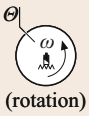 Flywheel (rotation)			Superheated steam
4	 Wheel on inclined plane (rot. + transl. + pot.)			
5	Metal spring 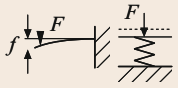	Other springs (compression of fluid + gas) 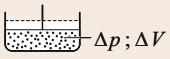		
6		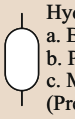 Hydraulic reservoir a. Bladder b. Piston c. Membrane (Pressure energy)		

tions that are characterized by organizational aspects or differentiating features. Such organizational aspects and/or differentiating features are, for example, types of energy as well as effective structural features (effective geometry, effective movement, and substance). One example of an order scheme of this nature is Zwicky's morphological box (Fig. 16.14).

The designer quickly arrives at solution proposals by adopting, developing, or adapting known and trusted solutions (with various levels of concretization and complexity) found in *construction catalogs* [16.2]. It is important that the selection schema used by the catalog allow appropriate selection of a solution for the required function or task (Table 16.5). Catalogs and databases also play an important role when searching for design options during the draft phase of product development.

Selection and Evaluation Methods

During each design phase or concretization stage of the development and construction process, selection methods are employed to assess and select solution variants for which further realization is worthwhile. Either rough selection or fine selection of appropriate solutions is performed, depending on how much is known about the characteristics of the solutions to be assessed. Rough selection is characterized by the tasks of rejecting (−) and preferring (+). Totally unsuitable solutions are first rejected with the aid of a selection list (Fig. 16.15). Rough selection processes have proven particularly useful for listing and/or designation in morphological boxes employed during the drafting of effective structures.

Solutions that are not eliminated during the rough selection process are preferred solutions. The selection criteria are tailored to the goals of product development and the company. More accurate selection of solution variations is performed using evaluation procedures, in particular VDI guideline 2225 [16.29] and utility analysis [16.30]. Table 16.6 compares these two procedures.

Design Principles

After evaluating the effective structures and/or principle solutions, a structure/solution is usually released for

Selection chart for a skin-mixer — Page: 1

Enter solution variant (Sv):

Solution variants (Sv) evaluated by by selection criteria

(+) Yes
(–) No
(?) Lack of information
(!) Check requirement lists

Decision

Mark solution variants (Sv)

(+) Pursue solution
(–) Eliminate solution
(?) Collect information (reevaluate solution)
(!) Check requirements list for changes

Compatibility assured
Fulfills demands of requirement list
Realizable in principle
Within permissible costs
Incorporates direct safety measures
Preferred by designer's company
Adequate information

Sv		A	B	C	D	E	F	G	Remarks (indications, reasons)	Decision
A1	1	+	+	+	+	+	+	+	Customary mixer function as an example	+
A2	2	+	–	+	–	–	–	–	Cleaning the inside wall with a knife is difficult	–
A3	3	+	–	+	–	–	–	–	High injury risk by a knife in the lid	–
A4	4	?	?	+	+	?	?	?	Insufficient knowledge	–
A5	5	?	–	+	–	+	?	?	To much water in the shaker	?
B1	6	+	+	+	+	+	+	+	240 V/50 Hz and 24 V DC power source available	+
B2	7	–	–	+	–	?	–	+	No source of hydraulics available in the theater	–
B3	8	+	+	+	+	+	+	+	Shop air pressure of 6–8 bar available	+

Fig. 16.15 Systematic selection chart (1, 2, and 3, etc. are solution variants)

Table 16.6 Points awarded in utility analysis and VDI guideline 2225 (after [16.8])

Utility analysis		VDI guideline 2225	
Pts.	**Meaning**	**Pts.**	**Meaning**
0	Absolutely useless solution	0	Unsatisfactory
1	Very inadequate solution		
2	Weak solution	1	Just tolerable
3	Tolerable solution		
4	Adequate solution	2	Adequate
5	Satisfactory solution		
6	Good solution with few drawbacks	3	Good
7	Good solution		
8	Very good solution	4	Very good (ideal)
9	Solution exceeding the requirement		
10	Ideal solution		

drafting. The design stage in the drafting of a product requires the use of mechanics and a knowledge of strength science, manufacturing technology, materials technology, and other fields. The fine design (the detailed design obtained by applying guidelines/regulations and norms, performing appropriate calculations, and considering the impact of auxiliary functions) is gradually generated from the rough design (which is spatially and significantly correct but lacks detail; it is a preliminary draft).

The process of generating the fine design is structured into individual working steps. The starting point is the principle solution. After clarifying the spatial conditions, the main functional elements and then the other main functional bodies are designed. If they are sufficiently specified, solutions for the auxiliary functional elements are sought [16.3]. These are often bought-in parts. The aim of this working step is to define the design of the principle solution, i.e., all of its geometric and material characteristics and condition.

The following methods and rules are recommendations, strategies, and hints that can facilitate successful product structure design [16.3].

Basic Design Rules. The basic rules are instructions that are always applicable; in other words, observing these rules promotes the generation of a successful solution, whereas ignoring them leads to major drawbacks. They are derived from general objectives of the construction process.

The basic rules can be summarized as follows:

- Easy
- Clear
- Safe.

Adhering to these principles leads to the fulfillment of the technical function of the product in a clear, cost-effective, and safe (to humans and the environment) manner.

Observing the basic rule *clear* helps the designer to reliably predict the effect and behavior of a structure. Figure 16.16 shows an example of a shaft–hub cross-compression connection. The inclusion of the parallel key does not make the connection any more secure; it causes sectional weakening. The notches (location B) complicate the stress conditions and handling (location C). As a result, the whole connection is insecure.

An additional basic rule *simple* could also be assumed to ensure the generation of a cost-effective and feasible solution. However, the functional performance of the solution takes precedence. Functional fulfillment determines the compliance threshold for the *easy* rule.

It is wise to adhere to the following basic guideline: *make the design simple, and minimize the number of parts*. Following this guideline often means finding the best compromise between the following two aspects:

- Functional fulfillment
- Economic efficiency.

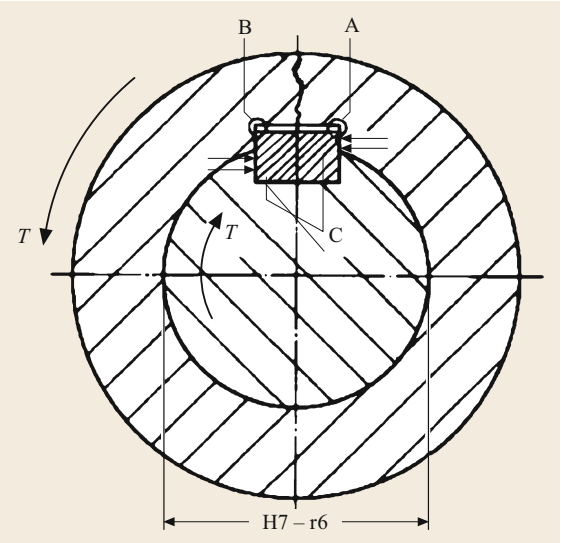

Fig. 16.16 Combined shaft–hub connection achieved using shrink fitting and a key: an example of not applying the principle of clarity

Functional fulfillment implies that the design includes the minimum number of parts that have the shapes required to fulfill the required function.

Economic efficiency requires that the parts comprising the design allow the product to be manufactured inexpensively and quickly (i.e., on schedule).

The demand for *safety* forces designers to continually consider part durability and reliability, the extent to which the part is free from accidents, as well as environmental protection. The following criteria are addressed by the designer at various levels [16.3]:

- Immediate safety engineering (*safe existence*, *limited failure*, *back-up arrangements*)
- Indirect safety engineering (protection systems, protective equipment)
- Indicative safety engineering (identifying the danger).

Figure 16.17 shows the key safety areas.

The designer always strives for immediate safety engineering. Three principles are applied to achieve this:

- *The principle of safe existence* (safe-life behavior) implies that that all components and their relationships within the product will survive the intended stress and operational life without failing or generating a fault.
- *The principle of limited failure* (fail-safe behavior) implies that a functional fault or damage can occur during the operational life of the product without causing serious damage to the product.

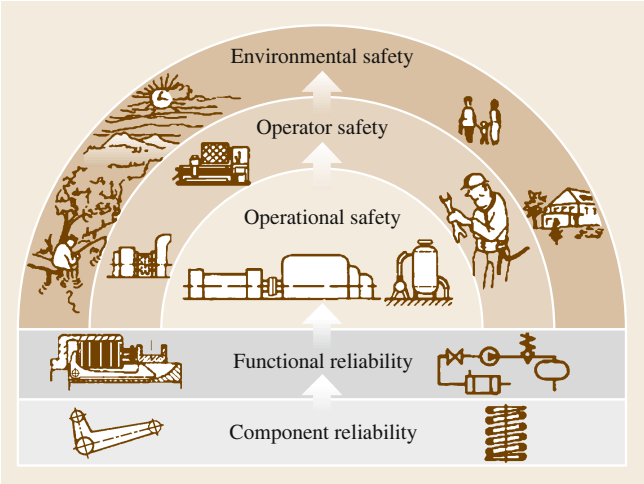

Fig. 16.17 Relationship between component and functional reliability on the one hand and operational, operator, and environmental safety on the other (after [16.8])

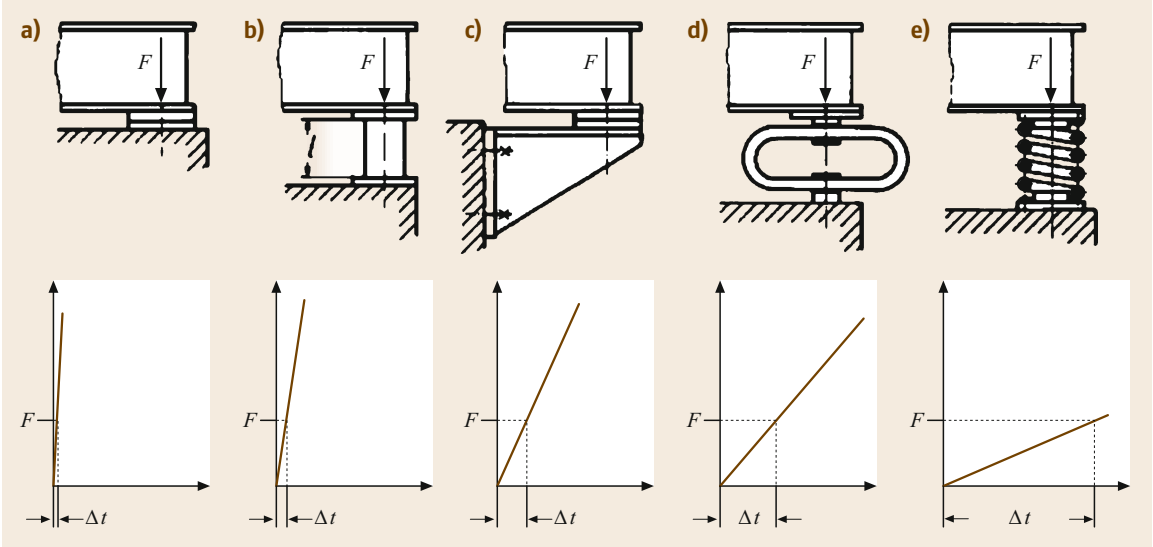

Fig. 16.18a–e Options for supporting a machine frame on a concrete foundation (after [16.8]). **(a)** A very rigid support due to a short force transmission path and low stress on the base plates. **(b)** A rigid support with tubes or box sections under compression, but with a longer force transmission path. **(c)** A less rigid support with pronounced bending deformation (a stiffer construction would require more material). **(d)** A more flexible support under bending stresses. **(e)** A very flexible support that uses a spring to transmit the load in torsion; this approach can be used to alter the resonance characteristics

- *The principle of redundancy* implies that the safety and security of the product is enhanced by including reserve elements that can fulfill some or all of the product's functions in case of failure. In the case of passive redundancy, the reserve element supports required functionality even when all components are functioning normally. With passive redundancy, the reserve element is only activated in the case of a failure. When the original and reserve elements operate according to differing modi operandii it is known and is the principle redundancy. Back-up elements can be employed in parallel, serial, quartet, cross-quartet, two-out-of-three and comparative redundancy.

If risk cannot be excluded by applying the three principles listed above, complementary indirect and indicative safety equipment is incorporated.

Design Guidelines. The principles used to develop a construction based on the effective structure as well as to define the nature and (especially) the setup of the functional body are:

- Force transmission
- Task division
- Self-help
- Stability and bistability
- Low-fault design.

Force transmission principles ensure uniform shape stability, cost-effective and load-favourable channeling of force/power-flow, adjustment of component shaping and equilibrium. It is also worth noting that the following force subfunctions are implemented in many machine-engineered products (including precision engineering):

- Pickup (induction)
- Channeling (onward channeling)
- Release (channel off).

Momentum is also considered in the context. When tackling power-channeling problems, it is often very helpful to use the concept of force flow. In this respect, the following guidelines should always be adhered to:

- The flow of force must always be closed.
- Sharp deflections in the flow of power should be avoided.
- Strong changes in the orientation of the power flow should be avoided.

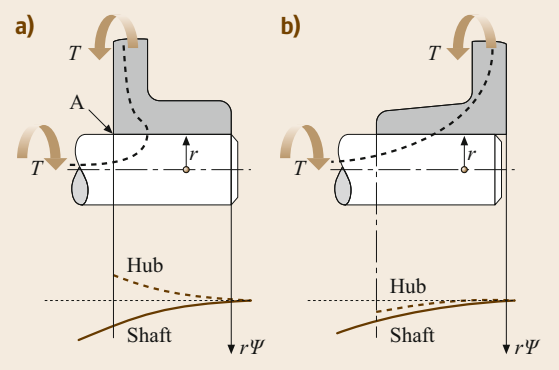

Fig. 16.19 **(a)** Shaft–hub connection with strong force flowline deflection. Torsional deformations of the shaft and the hub occur in opposite directions (Ψ = twist angle). **(b)** Shaft–hub connection with gradual force flowline deflection. Torsional deformations of the shaft and the hub occur in the same direction (after [16.3])

As well as utilizing this power flow concept, the following principles should be observed:

- The *principle of equal shape stability* implies that the same stable load is applied throughout the entire component. Economic aspects (costs) can hinder the application of this principle.
- The *principle of the direct and brief transmission of force* refers to the selection of the shortest and most direct path of channeled force (momentum), preferably using torsion/pressure stress to keep the deformation small and material expenses low by achieving a uniform stress distribution. Figure 16.18 shows these relationships for various brace supports for a machine frame, based on their compression stress–strain characteristics. Whether a more rigid or a more elastic solution is appropriate depends on the design requirements.
- In joint connections, the *principle of adjusted deformations* is applied when designing the components. This implies that, when the component is sujected to a load, extensive parallel and uniform deformation occurs. As an example, Fig. 16.19 shows torque-stressed shaft–hub connections (shaft-to-collar connections) in favorable and less favorable designs. Figure 16.20 shows options for adjusting the deformation in a crane drive mechanism. Such adjustments are necessary to stop the drives from running off the track due to the different torsion stiffnesses of the shaft sections I_1 (large) and I_2 (less than that of I_1), as shown in Fig. 16.20a. When torque is applied, the left wheel initially moves while the right wheel stands still, and the drive remains obliquely positioned. This deficiency can be overcome through a symmetrical arrangement (Fig. 16.20b) or by adjusting the torsion stiffness of each shaft section (Fig. 16.20c).
- The *principle of balancing force* aims, through the use of compensatory elements or a symmetrical arrangement, to limit the auxiliary variables that accompany the main function variables to an area that is as small as possible, so that construction costs and energy losses can be minimized (Fig. 16.21).

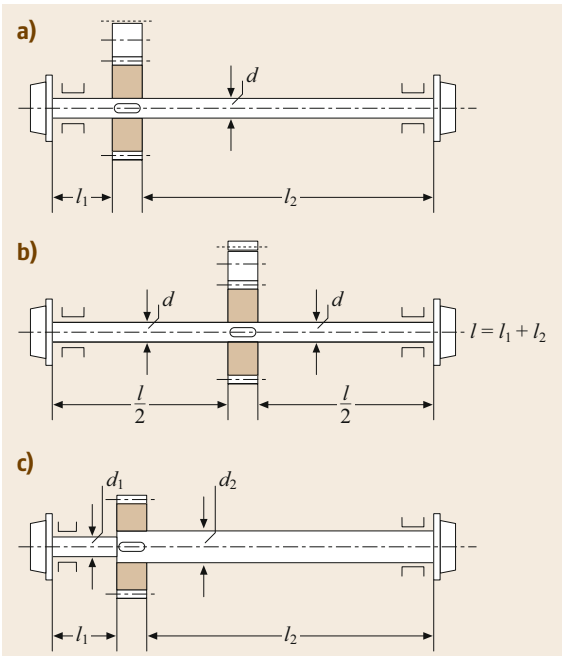

Fig. 16.20a–c Application of the principle of matched (equal here) deformations in crane drives: **(a)** unequal torsional deformation of lengths l_1 and l_2; **(b)** a symmetrical layout ensures equal torsional deformation; **(c)** an asymmetrical layout with equal torsional deformations achieved by appropriate adjustment of the torsional stiffnesses of both sections (after [16.3])

The *principle of sharing tasks* enables the clear and safe behavior of functional agents as well as improved efficiency and increased capacity by assigning components or assemblies, materials, or other construction elements to individual subfunctions of a solution concept. This *differential design* approach contrasts with the *integral design* approach, which is usually less expensive. The usefulness of the application should be tested on a case-by-case basis. By way of example, Fig. 16.22 shows a fixed bearing arrangement in which radial forces are transferred by a roller bearing and axial forces by a deep-groove ball bearing. At high loads, this arrangement is superior to the usual version in which a deep-groove ball bearing transfers both the radial and axial forces.

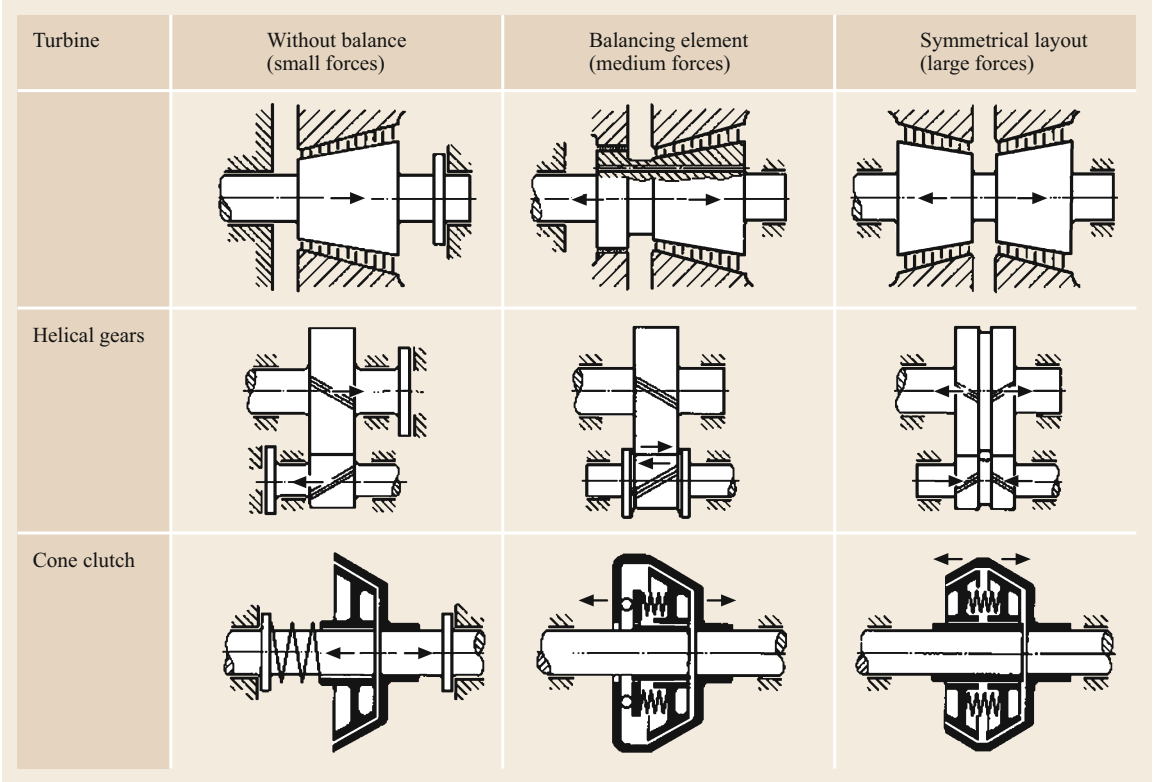

Fig. 16.21 Fundamental solutions for balancing associated forces, illustrated via a turbine, helical gears, and cone clutch (after [16.3])

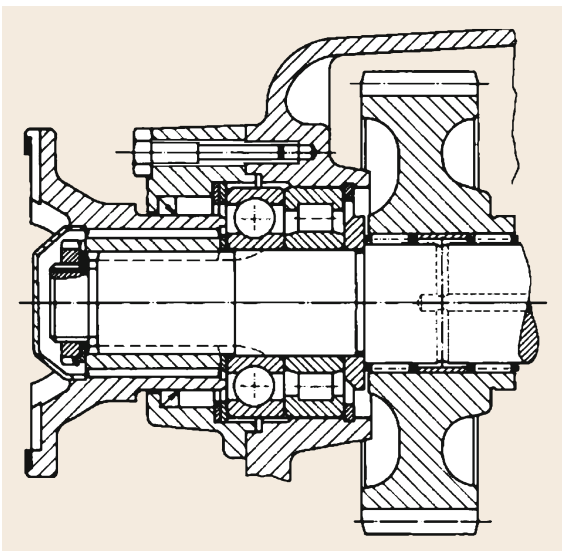

Fig. 16.22 A locating bearing with separate transmission paths for radial and axial forces (after [16.3])

The principle of sharing tasks is also applied to distribute the load onto several identical mechanical transmission elements when one of the mechanical transmission elements exceeds its load limit. This technique is used in, for example, split-torque multichannel drives and belt gears with several parallel V belts.

The *principle of self-help*, which is achieved through the appropriate selection and arrangement of components, promotes effective mutual support, thus permitting a function to be fulfilled in the best, safest, and most economical manner [16.31]. At the same time, a self-strengthening and self-compensating effect can be exploited under a normal load, and a self-protecting effect in an overload situation. Figure 16.23 illustrates a self-strengthening solution for pressure vessel closure, in which the sealing force of the lid increases in proportion to the internal pressure of the container.

An example of a self-compensating solution is an incorrectly clamped blade of a jet engine rotor. Slanting the blades leads to the generation of additional bending stress due to centrifugal force; this counteracts

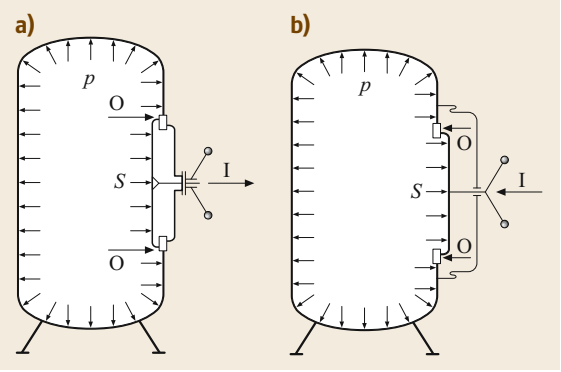

Fig. 16.23 **(a)** Self-helping and **(b)** self-damaging layout of an inspection cover; *I* is the initial effect, *O* is the overall effect, and *p* is the internal pressure (after [16.3])

and (partly) compensates for the bending stress from the tangential force, making the design more robust at higher tangential forces (i.e., blade forces) (Fig. 16.24).

A *self-protecting* solution protects an element from being overstressed by changing the type of stress present and restricting functionality. As an example, Fig. 16.25 shows how springs can enable a self-protecting solution.

The *principle of stability* implies that a self-neutralizing compensatory effect (or, at the very least, an alleviating effect) is induced in the event of a fault. Figure 16.26 shows an example of the application of this principle: a compensation piston seal either starts to grind (unstable solution) or lift itself away from the ineffective area (stable solution) when heated (i.e., during a fault). Figure 16.26a shows that the frictional heat caused by rubbing (the fault) primarily flows into the inner part, causing additional warming of that part. The resulting expansion reinforces the fault and leads to unstable behavior. In Fig. 16.26b, we can see that the frictional heat due to rubbing (the fault) is primarily transferred to the outer part, causing its temperature to increase. The resulting expansion reduces the fault, leading to stable behavior.

In the *principle of bistability*, triggering a fault deliberately causes effects that reinforce the fault. This allows the system to jump directly from one state to another very different state without having to pass through unwanted intermediate states. As such the principle also

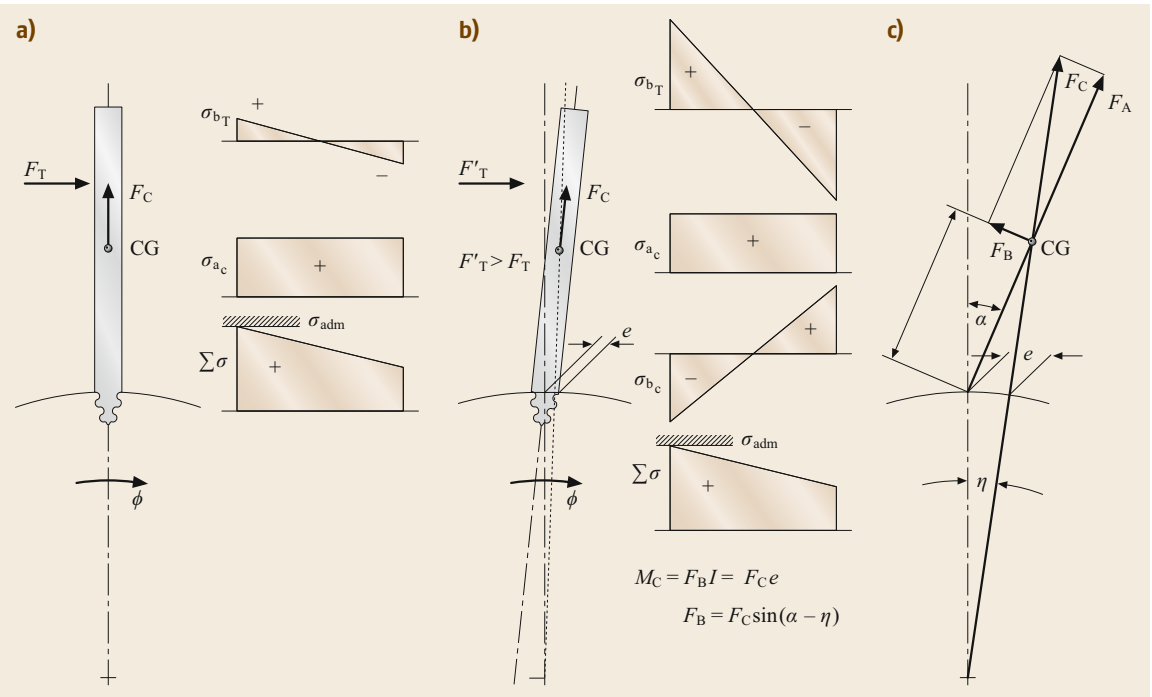

Fig. 16.24a–c Self-compensating solution for turbine blades. In contrast to the conventional solution shown in **(a)**, the use of slanted blades, as depicted in **(b)**, leads to the production of additional bending stresses by the centrifugal inertial force σ_{b_C} that oppose (i.e., help to compensate for) the bending stresses caused by the tangential force σ_{b_T}. **(c)** Diagram of forces. Here, CG is the center of gravity, F_T is the tangential force, F_C is the centrifugal inertial force, σ_{b_T} is the bending stress due to F_T, σ_{a_c} is the axial stress due to F_C, σ_{b_c} is the bending stress due to F_C, F_A is the axial component to F_C, and F_B is the bending component to F_C

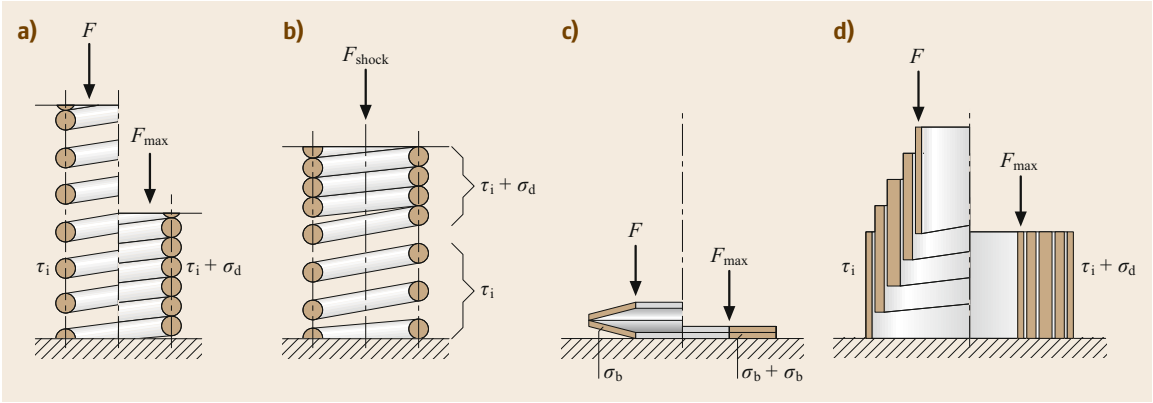

Fig. 16.25a–d Self-protecting solution achieved via springs. **(a–d)** show how the force transmission path is changed, causing normal function to be suspended or limited in the presence of excess loading (after [16.3])

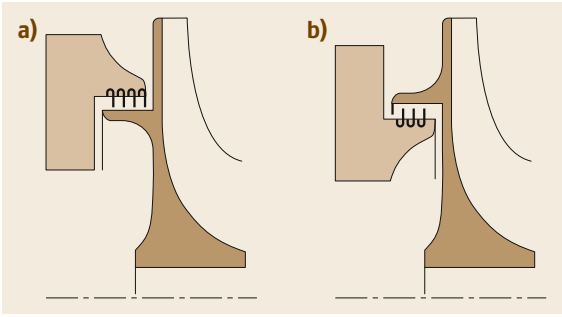

Fig. 16.26a,b Different seal designs for a turbocharger (after [16.3]): **(a)** heat-labile arrangement, **(b)** heat-resistant arrangement

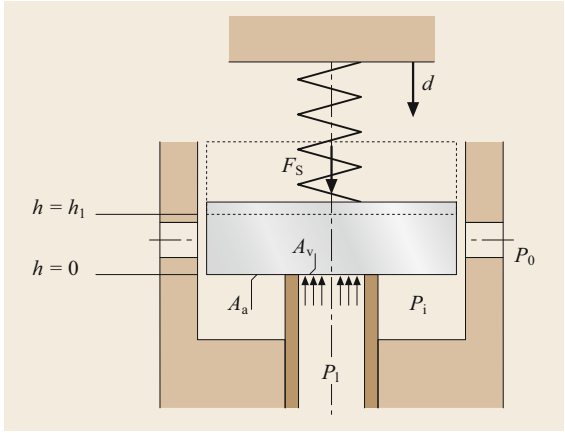

Fig. 16.27 Solution principle for a valve with an unstable opening mechanism (d is the precompression of the spring, s is the stiffness of the spring, F_S is the spring force, h is the height that the valve head is lifted, p is the pressure on the valve, p_l is the limiting pressure that is just sufficient to open the valve, p_i is the intermediate pressure upon opening the valve, p' is the pressure after opening the valve, p_0 is the atmospheric pressure, A_v is the surface area of the valve opening, A_a is the additional surface area). Valve closed: $F_S = sd > pA_v$, $h = 0$; valve just open: $F_S = sdp_l A_v$, $h = 0$; valve opening fully: $F_S = s(d + h) < pA_v + p_i A_a$, $h = \pm h_1$; valve fully open: $F_S = s(d+h_1) = p'(A_v+A_a)$, $h = h_1$ (new equilibrium position) (after [16.3])

improves efficacy. As an example, Fig. 16.27 shows the principle of a safety valve, which needs to jump quickly from a closed borderline state to an open borderline state (due to the sudden increase in the pressure area, A_v to A_z, caused by lifting the valve plate).

More Recommended Design Guidelines. The following design guidelines are recommendations that should help designers to satisfy general and specific task objectives. A detailed description of these design guidelines is found in [16.3].

Design in accordance with stress implies that the initial aim should be to ascertain all longitudinal and transverse forces that act on the component, as well as bending and torque moments. This allows the normal stresses—the tensile, compression, and bending stresses, as well as tangential stresses such as shear and torsional stresses— to be calculated. This stress analysis provides the basis for determining the elastic and/or plastic deformation (strain analysis). In order to identify the level of safety from failure or to make lifetime predictions, these loads are contrasted with the applicable material threshold values for the load in the current case, with notching effects as well as surface and variable influences examined via stability hypotheses.

At the same time, the principle of *equal stability* should be strived for to ensure that all design areas are used to approximately the same extent.

Design in accordance with expansion means that thermal and tension-conditioned component expansion (especially relative expansion between the components)

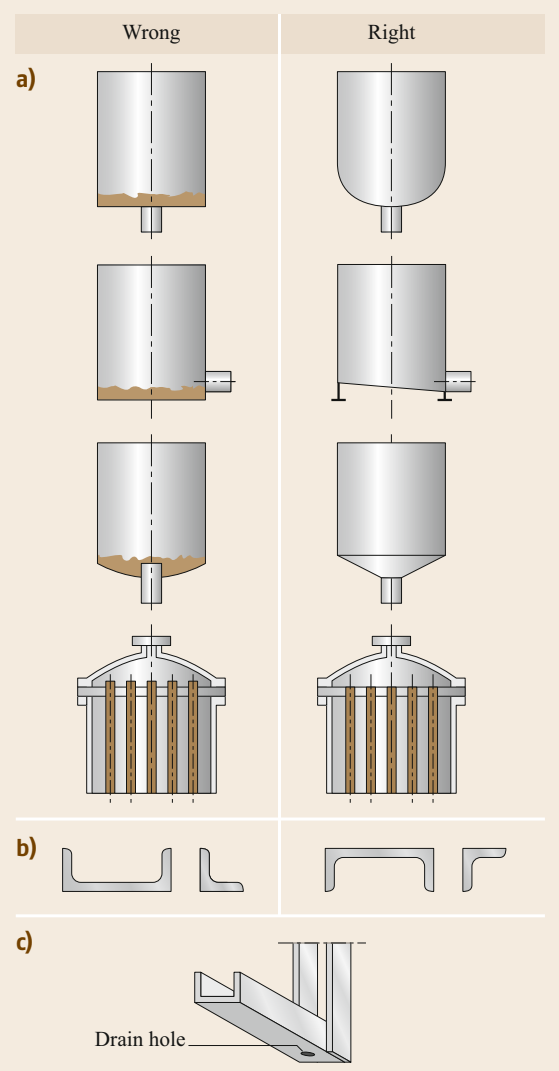

Fig. 16.28a–c Drainage of components that are susceptible to corrosion: **(a)** designs that encourage and impede corrosion; **(b)** incorrect and correct arrangements of steel sections; **(c)** a bracket made from a channel section with a drainage hole (after [16.3])

is compensated for by adopting channels and selecting materials such that there are no residual stresses, clamping, or other compelling conditions that could reduce the bearing strength of the structure. Channels should be arranged in the direction of expansion or along the line of symmetry of the thermally or mechanically conditioned distortion state of the component.

When there are transient temperature changes, the thermal time constants of adjacent components must be adjusted to avoid relative movements between these components [16.3].

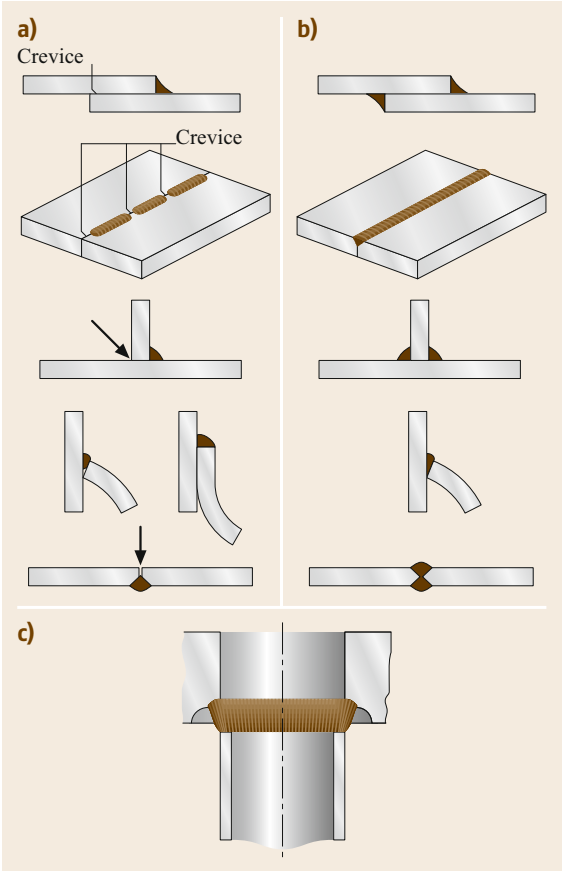

Fig. 16.29a–c Examples of welded joints that are susceptible and resistant to crevice corrosion: **(a)** design that encourages corrosion; **(b)** design that inhibits corrosion; **(c)** crevice-free welding of pipes, which improves resistance to stress corrosion cracking (after [16.3])

Design in accordance with creep requires that the time-related plastic deformation of individual materials (especially at higher temperatures) or the deformation of synthetic materials is accounted for through the appropriate selection of materials and design. In other words, the aim is to avoid any reduction in tension (relaxation) in stressed systems (screw connections, compressed connections) through the use of elastic flexibility reserves. Tertiary creep through extremes of load and temperature is avoided by the appropriate selection of materials and the application of stress–time testing [16.3].

Design in accordance with corrosion includes avoiding the causes of and/or preconditions for the various types of corrosion (primary measures) or selecting materials, coatings, or other protective/maintenance measures (secondary measures) that will reduce corrosion to a permissible level. Figure 16.28 illustrates design measures used to eliminate moisture collection

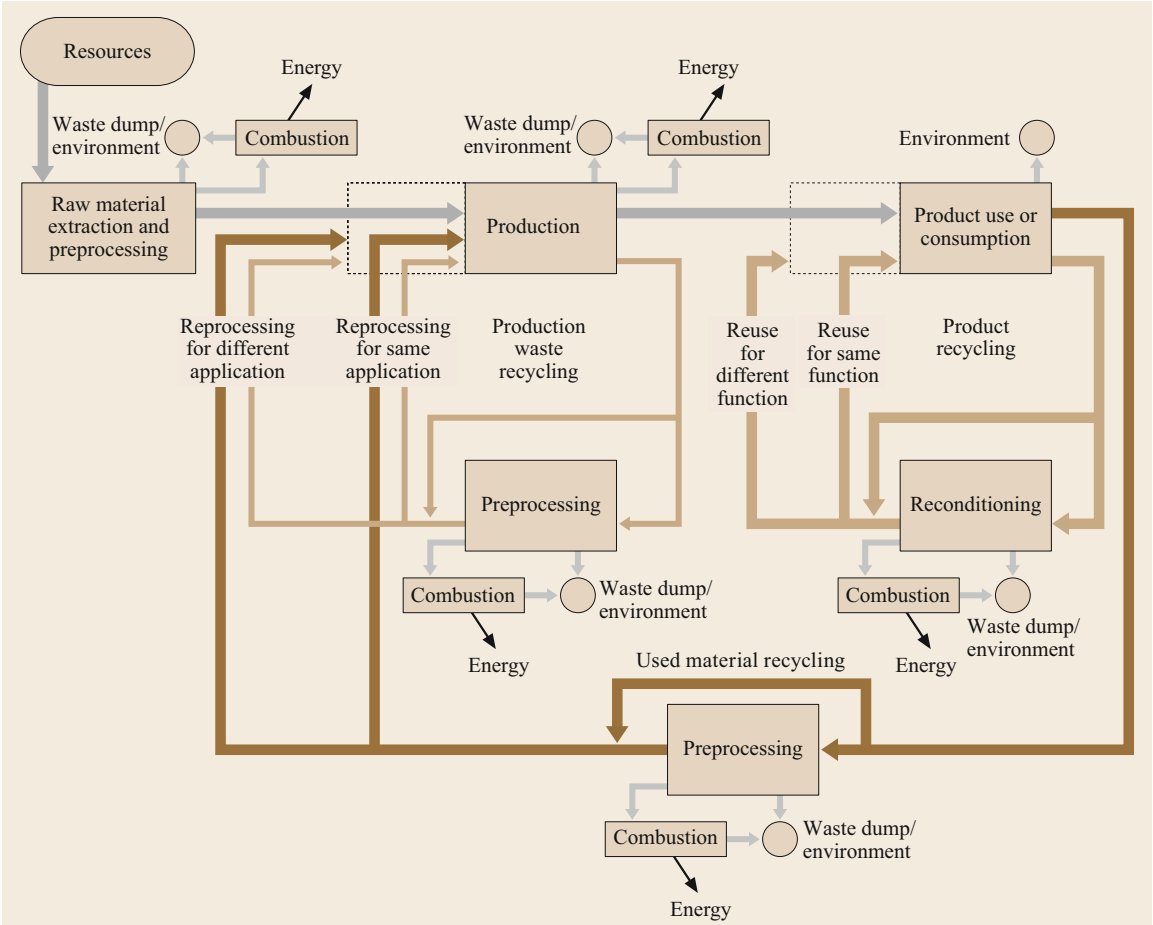

Fig. 16.30 Recycling options (after [16.3])

points, and Fig. 16.29 shows how to suppress crevice corrosion.

Design in accordance with wear and tear means ensuring that moving parts in the product are free to move as required for product operation while incurring as little wear and tear from their movements as possible. This is achieved through tribological measures based on the selection of optimal materials, surfaces, or lubricants. In this respect, the application of composite structures with high-strength boundary layers and design-giving basic materials often yields an economic solution [16.32].

Design in accordance with ergonomic considerations implies that the design takes the key characteristics, abilities, and needs of the people who will use the product into account. Biomechanical, physiological, and psychological aspects must therefore be considered. It is possible to differentiate between the active contribution of a person using the product (e.g., the operator) and passive relationships (i.e., retroactive and side effects of the product) [16.33].

Design in accordance with shape (industrial design [16.23, 34]) ensures that utensils not only serve a purpose but also have aesthetic appeal. This is especially true of the look (shape, color, and labeling) of the product.

Design in accordance with manufacturing considerations means that the significant influence of construction-related decisions on production costs, production times, and manufacturing qualities are accounted for when optimizing components [16.3]. In order to design parts (pieces) that are well suited to manufacturing processes, the designer must be aware of the nature of the relevant manufacturing procedures and the specific circumstances of each manufacturing plant (internal or external).

Design in accordance with assembly considerations involves designing a structure (especially in respect to its joints and joining parts) that allows assembly operations to be minimized, simplified, unified, and automated [16.3]. Aspects of the testing process and production monitoring are considered when attempting

to ensure that the parts can be produced and the product assembled in a relatively straightforward manner.

Design in accordance with norms implies that the design complies with norms that are observed for safety, usage, and economic reasons and with other technical rules (e.g., recognized engineering rules) that are in the best interests of manufacturers and users.

Design in accordance with transportation and packing considerations means that the design accounts for the use of standardized packaging and loading units (containers, pallets) during serial production processes, as well as for the transportation options available for large machinery [16.3].

Design in accordance with recycling considerations ensures that the design considers the nature of processing and reclamation procedures and supports their use through the utilization of appropriate assemblies and component design (shape, joints, and materials). At the same time, the application of reclamation-friendly construction measures (i.e., those facilitating dismantling and reassembling, cleaning, testing, and postprocessing or exchange processes) facilitates maintenance-compatible design (inspection, servicing, and repairs). Figure 16.30 shows recycling options for material products; recycling is only possible if accounted for in the design [16.35–38].

16.2 Engineering Design Basics

Virtually all design departments employ a methodical approach to the development and design of technical systems (engineering design). Indeed, imparting a specialized knowledge of methodical design is a core aim of engineering science courses taught in universities and technical colleges.

A large number of approaches to design methodology are documented in the technical literature. For example, *Ehrlenspiel* [16.1] focuses more on the cost approach to product development. One way of reducing and identifying costs early, according to Ehrlenspiel, is to perform integrated product development. On the other hand, *Roth* [16.2] divides the design process into many smaller steps, and strongly emphasizes the incorporation of design catalogs into the solution process. *Pahl* et al. [16.3], who worked very actively on the German guidelines VDI 2221 [16.7] and VDI 2222 [16.39], subdivide the design process into individual activities to which detailed methods are assigned. Other design methodology approaches include those from *Koller* [16.6], *Gierse* [16.40], *Hubka* [16.41], *Hansen* [16.42], and *Rugenstein* [16.43]. The essential aspect of all of these approaches is the structuring of the task, which may be achieved by drawing flow diagrams or applying methodical structuring aids such as functional structures, efficacy structures, or classification diagrams [16.44].

In this section, the methodical approach to the development of a technical system is illustrated by applying the approach expounded by *Pahl* et al. [16.3] to a practical example from the interdisciplinary field of biomedical engineering. According to Pahl et al., the design process can be divided into four stages:

- Problem identification (i.e., precisely defining the task)
- The concept stage
- The design stage
- Detailed design (i.e., drawing up the final solution).

As the example involves an interdisciplinary development project, it is particularly important to draw up a few (but nevertheless all) of the problem or work-related (sub)functions required to adequately structure the task and to represent them in a functional structure. It is also necessary to use a generally understood vocabulary. This ensures that people who are not yet involved in the process or those with no engineering training (e.g., medical experts or biologists) can easily understand the process. This integration of employees from various specialized fields is needed in order to implement all medical and biological requirements to a high standard.

16.3 Precisely Defining the Task

16.3.1 The Task

The engineering system to be developed is a test setup for experiments with live human cells. The task (problem) for the designers was drawn up by the medical experts involved in the experiments. An extract from this is shown below.

For decades it has been known that certain cells in the human immune system are practically incapable of functioning in weightlessness. This can pose a serious problem for long-term stays in space on the International Space Station (ISS), or flights to Mars. The basic mechanism is to be investigated by means of weightlessness experiments with the help of parabolic (ballistic)

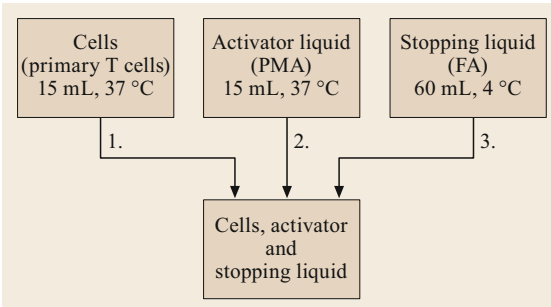

Fig. 16.31 Liquids to be mixed

flights. To this end, experimental equipment is to be designed with which tests on live cells can be performed onboard parabolic flights and in weightlessness. These experiments should also answer the question of whether humans are at all capable of living in weightlessness for any lengthy period. The findings can also be used in therapy for diseases of the immune system. It is necessary to mix the living human cells with an activator liquid and with a stopping liquid after a certain time. All the necessary safety requirements must be observed.

The task of the designer is to precisely define this problem, meaning that they must first draw up a functional engineering description. The aim is to derive the whole function and all input and output variables for the engineering system to be developed.

16.3.2 Functional Description

The functional engineering description is drawn up by the designer. This description is used to clearly define the task or problem the designer has been set and to provide a basis for discussion with other team members. This makes it is possible to quickly identify any potential communication problems. In interdisciplinary projects, it is particularly important to integrate the information from team members without an engineering science background into the technical preparations and thus provide the basis for a methodical approach. For instance, in the project discussed here, the medical experts/biologists and engineers have to *speak the same language*. The functional description is usually verbal. Diagrams or initial sketches are frequently also produced to transparently depict the whole function to be fulfilled. Figure 16.31 shows an outline of the technology needed for the test setup developed in the project discussed here.

This rough structuring was conceived based on notes taken during team meetings and a functional structure drawn up by one of the medical-biological team members (Fig. 16.32).

This description is already very finely structured. However, it is not drawn up in the usual form employed in design methodology [16.3]. Further, such a precise description of a possible solution excludes other approaches and solutions in advance. The func-

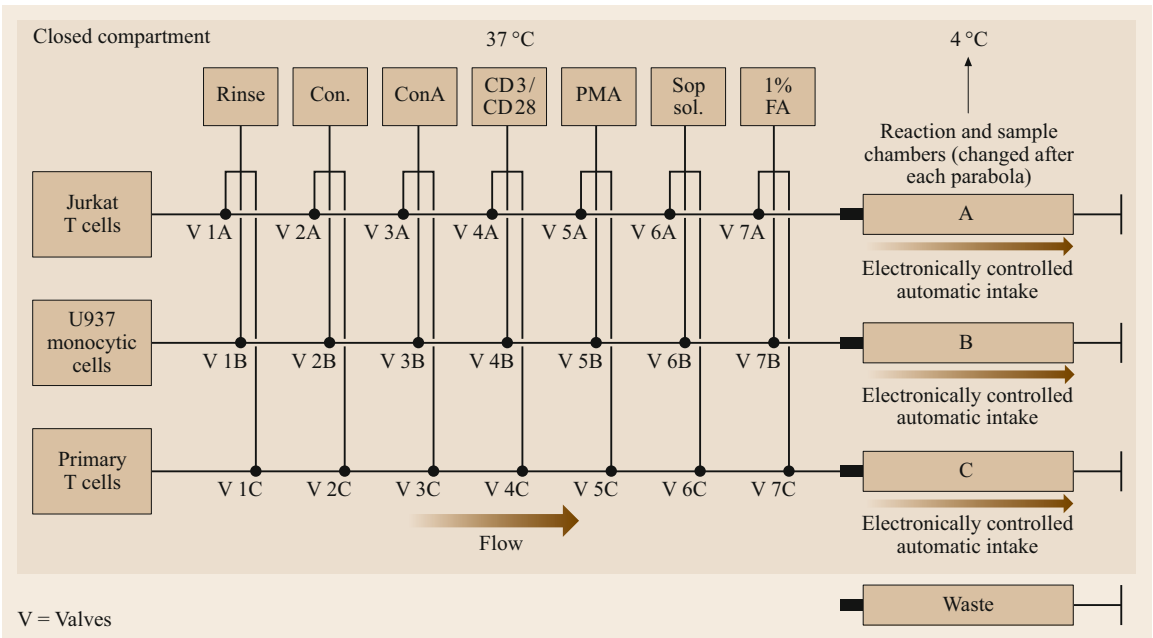

Fig. 16.32 Functional description from a medical point of view

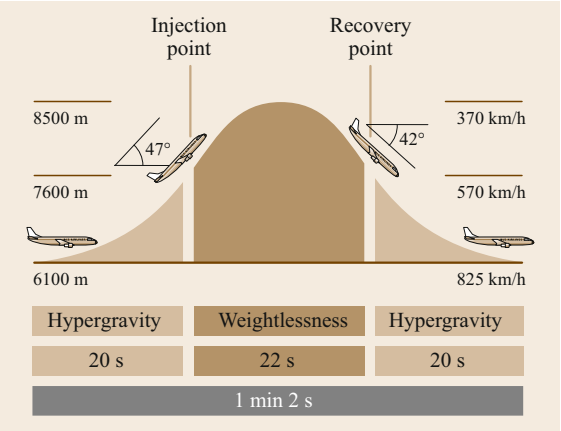

Fig. 16.33 Flight parabola used to generate weightlessness (microgravity) onboard the aircraft (after [16.45])

tional engineering description or the overall function to be fulfilled by the test setup can be described as follows:

A test setup is to be developed that enables three different cell lines to be mixed, to a large extent homogeneously, with certain activator liquids at the start of the weightlessness phase. Just before the end of the weightlessness phase, a stopping liquid is to be added to the cell vessels filled with a cell type and an activator liquid.

In order to fulfill the specified medical requirements, combinations of three different cell liquids, three different activator liquids, and two stopping liquids (Fig. 16.31) must be realized.

Weightlessness was to be achieved by performing the experiments during parabolic flights (i.e., onboard an aircraft flying in a precisely defined parabola), with approximately 22–25 s of weightlessness (microgravity) available per flight (Fig. 16.33).

It was extremely important to ensure that all safety requirements were fulfilled by the test setup; primarily, liquids must not escape from the test setup during the parabolic flights under any circumstances. Some of the cell lines used are genetically modified tumor cells and immune cells isolated from blood donors, and toxic liquids such as formaldehyde are employed in the experiments. These could pose a risk to flight personnel during the weightless phase. This means that any part that comes into contact with the media or cells, activator, or stopping liquids had to have double walls.

A further requirement was that the temperatures of the cell and activator liquids must be 37 °C and the temperature of the stopping liquid must be 4 °C (Fig. 16.31). The following requirements were also stated in the initial functional engineering description:

- Rapid and easy provision of the system with liquids
- The direct safety stage [16.3] should be realized, i.e., the system should be leakproof under the conditions experienced in the aircraft
- Clear functional sequences
- Good miscibility of the liquids in the cell culture bag during the experiment
- Filling can be performed in the absence of air
- Largely transparent construction to allow checks for any unwanted air in the system
- Low weight (mass)
- Small space requirement
- Good cost-effectiveness.

This initial functional description provided the basis for drawing up a requirements list.

16.3.3 Requirements List

After defining the task or problem more precisely, other individual characteristic values and special requirements are determined. It is necessary to adequately describe all of the requirements that have been set, both qualitatively and quantitatively. This was achieved in the project described here through:

	Product: *Parabolic Flight*		Date: 06.02.06	Sheet 03
	Requirements			Source Responsibility
	No.	Descriptive information	Numerical info/comments	
Overall space required/ connection dimensions/ installation conditions		Aircraft door width	– 1.07 m	
		Aircraft door height	– 1.93 m	
		Cabin length	– 20 m	
		Maximum rack height	– 1500 mm	
		Fixing points for experimental setup	– Mean rail spacing (y-axis) a) 503 mm b) 1006 mm – Hole diameter for screw M10 = 12 mm – Hole spacing in x direction = $n \times 25.4$ mm > 20 in (1 in = 25.4 mm)	
		Maximum load per unit area over 1 m fixing rail length	– 100 kg	
		Rack structure	– Baseplate or frame connected to the seat rail system of the aircraft – There must not be any parts protruding from the baseplate in the direction of the flooring	

Fig. 16.34 Extract from the requirements list

- Discussions with the other team members (biologists, medical experts)
- Literature and patent research
- Analysis and evaluation of all applicable rules, regulations, etc. (the technical requirements of the aircraft operator) [16.46].

The results of precisely defining the task are documented in the requirements list. This usually contains the objectives to be realized and the prevailing conditions in the form of requirements and wishes [16.3]. The requirements must always be fulfilled, whereas the wishes are to be realized if possible. However, the boundary between requirements and wishes is often difficult to define clearly, especially in interdisciplinary projects. For this reason, this differentiation was ignored for the present project. An extract from the requirements list for this project is shown in Fig. 16.34. At the same time, the requirements list provides the legal basis for all further activities.

16.4 Conceptual Design

The overall function is structured during the conceptual design stage. The result is a functional structure (Fig. 16.35) in which the system is divided into subfunctions and the links between them.

This procedure enables optimum analysis of the whole system. Efficacy principles are then assigned to the subfunctions.

Efficacy principles are usually based on physical effects that enable the function to be fulfilled. These are combined with geometric and material characteristics. In the present project, conventional (e.g., literature or patent research), intuitive (e.g., brainstorming), and discursive (e.g., the use of design catalogs) solution-finding methods [16.3, 47] were used to derive suitable action principles.

When efficacy principles that are suitable for fulfilling the function have been determined, they are assigned to subfunctions in a classification diagram. In this project, the morphological box (Fig. 16.36) was used to perform this assignment.

The efficacy principles drawn up to fulfill the individual subfunctions must then be purposefully linked to each other. When drawing up the concept for the test setup, it was important to ensure that the high safety requirements were fulfilled with all of the selected efficacy principles. This resulted in various possible efficacy structures. In practice, it is usual to draw up a maximum of three efficacy structures. Figure 16.37 shows the path through the morphological box.

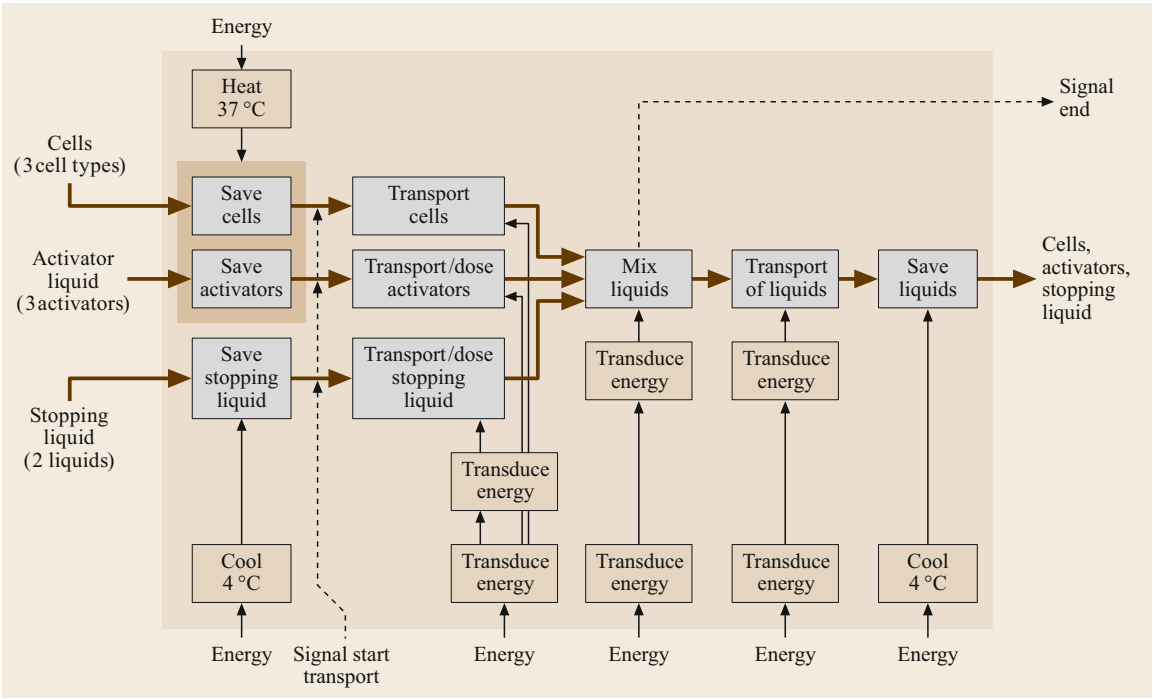

Fig. 16.35 Simplified functional structure

Function	Option	1.	2.	3.	4.
	Cool	Cooling accumulators Source: Novodirect	Peltier cooler Source: Rübsamen & Herr GmbH	Cryogenics	Refrigerator principle (compressor + heat exchanger)
	Heat	Sheet-type heating elements (silicon heating mats) Source: Hewid GmbH	Heat cartridges Source: Hewid GmbH	Infrared radiators Source: Hewid GmbH	Chemical reaction (thermal accumulators) Source: www.riedborn-apotheke.de
	Transport/ meter	Flexible tube pump Source: ismatec	Piston pump Source: Novodirect	Diaphragm pump Source: Novodirect	Gear pump Source: Novodirect
	Mix	Use of the pumps, pressure surge	Magnetic stirrer principle Source: Novodirect	Swivel movement of the vessels (shaker, vibrator)	

Fig. 16.36 Morphological box

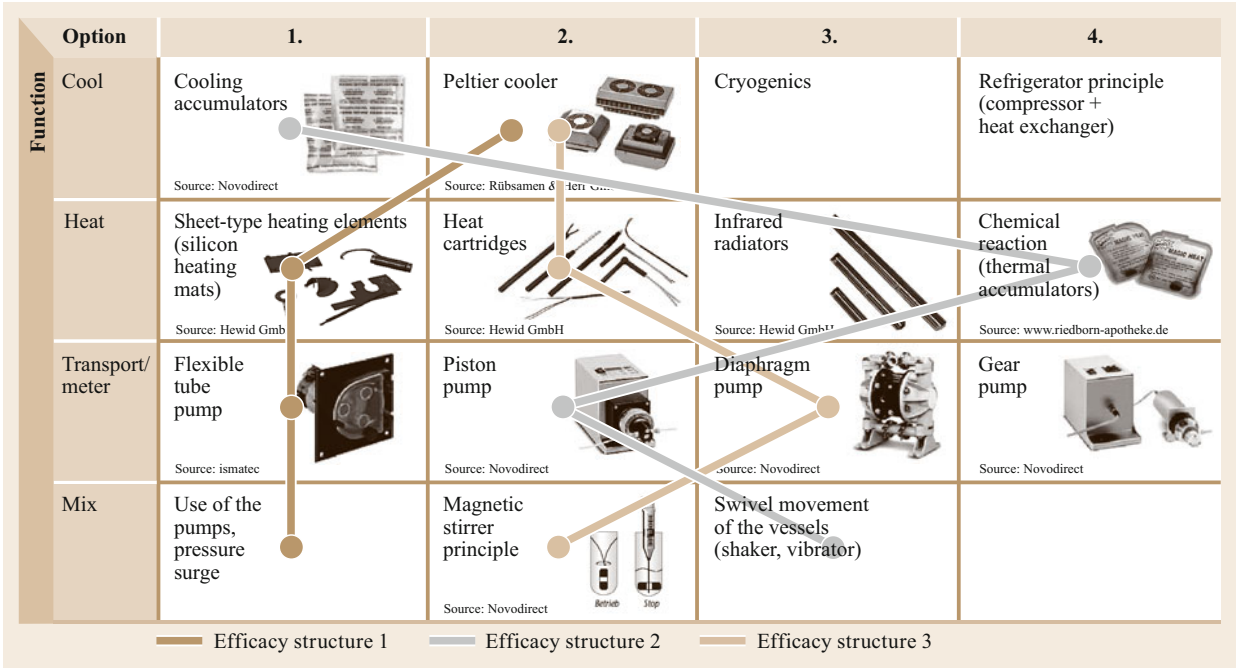

Fig. 16.37 Path through the morphological box

The efficacy structures generated are then specified in greater detail and developed further to produce basic solutions. The individual basic solutions are then assessed. An extract of the assessment (rating) undertaken in the present project is shown in Fig. 16.38. The assessment criteria were defined and the assessment itself was carried out by the whole project team.

As a result, a basic solution was released to be drawn up. In general (and in the present project), this is the efficacy structure with the best rating, which forms

Assessment criteria	Weighting (W)	Opt. 1		Opt. 2		Opt. 3	
		Item (P)	$W \times P$	Item (P)	$W \times P$	Item (P)	$W \times P$
37 °C uniformly distributed in the area of the cell storage and the activator liquids	0.8	4	**3.2**	1	**0.8**	3	**2.4**
4 °C uniformly distributed in the area of the stopping liquids and in the subsequent storage system	1.0	4	**4**	1	**1**	4	**4**
Low energy requirements	0.6	2	**1.2**	4	**2.4**	2	**1.2**
Low mass	0.7	3	**2.1**	3	**2.1**	2	**1.4**
Sterile pumping system with few mechanical components in area of contact with the pumped media	0.5	4	**2**	2	**1**	2	**1**
Total			30.0		25.3		27.1
Percent			0.83		0.70		0.75

Fig. 16.38 Extract from the assessment list

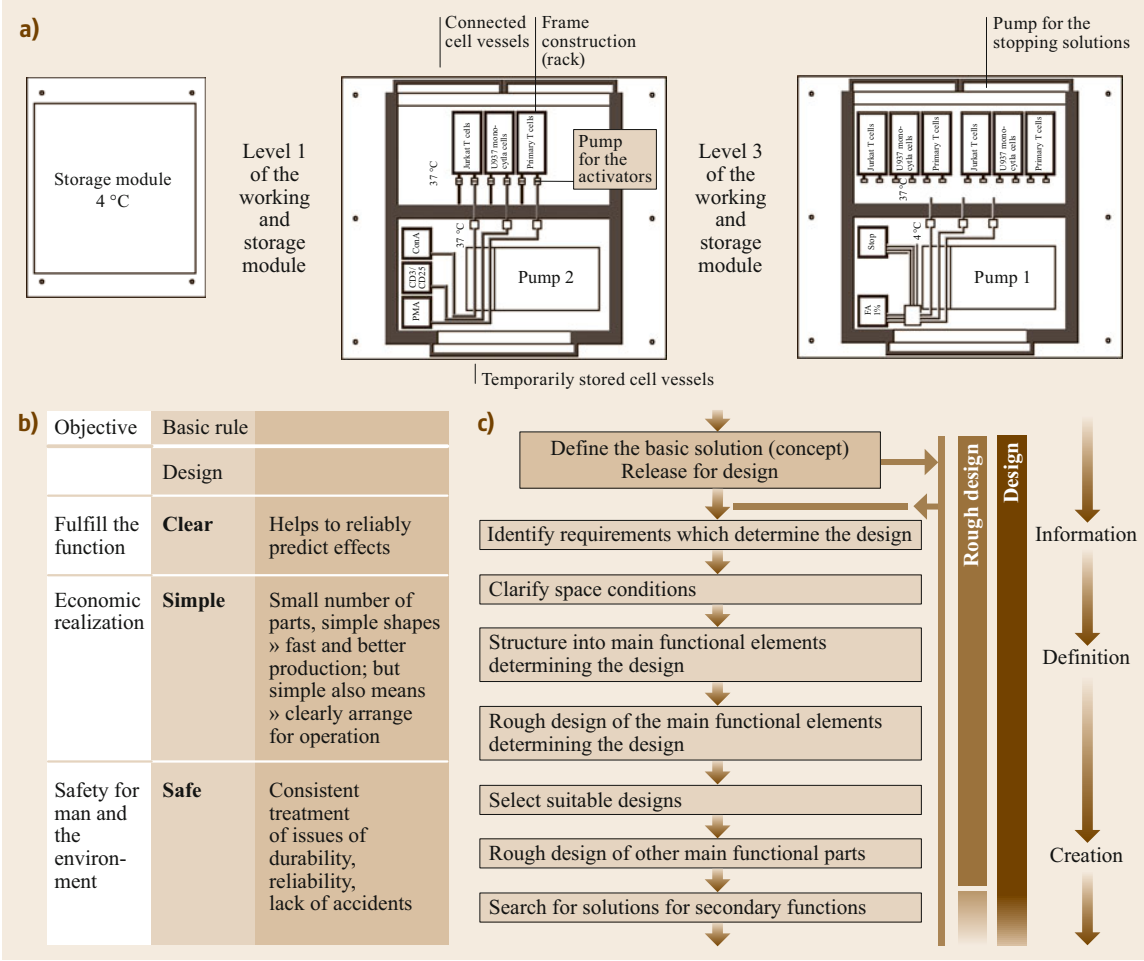

Fig. 16.39 (a) Basic solution that was released to be drawn up, (b) basic design rules, and (c) extract from the main design activities (after [16.3])

the basis of the design stage. This basic solution is shown in Fig. 16.39a.

The basic solution consists of two separate modules. The first module is the actual working module; the cells, the activator and stopping liquids, and all the necessary units are installed into this module for pumping. It is divided into three levels/submodules, which are stacked on top of each other. Level 1 contains the pump for the stopping liquids and unfilled cell vessels in storage, which are separated from the pump by a wall. Above this is the level for the power supply and controls. The top area contains the pump for the activators and connected cell vessels that are ready to be filled, which are separated from the pump by a wall. Upon consulting the medical experts, it was discovered that three individual cell vessels were to be filled in parallel. The second module is the cooling module, where all of the filled cell vessels are stored at 4 °C after the experiment.

An important aspect of this design is the joint specification from the medical experts and engineers in the project team that a predefined precise quantity of the cell liquid should already be present in special cell vessels. The activator and stopping liquids are then pumped into these. The result is a simpler and better solution than that previously proposed by the medical experts in Fig. 16.32. This arose as a direct consequence of the methodical approach described in Sect. 16.3.2. The new solution prevents the cells from being metered into the installed cell vessels by the pump, which would generate shear forces that would have negative effects on the cells, exposing them to considerable stresses. In addition, it avoids repeated flushing of the pipes/lines for liquid transport, thus minimizing the number of components (pumps, valves, and lines) needed and the costs incurred. This approach also minimizes the costs associated with the liquids to be pumped (less flushing means less waste). This was an important aspect of fulfilling the basic design rule *in the simplest manner*. The content of the design is discussed in the next section.

16.5 Design

The design stage is divided into the following phases:

- Rough design
- Detailed design
- Complete and check.

The solution is defined more and more precisely during the design stage until a complete structure is obtained [16.3]. All technical and economic requirements must be clearly and completely drawn up. The result is the design of the solution option, with all of its geometric and material characteristics and conditions defined. During this stage, the following three basic design rules must be observed: *simple*, *clear*, and *safe* [16.3].

Figure 16.40 shows an extract of the main design activities.

The individual activities performed to develop the test setup for experiments with human cells are now described.

16.5.1 Identification of Requirements that Determine the Design and Clarification of the Spatial Conditions

The decisive requirements are essentially set by the ambient conditions, e.g., available space, effective and allowable stresses and loads, and the requirements set by the work sequence. The main requirements for the

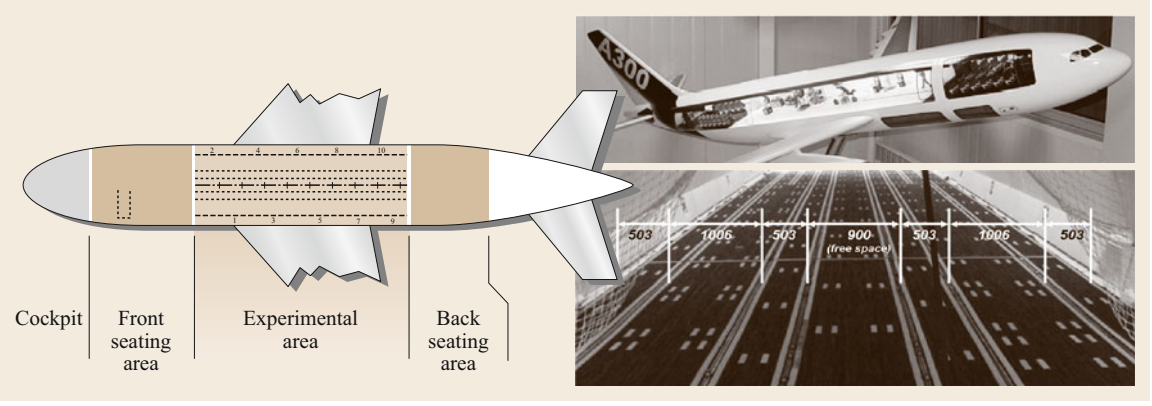

Fig. 16.40 Available (free) space and fixing options in the Airbus A300 of Novespace [16.45]

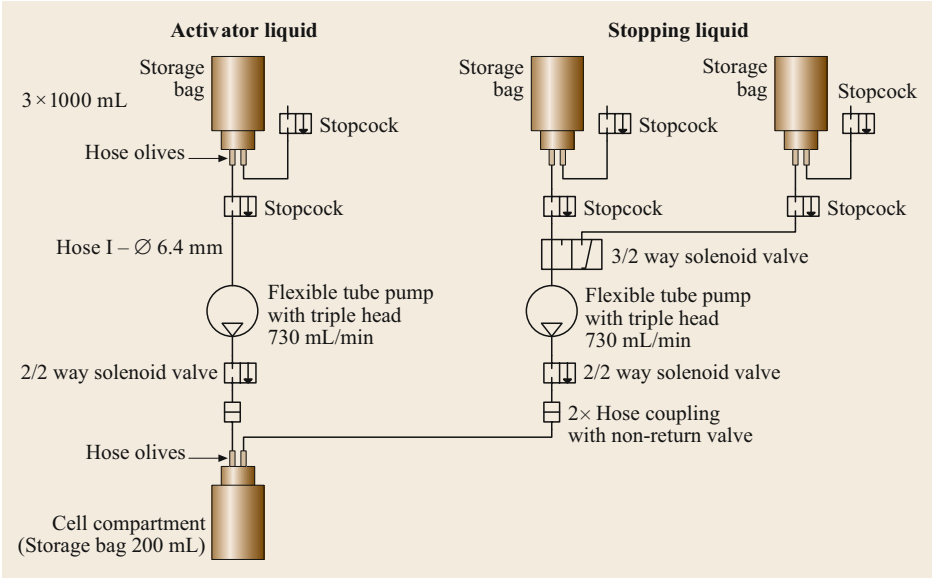

Fig. 16.41 Flow diagram showing how a cell vessel is filled

test setup were specified by the information in the aircraft operator's user manual. This document provided information on, for example, the internal dimensions of the aircraft frame and therefore the maximum effective heights and widths, the types and locations of the fixing points, door dimensions for loading, the maximum allowable load per unit area, and details of the power supply (Fig. 16.40).

Requirements determined by the layout, such as the flow directions and handling sequences, were specified by the biomedical description of the experiment.

16.5.2 Structuring and Rough Design of the Main Functional Elements and Selection of Suitable Designs

In this activity, a roughly structured diagram of the main material flow that was labeled with the main components selected beforehand was drawn up (Fig. 16.41). The main material flow is the pumping of activator and stopping liquids from storage into the cell vessel. Flexible tube pumps and suitable valves and hoses were selected for this task. The pump and valve sizes were chosen according to the time and delivery rate requirements imposed by the biomedical process variables. Because of these specifications, instead of the original idea of using a flexible tube pump with a triple head for all activators and the same pump for all stopping liquids, six separate pumps had to be selected to achieve the objective.

Another main functional element was the frame (rack) for the modules. Extruded aluminum sections and accessories that are available as a modular system and are frequently used for automation engineering were used in the design. The section size was chosen

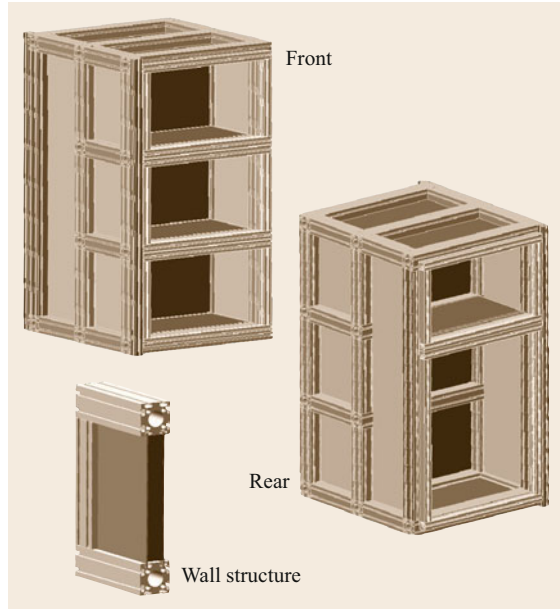

Fig. 16.42 Working module rack: front, rear, and wall structure

based on the calculated loads. Figure 16.42 shows the initial design of the working module.

16.5.3 Detailed Design of the Main and Secondary Functional Elements

Main and secondary functional element design is a process that takes place in parallel with everyday design, as both groups can strongly influence each other. The pump–valve module (Fig. 16.43) is one of the main

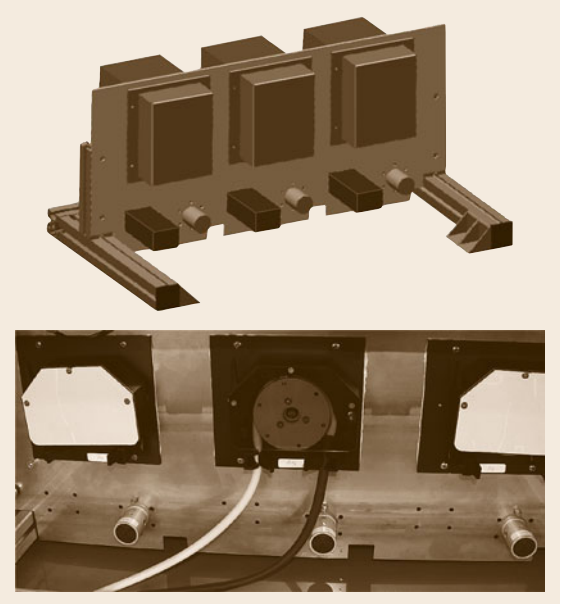

Fig. 16.43 Pump–valve module during development and assembly

functional elements in the system of interest. Its decisive design requirements are those resulting from the biomedical process variables (size of the metered volume) and the boundary conditions resulting from the technical requirements (e.g., low mass, small space requirement).

A secondary functional element is the cell vessel, which initially contains 15 mL of cell liquid. The activator is injected into this vessel before the onset of weightlessness, and the stopping solution is injected after approximately 22–25 s. The ability to fill the vessel in the absence of air and under sterile conditions was a prerequisite. Further, the safety requirements necessitated that this vessel was double walled and that the liquids inside it were quickly removed after the experiment. For biological and economic reasons, the inner part of the vessel had to be a one-off (disposable) product and the outer part had to be reusable. Due to these requirements, further solutions were conceived and tested (Fig. 16.44).

Option 1 consisted of an inner infusion bag integrated into a conventional 1 L plastic bottle. The connections were realized via hose olives screwed into the bottle lid. Option 2 had a similar structure except that the second wall was provided by a second liquid bag with a screw lid. In the third solution, the outer enclosure consisted of a specially produced plastic enclosure made using a rapid prototyping method.

The first two options were very cost-effective, as all of the components are production items. However, they contained substantial defects in terms of functional fulfillment (filling under the exclusion of air). This was because the inner infusion bag irreversibly twisted when it was screwed in. As a result, unrestrained material flow was not possible; i.e., the design was not *clear*. The third option was the most costly, but it enabled complete functional fulfillment according to the requirements. Therefore, it was the preferred option and was released for design optimization. The design obtained following a continuous functional test during the optimization phase is shown in Fig. 16.45.

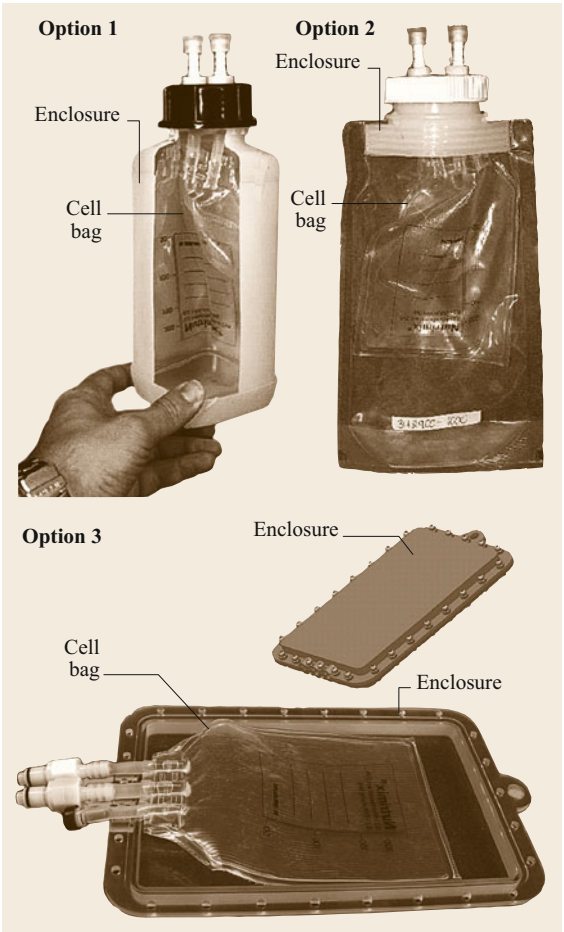

Fig. 16.44 Possible options for the cell vessel (cell compartment), a secondary functional element

16.5.4 Evaluation According to Technical and Economic Criteria and Specification of the Preliminary Overall Design

During the design and associated continuous testing and control process, it was found that some technical requirements could not be realized, such as:

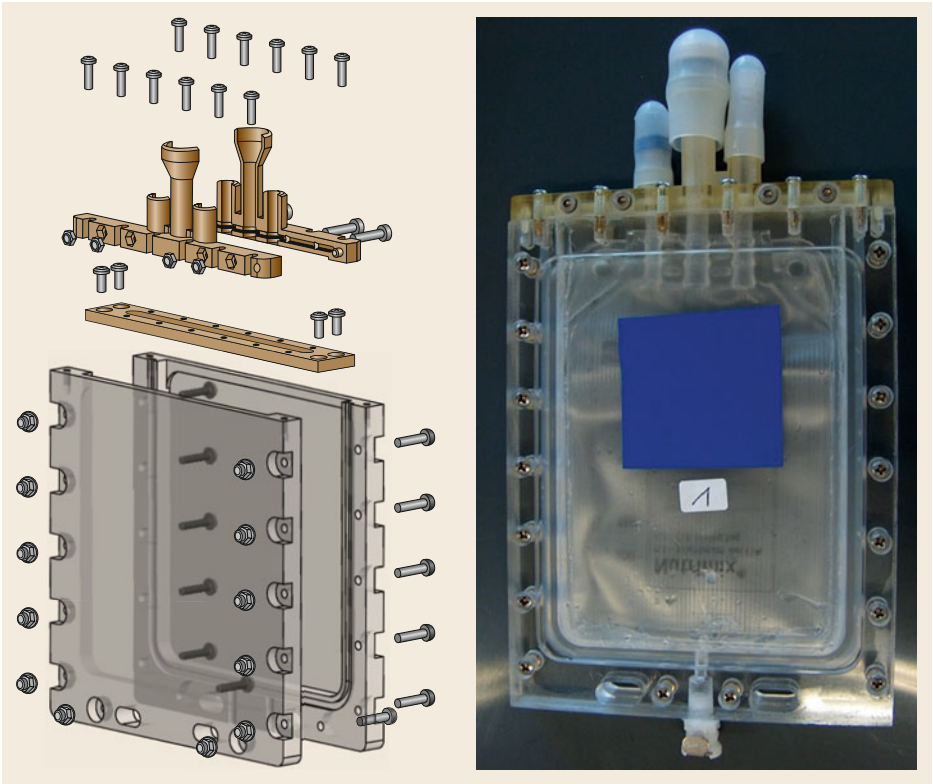

Fig. 16.45 Cell vessel structure

- Compliance with the maximum module dimensions
- Compliance with the maximum mass
- Compliance with the electricity consumption.

In other words, deviations from the requirements list were found.

Furthermore, the functional fulfillment was checked during this phase of the development work. No deviations from the requirements list were found. The specified delivery rates of the pumps were fulfilled. The temperature ranges to be realized were achieved, and the whole operational sequence was clear.

There were also no deviations from the requirements list with respect to the economic criteria to be realized. All the specifications—such as material, production, and assembly costs—were met.

A second design was drawn up based on the deviations from the requirements list. This design consisted of three separate modules (Fig. 16.46):

- *Module 1*: The heating module, where the cell compartments are stored at 37 °C before the experiment (i.e., an incubator)
- *Module 2*: The working module, where the cell vessels are filled
- *Module 3*: The cooling module, where the cell vessels are stored at 4 °C after the experiment.

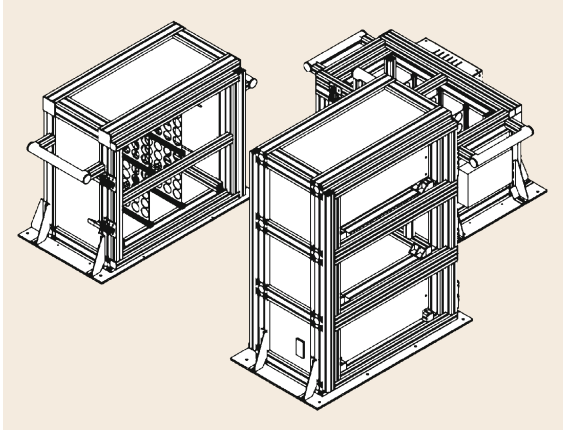

Fig. 16.46 Design of the experimental modules

This design was able to fulfill all of the technical and economic requirements, and was released for further design work.

During the final phase of the design stage, it is necessary to adapt the solution to existing standards and regulations. The individual components are assigned binding materials. During this phase, among other things, the drawings needed for production are completed and the product documentation is produced. Figure 16.47 shows the result of the development.

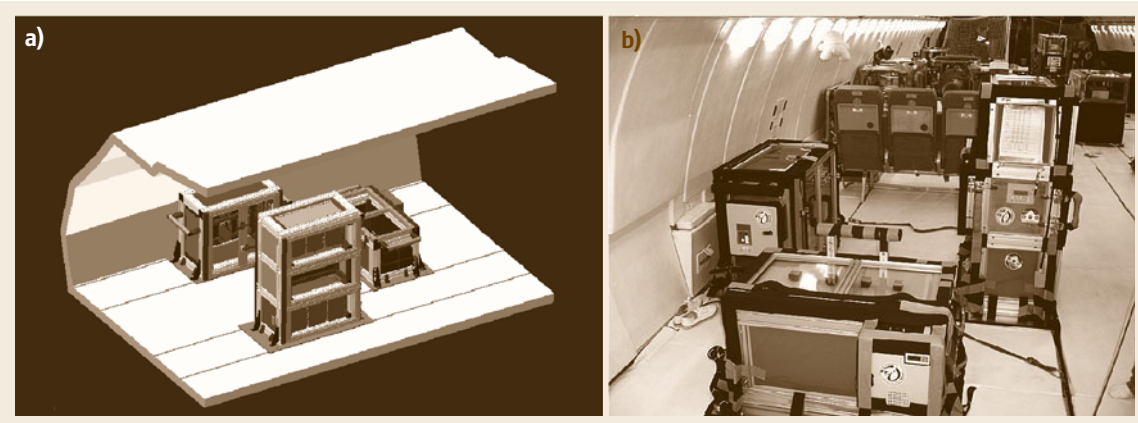

Fig. 16.47a,b Experimental modules: **(a)** computer simulation, **(b)** installed in aircraft

16.5.5 Subsequent Consideration, Error Analysis, and Improvement

The main activities performed during the design phase according to [16.3] include *checking for errors and disrupting effects*. This is a meaningful and necessary activity during design as it prevents abortive development. However, only a limited systematic error analysis was possible for the developed modules. Unlike other projects in which there are already empirical values, process sequences are easy to follow or test, and preliminary trials performed in parallel with the development process can be used to check for errors or faults, the analyses carried out for the experiment modules described here were largely based on assumptions—it was not possible to produce microgravity while testing the modules of the test setup during the development phase. For this reason, it was important to document and analyze the module sequence and function during parabolic flights. This was the only way to facilitate error correction and improvements. Examples of modifications that are to be made to the modules in subsequent flights include:

- Most of the hoses from the medium are to be replaced with rigid pipes
- Safety sensors will be added to check for the presence of the vessels to be filled before injection is initiated
- The manually opened venting valves in the cell vessels are to be replaced with automatically opening valves
- The method used to fix the cell vessels in place (stoppers) in the heating and cooling modules will be improved.

It is useful to develop and design engineering systems according to methodical aspects based on information from the literature [16.1–3]. Design methodology guidelines were also applied in this interdisciplinary development project, together with design methodology tools such as the requirements list, functional structure, and morphological box (to name just a few). During the design phase of the product development process, it was important to comply with the basic design rules: *simple*, *clear*, and *safe* [16.3]. The following aspects clearly show the realization of these three criteria in the present project:

1. Simple:
   - The use of a modular system for the rack design
   - Only 15% of the required components were specially made (turned or milled parts)
2. Clear:
   - The liquid flow path was clear and did not lead to undefinable conditions
3. Safe:
   - A redundant arrangement of parts that absorbed forces was employed
   - Moving parts (cell vessels) were fixed in position using stoppers.

The realization of the direct safety requirements during the development activity was considered to be of primary importance. This task was successfully solved.

However, practical experience shows that, especially during the conceptual and design phases, the experience and intuition of the designer are increasingly used to find the solution, whereas systematic development is consciously dispensed with. This is not because theoretical procedures are generally impractical; it is due to increas-

ing time and cost pressures during development. It is often not possible for the designer to define several options for all main and secondary functions or to produce designs for the overall and part solutions and still present a solution on schedule and within the cost framework. In this case, there is a risk that better solutions (both technically and economically) are overlooked. One example from the project above is the fixing mechanism (stoppers, Fig. 16.48) used to limit the sixth degree of freedom of movement and thus secure the cell vessels in place in the working and heating modules. Several optional solutions were not determined for this secondary functional element in advance; instead, the *first best* solution was used. In the technical test evaluations performed after the flights, the operators complained that the stoppers were difficult to undo and refasten due to the high stresses that occurred during parabolic flight. This solution had worked, but not optimally, and will be changed for the next series of flights.

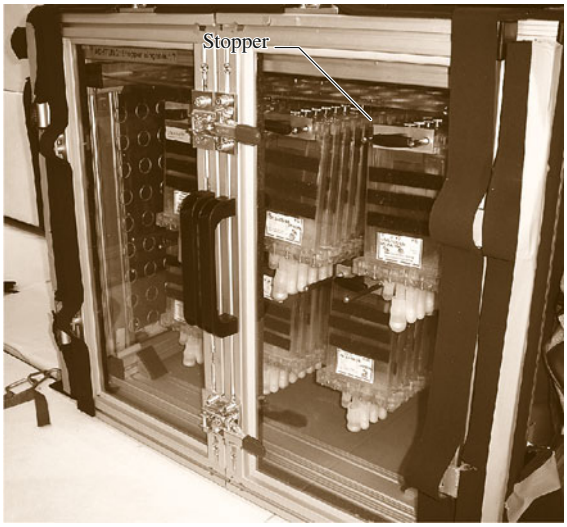

Fig. 16.48 Stopper used in the heat module

16.6 Design and Manufacturing for the Environment

The environment can be envisioned as interacting with human society in two ways: as a *source* of natural resources and as a *sink* for emissions and wastes. The environmental problems addressed here are all related to the overuse of both sources and sinks. Overuse of sources shows up as depletion and therefore as reductions in the quantity and quality of resources. Overuse of sinks shows up as an unbalancing of the harmony of previously natural processes. The change in balance often takes years to detect and can be influenced by a variety of factors, making isolating and identifying the problems difficult and sometimes controversial. Nevertheless, many of these problems have been identified over time. They include ozone depletion, global warming, acidification, and eutrophication, among others. Corrective action often involves changing the types of materials and energy and the ways in which they are used during the production, use, and disposal of products. Table 16.7 lists commonly agreed environmental concerns and aspects of production, consumer use, and disposal that contribute to those concerns.

Table 16.7 clearly conveys the message that many of our environmental problems are directly related to our use of materials, including energetic materials. In particular, note that several prominent concerns listed in Table 16.7 are directly related to our use of fossil fuels to generate energy. These include CO_2 and NO_x emissions from the combustion of all fossil fuels as well as the deposition of SO_x and several heavy metals (including As, Cd, Cr, and Hg) onto the land following

Table 16.7 List of environmental concerns and links to manufacturing processes

Environmental concern	Links to manufacturing processes
1. Global climate change	Greenhouse gas (GHG) emissions from direct and indirect energy use, landfill gases, etc.
2. Human organism damage	Emission of toxins, carcinogens, etc., including the use of heavy metals, acids, and solvents as well as coal burning
3. Water availability and quality	Water usage and discharges, e.g., water used for cooling and cleaning in particular
4. Depletion of fossil fuel resources	Electricity and direct fossil fuel usage, e.g., power and heating requirements, reducing agents
5. Loss of biodiversity	Land use, water usage, acid deposition, thermal pollution
6. Stratospheric ozone depletion	Emissions of chlorofluorocarbons (CFCs), hydrochlorofluorocarbons (HCFCs), halons, and nitrous oxides (used, e.g., in cooling equipment as refrigerants, in cleaning methods, and for fluorine compounds)
7. Land use patterns	Land appropriated for mining, biomaterial growth, manufacturing, and waste disposal
8. Depletion of non-fossil fuel resources	Materials usage and waste
9. Acid disposition	Sulfur and NO_x emissions from smelting and fossil fuels, acid leaching, and cleaning

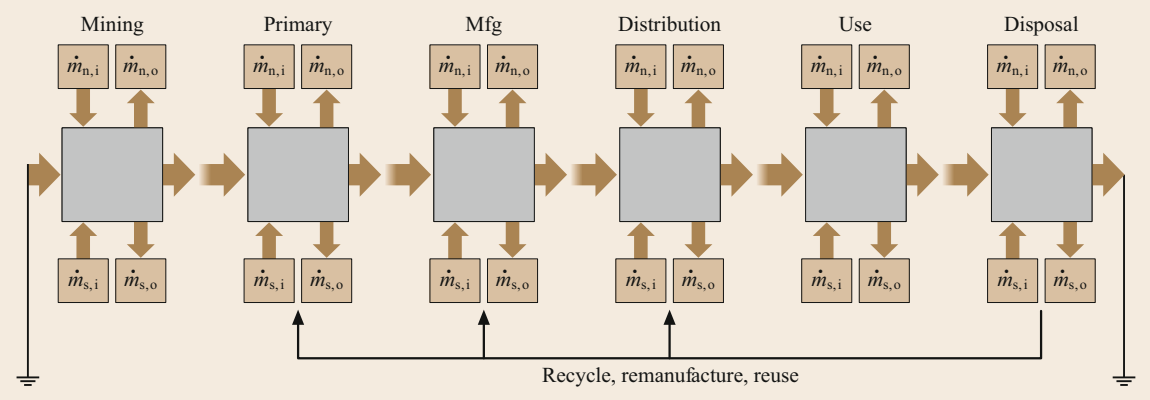

Fig. 16.49 Product life cycle material flows (m_n represent exchanges with nature, m_s represent exchanges with society)

the combustion of coal [16.48, 49]. In fact, at least four (numbers 1, 2, 4, and 9) of the nine concerns listed in the table are related to fossil fuel use. Because of this overriding importance, we now take a close look at the utilization of energy during the life cycles of products.

16.6.1 Life Cycle Format for Product Evaluation

A very important aspect of environmental analysis involves simply *connecting the dots*; in other words, showing the interconnectivity of human activities and, in particular, material flows. Few people contemplate where resources come from or where they go after they are used, but these are essential aspects of life cycle analysis. Using a life cycle accounting scheme, any product or activity can be assigned an environmental load. This information can in turn be used to answer the following question: *is the utility gained from this product or activity worth the associated environmental load*? Although conceptually simple, this task is actually quite complex. The major complexities are:

1. Establishing system boundaries
2. Obtaining accurate data
3. Representing the data with concise descriptors that accurately assign responsibility
4. Appropriately evaluating the results.

Our approach will be to represent the product using material flow diagrams that capture the major inputs and outputs. In general, we will not attempt to relate these inputs and outputs to specific levels of environmental harm; we will only identify them as *environmental loads* that are known to cause harm and are excellent targets for technical improvement. When specific amounts of inputs used or outputs emitted are given, the associated analysis is called a life cycle inventory (LCI). Full life cycle analysis (LCA) comprises the LCI, the connection between the loads produced and the associated harm caused, and often ranking values relating to the different types of harm. Some LCA methods use these ranking values to generate a single numerical result. This can greatly ease decision-making but requires agreement with all of the implied value tradeoffs, which is often difficult.

Before proceeding further, it is important to more clearly establish the idea of a product life cycle. This is generally a materials flow process that starts with the extraction of raw materials from the earth and ends with the disposal of the waste products back into the earth. The general stages of this linear *once-through* cycle are:

1. Material extraction
2. Primary processing and refining
3. Manufacturing
4. Product distribution
5. Use
6. Final disposition.

This sequence follows the principal product material flow, but of course there are multiple crossflows (consider the materials used by products, e.g., paper in printers and gasoline in automobiles) as well as backflows (such as product reuse, component remanufacturing, and material recycling). Figure 16.49 illustrates these flows in a general way, indicating crossflows from both nature and society as well as the major recycling flows. Society can then be represented by a vast array of these networks, interconnected but ultimately all originating from and leading to the ground. This thought experiment clearly suggests the complexity of our problem. In practice, this task is simplified by clearly defining the system boundaries and the objectives of the life cycle study. Problems can arise when the system considered is too large due to the interconnectiv-

Table 16.8 The environmentally responsible product assessment matrix [16.50]

Life cycle stage	Environmental stressor				
	Choice of materials	Energy use	Solid residues	Liquid residues	Gaseous residues
Premanufacture	11	12	13	14	15
Product manufacture	21	22	23	24	25
Product delivery	31	32	33	34	35
Product use	41	42	43	44	45
Refurbishment, recycling, disposal	51	52	53	54	55

The numbers are the indices for the matrix element M_{ij}

ity of materials systems or when the system considered is too small due to truncation. Matrix inversion methods (identical to those used in economic input–output analysis [16.51]) along with high-level summary statistics have been called upon to help with the first problem [16.52, 53], while experience, iteration, and hybrid approaches are used to address the second [16.54, 55].

The commonest practice among LCA practitioners is to develop process flow diagrams similar to Fig. 16.49 for the product and trace the major input and output paths to the earth. This requires data such as a bill of materials and lists of manufacturing processes, common use scenarios, distribution channels, and end-of-life characteristics for the product. The output is then a long list of material and energy inputs as well as emissions to the environment. These lists can easily include hundreds of materials, which then require some simplification and aggregation for interpretation. In this section, we will use a simplified format suggested by *Graedel* in his book on streamlined life cycle analysis (SLCA) [16.50]. This involves examining each stage of the life cycle and identifying major impacts and opportunities for improvement in five categories:

1. Materials choice
2. Energy use
3. Solid residues
4. Liquid residues
5. Gaseous residues.

Graedel then suggests scoring each stage of the life cycle for each of the five categories with a numerical score from 0 (the worst) to 4 (the best). These scores are given relative to the best practice for the product under consideration. In general, a score of 0 is reserved for a blatantly poor and/or uninformed practice that raises significant environmental concerns, while a score of 4 indicates excellent environmental performance with no known serious concerns. A perfect product would thus obtain a score of 100. Graedel gives more detailed guidance on how to score each element of the 5×5 matrix, as shown in Table 16.8, which represents the product.

16.6.2 Life Cycle Stages for a Product

In this section we will identify some of the major environmental issues that appear during each of the five stages of a product's life cycle. Product scores in SLCA depend on the extent to which the designer and manufacturer make an effort to avoid these issues and employ alternative materials and technology where possible.

Premanufacture: Material Extraction and Primary Processing

Many of the environmental impacts associated with the choice of materials occur during the very early stages of the material life cycle. This can be surmised by reviewing United States national statistics on energy use, pollutants, and hazardous materials for various industrial sectors.

For example, Fig. 16.50 shows that raw material production industries such as metal mining, the manufacture of chemicals, and the manufacture of primary metals are responsible for a significantly higher pro-

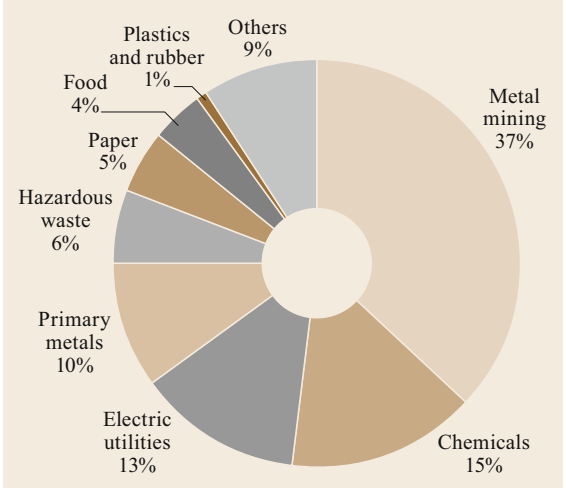

Fig. 16.50 Amount of CO_2 and toxic materials released by each manufacturing industry as a proportion of the total amount of CO_2 and toxic materials released by all industries in 2015

Table 16.9 Typical energy requirements for the production of some common materials [16.57]

Material	Energy required for production (MJ/kg)	Made or extracted from
Aluminum	227–342	Bauxite
Copper	60–125	Sulfide ore
Glass	18–35	Sand, etc.
Iron	20–25	Iron ore
Nickel	230–70	Ore concentrate
Paper	25–50	Standing timber
Polyethylene	87–115	Crude oil
Polystyrene	62–108	Crude oil
Polyvinylchloride	85–107	Crude oil
Silicon	230–235	Silica
Steel	20–50	Iron
Titanium	900–940	Ore concentrate
Wood	3–7	Standing timber

Table 16.10 Toxicity ratings for some elements [16.49]

Toxicity rating	Elements
High toxicity	Beryllium, arsenic, cadmium, mercury, lead
Moderate toxicity	Lithium, boron, chromium, cobalt, nickel, copper, bismuth
Low toxicity	Aluminum, silicon, titanium, iron, zinc, bromine, silver, tin, tungsten, gold

portion of the total amount of CO_2 and toxic materials released by industry than, for example, paper manufacturing, the food industry, or the production of rubber and plastic [16.56].

These large normalized impacts can be explained by two factors: relatively large emissions and relatively low prices. Primary processing industries handle very large quantities of materials, which introduces many opportunities for economies of scale. At the same time, this high usage of materials leads to high waste and emissions levels. For example, mining is very material intensive, with ore waste-to-metal ratios ranging from about 3 : 1 for iron and aluminum to 10 000 : 1 for gold. In addition, many metals exist as, or occur in association with, metallic sulfides. Once these materials are exposed to the air, they can oxidize into sulfates and sulfuric acid runoff, causing significant damage through acid mine drainage. In fact, acid mine drainage can result from the mining of many of the commonest metals, including copper, iron, nickel, lead, and zinc. Also, some of the initial processes used by primary processing industries can involve other hazardous materials. If those materials escape, widespread environmental damage can occur. For example, toxic cyanide compounds are used in the leaching of gold.

Similarly, primary materials processing can be both materials and energy intensive. For example, the production of 1 kg of aluminum requires on the order of 12 kg of input materials and 290 MJ of energy [16.57]. The generation of the energy required for aluminum production plus other processing effects leads to the release of about 15 kg of CO_2 equivalent for every kg of aluminum produced [16.58]. Table 16.9 gives the energy requirements for some materials. Note that aluminum is among the most energy intensive of these materials to produce—similar to silicon but substantially less energy intensive to produce than titanium. Recycling materials can greatly reduce this energy requirement. Conversely, the requirement for ultrahigh purity can greatly increase the energy requirement. For example, the ratio of the energy required to recycle versus that required to produce *virgin* material is about 5% for aluminum and 30% for steel [16.59], while the energy required to produce the wafer-grade silicon used in the semiconductor industry is about 33 times that required to produce commercial-grade silicon [16.60]. Hence, the mere act of selecting the materials to use in a product can largely define the environmental footprint of that product.

Graedel and *Allenby* suggest several other criteria to consider when selecting materials, including toxicity and abundance [16.49]. The toxicity and abundance ratings for some elements are given in Tables 16.10 and 16.11, respectively.

Table 16.11 Supply levels of some elements [16.49]

Global supply level	Elements
Infinite supply	Bromine, calcium, chlorine, krypton, magnesium, silicon
Ample supply	Aluminum (gallium), carbon, iron, potassium, sulfur, titanium
Adequate supply	Lithium, phosphorus
Potentially limited supply	Cobalt[a], chromium[b], nickel[a], lead (arsenic, bismuth), platinum[b], zirconium
Potentially highly limited supply	Silver, gold, copper, mercury, tin, zinc (cadmium)

Note that materials in parentheses are mined together; the parent material is listed first. [a] Supply is adequate, but virtually all cobalt and nickel comes from South Africa and Zimbabwe, meaning that supplies of these metals are potentially subject to cartel control [b] If supplies are to be maintained, seafloor nodules will need to be mined.

Manufacturing Processes

As a group, manufacturing processes appear to be quite benign from an environmental perspective compared to materials extraction and primary processing, as indicated in Fig. 16.50. However, manufacturing processes often set many of the requirements for primary processing outputs. For example, manufacturing processes with higher scrap rates require more energy during primary processing. Alternatively, manufacturing processes that use large quantities of recycled materials will have greatly reduced primary energy needs. This concept can be illustrated more rigorously by writing an equation for the embodied energy content of a hypothetical manufacturing process that uses E_m energy per kilogram of product produced. It has become common to discuss the energy *used up* by a process, but the first law of thermodynamics implies that the energy is not actually lost—it becomes unavailable. A more accurate thermodynamic quantity, the *exergy*, can be used up, and this is what we are actually referring to in our discussion of energy used up. Let the waste fractions be: α to ground, γ to recycle, and β to *prompt scrap* (recycled within the factory). This process uses a fraction ϕ of primary material with embodied energy E_p and a fraction $(1-\phi)$ of recycled material with embodied energy E_r, where in general $E_r \leq E_p$. From this, the total energy E_s required to produce one kilogram of product is (Fig. 16.51)

$$E_s = [\phi E_p + (1-\phi)\, E_r]\,(1+\alpha+\gamma) + E_m\,(1+\alpha+\beta+\gamma)\,. \tag{16.1}$$

Hence, even though E_m may be much less than E_p, (16.1) illustrates that the manufacturing process influences stages both before and after it in the product life cycle. As an example, consider the difference between machining and casting a part. While $E_{m\,\text{casting}}$ may be larger than $E_{m\,\text{machining}}$, $\phi_{\text{machining}}$ is generally much much larger than ϕ_{casting}. Furthermore, the waste from machining—in particular α and γ, which appear in the first part of (16.1)—can be quite large. In contrast, for large casting operations, most metal waste shows up in β, which does not occur in the first term. Hence, quite counterintuitively, casting may be a more environmentally benign process than machining in some situations. Of course, this statement is based only on embodied energy usage and ignores other possible emissions.

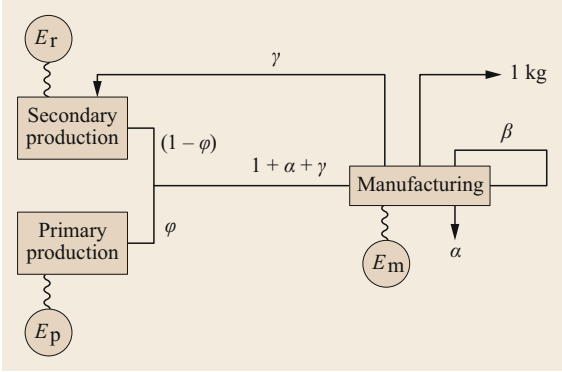

Fig. 16.51 System energy requirements for a manufacturing process

Generally speaking, however, while primary processing adds approximately 100 MJ/kg of energy (E_p) to any product, manufacturing adds around 10 MJ/kg of energy (E_m) [16.61, 62]. The real role of manufacturing is that it draws in materials and energy that are not directly incorporated into the product and then expels them, often as wastes or emissions to the environment.

In addition to fossil fuel usage, a second environmentally important class of materials used in manufacturing is cleaning fluids and coatings. Manufacturing often involves the cleaning and preparation of surfaces. Of particular concern are many of the solvents that are used to remove cutting fluids, lubricants, and other materials from the surfaces of parts. In order to avoid the use of hazardous materials, many manufacturers have replaced organics with water-based and mechanical cleaning methods [16.63].

Product Delivery

Product delivery involves two important types of environmental loads: transportation and packaging. The transportation of products around the world provides jobs and opportunities for many, but it also uses a considerable amount of energy and produces substantial emissions. Furthermore, the geographical separation of product use from manufacturing can create significant barriers to the recycling of some materials.

Packaging waste is particularly egregious because of the large amount of materials used for only a very short intended lifetime. Furthermore, the customer gets the opportunity to experience this waste first hand.

Product Use

It is probably true that the vast majority of consumer appliances, electrical products, vehicles, lawn equipment, power tools, etc.—in short anything that has a power cord or runs on gasoline—has its largest or second largest impact during the use phase. Products with power cords draw energy from utility stations, which, in the US, have an average efficiency of about 35% and still burn 50% coal. These two facts alone often completely dominate the environmental impact of some products. Furthermore, powered devices can consume other materials, e.g., paper and ink in printers, coffee in espresso machines, water in refrigerators with electric ice makers, etc. By and large, these automated

appliances are considered desirable conveniences, but automated usage often (unintentionally) leads to automated waste too.

Disposal

Most products in the United States end up in landfills, some are incinerated, and a few are recycled. In general, US landfill access has been significantly diminishing, particularly in the highly populated northeast. Many states have been closing landfills faster than they are opening new ones. Some states have moratoriums on new landfill development, and many ship their waste out of state. Furthermore, lined landfill sites for the collection of hazardous materials are highly restricted, leading to very high transportation and disposal costs for hazardous substances.

While incineration is not very popular in the USA, particularly in well-to-do communities, it is very much an active option for a significant portion of the municipal solid waste (MSW) generated. Incineration can be performed in an electrical generation facility to produce power. Furthermore, the emissions can be scrubbed to remove various gases that should not be released into the atmosphere. Nevertheless, it is difficult to tightly control the incoming waste stream, so a wide variety of emissions—some of which are not anticipated—can occur. In addition, it is well known that municipal incinerators are one of the top producers of dioxins in the US, and these dioxins are extremely expensive to scrub [16.64, 65]. Dioxins are a group of chemicals that have been found to be highly persistent, toxic, and carcinogenic.

A number of products are widely recycled in the USA. These include automobiles, tires (as a fuel to generate energy), newspapers, aluminum cans, and—to a lesser extent—mixed paper and high-density polyethylene (HDPE) and polyethylene terephthalate (PET) bottles.

16.6.3 Product Example: Passive House

One example of environmentally compatible design is the *passive house* building concept. By using particularly energy-efficient structural members and special ventilation engineering, energy savings (due to a reduced need for heating) of over 80% can be achieved compared to legally specified new-build standards. In addition to its energy efficiency, the passive house is characterized by economic efficiency and environmental friendliness [16.66].

The passive house principle is based on using the heat produced by a household as effectively as possible. In addition to solar energy, heat from internal sources can also be recovered. This includes not only the waste heat produced by electrical appliances but also the thermal energy emitted by people.

To obtain an energy-efficient structure, the heat lost from the structure must be kept to a minimum. Heat losses include, among other things, transmission losses; i.e., heat lost through structural parts such as the floor, walls, roof, and windows. The losses resulting from ventilation must also be considered in the heat loss calculation. Thus, the heat energy requirement calculation is as follows: heat energy requirement = heat losses − heat gains [16.67].

To keep the external heat requirement as low as possible, the heat losses must be minimized and the heat gains maximized. Transmission losses can be reduced by fitting thick thermal insulation and properly insulated windows and through the application of a compact building shape. Otherwise, the most important component of a passive house is a special ventilation system that enables the heat present in the extracted air to be transferred to the incoming fresh air, reducing heat losses due to ventilation.

Heat gains can be maximized by ensuring that the main façades have a southerly aspect and that there are large windows on the south side. It is also important to stop any shadows from being cast on the building. In order to use the solar energy optimally, shadows caused by protruding building elements, balconies, and roof overhangs should be eliminated. The individual components of the passive house are now discussed [16.66].

Components

Building Envelope. The building envelope plays an important role in the reduction of heat losses. To retain as much heat as possible within the building, particular attention should be paid to thermal insulation and airtightness.

In addition to ensuring that it is sufficiently thick, attention should also be paid to avoiding thermal bridges when designing the thermal insulation. Thermal bridges at edges, corners, junctions, connections, and penetrations can be reduced by various measures. For example, balcony slabs should always be thermally isolated or separated rather than having them penetrate into the insulation, which causes large amounts of heat to be transferred out of the building. Thermal separation can be achieved by supporting balconies on separate columns or by using certified insulated reinforcement cages [16.68, 69].

Besides thermal insulation, airtightness is very important in passive houses. As the insulation layer is not airtight in most cases, an airtight envelope is required in addition to a thermally insulated envelope (Fig. 16.52).

Increasing the airtightness also reduces heat losses and susceptibility to structural damage and improves

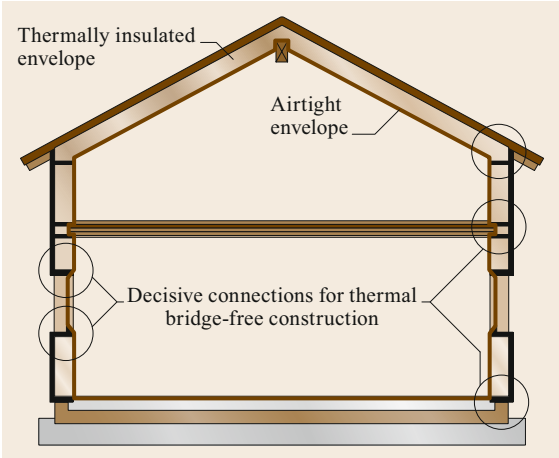

Fig. 16.52 Building envelope (after [16.69])

sound insulation. Various measures are used to achieve the required airtightness. In addition to full plastering of internal surfaces, membranes (flexible liner sheets) or wood-based panels that are jointed airtight can be used. It is also important for all materials and components (e.g., doors and windows) to be installed and joined in an airtight manner [16.68].

Windows. Alongside suitable insulation of the building envelope, the design of the installed windows must be optimized to minimize the energy needed for heating. Windows must satisfy strict thermal insulation requirements that are designed to suppress heat losses through windows. They must have a U value, also called the thermal transmittance (the thermal energy lost through one square meter of a building element at a temperature difference of 1 °C [16.67]), of less than $0.85\,\mathrm{W/(m^2\,K)}$, and the mean temperature on the interior surface of the windows must not fall below 17 °C, even during a cold winter [16.68].

The window frame and the spacers between the pane and frame are also important in the window design. The frame is an element whose importance is often underrated, given that it accounts for roughly 30–40% percent of the area of typical window. To achieve a low U value for the frame, it should be insulated. The heat losses at the crossover between the pane and frame should be minimized by using suitable spacers. The spacer material is important: while the most frequently used spacer material—aluminum—leads to large losses, they can be reduced by using materials such as stainless steel or plastic in spacers.

Finally, several factors must be considered when installing the windows in the wall or significant thermal bridges could result. To this end, the windows should be integrated into the thermal insulation of the external building elements, e.g., by insulating the outside of the window casement [16.67]. Figure 16.53 shows an overview of the aspects that require attention in a passive house window.

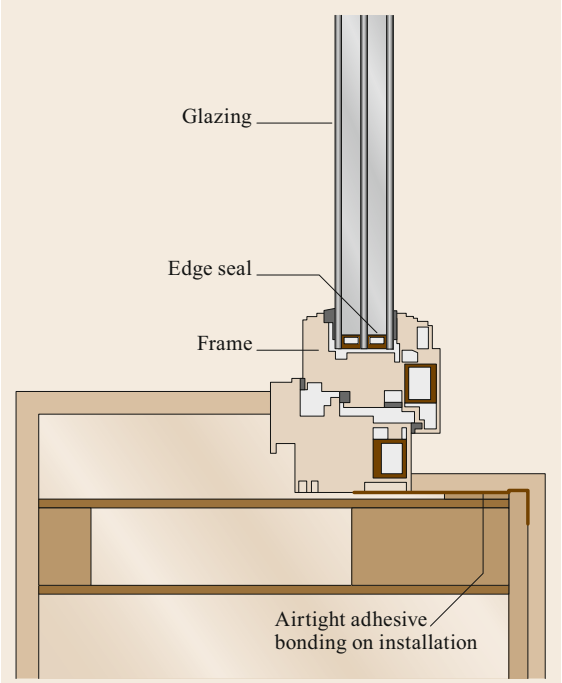

Fig. 16.53 Aspects of passive house windows (after [16.68])

Ventilation. The final decisive component in a passive house is the ventilation system installed. To ensure hygienic air and to minimize ventilation heat losses, the system should be well thought through and designed.

It is important for moisture and odors to be removed where they occur.

Accordingly, air should enter the house in the living room, bedrooms, and children's rooms and leave the house in the kitchen and bathrooms. The individual rooms are connected by so-called air transfer zones (e.g., the hallway). Doors should be fitted with suitable overflow air openings to prevent obstruction of the air flow.

The main reason for installing a ventilation system is to minimize ventilation heat losses, as described above. To achieve this objective, as much of the heat in the exhaust air as possible should be transferred to the fresh air. Depending on the heat exchanger used, up to 90% of the heat can be passed on. The supply air and exhaust air should be clearly separated in the exchanger to avoid mixing. In addition to efficient heat transfer, minimizing the noise emissions produced by

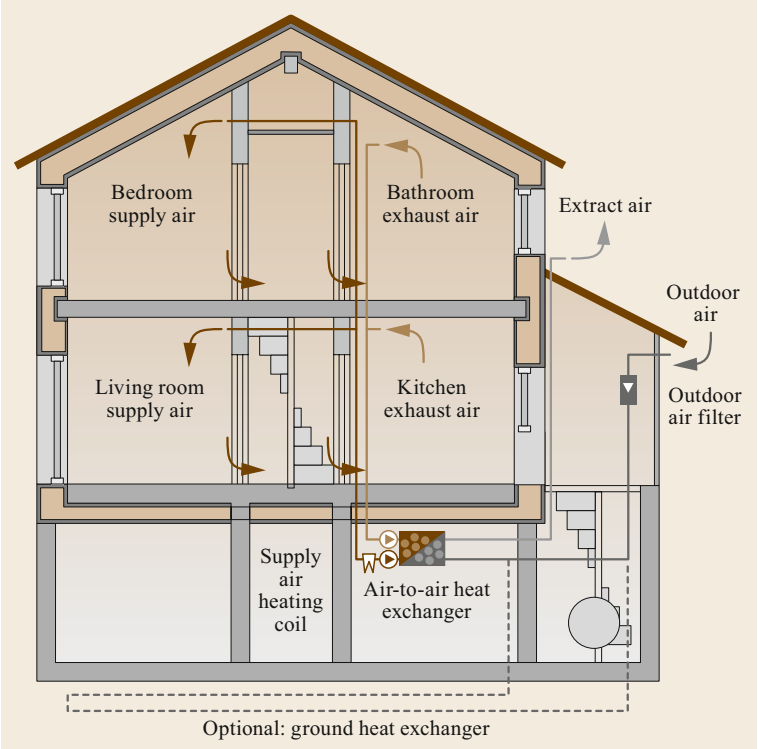

Fig. 16.54 Ventilation system in a passive house (after [16.69])

the ventilation is a very important issue, as this can help to ensure a pleasant living environment. A maximum noise level of 25 dB(A) due to the ventilation system has proven to be acceptable [16.68].

It can also be worthwhile to use the ventilation system to cover the additional heat energy requirement. This can be achieved, for example, by using a heating coil. An example of a practical and worthwhile ventilation system is shown in Figure 16.54.

Examples of Passive House Estates

A large number of statistically assured measurement results have been gathered to determine the effectiveness of the passive house concept. For example, measurements taken in various German passive house estates have allowed the average annual heat energy consumption of a passive house to be calculated.

Figure 16.55 clearly shows that the average heat energy consumption of a passive house on a German estate is significantly below the current (2015) average energy consumption for space heating in Germany. Buildings in Germany supplied with natural gas or heating oil have values of 134 and 132 kWh/(m^2 a), respectively, while buildings with a district heating supply consume around 109 kWh/(m^2 a) [16.71].

While 120.3 million housing units in Germany use natural gas as an energy source, heating oil is used to generate heat in 10.8 million households. By contrast, district heating is used as an energy source in only 5.5 million housing units. Based on these values, an average heat energy demand of 129.4 kWh/(m^2 a) per unit can be calculated for Germany [16.70].

With a heat energy consumption of 12.8 kWh/(m^2 a) in Hanover-Kronsberg, 14.9 kWh/(m^2 a) in Heidelberg, 11.4 kWh/(m^2 a) in Nuremberg-Wetzendorf and 12.2 kWh/(m^2 a) in Frankfurt am Main, the consumption of a passive house is thus approximately 90% below the current national average [16.72].

16.6.4 Design for the Environment (DFE)

Design for the environment, like design for manufacturing or design for assembly, is a set of guidelines to help designers meet particular design goals. Often, these guidelines are reduced to simple rules that aid understanding. However, behind these rules are observations and models that capture how the product can be expected to perform as the result of certain design decisions.

To a certain extent, this whole section aims to impart an understanding of how products and product decisions result in environmental loads. However, there can be different environmental goals. For example, designing an automobile for lower fuel consumption may lead

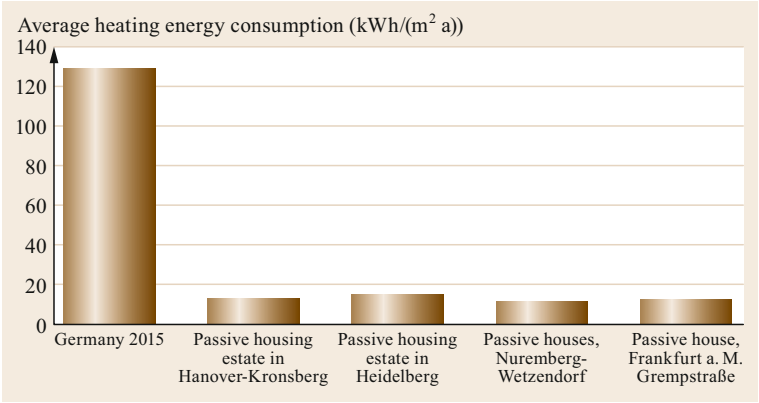

Fig. 16.55 Average heating consumption (after [16.69, 70])

to the use of structural composite materials for weight reduction, whereas designing for recyclability would probably lead to the use of metals for structural components. We now outline some of the generally agreed upon guidelines for two important environmental goals: reduced hydrocarbon fuel consumption and increased recyclability. These are summarized in Tables 16.12 and 16.13.

16.6.5 System-Level Observations

In this section, we have presented an overview of engineering actions that reduce the impacts of materials use, manufacturing, and design decisions on the environment. One of the goals of this section has been to identify the connections between a product life cycle and the associated environmental loads. To do this, we

Table 16.12 Energy efficiency guidelines [16.49, 73, 74]

Action	Reason
Perform SLCA/LCI/LCA for product	Identifies energy usage
Encourage use of clean renewable energy sources	Reduces harmful by-products and preserves resources
Choose the least harmful source of energy (the cleanest fossil fuel is natural gas, followed by oil products and then coal)	Reduces harmful by-products
Have subsystems power down when not in use	Reduces energy usage and fossil fuel consumption
Permit users to turn off systems in part or full	Reduces energy usage and fossil fuel consumption
Avoid high-energy materials	Reduces energy and preserves resources
Avoid high-energy processes	Reduces energy
Specify best-in-class energy efficiency components	Reduces energy usage and fossil fuel consumption
Insulate and/or use waste heat	Reduces losses/increases efficiency

Table 16.13 Recyclability guidelines [16.49, 73, 74]

Rating	Description or action	Reason or comment
Good	Product is reusable/remanufacturable	Extends life of product
Good	Some materials are recyclable with a clearly defined technology and infrastructure	Most metals and some plastics, e.g., PET and HDPE
Good	No toxic materials, or, if present, they are clearly labeled and easy to remove	Avoid Pb, Hg, Cd
Good	Allow easy removal of materials, avoid adhesives and joining methods which cannot be reversed	Facilitates separation and sorting
Less good	Material is technically feasible to recycle but the infrastructure needed to support recycling is not available	Most thermoplastics, some glass
Less good	Material is organic—it can be used for energy recovery but cannot be recycled	Thermoplastics, rubber, wood products
Avoid	Avoid mixtures that cause contamination as well as painting and coatings that are difficult to remove	For example, polyvinylchloride (PVC) in PET, Cu in steel, painted plastics
Avoid	Material has no known or very limited technology for recycling	Heated glass, fiberglass, thermoset plastics, composite materials

have frequently normalized environmentally sensitive parameters such as energy requirements or emissions to some measure of useful output such as the output weight, the economic activity, or, in some cases, the product itself. This scheme helps to assign responsibility and allows us to track progress by enabling comparisons.

At the same time, however, if the environmental load is measured too narrowly, there is a danger of missing the overall trend. One way of making this point is by writing the environmental impact in terms of several normalized parameters. For example, consider

$$\text{Impact} = \text{population}\,\frac{\text{wealth}}{\text{person}}\,\frac{\text{impact}}{\text{wealth}}\,. \qquad (16.2)$$

This mathematical identity, known as the IPAT equation, associates the impact I with three important elements: P for population, A for affluence, and T for technology. Our focus has been on the last term—impact/wealth (or impact/product, etc.). Many variations on the IPAT equation are possible, e.g., $A =$ products/person, $T =$ impact/product, etc. It is the collection of the terms on the right-hand side that give the impact. Hence, a technology improvement could be offset by increases in population and/or wealth/person. This is unfortunate, but does not appears to be in the domain of the engineer. If this was all there was to the story, the IPAT equation would be a neat way to subdivide responsibility. The implication is that engineers have done their job if they have improved the technology term. Unfortunately, the actual picture is much more complicated, as technological advances not only improve the environment but also play an important role in stimulating the economy. In fact, relatively recent economic growth theories pioneered by the Nobel laureate Robert Solow give primary importance to technological change [16.75, 76]. Hence, the very act of improving the performance of a product could, and often does, stimulate increased production and consumption of the product. Some versions of this effect are called the *rebound effect* or *Jevon's paradox*, after the nineteenth century economist who noted that more efficient production and use of a resource (coal in his case) stimulated more consumption of the resource, not less [16.77].

In a similar vein, one can observe that, taken as a whole, labor-saving technological progress in developed countries has not led to less employment (although it has led to increased income). The general rule is that people respond to incentives, and all the incentives in a market economy point toward increasing investment and output rather than decreasing employment or resource use [16.76].

If society wants to reduce resource use, or emissions, or toxic waste, etc., it will need to provide the incentives to do this, most likely through policy instruments. There are many successful examples that illustrate this point. The US has reduced emissions of lead and sulfur dioxide and the energy consumed by refrigerators, and the world has stabilized the levels of ozone in the upper atmosphere through the implementation of the 1976 Montreal Protocol. Hence, the engineering actions described in this chapter should be taken in conjunction with a wider incentive and policy system that will preserve the engineering efficiency gains.

16.7 Failure Mode and Effect Analysis for Capital Goods

Failure mode and effect analysis (FMEA) [16.78, 79] is a method used to recognize and eliminate mistakes or causes of faults during the product design process, particularly during the earliest stages.

This method was developed in the US in 1963 by the National Aeronautics and Space Agency (NASA) during the Apollo space program as a means to design products without design failures. This is especially important when the products cannot be repaired easily (e.g., satellites or spaceships). The method was later adopted by the aviation industry, the automotive industry, in medicine and nuclear technology, as well as by the armaments industry [16.79, 80]. Today, this method is increasingly used in all fields of the development processes of consumer and capital goods [16.78, 81–83].

With regard to the rework of the initially developed and applied approach, see [16.83, 84].

16.7.1 General Innovations for the Application of FMEA

Many products are very complex because they are mechatronic in nature and they involve the simultaneous application of engineering concepts. This complexity blurs the distinction between the three traditional types of FMEA: system FMEA, design FMEA, and process FMEA (Fig. 16.56). In addition, many FMEA sessions mix all three of these fields [16.84].

Instead of making this distinction, a continuous form of FMEA must therefore be implemented. The form of FMEA becomes more detailed as knowledge increases during the product development process. As the design of a product proceeds and product knowledge grows, the danger of errors increases, as does the need for their recognition and elimination. This

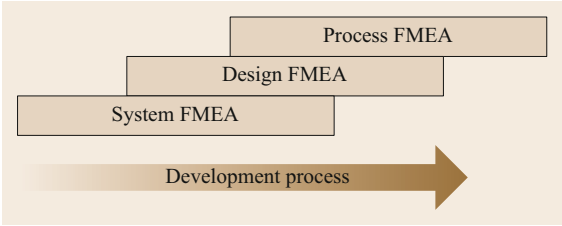

Fig. 16.56 FMEA separated into subprocesses (traditional form)

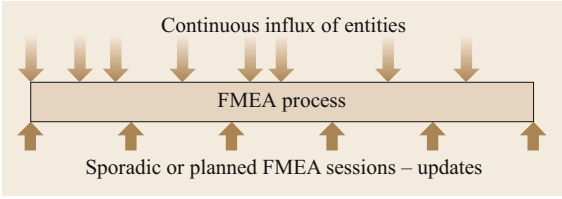

Fig. 16.57 FMEA as a continuous process

leads to the concept of a continuous FMEA process (Fig. 16.57).

Such continuity produces the best results if the group of people involved stays the same. In practice, it turns out that it is reasonable to apply competence in manufacturing or quality control in FMEA at the concept stage. This does not contradict the demand that specialists must be consulted for specific questions. An additional benefit of this approach is that all team members become acquainted with the product.

In general, the early stages of the product development process and the stages during and after market launch are not covered by traditional FMEA. The early phases of the product development process (idea generation and market assessment) include many sources of error that influence the success or failure (not only technically) of a new product.

The traditional form of FMEA does not take the costs of possible damage as well as the costs of avoiding this damage into account. Before deciding on appropriate trouble-shooting actions, it is important to gain an economic understanding of FMEA and its consequences.

This new form of FMEA, which is based on the original form of FMEA but incorporates an economic perspective, is schematized and formalized in Fig. 16.58.

16.7.2 General Rules for Carrying Out FMEA

Observations of FMEA sessions in companies indicate that clear separation into the three fields of system, design, and process is not attempted; nor is it reasonable. This is because each failure affects the system FMEA, the design FMEA, and the process FMEA.

Since the system FMEA is carried out before the design FMEA, this new influence on the system and its effects are not considered. Only a completed process FMEA will discover the actual source of error (e.g., an unsuitable die-casting machine), but the influence of the elimination of this failure mechanism is not considered in the system and design FMEAs.

For these reasons, it is not logical to separate the three individual FMEA methods—it is better to carry them out simultaneously in order to benefit from synergy within the group.

Prerequisites for a FMEA

The following are strict prerequisites for the FMEA process:

1. FMEA participants must be competent and it should be confirmed that they will be continuously available throughout the FMEA [16.85, 86]. The *risk*

Company project	**Failure mode and effect analysis – FMEA** Project- and lifecycle – FMEA									Name of functions / working principles / assemblies Ident-No.						
	Generating department:									Generated by:		Date:				
Failure location Ident-No. Entity	Type of failure	Impact of failure	Cause of failure	Present status Means of control	A	B	E	K	RPZ	Remedial action	Improved status Realized action	A	B	E	K*	RPZ*
1	2	3	4	5	6	7	8	9	10	11	12	13	14	15	16	17

Fig. 16.58 FMEA form with additional columns K and K* to account for cost influences in decision-making

	Examples		
Action	Operate	View	Hear
Function	Amplify	Shine	Ring
Principle	Hydraulic	Electric	Acoustic
Effect, physical principle	Static pressure	Ohm's law	Sound wave
Formula	$P_2 = P_1 (A_2/A_1)$	$U = RI$	$E = J/(f\mu)$

Fig. 16.59 Heuristic approach to the product development process: the five stages of solution finding at the concept stage

priority number (RPZ) (see Sect. 16.7.3) is defined subjectively and thus randomly. Therefore, FMEA participants must be carefully selected to incorporate different views and issues and to obtain a realistic RPZ. This problem is similar to that associated with the evaluation process [16.85, 86].

2. The product idea should be defined and understood by all FMEA participants.
3. The market performance process for a new product should be available.
4. There must be a clear list of demands (requirements) that have been tested for interrelationships [16.87].
5. There should be a use analysis [16.88].
6. The results of a functional analysis should be available (in the form of a functional diagram if possible).
7. The product development process should be approached heuristically. The operational modes between the individual components and units, as well as external (product usage) and internal (operation modes, effects and timings) ones (Fig. 16.59) cannot be represented by conventional forms, so the use of such forms will result in errors.
8. There should be complete documentation of the state of development.

Improving Error Recognition

Strictly speaking, a formal FMEA carried out with conventional forms [16.78] will be incomplete, since there is no suitable inspection of completeness. This affects the applicability of methodologies and passive error detection. Some ways of improving error recognition rates include:

1. Drawing upon the experience of the FMEA participants
2. Including other specialists
3. Improving knowledge of or becoming acquainted with the product to be analyzed

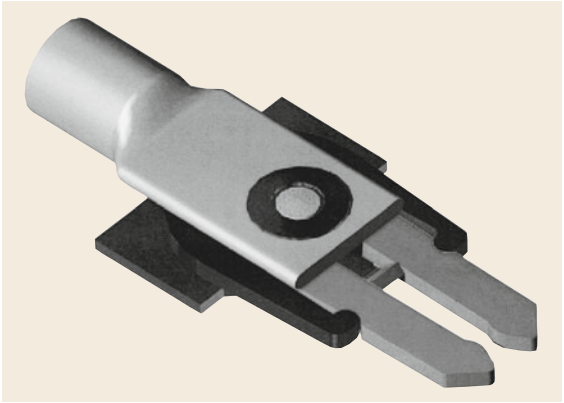

Fig. 16.60 Small product: plug-in contact (source: ABB, Baden)

4. Integrating customer-oriented departments and the customers themselves
5. Recording mistakes and experiences in databases and analyzing them
6. Studying the product history (test reports, complaint reports, etc.)
7. Concurrently applying heuristic support tools (e.g., *Goldfire*, Invention Machine, Boston).

Including All Secondary Fields of Development

A FMEA focuses only on hardware—not documentation, services, software logistics, test programs, manufacturing methods, production plants, and machines. Measurement and checking facilities, experimental setups, and devices are not covered by a FMEA, even though they could be sources of many errors. This situation can only be improved by including these new fields.

16.7.3 Procedure

The procedure used to identify the risks during the lifetime of a product, from the first design concept to product use, is always the same, regardless of the product size: it is the same for a small product such as a plug-in contact (Fig. 16.60) or a large technical system such as a machine tool (Fig. 16.61).

16.7.4 Description of the Project

Nomination of the FMEA Moderator

The moderator is nominated with the agreement of the relevant project manager.

Putting Together the FMEA Team

The team (Table 16.14) is put together by the project manager with the agreement of the FMEA moderator. The visibility of the team within the organization is

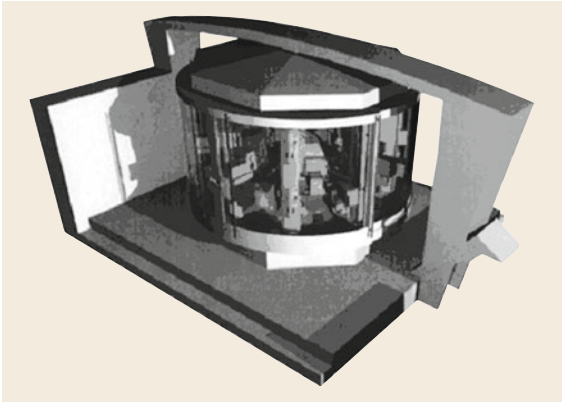

Fig. 16.61 Large product: machine tool (source: A. Breiing, Mikron, Biel)

Table 16.14 Visualization of the team members

No.	Faculty/customer	Name, company
1	Project management	
2	Design, construction, and calculation	
3	Manufacturing preparation	
4	Manufacturing	
5	Quality control and presentation of FMEA	
6	Purchase department	
7	Sales department	
8	Customer support (inauguration, maintenance, repair)	

important (Table 16.14). Each department should contribute at least one continuous FMEA team member.

Structuring Functions. In FMEA, a functional analysis of the investigated product is performed, implying that functional modules or submodules must be specified. This may be achieved using a hierarchical functional diagram (Fig. 16.62) or a a process-orientated diagram (Fig. 16.63), for example.

Filling Out the FMEA Form.

Column 1. This column lists all possible sources of error, as shown in Table 16.15. Because errors can occur even during the early stages of product development, but particularly during idea generation and when determining the market performance profile, the corresponding entities must be entered into this column (the first block). Sources of error can also occur during the development phase (second block), during market launch (third block), and (especially) during the usage phase up to product disposal (fourth block).

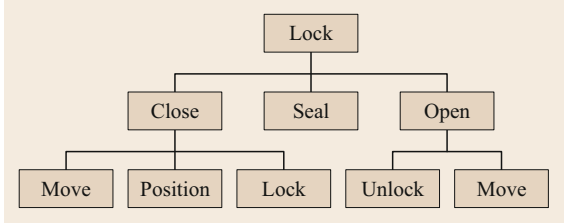

Fig. 16.62 Example of the hierarchical functional structure of an autoclave door [16.89]

Columns 2–4. These columns are filled in upon analyzing all possible potential failures. Examples of potential failures are listed below.

Possible Errors During the Planning Stage.

- The concept for a new product cannot be realized due to physical, chemical, biological, ethical, legal, or cultural constraints or restrictions
- The concept has already been realized by competitors
- The concept is protected by competitors through patents, petty patents, and/or design patents
- There is no market potential and/or no market gap available
- The time is not ripe
- No foe image available or not relevant enough (for military development)
- Materials used in the product are scarce
- No sustainable environment

Possible Errors During the Development Process.

- Internal functions from a function analysis (hierarchical and/or process functional structure)
- External functions from a use analysis
- Assembly of the product structure
- Assembly/disassembly:
  - Assembly/disassembly operation
  - Assembly/disassembly regulations
  - Utilities (e.g., oil for the removal of bearings)
  - Assembly/disassembly devices
  - Control and/or measuring devices (e.g., torque wrench)
  - Additional means (e.g., hoisting devices)
- Components from the product structure and/or parts list
- Manufacturing:
  - Manufacturing processes (e.g., lapping)
  - Manufacturing operations (for manual manufacturing, e.g., deburring)
  - Manufacturing regulations

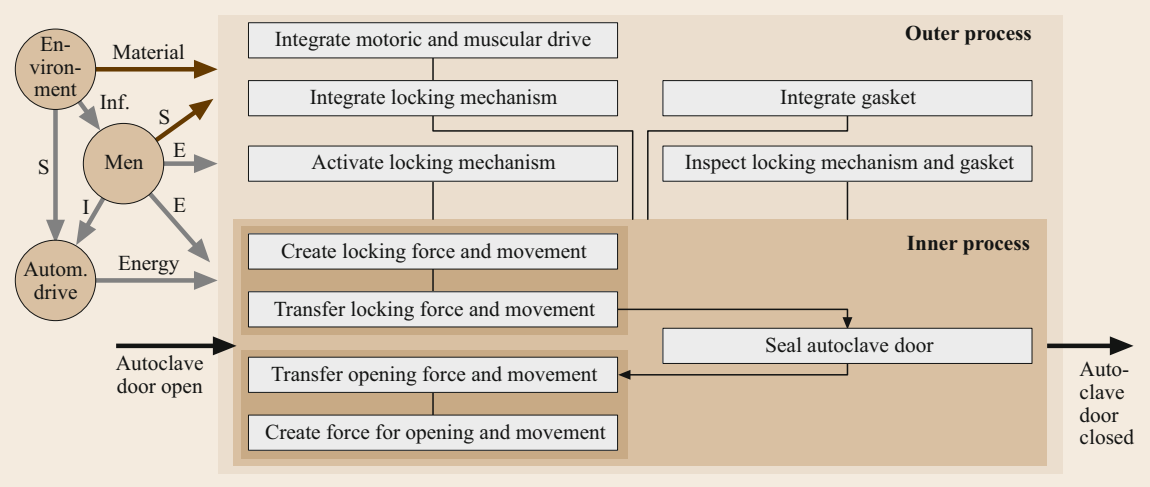

Fig. 16.63 Example of the process functional structure of an autoclave door [16.89], as generated from Fig. 16.61

Table 16.15 Example of a FMEA form showing entities across the full life cycle of a product

Company project	**Failure mode and effect analysis (FMEA)**			
Failure location	Impact of failure	Type of failure	Failure cause	Means of control
Identification number				
Entity				
1	2	3	4	5
Idea Market analysis Cost planning Time scheduling Strategy				
Inner functions Outer functions Module Assembly Component Manufacturing process				
Storage Transport Mounting Initiation				
Implementing Operation Controlling Maintenance Repair Recycling or liquidation				

- Manufacturing means and devices (e.g., drilling patterns)
- Auxiliary manufacturing requirements (e.g., coolant)
- Control and measuring devices (e.g., calipers).

The *outer function* takes into account the imperfect behavior of users (i.e., humans) during the life of the product. This must be included in the FMEA. The user is a component of the system; (s)he influences all of the processes, from idea generation through develop-

Table 16.16 Use analysis of a nutcracker

No.	First-order subfunction	Man–product relationship: required activities	Man–machine interface	Affiliated requirement	Required functions or possible carriers of function
1	Detect (the object)	Nutcracker: Seek Ask for Find	Eye–object Sense of touch–object	Noticeable design Recognizable design Shiny color	Color Contrast Grade of reflection
2	Transport/place (the object)	Nutcracker: Grasp, lift, carry Put down Slacken	Hand–handle Hand–object body Eye–hand–handle	Light weight, ergonomic handle, convenient to use surfaces, *crack protection* Stable stand	Lightweight construction Handle–lever Corrugated surface Platform
3	Equip (with a nut)	Open nutcracker Insert nut	Hand–object Hand–nut	Easy to equip Safe to equip	Trough Stop
4	Locate (the nut)	Hold nut Press against stop Clamp nut	Finger–nut Hand–nut Eye–finger–nut	Easy to use Secure fixation of nut Limit clamping force	Trough Clamping claw Vise
5	Produce (opening) force	Move lever Hit against anvil Turn knob	Hand–lever Fist–anvil Hand/finger–knob	Secure application of force Note finger/hand span	Handle Lever
6	Guide force/amplify force	Inner function	–	Force (N) Distance (mm) Limit force/distance	Lever Spline Screw
7	Open nut by: – pressure – effect of spline	Inner function	–	Selection of effective functionalities that can be realized inexpensively	Thrust piece Splines Blade Clamping screw
8	Remove (result)	Remove cracked nut Remove nut and shell	Finger–cracked nut Hand–cracked nut Eye–finger–cracked nut	Easy to remove Certain removal	Collecting pan, sack Basin Flap Opening
9	Clean	Hold nutcracker Shake out cavity that holds nut Clean cavity	Hand–nutcracker Finger/hand–cleaning device	Easy to handle No unreachable corners Easy-to-clean surface	*Nut cavity design* Shape of surface Surface roughness

ment and usage until the end of the product's life cycle. The user can cause failures and errors at any stage. The available use analysis (Table 16.16), which covers all product life cycle stages [16.88], can be used to account for all possible sources of error during assembly, maintenance, and repair (Table 16.15, fourth block).

In order to identify these potential sources of error systematically, the FMEA is expanded through the incorporation of the use analysis. These entities can then be taken from the tabulated record of man–machine interfaces.

Moreover, each part, assembly, and product has technical documentation that must be checked for errors.

Possible Errors Within the Technical Documentation. It is important to check the:

- Manufacturing documents (drawings and lists)
- Documents for assembly/disassembly (e.g., instruction sheets)
- Calculation documents, such as:
  - Load assumptions
  - Verification of strength
  - Verification of deformation
  - Verification of stability (e.g., buckling, bending, stability)
- Balances, such as:
  - Balance of performance
  - Balance of weight

- Positions of the centers of gravity
- Balance of the moments of inertia
- Balance of temperature
- Balance of coolant

- Documents such as:
  - Manufacturing documents
  - Instruction sheets
  - Instructions for maintenance and service
  - The spare-part catalog.

Possible Errors During Market Launch.

- Storage:
  - Activities
  - Apparatus (e.g., bearing block)
  - Racks, halls, stacks (e.g., storage rooms with air conditioning)
- Transport:
  - Activities
  - Apparatus (e.g., lifting gear)
  - Means of transportation (e.g., overhead crane)
- Mounting:
  - Activities
  - Mounting regulations and instructions
  - Apparatus (e.g., lifting gear)
  - Measuring and test equipment (e.g., theodolite)
- Initial operation:
  - Activities and testing in accordance with the:
    Instruction manual (*Initial Setup* chapter)
    Checklist
    User handbook
    Maintenance instructions.

Possible Errors During the Use Stage and Decommissioning.

- Initial operation:
  - Activities in accordance with the:
    Instruction manual (*Initial Setup* chapter)
    Checklist
    Maintenance history
    Document
- Operation:
  - Activities in accordance with the:
    Instruction manual
    User handbook
- Maintenance:
  - Activities and testing in accordance with the:
    Instruction manual
    User handbook
    Service documentation
    Maintenance history (e.g., exhaust emissions document for an automobile)
- Service:
  - Activities and testing in accordance with the:
    Instruction manual
    User handbook
    Service manual and spare-part catalog
    Logistics documents (e.g., global workshop catalog).

Column 5. The status of each failure measure and each test procedure that is currently used is entered here. These entries are used to reduce the causes of failure in column 4 and to detect possible sources of error.

Columns 6–10. These columns are used to calculate the risk priority number (RPZ).

Before deciding on the troubleshooting actions that are to be taken, it is very important to obtain an economic perspective on the consequences of those actions. When the FMEA is extended by including a cost calculation, the form will include an additional column that lists values of K, the probable cost of an error.

The RPZ values in column 10 are calculated via

$$\mathrm{RPZ} = ABEK\,, \tag{16.3}$$

where A is the probability that the failure will occur, which takes the following values:

1 Unlikely
2 Very low
3 Low
4 Medium
5 High
6 Very high.

B is the impact of that failure on the customer, which takes the following values:

1 Customer does not notice the consequences
2 Insignificant inconvenience to the customer
3 Minor inconvenience to the customer
4 Significant inconvenience to the customer
5 Irritation of the customer
6 Possible loss of the customer.

E is the probability of detecting the failure, which takes the following values:

1 Very high
2 High
3 Medium
4 Low
5 Very low
6 Unlikely.

Finally, K is the probable cost of the failure, which takes the following values:

1 No or negligible increase in costs
2 Minor additional costs
3 Moderate additional costs
4 High additional costs
5 Extremely high additional costs
6 Costs are not budgeted for.

Instead of values ranging from 1 to 6, a value range of 1–10 can also be applied, although this is only reasonable if detailed knowledge is available (e.g., from the FMEA at the end of the product development process).

A RPZ value in the range 1296–10 000 is considered to be unacceptably high; the range 256–1295 corresponds to medium RPZ; and a RPZ value in the range 1–255 is low. In practice, the threshold RPZ value below which a failure is ignored because it is not profitable to address it can be anywhere between 81 and 625.

Column 11. The troubleshooting actions that should be performed in the case of an error are entered into this column.

Columns 12–17. If any of the recommended troubleshooting actions listed in column 11 are performed, those actions are described in column 12 and the RPZ value is recalculated (yielding RPZ*) and listed in columns 13–17. Values of RPZ* listed in column 17 are calculated via

$$\mathrm{RPZ}^* = ABEK^* \,. \tag{16.4}$$

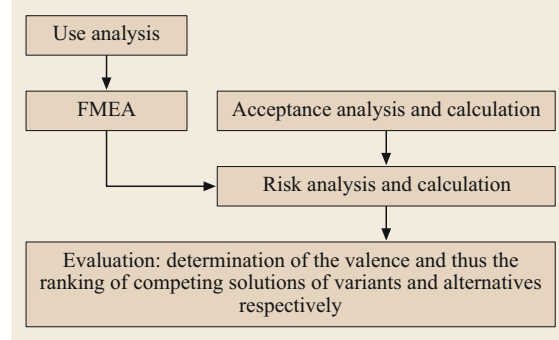

Fig. 16.64 Relationship between acceptance, risk, and evaluation

Here, K^* is the probable cost of implementing the measures required to avoid or minimize a probable error. Both K and K^* have the same range of risk factors. Values of RPZ* are categorized in a similar manner to those of RPZ, meaning that the measures are accepted if RPZ* is below approximately 81–625. If RPZ* is higher than RPZ, the measures applied to avoid or to minimize the error should be reconsidered.

16.7.5 Further Use of FMEA Results

Several competing solutions or alternatives are available during the concept and sketching phases. In order to identify the best solution, a ranking procedure is carried out. If the ranking procedure takes *risk* into account, it is reasonable to use the sum of the RPZ or RPZ* values for a particular solution to calculate the risk associated with that solution.

The relationship between acceptance, risk, and weighting is shown in Fig. 16.64.

16.8 Bioindustrial Design: Challenges and Vision

Nature did not invent the wheel because it did not need the wheel: the main methods by which organisms move—flying, swimming, diving, running, and gliding—have been perfected over the course of millions of years of continuous (and ongoing) evolution. Mankind's technical achievements pale in comparison to those of nature. *Think tanks* aimed at promoting technological development (which often ends in a dead-end street) are wisely drawing upon natural phenomena, implying that biotechnology (bionics) will be one of the main preoccupations of future engineers.

For instance, an international oil company is investigating hydrodynamic molds for lowering giant submerged tankers into shallow, calm depths to shield them from destructive conditions at the surface of the water (the interface between two media). Our own experiences underwater suggest that man-made vessels (even the latest submarines) have nonoptimal designs, as they leave kilometer-long white trails behind them in the semisubmerged state due to poor hydrodynamics. In contrast, orcas and belugas (for example) do not create large water waves when semisubmerged; they glide in the exact same manner as when they are fully submerged. This demonstrates that is it possible to further optimize the design and construction of propellers. Here, as in other comparisons, nature puts the engineering world in the shade.

Even the pressure equalization processes used by the largest mammals in the world—whales—during rapid submerging and surfacing are yet to be studied in detail and imitated in technology. Another water-based example: no complex technical device would survive unscathed the rapid vertical immersion experienced by waterfowl hunting food, nor the rapid change in media that occurs when waterfowl resurface.

The shape of the manta ray has long been held up by aircraft manufacturers as the ideal silhouette for a passenger airplane. Indeed, investigations of the manta ray by Hugo Junkers in the early twentieth century inspired him to design *wing-only airplanes*. In 1920, he broke new ground with the development of the Junkers D-2500: an (almost) wing-only airplane in which passengers sat in cabins located in the front sections of the wings! In the US, the wing-only concept has been applied in Northrop's B1 and B2 bombers.

In the construction industry too, nature serves as a role model for design and construction. For instance, termite structures—with their ventilation systems that allow the termites to survive low external temperatures unharmed and their fermentation fields that provide a ready supply of food—are essentially *giant skyscrapers* with approximately 1000 floors. The human equivalent of such a skyscraper would be 3000 m high!

The famous industrial designer Luigi Colani was introduced by the biologist Ernst Haeckel to the miraculous world of microscopic lime structures: architectural inspirations that have been developing in the depths of the oceans for eons. The vast majority of the world's oceans is unexplored, which raises the question of the benefits of space research, given that the survival of mankind depends more on the careful treatment of our oceans that cover 70% of the Earth's surface. Unfortunately, the's extensive lectures and seminars on Bauhaus new beginnings at the Hochschule für Bildende Künste Berlin (later the Academy of Fine Arts and the University of the Arts) could not be realized at that time. Many years later, it should be noted that among the cheerful trilogy of colorful cubes, pyramids, and spheres laid down by Kandinsky, only the cube is left, and was often taught as *Bauhaus style* in universities and used by leading design teams. The new forms are orthogonal, the materials steel and glass, and the color *gray*.

German engineering sciences are world leading in many technical fields, but German design will probably never again reach the level of design and color delivered by the Bauhaus in Weimar in the early 1930s, where a colorful group of young, brilliant, international creatives gathered around Walter Gropius to turn conventional *petty bourgeois design* on its head. Wassily Kandinsky, a Russian artist, designed the ultimate visualization of the Bauhaus approach—a brightly colored logo for the school, to act as a goal and a legacy. However, the novel methods espoused by the Bauhaus were deemed too *un-German* by the Nazis striving for power and were thus forbidden, causing the intellectual founders of the school to become scattered around the world. After World War II, incomprehensibly, only the cube from Kandinsky's triple form (*cube, pyramid, and sphere*) was adopted and cultivated by German designers after World War II, prompting a new—false—identity to be attributed to the true *universal Bauhaus* design philosophy. Bauhaus became associated with squares and cubes, with steel and glass, with gray. Therefore, only 33% of the original Bauhaus principle has survived. This falsification of the power of shape and color has become the backbone of German design. The corresponding design philosophy can be observed, for example, in the sharp-edged forms of sanitary ceramics and fittings.

However, not all supporters of the *old Bauhaus* followed suit; for instance, the author—an aerodynamicist and aircraft builder—returned to design to represent the original Bauhaus philosophy with technical competence

Fig. 16.65 Futuristic sports car design by L. Colani

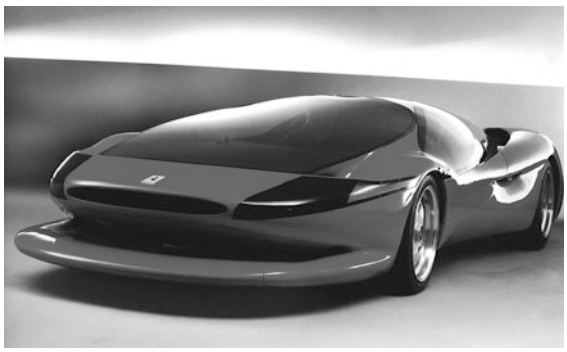

Fig. 16.66 Design of a Ferrari sports car from 1989 by L. Colani

and steadfastness. The idea of *going back to go forward*, which the author considers to be crucial to enhancing German design, has only partly been adopted by German industry. That said, the original Bauhaus philosophy has often been applied in other countries, and has led to spectacular new developments (e.g., in the design of sports cars; see Figs. 16.65 and 16.66). From the Design Center in Milan, the author is orchestrating the creation of think tanks aimed at encouraging a better Bauhaus design philosophy and demonstrating the tradition of Bauhaus design around the world, in line with the motto [16.90–96]: *long live the original Bauhaus*!

References

16.1 K. Ehrlenspiel: *Integrierte Produktentwicklung: Denkabläufe, Methodeneinsatz, Zusammenarbeit*, 4th edn. (Hanser, München 2009), in German

16.2 K. Roth: *Konstruieren mit Konstruktionskatalogen: Konstruktionslehre*, 3rd edn. (Springer, Berlin, Heidelberg 2001), in German

16.3 G. Pahl, W. Beitz, J. Feldhusen, K.-H. Grote: *Konstruktionslehre*, 8th edn. (Springer, Berlin, Heidelberg 2013), in German

16.4 F. Kramer: *Innovative Produktpolitik* (Springer, Berlin, Heidelberg 1988), in German

16.5 W. Rodenacker: *Methodisches Konstruieren*, 4th edn. (Springer, Berlin, Heidelberg 1991), in German

16.6 R. Koller: *Konstruktionslehre für den Maschinenbau*, 4th edn. (Springer, Berlin, Heidelberg 1998), in German

16.7 VDI: *VDI 2221: Methodik zum Entwickeln und Konstruieren technischer Systeme und Produkte* (VDI, Düsseldorf 1993), in German

16.8 G. Pahl, W. Beitz, J. Feldhusen, K.-H. Grote: *Konstruktionslehre*, 7th edn. (Springer, Berlin, Heidelberg 2007), in German

16.9 K.-H. Grote, J. Feldhusen (Eds.): *Dubbel: Taschenbuch für den Maschinenbau*, 24th edn. (Springer, Berlin, Heidelberg 2014), in German

16.10 H. Petra: *Systematik, Erweiterung und Einschränkung von Lastausgleichslösungen für Standgetriebe mit zwei Leistungswegen*, Dissertation (TU München, München 1981), in German

16.11 DIN: *DIN EN 1325: Value Management* (Beuth, Berlin 2014), in German

16.12 DIN: *Sachmerkmale, DIN 4000 – Anwendung in der Praxis* (Beuth, Berlin 2006), in German

16.13 DIN: *DIN 4000 (z. Zt. mit Entwürfen 163 Teile): Sachmerkmal-Leisten [für Norm- und Konstruktionsteile]* (Beuth, Berlin 2006), in German

16.14 D. Krauser: *Methodik zur Merkmalbeschreibung technischer Gegenstände* (Beuth, Berlin 1986), in German

16.15 H. Czichos, M. Hennecke: *Hütte – Das Ingenieurwissen*, 34th edn. (Springer, Berlin, Heidelberg 2012), in German

16.16 H. Holliger-Uebersax: *Handbuch der allgemeinen Morphologie*, 4th edn. (MIZ, Zürich 1980), in German

16.17 J. Müller: *Grundlagen der systematischen Heuristik* (Dietz, Berlin 1970), in German

16.18 H.G. Schmidt: *Heuristische Methoden als Hilfen zur Entscheidungsfindung beim Konzipieren technischer Produkte* (TU Berlin, Berlin 1980), in German

16.19 V. Krick: *An Introduction to Engineering and Engineering Design*, 2nd edn. (Wiley, New York 1969)

16.20 R.K. Penny: Principles of engineering design, Postgrad. Med. J. **46**, 344–349 (1970)

16.21 W.F. Daenzer: *Systems Engineering*, 6th edn. (Industrielle Organisation, Zürich 1989)

16.22 F. Zwicky: *Entdecken, Erfinden, Forschen im morphologischen Weltbild*, 2nd edn. (Baeschlin, Glarus 1989), in German

16.23 H. Seeger: *Industrie-Designs* (Expert, Grafenau 1983), in German

16.24 H. Hertel: *Biologie und Technik* (Krausskopf, Mainz 1963), in German

16.25 P. Kerz: Konstruktionselemente und -prinzipien in Natur und Technik, Konstruktion **39**, 474–478 (1987), in German

16.26 P. Kerz: Natürliche und technische Konstruktionen in Sandwichbauweise, Konstruktion **40**, 41–47 (1988), in German

16.27 P. Kerz: Zugbeanspruchte Konstruktionen in Natur und Technik, Konstruktion **40**, 277–284 (1988), in German

16.28 W. Kroy: Abbau von Kreativitätshemmungen in Organisationen. In: *Personal-Management in der industriellen Forschung und Entwicklung*, ed. by M.E. Domsch (Heymanns, Köln 1984), in German

16.29 VDI: *VDI 2225 Blatt 1 und 2: Technisch-wirtschaftliches Konstruieren* (VDI, Düsseldorf 1998), in German

16.30 C. Zangemeister: *Nutzwertanalyse in der Systemtechnik*, 4th edn. (Wittemann, München 1976), in German

16.31 R. Kühnpast: *Das System der selbsthelfenden Lösungen in der maschinenbaulichen Konstruktion*, Dissertation (TH Darmstadt, Darmstadt 1968), in German

16.32 K.-H. Habig: *Verschleiß und Härte von Werkstoffen* (Hanser, München 1980), in German

16.33 VDI: *VDI 2242 Blatt 1 und 2: Konstruieren ergonomiegerechter Erzeugnisse* (VDI, Düsseldorf 1986), in German; Current draft: VDI 2242:2016-06

16.34 I. Klöcker: *Produktgestaltung* (Springer, Berlin, Heidelberg 1981), in German

16.35 VDI: *VDI 2243 Blatt 1: Recyclingorientierte Produktentwicklung* (VDI, Düsseldorf 2002), in German

16.36 H. Meyer: *Recyclingorientierte Produktgestaltung* (VDI, Düsseldorf 1983), in German

16.37 M. Pourshirazi: *Recycling und Werkstoffsubstitution bei technischen Produkten als Beitrag zur Ressourcenschonung* (TU Berlin, Berlin 1987), in German

16.38 R.-D. Weege: *Recyclinggerechtes Konstruieren* (VDI, Düsseldorf 1981), in German
16.39 VDI: *VDI 2222: Methodisches Entwickeln von Lösungsprinzipien* (VDI, Düsseldorf 1997), in German
16.40 F.J. Gierse: *Funktionen und Funktionsstrukturen, zentrale Werkzeuge der Wertanalyse*, VDI-Berichte, Vol. 849 (VDI, Düsseldorf 1990), in German
16.41 V. Hubka: *Theorie Technischer Systeme: Grundlagen einer wissenschaftlichen Konstruktionslehre*, 2nd edn. (Springer, Berlin, Heidelberg 1984), in German
16.42 F. Hansen: *Konstruktionssystematik: Grundlagen für eine allgemeine Konstruktionslehre*, 2nd edn. (VEB Verlag Technik, Berlin 1965), in German
16.43 J. Rugenstein (Ed.): *Arbeitsblätter Konstruktionstechnik* (Technische Hochschule Magdeburg, Magdeburg 1979), in German
16.44 F. Engelmann: *Produktplanung und Produktentwicklung in kleinen und mittleren Unternehmen* (Shaker, Aachen 1999), in German
16.45 Novespace: *Parabolic Flight Campaign with A300 ZERO-G User's Manual*, 5th edn. (Novespace, Paris 1999)
16.46 R. Bjärnemo: *Evaluation and Decision Techniques in the Engineering Design Process* (Heurista, Zürich 1991)
16.47 A.F. Osborn: *Applied Imagination—Principles and Procedures of Creative Thinking* (Scribner, New York 1957)
16.48 J.O. Nriagu, J.M. Pacyna: Quantitative assessment of worldwide contamination of air, water and soils by trace metals, Nature **333**, 134–149 (1988)
16.49 T.E. Graedel, B.R. Allenby: *Design for Environment* (Prentice Hall, New York 1998)
16.50 T.E. Graedel: *Streamlined Life-Cycle Assessment* (Prentice Hall, New York 1998)
16.51 W. Leontief: *Input-Output Economics*, 2nd edn. (Oxford Univ. Press, Oxford 1986)
16.52 C. Hendrickson, A. Horvath, S. Joshi, L. Lave: Economic input-output models for life-cycle assessment, Environ. Sci. Technol. **13**(4), 184A–191A (1998)
16.53 R. Miller, P. Blair: Input-output analysis: foundations and extensions. In: *Environmental Input-Output Analysis* (Prentice Hall, New York 1985) pp. 236–260, Chap. 7
16.54 S. Joshi: Product environmental life-cycle assessment using input-output techniques, J. Ind. Ecol. **3**(2/3), 95–120 (2000)
16.55 S. Suh, G. Huppes: Methods for life cycle inventory of a product, J. Cleaner Prod. **13**, 687–697 (2005)
16.56 Environmental Protection Agency: EPA TRI 2015 Data release web page, http://www.epa.gov/tri/ (2015)
16.57 V. Smil: *Energies—An Illustrated Guide to the Biosphere and Civilization* (MIT Press, Cambridge 1999)
16.58 K.J. Martchek, E.S. Fisher, D. Klocko: Alcoa's worldwide life cycle information initiative, SAE Conf. Proc. **339**, 121–126 (1998)
16.59 P.F. Chapman, F. Roberts: *Metals Resources and Energy* (Butterworth-Heinemann, London 1983)
16.60 E. Williams, R. Ayres, H. Heller: The 1.7 kg microchip: energy and chemical use in the production of semiconductors, Environ. Sci. Technol. **36**(24), 5504–5510 (2002)
16.61 J. Dahmus, T. Gutowski: An environmental analysis of machining. In: *ASME Int. Mech. Eng. Congr*, ed. by L. Yao (ASME, New York 2004)
16.62 S. Dalquist, T. Gutowski: Life cycle analysis of conventional manufacturing techniques: sand casting. In: *ASME Int. Mech. Eng. Congr*, ed. by L. Yao (ASME, New York 2004)
16.63 J. Sherman, B. Chin, P.D.T. Huibers, R. Garcia-Valls, T.A. Hatton: Solvent replacement for green processing, Environ. Health Persp. **106**(Suppl. 1), 253–271 (1998)
16.64 V.M. Thomas, T.G. Spiro: The U.S. dioxin inventory: Are there missing sources?, Environ. Sci. Technol. **30**(2), 82A–85A (1996)
16.65 A. Grubler: *Technology and Global Change* (Cambridge Univ. Press, Cambridge 1998)
16.66 Passivhaus Institut: Passipedia – Die Passivhaus-Wissensdatenbank, https://passipedia.de/ (2017), in German
16.67 A. Graf: *Das Passivhaus – Wohnen ohne Heizung* (Callwey, München 2000), in German
16.68 Informations-Gemeinschaft Passivhaus Deutschland: *Aktiv für mehr Behaglichkeit: Das Passivhaus*, 9th edn. (IG Passivhaus Deutschland, Darmstadt 2016), in German
16.69 Passivhaus Institut: http://www.passiv.de
16.70 Bundesverband der Energie- und Wasserwirtschaft e. V.: *„Wie heizt Deutschland?" – BDEW-Studie zum Heizungsmarkt* (BDEW, Berlin 2015)
16.71 Techem Energy Services: *Energiekennwerte 2016. Eine Studie von Techem zum Wärme- und Energieverbrauch in Mehrfamilienhäusern* (Techem, Eschborn 2016), in German
16.72 R. Kuehr, E. Williams (Eds.): *Computers and the Environment: Understanding and Managing their Impacts* (Kluwer Academic, Dordrecht 2004)
16.73 Microelectronics, Computer Technology Corporation: *Life Cycle Assessment of a Computer Workstation*, Report HVE-059-094 (MCC, Austin 1994)
16.74 K. Kawamoto, J. Koomey, B. Nordman, A. Meier: Electricity used by office equipment and network equipment in the U.S. In: *2000 Summer Study on Energy Efficiency in Buildings* (ACEEE, Washington 2000)
16.75 E. Williams: Environmental impacts in the production of personal computers. In: *Computers and the Environment: Understanding and Managing Their Impacts*, ed. by R. Kuehr, E. Williams (Kluwer Academic, Dordrecht 2004) pp. 41–72
16.76 Environmental Protection Agency: *EPA egrid 2004* (EPA, Washington 1998)
16.77 W.S. Jevons: *The Coal Question: An Inquiry Concerning the Progress of the Nation, and the Probable Exhaustion of our Coal-mines*, Reprints of Economic Classics (Kelley, Fairfield 1906)
16.78 DIN: *DIN EN 60812: Fehlzustandsart- und -auswirkungsanalyse (FMEA)* (Beuth, Berlin 2006), in German; Current draft: DIN EN 60812:2015-08
16.79 Department of Defense: *Procedures for Performing a Failure Mode, Effects and Criticality Analysis (FMECA)*, MIL Std., Vol. 1629A (Department of Defense, Washington 1980)

16.80 P. Conrad, P.E. Hedderich: *Navy Proactive Maintenance* (US Navy, Washington 2000)
16.81 N. Berens: *Anwendung der FMEA in Entwicklung und Produktion* (Verlag Moderne Industrie, Landsberg 1989), in German
16.82 C.H. Kepner, B.B. Tregoe: *Entscheidungen vorbereiten und richtig treffen* (Verlag Moderne Industrie, Landsberg 1988), in German
16.83 M. Schubert: *FMEA – Fehlermöglichkeits- und Einflußanalyse* (Deutsche Gesellschaft für Qualität, Frankfurt 1993), in German
16.84 A. Breiing: *Die FMEA in sinnvoller Form für Investitionsgüter* (Institut für Mechanische Systeme, ETH Zürich, Zürich 2003), in German
16.85 A. Breiing: The evaluators influence on the results of evaluation. In: *MCE 2000, Neukirchen* (2000)
16.86 A. Breiing: Who evaluate the evaluators? In: *Int. Conf. Comput. Integr. Manuf., Zakopane* (2001)
16.87 A. Breiing, R. Knosala: *Bewerten Technischer Systeme* (Springer, Berlin, Heidelberg 1997), in German
16.88 A. Breiing: *Vertiefungsvorlesung Produkte-Design* (Institut für Mechanische Systeme, ETH Zürich, Zürich 2000), in German
16.89 A. Breiing, M. Flemming: *Theorie und Methoden des Konstruierens* (Springer, Berlin, Heidelberg 1993), in German
16.90 L. Colani, A. Fujimoto (Eds.): *Part 1—Designing Tomorrow: Car Styling*, Tomorrow, Vol. 23 (Sanei Shobo, Tokyo 1978)
16.91 L. Colani, A. Fujimoto (Eds.): *Part 2—For a Brighter Tomorrow: Car Styling*, Tomorrow, Vol. 34 (Sanei Shobo, Tokyo 1981)
16.92 L. Colani, A. Fujimoto (Eds.): *Part 3—Bio-design of Tomorrow: Car Styling*, Tomorrow, Vol. 46 (Sanei Shobo, Tokyo 1984)
16.93 A. Bangert: *Colani—Fifty Years of Designing the Future* (Thames Hudson, London 2004)
16.94 A. Bangert: *Colani—Form Follows Nature* (Bangert, Schopfheim 2009)
16.95 L. Colani, A. Bangert: *Colani—The Art of Shaping the Future* (Bangert, Schopfheim 2004)
16.96 L. Colani: Bio-Industrie-Design: Herausforderungen und Visionen. In: *Dubbel – Taschenbuch für den Maschinenbau*, 24th edn., ed. by K.-H. Grote, J. Feldhusen (Vieweg, Wiesbaden 2014), in German

Frank Engelmann

Industrial Engineering
Ernst-Abbe-Hochschule Jena University of Applied Science
Jena, Germany
frank.engelmann@eah-jena.de

Frank Engelmann studied mechanical engineering at the Engineering Department of the University of Magdeburg. He then obtained a PhD at the same institution while working as the managing Director of a production business. His research activities focus on secondary explosion protection and biomedical technology. In October 2007, Frank Engelmann joined the University of Applied Sciences in Jena, Germany, as a full professor.

Alois Breiing

breiing@imes.mavt.ethz.ch

Alois Breiing is a retired professor at ETH Zürich who lectured on machine design. His research focused on evaluation and decision processes. In 1985, he began work as a senior researcher and section leader at the Institute of Design and Construction Methods (now the Institute of Mechanical Systems), ETH Zurich. He received a PhD in 1991. He also worked as an aerospace engineer for the company Dornier for 23 years.

Timothy Gutowski

Department of Mechanical Engineering
Massachusetts Institute of Technology
Cambridge, MA, USA
gutowski@mit.edu

Timothy Gutowski is a Professor of Mechanical Engineering at MIT, where his research focuses on the relationship between manufacturing and the environment. He was Director of MIT's Laboratory for Manufacturing and Productivity for 10 years and Associate Department Head of Mechanical Engineering from 2001 to 2005. He has a PhD in Mechanical Engineering from MIT, a MS degree in Theoretical and Applied Mechanics, and a BSc degree in Mathematics.

17. Piston Machines

Helmut Tschöke, Vince Piacenti, Brent Keppy, Aneel A. Singh, Steven D. White, Justin Kern, Jon H. van Gerpen

Piston machines are the most used power and work machines in the mechanical engineering industry. Piston machines are divided into so-called reciprocating and rotary piston machines. With the first type, a reciprocating motion is transformed to a rotary motion in the case of the power machine and conversely in the case of the working machine. Today, rotary piston machines are almost exclusively used as work machines. Important innovations and intensive research are practiced in particular for the use of piston machines as an internal combustion engine. Therefore, mixture formation and the combustion process, with their consequences in terms of emission and fuel consumption, are in the center of attention.

17.1 **Foundations of Piston Machines** 683
17.1.1 Definitions 683
17.1.2 Ideal and Real Piston Machines 685
17.1.3 Reciprocating Machines 688
17.1.4 Selected Elements of Reciprocating Machines 694
17.2 **Positive Displacement Pumps** 697
17.2.1 Types and Applications 697
17.2.2 Basic Design Parameters 699
17.2.3 Components and Construction of Positive Displacement Pumps 705
17.3 **Compressors** 713
17.3.1 Cycle Description 713
17.3.2 Multistaging 714
17.3.3 Design Factors 715
17.4 **Internal Combustion Engines** 715
17.4.1 Basic Engine Types 716
17.4.2 Performance Parameters 717
17.4.3 Air Systems 718
17.4.4 Fuel Systems 722
17.4.5 Natural Gas Fuel Systems 729
17.4.6 Ignition Systems 731
17.4.7 Mixture Formation and Combustion Processes 733
17.4.8 Fuels 735
17.4.9 Emissions 738
17.4.10 Selected Examples of Combustion Engines 745
References 750

17.1 Foundations of Piston Machines

17.1.1 Definitions

Piston machines employ a moving displacer (also called a piston) to convert a medium's potential energy into kinetic energy or vice versa, i.e., they use the movement of the displacer to increase the energy content of the medium. This occurs in a working chamber that can be altered by the displacer motion.

In piston machines, the moving displacer effects both the charge cycle (filling and draining of the medium) and the work cycle (expansion and compression). The characteristic mode of operation for piston machines is a self-contained working chamber that varies periodically due the piston's movement.

Piston machines can be classified according to their method of operation, the piston motion and the medium used (Fig. 17.1). When piston machines are classified according to their method of operation, then power and work machines are differentiated.

A power machine converts a medium's potential energy into mechanical energy. Power machines include engines (pneumatic engines, hydraulic motors) and thermal machines (steam engines, combustion engines). Work machines, on the other hand, utilize mechanical energy to increase the energy of the medium being conveyed. Work machines include compressors and pumps. Rotating and oscillating displacer motions are another potential classification. In addition, piston

K.-H. Grote, H. Hefazi (Eds.), *Springer Handbook of Mechanical Engineering*, Springer Handbooks,
https://doi.org/10.1007/978-3-030-47035-7_17

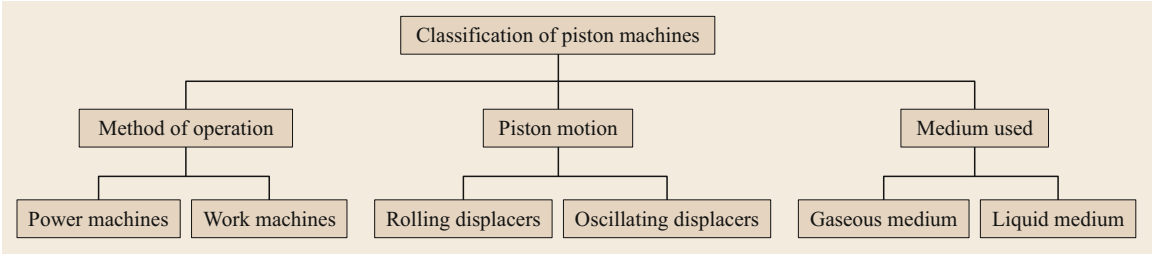

Fig. 17.1 Classification of piston machines (after [17.1])

machines can be classified according to the medium used, which can be gaseous or liquid.

Reciprocating Machines

When a piston machine's oscillating displacer executes a linear motion, it is called a reciprocating machine (Fig. 17.2). A cylindrical displacer that moves between two end positions, top and bottom dead center (TDC and BDC), is characteristic. The working chamber is calculated from the piston diameter and the distance between the two dead centers, the so-called stroke s (Sect. 17.1 *Working Chamber*), and is, therefore, also referred to as the displacement.

Rotary Piston Machines

Machines of this type are characterized by a rotating displacer. The medium can flow axially or radially to the piston axis. An axial direction of flow is found, for instance, in screw-type compressors, screw pumps, or eccentric screw pumps. Rotary piston compressors, roots blowers, and gear pumps are examples in which the medium flows radially to the piston axis. In Wankel engines (Fig. 17.3), however, the medium flows axially as well as radially, depending on the design.

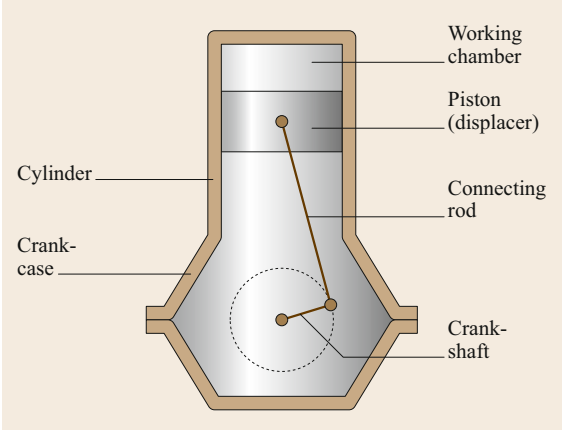

Fig. 17.2 Reciprocating machine (after [17.1])

Cylinder Configuration

Configuring differently (Fig. 17.4) the interrelation of the cylinders makes it possible to produce various types of piston machines.

The inline and V configuration in particular, to a lesser degree the boxer variant (opposed-cylinder machine), are choices for combustion engines. The V design is compact and produces high output per unit volume. However, its compact design makes manufacturing it more complex and expensive. Moreover, accessibility is impaired, as a result of which the time and effort required for maintenance increase along with maintenance costs. The advantages of the boxer engine are its overall length and height, although at the expense of width. The W configuration is frequently employed for piston compressors, yet relatively infrequently for combustion engines. The radial configuration is considered obsolete. It was used early on for aircraft engines because of the good air cooling resulting from the design and the minimal axial extension.

A multicylinder design helps increase machine performance for combustion engines. In compressors, multistage compression is achieved by additionally using varying piston diameters. Increasing the number of cylinders boosts running smoothness. A larger number of cylinders adversely affects production and main-

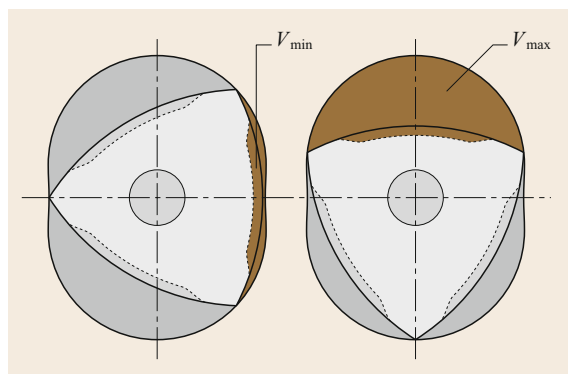

Fig. 17.3 Wankel engine as an example of a rotary piston machine (after [17.2])

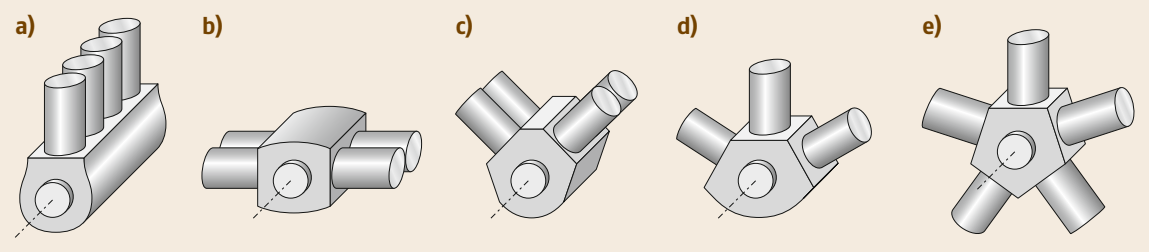

Fig. 17.4a–e Cylinder configurations (after [17.1]). **(a)** In-line machine, **(b)** opposed-cylinder machine, **(c)** V machine, **(d)** W-machine, and **(e)** radial machine

tenance costs. Moreover, a more complex design increases susceptibility to failure. Cylinder configuration, unit size, and the stiffness of the crankshaft can limit the number of cylinders.

Working Chamber

The displacer's movement causes the actual working chamber volume V_a to vary between the volume limits V_{min} and V_{max}; V_{min} can be a design-related clearance volume V_S or, in the case of combustion engines, a compression volume V_c contingent on the working process. Thus, $V_{min} \leq V_a \leq V_{max}$ applies.

In a reciprocating machine, the maximum piston displacement V_A or swept volume V_h corresponds to the volume resulting from the product of the piston surface A_p and the stroke s (17.1). The stroke corresponds to the distance that the piston covers between the top and bottom dead centers (Fig. 17.5)

$$V_A = V_h = A_p s = s\pi\frac{D^2}{4} . \tag{17.1}$$

Defining a cylinder's volume (corresponding to the maximum volume) requires the incorporation of the minimum volume

$$V_{cyl} = V_{max} = V_h + V_{min} . \tag{17.2}$$

For machines with a multicylinder design, the total piston swept volume V_H follows from the number of cylinders z and the swept piston volume V_h

$$V_H = zV_h = zA_p s . \tag{17.3}$$

Using (17.2), the total working chamber of a combustion engine is calculated as

$$V_{working\text{-}chamber} = V_h + V_{min} . \tag{17.4}$$

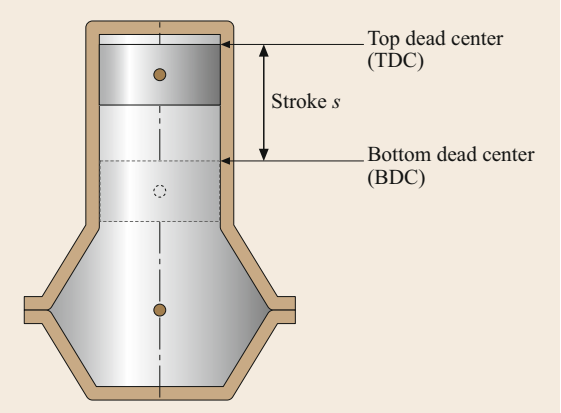

Fig. 17.5 The stroke s corresponds to the distance between top and bottom dead centers (after [17.1])

17.1.2 Ideal and Real Piston Machines

The Ideal Combustion Cycle

A cycle is a succession of a material's changes of state until it returns to its initial state. The cycle serves as the foundation for evaluating the thermodynamics of processes. The p–V diagram is used to represent the development of cycles (Fig. 17.6). Its enclosed area corresponds to the cycle work W.

Figure 17.6 is a general representation of the development of the cycles of a power and a work machine. The different direction of rotation of each process and the resultant sign of the cycle work are characteristic here. Since the work done by the machine's piston can be utilized (effective work), it is defined negatively, while the work expended on the working material is defined positively. The cycle work is calculated from the total of both values and corresponds to the area within the circle

$$W = W_{at\text{-}the\text{-}piston} + W_{at\text{-}the\text{-}working\text{-}material} , \tag{17.5}$$

$$W = \oint V\mathrm{d}p = -\oint p\mathrm{d}V . \tag{17.6}$$

A clockwise cycle profile with negative cycle work results for the power machine, while a counterclockwise cycle profile with positive cycle work results for the work machine.

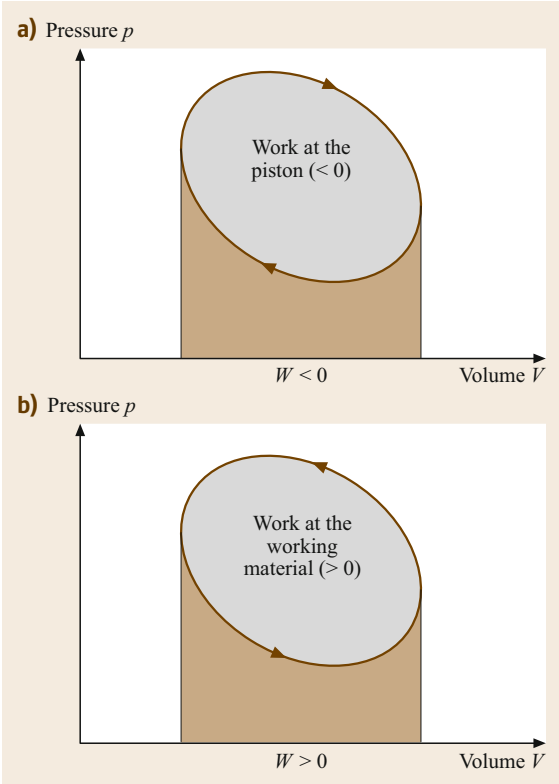

Fig. 17.6a,b The p–V diagrams of power and work machines. **(a)** Power machine (clockwise), **(b)** working machine (counterclockwise) (after [17.3])

Three examples of cycles based on the Carnot process (Chap. 4) are described below and are referred to as reference cycles. They are subject to the following premises:

1. State changes are infinitely slow.
2. The working chamber is adiabatically and hermetically sealed.
3. Fluid is exchanged without any change in the state variables (mass, pressure, temperature).

Combustion Engines. The Seiliger process constitutes a reference process for diesel engines (Fig. 17.7). Adiabatic compression causes the pressure to rise until it is slightly below the maximum cylinder pressure. The internal combustion of a fuel mass is followed by an isochoric and isobaric input of heat, as a result of which the maximum cylinder pressure is reached. This is followed by an isentropic expansion up to the initial volume. The initial state is reached again when the heat extraction is isochoric.

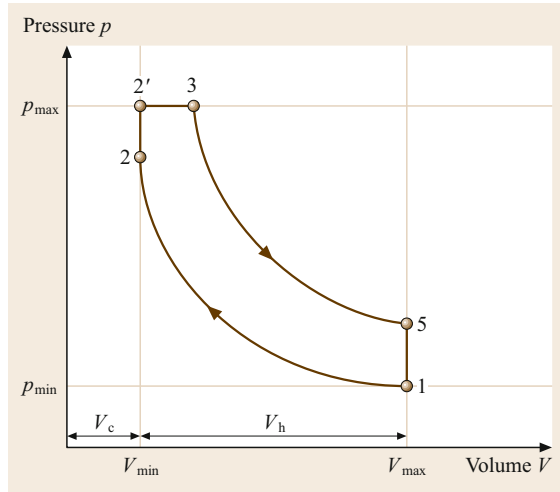

Fig. 17.7 The p–V diagram of a combustion engine (Seiliger process) (after [17.4])

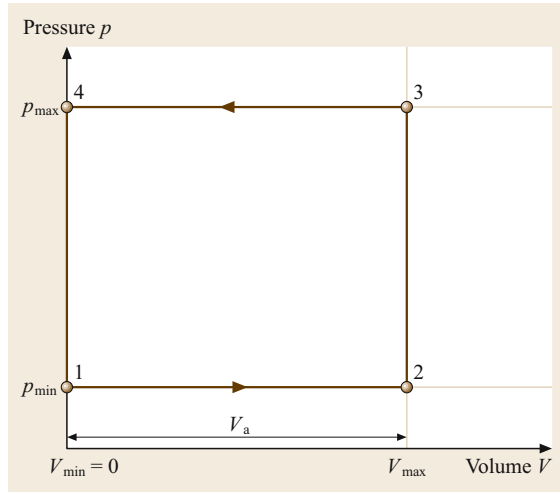

Fig. 17.8 The p–V diagram of a positive displacement pump (after [17.4])

Positive Displacement Pump. In an initial step, the working chamber is filled with an incompressible fluid (Fig. 17.8). When the maximum volume V_{max} is reached, the pressure climbs isochorically to the maximum pressure p_{max}. The fluid is expelled at the maximum pressure. When the working chamber has been completely discharged, the pressure falls isochorically, returning to the initial state.

Positive Displacement Compressor. Analogously to the positive displacement pump, the working chamber is filled isobarically with a fluid up to the volume limit

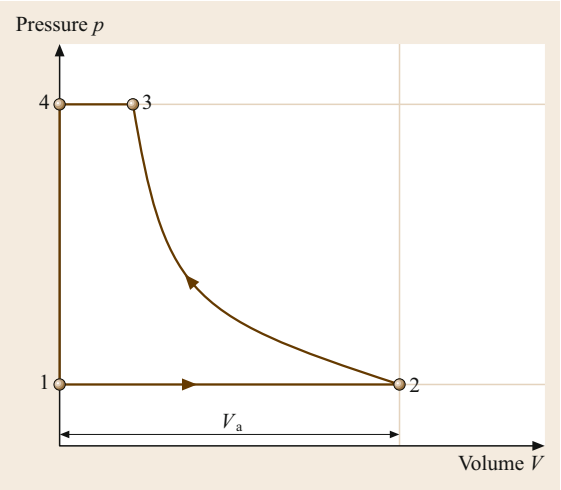

Fig. 17.9 The p–V diagram of a positive displacement compressor (after [17.4])

(Fig. 17.9). When the positive displacement compressor's cycle is ideal, the low-compression work causes the pressure to rise isothermally. When the maximum pressure has been reached, the fluid becomes isobaric and is expelled isochorically until it has been completely discharged.

Real Machines

While lossless state changes are assumed for an ideal combustion cycle, losses in the real machine occur as irreversible subcycles when the state changes. Infinitely slow (quasistatic) state changes would be needed to prevent irreversible cycles.

Deviations from the ideal cycle occurring in real machines are caused by:

1. Wall heat losses, i.e., heat exchange with the system boundaries (e.g., with the working chamber's walls and the piston)
2. Irreversibilities when states change; changing material values during the cycle
3. Losses when energy is transferred (e.g., friction in the machine, flow losses)
4. Leaks because the working chamber is not absolutely sealed.

Efficiency

The aforementioned deviations are expressed by the efficiency, which represents the relationship between utility and effort. For heat engines, the total effort corresponds to the total quantity of input heat, while the utility is the outcome of an energy conversion process.

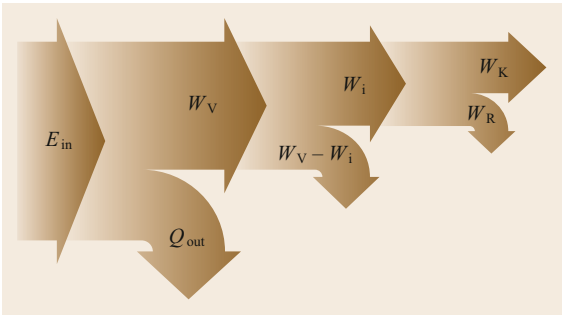

Fig. 17.10 A real power machine's losses (combustion engine) (after [17.3])

Power Machines. Figure 17.10 is a schematic diagram of a real power machine's losses.

Heat exchange with the system boundaries represents the greatest percentage loss of input energy. The relationship between the cycle energy of an ideal power machine's reference cycle and the input energy is expressed with the efficiency of the reference cycle and is referred to as the efficiency of the ideal machine

$$\eta_v = \frac{W_v}{E_{in}} . \tag{17.7}$$

The irreversibilities of a cycle's state changes cause further losses. The related efficiency specifies the indicated cycle's approximation of the reference cycle and is referred to as a cycle's efficiency

$$\eta_g = \frac{W_i}{W_v} . \tag{17.8}$$

The work against friction W_R subsumes the losses occurring during the transfer of energy. The relationship between the effective work or the useful work that can be extracted at the clutch W_K and the indicated work is referred to as the mechanical efficiency

$$\eta_m = \frac{W_K}{W_i} . \tag{17.9}$$

Consequently, a real power machine's coupling efficiency is calculated from the efficiency chain

$$\eta_K = \eta_v \eta_g \eta_m = \left(\frac{W_v}{E_{in}}\right)\left(\frac{W_i}{W_v}\right)\left(\frac{W_K}{W_i}\right) = \frac{W_K}{E_{in}} . \tag{17.10}$$

This efficiency represents all losses occurring in the power machine, which leads to the output useful work (clutch work) W_K.

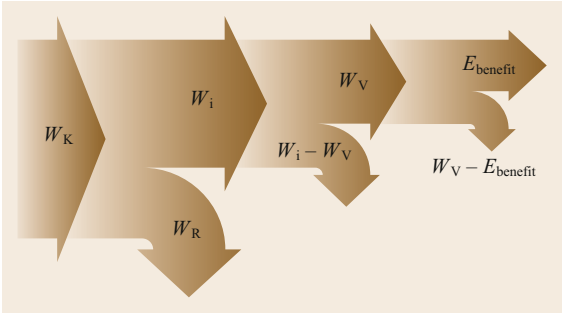

Fig. 17.11 A real work machine's losses (after [17.3])

Work Machines. Figure 17.11 is a schematic diagram of a real work machine's losses.

The following relationships likewise apply to the mechanical efficiency

$$\eta_m = \frac{W_i}{W_K} , \tag{17.11}$$

internal efficiency

$$\eta_g = \frac{W_V}{W_i} , \tag{17.12}$$

and system efficiency

$$\eta_A = \frac{E_{benefit}}{W_V} . \tag{17.13}$$

Consequently, a work machine's total efficiency is calculated from the chain of efficiencies

$$\eta = \eta_m \eta_g \eta_A = \left(\frac{W_i}{W_K}\right)\left(\frac{W_V}{W_i}\right)\left(\frac{E_{benefit}}{W_V}\right) = \frac{E_{benefit}}{W_K} . \tag{17.14}$$

Specific energy

The relationship between the piston machine's output energy W_e and the corresponding piston swept volume is referred to as the volume-specific energy w_e

$$w_e = \frac{W_e}{V_H} . \tag{17.15}$$

In combustion engines, the unit of the volume-specific energy w_e is denoted as kJ/dm^3. Work machines' mass-specific energy w' is obtained from the relationship of the requisite work energy W_a and the mass of the fluid delivered per working cycle m_f. It is specified, for instance, in kJ/kg

$$w' = \frac{W_a}{m_f} . \tag{17.16}$$

The more losses that occur in the work machine, the more energy is needed to deliver the same amount of fluid. Consequently, the mass-specific work also increases as losses occur.

Power

A machine's power corresponds to the energy output (power machine) or input (work machine) per unit time

$$P = \frac{W}{t} . \tag{17.17}$$

Moreover, the power can be calculated using the product of the torque M_d and angular velocity ω

$$P = M_d \omega = M_d 2\pi n , \tag{17.18}$$

where ω is the angular velocity, and n is the engine speed; or with the aid of the cycle energy W_K

$$P = \frac{W_K}{t_{ASP}} = W_K f_{ASP} , \tag{17.19}$$

where $t_{ASP} = i/2n$ is the time for one working cycle, and $f_{ASP} = 1/t_{ASP}$ is the working cycle frequency; i is the number of cycles or piston strokes per working cycle. Expressing this using the mass flow $\dot{m}$ and the mass delivered per working cycle m_{ASP} leads to

$$P = \frac{W_K}{m_{ASP}} \dot{m} . \tag{17.20}$$

17.1.3 Reciprocating Machines

Types of Transmissions

Different types of transmissions transmit energy between piston and crankshaft, e.g., crankshaft drive, swash plate drive, cam drive, and eccentric drive. The simple engineering and dimensioning of a reciprocating machine's important parameters (e.g., stroke and compression) are the reason why a crankshaft drive is frequently used as the transmission.

The connecting rod transmits energy between the piston and crankshaft (Fig. 17.2). In the process, the piston's oscillating motion is converted into the crankshaft's rotating motion in order to improve the further transmission of energy. Accordingly, the motion is transformed conversely when energy is transmitted from the crankshaft to the piston. The crankshaft drive can be constructed as a plunger piston or crosshead version. The crosshead serves to relieve the piston from the lateral piston force, particularly in large piston machines.

Kinematics

The piston executes a motion characterized by accelerations and decelerations between the two dead centers. The piston's linear, irregular motion at the crankshaft is converted by the connecting rod into a rotating motion with constant angular velocity. The instantaneous distance covered by the piston, related to the top dead center, is designated as the piston travel x (Fig. 17.12). The maximum piston travel, i.e., the distance between the two dead centers, is defined as the stroke s. This corresponds to twice the distance between crankshaft journal and shaft journal (crank radius r).

Piston travel can be specified as a function of the piston angle α

$$x = l + r - (l\cos\beta + r\cos\alpha)\,. \tag{17.21}$$

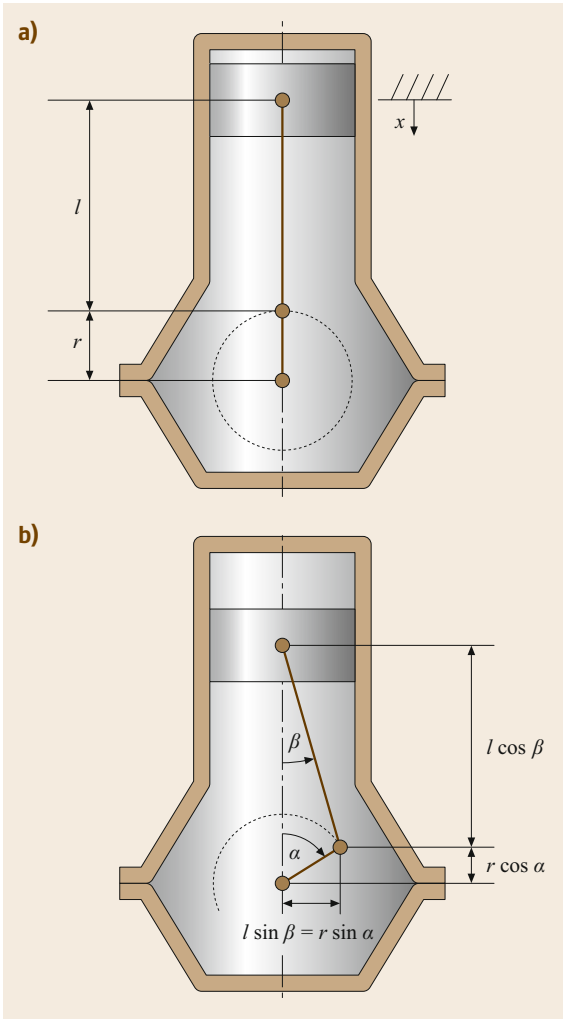

Fig. 17.12 (**a**) Piston travel x, (**b**) crankshaft drive geometry

By substituting the connection rod angular travel β with α by using the relation

$$l\sin\beta = r\sin\alpha \tag{17.22}$$

and the connecting rod ratio

$$\lambda = \frac{r}{l}\,, \tag{17.23}$$

the formula for piston travel is obtained as

$$x = r(1-\cos\alpha) + l\left(1 - \sqrt{1-\lambda^2\sin^2\alpha}\right), \tag{17.24}$$

where $\sin\beta = \lambda\sin\alpha$ and $\cos\beta = \sqrt{1-\lambda^2\sin^2\alpha}$.

Expanding the expression under the root into a Taylor polynomial produces a complex equation. In practice, only the first two orders of the Taylor polynomial are applied since they already yield sufficiently precise results for the piston travel x

$$x \approx r\left(1 - \cos\alpha + \frac{\lambda}{2}\sin^2\alpha\right). \tag{17.25}$$

Piston speed can be stated as an average or instantaneous speed.

The average piston speed is calculated based on the simple relation between distance covered and the necessary time expended. Twice the piston stroke is covered during one revolution. This yields the formula for the average piston speed

$$c_\mathrm{m} = \frac{2s}{\frac{1}{n}} = 2sn\,. \tag{17.26}$$

The following numerical value equation is also frequently applied

$$c_\mathrm{m} = \frac{sn}{30}\,. \tag{17.27}$$

The unit of revolution has to be specified in $1/\mathrm{min}$ or min^{-1} and rpm, respectively, in order to obtain the average piston speed in m/s, if the unit of stroke is m.

If the actual piston speed v is required, piston travel must be differentiated with respect to the time t, remembering that piston travel is only a function of the piston angle

$$v = \frac{\mathrm{d}s}{\mathrm{d}t} = \frac{\mathrm{d}s}{\mathrm{d}\alpha}\frac{\mathrm{d}\alpha}{\mathrm{d}t}\,, \tag{17.28}$$

where $\mathrm{d}\alpha/\mathrm{d}t$ is the crankshaft angular velocity ω.

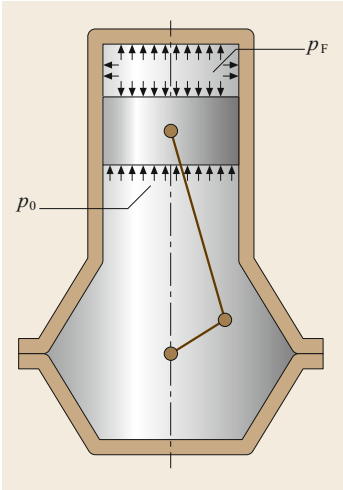

Fig. 17.13 Pressures on the piston

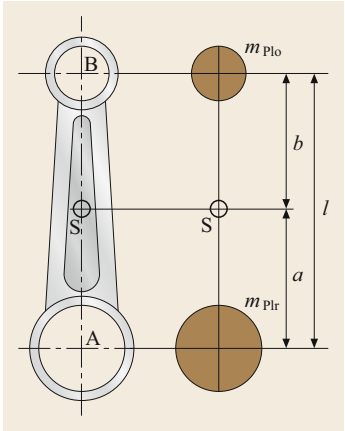

Fig. 17.14 Distribution of the connecting rod mass (after [17.5])

Differentiating (17.25) yields an approximate equation for the piston speed

$$v \approx \omega r \left[\sin\alpha + \frac{\lambda}{2} \sin(2\alpha) \right] . \tag{17.29}$$

Analogously to the piston speed, an approximate value can be derived for the piston acceleration

$$a \approx \omega^2 r [\cos\alpha + \lambda \cos(2\alpha)] . \tag{17.30}$$

Equations (17.25), (17.29), and (17.30) do not yield any precise results when speeds are high (e.g., racing engines). The exact piston travel and the corresponding derivatives for speed and acceleration have to be used for this application.

Forces

Fluid Forces. The state change of the fluid enclosed in the working chamber induced by the oscillating motion of the displacer causes a force that is dependent on the piston surface A_K and the fluid pressure p_F exerted on the piston. Allowing for the atmospheric pressure p_0, the fluid force F_F of a single-action piston is calculated with the following equation

$$F_F = A_K (p_F - p_0) . \tag{17.31}$$

An equal force acts on the cylinder cover. The bolted connections, e.g., between the cylinder cover and the housing, create a closed linkage so that the forces in the machine balance (Fig. 17.13).

Inertial Forces. The irregular motions of the translationally moving structural parts cause periodic inertial forces to arise, which act as oscillators. The centripetal acceleration generates rotary inertial forces on the connecting rod and crankshaft suspensions. Therefore, they have to be balanced. This can be easily and completely done for rotary piston machines, but only partially or with considerable effort for reciprocating machines. The inertial forces are classified as rotating and oscillating based on the different types of motion of the transmission components.

The rotating inertial forces F_{mr} are calculated with the formula

$$F_{mr} = m_r r \omega^2 . \tag{17.32}$$

The rotating masses m_r are concentrated in the crankshaft journal at the distance r from the center of rotation and consist of the masses of the crankshaft journal m_z, the crankshaft web (converted to the crank radius), and the rotating portion of the connecting rod (17.36).

The oscillating and rotating motion of the connecting rod cause the mass to be distributed to two points

$$m_{Pl} = m_{Plo} + m_{Plr} , \tag{17.33}$$

where m_{Pl} is the connecting rod mass, m_{Plo} is the oscillating mass fraction, m_{Plr} is the rotating mass fraction, a and b are the distances to the connecting rod gravity center S, and l is the distance between the two connecting rod eyes (Fig. 17.14).

The mass m_{Plo} is located in the piston pin and is only involved in the oscillating motion, while m_{Plr} on the crankshaft journal executes a purely rotary motion. Since the distances from the center and the total moment of inertia are maintained, the masses are calculated based on

$$m_{Plo} = \frac{m_{Pl} a}{l} \tag{17.34a}$$

and

$$m_{\mathrm{Plr}} = \frac{m_{\mathrm{Pl}} b}{l} \,. \tag{17.34b}$$

As a result, a substitute connecting rod is obtained, the dynamic behavior of which is approximately comparable with a real connecting rod.

Since the center of the web masses m_{W} does not lie at the center of the crankshaft axis, the masses must be converted to the crank radius. Using the distance x between the center of the web masses and the crankshaft axis as well as the crank radius, the reduced mass m_{WE} is calculated as

$$m_{\mathrm{WE}} = m_{\mathrm{W}} \frac{x}{r} \,. \tag{17.35}$$

Taking the preceding observations and allowing for two web masses, the following result ensues for the rotating inertial forces of the reciprocating machine

$$F_{\mathrm{mr}} = (m_{\mathrm{Z}} + m_{\mathrm{Plr}} + 2m_{\mathrm{WE}})\, r\omega^2 \,. \tag{17.36}$$

The irregular piston motion generates oscillating inertial forces F_{mo} as a function of the piston acceleration a

$$F_{\mathrm{mo}} = m_{\mathrm{o}} a \,, \tag{17.37}$$

where $m_{\mathrm{o}} = m_{\mathrm{K}} + m_{\mathrm{Plo}}$ are the oscillating masses.

Taking the piston acceleration (17.30), the following ensues for the oscillating inertial force

$$F_{\mathrm{mo}} \approx m_{\mathrm{o}} \omega^2 r [\cos\alpha + \lambda \cos(2\alpha)] \,. \tag{17.38}$$

It is divided into oscillating inertial forces of first and second order (I and II)

$$F_{\mathrm{moI}} = m_{\mathrm{o}} \omega^2 r \cos\alpha = F_{\mathrm{I}} \cos\alpha \,, \tag{17.39a}$$

$$F_{\mathrm{moII}} = m_{\mathrm{o}} \omega^2 r \lambda \cos(2\alpha) = F_{\mathrm{II}} \cos(2\alpha) \,. \tag{17.39b}$$

The frequency of the first-order forces of inertia corresponds to the crankshaft speed, while the second-order forces of inertia change as the crankshaft speed doubles.

The influence of the stroke–connecting rod ratio λ (17.23) makes the amplitude of the second-order forces of inertia less than that of the first-order forces. The extreme values for F_{moI} are in the top and bottom dead center, i.e., at $\alpha = 0°$, and $\alpha = 180°$. Since the frequency of F_{moII} is doubled, the maximum amplitudes are at $\alpha = 0°$, 90°, 180°, and 270°. This yields the following for the oscillating inertial forces at top dead center

$$F_{\mathrm{mo}} = F_{\mathrm{moI}} + F_{\mathrm{moII}} \,, \tag{17.40}$$

and the following at bottom dead center

$$F_{\mathrm{mo}} = F_{\mathrm{moI}} - F_{\mathrm{moII}} \,. \tag{17.41}$$

Since there is no closed linkage, the oscillating inertial forces cause the crankcase to oscillate and, thus, exerts a load on the external engine suspension.

Forces on the Transmission. The piston force F_{K} consists of the fluid force F_{F} and the oscillating inertial force F_{os}. It is broken down into a lateral force F_{N} and a connecting rod force F_{S} as follows (Fig. 17.15)

$$F_{\mathrm{N}} = F_{\mathrm{K}} \tan\beta \,, \tag{17.42a}$$

$$F_{\mathrm{S}} = \frac{F_{\mathrm{K}}}{\cos\beta} \,. \tag{17.42b}$$

The cylinder wall absorbs the normal force. The connecting rod force divides at the crankshaft journal into a radial and a tangential component (F_{R} and F_{T})

$$F_{\mathrm{R}} = F_{\mathrm{S}} \cos(\alpha+\beta) = F_{\mathrm{K}} \frac{\cos(\alpha+\beta)}{\cos\beta} \,, \tag{17.43a}$$

$$F_{\mathrm{T}} = F_{\mathrm{S}} \sin(\alpha+\beta) = F_{\mathrm{K}} \frac{\sin(\alpha+\beta)}{\cos\beta} \,. \tag{17.43b}$$

The tangential force and the crank radius produce the torque

$$M_{\mathrm{d}} = F_{\mathrm{T}} r \,. \tag{17.44}$$

The direction of the force F_{T} corresponds to the direction of rotation. The normal force generates the corresponding reaction torque, which acts as a tilting moment on the housing and must be absorbed by the housing suspension.

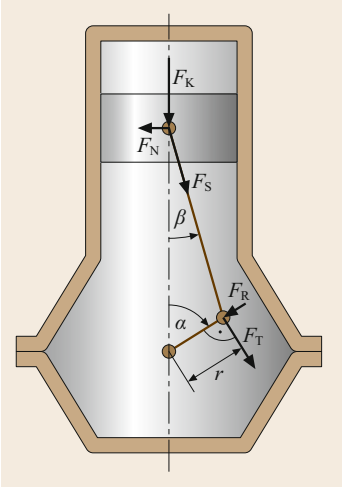

Fig. 17.15 Forces on the transmission

Mass Balancing

The periodically varying inertial forces and moments of the transmission's moving points can cause oscillations, which have an effect on the engine suspension and substructures. This load can be counteracted by balancing masses at the crankshaft webs. The configuration of this mass balancing depends on the number and arrangement of the cylinders as well as the distribution of the crank throw.

Inertial Force Balancing on Single-Cylinder Machines. Only rotating and oscillating inertial forces, but no moments of inertia, occur on a single-cylinder machine, since the plane of symmetry lies in the cylinder axis. The rotating inertial forces can be balanced relatively easily and completely by two counterweights m_{rG} on the crankshaft (Fig. 17.16). These are offset by 180° with respect to the crankshaft journal and are calculated from the rotating mass m_r and the corresponding distances from the center of rotation as

$$m_{rG} = 0.5 m_r \frac{r}{r_G} , \tag{17.45}$$

where r is the crank radius and r_G is the distance of the counterweights from the center of rotation.

The distribution of the balancing masses to individual counterweights with the mass m_{rG} is incorporated to prevent an additional moment.

To balance the oscillating inertial forces, (17.38) is applied and broken down into first and second-order forces of inertia. The change of the first-order forces of inertia corresponds to the frequency of the crankshaft

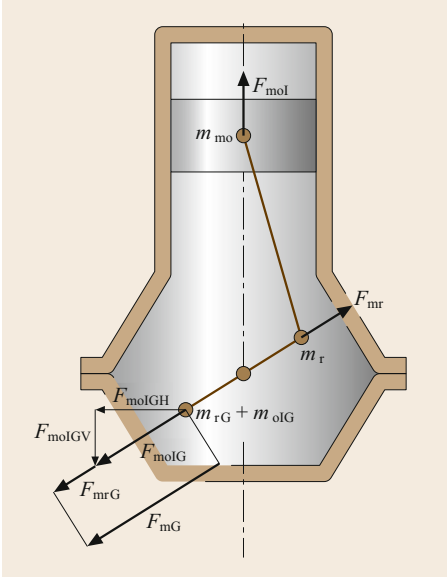

Fig. 17.16 Counterweight and forces

speed and can, consequently, be partially balanced by counterweights on the crankshaft. Second-order forces of inertia change twice as fast. Therefore, they cannot be balanced by counterweights on the crankshaft.

The oscillating inertial forces act in the direction of the cylinder axis. Hence, only the perpendicular force components of the rotating counterweights can be used as mass balancing. The horizontal force components also generated represent an interfering force. The following equation is used to calculate the counterweights m_{oIG} per web to balance the first-order forces of inertia

$$m_{oIG} = 0.5 m_o \varphi \frac{r}{r_G} , \tag{17.46}$$

where φ represents the proportion of the first-order forces of inertia being balanced. This prevents the influence of the interfering horizontal force components from becoming too great.

Mass Balancing on Multicylinder Machines. To balance masses for multicylinder engines, the inertial forces are calculated for every cylinder and consolidated in a resultant. The aim of mass balancing is to compensate the inertial forces reciprocally and to keep the resultants as small as possible. Furthermore, the concentrated loads not engaging in the center of mass cause additional moments of inertia. These are also consolidated into resultants.

The radial and axial arrangement of the crank throw strongly influence the value of the resultants. When designing the crankshaft, attention has to be paid to balancing the concentrated loads. One simple way to do this is by projecting the crankshaft radially and axially. Cross and longitudinal sections of the crankshaft are drawn (Fig. 17.17). The cross section (the left-hand image in Fig. 17.17) is called a throw diagram because of its shape. Along the longitudinal section (the right-hand image in Fig. 17.17) of the crankshaft, the crank throws are numbered from left to right and subsequently transferred to the throw diagram.

Resultants from the Rotating Inertial Forces. The rotating inertial forces calculated with (17.32) are transferred in parallel to a common cross-sectional plane. By adding the vectors, the individual forces are consolidated into a resultant F_{mrR} (Fig. 17.18).

The resultant rotates with the crankshaft speed and has a constant value. Hence, it does not have to be determined anew for other crankshaft positions, but only rotated by the corresponding angle (Fig. 17.18).

Resultants from the First-Order Forces of Inertia. The specific instantaneous value in the cylinder axis is

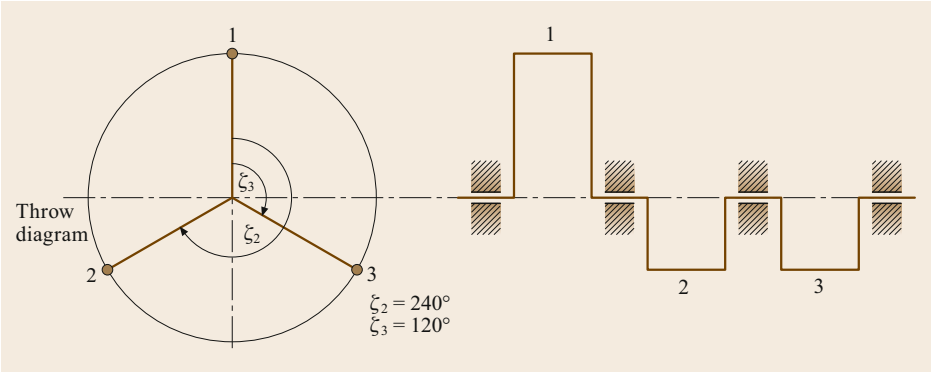

Fig. 17.17 Cross and longitudinal sections of a three-cylinder crankshaft (after [17.3])

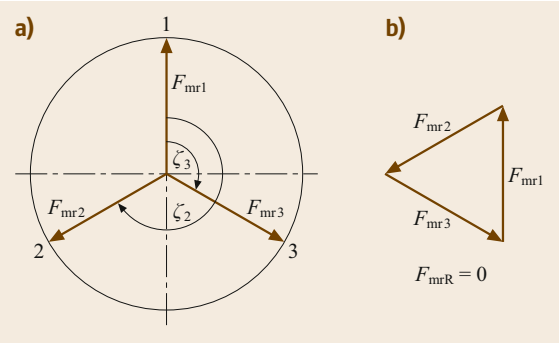

Fig. 17.18a,b Determination of the resultants from the rotating inertial forces. **(a)** Position diagram, **(b)** force diagram (after [17.3])

calculated by projection onto these, and the total first-order inertial forces in the direction of the cylinder axis is determined by adding their vectors. The maximum value of the first-order forces of inertia is calculated with

$$F_{\mathrm{moI\_max}} = m_{\mathrm{o}}\omega^2 r\,. \qquad (17.47)$$

A simpler approach is often used in practice. The maximum values are likewise applied in the direction of the crank arm. Adding these forces yields a resultant of the maximum values $F_{\mathrm{moI\_maxR}}$ that is projected onto the cylinder axis. The force calculated in this way is the resultant of the first-order forces of inertia F_{moIR} (Fig. 17.19).

The resultant of the maximum values rotates together with the crankshaft as it rotates. In the corresponding crank position, it must be projected anew onto the cylinder axis in order to obtain the corresponding resultant of the first-order forces of inertia.

Resultants from the Second-Order Forces of Inertia. The resultant of the second-order forces is calculated in the same way as the resultant from the first-order forces of inertia. However, the second-order forces of inertia change their value as the crankshaft's angle of rotation doubles. Therefore, they cannot be applied in the direction of the crank arms. Rather, they have to be drawn at twice the angle. A force plan is again used to calculate the resultant of the maximum values, which is subsequently transferred to the position diagram. Projection onto the cylinder axis yields the resultant of the second-order forces of inertia. The rotation of the resultant of the maximum values has to be entered on the site plan at twice the crankshaft angle. The resultant sought is calculated by projection onto the cylinder axis.

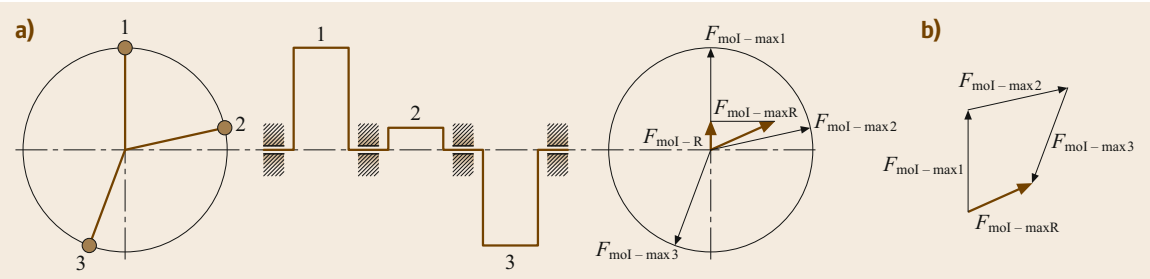

Fig. 17.19a,b Determination of the resultants from the first-order forces of inertia. **(a)** Throw diagram (*left*) and position diagram (*right*), **(b)** force diagram (after [17.6])

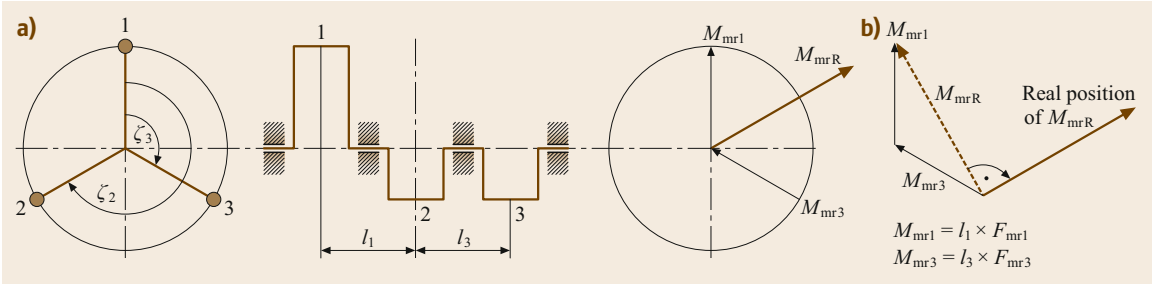

Fig. 17.20a,b Determination of the resultant moment of inertia from the rotating inertial forces. **(a)** Throw diagram (*left*) and position diagram (*right*), **(b)** moment diagram (after [17.6])

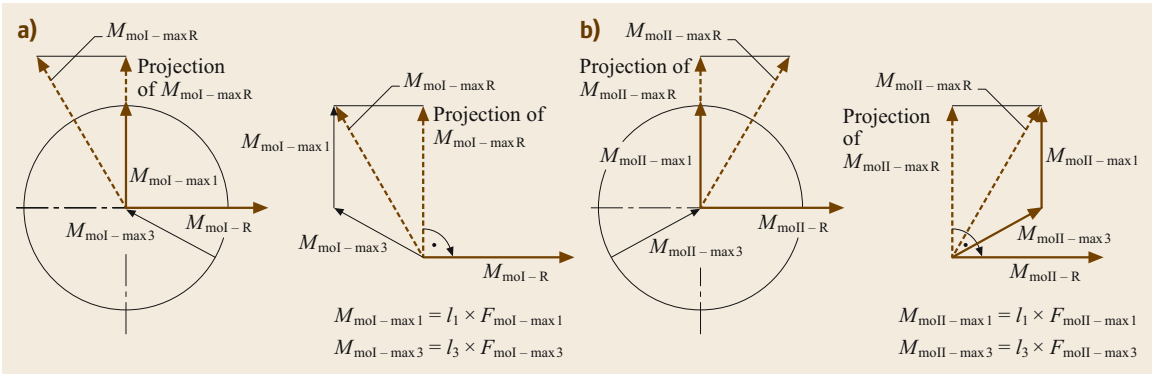

Fig. 17.21a,b Determination of the resultant moment of inertia from the oscillating **(a)** first and **(b)** second-order inertial forces. Position diagrams are shown on the *left* and motion diagrams are shown on the *right* (after [17.6])

Resultant Moment of Inertia. The inertial forces in multicylinder engines act at a specific distance to the machine's center of gravity and cause moments of inertia. Since their precise determination is extremely involved, a simplified assumption places the center of gravity in the longitudinal section in the crankshaft axis (e.g., the second cylinder's axis in a three-cylinder machine; see the longitudinal crankshaft section in Fig. 17.20). The resulting error is negligible in most cases.

The moment vectors are applied corresponding to the crank arms taken from the throw diagram in the site plan. The direction of the vectors is determined as follows. The vectors in the longitudinal section to the left of the reference point point outward, while the vectors to the right of the reference point point toward the center of the throw diagram.

The value of the resultant moment of inertia is obtained by adding the vectors in the moment diagram. The vector is given its correct position by rotating it clockwise by 90°.

A similar approach is employed to determine the resultant first-order moment of inertia. However, the resultant of the maximum values of the moments is projected onto the cylinder axis and then rotated clockwise by 90° (left-hand position and moment diagram in Fig. 17.21).

When the resultant second-order moment of inertia is calculated, the moment vectors must be entered at twice the crank angle (see the right-hand position and moment diagram in Fig. 17.21). Just as with the resultant first-order moment of inertia, the resultant of the maximum values is projected onto the cylinder axis and rotated by 90°.

17.1.4 Selected Elements of Reciprocating Machines

Crankshaft Drive

The crankshaft drive can be constructed in a plunger piston or crosshead design. The crosshead relieves the piston from lateral piston force, especially in large piston machines (Fig. 17.23).

Crankshaft

The crankshaft shown in Fig. 17.22 has a shaft journal running in bearings connected by webs to the crankshaft journal. Counterweights on the webs balance

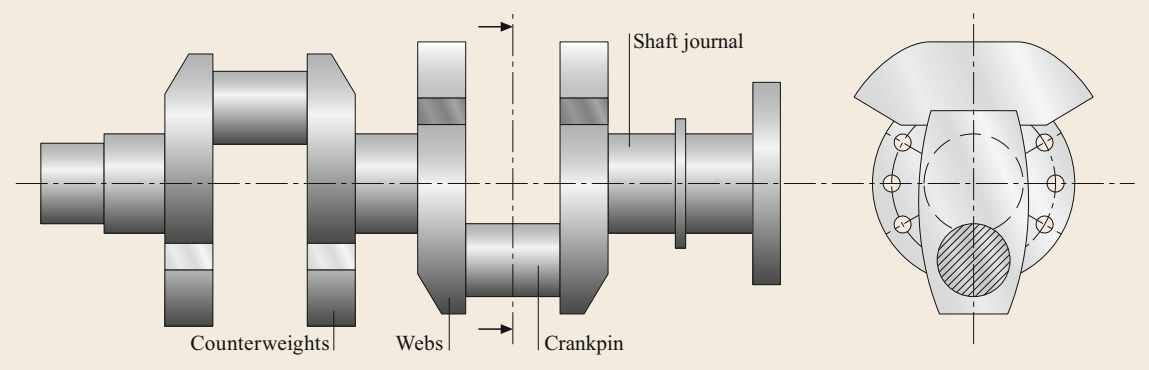

Fig. 17.22 Elements of a crankshaft (after [17.4])

the rotating inertial forces. As a rule, the crankshaft is suspended normally by $z + 1$ main bearings, where z is the number of cylinders.

The crankshaft is under stress from forces and bending and torsional moments. The webs are dimensioned accordingly to handle the high stresses.

Different methods are used to manufacture crankshaft blanks. A difference is principally made between cast and forged crankshafts. Cast crankshafts weigh 10% less than forged ones because of the low density of the nodular graphite cast iron frequently used. Giving cast crankshafts a hollow design can boost this even more. A significant disadvantage of cast over forged crankshafts is the low elastic modulus of penetration and associated lower stiffness. In Europe, the market share of cast-iron car and truck crankshafts that are not highly stressed is 60% [17.7].

The most important forging methods can be classified as open die forging and closed die forging. While hammer forging is only used for prototypes and custom-made pieces, closed die forged crankshafts are primarily used in cars and trucks in conjunction with large lot sizes. If the size of the crankshaft being produced exceeds the production possibilities of forging and casting, the shaft and crankshaft journal are directly connected to one another by the webs. These so-called multipiece crankshafts are primarily used in the manufacture of large diesel engines.

Forged and cast crankshafts are subjected to different postprocessing in order to increase a crankshaft's component strength. Apart from inductive hardening to increase the bearing journal's resistance to wear, rolling the radii in the transition bearing journal and web and nitriding build up residual compressive stresses in the journal and radii zone. As a result, the fatigue strength can be increased considerably in these highly stressed zones.

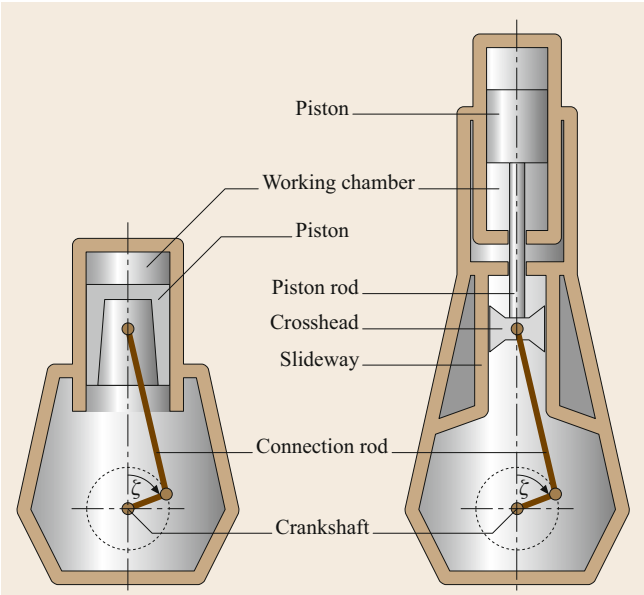

Fig. 17.23 Plunger piston and crosshead crankshaft drive (after [17.6])

Connecting Rod

The connecting rod transmits forces between the piston and crankshaft journal. It is not only under stress from tension and compressive forces but is also subjected to bending by the respective inertial forces. This necessitates a design that is both rigid and light, especially in high-speed combustion engines.

The connecting rod (Fig. 17.24) consists of a shank and two conrod eyes, which act to connect the piston and the crankshaft. It is cast, die forged, or sintered. Heat-treated steel, as well as gray cast iron, malleable iron, and light metals are used as materials. Fracture separations, also called cracks, separate (straight or

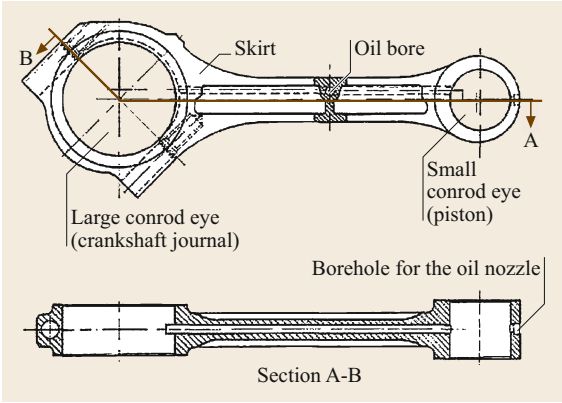

Fig. 17.24 Connecting rod design (after [17.6])

obliquely) the bottom (large) small-end bearing. Antifatigue bolts hold the halves of the large conrod eye together.

Piston

The piston's job is to transmit fluid forces to the connecting rod or connecting rod forces to the fluid (Fig. 17.25).

In addition, the piston seals the working chamber by means of piston rings. The number of piston rings is dependent on the pressure difference between the upper surface and the bottom surface. In combustion engines, for example, the piston rings dissipate the heat generated in the pistons, which piston cooling can subsequently pass to the motor oil. Hence, a high resistance to wear and resistance to heat as well being able to conduct heat and being lightweight are the most important requirements on a piston. This is why pistons are usually made of light alloys and less often gray cast iron (smaller pistons). Low piston weight has a positive effect on the oscillating inertial forces. Steel and cast steel are mostly used for the top part of multipiece pistons or for plunger pistons. Recently, steel pistons are being used as a mono material for high powered engines in trucks and passenger cars (PC).

Lubrication

The lubrication of piston machines serves the following functions:

- Forming a stable lubricating film between the structural parts
- Reducing friction
- Reducing wear in the machine
- Cooling and cleaning bearings and sliding surfaces
- Forming a seal between the piston ring and cylinder wall.

Pressure circulation lubrication is primarily used. The oil is delivered by a pump that is powered by a piston machine or electrically powered. It is purified, cooled, and subsequently pumped into the main oil gallery. From there, it reaches the lubricating points such as the crankshaft, valve gear, and piston.

Cooling

The heat losses occurring on the walls of the working chamber necessitate cooling of the corresponding components. The heat flow dissipated is dependent on the surface, the heat transfer coefficients, and the temperature difference. Water and air are mainly used as coolants and prevent overheating of the components and lubricant, as well as power losses caused by filling losses. However, the better cooling effect of water increases the complexity of the design and manufacture of the machine. Water-cooled machines are given a cooling jacket through which water is pumped. In the case of air cooling, the design of the fins enlarges the surface of the components being cooled.

Suspension

As a rule, a split bearing is used for the suspension in reciprocating machines because of the offset shape of the crankshaft. Exceptions are multipiece crankshafts or small and medium-sized piston compressors in which antifriction bearings, among others, can be used. Their simple design and the small space required in the crankcase, their ability to absorb impacts and vibra-

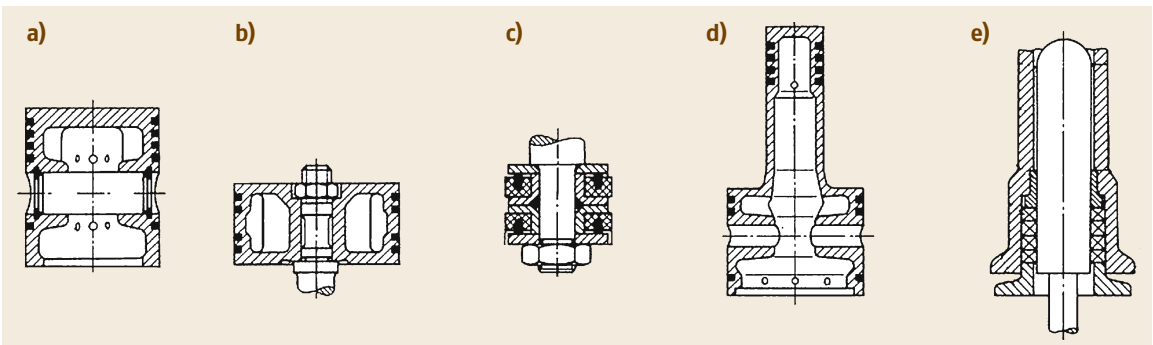

Fig. 17.25a–e Piston variants (after [17.4]). **(a)** Plunger, **(b,c)** disc pistons, **(d)** stepped piston, **(e)** plunger piston

tions, as well as their low mass, are increasingly leading to friction bearings with hydrodynamic lubrication being used in reciprocating machines.

Apart from great strength, the materials used must also have optimal tribological properties. Hence, friction bearings are usually designed with a harder matrix (e.g., CuSn, AlCu) into which a soft, low-melting-point material (e.g., Pb, Sn) is incorporated. The suspension's reliability is crucial for guaranteeing a piston machine's operation. Hence, optimal engineering utilizes improved bearing materials and state-of-the-art calculation methods.

17.2 Positive Displacement Pumps

17.2.1 Types and Applications

A positive displacement pump is a work machine for liquid media (fluids), the working chamber of which is periodically altered by the displacer (piston). The displacer's motion can be either oscillating (reciprocating pump) or rotating (rotary piston pump). Reciprocating pumps mainly use automatically operating, pressure-controlled valves to control the process, i.e., to connect and disconnect the working chamber to the suction and the pressure line. Rotary piston pumps use ports to do this. In each case, the discharge of the medium directly follows the characteristic of the displacer's motion (volume displacement). Theoretically, the maximum pressure achievable with positive displacement pumps is unlimited and determined only by internal leakage losses, the medium's compressibility, the component strength, and the motive power.

During delivery, mechanical energy is transferred to the medium as potential energy, which serves to compensate for level or pressure differences. A difference is made between reciprocating pumps with rigid pistons (disc and plunger pistons and plungers, Fig. 17.26) and with elastic pistons (diaphragm, hose, Fig. 17.27).

Radial and axial piston pumps in which the piston is typically designed as a plunger are also used in high-pressure hydraulics. Depending on the design (radial or axial), the stroke motion in these pumps is generated

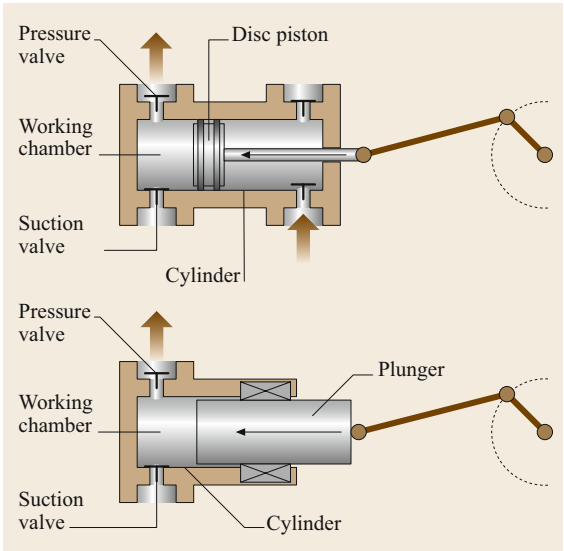

Fig. 17.26 Rigid piston design

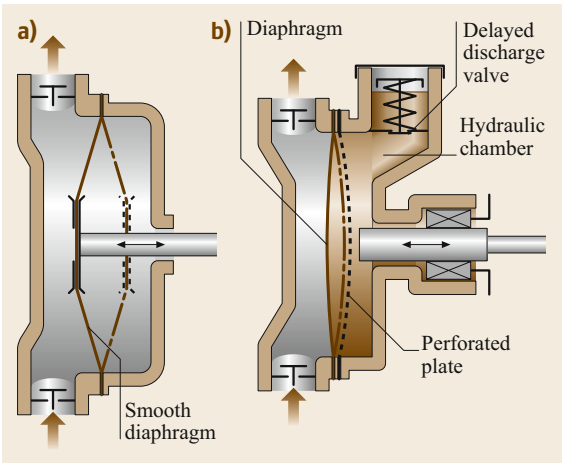

Fig. 17.27a,b Diaphragm designs. **(a)** Mechanical drive, **(b)** hydraulic drive

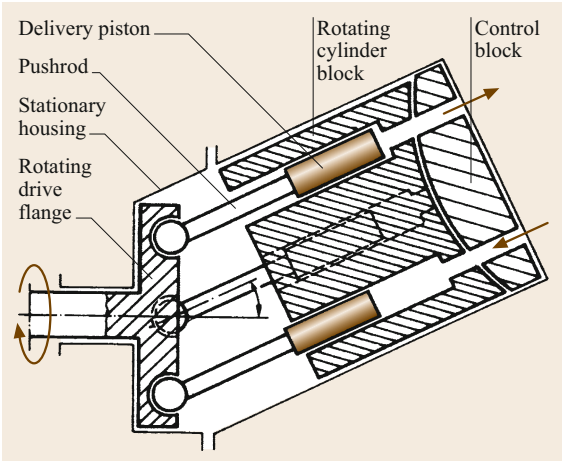

Fig. 17.28 Axial piston pump

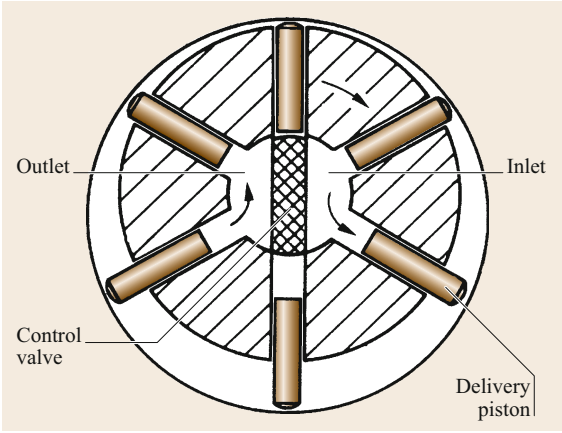

Fig. 17.29 Radial piston pump

by a rotating eccentric cam or a swash plate and a fixed cylinder unit, i.e., similarly to reciprocating pumps with crankshaft drive.

In part, the lift stroke for a fixed eccentric or swash plate is also produced with a rotating cylinder unit (drum/star). In systems with a rotating cylinder unit, control blocks with ports are used instead of the working valves otherwise customary in reciprocating pumps (Figs. 17.28 and 17.29).

Rotary piston pumps are classified according to the primary motion of the displacer as single-rotation piston machines, planetary rotation piston machines, and circulation piston machines (Figs. 17.30–17.33).

Other designs for delivering media with solid fractions, or for liquefied gases, or even with direct drive without crankshaft drive, e.g., steam and pneumatic

Single-rotation piston machines	Planetary rotational piston machine	Circulation piston machine
Moving parts induce uniform rotation around their centers of mass.	The center of gravity of the uniformly rotating displace describes a circular path.	Along with uniformly rotating parts there are also irregularly moving parts that execute circular or circle-like, or even oscillating motions.
Moving parts are directly balanced: bearings and shafts are not subjected to stress from centrifugal forces → High speeds are possible.	The rotary imbalance can only be directly balanced. Increased stresses on bearings caused by centrifugal forces. Speeds are limited.	Increased friction in the machine → overall efficiency decreases. Wear increases.
Examples: gear pump, screw design, roots blower, gear tooth design, liquid ring design.	Examples: trochoidal-type design, eccentric screw pump, eccentric design, rolling piston design.	Examples: multicell or impeller cell design, rotary valve design, external-vane design.
Operating principle 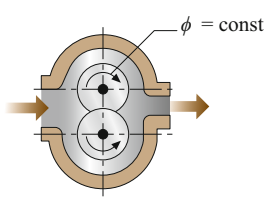 (Gear pump)	Operating principle 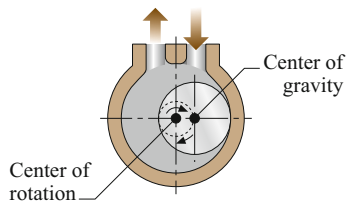 (Eccenter-type design)	Operating principle 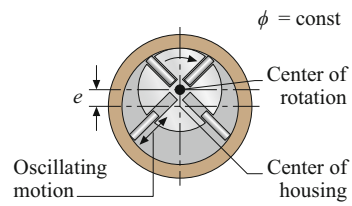 (Vane-type design)

Fig. 17.30 Rotary piston machines

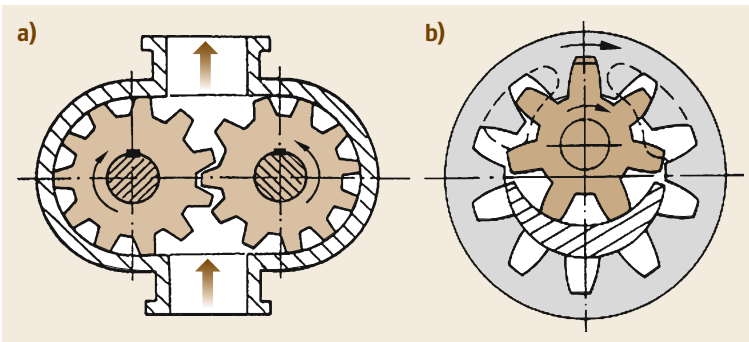

Fig. 17.31a,b Single-rotation piston design. **(a)** External gear, **(b)** internal gear

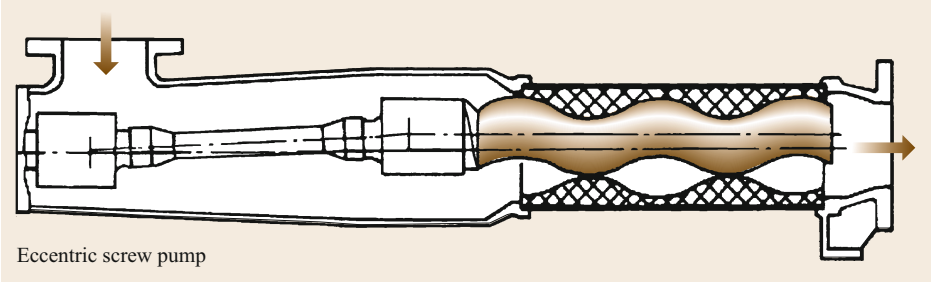

Fig. 17.32 Planetary rotation piston design

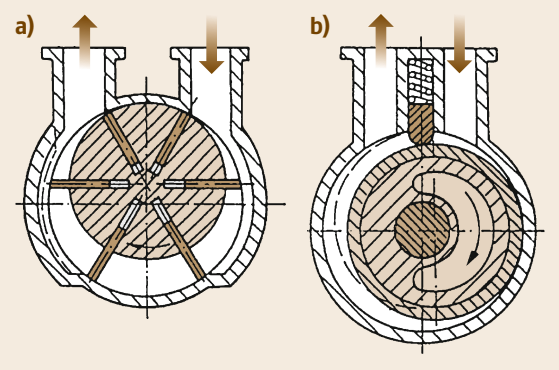

Fig. 17.33a,b Circulation piston design. **(a)** Cell pump, **(b)** rotary piston pump

pumps or hand pumps, are characterized in every configuration by special requirements and have different, usually oscillating types of motion, which for the most part are directly generated without a crankshaft drive or the like (Fig. 17.34).

Furthermore, other designs exist that cannot be directly classified into the categories cited because of their types of motion. One example is the peristaltic pump used in medicine and laboratories (Fig. 17.35).

The vane pump, primarily used for garden irrigation and in small boats, is simple in design and durable in operation (Fig. 17.36).

17.2.2 Basic Design Parameters

Figure 17.37 presents the principle of reciprocating pump operation.

The crankshaft drive, consisting of the crankshaft, connecting rod, and crosshead, converts rotary drive motion into an oscillating motion, which the piston rod transmits to the piston. In the cylinder, the piston executes a motion between the two dead center positions, the crank dead center (CDC), and the head dead center (HDC), whereby the volume trapped between piston and cylinder cover diminishes and expands periodically.

In principle, the function and process are identical for rotary positive displacement pumps. The resultant working cycle can be broken down as follows:

1. Induction. The volume of the working chamber expands during the piston's motion from CDC to HDC. This produces a vacuum in the working chamber causing the suction valve (SV) to open. This vacuum causes the fluid delivered from the

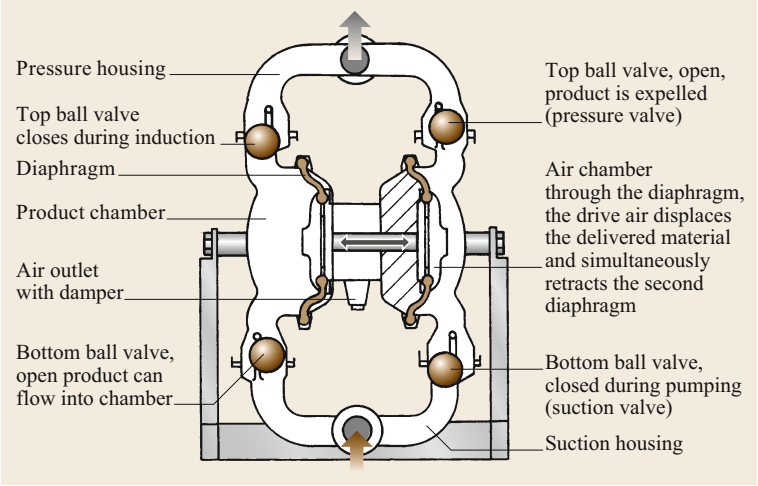

Fig. 17.34 Compressed-air diaphragm pump (after [17.8, 9])

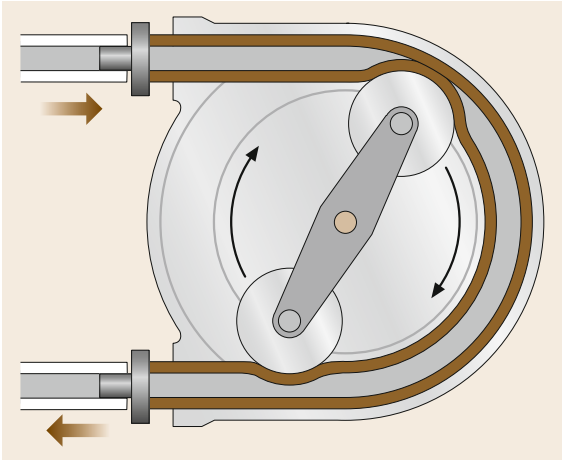

Fig. 17.35 Peristaltic pump (after [17.10])

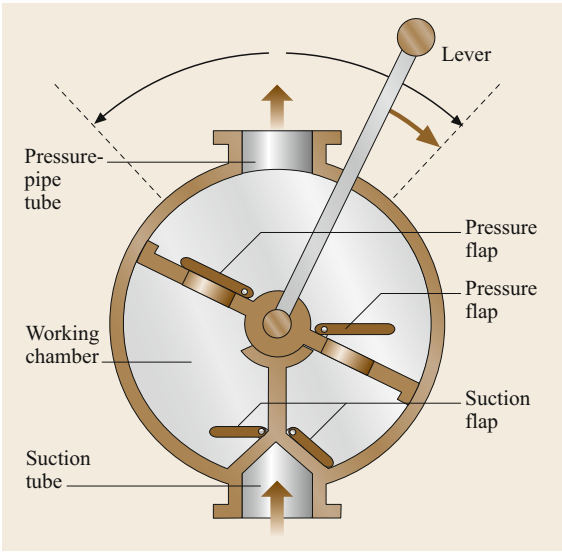

Fig. 17.36 Sliding vane pump

suction line to flow into the cylinder. At nearly constant pressure, induction theoretically occurs during the complete piston stroke (corresponding to line 1–2 in the p–V diagram).

2. Pressure rise. The piston motion reverses in the crank dead center. The resultant reduction in volume causes the pressure in the working chamber to rise and the suction valve to consequently close. Since liquids are theoretically incompressible, the pressure rises at a constant volume to the pressure at the pressure valve (PV) (corresponding to line 2–3 in the p–V diagram).
3. Expulsion. The reduction in volume during the piston's motion from CDC to HDC causes the pressure in the working chamber to increase. When a pressure is attained, which dominates on the pressure side of the pump, the pressure valve opens. The fluid is expelled approaching the pressure, which dominates at the outlet (corresponding to line 3–4 in the p–V diagram).
4. Pressure drop. When the head dead center is reached, the piston motion reverses again so that the pressure drops at constant volume causing the pressure valve to close and the suction valve to open (corresponding to line 4–1 in the p–V diagram).

Whereas the crankshaft has a constant angular velocity (speed), the piston speed in the cylinder is not constant. It is zero at the dead centers. During its motion from one dead center to the other, there is acceleration and deceleration, each corresponding to the crankshaft's law of motion (Sect. 17.1.3). The piston speed is a function of the angle of rotation α and, as a function of the crankshaft drive's connecting rod ratio (17.23), has an approximately sinusoidal characteristic line.

Operating Behavior

The p–V diagram in Fig. 17.37 represents an ideal development of pressure, presuming a massless fluid flows without loss. Since losses and inertial forces always have an effect under real conditions, the real p–V diagram of a piston pump in Fig. 17.38 is produced. The ideal pressure development from Fig. 17.37 has been incorporated for comparison.

- Since the frictional losses in the suction line and the suction valve have to be compensated for, suction occurs at a pressure lower than the suction tank pressure. Moreover, another drop in pressure is needed to open the suction valve since the valve opening resistance (valve acceleration, surface ratios at the valve seat, valve elastic force) has to be overcome. The mass inertia of the decelerated liquid column or the suction pressure can also cause a slight rise in pressure toward the end of the intake stroke.
- Since the mass inertia does not cause the suction valve to close abruptly when the CDC is reached, and a real fluid is not fully compressible, the pressure does not rise at a constant volume. Moreover, fluids frequently contain small quantities of gas that cannot be compressed. As a result, the real pressure rise from 2′ to 3′ is not isochoric.
- Expulsion occurs at a higher pressure than on the pressure side of the pump, since the corresponding losses again have an effect here. Analogously to the suction valve, an additional increase in pressure is needed to open the pressure valve.

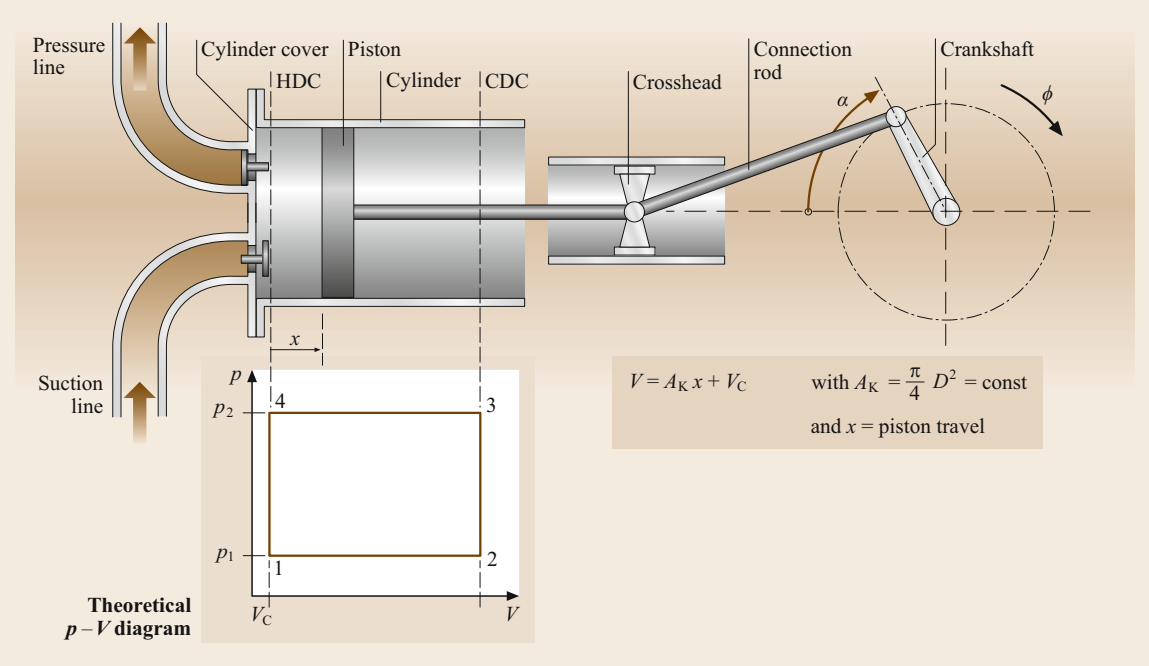

Fig. 17.37 Principle of reciprocating pump operation

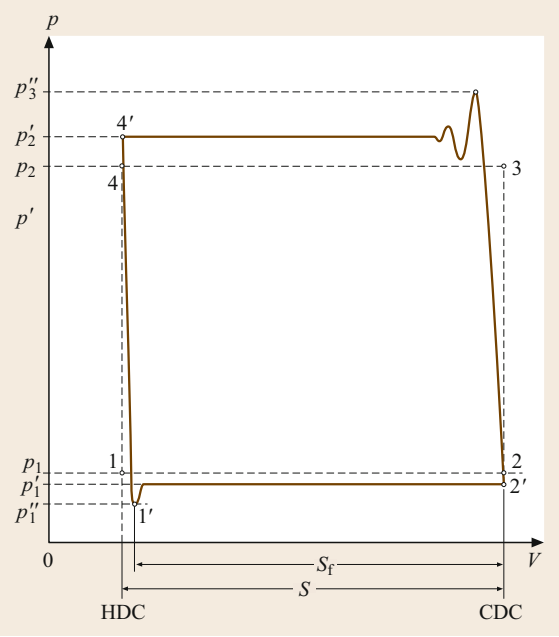

Fig. 17.38 Ideal and real piston pump p–V diagram

- In turn, the pressure cannot drop at a constant volume, since there are inertial forces and potential backflows from the pressure line when the pressure valve closes and the gas fractions reexpand. As a result, the ideally isochoric pressure drop from 4′ to 1′ is not isochoric.

In contrast to centrifugal pumps, piston pumps have a characteristic curve with a delivery rate that is nearly independent of delivery pressure. As a result of the displacement, the delivery rate is calculated as the product of the piston surface s, stroke, and rotational speed n

$$\dot{v} = Q = A_K s n \,. \tag{17.48}$$

Consequently, throttling, i.e., changing the system head curve, cannot regulate the delivery rate. On the other hand, an inordinate rise in pressure has to be prevented from destroying the pump and system components. Hence, any time a piston pump is used, a *safety valve* must be incorporated on the system's pressure side.

Energy and Efficiency

Specific Effective Energy of the Complete System w_{st}. Figure 17.39 shows a simple pump system.

The pump feeds mechanical work to the fluid in order to increase the pressure of the potential energy, i.e., to facilitate delivery and/or a rise in pressure. If this work is applied to the fluid's mass (disregarding changes in density), then the specific effective energy of the system is obtained

$$w_{st} = w_{geo} + \frac{(p_a - p_e)}{\rho} \,, \tag{17.49}$$

$$w_{geo} = H_{geo} g \,, \tag{17.50}$$

where w_{geo} is the specific geodetic delivery work, p_e is the pressure on the fluid in the suction tank, p_a is

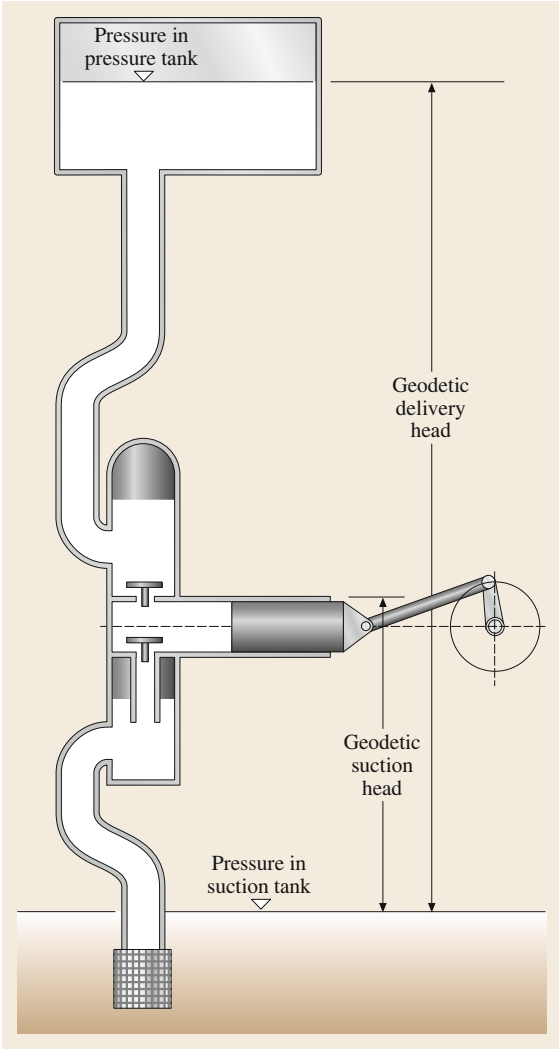

Fig. 17.39 Piston pump system

the pressure on the fluid in the pressure tank, ρ is the density of the pumped medium, g is the gravitational acceleration, and H_{geo} is the level difference.

Expressed in pressures and levels, the following ensues

$$p_{st} = H_{geo}\rho g + p_a - p_e \,, \tag{17.51}$$

$$H_{st} = H_{geo} + \frac{(p_a - p_e)}{\rho g} \,. \tag{17.52}$$

The system's specific effective energy is independent of the type of pump, the size of the delivery flow, and the layout of the pipe system.

Specific Effective Energy of the Pump w. The specific delivery work required to deliver the mass flow of the fluid in the selected system is referred to as the specific effective energy of the pump. The proportions of energy loss and velocity energy are taken into account here

$$w = w_{st} + w_{dyn} + w_V \,, \tag{17.53}$$

$$w_{dyn} = 0.5\left(v_2^2 - v_1^2\right), \tag{17.54}$$

where v_2 and v_1 are the velocities in the suction and pressure tubes, respectively, and w_v is the specific energy loss in the suction and pressure lines.

The pump's specific effective energy depends on:

1. The type of pump
2. The size of the delivery flow
3. The layout of the pipe system.

Delivery rate η_{Vol}. As a result of volume losses, a pump's effective delivery rate is lower than the theoretical rate. These losses are caused by the following:

1. Leaks or valve-closing delays (volumetric efficiency λ_L)
2. The presence of gases or incomplete filling (λ_F).

The product of λ_L and λ_F constitutes the delivery rate η_{Vol}. The following empirical values apply to the delivery rate η_{Vol}:

1. 0.88–0.92 for small pumps
2. 0.92–0.96 for medium-sized pumps
3. 0.96–0.98 for large pumps.

Indicated efficiency η_i. Indicated efficiency expresses the ratio of a system's effective power to a pump's indicated power (determined from the indicator diagram). Thus, hydraulic losses are also taken into account.

$$\eta_i = \frac{P_Q}{P_i}, \tag{17.55}$$

$$P_Q = \rho Q w_{st} \,, \tag{17.56}$$

where Q is the feed rate and P_i is the indicated power (from the indicator diagram).

Mechanical efficiency η_m. Mechanical efficiency expresses all the losses caused by *mechanical friction* inside the pump. In the process, the ratio of indicated power to coupling power (input power) is expressed by

$$\eta_m = \frac{P_i}{P_{input}} \,. \tag{17.57}$$

Experience has shown that pumps with crankshaft drive have a mechanical efficiency in the range

$$\eta_m = 0.85–0.95\,. \tag{17.58}$$

Total efficiency of the pump η. Total efficiency η is expressed by the ratio of the effective power to the input power

$$\eta = \frac{P_Q}{P_{input}}\,. \tag{17.59}$$

Experience has shown that a pump with crankshaft drive has a total efficiency in the range of $\eta = 0.70–0.80$.

Mass Actions

On the one hand, the reciprocating pump's discontinuous working process results in a constantly fluctuating speed of the pumped medium in the connected lines. On the other hand, the portions of the pumped medium subjected to accelerations undergo a mass action. The time-varying delivery rate follows the laws of piston motion up to a fixed limit (the vapor pressure), so that the time progression of the volumetric delivery corresponds exactly to the piston velocity. The valves' action is used to allocate the positive and negative fractions to the intake and the delivery stroke (Fig. 17.40).

The crankshaft's rotation is split into the intake and the delivery stroke. Thus, the total delivery rate must be pumped during a half-rotation of the crankshaft. The maximum value of the speed is considerably larger than the average value. There are only two times during both the intake and the delivery stroke at which the instantaneous delivery rate corresponds exactly to the average volumetric flow. This is not the case at any other time.

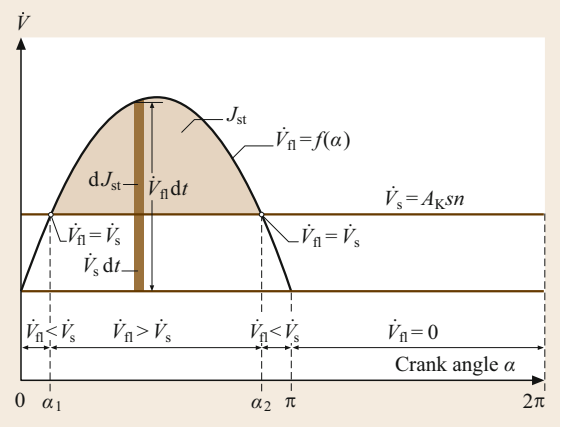

Fig. 17.40 Time progression of the volumetric delivery of a single-action, one-cylinder pump

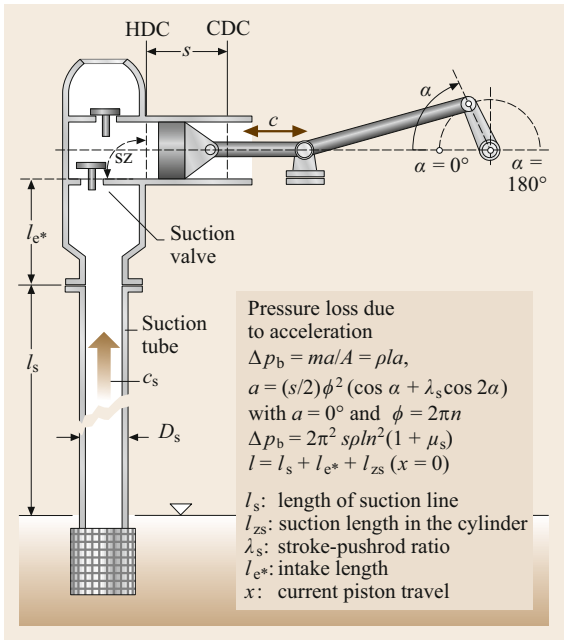

Fig. 17.41 Suction side of a reciprocating pump system

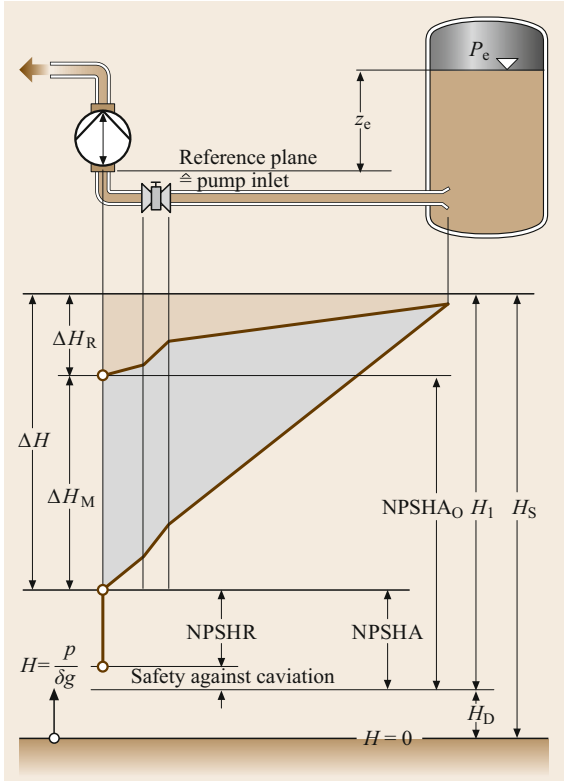

Fig. 17.42 NPSH value of the intake tract of a pump system (after [17.11])

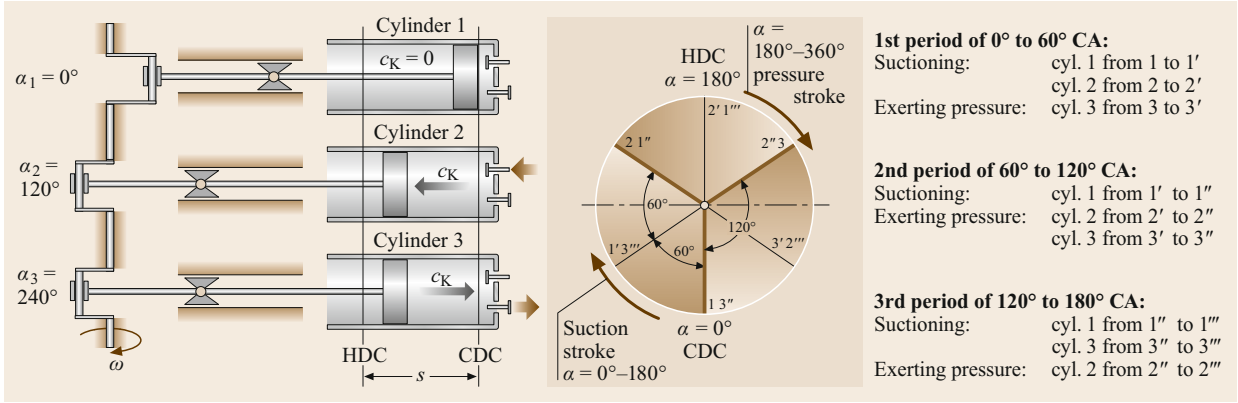

Fig. 17.43 Function of a three-cylinder pump

The maximum acceleration is at a crank angle of 0°, i.e., the theoretical start of the intake stroke. However, a maximum acceleration of the amount of fluid also corresponds to a maximum mass action, which results in a maximum reduction in the pressure in the working chamber (Fig. 17.41).

To prevent cavitation, the so-called vapor pressure p_0 of the fluid must not be reached during pump operation. Consequently, the piston acceleration and the mass of the fluid present in the intake tract yield the maximum permissible suction head. Conversely, when the suction head is known, it yields the maximum permissible speed for the pump.

The net positive suction head (NPSH; Fig. 17.42) is used to designate a pump's volume flow rate. The difference between the actual NPSH and the required NPSH is a measure of protection against cavitation.

When several working cylinders are employed, conditions change with the effect that several cylinders are able to draw from one suction line at the same time (Fig. 17.43). Here, the drop in pressure as a result of the mass action must be determined individually for the single parts of the intake tract. Employing several cylinders improves the overall balance, since the entire amount of fluid is not subjected to maximum acceleration and, when there are upwards of three working chambers, the flow velocity in the suction line is never zero.

To reduce the pulsation of the delivery rate both on the suction and the pressure side, employing several cylinders is expedient. If using several cylinders proves insufficient, then installing elastic components, the so-called expansion chamber, is advisable. Here, interconnecting an elastic accumulator (gas cushion) achieves a homogenization of the delivery rate.

The cyclic irregularity of the pressure on the piston is considered as a decision criterion for integrating an

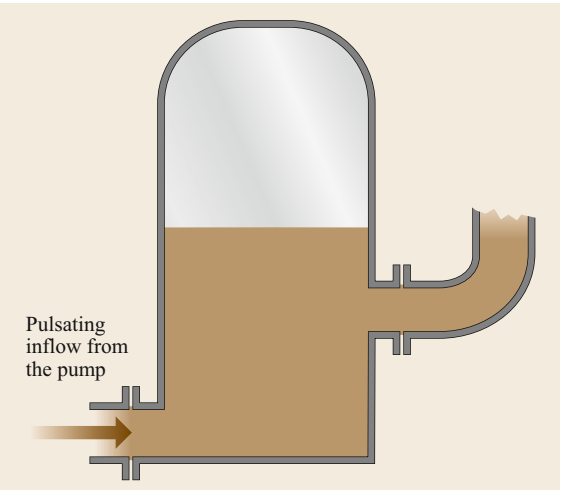

Fig. 17.44 Pressurized air chamber

expansion chamber

$$\delta_p = \frac{(p_{K-max} - p_{K-min})}{p_{K-m}} , \tag{17.60}$$

where

$$p_{K-m} = \frac{p_{K-max} + p_{K-min}}{2} . \tag{17.61}$$

This applies to both the suction side and the pressure side.

The cyclic irregularities considered limit values for the use of expansion chambers are $\delta_{p-s} \leq 0.1–0.05$ (suction side), and $\delta_{p-d} \leq 0.05–0.02$ (pressure side). The expansion chambers can be constructed both as a simple air tank open toward the fluid (Fig. 17.44) or as a diaphragm or bladder accumulator (Fig. 17.45).

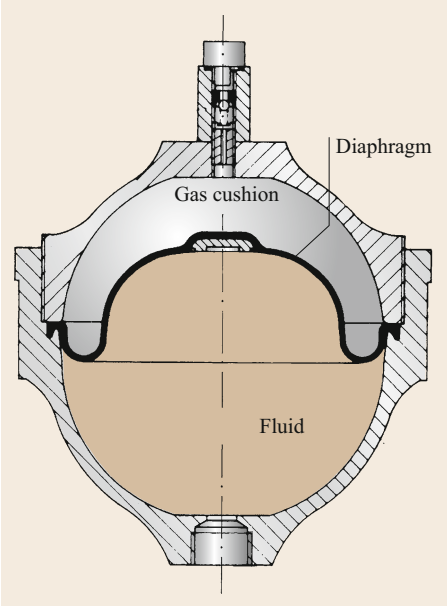

Fig. 17.45 Diaphragm accumulator (after [17.12])

17.2.3 Components and Construction of Positive Displacement Pumps

Working Valves

Automatically operating, pressure-controlled valves are used in reciprocating pumps to separate the suction and expulsion processes. These valves can be constructed as flat seats, conical seats, or ball valves. Both elastic force and gravitational force can trigger their closing forces (Fig. 17.46).

Multiple annular valves (Fig. 17.47) are also used to reduce the force of acceleration at the valve and above all to lower their speed when they close. These make large openings possible when strokes are small.

To open such a valve, a pressure differential must always be present, which essentially depends on the elastic force, the friction, and the valve face (Fig. 17.48).

Reciprocating Pumps

Compression Pumps. Compression pumps are pumps, such as boiler feed pumps, for example, that work approaching pressures up to 7000 bar and achieve

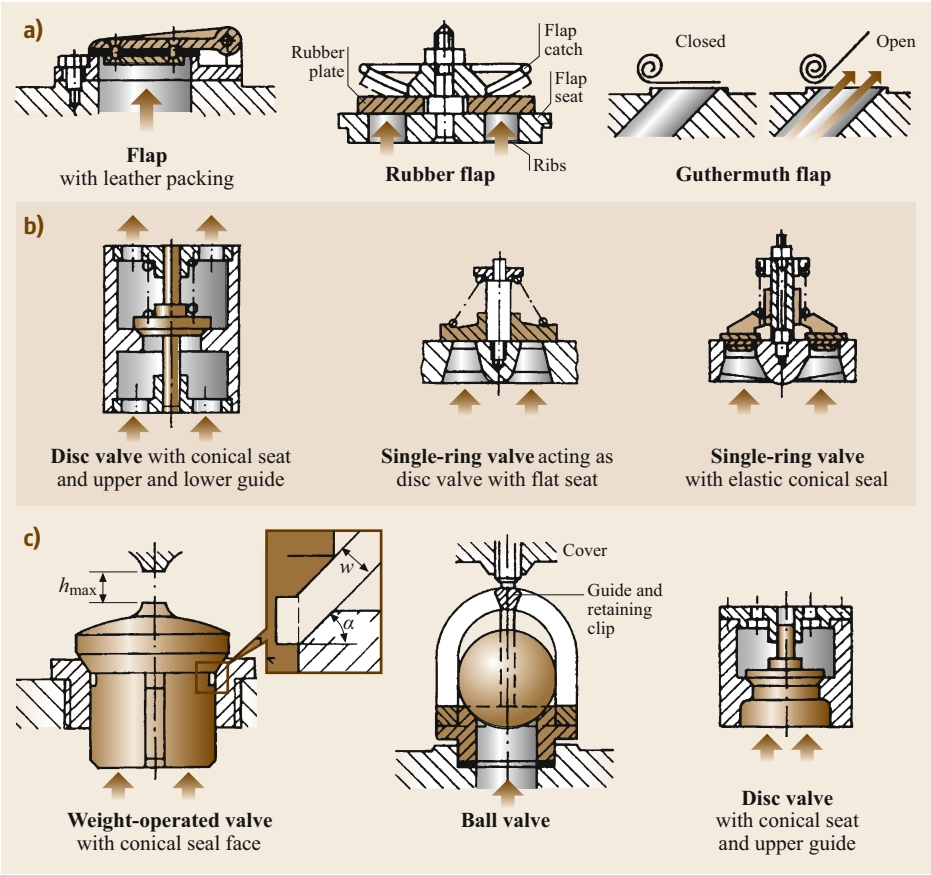

Fig. 17.46a–c Valve types. **(a)** Flaps, **(b)** spring-loaded valves, **(c)** weight-loaded valves (after [17.13])

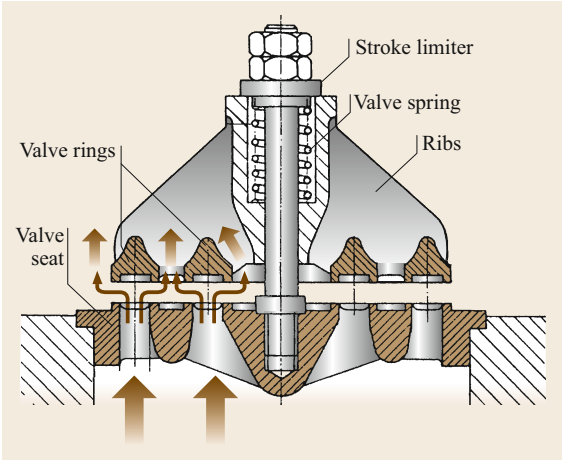

Fig. 17.47 Multiple annular valves (after [17.13])

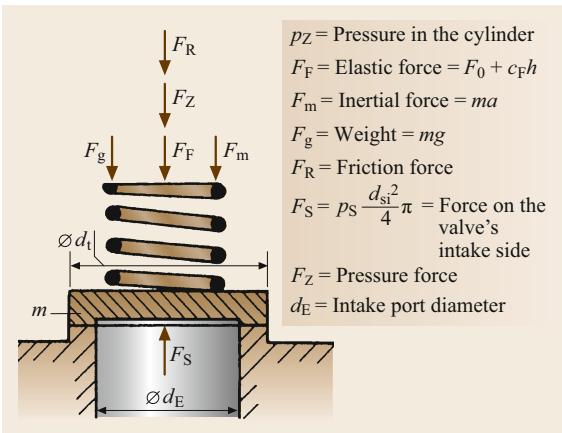

Fig. 17.48 Forces at the suction valve

delivery flows of 0.01–160 m^3/h. As a result, pump components are under the most extreme stresses, most notably in the cylinder (called the pump head here), the valves, and the plunger seal (stuffing box). In view of the high pulsating stress of the components, the design not only has to apply appropriate methods of calculation and employ the requisite material but also produce particular surface finishes to ensure sufficient operational reliability.

For economic reasons, such pumps, which are usually only manufactured in small quantities, are often engineered based on *standardized* engines with crossheads. They are, thus, then designed for specific forces along the rod (piston forces). When standard engines are used for different pumps, a specific maximum piston diameter is produced for every pressure to be reached. The number of cylinders and the speed determine the delivery flow pumped. By combining pump heads in these engines, appropriate pumps can be assembled (modular system) for the widest variety of applications with relatively little effort.

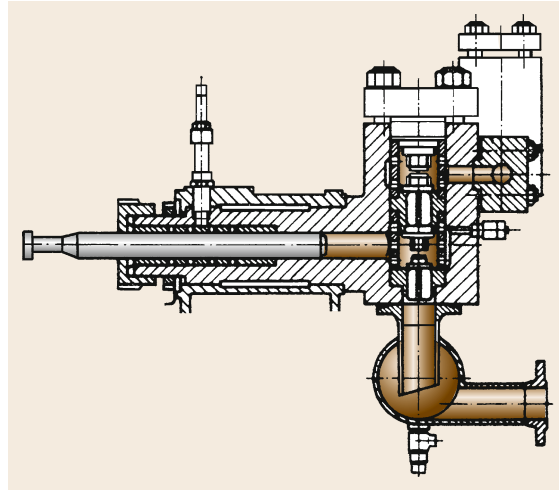

Fig. 17.49 Maximum pressure piston pump for pressures up to 7000 bar (after [17.14])

The design engineering and material selection for individual components such as the plunger, pump cylinder, valves, etc., are extremely important for pumps with higher pressures. Composite materials or prestressed components are used at extreme pressures (Fig. 17.49).

An important aspect of design is making the disassembly of wearing parts (valves, stuffing box packing) as easy as possible. Above all, it is essential to avoid having to disassemble the suction and pressure lines when removing the valve, since these are very rigid at extreme pressures. The stuffing box packing in compression pumps is under extreme stress and, therefore, may not be used as a plunger guide. To this end, a corresponding guide bushing (not functioning as a seal) is used.

Metering Pumps. The chemical industry as well as the food processing industry need metering pumps on a large scale to ensure fluid is metered precisely and consistently. Delivery pressures of up to 4000 bar and precisely repeatable metered quantities of 0.001 L/h or 0.2 mg/stroke up to 200 000 L/h have to be achieved. The required metered quantities are regulated by adjusting the speed or more frequently the plunger stroke. While continuously variable transmissions or frequency converters are widely used to adjust the speed, different variants are used to adjust the piston stroke, which, depending on their design, operate with the *fixed mean position of the piston* or with the *fixed dead center of the piston* from stroke zero onward. Both plunger and diaphragm-type metering pumps are constructed.

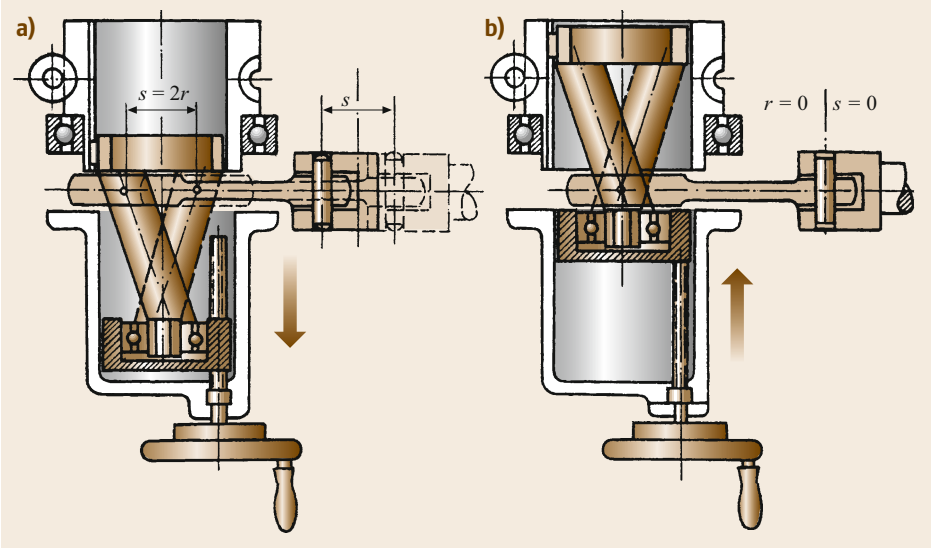

Fig. 17.50a,b Adjustable crank radius. **(a)** 100% stroke, **(b)** 0% stroke (after [17.12])

The stroke can be adjusted in different ways, e.g.:

- Crankshaft drive with adjustable crank radius (Fig. 17.50).
- Double eccentric with adjustable eccentricity (Fig. 17.51).
- Radially adjustable rotary eccentric (Fig. 17.52).
- Spring cam drive units (Fig. 17.53) are often used for simple, primarily smaller diaphragm metering pumps. An adjustable limiting bolt mechanically adjusts the stroke. The stroke can be adjusted by using the limiting bolt to increase or decrease the distance between the follower and the cam's basic circular path. A rotary eccentric cam is the cam shape used. A so-called phase angle occurs in which only part of the stroke is utilized. However, strong forces of acceleration act in this drive unit at the start of the effective stroke so that the range of adjustment at higher pressures is limited to values between a complete stroke and a maximum of 50% of the stroke.

Diaphragm metering pumps are used for applications in which the delivery chamber must be absolutely impermeable to the environment. The diaphragm can be operated mechanically as well as hydraulically (Figs. 17.54 and 17.55).

The delivery pressure in mechanical drives subjects the membrane edge to great stress. A hydraulic drive does not subject the diaphragm to great stress, and considerably higher delivery pressures are possible.

With regard to adjusting the stroke, the same applies to hydraulically powered diaphragms as to mechanically powered diaphragms. The hydraulic system is simply

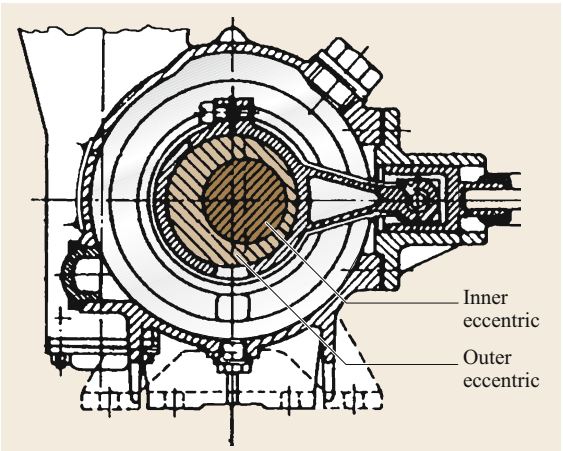

Fig. 17.51 Double eccentric (after [17.15])

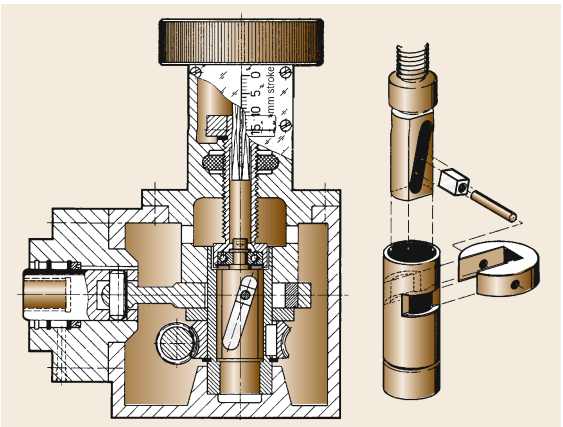

Fig. 17.52 Adjustable rotary eccentric (after [17.15])

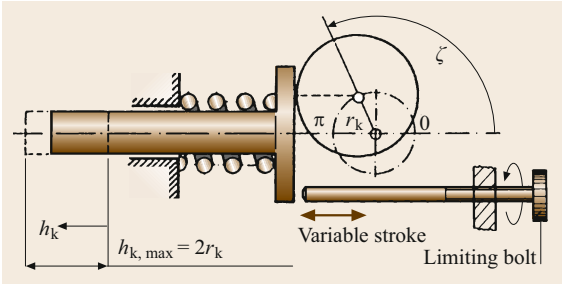

Fig. 17.53 Flexible cam drive unit

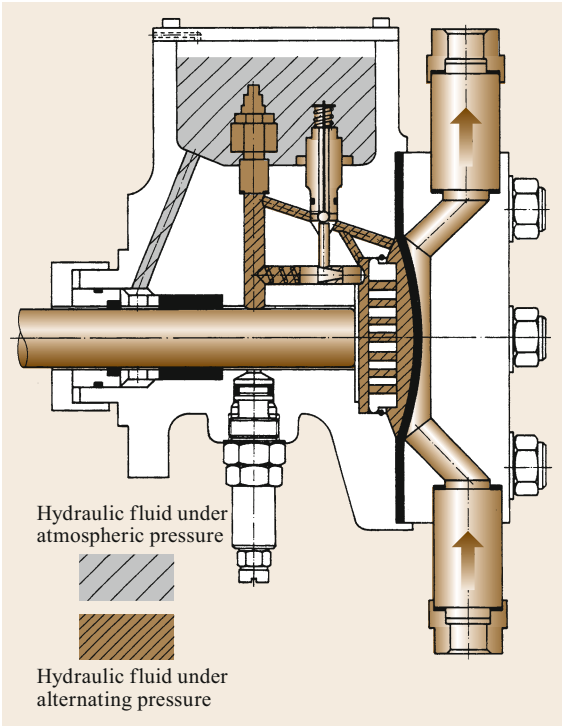

Fig. 17.54 Diaphragm metering pump with diaphragm position control (after [17.12])

connected between the plunger and the diaphragm and serves to transfer the quantity pumped in a ratio to the volume of 1 : 1. The force and travel ratios follow the continuity equation. The amount of leakage potentially occurring in the hydraulic system is replenished from the storage tank during each stroke so that the diaphragm's stroke motion is retained with its end positions. Frequently, there is a diaphragm position control. Employing a device to redefine the diaphragm's end position during each stroke prevents overloading of the diaphragm.

A multiple membrane with an inserted control medium is used for cases in which contamination of the pumped fluid by the hydraulic fluid must be prevented or emergency operation guaranteed.

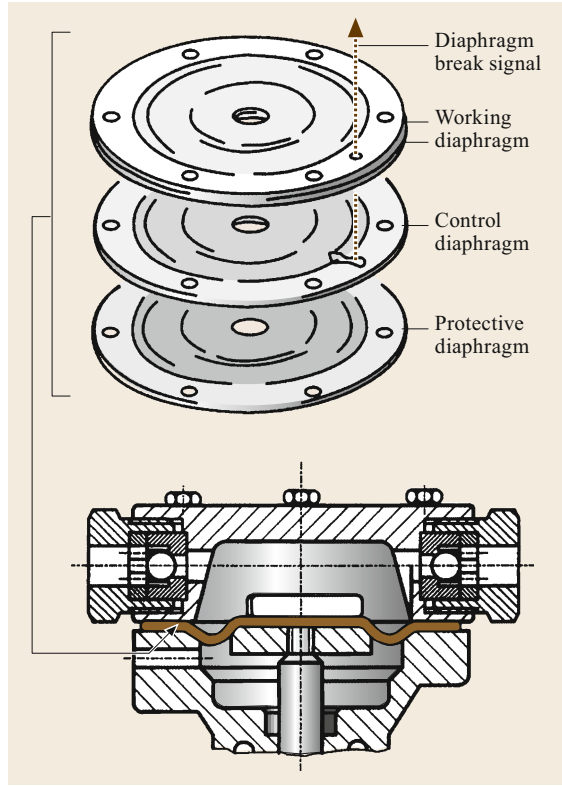

Fig. 17.55 Multidiaphragm pump (after [17.12])

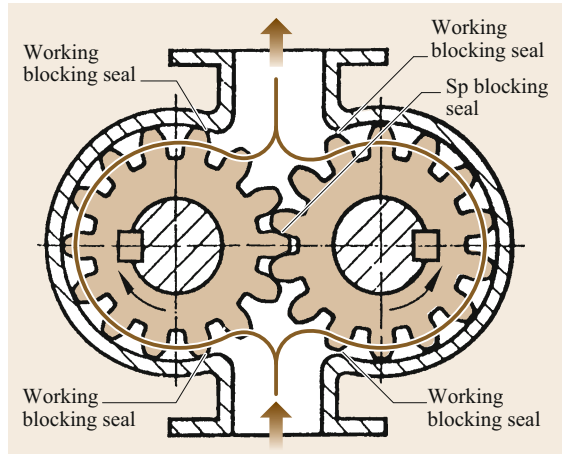

Fig. 17.56 Principle of the gear pump

Rotary Piston Pumps

Along with the type of motion, the absence of working valves is a significant feature of piston pumps with rotary displacers. Ports control the suction and pressure process. As a result, when a pressure difference exists in the adjacent medium, these machines can also function as power machines. In order to prevent this, nonreturn

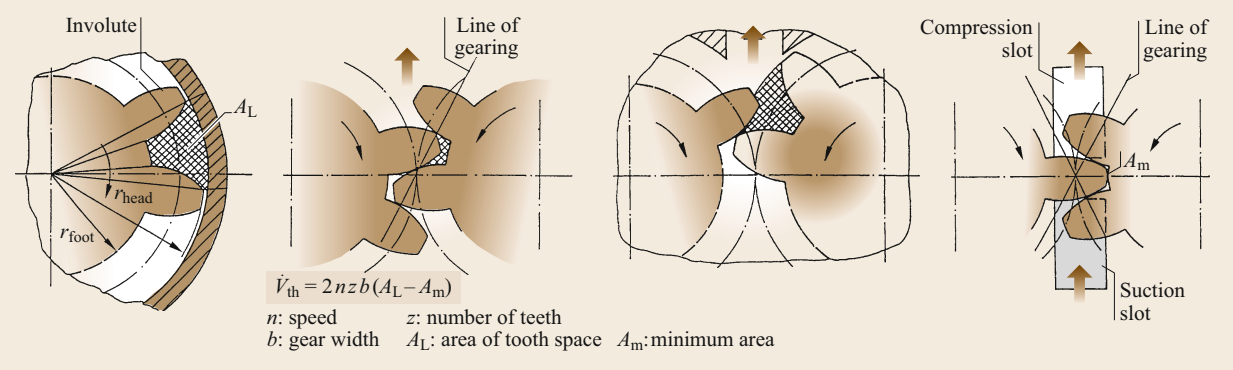

Fig. 17.57 Displacement in a gear pump

valves (that do not have the function of working valves) are used.

Single-Rotation Piston Machines.

Gear pumps. A gear pump consists of two or more gearwheels arranged in a housing and intermeshed. The driveshaft is attached outside the housing, the remaining gearwheels being driven by the gearing. The suction and pressure sides are separated by the meshing and the sealing gap between the tooth tips, gear-side surfaces, and housing.

The rotating gearwheels cause the pumped medium to be delivered from the suction side to the pressure side. In the zone of gear meshing, the teeth displace the medium from the tooth gaps (displacement effect). Simultaneously, the intermeshed tooth flanks seal the suction chamber off from the pressure chamber (Fig. 17.56 (Sp)). Moreover, the tooth tips seal the individual volumes off from the housing (Fig. 17.56). In addition, the axial gap must be confined to narrow limits by maintaining slight axial clearances. An optimal seal enables the gear pump to attain high delivery rates (volumetric efficiencies).

As a rule, the same involute profile used for transmission gears is used for the tooth flank profile of gear pumps. Thus, the gearwheels can be manufactured cost effectively by using the same tools on identical machines. Other, more expensive profiles are reverted to only for special applications such as pulsation-free sine pumps. Helical gears are also rarely used. While intended to achieve smoother running, they generate an axial thrust to the gearwheels and

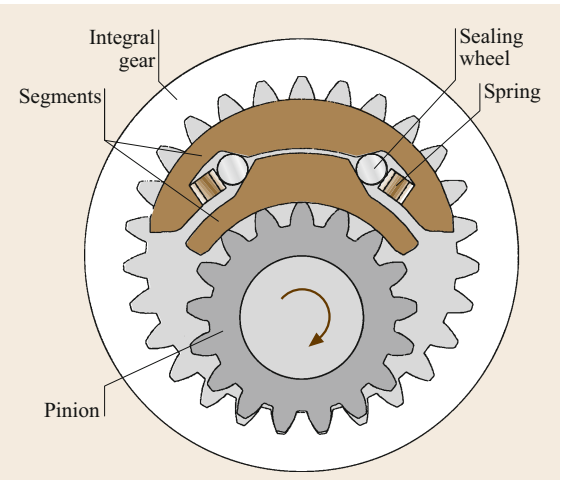

Fig. 17.58 Internal gear pump with clearance compensation (after [17.16])

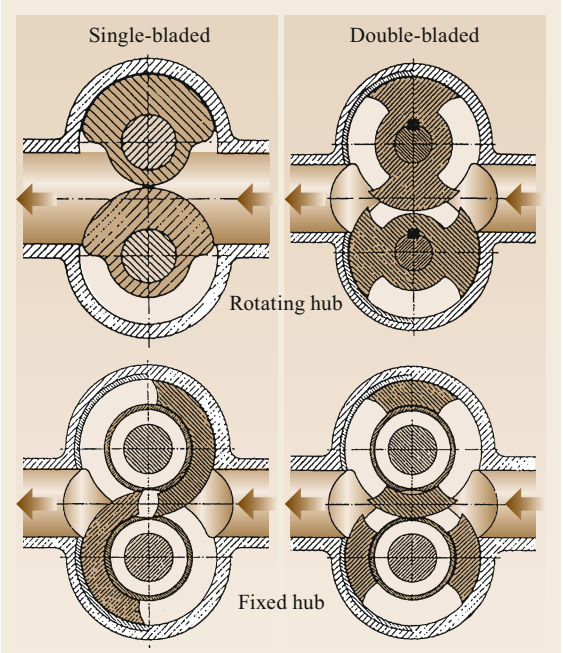

Fig. 17.59 Variants of rotational motion piston pumps (after [17.17])

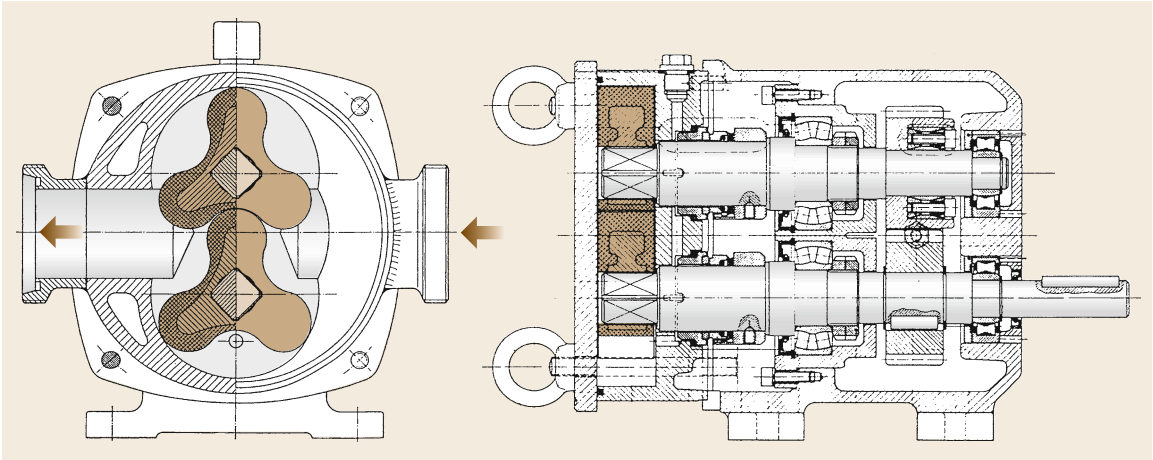

Fig. 17.60 Rotational motion piston pump for food, and cross and longitudinal sections (after [17.17])

bearings, as well as unequal axial gap widths. When rolling, a self-contained volume is produced in the tooth gap into which the opposing tooth immerses. This causes a change of volume. Since a change of volume in enclosed spaces cannot be tolerated when fluid is being pumped, appropriate measures must ensure fluid is supplied to and removed from the tooth gap (Fig. 17.57).

To this end, either so-called compression slots are made in the side panels of the pump or on the teeth flanks or boreholes are made in the bottom land of a gear, which the grooves in a fixed axis connect to the suction or pressure chamber. Alternatively, the tooth flank clearances are made sufficiently large. When they are being engineered, the clearances between the components must be dimensioned to correspond to the viscosity of the pumped medium and the delivery pressure. This can lead to problems, most notably when there is axial play.

Axial hydraulic clearance compensation is applied to improve impermeability at high pressures and to simultaneously reduce friction during starting. Thus, delivery pressure is utilized to reduce running clearance. Internal gear pumps can additionally be given radial hydraulic clearance compensation (Fig. 17.58).

Low-pressure pumps ($\Delta p < 16$ bar) are usually designed with 8 to 14 teeth, while medium to high-pressure pumps ($\Delta p > 160$ bar) have 16–25 teeth.

Single-rotation piston pumps. Rotational motion piston pumps are often incorrectly called eccentric rotational motion piston pumps. Since they are frequently positively driven by external gears, the sliding of their plungers past one another without contact is common to all rotational motion piston pumps. As a result, these pumps are well suited for delivering nonlubricating and abrasive liquids. This aspect fundamentally distinguishes this type of pump from gear pumps. The types are classified according to the number of impellers and the type of hub design (Fig. 17.59).

In some cases, the design selected for the displacer ranges from a multi-impeller to a gear type. However, the rotational motion piston pump is not a gear pump, since exterior synchronizer gears enable the displacer to run without contact. The fixed hub produces a seal covering the space between the displacers. The plunger shape creates a flat seal in the space between the housing and the displacer so that the fixed hub is able to achieve better inner impermeability. These pumps are used, for instance, to deliver finishes, paints, oils, gasoline, food, and alcohol, and for foaming liquid–gas mixtures. The pressure range of these pumps reaches 20 bar at delivery rates up to 500 m^3/h. They can pump media with very high viscosities.

Other displacer forms, some without dead space, are also used for special applications such as those in the food processing industry (Fig. 17.60).

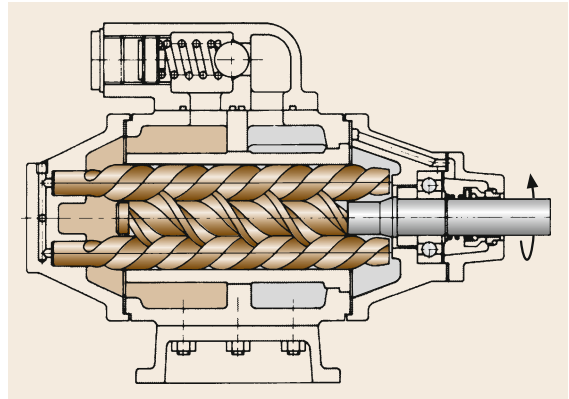

Fig. 17.61 Rotary screw pumps with three spindles (after [17.18])

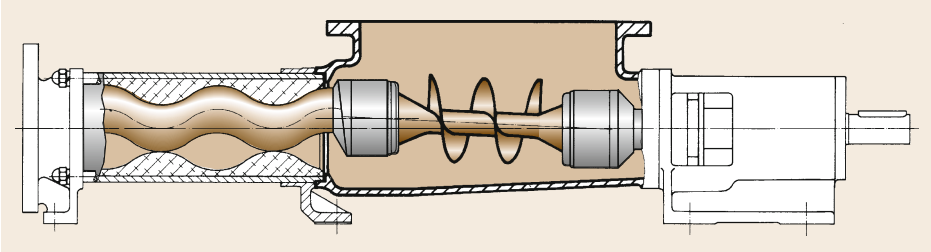

Fig. 17.62 Eccentric screw pump (after [17.19])

Rotary screw pumps. Among other things, rotary screw pumps are called *degenerate* gear pumps with helical gears and few teeth. The interrotating profiles effect an axial delivery. Rotary screw pumps are constructed with two, three, or five spindles. The design with two or three spindles is most widespread. The secondary spindles are arranged around the main spindle (Fig. 17.61).

These pumps are engineered both with single and dual flow to compensate for the axial thrust. The main spindle is usually double-threaded; the secondary spindles double or triple-threaded. Depending on the pumped medium, pitch, and profile, they are constructed with or without synchronizer gears.

Basically three profiles are used:

- Involute profile, without synchronizer gears (e.g., Leistritz)
- Epicycloidal profile (e.g., IMO AB, Stockholm: manufacturer of rotary positive three-screw pumps)
- Trapezoidal or rectangular profile, only with synchronizer gears (e.g., Bornemann).

Rotary screw pumps are constructed for:

- Delivery rates of $10-150\,m^3/h$
- Pressures of $15-150\,bar$
- Speeds of $500-1500\,min^{-1}$
- Viscosities of $25\times10^{-6}-5\times10^{-3}\,m^2/s$.

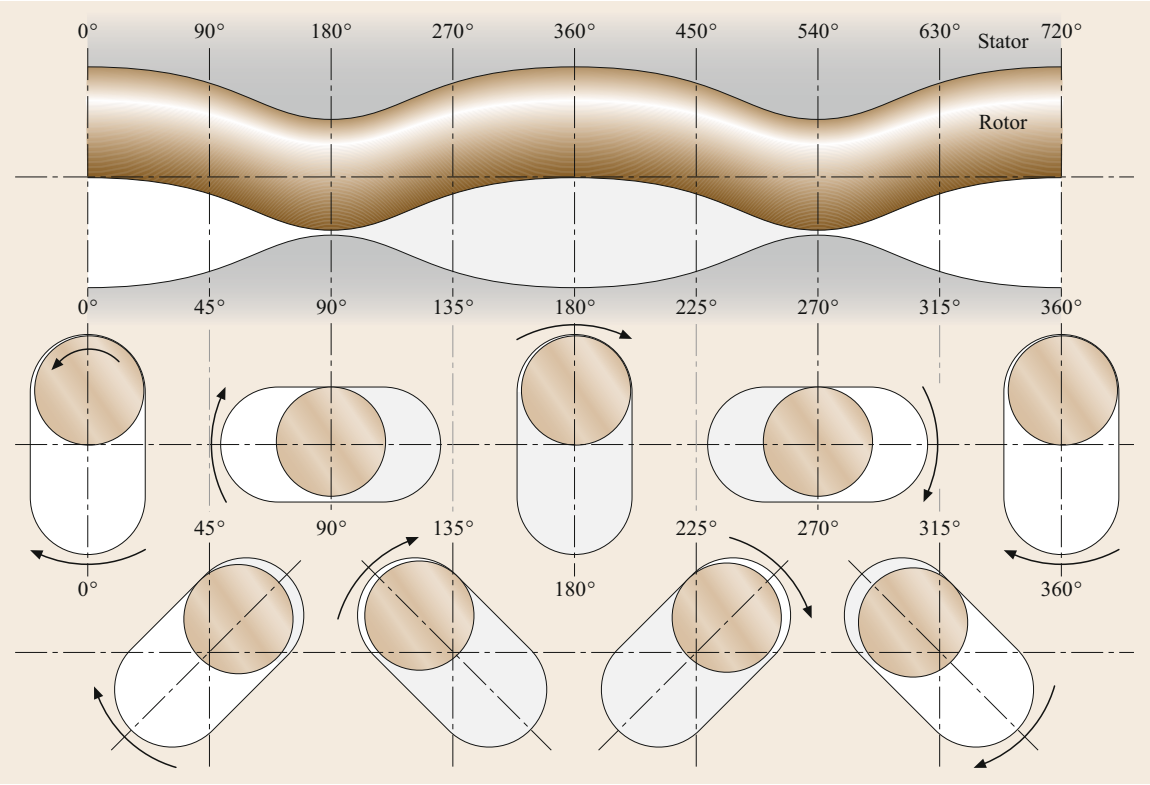

Fig. 17.63 Displacement effect of the eccentric screw pump (after [17.19])

Planetary rotation piston machine. *Eccentric screw pumps.* The principle of the eccentric screw pump (Fig. 17.62) goes back to the Frenchman Moineau. A rotor with a single-threaded diamond knurl rotates in a housing (stator) with a double-threaded diamond knurl. An alternative name for the eccentric screw pump is the single-spindle pump. Depending on its design, this pump is an eccentric rotational motion piston pump.

At every point, the rotor has a circular section with its center lying on the rotor axis on a helix. The housing has an oval section and twice the pitch of the rotor. Eccentric screw pumps attain delivery rates of $0.6-1000\,m^3/h$ at pressures of up to 40 bar. Apart from being able to deliver abrasive and highly viscose media, the eccentric screw pump provides the advantage of a pulsation-free delivery rate (Fig. 17.63). Since dry running the pump has to be avoided in any operational situation, the suction and compression flanges in this type of pump are frequently arranged on the top side of the housing.

Typically, the rotors are made of CrNi steel or cast iron and the housing of red brass or cast iron. The stator is made of elastic material such as rubber, polytetrafluoroethylene (PTFE), or neoprene. The medium may contain a solid content of up to 45%. However, this leads to a sharp power increase and causes low speeds. The elastic stator makes it possible to attain high impermeability and a suction head of up to 8.5 m.

The rotor executes a circular motion with its center axle so that it must be driven by cardan joints. In some cases, only one cardan joint is used in smaller units. As a result, the stator must absorb part of the motion. In addition, a joint can be used, which compensates for a parallel axle offset. Impellers or screws that improve the feeding of the pumped substance are often mounted on the cardan shafts. Eccentric screw pumps are used to pump mortar, among other things.

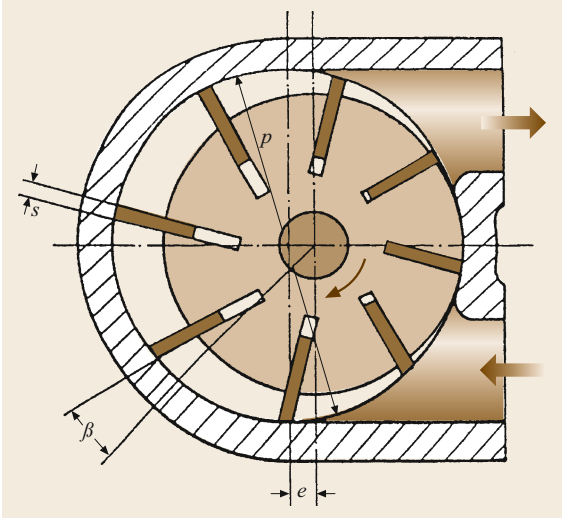

Fig. 17.64 Cell pump

Circulation piston machine. *Cell pumps.* Cell pumps (Fig. 17.64) are frequently used for low delivery rates of up to $25\,m^3/h$. As a rule, four to six slide valves are employed. Up to 12 slide valves are used at higher pressures of up to 100 bar. In some cases, even two slide valves per channel are used to increase impermeability.

Normally, the centrifugal force alone lifts the slide valves negatively. As a result, these pumps are relatively leaky at low speeds. The principle is broadly applied to fuel feed pumps, for instance. The roller cell pump is another common type. Rollers are used instead of slide valves. Their shape gives them advantages over slide valves in terms of wear. This type of pump is used, for example, as an electric fuel pump to pump gasoline in cars (Fig. 17.65).

So-called impeller pumps are also used when delivery flows are smaller, e.g., for garden pumps or coolant pumps for boat engines (Fig. 17.66).

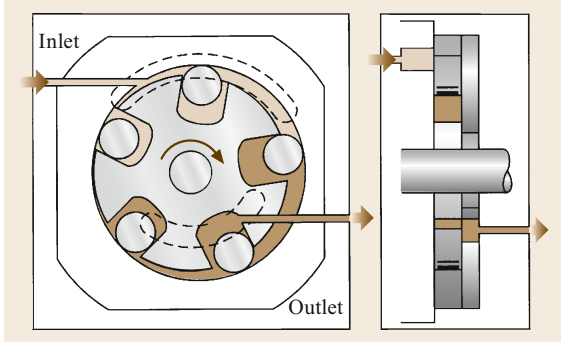

Fig. 17.65 Roller-cell fuel pump (after [17.20])

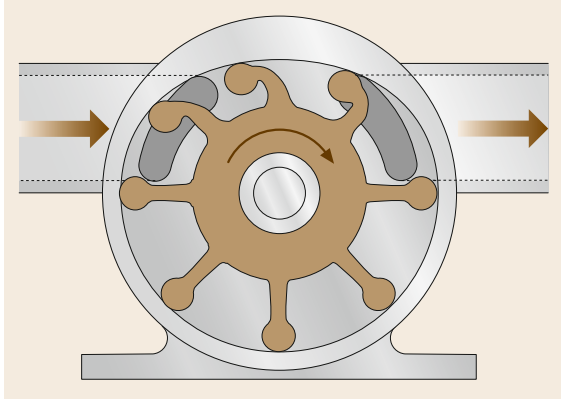

Fig. 17.66 Impeller pumps (after [17.21])

The working chamber changes volume by bending the rotor's elastic, usually rubber, impellers against the sickle-shaped part of the housing deviating from a circular shape. The rotor is installed axially without any gap in order to guarantee high impermeability. Thus, these pumps are self-priming. The impellers' ability to upright themselves determines the maximum speed. The delivery pressure depends on the flexural strength of the impellers. These pumps are insensitive to contamination of the pumped medium but can only reach low pressures of approximately 4 bar. They are used as boat motor seawater pumps and as garden pumps.

17.3 Compressors

Compressors can be divided into two general categories: positive displacement types and nonpositive displacement types. Positive displacement compressors deliver essentially the same volume of air regardless of the pressure ratio, while nonpositive displacement compressors will have reduced flow at higher delivery pressures. Axial flow and centrifugal compressors are nonpositive displacement types and reciprocating, rotary screw, and diaphragm compressors are of the positive displacement type. This section discusses the characteristics of positive displacement reciprocating compressors.

Reciprocating compressors are frequently used when high pressures are needed, although they generally use multiple stages of compression to limit the power required for the process. The basic compression process can be visualized as occurring in a piston–cylinder configuration that is similar to that of an internal combustion engine. In practice, reciprocating compressors frequently use both sides of the piston in *double-acting* systems. Inlet and discharge valves are spring-loaded so that they will automatically open when there is an appropriate pressure in the cylinder. The inlet valve will open when the cylinder pressure drops below the inlet pressure, and the discharge valve will open when the cylinder pressure exceeds the receiver pressure.

17.3.1 Cycle Description

Figure 17.67 shows the sequence of processes followed by reciprocating compressors. The upper part of each diagram shows the piston position in the cylinder and whether the valves are open or closed. The lower part of each diagram shows the corresponding pressure–volume diagram for the process. In Fig. 17.67a, the piston moves to decrease the volume with the valves closed. The pressure rises from state 1 to state 2 following a process line that depends on the amount of heat loss during the compression process. When the cylinder pressure exceeds the receiver pressure, the discharge valve will be forced open, and the gas is discharged at constant pressure, as shown in Fig. 17.67b. When the piston reaches the point of minimum volume, the cylinder volume is equal to the clearance volume. This is the starting point for the expansion process from state 3 to state 4, as shown in Fig. 17.67c, where the pressure falls from the receiver pressure to the intake pressure. Finally, when the cylinder pressure has dropped to the inlet pressure, the intake valve opens and fresh air is drawn into the cylinder, as shown in Fig. 17.67d.

The compression process for a reciprocating compressor will generally follow a polytropic process line that is between a reversible adiabatic process (isentropic) and a constant temperature (isothermal) process, as shown in Fig. 17.68. The isothermal process accomplishes the compression with the least work input. Ideal gases follow the relationship

$$pV = RT\,. \tag{17.62}$$

When an ideal gas is compressed it usually follows a polytropic process line that is modeled as

$$pV^n = \text{const}\,. \tag{17.63}$$

The usual values for n are between 1, which corresponds to an isothermal process, and k, which is the ratio of specific heats and is equal to 1.4 for air at 25 °C.

For the polytropic process, the pressure at the end of the compression process will depend on the compression ratio $r_\mathrm{v} = V_1/V_2$ according to the following equation

$$p_2 = p_1\left(\frac{V_1}{V_2}\right)^n = p_1 r_\mathrm{v}^n\,. \tag{17.64}$$

The final temperature can be calculated as

$$T_2 = T_1 r_\mathrm{v}^{n-1} = T_1\left(\frac{p_2}{p_1}\right)^{\frac{n-1}{n}} = T_1 r_\mathrm{p}^{\frac{n-1}{n}}\,. \tag{17.65}$$

The power required for the compression process is

$$\mathrm{Pwr} = p_1\dot{v}_1\left(\frac{n-1}{n}\right)\left(r_\mathrm{p}^{\frac{n-1}{n}} - 1\right), \tag{17.66}$$

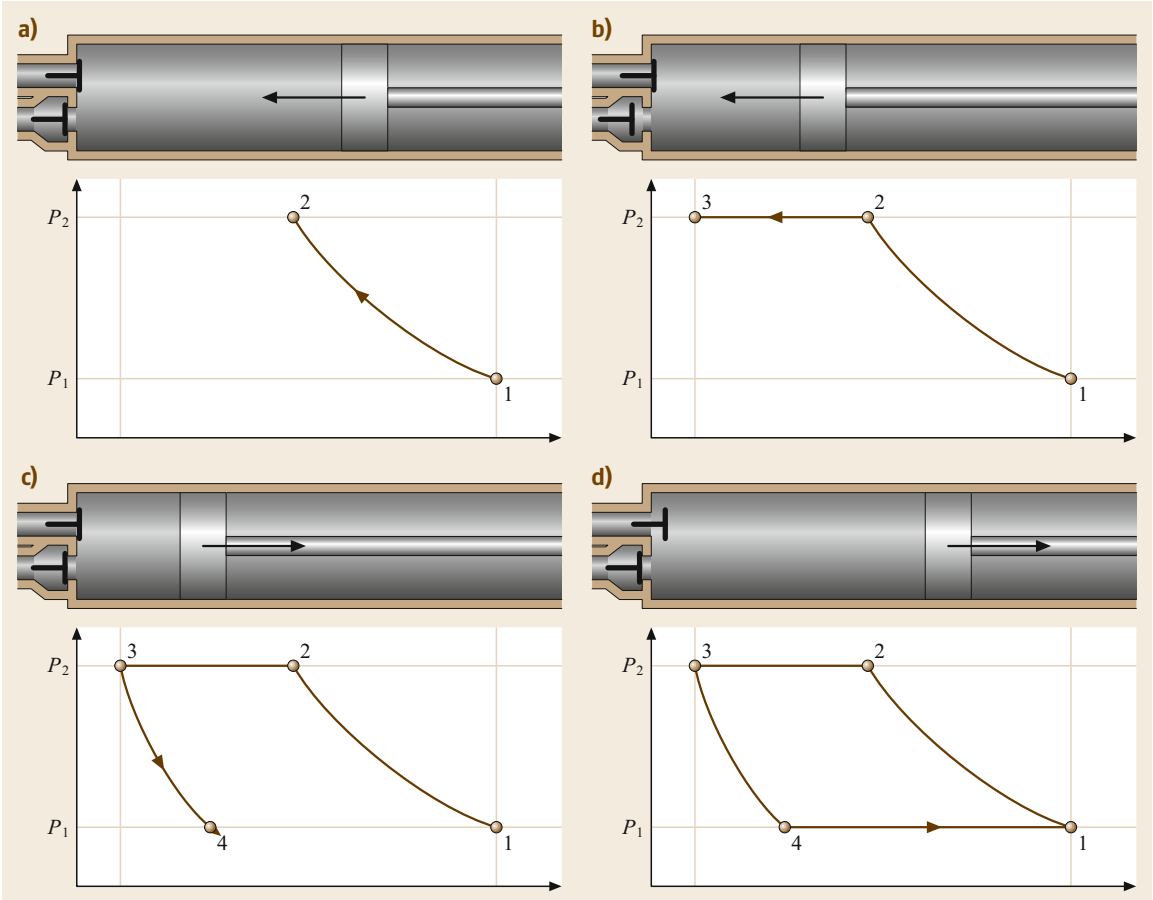

Fig. 17.67a–d Reciprocating compression processes. **(a)** Compression, **(b)** discharge, **(c)** expansion, **(d)** intake

where $\dot{v}_1$ is the volumetric flow rate entering the compressor, r_p is the pressure ratio p_2/p_1, n is the polytropic exponent, and p_1 and p_2 are the pressures at states 1 and 2, respectively.

At high pressures, many gases will deviate considerably from ideal gas behavior. Usually, these deviations are incorporated into the calculation through the use of a compressibility factor Z. The equation between temperature, pressure, and volume becomes

$$pV = ZRT \,. \tag{17.67}$$

The value of Z depends on the state, and charts are widely available for most common gases.

While reciprocating compressors are usually designed to encourage heat rejection, it is more common to have an intercooler between separate stages of compression. The intercoolers and multiple compressor stages are usually integrated into a common assembly that may take advantage of double-acting pistons.

17.3.2 Multistaging

Compression at constant temperature requires less work input than when the temperature is allowed to rise. In practice, isothermal compression is difficult to achieve. However, incorporating intercooling between multiple stages of compression can approximate isothermal compression.

In the limiting case of an infinite number of compression stages that include intercooling back to the inlet temperature, the total work required will be equal to that for isothermal compression. Even the division of a compression process into two stages can save considerable work input.

A two-stage compression process is depicted in Fig. 17.69. The compression process begins at stage 1, which corresponds to the piston at BDC and inlet pressure. The gas is compressed in the first stage to the intercooler discharge pressure at stage 2. The gas is then discharged at p_2 into an intercooler before en-

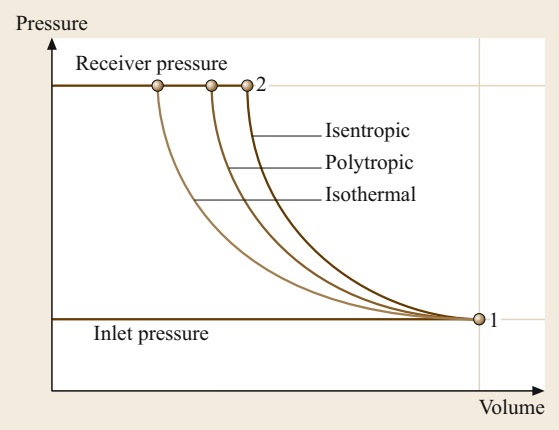

Fig. 17.68 Compression process lines

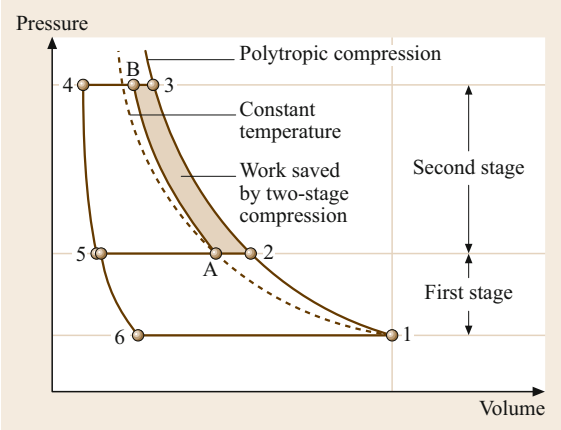

Fig. 17.69 Two-stage compression

tering the second compressor stage at state A. In this idealized case, the intercooler is assumed to operate at constant pressure, but the volume of gas is decreased due to the drop in temperature to the initial temperature of the gas. Then, the gas is compressed to state B before being discharged at p_B. If the pressure increase had been attempted with a single stage of compression, then the process line would pass through stages 1, 2, and 3. Since the area enclosed on the p–V diagram is the work needed to accomplish the process, the shaded area is the difference in work between the single-stage and two-stage compression processes. Clearly, the two-stage compression is more efficient.

The optimum pressure for intercooling is generally assumed to correspond to an equal pressure ratio for each stage. This assumes that the intercooling is able to reduce the gas temperature to the inlet temperature at each stage. If r_s is the pressure ratio for each stage, r_t is the overall pressure ratio, and s is the number of stages, then

$$r_s = \sqrt[s]{r_t} \,. \tag{17.68}$$

17.3.3 Design Factors

At the end of the compressor's discharge stroke, shown in Fig. 17.67b, gas fills the clearance volume at the discharge pressure. This gas expands as the piston moves away from the cylinder head until its pressure drops below the inlet pressure when the intake valve opens. The induction of fresh charge does not begin until this point is reached, so the full volume displaced by the piston is not utilized. When the clearance volume is large, then the capacity of the compressor is less.

The volumetric efficiency of a compressor can be approximated as

$$\eta_v = 1 - \frac{V_{\text{Clearance}}}{V_{\text{Displ}}}\left(r_p^{1/k} - 1\right) - \text{Leakage} \,, \tag{17.69}$$

where the leakage can generally be assumed to be between 0.03 and 0.05. Lower molecular weight gases usually have higher leakage.

It can be seen from the equation for η_v that an increase in clearance volume directly causes a decrease in volumetric efficiency. Its significance is much greater for high values of the pressure ratio r_p.

Although compressor designers try to minimize it, the clearance volume cannot be entirely eliminated. Reducing it to less than 4% of the displacement volume is difficult. The amount of clearance volume will affect the capacity of the compressor and its efficiency. Overall compression efficiency is improved when valve flow area is large. However, the desire to minimize the clearance volume conflicts with the desire to maintain large valves. Thus, there is often a tradeoff between volumetric efficiency and compression efficiency, which determines the actual value of the clearance volume.

17.4 Internal Combustion Engines

In an internal combustion engine, the working fluid consists of a fuel–air mixture and the combustion products of this mixture. Although many cycles have been proposed, the traditional two-stroke and four-stroke cycles still dominate current use. Depending on their design and application, internal combustion engines provide

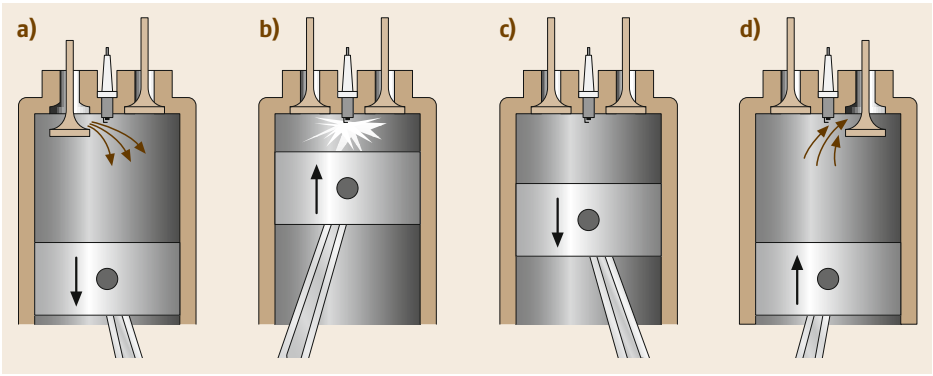

Fig. 17.70a–d Four-stroke cycle events. **(a)** Intake, **(b)** compression, **(c)** expansion, **(d)** exhaust

excellent portability, power density, and fuel economy. Vehicles that utilize internal combustion engines provide unsurpassed range, drivability, and driver comfort while maintaining low levels of hazardous pollutants.

17.4.1 Basic Engine Types

Engines can be categorized in many different ways. The number of cylinders, the type of valve actuation, and whether the engine is turbocharged or naturally aspirated are all possible choices. Some engines are spark-ignited and utilize a homogeneous fuel–air mixture, and some are compression-ignited, also called diesel engines, and utilize a heterogeneous fuel–air mixture. Another characteristic is whether the engine uses the two-stroke or four-stroke engine cycle.

All reciprocating internal combustion engines need to go through the four processes of intake, compression, expansion, and exhaust. The basic difference between two-stroke and four-stroke cycle engines is that the two-stroke engine accomplishes the four processes in a single revolution, or two strokes of the piston (one up and one down). The four-stroke engine needs two revolutions to complete the cycle.

The processes are shown in Fig. 17.70 for a four-stroke cycle. In Fig. 17.70a, the intake valve is open and fresh charge is drawn in as the piston moves downward toward the bottom dead center (BDC) position. After BDC, the intake valve closes, and the piston compresses the air on its upward compression stroke. Near the end of the compression stroke, close to top dead center (TDC), the spark plug fires and ignites the fuel–air mixture. In a diesel engine, only air is drawn in through the intake valve and fuel is injected into the air near the end of the compression stroke. The mixture self-ignites after a short delay. For both spark-ignited and diesel engines, the combustion products work on the piston as it moves out for the expansion stroke, as shown in Fig. 17.70c. In Fig. 17.70d, the exhaust valve opens near BDC and the combustion products are expelled from the cylinder by the upward motion of the piston. At the end of the exhaust stroke, the intake valve opens, and the cycle is repeated with another intake stroke.

The two-stroke cycle is depicted in Fig. 17.71. When the piston is near the BDC position, air enters the cylinder from a port in the cylinder wall. There is a deflector on the top of the piston to inhibit the direct passage of the fresh charge across the cylinder and out the exhaust port on the other side. As the piston moves upward, it covers the intake and exhaust ports and compresses the fuel–air mixture. Near TDC, the spark fires to start the combustion process. In a two-stroke diesel

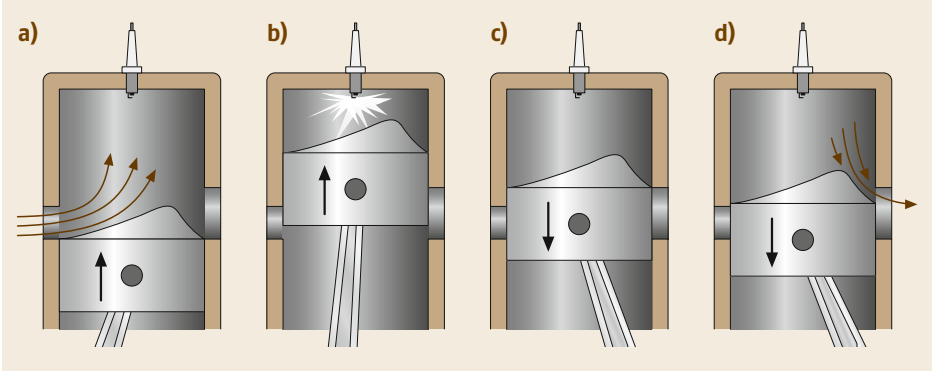

Fig. 17.71a–d Two-stroke cycle events. **(a)** Intake, **(b)** compression, **(c)** expansion, **(d)** exhaust

engine, the fuel is injected into the compressed air at this point. For both types of engines, the combustion products expand and work on the piston surface until the point where the piston uncovers the upper edge of the exhaust port. At this point, the gases in the cylinder rapidly blow down until the pressure in the cylinder is close to the exhaust pressure. As the piston continues its downward motion, it uncovers the intake port, so fresh charge can enter the cylinder and repeat the cycle.

Because the two-stroke engine needs to complete all four processes in a single revolution, it must start the exhaust process well before the piston has reached bottom dead center. A four-stroke engine can wait until about 140° after TDC before starting to open the exhaust valve, since the primary criterion is that the period of rapid pressure equalization that occurs when the valve is first opened, called the blowdown, is essentially complete by BDC. A two-stroke engine must start opening the exhaust port at about 90° after TDC to provide sufficient time for the blowdown before the intake port opens and the intake process starts. Opening the exhaust valve early so that the cylinder pressure is throttled down to ambient allows no recovery of the energy in those hot gases and is the major reason why two-stroke engines are less efficient than four-stroke engines.

In four-stroke engines, almost the entire cylinder contents of burned product gases, called residual gases, is expelled when the piston reaches TDC at the end of the exhaust stroke. Then, as the piston moves away from TDC, it produces a low pressure in the cylinder, which draws in a fresh air charge through the intake valve. Four-stroke engines are said to be self-scavenging. That is, the piston motion is directly responsible for moving the exhaust gases out of the engine and drawing in fresh air. Two stroke engines are not self-scavenging. Some mechanism other than piston motion is needed to exchange the gases in the cylinder. By opening the exhaust valve early, while the cylinder pressure is still high, most of the residual gases can be expelled. The fresh charge must be forced into the cylinder from a pressurized source, which might be a crankcase that is pressurized by the downward motion of the piston as in the single-cylinder two-stroke engines used for hand-held power equipment. It might also be from an engine-driven blower as is common in diesel two-stroke engines.

17.4.2 Performance Parameters

Engine speed and torque are the two most fundamental quantities of engine performance. Both are usually measured quantities, with speed given in revolutions per minute (rpm) and torque in newton meters (Nm). Power is defined as torque times rotational speed. When the torque is measured at the engine flywheel, it is called the *brake torque*, and the power calculated from it is the brake power, as

$$P_b = T_b\omega = T_b 2\pi N \,, \tag{17.70}$$

where P_b is the brake power, T_b is the brake torque, ω is the rotational speed, usually in radians/unit time, and N is the rotational speed in rev/unit time.

The source of power in the engine is the work done on the piston by the expanding combustion gases. The power associated with this piston work is called the *indicated power*. The difference between the indicated power and the brake power is the power required to overcome friction and to drive the accessories including e.g., the water and oil pumps

$$P_i = P_b + P_f \,, \tag{17.71}$$

where P_i is the indicated power, P_b is the brake power, and P_f is the friction power.

Direct calculation of the indicated power requires measurement of the cylinder pressure. The brake power can be calculated from the measured engine torque and speed. The friction power must be calculated from the difference of the indicated and brake power.

Generally, small engines run at high rotating speeds and large engines run at low rotating speeds. To allow comparisons between engines of different sizes, it is common to calculate the *mean piston speed* (MPS), which is the average velocity of the piston as the engine makes one revolution

$$\text{MPS} = \frac{2S}{\text{time for one revolution}} = 2SN \,, \tag{17.72}$$

where S is the stroke, and N is the engine rotating speed.

The *mean effective pressure* (MEP) is a way to normalize the work done by the engine against the size of the engine. It is intended as a measure of engine loading. The MEP is defined as the ratio of the work done by the engine in one cycle to the displacement volume. A four-stroke engine undergoes one cycle in two revolutions (or 4π radians), so the work done is equal to the torque times the angular displacement. When the brake torque is used, the quantity is known as the *break mean effective pressure* (BMEP)

$$\text{BMEP} = \frac{4\pi T_b}{V_d} \,. \tag{17.73}$$

Since work is measured in Nm and volume in m^3, the ratio has units of pressure N/m^2. The MEP is sometimes described as the pressure which, if applied as

a constant pressure during the expansion stroke, would give the same work as is actually produced by the engine.

The *mechanical efficiency* is a measure of how much of the power produced by the combustion process is delivered to the output shaft. It is defined as the ratio of the brake power to the indicated power

$$\eta_m = \frac{P_b}{P_i} = 1 - \frac{P_f}{P_i} , \tag{17.74}$$

where η_m is the mechanical efficiency, P_b is the brake power, P_i is the indicated power, and P_f is the friction power.

The *thermal efficiency* is defined as the ratio of the power produced by the engine to the rate at which fuel energy is supplied to the engine, as indicated by the lower heating value (LHV). When the brake power is used, the quantity is known as the brake thermal efficiency

$$\eta_{bt} = \frac{P_b}{\dot{m}_{fuel}(\text{LHV})} . \tag{17.75}$$

Mechanical and thermal efficiencies are sometimes confused. For a modern engine running at full load, the mechanical efficiency may be 90% or higher. However, the brake thermal efficiency will generally be 30–50%.

The *specific fuel consumption* (SFC) is the ratio of the fuel flow rate to the power of the engine. When brake power is used, the quantity is known as the brake specific fuel consumption

$$\text{BSFC} = \frac{\dot{m}_{fuel}}{P_b} . \tag{17.76}$$

The BSFC is similar to an efficiency in that it measures how little fuel may be required to do a certain quantity of work. The lower the BSFC, the more efficient the engine.

The *volumetric efficiency* is a measure of how well air moves through the engine. For a four-stroke engine

$$\eta_v = \frac{\dot{m}_{actual}}{\dot{m}_{ideal}} = \frac{\dot{m}_{actual}}{\rho_{ref} V_d \left(\frac{\text{rpm}}{2}\right)} , \tag{17.77}$$

where η_v is the volumetric efficiency, $\dot{m}_{actual}$ is the actual mass flow rate of air (or air–fuel mixture) entering the engine, $\dot{m}_{ideal}$ is the ideal mass flow rate of air (or air–fuel mixture), ρ_{ref} is a reference density, V_d is the displacement volume, and rpm/2 is the number of engine cycles per minute.

For manifold-injection spark-ignited engines, the values of $\dot{m}_{actual}$ and $\dot{m}_{ideal}$ refer to the fuel–air mixture entering the engine. For diesel engines and DI gasoline engines, they refer only to the air entering the engine.

The volumetric efficiency tends to be ambiguous for several reasons:

1. There is uncertainty about where the reference density should be calculated. Some sources suggest using ambient conditions, while others suggest using the average intake manifold pressure and temperature.
2. Although it is considered to be an efficiency, there is no reason why the volumetric efficiency cannot be greater than 1. If the ambient density is used to compute the volumetric efficiency of a turbocharged engine, the volumetric efficiency may be as high as 2 or 4. Even a naturally aspirated engine with a tuned intake system can have a volumetric efficiency of 1.2 or 1.3.
3. In engines with a large valve overlap period, a significant amount of air can blow through the engine directly from the intake to the exhaust without participating in a combustion process. This air could contribute to a high volumetric efficiency but is not available for combustion.

17.4.3 Air Systems

The power produced by all internal combustion engines is limited by their ability to draw air from the atmosphere. Fuel systems can always be designed to provide the amount of fuel appropriate to this air flow. To increase the power produced by an engine of a certain displacement volume, the air flow needs to be increased. This can be done with passive techniques that are incorporated into the engine's design or through the addition of external devices, such as a supercharger.

Natural Aspiration

In a naturally aspirated engine, the air flows into the cylinder through the intake manifold and intake ports without the use of an external compressor of blower. At high engine speed this air moves at high velocity. When the piston approaches the end of the intake stroke, the momentum of the air keeps the air moving toward the cylinder and can continue to force air into the cylinder after the piston has started upward on the compression stroke. By properly timing the closing of the intake valve, the amount of air trapped in the cylinder can be increased beyond that which would be predicted based on ambient air density. This phenomenon, called the *ram effect*, increases with air velocity and, therefore, with engine speed.

A second effect that can be utilized to increase engine air flow is to take advantage of the pressure waves

that are induced in the intake and exhaust system due to valve opening and closing events and piston motion. For example, the high-pressure wave created when the exhaust valve opens and rapidly blows down the cylinder contents travels to the end of the exhaust pipe and is reflected as a low-pressure wave or rarefaction wave. If this wave is timed to enter the cylinder near the end of the exhaust stroke, it can assist in evacuating the residual gases and draw in fresh charge as the intake valve opens. Similarly, rarefaction waves in the intake system are reflected from the open end of the intake as pressure waves that will force more air into the cylinder. This process, known as tuning, is highly dependent on the relationship between valve timing, pipe lengths, and the speed of sound in the intake and exhaust gases. As a result, the benefits of tuning tend to be concentrated at specific engine speeds, and the effects at other speeds may actually be negative. Other passive effects involving resonator cavities connected to the intake and exhaust pipes can also be used to raise the air flow to the engine. The engine air flow can also be increased with the addition of a compressor in a technique known as supercharging, which will be discussed later.

Effect of Speed on Volumetric Efficiency

Engine volumetric efficiency is affected by engine speed. At higher speeds, the pressure drop resulting from frictional effects associated with higher flow velocity tends to cause less air–fuel mixture to enter the cylinder. Up to a certain speed, this effect can be offset by the ram effect and tuned intake and exhaust pipes. These flow enhancing effects can keep the volumetric efficiency relatively high over most of the engine's operating range, but at a certain speed, which depends mostly on valve area and mean piston speed, the volumetric efficiency drops off sharply.

Poppet Valves

Flow through a poppet valve is usually modeled as the product of isentropic flow through a restricted area passage and a flow coefficient that varies with valve lift and geometry. This equation is valid through all flow ranges, except when the flow is choked

$$\dot{m} = C_D \rho_0 c_0 A_x \times \sqrt{\frac{2}{k-1}\left[\left(\frac{P_x}{P_0}\right)^{\frac{2}{k}} - \left(\frac{P_x}{P_0}\right)^{\frac{k-1}{k}}\right]}, \qquad (17.78)$$

where $\dot{m}$ is the actual mass flow rate through the valve; C_D is the discharge coefficient for the valve, ρ_0 is the density at the upstream stagnation state, c_0 is the speed of sound at the upstream stagnation state, A_x is the minimum flow area between the valve and seat, k is the ratio of specific heats C_p/C_V, P_x is the downstream static pressure, and P_0 is the upstream stagnation pressure; C_D is greatest at low valve lifts. Under these conditions, the air flow fills the entire flow channel without the separations that reduce the effective flow area. As the valve opens further, the flow separates from the valve edge and the seat, which reduces the actual flow area and decreases C_D. The value of C_D tends to be independent of the flow Reynolds number, except at low lift, where C_D decreases as the Reynolds number increases, reflecting a greater significance of boundary layers on the flow.

Valve Timing

The timing for the opening and closing of the intake and exhaust valves can have a major impact on the engine performance. In four-stroke engines, the exhaust valve opens at about 120°–140° after TDC. Earlier timing will reduce expansion work and may later delay the exhaust blowdown, so that high cylinder pressures early in the exhaust stroke increase the pumping work. Intake valve closing typically occurs at 20°–60° after BDC and has a strong effect on the engine's volumetric efficiency. Earlier closing may reduce the air flow into the cylinder due to the ram effect described earlier, especially at high engine speeds. The Miller cycle, early closing of intake valve, for diesel engines is an effective measure to lower the effective compression ratio and NO_x emissions as a result. Later closing delays the start of the compression process and may allow some of the fresh charge to flow back into the intake manifold. The timings for closing the exhaust valve and opening the intake valve are not as critical for engine performance.

Supercharging

Supercharging is a general term for a variety of techniques used to boost the pressure of the air entering the cylinder to increase the engine's power. In some cases, this involves devices to compress the air that might be driven directly by the engine or by the engine's exhaust gas. These devices are known as superchargers. When the device is driven by exhaust gas, it is called a turbosupercharger or just a turbocharger [17.22].

Figure 17.72 shows a schematic of an engine-driven supercharger that is driven by a set of gears, although belts are also frequently used. Engine-driven superchargers have the advantage that they provide air flow even at low speeds, so they can be used to provide the scavenging needed for two-stroke engines during startup. They also do not have the acceleration lag often noted with exhaust-driven turbochargers.

Turbocharging

A specific type of supercharging that utilizes power recovered from expanding the exhaust gas to atmospheric

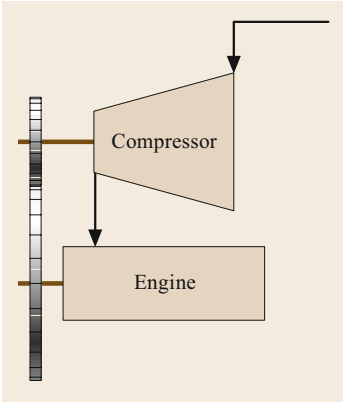

Fig. 17.72 Engine-driven supercharger

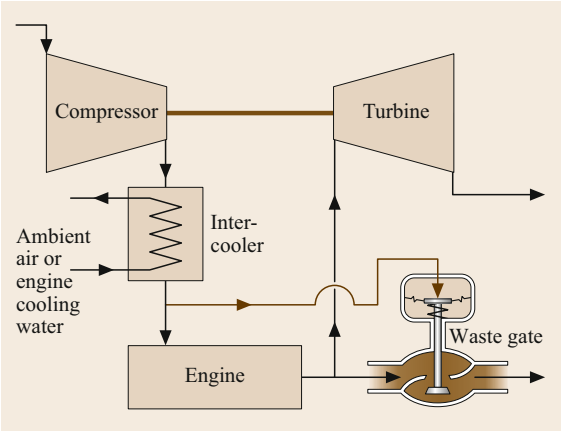

Fig. 17.74 Turbocharged engine with intercooler and waste gate

pressure is called *turbocharging*. Figure 17.73 shows a schematic of a typical system. Air, after being filtered, is compressed and then supplied to the engine. Single-stage radial-design compressors are the most common and are generally capable of 3 : 1 pressure ratios. The compressor is directly coupled to an expansion turbine that provides the work to drive the compressor. While the turbine imposes a back pressure on the engine, this is more than offset by the higher potential power available from the increased pressure in the intake system.

In diesel engines, the air supplied by the turbocharger is more dense and allows more fuel to be injected, while still maintaining the air–fuel ratio limits imposed by concerns about exhaust emissions. In fact, due to the greater availability of air, turbocharged engines can usually be operated at higher air–fuel ratios than naturally aspirated engines, which improves both particulate and NO_x emissions. Although engine power can be increased by a factor of 2–3 over a similarly sized naturally aspirated engine, fuel economy improves only slightly. This improvement is generally associated with the fact that friction losses do not increase proportionately with the increase in overall power, so the mechanical efficiency of the engine improves. Turbocharging offers additional benefits of improved scavenging and piston cooling by allowing a portion of the compressed charge to short circuit through the cylinder during the valve overlap period. Another notable benefit is performance at altitude, where a naturally aspirated engine lacks sufficient air, and the turbocharger is able to provide the desired air even at lower atmospheric pressure conditions.

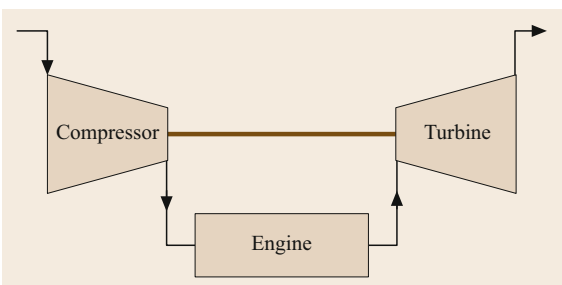

Fig. 17.73 Typical turbocharger configuration

Part of the density increase potential of the turbocharger is lessened by the fact that the air leaving the compressor is at a high temperature. It is common to insert a heat exchanger, called an intercooler or aftercooler, into the airstream after the compressor. Figure 17.74 shows this configuration. The compressed air may be cooled by engine coolant, or more commonly in heavy-duty applications, by ambient air.

A waste gate is also shown in Fig. 17.74. This device allows a portion of the engine's exhaust gas to bypass the turbine. A diaphragm actuator senses compressor boost pressure and releases a portion of the exhaust gas so that the boost pressure does not become excessive. A similar device, known as a compressor recirculation valve, is frequently used on the compressor side to recirculate high pressure air from the compressor outlet back to the compressor inlet during certain load cases to prevent a phenomenon known as surge. Surge is a condition in turbocharger operation when an engine at operation suddenly lifts off the throttle. In this situation, high pressure air in the intake system can be forced back to the compressor causing rapid deceleration, and even stalling, of the compressor wheel. Turbocharger design and matching to a specific engine is usually a compromise between providing sufficient air at the low-speed peak-torque condition while not delivering excessive pressure at the high-speed high-load conditions that will cause high-peak cylinder pressures.

One way to optimize turbochargers for low-speed torque that is gaining in popularity is to use variable

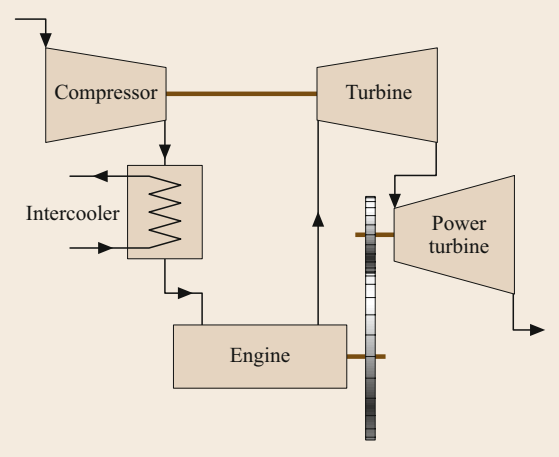

Fig. 17.75 A turbocompounded engine

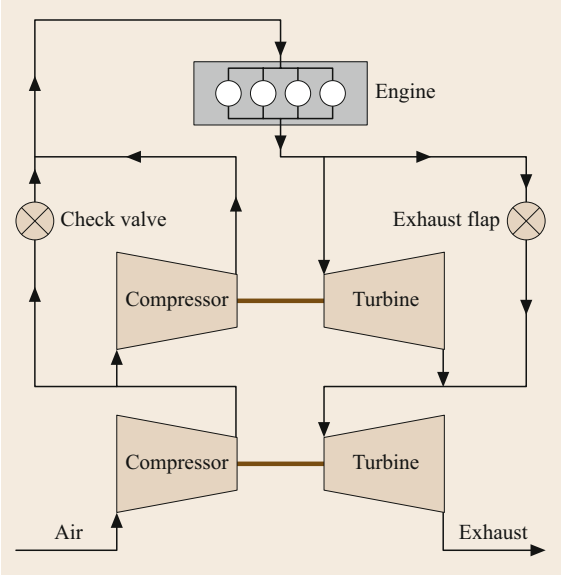

Fig. 17.76 Twin turbocharger configuration

turbine geometry (standard for PC with diesel engines and a few for gasoline engines). Vanes in the turbine housing assembly adjust to create a narrower or wider path for exhaust flow to the turbine wheel. When vanes create a narrow pathway, exhaust gas accelerates as it passes through and, thus, spin the turbine wheel at a greater rotational speed. This allows larger turbochargers to reach desired speeds faster, reducing the lag typically experienced in large applications without such technology. For engines that are consistently operated at high loads, there is more energy available in the exhaust gas than is needed to operate the compressor. One option to utilize this excess energy is to add a second turbine, sometimes known as the power turbine, which will recover energy from the exhaust gas leaving the first turbine, which drives the compressor. As shown in Fig. 17.75, the power turbine is connected to the engine's drive train through a mechanical connection so the power can be delivered to the engine's output shaft. This technique is often referred to as *turbocompounding*. The fuel economy benefits of turbocompounding can be significant, especially when the engine is designed for minimum heat rejection, which tends to increase exhaust energy. However, at current fuel prices, the savings in operational cost has not been enough to justify widespread acceptance of this technology.

Other technologies have been developed to provide optimum turbocharger performance over a larger fraction of the engine's operating range. Figure 17.76 shows a twin-turbocharger technology developed by Opel that utilizes two turbochargers. As shown in the figure, exhaust gas from the engine is directed through two separate passageways to two turbochargers. The passage to the larger turbocharger is equipped with a flapper valve to limit the flow. At light load conditions, the flapper is mostly closed, which forces most of the exhaust flow through the small turbocharger so it has sufficient flow to operate at its most efficient condition. The large turbocharger is essentially free-spinning at this point and not providing much compression. As the engine speed and load increase, the exhaust flapper is opened, allowing the larger turbocharger to become active so that it can supply air for the high power condition. A check valve is provided in the intake pipe so that the high air flow does not all have to pass through the small turbocharger compressor. This arrangement provides efficient operation over a wide range of engine operating conditions. In the meantime, variable turbine geometric devices control the small turbochargers.

Advancements have also been made in turbocharger regulation and control. As mentioned, turbocharger waste gates often use pneumatic diaphragm actuators to control waste gate operation and exhaust flow. However, many manufacturers have begun to use electric actuators for this purpose. These actuators use engine speed data to control the position of the waste gate valve more precisely than pneumatic actuators. Electric actuators also allow the waste gate to be opened during ignition when the engine is at low speeds. This is often done to quickly heat up the catalyst by allowing hot exhaust gas to bypass the turbocharger and flow directly through the catalyst. Electric rotary and linear actuators are commonly used in today's waste gate and variable turbine geometry applications, and solenoid valves are used for compressor recirculation valve applications.

Efficiency Definitions

The efficiency of a turbocharger is determined by the efficiency of its various elements. The efficiency of the compressor is calculated from the ratio of the work that would be required for a reversible adiabatic (isentropic) process divided by the actual work for the process. The compressor efficiency can be calculated using stagnation states at the inlet and the outlet, or since the kinetic energy leaving the compressor is not recovered, the efficiency can be calculated from the inlet stagnation state to the outlet static state. The latter choice is more conservative and allows the effectiveness of the compressor outlet diffuser to be included in the efficiency. The equation for compressor efficiency is provided below based on the state definitions given in Fig. 17.77

$$\eta_C = \frac{h_{2s} - h_{01}}{h_{02} - h_{01}} \,. \tag{17.79}$$

In a similar manner, the efficiency of the turbine from the inlet stagnation state to the outlet static state can be written as

$$\eta_T = \frac{h_{03} - h_{04}}{h_{03} - h_{4s}} \,. \tag{17.80}$$

Although the simple design of the turbocharger offers little opportunity for frictional losses, a mechanical efficiency can be defined that consists of the power delivered to the compressor divided by the power produced by the turbine

$$\eta_M = \frac{-\dot{W}_C}{\dot{W}_T} \,. \tag{17.81}$$

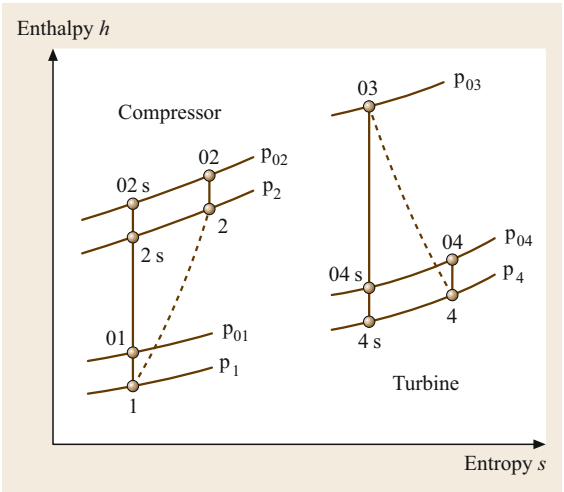

Fig. 17.77 State definitions for compressor and turbine efficiencies

17.4.4 Fuel Systems

This section will cover gasoline and diesel fuel systems. The principles, main designs, key operating characteristics, and controls of each system will be explained. Other important adjuncts such as low-pressure systems, filtration, and sensors will also be covered.

Gasoline systems are divided into carburation and fuel injection; fuel injection is further broken down into the throttle body, port injection, and direct injection.

Diesel systems are divided into cam-driven and common-rail systems; cam-driven systems are further divided into two main groups: pump-line-nozzle (inline, distributor, unit pump) and unit injector.

Gasoline Fuel Systems

Principle. Gasoline fuel systems can be divided into two main types: carburation and fuel injection. For all systems, the goal is, in principle, to achieve a stoichiometric air–fuel ratio, which is the ideal ratio whereby all of the fuel is completely mixed and burned. For normal gasoline, this is usually around 14.7 : 1 air mass to fuel mass, however, some engines are moving towards the lean-burn principle.

Carburation. The simplest of all systems is the carburetor, which consists of the following subsystems:

- Inlet system to maintain a constant level of fuel in the reservoir
- Metering system to maintain the desired air–fuel ratio
- Accelerator-pump system to provide extra fuel during acceleration
- Power enrichment system to provide extra fuel during periods of high demand
- Choke system to provide a rich mixture for start and cold-engine operation.

The carburetor uses the venturi principle: the inlet air flows through a necked-down area (venturi), where the flow increases in speed and decreases in pressure. A passage connects the fuel reservoir to the venturi; since the fuel in the reservoir is at atmospheric pressure, fuel flows from the reservoir to the lower-pressure area inside the venturi and then into the engine. The pressure drop at the venturi increases with engine speed and with throttle position, thus causing fuel flow from the reservoir to the venturi to increase as engine speed and throttle position increase [17.23].

Fuel Injection. Fuel injection can be divided into two basic types: manifold (throttle body and port) and gaso-

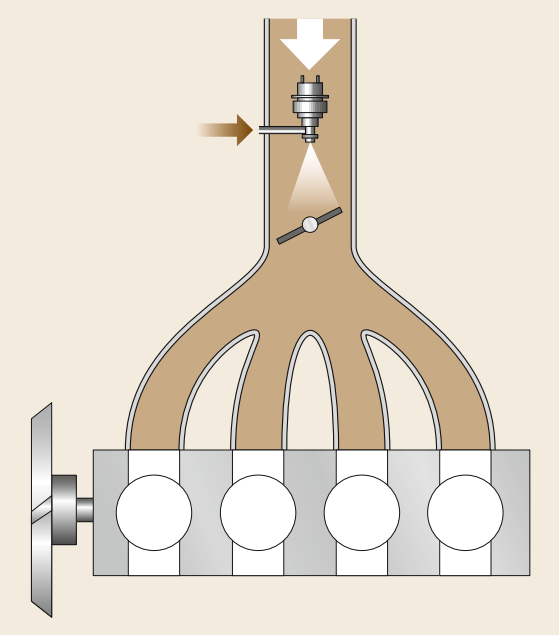

Fig. 17.78 Throttle body injection

line direct injection (GDI). Manifold injection systems allow only a homogeneous operating mode; GDI allows this and several other modes as well [17.24].

Throttle Body Injection. Throttle body fuel injection is also known as single-point injection because there is a central point of injection: a single, electromagnetically operated injector is located directly above the throttle valve (Fig. 17.78).

Port Injection. Port injection is also known as multipoint injection because fuel is injected into every intake port, i.e., onto the cylinder's intake valve (Fig. 17.79).

There are four types of port injection:

- Simultaneous fuel injection: all injectors open and close together. Half of the fuel quantity is injected in one engine revolution; the remaining half is injected in the next revolution.
- Group fuel injection: the injectors are combined into two groups. All injectors in a group open and close together. One injector group injects the total fuel quantity needed for its cylinders in one engine revolution, then the second set injects its total fuel quantity in the next revolution.
- Sequential fuel injection (SEFI): fuel is injected individually for each cylinder. Injectors are triggered in the same sequence as the firing order. Duration and start of injection (relative to each cylinder's top dead center) are the same for all cylinders.

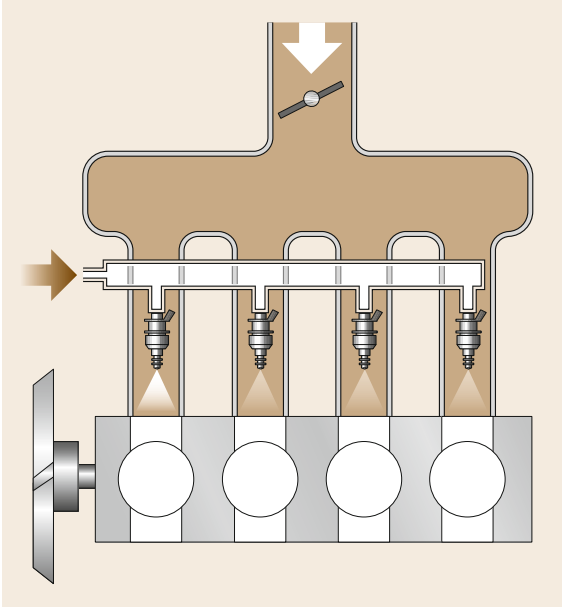

Fig. 17.79 Port injection

- Cylinder-individual fuel injection (CIFI): the duration of injection (i.e., fuel quantity) can be varied for each individual cylinder.

Gasoline Direct Injection. Fuel is injected directly into each cylinder's combustion chamber (Fig. 17.80 [17.25]).

An electric fuel pump delivers fuel to the high-pressure pump, which pressurizes the fuel to 50–350 bar

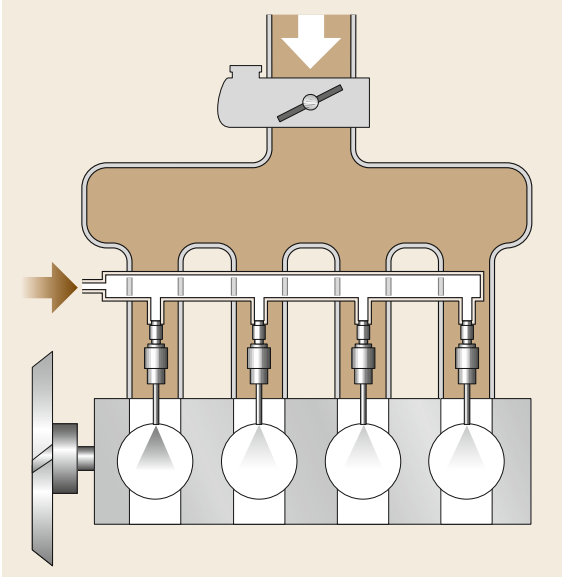

Fig. 17.80 Gasoline direct injection

(depending upon the engine operating condition) and sends this fuel on to the accumulator rail. Since all injectors are connected in parallel to the rail, they are all constantly pressurized and inject only when an electric signal is sent to each injector.

GDI allows not only homogeneous operation but also stratified charge, homogeneous stratified charge, homogeneous antiknock, and stratified-charge/catalyst heating.

Fuel Injection Control System. The injected fuel quantity is determined by the control system, which consists of sensors that measure various input parameters, a processor to determine the optimum fuel quantity based upon the sensor input, and actuators that carry out the commands of the processor.

Examples of sensors: inlet air temperature, airflow, accelerator pedal position, throttle-valve angle, rail-pressure, lambda, coolant temperature, etc. Examples of actuators: injectors, idle-air control valve, throttle valve, fuel-pressure regulator, etc.

The control system has to maintain the proper air–fuel ratio under the following engine operating modes:

- Start and warm-up
- Idle and part load
- Full load
- Acceleration and deceleration
- Overrun.

The fuel injection control system may be combined with the ignition control system to allow for coordinated total engine management. The image in Fig. 17.81a shows such a system for port injection, and the image in Fig. 17.81b shows a system for direct injection.

Fuel Supply System. For both carburetors and fuel injection, the fuel must be pumped from the storage tank by a mechanical or electrical pump and must pass through a filter for impurities to be removed. The fuel pressure is regulated to a constant value.

Diesel Fuel Injection Systems

Principle. There are essentially two types of diesel fuel injection: indirect and direct. Since the indirect diesel injection (IDI) is for prechamber or whirl-chamber engines, both of which are seldom applied today, we will concentrate on direct injection (DI) [17.26].

In the DI process, the fuel is injected directly into the highly compressed hot air in the combustion chamber above the piston (Fig. 17.82). A multihole nozzle is used to distribute the fuel uniformly in the combustion chamber to ensure rapid mixing. Very high injection pressures (up to 2500 bar) are required to properly and completely atomize the fuel.

For any combination of engine operating parameters, the fuel injection system must deliver the correct amount of fuel, at the correct time, at the correct injection pressure, with the correct timing pattern, and at the correct point in each cylinder's combustion chamber. Limits such as emissions, combustion pressure, exhaust temperature, engine speed and torque, and vehicle-specific loads may need to be taken into account when determining the proper fuel injection.

Injection Characteristics. The key parameters and their corresponding units for every fuel injection system are:

- Injected fuel quantity (mm^3/injection or mg/injection)
- Injection pressure (bar or psi)
- Injection duration (degrees crank angle)
- Injection timing (degrees before or after the engine piston's TDC)
- Injection spray plume:
  - Number of plumes
  - The plume angle (degrees)
  - Location of the plume in the combustion chamber (height above piston bowl, position in cylinder)
  - The shape of the plume itself.

Depending upon the type of fuel injection system, one or more additional injection characteristics may be available:

- Injection rate shape (mm^3 as a function of crank or cam angle)
- Injection pattern (number and form of injections during each combustion cycle, Fig. 17.83; up to ten injections per combustion cycle may be required)
- Preinjection 1: to reduce noise, improve warm-up (by avoiding misfire and white smoke)
- Pre-injection 2: to further reduce noise, improve warm-up (by avoiding misfire and white smoke)
- Main injection
- Post-injection 1 (close after the main injection): to reduce soot emissions
- Post-injection 2 (retarded): to act as a reducing agent for an after-treatment device.

Digital rate shaping refers to splitting the main injection into two very closely-coupled smaller injections of lower pressure to further control the rate of heat release and, thus, further lower noise while maintaining soot emissions.

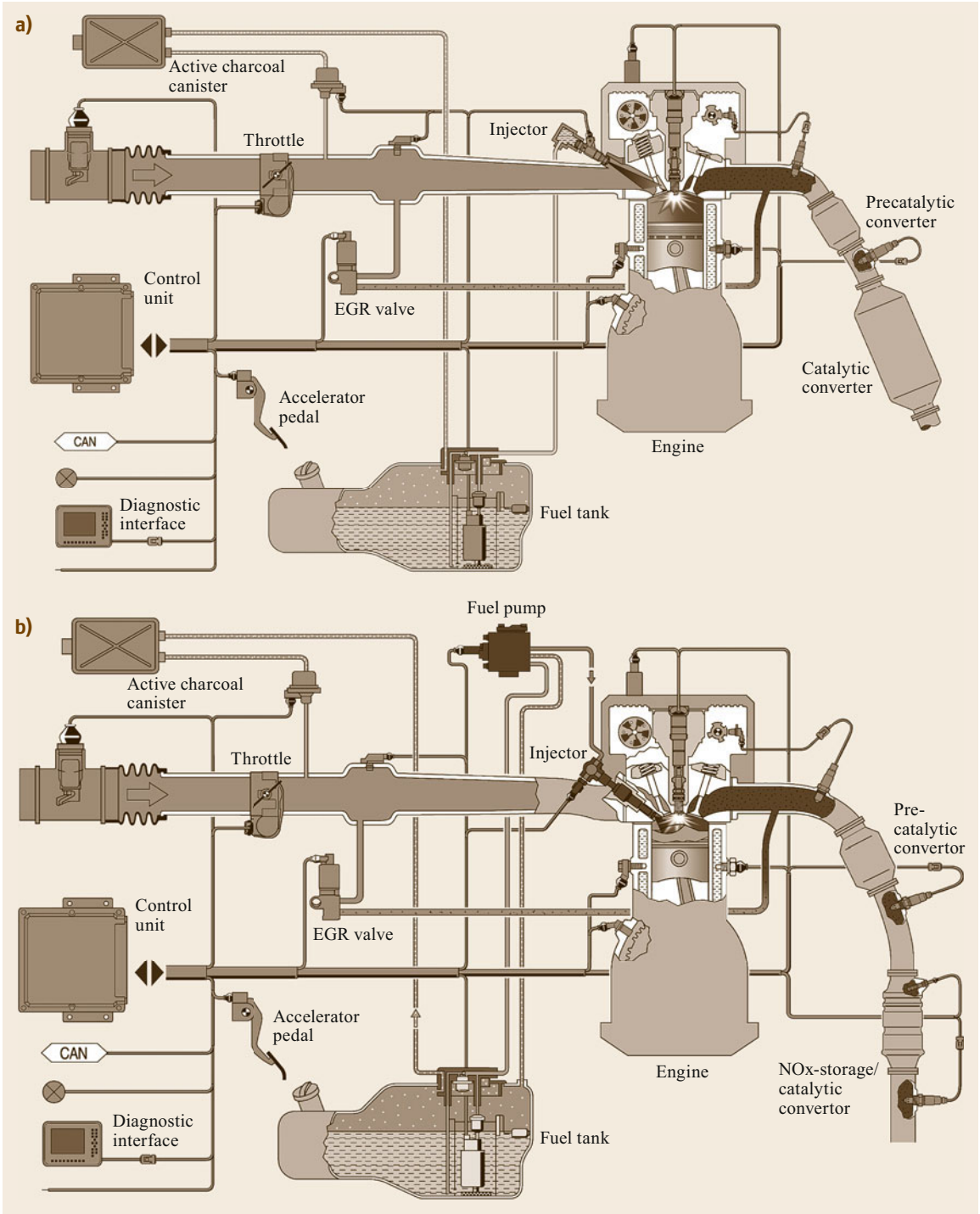

Fig. 17.81a,b Fuel injection control system. **(a)** Port injection; **(b)** direct injection

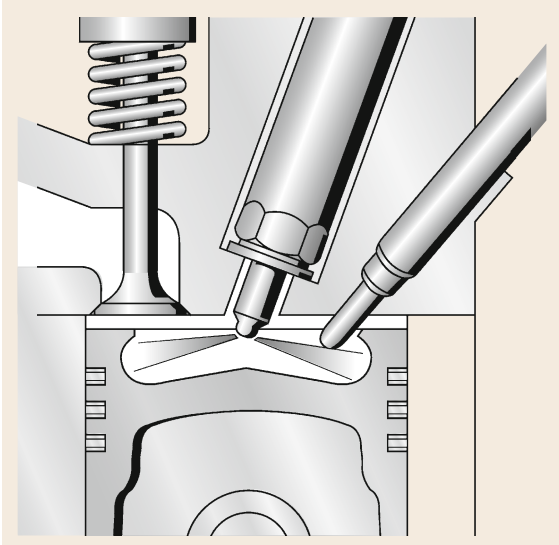

Fig. 17.82 Direct injection process

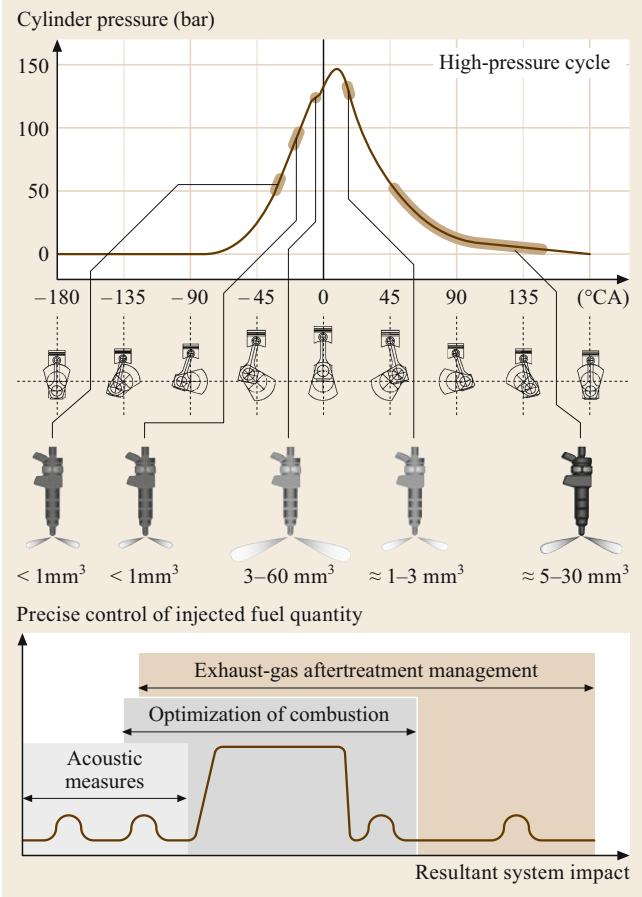

Fig. 17.83 Injection pattern

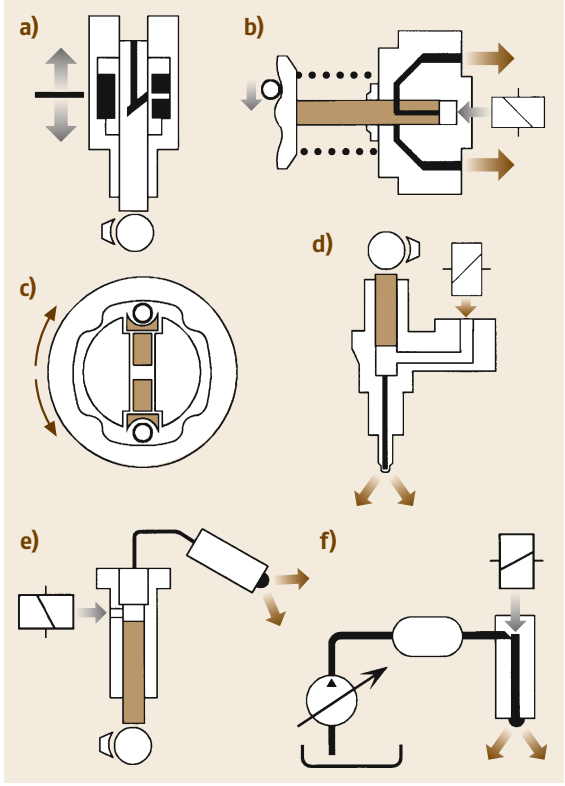

Fig. 17.84a–f Fuel injection systems. **(a)** In-line control sleeve injection pump (electr., helix-controlled), **(b)** distributor-type injection pump (solenoid valve), **(c)** radial-piston pump (solenoid valve), **(d)** unit injector, **(e)** unit pump, **(f)** common-rail (solenoid valve, piezo)

Fuel Injection System Designs. To cover the wide variety of diesel engines in the marketplace (from stationary engines with 1 kW/cylinder up to large two-stroke engines with up to 6000 kW/cylinder), there is a corresponding variety of fuel injection designs [17.27]. Figure 17.84 shows the various designs, and Fig. 17.85 shows the development of pressure capability over the years. These can be divided into two main groups: cam-driven and common-rail.

Cam-Driven Systems. The cam-driven pumps can be further divided into two main groups: pump-line-nozzle and unit injector.

Pumping Arrangement of Cam-Driven Systems. The different designs within the pump-line-nozzle group:

- Inline fuel-injection pumps: one pumping unit per engine cylinder, mounted in a common housing

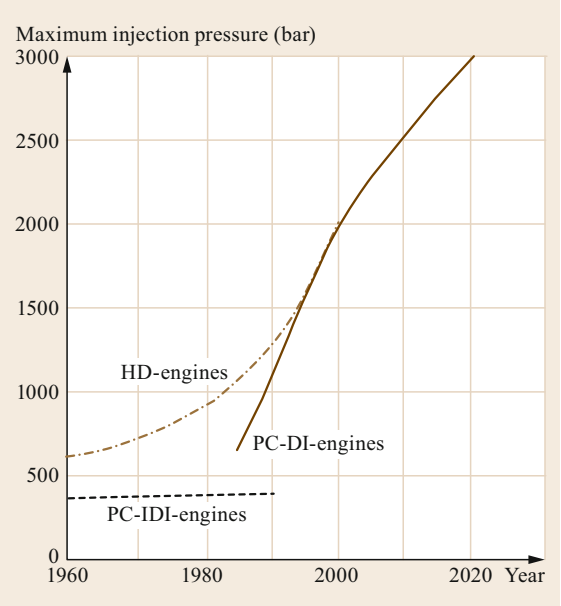

Fig. 17.85 Pressure ranges of fuel injection systems

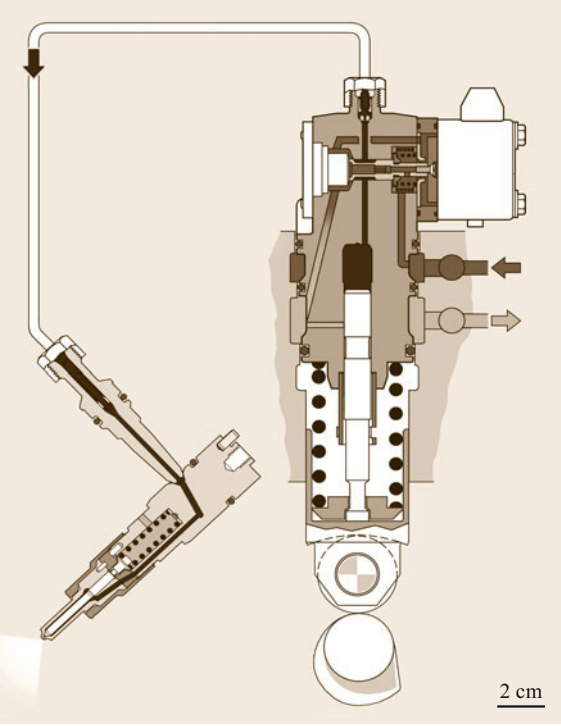

Fig. 17.86 Individual-cylinder pump

- Rotary fuel-injection pumps (axial-piston and radial-piston): one pumping unit for all engine cylinders; the fuel is distributed to each cylinder by a rotating shaft

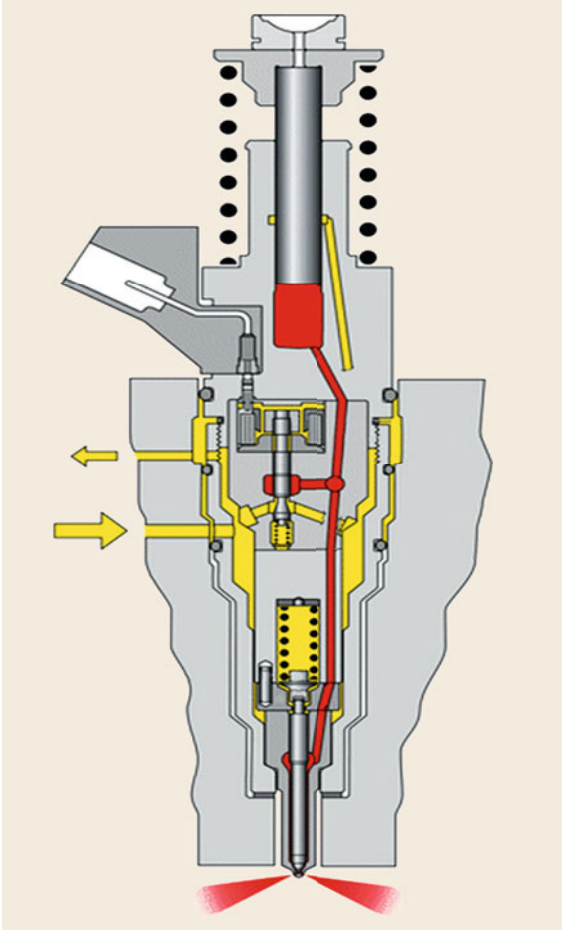

Fig. 17.87 Unit injector, *small arrow*: fuel return, *big arrow*: fuel supply

- Individual-cylinder pumps: one pumping unit per engine cylinder, mounted separately and usually actuated by separate cam lobes on a common camshaft (Fig. 17.86).

Each of the above has a high-pressure line to connect each pumping mechanism to its corresponding nozzle.

The unit injector combines the pumping unit and nozzle in one assembly for each engine cylinder; each unit injector is actuated by a separate cam lobe on a common camshaft (Fig. 17.87).

Pumping Principle of Cam-Driven Systems. The pumping principle is essentially the same for all cam-driven systems: the cam lobe, which is driven by the engine's crankshaft and is, thus, phased to the crankshaft, pushes a plunger which pressurizes the fuel. This pressurized fuel travels to the nozzle, and as soon as the

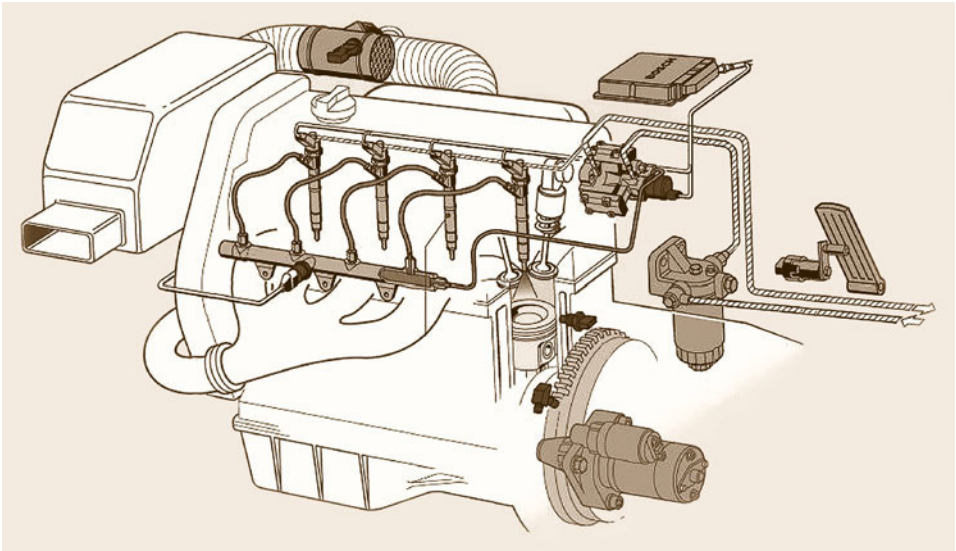

Fig. 17.88
Common-rail system

pressure exceeds the nozzle's opening pressure, the nozzle needle lifts and fuel is injected into the engine.

Control System of Cam-Driven Systems. The fuel quantity is controlled by varying the length of delivery, which is accomplished by varying either the beginning of delivery (and keeping the end constant), the end of delivery (keeping the beginning of delivery constant), or by varying both. Governing can be mechanical, pneumatic, electromechanical, or electronic, whereby the majority of new applications are electronic.

In addition to fuel control, the timing may also be controllable, either by changing the phasing of the pumping cam to the crankshaft or by changing the point at which pressure starts to build up on the pumping cam. The injection rate and pilot injection may also be controlled in some instances.

Common-Rail Systems. This system offers the greatest flexibility in the choice of fuel-injection parameters.

Pumping Arrangement. The common-rail (CR) system utilizes a single pump to pressurize the fuel, which is delivered to an accumulator rail. One injector per engine cylinder is connected to this rail by means of a high-pressure line (Fig. 17.88).

Pumping Principle. Fuel is delivered by the low-pressure system to the high-pressure pump, where it is pressurized by the pumping plungers (arranged either radially or inline) and sent from there to the accumulator rail. Since all injectors are connected in parallel to the rail, they are all constantly pressurized and inject only when an electric signal is sent to each injector. Pressures range from 1400 bar (20 305 psi) to 2500 bar (36 260 psi) and even higher pressures are in development.

Control System. The start of injection (timing) and duration of injection (fueling) is controlled by an actuated valve (electromagnetic or piezo) on each injector. When the actuating signal is sent to the injector, a coil or piezo stack inside the injector is energized, upsetting the pressure balance (on both sides of the nozzle needle) that was holding the nozzle closed. The needle then lifts, and the injector delivers fuel to the engine. When the signal ceases, the pressure above the needle increases, forcing the needle closed and, thus, ending injection.

In addition, a sensor in the high-pressure circuit monitors the system pressure and sends this information to the electronic control unit (ECU) so that the pressure can be regulated to a value that is optimal for the engine's operating condition.

Low-Pressure System. Regardless of the fuel injection design, all fuel injection systems require a primary fuel pump to deliver the fuel from the fuel tank through the fuel filter to the injection pump.

Primary Fuel Pump. The primary fuel pump can be either mechanical or electric; the electric pump can be inside the fuel tank, mounted on the engine, or mounted on the vehicle.

Fuel Filter. The fuel filter must strain out impurities in the fuel, as contamination will cause wear, orifice plugging, component sticking, and seizures. The filter medium must be fine enough to trap small particles,

and the filter size must be large enough to assure adequate service life. Often, a preliminary filter is used in addition to the main filter to extend the filter change interval. In addition, filters should have the ability to separate water out of the fuel, as water will cause wear, corrosion, and seizures. Many filters today have water separation, a water-in-fuel indicator, and a heater combined in one unit.

17.4.5 Natural Gas Fuel Systems

Natural gas is a suitable fuel for many different combustion concepts, each with different features required for the fuel delivery system. The current, most popular concept for natural gas engines, especially in the light to medium-duty segments, is homogeneous spark-ignited combustion. This combustion concept exists in regular production with both stoichiometric and lean air–fuel ratios, and with different fuel delivery systems. Another popular way for natural gas combustion, common in large-engine applications, is homogenous natural gas combustion with diesel pilot ignition. This *dual fuel* concept is an advantage for durability, as it eliminates the sparkplug and maintenance requirements of the spark ignition system. Finally, different types of natural gas direct injection combustion are under development, with one system having been in production [17.26, 28]. The following sections describe the fuel system features for these different natural gas combustion concepts.

Natural Gas Fuel Systems – Premix for Homogenous Combustion

The most basic fuel delivery for natural gas engines is commonly labeled the *central-point* fuel system. This fuel system introduces gaseous fuel into the air stream going into the engine, usually upstream of the throttle valve in an SI application, or at least upstream of the intake manifold in dual-fuel applications, which do not use an intake throttle. This introduction of the fuel into the airstream before the air splits into multiple streams for each cylinder is convenient in that the fuel metering and air–fuel mixing can all be done at one point in the intake system. Central point fuel systems can use either fuel injectors or continuous flow valves to meter the fuel quantity, and usually include specific geometric features to enhance the mixing of the fuel and air. In a CPI system, the continuous air flow though the intake system provides the opportunity to have an active mixing device, with the mixing of the fuel and air at one point in the intake system for all cylinders. Systems of this type using fuel injectors for fuel metering are often called *central-point injection* (CPI) fuel systems. CPI can be used with stoichiometric and lean combustion concepts, and with either spark ignition or diesel-pilot ignition.

The next common system for fuel metering of natural gas is multipoint injection. Multipoint injection precharges the intake manifold runner for each cylinder with the amount of fuel required for the next combustion cycle of a single cylinder. This type of fuel system relies on the fuel injector to meter the fuel quantity on a cylinder-individual basis, and the mixing of the fuel and air occur independently for each cylinder. In traditional MPI systems, the fuel is injected during the time when the intake valve is closed. This provides sufficient time for the injection to occur with relatively low flow-rate injectors, and allows time for the fuel and air to mix through diffusion.

A variant of multipoint injection where the injection flow rate is sufficiently high to inject only during the suction-stroke is called *multipoint open-valve injection* (MP-OVI). For engines that are converted from diesel applications, there is commonly no intake runner length to provide cylinder-to-cylinder separation of the fuel delivered, as required in a pre-charge MPI system. Therefore, a concept with injection only during the intake valve opening is an enabler for equipping engines converted from diesel with natural gas multipoint injection. With MP-OVI, the fuel and air mixing is dependent on the in-cylinder mixture motion only, where with MPI or CPI, there are other mechanism available for mixing.

The complete fuel system for a spark-ignited or diesel pilot natural gas engine includes multiple components between the fuel storage and the fuel metering device. A typical fuel system includes shutoff valves, filters, and at least one fuel pressure regulator. For a CNG (compressed natural gas) storage system, a high-pressure manual shutoff valve and shutoff solenoid are located at the outlet of the fuel tank, as well as other safety components required with high-pressure storage. This is typically followed by a high-pressure filter, suitable for removing any contaminates that might degrade the function of the fuel pressure regulator. There are different types of fuel pressure regulators for CNG storage systems. These include mechanical fixed-pressure, engine-manifold referenced mechanical regulators, which provide a fuel pressure increase as intake manifold pressure is increased, and also electronic variable pressure regulators, which can adjust the fuel pressure independently based on requirements determined from an electronic engine control unit. After the fuel pressure regulator, there is typically a low-pressure fuel shutoff solenoid and a low-pressure filter suitable for ensuring that the fuel injectors are not contaminated. This low-pressure filter can also be a coalescing oil separator if the injectors require oil-free fuel. The fuel injectors themselves are typically electromagnetic operated, with a constant flow rate due to supercriti-

cal operation, with a sealing mechanism optimized for a gaseous medium. In some production systems a variable fuel metering valve is used as an alternative to the digital fuel metering of an injector-based system. With either of these fuel metering devices in a CPI system, the quantity of fuel is determined by an electronic control unit, by using a measurement or calculation of the engine air flow, and typically with an exhaust gas oxygen sensor to provide closed-loop fuel control.

The components for an LNG (liquefied natural gas) storage based system are different due to the fuel being stored as a cryogenic liquid. LNG is stored at a low pressure and temperature, and a heat exchanger is required to vaporize the fuel before it is used in the engine. After the fuel is vaporized, a pressure-limiting device is used instead of a regulator, and then the low-pressure components are similar to a CNG-based system, including the low-pressure electronic shutoff solenoid and filter. The LNG tank storage system also includes multiple components for filling and safety of the system.

Natural Gas Fuel Systems—Direct Injection

The term *natural gas direct injection* (NGDI) has been used recently to describe multiple different types of fuel injection and combustion concepts. The NGDI realm includes both premix spark-ignited and diffusion burn combustion concepts. Each of these combustion concepts has different fuel delivery system requirements, and they are further differentiated with a complete description.

The first type discussed here, low-pressure spark-ignited homogeneous-charge NGDI is similar to MPI, with the additional feature that the premix injection range is extended to include the beginning of the compression stroke after the intake valve closes. At this point in the engine cycle, an MPI or MP-OVI system would not be able to deliver fuel into the cylinder. With a modest rail pressure (e.g., < 100 bar), injection during the first part of the compression stroke is possible. With this combustion concept, an injector with gaseous fuel that can seal against combustion pressure, withstand combustion temperatures, and is suitably durable is required. Compressed gas storage can be used to provide the necessarily higher rail pressure than a multipoint system, however with a higher minimum pressure, the usable fuel volume from the storage is limited, consequently limiting vehicle range.

The next type of NGDI is high pressure, spark-ignited combustion. This system type enables injection throughout the compression stroke by use of an even higher rail pressure (e.g., > 100 bar). This provides the opportunity to introduce stratified mixtures into the combustion chamber and also the ability to increase the charge in the cylinder by delaying injection of the fuel until the cylinder is filled with air, and the intake valve closes. A fuel pressure increasing device would be necessary to maintain the required high-injection pressure.

Finally, yet another injection and combustion type is also called NGDI, or HPDI (high-pressure direct injection). This type of injection uses compression ignition of a diesel pilot injection, followed by high-pressure natural gas injection. Both fuels combust with a diffusion burn type of heat release. This combustion system has the potential of having the highest engine efficiency out of all natural gas combustion types. The fuel system for this combustion type is the most complex of all that have been discussed. The primary enabling component is a dual acting injection with two concentric fuel outlets and actuators: one actuator and outlet for the diesel pilot injection to initiate combustion, and a second actuator and fuel outlet for the natural gas injection for the majority of the heat release. The fuel system requires a high-pressure diesel fuel system consisting of a pump, pressure regulation, and a common rail to supply the first fuel to the dual-fuel injector. In addition to the complete diesel system, a high-pressure natural gas common rail is also required to deliver the second fuel to the injector, with some mechanism for developing the high pressure. The one concept for the high-pressure NG (natural gas), which has been used by Westport in their HPDI system, is to generate the high pressure onboard the vehicle from LNG storage. This is achieved by using a cryogenic pump in the fuel tank, which pumps the liquid natural gas up to the required pressure. Then, a heat exchanger is used to gasify the fuel. From there, the high-pressure gaseous fuel can be used in the injection system. This is a complex fuel delivery system with specific components that increase the cost of the system. However, this combustion concept is still considered advantageous due to the engine efficiency potential.

Natural Gas Combustion—Emissions

The different types of natural gas engine combustion concepts each have different emission aftertreatment requirements.

Homogeneous, spark-ignited, stoichiometric combustion, with either CPI or MPI fuel systems, has been in production with a three-way catalyst as the single aftertreatment device. This combination has met the tightest emissions standards from both the EU and CARB (California Air Resource Board). With the addition of cooled external EGR, the Cummins-Westport ISL G NZ has achieved the CARB optional low-NO_x certification of 0.02 g/bhph, to which no other engine has been certified. This is an example of the emissions potential of NG combustion as an advantage over diesel.

The dual-fuel diffusion burn NGDI combustion concept requires emission aftertreatment systems similar to diesel. This is due to the lean overall mixture, for which a TWC (three-way catalyst) does not function. A urea-SCR-based lean-NO_x system is necessary; however, the potential low soot production may eliminate the need for a particulate filter.

17.4.6 Ignition Systems

This section will cover the principles of ignition and the two main design types. It will explain how the high voltage needed for ignition is generated and the importance of ignition timing. Lastly, it will cover spark plug design and function.

There are two basic types of ignition system: conventional coil and electronic. Conventional coil design can have one of three types of trigger; electronic design can either have a distributor or be distributorless. All designs use essentially the same method for generating high voltage, and all systems use the same design type of spark plug. In addition to the systems covered here, there are new systems in development such as microwave-assisted ignition and corona ignition.

Principle

A gasoline internal combustion engine needs a spark to ignite the compressed air–fuel mixture in the combustion chamber. The spark is a discharge between the two electrodes that protrude into the combustion chamber. The ignition system generates the high voltage (up to 30 000 V) [17.29, 30] needed to create the spark discharge and also initiates the spark to occur at the proper piston position (ignition timing).

Ignition System Design

Conventional Coil Ignition. This system consists of an ignition coil, an ignition distributor, and spark plugs; see Fig. 17.89. As the coil is similar for all types of systems, it is explained under point 3 (*high-voltage generation*).

The distributor rotates in sequence with the engine's crankshaft and at half of the crankshaft's speed for four-stroke engines or at crankshaft speed for two-stroke engines. One of three types of triggers is used in the distributor to control the current through the ignition coil:

- Mechanical breaker points: a mechanical switch that is closed and opened once per firing event by a cam located on the distributor shaft. The number of cam lobes equals the numbers of cylinders.
- Breaker-triggered transistorized ignition: this design is similar to mechanical breaker points except that the primary ignition circuit is controlled by a transistor instead of by the breaker points. Only the control current is switched by the breaker points; this extends the breaker-point life and allows higher primary currents to be controlled.
- Transistorized ignition with Hall-effect trigger or induction-type pulse generator: the breaker points are totally eliminated and replaced by either a Hall-effect sensor or an induction-type pulse generator located in the distributor. The sensor or generator create one signal per cylinder; this signal is used to charge and discharge the coil.

A mechanical advance and vacuum unit define the proper ignition point as a function of engine speed and load.

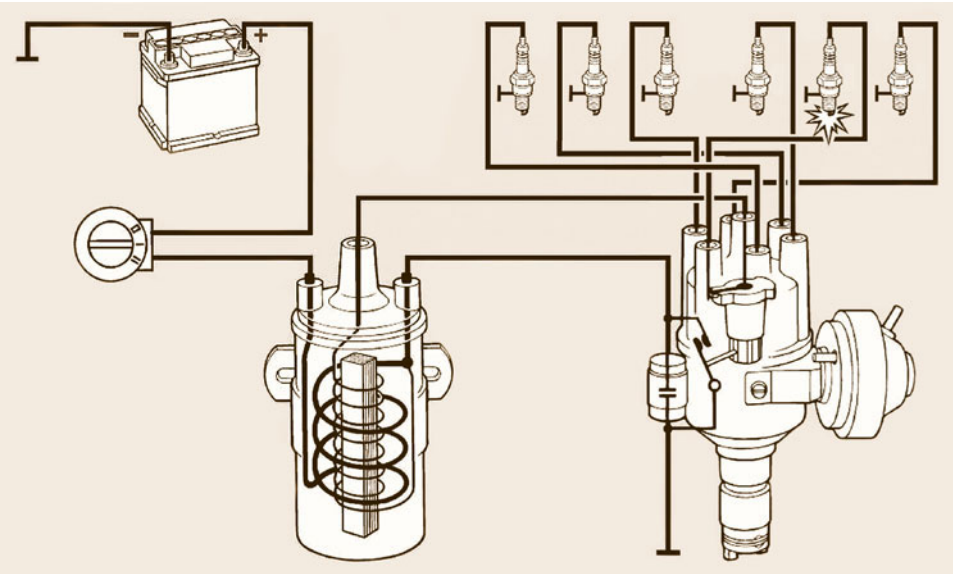

Fig. 17.89 Conventional coil ignition

Electronic Ignition. This system requires no centrifugal or vacuum-based timing control. Sensors monitor engine speed and load; these signals are sent to the ignition control unit, which determines the optimal ignition timing.

Engine speed is sensed by an inductive pulse sensor; engine load is sensed by a pressure (vacuum) sensor connected to the intake manifold. The ignition control unit uses these signals in a timing program map to determine optimal ignition timing for each speed/load point. Additional sensors may be used to monitor engine temperature, intake air temperature, throttle-plate position, and other operating parameters, which are then taken into consideration when determining ignition timing.

This system may utilize a distributor to contain the engine speed/position sensor and to distribute the high voltage (Fig. 17.90a), or may instead be distributorless (Fig. 17.90b). The latter system has a separate ignition coil for each cylinder or pair of cylinders. These coils may be mounted on the engine or directly attached to the spark plugs.

The ignition control system may be combined with the fuel-injection control system to allow for coordinated total engine management (Sect. 17.4.4).

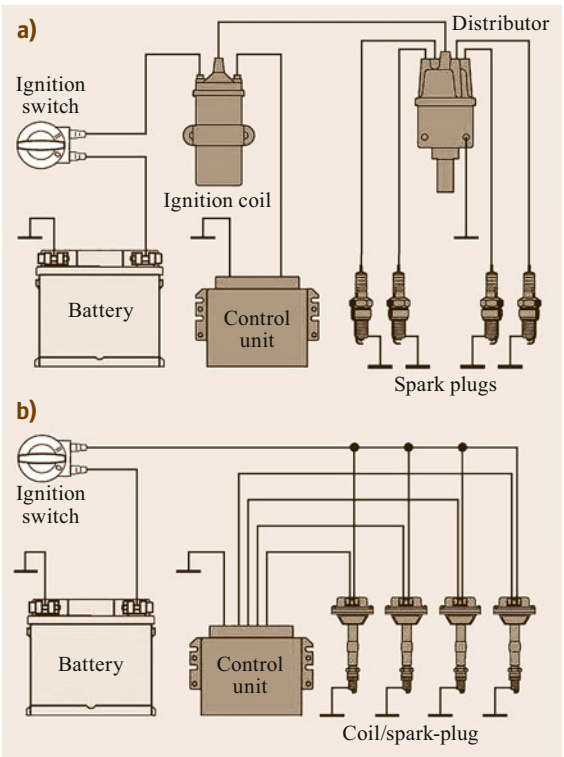

Fig. 17.90a,b Electronic ignition. **(a)** Separate coil and spark plugs; **(b)** unitized coil/spark plugs

High-Voltage Generation

The high voltage needed to bridge the spark-plug gap is typically generated by a coil. The coil consists of two copper windings (primary and secondary), an iron core, and a plastic casing. Energy is transferred from the primary winding to the secondary winding by means of magnetic induction. The current and voltage amplification from primary to secondary is the ratio of the number of coil windings.

Charging and discharging the coil to generate the high voltage needed for the spark plugs is essentially the same for all types of ignitions. The trigger closes and opens once for each cylinder's combustion event. When the trigger closes, current flows through the coil's primary winding and to ground. This produces a flux field in which ignition energy is stored. The time available for charging is determined by how long the trigger is closed (referred to as the dwell angle). The current is interrupted when the trigger opens.

The flux field in the primary winding produces high-tension voltage in the secondary winding. For a distributor-type system, this voltage is conducted to a center contact in the distributor cap. A rotor within the distributor rotates with engine rotation and distributes the high voltage to the spark plugs via the distributor cap and ignition wires. For a distributorless system, the voltage is fed directly to the spark plug.

Ignition Timing

As engine speed increases, ignition timing must be advanced relative to the piston's top dead center to allow the air–fuel mixture more time to burn. As the load increases, the ignition timing must be retarded to prevent detonation (knock). The effect of ignition timing on combustion pressure is illustrated in Fig. 17.91.

Spark Plug Design

All ignition system designs include a spark plug, which consists of the following:

- A terminal post that leads the current from the ignition wires to the center electrode.
- An insulator that is made of a ceramic material and insulates the center electrode and terminal post of the shell.
- A shell that houses the insulator and allows mounting to the cylinder head.
- A gasket and a seat that seals the combustion pressure.
- Electrodes that form a gap, which the high voltage must bridge to pass to ground, thus causing a spark.

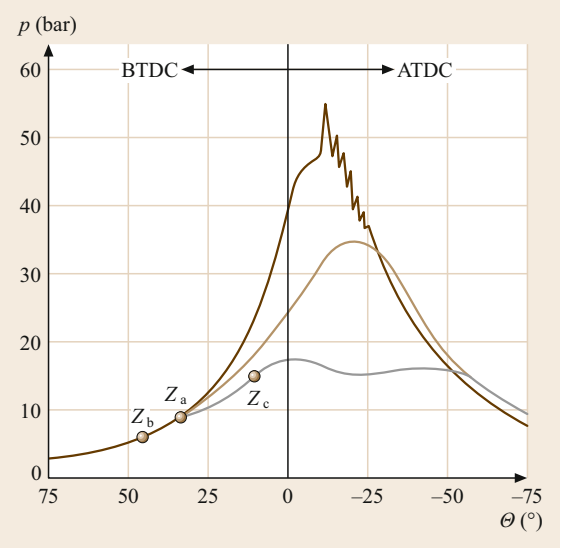

Fig. 17.91 Effect of ignition timing on combustion pressure

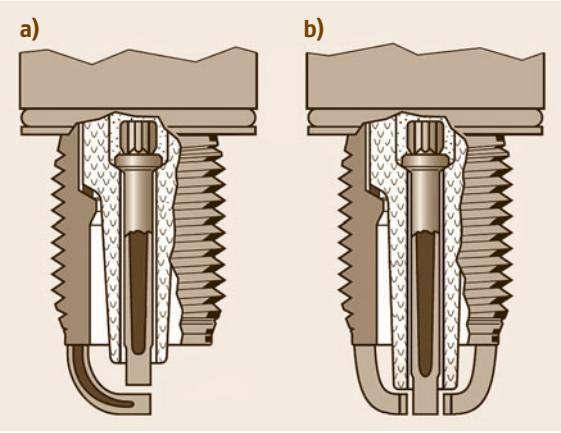

Fig. 17.92a,b Electrode designs: **(a)** single electrode, **(b)** dual electrodes

Electrodes may be made from a compound of corrosion-resistant nickel and copper, a composite with silver as a base, or platinum. The electrode gap determines the length of spark; the voltage required to jump the gap increases as the gap width increases.

A plasma spark is a high-voltage ignition spark with a very large ignition kernel with peak currents exceeding 20–30 A. The net energy output of a plasma spark is several hundred times greater than that of a conventional spark.

Figure 17.92 shows a spark-plug cross section of two different electrode designs (a front electrode and a side electrode).

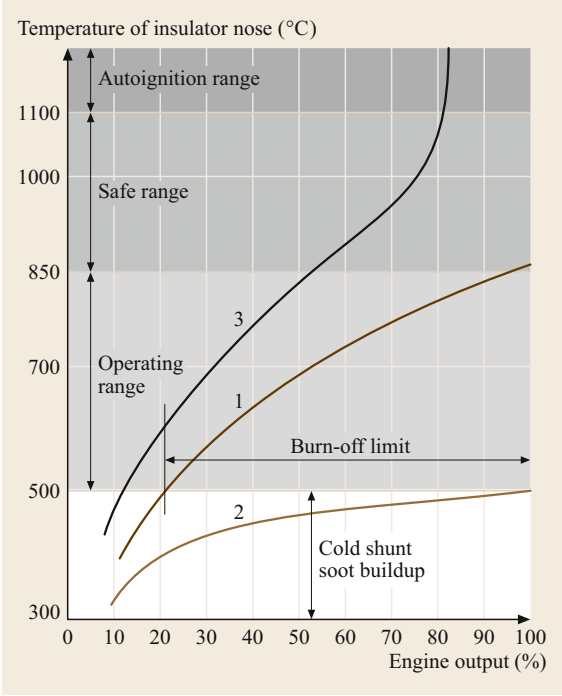

Fig. 17.93 Operating temperature of the spark plug's insulator nose

The heat range defines the operating temperature of the spark plug's insulator nose and should be chosen to maintain 500–900 °C. If the temperature is below 500 °C combustion residue will form on the insulator nose. If the temperature is above 900 °C, the hot combustion residue gases promote electrode oxidation. Above 1100 °C autoignition may result. Figure 17.93 shows the proper operating range.

17.4.7 Mixture Formation and Combustion Processes

All fuel–air mixtures have limits for the mixture ratios that can be used in engines. When there is too little fuel, the mixture is said to be *lean* and flame propagation is slow, and misfire is likely. When the fuel concentration is too high, the mixture is said to be *rich*, and the combustion produces products of incomplete combustion, such as carbon monoxide.

Spark Ignition Engines

In spark-ignited engines, a homogeneous charge of fuel and air is introduced into the cylinder, and a flame is initiated with a spark near the end of the compression process. The flame propagates outward from the spark source. Turbulence is required for the flame to achieve

the speed necessary to complete the combustion process before the exhaust valve opens. In the early part of the combustion process, immediately after ignition, the flame growth is slow. The combustion zone, called the flame kernel, is small, and very little energy has been released. The progress of combustion at this point is sensitive to the balance of energy released by combustion and the heat lost to the cooler surroundings. Leaner mixtures and lower temperatures and pressures can slow the energy release rate and increase the likelihood of misfire. Cycle-to-cycle variations in this critical phase of the combustion process can cause large differences in the development of the cylinder pressure.

In some cases, the combustion process may not proceed in the normal manner of a deflagration wave propagating away from the spark. In one such case, the gases in front of the flame front, which are compressed as the cylinder pressure rises from combustion of the gases behind the flame front, may spontaneously ignite. This *autoignition*, also called *knock*, can be extremely violent and significantly raises engine noise levels. If a large percentage of fuel is involved in the event, it can cause mechanical damage to the engine. Some fuels are more prone to autoignition than others. The resistance of the fuel to autoignition is characterized by the fuel's octane number. Fuels with high octane numbers can be operated with less chance of knock.

Basic thermodynamics indicates that engines with a high compression ratio should have better fuel economy and performance. However, the higher temperatures and pressures that result from the higher compression ratio increase the tendency of knock. High-octane fuels are needed for engines with elevated compression ratios. Because knocking combustion is so rapid, it tends to approximate the thermodynamic ideal of constant volume combustion. In fact, many engines demonstrate their highest efficiency when operated with light knock. However, as more fuel is consumed by autoignition, the pressure oscillations in the cylinder tend to disrupt the thermal boundary layers in the cylinder and increase the heat loss from the combustion gases.

Another type of abnormal combustion is known as preignition or surface ignition. In this case, the fuel–air mixture may be ignited by a hot surface in the cylinder. This might be a valve surface, a carbon deposit, or even a piece of head gasket that protrudes into the cylinder. Because the combustion may be earlier than the spark, the flame-caused pressure rise may occur during the compression process causing the cylinder pressure to become very high. It has been proposed that knock and preignition can be coupled. Knocking can increase heat transfer rates and raise surface temperatures so that preignition is more likely. The resulting preignition raises the gas temperatures in the cylinder and makes knock more likely to occur.

When the fuel–air mixture is too lean, the flame kernel grows slowly, and there is an increased probability of misfire in the engine. The mixture ratio where the misfire becomes unacceptable is the lean operating limit of the engine. There is a corresponding rich operating limit, where there is insufficient oxygen to sustain combustion. The chemically correct mixture is known as the *stoichiometric* mixture. The air–fuel ratio for maximum engine power falls on the rich side of the stoichiometric mixture, and the best fuel economy tends to be on the lean side.

In order for a spark-ignited engine to operate continuously, the air–fuel mixture must be between the two flammability limits. However, exhaust emission concerns dictate that the mixture be held close to stoichiometric. Except for cold starts and brief periods of high power demand, modern vehicles equipped with three-way catalysts and closed-loop control of air–fuel ratio operate in a narrow band around stoichiometric.

Figure 17.94 shows three different approaches to fuel–air mixture formation in spark-ignited engines. The traditional approach of introducing the fuel with a carburetor into the intake air stream is only used for small engines and is obsolete for larger engines that are subject to emissions controls. Most engines today use port fuel injection, as shown in Fig. 17.94b. This approach provides very uniform air–fuel mixture between cylinders and excellent atomization of the fuel at all speeds. Figure 17.94c shows direct injection of the fuel into the cylinder. The share of DI engines is continuously increased; this approach allows a homogeneous mixture or some degree of charge stratification in the cylinder and fuel economy that approaches the diesel engine.

Compression Ignition Engines

Compression ignition engines, also known as *diesel* engines, bring only air into the cylinder through the intake valve. The engines rely on compression of the air to produce a sufficiently temperature for the fuel to autoignite soon after it is injected near the end of the compression process. In contrast to the homogeneous charge spark-ignited engine, the air–fuel mixture in the diesel engine is always heterogeneous. Since there is a distribution of fuel–air ratios ranging from very lean to very rich, there is always some location in the cylinder where conditions are optimum for autoignition, and the cycle-to-cycle variability for diesel engines is very small.

Diesel engines run without throttles, so they have the advantage of low pumping losses. Load is controlled by varying the amount of fuel that is injected into the cylinder. At light load and idle, the air–fuel ratio may be

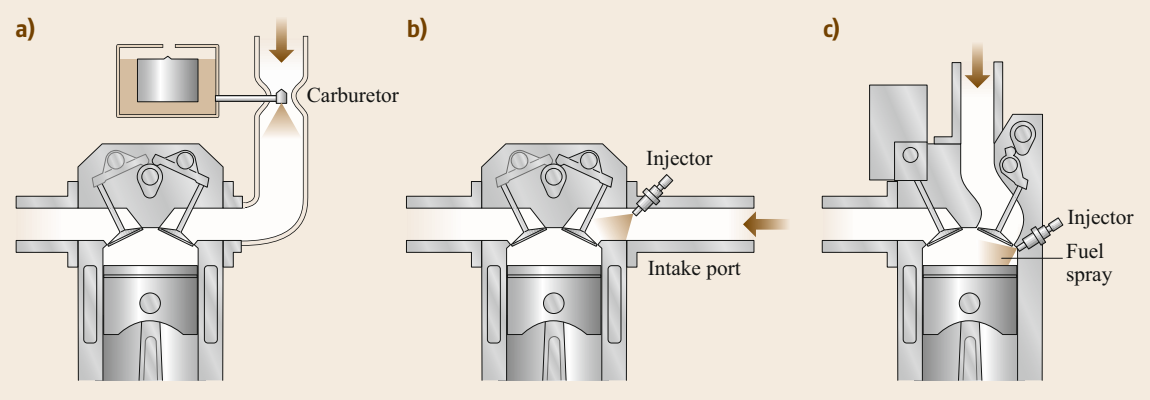

Fig. 17.94a–c Fuel–air mixture formation in spark-ignited engines: **(a)** carburetor injection, **(b)** port injection, **(c)** direct injection

70 : 1 or higher. At full load, the air–fuel ratio may be as low as 20 : 1. The stoichiometric ratio of 14.5–14.8 is generally not achieved because of high smoke levels.

Diesel engines can be categorized into direct injection (DI) and indirect injection (IDI) engines, although indirect injection designs are now mostly obsolete. IDI engines utilized a small chamber apart from the main chamber, called a prechamber or turbulence chamber, which was connected to the main chamber by a narrow passageway. Fuel was injected either into the separate chamber or into the passageway, and the rapid air motion between the two chambers caused by the piston motion, provided excellent fuel–air mixing. This rapid mixing allowed high-speed operation of the engines but heat transfer and throttling losses exacted a severe fuel-economy penalty on IDI engines. Advances in fuel-injection technology have allowed DI engines to operate at equivalent speeds with much better fuel economy. A DI engine with the fuel sprayed directly into a chamber in the cylinder formed by a toroidal recess in the piston is the most common configuration in modern diesel engines.

Alternative Combustion Systems

A major drawback of both spark-ignited and compression-ignited engines is their high NO_x emissions. Both engines require aftertreatment to reduce NO_x to acceptable levels. Combustion systems that are homogeneously charged, like spark-ignited engines, but utilize autoignition, like a compression-ignited engine, have been developed. These engines utilize an air–fuel mixture that would ordinarily be quite lean, but by controlling the temperature, it can be made to autoignite in a gradual and controlled manner towards the end of the compression stroke. The temperature and the air–fuel ratio can be optimized to reduce NO_x emissions to very low levels. Numerous concepts have demonstrated excellent benefits. However, real-world application has been hampered by the very strict and dynamic air and fuel controls that are required to adequately control combustion.

17.4.8 Fuels

This section will cover the basics of gasoline, diesel, natural gas, and renewable fuels [17.22]. It will start with the sources of petrochemical fuels and the refining process. The basic composition and key characteristics of gasoline and diesel fuels will then be explained. Lastly, an overview of fuel substitutes and alternate fuels will be given, whereby this cannot cover the plethora of newly emerging fuels in detail.

Petroleum Refining and Basic Organic Chemistry

Most conventional fuels are made from petroleum crude oils, consisting primarily of paraffinic, naphthenic, and aromatic hydrocarbons. Raw crude oils have a wide range of densities ranging from as thin as water to as thick as tar. Crude oil is converted into usable products by means of refining; the most important products are gasoline, jet fuel, and diesel fuel. Other valuable products are heating oils, liquefied petroleum gas, lubricating oils, and asphalt.

To convert crude oil the feedstock is typically distilled. Since the different components of crude oil (e.g., gasoline, diesel) have different boiling points, the lighter components (those with relatively low boiling points, e.g., propane and butane) rise to the top of the distillation column, where they are drawn off. The next-heavier components (e.g., gasoline) are drawn off lower on the column, and then the subsequently heavier components (kerosene and then diesel) are drawn off towards the bottom. The fuels must then be upgraded,

usually by hydroprocessing (which uses hydrogen with a catalyst) to remove undesired components. Fuels with higher boiling points are then cracked (broken down) into lower boiling points using very high temperatures and catalysts [17.31].

Gasoline

Gasoline fuels for spark-ignition engines are hydrocarbon compounds, which sometimes contain oxygenous components to enhance performance.

Key Characteristics.

- Grade: usually stated as regular or premium; an indication of antiknock properties.
- Octane number: the resistance to knock (preignition).
- Density: weight per unit volume; energy content increases as density increases.
- Volatility: how easily the fuel vaporizes. The fuel must vaporize quickly for good cold starting but not so quickly as to cause vapor lock. Volatility is characterized by the fuel's vapor pressure and/or evaporation point dependant upon temperature.
- Sulfur content: must be kept low to allow proper operation of the catalytic converter or other aftertreatment device.
- Additives: may be used to enhance one or more of the properties stated above, or to protect against aging, contamination or corrosion.

Diesel

Diesel fuels for compression-ignition engines are usually distilled from crude oil. They consist of a large number of different hydrocarbon compounds, including *n*-paraffins, olefins, naphthenes, and aromatic compounds. Diesel fuel ignites at $\approx 350\,^{\circ}\mathrm{C}$, much lower than gasoline, which ignites at $\approx 500\,^{\circ}\mathrm{C}$.

Key Characteristics.

- Grade: the standard to which the fuel must conform.
- Density: weight per unit volume; energy content increases as density increases.
- Viscosity: resistance to flow; low viscosity leads to leakage losses, while high viscosity may impair injection pump function.
- Cetane number: ease with which fuel ignites; combustibility increases as cetane number increases.
- Cold-filter plugging point: the temperature at which the fuel clogs the filter.
- Flash point: the storage temperature at which flammable vapors are produced.
- Water content: amount of water in fuel; water causes corrosion and poor lubrication, leading to wear and seizures.
- Contaminants: foreign particles in fuel; the particles cause erosive and abrasive wear.
- Lubricity: measure of the fuel's lubrication properties; low lubricity causes wear and seizures.
- Sulfur content: amount of sulfur in fuel; sulfur does not harm the fuel injection system but will harm most aftertreatment devices. Most on-road diesel fuels have a maximum of 10–15 ppm (parts per million) sulfur. The removal of sulfur by hydrogenation also removes the ionic fuel components that aid lubrication, reducing the lubricity properties of the fuel. Additives are, thus, needed to restore lubricity to a sufficient level.
- Oxidation stability: resistance to forming acids.
- Additives: may be used to enhance one or more of the properties stated above.

Renewable Fuels

In addition to standard fuels there are several alternatives to gasoline and diesel. These are often pursued in order to reduce emissions or to reduce consumption of nonrenewable fuels, as most alternate fuels are from a renewable source. It should be noted that renewable fuels are not always compatible with the fuel system (some require extensive modifications), and that they may increase one emission component while reducing another. They are often not as stable as petroleum-based fuels [17.26].

Alternate fuels can basically be divided into two categories: gasoline substitutes/additives and diesel substitutes/additives. A popular gasoline substitute is ethanol; this can comprise up to 10% of the gasoline and is commonly known as E10. Vehicles that have been designated as Flex-fuel can use blends of up to 85% ethanol (E85) [17.32]. Diesel renewable fuels include biodiesel, the feedstock of which is typically yellow grease, canola, or soy beans. Blends of up to 20% (B20) can be found. Other renewable diesel fuels are gas-to-liquid, (GTL), coal-to-liquid (CTL) and biomass-to-liquid (BTL), as well as paraffinic fuels.

Gasoline Substitutes/Additives.

- Coal hydrogenation: coal and coke.
- Liquefied petroleum gas (LPG): hydrocarbon mixtures (mostly propane) that are liquid at ambient temperatures under relatively low pressures.
- Liquefied natural gas (LNG): methane that is cooled to $< -160\,^{\circ}\mathrm{C}$ and condensed to a liquid by compression.

- Compressed natural gas (CNG): natural gas (mostly methane) compressed to high pressure.
- Hydrogen: produced by electrolysis of water or from natural gas/coal.
- Alcohol: methanol (usually made from natural gas but can also be made from biomass resources such as wood) and ethanol (made from grain or biomass). Either can be used alone or mixed with gasoline.

Diesel Substitutes.

- Alcohol: methanol and ethanol as described above; usually mixed with diesel.
- Fatty acid methyl ester (FAME): often known as biodiesel, made from many sources, the most popular of which are rapeseed, soybean, sunflower, and depleted cooking oils. Usually mixed with diesel in 5–50% concentrations, these bring lower PM emissions and improve lubricity but are critical regarding density, NO_x, water absorption, and stability.
- Diesel-water emulsions: reduce soot and NO_x but also lower power output.
- Dimethyl ether (DME): a gas-phase fuel, requiring extensive modification of the fuel-injection equipment.
- Oil sand/tar sand gasification.
- Synthetic fuels: methane gas-to-liquid (GTL, tradename *Synfuel*), biomass-to-liquid (BTL, tradename *Sunfuel*), and coal-to-liquid (CTL).

Natural Gas Fuels (Gaseous Fuels). Natural gas is a general term used to encompass a number of gaseous fuels. Each fuel type has specific technical properties and advantages or challenges and techniques to address them. Natural gas has attractiveness as a fuel due to its generally lower fuel costs and emissions advantages (primarily low NO_x), as well as greenhouse gas reductions (CO_2), along with essentially no particulate matter (PM) emissions. Abundant and growing discoveries of natural gas reserves also make it attractive for self-sufficiency and sustainability in some regions. Natural gas has varying levels of lower energy content when compared to gasoline.

Compressed Natural Gas (CNG). CNG is composed primarily of methane, typically around the 95% level, depending upon the source of the gas, blending. The remaining small amount of gas constituents affect the overall *gas quality* and can have an impact on the characteristics of the gas and the performance of the engine, such as heating value, injector mass flow, knock resistance, and related performance output. CNG is stored under pressure in the vehicle's fuel tank, and, thus, where its designation as compressed natural gas comes from.

Since the gas is still in a gaseous state, its energy density is lower than that of other fuels, and much larger vehicle storage tanks are required. Also, due to a higher pressure than other systems, more expensive storage tanks are required.

Due to its primary composition as methane, low NO_x emissions occur somewhat naturally, and there are essentially no particle emissions. Because methane has the lowest carbon content and highest hydrogen content of any current fuel type, it produces low CO_2 emissions. Methane also provides high antiknock properties as an attractive performance feature.

Liquefied Natural Gas (LNG). LNG is also methane-based and, therefore, has the same technical advantages as CNG, but is cooled and transported and stored in cryogenic liquid form. Methane must be cooled below −162 °C to liquefy it at atmospheric pressures. In liquid form, the energy density is significantly higher than CNG, thus requiring smaller vehicle storage tanks for LNG. LNG does have the drawback of boil off (it converts back to the gaseous form) if the tank heats up after several days without vehicle operation. Due to its storage system, it is more costly and complex than gasoline and other gaseous fuel systems. LNG is converted into gaseous form before being introduced to the engine.

Liquefied Petroleum Gas/Autogas/Propane (LPG). LPG is a mixture consisting primarily of propane and butane. By definition, it is a liquid fuel when stored at its lower pressure and requires a smaller tank than other gaseous fuels, and thus its storage system is more economic. LPG as a system is more closely related to gasoline engines. LPG is introduced to the engine in either liquid form or converted back into gas.

Renewable Natural Gas (RNG). RNG is gaining popularity in some regions due to sustainability and a neutral greenhouse-gas calculation impact. RNG is created from biomass, typically from landfills, and thus captures (as well as generates additional) methane discharged by decomposing waste. RNG has essentially the same properties and characteristics as CNG and can also be cooled to generate LNG.

Transportation and Filling Station Infrastructure. Transportation from the gas well to the refueling station and any final conditioning prior to refilling the vehicle varies between the gas types, depending on their various unique characteristics and conditions:

- *CNG* infrastructure allows it to by piped underground at low pressures to the retail location where it is compressed to higher pressures and stored. With this technique, there is less exposure to leakage at each off-loading point, due fewer transfer points in general. The cost of equipment is practical on the scale of retail locations.
- *LNG* is liquefied at a low temperature and, therefore, is transported at a lower pressure than CNG. However, due to the cost of the liquefaction process, it is only cost effective when this is performed on a large scale, and it is, thus, not practical at retail locations. The LNG is, therefore, liquefied near its point of extraction and shipped via truck or rail to retail locations. Each transfer point represents a fugitive emissions risk.
- *LPG* is liquefied by nature but only requires a low pressure to remain so, and, thus, a less expensive infrastructure is needed, but transfer emissions loss is still a concern due to the multiple transfer points on the way to the retail location and refilling.

Vehicle Storage. Vehicle storage requirements also vary among gas types, depending upon their various unique characteristics and conditions, with the storage pressure requirement being the key factor:

- *CNG* tanks require thick walls due to the high storage pressures required to gain practical levels of capacity, which drives the cost of the storage tanks to levels that are much higher than that for other fuels. The cost of the storage tank typically accounts for roughly half the total unique system costs. Due to its lower storage energy density, a CNG requires approximately four times the volume of conventional gasoline or diesel fuel tanks.
- *LNG* systems can be either cold (unsaturated) or saturated (warm) LNG fuel types, depending upon the operating region's availability or the fleet operation's preference. Cold LNG provides for a denser fuel storage and longer operating range, but requires unique system hardware, which is more expensive. Saturated LNG is stored at a higher pressure than cold LNG and has less storage capacity due to its less dense gas, but is slightly more economical. The difference between the two types is based on the storage temperature and resultant pressures, with cold CNG at a lower temperature and, thus, lower pressure than saturated LNG.
  While not as high pressure as CNG systems, cold LNG requires a cryogenic pump system as part of the tank to supply the gas to the engine, due to the lower cold pressure of the gas. LNG tanks also require insulation to maintain the lower storage temperatures. The addition of the pump, and tank insulation, in comparison to conventional fuels makes for a more expensive system. The further addition of a boil-off valve to manage pressures as temperatures rise with the vehicle off, represents additional costs to the system. An LNG storage tank requires about 1.7 times the tank volume of a gasoline or diesel tank.
  A saturated LNG system does not require a cryogenic pump due to its higher pressure as a result of its higher temperature, and relies on that pressure to supply gas to the engine, but has less storage capacity than a cold LNG system due to its higher pressures. However, there is a greater concern with venting due to the tank's lower storage temperature being at the boil-off temperature.
- *LPG* allows tanks with thinner wall thicknesses, and resultant lower costs, because it required even lower pressure. Storage tanks need to have about 1.4 times the capacity of conventional fuel tanks to approximate similar ranges.

Due to the pressures required to store the various gases, current tanks are of the cylindrical design. Because of this shape, and the extra capacity required to obtain acceptable driving ranges, the tanks take away some of the valuable vehicle storage space. To address this issue, and gain further driving ranges, other technologies such as ANG are being developed. ANG (absorbed natural gas) uses a porous sorbent, such as activated carbon, that has a high surface area to allow greater storage volume at lower storage pressures. This also allows for different tank shapes that may be able better fit in locations of the vehicle to not impact vehicle storage significantly. The metal-organic framework (MOF) is another technique to provide conformable tank technologies. Lower storage pressures are possible with these more efficient storage methods, which also reduces the cost of the compressor hardware at retail refueling locations.

17.4.9 Emissions

Emissions from engines are generally thought of as the harmful chemicals that are present in small amounts in the exhaust gas. However, vaporized fuel that is released during refueling or from leaks onboard the vehicle can also be a source of air pollution. Carbon dioxide, a major component of engine exhaust and an inevitable consequence of hydrocarbon combustion, was traditionally considered to be benign and not included as a hazardous air pollutant. Now that the role

of carbon dioxide from fossil resources in global climate change has been identified, much more attention is being paid to this gas.

Emission regulations can be placed into two categories: those that limit emissions from specific engines or vehicles, and those that limit the levels of emissions in specific spatial locations, without regard to their origin. The first category of regulations will be our primary focus, as these are the regulations that engine and vehicle manufacturers are required to meet in order to sell their products. The second category of regulations tend to be the responsibility of cities or states, and while they may impose restrictions on the types of vehicles that can be sold within their jurisdiction, the sources of pollution are not limited to engines and vehicles [17.22, 26].

Ambient Air Quality

Ozone has been the subject of what appears to be contradictory statements in popular media. Ozone is described as being essential as protection against skin cancer and is being depleted by chlorofluorocarbons (CFCs). At the same time, city dwellers are subject to warnings about high ozone levels. The resolution of this apparent contradiction lies with understanding the role of altitude as explained in Fig. 17.95. In the stratosphere, above 15 000 ft, the concentration of ozone can be very high, approaching 10 000 ppb (parts per billion). This ozone is formed by reactions involving sunlight and oxygen. It filters the ultraviolet solar radiation that causes skin cancer. Some researchers have argued that this ozone is destroyed by reactions with chlorine atoms originating from CFCs.

At lower altitudes, the natural concentration of ozone is up to three orders of magnitude lower than in the stratosphere. This is fortunate, since high levels of ozone interfere with plant growth and are a strong irritant. High levels of ozone can be produced at lower elevations by reaction of volatile organic compounds (VOCs), carbon monoxide, oxides of nitrogen (NO_x), and sunlight. This complex set of chemical reactions produces a large number of different chemical compounds, many of which are harmful and irritating to people. Ozone, although only one chemical compound, is widely used as a measure of the overall concentration of the complex chemical mixture, sometimes known as *smog*. The EPA recently reduced the maximum allowable ozone concentration from 120 ppb averaged over a 1 h period to 80 ppb averaged over an 8 h period. Normal background levels of ozone are typically 20–40 ppb and can exceed 200 ppb during severe smog episodes [17.29, 30].

Ozone is a secondary pollutant. It is not found in significant amounts in the exhaust of engines. However, compounds that are found in engine exhaust contribute to the formation of ozone, such as, VOCs, carbon monoxide, and NO_x. Another major source of VOCs is evaporative emissions. Evaporative emissions originate from losses of fuel during refueling as well as when the vehicle undergoes diurnal heating and cooling. These emissions are strongly tied to the Reid vapor pressure of the fuel, which is why it is now closely controlled

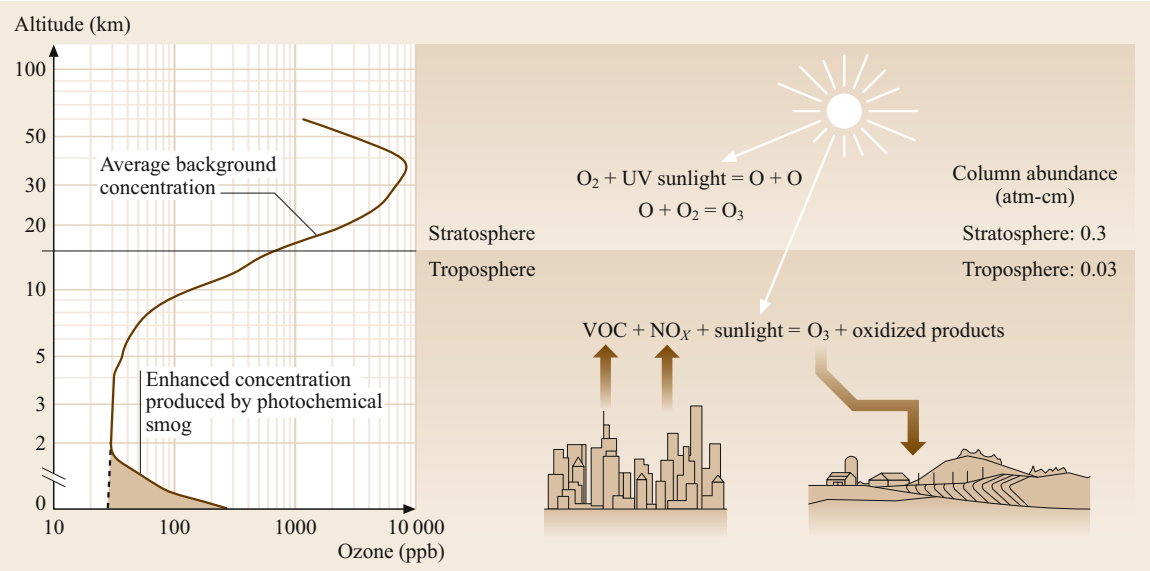

Fig. 17.95 Atmospheric ozone (after [17.33])

in areas where air pollution is a problem. Evaporative emissions are only a problem with volatile fuels such as gasoline and its blends with alcohol. Diesel fuel's vapor pressure is so low that it does not contribute to evaporative emissions.

Regulated Pollutants

The Environmental Protection Agency (EPA) regulates tailpipe emissions of both spark-ignition and compression-ignition engines in the United States. Regulated pollutants from spark-ignited engines include carbon monoxide, oxides of nitrogen, and unburned hydrocarbons. Compression ignited, or diesel engines must meet requirements for particulates as well as these gaseous species.

Carbon monoxide is primarily determined by the engine's air–fuel ratio. When the engine is operated fuel-rich there is insufficient oxygen to convert all of the carbon to carbon dioxide, so a portion is converted to carbon monoxide. Carbon monoxide is actually an intermediate product in the oxidation of hydrocarbons and is always present in significant amounts during the combustion process. Measured levels in the exhaust are usually higher than would be expected because the oxidation of the carbon monoxide tends to be a slow process that is limited by the rate of the reaction of CO with the OH radical, as shown in the following equation

$$CO + OH \rightarrow CO_2 + H \tag{17.82}$$

The concentration of the OH radical decreases rapidly as the in-cylinder temperature drops during expansion, leaving the CO frozen at an elevated level. An additional mechanism that affects homogeneous charge engines is the partial oxidation of trapped fuel that emerges from crevices or oil films during the expansion process when the temperature is too low to oxidize the fuel completely before the exhaust valve opens. In carbureted engines, rich-burning cylinders resulting from the nonuniform distribution of fuel between cylinders is an important source of carbon monoxide. Carbon monoxide emissions from diesel engines are generally well below regulation limits because diesels always operate with excess air.

Oxides of nitrogen (NO_x) consist primarily of nitric oxide (NO) and nitrogen dioxide (NO_2). Nitric oxide originates through three potential mechanisms that are usually categorized as fuel NO_x, prompt NO_x, and thermal NO_x. Fuel nitrogen can contribute to NO_x formation but is usually not important for engines because gasoline and diesel fuel contain small amounts of nitrogen. Prompt NO_x is formed by reactions between nitrogen and hydrocarbons during the combustion process. This mechanism also does not seem to be an important source of NO_x for engines. The primary source of engine NO_x emissions is thermal NO_x. This mechanism involves the following three reactions

$$O + N_2 \rightarrow NO + N \tag{17.83}$$

$$N + O_2 \rightarrow NO + O \tag{17.84}$$

$$N + OH \rightarrow NO + H \tag{17.85}$$

Since these reactions require significant concentrations of the radicals O, N, and OH, they only occur at high temperatures. The reactions also require significant time to equilibrate, so most of the NO formation occurs in the postflame gases. Virtually all NO_x control strategies, such as timing retard and exhaust gas recirculation (EGR), focus on reducing the temperature of the postflame gases.

Unburned hydrocarbon emissions from spark-ignited engines generally originate from fuel that is trapped in crevices, oil films, or deposits and is thus protected from combustion during the main combustion event. This sequestered fuel is released when the pressure drops during the expansion process but the temperature may be too low for complete combustion. Some of the fuel may burn to carbon monoxide but a significant portion will remain unburned or only partially burned, and this will be released in the engine exhaust. Some of the products of partial combustion, such as olefins and aldehydes, are highly reactive and are strong contributors to photochemical smog reactions. Occasional misfiring cycles can also be a significant source of unburned hydrocarbon (UHC) from spark-ignited engines. UHC from diesel engines generally originate from fuel that has been overmixed with air so that the mixture is too lean to burn under the conditions in the cylinder. These conditions are most likely to be encountered at idle and light loads. Reducing the engine compression ratio is an effective way to reduce combustion temperature (and NO_x), but also results in a tradeoff with increasing UHC.

Regulated emissions from compression-ignited or diesel engines include the CO, NO_x, and UHC described for spark ignition (SI) engines, but also include particulates. Particulates from diesel engines are operationally defined as whatever collects on a filter when the exhaust is cooled to 52 °C after the filter has had a chance to equilibrate in a temperature and humidity controlled environment. The primary constituent is carbonaceous matter, usually referred to as soot, that originates from high temperature pyrolysis reactions in the fuel-rich regions of the cylinder. The carbonaceous particles provide sites for the condensation and adsorption of high molecular weight hydrocarbons as the combustion products cool, and this portion of the particulate is often referred to as the soluble organic fraction (SOF) or

the volatile organic fraction (VOF). These high molecular weight hydrocarbons may originate from the fuel but are more frequently associated with the lubricating oil. Particulate may also contain sulfates resulting from the reaction of fuel-based sulfur-to-sulfur trioxide and then to a variety of sulfate compounds that may be observed as small droplets of sulfuric acid. Finally, the particulate may include inorganic compounds resulting from engine wear and lubricant additives. Many of the compounds identified in the SOF are known carcinogens, and the small size of the particulates (0.01–0.1 μm) increases the potential for their inhalation and retention in the lungs. For these reasons, the regulatory levels for particulate emissions have been progressively lowered so that after 2007, exhaust filtration technology has been required for most on-highway engines.

Measurement Instruments

A variety of instrumentation technologies has been developed to quantify the levels of pollutants in engine exhaust gases. Some techniques, such as Fourier transform infrared spectral analysis have broad applicability and are widely used for engine development. For emissions certification, specialized instruments are still used that have been developed to measure specific species, and often over limited ranges. Oxides of nitrogen are measured with devices that take advantage of the chemiluminescent reaction that occurs when NO reacts with ozone to form NO_2 and oxygen. The photon of light that is emitted by this chemical reaction can be measured and directly related to the concentration of NO. Total NO_x can be measured by passing the exhaust gas through a catalyst that converts NO_2 into NO before the gas is exposed to ozone.

Carbon monoxide and carbon dioxide are most commonly measured with nondispersive infrared (NDIR) absorption instruments that measure the amount of light of a specific wavelength that is absorbed by the exhaust gas. The wavelengths and path lengths for the light are chosen to provide the best sensitivity for the gas of interest. This technique requires that water vapor, a broadband absorber of infrared radiation, be removed before the measurement can be performed. The water is usually removed by cooling the gas to condense the water or passing the gas stream through a chemical desiccant.

Unburned hydrocarbons are measured using a flame ionization detector. These devices contain a small hydrogen flame located between two electrically charged plates. A small amount of the exhaust stream is fed into the hydrogen flame and the hydrocarbon-based carbon atoms produce flame ionization that can be measured as an electric current between the charged plates. The particle filters and all connecting lines must be heated to prevent condensation of the hydrocarbon vapors before they enter the flame. The heated flame ionization detector (HFID) measures the number of carbon atoms associated with hydrocarbons in the exhaust and, thus, requires an assumption to be made regarding the chemical composition of the hydrocarbons. Measurements performed on gasoline-fueled engines often assume the hydrocarbon has the same structure as hexane. Assuming that the unburned hydrocarbons have the same chemical structure as the fuel is also a common assumption for both gasoline and diesel engines.

Particulates are measured by filtering a portion of the exhaust gas and then weighing the increase in mass of the filter. The temperature of the filter is carefully controlled, because if it is too low, an excessive amount of the unburned hydrocarbon vapors may condense on the filter. The techniques used to capture a representative sample of the exhaust gas and allow the determination of the amount of particulate during a transient test cycle are described in the following section. For direct injection gasoline engines, the particulate number (PN) can be critical. With revelation that ultrafine particles may have adverse health effects, particulate mass (PM) is considered less appropriate than PN. Diesel combustion particulates are typically much larger in size. The measurement of PN is described in [17.26].

Test Cycles

Emissions from passenger cars and other light-duty vehicles are measured while the vehicle is operated on a chassis dynamometer. The chassis dynamometer connects the drive wheels of the vehicle to a load absorber through a set of rollers. The device allows the vehicle to be operated in a controlled laboratory but with an accurate simulation of actual in-use driving conditions. Flywheels and dissipative absorbers are used to simulate vehicle inertia and air resistance, so that the vehicle can be operated over transient driving cycles. Test cycles that involve following a vehicle speed versus time curve that models different driving conditions are used for emissions certification. Trained drivers can follow these curves very exactly, although most installations now use computerized accelerator pedal controllers.

The wide variety of transmission, drive line, and engine combinations used in heavy-duty applications precludes the emissions certification of vehicles. Heavy duty emissions testing focuses on testing the engine itself while it is outside the vehicle connected to a computer-controlled load absorber. The engine is operated over a 20 min cycle, where both the engine speed and torque are specified on a second-by-second basis. The 20 min test cycle consists of four 5-min segments that model different types of city and highway driving.

Exhaust emissions for both chassis dynamometer and engine dynamometer test systems involve injecting some or all of the exhaust gas stream into a dilution tunnel to lower the temperature of the exhaust gas and to simulate the particulate agglomeration processes that occur when the exhaust enters the atmosphere. These systems are equipped with flow control systems so that a constant volumetric flow rate is maintained for the sum of the engine exhaust and the dilution air. A sample of the diluted exhaust gas is filtered and the weight of the particulate is measured. In the case of chassis dynamometers, the pollutant is expressed as g/mile and for the engine dynamometer, it is expressed as g/hp-h or g/kWh. The denominator of the engine dynamometer term is the total amount of work performed by the engine during the test cycle.

Gaseous emissions are also sampled from the dilution tunnel. They may be collected in special chemically inert bags to obtain an integrated total for the cycle, or measured second by second to investigate the effect of different parts of the test cycle on a pollutant of interest.

Both chassis and engine dynamometer testing are conducted under carefully controlled laboratory conditions. There have been some claims that this testing is not representative of emissions from in-use vehicles, and attempts have been made to characterize in-use emissions using chassis dynamometers to test vehicles chosen at random from traffic flows. This experience has shown that a significant number of vehicles have improperly operating emission control systems, and actual emission levels are higher than would be expected from emission certification data. Measurements have been attempted using light absorption techniques from passing traffic but results have been mixed. Variability in measurement points, vehicle types, weather effects, etc., mean that extremely large numbers of measurements are required.

To better understand the real-world driving emissions (RDE), several suppliers have developed portable emissions measurement systems (PEMS) that attach to a vehicle that can be driven on the road with real-world driving. At the moment, new emissions regulations that include PEMS measurement of RDE are being developed. All vehicle manufacturers have added PEMS measurements to their development and calibration processes.

SI Engine Emissions Characteristics

The primary pollutants of regulatory concern for spark-ignited engines are carbon monoxide, oxides of nitrogen, and unburned hydrocarbons. The levels of these pollutants in the engine exhaust depend strongly on the engine's operating conditions such as spark timing, load, speed, and air–fuel ratio. While the engine speed and load are controlled by the operator (for manual transmission), the timing and air–fuel ratio are set by the engine's electronic control module (ECM) to keep the levels of the exhaust pollutants within the range allowed by emissions regulations while ensuring adequate vehicle performance. Under cold starting and high-power-demand conditions the air–fuel ratio is calibrated to be fuel rich. However, under all other operating conditions, the ECM maintains the air–fuel ratio close to the chemically correct, or stoichiometric, ratio.

The impact of timing, speed and most other operating parameters on carbon monoxide is secondary to the air–fuel ratio. There may be some effect on CO as these parameters are varied, but this is most likely due to changes in the air–fuel ratio or in causing the engine to operate at nonoptimum conditions for oxidation of the CO.

As described above, oxides of nitrogen from spark-ignited engines are almost entirely thermally based, and the two primary parameters that influence combustion temperature are spark timing and the air–fuel ratio. Over the normal range of variation of spark timing used in modern engines, earlier timing (advanced) always increases emissions of oxides of nitrogen (NO_x) and later timing (retarded) always decreases NO_x. Since the spark timing that provides best fuel economy is usually well advanced from the timing needed to keep NO_x at a tolerable level, engine designers are confronted by a trade-off between the desire to provide good fuel economy while still keeping NO_x emissions at a level that can be controlled by the catalytic converter.

While spark-ignited engine UHC emissions are primarily dependent on design factors such as piston ring position, which controls the size of the crevice volume, they can be affected by speed, timing, load, and the fuel–air ratio, as these will affect the amount of fuel that is sequestered in crevices and the tendency to misfire. As mentioned earlier, evaporative emissions are another source of UHC from spark-ignited engines. While these can be controlled during engine operation by venting the fuel tank through a carbon canister to absorb fuel vapors, vehicle refueling still usually involves a release of vapors, as capture systems are not required in most states. Evaporative emissions are best controlled by limiting the fuel's vapor pressure during warm weather.

In some parts of the United States, oxygenates are required to be added to gasoline to lower emissions. Ethanol is currently the most widely used fuel oxygenate. Methyl *t*-butyl ether (MTBE) is being rapidly phased out due to concerns about groundwater contamination resulting from fuel spills. Because of its lower oxygen requirement for combustion, ethanol decreases emissions of CO and UHC during cold starting and pe-

riods of high load. This is partially offset by higher evaporative emissions resulting from the higher vapor pressure when ethanol is blended with standard grades of unleaded gasoline.

Closed-Loop and Open-Loop Control. As described above, the pollutant species that need to be controlled from spark-ignited engines are carbon monoxide, unburned hydrocarbons, and oxides of nitrogen. It should be noted that the first two of these compounds need to have their oxidation process completed, while the third compound needs to be *unoxidized* or reduced. This conflict in objectives is what makes the simultaneous elimination of the three compounds so difficult. Completion of the oxidation process can be accomplished by providing an excess of oxygen and then passing the exhaust gas through an oxidizing catalyst such as platinum. Reducing the oxides of nitrogen requires an oxygen-poor environment and an easily oxidized compound, called a reducing agent, to assist in breaking down the nitric oxide.

Early technology to achieve simultaneous control of the three pollutants required two operations, as shown in Fig. 17.96.

The engine was operated somewhat rich so that conditions were suitable for the exhaust entering the reducing catalyst, which eliminated most of the nitric oxide. Then an air pump supplied additional air to the exhaust stream to create the oxygen-rich conditions needed by the oxidation catalyst.

Modern catalysts, called three-way catalysts, can combine the oxidation and reduction functions into a single catalyst structure but require that the air–fuel ratio be controlled precisely in a narrow band around the stoichiometric value, as shown in Fig. 17.97. Such exact control of the air–fuel ratio could not be achieved without feedback from an exhaust oxygen sensor and closed-loop electronic control of fuel injection. Figure 17.98 shows the typical configuration of an oxygen sensor that measures the fuel–air ratio in the exhaust gas, and then the engine's electronic control module adjusts the fuel injected to correspond to the air flow rate. This system maintains the air–fuel ratio entering the three-way catalyst in a narrow range around the stoichiometric ratio.

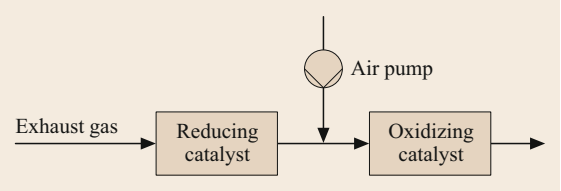

Fig. 17.96 Two-part catalytic converter

In reality, the nature of the oxygen sensor and the delay associated with the time required for changes in the air–fuel ratio to reach the oxygen sensor results in an oscillation of the air–fuel ratio around the stoichiometric condition. This oscillation between rich and lean conditions enhances the catalyst's ability to provide the oxygen-poor conditions needed to reduce the oxides of nitrogen while using oxygen stored during the periods of lean operation to eliminate carbon monoxide and unburned hydrocarbons. Recent advances in oxygen sensor technology have incorporated heaters to decrease the time needed for the sensor to reach operating temperature and wideband sensing of air–fuel ratios to provide greater flexibility in control strategies over conventional rich-lean dual state sensors.

A complementary technique for NO_x reduction is exhaust gas recirculation (EGR). This technique directs a portion of the engine's exhaust gas back to the intake where it mixes with and dilutes the incoming charge. It reduces the flame temperature and the availability of oxygen without the fuel economy penalty that would accompany the equivalent NO_x reduction from spark

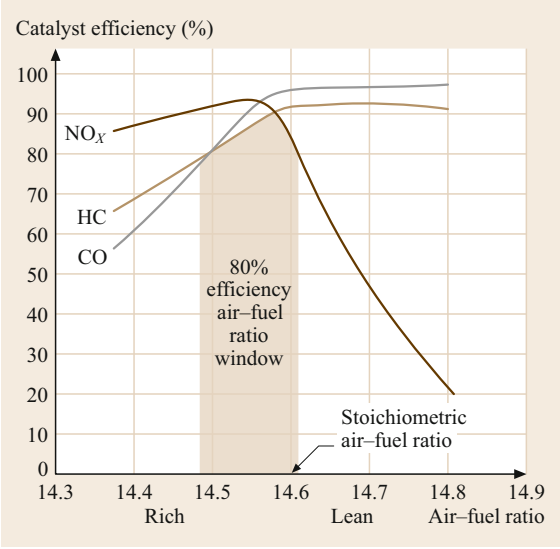

Fig. 17.97 Effect of the air–fuel ratio on a three-way catalyst (after [17.34])

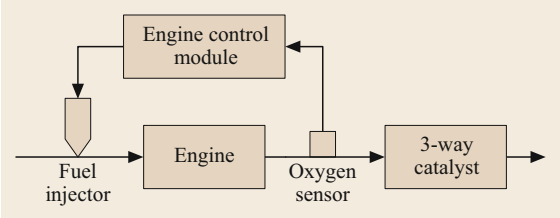

Fig. 17.98 Closed-loop engine control

timing retard. Exhaust gas recirculation is most effectively used under part-load conditions, where it allows the throttle to be more open and, thus, can actually improve fuel economy by reducing throttling losses.

Compression-Ignition (CI) Engine Emissions Characteristics

With the exception of carbon monoxide, exhaust emissions from compression-ignited engines will be strongly affected by engine operating conditions. Carbon monoxide emissions from diesel engines are always low. They tend to be limited by factors such as late-burning fuel that has insufficient time or temperature to combust completely. While more fuel is present at high load, the temperatures are lower at light load, and there is a greater availability of fuel that has mixed beyond its lean combustion limit and can, thus, only react slowly.

Unburned hydrocarbon emissions from diesel engines are primarily a light load problem. At heavy loads, the in-cylinder temperatures are high enough that the fuel readily burns to complete products. At light loads, fuel on the periphery of the fuel spray mixes with the large excess of air in the chamber and never reaches the temperature or the air–fuel ratio needed for rapid combustion. This fuel will be emitted as unburned or partially burned hydrocarbons. Engines with the greatly retarded timing needed for NO_x control may also have difficulty keeping the fuel–air mixture in the piston bowl because the piston may be well down on its expansion stroke while fuel injection is still underway. This allows the fuel–air mixture to enter the crevice above the top compression ring and evade combustion in a manner that is similar to spark-ignited engines.

As mentioned earlier, NO_x emissions are primarily dependent on in-cylinder temperatures. Since these temperatures are higher when the engine is operating at full load, the emissions of NO_x will be higher under these conditions. Diesel fuel injection timing is generally retarded to keep NO_x emissions low, in a manner that is similar to spark-timing retard in spark-ignited engines. EGR can be used very effectively to reduce NO_x in diesel engines, especially if the EGR is cooled before it is mixed with the intake air. The cooling is usually accomplished using engine coolant, so a portion of the exhaust energy is added to the engine's heat rejection load. EGR is usually accompanied by an increase in exhaust particulates.

Electronically controlled engines can vary the injection timing corresponding to speed, load, or other operating variables following detailed maps. This allows NO_x to be controlled with minimum impact on fuel economy and particulate emissions. NO_x is maximized when the fuel and air are mixed rapidly and combustion occurs near TDC. This is the condition that provides the best conditions for minimizing soot production and maximizing its subsequent oxidation. These conflicting effects give rise to the phenomenon known as the NO_x-particulate tradeoff. Those measures taken to minimize NO_x (timing retard, EGR, lower swirl, etc.) tend to increase particulates, and the converse is also true. Higher fuel injection pressures with smaller injector nozzle holes and lower intake air temperatures tend to move the NO_x-particulate tradeoff to more favorable operating points where both pollutants are reduced.

Exhaust gas recirculation can be problematic with diesel engines because the intake manifold pressure is frequently at a higher pressure than the exhaust manifold. Some systems direct the exhaust from upstream of the turbine to upstream of the compressor, which forces the exhaust gas to pass through the compressor. Other approaches use throttling to lower the pressure of the air entering the compressor so that exhaust can be drawn in from an ambient pressure source after the turbine.

Most diesel engines are equipped with turbochargers that allow demands for increased power to be met while still maintaining the air–fuel ratio at values that ensure low emissions. To meet NO_x emission standards, highly-rated engines use heat exchangers known as intercoolers or aftercoolers to reduce the temperature of the compressed air from the turbocharger compressor. Using ambient air as the exchange fluid for the intercoolers is the norm for most applications. Further improvements in engine air supply can be obtained from the use of variable geometry turbocharging. These turbochargers are equipped with variable area turbine nozzles, so the exhaust velocity entering the turbine can be optimally matched to the engine's speed and load. This provides greater intake air boost pressures over a wider range of operating conditions. However, this combination of high boost pressures and relatively low air mass (displaced by EGR) places the turbocharger operating point close to its surge line (where compressor performance and efficiency falls dramatically). The use of low pressure EGR is becoming more common to provide the necessary boost pressure and air–fuel ratio that modern low NO_x applications require. Low pressure EGR takes exhaust gas from downstream of the turbine and introduces it at the compressor inlet, thereby increasing the mass flows through the turbocharger system and improving system efficiency. This system is naturally more challenging to package and control due to the increased size and trapped volumes. Low-pressure EGR is usually used in combination with a high-pressure (from the exhaust manifold to the intake manifold) EGR loop, due to the different operating ranges where each provide benefits.

Diesel engines cannot use the three-way catalyst technology that is used for spark-ignited engines because diesel engines always operate with excess air, and it is difficult to reduce NO_x under lean conditions. Recent developments in catalyst technology have produced lean NO_x catalysts, but their low efficiency has limited their acceptance. Catalytic systems that absorb the NO_x and then periodically release it as harmless gases when the engine is momentarily operated rich have been more successful and may be used in the near future. Emissions-reduction durability with new catalyst concepts are often critical because catalysts are required to perform over a vehicle's useful lifetime. A catalyst that degrades by over 50% in useful life must, therefore, be overdesigned as needed to accommodate the shift, adding cost, weight, and packaging considerations.

Urea-based selective catalytic reduction (SCR) systems have proven to be exceptionally effective in reducing tailpipe NO_x emissions to levels even above 98% effectiveness. However, current catalyst formations do not perform until the exhaust temperature exceeds the *light-off* temperature of approximately 250 °C. The resulting emissions during the cold start phase of emissions test cycles can exceed the standard even before the catalyst reaches this state. As such, extensive efforts are made to rapidly heat up the exhaust to achieve catalyst light-off as quickly as possible. These efforts usually involve engine measures such as retarded combustion phasing, intake air throttling, and additional post injections of fuel. These measures are usually associated with an increase in fuel consumption, presenting a new tradeoff that must be carefully considered.

Particulate matter emissions (commonly referred to as smoke) have historically given diesel engines a bad reputation. DPFs have been extremely effective in reducing tailpipe emissions, even allowing OEM's (original equipment manufacturer) to shift the operating point on the NO_x/PM tradeoff to achieve additional NO_x reduction.

To clean out, or regenerate the DPF, two methods are commonly used. The first method is to use a late post injection, injecting fuel into the combustion chamber late in the cycle to effectively provide unburnt hydrocarbons to the oxidation catalyst. The exothermic reaction provides the necessary temperatures for DPF regeneration. There exists a practical limit to how much fuel can be injected via late post injection. Too much fuel results in wetting of the cylinder walls, which leads to unacceptable dilution of the engine oil. Larger diesel engines do not use late post injection for this reason. The second method is to employ an extra fuel injector in the exhaust system, upstream of the oxidation catalyst. This hydrocarbon injector is very effective, however, it adds cost and complexity over using post injections.

17.4.10 Selected Examples of Combustion Engines

PC Diesel Engines

The further development of the BMW Twin Turbo Technology (BMW 535d) led to a six-cylinder diesel engine with four turbochargers; the high-pressure TC (turbochargers) are controlled by VTG (variable turbine geometry). The engine's rated output is 296 kW (98 kW/L), and the maximum torque achieved is

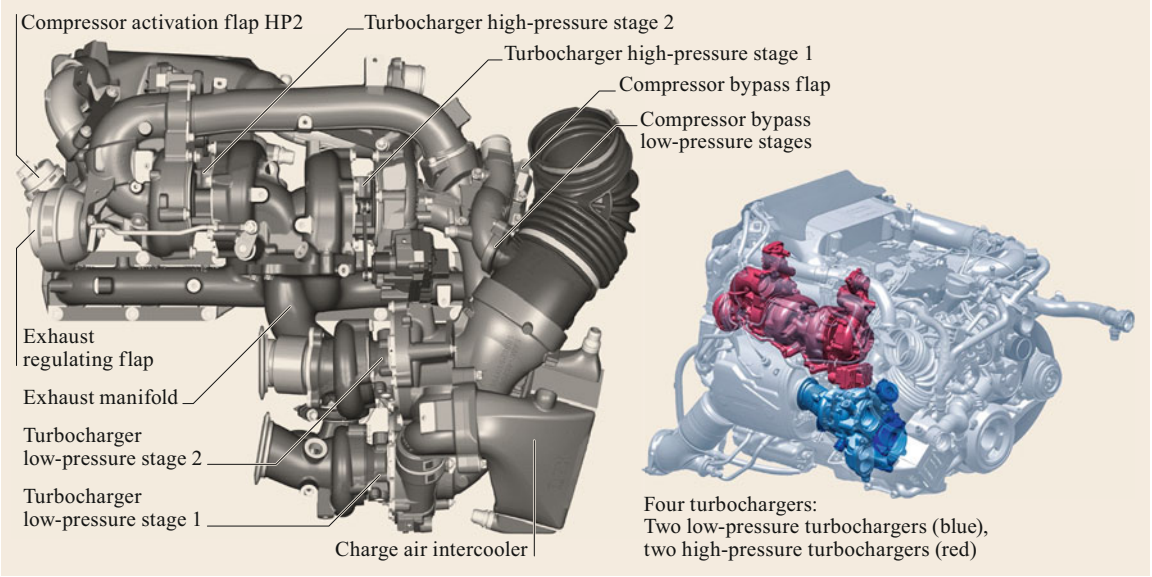

Fig. 17.99 Six-cylinder BMW diesel engine with four turbochargers (© BMW)

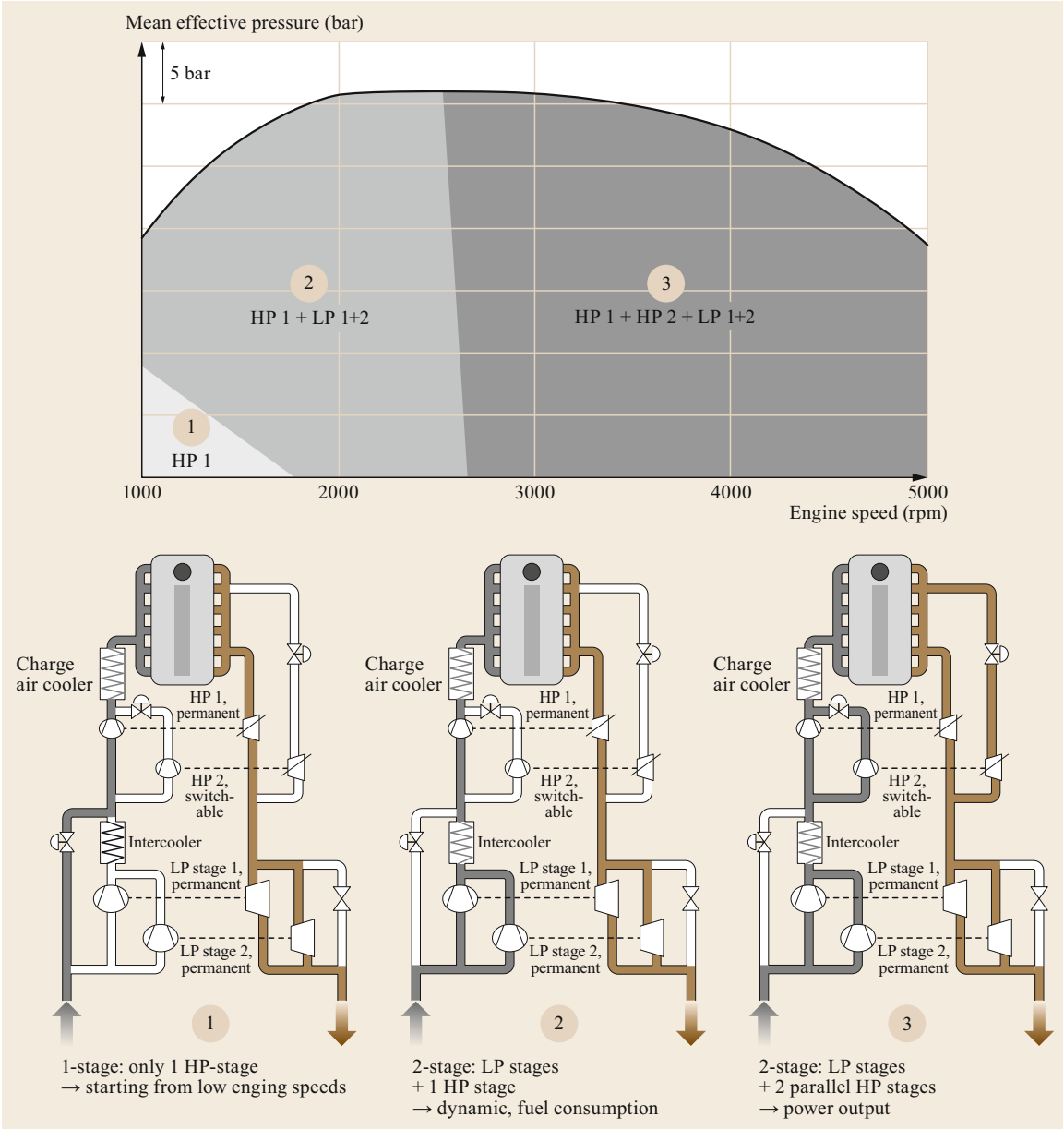

Fig. 17.100 Dynamic operating behavior (© BMW)

760 Nm. The maximum cylinder pressure rises up to 210 bar, and the injection pressure is up to 2500 bar (Figs. 17.99 and 17.100) [17.35].

Mercedes-Benz started a new diesel engine family with the OM 654 (Fig. 17.101 and 17.102 [17.36]).

Gasoline Engines

Figures 17.103 and 17.104 show the engine modules of the VW EA211-evo-engine family and the effect of turbocharging with VTG with benfit at the low-end-torque area. This is a four-cylinder DI gasoline engine with 1.5 L displacement, and 96 or 110 kW power output. The maximum torque achieved is 200 and 250 Nm, the compression ratio is 12.5 at lower power and 10.5 in the maximum power application [17.37].

Diesel Engine for Heavy-Duty Pickups

With 385 HP, the Cummins 6.7 L Turbo Diesel is one of the most powerful engines available for the pickup truck market (Fig. 17.105). Available as the engine in

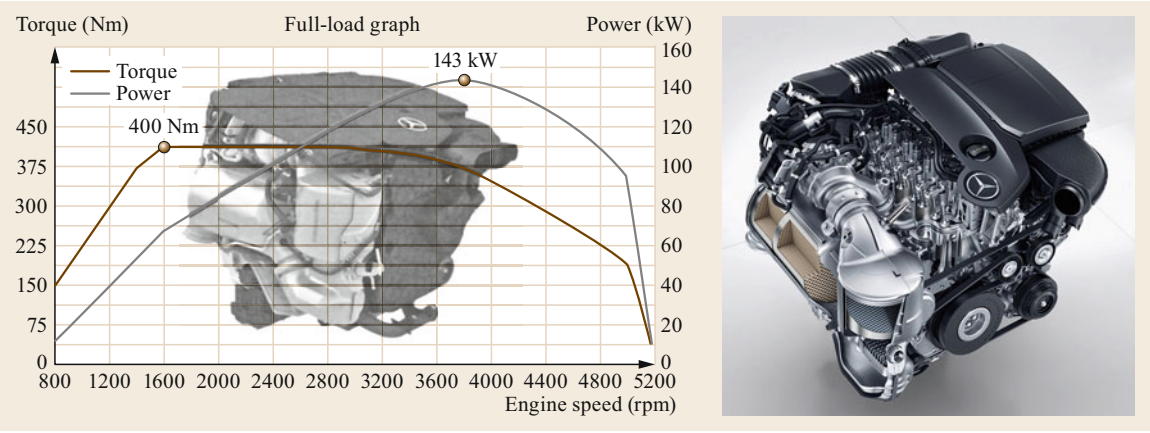

Fig. 17.101 Four-cylinder Mercedes-Benz diesel engine OM 654 (© Daimler)

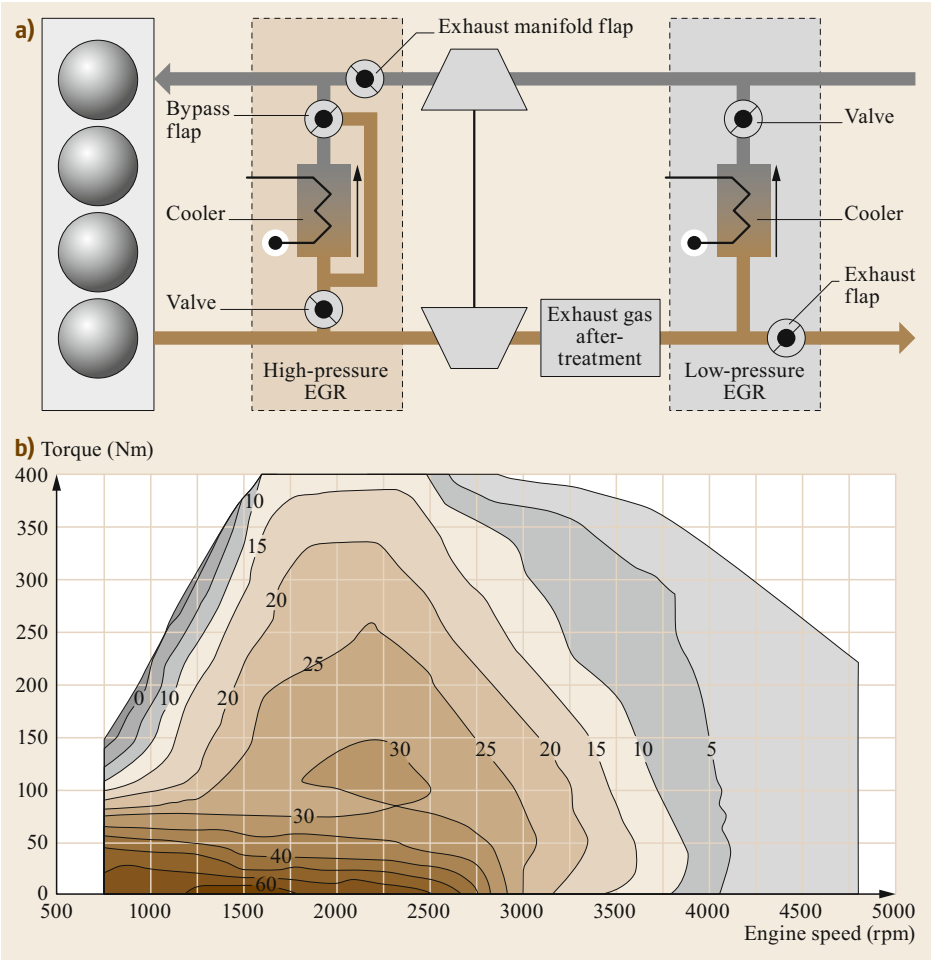

Fig. 17.102 **(a)** OM 654 EGR systems and **(b)** overall EGR rates (in %) (© Daimler)

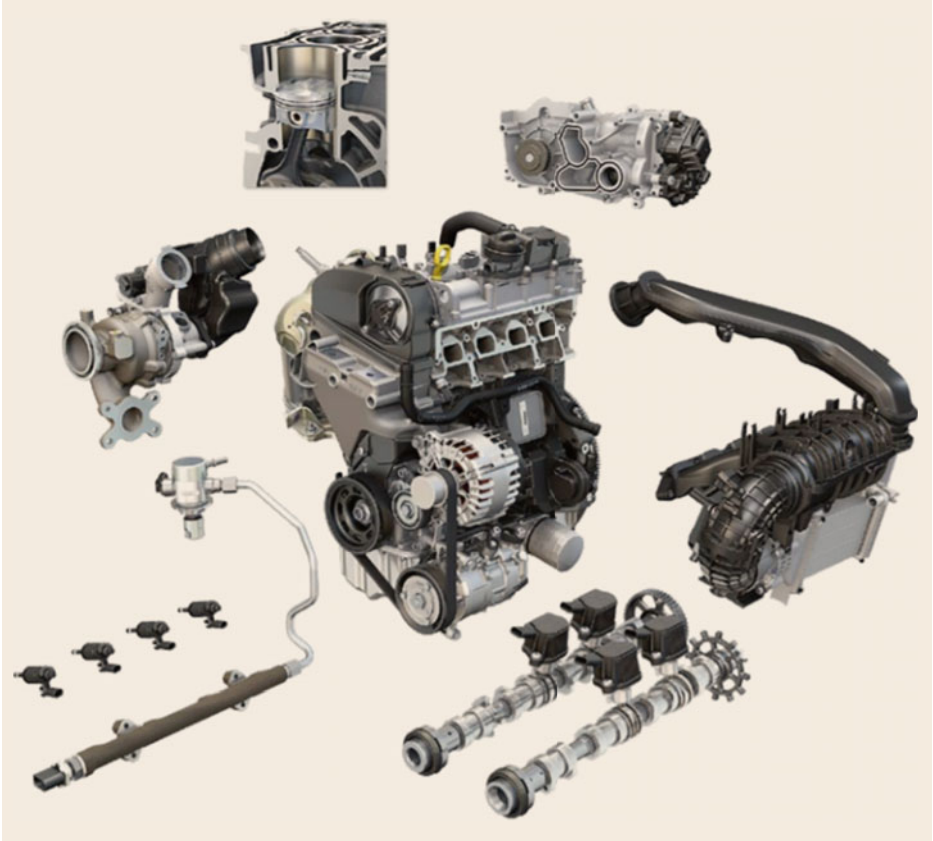

Fig. 17.103 Engine modules from the EA211 evo engine family (© Volkswagen)

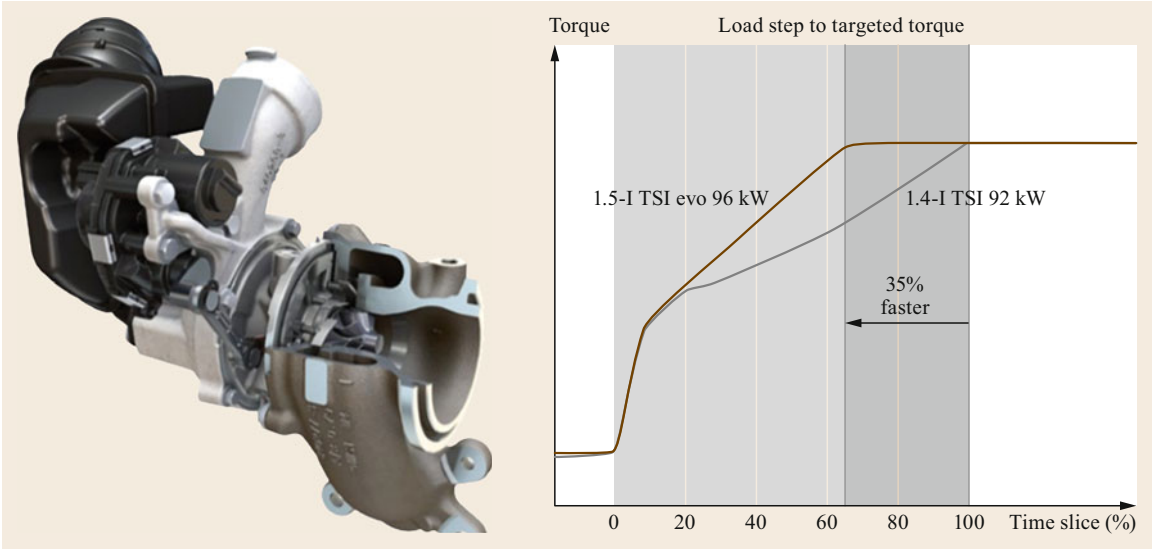

Fig. 17.104 Cut-away view of turbocharger with VTG and comparison of torque buildup between EA211 and EA211 TSI evo (© Volkswagen)

Fig. 17.105 Cummins 6.7 L Turbo Diesel

Fig. 17.106 Six-cylinder Navistar MaxxForce 13 heavy-duty engine for on-highway vehicles

the Dodge Ram heavy-duty pickup, this diesel engine generates a peak torque of up to 1220 Nm (900 ft lb).

Diesel Engine for Heavy-Duty On and Off-Highway

Figure 17.106 shows an example of a heavy-duty engine used in on-highway line-haul trucks.

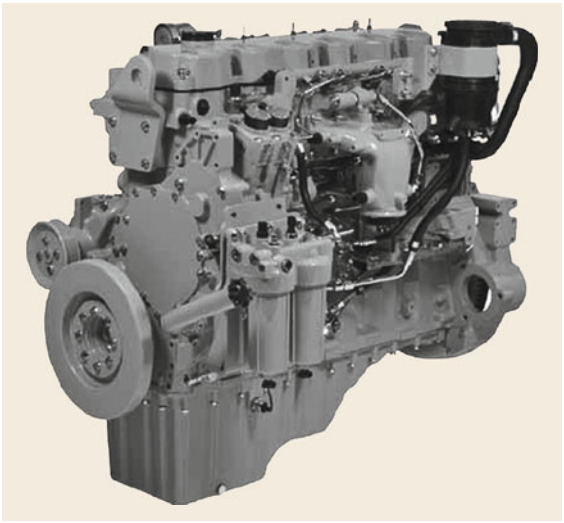

Fig. 17.107 Six-cylinder CAT® heavy-duty industrial diesel engine

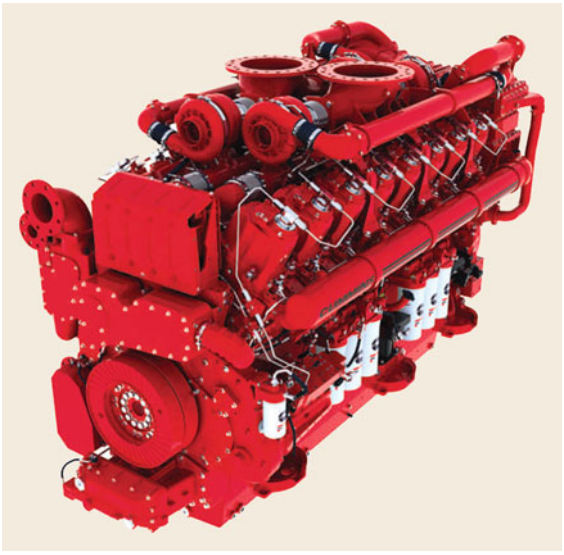

Fig. 17.108 Eight-cylinder Cummins QSK 95 large diesel engine for power generation of locomotives and marine applications

An example of a heavy-duty industrial engine used in construction equipment like wheel loaders, graders, and excavators is shown in Fig. 17.107. It is also used in power generation, water pumps, and forestry equipment.

Figures 17.108 and 17.109 show examples of a large engine used in power generation, locomotives, and marine.

Fig. 17.109 12-cylinder GE GEVO large diesel engine used in primarily in locomotives but also in power generation and marine applications

References

17.1 W. Eifler, E. Schlücker, U. Spicher, G. Will: *Kütt-ner Kolbenmaschinen*, 7th edn. (Vieweg+Teubner, Wiesbaden 2009), in German

17.2 H.T. Wagner, K.J. Fischer, J.D. von Frommann: *Strömungs- und Kolbenmaschinen*, 3rd edn. (Vieweg, Wiesbaden 1993), in German

17.3 H. Tschöke: *Vorlesungsskript Grundlagen Kolbenmaschinen* (Otto-von-Guericke-Universität, Magdeburg 2010), in German

17.4 K.-H. Grote, J. Feldhusen (Eds.): *Dubbel Taschenbuch für den Maschinenbau*, 24th edn. (Springer, Heidelberg, Berlin 2014), in German

17.5 V. Küntscher: *Kraftfahrzeugmotoren – Auslegung und Konstruktion*, 3rd edn. (Verlag Technik, Berlin 1995), in German

17.6 H. Grohe: *Otto- und Dieselmotoren*, 10th edn. (Vogel, Würzburg 1992), in German

17.7 R. van Basshuysen, F. Schäfer: *Lexikon Motortechnik – Der Verbrennungsmotor von A–Z*, 2nd edn. (Vieweg, Wiesbaden 2006), in German

17.8 KWW Crane GmbH: *DEPA-Druckluft-Membranpumpen* (CPFT, Düsseldorf 2005), in German

17.9 Crane Co.: DPEA® Air-operated double diaphragm pumps-brochure (EMEA), https://www.cranecpe.com/chem-energy/de/products/pumps/air-operated-diaphragm-pumps/depa-air-operated-diaphragm-pumps-cast-metal-pumps-series-m (2017)

17.10 Ponndorf Gerätetechnik GmbH: *Hose Pumps* (Ponndorf, Kassel 2005), http://www.ponndorf.de

17.11 G. Vetter: *Pumpen* (Vulkan, Essen 1992), in German

17.12 Alpha Laval Bran Lübbe GmbH: *Diaphragm Metering Pumps* (Bran Lübbe, Norderstedt 2005), http://www.bran-luebbe.de

17.13 W. Hinze: *Kolbenpumpen und -verdichter, Bildsammlung zur Vorlesung* (Technische Hochschule Magdeburg, Institut für Kolbenmaschine und Maschinenlaboratorium (IKM), Magdeburg 1990), in German

17.14 R. Prager: *Technisches Handbuch Pumpen*, 7th edn. (Verlag Technik, Berlin 1987), in German

17.15 LEWA Herbert Ott GmbH: *ecoflow – Die innovativen Dosierpumpen* (LEWA, Leonberg 2005), in German, http://www.lewa.de

17.16 Eckerle Industrie Elektronik GmbH: *Internal Gear Pumps* (Eckerle, Malsch 2006), http://www.eckerle.com

17.17 R. Neumaier: *Rotierende Vedrängerpumpen* (Lederle Hermetic, Gundelfingen 1991), in German, http://www.hermetic-pumpen.com

17.18 Kräutler GmbH: *Screw Pumps Series M* (Kräutler, Lustenau 2006), http://www.kral.at

17.19 Netzsch-Mohno GmbH: *Nemo®-Pumpen* (Netzsch, Waldkraigburg 2006), in German, http://pumpen.netsch.com

17.20 K. Reif: *Einspritzsysteme für Ottomotoren* (Vieweg, Wiesbaden 2015), in German

17.21 Johnson Pumpen GmbH: *Impeller Pumps* (Johnson Pumpen, Löhne 2006), global.johnson-pump.com

17.22 R. van Basshuysen, F. Schäfer (Eds.): *Internal Combustion Engine Handbook* (SAE International, Warrendale 2016)

17.23 M. Urich, B. Fisher: *Holley Carburetors and Manifolds* (HP, New York 1987)

17.24 K. Reif (Ed.): *Gasoline Engine Management Systems and Components* (Vieweg, Wiesbaden 2015)

17.25 R. von Basshuysen (Ed.): *Gasoline Engine with Direct Injection* (Vieweg, Wiesbaden 2009)

17.26 H. Tschöke, K. Mollenhauer, R. Maier (Eds.): *Handbuch Dieselmotoren*, 4th edn. (Vieweg, Wiesbaden 2018), in German

17.27 K. Reif (Ed.): *Diesel-Engine Management Systems and Components* (Vieweg, Wiesbaden 2015)

17.28 R. von Basshuysen (Ed.): *Natural Gas and Renewable Methan for Powertrains* (Springer, Wiesbaden 2015)

17.29 R. Bosch GmbH: *Ignition Systems for Gasoline Engines* (Bosch, Stuttgart 2003)

17.30 K. Reif (Ed.): *Zündsysteme für Ottomotoren* (Vieweg, Wiesbaden 2015), in German
17.31 R. Bosch GmbH: *Automotive Handbook*, 9th edn. (Society of Automotive Engineers, Warrendale 2014)
17.32 California Energy Commission: A student's guide to alternate fuel vehicles, http://www.energyquest.ca.gov/transportation/index.html (2006)
17.33 National Research Council: *Rethinking the Ozone Problem in Urban and Regional Air Pollution* (National Academy, Washington 1991)
17.34 J.T. Kummer: Catalysts for automobile emissions control, Prog. Energy Combust. Sci. **6**, 177–199 (1980)
17.35 F. Steinparzer, P. Nefischer, D. Hiemesch, E. Rechberger: The new BMW six-cylinder top engine with innovative turbocharging concept, MTZ Worldwide **77**(10), 38–45 (2016)
17.36 T. Eder, P. Lückert, M. Kemmner, H. Sass: OM 654 – launch of a new engine family by Mercedes-Benz, MTZ Worldwide **77**(3), 60 (2016)
17.37 W. Demmelbauer-Ebner, K. Persigehl, M. Görke, E. Werstat: The new 1.5-l four-cylinder TSI engine from Volkswagen, MTZ Worldwide **78**(2), 16 (2017)

Helmut Tschöke
Institute of Mobile Systems
Otto-von-Guericke University
Magdeburg, Germany
helmut.tschoeke@ovgu.de

Helmut Tschöke was a Professor of Reciprocating Machines at the University of Magdeburg from 1995 to 2011. Before that he worked with Bosch Diesel Division, where he was responsible for the development and production of distributor and inline pumps. He is an active member of VDI and member of SAE, and was the Head of the Automotive Research Program at the University of Magdeburg. He is currently a consultant.

Vince Piacenti
Powertrain Solutions
Bosch LLC
Farmington Hills, MI, USA
vince.piacenti@us.bosch.com

Vince Piacenti received his BS degree in Mechanical Engineering from Bradley University in 1976. He spent 7 years at Bosch's Headquarters in Stuttgart, Germany, working on diesel fuel injection. He is currently a Senior Manager at Bosch in Michigan, responsible for diesel hydraulic systems integration and engineering methods. He has experience in all forms of diesel fuel injection.

Brent Keppy
PS/ECW1-NA
Robert Bosch LLC
Waterford, MI, USA
brent.keppy@us.bosch.com

Brent Keppy is Manager of Powertrain Systems Engineering at Robert Bosch LLC in Michigan, USA. His responsibilities include diesel combustion development, and other advanced powertrain technologies for commercial vehicles. He received a BS in Agricultural Engineering, Power and Machinery from Iowa State University in 1994 and has been involved in diesel engine development since that time.

Aneel Singh
Powertrain Solutions
Robert Bosch, LLC
Farmington Hills, MI, USA
aneel.singh@us.bosch.com

Aneel Singh received his BS degree in Mechanical Engineering from the University of Michigan in 2015. He specialized in manufacturing systems and also pursued additional studies in multidisciplinary design. He has since worked at Bosch in Michigan as an Application Design Engineer, responsible for the design and development of turbocharger applications.

Justin Kern
West Bloomfield, MI, USA
steve.white@us.bosch.com

Justin Kern is a systems engineer at Robert Bosch LLC and has worked on engine controls and calibration for advanced powertrains. He is currently supporting commercial vehicle advanced powertrain projects, including alternative fuels and electric drive systems.

Jon Van Gerpen
Powertrain Solutions
Robert Bosch LLC
Farmington Hills, MI, USA
justin.kern@us.bosch.com

Jon Van Gerpen has been Professor and Department Head of Biological and Agricultural Engineering at the University of Idaho since July 2004. Before that he was a Professor of Mechanical Engineering at Iowa State University for 20 years. He received his PhD degree from the University of Wisconsin-Madison in 1984. His current research interests include the production and utilization of biofuels and the development of a nationwide biodiesel education program.

18. Pressure Vessels and Heat Exchangers

Ajay Mathur, Hamidreza Najafi

This chapter presents an overview of pressure vessels and heat exchangers and covers basic design concepts, loadings, and testing requirements relevant to such equipment. The principles of thermal design as well as mechanical design criteria, fabrication, testing, and the certification requirements of various standards/codes adopted in different countries are discussed on a comparative basis to bring out the similarities between their features.

To complete this overview, a brief discussion is also provided on commonly used construction materials and their welding practices along with updates on ongoing developments in this area.

18.1 **Pressure Vessels – General Design Concepts** 753
18.1.1 Thin-Shell Pressure Vessels 753
18.1.2 Thick-Walled Pressure Vessels 755
18.1.3 Heads 755
18.1.4 Conical Heads 756
18.1.5 Nozzles 756
18.1.6 Flanges 756
18.1.7 Loadings 756
18.1.8 External Local Loads 756
18.1.9 Fatigue Analysis 757
18.2 **Design of Tall Towers** 757
18.2.1 Combination of Design Loads 757
18.2.2 Wind-Induced Deflection 758
18.2.3 Wind-Induced Vibrations 758
18.3 **Testing Requirements** 758
18.3.1 Nondestructive Testing (NDT) 758
18.3.2 Destructive Testing of Welds 759
18.4 **Design Codes for Pressure Vessels** 759
18.4.1 ASME Boiler and Pressure Vessel Code 759
18.4.2 PED Directive and Harmonized Standard EN 13445 760
18.4.3 PD 5500 760
18.4.4 AD Merkblätter 762
18.5 **Heat Exchangers** 763
18.5.1 Thermal Design 766
18.5.2 Mechanical Design 769
18.6 **Construction Materials** 769
18.6.1 Carbon Steel 769
18.6.2 Low-Alloy Steel 770
18.6.3 NACE Standards 770
18.6.4 Comparative Standards for Steel 771
18.6.5 Stainless Steel 771
18.6.6 Ferritic and Martensitic Steels 773
18.6.7 Copper- and Nickel-Based Alloys 774
References 776

18.1 Pressure Vessels – General Design Concepts

Pressure vessels are closed structures, commonly in the form of spheres, cylinders, cones, ellipsoids, toroids, and/or combination thereof, and which contain liquids or gases under pressure. There are various other requirements such as end closures, openings for inlet/outlet pipes, internal/external attachments for support, and other accessories.

18.1.1 Thin-Shell Pressure Vessels

When the thickness of the vessel is less than about one-tenth of its mean radius, the vessel is called a thin-walled vessel and the associated stresses resulting from the contained pressure stress are called membrane stresses. The membrane stresses are assumed to be uniform across the vessel wall and act tangential to its surface.

Vessels Under Internal Pressure

The membrane stresses due to internal pressure can be derived from the application of equilibrium conditions to an appropriate element cut from the vessel shell, which in turn is considered as a *symmetrically loaded shell of revolution*. Figure 18.1 shows the resulting membrane stress for a thin-walled cylindrical shell, in both the axial axis (called the *meridional* stress) and circumferential direction (also called the *hoop stress*); the corresponding formulae are presented in Table 18.1. It can be seen that the thickness of the cylindrical vessel can be deter-

K.-H. Grote, H. Hefazi (Eds.), *Springer Handbook of Mechanical Engineering*, Springer Handbooks,
https://doi.org/10.1007/978-3-030-47035-7_18

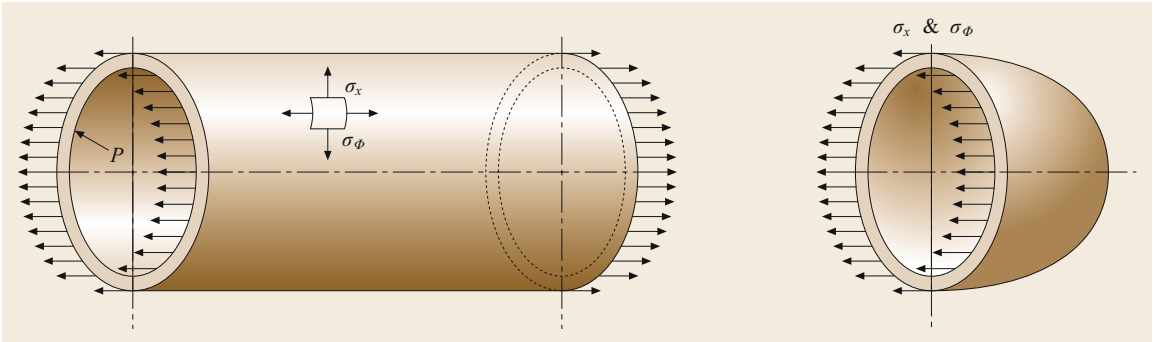

Fig. 18.1 Cylindrical shell with hemispherical heads

Table 18.1 General vessel formulae

Part		Stress formula	Thickness d	
			Inside radius	Outside radius
Shell	Longitudinal direction	$\sigma_x = \frac{PR_m}{2d}$	$\frac{PR_i}{2SE+0.4P}$	$\frac{PR_o}{2SE+1.4P}$
	Circumferential stress	$\sigma_\Phi = \frac{PR_m}{d}$	$\frac{PR_i}{SE-0.6P}$	$\frac{PR_o}{SE+0.4P}$
Heads	Hemisphere longitudinal stress = circumflex stress	$\sigma_x = \sigma_\Phi = \frac{PR_m}{2d}$	$\frac{PR_i}{2SE-0.2P}$	$\frac{PR_o}{2SE+0.8P}$
	Ellipsoidal		$\frac{PD_iK}{2SE-0.2P}$	$\frac{PD_oK}{2SE+2P(K-0.1)}$
	2:1 semiellipsoidal		$\frac{PD_i}{2SE-0.2P}$	$\frac{PD_o}{2SE+1.8P}$
	100%–6% torispherical		$\frac{0.885PL_i}{SE-0.1P}$	$\frac{0.885L_o}{SE+0.8P}$
	Torispherical $L/r < 16.66$		$\frac{PL_iM}{2SE-0.2P}$	$\frac{PL_oM}{2SE+P(M-0.2)}$
Cone	Longitudinal	$\sigma_x = \frac{PR_m}{2d\cos\alpha}$	$\frac{PD_i}{4\cos\alpha(SE+0.4P)}$	$\frac{PD_o}{4\cos\alpha(SE+1.4P)}$
	Circumferential	$\sigma_\Phi = \frac{PR_m}{2d\cos\alpha}$	$\frac{PD_i}{2\cos\alpha(SE-0.6P)}$	$\frac{PD_o}{2\cos\alpha(SE+0.4P)}$

mined based on the hoop stress, which is governing since its value is twice that of the meridional stress.

In the case of a spherical shell, the circumferential stress is identical in all directions and its magnitude is half the hoop stress of a cylinder of the same radius.

Because a thin shell is assumed to offer no resistance to bending, radial stresses, if present, are small compared with the membrane stresses and are generally ignored. This implies that thin-shell analysis considers only biaxial stresses and therefore follows the *maximum stress theory*, wherein stress failure depends on the numerical magnitude of the principal stresses, ignoring stresses in other directions.

Vessels Under External Pressure

Thin-walled vessels under external pressure fail at stresses much lower than the yield strength due to the instability of the shell. In addition to the physical properties of the construction material at the operating temperature, the principal factors governing the instability and critical (collapsing) pressure P_c are geometrical, namely the unsupported shell length L, the shell thickness t, and the outside diameter D_o. The solution to the theoretical elastic formula for the critical pressure at which a cylinder will collapse under external pressure depends on the number of lobes at collapse, which is a cumbersome exercise. To eliminate this dependence on the number of lobes, American Society of Mechanical Engineers (ASME) codes have adopted a simplified procedure using geometric charts developed for the critical stress ratio $(v/s)(L/D_o)$ for different values of the D_o/t ratio. This critical stress ratio in turn is related to the collapsing ratio for a particular material given in another chart, thus an estimate

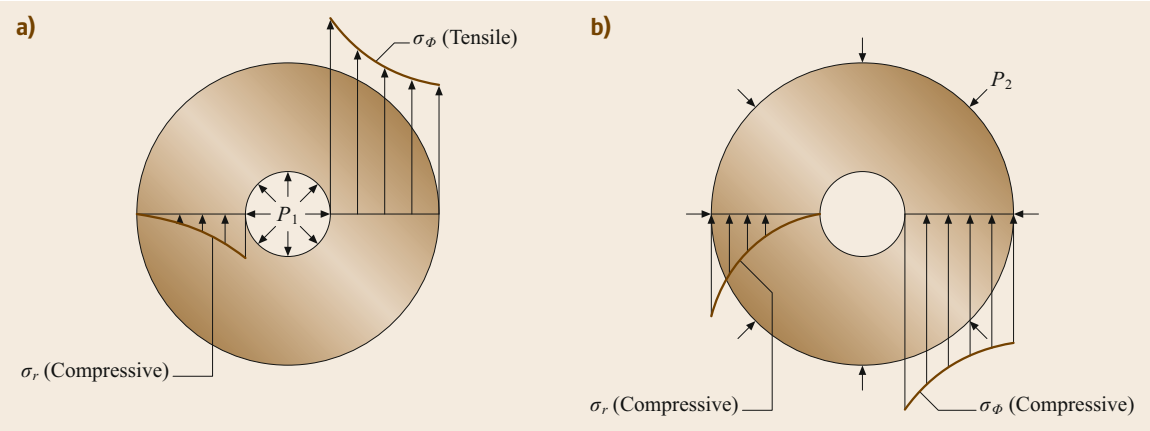

Fig. 18.2a,b Stress distribution for a thick shell under **(a)** internal pressure, **(b)** external pressure

for the maximum allowable pressure can be obtained for a given geometry. Several trials can be carried out to achieve an optimum solution for the shell thickness and the maximum unsupported length (or stiffener spacing) for a given external pressure.

18.1.2 Thick-Walled Pressure Vessels

The membrane stresses used to analyze thin shells cannot be used for thick-walled vessels (with thickness greater than their mean radius) subjected to internal pressure, since the radial stresses are significant and the stress distribution in the vessel walls varies through their thickness. The stress distributions through the thickness for a vessel for internal and external pressure conditions are shown in Fig. 18.2a,b.

From Fig. 18.2, it is evident that the maximum circumferential stress occurs at the inner surface of the cylinder, but it is tensile in nature for internal pressure conditions and compressive in the case of external pressure. As per Lamé's solution,

$$\sigma_\Phi = (+)\frac{PR_\mathrm{i}^2}{R_\mathrm{o}^2 - R_\mathrm{i}^2}\left(1 + \frac{R_\mathrm{o}^2}{R_\mathrm{i}^2}\right), \tag{18.1}$$

$$\sigma_r = (-)\frac{PR_\mathrm{i}^2}{R_\mathrm{o}^2 - R_\mathrm{i}^2}\left(1 - \frac{R_\mathrm{o}^2}{R_\mathrm{i}^2}\right), \tag{18.2}$$

the magnitude of the stress for a thick-walled vessel is a function of the ratio of the outer to inner radii.

Prestressing is a manufacturing technique by which compressive stresses are introduced into the inside shell of a multilayer/multiwall vessel and/or tensile stresses are created on the outside shell of this vessel operating under internal pressure. Such prestresses help to neutralize the peaks in the typical stress distribution, making the material stress almost uniform through the thickness, as shown in Fig. 18.3. This also considerably reduces the required wall thickness.

Prestressing can be carried out using the following methods:

- Shrink-fitting outer layers over the core, inner layer(s)
- Wire/coil wrapping
- Autofrettage.

A detailed introduction to the basic theory of membrane stress and its application to commonly encountered elements of pressures vessels is presented in [18.1]. However, a brief discussion on other vessel components such as heads, nozzles, and flanges is presented below.

18.1.3 Heads

There are three general categories of heads (also called dished ends):

Hemispherical: These dished ends are analyzed as the thin-walled spherical shells discussed above.

Ellipsoidal: Ellipsoidal heads are formed by the rotation of a semiellipse with a 2 : 1 ratio of major

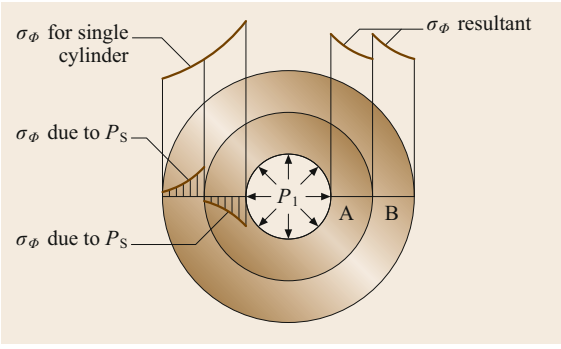

Fig. 18.3 Resultant stresses in a shrink-fit multiwall vessel

R to minor axis h. These heads are the most frequently used end closures in vessel design, particularly for internal pressures greater than 10 bar and also for bottom heads of tall, slender columns.

Torispherical: Torispherical heads have a meridian formed of two circular arcs, a knuckle section with radius r, and a spherical crown segment with a crown radius of L. The maximum crown radius equals the inside diameter, which results in the same maximum membrane stress in the crown region as in the cylindrical region. The minimum knuckle radius is 6% of the crown radius, although a 10% knuckle is the most commonly used.

18.1.4 Conical Heads

A conical head is generated by the rotation of a straight line intersecting the axis of rotation at an angle, α, which is the half-apex angle of the formed cone.

Formulae for computing the thickness of different types of heads under both internal and external pressure are provided in Table 18.1.

There is a failure phenomenon in the knuckle region due to tangential stress under compression, which can occur through elastic buckling (circumferential wrinkles) at a stress much lower than the yield strength or through plastic buckling. A reliable analysis method for predicting such buckling failure was introduced in the harmonized pressure vessel standard EN 13445, which is discussed below.

18.1.5 Nozzles

Nozzles or openings are provided in pressure vessels to satisfy certain process requirements such as inlet or outlet connections, manholes, hand holes, vents and drains, etc. These may be located on the shell or head according to the functional requirements and can be circular, elliptical, or rectangular in shape. The basic construction of a nozzle connection essentially consists of short pieces of pipes welded to the vessel wall at an opening made in the wall. The other side is normally a flanged end suitable for connection to the corresponding piping or to bolt on the blind cover (as in the case of a manhole). The complete nozzle may also be formed by rolling or forging to the required shape.

In addition to weakening the vessel wall, the nozzle opening also causes discontinuity in the wall and creates stress concentrations at the edges of the opening. This can be compensated by providing reinforcement pads around the nozzle necks, which are suitably attached to the vessel wall. Rules are provided in each pressure vessel code to calculate the reinforcement requirement for all nozzles. At times, additional thickness is provided at the base of the nozzle wall itself; such nozzles are called self-reinforced nozzles.

18.1.6 Flanges

Tall columns are usually constructed in detachable sections for ease of fabrication, transportation, erection, assembly, and internal maintenance. Like nozzles and the piping system, these sections (or heads) must be provided with end flanges with an arrangement for easy bolting and dismantling as required. A flanged joint therefore consists of a pair of flanges; each is attached to one of the components to be joined and is held securely in place by a series of bolts or studs. A gasket is interposed between the two adjoining flange faces. The joint must retain structural integrity with (zero) minimum leakage during service. Several flange configurations using various construction materials and a large variety of gaskets are available; the selection is mainly dependent upon the service requirements.

The main considerations for the design of a flanged joint are:

1. Ensuring a positive contact pressure at the gasket–flange interface to prevent leakage in service. The gasket must be able to withstand the required sealing force.
2. Provision of the gasket sealing force by bolt tightening but without overstressing.
3. Ensuring the structural integrity of the flange sections and minimizing flange deflections.

18.1.7 Loadings

Loadings or forces are the *causes* of stress in pressure vessels. It is important to identify the areas *where* and the times *when* these forces are applied to pressure vessels. The stresses produced by these loads, which could be *general* or *local*, are additive and define the overall stress state in the vessel or its components. The combined stresses are then compared with the allowable stress defined in the pressure vessel code.

An outline of the various categories and types of loadings is summarized in Tables 18.2 and 18.3, respectively.

18.1.8 External Local Loads

Stresses caused by external local loads at the points of attachment to the vessel must be assessed to keep them within prescribed limits. These loads are usually significant at nozzles, the vessel support region, brackets, lifting lugs, and saddle supports for horizontal vessels. Since the contact area of such attachments is relatively small compared with the vessel area, a simplified form

Table 18.2 Categories of loadings

General loads	Local loads
General loads are applied more or less continuously across a vessel section	Local loads are due to reactions from supports, internal components, attached piping, and equipment such as mixers, platforms, etc.
Examples	
Pressure loads – internal or external pressure (design, operating, hydrotesting, and hydrostatic head of liquid) Moment loads – due to wind, seismicity, erection, and transportation Compressive/tensile loads – due to dead weight, installed equipment, ladders, platforms, insulation, piping, and vessel contents Thermal loads – skirt head attachment	Radial load – inwards or outwards Shear load – longitudinal or circumferential Torsional load Tangential load Moment load – longitudinal or circumferential Thermal loads

Table 18.3 Types of loadings

Steady loads	Nonsteady loads
These loads are long term and continuous	These loads are short term and variable
Examples	
Internal/external pressure Dead weight Vessel contents Loading due to attached piping and equipment Loading to and from vessel supports Thermal loads Wind loads	Shop and field hydrotesting Earthquakes Erection Transportation Failures, emergencies Thermal loads Startup, shutdown

of the interface force distribution between the vessel and support is assumed. This analysis is based on elastic stress analysis, and stress categorization is used to compare the resultant stresses.

This approach is used in annexure G of the PD 5500 code and in the Welding Research Council (WRC) bulletins WRC 107 and 297 used in the design of the ASME code. In 1991, the WRC published another bulletin, WRC 368, for the evaluation of shell and nozzle stresses due to internal pressure.

The analytical solution for evaluating localized stresses in the shell wall above saddle supports for a horizontal vessel is based on the method developed by Zick and published in 1951.

The method used in the harmonized standard EN 13445-3 (clause 16) for evaluating nozzle loads is based on limit load analysis. This standard provides separate rules for calculating line loads for lifting eyes, supporting brackets, and saddle supports.

18.1.9 Fatigue Analysis

Vessels undergoing cyclic service and repeated loading may fail in fatigue due to progressive fracture of localized regions. The behavior of metals under such fatigue conditions varies significantly from the normal stress–strain relationship. Damage accumulates during each loading cycle and develops at localized regions of high stress until subsequent repetitions finally result in visible cracks, which grow, join, and spread.

Localized stresses at abrupt changes in section such as at the head junction or a nozzle opening, misalignment, defects during fabrication, and thermal gradients are probable causes of fatigue failure. Special attention should be paid to manufacturing tolerances, nondestructive testing, and in-service inspection of vessels designed for fatigue.

All pressure vessel codes have established specific criteria for determining when a vessel must be designed for fatigue. Each code has adopted a methodology for carrying out fatigue analysis based on the use of fatigue curves obtained from test specimens. The fatigue design rules of some of the pressure vessel codes are discussed below.

18.2 Design of Tall Towers

18.2.1 Combination of Design Loads

The shell thickness of tall columns as computed based on internal or external pressure is not usually sufficient to withstand the combined stresses produced by the operating pressure plus weight, and wind or seismic loads. Combined stresses in the longitudinal direction σ_L due to the pressure P, dead weight W, and applied moment M, with W and M taken at the elevation under consideration, are calculated as follows:

1. On the windward side

$$\sigma_L = \left(\frac{PD}{4d}\right) + \left(\frac{4M}{\pi D^2 d}\right) - \left(\frac{W}{\pi D d}\right), \qquad (18.3)$$

$$d = \frac{\left[\left(\frac{PD}{4}\right) + \left(\frac{4M}{\pi D^2}\right) - \left(\frac{W}{\pi D}\right)\right]}{\text{allowable stress}}. \qquad (18.4)$$

2. On the leeward side

$$\sigma_L = \left(\frac{PD}{4d}\right) - \left(\frac{4M}{\pi D^2 d}\right) - \left(\frac{W}{\pi D d}\right). \qquad (18.5)$$

For the design of a particular vessel, the value of the moment derived from either the wind or seismic load is used in these expressions. This is due to the assumption that wind and seismic loads are not expected to occur simultaneously, so the higher of the two moments is considered to be governing. These loads are based on site-specific data, which is obtained from one of the following national standards as applicable to the installation site.

Code for Wind Loads

- American Society of Civil Engineers (ASCE) 7, formerly American National Standards Institute (ANSI) A58.1
- Uniform building code (UBC)
- National building code (NBC)
- British standard (BS) 6399.

Code for Seismic Loads

- ASCE-7
- UBC/NBC
- International building code (IBC) 2000
- Response spectrum data.

Tall cylindrical vessels are normally designed to be self-supporting; they are supported on cylindrical or conical skirts with base rings resting on concrete foundations, firmly fixed to the foundations by anchor bolts. Detailed analytical methods for computing the thickness of the skirt components and sizing of the anchor bolts can be found in [18.2, 3], which also provide procedures for other types of support such as lugs, legs, and rings due to wind and seismic loads.

18.2.2 Wind-Induced Deflection

A sustained wind pressure will cause tall columns to deflect with the wind. Most engineering specifications limit such deflection to 150 mm per 30 m of column height. The vessel is assumed to be a cantilever beam firmly fixed to the concrete pedestal, and individual deflections induced by wind load and moments are calculated for each varying section of the vessel using the deflection formula for cantilever beams. The total deflection is then calculated using the method of superposition.

18.2.3 Wind-Induced Vibrations

Wind-induced vibrations can be caused by vortex shedding, the magnitude of which is dependent on the wind velocity and vessel diameter. Vortex shedding can result in severe oscillations, excessive deflections, structural damage, and even failure. When the natural frequency of a column or stack coincides with the frequency of vortex shedding, the amplitude of the resulting vibrations is greatly magnified. After a vessel has been designed statically, it is thus necessary to determine whether the vessel must be investigated dynamically for vibrations. Detailed methods for determining the need for dynamic analysis and a method for carrying out such analysis are provided in [18.3].

18.3 Testing Requirements

18.3.1 Nondestructive Testing (NDT)

NDT of the raw material, components, and finished vessel is important from the safety point of view. The most widely used methods for examination of plates, forgings, castings, and welds are briefly described below.

Radiographic examination is done using either x-rays or gamma rays. The former has greater penetrating power, but the latter is more portable. Single- or double-wall techniques are used for tubular components. Penetrameters, or image quality indicators, can be used to confirm the sensitivity of a radiographic technique to ensure that any defect will be visible.

Ultrasonic techniques use vibrations with a frequency between 0.5 and 20 MHz that are transmitted to the metal by a transducer. The instrument sends out a series of pulses, which are seen on a cathode-ray screen after being reflected from the other end of the member. Reflections from either a crack or an inclusion in the metal (or weld) can be detected on the screen; based on the magnitude and position of the signal, the location of the flaw can also be ascertained.

Liquid penetrant examination involves wetting the surface with a colored fluid that penetrates into open cracks. After wiping out excess fluid, the surface is coated with a developer fluid, which reveals the liquid that has penetrated the cracks. Another system uses a penetrant that becomes florescent under ultraviolet light.

Magnetic particle examination, which can only be used on magnetic materials, is carried out by using a probe to pass a magnetic flux through the part to be tested. Fine magnetic particles are dusted over the sur-

face and tend to concentrate at crack edges. To pick up all the cracks, the area is probed in two directions.

18.3.2 Destructive Testing of Welds

In contrast to NDT methods, which are essentially predictive techniques, the mechanical integrity of welds can also be checked by testing of sample test plates called *production test coupons*. The coupons are welded along with the actual vessel joint (usually a longitudinal seam) and are thus representative of the actual welding techniques employed for the vessel. The following tests are normally carried out on the test piece:

1. Tensile testing, which includes transverse tensile and all-weld tensile tests
2. Bend testing – transverse bend/side bending
3. Macroetching, hardness, and impact testing
4. Intergranular corrosion testing (IGC) for austenitic stainless-steel material/welds
5. Ferrite checking.

18.4 Design Codes for Pressure Vessels

In modern competitive industry, new process plants are being set up rapidly while existing units are continually being revamped, modernized, and refurbished for use in the chemical, petrochemical, pharmaceutical, energy, refinery, and nuclear industries worldwide. A variety of equipment is needed for the storage, handling, and processing of hydrocarbons and chemicals in these processing plants. Unfired pressure vessels such as storage tanks, Horton spheres, mounded bullets, reactors, autoclaves, distillation/fractionating columns, and heat exchangers are some of the basic components of any such process plant.

Various codes specifying the requirements for the design, materials, fabrication, inspection, and testing of pressure vessels have been written and adopted as national standards in various countries. Most international pressure vessel codes have been developed with a higher degree of technical similarity between them. Core features such as vessel classes, design criteria, and the requirements for independent inspection and certification are based on similar (but not identical) guiding principles.

A compilation of websites of various organizations, associations, technical standards, and current European Union (EU) legislation relating to the pressure equipment sector is presented in [18.4].

The subsequent subsections present a brief discussion of the key features of some of the international pressure vessel codes.

18.4.1 ASME Boiler and Pressure Vessel Code

The ASME boiler and pressure vessel code, section VIII, published by the American Society of Mechanical Engineers, also known as ASME International, is a widely accepted code in the USA and 80 other countries around the world. The code is written by voluntary engineering talent and is constantly upgraded by the corresponding committee members to include the latest developments in material and design methodology.

ASME section VIII is written against a well-defined theoretical background and is divided into three subdivisions: 1, 2, and 3. The important design rules of both codes are summarized in the respective appendices of each code. The contents of the three divisions are organized to cover specific pressure ranges, as illustrated in Table 18.4.

As can be seen from this code comparison table, division 2 permits higher working stresses at the expense of stringent material testing and more careful quality control. In addition to detailed design rules, division 2 provides for discontinuities, fatigue, and other stress analysis considerations, which are based on maximum shear stress theory. Division 2 also contains rules for vessels with layered construction (multiwalled vessels).

Fatigue Analysis

Clause AD-160 of division 2 provides several methods for exempting fatigue evaluations. If the cyclic operation does not meet all the conditions of AD-160, a fatigue evaluation method as per appendix 5 or 6 is added. The stress ranges are first determined for the specified cyclic operation, and then, using the fatigue curves presented in appendix 5, the associated number of allowable cycles and Miner's rule are used to determine the life fraction and cumulative damage. Fatigue curves up to 370 °C for carbon/low-alloy steel and 430 °C for austenitic stainless steel are provided in the code.

Division 3, which is a comparatively recent publication, provides a state-of-the-art code and is intended for high-pressure applications where fatigue and fracture dominate.

Table 18.4 Comparison of various divisions of ASME codes vis-à-vis EN13445

		Section VIII Division 1	Section VIII Division 2	Section VIII Division 3	EN 13445 part 3
First publication		< 1940	1968	1997	2002
Units adopted		°F and ksi			°C and N/mm^2
Pressure limits		Up to 3000 psig	No limits, usually + 600 psig	No limits, usually from 10 000 psig	For gas-PS up to 3000 bar and/or PS × V up to 3000 bar L For liquid-PS up to 1000 bar and/or PS × V up to 10 000 bar L
Design factor	Tensile strength	3.5	3.0		Ferritic/normalized steel – 2.4 Austenitic steel – 3
	Yield strength	1.5	1.5	Yield based with reduction factor for yield to tensile ratio less than 0.7	Ferritic/normalized steel – 1.5 Austenitic steel – 1.5 or 1.2 (depending on rupture elongation)
	Average stress for 1% creep in 100 000 h	1.0	1.0		Guidelines for design in creep range are under development
Allowable stress calculated by		Committee and provided in tables in section II C for individual grades and products			Designer
Testing groups		NDE requirement dependent on weld efficiency factor	Stringent NDE requirement	NDE requirement is even more stringent than division 2	Classified from I to IV in decreasing extent of NDT
Hydrostatic test		1.3 × design pressure	1.25 × design pressure	1.25 × design pressure	Greater of 1.43 × allowable pressure and 1.25 × temperature-adjusted pressure

18.4.2 PED Directive and Harmonized Standard EN 13445

The early phase of development of design codes and associated legislation in the pressure equipment sector was done predominantly at the national level. In view of the substantial economic potential of this sector, a need was felt in the European community to introduce a uniform and harmonized regulatory framework within the EU. The objective of the common legislation mechanism promulgated through directives was to minimize, if not eliminate, trade barriers between EU member states for pressure equipment, while at the same time meeting essential safety requirements stipulated by the new directives.

Of the several European directives enforced since 1987, the Pressure Equipment Directive (PED) (97/23/EC) and the Simple Pressure Vessel (SPV) Directive (87/404/EEC) are the two principal instruments for the pressure equipment sector. The approach of the directives includes the identification of the product, a prescription of the essential safety requirements (ESRs) to be met by technical standards, a demonstration of conformity, and CE marking. Technical standards adopted by the European Committee for Standardization (CEN/CENELEC), which provide means for the user to comply with the ESRs of the PED, are called *harmonized standards*.

EN 13445:2002 Unfired Pressure Vessel is a major harmonized product standard within the CEN pressure equipment portfolio. The standard utilizes expertise and best practices from across European member states as well other internationally accepted standards. The adoption of the first issue of this standard, published in 2002, was preceded by discussions between experts, who took nearly 10 years to achieve major technical convergence.

The various sections of EN 13445 along with a brief description of the respective contents are presented in Table 18.5, while Table 18.6 summarizes the essential features of the design rules for various pressure vessel components, as covered in part 3 of EN 13445. An excellent presentation of the background to the rules of EN 13445 part 3 is available [18.5].

18.4.3 PD 5500

PD 5500:2000, the *specification for unfired fusion-welded pressure vessels*, is a recent replacement for BS 5500:1997. It was issued under the status of a published document (PD) in anticipation of the simultaneous release of the harmonized standard EN 13445 for pressure equipment in Europe.

Although PD 5500 does not currently have formal status as a harmonized standard and compliance with its technical requirement does not qualify presumption of conformity with PED, it does include information

Table 18.5 EN 13445:2002 *Unfired pressure vessels* – a quick reference

Reference	Title	Contents/special features
EN 13445-1:2002	General	Scope, extent of testing with respect to weld joint coefficient, material grouping, etc.
EN 13445-2:2002	Materials	Materials listed include steels with sufficient ductility, cast iron, and aluminum Permitted or tabulated design stress are not provided A list of normative annexures is provided, including technical, inspection, and delivery condition Material listed in the CE harmonized product standard can be used for that product Material listed in the CE harmonized material standard, if appropriate to the product European approval of material (EAM) required for materials not listed in the harmonized standards Particular material appraisal (PMA) required for materials not listed in the harmonized standards or approved via EAM
EN 13445-3:2002	Design	See Table 18.6, listing features for individual components
EN 13445-4:2002	Fabrication	Provides weld designs, tolerances, production testing, postweld heat treatment, and repair requirements
EN 13445-5:2002	Inspection and testing	Specifies nondestructive testing, pressure testing, marking, and documentation requirements for noncyclic operation and special provisions for cyclic operations
EN 13445-6:2002	Requirements for design and fabrication of pressure vessels and pressure parts constructed of spheroidal graphite cast iron	
CR 13445-7:2002	Supporting standard for guidance on the use of the conformity procedures	
prEN 13445-8	Additional requirements for pressure vessels made of aluminum and aluminum alloys	

showing how its technical content would comply with the ESR of the directive.

Fatigue Analysis

Annexure C of the code presents criteria for exemption from fatigue analysis. A simplified fatigue analysis using design curves can be carried out using conservative estimates of the stress range due to pressure changes and thermal gradients. By using an appropriate design curve to obtain allowable cycles and satisfying a cumulative damage rule, a simplified analysis can be done.

A detailed analysis is required if the specified criterion is not satisfied. Detailed methods for determining stresses due to pressure, thermal gradients, and piping loads based on the use of stress concentration factors are provided in annexure G. Based on the individual stresses thus obtained, the maximum principal stress range for each individual cycle is determined and a fatigue evaluation carried out as per annexure C.

Table 18.6 A quick summary of EN 13445 part 3

Type of analysis	Component	Special features
Design by formulae for noncyclic loading (used in clauses 7–16) (fewer than 500 full-pressure cycles)	Dished ends	Additional formulae for knuckle and knuckle buckling
	Cones and conical ends	Based on limit analysis
	Opening in shells	Pressure area method
	Opening in flat ends	Replacement of section modulus
	Flanges	Modified Taylor forge method, alternate method also provided based on limit load analysis carrying out detailed assessment of flange–bolt–gasket system, useful for joints where bolt loads are monitored
	Weld joint efficiency	Linked to testing group I/II/III/IV
	Tubesheets	In addition to traditional method, a new method using limit analysis approach in which edge loads and restraints are addressed is provided Allowable tube loads are calculated
	Bellows	Covers both thin- and thick-walled bellows Rules are based on Expansion Joint Manufacturers Association (EJMA) standards
	Rectangular vessels	Covers both unreinforced and reinforced vessels where outside stiffeners are attached
	Nonpressure local loads	Local loads are assessed by comparison with allowable loads calculated based on limit load analysis

Table 18.6 (continued)

Type of analysis	Component	Special features
Design by formulae for cyclic loading (used in clauses 17 and 18) (more than 500 full-pressure cycles)	Simplified fatigue analysis (clause 17)	Fatigue strength calculated using fatigue curves, which are more conservative than those used in detailed fatigue analysis for the unwelded region Table provided for selecting stress factor for various design configurations
	Detailed fatigue analysis (clause 18)	Correction factors depending upon temperature, thickness, mean stress, and surface finish are applied on fatigue curves Cumulative damage calculated as per Miner's rule Guidance provided on bending stress calculations due to misalignment of weld and recommendation given for weld-toe grinding
Design by analysis (covered by annexes B and C)	Direct route (annex B)	New route based on Eurocode (for steel structure), which overcomes the shortcomings of the familiar stress categorization method and addresses failure modes directly by way of design checks under the influence of *actions* (all imposed thermomechanical quantities including pressure, thermal, and environmental) using partial safety factors depending on the nature of a single action or a combination of actions
	Stress categorization route (annex C)	Based on categorization of stresses into primary, secondary, and peak stress and comparing the same with specified limits A stress classification table is provided for a given component and its location depending upon the source load to help list and allocate stress categories

The fatigue curves are limited to 350 °C for ferritic steel and 430 °C for austenitic stainless steels.

18.4.4 AD Merkblätter

Arbeitsgemeinschaft Druckbehälter (AD) Merkblätter regulations are a set of generally accepted rules for technology related to pressure vessels and contain safety requirements for equipment design, manufacture, testing, and materials. These regulations are compiled by seven German trade associations, who together form the AD. The AD associations represent a balanced combination of material and pressure vessel manufacturers, operators, employer's liability insurers, and technical inspectorates.

To a large extent, the AD Merkblätter code is based on Deutsches Institut für Normung (DIN) standards and is continuously amended in keeping with technical progress. The associations have published a regulation called AD 2000 conforming to the safety requirements and other stipulations as laid down in the PED, which has been compulsory in Europe from May 2002 onwards.

A quick summary showing the key technical points of PD 5500 in comparison with the ASME section and AD Merkblätter code is presented in Table 18.7.

Table 18.7 Summary of salient features of ASME, PD 5500, and AD code

Information	ASME Section VIII Division 1		PD 5500		AD Merkblätter	
	Part	Summary	Section	Summary	Section	Summary
Responsibilities	UG-99	Responsibilities listed for manufacturer and authorized inspector (AI)	1.4	Responsibilities for code compliance is on manufacturer	Druckbehälter VO	Authorized inspector to issue final vessel certification
Certification	UG-115 to 120	Manufacturer to have *certificate of authorization* to construct ASME-stamped vessel	1.4	Code compliance is documented by use of form X issued by the manufacturer and countersigned by AI	Druckbehälter VO	Authorized inspector to issue final vessel certification
Construction categories	–	–	3.4	Three categories with different material and NDT requirements are defined	HP 0	Four testing groups I, II, III, and IV are defined

Table 18.7 (continued)

Information	ASME Section VIII Division 1		PD 5500		AD Merkblätter	
	Part	Summary	Section	Summary	Section	Summary
Joint types	UW-3	Defines categories A, B, C, and D with different NDT requirements; UW-12 gives joint efficiencies	5.6.4	Defines A and B welded joints, with different NDT requirements		
Weld joint details	UW-12, UW-13, and UW-16	Shows typical weld joints for guidance but are not mandatory	E.1(1)–E.1(6)	Shows typical weld joints for guidance but are not mandatory		
Welder's approval	UW-28, UW-29, UW-48	Weld procedure specification (WPS), procedure qualification record (PQR) and welder's qualification are required	5.2, 5.3	WPS, PQR, and welder's qualification are required	HP 2/1	WPS, PQR, and welder's qualification are required
Permissible materials	UG-4 and UG-10	UG-4 refers to materials specified in ASME section II	2.1.2	This section references British standard materials	W0 to W13 for metallic and N series for nonmetallic materials	W0 to W13 cover all types of alloyed/unalloyed steel, castings, forgings, and clad steel bolts and nuts, but not gaskets
Material identification	UG-94	Material for all pressure parts is marked and certified for traceability	4.1.2	Positive material identification is required for all pressure parts		
NDT techniques	UW-51 to 53, UW-11, and UW-42	NDT techniques are detailed in ASME section V	5.6.4	Ultrasonic testing (UT) and radiographic testing (RT) are both acceptable	HP 5/3	DIN standards are referenced for all NDT techniques
Assembly tolerance	UG-80, UW-33	Tolerances for circularity and alignment are specified	4.2.3	Tolerances for circularity and alignment are specified		
Pressure testing	UG-99, UW-50	Test pressures are specified along with other testing requirements	5.8.1	Test pressures are specified along with other testing requirements	HP 8/2, HP 30	
Heat treatment	UCS-56				HP 7/1 to HP 7/4	

18.5 Heat Exchangers

Heat exchangers provide a means for transferring heat between two fluids at different temperatures. They are amongst the most commonly used equipment in a variety of industries and can be classified based on different factors including the transfer process (direct or indirect contact), compactness (compact or noncompact), construction (tubular or plate), heat transfer mechanism, flow arrangement (parallel flow, counterflow, or crossflow), and application. These factors are briefly discussed in this section. More details about heat exchanger classifications can be found in *Shah* and *Sekulic* [18.6].

The transfer of heat in *indirect-contact* heat exchangers occurs through a surface (e.g., tubes or plates) that separates the two fluids. However, in *direct-contact* exchangers, the fluids are in close contact and are not separated, such as water and air in cooling towers. Another important classification of heat exchangers is based on their compactness. If the surface-to-volume ratio of a gas-to-fluid or liquid-to-liquid heat exchanger exceeds 700 or 400 m^2/m^3, respectively, its can be categorized as compact. Compact heat exchangers play an essential role in many applications, particularly where the available space is limited.

Schematics showing the structure of some of the most commonly used heat exchangers are depicted in Fig. 18.4. Heat exchangers may be built using a variety of constructions, including tubular, plate, and extended

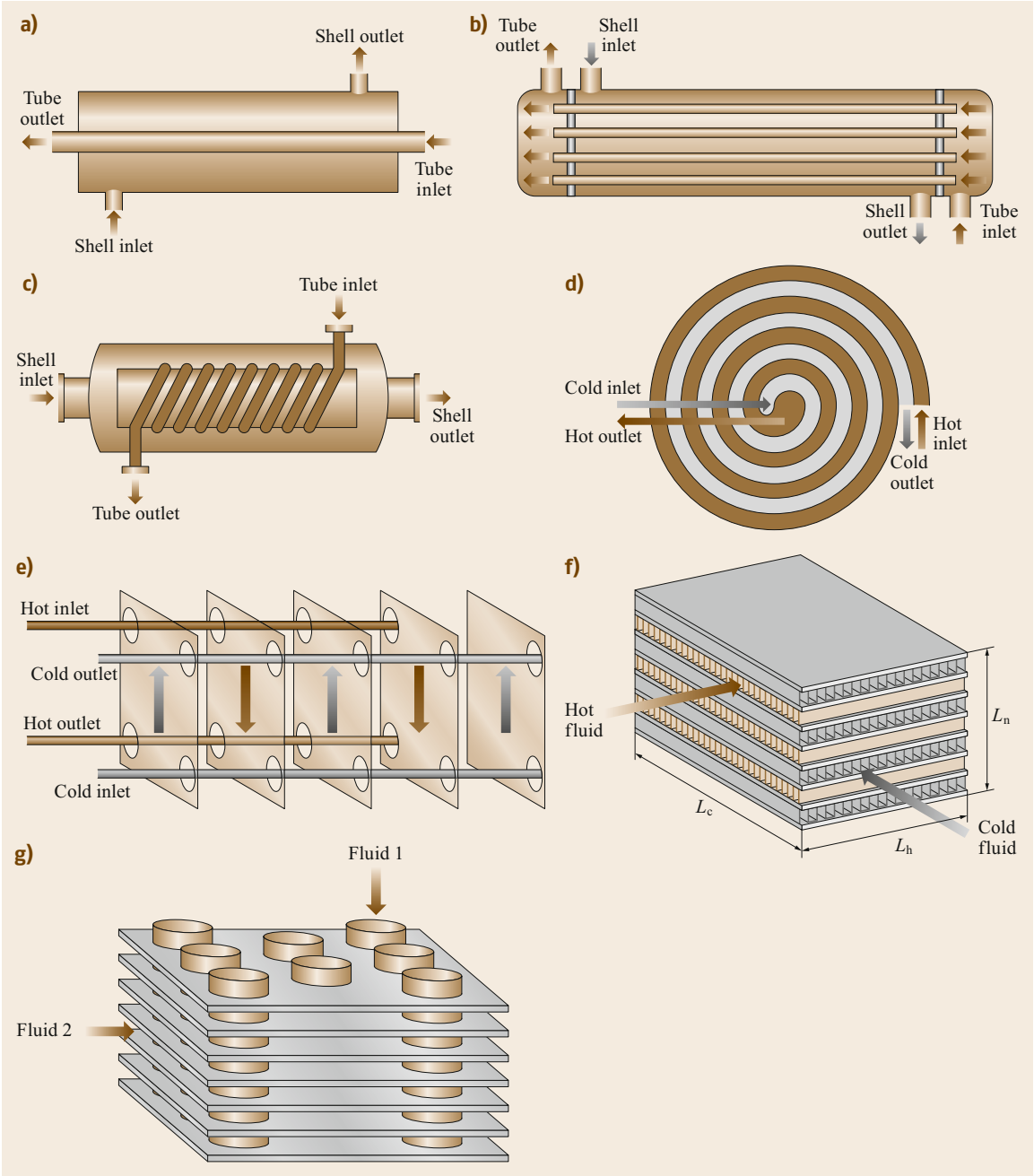

Fig. 18.4a–g Schematics of commonly used heat exchangers: **(a)** concentric tube (double-pipe) heat exchanger, **(b)** shell-and-tube heat exchanger, **(c)** shell and helical coiled tube heat exchanger, **(d)** spiral heat exchanger, **(e)** plate-and-frame heat exchanger, **(f)** plate-and-fin heat exchanger (reprinted from [18.7] with permission from Elsevier), **(g)** tube-fin heat exchanger

designs. Tubular exchangers are built using circular tubes. These are generally used for liquid-to-liquid or liquid-to-gas (or phase-change) applications. The simplest tubular heat exchanger is the *concentric tube heat exchanger* (also known as a double-pipe heat exchanger). Two fluids at different temperatures flow in the pipes, and heat is transferred through the surface of the pipe (Fig. 18.4a). Other well-known configura-

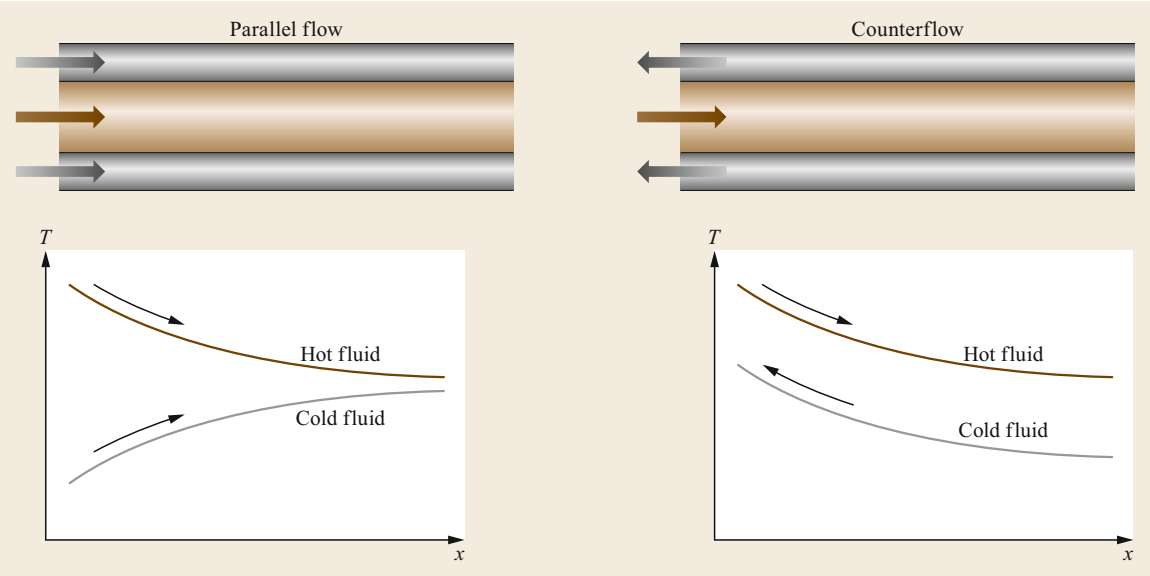

Fig. 18.5 Parallel flow and counterflow configurations with associated temperature profiles

tions of tubular heat exchangers include shell-and-tube and helical coiled tube heat exchangers. Shell-and-tube heat exchangers are widely used in industry (Fig. 18.4b) as they can be designed for high-pressure and high-temperature applications. A number of tubes may be placed inside a large pressure vessel (shell side), and a fluid passes from each side. The tubes are distributed within the tube sheet in a certain pattern, the three most common of which are the triangular, square, and rotated triangular. Designs for the joint between the tube and tube sheet vary widely and are chosen to be compatible with the severity of the service conditions. The joint may be expanded, welded, or a combination of both. There are various constructional details of welded joints, the choice of which is based upon the service conditions and environment. Various configurations and designs of shell-and-tube exchangers are covered extensively by the Tubular Exchanger Manufacturers Association (TEMA) [18.8]. A schematic of a helical coiled tube heat exchanger is shown in Fig. 18.4c. This class of heat exchanger offers higher efficiency compared with heat exchangers with straight tubes. The curvature of the tube creates secondary flow and allows a larger surface area between the two streams, which enhances the heat transfer process.

Plate-type heat exchangers are built from thin plates, which can be either smooth or corrugated. Although they usually cannot be used for very high-temperature or high-pressure applications, they are popular due to their compactness and high efficiency in many applications, including heating, ventilation, air-conditioning, and refrigeration (HVACR) and food industries. Plate heat exchangers can be classified based on their construction as gasketed, welded, or brazed. Two of the most commonly used plate-type heat exchangers are plate-and-frame heat exchangers and spiral plate heat exchangers. Plate-and-frame or gasketed plate heat exchangers (PHEs) consist of numerous corrugated plates mounted in a frame, being sealed by gaskets. A schematic of a PHE is shown in Fig. 18.4e. As seen, the hot and cold fluids flow through alternate channels, while the plates allow a very large surface area between the hot and cold fluids, thereby significantly enhancing the heat transfer rate. Another widely used plate-type exchanger is the spiral plate heat exchanger, which is demonstrated in Fig. 18.4d. The structure of a spiral plate heat exchanger allows a high surface area between the two streams and causes turbulence in the flow, which increases the heat transfer and reduces fouling.

Plate-fin exchangers and tube-fin exchangers, depicted in Fig. 18.4f and g respectively, are the most well-known types of extended surface heat exchanger. Plate-fin heat exchangers consist of several layers of flat plates and finned chambers. Owing to their high heat transfer surface area and the turbulence caused by the fins, this class of heat exchanger offers high thermal efficiency. Tube-fin exchangers include arrays of finned tubes and are usually applied when at least one of the fluids is a gas with a significantly lower convective heat transfer coefficient (Fig. 18.4g).

Heat exchangers may have different flow arrangements including parallel flow, counterflow, or crossflow. Figure 18.5 shows a schematic of a concentric tube heat

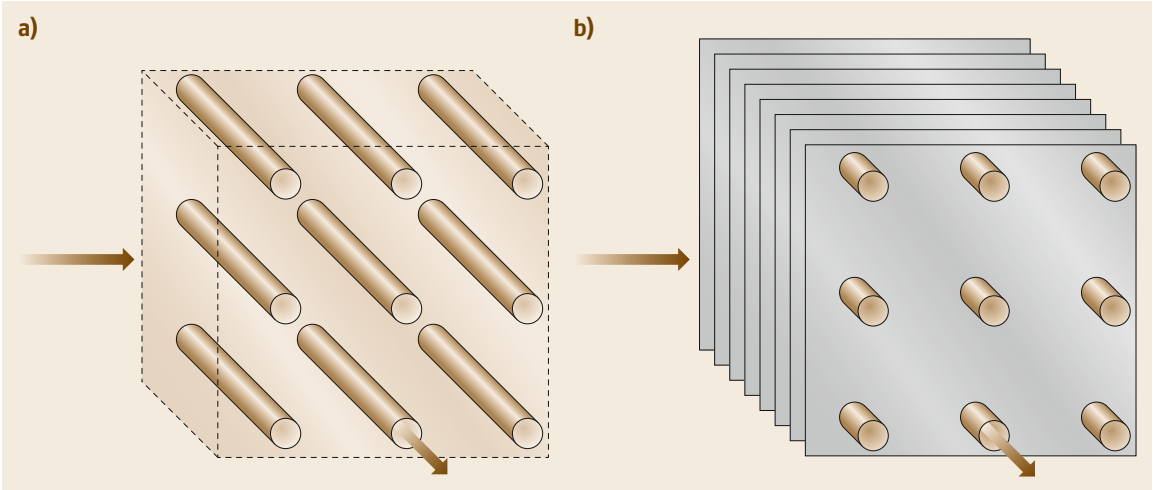

Fig. 18.6a,b Crossflow configuration associated with one fluid mixed (a) and both fluids unmixed (b)

exchanger with parallel and counterflow configurations along with the associated temperature profiles.

Note that, in the parallel flow configuration, the outlet temperature of the cold stream is always lower than the outlet temperature of the hot stream. However, in the counterflow configuration, the outlet temperature of the cold stream may exceed the outlet temperature of the hot stream. The counterflow configuration is more efficient than the parallel flow configuration as it maintains a considerable temperature gradient between the two streams throughout the entire length of the heat exchanger, unlike the parallel flow heat exchanger, in which the temperature difference between the two streams decreases continuously along the heat exchanger.

Figure 18.6 shows schematics of crossflow heat exchangers. In the crossflow configuration, the fluids flow perpendicular to one another and may be mixed or unmixed.

The appropriate type of heat exchanger for a particular application can be selected by considering the operating temperatures and pressures, flow rates, types of fluids, potential for fouling, materials, thermal effectiveness, pressure drop, and available space. The overall cost of the system is another important factor in the selection of heat exchangers. The analysis and design of a heat exchanger include thermal and mechanical design, each of which are briefly discussed in the next sections.

18.5.1 Thermal Design

The thermal design of a heat exchanger usually includes the determination of the type of heat exchanger, the heat transfer area, the dimensions of the tubes/plates, the number of passes, the number and geometry of fins and baffles, and the pressure drop, based on inputs such as the inlet/outlet temperatures, flow rates, and fluid properties.

The two primary objectives that must be addressed from the thermal/fluid perspectives are maximizing the heat transfer rate and minimizing the pressure loss, although these are often conflicting. In other words, any effort to increase the heat transfer rate between the hot and cold streams may result in a higher pressure loss, which in turn translates into a higher operational cost (pumping cost). An example is adding baffles to shell-and-tube heat exchangers. Baffles are perforated plates that increase the heat transfer surface between the two fluids and generate a turbulence effect that enhances the convective heat transfer coefficient and thereby the heat heat transfer rate between the fluids. However, using baffles may cause additional pressure loss. Therefore, careful design of heat exchangers is of interest to maximize the heat transfer rate while maintaining a low pressure loss.

An important thermal characteristic of heat exchangers is the overall heat transfer coefficient U, which is defined as the inverse of the total thermal resistance to heat transfer between the two fluids. The overall heat transfer coefficient can be calculated as

$$\frac{1}{UA} = \frac{1}{(UA)_c} = \frac{1}{(UA)_h} = \frac{1}{(hA)_c} + \frac{R''_{f,c}}{A_c} + R_w + \frac{R''_{f,h}}{A_h} + \frac{1}{(hA)_h}\,, \quad (18.6)$$

where A represents the heat transfer surface area, h is the convective heat transfer coefficient, R''_f is the thermal resistance due to fouling, and R_w refers to the

resistance to conduction through the wall between the two fluids, which may be found as $\ln(D_o/D_i)/(2\pi kL)$ for a concentric tube heat exchanger. The subscripts "i" and "o" indicate the inner and outer surfaces, while the subscripts "h" and "c" refer to hot and cold side of the heat exchanger.

Note that, here, fouling refers to the accumulation of undesirable deposits on the surface of the heat exchanger, which will increase the resistance to heat transfer between the two fluids. Fouling may occur due to corrosion, accumulation of solid particles that are mixed in the fluid, crystallization of salts in the process stream, growth of microorganisms (biofouling), or chemical reactions between the solid surface and fluid. Fouling reduces the effectiveness of the heat exchanger and increases the pressure loss. Fouling must be considered as an important factor when designing heat exchangers, and heat exchangers must be cleaned on a regular basis to minimize the effect of fouling on their performance. Fouling resistance can vary greatly based on the type of fluid, application, heat exchanger construction, etc. Fouling resistances for different industrial fluids can be found in [18.9], which may be used for design purposes.

If fins are added to either side of a heat exchanger, (18.6) may be written as

$$\frac{1}{UA} = \frac{1}{(\eta_0 hA)_c} + \frac{R''_{f,c}}{(\eta_0 A)_c} + R_w + \frac{R''_{f,h}}{(\eta_0 A)_h} + \frac{1}{(\eta_0 hA)_h} , \tag{18.7}$$

where η_0 is the overall surface efficiency with fins and can be found as

$$\eta_0 = 1 - \frac{A_f}{A}(1 - \eta_f) . \tag{18.8}$$

Here, A_f denotes the surface area of the fins, A represents the total surface area, and η_f is the efficiency of a single fin. For a straight or pin fin with the assumption of an adiabatic fin tip, the fin efficiency can be determined as

$$\eta_f = \frac{\tanh(mL)}{mL} , \tag{18.9}$$

where L is the length of the fin and m may be found as

$$m = \sqrt{\frac{2h}{k_f t}} . \tag{18.10}$$

Here, t is the thickness of the fin and k_f denotes the thermal conductivity of the fin.

Note that the convective heat transfer coefficient, h, can be calculated as

$$h = \frac{\mathrm{Nu}k}{D_h} , \tag{18.11}$$

where Nu is the Nusselt number (dimensionless heat transfer coefficient), k is the thermal conductivity of the fluid, and D_h is the hydraulic diameter. The Nusselt number is a function of the Prandtl number and Reynolds number. Several empirical correlations are available for calculating Nu for different geometries and flow regimes, many of which are listed by *Kakaç* et al. [18.9] and *Bergman* and *Lavine* [18.10].

There are a number of standard procedures for the thermal design and analysis of heat exchangers. The most common approaches include the log-mean temperature difference (LMTD) method and effectiveness–NTU method, which are briefly described below.

Log-Mean Temperature Difference

The temperature difference between the cold and hot fluids acts as the driving force for the heat exchange between them. From the thermodynamic perspective, assuming negligible heat transfer between the heat exchanger and its surroundings and negligible changes in potential and kinetic energy, the heat transfer rate between the hot and cold fluids can be obtained as

$$q = \dot{m}_h(i_{h,i} - i_{h,o}) = \dot{m}_c(i_{c,o} - i_{c,i}) , \tag{18.12}$$

where i represents the enthalpy of the fluid, the subscripts "h" and "c" refer to the hot and cold fluids, and the subscripts "i" and "o" refer to the inlet and outlet. Assuming constant specific heats and in the absence of phase changes, the above equation can be simplified to

$$q = \dot{m}_h c_{p,h}(T_{h,i} - T_{h,o}) = \dot{m}_c c_{p,c}(T_{c,o} - T_{c,i}) . \tag{18.13}$$

From the heat transfer perspective, the heat transfer rate between the two fluids in a heat exchanger can be obtained as

$$q = UA\overline{\Delta T} , \tag{18.14}$$

where $\overline{\Delta T}$ is the effective temperature difference. For concentric tube heat exchangers with a parallel or counterflow configuration, $\overline{\Delta T}$ is equivalent to the log-mean temperature difference, which can be found as

$$\Delta T_{LM} = \frac{\Delta T_2 - \Delta T_1}{\ln(\Delta T_2/\Delta T_1)} . \tag{18.15}$$

Here, for a parallel flow heat exchanger, $\Delta T_1 = T_{h,i} - T_{c,i}$ and $\Delta T_2 = T_{h,o} - T_{c,o}$, while for a counterflow

Table 18.8 Heat exchanger effectiveness relations [18.11]

Flow arrangement	Relation
Parallel flow	$\varepsilon = \dfrac{1-\exp[-\mathrm{NTU}(1+C_\mathrm{r})]}{1+C_\mathrm{r}}$
Counterflow	$\varepsilon = \dfrac{1-\exp[-\mathrm{NTU}(1-C_\mathrm{r})]}{1-C_\mathrm{r}\exp[-\mathrm{NTU}(1-C_\mathrm{r})]}\,, \quad C_\mathrm{r}<1$ $\varepsilon = \dfrac{\mathrm{NTU}}{1+\mathrm{NTU}}\,, \quad C_\mathrm{r}=1$
Shell-and-tube One shell pass (two, four, … tube passes)	$\varepsilon_1 = 2\left\{1+C_\mathrm{r}+\left(1+C_\mathrm{r}^2\right)^{0.5}\dfrac{1+\exp\left[-\mathrm{NTU}_1\left(1+C_\mathrm{r}^2\right)^{0.5}\right]}{1-\exp\left[-\mathrm{NTU}_1\left(1+C_\mathrm{r}^2\right)^{0.5}\right]}\right\}^{-1}$
Shell-and-tube n shell passes ($2n$, $4n$, … tube passes)	$\varepsilon = \left[\left(\dfrac{1-\varepsilon_1 C_\mathrm{r}}{1-\varepsilon_1}\right)^n - 1\right]\left[\left(\dfrac{1-\varepsilon_1 C_\mathrm{r}}{1-\varepsilon_1}\right)^n - C_\mathrm{r}\right]^{-1}$
Crossflow (both fluids unmixed)	$\varepsilon = 1-\exp\left(\dfrac{1}{C_\mathrm{r}}\mathrm{NTU}^{0.22}\{\exp[-C_\mathrm{r}(\mathrm{NTU})^{0.78}]-1\}\right)$
Crossflow (C_max mixed, C_min unmixed)	$\varepsilon = \left(\dfrac{1}{C_\mathrm{r}}\right)(1-\exp\{-C_\mathrm{r}[1-\exp(-\mathrm{NTU})]\})$
Crossflow (C_max unmixed, C_min mixed)	$\varepsilon = 1-\exp\left(-C_\mathrm{r}^{-1}\{1-\exp[-C_\mathrm{r}(\mathrm{NTU})]\}\right)$
All exchangers for $C_\mathrm{r}=0$	$\varepsilon = 1-\exp(-\mathrm{NTU})$

heat exchanger, $\Delta T_1 = T_{\mathrm{h,i}} - T_{\mathrm{c,o}}$ and $\Delta T_2 = T_{\mathrm{h,o}} - T_{\mathrm{c,i}}$. For other heat exchangers, including crossflow heat exchangers and multiple-pass shell-and-tube heat exchangers, a correction factor may be applied as

$$\overline{\Delta T} = F\Delta T_\mathrm{LM}\,, \tag{18.16}$$

where F is a correction factor that varies between 0.5 and 1 and depends on the type of heat exchanger as well as the inlet and outlet fluid temperatures. These correction factors are listed by *Bowman* et al. [18.12].

Effectiveness–NTU

An alternative approach for the analysis of heat exchangers is the effectiveness–NTU method. The effectiveness of a heat exchanger can be defined as the ratio of the actual heat transfer rate through the heat exchanger to the maximum possible heat transfer in an infinitely long counterflow heat exchanger

$$\varepsilon = \frac{q}{q_\mathrm{max}} = \frac{C_\mathrm{h}(T_{\mathrm{h,i}}-T_{\mathrm{h,o}})}{C_\mathrm{min}(T_{\mathrm{h,i}}-T_{\mathrm{c,i}})} = \frac{C_\mathrm{c}(T_{\mathrm{c,o}}-T_{\mathrm{c,i}})}{C_\mathrm{min}(T_{\mathrm{h,i}}-T_{\mathrm{c,i}})}\,, \tag{18.17}$$

where $C_\mathrm{h} = \dot{m}_\mathrm{h}c_{p,\mathrm{h}}$, $C_\mathrm{c} = \dot{m}_\mathrm{c}c_{p,\mathrm{c}}$, and $C_\mathrm{min} = \min(C_\mathrm{h}, C_\mathrm{c})$.

A dimensionless parameter known as the number of transfer units can then be defined as

$$\mathrm{NTU} = \frac{UA}{C_\mathrm{min}}\,. \tag{18.18}$$

It can be shown that, for any type of heat exchanger, the effectiveness is a function of the NTU and the ratio of the heat capacity rates, $C_\mathrm{r} = C_\mathrm{min}/C_\mathrm{max}$. The effectiveness–NTU relations are summarized in Table 18.8.

Note that $C_\mathrm{r} = 0$ refers to either phase-change conditions (when C_max is infinitely large) or when $C_\mathrm{min} \ll C_\mathrm{max}$.

Pressure Loss

The pressure loss is another important consideration when designing heat exchangers. The frictional pressure drop for a flow through a pipe/duct of length L can be found as

$$\Delta p = f\frac{L}{D}\frac{\rho u_\mathrm{m}^2}{2}\,, \tag{18.19}$$

where f is the friction coefficient, ρ is the density of the fluid, u_m is the mean velocity of the fluid, and D is the diameter. Note that, for noncircular cross sections, the hydraulic diameter (D_h) must be used instead of the diameter (D). The hydraulic diameter can be found as $D_\mathrm{h} = 4A_\mathrm{c}/p$, where A_c is the cross-sectional area and p is the wetted perimeter. The friction coefficient, f, for laminar flows can be found as

$$f = \frac{64}{\mathrm{Re}}\,. \tag{18.20}$$

For turbulent flows, f is a function of Re and the relative roughness (e/D) and can be obtained from a Moody diagram or from alternative equations such as the Colebrook equation [18.10]

$$\frac{1}{\sqrt{f}} = -2\log\left(\frac{e}{3.7D} + \frac{2.51}{\mathrm{Re}\sqrt{f}}\right). \tag{18.21}$$

Table 18.9 Design rules for tube sheets as per different codes

	TEMA	ASME section VIII division 1	EN 13445-3
U-tube tubesheet			
Reference section	Section 1999 edition	Appendix AA-1 edition 2001 and UHX-12 edition 2002 (mandatory)	Clause 13 D-2002 (based on Code français de construction des Appareils à Pression (CODAP)/unfired pressure vessel (UPV) rules)
Assumptions	Perforated tubesheet and unperforated rim not accounted for; the effect of tube sheet attachment with shell/channel not considered	Refined and rational analytical treatment is used after taking into account actual geometry (based on model proposed by F. Osweiller in 2000)	
Ligament efficiency	$0.45 \leq \eta \leq 0.60$	$0.25 \leq \mu \leq 0.35$	
Safety factor	2.6	1.5	2.0
Allowable stress		Stress classification of division 2 appendix 4	Based on primary and secondary stress as per appendix C
Remarks	TEMA approach leads to lower thickness than ASME due to higher ligament efficiency and high safety factor	Higher thickness obtained in ASME rules than UPV/CODAP due to lower allowable stress	
Fixed/floating tubesheet			
Reference section		Appendix AA-2 edition 1992	Clause 13 E-2002 (based on CODAP/UPV rules)
Assumption	Stiffening effect of tube bundle and weakening effect of tube holes are assumed to counterbalance each other, coefficient F is not dependent on the stiffness ratio X of the axial tube bundle rigidity to the bending rigidity of the tube sheet	Coefficient F is dependent on the stiffness ratio X	Coefficient F is dependent on the stiffness ratio X; the value of F is higher than ASME since tubes are assumed to be uniformly distributed over the whole tube sheet
Remarks	TEMA does not provide the same design margin for all cases, leading to overthickness for higher X and underthickness for lower X		

For an incompressible fluid with a mass flow rate of $\dot{m}$, the pumping work required to overcome a pressure loss of Δp can be determined as

$$W_p = \frac{\dot{m}}{\rho} \Delta p \frac{1}{\eta_\mathrm{p}} , \tag{18.22}$$

where η_p is the isentropic pump efficiency. Note that, to calculate the amount of electric power needed by the pump, the motor efficiency and drive efficiency must also be considered ($W_\mathrm{p}/(\eta_\mathrm{m}\eta_\mathrm{d})$).

Detailed correlations for calculating pressure losses through helical coils, spiral coils, flow over a tube bundle, bends, fittings, expansions, and contractions are discussed by *Kakaç* [18.9].

18.5.2 Mechanical Design

The mechanical design principles applied for most of the components of a heat exchanger are identical to those used in the design of a pressure vessel. However, the design of a tube sheet is typically different because of its constructional geometry. Design rules for tube sheets have been rationalized in recent years in various pressure vessel codes, as summarized in Table 18.9.

18.6 Construction Materials

18.6.1 Carbon Steel

Steel is formed from iron alloyed with carbon at a level of 0.05–2.0%. In addition, it contains smaller proportions of phosphorus, sulfur, silicon, aluminum, and manganese. Such steels are known as plain carbon steels, being classified as mild-, medium-, and high-carbon steels according to the percentage of carbon.

Mild steel has 0.05–0.3% carbon by weight, medium-carbon steel has a carbon content of 0.3–0.6%,

while high-carbon steel has more than 0.5%, up to a maximum of 2%, carbon content. Mild steels are the most versatile materials for the construction of pressure vessels due to their good ductility and relatively easy forming, rolling, forging, fabrication, and welding. They are also most well suited and economic for applications where the rate of corrosion is low. During the manufacture of these steels, silicon and/or aluminum are added to react with dissolved oxygen in the molten metal alloy to form a slag of Al_2O_3/SiO_2, which floats to the top and is removed; the resultant steel is called *killed steel*. A fully killed steel usually contains less than 150 ppm oxygen and at least 0.10% silicon. Besides being cleaner due to the formation of fewer oxides and inclusions, fully killed steels are much easier to weld due to a lower tendency to outgas during welding.

Welding

Mild-steel electrodes are grouped into those with a rutile-type flux covering and those with a low-hydrogen flux covering. Rutile-covered electrodes are used for general fabrication involving thinner sections and lower tensile strength, and in applications where there is no requirement for impact properties. For all other applications, where strength, impact properties, and weld quality are essential, low-hydrogen-type electrodes are employed. The flux covering eliminates potential sources of hydrogen and thus minimizes the chances of clod cracking.

18.6.2 Low-Alloy Steel

Low-alloy steel contains additions of the elements Ni, Cr, Si, Mo, and Mn in amounts totaling less than 5%. The added elements improve the mechanical properties, heat treatment response, and/or corrosion resistance. The weldability of low-alloy steels is also good; however since these steels can be hardened by heat treatment, careful attention must be paid to the welding procedure, including pre- and postweld heat treatment (PWHT) for stress relief, which is discussed below.

The workhorse alloys for pressure vessels, heat exchanger and heater tubes, and piping for service at elevated temperatures, usually greater than 250 °C, contain 0.5–9.0% chromium plus molybdenum. With increasing chromium content, the resistance to high-temperature hydrogen attack as well as sulfidation and oxidation increases.

Developments

There has been an increasing trend towards improved toughness properties and temper embrittlement resistance by restricting levels of impurity elements at the ladle.

To minimize the temper embrittlement of low-alloy steel, the phosphorous content is restricted to 0.010% or lower, while the combined phosphorous/tin content is limited to 0.010%.

The effects of tramp elements have been addressed using the Bruscato factors X and J, defined as

$$X = \frac{(10\mathrm{P} + 4\mathrm{Sn} + 5\mathrm{Sb} + \mathrm{As})}{100} \text{ (elements in ppm)} ,$$

$$J = (\mathrm{Si} + \mathrm{Mn})(\mathrm{P} + \mathrm{Sn}) \times 10^4 \text{ (elements in \%)} .$$

For this reason, PWHT is a must for all creep-resisting Cr-Mo-type alloy steels. PWHT also stabilizes and softens the microstructure in the heat-affected zone (HAZ) of the weld. If the base metal is quenched and tempered, higher PWHT temperatures can be specified for improved resistance to creep embrittlement.

Fabrication

In view of the criticality of preheating, postheating, and PWHT, it is prudent to employ specialized heat-treatment techniques using electrical resistance pads or induction coils, especially for thick piping sections.

18.6.3 NACE Standards

The National Association of Corrosion Engineers (NACE) is a worldwide technical organization that studies various aspects of corrosion in refineries, chemical plants, and other industrial systems.

NACE standard MR0175, entitled *Sulfide corrosion cracking resistant metallic material for oilfield equipment*, is widely used for applications in sour gas and oil environments. NACE compliance is recommended in systems where there is a likelihood of sulfide cracking due to the presence of a measurable amount of H_2S. Since the susceptibility of carbon, low-alloy, and austenitic stainless steels to sulfide corrosion is directly related to their strength and hardness level, these standards recommend that the hardness of the aforementioned plate materials should be restricted to 22 HRC (200 BHN). The cold working of these steels during forming/rolling shall be less than 5%. Postweld heat treatment is to be carried out for carbon steels in the case of greater cold working. A few duplex stainless and some nickel-based alloys are also acceptable according to the NACE criteria, subject to a maximum hardness level of 28 and 35 HRC, respectively.

Welding

All welding procedures must be qualified to meet the same hardness level standards as specified for the corresponding parent material.

Table 18.10 Comparative chart for material standards of flat products (plates) for pressurized use

Harmonized European standard Description			ASTM	DIN Standard	BS 1501 Grade
General requirement	EN 10028-1		SA 20		
				DIN 17155	
Nonalloy and alloy steels with elevated-temperature properties	EN 10028-2	P235GH	SA 283 Gr C/ SA 516 Gr 55	H I	161 Gr 360/ 164 Gr 360
		P265GH	SA 516 Gr 60	H II	161 Gr 400/ 164 Gr 400
		P295GH	SA 516 Gr 65	17Mn4	224 Gr 490
		P355GH	SA 414 Gr G	19Mn6	
		16Mo3	SA 204 Gr B	15Mo3	1503-243 B
		13CrMo4-5	SA 387 Gr 12	13CrMo4-4	620 Gr 27
		10CrMo9-10	SA 387 Gr 22	10CrMo9-10	620 Gr 31
				DIN 17102	
Weldable fine-grain, normalized	EN 10028-3	P275N		StE 285	224 Gr 400
		P275NH	SA 516 Gr 60	WStE 285	224 Gr 430
		P275NL1	SA 662 Gr A	TStE 285	
		P275NL2		EStE 285	
		P355N	SA 537 CL 1	StE 355	224 Gr 490
		P355NH	SA 662 Gr C	WStE 355	224 Gr 490
		P355NL1	SA 737 Gr B	TStE 355	224 Gr 490
		P355NL2		EStE 355	
		P460N		StE 460	
		P460NH		WStE 460	
		P460NL1		TStE 460	
		P460NL2		EStE 460	
				DIN 17280	
Nickel alloy steel with low-temperature properties	EN 10028-4	11MnNi5-3		13MnNi6	
		12Ni14	SA 203 Gr D,E,F	10Ni14	
		X12Ni5 (12Ni19)	SA 645	12Ni19	
		X8Ni9 NT	SA 353		
		X8Ni9 QT	SA 553		
Weldable fine grain, thermomechanically rolled	EN 10028-5	P355M/ML1/ML2			
		P420M/ML1/ML2			
		P460M/ML1/ML2			
Weldable fine grain, quenched, and tempered	EN 10028-6	P690Q/QH QL1/QL2	SA 517, SA 533, SA 724		
Stainless steel	EN 10028-7	Various grades (refer to Table 18.11)	SA 240	DIN 17440 DIN 17441	BS 1449-2 and BS 1501-3

Legend for steel grade to EN series:
G – other characteristics follow, N – normalized condition, H – elevated-temperature property required, M – thermomechanically rolled, QT – quenched and tempered, L1 – low-temperature property, impact testing at −50 °C, L2 – special low-temperature property, impact testing at −50 °C, enhanced requirement

18.6.4 Comparative Standards for Steel

This discussion on carbon steel material and the subsequent discussion on other construction materials are generally based on the generic composition of the materials without referring to any code of construction. It is difficult to furnish equivalence of any grade of material from one code to another; at best, steels grades can be compared based on the closest matching technical requirements. Tables 18.10 and 18.11 list some of the comparable standards for flat and tubular products commonly used in the fabrication of pressure vessels.

18.6.5 Stainless Steel

Alloys of iron and carbon with over 12% chromium, which resist rusting under most atmospheric conditions, are called stainless steels. These alloys become more corrosion resistant as the chromium level is increased. As more nickel is added, several phases are possible

Table 18.11 Comparative chart for material standards of tubular products for pressurized use

Harmonized European standard			ASTM		DIN	BS		
Description							Standard	Grade
Nonalloy for general use	EN 10216-1	P195 P235 P265	SA 53 Gr A/SA 106 Gr A SA 53 Gr B/SA 106 Gr B		 DIN 1629 St 37 DIN 1629 St 44	BS 3059-1 Gr 320 BS 3601 Gr 360 BS 3601 Gr 430		
					DIN 17175	*BS 3059-2 Carbon/alloy*	*BS 3602 C-Mn*	*BS 3606 Exchanger tube*
Unalloyed and alloyed for elevated temperature	EN 10216-2	P195GH P235GH P265GH	SA 179 – cold-drawn tubes for exchanger SA 192 – boiler tubes SA 210 Gr A1 – boiler/superheater tube SA 210 Gr C		 St 35.8 St 45.8 17Mn4	 360 440	 360 430	Gr 320 400 440
			Tube	*Pipe*				
		16Mo3 10CrMo5-5 13CrMo4-5 10CrMo9-10 X11CrMo5 X11CrMo9-1 X10CrMoVNb9-1	SA 209 T1 SA 213 T2 SA 213 T11 SA 213 T12 SA 213 T21 SA 213 T22 SA 213 T5 SA 213 T9 SA 213 T91	SA 335 P1 SA 335 P2 SA 335 P11 SA 335 P12 SA 335 P21 SA 335 P22 SA 335 P5 SA 335 P9 SA 335 P91	15Mo3 13CrMo44 10CrMo9-10 12CrMo195 X10CrMoVNb91	243 620–470 91	 BS 3604 (ferritic) 621 620 622 625 620–470	243 621 620 622 625
					DIN 17179			
Unalloyed and alloyed, fine grain	EN 10216-3	P275NL1/NL2 P355N/NH P355NL1/NL2 P460N/NH P460NL1/NL2			WStE/TStE 285 EStE/StE 355 WStE/TStE 355 EStE/StE 460 WStE/TStE 460			
			ASTM 333	*ASTM 334*	*DIN 17173*	*BS 3603 carbon/alloy*		
Unalloyed and alloyed, low temperature	EN 10216-4	P215 NL P265 NL 12Ni14 12Ni14 + QT X10Ni9 X10Ni9 + QT	Gr 1 Gr 6 Gr 3 Gr 3 Gr 8 Gr 8	Gr 1 Gr 6 Gr 3 Gr 3 Gr 8 Gr 8	TTSt35 N 10Ni14 10Ni14 X8Ni9 X8Ni9	 430 LT 530 LT 530 LT 509 LT 509 LT		

Legend for steel grade to EN series:
G – other characteristics follow, N – normalized condition, H – elevated-temperature property required, M – thermomechanically rolled, QT – quenched and tempered, L1 – low-temperature property, impact testing at −50 °C, L2 – special low-temperature property, impact testing at −50 °C, enhanced requirement

and the alloy may undergo transformation depending on the actual content of Cr–Ni–Fe and C. Gamma or austenitic stainless steel is an iron alloy containing at least 18% Cr and 8% Ni with up to 0.10% carbon. The austenitic structure provides a combination of excellent corrosion, oxidation, and sulfidation resistance with high creep resistance, toughness, and strength at temperatures up to 550 °C. The 18Cr-8Ni stainless alloys form a series known as the American Iron and Steel Institute (AISI) type 300 series, with varying amounts of carbon, molybdenum, and titanium added.

The 18-8 series show good formability, besides being readily weldable without stress relief; however they can be hardened by cold working. These steels are susceptible to grain-boundary chromium carbide precipitation, known as *sensitization*, when subjected to temperatures in the range of 535–800 °C. To prevent sensitization, low-carbon grades (C < 0.03%) and

stabilized grades with added niobium or titanium are used.

The traditional grades of stainless steel that are extensively used in the fabrication of chemical plants and equipment are AISI 304 type and the 2% molybdenum-bearing 316 types along with their low-carbon versions 304L and 316L or the stabilized grades 321 (with Ti) or 347 (with Nb) where intercrystalline corrosion is to be avoided.

Higher-alloyed grades such as AISI 309 and 310 have a higher chromium content that makes them suitable for high-temperature applications such as furnace liners, preheaters, and column trays.

Developments

Newer grades of stainless steel have been developed to overcome the limitations of low 0.2% proof stress, sensitivity to stress, and pitting corrosion especially in chloride media, inadequate corrosion resistance in reducing media, and preferential attack on the ferrite phase in strong oxidizing media.

Nitrogen alloyed steel such as AISI 304LN and 316LN have been developed with the addition of 0.2% nitrogen, resulting in an improvement of the proof stress by about 15%. Nitrogen alloyed steel finds wide applications in the transportation and storage industries.

For reactors, strippers, and condensers in urea applications, steels with higher chromium and nickel contents but nil ferrite have been developed. Modified compositions of AISI 310 steel such as SANDVIK 2RE69 and Assab 725 LN have been developed for strong oxidizing conditions in fertilizer plants.

For elevated-temperature applications in furnaces, and hydrocarbon and steam reformers, where higher creep strength is also necessary, casting alloys such as HK-40 and IN657 have been developed.

Duplex stainless steels have been developed to combine the attractive properties of ferritic and austenitic stainless steels. In simple terms, the ferrite can be said to provide mechanical strength and stress corrosion resistance while the austenite provides ductility, and the two combine to produce a fine-grained, two-phase microstructure with high strength and good corrosion resistance. Of the many alloying elements, Cr and Mo enhance the formation of ferrite, while Ni and N stabilize the austenite. The resistance to pitting and crevice corrosion in chloride environments is increased, as expressed by the pitting resistance equivalent $PRE_N = \%\,Cr + 3.3 \times \%\,Mo + 16 \times \%\,N$.

This number is used to rank materials according to their expected resistance to pitting corrosion. A 23% Cr Mo-free grade would have a PRE_N value of about 25. Regular Mo-alloyed duplex grades have PRE_N values of 30–36. Steels having a PRE_N value higher than 40 are normally defined as superduplex stainless steels.

Welding

Duplex stainless-steel welds using a filler material with matching composition show high levels of ferrite, which has low toughness and poor ductility. Therefore all welding consumables for duplex materials are overalloyed with nickel, which allows more austenite to form so that the ferrite level in the welds is lowered and the welds show good ductility and corrosion resistance. It is recommended that a ferrite content of approximately 22–70% should be achieved, equivalent to 30–100 ferrite number (FN). In addition to the ferrite count, a corrosion test in ferric chloride is also carried out as per ASTM G48, which gives a good assessment of the corrosion resistance of the weld metal. As per this test, the critical pitting temperature (CPT) is specified as 22 °C for duplex and 35 °C for superduplex steel.

Preheating of duplex material is not required except where heavy loads on high-ferrite-containing welds may cause cracking. Postwelding solution annealing is required only in cases where the resultant weldment has deteriorated due to detrimental phase transformation and/or has high ferrite levels.

Root passes of nitrogen-alloyed stainless steel are welded with higher-alloyed filler, to compensate for the influence of nitrogen.

Urea-grade stainless steels and steels for use in high-temperature applications are welded using electrodes with matching composition but enriched with 4–5% manganese to counteract the tendency for microfissuring.

18.6.6 Ferritic and Martensitic Steels

Ferritic steels are chromium-iron stainless steels with little or no nickel and form a body-centered structure, unlike the face-centered structure of austenitic steel. When ferritic steels are modified by heat treatment, they become hardened and form *martensitic* steels.

Martensitic steels derive their excellent hardness from the high levels of carbon added to their alloy. The most commonly used martensitic steel is ASTM type 410 stainless steel, which is applied for the column tray and tower lining in crude refinery applications. The increased carbon level in 410 steel results in a much harder martensitic cutlery steel or tool steel type 420.

By increasing the percentage of chromium, transformation hardening is suppressed, as in ASTM types 430 and 446, which are essentially ferritic. These steels are resistant to chloride stress corrosion cracking; however they are subject to ductile–brittle temperature embrittlement, thereby restricting their mechanical properties.

The limiting values for the X and J factors are usually specified for welding consumables, although it would be preferable also to restrict these for the base material.

A step-cooling simulation treatment is performed on higher-thickness quenched and tempered plates to determine the susceptibility to embrittlement phenomena in terms of meeting the specified shift in the 40 ft–lb Charpy V-notch (CVN) transition temperature.

Welding

With increasing base and weld material strength and hardenability, the hydrogen diffusibility in the weldment is kept below 5 mL/100 g of deposited weld metal. The flux covering of all the electrodes is of the low-hydrogen type and employs binders that give high resistance to moisture absorption. Prior to use, they are dried or baked at the manufacturer's recommended temperature.

Although there are several theories for determining the optimum preheat temperature, the common industrial practice is to use the carbon equivalent to provide guidance regarding the temperature selection, as follows:

CE	Temperature (°C)
< 0.4	50
< 0.55	100
< 0.70	150
< 0.8	200
< 0.9	250

Maintaining the preheat after welding (also called postheating) for a specified period (generally 300–350 °C for 30 min) in some cases (say for pipe thicknesses greater than 12 mm with a chromium content of 2–7%) also helps to reduce hydrogen levels, thereby preventing cold cracks and stress corrosion cracking.

Martensitic steels can be welded, but caution needs to be exercised as they will produce a very hard and brittle zone adjacent to the weld. Cracking can occur in this zone (particularly in thicker sections), thus preheating and PWHT are recommended.

Although ferritic steels are less prone to cracking due to their lower strength and nonhardenability, the weldment suffers from excessive grain growth, sensitization, and a lack of ductility. Due to the excessive grain growth problem, only thin-gauge sheets are generally used. Filler material can be of a similar composition, or alternatively an austenitic grade can be used to help the weld toughness and increase the ductility.

Table 18.12 lists some of the comparable standards for stainless-steel grades commonly used in the fabrication of pressure vessels.

Developments

Since the ferritic grades do not exhibit good welding properties, hybrid utility ferritics such as 3CR12 with controlled martensite (dual-phase steel) have been developed to overcome these welding difficulties. Using new steel-refining techniques, along with the addition of titanium or niobium, it has been possible to develop extremely corrosion-resistant grades such as *superferritic stainless steel*.

18.6.7 Copper- and Nickel-Based Alloys

Brass

Brasses are commercially produced with varying percentages of copper and zinc to provide a range of properties depending on the end-use requirements.

Admiralty brass, which is widely used for tubes in water-cooled condensers for low water speeds, is an alloy brass containing 71% Cu, 28% Zn, and 1% Sn. To prevent dezincification, small amounts of arsenic, phosphorus, or antimony are added.

At high water speeds and when seawater contains air bubbles, aluminum brass containing 2% Al is more suitable due to the formation of a protective film. For tube plates in condensers and exchangers, it is usual practice to use high-zinc brasses, hot-rolled Muntz metal (60% Cu, 40% Zn) or naval brass (60% Cu, 39% Zn, and 1% Sn) to take advantage of their higher tensile strength, although the two-phase structure of these alloys cannot be satisfactorily inhibited against dezincification.

Bronze

Bronze is a tin alloy of copper with other elements such as aluminum added to obtain other properties. Because of the hardening effect of tin, hot-rolled bronze plates have greater strength than brass plates and therefore can be used for tube plates and channel material for exchangers.

Cu–Ni Alloys

Alloys of copper and nickel have historically been used in saltwater condensers as they show better resistance to saltwater than brasses. Increasing the nickel content was found to be beneficial, and 30% Ni alloy was adopted as the standard for naval vessels. The addition of iron and Mn was found to improve the resistance to impingement attack.

These alloys are used for tubes in heat exchangers, saltwater pipelines, and hydraulic lines as well as in several applications in marine and offshore platform services. Cupronickel tubes are superior to brass in terms of their better resistance to dezincification for water-cooled heat exchanger applications involving higher metal temperatures. They are also excellent materials for tube plates, and because of their good formability and weldability, they can be used in sheet

Table 18.12 Comparative chart for various stainless-steel grades

Structure	Hardenability	ASTM 240		EN 10028-7		Analysis built up from basic type
		Grade	UNS no.		Grade	Number
Austenitic	Hardenable by cold work	304	S 30400	X5CrNi18-10	1.4301	Cr 18% + Ni 8% basic type
		304L	S 30403	X2CrNi18-10	1.4303	304 with low carbon
		308	S 30800	X2CrNiMo8-14-3	1.4432	Higher Cr and Ni for more corrosion and scaling resistance
		309	S 30900	X2CrNiCuWN25-7-4	1.4501	Still higher Cr and Ni
		310	S 31000	X5CrNi25-21	1.4335	Highest Cr and Ni (Cr 25% + Ni 20%)
		316	S 31600	X5CrNiMo17-11-2	1.4401	Mo added for corrosion resistance
		316L	S 31603	X5CrNiMo17-12-2	1.4404	316 with low carbon
		316N	S 31603	X2CrNiMoN17-11-2	1.4406	316 with nitrogen added for low-temp. service
		321	S 32100	X6CrNiTi18-10	1.4541	Ti added to avoid carbide precipitation
		347	S 34700	X6CrNiNb18-10	1.4550	Cb added to avoid carbide precipitation
Martenstitic	Hardenable by heat treatment	410	S 41000	X12Cr13	1.4006	Cr 12% basic type
		420	S 42000	X46Cr13	1.4034	Higher C, cutlery applications
		431	S 43100	X4CrNiMo16-5-1	1.4418	Higher Cr and Ni added for improved ductility
Ferritic	Nonhardenable	405	S 40500	X6CrAl13	1.4402	Al added to Cr 12% to prevent hardening
		430	S 43000	X6Cr17	1.4016	Cr 17% basic type
		442	S 44200			Higher Cr to resist oxidation and
		446	S 44600			sulfidation at higher temperature
Precipitation-hardening steel	Age-hardenable	17-7 PH	S 17700	X7CrNiAl17-7	1.4568	
		14-8MoPH	S 13800	X8CrNiMoAl15-7-2	1.4532	

form for the fabrication of heat-exchanger shells and water boxes. Monel, a nickel-copper alloy (67% Ni, 30% Cu), shows good resistance to saltwater, and to hydrochloric and hydrofluoric acid under nonoxidizing conditions. Therefore they are excellent material for cladding and trays in towers handling acid vapors.

Other nickel-based alloys are classified as:

1. Chromium bearing as in Inconel 600, and Hastelloy C-22 and C-276
2. Containing chromium and molybdenum such as Inconel 625, Hastelloy B, and Incoly 825
3. Precipitation-hardening alloys such as Monel K-500, and Inconel 817.

These alloys show excellent resistance to pitting and stress corrosion cracking in chloride environments and retain strength at elevated temperatures. Therefore, they are excellent candidates for exchanger tubes, heat-transfer plates for plate heat exchangers (PHE), and pressure coils for steam/hydrocarbon reformers, naphtha-cracking furnaces, etc. in the petrochemical and fertilizer industries.

Welding

Gas tungsten arc (GTAW), gas metal arc (GMAW), and shielded metal arc (SMAW) processes are most commonly used for welding brasses and bronze. Whereas thin gauges are welded with GTAW using zinc-free fillers, heavier gauges are joined by a GMAW/SMAW process using zinc-free silicon bronze or aluminum bronze fillers/electrodes. Zinc-free fillers are prescribed since the evolution of zinc fumes makes the weld porous and affects visual observation of the welding process; moreover, zinc fumes are extremely hazardous to health. Argon and helium, either individually or in combination, are used for shielding in the case of the GTAW/GMAW process.

Welding consumables for welding of all Cu-Ni-based alloys are available with compositions matching the specific parent material with the generous addition of manganese and/or niobium, which are added inten-

tionally to provide resistance to hot cracking and raise hot strength. Most of these consumables are often used for dissimilar metal welding between the nickel base and most steels or between other ferrous and nonferrous alloys.

Carbon and silicon are controlled to low levels to minimize detrimental precipitates in the weld metal and HAZ for electrodes with specifications matching some of the high-molybdenum alloys such as Hastelloy C276 and Hastelloy B.

References

18.1 J.F. Harvey: *Theory and Design of Pressure Vessels* (Van Nostrand Reinhold, Amsterdam 1985)

18.2 D.R. Moss: *Pressure Vessel Design Manual* (Gulf, Houston 1987)

18.3 H.H. Bednar: *Pressure Vessel Design Handbook* (Van Nostrand Reinhold, Amsterdam 1986)

18.4 C. Matthews: *Engineer's Guide to Pressure Equipment – The Pocket Reference* (Professional Engineering, Suffolk 2001)

18.5 G. Baylac, D. Koplewicz (Eds.): *EN 13445: Unfired Pressure Vessels – Background to the Rules in Part 3 Design* (UNM, Paris 2002), Issue 2

18.6 R.K. Shah, D.P. Sekulic: *Fundamentals of Heat Exchanger Design* (Wiley, New York 2003)

18.7 T.A. Khan, W. Li: Optimal design of plate-fin heat exchanger by combining multi-objective algorithms, Int. J. Heat Mass Transf. **108**(B), 1560–1572 (2017)

18.8 Tubular Exchanger Manufacturers Association: *Standards of the Tubular Exchanger Manufacturers Association*, 9th edn. (TEMA, Tarrytown 2007)

18.9 S. Kakaç, H. Liu, A. Pramuanjaroenkij: *Heat Exchangers: Selection, Rating, and Thermal Design*, 3rd edn. (CRC, Boca Raton 2012)

18.10 T.L. Bergman, A.S. Lavine: *Fundamentals of Heat and Mass Transfer*, 8th edn. (Wiley, New York 2017)

18.11 W.M. Kays, A.L. London: *Compact Heat Exchangers*, 3rd edn. (McGraw-Hill, New York 1984)

18.12 R.A. Bowman, A.C. Mueller, W.M. Nagle: Mean temperature difference in design, Trans. ASME **62**(4), 283 (1940)

Ajay Mathur

HSE and Plant Engineering
Indohaan Technologies Pvt Ltd
Faridabad, India
amathur@indohaan.com

Ajay Mathur graduated in mechanical engineering from M. S. University–Baroda (India) and has over 33 years of experience in fabrication, engineering, and contracting industry. He is director of a consultancy organization handling health, safety, environmental, and sustainability studies. Previously, as head of plant engineering, he executed several process plants from detailed design to start-up and handover.

Hamidreza Najafi

Department of Mechanical and Civil Engineering
Florida Institute of Technology
Melbourne, FL, USA
hnajafi@fit.edu

Hamidreza Najafi is an Assistant Professor of Mechanical Engineering and Director of the Innovations in Sustainable Energy and Thermal Systems (I.S.E.T.S) Lab at Florida Institute of Technology. He conducts research and teaches courses in the areas of thermal sciences. His research works have been focused on design and optimization of thermal/energy systems, sustainable energy, and computational heat transfer.

19. Turbomachinery

Meinhard T. Schobeiri

The following chapter consists of two sections. Section 19.1 presents a concise treatment of the theory of turbomachinery stages including the energy transfer in absolute and relative systems. Contrary to the traditional approach that treats turbine and compressor stages of axial, radial or mixed configurations differently, these components are treated from a unifying point of view. A detailed instruction in Sect. 19.2 for turbine and compressor blade design concludes Sect. 19.1

Section 19.3 is dedicated to steady and unsteady performance of gas turbine engines, where the components are treated as generic modules. Thus, any arbitrary power generation or aircraft gas turbine engine with single or multiple shafts can be composed of these modules. Several examples show, how different gas turbine configurations can be constructed and dynamically simulated. Finally, a section about the new generation gas turbines shows, how the efficiency of gas turbines can be improved far beyond the existing level. This chapter is based on [19.1], where the reader can find detailed explanation of relevant aerodynamic aspects of turbomachines, their component losses and efficiencies, and the design and off-design performance calculations.

19.1 **Theory of Turbomachinery Stages** 777
19.1.1 Energy Transfer in Turbomachinery Stages 777
19.1.2 Energy Transfer in Relative Systems 778
19.1.3 General Treatment of Turbine and Compressor Stages 779
19.1.4 Dimensionless Stage Parameters 781
19.1.5 Relation Between Degree of Reaction and Blade Height for a Normal Stage Using Simple Radial Equilibrium 783
19.1.6 Effect of the Degree of Reaction on the Stage Configuration 784
19.1.7 Effect of the Stage Load Coefficient on Stage Power 785
19.1.8 Unified Description of a Turbomachinery Stage 786
19.1.9 Special Cases 788
19.1.10 Increase of the Stage Load Coefficient: Discussion 789

19.2 **Blade Design** 790
19.2.1 Compressor Blade Design 791
19.2.2 Turbine Blade Design 795
19.2.3 Assessment of Blades Aerodynamic Quality 798

19.3 **Gas Turbine Engines: Design and Dynamic Performance** 800
19.3.1 Gas Turbine Processes, Steady Design Operation 800
19.3.2 Nonlinear Gas Turbine Dynamic Simulation 809
19.3.3 Engine Components, Modular Concept, and Module Identification ... 809
19.3.4 Levels of Gas Turbine Engine Simulations, Cross Coupling 814
19.3.5 Nonlinear Dynamic Simulation Case Studies 814
19.3.6 New Generation Gas Turbines, Detailed Efficiency Calculation 823

References 827

19.1 Theory of Turbomachinery Stages

19.1.1 Energy Transfer in Turbomachinery Stages

Energy transfer in turbomachinery is established by means of a number of stages. A *turbomachinery stage* consists of a row of fixed, guide vanes called *stator blades*, and a row of rotating blades termed the *rotor blades*. To elevate the total pressure of a working fluid, *compressor stages* that partially convert the mechanical energy into potential energy are used. According to the law of conservation of energy, this energy increase requires an external energy input which must be added

K.-H. Grote, H. Hefazi (Eds.), *Springer Handbook of Mechanical Engineering*, Springer Handbooks,
https://doi.org/10.1007/978-3-030-47035-7_19

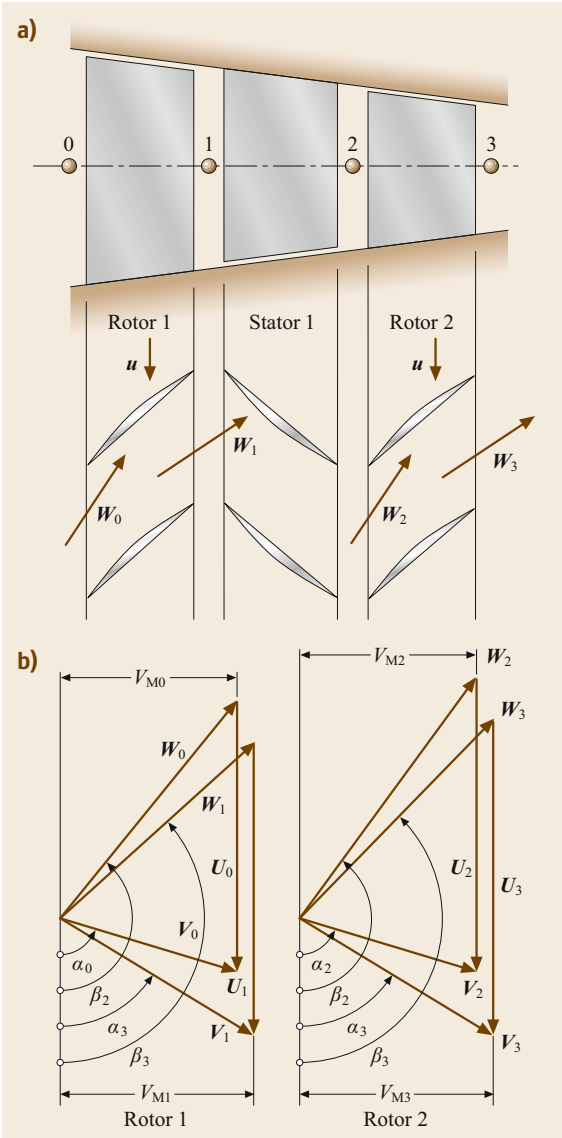

Fig. 19.1 **(a)** An axial compressor stage with a rotor–stator–rotor configuration and **(b)** velocity diagrams for the first and second rotor

to the system in the form of mechanical energy. Figure 19.1 shows a schematic of an axial compressor stage that consists of one stator and two rotor rows. In general, a *compressor component* starts with a rotor row followed by a stator row. Compressor configurations that start with an *inlet guide vane* are also found. To define a unified station nomenclature for the compressor and turbine stages, we identify station number 1 as the inlet of the stator, followed by station 2 as the rotor inlet, and station 3 as the rotor exit. The absolute and relative flow angles are counted counterclockwise from a horizontal line. This convention allows an easier calculation of the off-design behavior of compressor and turbine stages during a transient operation, as we will see later. Different angle conventions are used in the literature [19.2–5]. The working fluid enters the first rotor with an *absolute velocity* in the axial direction (Fig. 19.1b), where it is deflected in the direction of the rotor's leading edge. As a result of the rotational motion of the rotor, a major part of the mechanical energy input is converted into the potential energy of the working medium, causing the total pressure to rise. During the compression process, the absolute velocity within the stator and the relative velocity vector within the rotor decrease. To convert the total energy of a working medium into mechanical energy, *turbine stages* are used. Figure 19.2 exhibits a turbine stage within a multistage environment. As shown, the mean diameter may change from inlet to exit. The continuous increase in flow path cross section is due to the continuity requirement.

19.1.2 Energy Transfer in Relative Systems

Since the rotor operates in a relative frame of reference (relative system), the energy conversion mechanism is quite different from that of a stator (absolute system). A fluid particle that moves with a relative velocity $\boldsymbol{W}$ within the relative system that rotates with the angular velocity $\boldsymbol{\omega}$, has an absolute velocity

$$\boldsymbol{V} = \boldsymbol{W} + \boldsymbol{\omega} \times \boldsymbol{R} = \boldsymbol{W} + \boldsymbol{U}\,, \quad \boldsymbol{\omega} \times \boldsymbol{R} = \boldsymbol{U}\,, \tag{19.1}$$

where $\boldsymbol{R}$ is the radius vector of the particle in the relative system. Introducing the absolute velocity vector $\boldsymbol{V}$ in the equation of motion [19.6, Chap. 3, Eq. (3.37)] and multiplying the results with a relative differential displacement dR, we get the energy equation for an adiabatic steady flow within a relative system

$$\mathrm{d}\left(h + \frac{1}{2}W^2 - \frac{\omega^2 R^2}{2} + gz\right) = 0 \tag{19.2}$$

or the relative total enthalpy

$$H_\mathrm{r} = h + \frac{1}{2}W^2 - \frac{\omega^2 R^2}{2} + gz = \text{const}\,. \tag{19.3}$$

Neglecting the gravitational term, $gz \approx 0$, (19.3) can be written as

$$h_1 + \frac{1}{2}W_1^2 - \frac{1}{2}U_1^2 = h_2 + \frac{1}{2}W_2^2 - \frac{1}{2}U_2^2\,. \tag{19.4}$$

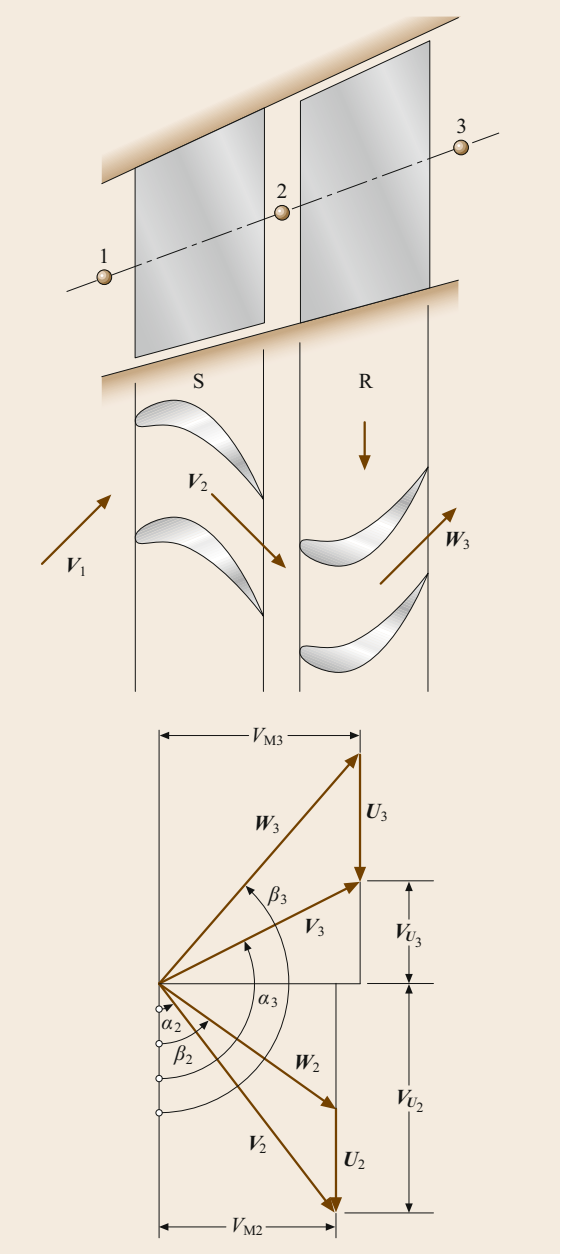

Fig. 19.2 An axial turbine stage with velocity diagram

Equation (19.4) is the equation for the energy transformed in a relative system. As can be seen, the transformation of kinetic energy undergoes a change while the transformation of static enthalpy is frame indifferent. With these equations together with the energy balance [19.1] we can analyze the energy transfer within an arbitrary turbine or compressor stage.

19.1.3 General Treatment of Turbine and Compressor Stages

In this chapter, compressor and turbine stages are treated from a unified physical point of view. Figures 19.3 and 19.4 show the decomposition of a turbine and a compressor stage into their stator and rotor rows. The primes $'$ and $''$ refer to stator and rotor rows, respectively. As seen, the difference between the isentropic and the polytropic enthalpy difference is expressed in terms of dissipation $\Delta h'_{\mathrm{d}} = \Delta h'_{\mathrm{s}} - \Delta h'$ for turbines and $\Delta h'_{\mathrm{d}} = \Delta h' - \Delta h'_{\mathrm{s}}$ for compressors. For the stator, the energy balance requires that $H_2 = H_1$. This leads to

$$h_1 - h_2 = \Delta h' = \frac{1}{2}\left(V_2^2 - V_1^2\right). \tag{19.5}$$

Moving to the relative frame of reference, the relative total enthalpy $H_{\mathrm{r}2} = H_{\mathrm{r}3}$ remains constant. Thus, the energy equation for the rotor is according to (19.4) (Fig. 19.4)

$$h_2 - h_3 = \Delta h'' = \frac{1}{2}\left(W_3^2 - W_2^2 + U_2^2 - U_3^2\right). \tag{19.6}$$

The stage specific mechanical energy balance requires (Fig. 19.5)

$$\begin{aligned} l_{\mathrm{m}} &= H_1 - H_3 \\ &= (h_1 - h_2) - (h_3 - h_2) + \frac{1}{2}\left(V_1^2 - V_3^2\right). \end{aligned} \tag{19.7}$$

Inserting (19.5) and (19.6) into (19.7) yields

$$l_{\mathrm{m}} = \frac{1}{2}\left[\left(V_2^2 - V_3^2\right) + \left(W_3^2 - W_2^2\right) + \left(U_2^2 - U_3^2\right)\right]. \tag{19.8}$$

Equation (19.8), known as the *Euler turbine equation*, indicates that the stage work can be expressed simply in terms of absolute, relative, and rotational kinetic energies. This equation is equally applicable to turbine stages that *generate* shaft power and to compressor stages that *consume* shaft power. In the case of a turbine stage, the sign of the specific mechanical energy l_{m} is negative, which indicates that energy is removed from the system (power generation). In compressor cases, it is positive because energy is added to the system (power consumption). Before proceeding with velocity diagrams, it is of interest to evaluate the individual kinetic energy differences in (19.8). If we wish to design a turbine or a compressor stage with a high specific mechanical energy l_{m} for a particular rotational speed, then we have two options:

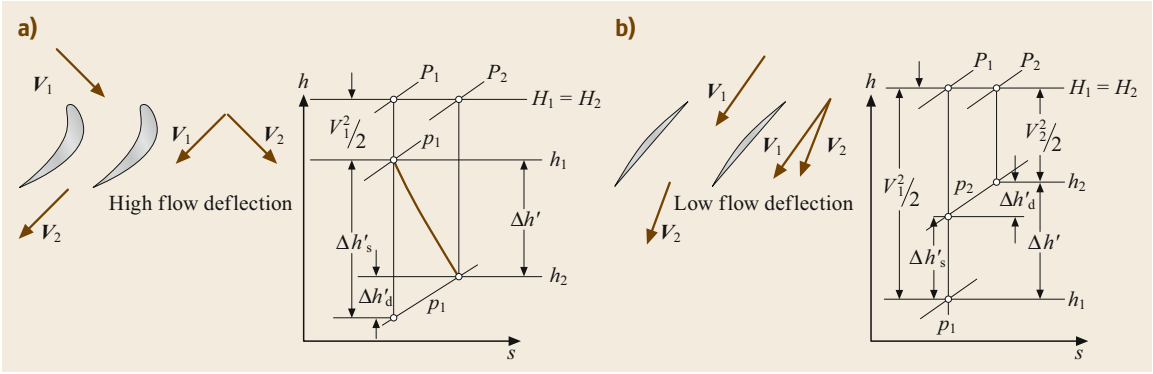

Fig. 19.3a,b Expansion and compression process through a turbine (**a**) and a compressor (**b**) stator row

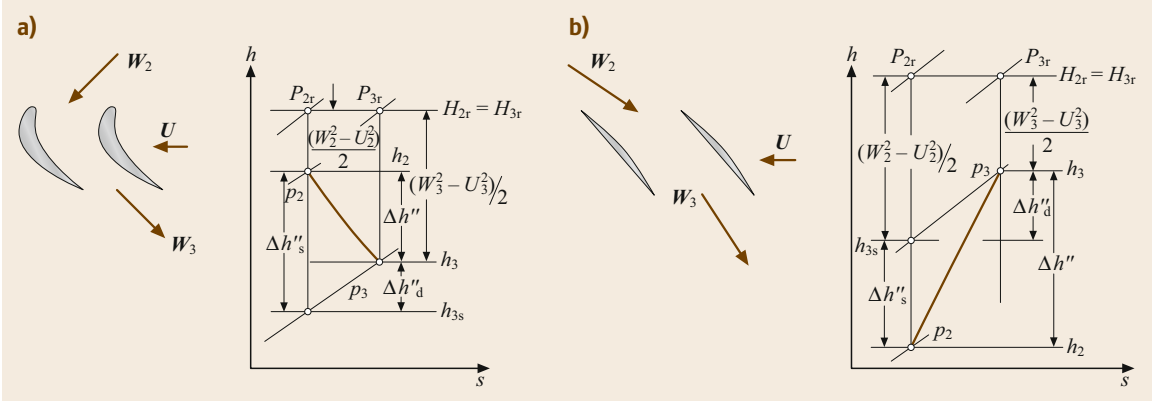

Fig. 19.4a,b Expansion and compression process through a turbine (**a**) and a compressor (**b**) rotor row

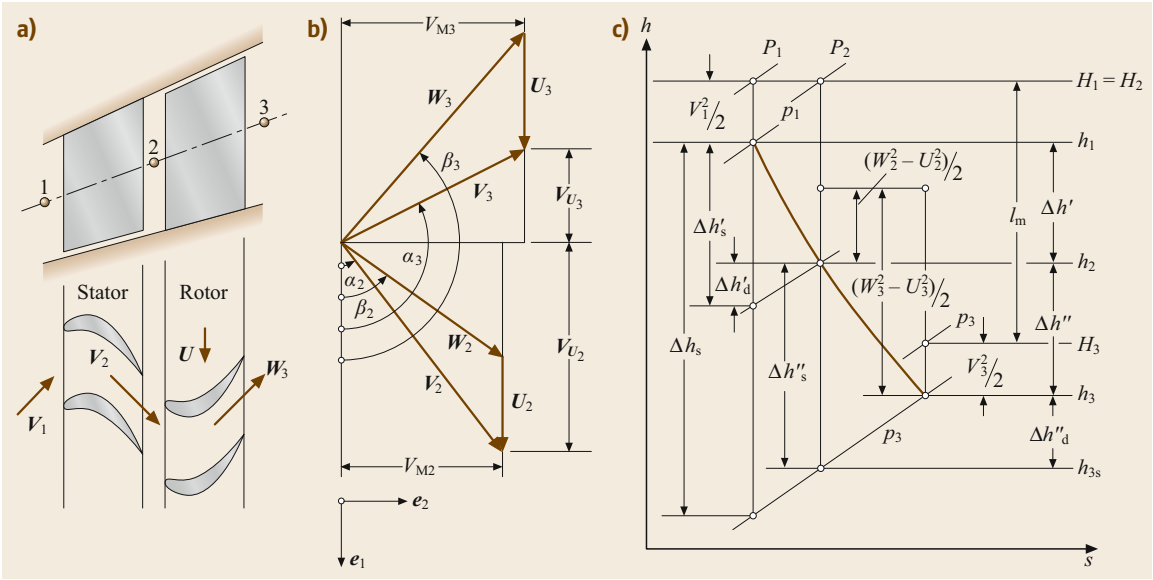

Fig. 19.5a–c A compressor stage (**a**) with the velocity diagram (**b**) and the expansion process (**c**). The direction of the unit vector e_1 is identical with the rotational direction

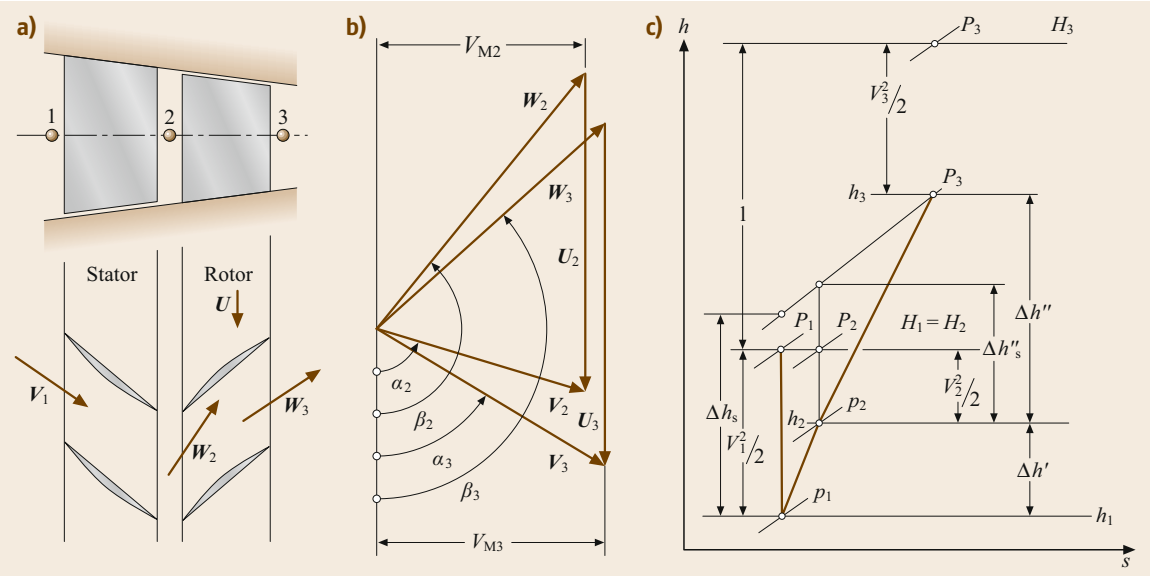

Fig. 19.6a–c A compressor stage (a) with the velocity diagram (b) and the expansion process (c). The direction of the unit vector $\boldsymbol{e}_1$ is identical with the rotational direction

1. We increase the *flow deflection*, which leads to an increase in $(V_2^2 - V_3^2)$.
2. We increase the radial difference that leads to a larger $(U_2^2 - U_3^2)$.

While option 1 is used in axial stages, option 2 is primarily applied to radial stages. These quantities are the characteristics of a stage velocity diagram at the corresponding radial section.

Using the trigonometric relation with the *angle convention* from the velocity diagram in Figs. 19.5 and 19.6, we determine the velocity components and vector relations from

$$
\begin{aligned}
&V_{\mathrm{m}2} = W_{\mathrm{m}2}\,, \quad V_{\mathrm{m}3} = W_{\mathrm{m}3}\,,\\
&\boldsymbol{W}_2 = e_1(V_{\mathrm{u}2} - U_2) + e_2 V_{\mathrm{m}2}\,,\\
&\boldsymbol{W}_3 = -e_1(V_{\mathrm{u}3} - U_3) + e_2 V_{\mathrm{m}3}\,. \qquad (19.9)
\end{aligned}
$$

In (19.9) V_{m}, W_{m} and V_{u}, W_{u} are the meridional and circumferential components of the absolute and relative velocities, respectively. The corresponding kinetic energy contributions are determined from

$$
\begin{aligned}
W_2^2 &= \left(V_{\mathrm{u}2}^2 + V_{\mathrm{m}2}^2\right) + U_2^2 - 2V_{\mathrm{u}2}U_2\\
&= V_2^2 + U_2^2 - 2V_{\mathrm{u}2}U_2\,,\\
W_3^2 &= V_{\mathrm{u}3}^2 + U_3^2 + 2V_{\mathrm{u}3}U_3 + V_{\mathrm{m}3}^2\,,\\
W_3^2 &= V_3^2 + U_3^2 + 2V_{\mathrm{u}3}U_3\,. \qquad (19.10)
\end{aligned}
$$

Incorporating (19.9) and (19.10) into (19.8) yields the *stage specific* work

$$
l_{\mathrm{m}} = U_2 V_{\mathrm{u}2} + U_3 V_{\mathrm{u}3}\,. \qquad (19.11)
$$

Equation (19.11) is valid for axial, radial, and mixed flow turbines and compressors. A similar relation is obtained from the scalar product of moment of momentum and the angular velocity. In conjunction with the equation of moment of momentum, one finds in the literature $l_{\mathrm{m}} = U_2 V_{\mathrm{u}2} - U_3 V_{\mathrm{u}3}$. In order to avoid confusion that may arise from different signs, it should be pointed out that the negative sign is the result of the formal derivation of the conservation law of moment of momentum. This negative sign implies that $V_{\mathrm{u}1}$ and $V_{\mathrm{u}2}$ point in the same direction. The unified angle convention introduced in Figs. 19.1 and 19.2, however, takes the actual direction of the velocity components with regard to a predefined coordinate system.

19.1.4 Dimensionless Stage Parameters

Equation (19.11) exhibits the direct relation between the specific stage work l_{m} and the kinetic energies. The velocities from which these kinetics energies are built can be taken from the corresponding stage velocity diagram. The objective of this chapter is to introduce dimensionless stage parameters that completely determine the stage velocity diagram. These stage pa-

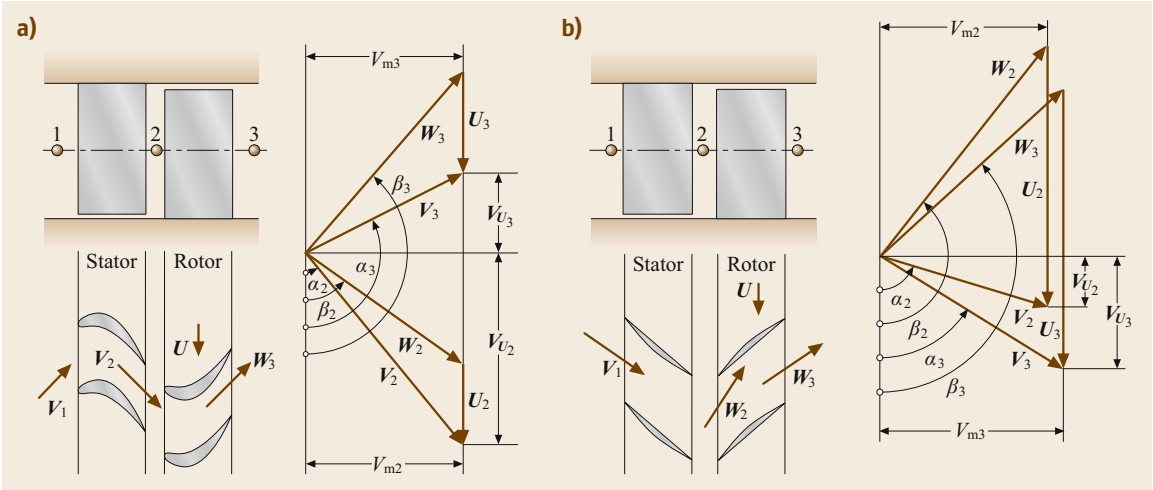

Fig. 19.7a,b Turbine (a) and compressor (b) stages with corresponding velocity diagrams

rameters exhibit unified relations for compressor and turbine stages, respectively.

Starting from a turbine or compressor stage with constant mean diameter and axial components (Fig. 19.7) we define the dimensionless stage parameters that describe the stage velocity diagram of a *normal stage* introduced by *Traupel* [19.3]. A normal stage is encountered within the high-pressure (HP) part of multistage turbines or compressor components and is characterized by $U_3 = U_2$, $V_3 = V_1$, $V_{m1} = V_{m3}$, and $\alpha_1 = \alpha_3$. The similarity of the velocity diagrams allows the same blade profile to be used throughout the HP turbine or compressor, thus significantly reducing manufacturing costs. We define the stage flow coefficient ϕ as the ratio of the meridional velocity component and the circumferential component. For this particular case, the meridional component is identical with the axial component

$$\phi = \frac{V_{m3}}{U_3} \,. \tag{19.12}$$

The stage flow coefficient ϕ in (19.12) is a characteristic of the mass flow behavior through the stage. The *stage load coefficient* λ is defined as the ratio of the specific stage mechanical energy l_m and the exit circumferential kinetic energy U_3^2. This coefficient directly relates the flow deflection given by the velocity diagram with the specific stage mechanical energy

$$\lambda = \frac{l_m}{U_3^2} \,. \tag{19.13}$$

The stage load coefficient λ in (19.13) describes the work capability of the stage. It is also a measure for the stage loading. The *stage enthalpy coefficient* Ψ represents the ratio of the isentropic stage mechanical energy and the exit circumferential kinetic energy U_3^2

$$\Psi = \frac{l_s}{U_3^2} \,. \tag{19.14}$$

The stage enthalpy coefficient represents the stage isentropic enthalpy difference within the stage. Furthermore, we define the *stage degree of reaction* r which is the ratio of the static enthalpy difference used in the rotor row divided by the static enthalpy difference used in the entire stage

$$r = \frac{\Delta h''}{\Delta h'' + \Delta h'} \,. \tag{19.15}$$

The degree of reaction r indicates the portion of energy transferred in the rotor blading. Using (19.5) and (19.6), we arrive at

$$r = \frac{\Delta h''}{\Delta h' + \Delta h''} = \frac{W_3^2 - W_2^2 + U_2^2 - U_3^2}{W_3^2 - W_2^2 + U_2^2 - U_3^2 + V_2^2 - V_1^2} \,. \tag{19.16}$$

Since for the stage type under consideration, $V_1 = V_3$ and $U_2 = U_3$, (19.16) can be simplified as

$$r = \frac{W_3^2 - W_2^2}{W_3^2 - W_2^2 + V_2^2 - V_3^2} \,. \tag{19.17}$$

The velocity vectors and the corresponding kinetic energies are determined from the stage velocity diagram

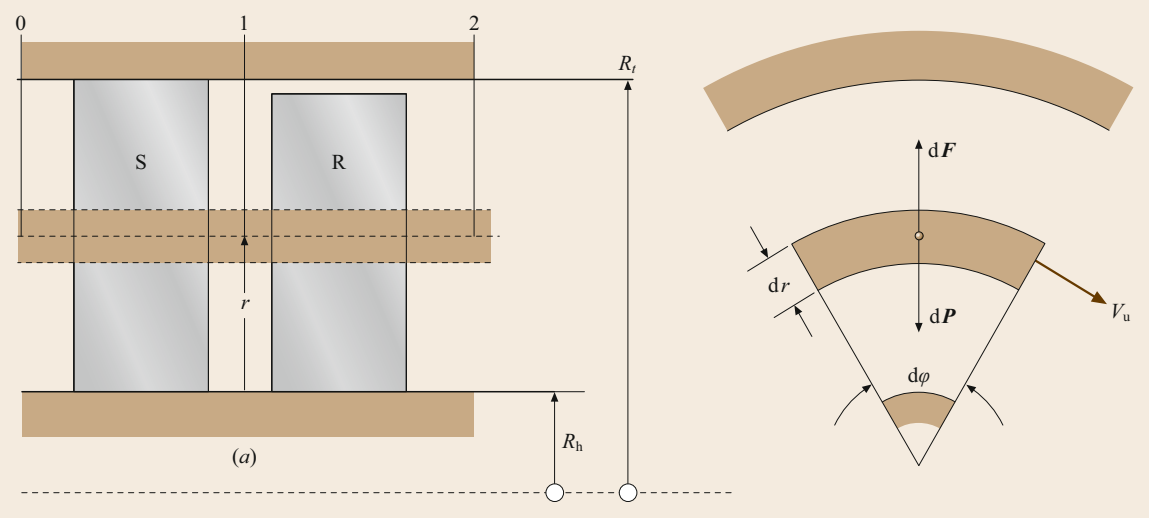

Fig. 19.8 Explanation for simple radial equilibrium

in connection with the angle and direction convention as follows

$$\begin{aligned} V_2 &= e_1(W_{u2} + U_2) + e_2 W_{m2}\,, \\ V_2^2 &= (W_{u2} + U_2)^2 + W_{m2}^2\,, \\ V_3 &= e_1(W_{u3} + U_3) + e_2 W_{m3}\,, \\ V_3^2 &= (W_{u3} + U_3)^2 + W_{m3}^2\,, \end{aligned} \tag{19.18}$$

since $U_2 = U_3 = U$,

$$V_2^2 - V_3^2 = W_2^2 - W_3^2 + 2UW_{u2} + 2UW_{u3}\,. \tag{19.19}$$

Using (19.18) and (19.19), (19.17) gives

$$r = \frac{W_3^2 - W_2^2}{2U(W_{u2} + W_{u3})} = \frac{W_{u3}^2 - W_{u2}^2}{2U(W_{u2} + W_{u3})}\,. \tag{19.20}$$

Rearranging (19.20) yields the final relationship for the particular stage we introduced above

$$r = \frac{1}{2}\frac{W_{u3} - W_{u2}}{U}\,. \tag{19.21}$$

19.1.5 Relation Between Degree of Reaction and Blade Height for a Normal Stage Using Simple Radial Equilibrium

In axial flow compressors or turbines, the working fluid has a rotational and translational motion. The rotating fluid is subjected to centrifugal forces that must be balanced by the pressure gradient in order to maintain the radial equilibrium. Consider an infinitesimal sector of an annulus with unit depth containing the fluid element which is rotating with tangential velocity V_u.

The centrifugal force acting on the element is shown in Fig. 19.8. Since the fluid element is in radial equilibrium, the centrifugal force is obtained from

$$\mathrm{d}F = \mathrm{d}m\frac{V_u^2}{R} \tag{19.22}$$

with $\mathrm{d}m = \rho R\,\mathrm{d}R\,\mathrm{d}\phi$. The centrifugal force is kept in balance by the pressure forces

$$\frac{\mathrm{d}\rho}{\mathrm{d}R} = p\frac{\mathrm{d}p}{\mathrm{d}\rho}\frac{V_u^2}{R}\,. \tag{19.23}$$

This result can also be obtained by decomposing the Euler equation of motion [19.1, Chap. 3, Eq. (3.51)] for inviscid flows into its three components in a cylindrical coordinate system. The Euler equation is expressed as

$$\boldsymbol{V}\cdot\nabla\boldsymbol{V} = -\frac{1}{\rho}\nabla p\,. \tag{19.24}$$

In the radial direction

$$V_r\frac{\partial V_r}{\partial R} + V_u\frac{\partial V_r}{R\partial\varphi} + V_z\frac{\partial V_r}{\partial z} - \frac{V_u^2}{R} = -\frac{1}{\rho}\frac{\partial p}{\partial R}\,. \tag{19.25}$$

The assumptions needed to arrive at (19.23) are

$$\frac{\partial V_r}{\partial R} \approx 0\,,\ \text{axial symmetric:}\ \frac{\partial V_r}{\partial\varphi} = 0\,,\quad \frac{\partial V_r}{\partial z} \approx 0\,. \tag{19.26}$$

With these assumptions, (19.24) yields

$$\frac{1}{\rho}\frac{\partial p}{\partial R} = \frac{V_u^2}{R}\,. \tag{19.27}$$

Equation (19.27) is identical with (19.23). Calculation of a static pressure gradient requires additional information from the total pressure relation. For this purpose, we apply the Bernoulli equation neglecting the gravitational term

$$P = p + \frac{1}{2}\rho V^2 = p + \frac{1}{2}\rho\left(V_\mathrm{u}^2 + V_\mathrm{ax}^2\right). \tag{19.28}$$

Using (19.28), the change in radial direction is

$$\frac{\mathrm{d}p_0}{\mathrm{d}R} = \frac{\mathrm{d}p}{\mathrm{d}R} + \rho V_\mathrm{u}\frac{\mathrm{d}V_\mathrm{u}}{\mathrm{d}R} + \rho V_\mathrm{ax}\frac{\mathrm{d}V_\mathrm{ax}}{\mathrm{d}R}. \tag{19.29}$$

If the stagnation or total pressure $P = p_0 = \text{const}$ and $V_\mathrm{ax} = \text{const}$, (19.29) yields

$$\frac{\mathrm{d}p}{\mathrm{d}R} + \rho V_\mathrm{u}\frac{\mathrm{d}V_\mathrm{u}}{\mathrm{d}R} = 0, \quad \text{or} \quad \frac{\mathrm{d}p}{\mathrm{d}R} = -\rho V_\mathrm{u}\frac{\mathrm{d}V_\mathrm{u}}{\mathrm{d}R}. \tag{19.30}$$

Equating (19.30) and (19.23) results in

$$V_\mathrm{u}\frac{\mathrm{d}V_\mathrm{u}}{\mathrm{d}R} + \frac{V_\mathrm{u}^2}{R} = 0 \tag{19.31}$$

or

$$\frac{\mathrm{d}V_\mathrm{u}}{V_\mathrm{u}} + \frac{\mathrm{d}R}{R} = 0. \tag{19.32}$$

The integration of (19.32) leads to $V_\mathrm{u}R = \text{const}$. This type of flow is called free vortex flow and fulfills the requirement to be potential flow, $\nabla \times V = 0$. We use this relation to rearrange the specific stage mechanical energy

$$l_\mathrm{m} = U_2 V_{\mathrm{u}2} + U_3 V_{\mathrm{u}3} = \omega(R_2 V_{\mathrm{u}2} + R_3 V_{\mathrm{u}3}). \tag{19.33}$$

At station 2 (Fig. 19.7a) the swirl is $R_2 V_{\mathrm{u}2} = \text{const} = K_2$; likewise at station 3 the swirl is $R_3 V_{\mathrm{u}3} = K_3$. Since $\omega = \text{const}$, the specific stage mechanical energy is constant

$$l_\mathrm{m} = (K_2 + K_3)\omega = \text{const}. \tag{19.34}$$

Equation (19.34) implies that, for a stage with constant spanwise meridional components and constant total pressure from hub to tip, the specific stage mechanical energy is constant over the entire blade height. To express the degree of reaction in the spanwise direction, we replace the enthalpy differences in (19.15) by pressure differences. For this purpose we apply the first law for an adiabatic process through stator and rotor blades expressed in terms of $\Delta h'' = \bar{v}''\Delta p''$ and $\Delta h' = \bar{v}'\Delta p'$. This leads to

$$r = \frac{\bar{v}''\Delta p''}{\bar{v}''\Delta p'' + \bar{v}'\Delta p'} = \frac{\Delta p''}{\Delta p'' + \frac{\bar{v}'}{\bar{v}''}\Delta p'} \approx \frac{p_2 - p_3}{p_1 - p_3}. \tag{19.35}$$

In (19.35), the ratio of specific volumes was approximated as $\bar{v}'/\bar{v}'' \approx 1$. This approximation is admissible for low Mach number ranges. Considering $R_2 V_{\mathrm{u}2} = \text{const}$, the integration of (19.23) for station 1 from an arbitrary diameter R to the mean diameter R_m yields

$$(p_1 - p_{\mathrm{m}1}) = \frac{\rho}{2}(V_\mathrm{um})_1^2\left(1 - \frac{R_\mathrm{m}^2}{R^2}\right)_1. \tag{19.36}$$

At station 2 we have

$$(p_2 - p_{\mathrm{m}2}) = \frac{\rho}{2}(V_\mathrm{um})_2^2\left(1 - \frac{R_\mathrm{m}^2}{R^2}\right)_2 \tag{19.37}$$

and finally, at station 3 we arrive at

$$(p_3 - p_{\mathrm{m}3}) = \frac{\rho}{2}(V_\mathrm{um})_3^2\left(1 - \frac{R_\mathrm{m}^2}{R^2}\right)_3, \tag{19.38}$$

with $(R_\mathrm{m})_1 = (R_\mathrm{m})_2 = (R_\mathrm{m})_3$ and $V_{\mathrm{um}3} = V_{\mathrm{um}1}$. Introducing (19.36)–(19.38) into (19.35), we finally arrive at a simple relationship for the degree of reaction

$$\frac{1-r}{1-r_\mathrm{m}} - \frac{R_\mathrm{m}^2}{R^2}. \tag{19.39}$$

From a turbine design point of view, it is of interest to estimate the degree of reaction at the hub and tip radius by inserting the corresponding radii into (19.39). As a result, we find

$$\frac{1-r_\mathrm{h}}{1-r_\mathrm{m}} = \left(\frac{R_\mathrm{m}}{R_\mathrm{h}}\right)^2, \quad \frac{1-r_\mathrm{t}}{1-r_\mathrm{m}} = \left(\frac{R_\mathrm{m}}{R_\mathrm{t}}\right)^2. \tag{19.40}$$

Equation (19.40) represents a simple radial equilibrium condition which allows the calculation of the inlet flow angle in a radial direction by integrating (19.32)

$$V_\mathrm{u}R = \text{const}, \quad R = \frac{\text{const}}{V_\mathrm{u}}. \tag{19.41}$$

This leads to the determination of the inlet flow angle in a spanwise direction as

$$\frac{R_\mathrm{m}}{R} = \frac{\cot\alpha_1}{\cot\alpha_\mathrm{m}}. \tag{19.42}$$

19.1.6 Effect of the Degree of Reaction on the Stage Configuration

The distribution of the degree of reaction can also be obtained simply by using the velocity ratio for r. If, for example, the degree of reaction at the mean diameter is set at $r = 50\%$, (19.40) immediately calculates r at

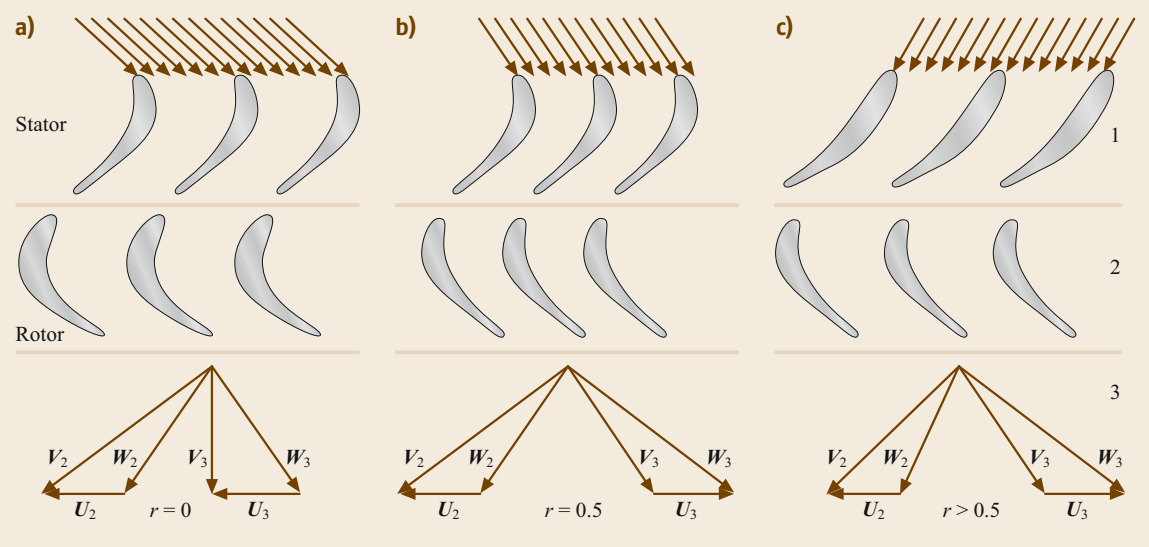

Fig. 19.9a–c Effect of degree of reaction on the stage configuration

the hub and tip for the simple radial equilibrium condition $V_u R = \text{const}$, as presented above. It should be mentioned that for a turbine a negative degree of reaction at the hub may lead to flow separation and is not desired. Likewise, for a compressor, r should not exceed the value of 100%. The value of r has major design consequences. For turbine blades with $r = 0$, as shown in Figs. 19.9a and 19.10, the flow is deflected in the rotor and exit velocity vectors have the same magnitude but opposite directions. The entire stage static enthalpy difference is partially converted within the stator row. Note that the flow channel cross section remains constant. For $r = 0.5$, shown in Fig. 19.9b, a fully symmetric blade configuration is established. Figure 19.9c shows a turbine stage with $r > 0.5$. In this case, the flow deflection inside the rotor row is much greater than the one inside the stator row. Figure 19.10 shows the flow deflection within a high-speed rotor cascade. In the past, mainly two types of stages were common designs in steam turbines. The stage with a constant pressure across the rotor blading ($p_2 = p_3$), called an *action stage*, was used frequently. This turbine stage was designed such that the exit absolute velocity vector V_3 was swirl free. It is most appropriate for the design of single-stage turbines and as the last stage of a multistage turbine. The *exit loss*, which corresponds to the kinetic energy of the exiting mass flow, becomes a minimum by using a swirl-free absolute velocity. The stage with $r = 0.5$ is called the *reaction stage*.

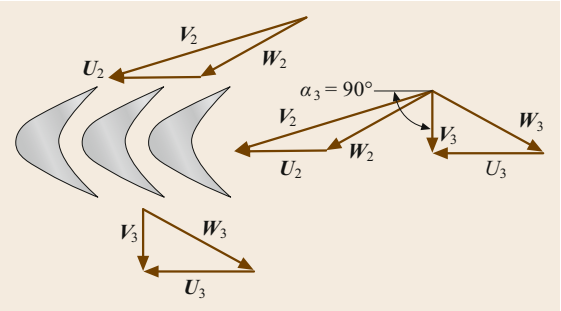

Fig. 19.10 Flow through a high-speed turbine rotor with a degree of reaction $r = 0.0$, note that $\alpha_3 = 90°$ and $|W_2| = |W_3|$

19.1.7 Effect of the Stage Load Coefficient on Stage Power

The stage load coefficient λ defined in (19.13) is an important parameter, which describes the capability of the stage to generate/consume shaft power. A turbine stage with low flow deflection, and thus low specific stage load coefficient λ, generates lower specific mechanical energy. To increase the stage mechanical energy l_m, blades with higher flow deflection are used that produce a higher stage load coefficient λ. The effect of an increased λ is shown in Fig. 19.11, where three different bladings are plotted.

The top blading with the stage load coefficient $\lambda = 1$ has lower deflection. The middle blading has a moderate flow deflection and moderate $\lambda = 2$, which delivers twice as much stage power as the top blading. Finally, the bottom blading with $\lambda = 3$ delivers three times the stage power as the first one. In the practice of turbine design, among other things, two major parameters must

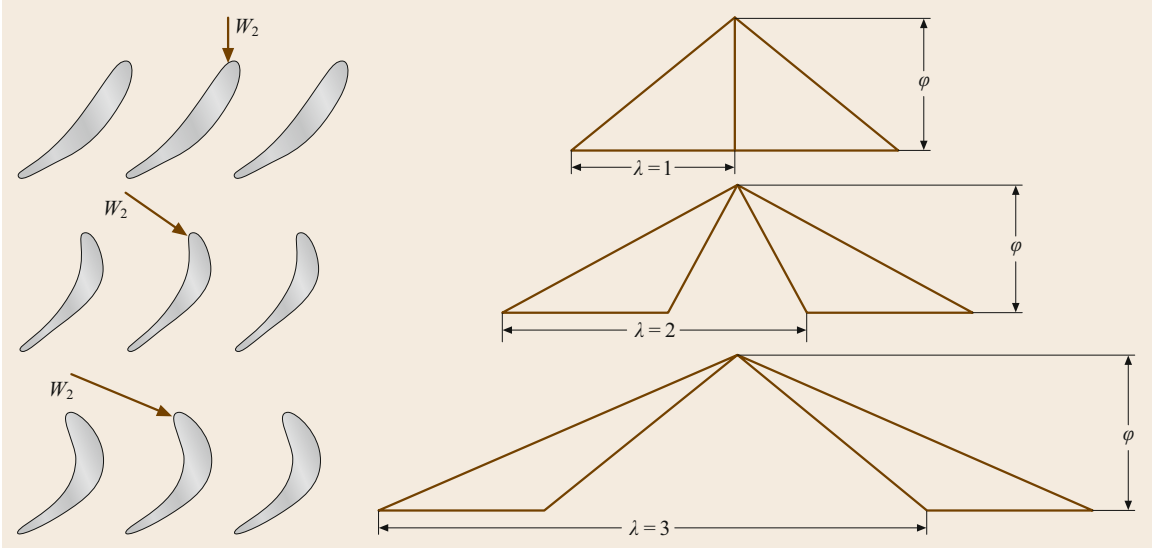

Fig. 19.11 Dimensionless stage velocity diagram to explain the effect of the stage load coefficient λ on flow deflection and blade geometry, $r = 0.5$

be considered: the specific load coefficients and the stage polytropic efficiencies.

Lower deflection generally yields higher stage polytropic efficiency, but many stages are needed to produce the required turbine power. However, the same turbine power may be established by a higher stage flow deflection, and thus a higher λ, at the expense of the stage efficiency. Increasing the stage load coefficient has the advantage of significantly reducing the stage number, thus lowering the engine weight and manufacturing cost. In aircraft engine design practice, one of the most critical issues besides the thermal efficiency of the engine is the thrust-to-weight ratio. Reducing the number of stages may lead to a desired thrust-to-weight ratio. While a high turbine stage efficiency has top priority in power generation steam and gas turbine design, the thrust-to-weight ratio is the major parameter for aircraft engine designers.

19.1.8 Unified Description of a Turbomachinery Stage

The following sections treat turbine and compressor stages from a unified standpoint. Axial, mixed flow, and radial flow turbines and compressors follow the same thermodynamic conservation principles. Special treatments are indicated when dealing with aerodynamic behavior and loss mechanisms. While turbine aerodynamics are characterized by negative (favorable) pressure gradient environments, the compression process operates in a positive (adverse) pressure gradient environment. As a consequence, partial or total flow separation may occur on compressor blade surfaces, leading to partial stall or surge. On the other hand, with the exception of some minor local separation bubbles on the suction surface of highly loaded low-pressure turbines blades, a turbine normally operates without major flow separation or breakdown. These two distinctively different aerodynamic behaviors are due to the different pressure gradient environments. Turbine and compressor cascade aerodynamics and losses are extensively treated in [19.1, Chaps. 7, 16]. In this section, we will first present a set of algebraic equations that describes turbine and compressor stages with constant mean diameter and then extend the approach to general cases where the mean stage diameter changes.

Unified Description of Stages with Constant Mean Diameter

For a turbine or compressor stage with constant mean diameter (Fig. 19.7), we present a set of equations that describe the stage by means of dimensionless parameters such as stage flow coefficient ϕ, stage load coefficient λ, degree of reaction r, and the flow angles. From the velocity diagram with the angle definition in Fig. 19.7, we obtain the flow angles

$$\begin{aligned}
\cot\alpha_2 &= \frac{U_2 + W_{u2}}{V_{ax}} = \frac{1}{\phi}\left(1 + \frac{W_{u2}}{U}\right) \\
&= \frac{1}{\phi}\left(1 - r + \frac{\lambda}{2}\right), \\
\cot\alpha_3 &= -\frac{W_{u2} - U_2}{V_{ax}} = -\frac{1}{\phi}\left(\frac{W_{u3} - U}{U}\right) \\
&= \frac{1}{\phi}\left(1 - r - \frac{\lambda}{2}\right).
\end{aligned} \tag{19.43}$$

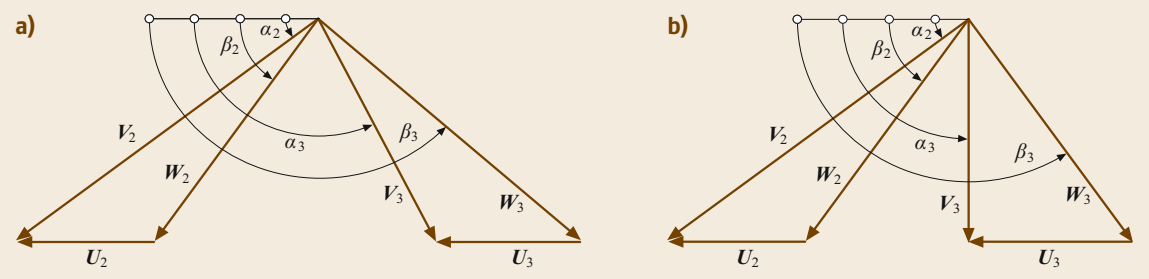

Fig. 19.12a,b Turbine stage velocity diagrams: **(a)** for a normal stage, and **(b)** for the last stage of a multistage turbine

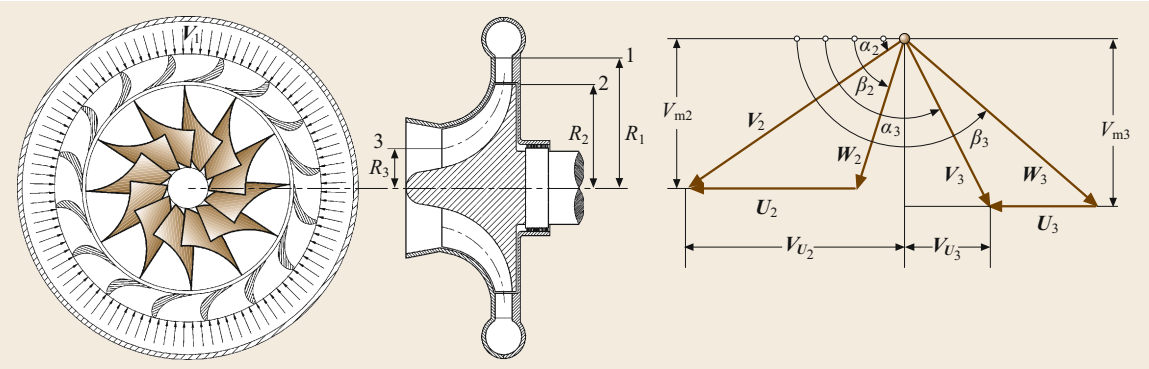

Fig. 19.13 A centripetal turbine stage with cross section and velocity diagram

The other flow angles can be found similarly, thus we summarize

$$\cot\alpha_2 = \frac{1}{\phi}\left(1 - r + \frac{\lambda}{2}\right), \tag{19.44}$$

$$\cot\alpha_3 = \frac{1}{\phi}\left(1 - \frac{\lambda}{2} - r\right), \tag{19.45}$$

$$\cot\beta_2 = \frac{1}{\phi}\left(\frac{\lambda}{2} - r\right), \tag{19.46}$$

$$\cot\beta_3 = -\frac{1}{\phi}\left(\frac{\lambda}{2} + r\right). \tag{19.47}$$

The stage load coefficient can be calculated from

$$\lambda = \phi(\cot\alpha_2 - \cot\beta_3) - 1\,. \tag{19.48}$$

The velocity diagram of the last stage of a compressor or a turbine differs considerably from the normal stage. As mentioned in the previous section, to minimize the *exit losses*, the last stage usually has an exit flow angle of $\alpha_3 = 90°$. Figure 19.12 compares the velocity diagram of a normal stage with the one in the last stage of the same turbine component. As shown, by changing the exit flow angle to $\alpha_3 = 90°$ a substantial reduction in exit velocity vector V_3, and thus the exit kinetic energy V_3^2, can be achieved. This subject is treated in [19.6, Chap. 7] in detail.

Generalized Dimensionless Stage Parameters

Now we extend the foregoing consideration to compressor and turbine stages where the diameter, circumferential velocities, and meridional velocities are not constant. Examples are axial flow turbine and compressors (Figs. 19.5 and 19.6), radial inflow (centripetal) turbines (Fig. 19.13), and centrifugal compressors (Fig. 19.14).

In the following, we develop a set of unifying equations that describes the above axial turbine and compressor stages, as well as the centripetal turbine and centrifugal compressor stages shown in Figs. 19.13 and 19.14. We introduce new dimensionless parameters

$$\mu = \frac{V_{m2}}{V_{m3}}\,,\ \nu = \frac{R_2}{R_3} = \frac{U_2}{U_3}\,,\ \phi = \frac{V_{m3}}{U_3}\,,$$
$$\lambda = \frac{l_m}{U_3^2}\,,\ r = \frac{\Delta h''}{\Delta h' + \Delta h''}\,, \tag{19.49}$$

with V_m, U from the velocity diagrams and $\Delta h'$ and $\Delta h''$ as the specific static enthalpy difference in the rotor and stator, respectively. The dimensionless parameter μ represents the meridional velocity ratio for the stator and rotor, respectively, ν is the circumferential velocity ratio, ϕ is the stage flow coefficient, λ is the stage load coefficient, and r is the degree of reaction. Introduc-

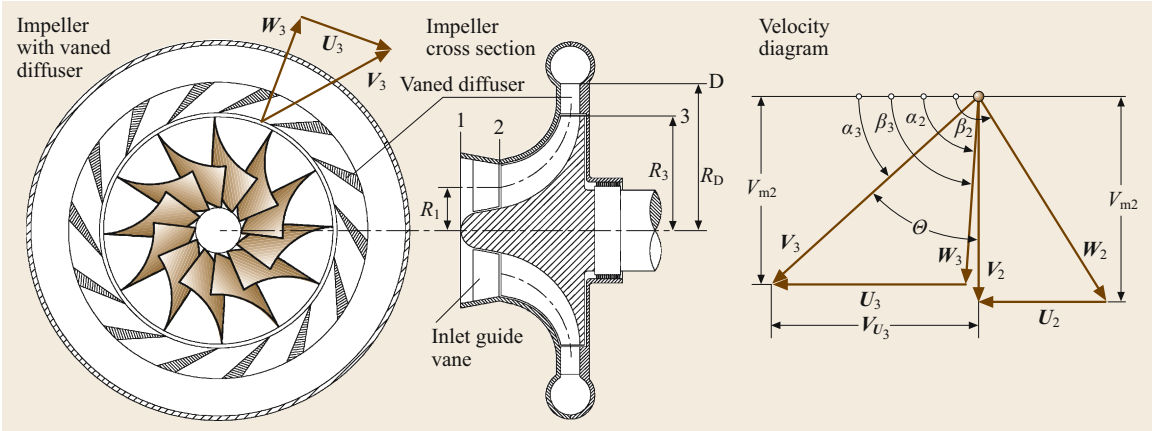

Fig. 19.14 A centrifugal compressor stage with cross section and velocity diagram

ing these parameters into the equations of continuity, moment of momentum, and the relation for degree of reaction, the stage is completely defined by a set of four equations

$$\cot\alpha_2 - \cot\beta_2 = \frac{\nu}{\mu\,\phi}\,, \tag{19.50}$$

$$\cot\alpha_3 - \cot\beta_3 = \frac{1}{\phi}\,, \tag{19.51}$$

$$r = 1 + \frac{\phi^2}{2\lambda}\left[1 + \cot^2\alpha_3 - \mu^2\left(1 + \cot^2\alpha_2\right)\right], \tag{19.52}$$

$$\lambda = \phi(\mu\nu\cot\alpha_2 - \cot\beta_3) - 1\,. \tag{19.53}$$

While (19.50), (19.51) and (19.53) are exact, (19.52) is only an approximation. However, its exact value can be obtained by solving equation system (19.54). The system of (19.50)–(19.53) contains nine unknown stage parameters. To find a solution, five parameters must be guessed. Appropriate candidates for the first guess are: the diameter ratio, $\nu = R_2/R_3 = U_2/U_3$, the stator and rotor exit angles α_2 and β_3, the exit flow angle α_3, and the stage degree of reaction r. In addition, the stage flow coefficient ϕ can be estimated by implementing the information about the mass flow and using the continuity equation. Likewise, the stage load coefficient λ can be estimated for turbine or compressor stages by employing the information about the compressor pressure ratio or turbine power. Once the five parameters are guessed, the rest of the four parameters are determined by solving the above equation system. In this case, the four parameters calculated fulfill the conservation laws for the particular compressor or turbine blade geometry for which the five stage parameters were guessed. This preliminary estimation of stage parameters, however, is considered the first iteration toward an optimum design. A subsequent loss and efficiency calculation, presented in [19.6, Chap. 8], will clearly show if the guessed parameters were useful or not. In fact, a few iterations are necessary to find the optimum configuration that fulfills the efficiency requirement set by the compressor or turbine designer. Equations (19.50)–(19.53) can be expressed in terms of the flow angles α_2, α_3, β_2, and β_3, which lead to a set of four nonlinear equations

$$\begin{aligned}
&\mu^2\phi^2(1-\nu^2)\cot^2\alpha_2 + 2\mu\nu\,\phi\,\lambda\cot\alpha_2 \\
&\quad -\lambda^2 - 2(1-r)\lambda + (\mu^2-1)\phi^2 = 0\,, \\
&\phi^2(1-\nu^2)\cot^2\alpha_3 + 2\phi\,\lambda\cot\alpha_3 \\
&\quad +\lambda^2 - 2(1-r)\lambda\nu^2 + (\mu^2-1)\phi^2\nu^2 = 0\,, \\
&(1-\nu^2)(\mu\,\phi\cot\beta_2 + \nu)^2 + 2\nu\,\lambda(\phi\,\mu\cot\beta_2 + \nu) \\
&\quad -\lambda^2 - 2(1-r)\lambda + (\mu^2-1)\phi^2 = 0\,, \\
&(1-\nu^2)(\phi\cot\beta_3 + 1)^2 + 2\lambda(\phi\cot\beta_3 + 1) \\
&\quad +\lambda^2 - 2(1-r)\lambda\nu^2 + (\mu^2-1)\phi^2\nu^2 = 0\,.
\end{aligned} \tag{19.54}$$

19.1.9 Special Cases

Equations (19.50)–(19.54) are equally valid for axial, radial, and mixed flow turbine and compressor stages. Special stages with corresponding dimensionless parameters are described as special cases as listed below.

Case 1: Constant Mean Diameter

In this special case, the diameter remains constant, leading to the circumferential velocity ratio of $\nu = U_2/U_3 = 1$. The meridional velocity ratio is $\mu = V_{m2}/V_{m3} \neq 1$. The flow angles expressed in terms of

other dimensionless parameters are

$$\cot\alpha_2 = \frac{1}{\phi\,\mu}\left[\frac{\lambda}{2} + (1-r) - (\mu^2-1)\frac{\phi^2}{2\lambda}\right],$$
$$\cot\alpha_3 = \frac{1}{\phi}\left[-\frac{\lambda}{2} - (1-r) - (\mu^2-1)\frac{\phi}{2\lambda}\right],$$
$$\cot\beta_2 = \frac{1}{\mu\,\phi}\left[\frac{\lambda}{2} + (1-r) - (\mu^2-1)\frac{\phi^2}{2\lambda} - 1\right],$$
$$\cot\beta_3 = \frac{1}{\phi}\left[-\frac{\lambda}{2} + (1-r) - (\mu^2-1)\frac{\phi}{2\lambda} - 1\right]. \quad (19.55)$$

The stage load coefficient is calculated from

$$\lambda = \phi(\mu\cot\alpha_2 - \cot\beta_3) - 1 \quad \text{for } \nu = 1 \text{ and } \mu \neq 1\,. \quad (19.56)$$

Case 2: Constant Mean Diameter and Meridional Velocity Ratio

In this special case, the circumferential and meridional velocities are equal, leading to $\nu = U_2/U_3 = 1$, $\mu = V_{m2}/V_{m3} = 1$. The flow angles are calculated from

$$\cot\alpha_2 = \frac{1}{\phi}\left(\frac{\lambda}{2} - r + 1\right),$$
$$\cot\alpha_3 = \frac{1}{\phi}\left(-\frac{\lambda}{2} - r + 1\right). \quad (19.57)$$

The stage load coefficient is calculated from

$$\lambda = \phi(\cot\alpha_2 - \cot\beta_3) - 1 \quad \text{for } \nu = 1 \text{ and } \mu = 1\,. \quad (19.58)$$

The generalized stage load coefficient for different μ, ν-cases can be summarized as

$$\lambda = \phi[\mu\nu\cot\alpha_2 - \cot\beta_3] - 1 \quad \text{for } \nu \neq 1 \text{ and } \mu \neq 1\,,$$
$$\lambda = \phi[\mu\cot\alpha_2 - \cot\beta_3] - 1 \quad \text{for } \nu = 1 \text{ and } \mu \neq 1\,,$$
$$\lambda = \phi[\nu\cot\alpha_2 - \cot\beta_3] - 1 \quad \text{for } \nu \neq 1 \text{ and } \mu = 1\,,$$
$$\lambda = \phi[\cot\alpha_2 - \cot\beta_3] - 1 \quad \text{for } \nu = 1 \text{ and } \mu = 1\,. \quad (19.59)$$

19.1.10 Increase of the Stage Load Coefficient: Discussion

Following the discussion in Sect. 19.1.3 regarding the increase of the specific stage mechanical energy and the subsequent discussion in Sect. 19.1.8, we proceed with (19.53), where the stage load parameter λ is expressed in terms of μ and ν and the blade angle α_2 and β_3 as

$$\lambda = \phi(\mu\nu\cot\alpha_2 - \cot\beta_3) - 1\,. \quad (19.60)$$

The effect of flow deflection on the stage load coefficient of axial flow turbines was already discussed in

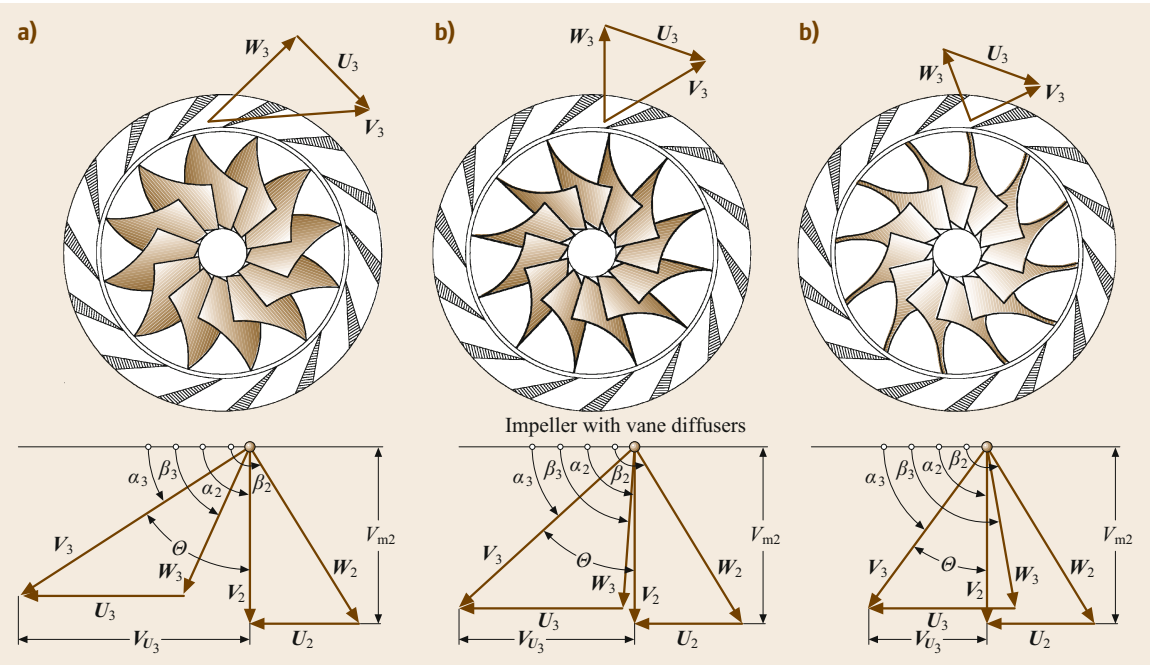

Fig. 19.15a–c Centrifugal compressor stage with velocity diagrams: **(a)** forward lean, **(b)** radial zero lean, and **(c)** backward lean

Sect. 19.1.8. As we saw, turbine blades can be designed with stage load coefficients λ as high as 3 or more. In turbine blades with high λ and Reynolds numbers $\mathrm{Re} = V_{\mathrm{exit}}\, c/\nu > 150\,000$, the governing strong negative pressure gradient prevents major separation from occurring in the flow. However, if the same type of blade operates at lower Reynolds numbers, flow separation that results in a noticeable increase of profile losses may occur. For high-pressure turbines (HPT), the strong favorable pressure gradient within the blade channels prevents major separation from occurring in the flow. However, low-pressure turbine (LPT) blades, particularly those of aircraft gas turbine engines that operate at low Reynolds numbers (cruise conditions up to $\mathrm{Re} = 120\,000$), are subjected to laminar flow separation and turbulent reattachment. While axial turbine blades can be designed with relatively high positive λ, the flow through axial compressor blade channels is susceptible to flow separation, even at relatively low λ. This is primarily due to a positive pressure gradient in the streamwise direction that causes the boundary layer to separate once a certain deflection limit or a *diffusion factor* (see [19.1, Chaps. 5, 16]) has been exceeded. To achieve a higher λ, and thus a higher stage pressure ratio, a smaller diameter ratio $\nu = D_2/D_3 = U_2/U_3$ can be applied. Using a moderate diameter ratio range of $\nu = 0.85$–0.75 results in a mixed flow configuration. At a lower range of ν, such as $\nu = 0.75$–0.4, a centrifugal compressor configuration is designed.

Figure 19.15 shows, schematically, three centrifugal compressors with three different exit flow angles and the corresponding velocity diagrams. Figure 19.15a shows a centrifugal impeller in which the trailing edge portion is forward leaning with a negative lean angle of $\Delta\beta = \beta_3 - 90° < 0$. The reference configuration Fig. 19.15b shows an impeller with a radial exit flow angle $\beta_3 = 90°$ and thus $\Delta\beta = 0$. Finally, Fig. 19.15c shows an impeller with a backward-leaned trailing edge portion with a positive lean angle of

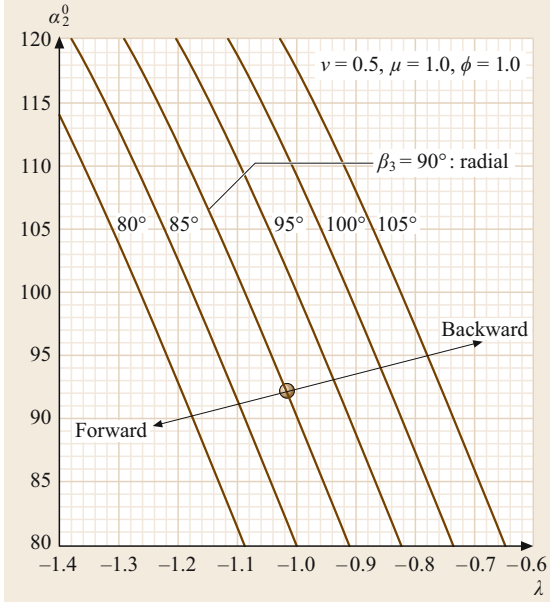

Fig. 19.16 Influence of lean angle on λ: forward lean with $\beta_3 < 90°$, backward lean $\beta_3 > 90°$, and zero lean $\beta_3 = 90°$

$\Delta\beta = \beta_3 - 90° > 0$. All three impellers have the same diameter ratio ν and the same rotational speed ω. The λ-behavior of these impellers is shown in Fig. 19.16, where the relative exit flow angle is varied in the range of $\beta_3 = 80$–$105°$. As shown, forward lean results in higher deflection Θ, larger ΔV_{u}, and thus higher negative λ, which is associated with a higher profile loss. Backward lean, however, reduces the flow deflection Θ and ΔV_{u}. As a result, the stage load coefficient λ is reduced. For the comparison, the radial exit case with $\beta_3 = 90°$ is plotted. In calculating the stage load coefficient λ, the influence of the radius ratio $\nu = R_2/R_3 = U_2/U_3$ on the stage load coefficient becomes clear.

19.2 Blade Design

Power generation and consumption by turbine and compressor components are accomplished by stages that consist of stator and rotor rows with the corresponding blades. The geometric configuration of the blades provides the prescribed flow deflection that is essential for energy conversion in both machines. The blade geometry includes the inlet and exit camber angles, stagger angle, camberline, and thickness distribution from leading to trailing edge of the blade. The blade geometry is adjusted to the stage velocity diagram which is designed for specific turbine or compressor flow applications. Simple blade design methods are available in the open literature (see References). However, advanced blade designs developed by engine manufacturers are generally proprietary and thus, are not available to the public. The subject of this section is to provide engineers with the necessary information to design high efficiency turbine and compressor blades. An earlier theoretical approach by Joukowsky [19.7] used the method of conformal transformation to ob-

tain cambered profiles that can generate lift force. The mathematical limitations of the conformal transformation do not allow modifications of a cambered profile to produce the desired pressure distribution required by a turbine or a compressor blade design. In the following, a simple method is presented that is equally applicable for designing compressor and turbine blades. The method is based on (a) constructing the blade camberline and (b) superimposing a predefined base profile on the camberline. With regard to generating a base profile, the conformal transformation can be used to produce useful profiles for superposition purposes. Detailed instruction on designing appropriate base profiles for turbines and compressor blades are given in [19.1] with a few examples in this chapter.

In the following sections we present the compressor blade design, followed by the turbine blade design process.

19.2.1 Compressor Blade Design

The major parameter for determining the shape of a compressor blade is the Mach number. For low- to intermediate-subsonic Mach range ($M_1 = 0.1$–0.6), NACA-65 profiles [19.8] provide a relatively high pressure at a reasonably high efficiency. For intermediate Mach numbers, double-circular arc (DCA) and multi-circular arc (MCA) profiles may be used. Surface pressure measurements show that at an inlet Mach number of $M_1 = 0.6$ and at the design incidence, the NACA-65 and DCA profiles have comparable pressure distributions. However, due to a sharp leading edge, the DCA-profiles have higher profile losses than the NACA-65 series when operating at off-design conditions. For high subsonic Mach range $M_1 > 0.6$, DCA or MCA profiles are used. Controlled diffusion profiles CD are used for transonic Mach ranges in order to reduce the shock losses. Supersonic compressors require s-shaped blades with sharp leading edges to avoid shock detachment, [19.1].

Low Subsonic Compressor Blade Design

In [19.1], it was shown that for an inviscid flow, the lift force can be expressed as

$$F = \rho V_\infty \times \Gamma, \text{ where } \Gamma = \oint_C V \cdot \mathrm{d}c \tag{19.61}$$

with V_∞ as the mean velocity between the inlet and the exit of the blade row and Γ as the circulation. This relation shows that a lift force always exists if there is circulation around the airfoil. The circulation is directly related to the flow deflection from the blade inlet to the exit as shown in Fig. 19.17.

As discussed in [19.1], for an incidence free ($i = 0$) flow, the velocity vector at the inlet is tangent to the camberline. Likewise, for a deviation free angle ($\delta = 0$) exit flow, the velocity vector is tangent to the camberline at the cascade exit, as seen in Fig. 19.17. Once the compressor stage velocity diagram is constructed, the deflection angle θ and, thus, the circulation Γ is known. The problem now is to find the corresponding blade profile for a given circulation. For a compressor blade which generally has a small flow deflection, the circulation Γ can be thought of as the sum of differential circulations $\mathrm{d}\Gamma$ generated by infinitesimally small vortices. If we distribute the vortices along the blade chord and consider the specific circulation at an arbitrary point x to be

$$\gamma(x) = \frac{\mathrm{d}\Gamma}{\mathrm{d}x}. \tag{19.62}$$

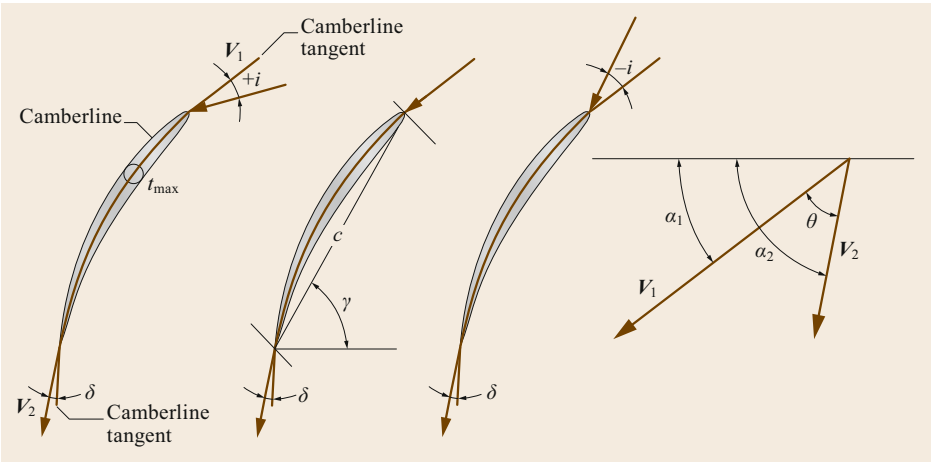

Fig. 19.17 Compressor cascade nomenclature, c = chord length, t_{max} = maximum thickness, γ = cascade stagger angle, θ = cascade flow deflection angle, i = flow incidence angle, δ = flow deviation angle. For $i > 0$ the actual deflection of $\theta > \theta_{design}$

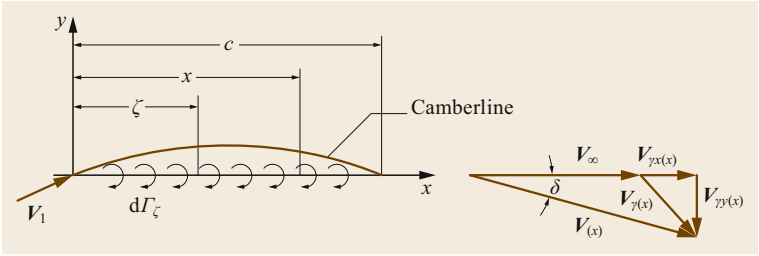

Fig. 19.18 Vortex distribution along the blade chord and induced velocity

Integrating (19.62) yields

$$\Gamma = \int_0^c \gamma(x)\mathrm{d}x. \tag{19.63}$$

with c as the blade chord. The vortex with the strength $\mathrm{d}\Gamma$, located at the point ζ induces a velocity at an arbitrary point x that can be calculated from Biot–Savart's law. Figure 19.18 shows the distribution of the discrete vortices along the chord (left) and their induced velocity vector $V_{\gamma(x)}$ with its components $V_{\gamma x(x)}$ and $V_{\gamma(y)}$ (right).

The induced velocity in the y-direction is

$$\mathrm{d}V_{\gamma y}(x) = -\frac{\mathrm{d}\Gamma_\zeta}{2\pi(x-\zeta)} \tag{19.64}$$

and in the x-direction

$$V_{\gamma x}(x) = \pm\frac{\gamma(x)}{2} \quad (-\text{ sign for } x > \zeta). \tag{19.65}$$

The integration of (19.65) along the blade chord gives the total velocity induced at x by the vortices distributed at ζ

$$V_{\gamma y}(x) = -\frac{1}{2\pi}\int_0^c \frac{\gamma(\zeta)\mathrm{d}\zeta}{(x-\zeta)}. \tag{19.66}$$

The induced velocity for the incidence angle $i = 0$ is shown in Fig. 19.18. Superimposing the induced velocity $V(x)$ on V_1, we get the contour velocity $V(x)$ around the profile. Since the direction of this velocity must be identical with the slope of the camberline,

$$\tan\delta = \frac{\mathrm{d}y(x)}{\mathrm{d}x} = \frac{V_{\gamma y}(x)}{V_1 + V_{\gamma x}(x)} \tag{19.67}$$

and since the induced velocity component $V_{\gamma y} \ll V_1$, it follows that

$$\frac{\mathrm{d}y(x)}{\mathrm{d}x} = \frac{V_{\gamma y}(x)}{V_1}. \tag{19.68}$$

Introducing (19.66) into (19.68),

$$\frac{\mathrm{d}y(x)}{\mathrm{d}x} = -\frac{1}{2\pi V_1}\int_0^c \frac{\gamma(\zeta)\mathrm{d}\zeta}{x-\zeta} \text{ for } i = 0 \tag{19.69}$$

and for considering a small incidence angle i, we find

$$1 + \frac{\mathrm{d}y(x)}{\mathrm{d}x} = -\frac{1}{2\pi V - 1}\int_0^c \frac{\gamma(\zeta)\mathrm{d}\zeta}{x-\zeta}. \tag{19.70}$$

Now, we introduce the lift coefficient for the camberline and label it with the superscript $*$ (for detail see [19.1])

$$C_\mathrm{L}^* = \frac{F^*}{\frac{\rho}{2}V_1^2 c} = \frac{\rho\Gamma V_1}{\frac{\rho}{2}V_1^2} = \frac{2\Gamma}{V_1 c}. \tag{19.71}$$

We assume that the lift force induced by a discrete vortex is linearly proportional to the blade lift. This uniform lift distribution assumption results in

$$\frac{\mathrm{d}\Gamma_\zeta}{\mathrm{d}\zeta} = \frac{\Gamma}{c} \tag{19.72}$$

and so

$$\frac{\mathrm{d}\Gamma_\zeta}{\mathrm{d}_\zeta} = \gamma(\zeta) = \frac{C_\mathrm{L}^*}{2}V_1. \tag{19.73}$$

Inserting (19.73) into (19.70) and setting $i = 0$ for an incidence free inlet flow condition, we find

$$\frac{\mathrm{d}y(x)}{\mathrm{d}x} = \frac{C_\mathrm{L}^*}{4\pi}\int_0^c \frac{\mathrm{d}\zeta}{x-\zeta}. \tag{19.74}$$

The first integration of (19.74) yields

$$\frac{\mathrm{d}y(x)}{\mathrm{d}x} = \frac{C_\mathrm{L}^*}{4\pi}\ln\left(\frac{1-\frac{x}{c}}{\frac{x}{c}}\right). \tag{19.75}$$

The integration of (19.75) determines the coordinate for the camberline

$$\frac{y(x)}{c} = -\frac{C_\mathrm{L}^*}{4\pi}\left[\left(1-\frac{x}{c}\right)\ln\left(1-\frac{x}{c}\right) + \frac{x}{c}\ln\left(\frac{x}{c}\right)\right]. \tag{19.76}$$

This is the equation of the camberline for the NACA-compressor blades. The maximum camber is at $x/c = 0.5$

$$\frac{y_{max}}{c} = \frac{C_L^*}{4\pi} \ln 2. \tag{19.77}$$

Generation of Base Profiles

A set of base profiles can be constructed by using the *conformal transformation* detailed in [19.1] that is briefly summarized. To this end we use a *reference circle* with radius a and a *mapping circle* with radius b. The center of the mapping circle is shifted by Δx along the x-axis relative to the *reference* circle with its origin at the coordinate system as its center. An eccentricity $\epsilon = e/a$ with $e = \Delta x$ is defined that determines the thickness of the airfoil. The radius of the mapping circle is determined by

$$b = (1 + \epsilon)a. \tag{19.78}$$

Thus, the magnitude of the eccentricity defines the slenderness of the airfoil. For $\epsilon = 0$, the circle is mapped into a slit. Increasing the eccentricity causes the base profile to become thicker. Due to zero flow deflection, the symmetrical *base profiles* at zero-angle of attack do not generate circulation and, therefore, no lift. Similar profiles can be used as *base profiles* in compressor and turbine blade design to be superimposed on the *camberline*. Figure 19.19 exhibits a systematic generation of base profiles by varying the eccentricity ϵ. Turbine blades that are exposed to a frequent off-design operation conditions have generally a larger leading edge

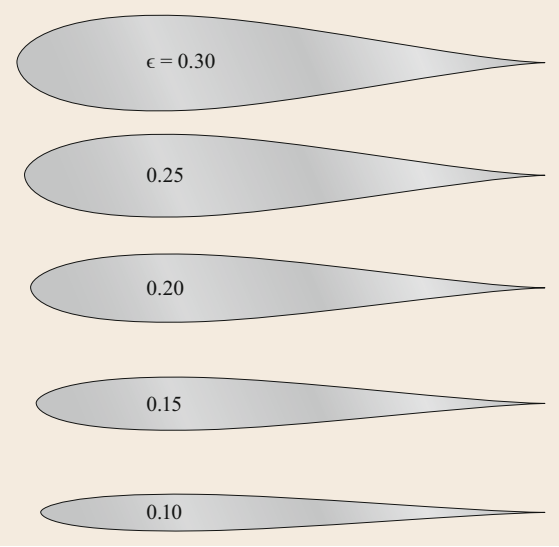

Fig. 19.19 Example of a systematic generation of base profiles by varying the eccentricity ϵ

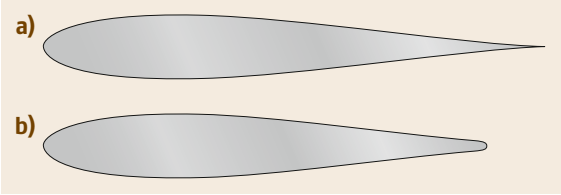

Fig. 19.20a,b A base profile before **(a)** and after adding a trailing edge circle **(b)**

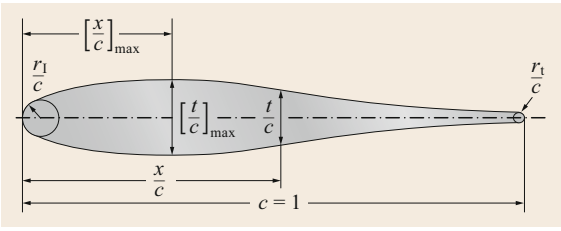

Fig. 19.21 Schematic of a base profile to be superimposed on camberline, $\xi = x/c$ and $(t/c)/2 = f(\xi)$

radii. In this case, $\epsilon > 0.15$ may be chosen. It should be noted that the base profiles with lower eccentricity shown in Fig. 19.19 may be used for subsonic compressor design. Blades with sharp trailing edges are subject to high stress concentration. An excessive stress concentration leads to cracks that propagates from the blade hub to tip resulting in mechanical failure of the blade. To avoid a high level of stress concentration, a circle with a radius of 0.5–1.2 mm (based on the blade chord length) may be drawn tangent to the suction and pressure surfaces of the blade trailing edge. This can be done before superimposing the base profile. Figure 19.20 shows a base profile before and after adding a trailing edge thickness.

In addition to the base profiles listed above, a NACA-base profile for subsonic compressors and a base profile for subsonic turbines used in industrial practice as well as in research are listed in Tables 19.1 and 19.2 with the nomenclature shown in Fig. 19.21. The maximum thickness for compressors is around $t_{max}/c = 10\%$, whereas for turbines it may vary from 15 to 18%.

Superimposing the Base Profile on the Camberline. With (19.76), we are able to design the compressor blade camberline at a particular position where the lift coefficient is already calculated. To construct the profile, we superimpose a base profile on the camber. The base profile may be taken from the conformal transformation or from Table 1. For a profile with the chord c, the camberline coordinates are

$$x_c = \frac{x}{c}c\,, \quad y_c = \frac{y}{c}c\,, \tag{19.79}$$

Table 19.1 Thickness distribution of a NACA-65 compressor

ξ	0.0	0.50	0.75	1.25	2.5	5.0	7.5	10	15	20
$f(\xi)$	0.0	0.772	0.932	1.690	1.574	2.177	2.641	3.040	3.666	4.1
ξ	25	30	35	40	45	50	55	60	65	70
$f(\xi)$	4.50	4.76	4.92	4.99	4.96	4.81	4.53	4.14	3.6	3.15
ξ	75	80	85	90	95	100				
$f(\xi)$	2.58	1.98	1.38	0.81	0.30	0				

Table 19.2 Thickness distribution of a turbine base profile

ξ	0.00	5.0	10.00	15.00	20.00	25.00	30.00	35.00	40.00	45.0
$f(\xi)$	0.00	4.2	5.55	6.50	7.20	7.45	7.50	7.20	6.75	6.2
ξ	50.00	55.00	60.00	65.00	70.00	75.00	85.00	90.00	95.0	100.00
$f(\xi)$	5.6	5.05	4.45	3.85	3.35	2.85	1.9	1.5	1.05	0.00

$r_L/c = 0.030$, $r_T/c = 0.009$, $t_{max}/c = 0.15$

where the subscript c represents the camberline of the blade to be designed. If the maximum thickness $(t/c)_{max}$ of the actual blade is different from the reference maximum thickness $(t/c)_{max\ ref}$ of the base profile, the thickness distribution of the actual profile can be determined by

$$\frac{t}{c} = \left(\frac{t}{c}\right)_{ref} \frac{\left(\frac{t}{c}\right)_{max}}{\left(\frac{t}{c}\right)_{max\,ref}}. \tag{19.80}$$

The superposition procedure is sketched in Fig. 19.21 where a piece of the camberline is shown, on which the thickness is superimposed.

For the suction side, Fig. 19.22, where $sc = t/2$ the blade coordinates are

$$x = x_c - \left(\frac{t}{2}\right)\sin\varphi$$
$$y = y_c + \left(\frac{t}{2}\right)\cos\varphi \tag{19.81}$$

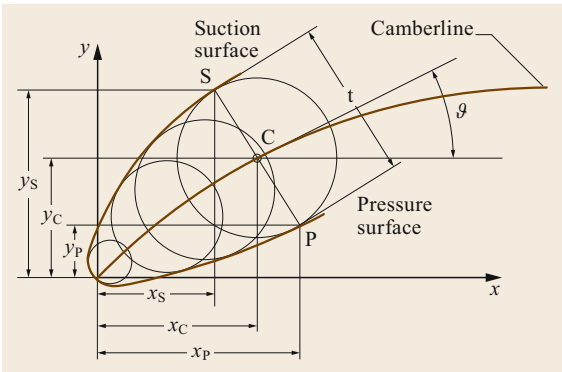

Fig. 19.22 Superposition of a base profile on the camberline

and for the pressure side, where $sp = t/2$

$$x = x_c - \left(\frac{t}{2}\right)\sin\varphi$$
$$y = y_c + \left(\frac{t}{2}\right)\cos\varphi. \tag{19.82}$$

The angle φ is calculated from (19.75)

$$\frac{dy(x)}{dx} = tg\varphi = \frac{C_L^*}{4\pi}\ln\left(\frac{1-\frac{x_c}{c}}{\frac{x_c}{c}}\right). \tag{19.83}$$

The above procedure is also equally valid for the turbine profile design.

Compressor Blades for High Subsonic Mach Number

Double-circular arc (DCA) and multi-circular arc (MCA) profiles are used particularly for compressors operating at intermediate and high subsonic inlet Mach numbers ($M > 0.6$). Considering a particular cross section through a compressor cascade as shown in Fig. 19.23, the suction and pressure surfaces of a DCA-profile consist of two circular arcs. The suction and pressure surfaces of MCA-profiles however, may consist of several circular arcs. The arc must have the same slopes at the joints to avoid surface discontinuities. This can be assured by plotting the first surface derivative.

The following criteria dictate the selection of a particular profile for high subsonic compression application:

1. The inlet Mach number
2. Incidence tolerance with regard to the profile losses
3. Pressure distribution determining the lift coefficient
4. Drag forces determining the blade profile loss.

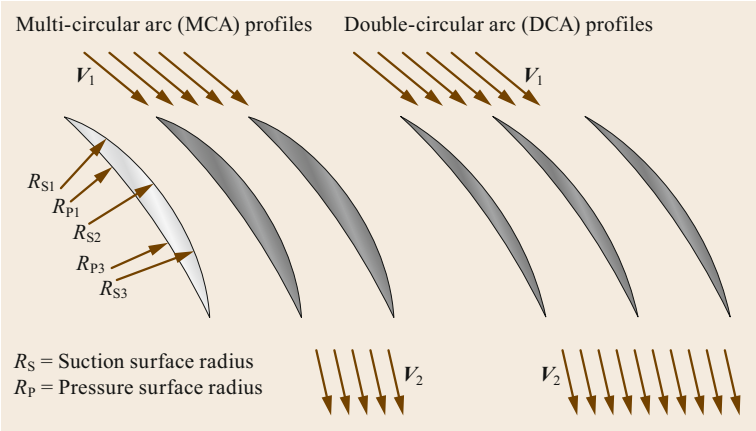

Fig. 19.23 MCA and DCA profiles for high subsonic Mach number applications

1. and 4. can be combined to arrive at the optimum lift/drag ratio.

Transonic, Supersonic Compressor Blades

For compressors operating at transonic and supersonic Mach numbers, blade design efforts are concentrated on keeping the shock losses at a minimum level. In doing so, it is important to accurately determine the shock angle. This topic is extensively discussed in [19.1, Chap. 16]. Figure 19.24 shows a supersonic compressor cascade with an inlet Mach number $M_4 > 1$. The incoming supersonic flow impinges on the sharp leading edge and forms weak oblique shocks, followed by an expansion fan. Passing through the shock front, the Mach number, although smaller, remains supersonic. Expansion waves are formed along the suction surface (convex side) of the blade from the leading edge L to the point e where the subsequent Mach wave at point e intersects the adjacent blade leading edge.

Regarding the transonic compressors, the research efforts resulted in the design of controlled diffusion blades that almost eliminate shock losses [19.9–11].

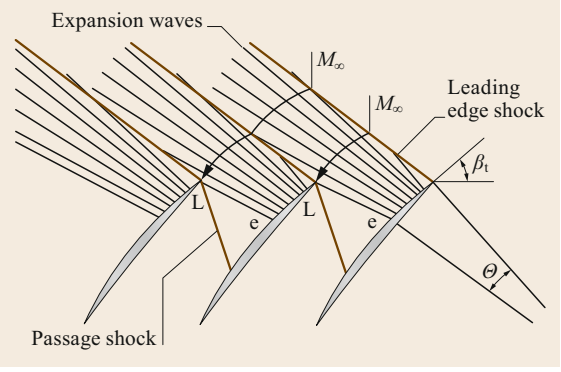

Fig. 19.24 Schematic of a supersonic compressor cascade, the supersonic inlet Mach number, expansion wave and passage shocks

For compressors operating in the supersonic Mach range, the so called S-profiles with sharp leading edges are used. The pressure and suction surfaces consist of multi-circular arcs with very small curvatures (large radii). Particular attention must be paid to the shock losses, as discussed in [19.1, Chap. 6] and [19.12]. The flow decelerates within the convergent part by a system of oblique shock waves followed by a normal shock. Further deceleration is achieved by diffusion within the divergent part. As seen, these profiles have a slightly convergent inlet tangent to a throat which is followed by a slightly divergent channel.

19.2.2 Turbine Blade Design

Different turbine blade designs are discussed in the literature, [19.13–17]. Given the stage velocity diagram with the flow velocity vectors and angles, the corresponding blade profiles are constructed such that the flow angles at the inlet and exit are realized. This includes the incorporation of the design incidence and deviation into the design process as discussed in [19.1, Chap. 9]. Figure 19.25 schematically shows the velocity diagram and the corresponding stator and rotor blades. Analogous to Sect. 19.1, the task here is designing the camberline on which a base profile will be superimposed. The camberline can be constructed from the inlet and exit flow angles under consideration of the incidence and deviation. This can be done graphically or numerically. Both methods are discussed in the following section.

Steps for Designing the Camberline

Step Ia. This step determines the stagger angle γ graphically. Given the inlet and the exit velocity vectors V_1, V_2 with the flow angle α_1, α_2 for a stator blade and β_2, β_3 for the rotor blade, the stagger angle γ must first be determined. For this purpose, the location of the maximum thickness $(t/c)_{max}$ of the base

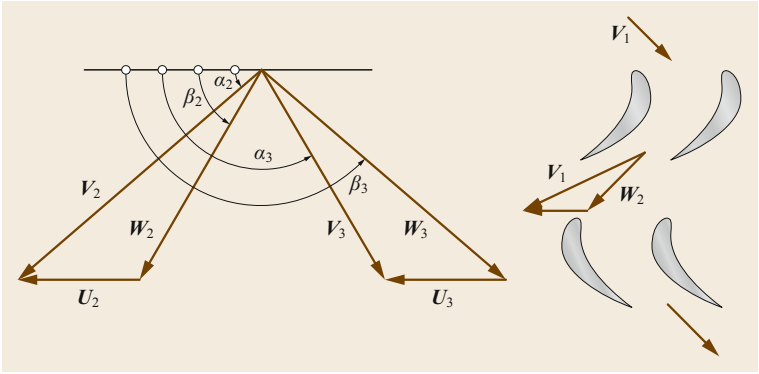

Fig. 19.25 Allocation of a set of stator and rotor blades to a given velocity diagram

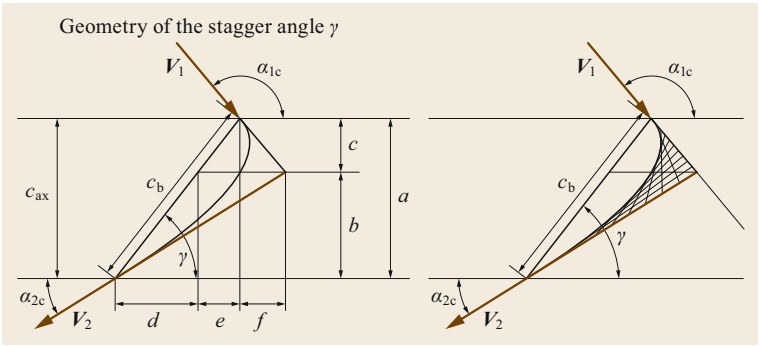

Fig. 19.26 Geometry for calculating the stagger angle

profile $(x/c)_{max}$ is an appropriate guideline for determining γ. As an example, we choose an axial chord of $c_{ax} = c \sin\gamma = a$ as shown in Fig. 19.26 and assume the position of $(x/c)_{max} = c$ and draw a line parallel to the cascade front. Then we intersect the continuation of the inlet velocity vector with that line. At the point of intersection we draw a line parallel to the exit velocity vector and find immediately the stagger angle γ as shown in Fig. 19.26.

Step Ib. These steps determines the stagger angle computationally. With the geometry from Fig. 19.26, the stagger angle can be computed as follows. Using the flow angles tangent to the camber leading edge and trailing edge α_{1c}, α_{2c} for the stator row and β_{2c}, β_{3c} for the rotor row along with the axial chord a, the distance of the maximum camber from the leading edge c and the trailing edge b with $b = a - c$, the stagger angle is calculated as

$$\tan\gamma = \frac{a}{\frac{a-c}{\tan\alpha_2} - \frac{c}{\tan(\pi-\alpha_1)}}. \qquad (19.84)$$

In (19.84) the distances a, and c are dimensional parameters. They can be non-dimensionalized by dividing the nominator and denominator in (19.84) by a and defining the ratio c/a as the fraction of the axial cord $F = c/a$ to arrive at

$$\tan\gamma = \frac{1}{\frac{1-F}{\tan\alpha_2} - \frac{F}{\tan(\pi-\alpha_1)}} \qquad (19.85)$$

from which the stagger angle γ is calculated immediately. For the first estimation, the fraction F may assume a value from 0.2 to 0.5. The resulting stagger angle may or may not be the appropriate one. To find the optimum F and thus the optimum stagger angle, the blade pressure distribution must be determined as detailed in Sect. 19.3.

Step II. This step prepares the geometry detailed in Figs. 19.26 and 19.27 for constructing the camberline. Given the chord length c and the stagger angle from the previous step, the tangents to the leading- and trailing-edge of the camberline to be determined are constructed by the inlet and exit metal angles as shown in Fig. 19.27. The latter is found from the stage velocity diagram under consideration of incidence and deviation angles, leading to camber angle α_{1c} and α_{2c}. The tangents intersect each other at the point P_1 and are subdivided into $n-1$ equal distances. Starting with the first point 1 at the leading edge (LE) tangent, a line is drawn to intersect the trailing edge (TE) tangent at point n. The following lines start at the second point on the LE-tangent and

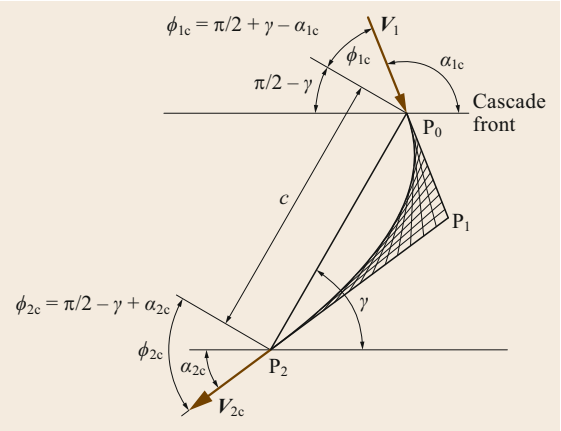

Fig. 19.27 Camber angle definitions: α_{1c}, α_{2c} are camber angles at the cascade inlet and exit, angle ϕ_{1c} and ϕ_{2c} are auxiliary angles required for camberline construction

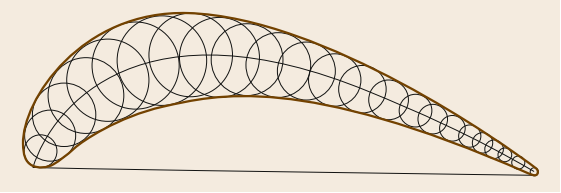

Fig. 19.28 Superposition of the base profile on the camber

intersects the TE-tangent at $n-1$ and so on. The envelope of the inner region of the connecting lines is the camberline shown in Fig. 19.28.

Step III. Prepares the camberline for the superimposing the base profile on camber line. This step requires turning the chord c counter clockwise by an angle of $180^\circ - \gamma$ making the axial chord the reference line. It is important to keep the entire angle configuration as detailed in Figs. 19.26 and 19.27, while turning the cascade to a horizontal position. Superimposing the base profile on the camberline delivers the turbine profile as shown in Fig. 19.28.

Camberline Coordinates Using a Bézier Function

A similar camberline is constructed by using the Bézier polynomial presented in [19.18]. The general Bézier polynomial of degree n is given as

$$B(t) = \sum_{i=0}^{n} \binom{n}{i} (1-t)^{n-i} t^i \mathrm{P}_i \qquad (19.86)$$

with P_i as the given points in Fig. 19.29, with $t \in [0, 1]$ the curve parameter, and $B(t)$ the position vector of

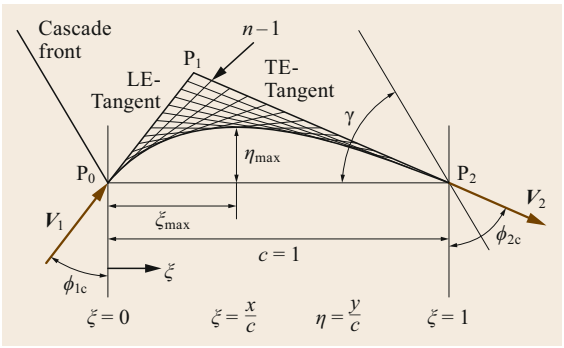

Fig. 19.29 Figure is turned counter clockwise by an angle of $180^\circ - \gamma$

the Bézier curve at the curve parameter t. For the purpose of designing the camberline, a quadratic Bézier curve is quite appropriate for a conventional turbine blade design. However, for the blades with high flow deflections, cubic Bézier curves may be utilized. The quadratic Bézier function reads

$$B(t) = (1-t)^2 \mathrm{P}_0 + 2(1-t)t\mathrm{P}_1 + t^2 \mathrm{P}_2. \qquad (19.87)$$

Before re-writing the Bézier formulation in terms of our nomenclature, we refer to Fig. 19.29, where the camber and Bézier quantities are shown. Thus, (19.87) reads as

$$\begin{aligned} B_\xi(\xi) &= (1-\xi)^2 \mathrm{P}_{0_\xi} + 2(1-\xi)\xi \mathrm{P}_{1_\xi} + \xi^2 \mathrm{P}_{2_\xi} \\ B_\eta(\xi) &= (1-\xi)^2 \mathrm{P}_{0_\eta} + 2(1-\xi)\xi \mathrm{P}_{1_\eta} + \xi^2 \mathrm{P}_{2_\eta}. \end{aligned} \qquad (19.88)$$

Considering the nomenclature in Fig. 19.29, the boundary conditions are

$$\begin{aligned} &\text{For } \mathrm{P}_0: \quad \xi = 0\text{: } \mathrm{P}_{0_\xi} = 0,\ \mathrm{P}_{0_\eta} = 0 \\ &\text{For } \mathrm{P}_1: \quad \mathrm{P}_{1\xi} = \frac{1}{1 + \frac{\cot\phi_{1c}}{\cot\phi_{2c}}},\ \mathrm{P}_{1\eta} = \frac{\cot\phi_{1c}}{1 + \frac{\cot\phi_{1c}}{\cot\phi_{2c}}} \\ &\text{For } \mathrm{P}_2: \quad \xi = 1\text{: } \mathrm{P}_{2_\xi} = 1,\ \mathrm{P}_{2_\eta} = 0. \end{aligned} \qquad (19.89)$$

With (19.88) and (19.89), the coordinates of the camberline are calculated by varying the dimensionless variable ξ from 0 to 1. A smooth camberline is obtained by introducing a small increment of $\xi = 0.01$ or less.

Figure 19.30 shows the construction of a turbine blade profile for the stator row using α_{1c}, α_{2c}, the stagger angle from (19.85) and the Bézier function. For designing the rotor blade the relative rotor angles, β_{2c}, β_{3c} along with the stagger angle equation (19.85) are used. In both cases, coordinate transformations facilitate rotation of the blades into correct positions as shown in Fig. 19.30. As seen the blades have very sharp trailing edges. This is the result of superimposing the base

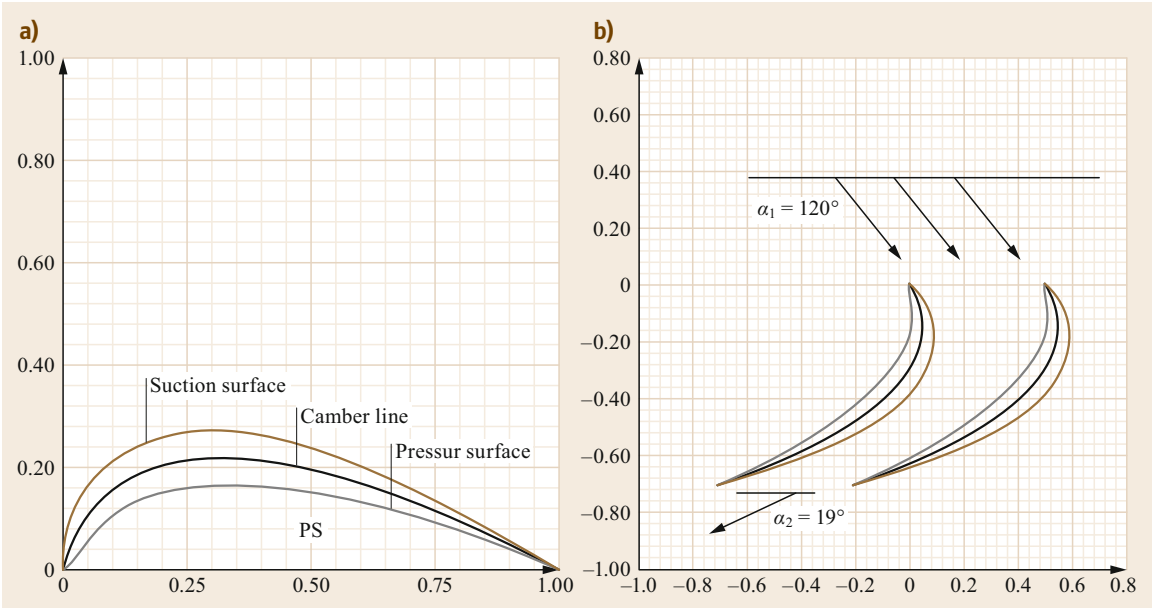

Fig. 19.30a,b Generation of a turbine stator blade profile using a Bezier function for the construction of camber, with stagger angle $\gamma = 45°$. **(a)** Profile of a medium loaded turbine, **(b)** cascade of highly loaded turbine blades

profile, which was obtained from the conformal transformation with zero trailing edge thickness. Blades with sharp trailing edges are subject to high stress concentration. To avoided the high level of stress concentration, a circle with a radius of 0.5−1.2 mm (based on the blade chord length) may be drawn tangent to the suction and pressure surfaces of the blade trailing edge.

19.2.3 Assessment of Blades Aerodynamic Quality

The objective of a turbine stator or rotor blade design is to accomplish a certain flow deflection that is required to produce a prescribed amount of power per stage. Given the inlet and the exit flow angles resulting in a given flow deflection, infinite number of blades with different shapes can be constructed that realize the above flow deflection. These blades, however, will have a different stagger angle with boundary layer distributions on suction and pressure surfaces and, thus, different profile loss coefficients. Among the numerous possible designs, only one has the lowest loss coefficient, i.e., the optimum efficiency at the design operating point only. Figure 19.31 shows the pressure distribution along the suction and pressure surfaces of a high efficiency turbine blade at the design point. This blade type is sensitive to incidence changes caused by off-design operation.

A change in operation condition results in a change of incidence angle and an increase in profile losses.

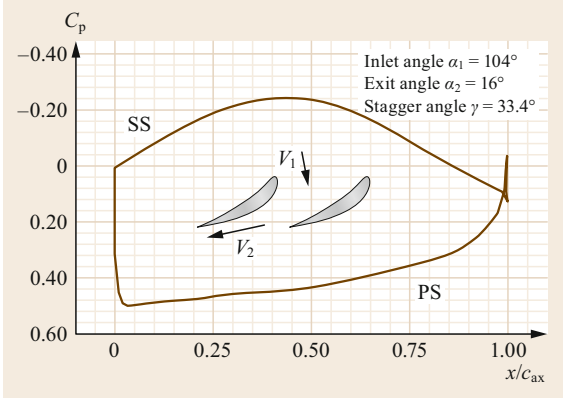

Fig. 19.31 Pressure distribution along the suction and pressure surfaces of a turbine blade

Thus, the operation condition of a turbine plays a crucial role in designing the blade. If the mass flow or the pressure ratio of a turbine component undergo frequent changes, the blades must be designed in such a way that their profile losses do not experience significant increases. Parameters determining the efficiency and performance behavior of a turbine as a result of the boundary layer development on the suction and pressure surface are, the Reynolds number, Mach number, pressure gradient, turbulence intensity and unsteady inlet flow conditions. Of the above parameters, the blade geometry defines the pressure gradient which is, in the first place, responsible for the boundary layer

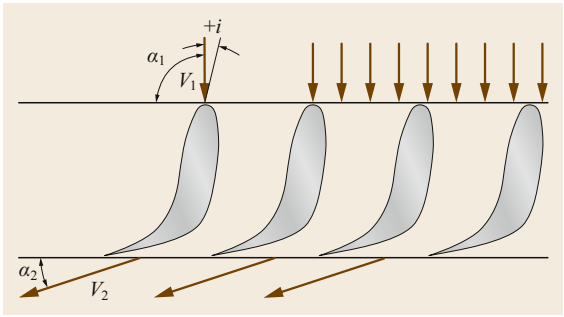

Fig. 19.32 A turbine cascade that fulfills the criteria 1. through 3.

development, separation and re-attachment. Since the pressure distribution is determined by the geometry and vice versa, the question arises as to how the blade geometry should be configured in order to establish a desired pressure distribution. This question has been the subject of numerous papers dealing with the *inverse blade design*, particularly for subcritical and supercritical compressor cascades [19.19–21]. In the context of this Chapter, we treat the question of the pressure distribution versus geometry from a simple physical point of view to establish a few criteria as a guideline for turbine blade design. The following example should demonstrate what criteria should be used in order to design

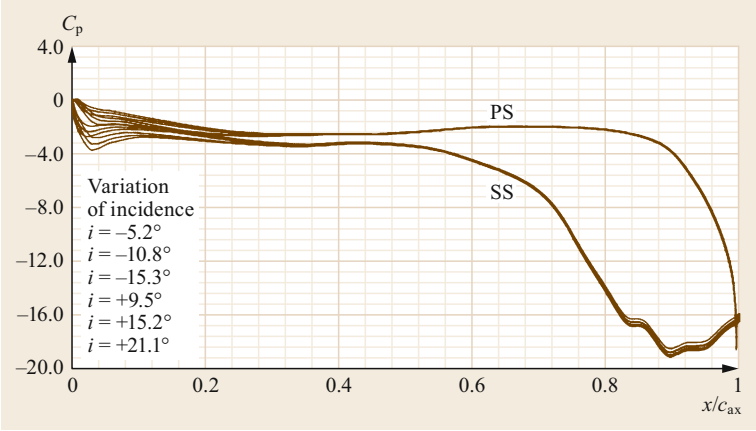

Fig. 19.33 Pressure distribution as a function of dimensionless axial chord with the incidence angle as the parameter, TPFL-design

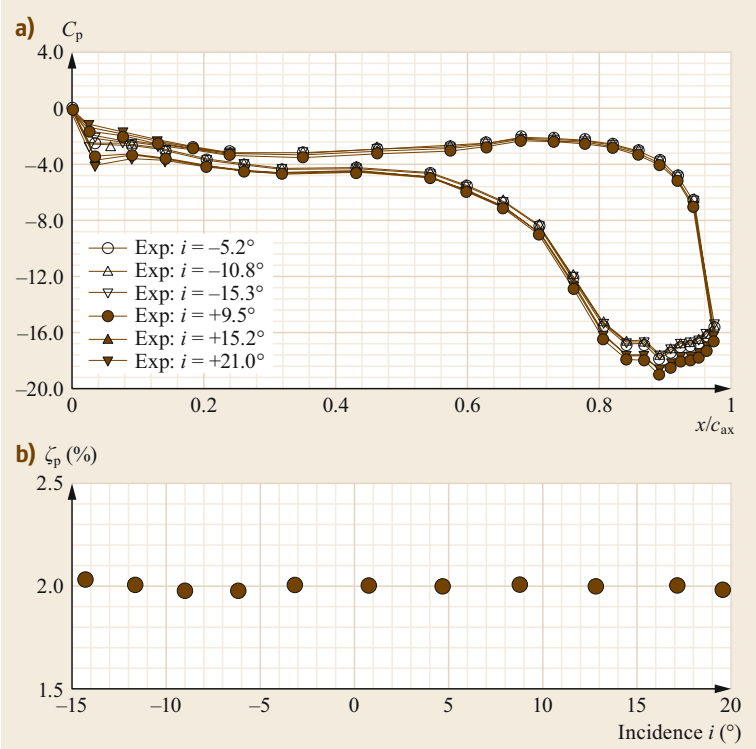

Fig. 19.34a,b Experimental pressure distribution as a function of dimensionless surface **(a)**, total pressure loss coefficient as a function of incidence angle **(b)**

a turbine blade that operates at a wide range of incidence changes without a substantial decrease of its efficiency:

1. With the exception of the leading edge portion, the pressure gradient on the pressure and suction surfaces should not experience sign changes over a range of 60–70% of the blades axial chord.
2. Over the above range, the pressure gradient should be close to zero. This means that flow on both surfaces neither accelerates nor decelerates.
3. Over the remaining 30–40% of the blade surface, the flow should strongly accelerate.

Applying criteria 1. through 3., associated with a moderately thick leading edge radius, provides a turbine blade that is insensitive to adverse off-design operation conditions at a relatively high efficiency, Fig. 19.32.

Figure 19.33 shows the numerical calculation of the pressure coefficient versus the dimensionless axial chord. As seen, with the exception of the leading edge portion, the pressure distributions do not change over a wide range of incidence from −15 to +21°. This numerical result is verified experimentally and presented in Fig. 19.33.

Figure 19.34 shows the experimental verification of the numerical results presented in Fig. 19.33. It also shows the profile loss coefficient ζ_p as a function of the incidence angle. Here as in Fig. 19.33, the pressure distributions do not change over a wide range of incidences from −15 to +21°. The results are in reasonable agreement with the numerical results, resulting in an approximate constant loss coefficient of 2%.

19.3 Gas Turbine Engines: Design and Dynamic Performance

A gas turbine engine is a system that consists of several turbomachinery components and auxiliary subsystems. Air enters the compressor component, which is driven by a turbine component that is placed on the same shaft. Air exits the compressor at a higher pressure and enters the combustion chamber, where the chemical energy of the fuel is converted into thermal energy, producing combustion gas at a temperature that corresponds to the turbine inlet design temperature. The combustion gas expands in the following turbine component, where its total energy is partially converted into shaft work and exit kinetic energy. For power generation gas turbines, the shaft work is the major portion of the above energy forms. It covers the total work required by the compressor component, the bearing frictions, several auxiliary subsystems, and the generator. In aircraft gas turbines, a major portion of the total energy goes toward generation of high exit kinetic energy, which is essential for thrust generation.

Gas turbines are designed for particular applications that determine their design configurations. For power generation purposes, the gas turbine usually has a *single spool*. A spool combines a compressor and a turbine that are connected together via a shaft. Figure 19.35 exhibits a single-spool power generation gas turbine, where a 14-stage compressor shares the same shaft with a three-stage turbine.

While in power generation gas turbine design the power-to-weight ratio does not play an important role, the thrust-to-weight ratio is a primary parameter in designing an aircraft gas turbine. High-performance aircraft gas turbine engines generally have twin-spool or multispool arrangements. The spools are usually rotating at different angular velocities and are connected with each other aerodynamically via air or combustion gas. Figure 19.36 exhibits a typical high-performance twin-spool aircraft gas turbine with a *ducted front fan* as the main thrust generator. Gas turbine engines with power capacities less than 20 MW might have a *split shaft* configuration that consists of a *gas generation spool* and a *power shaft*. While the turbine of the gas generation spool provides the shaft work necessary to drive the compressor, the power shaft produces the net power. In addition to the above design configurations, a variety of engine derivatives can be constructed using a core engine as shown in Fig. 19.37.

19.3.1 Gas Turbine Processes, Steady Design Operation

Starting with the single-spool power generation gas turbine that consists of a multistage compressor, a combustion chamber, and a turbine, the *h–s* diagram is shown in Fig. 19.38a.

The compression process from 1 to 2 is accomplished by the compressor with a polytropic efficiency η_{pol} that can be accurately calculated using the row-by-row or stage-by-stage methods discussed in [19.1]. The combustion process from 2 to 3 is associated with certain total pressure loss coefficient ζ_{comb}, thus it is not considered isobaric. The expansion process from 3 to 4 causes an entropy increase that is determined by the turbine efficiency. Figure 19.38b shows the *h–s* diagram for a twin-spool aircraft engine. In contrast to the

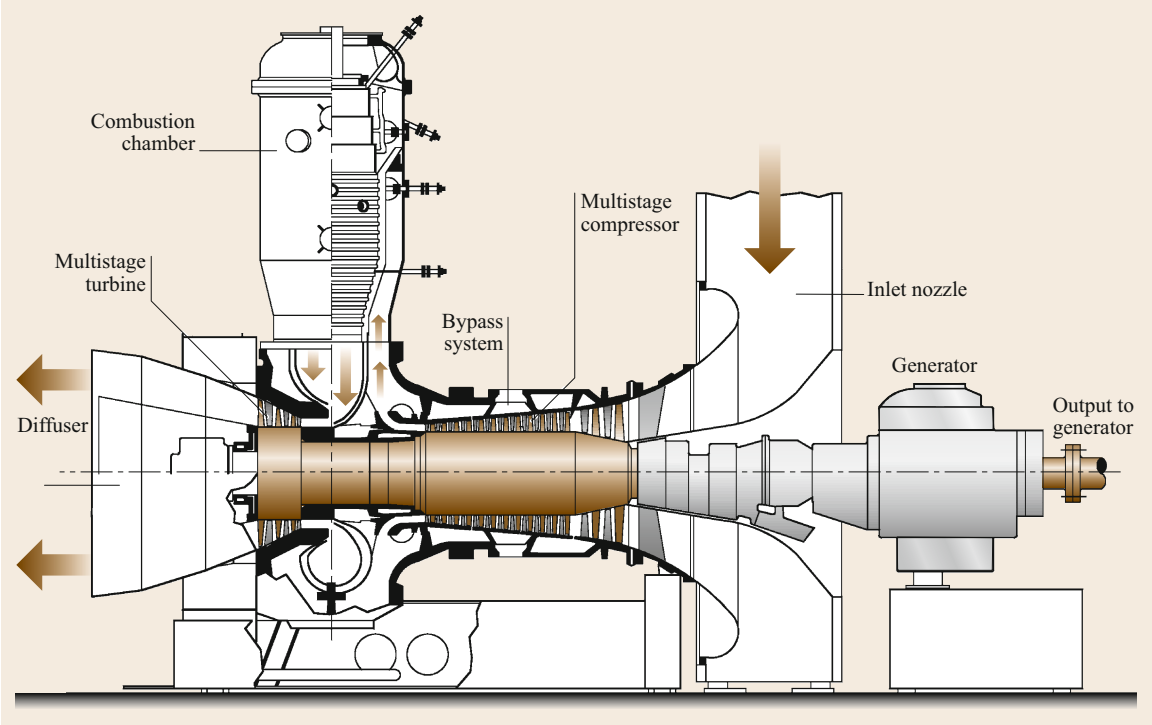

Fig. 19.35 A single-spool power generation gas turbine BBC-GT9

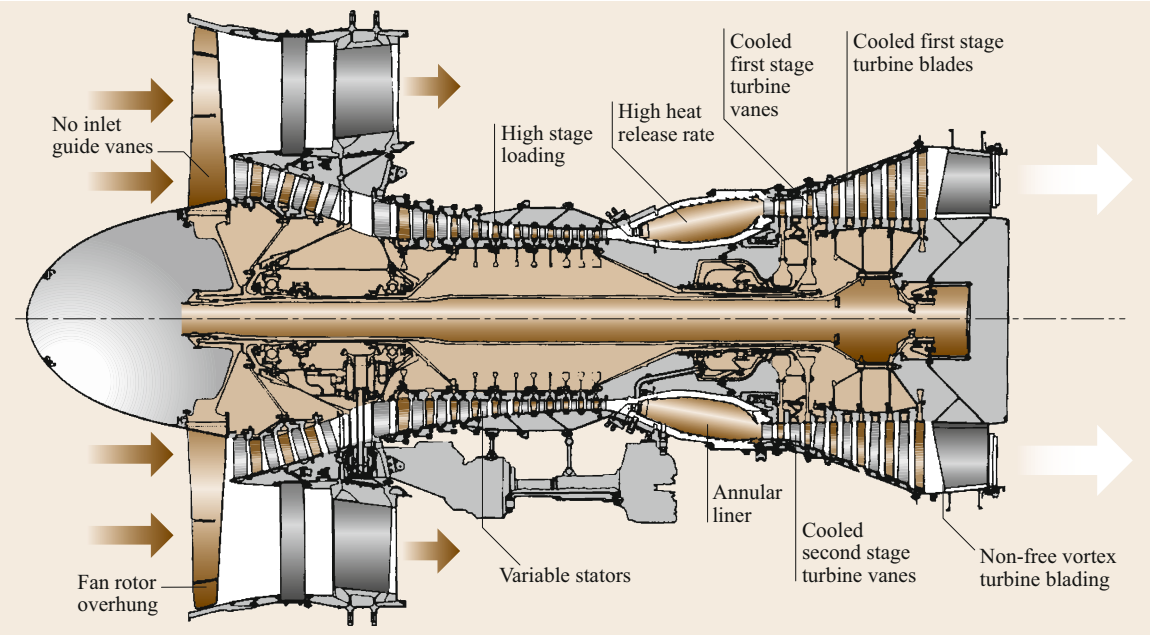

Fig. 19.36 A twin-spool Pratt & Whitney high-bypass-ratio aircraft engine with multistage compressors and turbines

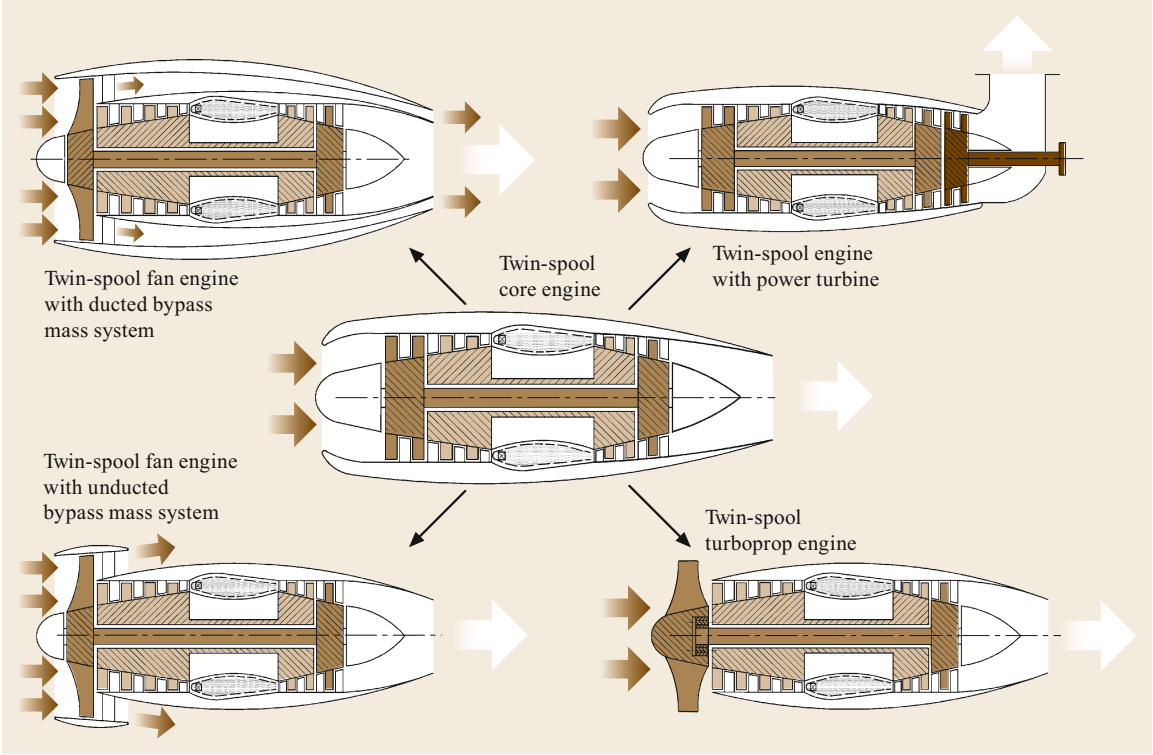

Fig. 19.37 Schematic of a twin-spool core engine with its derivatives

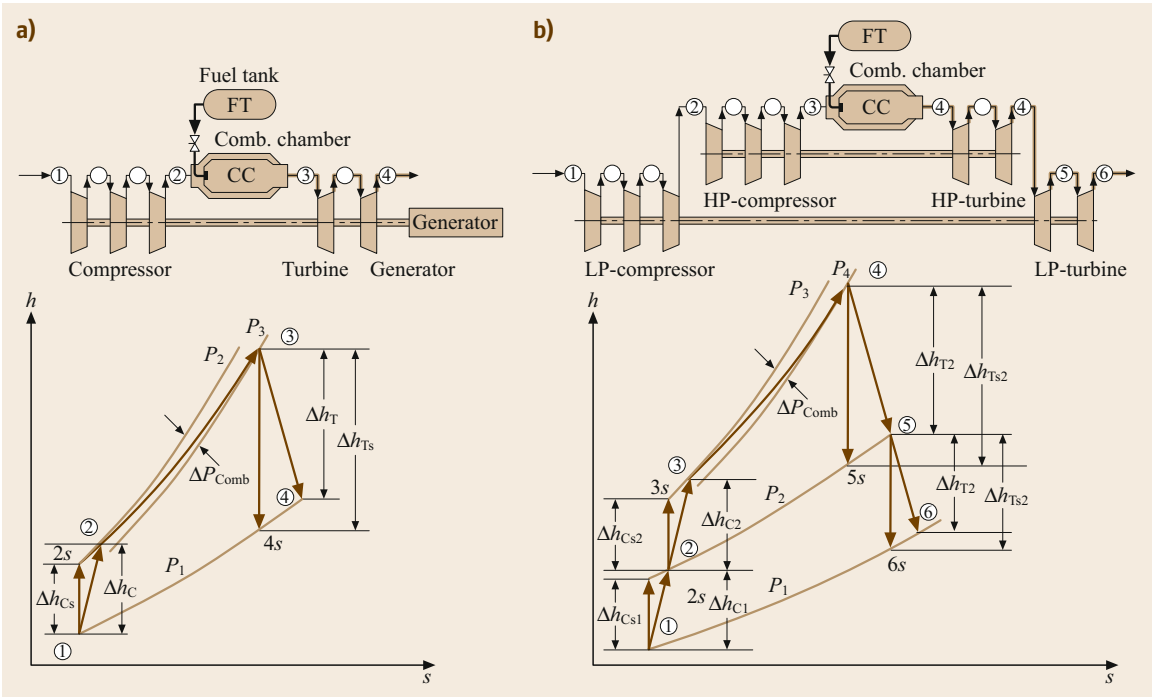

Fig. 19.38a,b *h–s* diagram of (**a**) a single-spool power generation gas turbine and (**b**) a twin-spool aircraft engine

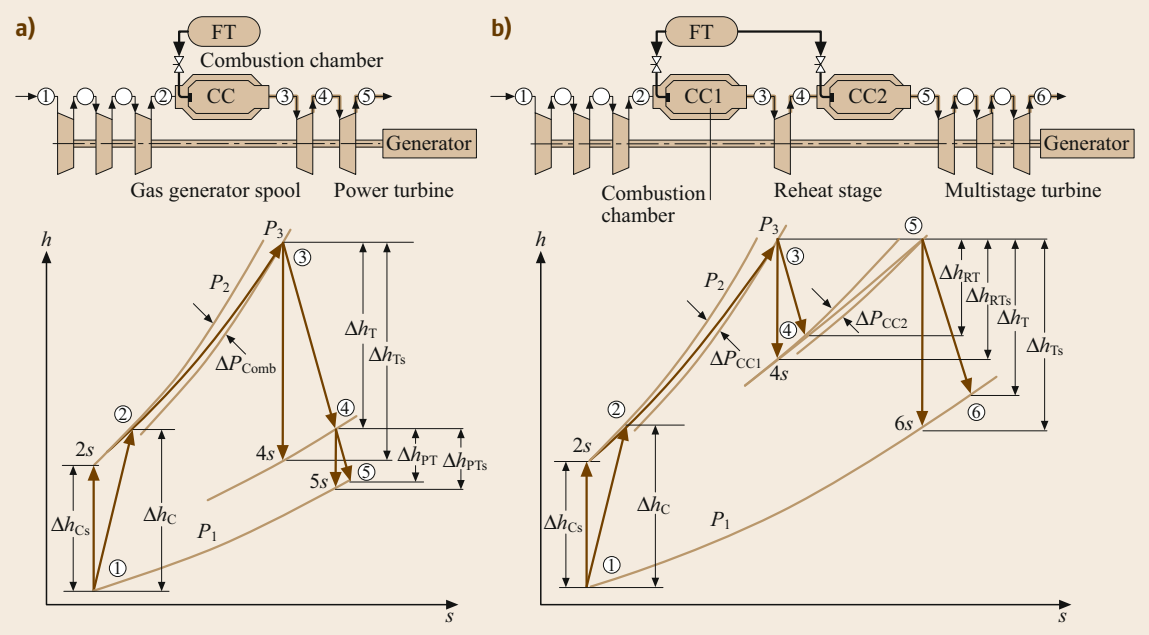

Fig. 19.39a,b *h–s* diagram of **(a)** a single-spool power generation gas turbine with a power shaft and **(b)** a single-spool power generation gas turbine with a reheat stage and two combustion chambers

single-spool engine, the compression process is accomplished by two compressors that are operating at two different angular velocities. Air enters the low-pressure (LP) compressor driven by the LP turbine and is compressed from 1 to 2. Further compression from 2 to 3 occurs in the high-pressure compressor (HP compressor) driven by the HP turbine. After addition of fuel in the combustion chamber, the first expansion occurs in the HP turbine, whose power exactly matches the sum of the HP compressor power and the power required to compensate bearing frictions. The second expansion in the LP turbine matches the power by the LP compressor, bearing friction, and the auxiliary subsystems. In off-design operation, there is always a dynamic mismatch between the turbine and compressor power that changes the spool rotational speed. This dynamic mismatch is brought to an equilibrium by taking appropriate control measures, as discussed in the following sections. As mentioned briefly, small gas turbines may have a split shaft configuration, as shown in Fig. 19.39. The single-spool gas generator unit provides the power turbine with combustion gas that has the required pressure and temperature to produce the power. As seen in Fig. 19.39a, the specific turbine enthalpy difference is $\Delta h_T \approx \Delta h_C$, leaving the remaining enthalpy difference Δh_{PT} for power generation.

Figure 19.39b shows the *h–s* diagram of a high-efficiency power generation gas turbine. The schematic cross section of this gas turbine is shown in Fig. 19.43. It consists of a multistage compressor C and a combustion chamber CC1, providing a lean combustion gas that expands in a single-stage reheat turbine (RT). The exhaust gas from the RT enters the second combustion chamber CC2, where the remaining fuel is added to ensure a stoichiometric combustion. It expands in the multistage turbine, which produces the major portion of power. As seen in the following sections, the implementation of the reheat process substantially increases the thermal efficiency of gas turbines. The underlying thermodynamic principles of this concept is the reheat process, which has been very well known in steam turbine design for more than a century. However, in gas turbine design, adding a second combustion chamber to a conventionally designed gas turbine seemed to be associated with unforeseeable problems. Based on design experiences with *compressed air energy storage* (CAES) gas turbines with two combustion chambers, *Brown Boveri* designed and successfully manufactured the first series of power generation gas turbines with a reheat stage and two combustion chambers.

Gas Turbine Process

Accurate prediction of the thermal efficiency of a gas turbine engine requires knowledge of the compressor, combustion chamber, and turbine efficiencies as well as the bearing losses and the losses in auxiliary systems. Furthermore, detailed knowledge of the amount of mass

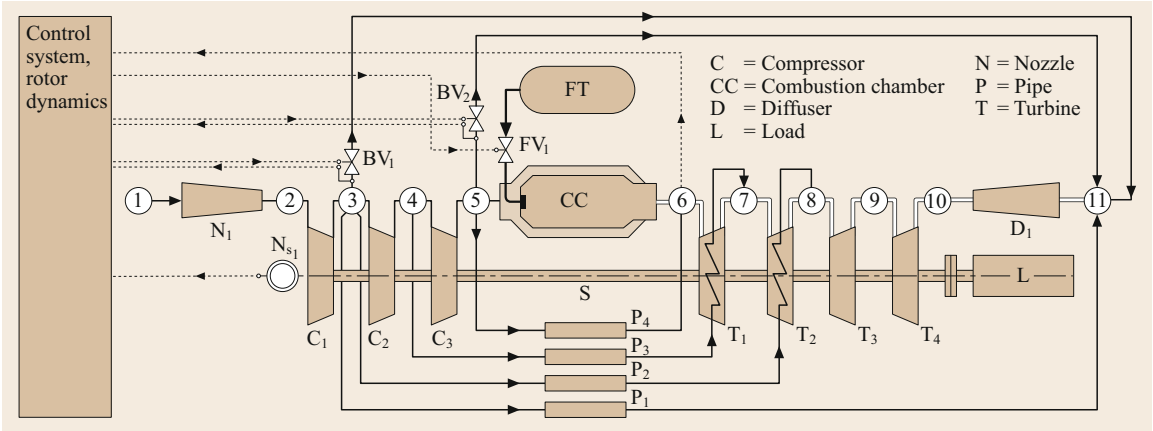

Fig. 19.40 Schematic of a single-spool gas turbine illustrating the mass flow extraction from the compressor for different cooling purposes

flows with their extraction and injection pressures for cooling the turbine blades and the rotor discs are necessary. In addition, a detailed gas table that accounts for thermodynamic properties of humid air as well as the properties of the combustion gas must be implemented into the calculation procedure. Assuming that air and combustion gas are calorically perfect gases results in significant errors. Figure 19.40 exhibits a schematic diagram that shows in detail the extraction of different cooling mass flows and their injection locations.

Mass flow through P1 extracted from plenum 3 cools the rotor and does not participate in power generation; mass flows through P2 and P3 cool the second and first turbine stages and remain in the system; and finally, mass flow through P4 reduces the combustion chamber exit temperature before it enters the turbine. At stations 6–8 and 11 humid air is mixed with combustion gas resulting in a local change of water-to-air and fuel-to-air ratios, therefore changing the entire thermodynamic properties including the special gas constant R. In the absence of the above information, reasonable assumptions relative to component efficiencies can be made to qualitatively determine the thermal efficiency and its tendency with regard to parameter variation. In the following section, a simple thermal efficiency calculation procedure is derived that is appropriate for varying different parameters and qualitatively determining their impacts on thermal efficiency.

The gas turbine with its corresponding process is sketched in Fig. 19.41. It consists of a compressor, a recuperator, a combustion chamber, and a turbine. Exhaust gas from the turbine is diverted into the recuperator, heating up the compressed air before entering the combustion chamber. The individual processes are compression, expansion, fuel addition and combustion, and heat exchange in the recuperator. The compressor and turbine enthalpy differences are calculated from

$$h_2 - h_1 = \frac{h_{2s} - h_1}{\eta_c} ,$$
$$h_3 - h_4 = (h_3 - h_{4s})\eta_T . \qquad (19.90)$$

We introduce the following definitions for the recuperator air and gas side (RA, RG), as well as combustion chamber (CC) pressure loss coefficients

$$\zeta_{RA} = \frac{\Delta P_{RA}}{P_2} , \quad \text{with } \Delta P_{RA} = P_2 - P_5 ,$$
$$\zeta_{RG} = \frac{\Delta P_{RG}}{P_1} , \quad \text{with } \Delta P_{RG} = P_4 - P_6 ,$$
$$\zeta_{CC} = \frac{\Delta P_{CC}}{P_2} , \quad \text{with } \Delta P_{CC} = P_5 - P_3 . \qquad (19.91)$$

The thermal efficiency is defined as

$$\eta_{in} = \frac{L_{net}}{\dot{Q}_{in}} = \frac{L_T - L_C}{\dot{Q}_{in}} = \frac{\dot{m}_T l_T - \dot{m}_C l_C}{\dot{Q}_{in}} . \qquad (19.92)$$

The specific net power is calculated from

$$\frac{L_{net}}{\dot{m}_1} = \frac{L_T - L_c}{\dot{m}_1} = \frac{\dot{m}_3 l_T - m_1 l_C}{\dot{m}_1}$$
$$= (1+\beta) l_T - l_c , \qquad (19.93)$$

with the fuel air ratio $\beta = \dot{m}_f/\dot{m}_1$. Replacing the specific turbine power l_T by the enthalpy difference from (19.90), we find

$$\frac{\dot{m}_3}{\dot{m}_1} l_T = (1+\beta)(h_3 - h_4) = \eta_T (1+\beta)(h_3 - h_{4s}) ,$$
$$\frac{\dot{m}_3}{\dot{m}_1} l_T = \eta_T (1+\beta)\bar{c}_{PT}(T_3 - T_{4s}) ,$$
$$\frac{\dot{m}_3}{\dot{m}_1} l_T = \eta_T (1+\beta)\bar{c}_{PT} T_3 \left(1 - \frac{T_{4s}}{T_3}\right) . \qquad (19.94)$$

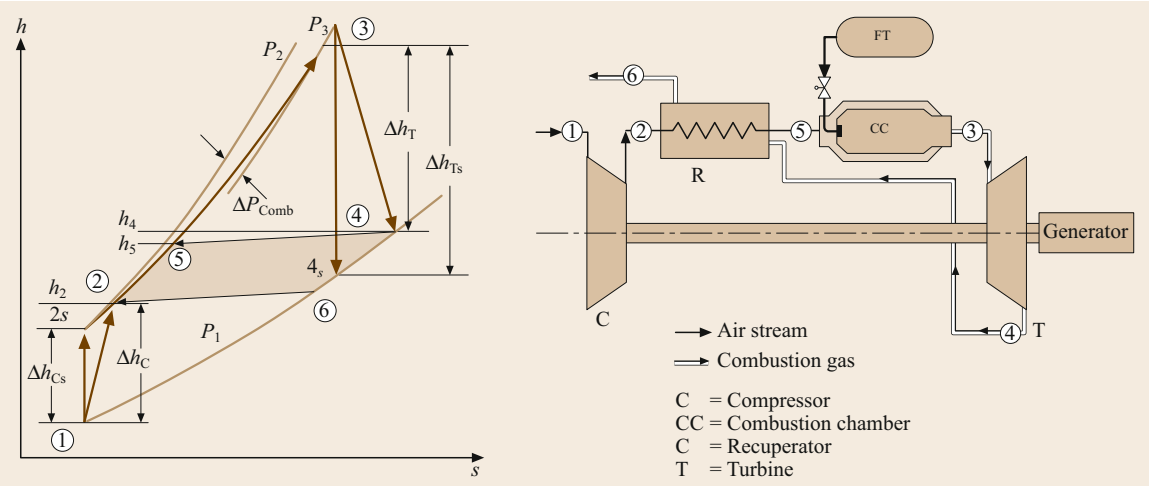

Fig. 19.41 Simple sketch of a gas turbine with recuperator

Equation (19.94) expresses the isentropic enthalpy difference in terms of a product of averaged specific heat at constant pressure and the isentropic temperature difference. The specific heat in (19.94) exhibits an averaged value between the two given temperatures

$$\bar{c}_{\mathrm{PT}} = \frac{h_3 - h_{4\mathrm{s}}}{T_3 - T_{4\mathrm{s}}} \,. \tag{19.95}$$

The temperature ratio in (19.94) can be related to the pressure ratio by

$$\frac{T_3}{T_{4\mathrm{s}}} = \left(\frac{p_3}{p_4}\right)^{\left(\frac{k-1}{k}\right)_{\mathrm{T}}} = \pi_{\mathrm{T}}^{\left(\frac{k-1}{k}\right)_{\mathrm{T}}} = \pi_{\mathrm{T}}^{m_{\mathrm{T}}} \,,$$
$$\text{with } m_{\mathrm{T}} \equiv \left(\frac{k-1}{k}\right)_{\mathrm{T}} \,. \tag{19.96}$$

With (19.96), (19.94) becomes

$$\frac{\dot{m}_3}{\dot{m}_1} l_{\mathrm{T}} = \eta_{\mathrm{T}} (1+\beta) \bar{c}_{\mathrm{PT}} T_3 \left(1 - \pi_{\mathrm{T}}^{-m_{\mathrm{T}}}\right) . \tag{19.97}$$

Because of the pressure losses across the combustion chamber, the turbine and compressor pressure ratios are not the same ($\pi_{\mathrm{T}} \neq \pi_{\mathrm{c}}$). Implementing the pressure losses of the combustion chamber and recuperator air side, we find

$$\begin{aligned} \pi_{\mathrm{T}} &= \frac{p_3}{p_4} = \frac{p_2 - \Delta p_{\mathrm{RA}} - \Delta p_{\mathrm{CC}}}{p_1 + \Delta p_{\mathrm{RA}}} \\ &= \frac{p_2}{p_1} \left(\frac{1 - \zeta_{\mathrm{RA}} - \zeta_{\mathrm{CC}}}{1 + \zeta_{\mathrm{RA}}}\right) \\ &= \pi_{\mathrm{c}} \frac{1 - \zeta_{\mathrm{RA}} - \zeta_{\mathrm{CC}}}{1 + \zeta_{\mathrm{RA}}} \,. \end{aligned} \tag{19.98}$$

We set the fraction on the right-hand side of (19.98) as

$$\epsilon = \frac{1 - \zeta_{\mathrm{RA}} - \zeta_{\mathrm{CC}}}{1 + \zeta_{\mathrm{RA}}} \tag{19.99}$$

and arrive at

$$\pi_{\mathrm{T}} = \epsilon \pi_{\mathrm{c}} \quad \begin{array}{l} \text{for } \epsilon = 0 \,,\ \zeta_{\mathrm{RA}} = \zeta_{\mathrm{CC}} = \zeta_{\mathrm{RA}} = 0 \\ \text{and for } \epsilon > 0 \,,\ \zeta_{\mathrm{RA}} \neq 0 \,,\ \zeta_{\mathrm{CC}} \neq 0 \,. \end{array} \tag{19.100}$$

For parameter variation, the following values may be used: $\zeta_{\mathrm{RA}} \approx \zeta_{\mathrm{RG}} = 2\text{–}8\%$ and $\zeta_{\mathrm{CC}} \approx 5\text{–}10\%$. Following exactly the same procedure defined by (19.93)–(19.100), we find the compressor specific work as

$$l_{\mathrm{C}} = \frac{1}{\eta_{\mathrm{C}}} \bar{c}_{\mathrm{Pc}} T_1 \left(\pi_{\mathrm{C}}^{m_{\mathrm{C}}} - 1\right) , \text{ with } m_{\mathrm{C}} = \left(\frac{k-1}{k}\right)_{\mathrm{C}} \,. \tag{19.101}$$

Inserting (19.97) and (19.101) into (19.93), we arrive at

$$\begin{aligned} \eta_{\mathrm{th}} = {} & \frac{\eta_{\mathrm{T}} \bar{c}_{\mathrm{PT}} T_3 \left[1 - (\epsilon \pi_{\mathrm{c}})^{-m_{\mathrm{T}}}\right] (1+\beta)}{\bar{c}_{\mathrm{PCC}} T_1 \left[(1+\beta)\frac{T_3}{T_1} - \frac{T_5}{T_1}\right]} \\ & - \frac{\frac{1}{\eta_{\mathrm{c}}} \bar{c}_{\mathrm{Pc}} T_1 \left(\pi_{\mathrm{c}}^{m_{\mathrm{c}}} - 1\right)}{\bar{c}_{\mathrm{PCC}} T_1 \left[(1+\beta)\frac{T_3}{T_1} - \frac{T_5}{T_1}\right]} \,. \end{aligned} \tag{19.102}$$

The turbine inlet temperature T_3 and the environmental temperature T_1, and thus their ratio T_3/T_1, is considered as a known parameter. This parameter can also be used for parametric studies. Therefore it is desirable to

express the ratio T_5/T_1 in terms of T_3/T_1. We find this ratio by utilizing the recuperator effectiveness η_R

$$\eta_R = \frac{h_5 - h_2}{h_4 - h_2} \approx \frac{T_5 - T_2}{T_4 - T_2} \,. \tag{19.103}$$

From the compressor and turbine energy balance in (19.90) we find

$$\begin{aligned} T_2 &= T_1 + (T_{2s} - T_1)\frac{1}{\eta_c} = T_1 + T_1\left(\pi_c^{m_c} - 1\right)\frac{1}{\eta_c} \,, \\ T_4 &= T_3 - (T_3 - T_{4s})\eta_T = T_3 - T_3\left[1 - (\epsilon\pi_c)^{-m_T}\right]\eta_t \,. \end{aligned} \tag{19.104}$$

Equation (19.104) in dimensionless form yields

$$\begin{aligned} \frac{T_2}{T_1} &= 1 + \frac{1}{\eta_c}\left(\pi_c^{m_c} - 1\right) , \\ \frac{T_4}{T_1} &= \frac{T_3}{T_1} - \frac{T_3}{T_1}\eta_T\left[1 - (\epsilon\pi_c)^{-m_T}\right] . \end{aligned} \tag{19.105}$$

Introducing the temperature ratio $\theta = T_3/T_1$, the temperature ratio T_4/T_1 (19.105) becomes

$$\frac{T_4}{T_1} = \theta\left\{1 - \left[1 - (\epsilon\pi_c)^{-m_T}\right]\eta_T\right\} . \tag{19.106}$$

To determine the temperature ratio T_5/T_1, we rearrange (19.103) to obtain

$$\frac{T_5}{T_1} = \eta_R\left(\frac{T_4}{T_1} - \frac{T_2}{T_1}\right) + \frac{T_2}{T_1} \,. \tag{19.107}$$

Using (19.105) and (19.106), (19.107) can be rearranged to

$$\begin{aligned} \frac{T_5}{T_1} = \eta_R\Bigg(&\theta\left\{1 - \left[1 - (\epsilon\pi_c)^{-m_T}\right]\epsilon_T\right\} - 1 \\ &- \frac{1}{\eta_c}\left(\pi_c^{m_c} - 1\right)\Bigg) + 1 + \frac{1}{\eta_c}\left(\pi_c^{m_c} - 1\right) . \end{aligned} \tag{19.108}$$

Introducing (19.108) and the definition $\theta = T_3/T_1$ into (19.102), the thermal efficiency equation for a gas turbine with a recuperator is written as

$$\begin{aligned} \eta_{th} = &\left\{\bar{c}_{PT}\eta_T\theta\left[1 - (\epsilon\pi_c)^{-m_T}\right](1 + \beta)\right. \\ &\left. - \frac{1}{\eta_c}\bar{c}_{Pc}\left(\pi_c^{m_c} - 1\right)\right\} \\ &\times\Bigg(\bar{c}_{PCC}\Big\{\theta(1 + \beta - \eta_R) \\ &- \left[1 + \frac{1}{\eta_c}\left(\pi_c^{m_c} - 1\right)\right](1 - \eta_R) \\ &+ \theta\eta_R\eta_T\left[1 - (\epsilon\pi_c)^{-m_T}\right]\Big\}\Bigg)^{-1} . \end{aligned} \tag{19.109}$$

From (19.109) special cases are obtained. Setting $\eta_R = 0$ gives the thermal efficiency of a gas turbine without a recuperator. The ideal case of the Brayton cycle is obtained by setting all loss coefficients equal to zero, all efficiencies equal to unity, and $\bar{c}_{PC} = \bar{c}_{PCC} = c_{PT} = \text{const}$. Equation (19.109) properly reflects the effects of individual parameters on the thermal efficiency and can be used for preliminary parameter studies. As an example, Fig. 19.8 shows the effect of pressure ratio, the turbine inlet temperature, and the component efficiency on thermal efficiency for two different cases. As Fig. 19.42 shows, for each turbine inlet temperature, there is one optimum pressure ratio. For temperature ratios up to $\theta = 3.5$ pronounced efficiency maxima are visible within a limited π-range. When approaching higher inlet temperature, however, this range widens significantly.

For a gas turbine without recuperator, the thermal efficiency (the solid curves in Fig. 19.42) shows that, for $\theta = 4.0$, increasing the pressure ratio above 15 does not yield a noticeable efficiency increase. However, this requires the compressor to have one or two more stages. The temperature ratio $\theta = 4.0$ corresponds to a turbine inlet temperature of $T_3 = 1200\,\text{K}$ at a compressor inlet temperature of $T_1 = 300\,\text{K}$.

The dashed curves in Fig. 19.42 indicate that tangibly higher thermal efficiencies at a substantially lower pressure ratio can be achieved by utilizing recuperators. This is particularly advantageous for small gas turbines (so called *microturbines*) with power ranging from 50 to 200 kW. The required low maximum pressure ratio can easily be achieved by a single-stage centrifugal compressor. Comparing cases 1 and 2 in Fig. 19.42 shows that thermal efficiency reduces if low-efficiency components are applied.

Improvement of Gas Turbine Thermal Efficiency

The above parameter study indicates that, for a conventional gas turbine with a near-optimum pressure ratio with or without a recuperator, the turbine inlet temperature is the parameter that determines the level of thermal efficiency. For small-size gas turbines, the recuperator is an inherent component of the gas turbine. For large power generation gas turbines, however, this is not a practical option. Using a recuperator in a large gas turbine requires a significantly lower pressure ratio, which results in a large-volume recuperator and turbine. As a result, in order to improve the thermal efficiency of conventional gas turbines, increasing the turbine inlet temperature seems to be the only option left. Considering this fact, in the past three decades, gas turbine manufacturers have been concentrating their efforts on introducing more sophisticated cooling tech-

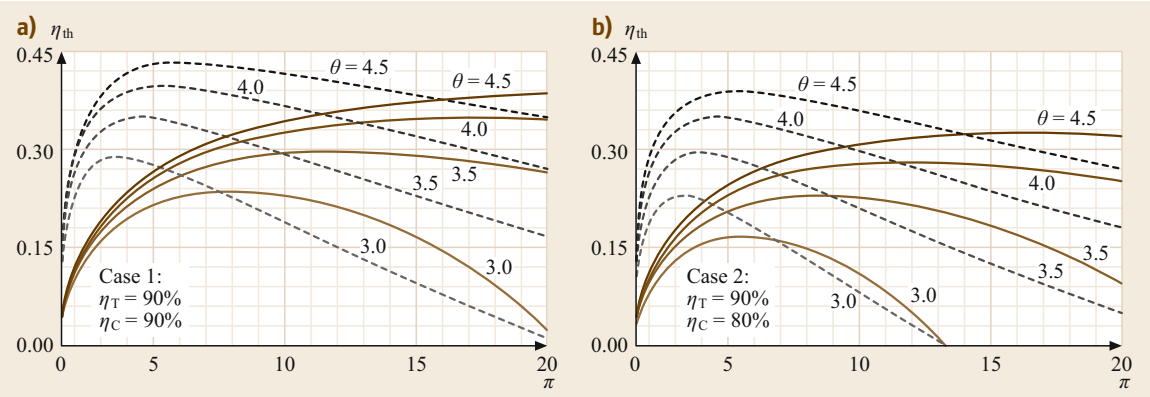

Fig. 19.42a,b Thermal efficiency as a function of pressure ratio with turbine inlet temperature ratio as a parameter for **(a)** a gas turbine with a recuperator (*dashed curves*) and **(b)** without a recuperator (*solid curves*). $\eta_R = 0.75$, $\zeta_{CC} = 0.05$, $\zeta_{RA} = \zeta_{RG} = 0.03$, for case 1 and case 2. In case 2 the turbine efficiency is lowered from 90% to 80%

nologies, which are essential for increasing the turbine inlet temperature of conventional gas turbines.

To improve the thermal efficiency substantially without a significant increase in turbine inlet temperature, the well-known reheat principle as a classical method for thermal efficiency augmentation is applied. Although this standard efficiency improvement method is routinely applied in steam turbine power generation, it did not find its way into aircraft and the power generation gas turbine design. The reason for this was the inherent problem of integrating a second combustion chamber into a conventionally designed gas turbine engine. This issue raised a number of unforeseeable design integrity and operational reliability concerns. ABB (formerly Brown Boveri & Cie) was the first to develop a gas turbine engine with one reheat stage turbine followed by a second combustion chamber and a multistage turbine (Fig. 19.43).

A comparative study in [19.22] emulates two conceptually different power generation gas turbine designs utilizing components whose detailed aerodynamic performance characteristics were known. The first is a conventional gas turbine, whereas the second one has a reheat turbine stage and a second combus-

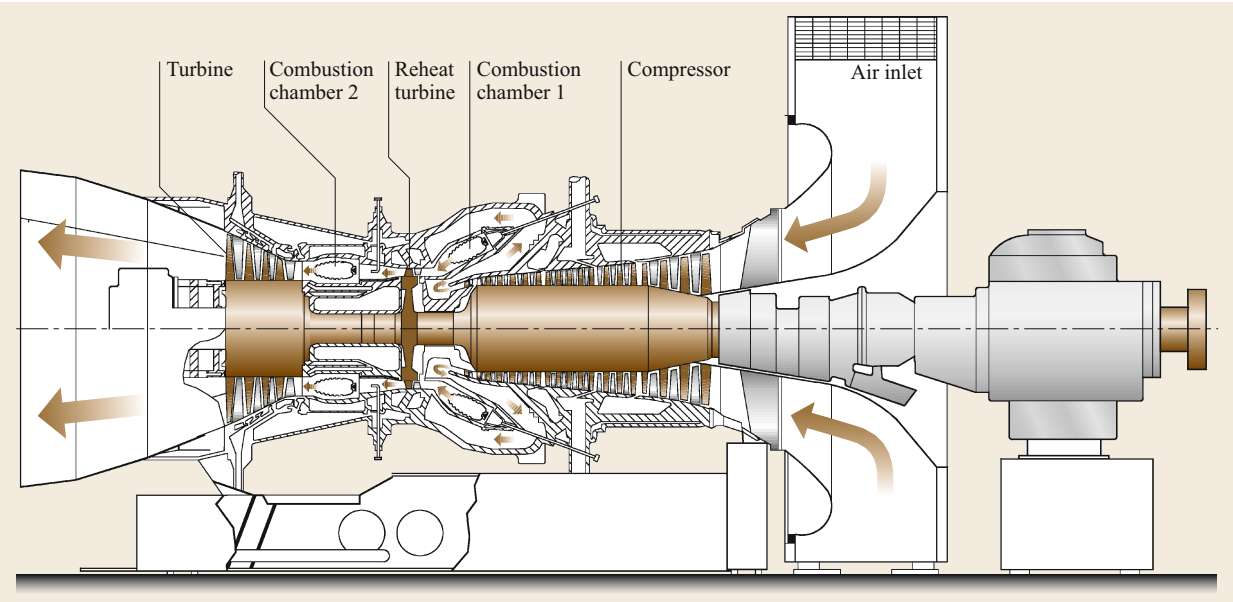

Fig. 19.43 A schematic cross section of the GT-24 gas turbine engine with a single-stage reheat turbine and a second combustion chamber

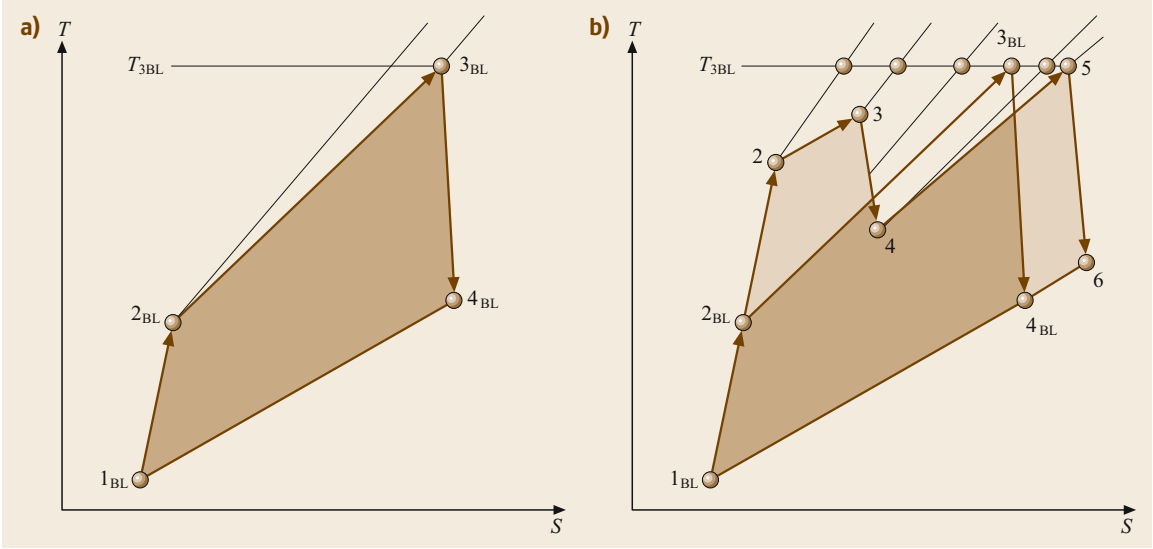

Fig. 19.44a,b Comparison of (a) a conventional baseline gas turbine process (b) with the GT-24 process after [19.22]

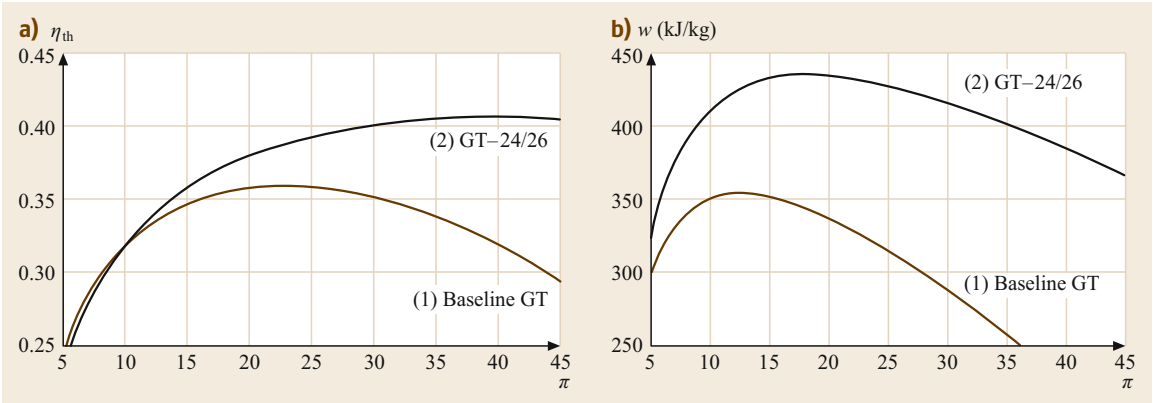

Fig. 19.45a,b Comparison of efficiency and specific work between a conventional baseline gas turbine and GT-24: (a) efficiency, (b) specific work

tion chamber resembling the GT-24 [19.23]. Starting from a given environmental condition (pressure, temperature) and a consolidated turbine inlet temperature $T_{3BL} = 1200\,°C$ for both engines (Fig. 19.44a) the thermal efficiency is determined by the compressor pressure ratio and the compressor and turbine polytropic efficiencies η_c and η_T and is plotted in Fig. 19.45a. As curve 1 shows, for the given pressure ratio, which is not identical with the optimum pressure ratio, an efficiency of $\eta_{th} = 35\%$ is calculated. Substantial efficiency improvement is achieved by introducing a single-stage reheat principal, as applied to the GT-24. Details of the process are sketched in Fig. 19.44b with the baseline process as the reference process. The bright dotted area in Fig. 19.44b translates into the efficiency improvement, which in the case of the GT-24 resulted in efficiency improvement of 5.5% above the baseline efficiency. A detailed dynamic engine simulation of the GT-24 gas turbine engine with GETRAN© [19.24] verified a thermal efficiency of $\eta_{th} = 40.5\%$ plotted in Fig. 19.45a, curve 2. This tremendous efficiency improvement was achieved despite the facts that (a) the compressor pressure ratio is much higher than the optimal one for a baseline engine and (b) the introduction of a second combustion chamber inherently causes additional total pressure losses. Further calculation showed that introducing a third combustion chamber would only result in a marginal improvement of 1–1.5% thermal efficiency, which does not justify the necessary research and development efforts to integrate a third combustion chamber. The specific work comparison is plotted in Fig. 19.45b, which shows a significant in-

crease in specific work. Additional efficiency improvement requires a technology change. Major improvement can be achieved by using the ultrahigh-efficiency gas turbine (UHEGT) technology [19.1]. This technology eliminates the combustion chambers altogether and places the combustion process inside the stator blade passages (Sect. 19.3.6).

19.3.2 Nonlinear Gas Turbine Dynamic Simulation

The continuous improvement of efficiency and performance of aircraft and power generation gas turbine systems during the past decades has led to engine designs that are subject to extreme load conditions. The engine components operate near their aerodynamic, thermal, and mechanical stress limits. Under these circumstances, any adverse dynamic operation causes excessive aerodynamic, thermal, and subsequent mechanical stresses that may affect the engine safety, and reliability if adequate precautionary actions are not taken. Considering these facts, an accurate prediction of the above stresses and their cause is critical at the early stages of design and development of the engine and its components. This section focuses on the simulation of the dynamic behavior of gas turbine engines and their components. The simulation spectrum encompasses single- and multispool gas turbine engines, turbofan engines, and power generation gas turbine engines. The simulation concept is based on a generic modularly structured system configurations. This concept is discussed in detail in [19.1], where the gas turbine components are represented by individual modules described mathematically by systems of differential equations. Based on these and other necessary modules, a generic concept is presented that provides the reader with necessary tools for developing computer codes for simulation of arbitrary engine and plant configurations ranging from single-spool thrust generation to multispool thrust/power generation engines under adverse dynamic operating conditions. It can easily be extended to rocket engines, combined cycles, cogeneration cycles, and steam power plants. In [19.1] a multilevel system simulation treats different degrees of complexity ranging from global adiabatic simulation to a detailed diabatic one. The dynamic behavior of the subject engine is calculated by solving a number of systems of partial differential equations which describe the unsteady behavior of the individual components. Accurate prediction of the dynamic behavior of the engine and the identification of critical parameters by using the method enables the engine designer to take appropriate steps using advanced control systems. This method may also be used to prove the design concept of the new generation of high-performance engines. The modular structure of the concept enables the user to independently develop new components and integrate them into the simulation code. As representative examples, four different case studies are presented that deal with dynamic simulation of a compressed air energy storage gas turbine. Different transient cases with single- and multispool thrust, and power generation engines were simulated. The transient cases range from operating with a prescribed fuel schedule, to extreme load changes and generator shut down.

19.3.3 Engine Components, Modular Concept, and Module Identification

A schematic component arrangement and modeling of a twin-spool core engine is shown in Fig. 19.46. The corresponding modules are implemented into the engine modular configuration schematic in Fig. 19.47. Figures 19.48 and 19.49 show the lists of components with their corresponding modular representations and symbols that are described by the method presented in [19.1]. They exhibit the basic components essential for generically configuring any possible aero- and power generation gas turbine engines. These modules are connected to each other with a plenum, which is a coupling component between two or more successive components. As briefly explained in [19.1], the primary function of the plenum is to couple the dynamic information of entering and exiting components such as mass flow, total pressure, total temperature, fuel-to-air ratio, and water-to-air ratio. After entering the plenum a mixing process takes place, where the aforementioned quantities reach their equilibrium values. These values are the same for all outlet components.

A survey of power and thrust generation gas turbine engines has led to the practical conclusion that any arbitrary aircraft or power generation gas turbine engine and its derivatives, regardless of configuration, i.e., number of spools and components, can be generically simulated by arranging the components according to the engine configuration of interest. The nonlinear dynamic method presented in [19.1] is based on this generic, modularly structured concept that simulates the transient behavior of existing and new engines and their derivatives. The modules are identified by their names, shaft number, and inlet and outlet plena. This information is vital for automatically generating the system of differential equations representing individual modules. Modules are then combined into a complete system which corresponds to the engine configuration. Each module is physically described by the conservation laws of thermo-fluid mechanics which result in a system of nonlinear partial differential or algebraic equations.

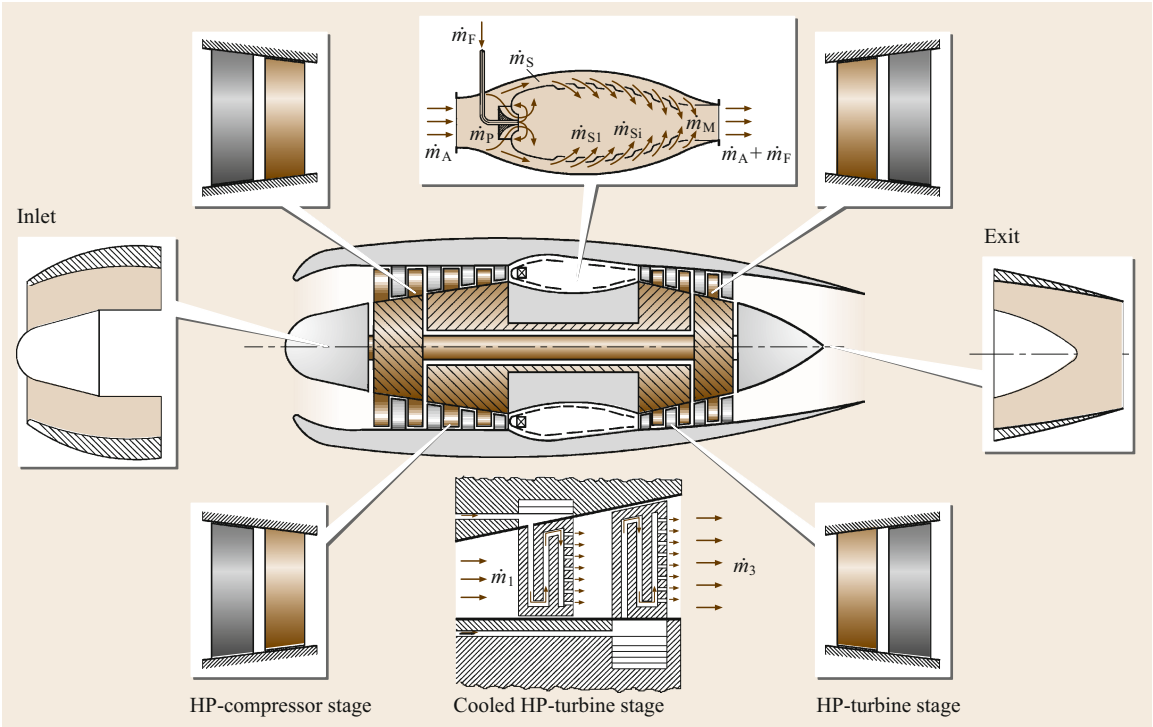

Fig. 19.46 Schematic of a twin-spool core engine, component decomposition

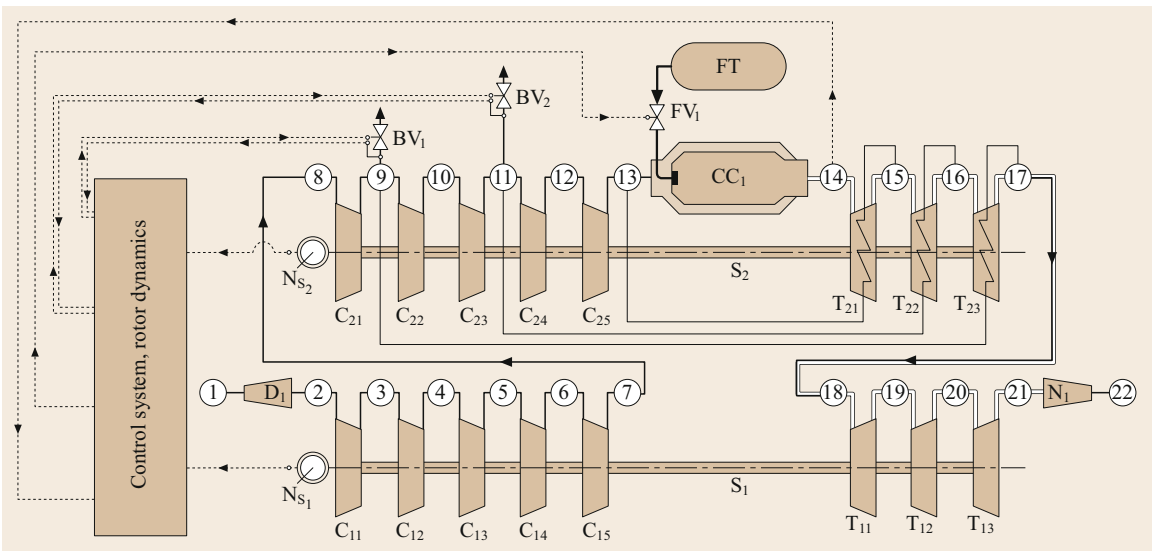

Fig. 19.47 Modular configuration of the engine exhibited in Fig. 19.46

Since an engine consists of a number of components, its modular arrangement leads to a system containing a number of sets of equations. The above concept can be systematically applied to any aircraft or power generation gas turbine engine.

The general application of the modular concept is illustrated in Figs. 19.46 and 19.47. The twin-spool engine shown in Fig. 19.46 exemplifies the modular extension of the single-spool base engine. It consists of two spools with shafts S_1 and S_2, on which the low- and high-pressure components such as compressors and turbines are assembled. The two shafts are coupled by the working media air and combustion gas. They rotate with different speeds, which are transferred to the

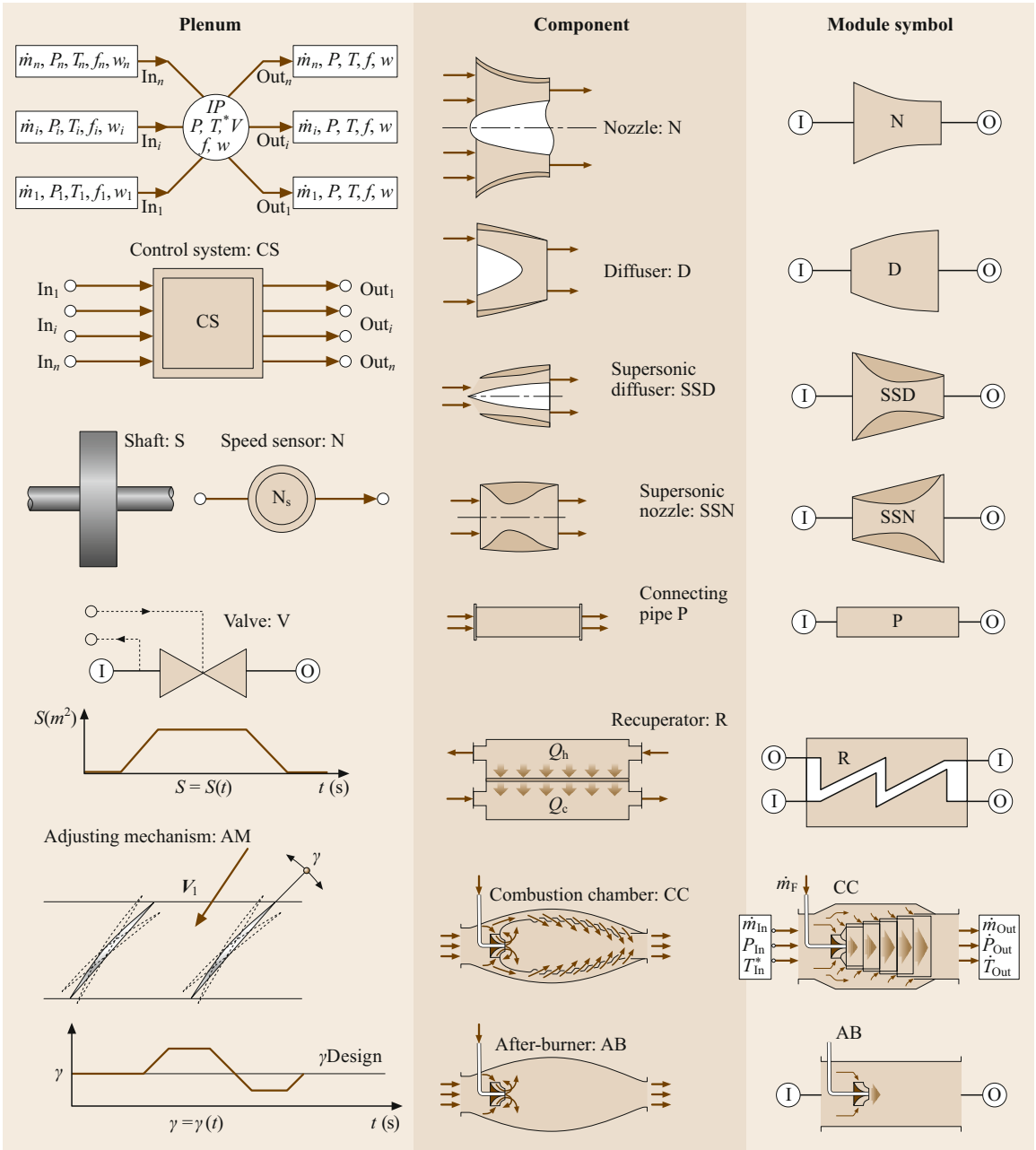

Fig. 19.48 Components, modules, and their symbols: plenum, control system CS, shaft S, with moment of inertia I and rotational velocity ω, speed sensor N, valve with an arbitrary ramp for closing and opening the cross section s, adjusting mechanism AM for stator blade adjustment, subsonic nozzle N, subsonic diffuser D, supersonic diffuser SSD, supersonic nozzle SSN, recuperator R, combustion chamber CC, and afterburner AB

control system by the sensors Ns_1 and Ns_2. Air enters the inlet diffuser D_1, which is connected with the multistage compressor assembled on S_1, and is decomposed in several compressor stages C_{1i}. The first index (1) refers to the spool number and the second index i marks the number of the compressor stage. After compression in the S_1 compressor stage group, the air enters the second compressor (HP compressor) assembled on the S_2 shaft, which consists of stages C_{21}–C_{25}. In the combustion chamber (CC_1) high-temperature combustion gas is produced by adding the fuel from the tank FT. The gas expands in the high-pressure turbine that

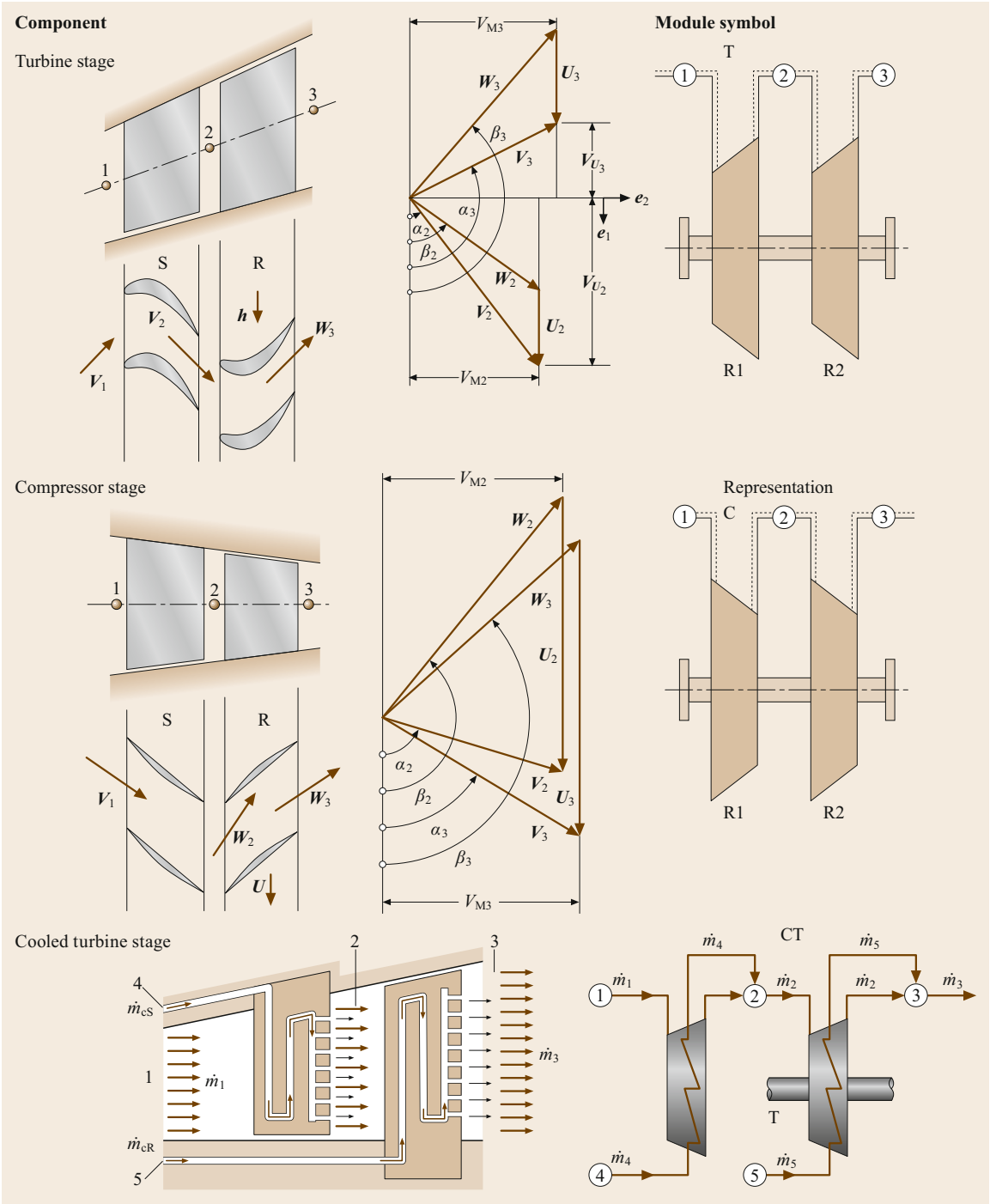

Fig. 19.49 Adiabatic turbine stage with module T, adiabatic compressor stage with module C, cooled turbine stage with module CT

consists of stages T_{21}–T_{23}. When exiting from the last stage of the HP turbine, the combustion gas enters the low-pressure turbine, consisting of stages T_{11}–T_{13} and is expanded through the exit nozzle. Two bypass valves, BV_1 and BV_2, are connected with the compressor stator blades for surge prevention. The fuel valve, FV_1, is placed between the fuel tank, FT, and the combustion chamber, CC_1. The pipes, P_i, serve for cooling air

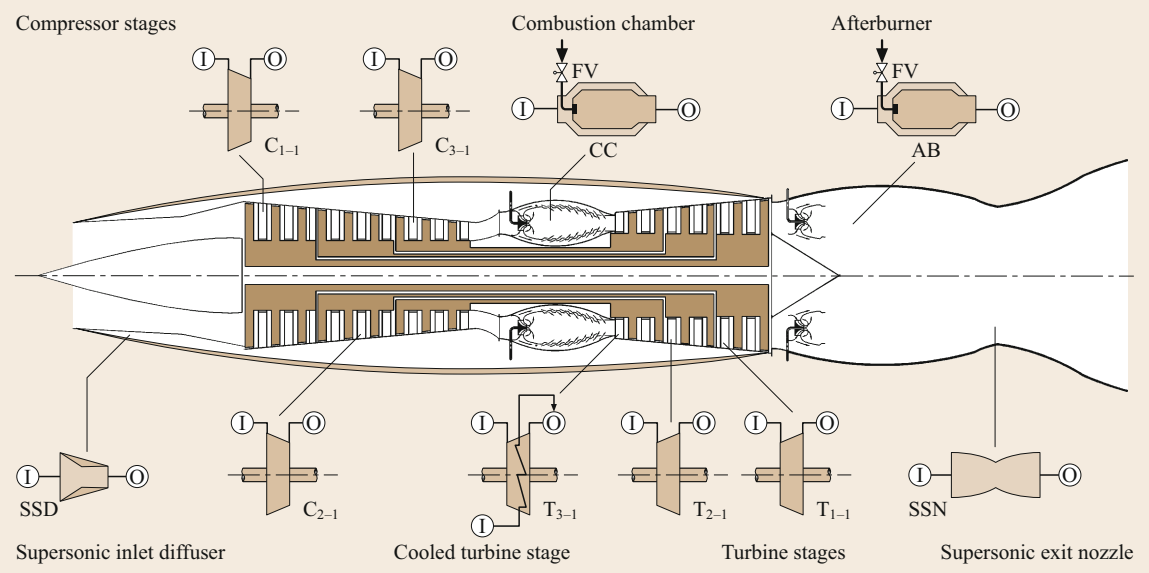

Fig. 19.50 Schematic of a three-spool high-performance core engine, component decomposition

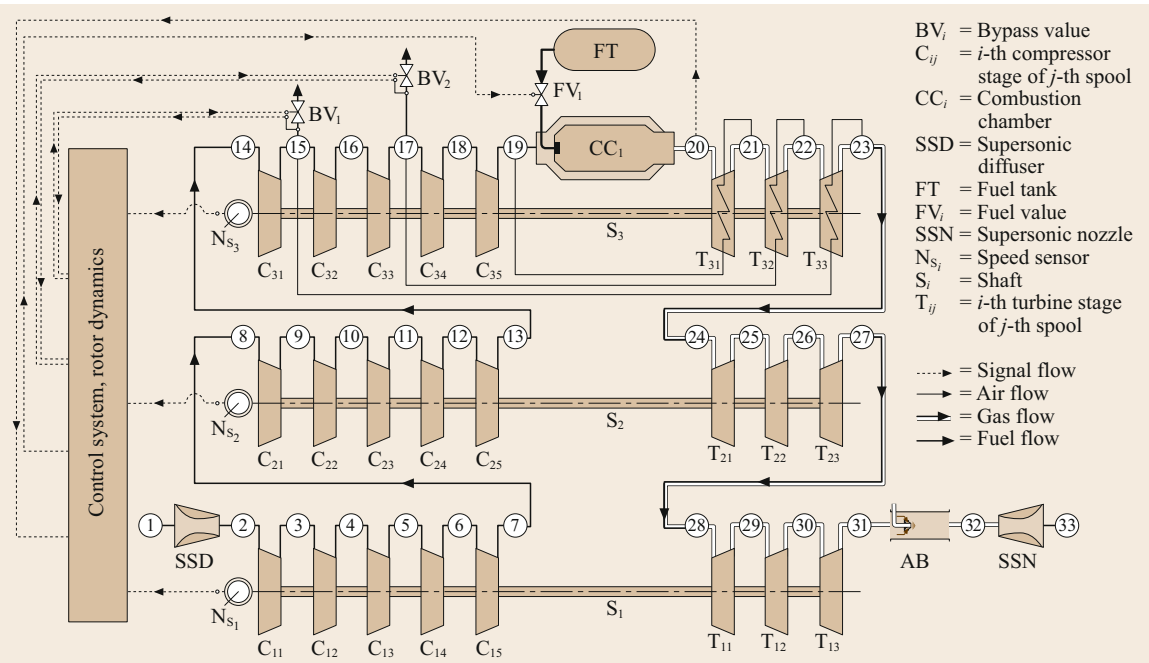

Fig. 19.51 Modular configuration of the three-spool engine shown in Fig. 19.50. The three compressors and turbines are connected aerodynamically. The plena addressing the spool number, and the component number uniquely identify the set of differential equations that describe the module

transport from the compressor to cooled turbines. The compressor stage pressures, the turbine inlet temperature, and the rotor speed are the input signals to the control system, which controls the valve cross sections and the fuel mass flow.

Figure 19.50 shows a more complex example of a three-spool supersonic engine with its modular decomposition. Figure 19.51 exhibits a systematic modular configuration of Fig. 19.50 that is represented by a large system of differential and algebraic equations.

19.3.4 Levels of Gas Turbine Engine Simulations, Cross Coupling

The accuracy of gas turbine dynamic simulation is determined by the level of component modeling. It increases by increasing the level of simulation complexity. Four levels of simulation are introduced:

- The *zeroth simulation level* is applied to simple cases utilizing a fixed system configuration with steady-state component characteristics that are described by algebraic equations, simplified differential equations, and lookup tables and maps. Furthermore, there is no dynamic coupling between the components. Since this simulation level does not account for engine dynamics, it will not be discussed further.
- The *first simulation level* uses the component global performance map only for turbines and compressors. The maps are generated using the row-by-row adiabatic calculation method detailed in [19.1]. The other components such as recuperators, coolers, combustion chambers, pipes, nozzles, and diffusers are simulated according to methods discussed in [19.1]. Primary air, secondary combustion gas, and metal temperature of the combustion chamber are calculated. All modules are coupled with plena, ensuring a dynamic information transfer to all modules involved. Modules are described by algebraic and differential equations.
- The *second simulation level* utilizes adiabatic row-by-row or stage-by-stage calculation for the compressor and turbine modules. For the combustion chamber, primary air, secondary combustion gas, and metal temperature are calculated. Dynamic calculations are performed throughout the simulation, where the modules are coupled by plena. Each module is described by differential and algebraic equations.
- The *third simulation level* uses diabatic row-by-row calculation for compressor and turbine modules. This level delivers very detailed diabatic information about the compressor and turbine component dynamic behavior. It utilizes cooled turbine and compressor stages and simultaneously calculates the blade temperatures. For the combustion chamber, primary air, secondary combustion gas, and metal temperature are calculated. Dynamic calculations are performed throughout the simulation, whereas the modules are coupled by plena. Each module is described by differential and algebraic equations. The details of information delivered by this level and degree of complexity is demonstrated by the following example. The first two stages of a four-stage turbine component of a high-performance gas turbine engine must be cooled. For the first four turbine rows we use the diabatic expansion process that requires three differential equations for describing the primary flow, three differential equations for describing the cooling flow, and one differential equation for describing the blade temperature. This leads to 28 differential equations from two cooled turbine stages.

The generic structure allows cross-coupling of levels 1 to 3. For example, we wish to simulate a gas turbine engine with a global compressor performance map but need to obtain detailed information about the turbine blade temperature, as this is needed to calculate the relative expansion between the blades and the casing, then we may use the diabatic calculation method. In this case, we cross-couple the first- and third-level simulation.

19.3.5 Nonlinear Dynamic Simulation Case Studies

Three case studies dealing with three completely different gas turbine systems are presented. Table 19.3 shows the matrix of the cases where the engine types and transient-type simulations are listed. These studies demonstrate the capability of the generic structured method discussed in [19.1] to simulate complex systems dynamically and with high accuracy. The case studies presented in this chapter are related to real-world engine simulation and are intended to provide the reader with an insight into nonlinear engine dynamic simulation. The selected cases ranging from zero-spool, single-shaft power generation to three-spool four-shaft thrust and power generation gas turbine engines provide detailed information about the engine behavior during design and off-design dynamic operation. For each engine configuration the simulation provides aerothermodynamic details of each individual component and its interaction with the other system components. Since

Table 19.3 Simulation case studies

Tests	Gas turbine type	Transient type
Case 1	CAES: Compressed air energy storage power generation gas turbine engine, zero-spool, single shaft, two turbines, two combustion chambers	Generator and turbine shut down
Case 2	Single-spool, single-shaft, power generation gas turbine engine, BBCGT9	Adverse load changes
Case 3	Three-pool, four-shaft, thrust and power generation core engine	Operation with fuel schedule

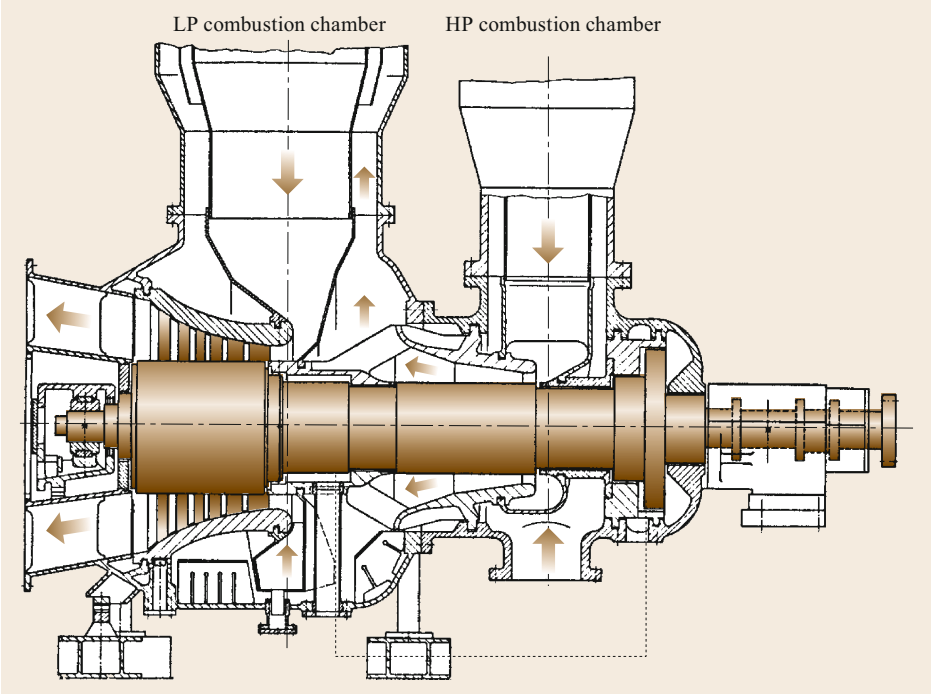

Fig. 19.52 BBC-CAES-Huntorf gas turbine engine after [19.1]

the presentation of the complete simulation results of the three cases listed in Table 19.3 would exceed the scope of this chapter, only a few selected plots will be displayed and discussed for each case.

Case Study 1: Compressed Air Energy Storage Gas Turbine

The subject of this case study is a zero-spool, single-shaft compressed air energy storage (CAES) gas turbine [19.6], which is utilized to efficiently cover peak electric energy demand during the day. Continuous increase of fuel costs have motivated the power generation industry to invest in technologies that result in fuel saving. Successful introduction of combined cycle gas turbines (CCGT) has drastically improved the thermal efficiency of steam power plants, which is equivalent to a significant fuel saving. Further saving is achieved by using the excess electrical energy available during the period of low electric energy demand (6–8 h during the night) to compress air into a large storage system. During periods of peak demand, the compressed air is injected into the combustion chambers and mixed with the fuel. After the ignition process is completed, the high-pressure high-temperature gas expands in the turbine, generating electric energy for about 2–4 h. In contrast to a CCGT, the period of operation of a CAES plant is restricted to a few hours per day, resulting in a daily startup followed by a shutdown procedure. This relatively high frequency of startups and shutdowns may cause structural damages resulting in reduced lifetime if the startup and shutdown procedures are not performed properly. The condition for a safe startup procedure is outlined in this study, which helps the engine and control system designer to integrate this into their design procedure. The CAES gas turbine system (Fig. 19.52) with the simulation schematic shown in Fig. 19.53 features a large-volume plenum (8) for storing the compressed air, a high-pressure combustion chamber (HPCC), a high-pressure turbine (HPT), a low-pressure combustion chamber (LPCC), a low-pressure turbine (LPT2), a cold-air preheater with a low- and high-pressure side (LPP and HPP side) and a generator (G). During steady-state turbine operation, cold air from the air-storage facility, plenum 8, passes through the shutdown valve (V_1) to the inlet plenum (1), where it is divided into combustion and cooling-air flows. The addition of fuel in the HPCC causes the combustion air to be heated to the combustion chamber's exit temperature. Immediately upstream of the HPT, the combustor mass flow is mixed with a portion of the cooling-air flow, which has already been preheated in the HPP. As a result, the gas temperature of the turbine mass flow lies below the combustion chamber's exit temperature. After expansion in the HPT, the combustion chamber (LPCC) mass flow is mixed in the LPT inlet plenum (4) with the rest of the preheated cooling-air flow and the sealing-air flow. After expansion in the LPT, the gas gives off some of its heat in the LPP before leaving the gas turbine system.

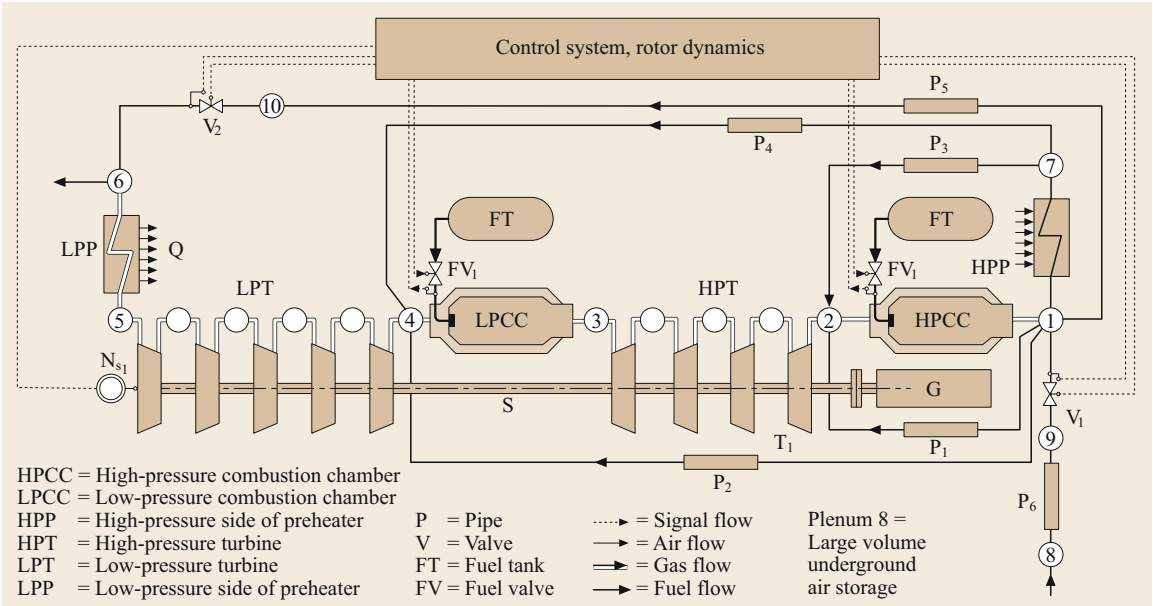

Fig. 19.53 Simulation schematic of the CAES shown in Fig. 19.52

Figure 19.53 shows how the various components are interconnected. Plenum 8, the air storage facility, is connected via two identical pipes (P6) to two shutdown valves (V_1). During steady-state operation, the blow-off valve (V_2) remains closed, being opened in the event of a disturbance likely to cause rapid shutdown. In such an event, the valve blows off some of the gas, thereby limiting the maximum rotor speed. For the sake of clarity, the preheater (P) has been separated into its air and gas sides, designated by HPP and LPP, respectively.

Simulation of Emergency Shutdown. Starting from a steady operating point, a generator trip with rapid shutdown was simulated, assuming a failure of the control system. This circumstance necessitates an intervention by the hydraulic emergency system. This incident simulates an extreme transient process within some of the components, as explained briefly. After the generator trip, the rotor is strongly accelerated because of the full turbine power acting on it (Fig. 19.54a).

The hydraulic emergency system intervenes only when the speed corresponding to the hydraulic emergency overspeed trip is reached. This intervention involves closing the fuel valves, FV_1 and FV_2, and air valves V_1, after which the system no longer receives any energy from outside (Fig. 19.54b). It also involves opening the bypass/blow-off valve V_2, which allows the high-pressure air contained in both large-volume

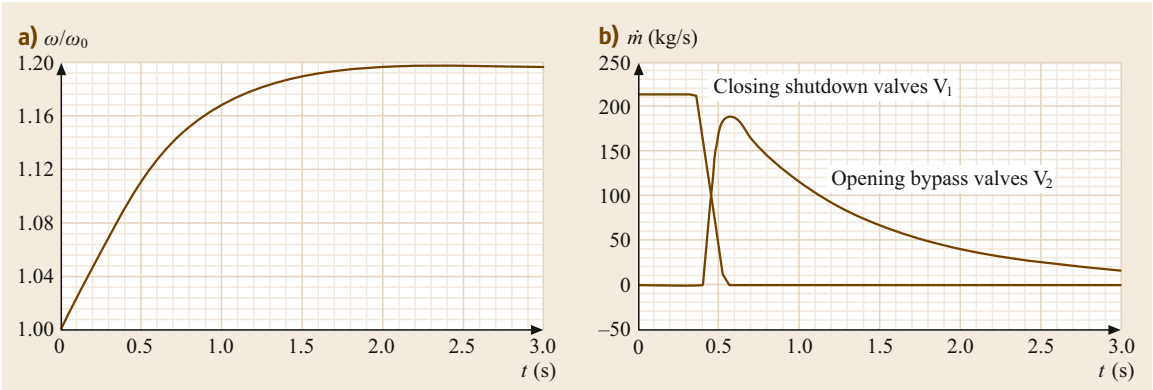

Fig. 19.54 **(a)** Relative angular velocity and **(b)** mass flows as functions of time. The inlet shutdown valves V_1 remain open until the trip speed at $t = 0.35$ s has been reached. The same procedure is true for opening the blow-off valves V_2. Closing the shutdown valves follow the ramp shown in **(b)**

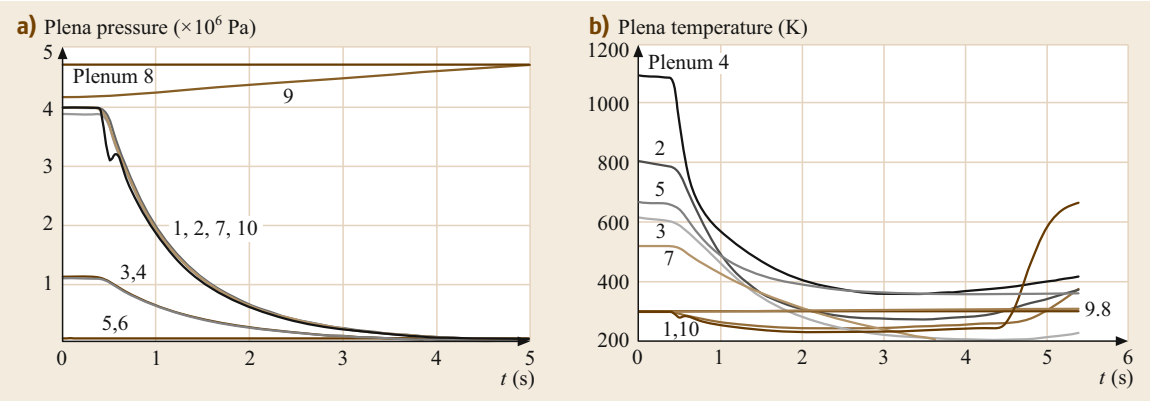

Fig. 19.55 **(a)** Plena pressure and **(b)** temperature as functions of time. The shutdown process causes rapid depressurization in the high-pressure plena 1, 2, 7, and 10

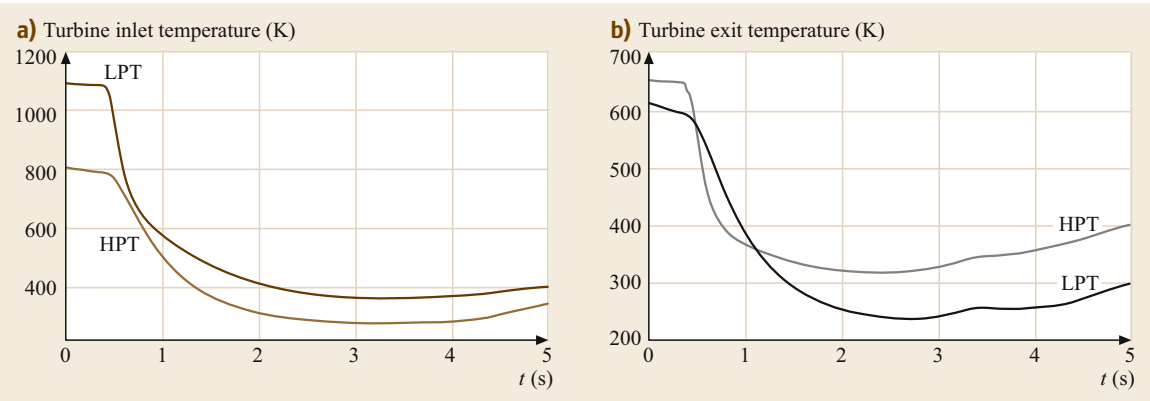

Fig. 19.56 **(a)** Turbine inlet and **(b)** exit temperature as functions of time. Note the changes of the exit temperature at $t = 3.4$ s

combustion chambers as well as in the HP side of the preheater to discharge.

The closing process of the inlet and shutdown valves and the opening of the bypass valves are shown in Fig. 19.54b. This process results in a steady drop in plena pressures and temperatures. As Fig. 19.55 shows, the pressure drop in the high-pressure section is initially steeper than in the low-pressure section. This means that the enthalpy difference of the high-pressure turbine is reduced more rapidly than that of the low-pressure turbine. Immediately after the blow-off valve is opened, an abrupt pressure drop takes place in plenum 10, which is connected to plenum 1 via pipe P_5. Thereafter, dynamic pressure equalization takes place between the two plena. This drop in pressure and temperature causes a corresponding drop in the shaft power and the mass flow throughout the engine. Figure 19.56 shows the resulting drop in turbine inlet and exit temperature. The continuous decrease in turbine mass flow causes a strong dissipation of shaft power, resulting in the excessive increase of turbine exit temperature. In order to avoid thermal damage to the blades, a small stream of cold air is injected into the turbine flow path, which causes a reduction in temperature gradient. This is shown in Fig. 19.56 for the exit temperature at $t = 3.4$ s.

Dynamic behavior of the rotor speed is generally determined by the turbine power acting on the rotor. How the rotor behaves in response to a generator trip depends, in particular, on how long the full turbine power is available, a process monitored by the control and safety monitoring system. When the control system functions normally, a trip is signaled without delay to the shutdown valve. Failure of the control system causes the hydraulic emergency system to intervene. The intervention begins only when the speed corresponding to the hydraulic emergency overspeed trip is reached. During this process, and also the subsequent valve dead time, the rotor receives the full turbine power. The closing phase is characterized by a steady

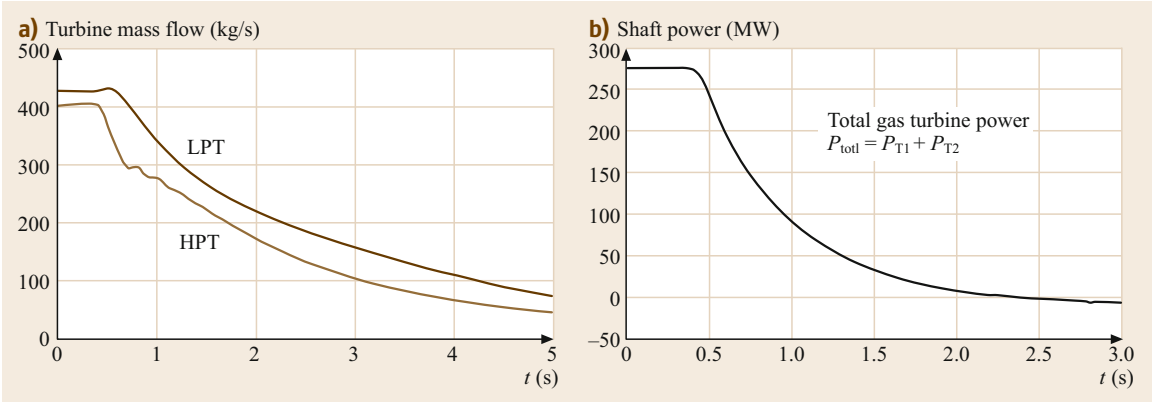

Fig. 19.57 **(a)** Turbine mass flow and **(b)** shaft power as functions of time

reduction in energy input from outside, which finally becomes zero. The total energy of the gases still contained in the system is converted by the two turbines into mechanical energy, causing the rotor speed to increase steadily (Fig. 19.54). When the instantaneous turbine power is just capable of balancing the friction and ventilation losses, the rotor speed reaches its maximum, after which it begins to decrease. Reducing the turbine mass flow (Fig. 19.57a) below the minimum value discussed in [19.25] causes the shaft power to dissipate completely as heat, resulting in negative values, as shown in Fig. 19.57b. From this point on, the rotational speed starts to decrease. Figure 19.57a depicts the mass flows through the HP and LT turbines that generate the total shaft power (Fig. 19.57b).

Case Study 2: Power Generation Gas Turbine Engine

The subject of this case study is the dynamic simulation of a BBC-GT9 gas turbine which is a single-spool single-shaft power generation gas turbine engine. It is utilized as a stand-alone power generator or in conjunction with combined cycle power generation. The engine shown in Fig. 19.58 consists mainly of three compressor stage groups, a combustion chamber, a turbine, a control system, and a generator.

The simulation schematic of this engine is presented in Fig. 19.59. The rotor speed and turbine inlet temperature are the input parameters for the controller, its output parameters are the fuel mass flow (fuel valve opening), and the mass flows of the bypass valves (bypass valve opening). The dynamic behavior of BBC-GT9 was experimentally determined for transient tests with extreme changes in its load. Its transient data was accurately documented by *Schobeiri* et al. [19.24]. Starting from a given network load schedule, the dynamic behavior of the gas turbine is predicted and the results are presented.

The engine under consideration consists mainly of three compressor stage groups, a combustion chamber, a turbine, a control system, and a generator. The simulation schematic of this engine is similar to that of Fig. 19.60. For dynamic simulation, the first, second, and third stage groups are simulated using the row-by-row technique [19.25]. A similar row-by-row calculation procedure is applied to the turbine component. The rotor speed and the turbine inlet temperature are the input parameters for the controller; its output parameters are the fuel mass flow (fuel valve opening) and the mass flows of the bypass valves (bypass valve opening).

Simulation of an Adverse Dynamic Operation. Starting from steady state, in accordance with the load schedule indicated in Fig. 19.60a (curve 1), after 1 s, a generator loss of load is simulated that lasts for 6 s. The rotor at first reacts with a corresponding increase in rotational speed (Fig. 19.60b), which results in a rapid closing of the fuel valve (Fig. 19.60b). The rotational speed is then brought to an idling point and held approximately constant. The process of control intervention lasts until a constant idling speed is attained. After that, there is an addition of load in sudden increases, such that the gas turbine is supplying approximately 25% of its rated load (Fig. 19.60). The rotor first reacts to this addition of load with a sharp decrease in rotational speed, as exhibited in Fig. 19.60, causing a quick opening of the fuel valve (Fig. 19.60). After completion of the transient process, the steady off-design state is reached.

Plena Pressure and Temperature Transients. The above adverse dynamic operation triggers temporal changes of the flow quantities within individual components. Figure 19.61 shows how the plena pressure and temperature change with time. Decrease of turbine power and increase of the shaft speed (Fig. 19.60) has

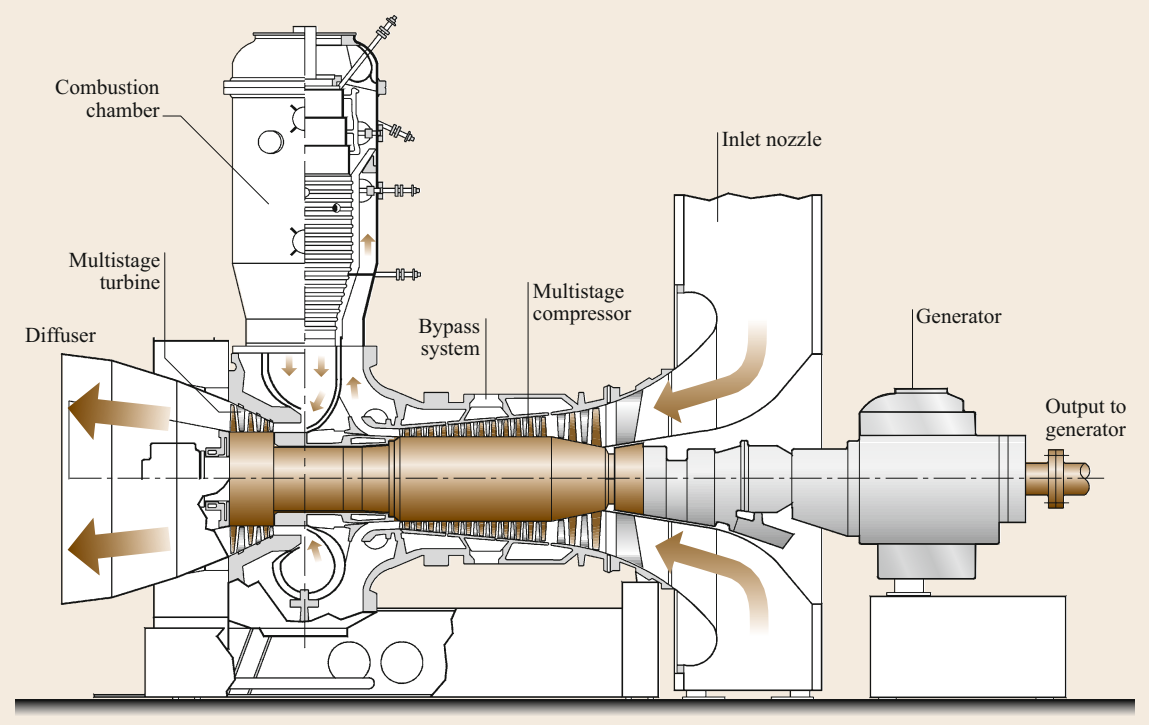

Fig. 19.58 A single-spool power generation gas turbine BBC-GT9

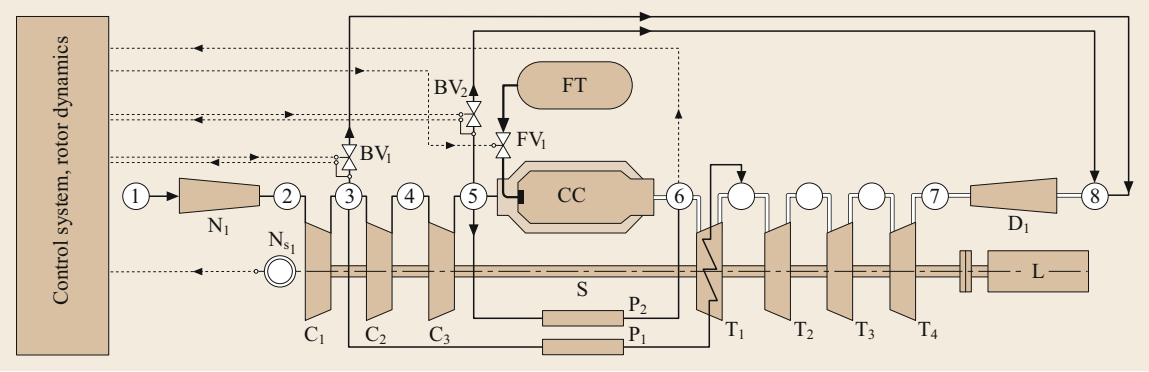

Fig. 19.59 Simulation schematic of BBC-GT9 shown in Fig. 19.58

caused the HP compressor exit pressure in plenum 5 to decrease. The temperature at the combustion chamber exit, plenum 6, and turbine exit, plenum 7, follow the course of fuel injection shown in Fig. 19.65b. The plena temperature upstream of the combustion chamber are not affected.

Compressor and Combustion Chamber Mass Flow Transients. Figure 19.62 exhibits the mass flow transients through low-pressure (LP), intermediate-pressure (IP), and high-pressure (HP) compressors. While the IP- and HP-stage groups have the same mass flow, the LP part has a greater mass flow. The difference of 1 kg/s is due to the cooling mass flow extraction. As briefly mentioned, the increase in shaft speed and the simultaneous decrease in compressor power consumption leading to the compressor pressure drop has caused an increase in the compressor mass flow during the process of loss of load that lasts up to $t = 6$ s. The sudden load addition reduces the compressor mass flow.

The combustion chamber mass flow shows a similar course with a substantial difference: a substantial

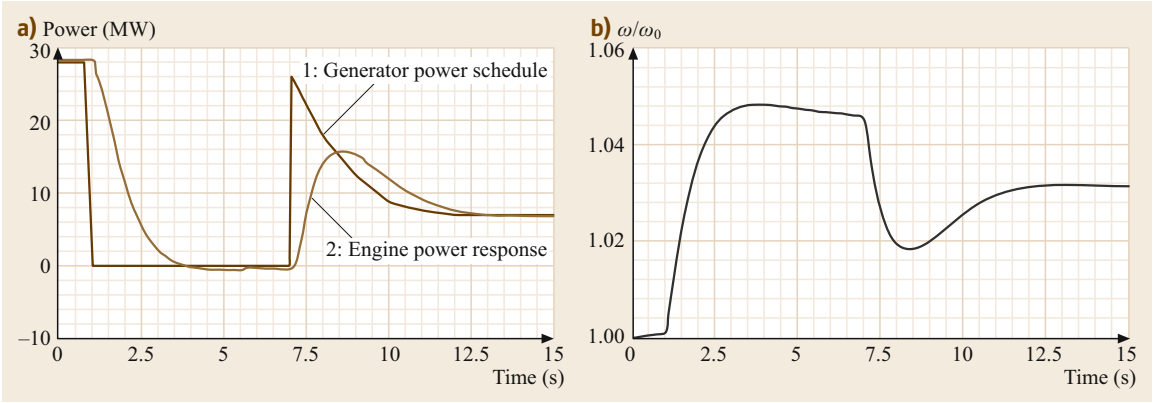

Fig. 19.60 **(a)** Generator load schedule (*curve* 1). Sequence of events: steady operation from 0 to 1 s, sudden loss of load, idle operation, sudden addition of load, continuous decrease of load to 25%. *Curve* 2: engine power response. **(b)** Relative shaft speed as a function of time

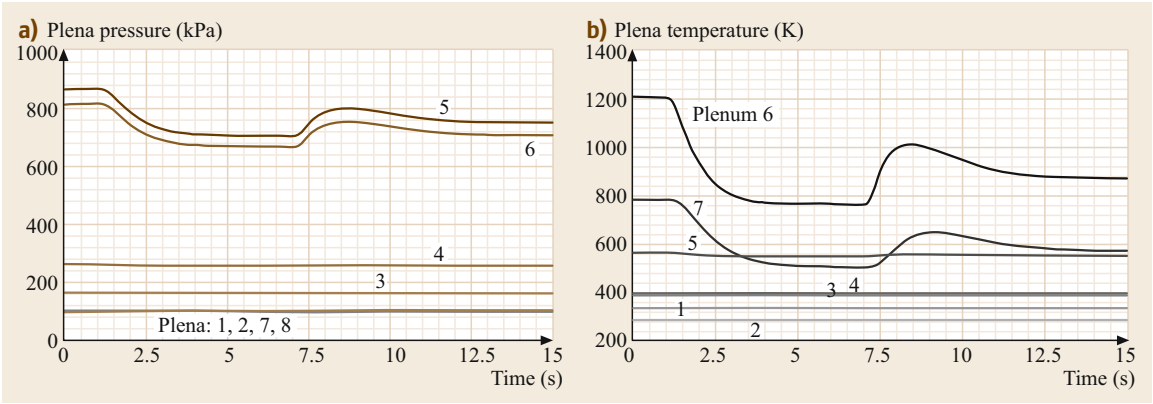

Fig. 19.61 **(a)** Plena pressure and **(b)** temperature as functions of time. Individual plena are labeled

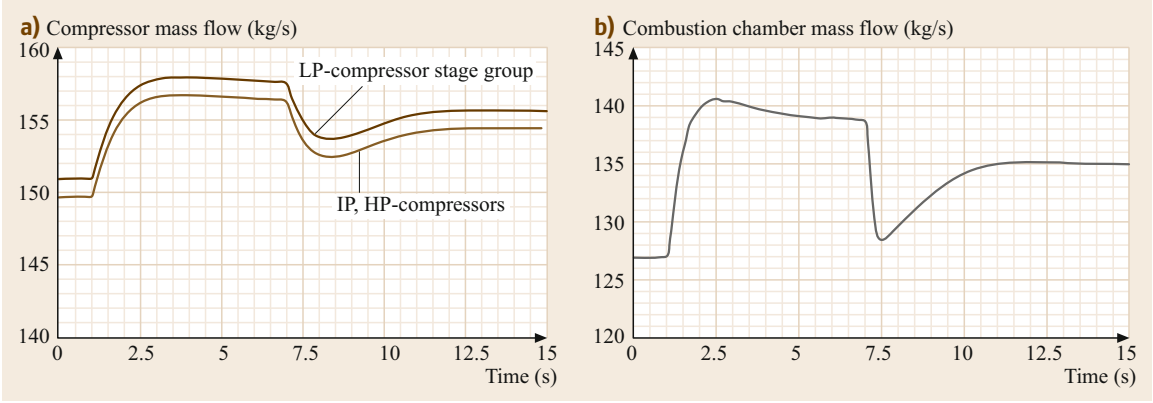

Fig. 19.62 **(a)** Compressor and **(b)** combustion chamber mass flows as functions of time

portion of the compressor mass flow is extracted for combustion chamber exit temperature mixing cooling.

Combustion Chamber Gas and Metal Temperature Transients. The combustion chamber component used in this simulation has three segments that separate the primary combustion zone from the secondary cooling air zone. Its module is shown in Fig. 19.63. Figure 19.64 exhibits the combustion chamber gas and metal temperatures as functions of time. Compressed air enters the combustion chamber at station 1 (Fig. 19.64). Fuel is added and the segment cooling occurs according to the procedure described in [19.25]. The secondary mass flow portions $\dot{m}_{Si}$ serve as cooling jets and are mixed with the combustion gas, thus reducing the gas temperature. Before exiting, the combustion gas is mixed with the mixing air stream $\dot{m}_M$, further reducing the temperature. Figure 19.64b shows the mean segment temperatures. In accordance with the measurements on this gas turbine, the flame length extends from station 1 to 3, which makes segment number 2 the hottest one. We assumed that all secondary cooling channels are open.

Turbine and Fuel Mass Flow Transients. Figure 19.65a exhibits the turbine mass flow transient, which is dictated by the compressor dynamic operation. The difference between the turbine and the compressor mass flow is the injected fuel mass flow. The particular course of fuel mass flow shown in Fig. 19.65b is due to the intervention of the control system. An increase in rotational speed causes the controller to close the fuel valve. Subsequent addition of generator load results in a steep drop of rotational speed, which causes an opening of the fuel valve.

Case Study 3: Simulation of a Multispool Gas Turbine Engine

The subject of this study is the nonlinear dynamic simulation of a gas turbine engine with a higher degree of complexity than the previous cases. For this purpose a three-spool thrust-generating gas turbine engine is designed that incorporates advanced components. The three-spool four-shaft high-performance gas turbine engine consists of a low-pressure spool that incorporates the LP compressor and turbine connected via shaft S_1. The intermediate pressure spool integrates the IP compressor and turbine connected via shaft S_2. The high-pressure spool carries the HP compressor and HP turbine on shaft S_3. To increase the level of engine complexity, a fourth shaft, S_4, with the power generating turbine T_4, was attached to the exit of the three-spool gas generating unit as shown in Fig. 19.66. The transient operation is controlled by a given fuel schedule. The component nomenclature for this configuration is the same as for the previous cases. The simulation schematics shown in Fig. 19.66 represents the modular configuration of the gas turbine.

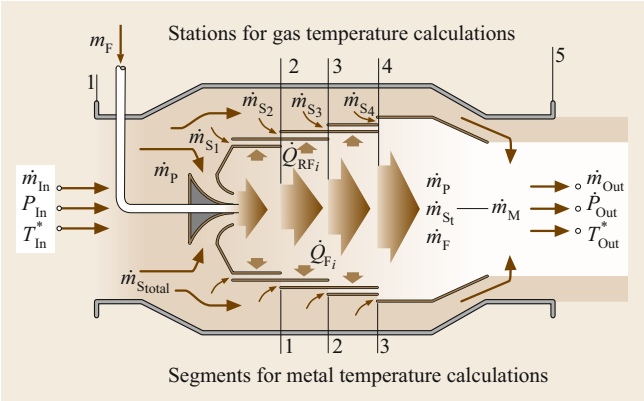

Fig. 19.63 Combustion chamber module, stations and segments, $\dot{m}_P$ – primary $\dot{m}_{S_{total}}$ – total secondary air, $\dot{m}_{S_i}$ – individual secondary air

Fuel Schedule and Rotor Response. The dynamic behavior of the above engine is simulated for an adverse acceleration–deceleration procedure (Fig. 19.67).

The transient operation is controlled by an open-loop fuel schedule shown in Fig. 19.67a. The three spools and the fourth shaft run independently at different rotational speed (Fig. 19.67b). The fuel schedule generated completely arbitrarily simulates an acceleration–deceleration procedure with emphasis on deceleration. We start with the steady-state operation and reduce the fuel mass flow to $\dot{m}_F = 2.8\,\mathrm{kg/s}$ for about 2 s. During this short period of time, the engine operates in a dynamic state which is followed by a cyclic acceleration–deceleration event with the ramps given in Fig. 19.67. The dynamic operation triggers a sequence of transient events within individual components that are discussed in the following sections.

Rotor Speed Behavior. The transient behavior of the three spools as well as the power shaft is determined by the net power acting on the corresponding rotor. For each individual spool, the cyclic acceleration–deceleration event has caused a dynamic mismatch between the required compressor power consumption and the turbine power generation, as shown in Fig. 19.68. While the LP and IP spools 2 and 3 decelerate under the influence of negative net power, the HP spool 3 reacts faster to the acceleration. Since the fuel schedule places special weight upon deceleration, the rotational

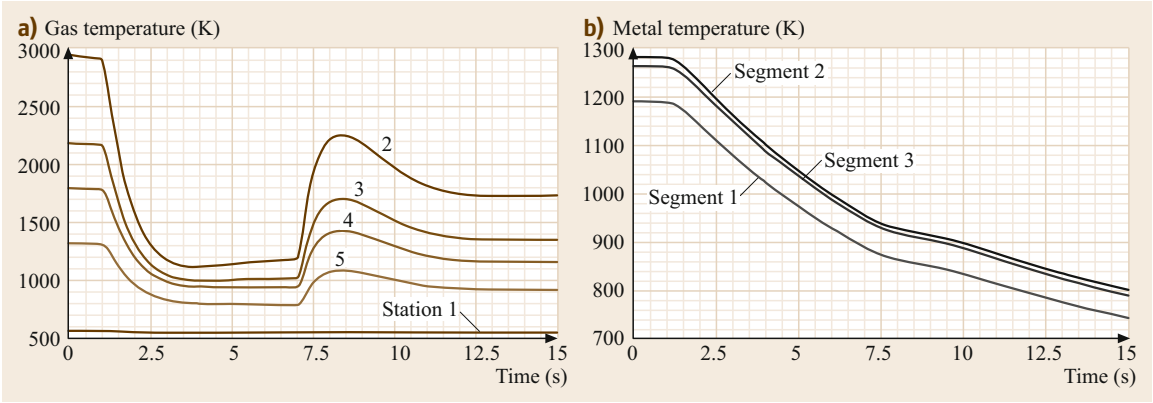

Fig. 19.64 (a) Combustion chamber gas and (b) metal temperature at different positions as functions of time

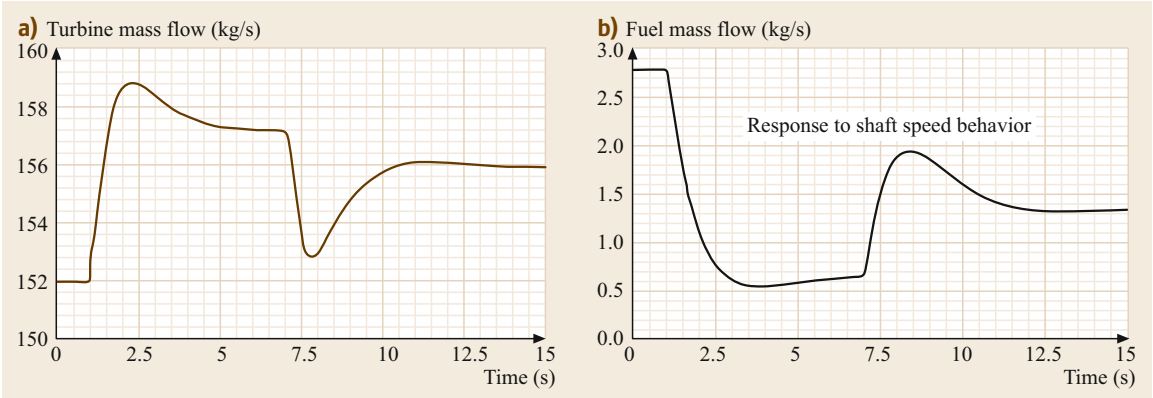

Fig. 19.65 (a) Turbine and (b) fuel mass flow as functions of time. The fuel mass flow is controlled by the shaft rotational speed

speeds of all three spools have a decelerating tendency as shown in Fig. 19.68.

Pressure and Temperature Transients Within Plena. The change in fuel mass flow triggers a chain of transient events within the plena, as shown in Fig. 19.69. Plena pressure 5 and 6, which corresponds to the exit pressure of the HP compressor and the combustion chamber, are strongly affected by the cyclic fuel change, whereas the other plena that correspond to the inlet and exit plena of the remaining components experience moderate changes. The plena temperature distributions downstream of the combustion chamber shown in Fig. 19.69b reflect the course of the fuel schedule.

Combustion Chamber Gas and Metal Temperature Transients. Figure 19.70 exhibits the combustion chamber gas and metal temperatures as functions of time. The combustion chamber component used in this simulation has three segments that separate the primary combustion zone from the secondary cooling air zone. Its module is shown in Fig. 19.65. Compressed air enters the combustion chamber at station 1 (Fig. 19.70a). Fuel is added and the segment's cooling occurs according to the procedure described in [19.25]. The secondary mass flow portions serve as cooling jets and are mixed with the combustion gas, thus reducing the gas temperature. Before exiting, the combustion gas is mixed with the mixing airstream, further reducing the temperature. Figure 19.70a shows the mean segment temperatures. The flame length extends from station 1 to 3, which makes segment number 2 the hottest one. As seen, the gas temperature at station 2 follows the sharp changes in the fuel schedule. By convecting downstream, these sharp changes are smoothed out. The wall temperatures shown in Fig. 19.70b exhibit similar tendencies.

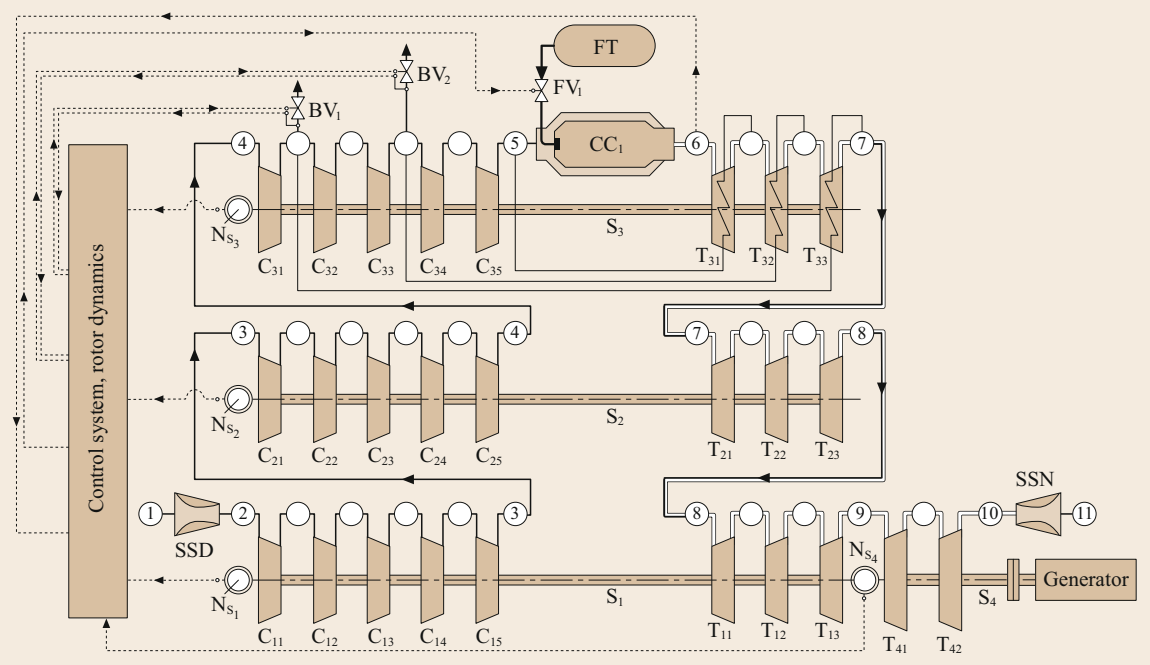

Fig. 19.66 Simulation schematic of three-spool four-shaft high-performance gas turbine engine. Spool 1 incorporates the LP compressor and LP turbine connected via shaft S_1; spool 2 incorporates the IP compressor and IP turbine connected via shaft S_2; spool 3 incorporates the HP compressor and HP turbine connected via shaft S_3

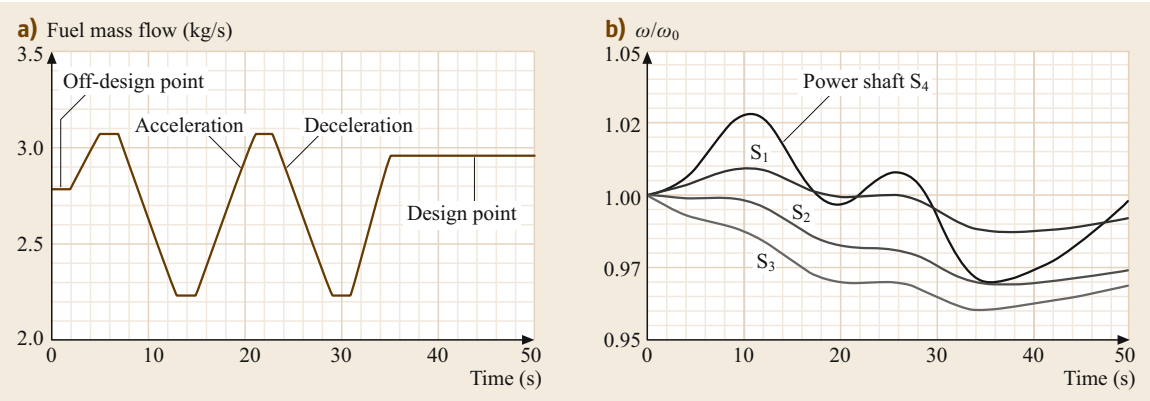

Fig. 19.67 **(a)** Fuel schedule starts with an off-design mass flow followed by a cyclic acceleration–deceleration procedure. **(b)** Rotational speed of the three spools and the power shaft

Compressor and Turbine Mass Flow Transients. Figure 19.71a exhibits the compressor mass flow transients, which are dictated by the compressor dynamic operation. The difference in compressor mass flow is due to the mass flow extraction for cooling purposes. Turbine mass flows are illustrated in Fig. 19.71b. Except for a minor time lag, they show identical distributions. The difference in turbine and compressor mass flow is due to the addition of fuel.

19.3.6 New Generation Gas Turbines, Detailed Efficiency Calculation

One of the interesting aspects of a dynamic simulation is the capability to calculate the gas turbine thermal efficiency dynamically during steady-state and dynamic operation. Such calculations are performed to compare the thermal efficiencies of four gas turbines with different design methodologies. The calculations are per-

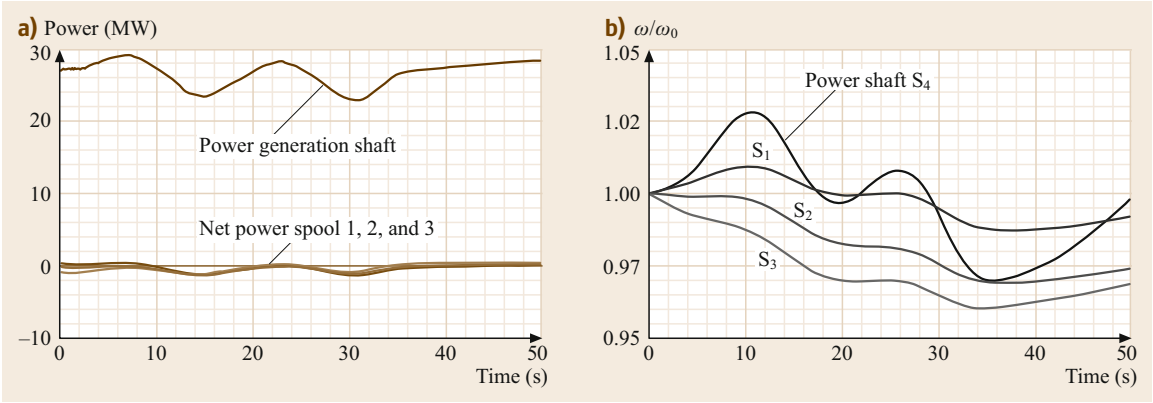

Fig. 19.68 **(a)** Net power acting on the three spools causing a dynamic mismatch and the power generated by the fourth shaft. **(b)** Relative rotor speed of three spools and the fourth shaft

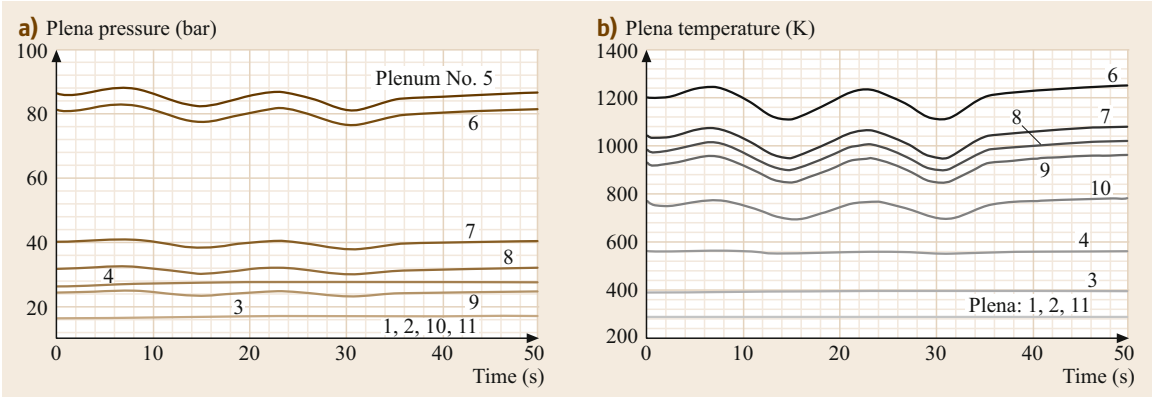

Fig. 19.69 **(a)** Plena pressure and **(b)** temperature as functions of time

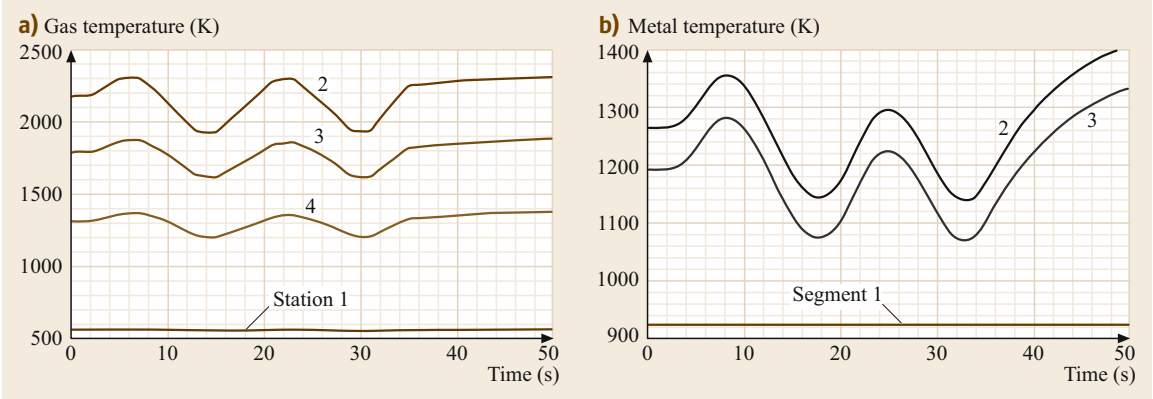

Fig. 19.70 **(a)** Combustion chamber gas and **(b)** metal temperature as functions of time

formed with the nonlinear dynamic code GETRAN©. The first gas turbine dynamically simulated for efficiency calculation is a conventional single-shaft, single-combustion chamber power generation gas turbine. The second one is the ABB GT 24/26. The third is an ultrahigh-efficiency gas turbine (UHEGT) with a precombustor, a reheat turbine stage, and an integrated stator internal combustion, as illustrated in Fig. 19.72. For the fourth gas turbine, the combustion process is placed entirely within the stator rows, thus eliminating

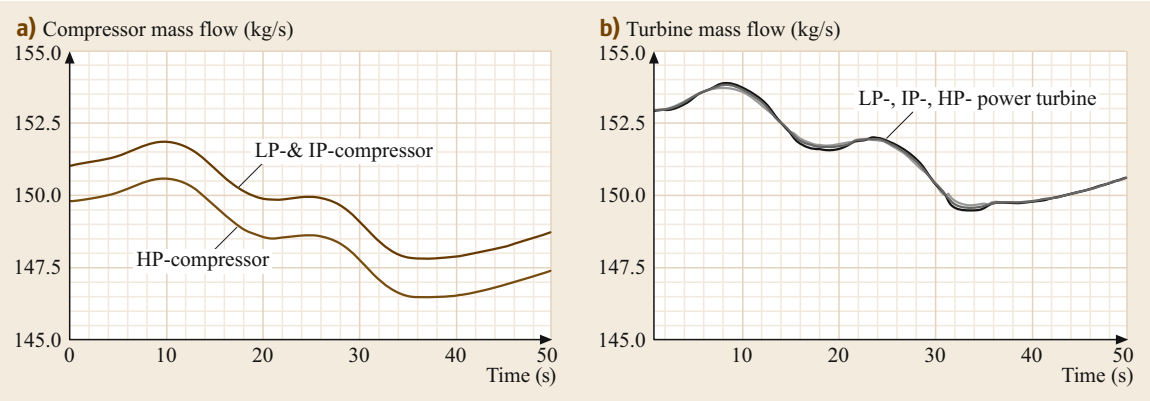

Fig. 19.71 **(a)** Compressor and **(b)** turbine mass flow as functions of time

the combustion chambers all together, Fig. 19.73. The dynamic efficiency calculation results are presented in Fig. 19.74. To accurately determine the thermal efficiency and specific work of the gas turbines, calculations are performed with GETRAN© and the results are presented in Fig. 19.74. To compare the degree of efficiency improvement, the thermal efficiency and specific work of a baseline GT, GT-24, and the three UHEGT gas turbines are included in the figures.

For a UHEGT with three-stator combustion, denoted by the curve UHEGT-0C3S, a thermal efficiency above 45% is calculated. This exhibits an increase of at least 5% above the gas turbine engine GT-24, which is close to 40.5%, as shown in Fig. 19.74a. Increasing the number of stators for internal combustion to four (curve labeled *UHEGT-0C4S*) raises the efficiency above 48%. This is an enormous increase compared with any existing gas turbine engine. In the course of this calculation, the UHEGT technology is applied to a gas turbine engine with a precombustion chamber, such as the first one in GT-24 (Fig. 19.72). Using this combustion chamber with two-stator combustion, the curve labeled *UHEGT-1C2S* shows an efficiency of 44%. This is particularly interesting for upgrading

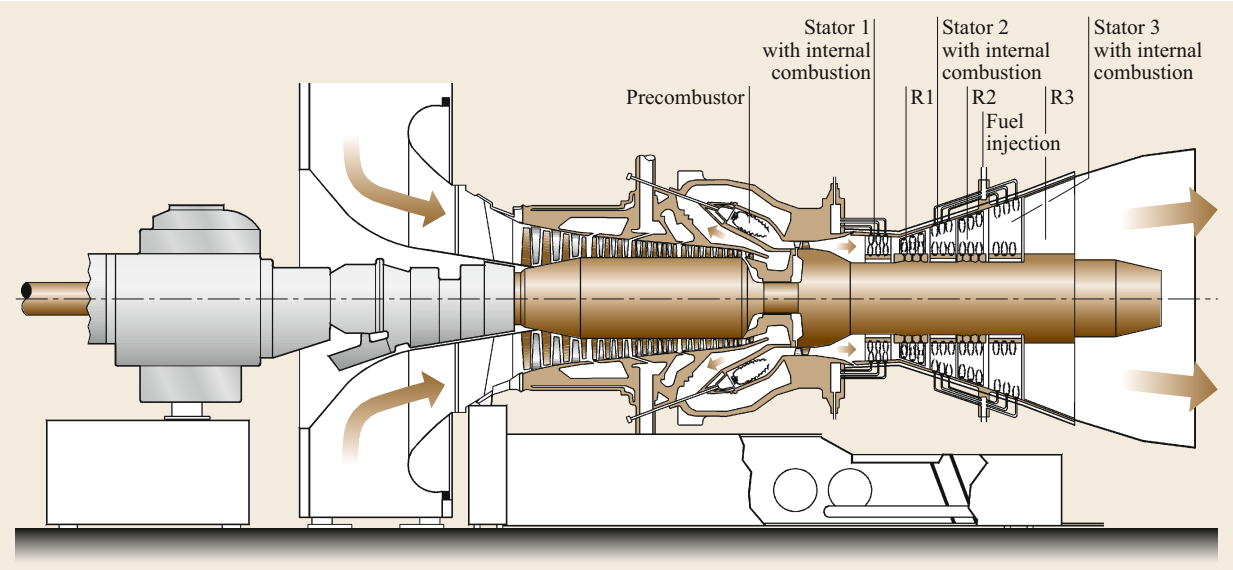

Fig. 19.72 A derivative of the ultrahigh-efficiency gas turbine engine with a multistage compressor, a conventional combustion chamber PC, a single-stage reheat turbine RT, a three-stage turbine with an integrated stator internal combustion. B1, B2: compressor bypass blow-off, Fl1, Fl2: fuel lines to stator. The combustion process takes place inside the precombustor and stator flow path (after [19.22])

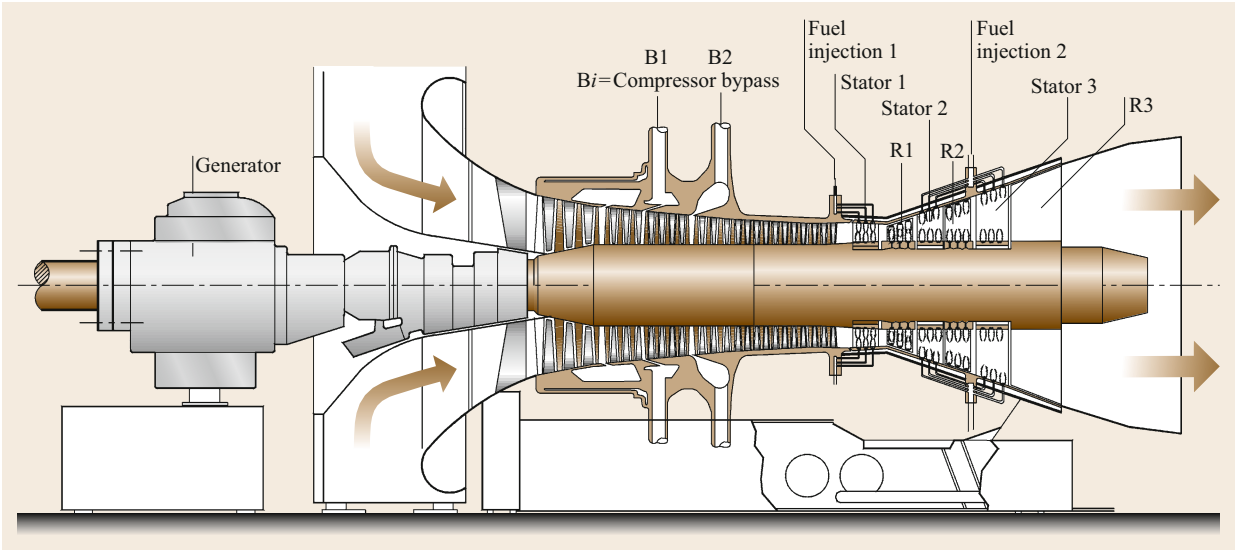

Fig. 19.73 An ultrahigh-efficiency gas turbine engine with a multistage compressor, and a three-stage turbine with an integrated stator internal combustion. B1, B2: compressor bypass blow-off, Fl1, Fl2: fuel lines to stator. The combustion process takes place inside the stator flow path (after *Schobeiri* [19.22])

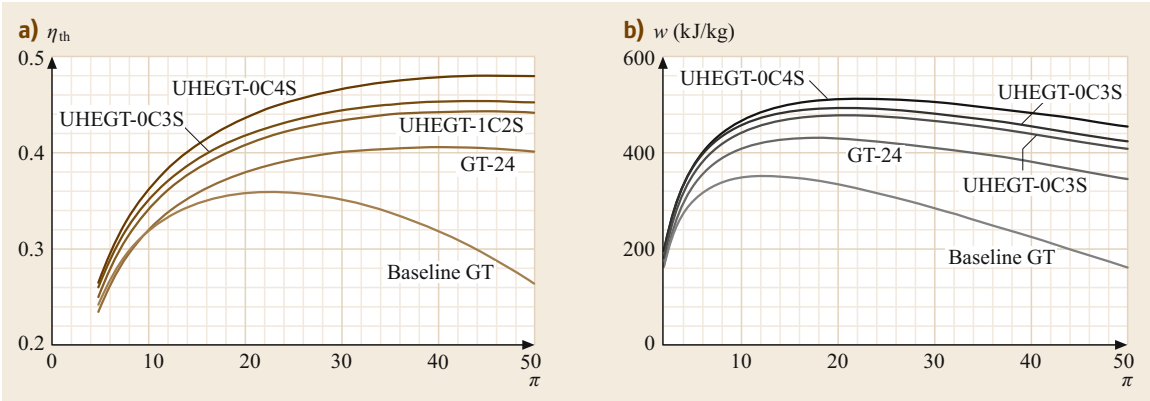

Fig. 19.74 **(a)** Thermal efficiency and **(b)** specific work as functions of compressor pressure ratio for the reference baseline gas turbine engine, the ABB-GT-24 with two combustion chambers, the UHEGT-1C2S with one conventional combustion chamber and two UHEGT-stator combustion, the UHEGT-03S with three-stator combustion, and the UHEGT-0C4S with four-stator combustion. Turbine inlet temperature = 1200 °C, calculation with GETRAN (after [19.24])

existing gas turbines with UHEGT technology. Figure 19.74b shows a comparison of the specific work for the gas turbines discussed above. Compared to the GT-24, UHEGT technology has about 20% higher specific work, making these engines very suitable for aircraft, stand-alone, as well as for combined cycle power generation applications. The evolution of the gas turbine efficiency improvement is summarized in the corresponding T–s-diagrams presented in Fig. 19.75a–c. In addition to the efficiency improvement brought about by utilizing a reheat turbine and two combustion chambers already discussed in conjunction with Fig. 19.44a,b further improvement is achieved by using stator internal combustion.

As shown in Fig. 19.72c, the UHEGT facilitates *quasi-Carnotising of the Brayton cycle*. It is interesting to note that this efficiency increase can be established at a compressor pressure ratio of $\Pi_{\text{UHEGT}} \approx 35\text{–}40$, which can be achieved easily by existing compressor design technology with high polytropic efficiency.

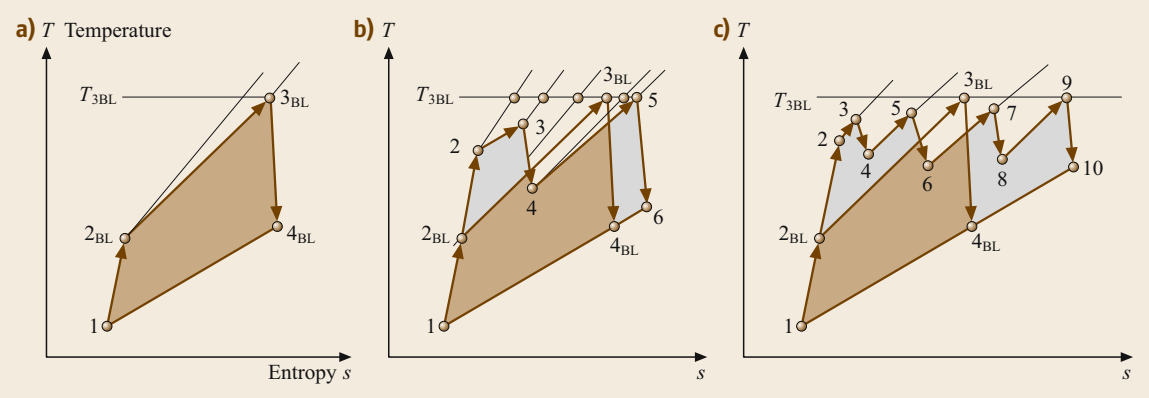

Fig. 19.75a–c Process comparison for **(a)** the baseline GT, **(b)** the GT-24, **(c)** the ultra high efficiency gas turbine technology (UHEGT) which has four stages with four integrated stator internal combustion

In performing the GETRAN© calculation, compressor and turbine efficiencies are calculated on a row-by-row basis. This automatically accounts for an increase of secondary flow losses based on aspect ratio decrease. Thus, in a compressor case, efficiency decrease with pressure ratio increase is inherently accounted for.

References

19.1 M.T. Schobeiri: *Turbomachinery Flow Physics and Dynamic Performance*, Vol. 2012, 2nd edn. (Springer, Berlin, Heidelberg 2012)

19.2 M.H. Vavra: *Aero-Thermodynamics and Flow in Turbomachines* (Wiley, New York 1960)

19.3 W. Traupel: *Thermische Turbomaschinen*, Vol. 1 (Springer, Berlin, Heidelberg 1977)

19.4 J.H. Horlock: *Axial Flow Compressors* (Butterworth, London 1966)

19.5 J.H. Horlock: *Axial Flow Turbine* (Butterworth, London 1966)

19.6 M.T. Schobeiri: *Turbomachinery Flow Physics and Dynamic Performance* (Springer, Berlin, Heidelberg 2004)

19.7 N.E. Joukowsky: Vortex Theory of Screw Propeller, IV, Trans. Office Aerodyn. Calc. Essays Super. Tech. School Mosc. **3**, 1–97 (1918), in Russian

19.8 R.O. Bullock, I.A. Johnsen: *Aerodynamic Design of Axial Flow Compressors*, NASA Report, Vol. NASA-SP-36 (NASA, Washington 1965)

19.9 D.E. Hobson: Shock free transonic flow in turbomachinery cascade, CUED/A-Turbo/TR 65 (1979)

19.10 J.F. Schmidt, T.F. Gelder, L.F. Donovan: Redesign and cascade tests of a supercritical controlled diffusion stator blade section, AIAA Paper (1984), https://doi.org/10.2514/6.1984-1207

19.11 B. Lakshminarayana: *Fluid Dynamics and Heat Transfer of Turbomachinery* (Wiley, New York 1995)

19.12 M.T. Schobeiri: Shock-loss model for transonic and supersonic axial compressors with curved blades, J. Propuls. Power **14**(4), 470–478 (1998)

19.13 A. Teufelberger: Choice of an optimum blade profile for steam turbines, Rev. Brown Boveri **2**, 126–128 (1976)

19.14 K. Kobayashi, M. Honjo, H. Tashiro, T. Nagayama: Verification of flow pattern for three-dimensional-designed blades. In: *ImechE Paper C423/015* (1991)

19.15 M. Jansen, W. Ulm: Modern blade design for improving steam turbine efficiency, VDI Berichte 1185 (1995)

19.16 R. Emunds, I.K. Jennions, D. Bohn, J. Gier: The computation of adjacent blade-row effects in a 1.5 stage axial flow turbine. In: *ASME Paper 97-GT-81, Orlando, Florida* (1997)

19.17 J.C. Dunavant, J.R. Erwin: Investigation of a related series of turbine-blade profiles in cascade. In: *NACA TN-3802* (1956)

19.18 F. Gerald: *Curves and Surfaces for Computer-aided Geometric Design*, 4th edn. (Academic, New York 1997)

19.19 F. Bauer, P. Garabedian, D. Korn: *Supercritical Wing Sections III* (Springer, New York 1977)

19.20 T. Dang, S. Damle, X. Qiu: Euler-based inverse method for turbomachine blades: part II—three dimensions, AIAA Journal **38**(11), 2007–2013 (2000)

19.21 A.J. Medd: *Enhanced Inverse Design Code and Development of Design Strategies for Transonic Compressor Blading*, Ph.D. Thesis (Syracuse Univ., Department of Mechanical Engineering, Syracuse 2002)

19.22 M.T. Schobeiri: The ultra-high efficiency gas turbine engine with stator internal combustion, UHEGT Patent 1389-TEES-99 (1999)

19.23 M.T. Schobeiri, S. Attia: Advances in nonlinear dynamic engine simulation technology. In: *ASME 96-GT-392, Int. Gas Turbine Aero-Engine Congr., Birmingham* (1996)

19.24 M.T. Schobeiri, M. Abouelkheir, C. Lippke: GETRAN: A generic, modularly structured computer code for simulation of dynamic behavior of aero- and power generation gas turbine engines, ASME Trans. J. Gas Turbine Power **1**, 483–494 (1994)

19.25 M.T. Schobeiri: Digital computer simulation of the dynamic operating behavior of gas turbines, Brown Boveri Rev. **74**(3), 161–173 (1987)

Meinhard T. Schobeiri

Department of Mechanical Engineering
Texas A&M University
College Station,Texas, USA
tschobeiri@tamu.edu

Dr Schobeiri, a Professor of mechanical engineering, received his entire engineering education at the Technical University Darmstadt, Germany. He was group leader for gas turbine aero-thermodynamic R&D at Brown Boveri Co., Baden, Switzerland. His area of expertise includes unsteady aerodynamics, turbine and compressor aerodynamics design, heat transfer and nonlinear gas turbine engine dynamic simulations. He is the author of four books, two dealing with turbomachinery design and two with advanced fluid mechanics. He is the author of more than 100 journal, conference and technical papers and reports. He is a member of VDI and a fellow of the ASME.

20. Conveying and Construction Machinery

André Katterfeld, Alan Roberts, Craig Wheeler, Kenneth Williams, Chris Wensrich, Jan Scholten, Mark Jones, Günter Kunze, Henning Strubelt, Dusan Ilic, Tim Donohue, Hendrik Otto, Jens Sumpf, Wei Chen, Bin Chen, Daniel Ausling

In this chapter, the fundamentals of design of conveying and construction machinery will be presented. Machines that fulfill transportation tasks in limited operating areas such as mines, ports, work and storage yards, as well as construction sites are most common and can be found in any type of industry. Hence, the diversity of conveying and construction machinery is very wide. However, the typical driving elements, machine components, and calculation concepts are similar.

The group of construction machinery covers many machines, e.g., concrete mixers or compactors that are not used for material transport. Such machines are not discussed in this chapter.

While the machinery belonging to the group of conveying technology is very diverse, many machine drives and parts are quite similar. The first aim of this chapter is to present a system for the classification of general materials handling equipment, which allows the understanding of the basic calculation methods. The two main groups of conveyors can be distinguished by their operational process: continuous and discontinuous conveyors. Another significant difference are the goods the equipment should handle: general cargo or bulk materials.

The second aim is the presentation of the basics of the design and calculation of conveying technology and their main mechanical elements and drives. To understand the design of bulk materials handling equipment, the necessary basics of bulk mechanics are described in Sect. 20.2. The design and calculation of basic machine elements of materials handling equipment (e.g., steel ropes, chains or wheels and tracks) are presented in Sect. 20.3. Section 20.4 presents the most important continuous conveying machinery, followed by discontinuous conveying machinery in Sect. 20.5. The necessary storage equipment is presented in Sect. 20.6.

20.1 **Background and Fundamentals** 830
20.1.1 Characterization of the Engineering Field 830
20.1.2 Historical Outline 831
20.1.3 Classification of Transported Goods 832
20.1.4 Classification of Basic Types of Machine and Transport Processes 833
20.1.5 General Drives of Conveying Machinery 834
20.1.6 General Introduction to Motion Resistance Theory 835
20.1.7 General Quantification of Transport Processes 835

20.2 **Bulk Solid Mechanics and Characterization** 837
20.2.1 Mechanical Sampling of Bulk Solid Materials 837
20.2.2 Characterization Parameters 838
20.2.3 Determination of Bulk Solid Properties 841
20.2.4 Regulatory Tests 843
20.2.5 Environmental/Occupational Exposure Tests and Procedures 845
20.2.6 Wear 846

20.3 **Basic Mechanical Elements** 848
20.3.1 Wire Ropes 848
20.3.2 Chains 856
20.3.3 Wheels and Track 859

20.4 **Continuous Conveyors** 863
20.4.1 Belt Conveyors 864
20.4.2 Bucket Elevators 876
20.4.3 Chain Conveyors 881
20.4.4 Overhead Conveyors 890
20.4.5 Screw Conveyors 894
20.4.6 Vibratory Conveyors 900
20.4.7 Pneumatic Conveyors 903
20.4.8 Chutes 915
20.4.9 Conveyors for General Cargo 920

20.5 **Discontinuous Conveyors** 923
20.5.1 Main Drives: Hoisting, Driving, and Slewing 923
20.5.2 Hoists and Cranes 926
20.5.3 Excavators and Loaders 941
20.5.4 Elevators 947
20.5.5 Trucks 949

K.-H. Grote, H. Hefazi (Eds.), *Springer Handbook of Mechanical Engineering*, Springer Handbooks,
https://doi.org/10.1007/978-3-030-47035-7_20

20.6 **Storage Systems** 955
20.6.1 Silos and Bunkers 955
20.6.2 Stockpiles 963
20.6.3 Feeders 968
20.6.4 Yards for General Cargo 970
20.6.5 Racking Systems 972

References 981

20.1 Background and Fundamentals

20.1.1 Characterization of the Engineering Field

Conveying machinery transports (conveys) goods or persons over a limited distance in spatially confined operation areas. Such confined operation areas could be, e.g., ports, factories, or mine sites. The engineering field that deals with conveying machinery can be called conveying technology but is better known as materials handling. Conveying machines can be combined to form materials handling systems. Material handling systems include not only conveying machines but also storage equipment and control and sensing technology to enable smooth material flow between the linked conveyors.

Confinement of the Engineering Field

There are other engineering fields that do not belong to the field of materials handling but also focus on the transport task. The transport of goods and persons over larger distances using cars, trucks, trains, planes, and ships is part of the engineering field of transport systems (see Chaps. 21–25 of this book). The transport of gases and liquids without any particle phase, such as natural gas or oil, is typically part of process engineering and is not covered in this chapter. Also, the precise manipulation and positioning of goods in a very close area—as it is often done by industrial robots—does not belong to the field of materials handling.

The field of materials handling includes machines for the transport of building materials and elements at construction sites. Such machines as the often-seen mobile or tower cranes belong to the group of materials handling but also to the wider group of construction machinery. However, only construction machines that fulfill a transport task belong to the group of materials handling equipment. Mining and construction machinery includes machines with the main task of excavating raw materials, e.g., ore from natural ground or rock. The excavation process is intensively studied in the field of mining and geotechnical engineering and is usually analyzed separately from the subsequent conveying process.

This chapter focuses on commonly used materials handling equipment. This equipment includes cranes, excavators, and loaders, which also belong to the group of construction machinery.

Logistics and Material Handling Systems

The field of materials handling is very wide and serves as an important link between transport systems (e.g., from train to ship), process technology (e.g., from crushing plants to mills), and manufacturing (e.g., from assembly to packaging). All machines in this field transport goods or persons from a source to a sink. While the source and sink could be within an operation area, they may also be far away. Transport chains, which combine materials handling equipment with transport technology, are often generated. The main operation within a transport chain is the actual transport itself, the handling between transport equipment, and the storage of goods.

For the correct selection and proper design of materials handling equipment, it is often necessary to analyze the material flow along the whole transport chain. However, an efficient transport chain is not only based on the flow of the physical goods, but also on the flow of information regarding the goods. A proper information flow is necessary to deliver:

- The right good
- In the right quality
- In the right amount
- At the right time
- To the right destination
- With acceptable costs and
- In an ecologically acceptable manner.

The holistic analysis and organization of these aspects of transport chains is the task of the field of logistics. The relations between logistics, materials handling systems, and conveying technology is shown in Fig. 20.1. The logistical requirements on materials handling systems and subsequently on conveying technology define the main machine parameters, such as capacity and speed.

Content of This Chapter

This chapter provides an overview of the different types of machine as well as general design concepts. The main design standards for many continuous and discontinuous conveyors and their important mechanical elements are presented. In addition to the transport of solids goods, many conveying and construction ma-

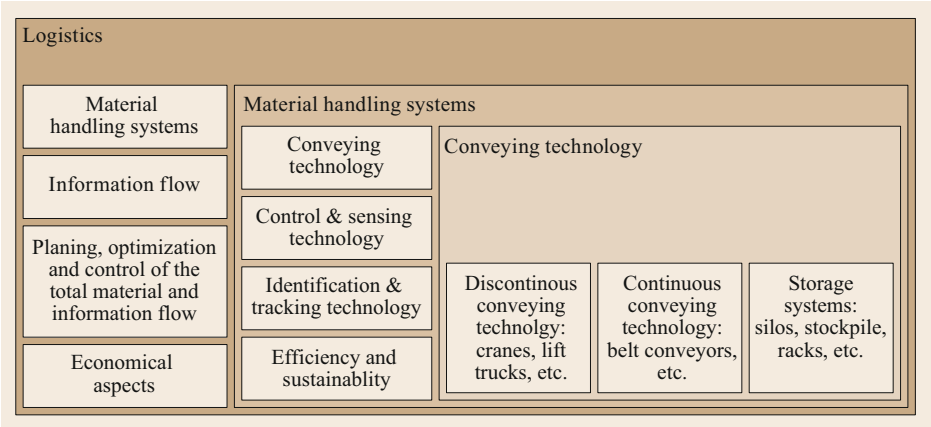

Fig. 20.1 Relationship between logistics, materials handling systems, and conveying technology (after [20.1])

chines are used to transport bulk materials. To store this type of material, stockpiles, silos and bunkers are used. The understanding of the special mechanical behavior of bulk materials is a key factor for the correct design of many types of conveying and construction machinery. Therefore, the basic properties and mechanical theories for bulk solids are also included in this chapter.

20.1.2 Historical Outline

Transport, transfer, storage, and excavation processes have been significant to humans since they have lived in settlements; attempts to ease the effort of lifting and transporting loads with muscle power are just as old.

The first aids were levers, wedges (inclined planes), and rolling elements (tree trunks). Later, wheels, ropes, and chains were added. They provided the premise for the first transport devices:

- Slideways
- Roller tracks
- Wagons
- Blocks and tackle
- Worms
- Norias
- Bucket conveyors.

Besides civil engineering, mining, and shipbuilding, materials handling was one of the first engineering sciences. The necessity of lifting heavy loads motivated the construction of the first hoisting gears many millennia ago. In the Middle Ages, crane engineering had already reached a significant level. Besides the construction industry, port operations (transfer and storage of goods) as well as mining (raw material excavation and transport) were the main development factors, until production plants gained importance due to the sudden industrialization of the 19th century.

The introduction of steel ropes and electrical drives enabled an abrupt progression in, e.g., crane engineering.

Over recent decades, materials handling has become an engineering discipline with cross-departmental and integrating functions in all branches of industry. The demand for automated materials handling systems and the planning and guidance of complex material flow processes led to the independent field of logistics.

In many branches of industry, materials handling is the main process (e.g., in mining, above and below ground, in port operations, in storage and silo operations, and in warehousing). In the production sector, materials handling has progressed from an auxiliary process to become one of the main processes:

- Manufacturing process
- Material handling process.

From a logistical point of view, material flows are strongly connected to the flow of information. Through logistics, we now understand the science of scheduling, controlling, and supervising the flow of materials, persons, energy, information, and finance in complex systems.

Material handling involves the project planning, design, and operation of materials handling systems.

Thanks to modern informatics, the holistic coalescence of material flows with preceding, accompanying, or subsequent information flows is enabled. In this way, materials handling systems have become an integrated factor in the effective production and distribution of goods.

Transport machines comprise elements that—once arranged in an appropriate chain—form modern materials handling systems. Since technological processes are often unavoidably linked to materials handling systems, they are covered well in many technologically oriented fields.

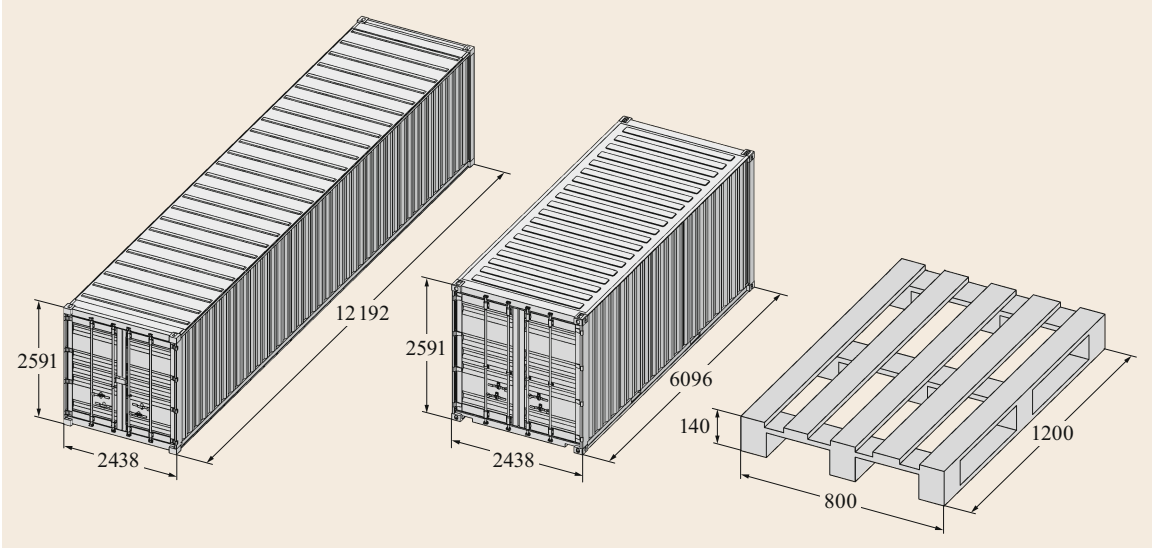

Fig. 20.2 Sizes (mm) of the most common load carriers: 40-ft and 20-ft container, and EUR palette

Today, environmental engineering places special demands on the development of materials handling equipment. This includes the environmentally friendly operation of individual transport machines and materials handling systems as well as the development of transport machines for specific environmental engineering tasks.

20.1.3 Classification of Transported Goods

The transport of goods is usually a necessary step in the value chain of a product. The best transport is the transport that is not necessary. However, since most products need many manufacturing or processing steps and the consumer of a product very rarely has the identical location of the producer, transport is almost always necessary. Therefore, materials handling equipment must be adopted to transport the goods.

Besides the transport of persons, which is associated with high demands in terms of security and safety, two major kinds of goods can be found:

- General cargo, which means goods handled piecewise
- Bulk solids, which means granular or particulate materials.

Goods with arbitrary shape and size are often transported in load supports or load carriers for easier handling. These load carriers can be bins, palettes, box palettes, or containers, which can also often be used to transport small amounts of bulk solids.

Although the variety of load carriers is very large, standardization of their sizes and loads is essential to allow worldwide use. The most important load carriers are reusable and part of a worldwide exchange cycle. The most often used palette is the so-called EUR palette according to ISO 6780 [20.2] with main dimensions of 1200 mm × 800 mm and a maximum load of approx. 1.5 t. The most often used intermodal containers are the 20- and 40-ft containers according to ISO 668 [20.3] with main dimensions as shown in Fig. 20.2 and a maximum load of approx. 21.67 t (20 ft) or 26.48 t (40 ft).

Often, load carriers will also be used if the packaging of the goods reduces the variety of shapes and sizes. Goods packaged in parcels are often transported on palettes. To secure the load on the flat palette, additional load securing equipment such as wires, ropes, straps, or stretch film is used.

To provide an idea of the importance of the two types of goods in terms of worldwide transport amounts, Fig. 20.3 shows the tonnages for general cargo, containers, and bulk materials at the Port of Rotterdam, the largest port in Europe. This explains the high logistic and economical importance of both kinds of goods.

To handle the different types of goods, specific materials handling equipment has been developed. The handling of solid goods (general cargo) is generally much simpler in comparison with the handling of bulk materials, because of the much more complex physical behavior of the latter. Section 20.2 explains the basics of bulk mechanics as an important requirement to understand and design bulk materials handling and storage equipment.

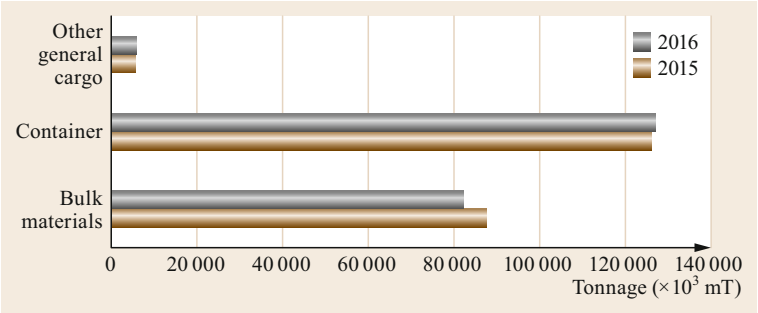

Fig. 20.3 Tonnages of general cargo, containers, and bulk materials at Port of Rotterdam (mT = metric ton) according to [20.4]

20.1.4 Classification of Basic Types of Machine and Transport Processes

There are basically two kinds of materials handling equipment:

- Discontinuous conveying machines
- Continuous conveying machines.

The difference between the two is the general working cycle of the machine considering its loading possibilities. The working cycle of a conveying machine includes all the operations that are necessary for:

1. The loading of the machine
2. The movement of the machine parts to fulfill the actual transport process
3. The unloading of the machine
4. The movement of the machine parts to return to the loading point.

Figure 20.4 shows a typical working cycle based on the example of a crane with grab equipment for bulk materials handling. The crane belongs to the group of discontinuous conveying machines.

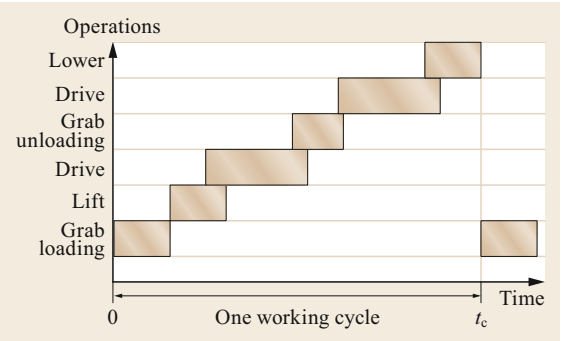

Fig. 20.4 Example working cycle for a crane with grab equipment for bulk materials handling (after [20.5])

Continuous conveying machines can be loaded continuously, and their drives usually show much longer steady-state times than discontinuous conveying machines (Fig. 20.5). The latter are typically characterized by a start-and-stop operation mode as well as by longer pauses between operations. Because of these pauses, this operation mode can be called intermittent. The operation mode significantly influences the choice of the motor for the drive, but also increases the effort required to control the machine as well as its dynamic loads.

Due to the wide variety of conveying machines, a classification system is important for better understanding and easier orientation. Figure 20.6 shows a classification system that includes the two main types

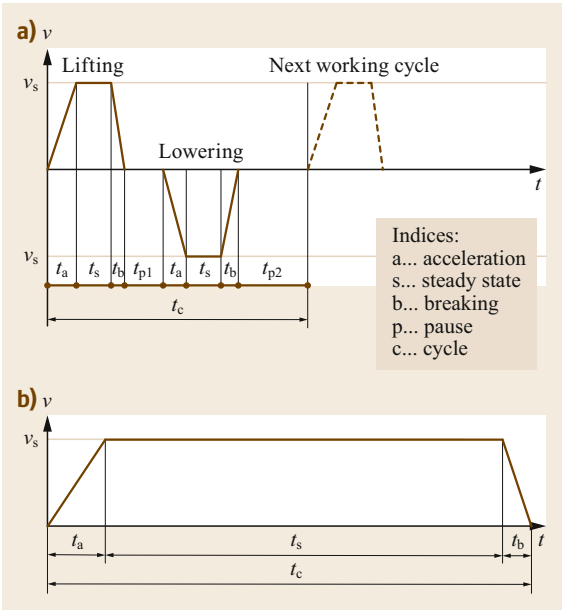

Fig. 20.5a,b Drive operation modes for **(a)** discontinuous (e.g., lift of a crane) and **(b)** continuous conveying machines (e.g., bucket elevator) shown on velocity versus time diagrams

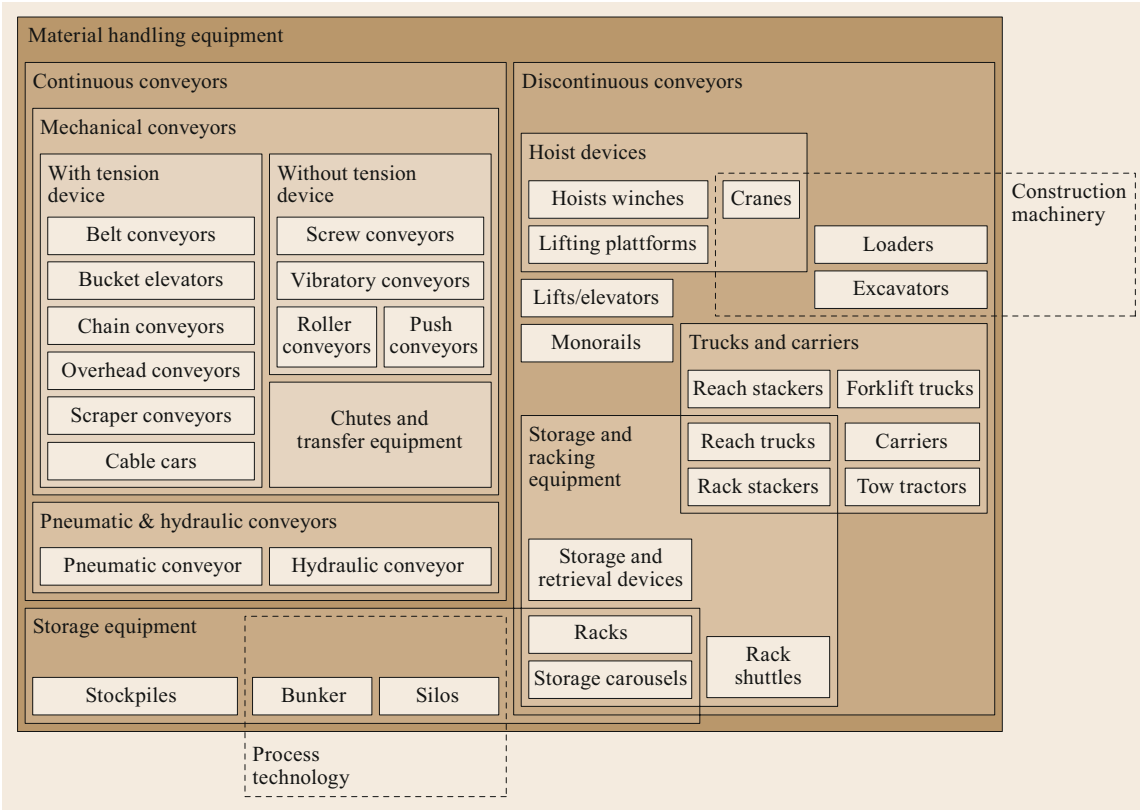

Fig. 20.6 Classification of types of machine in the materials handling field

of machine but also considers the field of application. This classification system does not claim to be complete but includes the most important conveying devices with their most usual terminology.

20.1.5 General Drives of Conveying Machinery

As shown in Fig. 20.6, the field of conveying machinery includes many devices that are very different in their function, design, and application. However, there are also some general similarities. All continuous and discontinuous conveyors consist of a load-supporting (steel) structure and drives that enable the motion of the load.

Continuous conveyors mostly have one main drive to—in whatever way—move the load along a defined route or path.

Discontinuous conveyors can generally move the load in four different ways and use different drives for this:

- Translational motion:
  - Vertical (hoist) → hoisting gear
  - Horizontal (drive) → chassis.
- Rotation around:
  - The vertical axis (slew) → slewing gear
  - The horizontal axis (retract) → retracting unit.

In addition, there are other, special drives: luffing gears, pushing gears, and tipping gears. All these drives perform work cycles in intermittent operation.

While the design of the machinery may be totally different, the main drive principle is the same, and thus also the calculation principle. One main task of a materials handling engineer is to calculate the drive power necessary to move the load as well as to define the size and speed of the conveyor drives to enable the transportation of a certain amount of cargo or bulk material.

Another main task is the proper design of the steel structure because of the static and dynamic forces occurring due to the movement of the load. While the design and calculation of steel structures is a general engineering task and very similar to such tasks in many engineering fields, the materials handling engineer still needs to define the load assumptions based on an understanding of the occurring forces, the necessary throughput, and the resulting working cycles.

20.1.6 General Introduction to Motion Resistance Theory

The design of drives for and the structure of materials handling equipment must consider the forces acting on the load and the machine parts. In the field of conveying and construction machinery, the term "motion resistance" is often used for the drive calculation. The term "motion resistance" describes the forces acting in or against the conveying direction. Motion resistances that act against the conveying direction are defined as positive forces, while those which act in the conveying direction are defined as negative, since these forces reduce the necessary drive power.

The general motion resistances of the drives during steady operation are:

- Gravitational forces
- Frictional forces
- Wind forces
- Excavation forces, etc.

Considering the transport velocities that are typical in the field of materials handling, these resistances are nearly independent of the transport speed but dependent on the:

- Moving mass
- Wind speed
- Friction conditions
- Bulk material properties
- Excavation resistances, etc.

Ongoing working cycles can result in irregularly changing countertorques. The occurrence of motion resistance depends on the conveyor type and the type of operation. The typical motion resistances for discontinuous and continuous materials handling equipment include:

- For discontinuous conveying machinery:
  - For hoisting gears: The gravitational force acts as an external force, being always downwards and independent of the direction of motion. However, the motion resistance caused by gravity will be positive if the load is hoisted but negative if the load is lowered. In the latter case, the hoisting gear must pick up potential energy (the drive power becomes negative).
  - For the chassis: The motion resistances due to friction remain positive, since they always act against the conveying direction. Even in reverse drive, the drive power remains positive. Under wind exposure and with a downhill force component, the resulting total motion resistance may be negative (resulting in negative drive power).
  - For slewing gears: The countertorque generally depends on the slewing angle, the angle of inclination of the jib (retracting unit), etc.
- For continuous conveying machinery: Gravitational and frictional resistances usually occur depending on the conveying route. Frictional resistances always act against the conveying direction, while gravitational resistances can act in or against the conveying direction. The actual physical process generating the frictional resistances is usually quite complex for bulk material handling equipment. Additional resistances may occur during the continuous loading and unloading processes.

During nonsteady operation, i.e., during start-up or stopping, additional acceleration forces due to inertia must be considered. For each drive, one must be calculate when the worst-case scenario will occur, i.e., in steady or nonsteady operation.

20.1.7 General Quantification of Transport Processes

All conveyor machinery is typically quantified by the amount of material or goods that can be transported. The amount of goods or material is measured in pieces per unit time or mass per unit time. The definition of pieces per unit time is, of course, only appropriate for piecewise handling of general cargo. The cargo flow rate Q_c is used to specify the amount of cargo transported per unit time. However, the mass flow rate Q_m is an even more common value, because many processes are evaluated based on the mass conveyed.

Although the mass flow rate is the most common parameter used to specify the transport amount, it is not the most basic one. All conveyor machinery works on a volumetric basis, because it provides a certain volume for the transport of cargo or bulk material. While the density of the goods or bulk material may vary, the volume does not. The volumetric flow rate Q_V as the volume conveyed per unit time is therefore independent of the bulk density of the transported bulk material or the packaging efficiency of the load carrier.

Material handling equipment is typically characterized based on its maximum cargo/mass/volumetric flow rate. This is the maximum flow rate of each conveying machine in a transport chain, and the arrangement of several linked conveyors in a materials handling system defines the maximum throughput of the system. This maximum throughput value is a theoretical technical value that does not consider, e.g., the technical

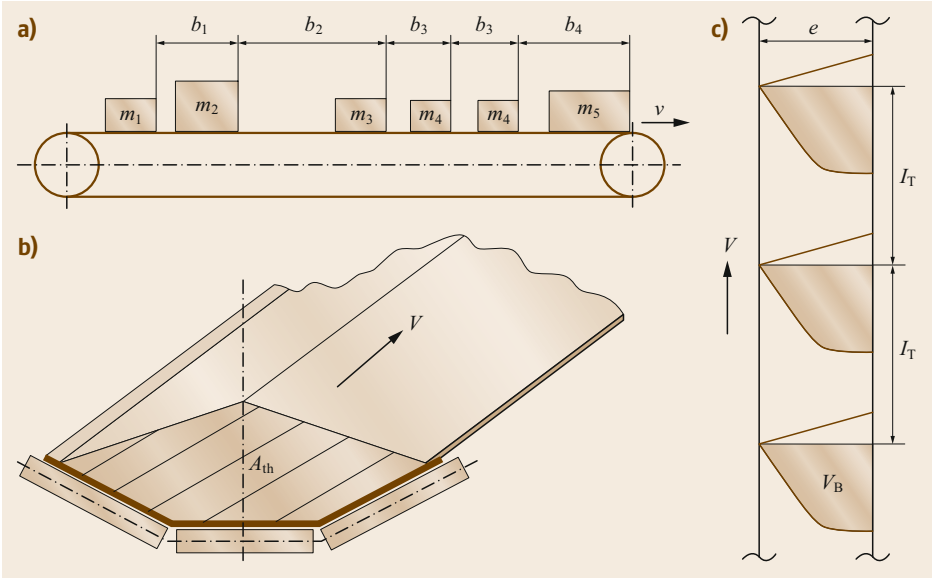

Fig. 20.7a–c Distribution of goods on continuous conveyors as the basis for the flow rate calculation when conveying **(a)** cargo on a flat belt conveyor and bulk material on **(b)** a troughed belt conveyor or **(c)** a bucket elevator (after [20.5])

reliability of the system. Indeed, the actual flow rate in a materials handling system might be smaller or equal to this maximum flow rate, often showing large fluctuations. The time-varying average flow rate is frequently used to describe the momentary throughput.

For discontinuous conveyors, the cargo flow rate can be determined from the average time required to complete one working cycle $\overline{t_c}$ as

$$Q_c = \frac{1}{\overline{t_c}} . \tag{20.1}$$

The mass flow rate can be derived from the cargo flow rate by considering the average mass of the cargo $\overline{m_c}$ as

$$Q_m = Q_c \overline{m_c} = \frac{\overline{m_c}}{\overline{t_c}} . \tag{20.2}$$

The cargo flow rate for continuous conveyors transporting general cargo according to Fig. 20.7a can be calculated from the average spacing or pitch between two goods $\overline{b}$ and the conveying velocity v. Their ratio is equal to the time required to transport each cargo, which can be interpreted as the working cycle for a continuous conveyor

$$Q_c = \frac{\overline{b}}{v} = \frac{1}{\overline{t_c}} . \tag{20.3}$$

Continuous transport of bulk materials is characterized by the volumetric flow rate, given by the product of the maximum cross-sectional area of the bulk material A at the conveyor, the filling level/filling efficiency η_F, and the conveying speed

$$Q_V = A v \eta_F . \tag{20.4}$$

The fundamental law of continuity of flow states that Q_V is constant for all continuous conveyors

$$Q_V = A_1 v_1 = A_2 v_2 = \text{const.} \tag{20.5}$$

The mass flow rate is defined based on the volumetric flow rate and the bulk density of the material ρ_b as

$$Q_m = Q_V \rho_b = A v \eta_F \rho_b . \tag{20.6}$$

Many conveyors for bulk materials handling use tubes or troughs to convey the material inside via the translational motion of scrapers attached to chains, ropes, or rotating parts such as screws (Fig. 20.8). Since the mechanical parts inside the trough require a certain volume, the calculation of the maximum cross-sectional

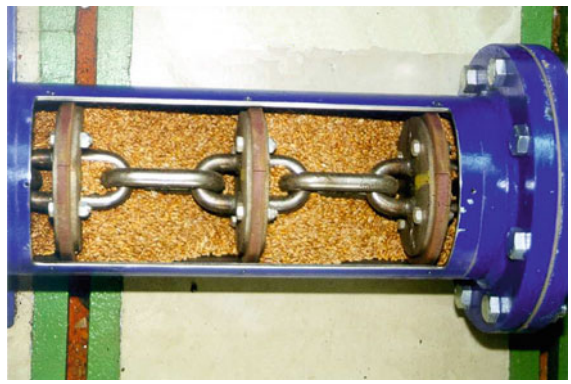

Fig. 20.8 Tube chain conveyor as an example of the need to consider the volumetric efficiency, because the chain and transport disks reduce the volume available for bulk material inside the tube [20.6]

area must only consider the volume that can be taken up by the bulk material. The volumetric efficiency η_V must therefore be introduced, being defined as the ratio of the real volume available for the bulk material to the ideal trough volume,

$$A = A_{\text{trough}}\,\eta_V = A_{\text{trough}}\,\frac{V_{\text{trough}} - V_{\text{parts}}}{V_{\text{trough}}}\,. \qquad (20.7)$$

For continuous conveyors with pulsatile material flow such as bucket elevators (Fig. 20.7c), it is possible to calculate the idealized theoretical cross-sectional area A_{th} by dividing the bulk material volume in the buckets V_B by the bucket spacing l_B,

$$A_{\text{th}} = \frac{V_B}{l_B}\,. \qquad (20.8)$$

20.2 Bulk Solid Mechanics and Characterization

Bulk solid handling operations perform an essential function in many different industries worldwide. As the nature of the application and the scale of the operation vary from one industry to another, as well as from one country to another, the relative costs of storing, handling, and transporting bulk materials differ significantly. For these reasons, it is important that handling systems be designed and operated to achieve the maximum efficiency and reliability.

While operations range across a broad spectrum of industries, the mining and mineral processing industries which handle coal and mineral ores at high throughputs are just as important as the transport of agricultural, pharmaceutical, and renewable materials such as grains, powders, and biomass. These industries make a major contribution to the exports and economic growth of a number of countries as well as fulfilling the evolving global energy and food requirements.

The previous 50 years have seen significant advances in the theory and practice of bulk solid handling. Reliable test procedures and equipment for determining the strength and flow properties of bulk solids have been developed, and analytical methods have been established to aid the design of bulk solid storage, handling, feeding, and transportation. Industry-wide acceptance of these testing and design procedures, and the numerous examples throughout the world of modern industrial bulk solid handling installations, reflect the impact of such technological developments. The procedures for the design of handling plants covering storage, gravity reclaim, feeding, and transfer are well established and follow four basic steps:

(i) Determination of the strength and flow properties of the bulk solid for the range of likely flow conditions expected to occur in practice
(ii) Determination of the bin, stockpile, feeder, or chute geometry to achieve the desired capacity, provide a flow pattern with acceptable characteristics, and ensure that the discharge is reliable and predictable
(iii) Estimation of the loads acting on the bin and hopper walls and on the feeders and chutes under operating conditions
(iv) Design and detailing of the handling plant, including its structure and equipment.

The general theory, characterization procedures, and design methodologies pertaining to gravity flow of bulk solids are presented below, and a selection of references are included at the end of this chapter [20.7–24].

20.2.1 Mechanical Sampling of Bulk Solid Materials

The first step in materials testing is to gather a bulk material sample. Depending on the conditions, a sample may need to represent only a small subset of the bulk solid, or alternatively, the sample may need to represent the average behavior of an entire ore body. Sampling methods include exploratory drill cores, on-site sample stations, belt cut samples, and stockpile drill core samples, to name but a few. The method used for the initial collection of material will often be determined by the conditions and what is available rather than best practice. The critical consideration is to take every precaution available to collect a sample that is considered to be representative of the bulk material to be tested. Regarding these methods, various standards and guidelines exist. The international standard ISO 11648 directly relates to the general principles and statistical requirements for sampling of bulk materials. Beyond these considerations, the tested good dictates or guides the sampling equipment and methods used; for example, AS 4264 is an Australian standard covering sampling procedures for Australian coal types. Further standards and guidelines that are specific to the considered good and application should be sought.

Once a bulk sample has been collected from the material to be transported, it becomes important to ensure that each subset of the sample that is tested is representative of the original sample and thus, ideally, of the

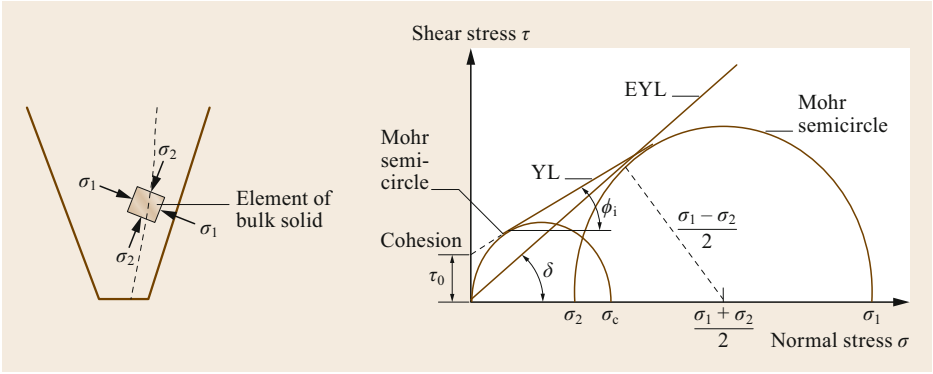

Fig. 20.9 Yield loci for consolidated bulk solid

bulk material as a whole. Again, numerous approaches can be used for such subsampling:

- Cone and quartering—an older technique that has been replaced by sampling devices
- Sample divider or riffler
- Table sampler
- Rotary sample divider.

Cone and quartering is an older technique that was commonly used before mechanical sampling devices became widely available. Current best practice uses a sample divider to split a sample before it is recombined. This procedure aims to ensure that a subsample to be tested in the laboratory is statistically representative of the larger bulk material sample. It is recommended to ensure that any laboratory utilizes a mechanical sampling device alongside a standard operating procedure that fulfills this goal.

20.2.2 Characterization Parameters

Yield Loci Defining Flow of Bulk Solid

A bulk solid flows by failing through internal shear or yielding. Within the solid mass, internal shear is present, whereas at the boundary wall of a hopper or chute, boundary shear occurs. Consider an element of bulk solid flowing by gravity in a symmetrical hopper as depicted in Fig. 20.9. The major and minor principal stresses are σ_1 and σ_2, respectively, with σ_1 being referred to as the major consolidating stress or pressure. As shown by *Jenike* [20.7, 8], a radial stress field exists and σ_1 and σ_2 are as depicted.

The yield locus (YL), or more specifically the instantaneous yield locus (IYL), defines the relationship between the normal and shear stresses during flow. The YL is tangential to the two Mohr semicircles, as indicated in Fig. 20.9. The principal stresses σ_1 and σ_2 define the major Mohr semicircle. The Mohr semicircle that passes through the origin, which is tangential to the YL, defines the unconfined yield strength σ_c. Extrapolation of the YL to the shear stress axis allows the cohesive stress τ_0 to be determined; τ_0 is the shear stress at zero normal stress.

The straight line through the origin and tangential to the major Mohr semicircle is the effective yield locus (EYL). The angle of its slope, defined by δ, is the effective angle of internal friction. For a free-flowing easy-to-handle bulk solid with no cohesion (e.g., dry sand or grain), both τ_0 and σ_c are zero and the internal angles of friction δ and ϕ_i are the same. For a cohesive bulk solid, the EYL may be thought of as the yield locus for an equivalent free-flowing bulk solid having properties similar to that of the actual bulk solid. In bulk solid analysis, δ is a more convenient parameter to use than the cohesive stress τ_0. The angle δ defines the major and minor principal stresses σ_1 and σ_2 as

$$\sin\delta = \frac{\sigma_1-\sigma_2}{\sigma_1+\sigma_2}\,, \tag{20.9}$$

hence

$$\frac{\sigma_2}{\sigma_1} = \frac{1-\sin\delta}{1+\sin\delta}\,. \tag{20.10}$$

Instantaneous Yield Locus (IYL) and Flow Function (FF)

Figure 20.10 shows the IYL for a bulk solid under three consolidation conditions defined by the major consolidation pressures $(\sigma_1)_1$, $(\sigma_1)_2$, and $(\sigma_1)_3$. The instantaneous condition is the instant at which the consolidation pressure acts. For a storage bin, this is the instant when flow occurs, immediately following the initial filling of the bin. The three consolidation conditions represent three positions of an element of flowing bulk solid in the lower hopper during discharge.

The Mohr stress semicircles passing through $(\sigma_1)_1$, $(\sigma_1)_2$, and $(\sigma_1)_3$ are tangential to the respective yield loci, as shown in Fig. 20.10. The Mohr semicircles passing through the origin and tangential to the IYL

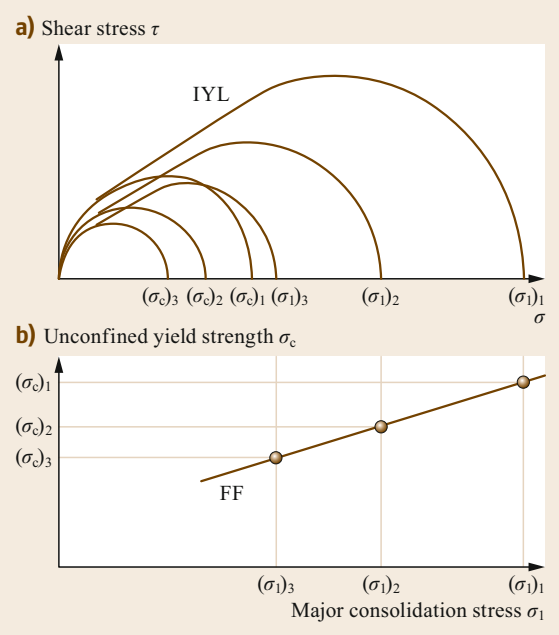

Fig. 20.10 **(a)** Yield loci and **(b)** flow function (FF)

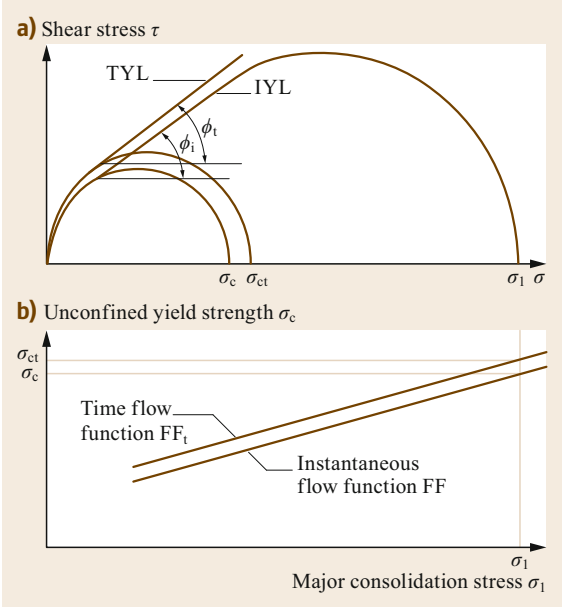

Fig. 20.11 **(a)** Time yield locus (TYL) and **(b)** time flow function (FF_t)

define the unconfined yield strength or stress, σ_c, corresponding to each consolidation condition. The three stresses $(\sigma_c)_1$, $(\sigma_c)_2$, and $(\sigma_c)_3$ correspond respectively to the three consolidation pressures $(\sigma_1)_1$, $(\sigma_1)_2$, and $(\sigma_1)_3$. The bulk strength, represented by the flow function (FF), is the unconfined yield strength σ_c expressed as a function of the major consolidation stress σ_1 obtained from the IYL, as shown in Fig. 20.10.

Time Yield Locus (TYL) and Flow Function (FF_t)

During storage, many cohesive bulk solids increase in strength. The application of the major consolidation pressure σ_1 over time will cause the unconfined yield strength to increase from σ_c to σ_{ct}, as shown in Fig. 20.11. The time yield locus (TYL) defines the yielding condition following undisturbed storage over time. In this case, the static angle of internal friction, ϕ_t, is defined by the slope of the TYL at the tangent point with the Mohr semicircle through σ_{ct}.

Types of Flow Function for Bulk Solids

Figure 20.12 illustrates various forms of the FF for common bulk solids. Most cohesive bulk solids tend towards a limiting strength as the consolidation pressure increases; their FF is convex upward in shape, as indicated by curve (a) in Fig. 20.12. Simple bulk solids have a linear FF over the range of consolidation pressures considered, as in curve (b). Free-flowing bulk solids have zero strength, and their FF coincides with

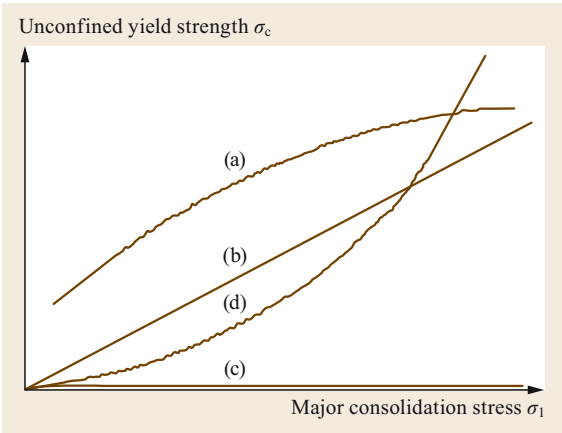

Fig. 20.12 Various forms of flow functions for bulk solids

the horizontal axis, as depicted in curve (c). Occasionally, the strength of a bulk solid increases nonlinearly with increasing consolidation pressure, as in curve (d). Such materials are free flowing under low consolidation pressures but tend to cake or bond together as the consolidating pressure increases. A typical material exhibiting these characteristics is ammonium nitrate prill [20.9]. Such materials are difficult to handle and when stored in mass-flow bins exhibit arching high up in the hopper where the consolidation stresses are high. As such, they should be stored in mass-flow bins without upper, cylindrical sections (hopper only).

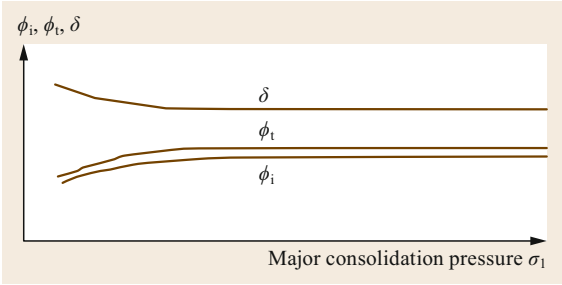

Fig. 20.13 Angles of internal friction

Flowability Index

A measure of the cohesive strength of a bulk solid material can define its flowability. The higher the cohesive strength, the more difficult the handling becomes. According to [20.10], the FF of a bulk material can be categorized based on the Jenike flowability classification, defined as

$$\mathrm{ff_c} = \frac{\sigma_1}{\sigma_c} \,. \tag{20.11}$$

The flowability can be categorized as follows:

- $\mathrm{ff_c} > 10$: free flowing, very low cohesion
- $4 < \mathrm{ff_c} < 10$: easy flowing, low cohesion
- $2 < \mathrm{ff_c} < 4$: cohesive
- $1 < \mathrm{ff_c} < 2$: very cohesive
- $\mathrm{ff_c} < 1$: not flowing.

According to recent research [20.11], a single $\mathrm{ff_c}$ value is not suitable to define the flowability of bulk solids, such as wet and sticky iron ore, for which the flow function spans two different classifications.

Angles of Internal Friction

Typically, the relationship between the angles of internal friction, ϕ_i, ϕ_t, and δ, and the major consolidation pressure, σ_1, is shown in graphical form as illustrated in Fig. 20.13.

Wall Yield Locus and Wall or Boundary Friction

At a boundary surface, such as the walls of a hopper or chute, the flow is characterized by the wall yield locus (WYL), which relates the shear stress to the corresponding normal stress or pressure. Figure 20.14 illustrates the flow channel, WYL, and stress conditions at the boundaries of a hopper and chute. Also shown are the yield functions and Mohr semicircles relating the normal and shear stresses at the wall to the principal stresses of the bulk solid.

The WYL for most bulk solids is slightly convex, as shown in Fig. 20.14c. In some cases, the extrapolated

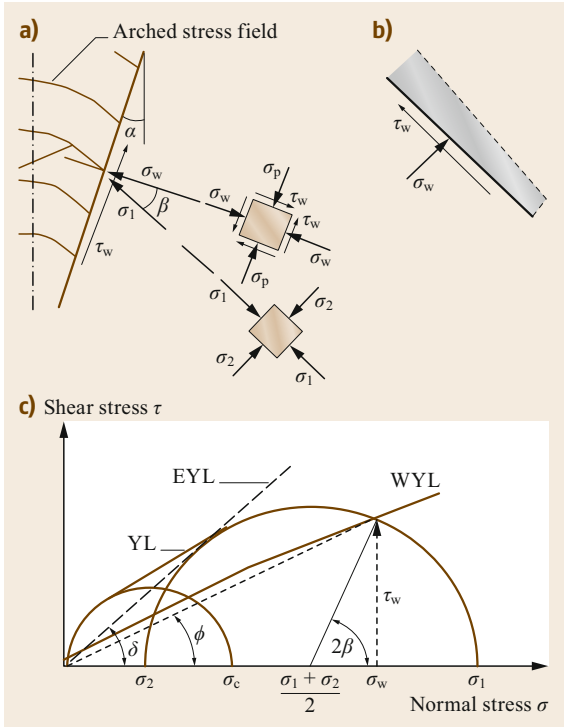

Fig. 20.14a–c Bulk solid yield and flow channels: **(a)** flow channel in hopper, **(b)** flow channel in chute, **(c)** yield loci

WYL does not pass through the origin, indicating adhesion (attraction between the bulk solid and the wall surface). To highlight this, the low-pressure or low-stress end of the WYL is shown diagrammatically in Fig. 20.15. For illustrative purposes, the WYL shown extends into the tensile normal stress region where the tensile stress (at zero shear stress) is denoted by σ_0 (adhesion). The cohesive stress τ_0 is the shear stress corresponding to zero normal stress and is also sometimes referred to as the adhesive stress. The wall friction angle, ϕ, is defined by

$$\phi = \tan^{-1}\left(\frac{\tau_w}{\sigma_w}\right) \,, \tag{20.12}$$

where

τ_w shear stress at the wall,
σ_w pressure acting normal to the wall.

Since the WYL for cohesive bulk solids is often convex upward in shape and, when extrapolated, intersects the shear stress axis at τ_0, then ϕ will decrease with an increase in normal pressure. Figure 20.16 illustrates this relationship. Note that ϕ cannot be larger than δ.

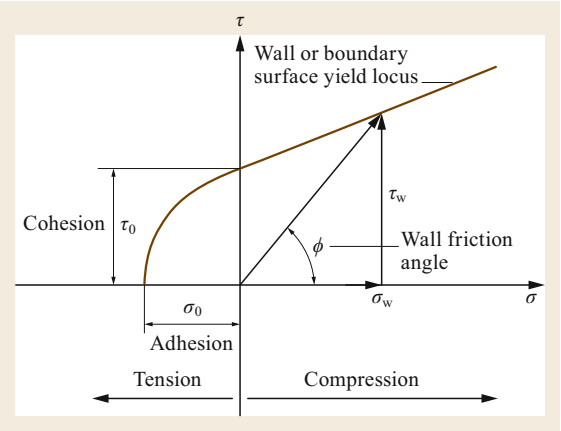

Fig. 20.15 Wall yield locus, cohesion, and adhesion

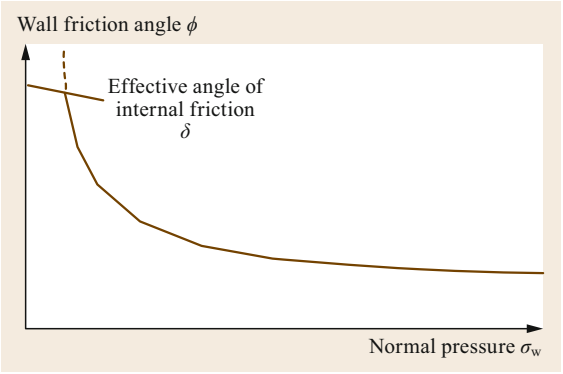

Fig. 20.16 Variation of wall friction angle with normal pressure

The angle δ is, therefore, an upper bound for ϕ. This means that, at low normal pressures, the bulk solid will flow by internal shear rather than by sliding against the wall.

20.2.3 Determination of Bulk Solid Properties

The flow properties of a bulk solid can be determined using a number of test methods. The primary output of such testing is a measure (or measures) of the internal strength of the bulk material. There are a number of testing options available that can provide the internal strength: the Jenike shear tester, the torsional (or ring) shear tester, the uniaxial shear tester, or the triaxial shear tester. Each test apparatus offers advantages and disadvantages in terms of operability and application, but their aim is the same: to provide a measure of the strength of a bulk material under different conditions. This typically involves varying the moisture content, which enables the determination of the condition of the bulk material that results in the maximum strength. The two commonest testing devices—the Jenike shear tester and torsional shear tester—are discussed further below.

Jenike-Type Direct Shear Tester

Among the methods mentioned above, the linear direct shear tester of the type developed by *Jenike* [20.7, 8, 25–27] is widely used, particularly for industrial design applications. The Jenike-type direct shear test apparatus employs a shear cell with a circular cross-section, as shown in Fig. 20.17. The test involves two phases: the filling of the cell and preconsolidation phase, as shown in Fig. 20.17a, and the shear consolidation followed by the shear phase, as shown in Fig. 20.17b. The normal load is applied to the top cover by means of a gravity load frame, while the shearing action is applied by means of an electromechanically driven loading stem, which is driven at a rate of 2.5 mm/min. The shear force is measured using a load cell and displayed on a computer via data logger equipment and software.

The shear consolidation phase involves shear deformation under the nominated load with the aim of bringing the sample to the critical state. As indicated in Fig. 20.17b, the consolidation phase commences with the shear ring offset, the objective being for the sample to reach the critical state condition by the time the shear ring becomes concentric with the base. Due to the limited travel for this condition to be reached, the sample must be preconsolidated. On completion of preconsolidation, the cell is then set up as indicated in Fig. 20.17b to complete the shear consolidation.

Following consolidation to the critical state condition, the sample is then sheared to failure under a nominated load that is smaller than the consolidation load. For time yield locus tests, each sample is consolidated as described above and then removed from the shear tester and placed in a consolidation bench. The consolidation load is applied, and the sample remains in the consolidation bench for the prescribed storage time. The sample is then removed from the consolidating bench, placed back in the shear tester, and sheared under the nominated load.

Torsional or Ring Shear Apparatus

A disadvantage of the Jenike-type direct shear tester is the limited travel it offers during the consolidation phase, as indicated above. The travel is limited, effectively, by the thickness of the shear ring. Torsional, or ring, shear testers have unlimited travel, enabling consolidation of the sample without the need for the preconsolidation phase applied in the Jenike-type shear test. However, torsional shear testers suffer from the following disadvantages:

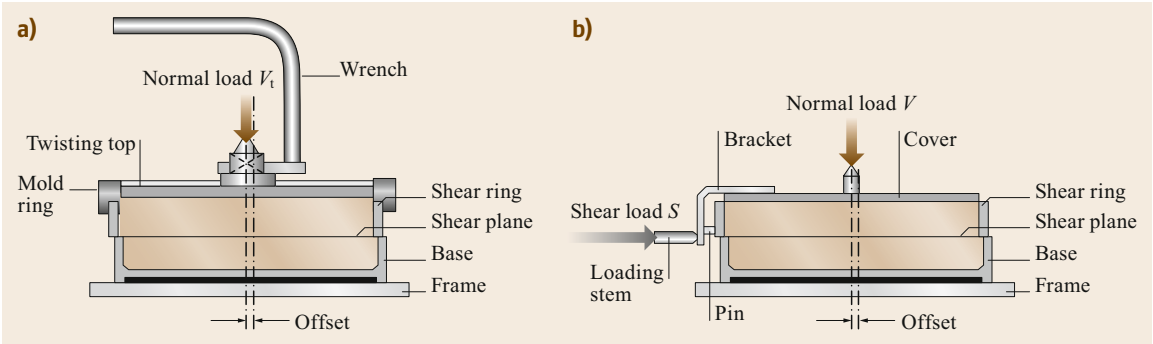

Fig. 20.17a,b Jenike-type direct shear test: (**a**) preconsolidation of sample, (**b**) shear consolidation followed by shear to failure

- Due to the rotational motion, the shear strain is not linear; rather, it is a function of radius and hence is not uniform for all regions of the bulk solid sample.
- Time consolidation tests are difficult to perform.
- Wall friction tests may be performed, but the rotary motion will mask out the unidirectional surface properties of the wall lining material.

Wall Friction Testing

The wall friction test replaces half of the shear test with a wall liner so that the shear load can be recorded as a function of normal load. The testing setup is illustrated in Fig. 20.18. This test is specific to the bulk material, wall liner, surface condition and roughness, bulk material moisture content, and method of operation of testing. It is strongly advisable to understand the surface conditions of any wall liner that is to be used in a materials handling system.

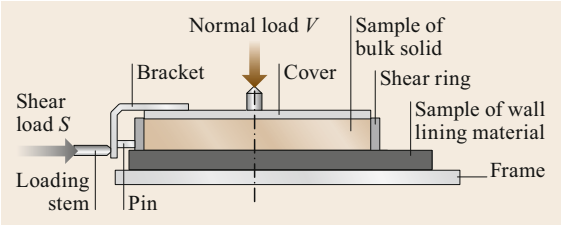

Fig. 20.18 Wall friction test arrangement

Bulk Density

The bulk density varies as a function of the consolidation pressure or normal load. This material property can be determined using a compressibility tester. Typical bulk density results are illustrated in Fig. 20.19. The minimum value is typically termed the *loose-poured* or unconsolidated bulk density, with a maximum value being approached as the consolidation pressure increases. Additionally, the particle density or solid density can be measured if required.

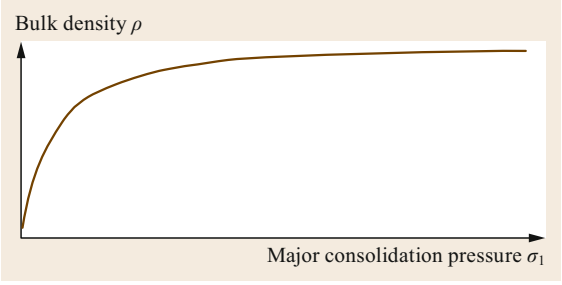

Fig. 20.19 Typical bulk density curve

Fluidization Test

In the case of fine powders, fluidization and de-aeration are properties that need to be measured. The settling and consolidation characteristics of fine powder-type bulk solids, when placed in storage, and their gravity discharge characteristics during flow from storage are governed, to a large extent, by the ability of air to permeate through the stored mass. A schematic of a fluidizing rig is shown in Fig. 20.20. The rig is 50 mm in diameter with three measurement points spaced 150 mm apart.

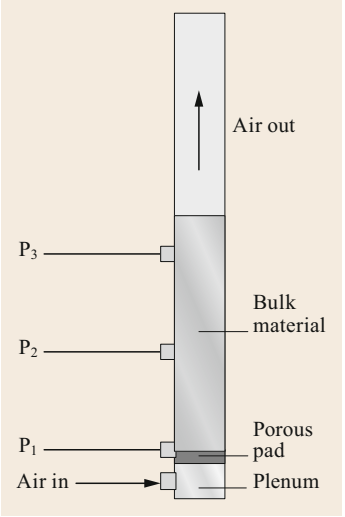

Fig. 20.20 Fluidization test rig

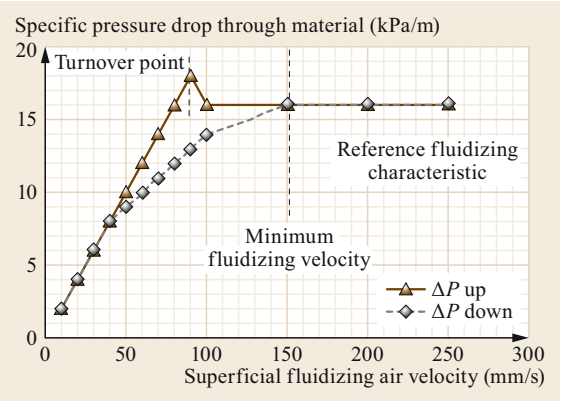

Fig. 20.21 Ideal fluidization characteristic

The tapping points at the levels of 150 and 300 mm are connected to a differential pressure transducer, resulting in a characteristic of the form shown in Fig. 20.21. The plot shown in Fig. 20.21 represents an ideal fluidization characteristic. As the superficial air velocity through the column of material is increased, the specific pressure drop steadily increases to the turnover point, beyond which the specific pressure drop reduces slightly and then remains constant with increasing air velocity. Beyond the minimum fluidization velocity shown on this graph, reducing the air velocity has no effect on the specific pressure drop. Reducing the air velocity below the minimum fluidization velocity results in a reducing specific pressure drop, as shown in the graph.

De-aeration Test

Using the fluidization rig shown in Fig. 20.20, the material can be fully fluidized by setting the superficial velocity above the minimum fluidizing velocity as determined by the fluidization test, then the air input port to the plenum is closed. The material is left in the rig to de-aerate while monitoring the pressure at the base of the column (P_1 in Fig. 20.20). Plotting the pressure per meter of bed depth against time then gives the material's characteristic de-aeration curve. The de-aeration time per meter of bed depth is generally taken as the time for the pressure to drop by 95% of its original value.

20.2.4 Regulatory Tests

Transportable Moisture Limit (TML)

The purpose of establishing a transportable moisture limit (TML) is to ensure the stability of the vessel under motion by ensuring that the bulk cargo moisture is below the level at which a dangerous shift or liquefaction could occur. TMLs are commonly defined for maritime transportation but can also be applied for road and rail transport of mineral ores, concentrates, coal, and other commodities.

For maritime transportation, TML test methods are specified in the International Maritime Solid Bulk Cargoes (IMSBC2017) code, detailing the test equipment and methodology required to determine the TML.

To judge whether a cargo needs to have its TML determined, the IMSBC code specifies three basic types of cargo:

- Class A—those materials which may liquefy
- Class B—materials which may represent chemical hazards
- Class C—materials which fall into neither of these categories but may pose other dangers.

The TML test methods contained in the IMSBC code provide five techniques to determine the TML of a range of bulk cargoes that have the potential to liquefy. These tests are identified below with size limits.

The following three tests shown in Fig. 20.22 can be used for all bulk commodities:

- Flow table test—all bulk commodities with a maximum particle size of 7 mm.
- Penetration test—using two cells:
  - Small cell—maximum particle size of 10 mm
  - Large cell—maximum particle size of 25 mm.
- Proctor–Fagerberg test—maximum particle size of 5 mm.
- The following test is applicable to iron ore fines only:
  - Modified Proctor–Fagerberg test for iron ore fines—no maximum particle size.
- The following test is applicable to black coal only:
  - Modified Proctor–Fagerberg test for coal—nominal maximum particle size of 50 mm.

Corrosion

Identifying the potential corrosion response of bulk materials is essential to identify the structural degradation that may affect their safe transport. A number of such test have been detailed to assess the corrosion rate and risk:

- ASTM G162-99 [20.28]—standard practice for conducting and evaluating laboratory corrosion tests in soils
- C.1 Test—UN Manual of Tests and Criteria for Transport of Dangerous Goods, section 37
- DIN 50929-3 [20.29]—corrosion of metals—probability of corrosion of metallic materials when subject to corrosion from the outside—buried and underwater pipelines and structural components

Fig. 20.22a–c IMO-specified TML test apparatuses: **(a)** flow table tester, **(b)** penetration tester, **(c)** Proctor–Fagerberg tester

- EN 12501 [20.30]—protection of metallic materials against corrosion—corrosion likelihood in soil
- MHB (CR)—IMSBC code, section 9.2.3.7.3.

When evaluating the appropriateness of any of the test methods prescribed above, consideration should be given to the applicability of the test to the transport conditions of the bulk material.

Self-heating

Dangerous self-heating in a bulk material occurs when the temperature of the bulk material reaches its spontaneous combustion temperature. To assess whether a bulk commodity and the associated storage and transport system are at risk of dangerous self-heating, a number of assessment methods and classifications have been proposed:

UN-N4 Test. This test assesses the ability of a substance to undergo oxidative self-heating. In this process, the sample is placed in a mesh container within an oven at the specified temperature. If, over a specified period, the temperature of the sample exceeds the ambient temperature of the oven by a specified amount, a positive result is given. To assess the volatility of a sample completely, a range of sample sizes, oven temperatures, and test durations are applied.

R70 Test. The R70 test assesses the reactivity of a bulk material sample to oxygen. This test dries a sample under nitrogen to remove moisture from the material, before passing an oxygen flow over the sample under adiabatic conditions. Starting at 40 °C, the temperature of the oven is programmed to match that of the sample. The R70 value is the average self-heating rate between 40 and 70 °C. Given that this test does not consider the moisture content or convective cooling due to air, it can only be used for indicative purposes in its current form.

Runaway Ignition Temperature (RIT). The runaway ignition temperature is typically derived from the temperature trace used to assess the R70 value, representing the temperature at which thermal runaway occurs. It is this temperature which is usually used to indicate the minimum threshold beyond which a bulk material could spontaneously combust.

Adiabatic Test Methods. Several procedures have been developed to assess the self-heating propensity of a bulk sample under adiabatic conditions. In contrast to the R70 method outlined above, these procedures test a sample in its *as-shipped* form, under a flow of air. The starting temperature of the test is matched approximately to the maximum loading or freight temperature, in order to simulate a site-specific environment. This test is considered to be particularly accurate for simulating the initial stages of in situ self-heating, during which heat losses are thought to be negligible.

Maritime Regulations. For maritime transportation, the current IMSBC code describes two self-heating classifications for bulk materials that are liable to self-heating:

- Class 4.2 (dangerous goods): substances liable to spontaneous combustion. Bulk materials in this class are materials, other than pyrophoric materials, which, in contact with air without energy supply, are liable to self-heating.
- Self-heating solids: MHB (SH)—these are bulk materials that self-heat when transported in bulk but

do not meet the criteria established for inclusion in class 4.2 above.

The IMSBC code specifies that the inclusion of bulk materials in these two categories should be assessed via the test method outlined in the United Nations Manual of Tests and Criteria, Part III, 33.3.1.6 [20.31].

20.2.5 Environmental/Occupational Exposure Tests and Procedures

Controlling the release of fine particles and dust emissions into the surrounding environment is a crucial consideration in the design and operation of bulk solid handling facilities. Minimizing exposure to airborne particulates is a key priority within the management of health, safety, and environmental policies of all the organizations involved and multiple levels of government. In addition, an ineffective dust management plan can have disastrous consequences for the safety of workers, surrounding communities, and the environment. Typically, water sprays are used to reduce fine particle release from exposed bulk solid storage systems such as streams and piles. An underestimate of the moisture requirements will likely result in increased dust emissions, while an overestimate will lead to increased materials handling problems and excessive water usage, and may exceed the bulk solid moisture level for safe maritime transportation (TML). Excessive moisture is also economically costly; for instance, in the case of export of Australian coal, every 1% of total moisture above the target equates to a potential revenue loss to all businesses in the supply chain of approximately AU$1 per t. From an environmental and community perspective, the consequence of inadequate dust management is a significant reduction in air quality, physical and psychological well-being, and the use of amenities, and from a human health perspective, chronic illness and a reduction in life expectancy.

To define exposure limits, dustiness classification schemes have been developed based on the relative inhalable, thoracic, and respirable fractions of particulate mass concentrations. These classifications, particularly used in Europe and focused on powders and (more recently) nanomaterials, are measured in mg/kg and are most frequently applied in the pharmaceutical and food industries. Such dustiness indices can be used to inform and evaluate dust exposure policies in the workplace.

The term "dustiness" has been described as having "no unique definition" [20.12] or the "ability of a material to generate dust during handling" [20.13, 14]. The definition that is most applicable to the discussion herein is that by the British Hygiene Society Technology Committee Working Group on Dustiness Estimation (BOHS) in 1985 as "the tendency of dry materials to liberate dust into the air when handled under specific conditions" [20.12]. The relationship between dustiness and exposure is strongly dependent on the test procedure as well as the method used to apply mechanical energy to generate dust. To address this, the European standard EN 15051 [20.15] was developed, based on rotating drum (EN 15051-2) and continuous drop (EN 15051-3) methods. The dustiness classification schemes in this standard were defined based on the results of testing over 200 different materials. Both methods classify dustiness according to inhalable, thoracic, and respirable mass fractions (concentrations), but the classification varies depending on which method is used [20.16]. Other testers in the same category and for similar purposes have been evaluated, notably the Heubach and Midway Research Institute (MRI) [20.17] testers, with each defining its own dustiness categories (ranging from very low to high) depending on the dust generation technique and energy supplied. These testers and others operating on similar principles have been related to different handling practices and a variety of procedures. Effectively, each method has its own classification system, with the aim of replicating an industrial process in order to define exposure.

In Australia, dustiness is typically evaluated using two methods, based on a rotating drum and wind tunnel, respectively. To evaluate active dust generation by transfer chutes or train and ship loaders, the rotating-drum dust extinction moisture (DEM) procedure outlined in AS 41566 [20.18] is used. The application of this standard involves tumbling a bulk solid material in a rotating drum to provide an evaluation of the dustiness and a moisture content at which dust is no longer generated. For passive dust generation caused by an air stream flowing over a static exposed surface, e.g., for stockpiles or train wagons, a wind tunnel test approach is used. The wind tunnel test method simulates the site conditions of an air stream passing over a static pile in a controlled environment. Importantly, *Djukic* and *Planner* [20.20] found a relationship between the dust suppression moisture obtained using the wind tunnel test and the DEM obtained using the method described in AS 4156.6.

The AS 41566 [20.18] method specifies a moisture content at which a handled bulk solid material does not emit dust. Initially developed by *Farrugia* et al. [20.19], and specifically for coal, it has since been successfully implemented for dust management at a number of Australian locations, including Dalrymple Bay and Hay Point in Queensland [20.21, 22], and also for other commodities and minerals such as iron ore. The ma-

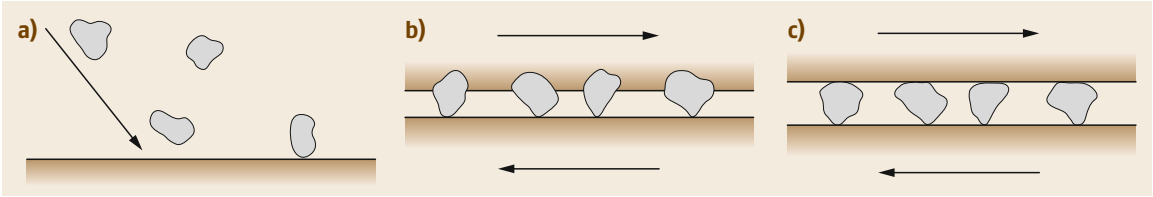

Fig. 20.23a–c Illustration of difference between (**a**) erosion, (**b**) two-body abrasion, and (**c**) three-body abrasion

terial samples tested typically contain larger particles compared with EN 15051 (maximum particle size of 6.3 mm for coal). Rather than a dustiness classification scheme based on the particulate size fractions collected, AS 4156.6 defines a moisture content that prevents (or minimizes) dust release, where dust is defined as particles entrained in an air stream having equivalent diameter of 150 µm or less. Subsequently, a review of this standard [20.23, 24] showed that the measured DEM is strongly influenced by the particle density of the material sample assessed. Unlike the European standard, AS 4156.6 does not aim to replicate a specific process.

The characteristics that define the difference between the discussed methods also include the lack of a unified classification for dustiness; for example, EN 15051 classifies dustiness according to a finite number of tested reference samples, while AS 4156.6 provides a dust number over a finite test period. The wind tunnel test currently does not have a standard. As such, further research in this field, including on the biological relevance of such dustiness classifications, is required.

20.2.6 Wear

Wear is a common and complex phenomenon in applied engineering science. It has been defined as damage to a solid surface, generally involving progressive loss of material, due to relative motion between that surface and a contacting substance or substances. Wear can be broadly divided into abrasion and erosion, depending on the interaction between the contacting surfaces. Due to the abrasive nature of many bulk materials, wear is a common problem in materials handling.

Abrasive and Erosive Wear Mechanisms

The erosive and abrasive wear mechanisms are illustrated in Fig. 20.23 [20.32]. Erosive wear occurs due to the impingement of particles on a surface. The particles can cut or deform the surface and, depending on their velocity and impact angle, then remain on or rebound from it. Abrasive wear occurs when the particles slide on the surface and damage it via cutting and deformation. Particle sliding (two-body abrasion) and rolling (three-body abrasion) are illustrated in

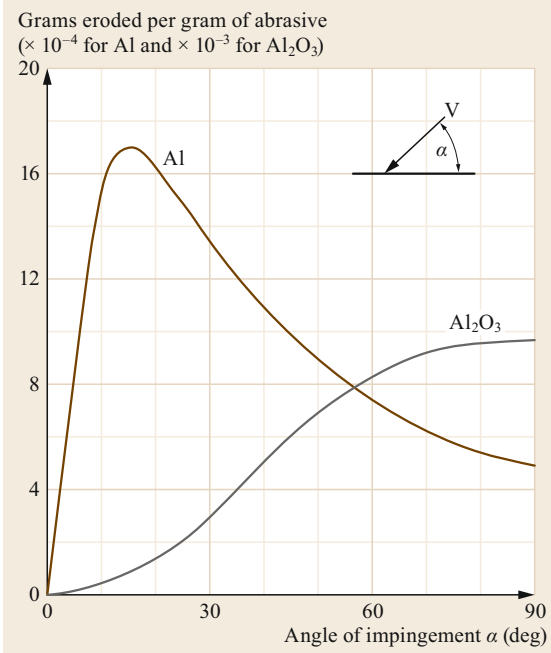

Fig. 20.24 Comparison of 1100-0 aluminum and aluminum oxide eroded by 127-µm (120-mesh) SiC particles at 152 m/s [20.33]

Fig. 20.23b,c [20.32]. In the case of two-body abrasion, the particle is attached to one surface but slides on the other. Relative motion is present between the particle and the sliding surface. In the case of three-body abrasion, the particle is free to roll between the surfaces and damage can occur to both surfaces.

Extensive work has been conducted to understand the erosive and abrasive wear mechanisms. A number of models have been proposed to explain the wear behavior of different materials in different situations. Although opinions on the actual material removal mechanisms differ, most researchers agree that cutting and deformation are the dominant wear mechanisms on ductile materials. For brittle materials, the formation of cracks and crack propagation are considered to be the dominant wear mechanisms.

Due to the differences between the wear mechanisms of ductile and brittle materials, the wear rates

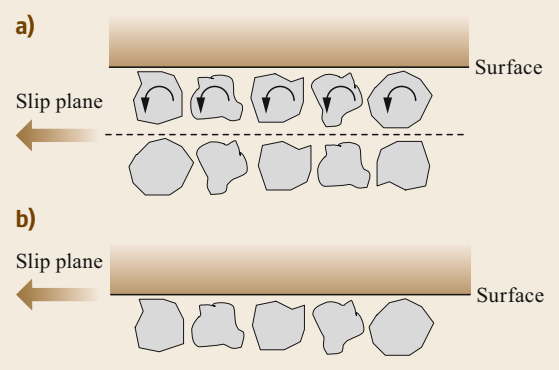

Fig. 20.25a,b Effects of internal friction (μ_i) and surface friction (μ_s) on wear mechanisms in bulk materials handling [20.34]: with **(a)** $\mu_s > \mu_i$ and **(b)** $\mu_s < \mu_i$

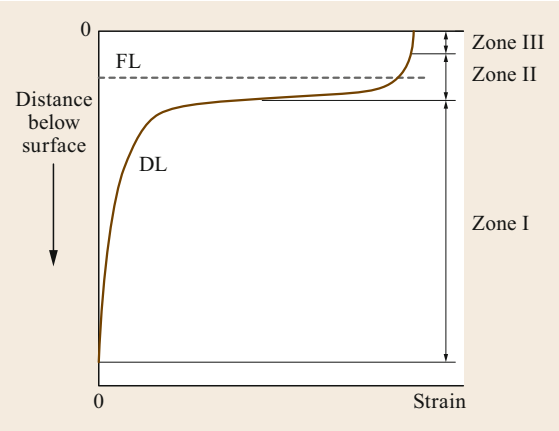

Fig. 20.26 Schematic diagram of strain distribution below the wear surface and regions defined as *deformed layer* (DL) and *fragment layer* (FL). Also shown approximately are regions referred to as zones I, II, and III

of these materials vary dramatically in different environments. Figure 20.24 shows the wear rate of two different materials for impact angles (α) from 0° to 90° [20.33]. This figure shows that the maximum erosive wear rate occurs in the impact angle range from 20° to 30° for the ductile material but at 90° for the brittle material under the same erosive wear conditions. Although the impact angle and velocity of the particles are the key factors determining the erosive wear rate, the surface properties and the properties of the particles also play substantial roles in determining the wear rate.

Depending on the particle loading conditions, both three- and two-body mechanisms can contribute to the wear. Figure 20.25 shows the rolling and sliding conditions for particles depending on the particle packing and loading conditions. The internal friction, particle interlocking, and surface friction play important roles in controlling the wear mechanisms during the conveyance of bulk solids [20.34].

If the surface friction is greater than the internal friction between the particles, a slip plane is created in the bulk material and the particles tend to roll along the surface. On the other hand, if the surface friction is lower than the internal friction between the particles, they act as a single body and slide along the surface. Figure 20.25a presents the situation of three-body abrasive wear, whereas Fig. 20.25b shows two-body wear in the case of bulk materials handling.

In the case of three-body abrasive wear, the particles are free to roll and slide on the surface, and the surface can be subjected to a loading–unloading cycle due to the rolling contact of the particles. This cyclic loading can cause microfatigue of the surface material, subsequently generating randomly shaped wear scars similar to those observed for the brittle fracture mechanism.

Another effect of the cutting and deformation mechanisms occurring on the surface is surface hardening. The complex stress cycles undergone by surfaces due to sliding and impacts of particles result in significant alterations to the surface and subsurface [20.35]. The material behavior and changes in the properties of the subsurface layer govern the formation of a new surface texture and hence the wear behavior. The cyclic accumulation of plastic deformation in the subsurface layer plays an important role in the wear behavior due to the plastic deformation of the surface. Based on the dislocation structures in the subsurface layer, three zones were defined by *Glardon* and *Finnie* [20.36], as shown schematically in Fig. 20.26.

According to Fig. 20.26, as zone I extends from the virgin material towards the surface, a subgrain substructure is formed. The size of this zone decreases as the strain increases towards the surface. In the upper part of zone I, subgrains elongated parallel to the surface are observed. The microstructures in zone II are similar to those in plastic deformation shear bands and can be considered to represent a superficial shear band. Zone III is described as a transfer layer which consists of ultrafine crystallites incorporating materials from the abrasive particles. Zones II and III correspond approximately to the fragmentation thickness and represent about 20% of the subsurface layer (i.e., the deformed layer).

20.3 Basic Mechanical Elements

A large amount of the equipment used in materials handling systems is made from the same basic mechanical elements. Since the design and calculation of most of these elements are usually not discussed in the field of machine elements (Chap. 15), the following sections present the necessary knowledge for the basic design of the most important mechanical elements: ropes, chains, belts, and the wheel/track system.

It should be noted that mechanical brakes such as drum, disk, cone, and band brakes are also essential mechanical parts for materials handling systems. However, brakes are not discussed in this chapter, because they are usually applied as a separated part, not necessarily integrated with the conveyor. Mechanical brakes can be seen as part of the drive system, which typically consists of a drive (mostly electrical but also hydraulic drives are also used, and rarely direct combustion engines), gear, and clutch.

20.3.1 Wire Ropes

Ropes are one of the oldest machine elements for materials handling. While ropes made of natural fibers have been used throughout history, the industrial use of ropes increased dramatically with the invention of the wire rope by the German Wilhelm Albert in 1834. Invented especially as an alternative lift element to chains for use in mines, wire ropes are now applied in mining, materials handling, and general mechanical engineering but also civil engineering. Compared with natural fibers, metal wires have much higher tensile strength. Natural fibers such as flax, hemp, or sisal are therefore rarely used today. However, synthetic fibers such as polypropylene, nylon, polyesters (e.g., PET), polyethylene (e.g., Dyneema®), aramids (e.g., Kevlar®), and acrylics (e.g., Dralon®) can be used today to produce ropes with very similar or higher tensile strength and strain rates compared with wire ropes but with much lower weight. It can be expected that—with the continuing development of synthetic fiber ropes—they will be increasingly applied in materials handling. However, for many applications in materials handling, the wear behavior of the ropes is also an important property, where wire ropes still show many advantages. The next sections therefore only focus on wire ropes. For additional information on the latest research results on fiber ropes, refer to [20.37–41].

In comparison with chains, wire ropes show the following advantages:

- Low weight with large breaking forces.
- Due to the fact that a wire rope consists of many (twisted) single wires with small diameter lying next to each other, failure of the rope because of the simultaneous breakage of all single wires is very unlikely.
- Smooth running of the rope even at high operational speeds.

Types of Wire Ropes

The design of a wire rope depends mainly on its application. Generally, four types of rope applications can be distinguished (see also Fig. 20.27):

- Running ropes (e.g., for lifting and hoisting devices such as cranes)
- Track or suspension ropes (e.g., to carry the gravitational load of a cable-car cabin, where the rope will undergo minimal deflection under the moving load)
- Sling ropes (e.g., to attach a load to a crane hook)
- Stationary or guy ropes (e.g., for structural support of crane booms or jigs, and suspension bridges).

Depending on its application, a wire rope must be

- Flexible to be continuously redirected via sheaves or pulleys (running ropes)

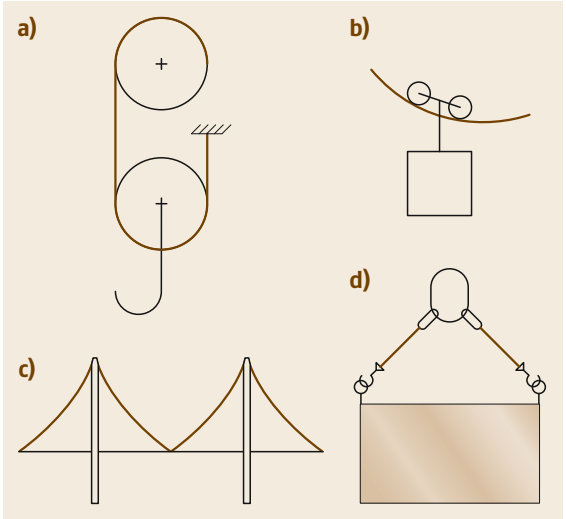

Fig. 20.27a–d Wire rope types: (a) running rope, (b) suspension ropes, (c) stationary ropes, and (d) sling ropes

- Smooth at the surface to allow a smooth running of equipment over it (track ropes)
- Resistant to sharp edges (sling ropes), or
- Strong to carry very high tensile forces (stationary ropes).

Running ropes are the most widely used and interesting ropes in materials handling, because they are used in the large machinery group of hoisting devices. This application area requires the redirection/deflection of ropes via sheaves, which can be arranged into a block and tackle, the storage and drive of the rope via a rope drum, or a single drive via a friction hoist. Besides the wire rope design, these elements will therefore also be discussed.

Basic Design of Wire Ropes

Wire ropes generally consist of several layers of metal wires that are helically twisted around a core. If the core is a single wire, it is called a king wire. However, other core materials (e.g., natural or synthetic fibers) can also be used. The result of this first step in rope manufacturing is called a strand. The twisting process is called laying, where a certain lay angle, lay length, and lay direction are used. In the second step, multiple layers of strands are laid around a rope core to create the final rope (see also Fig. 20.28). The main components of wire ropes are therefore the wires, the strands, and the core material of the rope and strands. While there are special triple-stranded ropes called cable-laid ropes for use in ship building, running ropes in materials handling are double stranded.

The design and main components of wire ropes are internationally standardized in ISO 2408 [20.42].

Rope Wire. A rope wire usually has a round cross-section, although Z-shaped, H-shaped, T-shaped, triangular, flat, or oval wire cross-sections can also be made. Nonround wires are called profile wires. The wire can be made from unalloyed carbon steel according to DIN EN ISO 16120-1 to -4 [20.43] or from alloyed austenitic steels. According to ISO 2408 [20.42], common wire tensile strengths are

$$R_0 = 1370;\ 1570;\ 1770;\ 1960;\ 2160\,\mathrm{N/mm^2}\,.$$

Since the bending stiffness is reduced with higher tensile strength, higher wire tensile strengths are typically not used. The tensile strength of the rope wire defines its rope grade.

The wire can be uncoated (bright) or zinc- and zinc-alloy coated. According to ISO 2408 [20.42], the typical diameter of rope wire ranges between 0.2 and 7 mm.

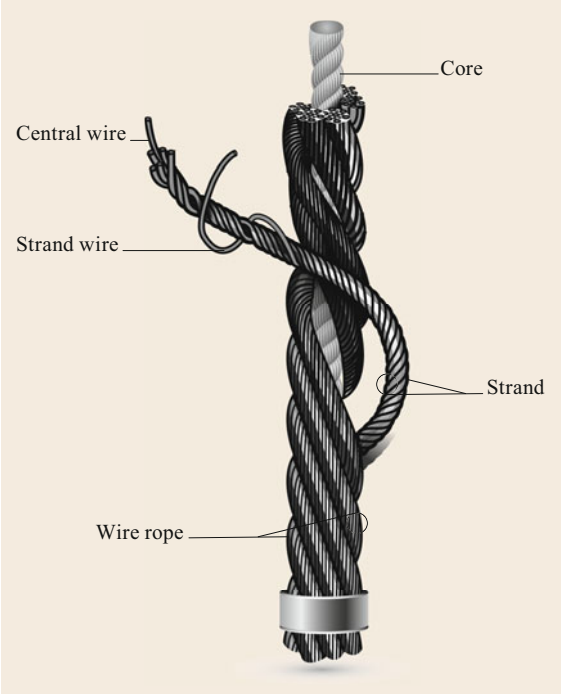

Fig. 20.28 Basic wire rope design

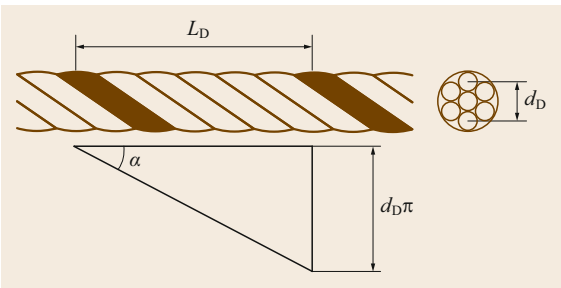

Fig. 20.29 Lay length L and lay angle α of the wires in a strand (after DIN EN 12385-2 [20.45])

Strands. The rope wires are laid helically around a strand core or king wire. The lay length, lay angle, and lay direction (Fig. 20.29) are important design parameters. Left-hand and right-hand lay are known. The standard direction of lay is right-hand lay [20.44]. The lay direction of the wires in the strand and the strands in the rope are very important and are explained in the rope section.

The lay length or lay angle can be kept constant for the lay of the strand. For standard strands—as shown in Fig. 20.30a—the lay length is kept constant, and common wires with the same diameter are used. In these strands, the wires touch each other at single points. This causes peak stresses at the point contacts, especially

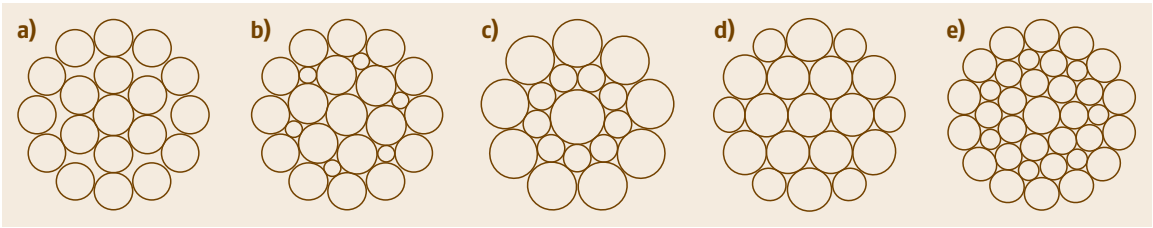

Fig. 20.30a–e Cross sections of standard-lay and parallel-lay strands: **(a)** standard strand, **(b)** parallel lay: Filler, **(c)** parallel lay: Seale, **(d)** parallel lay: Warrington, **(e)** parallel lay: Warrington–Seale (DIN EN 12385-2 [20.45])

during deflection of the strand, resulting in damage to the wires and thus a shorter lifetime. To avoid this problem, strands with parallel laid wire were developed. Here, the wires have the same lay angle but not the same lay length. The wires therefore touch each other along their whole length, resulting in a linear contact. For parallel-lay strands, wires with different diameters are used. Typical designs of parallel-lay strands are shown in Fig. 20.30b–e. Compound strands with at least three wire layers show a combination of parallel-lay and standard strands.

The strands can be produced with certain shapes, as shown in Fig. 20.31. Most often, round strands are used.

Conventional and compacted strands as shown in Fig. 20.32 can be manufactured. Compacted strands result from a compaction process (drawing, rolling, or hammering). The metallic cross section of the wires remains the same, in contrast to the wire form and the dimensions of the strand. Compacted strands show better surface properties, and prevent dirt from entering or lubricant from escaping, but the flexibility is decreased.

Strand Cores. The core of the strands can consist of natural or synthetic fibers or a single king wire. Fiber cores increase the flexibility of the strand and allow the storage of lubricants. Since corrosion of steel wires is a great problem, strand and rope lubrication is important.

Rope. The rope is built from strands that are laid helically around a rope core. The rope core can be made of steel or fiber. The lay direction of the strands in the rope with respect to the wires in the strand strongly influences the final properties of the rope. Lang's lay is when

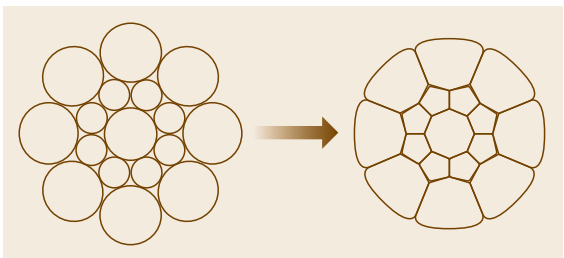

Fig. 20.32 Conventional and compacted strands (after DIN EN 12385-2 [20.45])

the lay direction of the rope and strand is the same. Ordinary lay is—according to ISO 2408—when the lay direction of the rope and strand are opposite. For easier identification of the lay type, the character S is used for left-hand lay and Z for right-hand lay. The standard direction of lay is right-hand lay. The characters are chosen due to the orientation of the center part of the character, which is the same as the orientation of the wires and strands in the rope—according to Fig. 20.33. For the lay direction of the wires in the strand, a small character is used, while a capital letter is used for the lay direction of the strands in the rope. Four combinations are therefore known as shown in Fig. 20.33.

The ordinary lay reduces the twist tendency of the rope. However, the different lay directions also result in worse contact at the wire level, and thus a decreased lifetime in comparison with Lang's lay ropes. Lang's lay ropes have the disadvantage of a higher twist tendency. They therefore cannot be used as a single rope on a hoist. The twist properties of the rope can be improved when an increasing number of strand layers in ordinary lay are used in a rope. Three kinds of

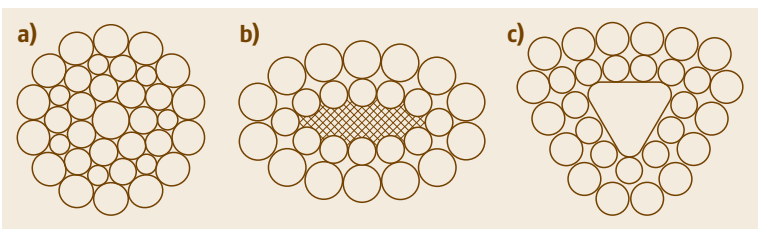

Fig. 20.31a–c Cross-sectional shapes of strands (after DIN EN 12385-2 [20.45]), **(a)** round strand with king wire, **(b)** oval strand with oval core, and **(c)** triangle strand with triangle-shaped king wire

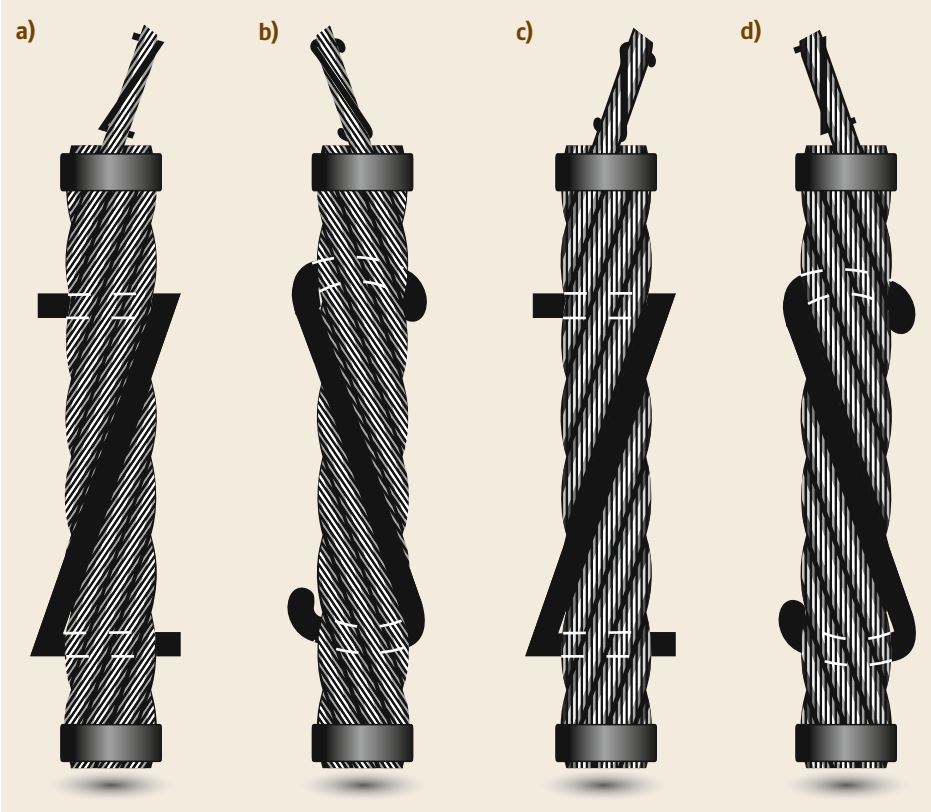

Fig. 20.33a–d Lay direction of wire in strands and of strands in wires, **(a)** zZ: right Lang's lay, **(b)** sS: left Lang's lay, **(c)** sZ: right ordinary lay, **(d)** zS: left ordinary lay

ropes are known—according to VDI 2358 [20.46]: non-rotation-resistant, semi-rotation-resistant, and rotation-resistant rope. A rotation-resistant rope will show no twist around its longitudinal axis if an unguided load is applied. For subsequent calculations of the rope diameter, the differentiation between non-rotation-resistant and rotation-resistant ropes is important.

If a rope may be exposed to intense damage (extreme wear or corrosion), its design must be adapted by adding thicker outer wires to the stranding. Since strands with parallel lay have a longer lifetime, they are the best choice for ropes in heavy-duty applications. Otherwise, ordinary-lay ropes are generally used in rope drives. If Lang's lay ropes are used to achieve a longer lifetime, one has to consider that they will also have a higher torque. If the ropes are to be arranged in pairs (e.g., in rope grabs), there must be an equal number of right-handed and left-handed ropes. A nonguided load on one rope requires a rotation-resistant or at least semirotation-resistant rope. Lang's lay ropes are used for rope drives when so-called low-stress ropes are required (see also VDI 2358 [20.46]).

Spiral Ropes. The simplest rope is basically a standard strand. Consisting of multiple layers of wire of the same diameter, the so-called spiral rope is manufactured in one lay step. The layers of wire can have different lay directions to improve the twist properties of the spiral rope. In comparison with ropes manufactured with two lay steps, spiral ropes have a high metal content per cross-sectional area. The tensile strength of such ropes is therefore high, but their flexibility is low. Therefore, such ropes are especially used for track/suspension ropes (e.g., cable cars) or as stationary ropes (e.g., cranes, bridges). To improve the smoothness of the rope surface and decrease the possibility of corrosion, semilocked or fully locked coil ropes can be produced by the use of form wires, as shown in Fig. 20.34.

Round-Strand Ropes. Round-strand ropes are the most common ropes used in materials handling. Single-layer round-strand ropes and multiple-layer round-strand ropes show increased flexibility. There are many different designs of round-strand ropes, giving the rope certain properties to fulfill the requirements of the intended application. Normative part 22 of ISO 2408 [20.42] includes commonly used designs for round-strand ropes with their dimensions and properties. Typical round-strand ropes are shown in Fig. 20.35.

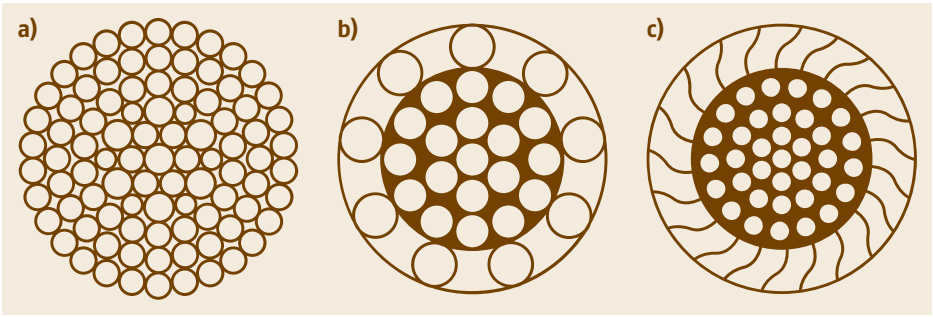

Fig. 20.34a–c Spiral rope types: **(a)** open spiral rope, **(b)** semilocked coil rope, and **(c)** fully locked coil rope (DIN EN 12385-2) [20.45]

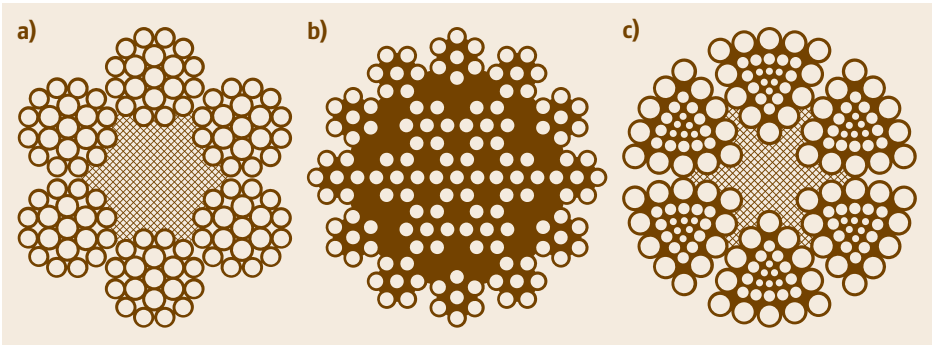

Fig. 20.35a–c Round-strand rope types: **(a)** single-layer round-strand rope (6 × 19 filler), **(b)** multiple-layer round-strand rope, and **(c)** triangular-strand rope (after ISO 2408 [20.42])

In hoists, wire ropes with six to eight outer strands and two or three layers of wire in each parallel-lay strand are most often used (Fig. 20.35a).

Shaped-Strand Ropes. For shaped-strand ropes, one uses strands with nonround cross-sections, such as triangular, oval, or flat strands, as shown in Fig. 20.35c. In comparison with round-strand ropes, shaped-strand ropes are not so commonly used but can offer certain advantages for special applications. ISO 2408 [20.42] contains only one commonly used shaped-strand rope in its normative part.

Rope Cores. The rope core can be made out of natural or synthetic fibers but can also consist of a strand (spiral rope) or a round-strand rope itself. Depending on the rope design, different rope cores such as those presented in Table 20.1 are possible.

Table 20.1 Rope cores and their international abbreviations

Core material	Abbreviation
Fiber core	FC
Natural fiber core	NFC
Synthetic fiber core	SFC
Full polymer core	SPC
Wire core	WC
Wire strand core	WSC
Independent wire rope core	IWRC
Parallel wire rope core	PWRC
Synthetic coated independent wire rope core	EPIWRC

To characterize the rope core, the abbreviations listed in Table 20.1 are used internationally. The rope core, and the strands themselves, can be covered by polymers to stabilize the rope, prevent water and dirt ingress, and thus decrease the risk of corrosion.

Monitoring and Examination of Ropes in Operation

Wire ropes for running and stationary purposes, as well as rope slings and suspensions, must be periodically examined and maintained (if necessary) before every use. Operational safety must be assessed based on:

- The type and number of wire breaks
- The position of any wire breaks
- A chronological log of the wire breaks
- The reduction int he rope diameter during the operation period
- The degree of corrosion
- The extent of abrasion
- The loosening of the rope structure
- The deformation of the rope
- Resting periods.

The general handling of wire ropes as well as their maintenance, inspection, and disposal are standardized in ISO 4309 [20.47].

Rope Calculations

The strength of a rope depends directly on its diameter and design, and the grade of the wire applied. According to ISO 2408 [20.42], a semiempirical method can be used to calculate the minimum breakage force for common types of rope.

For the application of running ropes in materials handling, the usage frequency and the number of redirections must also be considered during rope dimensioning. A calculation approach for the minimum rope diameter, including the minimum breakage force and a so-called design factor, is derived in ISO 16625 [20.48].

Breaking Force. The stress conditions inside wire ropes are complex due to the helical arrangement of the wires and strands, the contact conditions resulting from the stranding, and the rope design (with point or line contacts between the wires). The stresses inside a rope can be distinguished into stress components, resulting from:

- Pure tensional forces due to the load (which would also occur if the rope wire were arranged parallel without any twisting)
- Pure bending forces if the rope runs over the curvature of a drum or sheave
- Tensional forces that occur in the rope during stranding
- Tensile, compressive, and shear stresses occurring at the contacts between the wires in the rope as well as at its contact with sheaves or drums
- Shear stresses caused by the torque that occur when the helically laid wire and strands are tensioned
- Bending stresses due to the point contacts between wires caused by the rope design.

Due to these complex stress conditions, a fully analytical approach to the calculation of the rope breakage force does not exist. The following semiempirical approach for the calculation of the minimum breakage force F_{min} for a rope with diameter $d < 60\,mm$ as described in ISO 2408 [20.42] is therefore used

$$F_{min} = d^2 R_r K\,, \tag{20.13}$$

where

d rope diameter in mm,
R_r rope grade in N/mm^2
K minimum breaking force factor for a given rope class, being included for common rope designs with different rope cores and diameters in ISO 2408 [20.42]. DIN EN 12385 Part 4 [20.49] also includes further K values for other rope designs. Table 20.2 presents examples of K factors for some basic rope designs. Included in the minimum breaking factor is the cross-sectional metallic area factor C, which is also given separately in ISO 2408 [20.42], together with the weight factor W of the rope.

Table 20.2 Minimum breaking factor K for some basic rope designs according to ISO 2408 [20.42]

Rope design[a]	K		
	for fiber cores FC	for independent wire rope core IWRC	for wire strand cores WSC
Single-layer round steel wire ropes			
6 × 7	0.332	0.359	0.388
8 × 36	0.293	0.356	
Rotation-resistant round steel wire ropes			
4 × 19, 4 × 36	0.36		
18 × 7, 18 × 19	0.328		0.328

[a] Rope design nomenclature: Number of outer strands × number of wires in each outer strand. For more information regarding the full rope nomenclature, see DIN EN 12385-2 [20.45]

For rope diameters larger than 60 mm, special equations are available in ISO 2408 [20.42].

Rope Diameter in Hoisting Devices. For the design of hoisting equipment, the minimum rope diameter is calculated based on the maximum rope force F_r but also based on the actual application scenario. The maximum rope force F_r is defined as

- The maximum load
- The weight of the necessary suspension
- The weight of necessary load handling attachments
- The efficiency of the rope drive, especially if block and tackles are used.

The application scenario is characterized by two aspects:

- How often is the hoist/crane used?
- How often does the maximum load occur?

To consider these questions, the international standard ISO 16625 [20.48] introduces a so-called minimum design factor Z_P, which is an empirical factor given for certain rope designs and certain applications (stationary or mobile cranes, pure hoisting or boom hoisting/luffing, single- or multiple-layer spooling). The design factor is given for several group classifications of mechanism M1–M8 in accordance with ISO 4301 [20.50]. The so-called M classes take into account the total duration of full-load working cycles from 100

to 12 500 h. However, this old classification system does not sufficiently consider the situation where smaller loads are transported. ISO 4301 [20.50], in its last update from 2016, thus no longer contains this classification system. Rather, it includes a more sophisticated approach, where the so-called A classes are calculated based on the total number of working cycles and the typical load spectrum class. This new classification system of the international standard follows the approach of the German DIN 15020-1 [20.51]. However, because ISO 16625 [20.48] does not yet consider this new classification system, the M class must be derived from the A class. With the knowledge of the Z_P value, the minimum rope diameter can be calculated as

$$d = \sqrt{\frac{F_r Z_P}{R_r K}} \,. \tag{20.14}$$

For hoisting applications, Z_P for single-layer spooling on the rope drum, with both non-rotation-resistant and rotation-resistant ropes, can be roughly estimated depending on the total duration of full-load operation t_{flo} in h or M class using the equation

$$Z_P = 2 \times 10^{-12} t_{flo}^3 - 7 \times 10^{-8} t_{flo}^2 + 0.001 t_{flo} + 3.1444 \,. \tag{20.15}$$

The design factor for other applications is given in ISO 16625 [20.48].

Components of Rope Systems

If a wire rope is to be used in technical equipment such as a hoist, several other elements are required to:

- Fasten the rope via rope terminations
- Guide and redirect the rope via sheaves
- Drive the rope via rope drums or hoisting drums
- Reduce the rope force by employing a reeving system (block and tackle).

The design of these most important components of rope systems is briefly discussed in the following sections.

Assemblies and Terminations. Rope ends can only be connected frictionally to each other or with other machine parts. For stranded ropes, splicing is possible. Endless rope splicings are always more stressed than the rope itself due to the occuring pressings between the wires. Permanent and nonpermanent rope terminations are known. Many types of rope termination are standardized in DIN EN 13418 Part 1–8. The most basic rope termination is to build an eye and a permanent splice between the rope end and the rope. Other permanent rope terminations include metallic or resin sockets, sleeves, or clamps. The rope eye can be supported by thimbles. Clips and special sleeves can be unfastened and are used to terminate nonpermanent ropes. Wedges can be used together with clips to build a rope lock. It is very important to note that most rope terminations cause a reduction in the minimum breaking force of the rope.

Sheaves. Rope sheaves are designed to redirect the rope. Due to the bending stiffness of the rope, the minimum sheave diameter d_s must be calculated based on the rope diameter d. The M class must also be considered via a factor called h_2. This factor takes into account the occurrence of fully loaded operating conditions and varies between 12.5 and 28. Furthermore, ISO 16625 [20.48] introduces an additional influencing factor t, which takes into account the number of outer strands in the rope. t varies between 1.25 for three outer strands and 0.9 for eight to ten outer strands (with plastic impregnation).

$$d_s = h_2 t d \,. \tag{20.16}$$

However, other widely used standards such as DIN 15020 [20.51] propose the consideration of the number of bending cycles via an additional factor. This may lead to a slightly larger diameter for the case where a high number of bending cycles occurs in the rope drive (e.g., because of a high transmission ratio of the reeving system).

The radius of the groove r_g where the rope makes contact with the sheave must be large enough to prevent blockage but should still provide sufficient guidance for the rope as well. ISO 16625 [20.48] suggests the usage of the following groove radius

$$r_g = (0.525\text{–}0.55) d \,. \tag{20.17}$$

Rope Drums. Drums are used to drive and store rope. For typical hoist and crane ropes, drums with single-layer spooling are used. Drums with multilayer spooling are also possible but require special care regarding the spooling order to prevent rope damage caused by rope crossing. The diameter of the rope drum d_d depends on the rope diameter d and can be calculated similarly to the sheave diameter. However, the M class factor h_1 is smaller than for sheaves and varies depending on the M class between 11.2 and 25. ISO 16625 [20.48] defines the drum diameter as

$$d_d = h_1 t d \,. \tag{20.18}$$

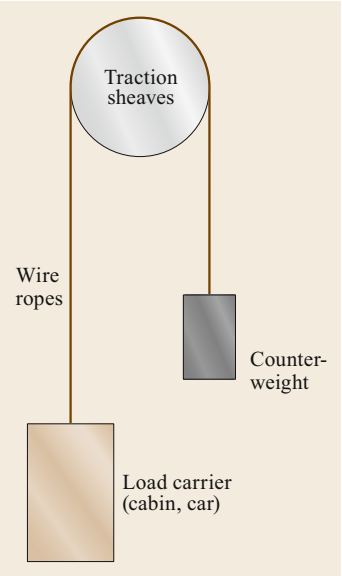

Fig. 20.36 Traction sheaves used in a lift

Traction Sheaves/Hoisting Drums. Hoisting drums allow the drive of an endless rope or a rope between two machine items *without* storing it. While a single traction sheave is principally a large sheave, the name hoisting drum is used because 4–8 ropes are often driven in parallel mode. Traction sheaves were invented in 1877 by the German mining engineer Carl Friedrich Koepe. Since then, they have most often been used for lifts in mines, but also to enable passenger transportation in taller buildings (Fig. 20.36).

In comparison with rope sheaves, traction sheaves usually have a larger diameter of at least $40d$. The basic characteristic of a traction sheave is that the friction between the drum and rope is large enough to prevent sliding. To achieve this, the ratio of the on- and off-going rope must be smaller than the transmission condition defined by the Euler–Eytelwein equation

$$\frac{F_1}{F_2} \leq \mathrm{e}^{\mu\alpha} \,. \tag{20.19}$$

The transmission condition can thus be increased by increasing the coefficient of friction μ between the rope and sheave but also by increasing the wrap angle α. To increase the friction, special kinds of liner materials can be used on the drum. The design of the groove can also positively influence the transmission condition. Round grooves, as well as V-grooves with and without undercut, are known. Furthermore, the increase of the normal force when using rope clamps or magnetic traction sheaves can be applied to improve the transmission ratio.

Reeving Systems (Block and Tackle). The Ancient Egyptians and Greeks used combinations of rope sheaves and drums as blocks and tackle for lifting heavy loads. Today, the term "block and tackle" is no longer used in English in materials handling. Rather, the term "reeving system" is applied to describe how a rope runs between a lower free-hanging sheave(s) and the fixed sheave(s) and drum(s). Common reeving systems are shown in Fig. 20.37. The transmission ratio of the reeving system can be calculated as

$$i_\mathrm{r} = \frac{z_\mathrm{lb}}{z_\mathrm{d}} \tag{20.20}$$

with

z_lb number of rope strands to the lower block
z_d number of rope strands that are spooled on a drum.

This simple equation leads to the given transmission ratio for the reeving systems shown in Fig. 20.37.

The greatest advantage of double- or twin-drum reevings—as shown in Fig. 20.37d–g—is that the load is lifted purely vertically. Single-drum reevings—as shown in Fig. 20.37a–c—cause a sideways movement of the load due to the change of the spooling position on the drum. Furthermore, the load is shared between two rope strands in double- or twin-drum reeving systems, halving the rope load. In all reeving systems, the maximum fleet angle φ of the rope between the drum and sheaves must be considered. According to DIN 15020, φ should be less than 4° for round-strand wire ropes but less than 1.5° for spiral ropes.

To calculate the maximum rope force, the efficiency of the rope drive must be considered. Given a defined efficiency of a sheave $\eta_\mathrm{s} = 0.98$ (roller bearing) or $\eta_\mathrm{s} = 0.96$ (plain bearing), the efficiency of the reeving system for *load lift*, usually the most critical operation mode, is given by

$$\eta_\mathrm{load,lift} = \frac{1}{i_\mathrm{r}} \frac{1-\eta_\mathrm{s}^{i_\mathrm{r}}}{1-\eta_\mathrm{s}} \,. \tag{20.21}$$

When the operation mode is lowering the lower block without a load, the efficiency is usually similar to $\eta_\mathrm{load,lift}$. However, for high transmission ratios, one must check whether there is a risk, e.g., with jib cranes, that the weight force of the empty hook, as a result of energy losses, will be insufficient to pull the rope through the reeving system [20.52].

The rope force increases due to the motion resistance of each sheave. The maximum rope force for a single- or double/twin-drum reeving system can be calculated as

$$F_{\mathrm{r}_\mathrm{max}} = \frac{F}{z_\mathrm{d} i_\mathrm{r} \eta_\mathrm{load,lift}} \,. \tag{20.22}$$

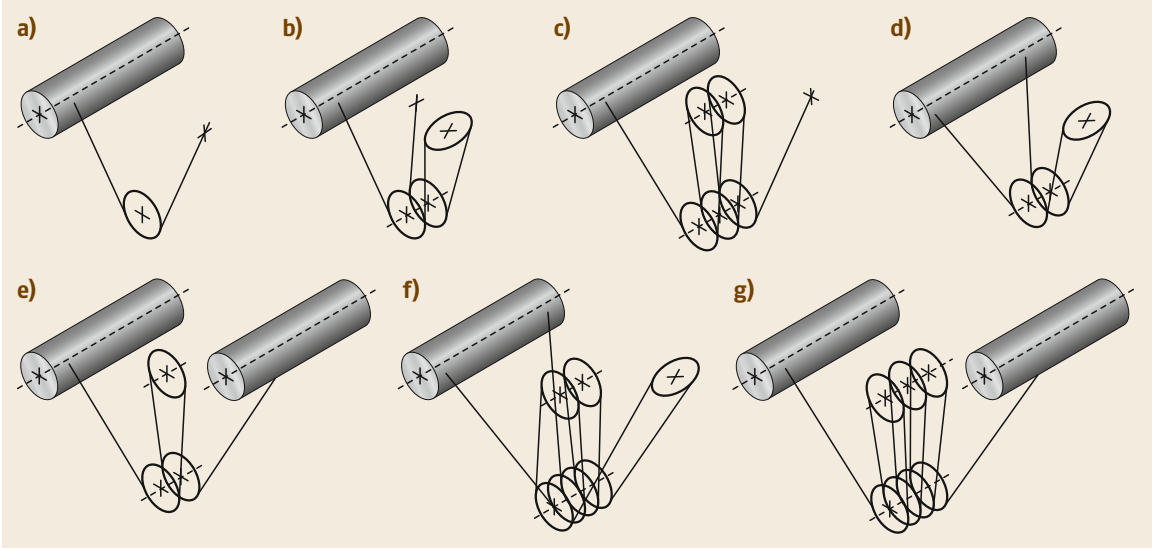

Fig. 20.37a–g Commonly used reeving systems for rope drives: **(a)** $i_r = 2$, single, **(b)** $i_r = 4$, single, **(c)** $i_r = 6$, single, **(d)** $i_r = 2$, double, **(e)** $i_r = 2$, twin, **(f)** $i_r = 4$, double, **(g)** $i_r = 4$, twin

In the case where the rope drive contains a number z_s of additional redirection sheaves (e.g., if the pulley is not mounted directly above the reeving system), the efficiency of these additional sheaves must also be considered

$$F^*_{r\max} = \frac{F_{r\max}}{\eta_s^{z_s}} \,. \tag{20.23}$$

20.3.2 Chains

Chains consist of many short joined links, being some of the oldest mechanical elements since the development of iron by mankind. Over the centuries, a large variety of chains have been developed. In comparison with ropes, chains offers the advantages of:

- High agility, allowing very small redirection diameters
- Good resistance to wear and corrosion
- Excellent heat resistance
- Form-fitting operation via sprocket wheels for drive and redirection
- Easy repair by exchanging individual chain links
- Simple connection to endless tension devices via chain locks or to attach additional accessories to (buckets, cleaner, scraper blades).

Their disadvantages in comparison with ropes are:

- Higher weight
- Difficulty in evaluating their condition regarding fracture and fatigue, thus increasing the risk of force rupture or fatigue fracture and requiring the use of higher safety factors, especially for hoist chains
- Alternating fluctuation of the speed of and force in the chain due to its movement over sprocket wheels with an endless pitch (polygonal effect), especially for large chain pitches and comparably small redirection diameters.

Polygonal Effect

The above-mentioned polygonal effect occurs in all chain drives due to the defined pitch length of the chain, which is essentially defined by the length of the chain links. The chain does not form a circular arc around the chain sprocket wheel but rather a polygonal line. The smaller the number of chain links that fit around the sprocket, the greater the deviation between this polygonal line and a circular arc, as shown in Fig. 20.38 for the example of a sprocket wheel with a teeth number of 6. For this teeth number, the percentage fluctuation in the speed, which is only dependent on the teeth number, can be calculated as

$$\Delta v(z = 6) = 1 - \cos\left(\frac{\pi}{z}\right) = 13.4\% \,. \tag{20.24}$$

The polygonal effect causes a periodic fluctuation of the chain speed and—due to the acceleration and deceleration—fluctuations of the chain force as well. Furthermore, the chain excites vibration due to the changing lateral position of the chain links in contact with the sprocket wheel. Therefore, the polygonal effect limits the velocity of chain drives. In materials

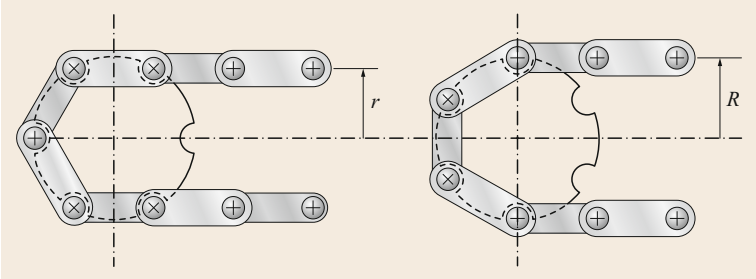

Fig. 20.38 Polygon effect in chain drives for a teeth number of 6

handling, belt or rope drives can usually operate at higher velocities. However, there are application, e.g., for scraper conveyors in underground mining, where a high polygonal effect is taken into account to use small sprocket wheels and thereby realize very shallow conveying systems.

Classification of Chains

Chains can be classified by their application area. These are typically:

- Transmission or drive chains: short distances, high speed, high tension loads
- Timing chains: very short distances, very high speed, low tension loads
- Load chains (lifting chains): medium distances, low speed, high loads
- Conveyor chains: long distances, medium speed, very high loads
- Sling chains for load attachment.

The following discussion focuses on hoist and conveyor chains only. For an overview of transmission and timing chains, the reader is referred to [20.53].

There are two main groups of chains, which can be distinguished by their design and manufacturing process:

- Round steel link chains
- Steel link chains.

Round Steel Link Chains

Round steel link chains are formed by round steel links made from usually round wires that are joined together before being fixed by welding. They permit movement in each direction (Fig. 20.39). Round steel link chains are connected with chain locks (with various constructions being possible). Their manufacture involves:

1. A welding process for links of approved chains: pressure butt welding (link consistency $d \leq 18\,\text{mm}$) and flash butt welding
2. After welding: normalizing or rather quenching and tempering or case-hardening in order to increase their resistance to abrasive wear.

For round steel link chains, the international standardization process given in the ISO standards, e.g., ISO 610 [20.55] and the group of standards developed by the ISO/TC 111 group, does not fully reflect the variety of the applications of this type of chain. More manufacturers produce round steel link chains according to national standards, whereas the German DIN standards are very often used. The following general information therefore refers to the DIN standards.

Tensile stressed chains for use in transport machines should be proof tested. The nominal breaking tensile stress σ_{Bn} can be calculated as

$$\sigma_{\text{Bn}} = \frac{F_{\text{B}}}{2A} = \frac{2F_{\text{B}}}{d^2\pi}\,, \tag{20.25}$$

where F_{B} is the breaking force, d is the chain link diameter, and A is the cross-sectional area of the chain link.

The chain tension is determined by the quality grade of usually 2, 3, 5, 6, or 8. This number indicates the first digit of the nominal breaking tension, being equivalent to the quality classes 250, 320, 500, 630, and $800\,\text{N/mm}^2$. According to DIN 17115 [20.56], the materials for round steel chains are unalloyed quality steels and low-alloyed high-grade steels. Chains that run over sprocket wheels are to be manufactured true to gauge.

True-to-gauge chains are calibrated after heat treatment, which means that a segment with a defined number of chain links is loaded with a superimposed

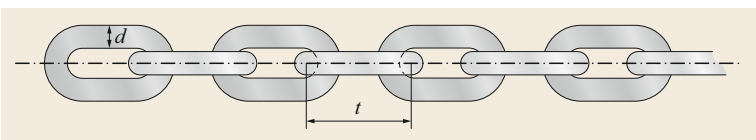

Fig. 20.39 General design of round steel link chain according to DIN 764-1 [20.54]: an example with a pitch-to-diameter ratio of 3.5, typical for a conveyor chain

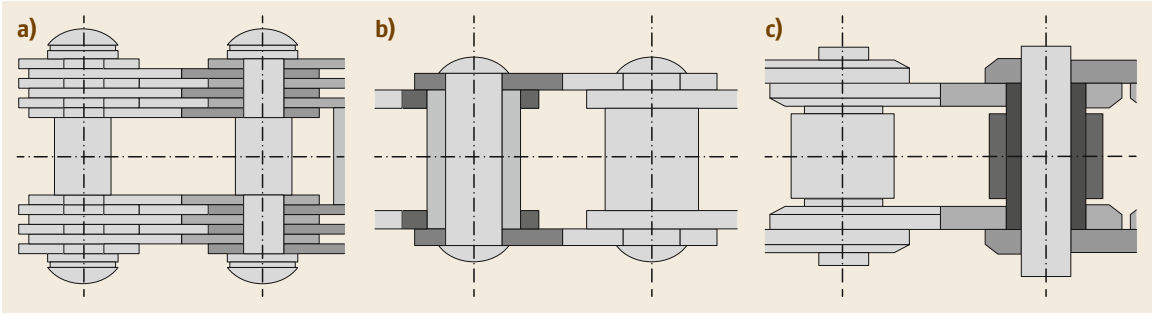

Fig. 20.40a–c General design of steel link chains: **(a)** leaf chain made out of several link plates and pin, **(b)** bush chain with link plates, pin and bush, and **(c)** roller chain with link plates, pin, bush, and roller

load. This causes a length change with a small plastic deformation, and thus a homogenization of the chain width and chain length.

Nominal sizes for round steel link chains vary in the different standards depending on their application. Generally, the chain size is defined by the nominal link thickness d and the pitch t, with typically $d = 4$–42 nm and a t/d ratio of 2.7–5. Chains that are driven by sprocket wheels should not exceed the value $t/d = 3$.

When labeling the strength characteristics of round steel link chains, the breaking force, production force, test force, and maximum operational force are defined by the standards.

Round steel chains for mining—according to DIN 22252 [20.57]—undergo an endurance test in addition to static testing. The criteria for discarding round steel link chains are based on wear (when the link thickness reaches 90% and the pitch increase t is about 2–5%).

In DIN 685-1, -2, -3, -4, -5, and -100 [20.58–63], the following application types of chain for use in transport machines are distinguished:

- Conveyor chains: DIN 762, 764, 766, calibrated [20.54, 64–66]
- Load chains (lifting chains): DIN 5684-1–3, calibrated [20.67–69]
- Sling chains: DIN 5687 (04/1996), usually not calibrated [20.70]
- Round steel chains for conveyor and extrication systems in mining: DIN 22252 [20.57], calibrated.

The main application fields for round steel link chains in continuous conveyors are bucket elevators, apron feeders, trough chain conveyors, tube chain conveyors, drag chain conveyors, overhead conveyors, and scraper conveyors.

Steel Link Chains

In the case of steel link chains, the rotational degree of freedom is spatially restricted. Such chains can mostly only be guided and diverted in two dimensions, rather than in all three dimensions like round steel link chains. Their structure, mainly consisting of link plates and pins, allows higher speeds and reliability as well as manyfold forms, which can be directly adopted, e.g., to the function of a continuous conveyor.

In comparison with round steel link chains, steel link chains have many fewer applications in the field of materials handling. They are not commonly used as hoisting or sling chains. Their use as lifting chains is mostly restricted to application in lift trucks. In materials handling, this type of chain is primarily used for continuous conveyors. However, the variety of different steel link chains is much greater than for round steel link chains. This section therefore focuses on the leaf chains standardized in ISO 4347 [20.71] and the conveyor chains standardized in ISO 1977 [20.72]. Furthermore, import chain designs for materials handling are presented. A very broad overview of the different types of steel link chain is provided in [20.53, 73].

Figure 20.40 shows the general steel link chain design consisting of link plates, pin, bush, and roller.

In a leaf chain, the pin is in direct contact with the link plates. Typically, two to eight link plates are used. Leaf chains therefore exhibit large breaking forces (up to 1500 kN), but the chain velocity is limited to 0.5 m/s due to high wear. Leaf chains are typically made from mild steel with low abrasion resistance (such chains are also called gall chains). If leaf chains are manufactured from unalloyed quality steels and low-alloyed high-grade steels, they can be heat treated and case hardened, which makes them more resistant to abrasive wear.

Typical conveyor steel link chains have link plates with a comparatively large pitch of 40–1000 mm. Such conveyor chains can normally be used without rollers or with larger roller wheels, which reduce the frictional forces during running. The conveyor chain can be used in trough conveyors or bucket elevators as a single- or double-stranded chain. The track width of double-stranded conveyor chains can be more than 2000 mm. Typical breaking forces range from 40 to 630 kN.

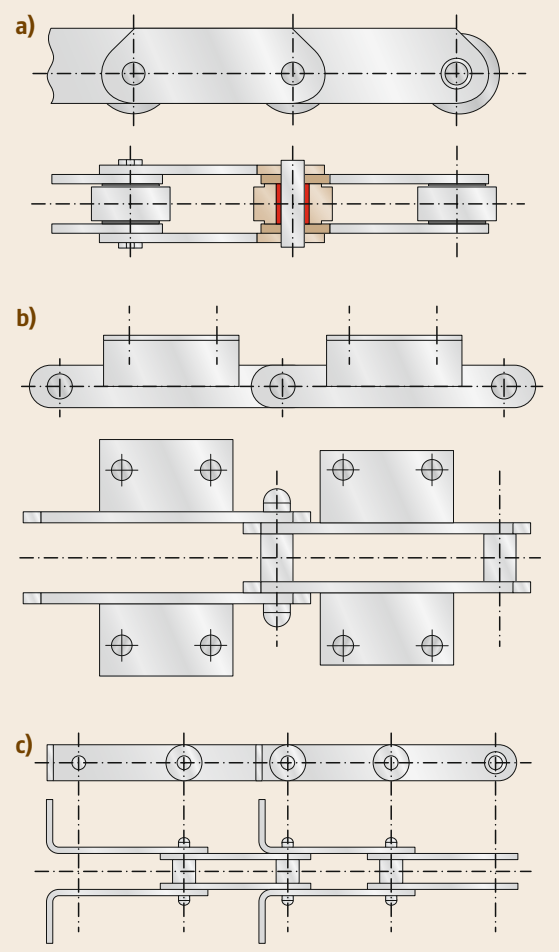

Fig. 20.41a–c Steel link chains with special link plates: **(a)** deep link chain, **(b)** link plate with horizontally cranked link plates for, e.g., bucket elevators and apron feeder-type conveyors, and **(c)** link plate with sidewards cranked link plates for, e.g., trough conveyors

Conveyor chains with cranked link plates (on one or both sides) allow the fastening of additional parts such as horizontal plates for the transport of general cargo (e.g., slat conveyors) as well as scraper blades or buckets for the transport of bulk materials. Figure 20.41 shows examples of such cranked steel link chains.

Besides the basic layout of the link plates, pins, bushes, and rollers, there are derived steel link chains for different purposes, e.g.:

- Top chains for continuous conveying of general cargo goods directly on top of the chain. Top chains can allow limited rotation around the vertical axis, thus enabling the realization of three-dimensional conveying routes. The top plate and the joint can be made out of steel or plastic. The use of modern plastic compounds with low friction, high strength, abrasion resistance, and—most importantly—low dead weight enables energy-efficient conveying. Due to their cost-efficient manufacturing process (injection molding), completely new chain designs are also possible [20.74, 75].
- Fork chains: Forged and hardened fork chains with high wear resistance and tensile strength that guarantees a long lifecycle for use in scraper and trough chain conveyors.
- Cardan chains: Chains with Cardan joints between the link plates, specially designed to allow three-dimensional routings for overhead (powered and free) conveyors.
- Chain belts are belt-like parts of continuous conveyors that consist of a series of chain links arranged to realize a certain width of the chain belt.

Drive and Redirection Wheels

Sprocket wheels are usually applied for the form-fitting drive of chains and thus the transmission of traction forces. The design of the sprocket, especially the tooth geometry, depends on the chain design. For round steel link chains, so-called pocket wheels are also available. At sprockets that support horizontal chain links (or free-standing vertical chain links), the forces at the points of contact are higher in comparison with the use of so-called pocket wheels with the support of vertical chain links (Fig. 20.42).

Wheels and slideways are used for guidance and redirection. Support rollers may be attached separately from the chain, in a support structure or on the chain itself. Different groove designs for guiding wheels or friction-type chain rollers for round steel link chains are possible (due to chain lubrication, a very low coefficient of friction $\mu = 0.06$–0.08 occurs for the frictional connection).

Polygonal sprockets (five- to eight-angular) are used for steel link chains with very large chain pitches.

20.3.3 Wheels and Track

Wheels and track are used across a wide range of materials transportation and handling systems due to their high energy efficiency. The most common application, of course, is trains (Chap. 12) used for long-distance transportation of goods and persons. In terms of conveying technology, wheels and tracks are used extensively in a number of materials handling systems. These uses can include the primary means for transportation in the cases of haulage skips, rail-supported conveyors, and rollers for the support of moving load support elements or, alternatively, for the movement of large

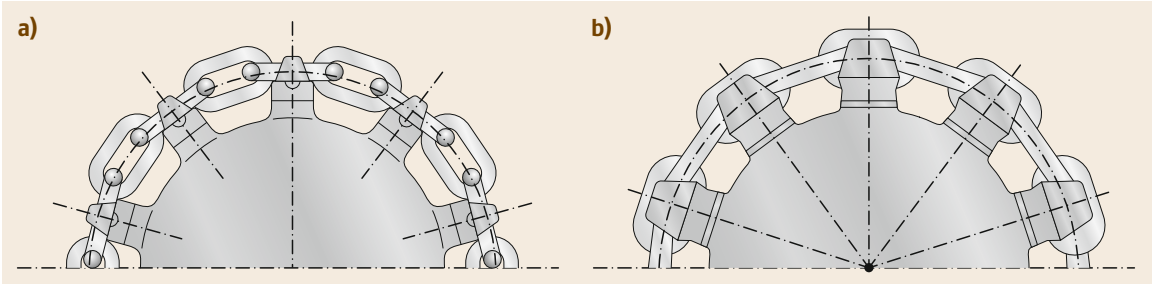

Fig. 20.42a,b Sprocket wheel (a) and pocket wheel (b) for driving round steel link chains

mobile materials handling equipment, such as cranes, stackers, and reclaimers, shuttle conveyors, trippers, and conveyor take-up pulleys.

Design

There are a variety of wheel types depending on the application and the type of track to be used. The combination of wheel and track determines the degree of axial restraint. Track wheel types include plain roller, and single- and double-flange track wheels, while typical grooved wheels include V and U profiles. The track is typically specific to the wheel, as shown in Fig. 20.43. Grooved track wheels are used in applications that require improved alignment accuracy, but they exhibit greater sliding friction, leading to increased friction and higher wear.

Wear

The high energy efficiency of wheel–track transportation is due to the low rolling losses between the hard surfaces of the wheels and track. This in turn leads to a relatively small contact area between the wheels and track, resulting in high contact stresses and wear. The interaction between the wheels and track is dependent on the profile of each element and determines the contact forces and relative motion between them. These forces and interactions induce cumulative damage to both the wheels and track. The contact stresses in the wheels may cause rolling contact fatigue in the surface layer or at subsurface locations, while the track may yield, leading to a change in its cross-sectional profile [20.76]. Tracks are subjected to a combination of local wheel contact stress and bending stresses.

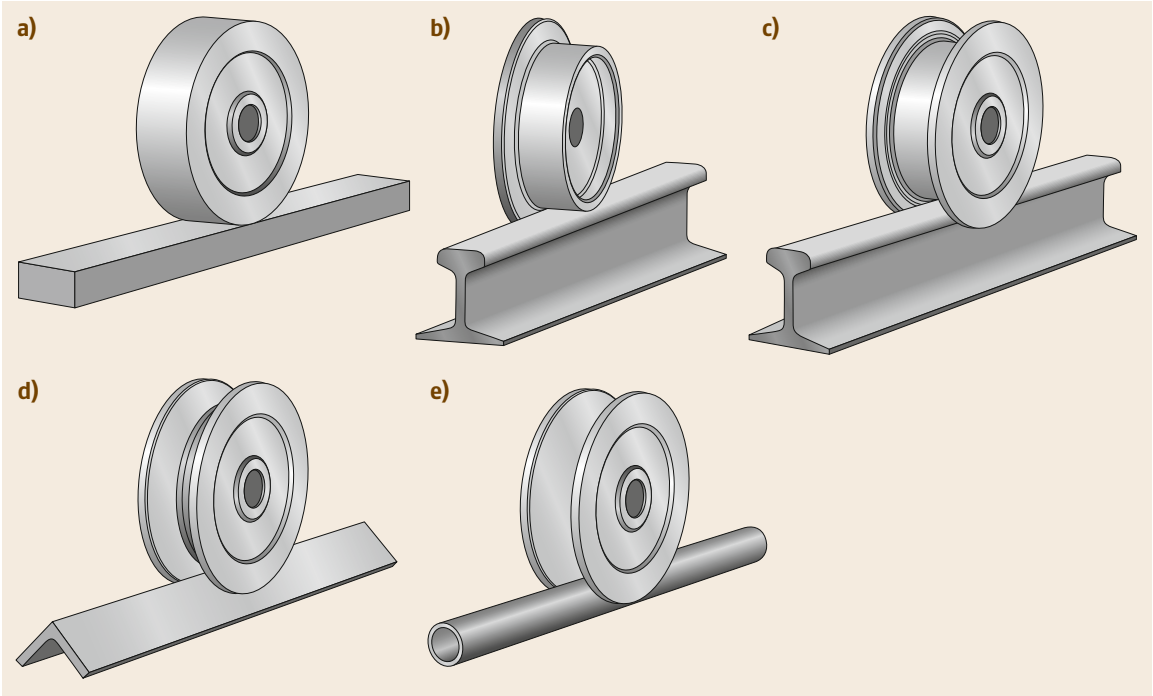

Fig. 20.43a–e Types of wheels and track: (a) plain roller track wheel, (b) single-flange track wheel, (c) double-flange track wheel, (d) V-groove track wheel, and (e) U-groove track wheel

Dimensioning

Rail wheels are dimensioned depending on the load of their running surface, while abrasion of the wheel flanges reduces their operational life. The criteria for calculating the compression strength is based on the exterior load that is endured during a certain number of rolling cycles. These criteria are derived from rolling element bearing and gear technology. The rail wheel size is selected to ensure that the wheel normal force N does not exceed the maximum force of

- The wheel body
- The shaft and
- The bearing.

The fundamental basis of wheel dimensioning is the Hertzian contact pressure for line and point contacts. For more information, refer to [20.52]. The dimensioning of crane wheels is standardized in ISO 16881 [20.77].

Rolling Resistance

The rolling resistance of a track wheel comprises a number of components, typically including:

- The resistance due to the rolling elements and lubrication in the bearings
- The seal resistance
- The rolling and sliding friction due to the interaction between the wheel and track (especially at the flanges)
- The energy loss due to the interaction of the track with its supporting structures.

The rolling resistance, or rolling friction, in relation to the track wheels is the force resisting the motion of the wheel as it rolls along the track. This resistance occurs since the energy of deformation is not fully recovered when the pressure is released. This results in hysteresis losses and an asymmetric pressure distribution in the contact zone that generates a moment that acts to retard the rolling motion. Additionally, rolling resistance can occur due to slip between the wheel and track, which dissipates energy. Like sliding friction, the rolling resistance is often expressed as a coefficient times the normal force.

Figure 20.44 shows a track wheel rolling on a track to the left at constant speed. N is the normal force, F is the pull force, r is the wheel radius, M_b is the rolling resistance moment from the bearing (depending on the bearing friction value μ_b and the shaft diameter d_s), and R is the force resulting from the nonuniform pressure at the wheel–track interface.

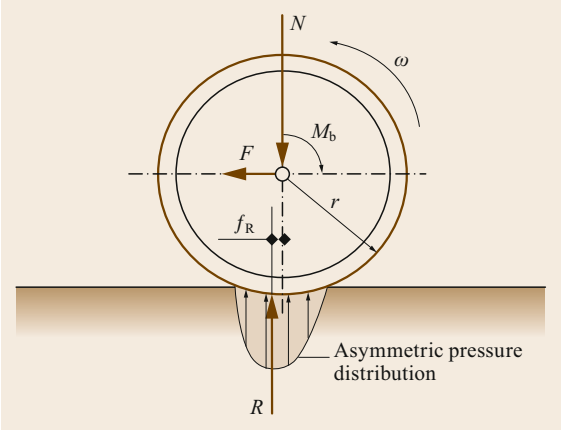

Fig. 20.44 Rolling resistance of a nondriven wheel

The contact pressure is shown, being greater towards the front of the wheel due to hysteresis. The eccentricity f_R of the resultant force R is often described as the *arm of the rolling friction*. The ratio of f_R to the wheel radius is defined as the rolling friction coefficient, often being used in the field of transport engineering. However, in the field of materials handling, this approach is also used to calculate the motion resistance for different (e.g., roller and wheel) conveyors. In these applications, a wider variety of goods are handled (e.g., wooden pallets on steel rollers), hence the definition of a material-dependent f_R value is more established.

Note that, in this simplified case, the energy loss due to the interaction of the track with its supporting structures is neglected.

The rolling resistance force, F_R, without consideration of the influence of the flange, can be expressed as

$$F_R = C_{rr}N + \frac{M_b}{r} = \frac{f_R}{r}N + \mu_b \frac{d_s}{2}\frac{1}{r}N\,, \qquad (20.26)$$

where

C_{rr} rolling resistance coefficient
N normal force
f_R arm of the rolling friction
μ_b friction value for the bearing
d_s shaft diameter

Typical values for μ_b are

$\mu_b = 0.003$ for roller bearings
$\mu_b = 0.08$ for plain bearings

Table 20.3 presents typical values of the rolling resistance coefficient for a number of track wheel applica-

Table 20.3 Rolling friction coefficients

Rolling friction coefficient C_{rr}	Description
0.0010–0.0024 [20.78, 79]	Railroad steel wheel on steel rail
0.0019–0.0065 [20.80]	Mine-car cast iron wheels on steel rail
0.005	Dirty tram rails with straights and curves
0.0045–0.008	Large truck tires
0.010–0.015 [20.81]	Passenger car tires on concrete

Table 20.4 Arm of the rolling friction for different material pairings

Material pairing	f_R (mm)
Steel/steel	0.5
Steel/steel (both hardened)	0.01
Wood/steel (roller conveyor)	1.2
Plastic/steel	2
Hard rubber/steel	7
Plastic/concrete	5
Hard rubber/steel	10–20
Medium hard rubber/steel	15–35

Table 20.5 Approximated virtual running friction coefficient for wheel/track systems in materials handling (valid for wheel diameters of 200–1250 mm) [20.52]

Wheel	Plain bearing	Roller bearing
Without flange	0.02	0.006
With flange, lubricated	0.025	0.009
With flange, not lubricated	0.030	0.012

tions, with truck and passenger vehicle tires included for comparison.

Table 20.4 presents typical f_R values for certain material pairings commonly used in the field of materials handling.

In the field of materials handling, the influence of the flange can be estimated via a flange factor κ according to [20.52]. Hence, the complete equation (20.26) can be extended to

$$F_R = N \underbrace{\left(\frac{f_R}{r} + \frac{\mu_b d_s}{2r} + \kappa \right)}_{\mu_t} . \qquad (20.27)$$

According to [20.52], κ values of 0.001–0.005 are typical, while the use of roller bearings results in lower κ values (0.001–0.002). To facilitate the calculation of the motion resistance, it is common in materials handling to summarize the bracketed term in (20.27) using a virtual running friction coefficient at the track μ_t. Typical virtual running friction coefficients are presented in Table 20.5.

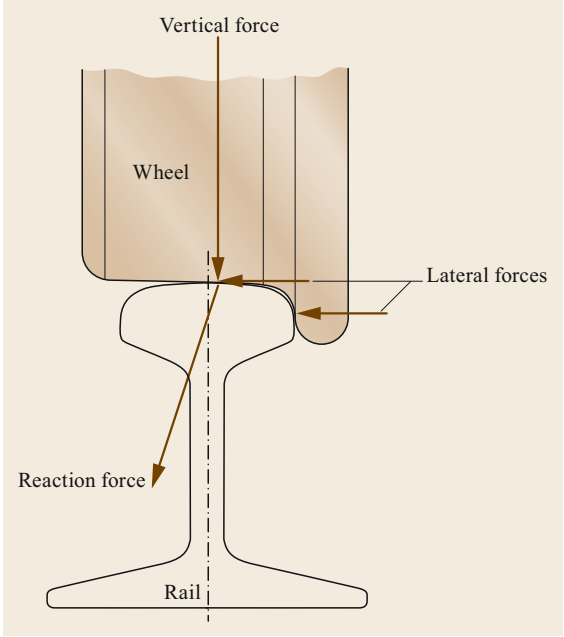

Fig. 20.45 Forces acting on a tapered rail wheel

Rail Wheels and Tracks

A rail wheel is a type of track wheel specially designed for use on rail tracks, for example, train wheels. Rail wheels are typically made of cast or forged steel heat-treated to a specific hardness, although Nylon and polyurethane can be used for applications operating under light loads, such as rail running conveyors. For self-guidance purposes, rail wheels are generally tapered and fixed to a common axle to form a wheelset. Rail wheels have a flange on one side to prevent wheel climb and possible derailment when the limits of the geometry-based alignment are reached.

Rails are typically made from hot-rolled steel with a cross sectional profile like that shown in Fig. 20.45. The rail head profile is designed to minimize wear, while the rail foot is designed to suit the supporting structure.

Figure 20.45 shows a free body diagram of the forces acting on a tapered rail wheel.

20.4 Continuous Conveyors

The continuous transport of goods without the need for nonloaded operation modes defines this large group of conveyors. As described in [20.82], manyfold different working principles are available to convey general cargo goods or bulk materials from a feeding point (inlet) to an outlet. Many of these conveyors allow the use of several in- and outlet points. However, the conveying route is very often fixed and can hardly be changed. Continuous conveyors are therefore usually permanently installed and much less mobile than common discontinuous conveyors (e.g., forklift trucks).

As described in Sect. 20.1, a throughput or volumetric flow rate, or rather a mass flow rate, is used to characterize the performance of a conveyor. The calculation of the power consumption for any continuous conveyor can be traced back to the analysis of the motion resistance, which depends on the physical effects of the conveying principle, the character of the goods, but also on the conveyor route. The routing of continuous conveyors is often adapted to the requirements of the environment. This can be the natural topography of the landscape for long belt conveyors, called overland conveyors, but consideration of the surrounding machines or plants can also strongly influence the conveyor routing. The calculation of the motion resistance for conveyors can even be done for complex routings by breaking down the conveyor routing into a number of parts, as shown in Fig. 20.46. In the calculations for these parts, the motion resistance should change only steadily.

Mechanical conveyors are the largest group of continuous conveyors, as shown in Fig. 20.47. The understanding of the working and calculation principles of this group will be increased if the tension and supporting devices are identified as the main components. While the tension device is responsible for the transmission of the motion resistance to the drive, the supporting device takes up the gravitational forces (for horizontal conveying).

The sum of all the motion resistances, or respectively the sum of all the energy losses during transport occurring over the whole conveyor route, defines the power consumption of the conveyor drive. The general power consumption P_n of a conveyor drive can be cal-

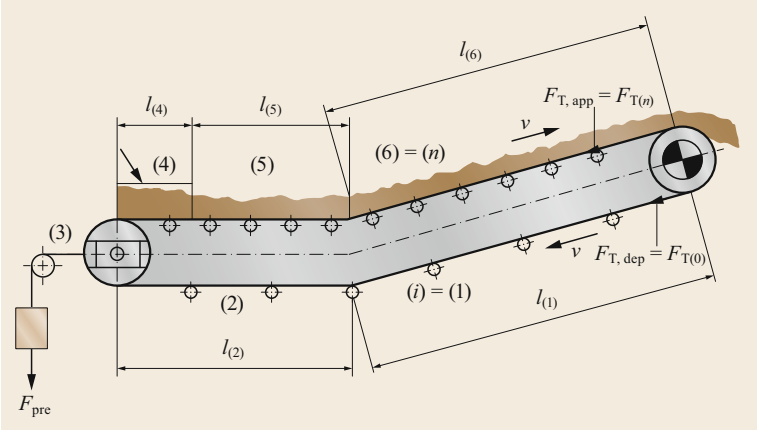

Fig. 20.46 Breaking down the routing of a belt conveyor into six calculation parts *i*

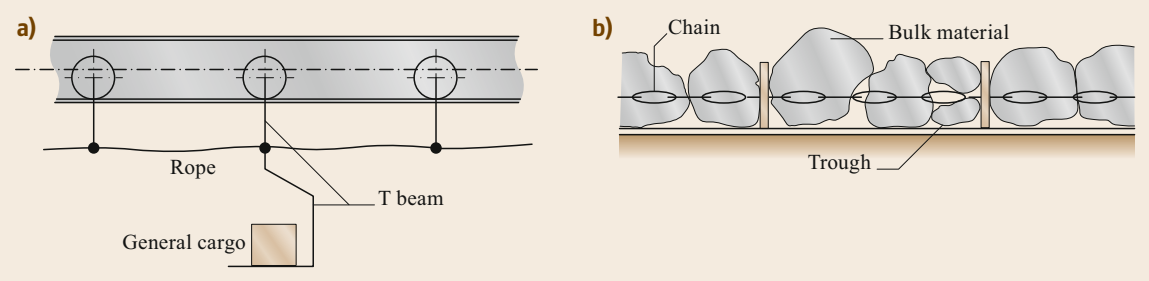

Fig. 20.47a,b General identification of main components of continuous mechanical conveyors using the examples of **(a)** an overhead conveyor (tension device: rope; support device: T beam; goods: general cargo) and **(b)** a scraper conveyor (tension device: chain; support device: trough; goods: bulk material)

culated as

$$P_n = \frac{F_{\text{total}}\, v}{\eta_{\text{drive}}}\,, \tag{20.28}$$

where

F_{total} sum of all motion resistances occurring over the conveyor route
v conveying speed
η_{drive} total efficiency of the used drive.

20.4.1 Belt Conveyors

Belt conveyors play a major role in bulk materials handling operations. They combine versatility and reliability and, in view of their inherent simplicity of operation, are suited to the conveying of a wide range of bulk materials. They may be used effectively for the movement of bulk materials over both short and long distances. In the latter case, the adaptability of their design and construction permits them to operate over undulating terrain.

The first documented use of belt conveyors dates back to 1830, when sawmills used flat belts sliding in steel troughs to transport refuse away from milling operations. The grain industry further developed belt conveyors in the 1850s, replacing the trough with a series of pulleys, with end disks separated by bent bars to form a cupped shape in order to hold leather belts. Further developments occurred from 1860 to 1880, leading to the introduction of wooden drums with shafts supported by bearings [20.83].

Conveyor belts were first employed to transport heavy bulk materials in 1891. Thomas Edison first used flat belts to transport iron ore, but the cotton belts and wooden idlers wore quickly due to the heavy abrasive ore. In the same year, Thomas Robbins worked with Edison to develop the first rubber-covered belt, consisting of a cotton duck belt with a $1/8''$ rubber cover. This greatly improved both the belt and roll life. Soon thereafter, Robins went on to develop the three-roll troughing idler set (Fig. 20.48a). These two innovations (the rubber-covered belt and the three-roll troughing idler set) established the foundations for modern belt conveying technology [20.83].

In addition to the ongoing development of conventional troughed belt conveyors, there has been much advancement of belt conveying technology with the development of specialized belt conveyors. These include pipe conveyors, air-supported conveyors, pouch conveyors, pocket conveyors, and cable- and rail-supported belt conveyor systems (Fig. 20.48). This array of specialized belt conveying systems provide the flexibility and advantages of continuous conveying in situations where conventional troughed belt conveyors are not technically or economically feasible.

There is no doubting the significant role that belt conveyors have, and will continue to play, in bulk materials handling operations throughout the world. Belt conveyors are by far the most widespread bulk material transportation system used across the mining, mineral processing, and power generation industries. Their continuous mode of operation makes them highly desirable for automated mining activities, and this continues to drive the technology towards higher capacities and longer transportation distances.

Design procedures in general are based on handbooks, for example, the North American Conveyor Equipment Manufacturers' Association Handbook [20.83] or standards such as ISO 5048 [20.86] and DIN 22101 [20.87]. The material presented in this section is intended to give an overview of the conventional approach to steady-state belt conveyor design.

Belt Carrying Capacity

The carrying capacity, or mass flow rate, of a belt conveyor is given by

$$Q_{\text{m}} = A v \eta_{\text{F}} \rho_{\text{b}} k \cos\alpha\,, \tag{20.29}$$

where

A cross-sectional area of material on the belt
v belt velocity
η_{F} filling efficiency
ρ_{b} bulk density of material
k slope factor
α slope angle

Considering the low inclination and declination angles of belt conveyors, the effect of slope on capacity is minimal. The capacity may therefore be expressed simply as

$$Q_{\text{m}} = A v \eta_{\text{F}} \rho_{\text{b}} k\,. \tag{20.30}$$

The cross-sectional area depends on the belt width and idler configuration. In general, the cross-sectional area is a function of the contact perimeter, b, of the material

Fig. 20.48a–h Different types of belt conveyor system: **(a)** conventional troughed belt conveyor, **(b)** pipe belt conveyor, **(c)** pouch belt conveyor, **(d)** air-supported belt conveyor, **(e)** pocket belt conveyor [20.5], **(f)** cable belt conveyor [20.84], **(g)** RopeCon® conveyor [20.5], and **(h)** rail conveyor [20.85] (reprinted by permission of Taylor & Francis Ltd.) ►

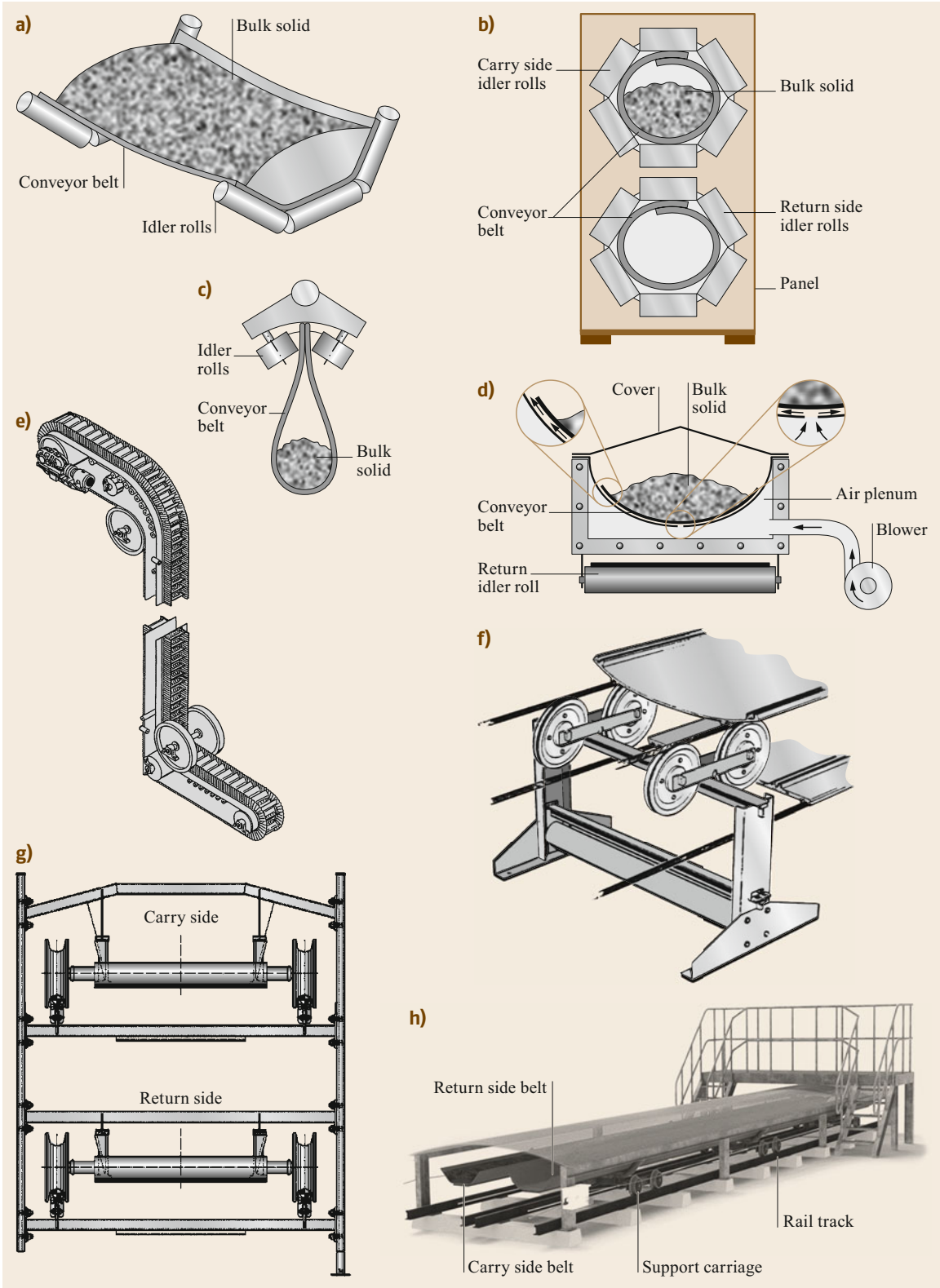
a)
Bulk solid
Conveyor belt
Idler rolls
b)
Carry side idler rolls
Bulk solid
Conveyor belt
Return side idler rolls
Panel
c)
Idler rolls
Conveyor belt
Bulk solid
d)
Cover
Bulk solid
Air plenum
Conveyor belt
Blower
Return idler roll
e)
f)
g)
Carry side
Return side
h)
Return side belt
Rail track
Carry side belt
Support carriage

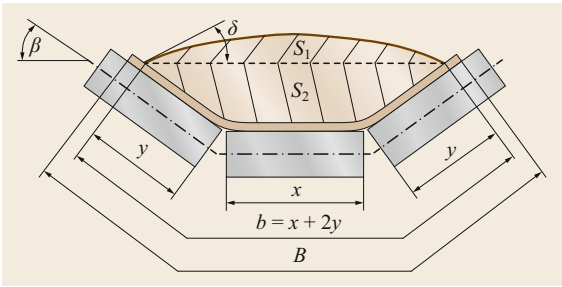

Fig. 20.49 Cross-sectional profile for a three-roll idler configuration

on the belt and can be expressed as

$$A = Ub^2 \,, \tag{20.31}$$

where

b contact perimeter
U nondimensional cross-sectional area shape factor

Expressions for the shape factor can be readily determined from the geometry of the cross section of the material on the belt, and for a three-idler roll configuration assuming symmetric loading and a surcharge with parabolic shape, as shown in Fig. 20.49, it can be shown that

$$U = \frac{1}{(1+2\lambda)^2}\left\{\lambda \sin\beta + \frac{\lambda^2}{2}\sin 2\beta + \frac{\tan\delta}{6}[1 + 4\lambda\cos\beta + 2\lambda^2(1+\cos 2\beta)]\right\} , \tag{20.32}$$

where $\lambda = y/x$.

Belt Width. For a given idler configuration and hence shape factor U together with a given belt speed, the necessary value of the contact perimeter b can be determined. The corresponding minimum belt width $B_{\min}$ from ISO 5048 [20.86] and DIN 22101 [20.87] is

$$\begin{aligned} B_{\min} &= 1.1b + 0.05 \quad \text{for } B_{\min} \le 2\,\text{m} \,, \\ B_{\min} &= b + 0.25 \quad \text{for } B_{\min} > 2\,\text{m} \,. \end{aligned} \tag{20.33}$$

It is necessary, of course, to select a standard belt width, B, where $B \ge B_{\min}$.

Belt Speed. Belt speeds depend largely on the characteristics of the material to be conveyed, the capacity or throughput, and the belt tension. Low speeds may be necessary to minimize dust lift-off in the case of powdery materials or to prevent fracture in the case of fragile materials. Limitations in speed may also be necessary to minimize belt wear and abrasion and to maintain satisfactory belt tracking. In addition, belt speeds have an influence on the effectiveness and maintainability of conveyor transfer points.

Belt Surcharge Angle. The belt surcharge angle, δ, for the bulk material is best measured, but may be estimated from a variety of references; for example, [20.83] approximates the surcharge angle to be 5°–15° less than the angle of repose θ_r of the bulk solid, ISO 5048 [20.86] assumes a value of 75% of the angle of repose, while *Colijn* [20.88] provides the empirical relationship

$$\delta = 1.11\theta_r - (0.1\beta + 18^\circ) \,, \tag{20.34}$$

where

θ_r angle of repose
β troughing angle

Belt Slope Factor. The slope factor, k, is determined by taking into account the decrease of the surcharge (top parabolic) section, S_1, when material is fed onto an inclined part of a belt

$$\begin{aligned} S_1 &= [x + (b-x)\cos\beta]^2 \frac{\tan\delta}{6} \,, \\ S_2 &= \left[x + \left(\frac{b-x}{2}\right)\cos\beta\right]\left[\left(\frac{b-x}{2}\right)\sin\beta\right] \,, \\ A &= S_1 + S_2 \,. \end{aligned} \tag{20.35}$$

The slope factor, k, is given by

$$k = 1 - \frac{S_1}{S_2}(1 - k_1) \,, \tag{20.36}$$

where k_1 is the reduction factor of the surcharge portion. For uniformly loaded, properly aligned conveyors handling middle lump size material, k_1 can be approximated as

$$k_1 = \sqrt{\frac{\cos^2\alpha - \cos^2\delta}{1 - \cos^2\delta}} \,. \tag{20.37}$$

When $\alpha = \beta$, the surcharge section S_1 becomes nonexistent and only the lower section S_2 can be utilized.

Bulk Material Characteristics. The carrying capacity shape factors presented in this section are idealized inasmuch as they do not take into account the particle size or distribution of the material being conveyed. The lump size may in some cases influence the belt width; the reader is referred to [20.83] for further information.

Resistances to Motion

The power required to convey a bulk material is utilized to overcome several resistances to motion that are present. These resistances include all those resulting from friction, the slope of the conveyor, and the need to accelerate the material onto the belt at the feed or intake end. Some of these resistances make major contributions as they occur along the length of the conveyor, while others are localized, such as those associated with the feeding and discharge of the material. The latter can often have a negligible effect.

Belt conveyor resistances are classified into five groups according to ISO 5048 [20.86] and DIN 22101 [20.87]:

- Main resistances F_H
- Secondary resistances F_N
- Special main resistances F_{S1}
- Special secondary resistances F_{S2}
- Slope resistance F_{St}.

The main and secondary resistances, F_H and F_N, occur on all belt conveyors, while the special resistances, $F_S = F_{S1} + F_{S2}$, are only present for certain installations. The main resistances F_H and F_{S1} occur continuously along the belt conveyor, whereas the secondary resistances F_N and F_{S2} are only present locally. The slope resistance F_{St} may have a positive, zero, or negative value, depending on the gradient of the conveyor. Furthermore, they can occur in a continuous manner along the whole conveyor or only arise in some sections along its length.

Main Resistances, F_H. The main resistances occur continuously along the length of the conveyor and include:

- The rotational resistance of the idler rolls due to the friction in the bearings and seals
- The indentation rolling resistance due to the deformation of the belt bottom cover as it passes over the idler rolls due to the weight of the belt and bulk material
- The flexure resistance of the conveyor belt and bulk solid due to the cyclic transverse and longitudinal movement as the belt progresses from one idler set to the next.

Figure 20.50 illustrates the main resistances of a belt conveyor and their location along the length of the system.

In view of the complexities of the main resistances of belt conveyors, ISO 5048 [20.86] and DIN 22101 [20.87] combine the above-mentioned components and express the resistance to motion in terms of an artificial Coulomb-type friction coefficient, f. Hence, the resistance to moving the empty belt is

$$F_{H1} = (q_{ro} + q_{ru} + 2q_b \cos\alpha) fLg \,, \tag{20.38}$$

where

q_{ro} mass per unit length of rotating parts of idler rolls along carrying side of conveyor
q_{ru} mass per unit length of rotating parts of idler rolls along return side of conveyor
q_b mass per unit length of conveyor belt
α slope angle
L belt conveyor length (center to center)
g acceleration due to gravity
f artificial friction coefficient

The resistance to moving the bulk material horizontally is

$$F_{H2} = q_m \cos\alpha fLg \,, \tag{20.39}$$

where

q_m mass of bulk material conveyed per unit length
$q_m = Q_m/v$

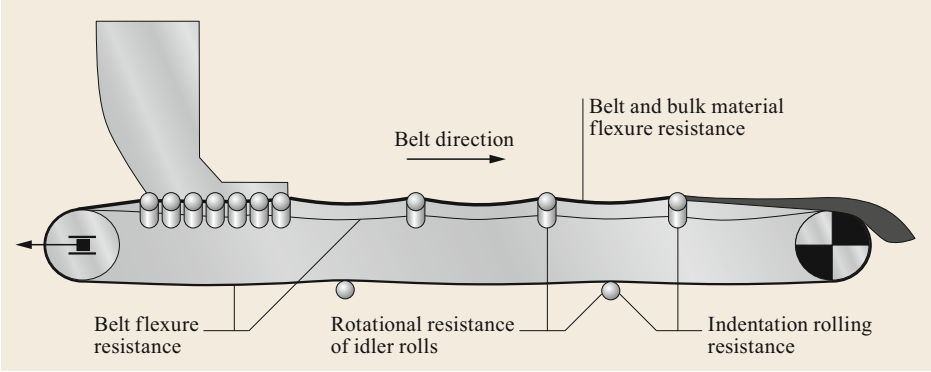

Fig. 20.50 Main resistances of a belt conveyor

Table 20.6 Guidance for selection of artificial friction coefficient, f, according to DIN22101 [20.87]

Characteristic	Classification		
Internal friction of bulk material	Medium	Low	High
Conveyor alignment	Medium	Good	Poor
Belt tension	Medium	High	Low
Operational conditions (dusty, cohesive)	Medium	High	Low
Idler roll diameter (mm)	108–159	> 159	< 108
Carry-side idler roll spacing (m)	1.0–1.5	< 1.0	> 1.5
Return-side idler roll spacing (m)	2.5–3.5	< 2.5	> 3.5
Belt speed (m/s)	4–6	< 4	> 6
Troughing angle (°)	25–35	< 25	> 35
Ambient temperature (°C)	15–25	> 25	< 15
Friction factor	Normal value ≈ 0.020	Results in a decrease of the friction factor f down to ≥ 0.010	an increase up to ≤ 0.040

The nominal value of the artificial friction coefficient, f, has been calculated to be 0.02, but it may be higher or lower according to the system configuration, belt construction and properties, idler roll construction and diameter, properties of the bulk material being conveyed, operating and maintenance conditions, and environmental conditions. Several methods and standards exist to predict and directly measure the individual components of the main resistance, in particular the idler roll rotating resistance and conveyor belt indentation rolling resistance. For methods to predict the idler roll rotating resistance, the reader is referred to [20.83, 89], while direct measurement methods are detailed in [20.83] and DIN 22112-3 [20.90]. Similarly, for the indentation rolling resistance of the conveyor belt, methods for direct measurement using large-scale belt samples are described by *Munzenberger* et al. [20.91], AS 1334-13 [20.92], and DIN 22123 [20.93], while *O'Shea* et al. [20.94] provide an analytical approximation. The bulk material flexure resistance, due to the difficulty in its isolation and measurement, is typically predicted using numerical methods, such as coupled continuum and finite difference [20.95] and coupled finite element and discrete element methods [20.96].

Table 20.6 provides guidance for selecting the artificial friction coefficient according to DIN 22101 [20.87].

According to ISO 5048 [20.86] and DIN 22101 [20.87], for downhill conveyors that require braking as a safety measure, an f value lower by 40% than that for a driven belt conveyor should be used.

Secondary Resistances, F_N. Secondary resistances are localized and include the effects of:

- Inertial and frictional resistances due to the acceleration of the material at the loading area
- Resistance due to the friction on the side walls of the chute at the loading area
- Pulley bearing resistance with the exception of the driving pulley bearings
- Resistance due to the wrapping of the belt on the pulleys.

According to ISO 5048 [20.86] and DIN 22101 [20.87], for long-center-distance conveyors (for example, over 80 m), the secondary resistances are of low order compared with the main resistances and can be calculated in a simplified way, without serious error. To account for the secondary resistances, a coefficient C that is dependent on the length of the belt conveyor is introduced. The determination of the coefficient C is discussed in the next section.

Special Main Resistances, F_{S1}. Special main resistances are present only in certain installations, but when present they occur continuously along the length of the conveyor and include:

- Drag resistance due to forward tilt of the idler in the direction of movement of the belt
- Resistance due to the friction against chute flaps or skirt plates, when present along the full length of the belt.

Special Secondary Resistances, F_{S2}. Special secondary resistances are present only in certain installations, are localized, and include:

- Resistance due to friction with belt and pulley cleaners
- Resistance due to friction with the chute flaps or skirt plate, when present along part of the length of the belt

- Resistance due to inverting the return strand of the belt
- Resistance due to discharge plows
- Resistance due to trippers.

Slope Resistance, F_{St}. The slope resistance results from the change in potential energy of the bulk material and belt and is given by

$$F_{St} = \pm(q_m + q_b)Hg\,, \tag{20.40}$$

where

H net change in elevation
$+$ denotes raising the material
$-$ denotes lowering the material

Driving Force

From the foregoing, an expression can be developed for the peripheral driving force, F_u, at the driving pulley(s). The total sum of the resistances present is given by

$$F_U = F_H + F_N + F_{S1} + F_{S2} + F_{St}\,. \tag{20.41}$$

When determining the driving force, the sum of the slope resistance of the belt is zero

$$F_U = fLg[q_{ro} + q_{ru} + (2q_b + q_m)\cos\alpha] + F_N + F_{S1} + F_{S2} \pm q_m Hg\,. \tag{20.42}$$

When the conveyor slope is less than about 18°, its effect is negligible, thus $\cos\alpha \approx 1$. Note that $\alpha = 18°$ generally represents the upper limit for smooth surface belt conveyors. If the conveyor slope angle exceeds 18°, the loads q_b and q_m should be multiplied by $\cos\alpha$.

As noted above, for long-center-distance conveyors (for example, over 80 m), the secondary resistances are of low order compared with the main resistances and can be calculated in a simplified way, without serious error. ISO 5048 [20.86] and DIN 22101 [20.87] introduce a coefficient, C, given by the ratio

$$C = \frac{F_H + F_N}{F_H}\,. \tag{20.43}$$

The conveyor driving force, F_U, can then be expressed as

$$F_U = CfLg[q_{ro} + q_{ru} + (2q_b + q_m)] + F_{S1} + F_{S2} \pm q_m Hg\,. \tag{20.44}$$

The secondary resistance coefficient, C, depends on the length of the conveyor, L, and is plotted in Fig. 20.50. The values plotted are derived from tests carried out on a variety of installations. The graph shows that, when calculating values of C, reliable values for the peripheral force at the driving pulley can only be obtained for conveyor lengths over 80 m.

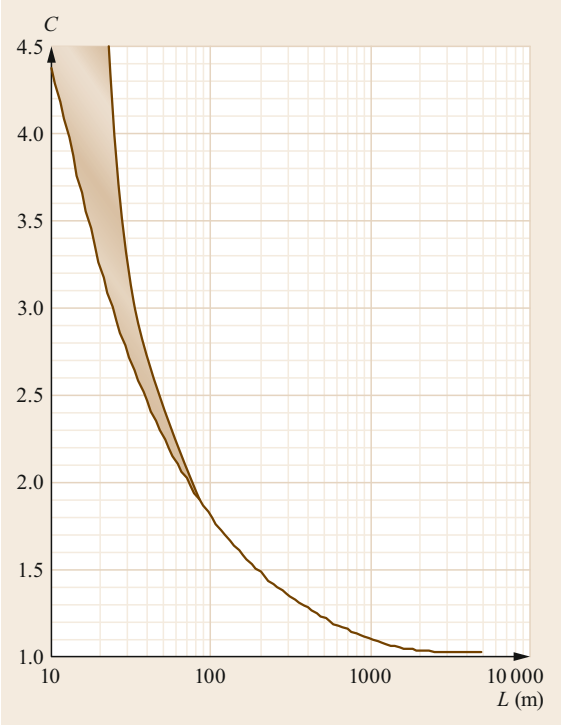

Fig. 20.51 Secondary resistance coefficient C, versus conveyor length L (ISO 5048 [20.86] and DIN 22101 [20.87])

For center distances of less than 80 m, the value of the coefficient C becomes uncertain, as indicated by the shaded area in Fig. 20.51. The uncertainty on the coefficient C for short-center conveyors is due to the large secondary resistances of such installations. The broken lines for the coefficient C do not represent boundary curves but rather indicate the growing uncertainty on C. For more precise calculations of the driving power of belt conveyors with center distances of less than 80 m, the reader is referred to ISO 5048 [20.86] and DIN 22101 [20.87].

For numerical computational purposes, an appropriate expression for C is

$$C = 0.85 + 13.31L^{-0.576} \quad \text{for } 80\,\text{m} \le L < 1500\,\text{m}\,,$$
$$C = 1.025 \quad \text{for } 1500\,\text{m} \le L \le 5000\,\text{m}\,. \tag{20.45}$$

This calculation of the peripheral driving force, F_U, is suitable for a uniformly and continuously loaded belt conveyor. Where the conveyor installation experiences

slope changes and/or partial loading, ISO 5048 [20.86] states that the peripheral driving force should be calculated for the full range of different operating conditions, for example:

- Empty
- Fully loaded along the length of the conveyor
- Loaded on the rising, level, and slightly descending runs, where each section requires a positive driving force, and empty on the remaining sections that would be regenerative if loaded
- Loaded on regenerative sections, and empty on sections that would require a positive driving force if loaded.

If one or more loading condition results in a negative driving force (i.e., the system becomes regenerative), the artificial friction coefficient, f, must be lowered by 40%. In these cases, the highest positive driving force and greatest negative braking force will be considered in the design of the driving and braking systems.

Operating Power Requirements

The operating power required at the driving pulley(s) is

$$P_A = F_U v \,. \tag{20.46}$$

The driving, or motor power, P_M, taking into account the efficiency, η, of the transmission equipment is as follows:

For conveyors requiring positive power

$$P_M = \frac{P_A}{\eta_1} \,. \tag{20.47}$$

For regenerative conveyors

$$P_M = P_A \eta_2 \,, \tag{20.48}$$

where

η_1 is generally selected between 0.90 and 0.98
η_2 is generally selected between 0.95 and 1

The selection of the efficiency factor, η, of the transmission equipment depends on the number and type of elements in the drive train, such as the gearbox and fluid coupling. Where multiple elements exist in series, their efficiencies are multiplied together.

Drive Tension Relationships and Belt Forces

The force required to drive a belt must be transmitted from the drive pulley, or pulleys, to the belt by means of friction between the two surfaces, as shown in Fig. 20.52. In the case of a downhill regenerative-type conveyor, the force is transmitted in exactly the same way but in the reverse sense. As in any belt drive arrangement, the power transmitted results from the difference in tension between the belt that approaches and the belt that departs the drive pulley.

Where power is transmitted from the pulley to the belt, the approaching portion of the belt will have a higher tension F_1 while the departing portion will have a lower tension F_2. In a regenerative situation, the power is transmitted from the belt to the pulley, and in this case, F_1 will be the departing-side tension and F_2 the approaching-side tension.

Figure 20.52 shows a single- and dual-pulley conveyor drive. With a single-pulley drive, the angle of wrap is limited to 180°, but this can be increased up to 240° by using a snub pulley, with much greater effective wrap angles being achievable using dual drives.

The drive tension relationship for a single-drive pulley is

$$F_U = F_1 - F_2 \tag{20.49}$$

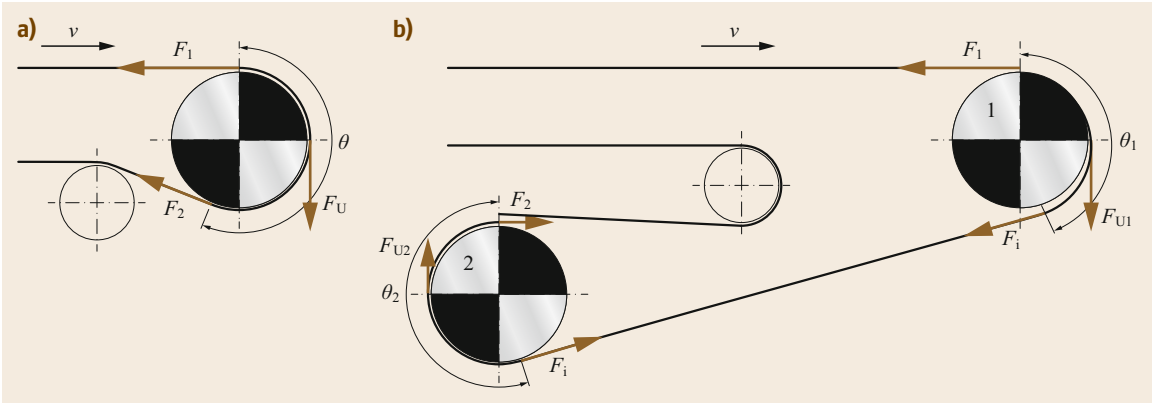

Fig. 20.52 **(a)** Single- and **(b)** dual-drive pulley tension relationship (F_i is the intermediate tension)

Table 20.7 Friction coefficient, μ, between driving pulley and belt (ISO 5048 [20.86] and DIN 22101 [20.87])

Operating condition	Pulley surface			
	Bare steel pulley (smooth)	Polyurethane lagging (herringbone grooves)	Rubber lagging (herringbone grooves)	Ceramic lagging (herringbone grooves)
Dry	0.35–0.4	0.35–0.4	0.4–0.45	0.4–0.45
Wet (pure water)	0.1	0.35	0.35	0.35–0.4
Wet (contaminated)	0.05–0.1	0.2	0.25–0.3	0.35

and

$$\frac{F_1}{F_2} \leq e^{\mu\theta} , \tag{20.50}$$

where

F_1 tight-side tension
F_2 slack-side tension
θ angle of wrap
μ effective friction coefficient

Meanwhile, the dual-drive tension relationship is

$$F_U = F_{U1} + F_{U2} \tag{20.51}$$

and

$$\frac{F_{U1}}{F_{U2}} = e^{\mu\theta_2} \frac{e^{\mu\theta_1} - 1}{e^{\mu\theta_2} - 1} . \tag{20.52}$$

The effective friction coefficient between the driving pulley and the belt depends on the conveyor operating condition and the pulley surface, being given by ISO 5048 [20.86] and DIN 22101 [20.87] as shown in Table 20.7.

To transmit the peripheral drive force, F_U, from the drive pulley to the belt, it is necessary to maintain a minimum F_2 on the return-side belt during startup and braking of the fully loaded conveyor. The minimum F_2 for driving is given by

$$F_{2,min} \geq F_{U,max} \frac{1}{e^{\mu\theta} - 1} , \tag{20.53}$$

where

$F_{U,max}$ maximum peripheral force that typically occurs during starting up or braking the fully loaded belt conveyor

During startup and braking, the peripheral force will be higher than during steady-state operation. To determine the forces during startup and braking, the reader is referred to ISO 5048 [20.86] and DIN 22101 [20.87].

Force to Limit Belt Sag. It is important that the idler spacing be such that the belt sag is limited between successive idler sets. The minimum tensile force to limit sag between idler sets is given as follows:

For the carrying-side belt

$$F_{min} \geq \frac{a_0(q_b + q_m)g}{8k_s} . \tag{20.54}$$

For the return-side belt

$$F_{min} \geq \frac{a_u q_b g}{8k_s} , \tag{20.55}$$

where

a_0 distance between carrying-side idler sets
a_u distance between return-side idler sets
k_s allowable belt sag ratio, typically between 0.005 to 0.02, depending on the belt properties

Force Variation. The tensile force distribution along the length of the belt conveyor is determined for each load case by suitably adding to, or subtracting from, the minimum forces acting on the belt the resistances to motion, the forces due to the weight of the belt and bulk material, and the peripheral forces applied to the drive pulley(s). The minimum tensile force is determined from either the minimum slack-side tension, $F_{2,min}$, required to drive the belt without slip or the minimum tensile force, F_{min}, to limit the sag between idler sets. Typically, $F_{max} = F_1$, the tight-side tension, but this is not always the case, and each conveyor configuration must be examined separately.

Conveyor Belt

The ultimate strength of conveyor belts is usually expressed in kN per meter width per ply for fabric-reinforced belts and in kN per meter width for steel-cord-reinforced belts. In addition to the maximum strength, belt selection is also determined by the maximum permissible length change of the belt during operation, the properties of the bulk material, the operating and loading conditions, and in the case of fabric belts, the minimum number of plies to support the load and the maximum number of plies for troughing.

Belt Constructions. The reinforcement within a conveyor belt is referred to as the carcass. The carcass not only provides the tensile strength of the belt but must also

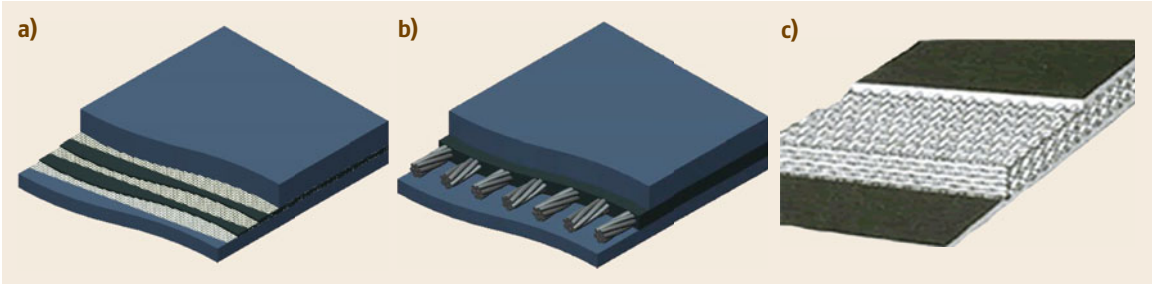

Fig. 20.53a–c Typical conveyor belt carcass constructions: **(a)** fabric ply conveyor belt, **(b)** steel cord conveyor belt, and **(c)** solid woven conveyor belt [20.97]

absorb the impact of the bulk material being loaded onto the belt, provide lateral stiffness to support the load, and provide adequate strength for the splice. Conveyor belt carcasses are typically categorized as either fabric ply, solid woven, or steel cord. Figure 20.53 shows the typical range of carcass constructions for belt conveyors.

Safety Factors for Belt and Splice. The operating strength of a conveyor belt is influenced by the strength of the splice under dynamic load. DIN 22101 [20.87] relies on measuring the dynamic splice efficiency for a specific type of belt and splice. For simplicity, the approach adopted by DIN 22101 (1982) [20.98] is presented here. DIN 22101 (1982) [20.98] provides belt safety factors for nonpermanent peak loading, S_{inst}, and steady-state operation, S_{sta}.

For steady-state operating conditions, the safety factor, S_{sta}, is given by

$$S_{\text{sta}} = \frac{1}{1-(r_0+r_1+r_2)}\,, \tag{20.56}$$

where

r_0 basic reduction considering fatigue strength of splice
r_1 reduction for additional elongations due to deflections of pulleys, troughing transitions, and curves
r_2 reduction due to dynamic loads (starting and stopping) in nonpermanent peak loading conditions

Similarly, for nonpermanent peak loading conditions, the safety factor, S_{insta}, is given by

$$S_{\text{insta}} = \frac{1}{1-(r_0+r_1)}\,. \tag{20.57}$$

Table 20.8 provides reduction factors and calculated safety factors for favorable, normal, and unfavorable operating conditions.

Belt Strength. The construction of the carcass determines the tensile strength of the conveyor belt. Figure 20.54 provides a typical range of rated braking strengths for conveyor belts in N/mm. However, the operating strength of the conveyor belt will be significantly lower due to the application of a safety factor that is dependent on the splice and operating conditions.

Splicing. Splicing is the term used to describe joining the two ends of a conveyor belt together. Splices can be either detachable or nondetachable joins, with nondetachable splices being able to withstand greater stress. There are three common methods for splicing conveyor belts, including mechanical splices, hot vulcanized splices, and cold splices.

Mechanical splices are detachable and quick to install, being recommended for conveyor belts that are frequently replaced, or shortened or lengthened, like

Table 20.8 Belt safety factors (DIN 22101 (1982) [20.98])

Carcass material	Operating condition	Safety factors and reductions					
		Basic reduction	Nonpermanent peak loading k_{inst}		Maximum loading in the steady-state operating condition k_{sta}		
		r_0	r_1	S_{inst}	r_1	r_2	S_{sta}
B (cotton)	Favorable	≥ 0.691	≥ 0.100	≥ 4.8	≥ 0.100	≥ 0.060	≥ 6.7
P (polyamide)	Normal	≥ 0.715		≥ 5.4			≥ 8.0
E (polyester)	Unfavorable	≥ 0.734		≥ 6.0			≥ 9.6
Steel cords	Favorable	≥ 0.641	≥ 0.150	≥ 4.8	≥ 0.150	≥ 0.060	≥ 6.7
	Normal	≥ 0.665		≥ 5.4			≥ 8.0
	Unfavorable	≥ 0.684		≥ 6.0			≥ 9.6

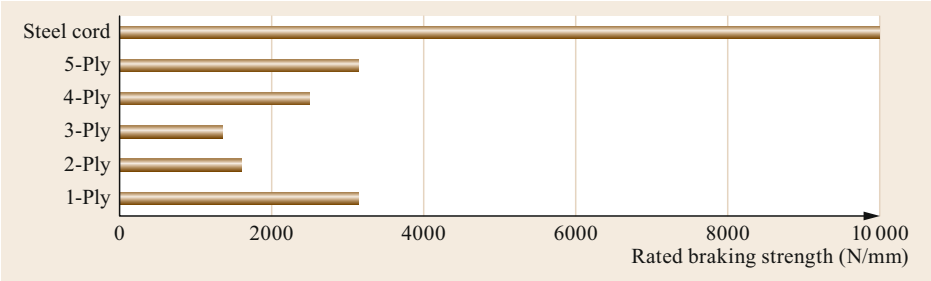

Fig. 20.54 Rated braking strengths of conveyor belt

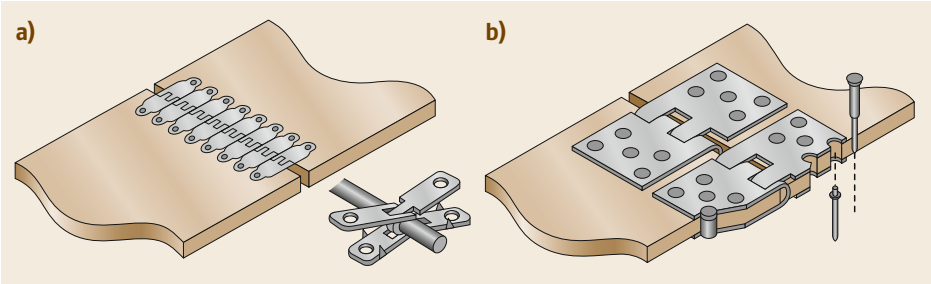

Fig. 20.55a,b Mechanical fastening of conveyor belts using **(a)** hinged plate fastener and **(b)** riveted plate fastener [20.99]

those in underground mines. Figure 20.55 shows examples of typical mechanical splices.

The more common and most efficient forms of joining fabric ply belts are the hot vulcanized splice and cold-bonded splice. Hot vulcanization involves heating and curing under pressure with a vulcanizing press. A cold splice uses a bonding agent and chemical reaction to form the splice. There are three different types of nondetachable splice that are suitable for fabric belts, including a stepped splice, overlapping splice, and finger splice. Figure 20.56 shows a finger splice and a two-step splice. Finger splices are typically used for solid woven conveyor belts.

Steel cord conveyor belt splices are hot vulcanized with cords laid parallel, as shown in Fig. 20.57. A one-step splice and two-step splice are shown, with the splice configuration determined by the belt manufacturer based on the strength of the belt.

Cover Properties. Covers protect the conveyor belt carcass and provide a means to transmit power from the drive pulley(s) or to the braking pulley(s). Belt covers need to withstand the impact of and abrasion from the bulk material on the carry side when being loaded and conveyed, protect the carcass from the idler rolls on the return side, while providing sufficient strength to transmit power at the drive or braking pulley(s). Belt covers are manufactured to standards with regards to tensile strength, elongation, and abrasion, as presented in Table 20.9. The belt cover thickness is selected based on the carcass construction, cover type, properties of the bulk material, length of the conveyor, and required belt life.

Take-Up Devices. Take-up devices are required to generate sufficient belt tension to avoid slip during driving, accelerating, and braking, and to ensure that the belt does not sag beyond allowable limits. Take-up de-

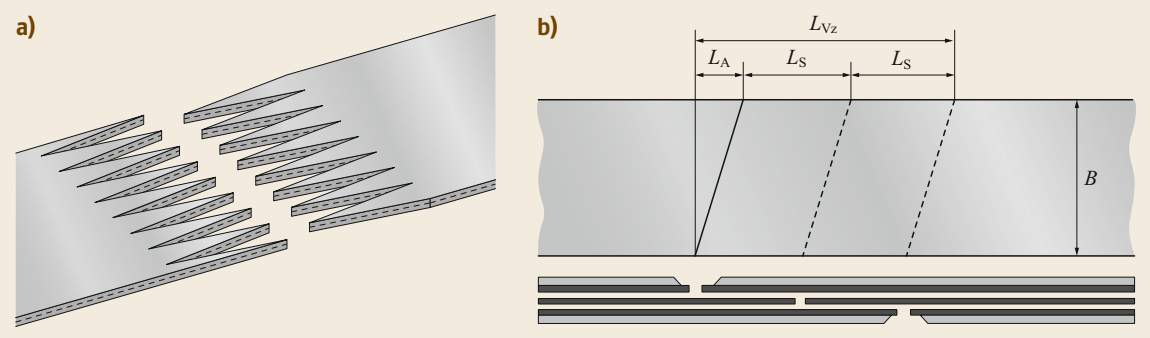

Fig. 20.56a,b Fabric conveyor belt splices: **(a)** finger splice, **(b)** two-step splice [20.99]

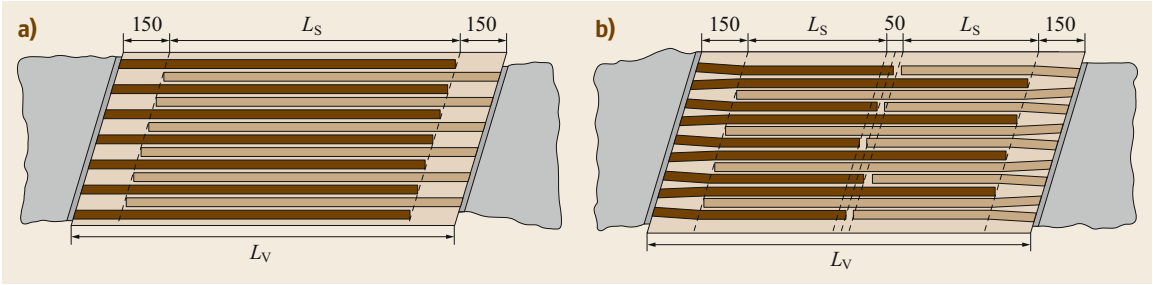

Fig. 20.57a,b Steel cord conveyor belt splices: **(a)** one-step splice, **(b)** two-step splice [20.99]

Table 20.9 Types and properties of conveyor belt covers [20.100]

Cover type DIN 22102, DIN 22131	ISO10247	Min. tensile strength (N/mm^2)	Min. elongation at break (%)	Max. abrasion loss (mm^3)
W	(D)	18 (18)	400 (400)	90 (100)
X	(H)	25 (24)	450 (450)	120 (120)
Y		20	400	150
Z	(L)	15 (15)	350 (350)	250 (200)
K		20	400	200

vices can have a moving take-up pulley, or alternatively, a fixed take-up pulley. Moving take-up pulleys include gravity, winch, and hydraulic take-ups, while a screw take-up is a common example of a fixed take-up used on short belt conveyors and belt feeders. Generally, take-up devices used on belt conveyors are of the moving pulley type, being designed with sufficient travel to absorb the elastic and permanent elongation of the belt.

Minimum Pulley Diameters. Pulley diameters are selected based on the type of pulley and location, belt operating tension, belt construction, and type of splice. The diameter of the pulley should be selected with reference to the belt manufacturer's recommendations and standards such as DIN 22101 (2000) [20.87].

Transition Lengths. Suitable transition lengths are necessary when conveyor belts transition from flat to trough and trough to flat. Conveyor belt transition distances should be sufficiently long to avoid overstressing the edges of the conveyor belt and buckling at the center. The transition distance is dependent on the geometry of the transition, the type of belt carcass, the belt tension, and the location of the transition. Readers are referred to [20.83] and DIN 22101 (2000) [20.87] for suitable transition distances.

Belt Mistracking

Belt mistracking like that shown in Fig. 20.58a is one of the most common problems when operating a belt conveyor. The problem of mistracking is similar to the tracking problems seen on flat belts for drive trains. Increasing the length increases the belt mistracking, as do the increasing number of factors that can disturb the straight run of the belt. The most common reasons for belt mistracking are [20.101, 102]:

- Noncentric belt loading
- Material build-up on idlers or pulleys
- Insufficient belt tension
- Extreme weather such as side wind or heavy rainfall
- Misalignment of idlers or head and tail pulley
- Belt cambers due to insufficient manufacturing accuracy.

A sideways movement of a flat belt or a troughed conveyor belt occurs when the belt has a nonperpendicular contact angle between the belt and a pulley or idler (Fig. 20.58b). The velocity of this sideways movement can be calculated from this angle and the belt velocity. The belt does not move relative to the idler, but a different point comes into contact when the belt is moving in the conveying direction. Due to the motion of the contact point, it appears that the belt is sliding sideways over the idlers.

The mistracking of a conveyor belt can have different reasons, which influence each other. The alignment of idlers has a major influence on belt tracking. Small deviations from the ideal aligned position can result in a large mistracking of the belt. The amount of mistracking is significantly higher for rotational than translational displacements. A misalignment in the lateral direction will shift the idler station relative to the belt center line. Mistracking will occur as an effect of the self-centering of the conveyor belt. The belt tries to follow the lowest points of the idler stations due to its

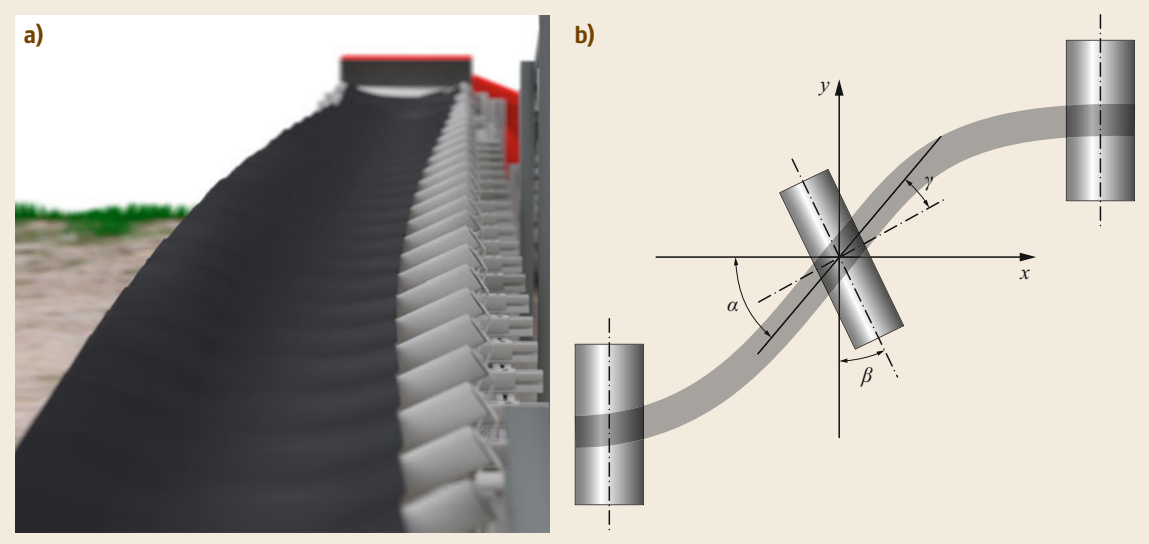

Fig. 20.58a,b Example of a mistracking conveyor belt on troughed idler stations **(a)** and example of the resulting contact angle on a mistracking belt **(b)**

self-centering behavior caused by the weight of the belt and bulk material.

Rotationally misaligned idlers are more critical. A rotational misalignment around the vertical axis is known as a skewed idler station. A skewed station will steer the belt in the direction normal to the idler. The sideways movement is directly proportional to the angle of skew (up to 6°–8°), as long as the force acting on the belt is smaller than the maximum frictional force between the belt and idler. Otherwise the belt will slip above the idler. This steering effect can be used as the output value for controlled training of idlers.

The rotation of an idler station around the axis perpendicular to the conveying direction is called a tilted idler station (Fig. 20.59). Depending on the conveying direction, the tilt of the idler station can have a positive influence on the self-centering of the belt. If idler stations are tilted forwards in the conveying direction, the belt has more contact area and force with the idler pointing against the direction of mistracking. This principle cannot be used for reversing drives, because the belt will exhibit a centering deformation in one conveying direction but unstable behavior in the other direction. The amount of tilting should not exceed 2°, otherwise the friction forces increase more than the steering effect increases [20.103]. The more stations are tilted, the more central the belt will run, but with increased energy consumption and wear. Tilting of idler stations is the method most commonly used for belt training.

Off-centered loading of the bulk material onto the belt is one of the major causes of belt mistracking,

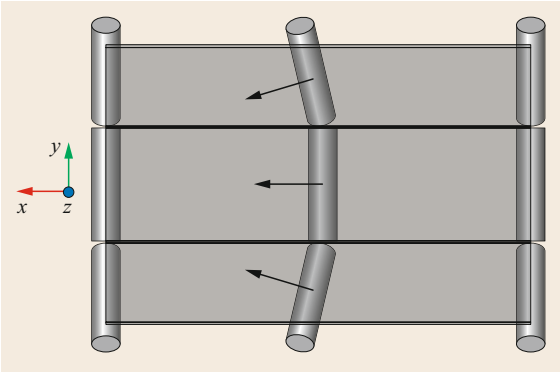

Fig. 20.59 Tilted idler stations have a positive influence as a self-centering method on the lateral running behavior

where the material is loaded eccentrically onto a centered belt due to incorrect settings or a poor design of the transfer chute. The weight force of the eccentric bulk material results in a belt deflection which causes a sideways movement. A self-intensifying eccentric belt movement results if the belt is not centered before the transfer chute, as the bulk material will be loaded eccentrically onto an already off-centered running belt. This can be solved by redesigning the transfer chute that loads the belt. To investigate the magnitude of the bulk material pushing the belt sideways, discrete element method (DEM) simulations can be used. The resulting forces can be simulated and plotted in relation to the eccentricity of the center of mass. Using this procedure, changes in the design of the transfer chute can be directly examined [20.104].

Extreme weather such as side winds, heavy rainfall, or even uneven sunlight can lead to belt mistracking due to lateral forces, reduced friction values, and uneven elongation of the belt. The best counteraction against side winds is wind guards or even hoods for all kinds of weather conditions.

Other reasons are misaligned pulleys, or a change in the shape of the idlers and pulleys due to the build-up of fine and cohesive material on their surfaces. The shape has a direct influence on the movement in the lateral direction. Crowned pulleys cause a self-centering effect, whereas tapered pulleys result in a constant sideways movement.

The construction of the belt has a strong influence on its running behavior. Some belts are produced with a small bend, so they will always run to one side. Another point of interest is the belt splice. If the splice is poorly built with an angle between the two belt ends, this point will change the sideways movement on an idler station immediately when it passes by.

Modern computational methods allow the simulation of belt mistracking behavior. The belt is modeled in a reduced system using finite element analysis (FEA). The sideways movement of the belt does not depend on the forces in contact, but rather on the geometric boundaries. The contact angle γ as shown in Fig. 20.58b is the direct value of the ratio between the feed and lateral travel. A frictional contact between the belt and an idler is used in such simulations [20.105, 106].

20.4.2 Bucket Elevators

Bucket elevators are mostly designed for steeply inclined or vertical transport of bulk materials. Vertical heights of more than 150 m can be realized. The volumetric flow rate is typically less than approx. 2000 m^3/h. Most commonly, a chain or belt is used as the tension device. The buckets are fixed on the tension device and act as the supporting devices for the bulk material, which rests in the buckets during the vertical transport. Relative motion between the buckets and the bulk material is only observed during feeding and emptying.

The bucket strand runs between driving and redirection sprockets when chains are used as the tension device (drive ring for the central chain). Pulleys will be used if a belt is the tension device. The drive station is commonly installed at the top of the bucket elevator (head), and the redirection station at the boot (Fig. 20.60). The buckets run in a closed casing (box-type casing or double casing for the conveying and return strand).

The following ISO standards exist for bucket elevators: ISO 7190 [20.107], ISO 5050 [20.108], and ISO 5051 [20.109]. National standards, e.g., VDI 2324 [20.110], describe and explain the full state of the art of such conveyors. There is also an American CEMA design guide for bucket elevators.

Applications

The design, size, and speed of the bucket elevator, and thus the mass flow rate, depend strongly on the properties of the bulk material. Fine-grained bulk solids and powders with low or medium density (grains, feed, granulates, and cement) generally allow the use of a belt as the tension device as well as higher conveying speeds up to 4 m/s. With these high velocities, volumetric flow rates of 2000 m^3/h and large conveying heights (150 m) can be realized. High-temperature belt bucket elevators can be used for constant operating temperatures in the casing < 130 °C. Heavy and coarser bulk materials (e.g., gravel, cement clinker, and ores) but also cohesive or adhesive materials require the use of chains and lower speeds, typically < 2 m/s. The use of chains allows higher temperatures in the casing (< 150 °C) with a much higher initial temperature of the bulk material (400–600 °C). Water filling of the buckets—as shown in Fig. 20.60—defines their 100% filling level. Due to the angle of repose of bulk materials, a filling level of > 100% can occur. Depending on the bucket geometry, the bucket spacing, and the filling mode applied, a vertical bucket conveyor can reach a bucket filling level of 70–90% for fine-grained and 40–80% for coarse-grained bulk material. The filling and discharge behavior of the buckets depend on the bucket velocity, design, size, and spacing as well as the diameter of the head sprocket or pulley.

Bucket Filling

Two feeding modes can generally be distinguished: scooping and dumping. During scooping, the bulk material starts to flow into the bucket during the redirection of the bucket in the boot. The boot section itself therefore needs to be filled with bulk material. The inlet position is commonly lower than the center of the boot sprocket or pulley and is installed at the conveyor strand side. However, for less abrasive material with medium weight, it is also possible to position the inlet at the return strand side. The material has to fill the boot section before scooping occurs. During scooping, the bulk material requires time to flow back into the scooping area between two bucket fillings; otherwise, the buckets will not be filled completely. Scooping operations therefore require relatively slow bucket velocities and large bucket spacings. The spacing is usually approx. $l = (2–4)h_1$. Scooping is suitable for coarse and heavy bulk materials such as cement clinker.

In dumping, the material flows directly into the bucket. This usually occurs in the vertical part of the conveying strand. The inlet position is therefore above the center of the boot sprocket or pulley. The material falls

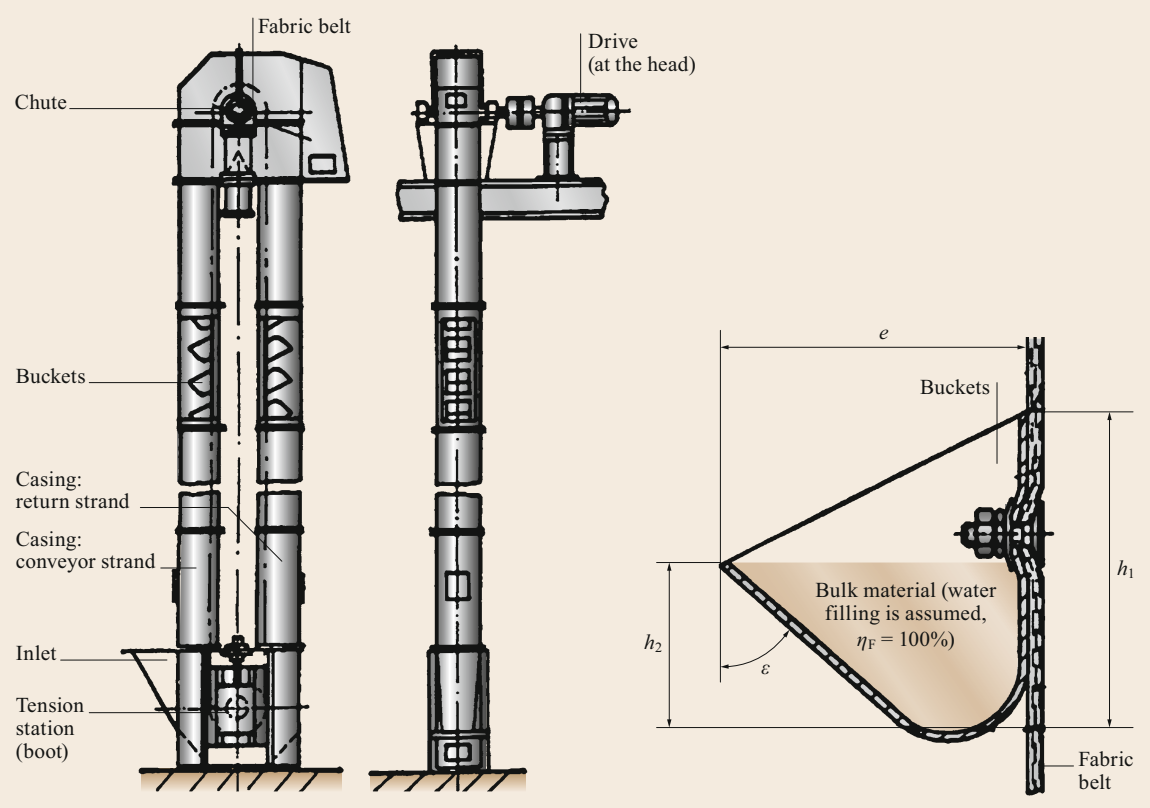

Fig. 20.60 Belt bucket elevator, e projection, ε bucket opening angle, h_1, h_2 bucket heights

with high speed into the buckets. The bucket spacing must be relatively small to prevent spillage. Continuous bucket elevators are also used with bucket spacings equal to the bucket height. So-called supercapacity continuous conveyors have very large buckets for increased throughput. However, if the buckets move through the dumped material stream, some particles will be redirected and fall into the boot of the elevator. The bucket velocity can be higher in comparison with the scooping mode.

Bucket Discharge

In the head section, the bulk material leaves the bucket. During the discharge, gravitational forces as well as centrifugal forces act on the particles. Two major discharge regimes can therefore be distinguished: gravitational and centrifugal discharge. Gravitational discharge occurs for low bucket velocities, while centrifugal discharge occurs for high bucket velocities. When both regimes occur at the same time (gravitational discharge for the particles at the back of the buckets but centrifugal discharge for the particles at the tip), the regime is called mixed discharge.

During gravitational discharge, the material leaves the bucket over the back and typically hits the front of the forerunner bucket, which directs the material into the discharge chute (Fig. 20.61a). During centrifugal discharge, all the particles leave the bucket via the bucket tip. The resulting shape of the particle stream is a logarithmic spiral. The material usually hits the elevator casing at high speed and falls into the outlet. Due to the character of these discharge regimes, gravitational discharge is commonly used for transport of heavy and abrasive materials (cement, cement clinker) while centrifugal discharge is used for grains. To reduce the wear on the buckets and casing as well as material attrition, mixed discharge is recommended.

To estimate the discharge regime, the Froude number describing the ratio of the centrifugal to gravitational forces can be applied

$$\mathrm{Fr}^2 = \frac{v^2}{r_\mathrm{i} g}\,, \tag{20.58}$$

where

v bucket speed
r_i inner radius at the back of the bucket as shown in Fig. 20.62.

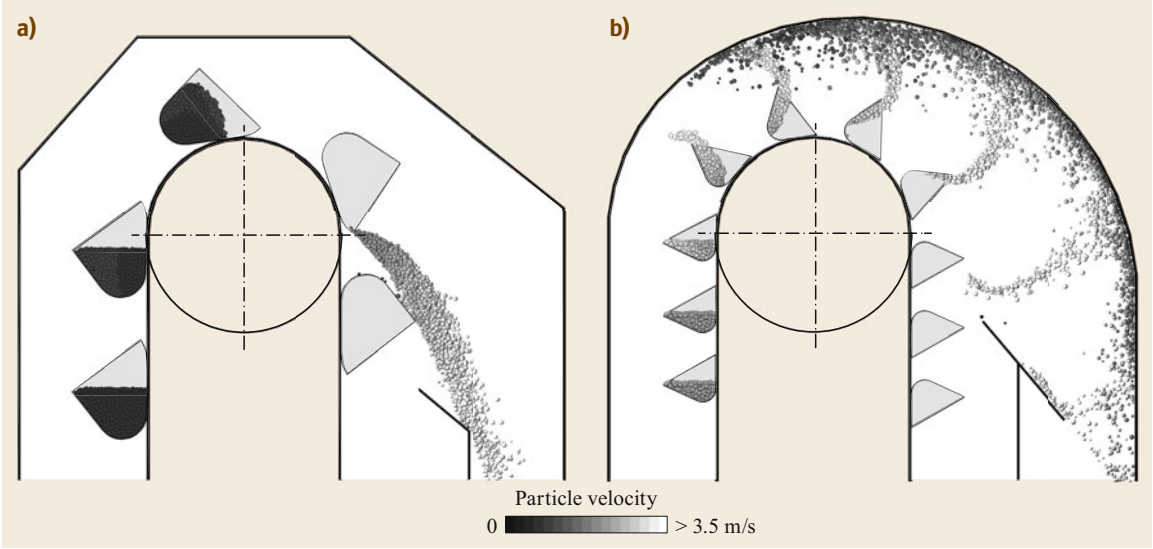

Fig. 20.61a,b DEM simulation of material flow during bucket discharge: **(a)** gravitational discharge with deep buckets according to DIN 15235, $v = 0.5\,\mathrm{m/s}$, **(b)** centrifugal discharge with flat bucket according to DIN 15231, $v = 2.5\,\mathrm{m/s}$

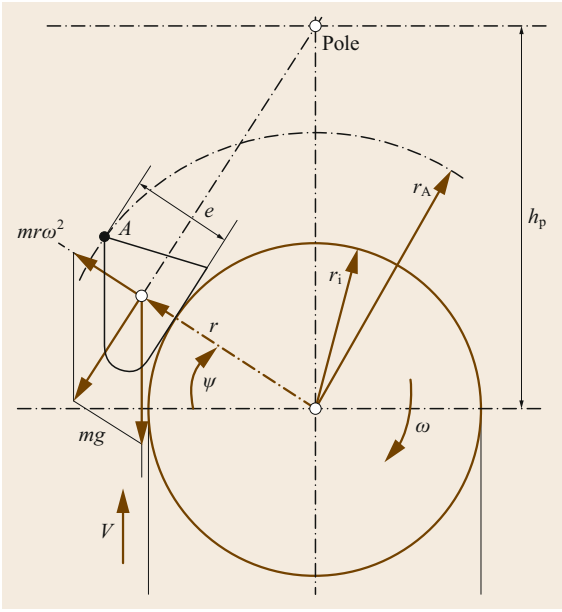

Fig. 20.62 DEM simulation of material flow during gravitational discharge

Figure 20.62 also clarifies the relation between the gravitational and centrifugal forces and the inner and outer radius. The intersection of the vertical symmetry line through the head sprocket/pulley center and the extended resulting force vector out of the gravitational and centrifugal forces is called the pole height h_P. The pole height can be calculated as the ratio g/ω^2, where ω is the angular velocity of the buckets. Table 20.10 summarizes the limits of the Froude number and pole height for the discharge regimes and hence characterizes them. To ensure that all the conveyed bulk material falls into the outlet, more sophisticated analysis is necessary to predict the precise behavior of the particles at discharge. As shown in Fig. 20.61, computer simulations based on the discrete element method (DEM) are an effective tool to analyze the bucket discharge [20.111] as well as filling process.

Table 20.10 Limits of Froude number and pole heights for the three discharge regimes of bucket elevators

Gravitational discharge	Mixed discharge	Centrifugal discharge
$\mathrm{Fr}^2 < \frac{r_i}{r_0}$	$\frac{r_i}{r_0} \le \mathrm{Fr}^2 \le 1$	$\mathrm{Fr}^2 > 1$
$h_P > r_0$	$r_i < h_P < r_0$	$h_P < r_i$

Tension

Belt bucket elevators commonly use fabric (EP) belts as the tension device. The buckets are commonly fixed by segment fastening and plate screw (DIN 15237) [20.112] fastening at the perforated belt (DIN EN ISO 15236-1) [20.113]. However, steel cord belts can also be used for large conveying heights. Steel cord belts need to have steel-cord-free zones to be perforated. Alternatively, rubber–metal connections can be used. Here, optimally shaped rubber profiles with an embedded metal rail are vulcanized on the belt. For more information, see VDI 2324 [20.110].

Bucket elevators with a chain as the tension device are built with one or two chain strands. The use of

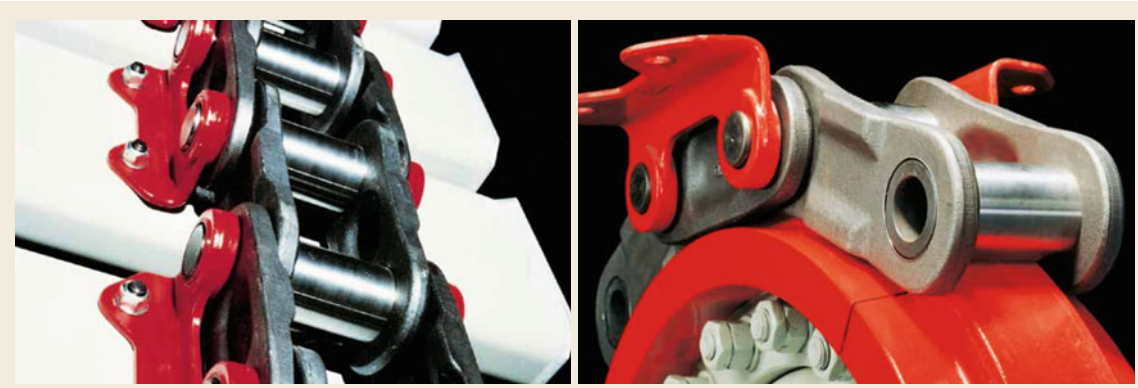

Fig. 20.63 Central chain for heavy-duty bucket elevators (Aumund Fördertechnik GmbH, Rheinberg/Germany)

two chain strands requires additional attention regarding their synchronized running, which must consider the uneven chain elongation on each side. The following chains are used for chain bucket elevators:

- Double-stranded round steel link chains according to DIN 764 [20.54] and DIN 766 [20.66] with chain brackets to fasten the buckets.
- Double-stranded (flat) bush chains attached directly to the sides of the buckets (via bolt/bush).
- Double-stranded steel link chains with special cranked link plates to attach the buckets via screws
- Single-stranded forged steel link chain (central chain) with brackets for bucket attachment. Unlike other chains, this type of chain is usually driven with a force-fit (nonpositive) drive ring (Fig. 20.63). The central chain is used for heavy-duty operation and provides higher conveying heights and larger capacities with the advantages of a single chain (with no synchronization of the chain strands being needed).

Buckets

The bucket geometry heavily influences the filling and discharge processes. Different bucket designs are therefore available for different operation modes. Flat buckets according to, e.g., DIN 15231 [20.114] and DIN 15232 [20.115], are used for light bulk materials and centrifugal discharge. Medium deep buckets according to, e.g., DIN 15233 [20.116], and deep buckets according to, e.g., DIN 15234 [20.117] and DIN 15235 [20.118], are used for medium to heavy bulk materials and mixed or gravitational discharge. Buckets can be made from mild steel or plastic. Nowadays, nonstandardized bucket designs are also used to allow optimal filling and discharge processes.

Drive and Tension Station

The drive shaft at the elevator head supports the drive pulley (belt), sprockets (chain), or ring (central chain). For power consumptions $P < 15\,\mathrm{kW}$, a geared motor (geared brake motor), and with bevel gearbox for larger powers is used. In the latter, a short-circuit rotor and usually a fluid coupling as a load-free motor starting aid as well as torque limitation (traction force limitation for the tension device) are used as the drive motor. A return lock or a self-acting brake during motor shutdown is always required.

The tensioning of the chain or belt at the lower redirection is realized by means of a weight-loaded parallel lever tensioning station or spring-loaded spindle tensioning station. Monitoring the speed of the shaft of the tension pulley/drum can indicate insufficient pretension.

Calculations

The mass flow rate can be calculated according to (20.6) and (20.8). To calculate the resistances to motion, a vertical bucket elevator with height H can be divided into two calculation parts, as shown in Fig. 20.64. The resistance to motion occurring in the conveyor strand is mainly caused by the gravitational resistance F_{g1} resulting from the weight of the bulk material q_m, buckets q_b, and tension device q_t,

$$F_{g1} = H(q_m + q_b + q_t)g\,. \tag{20.59}$$

In case of scooping, an additional scooping resistance, F_S, as described in VDI 2324 [20.110], must be considered. The pretension force F_T influences the maximum tensile force in the belt or chain. The pretension force must be chosen to prevent a loose belt or chain at the lower redirection. In case of scooping, it must also be considered that the interaction of the buckets and bulk material in the boot may result in an upwards force component, thus reducing the pretension force. Additional redirection resistances F_R and dynamical resistances F_{dyn} have to be considered when using chains.

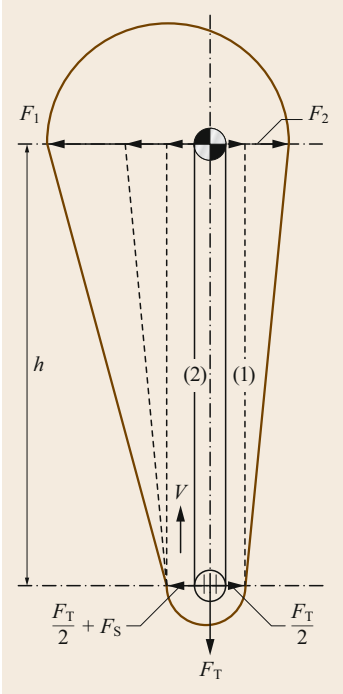

Fig. 20.64 Course of the tension force in a vertical belt bucket elevator

$$F_R = f[H(q_m + 2q_b + 2q_t)g + F_T] ,$$
$$F_{dyn} = \frac{2}{D^2} v^2 t H(q_m + 2q_b + 2q_t) , \qquad (20.60)$$

where

D sprocket diameter
t chain pitch
f friction value.

For typically chain bucket elevators, $f \approx 0.0035$ for small bucket widths but $f \approx 0.01$ for large widths. The maximum tensile force F_1 follows as

$$F_1 = F_{g1} + F_S + F_R + F_{dyn} + \frac{F_T}{2} . \qquad (20.61)$$

The scooping resistance, redirection resistance, and dynamical resistance are often less than 10% of the gravitational resistance. As a first estimate, it is therefore possible to assume that

$$F_1 = H(q_m + q_b + q_t)g + \frac{F_T}{2} . \qquad (20.62)$$

The power consumption by the drive results as the difference between F_1 and F_2,

$$P_M = \frac{(F_1 - F_2)v}{\eta} , \qquad (20.63)$$

where η is the drive efficiency and

$$F_2 = H(q_b + q_t)g + \frac{F_T}{2} . \qquad (20.64)$$

Using the estimation in (20.26), the power consumption can be approximated as

$$P_M = \frac{F_U v}{\eta} = \frac{H q_m g v}{\eta} . \qquad (20.65)$$

The maximum tensile force occurs during startup of the fully loaded conveyor, taking into account a startup factor for the fluid coupling of $p_{start} = \frac{F_{U\,start}}{F_U} = 1.6–2.0$ or higher without fluid coupling. Neglecting the acceleration forces in the return strand, the maximum tensile force can be calculated as

$$F_{max} = p_{start} H q_m g + H(q_b + q_t)g + \frac{F_T}{2} . \qquad (20.66)$$

For nonpositive drives, as used in bucket elevators with a belt or central chain, F_2 must be

$$F_2 \geq \frac{F_{U\,start}}{e^{\mu\alpha} - 1} , \qquad (20.67)$$

where

μ friction value (belt/pulley: 0.2 (wet)–0.35 (dry); chain/ring: 0.15 (wet)–0.3 (dry))
α angle of wrap.

The pretension force can thus be calculated as

$$F_T \geq \frac{2 p_{start} H q_m g}{e^{\mu\alpha} - 1} - 2H(q_b - q_t)g . \qquad (20.68)$$

Other Types of Bucket Elevator

Pendulum Bucket Elevators. Pendulum bucket elevators as shown in Fig. 20.65a have pivoted buckets between two chain strands. The buckets have a symmetric shape. The pivoting allows the change of the bucket orientation. Due to the low center of gravity, the bucket opening always points upwards independently of the conveyor routing. This allows the use of not only vertical but also inclined or horizontal conveyor routes. Very common are so-called Z-routings, which provide one vertical or inclined part and two horizontal parts for filling and discharge. The chain strands run on guides, tracks, or wheels. The pendulum bucket elevator operates with low speed, typically $< 0.2\,m/s$. The filling of the buckets is realized in the horizontal part of the conveyor route via dosing systems (rotary valve) or specially designed chutes. The material distribution in the bucket must be symmetric to prevent misalignment of the buckets. The discharge of the buckets is realized using tipping mechanisms which can be installed along the whole conveyor route. The tipping mechanisms can be controlled so that many discharge points can be automatically set. In the horizontal and inclined parts, additional motion resistances due to friction occur.

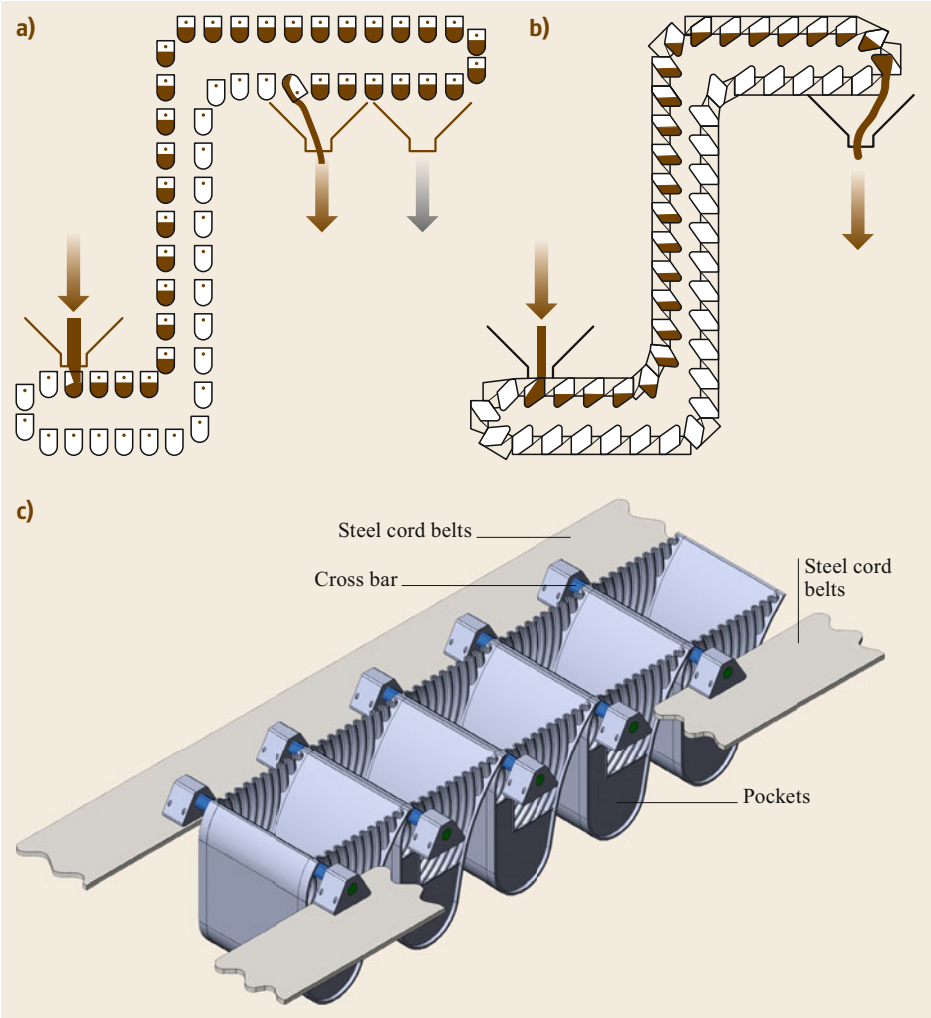

Fig. 20.65a–c Special types of bucket elevator: **(a)** pendulum bucket elevator [20.119], **(b)** bucket conveyor [20.119], and **(c)** detail of pocket bag conveyor Pocketlift® [20.120]

Bucket Conveyors. Bucket conveyors can transport bulk material not only vertically but also horizontally or along inclined routes. They use special bucket designs with overlaps and/or seals, which result in a closed continuous bucket strand as shown in Fig. 20.65b. The bucket strand is attached to two parallel chain strands. The bucket side walls, as well as the back, are so designed that no bulk material can fall out, except when the bucket is turned upside down. The material can therefore only leave the bucket at the head redirection. Gravitational or mixed discharge prevails in bucket conveyors. Often L- or Z-shaped routings are realized.

Pocket Bag Elevators. Pocket bag elevators such as Pocketlift® [20.120] as shown in Fig. 20.65c consist of two narrow steel cord belts as the tension device, which are connected with rigid triangular cross bars. The bulk material is fed into the fabric-reinforced rubber pockets, which are bolted at the center of the cross bars. Due to the resulting continuous bucket strand, horizontal and inclined conveying routes are possible. However, the greatest advantage of this system is the large lifting height of up to 700 m (276 m realized), which is limited by the strength of the used steel cord belt. Typically, Z-shaped conveying routes are used to feed the material in the lower and discharge the material at the end of the upper horizontal or inclined part of the conveying route. Depending on the bulk material properties, a longer discharge area is needed to achieve complete emptying of the deep pockets.

20.4.3 Chain Conveyors

The group of chain conveyors shows the greatest variety of all continuous conveyors. Two major groups can be distinguished for the:

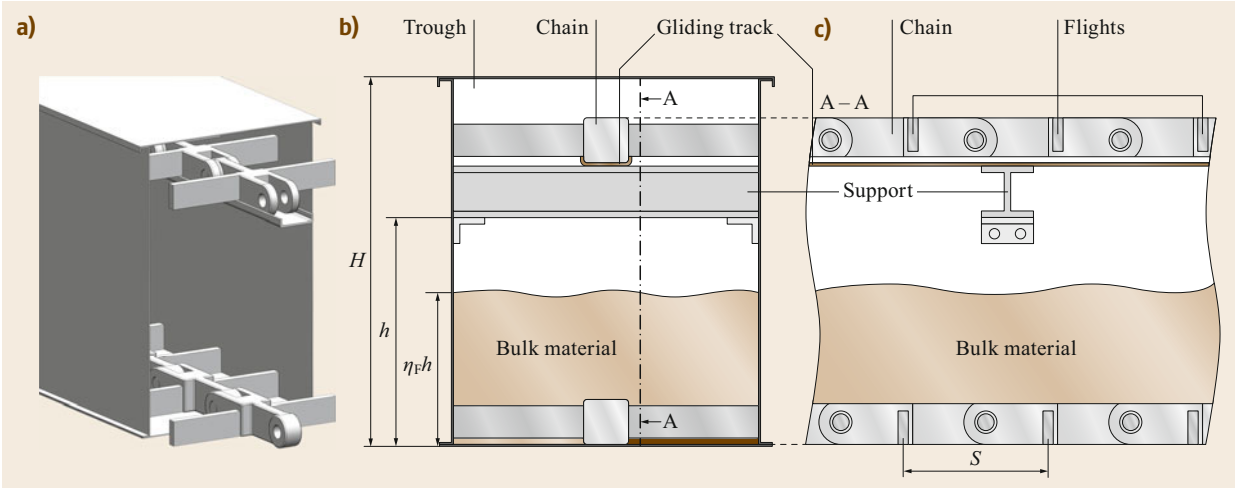

Fig. 20.66a–c Typical design of trough chain conveyor with single casing and one chain strand: **(a)** 3-D view, **(b,c)** cross sectional views

- Transport of bulk materials using:
  - Trough chain conveyors
  - Tube chain conveyors
  - Scraper conveyors (face conveyors in mining)
  - Scraper reclaimers (for stockpiles)
  - Apron and pan conveyors.
- Transport of general cargo using:
  - Carrier chain conveyors
  - Slat conveyors
  - Flat top chains
  - Chain belts.

All chain conveyors use one or two chains as the tension device and a positive drive via a sprocket or pocket wheel as discussed in Sect. 20.3.2. The positive drive principle requires the definition of a minimum tensile force. The chain tensile force along the conveyor route should not be lower than this value. The point of minimum tensile force is typically found in the return strand after downwards sections. From this point, the tensile forces over the whole conveying route can be calculated.

Trough Chain Conveyors

Trough chain conveyors, also known as En Masse conveyors or Redlers, transport powdery, fine-grained or coarse-grained bulk material. The bulk material is conveyed in a closed rectangular trough by a single chain strand (approx. trough width $B \leq 0.4\,\mathrm{m}$) or double-stranded chain ($B > 0.4\,\mathrm{m}$) with attached flights. To allow mostly friction-based transport of the material, the cross section of the flights is much smaller than that of the troughs. Trough chain conveyors are therefore characterized by high volumetric efficiency. The conveying and return strands run in one casing. The height of the conveyed bulk material bed is limited by the installation height of the tracks for the return strand (Fig. 20.66a).

Trough chain conveyors allow horizontal, inclined, and vertical conveying routes. Due to the rectangular casing, a three-dimensional conveying route is not possible. L-type routes are often found (Fig. 20.67). Their technical parameters including volumetric flow rates of $< 1600\,\mathrm{m^3/h}$ (grains), typical conveying speeds of $< 1\,\mathrm{m/s}$ (depending on the chain used), conveying lengths $< 150\,\mathrm{m}$, and bulk material temperatures $< 500\,^\circ\mathrm{C}$.

Depending on the properties of the bulk material, the mass flow rate, and the conveying route, different flight designs are used (Fig. 20.68). The higher the inclination, the higher the flight cross-section to prevent the back flow of the bulk material. Cohesive material requires less flight cross-section than free-flowing material. Very adhesive material causes great problems during emptying. The right chose of the flight geometry and flight pitch is essential for efficient conveying. Bush chains with cranked link plates (Fig. 20.68c) or fork chains will be used if the conveyor is equipped with a single chain strand. Round steel link chains or steel link chains are used for conveyors with double-stranded chains.

The bulk material is typically conveyed in the lower chain strand, while the upper strand is the return strand. The use of intermediate bottom plates allows conveying in both strands. Sieve bottom plates also allow the implementation of mass flow screening in the trough chain conveyor. Trough chain conveyors are also used to implement the cooling of the material stream.

Sprocket wheels are used for drive and redirection. The necessary pretension force is applied at the redirection station with a sprocket installed in a slide frame

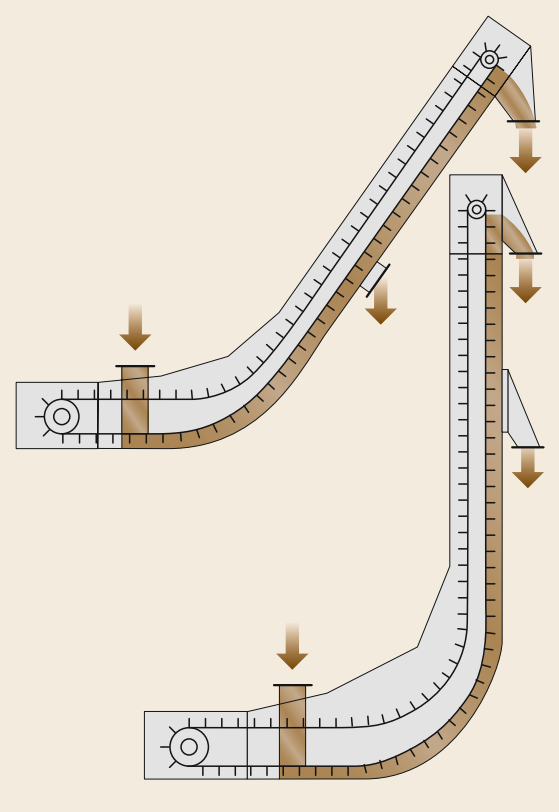

Fig. 20.67 Conveying routes of trough chain conveyors

tensioned by a spring-spindle mechanism or pneumatic/hydraulic cylinders. Simple screw tensioning cannot ensure a constant pretension force. Normally, a minimum tensile force of $F_{min} \geq 2\text{kN}$ is used to ensure a safe and efficient run of the chain without extensive wear, noise, or vibrations.

Flow Rate. The friction-based conveying principle implies that not all the bulk material is conveyed at the chain speed. A reduction factor c is therefore introduced into the calculation of the volumetric or mass flow rate. c depends on the bulk material properties, but also on the conveyor route. The following approximations for c are based on experience:

- Horizontal and low inclined routes: $0.6 < c < 0.9$ (higher values for medium- and coarse-grained material)
- Highly inclined ($> 45°$) and vertical routes: $0.4 < c < 0.7$ (lower values for powders).

The suggested chain velocities range from very low values, e.g., 0.05 m/s, for very abrasive material to 1.2 m/s for grains. Cement clinker is often transported with < 0.3 m/s, wood pellets with 0.5 m/s, and coal with 0.8 m/s.

Motion Resistance. Motion resistances occur due to the weight of the chain and bulk material and the friction:

- Between the chain and trough (sliding tracks)
- Between the bulk material and trough
- Inside the bulk material due to the backwards flow, especially in inclined parts.

A conservative approach to the calculation of the motion resistance F_i in a conveyor part i with any incli-

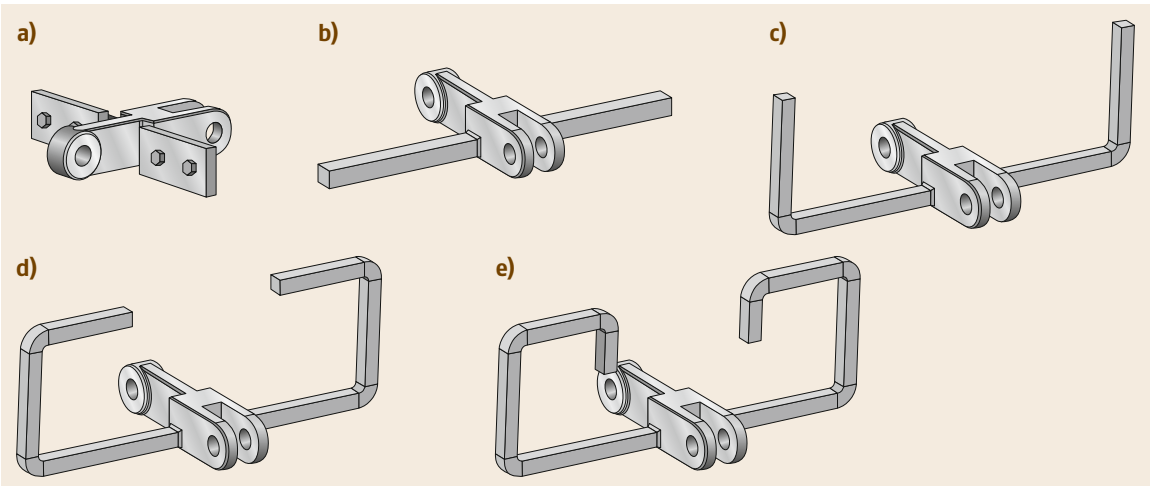

Fig. 20.68a–e Flight shapes for trough chain conveying with different routes: **(a,b)** horizontal, **(c)** low inclined, **(d)** steep inclined, and **(e)** vertical

nation δ can be given as

$$F_i = L_i \Bigg[q_c g(\mu_c \cos\delta \pm \sin\delta) + q_m g \Bigg(\mu_m \Bigg\{ 1 + \lambda_a \frac{\eta_F h}{B} \Bigg\} \cos\delta \pm \Bigg\{ 1 + [\mu_m + \mu_e] \Bigg[\lambda_a s (1 + e^{\mu_m \mu_e}) \frac{h+B}{hB} \Bigg] \Bigg\} \sin\delta \Bigg) \Bigg], \tag{20.69}$$

where

δ slope angle of the conveyor
L_i length of the route section
h maximum height of the material bed, defined by the trough height H minus the height of the returning chain strand
B width of the trough
s flight spacing, typically $s < h$
q_c meter weight of the chain(s)
μ_c friction value between chain and trough
q_m meter weight of the bulk material
μ_m wall friction value of the bulk material (against trough material)
μ_e effective internal friction value of the bulk material
$\lambda_a = \frac{1-\sin\mu_e}{1+\sin\mu_e}$ active stress ratio according to Rankine
η_F filling ratio

The approach considers the important bulk material properties, the wall friction μ_m, and the effective internal friction μ_e as well as the dimensions of the material bed defined by the trough width b and the height of the trough h. For vertical sections ($\delta = 90°$), it is assumed that a frictional motion resistance of the bulk material does occur at the trough walls and within the material due to the backflow.

Additional safety factors ranging from 2 for short conveying distances of 5 m to 1.22 for distances larger 40 m are used to consider the chain redirection resistances and the friction in the sprocket bearings.

Scraper Conveyors

Scraper conveyors are very similar to trough chain conveyors. The biggest differences are the open trough and the limitation to horizontal and inclined conveyor routes. The maximum slope angle is dependent on the bulk material. The material can be loaded over the whole length of the upper strand of the conveyor. The lower strand is the return strand. Scraper conveyors are typically used for heavy-duty operations, such as hopper discharge or in mining. Here, the so-called armored face conveyor is a central component of longwall mining equipment for transporting the claimed coal or ore (Fig. 20.69). Scraper conveyors are usually designed

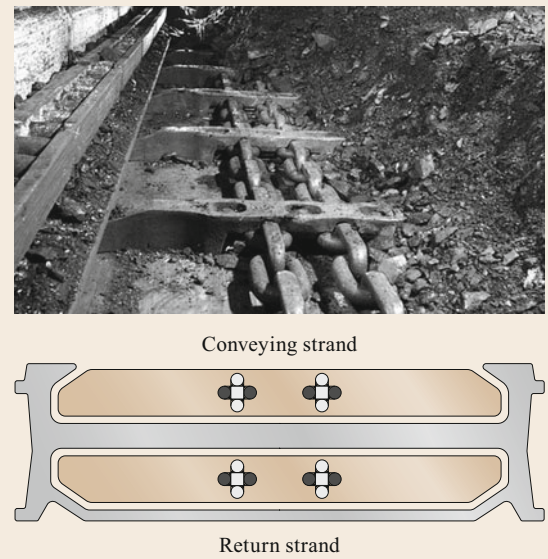

Fig. 20.69 The armored face conveyor for underground mining is the most powerful scraper conveyor

with double-stranded chains connected through the scraper flights. Bush chains are often used. For heavy-duty operation, special round steel link chains are also used (e.g., as standardized in DIN 22252 [20.57]). Here, two chain strands are commonly used, being centrically fastened at the scraper flights. The use of a round steel link chain allows three-dimensional conveyor routes with large radius of curvature. Therefore, e.g., armored face conveyors can adapt to underground conditions. Armored face conveyors show the longest conveying routes of all chain conveyors: up to 500 m conveying length. With common chain speeds of 1.2 m/s and conveying cross sections of 1.2 m^2, the mining conveyor can reach volumetric flow rates of more than 5000 m^3/h. The largest round steel link chains with special flat vertical chain links (to reduce the trough height in the return strand) and chain link diameter of up to 60 mm are used for armored face conveyors. Such chains can have a breakage force of up to 4500 kN.

Due to the high chain speed and small diameter of the sprockets used (for height reduction), large dynamical motion resistances occur in armored face conveyors. Furthermore, the very dynamic claiming process and the blocking and seizing of scraper flights in the special-shaped but narrow trough increase the motion resistances of such conveyors.

Scraper Reclaimers

Scraper reclaimers have no trough and are used for reclaiming longitudinal or circular stockpiles. A chain with scraper flights moves on top of the bulk material bed, as shown in Fig. 20.70.

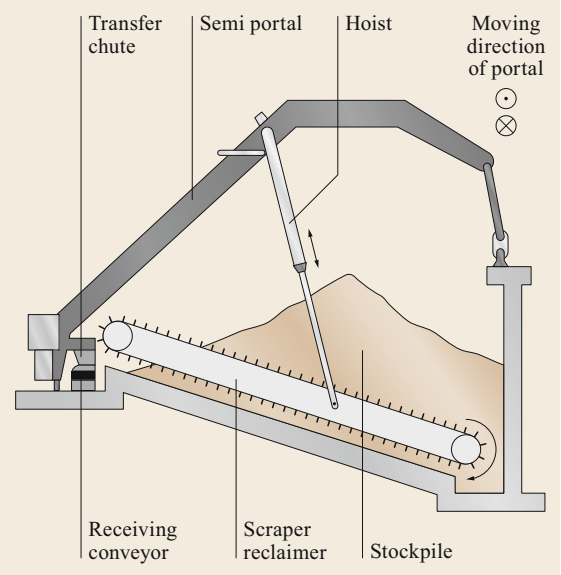

Fig. 20.70 Semiportal scraper reclaimer for lateral discharge of stockpile undercut operation is shown as the worst case for the design of scraper conveyors

There are two different types of machines:

- Hoisted scraper reclaimers fixed on a hoist to change the slope angle: such scraper conveyors are used as (semi)portal scraper reclaimers, side scraper reclaimers, slewing scraper reclaimers, or circular scraper reclaimers.
- Horizontal scraper reclaimers used as bridge-type reclaimers.

In contrast to scraper conveyors, scraper reclaimers are not loaded from the top but from the side over the whole conveying length. To realize this sideways loading, the scraper reclaimer is moved sideways along the stockpile surface (hoisted scraper reclaimers), or the bulk material flows from the stockpile sideways towards the horizontal conveyor at the base of the stockpile (bridge-type reclaimer). Due to the sideways movement, a span of the stockpile is reclaimed. To realize efficient scraper reclaimers, the scraper flight size and spacing must to be adapted to the speed of the sideways movement and the cutting depth of the scraper flights into the material bed. Commonly, the full volume between two scraper flights cannot be filled with bulk material, because the material would start to flow out earlier. The maximum filling level is estimated to be 70%. Scraper reclaimers can realize mass flow rates of up to 6000 t/h with a conveying length of 70 m. Typically, double-stranded bush chains with large chain pitches are used.

The motion resistances are calculated for the worst-case condition, viz. horizontal operation of the reclaimer, or if possible the so-called depth cut operation mode, where bulk material has to be transported upwards (see the design of the stockpile foundation in Fig. 20.70). For the design and calculation of scraper reclaimers, refer to [20.122].

Tube Chain Conveyors

Tube chain conveyors have a tube as a closed trough. The conveying and return strands run in separated tubes. Transportation disks are fixed on a chain that circulates axially through the tube. Bulk material can be filled via one or several inlets, and is conveyed to the outlet by the transportation disks in the direction of the chain movement (Fig. 20.71). The main difference between trough chain and scraper conveyors is the conveying principle. As the transportation disks have almost the same cross-sectional area as the tube, a positive (form-fit) conveying principle is used. These conveyors are used throughout industry with transport rates of up to medium volumetric flows (60 m^3/h). In contrast to trough chain conveyors, no reduction factor must be considered when calculating the flow rate as the material moves at the chain speed.

Typically, a round steel link chain is used as the tension device. Then, conveyor speeds of 0.01–0.4 m/s are applied. The main advantage of the tube chain convey-

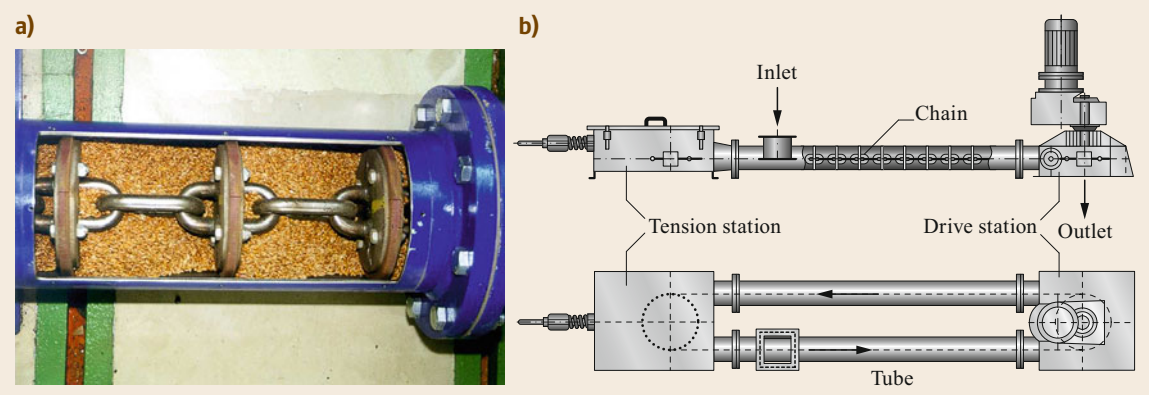

Fig. 20.71a,b Tube chain conveyor principle [20.6] (**a**) and general layout [20.121] (**b**)

ors with a round steel link chain is the possibility of realizing three-dimensional conveyor routes. However, bush chains with a smaller chain pitch can also be used, which allows higher conveyor speeds of up to 1 m/s but restricts the conveyor route to two-dimensional layouts.

For coarse-grained material with hard particles, blockage or seizing of the particles between the disks and tube can occur. This gap effect causes a significant increase of the motion resistances. Further details about the gap effect and how it can be estimated are described in [20.123, 124].

The motion resistance in a straight conveyor route segment i with length L_i and slope angle δ can be calculated as

$$F_i = L_i\left(q_c g\{\mu_c\cos\delta \pm \sin\delta\} + q_m g\left\{\mu_m\left[1+\lambda_a\frac{\eta_F}{\eta_V}\right]\cos\delta \pm\left[1+\frac{d_T}{4s\mu_m\eta_V\eta_F\lambda_a}\left(e^{\frac{4}{d_T}\mu_m\lambda_a\eta_V\eta_F s}-1\right)\right]\sin\delta\right\}\right), \tag{20.70}$$

where

d_T inner tube diameter
s spacing of the transportation disks, typically $s = (1\text{–}2)d_T$
η_V volumetric efficiency

Furthermore, the calculation of the motion resistances must also consider the redirections of the conveyor route. While trough chain and scraper conveyors typically only have one redirection section (curves or bends with large radius), bends are used more often in tube chain conveyors and typically have a smaller radius of approx. 800–2000 mm. It is very important to note that the motion resistances in bends increase exponentially. Hence, the larger the tensile force at the beginning of the bend, the larger the tensile force at the bend end. This important finding influences the design of tube chain conveyors significantly. The number of bends as well as their positioning thus have to be chosen carefully. A simple rule is to include the bends as early as possible, to reduce the chain force (motion resistance) at the beginning of the bend.

To calculate the motion resistance, the following general equation can be used

$$\begin{aligned} F_i &= F_B(\psi) \\ &= e^{\mu_c(\psi-\psi_0)}\left[F_B(\psi_0) + \frac{\mathcal{A}(\mu_c\sin\psi_0+\cos\psi_0)}{\mu_c^2+1} + \frac{\mathcal{B}(\mu_c\cos\psi_0-\sin\psi_0)}{\mu_c^2+1} + \frac{C}{\mu_c}\right] \\ &\quad - \frac{\mathcal{A}(\mu_c\sin\psi+\cos\psi)}{\mu_c^2+1} + \frac{\mathcal{B}(\sin\psi-\mu_c\cos\psi)}{\mu_c^2+1} + \frac{C}{\mu_c} \end{aligned} \tag{20.71}$$

with

$$\begin{aligned} \mathcal{A} &= \frac{r\cos\alpha q_m g d_T}{4\mu_m s\eta_V\eta_F\lambda_a}\left(e^{\frac{4}{d_T}\mu_m\lambda_a\eta_V\eta_F s}-1\right) \\ &\quad + r\sin\alpha q_m g\mu_m\left(1+\lambda_a\frac{\eta_F}{\eta_V}\right) + rq_c\cos\alpha\,, \\ \mathcal{B} &= rq_m g\mu_m\left(1+\lambda_a\frac{\eta_F}{\eta_V}\right) - rq_c g\mu_c\cos\alpha\,, \\ C &= rq_c g\mu_c\sin\alpha\,, \end{aligned}$$

where

r bend radius
α bend inclination angle against the vertical
ψ circumferential angle at the bend end
ψ_0 circumferential angle of the bend start
$F_B(\psi)$ chain force at the bend end
$F_B(\psi_0)$ chain force at the bend start

For further details, the reader is referred to [20.123, 124].

Apron and Pan Conveyors

If abrasive, very coarse, or very hot materials (< 1100 °C, e.g. cement clinker) are to be conveyed, the relative motion between the chain, trough, and bulk material should be as small as possible. Apron conveyors address this requirement with the following design features: Overlapping and interlocking plates are attached at the plate ends to two chain strands. Depending on the application, roller chains, gliding tracks, or fixed rollers are used to reduce the motion resistances of the chain. The bulk material is loaded onto the plates. The overlapping and interlocking design of the plates generates a leakproof continuous surface to convey the bulk material. Hence, the chains do not come into contact with the bulk material. The conveying principle varies. While smooth plates convey the material purely based on friction, plates with profiles allow the form-fitting transportation of the material. Different designs for the plate segments exist. Plates with relatively large side walls are called pans. Due to the additional side wall support, the conveyor can then be used for higher volumetric flow rates, but also over more inclined routes. If the pans are equipped with support walls that are transverse to the conveying direction, very high inclination angles can be realized. Such conveyors are very similar to the bucket conveyors described in Sect. 20.4.2. Apron feeders are often used for bunker and hopper discharge, but also as feeders for primary and secondary crushers in the mining industry. Here, the apron feeder is loaded via large dump trucks or ore draws, where large lumps (up to 2 m) can hit the feeder. The width of such apron feeders can be up to 3.4 m. For these applications, special heavy-duty chains (crawler chains) are used (Fig. 20.72). The chain speed for apron feeders is typically less than 0.4 m/s.

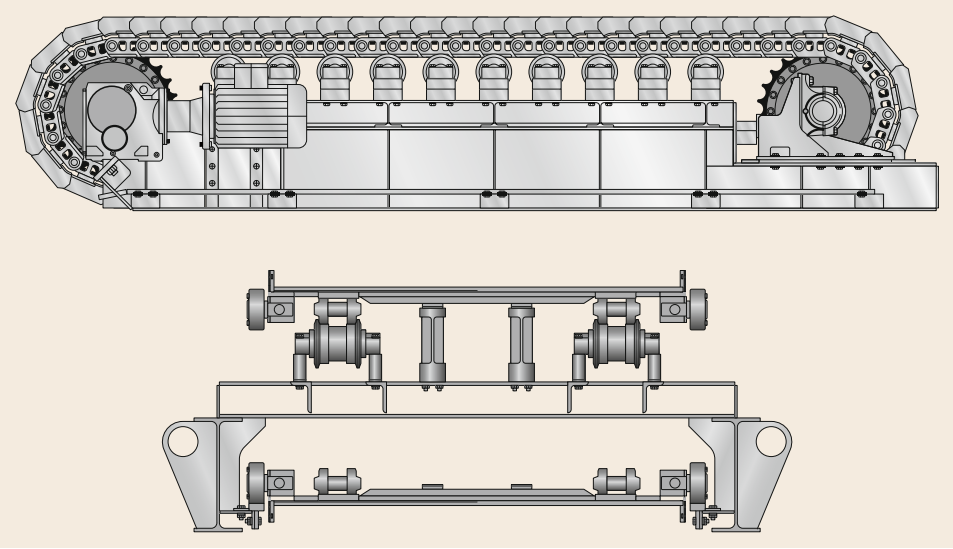

Fig. 20.72 Apron feeder for bunker discharge (heavy-duty crawler chain type)

The motion resistances on the apron feeder during hopper discharge mainly depend on the vertical and shear forces resulting from the bulk material. The latest results including analytical calculation approaches, simulations, as well as experimental results were published by *Guo* in [20.125, 126].

Carrier Chain Conveyors

For the transport of rigid and relatively large general cargo, carrier chain conveyors are one possible solution. In materials handling of general cargo, load carriers such as pallets are very often used. Carrier chain conveyors are mainly applied to handle pallets. This type of conveyor has a very simple design. As shown in Fig. 20.73, two strands of bush or roller chains with relatively small chain pitch run synchronized in two tracks. The cargo will be loaded on top of the conveyor. This design represents a simple possibility to realize accumulation of the goods as well, if special steel link chains with larger rollers are used. If the cargo transport is blocked, the chain can run under the accumulated good while generating only small backpressures.

Carrier chain conveyors are used for horizontal or slightly inclined transport. The conveying speed is typically $< 0.4\,\mathrm{m/s}$. Pallet weights of up to 2000 kg can be handled. The following equation allows the general calculation of the motion resistances

$$F_i = L_i(q_\mathrm{c} + q_\mathrm{g})g(\mu_\mathrm{c}\cos\delta \pm \sin\delta)\,, \qquad (20.72)$$

where

$q_\mathrm{g} = \frac{m_\mathrm{g}}{s}$ meter weight of the general cargo, defined as the ratio of the average weight of a single good m_g to

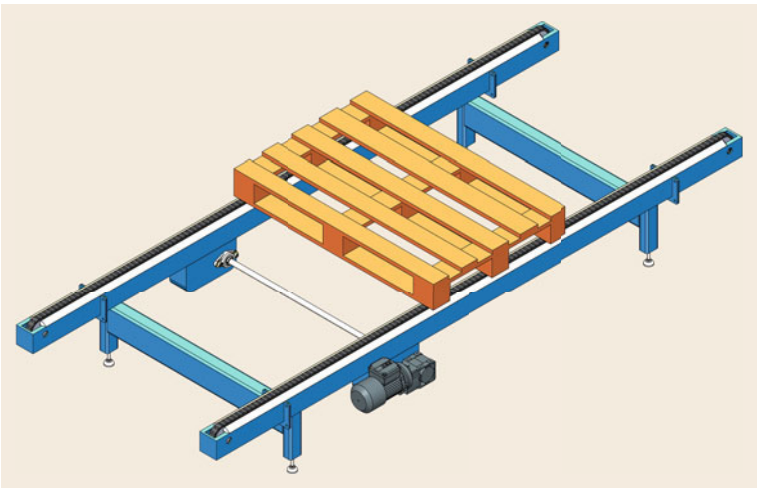

Fig. 20.73 Carrier chain conveyor

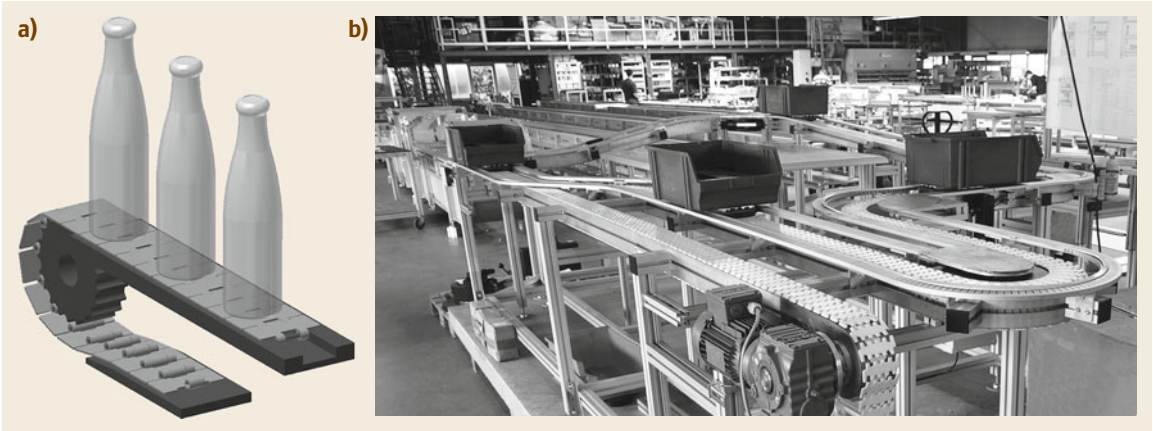

Fig. 20.74a,b General function of a flat-top chain conveyor **(a)**, conveying routes of multiflex chain conveyors **(b)**

the average spacing between two goods s_g, as shown in Fig. 20.74a

Often, carrier chain conveyors do not need additional pretension (take-up) units. Hence, the chain force during the run-off of the sprocket wheel is just determined by the weight of the chain or by a chain-tensioning ring.

Slat Conveyors

Slat conveyors have an operating principle similar to that of apron conveyors. However, they are designed for general cargo rather than bulk materials. Hence, the plates (or better slats) do not overlap and interlock. However, there are also slat conveyor designs in which the slats form a closed surface with very small gaps (not leakproof). Two strands of bush or roller chains are used. Slat conveyors with one chain strand can also be found. Then the slats are mounted on a frame with wheels running in tracks. The chain is attached at the center of the frame.

Slat conveyors can reach very large widths. Conveyors with 6-m-long slats are known. Slat conveyors are used in the automobile industry, where two synchronously moving slat strands (fixed on one frame) transport cars. The conveying speed is typically $< 0.8\,\mathrm{m/s}$. The heavier the good, the slower the conveyor.

The general design principle for a slat conveyor (a frame with wheels running in tracks towed by a chain) can be varied widely to form completely new conveyors, such as escalators (for transport of persons) or baggage conveyors (where special chains and overlapping scale-like slats with a special design allow running around horizontal and vertical curves). However, the principles of the calculation of the motion resistances are similar to (20.72).

Flat-Top Chain Conveyors

The large group of flat-top chain conveyors (synonyms: top chain or sliding chain conveyors) are increasingly used in materials handling for the transport of general cargo. Due to a new chain design and the application of new materials (plastics), top chain conveyors enable transport at relatively high speeds and the realization of complex conveyor routes with small radii of curvature, as shown in Fig. 20.74b. Such conveyors allow the connection of modern automated manufacturing machines, as well as the realization of high throughput rates as needed, e.g., in the beverage industry. An important advantage of plastic top chains is that they do not require external lubrication, making them suitable for use in sensitive areas, e.g., in the food, packaging, and pharmaceutical industries.

Flat-top chain conveyors basically consist of specially designed chain links forming an almost closed conveyor surface. To realize horizontal and vertical curves, the design of the top segment of the chain, where the material is loaded, must be adapted. Hinge chains as shown in Fig. 20.75 are traditionally used in top chain conveyors. The horizontal redirection of the hinge chains with a minimum radius of curvature of approx. 500 mm is realized using the corresponding joint play.

Another chain design, so-called multiflex chains, separate the function of transmitting the tensile forces and the support of the load, as shown in Fig. 20.76. The cardanic joint provides greater agility in comparison with hinge chains, as well as much smaller radii of curvature of approx. 150 mm. Therefore, wheel bends or curve wheels can be used instead of horizontal slide bends. This allows a significant reduction of the chain load due to the absence of radial friction at these curves. Multiflex chains are commonly guided by aluminum tracks with extruded plastic profiles. The

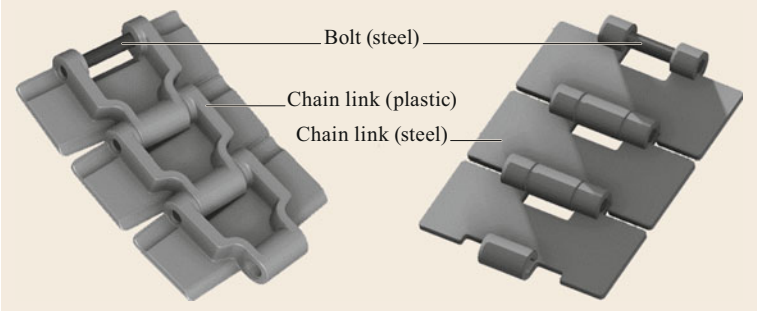

Fig. 20.75 Hinge chains made out of plastic (*left*) or steel (*right*)

conveyor design is modular and consists of straight sections, horizontal and vertical bends, curve wheels, drive units, redirection units, support, and supplementary elements. This modular design allows very easy configuration of three-dimensional conveyor routes.

The design of the support plates of top chain conveyors can be adapted for specific transport tasks and goods properties. Examples of this include steel and elastomeric adhesive linings, rollers for good accumulation over the conveying length, elastomeric elements for clamping conveyors, etc. Typical slide chains have a support plate width of about 80 mm, but widths up to about 200 mm are also possible.

Top chain conveyors can realize chain speeds of up to 2 m/s and conveying lengths of approx. 20 m. The length is limited by the maximum operational chain force, which can be estimated as 1000–2000 N for plastic chains and 4000–7000 N for steel chains. Many manufacturers of top chains publish only the breakage force of the chains. To calculate the maximum chain force for operation, a safety factor of typically 3–4 has to be taken into account. As for tube chain conveyors, special attention must be paid to the bends/slide curves when designing complex conveyor routes. In these sections, the chain forces increase exponentially and the maximum operational chain force can quickly be reached. Furthermore, the high radial force on the inner radius of the curve leads to strong heating, leading (in particular for plastic chains) to high wear or thermal failure and thus representing a frequent cause of failure.

In contrast to other chain conveyors, the run-off of the chain from the drive sprocket can be assumed to be force free. Hence, no minimum tensile force and no pretension need be considered in calculations for such chain conveyors. From the run-off, the motion resistances can be calculated using (20.36). Especially for the sliding curves, consideration of realistic friction values (also considering thermal effects) is important due to the exponential force increase according to

$$F_n(\varphi) = (F_{n-1} + C_F)e^{C_R\varphi} - C_F\,, \tag{20.73}$$

where

C_F force component
C_R friction factor
φ curve angle

For the definition of the force component C_F and the friction factor C_R, please refer to [20.127], which also includes recent research findings for plastic chains.

Modular Belt Conveyors

Modular belt conveyors consist of individual modules made of plastic, which are flexibly assembled into

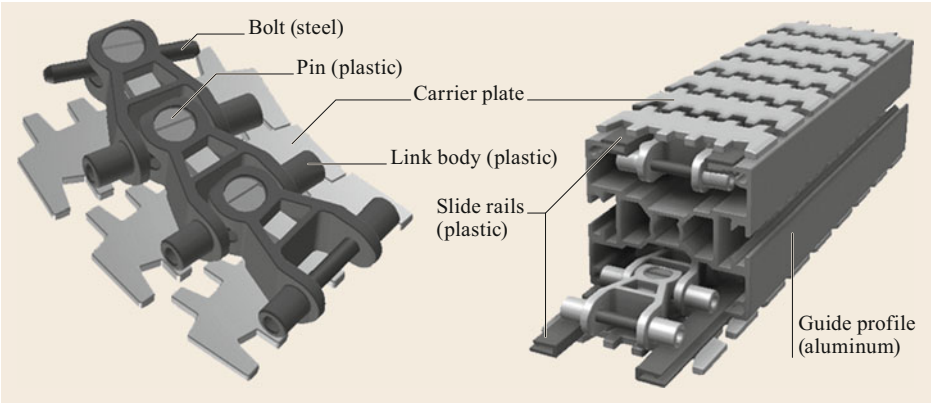

Fig. 20.76 Multiflex chains for top chain conveyor

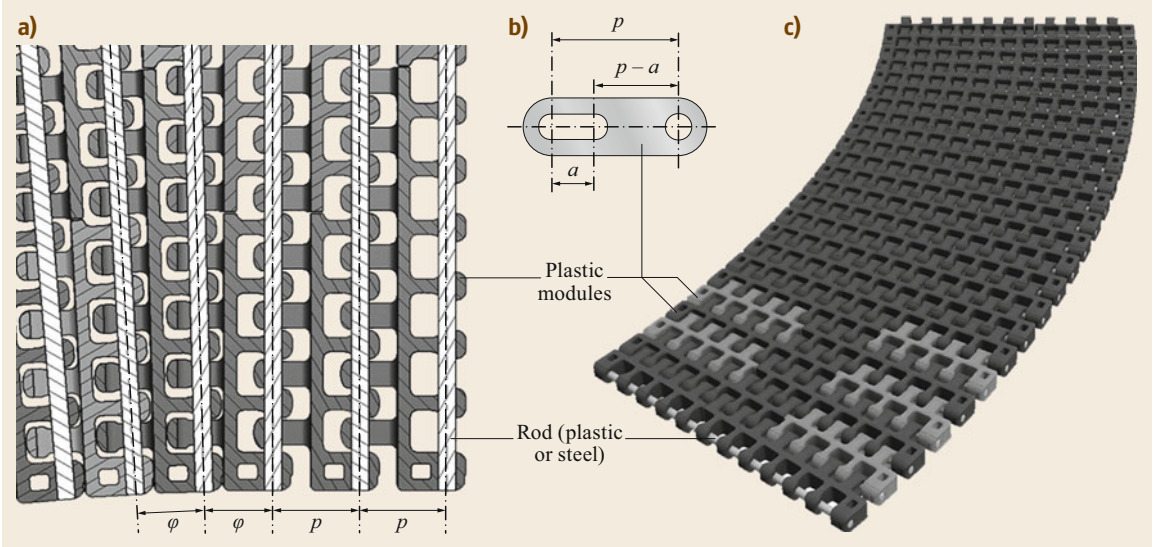

Fig. 20.77a–c Principle of operation (a,b) and construction (c) of a curved modular belt

a bricklay pattern and hinged together with rods made of plastic or metal. By means of a corresponding joint design with a slot, not only straight but also curved modular belts are possible (Fig. 20.77). The modular design allows the production of flexible tapes in widths of approx. 200–5000 mm. By using differently designed modules, band thicknesses of approx. 5–30 mm are possible, whereby a broad load spectrum can be covered. In conjunction with a positive drive via sprockets (also made of plastic), modular belt conveyors can thus be up to approx. 50 m long and load both filigree goods and heavy loads such as pallets, white goods (e.g., washing machines or refrigerators), or cars in automobile manufacturing plants.

Modular belt conveyors belong to the group of chain conveyors and often compete with belt conveyors. Significant advantages of these conveyors are the slip-free drive (meaning that no pretension is required), the possible realization of straight lines and curved sections using a single band, and easy installation by means of removable connecting chain pins. The disadvantages are the relatively loud noise and the polygon effect, which limits the maximum transport speed to about 1 m/s.

The use of plastic offers considerable advantages due to the wide diversity of such materials. Modular belt conveyors can usually be operated without additional lubrication and thus can be applied, amongst other sites, in clean areas such as in the paper and packaging industry. Many plastics are resistant to moisture and a variety of chemicals (e.g., acids, bases, and detergents) and are physiologically harmless; this means that they are suitable for direct contact with food, making such conveyors ideal for use in the food industry. Flame-retardant, antistatic, or detectable plastics are available as well. Another advantage is the great design freedom of the modules. As a result, e.g., straight and curved modular belts with almost closed surfaces or well-defined openings are available, thus enabling the integration of various processing processes such as washing/draining, cooling, drying, etc. during conveying.

As described above, the curve mobility of modular belts is achieved by elongated holes, whereby the rods obtain a certain mobility in the direction of travel. In straight runs, the rods are exactly the same spacing p apart. The tensile force is evenly distributed over the entire width of many joints, so that in total a very high force can be transmitted (depending on the design, up to about 25 kN/m). If the chain turns in a curve, the modules are pushed together in the inner radius of the curve and thus load free, whereby the entire chain tension can now only be transmitted over a narrow range at the outside radius of the curve. At the same time, a high radial force acts on the curve support, leading to friction-induced heating of the contact area. Therefore, a significant reduction of the permissible tensile force occurs at curves in relation to straight lines. Indeed, massive disturbances and failures often occur here as a result of overheating at the radial sliding support or a chain tear starting from the outside.

20.4.4 Overhead Conveyors

Overhead conveyors (or trolley conveyors) are highly versatile machines for transporting general cargo or bulk materials in bags or bins. Overhead conveyors are a central part of automated manufacturing systems, especially

assembly lines, but can also be found in paint and finishing lines, in the garment and food industry, etc. The greatest advantages of this type of conveyor are:

- Their ability to convey goods above the floor
- Their ability to realize relatively long (up to 3000 m) and very flexible three-dimensional conveyor routes
- Low power consumption due to small frictional motion resistances.

Overhead conveyors consist of four fundamental components:

1. A track and supports, mounted above the floor
2. Trolleys that move along the track system
3. A load attachment device, which is fastened to the trolley
4. A tension device, which is often a chain but can also be a rope or belt.

The trolleys and load attachment devices are support elements that transmit the gravitational force to the track system. The trolleys are towed by the tension device along the conveyor route, which is defined by the track system. The design of the load attachment device depends on the properties of the transported good. Multilevel platforms, racks, forks, hangers, hooks, hollows, containers, or bins can be used.

Certain drive, redirection, and pretension units can be applied depending on the components. Due to the large number of overhead conveyors using chains, the following explanation focuses on chain-based overhead conveyors. Two main types of overhead conveyor can be distinguished depending on the connection of the tension device to the trolleys. If the connection between these two components is not permanent, the conveyor is called a power and free conveyor to emphasis the presence of a powered and unpowered (free) track. A single-chain overhead conveyor has a permanent connection between the trolleys and chain.

Single-Chain Overhead Conveyors

Track System, Trolleys, Chain, and Load Attachment. Simple track systems can be made out of common I-beams. Trolley brackets with one roller pair run along the I-track, as shown in Fig. 20.78a. Closed track profiles as shown in Fig. 20.78b,c provide an easier connection of the track segments via flanges, but also better running conditions on complex routes due to the more enclosed system.

The load attachment device can be directly attached to the trolleys. If heavier goods are to be transported, the load can be shared between two or more trolleys by the use of load bars.

Profiled track systems can have a rectangular-, spherical-, or cross-shaped cross section. The different shapes allow the use of special trolleys or—more often—the use of a Cardan chain as the combination of the trolley and chain, as shown in Fig. 20.79. The load attachment device can be directly connected to the Cardan chain. As for the trolley–chain system, load bars are used to distribute the load over a certain amount of links of the Cardan chain.

If noncardanic chains are used, the chain design must allow three-dimensional redirection. Hence, round steel link chains or drop-forged rivetless chains could be used. Rivetless chains belong to the class of steel link chains and according to [20.52] allow limited redirection (up to 13°) in the third dimension (Fig. 20.80).

Drive. Sprocket wheels can be used to drive round steel link chains or rivetless chains, but not cardanic chains. Caterpillar drives as shown in Fig. 20.81 are an alternative here. The caterpillar drive consists of a steel link

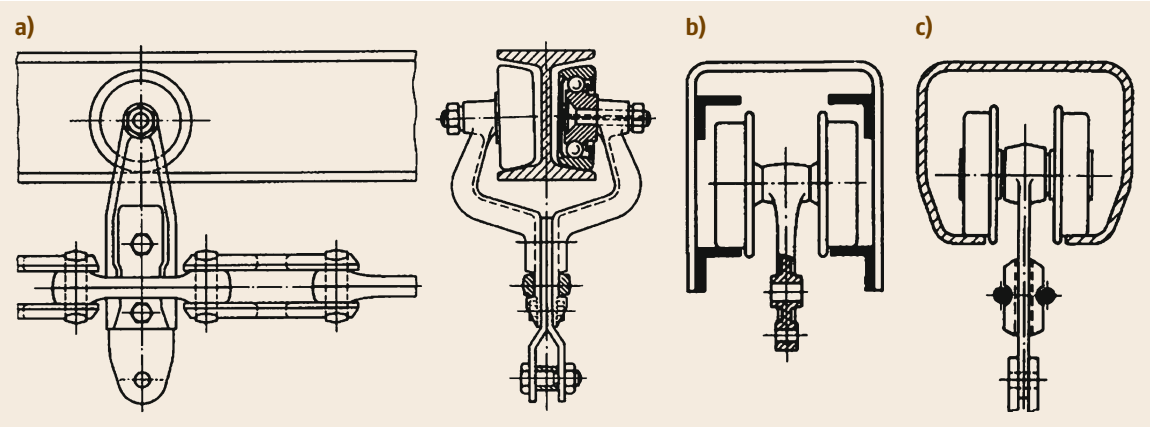

Fig. 20.78a–c Track systems for overhead conveyors, **(a)** I-beam track and trolley brackets, **(b)** U-shape profile with angle tacks, **(c)** rectangular profiled track [20.5]

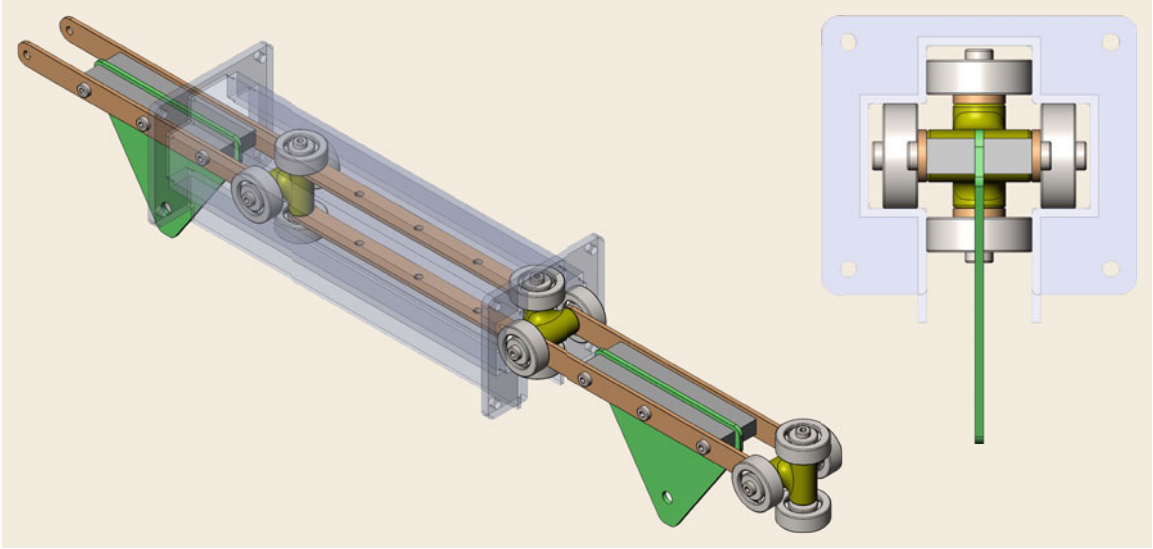

Fig. 20.79 Cardanic chain as merged element of trolley and chain

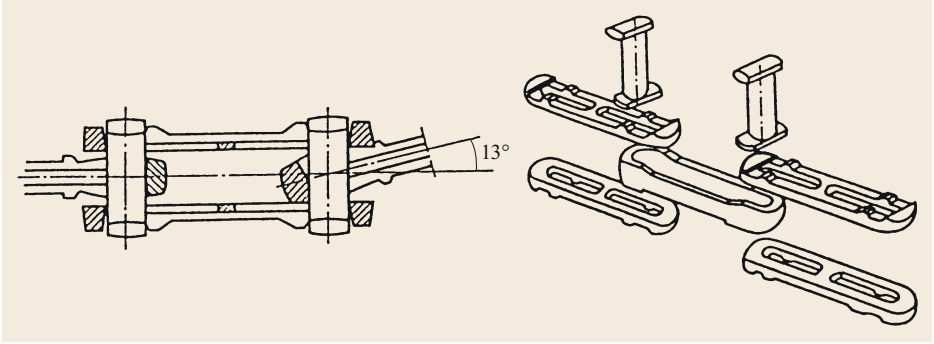

Fig. 20.80 Drop-forged riveted chain [20.52]

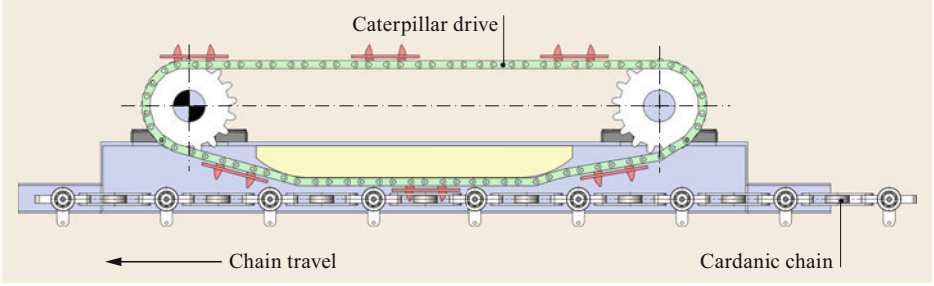

Fig. 20.81 Caterpillar drive for cardanic chains

chain with driving dogs. This power chain is driven by a sprocket wheel. The dogs engage with the conveyor chain and transport it in the conveying direction. The dogs can engage with the transport chain from the top, or from the left and right side if two synchronous power chains are used. Caterpillar drives offer certain advantages in comparison with common sprocket wheel drives:

- Easy application at almost any straight point of the conveyor routing, enabling the placement of the drive at the position where the highest chain tensile force occurs (independent of redirection)
- More cost effective than sprocket wheels due to lower torque requirements
- Reusability of the drive in case of modification of the conveyor route.

Table 20.11 Redirection coefficient for S-bends in overhead conveyors

Operation conditions	Redirection coefficient ξ depending on bend angle ψ		
	$\psi \leq 25°$	$\psi \leq 35°$	$\psi \leq 45°$
Good (clean, moderate temperature)	1.010	1.015	1.020
Normal	1.015	1.020	1.025
Poor (dirty, low temperature)	1.020	1.025	1.030

Tensioning Device. The pretension of the chain is realized during a 180° horizontal bend/curve of the track along the conveyor route. The curved track is mounted on a slide frame which is tensioned by a spring-spindle mechanism or pneumatic cylinders. Telescopic tracks can be realized for profiled track systems. I-beam tracks use expansion-type sliding joints.

Redirection. Redirection of the conveyor route is mainly realized by track bends/curves. The minimum radius of such horizontal and vertical curves must consider the chain turn angle (for rivetless and for cardanic chains), but also the dimensions of the load attachment and the good. The frictional forces during the curve can be reduced by using roller bends. Typically, so-called S-bends are used to realize the height difference between two horizontal levels of the conveyor route. The S-bend consists of two bends and a straight but inclined part. Inclination angles of $< 60°$ are commonly used to prevent collisions between the load attachment devices. Vertical sections are possible if the design allows a collision-free turn of the load attachment devices.

Calculations. Frictional motion resistances occur due to the rolling resistance of the trolley wheels. The tracks are made from steel, the trolley/chain wheels from steel or plastic (for noise reduction) with roller bearings. Therefore, friction factors can be calculated using (20.27) in Sect. 20.3.3. To estimate the motion resistances, the following friction factors μ_t for the trolley wheel motion can be applied depending on the operating conditions:

- Good conditions (clean, moderate temperature): $\mu_t = 0.02$
- Normal conditions: $\mu_t = 0.03$
- Poor conditions (dirty, low temperature): $\mu_t = 0.04$.

For straight and inclined sections, the motion resistances can be calculated as

$$F_i = L_i(q_c + q_t + q_a + q_g)g(\mu_t \cos\delta \pm \sin\delta) , \tag{20.74}$$

where

μ_t friction value of trolley wheels at the track
q_t meter weight of the trolleys
q_a meter weight of the load attachment device

For the S-bends described above, the chain tensile force at the end of the S-bend F_S can be calculated depending on the force at the start of the S-bend F_{S-1} via the use of the redirection factor ξ as

$$F_S = \left[F_{S-1} + L_i(q_c + q_t + q_a + q_g) \times g(\mu_t \cos\delta \pm \sin\delta)\right]\xi . \tag{20.75}$$

The values of ξ according to [20.128] are presented in Table 20.11, depending on the operating conditions and bend angle used.

To estimate the redirection resistance of the chain at sprockets or wheels, the redirection factor μ_R given by the following equation can be used

$$\mu_R = 2.1\left(\mu_{sh}\frac{d_{sh}}{d_{sw}}\sin\frac{\alpha}{2} + \mu_c\frac{d_c}{d_{sw}}\right) , \tag{20.76}$$

where

μ_{sh} friction at the shaft of sprocket wheel
d_{sh} diameter of the sprocket wheel shaft
d_{sw} diameter of the sprocket wheel
α redirection angle
μ_c friction in the chain joint
d_c diameter of the chain pin

According to [20.128], μ_{sh} and μ_c are given as presented in Table 20.12 depending on the operating conditions, the bearing, and the lubrication.

Table 20.12 Friction factors at chain and sprocket wheels of overhead conveyors

Operation conditions	μ_c		μ_{sh}		
	Roller bearing	Plain bearing	Continuous lubrication	Periodic lubrication	No lubrication
Good (clean, moderate temperature)	0.03	0.15	0.10	0.16	0.25
Normal	0.04	0.20	0.15	0.20	0.35
Poor (dirty, low temperature)	0.06	0.25	0.20	0.25	0.45

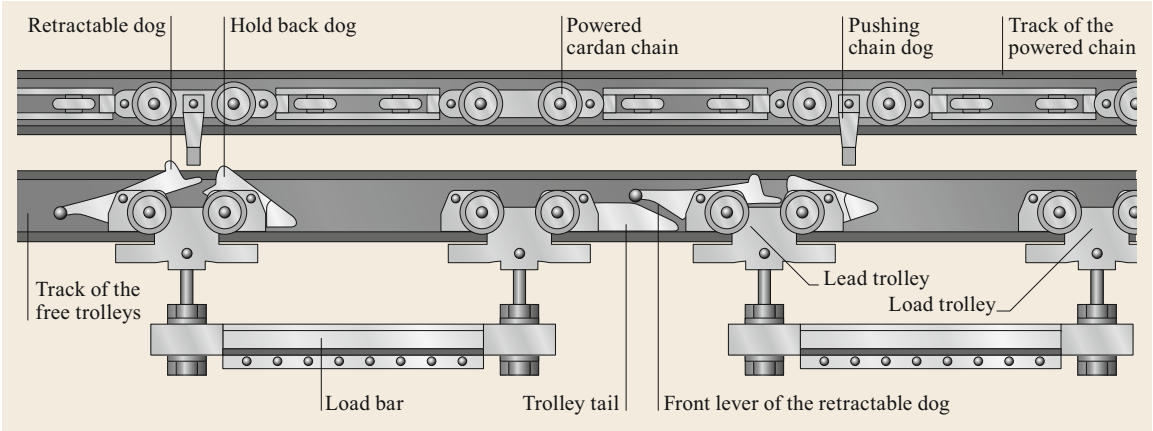

Fig. 20.82 Power and free conveyor components [20.5]

Power and Free Systems

The trolleys and chain can be separated and connected in power and free systems. Such systems allow the accumulation of trolleys with the goods in storage segments of the conveyor route, as well as the diversion of the trolleys in the conveying direction. This offers many advantages for the intermittent operation of many industrial and manufacturing processes.

For separation and connection, the chain is equipped with a pushing dog that can engage at the trolley dog, as shown in Fig. 20.82. The trolley dog is retractable and can be lowered via a front lever. If the trolley dog retracts, the trolley separates from the chain. During lowering of the retractable dog, a hold-back dog is lowered as well. The front lever can be lifted using controllable stopper blades or via the trolley tail of a fore- trolley. Hence, if one trolley is stopped and separated from the chain, the following trolley will also be stopped and separated if both trolleys come into contact. If trolleys are connected via load bars for load distribution, lead and load trolleys might be used, as shown in Fig. 20.79.

In power and free conveyors, the conveying route of the trolleys need not be fixed. Due to the installation of many powered chains, many route segments are possible. Trolleys can be diverted and merged via switches along the track.

The motion resistances of power and free systems can be calculated using the equation given for the single-chain overhead conveyor.

Inverted power and free conveyors do not work above floor but like other conveyors on the ground. The load attachment device is not hanging at the trolleys but rather sitting on top of them and forms a table on which the good can be placed. Inverted power and free conveyors are one possibility to create sorter conveyors, which are explained in more detail in Sect. 20.4.9.

20.4.5 Screw Conveyors

The principle of the screw conveyor dates back some 2200 years to the time of Archimedes, who developed the helical screw conveyor, mainly for pumping water for irrigation purposes. As illustrated in Fig. 20.83a, the Archimedean screw conveyor consists of a helical screw flight which is attached to a cylindrical casing, both rotating together. Its conveying action is by positive displacement, which can only be achieved at low elevation angles, thus restricting its use mainly to fluids or free-flowing granular materials. To handle and convey bulk materials over a range of elevation angles from horizontal to vertical, it is necessary for relative motion to occur between the rotating helical flight and the casing. This is normally achieved by fixing the casing while the screw rotates within it, as illustrated by the enclosed screw conveyor shown in Fig. 20.83b.

For enclosed screw conveyors, practical limitations require a generous clearance between the flight and the casing, and this has been shown to be beneficial rather than detrimental to their performance. The conveyor may be gravity fed, as shown in Fig. 20.83b, in which the screw flight projects beyond the casing at the lower or intake end, this projection being referred to as the *choke*. The screw must be immersed into the feed material at least to the level of the lower end of the casing, otherwise the conveyor will not elevate the bulk material. Better performance can be achieved by employing an efficient forced feeding system.

In an alternative type of screw conveyor that is widely used in industrial operations, the helical screw flight rotates in a U-shaped trough-type casing, as illustrated in Fig. 20.84a. The applications of such devices are limited to low angles of elevation, low speeds, and low fill ratios. The low fill ratios are to protect the hanger support bearings when long conveying distances

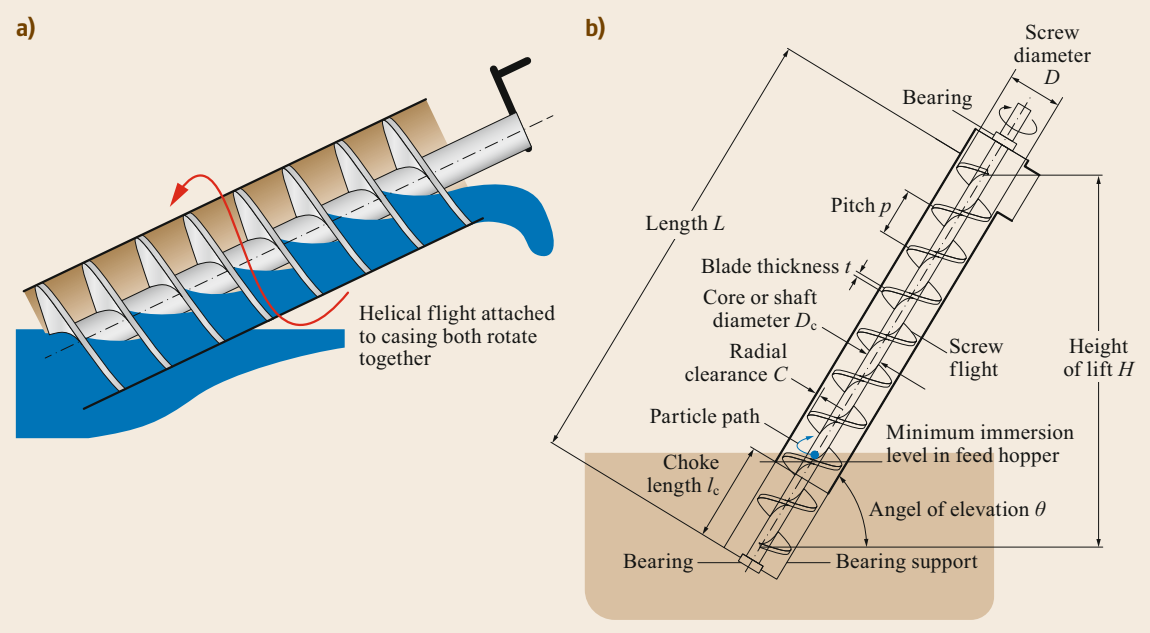

Fig. 20.83 **(a)** Archimedean screw pump, **(b)** enclosed screw conveyor

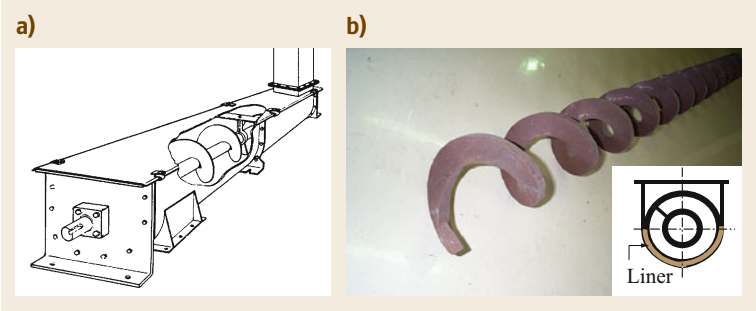

Fig. 20.84 **(a)** U-shaped trough-type screw conveyor, **(b)** shaftless screw

are employed. This problem can be overcome by using shaftless screws which employ helical flights with a heavy cross section that is necessary to resist the torsional, wind-up deformation imposed by the conveying action. The shaftless flight is supported on plastic, wear-resistant liners attached to the inside surface of the casing, as shown in Fig. 20.84b.

Of the various types and design of mechanical handling equipment employed in industrial operations, screw conveyors, in particular, play a major role in transport at low to medium throughput rates of up to 1000 m^3/h. Their application for conveying and elevating bulk materials for in-plant process requirements is well established and proven. Nonetheless, their mode of operation, while seeming to be obvious and simple, is in fact just the opposite, being quite intriguing and complex. It is particularly important, therefore, that conveyor designers, manufacturers, and users have some understanding of the basic mechanics governing their performance. This is essential to ensure their reliability and efficient operation. While screw conveyors are standardized in many international and national standards such as ISO 7119 [20.129], ANSI/CEMA 350 [20.130], DIN 15262 [20.131], and VDI 2330 [20.132], the design methodology is often limited to screw conveyors operating either horizontally or at low inclination angles. The influence of the bulk material is considered by a single factor (e.g. the "progress resistance factor λ" in ISO 7119 [20.129]). The VDI 2330 standard provides a relatively new empirical design approach for inclined and vertical screw conveying. However, the approach does not allow an understanding of important influencing parameters such as the wall friction of the bulk material (described in Sect. 20.2) versus the screw and casing. Hence, it seems appropriate to provide an overview of some salient performance and design as-

pects of screw conveyors, first dealing with the enclosed screw conveyor and second with the U-shaped trough conveyor. The content of these sections draws upon background research as presented in the selected references cited [20.133–138].

Enclosed Screw Conveyors for Steeply Inclined and Vertical Transport

Referring to the enclosed screw conveyor shown in Fig. 20.82b, the conveying of bulk materials is characterized by particles moving along a helical path with the opposite hand to that of the screw. The conveying action and throughput are dependent on the *braking effect* imposed by the casing friction, which can control and reduce the rotational component, the so-called vortex motion, imparted to the material by the rotating screw flight. The conveyor throughput is also influenced by the degree of fill or *fullness* of the screw. As the rotational speed of the conveyor increases, the losses due to the vortex motion decreases up to a limiting value, resulting in a more efficient conveying action. However, when a gravity feed is employed at the screw intake as in Fig. 20.83b, the feed rate cannot match the potential conveying capacity, and a reduction in fill ratio or *fullness* occurs. By employing a positive feed system to increase the *fullness*, the efficiency of the conveyor can be improved.

An appropriate forced feeding arrangement can be used to meet a specified throughput requirement, particularly when cohesive bulk solids are to be conveyed; for example, forced feeding is utilized in the Siwertell-type ship unloader, which employs a counterrotating lower casing with feed vanes that scoop the bulk material into the screw intake. The capacity of the screw conveyor is controlled by the feeding device rather than by the conveyor itself. To avoid blockages at the screw intake, it is essential that the conveyor speed be high enough to achieve a fill ratio $\eta_F < 1$.

In multiple conveyor installations where transfers are employed, it is most important that blockages be avoided. As an illustration, the transfer from a horizontal to a vertical screw conveyor as depicted in Fig. 20.85 is considered. Two design conditions need to be considered. Firstly, the discharge Q_1 from the horizontal conveyor will be cyclical at a frequency related to the conveyor rotational speed as indicated. Secondly, the conveying efficiency of the vertical conveyor will be less than that of the horizontal conveyor. To avoid blockages, it is recommended that the vertical conveyor be designed for a capacity, $Q_2 \geq 1.2Q_1$.

Conveyor Throughput. The typical characteristic of volumetric throughput Q_V versus speed is illustrated in Fig. 20.86. This figure shows the throughput versus speed plots for a screw conveyor with equal diameter and pitch of 152 mm when conveying wheat at

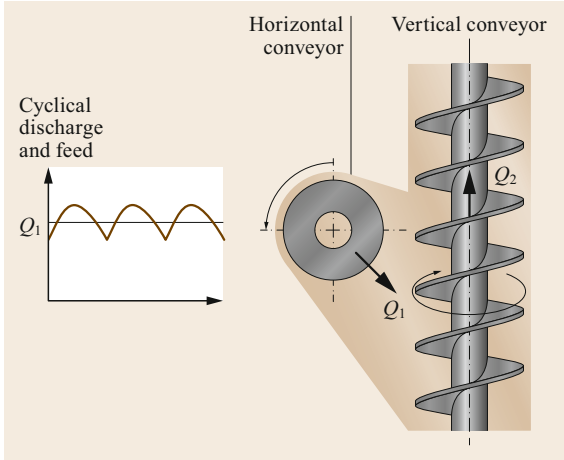

Fig. 20.85 Horizontal to vertical conveyor transfer

three angles of elevation: 30°, 60°, and 90°. Over the lower speed range, the throughput is nominally proportional to the speed, but it then becomes quite nonlinear and limited with further increase in speed, sometimes reaching a maximum then decreasing. Figure 20.85 also shows the maximum theoretical throughput Q_t for the conveyor running 100% full with the bulk material moving axially without rotation. While this is not possible in an actual conveyor in view of the influence of the friction due to the screw flight, it provides a basis for the determination of the conveying efficiency.

$$Q_V = Q_t \eta_v \,, \tag{20.77}$$

where

$$Q_t = 60\Gamma N D^2 \tag{20.78}$$

with

$$\Gamma = \frac{\pi}{4}\left[\left(1+2\frac{C}{D}\right)^2 - \left(\frac{D_c}{D}\right)^2\right]\left[\frac{p}{D} - \frac{t_s}{D}\right] , \tag{20.79}$$

Q_t maximum theoretical volumetric throughput (m^3/s)
η_v conveying efficiency of the volumetric flow rate
D screw diameter (m)
D_c core or shaft diameter (m)
p pitch (m)
N rotational speed of screw (rev/m)
C radial clearance (m)
t_s thickness of screw blade (m)

The mass flow rate Q_m can be calculated according to (20.6).

Effect of Conveyor Diameter–Corresponding Speeds. Corresponding speeds are given by the

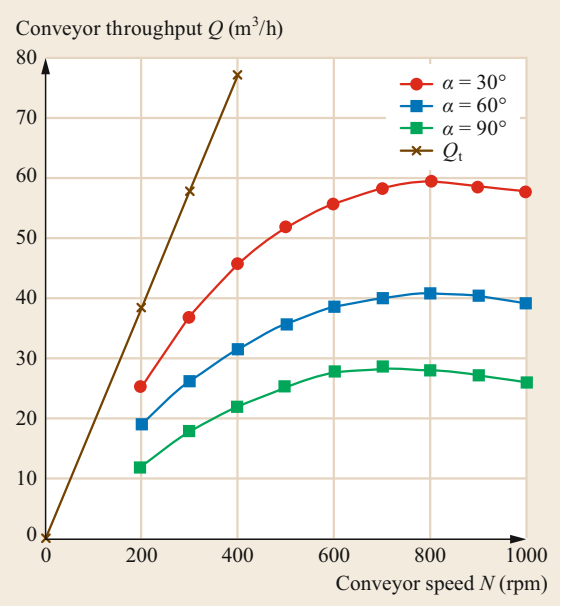

Fig. 20.86 Conveyor throughput for wheat $p = D = 0.152\,\text{m}$; $C = 0.097\,\text{m}$

nondimensional, specific speed number N_S defined as

$$N_S = \frac{\omega^2 R_0}{g} = \frac{N^2 D}{1789}\,, \tag{20.80}$$

where

R_0 outer radius
g gravitational acceleration
ω angular velocity (rad/s).

It follows from (20.80) that screw conveyors with large diameter attain their maximum output at lower speeds than conveyors with smaller diameter [20.133]; for example, for a scale of 4 : 1, the characteristic performance of the larger of the two conveyors would occur at half the speed of the corresponding, geometrically similar conveyor of one-quarter the size.

Conveying Efficiency of Volumetric Flow Rate. The conveying efficiency of the volumetric flow rate of a screw conveyor is the product of two components

$$\eta_v = \eta_{vR}\eta_F\,, \tag{20.81}$$

where

η_{vR} conveying efficiency accounting for the rotational or vortex motion
$\eta_F = h_{av}/p$ the filling efficiency or fullness,

defined by the ratio of the average height of material on the screw surface h_{av} and the pitch p.

To throw some light on the basic mechanics governing the performance of screw conveyors, the case of a vertical screw conveyor is now considered. The theory presented here is an overview of the theory presented in some detail in [20.135, 138].

Conveying Efficiency Considering the Rotational or Vortex Motion in Vertical Screw Conveyors. Figure 20.86 shows the conveying action within a vertical screw conveyor. The velocity diagram for a particle in contact with the screw surface at a particular location is also shown. v_S is the screw velocity due to its rotation, v_R is the relative velocity of the particle with respect to the screw surface, and v_A is the absolute velocity of the particle defined by the helix angle λ. The velocity diagram, reproduced in Fig. 20.87c, shows the absolute velocity resolved into two components: the useful conveying velocity v_L and the rotational component v_T. Since the helix angle λ of the screw flight varies with the radius, being smaller at the outer periphery and larger at the shaft, the angle λ will also vary in the radial direction from the outside of the flight to the shaft. This means that the rotational velocity v_T, in theory, will vary from the outside to the shaft. The variation in v_T with radius describes the vortex motion in the screw and is expressed by $v_T r^n = \text{const}$. The constant n is the vortex index.

It has been shown by *Roberts* [20.134, 135] that $n \approx 0$, that is, the velocity component v_T is approximately constant and, in fact, does not vary with the increase in radius from R_i at the shaft to R_0 at the outer periphery. This means that the height h of material on the screw flight is approximately constant and does not vary with the radius.

To determine the conveying efficiency, it is necessary to determine first the variation of the path helix angle λ as a function of the radius and rotational speed of the conveyor. This analysis can be simplified by lumping the rotational mass and resultant forces at the effective radius R_e defined by

$$R_e = \frac{2}{3}\frac{R_0^3 - R_i^3}{R_0^2 - R_i^2}\,, \tag{20.82}$$

where

R_0 outside radius of screw flight
R_i inner radius of radius of shaft.

The helix angle of the screw flight corresponding to R_e is

$$\alpha_e = \tan^{-1}\left(\frac{p}{\pi D}\frac{R_0}{R_e}\right)\,, \tag{20.83}$$

where

p pitch
$D = 2R_0$ screw flight diameter

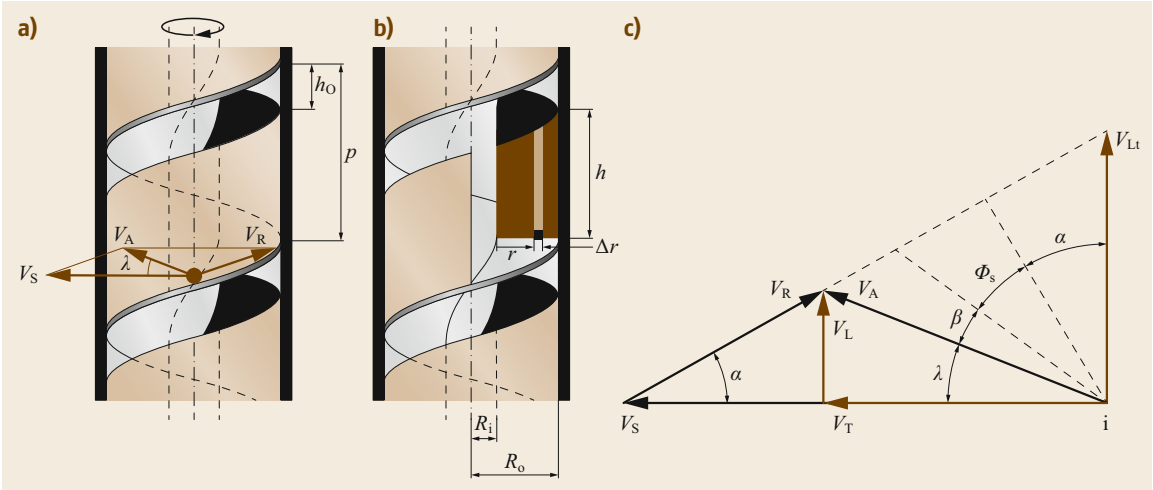

Fig. 20.87a–c Mechanics of conveying action on a vertical enclosed screw conveyor **(a)** (sectional view **(b)**) with the related velocity diagram **(c)**

The relationship between the helix angle λ of the path and the speed of rotation of the conveyor has been studied by *Roberts* [20.133–135]. The angle λ_e increases with the speed of rotation, asymptotically reaching a limiting value defined as

$$\text{as } N_S \to \infty\,, \quad \lambda_e \to 90° - (\alpha_e + \phi_s)\,, \tag{20.84}$$

ϕ_s friction angle for screw surface

That is, λ_e approaches a constant value defined by the helix angle of the screw and the friction angle of the bulk solid in contact with the screw surface.

The actual conveying velocity v_{Le} at the effective radius, when expressed as a ratio of the maximum theoretical conveying velocity v_{Lt}, provides a measure of the conveying efficiency, allowing for losses resulting from the rotational or vortex motion. It may be shown that

$$\eta_{vR} = \frac{v_{Le}}{v_{Lt}} = \frac{\tan\lambda_e}{\tan\alpha_e + \tan\lambda_e}\,. \tag{20.85}$$

The performance of screw conveyors is significantly influenced by the friction generated between the bulk material and the screw and casing surfaces. As shown in [20.139], increasing the friction between the bulk material and screw decreases η_{vR}, while increasing the friction at the casing causes an increase of η_{vR}. These results clearly show the advantages of low screw surface friction and high casing friction.

It should be noted that the surface friction angles for cohesive bulk solids are found to decrease with increasing normal pressure. It is important that the surface friction angles be measured and that the appropriate friction angles corresponding to the pressures generated at the screw and casing surfaces be used in the conveyor design.

Screw Torque and Power. The motion resistances in a vertical or steeply inclined screw conveyor arise mainly from the weight of the material, the friction at the casing induced by the centrifugal forces, and the friction between the bulk material and screw. The calculation of the resultant motion resistance F_R is described in detail in [20.136].

The total torque of screw conveyors consists of the screw torque T_{sc} and the torque at the shaft T_{sh}. The screw torque due to the bulk solid on the flight face can be determined from

$$T_{Sc} = \frac{L}{p} F_R R_e \tan(\alpha_e + \phi_s)\,, \tag{20.86}$$

where

ϕ_s friction angle for bulk solid on screw surface
R_e effective radius
α_e effective helix angle
L length of screw conveyor
p pitch

The torque due to the bulk solid moving relative to the shaft is

$$T_{Sc} = 2\pi R_i^2 L K \rho_b g p \eta_F\,. \tag{20.87}$$

K accounts for the pressure distribution around the shaft. It is assumed that $K = 0.4$.

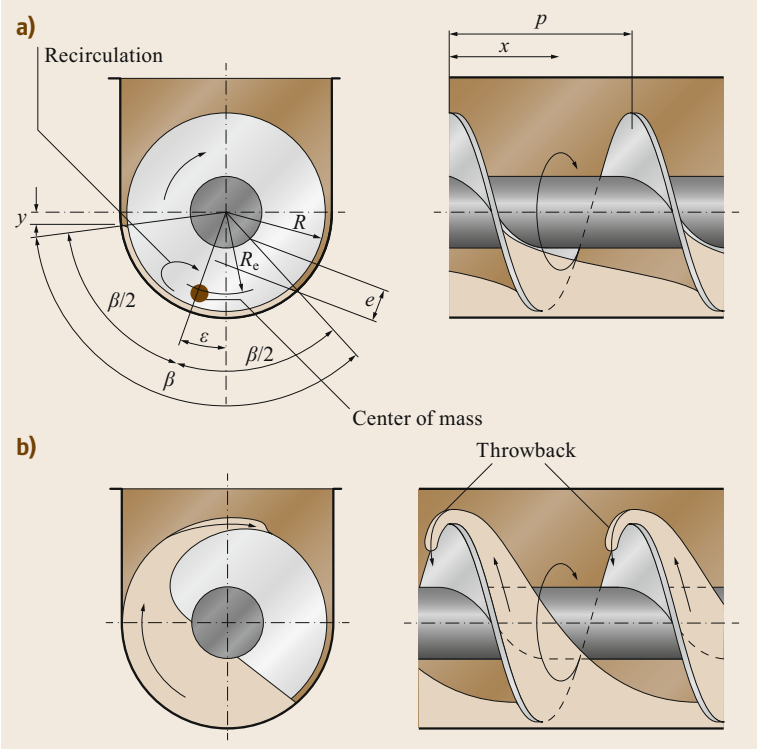

Fig. 20.88a,b Mechanics of U-shaped trough screw conveyor performance **(a)** and throwback, which decreases the conveying efficiency **(b)**

Considering the drive efficiency η_{drive}, the necessary drive power can be calculated as

$$P = \frac{(T_{sc} + T_{sh})\omega}{\eta_{drive}} . \qquad (20.88)$$

U-Shaped Trough Screw Conveyor for Horizontal or Slightly Inclined Transport

These conveyors operate in a horizontal position or a low elevation angle. The bulk solid assumes an offset position as indicated in Fig. 20.88a. It is important that the fill ratio be such that the surface of the bulk solid does not lead to overfilling of the conveyor, causing throw-back as shown in Fig. 20.88b. To avoid throw-back, the restraining torque due to the weight of the bulk solid and casing friction must be equal to or greater than the torque generated by the screw when the surface of the segment just intersects the horizontal center line, that is, when the dimension y in Fig. 20.88a equals zero.

The performance of such a conveyor is analyzed by concentrating the weight of material at the center of mass denoted by point P in Fig. 20.88. The effective radius R_e and corresponding effective helix angle α_e are given by

$$R_e = \frac{2}{3} R \frac{N_T}{\beta - \sin\beta} \quad \text{and}$$

$$\alpha_e = \tan^{-1}\left(\frac{p}{2\pi R_e}\right) . \qquad (20.89)$$

The mass flow rate of the conveyor is given by

$$Q_m = \rho_b A n p \eta_v , \qquad (20.90)$$

where

A cross-sectional area
n rotational speed (1/s)
p pitch
η_v conveying efficiency due to the rotational or vortex motion of the bulk material.

The cross-sectional area of the bulk material in the trough can be calculated via the angle β as shown in Fig. 20.88. β is the included angle of the segment of the bulk material. It is directly dependent on the filling level η_F and the volumetric efficiency η_V (defined in (20.7)) as well as the theoretical circular area of the trough A_c. Hence, A can be calculated as

$$A = \frac{R^2}{2}(\beta - \sin\beta) = A_c \eta_F \eta_V = \pi R^2 \eta_F \eta_V . \qquad (20.91)$$

The conveying efficiency of the volumetric flow rate is given by

$$\eta_v = \frac{1}{2}\left(1 + \frac{\tan\lambda_e}{\tan\alpha_e + \tan\lambda_e}\right) , \qquad (20.92)$$

where λ_e according to (20.84) is assumed to be

$$\lambda_e = \frac{\pi}{2} - (\alpha_e + \phi_s) . \qquad (20.93)$$

The nondimensional parameter N_T is known as the torque parameter and is given by

$$N_T = \beta - \frac{1}{2}\sin\beta - \cos^3\frac{\beta}{2}\ln\left[\tan\left(\frac{\pi}{4}+\frac{\beta}{4}\right)\right] . \quad (20.94)$$

The torque per pitch is given by

$$T = \frac{1}{3}\sigma_a R^3 \tan(\alpha_e + \phi_s) N_T , \quad (20.95)$$

where the axial pressure σ_a is given by

$$\sigma_a = \rho_b g p(\sin\theta + \mu_E \cos\theta) , \quad (20.96)$$

where the equivalent friction value μ_E can be calculated as

$$\mu_E = \mu_c\left[1 + K\left(1 - \cos\frac{\beta}{2}\right)\right] , \quad (20.97)$$

assuming a pressure ratio K of 0.4.

The total torque can than be calculated as

$$T_{total} = \frac{TL}{\eta_v p} . \quad (20.98)$$

Hence, the drive power is given by

$$P = \frac{T_{total}\omega}{\eta_{drive}} . \quad (20.99)$$

To prevent throw-back, it may be shown that

$$\sin\varepsilon + \mu\cos\varepsilon \geq (\sin\theta + \mu_E\cos\theta)\tan(\alpha_e + \phi_s) . \quad (20.100)$$

20.4.6 Vibratory Conveyors

Vibratory conveyors are used in many branches of industry to achieve low to medium mass flow rates with relatively low speeds ($< 0.4\,m/s$). The advantages of this conveyor are its relatively simple design, the lack of contact between the bulk material and sensitive machine parts (e.g., bearings), the possibility of transporting bulk material at high temperatures ($< 1000\,°C$), the possibility of safe and hermetic transport, and the possible combination of the transport process with other technological processes such as screening, mixing, and feeding. The disadvantages of this type of conveyor are the limited length, the high noise generation, and the complex dynamic interaction between the bulk material and trough, which may lead to a reduction of the throughput rate due to changes in the properties of the bulk solid.

In manufacturing and on assembly lines, vibratory conveyors are commonly used to transport small machine parts such as bolts, screws, rings, etc. A major advantage is the orientation of the machine parts during the transport process. With the help of guiding obstacles, it is possible to generate a material flow with the same orientation of all goods, which facilitates automation of the manufacturing/assembly process.

Vibratory conveyors can be used to realize straight linear conveying routes with rather small inclination angles (depending on the properties of the goods). Furthermore, vertical transport is possible if troughs with a spiral design are used, as shown in Fig. 20.89.

General Design

Vibratory conveyors basically consist of a vibrating trough or tube, which is flexibly supported, and the drive. The vibration motion can be generated electrically (using oscillators or electromagnets) or mechanically (e.g., using a slider-crank mechanism or a centrifugal drive with rotating unbalanced weights). The vibration occurs due to the generation of an exciting force acting on the trough or due to the direct displacement of the trough (Fig. 20.90). Displacement drives (e.g., using a slider-crank mechanism) can exert high loads on the mechanical parts of the conveyor. Exciting force drives—such as the centrifugal drive with rotating unbalanced weights—are therefore commonly used.

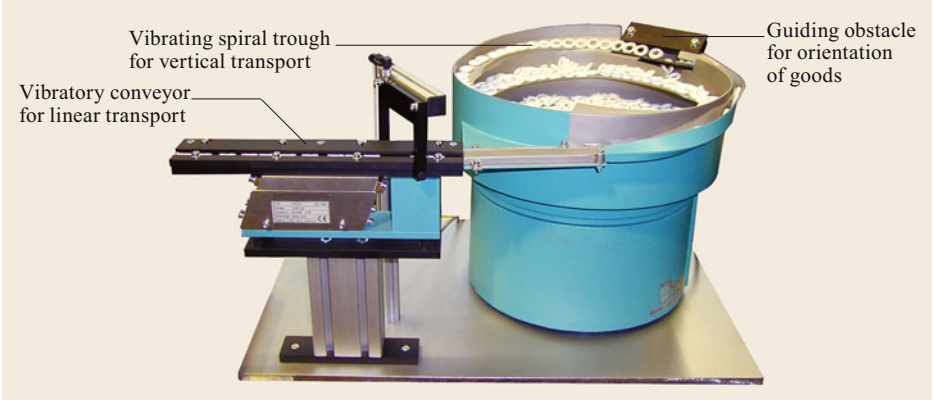

Fig. 20.89a,b Vibratory conveyors for the transport of small parts (AViTEQ Vibrationstechnik GmbH, Hattersheim)

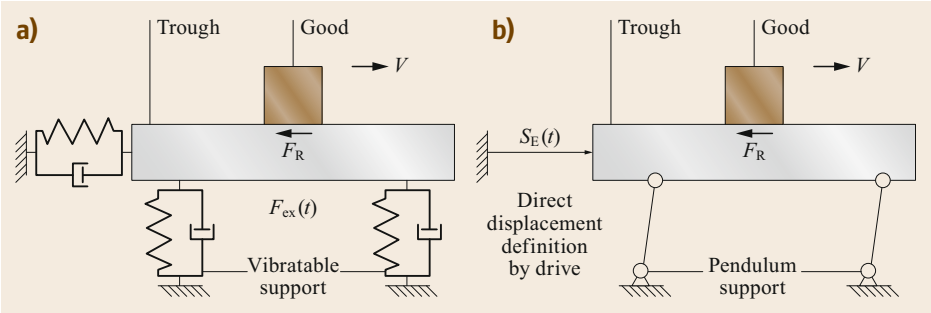

Fig. 20.90a,b Design principle of a vibratory conveyor with exciting force drive **(a)** or displacement drive **(b)** [20.140]

Conveying Principle

Two operation modes of vibratory conveyors can be distinguished: the gliding and the micro-throw regime. During gliding, the material never loses contact with the vibrating trough. If the material loses contact with the trough, the conveyor will operate in the micro-throw regime.

Notwithstanding the simplicity of the vibratory conveyor design, the question of the control and transportability of arbitrary bulk solid remains vital. The reason is the complex behavior of bulk solids on a vibrating surface, where the properties of the bulk solid, as well as induced air, may influence the transport process. Furthermore, the bulk material can influence the vibratory conveyor itself, namely its natural frequency, amplitude, and required drive power. This so-called reactive effect of the bulk material will occur especially if the conveyor is loaded with high filling heights. The reactive effect results partially in damping and partially in an increase of the trough mass due to the connected mass of the bulk solid. For further information, refer to [20.141]. The interaction of the bulk material with the vibrating trough can lead to nonharmonic motions that may negatively influence the conveying process.

Throughput Calculation

To calculate the volumetric flow rate according to (20.6), it is necessary to predict the velocity of the material stream. Different approaches are available. The most popular approach is the point-mass model, which has found practical application in many works covering the theory of vibratory conveyors. The model uses the following assumptions [20.142]:

- The trough is driven harmonically in horizontal and vertical directions.
- A particle can be considered as a point mass.
- The collisions between the particles and trough surface are completely plastic. No particle rebound occurs after collision.
- The particle does not rotate.
- The trough vibrating surface is ideally flat, and the trough side walls have no influence.
- The interparticle friction, the wall friction, the permeability to air, as well as the elastic damping properties of the particles can be neglected.

A characteristic parameter for the conveying behavior is the so-called throw number Γ

$$\Gamma = \frac{\Omega^2 A \sin\beta}{g} \qquad (20.101)$$

with

g acceleration of gravity
f_{dr} driving frequency
A amplitude
β vibration angle
Ω angular vibration frequency ($\Omega = 2\pi f_{dr}$).

The micro-throw regime will occur if the particles lose contact with the trough. This occurs when the reaction force between the trough and particle becomes equal to zero. Hence, $\Gamma < 1$ indicates gliding rather than throw operation, while $\Gamma \geq 1$ indicates that particle micro-throw occurs. In the latter case, the given vertical particle acceleration caused by the trough motion exceeds the acceleration due to gravity.

The periodic particle motion can be divided into characteristic phases: sliding, flight, collision, rest, and combined phases, as shown in Fig. 20.91. The start and end time of each characteristic point must be calculated. To do this, the equations of motion of the particle and trough as well as the momentum equations of the particle–trough interaction must be solved. A throw over the whole period results in values $\Gamma \geq 3.3$. This is commonly not beneficial due to the increase of the necessary drive power, which is not necessarily reflected in an increase of the volumetric flow rate.

A particle velocity can be computed for each of the characteristic phases of the motion cycle. The sum of all the phases defines the conveying speed. The basic

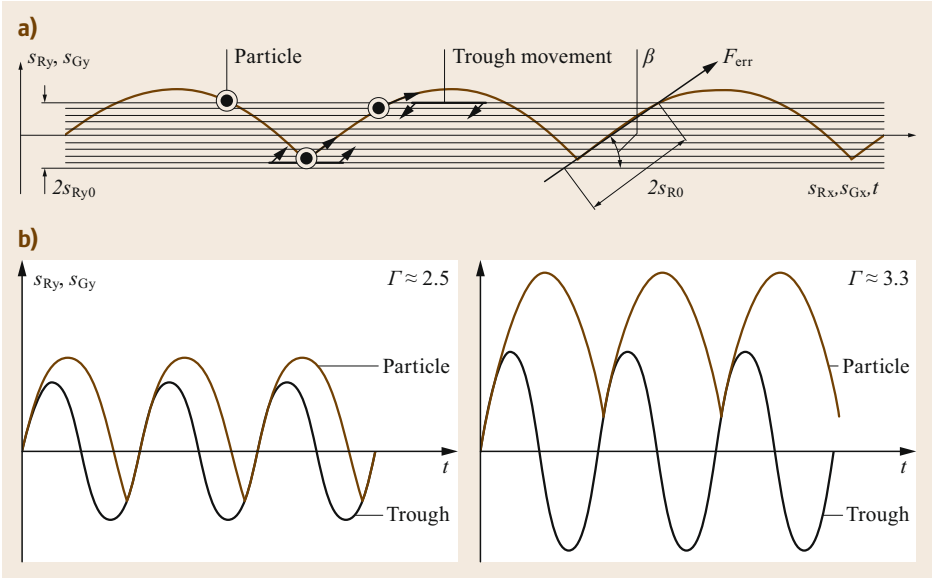

Fig. 20.91a,b Visualization of conveying process in micro-throw regime **(a)** and influence of throw number on conveying process **(b)** [20.143]

formula to determine the average conveying speed is therefore

$$v_{th} = \frac{g\overline{n}^2}{2f_{dr}} \cot\beta \quad \text{with } 0 \le \overline{n} \le 1 \tag{20.102}$$

with

$\overline{n}$ factor of throw time, which is a function of the throw number
f_{dr} driving frequency.

The inverse relation of $\overline{n}$ and Γ is defined as

$$\Gamma = \sqrt{\left(\frac{\cos(2\pi\overline{n}) + 2\pi^2\overline{n}^2 - 1}{2\pi\overline{n} - \sin(2\pi\overline{n})}\right)^2 + 1}\,. \tag{20.103}$$

The factor of the throw time indicates the relation of the pure throw time to the whole vibrating period. Figure 20.92 shows the relationship between $\overline{n}$ and Γ.

This theoretical average conveying speed will not be achieved, because many factors that are not accounted for will influence the motion of the bulk solid. The actual properties of the bulk solid and other parameters that influence the motion of the bulk solid can be considered by incorporating correction coefficients

$$v = v_{th} K_1 K_2 K_3 K_4 \tag{20.104}$$

with

v conveying speed achieved in practice
v_{th} theoretical conveying speed
K_1 coefficient due to bulk solid properties
K_2 coefficient due to percentage of fines in the bulk solid

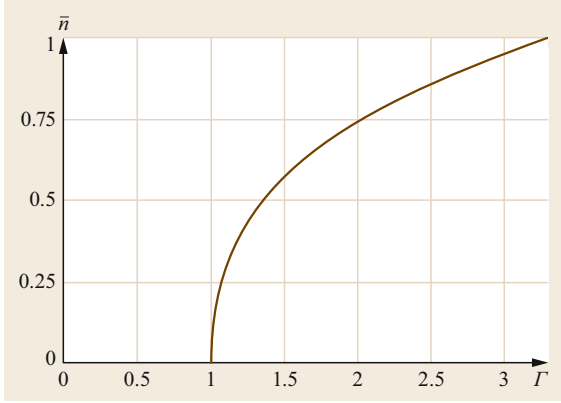

Fig. 20.92 Relationship between the factor of throw time $\overline{n}$ and throw number Γ [20.143]

K_3 coefficient due to the height of the load
K_4 coefficient due to trough inclination.

K_1 is determined experimentally for each bulk material for thin bed heights. Approximations for the other K factors are shown in Fig. 20.93.

The product of all the correction coefficients can range between 0.05 and values over 1.0. Numerous works in this field cover the definition of the influences of air permeability, friction, the bulk solid reaction on the trough motion, trough inclination, and other factors. Despite many works that recommend improved calculation theories, the basic formula for the average conveying speed is still used in practice. A detailed overview of the K coefficients as well as a presentation of alternative calculation approaches including DEM simulation is given in [20.143] for bulk materials and

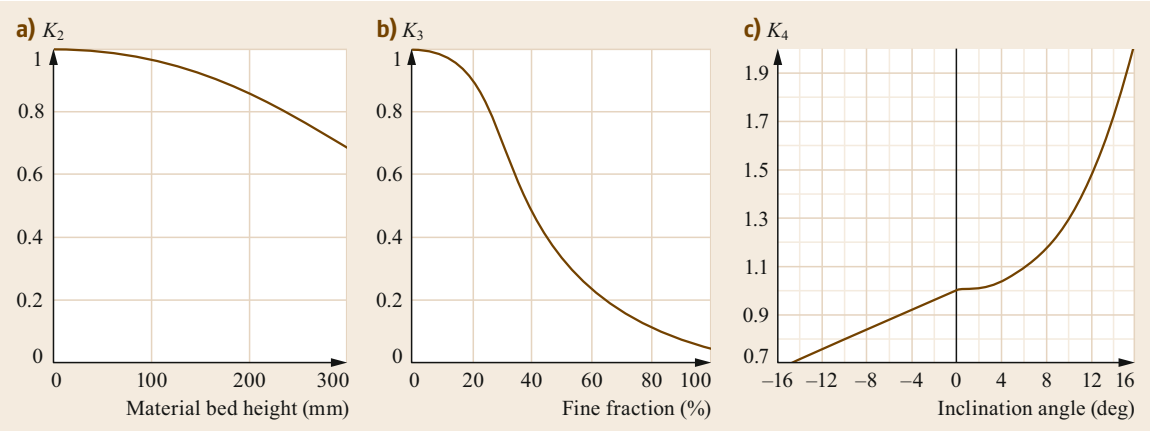

Fig. 20.93a–c Correction coefficients for the calculation of the mean conveying speed depending on **(a)** the bed height at the trough, **(b)** the percentage of the fine fraction <0.3 mm, and **(c)** the conveyor inclination angle [20.143]

for the transport of the small machine parts in single and bulk mode in [20.140, 144].

Estimation of Drive Power

In [20.145–147], based on a *semiempirical* approach, an estimation for the necessary drive power is given as

$$P = Q_{\mathrm{m}} g L(\mu_{\mathrm{total}} \pm \sin\delta) \qquad (20.105)$$

with

L conveyor length
δ inclination angle
μ_{total} virtual friction coefficient that summarizes all motion resistances.

According to [20.143], it is generally accepted that one can assume a conservative $\mu_{\mathrm{total}} = 1.5$ for a first estimation of the necessary drive power.

20.4.7 Pneumatic Conveyors

Pneumatic conveying is a common in-plant transport system for bulk material which has been used successfully in the chemical (soap powders, detergents), food (sugar, flour), cosmetics (talc, face powder), and energy (coal and ash) industries. The major advantages of pneumatic conveying systems are their enclosed nature, flexibility, and easy automation. There are two basic flow modes in pneumatic conveying: dilute phase (or suspension flow) and dense phase, where the predominant flow mechanism is a nonsuspension mode of flow. While dilute phase systems are generally the most reliable and offer the greatest flexibility in design, their relatively high conveying velocities (generally in excess of 15 m/s) lead to significant operational problems including particle attrition and erosive wear of pipelines.

The choice of whether to design for dilute phase or dense phase conditions can be a difficult choice for the designer. In general, dilute phase conveying has greater tolerance and can be safer with regard to reliability and the sensitivity of the system to changes in material properties. However, for materials that are erosive or abrasive and for materials that are fragile, dilute phase systems are generally not suitable. Lowering the conveying velocity can have a very significant effect in terms of reducing the unwanted side effects of product degradation (or attrition) and erosive wear of the system. In these situations, there is a strong case for using dense phase conveying.

The origins of modern pneumatic conveying systems can be traced back to the late 19th century in England, where a vacuum conveyor was installed to discharge grain from ships [20.148]. Throughout the 20th century, pneumatic conveying technology has grown enormously. In the 1970s, pneumatic conveying system installations boomed by an order of magnitude, partially because of the reinforcement of health and safety regulations for the working environment when handling explosive, toxic, and other hazardous materials [20.149]. The major advantages of the pneumatic conveying method are environmentally friendly operation, air as the required source, routing flexibility, low maintenance and labor costs, and easy automation/-control. However, some of the main disadvantages of this method include relatively high power consumption, limited conveying distance, and abrasion/wear of the system [20.150].

Components and Systems

A pneumatic conveying system generally consists of four sections: the prime mover which supplies the conveying gas, the feeding section, the conveying zone, and the discharge section. Figure 20.94 shows a basic pneumatic conveying components setup.

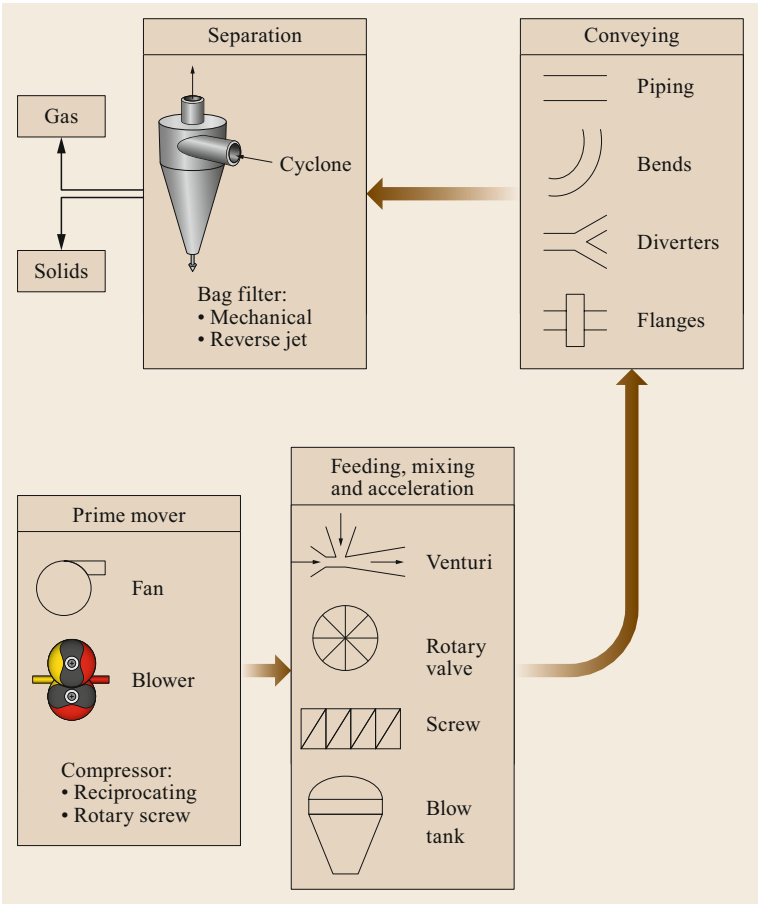

Fig. 20.94 Basic components of a pneumatic conveying system [20.151]

Firstly, in terms of the prime mover, a wide range of compressors, blowers, and fans are usually applied to provide the conveying gas. Depending on the location of the prime mover, positive- or negative-pressure systems can be established. The prime mover is commonly the most expensive single item in terms of capital and running costs. To provide a reliable and effective transport medium, it is critical to identify the gas flow rate and pressure required from the prime mover. To achieve this, it is essential to understand the theories of compressed gas pipeline flows, together with special product requirements such as gas driers, coolers, oil filters, etc.

Secondly, the feeding section that *inserts* the material into the conveying gas is a critical element of a pneumatic conveying system. For a particular type of feeder, it can only be operated in a certain range of differential pressures between the feed hopper and the pipeline. Incompatibility of the parameters of the feeder and the prime mover often leads to conveying system problems. As shown in Fig. 20.94, feeding devices such as venturi, rotary valve, screw feeder, and blow tanks are commonly used to suit particular pneumatic conveying applications.

Thirdly, the solid material is fed into the conveying zone. Within this zone, a large momentum transfer is induced by the conveying medium to accelerate the solids. Once accelerated, the material will pass various conveying zone configurations such as piping, bends, expansions, and diverters, within which the material may be decelerated or reaccelerated. The design of the conveying zone layout is largely dependent on the available routing space, minimum conveying velocity, pressure drop requirement, product abrasiveness, and product physical properties.

Regarding separation systems, cyclones and bag filters (typically shaking or pulse jet) are commonly used devices in the discharge section to separate the gas and solids at the end of the pipeline. In fine ash handling plants, electrostatic precipitators (ESP) are commonly used. In particle separation systems, the material will subsequently be conveyed to the receiving bin, with the conveying gas usually rejected to the atmosphere.

Modes of Flow

Determining the performance capability of a pneumatic conveying system for bulk materials in the dense phase

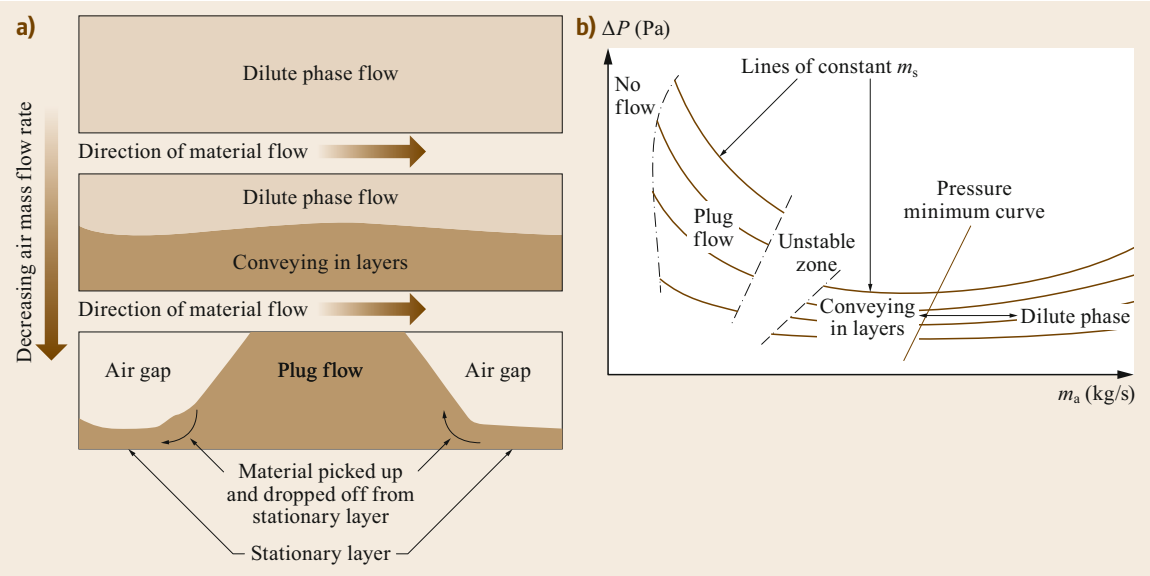

Fig. 20.95a,b Transition from dilute phase flow to plug flow [20.152]. **(a)** General structure of transition from dilute flow to plug flow within the pipeline. **(b)** Pneumatic conveying characteristic chart for transition from dilute flow to plug flow

is generally more challenging when compared with the same material in the dilute phase. It has long been recognized that there are two broad categories of dense phase flow that can be effectively used in pneumatic conveying systems: firstly, dense phase conveying of predominantly granular materials (plug flow) which exhibit a high degree of permeability, and secondly, a flow which is based largely on the fluidized nature of fine powders (fluidized dense phase flow). For granular material, the dense phase flow basically consists of full-bore conveying of material separated by air gaps. For the fine powder dense phase flow, the material generally flows in two layers which consist of a dense phase layer flowing at the bottom of the pipe and a dilute phase layer flowing in the upper layer.

Plug Flow. In fully developed dense phase pneumatic conveying of granular material, discrete full-bore lengths of material flow through the pipeline. These full-bore lengths of material have been characterized as plugs (or slugs) of material. In plug flow, the discrete plugs can vary in length and frequency and can merge with other plugs or be destroyed. These variations in plug behavior are generally dependent on the pneumatic conveying conditions through the pipeline, usually defined by the air pressure (P) and flow parameters such as the solid mass flow rate (m_s) and air (or gas) mass flow rate (m_a).

With respect to the conveying parameters described above, the transition behavior from dilute flow to plug flow conveying can vary considerable and be quite complex and difficult to measure. For instance, as shown in Fig. 20.95, as m_a is decreased, there is a (generally smooth) transition from the dilute phase flow to a mode of conveying characterized by a dense layer of particles traveling along the bottom of the pipeline (conveying in layers or strand flow) and a dilute phase layer flowing over the top. Further reduction of m_a can cause instabilities in the flow in a region known as the unstable zone. The characteristics of the flow of granular material in the unstable zone can vary, depending on the material type. For instance, for some sugars and sand, the unstable zone represents a *no go* region for pneumatic conveying while for other material such as plastic pellets, the transition is relatively smooth. For other materials, the unstable zone is characterized by significantly large pressure fluctuations and severe pipeline vibration. Further reduction of m_a below a critical value defines the dense phase steady-state region of plug flow, where each plug of material *picks* up particles from a stationary layer at the front and material falls off at the back of the plug.

Fluidized Dense Phase Flow. The general description of dense phase flow of fine powders is that it consists of two layers: a dilute phase layer flowing over a slower dense phase layer. The dense phase layer exhibits a wave (or dune)-like motion along the bottom of the pipe, as illustrated in Fig. 20.96. This two-phase flow can be discontinuous and interspersed with full-bore pulses of material. The composition of the material structure within the dense pulse varies with stratification of the density, increasing towards the bottom of the pipe. In essence, the transient pulsatile dune structure of the

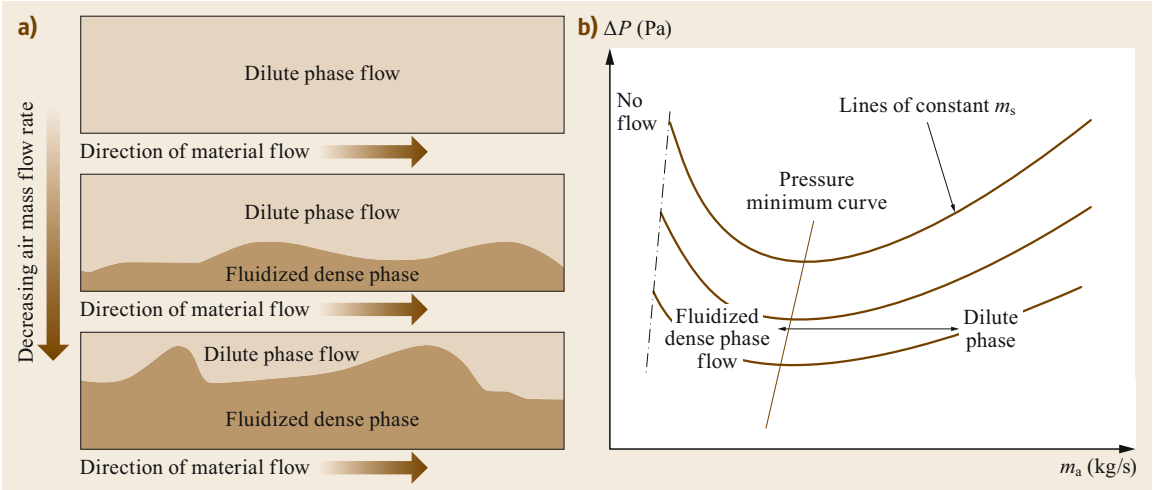

Fig. 20.96a,b Transition from dilute phase flow to fluidized dense phase flow [20.152]. **(a)** General structure of transition from dilute flow to fluidized dense phase flow within the pipeline. **(b)** Pneumatic conveying characteristic chart for transition from dilute flow to dilute flow to fluidized dense phase flow

flow re-aerates the powder, which effectively fluidizes the material, hence the term "fluidized dense phase".

Although the fluidized dense phase flow is a non-steady pulsatile flow, an averaged approach can be applied with respect to the global operating parameters of pressure, air mass flow rate, and solid mass flow rate. As shown in Fig. 20.97, the fluidized dense phase flow is similar to the *conveying in layers* behavior seen in plug flow conveying. The difference between the two modes lies in the continual smooth transition from dilute to dense phase conveying (i.e., without an unstable zone). With the exception of the full-bore pulses, the dense flowexhibits a two-layer structure where the majority of the particles are transported in the denser layer at the bottom of the pipeline with the upper layer dominated by the higher-velocity dilute flow.

Bulk material that can naturally be conveyed in a fluidized dense phase flow includes generally small particles (< 100 µm) with a large size distribution (e.g., cement, fly ash, flour, and alumina). In contrast to plug flow, researchers have found [20.24, 25, 153] that a high air retention capability is an important attribute for fluidized dense phase flow. This high air retention maintains the fluid-like nature of the material, which can be attributed to the smooth transition between this form of dense phase flow and dilute phase conditions.

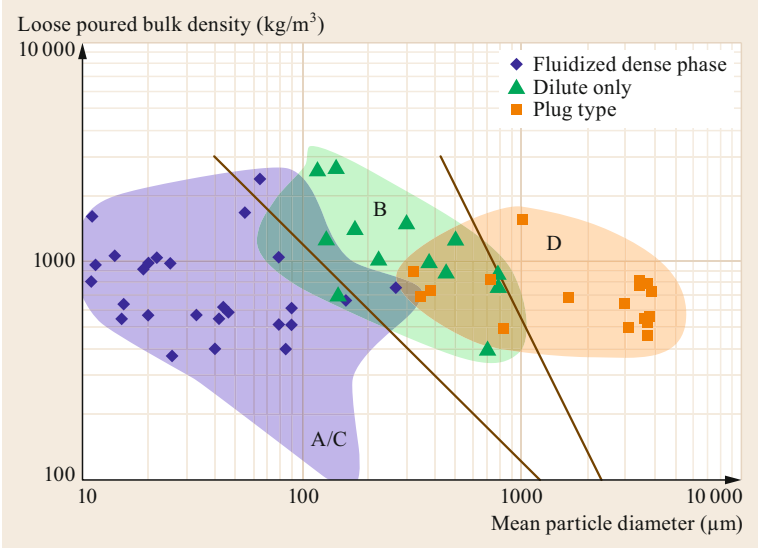

Fig. 20.97 Geldart-based flow mode prediction chart [20.152]

Flow Mode Prediction Charts

Different pneumatic conveying classification diagrams using various particle and bulk material parameters have been used to try to accurately predict the potential of a bulk material to be conveyed in a dense phase flow. The parameters used in these diagrams vary from basic particle properties such as size and density and the bulk density to more complex air–particle properties based on the fluidization and de-aeration behavior. The approach taken in predicting the flow mode based on these different particle and bulk parameters also varies significantly between researchers. The aim of this review is to describe each approach and assess the performance of such flow mode predictions against the known capability for a bulk material. Also, when fluid (or gas) properties (density, viscosity, and temperature) are required, the values associated with air at standard atmospheric conditions are used.

Basic Particle Parameter Charts. The first diagrams used to predict pneumatic conveying capabilities were constructed based on the pioneering work on bulk material fluidization behavior by *Geldart* [20.154] in 1973. Geldart derived a fluidization classification with four distinct groups (A, B, C, and D) using basic bulk material properties: the particle density and average particle diameter. The fluidizing behavior of materials within the groups identified by Geldart can also be extended to predict their pneumatic conveying behavior. Group A materials tend to exhibit high levels of air retention capability and therefore may be well suited to fluidized dense phase flow. Group C materials are rather more difficult to fluidize initially but also exhibit good air retention capabilities once fluidized, therefore also being potential candidates for fluidized dense phase. By contrast, group D materials tend to be highly permeable provided their size range is not too wide. Materials with very narrow size distributions that reside in group D tend to be potential candidates for the plug mode of dense phase conveying. Materials in group B usually exhibit poor air retention capability and are not particularly permeable. Materials in this category are generally not good candidates for dense phase conveying in conventional pipelines.

The boundaries in Geldart's diagram have been discussed and compared by numerous researchers using different techniques, but with the material classifications based on particle size and particle density remaining the same. In 1982, *Molerus* [20.155] specifically looked at the adhesion forces in determining some of the boundaries. In 1986, *Grace* [20.156] derived dimensionless parameters based on the superficial gas velocity and particle diameter to describe the boundaries of Geldart's bulk material classification. In 1979, *Dixon* [20.157] developed a slugging diagram, which is loosely based on and has the same axes as Geldart's diagram. Dixon's diagram classifies bulk materials according to their ability to slug in vertical columns. *Pan* in 1999 [20.158] and *William* in 2008 [20.152] developed diagrams which replaced the particle density with the bulk density to try to predict the likely mode of flow.

Charts Based on Aeration and De-aeration. To improve the accuracy of predicting the likely pneumatic conveying mode of flow, researchers have specifically investigated the air–particle behavior of a bulk material, in particular parameters associated with bench-scale fluidization and de-aeration tests. *Mainwaring* and *Reed* [20.159] proposed a two-diagram predictive technique using the parameters of steady-state pressure, permeability, and de-aeration, whereas *Jones* [20.160] developed a single-chart system which compared the permeability of a material with its de-aeration behavior under mechanical vibration. Single dimensionless parameters were also developed by *Chambers* et al. [20.161] and *Fargette* et al. [20.162], who utilized the combination of air–particle behaviors in permeability and de-aeration with the particle or bulk density. *Sanchez* et al. [20.163] developed a two-parameter dimensionless diagram using the permeability and de-aeration rate, gravitational forces, conveying gas properties, and particle size. These predictive diagrams based on air–particle properties are analyzed in more detail in the following paragraphs.

The flow mode data shown below in the selected diagrams are derived from the works of *Jones* [20.160], *Mainwaring* and *Reed* [20.159], and *Williams* [20.152]. Also, due to the various techniques used by the different researchers in determining the de-aeration value, normalized de-aeration values were calculated and are explained in the relevant references.

Mainwaring and Reed. In 1987, *Mainwaring* and *Reed* [20.159] developed a two-diagram predictive technique based on the determination of the steady-state fluidization pressure $(\Delta P/L)_{ss}$ and permeability (P_f) of a material using bench-scale fluidization tests. Mainwaring developed a de-aeration constant (A_f) which was based on a *best-fit* approach for determining the time (t) relationship in a plot showing the decay of the pressure drop from the fluidization pressure to atmospheric pressure, i.e.,

$$\frac{\Delta P}{L} t = A_f \,. \tag{20.106}$$

The first diagram in Mainwaring's technique was designed to distinguish between the high-permeability

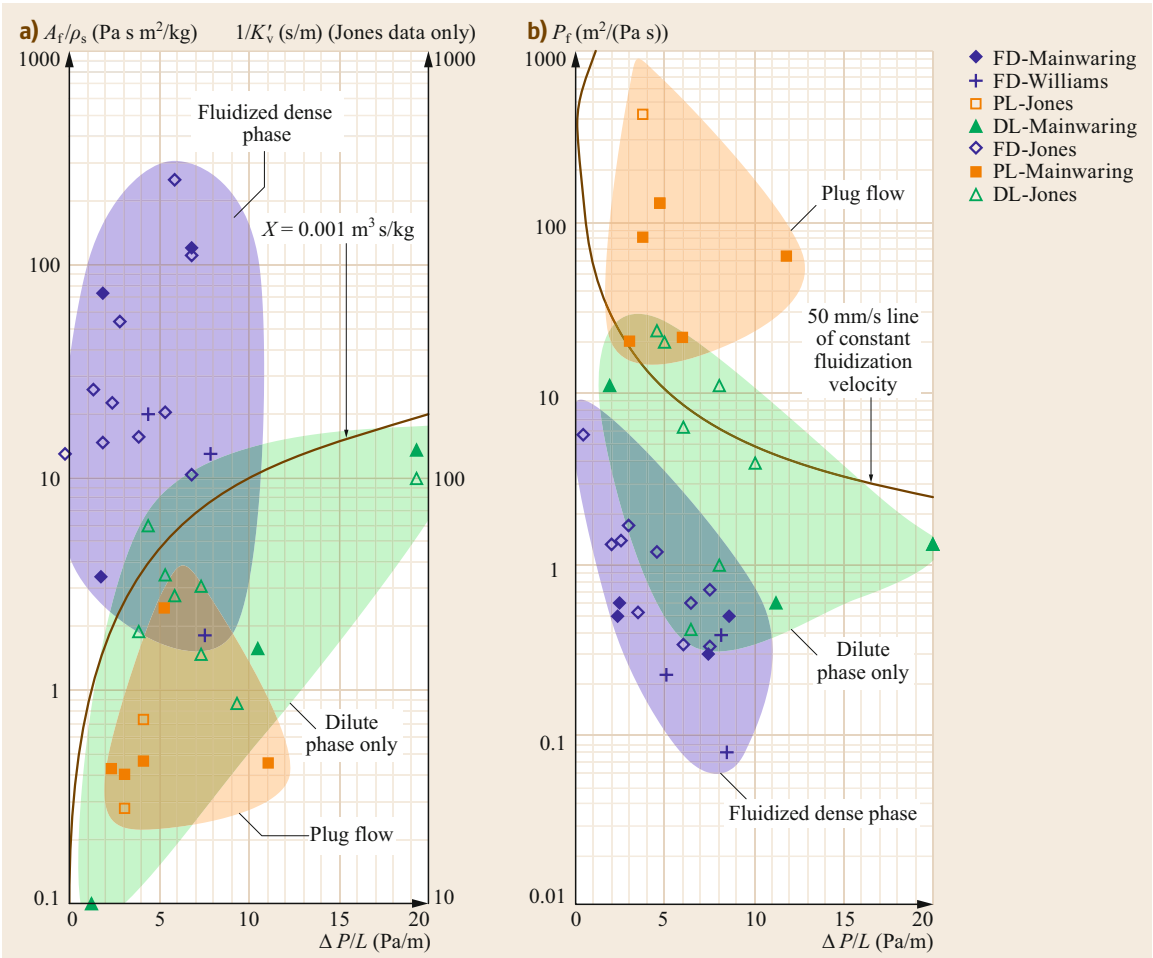

Fig. 20.98a,b Mainwaring and Reed two-diagram mode of flow prediction chart [20.152]. **(a)** De-aeration versus pressure drop chart. **(b)** Fluidization versus pressure drop chart

behavior of plug flow-capable material and the low-permeability behavior seen in dilute only and fluidized dense phase bulk material. As shown in Fig. 20.98a, the *mode of flow* data generally support Mainwaring's proposal that materials above the minimum fluidization velocity (v_{mf}) of 50 mm/s are plug flow capable, i.e.,

$$v_{mf} = P_f \left(\frac{\Delta P}{L}\right)_{ss} = 50\,\text{mm/s}\,. \qquad (20.107)$$

Chambers Diagram. In 1998, *Chambers* et al. [20.161] proposed the use of a single nondimensional parameter (N_c) based on the particle density, permeability, and a de-aeration value (t_{da}), defined as

$$N_c = \frac{\rho_s P_f}{t_{da}}\,. \qquad (20.108)$$

t_{da} was derived from the exponential time decay relationship with the change in bed height (ΔL), with an initial point defined by the bulk material fluidized bed height (ΔL_0), i.e.,

$$\frac{\Delta L}{\Delta L_0} \propto \exp\left(\frac{-t}{t_{da}}\right)\,. \qquad (20.109)$$

Chambers suggested that it was only necessary to estimate t_{da} in the range $1\,\text{s} < t_{da} < 10\,\text{s}$, as any material with a decay time greater than 10 s showed good air retention while those with values less than 1 s exhibited poor air retention properties. Unfortunately, there is no information on bed height for the *mode of flow* data to determine t_{da} using Chambers' approach, so a calculated time decay de-aeration value, t_c (in s), was determined from Mainwaring's de-aeration factor (A_f) and the steady-state fluidization pressure using the equation

$$t_c = A_f \left(\frac{\Delta P}{L}\right)^{-1}_{ss}\,. \qquad (20.110)$$

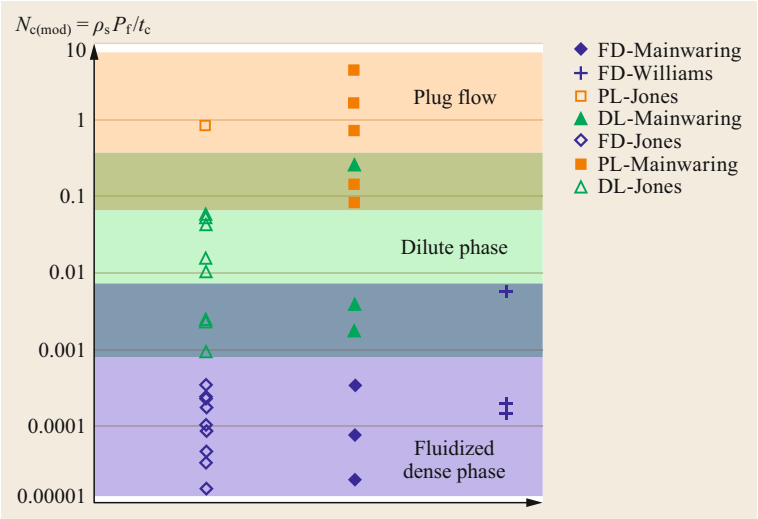

Fig. 20.99 Chambers et al. flow mode prediction chart [20.152]

Subsequently, (20.110) was used to replace the t_{da} value described in (20.107) and (20.108) to form a modified Chambers parameter ($N_{c(mod)}$), i.e.,

$$N_{c(mod)} = \frac{\rho_s P_f}{t_c} \,. \tag{20.111}$$

Figure 20.99 shows the values calculated for $N_{c(mod)}$ for the different flow modes. Figure 20.99 shows that $N_{c(mod)} < 8 \times 10^{-4}$ predicts all but one of the fluidized dense phase-capable materials, while all the materials with $N_{c(mod)} > 0.07$ (except one) are plug flow capable. This also indicates that $N_{c(mod)}$ can accurately predict dilute phase only-capable material ($0.07 < N_{c(mod)} < 8 \times 10^{-4}$) and overall is a good predictor of pneumatic conveying flow mode capability.

Sanchez Diagram. In 2003, *Sanchez* et al. [20.163] related pneumatic conveying predictive charts and their relationship to the Geldart fluidization classifications. Sanchez conducted nondimensional analysis on the basic and air–particle bulk material parameters and found that the best correlation to the Geldart groups was a three-dimensional relationship between the nondimensional parameters Grt (a de-aeration-based parameter), P^* (a permeability-based parameter), and Fr_{mf} (a minimum fluidization velocity-based Froude number), which were defined as

$$P^* = \frac{P_f \rho_s \sqrt{g d_p}}{d_p} \,, \tag{20.112}$$

$$Grt = \frac{\mu}{d_p \left(\rho_s + \rho_g/2\right)} t_{da} \,, \tag{20.113}$$

$$Fr_{mf} = \frac{v_{mf}}{\sqrt{g d_p}} \,. \tag{20.114}$$

Sanchez determines his de-aeration value from an exponential pressure drop decay equation of the form

$$\frac{\Delta P}{L_0} \propto \exp\left(\frac{-t}{t_{da}}\right) \,. \tag{20.115}$$

Similarly to the previous nondimensional value defined by Chambers, the value of t_c (20.124) replaced the t_{da} value for the analysis of the Grt parameter.

Due to the insufficient information on the minimum fluidization velocity for the flow mode of the material, the fluidization Froude number could not be adequately determined. However, a comparison between P^* and Grt and the flow mode data revealed good predictive capabilities, as shown in Fig. 20.100.

The clear clustering of the flow mode predictive performance using Sanchez's key parameters is clearly seen in Fig. 20.100, where there are very few data points in the regions shaded by any two of the modes of flow. Furthermore, a clear majority of fluidized dense phase materials can be determined to have Grt values greater than 0.2×10^{-3}, being relatively independent of the P^* values. Overall, the flow mode predictive performance is similar to the Chambers and Fargette analyses.

Innovative Conveying Systems

Many materials do not exhibit the physical properties for reliable conveyance in a low-velocity, dense-phase flow regime, because these non-dense phase-capable materials have either poor permeability or poor air retention capabilities. However, a dense-phase capability is desirable for materials, especially if they are erosive or fragile. For instance, wear is a critical issue for pneumatic conveying pipelines and must be minimized to achieve long service life with minimal maintenance requirements. In the chemical industry, many non-dense

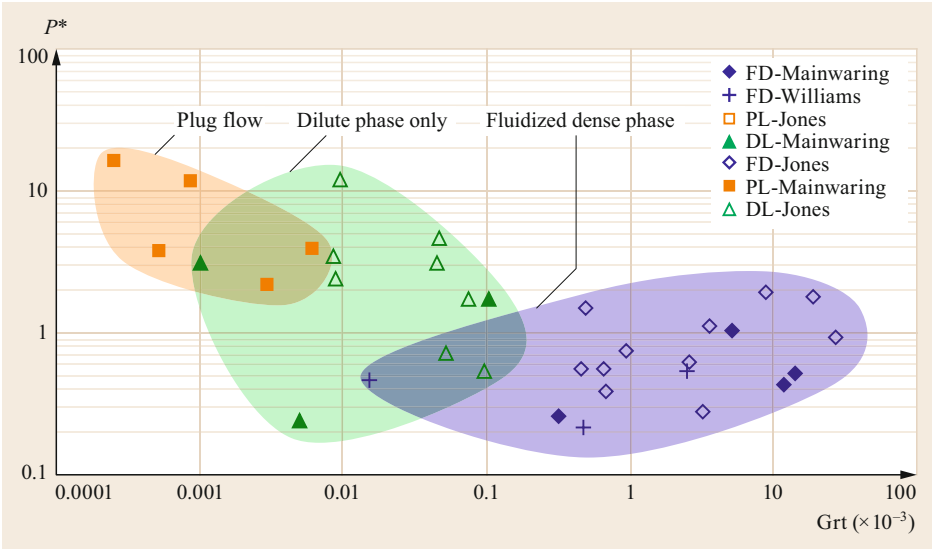

Fig. 20.100 Sanchez flow mode prediction chart [20.152]

phase-capable bulk materials, such as sand and alumina, are extremely abrasive. When these materials are conveyed in dilute phase mode at relatively high velocity, they can cause rapid pipe wear and holes in pipe elbows within only a few weeks. One common solution to this is to artificially increase either the air retention capability or permeability of such materials using air addition systems and bypass systems, respectively.

Air Addition Systems. Air addition systems are also referred to as air injection or booster systems [20.164]. These systems work by injecting air into the pipeline at regular intervals to keep the material fluidized. In most air addition systems, spring-controlled valves or pressure-actuated controlled valves are used to inject additional air into the pipeline at points where the pressure loss becomes high. However, such addition of air along the pipeline leads to a significant increase in the downstream conveying velocity; it is almost impossible to prevent large amounts of air being injected into the pipeline. In long-distance conveying systems, the air velocity increases along the pipeline as a result of the pressure decrease, with the flow mode becoming dilute when the air velocity exceeds a critical value. This increase in velocity is accentuated with air addition systems. An increase in the pipe diameter (stepped pipeline) will to some extent alleviate this gas expansion and associated increased velocities; however, a large number of pipe steps may be required. A potential for blockages has also been identified in these systems, especially under rough operating conditions, usually associated with the quantity of air injected, the injection period, and the overall control of the injection. These systems have been found to be unsuitable for low-velocity conveying of materials with very high solids loading ratio. The purpose of these air injection systems is to form uniformly spaced material plugs that travel along the pipeline. However, the plugs can become excessively long when they catch up to the next plug, with increasing length leading to greater loss of pressure and an increased risk of blockage in the pipeline. Moreover, the capital expenditure and maintenance costs are very high for these systems. Considering these shortcomings, air addition systems have seen limited use.

Bypass Systems. An alternative and much more satisfactory approach for dense phase conveying of naturally non-dense phase-capable materials, with reduced material degradation and pipe erosion, is the use of bypass systems [20.165]. Bypass pneumatic conveying systems both allow for dense phase transport of materials that are not naturally suited to dense phase flow and can be used to reduce the conveying velocity of materials that are naturally suited to dense phase flow. In both cases, the conveying velocities are lower, resulting in less particle degradation, lower pipeline wear, and reduced power consumption.

There are two basic types of bypass system: internal and external. In an internal bypass system, an inner air pipe is installed inside the conveying line (main pipe). The internal bypass pipe occupies space within the conveying line, reducing the area of the main pipe cross section, which affects the system's tonnage capabilities. In an external bypass system, the bypass pipe runs outside the conveying line, taking up space outside the main pipe. In both internal and external bypass systems, air can flow in the bypass and the main pipe simultaneously. Air flow occurs between the bypass and main pipelines through a series of flutes (openings) located at regular intervals along the length of the pipeline.

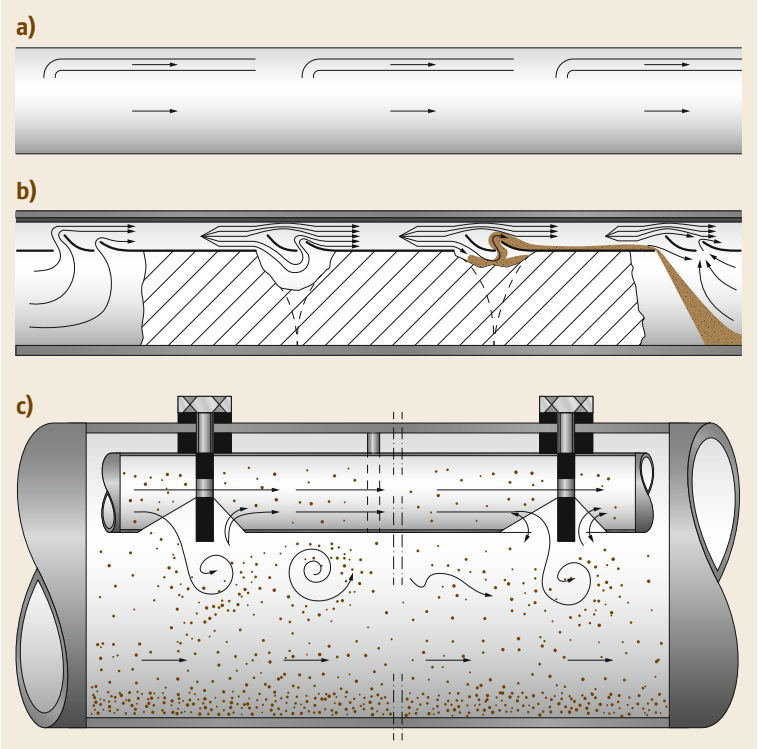

Fig. 20.101a–c Internal bypass arrangements: **(a)** *Lippert* and *Muschelknautz* [20.166], **(b)** Fluidstat (*Muschelknautz* [20.166]), **(c)** Turbuflow (*Möller* [20.167])

Bypass pneumatic conveying systems have been widely used in the process industry over the last few decades to convey cement, sand, alumina, fly ash, and other raw materials. A number of patents are available on bypass pneumatic conveying systems. For internal bypass systems, there are three representative patents:

- *Lippert* and *Muschelknautz* [20.166]
- *Muschelknautz* [20.166]
- *Möller* [20.167].

Their arrangements are shown in Fig. 20.101.

Figure 20.102 shows the arrangements for the patents available for external bypass systems:

- *Lippert* and *Muschelknautz* [20.166]
- *Merz* [20.168]
- *Rapp* et al. [20.169].

Among these patents, Fluidstat [20.168] in Fig. 20.101b and Turbuflow [20.167] in Fig. 20.101c are the most commercially available bypass pneumatic conveying systems.

Pneumatic Conveying Performance

When designing pneumatic conveying systems, the two primary aims are, firstly, to ensure the system operates reliably, and secondly, to ensure the system is as efficient as possible (i.e., optimized). Certainly, the ultimate aim of the user of the pneumatic conveying system is to achieve both reliability and performance, while the designer is limited by the available knowledge on pneumatic conveying behavior to ensure optimum efficiency. Also, the optimization parameters may vary, and are dependent on the user specifications, which can limit the available pipeline geometry options, e.g., in terms of pipeline routing and/or bend configuration. Further design constraints on the solid mass flow rate (or tonnage) requirements may also be imposed by the user, or the airflow rate and pressure capability may be restricted due to the available equipment.

However, once the geometric limits and tonnage requirements are known, determining the optimal pressure drop and air flow settings are the final challenge for the designer to determine the most economic air mover systems; for instance, if the combination of the air mass flow rate and pressure drop is too low, then the solids may block the pipeline.

Excessively high airflow rates and pressure drops will use excessive power for the flow required, increase particle degradation and/or pipeline wear, or convey a dense phase-capable material in a dilute phase mode. To determine the most accurate or optimal combination of pressure drop and air and solids (or particle)

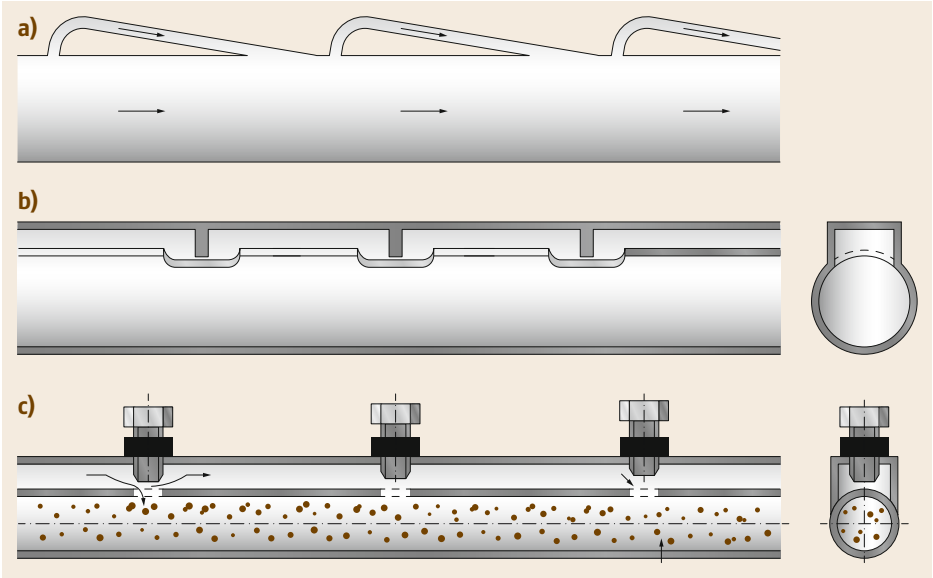

Fig. 20.102a–c External bypass arrangements: **(a)** *Lippert* and *Muschelknautz* [20.166], **(b)** *Merz* [20.168], **(c)** *Rapp* et al. [20.169]

mass flow rate, typically the approach has been to use either scale-up techniques utilizing experimental test rig data or to use empirical-based equations to predict the operating parameters. Generally, pressure prediction models use a superposition technique where the individual pressure losses are calculated separately and then added together. The most common individual pressure losses relate to the initial acceleration of the solids into the pipe, the frictional forces of the air and solids, the resistance due to the pipe bends, and finally the gravitational effect due to upward flow geometries. Also, although the flow is compressible along the pipeline, these techniques generally employ average or global conveying parameters. This average parameter approach includes single air density and velocity values, which essentially means that the flow is treated as incompressible, thus greatly simplifying the pressure drop calculation. In fluidized dense phase conveying, the most dominant pressure drop component is due to the solids friction losses. Typically, an empirically based friction factor has been used to determine the associated frictional pressure losses in fluidized dense phase pneumatic conveying. These friction factors are dominated by a power-law relationship; the values of the exponents associated with this power law, and the resultant pressure drop, are the focus of the paragraphs below.

Pressure Drop Determination. Pipeline pressure drop has been identified as one of the key parameters in pneumatic conveying system design. The total pressure drop or loss from the system will be a summation of the pressure drop across three major sections, the air only lines, the conveying pipeline, and the filter, and can be expressed as

$$\Delta P_{\text{total}} = \Delta P_{\text{air only lines}} + \Delta P_{\text{conveying line}} + \Delta P_{\text{filter}} .$$

To account for the solids and air components across the conveying lines, a common superposition method is used, as suggested by *Chambers* et al. [20.161]

$$\Delta P_{\text{conveying lines}} = \Delta P_{\text{a}} + \Delta P_{\text{z}} + \Delta P_{\text{l}} + \Delta P_{\text{b}} ,$$

where the components of the pressure equation above are defined below:

ΔP_{a} the acceleration pressure loss, accounting for the energy required to accelerate the particles when initially entrained into the air stream
ΔP_{z} the vertical pressure loss, accounting for the energy required to lift the material through vertical rising sections
ΔP_{b} the bend pressure loss, accounting for the energy required to re-accelerate the flow around the pipeline bends
ΔP_{l} the pipe friction pressure loss, accounting for the energy required to overcome the frictional resistance of the particles and the air interactions.

The components of the pressure loss can be calculated as follows:

Particle Acceleration Pressure Loss (ΔP_{a}).

$$\Delta P_{\text{a}} = \left(1 + 2m^* \frac{v_{\text{s}}}{v}\right) \frac{\rho v^2}{2} , \qquad (20.116)$$

m^* solids loading ratio
ρ air density (kg/m^3)
v air velocity (m/s)
v_s/v solids to air slip velocity, defined as

$$\frac{v_s}{v} = 1 - 0.008 d^{0.3} \rho_b^{0.5} , \tag{20.117}$$

d mean particle diameter (mm)
ρ_b bulk density (kg/m^3).

Bend Pressure Loss (ΔP_b).

$$\Delta P_b = NB(1 + m^*) \frac{\rho v^2}{2} , \tag{20.118}$$

N number of bends
B bend factor.

Gravitational pressure loss (ΔP_z).

$$\Delta P_z = m^* \rho L_v g \frac{v}{v_s} , \tag{20.119}$$

g acceleration due to gravity (9.81 m/s^2)
L_v vertical length.

For the frictional losses through the conveying pipeline, the pressure drop can be calculated using (20.120) below.

$$\Delta P_l = (\lambda_f + m^* \lambda_s) \frac{L}{D} \frac{\rho v^2}{2} , \tag{20.120}$$

where

λ_f gas friction factor
λ_s solids friction factor
L pipe length (m)
D pipe diameter (m).

This equation has also been used to calculate the pressure drop from the dilute phase to the fluidized dense phase.

In pneumatic conveying, the gas friction factor can be determined using the Blasius equation for smooth turbulent flow ($Re_f < 105$)

$$\lambda_f = \frac{0.316}{Re_f^{0.25}} , \tag{20.121}$$

where Re_f is the fluid Reynolds number.

$$Re_f = \frac{\rho v D}{\mu} , \tag{20.122}$$

where

μ dynamic viscosity of the fluid (Pa s).

Alternatively, for turbulent flow ($Re > 2300$), the fluid friction factor λ_f is used

$$\lambda_f = \frac{1.325}{\ln\left(\frac{5.74}{Re_f^{0.9}}\right)^2} . \tag{20.123}$$

For practical situations, $\lambda_f = 0.02$ can be assumed when Re_f is greater than 104 [20.149].

Pressure Drop due to Solid Particles.

To predict the pressure drop due to the presence of solids, the solids friction factor has been investigated by many researchers.

Stegmaier [20.170] investigated the solids friction factor in horizontal conventional pneumatic conveying pipelines, as subsequently reviewed and presented by *Weber* [20.171]. The correlation with the solids friction was established using the following relationships, which are only applicable to dilute phase flows

$$\lambda_s = 2.1 m^{*0.3} Fr^{-1} Fr_s^{0.25} \left(\frac{D}{d_s}\right)^{0.1} \quad \text{when } d_s < 0.5\,\text{mm} , \tag{20.124}$$

$$\lambda_s = 0.082 m^{*0.3} Fr^{-1.72} Fr_s^{0.25} \left(\frac{D}{d_s}\right)^{0.1} \quad \text{when } d_s > 0.5\,\text{mm} , \tag{20.125}$$

where

d_s particle diameter (m)
Fr_s Froude number of the particle
Fr Froude number of flow given by

$$Fr = \frac{v^2}{gD} \tag{20.126}$$

g gravity acceleration (m/s^2).

Fr_s can be derived from (20.127) by [20.171],

$$Fr_s = \frac{w_{fo}}{(d_s g)^2} , \tag{20.127}$$

where

w_{fo} single-particle settling (terminal) velocity in an undisturbed fluid (m/s).

The following conditions apply when using the energy equations defined above:

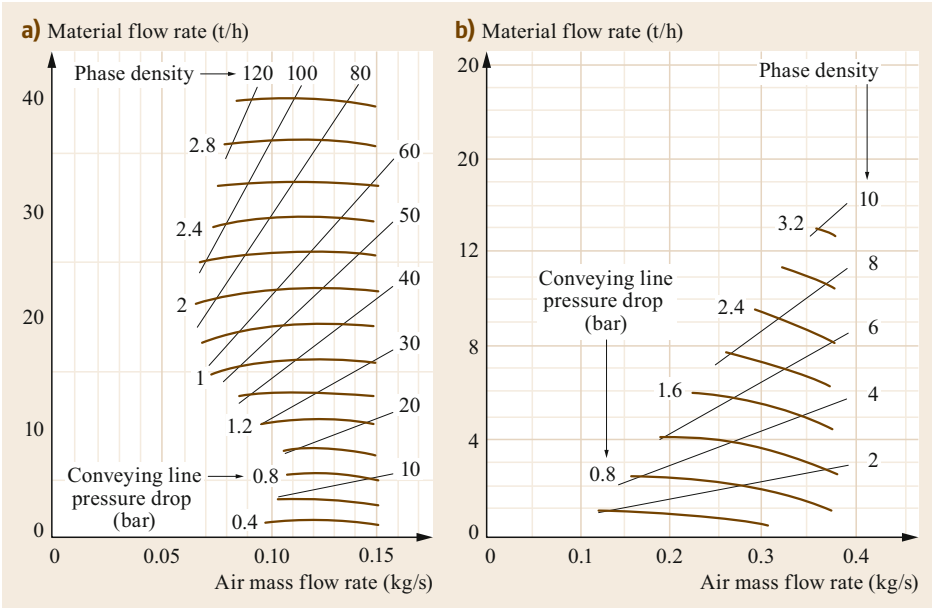

Fig. 20.103a,b Pneumatic conveying characteristic for a fine fly ash and a course fly ash. **(a)** Fluidized dense phase to dilute phase—pneumatic conveying characteristics for fine fly ash over 100 m through an 80-mm-bore pipeline [20.160]. **(b)** Dilute phase only—pneumatic conveying characteristics for coarse fly ash over 100 m through an 80-mm-bore pipeline [20.160]

- They are for incompressible, isothermal flows.
- They can be used for compressible, isothermal flows provided the gas density and velocity are based on the average pipeline pressure.
- These equations have been shown to hold predominantly for dilute phase conveying but may also be applicable to fluidized dense phase (moving bed-type flow) applications.

Pneumatic Conveying Characteristic Charts and Scaling

Another typical method to determine the pneumatic conveying performance of a pipeline is by applying a scaling technique based on pilot-scale data. This process typically follows the determination of the performance of the pilot-scale pipeline via the development of a pneumatic conveying characteristic (PCC) chart. This chart is produced by undertaking a range of tests through the pipeline with different air and solids flow rates and pressure drops for the specific material being conveyed. An example for dense phase-capable fly ash is shown in Fig. 20.103a, while a coarser, dilute phase-only fly ash is shown in Fig. 20.103b.

Scaling Equations

One of the early forms of scale-up techniques was developed by *Mason* et al. [20.172] and *Mills* et al. [20.173], who assumed that the ratio of the solids flow rate from the test to plant pipeline was inversely proportional to the pipeline lengths but proportional to their cross-sectional area. This assumption was based on the criteria that the air mass flow rate per cross"0sectional area and the pressure drop remained constant (i.e., constant m_a/D^2 and ΔP), which gives the following solids mass flow relationship between the two pipeline geometries

$$\frac{m_{s2}}{m_{s1}} = \frac{L_1}{L_2}\left(\frac{D_2}{D_1}\right)^2 , \qquad (20.128)$$

where the subscript "1" refers to the pilot-scale test pipeline and the subscript "2" refers to the full-scale pipeline.

Further investigation by *Wypych* and *Arnold* [20.174] found that (20.128) significantly underestimates the scale-up of the solids mass flow rate (m_{s2}) when conveying in large-bore pipelines; they developed a modified scale-up technique in which the diameter ratio exponent (or power index) is increased from 2 to 2.8. It is important to note that this increase in the diameter ratio exponent suggests that the frictional resistance of the solids per unit area decreases as the diameter is increased.

Therefore, assuming the same pipeline diameter, the scaling for pipeline length is

$$m_{s2} = m_{s1}\frac{L_1}{L_2} , \qquad (20.129)$$

while the scaling for pipeline bore is

$$m_{s2} = m_{s1}\left(\frac{D_2}{D_1}\right)^2 . \qquad (20.130)$$

Power Consumption

The operating energy cost in the pneumatic conveying process can be referred to as the energy requirement to move bulk materials from one place to another. It is possible to evaluate the operating energy cost in the pneumatic conveying process if all of the parameters necessary for the analysis are known. For a given pneumatic conveying system, the energy consumption varies depending on the operating conditions and material properties. Investigation of the manufacturer's literature is necessary to accurately assess the power needed, as different air movers have their own specific capacity and efficiency. However, it is relatively easy to approximately estimate the power associated with the operating conditions of the system, which can be calculated using (20.131), based on a simple model using isothermal compression [20.175].

$$\text{Power} = 2RTm_{\text{a}} \ln\left(\frac{P_1}{P_2}\right) , \tag{20.131}$$

where

m_{a} air mass flow rate (kg/s)
R universal gas constant, 0.287 kJ/(kg K)
T absolute temperature, 288 K
P_1 conveying line inlet absolute pressure (Pa)
P_2 conveying line outlet absolute pressure (Pa)

The model above can be used to illustrate the relationship between the power requirement and the air flow rate without a clear description of the impact of the different materials being transported.

The specific energy is defined as the energy required to convey a unit mass of material at a given pressure difference. This is considered to be a simple measure for comparing different conveying methods. The specific energy consumption of a conventional system can be estimated using (20.132), given by *Mills* [20.175],

$$\text{specific energy} = 2RT\frac{m_{\text{a}}}{m_{\text{s}}} \ln\left(\frac{P_1}{P_2}\right) . \tag{20.132}$$

20.4.8 Chutes

Gravity flow chutes play a major role in almost all bulk solids handling operations, including feeding, transfer, loading, and discharge. In these applications, efficient, trouble-free performance is required. Wear is controlled, flow blockage and spillage prevented, and maintenance costs are minimized. While the design of gravity flow chutes varies widely, their role in belt conveying operations is of particular significance. In feeding operations, the chute functions to accelerate the bulk solid from a slow-moving belt or apron feeder and directs the flow onto a faster-moving receiving belt conveyor. Transfer chutes are employed to direct the flow of bulk solids from one conveyor belt to another, often via a three-dimensional path. Discharge chutes direct the flow of bulk solids leaving the conveyor to the receiving bin, stockpile, truck, or rail wagon. In all cases, the chute design must suit a specific performance function as defined by the technical specification criteria. These criteria typically require adaptive designs to handle bulk solids of varying characteristics and a range of operating conditions. Consequently, the specification must be unique for the intended application, clearly defined, and based on the material characteristics of the bulk solids handled. To ensure system reliability, chute functionality is integral to the early stages of plant or facility layout design as much as other components such as conveyor pulleys, take-ups, and main structural elements. Chute technical design criteria, based on the work of *Ilic* [20.176], include specifying:

- Bulk solid flow properties, or minimum flow property testing requirements
- Minimum and maximum bulk solid velocities through the chute
- Minimum chute angles specific to each location-based bulk solid characteristics
- Maximum impact and shear pressures or energy densities for the chute and belt
- Bulk solid material stream velocity direction and variation during loading
- Hold points for acceptance of the arrangement, including minimum technical supporting evaluation [scale modeling, continuum mechanics, or simulation based on the discrete element method (DEM)].

The modern approach [20.177–179] to transfer chute design involves the following two steps:

(i) Employing a classical continuum mechanics methodology to analyze the variation in velocity and thickness of the flowing stream of bulk solids and predict the likely chute wear profile [20.180–183]
(ii) For the chute geometry examined in the continuum analysis, undertake DEM simulation to study the flow behavior and, by a process of correlation with the predictions determined in (i) above, *fine tune* the design to arrive at the best solution for the particular application.

These procedures are now briefly summarized.

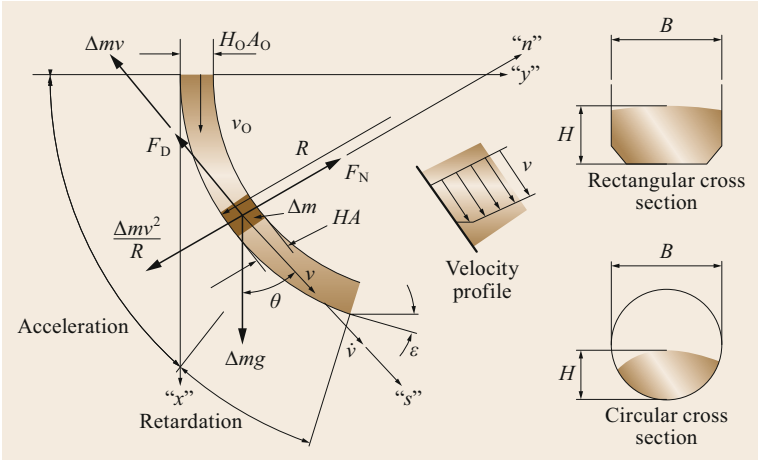

Fig. 20.104 Chute flow model

Basic Design Principles—The Continuum Approach

The aim of chute design [20.181, 182, 184] is to achieve accelerated, *fast flow* conditions, in which the bulk solid flows in contact with the chute bottom and sidewalls, as illustrated by the chute flow model in Fig. 20.104. Two flow zones are identified: the acceleration zone which corresponds to the steeper section of the chute profile, and the retardation zone which corresponds to the *flatter* section of the chute profile. In the acceleration zone, the stream velocity increases from an initial value V_0, with a rate of increase that reduces with a decrease in the chute slope. This is accompanied by a decrease in the stream depth or thickness, as illustrated. As the velocity of the stream reaches a maximum, the drag force F_D begins to dominate and retardation commences, leading to a buildup of stream thickness. This corresponds to a decreasing stream velocity. The buildup in the retardation zone is usually quite rapid so that, for a fully enclosed chute, a transformation to a fully choked, *slow flow* mode is a likely outcome. This of course equates to a high risk of blockage occurring.

Chute Cross-Sections. The two chute types are tubular and rectangular, as shown in Fig. 20.104. The tubular chute with a circular cross-sectional profile offers the advantage, by means of flanged connections, of rotating (if required) to even out any wear that occurs. A chute with a rectangular cross section offers certain advantages in that suitable wear-resistant material may be readily lined and replaced, as required, during maintenance. It is important that such rectangular chutes have chamfers in the corners, as shown in Fig. 20.104 to minimize the possibility of buildup occurring. To maintain *fast* accelerated flow, it is important that the chute cross-sectional dimensions be adequate to ensure shallow bed conditions. For rectangular profiles, the bed depth H should be less than the width B along the chute, preferably $H \leq B/2$. This also applies to chutes with a circular cross-section, where it is essential that the chute never runs more than half-full, particularly in the retardation zone. The ratio H/B may differ in specific applications, e.g., to minimize dust from free-flowing materials (grains).

Chute Flow Dynamics. In fast flow, the largest component of F_D occurs along the chute bottom. The sidewalls and interparticle friction contribute to a lesser extent. For this reason, it is acceptable to apply a lumped-parameter dynamics approach to model the flow. Here, an equivalent friction coefficient μ_E is introduced to account for the actual friction coefficient μ of the bulk material in contact with the chute walls, the material bed depth H, and the interparticle friction. From the work of *Roberts* [20.181, 182], the expression for μ_E which applies equally well for chutes of rectangular and circular cross-section is given by

$$\mu_E = \mu\left(1 + K_V \frac{H}{v}\right) = \mu\left(1 + \frac{C}{v}\right), \qquad (20.133)$$

where

μ $= \tan\phi$
ϕ chute wall friction angle
K_V ratio of normal pressure at the chute walls to the vertical pressure $= 0.4$–0.6

$$C = K_V \frac{v_0 H_0}{B}. \qquad (20.134)$$

Referring to the chute flow model shown in Fig. 20.104, the equation of motion can be derived for the coordinate system relevant to the chute geometry. For chutes of constant radius R, it is appropriate to select normal n

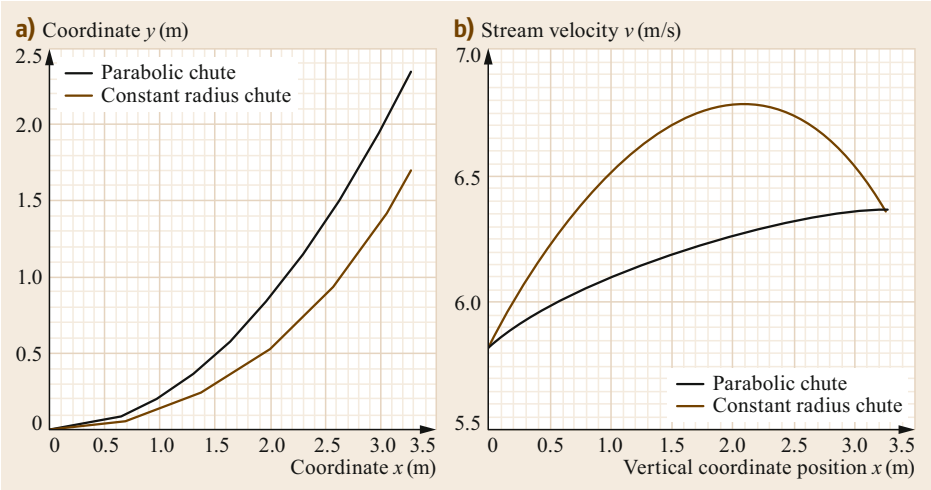

Fig. 20.105a,b Constant-radius and parabolic chute profile: **(a)** chute profiles, **(b)** stream velocities

and tangential $s = R\theta$ coordinates, for which the equation of motion is given by

$$\frac{dv}{d\theta} + \mu_E \theta = \frac{gR}{v}(\cos\theta - \mu_E \sin\theta) \,. \qquad (20.135)$$

A numerical solution of (20.135) can yield $v = f(\theta)$. Assuming that the bulk density is constant, the variation of the stream cross-sectional area is determined as

$$A = \frac{A_0 v_0}{v} \,, \qquad (20.136)$$

where

A_0 stream cross-sectional area
v_0 velocity at the point of material entry into the chute

An important aspect of chute design and performance is the interrelation between the chute radius of curvature R and the stream velocity v; for example, a chute with a parabolic profile and an increasing characteristic radius of curvature will generally perform better than a chute of constant radius when transferring bulk material from a slow-moving belt or apron feeder to a receiving belt conveyor. On the other hand, a chute with constant radius of curvature will perform better than a parabolic chute in the case of a high entry velocity such as a belt-to-belt conveyor transfer operation, particularly when the chute intake velocity is high. Note that, for chutes such as those with an optimized profile, e.g., parabolic, the alternative Cartesian coordinate form of the dynamic equation is employed rather than that represented by (20.133). It is important that the cutoff angle ε at the discharge end of the chute (the chute inclination at discharge, see Fig. 20.104) is sufficient to ensure flow under all operating conditions. The recommended cutoff angle depends on the friction acting in the chute,

$$\varepsilon = \tan^{-1}\mu_E + 5^\circ \,. \qquad (20.137)$$

To illustrate the foregoing discussion, the case of feeding a bulk solid material from an apron feeder onto a belt conveyor is considered. The performance of a constant-radius chute is compared with that of a chute with a parabolic profile. The initial velocity at the entry point of the chutes is 5.82 m/s, and the chute inclination at the exit of both chutes is the same. Figure 20.105a shows the two chute profiles, and Fig. 20.105b shows the corresponding stream velocities. The constant-radius chute shows a stream velocity that increases rapidly through the initial acceleration zone, reaching a maximum at the coordinate position $x = 2.1$ m, then decreases due to the stream retardation. On the other hand, the parabolic chute shows a stream velocity that increases steadily to the discharge point, with the bulk material accelerating from entry to discharge. Despite these different velocity profiles, the exit velocities for the two chutes are virtually the same at approximately 6.3 m/s.

Chute Wear. Chute wear is a combination of impact and abrasive wear. Impact wear may occur at points of entry or sudden change in direction. Abrasive wear is a function of the normal pressure, the friction coefficient, and the velocity at the chute boundaries. It can be expressed in nondimensional form as

$$N_{WR} = \left(\frac{v^2}{Rg} + \sin\theta\right) \,. \qquad (20.138)$$

As an example, the nondimensional wear profiles for the two chutes shown in Fig. 20.104 are plotted in

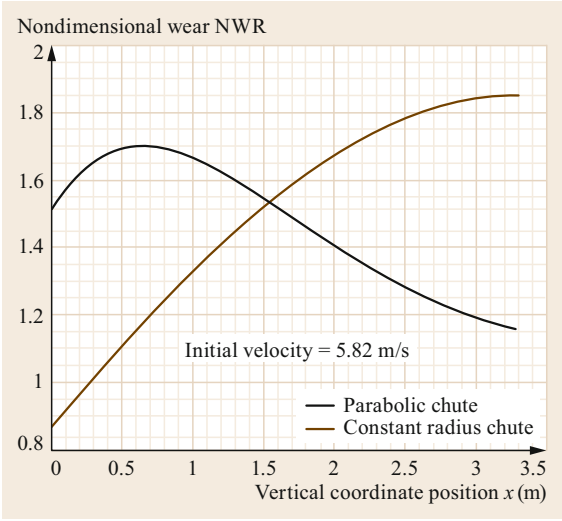

Fig. 20.106 Predicted wear profiles

Fig. 20.106. The constant-radius chute shows highly localized wear in the region of maximum stream velocity. On the other hand, the parabolic chute shows a high initial wear zone with maximum wear occurring at $x = 0.7$ m, but the wear then decreases toward the discharge point. The high initial wear is mainly due to the small chute radius of curvature in combination with the relatively fast initial velocity.

Other Chute Types. While the above flow models are applicable to generally softer and more free-flowing materials, other types of chute such as straight inclined chutes and cascading ledges, rock-box, or dead box designs are also common, particularly for hard ores. For a straight chute, the material stream at a distance, s, down the incline is given by

$$v = \sqrt{v_0^2 + 2as}\,, \qquad (20.139)$$

where the acceleration $a = g(\cos\theta - \mu_E \sin\theta)$ with θ being the chute inclination from the vertical. For internal shear flows, observed with rock-box-type chutes, μ_E is related to the effective angle of internal friction, δ, of the bulk material handled through $\mu_E = \sin\delta$.

Discrete Element (DEM) Analysis

The application of DEM to solve industrial problems has increased in line with the rise in computing resources, with the most common application being transfer chutes, with many publications including [20.177, 185–190]. Before a successful DEM simulation can be undertaken, it is first necessary to select the parameters in the DEM software such that they accurately represent the behavior of the real bulk material being handled. This process of matching of DEM parameters with experimental test results is referred to as calibration.

By way of background, the physical properties of the bulk material determine the previously discussed way in which it behaves during handling and flow. To obtain accurate quantitative predictions from DEM, the material parameters must be chosen to produce a model that behaves in the same manner as the physical material that it represents. Previous studies have established that DEM results in bulk handling applications are sensitive to the microproperties selected. *Grima* and *Wypych* [20.191] found that the loose poured bulk density and static angle of repose of monosized pellets are sensitive to the particle rolling resistance and interparticle friction, while *Coetzee* and *Els* [20.192, 193] showed that the angle of internal friction obtained from simulated shear tests on corn grains was dependent on the particle friction coefficients. Physical properties such as the internal friction angle, unconfined yield strength, and angle of repose can be obtained via proven laboratory tests such as direct shear and uniaxial tests. However, the results of these tests cannot be directly translated into DEM parameters. This problem is exacerbated when scaling. Also, simplification of the size distribution and shape of particles must be implemented in the DEM environment to reduce the computational expense.

The difficulty in relating DEM parameters to those measured experimentally means that parameters are often implemented without calibration to measured values or assumed without justification [20.194]. Due to these problems, the area of DEM calibration has been frequently studied during the last decade. This has mostly been approached by replicating experimental tests directly in DEM using various parameters to identify a unique set of parameters that yield the same result as the experimental tests. The calibration test itself has to show the same principal flow regime as in the final application. For transfer chute design and many other applications in materials handling, the fast flow regime of bulk materials under relatively low consolidation is the most important regime, as described in detail by *Katterfeld* et al. [20.195]. For cohesionless materials, the drawdown test as described in detail by *Roesler* [20.196] can be seen as a standard calibration test, as three independent test results for the angle of repose, shear angle, and mass flow rate can be obtained from a single test. Hence, the drawdown test allows a relatively easy determination of an unambiguous set of DEM parameters. For faster determination of DEM parameters, optimization algorithms can be used, as described in [20.197–199]. For cohesive materials, the calibration procedure is usually much more complex,

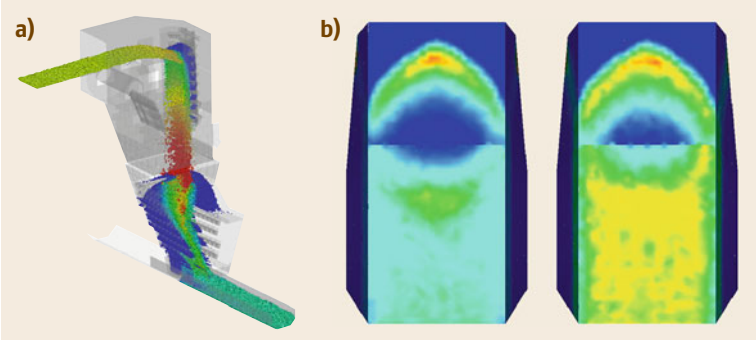

Fig. 20.107 (a) DEM flow and (b) wear pattern examples

as described in [20.200–202], and no standard calibration tests are available; more complex procedures thus need to be developed.

In general, when considering a DEM model for transfer chute analysis, the most important parameters in the software that need to be considered are the bulk density, particle size distribution, particle–particle friction, particle rolling resistance and/or particle shape, particle–wall friction, coefficient of restitution, and particle or loading stiffness. Some of these parameters can be determined directly, such as the bulk density and wall friction. However, others require that an assumption be made, such as the minimum particle size required due to computational restrictions, while some of these parameters (e.g., rolling resistance) need a sound calibration process to determine the correct values. For a DEM novice, the preceding discussion on calibration and associated references is an ideal starting point.

When applying the DEM model, there are a number of considerations to take into account (in addition to calibration). A number of assumptions are implicit in the DEM analysis tool, and there are limitations on the method as well. A good starting point for a simulation is to answer the following questions:

1. Can we capture the correct failure mode? For materials to flow, they must fail—is the failure mode by gravity alone or forced flow? Will the bulk material be failing internally or at a wall (boundary) surface?
2. What is the scale of the problem? Can it be modeled with enough resolution? This includes both the scale of the geometry as well as the scale of the particles.
3. What is the throughput? The trend is for higher throughputs ($> 20\,000\,\mathrm{t/h}$), so can this be modeled with small enough particles? Once again, is there enough resolution? Too small a throughput can also be problematic in terms of resolving the particle scale adequately with respect to the burden height.
4. Under what circumstances does the specific behavior we are looking at occur? That is, if we are trying to solve a problem using DEM, it is first necessary to establish that the problem can indeed be re-created in DEM.
5. Are the effects time dependent? If so, how much simulation time is needed to capture the behavior, and is this reasonable?

When a calibrated DEM model has been set up successfully, there are a number of analysis features extracted from the software:

1. Flow patterns can be visualized—see Fig. 20.107a. It is typical for particles to be colored by their velocity, with red being the maximum and blue being the minimum. Common features to look for in a transfer chute analysis are regions where possible flow choking or blockage can occur as well as any possible noncentral loading onto the receiving belt.
2. Wear patterns on surfaces are viewed—this can include transfer chute surfaces along with conveyor belt surfaces—see Fig. 20.107b. It is typical for surfaces also to be colored by their wear value, with red being maximum and blue minimum. Both impact wear and abrasive wear numerical data can be analyzed.
3. Forces due to the bulk solid interaction with surfaces can be extracted from the simulation data.
4. Breakage of particles is directly simulated. A detailed calibration process is used to quantify the breakage model parameters such that the DEM simulation can accurately predict the particle breakage (first the propensity to break, then the broken particle size distribution is modeled).

One of the main advantages of DEM is the ability to simulate many design iterations without the need to fabricate and install each transfer chute variation. This is particularly useful when wanting to investigate

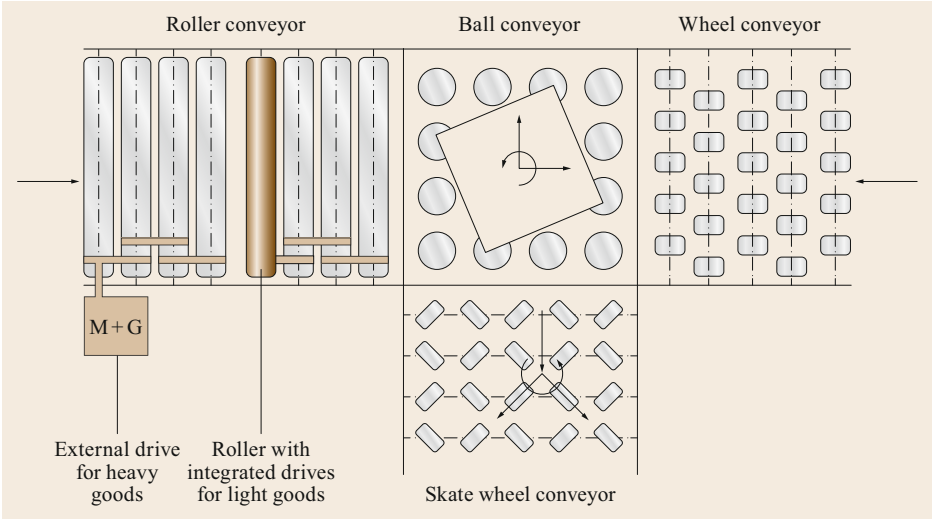

Fig. 20.108 Roller, wheel, and ball conveyor for handling of general cargo

minor design modifications or variations in the operating conditions or bulk solid characteristics. Evaluating a design change in the DEM environment is quick, and a new design can be evaluated within a single day. In the application of DEM to transfer chutes, a secondary verification tool such as the continuum method is recommended, as the combination of the two can lead to greater confidence in the transfer design decision-making process.

20.4.9 Conveyors for General Cargo

Besides the group of conveyors explained above, there are manyfold devices specially built for the handling of general cargo and that are often used in warehousing, distribution centers, and for baggage handling at airports. This section will focus on two special groups of such conveyors:

1. Roller, wheel, and ball conveyors
2. Conveyors for sorting.

Roller, Wheel, and Ball Conveyors

Roller, wheel, and ball conveyors belong to the continuous conveyor group without a tension device. The goods are placed on rollers, wheels, or balls which are mounted on a frame (Fig. 20.108). While rollers and wheels allow transport along a defined conveying route, ball conveyors (or ball tables/decks) allow two-dimensional arbitrary movement of the goods across the whole table size. The conveying route of roller and wheel conveyors can include horizontal and vertical curves. Typically, such conveyors are used for horizontal and downward inclined transport. This group of conveyors is characterized by a relatively simple design, allowing easy maintenance of the conveyor.

The dimensions and especially the mass of the goods determine the design of the rollers, wheels, and balls. For heavy goods, steel rollers and wheels are used, while aluminum and plastic rollers are preferred for medium and light goods. Instead of a single roller with the length as the dominant dimension, several smaller wheels aligned along an axis are used for the transport of small and lightweight goods. Typically, rollers are equipped with ball bearings to ensure easy running. Wheels are also available with plain bearings.

Ball tables use metal balls on a spherical bearing as shown in Fig. 20.109 or skate wheels for the realization of the planar movement.

The roller, wheel axis, or ball spacing must ensure that the goods are always in contact with at least three conveyor elements. Hence, the roller spacing is commonly defined as three times the smallest goods length. For the transport of EUR pallets, the roller spacing should not exceed 50 mm if the pallets are conveyed transversally or 150 mm if the pallets are transported longitudinally. The roller or wheel axis length should be at least 20 mm larger than the largest goods dimension.

The conveyors can be driven or nondriven. Nondriven conveyors use gravity or manual force for the realization of goods transport. Due to the low motion resistance of the rotating roller, the material can already be transported with very small inclination angles.

For the design of nondriven roller, wheel, as well as ball conveyors, the estimation of the critical inclination angle α is important. The critical inclination angle α is understood as the horizontal angle that is neces-

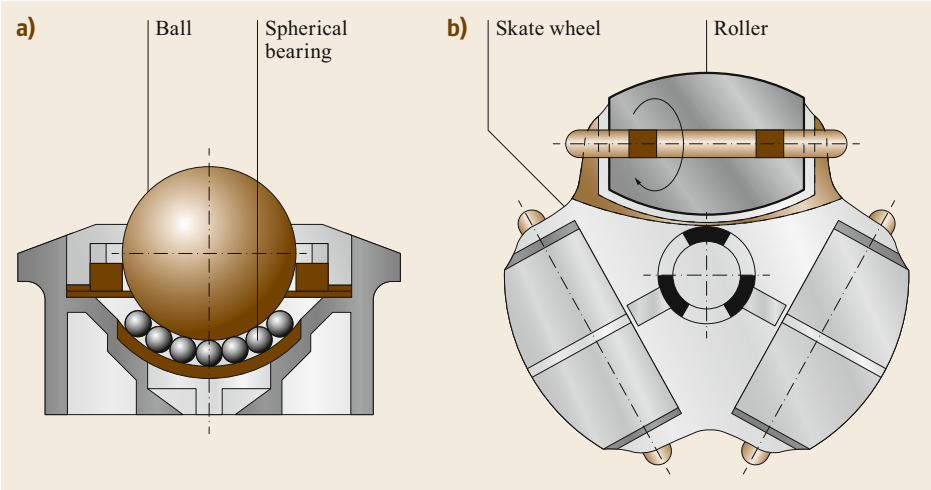

Fig. 20.109a,b Components for ball conveyors: **(a)** ball with spherical bearing, **(b)** skate wheel

sary to realize a constant speed of the goods down the conveyor. This assumption is required to maintain the throughput rate while conveying a series of densely spaced goods.

$$\alpha \geq \arcsin\left(\frac{m_G g \frac{2}{D} f_R + \left(\frac{L_G}{l_R} m_R + m_G\right) g \left(\frac{2}{D} \frac{\mu_b d_R}{2}\right) + m_R \frac{v^2}{l_R}}{m_G g}\right), \quad (20.140)$$

where

D roller diameter
f_R arm of the rolling friction according to Table 20.4 in Sect. 20.3.3
L_G goods length in conveying direction
m_G mass of a single good
m_R mass of a single roller
μ_b friction value of the roller bearing
d_R diameter of roller shaft

If higher inclination angles are used, it may become necessary to brake the goods during conveying downhill. For this task, special brake rollers are available. Their function can be based on purely mechanical principles (centrifugal brakes) or electrical principles (eddy-current brakes).

Driven roller conveyors use rollers with integrated drives, transmission belts, tooth belts, or chains depending on the transported goods, as shown in Fig. 20.110. Belts and chains can drive the rollers tangentially (Fig. 20.110b for light applications) or by wrapping roller pairs as shown in Fig. 20.108. For heavy applications, chain drive pairs are used. Depending on the goods dimensions, not every roller may be driven. If the rollers are driven pairwise, it must be considered that the drive efficiency is reduced by the efficiency of the belt or chain transmission η_{bc} to the power of the number x of drive pairs: η_{bc}^{x}. Common belt transmission efficiencies are $\eta_b \approx 0.8$–0.9, lower than chain transmission efficiencies of $\eta_c \approx 0.9$–0.98. Due to the relatively low motion resistance for the transport of the goods, the drives are often chosen based on the power necessary for acceleration of the completely loaded conveyor.

Roller conveyors can be used to accumulate goods along the conveying route. For this, a stopper blade can

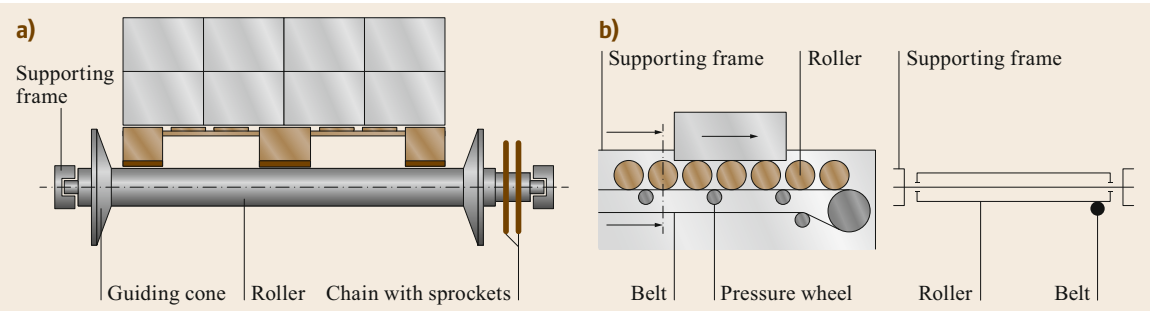

Fig. 20.110a,b Driving possibilities for roller conveyors: **(a)** heavy roller conveyor for pallets driven by chains, **(b)** roller conveyor for medium to light goods with nonpositive transmission belt [20.5]

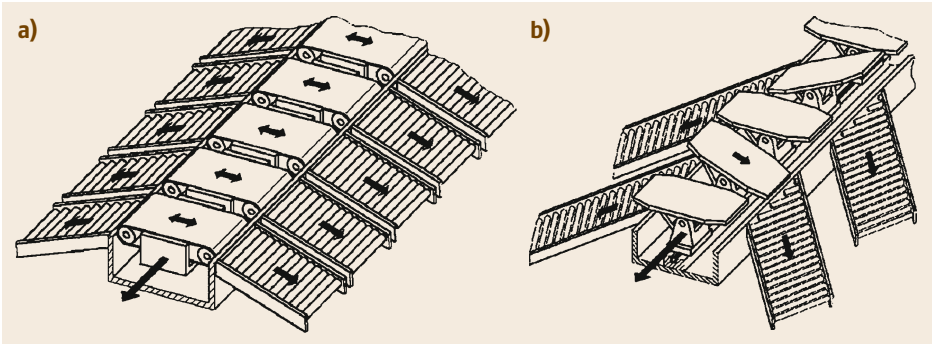

Fig. 20.111 (a) Cross-belt sorter, (b) tilt-table sorter [20.5]

be lifted between the rollers to stop the movement of the goods. Such accumulation usually requires a limitation on the accumulation pressure on the goods themselves when they cannot move but the rollers rotate below the goods queue. A reduction of the accumulation pressure can be easily realized if friction-based tangential drives are used as shown in Fig. 20.110b. Here, slip will occur between the transmission belt and roller if the roller cannot rotate due to the load of the stopped goods. For soft and sensitive goods, pressure-free accumulation can be realized if a series of short roller conveyor sections with separate drives and loading sensors are used.

Sorters

The distribution or sorting of goods is a central task of materials handling equipment in warehousing and distribution centers. Here, a very large number of goods with weights from a few grams (letters, mail) to many kilograms ($< 100\,\mathrm{kg}$, typically $< 30\,\mathrm{kg}$ for baggage) have to be conveyed to the correct assembly point for further transport. The necessary throughput rate is high. Due to the large number of possible assembly points, a central conveyor with many discharge positions is required. The decision regarding which goods are discharged at which discharge point requires the automated identification of the goods prior to the discharge point, as well as automated control over the discharge/deflector/diverter unit.

Classically, flat belt conveyors and roller conveyors were used for sorting. Special movable discharge devices such as pushers or diverters can be used to redirect the goods to the discharge point. Turntables with moving rollers can also be used to influence the goods direction. However, the possible throughput rate is relatively small, since pushers and diverters as well as turntables need some time to retract. The retraction time defines the spacing of the goods on the conveyor. Hence, such systems cannot be used for densely packed conveyors with small goods spacings.

To allow higher throughput rates, the discharge device must travel with the goods itself. This idea forms the basis for a special group of conveyors called sorters. Most conveyors of this group offer each good a single discrete transport position. These types of sorter are distinguished by their discharge principle. The most commonly used sorters with the highest throughput rates $> 10\,000\,\mathrm{h}^{-1}$ are:

- Brush sorter: The goods are loaded onto a horizontal table with a mechanical pusher arm discharging the goods.
- Cross-belt sorter (Fig. 20.111a): The goods are loaded onto a small horizontal flat belt conveyor (cross-belt). The conveying direction of the cross belt is transverse to the conveying direction and hence discharges the goods if switched on.
- Tilt-table sorter (Fig. 20.111b): The goods are loaded onto a curved table (typically made from wood). The table tilts at the discharge position, and the good flows down due to gravity.

All of these sorters allow an arrangement as a line (with an upper and lower strand, with one strand being used as the conveying strand and the other as the return strand) or planar circuit (one strand with straight sections and horizontal curves).

Depending on the arrangement, the sorter conveyor can be designed as:

- An inverted overhead conveyor with trolley units and discharge devices running in a track system connected by chains and one or several stationary drives along the conveyor route (e.g., caterpillar drive).
- A series of connected trolley units with discharge devices running in a track system. Several trolley units have attached drives connected to drive wheels in the track or other drive systems. More and more linear induction drives are used, where a metal blade on each trolley runs through a stationary linear motor and thus accelerates.

Furthermore, smaller sorters such as ring/rotating sorters or flap sorters are available [20.203].

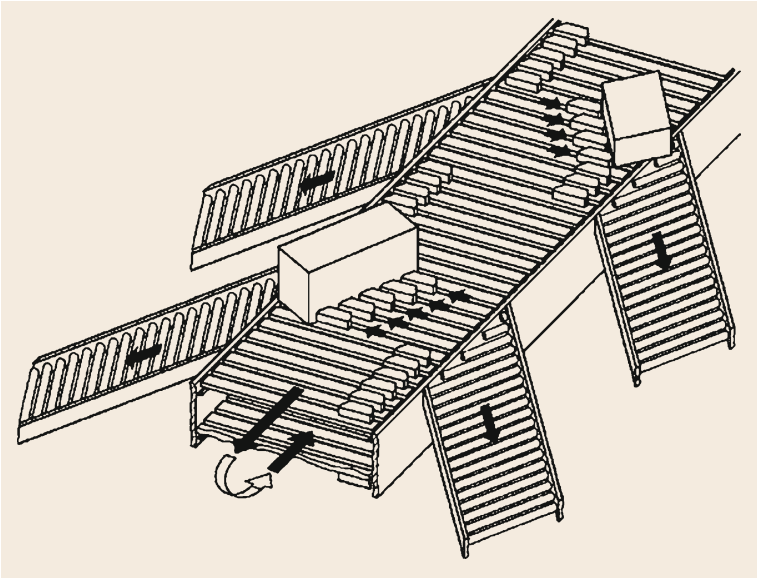

Fig. 20.112 Sliding shoe sorter [20.5]

The only sorter without single discrete transport positions but high throughput rates is called a sliding shoe sorter, as shown in Fig. 20.112. This is a special kind of slat conveyor (Sect. 20.4.3) with gliding shoes between the slats. Each shoe can be moved in a track system transverse to the conveying direction.

20.5 Discontinuous Conveyors

The group of discontinuous conveyors is even more diverse than the group of continuous conveyors. Many machines do not seem to have anything in common at first sight. However, all discontinuous conveying machines have drives and a supporting structure to carry the load. The main drives, as well as the specific features of the different types of machine, are presented in this section. The design and calculations of the supporting structure for discontinuous conveyors require deep understanding of the operating and boundary conditions for the specific equipment. However, this will not be discussed in detail in this section.

20.5.1 Main Drives: Hoisting, Driving, and Slewing

Hoisting Drives

The vertical movement of the load is realized by a hoisting drive. Different operating principles can be used for load lifting and lowering. For shorter distances, hydraulic or screw-type hoists are used. For longer distances, rack drives and the mostly used chain or rope hoists are applied. The hoist moves the load directly, while a luffing drive moves it indirectly by changing the inclination of a jib. The most common hoist drives are developed for rope drives. Hence, the next section focuses on this type of hoist drive.

Manually or motor-driven winches (rope drums) can apply tensile forces in any direction and store the rope that acts as the tension device. Hoists can be installed stationary or movable by mounting them on a trolley. Common hoist speeds are 0.8–40 m/min, and up to 180 m/min for dockside cranes. The hoisting drive consists of a motor, a coupling, a gear, and the rope or chain drive. Rope drives allow faster speeds and higher lifting heights. As described in more detail in Sect. 20.5.3, two hoist designs are known: standard hoists with an integrated assembly of standard components for production series, and individual hoists with an open design. Special hoists with several drums are necessary to use a grab as the load handling device for bulk materials handling.

The working cycle of a hoist is shown in Fig. 20.142a. As a common simplification, uniformly accelerated motion of the load is assumed. After an acceleration phase with typical acceleration times of 0.1–2 s, a stationary phase with constant velocity may occur. The nominal velocity for full load is the full stationary velocity v_f. Breaking times for stopping are typically shorter than the acceleration time.

The full stationary lifting power can be calculated as

$$P_f = \frac{(m_{Load} + m_{dead}) g v_f}{\eta_{total}} , \quad (20.141)$$

where

m_{Load} maximum load weight
m_{dead} deadweight of suspension and load handling device at the lower block
η_{total} total efficiency as the product of the rope drive efficiency η_r, the efficiency of an additional number z of rope sheaves η_s^z, the drum efficiency η_d, and the gear efficiency η_g

$$\eta_{total} = \eta_r \eta_s^z \eta_d \eta_d \approx 0.8–0.9 . \quad (20.142)$$

During acceleration, additional drive power is needed. The acceleration power can be calculated as

$$P_{acc} = \frac{(m_{Load} + m_{dead}) v_f + J_{red} \omega^2}{t_{acc} \eta_{total}} , \quad (20.143)$$

where

t_{acc} acceleration time
J_{red} mass moment of inertia of all rotating parts reduced to the moment of inertia of the motor
ω rotational speed.

As a first approximation, J_{red} can be assumed to be 1.5 times the moment of inertia of the motor rotor: $J_{red} = 1.5 J_{rotor}$. For hoist drives, $P_f \gg P_{acc}$. Hence, drive dimensioning is based on P_f but also on the relative duty cycle factor (DCF) which determines the thermal behavior of the motor due to the alternation of operation and pause. Standardized DCF values are $DCF_{stand} = 15$, 25, 40, 60, and 100%. The current duty cycle factor is calculated as

$$DCF = \frac{t_{acc} + t_f (+ t_{brake})}{t_{acc} + t_f + t_{brake} + t_{pause}} , \quad (20.144)$$

where

t_f time for full stationary operation
t_{brake} deceleration time
t_{pause} pause time between two working cycles.

The braking time in the numerator of (20.144) must be considered, if the electric motor is also used for braking.

The holding brake torque of a rope hoist is defined as

$$M_{hb} = \nu \frac{z_d (m_{load} + m_{dead}) g d_d \eta_{total}}{i_r i_g} , \quad (20.145)$$

where

ν safety factor (commonly $\nu = 2–2.5$ for hoists),
z_d amount of spooled ropes at the drum
d_d drum diameter
i_r transmission ratio of the reeving system defined by (20.20)
i_g gear transmission ratio.

Chassis Drive

In the field of materials handling, the term "chassis" is understood as the main drive for the mostly translational movement of the conveyor. The chassis (also called the running gear or simply drive) is often placed in an undercarriage. The chassis propels the conveyor along the prepared or nonprepared ground or along a track or runway which can be overhead mounted on support structures. Different operating principles are used for the conveyor movement: wheels on rail tracks (Sect. 20.3.3), tire drives, crawler tracks, and walking mechanisms. In addition to rail drives for cranes (Sect. 20.5.2), tire drives are used for industrial trucks (Sect. 20.5.5) and for many construction machines. Crawler track drives are used for excavation machines in construction and mining. Walking mechanisms are used in excavation machines in mining, but are of minor importance.

Rail drives require the greatest effort for preparing the track but can transmit the highest wheel force. The drive movement is predefined by the track path. The drive resistance of commonly used steel wheels on steel tracks is very low. Tire drives need a prepared ground allowing surface pressures of approx. $30\,N/cm^2$. The common air tires limit the wheel forces. Hence, full rubber tires are also used in materials handling. The drive direction is only limited by the dimensions of the prepared ground. The drive resistance is larger compared with rail drives. Rail and tire drives use three or more wheels to support the machine. For heavy machinery, a set of wheels is arranged in suspended bogies (especially for rail drives). Crawler track drives have a large contact area with the ground. Hence, the surface pressure is low (approx. $10\,N/cm^2$), allowing the drive to operate on unprepared ground. Crawler track drives are heavy devices which increase the weight significantly and cause a large drive resistance as well as high wear. This limits the drive speed. However, crawler track drives allow even more flexible movement of the equipment than a tire drive. The application benefits are operation at very high inclinations, turning on the spot (when the crawler tracks move in opposite directions), and the support of very large equipment (crawler cranes, bucket wheel excavators) with large working area due to their large and heavy jibs. The walking mechanism allows even lower surface pressure (approx.

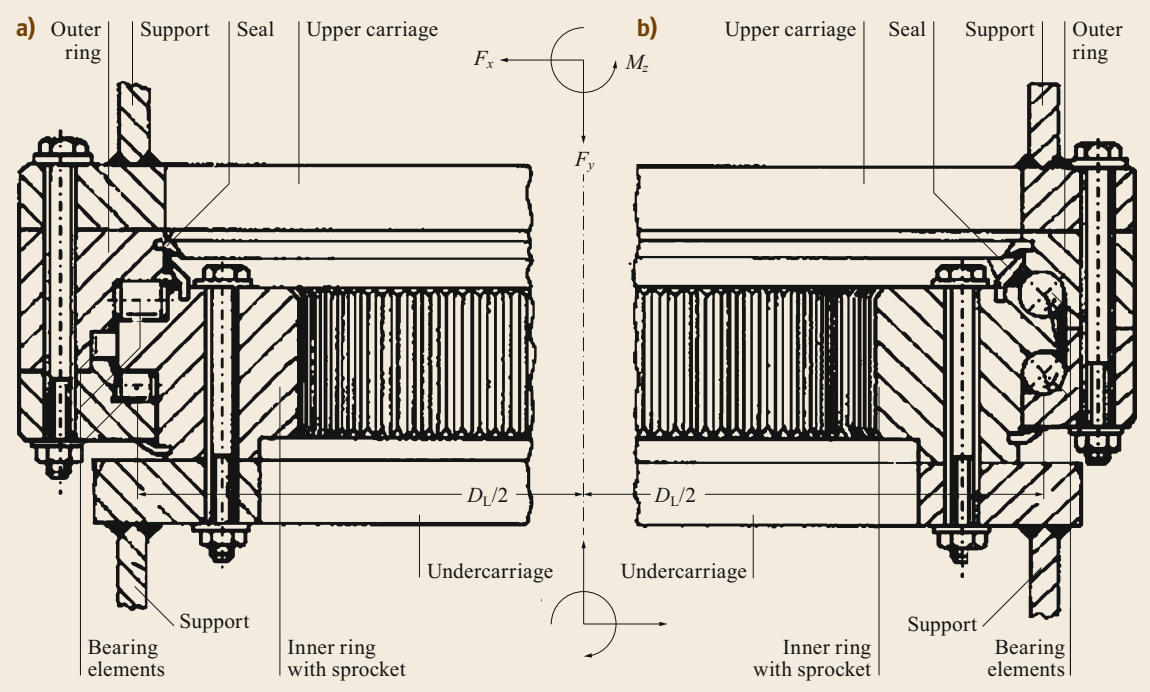

Fig. 20.113a,b Slewing bearing (Hoesch Rothe Erde): **(a)** three-row roller slewing bearing, **(b)** two-row ball slewing bearing [20.5]

5–10 N/cm^2) but also lower speeds then crawler track drives due to the larger contact area.

The chassis drive design influences not only the movability of the conveyor or construction machine but also significantly influences its stability. The arrangement of the wheels, wheel bogies, or crawler tracks determines the size of the area over which the resulting force from the load weight (e.g., at a jib) and the dead weight of the machine itself can be moved. If the resultant force moves outside this area, the machine will tip.

Hence, the design process of the chassis includes a stability assessment, the calculation of the driving resistance, and—for rail and tire drives—the calculation of the necessary wheels to distribute the load, as well as the calculation of the necessary number of driven and braked wheels. The latter implies the proof that the necessary driving force can be transmitted without significant slip between wheel and track/ground.

For the calculation of the driving resistance, the interaction between the wheel and track/ground has to be considered, as described in Sect. 20.3.3. Furthermore, slope resistances, wind forces, forces occurring in curves, and acceleration resistances must be taken into account. As an approximation, the driving resistances on horizontal paths can be calculated as

$$F_d = \mu_{drive}(m_{load} + m_{dead})g\,, \qquad (20.146)$$

where the drive resistance factor μ_{drive} can be estimated as 0.01–0.03 for rail drives and 0.02–0.08 for tire drives. For a rail drive on, e.g., a crane, the acceleration power (obtained using an approach similar to that applied in (20.143)) mostly determines the nominal power of the drive motor.

Slewing Gears

Generally, a slewing gear rotates around a vertical axis. The upper section can rotate in the opposite sense to the lower section. It can be fixed (e.g., a pillar slewing crane, or derrick), mounted on rails (e.g., a luffing slewing crane or railway crane), or mounted on a floating body (floating crane) or road chassis (mobile crane). The slewing gear consists of the mechanical parts of the slewing bearing and the slewing gear drive. Slewing bearings are large ball or roller bearings that transmit vertical forces, horizontal forces, and torques. The torques can be caused by the eccentric position of the center of gravity of the upper section and the load, by wind forces, and by inertial forces during turning and driving. Today, single- to three-row ball slewing bearings and two- and three-row roller slewing bearings are most frequently used (Fig. 20.113).

One of the two rings of these large roller bearings (with track diameter of up to 14 m) is bolted to the upper carriage, while the other one is bolted to the un-

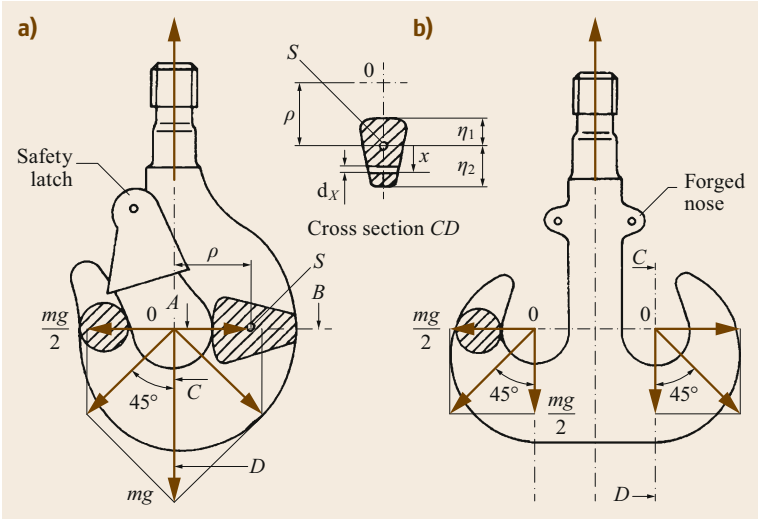

Fig. 20.114a,b Shapes of lifting hooks: **(a)** single lifting hook according to DIN 15401-1, -2 [20.204, 205], **(b)** double lifting hook according to DIN 15402-1, -2 [20.206, 207]; forged, optional forged nose for safety latches

dercarriage. The sprocket for the slewing gear is milled into one of the two rolling rings. The slewing gear drive is generally mounted on the upper carriage of the machine. It causes twisting of the upper carriage with respect to the lower carriage. Slewing gears are usually driven and braked by cage motors. The mechanical brake acts only as a holding brake. The maximum motor torque arises when the upper carriage is rotationally accelerated with the jib and load under a headwind. For further information see [20.52].

Retracting Units and Luffing Gears

Retracting units and luffing gears resemble each other in their constructional design, but luffing gears work at higher speeds and change the angle of inclination and the outreach of the jib. Like hoisting gears, they are primarily loaded by weight forces. The hoisting mass is affected by the jib weight. Rope, rack, and spindle drives, or hydraulic drives, are used to adjust the jib. To keep the lifting work as low as possible, the kinematics of the jib and hoist rope drive are designed such that the load moves on an almost horizontal path (lift height compensation) when changing the jib length. The forces or torques acting on the moved jib are determinants of the dimensioning. In contrast to a hoisting drive, the external forces acting on the drive element are not constant but change with the outreach. For further information, see [20.52].

20.5.2 Hoists and Cranes

Hooks and Load Handling Devices

To convey goods by means of hoists and cranes, the load must be attached to the lower part (hook block) of the hoist. Lifting hooks or other devices (shackles) are firmly connected to the hoist at the hook block. Auxiliary load attachments (slinging or rigging gear, e.g., ropes, chains, or textile slings) can also be used to connect the load to the lifting hook. Furthermore, special load handling devices (e.g., lifting magnets or grabs) may be used. The weight of the cargo plus the weight of the load handling device plus the load of the auxiliary load attachment must not exceed the rated load (capacity) of the hoist or crane. According to DIN 15020 [20.51], the weight of the hook block including the lifting hook reduces the capacity if its weight exceeds 5% of the nominal load.

Lifting Hooks. Forged single and double hooks (Fig. 20.114) made of age-resistant steel are commonly used for the transport of general cargo. Different national (e.g. DIN 15400 [20.208]) and international standards (e.g., ISO 4779 [20.209], ISO 7597 [20.210], and ISO 8539 [20.211]) specify the capacity and design parameters of hooks of different strength classes based on different mechanism groups (e.g., $1B_m$ to 5_m according to the FEM classification). Furthermore, the associated stress level in the hook and shank cross sections are taken into account.

Lifting hooks can pivot about the vertical and a horizontal axis in the lower hook block (Fig. 20.115).

The loads are transmitted through the hook (Fig. 20.115), the shank suspension nut (which is secured by a square bar), and the axial ball bearing into the hook beam. Pull straps connect the pivotally mounted hook beam to the axis of the rope sheaves. A casing prevents the loose rope from jumping out of the rope groove. The hook block and associated equipment are also specified in different national and international standards.

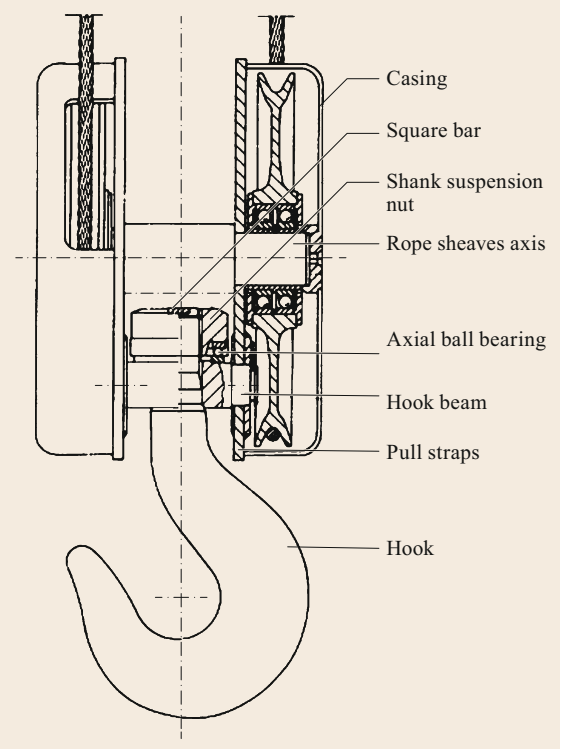

Fig. 20.115 Two-sheave hook block

For sea shipping, special loading hooks according to DIN 82017 [20.212] are used, in which a deflector prevents them from hanging on edges.

Laminated hooks, according to DIN 15407-1, -2 [20.213, 214], are used for the transport of molten metal (Fig. 20.116a). For safety reasons, they consist of several parallel plates (Fig. 20.116a) bolted together. They are made of age-resistant steel (e.g., P355N, according to DIN EN 10028-3 [20.215], for strength classes M or P, according to DIN 15400 [20.208]). A mouth saddle and impact protection prevent notches on the plate edge. C-hooks (Fig. 20.116b) are used to pick up ring-shaped loads, such as sheet metal and paper coils, as well as wire rolls.

Load Handling Devices for General Cargo. Tongs, grabs, and lifters are used to transport general cargo by friction or positive locking. Their design and function are adapted to the properties of the goods. Typical application examples include tongs and grabs for sheet metal and blocks, wood trunks, bales, bags, crates, and stone parts. Figure 20.117 shows a parallel gripper acting as tongs, based on the principle of the Nuremberg scissors.

Using the operating lever (Fig. 20.117), the scissors and the gripper itself can be locked in any position. The points of articulation of the scissors move parallel to each other during lifting. Therefore, the parallel gripper can be easily adapted to different transport tasks.

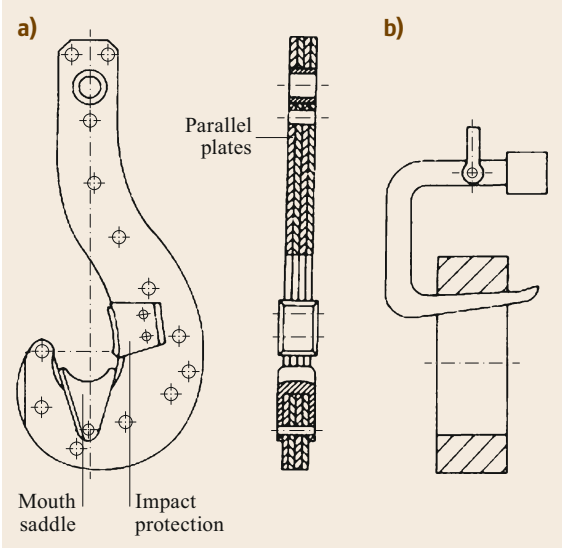

Fig. 20.116 **(a)** Laminated hooks, **(b)** C-hook (see text for explanations)

Vacuum lifters are suitable for picking up loads with smooth and low-porosity surfaces (e.g., sheet, glass, and chipboard). They are attached to rope hoists or chain hoists. In Fig. 20.118, a vacuum pump generates a negative pressure p in a space whose working surface A is sealed by rubber against atmospheric pressure p_0. The range of p is 0.2–0.4 times p_0. The load capacity is calculated as $A(p_0 - p)/S$, with a safety factor $S = 2$ for horizontal transport. In case of a vertical force surface, the capacity is reduced by approximately 50%. For goods with large surfaces, several vacuum elements can be mounted elastically on a load beam (traverse) supplied by one vacuum pump. An additional vacuum accumulator allows continuous operation of the vacuum pump and thus shorter working cycle times.

Lifting magnets pick up magnetizable goods such as slabs (< 600 °C), ingots, scrap, and chips. Their size is defined by the tear-off force as determined by VDE 0580 [20.216] or ISO 17096 [20.217]. The load capacity depends on the air gap between the magnetic base and the material, as well as on the shape of the material. With respect to the tear-off force, the load capacity is reduced by a factor of 2 or more. The highest capacity is achieved by round lifting magnets (Fig. 20.119), reaching up to 90 t at 17 t dead weight and 2.3 m diameter. The magnetic force is created by a shock-resistant electrified coil (Fig. 20.119) installed in a cast-steel or welded housing. A special coil arrangement, for example, in rectangular magnets, allows a defined orientation

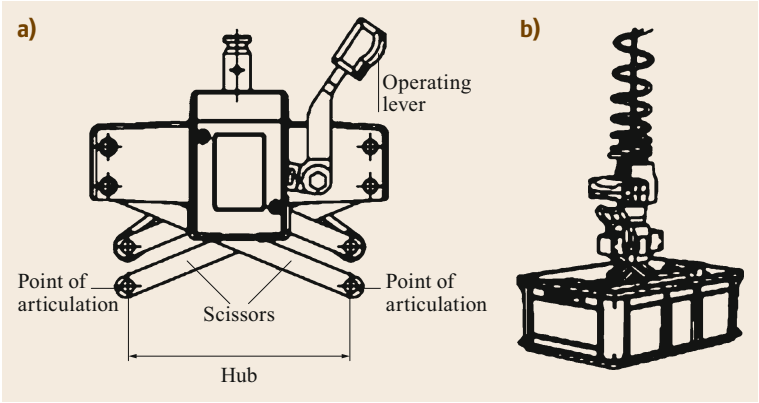

Fig. 20.117a,b Tongs (Demag Cranes & Components): **(a)** basic module for small loads, **(b)** parallel tongs for handling small containers

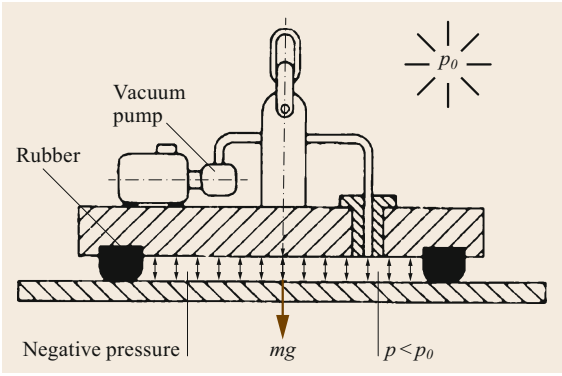

Fig. 20.118 Vacuum lifter (Fezer) (see text for explanation)

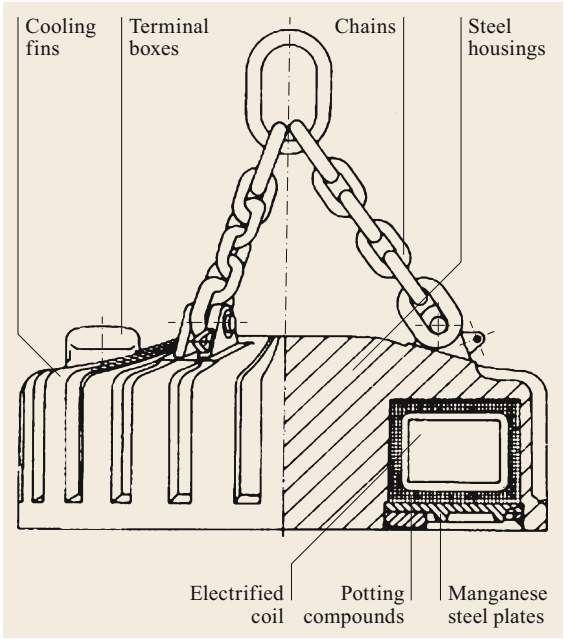

Fig. 20.119 Lifting magnet (Steinert)

of the force field in the longitudinal or transverse direction. In special cases, the shape of the receiving surface is adapted to the load (using profiling bars). In general, rectified mains voltage of 220 or 380 V is used for the power supply. In the event of a power cut, an additional backup battery extends the hold of the load. For transporting sheets or long profile strips, several magnets can be spring-suspended onto a (traverse) load beam. Battery-powered magnets or permanent magnets are used for small loads.

Load Handling Devices for Bulk Materials. Grabs are designed to handle bulk material. Two different types of grab can be distinguished based on the drive principle of the grab opening/closing: rope-driven grabs as shown in Fig. 20.120 are most commonly used, but there are also motor-driven grabs.

The common clamshell grab consists of two half-shells (Fig. 20.120) connected to each other in a rotatable manner. They form a transport container in the closed state.

For wear reasons, the half-shells are typically welded from S355. The cutting edges are made of S355 or high-strength fine-grained steel; in special cases, manganese hard-steel teeth are used. The joints are equipped with plain bearings, while the rope sheaves in general have roller bearings. The closing rope (S) and hoisting rope (H) are moved via the close and hoist drum, driven by two independent motors. The rope grab operation can be described as follows:

- Figure 20.120a: filling is carried out by pulling on the closing rope S with the loose hoisting rope H. Before closing the grab, it is fully opened and placed on the bulk material surface.
- Figure 20.120b: lifting the filled grab with both ropes S and H. Both ropes have approximately the same load distribution.

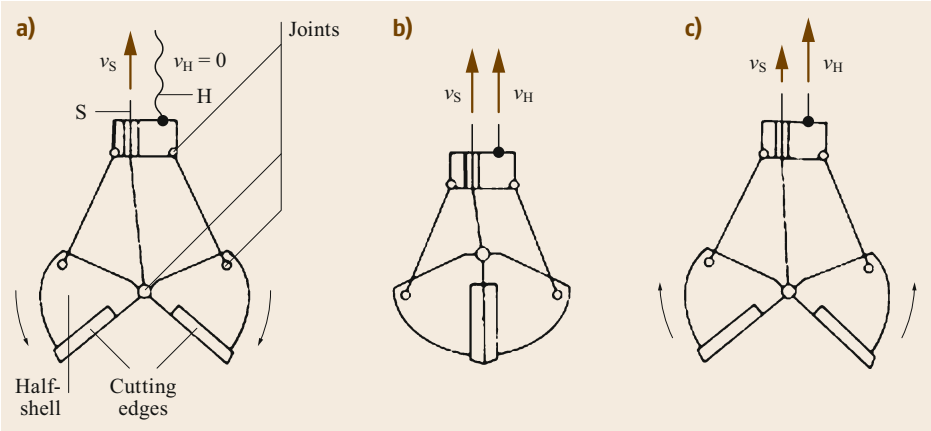

Fig. 20.120a–c Components and function of a rope-driven clamshell grab for bulk materials handling. **(a)** Filling process, **(b)** lifting process, **(c)** unloading process of a clamshell grab

- Figure 20.120c: the grab can be opened and closed during the lifting and lowering while applying different speeds v_S and v_H. The fully open grab hangs only on the hoisting rope.

Scissor grabs (Fig. 20.121) are preferably used for ship unloading of bulk material with difficult flow properties, high density, or high penetration resistance. Such materials are typically coal and ores, where higher forces are needed to close the grab. Capacities of up to 50 t are possible.

The spoon-like shells or buckets are mounted using a swivel joint and closed by a reeving system (here shown only for a closing rope S). The shells are connected with the load traverse using ropes. The grab is opened by releasing the closing rope.

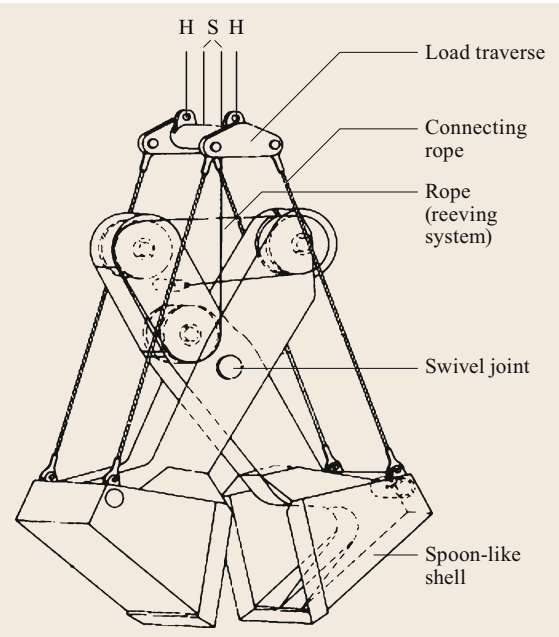

Fig. 20.121 Scissor grab (Peiner SMAG)

Peel grabs have several narrow, circularly arranged shells which are connected to a suspension frame and that rotate when the closing rope is pulled in. When closed, such shells with a large width form a completely enclosed space for the good, while smaller shell widths generate a partially open space (e.g., orange peel grabs). Peel grabs are used to handle natural soil, slag, scrap, garbage, stones, etc. They are also built as motor grabs (Fig. 20.122) that can be used with any simple hoisting gear. The closing mechanism is operated by a grab-integrated electrohydraulic power unit. Electrical power is supplied via cable stored on a cable drum.

Hoist Types

Hoists are machines used to lift and lower suspended loads over spatially limited distances. Ropes and chains are used as the actual lifting device. Chain hoists are typically used for smaller capacities and lower lifting heights. Hence, chain hoists are often used as auxiliary hoists.

Hoists can also be distinguished by their design. Chain and rope hoists are available with an integrated design where the components are densely assembled into a compact device. Such standard hoists are produced in large series with different model ranges and modular setup. In contrast, the individual (open) hoist design allows adaptation to special applications, meaning very large capacities (> 100 t) or special safety or redundancy requirements.

Hoists for, e.g., mobile cranes, tower cranes, or ship unloading cranes typically use winches that store the rope in multiple layers. The hoists in such cranes have a fixed position. The whole rope drive is integrated into the crane structure.

Motorized hoists are predominantly electrically driven in stationary applications or hydraulically driven

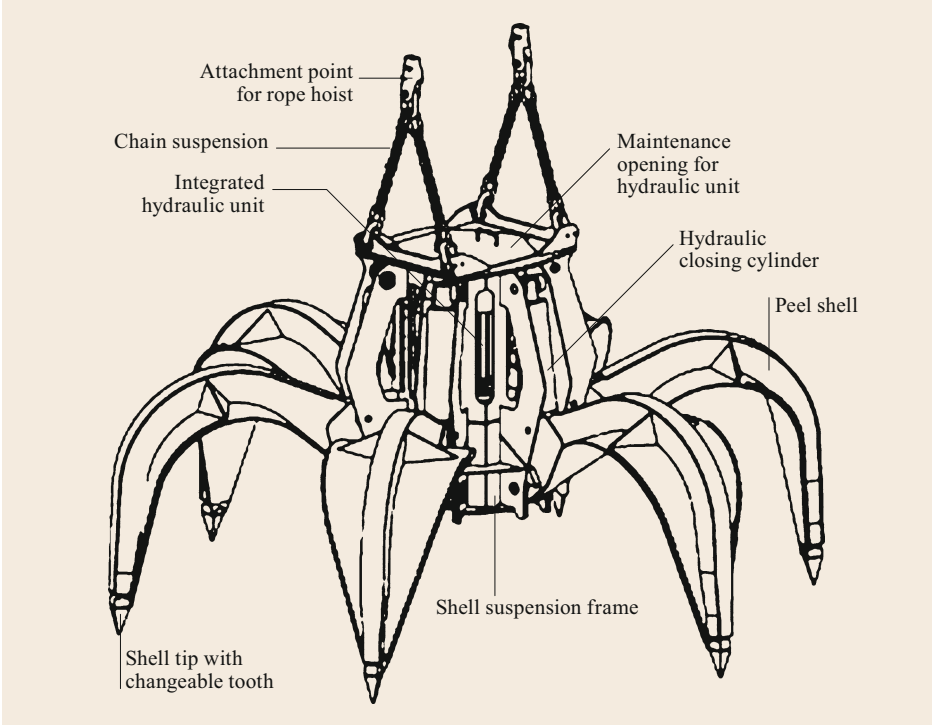

Fig. 20.122 Motor-driven peel grab for garbage (MRS Greifer GmbH)

in mobile applications. In explosion-risk areas, pneumatically driven hoists can be used, although electric drives are also possible if special protection measures (casings) are applied.

Standard Hoists. Due to their serial production, standard hoists are cost-effective and suitable for most applications. They are also used as crane hoists and can be integrated into a trolley or crab. The FEM product group Cranes and Hoists is used to define the grouping and dimensioning of standard hoists. FEM 9.511 [20.218] determines the rating mechanism group, FEM 9.661 [20.219] the sizes and the design of rope drives, and FEM 9.901 [20.220] the foundations for the general calculation. For an overview on powered hoists, see DIN EN 14 492-2 [20.221].

Electric Wire Rope Hoists. These can be distinguished by the arrangement of their components. There are three main types:

- Long designs with coaxial, serially arranged rope drum, gearbox, and motor with an integrated brake. This type can be characterized by a simple design and the use of standard components which are easily accessible (Fig. 20.123).
- Integrated designs with a coaxial arrangement. The gearbox, and sometimes the motor as well, are integrated into the rope drum, which is a weight- and space-saving solution.
- Compact or C-shaped designs (Fig. 20.124), where the motor and spur gear are arranged next to the rope drum, being easily accessible and cost-efficient.

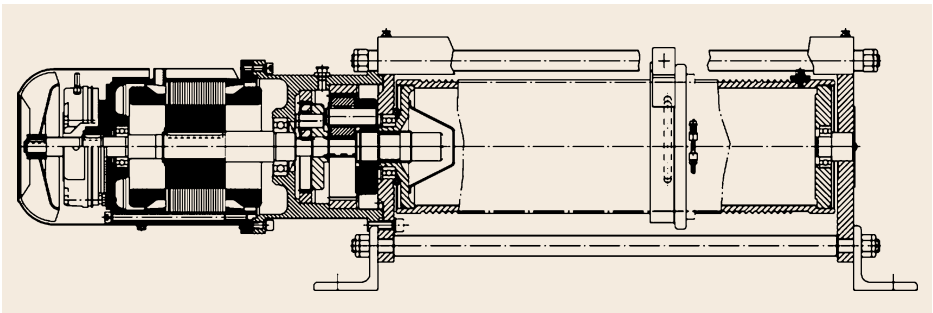

Fig. 20.123 Standard electric hoist with coaxial design (KULI Hebezeuge)

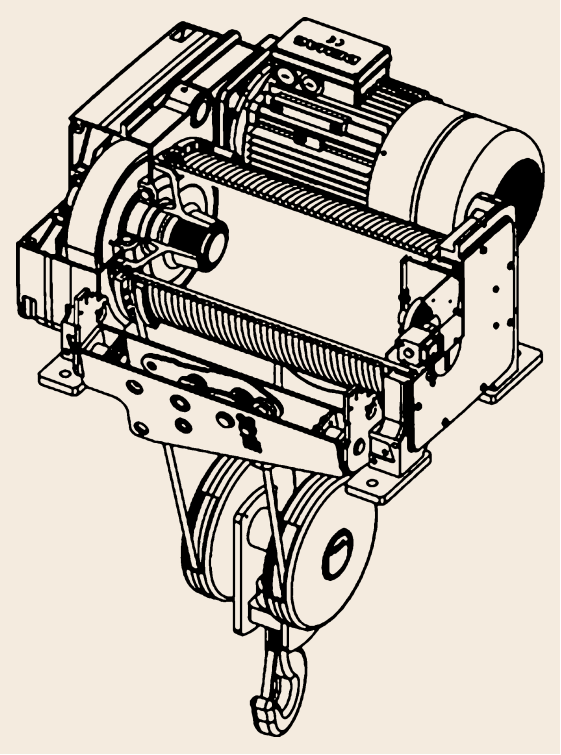

Fig. 20.124 Standard electric hoist with C-shaped design (Demag Cranes & Components, Solon, USA)

Electric rope hoists offer rated loads of approximately 1–100 t. The lifting speed ranges from 2 to 50 m/min, depending on the capacity. Drives are cylindrical-rotor motors with pole changing or motors with speed control via frequency converters. Mostly, single-layer spooling drums are used to store the wire rope.

Electric Chain Hoists (Fig. 20.125). An asynchronous motor drives a pocket wheel via an electrically monitored slip clutch and a transmission gearing. A single-disc brake located at the load side enables the holding function. Typically, a round steel link chain is used. A chain box receives the chain. A contactor control reduces the voltage at the control button to 24 V. Usual lifting heights are 4–8 m or, in special cases (e.g., for wind turbines), up to 180 m. Lifting speeds are up to 30 m/min. The rated load is up to 2500 kg with one chain, up to 5000 kg with two chain strands, and in special cases also up to 80 t.

Pneumatic Chain Hoists. A high-speed pneumatic vane motor powers a round steel link chain via a multistage planetary gearing and a pocket drive. The drive power of the hoist is 0.5–10 kW with nominal pressures of 4 or 6 bar. The lifting height is up to 50 m. The rated load ranges from 125 kg at 15 m/min to 100 t at 0.4 m/min. Continuous reduction of the lifting speed is possible by reducing the compressed air volume flow with overload protection via pressure difference detection in the motor. Pneumatic hoists are preferably used in explosive atmospheres (off-shore industry, mining, and foundries), and for special applications also underwater.

Individual Hoists. The conventional open design of an individual hoist as shown in Fig. 20.126 consists of a motor, a double-shoe brake or a disc brake on the drive side, a torsional flexible clutch, a spur gear, a rope drum, and the rope drive with the upper block and hook block. The lift displacement is limited by a gear limit switch, which is driven by the rope drum. The highest lifting position is usually monitored by an operating contact and an emergency stop switch. Compared with standard hoists, open hoists use symmetrical reeving systems with a twin or double drums, as described in Sect. 20.3.1. This avoids traveling and rotation of the load.

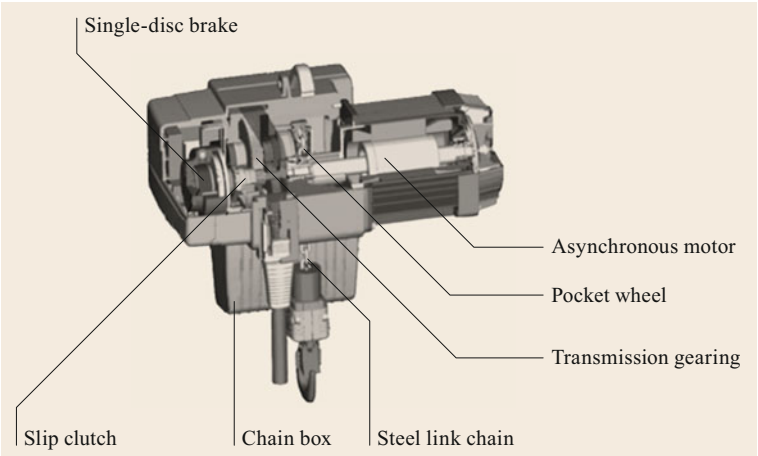

Fig. 20.125 Electric chain hoist (Demag Cranes & Components, Solon, USA)

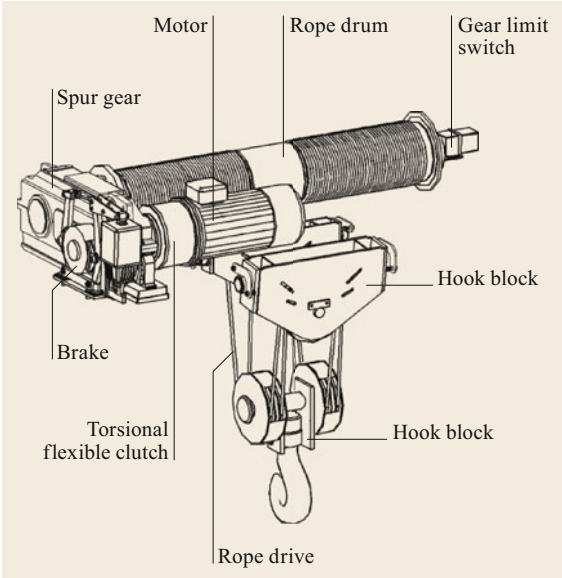

Fig. 20.126 Standard hoist with open design (Demag Cranes & Components, USA)

Individual hoists also typically use larger drums with single-layer rope spooling. If the size of the individual hoist is restricted, special drums with integrated gear motors can be used, similar to standard hoists. Due to their compact design, such integrated drums are used for mobile and ship cranes. In these applications, the wire rope is stored via multilayer spooling. Here, single-rope lifting forces of up to 2000 kN can be reached.

Redundant Hoists. Fully redundant hoists are equipped with two parallel powertrains and rope drives. If a safety-relevant component fails, the other system takes over the full load. Meanwhile, the load traverse maintains in a horizontal position. This is used, for example, for casting and reactor cranes. Partially redundant hoists only have two rope drives. A safety brake, which acts on the drum side wall, prevents the load from falling in the event of the failure of a part in the upper drive train. In the case of a rope break, the other rope takes the full load.

Crane Types

Cranes are discontinuous conveyors which can lift, lower, and move in one or more horizontal directions loads hanging from a suspension element. Slinging gears or special load handling devices are used to connect the suspension element (lifting hook) and the load (Sect. 20.5.2). Cranes can be moved on rails or be free (mobile and crawler cranes), or are mounted stationary or on floating bodies.

Crane types can be classified using different criteria. The following classification is according to DIN 15001-1 [20.222]. Several comprehensive standards exist for dimensioning of cranes and their components. At the European level, the basic standard DIN EN 13001 Crane Safety—Construction in General [20.223] should be mentioned. This standard includes parts about the general principles of and requirements for crane design (part 1), load assumptions (part 2), limit states and proof of competence of steel structures (part 3.1), the use of wire ropes in rope drives (Sect. 20.3.1), and the wheel/rail system (Sect. 20.3.3).

Furthermore, certain product standards (e.g., DIN EN 13000 Cranes—Mobile Cranes [20.223]) are to be used for specific types of cranes. A major difference between the now withdrawn DIN 15018 [20.224] and DIN EN 13001 [20.223] or ISO 20332 [20.225] at the international level lies in the assessment method. The European standard mainly uses the method of limit states, which allows a more differentiated safety level in the assessments [20.226, 227]. Risks resulting from the possible failure of components or the lack or failure of safety devices are prevented by inspection of cranes before their first commissioning and after significant changes, as well as through frequent inspections.

Acceptance tests are carried out according to national standards, e.g., DIN 15030 [20.228]. Technical inspection or other experts are authorized by the relevant trade association. Testing of structures and power units is performed with a suspended test load by moving the trolley or crab, as well as lifting and lowering of the test load, including a braking test with nominal lowering speed. The standards provide information regarding the test load.

Bridge and Gantry Cranes. Bridge cranes (overhead cranes) move guided by rails on high crane tracks. They can be equipped with one or more trolleys/crabs. As a hoist, manual chain hoists are rarely used. Typically, electrical and in some cases pneumatically or hydraulically operated hoists are applied. In general, motors with integrated brakes are used for the crane trolley and crab drives. Depending on the application, driving speeds range from 20 m/min to a maximum of 40 m/min for crabs and 40 m/min to a maximum of 120 m/min for crane bridges.

If overhead cranes are controlled from the floor, corded control units or increasingly radio remote controls are used. At crane speeds above 80 m/min, the crane is controlled from a control station which moves with the crane.

Various mechanical or electronic solutions exist to reduce swaying of the load. With the latter, an algorithm takes action in the crane control and affects the drives,

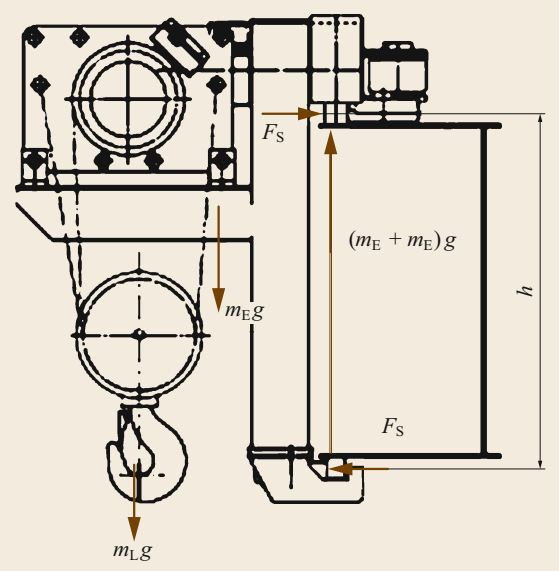

Fig. 20.127 Angular trolley for single-girder overhead cranes (KULI Hebezeuge)

depending on the load sway as recorded by an optical measuring system [20.229].

Single-girder overhead cranes with low capacity are usually equipped with a bottom flange trolley that drives on a single girder made of welded or rolled I-profiles. For cranes with an average capacity up to 20 t and maximum span of 40 m, a welded box girder is used. In addition to the bottom flange trolley, angular trolleys (Fig. 20.127) can also be used.

The wheel loads of the bottom boom trolley cause local bending stresses in the bottom flange of the main girder (so-called flange bending). Nonsymmetrical wheel loads result in an added torsional moment in the main girder, which must be considered in the design and dimensioning of the girder. Approaches to such flange bending calculation are described in DIN EN 15011 [20.230]. In case of large wheel loads, the rail must be supported by an additional I-beam (secondary girder) connected to the main girder at short intervals.

Angular trolleys as shown in Fig. 20.127 work next to a closed box girder. They only drive on one rail. The torsional moment M of the load m_L and dead weight m_E acting on the rail is supported by a pair of forces $F_S = M/h$ on the sidewards guide rollers. The forces F_S are applied as horizontal forces onto the upper and bottom flange of the main girder. The wheel blocks transmit the vertical forces of the load and dead weight to the rail. An arrester hook secures the track guidance during accidental events.

Double-girder overhead cranes have two parallel main beams with rails welded to the upper flanges, where a two-rail trolley (*crab*) runs. Two plate girders (I-beams) are often used as the main beams for light constructions. Here, the trolley rails are placed over the webs. Heavy twin-girder overhead cranes with load capacities of up to 100 t and spans of up to 36 m have two parallel rectangular box girders, as shown in Fig. 20.128a. The main girders are bolted or welded to the end carriages at both ends. The bridge wheels or wheel bogies are mounted at these ends. In general, half of the wheels are powered by the bridge drive. The trolley has one or two (e.g., casting crane) hoists. The power supply to the crane bridge and trolley is realized via power rails or trailing cables. The operation is controlled from a cab or by remote control. The trolley can be accessed via the upper flange of one of the main girders or a separate footbridge. Elastic–plastic buffers or hydraulic buffers dampen the impact in case of driving against the end stop or another crane. The trolley

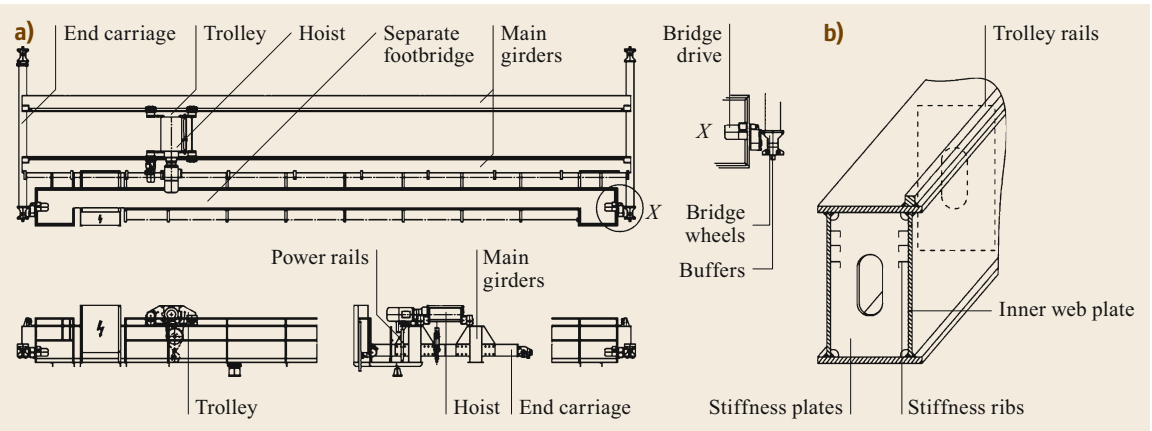

Fig. 20.128 **(a)** Double-girder overhead crane with two parallel box girders (KULI Hebezeuge), **(b)** cross-section of the box girder with stiffening plates and ribs

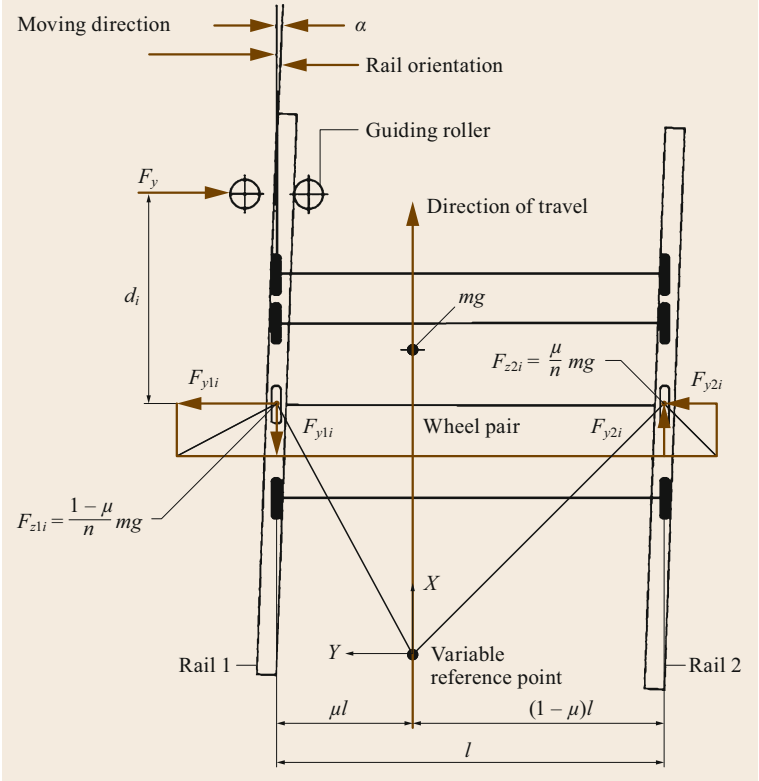

Fig. 20.129 Model to quantify the skew forces according to DIN EN 13001 [20.223]

rails generally lie over the inner web plate of the box girder (Fig. 20.128a,b). The eccentric transmission of wheel loads results in bending and torsional stress in the main girders. The shape of the box profile is maintained by stiffness plates, made of profiles or sheets. If wheel loads are introduced in the area between two stiffness plates, they are not borne by the whole box girder. Alternatively, the inner web and parts of the lower and upper flange in the section below the trolley rail can be assumed to be bearing (so-called secondary bending). Stiffness ribs welded in the longitudinal direction onto the inner side of the girder webs prevent the webs from bulging in the section between stiffness plates.

The wheel loads of the trolley are transmitted as Hertzian pressure. This results in local stresses in the trolley rail and at the connection between the rail and the main girders. To determine the stress, a simplified conical load profile below the wheel rail contact point can be assumed. Detailed calculation approaches are provided in DIN EN 15011 [20.230] and EN 13001 [20.223].

Lateral guiding of rail-bound cranes and trolleys is realized by wheel flanges or, in case of intense operation, by guide rollers. During skewing, the wheel flange or guide rollers come into contact with the rail. This also causes a displacement of the wheel contact area on the rail, which results in additional friction forces. According to DIN EN 13001 [20.223], skew forces are considered to be nonregular loads, although in individual cases, their frequency of occurrence may require a classification as regular loads. To quantify the skew forces, a simplified model can be used, which assumes a rigid crane supporting structure on a rigid crane runway.

The arrangement of the wheel pairs in reference to the moving direction of the front guides is described by the distances d_i (Fig. 20.129). In case of the use of wheels with flanges, $d_i = 0$. The weight force mg of the loaded crane acts at a distance μl from rail 1 and is distributed uniformly between the n wheels on each side of the crane runway. The crane moves under a skew angle α.

An equilibrium of moments exists between the track guiding force F_y on the front guide and the friction forces F_{x1i}, F_{y1i}, F_{x2i}, and F_{y2i} in relation to a variable reference point. According to DIN EN 13 001-2 [20.231],

$$F_y = vfmg\,, \tag{20.147}$$

where f is the friction coefficient of the wheel and $f = 0.3(1 - e^{250\alpha})$ applies. The coefficient v depends on the number of wheel pairs, their position relative to the front guide d_i, the type of drive (single-wheel

Fig. 20.130 Gantry crane as a loading bridge (KONECRANES)

drive, speed-coupled wheels, or free-running wheels), the axial mobility of the wheels (axially fixed or displaceable), and the position of the center of gravity of the crane (for the calculation of v see DIN EN 13 001-2 [20.231]).

Minimization of the track guiding force F_y and the wear on the running surfaces can be achieved by ensuring close tolerances on the axial parallelism of the wheels, by rigid design of the wheel connection, and by using small diagonal angles α. Hence, small crane runway tolerances and small clearances between the guiding elements and rail will minimize F_y. To achieve this, it is beneficial to guide the crane on only one rail. For tolerances for cranes and crane runways, see ISO 12488-1 [20.232]. According to DIN EN 13 001-2 [20.231], the skew angle should not exceed $\alpha = 0.015$ rad.

Gantry cranes are cranes with one or more horizontal girders supported at one (semi gantry crane) or two (full gantry cranes) supports. One of the supports can be a pendulum support, or both supports can be fully fixed to the main girder [20.233]. Gantry cranes are operated by remote control, via cable or from a control station. In some applications, e.g., in container terminals, automatic crane systems can also be found [20.234]. Here, precise load guidance for automatic positioning is important (compared with gantry cranes).

Loading bridges (Fig. 20.130) are full gantry cranes operating in larger storage areas (for steel, wood, and concrete parts) and ports (bulk goods and containers). Because of their large span, the main truss or box girder is mounted statically on a pendulum support and on a fully fixed support. The pendulum support transmits only vertical forces, while the fixed support also transmits horizontal forces in the trolley travel direction. The supporting forces are distributed over several wheel bogies. A synchronism control system limits the displacement difference between the two supports by decelerating the wheel drives of the leading side. Bridges with a small span and stiff frame construction do not require such a synchronism control system (e.g., the ship unloader shown in Fig. 20.132). Container handling gantry cranes are often equipped with a slewing trolley/crab (Fig. 20.130) with a special load handling device called a spreader (Fig. 20.131). The rotatability around the vertical axis allows aligning and positioning of the containers during transfer.

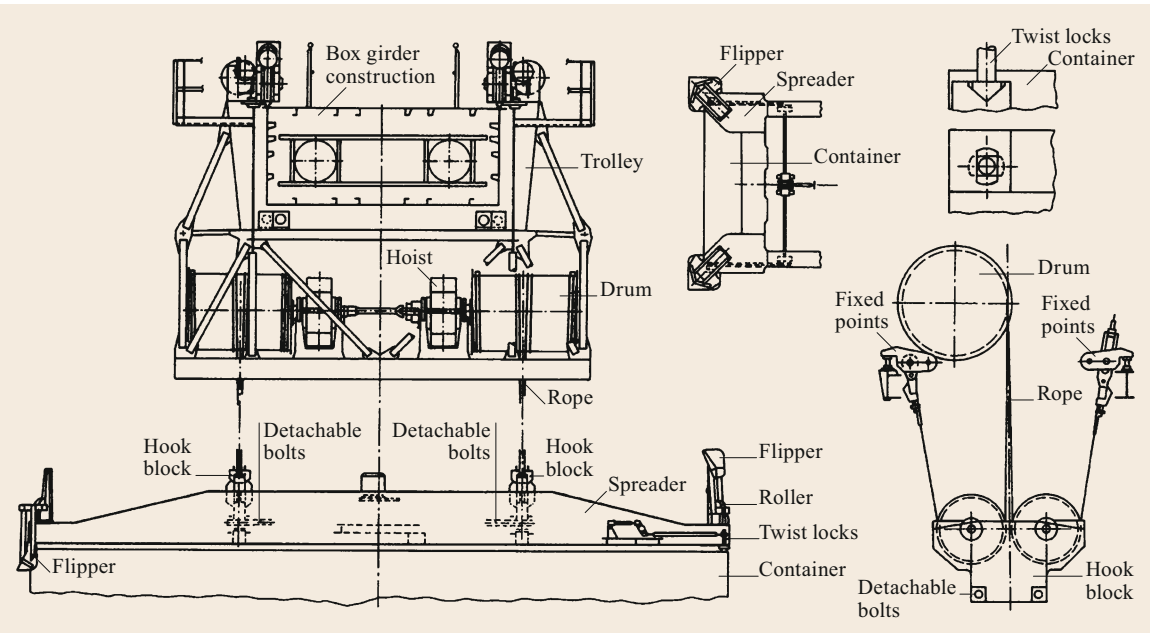

Fig. 20.131 Spreader for a container bridge (Vulkan Hafentechnik)

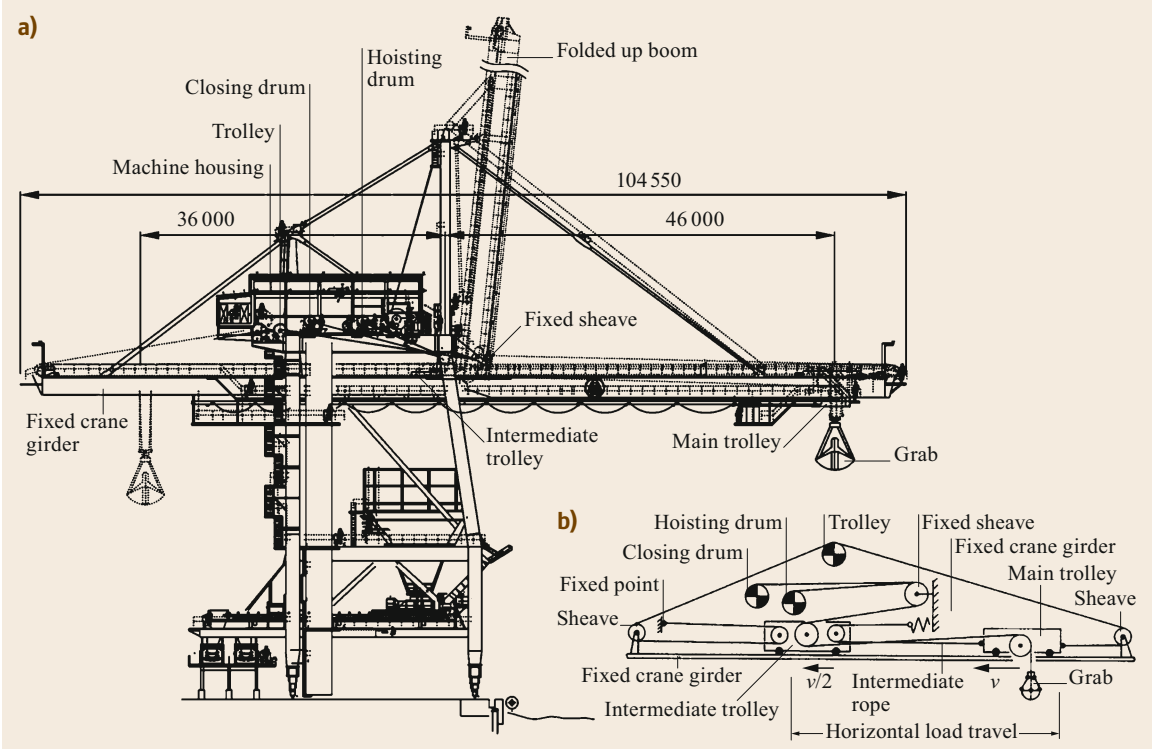

Fig. 20.132a,b Grab-type ship unloader with rope drive (Thyssenkrupp Industrial Solutions AG): **(a)** construction, **(b)** rope drive

Figure 20.131 shows a spreader which is used in container bridges with a box girder construction. The hoists are usually arranged on a trolley at the bottom flange of the main girder, and rarely stationary on the gantry. The capacity of the rope drive is 45–75 t. The lifting speed is 45–52 m/min for the nominal load and up to 180 m/min for the empty spreader. The speed of the trolley is 150–240 m/min. On average, 32 containers can be handled per hour [20.137]. Two ropes run from drums to fixed points across the hook block, which is connected to the spreader by detachable bolts. The link between the spreader and container is controlled remotely by the crane operator via hydraulically driven twist locks. Guide arms (flippers) are used to center the spreader on the container. For load attachment in the ship, the flippers are folded up. Then the spreader is guided over rollers, which run in the ship's own frame.

The length of fixed spreaders does not vary, but for heavier telescopic spreaders, the distance between the twist lock bolts can be adjusted hydraulically in the longitudinal direction so that 20′ (6 m), 30′ (9 m), 40′ (approx. 12 m), or 45′ (13.7 m) containers can be handled. The latest generation of spreaders is capable of handling two standard 20′ containers (twin lift) or even two 40′ containers (tandem lift).

For bulk materials handling in harbors, grab-type ship unloaders are in use. In these, rope-driven trolleys (Fig. 20.132a) work independently based on the friction forces between the wheel and rail. To reduce the weight of the trolley, the closing and hoisting drums are placed in a fixed machine housing. For horizontal travel of the grabs while moving the trolley, special rope drive systems are required (Fig. 20.132b). Those with two trolley drives are preferred. The hoisting and closing ropes run from the closing and hoisting drum via fixed sheaves to the intermediate trolley, then further via the main trolley to the grab. Two parallel ropes run from the trolley drum to the jib peak, and from there via sheaves to the main trolley. Two other ropes run from the trolley drum to the crane girder end, and from there via sheaves to the intermediate trolley and, after deflection, back again to a fixed point at the crane girder end. Thus, the main trolley travels with twice the speed as the intermediate trolley. The reduction in the grab rope length between the two trolleys is equal to the distance increase between the intermediate trolley and the fixed sheaves. Hence, the grab does not change its height position when the trolleys are moved. Intermediate ropes provide a preload in the trolley system. The hoist and trolley run using controlled drives with lifting

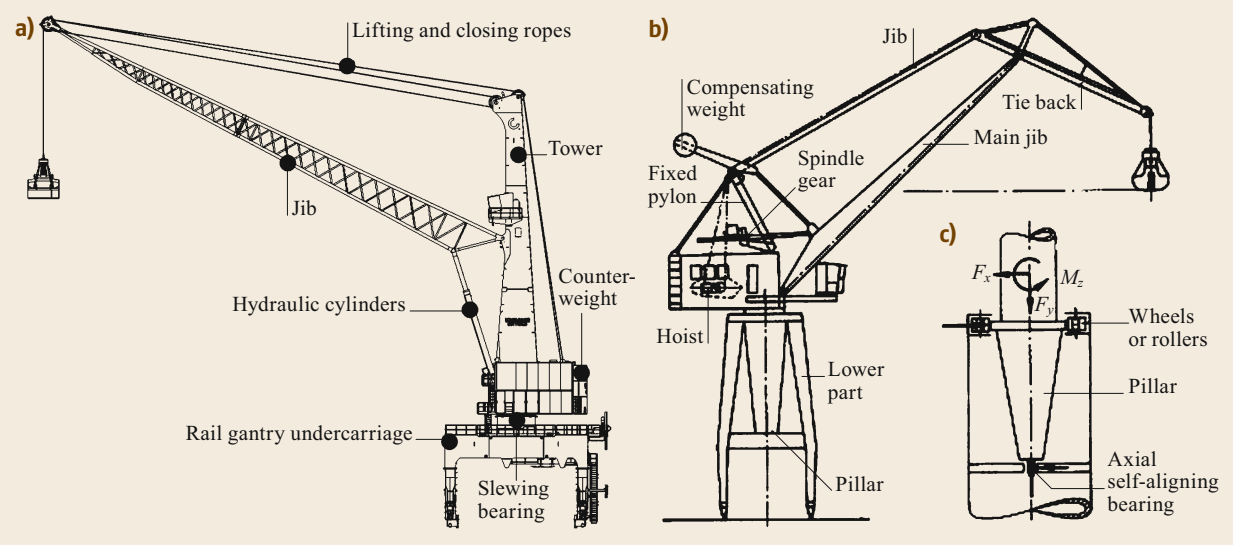

Fig. 20.133 **(a)** Luffing crane with rail drives for ports, **(b)** double-jib level luffing crane, **(c)** pillar slewing gear (KONECRANES)

speeds of up to 180 m/min and trolley speeds of up to 240 m/min (acceleration time 4 s). The best automatic suppression of grab sway is achieved when accelerating and braking the trolley with the eigenfrequency time of the grab [20.235]. A maximum performance of up to 2500 t/h can be achieved for short operation intervals. Trolley operations on a fixed crane girder are also possible when using a folded-up boom.

Slewing Cranes. Slewing cranes are cranes in which the upper part with the boom can turn around a vertical axis with respect to the lower part. Swinging (jib) cranes are preferred over slewing cranes when the angle of rotation is restricted (e.g., wall-mounted slewing cranes). The bottom of the crane can be fixed (as in a revolving jip pillar crane or tower crane), run on rails (e.g., a railway crane), or mounted on a floating body (floating crane) or a road chassis (mobile crane). For the design of tower cranes and slewing jib cranes, DIN EN 13001 [20.223] refers to special product standards. For the design of slewing pillar cranes and wall-mounted slewing cranes, the product standard for power-driven hoists (Sect. 20.5.1) is used.

The interface between the upper and lower part forms a driven slewing gear (Sect. 20.5.1). It transmits the vertical and horizontal forces and moments that arise from the eccentric center of gravity of the upper part and the load, from the inertial forces during slewing and driving, as well as from wind forces. Slewing bearings are most frequently used today. Slewing gears for heavy cranes are driven and braked via direct-current (DC) or slip-ring motors. The mechanical brake acts only as a holding brake. In the case of light cranes, cage motors with an intermediate flow coupling can be used. To prevent collisions in case of storms, the upper and lower parts of the crane are locked in the parking position using pins. In contrast, the brake is disabled on tower cranes so that the boom can self-adjust into the wind.

Wind loads must also be considered in the stability assessment, especially for jib cranes and all other cranes where there is a risk of tipping (e.g., mobile cranes). According to DIN EN 13001 [20.223], one must distinguish between wind loads for cranes in operation ($F = q(3)cA$) and those that are out of service ($F = q(z)cA$). In both cases, c describes the aerodynamic coefficient according to DIN EN 13 001-2 [20.231] and A is the active area. $q(3) = 0.5\rho v(3)^2$ represents the static pressure for a gust speed $v(3)$ over a period of three seconds for an air density of $\rho = 1.25\,\mathrm{kg/m^3}$. The equivalent static pressure in storm conditions ($q(z) = 0.5\rho v(z)^2$) mainly depends on the static equivalent wind speed $v(z)$, which changes with altitude above the ground and also depends on regional conditions and the frequency of storms.

Level luffing cranes (Fig. 20.133) are preferably used in ports and shipyards. Their structural parts are designed with plate, box, truss, or mixed construction. The portal-like gantry with typically four legs allows transit for rail or road traffic. The upper slewing part of the crane includes a luffing gear. The kinematics of the boom and hoisting rope drive is designed such that the load moves along an almost horizontal path when luffing the jib [20.236]. Hence, the luffing gear does not lift the load. The luffing crane shown in Fig. 20.133a consists of an upper part mounted on a rail gantry undercarriage. The crane operation can be fully electric, diesel, or a combi-

nation of both drive types. The jib is pivoted on the tower and is luffed by the hydraulic cylinders. The counterweight assists with stability and reduces the tilting moment of the slewing bearing. Almost horizontal (level) load displacement is achieved by triple reeving of the lifting and closing ropes. This involves storage of the rope in the reeving system between the sheaves located at the jib and tower tip. The luffing of the jib increases or decreases the distances between the sheaves. Hence, the length of rope stored on or released from the reeving system equalizes the lifting or lowering of the jip tip during luffing. The disadvantage of these simple level luffing cranes is that reeving systems to decrease the rope force cannot be used as the rope displacement would increase with the transmission rate.

In a double-jib level luffing crane (Fig. 20.133b), the ropes run from the hoist via the jibs and tie back to the load handling device. By coordinating the jib length of the squared four-beam linkage of the tie back, jib, main jib, and fixed pylon, the extension lines of the jib and main jib approximately intersect at the line of action of the load (momentary pole) in each steering position. This results in the desired, almost horizontal load path. As level luffing is realized by the kinematics of the jib system itself, the rope drive is not involved. Therefore, reeving systems can be used, in contrast to the single-jib level luffing cranes described above.

The magnitude of the movable compensating weight and the kinematics of its coupling to the main jib are adapted to the whole jib system such that approximate dead weight compensation is realized in each jib position. A spindle gear, double hydraulic cylinders, or closed pretensioned rope drives (for large cranes) are used as the actual luffing drive which changes the inclination of the jib system. The upper part of the crane is connected to the lower part via a robust slewing gear with a rotating pillar (Fig. 20.133c). As such, the upper part of the crane is supported below by the pillar on an axial self-aligning bearing and above by wheels or rollers distributed on the lower part.

Tower cranes (Fig. 20.134a) are used in civil engineering as construction machines (reach × lifting capacity: up to 5000 mt). Tower cranes have to be installed and dismantled relatively often and must be adapted to the requirements of the construction site (capacity, lifting height, and outreach). Thus, they must be designed using standardized modules that can be easily assembled. The counterweight, the weight of the hoist, and the weight of the counterboom form the countermoment to the weight of the main boom, trolley, and load. Overloading is prevented by switching off the lifting and trolley movements if the permissible load or permissible load torque is exceeded [20.236]. The load-bearing elements (Fig. 20.134e) are lightweight truss constructions, usually made of rectangular tubes or rarely still open rolled profiles. Rotating tower cranes can be firmly connected to a foundation (Fig. 20.134b), stationary on undercarriages, or movable on rails (Fig. 20.134a). Driving through curves is possible. They can also be mounted on a crawler undercarriage or the chassis of a mobile crane.

When equipped with climbing devices (Fig. 20.134), the height of tower cranes can be increased with the growing height of the building. For large heights, they can be braced against the building or climb inside the building. They may have an adjustable jib or, as preferred today, a fixed horizontally extending jib, on which a rope-driven trolley runs at up to 110 m/min.

As shown in Fig. 20.134c, the trolley rail generally consists of two rectangular tubes, which are welded with diagonal tubes and an overhead rectangular tube to form a triangular trolley jib.

Figure 20.134d shows how the hoist rope is guided from a drum via two fixed sheaves and in the tower, along the jib through the trolley, to the hook block, and to the fixed point A at the tip of the jib. The trolley is moved by the trolley drive via a closed rope system. The lifting speed is continuously adjusted to the load by means of frequency-controlled drives (up to 150 m/min). Often, the speed range is increased (up to 280 m/min) by remotely operated gear switching. In addition to frequency-controlled electric motors, slip-ring motors in conjunction with an eddy-current brake, pole-changing cage motors, or hydrostatic drives can also be used for the hoist and trolley drives.

Wall-mounted slewing cranes (Fig. 20.135) are available for loads of up to 5 t and jib lengths up to 10 m. The load moment is introduced into the wall via a bracket as a pair of forces. During assembly, it must be ensured that the support structure offers sufficient load bearing and rigidity to absorb the reaction forces, which change direction according to the different pivoting positions. The slewing of the jib is achieved manually or with slewing drives for larger loads. Wall swing cranes are commonly equipped with power-driven chain hoists or rope hoists, which hang from manually or electrically driven lower flange trolleys. If the console is equipped with running wheels on rails laid horizontally parallel to the wall, the crane is called a wall-mounted traveling crane. In such applications, the jib cannot be slewed.

Slewing pillar cranes are designed for loads of up to 6.3 t and outreach dimensions up to 10 m. Slewing pillar cranes are generally equipped with a rope or chain hoist, and are used in workshops or small storage areas. The fixed pillar, designed as a tube, transmits the load moment to the ground via anchor bolts. The pivot bearing receives the vertical force F_y and the horizontal force

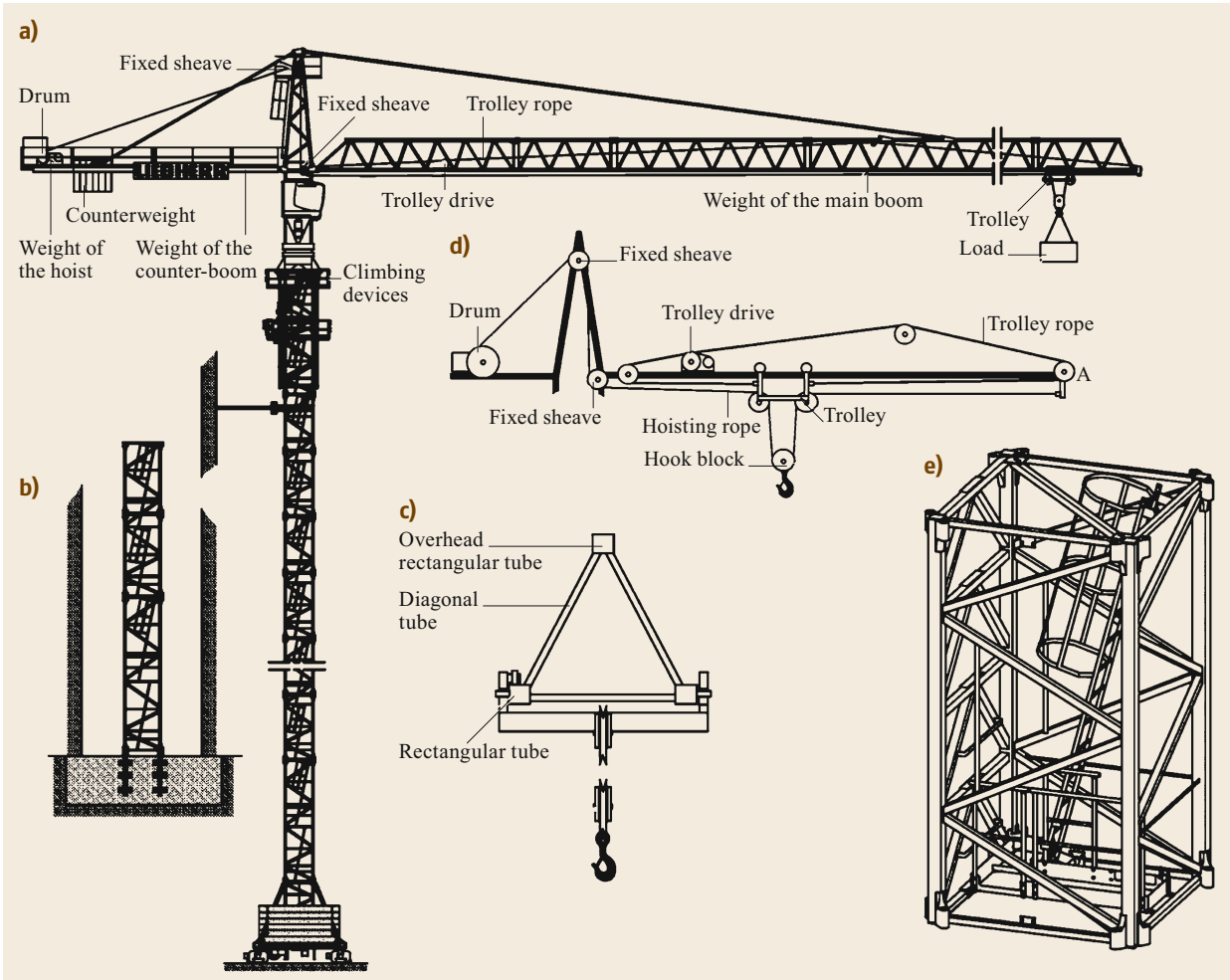

Fig. 20.134a–e Top slewing tower crane (Liebherr), **(a)** trolley jib tower crane, **(b)** crane tower on foundation anchors, **(c)** cut view of trolley jib, **(d)** rope drive of hoisting rope and trolley rope, **(e)** design of a tower section

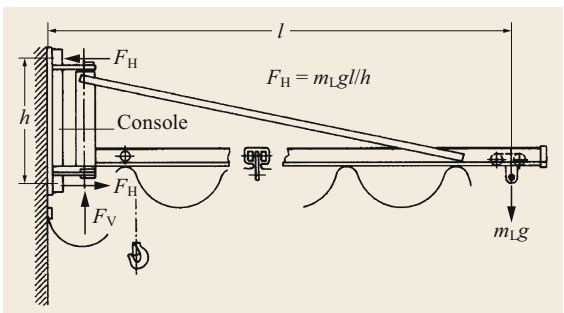

Fig. 20.135 Wall-mounted slewing crane (ABUS)

F_x. The jib is guided during rotation by two rollers in contact with a rail ring. Slewing is achieved manually or is motorized. In other constructions, the rotation is realized by a slewing bearing between a rotating jib and fixed pillar or between a rotating pillar and fixed base plate.

Mobile Cranes. Mobile cranes have lattice jibs or hydraulically extendable telescopic jibs with rated loads of 35–1200 t (or up to 3000 t for cranes with crawler undercarriages). For guidelines on their construction, see DIN EN 13000 [20.237]. The booms are designed according to beam theory. The cranes consist of an upper and undercarriage, which is equipped with a wheel or crawler drive (Sect. 20.5.1) to allow traveling on roads or moving over difficult terrain. Today, the majority of mobile cranes are truck cranes for road and level terrain, called all-terrain (AT) cranes. They have up to nine axles, all hydropneumatically suspended, while the main drive is a diesel engine with an automatic transmission, articulated shafts, transfer case, and blockable

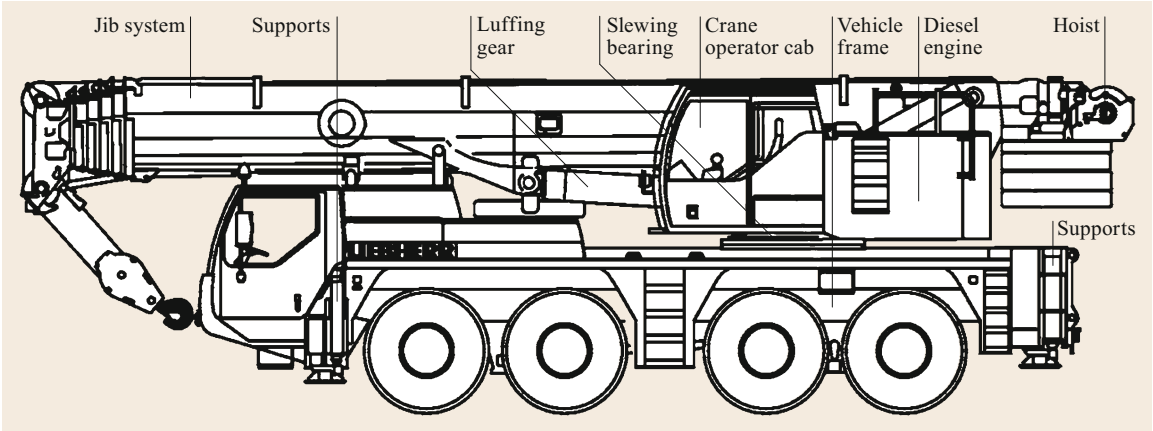

Fig. 20.136 Mobile crane (Liebherr)

differential gears; up to eight of the axles are steerable [20.236].

During operation, the forces and moments are transmitted from the upper carriage to the slewing bearing (Fig. 20.136), vehicle frame, and supports. The maximum rated load is limited by the stability of the system and the strength of the components, such as the jib, slewing bearing, and vehicle frame. The subassemblies for the main functions of the crane, such as the hoist, slewing gear, luffing gear, and jib system, are mounted on the upper carriage. The upper carriage frame also serves to accommodate the crane operator cab, upper carriage hydraulics, and another separate diesel engine for driving the hydraulic pumps in cranes with rated load of approximately 60–80 t. All crane functions are realized by hydraulic drives [20.236]. The telescopic jib is constructed from up to nine welded box girders made of fine-grained structural steel with yield strength of up to 1100 N/mm^2 (STE1100). For high rated loads, oval girder cross sections are used, making the use of stiffness ribs or material doubling unnecessary [20.238]. In addition to systems with multiple telescopic hydraulic cylinders or single-stage cylinders with a rope pull system, the current state of the art is a single-cylinder telescopic system with an automated securing and bolting unit. Different positions of the telescopic boom bolting can be used to achieve up to 1000 off-travel conditions. Due to the bolting, the standard forces only load the steel construction during operation but do not affect the hydraulic system. To increase the working range, telescopic booms can be extended with a lattice mast tip so that lifting heights of up to 146 m and outreaches of up to 126 m can be achieved. For cranes with higher rated loads, pure lattice mast booms are used. The maximum lifting height in this case is up to 193 m with an outreach of 136 m. Lattice mast cranes with a crawler undercarriage allow an outreach of 164 m and lifting heights of up to 226 m. To increase the rated load, additional guy ropes can be used [20.239]. The ropes from the head to the tensioning block are preloaded by winches.

Other Types of Crane. Overhead tracks are built according to a modular system, commonly equipped with ground-controlled chain hoists. They are used to supply workstations in production with loads of up to approximately 2000 kg. The chain hoists can be operated electrically, pneumatically, or hydraulically. The lanes of cold-formed rails are suspended or adjusted, pendulously or fixed by thread rods to ceilings or roof structures. Inside the rail or on the rail lower chord, a four-wheel trolley including a hoist is mounted and moved manually or driven by friction wheels.

Suspension Cranes. Manually moved or driven suspension cranes use the same support and driving elements, as well as the same energy supply and control, as the overhead tracks. The crane runway is realized in the form of swinging or fixed suspended track rails, which can also serve as a crane girder with the same design. The trolleys can, if necessary, change from one crane runway to another. By agile suspension of the crane runway, travel along sections with different suspension distances is possible. Depending on the span and load, the crane girder is designed as a single- or double-girder crane. For working loads above 2.0 t, suspension cranes are equipped with I-shaped crane girders and bottom flange trolleys.

Loading cranes (Fig. 20.137) are powered cranes with a rotatable pillar mounted on a crane base and a boom system attached to the top of the pillar. In general, loading cranes are mounted on a vehicle (including trailers) and are intended for loading and unloading it. If increased stability is required, supports

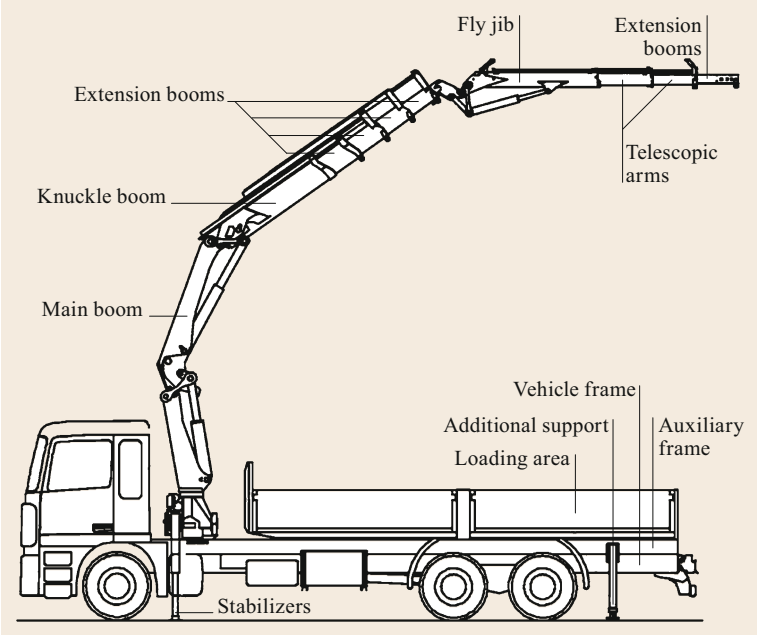

Fig. 20.137 Loading crane (Palfinger)

must be provided on the vehicle. Guidelines for their construction are provided by the product standard DIN EN 12999 [20.240].

Offshore cranes are less defined by their construction than by their place of use in predominantly maritime settings. The product standards DIN EN 13852-1, -2 [20.241, 242] for the design of such cranes distinguish between "offshore cranes for general use" (part 1) and "floating cranes" (part 2). Offshore cranes are permanently installed on drilling rigs and are generally designed as slewing cranes. Floating cranes are mounted on a specially designed floating body and are used during assembly or disassembly work. Both types of cranes are predominantly equipped with a sea tracking system and a rope tensioning system. The stability of floating cranes is particularly important. In the design phase, the load must be increased by using an increased dynamic coefficient that considers the relative speed between the crane basement and the lifted load.

20.5.3 Excavators and Loaders

Excavators and loaders form one of the most important groups of construction machines. They are used in different fields, and a clear separation between them is neither useful nor possible. Excavators are in general characterized by higher point loads on the material and moving larger volumes of material. On construction sites, excavators are used to demolish, dig, and load soil and bulk materials. Loaders are mainly used for loading but can also be used for other operations with a wide range of attachment tools. The forces, such as the excavation, digging, breakout, and loading forces, depend firstly on the machine mass and secondly on the engine and hydraulic system. As these building machines are not fixed to the ground, the maximum force is always limited by the mass of the machine, the working position of the tool, and the friction between the underlying ground and the machine. Therefore, heavy machines use crawler tracks to increase the frictional forces between the machine and the ground on the one hand, while on the other hand decreasing the soil pressure.

Forces when Digging and Loading

In the design process of a new construction machine, it is essential to proof the dynamic stability of the machine during its operation. This is necessary to ensure that the machine cannot roll over during its working process. One requirement for this kind of analysis is knowledge of all the masses of the machine components, their centers of mass, as well as all the forces and torques acting on the machine during its working process. The center of mass can be calculated using a three-dimensional (3-D) computer-aided design (CAD) model in most cases. Otherwise, it is also possible to measure the center of mass according to Fig. 20.138. Using this method, the axle loads are measured, as well as the distances between the axles. The position of the center of mass in the moving direction can then be easily calculated. The height of the center of mass can be measured in a second stage, if one axle of the machine is moved upwards. If the loads on

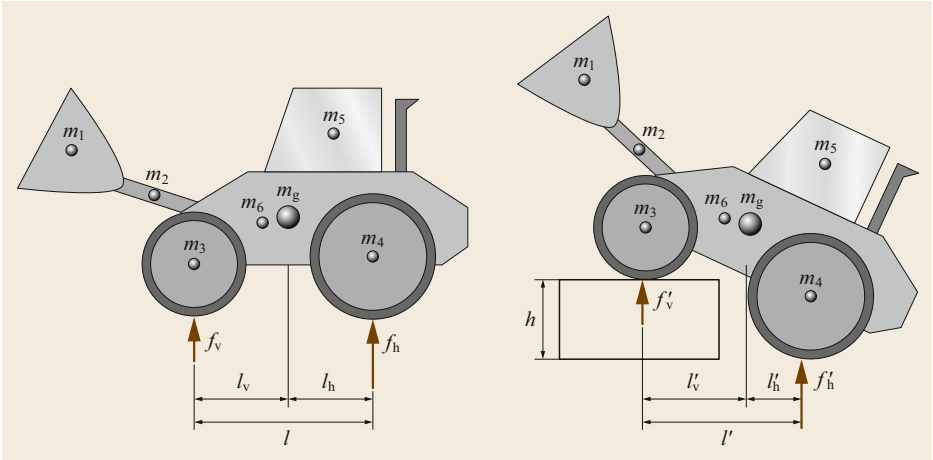

Fig. 20.138 Experimental measurement of the center of mass by lifting one axle

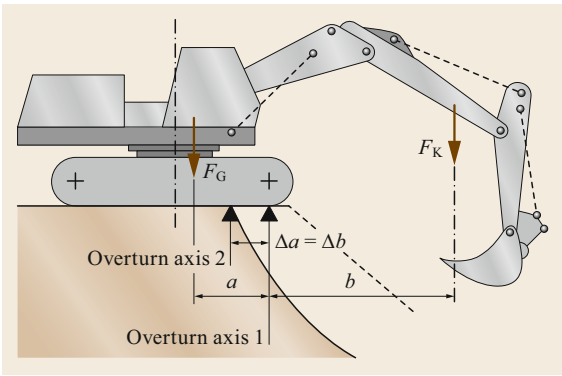

Fig. 20.139 An excavator with two different overturn axes: one is created and moving during the work process

the rear axle are measured, the equilibrium of moments around the front axle will solve the problem.

Once the center of mass is known, the next step in the calculation of the dynamic stability is the determination of the process loads. The process loads are mainly defined by the mass of the machine, the actuators, and the geometry of the tool, like the beam-and-stick combination of an excavator shown in Fig. 20.139. For many operations, it is necessary to avoid a positive torque around the overturn axis, if the gravitational force of the machine is considered, together with the process loads, the tool weight force, and the associated distances. For some machines, the dynamics of motion, and in special cases the acceleration forces, cannot be neglected when confirming their stability.

Computation of Process Forces

The excavation process is a combination of loosening the soil and filling the bucket. Different excavation processes with different tools lead to kinds of loosened material wedges that are very different in terms of size and shape. This depends on the soil parameters (e.g., strength), tool geometry, operational parameters of the excavation process (e.g., tool velocity), and system parameters of the machine. The excavation process is a combination of different processes that occur in parallel or successively. The forces generated by each process can be summed to obtain the resulting excavation force. The main forces are:

1. Cutting or loosening forces on the blade
2. Frictional forces between the tool and the underlying ground
3. Deformation and frictional forces during the flow of soil/bulk material into the tool
4. Gravitational forces of the tool
5. Acceleration forces.

While forces 4 and 5 can be calculated easily, the forces for cutting and the frictional deformational behavior of the loosened soil or bulk material cannot be calculated analytically. Analytical models are available to estimate these forces, as shown in [20.243]. The problem with these approaches is the degree of idealization. Indeed, the complex flow behavior of the mostly cohesive and consolidated soil or bulk materials interacting with real machine components with complex geometries and the superimposed movement of the components cannot be considered in such analytical models.

An alternative method to calculate the forces and material flow is the discrete element method (DEM). The DEM is capable of simulating the process forces acting on a machine during its operation. The DEM requires high computational effort but allows the consideration of cohesive material behavior as well as complex geometries and movements. Hence, the DEM can provide much better results than any analytical approach [20.244]. To simulate not only the bulk material

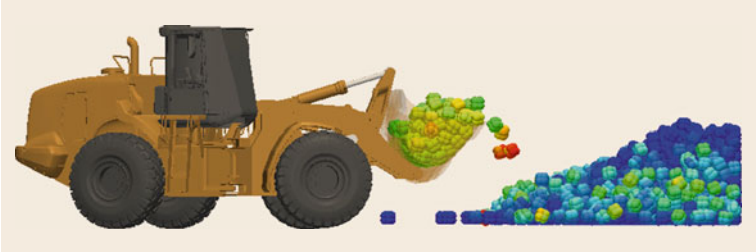

Fig. 20.140 Modeling of a wheel loader using multibody dynamic simulation coupled with a DEM simulation of the bulk material

flow but also the interaction of the bulk material with the machine, a combined simulation based on DEM with a multibody simulation (MBS) is necessary.

For many applications in the mining, exploration, conveying, and materials handling industries, multibody simulations (MBS) are the tool of choice to predict dynamic loads, power consumption, and stability. However, process loads can be neither calculated from multibody simulations nor identified by measurements, due to the dynamic interaction between the machinery and material. For accurate and sophisticated simulations, a model that considers the process, as well as the machine, is needed. FMI/FMU is a standard toolbox for interchange between different simulation programs to couple a multibody model of a machine to the DEM for the bulk material flow behavior [20.244, 245].

A DEM simulation can model and compute the interaction of particles of the bulk material to simulate its flow behavior. Using MBS, it is possible to model not only the mechanics but also the electric or hydraulic system of the machine that interacts with the bulk material (Fig. 20.140).

Such a coupled model can also be used to simulate the local forces acting on a tool of the machine. These forces, combined with a FEA model of the tool or machine part, are used to compute the local displacement and stress in the component [20.247].

Excavators

Excavators used on construction sites typically have a single bucket or a different tool. Given the large number of different tools available, excavators are multiuse vehicles applicable for nearly every kind of work except material transport over longer distances. Within the mining industry, excavators are mainly specialized for cutting soil, overburden, gravel, ore, or coal. These excavators usually have higher masses and workloads and operate with different working cycles. A mining excavator cuts the material with a face bucket or shovel in front of and away from the machine, while an excavator on a construction site (Fig. 20.141) cuts the material under and towards the machine with a backhoe bucket. In mining, bucket wheel excavators are used in open pit mines to achieve the highest mass flow rates. A bucket wheel excavator uses several face buckets mounted on a rotating wheel. This continuous mining process reaches much higher mass flow rates than a hydraulic bucket excavator can achieve. Bucket wheel excavators typically feed the bulk material to other, continuous conveyors such as belt conveyors. Excavators

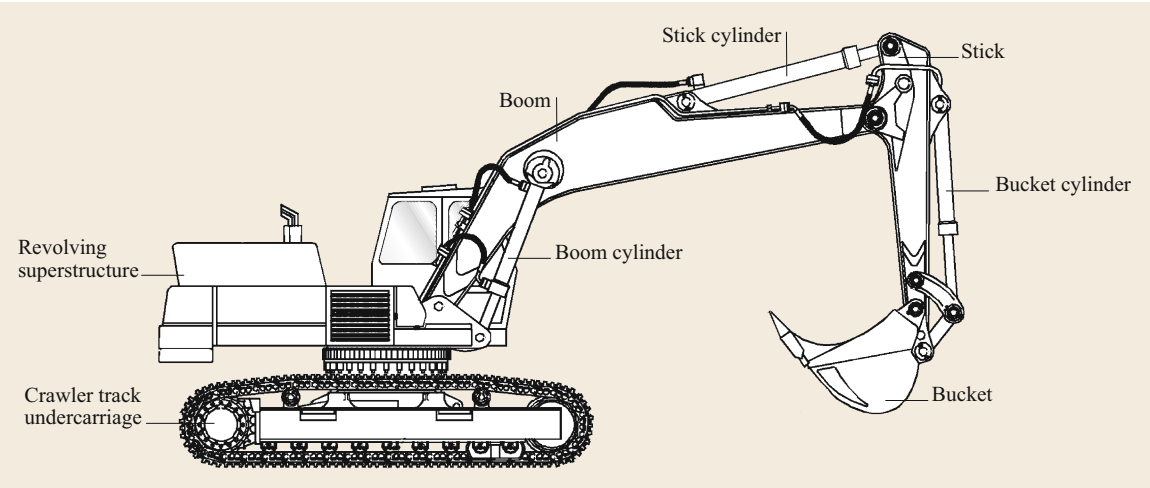

Fig. 20.141 Basic construction of a hydraulic excavator (after [20.246])

are built in sizes from less than 1 up to 40–50 t for construction sites and reach up to 1270 t with a front bucket volume of 63 m^3. Bucket wheel excavators can reach up to 14 200 t and can excavate 240 000 m^3 of overburden per day.

The excavators used on construction sites nowadays are commonly hydraulic. Such machines are often powered by a diesel engine with a hydrostatic system for all the work tools, as well as for the driving system. Hydraulic excavators can be classified based on their drive system. Crawler tracks are used on smaller and larger machines in all the weight size classes. The use of crawler tracks reduces the soil pressure, and allows higher frictional forces for the same mass by increasing the frictional coefficient. On small (mini) excavators the tracks are build out of rubber, while larger excavators use steel tracks, optionally with rubber plates to protect paved underlying ground. The crawler drive system with unsuspended wheels can only be used on site with driving velocities slower than 6 km/h. Higher velocities (usually less than 30 km/h) can be achieved if drives with air-pressured tires are used. These so-called mobile excavators make truck transport redundant, which reduces manpower and logistics costs. At railway construction sites, the mobile excavator can also be equipped with a railway drive system. These excavators are called two-way excavators. Further, special railway cranes are available with a fixed railway drive, typically designed for large loads.

Mobile excavators are the most variable machines in the class of excavators. If the machine can be equipped with a quick coupler, a tool change can be realized within a minute. The driver does not need to leave the machine to change the tool, even with an attached hydraulic system; for example, the change form a backhoe bucket to a hydraulic breaker to a grapple enables one machine to fulfill work tasks over a wide area [20.248].

Modern hydraulic excavators are steered by electric hydraulic systems which allow the driver to use predefined work cycles or motion sequences. Using common systems, the construction of defined slope angles is often challenging because the driver has to generate the superimposed motion of the tool via the independent control of three hydraulic cylinders [20.249, 250].

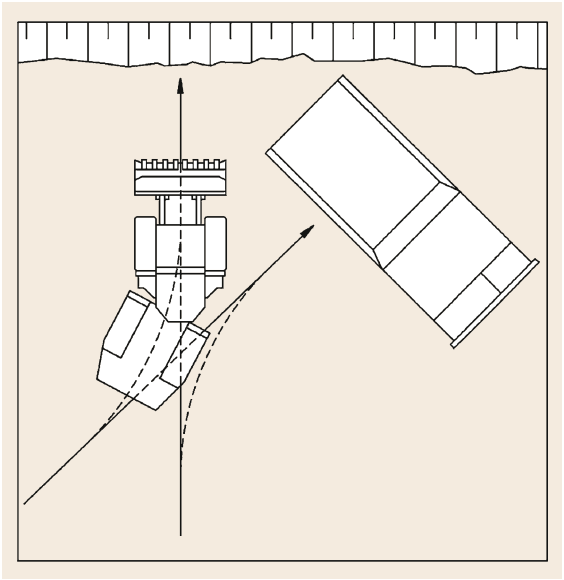

Fig. 20.142 Y cycles while loading a truck

Loaders

Loaders are used in soil moving and bulk materials handling for extraction, loading, and transport over short routes. The material is loaded by a forward movement of the loader into the material heap. The general operation cycle of loading and unloading often follows a Y-shaped curve, as shown in Fig. 20.142, consisting of a forward movement for loading, a bended reverse movement, a change in direction, and a bended forward movement towards the unloading point.

The work tool is a bucket which is connected to the machine via a frame that is supported by a hydraulic cylinder. The bucket is tilted using a hydraulic cylinder that is connected on a *parallel* or *z-kinematic*, as shown in Fig. 20.143. A *z*-kinematic leads to a higher excava-

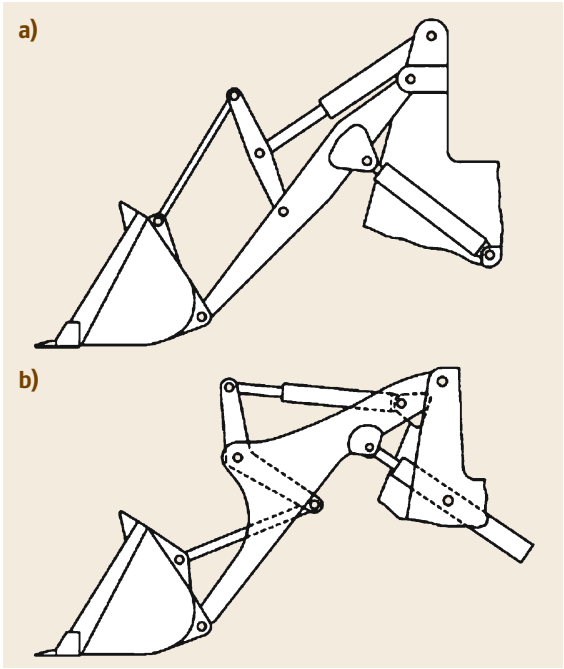

Fig. 20.143a,b Bucket kinematics of loaders: **(a)** parallel kinematic and **(b)** *z*-kinematic

tion force on the tip of the bucket because the hydraulic pressure can act on the larger circular area of the piston during the backwards tilting of the bucket. For the forwards tilting of the bucket, the smaller ring- area of the piston is used, so the discharge time of the bucket decreases when using a z-kinematic. The parallel kinematic works in the opposite way. The advantage is a much more precise movement of the attached tool due to the parallel movement of the tool and the hydraulic piston.

Wheel Loaders. The application of wheel loaders extends from construction through agriculture to mining. Wheel loaders can be characterized based on their chassis. The most common type is a wheel loader with a separate front and rear chassis and articulated steering. The steering is operated by a hydraulic system. The working tool is located on the front carriage, while the engine is placed on the rear carriage. Other types of steering include Ackermann steering combined with an oscillating axle on the rear wheels, or four-wheel steering. When four-wheel steering is used, the vehicle may also allow inverted steering angles on the front and rear axles to enabling parallel movement. This approach is mostly used in telescopic loaders. The cabin is positioned centrally above the machine, and in the case of articulated steering immediately above the rotating joint. However, its position can be either on the front or rear carriage. If the cabin is mounted on the front carriage, the view does not change on forwards movement. This type is used for difficult loading situations. A rear-mounted cabin as shown in Fig. 20.144 is applied to achieve a constant viewing angle on reverse driving, which makes backwards movement safer. The cabin must be designed with protective structure elements as described in DIN EN ISO 3164, 3449, and 3471 [20.251–253]. Wheel loaders are usually unsuspended, but a basic suspension is always supplied by the relatively large all-terrain tires. Their sizes range from small skit loaders to systems with a mass of 262 t and a bucket volume of over 40 m^3.

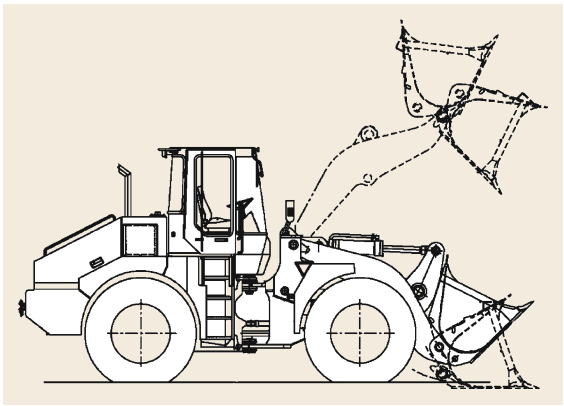

Fig. 20.144 Wheel loader with articulated steering (Liebherr, Bischofshofen, Austria)

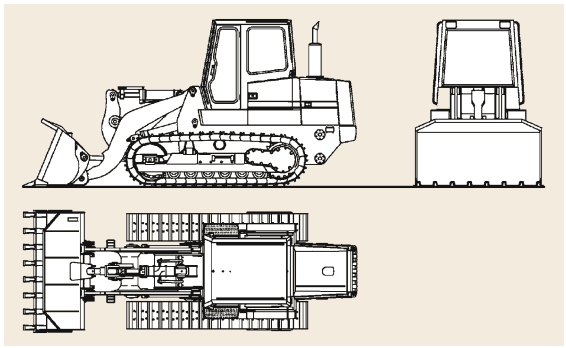

Fig. 20.145 Crawler track loader (Liebherr, Telfs, Austria)

Crawler Track Loaders. Track loaders such as that shown in Fig. 20.145 are used in environments with a rough surface or if the ground pressure must be kept low due to high moisture content. Surface irregularities can be compensated by the spring-suspended rear wheels on each crawler. The engine is located in the rear section of the loader to ensure an equal pressure distribution on the soil when the bucket of the machine is completely loaded, which is the case with the highest mass. To drive around curves, different steering options are possible, if the loader is operated by a mechanical drive train. For wide curves, the clutch on the crawler track can be opened. For narrow curves, the inner crawler track is reduced in speed or braked to stop off. If a hydraulic static drive system is installed, the loader can also change the speed of or reverse a single track to turn around the vehicle center. Crawler loaders belong to the class of heavy machinery equipment, operating under rough conditions, e.g., in mining. Such loaders thus have masses up to 30 t.

Backhoe Loaders. Backhoe loaders such as shown in Fig. 20.146 are multipurpose machines which have been developed from tractors with front loaders and an attached excavator beam. Nowadays, they are better classified as a combination of a wheel loader and hydraulic excavator. The beam of the excavator arm is often designed as a hydraulic telescopic extendable stick with two pieces, to reach a bigger working area while keeping the transport dimensions of the complete loader as small as possible. In contrast to an excavator, it is not possible to turn the upper part of the machine via a slewing gear. Instead, the excavator beam can be twisted at the loader. The driver seat can usually be twisted by 180° to ensure an independent working area for the operator with a good view to both sides. Some

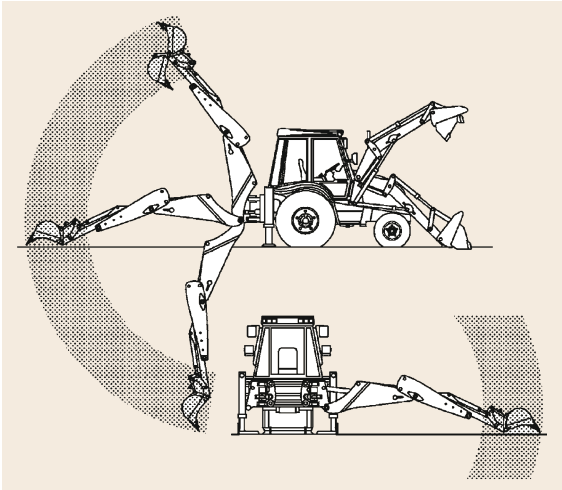

Fig. 20.146 Backhoe loader with area for possible tool usage (JCB, Köln, Germany)

backhoe loaders allow hydraulic sideways movement of the complete excavator section to reach a larger operation area without moving the vehicle. The hydraulic system is typically separated into a hydrostatic circuit for the working tools and a hydrodynamic part for the drive train. The typical mass class is less than 10 t.

Dozers and Graders

Dozers (Fig. 20.147) and graders (Fig. 20.148) are machines to remove thin layers of soil or ensure even planes on road or airport construction sites or sports fields. These machines work with a blade as a tool, which is basically designed like a very flat bucket but instead of filling the bucket, the material is basically pushed forwards. The conveying distance is usually less than 50 m. The blade is attached at the crawler drives on the side of the machine via two beams. In some dozers, a fully skewable U-carrier allows the blade to be skewed to both sides to discharge the material to one side. The carrier is steered mechanically or—more commonly—using hydraulic cylinders. The blade depth can be adjusted hydraulically on both machines. If the blade is tilted around the driving axis, the edge of the blade can be used to produce low-profile gullies.

The geometry of the blade is adapted to the kind of soil. Its curvature, height, and width depend on the soil and the mass and power of the machine. If heavy, claggy, or even rocky soil is present on the construction site, a tooth at the rear end of the machine can be forced into the ground to loosen the soil while driving. Armored dozers are also used by the military to clear soil of land mines or detonate improvised explosive devices. A reinforced blade is used as primary protection for the driver and machine. Dozers are built with masses from 10 to 100 t.

Graders are specialized dozers where the main blade is moved to between the axles. With a larger axial distance, the blade only moves a smaller amount in the vertical direction compared with the front axis when driving over a hump. This leads to a stable position of the blade. Hence, even an uncontrolled blade will produce a relatively even surface.

In graders, a fully skewable U-carrier allows the blade to be skewed to both sides to allow the material to flow to one side. The blade or even the blade edges can

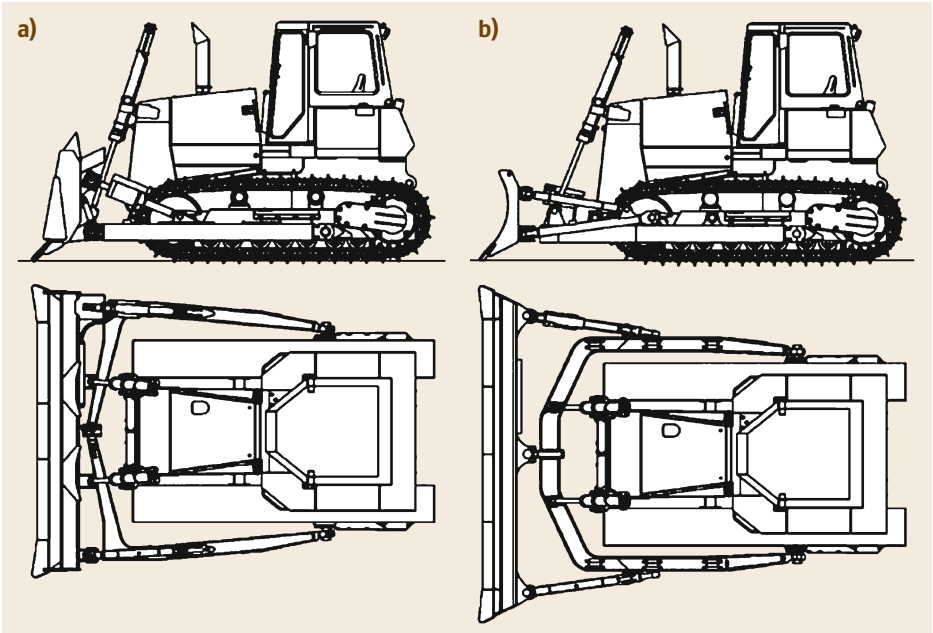

Fig. 20.147a,b Dozer with standard blade and hollow geometry **(a)** and skewable U-carrier and flat geometry **(b)** (Liebherr, Telfs, Austria)

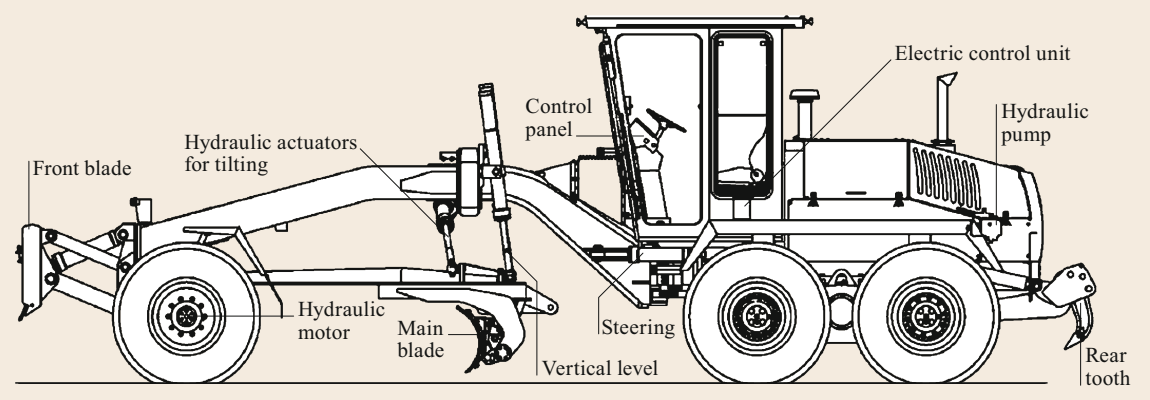

Fig. 20.148 Grader (HBM-Nobas, Nordhausen, Germany)

be shifted sideways, tilted, and lifted independently of the machine movement. A grader is front steered with Ackermann steering. In combination with articulated steering of the rear axis, crab steering becomes possible. Hence, graders must not drive over uneven surfaces.

In modern graders, laser-supported control systems are used to ensure an even surface even if the grader drives over an uneven surface. The control system keeps the blade in a steady vertical position by adjusting two hydraulic cylinders mounted at the edges of the blade. Most grades have a front blade to even out greater irregularities of the soil.

The rear axis is often build as a tandem axle which carries the engine block and driver cabin. The tandem axle is driven by a hydrodynamic drive train. Graders are built in sizes from 5 to 65 t. Larger graders are used in the mining field to build truck tracks.

20.5.4 Elevators

In the field of conveying technology, the machine group of elevators enables vertical and (strongly) inclined transport of passengers and freight. Hence, elevators (lifts) in buildings, construction elevators, shaft conveyor systems in mining, cable cars, cable railways, as well as escalators and moving walkways belong to this group. Cable cars include aerial tramways with reversing and cyclic operation using a suspension rope (fully closed spiral rope), and a tension rope. In the case of a monocable with detachable gondolas, the functions of the traction and suspension rope are combined into the tension rope. Chair lifts can be equipped with firmly connected or coupled load handling devices (velocities $> 2\,\mathrm{m/s}$). For cable railways or funicular railroads that are operated in reversing or cyclic operation, the wagons are track guided. For reversing operation, only one track is used over a long distance with a passing place provided in the middle. For escalators, step widths (600, 800, and 1000 mm) and gradients (30° and 35°) are specified with velocities of up to 0.7 m/s. The maximum gradient for moving walkways is 12° with velocity of $v \leq 0.75\,\mathrm{m/s}$. For gradients below 6°, the velocity can reach 1.0 m/s. Faster moving walkways are occasionally implemented with velocities of up to 2.5 m/s with special solutions for safe entry and exit, and the acceleration of passengers. The above-mentioned values are commonly used parameters (or parameter limits) according to [20.5].

In contrast to all other types of machinery, many of this type are primarily used for the transport of passengers, resulting in the consideration of different and stricter safety regulations during their design process. Furthermore, if installed in buildings, elevators are at the interface with the construction of the building, thus many boundary conditions are defined by its structural or architectural features. Elevators used for construction belong to the group of construction machines due to the close integration of this type of elevator with scaffolding. The many national standards, laws, and regulations make it difficult to provide general design advice. Hence, only an overview of the basic design of passenger and freight elevators is given in the next section. For more detailed information about dimensioning and capacity calculations, refer to [20.254].

Different types of elevator can be distinguished based on their driving concept: rope elevators, hydraulic elevators, spindle elevators, and rack (and pinion) elevators. Figure 20.149 shows six important types of elevator.

Rope and hydraulic elevators account for 98% of such machines. Hence, we will focus on these types.

Rope Elevators

In the case of rope elevators, one can distinguish between drum- and traction-type devices. Drum-type elevators use a common rope drum that drives and stores

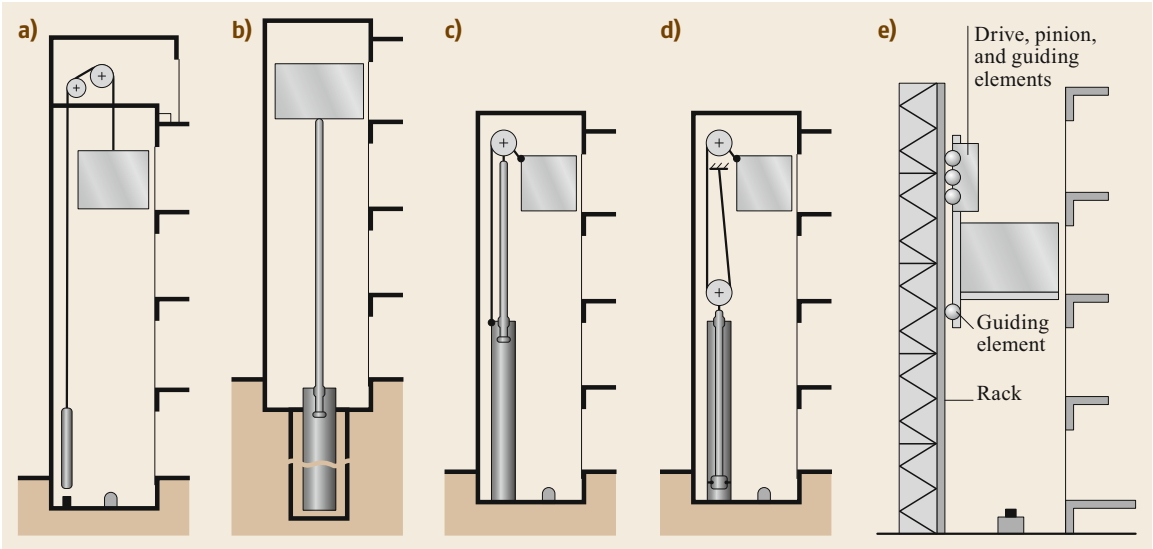

Fig. 20.149a–e Five important types of elevator: **(a)** traction type, **(b)** direct hydraulic drive, **(c)** indirect pushing hydraulic drive, **(d)** indirect pulling hydraulic drive, and **(e)** construction elevator based on a rack drive [20.255]

the rope. Hence, higher lifting heights need much larger drums, which represents a significant limitation on this type of rope elevator. Traction-type elevators do not suffer from this disadvantage, since the rope is driven by a traction sheave (= hoisting drum, Sect. 20.3.1). The relatively simple design principle of such traction-type elevators is shown in Fig. 20.149a. The car (cabin) is connected to the counterweight using at least six redundant wire ropes. The ropes are driven based on friction by the hoisting drum. The mass of the car and half of the maximum load is usually compensated by the counterweight. The drum is driven by a electric motor with or without a gear (gearless drive). Six ropes are used for security reasons. Each of the ropes could securely lift or lower the car. Although hoisting systems based on ropes have been known since ancient times, their use in passenger transport using elevators was long restricted due to the fear of a rope break and the crash of the car. This changed with the invention of a safety device by E.G. Otis 1852 (patent "Hoisting Apparatus"). The safety device invented by Otis braked the elevator car traveling on guide rails on both sides. The basic principle of this invention is still used today: the safety brake on the car is connected to a governor rope that drives a small traction sheave near the main elevator drive. A speed limiter is implemented in this auxiliary traction sheave (often centrifugal force limiters). This limiter stops the traction sheave and hence brakes the governor rope. This leads to a relative motion between the governor rope and the falling car, which activates the safety brakes at the bottom of the car and hence stops the car independent of the rope connection.

Today, typical safety devices are activated if the velocity of the car reaches 1.15 of the nominal lowering velocity. Uncontrolled upward driving motion must be decelerated by special measures. The cabin is separated from the hoistway by the cabin doors. The hoistway and the building are separated by the elevator shaft doors, which have special fire resistance requirements.

The rope drive shown in Fig. 20.149a can be adapted to high load with the help of reeving systems that reduce the rope forces, as described in Sect. 20.3.1.

Hydraulic Elevators

The usual construction methods for hydraulic elevators result in direct and indirect lifts (Fig. 20.149b–d). The directly driven hydraulic elevator with a piston in an earth-drilled hole is suitable for small hoisting heights. The construction method is quite simple, but the measures required to prevent entry of oil into groundwater or corrosion are exacting and costly. The indirect drive does not require an earth-drilled hole. One can distinguish between the pushing and pulling piston methods. For a pushing piston, the buckling stresses are crucial. For high hoisting heights, intermediate supports of the piston must be provided. However, the pulling piston with a smaller piston diameter requires higher oil pressures. A counterweight to compensate for the cabin weight can also be used. For high loads and cabin weights, several cylinders can be provided. The hoisting height is usually limited to about 25 m. The velocity only exceeds 1 m/s in exceptional cases.

The power of the hydraulic elevator drive without a counterbalance must be calculated for the sum of the

weight forces of the cabin, the additional load, and the pistons. Upward travel takes place with the drive running. The motor is off and the lift is controlled by valves when it travels downwards. Low-pulsation screw spindle pumps are often used in low-oil constructions. Measures against uncontrolled driving motion, i.e., overspeeds as a result of a pipe break or sinking at a stop when the doors are open, include a pipe breaking valve for a direct lift and the safety gear for an indirect lift.

Standardization

ISO 4190-1 [20.256] provides basic information about dimensioning and general design principles. However, national building regulations also define the basic properties of elevators, e.g., how many passengers can be transported in a car of given area. In the subject area of elevators, uniform European standards were introduced with the standard series EN 81 [20.257].

Shaft Hoisting Systems

Shaft hoisting systems can be operated using a Koepe hoisting sheave and a cylindrical or conical drum. According to [20.5], for material transport and the transport of passengers (elevator operation), shaft hoisting systems are operated with adapted velocities (up to 20 or $<10\,\mathrm{m/s}$) and rope safety ($v = 7.2 - 0.0005L$ or $v = 9.5 - 0.001L$ with $L =$ conveying depth). In Germany, typical shafts can reach up to approximately 1000 m in depth. However, in gold or gemstone mines, depths of up to 3000 m are reached using a series of shafts.

20.5.5 Trucks

This section deals with discontinuous, trackless, floor-level conveyors for general cargo. The task of these conveyors, which belong to the class of materials handling equipment and are sometimes also called industrial trucks, is the transport of goods—generally packed into or onto load carriers, such as parcels, palettes, boxes, or containers—inside or directly outside of a warehouse or factory. Industrial trucks are highly flexible as they have basically no route restrictions. They can be distinguished into trucks for indoor or outdoor use, into manual or powered, and finally into lifting and nonlifting trucks. Typical industrial trucks are pallet jacks, counterbalanced lift trucks, reach trucks, or tow tractors. For the terminology and basic definitions of powered industrial trucks see also DIN ISO 5053-1 [20.258] and DIN ISO 5053-2 [20.259].

Pallet Jacks

Pallet jacks, also known as hand pallet trucks or pump trucks, are widely known and employed for order picking and truck loading and unloading. They can be differentiated into manual (hand-powered) and electric (powered) pallet jacks. The main parts of a manual pallet jack are its two forks, wheels, hydraulic pump unit, and tow bar (Fig. 20.150).

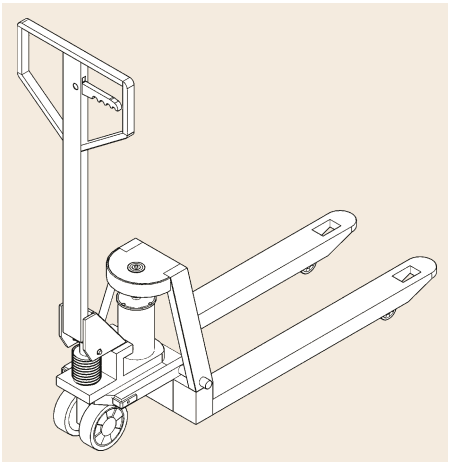

Fig. 20.150 Pallet jack

Pallet jacks are commonly employed to transport goods stacked on pallets, typically with weights of up to 3500 kg. They are simple in their operation. The operator slides the forks into and under the pallet, then uses the tow bar as a simple lever to pump the hydraulic pump unit, which lifts the forks off the ground. The two front wheels of the pallet jack are mounted in the front area of the forks. When the forks are lifted via the hydraulics, they move vertically relative to the wheels. The load is lifted until it leaves the ground and only rests on the forks. Then the pallet jack and its load are moved by pushing or pulling the tow bar. When the operator reaches the target destination, the forks are lowered to the ground by pulling the trigger at the tow bar handle, which opens the release valve. The pallet is set onto the ground, and the pallet jack can be slid out from under the pallet.

Powered pallet jacks can be differentiated again into pedestrian and ride-on pallet trucks. While the position of the operator for the pedestrian powered version remains unchanged from the hand-powered one, the operator of the ride-on pallet truck does not have to walk, but can enjoy the luxury of being driven by motor power, usually standing on a platform behind the bar handle. In general, operating powered pallet jacks is quite like operating manual pallet jacks. The difference is that the work of the lifting and movement of the pallet jacks (with or without a load) is carried out by the electric drive. The lifting movements are usually controlled by buttons, and the driving movements by paddles. The increased weight of the powered pallet jack—due to its electric drive—means it requires smoother and more even surfaces than the manually operated version. For

safety reasons, powered pallet trucks are equipped with so-called dead-man controls which stop the truck when the handle returns to its initial upright or its lowest position.

Hand Carts

A handcart or trolley is a simple wheel-mounted platform with operation-specific attachments for load bearing. They generally have four wheels on two axles, where one pair of wheels is not steerable. The other two wheels can be designed as steering castors or attached to a drawbar-guided turntable. The handcart features handles to push or pull it manually. Handcarts represent one of the simplest and least expensive modes of transport. They are used to transport materials over short stretches, preferably with level surfaces. They are also often used as interim storage between manufacturing operations.

Tow Tractors

Tow tractors for indoor use exist in several variants. They are fit with couplings and designed to haul carts or trailers. The most common tow tractors are three- and four-wheeled electric tractors. These are small and nimble industrial trucks with a driver's seat or standing platform. Three-wheeled electric tractors can reach speeds between 5 and 15 km/h, while four-wheeled electric tractors can attain higher speeds of up to 20 km/h. Generally, four-wheeled tractors offer greater traction and can thus move larger loads. Additional information on hauling of trailers, traction force, and trailer load can be found in DIN 15172 [20.260].

The combination of a tow tractor hauling a series of carts or trailers, usually between four and seven, is called a tractor–trailer train. The trailers can be lifted hydraulically or pneumatically and can accommodate various types of (rolling) load carriers. The most often used trailer type is probably the platform trailer. The combination of tow tractors with trailer trains permits one tow tractor to pull different trailer trains. The tow tractor may also be disconnected and move a different trailer train while the previously pulled one is (un)loaded. The load pickup process can be carried out manually or fully automatically. Tow tractor trains are normally used to supply several manufacturing stations with material.

Lifting Trucks

A great variety of lifting trucks exist, making it difficult to provide an overview. Lifting trucks range from pedestrian stackers and counterbalanced trucks to reach trucks and straddle carriers. In addition, there is—as of yet—no generally accepted classification for them. However, parts of their equipment are similar to one another. These components are explained in this section, before the individual lifting trucks are discussed.

In general, lifting trucks consist of a chassis, a power source, a transmission, wheels, loading equipment, and some kind of lifting arrangement. The power source can be electrical (battery power), a diesel engine, in rare cases a petrol engine, or a liquefied petroleum gas (LPG) engine. All of these have their individual advantages and drawbacks. Diesel engines, for example, are very powerful in relation to their weight, can run for long periods without needing to be refueled, and have comparatively low operating costs. Electrical power has great environmental advantages and provides better working conditions, especially indoors, as there is less noise and no direct exhaust pollution. Widely used loading equipment includes side-shifts, fork spreaders, and clamps. The loading equipment is mounted on a (fork) carriage on the lifting mast. Depending on the specific application field and corresponding equipment on the truck, the loading equipment can be tilted towards and away from the truck to allow for easier pickup and/or more secure transport of the load. For lifting the load, there are basically two different mast concepts: the single mast and the telescopic mast. The single mast consists of only one frame, while the telescopic mast consists of additional frames, often two, three, or four (double, triple, or quad mast), as shown in Fig. 20.151.

The frames of the lift mast slide inside one another, usually on roller bearings. In most cases, hydraulic cylinders provide the lifting power to slide the frames. Often, these masts can also be tilted. Tilting the mast toward the truck (backward tilt) brings the load center closer over the wheels of the truck, thus increasing its stability. Tilting the mast away from the truck (forward tilt) can make the load pickup or setdown process easier. Another aspect of the lifting arrangement is the freelift, i.e., the distance a loading device may be lifted

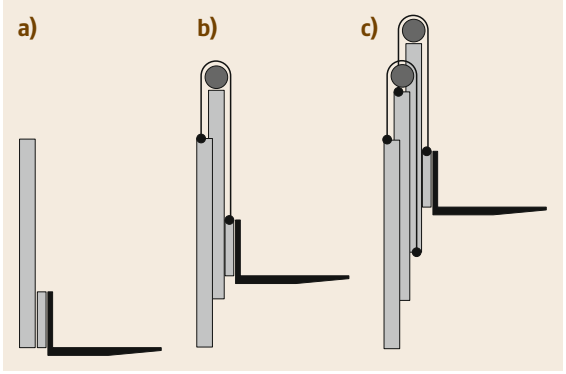

Fig. 20.151a–c Lift masts: (a) single mast, (b) double mast, and (c) triple mast [20.261]

off the floor without the mast exceeding its height in its retracted state. This is particularly relevant for operations in locations with low (head) heights, such as the loading and unloading of containers or trucks.

Powered Stackers

Powered stackers can be distinguished, just like powered pallet jacks, into pedestrian stackers (sometimes also called walkies), drawbar-guided vehicles for pedestrian operation, and ride-on stackers, i.e., vehicles with a collapsible standing platform or side-mounted seat.

There are pallet-based and straddle-based stackers. Pallet"0based stackers have two fixed front wheels mounted in the support arms (wheel arms), and the forks cover or enclose the arms from above (Fig. 20.152). When picking up pallets, both the forks and support arms slide into the pallet. Therefore, pallets with floor supports cannot be picked up from all four sides. Straddle-based stackers have support arms (outriggers), which are adjacent and outside the forks. This permits the forks to be lowered below the outriggers on load pickup. To achieve good space utilization, they carry their load inside the stability polygon.

Powered stackers are mainly used for storage, retrieval, and short-distance transport of pallets in floor or shelf storage warehouses where space is limited or throughput is low. To be able to lift loads to greater heights, powered stackers are equipped with a mast that is firmly attached to the vehicle frame. Typically, they are able to stack loads a maximum of three loads high. Their comparatively low investment costs make them very common.

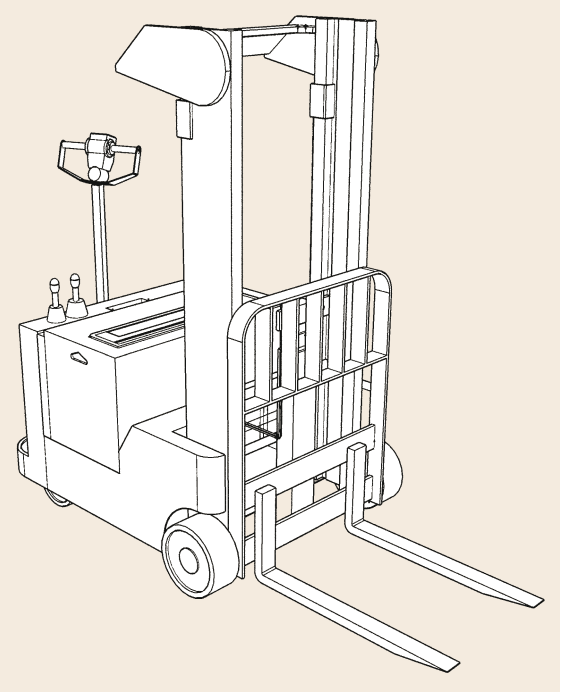

Fig. 20.152 Pedestrian stacker

Counterbalanced Lift Trucks

Counterbalanced trucks carry their load outside the chassis area and the stability polygon. The tendency to tip over forwards due to the load's weight is countered by a counterweight on the back of the truck. The load capacity can be increased by adding ballast to the rear of the truck [20.261]. The stability of counterbalanced trucks and their center of gravity for four- and three-wheeled versions are shown in Fig. 20.153.

Counterbalanced lift trucks are the most commonly applied lifting trucks in warehouses. Their operational flexibility makes them very popular, as they can be used to store and retrieve pallets from a warehouse and to load and unload trucks. As the operator rides on the truck, the transport distances can be longer than for pedestrian stackers. Generally, there are two possible modes of operation: sit-down and stand-up. Sit-down is better adapted to travel over longer distances where the operator does not frequently mount and dismount the truck (Fig. 20.154).

Stand-up trucks have a shorter wheelbase than sit-down trucks, resulting in a lower maximum capacity but improved maneuverability. In addition, four- and three-wheeled variants exist (Fig. 20.153). Three-wheeled counterbalanced trucks have a single drive wheel at the center of the rear of the truck. Generally, three-wheeled trucks have a smaller turning radius and therefore better maneuverability, but also lower maximum capacity.

The steering is usually servo-assisted to reduce the effort of the operator and enable enhanced visibility for the operator, as servo-assisted steering allows for narrower steering columns than unsupported steering.

Reach Trucks

Reach trucks are specialized to work efficiently in the tightest of spaces while reaching great heights. They can reach out into racking beyond their supporting wheel arms, hence the name. The mast can be pushed forwards to take the load and be lowered to the ground. Once the load has been absorbed, the mast can be retracted again and is therefore located between the two supporting arms (outriggers). Basically, two different types of reach trucks are available: the mast and the fork reach truck. On a mast reach truck, the mast is located inside the front-mounted support arms (outriggers) and is supported by the wheels. The entire mast is moved between the support arms. In contrast, on a fork reach truck, only the load-carrying equipment is moved, using a pantograph or scissor reach mechanism.

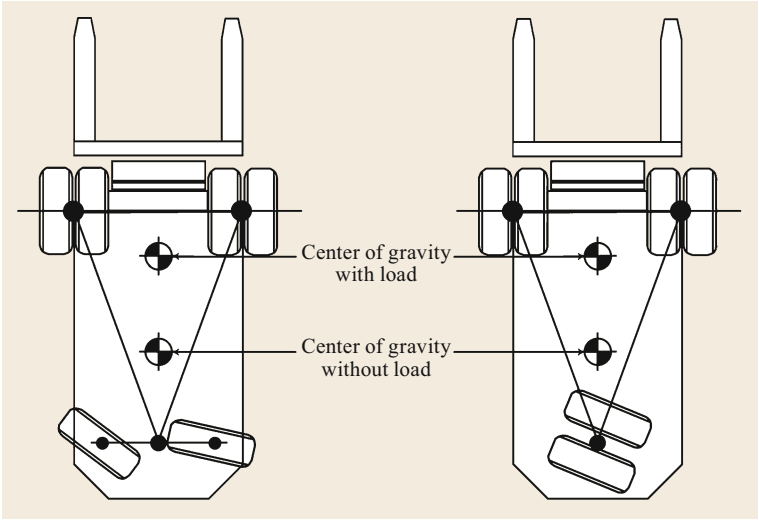

Fig. 20.153 Center of gravity of counterbalanced lift trucks [20.261]

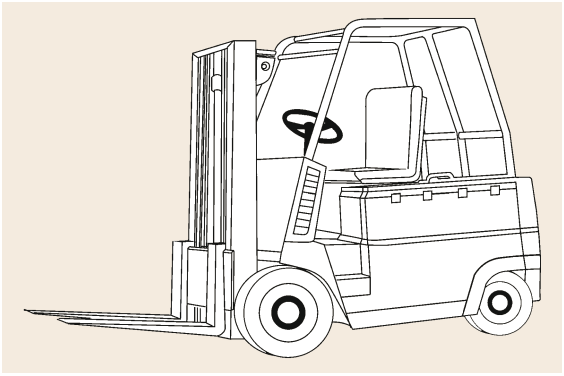

Fig. 20.154 Counterbalanced lift truck/forklift truck

Load handling using a reach truck is ideal for transporting pallets. Its construction requires a much smaller counterweight than other types of forklift such as the counterbalanced lift truck. This smaller counterweight means that the truck can be shorter and is therefore ideal for use in tighter spaces. Reach trucks are available in different versions with different capacities (generally up to 2.5 t), maximum heights (generally up to 14 m), and specifications. Among other things, the mast and the driver's seat can be installed laterally, making this variant particularly suitable for long loads. Note that the load capacity decreases with increasing lifting height.

Turret Trucks/Very Narrow Aisle Trucks

Turret trucks are used for storage and retrieval in high shelving racks with very narrow aisles (VNA). In general, they are built with a longer wheelbase for stability and are battery-operated using electric motors. There are basically two designs of turret truck: conventional and the man-up. The counterbalance weight of conventional turret trucks is provided by positioning the engine, battery, and operator at the rear. The design of the conventional turret truck leads to the operator being far away from the actual load handling operation, resulting in a possibly obscured view of the load. This requires the operator to rely on their best judgment or to apply supporting devices such as guide marks, height selectors, or cameras in order to position the load correctly. In the man-up version, the operator is positioned on an upfront platform at the front of the truck. When the mast is lifted, the operator is lifted with it. This allows for a clear view of the load handling operations. In addition, the man-up turret truck can not only be used for storage and retrieval processes, but also for order picking (Fig. 20.155).

Both versions of the turret truck have the advantage that they can move and lift at the same time. Their mast can reach lifting heights of up to 17 m, depending on the specific model and configuration. The load handling equipment (usually forks) is located at the front of the truck. The forks are mounted such that they can rotate by 180°. This allows the operator to access loads on both sides of the aisle without requiring the turret truck to turn in the aisle. This means that they only require very narrow aisles between shelves. To maximize both safety and operating speed, various systems are used to navigate the turret truck through the warehouse and avoid contact with obstacles; for example, ground-based laser or rail-guided systems are used to optimize navigation within the aisle and attain a maximum speed. Details concerning calculations of the working cycles of trucks in VNA warehouses can be found in VDI 2516 [20.262]. In general, turret trucks allow high throughput using the smallest possible space or very narrow aisles.

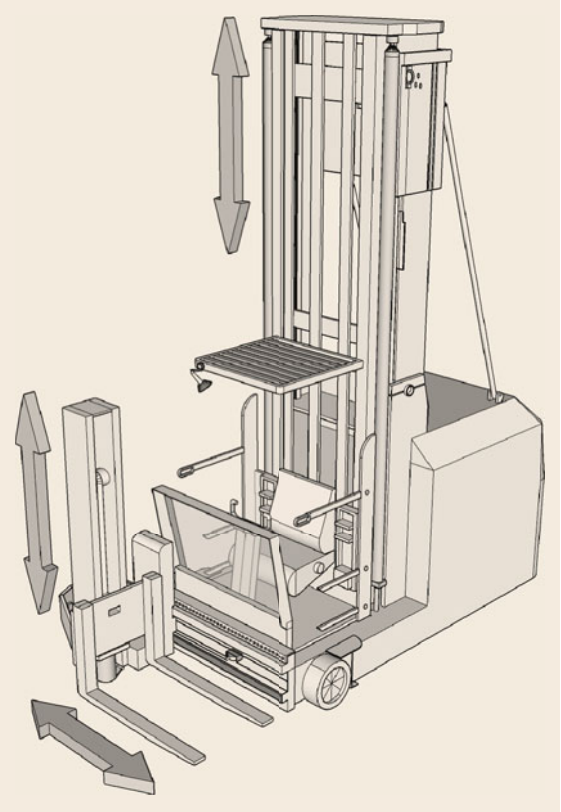

Fig. 20.155 Turret truck (man-up version)

Sideloaders

Sideloader trucks are specifically designed for the transport of long materials. They load and unload goods from one side. This allows them to drive to the storage location, then perform the handling operation, and drive off without turning in the aisle. The mast is positioned movable in a recess in the middle of the sideloader, perpendicular to the longitudinal axis of the vehicle. For the loading operation, the mast is pulled by hydraulic cylinders, moving on tracks transversely across the vehicle into the recess, and the load is placed on the vehicle platform. In another variant, forks are mounted protruding from a fixed mast on a scissor lift mechanism (pantograph). The advantage of sideloaders is their ability to handle long materials, such as beams, piping, or profiles.

AGVs for Warehouses or Factories

Automated guided vehicles (AGVs) are driverless and self-propelled transport vehicles. They can be realized in different forms, for example, as pallet trucks, fork trucks, unit load vehicles, towing vehicles, or platform vehicles.

They can independently load and unload themselves, drive to a destination, (un)load there, and return to their place of origin or continue to any other desired location. Inside production facilities, they are usually applied to transport materials between workstations or as mobile work platforms. Other application areas include the transport of materials between warehouse storage and the shipping/receiving and picking areas. Built-in safety systems allow AGVs to share factory aisles and roadways with other industrial trucks or personnel. The combination of several AGVs with their controlling station and the ground installation form an AGV system.

AGVs are very versatile transport vehicles, of which there is a great variety of designs. The range of designs covers a wide variety of criteria, which once again allow for a wide variety of different types. In addition to the aforementioned forms, other relevant criteria include, for example, the size of the vehicles, the control system, the various navigation options, and the styles of load handling. The possibilities of AGVs are also advancing with the development of new technologies. Not too long ago, the so-called (pre)determined fixed path method, then the market-dominant navigation option for AGVs, was used. Fixed-path guide paths are realized via a wire buried in the floor or via magnetic, reflective, or photofluorescent materials applied in stripes onto the floor. The wire in the floor is used as a transmitting antenna, while two receiving antennae are attached to the underside of the AGV. The AGV then steers along the buried wires by straddling the wire with its two receiving antennae. When using stripes on the floor, the AGV has a camera to detect them and have the vehicle follow the stripes. Both fixed-path solutions offer a good alternative to lift trucks as long as the transport routes can be well defined and are not or at least only very rarely changed. Changing the path is difficult and expensive, especially for the variant with a wire embedded in the ground. This means that fixed path navigation is not suitable for today's requirements, such as SmartFactories with constant changes and high demands on flexibility. This requires systems that can be adapted quickly and easily.

Autonomously managed AGVs offer this possibility. They can recognize stopping and turning points, notice obstructions, and monitor internal conditions such as current battery status or failures. Paths are described in a software environment model. The current position of the vehicle is constantly monitored and compared with points defined in the software. Position monitoring can be realized using different technologies, such as GPS, navigation by natural environmental features, or laser guidance. In case of position deviations, the control system automatically initiates the necessary steering movements of the AGV.

Several standards are relevant for the planning and operation of AGVs. These include DIN EN 1525:1997-

12 [20.263] regarding the safety of industrial trucks and in particular driverless trucks and their systems, as well as the two VDI standards VDI 2510:2005-10 [20.264] on AGV systems and VDI 2710:2010-04 [20.265] concerning the interdisciplinary design of AGV systems in all planning phases. Additional in-depth information on AGVs and AGV systems is discussed by *Ullrich* [20.266].

AGVs for Container Ports

AGVs deployed in container ports are basically larger versions of AGVs for warehouses. They are also known as automated container transporters. These AGVs are self-propelled, driverless, rubber-tired transport vehicles for receiving and transporting containers up to 45 ft long or two 20-ft containers. They can be divided into the following variants: single load carriers (SLCs), which can carry one standard container, multiload carriers (MLCs), which can carry several standard containers, and dual-load carriers (DLCs), which can transport exactly two containers. In most cases, they are diesel–hydraulically driven. Recently, however, electrically driven container transporters have also been increasingly used and tested. While the first electrically driven container transporters still used lead batteries, lithium-ion batteries are now being used. The advantage of lithium-ion technology over lead batteries is its lower weight and rapid charging capability.

Automated container transporters are used for horizontal transport of containers between the port quay and the handling equipment used there, typically container or gantry cranes, and the container storage yard where they are stacked. The driverless AGVs find their way to their destination, which is transmitted by radio, through a transponder network embedded in the ground and consisting of a grid of several thousand transponder position points. Alternatively and for support, GPS or radar can be deployed for positioning. The points of the transponder grid are then connected to form a logical driving course. A control center controls and monitors the movement of the AGVs and sends information about their start and destination positions with the help of planning and routing software. The area over which the AGVs travel is usually closed to persons for safety reasons.

The operation of AGVs can potentially reduce personnel and operating costs. The drawbacks of AGVs for container ports are their relatively low travel speeds of only up to 20 km/h and the increase in the surface space required due to that specifically reserved for driving tracks [20.267].

Straddle Carriers

Straddle carriers are the most frequently used container lifting trucks. They are also known as van carriers or gantry lifts. The construction of the straddle carrier can be described as a wheeled inverted U-frame, usually with six to eight pneumatic tires attached. The wheels are mounted in two-wheel carriers on turntables and are steered hydraulically. Straddle carriers often have a diesel–electric drive. The diesel engine and generator are located on the upper machine platform, while the electric traction motors are located in the wheel hubs or turntables. The driver's cab is located in the center or at the side of the front of the machine platform. The carrier straddles or drives over its load and can lift more than twice its own weight. The load is lifted between the tires with a spreader from above. Straddle carriers can stack containers up to four high. In addition to horizontal transport, straddle carriers are also ideally suited for stacking containers and loading and unloading trucks or railway wagons due to their all-wheel steering and associated maneuverability. Their use does not require any yard infrastructure, resulting in relatively low investment costs. Straddle carriers can also be automated: they are then called automatic guided straddle carriers (AGSCs). The driverless system can pick up, store, and transport containers at and to any point in the yard. Positioning and navigation are realized by an integrated system of differential GPS and dead reckoning. Semiautomated systems are also possible to support human operations. These include automatic braking over a container, automatic lowering of the spreader during braking, automatic braking with a container under the bridge, and automatic lifting of the spreader and acceleration.

The advantages of straddle carriers over other industrial trucks include their ability to pick up containers independently, transport them at up to 30 km/h, and drop them off at any point. Additionally, the straddle carrier has a spreader with hydraulic telescoping capability that allows it to pick up and move all kinds of containers. The use of twin-lift spreaders increases productivity as it enables the straddle carrier to transport two 20-ft containers at once.

Shuttle Carriers

The primary task of shuttle carriers is the horizontal transport of containers, but they can also handle the loading and unloading of trucks and railway wagons. They can stack containers up to two high. Shuttle carriers are ideally suited for integration into a system with automated stacking cranes or rubber-tired gantry cranes. The idea behind the shuttle carrier is that the transition of containers from crane to carrier can be achieved at a later point in time. As the shuttle carrier can pick up containers from the ground on its own, the crane need not place containers onto the carrier, but can simply place them on the ground in a buffer area. Thus, the crane does not lose time in the occasionally slow and difficult process of loading onto the carrier or while waiting for the carrier. The transition process can oc-

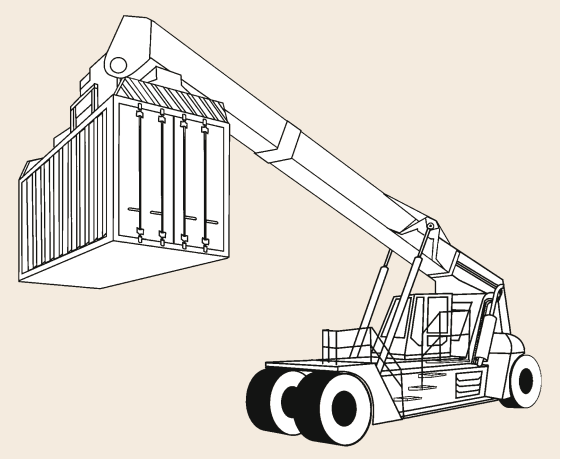

Fig. 20.156 Reach stacker

cur separately. For this particular application area, the shuttle carrier represents a good alternative to AGVs or straddle carriers. In contrast to AGVs, the shuttle carrier is able to pick up and set down containers independently. Furthermore, shuttle carriers are more flexible than AGVs due to their manual control, although this also leads to higher personnel costs in direct comparison. The advantages compared with straddle carriers are low investment and operating costs and, due to the lightweight construction of the shuttle carriers, higher travel speeds.

Container Stackers

Container stackers are constructed in the same way as forklifts, but instead of forks they are equipped with a hydraulic top or side spreader for picking up containers. In addition, container stackers are larger and have a higher load capacity than forklifts. Container stackers are available in lighter and heavier versions. The heavy versions, also known as laden container handlers, with lifting capacity of up to 45 t are usually applied for the transport of loaded containers. Smaller and lighter container stacker versions, also known as empty container handlers, can complement the more expensive larger and heavier container stacker versions. Their lifting capacity is usually only up to 10 t. Empty container handlers can handle single and double containers and can stack them up to eight (single) or six (double) high. Container stackers are used when the necessary handling capacity is so low that investment in more specialized industrial trucks such as straddle carriers would not be worthwhile. The advantages of container stackers are fast load handling, high maneuverability, and flexibility to be able to load and transport other goods as well by exchanging the attached loading devices [20.267]. They are also comparatively inexpensive and space-saving.

Reach Stackers

Reach stackers can stack loaded containers up to three rows one after the other and up to six on top of each other. This is made possible by their telescopic arm that can be lifted or lowered (Fig. 20.156). They have lifting capacities of up to 50 t.

The load is picked up from above by means of a rotating top spreader, so that the reach stacker does not have to stand at a specific angle to the container. This is particularly suitable for short transports with many stacking and unstacking operations. Reach stackers are therefore often used for transport means and stacking of empty containers [20.267]. When stacking trains or trucks, they offer the additional advantage of reaching across a track or truck thanks to their telescopic arm. This means that they can transfer containers directly from one train to another on a neighboring track, or from one parked truck to another one parked beside it. Due to their construction, they are also particularly maneuverable.

20.6 Storage Systems

20.6.1 Silos and Bunkers

Silos and bunkers are widely used for the storage of bulk solids in the mining, mineral processing, chemical, agricultural, and other industries. Silos and bunkers include various forms of bulk solids storage structures that may otherwise be referred to as bins. Although there is no generally accepted definition for these terms, shallow structures are often called bunkers, while tall structures are usually called silos. Silos are often constructed of steel, aluminum, or reinforced concrete. The capacity of silos and bunkers can range from a few to thousands of tons. The methods used to load and unload silos and bunkers depend largely on the type of material to be handled. Loading and discharging of bulk material to/from the silo or bunker may be done pneumatically, mechanically, or by gravity.

The procedures for the design of silos and bunkers are well established and follow four basic steps:

i. Determination of the strength and flow properties of the bulk solids for the worst likely flow conditions expected to occur in practice

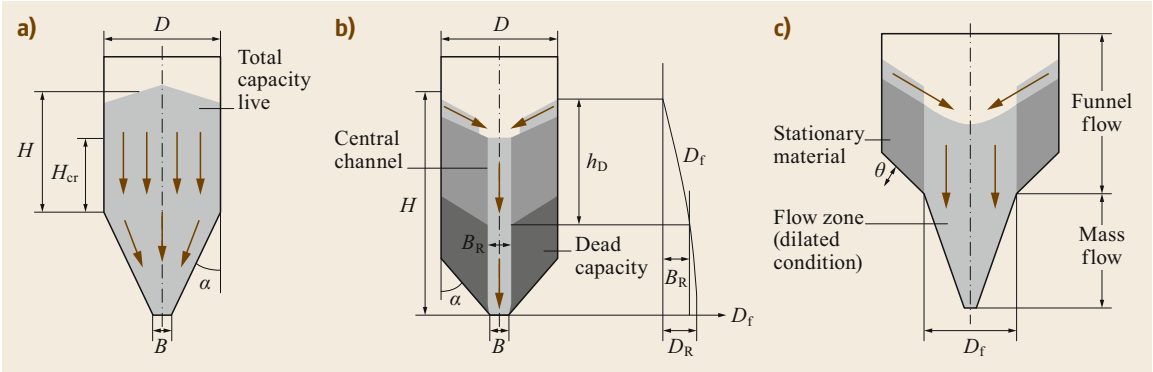

Fig. 20.157a–c Modes of flow: **(a)** mass flow, **(b)** funnel flow, **(c)** expanded flow

ii. Determination of the silo or bunker geometry to give the desired capacity, to provide a flow pattern with acceptable characteristics, and to ensure that the discharge is reliable and predictable
iii. Estimation of the loadings on the silo and bunker walls
iv. Design and detailing of the silo and bunker including the structure and equipment.

Flow Modes in Silos and Bunkers

The two principal modes of flow are mass flow and funnel flow. These are illustrated in Fig. 20.157a,b. During mass flow, the bulk solid is in motion at every point within the bin whenever material is drawn from the outlet. This implies a flow of bulk solid along the walls of the cylinder (the upper, parallel section of the bin) and the hopper (the lower, tapered section of the bin). Mass flow guarantees complete discharge of the bin contents at predictable flow rates. It is a *first-in, first-out* flow pattern; when properly designed, a mass-flow bin can remix the bulk solid during discharge should the solid become segregated upon filling of the bin. Mass flow requires steep, smooth hopper surfaces and no abrupt transitions or in-flowing valleys.

Mass-flow bins are classified according to the hopper shape and associated flow pattern. The two main hopper types are:

1. Conical hoppers which operate with axisymmetric flow
2. Wedged-shaped or chisel-shaped hoppers in which plane flow occurs.

In plane-flow bins, the hopper half-angle, α, required to achieve mass flow will typically be approximately 8°–10° larger than the corresponding value for axisymmetric bins. Plane flow therefore offers larger storage capacity for the same headroom compared with axisymmetric bins, although this advantage is somewhat offset by the long slotted opening which can give rise to feeding problems. Transition hoppers with plane-flow sides and conical ends can offer a good compromise. Pyramid-shaped hoppers, while simple to manufacture, are undesirable in view of the build-up of material that is likely to occur in the sharp corners or in-flowing valleys. This may be overcome by fitting triangular-shaped gusset plates in the valleys.

Funnel flow occurs when the hopper is not steeply sloped and the walls of the hopper are not smooth enough. In this case, the bulk solid sloughs off the top surface and falls through the vertical flow channel that forms above the opening. Such flow is generally erratic and gives rise to segregation problems. The flow will continue until the level of the bulk solid in the bin drops by an amount h_D equal to the drawdown. At this level, the bulk strength of the contained material is sufficient to sustain a stable rathole of diameter D_f, as illustrated in Fig. 20.157b. Once the level defined by h_D is reached, there is no further flow and the material below this level represents *dead* storage. This is a major disadvantage of funnel flow. For complete discharge, the bin opening needs to be at least equal to the critical rathole dimension determined at the bottom of the bin corresponding to the bulk strength at this level. However, for many cohesive bulk solids and for the normal consolidation heads occurring in practice, ratholes measuring several meters are often determined. This can make funnel flow impracticable. Funnel flow has the advantage of providing wear protection of the bin walls, since the material flows against stationary material. However, it is a *first-in, last-out* flow pattern, which is unsatisfactory for bulk solids that degrade over time. It is also unsatisfactory for fine bulk solids with low permeability. Such materials may aerate during discharge through the flow channel, which can give rise to flooding problems or uncontrolled discharge.

The disadvantages of funnel flow can be overcome by the use of expanded flow, as illustrated in

Fig. 20.157c. This combines the wall protection of funnel flow with the reliable discharge of mass flow. Expanded flow is ideal when large tonnages of bulk solid are to be stored. For complete discharge, the dimension at the transition of the funnel-flow and mass-flow sections must be at least equal to the critical rathole dimension D_f at that level. Expanded-flow bins are particularly suitable for storing large quantities of bulk solids while maintaining acceptable head heights. The concept of expanded flow may be used to advantage in the case of bins or bunkers with multiple outlets.

Mass-Flow and Funnel-Flow Limits for Symmetrical Bins

Mass-flow and funnel-flow limits have been defined by *Jenike* [20.7, 8] based on the assumption of a radial stress field in the hopper. These limits are well known and have been used extensively and successfully in bin design. The limits for axisymmetric or conical hoppers and hoppers with plane symmetry depend on the hopper half-angle α, the effective angle of internal friction, δ, and the wall friction angle, ϕ. Once the wall friction angle and effective angle of internal friction have been determined by laboratory tests, the hopper half-angle can be determined.

The bounds for conical and plane-flow hoppers are plotted for three values of δ in Fig. 20.158. As shown, the critical values of α are very sensitive to variations in the wall friction angle ϕ but relatively insensitive to variations in the effective angle of internal friction δ. In the case of conical or axisymmetric hoppers, it is recommended that the half-angle be chosen to be 3° less than the limiting value. For plane flow, the bounds between mass and funnel flow are much less critical than for conical hoppers. The larger hopper half-angles possible in plane-flow hoppers imply that the discharging bulk solid will undergo a significant change in direction as it moves from the upper section into the hopper. If the transition from the hopper to cylinder is sufficiently radiused such that the possibility for material buildup by adhesion is significantly reduced, then a half-angle up to 3°–4° larger than the limit may be chosen with caution.

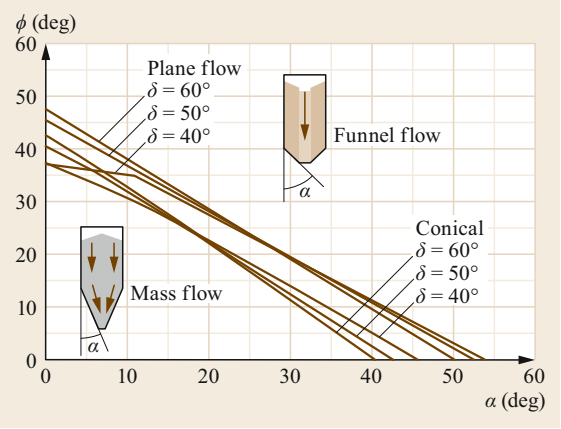

Fig. 20.158 Limits for mass flow for conical and plane-flow channels

Determination of Mass-Flow Hopper Geometry

The aim in mass-flow design is to determine the hopper half-angle α for flow along the walls and the minimum hopper opening dimension B to prevent a cohesive arch from forming. The hopper half-angle depends on the choice of the wall lining material and the measured wall friction angle ϕ as a function of normal pressure. The graph in Fig. 20.158 shows the variation of α with ϕ for mass flow.

The opening dimension for mass flow must be large enough to prevent cohesive or mechanical arches from forming across the outlet. A cohesive arch is one which forms as a result of the bulk strength gained by consolidation of the bulk solid. This should be distinguished from a mechanical arch which occurs as a result of the interlocking of solid particles. Mechanical and cohesive arches are illustrated in Fig. 20.159. To prevent a mechanical arch from forming, the opening dimension B should be at least four times the maximum particle or lump size. For coarse bulk solids (high permeability), the minimum or critical opening dimension, B_{cr}, is found when the stress acting in the arch, $\overline{\sigma}_1$, reaches the unconfined strength of the material, σ_c. This condition can be expressed in the form

$$B_{cr} = \frac{\sigma_c K(\alpha)}{\rho g}\,, \tag{20.148}$$

where

$K(\alpha)$ a factor dependent on the hopper half-angle
ρ bulk density
g acceleration due to gravity.

Since the wall friction angle decreases with increasing normal pressure, the relationship between the hopper half-angle α and the opening dimension B provides important information for hopper design. The application of (20.148) in conjunction with the flow property graphs provides the means for determining this relationship.

The steady-state flow rate for coarse, highly permeable, cohesive bulk solids can be estimated using a method proposed by *Johanson* [20.268] as

$$Q = \rho B^{1+m} L^{1-m} \left(\frac{\pi}{4}\right)^2 \sqrt{\frac{Bg}{2(m+1)\tan\alpha}\left(1-\frac{\mathrm{ff}}{\mathrm{ff_a}}\right)}\,, \tag{20.149}$$

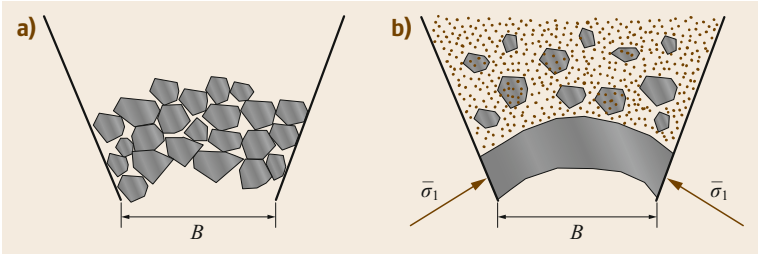

Fig. 20.159a,b Arches: **(a)** mechanical, **(b)** cohesive

where m equals 0 for a plane-flow hopper and 1 for an axisymmetric or conical hopper, B is the width of the slot or the diameter of the circular opening, L is the length of the slot in case of a plane-flow hopper, ff is the critical flow factor, and ff_a is the actual flow factor corresponding to the opening B. In the majority of cases, the flow rate thus determined for unimpeded discharge will be well in excess of plant requirements. For this reason, feeders are often used to control the discharge rate.

For fine powders with low permeability, actual flow rates can be much lower than suggested by (20.149). In this case, their prediction is much more complex and involves two-phase flow theory. In general, for the same flow rate, larger opening dimensions are required compared with an equivalent coarse bulk solid. In some cases, small quantities of air may be injected into the hopper with the aim of equalizing the pore pressure to atmospheric levels. However, caution is advised, as fine powders can be prone to flooding and uncontrollable discharge if allowed to aerate. For this reason, extreme care must be exercised in designing and installing any air permeation system.

Funnel-Flow and Expanded-Flow Bin Design

Funnel flow is characterized by material sloughing off the top surface and flowing down the central flow channel which forms above the opening. Flow will continue until the level of the bulk solid in the bin drops by an amount H_D equal to the drawdown. At this level, the bulk strength of the contained material is sufficient to sustain a stable pipe or *rathole* of diameter $D_f = B_R$ as illustrated in Fig. 20.157b. Once the level defined by H_D is reached, there is no further flow and the material below this level represents *dead* storage. For complete drawdown, B_f should be equal to D_R, which is the rathole diameter calculated for the base of the bin. However, for cohesive bulk solids, D_R is often several meters, rendering funnel flow impracticable. Expanded flow, as shown in Fig. 20.157 where D_R defines the minimum transition diameter, can provide a better proposition in this case.

In funnel flow, ratholes form over circular openings and across the diagonals of square and rectangular

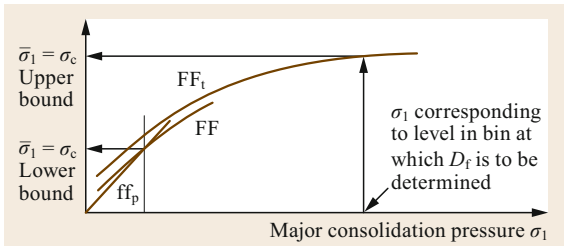

Fig. 20.160 Modes of flow: application of flow function for funnel-flow design

openings. The critical rathole dimension D_f is given by

$$D_f = \frac{\sigma_c G(\phi_t)}{\rho g} , \qquad (20.150)$$

where the function $G(\phi_t)$ can be represented by the empirical equation $G(\phi_t) = 4.3 \tan(\phi_t)$ (when $30° \leq \phi_t \leq 70°$), and ϕ_t is the static angle of internal friction. Once again, this relationship is based on the condition where the major consolidating stress within the rathole, $\overline{\sigma}_1$, reaches the unconfined yield strength of the material, σ_c. With reference to the flow function illustrated in Fig. 20.160, two cases can be considered:

(a) Case 1—upper bound D_f
This is the more conservative case and is based on the time flow function FF_t which defines the peak bulk strength under storage conditions. The condition $\overline{\sigma}_1 = \sigma_c$ depends on the major consolidation pressure σ_1 at the level of the bin at which D_f is to be computed. σ_1 is given by

$$\sigma_1 = \rho g h_f , \qquad (20.151)$$

where
h_f effective head of solids. For a funnel-flow bin, the effective head of solids, h_f, is defined as

$$h_f = \frac{R}{K_j \tan\phi}\left(1 - e^{-K_j \tan\phi h/R}\right) , \qquad (20.152)$$

R ratio of area of bin cross-section to perimeter of bin cross-section

j ratio of horizontal to vertical pressure in the bin, assumed to be 0.4
ϕ wall friction angle in degrees
h actual head of solids.

However, when the width of the storage bin is greater than or equal to the maximum height of the stored material, then h_f can be simplified to be equal to h; That is, the effective head, h_f, is equal to the *hydrostatic* head, h.

(b) Case 2—lower bound D_f

The lower bound value of D_f occurs for the case when the bin is, in effect, being emptied while it is being filled. A flow factor, ff_p, as defined in literature [20.7, 8, 269, 270], can be used to define the critical condition for which $\overline{\sigma}_1 = \sigma_c$. Usually, the instantaneous flow function FF applies in this case. For rectangular bin openings, arching may occur across the opening. In this case, a flow factor $ff_p = 1.7$ is applied. This assumes that the slope of the flow channel formed within the flow channel is not less than 30° at the sides of the rectangle. Such an angle is necessary to expand the crater from a width B_r to a diameter D_f, otherwise a stable pipe or rathole of smaller diameter will form. The application of $ff_p = 1.7$ in the flow function shown in Fig. 20.160 defines the condition for the stress acting in the arch $\overline{\sigma}_1 = \sigma_c$. B_f can then be calculated using (20.153) with $K(\alpha) = 1.15$, thus

$$B_f = \frac{1.15\overline{\sigma}_1}{\rho g} . \qquad (20.153)$$

Influence of Flow Properties on Bin Geometry

Many cohesive bulk solids gain strength due to consolidation during prolonged storage. This is illustrated in Fig. 20.161 for a typical run-of-mine coal with 10% moisture content. A small increase in strength is observed after two days of storage, however, after five days the strength gain is considerable. While it would be possible to design a satisfactory mass-flow bin to guarantee discharge after two days, it would be impossible to design a satisfactory bin to discharge the bin by gravity alone after five days of storage or longer. Some form of flow promotion would be necessary. Alternatively, periodic withdrawal of coal, say one to two minutes of flow each day, would help reconstitute the coal and reduce the effect of interparticle bonding. In this way, the influence of prolonged storage on the gain in bulk strength is minimized.

Changes in moisture content can significantly influence the strength of bulk solids. By way of illustration, the critical hopper opening dimension B for three coals plotted as a function of moisture content is shown in Fig. 20.162. This figure shows three coal samples, sample (1) being a raw open cut coal, sample (2) a washed version of (1) and sample (3), a blend of (2). The high strength of the raw, unwashed coal is clearly evident. Experience has shown that the peak bulk strength of coal may occur at a moisture content somewhere between 70% and 90% of the saturation limit. Washed coals such as those illustrated by the curves of samples (2) and (3) in Fig. 20.162 generally exhibit very little, if any, increase in bulk strength on storage.

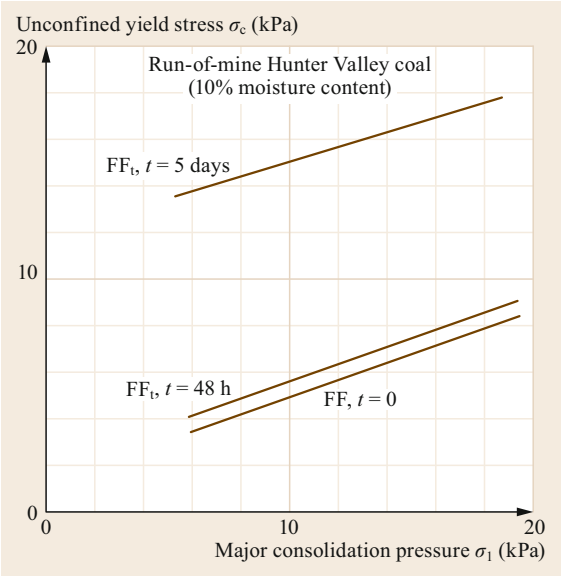

Fig. 20.161 Effect of storage time on strength of an unwashed coal

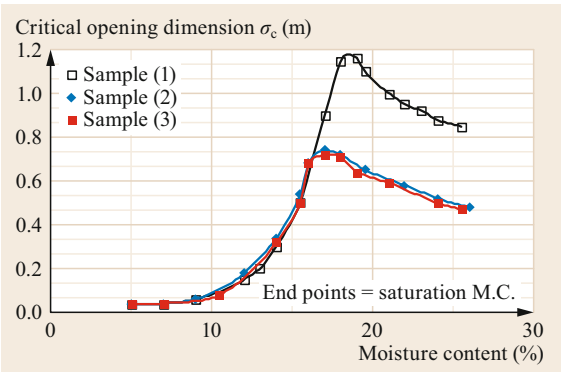

Fig. 20.162 Critical opening dimension as function of moisture content with stainless steel 304-2B lining. Moisture content determined on wet basis (wb)

Use of Inserts to Control Bin Flow Patterns

Inserts may be used in bins to achieve a desirable flow pattern. Often they are used in the form of a *retrofit* device to correct an undesirable flow pattern which is

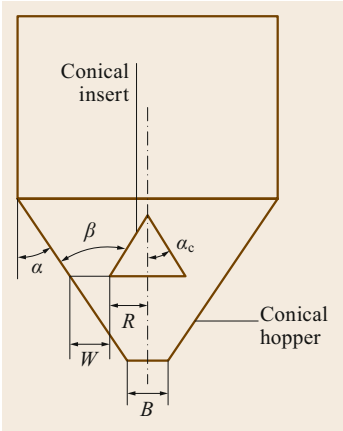

Fig. 20.163 Insert to correct hopper flow pattern

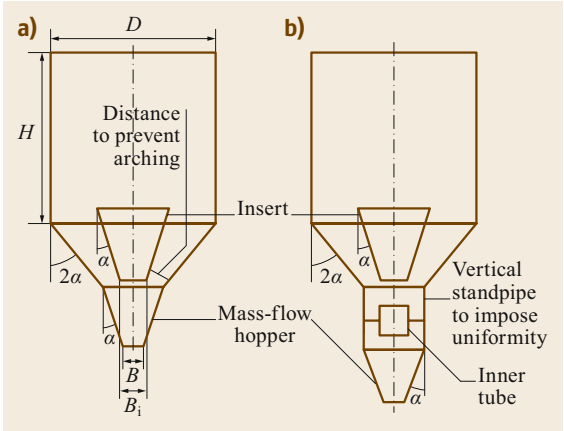

Fig. 20.164a,b Binsert for promoting mass flow and bin blending: **(a)** blending and mixing, **(b)** segregation control

giving rise to either flow blockages or dynamic wall loads of large magnitude. Knowledge of the flow properties of the bulk solid, together with an understanding of the conditions controlling bin flow patterns, permits the application of inserts with innovative designs for specific purposes.

An overriding consideration in the use of inserts within bins is the magnitude of the drawdown forces that can be generated. In the design of supporting structures, it should be noted that loads greater than hydrostatic can occur.

Inverted Cone Inserts. *Johanson* [20.271] proposed the use of inverted conical-shaped inserts to modify the flow in hoppers, as illustrated in Fig. 20.163. In effect, the insert converts a conical hopper into a pseudo-plane-flow hopper in which the slot is equivalent to a circular annulus. As indicated by the mass-flow limits shown in Fig. 20.158, the hopper half-angle for a plane-flow hopper is about 8°–10° larger than that of the equivalent conical hopper.

It is important to place the insert correctly. This requires consideration of the wall friction angle ϕ, insert cone angle α_c, insert base radius R, and spacing W, ensuring that the latter is sufficient to permit flow without arching. Procedures for designing and correctly placing inserts are described by *Johanson* [20.271].

Inverted conical inserts can also play a role in improving in-bin blending or correcting segregation issues, although this is an area requiring more research.

Cone-in-Cone. The cone-in-cone binsert is another common form of hopper insert. Invented by *Johanson* [20.272], this device can be used to modify and correct flow using arrangements such as those shown in Fig. 20.164.

The design of such an insert is based on achieving mass flow at all points within the bin. The half-angle α of the inner cone is determined by the mass-flow design requirements as outlined above. The half-angle of the outer cone can then be set to twice this value, provided the lining materials are the same or equivalent.

As a design tool, this allows large storage capacities to be achieved with much lower headroom than is possible with a conventional mass-flow bin. The concept is also very effective as a retrofit solution to correct problems associated with funnel flow. The cone-in-cone insert also offers many advantages in the area of blending and antisegregation control.

Energy-Assisted Discharge

Problems due to flow blockages such as arching and ratholing in bins may be solved by using active flow promotion devices. These may take the form of mechanical dischargers such as screws or scrapers, or other devices such as vibrators or air blasters that impart energy into the bulk solid in an effort to reduce its strength.

Flow Promotion by Mechanical Vibration. The application of mechanical vibration to promote the gravity flow of bulk solids has been studied by *Roberts* [20.273, 274] and *Rademacher* [20.275]. This work utilized a dynamic shear test apparatus that permits the measurement of shear strength in the presence of vibrations over a range of amplitudes and frequencies. Based on this work, Fig. 20.165a illustrates two yield loci for the same material: the unvibrated case (strength σ_c), and for the same consolidation conditions the case where vibrations are applied during shear (strength σ_{cf}).

The influence of mechanical vibration may induce flow by:

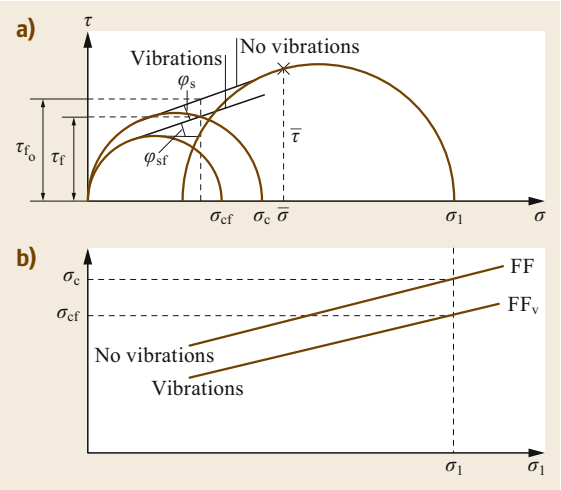

Fig. 20.165 **(a)** Yield loci and **(b)** flow functions

1. Improving the mass-flow performance of an existing mass-flow bin by reducing the wall friction angle and critical arching dimension
2. Improving the funnel-flow performance of an existing funnel-flow bin by reducing the critical rathole dimension
3. Lowering both the bulk strength and wall friction angle, converting an existing funnel-flow bin to mass flow.

Effective flow promotion depends on the ability to transmit vibration energy from the source to the region of the flow blockage. In the case of storage bins, it is usual to install the vibrator on the hopper wall; this provides an immediate benefit through the reduction in wall friction that may result. Furthermore, if the flow blockage is in the form of an arch, then vibration applied to the hopper wall at or near the outlet may cause the arch to fail and flow to occur. In this case, the vibration energy does not need to be transmitted any great distance. On the other hand, where funnel flow prevails and a stable rathole has formed, the vibration energy needs to be transmitted through the bulk mass.

To achieve the best results, higher modes of vibration should be used for flow promotion. The objective here is to create multiple (tensile) planes of failure, as illustrated in Fig. 20.166. Research to date has indicated that excitation frequencies on the order of 100 Hz or higher are necessary. There may be a tradeoff in the selection of the excitation frequency; the higher the frequency, the shorter the wavelength, hence the greater the number of failure zones; on the other hand, the transmitted vibration energy may suffer from greater attenuation at higher excitation frequencies.

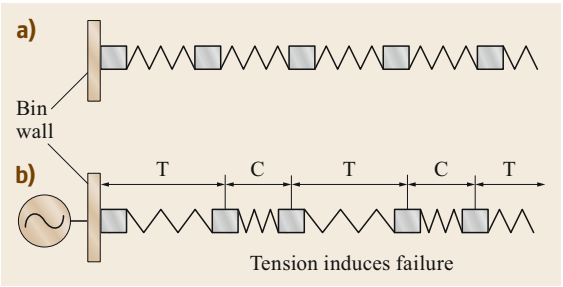

Fig. 20.166a,b Model to illustrate formation of failure zones: **(a)** static case, **(b)** dynamic case (T tension, C compression)

Use of Air Blasters for Flow Promotion. Air cannons or air blasters are commonly used to promote gravity flow in bins and stockpiles. In general, air blasters are used in retrofit situations to correct an inadequate design where flow blockages occur. In the case of a new design with some uncertainty in the expected variation in bulk solid properties or operating conditions, it is good practice to make provision in the design for a future installation of air blasters should they be found necessary.

Terziovski and *Arnold* [20.276] indicate that the sizing and placing of air blasters is often largely based on experience and guesswork, but some guidance is offered by their work in the form of a procedure for the correct selection of these devices based on measured flow properties and bin geometry.

Wall Loads

Many cases of bin failure occur each year. These not only involve loss of contained material but also loss of life in some instances. In many of these cases, the cause may be attributed to a lack of appreciation of the exact nature of the loads encountered by the bin walls during the design stage. This involves both the magnitude and variation of such loads, whose prediction continues to be a subject of considerable complexity. Consideration of the loads acting on the bin walls is thus a particularly important aspect of bin design.

Bin wall loads have been studied for over a century using a variety of approaches. Various attempts have been made to codify wall loads, resulting in several international standards. Australian Standard AS 3774 [20.277] and Eurocode EN 1991-4 [20.278] are the most modern and complete bin design codes in use today. These two standards are relatively comprehensive in terms of the range of loading conditions and bin types considered. They are backed up by the best available theory and underpinned by various large laboratory-scale experimental model studies, e.g., [20.279, 280].

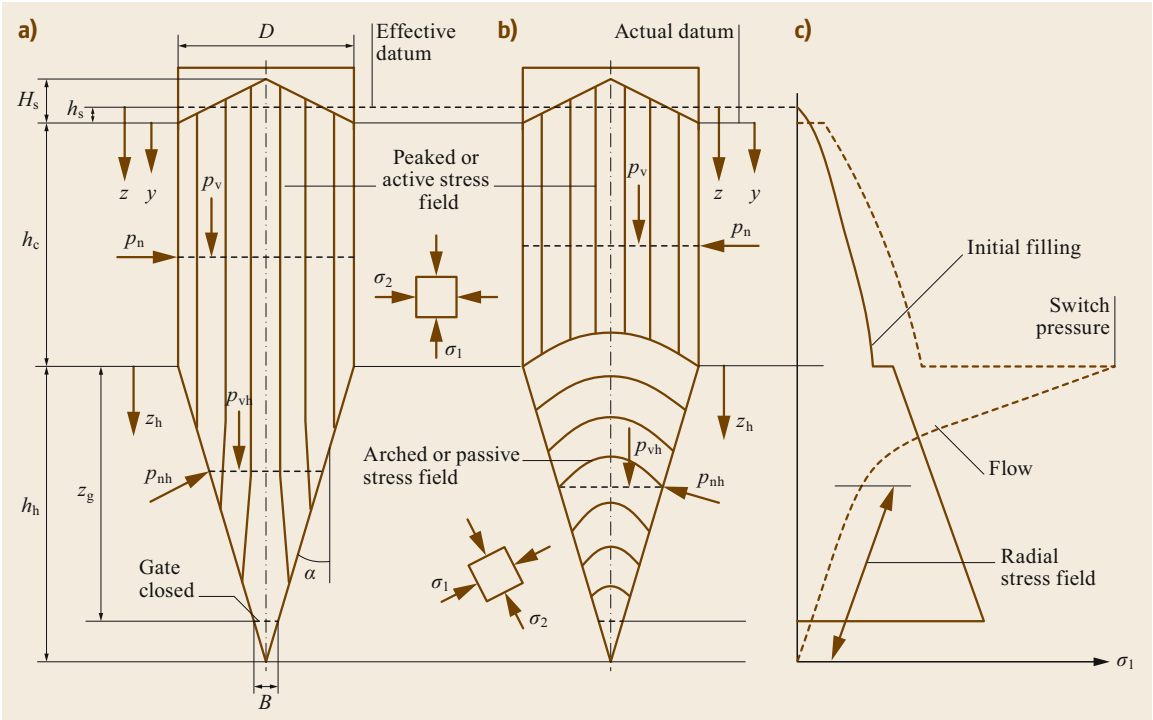

Fig. 20.167a–c Pressures acting in mass-flow bins: **(a)** initial filling, **(b)** flow, **(c)** normal wall pressure

With the advancement of simulation techniques, finite element analysis (FEA) based on plasticity theory and discrete element modeling (DEM) have become powerful techniques to estimate bin wall loads outside of the cases covered by standards, e.g., [20.281, 282].

The loads occurring within bins are directly related to the flow patterns, which are in turn dependent on the operating conditions, flow properties, and bin configuration. In general, the flow patterns (and hence wall loads) within mass-flow bins are easier to predict in comparison with funnel flow, especially if the bin has multiple outlet points, the loading of the bin is not central, and/or the bulk solid is prone to segregation. Unless there are compelling reasons to do otherwise, bin shapes should be kept simple and symmetric.

The stress fields and normal wall pressures occurring in a typical mass-flow bin during the initial fill and flow conditions are shown in Fig. 20.167. When a bin is initially filled from the empty condition, a peaked stress field occurs as shown in Fig. 20.167a; the major principal stress is almost vertical throughout the material. When flow occurs, the stress field in the hopper switches to an arched stress field, with the switch traveling up the hopper until it becomes fixed at the location of the transition as shown in Fig. 20.167b. In the arched stress field, the load is transmitted to the wall of the hopper, with the major principal stress acting closer to a horizontal direction.

In the cylinder, the peaked stress field remains, although imperfections in the cylinder wall which give rise to localized flow convergences can cause overpressures to occur. These imperfections may be due to manufacturing and/or construction details; examples include weld projections or plate shrinkages in the case of steel bins, and deformation of formwork in the case of concrete bins. Design codes generally employ overpressure factors to account for these effects.

Note that, when the bin discharges and the flow is stopped, the stress fields and corresponding pressures shown in Fig. 20.167b will remain. The stress field does not revert to that in Fig. 20.167a; this only occurs if the bin is completely emptied and then filled again.

Storage of bulk solids in large tonnages is often accomplished using multi-outlet bins with either flat or hopper bottoms. Multiple outlet bins and bins with an eccentric discharge point give rise to complex loading patterns as a result of the flow channels that develop above the outlets. Eccentric discharge of such a bin can lead to asymmetry in the normal pressure distribution around the bin walls. The nonuniformity and eccentricities of these wall loads can cause bending

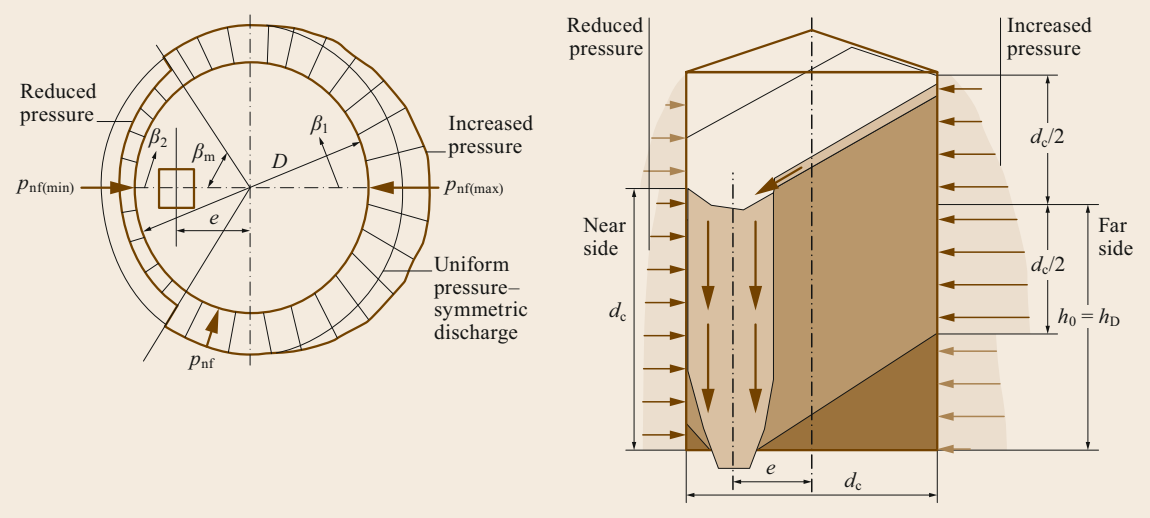

Fig. 20.168 Circumferential pressure variation due to operation of one eccentric outlet

stresses in the circumferential direction and other complexities that can have serious structural consequences. Understanding how wall loads are affected by eccentric discharge is an aspect of bin design of major importance.

The subject of eccentric loads in bins is addressed in AS 3774 [20.277]. As an example, the loading patterns illustrated in Fig. 20.168 are based on this standard. The pressures acting on the wall in the region of the outlet are of lower magnitude than the pressures that act in the region of the bin where there is no flow. As a consequence of this flow pattern, bending moments are induced in the walls, leading to distortion in the shape of the bin. The loss in cylindrical symmetry can place such a bin at a much higher risk of failure due to buckling.

Note that, where there are several symmetrically located outlets, the conservative approach to design is to assume that the possibility exists for only one of the outlets to operate at any particular instant.

Quaking

Silo quaking is a dynamic phenomenon that can occur in bins and silos of various geometries and operating conditions. A bin suffering from silo quaking may have a steady and reliable flow from the outlet, while material in the upper sections moves periodically in discrete quakes punctuated by periods of no motion. Material velocities during each individual quake can be orders of magnitude higher than the average value. Shock loads can be generated through the resulting material accelerations. These loads can range from a curious oddity, to a nuisance to neighboring areas, to levels where structural fatigue failure is of concern.

The problem is commonly associated with tall mass-flow silos, but it is not limited to this case. Examples of the phenomenon have been found in mass-flow, funnel-flow, expanded-flow, multi-outlet, and intermediate-flow bins; however the mechanisms involved can vary. In most cases, the period of the quakes is inversely proportional to the flow rate, and in tall silos, the magnitude grows exponentially with the height of the material column.

In a typical tall-silo example, silo quaking represents an example of slip–stick motion. Following each shock load, the bulk solid is well consolidated with a low level of wall friction required to support its weight. As material discharges from the outlet, the upper material is undermined and friction becomes mobilized. At some point, the limits of friction are reached and the material accelerates downwards. This occurs as a rarefaction wave which moves rapidly up through the material. As demonstrated by *Wensrich* [20.283], the mechanics of wall friction create a condition where this rarefaction wave grows exponentially with distance traveled. The subsequent compression waves have the tendency to form into shock fronts.

20.6.2 Stockpiles

In stockpiles, the reclaim is via gravity flow through hoppers, feeders, and/or chutes onto reclaim conveyors located below ground level. The mechanics of stockpile systems are often underestimated at the design stage, which can result in less than optimal reclaim performance. The design of stockpiles requires knowledge of the bulk solid material characteristics over a range of different operating conditions.

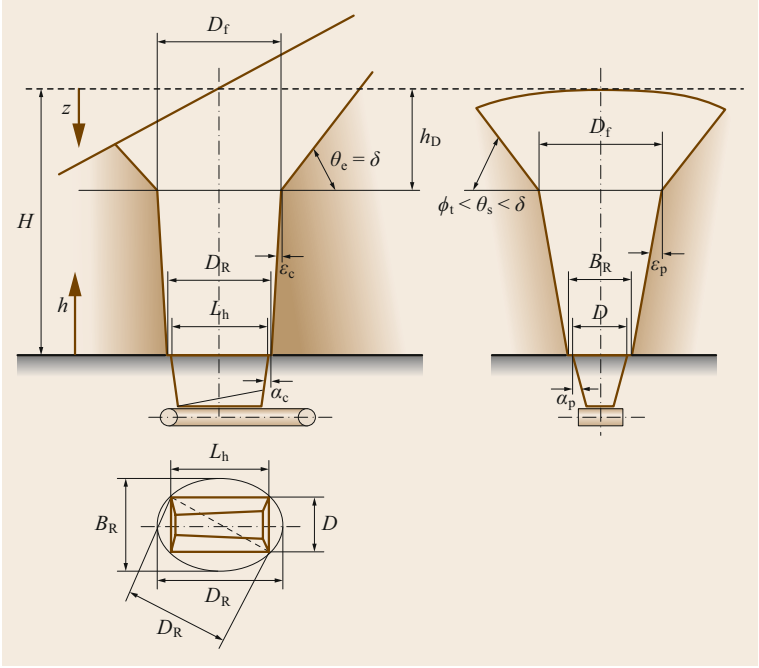

Fig. 20.169 Rathole geometry

Rathole Geometry

Following the work of *Roberts* [20.284], the general case of a rectangular opening associated with a hopper at the transition to a gravity reclaim stockpile is considered. The rathole forms at the top of the hopper across the diagonal D_R of the rectangle, such that

$$D_R = \sqrt{{L_h}^2 + D^2}\,, \tag{20.154}$$

where L_h is the length of the hopper transition and D is the width of the hopper transition.

While the actual shape of the rathole is quite complex, with the walls being slightly curved rather than straight, a close approximation to the shape can be obtained using the following assumptions based on the limiting rathole wall slope half-angles plotted in Fig. 20.169:

a) Immediately above the rectangular opening corresponding to the hopper transition, the rathole is approximately elliptical in shape with a major axis of D_R and a minor axis of B_R. The determination of B_R is based on the following assumptions:

- For a rectangular opening with $L_h \gg D$, the flow channel opens out at a half-angle of 30° along the sides, and at an average angle of 5° at the end.
- For a square opening, the flow channel opens out at an angle of 7° along the sides.
- For $D < L_h$, transitional arrangements apply.

On this basis, the following relationship can be proposed:

$$\frac{B_R}{D} = \frac{L_h}{D}\left\{1 + C_R\left[1 - \exp\left(-\frac{\frac{L_h}{D} - 1}{C_L}\right)\right]\right\} \times \left\{\sqrt{1 + \left[\frac{D}{L_h}\right]^2} - 1\right\} + 1\,, \tag{20.155}$$

where $C_R = 5.6$ and $C_L = 8$. Figure Fig. 20.170 shows plots of $\frac{D_R}{L_h}$ and $\frac{B_R}{D}$ as functions of $\frac{L_h}{D}$ based on (20.154) and (20.155), respectively.

b) The ratio of the area of the approximated ellipse to the area of the rectangular opening at the hopper transition (Fig. 20.171) is

$$A_R = \frac{\frac{\pi}{4} D_R B_R}{L_h D} = \frac{\pi}{4}\frac{B_R}{D}\sqrt{1 + \left(\frac{D}{L_h}\right)^2}\,, \tag{20.156}$$

c) The rathole opens out from the elliptical shape at the bottom to a circular shape of diameter D_f (the critical rathole diameter) at the top corresponding to the drawdown h_D.

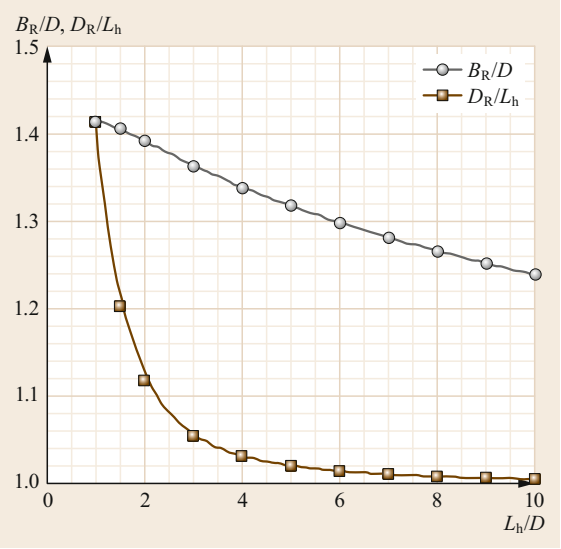

Fig. 20.170 Ratios D_R/L_h and B_R/D as functions of L_h/D

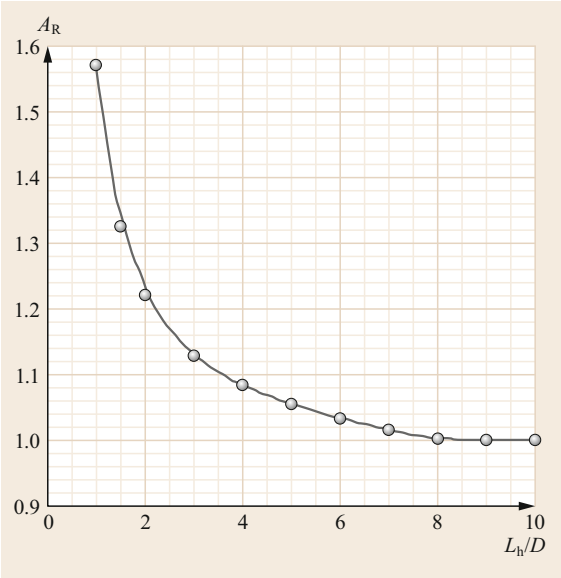

Fig. 20.171 Variation of area ratio with ratio L_h/D

d) The end walls of the rathole are sloped at an angle ε_c which is equal to or less than the limiting conical piping angle ψ_c.
e) The side walls of the rathole are sloped at an angle ε_p which is equal to or less than the limiting plane-flow piping angle ψ_p. Normally, $\varepsilon_p < \psi_p$, since the slope of the side walls is controlled by the rathole becoming circular at the drawdown transition.
f) Above the drawdown level, the crater sloughs off at an angle θ which normally ranges between the static angle of internal friction ϕ_t and the effective angle of internal friction δ. The limiting slope will normally be $\theta_s = \delta$ for the end slope. The slope of the sides is such that $\phi_t \leq \theta_s \leq \delta$.

Jenike [20.7] determined the flow factors ff_p for no piping and the corresponding limiting slope angles for the funnel-flow channel. Since in the case of funnel flow the slope of the flow channel is not defined, the Jenike limits are taken as upper-bound values for plane-flow and conical surfaces, respectively. Jenike assumed that, for a rectangular slot, the side walls of the rathole can slope out to allow the rathole to expand upward to a circular shape. He recommends that, in the design of rectangular outlets, a limiting $ff_p = 1.7$ be adopted. This corresponds to a half-slope angle for plane flow of $\psi_p = 30°$. This applies only to the transitional region immediately above the side walls of the opening but not to the side walls of the rathole that forms above the lower transition.

A more realistic, yet somewhat empirical, approach is to use the mass-flow limits as a guide. For instance, it is assumed that, as Jenike did, that at the surface of the rathole, the friction angle is given by

$$\phi_S = \tan^{-1}(\sin\delta)\,. \tag{20.157}$$

The assumption embodied in (20.157) is that failure by internal shear occurs at the maximum shear stress. Using the values of ϕ_S given by (20.157), the limiting half-slope angles for plane-flow and conical channels are plotted as curves 1 and 2, respectively, in Fig. 20.169. The 30° limit line for plane flow proposed by Jenike as previously discussed is also shown in Fig. 20.169.

Arching under Funnel Flow

In the case of bins with circular or square openings operating under funnel flow, arching over the opening will not normally occur. However, for a rectangular opening, while the rathole or flow channel forms across the diagonal, the width of the opening must be large enough to prevent a cohesive arch from forming. Following the discussion in the previous section, the procedure involves the application of the flow factor $ff_p = 1.7$ based on a half-slope-angle of 30° for the sides of the rectangle. The critical arching dimension B_r is computed as follows:

(a) Draw the $ff_p = 1.7$ line on the flow function graph (instantaneous or time dependent, whichever is relevant to the design). The value of σ_c at the intersection of ff_p and FF can then be read from the graph.

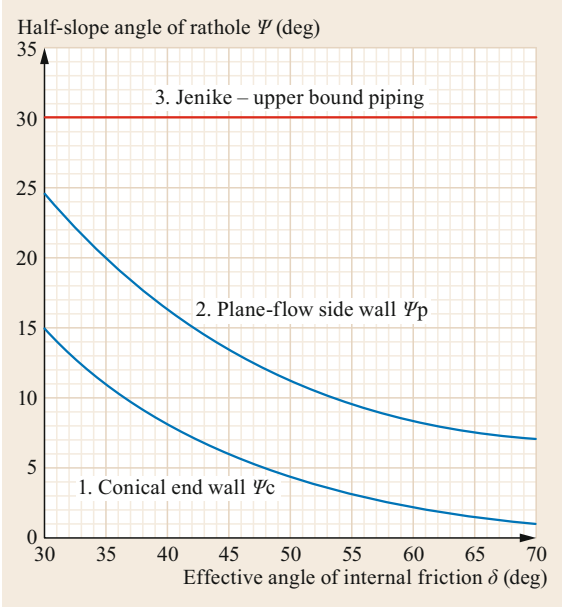

Fig. 20.172 Limiting half-slope angles for ratholes

(b) Compute B_r using (20.148) with $\overline{\sigma}_1 = \sigma_c$ and $H(\alpha) = 1.15$, when $\alpha = 30°$ for plane flow, thus

$$B_r = \frac{1.15\sigma_c}{\gamma} \,. \qquad (20.158)$$

Drawdown and Live Capacity

Assuming that the rathole geometry is as illustrated in Fig. 20.169 and choosing the slope of the end walls of the flow channel such that $\varepsilon_c \leq \psi_c$ and the side walls $\varepsilon_p \leq \psi_p$ as given by Fig. 20.172, the rathole diameter D_f and drawdown h_D can be determined as indicated in Fig. 20.173. The D_f versus h_D graph is drawn, and the expansion lines for the rathole side and end walls are drawn as indicated. The expansion lines intersect at the height h_c above the base, at which level the rathole becomes approximately circular in shape. The rathole then expands at the angle ε_c until the upper, critical intersection point is reached, as shown in Fig. 20.173. This defines the drawdown level h_D at which the rathole of diameter D_f starts to form. Above this level, the bulk solid has insufficient strength to form a stable rathole and the bulk solid sloughs off at an angle approaching the effective angle of internal friction, δ.

Having thus determined the various geometrical parameters defining the rathole geometry, the reclaimed volume can be calculated. The procedures outlined in [20.284–289] may be used for this purpose. One option is to use scale modeling as illustrated in [20.289]. However, it is now well established that the application of CAD geometrical modeling packages, coupled with flow property testing and rathole geometry analysis, as illustrated in Fig. 20.173, provides a ready means for simulating stockpile drawdown performance.

As an example, Fig. 20.174 shows the predicted and actual drawdown performance of a large, kidney-shaped, iron ore stockpile with twin outlets. Figure Fig. 20.174a shows the simulated CAD model of the stockpile generated using the measured flow properties of the iron ore. The model was produced in advance of the plant construction in order to predict the draw-

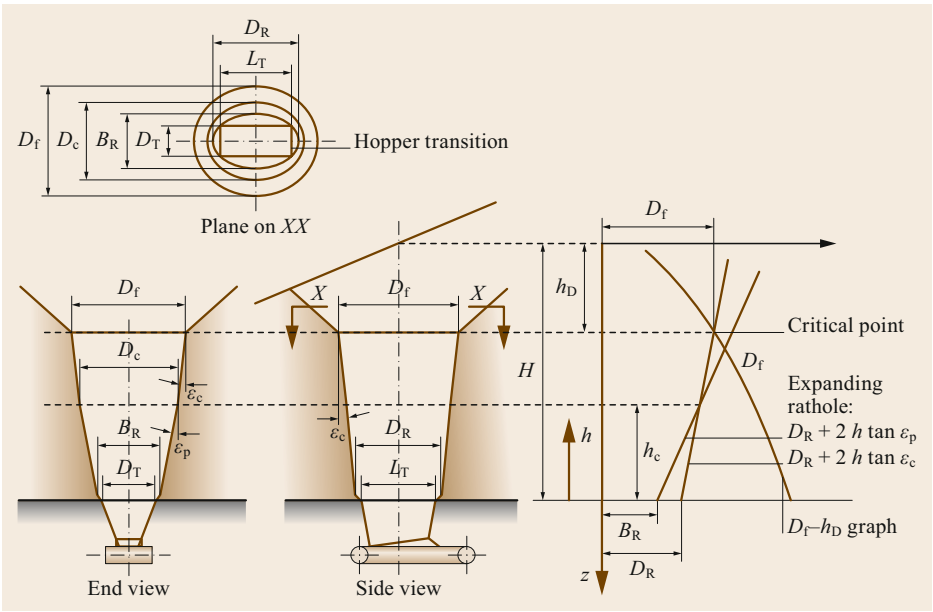

Fig. 20.173 Rathole diameter and drawdown determination

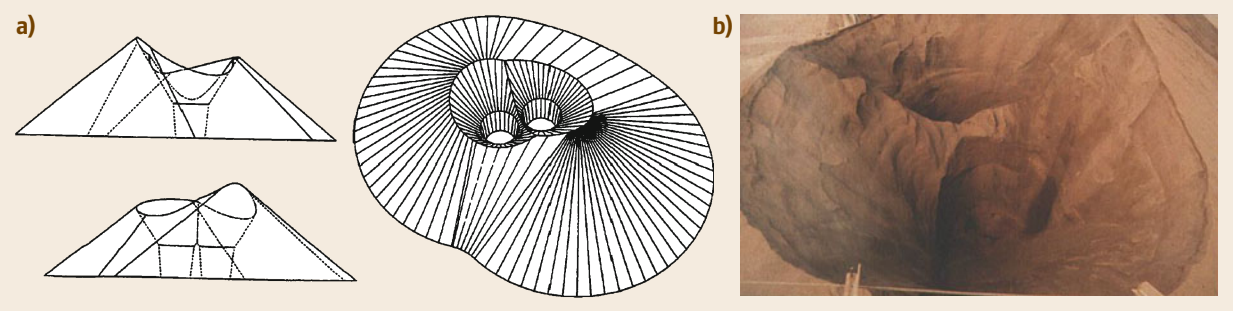

Fig. 20.174a,b Simulation and drawdown performance of iron ore stockpile: **(a)** CAD model simulation, **(b)** view of actual stockpile showing drawdown and craters

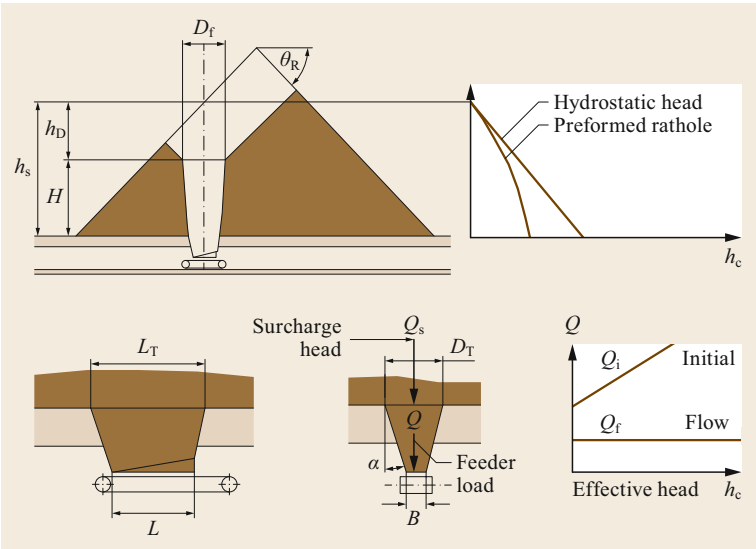

Fig. 20.175 Feeder loads

down and live capacity of the proposed stockpile. The photograph in Fig. 20.174b shows the drawdown of the stockpile after it had been in service. The comparison between the predicted and actual performance is shown to be quite good, confirming the validity of the design procedures outlined in this section.

Loads on Reclaim Hoppers and Feeders

The loads on reclaim hoppers and feeders and the corresponding power to drive the feeders varies from the *initial* to the *flow* condition as illustrated in Fig. 20.175. The initial load will correspond to the case when the stockpile or crater above the feeder is filled. The surcharge load Q_s will depend on the consolidation condition of the bulk solid in the stockpile. The worst case corresponds to the hydrostatic pressure. However, if a rathole has been preformed, the surcharge load will be reduced. When an arched or flow stressed field has been formed within the mass-flow reclaim hopper, the load on the feeder will be greatly reduced. Confirmation of the load conditions acting on reclaim hoppers can be obtained from model stockpile tests.

Load Analysis of Conveyor Support Structures Buried in Stockpiles

In many cases the load-out conveyor supplying the bulk solid to the stockpile is a boom conveyor supported by a vertical support structure located outside the peripheral area of the stockpile rill zone at ground level. The support structure is not in contact with the stored stockpile material. In other cases, particularly in the coal industry, the load-out conveyor is supported on trestle legs which are substantially buried in the stockpile. The work of *Roberts* [20.290] dealt with buried structural members which are square or rectangular in cross-section.

The loads acting on the trestle legs are quite complex and variable, being dependent on the following conditions:

- Variations in the flow properties of the material
- Loading and unloading history and mechanism for loading and unloading
- Slumping and avalanching during periods of heavy rain
- Length of time the bulk material remains undisturbed in the stockpile
- Degree of load support provided by the consolidation of the bulk solids acting around the trestle legs
- Rigidity of the stockpile base—whether any ground settlement has occurred
- Variations in stress fields from active to passive during filling and reclaim.

For these reasons, it is recommended that a conservative approach be taken to trestle leg load calculations.

20.6.3 Feeders

In bulk handling operations, feeders are used extensively to control the flow of bulk solids from storage bins and stockpiles. While the scale of operations in which feeders are used varies enormously from large feeders in mining operations to small feeders in powder processing, the underlying principles of feeder design remain the same. It is important that the interaction between the bin and feeder behavior be understood to achieve reliable and predictable flow. In this respect, the bin (and hoppers in particular) and feeder must be considered as one integral unit and designed accordingly. Feeders for controlling the flow of bulk solids require certain criteria to be met:

- Deliver the range of flow rates required;
- Handle the range of particle or lump size and flow properties expected;
- Deliver a stable flow rate for a given equipment setting;
- Permit the flow rate to be varied easily over the required range without affecting the performance of the bin or hopper from which it is feeding;
- Feed material onto the belt in the correct direction at the correct speed with the correct loading characteristic and under conditions that will produce the minimum impact, wear, and product degradation. Often, a feed chute is used in conjunction with the feeder to achieve these objectives;
- Fit into the available space.

The salient aspects of the various types of feeder commonly used to feed bulk solids onto belt conveyors are now briefly reviewed.

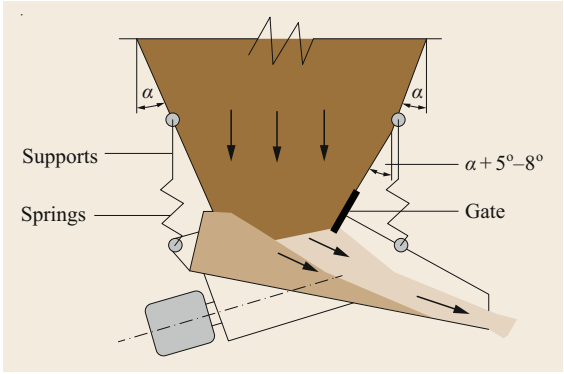

Fig. 20.176 Vibratory feeder and interfacing

Vibratory Feeders

Vibratory feeders, as illustrated in Fig. 20.176, are used extensively for controlling the discharge of bulk solids from bins and stockpiles and directing these materials onto conveyor belts. In general, vibratory feeders are classified as *brute force* or *tuned* depending on the manner in which the driving force imparts motion to the pan. As the name implies, *brute force*-type feeders involve the application of the driving force directly to the pan, while in the *tuned* feeder the exciter is attached to the feeder pan by means of springs. Brute force feeders have the following characteristics:

- Lower initial cost but higher operating costs;
- Greater forces to be accommodated in the design;
- Impact loads on the pan are transmitted to bearings on which out-of-balance masses rotate;
- Delivery rates are dependent on the feeder load due to bulk solids;
- Generally limited to applications requiring only one feed rate.

On the other hand, *tuned* vibrating feeders are more sophisticated in their operation inasmuch as the driving force is transmitted to the pan via connecting springs. In this way, they act essentially as a two-mass vibrating system and employ the principle of force magnification to impart motion to the pan. The primary driving force is provided by either an electromagnet or by a rotating an out-of-balance mass system.

Vibratory feeders are suitable for a broad range of bulk solids, being able to accommodate a range of particle sizes and being particularly suitable for abrasive materials. However, they are generally not suited to fine powders under 150–200 mesh where flooding can be a problem. Also, *sticky* cohesive materials may lead to buildup on the pan and thus a reduction in the flow rate.

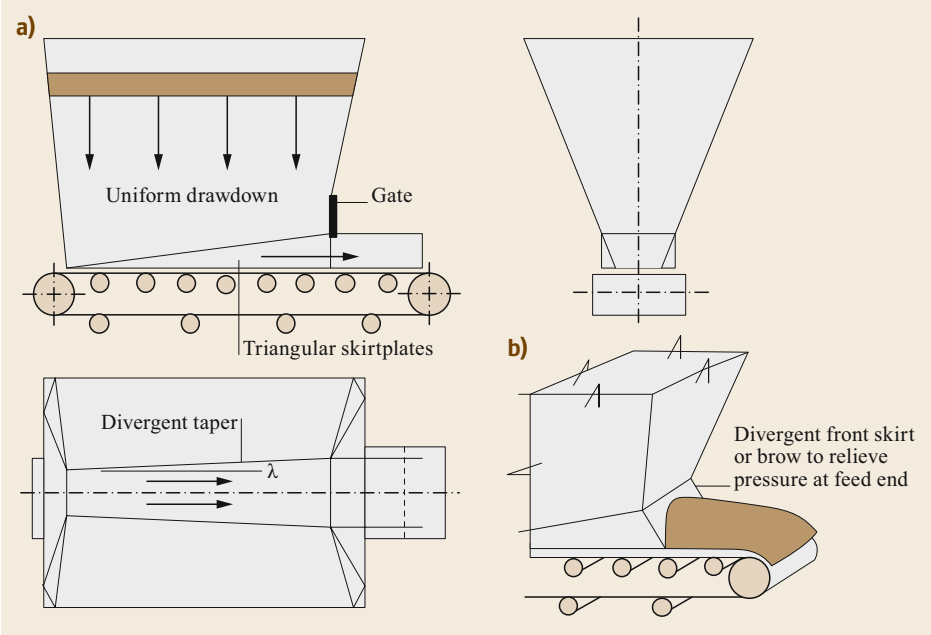

Fig. 20.177a,b Belt feeder **(a)** and alternative arrangement **(b)**

Bulk solids are conveyed along the pan of the feeder as a result of the vibrating motion imparted to the particles. The pan of the feeder is driven in an approximately sinusoidal fashion at some angle to the trough.

The converging velocity and throughput depend on the feeder drive frequency, amplitude or stroke, drive angle and trough inclination, coefficient of friction between the bulk solid and the pan, as well as the bulk solid parameters such as the bulk density, particle density, and general flow properties.

There are several aspects to note when designing feed hoppers for use with vibrating feeders. The effectiveness of the feeder, as with all feeders, depends largely on the hopper, which must be capable of delivering material to the feeder in an uninterrupted fashion. For a symmetrical hopper, there is a tendency for the feeder to draw material preferentially from the front of the hopper. Uniform draw can be achieved by making the hopper outlet asymmetrical with the back wall at the correct hopper half-angle and the front wall at an angle of $+5°$ to $+8°$. Alternatively, a symmetrical hopper may be made to feed approximately uniformly by using a rougher lining material on the front face.

Belt and Apron Feeders

Belt feeders, as illustrated in Fig. 20.177, are used to provide a controlled volumetric flow of bulk solids from storage bins and bunkers. They generally consist of a flat belt supported by closely spaced idlers and driven by end pulleys. While normally belt feeders are installed horizontally, on some occasions a feeder may be designed to operate at a low inclination angle. Some particular features of belt feeders include:

- Suitable for withdrawal of material along slotted hopper outlets when correctly designed;
- Can sustain high impact loads from large particles;
- Flat belt surface can be cleaned quite readily, allowing the feeding of cohesive materials;
- Suitable for abrasive bulk solids;
- Capable of providing a low initial cost feeder which is dependent on operation and suitable for automatic control.

The hopper and feeder interface geometry for long slots is critical if uniform draw is to be obtained. For this reason, a tapered opening is required, as illustrated in Fig. 20.177a. The triangular skirtplates in the hopper bottom are an effective way to achieve the required divergence angle. An important feature of the diverging skirts is the relief provided to skirtplate drag.

The gate on the front of the feeder is a flow trimming device and not a flow rate controller. The height of the gate is adjusted to give the required release angle and to achieve uniform draw along the slot. Once the gate is correctly adjusted, it should be fixed in position; the flow rate is then controlled by varying the speed of the feeder. This requirement places some limitations on belt feeders when very low flow rates are required, especially if the bulk solid is at all cohesive or contains large lumps. The use of a diverging front skirt or brow as illustrated in Fig. 20.177b has the advantage of re-

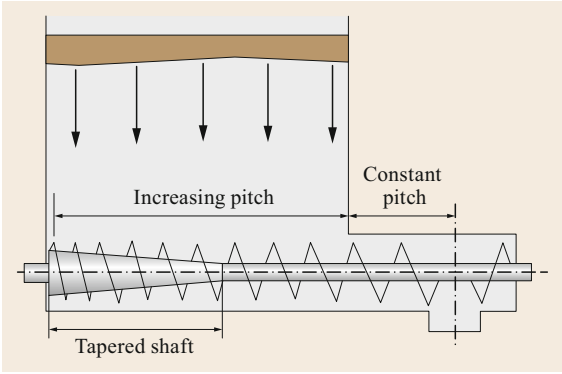

Fig. 20.178 Screw feeder with constant screw diameter, tapered shaft diameter, and expanding pitch, which results in uniform drawdown in hoppers

lieving the pressure at the feed end during discharge and forward flow.

Particular care is needed with the design of the hopper/feeder arrangement when handling fine powders in order to ensure that problems of flooding are avoided. If the bulk material tends to stick to the belt, spillage may be a problem with belt feeders. Therefore, if sufficient headroom is available, it is desirable to mount the feeder above the belt conveyor onto which it is feeding material in order that any material falling from the return side of the belt will automatically fall onto the conveyor belt.

Apron feeders are a type of large-scale belt feeder that is useful for feeding large tonnages of bulk solids, being particularly relevant for heavy abrasive ore-type bulk solids and materials requiring feeding at elevated temperatures. They are also able to sustain extreme impact loading. The remarks concerning the need for uniform draw and gate settings applicable to belt feeders are also applicable to apron feeders.

Screw Feeders

Screw feeders are widely used for bulk solids that show low or zero cohesion such as fine and granular materials which have to be dispensed under controlled conditions at low flow rates. However, as with belt feeders, design difficulties arise when the requirement is to feed along a slotted hopper outlet. An equal pitch, constant diameter screw has a tendency to draw material from the back of the hopper. To overcome this problem, the screw requires both a tapered shaft in addition to the expanding pitch as illustrated in Fig. 20.178.

The pitch variation is generally limited to the range between 0.3 and 1.5 diameters. This limits the length-to-diameter ratio for a screw feeder to about six, making them unsuitable for long slots. The section of the screw leading from the hopper to the feeder outlet is fundamental in determining the quantity of material discharged per revolution of the screw. At the point when the screw leaves the hopper, it is essential for control purposes to cover the screw, normally by a *choke* section having the same radial clearance as the trough. This choke section should extend for at least one pitch to prevent material cascading over the flights.

As a screw feeder relies on friction to transport material, it has very low efficiency in terms of energy requirements. Furthermore, the volumetric efficiency is impaired somewhat due to the rotary motion imparted to the bulk material during the feeding operation.

Since screw feeders are generally fully enclosed, relatively good dust control is achieved. However, due to the high frictional losses, abrasive-type bulk solids can effectively reduce the life of the feeder due to abrasive wear. Fine powders that tend to flood are difficult to control in a screw feeder in flooding situations.

20.6.4 Yards for General Cargo

This section deals with general cargo storage without the support of auxiliary means or accessories. This concerns the storage of general cargo without any kind of racking or other storage technology. Only load carriers, such as cardboard boxes, pallets, or containers, that allow goods to be stacked, and operating technology for the storage process itself, e.g. for lifting, are used.

Floor Storage: Block Stacking and Row Stacking

In floor storage, the goods to be stored are placed and stored directly on the floor without the need for any auxiliary equipment. This is the simplest and oldest form of storage. Two arrangement schemes can be used for floor storage: block stacking and row stacking, as shown in Fig. 20.179. Depending on the goods to be stored and the loading equipment used, both types of storage can be used both indoors and outdoors. Both block and row stacking are used for goods with particularly high throughput. The main difference between block and row stacking is the accessibility of the stored goods. When applying block stacking, the goods or load carriers are stacked in rows so that each row contacts another. No clearance or space is left between the rows. This saves space but should only be used when storing large quantities per stock keeping unit (SKU), as SKUs are only accessible according to the last-in first-out (LIFO) principle. Row stacking on the other hand leaves space between rows of stacked goods, and each row can be accessed by the operating technology in use.

With both block and row stacking, only a limited amount of stacking is possible, dependent on the goods stored. The stacking height depends on the properties and fragility of the stored goods, such as their load

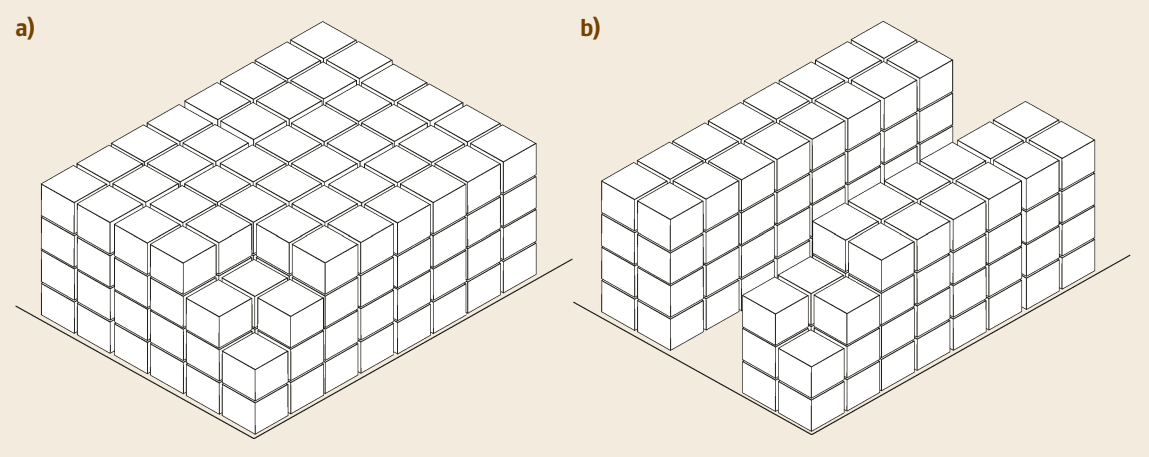

Fig. 20.179a,b Examples of block stacking **(a)** and row stacking **(b)**

strength (crushability), load weight, and load stability. Load carriers, such as carton boxes, pallets, or container, can be used as supports and thus increase the stacking height or allow stacking in the first place. The stacking height is further influenced by the operating technology used, such as cranes or forklifts, and the spatial conditions, such as floor loading restrictions, building heights, or weather (wind, rain, or humidity) [20.291].

Stacks can be arranged in two variations. By default, stacks are arranged vertically to the aisles, also known as parallel stacking. Only with narrow aisles are the individual stacks arranged at an angle (30° or 45° stacking) as shown in Fig. 20.180.

The servicing equipment most often used comprises forklifts with different and special attachments, such as roller or cardboard clamps, depending on the stored goods [20.292]. The aisle width then depends on the specifications of the servicing equipment. Also, the aisle width generally decreases with increasing angle of the stacks. This is illustrated in Fig. 20.180, where the aisle width decreases as the angle is increased from 0° (b_0) to 30° (b_{30}) to 45° (b_{45}).

In general, the block stacking scheme is a form with a very high surface area and space utilization rate, the latter of which can even be 100% when storing a single article: The smaller the assortment and the higher the stacking can be, the greater the efficiency [20.292].

Floor storage is typically used in the finished goods industry, where the goods are stored in standardized cartons on standardized pallets. This type of storage is also suitable for paper rolls, barrels, beverage pallets, material pallets, and pallet cages in mass production [20.293]. In this process, floor storage is used for a small range of goods and large product bundles with a high turnover rate, either as a stacked storage

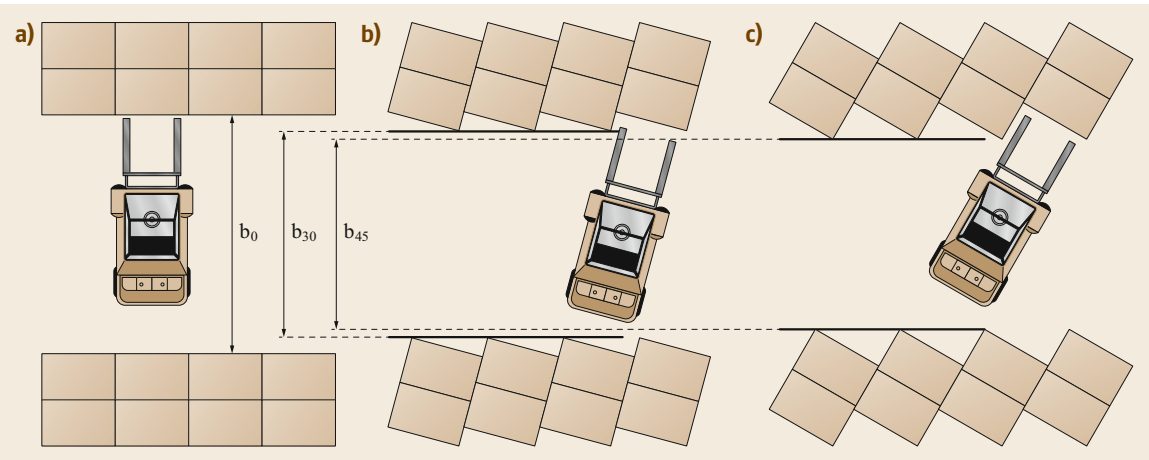

Fig. 20.180a–c Variants of stacking in floor storage: **(a)** parallel stacking, **(b)** 30° stacking, **(c)** 45° stacking [20.292]

unit or as an unstacked commissioning area/picking warehouse [20.292]. This storage type is used—among others—in:

- The beverage industry
- Paper production
- Sheet metal working and processing
- The food industry
- Construction materials trade [20.293].

Outdoors, container yards are probably the best-known block and row stacking applications. They form the interface between the quayside (water-based transport) and landside processes (hinterland transport) of larger container terminals. Standard shipping containers are temporarily stored in the yard, commonly in the form of block or row stacking. The containers have corner fittings on all eight corners. Using semiautomatic twistlocks, the containers can be secured to the deck or to each other in a stacked fashion.

The main advantage of floor storage is that no special storage equipment is required, making it the cheapest form of storage with low investment costs. Disadvantages especially relevant for block stacking are that only a limited number of stored goods are directly accessible, the poor possibility of automatization, and the so-called honeycombing phenomenon. Honeycombing refers to empty spaces, resulting from goods retrieval, which cannot directly be used for storing additional goods. Since only one SKU can effectively be stored in one row at a time, empty spaces are created during the retrieval of goods, which can only be filled with a new SKU when the entire row has been emptied. Therefore, it is advisable to withdraw goods row by row starting from the aisle and not across the front of the stacks. To achieve the highest possible storage capacity utilization, it is therefore necessary to plan the depth of the warehouse (the number of storage locations/goods in the depth starting from the aisle/access point) as carefully as possible beforehand.

20.6.5 Racking Systems

This section deals with general cargo storage with the support of auxiliary equipment. This can be differentiated into static and dynamic storage, based on how the storage locations are accessed (directly or indirectly), and into manually operated and automatically operated. Static storage is characterized by stationary stored goods, while dynamic storage is characterized by the movement of the stored goods by gravity or drive systems. Operator access to the stored goods can be differentiated into direct and indirect. Direct access storage allows the operator to access stored goods by themselves without additional support from the racking system. Manually operated racking systems include storage on all shelves or racks, where servicing must be done by staff. This also means that manually operated racking systems are operated according to the man-to-goods principle, where the operator moves to the storage location to store or retrieve the goods. Automatically operated storage systems are self-contained machines made up of various components that enable goods including their loading aids to be stored, retrieved, and made available at a picking station, thus implementing the goods-to-man principle. The goods-to-man principle reduces walking or driving distances for the operator as the goods are transported to the operator using conveying technology.

The variety of racking systems available and their variants makes it impossible to discuss all of them, thus prominent representatives are chosen and discussed. Their placement according to the three differentiation criteria is presented in Table 20.13.

To assess the performance of racking systems, to compare them based on actual performance data, and to assess their suitability for specific storage tasks, a variety of indicators have been developed. Typical key performance indicators to measure the performance and structure/capacity of racking systems are:

- Storage capacity: describes the maximum quantity of goods stored, usually as the number of storage locations or number of loading units (LU).
- Access time: describes the time needed to access specific storage locations or LUs. The access time can be given as average, minimum, or maximum values.
- inventory turnover rate (per year)
$$= \frac{\text{inventory turnover (LU per year)}}{\text{average inventory on hand (LU)}} . \quad (20.159)$$
- turnover period (days)
$$= \frac{\text{no. of days per year}}{\text{inventory turnover rate (per year)}} . \quad (20.160)$$
- average stock range (days)
$$= \frac{\text{average inventory on hand (LU)}}{\text{inventory turnover (LU per day)}} . \quad (20.161)$$
- storage utilization
$$= \frac{\text{no. of occupied storage locations}}{\text{storage capacity}} . \quad (20.162)$$

Table 20.13 Characterization of racking systems

Racking system	Criterion					
	Static storage	Dynamic storage	Direct access	Indirect access	Manually operated	Automatically operated
Shelf racking	×		×		×	
Bin shelving	×		×		×	
Pallet rack	×		×		×	
Drive-in & drive-through rack	×			×	×	
Gravity flow rack		×		×	×	
Push-back rack		×		×	×	
Mobile rack		×		×	×	
VNA storage	×		×		×	
Honeycomb rack	×		×		×	
Cantilever rack	×		×		×	
Carousels		×		×		×
Automated miniload system		×		×		×
Automated high bay warehouse		×		×		×
Automated storage and retrieval systems		×		×		×
Shuttle system		×		×		×

- floor space utilization

$$= \frac{\text{floor space used for storage}}{\text{total storage floor space}} . \qquad (20.163)$$

- space utilization

$$= \frac{\text{volume of space used for storage}}{\text{total storage volume}} . \qquad (20.164)$$

In the following paragraphs, the racking systems included in Table 20.13 are discussed in detail, beginning with the manually operated storage systems before this section ends with the automatically operated storage systems.

Manually Operated Storage Systems

Shelf Racking Systems. Shelf storage is constructed from modular parts that can be plugged or bolted together to form the system. In general, shelving consists of posts of formed or rolled sheet steel, shelf surfaces, and end bracings, back bracings, end panels, and/or base panels. For details on safety-related technical specifications for shelf racking systems and all other static steel storage systems, see DIN EN 15629:2010-09 [20.294]. Boltless (or snap-in) shelf racking systems are easy to assemble by simply putting the individual parts together and can be reconfigured without any major conversion work. Bolted shelving, on the other hand, requires that the modular individual parts be linked using bolts and nuts, leading to a higher installation effort, which increases again when the system is changed or modified. Shelf storage is particularly suitable for small to medium-sized goods with a low to medium handling frequency stored in bins, boxes, or packages, as shown in Fig. 20.181.

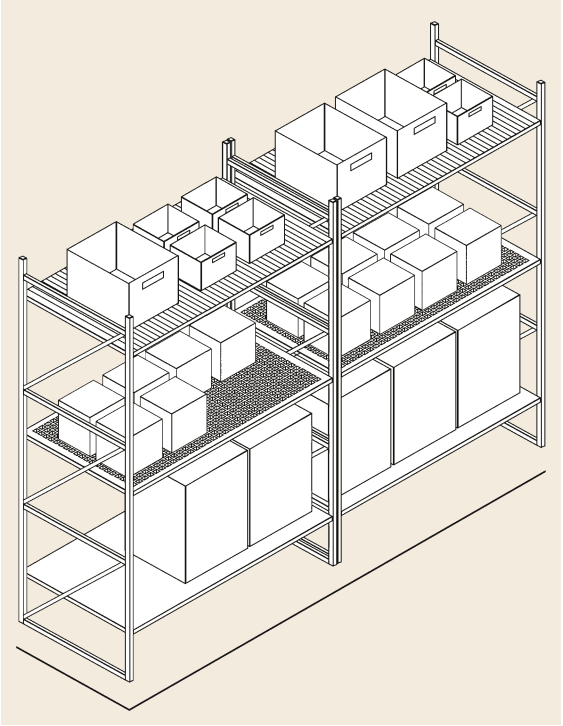

Fig. 20.181 Shelving rack

The shelves themselves (shelf surfaces) can vary in depth and load-bearing capacity and are usually made of sheet steel or wood (in some cases also grates are used) on which the goods or containers are stored. Reinforcement elements can be used to increase the load-

bearing capacity. The individual compartment heights are flexibly adjustable and can be adapted to the stored goods. The width of a compartment is usually between 800 and 1200 mm. Often, adaptable dividers are used to arrange the individual shelves. Other accessories, such as drawers, can be used to provide protection against dust, dirt, ultraviolet (UV) radiation, or theft. The height of the shelving racks is not standardized and can be chosen freely. However, the height should consider and not exceed the maximum height reachable by the operator, which is usually around 2000 mm. Higher shelving requires further servicing equipment—ladders or steps are used most often—to reach the topmost goods.

To utilize the height of and increase the storage density in the warehouse, so-called shelving catwalk mezzanines can be installed. These allow for a doubling of the shelving and the size of the floorspace by double decking the shelving, resulting in a multilevel system. In this way, the warehouse's vertical space can be used by installing catwalk aisles and employee access stairways. The distance between the mezzanine levels is generally around normal room height, between 2200 and 2600 mm, while the racks are usually used up to the gripping height of the operators.

Shelving systems are characterized by low investment costs, good space utilization, especially when mezzanine floors are used, and simple adaptation possibilities, which applies in particular to boltless shelf racking systems. Furthermore, they offer adaptable access, as the number of persons accessing the rack storage locations simultaneously within an aisle can be increased or decreased relatively easily. From an ergonomic point of view, one drawback of manually operated shelf racking is that only the middle height area of the rack is conveniently accessible for pickers. It is therefore important to ensure that articles with particularly high access frequency are stored in this area, while particularly heavy articles should not be stored on the higher shelves.

Bin Shelving. Bin shelving is primarily used for the storage of small parts and is therefore sometimes also called small parts storage. The type of loading equipment used is not limited to conventional bins, but also includes crates, cassettes, and trays. The selection of the load carrier depends on the application. The load carriers are placed single-place or multi-place in a rack. A bin shelf can include different types of load carriers, with the shelf divided into different fields, each field containing one type of load carrier.

The system can be flexibly modified, as the struts can be mounted in a grid pattern. This enables the system to be easily adjusted to changing requirements. Bin shelving has low investment costs and requires very little maintenance. This type of storage is particularly suitable for lightweight articles, so that the containers can be pulled out of the shelf, the articles removed, and the container pushed back into the shelf. This can be supported by means of a drawing technique using bars, handles, or a pincer mechanism. The comparably low space utilization is a drawback of bin shelving. Also, both picking and restocking operations access the bin shelves from the picking side, which can lead to interference. Item security problems and possible long travel distances for the pickers should also be considered when deciding on this storage system.

Pallet Rack Storage. Pallet rack storage is the most frequently used practice next to shelf storage. As with shelf storage, the pallet rack consists of modular individual parts and can therefore be adapted to the size or dimensions of the loading unit (usually a standard pallet or cage pallet). The racking system is offered in one- to three-spot versions and in four- to five-spot versions for very lightweight pallets. The pallet rack is a simple construction of metal uprights and cross-members providing direct access to each storage location. The principles for the structural design of adjustable pallet racking are defined in DIN EN 15512:2010-09 [20.295], while details on tolerances, deformations, and clearances can be found in DIN EN 15620:2010-05 [20.296]. In the pallet rack, the pallet is borne by shelf traverses or angle profiles and is only supported at the end faces. The pallet can be stored with both the longer edge—lengthwise—or the shorter edge—crosswise—facing the aisle. For lengthwise storage, the traverses are mounted between the front and back vertical uprights which form the shelving. The loading units are stored beside each other on these traverses. Lengthwise storage is generally used for standard pallets. Several loading units may be stored directly adjacent to each other (multi-spot storage), Fig. 20.182.

For crosswise storage, an angular support is attached between a front and back upright, and the storage unit is put into the storage spot laterally relative to the support. In this case there is usually only one storage unit between the uprights (one-spot storage). Lengthwise storage usually results in more effective space utilization. When operating equipment such as counterbalanced trucks is used, lengthwise storage is usually practiced. For manual picking, crosswise storage is recommended to limit the access depth and increase the accessibility of the goods. Table 20.14 presents the advantages and disadvantages of both storage versions.

Besides the described possibilities of storing lengthwise or crosswise in the pallet rack, there is also the possibility of using double-deep pallet racks. Double-deep pallet racks are simply two pallet positions deep, which allows for higher floor space utilization as fewer

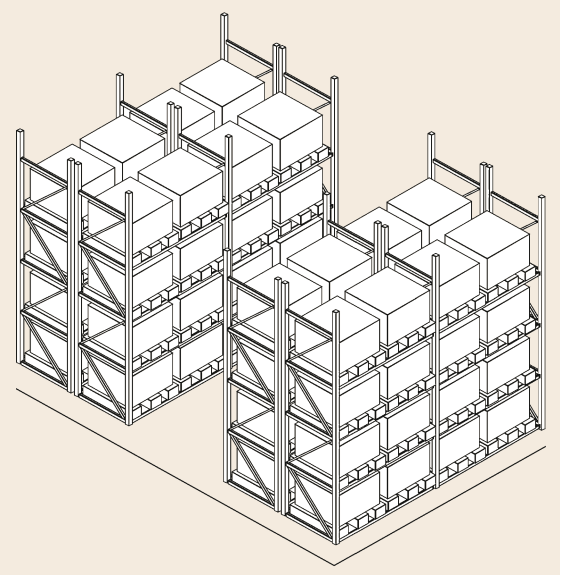

Fig. 20.182 Pallet rack storage in a two-spot version

Table 20.14 Advantages and disadvantages of lengthwise and crosswise storage [20.293]

	Lengthwise storage	Crosswise storage
Advantages	More pallets per rack Pallets can be picked up by forklifts easily	Only small aisles necessary
Disadvantages	Wider aisles necessary for front-loading forklifts	If forklifts are used, the fork may be longer than the pallet, causing damage Fewer pallets per rack

aisles are needed. However, in double-deep racks, either only the front pallet can be accessed directly or both pallets must be retrieved at once, requiring a double-reach forklift. The type of pallet rack storage chosen depends on the individual case. Depending on the dimensions of the storage area and the possible use of operating technology (such as counterbalance trucks), one or the other type of storage is more suitable.

Drive-In and Drive-Thru Racks. Drive-in racks and drive-thru racks are a combination of pallet racks and block storage and are suitable for palletized goods and stable uniform loading equipment such as crates or cage pallets. The goods are stored as in pallet racking, usually two to five pallets high with four to ten pallets being placed one after the other in the depth of one storage lane. Within the aisles, floor rails are used to guide the lifting truck and protect the shelves from damage. This type of shelf can only be serviced from the end faces, as shown in Fig. 20.183. With a drive-in rack, the shelf can only be serviced from one of the front sides; with a drive-thru rack, both end sides can be serviced.

This type of storage requires a stack to be completed before a new one can be started. Otherwise loading units are placed in front of empty storage locations, leading to honeycombing losses. It is recommended to store only one SKU per lane. In the case of a drive-in rack, storage and retrieval are carried out on the same end face, leading to the LIFO principle being applied, whereas in the case of a drive-thru rack, storage is carried out on one end face and retrieval on the other end face, ensuring the first-in first-out (FIFO) principle. This type of storage system is particularly suitable for large quantities of goods with a small variety of articles and a low turnover rate.

Both drive-in and drive-thru storage have similarities to block stacking, but differ in that they also allow for the storage of goods that are difficult to stack or cannot be stacked. Similar to block stacking are the low investment costs for the storage equipment and the high theoretically achievable utilization of space. In practice, however, the lanes can only be used for one SKU each and are rarely filled completely, so this theoretically high utilization of space is rarely achieved. In addition, only the front- and/or rearmost pallet is accessible with this type of storage, which only allows limited access. Although guide rails are used, the operating equipment used must thread precisely into the entry channels in order to store or remove the goods—a complicated and time-consuming process [20.293].

Gravity Flow Racks/Pallet Flow Racks. Gravity flow racks operate by gravity and are suitable for goods in crates or cartons, on pallets, and on/in other roller-suitable loading aids. The racks are built with a higher and a lower side, resulting in a slanted storage area. Goods are stored on the higher side and retrieved from the lower side, ensuring the FIFO principle. Also in this way stocking of the rack does not hinder retrieval. The shelving system consists of shelving supports between which roller conveyors, skate wheel conveyor, or rails are mounted. These are mounted from one end of each rack lane to the other at a slight inclination of usually up to 5°. Goods pushed in on the higher side slide until meeting other goods or until reaching the end of the lane (Fig. 20.184). If goods are retrieved, those next in line slide down consequently. To avoid damage to the goods, roller conveyors or rails are equipped with braking rollers to limit load speeds. Often, centrifugal-type brakes are used for this purpose. Alternatively, brake rollers can also control the speed along the entire gravity roller conveyor by keeping the conveyed goods at a constant speed. The braking effect can be generated by eddy current, hydraulics, or centrifugal force. In ad-

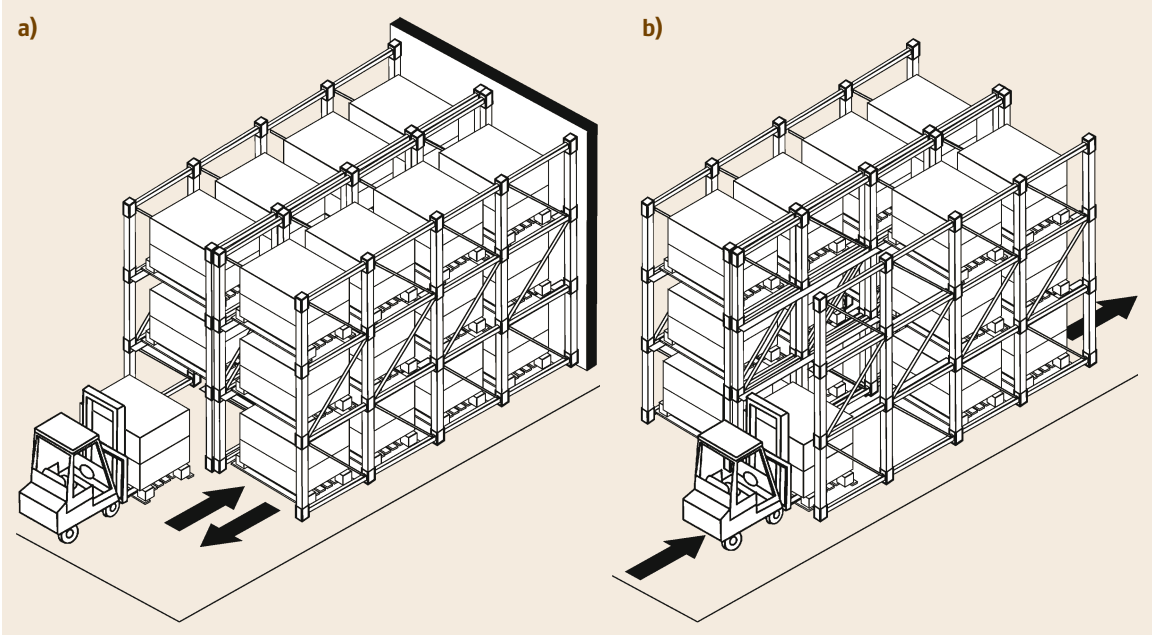

Fig. 20.183 (a) Drive-in and (b) drive-thru rack

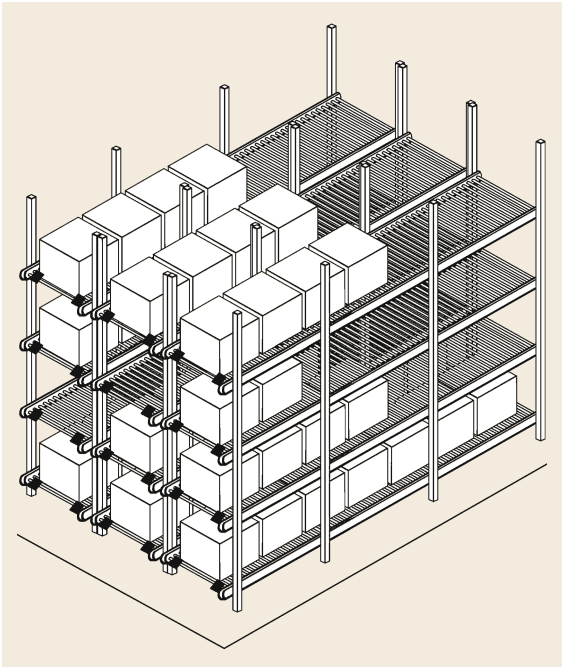

Fig. 20.184 Gravity flow rack

dition, to allow for easy access and retrieval of the goods without the gravitational pressure of other goods, separation devices are placed at the end of each lane to separate the front-most pallet from the rest of the pallets in the lane.

All individual goods in a lane should have equal weight. As goods are automatically moved forward by gravity, major differences in the weight of the goods can lead to goods damaging each other during transit and impact. For loosely stacked goods on pallets, it is also necessary to attach them to the pallet, for example by applying shrink or cling wrapping.

Gravity flow racks provide good floor space utilization. With storage and retrieval operations conducted on opposing sides, gravity flow racks enable high access and retrieval performance. Therefore, gravity flow racks are suitable for a high throughput of goods and hence for goods with high inventory turnover. The main disadvantage of gravity flow racks are their comparably high investment costs per storage position.

Push-Back Racks. Storage in a push-back rack adheres to the LIFO principle. The push-back rack is similar in its construction to the gravity flow rack, but it is only serviced from one side. Pallets are pushed from the low side into the storage lanes, and pallets already stored in the lanes are pushed back further. When one pallet is retrieved from the front of the storage lane, the remaining pallets automatically move due to their weight and the angle of the lane (usually up to 5°) to the rack face. Push-back rack storage lanes are usually two to five pallets deep.

In most cases, counterbalanced lift trucks are used as operating equipment for push-back racks. No special truck attachments are required, as storage and retrieval

take place at the rack face and only one pallet is stored or retrieved at a time. Also, usually only two end stops are required as safety elements.

This type of storage is only suitable for homogeneous and sometimes even batchwise storage of goods. Usually, palleted and less shock-sensitive goods are stored and, owing to the LIFO principle, mostly goods without a shelf life limit. As with gravity flow racks, compact storage and good floor space utilization can be achieved. It needs to be considered that the goods and/or load carrier can rub against each other during storage and retrieval, which can lead to damage to the goods or load carriers or even to the interlocking of load carriers. Therefore, only smooth-walled and robust load carriers are suitable for this type of rack [20.293].

Mobile (Pallet) Racks. The concept of mobile (pallet) racks allows for the maximum space utilization, while each individual stored good can still be accessed. Mobile racks consist of the racks, trolleys, runners and guide rails, and control and safety devices (e.g., for operator security, safety barriers are usually installed). Each rack can be moved either manually or mechanically to allow access to the storage locations. By moving the racks, generally only one aisle is opened, resulting in only the space for one aisle for storage and retrieval of goods being required, while the remaining space within the storage area is utilized with actual storage. Generally mobile racks are either shelving, pallet, or cantilever racks. Another frequent field of application is document archives.

The main advantage of mobile racks is their very high storage density and excellent space utilization, as only a very limited amount of floorspace is devoted to aisles. A comparably low storage and retrieval productivity, resulting from the often-required movement of the racks to generate the access aisle, is the main drawback. Mobile racks should be considered for slow-moving goods and when warehouse space is scarce.

Very Narrow Aisle (VNA) Storage. The (very) narrow aisle warehouse is characterized by its narrow aisle width of typically 1.4–1.8 m and can have shelf heights of up to 15 m. It is typically used to store standard pallets and pallet cages and, depending on the weight of the goods, it is designed with single or multiple deep storage places. Automation of the VNA warehouse is possible, but in practice very seldom applied. Picking, storage, and retrieval are usually carried out by suitable narrow aisle lifting trucks, also referred to as turret trucks, with swiveling forks. During operation in the aisle, the trucks' axis runs parallel to the shelving. Due to the very close distance of the driveway to the racks, inductive or mechanical guides are used. The guidance of the trucks ensures high driving and lifting speeds and as safe as possible operation of the VNA storage. Using inductive guidance, the lifting truck is guided by a wire laid in the ground. That wire is fed by a frequency generator with a high-frequency alternating current that generates a concentric electromagnetic alternating field. Sensors on the lifting truck detect this alternating field, and can so register any change in position of the lifting truck. An automatic compensation steering system is used. The lifting truck is thus safely guided in the aisle. The mechanical guidance is realized by means of two steel profiles bolted to the floor. On the lifting truck chassis, two rollers are attached to each side of the lifting truck, which hold the lifting truck between the steel profiles in the middle of the aisle.

The advantages are the very low space requirement and the medium to high degree of space utilization. In addition, a medium to high throughput rate can be achieved. Individual access is possible at any time to any pallet location. The disadvantage lies in the average investment costs that arise. In addition, floors with an utmost degree of planarity are necessary.

Honeycomb Racks. The honeycomb rack, also known as bar storage rack, consists of shelf levels with low individual heights arranged on top of each other. The arrangement of the shelf levels resembles a honeycomb on the front side, hence the shelf name. This type of racking is preferably used for lengthy goods such as profiles, iron bars etc., usually with a length of 3–8 m.

Long goods are stored in the honeycomb rack in a clear and space-saving way. The use of dividers also allows for the clearly arranged storage of different materials, while the open rack face enables a good overview of the current stock level. If long good cassettes (extractable cassettes) are used, the long goods can be retrieved and stored again quickly and conveniently by hand (removal of individual bars, profiles, etc.) or with a lifting truck or crane (removal of heavy long goods or bundles) after the cassette has been extended with a roller block or rack serve carrier attached to the honeycomb store.

This type of storage makes it possible to store different long goods in a particularly compact manner. Even for smaller warehouses or storage areas, a honeycomb rack offers optimal use of space especially for storing long goods with smaller diameters. The advantages of the honeycomb racking lie in the possibility of compact storage of long goods and the high utilization of spatial volume. Likewise, every article can be accessed at any time and high access performance is possible. Modularly constructed honeycomb racks can easily be expanded or adapted to changing storage volumes and location requirements.

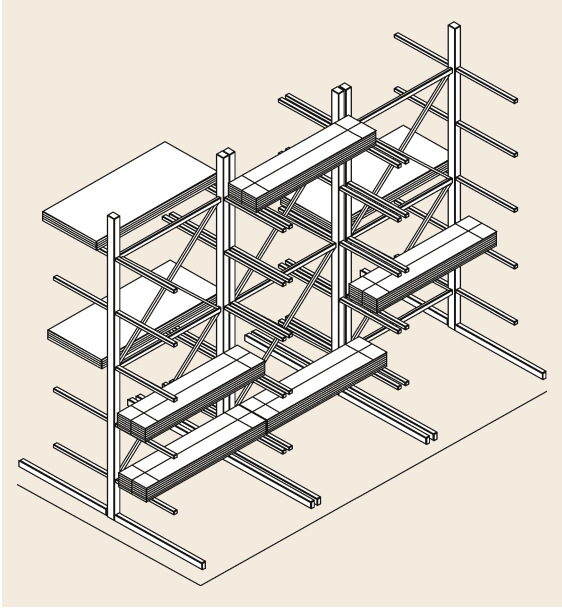

Fig. 20.185 Cantilever rack

Cantilever Racks. Cantilever shelving units are T-shaped rack stands, consisting of the rack stand, the stand feet, straight connectors, and crossing struts, which are equipped with cantilever arms (Fig. 20.185). The rack stand can be one- or two-sided, and its feet are mounted to the floor. The cantilever arms are bolted to the rack stand and are used for storing long or bulky goods. Depending on the weight of the goods, the cantilever arms can be single or double deep. Towards the top of the rack, the arms often become shorter to improve access.

Storage and retrieval are carried out at right angles to the cantilever rack and usually by sideloader trucks, cranes, or permanently installed storage and retrieval systems. In practice, this type of shelving is often used for the storage of boards, beams, tubes, and profiles. Advantages of cantilever racks are comparatively low investment costs, and the possibility of storing long or bulky goods with individual access to each item at any time. The biggest disadvantages are the space required for the operating aisles and the protrusion of the cantilever arms into the storage space, both resulting in a loss of spatial volume utilization.

Automatically Operated Storage Systems

Carousels. Carousels rotate in a circular pattern and can roughly be distinguished into horizontal and vertical carousels. While horizontal carousels rotate around an axis perpendicular to the floor, vertical carousels rotate around an axis parallel to the floor. Both are motorized, often computer controlled, independently rotating aisles of shelving.

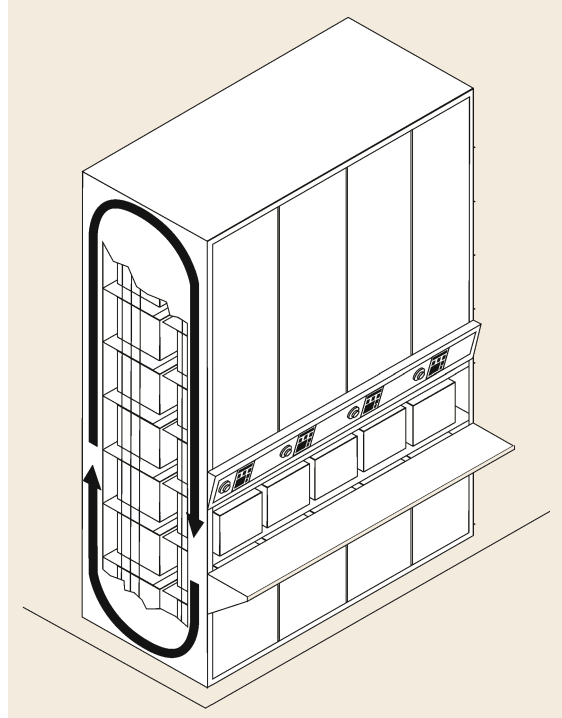

Fig. 20.186 Vertical carousel/paternoster rack

Vertical carousels, also known as paternoster racks, consist of two endless chains, running in parallel and connected by rods, on which the load handling devices are located. These vary according to the type of goods and may be shelves, cassettes, or drawers. Paternoster racks are reversible, which allows for particularly fast access. To prevent one-sided overloading of the shelving, overload protection is absolutely necessary [20.292].

Servicing can be done manually or fully automatized by information technology (IT)-supported systems such as warehouse management software or enterprise resource planning (ERP) systems. In practice, these types of shelving are often used for goods with medium to slow turnover and as order picking storage for small parts and micromaterial. Due to the construction of the paternoster rack, it forms a self-contained unit, limiting access to authorized personnel and thus reducing the risk of theft. In addition, goods are protected from dust and other dirt particles (Fig. 20.186).

Carousels carry the goods to the picker, following the goods-to-man principle, so there is no need for the operator to walk to the goods. They offer good space utilization and also take ergonomic working heights into account. Disadvantages of carousels are the comparably high investment costs, especially for the fully automatic variant of the paternoster rack. Due to the

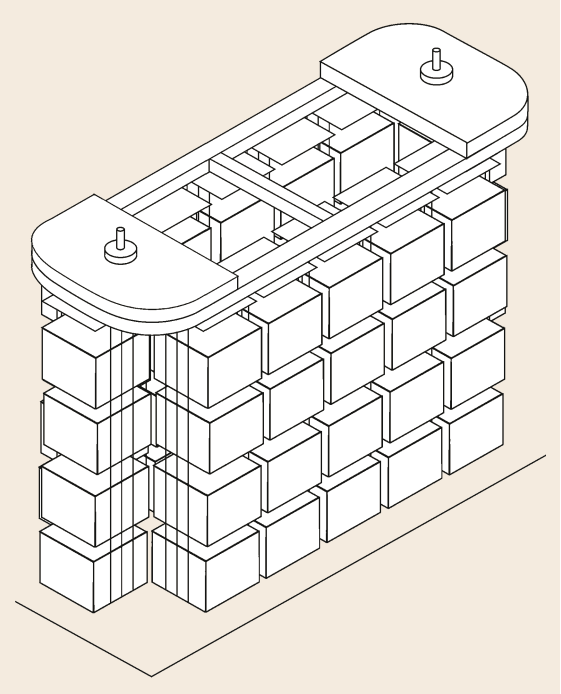

Fig. 20.187 Horizontal carousel

construction of the rack, direct access to all articles at the same time is not possible and restocking interleaves with picking operations. Also, in the event of a system malfunction, goods can no longer be withdrawn. Another drawback is that the pick rate cannot be significantly increased by adding operators, because carousels are generally designed to be operated by a single person. This makes it difficult to respond to increases in picking volume.

Horizontal carousels or carousel racks are horizontal circular conveyors (Fig. 20.187). As hangers they have shelving racks, which can be guided by a floor rail for stability. The carousel racks are only serviced from a defined location, again following the goods-to-man principle. The combination of several shelves potentially reduces the waiting time of the operator [20.292].

Carousel racks can be controlled manually, semiautomatically, or fully automatically. The rack is operated manually with buttons for start and stop. Semiautomatic operation to increase handling performance can be realized by means of an operating panel and a partially supported IT control. Fully automated carousel racks offer the highest handling performance and are completely computer controlled [20.292]. In the standard setup, horizontal carousels do not protect the goods from dust and dirt. However, such protection can be realized by introducing supplemental walls and window elements. Carousel racking for goods with slow to medium turnover is used in order picking warehouses with high turnover and in low-ceilinged rooms. The advantages and disadvantages of horizontal carousels resemble those of vertical carousels.

Automated Miniload System (AMS)/Automated Small Parts Warehouse. Automated miniload systems (AMS) or automated small parts warehouses are self-contained automated systems specially designed for storing small-volume goods of low to medium weight. The goods are usually stored in small parts containers, cartons, cassettes, or trays. AMS are often operated via IT terminals, which are directly linked to the company's ERP system. Storage and retrieval are carried out under IT control. When a retrieval order is processed by the IT system, the load carriers of the required small parts are automatically retrieved by the control software of the warehouse management system and are transferred directly to the operator according to the goods-to-man principle. The operator picks the required amount,s and the load carriers are then returned into the AMS.

AMS can be operated either by rail-mounted automated storage and retrieval systems (AS/RS) or by shuttles. They are realized as single- and multistation systems with storage depths ranging from single to multiple locations deep. They allow very good space utilization, as they can optimally use the available warehouse height. Further advantages of AMS are short access and delivery times, as well as high turnover performance. Drawbacks of AMS are the comparably high investment costs and dependence on IT control and permanent electric supply.

Automated High Bay Warehouses/High-Level Pallet Racking. High bay warehouses or high-level pallet racks are widely employed logistics systems. They are often used in buildings with high ceiling heights. A high bay warehouse may be as tall as 50 m and can contain several hundreds to thousands of pallet storage spots. A wide variety of configurations of automated high bay warehouses, ranging from single-deep and multi-deep storage locations to specifically configured compartment widths, exists. First and foremost, automated high bay warehouses can be differentiated based on their construction, as they can be installed in an (existing) building or as a silo system. With silo systems, the rack itself serves as the supporting structure for the building (walls and roof), and no separate building needs to be constructed. Starting from a height of ≈ 20 m, a silo design should be considered as an alternative to the classical warehouse design. High bay warehouses constructed in the silo design often exceed heights of 40 m. For the operation of these installations, it is indis-

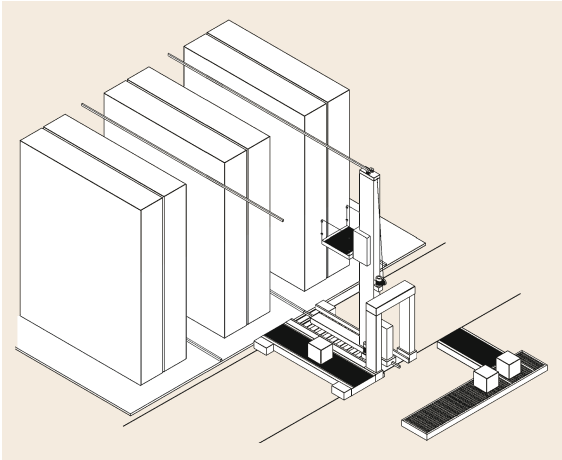

Fig. 20.188 AS/RS

pensable to incorporate specific protection against fire, such as smoke detectors and sprinkler units.

The aisles between the shelves give automated storage and retrieval systems (AS/RS) or shuttles access to the storage locations. Storage and retrieval of goods is fully automated. IT control decides which goods are to be stored in which positions and in which sequence they are to be retrieved. In most cases, each aisle possesses an input/output (I/O) point. This input/output point connects the high bay warehouse with the storage prezone, mostly realized by conveyor technology. Like AMS, the high bay warehouse operates according to the goods-to-man principle. The benefits are high storage density and high storage utilization, as well as high process speeds, short access and retrieval times, and direct access to every storage location. The drawbacks, also similar to the AMS, are high investment costs and dependence on IT control.

Automated Storage and Retrieval Systems (AS/RS). Automated storage and retrieval systems (AS/RS) ensure the automatic storage and retrieval of goods from high bay warehouses or AMS. The storage and retrieval machines can be equipped with various load lifting equipment, always depending on the specific task at hand. They are applied for all kinds of goods independent of their processing status: for raw materials, for work-in-process, as well as for finished goods. Storage and retrieval in the aisles can be realized in different ways. Most commonly this is done by a machine consisting of a floor-running traveling frame or a vertical mast with the specific loading equipment attached to it. Automated storage and retrieval machines run on fixed paths on rails in the aisles between the storage racks (Fig. 20.188).

They can travel three to six times faster longitudinally than they can lift with load. However, they are

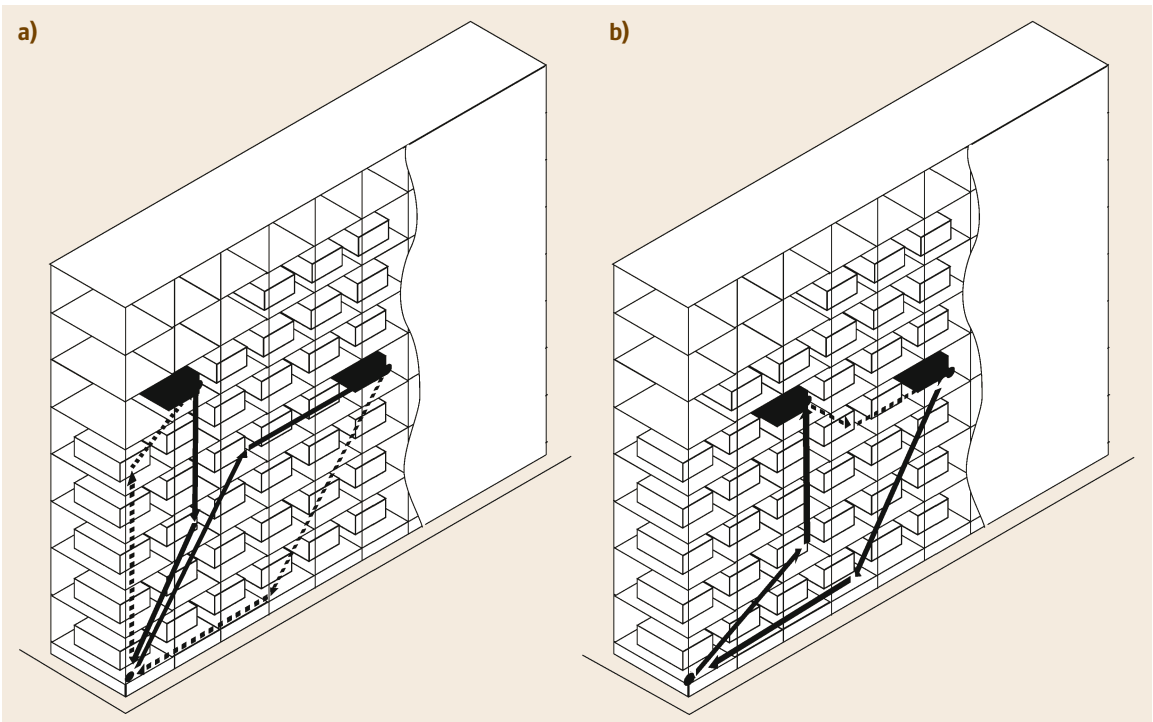

Fig. 20.189 (**a**) Single versus (**b**) dual command operation

typically able to travel simultaneously in vertical and horizontal directions. In addition, they can compute dual command operations (dual cycles). This means the AS/RS machine picks up a load at the input/output (I/O) point, transports it to and deposits it at its desired storage location, and before returning to the I/O point, travels empty to the location of the desired retrieval, retrieves the load out of the rack and brings it to the I/O point (Fig. 20.189). This combination of storage and retrieval operations, called dual command or dual cycle, is used to avoid unproductive travel wherever possible. For details concerning the calculation of the operating cycles of AS/RS, see VDI 3561 [20.297].

The operations of automated storage and retrieval systems are fully computer controlled. They automatically store and retrieve goods from defined storage locations. In practice, one AS/RS unit is often used per aisle. If fewer AS/RS units are used than there are aisles in the storage area, the units are usually moved between the individual rack aisles by means of transfer trolleys. An alternative to the application of transfer trolleys is curve-going AS/RS units, which are able to service several aisles autonomously. Additional information on the operation of several aisles in a high bay warehouse by using curve-going AS/RS units or by transfer trolleys can be found in VDI 3658 [20.298].

Shuttle Systems. The special characteristic of the shuttle system is the operation of individual storage levels by autonomous vehicles (shuttles) within a static linear rack warehouse. The transports between the individual storage levels and to the storage prezone are carried out by vertical conveyors. The shuttle vehicles travel on rails, but independent of the rack structure on storage levels. The rails not only guide the shuttle but simultaneously supply their electric motors with the required energy and also perform the tasks of position detection and fine positioning [20.299]. They also provide additional protection for the rail ends. These types of rails are also called multifunctional rails. Like AS/RS machines, the shuttle vehicles move within shelf aisles, but on various levels.

This complex system is fully IT controlled, and the shuttles are controlled via radio or a wireless local area network. The shuttle can be used to load or unload goods by means of various load handling devices, such as belt conveyors or diverse pulling mechanisms. The shuttles may be moved to other storage levels or even into other aisles by lifting or positioning devices. Several shuttles may be operated in one aisle. This allows for the adaptation of the system's performance to current requirements by simply adding or removing individual shuttles.

The greatest advantage of shuttle systems is their flexibility and scalability, as they can be adapted to changing requirements. In case of peak demand, additional shuttles can be deployed. Thanks to these advantages, shuttle systems are an alternative to AS/RS systems.

References

20.1 W.A. Günthner, K. Heptner: *Technische Innovationen für die Logistik* (Huss, München 2007)

20.2 ISO 6780: Flat pallets for intercontinental materials handling–Principal dimensions and tolerances (2003)

20.3 ISO 668: Series 1 freight containers–Classification, dimensions and ratings (2013)

20.4 Port of Rotterdam: Homepage, http://www.portofrotterdam.com (2016)

20.5 K.-H. Grote, J. Feldhusen (Eds.): *Dubbel – Taschenbuch für den Maschinenbau*, 24th edn. (Springer, Berlin, Heidelberg 2014)

20.6 A. Katterfeld, K. Williams: Functional analysis of tube chain conveyors part 1: General design and calculation principles, Bulk Solids Powder Sci. Technol. **2**(3), 23–32 (2008)

20.7 A.W. Jenike: *Gravity Flow of Bulk Solids*. Bulletin of the Utah Engineering Experiment Station, vol. 108 (Univ. Utah, 1961)

20.8 A.W. Jenike: *Storage and Flow of Solids*. Bulletin of the Utah Engineering Experiment Station, vol. 123 (Univ. Utah, 1964)

20.9 A.W. Roberts, O.J. Scott, W. Tiedemann: Bulk handling of ammonium nitrate: Flow properties and storage bin design criteria. In: *Int. Powder Bulk Solids Conf., Philadelphia, USA, May 1979* (1979)

20.10 D. Schulze: *Flow properties of powders and bulk solids* (Univ. Applied Sciences, Braunschweig, Wolfenbüttel 2006)

20.11 W. Chen, J. Miller, K. Williams, A. Roberts: Rapid and reliable flow property testing – A modified uniaxial approach. In: *Proceedings of Iron Ore* (2017)

20.12 K.Y. Chung, G.J. Burdett: Dustiness testing and moving towards a biologically relevant dustiness index, Ann. Occup. Hyg. **38**(6), 945–949 (1994)

20.13 C.P. Lyons, D. Mark, K.Y.K. Chung, G. Burdett: The application of health-related size fractions to dustiness measurement, J. Aerosol Sci. **23**(1), S607–S610 (1992)

20.14 M.A.E. Plinke, D. Leith, D.B. Holstein, M.G. Boundy: Experimental examination of factors that affect dust generation, Am. Ind. Hyg. Assoc. J. **52**(12), 521–528 (1991)

20.15 I.S. EN 15051: Workplace exposure – measurement of the dustiness of bulk materials (Parts 1 to 3) (The National Standards Authority of Ireland, Dublin 2013)

20.16 I. Pensis, J. Mareels, D. Dahmann, D. Mark: Comparative evaluation of the dustiness of industrial minerals according to European Standard EN 15051, 2006, Ann. Occup. Hyg. **54**(2), 204–216 (2010)

20.17 W.A. Heitbrink, W.F. Todd, T.C. Cooper, D.M. O'Brien: The application of dustiness tests to the prediction of worker dust exposure, Am. Ind. Hyg. Assoc. J. **51**(4), 217–223 (1990)

20.18 AS 4156.6: Coal Preparation – Part 6: Determination of dust/moisture relationship for coal, Standards Australia (2013)

20.19 T.R. Farrugia, N. Ahmed, G.J. Jameson: A new technique for measuring dustiness of coal, J. Coal Qual. **8**(2), 51–55 (1989)

20.20 M. Djukic, J.H. Planner: Evaluation of dust emission from coal wagons. In: *3rd Int. Conf. Storing Handl. Transp. Bulk, BulkSolids Europe 2010, 9–10 September 2010, Glasgow* (2010)

20.21 J.H. Planner: A sustainable approach to manage dust emission during handling and transport of coal and iron ore. In: *20th Int. Clean Air Environ. Conf., Clean Air Society of Australia and New Zealand (CASANZ), 31 July–2 August 2011, Auckland, New Zealand* (2011)

20.22 J.H. Planner: Improving air quality for communities adjacent to coal terminals in Hay Point Queensland. In: *11th Int. Congr. Bulk Mater. Storage Handl. Transp. (ICBMH), 2–4 July 2013, Univ. Newcastle, Australia* (2013)

20.23 D. Ilic, J. Planner, A. Roberts: Revision of AS 4156.6 dustiness test – final report, ACARP Project C23054, Univ. Newcastle, Australia (2015)

20.24 D. Ilic, J. Planner, S. Biswas, S. Reid: Revision of AS 4156.6 Coal preparation – Part 6: Determination of dust/moisture relationship for coal. In: *Proc. 12th ICBMH, ACT, Barton* (2016)

20.25 AS 3880-1991: Bin flow properties of coal (1991)

20.26 Institution of Chemical Engineers: *Standard Shear Testing Procedure for Particulate Solids Using the Jenike Shear Cell* (Institution of Chemical Engineers, Rugby 1989)

20.27 D6128-00: Standard Method for Shear Testing Using the Jenike Shear Cell, ASTM International, USA (2003)

20.28 ASTM G162-99: Standard practice for conducting and evaluating laboratory corrosion tests in soils (2010)

20.29 DIN 50929-3: Corrosion of metals–Probability of corrosion of metallic materials when subject to corrosion from the outside–Buried and underwater pipelines and structural components (1985)

20.30 EN 12501: Protection of metallic materials against corrosion–Corrosion likelihood in soil (2003)

20.31 United Nations: United Nations Manual of Tests and Criteria (2009) pp 364–365

20.32 G.P. Tilly: Erosion caused by impact of solid particles. In: *Treatise on Materials Science and Technology*, Vol. 13 (Academic Press, London 1979) pp. 287–319

20.33 G.P. Tilly, W. Sage: The interaction of particle and material behaviour in erosion process, Wear **16**, 447–465 (1970)

20.34 I.M. Hutchings: Wear by particulates, Chem. Eng. Sci. **42**(4), 859–878 (1987)

20.35 J.G.A. Bitter: A study of erosion phenomena part I, Wear **6**, 5–21 (1963)

20.36 R. Glardon, I. Finnie: A review of the recent literature on the lubricated sliding wear of dissimilar metals, ASME J. Eng. Mater. Technol. **103**(4), 333–340 (1981)

20.37 A. Finckh-Jung, G. Novak, S. Winter: Research results for the application of high tensile tension members and running fibre ropes. In: *Proceedings: IFAC (Int. Fibre Appl. Conf. 5th Ed., Antwerp, Belgium)* (2015)

20.38 G. Novak: Use of high-modulus fibre ropes in rope drives using the example of S/R-machines, Logist. J. (2016), https://doi.org/10.2195/lj_Proc_novak_de_201605_01

20.39 M. Wehr: Synthetische Faserseile unter hochdynamischer Beanspruchung, Logist. J. (2017), https://doi.org/10.2195/lj_Proc_wehr_de_201710_01

20.40 J.C. Weis, B. Ernst, K.H. Wehking: Use of high strength fibre ropes in multi-rope kinematic robot systems. In: *Cable-Driven Parallel Robots. Mechanisms and Machine Science*, Vol. 12, ed. by T. Bruckmann, A. Pott (Springer, Berlin, Heidelberg 2013)

20.41 A. Kretschmer: Einflussfaktoren auf die Lebensdauer laufender Faserseile, PhD thesis (TU Chemnitz, 2016)

20.42 ISO 2408: Steel wire ropes–Requirements (2017)

20.43 DIN EN ISO ISO 16120-1: Non-alloy steel wire rod for conversion to wire–Part 1: General requirements (2011)

20.44 K. Feyrer: *Wire Ropes: Tension, Endurance, Reliability* (Springer, Berlin, Heidelberg 2015)

20.45 DIN EN 12385-2: Steel wire ropes–Safety–Part 2: Definitions, designation and classification (2008)

20.46 VDI 2358: Wire ropes for materials-handling equipment (2012)

20.47 ISO 4309: Cranes–Wire ropes–Care and maintenance, inspection and discard (2017)

20.48 ISO 16625: Cranes and hoists – Selection of wire ropes, drums and sheaves (2013)

20.49 DIN EN 12385-4: Steel wire ropes–Safety–Part 4: Stranded ropes for general lifting applications (2008)

20.50 ISO 4301-1: Cranes Classification Part 1: General (2016)

20.51 DIN 15020: Hebezeuge; Grundsätze für Seiltriebe, Berechnung und Ausführung (1974)

20.52 M. Scheffler: *Grundlagen der Fördertechnik – Elemente und Triebwerke* (Wiesbaden, Vieweg 1994)

20.53 American Chain Association: *Standard Handbook of Chains: Chains for Power Transmission and Material Handling*, 2nd edn. (CRC Press, Boca Raton 2005)

20.54 DIN 764-1: Round steel link chains–Round steel link chains for chain conveyors–Part 1: Grade 3 (2010)

20.55 ISO 610: Hochfeste Rundstahlketten für Kettenförderer und Kohlenhobel (1990)

20.56 DIN 17115: Steels for welded round link chains and chain components – Technical delivery conditions (2012)

20.57 DIN 22252: Round steel link chains for use in continuous conveyors and winning equipment in mining (2012)

20.58 DIN 685-1: Geprüfte Rundstahlketten; Begriffe (1981)

20.59 DIN 685-2: Geprüfte Rundstahlketten – Teil 2: Sicherheitstechnische Anforderungen (2001)

20.60 DIN 685-3: Geprüfte Rundstahlketten – Teil 3: Prüfung (2001)

20.61 DIN 685-4: Geprüfte Rundstahlketten – Teil 4: Kennzeichnung, Prüfzeugnis (2001)

20.62 DIN 685-5: Geprüfte Rundstahlketten; Benutzung (1981)

20.63 DIN 685-100: Geprüfte Rundstahlketten – Teil 100: Zusätzliche Begriffe (2011)

20.64 DIN 762-1: Round steel link chains–Round steel link chains, pitch 5d, for chain conveyors –Part 1: Grade 3, quenched and tempered (2015)

20.65 DIN 762-2: Round steel link chains–Round steel link chains, pitch 5d, for chain conveyors–Part 2: Grade 5, quenched and tempered (2015)

20.66 DIN 766: Round steel link chains–Round steel link chains, pitch 2,8d, for chain conveyors, grade 3, quenched and tempered (2015)

20.67 DIN 5684-1: Rundstahlketten für Hebezeuge; Güteklasse 5, lehrenhaltig, geprüft (1984)

20.68 DIN 5684-2: Rundstahlketten für Hebezeuge; Güteklasse 6, lehrenhaltig, geprüft (1984)

20.69 DIN 5684-3: Round steel link chains–Fine tolerance hoistchains–Part 3: Grade T (Types T, DAT and DT) (2013)

20.70 DIN 5687-1: Rundstahlketten – Teil 1: Güteklasse 5, mittel toleriert, geprüft (1996)

20.71 ISO 4347: Leaf chaines, clevises and sheaves–Dimensions, measuring forces, tensile strengths and dynamic strengths (2015)

20.72 ISO 1977: Conveyor chains, attachments and sprockets (2006)

20.73 S. Shimura: *The Complete Guide to Chain* (U.S. Tsubaki, Wheeling 1997)

20.74 C. Rohne, M. Schreiter, J. Sumpf, K. Nendel, L. Kroll: Hybrid conveyor chains – Calculation, design and manufacturing. In: *Conf. Proc. 3. Int. Symp. Plastic-Slide-Chains Tribol. Conveyor Syst., Chemnitz, 11./22. April* (2017) pp. 65–77

20.75 J. Strobel, J. Sumpf: Dynamic studies on a slide chain conveyor system. In: *Conf. Proc. 3. Int. Symp. Plastic-Slide-Chains Tribol. Conveyor Syst., Chemnitz, 11./22. April 2017* (2017) pp. 180–186

20.76 R. Lewis, U. Olofsson: *Wheel-Rail Interface Handbook* (Woodhead, Sawston 2009)

20.77 ISO 16881: Cranes–Design calculation for rail wheels and associated trolley track supporting structure–Part 1: General (2005)

20.78 W. Hay: *Railroad Engineering* (Wiley, New York 1953)

20.79 Астахов П.Н.: Сопротивление движению железнодорожного подвижного состава (Resistance to motion of railway rolling stock) Труды ЦНИИ МПС (ISSN 0372-3305). Выпуск 311 (Vol. 311) (Транспорт, Москва, 1966). In Russian

20.80 M.D. Hersey: Rolling friction. In: *Transactions of the ASME* (1969) pp. 260–275

20.81 T.D. Gillespie: *Fundamentals of Vehicle Dynamics* (Society of Automotive Engineers, Warrendale 1992)

20.82 J. Pajer, H. Kuhn, F. Kurth: *Stetigförderer*, Vol. 5 (Verlag Technik, Berlin 1988)

20.83 CEMA: *Belt Conveyors for Bulk Materials*, 7th edn. (Conveyor Equipment Manufacturers Association, Naples 2014)

20.84 I.M. Thomson: Development of the cable belt conveyor. In: *Proc. BeltCon1, South Africa* (1981)

20.85 C.A. Wheeler: Development of the rail conveyor technology, Int. J. Min. Reclam. Env. **2017**, 1–15 (2017)

20.86 ISO 5048: Continuous mechanical handling equipment–Belt conveyors with carry idlers–Calculation of operating power and tensile forces, International Standard, Switzerland (1989)

20.87 DIN 22101: Continuous conveyors – Belt conveyors for loose bulk materials – Basis for calculation and dimensioning (2011)

20.88 H. Colijn: *Mechanical Conveyors for Bulk Solids* (Elsevier, Amsterdam 1995)

20.89 C.A. Wheeler: Rotating resistance of belt conveyor idler rolls, J. Manuf. Sci. Eng. **138**(2015), 1–8 (2015)

20.90 DIN 22113-3: Belt conveyors–Part 3: Belt conveyors for underground coalmining; idlers; testing (1996)

20.91 P.J. Munzenberger, C.A. Wheeler: Laboratory measurement of the indentation rolling resistance of conveyor belts, Int. J. Meas. **94**, 909–918 (2016)

20.92 AS 1334-13: Methods of testing conveyor and elevator belting. Determination of indentation rolling resistance of conveyor belting (2017)

20.93 DIN 22123, Conveyor belts – Indentation rolling resistances of conveyor belts related to beltwidth–Requirements, testing (2011). Withdrawn, replaced by DIN EN 16974

20.94 J.I. O'Shea, C.A. Wheeler, P.J. Munzenberger, D.G. Ausling: The influence of viscoelastic property measurements on the predicted rolling resistance of belt conveyors, J. Appl. Poly. Sci. **13**, 9170–9178 (2014)

20.95 C.A. Wheeler, A.W. Roberts, M.G. Jones: Calculating the flexure resistance of bulk solids transported on belt conveyors, Part. Part. Syst. Charact. **21**, 340–347 (2004)

20.96 M. Dratt, A. Katterfeld, C.A. Wheeler: Determination of the bulk flexure resistance via coupled FEM-DEM simulation, Bulk Solids Handl. **3**, 52–60 (2016)

20.97 P. J. Munzenberger: Three dimensional numerical modelling of conveyor belt indentation rolling resistance, PhD thesis (Univ. Newcastle, 2016)

20.98 DIN 22101: Continuous conveyors – Belt conveyors for loose bulk materials – Basis for calculation and dimensioning (1982)
20.99 Contitech: *Installing and splicing textile conveyor belts* (Contitech, Hannover 2010)
20.100 Phoenix: *Phoenix Conveyor Belts Design Fundamentals* (Phoenix, Hamburg 2004)
20.101 M. Selby: Introduction to tracking a conveyor belt. In: *Australian Bulk Solid Handlings* (2010)
20.102 Engineerdo: Reasons for belt mistracking, https://www.engineerdo.com/2019/10/04/belt-mistracking/ (2019)
20.103 T. Swindermann, L. Goldbeck, D. Marshall, M. Strebel: *Foundations, Volume 4* (Martin Engineering, Neponset, 2011)
20.104 H. Otto, A. Katterfeld: Prediction and simulation of the mistracking of conveyors belts. In: *8th Int. Conf. Conveying Handl. Part. Solids (CHOPS 2015), Tel-Aviv* (2015), Art. 139
20.105 H. Otto, A. Katterfeld: Analysis and simulation of belt tracking of conveyor belts, World Min. Surf. Underg. **67**(1), 53–59 (2015)
20.106 M. Egger: *Laufverhalten von Flachbändern: Lenkmechanismen beim seitlichen Führen von Bändern*, Stahleisen Communications (Verlag Stahleisen, Düsseldorf 2008)
20.107 ISO 7190: Continuous mechanical handling equipment; Bucket elevators; Classification Bilingual edition (1981)
20.108 ISO 5050: Continuous mechanical handling equipment; Vertical bucket elevators with calibrated round steel link chains; General characteristics (1981)
20.109 ISO 5051: Continuous mechanical handling equipment; Deep elevator bucket with flat rear wall; Main dimensions (1981)
20.110 VDI 2324: Vertical bucket elevators (2001)
20.111 A. Katterfeld, T. Gröger: Application of the discrete element method in materials handling: Bucket elevators and scraper conveyors, Bulk Solid Handl. **27**(4), 228–234 (2007)
20.112 DIN 15237-1: Steel cord conveyor belts–Part 1: Design, dimensions and mechanical requirements for conveyor belts for general use (2017)
20.113 DIN EN ISO 15236-1: Steel cord conveyor belts–Part 1: Design, dimensions and mechanical requirements for conveyor belts for general use (2017)
20.114 DIN 15231: Continuous mechanical handling equipment; bucket elevators, shallow buckets (1980)
20.115 DIN 15232: Continuous mechanical handling equipment; bucket elevators, shallow, rounded buckets (1980)
20.116 DIN 15233: Continuous mechanical handling equipment; bucket elevators, medium deep buckets (1980)
20.117 DIN 15234: Continuous mechanical handling equipment; bucket elevators, deep buckets with flat rear wall (1980)
20.118 DIN 15235: Continuous mechanical handling equipment; bucket elevators, deep buckets with curved rear wall (1980)
20.119 Nerak GmbH: Systeme für Schüttgüter, http://www.nerak.de/schuettgut.html (2017)
20.120 ContiTech Transportbandsysteme GmbH: POCKET-LIFT® The innovation in highend vertical conveying, http://apps.contitech-online.com/pages/produkte/transportbaender/brochures/WT7836_ContiTech_Pocketlift_en.pdf (2017)
20.121 Schrage Rohrkettensysteme GmbH: *Firmenschrift* (Firma Schrage Rohrkettensysteme GmbH, Friedeburg 2000)
20.122 F. Krause: Schüttgutumschlag, FAM Förderanlagen Magdeburg GmbH (2012)
20.123 A. Katterfeld, K. Williams: Functional analysis of tube chain conveyors part 1: General design and calculation principles, Bulk Solids Powder Sci. Technol. **2**(3), 23–32 (2008)
20.124 A. Katterfeld, K. Williams: Functional analysis of tube chain conveyors part 2: Experimental research and final recommendation for the calculation, Bulk Solids Powder Sci. Technol. **2**(3), 74–82 (2008)
20.125 Guo, J.: Investigation of arching behaviour under surcharge pressure in mass-flow bins and stress states at hopper/feeder interface, PhD thesis (Univ. Newcastle 2014)
20.126 J. Guo, A.W. Roberts, J.-D. Prigge: Experimental and simulation investigation of flow patterns and feeder loads at hopper/feeder interface. In: *Proceedings of the 11th Int. Congr. Bulk Mater. Storage Handl.Transp. The Univ. Newcastle* (2013)
20.127 R. Bartsch: Erweiterung der Dimensionierungsgrundlagen für Gleitkettenfördersysteme, PhD thesis (TU Chemnitz, 2017)
20.128 H.-J. Zebisch: *Fördertechnik 2: Stetigförderer* (Vogel, Würzburg 1972)
20.129 ISO 7119: Continuous mechanical handling equipment for loose bulk materials–Screw conveyors–Design rules for drive power (1981)
20.130 ANSI/CEMA Standard #350: Screw conveyors for bulk materials (2015)
20.131 DIN 15262: Continuous mechanical handling equipment; Screw conveyors for loose bulk materials; Design principles (1983)
20.132 VDI 2330 Part 1–4: Screw conveyors for bulk materials (09/2013, 05/2015, 03/2016)
20.133 A.W. Roberts, A.H. Willis: Performance of grain augers, Proc. Inst. Mech. Eng. **176**, 165 (1962)
20.134 A.W. Roberts: An investigation of grain vortex motion with relation to the performance within vertical grain augers, Proc. Inst. Mech. Eng. **178**, 293 (1964)
20.135 A.W. Roberts: The influence of granular vortex motion on the volumetric performance of enclosed screw conveyors, Powder Technol. **104**, 56–67 (1999)
20.136 A.W. Roberts: Design and performance criteria for screw conveyors in bulk solids operation, Bulk Solids Handl. **22**, 436–444 (2002)
20.137 D. Schlesinger, A. Papkov: Screw conveyor calculation based on actual material properties, Powder Handl. Process. **9**(4), 321–325 (1997)

20.138 A.W. Roberts, S.J. Wiche, D.D. Ilic, S.R. Plint: Flow dynamics and wear considerations in transfer chute design. In: *Proc. 8th ICBMH 2004, Institution of Engineers, Australia* (2004) pp. 330–334

20.139 A.W. Roberts: Bulk solids: Opitimizing screw conveyors, Chem. Eng. **122**, 62–68 (2015)

20.140 T. Risch: Zweidimensionale Bewegungsformen in der Vibrationsfördertechnik, Ph.D. thesis (TU Chemnitz, 2011), http://www.qucosa.de/fileadmin/data/qucosa/documents/6549/Diss_Risch.pdf

20.141 G. Uryadov, A. Katterfeld, F. Krause: Experimental investigations of the bulk solid reaction on vibratory conveyors. In: *Conf. Proc. 6th Int. Conf. Conveying Handl. Part. Solids (CHoPS). Brisbane* (2009) pp. 411–416

20.142 S. Böttcher: Beitrag zur Klärung der Gutbewegung auf Schwingrinnen, Fördern und Heben **8** (1958). PhD Thesis (TH Hannover, 1957)

20.143 G. Uryadov: Analyse der Schüttrückwirkung bei Vibrationsförderern, Ph.D. thesis (Univ. Magdeburg, 2014)

20.144 N. Dallinger: Diskrete Elemente Methode als Simulationsmethode in der Vibrationsfördertechnik, PhD thesis (TU Chemnitz, 2017)

20.145 K. Hoffmann, E. Krenn, G. Stanker: *Fördertechnik 2: Maschinensätze, Fördermittel, Tragkonstruktionen, Logistik* (Vieweg, Braunschweig, Wiesbaden 1998)

20.146 G. Reitor: *Fördertechnik. Hebezeuge, Stetigförderer, Lagertechnik* (Hanser, München, Wien 1993)

20.147 E. Zilich: Fördertechnik für Studium und Praxis. In: *Mechanisch arbeitende Stetigförderer*, Vol. 2 (Werner, Düsseldorf 1972)

20.148 P.W. Wypych: Introduction to pneumatic conveying, short course notes (2008)

20.149 R.D. Marcus, L.S. Leung, G.E. Klinzing, F. Rizk: *Pneumatic conveying of solids*, Vol. 507 (Chapman Hall, London 1990)

20.150 J.S. Mason: Introduction to pneumatic conveying. In: *Von Karman Inst. Fluid Dyn. Gas-Solid Suspens.*, Vol. 1 (1976) p. 12, N79-19286 10–34

20.151 W. Chen: Rheology of aerated fine powders: Theories and application in pneumatic conveying systems, PhD thesis (Univ. Newcastle, Australia 2013)

20.152 K.C. Williams: Dense phase pneumatic conveying of powders: Design aspects and phenomena, Ph.D. thesis (Univ. Newcastle 2008)

20.153 UN: C.1 Test–UN manual of tests and criteria for transport of dangerous goods, section 37

20.154 D. Geldart: Types of gas fluidisation, Powder Technol. **7**, 285–292 (1973)

20.155 O. Molerus: Interpretation of Geldart's type A, B, C and D powders taking into account interparticle cohesion force, Powder Technol. **33**, 81–87 (1982)

20.156 J.R. Grace: Contacting modes of behaviour classification of gas-solid and other two-phase suspensions, Can. J. Chem. Eng. **64**, 353–363 (1986)

20.157 G. Dixon: The impact of powder properties on dense phase flow. In: *Proc. Int. Conf. Pneum. Convey., London, UK* (1979)

20.158 R. Pan: Material properties and flow modes in pneumatic conveying, Powder Technol. **104**, 157–163 (1999)

20.159 N.J. Mainwaring, A.R. Reed: Permeability and air retention characteristics of bulk solid materials in relation to modes of dense phase pneumatic conveying, Bulk Solids Handl. **7**(3), 415–425 (1987)

20.160 M.G. Jones: The influence of bulk particulate properties on pneumatic conveying performance, Ph.D. thesis (Thames Polytechnic, 1988)

20.161 A.J. Chambers, S. Keys, R. Pan: The influence of material properties on conveying characteristics. In: *6th International Conference on Bulk Materials Storage, Handling and Transportation, Wollongong, Australia* (1998) pp. 309–319

20.162 C. Fargette, M.G. Jones, G. Nussbaum: Bench scale tests assessment of pneumatic conveying behavior of powders, Powder Handl. Process. **9**(2), 103–110 (1997)

20.163 L. Sanchez, N. Vasquez, G.E. Klinzing, S. Dhodapkar: Characterization of bulk solids to assess dense phase pneumatic conveying, Powder Technol. **138**, 93–117 (2003)

20.164 S. Barton: The effect of pipeline flow conditioning on dense phase pneumatic conveying (Glasgow Caledonian University, 1997)

20.165 J. Klintworth, R.D. Marcus: A review of low-velocity pneumatic conveying system, Bulk Solids Handl. **5**(4), 747–753 (1995)

20.166 A. Lippert, E. Muschelknautz: Process for automatically separating a column of granular or pulverulent material. US Patent No 3240531 (1966)

20.167 H. Möller: Device for pneumatic and hydraulic feeding of bulk goods, US Patent No 4595317 (1986)

20.168 W. Merz: Conveyance system for transporting powdery or granular material. Swiss Aluminium Ltd., Chippis, Switzerland, US Patent No 4615648 (1984)

20.169 H. Rapp, W. Allenspach: Pipeline construction for pneumatic and hydraulic conveyance of solid material, US Patent No 3524478 (1970)

20.170 W. Stegmaier: Zur Berechnung der horizontalen pneumatischen Förderung feinkörniger Stoffe, Fördern Heb. **28**, 363 (1978)

20.171 M. Weber: Principles of hydraulic and pneumatic conveying in pipes, Bulk Solids Handl. **1**(1), 57–63 (1981)

20.172 J.S. Mason, D. Mills, R.A. Reed, C.R. Woodcock: Introduction to pneumatic conveying, Powder Eur. **80**, 1–57 (1980)

20.173 D. Mills, J.S. Mason, R.B. Stacey: A design study for the pneumatic conveying of a fine particulate material. In: *The Solids Handling Conference–Solidex 82, Harogate, England* (1982) pp. C1–C75

20.174 P.W. Wypych, P.C. Arnold: On improving scale-up procedures for pneumatic conveying design, Powder Technol. **50**, 281–294 (1987)

20.175 D. Mills: *Pneumatic Conveying Design Guide* (Elsevier, Oxford 2004)

20.176 D. Ilic, T.J. Hicks: Towards the development of design criteria for reduced wear in iron ore transfers.

In: *17th Iron Ore Conf., ABM Week 2016, Rio De Janeiro, Brazil* (2016)
20.177 T.J. Donohue, D. Ilic, R. Bell, L. Newman: The use of DEM in the design and analysis of WEARBACK transfer chutes, Aust. Bulk Handl. Rev. **11**(12), 62–67 (2010)
20.178 D. Ilic, T. Donohue: Transfer chute analysis – Current practices involving continuum, DEM and practical validation. In: *Aust. Bulk Handl. Rev.*, Vol. 1/2 (2012)
20.179 Ilic, D.: Bulk solid interactions in belt conveying systems, PhD thesis (Univ. Newcastle 2013)
20.180 A.W. Roberts: An investigation into the gravity flow of non-cohesive granular materials through discharge chutes, J. Eng. Ind. **91**(2), 373–381 (1969)
20.181 A.W. Roberts: Chute design considerations for feeding and transfer. In: *Proc. BeltCon 11 Conf., Randburg, Republic of South Africa* (2001)
20.182 A.W. Roberts: Chute performance and design for rapid flow conditions, Chem. Eng. Technol. **26**(2), 163–170 (2003)
20.183 A.W. Roberts, O.J. Scott: Flow of bulk solids through transfer chutes of variable geometry and profile, Bulk Solids Handl. **1**(4), 715–727 (1981)
20.184 A.W. Roberts: Predicting abrasive wear in enclosed screw conveyors, Bulk Solids Powder Sci. Technol. **1**, 32–43 (2004)
20.185 A.I. Hustrulid, G.W. Mustoe: Engineering analysis of transfer points using discrete element analysis. In: *Proc. Annu. Meet. Soc. Min. Eng. (SME), Phoenix, AZ, 1996* (1996) pp. 9–13, Chap. 2
20.186 A.I. Hustrulid: Transfer station analysis. In: *Proc. Annu. Meet. Soc. Min. Eng. (SME), Orlando, FL* (1998) pp. 33–53
20.187 L.K. Nordell: Palabora installs curved transfer chute in hard rock to minimize belt cover wear, Bulk Solids Handl. **14**(4), 739–743 (1994)
20.188 A. Katterfeld, T. Gröger, A. Minkin: Discrete element simulation of transfer stations and their verification, Bulk Solids Powder Sci. Technol. **2**, 137–143 (2007)
20.189 F. Kessler, M. Prenner: DEM–Simulation of conveyor transfer chutes. In: *FME Transactions*, Vol. 37 (2009) pp. 185–192
20.190 D. Ilic, W. McBride, A. Katterfeld: Validation of continuum methods utilising discrete element simulations as applied to a slewing stacker transfer chute. In: *9th ICBMH 2007, Conf. Proc. (USB), Univ. Newcastle, Australia* (2007)
20.191 A.P. Grima, P.W. Wypych: Discrete element simulations of granular pile formation: Method for calibrating discrete element models, Eng. Comput. **28**(3), 314–339 (2011)
20.192 C.J. Coetzee, D.N.J. Els: Calibration of discrete element parameters and the modelling of silo discharge and bucket filling, Comput. Electron. Agric. **65**(2), 198–212 (2009)
20.193 C.J. Coetzee, D.N.J. Els: Calibration of granular material parameters for DEM modelling and numerical verification by blade-granular material interaction, J. Terramech. **46**(1), 15–26 (2009)
20.194 Y.C. Chung, J. Ooi: Influence of discrete element model parameters on bulk behavior of a granular solid under confined compression, Part. Sci. Technol. **26**(1), 83–96 (2008)
20.195 A. Katterfeld, C.J. Coetzee, T. Donohue, J. Fottner, A. Grima, Á. Ramírez-Gómez, D. Ilic, R. Kačianauskas, J. Necas, D. Schott, K. Williams, J. Zegzulka: White Paper: Calibration of DEM parameters for cohesionless bulk materials under rapid flow conditions and low consolidation (2019), https://doi.org/10.13140/RG.2.2.26318.31048/1
20.196 T. Roessler, C. Richter, A. Katterfeld, F. Will: Development of a standard calibration procedure for the DEM parameters of cohesionless bulk materials – Part I: Solving the problem of ambiguous parameter combinations, Powder Technol. **343**, 803–812 (2019), https://doi.org/10.1016/j.powtec.2018.11.034
20.197 M. Rackl, K.J. Hanley: A methodical calibration procedure for discrete element models, PowTech **307**, 73–83 (2017)
20.198 H.Q. Do, A.M. Aragaon, D.L. Schott: Automated discrete element method calibration using genetic and optimization algorithms. In: *Powders and Grains 2017, EPJ Web of Conferences, 140:15011* (2017)
20.199 C. Richter, T. Roessler, A. Katterfeld, F. Will: Development of a standard calibration procedure for the DEM parameters of cohesionless bulk materials – Part II: Efficient optimization-based calibration, Powder Technol. **360**, 967–976 (2020), https://doi.org/10.1016/j.powtec.2019.10.052
20.200 T. Roessler, A. Katterfeld: DEM parameter calibration of cohesive bulk materials using a simple angle of repose test, Particuology **45**, 105–115 (2019), https://doi.org/10.1016/J.PARTIC.2018.08.005
20.201 M. Carr, T. Roessler, H. Otto, C. Richter, A. Katterfeld, C.A. Wheeler, K. Williams, G. Elphick, K. Nettletone: Calibration procedure of discrete element method (DEM) – Parameters for cohesive bulk materials. In: *Proc. ICBMH 2019. Gold Coast. Institution of Engineers Australia* (2019)
20.202 M.J. Carr, W. Chen, K. Williams, A. Katterfeld: Comparative investigation on modelling wet and sticky material behaviours with a simplified JKR cohesion model and liquid bridging cohesion model in DEM. In: *ICBMH 2016 Barton, A.C.T. Engineers Australia* (2016)
20.203 D. Jodin, M. Hompel: *Sortier- und Verteilsysteme: Grundlagen, Aufbau, Berechnung und Realisierung* (Springer, Berlin, Heidelberg 2006)
20.204 DIN15401-1: Lasthaken für Hebezeuge; Einfachhaken; Rohteile (1982)
20.205 DIN15401-2: Lasthaken für Hebezeuge; Einfachhaken; Fertigteile mit Gewindeschaft (1983)
20.206 DIN15402-1: Lasthaken für Hebezeuge; Doppelhaken; Rohteile (1982)
20.207 DIN 15402-2: Lasthaken für Hebezeuge; Doppelhaken; Fertigteile mit Gewindeschaft (1983)

20.208 DIN 15 400: Lasthaken für Hebezeuge; Mechanische Eigenschaften, Werkstoffe, Tragfähigkeiten und vorhandene Spannungen (1990)

20.209 ISO 4779: Geschmiedete Ösenhaken aus Stahl zum Heben für den Einsatz in Rundstahlketten der Güteklasse M(4) (1986)

20.210 ISO 7597: Forged steel lifting hooks with latch, grade 8 (2013)

20.211 ISO 8539: Forged steel lifting components for use with Grade 8 chain (2009)

20.212 DIN 82017: Ladegeschirr – Zubehör- und Beschlagteile zum Heben – Ladehaken (2010)

20.213 DIN 15407-1: Lasthaken für Krane; Lamellen-Einfachhaken für Roheisen- und Stahlgießpfannen; Zusammenstellung, Hauptmaße (1977)

20.214 DIN 15407-2: Lasthaken für Krane; Lamellen-Einfachhaken für Roheisen- und Stahlgießpfannen; Einzelteile (1989)

20.215 DIN EN 10028-3: Flat products made of steels for pressure purposes–Part 3: Weldable fine grain steels, normalized (2017)

20.216 VDE 0580: Elektromagnetische Geräte und Komponenten – Allgemeine Bestimmungen (2011)

20.217 ISO 17096: Cranes–Safety–Load lifting attachments (2015)

20.218 FEM 9.511: Berechnungsgrundlagen für Serienhebezeuge (1986)

20.219 FEM 9.661: Berechnungsgrundlagen für Serienhebezeuge – Baugrößen und Ausführung von Seiltrieben (1986)

20.220 FEM 9.901: Berechnungsgrundlagen für Serienhebezeuge und Krane mit Serienhebezeugen (1991)

20.221 DIN EN 14492-2: Cranes–Power driven winches and hoists–Part 2: Power driven hoists (2010)

20.222 DIN 15001-1: Krane; Begriffe, Einteilung nach der Bauart (1973)

20.223 DIN EN 13001: Cranes–Part 1–3 (2012)

20.224 DIN 15018: Krane; Grundsätze für Stahltragwerke; Berechnung von Fahrzeugkranen (1984)

20.225 ISO 20332: Cranes–Proof of competence of steel structures (2016)

20.226 O. Kempkes, J. Scholten, G. Wagner: *Europäische Krannorm DIN EN 13 001–Wege zur Konstruktion sicherer und wirtschaftlicher Krane*, Hebezeug Fördermittel, Vol. 7–8 (HUSS-Medien, Berlin 2005) pp. 356–358

20.227 M. Golder: Die praktische Anwendung der EN 13 001 am Beispiel von Brückenkrananlagen. In: *12. Int. Kranfachtagung, Tagungsband*, ed. by G. Wagner, J. Scholten (Selbstverlag der Ruhr-Universität Bochum, Bochum 2004)

20.228 DIN 15030: Hebezeuge; Abnahmeprüfung von Krananlagen, Grundsätze (1977)

20.229 D. Smolyaninov, P. Horn, F. Krause, F. Palis: Ergebnisse der Untersuchungen zur Pendeldämpfung bei Drehkranen. In: *11. Internationale Kranfachtagung, Tagungsbeiträge*, ed. by H.-G. Marquardt (Selbstverlag der TU Dresden, Dresden 2003)

20.230 DIN EN 15011: Cranes–Bridge and gantry cranes (2014)

20.231 DIN EN 13001-2: Crane safety–General design–Part 2: Load actions (2014)

20.232 ISO 12488-1: Cranes–Tolerances for wheels and travel and traversing tracks–Part 1: General (2012)

20.233 I. Brötzmann: Portalkrane – Einsatzgebiete, Arbeitsaufgaben und Problemlösungen. In: *12. Internationale Kranfachtagung, Tagungsband*, ed. by G. Wagner, J. Scholten (Selbstverlag Ruhr-Universität Bochum, Bochum 2004)

20.234 T. Koch: Einsatz automatisierter Krananlagen im Yard des Container-Terminals Altenwerder – Funktion und erste Betriebserfahrungen. In: *12. Int. Kranfachtagung, Tagungsband*, ed. by G. Wagner, J. Scholten (Selbstverlag der Ruhr-Universität Bochum, Bochum 2004)

20.235 Traunitz, W.: Seeschiffsentlader mit automatischer Steuerung. Siemens-Zeitung **48**(2) (1974)

20.236 K. Malcher, T. Nogiec: Wippdrehkrane: Lastausgleich bei idealem Lastweg, Fördern Heb. **34**(3), 150–152 (1986)

20.237 DIN EN 13000: Cranes–Mobile Cranes (2014)

20.238 G. Wagner, J. Scholten: Neue Entwicklungstendenzen in der Fördertechnik, Hebezeug Förderm. **6**, 262–264 (2003)

20.239 O. Fries: Traglaststeigernde Systeme für Fahrzeugkranausleger. In: *11. Int. Kranfachtagung, Tagungsband*, ed. by H.-G. Marquardt (Selbstverlag der TU Dresden, Dresden 2003)

20.240 DIN EN 12999: Cranes–Loader cranes (2013)

20.241 DIN EN 13852-1: Cranes–Offshore cranes–Part 1: General-purpose offshore cranes (2014)

20.242 DIN EN 13852-2: Krane – Offshore-Krane – Teil 2: Schwimmende Krane (2015)

20.243 G. Kunze, H. Göhrung, K. Jacob, M. Scheffler (Eds.): *Baumaschinen Erdbau- und Tagebaumaschinen* (Vieweg, Braunschweig 2003)

20.244 G. Heß, C. Richter, A. Katterfeld: Simulation of the dynamic interaction between bulk material and heavy equipment–calibration and validation. In: *ICBMH 2016. 12th Int. Conf. Bulk Mater. Storage Handl. Transp.; Proceedings; Darwin, Australia, 11–14 July 2016*, ed. by D. Hastie (The Institution of Engineers, Australia, Barton 2016) pp. 427–436

20.245 G. Kunze, A. Katterfeld, C. Richter, H. Otto, C. Schubert: Plattform- und softwareunabhängige Simulation der Erdstoff-Maschine Interaktion. In: *Fachtagung Baumaschinentechnik Dresden* (2012)

20.246 C. Holländer: *Untersuchungen zur Beurteilung und Optimierung von Baggerhydrauliksystemen*, Fortschritt-Ber. VDI Reihe 1, Vol. 307 (VDI, Düsseldorf 1998)

20.247 M. Dratt, A. Katterfeld: Coupling of FEM and DEM simulations to consider dynamic deformations under particle load. In: *Granular Matter*, Vol. 19 (Springer, Berlin 2017), Art. 49

20.248 DIN 24080: Earth-Moving Machinery (1979), withdrawn

20.249 J. Forche: Antriebsmanagement für Hydraulikbagger, Baumaschinentechnik **26**, 33–40 (2004)

20.250 J. Weber, E. Lautner: Intelligente Baumaschinensteuerungen und alternative Antriebssysteme. In: *Baumaschinentechnik 2004*, Schriftenreihe

der Forschungsvereinigung Bau- und Baustoffmaschinen, Vol. 26 (2004) pp. 41–48
20.251 DIN EN ISO 3164: Earth-moving machinery–Laboratory evaluations of protective structures–Specifications for deflection-limiting volume (2013)
20.252 DIN EN ISO 3449: Erdbaumaschinen – Schutzaufbauten gegen herabfallende Gegenstände – Prüfungen und Anforderungen (2009)
20.253 DIN EN ISO 3471: Earth-moving machinery–Roll-over protective structures–Laboratory tests and performance requirements (2010)
20.254 G.R. Strakosch (Ed.): *The Vertical Transportation Handbook*, 3rd edn. (Wiley, New York 1998)
20.255 M. Scheffler, K. Feyrer, K. Matthias: *Fördermaschinen – Hebe- und Flurförderzeuge* (Vieweg, Wiesbaden 1998)
20.256 ISO 4190-1: Lift (elevator) installation–Part 1: Class I, II, III and VI lifts (2010)
20.257 EN 81: Safety rules for the construction and installation of lifts (2016)
20.258 DIN ISO 5053-1:2015-11: Industrial trucks-Terminology and classification-Part 1: Types of industrial trucks (2015)
20.259 DIN ISO 5053-2: Industrial trucks–Terminology and classification–Part 2: Fork arms and attachements (2017)
20.260 DIN 15172:1988-12: Powered industrial trucks; tractors and other trucks used for hauling trailers; traction force, trailer load (1988)
20.261 R.G.T. Lindkvist: *Handbook of Materials Handling*, Ellis Horwood Series in Applied Science and Industrial Technology (Ellis Horwood, Chichester 1985)
20.262 VDI 2516:2003-09: Floor conveyors for storage and retrieval-Cycle time calculation in narrow aisles (2003)
20.263 DIN EN 1525:1997-12: Safety of industrial trucks-Driverless trucks and their systems (1997)
20.264 VDI 2510:2005-10: Automated Guided Vehicle Systems (AGVS) (2005)
20.265 VDI 2710:2010-04: Interdisciplinary design of automated guided vehicle systems (AGVS) (2010)
20.266 G. Ullrich: *Automated Guided Vehicle Systems–A Primer with Practical Applications*, Vol. 2 (Springer Vieweg, Heidelberg, New York 2015)
20.267 B. Brinkmann: *Seehäfen – Planung und Entwurf* (Springer, Berlin, Heidelberg 2005)
20.268 J.R. Johanson: Method of calculating rate of discharge from hoppers and bins, Trans. Min. Eng. AIME **232**, 69–80 (1965)
20.269 P.C. Arnold, A.G. McLean, A.W. Roberts: *Bulk Solids: Storage, Flow and Handling* (TUNRA, Newcastle 1982)
20.270 A.W. Roberts: *Modern Concepts in the Design and Engineering of Bulk Solids Handling Systems* (TUNRA Bulk Solids Research, Newcastle 1988)
20.271 J.R. Johanson: The use of flow-corrective inserts in bins, J. Eng. Ind. **88**(2), 224–230 (1966)
20.272 J.R. Johanson: Controlling flow patterns in bins by the use of an insert, Int. J. Bulk Solids Handl. **2**(3), 495–498 (1982)
20.273 A.W. Roberts: Vibrations of powders and bulk solids. In: *Handbook on Powder Science and Technology* (Van Nostrand, New York 1984), Chap. 6
20.274 A.W. Roberts, M. Ooms, O.J. Scott: Influence of vibrations on the strength and boundary friction characteristics of bulk solids and the effect on bin design, Int. J. Bulk Solids Handl. **6**(1), 161–169 (1986)
20.275 A.W. Roberts, F.J.C. Rademacher: Induced gravity flow by mechanical vibrations. In: *11th Annu. Powder Bulk Solids Conf., Chicago, USA, 12–15 May 1986* (1986) pp. 58–74
20.276 M. Terziovski, P.C. Arnold: On the effective sizing and placement of air blasters, Int. J. Bulk Solids Handl. **10**(2), 181–185 (1990)
20.277 AS 3774: *Loads on Bulk Solids Containers* (Standards Association of Australia, Sydney 1996)
20.278 EN 1991-4: Eurocode 1 actions on structures, Part 4 silos and tanks (2006)
20.279 J.Y. Ooi, L. Pham, J.M. Rotter: Systematic and random features of measured pressures on full-scale silo walls, Eng. Struct. **12**(2), 74–87 (1990)
20.280 A. Ramírez, J. Nielsen, F. Ayuga: Pressure measurements in steel silos with eccentric hoppers, Powder Technol. **201**(1), 7–20 (2010)
20.281 P. Vidal, E. Gallego, M. Guaita, F. Ayuga: Finite element analysis under different boundary conditions of the filling of cylindrical steel silos having an eccentric hopper, J. Construct. Steel Res. **64**(4), 480–492 (2008)
20.282 B. Chen, A. Roberts, T. Donohue: DEM modelling of silo loads asymmetry induced by eccentric discharge, presents the state of art of discrete element methods, Springer Proc. Phys. **188**, 1133–1141 (2017)
20.283 C.M. Wensrich: Analytical and numerical modelling of quaking in tall silos, PhD thesis (Univ. Newcastle, Newcastle, 2002)
20.284 A.W. Roberts: *Rathole Geometry and Draw-Down During Funnel-Flow in Bins and Gravity Reclaim Stockpiles*, Bulk Solids Handling (Systems and Design) Notes (Centre for Bulk Solids and Particulate Technologies, Newcastle 2000) pp. 609–618
20.285 W. McBride: *Effective gravity reclaim stockpile design*, Bulk Solids Handling (Systems and Design) Notes (Centre for Bulk Solids and Particulate Technologies, Newcastle 2000) pp. 635–644
20.286 A.W. Roberts, W. Mc. Bride: *Predicting the Performance of Gravity Reclaim Stockpiles*, Bulk Solids Handling (Systems and Design) Notes (Centre for Bulk Solids and Particulate Technologies, Newcastle 2000) pp. 645–652
20.287 A.W. Roberts: *Design Considerations for Maximum Reclaim Capacity of Gravity Reclaim Stockpiles*, Bulk Solids Handling (Systems and Design) Notes (Centre for Bulk Solids and Particulate Technologies, Newcastle 2000) pp. 653–675
20.288 W. McBride: Mechanics of bulk solids stockpiles, Ph.D. thesis (Univ. Newcastle, 2001)

20.289 A.W. Roberts: Dynamic modelling of bulk solids storage, discharge and handling systems, Bulk Solids Handl. **20**(2), 183–189 (2000)

20.290 A.W. Roberts: Loads on support structural elements buried in stockpiles, Part. Part. Syst. Charact. **24**, 352–359 (2007)

20.291 E. Frazelle: *World-Class Warehousing and Material Handling*, Vol. 1 (McGraw-Hill, New York 2001)

20.292 H. Martin: *Transport- und Lagerlogistik: Systematik, Einsatz und Wirtschaftlichkeit* (Springer Vieweg, Wiesbaden 2016)

20.293 K. Bichler, G. Riedel, F. Schöppach: *Kompakt Edition: Lagerwirtschaft – Grundlagen, Technologien und Verfahren* (Springer Gabler, Wiesbaden 2013)

20.294 DIN EN 15629:2010-09: Steel static storage systems-Specification of storage equipment (2010)

20.295 DIN EN 15512:2010-09: Steel static storage systems-Adjustable pallet racking systems-Principles for structural design (2010)

20.296 DIN EN 15620:2010-05: Steel static storage systems-Adjustable pallet racking-Tolerances, deformations and clearances (2010)

20.297 VDI 3561: Determination of cycle timesfor automated channel-type storage systems (2009)

20.298 VDI 3658: Equipment for inter-aisle transfer of storage and retrieval machines (1993)

20.299 M. ten Hompel, T. Schmidt, L. Nagel: *Materialflusssysteme, Förder- und Lagertechnik*, 3rd edn. (Springer, Berlin, Heidelberg 2007)

André Katterfeld

Institute of Logistics and Material Handling Systems
Otto-von-Guericke-Universität Magdeburg
Magdeburg, Germany
andre.katterfeld@ovgu.de

André Katterfeld holds the chair of Material Handling Systems at the Institute of Logistics and Material Handling Systems of Otto-von-Guericke-University Magdeburg. His PhD was on analysis of tube chain conveyors. He worked as an Associate Professor in Magdeburg and contributed intensively to the Discrete Element Method (DEM) in the field of bulk materials handling. His research focuses on understanding and modeling the interaction between goods and machinery in materials handling.

Alan Roberts

TUNRA Bulk Solids Handling Research Associates and Centre for Bulk Solids and Particulate Technologies
University of Newcastle
Callaghan, NSW, Australia
alan.roberts@newcastle.edu.au

Founding director of TUNRA Bulk Solids Handling Research Associates and formerly dean of the Faculty of Engineering of the University of Newcastle, Australia, Alan Roberts established a research and consulting group that has completed some 5000 projects for companies worldwide. He holds BE, PhD, DUniv, and HonDSc degrees and has over 50 years of experience in research and consulting in bulk solids handling.

Craig Wheeler

School of Engineering, Faculty of Engineering and Built Environment
University of Newcastle
Callaghan, NSW, Australia
craig.wheeler@newcastle.edu.au

Craig Wheeler is professor in the School of Engineering, University of Newcastle, Australia and associate director of TUNRA Bulk Solids and of the Centre for Bulk Solids and Particulate Technologies. He worked as a mechanical engineer for BHP Billiton. His PhD in mechanical engineering was on analyzing the motion resistances of belt conveyors. His research focuses on reducing the energy intensity and environmental impact of ore and mineral transportation.

Kenneth Williams

School of Engineering, Newcastle Institute for Energy and Resources
University of Newcastle
Callaghan, NSW, Australia
ken.williams@newcastle.edu.au

Kenneth Williams is associate professor at the Centre for Bulk Solids and Particulate Technologies and inaugural chair of the Doctoral Training Centre for Mining Equipment, Technology and Services at the University of Newcastle, Australia. His research includes transient modeling approaches, CFD of particulate flows, bulk solids characterization, robust modeling approaches to analyze transient flow behavior, prediction of bulk cargo surface and sub-surface failure, and self-heating of coal during marine transportation.

Chris Wensrich

School of Engineering, Faculty of Engineering and Built Environment
University of Newcastle
Callaghan, NSW, Australia
christopher.wensrich@newcastle.edu.au

Chris Wensrich is associate professor in mechanical engineering at the School of Engineering, University of Newcastle, Australia. After graduating in applied mathematics and engineering, he received a PhD in mechanics engineering on silo quaking. His research interests span granular mechanics, materials handling, DEM, residual stress analysis, and neutron-based strain measurements.

Jan Scholten

Group of Construction Machinery and Materials Handling
Ruhr-Universität Bochum
Bochum, Germany
jan.scholten@bmft.rub.de

Jan Scholten leads the construction machinery and materials handling group at Ruhr-University, Bochum, Germany. He received a PhD on stress determination for maintenance-free plain bearings in 2002. His research is in the area of product verification and focuses on the development of methods and tools for modeling, simulation, and evaluation of product behavior in the use phase, virtual damage simulation, modeling of tribomechanical systems, and acoustic simulations.

Mark Jones

School of Engineering, Faculty of Engineering and Built Environment
University of Newcastle
Callaghan, NSW, Australia
mark.jones@newcastle.edu.au

Mark Jones is head of the School of Engineering, director of TUNRA Bulk Solids and the Centre for Bulk Solids, and president of the Academic Senate at the University of Newcastle. He has held the Chair in Bulk Solids Handling at the University of Newcastle since 1999. His research interests span the broad area of bulk materials handling, and he specializes in pneumatic conveying.

Günter Kunze

Lehrstuhl für Baumaschinen- und Fördertechnik
TU Dresden
Dresden, Germany
guenter.kunze@tu-dresden.de

Günter Kunze graduated in mechanical engineering from the Technical University of Dresden in 1972 and obtained his doctorate in the field of rolling friction. As a senior engineer in industry, he worked on driver gear teeth problems. In 1993 he was awarded a professorship for mechanical engineering at TU Dresden. His research focuses on special machine elements and drive technology as well as the simulation of mobile construction machinery.

Henning Strubelt

Chair of Warehouse Technology, Warehouse Planning, Warehouse Organization
Bremerhaven University of Applied Sciences
Bremerhaven, Germany
hstrubelt@hs-bremerhaven.de

Henning Strubelt is professor for warehouse technology, warehouse planning and warehouse organization at the University of Applied Sciences Bremerhaven, Germany, visiting professor at Chiang Mai University, and teaches at Technical University of Applied Science Wildau, Germany and Vietnamese-German University, Vietnam. He received his doctorate in engineering for research on ramp-up management for job production. His research focuses on sustainable supply chain design, lean ramp-up, and material provision for multimodal production.

Dusan Ilic

School of Engineering, Newcastle Institute for Energy and Resources
University of Newcastle
Callaghan, NSW, Australia
dusan.ilic@newcastle.edu.au

Dusan Ilic is a senior research associate at the School of Engineering, University of Newcastle, Australia. He has established a globally recognized track record in troubleshooting, designing, and optimizing storage, handling, and transportation systems. His multidisciplinary research collaborations bring together engineering, environmental, biomedical, and biological sciences to influence society and the environment.

Tim Donohue

TUNRA Bulk Solids
University of Newcastle
Shortland, NSW, Australia
timothy.donohue@newcastle.edu.au

Tim Donohue is conjoint lecturer at the University of Newcastle, Australia, and general manager of TUNRA Bulk Solids. He received his PhD in 2008 on the topic of permeability of packed beds. His research focuses on conveyor transfer chutes, specifically passive dust control techniques and calibration of parameters for discrete element modeling (DEM). His research on dust control uses both computational fluid dynamics (CFD) and DEM.

Hendrik Otto

Institute for Logistics and Material Handling
Otto-von-Guericke Universität Magdeburg
Magdeburg, Germany
hendrik.otto@ovgu.de

Hendrik Otto is a mechanical engineer and researcher at the Institute of Logistics and Material Handling at Otto-von-Guericke University Magdeburg. Since 2012 he has worked on the analysis and simulation of belt mistracking in which he received a PhD in 2019. His research interests include modeling bulk material flow by DEM as well as analysis of the interaction between bulk materials and fluids by coupled CFD–DEM simulations.

Jens Sumpf

Institute of Materials Handling, Conveying and Plastics Engineering
Chemnitz University of Technology
Chemnitz, Germany
jens.sumpf@mb.tu-chemnitz.de

Jens Sumpf is head of the Traction Mechanisms and Tribology research team at the Institute of Materials Handling, Conveying, and Plastics Engineering at Chemnitz University of Technology. He received a PhD in mechanical engineering in 1999. His team works on dimensioning basics for continuous conveyor systems using belts, toothed belts, and conveyor chains, preferable made of plastics, and also specializes in the tribology of plastics.

Wei Chen

School of Engineering, Faculty of Engineering and Built Environment
University of Newcastle
Callaghan, NSW, Australia
w.chen@newcastle.edu.au

Wei Chen is conjoint senior lecture at the University of Newcastle, Australia and global DEM design engineer at Bradken Resource Limited. He received a PhD in mechanical engineering in 2014. His research interests cover general bulk solids handling, pneumatic conveying, and discrete element modeling, with a particular focus on industrial applications.

Bin Chen

TUNRA Bulk Solids
Shortland, NSW, Australia

Bin Chen is a senior consulting engineer at TUNRA Bulk Solids and conjoint lecturer at the University of Newcastle, Australia. His research and consultancy activities have covered a broad area of bulk materials storage, handling, and transportation. His focus is to develop techniques to guide the design of these systems and ultimately solve industrial problems. He has over 40 publications including patents, book chapters, and research papers.

Daniel Ausling

TUNRA Bulk Solids
The University of Newcastle
Shortland, NSW, Australia
daniel.ausling@newcastle.edu.au

Daniel Ausling has been with TBS since 2003 and is currently a senior consulting engineer. After his degree in mechanical engineering, his PhD focused on overland conveyors, during which he contributed to different consultancy projects in this area. He specializes in materials handling and testing, conveyor belts, and idler testing, as well as overland conveyor, hopper, and transfer chute conceptual design.

Part E Transport

Part E Transportation – Mobility

21 **Trends and Challenges in Mobility and Transportation**
Marc Claus Schmitt, Munich, Germany
Stefan Pischinger, Aachen, Germany

22 **Automotive Engineering**
Gritt Ahrens, Neu-Ulm, Germany

23 **Railway Systems–Railway Engineering**
Markus Hecht, Berlin, Germany

24 **Aerospace Engineering**
Hamid Hefazi, Incheon, Republic of Korea

25 **Ships and Maritime Transportation**
Jean-Baptiste R. G. Souppez, Birmingham, UK

21. Trends and Challenges in Mobility and Transportation

Marc Claus Schmitt, Stefan Pischinger

This chapter provides a short overview of the three most important transportation technologies: automotive, aerospace, and rail. It initially examines the economic impact of transportation. A strong economy is usually highly dependent on the transportation of people and goods. The effects of environmental and safety legislation on transportation technologies are also discussed. Processes that will transform transportation over the coming decades are then considered.

After that, relevant legislation for and development trends in automotive, aerospace, and rail technologies are described and analyzed, and the processes used to develop new automotive vehicles, aircraft, and rail vehicles are outlined. More specifically, a section on automotive technology explores the different types of powertrains used in automotive transportation, current trends in the development of automobile bodies, chassis, advanced driver-assistance systems, combustion engines, and electric drives, as well as the automotive vehicle development process. A section on aerospace technology considers the relationship between air transportation and society before discussing the history of and challenges facing aeronautical engineering. A generic development process for aerospace technologies is then signposted. Finally, a section on rail technology describes basic technologies relating to the efficiency of and resistance and traction forces associated with rail transportation. Other important factors in rail transportation are then discussed, such as guidance, the braking system, train protection, management, rail vehicle structure, and coupling, before the development process for rail vehicles is detailed.

21.1 **Overview** 995
21.1.1 Transportation as an Economic Factor.. 996
21.2 **Impact of Safety and Environmental Legislation on Transportation Technologies** 997
21.3 **Upcoming Changes in Transportation** . 998
21.3.1 Automated..... 999
21.3.2 Connected 999
21.3.3 Electrified 999
21.3.4 Shared/Services 1000
21.4 **Automotive Technology** 1000
21.4.1 Automotive Technology, Legislation, and Development Trends..... 1000
21.4.2 The Automotive Vehicle Development Process 1004
21.5 **Aerospace Technology** 1005
21.5.1 Aerospace Technology, Legislation, and Development Trends..... 1006
21.5.2 The Aerospace Development Process.... 1008
21.6 **Rail Technology** 1009
21.6.1 Rail Technology, Legislation, and Development Trends..... 1009
21.6.2 The Rail Vehicle Development Process . 1012
References..... 1013

21.1 Overview

Transportation is the process of conveying humans, animals, or goods from one place to another (the word is derived from the Latin *portare*, meaning 'carry,' and *trans*, meaning 'between'). It is one of the most basic human needs, and it has a significant impact on any economy: productivity and economic strength are usually strongly correlated with the amount of people and goods that are transported in an economy. Transportation can be performed on the ground (by road or rail), across the sea, or through the air, leading to four main transportation technologies: automotive, rail, marine, and aerospace. These technologies face severe challenges in the near future due to (i) increased customer requirements and an ever-greater demand for transportation, (ii) energy shortages

K.-H. Grote, H. Hefazi (Eds.), *Springer Handbook of Mechanical Engineering*, Springer Handbooks,
https://doi.org/10.1007/978-3-030-47035-7_21

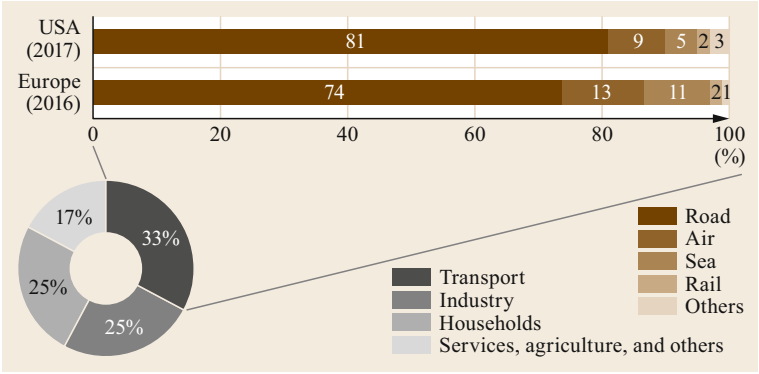

Fig. 21.1 Energy demand of the transportation sector as a proportion of the total energy demand in Europe, and the energy demand of each transportation mode as a proportion of the total energy demand of the transportation sector in Europe and the US (after [21.1, 2])

and rising fuel prices, (iii) more stringent legislative requirements such as those relating to pollutant and noise emissions and safety issues, and (iv) the imminent automatization and digitalization of transportation, which will involve seamlessly linking the transportation sectors together to enhance mobility and the transportation of goods.

In the first part of this chapter, we discuss the economics of transportation. After that, environmental and legislative issues relating to transportation are considered. The final part of the chapter will discuss upcoming changes in the transportation sector.

21.1.1 Transportation as an Economic Factor

The forecast increase in the world's population and the industrialization of large parts of the world are the main drivers for the predicted rise in demand for transportation. The potential environmental effects and risks to energy supplies caused by such an increase in demand for transportation are major concerns. As shown in Fig. 21.1, one-third of the total demand for primary energy in Europe in the year 2016 originated from transportation. In particular, road transportation consumes 74% and 81% of the overall energy demand from transportation in Europe and the United States, respectively.

Figure 21.2 shows the growth in various passenger and freight transportation modes in Europe between the years 1990 and 2020 (including some predicted data). For passenger travel, steady increases in both road and air transportation (in passenger kilometer) can be discerned, while the levels of rail and public transportation have remained more or less constant. An increase in freight transportation is also apparent, with the largest proportion (in ton kilometer) of this increase deriving from freight transportation up to the year 2020. However, it should also be noted that air transportation is forecast to double in the same period.

In Fig. 21.3, the predicted rise in the energy demand of the transportation sector during the period from 2004

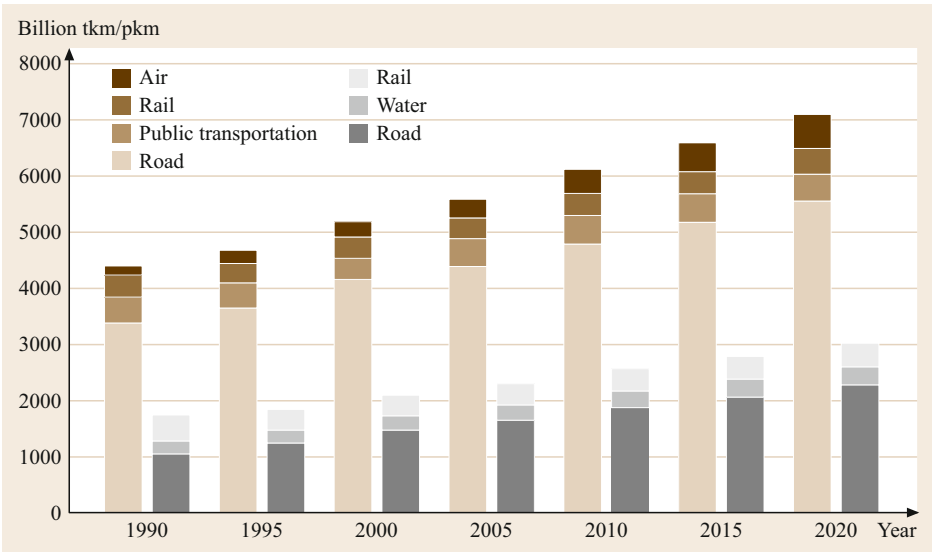

Fig. 21.2 Growth in various passenger (*left-hand bars for each year*) and freight (*right-hand bars for each year*) transportation modes in Europe between the years 1990 and 2020 (tkm: ton kilometer; pkm: passenger kilometer). Source: [21.3]

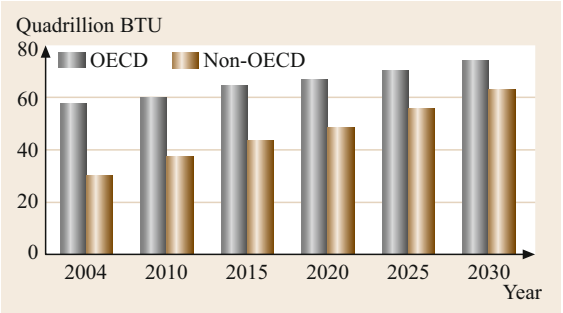

Fig. 21.3 Energy consumed by the transportation sectors of OECD and non-OECD countries during the period 2004–2030 (after [21.4]) ►

to 2030 is shown for Organisation for Economic Co-operation and Development (OECD) countries and for non-OECD countries. For OECD countries, an increase of 48% is envisioned, whereas growth of 66% is predicted for non-OECD countries. Such large increases imply that it is necessary to improve transportation efficiency and to search for new sources of energy.

21.2 Impact of Safety and Environmental Legislation on Transportation Technologies

In Fig. 21.4, greenhouse gas emissions in g/pkm (grams of CO_2 per person kilometer) are shown for various modes of transportation in Germany, based on statistical data from 2017. The plot shows that traveling by plane yields the largest greenhouse gas emissions in g/pkm, and that rail transportation is more efficient in terms of emissions than road transportation. However, it is difficult to accurately compare the emissions of different transport modes (road, rail, and aviation) because calculations of emissions are based on a range of assumptions (e.g., the distance traveled, the transportation speed, and the average occupation of the vehicle, train, or plane), and modifications to these assumed values can have major effects on the calculated emissions. For instance, a small change in the occupation of a small vehicle (e.g., a car) has a huge impact on the calculated emissions (in g/pkm), whereas a small change in the occupation of a train or plane has no noticeable impact on the calculated emissions (in g/pkm).

A combination of economic aspects (e.g., energy efficiency, cost efficiency, investment required, transportation speed, and space required) jointly determine the transportation mode that will become dominant in a particular area. In addition, legislative requirements are placing increasing constraints on all areas of transportation. For instance, limits on the emission levels of pollutants (e.g., nitrogen oxides, unburned hydrocarbons, carbon monoxide, and particulates resulting from the combustion of hydrocarbon-based fuels with air) from vehicles are gradually decreasing around the world.

Figure 21.5 shows that the CO_2 emission levels (in g/km) from new registered cars in Europe dropped considerably (by about 25%) from 2006 to 2015. Future EU legislation aims to decrease CO_2 emissions of new registered vehicles even further. For 2021, new cars must release no more than 95 g/km CO_2 on average or the manufacturers of those cars will face financial penalties. This permitted level of CO_2 emissions is set to decrease by 15% in 2025 and by 37.5% in 2030.

Besides CO_2 emissions, which are related to the efficiency of the powertrain, legislation is increasingly focusing on reducing the emissions of gases that are harmful to human health. Figure 21.6 shows how the

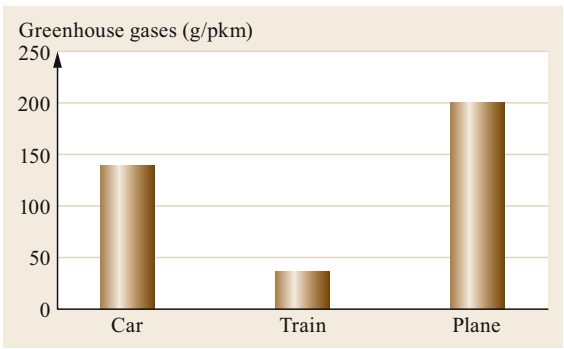

Fig. 21.4 Comparison of the greenhouse gas emissions (in g/pkm) from various modes of passenger transportation (after [21.5])

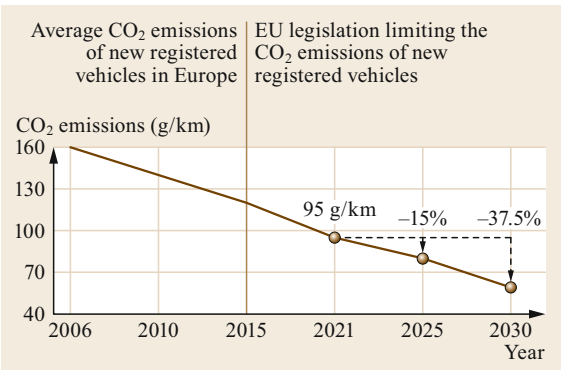

Fig. 21.5 Drop in CO_2 emission levels (in g/km) from new registered vehicles in Europe from 2006 to 2015, and prospective legislative limits on the CO_2 emissions of new registered vehicles in Europe from 2021 on (after [21.6])

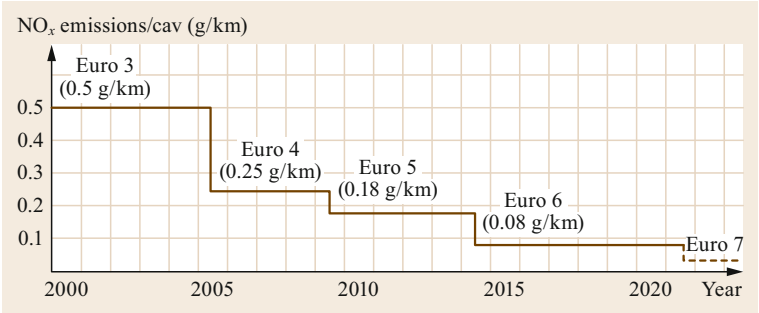

Fig. 21.6 Evolution of the EU limit on NO_x emissions from diesel-powered passenger cars since the year 2000, starting with the introduction of the EU legislation Euro 3; the implementation of Euro 7 is imminent in 2021 (after [21.7])

EU limit on nitrogen oxide (NO_x) emissions from diesel-powered passenger vehicles has evolved since the year 2000. Within 14 years of the first legislation, Euro 3, the limit on NO_x emissions had decreased by 84% from 0.5 to 0.08 g/km (Euro 6). This limit is set to decrease even further in 2021 with the introduction of the Euro 7 legislation.

These graphs illustrate a common trend among the industrialized nations to reduce the limits on pollutants emitted by vehicles. This means that car manufacturers must direct increasing resources into developing technologies that can fulfill all of their legislative requirements.

Besides chemical emissions, noise is also produced by the various modes of transportation. Although noise levels of 130–140 dB(A) are painful to humans, lower noise levels are also considered harmful because they annoy (leading to aggression and high stress levels), cause hearing loss, and have other harmful effects, depending on the noise level and duration of exposure. Major sources of transportation-related noise emissions are road, rail, and aircraft traffic.

Over the years, noise limits have been tightened for all transportation technologies. EU regulation Nr. 540/2014, for example, significantly reduces the permitted level of noise from a car. On the other hand, the regulation also mandates that all electric and hybrid cars (which are generally much quieter than cars that are entirely powered by petrol or diesel) must be equipped with an acoustic vehicle alerting system (AVAS) to warn pedestrians of their presence. In another example, in 1971, the International Civil Aviation Organization (ICAO), an agency of the United Nations that codifies the principles and techniques of international air navigation, established regulations limiting the noise emitted by different classes of civil aircraft.

Finally, safety issues should be mentioned as a major driver of transportation technology development. Improvements in transportation safety are imposed by legislation or prompted by customer requirements. In general, we can differentiate between measures that enable the safe use of the transportation mode of interest and measures that reduce the likelihood of harming a third party who is using the same mode, a different mode, or no mode of transportation. If we take aircraft as an example, measures aimed at improving safety when using this mode of transportation—including stringent servicing routines and heavily scrutinized development processes—are the main focus, rather than measures to reduce the probability of harming a third party. On the one hand, this is because any severe failure in the air would almost certainly cause a large number of casualties; on the other hand, the potential of an airplane to harm third parties cannot be significantly reduced by altering its design. Other measures must be taken to ensure the safety of third parties; for instance, air-traffic control is responsible for ensuring that two aircraft do not collide. In contrast, a road vehicle will often move through dense traffic, and the safety of the vehicle when it is passing through such traffic is largely dependent on the awareness of its driver (although there are various regulations concerning regular vehicle servicing). However, cars are increasingly being fitted with technological support for the driver (such as an automatic emergency braking system and a driver alert system) that lowers the probability of an accident.

21.3 Upcoming Changes in Transportation

When used in combination with fast and comprehensive mobile communications technology, digitalization enables digital networks, automation, artificial intelligence, and predictive analysis of a huge amount of data. Digitalization is therefore leading to a mobility revolution in the transportation of goods and people. The predicted changes in mobility can be summarized by the buzzword ACES, which is an acronym for *automated, connected, electrified, shared/services*. We now consider these four aspects of mobility in turn.

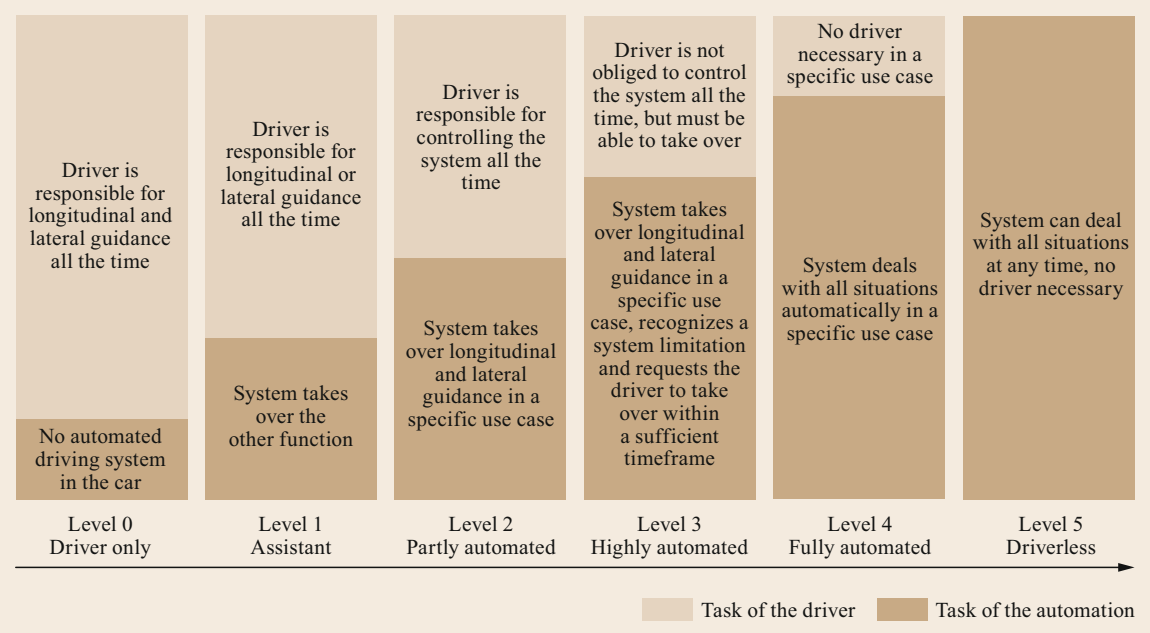

Fig. 21.7 Different levels of automated driving (after [21.8, 9])

21.3.1 Automated

Automation is central to future developments in transportation mobility, and it implies a major change in the use of the traffic infrastructure. In automation, the various tasks involved in driving are gradually transferred from the driver to the vehicle. Five different levels of automation can be distinguished. At level 0 (driver only), the driver is responsible for longitudinal and lateral guidance of the vehicle at all times; there is no active technology in the car that interferes with the driving. At level 1 (assistant), the driver is responsible for longitudinal or lateral guidance, whereas an onboard system is responsible for the other function (e.g., cruise control). Level 2 (partly automated), which is already implemented in modern premium cars, implies that the car can perform longitudinal and lateral guidance under certain circumstances, but the driver always has ultimate control of the system. At level 3 (highly automated), the system performs longitudinal and lateral guidance under certain circumstances, recognizes system limitations, and requests for the driver to take over within a sufficient timeframe. At level 4 (fully automated), the system can deal with all situations encountered while driving automatically in a specific use case (e.g., on a standard motorway). In this specific use case, no driver is necessary but the vehicle must be occupied. At level 5 (driverless), no driver is necessary, and the system can deal with any situation at any time. The different levels are shown in Fig. 21.7.

Level 4 or 5 automation of driving potentially has huge benefits. For instance, trucks can be driven together as a platoon on a motorway to make transportation safer, easier, and cheaper. Former drivers of private cars can use the time that they would have spent driving working or relaxing instead. However, various technical and legal difficulties will need to be solved before safe and reliable level 5 automation is achieved for cars; we may have to wait until at least 2030 for the advent of this level of car automation.

21.3.2 Connected

In the future, vehicle production per se will become less profitable, but, given that automation will relieve the occupants of the vehicle of the need to perform many/any of tasks associated with driving, more revenue will be earned by providing in-car services to the occupants through interconnectivity (e.g., via streaming services). In other words, in the future, business models for the automotive industry will largely focus on providing services on the move.

21.3.3 Electrified

It is very likely that in the medium-to-long term, electromobility will provide the solution to many of the problems with present-day road transportation technologies, including air and noise pollution. One of the major issues with current electric vehicles—their short ranges—

should be solved through future improvements in battery technology. Automation could allow electric vehicles to drive themselves to charging stations between transportation tasks. Especially in the US and Asia, new players are entering the electric vehicle industry, which is driving advances in electromobility technology. However, there is still a range of technical issues with electromobility to address, such as the charging infrastructure and the generation of green electricity.

21.3.4 Shared/Services

The predicted advances mentioned above should enable the operation of huge autonomous car fleets in a manifold and intermodal manner. In urban areas, young people in particular would prefer not to own a car but to be able to hire the transportation they require on a pay-per-use basis. The transportation systems, including cars, envisaged for such a scheme should be ecological, efficient, cheap, and flexible (in terms of mode of usage). Car sharing and ride hailing are becoming increasingly popular in big cities. Many companies already provide transportation as a service, hiring out cars with or without a driver. There is a strong drive to incorporate automated cars into this model to improve the service and optimize costs.

These aspects could lead to an intermodal transportation system that is booked on one platform as a single service; for instance, a trip involving a long-distance flight, an autonomous car ride from the airport to a bike rental facility, and then a bike ride to a hotel in a district in which cars are banned could all be booked in one go as a single service. Huge changes are also foreseen to the transportation of goods. For example, deliveries may be transported by an autonomous truck that passes the goods to a drone stationed within a mile or so of the final delivery address. The drone then delivers the goods directly to that address.

In the next section, we focus on vehicle technology and development.

21.4 Automotive Technology

By far the biggest proportion of all transportation (of passengers and goods) is carried out via the road network, as it is still the most flexible and least expensive way to meet transportation demands (Fig. 21.2). There has been a steady increase in passenger and goods traffic over the years. In this section, we begin by describing the basic technology of, legislation associated with, and development trends in automotive vehicles. After that, trends in automobile body design are discussed, before the automotive vehicle development process is outlined.

21.4.1 Automotive Technology, Legislation, and Development Trends

The automotive industry is a key global industry. In order to compete in the steadily growing automotive market, original equipment manufacturers (OEMs) and suppliers need to generate innovations.

Tougher emission legislation has resulted in a shift from conventional vehicles powered only by an internal combustion engine to more electrified powertrains. As shown in Fig. 21.8, hybrid vehicles contain both an electric drivetrain (with a range of up to 80 km using batteries) with an internal combustion engine (thus increasing the range of the vehicle beyond that achieved using the batteries). The batteries in a hybrid vehicle are charged by recuperation or by the internal combustion engine. If the vehicle can also be charged from a plug socket, it is known as a plug-in hybrid vehicle (PHEV).

A battery electric vehicle (BEV) contains no internal combustion engine; it is driven directly by electrical energy and has a range of up to 500 km. A fuel cell vehicle generates electrical energy by converting hydrogen in a fuel cell to water and energy. This energy is stored in a battery and used to drive an electric engine. The range of a fuel cell vehicle is comparable to that of a vehicle with a conventional drivetrain.

The most important parts of an automobile in terms of technological developments and future challenges are shown in Fig. 21.9; they include the body, chassis, advanced driver assistance system, internal combustion engine, and electric motor. Development trends for these vehicle parts are now described in detail.

Development Trends in Automobile Bodies

The body is not only the load-carrying part of an automobile; it also determines the vehicle's capacity for passenger and/or freight transport, dominates the outer appearance of the vehicle, and has an important influence on safety and driving comfort. The need for passive safety (noise–vibration–harshness, NVH), driving comfort, and dynamics determine the design of the body.

Another aspect of vehicle safety that is growing in importance is pedestrian protection. The introduction of regulations relating to pedestrian protection in Europe and in Japan has already prompted major changes to the design of the front of the body in many car models. As these regulations become increasingly stringent,

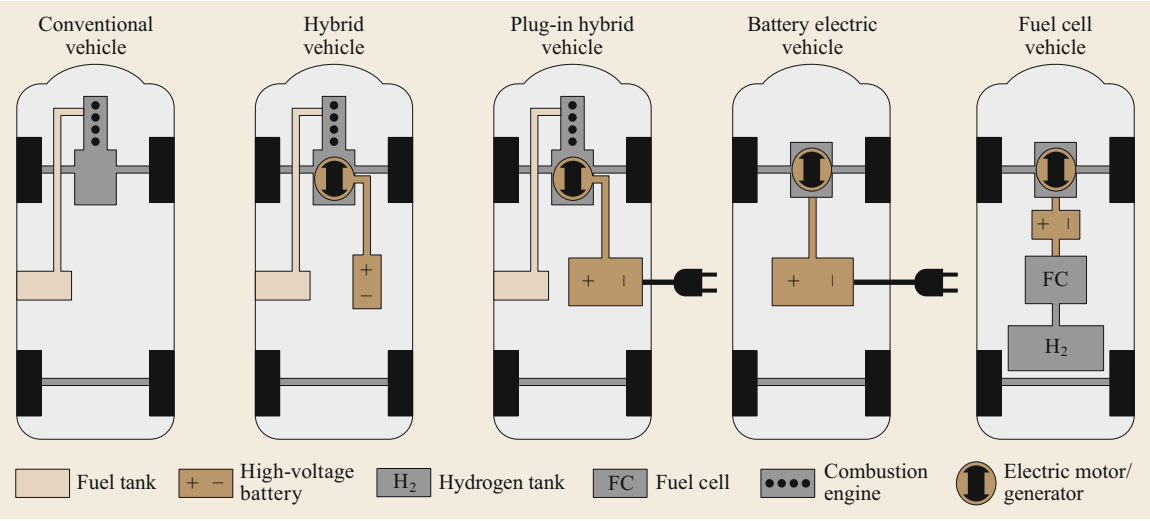

Fig. 21.8 Overview of various powertrain technologies (after [21.9])

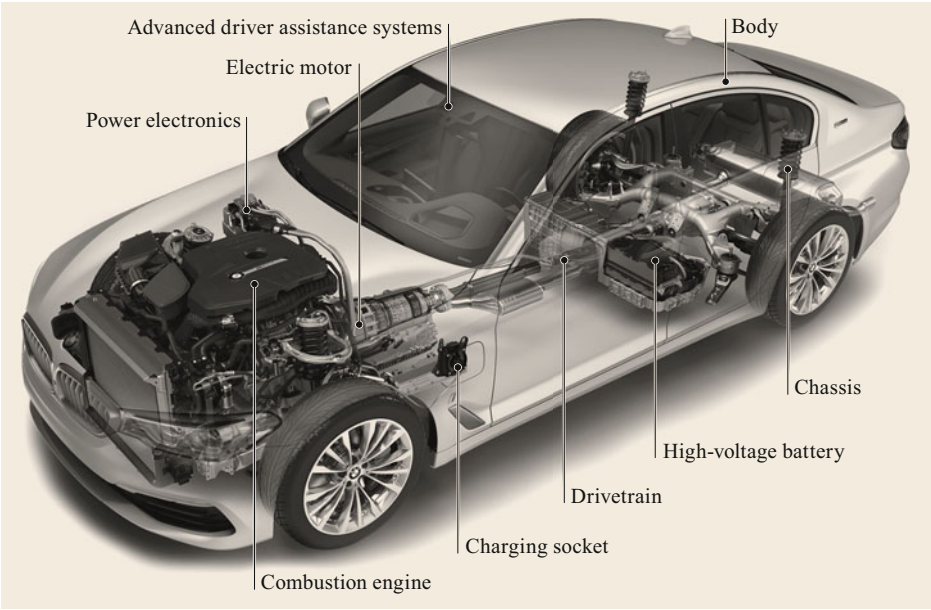

Fig. 21.9 Automobile parts that are currently undergoing prominent technological development; the vehicle shown in the figure is a BMW 5 Series plug-in hybrid (after [21.10])

additional pedestrian safety measures will be launched in the coming years. Moreover, crash compatibility in vehicle-to-vehicle collisions will become an important safety issue in the future, and is likely to influence body design significantly.

While fitting extra safety measures tends to increase the mass of the vehicle, there is a strong drive to reduce vehicle weight in order to improve handling characteristics, driving performance, and—last but not least—fuel consumption and CO_2 emissions. However, over the last three decades, the average unladen weight of a passenger car has steadily increased, despite intensive efforts to produce lightweight body structures. A major challenge in vehicle engineering is to reduce vehicle weight in spite of the push to add extra functionality, the need to fulfill new requirements, and the pressure to keep the cost of a vehicle as low as possible. The standard design concept for high-volume cars is a steel unibody. Substantial improvements in the crash behavior of steel unibodies and weight savings have already been realized through the application of new high- and ultrahigh-strength steels. Rolled profiles and hydroformed tubes are employed due to their superior strength and stiffness in comparison with conventional

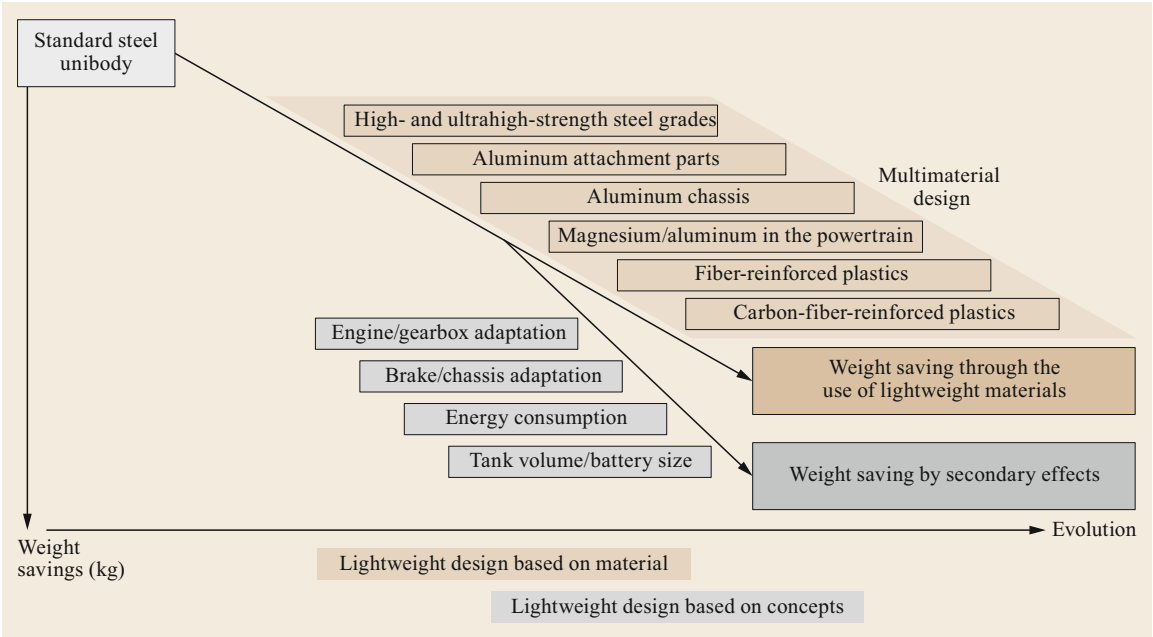

Fig. 21.10 Achieving lightweight vehicles through the application of appropriate materials and concepts (after [21.11])

spot-welded steel-sheet structures. In addition, a trend towards multimaterial design is apparent. In principle, this means that the most suitable material is selected for any particular body component or module, resulting in an intelligent mix of materials such as aluminum, magnesium, (carbon) fiber-reinforced plastics, and of course steel. Reducing the vehicle weight also has knock-on effects that allow even more weight to be saved; for instance, a lighter vehicle can achieve the required driving and braking performance using a smaller engine and gearbox and smaller brakes. Lowering the weight also reduces energy consumption, allowing the use of smaller fuel tanks or batteries to achieve the same range. Applying all of these weight-saving measures, which are summarized in Fig. 21.10, can reduce the vehicle weight by up to 200 kg.

Development Trends in Automobile Chassis

For decades, the trade-off between safety (roadholding) and comfort (soft suspension and noise insulation) presented the greatest challenge to every chassis engineer. However, this trade-off is gradually becoming irrelevant due to the use of adaptive components and active chassis systems. Over the next decade, the cost of electronic systems built into the chassis is predicted to increase fivefold compared to today (Fig. 21.11). As chassis control systems become more intelligent, there is an increasing need for an integrated control strategy. The next step is to link these systems to passive systems.

The electronic stability program (ESP), for instance, can be linked to active steering or electric power steering to allow combined steering and braking input, or to adaptive air suspension or variable damping systems to facilitate roll-angle adjustment. Also, ESP sensors can detect the risk of an accident and activate passive systems. The MacPherson strut (which is used in 85% of all automobiles) and double-wishbone suspension are the most commonly used front suspension types, while twist beam suspension and multilink suspension are the main choices for the rear suspension. Multilink rear suspension is expected to gradually grow in prominence until it is used in over 55% of all automobiles. Advances in braking, steering, and damping systems are facilitating the development of the so-called *dry* chassis, in which hydraulic actuation is replaced with electric motors. This enables greater chassis control and system integration.

Development Trends in Advanced Driver-Assistance Systems

Due to increasing traffic and the growing complexity of driving tasks, technical systems that support the driver and relieve him or her of some of those tasks have been developed. Such advanced driver-assistance systems (ADASs) include systems that automatically stop or accelerate the vehicle when appropriate as well as active safety measures (e.g., those focusing on pedestrian and cyclist safety). To fully realize such systems, further advances in recognition systems (e.g., front,

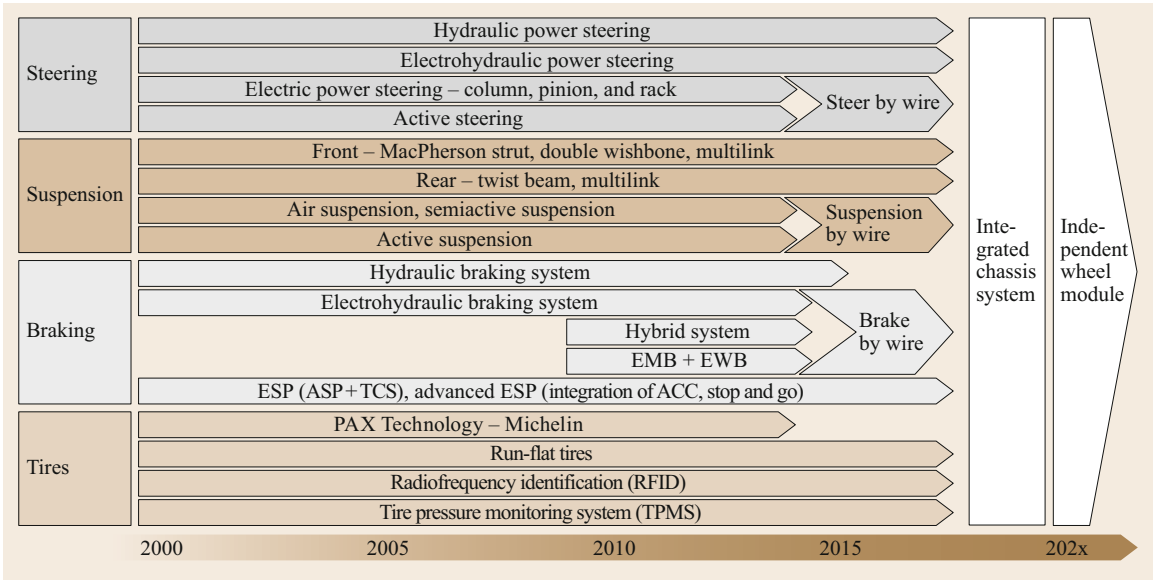

Fig. 21.11 Evolution of chassis components (after [21.12])

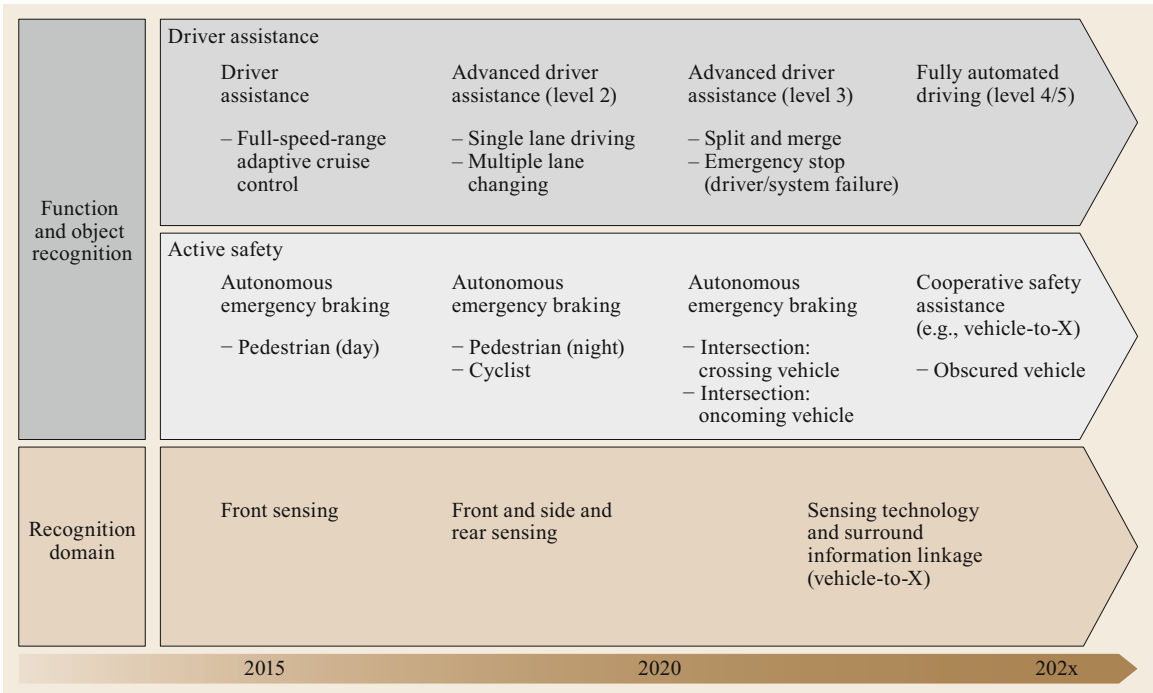

Fig. 21.12 Automation roadmap for advanced driver-assistance systems (according to [21.13])

side, and rear sensing and vehicle-to-X communication) are necessary. The long-term goal is to fully automate driving in order to increase safety and avoid accidents. The automation roadmap for ADASs is shown in Fig. 21.12.

Development Trends in Internal Combustion Engines

Figure 21.13 provides an overview of current development trends for internal combustion engines. The overall aim is to reduce fuel consumption and thus

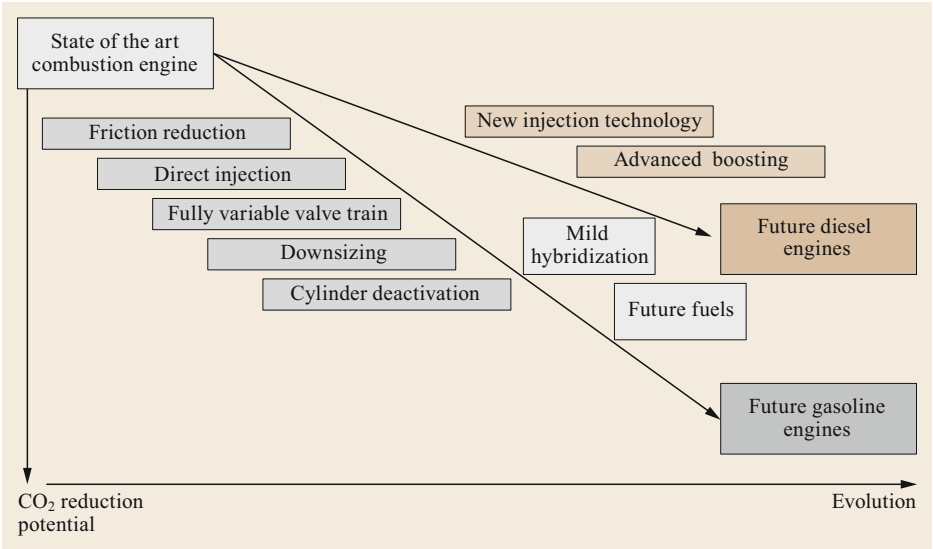

Fig. 21.13 Techniques for reducing CO_2 emissions from combustion engines (according to [21.14, 15])

CO_2 emissions from diesel and gasoline engines. The main targets of gasoline engine development are direct injection combined with advanced boosting strategies, increased variability (e.g., a variable valve train and a variable compression ratio), cylinder deactivation, and an increased level of mild hybridization (increasing the onboard power supply in the car from the current standard, 12 V, to 48 V enables more electrical energy to be recuperated, supporting the internal combustion engine and thus reducing fuel consumption and CO_2 emissions). For diesel engines, research and development is focusing on advanced injection systems (increased injection pressures and higher degrees of variability), boosting technology, and an increasing level of mild hybridization. Additional improvements to both gasoline and diesel engines should be possible through the use of future fuels, such as tailored fuels produced from biomass.

Development Trends in Electric Drives

Electric vehicles are still more expensive than conventional vehicles with internal combustion engines. In addition, they have significantly smaller ranges. These two factors are the two biggest challenges to the widespread adoption of electric vehicles. However, battery costs have substantially decreased recently (they have dropped by about 50% over the last 8 years), while battery energy density and thus the average range of an electric drive have markedly improved (on average by about 100% over the last 8 years; an increasing number of electric cars with a minimum range of over 300 km are now on the market or have been announced by manufacturers). Figure 21.14 implies that these two trends are likely to continue in the future. Therefore, even though there is still a huge gap in price between internal combustion engine powertrains and electric vehicles, this gap is gradually decreasing.

Another factor in the widespread adoption of electric vehicles is the charging process and infrastructure. The recharging process needs to be fast and easy to perform, just like refueling a conventional gasoline- or diesel-powered car. This means further technical advances that enable a high charging power are required. In addition, recharging stations must be easy to find and readily available, similar to gas stations today.

21.4.2 The Automotive Vehicle Development Process

The standard development process for a vehicle, as shown in Fig. 21.15, takes about 5 years, although it can be shorter or longer depending on the technical changes required and whether it is a completely new model or it is derived from an existing model. Generic processes such as strategic discussions and decisions, research into new technologies, and innovation management are always underway at an OEM. These inputs are available at milestone 0, the start of the product development process. During the following 6 months, the exact product goals and a rough product definition are established. Inputs at this stage include legislative issues such as emission thresholds and safety standards as well as customer requirements. The activities of competitors are also considered. When this stage is finished, i.e., the goals and the product have been defined, milestone 1 has been achieved. After that, further 6 months are devoted to precisely defining the product concept that fulfills the agreed goals. The rough product defini-

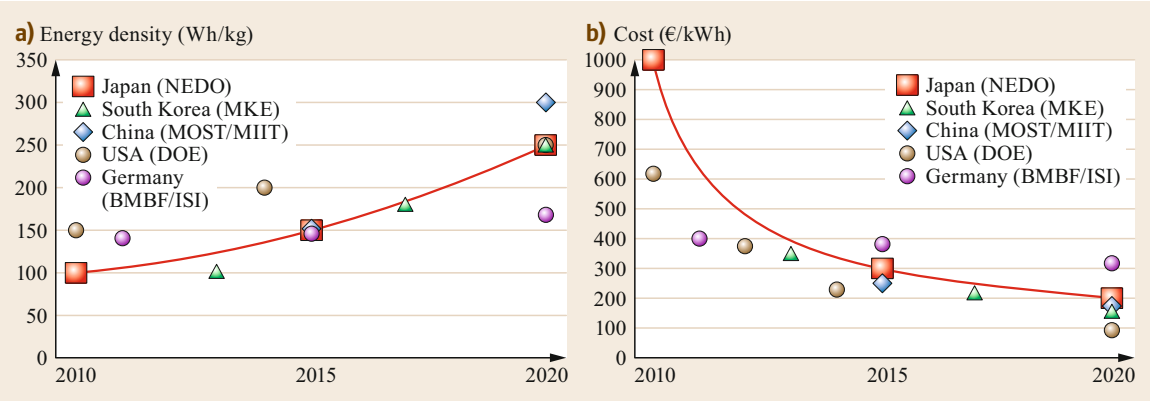

Fig. 21.14a,b Plots showing how **(a)** Li-ion battery energy density (Wh/kg) targets and **(b)** Li-ion battery cost (€/kWh) targets of various countries involved in the development of large-scale third-generation Li-ion batteries for application in BEVs/PHEVs have evolved since 2010. Note that the data were derived based on different definitions of market maturity and different numbers of units (e.g., some data were obtained based on battery prototypes with only a small number of units, while others were obtained based on a larger number of batteries comprising a market-entry/small-scale series) (after [21.16])

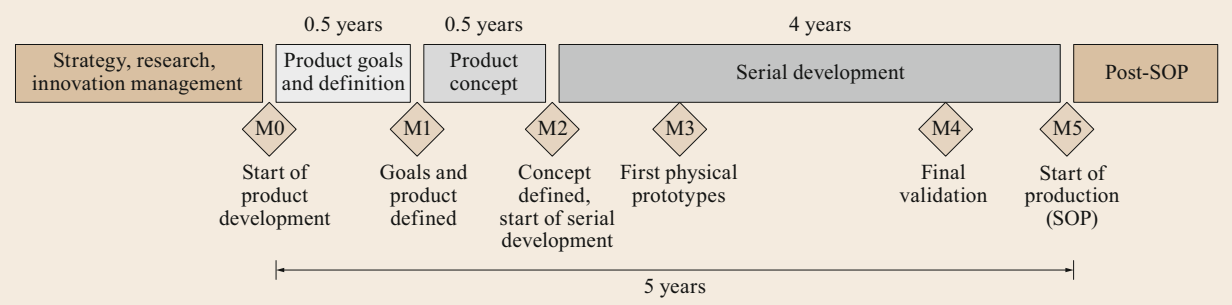

Fig. 21.15 The development process of a car (after [21.15, 17])

tion produced in the previous stage provides additional guidelines. At the end of this phase (milestone 2), the concept has been defined in detail and serial development can begin. Concrete constructions are realized, including a production concept, and negotiations with suppliers are initiated. The first physical prototypes are created (milestone 3) to test the product. At the end of the serial development process, a final validation is carried out (milestone 4) to check the quality of the final concept; then, assuming that the product is validated, the process moves to milestone 5, the start of production (SOP). The serial development process takes about 4 years. After that, post-SOP activities are carried out, such as facelifts of the product.

We now move on to describe aerospace technology and development.

21.5 Aerospace Technology

The wealth of modern society is based on the fast and reliable transport of information, passengers, and freight in an environmentally acceptable way. Products of the aerospace industry are a crucial element of the global transportation system: satellites provide weather information and navigation signals and transmit messages worldwide; aircraft permit the fast and safe transportation of passengers and/or freight across borders; and military aerospace technology is an important part of any military strategy. In commercial terms, the future of aviation is bright: passenger traffic has been increasing at a stable rate of around 5% per year for three decades, and this trend is forecast to continue for the next few decades; cargo transportation is growing at a faster rate, around 6% per year. From Fig. 21.2, it is apparent that the number of passengers that are

transported annually by aircraft surpassed the number transported annually by rail and public transport in 2015. In this section, aerospace technology, legislation, and development trends are explored. The aerospace development process is also described.

21.5.1 Aerospace Technology, Legislation, and Development Trends

In the following, the relationship between aerospace technology and society is considered, especially from the perspective of pollution and noise. After that, different aerospace disciplines are described, and then challenges in aeronautical engineering are discussed and analyzed by dividing the historical development of this field into four different phases.

Aerospace Technology and Society

Space vehicle launches are undeniably spectacular, but they are limited to only a few locations in the world. Therefore, the public takes considerable interest in these launches, because it is linked to that dream of mankind mentioned before. On the other hand, even though aircraft are also part of that dream and are mandatory for modern life, they tend to receive greater criticism than many other modes of transport. Whereas, for example, railway noise is generally accepted (even in city centers at midnight), aircraft noise is often said to be annoying, even when it is barely noticeable. The public has largely accepted the drawbacks of all other forms of traffic, but noise and emissions from aircraft seem to generate a disproportionate amount of irritation considering the contribution of air travel to the overall transport system. This may be due to the fact that the human desire to fly is rooted in observations of birds soaring in the sky, which they appear to do with an elegant ease and weightlessness. Thus, people react more sensitively to aircraft noise and pollution than to pollution from any other means of transport. In reality, much progress has been made in this area in recent decades. Noise from aircraft has been drastically reduced, with the aim being to keep most of the noise contour within the airport area (Fig. 21.16). For instance, the Airbus A350-900 has a 40–50% smaller noise contour than its predecessor models (the A-340-600 and A340-300). Exhaust emissions have also been decoupled from the number of aircraft, as illustrated for aircraft of the Lufthansa Group in Fig. 21.17. However, the overall fuel consumption of aircraft is still rising.

As in other fields, the tasks involved in aerospace engineering can be discussed from various perspectives. We can consider the work of specialists in many fields, or we can adopt a system approach in which various disciplines contribute to the creation of increasingly

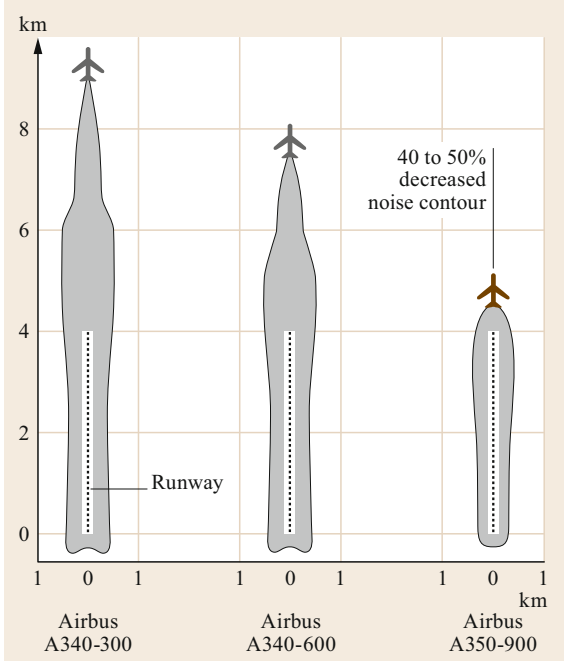

Fig. 21.16 Noise contour of a state-of-the-art Airbus A350-900 as compared to those of its predecessor models, the A340-300 and A340-600 (after [21.18])

complex components up to the level of the final vehicle. Finally, we can also employ a *system-of-systems* approach when contemplating the air transport system (ATS). In astronautics, this system-of-systems approach includes the vehicle, payload, transfer, and ground support. In any case, the overall lifetime of the aircraft must be addressed, from its first flight or launch to the period in which it is operating as envisaged and finally to the disposal of the aircraft. The disposal process is becoming increasingly important in both aeronautics and astronautics due to the need for global resource management and the issue of space debris, respectively.

Aerospace Disciplines

Aerospace in general is an integrated or so-called integration subject that includes aeronautics and astronautics as particular activities. Aircraft design is carried out based on inputs from the fundamental engineering disciplines of aerodynamics, structures, and systems, which in turn include flight mechanics, statics, kinematics, and other subdisciplines. In addition, combinations of those fundamental disciplines have emerged, such as aeroelastics and aeroacoustics. Advances have been made in all of these disciplines, such as new flow control methods, new materials, and new electronic systems. Components are designed and created based on

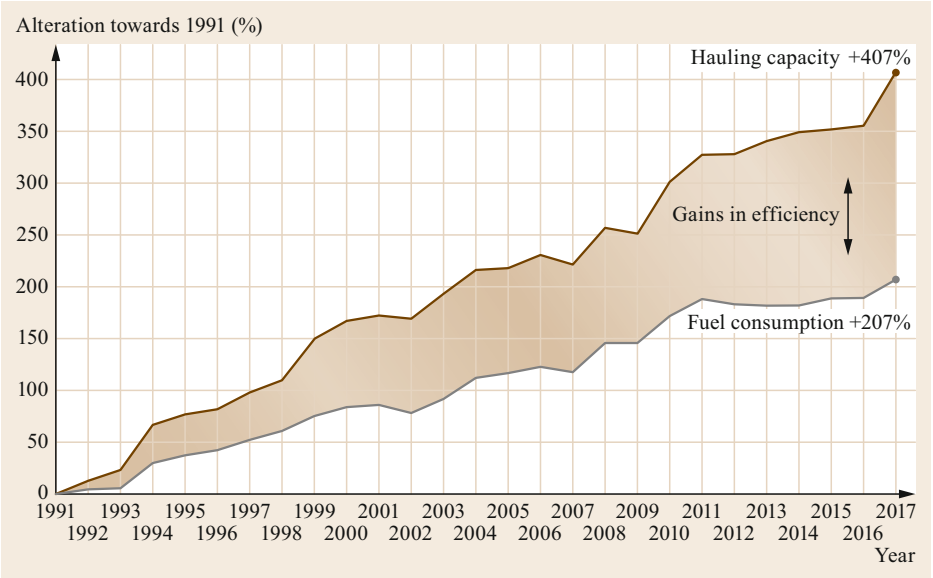

Fig. 21.17 Decoupling of fuel consumption from hauling capacity for the fleet of the Lufthansa Group since 1991 (after [21.18])

work done in the individual disciplines. This process is an interdisciplinary task; for example, a knowledge of aerodynamic performance and structure, including the kinematics and actuators on the systems side, is required when developing an aircraft flap. In aeronautics, the largest components are the complete aircraft structure and the engine, which are developed and manufactured separately.

The development of components and the process of combining those components to construct an aeroplane are multidisciplinary and interdisciplinary tasks. New aircraft are constructed from materials and components generated by monodisciplinary research (such as new materials, new actuators, or a specific aerodynamic vortex generator) and from integrated technologies. For example, fly-by-wire technology was required for the European supersonic airliner Concorde in the 1960s. Without this technology, it would not have been possible for pilots to fly Concorde in various flight regimes (e.g., taking off, cruising, and descending), given that the control behavior of the aircraft changes with the flight regime. Afterwards, this immature technology was introduced into the Airbus A310; then, when the technology had matured, it was fitted to the Airbus A320, which made its maiden flight in 1987.

Flow control technology and artificial instability are other examples of technological development in this field, and manufacturing technologies such as friction steel welding, laser beam welding, advanced bonding, and surface coating have been developed and are now part of the production process.

Following complete vehicle assembly, the aircraft is then operated in a diverse system.

Aircraft navigate with the aid of air-traffic control, and they are linked to other traffic in the air and on the ground, especially in the vicinity of airports. They need to be loaded and unloaded. They are also included in the concept of intermodality, in which personal and public ground transportation is linked to air or sea transportation.

Challenges in Aeronautical Engineering

The history of aeronautics can be divided into three phases. During the first phase, which lasted from the inception of aeronautics until the end of World War II, the main aim was to gain a physical understanding of powered flight. This began with daring pilots in *fantastic flying machines* who were constantly trying to break range, speed, and altitude records. The next phase coincided with the introduction of jet engines and the emergence of commercial aeronautics. Many different aircraft configurations were studied, including vertical take-off and landing (VTOL) aircraft such as the Dornier Do 31, supersonic transport such as Concorde, and flying wings such as the Northrop YB-49. This led to the third phase, corresponding to a mature commercial aviation industry based on aircraft that all look rather similar regardless of the manufacturer. This optimal aircraft configuration is the pay-off from all of the expensive civil aircraft design and manufacturing studies performed in the previous phase.

Due to the success of commercial air transportation, three other issues have emerged. First, airports are more often operating at their capacity limits, so it is questionable whether it is possible for air traffic to increase, even if there is a demand for it. The second issue is linked to

this: even though the contribution of aviation to global emissions is relatively small (about 2%), it is still the focus of intense debate. The third issue is that of safety, which is becoming an increasingly important topic in aviation, and is one that is again linked to the growth of air transportation. The current reliability rate for critical aerospace components (10^{-9} failures per flight hour) will not be sufficient if the number of aircraft doubles within a decade. In order to reduce the number of accidents as the number of aircraft increases, functional hazard analysis must become more reliable. This must be achieved for single components such as an actuator, subsystems such as an aileron, and the complete aircraft system and structure.

These issues are addressed by the European Commission in its *Vision 2020* on aeronautics and by the National Aeronautics and Space Administration (NASA) in its *Aeronautics Blueprint*. Both draw similar conclusions: given the importance of air transportation to the wealth of society on the one hand and the environmental issues that are linked to the aviation industry on the other, additional top-level aircraft requirements (TLAR) will be required to balance transport needs with societal needs (i.e., safety and security) and environmental protection. These additional TLAR may lead to different aircraft configurations as well as new ways of operating them. In addition, a system approach is needed to address these issues; for example, in contrast to road and rail transport, security will play an increasingly important role in commercial aviation. There are an increasing number of studies of seamless air transport, which will require new ground procedures and probably new aircraft designs. Defining the new TLAR and ensuring that the overall vehicle and system composition complies with those TLAR will be a demanding task for all aerospace disciplines, including both aeronautics and astronautics. With the implementation of the new TLAR, we can expect a fourth phase to begin: *sustainable growth*.

21.5.2 The Aerospace Development Process

Just like other product development processes, the general process of designing an aircraft or spacecraft has been established over the past few decades. Initially, there is a market analysis that searches for desirable products that are currently missing from or understocked in the market. In aeronautics, this may be defined by the so-called *transport task*, i.e., the requirement to move a given payload across a given distance within a given time. In astronautics, aside from the vehicle, the payload itself (such as a satellite) may be the product that needs to be developed. The TLAR can then be derived from these general requirements set by market demands, and these TLAR provide the basis for future project office (FPO) work. The general arrangement (GA) of the vehicle to be designed is then derived using tools based mainly on statistics and/or simple calculation methods. This GA will then be passed to various departments, such as flight physics or structures. Together with aircraft program management, they will start developing components using test rigs or simulators and by performing wind tunnel tests. At this stage, new technologies that have been made available by various disciplines can be included in the design process. Digital mock-ups (DMU) are increasingly used in the first part of the development phase instead of hardware.

When the GA and first performance estimates are available, launching customers must be found. The needs of those customers will influence the final design. When a certain number (which depends on the product size and cost) of products have been sold, the actual development of the product begins with the program *go-ahead*, which occurs almost in parallel with the production of the first parts. Specific tests will be carried out on prototypes, which may require some final (hopefully minor) changes in the design. The last step is the certification process, which ends with product entry into service (EIS). The overall development process as outlined above is almost the same for any aircraft manufacturer, and can be seen as a series of milestones, as shown in Fig. 21.18.

At present, the market analysis stage can last for 2 years, the predevelopment stage for 3 years, the development and manufacturing stage for about 5 years, and the certification stage for another year. Just before a program is initiated, technology development may be carried out, with technological feasibility considered in a first step and technology application studies performed in the final step. Overall, the time between the first suggestion that a new aircraft should be developed and the EIS is approximately 10–15 years. For example, the first document proposing what would become the Airbus A380 was published in 1989; at that point the proposal was for an ultra-high-capacity aircraft (UHCA) called the Megaliner. Later it became the Very Large Commercial Transport (VLCT), a joint feasibility study by Airbus and Boeing. The committed program started in 2000, and the A380 was finally introduced into airline service in 2007, corresponding to a total of 18 years of development. Of course, all manufacturers try to speed up this process. Further optimization of the development process for aircraft based on the already highly optimized standard configuration (i.e., fuselage, wing, engines, and tailplane) is possible mainly through improvements to the design chain, including supplier management.

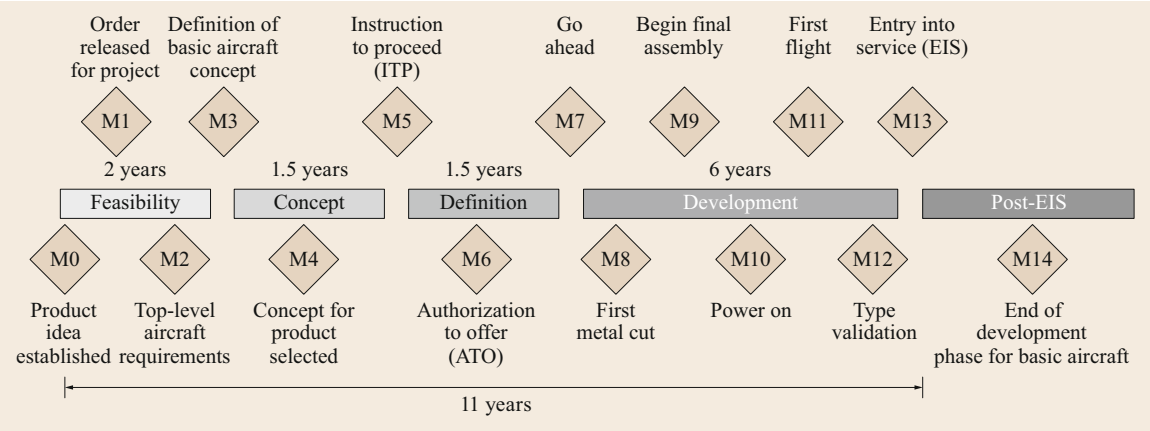

Fig. 21.18 Development process for an airplane

21.6 Rail Technology

As shown in Fig. 21.2, the amount of goods and people transported by rail in Europe has remained stable for a considerable amount of time. In this section, we discuss the basic technology and legislation associated with rail transportation and we consider the development of vehicles used in rail transportation.

21.6.1 Rail Technology, Legislation, and Development Trends

The main difference between rail and other means of transportation is the automatic guidance of rail vehicles along the track, which leaves only one degree of freedom for any rail vehicle—its velocity. This automatic guidance from the track keeps the vehicle on a particular course defined by the rail infrastructure, but it also means that it is not possible for the vehicle to sidestep other rail vehicles spontaneously; rail vehicles can only pass each other at specially equipped locations along the track. To prevent system deadlock, it is necessary to implement a schedule of rail vehicle movements—a timetable. Together with the timetable, there is a need for a protection system that prevents head-on collisions of trains on the same track.

Efficiency, Resistance, and Traction Forces

One advantage of using a railway schedule is that trains can run almost nonstop from one station to another (as long as the schedule works properly!). Thus, long and heavy trains can be operated in an energy-saving manner as they do not have to perform multiple accelerations and decelerations between stops. This is also important because the traction needed to accelerate a train must be generated from the friction between the wheels and the track, meaning that the acceleration of a train is limited. The frictional coefficient between rolling steel bodies is always correlated with the relative velocity (slippage) between the bodies (Fig. 21.19). The maximum coefficient of friction for steel wheels on dry rails is about $f_x \approx 0.45$; if the rails are wet or polluted, this can decrease to $f_x \approx 0.1$. This also means that a maximum deceleration b (where all wheel axles are braked) of $\approx 1\,\mathrm{m/s^2}$ can be achieved, as shown below.

$$F_\mathrm{B} = mb = f_x mg$$
$$\Rightarrow\ b = f_x g = 0.1 \times 9.81\,\mathrm{m/s^2} = 0.981\,\mathrm{m/s^2} \tag{21.1}$$

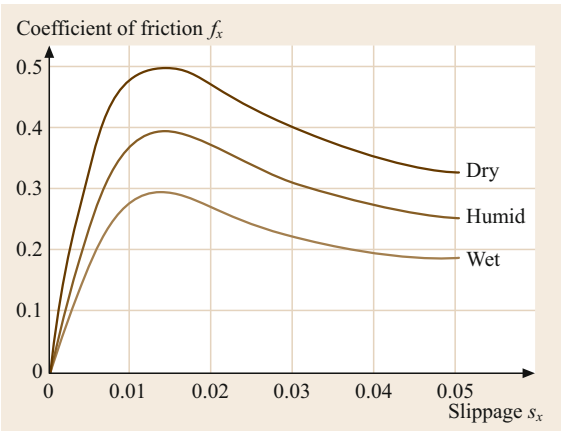

Fig. 21.19 Coefficient of friction of steel wheels on a dry, humid, or wet steel railway track

Table 21.1 Rolling resistances of different vehicles ($F_R = f_R mg$)

Wheel type	f_R	Example of contact pair
Heavy rail	0.002	Intercity train on track
Light rail	0.008	Tram on tram track
Tire	0.01	Tire on tarmac
Tire	0.2	Tire on unfortified road
Tire	0.007	Racing bicycle on tarmac

Besides the traction, the maximum acceleration depends on the number of powered axles and the friction conditions. For passenger trains, this problem is increasingly being solved through the use of multiple train units in which the traction is distributed across the whole length of the train. Freight trains are still equipped with conventional locomotives, meaning that only four or six powered axles pull the entire train. Once a train is in motion, the low frictional force of the wheel–rail contact is highly advantageous due to the low rolling resistance of steel on steel. Compared with road transportation (in which rubber tires are rolling on tarmac), resistance is marginal, which is especially useful for transporting heavy loads. Therefore, only a small amount of traction is needed to keep the train moving when it reaches its cruising speed (Table 21.1).

Guidance

Automatic guidance is another effect of the wheel–rail interaction. A conventional wheelset (i.e., a pair of torsion-resistant wheels fixed on a shaft) is guided by an effect called *sinusoidal movement*, which is caused by the wheel profile. In a simplified approach, wheel profiles can be regarded as conic, so that deflection of the wheelset causes the wheels to have different circumferential speeds. Together with the slippage–adhesion correlation, this leads to different traction forces on both wheels and thus a turning torque acts on the wheelset. As shown in Fig. 21.20, this torque on the wheelset always acts to push the deflected wheelset back towards the centerline of the track. After passing the centerline, the direction of the torque will change such that it will push the wheelset back into an offset position that is aligned with the centerline of the track. The whole deflection process will then start again, albeit in the opposite direction. The resulting motion of the wheelset with respect to the track's centerline is wavelike (i.e., sinusoidal).

Besides this desired effect (guidance), the sinusoidal movement causes lateral forces that disturb the comfort of passengers riding on the rail vehicle and can lead to the derailment of the wheelset when a certain velocity is exceeded. To achieve higher speeds and to increase riding comfort, it is therefore necessary to damp this sinusoidal movement. As sinusoidal movement always coincides with slippage and tangential forces, energy dissipation from noise and wear will occur. The vast majority of rail vehicles are equipped with wheelsets; however, a few rail vehicles have single wheels that are independently joined to the axle (Fig. 21.21). Here, guidance is achieved by geometrically induced forces. The inclination of the wheel profile increases towards the wheel flange. When the wheel flange approaches the rail, the lateral normal force between the wheel and rail will be greater than the lateral normal force for the opposite wheel, as the flange of the latter is further away from the rail and thus the inclination of the wheel profile is smaller. Therefore, the pair of wheels are pushed back towards the centerline of the track.

As a single wheel does not need an axle connecting it to another wheel, single wheels are primarily used in trams to facilitate a low-floor design without any steps between the wheels. Only the Spanish manufacturer Talgo provides vehicles with single wheels that are in-

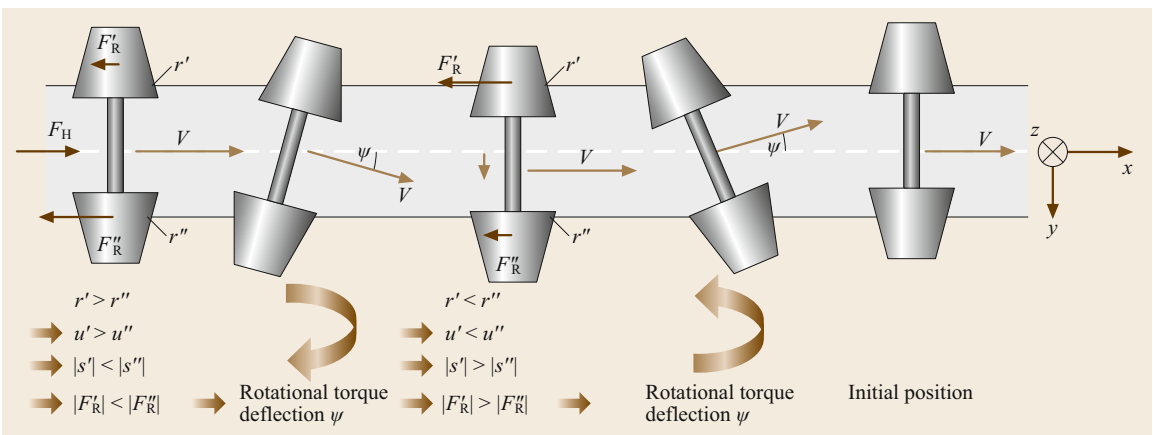

Fig. 21.20 Sinusoidal movement of a (powered) wheelset (circumferential velocity u > translational velocity v)

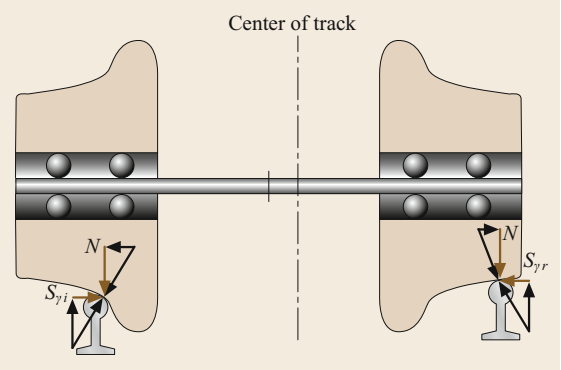

Fig. 21.21 Guidance of single wheels along a railway track

tended for heavy rail applications; here, the advantage is that the single wheels result in smoother guidance along straight tracks due to the lack of sinusoidal movement.

Braking Systems

Because rail vehicles are automatically guided, the system's safest state is at standstill. Therefore, railways are designed to default to a standstill in the case of a severe failure. Braking systems play a major role in achieving this failsafe behavior, so the braking systems themselves must also exhibit failsafe behavior. In the past, braking systems have been improved after almost every serious rail accident to prevent the specific failure that led to the accident from occurring in the future. This has, in turn, led to the current situation in which railway brake regulations are very strict, rendering almost any technical solution other than pneumatic brake systems inapplicable.

One of the main characteristics of a pneumatic railway brake is the main air pipe (MAP), which is a pressure line that runs along the full length of the train (Fig. 21.22). The pressure within the main air pipe controls the driver's brake valve such that, for detached brakes, the maximum pressure is 5 bar. To apply the brakes, the pressure in the pipe is decreased and the distributor valve transmits the pressure of the reservoir to the brake cylinder. This engineering methodology makes the train failsafe: a loss of energy within the MAP causes the brakes to be applied.

Two different devices are used to convert the pressure in the cylinder into a braking torque. For ordinary rail vehicles, a tread brake is used, where a brake pad is pressed directly onto the running surface (the tread) of the wheel. However, this causes wear and ripples on the running surface of the wheel, which lead to a noisier rail vehicle during use, and the thermal energy that must be absorbed by the brake when it is applied can damage the wheel. For passenger cars, the braking torque is usually generated by a disc brake, where two brake

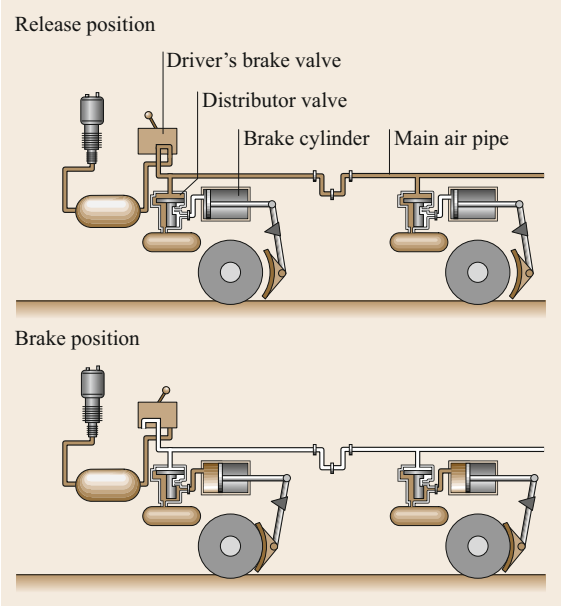

Fig. 21.22 Pneumatic braking system used in rail vehicles

pads are applied to a disc mounted on the wheelset. This eliminates the chance of causing mechanical damage to the wheel upon applying the brake, but damage can still be induced if the brake locks up and forces the wheel to slide on the rail, as this can cause the wheel to be planed. Wheel-slide protection (WSP) is therefore needed to avoid wheel flats.

Its failsafe behavior aside, the pneumatic brake has various disadvantages, including its relatively long response time. Not only does it have poor controllability for purposes such as WSP, but braking performance also suffers due to the length of time it takes for the pneumatic signal to reach the last car (for freight trains, a delay of approximately 30 s until the last car has reached full braking performance can be expected). To improve the performance of a conventional pneumatic brake, passenger trains are usually equipped with additional braking devices such as electropneumatic brakes, in which the brake signal is transmitted electronically to achieve better response times. Furthermore, powered cars are equipped with regenerative brakes and retarder brakes to increase the efficiency of and decrease the wear and thermal stress on the brakes.

Train Protection and Management

As mentioned above, a train schedule must be imposed to protect the system from deadlocks and to make sure that there is only one train per section of track. Also, to ensure safe operation when trains are not running on time, a train protection system is applied. Interlocks ensure that a train cannot enter a section that is al-

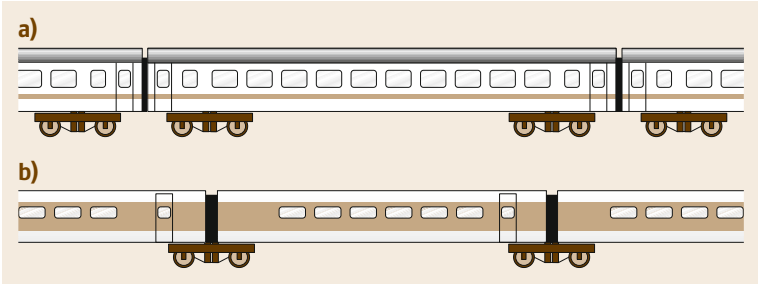

Fig. 21.23 **(a)** Conventional passenger car. **(b)** Passenger car with Jacobs bogies

ready occupied by another train. Entry to each section is guarded by a signal that allows or denies access to the block. As a crash is hard to avoid once two trains are on the same track, railway signals are even more important to rail safety than traffic lights are to road safety. To avoid human mistakes, railway signals are equipped with automatic train protection devices that can stop a train automatically if the driver does not react properly to a signal. These systems can differ from country to country and thus restrain international rail traffic. Because of their long stopping distances, trains cannot stop within their range of visibility. Thus, approach signals are installed several hundred meters before an event to give the engine driver ample time to adjust to the upcoming event. As the train has to come to a standstill within the approach distance to the main signal, this distance has to be the stopping distance of the train, which is one parameter that defines the maximum allowable speed of the train, along with the minimum curve radius of the track. To ensure passenger comfort and to prevent cargo from slipping, the maximum lateral acceleration of a train is limited to $1.0\,\mathrm{m/s^2}$.

Rail Vehicle Structure

The appearance of a rail vehicle is primarily dominated by the car body. The size of the car body is determined to a large extent by the rail infrastructure: the maximum height and width of the car must be within the clearance outline and the distance from the track that is guaranteed to be free from obstacles (e.g., platforms, bridges, and signal posts). As the vehicle must also travel along curves with specified clearance lines, the length of the vehicle is defined by these parameters. A rail vehicle must be designed such that it does not touch the clearance line, even on narrow curves. This has led to the establishment of typical dimensions for a passenger car running on European standard-gage tracks: a length of 26.4 m, a width of 3 m, and a height of 4 m. Such cars are usually carried by two bogies with two axles each.

Furthermore, the mass of a rail vehicle is limited by the permitted axle load. In Europe, the load is usually limited to 22.5 t per axle, meaning that a conventional four-axle car has a maximum weight of 90 t. Passenger cars and freight cars with small payloads may, however, use different axle arrangements to reduce the tare weight by minimizing the number of axles. Aside from the four-axle car, the most common type is the articulated train with Jacobs bogies, where two car bodies share one bogie (Fig. 21.23). The disadvantage of this arrangement is that the bodies can only be separated in the workshop, as the link to the bogie replaces the coupling between the cars.

Coupling

The most obvious use of a coupling is to create a detachable connection between cars. Couplings are also used to transmit longitudinal forces within the train and to prevent the train from being exposed to forces that exceed its specifications. If tensile forces become too high (e.g., if the pulled train is too heavy), the coupler will break; if compressive forces are exceeded (for example during a crash), the coupling can absorb some of the energy. Another important function of a coupling is data transmission. Conventional couplings only transmit the pneumatic signal and energy of the brake's main air pipe. For passenger cars, there is also an electric coupling that links the car to an energy supply and various types of signal cables. A manually operated screw coupling that offers the ability to combine all cars without limitation is used as standard in Europe. This standardization compensates for the disadvantage that this type of coupling cannot be automated. In Europe, automatic couplings are only fitted to multiple-unit passenger trains that must only be coupled to other units of a similar type. In the US and in countries that were formerly in the USSR, automatic couplings are also used for conventional passenger and freight trains.

21.6.2 The Rail Vehicle Development Process

Figure 21.24 shows a idealized development process for a rail vehicle. At the start of the process, the requirements aligned with those of the potential customer (usually a big railway undertaking). Milestone 1 is reached if the offer and the requirements are clear. Then the process enters the concept phase, which finishes at milestone 2,

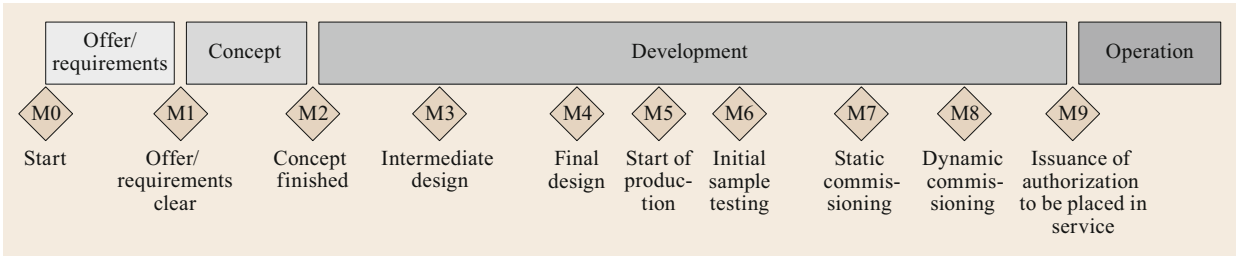

Fig. 21.24 Development process for a rail vehicle (after [21.19])

when the concept has been fixed. After that, the development phase can start. At milestone 3, an intermediate design has been developed. The final design is then fixed (milestone 4), and production of the rail vehicle is initiated (milestone 5). The beginning of the production process includes the initial sample testing (milestone 6). The development process then continues until static vehicle commissioning is performed to check that all of the functions of the vehicle work (milestone 7). If this vehicle function check is successful, dynamic commissioning is implemented (milestone 8). If all further tests carried out during the development process are successful, milestone 9 is reached, at which point the vehicle is authorized to be placed in service. After that, the vehicle can be operated with regularly scheduled maintenance by the railway undertaking. As the length of the development process is largely dependent on customer requirements and technical details, it is difficult to pinpoint the typical length of the rail vehicle development process.

References

21.1 Eurostat: *Consumption of Energy* (Eurostat, Luxembourg 2017)

21.2 U.S. Energy Information Administration: *Annual Energy Outlook 2018* (EIA, Washington 2018)

21.3 European Commission: *Statistical Pocketbook EU: Transport in Figures* (Publications Office of the European Union, Luxembourg 2017), available at https://ec.europa.eu/transport/facts-fundings/statistics/pocketbook-2017_en

21.4 U.S. Energy Information Administration: *International Energy Annual* (EIA, Washington 2006)

21.5 German Federal Environment Office: *Comparison of Average Emissions of Means of Transportation in Passenger Service* (Umweltbundesamt, Berlin 2017), in German

21.6 German Association of the Automotive Industry: *More Climate Protection by a Improved and Comprehensive C02 Regulation* (German Association of the Automotive Industry, Berlin 2017), in German

21.7 German Federal Environment Office: *Thresholds for Pollutant Emissions of Passenger Cars* (Umweltbundesamt, Berlin 2016), available at https://www.umweltbundesamt.de/sites/default/files/medien/376/bilder/dateien/tabelle_grenzwerte_fuer_schadstoffemissionen_von_pkw.pdf

21.8 R. Bormann, P. Fink, H. Holzapfel, S. Rammler, T. Sauter-Servaes, H. Tiemann, T. Waschke, B. Weirauch: *The Future of the German Automotive Industry* (Friedrich-Ebert-Foundation, Bonn 2018), available at http://library.fes.de/pdf-files/wiso/14450.pdf

21.9 Bavarian Business Association: *Changes in the Bavarian Automotive Industry Driven by Automotive Megatrends* (Bavarian Business Association, Munich 2018), in German

21.10 BMW Press Club Germany: *Der BMW 530e iPerformance* (BMW Press Club Germany, Munich 2016), available at https://www.press.bmwgroup.com/deutschland/article/detail/T0266487DE/der-bmw-530e-iperformance

21.11 F. Henning, E. Moeller (Eds.): *Handbuch Leichtbau: Methoden, Werkstoffe, Fertigung* (Hanser, Munich 2019)

21.12 Frost & Sullivan Consulting: *Evolution of Chassis Components* (Frost & Sullivan Consulting, Mountain View 2007)

21.13 ASEAN NCAP: *ASEAN NCAP 2021–2030 Draft Roadmap* (ASEAN NCAP, Kajang 2017), available at http://www.aseancap.org/v2/wp-content/uploads/2017/09/ASEAN-NCAP-2021-2030-Draft-Roadmap-for-Discussion.pdf

21.14 G.P. Merker, R. Teichmann (Eds.): *Grundlagen Verbrennungsmotoren* (Springer Vieweg, Wiesbaden 2019)

21.15 H.-H. Braess, U. Seiffert (Eds.): *Vieweg Handbuch der Kraftfahrzeugtechnik* (Vieweg, Wiesbaden 2011)

21.16 Fraunhofer Institute for Systems and Innovation Research ISI: *Technology Roadmap Energy Storage for Electric Mobility 2030* (Fraunhofer ISI, Karlsruhe 2012), available at https://www.isi.fraunhofer.de/content/dam/isi/dokumente/cct/lib/TRM-ESEM-2030_en.pdf

21.17 G. Pahl, W. Beitz, J. Feldhusen, K.-H. Grote (Eds.): *Engineering Design: A Systematic Approach* (Springer Vieweg, Wiesbaden 2014)
21.18 Lufthansa Group Communications: Balance Sustainability Report 2018, https://www.lufthansagroup.com/fileadmin/downloads/en/responsibility/LH-sustainability-report-2018.pdf (2018)
21.19 Verband der Bahnindustrie in Deutschland: *VDB-Leitfaden: Quality Engineering in der Entwicklung von Schienenfahrzeugen und ihren Systemen* (Verband der Bahnindustrie in Deutschland, Berlin 2015)

Marc Claus Schmitt

Powertrain
BMW Group
Munich, Germany
marc-claus.schmitt@bmw.de

Marc Claus Schmitt works for the BMW Group on powertrain strategy. He was previously employed by BMW in Germany and China as an innovation manager in R&D and a project leader for powertrain test-bed projects. He received a PhD in Engineering from the University of Magdeburg. He studied industrial engineering in Kaiserslautern and Brussels and has also worked for Liebherr and Porsche Engineering, among other companies.

Stefan Pischinger

Institute for Combustion Engines
RWTH Aachen University
Aachen, Germany
pischinger@vka.rwth-aachen.de

Professor Pischinger studied mechanical engineering at RWTH Aachen University and received a PhD for his work on spark ignition at the Sloan Automotive Laboratory (MIT). He worked on engine development and was project leader for the new common rail V8 diesel engine at Daimler. He is currently a Professor at RWTH Aachen University, Director of the Institute for Combustion Engines, and President and CEO of FEV Group GmbH.

22. Automotive Engineering

Gritt Ahrens

The development of vehicles, both passenger cars and commercial vehicles, has a history of more than 130 years. Changing demands and continuous improvement have led to many innovations and made vehicles more reliable and affordable, more beautiful and comfortable, and safer and less polluting.

Today, the automotive industry is most influenced by two megatrends: urbanization and sustainability.

Traffic in urban areas worldwide is becoming more dense, and the awareness that available resources are limited is increasing. Both trends have a major impact on the automotive industry.

This chapter will focus on current major targets of the automotive industry and specific challenges resulting from that. Emphasis is put on technology areas that are of essential importance in this context. The development of cars is quite specific, since the product is a high-technology mass product which at the same time is subject to massive individualization and, thus, high complexity. In order to generate a better understanding of how this specific development will be undertaken, insight is provided into the processes and methods applied in automotive development.

22.1 **Characteristics and Trends of Car Development** 1015
22.2 **Targets and Challenges for Car Development** 1017
22.2.1 Customer Demands 1018
22.2.2 Regulations 1018
22.2.3 Technical Requirements 1020
22.3 **Car Development Processes** 1033
22.3.1 Project-Independent Predevelopment 1036
22.3.2 Project-Specific Predevelopment 1038
22.3.3 Concept Development 1038
22.3.4 Series Development 1038
22.3.5 Development of Vehicle Software and IT 1039
22.3.6 Activities After Start of Production 1040
22.4 **Methods for Car Development** 1040
22.4.1 Methods for Product Layout and Conceptual Development 1040
22.4.2 Methods for Series Development 1046
22.4.3 Cross-Functional Methods 1048
References 1054

22.1 Characteristics and Trends of Car Development

Today, every technical device is subject to innovation, development, and production, which are the basics of engineering in general. However, there are differences between cars and their development compared with other technical products.

First of all, a car is a *highly complex* product that has developed tremendously since the days that it simply had to transport its load from one point to another. Today, the passenger and their satisfaction are the focus. The passenger is not only kept safe, dry, and warm, but is also comfortable in their seat, entertained, informed, and even supported in driving functions. The function of transport seems to have become secondary. Still, its realization has gained complexity as well. In Sect. 22.2, an overview of the targets and challenges facing the automotive industry is presented.

Buying a car is normally a *highly individual* process. Thousands of models of hundreds of brands are available. After having decided on a certain brand and a specific model, again, there are thousands of possibilities for configuring one's individual car (at least for premium European car brands).

Furthermore, a car is a *mass product*. Every year, millions of cars are produced and sold in countries all over the world. Characteristics of mass products include (a) a high number of units produced per year and (b) the

K.-H. Grote, H. Hefazi (Eds.), *Springer Handbook of Mechanical Engineering*, Springer Handbooks,
https://doi.org/10.1007/978-3-030-47035-7_22

fact that there is no direct customer for the development (i.e., there is only a customer for an individual car) but the company itself.

Moreover, cars are *durable products*. About 20 years go by from the first concept to the recycling of cars, and some of the cars remaining at this point even start a second career as classics after this long period of time. In order to achieve this level of durability, the development team has to have *a look into the future*: which features will be demanded 3–5 years later? How much is the customer willing/able to pay for a specific feature? Are the development departments of other original equipment manufacturers (OEMs) working on similar features, and what will the specifics of those be? Will there be regulations that might prohibit the use of this feature?

Because of its complexity, required quality, and resulting high development and production costs, the car is quite an *expensive* product.

Considering the sum of these characteristics – the car is an expensive, highly complex, and highly individualized mass product – a tremendous number of *jobs* depend on the automotive industry, and not only in the many industrialized countries. In 2015, for example, automotive manufactures employed more than 800 000 people as permanent staff and produced 5.7 million vehicles in Germany alone [22.1]. As a consequence, the automotive industry has an immense influence on society.

To achieve the countless functions and features, design the car and its variants, and set trends in styling, a huge *variety of expertise* is needed. In order to bundle this expertise, a *well-organized development process* is needed, which again consists of *adapted methods*. Sections 22.3 and 22.4 provide details regarding the characteristics of car development and the methods applied.

As cars are such complex products, a large number of components are *developed externally*, meaning that specialized companies supply their expertise to the OEM to develop components – usually complex, special components such as the brake system ESP (electronic stability program) – and integrate them in association with the OEM into the car context.

Because a car is a product in everyday use, there are thousands of *regulations* to ensure its safe and convenient use and to afford the necessary protection of the *environment*. The consideration of these regulations again increases the challenge in producing the functions and features that meet all existing requirements (function, low cost, etc.).

The complexity of a car and its development naturally also affect the costs of development and production. The *high investment* required to produce an entire new car can be up to five billion euros. Only the aerospace or military industry can boast similar numbers, but have entirely different customers.

Fig. 22.1 Benz and Daimler carriage (courtesy of Daimler AG)

The specifications for new car development include several important points: technical reliability, an appealing style that encourages the customer to buy the car, safety for the passengers and other traffic participants, fuel-saving features, good economics, and environmental compatibility. Beyond that, a car should also be individualized but nevertheless affordable. An overview of car development over the last 130 years will be given based on these main points.

The first cars built by Daimler and Benz in 1886 were nothing more than coaches with a slow-running Otto engine. These motor carriages had no roof and were not much faster than traditional horse-powered carriages (Fig. 22.1).

One of the first goals of car companies, of which there were increasing numbers in the 1890s, was to achieve greater technical reliability and more comfort for car users. Because no one had experience in developing cars and no development methods were known, the old-fashioned approach of *trial and error* was used to develop cars (Fig. 22.2).

In the mid-1960s, after the release of a book about car safety titled *Unsafe at any Speed* [22.2], the US government took measures to make cars safer: cars had to pass standardized crash tests, which were tightened every 2–3 years. Every car company selling cars in the USA had to pass these tests in order to obtain the approval of the US Department of Transportation. Almost immediately, all car companies optimized their current car types to pass the government safety tests. Research was set up to manufacture safer cars.

In 1973 there was an oil crisis. The oil-exporting nations reduced the amount of oil produced to a minimum, and as a consequence, the price of oil and fuel rose tremendously. People could not afford to run their cars in the way they were used to. Now everyone tried to save oil and fuel. In Germany, for example, four car-free Sundays were installed in the autumn of 1973. This nat-

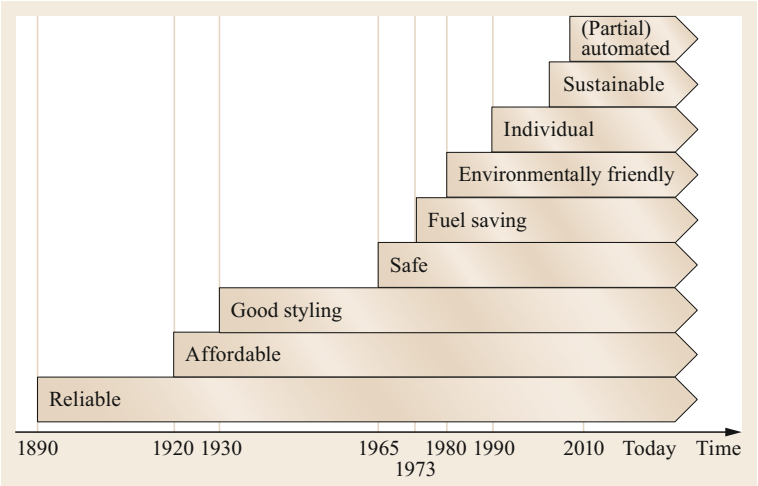

Fig. 22.2 Main aspects of car development and the points in time when they increased in importance

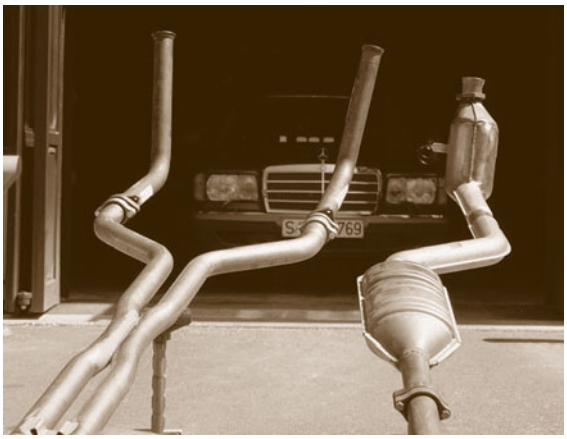

Fig. 22.3 Exhaust system without (*left*) and with (*right*) catalytic converter (courtesy of Daimler AG)

urally also affected the car industry. Several measures were taken by the automobile industry to develop cars that were more economical.

A phenomenon unknown until that time emerged in the early 1980s: the dying of forests caused by acid rain, which itself was the consequence of industrial waste gases and as car exhaust. Measures had to be taken to reduce air pollution.

This trend influenced car development: the catalytic converter for cars with gasoline engines, which had been in use since the mid-1970s in the USA, was now used in Europe as well (Fig. 22.3).

In the late 1980s, the common car changed due to a change in society in the industrialized nations: the demand for more individual products. Throughout the 1980s there were several studies for new, small fun cars.

Today the demand for low fuel consumption continues unbroken, even increasing every year. The reasons for this are two megatrends: urbanization and sustainability. Cities are becoming ever larger as people move from poor areas into urban areas where the potential for employment is higher. Individual transportation is still of great value to people, and many families can afford to have more than one car. The consequences are both megacities and normal cities filled with traffic and pollution. Legislators around the world are establishing increasingly stringent regulations for CO_2 emissions such that alternative propulsion engines are needed to fulfill the requirements.

22.2 Targets and Challenges for Car Development

Product development starts with a huge set of targets having different origins. The intent to meet the demands of customers and to comply with the existing regulations in the markets the vehicles will be sold in, and the technical requirements resulting either from the technical realization of the first two targets or from innovations that the vehicle manufacturer wants to introduce, are three fundamental target origins for which an overview will be provided in this chapter. Emphasis is placed on the challenges resulting from the complexity of the vehicle as a product on the one hand, and from current technological development and megatrends on the other hand, because the consequences to the automotive industry, and with it on car develop-

ment, are the most vital. The topic cannot be dealt with to the full extent in this book; therefore, the subjects presented are either of central importance in the development of vehicles today or are currently undergoing massive change.

22.2.1 Customer Demands

Customer demands are the most crucial targets for car development. Methods for the translation of customer demands to technical requirements are described in the literature, namely the House of Quality [22.3].

When clustering the demands that customers and society put on cars, one can identify different target conflicts. What is needed are:

- Safe cars
- Emotional cars
- Comfortable cars
- High-quality cars
- Highly reliable cars
- Low-emission cars
- Low-noise cars
- Cars which are highly recyclable
- Cars with decent driving performance and load capacity
- Low-cost cars – both in acquisition and utilization.

A rough overview of the major design requirements in different market segments is shown in Table 22.1.

22.2.2 Regulations

Regulations from legislation, car associations, and consumer groups are a major influence on car development and the final products themselves. In different countries, different regulations have to be taken into account regarding:

- The ability to bring a car model (line) in this specific domestic market at all
- The ability to fulfill consumer expectations, especially concerning safety and fuel economy.

The United Nations Economic Commission for Europe (UNECE) [22.5] has published more than 50 regulations concerning active and passive car safety (prevention of accident, reduction of consequences of accidents) and additional regulations on fuel economy and pollutant car emissions (both exterior and interior).

The reasons for regulations are manifold: from protection of people (driver, passenger, and pedestrian) to the environment and traffic, up to the protection of the domestic markets and its car manufacturers.

The challenge for the manufacturer, however, is not only the number of regulations to be taken into account, but the continuous change in the set of requirements that must be dealt with. In the European Union, for example, the General Safety Regulation, which clusters the safety requirements to be fulfilled in order to obtain a whole vehicle type approval [22.6], was adopted in 2019. Several mandatory safety features are included, such as driver drowsiness and distraction warning (e.g., smartphone use while driving), intelligent speed assistance, reversing safety with camera or sensors and data recorder in case of an accident (black box), lane-keeping assistance, and the demand for advanced emergency braking. Most of the new safety features will become mandatory beginning in 2022 [22.7].

The general trend toward reducing greenhouse gas emissions and improving air quality in the cities also led to regulations requiring further significant reductions of emissions. For CO_2 emissions, for example, which are proportionally linked to fuel consumption, the thresholds for 2020 are reduced approximately 20% in the USA to 27% in the EU and China in comparison to 2014/2015. The lowest threshold will be required in the EU with 95 g CO_2/km using the current NEFZ (Neuer Europäischer Fahrzyklus) test procedure in 2020. Authorities are currently in discussion about even stricter requirements for 2025.

In parallel to the threshold definition, supplementary regulations are updated with respect to greater transparency and determining more realistic fuel consumption values.

Transparency is achieved, for example, by obligatory fuel economy labels that must be displayed on every new car to be sold. Figure 22.4 shows two examples of these labels required by the EPA (Environmental Protection Agency), an operating unit of the Department of Transportation (DoT) of the US government.

Adapted test procedures will be introduced that provide test data for fuel consumption and emissions that are closer to what a customer experiences in reality. In 2017, the WLTP (Worldwide Harmonized Light-Duty Vehicles Test Procedure [22.10]) became effective in the EU, and other countries including Australia, India, Japan, Russia, and South Africa will also introduce this new standard. The WLTP includes the actual mass of the specific vehicle, including built-in optional equipment, aerodynamic influences, and rolling resistance of the wheels. Furthermore, a generally representative test procedure is applied that includes different driving scenarios such as in city traffic and on highway and rural roads. The consequences are effectively higher requirements with respect to emissions and the need to set up a process that enables the manufacturer to provide the required CO_2 data for each individual vehicle, consider-

Table 22.1 Design requirements in different market segments (following [22.4])

Micro car	Small car	Family car	Luxury car	Performance sedan	Sports car/coupe	Rally or track car
Versatile accommodation	Versatile accommodation	Versatile accommodation	Distinctive style	Fast appearance	Sleek styling	Priority to function
Small frontal area	Small frontal area	Low c_d and reasonable area	Low c_d	Low c_d	Low c_d	Ground effect and low c_d
Small ICE or e-drive	Small ICE	Choice of ICEs including diesel option	Wide choice of ICEs, optional with (plug-in) hybrid	Large ICE with fuel injection and/or turbo and optional with plug-in hybrid	Large ICE with fuel injection and/or turbo or e-drive	Maximum power output
Good performance	Good performance	Good performance	Smooth performance	Fun to drive	Fun to drive	Quick response, ultimate handling
Maximum fuel economy	Good fuel economy	Good fuel economy	Good fuel economy for class	Good fuel economy for class	Performance first	Performance first
Low cost	Low cost	Low cost	Value for money	Value for money	Cost secondary	Cost no object
Ride secondary	Adequate ride	Good ride	Good ride	Good handling	Good handling	Maximum road holding
Easy to service and repair	Easy to service and repair	Easy to service and repair				Fast repairs at pit or service stops
Minimum mass	Minimum mass	Minimum mass	Controlled mass	Good power-to-mass ratio	Good power-to-mass ratio	Low mass
Maximum package for size	Maximum package for size	Maximum package for size	Maximum package for size	Reasonable luggage space	Reasonable luggage space	To carry long-range fuel tank and large-section spare tire
Some noise acceptable	Reasonable noise	Low noise	Very quiet interior	Quiet at high speed	Quiet at high speed	Noise not important
4 seats at max.	4 seats	5 seats	5 seats	"2 + 2"	"2 + 2"	2 seats only
FWD	FWD	FWD or RWD (possibly 4WD)	FWD/RWD/4WD	FWD/RWD/4WD	RWD/4WD	RWD/4WD

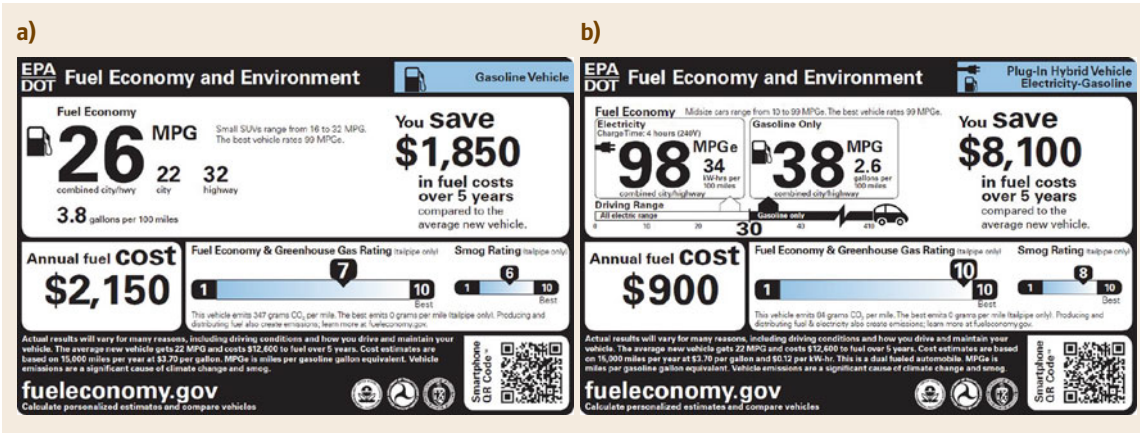

Fig. 22.4a,b Examples of fuel economy and environment labels: for gasoline vehicles **(a)**, for plug-in hybrid vehicle **(b)**, issued by EPA [22.8, 9]

ing the specific configuration and its impact on weight, aerodynamics, and rolling resistance.

The calculated CO_2 emissions must be provided for the Whole Vehicle Type Approval of the vehicle and will be used to determine the fleet fuel consumption for a manufacturer. Exceeding the fleet fuel consumption maximum leads to penalties.

Because the required improvement in CO_2 emissions cannot be realized by optimization of combustion engines within the given time frame, and first markets also claim quotas for battery electric vehicles (BEV), fuel cell vehicles (FCV), plug-in hybrid electric vehicles (PHEV), and others, car manufacturers are pushed to intensify the development of alternative engine concepts.

In the emerging markets, new regulations are introduced at high speed and frequency. The lead time for the implementation of regulations in China, for example, is rarely more than a year. Combined with the short drafting time of the regulations, the specifications lack clarity, leaving plenty of room for interpretation. As a result, industry is obliged to meet the changing specifications for the car and its components at a very late development stage, incurring high costs without knowing for certain whether their interpretation of the requirement meets the understanding of the legislation.

A positive development with respect to the number of relevant regulations is the attempt to standardize regulations worldwide, which is carried out by the World Forum for Harmonization of Vehicle Regulations (WP29), a permanent working party of the UNECE. Under the 1998 Agreement on vehicle construction, so-called Global Technical Regulations (GTRs) are developed, which set forth vehicle safety and environmental stipulations required for approval. The agreement currently has 34 contracting parties (including the EU, Japan, Russia, South Korea, China, India, and the USA) that are involved in the specification of these regulations. Once a contracting party votes in favor of establishing a GTR, it must expeditiously adopt this regulation within its own laws or regulations. Details regarding the agreement, the implementation provision, and current GTRs can be found at the official website of the UNECE WP29 [22.11].

22.2.3 Technical Requirements

Technical requirements for car development are derived from a number of external and internal influences on the vehicle and its operation. Car type, customer demand and use cases, functions to be integrated, and regulations define the framework for vehicle development. In the process of concretization, technological solutions, working concepts, materials, physical and chemical characteristics, etc., must be considered, selected, applied, and adapted in order to develop a vehicle that can be produced, shipped to the market, used according to its specification, maintained, and recycled.

Some examples are given below that indicate the wide range of technical requirements to be considered and demonstrate their interdependence. In addition to illustrating how all-encompassing the collection and specification of technical requirements has to be, the intention of this chapter is to point out major aspects of the evolution currently taking place in automotive engineering.

The examples used in this chapter start with the usual *core* requirements and are then extended to include complex issues, offering a view into the future of automotive development, which itself is undergoing a revolution in

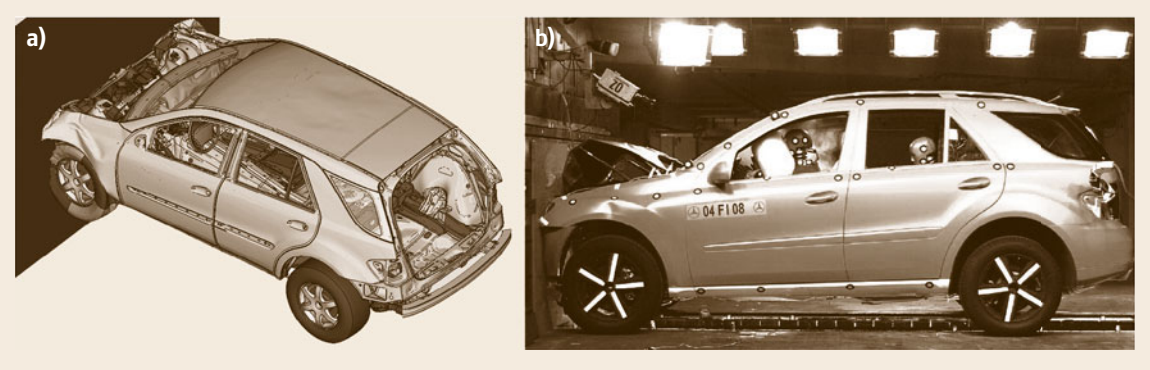

Fig. 22.5 **(a)** Crash simulation and **(b)** hardware crash (courtesy of Mercedes Car Group)

order to meet the expected demands resulting from new business models of the car industry as a whole.

Example: Climate Stress

A vehicle and its components are exposed to a multitude of external factors in terms of climate stress. The strength of these factors depends on the planned operating area of the vehicle and has to be taken into account when in its designing:

- Temperature: the maximum and minimum operating temperature and the temperature levels where the vehicle and its components are kept (e.g., during transport).
- Humidity: from extremely dry conditions (e.g., Mojave Desert) to tropical conditions – the most stressful environment is a hot, humid climate.
- Water: rain, car wash (with different kinds of washing equipment).
- Sand and dust: a challenge for layout of seals (e.g., keeping the passenger compartment free of dust, and taking care of the air convection in the cooling system not to be covered with dust).
- Sun: especially for interior parts in the cockpit, high temperatures up to 80 °C and above lead to thermal stress and aging.
- Corrosion: especially car operation on salted winter roads and in coastal climates.
- Chemical fluids: engine oil and fuel can come in contact with certain areas of the car.
- Air pressure: extreme operating conditions in high-altitude areas have to be taken into account when designing seals and membranes.

Example: Passive Safety

In the conventional understanding of passive safety, principles are applied to reduce the consequences of an accident on occupants. The overall technical requirements are derived from:

- General use case and the function of the specific part of the vehicle to be fulfilled
- Regulations
- Research on real-world accidents.

The criticality of body stresses induced by an accident is described with different coefficients, and regulations demand that the test data are below a certain level for each of these coefficients. These include the HPC (head protection criterion), the TCC (thorax compression criterion), and the TCFC (tibia compression force criterion).

Designing the vehicle to meet these regulatory demands, the vehicle structure, the materials, and the shape and location of interior components are impacted, and safety measures like airbags and deployment algorithms must be adopted.

For verification and validation of the crash performance of a vehicle, crash simulation and hardware crashes are used (Figs. 22.5 and 22.6).

While the primary passive safety features were strictly passive, such as seat belts that restrain the passenger in the seat, in further developments movement sensors and active functionality were integrated. A good example is the airbag. In the event of contact with a certain severity of force, a sensor supplies a signal to the airbag, where a gas explosion fills the airbag before the passenger moves forward as a reaction to the impact with the obstacle.

This development has been taken further. Today, the intention is even to use the time before the accident to prepare the vehicle and its interior for the accident. For this purpose, multiple data regarding the status of the vehicle and its surroundings, which will often be collected for other reasons, will be used to detect when an accident is most likely to happen and to actively influence the load on vehicle and persons. Windows will be closed, seats moved into an optimal position, and passengers will be fixed to the seats by the tightened belts

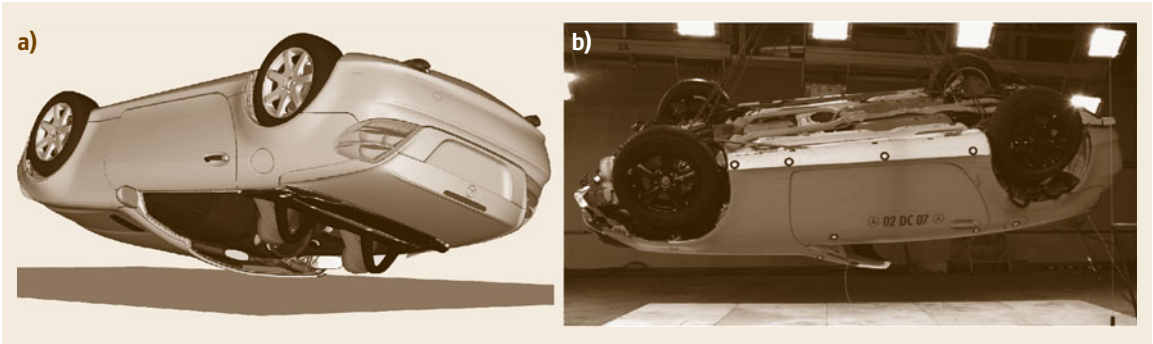

Fig. 22.6 (a) Crash simulation and (b) hardware crash of a convertible (courtesy of Daimler AG)

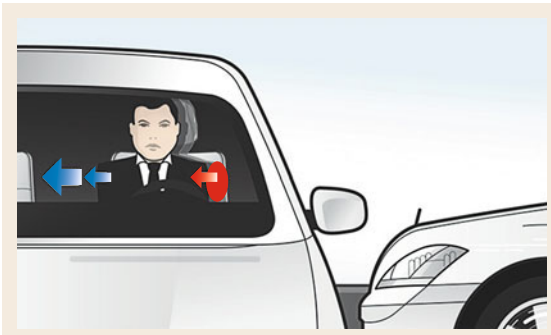

Fig. 22.7 Visualization of a safety feature for side impacts (PRE-SAFE® Impulse): If the vehicle sensors report that a side collision is unavoidable, air chambers in the side bolsters of the seat backrest inflate in a fraction of a second, thereby giving the occupant a slight nudge in the side, increasing the distance to the door at the moment of collision. (courtesy of Daimler AG)

or pushed away from an imminent side impact shortly before the vehicle is hit (Fig. 22.7), to name some examples of an active support of passive safety. In these cases, the technical requirements are derived from the aim of reducing the forces applied to the occupants of the vehicle and, hence, to reduce the severity of the resulting injuries to the passengers.

The requirements specified in new car assessment programs (NCAPs) that exist for several markets, including Europe [22.12], the USA [22.13], China, and South Korea, rate new cars by safety features. The scope is broadening continuously, including vulnerable road users today. Features for reducing the severity of the impact of a pedestrian or cyclist who collides with the vehicle are additionally requested. An example of achieving that kind of force reduction during an impact is an active bonnet that opens the bonnet near the wind screen, thereby increasing the deformation space, which leads to energy absorption and as such can help to substantially reduce the severity of injury. It is obvious that the specific technical requirements must also be deduced from medical knowledge, and often cooperation with hospitals helps in understanding what is needed, and from that to specify how to design interior parts in shape and material.

In general, the realization of passive safety is a holistic attempt, whereby the body of the car has to reduce as much energy as possible and lead the remaining load around the passenger cell, and the interior must provide space for the legs and moving body parts and be soft enough to also absorb energy in the case of contact. The seat and seatbelt combination must keep the occupant in position without applying too much force on the upper body and stomach.

The challenge is to achieve this integrated supportive approach, realized by many different departments in development. In the following, the body design, as one contributing element, will be given a more detailed look with respect to the technical requirements.

Targets for body design can be divided into two classes: targets relevant from an end-customer perspective, and those related to internal optimized production [22.14].

Targets relevant for customers include:

- Appealing design
- Maximum safety
- Minimal fuel consumption
- High comfort
- High level of functionality
- High quality and long lifetime
- Attractive/acceptable price
- Low maintenance costs
- Low noise emissions
- Everyday usability.

Targets relevant for production include:

- Easy assemblability
- Utilization of existing production machinery

Fig. 22.8 Simulation of an offset frontal crash of a large and a very small vehicle, in this case a Mercedes-Benz S-Class and a Smart (courtesy of Daimler AG)

- Small number of different parts
- Easy manufacturability
- Consistent high process quality
- Carryover parts and platform strategies
- Optimized utilization of materials
- Low production cost.

The basic layout of the body is influenced by the basic load cases of a vehicle: bending case, torsion case, combined bending and torsion, lateral loading, and fore and aft loading [22.15]. These load cases lead to stresses in the vehicle body structure. These stresses must be kept within acceptable limits under the worst load conditions. The torsional and bending stiffness of the vehicle structure is a major influence on the noise-vibration-harshness (NVH) performance of a vehicle and the tightness of seals and high-speed performance, especially of convertibles [22.16–18].

However, the worst load conditions do not occur in regular use cases, i.e., during driving, but in the case of accidents. In regulations, specific crash scenarios are defined, such as frontal crash (straight-on, full-width or with an offset; oblique; with fixed or deformable barrier) or side impact. The requirements are manifold: for example, the passenger cell should be intact and the doors should stay closed, but just as important is keeping the load on the bodies of the occupants as low as possible and preventing the head from touching the interior.

Designing a vehicle under consideration of regulatory requirements would only consider what is necessary to achieve a whole vehicle type approval. A wider variety of real-world accident types and their specifics can be derived from data collected by insurance companies and private testing experts [22.19, 20], and research conducted by authorities such the special crash investigation (SCI) by the National Highway Traffic Safety Administration (NHTSA) [22.21] or by the Initiative for the Global Harmonisation of Accident Data (IGLAD). IGLAD, which was initiated in 2010 by European car manufacturers, collects in-depth traffic accident data from all over the world in a standardized data scheme, thus enabling comparisons between data sets even from different countries. The collected data contain 93 variables regarding the accidents, roads, participants (vehicles or vulnerable road users), occupants, and safety systems [22.22]. For the design of the body structure, the data defining the deformation, severity of injuries, and severity of the accident are the most relevant.

The compatibility of different vehicle sizes is very important in the context of body and crash. Both compact cars and huge sports utility vehicles (SUVs) enjoy great popularity today. In the event of an accident, both types of vehicles should be able to provide for the safety of the occupants (Fig. 22.8). This aspect is becoming increasingly important as space in urban areas continues to shrink, but the need for individual transportation persists. A new car type, micro cars, will present a challenge in this context, since these cars differ strongly in shape and are extremely light by definition.

In the context of e-mobility, battery safety is an additional requirement for body design. High-voltage batteries have a huge energy load, which leads to fire when crushed strongly or penetrated. The fire itself is much more dangerous due to the chemicals inside the batteries combined with the electrical potential. Consequently, the body of the vehicle has to be designed in such a way that the battery is specifically protected. That can be achieved, for example, by some kind of framework or cage. In order to keep the dimensions of this cage as manageable as possible, especially with respect to weight, the battery should be positioned in a safe place. Again, accident data can be used to determine this safe position. Consequently, independent from the vehicle type, the database must provide detailed data on the characteristics of the deformations and must have a number of data sets that is high enough to be statistically relevant. In the German In-Depth Accident Study (GIDAS), a cooperative research project of the Research Association for Automotive Technology (Forschungsvereinigung Automobiltechnik e. V., FAT) and the Federal Highway Research

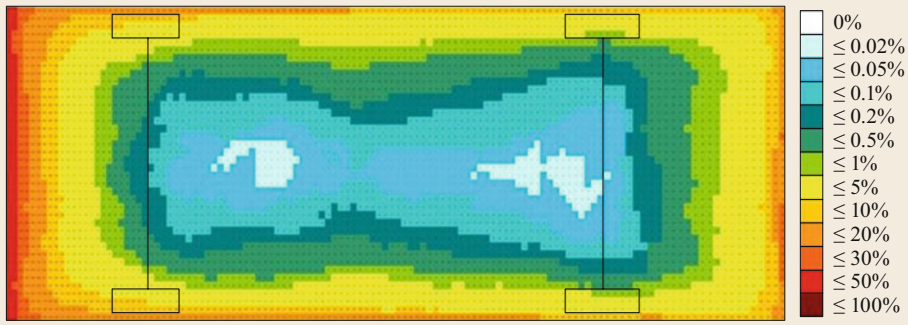

Fig. 22.9 Deformation grid (top view, vehicle front on the left) and cell frequency matrix of the GIDAS data sample containing 8612 passenger cars. The frequency is heat-color-coded ranging from red for the highest frequency to light blue for the lowest frequency [22.23]

Institute (Bundesanstalt für Straßenwesen, BASt), the vehicle is divided into deformation zones with respect to the specific function zones of the car in all three dimensions. The independent grid generated can be applied to all vehicle types and the collected deformation matrix from the vehicle involved in an accident applied. Figure 22.9 shows the results of analysis of the GIDAS data with respect to the occurrence of the potential damage caused in the different areas (cells of the grid) of a vehicle [22.23].

There are different basic concepts for the layout of body types. The ladder frame, historically the first and most flexible layout for the construction of car bodies, had its disadvantages, especially in terms of weight. Thus, today, in most cases, the body of a car is an integral structure with sheet steel parts spot-welded together, providing structural and other functions. Since integral structures – due to their flexibility in design and utilization of different materials – are very complex, traditional mechanical analysis cannot be used to predict their behavior in the layout phase; rather, finite element analysis (FEA) is used to determine the optimal shape and material used (in Figs. 22.10 and 22.11, load paths of different accident situations are visualized). This is also valid for the crash simulation of the body.

The body exterior is defined by three major influences: styling, aerodynamics, and packaging. Together with the body design itself, they simultaneously govern the development processes, with strong interdependencies, in the early phase of car development.

When optimizing stability and crash performance, weight reduction is a challenge that cannot be met using conventional steel bodies. Lightweight design, for example, using aluminum or tailored blanks, influences weight, stiffness, and crash performance in a positive way (e.g., see Fig. 22.12), but must be applied in a well-considered manner in order to contain production costs.

Since sheet metal stamping of body shell parts for the car assembly process is partly outsourced, modules are defined during the car body development process, which are delivered preassembled by suppliers and then are joined in one assembly step to the other body parts. A typical example is the front bumper, where often, besides the body sheet metal parts, electrical components

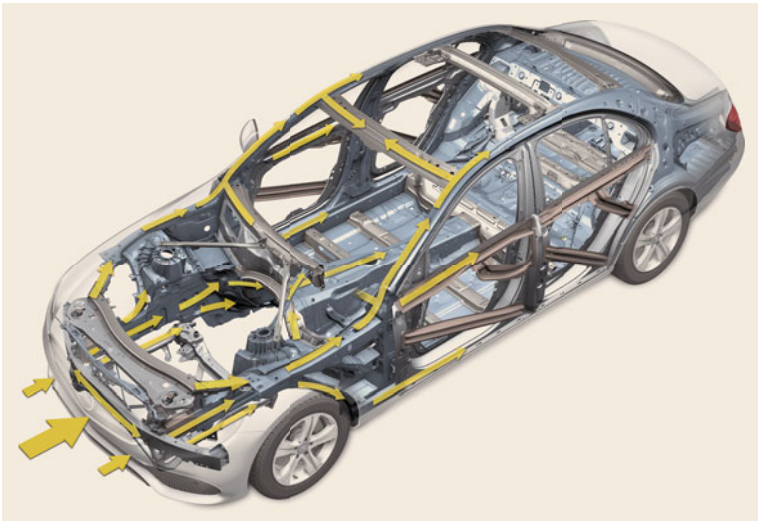

Fig. 22.10 Visualization of the load paths in a frontal crash situation in the car body (sedan) (courtesy of Daimler AG)

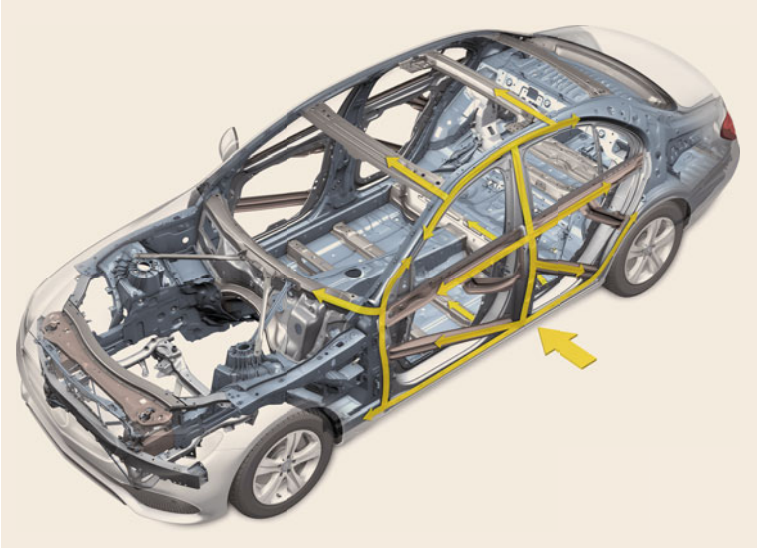

Fig. 22.11 Visualization of the load paths in a side impact situation in the car body (sedan) (courtesy of Daimler AG)

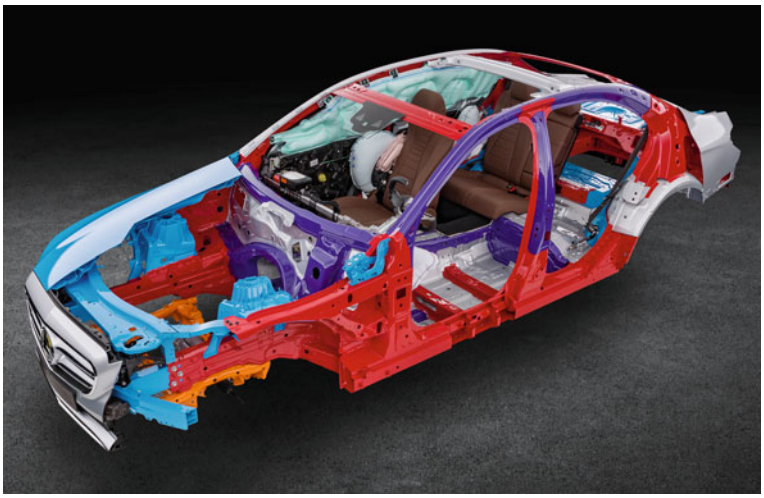

Fig. 22.12 Car body of a limousine, with colors representing different materials and strength: *light blue*: aluminum, *purple*: ultra-high-strength, heat-formed steel, *red*: high-strength steel, structures that are crash-relevant (courtesy of Daimler AG)

like the front lights, the ventilation device, and crash deformation elements fabricated from plastic material are integrated in one module, which will be delivered just in time and just in sequence to the production line of the car manufacturer.

Example: Active Safety

The intention of active safety is to prevent accidents altogether or, if that is not possible, to reduce the speed before impact as much as is achievable. This is the most efficient way to reduce the load on the car and injury to its occupants. Figure 22.13 gives an overview of the field of automotive safety.

The first active safety functions were control functions, the purpose of which was to support or increase the efficiency of a specific function of the core driving process. Examples of these functions include braking, made more efficient by antilock braking systems (ABS), and keeping the vehicle stable and on the road, supported by stability control programs. The necessary input for these functions was information on the status of the vehicle such as speed, grip of the tires or effective force, and data regarding the surroundings such as temperature. The detection of this data during operation ushered in a new area of traffic safety.

Today, the data captured exceed the system borders of the vehicle by far. Different types of sensors and radar, cameras, and ultrasonic sound systems enable the generation of an almost 360° surround view (Fig. 22.14). Obstacles in general, vehicles, pedestrians, and animals of a certain size can be detected, their speed and direction of movement distinguished, and

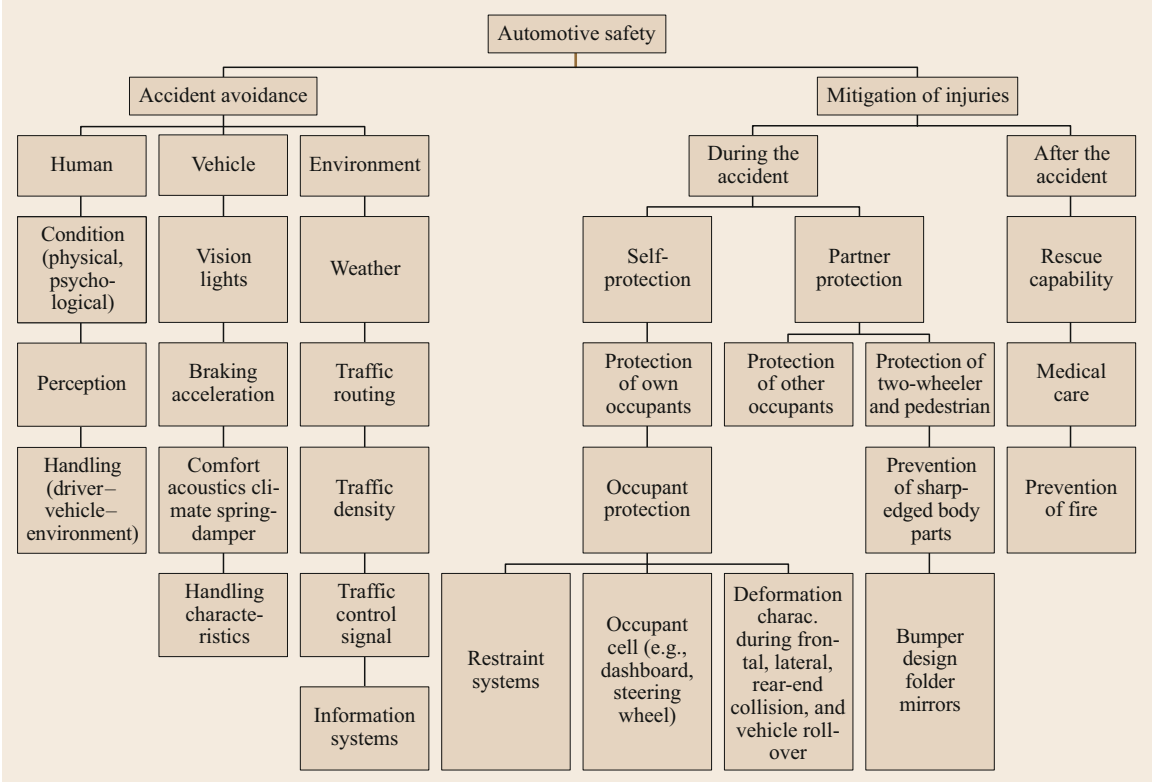

Fig. 22.13 The field of automotive safety [22.24]

road markings and traffic signs can be recognized and interpreted. The aim is to assist the driver in any way possible. Some of the available features include:

- Adaptive speed control not only maintains a set speed, but adjusts it when slower vehicles are in front and accelerates again when the obstacle is out of the way.
- A sound warns the driver when a vehicle in front decelerates abruptly and the driver does not react adequately.
- If the brake is operated and the force applied to the pedal does not correlate with the needed pressure in the braking system for the deceleration required to prevent an unavoidable collision, the system provides the needed delta of the force and pressure.
- If a vehicle enters a blind spot area, an optical warning signal will be displayed to the driver.
- Traffic sign identification provides the current speed limit or warning information if the driver enters a motorway in the wrong direction.

As sensor technology is developing rapidly, processor performance is becoming less expensive and can be provided in small size and weight, mobile services can be integrated in vehicles, and services like Bluetooth enable the connectivity of further systems in the car. As much as industry is pushing this development path, regulators pull at the same time, since the safety benefit of this kind of functionality is obvious.

Example: Autonomous Driving

The idea of assisting the driver in his or her duties automatically leads to the concept of autonomous driving. The vision of traffic that is entirely autonomous promises an almost completely safe traffic scenario.

The transition to get there, however, involves dealing with technical prerequisites and requirements as well as with social aspects. A world in which traffic is completely autonomous would look different from what we know today. Either pedestrians would be completely separated from the driving routes, or the traveling speed would be reduced to less than 30 km/h in areas where interaction between vehicles and pedestrians is likely. Since both city design and infrastructure would have to be adapted, the transition cannot be done in one step. A more realistic development will be an evolutionary approach. Vehicles will be equipped with functions that take over specific driving tasks step by step and level by level.

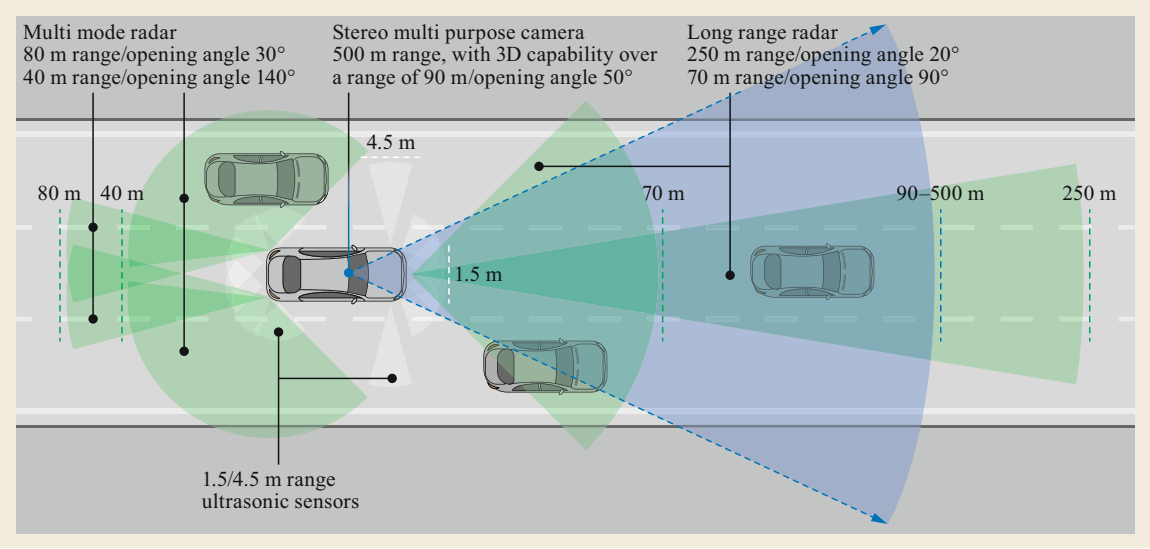

Fig. 22.14 Schematic illustration of the coverage of the vehicle surroundings achieved by different types of sensors, radar, and camera systems in a luxury car, in this case the Mercedes-Benz E-Class (courtesy of Daimler AG)

The definitions of the levels of automation in Europe and the USA differ slightly, but still follow the same line of thought. Table 22.2 shows the approach published by SAE International in the J3016 standard [22.25].

The functionality that operates a vehicle autonomously has to combine many functional systems of a conventional vehicle, adding the capability of seeing, acting, and reacting. All functions involved must guarantee a very low failure rate; the most relevant functions such steering and braking must even be provided redundantly. In the cases of high and full automation (levels 4 and 5 in Table 22.2), the driver is by definition no longer responsible for the operation of the vehicle and, hence, completely eliminated from the system, functioning as a fallback for unforeseen situations. The overall system enabling the autonomous driving process must be capable of handling any situation, and must be much more robust than any of the systems used for the separate functions in a vehicle today.

That a technical system can be designed to handle any possible real-world situation such that the vehicle will not be involved in an accident is simply not possible. There will always be situations which are so abrupt, close to the vehicle, or in other ways unsolvable that the system cannot prevent a collision. Examples include load falling off a truck on a highway in front of a vehicle, the sudden appearance of ice on a rural road due to freezing rain or in a city environment, the situation in which – with having oncoming traffic – a person runs onto the road in front of the car. The functionality will be designed to avoid a collision primarily by stopping or veering to the side, and if that is not possible, to reduce speed and thus reduce the severity of potential injuries or fatalities.

Nevertheless, for society, the circumstance in which a robot might be *responsible* for the death of person is entirely unfamiliar. The fact that vehicle automation will increase safety on the road statistically does not really help in this emotional debate. Society must adapt to the new technology, the same way it had to learn to deal with combustion-engine vehicles 130 years ago.

The reliability of the functional system is another challenge. The validation of autonomous vehicles by test driving is unrealistic given the complexity of functionality and real-world situations that also include bright sunlight, darkness, and numerous weather conditions. Hundreds of millions of miles would have to be driven to demonstrate the reliability. Even under

> aggressive testing assumptions, existing fleets would take tens and sometimes hundreds of years to drive these miles – an impossible proposition if the aim is to demonstrate their performance prior to releasing them on the roads … [22.26].

Testing on roads has to be combined with testing in the laboratory such as hardware-in-the-loop as well as functional tests of subfunctions and components. Sufficient validation of autonomous vehicles is still a matter of research and discussion. One approach to addressing this task is to reduce the parameters in a first step

Table 22.2 Overview of the levels of driving automation as defined in SAE International Standard J3016 [22.25]

SAE level	Name	Narrative definition	Execution of steering and acceleration/ deceleration	*Monitoring* of driving environment	Fallback Performance of *dynamic driving task*	System capability (*driving modes*)
Human driver monitors the driving environment						
0	No automation	The full-time performance by the *human driver* of all aspects of the *dynamic driving task*, even when enhanced by warning or intervention systems	Human driver	Human driver	Human driver	n/a
1	Driver assistance	The *driving mode*-specific execution by a driver assistance system of either steering or acceleration/ deceleration using information about the driving environment and with the expectation that the *human driver* perform an remaining aspects of the *dynamic driving* task	Human driver and system	Human driver	Human driver	Some driving modes
2	Partial automation	The *driving mode*-specific execution by one or more driver assistance systems of both steering and acceleration/deceleration using information about the driving environment and with the expectation that the *human driver* perform all remaining aspects of the *dynamic driving task*	**System**	Human driver	Human driver	Some driving modes
Automated driving system ("*system*") monitors the driving environment						
3	Conditional automation	The *driving mode*-specific performance by an *automated driving system* of all aspects of the dynamic driving task with the expectation that the *human driver* will respond appropriately to a *request to intervene*	System	**System**	Human driver	Some driving modes
4	High automation	The *driving mode*-specific performance by an automated driving system of all aspects of the *dynamic driving task*, even if a *human driver* does not respond appropriately to a *request to intervene*	System	System	**System**	Some driving modes
5	Full automation	The full-time performance by an *automated driving system* of all aspects of the *dynamic driving task* under an roadway and environmental conditions that can be managed by a *human driver*	System	System	System	**All driving modes**

and concentrate on conditional automation functionality (level 3, see Table 22.2). In this case, specific tasks will be carried out autonomously, with the driver still in the loop as a fallback. An example of this research is the government-funded PEGASUS project (by the Federal Ministry for Economic Affairs and Energy) that focuses on the establishment of accepted testing and validation criteria for level 3 highway systems [22.27]. The core question to be answered here, before a suitable testing scenario can be determined, is what level of safety is sufficient and acceptable to society. When the ability of a *good* driver is the level of safety that must be achieved from a statistical point of view, that does not necessarily mean that society is able to appreciate this transfer and would thus accept that safety level. Figure 22.15 illustrates the influencing factors for accepted safety levels of autonomous driving functions, represented by flags, that constitute the milestones in the project PEGASUS, and Fig. 22.16 shows the status of the project as of today.

The answer to this central questions defines the level of requested safety. The determination of testing and validation scenarios produce the needed evidence that this level of safety is provided by the autonomous function or vehicle. Figure 22.17 shows the dependence of uncertainties due to real-world application and necessary simplifications and the efforts to cover all relevant scenarios and environments.

Example: Emission

Besides the technical requirements arising from the goal of keeping the occupants and other vulnerable road users safe and the ability to use the vehicle in most weather conditions without functional constraints, the vehicle has one major function from which technical requirements arise: moving people and load from one point to another.

From that functional demand, the power train was developed.

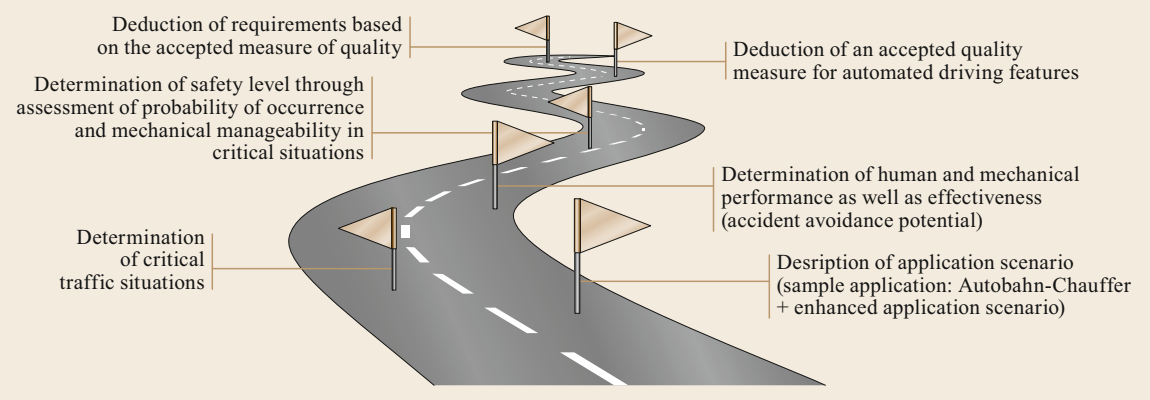

Fig. 22.15 Goals and work contents of PEGASUS – Scenario analysis and quality measures [22.28]

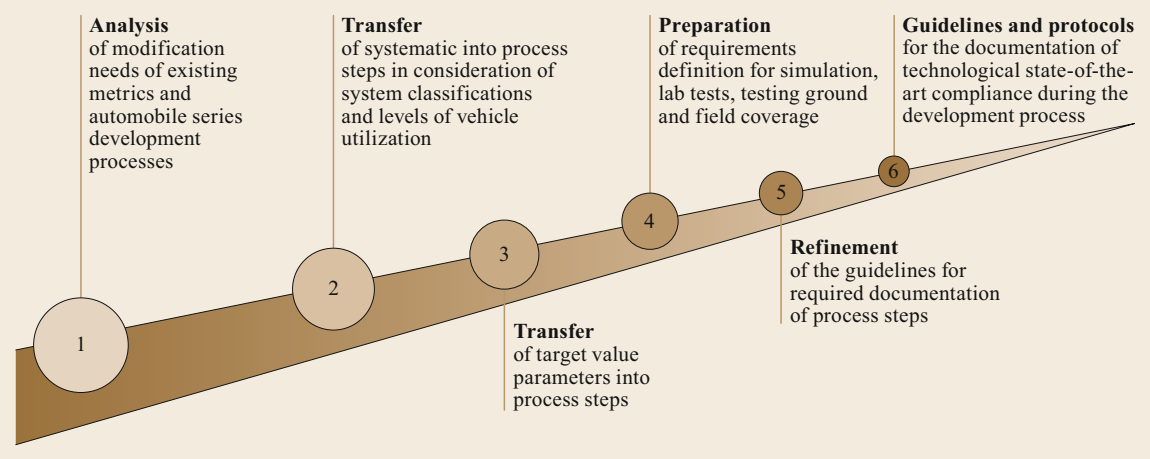

Fig. 22.16 Goals and work contents of Pegasus – Implementation process [22.28]

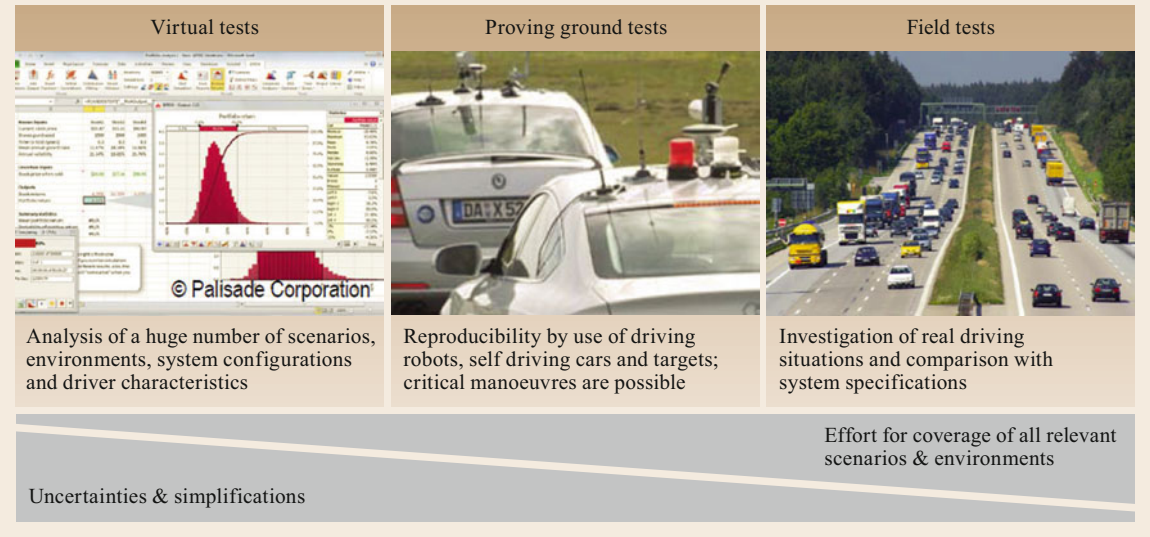

Fig. 22.17 Characteristics of test levels for the validation of autonomous driving functions [22.29]

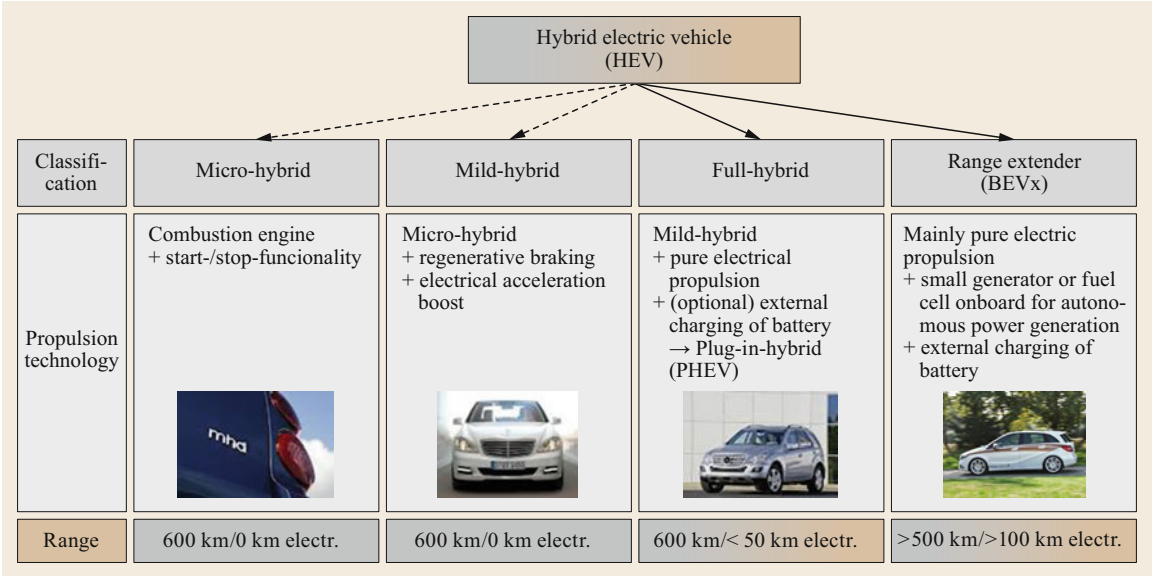

Fig. 22.18 Principle overview of hybrid electric vehicles (HEVs, pictures courtesy of Daimler AG)

The main requirements for the power train in a vehicle are as follows:

- Accelerate the vehicle from standstill to an arbitrary speed
- Allow for quick regulation of torque and engine speed for good dynamic behavior
- Provide good efficiency in terms of space consumption inside the vehicle as well as energy efficiency and low mass of the components used
- Ability to deal with shocks and extreme temperature conditions.

The conventional power train basically consists of the engine, transmission, and clutch. However, the megatrends of sustainability and urbanization have led to a strong emphasis on the massive reduction of emissions. In the context of transportation, this results in the priority objective of CO_2 reduction, which is directly linked to the fuel consumption of a vehicle (for details see chapter *Regulations*). Over the past 20 years, a number of regulations have been implemented to dramatically reduce fuel consumption, which have led to optimization of engine efficiency, improved combustion processes, and reduced friction and moving parts throughout the power train. But the effort did not stop at the power train. The design of the vehicle involved optimizing the power-to-wind ratio of all relevant parts (c_d value), and improving the efficiency of the numerous electronic consumers in the vehicle.

The combination of the megatrends and the fact that people are increasingly able to afford more than one car per household have made further regulatory steps for reducing fuel consumption inevitable. The technical solutions for further improvement, however, are not as productive or are too expensive, or both. With customer demand for an increasing number of standard features, the weight of vehicles continues to increase, putting additional strain on the ability to meet efficiency objectives.

A shifting strategy in power train development has been taking place for some years now, generating more momentum every day. The vision is the electrification of transportation. The evolutionary movement in this direction is realized by hybrid electric vehicles (HEV), enabling either supporting functions for the combustion engine (stop-and-start function, boosting, and recuperation) or additionally allowing electrically powered driving (see Fig. 22.18 for an overview of HEVs). A revolutionary step has been taken in the development of pure battery electric vehicles (BEVs) without alternative power sources, which are small in size, and because of the range available are predestined for city use or close-range delivery.

The reasons for the restricted range of the BEVs are the efficiency of the battery (ratio of power to needed space) and the price, but development is proceeding, and with it both the range and the size of the electrified cars is increasing. From the perspective of truly trying to reduce CO_2 emissions, the functional system vehicle is limited, focusing only on the tank-to-wheel ratio. If the well-to-tank ratio is not included, the effect on the environment might even be negative if the energy used for charging the battery is produced, for example, by coal-fired power plants. This is motivating car manufacturers to invest in alternative energy production.

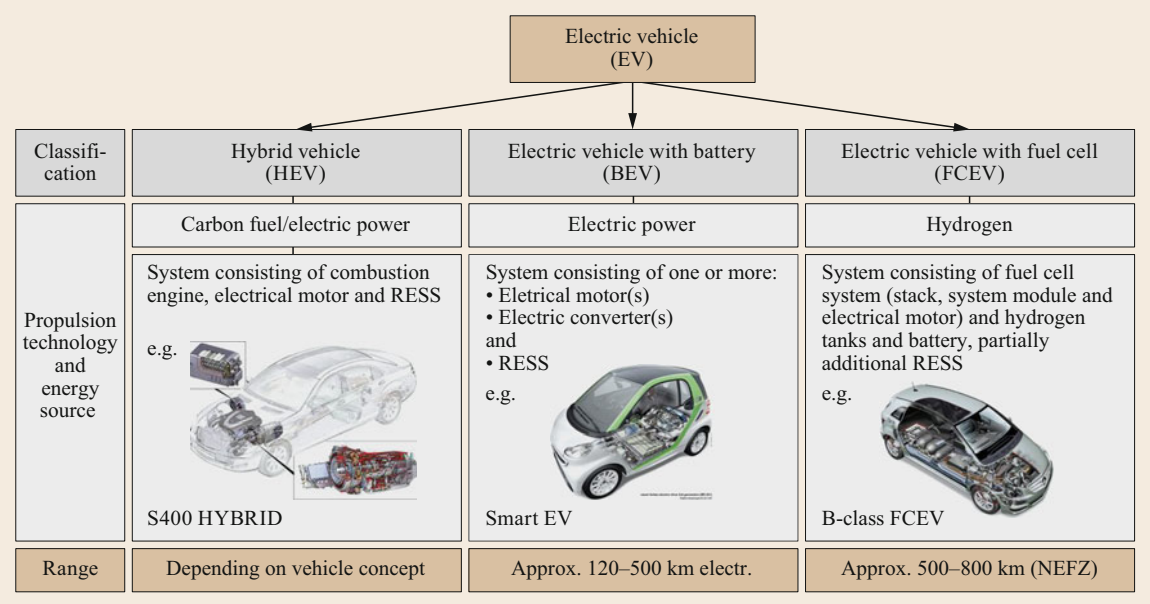

Fig. 22.19 Overview of electric vehicles (EV), RESS – Rechargeable energy storage system (pictures courtesy of Daimler AG)

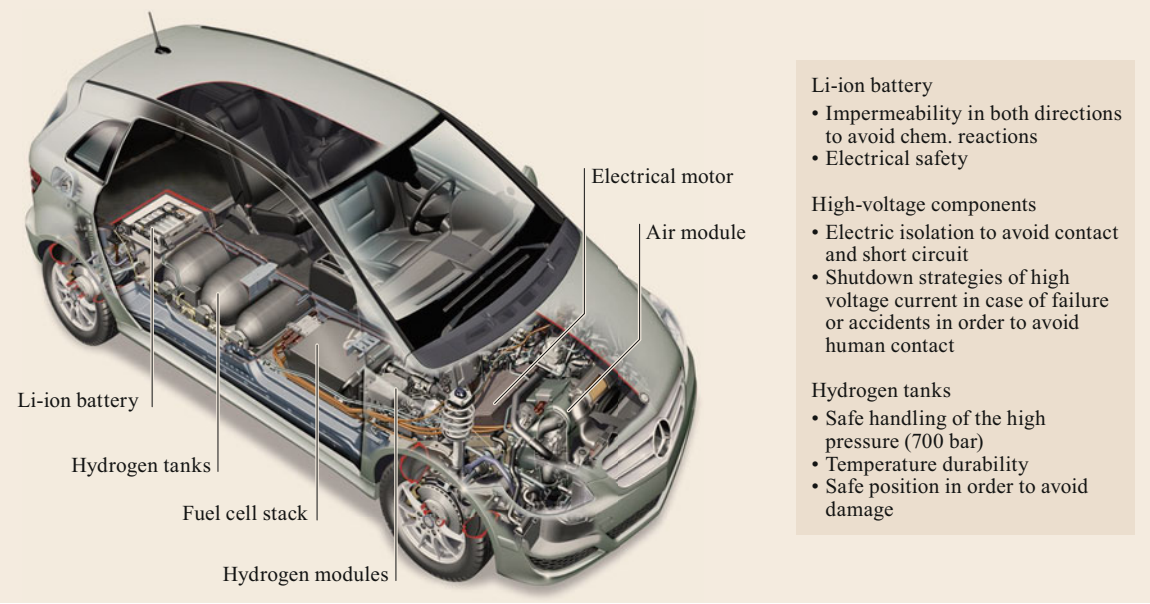

Fig. 22.20 Example of the packaging of the components of a fuel cell electric vehicle (FCEV) and the specific technical requirements (pictures courtesy of Daimler AG)

One alternative propulsion system is the fuel cell electric drive. An overview of electrically driven vehicles is given in Fig. 22.19. The fuel in this case is hydrogen, and the energy produced is either directly transformed into movement or temporarily stored in a traction battery. The fuel has to be stored in pressure tanks. Figure 22.20 shows a fuel cell electric vehicle (FCEV), an example of the packaging of the components, and specific technical requirements for this type of power train. The production of hydrogen again has an impact on the well-to-wheel ratio. In this case, the efficient and effective (with respect to energy con-

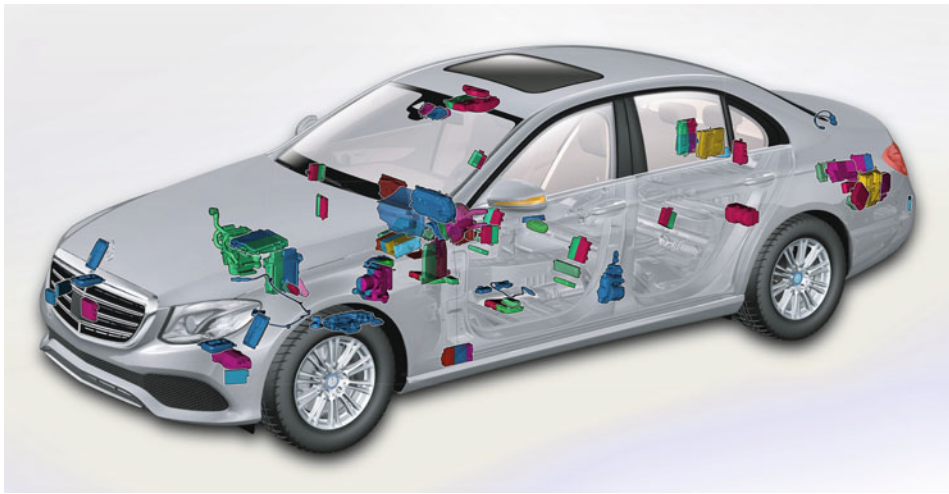

Fig. 22.21
Visualization of the hardware components of the interconnectedness of a modern luxury vehicle: For a modern luxury car, more than 80 control units are developed and integrated in the vehicle, dependent on the selected equipment (courtesy of Daimler AG)

sumption) mass production of hydrogen is still being developed.

The existence of a reasonable infrastructure of *fueling* points is necessary for BEVs and FCEVs to be competitive with conventional vehicles. The setup of an infrastructure for fuel is controlled by a different industry, which to date is unwilling to invest in those new forms of fuel supply. The energy-producing sector is only starting to see the new business model and, together with government and car manufacturers, investing in the development of infrastructure.

Example: Electrics/Electronics, Software, and IT

Many of today's functions in modern vehicles cannot be realized without the intensive use of electronic components for implementing the function, controlling the function and integrating the functions into a system.

The continuously rising demands for reliability, comfort, safety, information provision, reduction of fuel consumption, and reduction of environmental pollution cannot be satisfied by purely mechanically operating systems. Modern safety features like dynamic stability programs, automated emergency braking, or adaptive cruise control cannot operate without heavy use of electronics and microcomputers (Fig. 22.14 on surround view). Figure 22.21 shows the hardware components of the electrical interconnectedness in a modern vehicle.

With the high number of electrical and electronic components in a vehicle, the electrical energy consumption becomes a critical issue. Even during standstill, most modern cars need a certain voltage to be in a standby position for remote opening systems and for theft protection devices. Since in cold outside temperatures in particular, the driver and the passenger demand a high number of electrically supported functions (defrost, seat heating etc.), the management of these units to meet the demands of the passengers while enabling the car to achieve a stable operating condition is a challenging task. The time required for operating conditions in the electric network of the vehicle to reach a stable – i.e., constant – state is sometimes over 1 hour. A need for a further increase in electrical power in the car leads to the development of 48 V electric systems instead of today's 12 V electric system [22.30].

The rapid development of computers, mobile cellular telephones, and smartphones and the services provided with this technology, along with the massive increase in the effectiveness and the expansion of mobile communication networks, has also affected in-vehicle development. Most modern vehicles are connected today via mobile communication networks. The benefit for the customer is that there is one interface which – in most cases – is designed to meet the demands of control while driving (location of display and controls, size and color of text etc.), and because of the tight integration of this interface in the vehicle setup, different comfort functions can be realized more easily. An example is the integration of the radio service TMC (traffic message channel) with the navigation system, allowing for a dynamic route adjustment in the navigation system as a result of TMC-based information on traffic jams. Other examples include the hands-free use of the personal cellular/smartphone connected via Bluetooth® or the setup of an in-vehicle hot spot for the general use of internet and services by all passengers. The combination of mobile devices and the connectivity of the car enables communication and interaction even when not inside the car. The check of vehicle status, such as the filling or charging level of the vehicle, or even the control of specific functions via smart-

phones such as maneuvering the vehicle into a parking space while standing outside the vehicle, provide only a glimpse of the functional possibilities opened up by this development step.

Three categories of services can be differentiated with respect to specific terms of use:

Basic services (service provided at an incident):

- Maintenance management
- Remote diagnostics
- Accident management
- Breakdown management

Remote services (for use by customer):

- Remote inquiry of vehicle status
- Programming of auxiliary heater
- Programming of charging adjustments and preheating/-cooling

Locating services:

- Vehicle position
- Locating of vehicle position

For the vehicle manufacturer, this connection opens up an even wider field of utilization, including new business models. Predictive maintenance is one example, using the onboard information regarding the state of the car to determine the need for maintenance before a breakdown of the vehicle as in the case of engine problems or sensor check due to detected malfunctions. The driver can be informed, even offered the arrangement of an appointment in the dealer's garage. The monitoring of car fleet data can be used to analyze the actual use of the vehicles, identifying the most important use scenarios and the extremes, thus making it possible to determine technical requirements for the development of the next vehicle generation.

Connectivity, however, can have negative effects as well. It is also the basic path hackers use to manipulate anything implemented in the in-vehicle network.

Modern vehicles consist of numerous electric control units (ECU, see also Fig. 22.21) that enable the control of functions including steering support, vehicle stability, braking, distance to vehicle in front, or the parking process, to name only a few. At a minimum, all safety-related functions and systems and all interactions between them must therefore be designed modularly, separating them from open systems assessable via the internet and ensuring the validity, authenticity, and plausibility of data exchanged and used. General standards (e.g., ISO 26262 *Road vehicles – Functional safety* [22.31]) and encryption protocols are in place to support the design and validation of such systems.

A single mandatory definition of a secure system would be inappropriate, since that would make it very easy for hackers to attack. Systems are more secure the more they differ in design and are regularly updated.

Consequently, standards addressing the aspect of cybersecurity specifically define how a secure system can be developed, outlining relevant steps and aspects to consider. However, all attempts are still in progress today. An example is the development of the standard ISO/IAW 21434 *Road vehicles cybersecurity engineering*, which is a joint effort between ISO and SAE [22.32].

22.3 Car Development Processes

As with any product development, the development of cars is company-specific. Many factors influence the process, such as the size and level of globalization of the company, its product portfolio, the number of cars produced, and the proportion of outsourcing during the manufacturing process.

Generally, the development of cars consists of three main elements:

- The strategic phase
- The car development project
- The adaptation phase

Figure 22.22 gives an overview of the car development process (CDP). Like any other product development process, car development starts from a global perspective and a rough concept.

During the strategic phase, the car is planned, one could say, from above. Aspects considered at this stage relate to the environment, the market, and the company itself, and lead to the strategic specification of the car.

Aspects that influence strategic decisions include social trends such as increasing environmental awareness or the increasing need for safety, the need to update technologies as a consequence of improvements or as a result of legislation (e.g., the electric drive or fuel cell as alternative drive mechanisms), the product portfolio of competitors, rationalization of the company's own workflow, and new functions to be implemented in or-

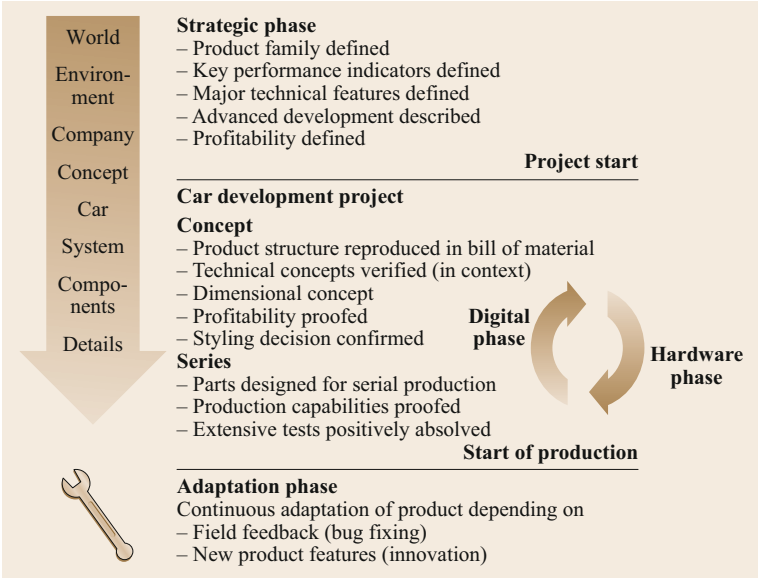

Fig. 22.22 Car development process

der to make the product more attractive, such as active high-beam lights or headway control.

The variety of aspects influencing the strategic definition of the car is huge, but there are just as many approved methods to support this phase of economical and political decisions. The methods are general, and there are many good summaries on this topic in the literature [22.33].

The main specifications to be defined during the strategic phase of vehicle development are summarized in Fig. 22.22. One important boundary condition for the development of a car is the definition of the product family. For this step, the needs and trends of the market have to be analyzed, competitor product portfolios must compared with the company's own portfolio and the profitability of the various scenarios must be calculated.

By defining the key performance indicators, the characteristics of a car are determined based upon the target customer group. In addition to price, the design and general affection for the brand have a large influence. Examples include the horsepower to be supplied, the noise and consumption allowances, the NCAP result aimed for, the loading capacity, the kind of air-conditioning system, and the need for automatic locking of the entire car. The basis for defining the key performance indicators and the major technical features to be implemented are again the general trends and circumstances in the market. Moreover, methods and technology are advanced in principle in order to achieve a competitive advantage. Section 22.3.1 focuses on car-specific development in this context.

If an advantage is to be expected when, for example, an important customer need will be fulfilled (e.g., providing driving comfort in what is actually a sporty car by an additional feature called active body control, or even automated driving functions) or requirements resulting from political discussions can be satisfied (e.g., discussions about environmentally friendly solutions for the end of life of vehicles [22.34–36]), then advanced development will be described. The aim in this context may be the result of project-independent or project-specific predevelopment, but is also a topic of general research. In this case, the results are not available at the time of description. During the verification of the concept, which is an early stage of the car development project, it must be established whether research has reached a stage of maturity such that it can be realized. In Sect. 22.3.2, the aim of this kind of development will be elucidated and examples will be described.

A further fundamental declaration at this stage of car development is that the project promises to be profitable. A car can be profitable when it achieves a monetary profit due to the price and the calculated number of units planned. On the other hand, the profit can also be nonmonetary, as is the case when it is of strategic importance (for example, the SLR for the Mercedes Car Group, or the Tesla Model S).

The car development project describes the period during which the car and its production is specified in all necessary detail in order to start the so-called *job number one*, meaning manufacturing.

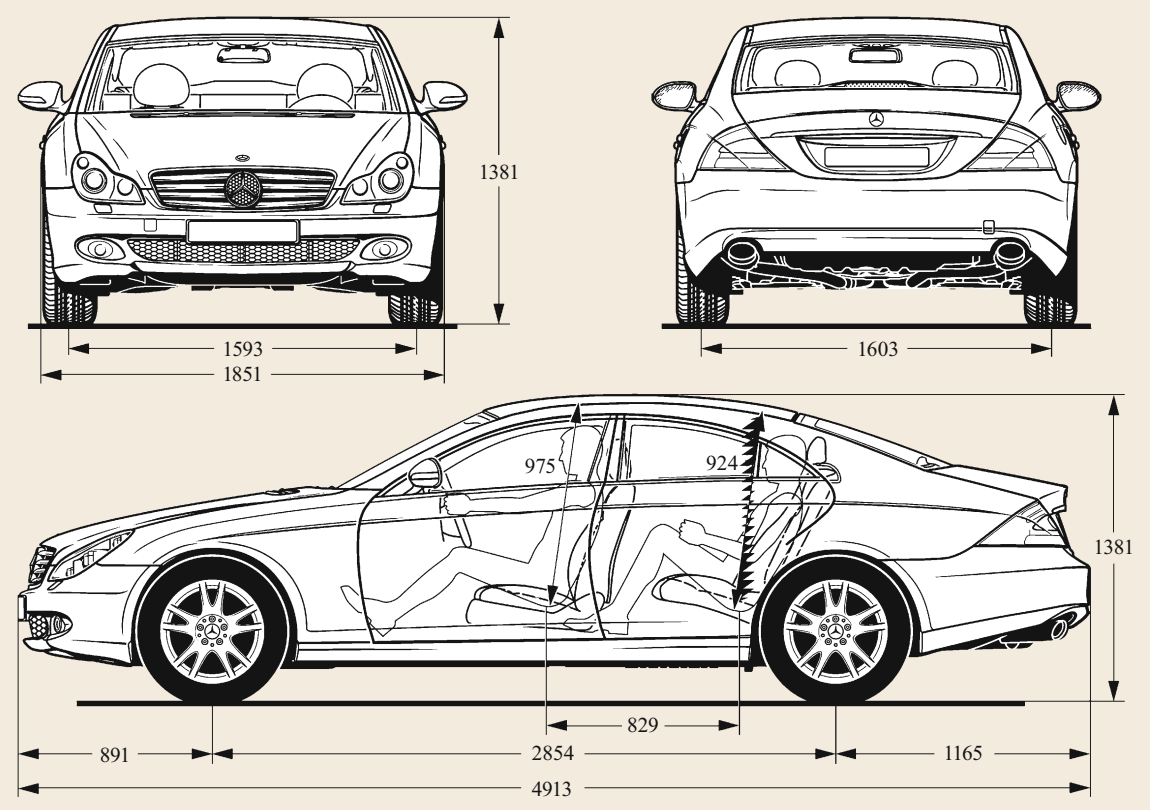

Fig. 22.23 Dimensional concept of Mercedes CLS (courtesy of Daimler AG)

The car development project (CDP) is generally carried out in two steps: development of concept and series (Fig. 22.22).

In the concept phase, it is determined whether the set of rough outlines and technical features defined during the strategic phase are compatible. For this purpose, the dependent system or even the entire car has to be investigated in context. By defining the dimensions of the concept, the size of the car is determined and with it one major specification of the entire car set. Already at this stage of development, all outer measurements are fixed and the functional spaces inside the car, such as overhead space, leg room, or trunk capacity, are provided (Fig. 22.23).

Parts and components are defined and created. The basis for car development, however, is the product structure of the vehicle, which is reproduced in the bill of materials (BOM). The bill of materials is the connection to production, regardless of whether it is a prototype or the series model that is to be manufactured. Since the configuration of the car and its possible variants are realized within the BOM, the BOM is used to order materials, parts, and components, and hence forms the basis for logistical processes. In Sect. 22.4.3 *Product Structure and Bill of Materials*, the importance of the product structure with respect to the BOM is clarified.

Furthermore, styling decisions generally have to be confirmed during the concept phase. One must ensure that the functional components can be accommodated and that the dimensional concept can be realized within the body prepared by the styling. Although changes in design will be accepted during the concept development, the fundamental design features are agreed upon before the car project starts.

Two main streams of development overlap in the development of both the concept and the series vehicles: the digital and hardware phases (Fig. 22.24).

Development always starts with the digital phase. Parts and components are designed for prototype or serial production in computer-aided design (CAD) systems. Assemblies are generated using the bill of materials, product data management (PDM), and CAD functionality (Sect. 22.4.3 *Product Structure and Bill of Materials*).

The digital model of the car is used for simulations such as package investigations via a digital mock-up (DMU), calculations to ensure stability such as in

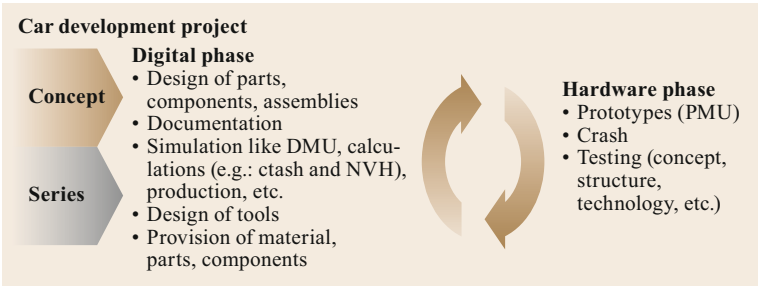

Fig. 22.24 Car development project (CDP)

specific crash situations, to check thermal behavior, vibrations or noise of the vehicle and the effects inside it, or kinematic examinations to verify the effects of open/closed doors or convertible (soft/hard) tops in specific use cases such as driving or parking off-road, as well as simulations to plan the production process.

After a certain delay, the hardware phase starts. Here the digital models are physically generated (in the form of a physical mock-up) in order to verify the digital simulations. The tests conducted vary depending on the level of progress of development. Examples include tests of concept and structure, functional tests of components on a mule or in a running car, and crash tests to ensure the safety features of the car in different accident situations and for different passenger combinations or vulnerable road users. The results of these tests are used to optimize the simulation models for the digital testing (for more details on interactions between the digital and hardware phases see also Sect. 22.4).

When the concept is verified, the series development starts, which means that parts and components are now redesigned for serial production using the results from tests carried out during the concept phase. Extensive tests are used to ensure the quality of the mature product. Systems containing electrical/electronic (E/E), software, and information technology (IT) systems are validated extensively in model setups (see also Sect. 22.4.2 *HIL*). Whether specific noise requirements are met, the car works under extreme climatic conditions, or the braking distance correlates with the requirements can only be fully verified by testing the car in its final realization. In preparation for production, the capability of plants must also be verified.

After a specific level of development is reached, the tools to produce the parts will be designed, and materials, parts, and components delivered by suppliers are ordered on the basis of the digital models, organized in the product structure of the BOM. Samples of parts and assemblies produced according to the specifications and with serial production tools will be finally and conclusively checked and tested. Development is gradually concluded with the certification of the type approval relevant aspects which relate either to the characteristics of components, systems, or the whole vehicle, or to its behavior in requested circumstances.

At a certain point, with the start of production (SOP), the development has to be completed, i.e., the parts, components, and systems have to be released (see also Sect. 22.4.3 *Release*), and the car will be produced. The development, however, is not yet finished, because continuous adaptations of the product are necessary as a result of field feedback (bug fixing) and innovations that should be implemented in order to stay competitive.

22.3.1 Project-Independent Predevelopment

Aside from vehicle development projects aimed at series production of vehicles for end consumers, there are complementary development activities prior to that.

These activities can generally be divided into different classes (Fig. 22.25).

The main distinction in project-independent predevelopment is between methods, technology, and styling concepts.

The definition of key technologies and features where there is substantial differentiation from other OEMs is a strategic trigger for the definition of predevelopment projects.

Road maps of pending regulations in the different markets are also used to derive predevelopment projects.

Methods

The demand for shortening product development time, reducing cost and development risk, providing new features (e.g., fuel cell for energy supply and electric drive), and meeting new regulations (e.g., pedestrian protection) lead to the need to develop new methods to satisfy these demands. Thus, the methods can also be divided into those for improving efficiency and those for meeting new demands.

Typically, all of these methods are developed with a specific target car development project in mind, where they will be used for the first time. Method evaluation is either a separate project or is done during the

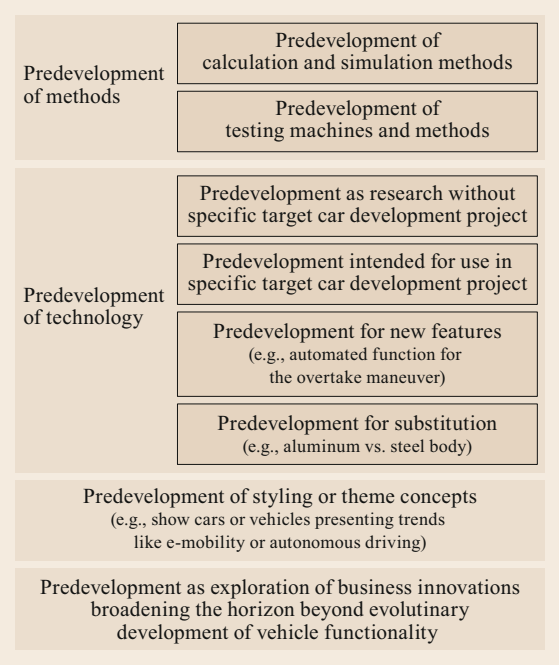

Fig. 22.25 Different types of predevelopment

real application of the methods in a car development project, in many cases accompanied by conventional fallback or backup methods if the new method does not work properly. An example is the use of computational fluid dynamics (CFD) methods for aerodynamic layout, where the fallback method is a scaled model in a wind tunnel.

However, general research done outside the OEMs also influences car development; for example, the development of new materials (plastics or sandwich materials with carbon or natural fiber), new manufacturing techniques that achieve greater stability (tailored blanks), and mathematic algorithms such as finite element analysis (FEA) for calculating stress and strength in parts are successfully applied in car development today.

Technologies

Technologies are predeveloped, driven either by external demands such as regulations or by the company's own impulse. One internal trigger may be the need to reduce weight in a certain area of the car in order to meet future weight and weight allocation targets for new car concepts, thus leading to the development of substitute materials, part structures, connection technologies, and production technologies. Another trigger is the fulfillment of expected customer needs for comfort (automatically shading roof glass), safety (lane departure warning systems), economy (gear shift indicator), and

Fig. 22.26 Mercedes-Benz F015, vision car on *luxury in motion* thinking ahead of the prospects arising from autonomous driving (courtesy Daimler AG)

entertainment (Bluetooth connectivity of personal mobile devices) [22.37, 38].

Styling and Theme Concepts

Styling and theme concepts are developed:

- In order to check whether a certain styling proportion or styling theme will appeal to customer tastes, especially the intended market segment
- To identify whether there is customer acceptance for a completely new car (and thus styling) concept
- To generate a vision of the integration of new trends in the vehicle (e.g., Mercedes Benz F015 for autonomous driving, see Fig. 22.26), present this to the market and thus initiate a process of consumer familiarization and consideration
- To show the fitness of the automotive company, and for marketing purposes.

Styling concepts that receive resonate positively with the customer base are often used for car development projects. Here it is especially important to reach the SOP within a short period due to shifting customer tastes. Theme concepts are used to prepare the customer, and with them society, for the introduction of fundamentally new technology. It is reasonable to present these concepts well in advance, especially when it involves changes in patterns, as in the case of e-mobility, when the vehicle fueling and charging process takes at least four times as long, or in the case of automated driving when both the customer and society in general must get used to the fact that a machine takes over the control.

Motor shows such as those in Detroit or Geneva are often used to present these styling or theme concepts to a broad group of people and obtain the desired feedback through the press.

Dependencies

One previous example of the need to develop new methods and technologies was establishing regulations for pedestrian protection, which is gradually being implemented in different stages. To meet the demands of pedestrian protection, various predevelopment steps had to be undertaken, including:

- Methods for simulating the body under contact with the car front and the resulting load on the car body parts
- Methods for calculating the critical points in the car exterior that must be analyzed
- Methods for testing a real car front with a dummy head and measuring the deceleration of the head
- Car concepts and technologies to meet the demand for deformation zones in the affected area of the car front (passive technologies such as providing enough space between the exterior shell and the underlying stiff components, and active technologies such as parts of the car front being raised during impact to enlarge the deformation zone and distance)
- Styling concepts for different variants of car fronts, taking passive technology with larger deformation zones into account.

22.3.2 Project-Specific Predevelopment

Unlike project-independent predevelopment, activities in project-specific predevelopment focus on the approval for the start of a car development project.

In project-specific predevelopment, various vehicle-specific activities take place, including:

- The packaging concept for the car is roughly defined.
- Technologies to be used in the car – also from project-independent predevelopment – are identified and decided on.
- Styling proportions and major styling elements are decided on.
- Targets for cost and weight are defined in the upper levels of the product structure.
- Strategic development partners for specific components and/or modules are selected.
- The time frames for car development until SOP and major milestones are defined.
- The project organization is defined at least at the upper levels; the need for engineering resources is roughly estimated.
- The expected economics of the project over its lifetime until end of production and spare parts provision are calculated based on extrapolation from previous car projects.

If the technological and styling concepts meet the expectations of management, the economics are expected to be above the margin defined in the automotive company, and if the project can be handled with the existing resources, the project is likely to be approved.

22.3.3 Concept Development

Concept development starts when the car development project starts, and ends when series development starts, usually with the milestone of *styling freeze*, at which point styling hands over leadership to body-in-white (BiW) development. Its main goal is to define the technological concepts and secure their function in the context of the vehicle.

At the start of concept development, many activities are initiated in parallel. Exterior and interior styling, packaging and ergonomics, body-in-white design and aero-/thermodynamics, along with concepts of all other technology departments, are defined and validated in the functional context of other concepts and taking space restrictions into account.

In Fig. 22.27, the main activities of concept development are shown at an abstract level.

Package freeze is a milestone in concept development when all space demands from all parties have been announced, and conflicts have been resolved by trade-offs under guidance from packaging. From this point onwards, violations of space utilization are monitored by packaging, and measures for resolving the conflicts identified.

Near the end of concept development, the first hardware prototype is crashed to confirm the structural concept of the car.

During concept development, the set of options from which the customer will be able to choose when ordering a vehicle is confirmed. The options differ for the markets the vehicle will be introduced to. The entire set of options will also be determined during the car development project, bearing in mind that there will be additional SOPs for some of the options after the SOP of the vehicle with the first set of options to be offered, normally at the home market. During series development, further options might be decided upon, resulting from market research and customer feedback.

22.3.4 Series Development

Depending on the internal definitions of the automotive company, series development starts with the milestone of styling freeze or styling release and ends at the start of series production (SOP). The major task during series development is to transfer a vehicle concept that has been proved during concept development to a vehicle

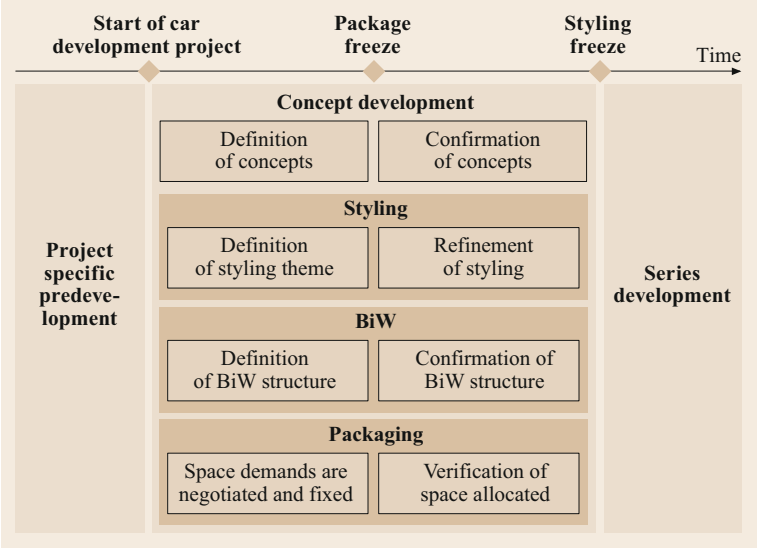

Fig. 22.27 Overview of activities of concept development

series that can be manufactured under series conditions in high volume, at high quality, in the variants offered to the customer, at a competitive production cost.

For this purpose, a number of milestones must be passed during series development:

- Prototype tests are finished, with positive results.
- Tools for series production are released.
- Contracts with the suppliers for series production are concluded.
- All regulations and country-specific requirements are fulfilled.
- Sample delivery of parts produced with series tools are positively approved.
- Logistics processes are defined and verified; the ability to handle the logistics according to the planned production volume and the special conditions in the production plant is verified.
- The marketing concept (advertising strategy) is defined.
- The dealer organization is informed about the product and its maintenance.

Series development is carried out in even closer cooperation with the suppliers than concept development, since sourcing for all parts is defined during series development, whereas often during concept development only strategic suppliers are directly integrated within the car development process.

With the start of series development at the latest, the project team structure is defined and fully operational. The teams consist of members of design, production, sales, purchasing, and quality, and are responsible for the development of the assigned components within the given limits of cost, time, quality, functionality, and performance.

22.3.5 Development of Vehicle Software and IT

The integration of software and IT in vehicles has been on the rise for years. As far as software that controls or steers vehicle functions is concerned (e.g., stability control, active high beam, or distance control), the development follows the same milestone framework as the hardware in order to have the software implemented, tested and, if necessary, certified on time for series production.

The development of telematics, however, is increasingly following a separate development process with different milestones (see also Sect. 22.4) and much shorter development cycles. This is because the development of vehicle telematics must be competitive with product development in the IT sector. An update cycle of 3–5 years is not acceptable, since manufacturers of smartphones and other electronic devices now provide new products every year. Keeping the interfaces defined, especially on the hardware side, the software development, the offer of applications and services for use in the car, and updating changing data such as maps or security services and their secure integration in the vehicle have to be organized.

Since in-car telematics support must provide tools for vehicle-specific functions or aspects, the interfaces, data supplied, exchange procedures, and protocols have to be defined. This definition is made vehicle-indepen-

dent so that the tools developed can be implemented in all vehicle types on the market at the time. Both application support and security features must work consistently with the driving-specific functions of the car and must not influence driving features in any way.

22.3.6 Activities After Start of Production

After the start of production, the car development project is finished. At this point, two major activities are still ongoing:

- Development of further options to be offered to the customers at a later point
- Optimization and continuous development of vehicle software (e.g., telematics, engine control unit, safety features to prevent vehicles from being hacked)
- Support of series production.

Further options are usually planned with the car development project in total. The production schedule of these options is integrated into the overall production scenario of how many cars will be sold at which time in what markets. Support of series production is an ongoing activity which is usually not planned in conjunction with the car development project, but is rather a support function that is continuously improved. Here:

- Changes of parts are made in order to optimize production processes in terms of cost and reliability.
- Design changes based on feedback from customers and dealers are implemented.
- Design is optimized in order to reduce material cost.

Depending on the type of change of the part design, effects have to be taken into account. Thus each change is evaluated in detail in terms of:

- Functionality and validation in system and vehicle context
- Certification (e.g., is update of certificate needed and what length of time is required to obtain the certification)
- Spare parts provision (e.g., spare parts supply considered in design and in eventually needed separate certifications)
- Overall cost
- Economical benefit.

Depending on the product life cycle and competitors' product developments, facelift projects are established in order to upgrade a vehicle that has been in the marketplace for a certain time with additional features, better performance, and adapted styling. After another period of time, the next generation of car development starts.

22.4 Methods for Car Development

As with the development of most technical artifacts, car development makes use of various methods for defining and verifying form, function, and performance. These methods can be categorized into:

- Virtual methods
- Hardware methods.

Virtual methods operate on a product description, usually contained in a computer-based product definition. Computer-aided tools are used to generate and verify the current state of the product definition (Fig. 22.28).

Hardware methods make use of real parts, components, assemblies, or products (in car development projects, usually prototypes and pre-series vehicles). On testing machines, on special driving courses, or out on the street, the product or parts of it are tested for function, performance, and durability (Fig. 22.28).

Virtual and hardware methods usually go hand in hand when a car is being developed (Fig. 22.29).

Generally, with virtual methods, a large number of design alternatives can be generated and/or evaluated in a comparatively short amount of time, whereas hardware methods involve more aspects of the real behavior of the product, since not all aspects of product behavior are modeled in the virtual methods.

In the following, some of the most important methods for car development will be highlighted, and their use in the development process will be explained.

22.4.1 Methods for Product Layout and Conceptual Development

In the early phase of a car development project, styling, package, the body-in-white structure, and aero- and thermodynamics are the key factors that must be harmonized in order to generate a suitable overall car concept.

Styling

Virtual. Computer-aided styling (CAS) tools allow the definition and manipulation of two-dimensional (2-D)

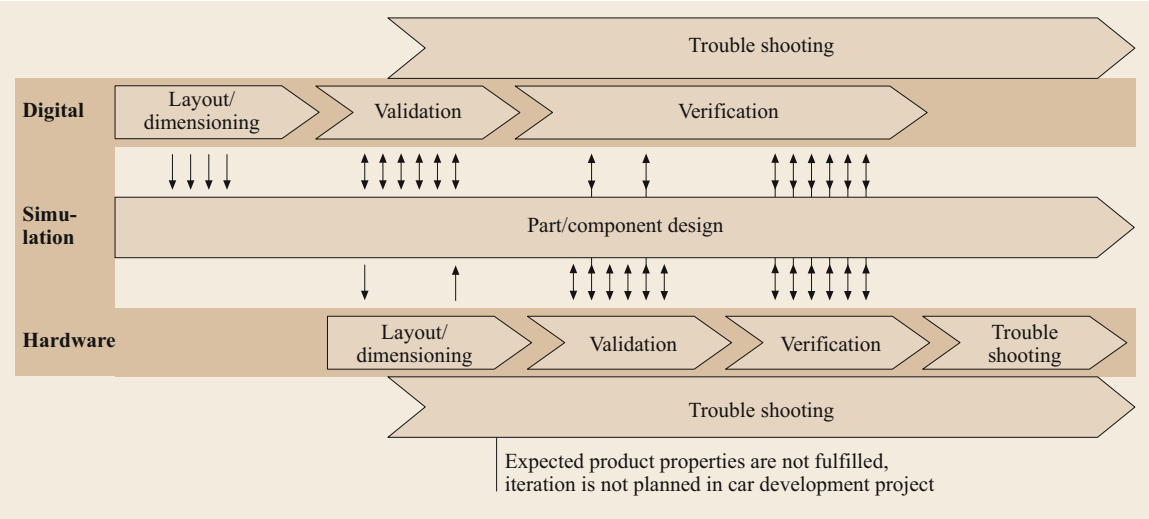

Fig. 22.28 Support of part and component design by virtual and hardware methods

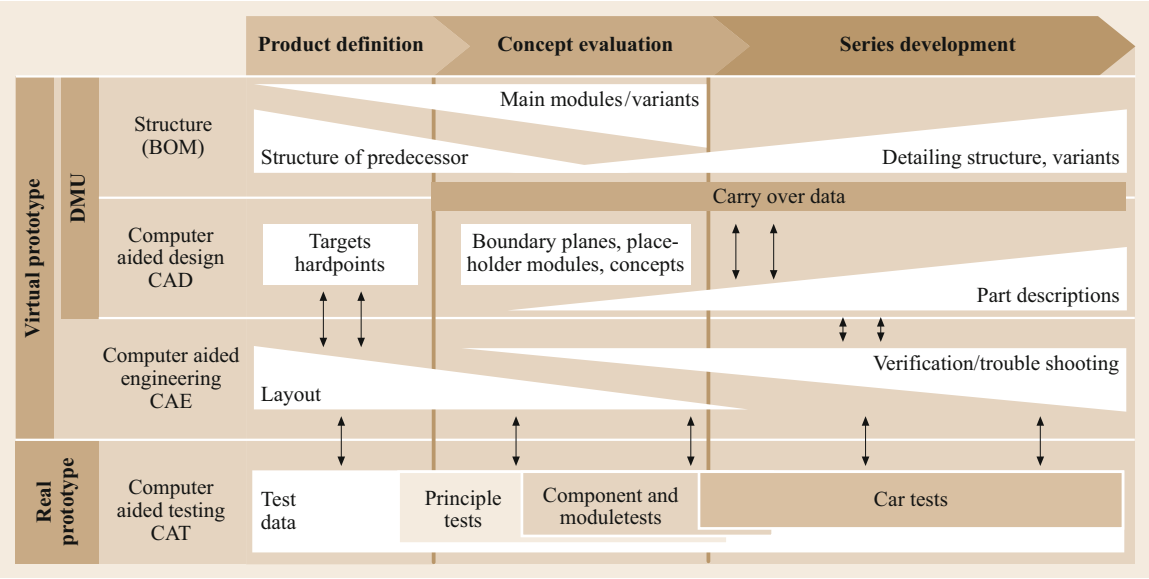

Fig. 22.29 Milestones of virtual development and verification in hardware [22.39]

sketches and three-dimensional (3-D) geometry, and have special capabilities for texturing and shading in order to obtain the most realistic pictures or models from the styling definition. Visualization can be done using high-definition printers or monitors, and for realistic 3-D viewing, virtual reality (VR) equipment can be used. CAS tools allow for the direct conversion of styling data into CAD data, thus making it possible to shorten the time between finishing a styling model and checking, for example, that the vehicle package complies with it. The data transferred into more technically oriented CAD programs can be used as a base for the design of metal sheets for the body shell. This is a method to define the geometry needed for final milling of the stamps for the outer shell parts, for example. Also, the airflow around and through the vehicle can be simulated using these models.

The major shortcoming of the virtual styling process today is that the evaluation of a virtual styling model is far more difficult than that of a hardware styling model. Even most sophisticated VR applications and equipment still do not give the same impression as a real vehicle model in real-world surroundings. Therefore, hardware styling models are essential in the styling process as well [22.40].

Hardware. In the early phases of the styling process, scale models (1 : 4 to 1 : 3) can be used to show different proportions and styling topics of a vehicle to be developed. One (or more) of these will be selected and then refined and used as the base for further styling activities.

Tape drawing is a method for defining the main contours of a car or areas of a car at a scale of 1 : 1 as 2-D models. Black tape is glued to a white surface for the development of styling concepts and their fast visualization and adaptation.

Styling models at a scale of 1 : 1 are mostly made of clay, and then finished with painted foil to give the styling model a more realistic appearance. Evaluation of the styling model should be done under different light conditions in different surroundings. With special preparation, the styling model can also be used for aerodynamic evaluation. Changes in the hardware styling model to address aerodynamic needs are less easily implemented compared with the adaptability of a virtual model.

Interaction Between Virtual and Hardware Models. Virtual styling models can be milled in styling foam, a painted foil can be applied, and the model can then be used for evaluation purposes. The hardware model can also be combined with augmented reality (AR) or virtual reality (VR) applications, both of which are used for the evaluation of styling variants. AR can be used, for example, to project variants of the front apron to the clay or milled vehicle model. VR is applied for the evaluation of interior alternatives using a hardware model of the front part of the car in which seats and some interior parts are installed, called a seat box, and with VR goggles the view of the interior can be completed in different styles, and in this way can be virtually experienced (Fig. 22.30).

Fig. 22.30 Utilization of VR for visualization of interior concepts of the vehicle, in this case for an evaluation of an operating concept using gestures [22.41]

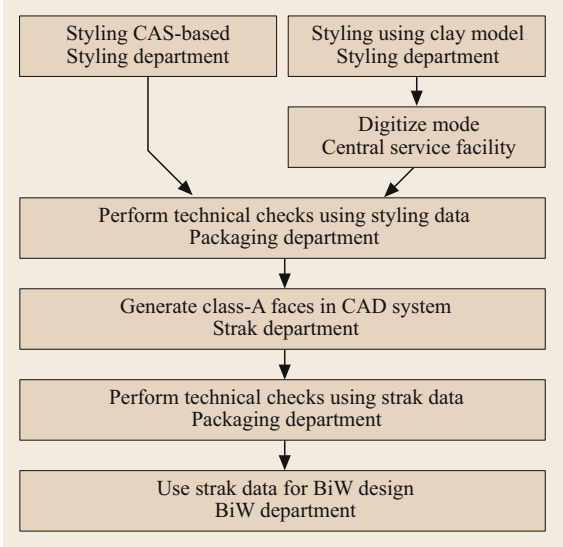

Fig. 22.31 Proceeding from styling data to technical data

Milled models can also be further developed with conventional methods, and later the modified model can be digitized with 3-D digitizing machines (3-D scanning).

For interaction with other processes in car development (technical checks on the car package, straken), it is important to ensure that the version of the styling model evaluated is the same version as that used for technical checks and strak activities. For this purpose, team data management systems are used.

Both virtual and hardware models are used (Fig. 22.31):

- For purposes internal to styling (evaluation, discussion)
- For evaluation by management
- For checking the acceptance of the styling by potential customers (car clinics).

During these car clinics, one or more alternative styling models intended for use in a car development project are usually presented, together with models of the main competitors in the target market segment. Customer responses are used to verify that the styling appeals to the customer tastes and is sufficiently differentiated from that of the competitors' vehicles.

Packaging and Ergonomics

Virtual. Packaging in the early phase of a car development process means defining prescriptions for space utilization by the different technical departments. Also, the main space features of a car, such as the size of

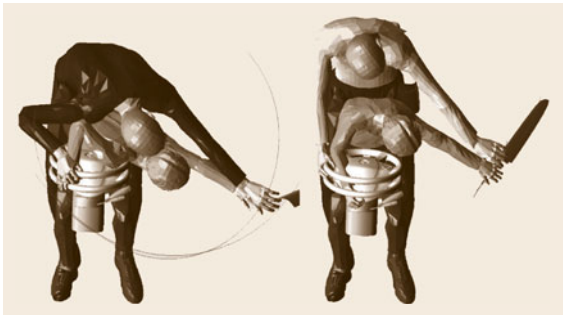

Fig. 22.32 RAMSIS application for verification of accessibility of door closing mechanism [22.42]

Fig. 22.33 RAMSIS application for verification of accessibility of rear door closing grip [22.42]

the trunk, are defined here. Space prescription is usually done using packaging boundary shapes, which are used to define the most critical areas in terms of building space in a car. They also reflect geometric demands derived from regulations such as minimum sight angle.

The ergonomics of a car (driver position, accessibility of steering wheel and switches, driver's view) are checked using virtual manikins, which are representations of human bodies derived from a statistical analysis of the main geometric body features of humans, such as 5% female and 95% male representing very short women and men of particular height. One example is manikin RAMSIS [22.42], which is a software package that can be used for any kind of geometric simulation of a human, and can be integrated into CAD models (Figs. 22.32 and 22.33).

Various methods and tools are used in car development to identify the needs of the customers and thereby to derive guidelines for the design, shape, and location of interior components. Table 22.3 gives an overview of methods for ergonomics development.

Packaging in the early phase is also responsible for the interface between the *technical world* and the *styling world* and trade-offs between them.

During the car development project, the packaging activities change from prescription to verification, ensuring that the parts developed will fit together in the virtual and hardware assembly.

A digital geometric product description, a combination of all 3-D models of all relevant parts in their correct position in space, is called a digital mock-up (DMU), and is used for the detection of collision between parts and for the simulation of the assembly process (Fig. 22.34).

To build up a DMU, it is necessary to have a bill of materials for the specific car. It can then be analyzed whether all part geometries necessary for a complete DMU have been provided by the engineering design or whether any part geometry is missing (Table 22.4).

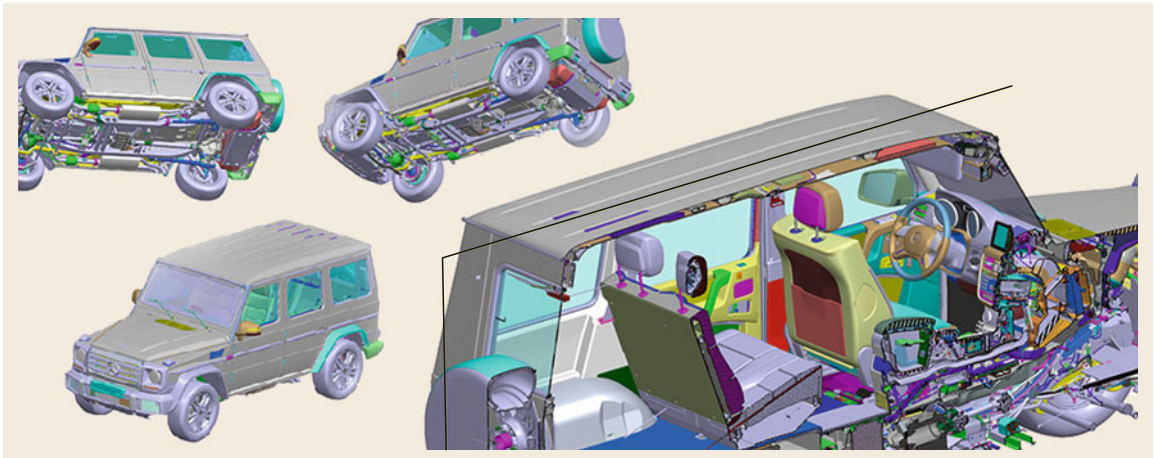

Fig. 22.34 DMU visualization of the entire vehicle Mercedes-Benz G-class with all parts assembled (courtesy of Daimler AG)

Table 22.3 Strengths and weaknesses of various methods and tools for ergonomics development [22.43]

Method/tool	Strengths	Weaknesses
Design recommendations and checklists	• Quick • Easy to use	• Relevance to specific users, tasks or vehicle type may be dubious • May have little scientific validity • No account taken of compromises • Either too specific (e.g., should be 457.2 mm) or too general (e.g., should be comfortable)
Anthropometry and biomechanics	• Quick • Good for novel designs • Useful for assessing the influence of age, sex, race, etc., on design	• May be a lack of data relevant to user or task • Data may be out of date • Data often relate to standardized postures, not necessarily working postures • Design may become too academic, mistakes being hard to identify
3-D human modeling CAD systems	• User- and task-specific predictions, quick and accurate for geometric issues such as fit, reach and vision • Enables effective communication at an early stage • Compromises can be objectively explored	• Expensive to set up (hardware, software, training), but very cost-effective thereafter • Does not assess personal preferences, psychological space, fatigue, task performance
Mock-ups and fitting trials	• Control selection of users and their tasks • Study comfort and performance over time • Sound basis for identifying good and poor designs using both objective and subjective methods • Essential for novel designs • Compromises can be investigated • Design problems are quickly identified	• Can be time-consuming and expensive • Can be difficult to obtain representative subjects • May not be a very realistic simulation of task or environment
Owner questionnaires and interviews	• Valuable information direct from the user population • Small details may be detected which the casual observer may have overlooked • User involvement	• User may take poor design for granted • Opinions can be strongly biased • Cannot be used for novel designs until after production • Biased sample – does not include those people who chose not to use the existing equipment • Biased sample – low response rate from postal questionnaires, who returns them? • No detailed assessment of body size, performance, or comfort
User trials and road trials	• Control selection of users and their tasks • Study comfort and performance over time • Sound basis for identifying good and poor designs using both objective and subjective methods • Allows comparative testing	• Can be time-consuming • Require production and/or prototype vehicles to test • Can be difficult to obtain representative subjects

Table 22.4 Sample chart for definition of car configurations for geometric space checks using DMU

Geometry influencing specifications	Car configuration									
	1	2	3	4	5	6	7	8	9	10
Left-hand drive	✓	✓	✓	✓	✓	✓				
Right-hand drive							✓	✓	✓	✓
Rear wheel drive	✓	✓	✓	✓			✓	✓	✓	
4 wheel drive					✓	✓				✓
Small gasoline engine	✓			✓			✓			
Large gasoline engine		✓			✓			✓		
Diesel engine			✓			✓				✓
Electric drive				✓					✓	

Since car development usually involves the development of a number of different vehicle variants (left- and right-hand drive, automatic and manual transmission, different engines, and different customer-specific equipment), packaging has to define the most critical (in terms of space) car configurations, and will track the fitting of parts with respect to one another on the basis of these configurations. Based on experience, a trade-off is made between complete coverage of all car variants that are potentially critical and the expense of this level of coverage.

In order to be able to generate a DMU automatically, the designer has to assign his 3-D CAD model to a node in the bill of materials, and has to position it in each relevant car configuration. Positioning can be done either in absolute coordinates (relative to the vehicle null point) or in relative coordinates describing the position relative to another part, for example, on which it is mounted.

Part collisions can be checked on demand (when the designer wants to verify his part design in his specific geometric surrounding), or on a regular basis as a complete geometric car check. Conflicts between two parts are documented, and a recommended action is communicated by packaging to the two part owners.

Hardware. Most automotive companies use hardware to verify the space allocation of parts and the ergonomic suitability of the position of interior components. One example is the engine bay, which contains flexible parts (cables, tubes) that today cannot be modeled in CAD systems such that behavior due to surface texture and flexibility can be evaluated. The seat box is another example, where hardware verification is used in order to check the ergonomic position of every element in the future seat. Both have their virtual counterparts, which are used earlier in the process.

Body Structure

The main physical structure of a car is the body-in-white structure (BiW structure). With the layout of this structure, the basic performance features of a car are also determined. To a certain extent, the BiW structure accounts for the weight of a vehicle, the bending and torsion stiffness, and its crash behavior. If changes in the layout of the BiW structure are necessary later in the process due to conflicts in space management or unsatisfactory crash performance, these changes result in heavy additional cost, since changing this structure leads to necessary changes in all other sections of the car connected with the BiW structure and in the highly automated manufacturing lines in the factory that are planned, ordered, and built early in the process as well. Thus, methods for a thorough layout of this structure according to the goals defined for the vehicle to be developed are used.

Virtual. Since body-in-white structures are developed in the early phases of car development, when no hardware is yet available, the focus for layout of the BiW structure is on virtual methods. For the layout of a structure, generative algorithms can be used. According to the definition of load cases, material coefficients, and major geometric boundary conditions such as free space for the passenger compartment and trunk, the algorithm identifies at which points of space material is needed in order to fulfill the demands for smooth load flow and minimum deflection of the beams of the BiW structure. The result of this algorithm is a space structure that can then be used for a first layout of the structure in the CAD system. The result of this structure is then subjected to finite element analysis to prove that the performance criteria are still met after the structure has been designed in such a way that it can also be manufactured.

Modal analysis of the BiW structure will show which frequencies will lead to resonance reactions, resulting in noise and discomfort for the passengers, and which therefore must be avoided when guiding the load path into the BiW structure.

Depending on the car family the BiW structure is intended for, precautions for reinforcements in the structure have to be taken into account. An example is the need for reinforcement when the BiW structure of a coupe is intended for use in a convertible, since bending and torsion stiffness will decrease in this case due to the absence of a roof, in order to give the coupe additional stability.

Hardware. To ensure that the results of the calculation are correct, one of the first BiW structures to be manufactured as a prototype structure is often used for the verification of bending and torsion stiffness on testing machines. Since these tests are also quite inexpensive, and the correct layout of the BiW structure is fundamental, this approach is reasonable. The first prototype with the new BiW structure, in most cases built shortly before the end of the concept phase, is used for first driving tests and, most importantly for the verification of the structure, in the case of accidents. Because of the highly dynamic processes and high dependence on dynamic material properties, the results of a crash simulation are uncertain, which is why hardware verification is still needed before series development can start.

Aero/Thermodynamics

The basic aero- and thermodynamic behavior of a vehicle is determined by the layout of the exterior, the

Fig. 22.35 Visualization of airflow (courtesy of Daimler AG)

main air channels inside the car, and the position of the engine and other power train components. Thus, this behavior has to be checked early in the process, when the styling process is not yet finished, in order to allow for necessary design changes due to flaws in the aerodynamic performance [22.44–46].

Virtual. For prediction of the aero- and thermodynamic behavior of a vehicle, computational fluid dynamics (CFD) methods are used. With the help of these methods, the airflow around and inside a vehicle can be visualized, a key vehicle performance indicator – the c_w coefficient which contributes to the fuel consumption, especially at high speeds – can be determined, and airflow can be analyzed. Minimum air mass flows are defined, for example, for the cooling needs of the engine through the radiator and of the brakes.

The normal force to the road consists of the weight of the car and the force generated by the airflow, the downforce. The downforce is also calculated in the early phase, as it is critical for driving stability at high speeds. Changes in the exterior car shape and additional aerodynamic spoiler can affect the downforce.

Hardware. In order to analyze the airflow around and inside a car, flow analysis models can be used. Early in the process, scaled models can be used to evaluate exterior airflow and provide criteria for selecting a styling alternative that is most suitable in terms of aerodynamic performance. Later in the process, both 1 : 1 scale models and hardware prototypes can be used for analyzing both exterior and interior airflow (Fig. 22.35).

The hardware-based approach is losing favor against the use of virtual simulations.

22.4.2 Methods for Series Development

With the concept confirmed, the series phase starts. Virtual methods are increasingly being substituted for and complemented by hardware methods.

A huge number of different development and testing methods are used in series development to ensure that the components developed will meet functional, performance, and quality targets. Each automotive company has its own particular approach in terms of which methods are used for what kind of evaluation at which point in time. Figures 22.36–22.39 give an overview of different tests to be performed.

Fig. 22.36 Test with Mercedes Benz E-Class cabriolet to verify performance in dry and dusty environment; the convertible soft top will be opened and closed 500 times per vehicle during this test phase (courtesy of Daimler AG)

Fig. 22.37 Test with vehicle to verify performance in all weather conditions (courtesy of Daimler AG)

Fig. 22.38 Test with autonomously steered vehicle to verify performance in situations that could be dangerous for the test driver (courtesy of Daimler AG)

Fig. 22.39 Test with sports utility vehicle to verify performance under extreme terrain conditions (courtesy of Daimler AG)

Using three examples, general insight into the methods for series development is provided below.

Climate Simulation

A climate chamber (Fig. 22.40) is used to simulate extreme climate conditions. Heat and cold are simulated, together with different levels of humidity and sunlight incidence. Different kinds of behavior are analyzed in the climate chamber: car functions such as door opening, and heating and cooling of the passenger cell are analyzed, as well as engine startup performance under extreme conditions. An extension of the climate chamber is the climate wind tunnel, in which different wind flow conditions can additionally be generated with the car standing still or using its engine to turn the wheels on rollers mounted to the floor.

Climate simulation on the test track is usually combined with analysis of the behavior of the car and especially its cooling system at high speeds. To simulate the vehicle being parked in a garage with a hot engine, after these tests the vehicle can be put into a closed chamber to simulate this extreme operating condition.

Climate simulation is also done in extensive tests in different climate zones in the world such as Scandinavia and Africa or Death Valley in the USA. Here, it is important to minimize the effort in transporting the test vehicles between the different test locations while maximizing the difference in climatic conditions, in order to minimize cost and time lost during transportation. Snow, sand, different road conditions, and stop-and-go traffic in metropolitan areas are also covered during these tests.

Fig. 22.40 Car test in climate chamber (courtesy of Mercedes-Benz Cars)

Chassis Tuning

For tuning of the chassis system, different driving situations are simulated by test drivers. Additional adaptations in terms of springs, dampers, and most importantly, electronic stability systems are derived. In order to cover all combinations in which a vehicle can be driven by a customer, the variants of tire size and type, usage of winter chains, and the different engine, chassis, and body types have to be taken into consideration. Therefore, with the large number of car variants that a customer can order, the effort required to tune the chassis can increase substantially.

Apart from tuning of the chassis, it must also be verified that there is enough space between the tire (all potentially usable tires) and the fender liner under all driving conditions. For this purpose, early in the process, wheel covers are generated as boundary faces for the movement of the tire under every condition in the CAD system, on the basis of which the fender liner is designed. The correct sizing of the fender liner is then later verified in hardware tests. Most critical in terms of space needed are large tire sizes with a sporty chassis layout and the usage of winter chains.

Hardware-in-the-Loop

Hardware-in-the-loop (HIL) is an approach to test certain hardware components in their future operating environment when this environment is not yet available, i.e., when other interoperating components are not yet

Fig. 22.41 Hardware-in-the-loop (HIL) of a vehicle-specific system relevant in the driving process. A predefined testing program is used to systematically test the system by simulating different driving situations, using both everyday situations and rare events to discover potential malfunctions. (courtesy of Daimler AG)

available. In this case, the other components and the environmental conditions are simulated by a computer program in real time, and the simulation parameters are input to the component to be tested. HIL is used for mechanical, electronic, and electromechanical components.

The HIL approach is used to decouple the behavior of components such as controllers in an interconnected network (for example, the Controller Area Network, or CAN bus). With clearly defined interfaces between the components and the definition of the communication bus structure, the HIL method is similar to the methods used in software engineering for some time already.

An example of the utilization of HIL is the testing of controllers for active body control in a test-bed with simulated signals from sensors and actuators before the controller is put into the networked car environment in a prototype (Fig. 22.41).

Tests of a component can be reproduced, and thus critical conditions in terms of operating behavior can also be reproduced and used as test criteria for approving the release of the component.

With the decoupling approach of HIL, product development time can be reduced, since it is not necessary to wait for the last component in a network to be available in hardware. Also, due to the modular structure of the network of components, the complex interaction of components can be controlled.

22.4.3 Cross-Functional Methods

Product Structure and Bill of Materials

The vehicle is logically and/or functionally structured. The power train, the doors, and the cockpit may be high-level elements of this structure, which are further divided into substructures. The leaves of the structure tree represent the parts or components. The part or component describing the data is matched via PDM software, and transformations describing the position of the specific part or component are added. The functionality of the PDM software enables the digital generation of assemblies or the entire car. For this purpose, the product structure will be interpreted, and the geometric description of the parts and components can be loaded and positioned element by element using the attached transformations. This functionality is the basis for all types of simulations (Fig. 22.42).

The product structure again is the basis for the BOM (Fig. 22.43). In the bill of material, the leaves of the structure of the car are focused upon. The geometric description itself is neglected; its existence and the level of quality are of importance and, hence, represented. Instead, further information is added which enables the configuration of the car. The BOM describes the contents of the accessory packages to be offered, the specifics of the American, European, or Japanese versions, the colors that will be available, the options that can be chosen from, and the dependencies that exist between these configurations.

The BOM, and the system in which it is handled, forms the basis for all logistical activities. Material and supplier parts are ordered using the BOM for both prototypes and the final customer-specific car. The plants in which the cars will be assembled can be planned with respect to capacities, required tools, robots, etc., and manufacturing costs can be calculated, since the parts-specific costs can also be added to the BOM, to name just a few applications of the BOM.

Since the role of the BOM is essential, its quality is a major aim in car development.

Data Quality

Because the virtual models of parts, components, and assemblies are used for diverse simulations

(Sect. 22.4.1 *Methods for Product Layout and Conceptual Development*), the representation of the real pendant has to be of high quality. Only by guaranteeing high data quality can costs be effectively contained by substituting physical prototypes with virtual ones early in the process.

The parts have to be *technically* mature, which means they have to meet the requirements by fulfilling the function specified and have to be producible. With respect to the car, they have to fit in the system, and their assembly has to be possible. On the other hand, the parts must be of high quality with respect to *formal* demands. For example, it is important that guidelines, both general and company-specific, have been taken into consideration in order to prevent unnecessary correction iterations. The parts have to be described completely, and all required extended information must be provided. This information completes the geometric description of the part, component, or assembly, and gains importance during the development process.

Examples are material, weight, center of gravity, and tolerances, as well as metadata such as the person in charge of the part, the supplier name, or in which context the part will be used or assembled (depending on the type of car, accessory package, or options to be chosen by the customer).

The responsibility for the quality of the data belongs to the part owner. To achieve technical quality, the part owner is supported by departments that investigate the packaging (Sect. 22.4.1 *Packaging and Ergonomics*) and digitally secure the assemblability. Companies often use tools to check the quality of the geometric data, particularly when data come from suppliers. These tools check whether planes are closed, parameters are set, and so forth. The formal quality can be controlled by monitoring tools that check specifically defined parameters. Sometimes the part owner is actively supported in completing the nongeometric information by departments that are in charge of product data management. These departments ultimately check the data set of a part, component and assembly. The positive result of a check leads to the release of the part, component, or assembly. This release also means that the digital model is reliable and can be used in further development (see the following section).

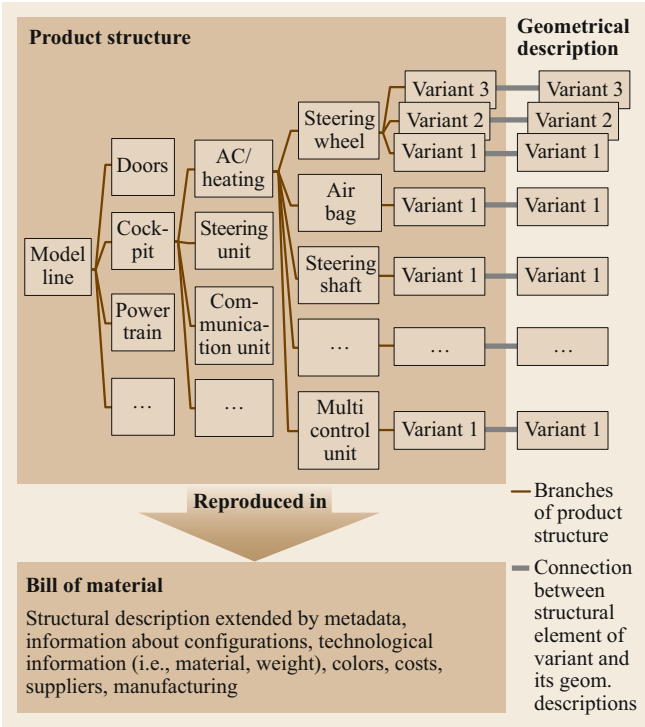

Fig. 22.42 Connection between product structure and virtual model

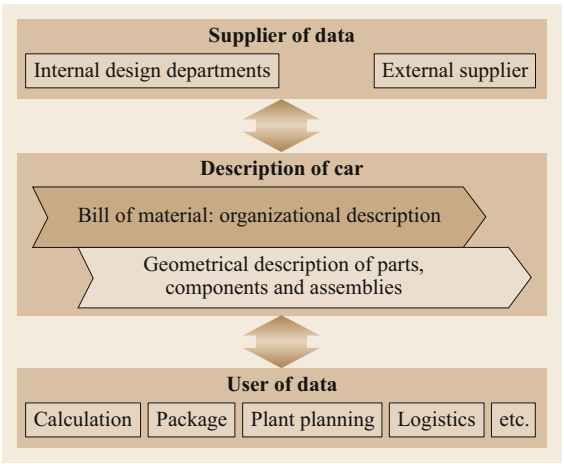

Fig. 22.43 Central role of the BOM in the car development process

Release

The importance of high data quality has already been discussed (Sect. 22.4.3 *Data Quality*). The measure by which the required quality of data and the conformity of documentation with hardware, if required, will be finally checked is the release, which concludes the development-specific activities at a certain version of the part, component, assembly, or system. The label *released* for an object makes the virtual model visible for downstream processes such as design of tools, logistical processes and planning of manufacturing units and plants. The released model is guaranteed to have the required level of maturity and quality in order to start hardware processes. Hence, every part that is needed to be manufactured and/or assembled has to be re-

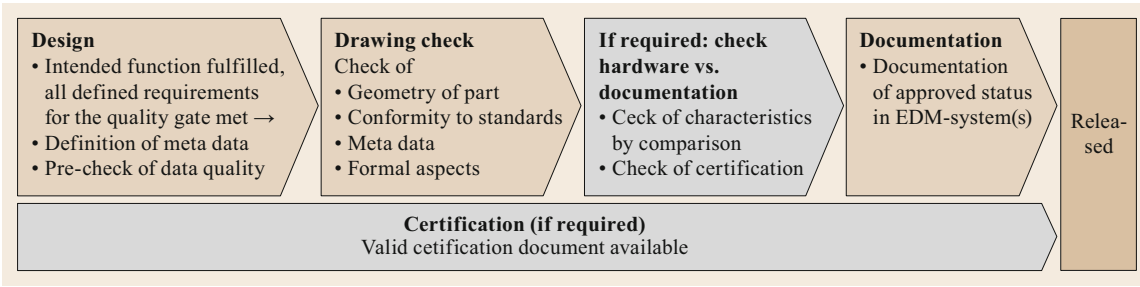

Fig. 22.44 General proceeding of a release of hardware during car development

leased. Only released parts can be ordered, regardless of whether the part is used for the production of a prototype or the final assembly of the car.

The release processes differ slightly from OEM to OEM. Nevertheless, a general process can be recognized. The release process described below is a generalized example that demonstrates the major characteristics of the process.

The prerequisite for the common release process for hardware is the completed design of the part, component, or assembly. It must fulfill its function(s) and meet all defined requirements at the specific point of development (so-called quality gates). The geometric description has to be complemented by the documentation of all required information. What this information is, depends on the point of development; for example, only a few pieces of technological information, such as tolerances and connecting details, are required in the early phases, whereas the weight and the center of gravity have to be available as precisely as possible from the start of design.

The release itself requires a positive evaluation over several steps. An overview of the process is presented in Fig. 22.44.

Design includes the *invention* of the part and must ensure the intended function. Furthermore, several influencing aspects must be considered before the release process is started. Table 22.5 shows examples of these aspects. An important part of the release process is that the principals of the engineer in charge of the development of the part or component confirm the evaluation of the expert. This is important in order to double-check whether all aspects are taken into account, even recent management decisions.

When the part has the required maturity and will be released, the person in charge of the part has to lock the model in order to prevent further manipulation. At this time, the required data quality must be secured by design or related departments. Data must be checked visually or with specific tools for the aspects to be considered (Table 22.5). Depending on the process specifications and the specific release level during the car development process, these aspects differ with respect to the expected maturity of data (Fig. 22.46).

Table 22.5 List of requirements to be checked before starting a release process for a part/assembly (not all aspects are always appropriate)

Weight targets fulfilled
Design for manufacturability (DFM) checked
Relevant laws and regulations checked and fulfilled
Carryover part contained
Safety aspects taken into account
Open points from design reviews settled
Cost targets fulfilled
Failure mode and effects analysis (FMEA) carried out
Standards checked
Production process capability proofed
Part assigned to car variants
Tests successfully completed

The locked and prechecked part will then be passed on to the *drawing check*. Now the model can, for example, be checked for:

- The manufacturing-specific design of the part
- The conformity of geometry, material, etc., to standards
- The existence of the required technological data
- The existence of the required metadata
- The existence of the required attributes.

At the end of development, the hardware has to be checked against its documentation. Samples produced on series production tools will be analyzed with respect to the characteristics documented by visual inspection by a quality department. Form, weight, dimensions, material, color, labels, and availability of variant tables are some examples of the checks conducted. In that case that the part or component is subject to certification, the availability of a valid certification for all the markets the part or component shall be distributed to has to be checked.

When the confirmation release is successful, this information is documented in the engineering data management (EDM) system. The part, component, or

Release without application	
→ New part	(general design, i.e., standard parts or generally applicable parts like tubes, clamps, surgical gloves, washer fluid)
Release with application	
→ New part	(specific design, i.e., body parts or the specifically adjusted tube)
→ New application of existing part	
→ Change of design	(part has to be replaceable in all applications)
→ Change of level of maturity	(no changes of design have been made, development phase changes by definition)
Examples	
→ Part looses validity	(for a specific application, another application might stay valid)
→ Exchange of part	(for a specific application)
→ Change of relevant equipment package	
→ Change of quality	

Fig. 22.45 Kinds of release

assembly is now labeled as *released*. This attribute is also transferred to the BOM. In this way, downstream processes can now access the geometric description of the part, and the release process is completed.

The various forms of releases are differentiated in Fig. 22.45.

Car development is a complex process in which suppliers develop a large share of the car. The parts, components, or assemblies will be designed at the OEM or be provided to the OEM by the supplier. Although the supplier naturally checks the required maturity for the development to be delivered, the release of the data is done by the OEM in order to achieve uniform data quality supplied to the process.

As mentioned above, the aspects to be checked in a release depend on the specific milestones of the car development process of the particular OEM. Figure 22.46 shows some examples of the form of a release with respect to maturity of car development.

Prototype and Test Management

The different departments in car development have special needs for tests. During tests, certain aspects of the behavior of the car are analyzed. In order to achieve the most efficient utilization of prototypes, tests are scheduled and assigned to prototypes in a way that minimizes the number of prototypes and the effort required to rebuild prototypes, while maximizing the usability and special needs of prototype equipment and maturity for the design departments. Prototype and test management is usually a central facility that covers all car development projects.

Weight Management

The weight of a vehicle is a basic layout parameter and influences fuel consumption, and the distribution of the weight between the front and rear axles of the vehicle is a parameter that influences the driving performance of the car.

Therefore, the definition of weight targets and weight management during the car development process is important to ensure that the vehicle will meet the expected performance criteria.

In the target building process, the weight target for a vehicle is defined by:

- Benchmarking of car weight of competitors in the market segment
- Key performance parameters of the car to be met (such as fuel consumption)
- Top-down definition of targets by proportional ratio of weight from the predecessor car
- Consideration of negative and positive weight contribution of new components (such as infotainment components) or technologies (aluminum body structure).

Weight targets are broken down from the whole car into modules and components to parts, and the designer has to meet the weight target while keeping the cost and time targets as well as the function in mind.

As soon as weight targets are defined and agreed upon, weight management is started in order to control the current status of the car weight at each step of the car development process. The quality of the weight status can be divided into three categories. In the early phases, when there is no 3-D part geometry available, the weight declaration is in the state of *estimate*. With engineering judgment, the responsible designer will feed this value into the weight management process.

As soon as a reasonable 3-D part geometry is available and the material is defined, the weight can be *calculated* by using CAD functionality for calculating the volume times the material density. The third level of weight status is reached as soon as parts are available in hardware. The weight can then be measured using a scale. The quality of the weight state *weighed* depends on whether the parts are made out of series material and series tools, or whether prototype material and tools are used, and eventually corrective factors are used to forecast the final part weight (Fig. 22.47).

During most of the car development process, there will be parts concurrently in the state of *estimated* and *calculated* or *calculated* and *weighed*, making the over-

Proceeding of product development

Kind of release	Release for planning	Release for tools	Release for purchasing	Release for disposition
Prerequisites	Part design is mature for testing	Results of testing positive for step-by-step release	Part desing finished, test results are sufficient	Evaluation by production is positive
Activities before starting release process	– CAD model created – Part information defined – BOM adapted – Signatures by principals given	– CAD model, BOM and part information changed due to results from testing – Signatures by principals given	– Part design finished – BOM and part information finally adapted – Signatures by principals given	– Sample delivery and testing positive – Signatures by principals given – If required: certification completed
		Release		
Activities triggered by release	– Evaluation in terms of DFM by production – Definition of production methods and tools – Purchasing of prototype parts – Disposition for tests – Check series delivery capabilities of supplier	– Generation of manufacturing BOM – Order of tools for series production – Finish planning for logistics processes	– Adaptation of manufacturing BOM – Planning of SOP – Planning of production capacity – Securing of ramp up of series production by contrasts – Purchasing of pre-series parts	– Contract for unlimited part delivery according to volume planned

Fig. 22.46 Kinds of release with respect to maturity

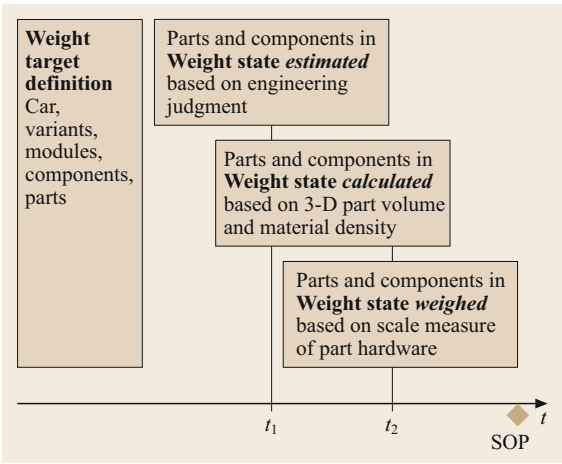

Fig. 22.47 Total weight state based on different part weight states (examples t_1 and t_2)

all weight state a combination of both states until near the start of production (SOP).

Weight is usually tracked in the BOM.

Weight targets are defined for a number of different car variants, and these have to be checked continuously. Finally, it is important to meet the needs of homologation of a car in the different countries to which the car will be exported, and the different regulations for measuring the car weight (tank full or empty, supposed number and weight of passengers).

Engineering Change Management

The dynamics of car development do not end with its introduction to the market. A car will continuously be developed further. On average, each part of a car will be changed approximately three times, and engine parts about eight times. Up to the point that a car model line ends, the number of spare parts increases by a factor of five.

Changes can become necessary because of field feedback (guarantee and warranty, quality, customer expectations, requirements from sales), measures due to legislation, optimization (costs, production, and quality), and technical development.

Change requests always have their reason. Nevertheless, not each request can be realized, since each change requires an enormous effort, as a complex process is necessary to realize a change and to ensure that it has no unintended impact on other parts or functions of the car. An idea of what has to be carried out to implement a change in a new car is presented in Fig. 22.48.

When a change request (Fig. 22.48 (4)) is generated for a model line that is in production (3), the change process starts in development again (5). Although the process of adaptation (6) differs slightly

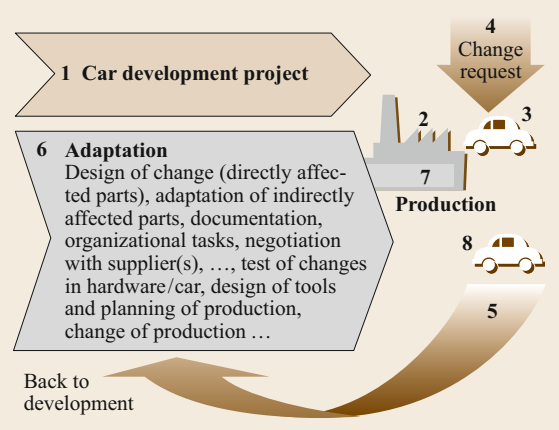

Fig. 22.48 Effort resulting from the realization of a change intention

from the general development process, the main steps are the same as shown in Fig. 22.48 (6). When the necessary adaptations of production tools and proceedings are implemented, the changed car (8) can finally be manufactured (7).

The entire process of realization of a single intention to change costs about 20 000–50 000 euros. This is why a change request has to be considered carefully. It must be determined whether the reason to change specific features of a car is profitable enough to cover the costs resulting from the process necessary for its realization.

In Fig. 22.49, the main steps for evaluating an intended change are shown. The two-level release process helps to extract unnecessary or unprofitable change requests early in the process. When the change request or intention is described by an expert, for example, a principal of the specific design department can evaluate it. This evaluation functions as an early filter, when only a small effort is invested. An approval leads to a phase of detailing of the design of the intended change. The detailed change request is then evaluated by all affected departments, as shown in the figure. Due to the more detailed specification, an evaluation of the intended change with respect to affected topics by the experts is now possible. When these experts approve the request, the realization of the intended change starts with the design.

The process of the evaluation and realization of a single change itself requires enormous effort. However, during the car's life cycle and in the various departments involved in car development, many change requests are generated. Since there are about 8000 changes in one car model line, and approximately 50% of that after the start of production, one can imagine that it is not possible to realize each change intent in the production line once it is completely defined. A change in production might, in the worst case, request a standstill of the line. This is expensive and must be coordinated so that many changes are carried out at the same time.

Another aspect that needs coordination is the testing of changes in hardware. In order to keep costs low, several changes should be tested in one production vehicle used for testing series aspects. A prerequisite is that the changes do not affect one another.

Furthermore, if the change has an impact on an existing certification, both the certification and the whole vehicle type approval in all relevant markets must be updated. This process has to be completed before a car in which the change is realized can be given into the hands of a customer. Hence, the realization of changes has to be planned in detail.

Integration of Development Partners

Tier 1 suppliers today have in-depth knowledge of their technologies and components and their respective application in a vehicle, which automotive companies can typically no longer afford because of the extreme specialization required for the different technologies. Therefore, the integration of these suppliers into the

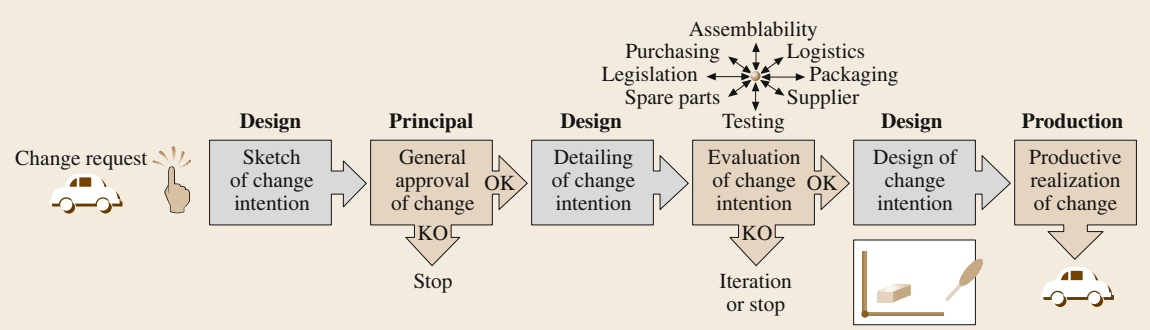

Fig. 22.49 Example of a change approval and realization process (after CAD/CAE in Automotive Industry, Technical University of Berlin, Institute of Vehicle Technology) (KO = knock-out)

Table 22.6 Non-engineering functions to support car development

Purchasing	In the early phase of the car development project, engineering partners and system suppliers who collaborate in concept development are sourced by purchasing. Contracts are established regarding the content of engineering service provided up to the provision of prototype parts for first hardware tests. Afterwards, most automotive companies have a global sourcing process in order to identify which supplier will provide the parts for series production, and select this supplier on the basis of reliability of supply and price.
Marketing	Marketing represents the voice of the customer. It is mainly involved in the definition of the car development project (positioning of the car to be developed in the market, definition of target price, definition of options to be offered).
Controlling	Each car development project is measured by a number of different parameters, one of the most important being cost. In most automotive companies, budgets are assigned for each respective engineering team responsible for a specific area of the car. These budgets consist basically of engineering cost (internal and external), prototype material cost and investment for sourced parts and for production machinery. Controlling keeps track of the predicted budget consumption against real consumption, and provides valuable information to the team for taking necessary corrective actions to meet the cost targets.

car development project from the very start is of vital importance. Examples of technologies and components developed by suppliers are headlamps and electromechanical components such as antilock braking systems.

When integrating suppliers into car development, one has to consider:

- The product substance
- Its extent in terms of engineering service
- The interaction between the supplier and the OEM.

Depending on this, the following aspects have to be agreed upon in contracts with the supplier:

- The kind of data exchange (mail, direct access to systems from the outside or by resident engineers)
- The kind, form, and content of the results to be delivered by the supplier
- The kinds of simulations and tests to prove the suitability of the concept and its application in the context of the car
- Delivery of prototype parts, if applicable and necessary
- Delivery of parts for series production, if the supplier will also source the component for series supply (including proof of quality assurance).

In order to integrate development partners successfully, there has to be a trade-off between open transfer of information and the retention of specific expertise between the OEM and the relevant supplier.

Non-Engineering Support of Car Development

During car development, the engineering departments are supported by various non-engineering functions in the company. Table 22.6 briefly describes the most important functions.

References

22.1 Verband der Automobilindustrie e.V. (VDA): Jahresbericht 2016 – Die Automobilindustrie in Daten und Fakten (Berlin 2016), in German and English, https://www.vda.de/de/services/Publikationen/jahresbericht-2016.html (2016)

22.2 R. Nader: *Unsafe at Any Speed* (Grossman, New York 1965)

22.3 D. Clausing: *Total Quality Development* (ASME, New York 1994)

22.4 D. Bastow, G. Howard, J.P. Whitehead: *Car Suspension and Handling*, 4th edn. (Wiley, Hoboken 2004)

22.5 UNECE, Inland Transport Committee, WP 29: Addenda to the 1958 Agreement, https://www.unece.org/trans/main/wp29/wp29regs.html (2017)

22.6 European Parliament and Council: Regulation (EC) No 661/2009 of 13 July 2009 concerning type-approval requirements for the general safety of motor vehicles, their trailers and systems, components and separate technical units intended therefore (EC, Brussels 2017), http://eur-lex.europa.eu/legal-content/EN/TXT/PDF/?uri=CELEX:32009R0661&from=DE

22.7 European Commission: Motor Vehicle Safety (EC, Brussels 2019), https://ec.europa.eu/growth/sectors/automotive/safety_en

22.8 DoE and EPA: Gasoline vehicle – Learn more about the new label, https://www.fueleconomy.gov/feg/label/learn-more-gasoline-label.shtml (2017)

22.9 US DoE and Environmental Protection Agency: Plug-in hybrid electric vehicles – Learn more about the new label, https://www.fueleconomy.gov/feg/label/learn-more-PHEV-label.shtml (2017)

22.10 United Nations: Global technical regulation No. 15 worldwide harmonized light vehicles test procedure (established in the Global Registry on 12 March 2014), https://www.unece.org/fileadmin/DAM/trans/main/wp29/wp29r-1998agr-rules/ECE-TRANS-180a15e.pdf (2014)

22.11 UNECE, Inland Transport Committee, WP 29: Global Technical Regulations, https://www.unece.org/trans/main/wp29/wp29wgs/wp29gen/wp29glob_registry.html (2017)

22.12 Euro NCAP: The official site of the European New Car Assessment Programme, http://www.euroncap.com/ (2017)

22.13 US DoT and National Highway Traffic Safety Administration: Safety ratings, https://www.nhtsa.gov/ratings (2017)

22.14 H.-H. Braess, U. Seiffert (Eds.): *Vieweg Handbuch der Kraftfahrzeugtechnik*, 7th edn. (Vieweg, Wiesbaden 2013), in German

22.15 J. Happian-Smith (Ed.): *An Introduction to Modern Vehicle Design* (Butterworth-Heinemann, Oxford 2002)

22.16 I.L. Ver, L.L. Beranek (Eds.): *Noise and Vibration Control Engineering*, 2nd edn. (Wiley, Hoboken 2005)

22.17 A.D. Dimaragonas: *Vibration for Engineers*, 2nd edn. (Prentice Hall, Englewood-Cliffs 1996)

22.18 B. Hall: Noise vibration and harshness. In: *An Introduction to Modern Vehicle Design*, ed. by J. Happian-Smith (Butterworth-Heinemann, Oxford 2002)

22.19 German Insurers Accident Research: Homepage, https://udv.de/en (2017)

22.20 DEKRA: DEKRA Road Safety Report 2016, http://www.dekra.de/en/verkehrssicherheitsreport-2016 (2017)

22.21 National Highway Traffic Safety Administration: Special Crash Investigation (SCI), https://www.nhtsa.gov/research-data/special-crash-investigations-sci (2017)

22.22 Initiative for the Global Harmonisation of Accident Data: Homepage, http://www.iglad.net/ (2017)

22.23 J. Bakker, C. Sachs, D. Otte, R. Justen, L. Hannawald, F. Friesen: Analysis of fuel cell vehicles equipped with compressed hydrogen storage systems from a road accident safety perspective, SAE Int. J. Passeng. Cars Mech. Syst. **4**(1), 332–342 (2011)

22.24 U. Seiffert, L. Wech: *Automotive Safety Handbook* (Society of Automotive Engineers, Warrendale 2003)

22.25 SAE International: Automated driving – Levels of automation are defined in new SAE International Standard J3016, https://www.sae.org/misc/pdfs/automated_driving.pdf (2017)

22.26 N. Kalra, S. Paddock: Driving to safety – How many miles of driving would it take to demonstrate autonomous vehicle reliability? (RAND Corporation), http://www.rand.org/pubs/research_reports/RR1478.html (2017)

22.27 PEGASUS: PEGASUS Research Project – Securing automated driving effectively, http://www.pegasus-projekt.info/en/about-PEGASUS (2017)

22.28 H. Winner: Safety assurance for highly automated driving (in PEGASUS Lectures/Publications 2017), http://www.pegasus-projekt.info/files/tmpl/pdf/TRB%20Annual%20Meeting%202017%20Folien.pdf (2017)

22.29 U. Steininger, H.-P. Schöner, M. Schiementz: Dependency of uncertainties due to real world application resp. necessary simplifications and the effort to put into the coverage of all relevant scenarios and environments (in PEGASUS Lectures/Publications 2017), http://www.pegasus-projekt.info/files/tmpl/pdf/7.Tagung%20Fahrerassistenz%20Praesentation.pdf (2017)

22.30 A. Vollmer: Deutsche OEMs setzen Standards – 48V-Bordnetz, Teilnetzbetrieb und Ladeschnittstelle, http://www.all-electronics.de/deutsche-oems-setzen-standards/ (2011)

22.31 ISO 26262-4: Road vehicles – Functional safety – Part 4: Product development at the system level (Beuth, Berlin 2011)

22.32 ISO/AWI 21434: Road vehicles – Automotive security engineering (ISO, Geneva 2017), https://www.iso.org/standard/70918.html

22.33 G. Pahl, W. Beitz, J. Feldhusen, K.-H. Grote: *Engineering Design* (Springer, Switzerland 2007)

22.34 European Parliament and Council: Directive 2000/53/EC on end-of-life vehicles, http://eur-lex.europa.eu/legal-content/DE/TXT/?uri=URISERV%3Al21225 (2017)

22.35 European Commisson: Decision 2002/151/EG on minimum requirements for the certificate of destruction issued in accordance with Article 5(3) of Directive 2000/53/EC of the European Parliament and of the Council on end-of-life vehicles, http://eur-lex.europa.eu/legal-content/DE/TXT/?uri=celex:32002D0151 (2017)

22.36 End of Life Solutions Corporation (ELVS): Homepage, http://elvsolutions.org/ (2017)

22.37 L. Sage: *Winning the Innovation Race: Lessons from the Automotive Industry's Best Companies* (Wiley, Hoboken 2001)

22.38 M. Maurer, C. Stiller (Eds.): *Fahrerassistenzsysteme mit maschineller Wahrnehmung* (Springer, Heidelberg, Berlin, New York 2005), in German

22.39 G. Döllner, C. Gümbel, O. Tegel: Prozesse und Bausteine des CAx-Datenmanagements in der Digitalen Produktentwicklung. In: *6. Automobiltechnische Konferenz „Virtual Product Creation 2002" (Berlin 2002)*, in German

22.40 C.E. Armi: *American Car Design Now: Inside the Studios of America's Top Car Designers* (Rizzoli, New York 2004)

22.41 Daimler: Wie autonomes Fahren das Interieur revolutioniert – TecDay „Autonome Mobilität", http://www.nu-x.de/102-wie-autonomes-fahren-das-interieur-revolutioniert-tecday-autonome-mobilitaet.html (2014), in German

22.42 A. Parnow: Nutzen und Einsatz von RAMSIS bei DaimlerChrysler. In: *RAMSIS User Conference (Kaiserslautern 2004)* (2004), in German

22.43 J.M. Porter, C.S. Porter: Occupant accommodation: an ergonomics approach. In: *An Introduction to Modern Vehicle Design*, ed. by J. Happian-Smith (Butterworth-Heinemann, Oxford 2002)

22.44 M.B. Abbott, D.R. Basco: *Computational Fluid Dynamics* (Longman, Harlow 1997)

22.45 R.H. Barnard: *Road Vehicle Aerodynamic Design*, 2nd edn. (MechAero, St. Albans 2001)

22.46 W.H. Hucho (Ed.): *Aerodynamics of Road Vehicles – from Fluid Mechanics to Vehicle Engineering*, 4th edn. (Society of Automotive Engineers, Warrendale 1998)

Gritt Ahrens

EvoBus GmbH
Corporate Quality Daimler Buses
Neu-Ulm, Germany
gritt.ahrens@daimler.com

The author studied Mechanical Engineering at Technical University of Berlin and earned the PhD on a topic in design methodology. She started her career in R&D at Mercedes-Benz Cars and gained expertise in PDM, E/E, safety certification, worldwide homologation and was involved in numerous cross functional projects. Today she is responsible for Corporate Quality of Daimler Buses.

23. Railway Systems–Railway Engineering

Markus Hecht

Railway travel is the smallest mode of transport but is becoming increasingly important. Urbanization needs more powerful urban rail systems, while intercity traffic needs fast, reliable, and high-performance long-distance train systems. Also, transport of freight by rail over long distances is increasing. The reason for this is the high transportation capacity with small infrastructure cross section because of their guided nature and high energy efficiency based on low running resistance and regenerative braking, which can transform kinetic energy into electric power with very high efficiency. Also, green electric energy can be used directly.

This chapter argues that railways require good organization not only in operation but also in the construction of vehicles and infrastructure. Special subjects such as wheel–rail interactions are introduced. The basic functions of different elements such as tracks, bogies, bodyshells and their subparts including gearboxes, wheelsets, doors, air conditioning, pneumatic brake systems, etc. for mainline (passenger and freight), metros, and trams are presented using up-to-date examples with modern and widespread applications. Also, safety and environmental issues such as airborne noise reduction and type testing are tackled.

23.1 **General Interactions of Modules of a Railway System with Surroundings** 1057
23.1.1 Duration of Passenger Exchange 1058
23.1.2 Lifecycle Costs 1059
23.1.3 Reliability, Availability, and Safety 1059

23.2 **Track** 1061
23.2.1 Track Geometry Components 1061
23.2.2 Track Bed Configuration 1061
23.2.3 Switches 1063
23.2.4 Track Irregularities 1064

23.3 **Running Gears** 1066
23.3.1 Wheel–Rail Interaction 1066
23.3.2 Bogie Principle 1066
23.3.3 Constructive Elements 1069
23.3.4 Bogies 1070

23.4 **Superstructures** 1074
23.4.1 Principle 1074

23.5 **Vehicles** 1074

23.6 **Coupling Systems** 1077
23.6.1 Coupling 1077
23.6.2 Coupled 1077
23.6.3 Uncoupling 1079

23.7 **Safety** 1080
23.7.1 Active Safety Systems/Brakes 1080
23.7.2 Passive Safety 1081

23.8 **Air Conditioning** 1081
23.8.1 Process Air Loop 1081

References 1083

23.1 General Interactions of Modules of a Railway System with Surroundings

Railways have many technical and economical interfaces with their surroundings, as indicated in Fig. 23.1. The aims of a railway are usually defined externally, based on policy and economics with the consideration of markets, finances, and the environment. These aims are then transformed into strategies by the management of a railway company, who will provide instructions to several subareas such as marketing to define the product in terms of timetable and comfort. The timetable provides lots of information; it defines the locations to be connected and the distances to be overcome. By defining the times of departure and arrival, the travel speed is fixed. Also, the frequency of operation of the trains is defined.

The operation of a railway must be able to fulfill these requirements by providing adequate, educated

K.-H. Grote, H. Hefazi (Eds.), *Springer Handbook of Mechanical Engineering*, Springer Handbooks,
https://doi.org/10.1007/978-3-030-47035-7_23

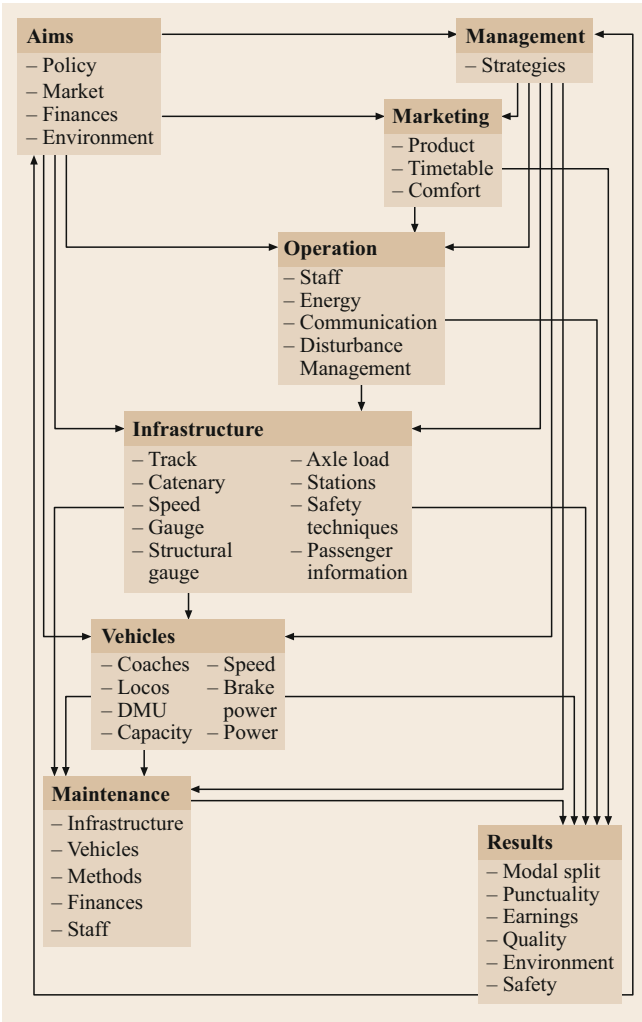

Fig. 23.1 Railway transportation—a system with strong interference

staff on trains and at fixed locations. Also, the energy to move the trains must be provided at the right locations. Communication must be enabled over one or even several lines with many trains. If the schedule fails, disturbance management must be able to restore the system to proper operation as soon as possible, whether the failure is caused for exterior or interior reasons.

Infrastructure such as tracks, perhaps catenary, the design speed of the track and its gauge, the structural gauge, the axle loads, and stations for passengers and/or loading/unloading facilities for goods must all fit the demands of the system. Information technologies for passengers are also gaining in importance.

The type of vehicles chosen must be adequate for the required operation, for instance locomotives, coaches or diesel multiple units (DMUs). The vehicles must fit the infrastructure and its operation in terms of speed, axle load, etc.

Maintenance must provide reliable system elements to avoid failures because of the effects of wear. Maintenance is increasingly being outsourced today.

If all of the elements shown in the boxes on the diagonal in Fig. 23.1 are provided by one company, the system is called an integrated railway; otherwise, it is known as a segmented railway.

The interaction of these elements produces results in terms of earnings and the quality of the process (for example, punctuality).

Because of high cost pressures, the aim for an economically sound railway system is to run as fast (km/(vehicle of the fleet × day)) and reliably as possible.

A high number of kilometers per vehicle in the fleet is important, as the costs for vehicles, stationary equipment, and operational staff are a function of time, whereas the earnings from passenger and freight traffic is more or less a function of distance. Also, fast running in the form of fast point-to-point transportation is itself attractive for passengers and goods.

Good reliability reduces the number of spare vehicles and spare staff required and also reduces the operational risk. Of course, this is also an important quality measure for clients in passenger and freight operations.

Rail vehicles must therefore be designed according to these requirements.

23.1.1 Duration of Passenger Exchange

As the stopping time has a negative effect on the aim mentioned above (covering as long distances as possible per vehicle and day), it should be as short as possible, which results in many technical and operational constraints.

As an example, the different elements or modules that define the stopping time of a train are shown in Fig. 23.1.

The duration of stops (intermediate stops and in the terminus/stations) is affected by the following parameters:

1. The height difference between the platform and train level, which should be as small as possible.
2. The gap between the train entrance and platform, which should be as small as possible (the ideal being gapless, high-level platforms in a straight line and without curves).
3. The ability of passengers to handle the process; large amounts of luggage and disabled persons slow down the loading and unloading process, as do small children and older persons.

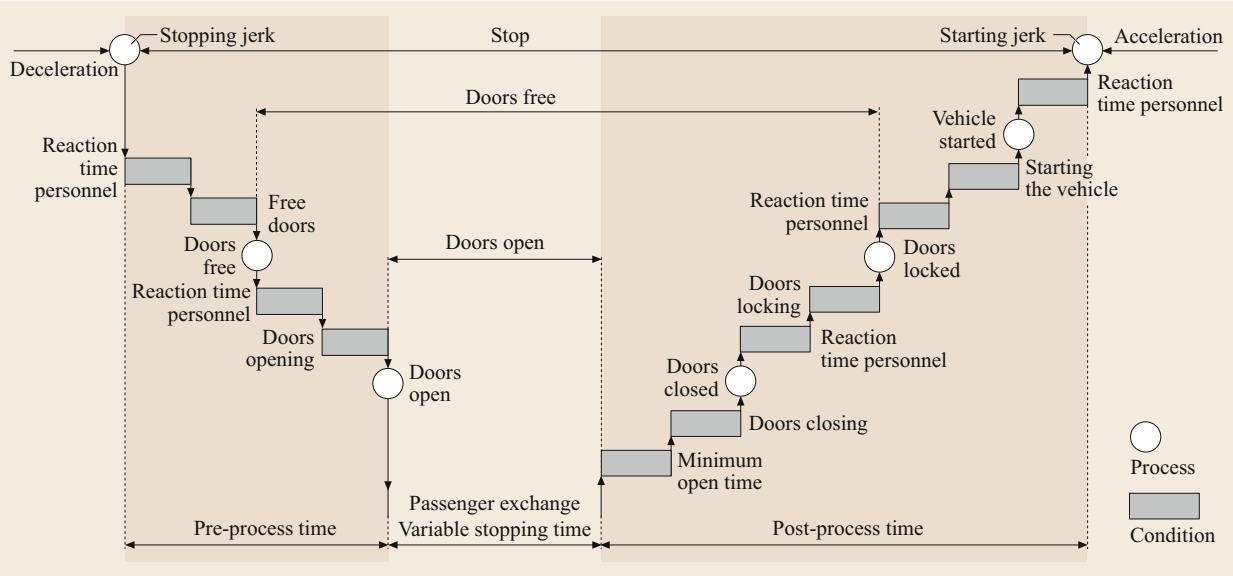

Fig. 23.2 Stopping, door opening/closing, and passenger exchange (after [23.1])

4. The duration of the door opening and closing process. Modern semiconductor-controlled doors often have very lengthy closing procedures, for instance, 20 s for InterCity Express 1 and 2 (ICE 1/2) trains in Germany, and similar values for the *train à grande vitesse* (TGV) in France. The reasons for this are the slow processors used for door control and the connection to the vehicle bus.
5. The number of doors. The number of doors should not be to small because of the possibility of door failures, but for long-distance traffic, doors are costly because of the costs of the doors themselves as well as the space behind the door, which is not usable as passenger seating space.

Especially for trains with frequent stops, it is very efficient to have short stopping times. The preprocess and postprocess time is clearly not productive at all, and the exchange of a given number of passengers is more effective the shorter this time (Fig. 23.2).

23.1.2 Lifecycle Costs

The annual distance traveled by rail vehicles is rather high, from 100 000 km/year for tram cars, over 200 000 km/year for regional trains and freight locomotives, and up to 500 000 km/year for high-speed rolling stock. For freight cars, it may range between 10 000 and 200 000 km/year. Lifetime is typically 30 and sometimes 40 years. Investment costs are rather high and typically account for one-quarter to one-third of the lifecycle costs, the other costs being maintenance and operation. In countries where wear- and noise-related track prices are charged, at least the difference between the cheapest and actual vehicle must be included as a new component of the lifecycle cost.

23.1.3 Reliability, Availability, and Safety

The basis for reliability, availability, maintainability, and safety (RAMS) is the European standard EN 50126 *Railway applications – The Specification and Demonstration of Reliability, Availability, Maintainability and Safety (RAMS)* (September 1999) [23.2] (Fig. 23.3).

RAMS is needed due to the increasing complexity of railway systems and to achieve a high-quality process. In a competitive environment (mainly from other modes of transport such as road, air, and even water), this is essential to survive economically. Very reliable transport (for instance, 99% or even more of trains on time) with high speeds and therefore little standby time must be achieved. Good reliability reduces the need for spare units and personnel; high speeds increase productivity, as payments are received on the

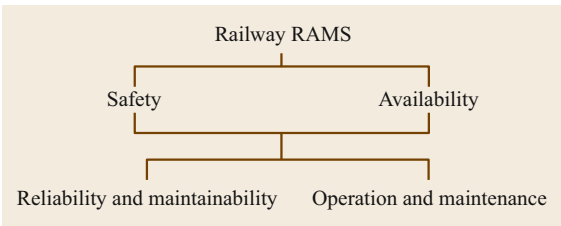

Fig. 23.3 Interrelation of railway RAMS elements

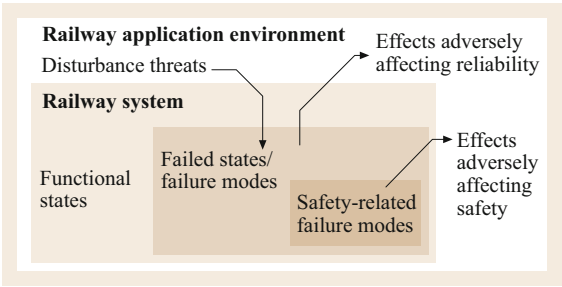

Fig. 23.4 Effects of failures within a system

basis of passenger-km or ton-km measures, whereas the expenses for equipment, including both trains and infrastructure, and also personnel occur on a time basis.

Here, mainly the process is discussed; targets are only mentioned as an example. RAMS covers the whole lifecycle of a system, and must be followed by the railway authorities (track and train operators) and the railway industry (system houses and suppliers).

The following definitions are used (Fig. 23.4):

- *Reliability*: the probability that an item can perform a required function under given conditions for a given time interval (t_1, t_2)
- *Availability*: the ability of a product to be in a state to perform a required function under given conditions at a given instant of time or over a given time interval, assuming that the required external resources are provided
- *Maintainability*: the probability that a given active maintenance action, for an item under given conditions of use, can be carried out within a stated time interval when the maintenance is performed under stated conditions and using stated procedures and resources
- *Safety*: freedom from unacceptable risk of harm (note that safety does not mean that no accident occurs at all).

Risk is defined as the product of the size of the resulting destruction and the likelihood of the occurrence of the event. This likelihood of occurrence may be reduced by huge safety margins or by diagnosis that improves the probability of the recognition of a defect at an early and still not dangerous stage.

Around 1980, railways demanded the availability of about 80% of their fleet. Some railways operating under difficult conditions, for instance when suffering from the requisition of spare parts for cannibalization for other units, often did not reach 50%. Today, figures of 95% for electric rolling stock and 92% for diesel rolling stock or even higher are demanded.

The definition of availability does not include accidents (for instance, at points during shunting) or

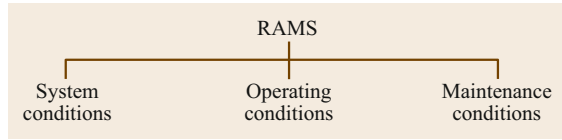

Fig. 23.5 Influences on RAMS

vandalism (for instance, broken windows or broken chairs due to rioting). Operational retardation is also not included. Because of all of these reasons, the number of spare units which are neither available nor down is greater than zero.

The basic equation for availability is

$$\text{availability} = \frac{\text{MTBF}}{\text{MTBF} + \text{MDT}}\,, \tag{23.1}$$

where MTBF is the mean time between failures, and MDT is the mean downtime.

Technical concepts of availability are based on a knowledge of:

1. Reliability in terms of:
   - All possible system failure modes in the specified application and environment
   - The probability of occurrence of each failure or, alternatively, the rate of occurrence of each failure
   - The effect of the failure on the functionality of the system
2. Maintainability in terms of:
   - Time for the performance of planned maintenance
   - Time for detection, identification, and location of faults
   - Time for the restoration of the failed system (unplanned maintenance)
3. Operation and maintenance in terms of:
   - All possible operation modes and required maintenance, over the system lifecycle
   - Human factor issues.

RAMS is influenced by the system conditions (vehicle and track, mainly influenced be the vehicle and track producers), operating conditions (the knowledge of the onboard personnel and the available data), and maintenance conditions (knowledge of the maintenance personnel and equipment of the maintenance facilities) (Fig. 23.5).

Methods to reduce downtime include:

1. Improving information to reduce inspection time by diagnosis
2. Parallel maintenance processes, including simultaneous processes of repair, inspection, refilling of water, sand, fuel etc.

For instance, cleaning of the interior (and probably the exterior) and toilets should be done simultaneous with refilling of water, sand, and probably fuel (while ensuring safety), a small overhaul, and module exchange (wheelsets, drive components, air-conditioning modules, etc.).

Simultaneous maintenance of fixed train sets (the locomotive plus wagons) and not locomotives separately from wagons avoids uncoupling and coupling time.

Systems diagnosis is becoming a major issue, and technical systems are becoming increasingly complex. Fault conditions are more difficult to reproduce, but fault analysis times should be reduced. Diagnosis systems for rail vehicles should have three levels:

1. Diagnosis for train personnel, to provide information for greater availability, and advice regarding redundant system operation
2. Diagnosis for maintenance personnel, to provide direct advice for required maintenance operations
3. Diagnosis for technical management, to provide data for reliability statistics as a basis for system improvements or at least spare-parts management (to enable the greatest reduction of spare-parts storage).

Two requirements of the diagnosis system that must be fulfilled are:

1. All data must be collected in one system for the whole vehicle (not separate systems, for instance, for the diesel motor, drive, doors, toilets, etc.).
2. The diagnosis criteria must be adaptable live during vehicle operation. This means that software skills must be available in the maintenance groups.

The reason for this is that the supplier cannot deliver a diagnosis system fulfilling all the needs of the operator because:

1. Not all operation circumstances are clear for the producer or even the operator.
2. Operation conditions may alter during vehicle operation (for instance, due to speed increases, longer trains, or movement from full to inferior service after 10 years or more).

It is recommended to order two or even more releases of diagnosis software after vehicle acceptance (and homologation) has been achieved. Operation experience can then be integrated, and the correct level of information attained.

Useless statements should be avoided, ensuring that information is given for real problems. Also, transfer from industry personnel to railway personnel must be achieved.

23.2 Track

23.2.1 Track Geometry Components

The track geometry defines the position of the track in the landscape [23.3]. The following components are used:

1. Vertical: level track, gradients, and gradient changes
2. Curves: radius R, transition curves with continually adapted curve radius, curvature k as inverse radius $k = 1/R$. Clothoid for the curvature of transition curves $k = L/A^2$, where A is the clothoid parameter that limits the jerk r (change of acceleration) in the lateral direction (m/s^3); limit $\leq 1\,m/s^3$ (Fig. 23.6)
3. Lateral: cant to reduce lateral accelerations (maximum for standard gauge with mixed traffic 150 mm) in transition curves ramps must be foreseen (Fig. 23.7).

23.2.2 Track Bed Configuration

The sleeper in the track bed (Fig. 23.8) distributes the weight not only in the vertical and lateral directions but also in the longitudinal direction. All forces caused by thermal stresses in the continuously welded rail must be transferred via the sleepers to the ballast. The continuous welding process is carried out at medium temperatures to minimize temperature effects. At high temperatures in summer, buckling of the track is avoided by high lateral resistance.

Rails are denoted by letters, which define the shape of the rail, and a figure, which normally gives the weight per meter in kg or lb (Fig. 23.9).

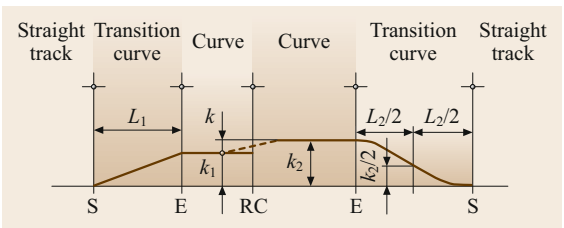

Fig. 23.6 Transition curves and ramps shown as curvature $k = 1/R$. RC – radius change; S – start transition curve; E – end transition curve

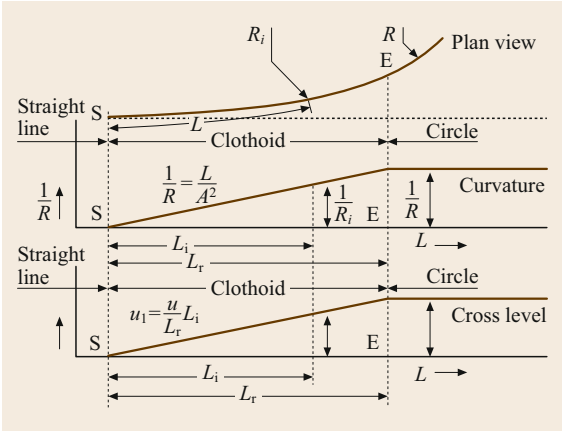

Fig. 23.7 Transition curve with linear ramp, *top* plan view, *middle* curvature, *below* cross level

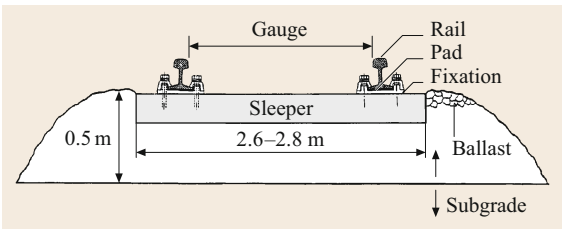

Fig. 23.8 Ballasted track bed (Table 23.1)

Table 23.1 Explanation for Fig. 23.8

Element	Function (construction)
Rail	Guidance of the vehicle, load distribution (rail 1 : 20 or 1 : 40 tilted)
Sleeper	Load distribution
Ballast	Load distribution, elastic element and damping device, distribution of the rail forces in all three directions, noise absorption of rolling noise and gearbox noise

The VST36 is a rail for light axle load, for instance Swiss narrow-gauge railways. The 49E1 is applied on lightly used European standard-gauge lines. The 60E2 is a rail for European main lines, and the AREA141AB is a rail for American mainlines.

The 60Ri2 is a grooved rail for tramway applications. Though the axle load of trams seldom exceeds 8 t, the stiffness of the tram rail is similar to that of other rails. In this way, much smaller displacements of the rail are achieved in the street plane.

Rails today are rolled as long as possible, typically 120 m long, to reduce the number of weld spots along the line as much as possible. Not only is welding on the line costly, but also the welds are more crack sensitive than the rolled rail.

Concrete sleepers are very durable and environmentally friendly; therefore, they have replaced wooden

Rail profile	VST36	49E1 (S49)	60E2	AREA141AB	60Ri2 (Ri60-13, Ri60N)
	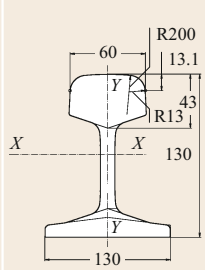	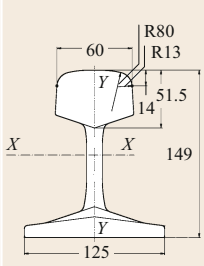	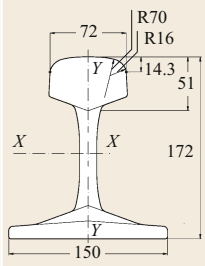	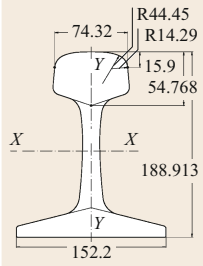	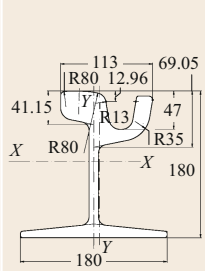
	Flat bottom rail	Flat bottom rail	Flat bottom rail	Flat bottom rail	Grooved rail
Mass (kg/m)	35.82	49.39	60.05	69.88	59.75
Area (cm^2)	45.63	62.92	76.5	89.02	76.11
Moment of inertia $X–X$ (cm^4) $Y–Y$ (cm^4)	1009.3 157.7	1816.0 319.1	3022 511.3	4180.0 620.7	3298.1 920.1

Fig. 23.9 Common rails with specific data. Rail profile, *TSTG-Profile-Handbook* (TSTG Schienen Technik, Duisburg)

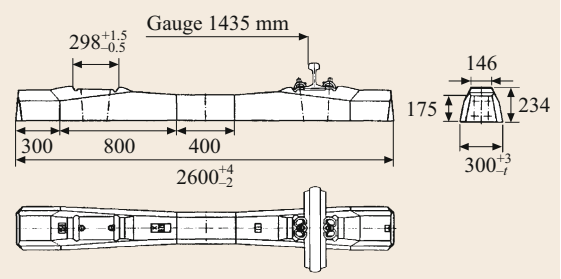

Fig. 23.10 B70 concrete sleeper, weight 445 kg (Pfleiderer Infrastrukturtechnik GmbH & Co KG, Neumarkt)

sleepers in many cases. Their large weight makes assembly difficult but provides good track stability (Fig. 23.10).

Today, the most commonly used sleeper type is concrete, but wood is still used also, and Y-steel sleepers have a growing market share. Y-steel sleepers offer much higher lateral resistance than concrete or wood, thus no ballast is required to avoid sideways buckling at high temperatures. Also, because of the lower height of the sleeper, less ballast is used in the track bed itself (Fig. 23.11). This is an advantage in tunnel construction. On intensively used lines, ballast-less track construction has the advantage of less maintenance effort compared with ballasted tracks (Fig. 23.12).

23.2.3 Switches

To enable networks, switches are essential. Compared with other guided transport modes where switches are large and heavy, on a railway switch only the switch blades must be moved. This is done by bending the blades elastically. Relatively small electric motors with gearboxes apply these forces.

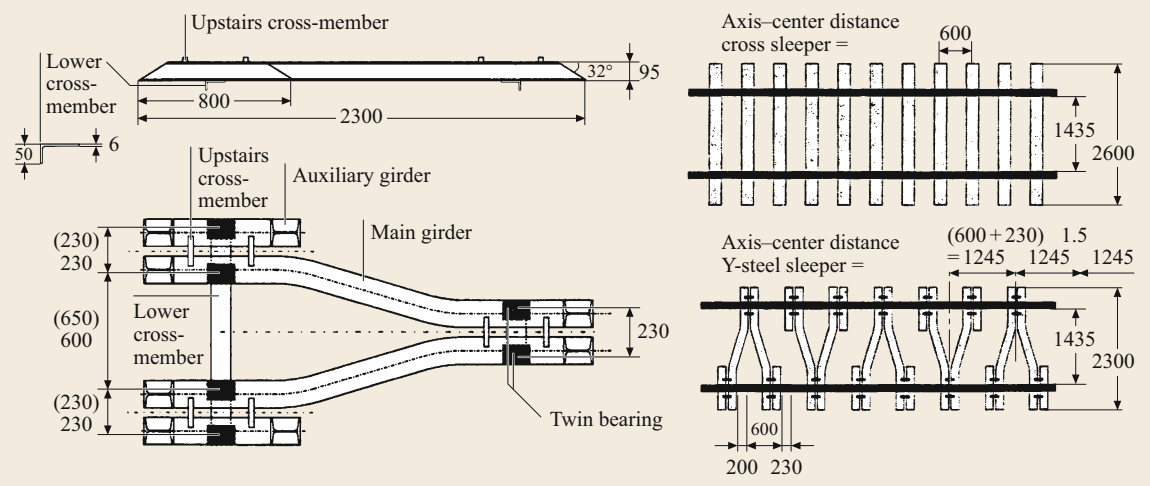

Fig. 23.11 Y-steel sleeper and comparison of steel, wood, and concrete sleeper track beds [23.4]

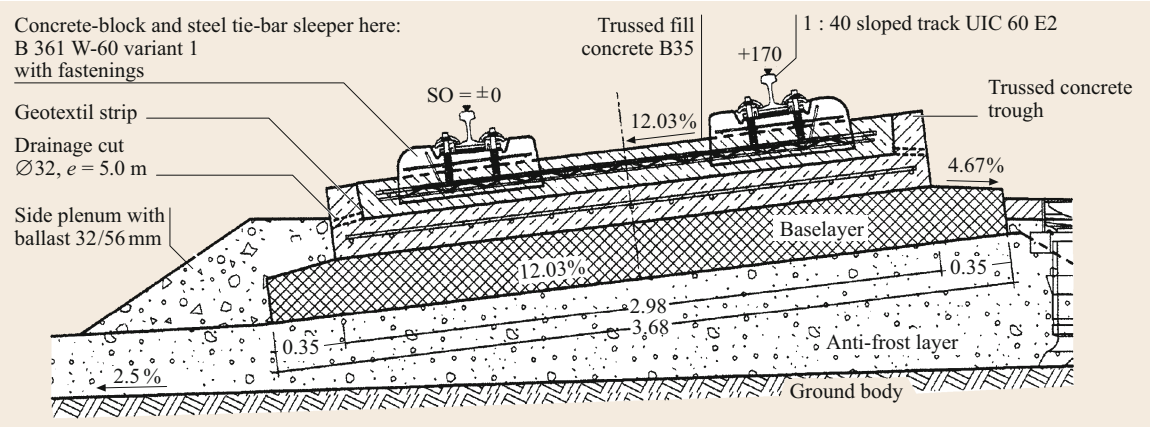

Fig. 23.12 Ballast-less track at the Cologne–Frankfurt high-speed line in a curve with maximum superelevation of 170 mm (Walter-Heilit, Munich) [23.5] (UIC – Union internationale des Chemins de fer)

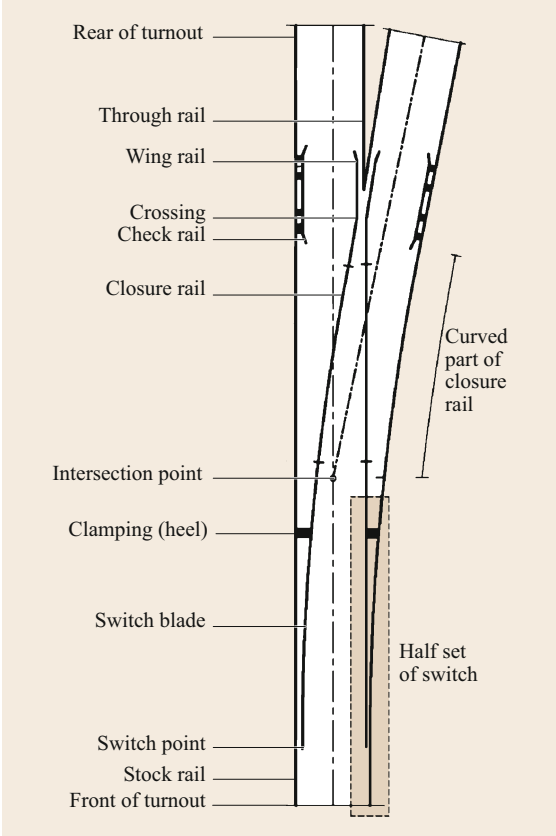

Fig. 23.13 Switches and their elements

In the crossing (also called a frog) itself, there is a gap where no lateral guidance of the wheel flange occurs. Here, check rails and the running rail provide guidance on both sides of the other wheel of the wheelset (Fig. 23.13).

23.2.4 Track Irregularities

The four degrees of freedom of the track are: gauge s, cant m_φ, alignment u, and level h (Fig. 23.14).

The gauge is defined as the smallest distance between the rail heads in a track 0–14 mm under the top of rail (TOR). The cant m_φ is the height difference between the two rails (Table 23.2). The twist is a function of the cant over distance

$$\text{cant} = \frac{m_\varphi(x_1) - m_\varphi(x_2)}{x_2 - x_1} \quad [-]$$

in units of mm/m = ‰.

Track irregularities are defined as a function of wavelength L or spatial frequency $\Omega = 2\pi/L$. With increasing wavelength, the amplitude of track irregularities increases (Figs. 23.15 and 23.16).

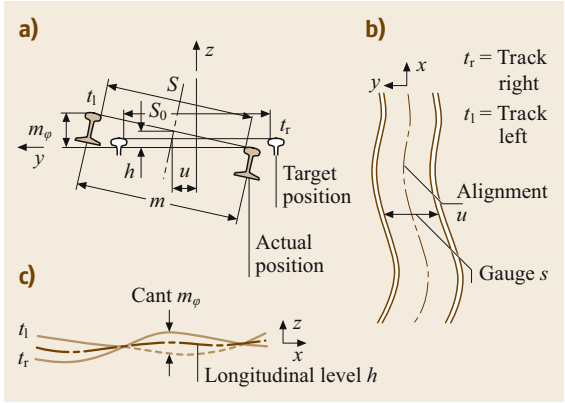

Fig. 23.14a–c Geometric track components: **(a)** coordinates in the measurement plane, **(b)** horizontal track coordinates: gauge s and alignment u, **(c)** vertical track coordinates: level h and cant m_φ

Table 23.2 Nominal international gauge distribution (caution: large tolerances between −3 and +35 mm are possible)

Name	Metric (mm)	British (inch)	Worldwide (%)
Meter gauge	1000	$3–3\frac{3}{8}$	7.5
CAP (gauge)	1067	3–6	7.7
Standard gauge	1435	$4–8\frac{1}{2}$	64
Russian broad gauge	1524[a]	5	11.8

[a] New 1520, since about 1980

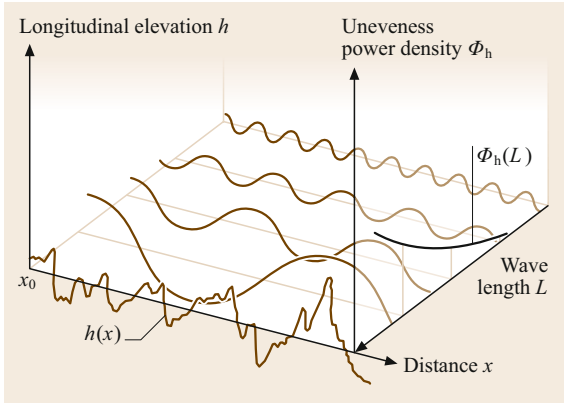

Fig. 23.15 Principle of calculation of power spectral densities (PSD) $\phi_h(L)$ from the displacement curve $h(x)$

The following track irregularities are common [23.6]:

- Level

$$\Phi_z(\bar{\Omega}) = \frac{A_V \Omega_c^2}{(\bar{\Omega}^2 + \Omega_r^2)(\bar{\Omega}^2 + \Omega_c^2)} A,$$

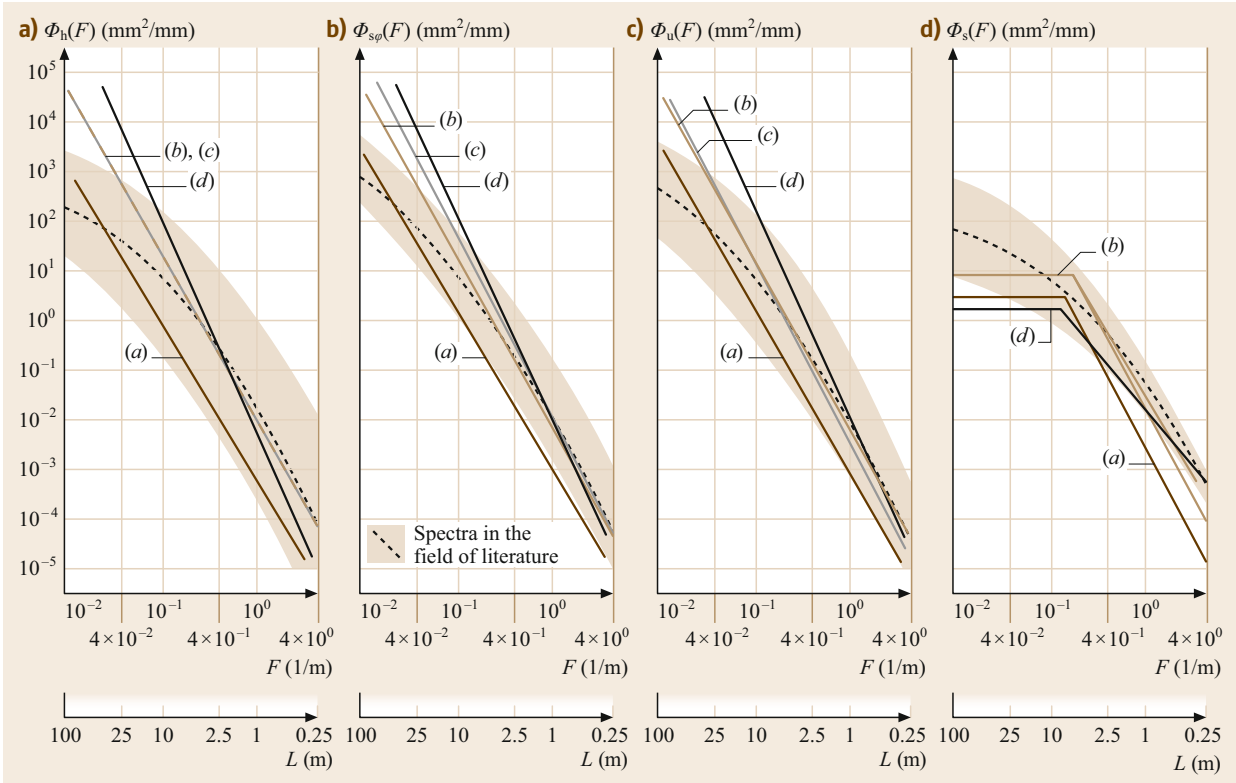

Fig. 23.16a–d Examples of track power spectral densities: **(a)** longitudinal level Φ_h, **(b)** cant $\Phi_{s\varphi}$, **(c)** alignment Φ_u, **(d)** gauge Φ_s. *Curve a* – standard gauge; *curve b* – city railway flat bottom rails (route track); *curve c* – city railway flat bottom rails (driving school track); *curve d* – city railway grooved tramway rails track

- Alignment

$$\Phi_y(\bar{\Omega}) = \frac{A_A \Omega_c^2}{(\bar{\Omega}^2 + \Omega_r^2)(\bar{\Omega}^2 + \Omega_c^2)}$$

- Cant in radians

$$\Phi_\rho(\Omega) = \frac{(A_C/a^2)\Omega_c^2 \bar{\Omega}}{(\bar{\Omega}^2 + \Omega_r^2)(\bar{\Omega}^2 + \Omega_c^2)(\bar{\Omega}^2 + \Omega_s^2)} ,$$

with the following data for a conventional track in good conditions:

$$\Omega_s = 0.4380\,\text{rad/m}\,, \quad \Omega_c = 0.8246\,\text{rad/m}\,,$$
$$\Omega_r = 0.0206\,\text{rad/m}\,,$$
$$A_V = A_A = A_C = 5.9233 \times 10^{-7}\,\text{m rad}\,,$$
$$a = 0.75\,\text{m}\,.$$

Impact of the increase in speed (Fig. 23.17):

(a) Without track quality improvement
(b) With track quality improvement

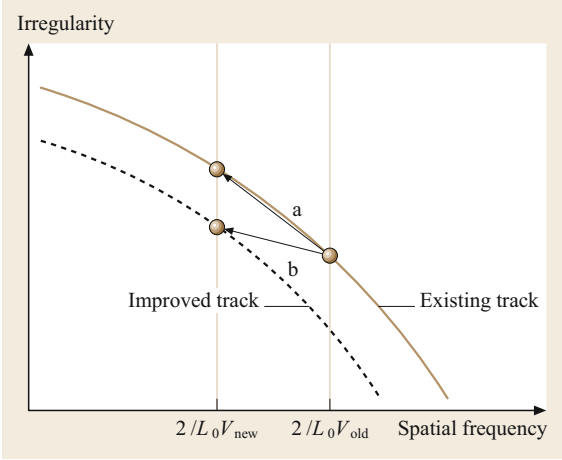

Fig. 23.17 Effect of speed increase on track amplitudes for a specific eigenfrequency of the vehicle

The relevant wavelength L_0 increases as the eigenfrequencies f_0 of the vehicles are time invariant

$$f_0 = \frac{V}{L_0} .$$

23.3 Running Gears

23.3.1 Wheel–Rail Interaction

The standard element of railway running gears is a wheelset, consisting of a rotating shaft on which two wheels are fixed by a press or shrink fit.

Additionally, the wheel profile together with the rail profile generates a steering effect (Fig. 23.18).

To introduce this effect, a conical thread geometry is first assumed.

The difference in radius Δr between the two rolling wheels leads to a self-steering effect, as both wheels have the same rotational speed but the outer wheel is running on a larger radius than the inner wheel.

This desirable behavior is superimposed by an effect called sinus running for conical profiles or wave running for practical profiles.

Equivalent Conicity

The wavelength of the real profile is equal to the wavelength of a wheel profile with constant conicity, as shown in Fig. 23.19.

To characterize the interaction between the wheel and rail for different wheel and rail profile shapes, Figs. 23.20 and 23.21 show examples for two different rail inclinations. The desired behavior is that the surfaces of the wheel and rail make contact on a rather broad level and that the difference in radius Δr reaches high values before flange contact occurs. If the angle of attack between the wheel and rail is large, then a two-point contact occurs (Fig. 23.22).

The running gears of a two-axle wagon are of link suspension type (Fig. 23.23). The links admit not only lateral but also longitudinal movements. In this way, self-steering of the individual wheelsets is enabled. The system is damped by friction, which is load sensitive; the higher the load, the greater the friction force. The diameter of the link is increased in the contact zones to increase the friction force.

The spring constant is very much a function of the amplitude. For small amplitudes, caused for instance by small track irregularities, the system is very stiff. For large amplitudes, caused for instance by severe rail twist, the system becomes rather soft [23.8] (Fig. 23.24).

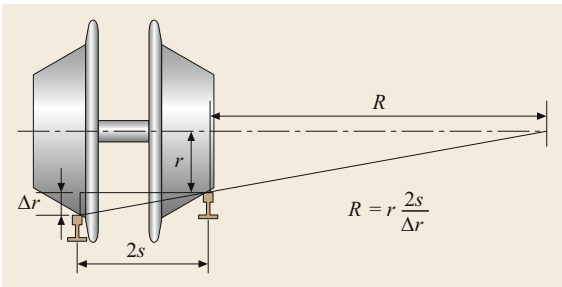

Fig. 23.18 Steering effect of a slip-free wheelset on a tight curve (radius R) related to the inner rail; $2s$ is the distance of contact points (typically 1500 mm at standard gauge); r is the rolling radius at the inner wheel; Δr is the radius difference between the outer and inner wheel

23.3.2 Bogie Principle

The wheelsets are spaced with an axial distance $2a$ and situated in a frame (Fig. 23.25). This frame together with the wheelsets forms the bogie. The vehicle body in general is supported in the middle of the bogie

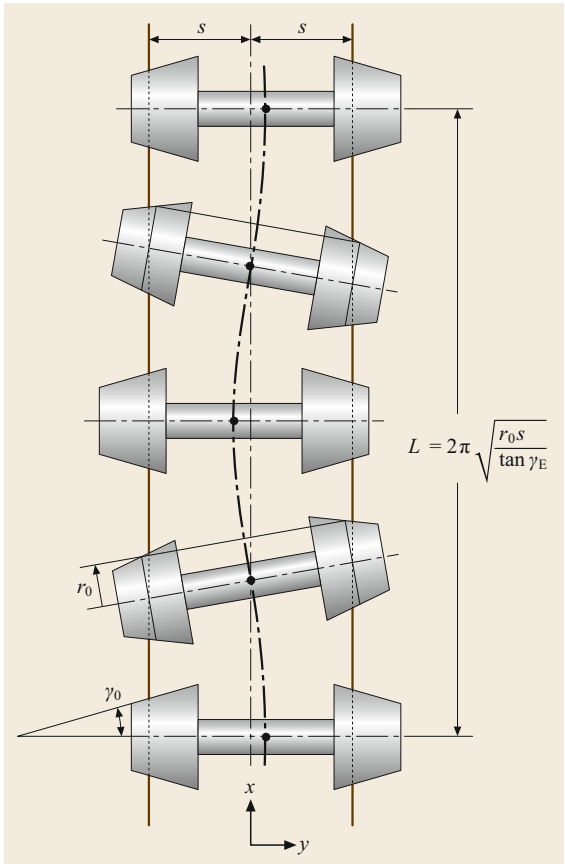

Fig. 23.19 Idealized wheelset moving: the wavelength L which occurs in slip-free movement [23.7]

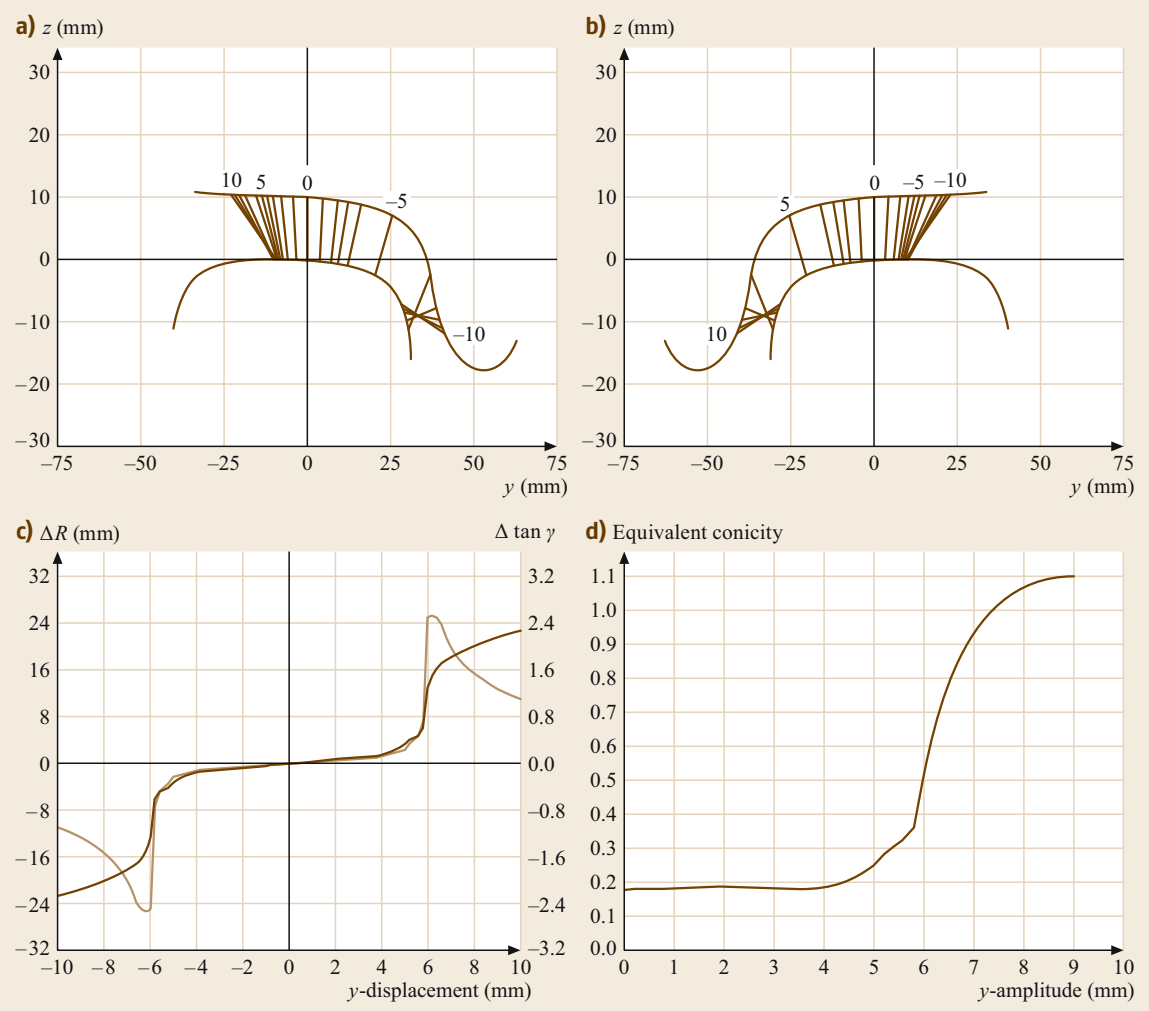

Fig. 23.20a–d Wheel–rail contact for S1002/UIC 60 1 : 40 inclined. Contact points and contact functions of wheel and rail, wheel profile S1002 (wheel diameter 700 mm, flange gauge 1426 mm, wheel load 175 kN), rail UIC 60, 1 : 40 inclined, track gauge 1435 mm. **(a)** Left contact point, **(b)** right contact point, **(c)** difference of contact radii ΔR (dark brown curve) and contact angle difference $\Delta \tan \gamma$ (light brown curve), **(d)** equivalent conicity

frame at z_P. This geometrical configuration leads to the reduction of track regularities. As a function of their wavelength, track irregularities are reduced between two extremes: no reduction at all (for wavelengths equal to the wheelset distance $2a$) and complete reduction (for wavelengths equal to half of the wheelset distance), as illustrated by the equations below:

Geometrical transfer function of a bogie

$$z_P(x_0) = \left[z(x_0 - a) + z(x_0 + a)\right]\frac{1}{2} .$$

Track irregularity $z(x)$

$$z_P(x_0) = \frac{1}{2}\left(z e^{i\Omega(x_0-a)} + z e^{i\Omega(x_0+a)}\right) ,$$

$$z(x) = z e^{i\Omega x} , \quad \Omega = \frac{2\pi}{L} ,$$

$$z e^{i\Omega(x_0-a)} = z e^{i\Omega x_0} e^{-i\Omega a} ,$$

$$z_P(x_0) = \frac{1}{2} z e^{i\Omega x_0}\left(e^{-i\Omega a} + e^{i\Omega a}\right) ,$$

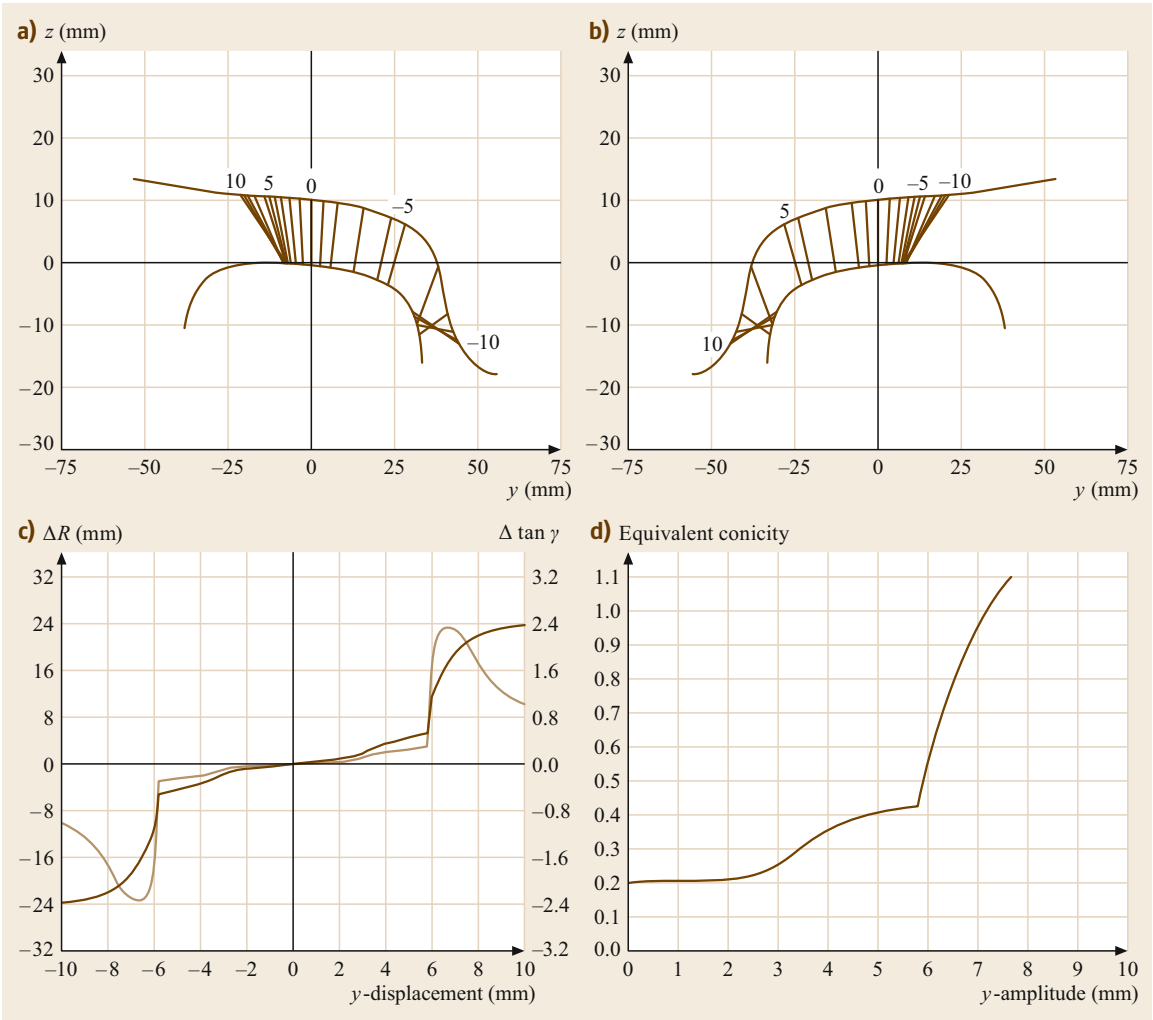

Fig. 23.21a–d Profile combination KKVMZ–UIC 60 1 : 20 (track gauge 1435 mm). Contact points and contact functions of wheel and rail, wheel profile KKVMZ (wheel diameter 700 mm, flange gauge 1426 mm, wheel load 175 kN), rail UIC 60, 1 : 20 inclined, track gauge 1435 mm. **(a)** Left contact point, **(b)** right contact point, **(c)** difference of contact radii ΔR (dark brown curve) and contact angle difference $\Delta \tan \gamma$ (light brown curve), **(d)** equivalent conicity

$$H = \frac{\text{Output}}{\text{Input}} ,$$

$$H = \frac{1}{2}\left(e^{-i\Omega a} + e^{i\Omega a}\right) ,$$

$$e^{i\Omega a} = \cos \Omega a + i \sin \Omega a ,$$

$$H = \frac{1}{2}(\cos \Omega a \, i \sin \Omega a + \cos \Omega a + i \sin \Omega a)$$

$$= \cos \Omega a$$

$$= \cos \frac{2\pi a}{L} .$$

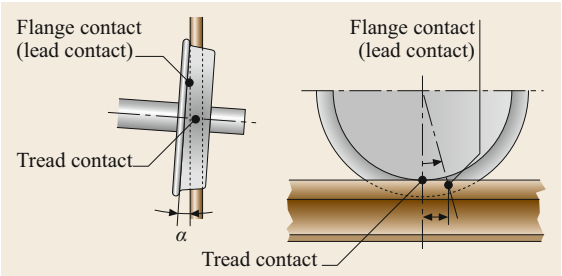

Fig. 23.22 Two points of contact in different planes, if the angle of attack between the wheel and rail α exceeds a certain value. Lead contact in the flange

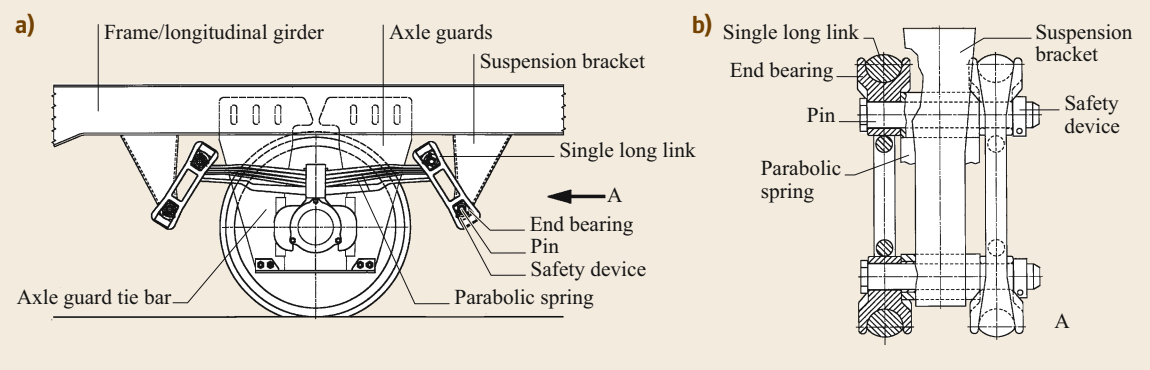

Fig. 23.23a,b Running gear for two-axle wagons with single long-link suspension *Niesky2* (Waggonbau Niesky GmbH, Niesky): **(a)** side view, **(b)** top view

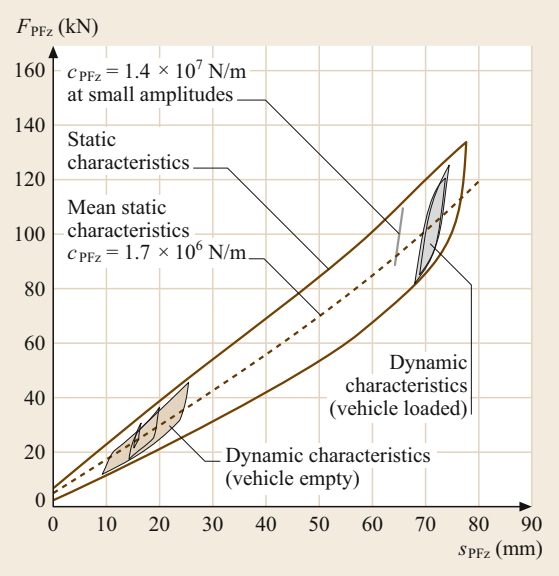

Fig. 23.24 Measured force–displacement diagram in the vertical direction of a leaf spring–link suspension system: spring constant and friction damping

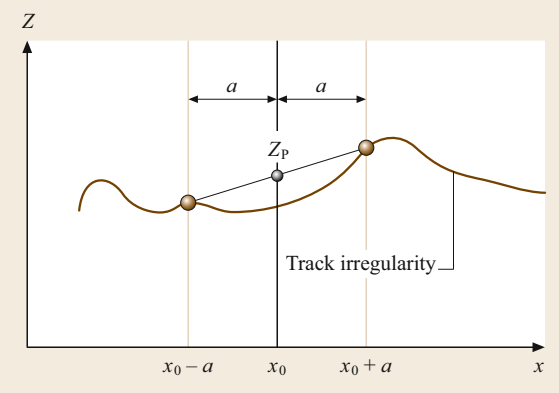

Fig. 23.25 A bogie with two wheelsets spaced from the bogie center

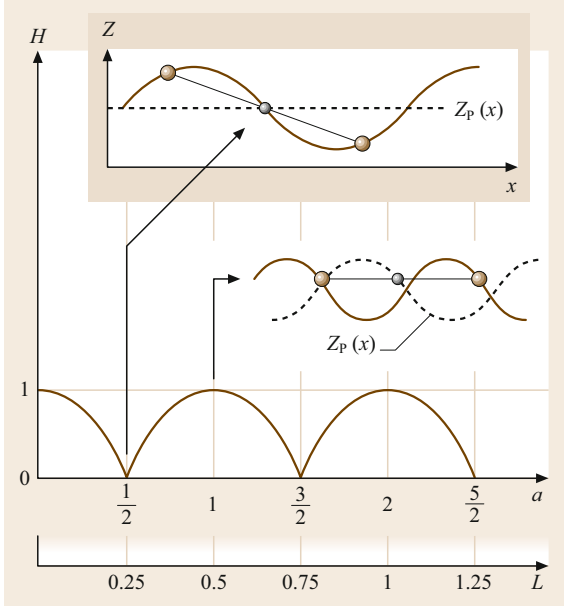

Fig. 23.26 Geometrical transfer function with values between 0 (no transfer of track irregularities) to 1 (all track irregularities are fully transferred, but not amplified)

For railways, very often the lateral dynamics is even more important than the vertical dynamics, and this good behavior of a bogie also applies for the lateral direction (Fig. 23.26).

23.3.3 Constructive Elements

Wheelsets

For tramways, where the track is always very stiff and therefore rather soft, rubber-cushioned wheels must be used. They also reduce noise (Fig. 23.27).

Low-floor trams cannot use wheelsets but instead use cranked axles, so that the height of the floor can be reduced (Fig. 23.28).

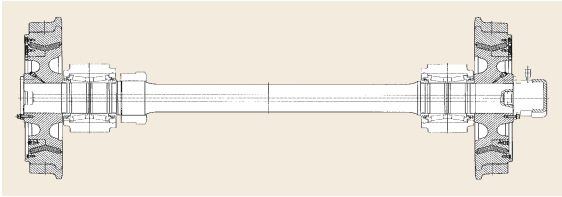

Fig. 23.27 Driven wheelset with inside bearings and rubber elastic wheels for the low-floor tram Schwerin (Germany), wheel type B02000, running circle new 600 mm, gauge 1435 mm, weight 552 kg, without bearings, wheel stiffness 20.0 kN/mm radial and 20 kN/mm axial (Bochumer Verein, BVV, Bochum)

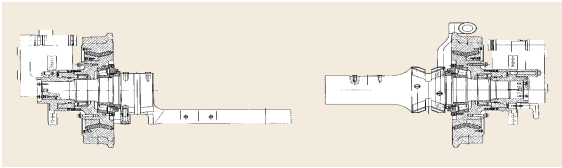

Fig. 23.28 Idle wheels with cranked axle for low-floor tram Schwerin with rubber-cushioned individual turning wheels of type BO2000, wheel diameter new 600 mm, gauge 1435 mm, weight 897 kg, with bearings and brake system, wheel stiffness 200 kN/mm radial and 20 kN/mm axial (Bochumer Verein, BVV, Bochum)

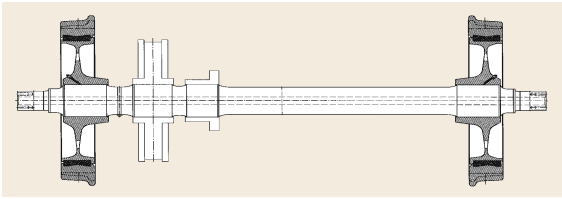

Fig. 23.29 Driven wheelset with brake disk from the Vienna Metro, rubber sprung wheels of type BO54, wheel diameter 840 mm new, gauge 1435 mm, weight 852 kg, wheel stiffness 75 kN/mm radial and 8 kN/mm axial (Bochumer Verein, BVV, Bochum)

Many wheelsets are hollow-bored. This reduces weight and also enables ultrasonic testing (Figs. 23.29–23.32).

23.3.4 Bogies

Figure 23.34 shows the so-called three-piece bogie. This is the most common freight bogie type in the world. Several million bogies of this type are running outside Europe. There is only a secondary spring according to Fig. 23.33a. The three pieces that give the name to the bogie are the two side frames and the bolster assembly. The wedge (Fig. 23.34) applies load-sensitive damping.

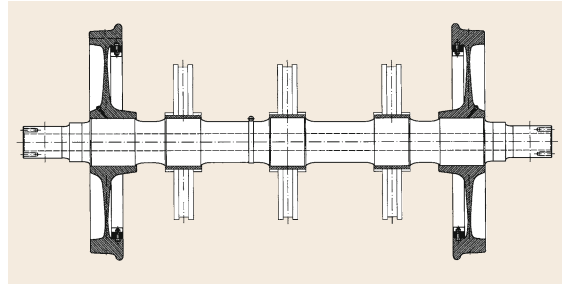

Fig. 23.30 High-speed wheelset with seats for three brake disks and wheels with sound absorbers. The shaft is hollow-bored for weight reduction and to enable ultrasonic crack detection, wheel diameter 920 mm new, gauge 1435 mm, weight 948 kg without brake discs (Bochumer Verein, BVV, Bochum)

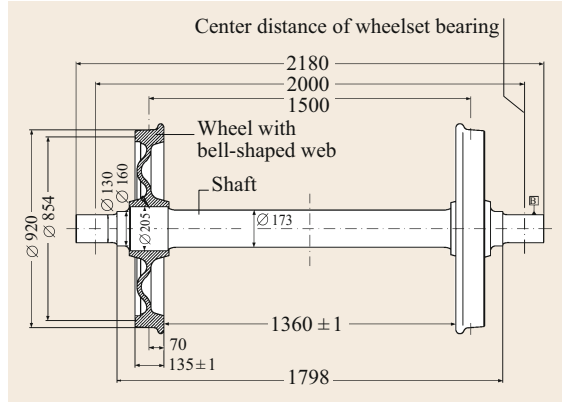

Fig. 23.31 Standard freight car wheelset type BA 304 for 25-t axle load (wheel with bell-shaped web to reduce stresses from block braking), wheel diameter 920 mm new, 854 mm worn, weight 1003 kg (Radsatzfabrik Ilsenburg Rafil)

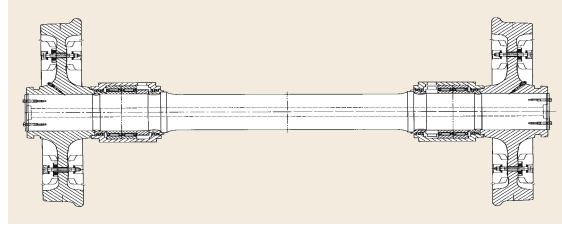

Fig. 23.32 Leila freight car wheelset for 22.5-t axle load with inside bearings and wheel brake disks 920-mm wheel diameter new, gauge 1435 mm, weight 1392 kg with bearings and aluminum brake discs (not to scale)

The three-piece bogie has unsuspended side frames, whereas the Y 25 bogie (Fig. 23.35) has individual suspended axle boxes, so-called primary suspension, according to Fig. 23.33b.

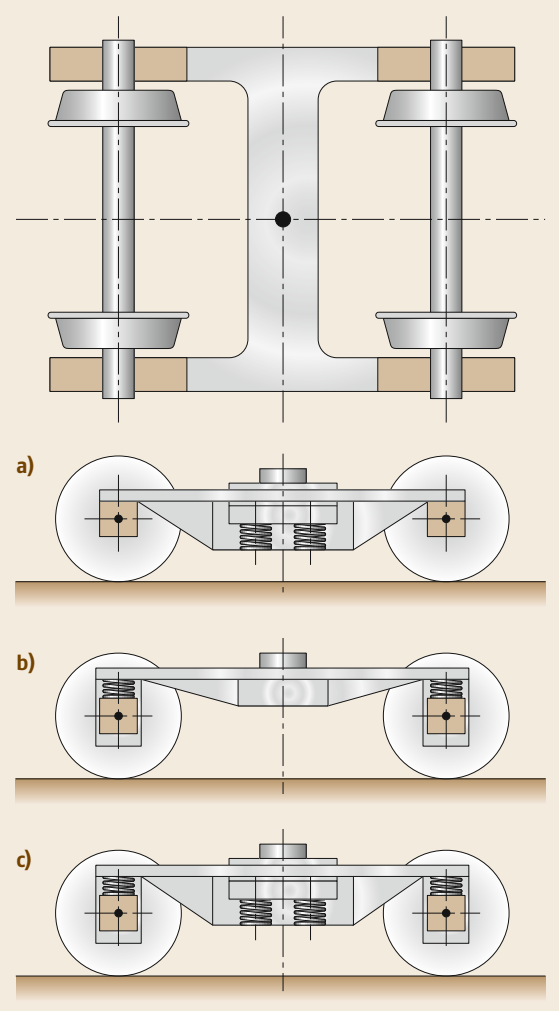

Fig. 23.33a–c Basic concepts of bogie suspension: **(a)** only secondary sprung (three-piece bogie), **(b)** only primary suspension (Union international des Chemin de fer (UIC) freight bogie), **(c)** with primary and secondary suspension; all in longitudinal stiff design

The bogie type mainly used in Europe is the so-called Y 25 (Fig. 23.35). The helical springs are responsible for vertical and lateral suspension. Over the inclined links in Fig. 23.33a, longitudinal friction force is caused in the axle guides, which damps the vertical and lateral movements. This force is load related.

The Leila freight bogie (Fig. 23.36) enables better load distribution by internal bearings and radial steering by the cross arm. The wheelsets are those from Fig. 23.32.

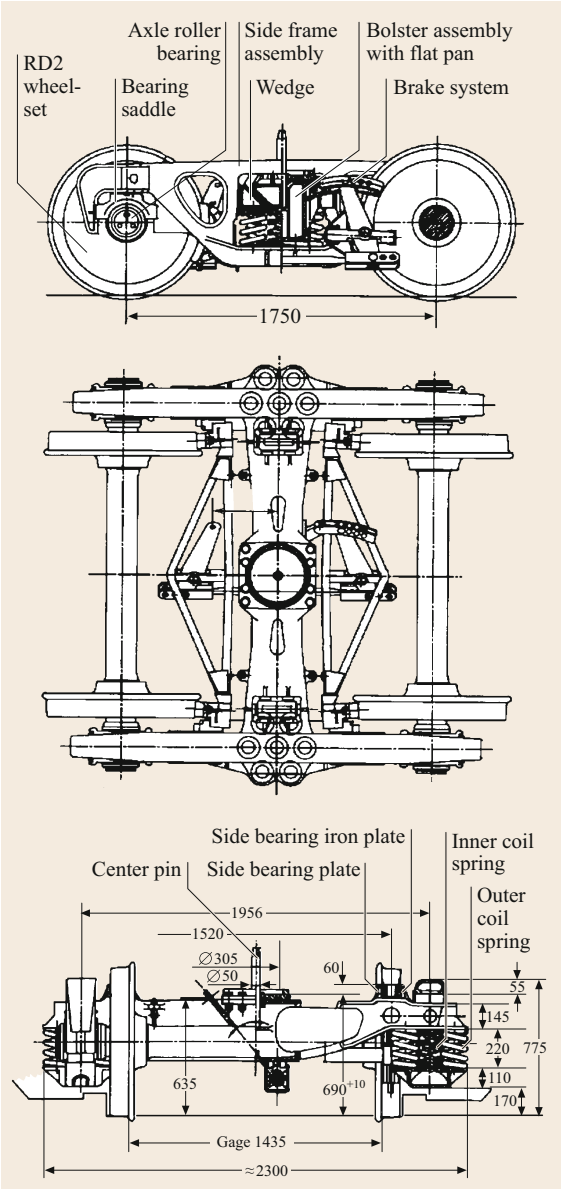

Fig. 23.34 Z8A freight car bogie (China) weight 4100 kg, max. axle load 210 kN (Qiqihar railway rolling stock Co., China) (RD2 is a wheelset type name)

In passenger transport as well, interior bearings offer huge benefits with about 30% lower bogie weight (Fig. 23.37).

The driving motor is located in the body shell, and the momentum is transferred to the axle-hung gearbox via a Cardan shaft (Fig. 23.37).

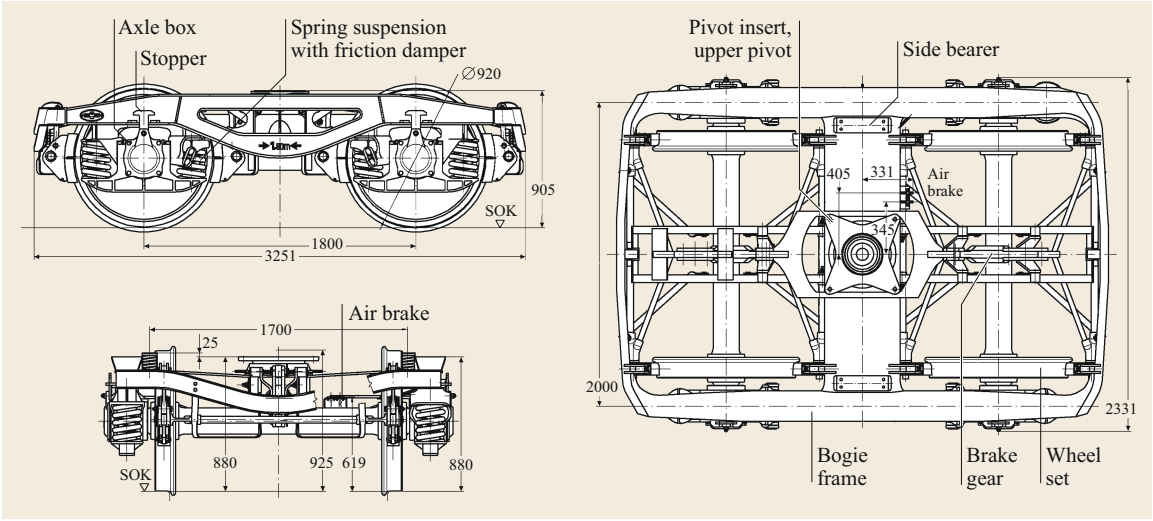

Fig. 23.35 Freight bogie Y25Lsd1-K with K-brake block insert in single brake block arrangement for axle load 22.5 t, mass 4390 kg (with wheelsets type BA 004 and pivot) (Eisenbahn Laufwerke Halle, ELH)

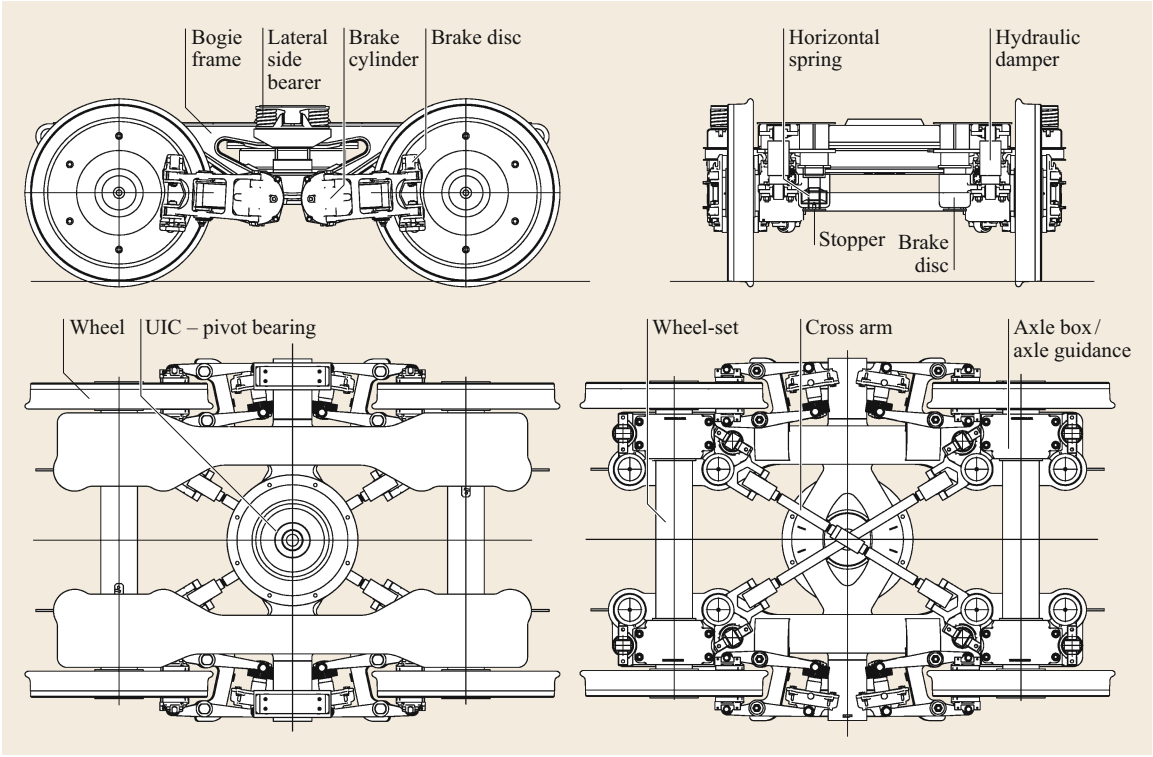

Fig. 23.36 Leila freight bogie (Josef Meyer Waggon AG, Rheinfelden)

Figure 23.37 shows a bogie for high-speed tilting trains with internal bearing wheelsets. This assembly offers huge benefits in terms of weight reduction and good access to the wheels.

The bogie shown in Fig. 23.38 is a very-high-speed bogie for the fastest scheduled passenger service today.

Low-floor trams need bogies with free space in the center (Fig. 23.39).

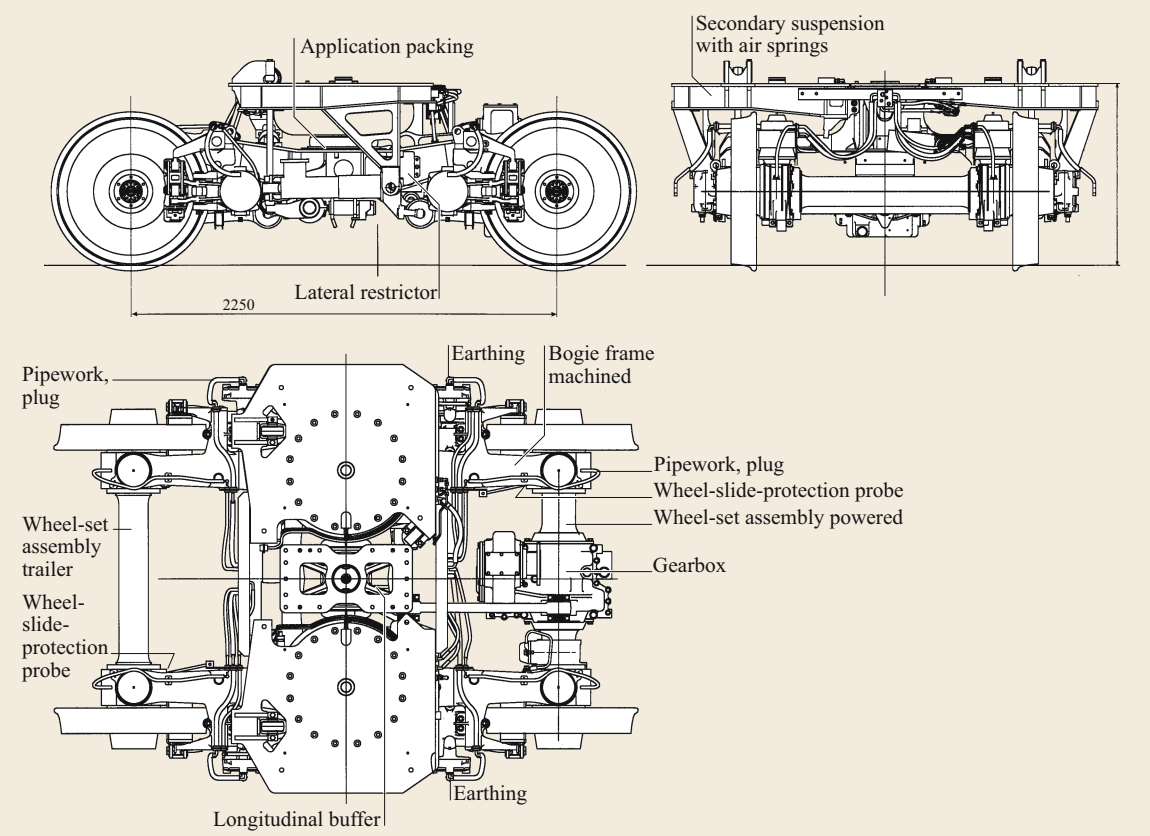

Fig. 23.37 Bogie assembly type A type B5000 for axle load 16 t, weight 4700 kg powered, wheel diameter new 780 mm, worn 716 mm, wheelbase 2250 mm, V_{max} 200 km/h (Bombardier Transportation, Berlin)

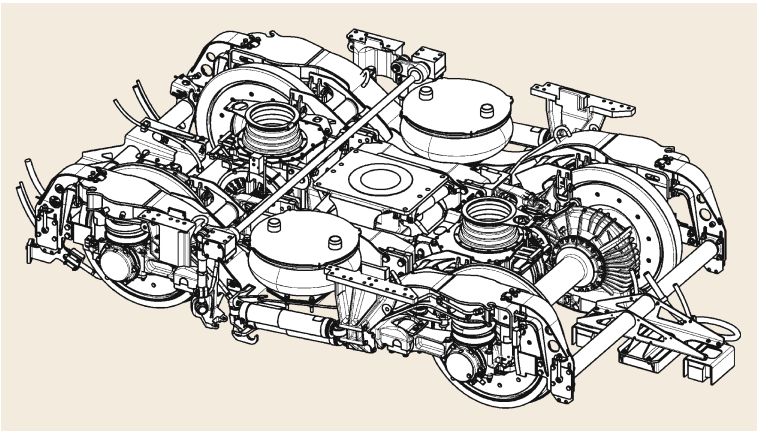

Fig. 23.38 Running gear SF 500-type motor bogie for operating speed up to 350 km/h, wheelset load maximum 17 t, continuous power per wheelset up to 500 kW, maximal starting tractive effort per wheelset 19 kN, wheelset distance 2500 mm, gauge 1435 mm, wheel diameter new/worn 920/830 mm minimal curve radius service/workshop 150/120 m, weight with pivot and traverse 9.2 t (Siemens Transportation Systems, Erlangen)

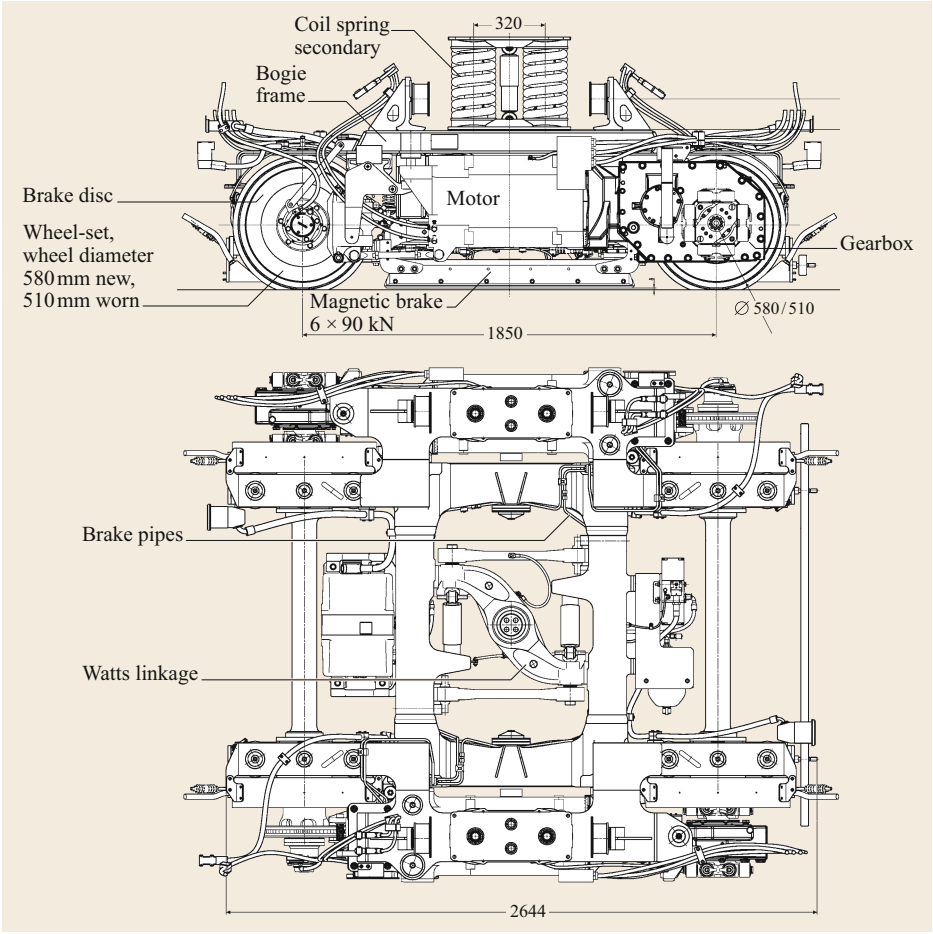

Fig. 23.39 Bogie assembly type S1000 BM1000 tram Marseille MB, weight 4700 kg powered, maximum speed 70 km/h (Bombardier Transportation, Berlin)

23.4 Superstructures

23.4.1 Principle

With articulated vehicles (Fig. 23.40), normally fewer wheelsets than with standard designs are needed. Fewer wheelsets per car length means less weight, less cost, and less noise, but the maintenance process is more complicated.

The body shells are made either from aluminum intrusion profiles [23.9] or from weldable steel in a sheet and stringer design. This design offers more possibilities to adapt the structure to the load requirements and enables simpler repairs (Fig. 23.41).

23.5 Vehicles

Figure 23.42 shows a freight wagon as an example of a very lightweight construction. The empty wagon weighs only 20% of the fully loaded vehicle. For both situations, loaded and empty, the safety requirements must be fulfilled.

To reduce operation expenses, modern metro systems are planned as driverless systems. In this way no space is lost for the driver cabin and all the space may be used for passengers (Fig. 23.43).

Modern tram cars are built in a modular manner so that capacity can be adapted to local needs. This means that the tram shown in Fig. 23.44 can be lengthened or shortened by further bogie and suspended modules.

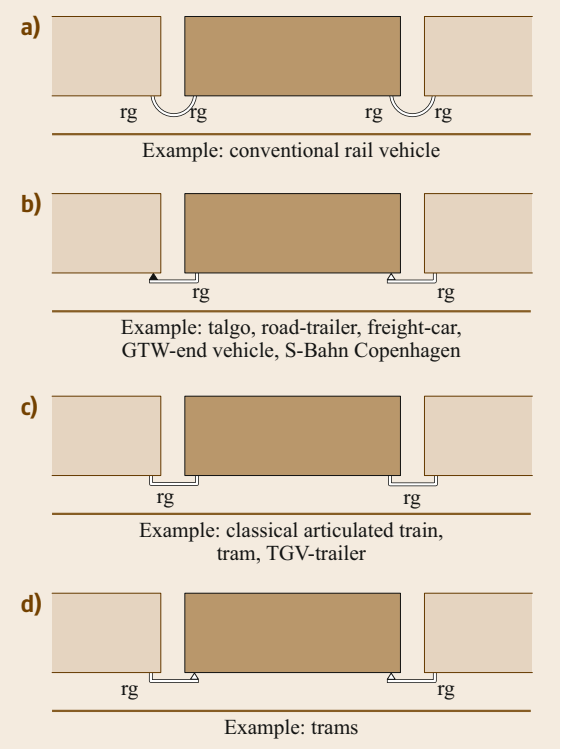

Fig. 23.40 **(a)** Single vehicle (vehicles separable in operation) supported by at least two running gears, rg (single wheelsets or bogies). Articulated vehicles (trains only separable in workshop): **(b)** saddle principle, semi-trailer, one end vehicle with two running gears (GTW – Gelenktriebwagen (German) – articulated vehicle), **(c)** Jacobs principle (bridge vehicle), **(d)** suspended modules

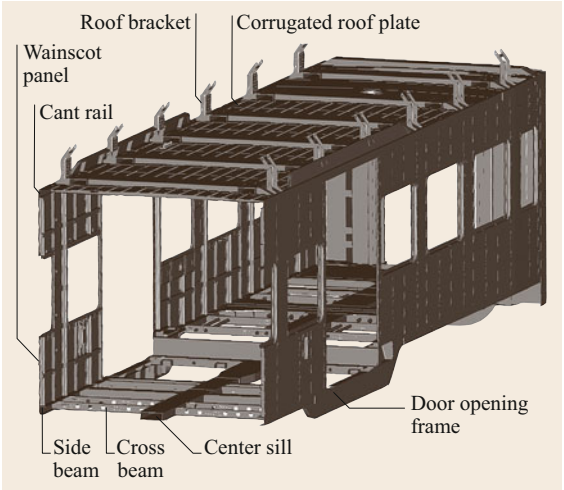

Fig. 23.41 Sheet and stringer design in steel (FTD Fahrzeugtechnik Dessau AG)

Electric locomotives are more powerful than diesel locomotives. To enable free running across borders, they are usually equipped to cover all four electric systems in use in Europe (Figs. 23.45 and 23.46). Modern locomotives also fulfill crash concepts; see Sect. 23.7.2 and [23.10].

Diesel locomotives are increasingly being replaced by hybrid catenary locomotives (Fig. 23.47). Catenary operative expenses are much lower, and regenerative braking can feed the braking energy back to the catenary.

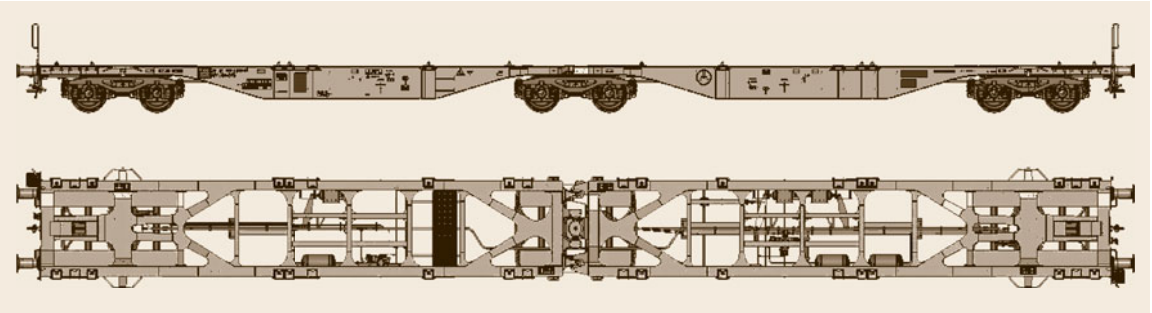

Fig. 23.42 Six-axle, three-bogie articulated flat-bodied Sggmrss-90 unit for container and swap bodies: axle load 22.5 t, load height 1155 mm, length over buffers 29 590 mm, empty weight 27.6 t, V_{max} 120 km/h (with 20 t axle load), bogie type Y25Ls(s)d1 (Trinity Rail Europe)

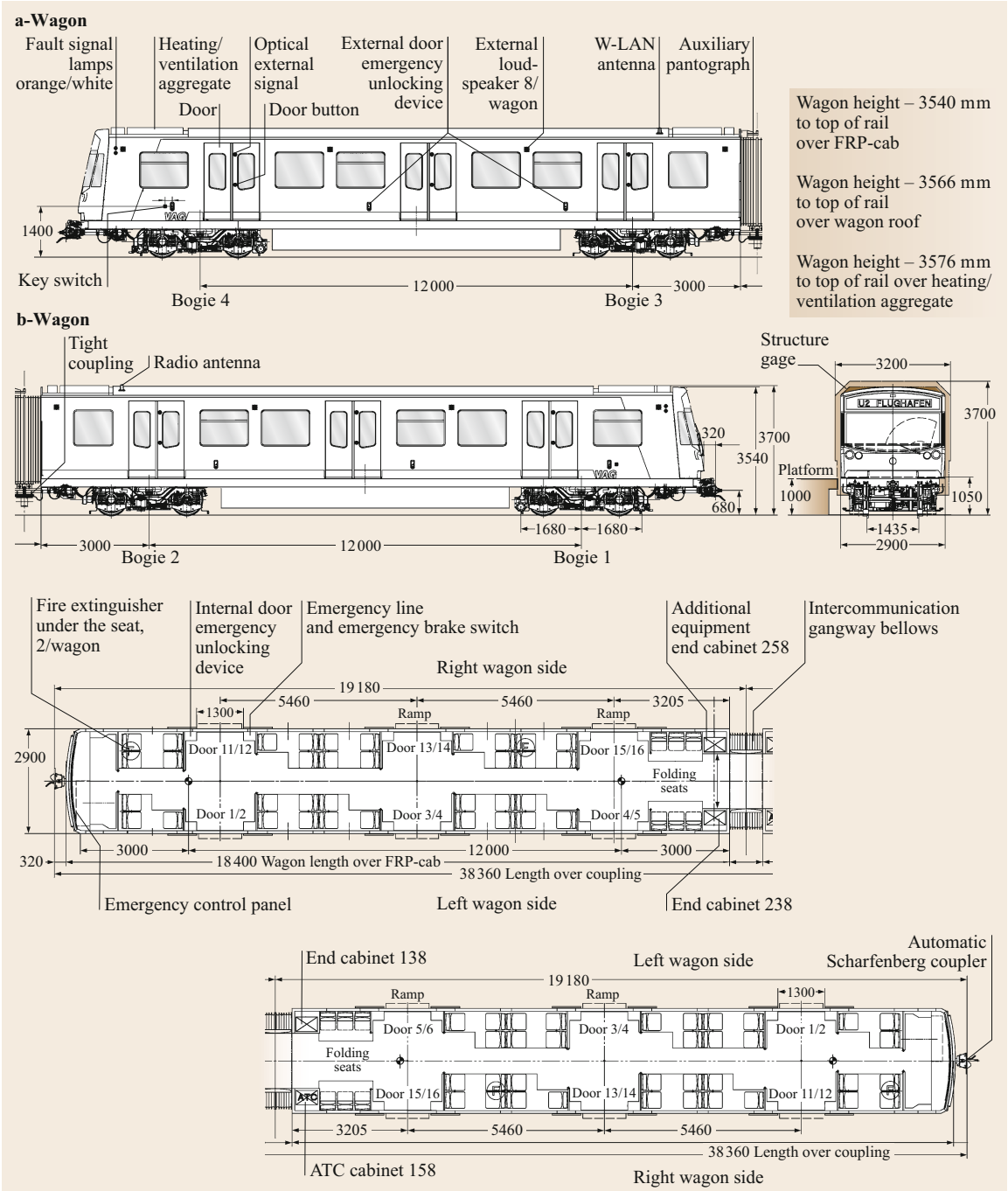

Fig. 23.43 DT3 RUBIN (automatic, driverless metro system) Nürnberg with auxiliary driver desks, but no cabs. Body-shell aluminum extrusion profiles, empty weight 59.2 t, loaded weight 98.4 t, 82 seats, capacity 424 passengers (6 /m^2) (Siemens Transportation Systems, Erlangen) (ATC – automatic train control, FRP – fiber-reinforced plastic)

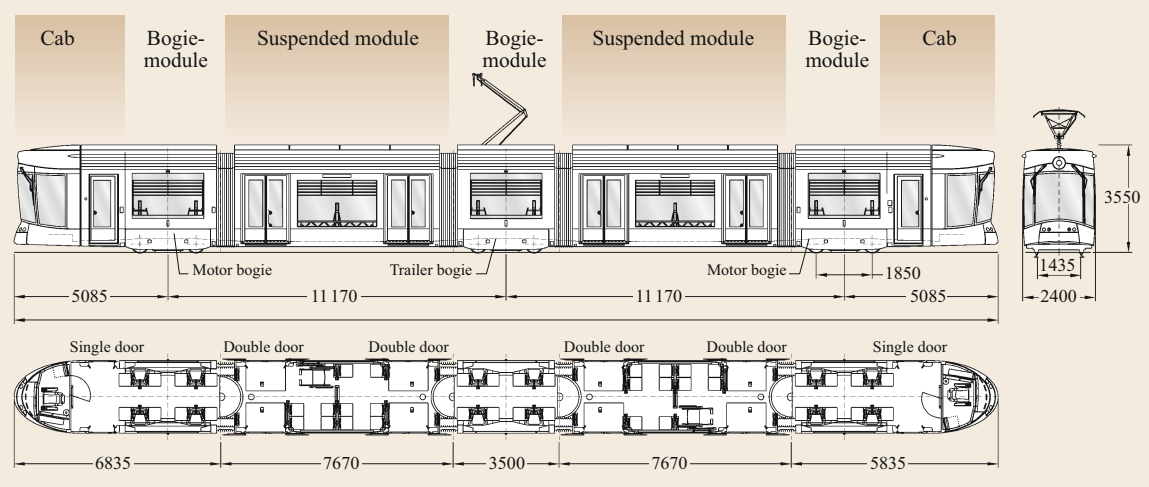

Fig. 23.44 Type of vehicle: Bombardier Flexity outlook, model Marseille: bidirectional, length 32.5 m, height 3.5 m, width 2.4 m, floor height above top of rail (low floor entrance) 320 mm, wheel diameter new/worn 580/520 mm, gauge 1435 mm, car weight (empty) 40 t, car weight (loaded) (4 pass./m^2) 54.3 t, maximum axle load 11 t, minimum horizontal curve radius 25 m, minimum vertical curve radius, crest 450 m, minimum vertical curve radius, sag 350 m, maximum speed 70 km/h, maximum gradient 80‰, nominal current supply: 750 $V_{=}$, regeneration of energy, low voltage: 24 $V_{=}$, four three-phase asynchronous motors, motor power: 4 × 115 kW, air-cooled motor, two powered bogies/one trailer bogie, rubber/metal primary suspension, coil spring secondary suspension, eight sanders, antislip, antiskid system, electrical service brake: regenerative, mechanical service brake: disc brake, magnetic brake: 6 × 90 kN (Bombardier Transportation)

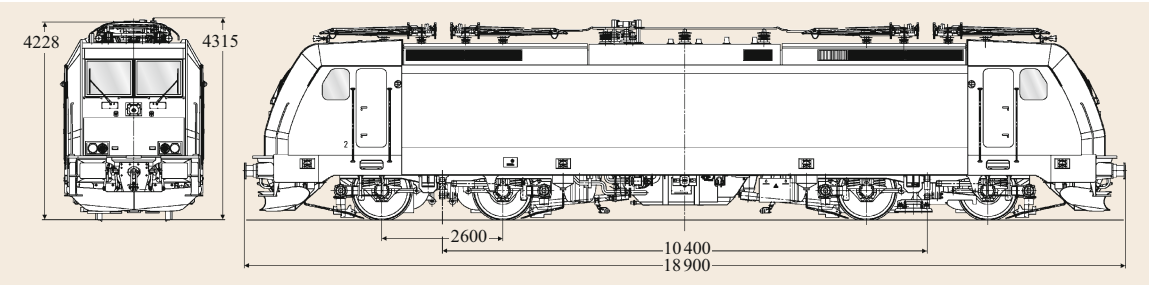

Fig. 23.45 Bombardier Traxx locomotive family, freight and passenger locomotive: weight 86 t, power 5600 kW, max. traction force 300 kN, speed 140, 160 or 200 km/h

23.6 Coupling Systems

As trains are formed from several vehicles, the coupling device used between the vehicles is essential. It transmits not only high forces, but also data channels. Coupling and uncoupling must be done very reliable (Figs. 23.48–23.50).

23.6.1 Coupling

The cone-and-funnel shape of the coupler front face profile ensures a generous gathering range both horizontally and vertically and allows automatic coupling on curves, even with vertical mismatch and very low speed. Minimal force is required for successful coupling.

23.6.2 Coupled

The coupler faces and the locking system form a rigid connection both vertically and horizontally. The parallelogram arrangement of the coupler link provides

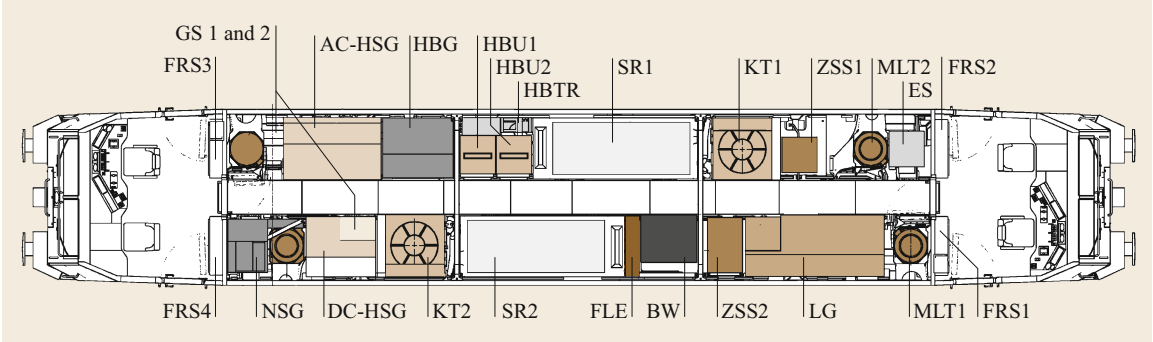

Fig. 23.46 Bombardier transportation (GS 1 and 2 – various nonpermanent equipment (inventory) such as track shoes, earthing rod gloves, tools, etc.; AC-HSG – high-voltage AC cell; AC – alternative current; HBG – auxiliary power distribution and battery charger; HBU1 and 2 – auxiliary converter; HBTR – auxiliary energy supply transformer; SR1 and 2 – traction converter; KT1 and 2 – cooling tower with blower; ZSS1 and 2 – signal equipment (automatic train control); MLT1 and 2 – traction motor blower; ES – electronic control equipment; NSG, NSGAT – low-voltage DC distribution; DC – direct current; DC-HSG high-voltage DC cell; FLE – fire detection and extinguishing equipment; BW – braking resistor; LG – compressed-air supply and braking equipment; FRS 1, 2, 3, 4 – cab rear wall cabinets)

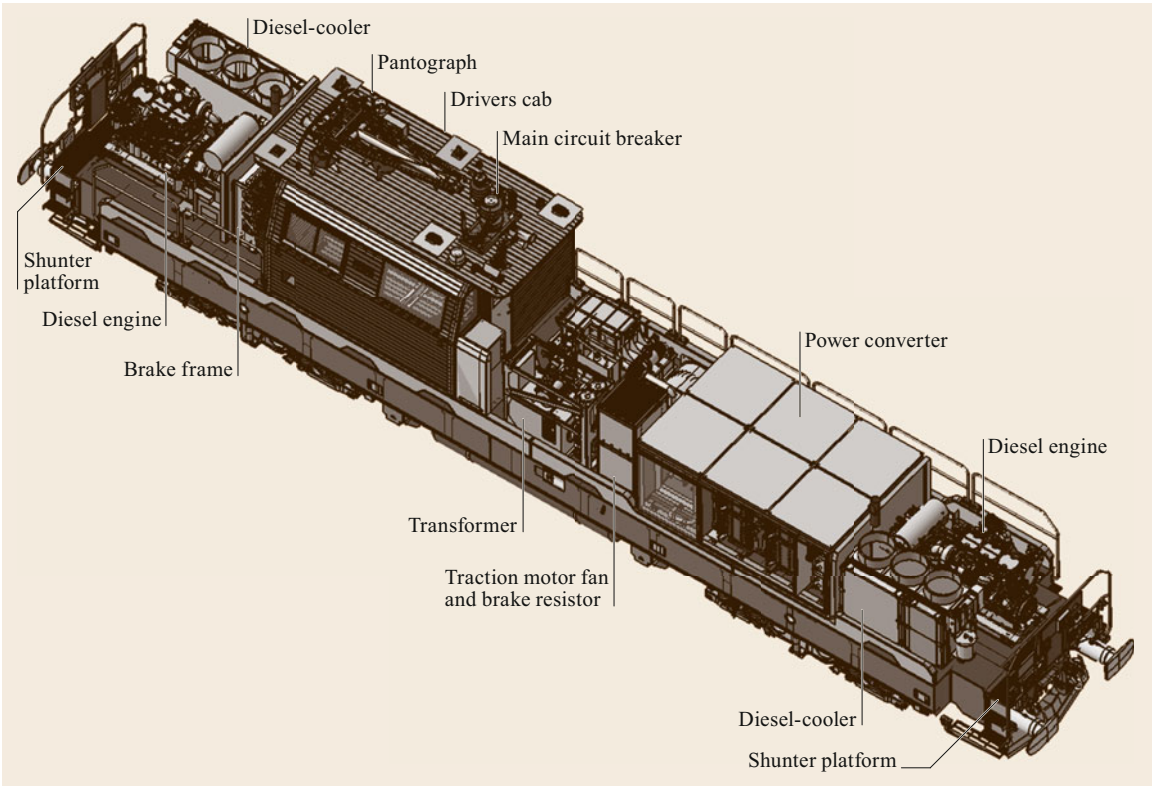

Fig. 23.47 Alstom Hybrid Loco Prima H4 bi-mode, power from catenary (16.7 Hz, 15 kV or 50 Hz, 25 kV) 2000 kW, Diesel 2 × 500 kW, traction force 300 kN, mass 80 t, mass with ballast 90 t, length over buffers 18 750 mm, width 2955 mm, height 4478 mm, bogie center distance 10 500 mm, wheelset distance in bogie 2500 mm, gauge 1435 mm, wheel diameter new 1000 mm, worn 920 mm, min. curve radius 80 m, max. speed 120 km/h, tank capacity 3000 L, operating temperature range −25 °C to 40 °C, multiple operation up to four locomotives (with permission from *ALSTOM* Schienenfahrzeuge AG, Neuhausen am Rheinfall, Switzerland)

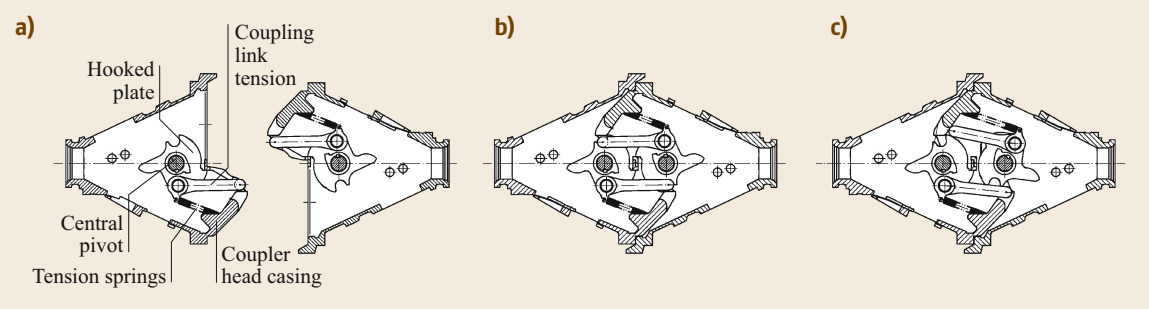

Fig. 23.48a–c Scharfenberg coupler, working principle (Voith Turbo): (a) ready to couple, (b) coupled, (c) uncoupled

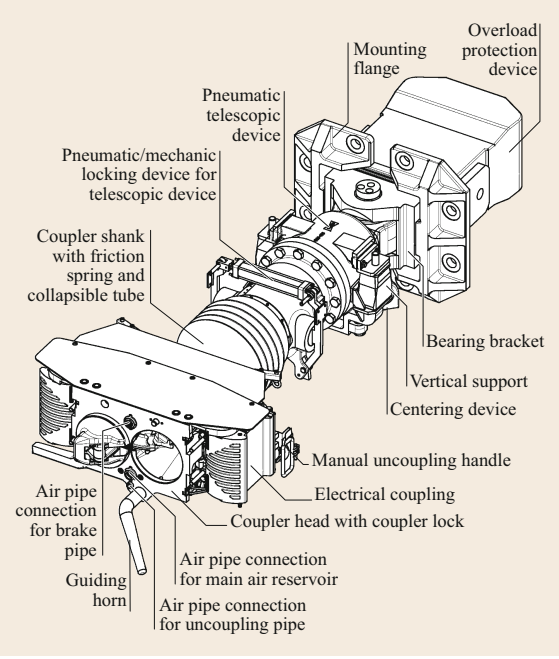

Fig. 23.49 Scharfenberg coupler for high-speed trains ICE 3 (ET-415/417)/Velaro S (AVE S 103)/Talgo 350 (AVE S 102) (Voith Turbo)

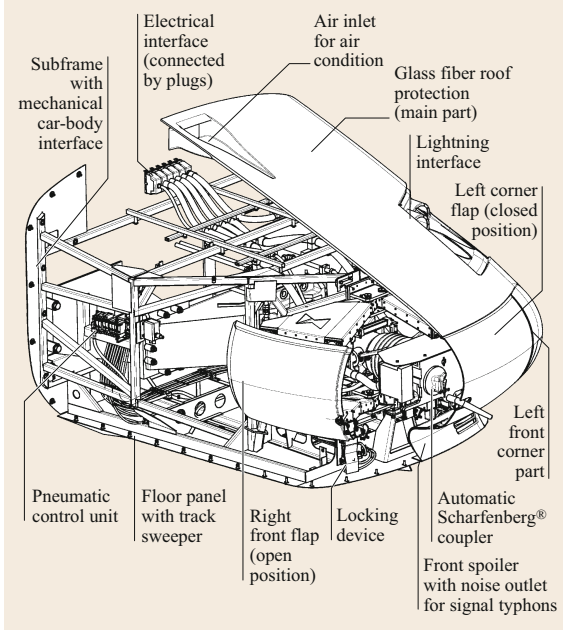

Fig. 23.50 Scharfenberg front nose for high-speed trains Talgo 350 (AVE S 102) (Voith Turbo). Technical data: overall length 2985 mm, overall hight 2042 mm, overall width 2866 mm, weight 1020 kg (without coupler), maximum train speed > 350 km/h, aerodynamic loads ±11 kPa, mechanical carbody interface 10 screws M 16, front flaps opening angle 64°, material of outside parts, GRP (glass fiber-reinforced plastic) sandwich laminate, fire protection according to DIN 5510 S4

uniform distribution of the draft load. This coupler link design ensures minimal wear and maximum coupler longevity. The rigid and slack-free connection enables jerk-free acceleration and braking, and offers optimum ride comfort. It also prevents the cars from overriding one another in the case of an accident.

23.6.3 Uncoupling

The geometry of the coupler lock enables automatic uncoupling even under traction load. Automatic uncoupling is ensured when misaligned, even on gradient changes. The uncoupling operation is irreversible. Schaku's safety philosophy does not allow recoupling, unless the cars have moved apart and the couplers have separated.

23.7 Safety

23.7.1 Active Safety Systems/Brakes

Brakes transform the kinetic energy of a train into other forms of energy. There are three principal tasks for a brake: bringing the train to a halt (stop braking), maintaining the speed of the train on a gradient (downhill braking), and preventing a stationary train from moving (park braking).

From the mechanical point of view, brakes can be categorized into adhesion-dependent and non-adhesion-dependent brakes. The former type always work via brake moments to wheels, whereas the latter are track brakes or aerodynamic brakes. Adhesion-dependent brakes may be friction brakes (tread or disc brakes) or dynamic brakes (electrodynamic brakes, where a motor works as a generator, or hydrodynamic brakes, which have a hydraulic retarder).

For safety reasons, all rail vehicles must be equipped with an indirectly acting pneumatic brake and the brake pipe must run through the entire train (Fig. 23.51).

The indirectly acting brake operates according to the following principle: If the full brake pressure (typically 5 bar) is available and the brake pipe is at that pressure, then the same pressure is present in the supply air reservoir and the brake cylinder is released by a mechanical spring in the brake cylinder. If the brake pressure is reduced, for instance, by the brake operating device, then the distributor valve connects the supply air reservoir to the brake cylinder and the brake is applied.

The brake is released by increasing the brake pipe pressure again. Then the distributor valve releases the pressure from the brake cylinder into the atmosphere and simultaneously refills the supply air reservoir with the brake pipe pressure. Because of this indirect or automatic behavior, the brakes are also applied if the train breaks apart and the pipe is separated.

Also, the brake can be applied from any location along the brake pipe, for instance, by a control van or by an emergency brake device.

The disadvantage of an indirect brake is that it takes a long time for application (up to 30 s for freight trains) and release (up to 60 s for freight trains). Therefore, vehicles that must be controlled quickly and precisely, for instance, locomotives, must be equipped with an additional direct brake device.

Brake actuators may operate through one-sided (Fig. 23.34) or two-sided (Fig. 23.35) brake blocks. Because of wear and noise demands, modern brake blocks are no longer made from cast iron but from composite materials.

Higher thermal capacity can be achieved by disk brakes: either wheel disk brakes (Figs. 23.36 or 23.37) or shaft disc brakes (Fig. 23.30).

To reduce the braking distance further, rail brakes can be used as they are not dependent on the wheel–rail friction coefficient (Fig. 23.52). If the brake is not used, pneumatic cylinders lift the brake to avoid contact because of track irregularities. The magnets are excited by direct current from batteries. The friction force between

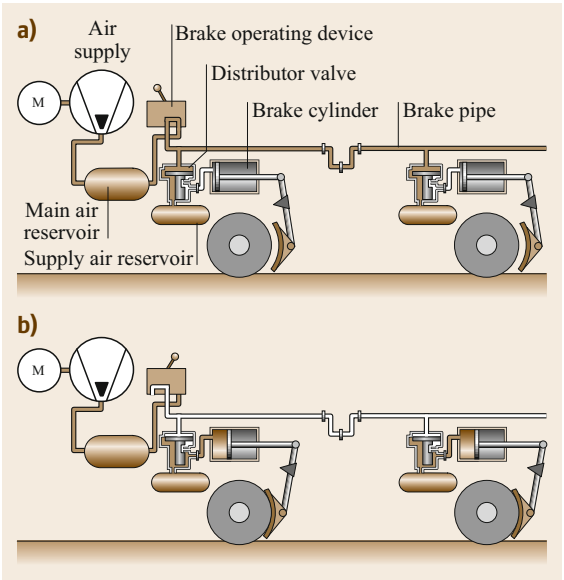

Fig. 23.51a,b Indirect (automatic) train brake. **(a)** Release position, **(b)** brake position

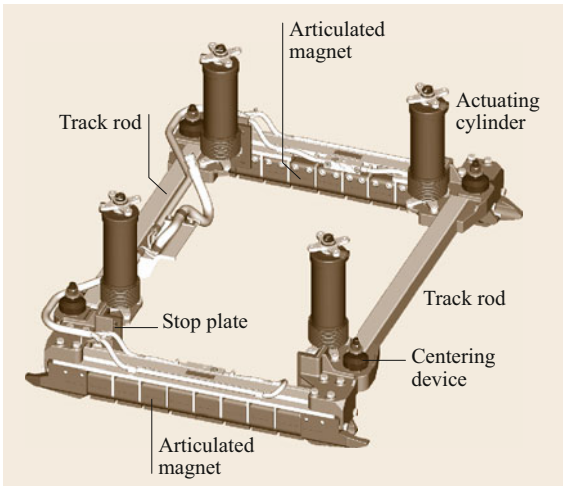

Fig. 23.52 Track brake, speed up to 200 km/h

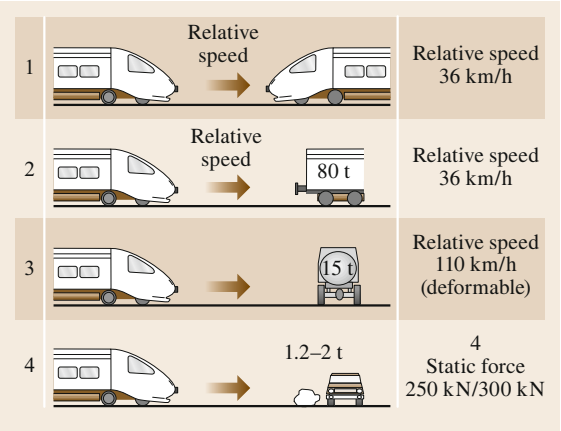

Fig. 23.53 Crash scenarios, main definitions of EN 15277 2016 (weights are given in units of metric tons)

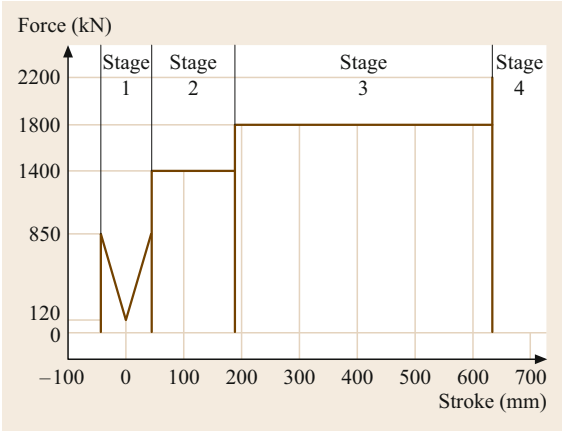

Fig. 23.54 Energy absorption of the coupler from Fig. 23.49. Overall length 2345 mm, telescopic stroke 200 mm, weight 960 kg, vertical swing ±6°, horizontal swing ±20°, tensile strength 850 kN (braking strength 1000 kN), compressive strength 1400 kN (braking strength 2000 kN), minimum coupling speed 0.6 km/h, admissible impact speed allowing buffer to regenerate: 5 km/h, admissible impact speed before coupler tear-off: 20 km/h. Energy absorption capacity. Stage 1: friction spring 120–850 kN, 44 mm stroke; Stage 2: collapsible tube 1400 kN, 145 mm stroke; Stage 3: collapsible tube 1800 kN, 445 mm stroke; Stage 4: shear-off elements 2200 kN; total energy absorption 1025 kJ

the magnet and the rail because of the magnetic forces causes the brake force.

For trams, the lifting device can be avoided because of the lower speeds (Fig. 23.39).

23.7.2 Passive Safety

Though the active safety provision of railway systems is very high due to the implementation of signals, brakes, and train control systems [23.11], collisions cannot be totally avoided. Therefore, it makes sense to reduce the potential human factor through the use of safety devices.

For various crash scenarios (Fig. 23.53), one must ensure that no severe injuries occur to passengers or staff.

Crash Scenarios

- Scenario 1: collision between two identical trains (single-unit train sets or defined formation) at a relative speed of 36 km/h.
- Scenario 2: collision between a train (single-unit train sets or defined formation) and a railway vehicle equipped with side buffers at a speed of 36 km/h. The railway vehicle shall be a four-axle freight wagon with a mass of 80 t.
- Scenario 3: collision at a speed of 110 km/h, on a level crossing, with an obstacle equivalent to a 15 t specially defined lorry.
- Scenario 4: collision with a small or low obstacle such as a car or animal, which shall be addressed by defining the characteristics of an obstacle deflector.

To fulfill these scenarios, a certain energy-absorbing capacity must be achieved by the couplers and body shells. Figure 23.54 shows an example of energy absorption.

23.8 Air Conditioning

For high-speed rail vehicles, closed body shells with fixed windows are essential for safety reasons. Air conditioning is therefore a must. For environmental reasons, air is also used for cooling purposes (Figs. 23.55 and 23.56).

23.8.1 Process Air Loop

In the cooling circuit, the process air is first expanded in the motorized air cycle machine (MAM), and thus cooled. The cold process air then passes through the

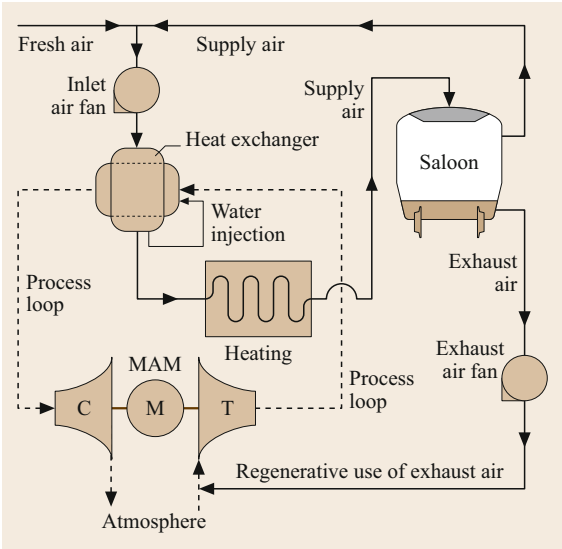

Fig. 23.55 Air cycle concept (Liebherr) (C – compressor; M – motor, T – turbine, MAM – motorized air cycle machine)

downstream heat exchanger to chill the air supply to the passenger saloon. Subsequently, the now heated process air is taken in by the turbocompressor and released to ambient.

The cooling process is controlled by the air cycle machine speed. The cooling power is thus infinitely variable between 0 and 100%.

Supply Air Loop

The supply air is a mixture of ambient fresh air and recirculated air from the vehicle. The supply air fan delivers the supply air through a supply air filter to the heat exchanger, where the required temperature reduction is performed in cooling mode.

The conditioned supply air is passed through an air silencer to the passenger compartment. In heating mode, the MAM is turned off so that the cooling process is deactivated. Controlled operation of the main heater adds the required amount of heat to the air flow.

To balance the air flow to the saloon, an amount of air equivalent to the amount of fresh air added must be exhausted. The cooling energy contained in the exhaust air will be used regeneratively in the process loop to improve the system's efficiency.

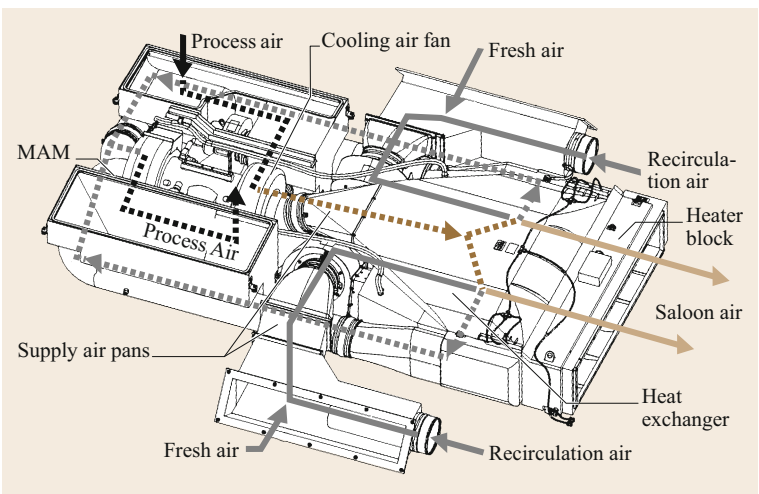

Fig. 23.56 Components and air flow (Liebherr). Roof-mounted air-conditioning unit for high-speed trains, weight 550 kg

References

23.1 U. Weidmann: *Grundlagen zur Berechnung der Fahrgastwechselzeiten*, Vol. 106 (IVT, Zürich 1995), in German

23.2 EN: *EN 50126: Railway Applications – The Specification and Demonstration of Reliability, Availability, Maintainability and Safety (RAMS)* (Beuth, Berlin 1999)

23.3 K. Tzanakakis: *The Railway Track and Its Long Term Behaviour: A Handbook for a Railway Track of High Quality* (Springer, Heidelberg, Berlin 2013)

23.4 K. Endmann: Bewährung des Y-Stahlschwellenoberbaus, Eisenbahningenieur **10**, 25–30 (2000), in German

23.5 A. van Wilcken, F. Fleischer, H. Lieschke: Herstellung Feste Fahrbahn Rheda, Type Walter-Heilit with bibloc sleeper used for Köln-Rhein/Main, with 300 km/h regular train speed, Eisenbahntech. Rundsch. **51**, 172–182 (2002), in German

23.6 Arbeitsgemeinschaft Rheine-Freren: *Rad/Schiene-Versuchs- und Demonstrationsfahrzeug Definitionsphase R/S-VD*, Ergebnisbericht (Arbeitsgruppe Lauftechnik, Minden 1980), in German

23.7 S. Stichel, K. Knothe: *Rail Vehicle Dynamics* (Springer, Cham 2017)

23.8 M. Hecht: New freight bogie is an important contribution for growth of rail-freight, Eur. Railw. Rev. **4**, 61–64 (2002)

23.9 K.H. Grote, B. Bender, D. Göhlich: *Dubbel Taschenbuch für den Maschinenbau*, 25th edn. (Springer, Heidelberg, Berlin 2018)

23.10 C. Schindler (Ed.): *Handbuch Schienenfahrzeuge – Entwicklung Produktion Instandhaltung* (DVV-Media Group, Hamburg 2014)

23.11 J. Pachl: *Systemtechnik des Schienenverkehrs, Bahnbetrieb planen, steuern und sichern*, 8th edn. (Springer Vieweg, Wiesbaden 2014), in German

Markus Hecht

Institute of Land and Sea Transport Systems, Department of Rail Vehicles
Berlin University of Technology
Berlin, Germany
markus.hecht@tu-berlin.de

Markus Hecht obtained industrial experience at the Swiss Locomotive and Machine Works Winterthur. Since 1997, he has been Professor for Rail Vehicles at Berlin TU, working on wheel–rail interaction, vehicle design and acoustics, and safety as well as several EU projects. He is a railway mechanics expert at the Swiss and German accreditation authorities, member of the European Railway Research Advisory Board, and lecturer at TUM ASIA Singapore.

24. Aerospace Engineering

Hamid Hefazi

This chapter focuses on the commercial aviation sector of the aerospace industry. Following a brief introduction, basic definitions and terminology are discussed in Sects. 24.1–24.5. Sections 24.6 and 24.7 focus on the aerodynamic characteristics of flight, followed by the general configuration of airplanes in Sect. 24.8. Weight definitions and the related performance of aircrafts are discussed in Sects. 24.9 and 24.10. Section 24.11 is on the stability and control of airplanes, followed by a description of loads in Sect. 24.12. Finally, Sect. 24.13 reviews aircraft structure and Sect. 24.14 describes basic maintenance checks for commercial airplanes.

24.1 **Aerospace Industry** 1086
24.2 **Aerospace Technology and Development** 1087
24.2.1 Aerospace and Society 1087
24.2.2 Aerospace Disciplines and the Design Process 1088
24.2.3 Challenges in Aeronautical Engineering 1090
24.3 **Aircraft** 1091
24.3.1 Aircraft Types 1091
24.4 **Spacecraft** 1093
24.5 **Definitions** 1093
24.5.1 Units 1093
24.5.2 Flight Speed Terminology 1093
24.5.3 Axis Systems 1096
24.5.4 Aerodynamic Forces and Moments 1098
24.5.5 Relative Wind 1099
24.5.6 Dynamic Pressure 1099
24.5.7 Airspeed Terminology 1100
24.6 **Flight Performance Equations** 1102
24.7 **Airplane Aerodynamic Characteristics** 1102
24.7.1 Airplane Lift Curve 1102
24.7.2 Airplane Drag Curve 1103
24.7.3 Mach Number Effects on Lift and Drag Curves 1104
24.8 **Airplane General Configurations** 1107
24.8.1 Aircraft Component Nomenclature 1107
24.8.2 Wing Geometric Characteristics 1107
24.8.3 Fuselage Geometry 1112
24.8.4 Empennage Geometry 1112
24.8.5 Landing Gear 1113
24.8.6 Propulsion Systems 1113
24.9 **Weights** 1113
24.9.1 Weight Definitions 1113
24.9.2 Weight Fractions 1114
24.9.3 Weight Estimation and Control 1114
24.9.4 Balance Diagram and C.G. Limits 1114
24.10 **Aircraft Performance** 1115
24.10.1 Level-Flight Performance 1115
24.10.2 Climb and Descent Performance 1116
24.10.3 Range 1118
24.10.4 Endurance 1120
24.10.5 Take-Off Performance 1121
24.10.6 Landing Performance 1122
24.11 **Stability and Control** 1123
24.11.1 Static Longitudinal Stability 1123
24.11.2 Longitudinal Control 1125
24.11.3 Static Directional Stability 1126
24.11.4 Directional Control 1127
24.11.5 Longitudinal Dynamics 1127
24.11.6 Lateral Dynamics 1128
24.11.7 Maneuverability and Turning 1128
24.12 **Loads** 1129
24.12.1 Air Loads 1129
24.12.2 Design Airspeeds 1131
24.12.3 Ground Loads 1132
24.13 **Airplane Structure** 1132
24.13.1 Structural Design 1132
24.13.2 Structural Analysis 1134
24.13.3 Structural Materials 1135
24.14 **Airplane Maintenance Checks** 1136
References 1136

K.-H. Grote, H. Hefazi (Eds.), *Springer Handbook of Mechanical Engineering*, Springer Handbooks,
https://doi.org/10.1007/978-3-030-47035-7_24

24.1 Aerospace Industry

Aerospace engineering is a branch of engineering that deals with the design, construction, and operation of aerospace vehicles.

The aerospace industry comprises a collection of organizations involved in the research, design, construction, testing, and operation of aerospace vehicles. In the USA, the aerospace industry consists of 20 prime contractors, 18 major airlines carriers that posted more than US $1 billion in revenue during the fiscal year 2016 (consisting of mainline, regional, and freight carriers), a large government-supported research agency, and thousands of smaller companies that supply special components to these primary contractors. A number of private space flight companies have also been added to this mix since the year 2000. The total (direct and induced) employment by the industry varies somewhat with changing business conditions, but in recent years has averaged about 2.5 million people, of whom approximately 70 000 are employed as engineers. According to a 2016 report by the Aerospace Industry Association [24.1], the total direct employment by the US aerospace and defense (A&D) sector in 2015 was 1.65 million. Additionally, the induced employment by the sector was estimated at 1.13 million. The aerospace industries in developed countries such as Russia, Japan, and European countries are not quite as large as that of the USA in terms of number of employees, but are similar in nearly every respect. Aerospace industries are also growing rapidly in populous countries such as China and India.

The products of the aerospace industry are many and varied, meeting a number of mission requirements. The broadest product classifications are related to the customer purchasing the product, giving rise to a classification into civil and military products. More specific product classifications can be derived from the type of aerospace vehicle and the particular use to which it is put. This section is organized in this manner.

Globally, more than 45 countries have notable levels of aerospace industry activities (Fig. 24.1). These activities include aircraft manufacturing, spacecraft manufacturing, missile and unmanned air vehicle (UAV) manufacturing (including engines, systems, aerostructures, and subtier suppliers), airborne defense electronics, simulator and ground support equipment, research and development, as well as maintenance and repair operations (MRO) for transport, military, and business and general aviation (BGA) aircraft.

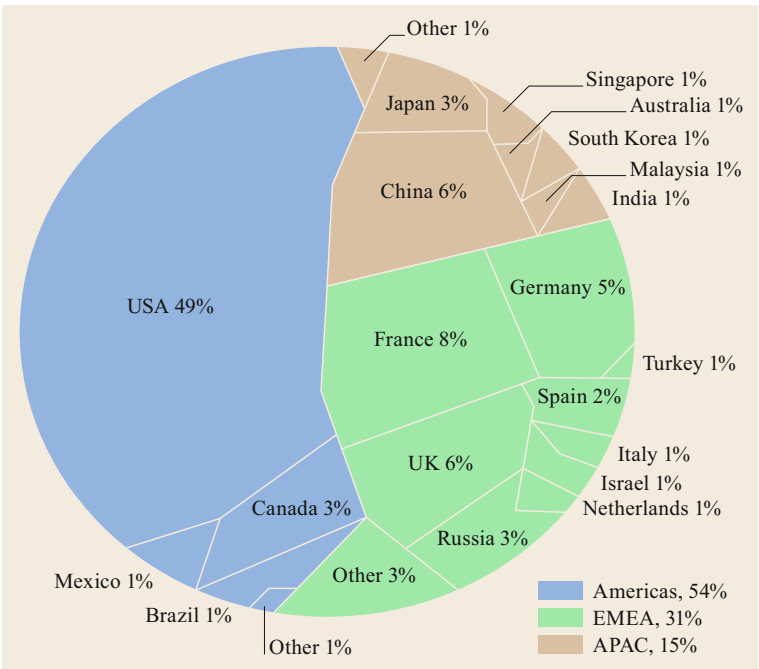

Fig. 24.1 The 2017 global aerospace industry – US$ 838 billion (Source: AeroDynamic Advisory & Teal Group 2018) [24.1–3]

24.2 Aerospace Technology and Development

24.2.1 Aerospace and Society

The wealth of any modern society is to a large extent based on fast and reliable transport of information, passengers, and freight in an environmentally acceptable way. Aerospace is a mandatory part of the overall transportation system: satellites provide weather information, navigation signals, and transmit messages worldwide; transport aircraft provide fast and safe transportation of passengers and/or freight across borders; and military aerospace will be part of any strategy for many years to come. In commercial terms, the future of aeronautics is bright: the increase of passenger traffic has been stable at some 5% per year over the past three decades, and is forecast to continue this trend over the coming decades. The International Air Transport Association (IATA) passenger growth forecast projects that passenger numbers are expected to reach 8.2 billion by 2031 with a 3.7% average annual growth in demand (2014 baseline year). This is more than double the 3.8 billion who flew in 2016. Cargo growth is even higher, at 6% per year [24.2]. From Fig. 24.2 it can be seen that, in Europe, passenger transport by aeronautics has exceeded that by rail and public transport since 2015.

In addition, aeronautics has always touched the human imagination: from the story of Daedalus through Leonardo da Vinci to Antoine de Saint-Exupéry. It is an ancient wish of mankind to be able to fly, and space has inspired human thought for a long time as well, from ancient cultures, which already knew much about the stars, up to today, where we think about an ever-expanding or finally collapsing universe.

In some fields of activity, aeronautics and space systems merge. After launch, space payload carriers not built in space have to cross the atmosphere, coping with gravity and air friction, similar to aeronautic vehicles. More specifically, common interests include space tourism, hypersonic transport, and rail guns as satellite launchers.

The launch of space vehicles is somehow spectacular and, in the past, has been limited to government agencies and a few places in the world. Therefore, the public takes quite some interest in such launches, because they are linked to the above-mentioned dream of mankind. Furthermore, since the year 2000, a robust and competitive commercial space sector has developed, promising to generate new global markets and innovation-driven entrepreneurship. On the other hand, and even though aeronautic vehicles are also part of that dream and are mandatory for modern life, their operation is more heavily criticized. Whereas, for example, railway noise is accepted even in the heart of cities at midnight, aircraft noise seems to be annoying even if hardly noticeable. The public is used to all other kinds of traffic and has accepted their drawbacks, but noise and emissions from aeronautics are more in the focus of today's discussion than merited by their share of the overall transport system. This may be due to the fact that the basis of one's desire to fly is the

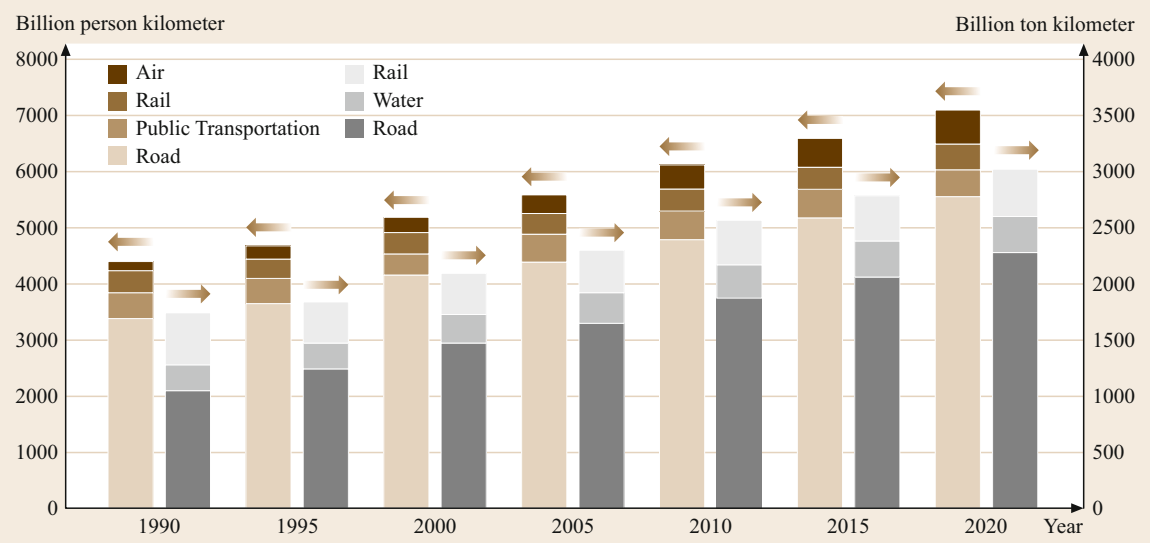

Fig. 24.2 Share of different modes of passenger and freight transportation in Europe (EU-25) (source: European Commission)

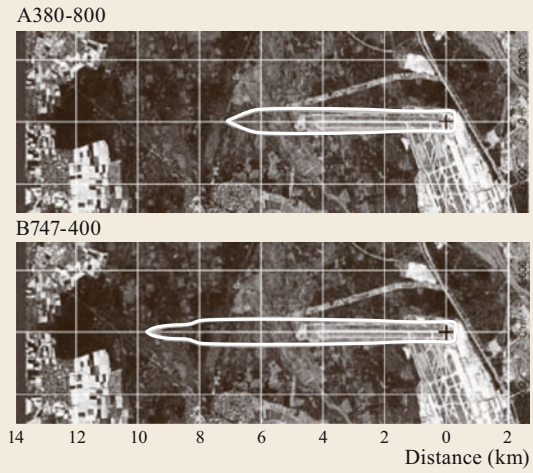

Fig. 24.3 Noise carpet at Frankfurt airport. The sound pressure is 85 dB(A) or higher within the marked region (source: DLH)

ease and weightlessness of a bird soaring in the sky. Thus, humans react more sensitively to aircraft noise and pollution than to pollution from any other means of transport. In reality, much progress has been made over recent decades. Noise has been drastically reduced with the target of keeping the major part of the noise carpet within the airport area (Fig. 24.3). While the amount of exhaust emissions has even been decoupled from the number of aircraft, overall aviation emissions remain a challenge due to increased demand for air travel (Fig. 24.4) [24.3].

As in other fields, there are many ways to look at aerospace engineering. Firstly, there is the work of specialists in many fields, but one can also consider a system approach, combining disciplines into increasingly complex components up to the level of the final vehicles; finally, there is the system-of-systems approach, when talking about the air transport system (ATS). In astronautics, this system-of-systems approach includes the vehicle, payload, transfer, and ground support. In any case, the total life cycle has to be addressed, from the first flight or launch via planned operation up to the disposal of the vehicle. The importance of the last topic is increasing, in aeronautics due to the issue of global resource management and in astronautics due to the issue of space debris.

24.2.2 Aerospace Disciplines and the Design Process

Aerospace in general is an integrated or so-called integration subject, with aeronautics and astronautics as particular fields of activity. Vehicle design is based on inputs from the fundamental engineering disciplines, namely aerodynamics, structures, and systems. As subgroups, flight mechanics, propulsion, guidance navigation and control (GNC), and others are found but can be allocated to the first three disciplines. In addition, combinations of the original disciplines have emerged, such as aeroelastics and aeroacoustics. Within each of these disciplines, progress has been made in the past, such as new flow control means, new materials, and new electronics systems.

Building on the foundations laid by work in the individual disciplines, components are created. This is already an interdisciplinary task; e.g., for an aircraft flap, aerodynamic performance is needed as well as the structure, including the kinematics and actuators on the systems side. Today, in aeronautics the largest components are the complete aircraft structure and the engines, which are developed and manufactured sepa-

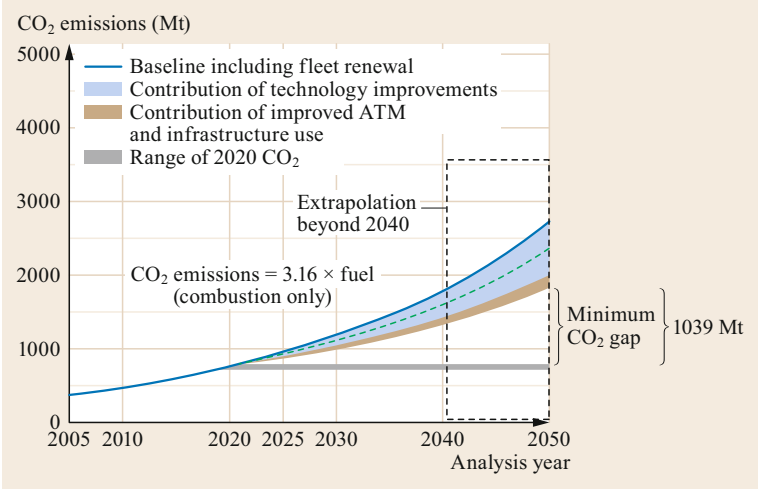

Fig. 24.4 CO_2 emissions trends from international aviation, 2005–2050

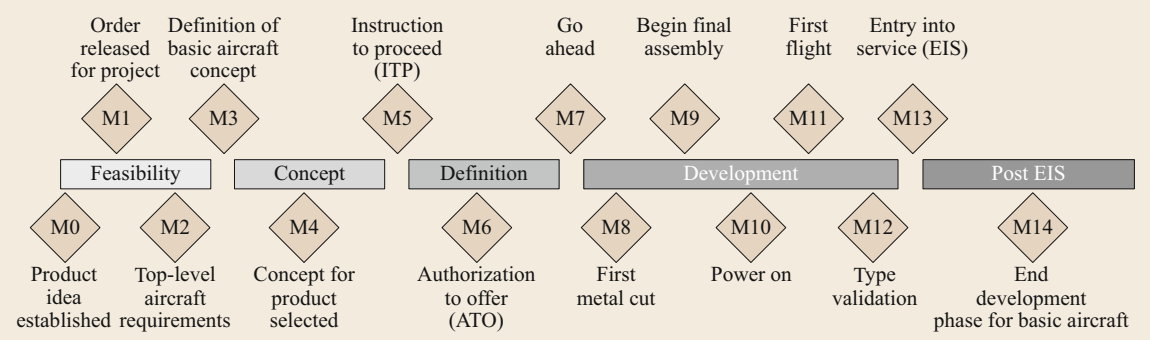

Fig. 24.5 Development process

rately. As for components, their development and final composition into a complete vehicle is a multidisciplinary and interdisciplinary task.

As for most other product developments, aircraft or spacecraft design follows a process which has been set up throughout recent decades. Initially, there is a market analysis, looking for what is missing in the present set of products. In aeronautics, this may be defined by the so-called transport task, i.e., the requirement to move a given payload in a given time across a given distance. In astronautics, apart from the vehicle, the payload itself can be the product to be developed, such as a satellite.

From these general requirements set by the market demands, the so-called top-level aircraft requirements (TLAR) can be derived as a basis for the future project office (FPO) work that will construct the general arrangement (GA) of the vehicle to be designed, working with tools mainly based on statistics and/or simple calculation methods.

This GA will then be given to various departments, such as flight dynamics or structures. Together with the aircraft program management, they will start component development, accompanied by tests using wind tunnels, test rigs, or simulators. At this stage, new technologies already available in the respective disciplines can be included in the design process. Increasingly, digital mock-ups (DMU) are used in the first part of the development phase instead of hardware.

With the GA and first performance estimates available, launching customers have to be found. They will influence the final design by their own needs. Depending on the product size and cost, with a certain number of products sold, the actual development starts with the program go-ahead, almost in parallel with the production of the first parts. At the end, specific tests will be carried out on prototypes, which may require some final, hopefully minor, changes to the design. The last step is the certification process, which ends with entry into service (EIS).

The whole development process as outlined above is almost the same for any aircraft manufacturer, and can be seen as a series of milestones as shown in Fig. 24.5.

At present, the market analysis may last for 2 years, the predevelopment for some 3 years, the development and manufacture for about 5 years, and the certification for another year. Just before the committed start of a program, technology development may take place, with technology feasibility or prematurity as a first step, and technology application studies as the final step. Overall, the time between the first thought about a new aircraft and the EIS is approximately 10–15 years.

For example, first thoughts on the Airbus A380 were published in 1989; at that time it was called the megaliner, ultrahigh-capacity aircraft (UHCA). Later it became the very large commercial transport (VLCT), as a common Airbus–Boeing feasibility study.

The committed program start occurred in 2000, and finally the A380 was introduced into airline service in 2007, corresponding to a total of 18 years. Of course, all manufacturers try to speed up this process. For the given and already highly optimized standard aircraft configuration, i.e., the fuselage, wing, engines, and tailplane as present in today's aircraft, further optimization is possible mainly by improving the design chain, including supplier management. However, for a completely new design, such as a blended wing body (BWB) (Fig. 24.6) or an oblique flying wing (OFW), the exhaustive time scale as described above is likely to remain.

Apart from monodisciplinary technologies such as new materials, actuators, or a specific aerodynamic vortex generator, integrated technologies make their way into the product, too; for example, fly-by-wire technology was a must for the European supersonic transport aircraft Concorde in the 1960s. Without it, it would not have been possible for the pilots to fly this aircraft in all the different flight regimes, in each of which the aircraft control behavior is different. Afterwards, in a first attempt, this technology was introduced into the

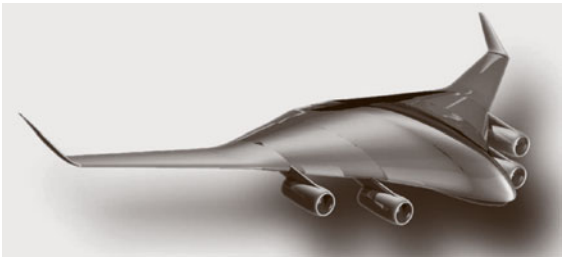

Fig. 24.6 Blended wing body (source: DLR)

Airbus A310, until it finally became mature in the Airbus A320, which made its maiden flight in 1987. Flow control technology or artificial instability are other examples of technology development, and manufacturing technologies such as friction stir welding or laser beam welding, advanced bonding or surface coating have been developed in the past and are part of the production process today.

Following its complete assembly, the vehicle will be operated in a larger system. Aircraft navigate with the help of air-traffic control, they are linked to other traffic in the air, and on the ground, especially in the vicinity of airports, they need to be loaded and unloaded, and they are part of a so-called intermodality concept that links personal and public transport on the ground with air or sea transport.

Design integration and connectivity of aircraft systems through the Internet of Things (IoT) are among the key enablers that impact the next-generation aircraft design process. Multidisciplinary design and optimization (MDO) and digital design are among the technologies that are at various levels of maturity in order to support the next-generation aircraft design process. Furthermore, a new area of the industry, focused on unmanned aircraft systems (UASs) – commonly know as drones or unmanned aerial vehicles (UAVs) – has also emerged in recent years. However, applications of these systems have mostly been limited to military and a few other commercial activities, as opposed to passenger or cargo transportation.

24.2.3 Challenges in Aeronautical Engineering

Looking at the history of aeronautics, it can be structured into three blocks. From its beginning until the end of World War II, physical understanding was the dominant driver. This began with daring pilots in fantastic flying machines, permanently hunting for records in range, speed, and altitude. As the next phase, coinciding with the introduction of jet engines, commercial aeronautics emerged. Many different configurations have been studied, including vertical take-off and landing (VTOL) aircraft such as the Dornier Do 31, supersonic transport in the shape of Concorde, and flying wings such as the Northrop YB-49. This led to the third phase, which is based on today's configuration of a commercial transport aircraft, all looking very much the same regardless of the manufacturing company. This configuration has reached a high level of maturity, so after all the expensive configuration studies, finally civil transport aircraft design and manufacturing has paid off.

However, with the success of commercial transport, three other issues have emerged. Firstly, airports are increasingly operating at their capacity limits, so it is questionable whether there is any chance to increase air traffic, even if there is a demand for it. Secondly, linked to this, environmental aspects play a leading role, even though the contribution of aeronautics to global emissions may be small, i.e., about 2% today. However, the 2015 Intergovernmental Panel on Climate Change (IPCC) estimated that aviation's contribution could grow to 5% of the total by 2050 if action is not taken to tackle these emissions. Thirdly, and still linked to growth, safety issues are of increasing importance. Today's reliability rate of 10^{-9} failures per flight hour for critical components will not be sufficient if the number of aircraft doubles within a decade. In order to reduce the number of accidents in parallel with an increasing number of vehicles, functional hazard analysis must yield greater reliability. This holds true for single components such as an actuator, up to subsystems such as an aileron, and also the complete aircraft system and structure.

Almost at the same time, the European Commission published its Vision 2020 [24.4] on aeronautics and the National Aeronautics and Space Administration (NASA) published its Aeronautics Blueprint on these issues. Both came to similar conclusions: with aeronautics being a vital element for the wealth of society on one side, and the environmental issues linked to it on the other side, in the future there will be additional TLAR, in order to balance transport needs, societal needs in terms of safety and security, and environment protection. These additional TLAR may ask for totally different vehicle configurations as well as for new ways of operating these vehicles. In addition, all of these issues ask for a system approach; for example, in contrast to road and rail transport, security will play an increasingly important role in aeronautics. There are an increasing number of studies on seamless air transport which ask for new ground procedures and probably even new vehicle designs. To define and finally solve all the new TLAR will be a demanding task for any discipline as well as for the overall vehicle and system composition, in aeronautics as well as in astronautics. Therefore, a fourth phase can be expected, aiming for sustainable growth.

24.3 Aircraft

The term "aircraft" is an all-inclusive term for any form of craft designed for navigation in the air. In the years since the first actual man-carrying flight in a hot-air balloon in the late 1700s, there have been a number of types of aircraft that have provided the means for aerial navigation. A brief recap includes the hot-air balloon ascension of de Rozier and d'Arlandes in 1783, the hydrogen balloon flight of J.A.C. Charles and M.N. Robert in 1783, and the successful steam-engine-powered airship (balloon) of Giffard in 1852. The German Otto Lilienthal developed a man-carrying glider that made over 2000 glides before suffering a fatal crash in 1896 [24.5]. As has been well documented, it was the Wright brothers, Orville and Wilbur, who made the first controlled powered flights of an airplane in 1903. Progress in aircraft design was slow in the first few years after the Wright flights, but by the start of World War I (WWI), many flying machines of various types and configurations had been successfully built and flown. During WWI, military requirements gave rise to the development of numerous types of aircraft with very specialized capabilities, which were produced in their thousands. Following the war, aircraft for the transportation of passengers came into widespread use, with the establishment of airline companies and air routes, first between major European cities, but later in America and other parts of the world as well. In the period between World War I and World War II, specialized aircraft were used to set nonstop distance records between continents, while other specialized aircraft set records for speed and altitude. World War II saw the introduction of new technology in aircraft design with the advent of practical helicopters, jet engines, rocket propulsion systems, and guided missiles. Following World War II, there was significant growth in private, recreational flying, expansion of the international commercial air transportation system, as well as continuing development of experimental aircraft that flew higher, faster, and farther than previous aircraft. With the creation of the National Aeronautics and Space Administration (NASA) in 1958, a variety of unique aircraft and spacecraft were designed to meet very specific mission objectives laid down by the agency. In recent years, there has been increasing military interest in unmanned combat air vehicles (UCAVs).

24.3.1 Aircraft Types

The two major categories of aircraft types are lighter than air (LTA) and heavier than air (HTA). A lighter-than-air craft is one that rises aloft by making use of Archimedes' principle, that is, by displacing a weight of air that is greater than the weight of the craft itself, thus creating a buoyant force. A heavier-than-air aircraft is one that rises aloft due to Bernoulli's principle acting on the aircraft's lifting surfaces, creating suction on the upper surface and pressure on the lower surface relative to the ambient air pressure. The design and operation of civil aircraft in the USA is subject to numerous regulations promulgated by the Federal Aviation Administration (FAA) of the Department of Transportation [24.6]. Table 24.1 presents a summary of the various types of FAA regulations.

Table 24.1 Summary of Federal Aviation Regulatory (FAR) categories

Regulatory category	FAR part
Certification procedures for products and parts	21
Airworthiness standards, normal, utility, acrobatic, and commuters	23
Airworthiness standards, transport category airplanes	25
Airworthiness standards, normal category rotorcraft	27
Airworthiness standards, transport category rotorcraft	29
Airworthiness standards, manned free balloons	31
Airworthiness standards, aircraft engines	33
Airworthiness standards, propellers	35
Noise standards, aircraft type, and airworthiness standards	36
Airworthiness directives	39
Maintenance, preventive maintenance, rebuilding, and alteration	43
Identification and registration marking	45
Aircraft registration	47
General operating and flight rules	91
Special air-traffic rules and airport traffic patterns	93
Instrument flight rules (IFR) altitudes	95
Standard instrument approach procedures	97
Ultralight vehicles	103
Certification and operation, domestic, flag, and supplemental air carriers, and commercial operators of large aircraft	121
Certification and operation, airplanes having seating capacity of 20 or more passengers, or a maximum payload capacity of 6000 lb or more	125
Certification and operation of scheduled air carrier helicopters	127
Air taxi operators and commercial operators	135
Agricultural aircraft operations	139

Lighter-than-Air Aircraft

One can distinguish between the following types of LTA aircraft:

- Hot-air balloon, which consists of a large envelope made of lightweight fabric to contain the hot air, a burner located below the envelope, usually fueled by kerosene, to heat ambient air, causing it to rise into the envelope. A basket hung underneath the burner is provided for the pilot and passengers.
- Light-gas balloon, which is similar in arrangement to a hot-air balloon, but without the burner. The buoyant force is generated by the use of light gases such as helium in the envelope, which displace the relatively heavier ambient air.
- Blimp or nonrigid airship, which is basically a large gas balloon whose streamlined shape is maintained by internal gas pressure. In addition to the gas envelope, the blimp has a car attached to the lower part of the envelope for the crew and passengers, engines and propellers to develop forward speed, and fins with hinged aft portions for control.
- Rigid airship, a lighter-than-air aircraft with a rigid frame to maintain its shape and provide a volume for the internal placement of light gasbags. The rigid airship also has a car attached to the lower part of the rigid frame for the crew and passengers, engines, propellers, and tail fins similar to the blimp. Rigid airships reached the peak of their development in the mid-1930s, but several spectacular accidents curtailed further development.

Heavier-than-Air Craft

HTA aircraft can be divided into three main categories.

A *glider* is an aircraft that flies without an engine. The simplest form of a glider is the hang glider, which consists of a wing, a control frame, and a pilot harness. The pilot is zipped into the harness and literally hangs beneath the wing, with his hands on the control bar of the control frame. The wing has an aluminum frame that supports the wing fabric, and internal battens to provide a proper shape to the fabric. Hang gliders are usually launched from a very steep hill or a cliff that affords sufficient altitude for gliding flight. Simple utility gliders which have rigid structural elements similar to an airplane are used primarily for training. These gliders are launched into the air by being towed by a power winch, an automobile, or an airplane. Extremely refined sailplanes, usually made of very lightweight materials and featuring very long thin wings, take advantage of rising air currents, and can soar for a long time and cover distances of hundred of miles in a single flight. A variation of the sailplane is the *motorglider*, basically a sailplane with a small motor and propeller, which is used for take-off and climb to soaring altitude, whereupon the motor is shut off, and then retracted along with the propeller to revert to the sailplane configuration.

An *airplane* is an air vehicle that incorporates a propulsion system and fixed wings, and is supported by aerodynamic forces acting on the wings. Airplane propulsion systems may be a piston engine driving a propeller, a turbojet engine, or a rocket engine, depending on the required mission. Airplanes range in form from small general aviation aircraft, usually privately owned, with one or two engines, to larger commercially operated air transport aircraft that can carry from 20 to upwards of 500 passengers and can fly distances from 500 to over 8000 miles nonstop. In addition to these civil aircraft types, there a number of military aircraft types designed for different missions, such as fighter, attack, bomber, reconnaissance, transport, and trainer. A very small class of airplanes, known as experimental research aircraft, usually powered by rocket engines, has been built to obtain flight test data at extremely high speeds and altitudes. The ultimate development in this area is the US Space Shuttle, which is a rocket-powered spacecraft for most of its mission, and an unpowered glider for the approach and landing phase of the flight. A number of supersonic transport aircrafts such as Lockheed Martin's X-59 (QueSST, quiet supersonic transport) and Boom Technology's Overture (https://boomsupersonic.com/overture) are at various stages of development.

A *helicopter* is an aircraft that is supported by aerodynamic forces generated by long thin blades rotating about a vertical axis. The rotor blades are driven by the helicopter's propulsion system, usually a piston or gas turbine engine. Helicopters range in size from small, two-seat personal utility models to large transport types that can carry up to 40 people. Large heavy-lift helicopters are often used in specialized hauling and construction tasks, where their ability to remain airborne over a fixed spot for extended periods of time is unique. Helicopters have also been used in several military applications such as air–sea rescue, medical evacuation, as battlefield gunships, and for special-operations troop transport. Recent developments in helicopter technology have led to hybrid helicopter craft called the tilt rotor. In this machine, there are two rotors to provide the vertical forces required for take-off and landing, but as the name implies, these rotors may be tilted to varying degrees until they are aligned in the direction of flight, acting like the propellers on a conventional airplane. The tilt rotor has small wings to provide the aerodynamic lift required during cruise flight, during which the rotors are used to provide forward thrust.

24.4 Spacecraft

Spacecraft fall into two major categories, unmanned, with no humans aboard, and manned, with humans aboard. Examples of unmanned spacecraft include civil communication satellites, military reconnaissance satellites, and scientific probes that gather information on our solar system. Examples of unmanned spacecraft include the Eutelsat civil communication satellites, the Aquila and Kosmos military reconnaissance satellites, the Hubble Space Telescope and Mars Global Surveyor and Starlink satellites. Examples of manned spacecraft include the Soyuz, Mir, Mercury, Gemini, Apollo, Space Shuttle SpaceX's Crew Dragon and Boeing's Starlines.

24.5 Definitions

The following are some important definitions related to a good understanding of aerospace engineering.

24.5.1 Units

Although there has been a policy in the USA in recent years to convert to the International System of Units (SI), the US aerospace industry continues to use English units in its work. This publication will use English units as primary, since most American engineers are familiar with this terminology. A list of conversion factors between SI and English units is given in Table 24.2.

24.5.2 Flight Speed Terminology

One of the key performance parameters for an airplane is its maximum level-flight speed [24.7]. For a variety of technical and economic reasons, various airplanes are designed to operate at speeds most appropriate to their design missions. Modern airplanes operate at speeds ranging from a low of around 60 kn to highs of around 1450 kn. Over such a wide range of flight speeds, the characteristics of the airflow around the airplane change dramatically. These changes, associated with the compressible nature of air, are directly related to the flight Mach number, defined as the flight speed divided by the speed of sound in the ambient air in which the airplane is flying. This situation has given rise to some general terms to describe airplane flight speeds in terms of Mach number, as shown in Fig. 24.7 [24.8]. Also shown are the types of airplanes having maximum level-flight speeds within the various speed regimes.

Standard Atmosphere

For design and performance calculations, it is appropriate to establish a standard set of characteristics for the Earth's atmosphere in which aircraft operate. The US standard atmosphere is a widely used set whose essential characteristics, that is, the temperature, pressure, density, and viscosity, as a function of altitude have been derived using

$$p = \rho RT \,,$$
$$\mathrm{d}p = -\rho g \,\mathrm{d}h \,,$$

where

p = pressure in $\mathrm{lb/ft^2}$,
ρ = density in $\mathrm{slug/ft^3}$,
T = absolute temperature in °Ra ,
R = gas constant (1718 ft lb/(slug °Ra)) for air ,
g = gravitational constant ($32.17\,\mathrm{ft/s^2}$),
h = height above sea level in feet.

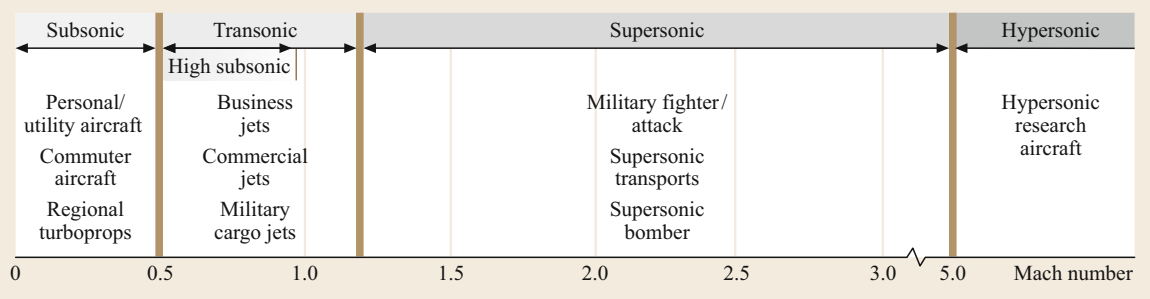

Fig. 24.7 Flight speed terminology

Table 24.2 Conversion factors between SI and English units

Conversion factor	
Mass	1.00 kg = 0.06852 slug 1.00 slug = 14.594 kg At the surface of the Earth, an object with a mass of 1.00 kg weighs 9.80 N or 2.205 lb, and an object with a mass of 1.00 slug weighs 32.17 lb or 143.10 N
Length	1.00 m = 3.2808 ft 1.00 ft = 0.3048 m = 30.48 cm
Force	1.00 N = 0.2248 lb 1.00 lb = 4.4482 N
Temperature	1.00 K = 1.8 °R °R = °F + 460 1.0 °R = 0.5556 K K = °C + 273
Pressure	$1.00\,N/m^2 = 1.4504 \times 10^{-4}\,lb/in^2 = 2.0886 \times 10^{-2}\,lb/ft^2$ $1.00\,lb/in^2 = 6.8947 \times 10^3\,N/m^2$ $1.00\,lb/ft^2 = 47.88\,N/m^2$
Velocity	1.00 m/s = 3.2808 ft/s = 2.2369 mi/h 1.00 ft/s = 0.6818 mi/h = 0.3048 m/s
Density	$1.00\,kg/m^3 = 1.9404 \times 10^{-3}\,slug/ft^3$ $1.00\,slug/ft^3 = 515.36\,kg/m^3$
Viscosity	$1.00\,kg/(m\,s) = 20.886 \times 10^2\,lbf\,s/ft^2$ $1.00\,lbf\,s/ft^2 = 47.879\,kg/(m\,s)$
Specific heat	$1.00\,N\,m/(kg\,K) = 1.00\,J/(kg\,K) = 2.3928\,Btu/(lb_m\,°R) = 5.9895\,ft\,lb_f/(slug\,°R)$ $1.00\,ft\,lb/(slug\,°R) = 1.6728 \times 10^{-1}\,N\,m/(kg\,K) = 1.6728 \times 10^{-1}\,J/(kg\,K)$
Frequently used equivalents	
1 bhp	550 ft lb/s = 33 000 ft lb/min
1 kn	1.152 mi (stat.)/h
1 kn	1.69 ft/s
1 mi (stat.)/h	0.868 kn
1 mi (stat.)/h	1.467 ft/s
1 ft/s	0.682 mi (stat.)/h
1 ft/s	0.592 kn
1 km	0.621 mi (stat.)
1 km	0.539 mi (naut.)
1 mi (stat.)	1.609 km
1 mi (naut.)	1.854 km
1 rad	57.3°
Note that the preceding values are *equivalents*. The conversion factors are the reciprocals.	
Frequently used constants	
γ	1.4 (air)
Gas constant R (air)	287.05 N m/(kg K) = 1718 ft lb/(slug °R)
Specific heat c_p (air)	1004.7 N m/(kg K) (J/(kg K)) = 6006 ft lb/(slug °R)
Gravitational constant at sea level g_0	$9.80\,m/s^2 = 32.17\,ft/s^2$
Radius of the Earth r_0	6.378×10^6 m = 20.92×10^6 ft

mi (stat.) = statute mile, nmi = nautical mile, kn = nautical mile per hour

With these equations, only a defined variation of T with altitude is required to establish the standard atmosphere. The defined variation, based on experimental data, is shown in Fig. 24.8.

Once the temperature variation with altitude is defined, the characteristics of the standard atmosphere can be calculated directly.

The characteristics of the US standard atmosphere are presented in Table 24.3. From sea level to 36 089 ft, the temperature decreases linearly with altitude. This region is called the troposphere. Above 36 089 ft, the temperature is constant up to 65 617 ft in the region called the stratosphere. Above 65 617 ft, the temperature increases linearly to 100 000 ft, the upper level of interest for current or foreseeable aircraft.

Although the concept of geometric altitude, the altitude above sea level as determined by a tape measure, is most familiar, of prime importance for aircraft design and performance calculations is the pressure altitude, i.e., the geometric altitude on a standard day for which

Table 24.3 Characteristics of the US standard atmosphere

Altitude	Temperature		Pressure	Density	Density ratio	Kinematic viscosity	q/M^2	Sonic velocity	
(ft)	(°F)	(°R)	(psf)	(slug/cu ft)		(ft^2/s)	(lb/ft^2)	(ft/s)	(kn)
0	59.0	518.7	2116.2	0.0023769	1.0000	0.0001572	1481.0	1116.4	661.5
1000	55.4	515.1	2040.9	0.0023081	0.9710	0.0001610	1429.0	1112.6	659.2
2000	51.9	511.6	1967.7	0.0022409	0.9427	0.0001650	1377.0	1108.7	656.9
3000	48.3	508.0	1896.7	0.0021752	0.9151	0.0001691	1328.0	1104.9	654.6
4000	44.7	504.4	1827.7	0.0021110	0.8881	0.0001732	1279.0	1101.0	652.3
5000	41.2	500.9	1760.9	0.0020482	0.8616	0.0001776	1233.0	1097.1	650.0
6000	37.6	497.3	1696.0	0.0019869	0.8358	0.0001820	1187.0	1093.2	647.7
7000	34.0	493.7	1633.1	0.0019270	0.8106	0.0001866	1143.0	1089.3	645.4
8000	30.5	490.2	1572.1	0.0018685	0.7860	0.0001914	1100.0	1085.3	643.0
9000	26.9	486.6	1512.9	0.0018113	0.7619	0.0001963	1059.0	1081.4	640.7
10 000	23.3	483.0	1455.6	0.0017556	0.7385	0.0002013	1019.0	1077.4	638.3
11 000	19.8	479.5	1400.0	0.0017011	0.7155	0.0002066	979.8	1073.4	636.0
12 000	16.2	475.9	1346.2	0.0016480	0.6932	0.0002120	942.1	1069.4	633.4
13 000	12.6	472.4	1294.1	0.0015961	0.6713	0.0002175	905.6	1065.4	631.4
14 000	9.1	468.8	1243.6	0.0015455	0.6500	0.0002233	870.2	1061.4	628.8
15 000	5.5	465.2	1194.8	0.0014962	0.6292	0.0002293	836.0	1057.4	626.4
16 000	1.9	461.7	1147.5	0.0014480	0.6089	0.0002354	802.9	1053.3	624.0
17 000	−1.6	458.1	1101.7	0.0014011	0.5892	0.0002418	770.8	1049.2	621.6
18 000	−5.2	454.6	1057.5	0.0013553	0.5699	0.0002484	739.8	1045.1	619.2
19 000	−8.8	451.0	1014.7	0.0013107	0.5511	0.0002553	709.8	1041.0	616.7
20 000	−12.3	447.4	973.3	0.0012673	0.5328	0.0002623	680.8	1036.9	614.3
21 000	−15.9	443.9	933.3	0.0012249	0.5150	0.0002697	652.7	1032.8	611.9
22 000	−19.5	440.3	894.6	0.0011836	0.4976	0.0002772	625.6	1028.6	609.4
23 000	−23.0	436.8	857.2	0.0011435	0.4806	0.0002851	599.4	1024.5	606.9
24 000	−26.6	433.2	821.2	0.0011043	0.4642	0.0002932	574.1	1020.3	604.4
25 000	−30.2	429.6	786.3	0.0010663	0.4481	0.0003017	549.7	1016.1	601.9
26 000	−33.7	426.1	752.7	0.0010292	0.4325	0.0003104	526.2	1011.9	599.4
27 000	−37.3	422.5	720.3	0.0009931	0.4173	0.0003195	503.4	1007.7	596.9
28 000	−40.9	419.0	689.0	0.0009580	0.4025	0.0003289	481.5	1003.4	594.4
29 000	−44.3	415.4	658.8	0.0009239	0.3881	0.0003387	460.3	999.1	591.9
30 000	−48.0	411.9	629.7	0.0008907	0.3741	0.0003488	439.9	994.8	589.3
31 000	−51.6	408.3	601.6	0.0008584	0.3605	0.0003594	420.3	990.5	586.8
32 000	−55.1	404.8	574.6	0.0008270	0.3473	0.0003703	401.3	986.2	584.2
33 000	−58.7	401.2	548.5	0.0007966	0.3345	0.0003817	383.1	981.9	581.6
34 000	−62.3	397.6	523.5	0.0007670	0.3220	0.0003935	365.5	977.5	579.0
35 000	−65.8	394.1	499.3	0.0007382	0.3099	0.0004058	348.6	973.1	576.4
36 000	−69.4	390.5	476.1	0.0007103	0.2981	0.0004185	332.3	968.8	573.8
37 000	−69.7	390.0	453.9	0.0006780	0.2843	0.0004379	330.9	968.1	573.6
38 000	−69.7	390.0	432.6	0.0006463	0.2710	0.0004594	316.7	968.1	573.6
39 000	−69.7	390.0	412.4	0.0006161	0.2583	0.0004820	301.8	968.1	573.6
40 000	−69.7	390.0	393.1	0.0005873	0.2462	0.0005056	287.7	968.1	573.6
41 000	−69.7	390.0	374.6	0.0005598	0.2346	0.0005304	274.2	968.1	573.6
42 000	−69.7	390.0	357.2	0.0005336	0.2236	0.0005564	261.3	968.1	573.6
43 000	−69.7	390.0	340.5	0.0005087	0.2131	0.0005837	249.0	968.1	573.6
44 000	−69.7	390.0	324.6	0.0004849	0.2031	0.0006123	237.4	968.1	573.6
45 000	−69.7	390.0	309.4	0.0004623	0.1936	0.0006423	226.2	968.1	573.6
46 000	−69.7	390.0	295.0	0.0004407	0.1845	0.0006738	215.6	968.1	573.6
47 000	−69.7	390.0	281.2	0.0004201	0.1758	0.0007068	205.5	968.1	573.6
48 000	−69.7	390.0	268.1	0.0004004	0.1676	0.0007415	195.8	968.1	573.6
49 000	−69.7	390.0	255.5	0.0003818	0.1597	0.0007778	186.7	968.1	573.6
50 000	−69.7	390.0	243.6	0.0003639	0.1522	0.0008159	177.9	968.1	573.6

Table 24.3 (continued)

Altitude (ft)	Temperature (°F)	(°R)	Pressure (psf)	Density (slug/cu ft)	Density ratio	Kinematic viscosity (ft^2/s)	q/M^2 (lb/ft^2)	Sonic velocity (ft/s)	(kn)
51 000	−69.7	390.0	232.2	0.0003469	0.1451	0.0008559	169.5	968.1	573.6
52 000	−69.7	390.0	221.4	0.0003307	0.1383	0.0008978	161.6	968.1	573.6
53 000	−69.7	390.0	211.0	0.0003153	0.1318	0.0009418	154.0	968.1	573.6
54 000	−69.7	390.0	201.2	0.0003006	0.1256	0.0009879	146.8	968.1	573.6
55 000	−69.7	390.0	191.8	0.0002865	0.1197	0.0010360	139.9	968.1	573.6
56 000	−69.7	390.0	182.8	0.0002731	0.1141	0.0010871	133.3	968.1	573.6
57 000	−69.7	390.0	174.3	0.0002604	0.1087	0.0011403	127.1	968.1	573.6
58 000	−69.7	390.0	166.2	0.0002482	0.1036	0.0011961	121.1	968.1	573.6
59 000	−69.7	390.0	158.4	0.0002366	0.0988	0.0012547	115.4	968.1	573.6
60 000	−69.7	390.0	151.0	0.0002256	0.0841	0.0013161	110.0	968.1	573.6
61 000	−69.7	390.0	144.0	0.0002151	0.0897	0.0013805	104.8	968.1	573.6
62 000	−69.7	390.0	137.3	0.0002050	0.0855	0.0014481	99.9	968.1	573.6
63 000	−69.7	390.0	130.9	0.0001955	0.0815	0.0015189	95.2	968.1	573.6
64 000	−69.7	390.0	124.8	0.0001834	0.0777	0.0015932	90.8	968.1	573.6
65 000	−69.7	390.0	118.9	0.0001777	0.0740	0.0016712	86.5	968.1	573.6
70 000	−67.3	392.4	92.7	0.0001376	0.0579	0.0021219	82.4	971.0	575.3
75 000	−64.6	395.1	73.0	0.0001077	0.0453	0.0026938	64.9	974.4	577.3

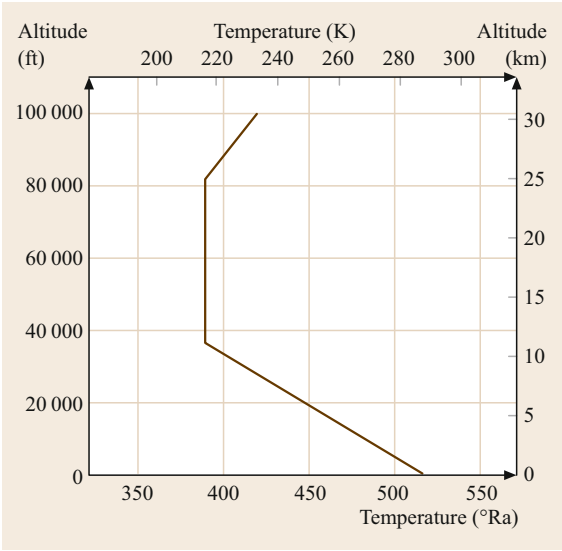

Fig. 24.8 Temperature variation with altitude in the US standard atmosphere

the pressure is equal to the ambient atmospheric pressure. Aircraft altimeters are pressure gages calibrated to read pressure altitude. Also important is the density altitude, the geometric altitude on a standard day for which the density is equal to the ambient air density. Pressure altitude, density altitude, and temperature are related through the equation of state $p = \rho RT$.

It should be noted that another standard atmosphere has been defined by the International Civil Aviation Organization (ICAO). The ICAO standard atmosphere and the US standard atmosphere are identical up to 65 617 ft. Beyond 65 617 ft, the ICAO standard atmosphere maintains a constant temperature up to 82 300 ft, while the US standard atmosphere reflects an increasing temperature with a constant gradient to beyond 100 000 ft.

24.5.3 Axis Systems

The airplane design process, with respect to achieving performance objectives of altitude, speed, range, payload, and take-off and landing distances, requires analysis of the airplane in motion. The Newtonian laws of motion state that the summation of all external forces in any direction must equal the time rate of change of momentum, and that the summation of all of the moments of the external forces must equal the time rate of change of the angular momentum, all measured with respect to axes fixed in space. However, if the motion of the airplane is described relative to axes fixed in space, the mathematics becomes extremely unwieldy, as the moments and products of inertia vary from instant to instant. To overcome this difficulty, use is made of moving or Eulerian axes that coincide in some particular manner from instant to instant with a definite set of axes fixed with respect to the airplane. The most common choice is to select a set of mutually perpendicular axes defined within the airplane as shown in Fig. 24.9, with their origin at the airplane's center of gravity (c.g.). The airplane's motion in space is defined by six components of velocity. This is a right-handed axis system with the positive x- and z-axes in the plane of symmetry and the x-axis point-

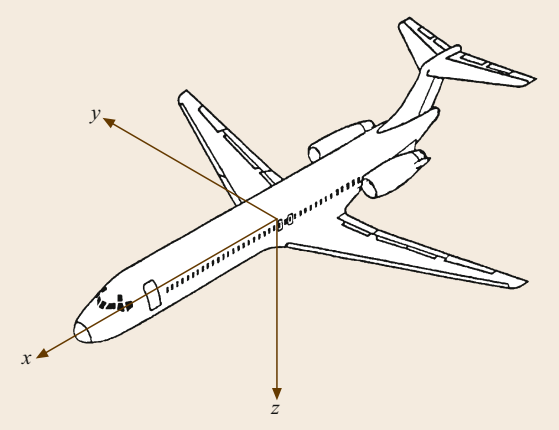

Fig. 24.9 Airplane axis system

ing out of the nose of the airplane along the flight path. This is called a wind axis system, since the x-axis always coincides with the airplane's velocity vector. The z-axis is perpendicular to the x-axis, positive downward, while the positive y-axis is out the right-hand wing, perpendicular to the plane of symmetry.

For most aircraft design analyses, the airplane is considered to be a rigid body with six degrees of freedom: three linear velocity components along these axes, and three angular velocity components around these axes. The angular motion around the y-axis is called pitch; the angular motion about the x-axis is called roll; and the angular motion about the z-axis is called yaw. Nearly all airplane motions encountered in preliminary aircraft design and performance analyses are in the plane of symmetry. The other three components of the airplane's motion lie outside the plane of symmetry. The symmetric degrees of freedom are referred to as the longitudinal motion, and the asymmetric degrees of freedom are referred to as lateral-directional motion.

In the plane of symmetry (Fig. 24.10), the inclination of the flight path to the horizontal is the flight path angle γ while the angle between the flight path and the airplane reference line is the angle of attack α. The angle between the airplane reference line and the horizontal is the airplane's pitch angle θ.

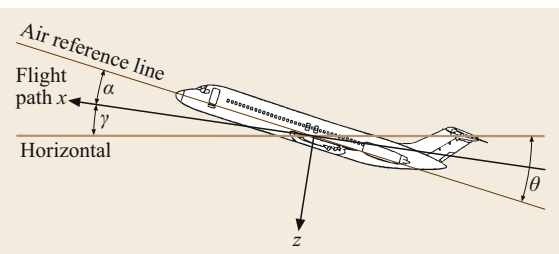

Fig. 24.10 Axis system in the plane of symmetry

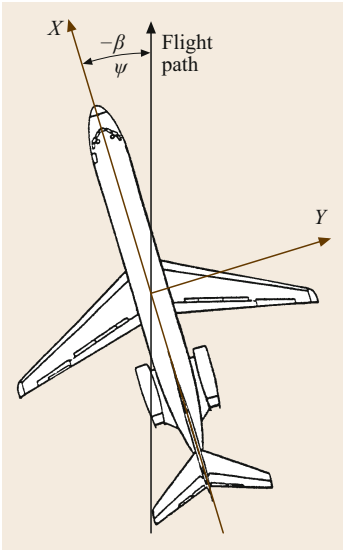

Fig. 24.11 Axis system in asymmetric flight

When the flight path does not lie in the plane of symmetry (Fig. 24.11), the angle between the flight path and the airplane's centerline is the yaw angle ψ. For straight flight in this situation, the yaw angle is equal in magnitude but opposite in sign to the sideslip angle β. In roll about the flight path, the angle between the y-axis and the horizontal is the roll or bank angle. A summary of all of the angles involved in flight performance and flight mechanics calculations is presented in Table 24.4.

The other three components of the airplane's motion lie outside the plane of symmetry. The symmetric degrees of freedom are referred to as the longitudinal motion, while the asymmetric degrees of freedom are referred to as lateral-directional motion. In the plane of symmetry (Fig. 24.10), the inclination of the flight path to the horizontal is the flight path angle γ and the angle between the flight path and the airplane reference line is the angle of attack α.

Table 24.4 Summary and definition of angles involved in flight performance and flight mechanics calculations

In the plane of symmetry		
γ	Flight path angle	Angle between the horizon and the velocity vector
θ	Pitch angle	Angle between the airplane reference line and the horizon
α	Angle of attack	Angle between the airplane reference line and the velocity vector
In asymmetric flight		
β	Angle of sideslip	Angle between the airplane centerline and the velocity vector
φ	Angle of roll	Angle between the airplane's y-axis and the horizon

24.5.4 Aerodynamic Forces and Moments

The aerodynamic forces acting on an aircraft consist of two types: pressure forces, which act normal to the aircraft surface, and viscous or shear forces, which act tangentially to the aircraft surface.

The physical parameters that govern the aerodynamic forces and moments acting on an aircraft have been developed through a method called dimensional analysis. This procedure is treated in detail in many textbooks on aerodynamics, and will only be summarized here. Dimensional analysis considers the dimensions or units of the physical quantities involved in the development of aerodynamic forces and moments, and divides them into two groups: fundamental and derived. The fundamental units are mass, length, and time, and all physical quantities have dimensions that are derived from a combination of these three fundamental units. Equations that express physical relationships must have dimensional homogeneity; that is, each term in the equation must have the same units in order for the equation to have physical significance. The broad physical relationships are postulated by logic, reason, or perhaps some experimental evidence, then the specific relationships are derived by dimensional analysis. For aerodynamic forces and moments acting on an aircraft in the plane of symmetry, the broad physical relationships are postulated as

$$F_{\text{aero}},\ M_{\text{aero}} = f(\text{shape, size, altitude, velocity, fluid properties})\ .$$

The specific relationship for aerodynamic forces, derived from dimensional analysis, is

$$F_{\text{aero}} = K\rho V^2 L^2 f\left(\alpha, \frac{\rho VL}{\mu}, \frac{V}{a}\right)\ ,$$

where K is a constant of proportionality or dimensionless coefficient, V is the velocity of the aircraft, L is an arbitrary characteristic length, ρ is the air density, μ is the coefficient of viscosity for air, α is the attitude of the airplane with respect to the flight path, $\rho VL/\mu$ is a dimensionless quantity called the Reynolds number (Re), a is the speed of sound in air, and V/a is a dimensionless quantity called the Mach number (Ma) [24.9].

The aerodynamic forces and moments acting on the airplane in the plane of symmetry are shown in Fig. 24.12. The resultant of the aerodynamic forces is resolved into the lift component, acting perpendicular to the flight path or velocity vector, and the drag component, acting parallel to the velocity vector. The lift and drag components are defined as acting at the airplane's center of gravity, while all of the moments acting on the airplane are lumped into one couple acting around the airplane's center of gravity. The equations for the lift and drag on the airplane may be written as

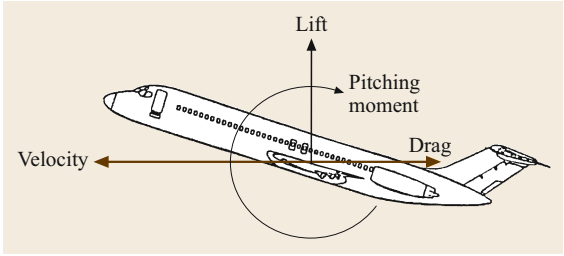

Fig. 24.12 Aerodynamic forces and moments in the plane of symmetry

$$\text{lift} = C_{\text{L}}\frac{\rho}{2}V^2 S\ ,$$

$$\text{drag} = C_{\text{D}}\frac{\rho}{2}V^2 S\ ,$$

where C_{L} and C_{D} are the lift and drag coefficients, respectively, and the area term in the equation is arbitrarily taken to be the wing area, S. To make the equation for the aerodynamic moment about the center of gravity dimensionally correct, the length of the wing mean chord, c, i.e., the mean distance from the leading edge to the trailing edge at the wing, is arbitrarily selected. The moment equation in the plane of symmetry is

$$\text{Moment} = M_{\text{cg}} = C_{\text{m}}\frac{\rho}{2}V^2 Sc\ ,$$

where C_{m} is defined as the pitching moment coefficient. As noted above, while the primary relationship between the physical quantities involved in the development of aerodynamic forces and moments is expressed in terms of the dimensionless coefficients, these coefficients are functions of both the Reynolds and Mach number. The aerodynamic forces and moments acting on the airplane in asymmetric flight are shown in Fig. 24.13. The side force acts normal to the airplane centerline, while the aerodynamic moments acting around the z-axis through the c.g. are lumped together and called the yawing moment. In addition, the aerodynamic moments acting around the x-axis are lumped together and are called the rolling moment.

The equations for the side force, yawing moment, and rolling moment are

$$\text{side force} = C_{\gamma}\frac{\rho}{2}V^2 S\ ,$$

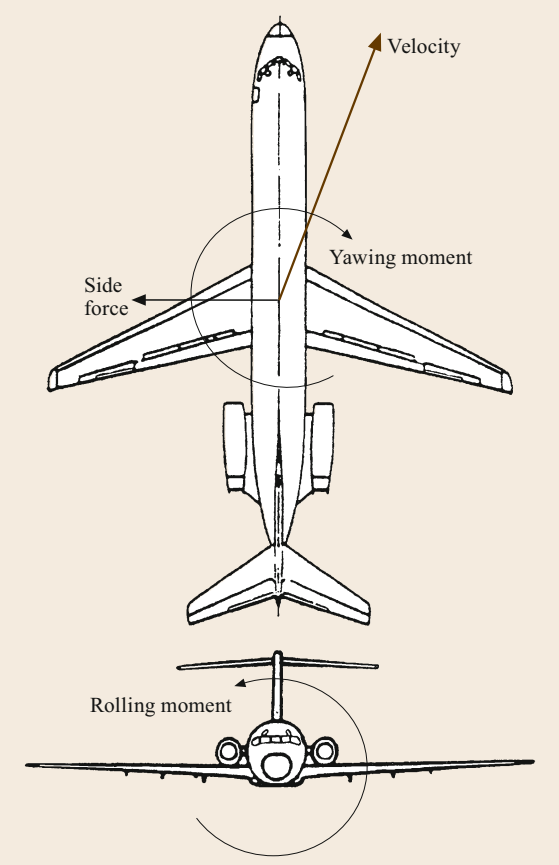

Fig. 24.13 Aerodynamic forces and moments in asymmetric flight

$$\text{yawing moment} = C_\text{n}\frac{\rho}{2}V^2Sb\,,$$

$$\text{rolling moment} = C_\text{l}\frac{\rho}{2}V^2Sb\,,$$

where C_γ, C_n, and C_l are the side force, yawing moment, and rolling moment coefficient, respectively, and b is the airplane wing span, selected as more appropriate than the wing mean chord for use with the asymmetric moment coefficients.

In summary, then, there are three defined aerodynamic forces acting along the airplane axes, and three aerodynamic moments acting around the airplane axes (Table 24.5).

24.5.5 Relative Wind

Up to now, the aerodynamic forces acting on the airplane have been defined in terms of the airplane velocity vector. It should be noted that the aerodynamic forces and moments depend only on the relative velocity between the airplane and the air that it is flying through. The same aerodynamic forces are generated if the airplane moves through the air with a velocity, V, or if the airplane is held fixed in space, as in a wind tunnel, and the air moves past the airplane, coming from the direction of the relative wind, opposite to the flight path, with a velocity, V, equal and opposite to the actual velocity, as shown in Fig. 24.14.

Table 24.5 Aerodynamic forces acting along and moments acting around the airplane axes

Axis	Force along	Moment around
x	Drag	Rolling moment
y	Side force	Pitching moment
z	Lift	Yawing moment

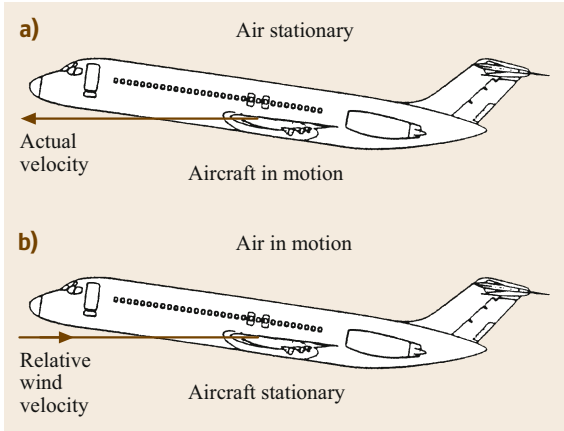

Fig. 24.14a,b **(a)** Actual velocity and **(b)** relative wind velocity

24.5.6 Dynamic Pressure

In the discussion on aerodynamic forces and moments, the expressions for all of them show a dependence on the quantity $(\rho V^2)/2$. This quantity, which appears throughout aerodynamic theory, is equal to the kinetic energy of a unit volume of air, and is defined as the dynamic pressure

$$q = \frac{\rho}{2}V^2\,.$$

Another form of the equation for dynamic pressure which is especially useful in aircraft design and performance calculations is

$$q = \frac{\gamma}{2}p\text{Ma}^2,$$

where γ is the ratio of specific heats for air, equal to 1.4, p is the ambient pressure, and Ma is the flight Mach number.

24.5.7 Airspeed Terminology

Since the very early days, airplanes have been equipped with airspeed indicators, which operate based on the difference between two pressures sensed by devices mounted on the airplane. One pressure used in airspeed measurement is the impact or total pressure, usually sensed by a Pitot or total head tube (Fig. 24.15a), which has an open hole at the front end to capture the total pressure. The other pressure used is the static pressure, that is, the ambient pressure at the operating altitude of the airplane, usually sensed by small flush holes located on a static tube (Fig. 24.15b). On many airplanes, the Pitot tube and the static tube are integrated into one device called the Pitot–static tube (Fig. 24.15c). On larger aircraft, the static pressure is sensed by flush holes in the fuselage called static ports (Fig. 24.15d), which are located in an area where the static pressure is equal to the ambient static pressure. Airspeed indicators are calibrated to read the airspeed as a function of the difference between the total and static pressure. To develop some meaningful definitions of airspeed over a range of aircraft operational altitudes, some specific terminology has been adopted as follows.

Indicated Airspeed (IAS)

This is the airspeed registered on the cockpit instrument, corrected for any instrument calibration errors.

Calibrated Airspeed (CAS)

This is the indicated airspeed reading corrected for static source position errors. Usually it is not possible to locate a Pitot–static tube or a static port in a place that senses the exact ambient static pressure, so corrections for this so-called position error are made. Calibrated airspeed refers to the fact that airspeed indicators are calibrated in airspeed units, usually knots, through the difference between total and static pressure at sea-level standard day conditions by [24.10]

$$V_{\text{cal}} = \sqrt{\frac{2\,(P_{\text{total}} - P_{\text{static}})}{\rho_{\text{sea-level}}}}\,V_{\text{true}}\,.$$

Equivalent Airspeed (EAS)

This is the calibrated airspeed adjusted for what are termed compressibility effects. Equivalent airspeed is a very important parameter in aircraft preliminary design and performance calculations. Equivalent airspeed is defined as

$$V_{\text{EAS}} = \sqrt{\frac{\rho_{\text{ambient}}}{\rho_{\text{sea-level}}}}\,V_{\text{true}}\,.$$

The idea behind equivalent airspeed is that, for any flight condition, i.e., any combination of true airspeed and ambient density, and therefore dynamic pressure, there is an equivalent airspeed at sea-level standard day conditions that produces the same dynamic pressure. In equation form

$$q = \frac{\rho_{\text{ambient}}}{2}V_{\text{true}}^2 = \frac{\rho_{\text{sea-level}}}{2}V_{\text{EAS}}^2\,.$$

A chart showing the relationship between V_{EAS} and V_{true} for the US standard atmosphere is shown in Fig. 24.16

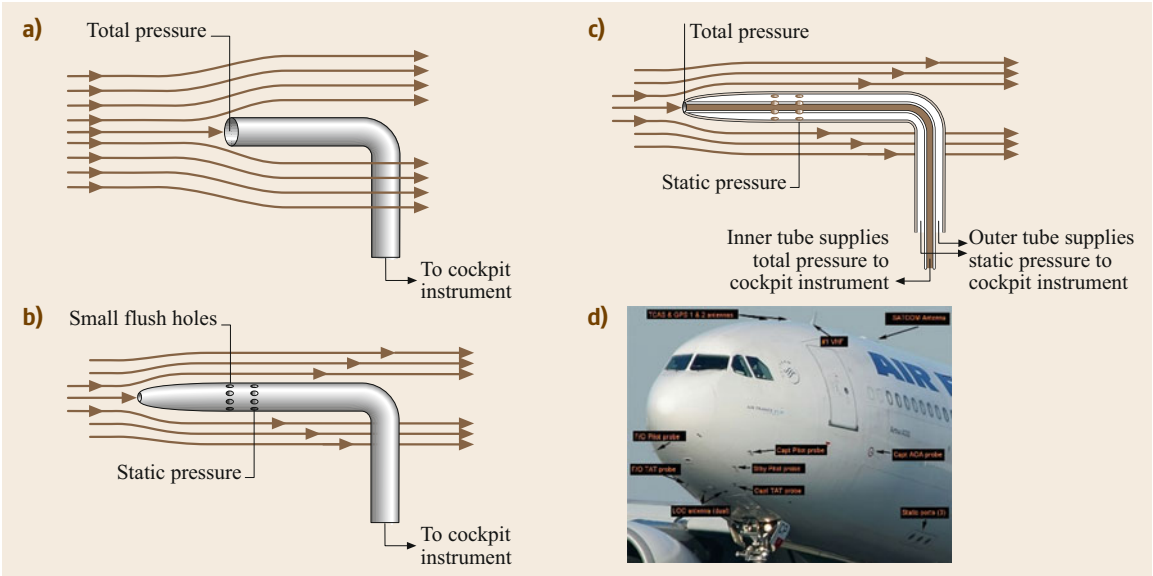

Fig. 24.15a–d Airspeed sensors. **(a)** Pitot tube, **(b)** static tube, **(c)** Pitot–static tube, **(d)** static ports

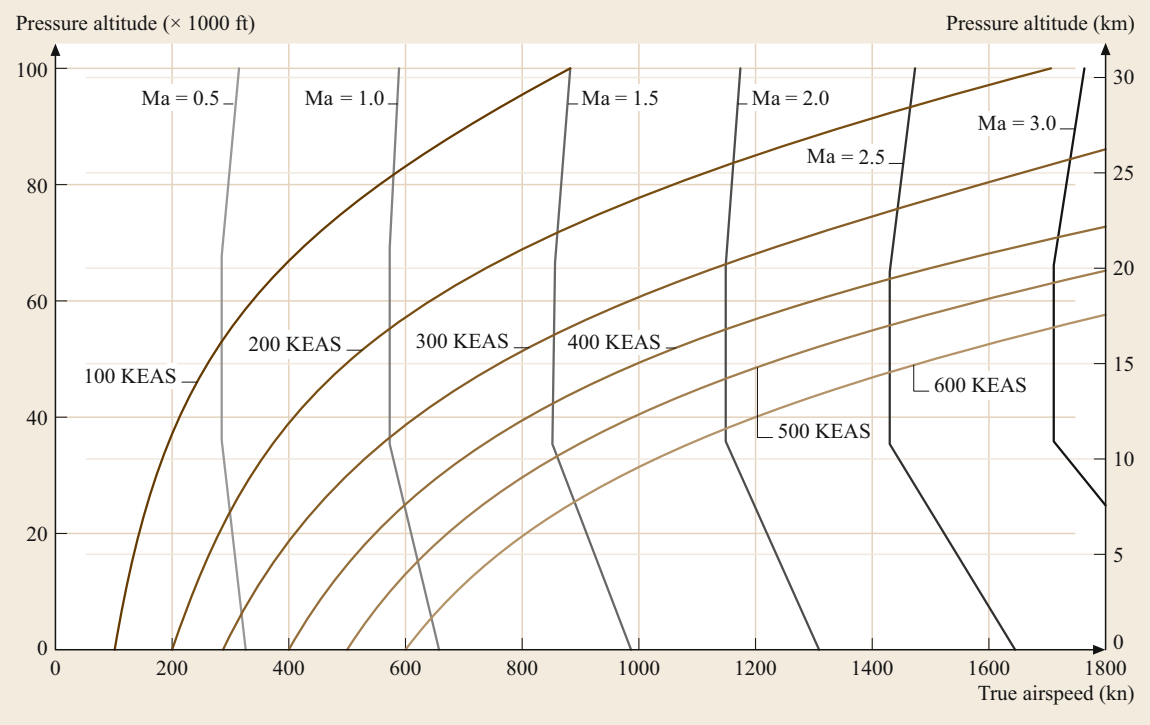

Fig. 24.16 Relationship between V_{EAS} and V_{true} for the US standard atmosphere

[24.11]. Equivalent airspeeds are reasonably close to the indicated airspeeds shown by the cockpit instrument.

The difference is the compressibility correction to the CAS in order to obtain the EAS. The compressibility increment, ΔV_C, is a function of both the Mach number and altitude, as shown in Fig. 24.17. This correction arises as follows.

For a compressible fluid such as air,

$$P_{total} - P_{static} = \frac{\gamma}{2} p \mathrm{Ma}^2 \left(1 + \frac{\mathrm{Ma}^2}{4} + \frac{\mathrm{Ma}^4}{40} + \frac{\mathrm{Ma}^6}{1600} + \dots\right).$$

Since the CAS is directly related to $(P_{total} - P_{static})$ and the EAS is directly related to the dynamic pressure q, the correction is the Mach number series in the brackets [24.12].

True Airspeed (TAS)

The true airspeed is the actual airspeed of the airplane at ambient conditions in the atmosphere, and may be obtained by converting or correcting the equivalent airspeed as follows

$$V_{true} = V_{EAS} \sqrt{\frac{\rho_{sea\text{-}level}}{\rho_{ambient}}}\,.$$

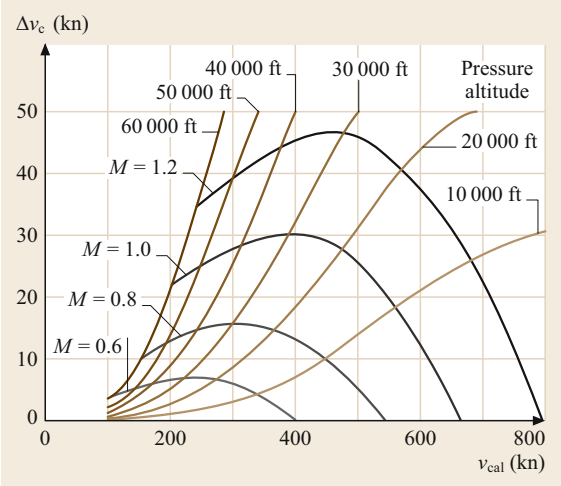

Fig. 24.17 Airspeed compressibility correction: subtract the compressibility from CAS to obtain EAS

At sealevel and at lower speeds where constant air density can be assumed, V_{true} equals CAS. At speeds above 100 kn (190 km/h), V_{true} is calculated by a flight computer or can be estimated by adding 2% to CAS for each 1000 ft (30.5 m) of altitude.

24.6 Flight Performance Equations

In order to examine the major characteristics of an airplane's performance, equations involving the summation of forces and moments in the plane of symmetry have been developed, so that Newton's laws of motion may be utilized. For unaccelerated symmetric flight along a straight path, the complete forces and moments are as shown in Fig. 24.18.

The summation of the forces and moments for static equilibrium may be written as

$$\sum F_x = T\cos\alpha - D - W\sin\gamma = 0\,,$$
$$\sum F_z = W\cos\gamma - L - T\sin\alpha = 0\,, \quad \sum M_{cg} = 0\,.$$

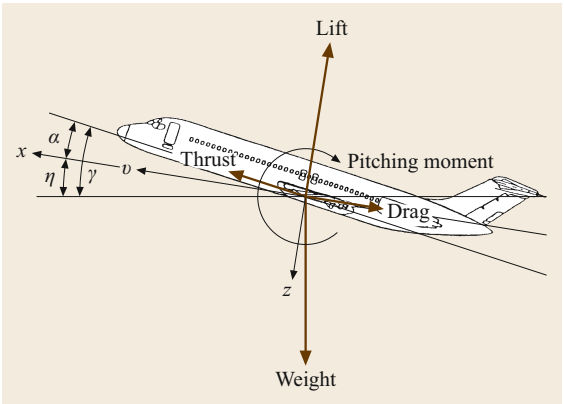

Fig. 24.18 Aerodynamic forces and moments in unaccelerated straight flight

If the assumption is made that the angle of attack is always a relatively small angle, then $\cos\alpha = 1$ and $\sin\alpha = 0$. With this assumption, the force equations reduce to

$$T - D = W\sin\gamma\,,$$
$$L = W\cos\gamma\,. \tag{24.1}$$

With the small-angle assumption of $\sin\gamma = \gamma$, (24.1) may be transformed into an expression for the gradient of climb, that is the gain in altitude over a given distance covered in the horizontal direction.

The climb gradient is $\gamma = (T-D)/W$ and the climb velocity, or rate of climb, is

$$\frac{R}{C} = \frac{(T-D)}{W}V\,. \tag{24.2}$$

If this is expressed in terms of the lift coefficient, then

$$C_L = \frac{W}{Sq}\cos\gamma\,,$$

or with the small-angle assumption ($\cos\gamma = 1$)

$$C_L = \frac{W}{Sq}\,.$$

24.7 Airplane Aerodynamic Characteristics

The concepts associated with the aerodynamic forces and moments acting on an airplane give rise to some of its important aerodynamic characteristics.

24.7.1 Airplane Lift Curve

In the discussion of aerodynamic forces and moments, it was noted that the lift coefficient is primarily a function of the angle of attack α. The variation of the lift coefficient with the angle of attack is a very important aerodynamic characteristic of an airplane, and is described in a plot such as that shown in Fig. 24.19, called the airplane lift curve.

It was also noted that the airplane lift coefficient is also dependent on the Mach and Reynolds numbers, which are discussed below, but for now, we focus on the lift curve for a specific Mach number and Reynolds number corresponding to full-scale airplane operation.

As seen from Fig. 24.19, the lift curve has a zero value at some, usually negative, angle of attack, a linear region with a well-defined slope $dC_L/d\alpha$, and a departure from the linear slope as the maximum lift coefficient $C_{L_{max}}$ is approached. The characteristics of the lift curve, namely the zero-lift angle, the slope $dC_L/d\alpha$, and $C_{L_{max}}$, depend on certain geometric characteristics of the airplane and its components, as shown below. The airplane lift curve has a special relationship to its operation in steady, unaccelerated flight. As we have seen for these steady conditions, the variation of the lift coefficient required to balance the weight at various steady flight speeds is as shown in Fig. 24.20. The lowest steady flight speed is called the stalling speed V_{stall} and corresponds to the operation of the airplane at its maximum lift coefficient $C_{L_{max}}$. At high flight speeds, and hence dynamic pressures, the lift coefficient required to balance the weight reduces as $1/q$ or $1/V^2$. Therefore,

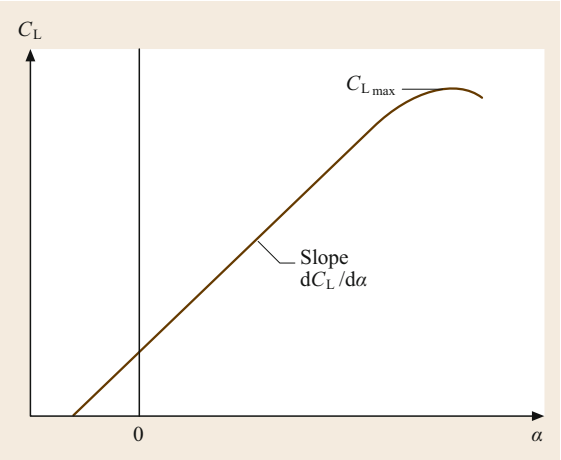

Fig. 24.19 Airplane lift curve

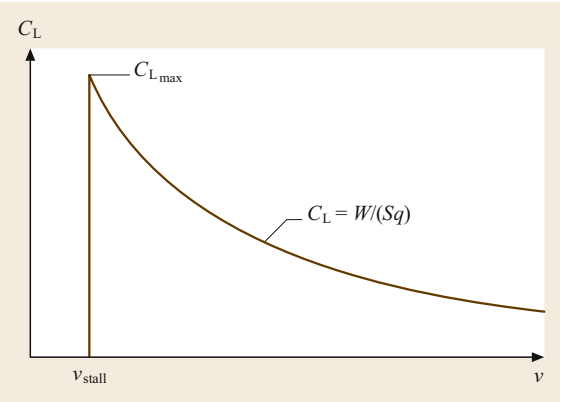

Fig. 24.20 Variation of C_L with airspeed in unaccelerated level flight

the airplane's speed along shallow, unaccelerated flight paths is primarily a function of the lift coefficient, or angle of attack. In order to control the airplane's speed, the pilot must be able to control the equilibrium lift coefficient or angle of attack.

Going back to (24.2), it can be seen that whether the airplane climbs or descends at a given speed depends on the difference between the thrust and drag at that speed. If the thrust just equals the drag ($T = D$), then the rate of climb will be zero and the airplane will be in level flight. Since the thrust is basically a function of the cockpit throttle setting, under steady unaccelerated flight conditions, the airplane speed is determined by the value of the equilibrium lift coefficient, and the rate of climb or descent is regulated primarily through the throttle [24.13]. For very large angles of climb or descent, this simple picture does not correspond to actuality, but for the performance methods presented in this chapter, it is a valid concept.

24.7.2 Airplane Drag Curve

Another aerodynamic characteristic of the airplane which is important for its range and climb performance is the drag curve or drag polar, viz. a plot of the drag coefficient versus the lift coefficient. As noted above, the drag varies with the angle of attack α, but since in the normal operating range of angle of attack C_L varies linearly with α, it has been found to be more convenient to describe the drag coefficient as a function of the lift coefficient instead of the angle of attack. The airplane drag curve, shown schematically in Fig. 24.21, has a value of C_D at zero C_L, called the zero-lift or parasite drag coefficient, C_{D_p}. At higher C_L, the drag coefficient exhibits a parabolic variation with C_L, due to the induced drag or drag due to the lift coefficient, C_{D_i}, which varies as the square of the lift coefficient. As is the case with the lift curve, the drag curve varies in shape with both the Mach number and Reynolds number, but for now we focus on the drag curve that is typical for full-scale airplane operation at one particular Mach number and Reynolds number.

A summary of the physical makeup of airplane drag is presented in Table 24.6.

An important parameter in the cruise performance of an airplane, as well as certain aspects of its climb performance, is the lift-to-drag ratio L/D. This ratio can be visualized from the drag polar as shown in Fig. 24.22. At any point on the drag curve, L/D is defined by the ratio C_L/C_D at that point, and also by the slope of a line from the origin to the point in question.

If the L/D values are determined at various points along the airplane drag curve, a plot of the airplane L/D ratio versus the lift coefficient C_L can be constructed. The L/D value is zero at $C_L = 0$, reaches a maximum value of $(L/D)_{max}$ at some C_L, then decreases at higher

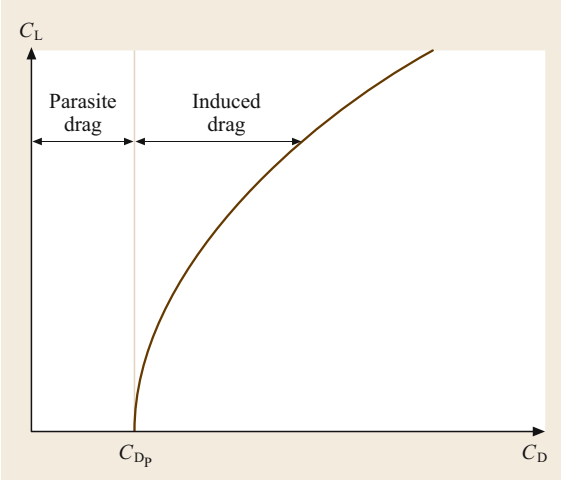

Fig. 24.21 Airplane drag curve

Table 24.6 Physical definition of airplane drag elements

Cruise speed of Ma = 0.5 or less	
Zero-lift drag	Skin friction plus pressure drag
Drag due to lift	Subsonic induced drag
Cruise speed between Ma = 0.5 and Ma = 1.0	
Zero-lift drag	Skin friction plus pressure drag
Drag due to lift	Subsonic induced drag
Compressibility drag	Drag from local shock waves
Cruise speed greater than Ma = 1.0	
Zero-lift drag	Skin friction plus pressure drag Supersonic wave drag
Drag due to lift	Supersonic wave drag due to lift Subsonic induced drag

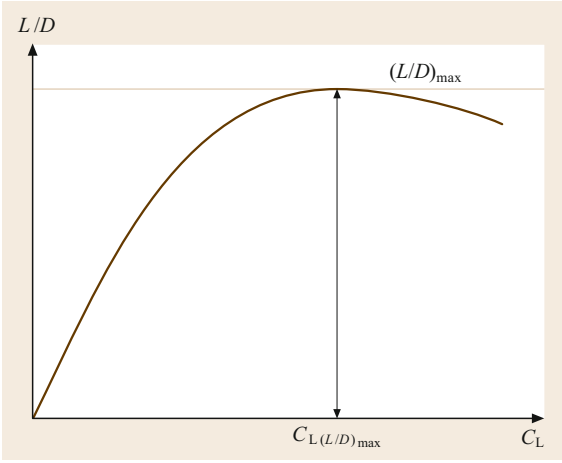

Fig. 24.22 Airplane L/D curve

C_L values. Both the value of $(L/D)_{max}$ as well as the C_L value at which it occurs, i.e., $C_{L(L/D)_{max}}$, are important aerodynamic characteristics of the airplane [24.11].

24.7.3 Mach Number Effects on Lift and Drag Curves

As noted in the section on flight speed terminology, the characteristics of the airflow around the airplane change dramatically as the flight Mach number is increased due to the compressible nature of air. These changes in the airflow have a significant effect on the airplane lift and drag curves in the various Mach number ranges. For airplanes that operate entirely within the subsonic speed range, there are no significant effects of the compressibility of air on the airplane lift and drag curves, and a single lift curve as shown in Fig. 24.19 and a single drag curve as shown in Fig. 24.21 describe the lift and drag characteristics of the airplane. For airplanes that operate at high subsonic speeds, i.e., in the transonic speed region, the airplane lift and drag curves will vary as the flight Mach number is increased due to the compressible nature of air, so there is a family of lift curves

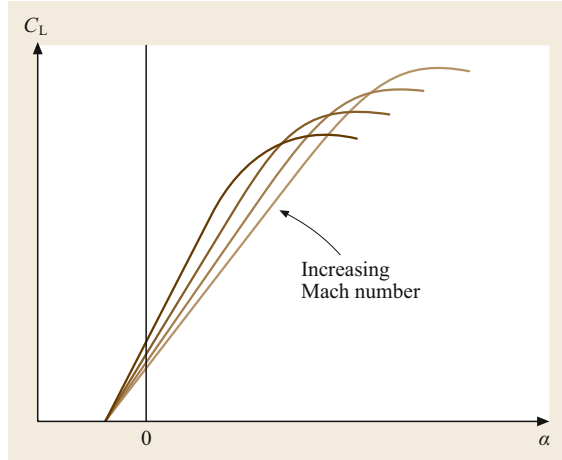

Fig. 24.23 Airplane lift curves at high subsonic Mach numbers

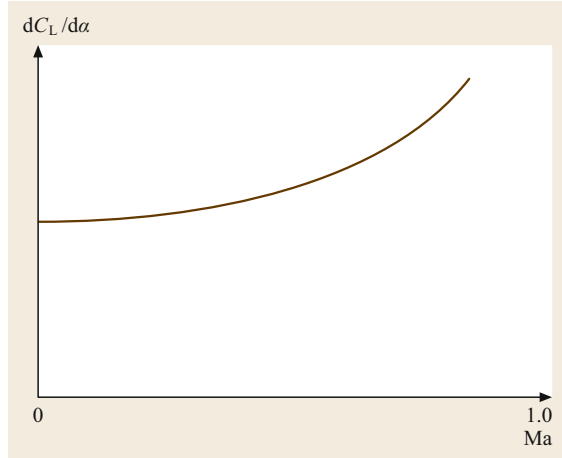

Fig. 24.24 Mach number effect on lift curve slope at high subsonic speeds

and a family of drag curves, one for each flight Mach number of interest. The family of lift curves is characterized by an increase in the slope of the lift curve $dC_L/d\alpha$ and a decrease in the maximum lift coefficient $C_{L_{max}}$ as the Mach number is increased in the high subsonic region, as shown schematically in Fig. 24.23.

The Mach number effects can be shown more specifically by plotting the significant parameters as a function of the Mach number; For example, the effect of the Mach number in increasing the lift curve slope is shown in Fig. 24.24, while the effect of the Mach number in decreasing the maximum lift coefficient $C_{L_{max}}$ is shown in Fig. 24.25.

The family of drag curves are characterized by increases in the parasite drag coefficient, C_{D_p}, and significant increases in the drag coefficient at higher C_L values as the Mach number is increased, as shown in Fig. 24.26.

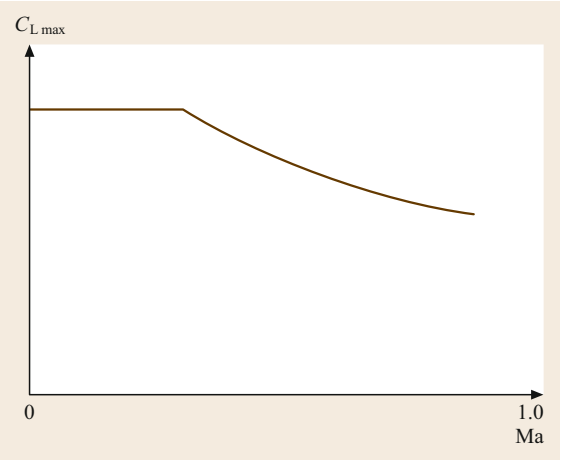

Fig. 24.25 Mach number effect on maximum lift coefficient at high subsonic speeds

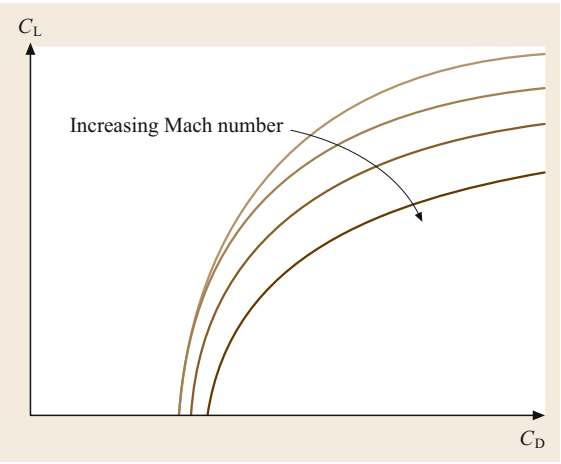

Fig. 24.26 Airplane drag curves at high subsonic speeds

For the drag curves, the Mach number effects are usually shown in the form of C_D versus the Mach number for various values of the lift coefficient, as shown in Fig. 24.27.

An explanation for these Mach number effects on the lift and drag curves has been derived from the theory of compressible flow [24.12], and confirmed by experimental data obtained in wind tunnels and from flight tests. It can be shown that, for an airplane at a given angle of attack, the lift coefficient will increase as the Mach number increases, because the suction on the wing upper surface and the pressure on the wing lower surface tend to grow with the Mach number, roughly by a factor of $1/\sqrt{1-\mathrm{Ma}^2}$ in the high subsonic speed range, which results in the increase in the lift curve slope as shown in Figs. 24.23 and 24.24. Also, as the Mach number increases, at some flight Mach number, the local velocities on the wing near the leading edge, at high angles of attack near the maximum lift coefficient, become supersonic, which leads to local shock waves and separation, limiting the attainable maximum lift coefficient as shown in Fig. 24.25. In the drag curves, the Mach number effects are due to the development of local supersonic flow around the wing, which eventually produces normal shock waves, and finally separated flow. Because of the energy loss in the shock wave, and the added pressure drag due to the separated flow, there are significant increases in the drag coefficient at a given lift coefficient as the flight Mach number is increased, as shown in Fig. 24.27. The development of these conditions for a wing airfoil section typical of those used on many current jet transports and business jets is shown in Fig. 24.28. There are some important concepts and definitions associated with the sketches in Fig. 24.28. At the condition shown in Fig. 24.28b, the condition of the lift coefficient and the flight Mach number where the maximum local velocity on the wing surface is equal to the sonic velocity is called the critical Mach number Ma_C. At a higher Mach number, in the conditions shown in Fig. 24.28c, with a local region of supersonic flow terminated by a normal shock wave, and the very beginning of flow separation behind the normal shock, the drag begins to rise abruptly. This condition is called the drag divergence Mach number Ma_{DIV}, for that particular lift coefficient. At higher flight Mach numbers (Fig. 24.28d,e), the supersonic zones are larger, the normal shocks are stronger, and the drag continues to rise very strongly. Although the wing is the primary source of local supersonic flow, shock waves, and the associated drag increase, all parts of the airplane, i.e., the fuselage, tail surfaces, and engine nacelles, will eventually experience these conditions as the flight Mach number approaches 1.0.

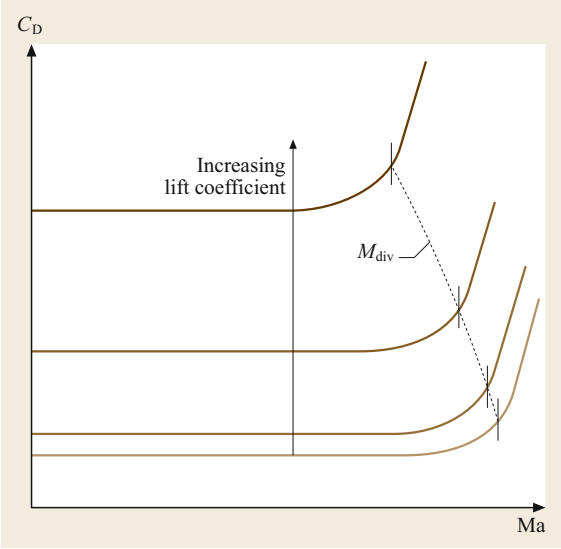

Fig. 24.27 Mach number effect on drag curves at high subsonic speeds

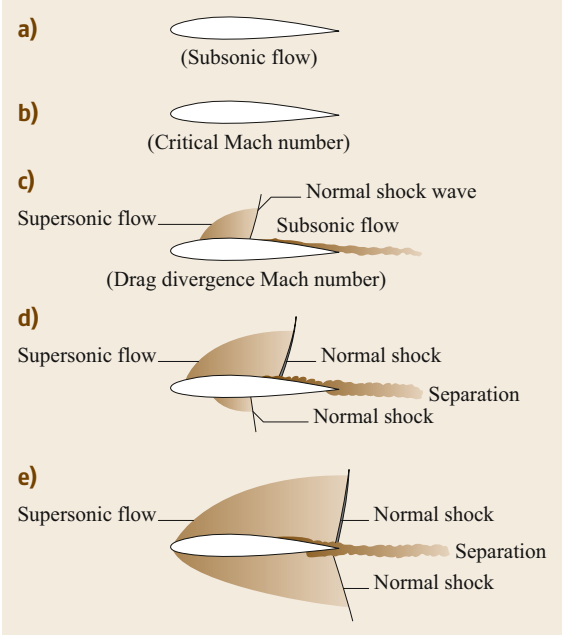

Fig. 24.28a–e Development of flow conditions around a wing airfoil section at high subsonic speeds. **(a)** Maximum local velocity is less than sonic; **(b)** maximum local velocity is equal to sonic; **(c)** supersonic velocities upper surface; **(d)** supersonic velocities upper and lower surfaces; **(e)** all velocities are supersonic

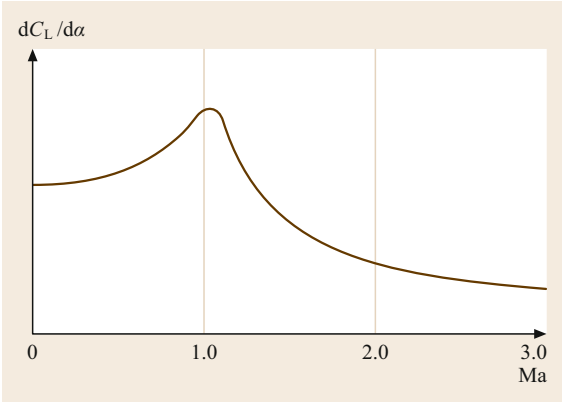

Fig. 24.29 Mach number effects on lift curve slope at subsonic and supersonic speeds

For airplanes that are designed to operate at supersonic speeds, the lift and drag curves also vary with the flight Mach number. The slopes of the curves are similar to those of subsonic speed designs, but the significant parameters show a different trend at supersonic speeds. The pressure on the wing upper and lower surfaces tend to reduce as the Mach number is increased supersonically, roughly by a factor of $1/\sqrt{\mathrm{Ma}^2-1}$, so that the lift curve slope, which increases at high subsonic speeds, decreases beyond Mach 1.0, as shown in Fig. 24.29. The maximum lift capability supersonically is described in terms of the maximum usable lift coefficient, which results from detached shock waves and unsteady flow at high angles of attack [24.14]. The drag curves at supersonic speeds are basically parabolic in shape, but with very high values of parasite drag coefficient because of the added element of supersonic wave drag, as shown in Fig. 24.30, and very high drag levels at operating lift coefficients due to the wave drag element that increases with the lift coefficient. The presence of wave drag at supersonic speeds has a significant impact on the maximum lift-to-drag ratio $(L/D)_{\max}$ referred to in Fig. 24.22. Because of this added drag element, the $(L/D)_{\max}$ values at supersonic speeds are usually less than half of the values at subsonic speeds, for any specific configuration.

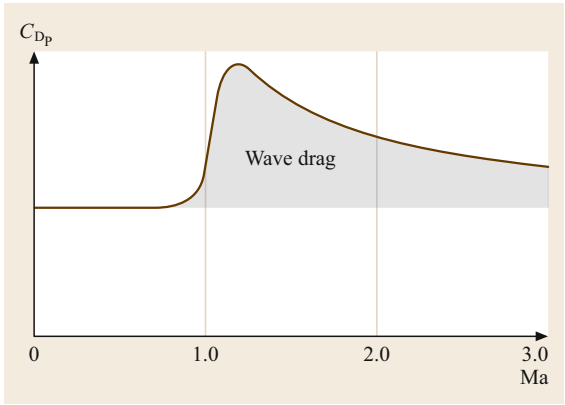

Fig. 24.30 Mach number effects on parasite drag coefficient

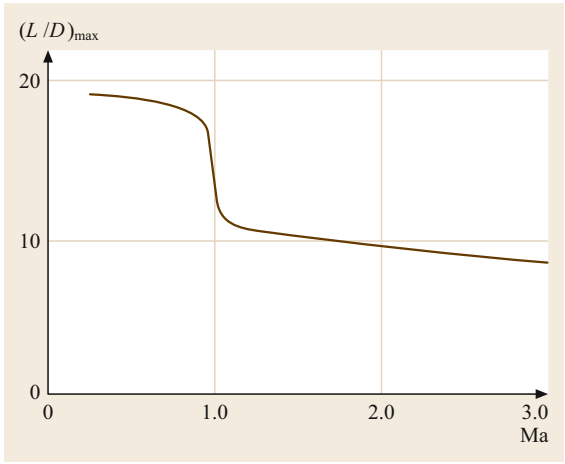

Fig. 24.31 Mach number effects on maximum lift-to-drag ratio

For jet transports, the $(L/D)_{\max}$ values subsonically are just under 20, while the best supersonic transport values are less than 10, as shown in Fig. 24.31.

24.8 Airplane General Configurations

Airplanes are often described by their general configuration. Figure 24.32 shows various aircraft types classified by the number of wings, their location on the fuselage, and the number of engines [24.15].

24.8.1 Aircraft Component Nomenclature

The various components of an airplane have unique names. Figure 24.33 indicates the names of the various components of a modern commercial transport aircraft.

Some specific geometric characteristics are defined in Table 24.7 and shown schematically in Fig. 24.34.

24.8.2 Wing Geometric Characteristics

The wing geometric characteristics include the wing area, aspect ratio, taper ratio, airfoil sections, thickness distribution, sweepback angle, aerodynamic twist, and dihedral angle. Other important elements that are incorporated into the geometric definition of the wing are high-lift system devices and lateral control system components.

Wing Area

The wing area is usually taken to be the total planform area of the wing from the fuselage centerline to the wing tip, including the area encompassed by the fuselage, as shown in Fig. 24.34.

Aspect Ratio

The wing aspect ratio (AR) is defined as the square of the wing span b divided by the wing area S

$$\mathrm{AR} = \frac{b^2}{S} \,.$$

Aspect ratio selection is basically a compromise between aerodynamic efficiency, in the form of high cruise L/D, and wing structural weight associated with the bending moments due to air loads for a given wing area.

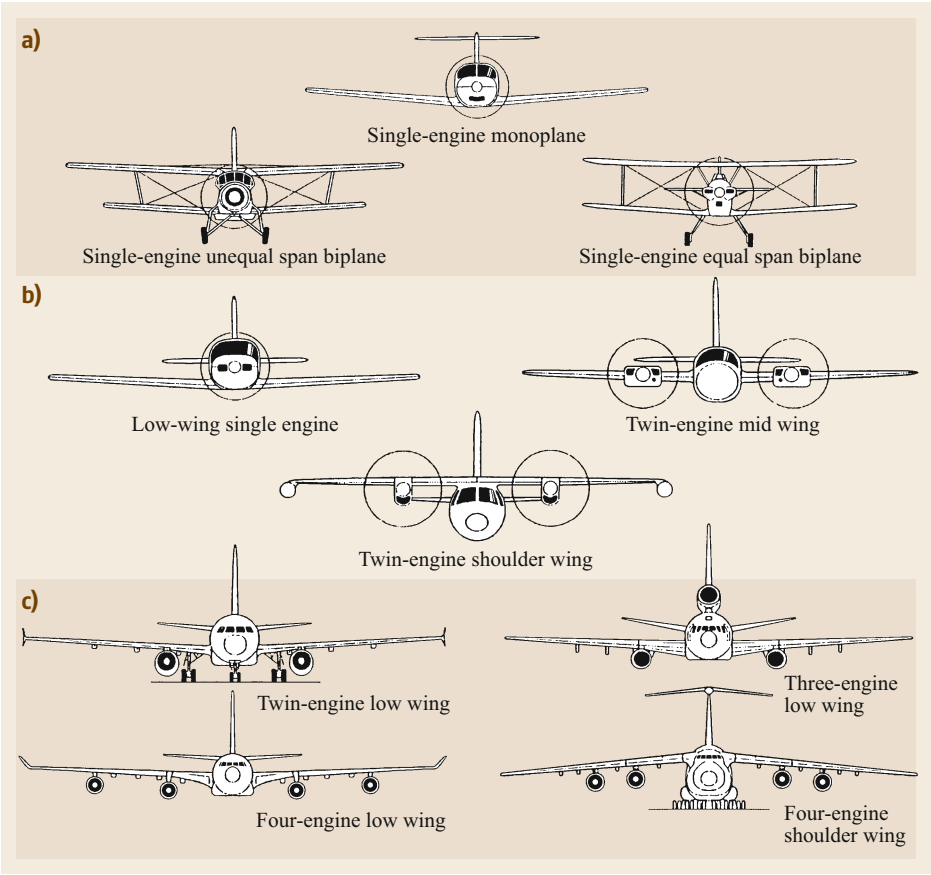

Fig. 24.32a–c Aircraft general configurations classified by the **(a)** number of wings, **(b)** their placement, and **(c)** the number and placement of engines

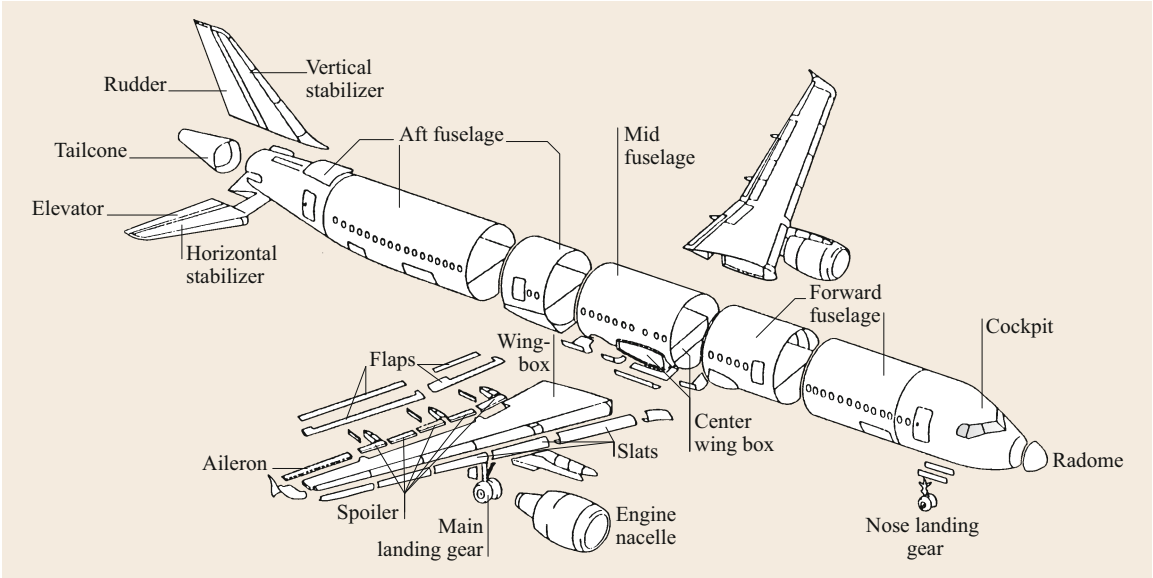

Fig. 24.33 Airplane component nomenclature

Table 24.7 Airplane geometric definitions

b	Wing span
$b/2$	Wing semispan
S	Wing area
b_H	Horizontal tail span
S_H	Horizontal tail area
l_H	Horizontal tail length
S_V	Vertical tail area
l_V	Vertical tail length
c	Wing mean aerodynamic chord
c_H	Horizontal tail mean aerodynamic chord
c_V	Vertical tail mean aerodynamic chord
l_{oa}	Overall length
l_{fus}	Fuselage length
h	Height
V_H	Horizontal tail volume
V_V	Vertical tail volume

Taper Ratio

The taper ratio λ is defined as the ratio of the chord at the tip of the wing to the chord at the airplane centerline, called the root chord

$$\lambda = \frac{c_t}{c_r} .$$

The taper ratio is also a compromise between aerodynamic considerations, primarily the span load distribution, which is important for cruise efficiency, stall characteristics, and bending moments due to air loads and structural considerations primarily associated with the bending moments.

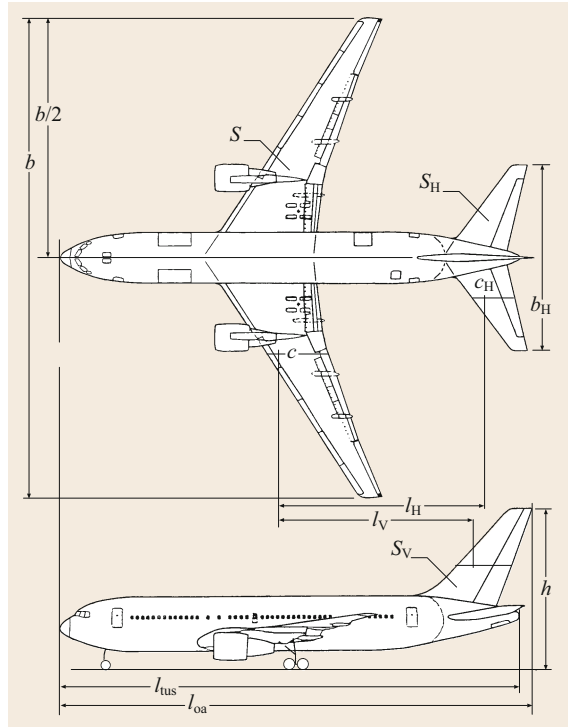

Fig. 24.34 Airplane geometric characteristics

Airfoil Sections

The wing airfoil sections are the cross-sectional shapes of the wing in planes parallel to the airplane centerline and normal to the wing reference plan. The wing airfoil sections provide the wing lift by creating suction

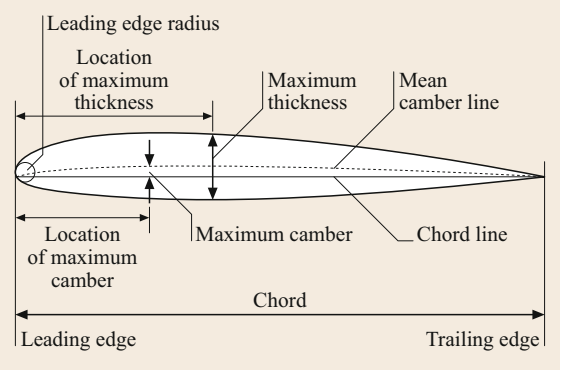

Fig. 24.35 Airfoil section geometric parameters

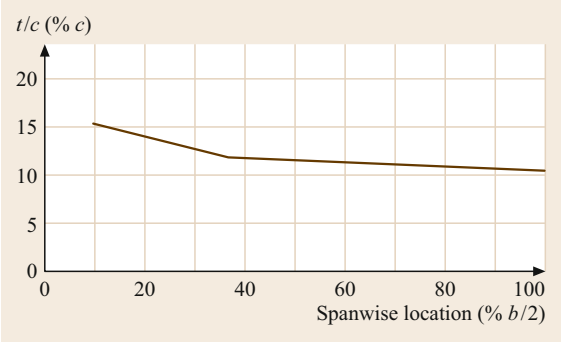

Fig. 24.37 Typical wing thickness distribution for a jet transport

on the wing upper surface and pressure on the lower surface. The wing airfoil geometry determines the detailed pressure distribution on the wing upper and lower surfaces, which in turn may have a significant influence on some of the important aerodynamic characteristics of the wing. Airfoil geometric parameters are defined in Fig. 24.35 [24.16].

Mean Aerodynamic Chord

An important wing geometric parameter is the mean aerodynamic chord (m.a.c.). The m.a.c. is the chord of an imaginary wing with a constant chord which would have the same aerodynamic characteristics as the actual wing. The m.a.c. can be defined graphically as shown in Fig. 24.36.

The wing span b is $b = \sqrt{\mathrm{AR}S}$, where AR is the wing aspect ratio and S is the reference wing area.

The root chord length is $C_{\mathrm{root}} = 2S/[b(1+\lambda)]$, where λ is the wing taper ratio.

The tip chord length is $C_{\mathrm{tip}} = \lambda C_{\mathrm{root}}$.

For trapezoidal planforms, the wing m.a.c. length is

$$\overline{C} = \left(\frac{2}{3}\right) C_{\mathrm{root}} \frac{1+\lambda+\lambda^2}{1+\lambda} .$$

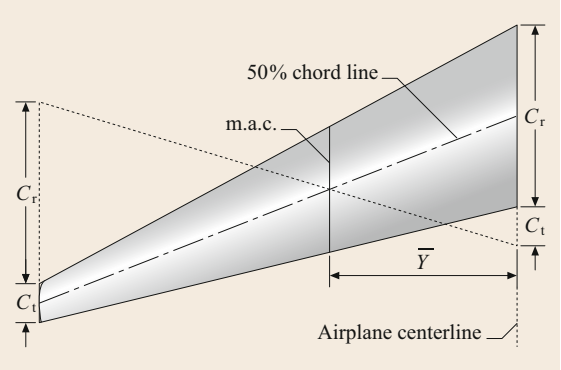

Fig. 24.36 Wing m.a.c. determination

The distance from the centerline to the m.a.c. location is

$$\overline{Y} = \left(\frac{b}{6}\right) \frac{1+2\lambda}{1+\lambda} .$$

Thickness Distribution

Another wing geometric characteristic is the variation of the airfoil thickness ratio across the span of each wing panel. Of course the simplest wing geometry, still found on many small personal/utility airplanes, is a constant-chord constant-thickness-ratio configuration. More sophisticated personal/utility aircraft, as well as commuters, regional turboprops, business jets, and jet transports, have wing designs in which the airfoil section thickness ratio (t/c) varies across the span, primarily to obtain greater depth for the airfoil sections at the wing root. This greater depth provides for a more efficient structural beam to resist the bending moments due to wing air loads. For straight-wing propeller-driven aircraft, the wing is usually defined by two airfoil sections, one at the wing root, and one at the wing tip, connected by straight-line elements through the constant-percentage chord points.

For business jets and jet transports which cruise at high subsonic speed, the wing is usually defined by three or more airfoil sections, one at the side of the fuselage, one at the tip, and one or more at intermediate spanwise locations. The purpose of the additional defining airfoils is to produce wing upper-surface pressure distributions that maintain as far as possible uniformly swept lines of constant pressure (isobars) at cruise conditions, so that the entire wing reaches its $\mathrm{Ma_{DIV}}$ at the same point. A typical wing thickness distribution for a commercial jet transport is shown in Fig. 24.37.

Sweepback Angle

Two very important wing geometric parameters, especially for airplanes that cruise at high subsonic speeds,

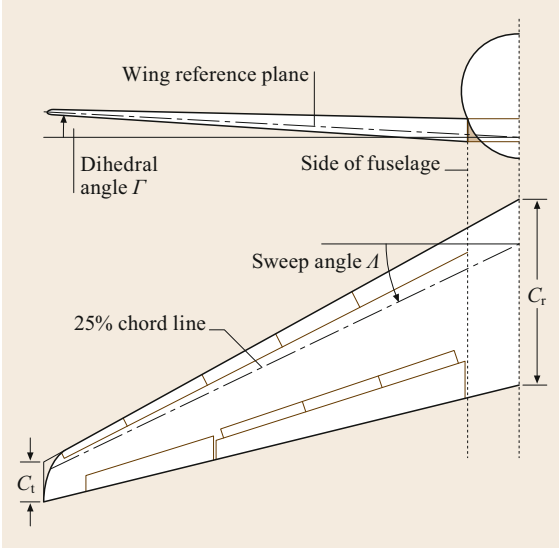

Fig. 24.38 Wing planform parameters

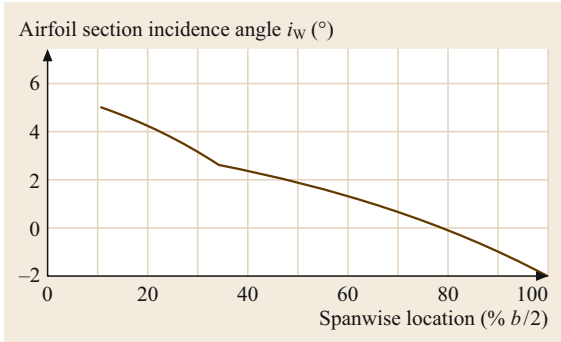

Fig. 24.39 Typical wing twist distribution for a jet transport

are the wing sweepback angle and the average thickness. The wing sweepback or sweep angle is defined in the plan view as the angle between a line perpendicular to the airplane centerline and the constant 25% chord line of the wing airfoil sections, as shown in Fig. 24.38. Nearly all high-subsonic-speed aircraft have wings with some amount of sweep, because sweep increases the wing drag divergence Mach number Ma_{DIV} for a given streamwise airfoil thickness.

Geometric Twist

Nearly all wing designs incorporate some degree of geometric twist, that is, a change in the orientation of the airfoil section chord lines from root to tip, with the tip airfoils having less of an angle of incidence than the root, as shown in Fig. 24.39. This geometric twist is used to avoid initial stalling at the wing tip as the airplane $C_{L_{max}}$ is reached. Typical values of wing twist vary from 3° for personal/utility, commuters, and regional turboprops to as much as 7° for business jets and jet transports. Supersonic military fighter/attack aircraft usually have little or no twist, depending on other means to provide satisfactory stall characteristics.

Dihedral Angle

The dihedral angle is defined in the front view of the airplane as the angle between the horizontal and a line midway between the upper and lower surfaces of the wing, as shown in Fig. 24.38. The dihedral angle primarily affects the lateral stability characteristics of the airplane. If the wing tips are higher than the wing root, the wing is said to have positive dihedral, which produces effective lateral stability. For low-wing airplanes with low horizontal tails, nearly all of the lateral stability comes from the wing dihedral angle, which is usually set around 5° for these types. For low-wing airplanes with high-mounted horizontal tails (tee tails), a significant amount of lateral stability is generated by the intersection between the horizontal and vertical tail sections, so that the wing dihedral angle for these types is usually reduced to around 2°. For high-wing airplanes, especially those with tee-tail arrangements, there is sufficient lateral stability generated by the wing–fuselage intersection and the horizontal tail–vertical tail intersection that the wing dihedral angle can be set at negative angles ranging from −2° to −5° [24.17].

Spar Locations

The front and rear spars, along with the upper and lower wing skins, are the major elements of the wing structural *box*, which resists the applied wing loads in bending and torsion. The distance between the wing spars is important structurally, but also has a significant impact on the space available for high-lift and lateral control devices, and on the volume available for internal wing fuel tankage. Typical locations for the front spar are 16–22% of local chord, while typical rear spar locations range from 60% to 75% of the local chord.

High-Lift Systems

Nearly all modern aircraft incorporate devices that fit within the wing to increase the maximum lift coefficient in the take-off and landing configuration. These devices are collectively called the high-lift system. High-lift devices fall into two categories: trailing-edge devices located at the rear portion of the wing, and leading-edge devices located at the forward portion of the wing. Trailing-edge devices include single-,

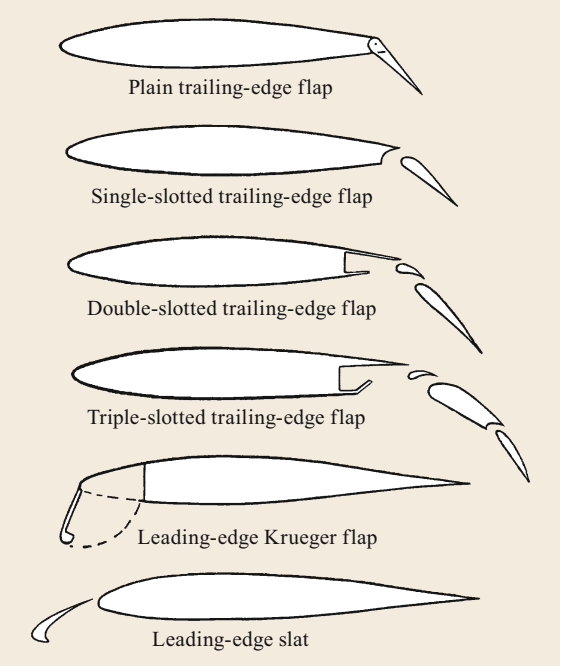

Fig. 24.40 Typical high-lift devices

double-, and triple-slotted flaps, as shown in Fig. 24.40. Single-slotted flaps are standard for personal/utility airplanes. Single-slotted flap chords are usually in the range of 25–30% of chord, and have a maximum deflection of 35°. For commuters, regional turboprops, business jets, and jet transports, more powerful double-slotted trailing-edge flaps are usually employed. Double-slotted flap chords are in the range of 30–35% chord with maximum deflections of 45°–50° [24.18, 19]. Some jet transports with design mission specifications that call for extremely low landing approach speeds and short landing distances have utilized triple-slotted trailing-edge flaps to achieve very high $C_{L_{max}}$ values in the landing configuration. Flap chords up to 40% may be used in triple-slotted flap designs, with maximum deflections of the aft flap segment of up to 55°. The effectiveness of trailing-edge flaps can be enhanced by selecting a large percentage of chord dimension for the flap, and utilizing as much flap span as possible, considering the need for lateral control ailerons on the outboard wing trailing edge.

Significant increases in $C_{L_{max}}$ can also be achieved through the application of leading-edge high-lift devices. The simplest leading-edge device is the plain leading-edge flap, used on a number of military fighter/attack aircraft. Some jet transports have used leading-edge Krueger flaps. A more effective, but more complicated, leading-edge device is the slat, which is used on all modern jet transports. The maximum effectiveness of leading-edge flaps and slats is usually achieved with flap and slat chords of 12–15%, and deflections ranging from 20° for slats to 30° for plain leading-edge flaps to 60° for Krueger flaps. Leading-edge flaps and slats must extend for the full span of the wing to be effective in increasing $C_{L_{max}}$. Typical high-lift devices are shown in Fig. 24.40.

Lateral Control Devices

An additional consideration during preliminary wing design is the provision of lateral control devices which produce rolling moments about the airplane's x-axis. The most common lateral control devices are ailerons, essentially a plain trailing-edge flap, and spoilers, basically a portion of the wing upper surface, hinged at its leading edge, which reduces the lift in the affected area of the wing when the spoiler is deflected. When deflected asymmetrically, spoilers can produce significant rolling moments, especially if they are located ahead of deflected trailing-edge flaps. Spoilers have additional uses when deflected symmetrically as drag-producing devices to allow the airplane to slow down in level flight, or to increase the rate of descent at the end of cruise. Spoilers are also used symmetrically to reduce the airplane's lift during landing ground roll, which improves braking effectiveness.

For personal/utility, commuters, and regional turboprops, the usual lateral control device is the aileron, with aileron spans ranging from 55% to 90% of the wing semispan. For business jets and jet transports, spoilers are generally used in conjunction with ailerons. Furthermore, since ailerons located on the outer part of the wing trailing edge tend to twist the wing as they are deflected to produce rolling moments at high dynamic pressure, or high-q conditions, thereby reducing there effectiveness, most jet transports utilize smaller ailerons located further inboard in addition to the outboard ailerons for high-q lateral control and trim.

Inboard Trailing-Edge Extensions

Wing inboard trailing-edge extensions are often used on business jets and jet transports with wing sweep angles greater then 30°. The need for an inboard trailing-edge extension arises from the required main landing gear leg upper pivot point location, which would be very near the wing trailing edge on a trapezoidal planform. By incorporating an inboard trailing-edge extension, a suitable structural arrangement may be designed to provide the necessary gear pivot location. This situation is shown in Fig. 24.41.

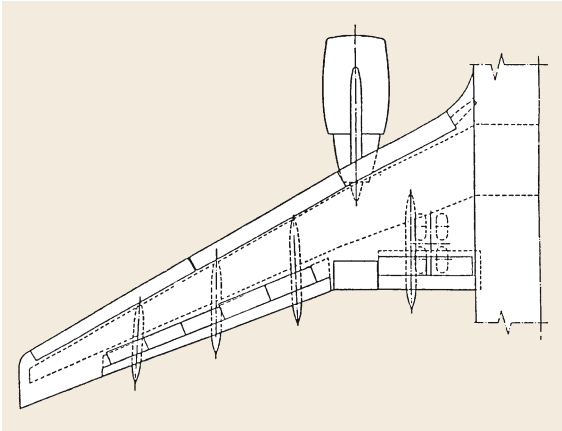

Fig. 24.41 Inboard wing trailing-edge extension

24.8.3 Fuselage Geometry

Primary requirements for the fuselage are to provide accommodation for the crew station, passengers, other payload to be carried in the fuselage, and for some designs the engine/propulsion system as well. For single-engine propeller-driven airplanes, the fuselage accommodates the engine/propeller installation forward, the pilot and passenger cabin next, followed by the aft fuselage, which serves mainly as a convenient structure for locating the horizontal and vertical tail well aft of the wing. For larger transport airplanes, the fuselage is made up of three distinct sections:

(1) the nose section
(2) a constant-section passenger compartment, and
(3) the afterbody or tail cone.

The nose section on larger airplanes usually contains the crew station, with crew seats, control yoke and wheel, or control stick, rudder pedals, instrument panel, glare shield, plus a variety of levers, knobs, and switches to operate various aircraft systems. Specific requirements for pilot field of view and downward vision from the defined pilot design eye position are contained in the Federal Air Regulations (FARs) and the military specifications (Mil Specs). The constant-section passenger compartment for larger airplanes is usually pressurized, and circular or near-circular in cross section, because of the structural weight efficiency of this shape for pressure vessels. For larger-capacity long-range jet transports, two aisles are provided for greater passenger mobility, and for ease of entry and exit from multiple adjacent seats. These larger circular cross sections provide significant space below the passenger deck to carry large amounts of revenue cargo, either in special containers or stacked on flat pallets. A typical cross section for a twin-aisle transport is shown in Fig. 24.42.

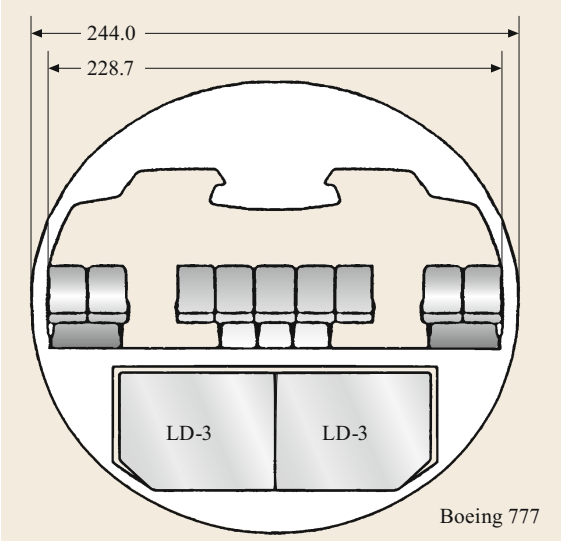

Fig. 24.42 Twin-aisle transport fuselage cross section

The length of the passenger compartment must be sufficient to accommodate the required number of passengers, allow for galley space, lavatories, coat rooms, plus passenger entrance doors, and emergency exits.

There are specific requirements in the FARs for emergency exits to be used in survivable accidents. The aft fuselage or afterbody is influenced by conflicting requirements of aerodynamic performance and structural weight. The afterbody should be long enough to avoid severe curvature and separation drag, while being as short as possible to avoid limiting the airplane pitch attitude on the ground during normal take-offs, as well as avoiding excessive weight from a long afterbody.

24.8.4 Empennage Geometry

For conventional aft-tail configurations, the horizontal and vertical tail arrangement, called the empennage, is the major element for providing both static aerodynamic stability in pitch and yaw as well as aerodynamic control moments in pitch and yaw. For unconventional configurations such as *flying wings* or forward horizontal tail *canards*, the static aerodynamic stability and control are provided by other means.

The aft horizontal tail is the major contributor to static aerodynamic stability in pitch. This is quite logical, since static longitudinal stability involves the generation of aerodynamic restoring moments which are dependent on an aerodynamic force from the horizontal tail (proportional to the horizontal tail area) and a moment arm (proportional to the distance from the

airplane center of gravity to the horizontal tail m.a.c.). The horizontal tail also provides the aerodynamic control moments to allow the pilot to achieve equilibrium in pitch at any desired lift coefficient, allowing the control of airspeed in steady unaccelerated flight, and the curvature of the flight path in accelerated flight. Longitudinal control is usually provided through the hinged, movable, aft portion of the horizontal tail called the elevator, although some designs move the entire horizontal tail about a fixed pivot point. This arrangement is called an all-movable horizontal, or a stabilator.

24.8.5 Landing Gear

Most modern airplanes use a tricycle landing gear configuration, that is, one with two main wheels aft of the c.g. and one forward [24.20]. Except for small airplanes with low cruise speed, landing gears are usually retracted for climb and cruise flight. The landing gear wheels and tires must be adequate to handle a variety of taxi, take-off, and landing loads prescribed by the FARs, as well as spreading the reaction loads from the gear sufficiently so as not to overstress the runway pavement. The landing gear also has to house the brakes.

24.8.6 Propulsion Systems

Propulsion systems for modern airplanes are of one of the following types [24.21]:

- Piston engine–propeller
- Turbine engine–propeller
- Turbojet engine
- Turbofan engine
- Turbofan engine with afterburner.

Small personal utility or acrobatic airplanes are usually powered by piston engine–propeller combinations, while larger personal utility and smaller commuter airplanes are usually powered by turboprop propulsion. Business jets and larger jet transports are powered by turbofans. High-performance military airplanes are usually powered by low-bypass turbofans equipped with afterburners. The key parameter for the propulsion system is the *specific fuel consumption* c, i.e., the amount of fuel burned per hour, per unit of output of the propulsion system [24.22].

For piston engines and turboprops, c is expressed in $\mathrm{lb}/(\mathrm{bh_p\,h})$, while for turbojets and turbofans, it is expressed in $\mathrm{lb}/(\mathrm{h\,lb_{thrust}})$.

24.9 Weights

The weight of an airplane, especially its empty weight, is a vital parameter in the performance and economics of the design. The following paragraphs provide information on the various aspects of aircraft weight.

24.9.1 Weight Definitions

Figure 24.43 shows a simple bar chart illustrating the elements of the weight buildup to the maximum take-off weight W_{to} required for a specific design mission. Also noted to the right of the bar chart are some important structural weight definitions that are related to the weight buildup, for a typical commercial jet transport. Other aircraft types have similar structural weight definitions.

Note that the operating weight empty includes both the manufacturer's weight empty (MWE), plus the operator's items, which include the flight crew, cabin crew, food, galley service items, drinkable water, cargo containers and pallets, plus life vests, life rafts, emergency transmitters, and the unusable fuel trapped in the fuel system and unavailable for use by the engines. When all the payload is loaded, that is, all available passenger seats are filled at the *standard* passenger + baggage weight and all the available revenue cargo volume is filled at some selected cargo density, the aircraft has reached its space limit payload (SLPL), which usually coincides with another key weight definition, the maximum zero-fuel weight (MZFW), the maximum design weight for the aircraft with no fuel on board. Loading

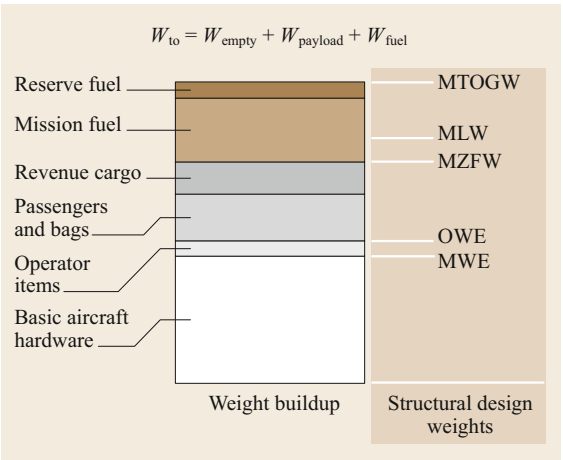

Fig. 24.43 Typical weight buildup – jet transport

on the fuel required for the mission, the mission fuel, plus the required reserves, brings the aircraft to W_{to}, the maximum take-off gross weight required to perform the specified design mission. The design maximum landing weight (MLW) for most smaller aircraft, such as private propeller-driven aircraft and short-range commuters, is usually the same as the MTOGW. However, for larger, long-range aircraft, where the mission fuel is a large percentage of the MTOGW, a somewhat lower MLW is selected to minimize the structural weight impact of designing all the structure to withstand the loads associated with landing at MTOGW. For this design choice, a fuel dump system, which allows fuel to be jettisoned overboard in an emergency following a high-gross-weight take-off, allows the aircraft to reduce its weight to the MLW without having to burn off large amounts of mission fuel. A summary of the airplane weight definitions is given in Table 24.8.

24.9.2 Weight Fractions

The maximum take-off weight required for a specific design mission (W_{to}) may be written as

$$W_{to} = W_{empty} + W_{payload} + W_{fuel}$$

or

$$\frac{W_{empty}}{W_{to}} + \frac{W_{payload}}{W_{to}} + \frac{W_{fuel}}{W_{to}} = 1 \,,$$

where

$$\frac{W_{empty}}{W_{to}} = \text{weight empty fraction} \,,$$

$$\frac{W_{payload}}{W_{to}} = \text{payload fraction} \,,$$

$$\frac{W_{fuel}}{W_{to}} = \text{fuel fraction} \,.$$

and W_{empty} is the operating weight empty (OWE), the basic aircraft hardware plus other items required to allow the aircraft to perform the design mission, $W_{payload}$ is the passengers + bags + revenue cargo (commercial) or bombs, missiles, cargo (military), and W_{fuel} is the total fuel on board for the mission, that is, fuel burned + reserve fuel.

24.9.3 Weight Estimation and Control

In order to begin design work on a specific aircraft project, there is a need to establish the weight of the various components and systems that make up the aircraft empty weight. This process, usually conducted by aircraft weight engineers, initially involves much reliance on empirical data from actual aircraft, correlated with appropriate physical parameters. These data are assembled into a group weight statement, a list of weights of the major elements that make up the MWE. Examples are shown in Table 24.9.

As the design work progresses, the group weights are updated as various parts of the aircraft are specifically defined. Major effort is required to ensure that the initial target weight for the entire aircraft is not exceeded during the design and manufacturing phase of the project.

24.9.4 Balance Diagram and C.G. Limits

The airplane balance diagram is used to ensure that the airplane center of gravity (c.g.) is in the proper location for all of the probable loading conditions considering the OWE c.g. location, fuel loading and usage, passenger loading, and cargo loading. The OWE c.g. is usually set by designers based on experience for a specific airplane design. Then the extreme excursions of the c.g. due to the most probable adverse loading conditions that move the c.g. forward and aft are examined by calculation to establish forward and aft limits for c.g. travel. The results of these calculations are plotted on a chart of airplane gross weight versus c.g. location so that appropriate c.g. limits can be established. Stability and control and structural design criteria must be met at these c.g. limits.

Table 24.8 Airplane weight definitions

Weight	Symbol	Definition
Manufacturer's weight empty	MWE	Airplane weight at the end of the manufacturing process
Operating weight empty	OWE	Airplane weight ready for operation, including flight crew, cabin crew, food, galley service items, potable water, cargo containers and pallets, life vests, life rafts, emergency transmitter, lavatory fluids, and unusable fuel
Maximum zero-fuel weight	MZFW	Airplane weight with maximum design payload on board, but no fuel; the design payload includes all passengers and their baggage, plus the maximum design cargo weight
Maximum landing weight	MLW	Airplane weight defined as the maximum for which the airplane meets all of the structural design requirements for landing, usually being somewhat higher than the MZFW
Maximum take-off gross weight	MTOGW	Airplane weight defined as the maximum for which the airplane meets all of the structural design and performance requirements for takeoff; this includes the maximum design payloads plus the fuel required to fly the design mission plus the required reserve fuel.

Table 24.9 Summary of group weight statements. Transport airlines in lb

Weight elements	DC-9-30	737-200	727-100	727-200	707-320	DC-8-55	DC-8-62	DC-10-10	L-1011-1	DC-10-30	747-100
Wing group	11 391	11 164	17 682	18 529	28 647	34 909	36 247	48 990	47 401	57 748	88 741
Tail group	2790	2777	4148	4142	6004	4952	4930	13 657	8570	14 454	11 958
Body group	11 118	11 920	17 589	22 415	22 299	22 246	23 704	44 790	49 432	46 522	68 452
Landing gear	4182	4038	7244	7948	11 216	11 682	11 449	18 581	19 923	25 085	32 220
Nacelle group	1462	1515	2226	2225	3176	4644	6648	8493	8916	9328	10 830
Propulsion group	2190	1721	3052	3022	5306	9410	7840	7673	8279	13 503	9605
Flight controls	1434	2325	2836	2984	2139	2035	2098	5120	5068	5188	6886
Auxiliary power	817	855	0	849	0	0	0	1589	1202	1592	1797
Instruments	575	518	723	827	550	1002	916	1349	1016	1645	1486
Hydraulic system	753	835	1054	1147	1557	2250	1744	4150	4401	4346	5067
Electrical system	1715	2156	2988	2844	3944	2414	2752	5366	5490	5293	5305
Avionics	1108	1100	1844	1896	1815	1870	2058	2827	2801	3186	4134
Furnishings	8594	9119	11 962	14 702	16 875	15 884	15 340	38 072	32 829	33 114	48 007
Air conditioning	1110	1084	1526	1802	1602	2388	2296	2386	3344	2527	3634
Antiicing system	474	113	639	666	626	794	673	416	296	555	413
Load and handling	57	–	15	19	–	55	54	62	–	62	228
Empty weight (less dry engine)	49 770	51 240	75 528	86 017	105 756	116 535	118 749	203 521	198 968	224 148	297 867
Dry engine	6160	6212	9322	9678	19 420	16 936	17 316	23 229	30 046	25 587	35 700
MWE	55 930	57 452	84 850	95 695	125 176	133 471	136 065	226 750	229 014	249 735	333 567
MTOGW	108 000	104 000	161 000	175 000	312 000	325 000	335 000	430 000	430 000	565 000	775 000

24.10 Aircraft Performance

Aircraft performance is the part of the subject of flight mechanics that deals with parameters such as speed, rate of climb, range, fuel consumption, and runway length requirements.

24.10.1 Level-Flight Performance

The simplest performance condition is steady level-flight cruise, when all forces are in equilibrium as the aircraft moves at a constant speed and altitude. From Fig. 24.18, equilibrium requires that

$$\text{lift } L = \text{weight } W = C_L \frac{\rho}{2} V^2 S\,, \quad C_L = \frac{W}{(\rho V^2/2)\,S}\,,$$

and

$$\text{thrust } T = \text{drag } D = C_D \frac{\rho}{2} V^2 S \quad \text{subsonic flight}\,.$$

For any given weight, C_L may be found and substituted into the induced drag term. ΔC_{D_C}, the empirical compressibility drag coefficient, is dependent on C_L and the Mach number.

Several fundamental airplane characteristics can be derived from the drag equation [24.23]. One major objective of airplane design is to minimize the drag for any required lift. At any altitude and speed, the ratio of drag to lift depends only on the ratio of C_D to C_L. At low Mach numbers, $\Delta C_{D_C} = 0$ and

$$C_D = C_{D_p} + \frac{C_L^2}{\pi e \mathrm{AR}}\,.$$

where AR is the aspect ratio and e is an efficiency factor. Generally, $e < 1$ but for elliptic wings $e = 1$.

For minimum drag, C_D/C_L is a minimum. Now

$$\frac{C_D}{C_L} = \frac{C_{D_p}}{C_L} + \frac{C_L}{\pi e \mathrm{AR}} .$$

At the value of C_L for which C_D/C_L is a minimum, $\mathrm{d}(C_D/C_L)/\mathrm{d}C_L = 0$. Then

$$\frac{\mathrm{d}\,(C_D/C_L)}{\mathrm{d}C_L} = -\frac{C_{D_p}}{C_L^2} + \frac{1}{\pi e \mathrm{AR}} = 0 .$$

And for $L/D =$ maximum,

$$C_{D_p} = \frac{C_L^2}{\pi e \mathrm{AR}} .$$

Thus, for minimum drag, the lift coefficient is the value for which the drag due to lift is equal to the parasite drag. For this condition,

$$C_{L_{(L/D)_{max}}} = \sqrt{C_{D_p} \pi e \mathrm{AR}} .$$

The value of L/D is

$$\frac{L}{D} = \frac{C_L}{C_D} = \frac{C_L}{C_{D_p} + C_L^2/(\pi e \mathrm{AR})} ,$$

for $L/D =$ maximum

$$C_L = \sqrt{C_{D_p} \pi e \mathrm{AR}}$$

and

$$C_{D_p} = \frac{C_L^2}{\pi e \mathrm{AR}} .$$

Thus,

$$\left(\frac{L}{D}\right)_{max} = \frac{\sqrt{C_{D_p} \pi e \mathrm{AR}}}{2C_{D_p}} .$$

To obtain this minimum drag in flight, one must fly at the speed corresponding to the C_L given above. This speed is designated as $V_{(L/D)_{max}}$. Then

$$\sqrt{\frac{2W}{\sqrt{C_{D_P} \pi e \mathrm{AR}}\rho S}} .$$

Propeller-driven airplanes achieve their best range at the lift coefficient and corresponding speed for $(L/D)_{max}$.

It is customary to study the performance of propeller-driven airplanes in terms of power, since they operate with engines that produce power rather than thrust. The thrust horsepower required for level flight is the drag times the distance covered per unit time, so

$$550\,\mathrm{thp}_{req} = \mathrm{DV} = C_{D_p}\frac{\rho}{2}V^3 S + \frac{C_L^2}{\pi e \mathrm{AR}}\frac{\rho}{2}V^3 S .$$

Then $V = \sqrt{2W/C_L \rho S}$, and we obtain

$$\mathrm{thp}_{req} = \frac{1}{550}\sqrt{\frac{2W^3}{\rho S}}\left(\frac{C_{D_p}}{C_L^{3/2}} + \frac{C_L^{1/2}}{\pi e \mathrm{AR}}\right) .$$

The constant 550 is included to keep the units in thrust horsepower and the other units in the corresponding English system units. The minimum power will be obtained when the term in parenthesis is a minimum. Taking the derivative of that term with respect to C_L, equating it to zero, and defining $C_{L_{mp}}$ as the lift coefficient for minimum power required leads to

$$-\frac{3}{2}\frac{C_{D_r}}{C_{L_{mp}}^{5/2}} + \frac{1}{2}\frac{1}{\pi e \mathrm{AR} C_{L_{mp}}^{1/2}} = 0 .$$

Therefore,

$$C_{L_{mp}}^2 = 3\pi C_{D_p} e \mathrm{AR} ,$$

and

$$C_{L_{mp}} = \sqrt{3\pi C_{D_p} e \mathrm{AR}} = \sqrt{3C_{L_{(L/D)_{max}}}} .$$

Substituting in the induced drag coefficient portion of the equation gives

$$C_{D_{imp}} = \frac{3\pi C_{D_p} e \mathrm{AR}}{\pi e \mathrm{AR}} = 3C_{D_p} .$$

At the minimum-power condition, the induced drag coefficient is three times as large as the parasite drag coefficient. This contrasts with the minimum drag condition, for which they are equal. Since, for a given total lift, the speed varies inversely as the square root of the lift coefficient, the speed for minimum power is lower than the speed for minimum drag by the ratio $1/3^{1/4} = 0.76$. Taking the inverse, the minimum drag speed is 1.32 times the minimum-power speed.

24.10.2 Climb and Descent Performance

Figure 24.18 illustrates the force on an airplane in steady-state constant-speed climb. The thrust is shown acting parallel to the flight path direction. In general, this is not quite true, but in conventional aircraft the

effects of an inclination of the thrust vector are small enough to be neglected.

Equating forces perpendicular and parallel to the flight path

$$L = W\cos\gamma\ ,$$
$$T = D + W\sin\gamma\ .$$

Then,

$$\sin\gamma = \frac{T-D}{W} = \frac{T}{W} - \frac{D}{W} = \frac{T}{W} - \frac{D}{L}\ ,$$

γ is the flight path angle or angle of climb. We may assume that γ is sufficiently small so that $\cos\gamma$ is approximately equal to 1.0. Then, $L = W$ and

$$\text{Rate of climb, RC} = V\sin\gamma = \frac{V(T-D)}{W}\ .$$

For propeller-driven aircraft, it is convenient to use power rather than thrust and drag. If RC is to be determined in feet per minute, the usual units, then with V in feet per second,

$$\begin{aligned}\text{RC (ft/min)} &= 60\left(\frac{\text{TV}-\text{DV}}{W}\right)\\ &= \frac{\text{thp}_{\text{avail}}-\text{thp}_{\text{req}}}{W}(33\,000)\\ &= \frac{\text{thp}_{\text{excess}}}{W}(33\,000)\ ,\end{aligned}$$

where $\text{thp}_{\text{excess}}$ is the thrust horsepower available for climbing; W is given in lb.

The preceding equations are based on an airplane climbing at constant true airspeed. In practical operations, climbing flight is done at constant indicated airspeed or constant Mach number. This provides the pilot with a simple guide to the proper climb speed, whereas a constant true speed would mean an ever-changing indicator reading as the altitude increases. A constant indicated speed essentially corresponds to a constant calibrated airspeed. At low Mach numbers, this is the same as a constant equivalent airspeed, since the compressibility correction to airspeed is very small.

With a constant equivalent airspeed, the airplane continually accelerates as the altitude increases. The equilibrium equation along the flight path must then include an inertial term. Thus

$$T = D + W\sin\gamma + \frac{W}{g}\frac{\mathrm{d}V}{\mathrm{d}t}\ .$$

Since

$$\frac{\mathrm{d}V}{\mathrm{d}t} = \frac{\mathrm{d}V}{\mathrm{d}h}\frac{\mathrm{d}h}{\mathrm{d}t} \quad\text{and}\quad \frac{\mathrm{d}h}{\mathrm{d}t} = V\sin\gamma\ ,$$

Table 24.10 Kinetic-energy correction factors for climb

Climb operation	Altitude (ft)	$(V/g)(\mathrm{d}V/\mathrm{d}h)$ (approx.)
Constant true speed	All	0
Constant v_{E}	Above 36 150	0.7Ma^2
Constant v_{E}	Below 36 150	0.567Ma^2
Constant Ma	Above 36 150	0
Constant Ma	Below 36 150	-0.133Ma^2

we can write

$$\sin\gamma = \frac{(T-D)/W}{1+(V/g)\,(\mathrm{d}V/\mathrm{d}h)} = \frac{T-D}{W}\quad\text{(K.E. factor)}\ .$$

This equation differs from the previous rate-of-climb equation at constant true speed by the kinetic-energy correction factor $[1+(V/g)(\mathrm{d}V/\mathrm{d}h)]^{-1}$. Approximate values of the term $(V/g)(\mathrm{d}V/\mathrm{d}h)$ are given as functions of the Mach number in Table 24.10 for various types of climb paths [24.24]. Note that, for constant-Mach-number climb below the isothermal atmosphere, the correction increases the rate of climb. In this region, constant Mach number means decreasing velocity as altitude increases, because the speed of sound is decreasing. The airplane is losing kinetic energy and trading it for an increased rate of climb. When applicable, the kinetic-energy correction factor is applied to gradient-of-climb and rate-of-climb calculations.

The foregoing equations include a surprisingly large amount of useful information. First, the Federal Air Regulations (FARs) specify minimum permissible performance for commercial aircraft in terms of minimum climb gradients, primarily after failure of one engine. A gradient is the tangent of an angle. For small to moderate flight path angles, the sine of the angle is essentially equal to the tangent, so

$$\begin{aligned}\text{gradient}\ \gamma &= \tan\gamma = \sin\gamma\\ &= \frac{T-D}{W}\quad\text{(K.E. factor)}\\ &= \left(\frac{T}{W}-\frac{D}{W}\right)\quad\text{(K.E. factor)}\ .\end{aligned}$$

Thus, the gradient depends on the thrust-to-weight ratio minus the inverse of the lift-to-drag ratio.

There are three conditions that are related to an airplane's climb performance. The first is the gradient of climb, which is important for clearing obstacles close to the ground. The second is the rate of climb, which is important for reaching cruise altitude as soon as possible. The third is the best economy of climb, climbing at a higher speed than the best rate of climb speed, but covering more distance in the climb for a given amount of fuel burned. These climb speeds are shown in Fig. 24.44.

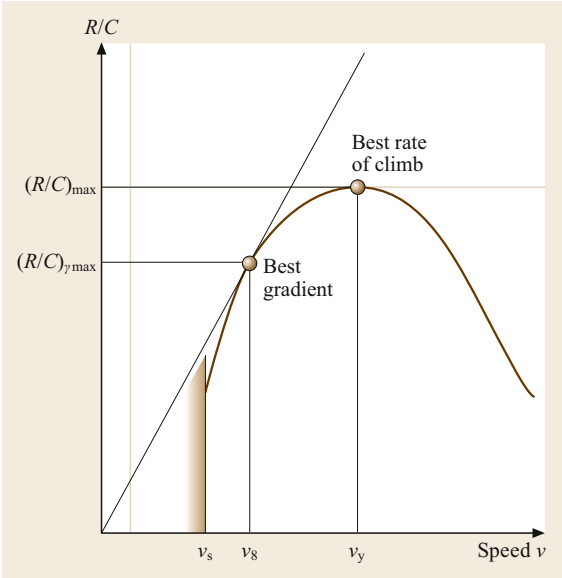

Fig. 24.44 Climb speed diagram

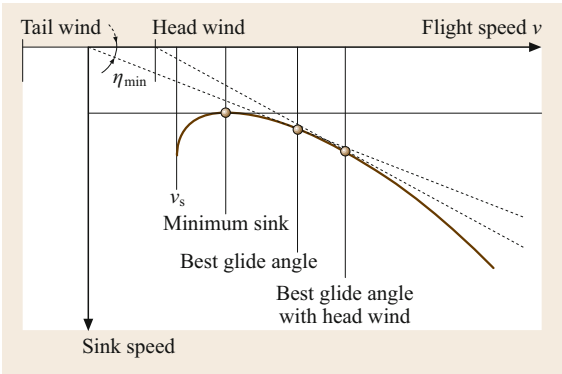

Fig. 24.45 Glider performance chart

Other important performance characteristics can be found from the climb gradient and rate-of-climb equations. If the thrust is zero, then the flight path gradient is the inverse of the L/D ratio, and the rate of descent or sink speed is given by the expression

$$\text{rate of descent} = \frac{V}{L/D} .$$

For gliders and sailplanes, these equations are used to develop charts such as the one shown in Fig. 24.45, which provide the essential performance data for these aircraft.

24.10.3 Range

The total range capability of an airplane consists of the climb, cruise, and descent segments. The cruise range is equal to the summation of the range increments obtained by multiplying the miles flown per pound of fuel used (mi/lb) at selected average weights by the appropriate incremental fuel quantity. The value of the miles per pound is called the specific range and is defined as follows.

For jet or turbofan aircraft,

$$\frac{\text{mi}}{\text{lb}} = \frac{\text{miles flown per hour}}{\text{fuel flow (lb/h)}} = \frac{V}{cT} = \frac{V}{cD} ,$$

where c is the specific fuel consumption (SFC) in pounds of fuel per pound of thrust per hour (lb/(lb h)).

The SFC used in the performance equations is the installed specific fuel consumption. *Installed* means that all adverse effects on SFC associated with the engine installation are included. A typical markup on engine specification SFC for jet and turbofan transports is 3% (i.e., installed SFC equals 1.03 times bare engine SFC). In some cases, for which the engine data are based on zero inlet and nozzle losses, the markup may be twice that amount.

Also,

$$D = \frac{W}{L/D} = \frac{D}{L} W$$

and thus

$$\frac{\text{nmi}}{\text{lb}} = \frac{V}{c(D/L)W} = \frac{V}{c}\frac{L}{D}\frac{1}{W} \quad \text{(jet)} .$$

The term $(V/c)(L/D)$ is called the range factor and is a measure of the aerodynamic and propulsive system range efficiency. If V is in knots, the range in miles per pound will be in nautical miles per pound of fuel.

For a propeller-driven airplane,

$$\frac{\text{nmi}}{\text{lb}} = \frac{V}{c\text{bhp}} ,$$

where c is the specific fuel consumption in pounds of fuel per horsepower per hour (lb/(bh$_p$ h)). Then the range in nautical miles per pound of fuel is

$$\frac{\text{nmi}}{\text{lb}} = \frac{V(\text{kn})}{c(\text{thp}/\eta)} = \frac{\eta}{c}\left(\frac{V(550)}{DV \times 1.69}\right) = 325\frac{\eta}{c}\frac{1}{D} = 325\frac{\eta}{c}\frac{L}{D}\frac{1}{W} \text{ (propeller)} .$$

For propeller-driven airplanes, the specific range depends only on the propeller efficiency, SFC, and L/D; speed is not a factor. Since the propeller efficiency and SFC are essentially constant in cruise, the range is determined by L/D.

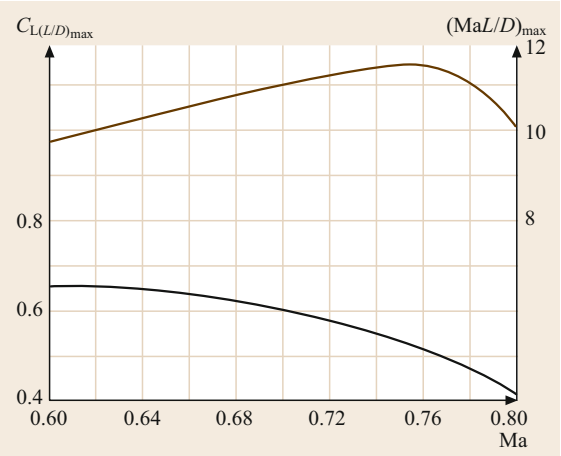

Fig. 24.46 $(MaL/D)_{max}$ and $C_{L(L/D)_{max}}$ for maximum range of jet airplanes (Ma is the cruise Mach number)

The specific range equation for jet airplanes can also be written as

$$\frac{\text{nmi}}{\text{lb}} = a\frac{\text{Ma}}{c}\frac{L}{D}\frac{1}{W} ,$$

where a is the speed of sound and Ma is the cruise Mach number. The expression (MaL/D) is a measure of the specific range capability due to the aerodynamic characteristics of jet-powered airplanes. Curves of (MaL/D) versus lift coefficient at various Mach numbers show that jet range is increased by high speed as well as high L/D up to the point where the adverse compressibility drag effect on L/D overpowers the beneficial effect of higher speed. This situation can be summarized on a chart such as that in Fig. 24.46, which shows that, if the SFC is constant with Mach number, the maximum mi/lb value for a jet airplane occurs at a Mach number and lift coefficient where the maximum value of (MaL/D) at each Mach number reaches its peak. However, the turbofan SFC increases slowly with Mach number, so that the optimum range will be obtained at a slightly lower Mach number than indicated in Fig. 24.46.

The total cruise range is given by

$$\text{range} = \int_{w_f}^{w_i} \frac{\text{nmi}}{\text{lb}} \mathrm{d}W .$$

If average values of η, c, and L/D can be chosen, the cruise range may be found analytically. For jets,

$$R\ (\text{nmi}) = \int_{w_f}^{w_i} \frac{\text{nmi}}{\text{lb}} \mathrm{d}W = \int_{w_f}^{w_i} \frac{V}{c}\frac{L}{D}\frac{\mathrm{d}W}{W}$$
$$= \frac{V}{c}\frac{L}{D}\ln\frac{W_i}{W_f} .$$

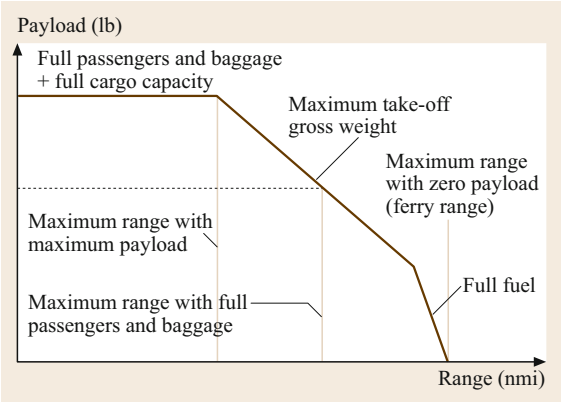

Fig. 24.47 Payload–range curve

For propeller-driven planes,

$$R\ (\text{nmi}) = \int_{w_f}^{w_i} 325\frac{\eta}{c}\frac{L}{D}\frac{\mathrm{d}W}{W}$$
$$= 325\frac{\eta}{c}\frac{L}{D}\ln\frac{W_i}{W_f} \quad \text{(Breguet formula)} ,$$

where η, c, and L/D are assumed constant throughout the flight or, more realistically, are taken as effective averages; V is in knots; and c is in lb/(lb h) or (lb/(bhp h)), as appropriate. The range formula for propeller-driven aircraft is called the Breguet formula, after its originator. The analogous jet formula is often similarly labeled.

The total range includes the cruise range plus the distance covered in climb and descent. For long flights, where the cruise portion is dominant, the lower mi/lb in climb due to the higher power being used, and the higher mi/lb in descent due to lower power being used, may be assumed to cancel, allowing the range to be estimated directly from the Breguet range equation, using the appropriate parameters chosen at an average weight. For short flights, where climb is a large portion of the total trip, this approximation may result in a significant error.

A summary of the payload–range characteristics of an airplane is shown in Fig. 24.47. The payload–range curve is one of the most important performance curves for a commercial transport or business jet. It establishes the envelope which shows how far the airplane can carry a given payload, or how much payload it can carry over a given range.

The payload–range curve applies to a specific airplane–engine combination (MWE, OWE, interior seating arrangement, fuel-tank configuration, MTOGW), operating under specific flight rules (cruise Mach number, altitude, altitude steps, alternate dis-

tance). The maximum payload is usually the volume or space limit payload (full passengers + bags and full cargo containers or pallets at some standard cargo density, i.e., 10 lb/ft^3) or the maximum zero-fuel weight limit payload, based on the structural limit of maximum zero-fuel weight. When operating on the maximum take-off weight limit, it is necessary to trade payload for fuel if greater range is desired. Operating on the fuel capacity limit line requires large reductions in payload to achieve small increases in range, due to modest improvements in cruise efficiency achieved by reductions in cruise weight. The key points on the payload range curve are calculated using the Breguet range equation for jet aircraft

$$R\ (\text{nmi}) = \left(\frac{V}{c}\right)\left(\frac{L}{D}\right)\ln\frac{W_\text{i}}{W_\text{f}}\,.$$

For a specific design on a particular cruise operation V, c, and L/D are usually taken as constants, and W_initial and W_final are derived from known weights, i.e., OWE, payload, reserve fuel, maximum take-off weight, and maximum fuel capacity. From this equation, it can be seen that the maximum range is achieved by cruising at a point where the quantity VL/D is a maximum.

Some key ideas about payload–range curves are as follows:

- Weight-limited payload = MZFW – OWE.
- Space-limited payload is slightly lower.
- Passengers + bags range is usually set by MTOGW.
- Greater passengers + bags range can be achieved by increasing MTOGW (allows more fuel to be carried).
- If passenger + bags range is limited by maximum fuel capacity, greater range can be achieved only through increased fuel capacity.

24.10.4 Endurance

The endurance problem is similar to the range problem except that we are trying to determine how long the aircraft will fly rather than how far it will fly. The quantity analogous to specific range is specific endurance, the hours flown per unit quantity of fuel. In the usual units, specific endurance is measured in hours per pound of fuel.

To maximize endurance, fuel flow per unit time must be minimized. Since the specific fuel consumption is nearly constant, the drag must be minimized for jet aircraft, while thrust horsepower must be as small as possible for propeller-driven aircraft. The endurance t_e for turbojet or turbofan aircraft is

$$\begin{aligned} t_\text{e} &= \int_{w_\text{f}}^{w_\text{i}} \frac{\text{h}}{\text{lb fuel}}\,\text{d}W = \int_{w_\text{f}}^{w_\text{i}} \frac{1}{Dc}\text{d}W \\ &= \int_{w_\text{f}}^{w_\text{i}} \frac{1}{[W/(L/D)]c}\text{d}W \\ &= \int_{w_\text{f}}^{w_\text{i}} \frac{1}{c}\frac{L}{D}\frac{\text{d}W}{W} = \frac{1}{c}\frac{L}{D}\ln\frac{W_\text{i}}{W_\text{f}}\,. \end{aligned}$$

Again, c and L/D are assumed to be constant throughout the flight, or taken as average values. Note the similarity between this equation and the jet range equation.

Endurance is simply range divided by speed. For the greatest endurance, the aircraft should obviously fly at the speed for minimum drag. This, of course, assumes that c is a constant with speed, a good assumption for jets but not quite true for turbofans. In addition, at very low engine thrust levels, c tends to increase as the thrust is decreased. This may also influence the speed for best endurance.

For propeller-driven aircraft, endurance is

$$\begin{aligned} t_\text{e} &= \int_{w_\text{f}}^{w_\text{i}} \frac{1}{\text{thp}\,c/\eta}\text{d}W = \int_{w_\text{f}}^{w_\text{i}} \frac{\eta}{c}\left(\frac{550}{DV\times 1.69}\right)\text{d}W \\ &= \int_{w_\text{f}}^{w_\text{i}} 325\frac{\eta}{c}\frac{L}{DV}\frac{1}{W}\text{d}W\,, \end{aligned}$$

where V is in knots and c is in pounds of fuel per brake horsepower per hour. We cannot assume that L/DV is a constant. L/DV is the ratio of lift to thrust power required, and we have shown that thp_req is a nonlinear function of weight. At any given lift coefficient, power required varies with $W^{3/2}$. However, it has been shown that, if V is expressed as $\sqrt{2W/(C_\text{L}\rho S)}$, t_e is given by [24.25]

$$t_\text{e}(s) = \frac{\eta}{c}\frac{C_\text{L}^{3/2}}{C_\text{D}}\sqrt{\frac{2\sigma S}{W_\text{i}}}\left[\left(\frac{W_\text{i}}{W_\text{f}}\right)^{1/2} - 1\right].$$

Here we see that, for best endurance, a propeller-driven airplane should be flown at the flight condition for maximum $C_\text{L}^{3/2}/C_\text{D}$. This is a maximum when the lift coefficient is $\sqrt{3}$ times the value for maximum lift-to-drag ratio. Since low speed as well as a particular lift

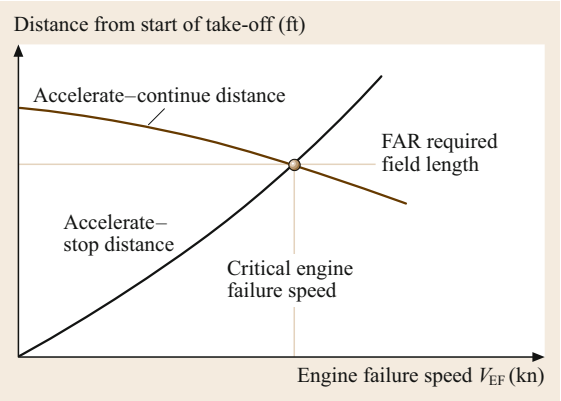

Fig. 24.48 Determination of FAR balanced field length with engine failure

coefficient is desirable for minimum power required, best endurance occurs at a high density (i.e., low altitude). Therefore, propeller aircraft endurance is best at low altitudes.

24.10.5 Take-Off Performance

The take-off performance problem is basically an acceleration to the required speed plus a transition to climb at a 35 ft height for civil turbine-powered transports, or a 50 ft height for piston-engine general aviation or military airplanes. The required runway length is defined as the distance from the start of take-off to the point where these *obstacle* heights are reached. The take-off field length required by FARs for jet transport operation is the greater of:

1. The all-engine take-off distance ×1.15
2. The take-off distance with an engine failure at the *most critical point* in the take-off.

The most critical point is where the distance to stop on the runway is equal to the distance to continue the take-off with one engine failed to a height of 35 ft. This situation is called the balanced field length concept. The most critical point in a given take-off, where the *accelerate–stop* distance is equal to the *accelerate–continue* distance, is found by plotting the accelerate–stop distance and accelerate–continue distance versus the engine failure speed, as shown in Fig. 24.48.

For propeller-driven transports, the FAR balanced field length concept is the same, but the speed at 35 ft is $1.15V_S$ for four or more engines, and $1.2V_S$ for two or three engines.

For single- and multiengine normal, utility, and acrobatic aircraft under 12 500 lb maximum gross weight, FAR 23 specifies only the all-engine take-off distance

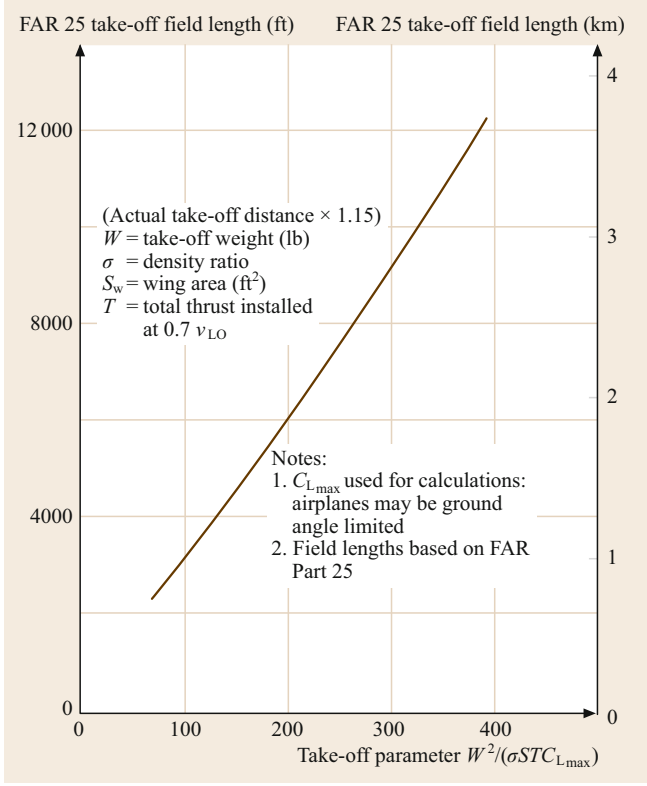

Fig. 24.49 FAR 25 all-engines-operating take-off field length to a 35 ft height

to a height of 50 ft with a speed equal to or greater than $1.3V_S$ at 50 ft. For FAR 23 commuter-category aircraft, the balanced field length concept is applied and the criteria for take-off are basically the same as for FAR 25, except that the take-off distance is defined to a 50 ft height, and the speed at 50 ft must be at least $1.3V_S$.

Analysis and flight tests suggest that the distance to liftoff is a function of several airplane factors, namely

$$d_{LO} = f\left(\frac{W^2}{\sigma S C_{L_{max}} T}\right) ,$$

where $\sigma = \rho/\rho_s$ and T is the thrust at $0.7V_{LO}$ [24.11]. Since the ground run distance to lift-off is about 80% of the total distance to the 35 ft height, it has been shown that this parameter works very well in correlating the required runway length results for many aircraft. Figure 24.49 shows the FAR all-engines-operating take-off field length to a 35 ft height d_{35} for jet or turbofan aircraft as a function of $W^2/(\sigma S C_{L_{max}} T_{0.7V_{LO}})$. This chart applies to normal take-off without engine failure and includes a 15% increase above the actual performance in accordance with the air transport requirements of FAR 25.

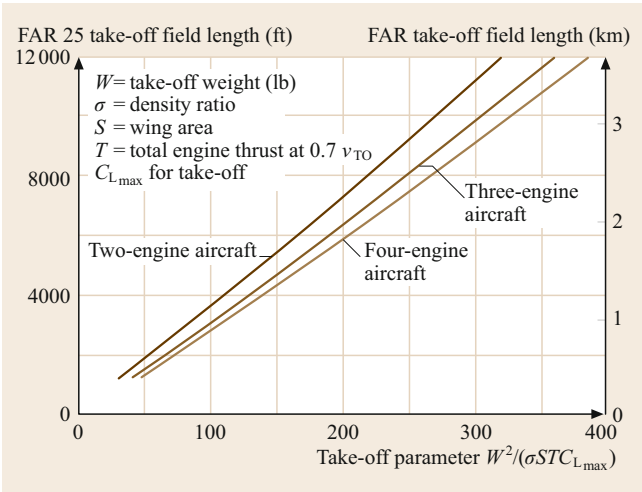

Fig. 24.50 FAR 25 one-engine-inoperative take-off field length. Two-, three-, and four-engine jet transports take-off distance to a 35 ft height balanced field length with engine failure

The actual distance is the distance determined from Fig. 24.49 divided by 1.15. Figure 24.50 shows the FAR one-engine-inoperative take-off field length for two-, three-, and four-engine transports.

For propeller-driven aircraft, a comparable analysis shows that take-off distance is a function of $W^2/(\sigma S C_{L_{max}} P)$, where P is the total brake horsepower. This is a less accurate approximation, since the effectiveness of the power depends on the propeller efficiency during take-off. Use of this parameter assumes that all propellers are designed to attain a similar level of efficiency in take-off.

24.10.6 Landing Performance

Landing distances consist basically of two segments: the air run from a height of 50 ft to the surface accompanied by a slight deceleration and flare, and the ground deceleration from the touchdown speed to a stop. Landing runway lengths are required by FAR 25 for commercial aircraft to be demonstrated by flight tests. The air distance d_{air} can be approximated by a steady-state glide distance d_{GL} plus an air deceleration distance d_{decel} at constant altitude, as shown in Fig. 24.51.

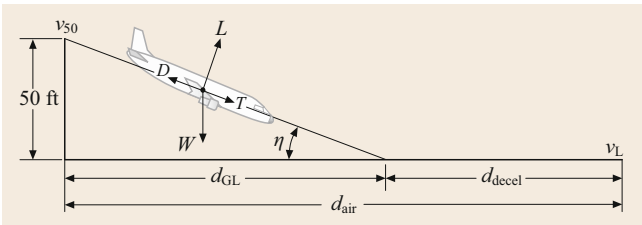

Fig. 24.51 Landing air distance

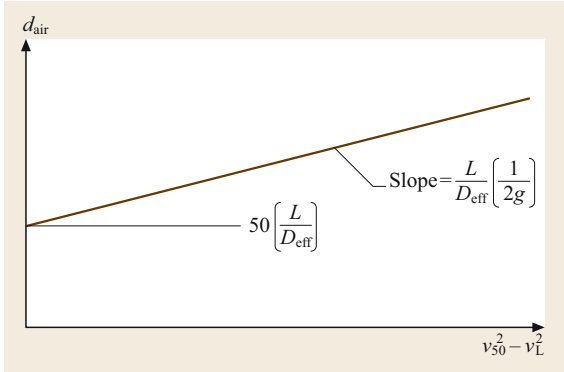

Fig. 24.52 Landing air run determination

V_{50} is the speed at the 50 ft height. In accordance with FAR 25, V_{50} must be at least $1.3V_S$. In practice, it is taken as equal to $1.3V_S$. V_L is the landing or touchdown speed and is usually about $1.25V_S$. The glide distance is

$$d_{GL} = 50\left(\frac{L}{D_{eff}}\right),$$

where $D_{eff} = D - T$,

$$d_{decel} = \frac{V_{50}^2}{2a} - \frac{V_L^2}{2a} = \frac{\frac{1}{2}\left(\frac{W}{g}\right)V_{50}^2 - \frac{1}{2}\left(\frac{W}{g}\right)V_L^2}{D_{eff}}.$$

Since lift is essentially equal to the weight,

$$d_{air} = 50\frac{L}{D_{eff}} + \frac{1}{2g}\left(V_{50}^2 - V_L^2\right)\frac{L}{D_{eff}}$$
$$= \frac{L}{D_{eff}}\left[50 + \frac{1}{2g}\left(V_{50}^2 - V_L^2\right)\right].$$

L/D_{eff} is the effective L/D ratio during the air run. It can be determined from flight test air runs by plotting flight test air run distances versus $(V_{50}^2 - V_L^2)$, as illustrated in Fig. 24.52.

The ground deceleration distance is

$$d_G = \frac{V_L^2}{2a} = \frac{V_L^2}{2\,[R/(W/g)]},$$

where R is the effective average resistance or total stopping force $= \mu(W-L) + D$, μ is the braking coefficient of friction (Table 24.11), and D is the drag, including the drag of flaps, slats, landing gear, and spoilers.

Note that both d_{air}, i.e., the air distance, and d_G, i.e., the ground stopping distance, are directly proportional to V_{50}^2 and/or V_L^2. Both V_{50}^2 and V_L^2 are fixed percentages above V_S for safety reasons. Thus, landing distance is linear in V_S^2 except for the glide distance from 50 ft, which depends only on the L/D ratio in the landing configuration. Thus, for similar airplanes with similar L/D values and equivalent braking systems (i.e., similar μ),

Table 24.11 Runway friction coefficients

Surface	μ typical values	
	Rolling (brakes off)	Brakes on
Dry concrete/asphalt	0.03–0.05	0.3–0.5
Wet concrete/asphalt	0.05	0.15–0.3
Icy concrete/asphalt	0.02	0.06–0.10
Hard turf	0.05	0.4
Firm dirt	0.04	0.3
Soft turf	0.07	0.2
Wet grass	0.08	0.2

landing distances can be expressed in the form

$$d_{\text{land}} = A + BV_S^2 ,$$

where $A = 50(L/D)_{\text{eff}}$.

The FAR 121 scheduled landing field length is defined as the actual FAR 25 demonstrated distance from a 50 ft height to a full stop on a dry, hard surface runway, increased by a factor of 1/0.60, i.e., a 67% increase. Curves of landing field length versus V_S^2 based on flight tests (Fig. 24.53) are linear, but vary between airplanes due to the effective L/D ratio in the air run, the effective coefficient of friction, and the drag in the ground deceleration. It should be noted that the FAR dry runway tests do not allow the use of engine thrust reversers. FAR dry runway distances must be increased by 15% for operation on wet runways.

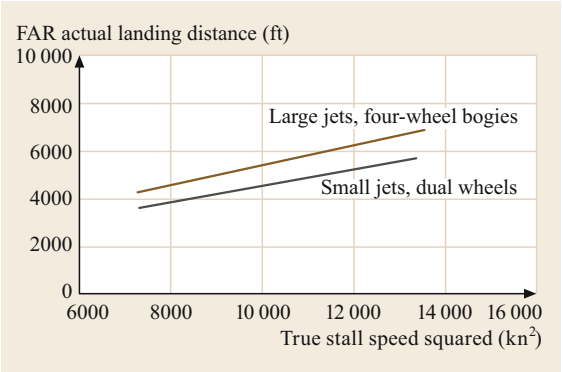

Fig. 24.53 FAR 25 demonstrated landing distance on dry, hard surface runways

24.11 Stability and Control

The subject of airplane stability and control deals with the ability of an airplane to fly straight with wings level without pilot input (stability) and the ability of the pilot to produce moments about the various airplane axes (control). *Static stability* refers to the initial tendency of the airplane to return or move away from its equilibrium position following a disturbance. *Dynamic stability* is concerned with the entire history of the airplane motion, in particular whether the motion subsides or diverges. In the following discussion, the airplane will usually be treated as a rigid body, a reasonable assumption for the majority of conditions studied. However, at high dynamic pressures, many of the structural elements deflect under aerodynamic loads, which further complicates stability and control analysis. The study of the behavior of the structural elements under load and the interaction with aerodynamic load is called *aeroelasticity*. Aeroelastic effects usually tend to reduce static stability. In extreme cases, this interaction may lead to dangerous undamped structural oscillations called *flutter*. The rigid-body motions of an airplane may be divided into two classifications: longitudinal and lateral motions. *Longitudinal motions* occur in the plane of symmetry, whereas *lateral motions* displace the plane of symmetry. For normal symmetric airplanes, with small displacements from equilibrium, these two types of motions are independent of each other.

24.11.1 Static Longitudinal Stability

Static aerodynamic stability in pitch, more commonly known as static longitudinal stability, is most easily achieved through the use of an aft-mounted horizontal tail. In concept, static longitudinal stability may be defined as the tendency of the airplane to return to its original flight condition without pilot input, when disturbed from steady, unaccelerated flight. While not an absolute requirement for sustained, controlled flight, static longitudinal stability has been found to be a desirable characteristic for ease of flight, since the variation of the airplane pitching moment coefficient C_m with the airplane lift coefficient C_L has a negative slope, as shown on the pitching moment diagram in Fig. 24.54.

It should be noted that the pitching moment coefficient is defined with respect to the airplane center of gravity (c.g.) location, expressed as a percentage of the wing mean aerodynamic chord (m.a.c.) aft of the leading edge. For example, with a c.g. location expressed as 25% m.a.c., the c.g. is located at a distance of 25% of the m.a.c. length aft of the leading edge of the m.a.c. Using the sign convention noted earlier, the negative slope of the pitching moment curve means that, for an airplane in equilibrium (pitching moment equal to zero) in steady, unaccelerated flight at a given lift coefficient, any disturbance which increases the airplane lift coef-

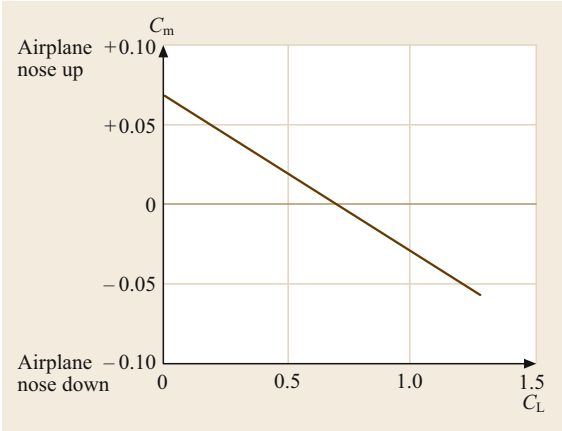

Fig. 24.54 Airplane pitching moment curve for a statically stable aircraft

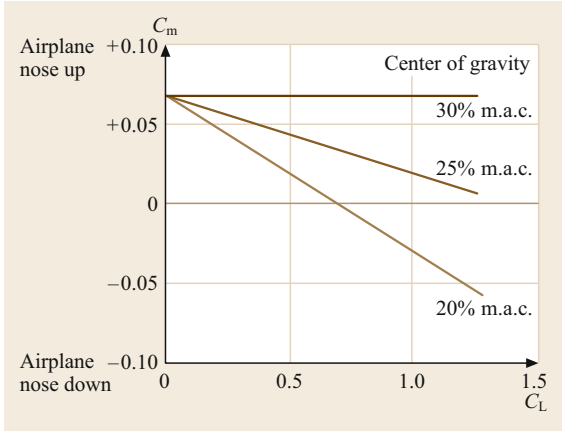

Fig. 24.55 Effect of c.g. location on airplane pitching moments

ficient will result in a negative, or airplane nose down (AND), pitching moment coefficient.

Effect of C.G. Location

It can be shown by analysis of the equation for the airplane pitching moment coefficient versus lift coefficient that the airplane c.g. location has a powerful effect on static longitudinal stability [24.26]. The results of this analysis show that, for every 1% of m.a.c. that the c.g. is moved forward, the slope of the pitching moment curve, dC_m/dC_L about that c.g. will become more negative by 0.01. This point is illustrated for a typical airplane configuration in Fig. 24.55. In this figure, the pitching moment curve with the c.g. located at 25% m.a.c. shows a negative (stable) slope of -0.05. If the c.g. is moved forward to 20% m.a.c., the pitching moment curve about this c.g. location shows a negative (stable) slope of -0.10, indicating that a 5% forward movement in the c.g. location results in a pitching moment curve that is more negative by 0.05. Similarly, if the c.g. is moved aft, the pitching moment curve will have a less stable (negative) slope about that c.g. location. In Fig. 24.55, if the c.g. location is moved aft to 30% m.a.c., then the slope of the pitching moment curve about this c.g. location is zero.

This situation illustrates another important concept in the discussion of static longitudinal stability, that of aerodynamic center.

Aerodynamic Center

From basic aerodynamics, the aerodynamic center location for any configuration is defined as the center of constant pitching moments, that is, the c.g. location where the pitching moment coefficient remains constant as the lift coefficient varies. In the illustration of Fig. 24.55, the aerodynamic center for the configuration shown is at 30% m.a.c., since for this c.g. location the pitching moment coefficient, C_m, is constant as the lift coefficient varies [24.27]. For any aircraft configuration, the criterion for achieving static longitudinal stability is that the aircraft c.g. must be located forward of the airplane aerodynamic center (a.c.). This criterion applies to all types of configurations, conventional aft-tail arrangements as well as canards, three-surface layouts, and even flying wings. However, as we shall see, this stability criterion is most easily met using a conventional aft-mounted horizontal tail. Again referring to Fig. 24.55, with the c.g. located at 25% m.a.c. and the a.c. located at 30% m.a.c., this configuration meets the criterion for static longitudinal stability, and with dC_m/dC_L equal to -0.05 is said to be stable by 5% m.a.c. With the c.g. located at 20% m.a.c. and the a.c. at 30% m.a.c., dC_m/dC_L is -0.10 and the configuration is said to be stable by 10% m.a.c. Expressed in equation form

$$\frac{dC_m}{dC_L} = X_{c.g.} - X_{a.c.} ,$$

where X is expressed in terms of a percentage of the m.a.c.

Aerodynamic Center Buildup

The aerodynamic center location for a complete airplane configuration is determined by the contribution of the various elements of the configuration in pitch. The contributions of these elements can be calculated with reasonable accuracy, but are usually verified by wind-tunnel model tests very early in the preliminary design phase. The major contributors to the complete configuration aerodynamic center are the wing, fuselage, engine nacelles, and horizontal tail. A typical wind-tunnel model

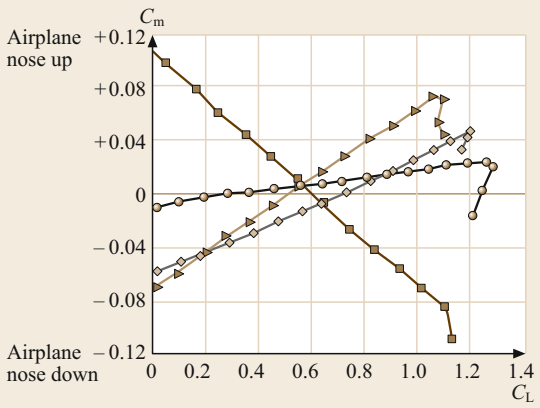

Configuration	p.m. curve slope dC_m/dC_L	a.c. location % m.a.c.	Effect of element on a.c. location
W	+0.024	22.6	–
W F	+0.087	16.3	$(-6.3\%)_{\text{fuselage}}$
W F N	+0.140	11.0	$(-5.3\%)_{\text{nacelles}}$
W F N H V	−0.177	42.7	$(+31.7\%)_{\text{horiz. tail}}$

Fig. 24.56 Aerodynamic center buildup. Straight wing, four-engine, propeller-driven transport model, center of gravity at 25% m.a.c.

buildup to determine the contributions of these elements to the complete configuration a.c. is shown in Fig. 24.56. These data are all referred to a c.g. location of 25% m.a.c. By measuring the slope of the pitching moment curve about this c.g., one can obtain the a.c. location for any configuration made up of the major elements that contribute to the a.c. location as

$$X_{\text{a.c.}} = 0.25 - \left(\frac{dC_m}{dC_L}\right) .$$

Figure 24.56 summarizes the a.c. locations for the various partial configurations, leading up to the complete configuration a.c. Also shown is the contribution of the various elements to the complete airplane a.c.

The wing-alone a.c. is at 22.6% m.a.c. The wing plus fuselage a.c. is at 16.3% m.a.c., indicating that the fuselage has a destabilizing or unstable contribution of 0.063 or 6.3% m.a.c. The wing plus fuselage plus engine nacelles have an a.c. location of 11.0% m.a.c., indicating that the nacelles have an unstable contribution of 5.3% m.a.c. to the a.c. location. The addition of the horizontal and vertical tails to the model results in an a.c. location for the complete configuration of 42.7% m.a.c. Since the vertical tail has no aerodynamic contribution in pitch, the horizontal tail provides a strong stabilizing contribution of 31.7% m.a.c. Some generalizations may be made from the data. First, the wing-only a.c. is usually around 25% m.a.c., not surprising since the a.c. for nearly all airfoil sections which make up the wing is within 1% m.a.c. or so of the 25% m.a.c. point. Wing sweep may also move the wing-alone a.c. by a percentage point or two, usually aft. Secondly, fuselages are destabilizing contributors, tending to move the a.c. location forward. The larger the fuselage relative to the wing, the more destabilizing its contribution to the complete airplane a.c. Forward-mounted nacelles, like the ones shown on the model in Fig. 24.56, are also destabilizing, although aft fuselage-mounted nacelles are usually stabilizing. Finally, the aft horizontal tail is a major stabilizing contributor to the complete airplane a.c. location. It can be shown that the horizontal tail contribution to static longitudinal stability is dependent on the distance between the 25% chord point on the wing m.a.c. and the 25% m.a.c. point on the horizontal tail, called the horizontal tail length l_H, and the horizontal tail area S_H. This is quite logical since static longitudinal stability involves the generation of aerodynamic restoring moments which are dependent on an aerodynamic force from the horizontal tail (proportional to the horizontal tail area) and a moment arm (proportional to the horizontal tail length).

24.11.2 Longitudinal Control

In addition to providing a major contribution to static longitudinal stability, the horizontal tail is also a source of longitudinal control moments. These control moments are used by the pilot to achieve equilibrium in pitch ($C_m = 0$) at any desired lift coefficient, allowing control of airspeed in unaccelerated flight, and the curvature of the flight path in accelerated flight. A typical pitching moment diagram illustrating the control moment required to balance the pitching moment at another lift coefficient is shown in Fig. 24.57.

This airplane is stable about its c.g. with a dC_m/dC_L equal to -0.10, and is in equilibrium ($C_m = 0$) at a lift coefficient $C_L = 0.5$. This means that the airplane will fly steadily at a speed corresponding to this lift coefficient, and its static longitudinal stability will resist any disturbances tending to deviate from this speed. If the pilot desires to slow the airplane down, and fly at

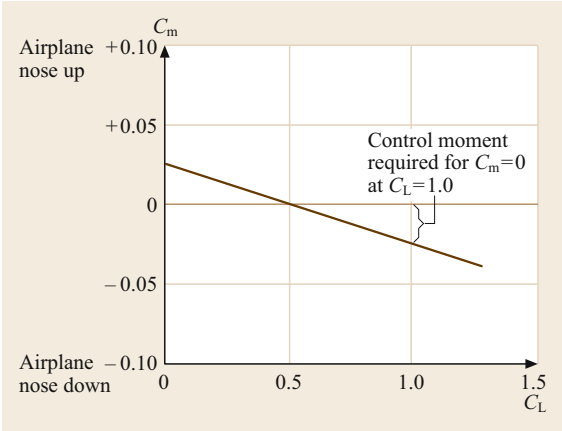

Fig. 24.57 Airplane pitching moment diagram, control moment requirement

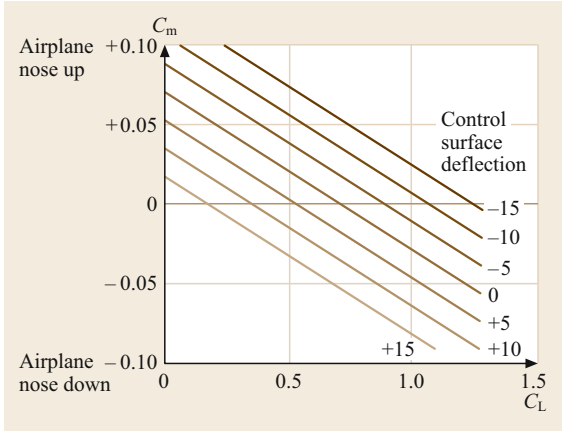

Fig. 24.58 Pitching moment diagram – effect of control deflections

a $C_L = 1.0$, he must be equipped with some type of control that can overcome the airplane nose-down moment coefficient of -0.05 at a $C_L = 1.0$, as shown in Fig. 24.57, in order to establish equilibrium at $C_L = 1.0$. Obviously, the more stable the airplane, the more control power must be provided to change the equilibrium lift coefficient. Thus, the designer must achieve a proper balance between the amount of static longitudinal stability provided and the amount of control power available. Longitudinal control power is usually provided through the hinged, movable aft portion of the horizontal tail (elevators), although in some designs the control power is provided by moving the entire horizontal tail about a fixed pivot point (all-movable horizontal tail or stabilator).

The longitudinal control capability for a specific configuration may be shown on a pitching moment diagram (Fig. 24.58), in which the pitching moment curves with various control surface deflections show the control deflection required to obtain equilibrium at various lift coefficients. Notice that a negative (trailing-edge-up) control deflection produces a positive (airplane-nose-up) pitching moment.

24.11.3 Static Directional Stability

Static directional stability for an airplane is defined as its tendency to develop restoring moments when disturbed from its equilibrium sideslip angle, normally zero. The static directional stability of an airplane is assessed from a chart of yawing moment coefficient, C_n, versus sideslip angle β as shown in Fig. 24.59. Using the sign convention of Figs. 24.11 and 24.13, a positive value of $dC_n/d\beta$ is required for static directional stability; i.e., a positive (airplane-nose-left) sideslip produces a positive (airplane-nose-right) yawing moment.

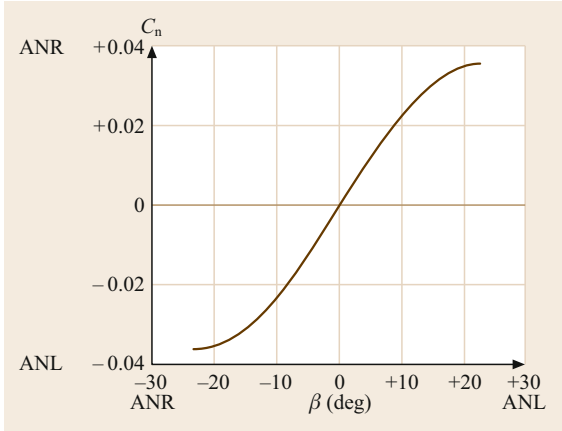

Fig. 24.59 Typical directional stability diagram (ANL = airplane nose left, ANR = airplane nose right)

Similar to the longitudinal case, the static directional stability of an airplane may be determined by adding up the contributions of the various elements of the configuration in sideslip. Analysis has shown that the main contributors to the airplane static directional stability are the fuselage and the vertical tail. The wing, a major element in longitudinal stability, has a negligible effect on the directional stability. This is due to the fact that an angle of sideslip produces very small cross-wind forces on the wing, whereas an angle of attack can produce very large lift forces. The fuselage is a major contributor to static directional stability, and its contribution is always unstable (destabilizing). The stabilizing contributor to static directional stability is the vertical tail, in reality a low-aspect-ratio wing attached to the aft fuselage. The contribution of the major elements is shown in Fig. 24.60. When a sideslip angle develops due to a disturbance, the vertical tail experi-

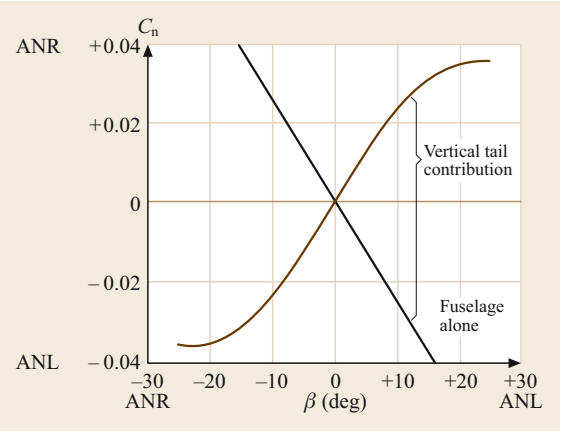

Fig. 24.60 Directional stability buildup (ANL = airplane nose left, ANR = airplane nose right)

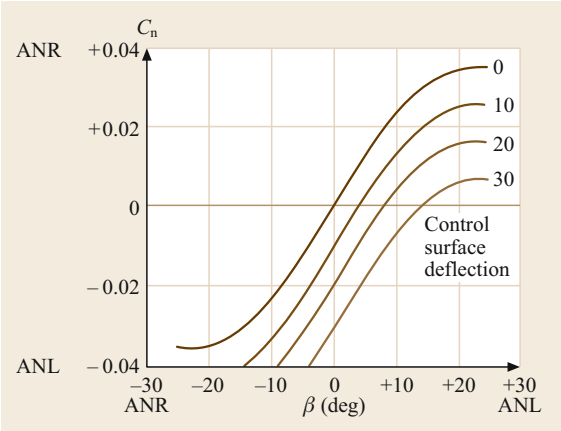

Fig. 24.61 Directional stability diagram – effect of control deflections (in degrees)

ences an increase in its angle of attack, and produces a restoring moment. The loss in directional stability at high sideslip angles, the *roundover* of the directional stability curve, is due to the vertical tail reaching its maximum lift capability, and stalling as the sideslip angle is increased. This roundover is not desirable and is often offset by the addition of a dorsal fin located at the intersection of the vertical tail leading edge and the fuselage. The magnitude of the restoring moment generated by the vertical tail depends on the distance from the airplane c.g. to the 25% m.a.c. point on the vertical tail, called the vertical tail length l_v and the vertical tail area S_v. For convenience, l_v is usually taken from the 25% m.a.c. point on the wing, rather than the c.g.

24.11.4 Directional Control

The vertical tail also provides the means for directional control. The predominant means is through a hinged, movable aft portion of the vertical tail (rudder), although some advanced military aircraft use all-movable verticals. As shown in Fig. 24.61, directional control is used to obtain equilibrium ($C_n = 0$) in steady sideslips. This figure shows that 30° of left rudder produces about 14° of positive sideslip.

Another requirement for directional control is to offset the asymmetric thrust moment which develops on a multiengine airplane when one engine becomes inoperative. In this situation, the aerodynamic moment from the vertical tail at or near zero sideslip with the control surface deflected must balance the thrust moment caused by the loss of one engine. This situation is most critical at low speeds during take-off. The minimum speed for which it is possible to maintain directional equilibrium ($C_n = 0$) during take-off with one engine inoperative is called the minimum control speed V_{mc},

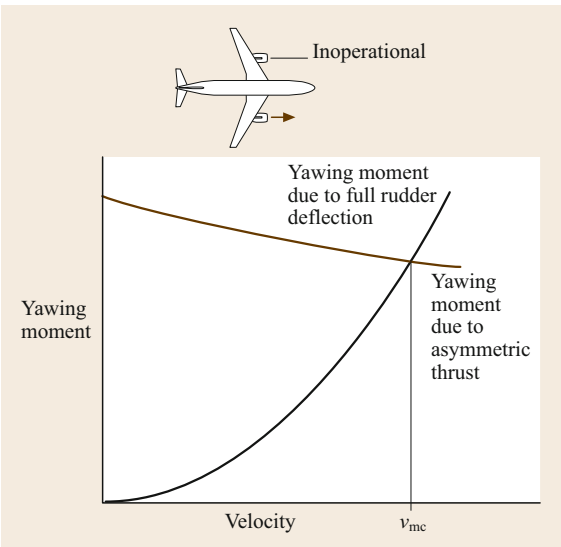

Fig. 24.62 Determination of ground minimum control speed

which may be obtained graphically by the intersection of the yawing moment due to the inoperative engine and the yawing moment due to full directional control, as shown in Fig. 24.62.

A summary of typical pilot control systems for airplanes is shown in Table 24.12.

24.11.5 Longitudinal Dynamics

In order to understand the requirements for static stability and control, it is necessary to study the dynamic characteristics of the airplane, investigating the types of motion that characterize the response of the airplane to a disturbance from some equilibrium flight condition

Table 24.12 Typical pilot control systems

Control about	Cockpit controller	Control direction	Airplane response
Lateral axis	Stick pull Stick push	Pitch	Nose up Nose down
Longitudinal axis	Stick right Stick left	Roll	Bank rwd Bank lwd
Vertical axis	Pedal right Pedal left	Yaw	Nose right Nose left

and the nature of the transient responses of the airplane to the movement of its controls. Dynamic systems in general have four different modes of motion when responding to a disturbance from an equilibrium condition. These modes are oscillatory or periodic, damped or undamped, as shown in Fig. 24.63.

The characteristic modes for nearly all airplanes are two oscillations, one of long period with poor damping, called the *phugoid*, and one of short period with heavy damping, called the *short period*. The *phugoid* oscillation is one in which there is a large-amplitude variation in airspeed, pitch angle, and altitude. The short period is a heavily damped oscillation in which the angle of attack varies at nearly constant speed.

24.11.6 Lateral Dynamics

There are two types of lateral dynamic motions. The first is called the *spiral mode*, which involves variations in bank angle and sideslip. This mode is usually a pure divergence, starting with a slow spiral in the direction of the disturbance, which if uncorrected, will develop into a high-speed spiral dive. The second motion is called the *Dutch roll*, because of its similarity to the well-known ice skating figure. This is an oscillatory motion involving variations in roll and yaw angles that for straight-wing propeller-driven airplanes is usually damped. However, for swept-wing airplanes, the Dutch roll oscillation is often lightly damped or mildly divergent, requiring the installation of a supplemental *yaw damper* system to provide satisfactory damping.

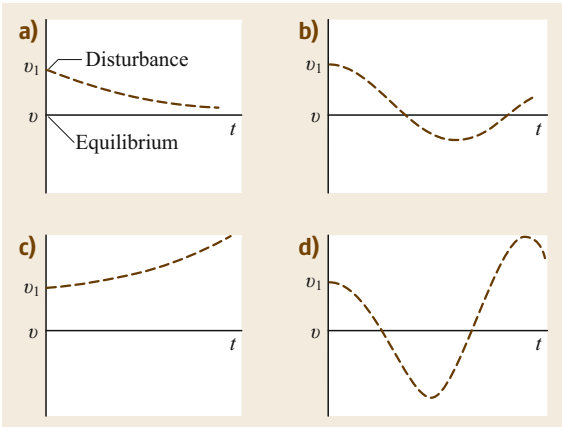

Fig. 24.63 Typical modes of motion. (a) Pure convergence; (b) damped oscillation; (c) divergence; (d) increasing oscillation

24.11.7 Maneuverability and Turning

The airplane flight path is controlled by varying the magnitude of the lift vector and by varying the output of the power plant. The magnitude of the lift vector is directly related to the lift coefficient through the angle of attack. The pilot can vary the angle of attack by controlling the pitching moment contributed by the control surfaces so that the pitching moment for the complete airplane is zero at the desired lift coefficient. From a steady unaccelerated level-flight condition, a maneuver in the plane of symmetry is initiated by a pilot control input to produce a positive nose-up pitching moment. This nose-up pitching moment will be balanced at some higher lift coefficient by the airplane's static longitudinal stability. If the longitudinal control input is made fairly rapidly, the speed will not have time to reduce to the speed required for equilibrium, and the lift will exceed the weight. With lift greater than weight, the airplane will experience a vertical acceleration. The maneuver just described is called an *abrupt pull-up* and may be the start of more complicated maneuvers. For a level-flight turn, referring to Fig. 24.64, the horizontal component of the lift vector accelerates the airplane laterally and curves the flight path. In a turn of radius R, the lateral force $L\sin\phi$, where ϕ is the angle of bank, must balance the centrifugal force on the airplane. Thus,

$$L\sin\phi = \frac{(W/g)V^2}{R}\,. \tag{24.3}$$

For a level-flight turn, the weight W must be equal to the vertical component of the lift $L\cos\phi$. Substitut-

Load factors in level flight turns

ϕ (deg)	$n = L/W = 1/\cos(\phi)$
0	1.000
15	1.035
30	1.155
45	1.414
60	2.000
75	5.464
90	∞

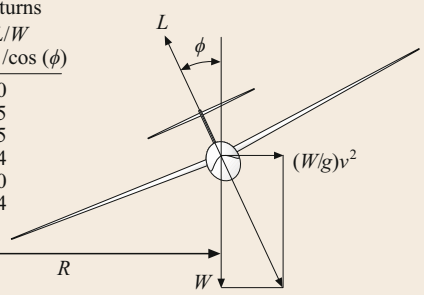

Fig. 24.64 Forces and load factors in level-flight turns

ing into (24.3), we obtain

$$L\sin\phi = \frac{[(L\cos\phi)/g]V^2}{R}\,, \quad \tan\phi = \frac{V^2}{\mathrm{gR}}\,. \quad (24.4)$$

Equation (24.4) specifies the angle of bank required for any speed and radius of turn. Conversely, the radius of turn is given by

$$R = \frac{V^2}{g\tan\phi}\,.$$

Also, since for a level-flight turn

$$W = L\cos\phi\,,$$

it follows that the lift for such a turn must be given by $L = W/\cos\phi$ and

$$\frac{L}{W} = \frac{1}{\cos\phi} = n\,.$$

As we shall see below, the quantity $n = L/W$ is an important parameter defined as the *load factor*.

24.12 Loads

Aircraft structures must be designed to withstand the most serious of the infinite number of possible combinations of external loads that may act on it in flight and when landing. Experience, accumulated over many years of design, analysis, and research, has led to the formulation of a very rational set of procedures that determine the design loads and define the airspeeds for which the design loads are imposed. For civil aircraft, these requirements and procedures are described in the FAR part 23 and part 25 *Airworthiness Standards, Airplanes*. For military aircraft, these requirements and procedures are described in MIL-A-8660, *Airplane Strength and Rigidity, General Specification For* and MIL-A-8661, *Airplane Strength and Rigidity, Flight Loads*. The requirements are, in most cases, nearly identical in both the civil and military documents. The information that follows is based on FAR 23 and 25, with information from MIL-A-8660 and MIL-A-8661 added where significant differences exist [24.26]:

- Flight conditions (FAR 25.331–25.459):
  - Maneuver load generated by intentional pilot application of controls
  - Gust load generated bya sudden change in angle of attack due to encountering a *gust*
- Landing conditions (FAR 25.473–25.511):
  - Level landing
  - Tail-down landing
  - One-wheel landing
  - Side load conditions
  - Braked roll conditions
  - Yawing conditions

24.12.1 Air Loads

Flight Load Factor

An important concept in the analysis of air loads imposed under various flight conditions is the flight load factor n, which is defined as

$$n = \frac{\text{aerodynamic force } \perp \text{ longitudinal axis}}{\text{aircraft weight}}\,.$$

For an aircraft in steady, level flight, the aerodynamic force perpendicular to the longitudinal axis is given by the lift, which is equal to the weight. Since the weight is due to the force of gravity, the aircraft is said to be in $1g$ flight. If the lift is four times the weight, the aircraft is subjected to $4g$. In a simpler form,

$$n = \frac{\text{lift}}{\text{weight}}\,.$$

V–n Diagrams

The analysis of the critical design air loads for an aircraft employs a chart known as the V–n diagram [24.26]. These charts show flight load factors as a function of equivalent airspeed and represent the maximum load factors expected in service, based on the requirements of the applicable specifications. These load factors are called *limit* load factors. The airplane structure must withstand these loads without damage. These limit loads are multiplied by a safety factor of 1.5 to define *ultimate* or failure loads. There are two types of V–n diagrams: one to define maneuver load factors, and one to define gust load factors.

V–n Diagram: Maneuver Envelope FAR 23.333 and FAR 25.333

The V–n diagram showing the maximum maneuver load factors that must be used for structural design (Fig. 24.65) is an envelope defined by various lines and points which have a specific relationship to the design load factors. A brief explanation of the key portions of the maneuvering envelope is given here.

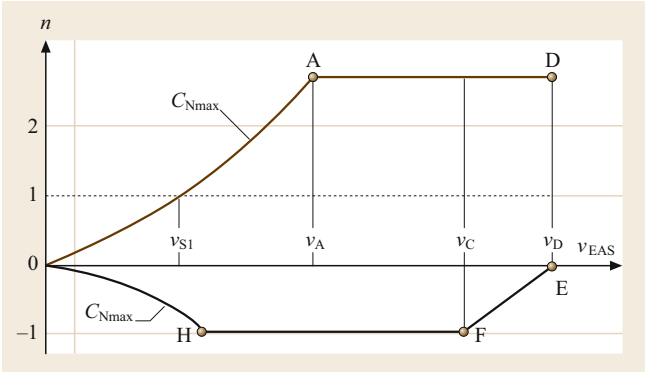

Fig. 24.65 *V–n* diagram: maneuvering envelope

Line O–A

This line describes the load factor that results when the aircraft is maneuvered to its maximum normal force coefficient $C_{N_{max}}$ in the clean or cruise configuration. Since this is the maximum normal force that can be generated by the aerodynamic characteristics of the configuration, it is the maximum load factor that can be generated by the pilot. The equation of this line is $n = C_{N_{max}} qS/W$.

Point A

This is the intersection of the pull up to $C_{N_{max}}$ with the maximum positive maneuver load factor specified in the requirements for the particular type of aircraft being designed. It should be noted that point A is not selected by the designer, but is determined uniquely by the aircraft parameters and the maneuver limit load factor for the type.

Table 24.13 Maximum maneuver load factors

Aircraft type	Max. positive	Max. negative
Normal	3.8	1.52
Acrobatic	6.0	3.00
Commuter	3.8	1.52
Utility	4.4	1.76

Line A–D

This is the maximum positive maneuver load factor for the type. The design limit load factors for various aircraft types were determined many years ago from flight tests of a number of airplanes of various types, each subjected to a number of typical maneuvers. These tests were made with an accelerometer placed at or near the airplane center of gravity, which recorded the imposed accelerations. Experience has indicated that these load factors result in highly satisfactory designs.

Line O–H

This line describes the load factor generated when the airplane is maneuvered to its maximum negative $C_{N_{max}}$ value. Since wing design is focused on using airfoils that have high values of positive $C_{N_{max}}$, the maximum values of negative $C_{N_{max}}$ are usually about 0.7 times the positive $C_{N_{max}}$ values.

Line H–F

This line describes the maximum negative maneuver load factor, again determined from flight tests as noted above.

The maximum maneuver load factors vary with aircraft type (Table 24.13). For FAR 23 aircraft, the maximum positive and negative maneuver load factors are listed in Table 24.14.

For FAR 25 aircraft, the maximum positive maneuver load factor varies with the design gross weight. The maximum value is 3.8 up to a gross weight of 4100 lb. At higher gross weights, the maximum value varies according to the relation up to a gross weight of 50 000 lb where the maximum becomes a constant value of 2.5. The maximum negative maneuver load factor for FAR part 25 aircraft is -1.0. Corresponding maneuver load factors for military aircraft are shown in Table 24.14.

V–n Diagram: Gust Envelope FAR 23.333 and FAR 25.333

In addition to the load factors imposed by intentional maneuvers controlled by the pilot, appreciable

Table 24.14 Design maneuver load factors for military airplanes

Aircraft type	Basic flight design weight		All weights	Max. design weight		Max. ordnance weight	
	Max.	Min. at V_H	Min. at V_H	Max.	Min. at V_H	Max.	Min. at V_H
Fighter/attack (subsonic)	8.00	−3.00	−1.00	4.00	−2.00	5.50	−2.00
Fighter/attack (supersonic)	6.50	−3.00	−1.00	4.00	−2.00	5.50	−2.00
Observation trainers	6.00	−3.00	−1.00	3.00	−1.00		
Utility	4.00	−2.00	0	2.50	−1.00		
Tactical bomber	4.00	−2.00	0	2.50	−1.00		
Strategic bomber	3.00	−1.00	0	2.00	0		
Assault transport	3.00	−1.00	0	2.00	0		
Conventional transport	2.50	−1.00	0	2.00	0		

increases in effective angle of attack result from entering a *gust*, or current of air having a velocity component normal to the line of flight. The resulting increase in load factor depends primarily on the vertical velocity of the gust, and especially for business jets and jet transports, it may exceed the maximum due to intentional maneuvers. These load factors are summarized on a *V*–*n* gust envelope diagram (Fig. 24.66).

The load factors produced by gusts vary directly with the equivalent airspeed, and are computed using the gust load factor equation given in FAR 23.341 and FAR 25.343.

The equation is

$$n = 1 + \frac{K_g U_{gE} V_E a}{498(W/S)} ,$$

where

$$K_g = \frac{0.88\mu_g}{5.3 + \mu_g} = \text{gust alleviation factor} ,$$

$$\mu_g = \frac{2(W/S)}{\rho \overline{C}_{ag}} = \text{airplane mass ratio} ,$$

U_{gE} = equivalent gust velocity (ft/s) ,

ρ = density of the air $\left(\text{slug/ft}^3\right)$,

$\frac{W}{S}$ = wing loading $\left(\text{lb/ft}^2\right)$,

$\overline{C}$ = mean geometric chord (ft) ,

g = acceleration due to gravity $\left(\text{ft/s}^2\right)$,

V_E = aircraft equivalent airspeed (kn) ,

a = slope of the airplane normal force curve per radian .

The *V*–*n* diagram for the gust envelope is shown in Fig. 24.66.

The designer must assume a symmetrical vertical gust of:

- 66 fps at V_B from sea level (S.L.) to 20 000 ft, decreasing to 38 fps at 50 000 ft
- 50 fps at V_C from S.L. to 20 000 ft, decreasing to 25 fps at 50 000 ft
- 25 fps at V_D from S.L. to 20 000 ft, decreasing to 12.5 fps at 50 000 ft.

The key points of the gust envelope are as follows.

Line 0–B′

As in the maneuver envelope, this line describes the maximum load factor that can be generated by a gust which causes the airplane to reach its $C_{N_{max}}$.

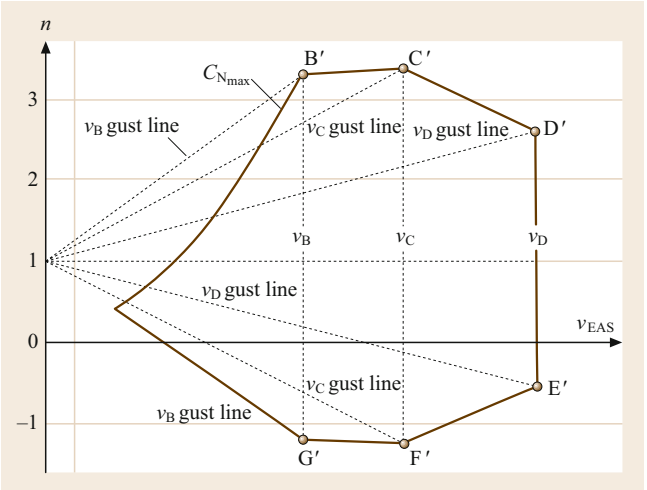

Fig. 24.66 *V*–*n* diagram: gust envelope

Point B′

This point is the intersection of the load factor for $C_{N_{max}}$ and the load factor for a 66 fps gust. This point determines V_B, the design speed for maximum gust intensity.

Point C′

This point is the intersection of the load factor due to a 50 fps gust and the design cruising speed V_C.

Point D′

This point is the intersection of the load factor due to a 25 fps gust and the design dive speed, V_D.

Points E′, F′, and G′

These points are the corresponding intersections for negative gusts at the designated speeds.

The maneuver and gust envelopes are superimposed to determine the highest load factors for design at all speeds within the flight envelope and the entire aircraft structure analyzed for these load factors.

In addition to these major air loads imposed on the airplane by intentional maneuvers and gusts, there are other conditions associated with abrupt control inputs in pitch, roll, and yaw that must be accounted for in the structural design.

24.12.2 Design Airspeeds

The airspeeds associated with the *V*–*n* diagram except for V_A and V_B are chosen by the designer, but must meet certain definitions and criteria contained in the FARs. The following list is a simplified summary.

Design airspeeds – EAS:

V_S Stalling speed or minimum steady flight speed
V_A Maneuver speed or full control deflection speed

V_B Design speed for maximum gust intensity
V_{FE} Design flap-extended speed
V_{LE} Design landing-gear-extended speed
V_{LO} Design landing-gear-operating speed (if different from V_{LE})
V_C Design cruising speed ($\geq V_B + 43$ kts)
V_{MO} Maximum operating limit speed (*barber's pole* speed)
V_{FC} Maximum speed at which flight characteristics requirements must be met
V_D Design dive speed, $\geq V_C/0.80$, or speed reached in 7.5° dive for 20 s from V_C, followed by 1.5g recovery.

The military speed definitions are basically the same, although MIL-A-8660B combines V_C and V_{MO} into a maximum level flight speed V_H, and replaces V_D with the *limit speed* V_L.

For subsonic airplanes, the design airspeeds are usually constant for the entire flight envelope. For high-subsonic and supersonic airplanes, the design airspeeds are varied throughout the flight envelope, since equivalent airspeeds that are appropriate at sea level and lower altitudes are beyond the performance capabilities of the airplane at higher altitudes. Therefore, the design airspeeds for these types are usually defined in terms of Mach number at higher altitudes; for example, the maximum operating limit speed is defined by a V_{MO}/Ma_{MO} line that is a function of altitude. As noted earlier, the design cruise speed (Mach number) need not be higher than the maximum speed in level flight at that altitude with maximum cruise power. This provision usually sets Ma_C. V_{MO} is usually set at or slightly above (0.01 or 0.02 Mach number) Ma_C, providing a margin on the order of 0.08 Mach number between the best long-range cruise Mach number and Ma_{MO}. The design dive Mach number is usually about 0.05 Mach number higher than Ma_{MO}.

24.12.3 Ground Loads

There are a range of take-off and landing conditions that must be considered in the structural design of the airplane. These conditions are described in detail in the appropriate sections of the Federal Aviation Regulations. These loads may be classified as vertical loads due to descent rates at touchdown and taxiing over rough surfaces, longitudinal loads caused by wheel spin-up loads on landing, braking loads, and rolling friction loads, and lateral loads caused by landing with some sideslip angle, cross-wind taxiing, and turning on the ground.

24.13 Airplane Structure

The structure of an aircraft must withstand the applied aerodynamic and ground reaction loads encountered in normal operation, as well as those that may be encountered very rarely. The essential character of aircraft structure is light weight, because weight plays such an important role in the performance and economics of the airplane. This critical significance of structural weight is the major difference between aircraft structural design and other types of structural design [24.28].

Overall aircraft structural loads consist of shear, bending, and torsion. Aircraft structural design has always sought to meet the applied load requirements with a minimum acceptable margin of safety and the least weight. However, the potentially disastrous effect of an aircraft structural failure requires that the structure must be designed for long life either with safe life criteria or fail-safe design. Safe life means that the stresses in a component are so low that fatigue failure is not possible over the anticipated life of the airplane, or at least until some period has passed after which a part replacement is required. Fail-safe means that the structure has alternate load paths so that no single failure of a part will be hazardous to the airplane. This is accomplished by designing the structure so that no one part carries most of the maximum load. Therefore, if one part fails, the remainder of the structure can still carry most of the maximum load. Since the maximum load is rarely encountered, and the structure has a safety factor of 1.5, the structure remains safe until the failure is found and repaired.

24.13.1 Structural Design

Aircraft structures are composed of three basic types of structural elements: stiffened shells, stiffened plates, and beams. The terms "stiffened shells" and "stiffened plates" refer to the fact that, under compressive loading, the thin skins of the shells and plates generally buckle before reaching the compressive failure stress of the material. To avoid this condition, stiffeners are attached to the thin skins. Stiffeners not only carry their own load, but by preventing early buckling of the skin, they increase the stress that can be supported in compression before buckling occurs. The primary wing structural element, the wing *box*, is essentially a hollow beam, consisting of the upper and lower wing skins, ribs, wing

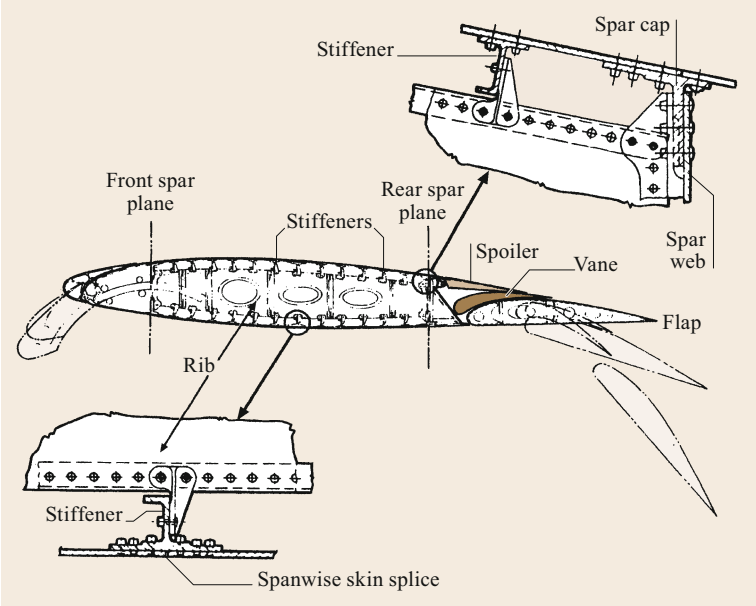

Fig. 24.67 Wing box structural elements

skin stiffeners, spar caps, and spar webs, as shown in Fig. 24.67.

The wing skins transfer the external air loads to the wing box structure. The fuselage is generally a semimonocoque structure (Fig. 24.68) that consists of frames which maintain the cross-sectional shape, to which are attached various longitudinal stiffeners called stringers or longerons. Loads on the fuselage floor are supported by floor beams, with other beam elements to accommodate cutouts in the fuselage shell. The horizontal and vertical tail structure is very similar to the wing structure, employing skins, ribs, stiffeners, spars, spar caps, and spar webs.

An overview of the semimonocoque construction of a Boeing KC-767a jet is shown in Fig. 24.69.

Another important aspect of structural design is the need to design for long fatigue life. Metals suffer gradual deterioration under repeated application and removal of loads. Modern commercial transports may fly for many thousands of hours and take-off and landing cycles, so that often fatigue life, rather than strength requirements, dominate the structural design. The number of load cycles a material can tolerate depends on the stress level. The lower the stress level, the greater the number of cycles that the part can withstand. The results of a typical fatigue test (Fig. 24.70) show the

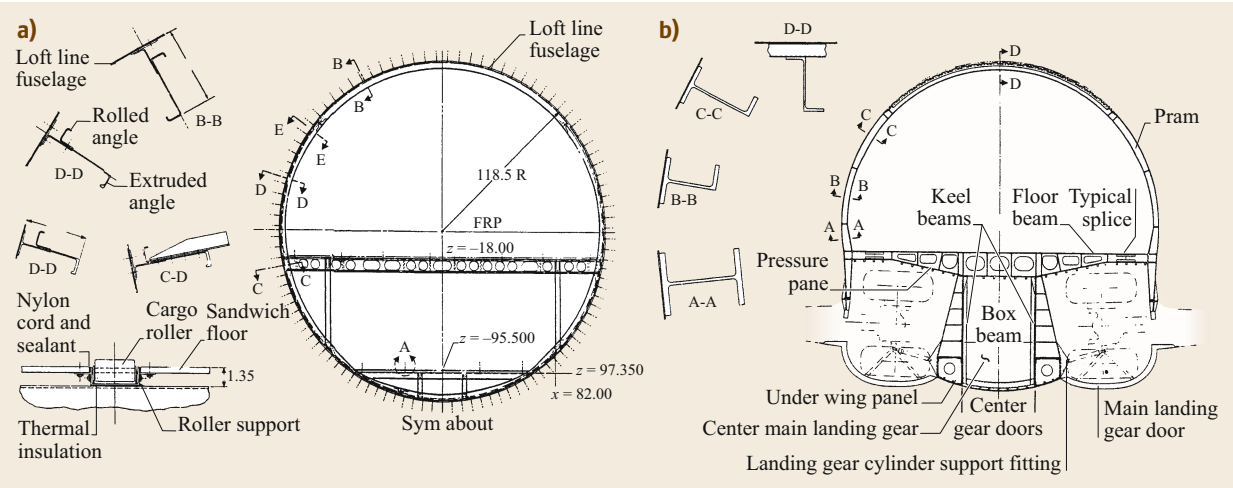

Fig. 24.68a,b Fuselage structural elements: **(a)** Typical fuselage cross section; **(b)** section through wheel wall

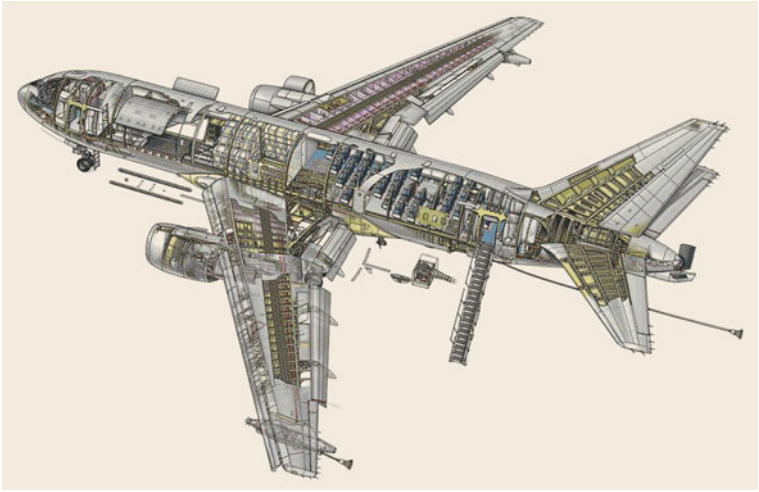

Fig. 24.69 Semimonocoque construction of a Boeing KC-767a jet (Flight International, © 2006 Reed Business Information)

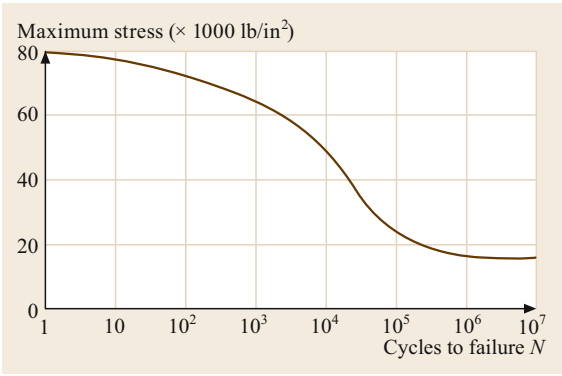

Fig. 24.70 Fatigue test results

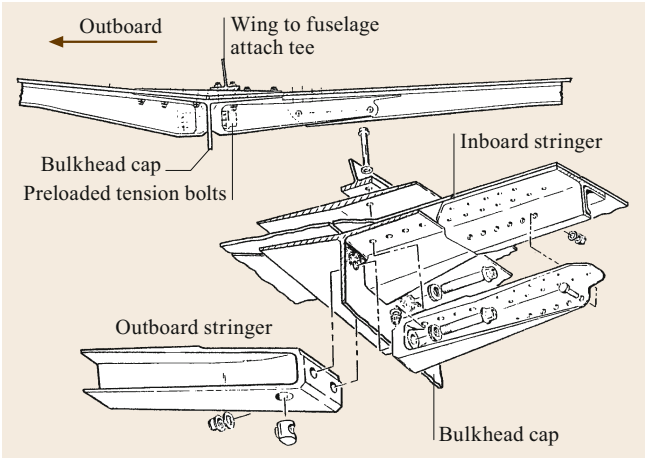

Fig. 24.71 Wing–fuselage joint fitting

tremendous improvement in fatigue life that can be obtained by limiting a material to cyclic stress levels that are well below the ultimate strength.

If fatigue is critical, a less strong material with better fatigue resistance may result in a lighter structure. Excessive stress levels conducive to early fatigue failure may arise not only from an overall high stress level, but also from stress concentrations at local points in the structure. Fittings and joints, which serve to carry loads from one structural component to another, may, if not designed very carefully, introduce increased local stresses leading to fatigue failure long before any problem occurs in the basic structure. A major part of the design of aircraft structure is the avoidance of stress concentrations by careful detail design. One approach is to lower the stress level approaching a hole or fitting by adding an extra sheet or thickness of metal called a *doubler* to the inside surface of a wing skin around an access hole or to the fuselage skin around a window. Special attention is given to fitting design (Fig. 24.71). In spite of the care taken in detailed structural design, a vital part of aircraft maintenance is the continuing search on a scheduled basis for structural cracks.

24.13.2 Structural Analysis

In the design and analysis of a real aircraft structure, which is usually a large assemblage composed of various structural elements such as stiffened shells, stiffened plates, and beams, the overall geometry becomes extremely complex and cannot be represented by a single mathematical expression. In addition, these built-up structures are characterized as having material and structural discontinuities such as cutouts, thickness variations in the members, as well as discontinuities in loading and support structures. It is apparent that classical methods can no longer be used, particularly those which require the formulation and solution of govern-

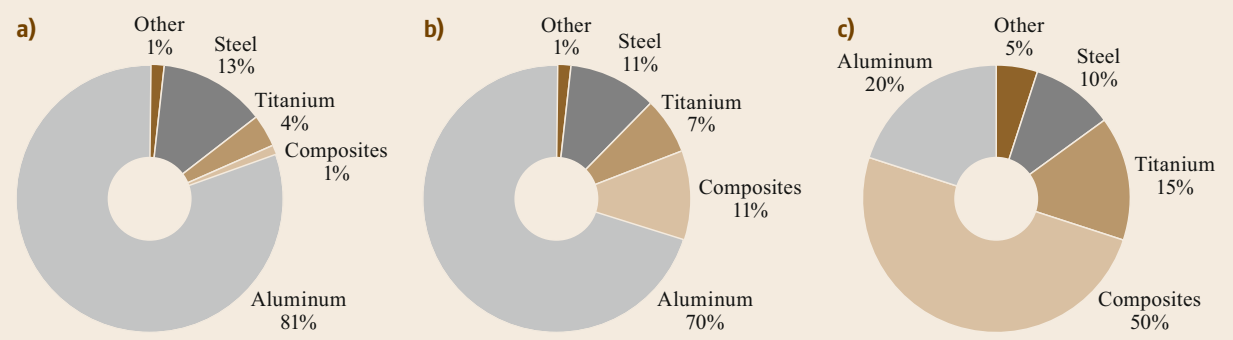

Fig. 24.72a–c Comparison of structural materials distribution – commercial transports. **(a)** Boeing 747, **(b)** Boeing 777, and **(c)** Boeing 787 Dreamliner

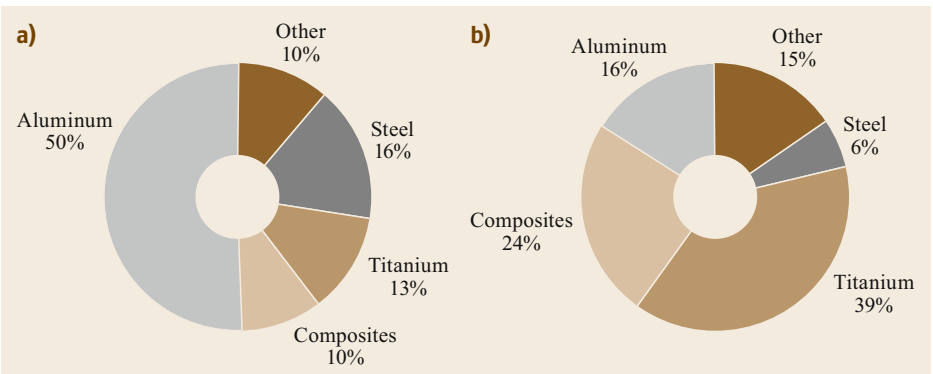

Fig. 24.73a,b Comparison of structural materials distribution – military fighters. McDonnel Douglas F-18, **(a)** Lockheed Martin F-22

ing differential equations. For complex structures, the preferred method of analysis is called the finite element stiffness method. With the advent of high-speed large-storage-capacity digital computers, finite element matrix methods have become the most widely used tools in the analysis of complex structures.

24.13.3 Structural Materials

Modern aircraft are constructed from a variety of materials, chosen based on considerations such as density, mechanical properties, corrosion resistance, ease of fabrication, and cost. The most used materials are the light metals, aluminum alloys, and titanium, although for some applications where high strength is required, steel alloys are used. Structural composite materials are being used more because of their low density and good mechanical properties. Composites generally consist of a plastic matrix of epoxy resin, reinforced by many high-strength fibers of carbon, Kevlar, glass, or boron. The distribution of materials used in aircraft construction has been changing over the years as materials science researchers have developed more attractive products. Figure 24.72 shows a comparison of the structural materials distribution between the Boeing 747 of 1969, the Boeing 777 of 1994, and the Boeing 787 of 2009. In the 40 years between the design of these three transport aircraft, the most notable difference in materials use is the large increase in composites and titanium, and a significant reduction in the use of aluminum.

An even more startling change in the structural materials distribution has taken place in military aircraft design. Figure 24.73 shows the distribution of structural materials in the McDonnell Douglas F-18 of 1978 and the Lockheed Martin F-22 of 2003. The most startling difference in the materials use between these two aircraft is the large reduction in the use of aluminum alloy and steel in the F-22 and the large increase in the use of titanium and composites.

In addition to the introduction of newer, nontraditional materials, several new processes for producing parts from these new materials have been introduced, which reduce the number of parts required and also reduce the amount of labor required to produce each part. Examples of these new processes are *resin transfer molding* (RTM) for producing composite parts, and *hot isostatic pressing* (HIP) for producing large high-quality castings.

24.14 Airplane Maintenance Checks

As noted earlier, in order to ensure safe operations, especially for commercial transport aircraft, regular formal maintenance checks are carried out on airplanes' systems and structure. These checks range from the very simple *preflight* check of the aircraft conducted by the flight crew prior to each flight, to the extensive, detailed maintenance inspection checks conducted by technical specialists at major maintenance facilities. A summary of the various types of maintenance checks that are conducted by airline operators is presented in Table 24.15.

Table 24.15 Summary of typical maintenance checks for transport airplanes

	B 737	B 747	A 300	A 320	Time required	Man-hours
A-Check	350 h	650 h	350 h	350 h	Overnight	20–130
B-Check	5.5 m	1800 h	1000 h	–	One day	200–1000
C-Check	15 m	18 m	18 m	15 m	A few days	600–1400
D-Check	22 000 h 25 000 ldg 108 m	31 000 h 72 m –	25 000 h 12 500 loading 108 m	– – 102 m	≈ 6 weeks	50 000

References

24.1 AIA: Manufacturing Workforce – Aerospace Industry Association Rep. (AIA, Arlington 2019), https://www.aia-aerospace.org/research-center/statistics/industry-data/workforce/

24.2 IATA: International Air Transport Association Rep. 62 (IATA, Geneva 2018), https://www.iata.org/en/pressroom/pr/2018-10-24-02/

24.3 P. Moran: Environmental Trends in Aviation 2050, FAA Office of Environment and Energy Report (2019), https://www.icao.int/Meetings/EnvironmentalWorkshops/Documents/Env-Seminars-Lima-Mexico/Mexico/08_UnitedStates_EnvironmentTrends.pdf

24.4 P. Argüelles, J. Lumsden, M. Bischoff: *European Aeronautics: A Vision for 2020* (Office for Official Publications of the European Communities, Luxembourg 2001)

24.5 D.P. Raymer: *Aircraft Design: A Conceptual Approach* (American Institute of Aeronautics and Astronautics, Reston 2006)

24.6 Federal Aviation Administration: *Code of Federal Regulations, Title 14, Aeronautics and Space* (Office of the Federal Register: Federal Aviation Administration, Washington 1997)

24.7 D. Küchemann: *The Aerodynamic Design of Aircraft* (Pergamon, Oxford 1978)

24.8 C.B. Millikan: *Aerodynamics of the Airplane* (Wiley, New York 1941)

24.9 A.M. Kuethe, J.D. Schetzer: *Foundations of Aerodynamics* (Wiley, New York 1950)

24.10 L.M. Nicolai: *Fundamentals of Aircraft Design* (METS, San Jose 1984)

24.11 R.D. Schaufele: *The Elements of Aircraft Preliminary Design* (Aries Publications, Santa Ana 2000)

24.12 H.W. Liepmann, A.E. Puckett: *Aerodynamics of a Compressible Fluid* (Wiley, New York 1947)

24.13 L.K. Loftin Jr.: *Subsonic Aircraft: Evolution and the Matching of Size to Performance* (NASA, Arlington 1980), (NASA Reference Publication 1060)

24.14 D.P. Raymer: *Aircraft Design: A Conceptual Approach* (AIAA, Washington 1989)

24.15 J. Roskam: *Airplane Design: Part I, Preliminary Sizing of Airplanes* (Roskam Aviation and Engineering, Ottawa 1989)

24.16 I.H. Abbott, A.E. Von Doenhoff: *Theory of Wing Sections* (Dover, New York 1959)

24.17 R.D. Schaufele, A.W. Ebeling: *Aerodynamic Design of the DC-9 Wiing and High Lift System, SAE Paper No. 67-0846* 1967), (Aeronautics and Space Engineering Meeting, Los Angeles)

24.18 Anonymous: *The DC-9 Handbook* (Douglas Aircraft, Long Beach 1991)

24.19 Anonymous: *The DC-10 Handbook* (Douglas Aircraft, Long Beach 1986)

24.20 N.S. Currey: *Aircraft Landing Gear Design: Principles and Practices* (AIAA, Washington 1988)

24.21 J. Roskam: *Airplane Design, Part IV; Layout Design of the Landing Gear and Systems* (Roskam Aviation and Engineering, Ottawa 1989)

24.22 A.P. Fraas: *Aircraft Power Plants* (McGraw-Hill, New York 1943)

24.23 Anonymous: *Brief Methods of Estimating Airplane Performance, Report No. SM-13515* (Douglas Aircraft, Santa Monica 1949)

24.24 Anonymous: *DC-9-30 Performance Handbook* (Douglas Aircraft, Long Beach 1969)

24.25 R.S. Shevell, I. Kroo: *Introduction to Aircraft Design Synthesis and Analysis, Course Notes* (Stanford Univ. Press, Palo Alto 1981)

24.26 C.D. Perkins, R.E. Hage: *Airplane Performance Stability and Control* (Wiley, New York 1949)

24.27 R.S. Shevell: *Fundamentals of Flight* (Prentice Hall, Englewood Cliffs 1989)

24.28 D.J. Peery, J.J. Azar: *Aircraft Structures* (McGraw-Hill, New York 1982)

Hamid Hefazi

Mechanical Engineering Department
State University of New York (SUNY)–Korea
Incheon, Republic of Korea
hamid.hefazi@sunykorea.ac.kr

Hamid Hefazi received the PhD degree in Aerospace Engineering from the University of Southern California in 1985. He is currently Professor and Chair of mechanical engineering department at SUNY-Korea. His research areas include computational fluid dynamics (CFD), aerodynamic design optimization, aeroacoustics, hydrodynamics, neural networks, and advanced optimization methods.

25. Ships and Maritime Transportation

Jean-Baptiste R. G. Souppez

This chapter offers insight into how ships are designed by naval architects to address the ever-growing demand for maritime transportation. The terminology associated with ships is introduced, together with some of the main design characteristics of ships. The stability of marine vessels at both small and large angles of heel is explored. Furthermore, the main resistance and propulsion concepts that must be utilized effectively to ensure that the vessel can achieve its target speed are presented. Elements of ship structure as well as structural design and optimization considerations are discussed. Finally, additional aspects that impact ship design are outlined, including the environment, seakeeping, maneuverability, and damage stability.

25.1 **Overview** 1139

25.2 **Ship Geometry and Definitions** 1141
25.2.1 Geometry and Nomenclature 1141
25.2.2 Form Coefficients 1142
25.2.3 Lines Plan 1143
25.2.4 Sectional Area Curve 1144
25.2.5 Gross Tonnage 1145
25.2.6 Axis System 1145

25.3 **Hydrostatics and Stability** 1145
25.3.1 Archimedes' Principle 1145
25.3.2 Definitions 1146
25.3.3 Transverse Stability at Small Angles 1146
25.3.4 Impact of $\overline{GM}$ on Comfort 1147
25.3.5 Transverse Stability at Large Angles 1147
25.3.6 Angle of List 1148
25.3.7 Weight Estimate 1149
25.3.8 Inclining Experiment 1149
25.3.9 Free Surface Effect 1150
25.3.10 Stability Curves 1150
25.3.11 Longitudinal Stability 1151
25.3.12 Plimsoll Mark 1152

25.4 **Resistance and Powering** 1152
25.4.1 Speed and the Froude Number 1152
25.4.2 Froude Resistance Model 1152
25.4.3 ITTC Resistance Model 1153
25.4.4 Towing Tank Testing 1153
25.4.5 Additional Resistance Components 1154
25.4.6 Wave Interference 1155
25.4.7 Powering 1156

25.5 **Structure** 1157
25.5.1 Structural Design 1157
25.5.2 Materials 1158
25.5.3 Global Loads 1158
25.5.4 Local Loads 1159
25.5.5 Design Optimization 1160
25.5.6 Midship Section 1160

25.6 **Additional Considerations** 1161
25.6.1 The Environment 1161
25.6.2 Seakeeping 1161
25.6.3 Maneuverability 1162
25.6.4 Damage Stability 1162

25.7 **Summary** 1162

References 1163

25.1 Overview

Maritime transportation has historically been at the heart of the world's economy, and it retains this status today; for instance, close to 90% of all the freight shipped globally in 2016 was transported by a fleet of over 50 000 marine vessels. Due to the diverse nature of the cargos shipped by sea, a range of specific ship designs have been developed to suit specific demands. A breakdown of the number of ships of each type is presented in Fig. 25.1.

The amount of freight carried by a ship is referred to as the deadweight (DWT). For container carriers, the amount of cargo is commonly quantified in terms of twenty-foot equivalent units (TEUs), where a TEU represents a standard 20 ft container.

In order to cope with the exponential growth in global trade and the resulting demand for ships, they have become larger over time. In the 1950s, a typical container carrier was 130 m long and would accommo-

K.-H. Grote, H. Hefazi (Eds.), *Springer Handbook of Mechanical Engineering*, Springer Handbooks,
https://doi.org/10.1007/978-3-030-47035-7_25

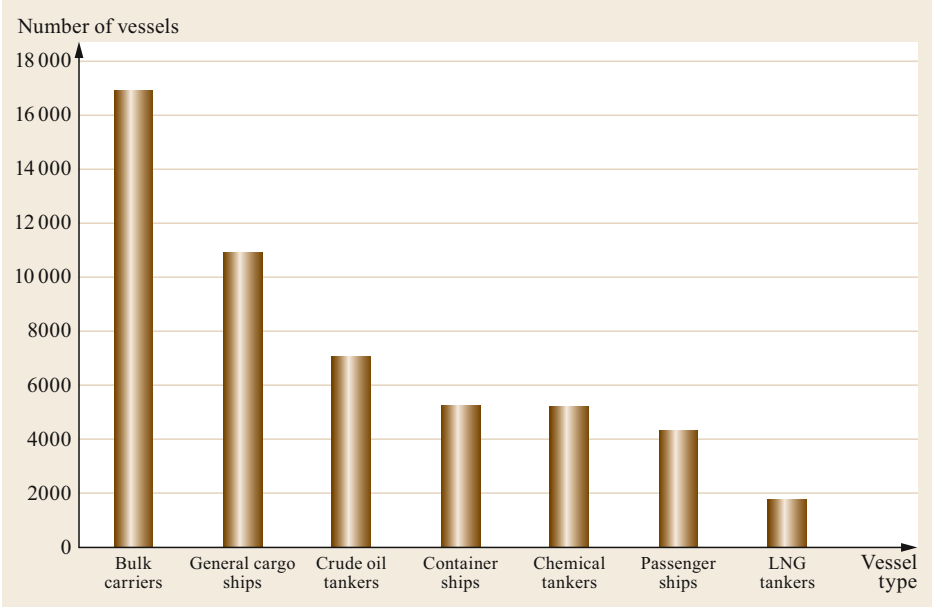

Fig. 25.1 Number of ships of each type in 2016

date in the region of 800 TEUs. However, the latest ships are close to 400 m long and carry in excess of 18 000 TEUs. The evolution in cargo capacity over the last 50 years is depicted in Fig. 25.2.

Ever-increasing ship sizes and the resulting need to improve their performance has created an array of challenges for naval architects and marine engineers. Furthermore, ship design is rigorously defined by international standards and class societies, and designs must comply with the relevant rules and regulations. Some of these regulations were established in response to tragedies; for example, the Safety Of Life At Sea (SOLAS) treaty [25.1] dates back to 1914, as it was a response to the sinking of the RMS *Titanic* two years earlier [25.2]. New regulations have also been brought forward due to modern environmental considerations. As a result, there are new constraints on emission levels that must be met, particularly for NO_x (nitrogen oxides) and SO_x (sulfur oxides).

International regulations are published by the International Maritime Organization (IMO), the United Nations' agency in charge of shipping regulation. Some of the most influential class societies in the context of shipping include Lloyd's Register (LR), the American Bureau of Shipping (ABS), Det Norske Veritas Germanischer Lloyd (DNV GL), Bureau Veritas (BV), Registro Italiano Navale (RINa), and Nippon Kaiji Kyokai (Class NK).

In order for a vessel to satisfy the present demands on maritime transportation, its design must also meet a set of preestablished requirements agreed upon by the various stakeholders. This set of requirements is known as the design brief. Furthermore, a ship must represent value for money and be stable, structurally sound, safe, and reliable without being overengineered. An excessively heavy structure will be more costly than necessary and will require extra power and consequently more fuel during operation, meaning that it will not be able to accommodate as much cargo as a less heavy structure. Nevertheless, the vessel must be strong enough to complete its intended service life and thus represent a good financial investment. In addition, ships must be as fuel efficient as possible to maximize profits; oil prices are therefore a primary driver of ship design. This has prompted innovations to reduce vessel drag or augment propulsive efficiency, including investigations into greener propulsion methods, such as kites and Flettner rotors.

In this chapter, to provide insights into the application of mechanical engineering to the design of ships and naval architecture in general, important terminology associated with ships is initially defined, along with key design ratios. Elements of ship stability that ensure the safe operation of vessels in service are then introduced, with particular emphasis placed on the challenges induced by fluctuating loading conditions. Moreover, the main aspects of resistance and powering calculations performed to ensure that the required ship speed is reached in the most fuel-efficient way are outlined. Moreover, an overview of ship structural design is provided, featuring some of the main aspects of the scantlings (i.e., the dimensions of the structural components of a vessel). Finally, other areas of ship design are briefly discussed. This chapter therefore encapsulates the major aspects of engineering in the field of naval architecture and maritime transportation.

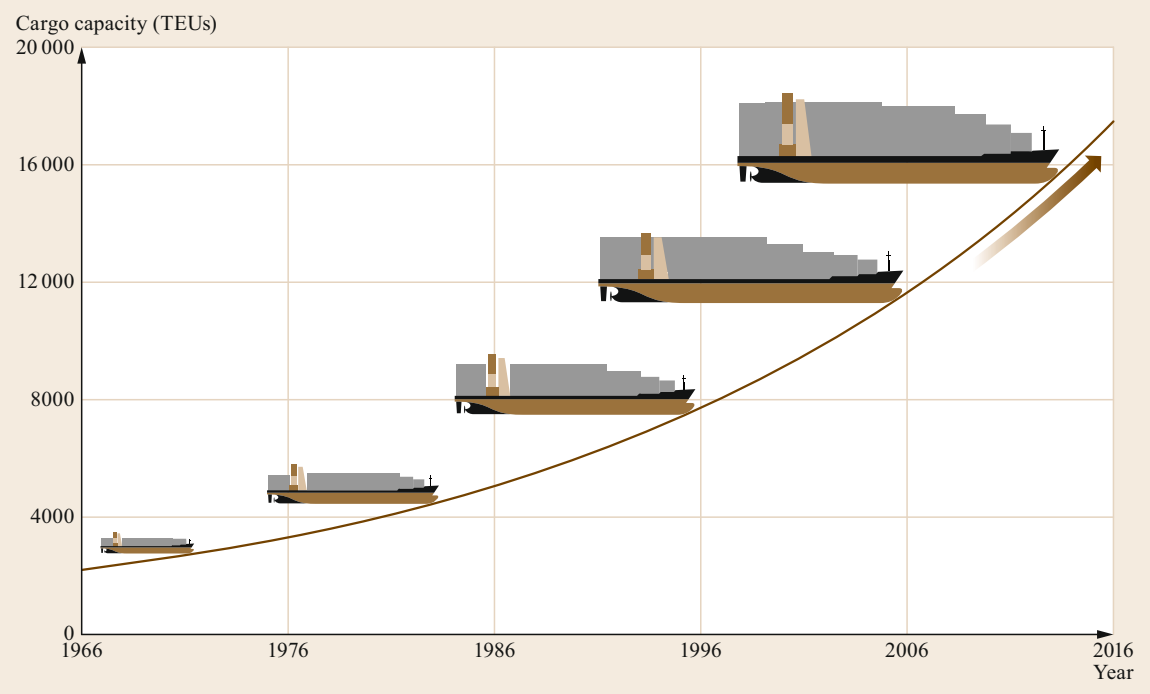

Fig. 25.2 Evolution of the cargo capacity of container ships over the past 50 years

25.2 Ship Geometry and Definitions

25.2.1 Geometry and Nomenclature

Ships are sizable and complex vessels with highly specific terminology. For instance, the length of a ship between its forward (the bow or stem) and aft (the stern) ends is defined in a number of ways. The overall length L_{OA} is the maximum length of the ship. The length at the waterline L_{WL} is measured at the waterline of the vessel while it is floating; this value is considered for hydrostatic and hydrodynamic purposes. Finally, the length between perpendiculars L_{BP} is the distance between the forward perpendicular (the intersection of the loaded waterline and the stem) and the aft perpendicular (commonly taken to be the rudder stock axis). The length between perpendiculars is noteworthy as it provides a preliminary idea of the volume available to carry cargo. The midway point between the perpendiculars is termed *amidships*, as pictured in Fig. 25.3.

As the hull is a three-dimensional (3-D) body, additional dimensions are required to better characterize the volume of the hull. The width of the hull is the molded breadth B, while the maximum overall breadth of the vessel is termed the extreme breadth B_E. Moreover, the beam at the waterline is labeled B_{WL}. The depth of the hull is referred to as the molded depth D, which is further divided into the freeboard F, measured from the waterline to the sheerline (the edge between the side of the vessel and the deck) and the draft T (the distance from the waterline to the lowest point on the keel). These parameters are presented in Fig. 25.4. The notion of the air draft T_A is also essential when attempting to define the overall size of the vessel, which represents the distance between the waterline and the highest point on the ship.

These dimensions are crucial to ship design. Vessels are intended for specific areas of operation and routes around the globe with precise environmental restrictions. For instance, the New Panamax vessels are specifically designed to be the largest vessels that still fit within the new lock restrictions of the Panama Canal: a length of 366 m, a breadth of 49 m, a draft of 15.2 m, and an air draft of 57.91 m. Ships in this class must be designed to fit within these restrictions imposed by the Panama Canal; any vessel that exceeds any of these dimensions requires an alternative trade route. Ship design therefore needs to acknowledge environmental constraints in order to produce suitable vessels.

The naval architect is also concerned with the dimensions of the part of the vessel that is underwater, such as the volume of water displaced, which allows

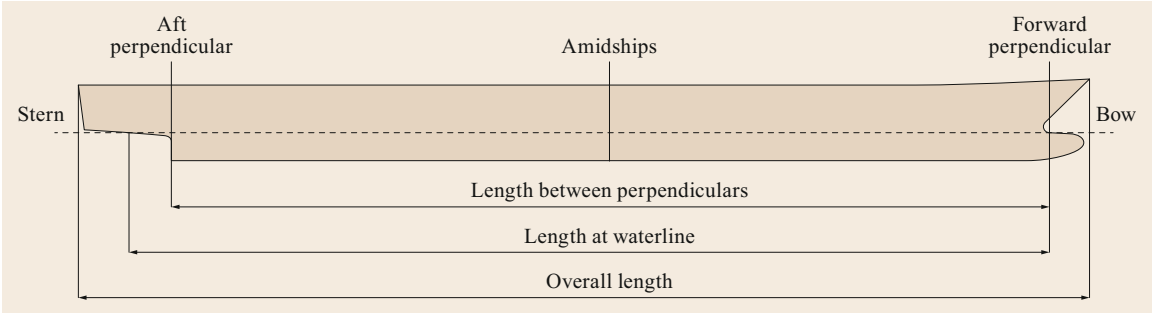

Fig. 25.3 Profile view of a ship and important definitions

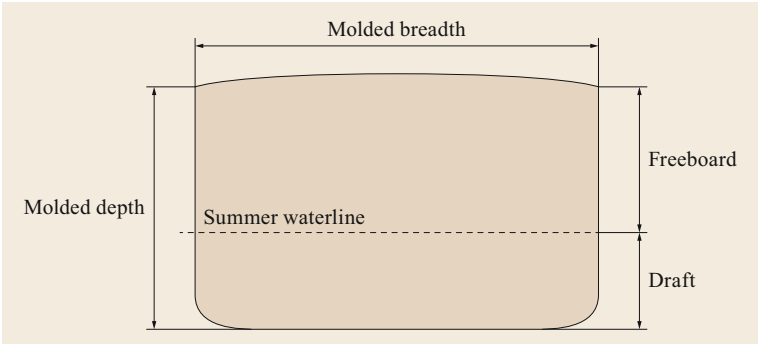

Fig. 25.4 Cross-section of a ship and definitions of various dimensions

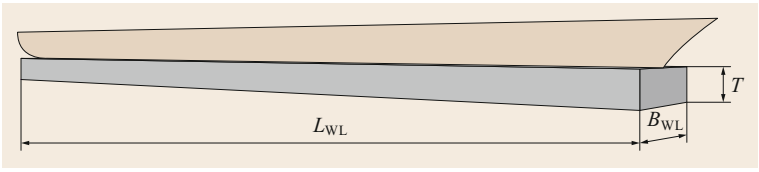

Fig. 25.5 Block coefficient

Archimedes' principle to be employed to determine the acceptable weight of the vessel (i.e., the weight that causes the vessel to float at its intended waterline). Knowledge of the dimensions of the immersed part of the ship and the primary design ratios (which must be within the expected range for this type of vessel) facilitate early hydrostatic and hydrodynamic calculations and support the decision-making process for certain aspects of the ship. Consequently, a number of form coefficients are defined, including the block coefficient C_B, the midship area coefficient C_M, the prismatic coefficient C_P, and the waterplane area coefficient C_{WPA}.

25.2.2 Form Coefficients

The block coefficient represents the nondimensional ratio of the immersed volume of the hull ∇ to the volume of a box of length L_{WL}, breadth B_{WL}, and draft T. A low block coefficient is associated with a lower resistance, thus enabling higher speeds to be reached, whereas a higher block coefficient indicates greater drag but also a larger cargo carrying capacity. The block coefficient is illustrated in Fig. 25.5 and is given by the equation

$$C_B = \frac{\nabla}{L_{WL} B_{WL} T} .$$

The midship area coefficient compares the immersed sectional area at midships A_M with the rectangle formed by the waterline breadth and draft, as shown in Fig. 25.6.

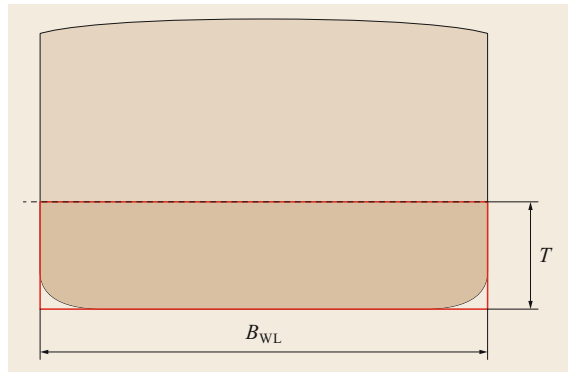

Fig. 25.6 Midship area coefficient

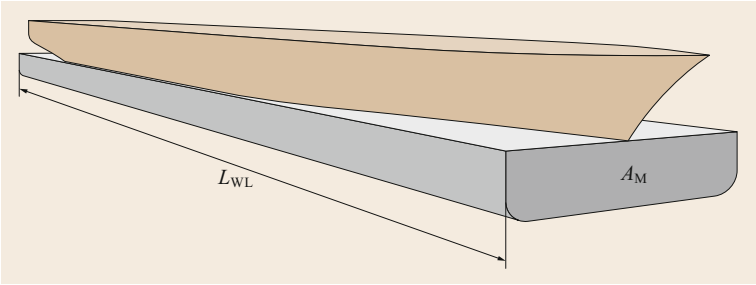

Fig. 25.7 Prismatic coefficient

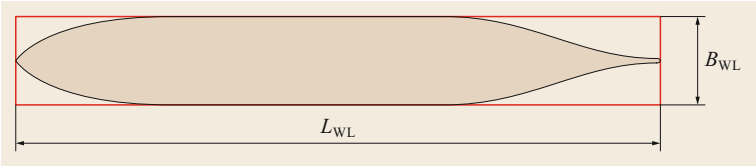

Fig. 25.8 Waterplane area coefficient

Because ships aim to transport as much freight as possible, values for the midship coefficient ordinarily range between 0.97 and 0.99 for tankers and bulk carriers. The midship area coefficient is found using

$$C_M = \frac{A_M}{B_{WL} T} .$$

The prismatic coefficient, which is commonly used in yacht and small craft design but not as much in ship design, allows better characterization of the underwater body, particularly the fullness of the ends. This coefficient is the ratio of the block and midship area coefficients, which simplifies to the ratio of the displaced volume ∇ to the midship area extruded along the length at the waterline, as depicted in Fig. 25.7. The prismatic coefficient is numerically expressed as

$$C_P = \frac{C_B}{C_M} = \frac{\nabla}{A_M L_{WL}} .$$

The ratio of the waterplane area and the product of the length and breadth at the waterline is termed the waterplane area coefficient C_{WPA}, and is illustrated in Fig. 25.8. This ratio plays a fundamental role in the draft variations of ships as they are loaded and unloaded, and features in early stability assessment. The waterplane area coefficient is quantified using

$$C_{WPA} = \frac{A_{WP}}{L_{WL} B_{WL}} .$$

Finally, to gain a better idea of the slenderness or fineness of the vessel, which is directly related to its hydrodynamic performance, the nondimensional length to displacement ratio

$$\frac{L_{WL}}{\nabla^{1/3}}$$

is utilized.

These ratios enable the 3-D shape of a vessel to be evaluated and hydrodynamic aspects to be considered at an early stage in the design process. Given the widespread use of computer-aided design (CAD), and the substantial role played by numerical methods such as computational fluid dynamics (CFD) and finite element analysis (FEA) in ship design, the 3-D modeling of the vessel is extremely important. Nevertheless, the design of a ship must still be conveyed in a 2-D drawing known as the lines plan.

25.2.3 Lines Plan

The lines plan is the primary way to communicate and represent the shape of any vessel, and comprises three views:

- A side elevation named the *sheer profile*, which represents the contour of the hull together with buttocklines
- A plan view, the *half-breadth*, which depicts one-half of the vessel with a series of waterlines
- An end elevation, the *body plan*, which depicts the forward half of the vessel on the right-hand side and the aft part on the left-hand side with a series of stations.

Specific cutting planes through the hull are presented in each view to clearly indicate the shape of the hull. These planes are:

- The *buttocklines* – evenly spaced vertical cutting planes parallel to the plane of symmetry.
- The *waterlines* – evenly spaced horizontal cutting planes parallel to the summer waterline (the latter is

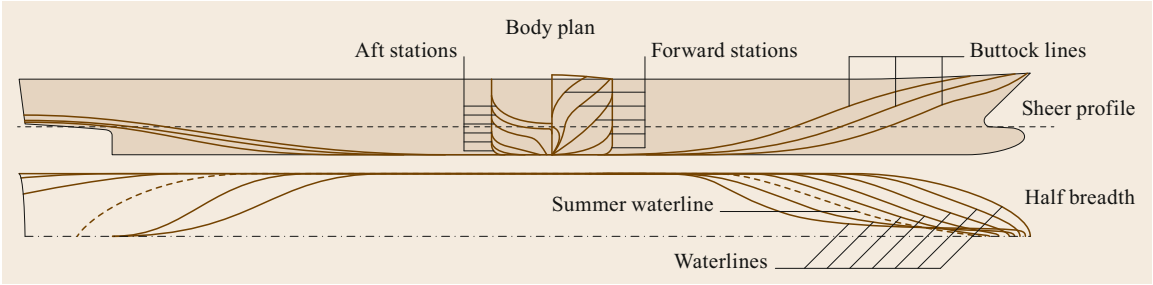

Fig. 25.9 The lines plan of a ship

usually depicted using a a different line weight or line type, e.g., the dashed line in Fig. 25.9).

- The *stations* – evenly spaced vertical cutting planes that are perpendicular to the plane of symmetry and are distributed along the length of the vessel. On ships, eleven stations are customarily represented, starting at the aft perpendicular (station 0) and ending at the forward perpendicular (station 10). Due to the rapid changes in shape at the bow and the stern, it is common to find half-stations in the bow region (stations 8.5 and 9.5) and at the stern (stations 0.5 and 1.5).

An example of a lines plan is presented in Fig. 25.9.

25.2.4 Sectional Area Curve

In order to further define the underwater body of the hull at an early design stage, a sectional area curve is developed. This involves assessing the cross-sectional area of the immersed hull at each station defined on the lines plan and then plotting the resulting areas along the waterline length of the vessel. The resulting sectional area curve of the vessel is given in either a dimensional form (featuring the actual cross-sectional areas) or a nondimensional form (expressed as a percentage of the maximum area; see Fig. 25.10).

The sectional area curve clearly shows the parallel midbody. The immersed part of the forward region of the hull is named the entrance, and the corresponding part of the aft is termed the run. Visually, the SAC provides the experienced naval architect with important information on the shape of the hull. This can also be quantified using a number of parameters via quadrature methods such as Simpson's rule [25.3]. The parameters include the prismatic coefficient, the waterplane area, and the immersed volume of the hull – all key design parameters for any vessel.

Moreover, the longitudinal center of buoyancy (LCB) is also ascertained from the sectional area curve. The LCB represents the center of the immersed volume of the hull and corresponds to where the upward buoyancy force is assumed to act. The location of the LCB is reported as a percentage of the waterline length from amidships, with a positive value being forward and a negative value being aft. Due to its impact on the resistance, the position of the LCB needs to be accurately determined. The LCB is generally a function of the vessel's speed; faster vessels exhibit LCB values of around −2%, whereas slower vessels present LCBs of between 2 and 3% forward of amidships. The speed of a ship is commonly linked to the nature of the cargo: container ships carrying perishable goods must operate at higher speeds. Conversely, bulk carriers or tankers can afford to operate at lower velocities.

The form coefficients and design ratios considered so far are of primary use to the naval architect from a design perspective. However, there are other factors

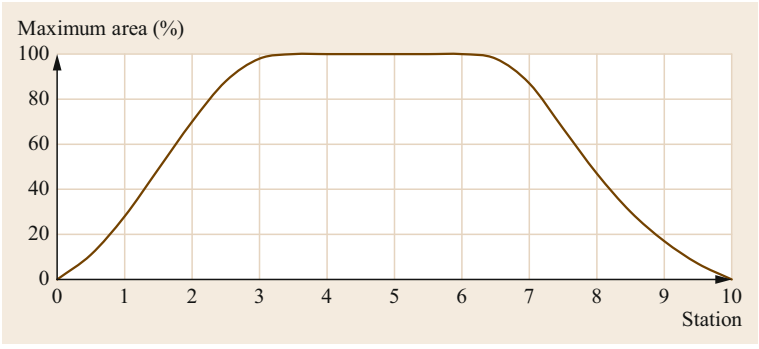

Fig. 25.10 Nondimensional sectional area curve

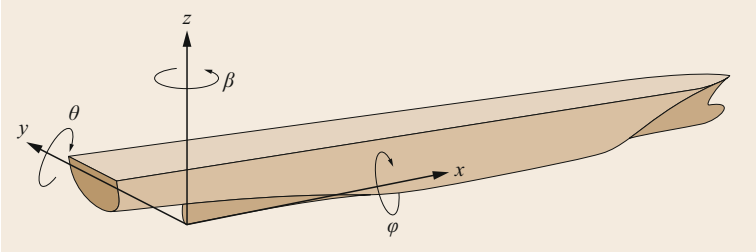

Fig. 25.11 Reference point and coordinate system

to consider that have decisive regulatory implications, such as the gross tonnage.

25.2.5 Gross Tonnage

The gross tonnage (gt) of a vessel must be established for regulatory purposes. It is a function of the ship's volume, and its value can impact on the applicability of regulations. For instance, SOLAS is only applicable for vessels over 300 gt.

The gross tonnage is defined by the International Convention on Tonnage Measurement of Ships [25.4] as being a function of the total volume of the ship V such that

$$\mathrm{gt} = KV\,,$$

where K is a multiplier between 0.22 and 0.32 given by

$$K = 0.2 + 0.02\log_{10} V\,.$$

Combining both equations, the gross tonnage is ascertained via

$$\mathrm{gt} = (0.2 + 0.02\log_{10} V)V\,.$$

25.2.6 Axis System

As it is a rigid body moving in space, the motion of a ship is defined by six degrees of freedom: three velocities and three angular motions. It is also necessary to define the reference point and sign convention; a typical right-handed coordinate system is used here.

Due to the varying loads of a ship and the resulting changes in draft, its waterline is not used as a datum point; instead, a fixed vertical baseline reference at the lowest point of the keel is adopted. Furthermore, as per the station numbering, the aft perpendicular is taken to be the longitudinal reference. Finally, due to symmetry, the transverse datum is located on the centerline. The intersection of the centerline of the ship with the aft perpendicular and the keel baseline is taken to be the zero point.

In order to specify the sign conventions used, additional terminology needs to be defined. When looking towards the bow, the left-hand side of the vessel is known as port and the right-hand side as starboard. From there, the six degrees of freedom and their respective sign conventions can be assigned as presented in Table 25.1 and Fig. 25.11.

Table 25.1 Sign convention

Degree of freedom	Name	Symbol	Sign convention
Linear velocity along the x-axis	Surge	x	Positive forward
Linear velocity along the y-axis	Sway	y	Positive to port
Linear velocity along the z-axis	Heave	z	Positive upwards
Angular motion around the x-axis	Roll	φ	Positive to starboard
Angular motion around the y-axis	Pitch	θ	Positive bow down
Angular motion around the z-axis	Yaw	β	Positive to port

25.3 Hydrostatics and Stability

25.3.1 Archimedes' Principle

Ship design relies on one of the most fundamental principles of physics, established by Archimedes of Syracuse circa 250 BC. This principle states that *any object wholly or partially immersed in a fluid is buoyed up by a force equal to the weight of the fluid displaced by the object.* The upwards force experienced by the immersed part of ship, known as the buoyancy, is therefore equal to the weight of the volume of fluid displaced, i.e.,

$$\text{bouyancy} = \nabla\rho g\,.$$

For a ship to float in equilibrium, the downward force exerted by the mass of the vessel Δ must be equal and

opposite to the buoyancy force, i.e.,

$$\Delta g = \nabla \rho g \, .$$

Simplifying for gravity gives one of the elementary principles of naval architecture, namely that mass is equal to the product of the immersed volume and the density of the fluid; in other words

$$\Delta = \nabla \rho \, .$$

25.3.2 Definitions

Vessel stability must be assessed to ensure that it complies with the relevant regulations and to guarantee its safety while in operation. The specific terminology associated with the key points and distances considered when evaluating ship stability are listed below (and illustrated for an upright ship in Fig. 25.12):

- B is the vertical center of buoyancy
- G is the vertical center of gravity
- M is the transverse metacenter
- K is the baseline reference
- $\overline{\mathrm{BM}}$ is the metacentric radius
- $\overline{\mathrm{GM}}$ is the metacentric height
- $\overline{\mathrm{Gz}}$ is the righting lever
- $\overline{\mathrm{KN}}$ is the baseline righting lever.

We focus here on the intact stability, meaning that the vessel is operating as designed. Another branch of ship stability, namely damage stability, deals with the impact of flooded compartments. The regulatory requirements for a given ship will require it to be sufficiently stable even when one or several compartments are flooded. This necessitates further analysis of the vessel's behavior, which will impact on the vessel's internal watertight subdivisions. However, these aspects are not tackled here and only the intact stability of ships under static conditions is considered.

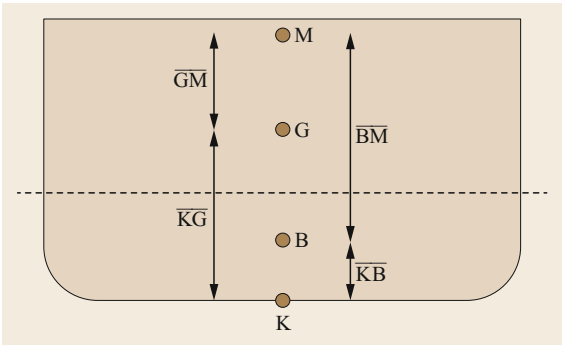

Fig. 25.12 Upright ship stability nomenclature

25.3.3 Transverse Stability at Small Angles

The transverse stability is first assessed based on small angle theory. As the ship rolls, the gravitational force acting through the center of gravity G remains constant, whereas the vertical force applied via the center of buoyancy shifts transversely from the upright center of buoyancy B to the inclined center of buoyancy B′. This causes a righting moment that brings the boat back upright, as depicted in Fig. 25.13. The intersection of the inclined vertical buoyancy force acting through B′ with the original line of action of the upright buoyancy force gives the location of the metacenter M, which is assumed to be fixed for small angles.

When the ship is upright, the center of gravity of the vessel G should always be located below the metacenter M for the boat to remain stable, implying that the metacentric height $\overline{\mathrm{GM}}$ is a crucial influence on the stability: a positive value of $\overline{\mathrm{GM}}$ indicates a stable boat whereas a negative $\overline{\mathrm{GM}}$ is characteristic of an unstable boat, as illustrated in Fig. 25.14.

The metacentric height $\overline{\mathrm{GM}}$ is determined by three variables – the vertical center of buoyancy $\overline{\mathrm{KB}}$, the metacentric radius $\overline{\mathrm{BM}}$, and the vertical center of gravity $\overline{\mathrm{KG}}$ – such that

$$\overline{\mathrm{GM}} = \overline{\mathrm{KB}} + \overline{\mathrm{BM}} - \overline{\mathrm{KG}} \, .$$

$\overline{\mathrm{KB}}$ can be found if the location of the center of buoyancy – i.e., the center of the submersed volume of the hull, where Archimedes' thrust is assumed to act – is known.

The metacentric radius $\overline{\mathrm{BM}}$ is a function of the transverse second moment of area of the waterplane about the centerline as well as the immersed volume

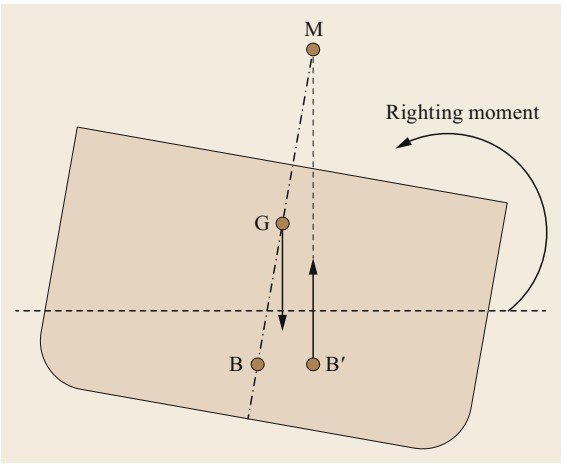

Fig. 25.13 Righting moment

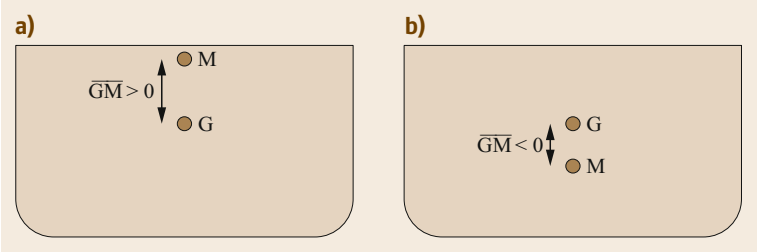

Fig. 25.14a,b Impact of $\overline{GM}$ on ship stability: **(a)** stable, **(b)** unstable

of the ship such that

$$\overline{BM} = \frac{I_{XX}}{\nabla} ,$$

where I_{XX} can be approximated as the second moment of area of a rectangle of length L_{WL} and breadth B_{WL} multiplied by the waterplane area coefficient squared, i.e.,

$$I_{XX} = \frac{L_{WL} {B_{WL}}^3}{12} {C_{WPA}}^2 .$$

Finally, $\overline{KG}$ depends on the location of the center of gravity of the ship. This is assessed at the design stage using the weight estimate; however, once built, the ship undergoes an *inclining experiment* to precisely determine the center of gravity. Both of these aspects will be discussed in further detail in subsequent sections.

25.3.4 Impact of $\overline{GM}$ on Comfort

Class rules define the minimum positive $\overline{GM}$ that is required to ensure that the vessel is stable, as a negative or only marginally positive $\overline{GM}$ could cause the boat to overturn, i.e., to capsize. For most passenger vessels and general cargo ships, the minimum regulatory requirement for the metacentric height is 150 mm. Other types of vessels, such as bulk carriers containing grains, are required to have a larger minimum $\overline{GM}$ of 300 mm because grain cargo tends to shift due to the motion of the vessel, leading to asymmetric loading and an additional rolling moment [25.5].

However, while a greater value of $\overline{GM}$ translates into a more stable boat, it also negatively impacts the roll period T of the ship, given by

$$T = \frac{2\pi k}{\sqrt{g\overline{GM}}} ,$$

where k is the radius of gyration (or gyradius) of the vessel. Shorter roll periods due to a large $\overline{GM}$ induce angular accelerations that exceed the comfort threshold of passengers, eventually resulting in motion-induced sickness. This should be avoided, especially on vessels carrying paying passengers. Consequently, cruise liners tend to minimize $\overline{GM}$ to achieve greater passenger comfort while traveling through waves, whereas a slightly higher $\overline{GM}$ and therefore shorter roll period is deemed acceptable for commercial freight ships operated by a professional crew.

25.3.5 Transverse Stability at Large Angles

The assumptions inherent to stability at small angles – for instance, the constant position of the metacenter or the fact that the upright and inclined waterlines intersect on the centerline – are not valid at larger angles, thus calling for additional theory.

As the boat rolls, its stability can be expressed as a function of the righting lever $\overline{Gz}$, defined as the horizontal distance between the center of gravity and the vertical line of action of the buoyancy force, as illustrated in Fig. 25.15. From simple trigonometry, the righting lever $\overline{Gz}$ is

$$\overline{Gz} = \overline{GM} \sin\varphi .$$

However, the vertical center of gravity of a ship varies over time because the amount and distribution of the cargo it carries will change substantially from journey to journey. In addition, considerable quantities of fuel are burnt by the ship while it is at sea. To compensate for this burnt fuel, water ballasts are employed to lower the center of gravity and retain stability. Thus, the center of gravity of a ship will vary over time for various reasons. As a result, $\overline{Gz}$ is often replaced with $\overline{KN}$, the baseline righting lever. This lever is measured from the baseline reference and is therefore not affected by the significant changes in the vertical center of gravity over time.

It should be noted that applying trigonometry to the case presented in Fig. 25.15 allows $\overline{Gz}$ to be related to $\overline{KN}$ via

$$\overline{Gz} = \overline{KN} - \overline{KG} \sin\varphi .$$

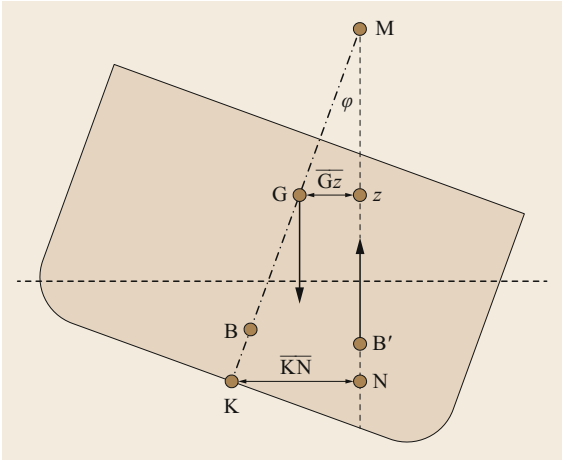

Fig. 25.15 Transverse stability at large angles

Figure 25.16 shows a $\overline{Gz}$ curve up to 180° of inclination (i.e., an inverted vessel). When it is upright, the vessel has no righting lever. However, the lever increases as the boat rolls to the maximum $\overline{Gz}$ (i.e., $\overline{Gz}_{MAX}$) and then decreases. The point at which $\overline{Gz}$ becomes negative is the angle of vanishing stability (AVS). Past this point, the negative righting lever starts to act as a capsizing lever: it tends to roll the boat even further. Moreover, the range of roll angles from the origin to the AVS is known as the range of stability of the ship. In addition to the upright $\overline{GM}$, intact stability regulations also consider the value of $\overline{Gz}_{MAX}$ and the angle at which it occurs, the range of stability, the angle at which downflooding occurs, as well as the area under the $\overline{Gz}$ curve. This is a measure of the amount of energy required to capsize the vessel and consequently a good indication of the stability of the ship.

When a vessel has a negative $\overline{GM}$ in the upright position, the vessel will roll until a neutral $\overline{GM}$ is achieved ($\overline{GM} = 0$), in which case the vessel is said to adopt an angle of loll. On the other hand, if the vessel has a static roll angle due to asymmetric loading (i.e., a transverse center of gravity offset from the centerline), an angle of list will result.

25.3.6 Angle of List

Shifting masses transversely across the vessel causes the transverse center of gravity (TCG) to move away from the ship's centerline, creating a moment. The ship therefore rolls until the vessel reaches equilibrium at an angle of list, as depicted in Fig. 25.17.

The angle of list φ is related to the metacentric height and the transverse center of gravity via

$$\tan\varphi = \frac{\mathrm{TCG}}{\overline{\mathrm{GM}}} .$$

Moreover, the TCG is a function of the moment created by moving a known mass m over a precise distance d, i.e.,

$$\mathrm{TCG} = \frac{md}{\Delta} .$$

Combining both of these equations gives the angle of list as

$$\tan\varphi = \frac{md}{\overline{\mathrm{GM}}\Delta} .$$

The theory associated with list angles provides the basis for the inclining experiment performed upon the

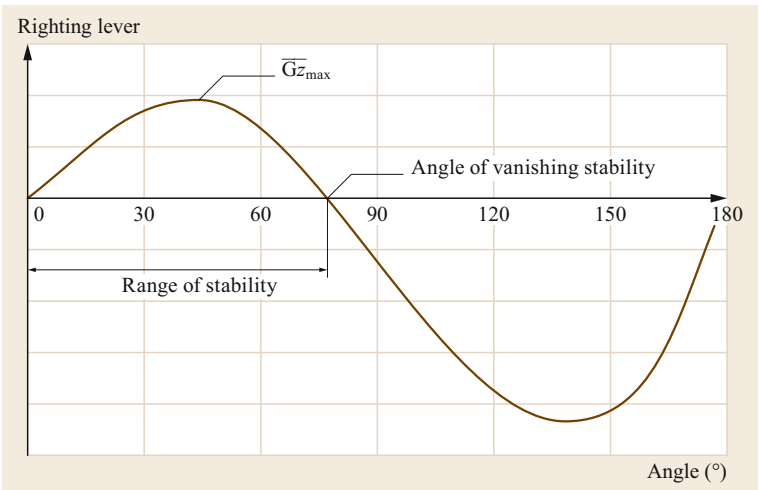

Fig. 25.16 $\overline{Gz}$ curve

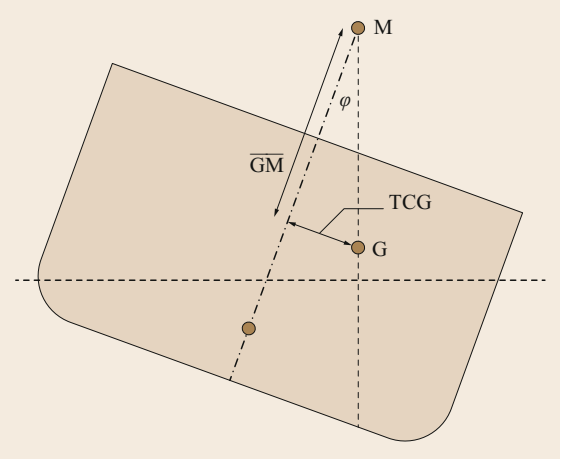

Fig. 25.17 Angle of list

completion of the ship to determine the location of the vertical center of gravity.

25.3.7 Weight Estimate

The purpose of the weight estimate is to locate the center of gravity in each of the three dimensions, i.e., the longitudinal center of gravity (LCG), the transverse center of gravity (TCG), and the vertical center of gravity (VCG). This is achieved by listing the mass M_i and the longitudinal, transverse, and vertical centers of gravity (labeled X_i, Y_i, and Z_i, respectively) of every single item and component of the vessel. The centers of gravity are then calculated via

$$\mathrm{LCG} = \frac{\sum(M_i X_i)}{\sum M_i} ,$$

$$\mathrm{TCG} = \frac{\sum(M_i Y_i)}{\sum M_i} ,$$

$$\mathrm{VCG} = \frac{\sum(M_i Z_i)}{\sum M_i} .$$

However, considering that ships are very large and complex (some ships measure close to 400 m and weigh in excess of 100 000 t), such a weight estimate has an inherent uncertainty. Therefore, once it has been launched, a marine vessel must undergo an inclining experiment. This is a mandatory regulatory requirement set in the International Code on Intact Stability [25.6], referred to as the IS Code.

25.3.8 Inclining Experiment

Ship stability assessment at small or large angles requires that the location of the center of gravity – which is the keystone of vessel stability – is known. This is assessed during the design stage via a weight estimate. Once built, the vessel undergoes an inclining experiment, a procedure that is used to accurately establish the location of the vertical center of gravity, which will then be used as a reference for loading calculations throughout the vessel's service life [25.7].

The theory behind the inclining experiment is simple: by creating a rolling moment and measuring the inclination angle once the vessel is in equilibrium, the righting moment can be deduced. The metacentric height $\overline{\mathrm{GM}}$ can then be found, allowing the position of the vertical center of gravity to be evaluated.

The inclining experiment relies on the fact that the metacenter is fixed for small angles of roll, hence the requirement of the IS Code for angles of inclination of between a minimum of 1° and a maximum of 4° [25.6]. The aim is to quantify the metacentric height $\overline{\mathrm{GM}}$ by creating a known moment and then measuring the resulting roll angle with a pendulum. The moment is created by shifting masses across the deck.

From list theory, the metacentric height is

$$\overline{\mathrm{GM}} = \frac{md}{\Delta \tan\varphi} .$$

During the inclining experiment, the angle of inclination adopted by the ship is measured with a pendulum of length l, which is deflected a distance x. Since $\tan\varphi = x/l$, the metacentric height and therefore the location of the center of gravity is ascertained using

$$\overline{\mathrm{GM}} = \frac{mdl}{\Delta x} .$$

Note that this is the metacentric height of the vessel with inclining weights onboard; these are normally added for the purpose of the experiment. In order to measure the actual $\overline{\mathrm{GM}}$ of the boat, the height of the center of gravity must be corrected by removing the inclining weights, resulting in a shift in the vertical center of gravity $\overline{\mathrm{GG'}}$ given by

$$\overline{\mathrm{GG'}} = -\frac{\overline{\mathrm{Gg}}m}{\Delta - m} ,$$

where $\overline{\mathrm{Gg}}$ is the vertical distance between the evaluated overall center of gravity and the center of gravity of the inclining weights (of mass m).

In order to maximize the accuracy of the inclining experiment once the ship has been constructed, it should be realized in calm water with no wind to avoid environmental interference with the results. The draft is

measured along the length of the vessel, and the density of the water is recorded, as this allows the volume of water displaced and therefore the mass of the vessel to be ascertained precisely. Vessel motion should not be restricted: mooring lines should be slack and gangways should be removed. Furthermore, all loose equipment should be secured and tanks should either be empty or full. The minimum number of crew should be present in a predetermined and fixed location onboard to avoid any interference with the experiment. The inclining weights can be shifted across the deck to preestablished positions, or the ballast tanks can be filled. The pendulums are located forward and aft. The plumb bob of each pendulum is commonly immersed in water or oil to damp oscillations, allowing the angle adopted by the vessel to be read more quickly and accurately, which in turn allows the location of the center of gravity to be pinpointed. Note that U-tubes and inclinometers are used in conjunction with the pendulums to measure the angle adopted by the vessel as the series of masses are shifted across the deck [25.8].

As previously highlighted, bulk carriers containing grain require a higher initial $\overline{\mathrm{GM}}$ to account for the shifting of the grain as the vessel moves. Partially full tanks can have a similar impact. This shifting of material onboard a ship as it moves is known as the free surface effect and is the reason why only empty or full tanks are permitted during inclining experiments.

25.3.9 Free Surface Effect

As a vessel rolls, the fluid in a partially full tank will shift to the lower side. This creates a transverse movement of the center of gravity toward the center of buoyancy, effectively decreasing the righting lever $\overline{\mathrm{G}z}$ and consequently the stability of the boat. The free surface effect is capable of rendering a vessel unstable by reducing the actual $\overline{\mathrm{GM}}$ of the boat. It causes an artificial reduction in the metacentric height $\overline{\mathrm{GM}}$ due to a shift in the center of gravity upwards from its original position G to a virtual position $\mathrm{G_V}$, which is quantified via

$$\overline{\mathrm{GG_V}} = \frac{\rho_{\mathrm{tank}} I_{\mathrm{tank}}}{\Delta} .$$

For a ship that has a given displacement and is carrying a specific type of fluid, the impact of the free surface effect can be minimized by reducing the second moment of area of the tanks. For a rectangle, the second moment of area about an axis parallel to the base passing through the centroid is

$$I_{\mathrm{rectangle}} = \frac{LB^3}{12} .$$

It is therefore critical to minimize the transverse width of the tanks due to the dramatic impact of the breadth on the free surface effect and the consequent reduction in $\overline{\mathrm{GM}}$.

25.3.10 Stability Curves

It is common practice to calculate the hydrostatics of a vessel for a range of waterlines, given that the displacement of the ship will vary over time. The results are then plotted against a range of drafts. Examples of hydrostatic curves are presented in Fig. 25.18.

Furthermore, in order to quantify the impact of loading on the vessel's draft, the tonnes per centimeter (TPC) of the ship is assessed. The TPC is the mass that must be added or removed to cause a change in draft of one centimeter. It is established using Archimedes' principle and by considering the volume corresponding to the extrusion of the waterplane area by one centimeter, assuming that the shape of the ship does not vary significantly. After introducing a conversion factor of 100 (to obtain a result in centimeters) and the density of the water ρ (to achieve a mass), the TPC is calculated as

$$\mathrm{TPC} = \frac{A_{\mathrm{WP}} \rho}{100} .$$

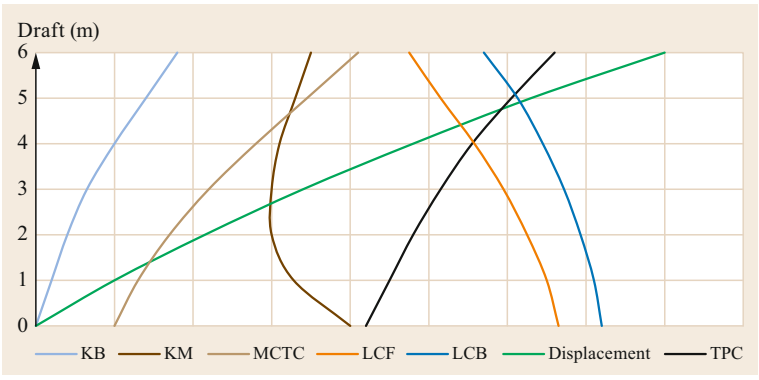

Fig. 25.18 Hydrostatic curves

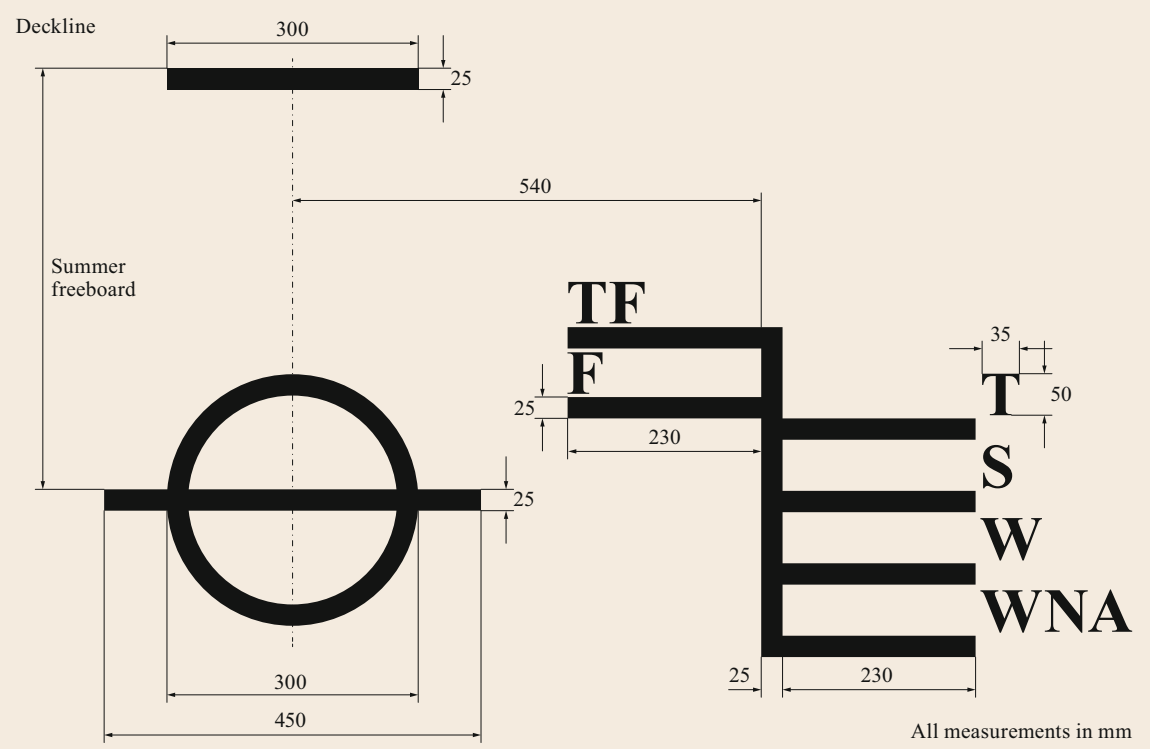

Fig. 25.19 The Plimsoll mark defined by the Load Lines regulation. (Reproduced after [25.9])

25.3.11 Longitudinal Stability

So far, the stability of the vessel has only been considered from a transverse point of view. The transverse stability is undoubtedly very important, but the longitudinal stability of the vessel should also be investigated. While the transverse roll of the ship is measured as an angle in degrees, changes in longitudinal trim are expressed in terms of the resulting change in draft. When the draft aft is greater than the draft at the stem, the ship is said to trim by the stern. Conversely, if the draft is larger at the bow than at the stern, the ship is trimming by the bow.

Similar principles to those for the transverse stability apply in this case too. The longitudinal metacentric radius $\overline{\mathrm{BM_L}}$ is found using

$$\overline{\mathrm{BM_L}} = \frac{I_{\mathrm{YY}}}{\nabla} ,$$

and the longitudinal metacentric height $\overline{\mathrm{GM_L}}$ is given by

$$\overline{\mathrm{GM_L}} = \overline{\mathrm{KB}} + \overline{\mathrm{BM_L}} - \overline{\mathrm{KG}} .$$

The vessel trims about the longitudinal center of flotation (LCF), defined as the transverse neutral axis of the waterplane. The moment to change the trim by one centimeter (MCTC) is calculated in a similar manner to the TPC. The trim angle θ generated by a change in draft x over the length of the ship L is simply

$$\tan\theta = \frac{x}{L} .$$

As per the transverse stability theory, this can also be expressed as a function of the trimming moment generated such that

$$\tan\theta = \frac{md}{\Delta\overline{\mathrm{GM_L}}} .$$

Solving for the change in trim x and introducing the relevant conversion factor to achieve a change in trim of one centimeter yields

$$x = 1 = \frac{mdL\,100}{\Delta\overline{\mathrm{GM_L}}} .$$

The product of the mass m and the distance d shifted is the moment needed to change the trim by one centimeter (the MCTC), i.e.,

$$\mathrm{MCTC} = \frac{\Delta\overline{\mathrm{GM_L}}}{100L} .$$

Calculating the trim of the vessel allows the draft as well as the freeboard forward and aft – which are important factors in the survivability of ships in rough weather for instance – to be quantified.

25.3.12 Plimsoll Mark

The Load Lines regulation published by the IMO [25.9] aims to ensure ship safety. The financial incentive to carry more cargo per trip in order to maximize revenues can have a negative impact on the safety of a vessel and its crew. As the cargo increases, so does the draft, resulting in a lower freeboard, which reduces the wave height that can confidently be encountered by the vessel. As a result, the Load Lines convention defines the minimum statutory freeboard according to the area of operation (the minimum statutory freeboard is adjusted to account for variations in typical weather conditions and water salinity around the globe).

All ships (with some exceptions, such as pleasure craft, fishing vessels, and warships) must therefore display the Plimsoll mark (pictured in Fig. 25.19) on their hulls. The Plimsoll mark establishes the minimum freeboard for the ship; this minimum freeboard depends on the ship's operational environment – either tropical freshwater (TF), freshwater (F), tropical saltwater (T), summer saltwater (S), winter saltwater (W), or winter North Atlantic saltwater (WNA).

25.4 Resistance and Powering

25.4.1 Speed and the Froude Number

In order to ensure that a ship can be propelled at a specified speed, the resistance generated by the water and air opposing the motion of the vessel must be assessed. The preferred unit of speed for nautical applications is the knot, equivalent to 1.852 km/h, 1.151 mi/h, or 0.5144 m/s. From an operational point of view, both the speed over the ground (SOG; the speed relative to the surface of the Earth) and the speed through water (STW; the speed relative to the water) are given in knots. However, the speed in knots does not allow the naval architect to fully characterize the behavior of the ship, as it does not account for the length of the vessel. Therefore, the speed is customarily expressed as a function of the Froude number, a nondimensional speed-to-length ratio that relates the wave pattern to the speed of a vessel. The Froude number is defined as

$$\mathrm{Fr} = \frac{V}{\sqrt{gL_{\mathrm{WL}}}} \,.$$

Two separate models are employed for the drag components of the hydrodynamic resistance of the hull: the Froude model and the ITTC model.

25.4.2 Froude Resistance Model

The Froude model is named after *William Froude* (1810–1879), who is considered a pioneer of modern naval architecture and hydrodynamics. The model splits the hydrodynamic resistance of the hull into two components: the friction resistance R_{F} and the residuary resistance R_{R} [25.10, 11].

The frictional resistance, which results from the tangential shear force applied to the hull, is assumed by Froude to be equal to the resistance of a flat plate with the same wetted surface area as the ship. The other components of the hydrodynamic resistance of the hull, which are primarily due to the form of the hull and the waves, are collected in the residuary resistance term. After testing a wide range of flat plates, Froude derived a formula for estimating the frictional resistance based on the wetted area Sc and the velocity V,

$$R_{\mathrm{F}} = f\mathrm{Sc}V^{1.825} \,,$$

where f is the friction coefficient, given by

$$f = \frac{1}{1000}\left[\left(0.1392 + \frac{0.258}{2.68 + L_{\mathrm{WL}}}\right)\rho_{\mathrm{water}}\right] .$$

While Froude's model is still valid and employed in several empirical resistance estimation methods, the expression for the friction coefficient has been refined over the years. A major step forward was achieved in 1883 with the definition of the Reynolds number [25.12]

$$\mathrm{Re} = \frac{\rho V L_{\mathrm{WL}}}{\mu} \,.$$

Also, in 1957, after decades of refinement, the International Towing Tank Conference (ITTC) [25.13] adopted the friction coefficient

$$C_{\mathrm{F}} = \frac{0.075}{(\log_{10}\mathrm{Re} - 2)^2} \,.$$

The expression for the friction coefficient has remained unchanged since it was first adopted, and was used to develop the ITTC resistance model.

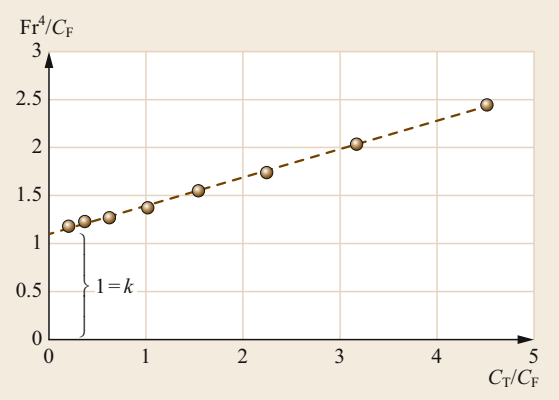

Fig. 25.20 Use of the Prohaska plot to ascertain the form factor $1 + k$

25.4.3 ITTC Resistance Model

The ITTC 1978 [25.14] method partitions the hull resistance into a viscous component and a wave component. The viscous component is defined as the impact of the 3-D shape of the hull on the friction resistance (as opposed to the 2-D flat plate assumed by Froude); this is known as the form factor (denoted $1 + k$). The viscous resistance R_V is given by

$$R_V = R_F(1 + k) = \frac{1}{2}\rho A V^2 C_F(1 + k) \,.$$

The form factor is experimentally assessed using the *Prohaska* method [25.15] during towing tank testing. If Fr^4/C_F is plotted against C_T/C_F, the y-intercept of the best-fit line will give the form factor $1 + k$. The resulting graph is a Prohaska plot, an example of which is presented in Fig. 25.20. This approach is only valid for slow speeds where the wave resistance is negligible and the viscous drag is the dominant component of the resistance.

The viscous component of the hull resistance can therefore be assessed. The other component – the wave resistance – is equal to

$$R_W = \frac{1}{2}\rho A V^2 C_W \,,$$

where the wave resistance coefficient C_W is ascertained experimentally via towing tank testing. The wave resistance coefficient of a ship with a given Froude number is the same regardless of the scale of the model used in the testing, which explains the benefit of carrying out towing tank testing.

25.4.4 Towing Tank Testing

Ship resistance assessment is a fundamental part of the design phase, as the results are needed to achieve appropriate powering. While new analytical methods such as computation fluid dynamics are available, the physical towing tank testing of a scale model is still crucially important.

As highlighted in our discussion of the resistance components above, the total drag is a function of both the Reynolds and the Froude numbers; the former is proportional to the length, while the latter varies with the inverse of the square root of the length. This presents a challenge during testing, as complete dynamic similarity of the model to the full-size vessel cannot be achieved. Because the correct Froude number is needed to achieve the appropriate wave pattern, model tests in towing tanks models always use the correct Froude number. As a consequence, the Reynolds number of the model is much smaller than that for the full-size ship, delaying the transition between laminar and turbulent flow. Therefore, at the model scale, the transition between flow regimes must be stimulated artificially using either studs or sand paper [25.16] (the former is illustrated in Fig. 25.21) in order to achieve more realistic modeling of the flow around the vessel and to obtain an accurate resistance measurement.

Both the form factor and the wave resistance coefficients can be established from towing tank testing. Since those two quantities will be the same as those for the full-scale vessel, and the friction coefficient can be

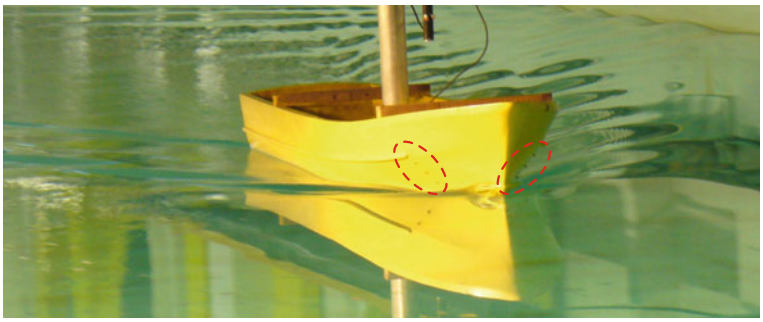

Fig. 25.21 Model fitted with studs (*circled*)

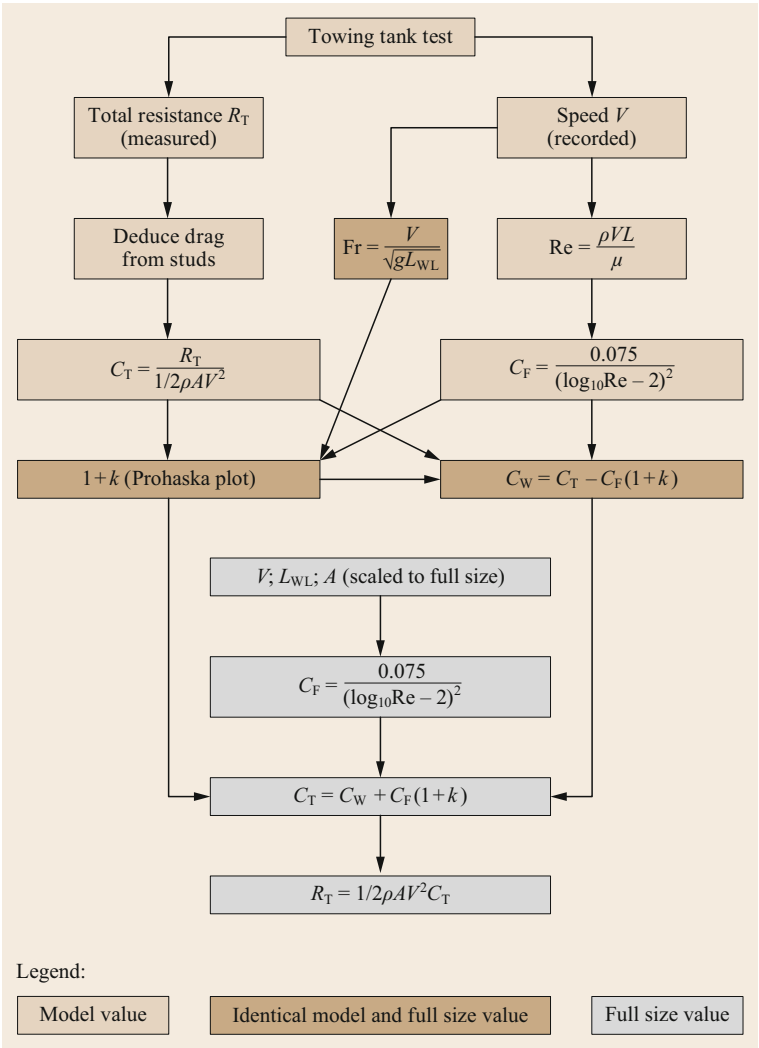

Fig. 25.22 Flow chart for towing tank testing

calculated directly for the full-size ship, the total resistance coefficient C_T is given by

$$C_T = C_W + C_F(1+k) \,.$$

The total resistance of the ship is finally found using

$$R_T = \frac{1}{2}\rho AV^2 C_T \,.$$

Figure 25.22 presents a flow chart of the calculations performed in the towing tank testing process, starting with the model tests and ending with the derivation of the resistance of the full-size ship.

The process is repeated over a range of speeds representative of the vessel's normal operation in order to achieve a resistance curve and subsequently a powering curve. Nevertheless, other resistance components also need to be considered.

25.4.5 Additional Resistance Components

Aside from the previously discussed hydrodynamic resistance of the hull, there are a number of other sources of drag, such as the hull roughness, appendages, and air resistance.

The hull of any vessel, particularly a ship, is far from perfectly smooth. Plate buckling, the paint surface, weld beads, corrosion, and in particular marine growth all increase the roughness of the hull, which translates into additional resistance. The roughness resistance is evaluated assuming a typical roughness coefficient of 0.0004.

The roughness of the hull has a substantial impact on the frictional resistance of the ship. The presence of this resistance means that more power must be supplied by the ship to reach the desired speed, leading to

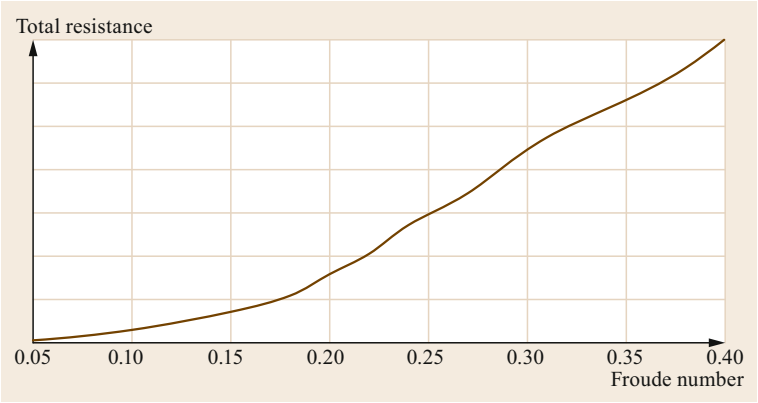

Fig. 25.23 Resistance curve

greater fuel consumption. This is costly and results in increased pollutant emissions. Due to increased environmental concerns, ship emissions have been subject to greater regulatory pressures in recent years; for instance, an energy efficiency operation index (EEOI) has been introduced by the IMO.

In addition to the hull, a number of appendages will generate drag, such as rudders, shafts, propellers, and stabilizers. Each of these must be accounted for in the resistance of the ship, as each has a non-negligible impact on the overall resistance.

Furthermore, while all of the components of the resistance discussed so far are immersed, the part of the vessel above the waterline also creates drag that must be overcome. On container carriers, for instance, the frontal and lateral areas of the vessel are considerable, leading to substantial drag in strong winds. The projected areas of the vessel are therefore utilized when assessing the air resistance.

Finally, all of the resistance components for the vessel are summed, allowing a resistance curve to be plotted for the vessel over a range of Froude numbers, as illustrated in Fig. 25.23.

Looking closely at the resistance curve, a series of small humps and hollows can be seen. These are the result of wave interactions around the vessel – a feature that plays a major role in the design phase.

25.4.6 Wave Interference

It is worth noting that for any vessel, the wave pattern generated as the boat travels through water is always the same: a series of divergent and transverse waves at the same angles. This is known as the Kelvin wave pattern, and it is illustrated for both the bow and stern wave systems in Fig. 25.24.

There is a strong interaction between the wave pattern generated at the bow and that generated at the stern. This can lead to wave superposition (also known as constructive interference), where the bow and stern wave crests line up, resulting in increased wave resistance. Conversely, it can also yield destructive interference, which is when a crest and trough cancel each other out, minimizing the wave height and thus the drag [25.17]. Constructive and destructive interference are shown in Figs. 25.25 and 25.26, respectively.

This phenomenon has a clear impact on the resistance curves of ships, as it causes a series of prismatic humps and hollows to occur at particular Froude numbers. These Froude numbers can be determined.

First, the wavelength λ is

$$\lambda = \frac{2\pi V^2}{g} .$$

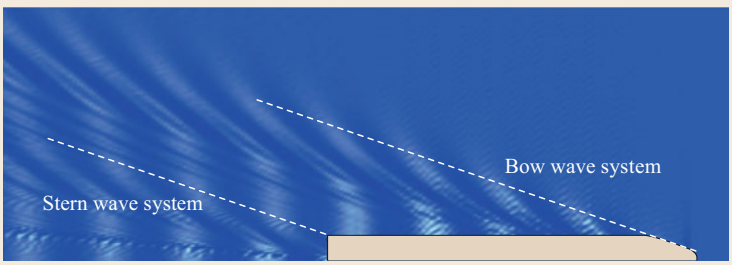

Fig. 25.24 Kelvin wave pattern

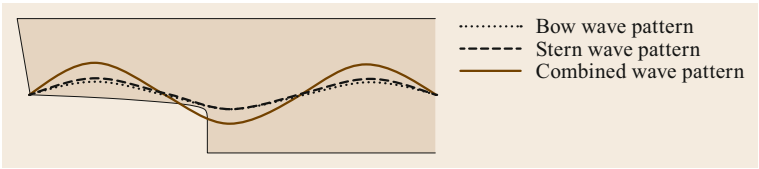

Fig. 25.25 Constructive interference

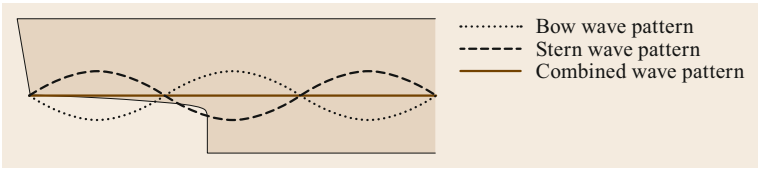

Fig. 25.26 Destructive interference

To introduce the Froude number into the equation, both sides are divided by the waterline length, i.e.,

$$\frac{\lambda}{L_{\mathrm{WL}}} = 2\pi\frac{V^2}{gL_{\mathrm{WL}}} = 2\pi\mathrm{Fr}^2 .$$

The Froude number is therefore

$$\mathrm{Fr} = \sqrt{\frac{\lambda}{2\pi L_{\mathrm{WL}}}} .$$

A resistance hump occurs when $\lambda = L_{\mathrm{WM}}/(n+0.5)$, where n is an integer. In other words,

$$\mathrm{Fr}_{\mathrm{HUMP}} = \sqrt{\frac{L_{\mathrm{WM}}}{2\pi L_{\mathrm{WL}}(n+0.5)}} , \quad n \in \mathbb{Z} .$$

Conversely, a resistance hollow occurs when $\lambda = L_{\mathrm{WM}}/n$ (where n is again an integer), so

$$\mathrm{Fr}_{\mathrm{HOLLOW}} = \sqrt{\frac{L_{\mathrm{WM}}}{2\pi L_{\mathrm{WL}} n}} , \quad n \in \mathbb{Z} .$$

The Froude numbers at which prismatic humps and hollows occur can therefore be predicted as a function of the number of whole waves n, the waterline length of the ship L_{WL}, and its wavemaking length L_{WM}, which is typically between 85 and 95% of the waterline length. The prismatic humps and hollows can be visualized in the wave resistance curve of the vessel; these humps and hollows are presented in an exaggerated fashion in Fig. 25.27.

In order to achieve greater fuel efficiency, the cruising speed is chosen to correspond to a resistance hollow. This idea can be taken a step further by employing a bulbous bow. While the bow-wave system can cancel out some of the stern-wave system, there is still a lot of wave resistance at the bow; hence the addition of a bulbous bow. This feature is designed to create a wave system that promotes destructive interference at the bow and thus reduce wave resistance, as illustrated in Fig. 25.28.

25.4.7 Powering

The purpose of the resistance calculation is to guarantee that the vessel will be fitted with an appropriate engine power to achieve the required speed. This is why it is important that the resistance is calculated accurately. Too little power and the boat will not reach its

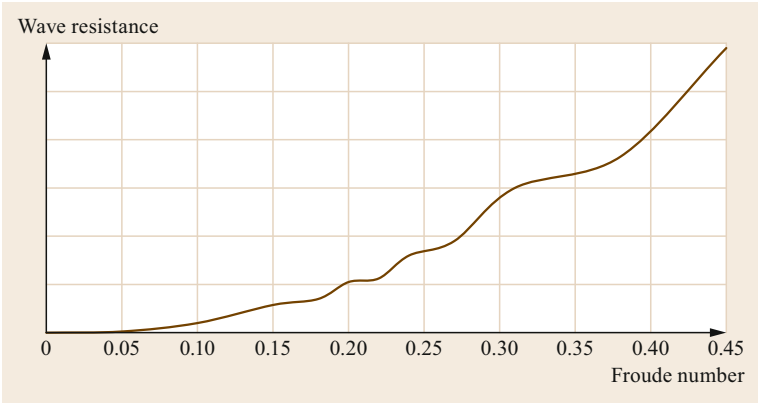

Fig. 25.27 Prismatic humps and hollows on a resistance curve (the humps and hollows are exaggerated to improve clarity)

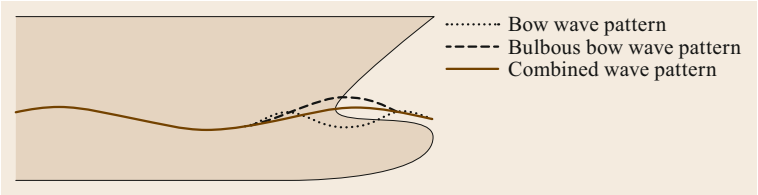

Fig. 25.28 Impact of a bulbous bow on the wave pattern

operational speed, meaning that it will take longer to complete a given route, negatively impacting the profit that can be made. Conversely, an engine that is too large will result in unnecessary additional power and potentially greater fuel consumption, leading to the need for more fuel onboard as well as increased expenses and less cargo space. It is therefore crucial to precisely assess the power that needs to be installed in the vessel so that a suitable engine can be selected. The power needed to overcome the resistance of the ship at a specific speed is

$$P_E = R_T V \,.$$

This is termed the effective power, labeled P_E, needed to propel the ship forward. It is substantially smaller than the installed engine power due to a number of losses that are quantified in term of efficiencies.

First of all, the efficiency of the propeller is a critical factor when attempting to generate the thrust that will propel the ship through the water. There are three efficiencies of the propeller: the open water, the rotary, and the hull efficiencies. The open water efficiency of a propeller η_O considers the propeller with no hull forward and no interference in the flow. The impact of nonhomogeneous flow is quantified by the rotary efficiency η_R. Finally, the effect of the presence of the hull is accounted for by the hull efficiency η_H. The product of those three individual efficiencies is the quasi-propulsive coefficient (QPC), i.e.,

$$\mathrm{QPC} = \eta_O \eta_R \eta_H \,.$$

Using the QPC, the power delivered at the propeller P_D can be calculated via

$$P_D = \frac{P_E}{\mathrm{QPC}} \,.$$

On the other hand, a number of losses occur at couplings, bearings, and stern tubes in the drive train (such as the losses in the gearbox or friction losses at the shaft). Accounting for those transmission losses enables the elucidation of the installed power P_I, which will be greater than the delivered power and considerably higher than the effective power.

As propeller efficiencies typically range from 50 to 70%, improving propeller efficiency in order to achieve a higher QPC is a significant area of research and development. The refinement and optimization of propeller design has been made possible by advances in computational fluid dynamics. Furthermore, alternatives to traditional screw propellers are becoming more popular. Controllable pitch propellers (CPP), also named variable pitch propellers (VPP), allow the pitch of the propeller blades to be altered, resulting in a more versatile propeller that is able to maximize its efficiency at all speeds. Ducted propellers, generally termed Kort nozzle propellers, can provide increased efficiency at low vessel speeds due to the presence of a foil-shaped duct that helps to accelerate the flow velocity. Another example is the use of forward-facing propellers mounted onto pods, meaning that the propellers operate in a less disturbed flow than that at the rear of the vessel. These options all aim to reduce the power that must be installed in the vessel and its fuel consumption.

25.5 Structure

25.5.1 Structural Design

The deadweight carried by a ship is a very important influence on efficient maritime transportation; the structural weight of the ship should be kept light enough to maximize the cargo carrying capacity. The structural design is, however, subject to a number of compromises, starting with the potentially conflicting perceptions of the various stakeholders, such as the shipyard and the owner, about what the optimal design should achieve. Furthermore, the trade-off between the weight and cost can have an impact on the vessel's structural design philosophy. A ship could be designed to have a relatively low acquisition cost but a high operating cost, which is not the most cost-efficient option in the long term. As a result, the idea of a minimum life cycle cost is applied to encourage a compromise between the initial investment required and the operating cost and

reduce expenses in the long run. The desire to achieve a very light structure impacts on the complexity and time frame of the design approach, which should also be factored in.

While many engineering fields have elected to adopt a direct analysis approach to the design of structures, ship conception remains heavily driven by rules-based design [25.16], although alternatives for direct analysis are now being incorporated into the rules issued by classification societies. Therefore, just as they do for ship stability, rules and regulations have a significant impact on the design undertaken by the naval architect.

25.5.2 Materials

Modern ship building almost exclusively utilizes steel, so it is necessary to understand the behavior of this isotropic material (i.e., it has identical properties regardless of its orientation). When subjected to a stress σ, a deformation known as the strain ε will occur. Consequently, material properties are customarily related to a stress–strain graph; an idealized version is presented in Fig. 25.29.

As loading is applied, the material first exhibits linear elastic deformation, meaning that the sample will return to its original dimensions when it is unloaded. The linear relationship between the stress and strain is a measure of the material's stiffness and is denoted the modulus of elasticity or Young's modulus E. Young's modulus is given by the slope of the stress–strain curve in the elastic deformation region, i.e.,

$$E = \frac{\sigma}{\varepsilon} .$$

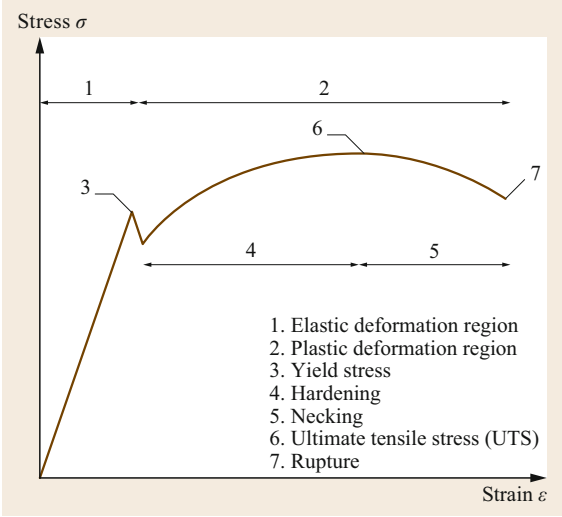

Fig. 25.29 Idealized stress–strain curve

The elastic deformation continues until the yield point is attained, after which the material reaches its plastic deformation region. Upon entering this region, the material becomes permanently deformed – it does not return to its original dimensions when unloaded. In the plastic region, the material first undergoes strain hardening, which causes the material to strengthen and leads to the ultimate tensile stress (UTS). Then necking occurs, with localized plastic deformation, ultimately resulting in rupture.

In rules-based structural design, a percentage of the yield or ultimate stress is normally allowed as the material's design stress used in the structural design. However, while the yield point and yield stress are very clear in some materials, this is not the case for all materials. For the latter, the normal practice is to define the yield stress as the 0.2% proof stress, which is obtained by offsetting the straight line of the stress–strain curve by 0.2% stain to give the stress required to produce a permanent strain of 0.2%.

Of course, vessels should not be designed for stresses within the plastic region, as permanent deformation could render the ship inoperable and unsafe. There are, however, some very limited areas where designing for plastic deformation may be tolerable. One example is the design of a watertight bulkhead on a warship, where the primary aim is to ensure that sufficient vessel buoyancy is maintained following a collision or blast.

It is also worth noting that the structure should allow for deterioration in service, with corrosion being a major concern for steel ships. In addition to the corrosion protection put into place when in operation, corrosion margins are included at the design stage to account for in-service deterioration. Given the intended life span of the vessel, sufficient thickness is added to ensure that structural integrity is maintained despite corrosion.

To ensure the structure is fit for purpose, a range of load cases and failure modes are considered, based on the mechanical properties of the material. Strength, stiffness, buckling, fatigue, grounding, and vibration are taken into account. The loads examined for the structural design are divided into two main categories, namely global and local loads.

25.5.3 Global Loads

Global loads, also referred to as primary loads, consider the impact of loading on the ship as a whole. One of the major load cases for global loads is the hull girder longitudinal strength, where the vessel is assumed to be a beam in a quasistatic analysis [25.19] performed during rules-based design. Two scenarios are investigated: crest landing and trough landing.

The crest landing load case assumes that the vessel is supported at each extremity by the buoyancy force

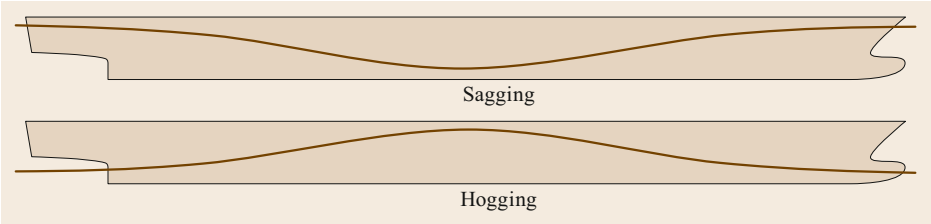

Fig. 25.30 Sagging and hogging of a ship as it statically balances on wave crests and troughs

exerted by wave crests. Since the load of the vessel acts in an unsupported area, the vessel sags. On the other hand, trough landing considers the scenario where the ends of the vessel are unsupported and buoyancy is applied amidships, causing the vessel to hog. Both cases are depicted graphically in Fig. 25.30.

In each case, a load function is obtained from the difference between the weight and the buoyancy distribution along the length of the vessel. Integrating the load curve q yields the shear force on the vessel F. Moreover, integrating the shear force gives the still-water bending moment M of the vessel. Mathematically,

$$F(x) = \int q(x)\,\mathrm{d}x\,,$$
$$M(x) = \int F(x)\,\mathrm{d}x\,.$$

These values provide the loading applied to the ship as a whole, and enable the naval architect to determine the longitudinal structure required to achieve a hull section modulus that will resist bending and prevent unreasonable hogging or sagging of the vessel.

25.5.4 Local Loads

Local loads are applied to localized structural components or supporting structures, such as hull panels and stiffeners. The hydrostatic pressure exerted by the sea on the hull shell is an example of a local load, as is the internal load that a liquid cargo or fuel in a tank exerts on the structure of the tank. In both cases, the hydrostatic pressure P resulting from the height of fluid h is given by

$$P = \rho g h\,.$$

Local loads are then used to evaluate the scantlings required for the hull plating and supporting structures at a localized level (each panel and stiffener are treated individually). Two types of designs can be distinguished: strength-driven designs, which aim to maintain the stresses at an acceptable level, and stiffness-driven designs, which limit deflection [25.20].

Each regulation relating to the strength-driven plating thickness has its own requirements, but these requirements are all are of a similar form, derived from beam theory. For the sake of simplification, the panel can be considered a beam when the aspect ratio of the panel is sufficiently large (greater than 2). Assuming that a built-in beam of span s is under a uniformly distributed load P, the maximum bending moment is

$$M_{\mathrm{MAX}} = \frac{Ps^2}{12}\,.$$

The minimum section modulus per unit width for a plate of thickness t is

$$\mathrm{SM}_{\mathrm{MIN}} = \frac{t^2}{6}\,.$$

Consequently, the design stress can be expressed as

$$\sigma_{\mathrm{DES}} = \frac{M_{\mathrm{MAX}}}{\mathrm{SM}_{\mathrm{MIN}}} = \frac{6Ps^2}{12t^2}\,.$$

Solving for the plate thickness yields

$$t = s\sqrt{\frac{kP}{\sigma_{\mathrm{DES}}}}\,,$$

where k would be 0.5 in this instance due to the boundary conditions assumed, which may vary depending on the regulatory body [25.21]. A strength-driven criterion for the design of the hull plating can therefore be provided. Nevertheless, in certain areas, or for particular materials, the analysis is supplemented with a stiffness-driven criterion. For the boundary and loading conditions assumed previously, namely a built-in beam under a uniformly distributed load, the maximum deflection ω_{MAX} is given by

$$\omega_{\mathrm{MAX}} = \frac{Ps^4}{384EI}\,.$$

However, the stresses across the plate lead to Poisson's ratio effects, where Poisson's ratio ν is the ratio of the transverse and axial strains, which is generally taken to be 0.3 for most metals. The term EI should therefore be replaced by the plate flexural rigidity D, where

$$D = \frac{Et^3}{12(1-\nu^2)} = \frac{Et^3}{10.92}\,.$$

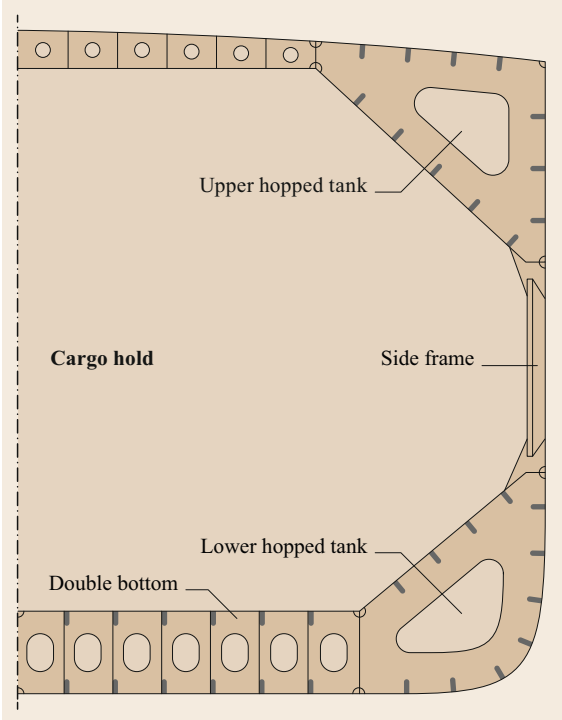

Fig. 25.31 Bulk carrier midship section

Furthermore, assuming a maximum deflection under load of 1% of the span and substituting for D, the original deflection equation becomes

$$0.01s = \frac{10.92Ps^4}{384Et^3} ,$$

which simplifies to

$$0.01 = \frac{0.028P}{E}\left(\frac{s}{t}\right)^3 .$$

Finally, solving for the plating thickness yields

$$t = s\sqrt[3]{\frac{0.028P}{0.01E}} .$$

Therefore, although they take various forms depending on the individual rules applied and inherent assumptions made, the strength and stiffness criteria can be employed to design a ship structure that is able to withstand local loads.

25.5.5 Design Optimization

The discussion of global and local loads provided above briefly summarized elements of the structural design of ships. Both types of loads were calculated via beam theory. Additional methods such as grillage theory and Euler's critical buckling are employed to analyze the hull plating in conjunction with its supporting structure. There are, however, a multitude of load cases and failure modes to consider when designing ships. For instance, one very important element is fatigue, as repeated loading cycles can lead to fatigue failure over time.

Even though a structural design complies with the regulatory requirements, it may not be a satisfactory design, as elements such as the weight or cost are yet to be incorporated. The structure must be both light enough to maximize the cargo carrying capacity and affordable to construct if the design is to be an attractive investment. The structural design must be refined, employing objective functions to identify the optimum compromise based on the various factors considered in the design. Furthermore, the use of more advanced analytical methods (FEA for example) is advised and is becoming increasingly common, even for small craft [25.22]. This permits a more rational and direct approach to the analysis of the structure while also enabling additional factors to be accounted for, such as vibrations.

Finally, an important aspect of the structural design, indeed ship design as a whole, is that automated iterations are carried out to refine and hone the design. Ship design is not a linear process but an iterative one, consistently described as a design spiral. A vast number of iterations are carried out, as slight changes in one area have a significant impact on the whole design. For instance, upon the completion of a new structural design iteration, the weight and center of gravity estimate will need to be updated, which will in turn affect the displacement and hydrostatics of the vessel. Increasing the displacement may reduce the cargo capacity and increase the draft of the vessel. Consequently, a more powerful engine will be required to achieve the same speed, which will have tremendous effects on the stability of the vessel because, for example, the location of the center of gravity will change. It is therefore crucial to introduce automation and optimization into the ship design spiral.

25.5.6 Midship Section

Once determined, the structure and main structural components of the ship are represented in a midship section. This particular drawing presents a cross-section of the vessel at midship in order to detail the scantlings and arrangement of the structural components. A simplified midship section for a double-bottom single-hull bulk carrier is depicted in Fig. 25.31.

25.6 Additional Considerations

25.6.1 The Environment

The environment represents a major unknown in the design of ships and ocean-going vessels. Both the wind and waves can negatively impact the stability of the vessel, increase its resistance, and induce greater structural loads. These environmental conditions must therefore be accounted for at the design stage. Two scales are used to express the wind strength or sea state: the Beaufort scale, which defines a range of wind forces, and the Douglas sea scale, which distinguishes between ten sea states. The Beaufort scale and Douglas sea scale are defined in Tables 25.2 and 25.3, respectively.

It should be noted that the Douglas sea scale defines a small wave as being less than 2 m in height, a medium wave as being between 2 and 4 m high, and a high wave as being in excess of 4 m high. In reality, much higher waves will be encountered, but it is extremely difficult to define and quantify the impact of a particular wave height and to choose the particular height to design to. Consequently, the concept of a significant wave height, labeled SWH or $H_{1/3}$, is used, which is defined as the mean wave height of the top third of all statistically encounterable wave heights. This enables the ship to be designed for the most statistically probable waves, but it does not account for larger waves that the vessel could encounter during its service life.

Table 25.2 Beaufort scale

Beaufort force	Description	Wind speed	
		kn	km/h
0	Calm	< 1	< 1
1	Light air	1–3	1–5
2	Light breeze	4–6	6–11
3	Gentle breeze	7–10	12–19
4	Moderate breeze	11–16	20–28
5	Fresh breeze	17–21	29–38
6	Strong breeze	22–27	38–49
7	Near gale	28–33	50–61
8	Gale	34–40	62–74
9	Strong gale	41–47	75–88
10	Storm	48–55	89–102
11	Violent storm	56–63	103–117
12	Hurricane	64+	118+

25.6.2 Seakeeping

The seakeeping behavior of a boat (considered a rigid body in a seaway) can be investigated for a given set of environmental conditions (sea spectrum). The aim of this is to define the vessel's response (or the response amplitude operator, RAO) to the external environment. Idealized wave spectra (such as JONSWAP or Bretschneider) are utilized in physical or numerical analysis to quantify the ship's motion.

Among other parameters, accelerations are assessed at various locations, as these accelerations are a critical influence on the design of the vessel. On the one hand, there are loading implications of higher accelerations. Quantifying the accelerations and therefore the loads acting on the structure more precisely facilitates a more refined design. Moreover, seakeeping analysis can ascertain deck wetness and inherent green water (solid sea water, rather than just foam or spray, on deck), thus allowing additional structural load cases to be defined.

On the other hand, the frequency of acceleration of the vessel at any given location onboard can be related to the number of individuals who become seasick through the motion sickness incidence (MSI). This is vital information for ensuring that fee-paying passengers (e.g., on a cruise ship) will not be seasick in moderate sea conditions.

Furthermore, seakeeping analysis allows the human factor to be accounted for in ship design, thus ensuring that the vessel's crew is fully able to operate the vessel. For example, it can be used to check that the bridge –

Table 25.3 Douglas sea scale

Douglas degree	Sea state (wind and sea)		Swell
	Wave height (m)	Description	Description
0	No wave	Calm (glassy)	No swell
1	0–0.1	Calm (rippled)	Very low (short or average and low wave)
2	0.1–0.5	Smooth	Low (long and low wave)
3	0.5–1.25	Slight	Light (short and moderate wave)
4	1.25–2.5	Moderate	Moderate (average and moderate wave)
5	2.5–4.0	Rough	Moderate rough (long and moderate wave)
6	4.0–6.0	Very rough	Rough (short and high wave)
7	6.0–9.0	High	High (average and high wave)
8	9.0–14.0	Very high	Very high (long and high wave)
9	14.0+	Phenomenal	Confused (wavelength and height indefinable)

the command center of the vessel – is located in the most suitable position. Since the vessel pitches about the LCF, much smaller accelerations will be experienced closer to the LCF, regardless of the sea spectrum. However, the stem of the boat will experience much higher accelerations, hence the preferred location of the bridge nearer the LCF.

Based on the results of the seakeeping analysis, limiting operational conditions can be defined, such as the maximum speed in a defined sea state. The ability of the crew to operate the vessel and the response of the vessel to the environment also affect the maneuverability of the ship, which is of considerable importance to its design.

25.6.3 Maneuverability

The maneuverability of a ship refers to how well the vessel responds to commands from the operator to change course. Some of the main areas of interest in this context include the ability of the vessel to remain on course, motions created by bow thrusters and other control devices, and the vessel's capacity to start or stop a turn, as well as the turn radius that can be achieved. A rudder (or rudders) is (are) used to maneuver the vessel. A rudder has a symmetrical aerofoil section. Inducing an angle of attack results in the generation of a lift force

$$L_{\mathrm{RUDDER}} = \frac{1}{2}\rho A V^2 C_{\mathrm{L}} ,$$

where C_{L} is the rudder lift coefficient at a given angle of attack. The lift can then be resolved into its components, including the transverse component that alters the course of the vessel. The rudder forces generated are transferred to the hull via the rudder stock, a structural component that must be designed to cope with both the bending and torque generated. Note that ship rudder movement is typically constrained to 35° either side of the centerline, as the rudder would stall beyond this point – the maneuverability does not improve, and the torque becomes much greater. This can be seen as a fail-safe to prevent structural impairment of the rudder, which could result in a loss of steering. A similar safety and reliability approach is adopted for damage stability.

25.6.4 Damage Stability

In order to prevent the loss of lives and vessels, regulatory requirements for the damage stability of ships have been implemented. For instance, a ship should be suitably subdivided into watertight compartments, and it should be able to withstand the flooding of a number of those compartments (this number depends on how the ship is operated). This regulation is particularly rigorous for passenger vessels, and is an important part of SOLAS [25.1].

The concept of a margin line is used to assess damage stability. This can be defined as an imaginary line that is 76 mm (3 inches) below the upper surface of the bulkhead deck at the side. Under no circumstances should the margin line become immersed, as it is assumed that the vessel will be lost if it is immersed past that point. The naval architect therefore needs to ascertain the floodable length of the vessel, i.e., the maximum length of the vessel that can be flooded for the margin line to remain above water.

Ballasting plays a substantial role in damage stability. Water ingress on one side of the vessel would shift the center of gravity away from the centerline, causing the vessel to adopt an angle of list, thus making it less safe for crew and passengers. Ballasting and cross-flooding methods must therefore be provided to cancel out any angle of list and achieve parallel sinkage. Consequently, sufficient freeboard must be available to account for the lost buoyancy. Furthermore, the vessel must retain sufficient transverse and longitudinal stability even when damaged. The purpose of those regulatory requirements is to improve the chances of the crew, passengers, and vessel surviving in the most statistically probable conditions.

25.7 Summary

Maritime transportation has seen exponential growth since the mid-twentieth century, with around 90% of the world's freight being transported by sea. Meeting this demand requires the construction of ever-larger vessels that are able to carry ever-increasing amounts of cargo. Such vessels present new challenges for naval architects from design and regulatory perspectives.

In this chapter, the terminology and form coefficients used to characterize the design of a hull were introduced. It was shown that this characterization of the hull design is followed by the generation of a lines plan. The crucial importance of stability was explained, emphasizing the effect of the constantly varying ship displacement. The definitions of the various drag components were shown to lead to a resistance curve for the vessel. The resistance can be optimized by ensuring that wave interactions lead to destructive interference that minimizes the wave resistance component. Moreover, by accounting for various

efficiencies, it is possible to calculate the installed power from the delivered power to check that the target speed of the vessel can be reached.

The structural design of ships was also considered in this chapter, with beam theory applied at various levels to both global and local loads. The strength and stiffness aspects of the latter were investigated. Optimizing the structural design is an essential part of the design process.

Finally, additional areas that should be considered by the naval architect were outlined, such as the environment, seakeeping, and maneuverability. Thus, the responses of a vessel to the environment and the operator's actions were discussed, as was damage stability, including the relevant safety regulations.

Ship design also involves numerous other fields; for instance, the propulsion configuration and the vast and complex arrangement of systems onboard must be analyzed in detail. Specific elements such as propeller design can also be targeted in major investigations. Lastly, ship building and construction play a major role in the design, and these aspects are always evolving in ways that permit better build quality to be achieved in a shorter time frame.

With the development of analytical methods (finite element analysis or computational fluid dynamics), further refinement of ship optimization has become possible, and the demand for larger, lighter, faster, and more efficient vessels can be met. A number of new research areas are also being driven by the increasing regulatory framework associated with ship design. For instance, one such area of research aims to minimize the environmental impact of ships by reducing emissions. Therefore, it appears that one of the main challenges in ship design and maritime transportation in the twenty-first century will be to enhance sustainability.

References

25.1 International Maritime Organisation: *International Convention for the Safety of Life at Sea* (International Maritime Organisation, London 1974)

25.2 J.-B. Souppez: Structural assessment and scantlings of traditional small crafts. In: *Proceedings of Historic Ships. The Royal Institution of Naval Architects, London, UK* (2020)

25.3 K.J. Rawson, E.C. Tupper: *Basic Ship Theory* (Butterworth-Heinemann, Boston 2001)

25.4 International Maritime Organisation: *International Convention on Tonnage Measurement of Ships* (International Maritime Organisation, London 2009)

25.5 C.J. Patterson, J.D. Ridley: *Ship Stability, Powering and Resistance* (Adlard Coles Nautical, Bloomsbury, London 2014)

25.6 International Maritime Organisation: *International Code on Intact Stability* (International Maritime Organisation, London 2009)

25.7 M.D. Woodward, M. van Rijsbergen, K.W. Hutchinson, A. Scott: Uncertainty analysis procedure for the ship inclining experiment, Ocean Eng. **114**, 79–86 (2016)

25.8 R. Munro-Smith: *Ships and Naval Architecture* (IME, London 1973)

25.9 International Maritime Organisation: *International Convention on Load Lines* (International Maritime Organisation, London 2005)

25.10 W. Froude: *Experiments of the Surface Friction Experienced by a Plane Moving through Water*, Report to the British Association for the Advancement of Science (London 1872)

25.11 W. Froude: *Report to the Lords Commissioners of the Admiralty on Experiments for the Determination of the Frictional Resistance of the Water on a Surface Under Various Conditions*, Report to the British Association for the Advancement of Science (London 1874)

25.12 O. Reynolds: An experimental investigation of the circumstances which determine whether the motion of water shall be direct or sinuous, and of the law of resistance in parallel channels, Philos. Trans. R. Soc. **174**, 935–982 (1883)

25.13 J.B. Hadler: *Coefficient for International Towing Tank Conference 1957 Model-Ship Correlation Line*, Vol. 1185 (David Taylor Model Basin, Navy Department, Washington DC 1958)

25.14 International Towing Tank Conference: Report of the resistance committee. In: *15th Int. Towing Tank Conf., The Hague* (1978)

25.15 C.W. Prohaska: A simple method for the evaluation of the form factor and low speed wave resistance. In: *11th Int. Towing Tank Conf., Tokyo* (1966)

25.16 J. Dewavrin, J.-B. Souppez: Experimental investigation into modern hydrofoils-assisted monohulls: How hydrodynamically efficient are they?, Trans. RINA Int. J. Small Craft Technol. **160**(B2), 111–120 (2018), https://doi.org/10.3940/rina.ijsct.2018.b2.223

25.17 A.F. Molland, S.R. Turnock, D.A. Hudson: *Ship Resistance and Propulsion: Practical Estimation of Propulsive Power* (Cambridge Univ. Press, Cambridge 2011)

25.18 J.-B. Souppez, E. Begovic, S. Pradeep, F. Wang, A. Rosén: Comparative assessment of rule-based design on the pressure and resulting scantlings of high speed powercrafts. In: *Proceedings of the Symposium of High Speed Marine Vehicles, Naples, Italy* (2020)

25.19 E.C. Tupper: *Introduction to Naval Architecture*, 5th edn. (Butterworth-Heinemann, Oxford 2013)
25.20 J.-B. Souppez: Structural design of high performance composite sailing yachts under the new BS EN ISO 12215-5, SNAME J. Sail. Technol. **2**, 1–18 (2018)
25.21 Lloyd's Register: *Rules and Regulations for the Classification on Ships* (Lloyd's Register Group, London 2016)
25.22 J.-B. Souppez: Designing the next generation of small pleasure and commercial powerboats with the latest ISO 12215-5 for hull construction and scantlings. In: *Proceedings of the 1st SNAME/IBEX Symposium* (2019)

Jean-Baptiste R. G. Souppez

Mechanical, Biomedical & Design Department, School of Engineering and Technology, College of Engineering and Physical Sciences
Aston University
Birmingham, UK
j.souppez@aston.ac.uk

Jean-Baptiste R. G. Souppez is the Senior Teaching Fellow in Mechanical Engineering and Design at Aston University. He is also the UK Principal Expert in small craft structures, the Deputy Editor-in-Chief of the SNAME Journal of Sailing Technology, and contributes to the EMship+ Master in Ship Design as a visiting Professor. His research in fluid dynamics has driven his expertise inhydrofoils and award-winning work on yacht sails' aerodynamics.

Part F Related Engineering Fields

26 **Electrical Engineering**
Martin Poppe, Steinfurt, Germany

27 **Power Generation**
Asfaw Beyene, San Diego, USA
Dwarkadas Kothari, Vellore, India
P.M.V. Subbarao, New Delhi, India

26. Electrical Engineering

Martin Poppe

Some of the most sophisticated systems are the result of close cooperation between mechanical and electrical engineers. This chapter aims to provide mechanical engineers with an introduction to electrical engineering. It explains its basic laws and components, and how they are used to create electrical and electronic systems.

The fundamental laws of electrodynamics are presented using terminology that is also common to mechanical engineers. In this way, the reader will, for example, understand why inductors are made by winding wires around a core and why, in different applications, completely different types of capacitors and resistors are used.

This chapter not only explains how electrical machines and generators work. It also shows how strong machines may become intelligent strong machines. For this purpose, it describes the functioning of transistors and shows how electronic networks can be analyzed. It also explains how semiconductor devices are able to switch and steer high tensions and large currents.

The chapter ends with a glance at one of the most challenging fields common to electrical and mechanical engineers: the storage of power.

26.1 **Fundamental Laws** 1167
26.1.1 Charge 1168
26.1.2 Forces and Fields 1169
26.1.3 Integral Formulation of Field Generation 1170
26.1.4 Potentials and Tensions 1173
26.2 **Capacitors, Resistors, and Inductors** .. 1174
26.2.1 Matter and Fields 1174
26.2.2 Resistors 1176
26.2.3 Capacitors 1177
26.2.4 Inductors 1179
26.2.5 Alternating-Current Behavior 1181
26.2.6 Parasitics 1182
26.3 **Semiconductor Devices** 1183
26.3.1 Semiconductors 1183
26.3.2 Doping, the Key to Top Performance 1184
26.3.3 Diodes 1185
26.3.4 Bipolar Transistors 1187
26.3.5 Metal–Oxide–Semiconductor Transistors 1189
26.3.6 Power Semiconductor Devices 1191
26.4 **Networks** 1194
26.4.1 Network Terminology and Reference Directions 1194
26.4.2 Kirchhoff's Rules 1195
26.4.3 Nonideal Voltage and Current Sources . 1196
26.4.4 Network Analysis Algorithms 1197
26.4.5 Alternating-Current Networks 1201
26.4.6 Transformers 1202
26.4.7 Three-Phase Alternating-Current Systems 1204
26.5 **Electrical Machines** 1205
26.5.1 How Wires Are Forced to Move 1205
26.5.2 DC Machines 1207
26.5.3 Asynchronous Machines 1208
26.5.4 Synchronous Machines 1210
26.6 **Energy Storage** 1214
26.6.1 Introductory Remarks 1214
26.6.2 Mechanical Storage: Water 1215
26.6.3 Electric Storage: Supercapacitors 1216
26.6.4 Electrochemical Storage: Batteries, Accumulators, and Fuel Cells 1217
References 1221

26.1 Fundamental Laws

Electrical engineering is the practical application of the laws of electrodynamics for the design of machines and systems. And electrodynamics is that part of physics that analyzes a single property of matter named *charge*. In this section, the fundamental properties of charged objects are discussed. This includes the formation of electric and magnetic fields by charges as well as their influence on the motion of charges. In this context, potentials, tensions, and currents are introduced.

K.-H. Grote, H. Hefazi (Eds.), *Springer Handbook of Mechanical Engineering*, Springer Handbooks,
https://doi.org/10.1007/978-3-030-47035-7_26

26.1.1 Charge

Charge, denoted by the letter Q and measured in coulombs (C), is a signed quantity, as it exists in both positive (+) and negative (−) forms. If charges move from one end of a wire to the other, the first end will lose charge while the other end gains charge. The rate of change is called the *current*

$$I = \frac{\mathrm{d}Q}{\mathrm{d}t} \tag{26.1}$$

and is measured in amperes (A) or coulombs per second. In technical applications, the transport of charges is done by elementary particles called *electrons*, named after the Greek word for amber, as amber charges up when being rubbed against wool. Electrons come in vast numbers, each carrying the same negative amount of charge called the *elementary charge* e.

$$e = 1.6021766 \times 10^{-19}\,\mathrm{C}\,. \tag{26.2}$$

Hence, if there is a current of 1 A from a plug to a lamp, some 6.25×10^{18} electrons per second will move from the lamp to the plug (electrons always move in the direction opposite to the current due to their negative charge). In the presence of such large numbers, rather than looking at individual electrons, it is meaningful to work with the density of charge per volume V

$$\rho = \frac{Q}{V} = \frac{-eN}{V} = -en\,, \tag{26.3}$$

where N is the number of electrons and $n = N/V$ is the density of electrons. It is know from experience that the current at one end of a wire is always the same as that at the other. In other words, no charge is ever lost. This statement, usually called *charge conservation*, is assumed to be a law of Nature.

Conservation of charge leads to a fundamental equation of electrodynamics: the *continuity equation*. This equation relates the loss of charge density in a small volume to the current density through the surface of this volume. It may be deduced from the following mathematical rearrangement: For any constant and stationary volume V, one can write

$$\frac{\mathrm{d}Q}{\mathrm{d}t} = 0$$

$$\rightarrow \quad \frac{\mathrm{d}}{\mathrm{d}t} \iiint \rho \mathrm{d}V = \iiint \left[\frac{\partial \rho}{\partial t} + \nabla \cdot (\rho \boldsymbol{v}) \right] \mathrm{d}V = 0$$

$$\rightarrow \quad \frac{\partial \rho}{\partial t} + \nabla \cdot (\rho \boldsymbol{v}) = 0\,. \tag{26.4}$$

The integrand must be zero because the integral equation is to be zero for an arbitrary volume. Mathematically, the vector $\boldsymbol{v}$ appearing in (26.4) is the speed of the points at which the density is calculated. Physically, this speed may be identified as the speed of the carriers of charge.

The bottom line of (26.4) is the continuity equation. It states that, for any infinitesimal volume, the rate of loss of charge density $-\partial\rho/\partial t$ inside that volume equals the divergence of the charge density multiplied by the speed of the charges $\boldsymbol{v}$. In plain terms, i.e., applied to a finite volume: the loss of charge in a given volume equals the current passing through its boundaries.

The product occurring in the continuity equation is called the *current density*

$$\boldsymbol{J} = \rho \boldsymbol{v}\,. \tag{26.5}$$

Hence, the continuity equation is often written

$$\frac{\partial \rho}{\partial t} + \nabla \cdot \boldsymbol{J} = 0\,. \tag{26.6}$$

This equation describes the effect of charge conservation for very small volumes. The current density is a quantity of great practical importance, as it connects the motion of carriers of charge to the electric current I. The current passing through an oriented area $\boldsymbol{A}$ is given by

$$I = \iint (\rho \boldsymbol{v}) \cdot \mathrm{d}\boldsymbol{A} = \iint \boldsymbol{J} \cdot \mathrm{d}\boldsymbol{A}\,. \tag{26.7}$$

Integrals of the type used in (26.7) are called *fluxes*, being represented by the Greek letter Φ. Mathematically speaking, a current I is the flux of a current density $\boldsymbol{J}$ through the oriented surface $\boldsymbol{A}$. For a mathematician, $I = \Phi_{\boldsymbol{J}}$.

While the current density $\boldsymbol{J}$ is a vector, the current I is not. Although it is said to have a direction, this simply expresses whether the change of charge balance between the two faces of a plane is meant to increase from left to right or from right to left. However, the quantity *current* does not contain any information about the angle between the electrons' movements and the surface they cross.

Application Example: The Speed of Electrons in a Power Supply Cable

If a current passes along a wire, electrons move in a direction perpendicular to its cross section A, as shown in Fig. 26.1. In this case, the equation relating the current and current density, (26.7), simplifies to $I = \rho v A = -envA$, where n is now the density of electrons. The evaluation of this product becomes simple if the following geometrical relation is understood: the number ΔN of electrons passing through the surface $\boldsymbol{A}$ per time

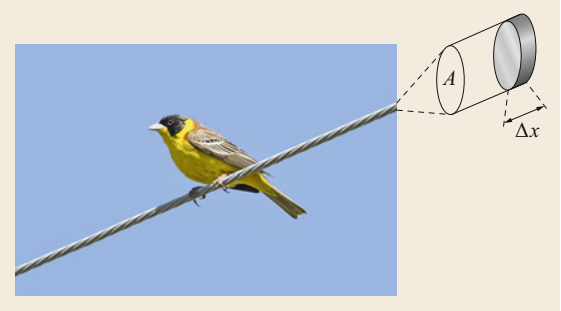

Fig. 26.1 A power cable with cross section A. The volume $V = A\Delta x$ is filled with electrons in a time $\delta t = \Delta x/v$, where v is the speed of the electrons (photo: © bennytrapp/stock.adobe.com)

interval Δt equals the number $\Delta N = n\Delta V$ of electrons in a volume $\Delta V = A\Delta x = Av\Delta t$. Therefore,

$$I = \frac{\Delta Q}{\Delta t} = -\frac{e\Delta N}{\Delta t} = -envA\,.$$

Clearly, n differs from material to material. Aluminum, for example has a chemical valence of 3 and a molar volume of $V_{\text{mol}} = 10.0\,\text{cm}^3/\text{mol}$, so its electron density is

$$\begin{aligned} n &= 3\frac{N_\text{A}}{V_\text{mol}} = 3\frac{6.02\times10^{23}\,\text{mol}^{-1}}{10.0(0.01\,\text{m})^3\,\text{mol}^{-1}} \\ &= 1.81\times10^{29}\,\text{m}^{-3}\,, \end{aligned}$$

with N_A being the Avogadro number. Assuming a current of 100 A traversing an aluminum wire with a cross section of $A = 1\,\text{cm}^2$, the velocity of electrons turns out to be surprisingly small:

$$\begin{aligned} v &= \frac{I}{enA} \\ &= \frac{100\,\text{A}}{(1.6\times10^{-19}\,\text{C})(1.81\times10^{29}\,\text{m}^{-3})(10^{-4}\,\text{m}^2)} \\ &\approx 3.5\,\frac{\text{mm}}{\text{s}}\,. \end{aligned}$$

The scale of this speed is thus that of snails not cheetahs. And, with the exception of semiconductor devices, this remains true for almost all products of electrical engineering.

26.1.2 Forces and Fields

Charge would be a completely unknown quality of matter if it were not connected to a set of forces to which carriers of charge (and nothing else) are susceptible. The experimental proof of the presence of a charged body is the presence of forces from other charged bodies.

The question of *how a charged particle knows or feels the presence of another charged body* leads to a key concept of electromagnetism, viz. electromagnetic fields. Forces between carriers of charges are, roughly speaking, regarded as the result of a two-step process: every charge modifies the space in its neighborhood. And it it this very modification that makes any other charge feel its presence. No carriers of charge ever notice other charges directly; they only feel the modification of the space.

The modification of space around a charged particle is called a *field of force* because the effect of a force proves its existence. Electromagnetism defines two fields. The *field of the electric force* $\boldsymbol{E}$ is usually simply called the *electric field*. This field is generated by every charged particle. If carriers of charge are moving, i.e., if there is an electric current, a second field, the *field of the magnetic force* $\boldsymbol{B}$, is generated in addition to $\boldsymbol{E}$. For historical reasons, the field of the magnetic force is often called the *flux density*. The origin of this term is an analogy which was thought to be fundamental in the 19th century.

The force due to the electric field is called the *Coulomb force*, the force due to a magnetic field is called the *Lorentz force*, and both together form the *electrodynamic force*. The term "electrodynamic force" (German: *elektrodynamische Kraft*) was introduced by *Einstein* [26.1] when he realized that a description of electromagnetism is valid in all moving frames if, and only if, both the Coulomb force and Lorentz force are taken into account. This is not to be confused with the *electromotive force*, which is not a force but a highly misleading pseudotechnical term that, for the sake of consistency, will not be used in this book. For a carrier of charge Q traversing these fields at a velocity $\boldsymbol{v}$, one has

$$\begin{aligned} \boldsymbol{F}_\text{C} &= Q\boldsymbol{E} && \text{Coulomb force}\,, \\ \boldsymbol{F}_\text{L} &= Q(\boldsymbol{v}\times\boldsymbol{B}) && \text{Lorentz force}\,, \\ \boldsymbol{F}_\text{e} &= Q(\boldsymbol{E}+\boldsymbol{v}\times\boldsymbol{B}) && \text{Electrodynamic force}\,. \end{aligned} \qquad (26.8)$$

There is one fundamental difference between the Coulomb force and the Lorentz force: the Coulomb force can change the velocity of charge carriers and thereby their kinetic energy. In contrast, the Lorentz force always acts perpendicular to the direction of motion, leaving the speed and thus kinetic energy unchanged.

The generation of fields by charges is described by a set of four differential equations, called *Maxwell's equations* [26.2],

$$\begin{aligned} &\text{div}\,\varepsilon_0\boldsymbol{E} = \rho\,, && \text{div}\,\boldsymbol{B} = 0\,, \\ &\text{rot}\,\boldsymbol{E} = -\frac{\partial}{\partial t}\boldsymbol{B}\,, && \text{rot}(\mu_0^{-1}\boldsymbol{B}) = \boldsymbol{J} + \frac{\partial}{\partial t}\varepsilon_0\boldsymbol{E}\,. \end{aligned} \qquad (26.9)$$

In (26.9), ρ is the charge density, $\boldsymbol{J}$ is the current density, ε_0 is the permittivity of free space, and μ_0 is the permeability of free space. The linearity of these equations guarantees the principle of linear superposition (linear superposition may be used up to photon energies below the rest energy of two electrons [26.3]) to apply to charge densities, current densities, and the fields $\boldsymbol{E}$ and $\boldsymbol{B}$.

Equations (26.8) and (26.9) form the backbone of what is known as *classical electrodynamics*. Its successor, named *quantum electrodynamics*, is the most stringently tested theory in the world [26.4, 5]

The set of equations (26.9) may also be expressed with the help of the *nabla operator* $\nabla = (\partial/\partial x, \partial/\partial y, \partial/\partial z)$ as follows

$$\nabla \cdot \varepsilon_0 \boldsymbol{E} = \rho\,, \qquad \nabla \cdot \boldsymbol{B} = 0\,,$$
$$\nabla \times \boldsymbol{E} = -\frac{\partial}{\partial t}\boldsymbol{B}\,, \qquad \nabla \times (\mu_0^{-1}\boldsymbol{B}) = \boldsymbol{J} + \frac{\partial}{\partial t}\varepsilon_0 \boldsymbol{E}\,. \tag{26.10}$$

Figure 26.2 provides a pictorial interpretation of these equations. Figure 26.2a,b defines the source structure of the fields: while the electric field has sources, the magnetic field does not. Figure 26.2c,d describes the rotational structure. The electric field only has a rotational component if changing magnetic fields are present. The magnetic field is entirely rotational and may be generated either by currents or by changing electric fields.

The lines drawn in Fig. 26.2 are called *field lines*. An electrical field line indicates the direction of the force acting on a positively charged particle. The meaning of the magnetic field line is more complicated as the force on a charge is always perpendicular to the line. Later in this chapter, it will be shown that a magnetic dipole, like a compass needle, is subject to a torque that tries to align the dipole with the magnetic field lines.

26.1.3 Integral Formulation of Field Generation

Maxwell's equations may also be formulated in integral form. To do so, the following convention shall be adopted: an integral over a closed path (around an area) or around a finite volume shall be denoted by a $\oint$ symbol with a subscript indicating the path or surface. So $\oint_{\partial V}$ is an integral over the surface enclosing the volume V, and $\oint_{\partial A}$ is a line integral along the enclosure of the surface A.

Applying Gauss's theorem [26.7] to the two equations describing the source structure of the electric field

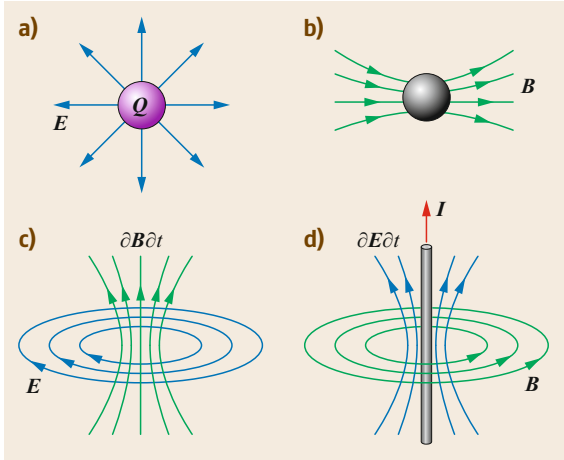

Fig. 26.2a–d Interpretation of Maxwell's equations according to [26.6]. **(a)** Charges are the sources of electric fields. $\nabla \cdot \boldsymbol{E} = \rho/\varepsilon_0$. **(b)** The magnetic field has no sources $\nabla \cdot \boldsymbol{B} = 0$; it is a purely rotational field. **(c)** Rotational electric fields are generated by changing magnetic fields $\nabla \times \boldsymbol{E} = -\partial \boldsymbol{B}/\partial t$. **(d)** Magnetic fields are created by both changing electric fields and moving charges (i.e., currents) $\nabla \times \boldsymbol{B} = \mu_0 \cdot \boldsymbol{J} + \varepsilon_0 \mu_0 \partial \boldsymbol{E}/\partial t$

and the magnetic field yields

$$\nabla \cdot \varepsilon_0 \boldsymbol{E} = \rho \quad \rightarrow \oint_{\partial V} \varepsilon_0 \boldsymbol{E} \cdot \mathrm{d}\boldsymbol{A} = Q\,,$$
$$\nabla \cdot \boldsymbol{B} = 0 \quad \rightarrow \oint_{\partial V} \boldsymbol{B} \cdot \mathrm{d}\boldsymbol{A} = 0\,. \tag{26.11}$$

Equations (26.11) are usually referred to as *Gauss's laws for the electric and magnetic field*. The most surprising aspect of these equations is that they connect the property of a volume (ρ is the density of charges within the volume) to an integral that is taken at the surface only. For the integrals in (26.11), the distribution of charges within the volume enclosed by the surface ∂V is completely irrelevant. Surface integrals of the type appearing in (26.11) are called *fluxes of a vector field* (here $\boldsymbol{E}$ or $\boldsymbol{B}$) through a surface $\boldsymbol{A}$. The reason is their formal similarity with physical fluxes such as water through the cross section of a river, grains through a tube, or charges through a wire as in (26.7).

Gauss's law for the electric field is an up-to-date version of a law found by Coulomb in 1784/1785. It states that the force between two point-like carriers of charges Q_1 and Q_2, situated at radii $\boldsymbol{r}_1$ and $\boldsymbol{r}_2$ as shown in Fig. 26.3, is

$$\boldsymbol{F_2} = -\boldsymbol{F_1} = \frac{Q_1 Q_2}{4\pi\varepsilon_0} \cdot \frac{\boldsymbol{r_2} - \boldsymbol{r_1}}{|r_{21}|^3}\,. \tag{26.12}$$

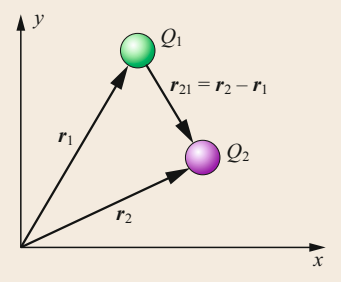

Fig. 26.3 Setup for the definition of the Coulomb force: two oppositely charged balls with centers placed at different locations $\boldsymbol{r}_1$ and $\boldsymbol{r}_2$

being know as *Coulomb's law*. Today, (26.12) is understood to be a consequence of Gauss's law for the electric field, together with the Coulomb force (see also (26.8)). In (26.12), $\boldsymbol{F_2}$ is the force acting on the carrier of Q_2. If the two charges have opposite signs, they attract each other; if not, the force is repelling. The force decreases with the square of the distance between the carriers of charge. The factor $1/(4\pi r_{21}^2)$ can be traced back to Gauss's law, as it is the inverse of the surface of a sphere or radius r_{21}.

If the forces on a positive charge are drawn as little arrows, one finds that these line up like strings ending on the charges. These lines are called *field lines*. Figure 26.4 shows the lines between a positive and a negative charge, and Fig. 26.5 the lines associated with two positive charges.

The *law of induction*, also known as the *law of Faraday and Henry* [26.8], is to some extent a consequence of the rotational part of the electric field. It is crucial for the functioning of a very wide range of electrical devices, as engines, generators, transformers, and solenoid antennas cannot operate without it:

$$U_{\text{ind}} = \oint_{\text{L}} \boldsymbol{E} \cdot \mathrm{d}\boldsymbol{\ell} = -\frac{\mathrm{d}}{\mathrm{d}t} \int_{A} \boldsymbol{B} \cdot \mathrm{d}\boldsymbol{A} = -\frac{\mathrm{d}\Phi_{\text{B}}}{\mathrm{d}t} \,. \tag{26.13}$$

The translation of this formula into plain English is: for a closed loop L of a conductor, placed in a magnetic field $\boldsymbol{B}$, the induced tension is given by the change of the magnetic flux Φ_{B} through any area $\boldsymbol{A}$ enclosed by this loop.

One reason for this wide variety of applications is the fact that the single formula (26.13) contains two completely different effects, which emerge if the derivative of the flux is worked out in detail. The terms remaining for the magnetic field are

$$\frac{\mathrm{d}}{\mathrm{d}t} \int_{A} \boldsymbol{B} \cdot \mathrm{d}\boldsymbol{A} = \int \left[\frac{\partial \boldsymbol{B}}{\partial t} - \nabla \times (\boldsymbol{v} \times \boldsymbol{B}) \right] \mathrm{d}\boldsymbol{A} \,. \tag{26.14}$$

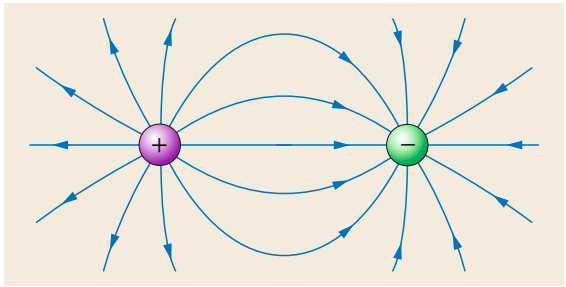

Fig. 26.4 Field lines between a positive and a negative charge

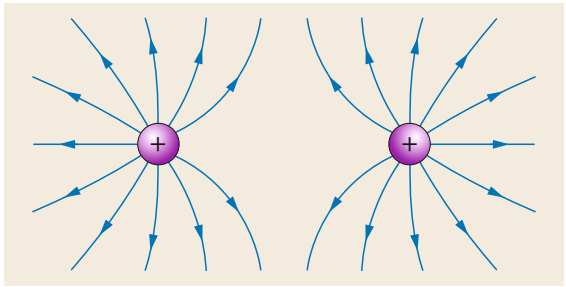

Fig. 26.5 Field lines associated with two positive charges

The mathematical origin of the velocity $\boldsymbol{v}$ is the contribution of the change of area to the total derivative. Its meaning is the speed of those points for which the flux elements are calculated. The physical meaning of (26.14) can be explored by translating the line integral in (26.13) into a surface integral $\oint_{\partial A} \boldsymbol{E} \cdot \mathrm{d}\boldsymbol{\ell} = \int (\nabla \times \boldsymbol{E}) \mathrm{d}\boldsymbol{A}$. So, one may conclude by comparison

$$\nabla \times \boldsymbol{E} = -\frac{\partial \boldsymbol{B}}{\partial t} + \nabla \times (\boldsymbol{v} \times \boldsymbol{B}) \,. \tag{26.15}$$

The outer terms may be interpreted as new descriptions of the Lorentz force:

$$\begin{aligned} & \boldsymbol{F} = Q\boldsymbol{v} \times \boldsymbol{B} \\ \rightarrow\ & \boldsymbol{E} = \boldsymbol{v} \times \boldsymbol{B} \\ \rightarrow\ & \nabla \times \boldsymbol{E} = \nabla \times (\boldsymbol{v} \times \boldsymbol{B}) \,. \end{aligned} \tag{26.16}$$

Equation (26.16) should, however, not be misunderstood as describing the appearance of an electric field. It simply means that, for a charge carrier traversing a magnetic field, there will be a force accelerating it in a direction perpendicular to its velocity and perpendicular to the magnetic field, and that the strength of this force is just the same as for the Lorentz force. In view of the theory of special relativity, this is more than a coincidence. According to Einstein, which fraction of an electromagnetic field is magnetic and which is electric varies with velocity. A force attributed to a mag-

netic field in one frame of reference may be entirely attributed to an electric field in another frame.

A practical result of (26.16) is that all forces appearing in electrical generators with permanent magnets can be calculated either using the Lorentz force on the charge carriers or using (26.13). The results must be identical.

The two terms on the left-hand side of (26.15) are crucial for the functioning of transformers. An oscillating magnetic field can be used to generate a tension in a closed conducting loop. These terms already appeared as one of Maxwell's equations in (26.10).

The fourth macroscopic law to be inspected is the law of *Ampère* and *Maxwell*:

$$\oint_{\partial A} (\mu_0^{-1}\boldsymbol{B}) \cdot \mathrm{d}\boldsymbol{\ell} = I + \int \frac{\partial(\varepsilon_0 \boldsymbol{E})}{\partial t} \mathrm{d}\boldsymbol{A} \,. \tag{26.17}$$

It describes the generation of a magnetic field $\boldsymbol{B}$ by both a current I and a time-dependent electric field $\boldsymbol{E}$, as shown in Fig. 26.2. In (26.17), $\mathrm{d}\ell$ is a small element of any line enclosing a current I, and $\mathrm{d}\boldsymbol{A}$ is a small element of any surface that is completely encircled by this line. Equation (26.17) can be identified with one of the known differential equations by converting all terms into surface integrals:

$$\int \left[\nabla \times (\mu_0^{-1}\boldsymbol{B})\right] \mathrm{d}\boldsymbol{A} = \int \left(\boldsymbol{J} + \frac{\partial(\varepsilon_0 \boldsymbol{E})}{\partial t}\right) \mathrm{d}\boldsymbol{A} \,. \tag{26.18}$$

Since this equation is to be valid for an arbitrary surface $\boldsymbol{A}$, the integrands must be identical

$$\nabla \times (\mu_0^{-1}\boldsymbol{B}) = \boldsymbol{J} + \frac{\partial(\varepsilon_0 \boldsymbol{E})}{\partial t} \,, \tag{26.19}$$

which is identical to the fourth equation in (26.10).

In the limit $\partial(\varepsilon_0 \boldsymbol{E})/\partial t = 0$, the above is often called *Ampère's law*. However, this naming convention may easily lead to misinterpretations, as the *law* is only valid in the absence of time-dependent electric fields, and if a magnetic field varies with no current present, the Ampère–Maxwell law requires the presence of a time-dependent electric field. So, what is referred to as Ampère's law is actually only an approximation that applies to the static case.

Application Example: Whistling Capacitors

Gauss's law for the electric field may be used to determine the forces between the electrodes of a capacitor. If the material between the plates is compressible, the plates will change their separation at the same frequency as the charging and discharging of the plates. If this frequency is below 10 kHz, such vibration can be heard, and the capacitor can thus be identified as being of poor quality.

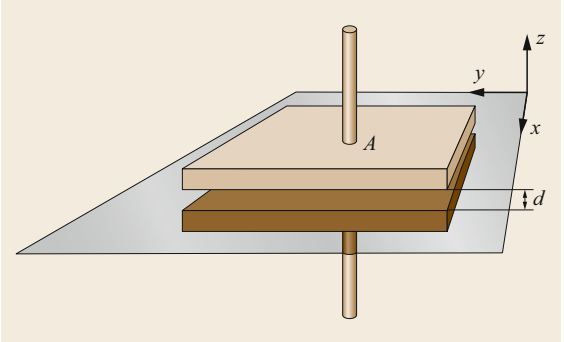

Fig. 26.6 Two electrodes forming a capacitor. All the electric field crosses the plane indicated between the electrodes, mostly traversing the area between the electrodes

Figure 26.6 shows the principal setup of a capacitor. It consists of two rather flat electrodes of area A, separated by a distance d. If a charge Q_1 is placed on the top electrode and a charge $Q_2 = -Q_1$ on the bottom, the electric field will be concentrated almost entirely in the region between the electrodes. For any surface enclosing the top electrode, the only significant contribution to the integral in Gauss's law will be the plane shown in gray in Fig. 26.6. The plane can be either close to one of the electrodes, or in the middle. One gets

$$Q_1 = \oint_{\partial V} \varepsilon_0 \boldsymbol{E} \cdot \mathrm{d}\boldsymbol{A} \approx \varepsilon_0 \boldsymbol{E} \cdot \boldsymbol{A} = \varepsilon_0 E_z A \,,$$

assuming an oriented area with $\boldsymbol{A} = (0, 0, A)$ and $E_z = -|\boldsymbol{E}|$ because the top plate is positively charged. The magnitude of the force $\boldsymbol{F}_2$ acting on the bottom plane is then

$$\boldsymbol{F}_2 = Q_2 \boldsymbol{E} = \varepsilon_0 Q_1 Q_2 \boldsymbol{A} = \varepsilon_0 Q^2 \boldsymbol{A} \quad (= -\boldsymbol{F}_1) \,.$$

If the electrodes carry oppositely signed charges, they will always attract each other, irrespective of which of the two electrodes is positively charged. Consequently, if the electrodes are charged with an alternating current of a certain frequency, the frequency at which the electrodes vibrate will be twice the frequency of the current. Actually, something similar can be heard close to old electrical locomotives. In that case, it is the oscillation of the magnetic field of the transformers that results in an audible mechanical frequency that is twice the frequency of the locomotive's power supply.

Table 26.1 Correspondence between electrostatics and gravitation

Electrostatics	Gravitation
$\boldsymbol{F} = Q\boldsymbol{E}$	$\boldsymbol{F} = m(0, 0, -g)$
Charge	Mass
Field strength $\lvert\boldsymbol{E}\rvert$	Acceleration g
Potential V	Height h
Tension U	Difference in height Δh

26.1.4 Potentials and Tensions

A charged particle in an electric field will gain potential energy when moving against the force of the field and loose potential energy when moving with the field. In other words: work is to be done if a charged body is to be moved along a path C through the field:

$$W = \int_{\mathrm{C}} -\boldsymbol{F}\cdot\mathrm{d}\boldsymbol{s} = -Q\int_{\mathrm{C}} \boldsymbol{E}\cdot\mathrm{d}\boldsymbol{s} \quad \text{(always)}\,. \tag{26.20}$$

If the electric field is static, it is bound to have no rotational component. Then, the dependence on the path vanishes and the value of the integral

$$\begin{aligned} W &= \int_a^b -\boldsymbol{F}\cdot\mathrm{d}\boldsymbol{s} \\ &= -Q\int_a^b \boldsymbol{E}\cdot\mathrm{d}\boldsymbol{s} \quad \text{(static field)} \end{aligned} \tag{26.21}$$

depends only on the starting point a and end point b. The minus sign in (26.21) indicates that energy is gained if the movement is *against* the direction of force.

For a given field $\boldsymbol{E}$, the work to be done only depends on the charge Q and the location of the two points a and b. Therefore, in the presence of a static electric field, one can assign a new property to each point in space called the *electric potential*, denoted by V. If one knows the potential at all points in space, one can easily calculate the energy gained by moving from one point to any other: it is the potential difference, multiplied by the charge, or just $V(b) - V(a) = W/Q$. The relation between $\boldsymbol{E}$ and V reveals a major practical use in its differential form. The equation

$$\boldsymbol{E} = -\nabla\cdot V \quad \text{(static field)} \tag{26.22}$$

shows that, if the (nondirectional) potential is known at every point in space, differentiation may be used to find both the strength and direction of the electric field.

The electric potential is only defined up to a constant, just as any indefinite integral. Physically, this freedom of choice simple means that one is free to choose an arbitrary starting point for the calculation of a potential. This freedom is lost when the difference of two potentials is calculated, as the constant of integration cancels out. The potential difference between two points is such an important quantity that it is given a name of its own, the *tension*

$$\begin{aligned} U_{ab} &= V(a) - V(b) \\ &= -\int_a^b \boldsymbol{E}\cdot\mathrm{d}\boldsymbol{s} \quad \text{(static field)} \end{aligned} \tag{26.23}$$

between two points.

The potential of a static electric field has a one-to-one correspondence with the height in the gravitational field of the Earth. Lines of equal potential correspond to lines of equal altitude in maps of mountains, as shown in Table 26.1.

As soon as the fields vary with time, the electric and magnetic fields are bound to appear together. In this case, it is helpful to define a *magnetic potential* $\boldsymbol{A}$, from which the magnetic field can be derived according to

$$\boldsymbol{B} = \nabla\times\boldsymbol{A}\,. \tag{26.24}$$

The electric field can now be written as

$$\boldsymbol{E} = -\nabla\cdot V + \frac{\partial\boldsymbol{A}}{\partial t} \quad \text{(always)}\,, \tag{26.25}$$

in a form that reveals the difference between electrostatics and electrodynamics: The second term in (26.25) accounts for the generation of a rotational electric field according to the Faraday–Henry law. It vanishes in the static case, leaving (26.22) only.

The major practical implication of (26.25) is that the idea of a tension between two points has to be dropped in the presence of varying magnetic fields. In fact, the stronger the rotational component of the electric field, the more important the path between two points becomes. Electric generators extensively use this fact by inducing high tensions (colloquially voltages) into wires that form a long path C in a time dependent magnetic field.

The instruction to "please switch off all electronic devices until the plane has reached its parking position" may be understood as a consequence of (26.25), as the functioning of electronic circuit boards relies on $\partial\boldsymbol{A}/\partial t$ being negligible.

26.2 Capacitors, Resistors, and Inductors

The functioning of the majority of basic circuit elements relies on the interaction between matter and electromagnetic fields. In this section, the influence of matter on electromagnetic fields will be analyzed and optimal geometries determined for resistors, capacitors, and inductors. The behavior of these circuit elements will be determined for direct-current (DC) and alternating-current (AC) networks. Finally, deviations from ideal circuit element properties are discussed.

26.2.1 Matter and Fields

Atoms and molecules consist of negatively charged electrons and positively charged nuclei. Therefore, even electrically neutral bodies will react to the presence of electric and magnetic fields. Figure 26.7 shows how an external field $\boldsymbol{E}_{\text{free}}$ applied to a neutral molecule will lead to the appearance of a new field $\boldsymbol{E}_{\text{bound}}$. Electrons that may move long distances (those that are *free* to leave molecular or atomic orbits) are held responsible for $\boldsymbol{E}_{\text{free}}$. In contrast, electrons and nuclei responsible for $\boldsymbol{E}_{\text{bound}}$ cannot move further than distances of about one nanometer, since they are *bound* to atoms. Both sets of carriers of charge are well distinct. The criterion is the value for the binding energy of electrons: those that are tightly bound will not be able to leave their orbit, while the others can. Usually, there is an energy gap between bound and free electrons. In mathematical terms, the bound and free electrons form distinct, nonoverlapping sets. Magnetization suggests a similar distinction for free and bound currents. In combination with a key characteristic of Maxwell's equations, viz. the principle of linear superposition, these distinctions form the basis for a practically usable formulation of fields in matter.

The principle of linear superposition states that the field resulting from two different sources may be calculated as their vector sum. Figure 26.8 shows the application of this principle to free and bound charges.

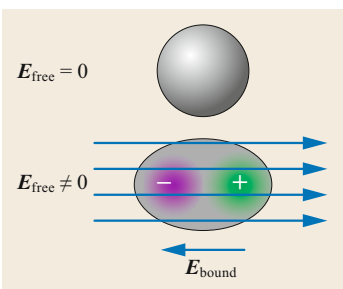

Fig. 26.7 Sketch of polarization: an external field $\boldsymbol{E}_{\text{free}}$ leads to a separation of charges bound within an atom or molecule. These charges produce a field $\boldsymbol{E}_{\text{bound}}$

The mathematical formulation is then

$$\rho = \rho_{\text{free}} + \rho_{\text{bound}} \quad \text{and} \quad \boldsymbol{E} = \boldsymbol{E}_{\text{free}} + \boldsymbol{E}_{\text{bound}} ,$$
$$\boldsymbol{J} = \boldsymbol{J}_{\text{free}} + \boldsymbol{J}_{\text{bound}} \quad \text{and} \quad \boldsymbol{B} = \boldsymbol{B}_{\text{free}} + \boldsymbol{B}_{\text{bound}} . \tag{26.26}$$

Maxwell's equations will hold for either subset, for example

$$\nabla \cdot \varepsilon_0 \boldsymbol{E}_{\text{free}} = \rho_{\text{free}} ,$$
$$\nabla \times (\mu_0^{-1} \boldsymbol{B}_{\text{free}}) = \boldsymbol{J}_{\text{free}} + \frac{\partial}{\partial t} \varepsilon_0 \boldsymbol{E}_{\text{free}} . \tag{26.27}$$

Inserting (26.26) into (26.27) yields

$$\nabla \cdot \varepsilon_0 (\boldsymbol{E} - \boldsymbol{E}_{\text{bound}}) = \rho_{\text{free}} ,$$
$$\nabla \times [\mu_0^{-1} (\boldsymbol{B} - \boldsymbol{B}_{\text{bound}})] = \boldsymbol{J}_{\text{free}} + \frac{\partial}{\partial t} \varepsilon_0 \boldsymbol{E}_{\text{free}} . \tag{26.28}$$

Equations (26.28) are usually presented in a different notation and are widely known as *Maxwell's equations in matter* in the form

$$\nabla \cdot (\varepsilon_0 \boldsymbol{E} + \boldsymbol{P}) = \nabla \cdot \boldsymbol{D} = \rho_{\text{free}} ,$$
$$\nabla \times (\mu_0^{-1} \boldsymbol{B} - \boldsymbol{M}) = \nabla \times \boldsymbol{H} = \boldsymbol{J}_{\text{free}} + \frac{\partial}{\partial t} \boldsymbol{D} . \tag{26.29}$$

This formulation has historical roots. In the 19th century, the entire world was assumed to be full of a strange substance called *ether* (not referring to the gas C_2H_6O). Electromagnetic waves would be transported by this substance, and it was assumed that charges would *displace* this substance. $\boldsymbol{D}$'s full name was the displacement current of the ether, while $\boldsymbol{H}$ (a little later) was assumed to be a stimulation of the ether. The name *magnetic field* for $\boldsymbol{H}$ is even older. It originates in symmetries which are now known to apply only to static

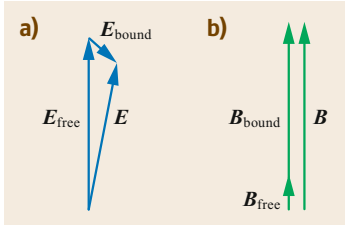

Fig. 26.8a,b In the presence of matter, the fields $\boldsymbol{E}$ and $\boldsymbol{B}$ are calculated as the vector sum of two contributions (taken from [26.6]) In **(a)**, the case of an electrically anisotropic material is shown, for **(b)**, a ferromagnetic substance is assumed

Table 26.2 Physical interpretation of traditional field quantities [26.6]

Traditional symbol	Meaning	Cause	Cause symbol
$\boldsymbol{H}$	$\mu_0^{-1}\boldsymbol{B}_{\text{free}}$	Free currents	$\boldsymbol{J}_{\text{free}}$
$\boldsymbol{D}$	$\varepsilon_0\boldsymbol{E}_{\text{free}}$	Free charges	ρ_{free}
$\boldsymbol{M}$	$\mu_0^{-1}\boldsymbol{B}_{\text{bound}}$	Bound currents	$\boldsymbol{J}_{\text{bound}}$
$\boldsymbol{P}$	$-\varepsilon_0\boldsymbol{E}_{\text{bound}}$	Bound charges	ρ_{bound}

fields. Over the last 100 years, the interpretation of $\boldsymbol{H}$ and $\boldsymbol{D}$ has gradually developed from *fields* [26.9], via *not so fundamental fields* [26.10] to *contributions to the fields* $\boldsymbol{B}$ *and* $\boldsymbol{E}$ [26.6].

Comparing the last two sets of equations leads to a physical interpretation of the traditional field quantities. These are summarized in Table 26.2. This table also explains why the equations found in the 19th century are still valid: there is a one-to-one correspondence between the quantities defined then and those which result from the present understanding of atoms and molecules.

For an understanding of electromagnetism in the context of current technological developments, it is important to realize that, when manufacturing techniques allow the creation of structures with the size of a single atom, $\boldsymbol{H}, \boldsymbol{D}, \boldsymbol{M}$, and $\boldsymbol{P}$ are no longer applicable. At such distances, the distinction between free and bound electrons becomes ambiguous. And if nuclear distances are probed, the distinction becomes completely irrelevant as the energies involved are much larger than atomic binding energies.

In Fig. 26.8, the modification of $\boldsymbol{E}_{\text{free}}$ to give the measurable $\boldsymbol{E}$ was achieved by adding field vectors from bound charges. But there is also a very popular alternative: the influence of matter may be formulated as a mapping of the fields from free charges onto the measurable ones. In the most general case, this mapping will include a rotation, and an elongation or shortening. It is written in the form

$$\begin{aligned}\boldsymbol{B} &= \mu_{\text{r}}\boldsymbol{B}_{\text{free}}\,,\\ \boldsymbol{E} &= \varepsilon_{\text{r}}^{-1}\boldsymbol{E}_{\text{free}}\,,\end{aligned} \tag{26.30}$$

where μ_{r} is called the *relative permeability* and ε_{r} is called the *relative permittivity*. In general, μ_{r} and ε_{r} are tensors depending on the field strength. In most cases, however, they are just numbers. A large value for μ_{r} means a *strengthening* of the magnetic field, while a large value for ε_{r} means a *weakening* of the electric field by matter.

Equation (26.30) can be used to derive a simple rule for the incorporation of matter into Maxwell's equations:

always		in matter
ρ	$\rightarrow$	ρ_{free}
$\boldsymbol{J}$	$\rightarrow$	$\boldsymbol{J}_{\text{free}}$
$(\varepsilon_0\boldsymbol{E})$	$\rightarrow$	$(\varepsilon_0\varepsilon_{\text{r}}\boldsymbol{E})$
$(\mu_0^{-1}\boldsymbol{B})$	$\rightarrow$	$[(\mu_0\mu_{\text{r}})^{-1}\boldsymbol{B}]$.

(26.31)

This substitution rule relates the measurable free charges and currents to the measurable electromagnetic fields. A consequent use of this rule allows a formulation of the whole of classical electromagnetism without ever mentioning the quantities $\boldsymbol{H}$ and $\boldsymbol{D}$, as done in [26.11]. When using (26.31) in integral equations, it is important to keep the quantities in brackets together, as shown.

In the presence of matter, Gauss's law for the electric field can now be written as

$$\oint_{\partial V} \varepsilon_0\varepsilon_{\text{r}}\boldsymbol{E}\cdot\mathrm{d}\boldsymbol{A} = Q\,, \tag{26.32}$$

while the law of Ampère and Maxwell in (26.17) may be written as

$$\oint_{\partial A} \left(\mu_0^{-1}\mu_{\text{r}}^{-1}\boldsymbol{B}\right)\cdot\mathrm{d}\boldsymbol{\ell} = I_{\text{free}} + \int \frac{\partial(\varepsilon_0\varepsilon_{\text{r}}\boldsymbol{E})}{\partial t}\mathrm{d}\boldsymbol{A}\,. \tag{26.33}$$

Gauss's law for the magnetic field and the law of Faraday and Henry remain unchanged in the presence of matter.

Currents flow if electrons are moving. If this happens within matter, the electrons will randomly collide with atoms, thus giving some of their kinetic energy to the body they traverse and being slowed down at the same time. In the case of the presence of an external electric field, the electrons will be accelerated between two collisions. It turns out that this ongoing sequence of collisions and acceleration leads to an average velocity of the electrons $\boldsymbol{v}_{\text{e}}$ that is proportional to the field strength. Therefore, the current density $\boldsymbol{J}$ due to electrons which have a density n_{e} is proportional to the field strength applied. The corresponding formula

$$\boldsymbol{J} = -n_{\text{e}}e\boldsymbol{v}_{\text{e}} = \sigma\boldsymbol{E} \tag{26.34}$$

is know as *Drude's law* [26.12]. The factor of proportionality σ is known as the *specific conductance*. Its inverse $\rho = 1/\sigma$ is called the *specific resistance*; due to the limited number of characters available, it is represented by the same letter as the charge density.

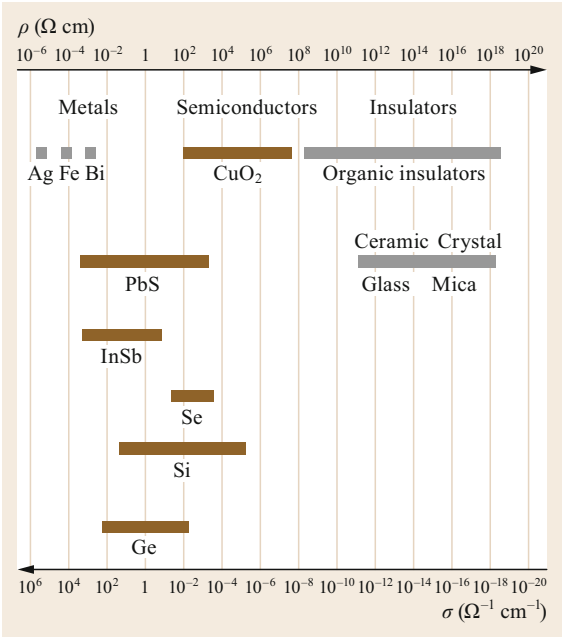

Fig. 26.9 Specific resistance of various materials

Materials are classified as *conductors* (usually metals), *semiconductors*, or *insulators*, depending on their specific resistance. Examples of classes of materials can be found in Fig. 26.9.

26.2.2 Resistors

Sending a current through a resistor is a bit like pulling a brake: the current becomes smaller the more resistors there are, and the resistors themselves become warm if current passes. The main use of resistors is to limit currents and to generate heat.

A resistor is called an *ohmic resistor* if the current is proportional to the voltage applied. Such behavior is a consequence of Drude's law. This will be shown for the example of a wire, as indicated in Fig. 26.10. An electric field $\boldsymbol{E}$ applied to a wire of length L and cross section $\boldsymbol{A}$ will provoke a current density $\boldsymbol{J} = \sigma\boldsymbol{E}$. As the tension between the two ends of the wire is $U = |\boldsymbol{E}|L$, one finds that the current

$$I = \boldsymbol{J}\cdot\boldsymbol{A} = \sigma\frac{A}{L}U \qquad (26.35)$$

is indeed proportional to the tension U applied. The proportionality factor is called the *conductance* G, and its inverse has the name *resistance*

$$R = \frac{L}{\sigma A} = \frac{1}{G}\,. \qquad (26.36)$$

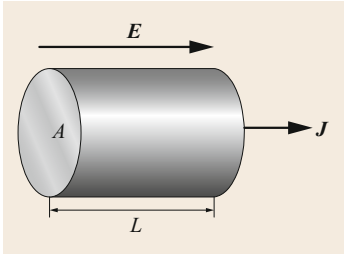

Fig. 26.10 A piece of conducting material of length L and cross section A exposed to an electric field $\boldsymbol{E}$ will have a current density $\boldsymbol{J}$ given by Drude's law

Equation (26.35) can then be written as

$$U = RI \quad \text{or} \quad I = GU\,, \qquad (26.37)$$

and in this form, it is known as *Ohm's law* [26.13].

Ohm's law is useful to describe circuit elements with fixed geometry, such as resistors *off the shelf*. In contrast, Drude's law may be applied to complicated geometries. Therefore, (26.34) is often referred to as the *differential form of Ohm's law*.

The resistance can be expressed in terms of the *electron mobility* $\mu_n = v/E$, which relates the field strength to the velocity v and density n of the electrons. The equation

$$R = \frac{1}{AEn\mu_n} \qquad (26.38)$$

shows very clearly that, the more electrons there are and the faster they move, the better the conductance becomes.

Resistors come in a variety of shapes, materials, and sizes. The size is determined by the heat produced: the more heat is produced, the larger a resistor needs to be in order to ensure that it will neither melt nor evaporate. The heating power generated for a constant field $\boldsymbol{E}$ parallel to the length L is, according to (26.20),

$$P_{\text{heat}} = \frac{\mathrm{d}W}{\mathrm{d}t} = \frac{-\mathrm{d}Q}{\mathrm{d}t}EL = -UI\,. \qquad (26.39)$$

The minus sign indicates that the heating power is *generated*. Clearly, this power must come from the circuit, i.e.,

$$P_{\text{circuit}} = UI\,, \qquad (26.40)$$

which means that a resistor transforms electric energy into heat energy. Unless otherwise mentioned, P is used for P_{circuit}.

Table 26.3 Temperature coefficients for selected materials [26.14]

Material	Temperature coefficient α ($°C^{-1}$)
Gold	0.0034
Copper, aluminum, lead	0.0039
Manganin	0.000002
Carbon (amorphous)	−0.0005
Silicon	≈ −0.075
Germanium	≈ −0.048

This is a general rule: a positive value for the power means that the circuit loses electrical energy to other forms of energy (for example, in a resistor), whereas a negative value indicates that the circuit gains energy (for example, from a battery).

Using (26.40), it can be deduced that the power of a resistor rises with both the square of the tension and the current

$$P = P_{\text{circuit}} = I^2 R = \frac{U^2}{R} \,. \tag{26.41}$$

The material used depends on price as well as the required accuracy and temperature independence of the resistance. For most conductors, the value of R increases with temperature. This may be understood as a consequence of the fact that the chance of an electron colliding with an atom increases as the atom moves (vibrates) faster when the temperature θ increases. For most purposes, it is accurate enough to describe this effect in a linear manner, starting at room temperature:

$$R(\theta) \approx R(25\,°\text{C})\,[1 + \alpha(\theta - 25\,°\text{C})] \,. \tag{26.42}$$

The factor α is called the *temperature coefficient*. It describes how the resistance increases with temperature.

Table 26.3 shows that, over a range of $\Delta\theta = 100\,°\text{C}$, the resistance of a metal wire may increase by more than one-third. It also shows that the conductivity of semiconductors increases as the temperature does.

Carbon composite resistors are the most common type, as they are quite robust and easy to manufacture. Figure 26.11 shows a cross section. The value for the resistance is determined by the fraction of carbon in the mixture and by the geometry. The colored rings indicate the value for R as well as the accuracy of this value. Carbon composite resistors have a very small parasitic inductance, thus making them ideally suited for high-frequency applications. Their main drawback is a lack of accuracy in the manufacturing process.

In contrast, *thin-film resistors* may be produced with high precision, often better than ±1%. They are produced by depositing a thin layer of metal onto a nonconducting substrate (Fig. 26.12). After deposition, a helix is engraved into the film. This increases both the resistance and parasitic inductance (see below).

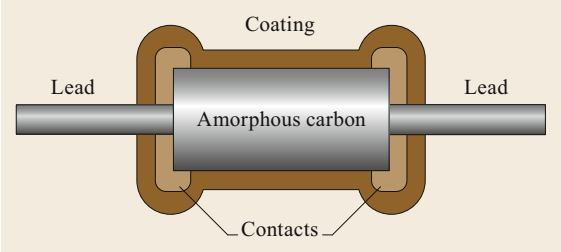

Fig. 26.11 Cross section through a carbon composite resistor

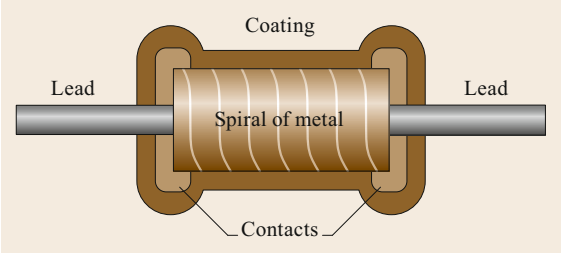

Fig. 26.12 Cross section through a thin-film resistor

For high-power, low-frequency applications, resistors can be made by winding wires to form a helix. These resistors are particularly suitable if low values ($< 100\,\Omega$) for the resistance are desired.

Some applications require resistors with a negative temperature coefficient. These can be made from impure semiconductor materials, as seen in Table 26.3.

26.2.3 Capacitors

Capacitors are used to store energy using an electric field. This is achieved by charge separation. A capacitor consists of two electrodes with a thin layer of a nonconducting substance called a dielectric between them, as shown in Fig. 26.6. A tension U between the two electrodes having an overlap area A and which are separated by a dielectric of thickness d with a relative permittivity ε_r makes one of them acquire a charge

$$Q = \varepsilon_0 \varepsilon_\text{r} \frac{A}{d} U \,. \tag{26.43}$$

The other electrode will have the same amount of charge, but with the opposite sign. This shows that an entire capacitor *separates charge*, rather than storing it.

The factors between U and Q in (26.43) are usually combined into a single factor called the *capacitance*

$$C = \frac{Q}{U} , \tag{26.44}$$

which for the setup shown in Fig. 26.6 means $C = \varepsilon_0 \varepsilon_r A/d$. Computing the time derivative of (26.44) yields

$$I = C\frac{\mathrm{d}U}{\mathrm{d}t} , \tag{26.45}$$

which reveals a typical feature of capacitors in circuits: the faster the tension changes, the more current will flow through a capacitor, while direct currents are not conducted at all.

The amount of energy stored can be calculated by computing how much work is needed to charge a capacitor. The result is

$$W = \frac{1}{2}CU^2 , \tag{26.46}$$

also demonstrating that the withstand voltage U_{max} of a capacitor is an important factor with regard to the maximum energy that can be stored. The electric field and the dielectric material can be identified as the place where the energy is stored. Comparing (26.46) with the strength $E = U/d$ of the electric field yields an energy density of

$$w = \frac{W}{V} = \frac{W}{Ad} = \frac{\varepsilon_0 \varepsilon_r}{2} E^2 , \tag{26.47}$$

which turns out to be a shorthand notation for two energy contributions. For $\varepsilon_r = 1$, the entire energy is stored in the field. For larger values, the elastic deformation of the dielectric molecules uses up the additional energy; for example, with $\varepsilon_r = 3$, the molecules contain twice as much energy as the field itself.

Capacitors may be connected in series or in parallel. In both cases, they can be treated as a single capacitor having a capacitance C_{total}. For a series of two capacitors with capacitances C_{s1} and C_{s2}, one gets

$$\frac{1}{C_{total}} = \frac{1}{C_{s1}} + \frac{1}{C_{s2}} \quad \text{(series)} , \tag{26.48}$$

while a connection of C_{p1} and C_{p2} in parallel gives

$$C_{total} = C_{p1} + C_{p2} \quad \text{(parallel)} . \tag{26.49}$$

The simplest form of a capacitor, the *film capacitor*, is achieved by rolling up two metal foil electrodes with a nonconducting substance placed in between. As the film between the electrodes is often made of plastic, these are also called *plastic film capacitors*, *film dielectric capacitors*, or *polymer film capacitors*. Such dielectric substances have relative permittivities ranging from $\varepsilon_r = 2.2$ for polypropylene (PP) to $\varepsilon_r = 3$ for polyethylene terephthalate (PET), i.e., polyester. In modern production lines, a plastic foil is given a metal coating by means of vacuum deposition and then wound up [26.15]. As both electrodes of such a capacitor form a helix, they will also produce a rather large parasitic inductance. For high-frequency applications, stacks of metal film layers are preferred despite their higher production costs.

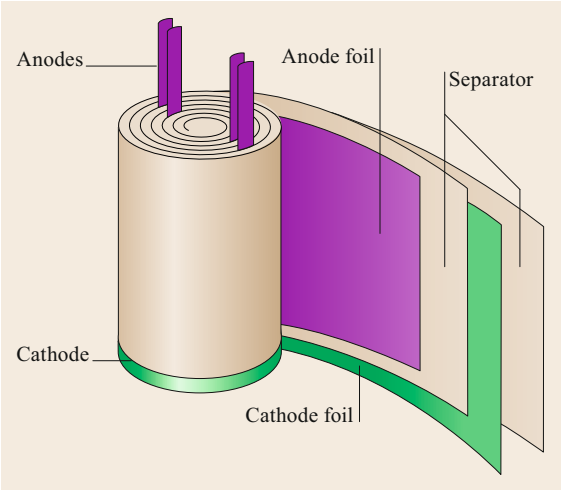

Fig. 26.13 Schematic illustration of geometry of an electrolytic capacitor

Substantially higher values for the capacitance may be achieved by *electrolytic capacitors*. The price is that these are *unipolar*, meaning that their cathode always needs to be connected to a potential that is lower than that of the anode. If the anode and cathode of an electrolytic capacitor are interchanged, the device may explode and poisonous substances may be released. Therefore, electrolytic capacitors have to be used in a careful manner.

Figure 26.13 shows the geometry of an electrolytic capacitor. Production details may be found in manufacturers' information [26.15]. Such a capacitor is formed by putting together a metal electrode, i.e., the anode, with a conducting liquid (the *electrolyte*) that has the property of forming a thin oxide layer on the surface of the metal. This layer is used as the dielectric. As the thickness of this layer is as little as a few atomic diameters, the C values of electrolytic capacitors are substantially larger than those of thin-film capacitors. They are, however, not suitable for high-frequency applications.

The top end of capacitor energy densities is marked by *double-layer capacitors*, branded as *gold caps*, *super*

caps, or *ultra caps*. Their features are discussed in the section on electrical energy storage.

26.2.4 Inductors

Inductors make use of the following relations between magnetic fields and currents. Time-dependent currents produce time-dependent magnetic fields. Also, time-dependent magnetic fields produce rotational electric fields in the wire conducting the current, thus actually reducing the strength of the current that produces the magnetic field. Therefore, in exact opposition to the behavior of capacitors, inductors conduct the better, the less the current changes. An ideal inductor acts like a short circuit in direct-current networks.

Inductors are made from helix-shaped wires that may or may not be placed around a core. This almost universal construction can be understood as ensuring the optimal use of the Faraday–Henry law (26.13), which states that the tension induced in a closed loop wire is given by the rate of change of the magnetic flux through the area spanned by this loop, and of the Ampère–Maxwell law (26.17), which states that the strength of the magnetic field along a field line is proportional to the current enclosed by this line. Each extra turn of a wire thus increases both the magnetic flux and the tension for a given change of flux. Ten times more turns will increase the effect by a factor $10^2 = 100$. Introducing extra core material may be used to increase the strength of the magnetic field even further.

The calculation of the magnetic fields from the current for a given wire geometry is a difficult exercise and hardly ever produces an exact result. In most cases, only numerical tools give satisfactory results. It is, however, known that, whatever the result, the induced tension must be proportional to the rate of change of the current. Therefore, all the factors that may be hard to determine can be summarized in a single quantity called the *inductance* L, and the equation

$$U = \pm L \frac{\mathrm{d}I}{\mathrm{d}t} \tag{26.50}$$

is correct irrespective of the geometrical details and uncertainties. In some parts of the literature, the induced tension is referred to as the *electromotive force*. This name will be omitted for the sake of consistent use of the term "force."

It may be irritating that, in the literature, (26.50) is written as often with a + sign as with a − sign. However, this is merely convention: If both the current and tension are given with respect to the same direction, the + sign applies. Otherwise, as usually indicated by the current arrow pointing in the opposite direction to the tension arrow, the − sign applies.

The amount of energy stored in the magnetic field of an inductor can be calculated from the energy that is needed to increase the current from zero to a certain value I. Starting from the definition of power $P = \mathrm{d}W/\mathrm{d}t = IU$, one gets

$$\begin{aligned} & \frac{\mathrm{d}W}{\mathrm{d}t} = IU = IL\frac{\mathrm{d}I}{\mathrm{d}t} \\ \rightarrow \quad & \mathrm{d}W = LI\mathrm{d}I \\ \rightarrow \quad & W = \frac{1}{2}LI^2 \,. \end{aligned} \tag{26.51}$$

The fact that $|\boldsymbol{B}| \approx I$ and $W \approx I^2$ suggests that $W \approx |\boldsymbol{B}|^2$, and in fact, a thorough analysis gives the result

$$w = \frac{W}{V} = \frac{1}{2\mu_0\mu_\mathrm{r}}\boldsymbol{B}^2 \,, \tag{26.52}$$

which not only seems natural but may also be severely misunderstood. At first glance, it seems to suggest that a large value of μ_r will lead to a reduction of the energy density of an inductor. However, can it be that putting iron into a coil will result in a reduction of the energy density? Of course, this is not the case, as can be shown as follows. In the presence of matter, the law of Ampère and Maxwell, (26.17), reads

$$\oint_{\partial A} (\mu_0^{-1}\mu_\mathrm{r}^{-1}\boldsymbol{B}) \cdot \mathrm{d}\boldsymbol{\ell} = I + \int \frac{\partial(\varepsilon_0\varepsilon_\mathrm{r}\boldsymbol{E})}{\partial t}\mathrm{d}\boldsymbol{A} \,, \tag{26.53}$$

indicating that, for a given inductor cross section A and in the absence of electric fields, $|\mu_\mathrm{r}^{-1}\boldsymbol{B}| \approx I$. Hence, doubling μ_r will increase $\boldsymbol{B}^2$ by a factor of 4 and consequently increase the energy density of the magnetic field according to (26.52) by a factor of 2. So, inspecting all the factors together, one finds that the energy density rises in proportion to μ_r.

As in the case of capacitors, networks of inductors may be treated as single inductors; for example, two inductors with inductances $L_{\mathrm{s}1}$ and $L_{\mathrm{s}2}$, placed in series, behave like a single one with an inductance

$$L_\mathrm{s} = L_{\mathrm{s}1} + L_{\mathrm{s}2} \quad \text{(inductors in series)} \,. \tag{26.54}$$

This may be understood as a consequence of the fact that the current is the same through both while the tensions add. Calculating the sum

$$\begin{aligned} U = U_1 + U_2 &= L_{\mathrm{s}1}\frac{\mathrm{d}I}{\mathrm{d}t} + L_{\mathrm{s}2}\frac{\mathrm{d}I}{\mathrm{d}t} \\ &= (L_{\mathrm{s}1} + L_{\mathrm{s}2})\frac{\mathrm{d}I}{\mathrm{d}t} \end{aligned} \tag{26.55}$$

shows the validity of (26.54).

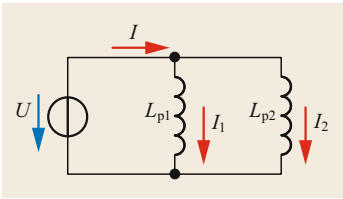

Fig. 26.14 Two inductors placed in parallel

If two coils are placed in parallel, they are both subject to the same tension U while, as shown in Fig. 26.14, their currents I_{p1} and I_{p2} add up to the total current I. If one eliminates I_{p1} from all the equations for the common tension, namely

$$U = L_{p1}\frac{dI_1}{dt} = L_{p2}\frac{dI_2}{dt} = L_p\frac{d}{dt}(I_1 + I_2)\,, \qquad (26.56)$$

one gets

$$\frac{1}{L_p} = \frac{1}{L_{p1}} + \frac{1}{L_{p2}} \quad \text{(inductors parallel)}\,, \qquad (26.57)$$

which also demonstrates that inductors and capacitors add in a complementary manner: inductances add when placed in series, whereas capacitances add when placed in parallel.

When choosing an inductor for a certain application, the diameter of the wire and the core material matter. The larger the current, the thicker the wire has to be for sufficient conductivity. At frequencies in or beyond the MHz region, two further effects matter. The *skin effect* describes the fact that the current is pushed towards the wire's surface, making its center useless for charge transport. Therefore, at high frequencies, bundles of insulated thin wires, called *Litz wires*, are used instead of single thick wires. Meanwhile, the *proximity effect* is observed if the conductivity of a wire is reduced by the presence of a high-frequency current close by. This effect can be counteracted by using special wiring geometries, often far from being solenoidal.

The core material is then mainly determined by the frequency of the application. At low frequencies (60 Hz, for example), iron cores are used to boost the magnetic inductance L by a factor of 1000 or even more. However, if a conduction material such as iron is exposed to an oscillating magnetic field, so-called *eddy currents* (or *Foucault currents*) are induced. The Faraday–Henry law describes the formation of rotational electric fields when magnetic fields oscillate. In a conductor, these rotational fields will push the electrons in the conductor to move along the field lines by means of the Coulomb force. In this manner, eddy currents are formed. Because the conductance of a material such as iron is finite, these eddy currents will produce heat: the larger the inductor's current and the larger the frequency, the more heat will be produced.

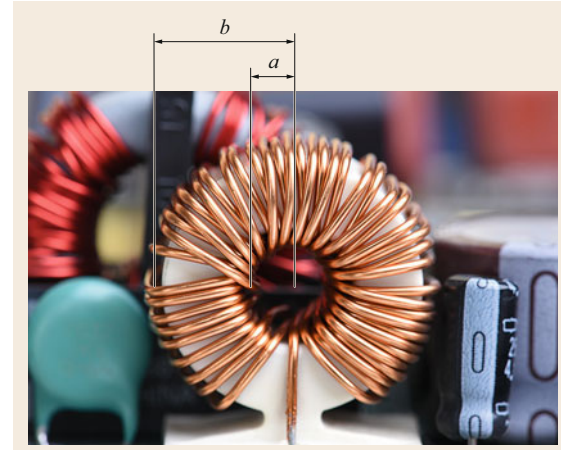

Fig. 26.15 Toroidal inductor with inner radius a and outer radius b. (Photo: © salita2010/stock.adobe.com)

The appearance of eddy currents can be reduced or even eliminated. If the iron core is laminated, i.e., if the core is produced as a stack of thin layers of oxidized iron, the currents cannot traverse the oxide layers. In this manner, the eddy currents are limited geometrically. However, for radio frequencies, this reduction is no longer sufficient. Instead of iron, nonconducting materials with large values of μ_r, i.e., *ferrites*, are used as the core material. These are ceramic compound materials of oxidized metals such as Fe_2O_3 (hematite, rust) and Fe_3O_4 (magnetite) or oxides including nickel or tin in addition to iron. Because they are insulators, there will be no eddy currents inside. At the high-frequency end of the spectrum, small values for the inductance are used and inductors do without cores.

Application Example: The Inductance of a Toroidal Inductor

Toroidal inductors are of special interest, as such devices may be (in fact, are) used to determine the values of μ_r of core materials experimentally.

For simplicity, the core is assumed to have a square-shaped cross section, as shown in Fig. 26.15. The inductance follows from the magnetic flux, which follows from the magnetic field. Hence, the field must be calculated first.

According to the law of Faraday and Henry, only the magnetic field enclosed by the current loops will contribute to the inductance (the field outside being negligible, anyway). The magnetic field lines must form circles with radii ranging from $r = a$ to $r = b$ and enclosing N turns of wire carrying a current I. According

to the Ampère–Maxwell law, the strength of the field is

$$B(r) = \frac{\mu_0 N I}{2\pi r} \,. \tag{26.58}$$

The magnetic flux may then be calculated as

$$\Phi_\mathrm{B} = (b-a)\int_a^b B(r)\mathrm{d}r = \frac{(b-a)\mu_0 N I}{2\pi} \ln\left(\frac{b}{a}\right) \,. \tag{26.59}$$

Now, the tension due to the change of the current can be computed. Every current loop adds a tension $U_\mathrm{ind}(1\ \mathrm{turn}) = \mathrm{d}\Phi_\mathrm{B}/\mathrm{d}t$, so that all the turns in series produce

$$U_\mathrm{ind} = N\frac{(b-a)\mu_0 N}{2\pi} \ln\left(\frac{b}{a}\right) \frac{\mathrm{d}I}{\mathrm{d}t} \,. \tag{26.60}$$

Comparing this result with the definition of the inductance shows that the factor preceding the time derivative is the inductance L. If a core with μ_r is placed between the windings, the inductance becomes

$$L = \frac{(b-a)\mu_0\mu_\mathrm{r} N^2}{2\pi} \ln\left(\frac{b}{a}\right) \,. \tag{26.61}$$

Equation (26.61) paves the way towards a measurement of μ_r. Its value for a given core material can be calculated as $\mu_\mathrm{r} = L\,(\text{with core})/L\,(\text{without core})$. Finally, if the torus is narrow, i.e., if the diameter $D = b - a \ll a$, then application of $\ln(1+x) \approx x$ yields

$$L \approx \mu_0\mu_\mathrm{r}\frac{N^2 D^2}{2\pi a} \,, \tag{26.62}$$

which also shows that, in this case, the shape of the individual turns no longer matters; indeed, the inductance depends only on the area D^2 and the radius of the torus a.

26.2.5 Alternating-Current Behavior

For a tension oscillating according to $u = \hat{U}\sin(\omega t)$, one has (by convention, a small u and a small i indicate sinusoidal forms of $U(t)$ and $I(t)$)

$$\begin{aligned}
R: u = Ri \;&\rightarrow\; i = \frac{1}{R}\hat{U}\sin(\omega t) \\
&\rightarrow\; \varphi_U - \varphi_I = 0 \,, \\
C: i = C\frac{\mathrm{d}U}{\mathrm{d}t} \;&\rightarrow\; i = \omega C\hat{U}\cos(\omega t) \\
&\rightarrow\; \varphi_U - \varphi_I = -90^\circ \,, \\
L: u = L\frac{\mathrm{d}i}{\mathrm{d}t} \;&\rightarrow\; i = \frac{1}{\omega L}\hat{U}[-\cos(\omega t)] \\
&\rightarrow\; \varphi_U - \varphi_I = 90^\circ \,.
\end{aligned} \tag{26.63}$$

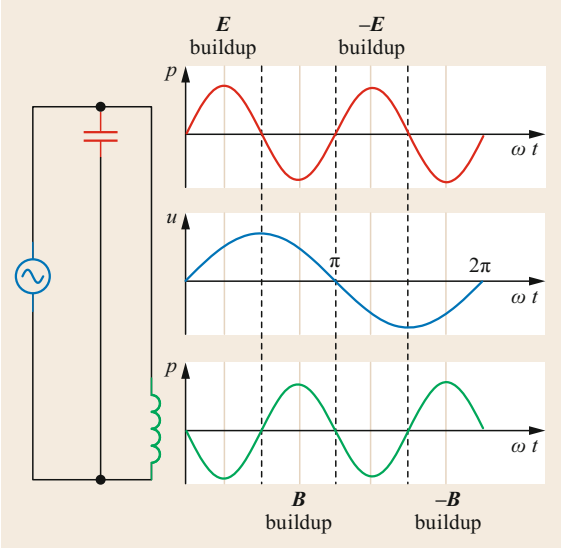

Fig. 26.16 Instantaneous power of an ideal capacitor (*top*) and an ideal inductor (*bottom*), compared with the instantaneous tension (*middle*)

So, ideally, this should be $\varphi_U - \varphi_I = \pm 90^\circ$ or zero. Such angles have surprising consequences for the time development of the instantaneous power $p(t) = i(t)u(t)$, as shown in Fig. 26.16. On average, the power is zero, meaning that there is a balanced flow of power in an out of the elements. When $p(t)$ is positive, energy is taken from the circuit and used to create fields; when it is negative, the fields give the energy back to the circuit. This behavior is in maximal contrast to that of a resistor, for which $p(t)$ is always positive, resulting in an average power of $\langle p\rangle = 1/2\hat{U}\hat{I}$, which is turned into heat by the resistor.

The calculations can be carried out in the most straightforward manner if the AC behavior of the circuit elements is considered in the complex plane. The reason is the simple behavior of the complex exponential function under differentiation and integration. Obviously, the three steps to take are:

- Transfer all equations into the complex plane, for example $\hat{U}\sin(\omega t + \varphi_u) \rightarrow \hat{U}\,\mathrm{e}^{\mathrm{j}\varphi_u}\mathrm{e}^{\mathrm{j}\omega t}$,
- Solve the complex equations, maybe with a result of the form $\hat{B}\,\mathrm{e}^{\mathrm{j}\beta}\mathrm{e}^{\mathrm{j}\omega t}$,
- Extract the result by taking the *imaginary part* of the complex result $\hat{B}\sin(\omega t + \beta) = \mathrm{Im}(\hat{B}\,\mathrm{e}^{\mathrm{j}\beta}\mathrm{e}^{\mathrm{j}\omega t})$.

A sinusoidal voltage is then represented as

$$\underline{u}(t) = \hat{U}\mathrm{e}^{\mathrm{j}\varphi_u}\mathrm{e}^{\mathrm{j}\omega t} = \underline{U}\mathrm{e}^{\mathrm{j}\omega t} \,, \tag{26.64}$$

where the *complex amplitude* $\underline{U} = \hat{U}\mathrm{e}^{\mathrm{j}\varphi_u}$ is the product of all the factors that do not depend on time. Note that

$u = \mathrm{Im}(\underline{u}) = \hat{U}\sin(\omega t + \varphi_u)$ and that complex quantities are indicated by being underlined.

The power of complex calculus is highlighted when applied to the model (26.45) and (26.50) for capacitors and inductors. By computing the derivatives

$$C: \quad \underline{i} = C\frac{\mathrm{d}\underline{u}}{\mathrm{d}t} \rightarrow \underline{u} = \frac{1}{\mathrm{j}\omega C}\underline{i}\,,$$

$$L: \quad \underline{u} = L\frac{\mathrm{d}\underline{i}}{\mathrm{d}t} \rightarrow \underline{u} = \mathrm{j}\omega L\underline{i}\,, \qquad (26.65)$$

one may deduce that, in the complex plane, inductors and capacitors may be treated as *complex resistors*. And as a formal add-on, due to $\mathrm{e}^{\mathrm{j}\pi/2} = \mathrm{j}$, (26.65) contain exactly the same phase relations as (26.63).

This idea has been generalized by introducing a complex resistance called the *impedance* $\underline{Z}$ and a complex conductivity called the *admittance*, $\underline{Y}$ as follows:

$$\begin{aligned} &\text{Original} && \rightarrow \text{Complex generalization} \\ &u = Ri && \rightarrow \underline{u} = \underline{Z}\,\underline{i} \\ &i = Gu && \rightarrow \underline{i} = \underline{Y}\,\underline{u}\,. \end{aligned} \qquad (26.66)$$

Sometimes, the real and imaginary parts are given separately

$$\begin{aligned} \underline{Z} &= R + \mathrm{j}X\,, \\ \underline{Y} &= G + \mathrm{j}B\,. \end{aligned} \qquad (26.67)$$

The factors for the imaginary parts are called the *reactance* X and *susceptance* B. According to (26.66), $\underline{Z} = 1/\underline{Y}$, leading to the following relations:

$$R = \frac{G}{G^2 + B^2}\,, \qquad X = \frac{-B}{G^2 + B^2}\,,$$

$$G = \frac{R}{R^2 + X^2}\,, \qquad B = \frac{-X}{R^2 + X^2}\,. \qquad (26.68)$$

The *power* may also be generalized to suit the complex plane. Recalling that the average power used by a resistor is $\langle P\rangle = R\langle i^2\rangle = R\hat{I}\langle\sin^2(\omega t)\rangle = 1/2R\hat{I}^2$, the following definitions for the *apparent power* $\underline{S}$, the *real or average power* P, and the *reactive power* Q have proven to be useful:

$$\begin{aligned} &\text{Original} && \rightarrow \text{Complex generalization} \\ &P = \langle ui\rangle && \rightarrow \underline{S} = P + \mathrm{j}Q \\ & && \rightarrow P = \mathrm{Re}(\underline{S}) = |\underline{S}|\cos(\varphi_U - \varphi_I) \\ & && \rightarrow Q = \mathrm{Im}(\underline{S}) = |\underline{S}|\sin(\varphi_U - \varphi_I)\,. \end{aligned} \qquad (26.69)$$

To make a long story short, P is exactly what is called the power in mechanics, while Q is a measure of the energy oscillation in an out of a circuit element.

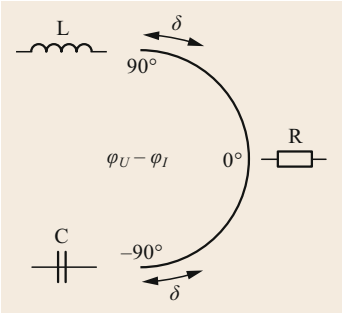

Fig. 26.17 The angle between tension and current in AC networks for the three basic circuit elements R, L, and C. The angular difference δ from the ideal values of $\pm 90°$ is called the loss angle

26.2.6 Parasitics

The behavior of real i.e., nonideal circuit elements is a mixture of what it should be and deviations due to *parasitic elements*. The finite conductivity of connecting wires will force any element to retain a little bit of resistor behavior, the helical shape of wound capacitors will add some inductive behavior, and the closeness of the wires in a coil will add a small capacitance to an inductor.

In alternating-current networks, the effect of such imperfections is most conveniently described by the deviation of the angle between the current and tension. Any deviation from the angles given in (26.63) can be interpreted as a result of imperfections or parasitic elements. The difference from the ideal values for the angle is called the *loss angle* and appears as δ in Fig. 26.17. Often, the *dissipation factor* D or the *quality factor* Q are given instead of δ. Because of

$$D = \frac{1}{Q} = \tan\delta\,, \qquad (26.70)$$

all these terms stand for the same. The larger the quality Q, the less the element behaves like a resistor.

Calculations based on this description of the AC behavior in the complex plane can help to understand why D and δ are called the dissipation factor and loss angle. The effect of the finite conductivity of the materials used in a capacitor can be approximated by introducing a resistance R_R in series with an ideal capacitor C_R. Then, the (*real*) capacitor's impedance is the sum

$$\underline{Z} = R_\mathrm{R} + \frac{1}{\mathrm{j}\omega C_\mathrm{R}} \quad \text{(capacitor with ohmic parasite)} \qquad (26.71)$$

which may be represented by an addition of vectors in the complex $\underline{Z}$ plane, as shown in Fig. 26.18. This figure also demonstrates that the tangent of the loss angle δ is the ratio between the resistance R_R and the

reactance $X_C(C_R)$. For an inductor, exactly the same analysis may be carried out, yielding

$$\underline{Z} = R_R + j\omega L \quad \text{(inductance with ohmic parasitic)} , \tag{26.72}$$

leading to a physical interpretation of the dissipation factor D.

The dissipation factor is the ratio of the ohmic power to the reactive power

$$D = \frac{P}{Q} . \tag{26.73}$$

It turns out that the definition in (26.73) remains correct even if other models of parasitic elements are used, while (26.71) and (26.72) are tied to a single ohmic resistor in series.

Finally, at the top end of the frequency spectrum, parasitic capacitances dominate the admittance of inductors, while parasitic inductances begin to dominate the impedance of capacitors. In brief: capacitors become inductors and vice versa.

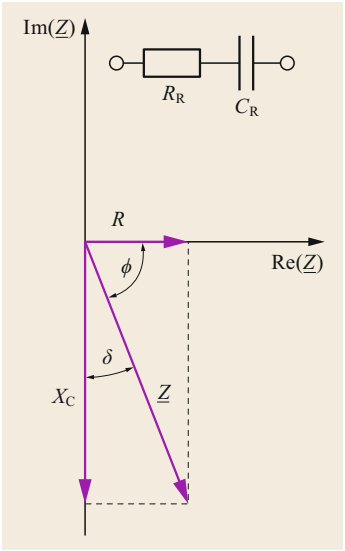

Fig. 26.18 Model of a *real* capacitor and a sketch of the corresponding addition of its impedance contributions in the complex plane, also indicating the meaning of the loss angle δ

26.3 Semiconductor Devices

All key elements of modern electronics are made from semiconductors. The features of most semiconductor devices are based on the special properties of highly purified monocrystalline silicon. Slices of these crystals, called *wafers*, are usually contaminated at the subthousandth level. This process is called *doping*. Most semiconductor functions can be traced back to an interaction of silicon areas with different doping materials and concentrations. In this section, the formation of diodes and bipolar transistors is discussed. Then, *metal–oxide–semiconductor (MOS) devices* are introduced as core elements of digital networks. These may be connected to electrical machines using *power semiconductor devices*.

26.3.1 Semiconductors

Semiconductors are materials that behave almost like insulators [26.16]. At 0 K, all their electrons are tightly connected, either to individual atoms or in binding orbitals. However, in contrast to an insulator, at room temperature, a tiny fraction of the electrons in binding orbitals in a semiconducting material are sufficiently energetic to move over large distances within the crystal.

The quantum-mechanical interpretation of this behavior is sketched in Fig. 26.19. As two orbits of two silicon atoms approach each other, new orbits are created, one with a slightly increased electron energy and another with a reduced energy. The latter will host both electrons. The more atoms that take part in this new orbit creation process, the more energy states will appear above and below the original energy level. It turns out that these energy states form two *energy bands*, the *valence band* and the *conduction band*, with a distinct *energy gap* between them. Energy bands denote regions of energy, where many energy states gather. While at 0 K the valence band hosts all the electrons, the energy gap to the conduction band is small enough for a tiny fraction at the top end of the electron's thermal energy spectrum to reach into the conduction band. Consequently, the number of conducting electrons increases with temperature. The energy that is halfway between the highest-energy state hosting electrons at 0 K and the lowest-energy empty state is called the *Fermi energy*.

Once an electron has reached the conduction band, it may follow the electric fields, just like an electron in a conductor. However, in a semiconductor, there is an additional type of conductance: whenever an electron *jumps* into the conductance band, it is missing from the valence band. In other words, it leaves a binding orbital with one electron too few. This deficit is called a *hole*, and it behaves similar to a carrier of positive charge: under the influence of an external field, the orbital may be refilled by an electron from an adjacent orbital, follow-

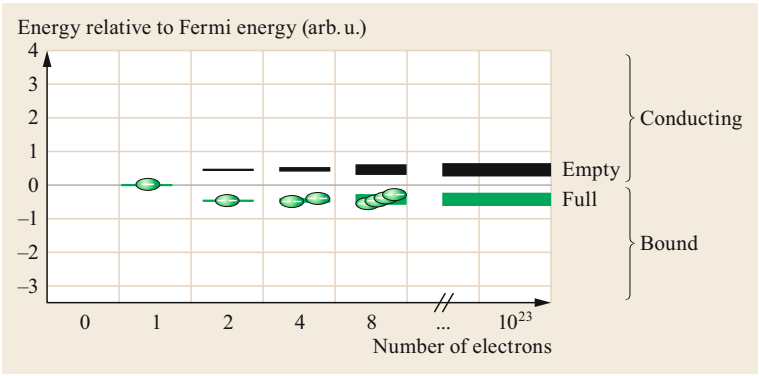

Fig. 26.19 Emergence of energy bands *from left to right*: Two energy states of electrons in silicon atoms combine to form two new states with slightly different energies. At 0 K, both electrons are found in the lower-energy orbit. The more atoms and electrons are combined, the more combined states result. These states turn out to form *energy bands*

ing that field. The net effect is that the positive charge has moved to the location where the refilling electron came from. If this process is repeated many times, the set of all refilling electrons moving in one direction have the same effect as a single positive carrier of charge moving in the opposite direction. This process is called *hole conduction*, and it is a unique feature of semiconductors. Consequently, the resistance of a piece of semiconductor material with a cross section A is determined by the concentrations n, p and mobilities μ_n, μ_p of negative electrons (n) and positive holes (p). The equation

$$R = \frac{1}{Ae}\frac{1}{p\mu_\mathrm{p} + n\mu_\mathrm{n}} \qquad (26.74)$$

reduces to the expression used for conductors in (26.38) when p is set to zero.

Apart from silicon, germanium and mixed crystals such as gallium arsenide may also be used as semiconductor substrates. Their advantage is a better electron mobility. However, for a single reason, silicon alone accounts for more than 90% of semiconductor sales. Oxidizing silicon gives quartz, one of the best insulators known. And it is exactly this property that allows efficient fabrication of metal–oxide–semiconductor (MOS) transistors. In this way, all modern processors are not only based on the properties of silicon itself, but also on its ability to form a well-insulating oxide.

26.3.2 Doping, the Key to Top Performance

While the structure of silicon forms the backbone of semiconductor devices, most electrons and holes responsible for the currents come from tiny impurities, introduced via a process called *doping*. In fact, when silicon is doped with a pentavalent substance such as phosphorus, the density of mobile electrons is almost identical to the density of doping atoms. For this reason, these substances are called *donors* (as they donate electrons). Meanwhile, if silicon is doped with a trivalent substance such as aluminum, the number of holes is almost equal to the number of aluminum atoms. These materials are called *acceptors*, as they *accept electrons* from the valence band. According to (26.74), the resistance can thus be adjusted by choosing the concentration of doping atoms.

The effect of doping is shown in Fig. 26.20. A pentavalent atom replacing one silicon atom will place four of its five outer electrons into the binding orbit, leaving one electron that does not fit into the structure. It turns out that the potential energy of this electron is slightly lower than the lower limit of the conduction band. Therefore, at room temperature, almost all the extra electrons will have sufficient thermal energy to be housed by the conduction band. The energies of all the pentavalent doping atoms together form a small band just below the conduction band. A piece of silicon having this extra band is called *n-doped*.

Holes will emerge due to doping with a trivalent substance. As the electrons in the neighborhood of an aluminum atom are not as tightly bound as those of a silicon atom, this type of doping will produce a small band of electron energies just above the valence band. Consequently, at room temperature, this new band will be almost completely filled with electrons from the valence band, leaving one hole per doping atom. Figure 26.21 shows the energetic structure of doped silicon.

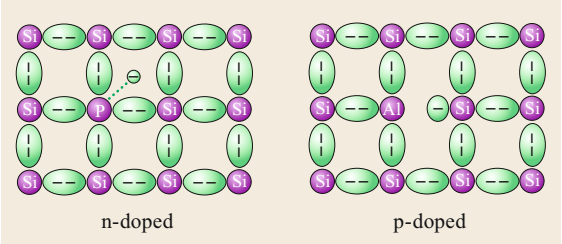

Fig. 26.20 Two-dimensional sketch of doping effect. An n-doped piece of silicon has some of its atoms replaced by pentavalent atoms. These will contribute extra electrons. In p-doped silicon, trivalent atoms mean that adjacent binding orbitals are filled by only a single electron

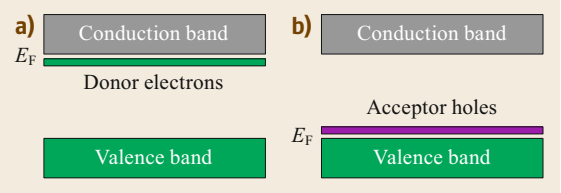

Fig. 26.21a,b Energy structure of n-doped silicon **(a)** and p-doped silicon **(b)**. At 0 K, the donor electron band is full, while the acceptor hole band is empty

Donor doping affects the concentration of holes as well as the number of electrons. Their relation is given by an equilibrium condition described by the *law of mass action*, which will be derived next. In pure silicon, the number of holes equals the number of electrons. This density of electron–hole pairs is called the *intrinsic density* n_i. The number is tiny, but grows strongly with temperature. The value of n_i is the result of a dynamic equilibrium that is reached when as many electron–hole pairs are thermally created as are eliminated by electrons dropping into holes. Now, if one doubles the density of electrons n by doping, the chance of a hole to be filled will double as well. So, the density of holes p will be halved. Tripling n will reduce p by a factor of there, and so on.

This reasoning can be generalized as follows: The law of mas action states that the product of the density of electrons and the density of holes equals the intrinsic density squared

$$np = n_i^2 \,. \tag{26.75}$$

Due to this law, an increase of the density of charge carriers of one type is always accompanied by a decrease of the density of the opposite type. Therefore, the corresponding holes or electrons are also called *majority carriers* and *minority carriers*.

26.3.3 Diodes

Diodes, bipolar transistors, and thyristors use the special properties that semiconductors acquire at the junctions between p regions and n regions. An understanding of the properties of this so-called p–n *junction* is thus crucial to understand these devices.

A *diode* consists of a p region adjacent to an n region, with both regions connected to the outside world, separately. Figure 26.22 indicates what happens if a p-doped region comes into contact with an n-doped region. At room temperature, both electrons and holes are in thermal motion. They move almost freely within the silicon crystal. This randomly orientated movement is called *diffusion*. If an electron happens to diffuse into

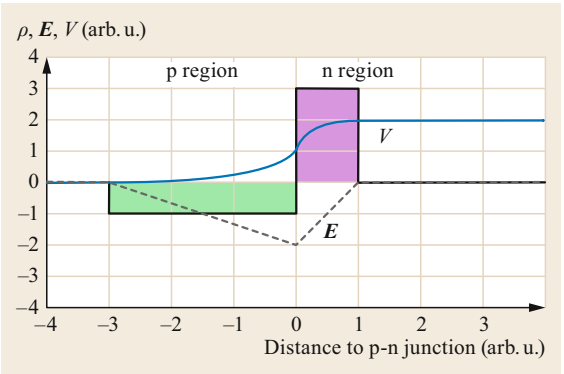

Fig. 26.22 Charge density, electric field, and electric potential near a p–n junction. In this example, the concentration of donor electrons is three times as large as the concentration of acceptor holes. The region with a nonzero electric field is called the *depletion region*

the p region, it will all of a sudden be exposed to a large number of holes to recombine with—and so it will. In this manner, an extra negative charge will be placed in the p region. This charge will also be missing from the n region. Similarly, a hole crossing the p–n junction will find many electrons to recombine with, thus placing an extra positive charge in the n region. In this manner, a region with locally bound positive charges will form in the n region next to the junction, while a region with negative charges will appear in the p region. As almost all freely moving charges close to the junction are trapped, such regions are called *depletion regions*.

According to Gauss's law, the locally bound charges will produce an electric field. A more elaborate analysis would show that the field produces a tension

$$U_D = \frac{kT}{e} \ln\left(\frac{n_A n_D}{n_i^2}\right) \tag{26.76}$$

between the regions. It is called the *diffusion voltage*. The factor kT, known from thermodynamics, shows that it is a result of thermal movement. The appearance of n_i and the doping densities n_A and n_D indicates that the value of U_D will result from a statistical equilibrium.

The equilibrium condition can be understood on the basis of the forces on the charge carriers in the depletion region. Figure 26.22 shows that, for electrons approaching the p–n junction from the n region, the local charges produce a potential barrier. The higher the tension, the smaller the fraction of electrons whose thermal energy suffices to cross the entire barrier. At the same time, holes from the n region, i.e., the minority carriers, will find themselves on a potential slide. All holes entering the depletion region from the n-doped side will be dragged into the p region. The complementary behavior will be found

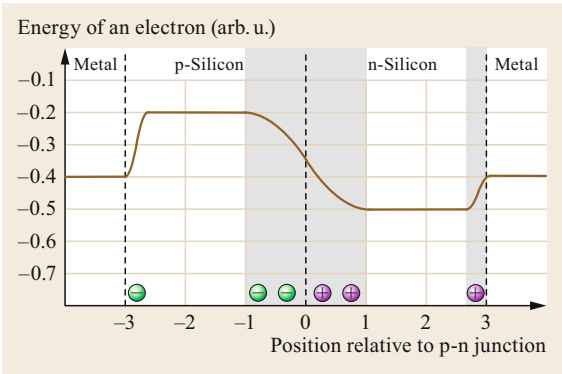

Fig. 26.23 Potential energy of an electron in doped silicon and adjacent metal. Energy conservation requires that the potentials at both ends be identical. Depletion regions (*gray*) and locally bound charges may occur at any of the junctions, depending on the materials chosen

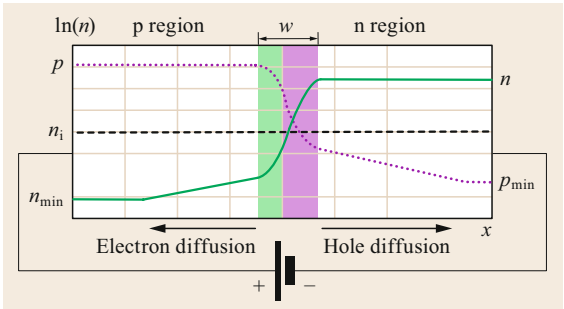

Fig. 26.24 Charge concentration in a forward-biased diode. The dropping of the densities in the depletion region is due to the electric field. The exponential decrease down to the level of the minority carriers is a result of diffusion and recombination

when analyzing the p side of the junction. Equilibrium is reached when the potential barrier for the majority carriers is so high that the number of these that can cross it equals the number of minority carriers moving in the same direction. As majority carriers outnumber minority carriers by many orders of magnitude, one finds the following rule: depletion regions reflect majority carriers, but they are transparent for minority carriers.

Finally, the value of U_D can never be measured directly. A voltmeter connected to a p–n junction (or a diode) will show 0 V. The reason is that the potential barrier at the p–n junction is exactly compensated by the potential jumps at the external connections of the silicon, i.e., the *contact potentials*. Figure 26.23 shows that this compensation must be exact due to energy conservation. An electron moving along a closed loop of metal → p-silicon → n-silicon → metal may neither gain nor lose energy.

If an external voltage U is applied to the p–n junction, the situation described in Fig. 26.23 may change significantly. A positive voltage applied to the p region relative to the n region reduces the width w of the depletion region. For an abrupt change of doping concentrations, one can determine the width of the depletion zone to be

$$w = \sqrt{\left(\frac{n_A + n_D}{n_A n_D}\right) \frac{2\varepsilon}{e}(U_D - U)} \,. \qquad (26.77)$$

At the same time, the height of the potential barrier for majority carriers is reduced—with drastic consequences: the number of majority carriers having enough energy to cross the potential barrier increases exponentially with the voltage applied. This is a consequence of the fact that all thermodynamic distribution functions have an exponentially falling *tail* at the upper end of the energy spectrum. Therefore, the current from majority carriers diffusing into the depletion region, named the *diffusion current*, increases exponentially with the voltage applied. The diode is then said to be *forward biased*. Figure 26.24 shows the density of charge carriers near the p–n junction for this case.

If the n region is given a higher potential than the p region, the diode is said to be *reverse biased*. Then, even fewer majority carriers cross the depletion region than in the equilibrium state. Quite in contrast, the current due to the minority carriers will remain constant, as all of them will move *down the potential slide*, irrespective of its height. As the carriers follow the field, this current is called the *field current*. The net effect is a reverse-bias current which, for large voltages, tends towards a constant value. This value is reached when the current due to majority carriers is negligible.

All together, the current of a diode is approximately given by the *Shockley equation*

$$I = I_S \left(e^{U/U_T} - 1\right) \,, \qquad (26.78)$$

where the *temperature voltage* U_T is a common abbreviation for $U_T = kT/e$. I_S is the current that should be measured in reverse-bias connection. Figure 26.25 shows that this is an approximation that is only valid for low voltages. If the diode is reverse biased, electron–hole pair creation due to thermal movement and impurities will dominate, while for large currents, the ohmic resistance of the silicon reduces the current. For almost all practical purposes though, the Shockley equation suffices. In the context of digital networks or power electronics, it is even sufficient to regard a diode as a device that conducts well above $U \approx 0.6$–0.7 V and not at all below this region.

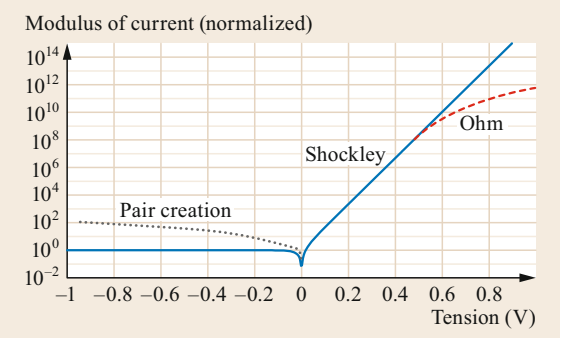

Fig. 26.25 The voltage–current characteristic of a diode, given approximately by the Shockley equation. Deviations are due to the creation of pairs in the depletion region and the ohmic resistance of the silicon

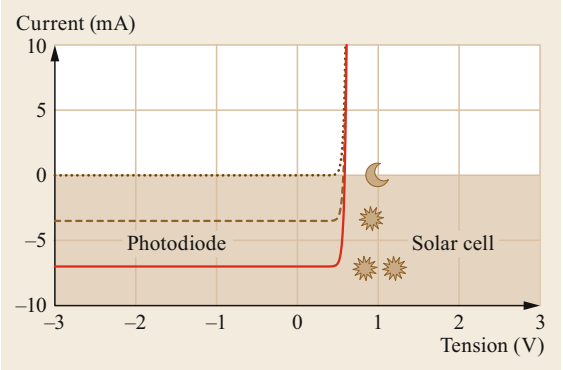

Fig. 26.26 Current–voltage characteristic of a light-sensitive diode. In the low-voltage forward-bias region, it is used as a solar cell. In the reverse-bias region, it acts as a photodiode

As a result of the steep increase of the current with voltage, the depletion zone around a p–n junction never disappears completely. A vanishing of the depletion region would be equivalent to the formation of a short circuit.

For certain semiconductor materials, efficient pair creation from incoming light is the design goal. Pairs produced in the depletion region will separate under the influence of the electric field, thus contributing to the field current. The number of pairs created is proportional to the number of incoming photons. As shown in Fig. 26.26, this can be used in either *solar cells* or *photodiodes*. In the region where the product $P = UI$ is negative, the diode acts as an electric power generator. In the reverse-biased region, it can be used as a light detector. In *light-emitting diodes* (LEDs), this process is reversed. Finally, there is a variety of types of diode apart from those presented here.

26.3.4 Bipolar Transistors

Bipolar transistors are used when large currents must be steered by small currents. They can be found wherever amplification is needed. Figure 26.27 shows that a transistor is a device with two p–n junctions, corresponding to two diodes connected *back to back*. Their terminals are called the *emitter* (E, emitting electrons), *base* (B, from fabrication history), and *collector* (C, collecting electrons). Two features turn this structure into an amplifying device:

1. The doping concentrations obey $n(\text{emitter}) \gg p(\text{base}) \gg n(\text{collector})$. The first $\gg$ sign ensures that, in forward-bias mode, most of the current through this junction is carried by electrons. So, when forward biased, the emitter emits electrons and the base receives them. On the contrary, a forward-biased junction between the collector and base will mainly have a hole-based current.
2. The p region in the middle (the base) is made so thin that an electron coming from the emitter has little chance to recombine before entering the depletion zone between the base and collector. With electrons being minority carriers in the base, whenever they reach the p–n junction to the collector, the field in the depletion zone will drag them into the collector, thus forcing it to collect electrons.

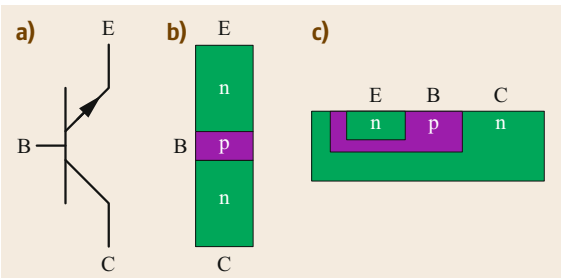

Fig. 26.27a–c The npn bipolar transistor symbol (**a**), its doping structure (**b**), and its geometry in planar technologies for integrated circuits (**c**). The *arrow* indicates the position of the emitter

The design of a transistor is optimized for a mode of operation called *forward active*. This mode is characterized by a forward-biased base–emitter junction but a reverse-biased base–collector junction. In Fig. 26.28, the tensions would then obey $U_{BE} \approx 0.6\,\text{V}$ and $U_{CB} > -0.6\,\text{V}$. A small current I_B entering the base is physically equivalent to a certain number of electrons entering the base from the emitter. Holes play a minor role here due to the concentration gradient. One would expect them to recombine in the base and thus close the

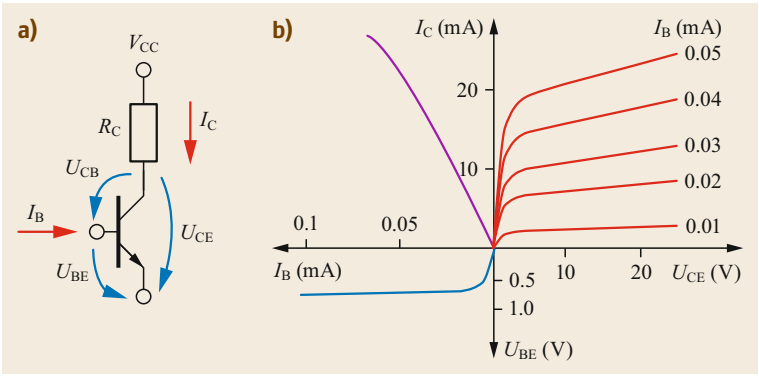

Fig. 26.28a,b Schematic of a transistor and a resistor **(a)** and the corresponding characteristics **(b)**

electrical circuit with the emitter. However, the special geometry of a transistor prevents the electrons from doing so. The base is so thin that most of the electrons will enter the depletion zone adjacent to the collector. Only one or a few percent of the current will make it to the base terminal. With the percentage of electrons being given by the geometry, the small fraction of the current passing through the emitter terminal and coming from the base terminal is also almost constant. In other words, a small value for the base–emitter current I_B determines a much larger value for the collector–emitter current I_C. Colloquially, this phenomenon is called *current amplification*, although *current steering* would be more precise.

The behavior of a transistor is usually summarized as shown in Fig. 26.28b. Starting with U_{BE} and moving clockwise, one finds the typical diode characteristics between U_{BE} and I_B (with axes interchanged). The top left quadrant shows the $I_B \leftrightarrow I_C$ characteristics. A constant current amplification would correspond to a straight line there. The ratio $B_f = I_C/I_B$ is called the *forward current amplification*, while the slope of the line, $\beta_f = \Delta I_C/\Delta I_B$, is called the *differential forward current amplification*. Finally, each value for the collector current depends on the collector emitter voltage U_{CE} as well as the base current I_B. Figure 26.28 shows that, for a fixed value of the base current, there is a separate characteristic $I_C \leftrightarrow U_{CE}$. In this quadrant, a flat line corresponds to constant amplification. Figure 26.29 shows that this is often a good approximation. The *Ebers–Moll model*

$$
\begin{aligned}
I_B &= I_{B,S}\left(e^{U_{BE}/U_T} - 1\right) \approx I_{B,S} e^{U_{BE}/U_T} \,, \\
I_C &= B_F I_B \approx B_F I_{B,S} e^{U_{BE}/U_T} \,, \\
I_E &= I_B + I_C
\end{aligned}
\qquad (26.79)
$$

reproduces the measured currents quite well. It is the first-choice starting point for the development of bipolar circuits.

Fig. 26.29 Photo of a transistor tracer. Here, the collector current is displayed as a function of the collector–emitter tension. Each of the almost horizontal lines corresponds to a fixed value of the base current I_B

Nevertheless, as shown in Fig. 26.29, there is always a slight increase of the current with U_{CE}. This increase is due to the fact that, as the collector–base tension increases, the depletion region adjacent to the collector zone becomes broader and reaches further into the base. As a result, the path along which electrons may recombine becomes shorter. The collector current increases relative to the base current. This phenomenon is called the *Early effect*.

Apart from the active mode, there are three more modes of operation. If both p–n junctions are forward biased, the transistor is said to be *in saturation*. This mode is characterized by almost constant voltages $U_{BE} \approx -U_{CB} \approx 0.6 \ldots 0.7\,\mathrm{V}$ and a current amplification less than the value for B_f given in the transistor's datasheet. Designers try to avoid this mode whenever speed is crucial. If both p–n junctions are reverse biased, no currents flow. The transistor is in the *cut-off* mode. Finally, if the base–collector diode is forward biased while the other junction is not, the transistor is in the *reverse active* mode. The amplification in this mode may have values well below one. For digital electronics

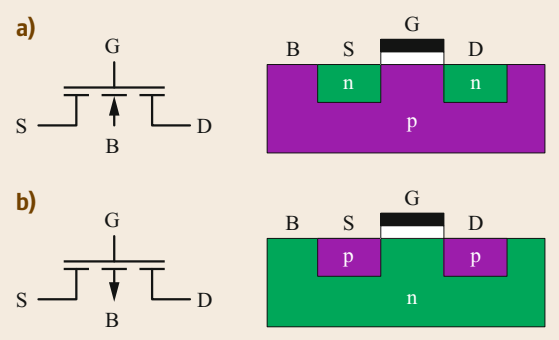

Fig. 26.30a,b Schematic symbol of **(a)** an NMOS transistor and its doping profile cross section and **(b)** the same for a PMOS transistor. The terminals are labeled B for *body*, S for *source*, G for *gate*, and D for *drain*

based on bipolar transistors (such as the 7400 series), a value close to zero is crucial for proper operation.

26.3.5 Metal–Oxide–Semiconductor Transistors

Metal–oxide–semiconductor (MOS) transistors are the workhorses of the digital world. They may be counted by the millions inside computers, smart phones, etc. for exactly one reason: reduced heat production. The steering of a MOS transistor does not require any permanent current. And a certain type of transistor circuit called CMOS (Fig. 26.33), once switched into a certain state, will keep it without further consumption of current. Hence—and this is the important point—there will be no further ohmic heat production. Modern processors have heating power densities exceeding those of electric cookers. So, a reduction of the heat production is crucial for an increase of transistor densities. And due to the finite value of the speed of light, a high density is a requirement for high clock rates. Without MOS, there would be no gigahertz processors.

MOS transistors come in two types with complementary doping profiles, the *n-channel (NMOS) transistor* and the *p-channel (PMOS) transistor*. Their schematic symbols and cross sections through the silicon setup are shown in Fig. 26.30. A MOS transistor has four terminals. The *body* insulates the two other doped areas, the *source* and the *drain*, from each other and from the rest of the chip. The insulation is the result of a reverse-biased (or 0 V) p–n junction forming a depletion region. An up-to-date transistor geometry is shown in Fig. 26.31. It minimizes the size of the p–n junctions and thus minimizes the (useless) current due to minority carriers.

The current through a MOS transistor is determined by a voltage rather than a steering current. The voltage

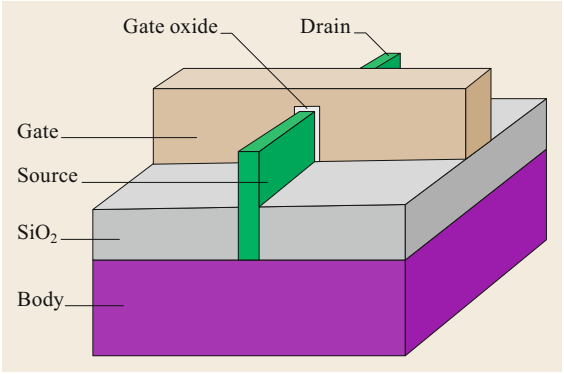

Fig. 26.31 A modern MOS transistor called a 3-D transistor by Intel [26.17]

is applied to a very thin layer of silicon dioxide. This layer is situated below a piece of metal connected to the *gate* terminal. It is called the *gate oxide*. If the potential at the gate of an NMOS transistor is larger than the potential of the body, the electric field through the oxide pushes the majority carriers of the body, the holes, away from the gate. A new depletion zone is thus created below the gate oxide. Above a certain value of the voltage, viz. the *threshold voltage* U_{Th}, the field is strong enough to form of a thin conducting layer of minority carriers (electrons) just below the gate oxide. This is called the *inversion layer*. It is formed if an electron loses more energy by moving to the gate oxide than is needed to leave its place in the valence band. Now, electrons are also the majority carriers of the adjacent n-doped regions named the source and drain. So, the emergence of this inversion layer leads to a conducting channel between the two n-doped regions. And this is what MOS transistors are about: the source and drain terminals are either connected or not, depending on the voltages involved. Technologically, there is no difference between the source and drain. Which of the two n-doped regions is the source is entirely determined by the tensions applied, The terminal with the lower potential is the source of an NMOS transistor, while that with the higher potential is the drain. Also, in some circumstances, they may even swap roles. In any case, the absolute value of the voltage between the gate and source will alway be larger than or equal to the value between the gate and drain. And, by definition, any current through an NMOS transistor will always flow from the drain to source. Therefore, the source is *the source of electrons* while the drain is *the drain of electrons*.

If the gate–source voltage is larger than the threshold voltage, and the gate–drain voltage is too, the tension across the gate oxide will suffice to form an inversion layer under the entire gate oxide. The transistor is then said to be in the *triode mode*. In this mode, the

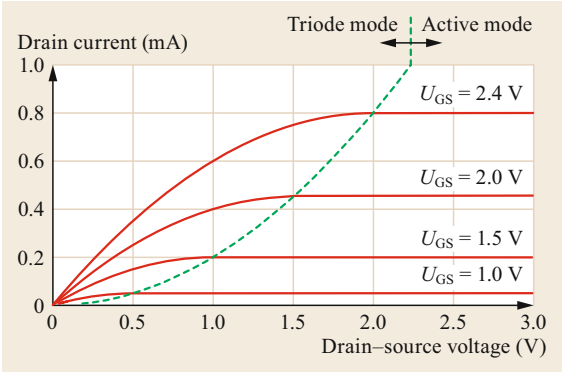

Fig. 26.32 Drain current of an NMOS transistor as a function of the drain–source voltage for various fixed values of the gate–source voltage U_{GS}

current from the drain to source is determined by the gate–source voltage U_{GS}, the drain–source voltage U_{DS}, and a technological factor β_N. The result

$$I_{DS} = \beta_N \left[(U_{GS} - U_{Th,N}) U_{DS} - \frac{1}{2} U_{DS}^2 \right] \qquad (26.80)$$

shows that the current plotted as a function of U_{DS} will give a parabola with a positive maximum. So, this formula accounts for the upper left part of the characteristics shown in Fig. 26.32. Clearly, (26.80) cannot account for the entire characteristic, as it predicts negative currents for large values of U_{DS}, which is not the case, as the discussion below suggests. For a given U_{GS}, the drain current reaches its maximum at $U_{GS} - U_{Th,N} = U_{DS}$. At this point, $U_{GD} = U_{Th,N}$; in other words, the maximal current is reached when the channel is about to be cut off from the drain. If U_{DS} is increased any further, the channel no longer reaches the drain. In this case, the conditions leading to (26.80) are no longer met.

For larger values of U_{DS}, the electrons reaching the end of the channel find themselves in a similar situation to those approaching the p–n junction of a bipolar transistor. They enter a depletion zone with a field dragging them towards the drain. As a result, all electrons entering the channel from the source side eventually reach the drain. Therefore, an incomplete channel goes along with an approximately constant current for a given value of U_{GS}, and the value of the current is given by the maximum that can be derived from (26.80).

$$I_{DS} = \frac{\beta_N}{2} (U_{GS} - U_{Th,N})^2 \,. \qquad (26.81)$$

The transistor is now said to be in the *active mode*, behaving almost like a current source between the drain and source terminals.

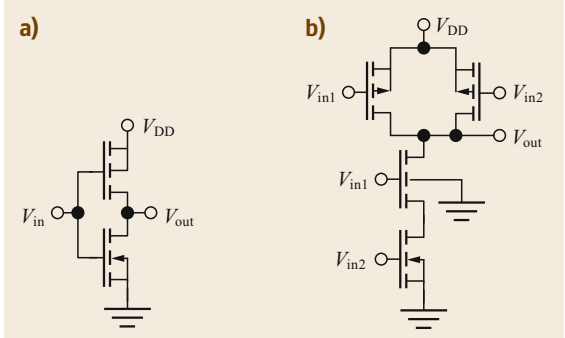

Fig. 26.33a,b Schematics of **(a)** a CMOS inverter and **(b)** a CMOS NAND (= not and) gate

Along the line $I_{DS} = \beta_N U_{DS}^2/2$, both (26.80) and (26.81) give the same current. When crossing this line, the mode changes from triode to active. In Fig. 26.32, this is shown by a dashed line.

Equation (26.81) can only be an approximation. The shorter the channel under the gate oxide becomes, the stronger the lateral field within the channel becomes (d gets smaller in $E = U/d$). Therefore, there is a slight current increase. Usually, a linear model of this increase, i.e.,

$$I_{DS} = \frac{\beta_N}{2} (U_{GS} - U_{Th,N})^2 (1 + \lambda_N U_{DS}) \,, \qquad (26.82)$$

is sufficiently accurate. The phenomenological factor λ_N is referred to as the *channel length modulation*.

Most digital electronic devices use a design technique in which there is one PMOS transistor complementing every NMOS transistor and vice versa. The result is called *complementary MOS* (CMOS). This is the most effective design method as far as energy consumption is concerned. Figure 26.33 shows the two most basic gates of this type, an inverter and a NAND gate. The key to understanding the way these gates work is to realize that, for each pair of complementary transistors connected to the same input potential V_{in}, only one is in a conducting mode. For $V_{in} = 0$, the PMOS transistor will be conducting. When the input changes from V_{DD} to 0, the PMOS switches from cut-off via active to triode mode while the NMOS is in a cut-off state. If $V_{in} = V_{DD}$, only the NMOS transistor conducts, and $V_{out} = 0$. So, if the voltages are associated with logical ones and zeros, the inverter will turn ones into zeros and vice versa, as the following table shows:

$$\begin{aligned} \text{Inverter:} \quad & V_{in} = V_{DD} \quad \rightarrow \; V_{out} = 0 \,, \\ & V_{in} = 0 \quad \rightarrow \; V_{out} = V_{DD} \,. \end{aligned}$$

The way the NAND gate works can be understood on the basis that a connection is established if either

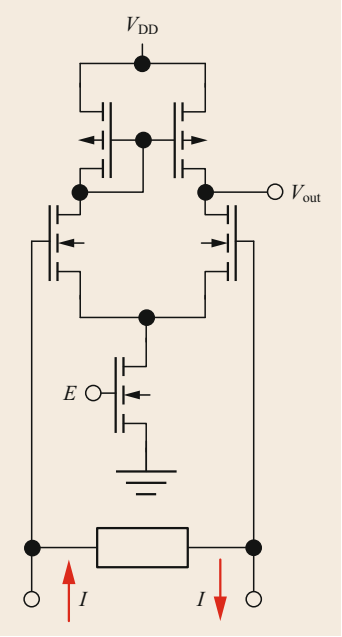

Fig. 26.34 A PCI Express receiver (body connections not shown). With $E = V_{DD}$, it is enabled. When the current I is positive, the resistor produces a potential difference, which is turned into $V_{out} \approx V_{DD}$ by the differential CMOS amplifier; if I is negative, $V_{out} \approx 0$

one of two parallel transistors conducts, or if both transistors in series conduct. The result

NAND gate:	V_{in1}	V_{in2}	$\rightarrow$	V_{out}
	0	0		V_{DD}
	0	V_{DD}		V_{DD}
	V_{DD}	0		V_{DD}
	V_{DD}	V_{DD}		0

may be interpreted as $V_{out} = \text{not } (V_{in1} \text{ and } V_{in2}) = V_{in1}$ NAND V_{in2}.

Whereas originally MOS transistors were used for digital circuits, the goal of integrating as many functions as possible onto a single chip led to increasing demand for analog CMOS circuits. An extensive discussion of these applications can be found in [26.18].

Application Example: A PCI Express Receiver

Peripheral Component Interconnect (PCI) Express is a point-to-point interface based on current loops. It can be found in almost any personal computer produced after 2010. A logical 1 is transmitted if the current flows in one direction, while a 0 corresponds to a current in the opposite direction. Figure 26.34 shows that, at the receiver end, a resistor turns the current into a voltage difference. And that is precisely what the transistor circuit can amplify well. Consider first the case of no current through the resistor: for symmetry reasons, both currents then have to be equal in both branches of the transistor circuit. The top left PMOS transistor has

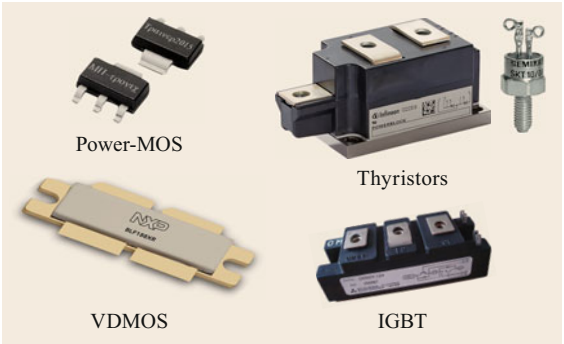

Fig. 26.35 Different types of power electronic devices

$U_{GD} = 0$ due to its wiring. It is therefore in the active mode, and so has to be the top right PMOS transistor, as it has the same U_{US} and the same current as the other one. Now assume that the current I in Fig. 26.34 reaches a small positive value. Then, the left NMOS transistors gets a larger U_{GS} than the right one. The NMOS transistor will therefore force the current in the left branch to be larger than that in the right branch. At the same time, the two PMOS transistors will keep the currents equal, *as long as the voltages in both branches are similar*. Because of the almost flat I_D versus U_{GD} characteristic of the PMOS transistors in the active mode (Fig. 26.32), a tiny decrease of I_D is necessarily accompanied by a large decrease of U_{GD}. But this is necessary, as the NMOS transistor connected to ground forces the sum of the currents through both branches to be constant. As a consequence, a little bit more current through the left branch will make V_{out} rise strongly. Consequently, $V_{out} \approx V_{DD}$ for $I > 0$ and $V_{out} \approx 0$ for for $I < 0$. This circuit is particularly popular, because V_{out} is stable, even if the surrounding is noisy.

26.3.6 Power Semiconductor Devices

Power semiconductor devices connect logical circuits to electrical machines. In this way, they turn strong machines into intelligent strong machines. Electromobility is unthinkable without power semiconductor devices. Figure 26.35 shows that power semiconductor devices are rather large. It may happen that an entire silicon wafer is turned into a single power device, rather than 100 microprocessors. The most popular power components are *thyristors*, *vertically double-diffused MOS (VDMOS)* transistors, and *insulated-gate bipolar transistors (IGBTs)*.

Thyristors behave like diodes that may be switched on or off. Once switched off, they may withstand several kV, whereas while being in the *on state*, they may conduct currents of several kA. Once a thyristor is in the on state, it will keep it until either the tension

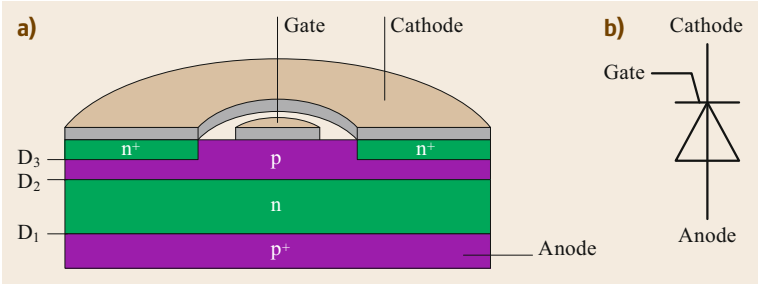

Fig. 26.36a,b Cross section through a thyristor **(a)** and schematic symbol **(b)**

approaches 0 V or the gate gets a reversed polarity. Figure 26.36 shows a cross section through a thyristor. Its four-layer npnp structure may be regarded as a series of three diodes. Either the outer two diodes (D_1 and D_3) are forward biased, or the one in the middle (D_2) is. One might therefore expect that a thyristor would never conduct at all. However, the setup may be turned into a switchable device by using the same techniques as known from bipolar transistors: the uppermost n layer is doped with a much higher concentration than the upper p layer. And because this p layer is thin, a small gate-to-cathode current will pass, along with the much larger current between the two n layers. So, the p–n junction labeled D_2 will be traversed by a large current despite being reverse biased. The result can be seen in the thyristor's characteristics, shown in Fig. 26.37. The lowermost junction serves as a current stabilizer, as can be understood in the following manner: because the lowermost p layer has a much higher doping concentration, any current traversing the D_1 p–n junction will be predominantly carried by holes. A large fraction of them will traverse the adjacent n layer and, being minority carriers there, also the depletion zone of the reverse-biased diode D_2. In this way, the current from the anode to cathode becomes quite independent of the current through the gate. In other words: a small gate-to-cathode current leads to an *ignition of the thyristor* by setting it into a permanent on state.

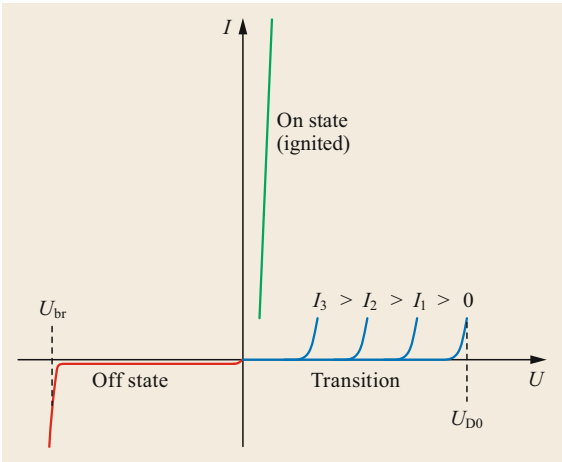

Fig. 26.37 Thyristor current as a function of the voltage between anode and cathode. If the reverse-bias voltage is smaller than the breakdown voltage U_{br}, the current is negligible. The larger the gate currents ($I_1, I_2, \ldots$), the lower the tension needed to ignite the device

In alternating-current networks, thyristors can only be in their on state for at most 50% of the time. For this case, which includes all home applications, the triode for alternating current (TRIAC) has been developed. Figure 26.38 shows that TRIACs can be regarded as antiparallel pairs of thyristors. The thyristor shown on the right of Fig. 26.38 will conduct current from terminal A_1 to terminal A_2, while the left one is responsible for the other direction.

The ignition of a thyristor is a process that cannot be influenced from the outside; in particular, it cannot be sped up by injecting more current into the gate. When timing is crucial, MOS solutions are preferred.

Power MOS transistors can operate at frequencies above 500 Hz, making them particularly suitable for switching power supplies. Figure 26.39 shows a cross section through the most powerful of these, an enhancement n-type vertical double-diffused metal–oxide–semiconductor (VDMOS) field-effect transistor. Seen from the top, the gate would appear as a disc, surrounded by a circular source. When U_{GS} is sufficiently large, an n-type inversion channel forms in the p region underneath the gate, thus forming a conducting channel to the central n region. Below that region, a highly doped n region helps to keep the contact resis-

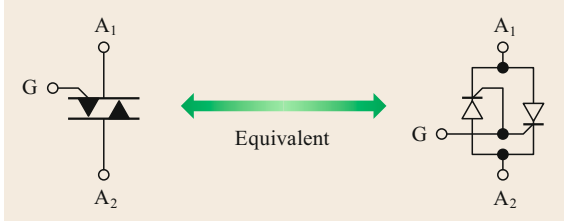

Fig. 26.38 The schematic symbol (*left*) and internal structure (*right*) of a TRIAC

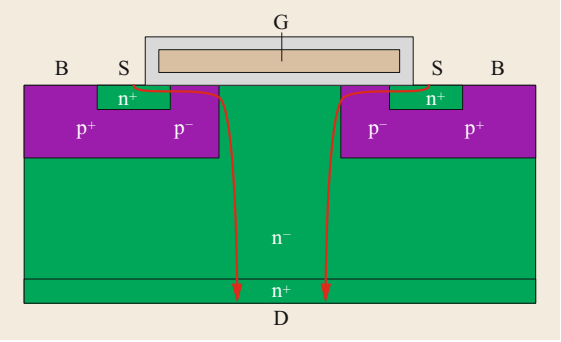

Fig. 26.39 Cross section through a VDMOS transistor with gate (G), source (S), body (B), and drain (D) terminals. The *arrows* indicate the path of electrons moving towards the drain

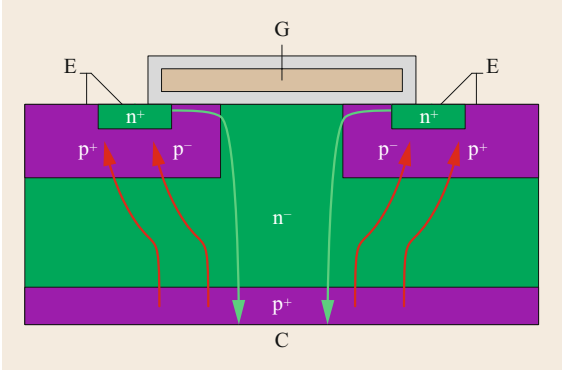

Fig. 26.41 Cross section through an IGBT with emitter (E), gate (G), and collector (C) terminals

tance to the drain terminal at a low level. The length of the channel is not determined by the size of gate, but rather by the geometry of the underlying diffusion regions. Usually, the body and source are attached to the same terminal, thus ensuring that there will always be a sufficiently large depletion zone between them.

As can be seen in Fig. 26.40, the characteristic of a power MOS device resembles that of a MOS transistor, the only exception being the larger saturation currents due to the junction areas' being many orders of magnitude larger.

When used for switching a large amount of power, the gate potential must change very quickly. In technical terms, if $P_{\text{loss}} = U_{\text{DS}}^2/R$ is to be small, then U_{DS} must reach a small value as quickly as possible. However, as long as the transistor is in the off state, there will be a large tension between the source and drain. If the power losses within the device are to be kept at a tolerable level, this tension has to drop fast, allowing the transition from the cut-off mode to active mode (incomplete channel) to triode mode to take place as fast

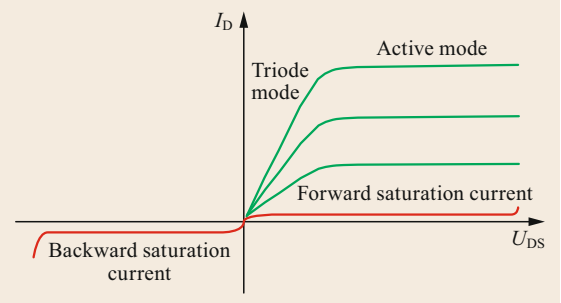

Fig. 26.40 Drain current as a function of the drain–source voltage of a VDMOS power transistor. The forward saturation current corresponds to $U_{\text{GS}} < U_{\text{Th}}$, and each line in the first quadrant corresponds to a fixed value of U_{GS}

as possible. Finally, in the triode mode, the remaining resistance $R_{\text{DS}}(\text{on}) = U_{\text{DS}}/I_{\text{D}}$ is mainly determined by the channel resistance and the conductivity of the low-doped drain region.

Often, entire silicon wafers are turned into massive parallel transistor arrays with densities of up to 800 000 transistors per cm^2. All the transistors together act like a single large transistor. Its power is limited by the power density in the channel, which is small, but has to carry the entire current. This limitation is overcome by the next technological advance.

A small technological modification turns a VDMOS transistor into another powerful semiconductor device, the *insulated-gate bipolar transistor* (IGBT). Figure 26.41 shows that it may be derived from a VDMOS transistor by replacing the lowermost n-doped area by a p-doped area. In this manner, another forward-biased p–n junction is introduced. This extra junction works like the afterburner of a jet engine. If, for example, the extra p layer has a doping concentration that is ten times higher than that in the n region above, for purely statistical reasons, each electron crossing the junction will pass about ten holes moving in the opposite direction. And because the number of electrons passing is entirely determined by the gate–source–body setup, the extra p–n junction will increase the current by a factor of $1 + 10 = 11$.

With the central n region having a sufficiently low doping concentration, most of the holes will reach the body, which is connected to the emitter terminal. The extra current due to holes coming from the collector terminal is particularly helpful because it does not have to pass through the channel underneath the gate. And a current distributed over a larger volume is equivalent to less concentrated heat production.

However, there is a price to pay for the efficient use of silicon in the production of IGBTs. The increased switch-off time compared with VDMOS devices is the

first drawback of an IGBT. It is imposed by the large number of minority carriers in the central n region in the on state. As all p–n junctions are transparent, an IGBT is only switched off after all the holes have left this region. The second drawback is the voltage drop across the forward-biased extra diode. A drop of 0.7 V exposed to a current of 1000 A will create a power loss of 700 W in the device. Nevertheless, for many power supply applications, IGBTs combine the best of the bipolar world with the best of the MOS world.

26.4 Networks

In this section, different types of networks are introduced. An explanation of technical terms used in networking is followed by a discussion of reference directions and the corresponding convention with respect to power. Kirchhoff's rules are presented in the context of conservation laws. It is shown how these rules form the basis of various network analysis methods. Finally, the properties of three-phase alternating-current networks are discussed.

26.4.1 Network Terminology and Reference Directions

Understanding networks is the first step towards understanding electrical and electronic systems. With up-to-date electronic systems having more than one billion components, computing techniques that can be automated are needed. In this section, the underlying rules are presented as well as some of the techniques themselves.

Schematics of electrical systems not only show the components and connections, they often show little arrows (often in red or blue) which seem to indicate directions. Such arrows are *not vectors*. They indicate a *reference direction*. Mathematically, they are simply a one-dimensional coordinate system. Thus, a red arrow (commonly used for currents) pointing to the right indicates that, if $I > 0$, the current also flows from left to right, while if $I < 0$, the current also flows in the opposite direction. A blue arrow (used for tensions) pointing from top to bottom corresponds to higher potential being at the top if $U > 0$.

There may be situations in which, at the same component, the reference directions for current and voltage are antiparallel. Physically, this is a modeling mistake: it means that two quantities (current and tension) are calculated in different coordinate systems. However, as shown in Fig. 26.42, there is an easy way to get it right again. Whenever the reference directions are antiparallel, the corresponding element equations need to be given an extra minus sign.

One might argue that these sign swaps are an artificial complication of the matter, as one might establish the rule that all reference directions should always be the same. Figure 26.43 may help to understand why electrical engineers have followed a different route. Each circuit gains energy from somewhere (battery, generator, ...) and loses it somewhere else (resistor). The gain of energy is always connected to a movement *against a force*. In mechanical examples, this is obvious. However, when capacitors or batteries are charged, the same principle applies to charge carriers: If a component delivers energy to a circuit, the current passing through will flow from the lower potential to the higher potential, i.e., *antiparallel to the tension*. Therefore, electrical engineers have adopted the convention that, for energy generators, the reference directions for current and tension should be antiparallel. If this convention is followed, the values for both the current and tension are positive in an energy source. However, as long as the rule indicated in Fig. 26.42 is followed, any combination of reference directions will also give correct results.

Networks are described using the technical terms illustrated in Fig. 26.44. Tensions may be measured between pairs of *terminals*. A *node* is characterized by having a certain potential. The connection between two nodes is called a *branch*. If several nodes are connected in series, the result is still a branch, unless the connection ends in a closed loop, as shown in Fig. 26.45. If (and only if) this *loop* does not contain another loop, it is called a *mesh*.

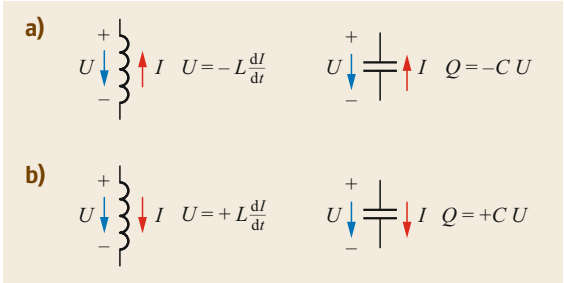

Fig. 26.42a,b The influence of reference directions of tension and current on the signs of element equations. Here, the arrows indicate the reference directions, representing one-dimensional coordinate systems for currents and tensions. If current and tension have the same reference direction, the equations have a + sign. **(a)** Generator, **(b)** consumer

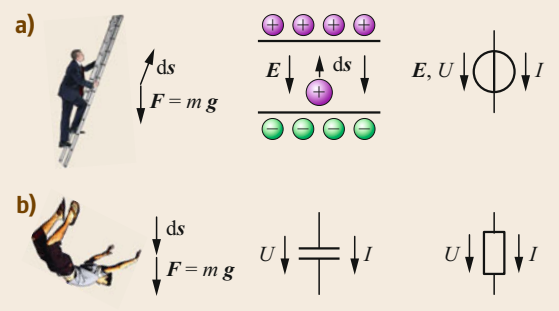

Fig. 26.43a,b Three examples for the transfer of energy. Potential energy is gained if there is a movement *against* a force. **(a)** Energy generation, gain, **(b)** energy consumption, loss

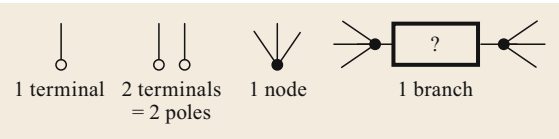

Fig. 26.44 Illustration of the meaning of electrical terminals, nodes, and branches

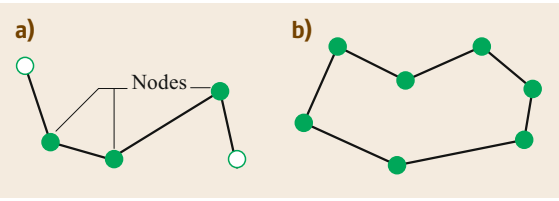

Fig. 26.45a,b Representation of a branch **(a)** and a mesh **(b)** made from nodes, terminals, and branches

26.4.2 Kirchhoff's Rules

The rules established by Gustav Robert Kirchhoff in the 19th century can be traced back to elementary conservation laws. They still form the basis of all methods to determine currents and potentials in a network.

Conservation of charge is the basis of Kirchhoff's first rule, the *node rule*. It is illustrated in Fig. 26.46,

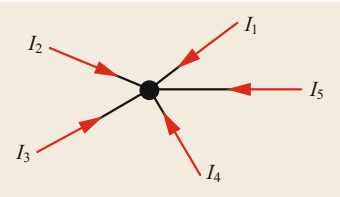

Fig. 26.46 Illustration of the node rule. If all the reference directions point into the node, the sum of all the currents must be zero

and it states that the sum of all currents flowing into a node must be zero:

$$\sum_i I_i = 0\,. \tag{26.83}$$

Clearly, this rule assumes that all reference directions point into the node (they might also all point outwards). It also implies that, at each node, there must be at least one current whose value is negative. A slight reformulation helps to find the relation to charge: For every node, the incoming currents must be balanced by the outgoing ones—just like a river has to carry all water that is supplied from smaller rivers at a river junction (Fig. 26.47). In this manner, it is guaranteed that neither water nor charge is lost or added.

Generally, in an open network with a number of k nodes, each node will have its own equation. Hence, the node rule will produce k equations. The majority of networks, however, are either closed or balanced with respect to the currents coming in and out (Fig. 26.48). This boundary condition makes one of the equations obsolete, leaving $(k-1)$ independent equations. Luckily, it is completely irrelevant which of the k node equations is left out for a determination of the currents in a closed network.

Conservation of energy is the basis of Kirchhoff's second rule, the *mesh rule*. As the static electric field is a conservative one, any charge traveling from one point to another and back again on a different path must have the same energy as at the beginning of the journey. As a consequence, any closed-loop movement back to the starting point may neither add nor subtract energy from the carrier of charge. Recalling that the electric potential is the potential energy per charge and that tension is

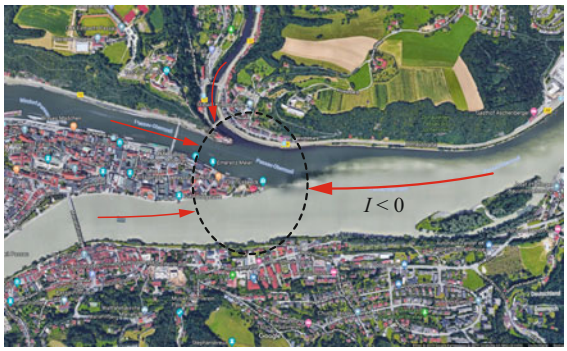

Fig. 26.47 Joining of three rivers in Passau, Germany. Analogously to the node rule, the value for the water flow on the *right* must be the negative sum of the flow of the three supplying rivers that can be seen on the *left* (©2019, Google, map data ©GeoBasis-DE/BKG (©2009))

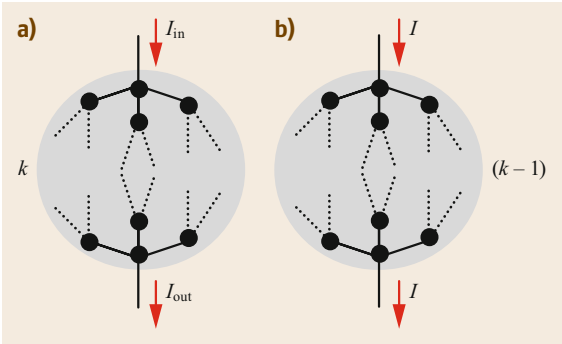

Fig. 26.48a,b Explanation of the number of node equations in a network. **(a)** In general, k nodes give k equations. **(b)** For networks with balanced input and output currents, there is one equation fewer. The latter includes closed networks ($I = 0$)

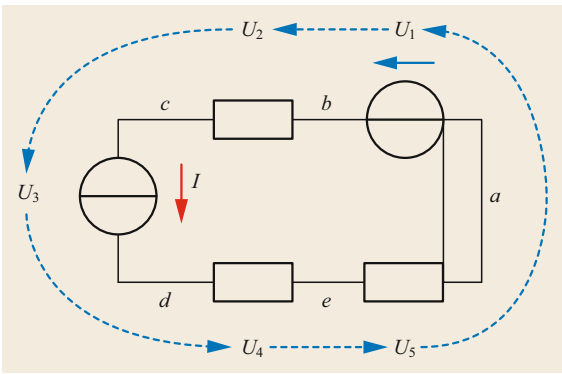

Fig. 26.49 Illustration of the mesh rule. If the reference directions for tensions form a closed loop, the sum of all tensions has to be zero

defined to be the difference of potentials, Kirchhoff's second rule seems self-evident, as it states that the sum of all tensions in a mesh is zero:

$$\sum_i U_i = 0\,. \tag{26.84}$$

An illustration of the rule is shown in Fig. 26.49. In a network with m meshes, the rule supplies m equations. This number strictly refers to the meshes, not to all loops.

While the validity of the node rule is limited by the alternating-current behavior of parasitic capacitors (e.g., long parallel wires), the use of the mesh rule is limited to the case where no strong alternating magnetic fields are present (see (26.25) and its explanation). The latter indicates a severe problem: electrical and electronic systems are developed by assuming that the mesh

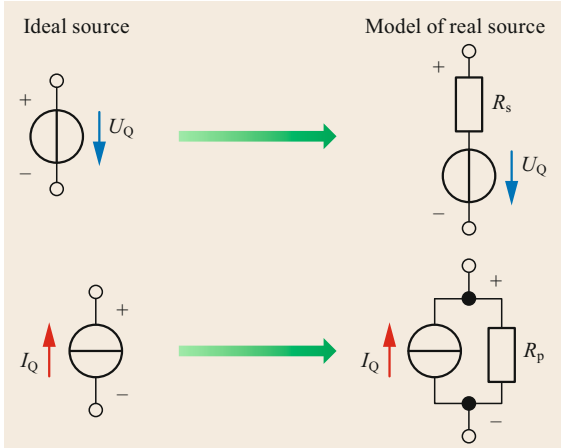

Fig. 26.50 Model of a nonideal voltage source (*top, right*) and model of a nonideal current source (*bottom right*)

rule applies. However, in the case of strong electromagnetic wave interference, the potentials start to oscillate, and this may lead to a malfunction or even destruction of the exposed device. This is why "please switch off all electronic devices" is an instruction commonly heard before takeoff.

In summary, one may conclude that, for a network with k nodes and m meshes, Kirchhoff's rules provide $k + m$ equations. If the network is closed, $(k-1) + m$ equations remain.

26.4.3 Nonideal Voltage and Current Sources

An *ideal voltage source* is a component that will deliver a constant voltage irrespective of the current passing through it. In reality, this can only be an approximation. The more current that flows, the smaller the tension will be. In almost all cases, it is sufficient to model such a nonideal voltage source as a series combination of an ideal source and an ohmic resistor, as shown in Fig. 26.50. Similarly, a real current source can be approximated by an ohmic resistor placed in parallel to an *ideal current source*. The voltage and current at the terminals of the real (nonideal) sources are then

$$\begin{aligned} U &= U_Q - R_s I \qquad \text{(real voltage source)}\,, \\ I &= I_Q - \frac{U}{R_p} \qquad \text{(real current source)}\,. \end{aligned} \tag{26.85}$$

As both real source models produce a linear dependence between voltage and current, it is always possible to exchange the two, as shown in Fig. 26.51. In fact, with

$$R_p = R_s \quad \text{and} \quad U_Q = R_S I_Q\,, \tag{26.86}$$

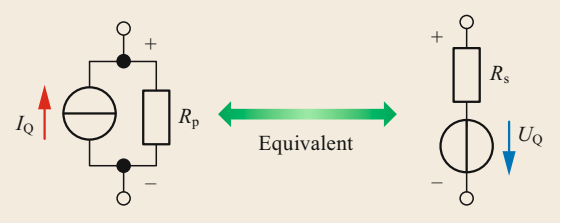

Fig. 26.51 Illustration of the fact that, for every real (linear) voltage source, a current source with the same behavior can be found

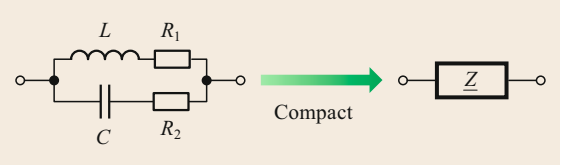

Fig. 26.52 Compaction of an electrical branch

one gets exactly the same behavior at the terminals of both sources. And in both cases, the value of the internal resistance R_i may by determined in the same manner. If the source is exposed to a variable resistor, a simultaneous measurement of the current and tension of either source will reveal its value, because

$$R_i = R_p = R_s = \frac{\Delta U}{\Delta I} = \frac{dU}{dI} \qquad (26.87)$$

is a direct consequence of (26.86).

When analyzing networks, it is always a good idea to replace internally complicated branches not only by real sources, but also by impedances, including the ones of inductors and capacitors. An example of such a compaction is shown in Fig. 26.52. For the analysis within a larger network, an entire branch can be replaced by a single impedance $\underline{Z}$. When the current and tension through $\underline{Z}$ are known, its components may by looked at in detail. In the case shown, one would have $\underline{Z} = (j\omega L + R_1) \parallel [1/(j\omega C) + R_2]$.

Application Example: Replacing Any Two-Terminal Network by Real Sources

A two-terminal network consisting of only sources and resistors has a linear current–voltage characteristic. It can therefore always be replaced by a real current source or a real voltage source. Figure 26.53 indicates a method to find these sources. The values for I_Q and U_Q can simply be determined by analyzing the behavior of the circuit for the two cases where the terminals are connected (short circuit) or disconnected (open circuit). This may be understood by a glance at Fig. 26.50. The behavior of the open circuit is independent of R_s, while R_p has no influence in the short-circuit current source. The method to determine the value for the internal resistance R_i can be understood to be a consequence of (26.87). An ideal current source has an infinite internal resistance. For the determination of R_i, it is replaced by an open switch, i.e., no connection. An ideal voltage source has $R_i = 0$ and is therefore replaced by a connection (short circuit). Both replacements together give the circuit shown on the top right of Fig. 26.53. An analysis of this circuit gives the value of R_i.

For the circuit shown, one thus gets

$$\begin{aligned} R_i &= (R_1 \parallel R_2) + R_3 \,, \\ I_Q &= \frac{1}{R_3}\left(I_B + \frac{U_B}{R_1}\right)(R_1 \parallel R_2 \parallel R_3) \,, \\ U_Q &= \frac{U_B + R_1 I_B}{1 + (R_1/R_2)} \,. \end{aligned} \qquad (26.88)$$

26.4.4 Network Analysis Algorithms

Using Kirchhoff's rules will always produce enough equations to determine all the currents and tensions in a given network. However, as networks get larger, the path towards the solution may become rather clumsy. For a network having k nodes and m meshes, a system of $m + k - 1$ equations has to be solved. And so the repeated emergence of the strategic question "which variable should be eliminated next?" may turn out to be rather nerve-racking.

There are two popular methods that allow the number of equations to be reduced. And, as long as linear elements such as R, L, C, and sources are the only components, these methods help to write down the equations in a manner that produces a system of equations that can be solved using matrix inversion. In the following, the methods will be presented with sources and resistors being the only components. All methods may, however, also be applied to alternating-current networks. In this case, impedances $\underline{Z}$ have to be used instead of resistances R.

The first algorithm, the technique of *mesh analysis*, also known as the *mesh current method*, reduces the number of equations to m by writing down all the mesh equations in a manner that makes the use of the node equations obsolete. Its principal idea is to interpret all the currents in a network as sums of so-called *mesh currents*. As shown in Fig. 26.54, the current through any component is written down as the sum of the currents of all meshes of which it is a part. So, the current through the resistor R_C in Fig. 26.54 would be $I_{M1} + I_{M2}$. Closer inspection also reveals that computing this sum is in fact the incorporation of the node rule. If the component is

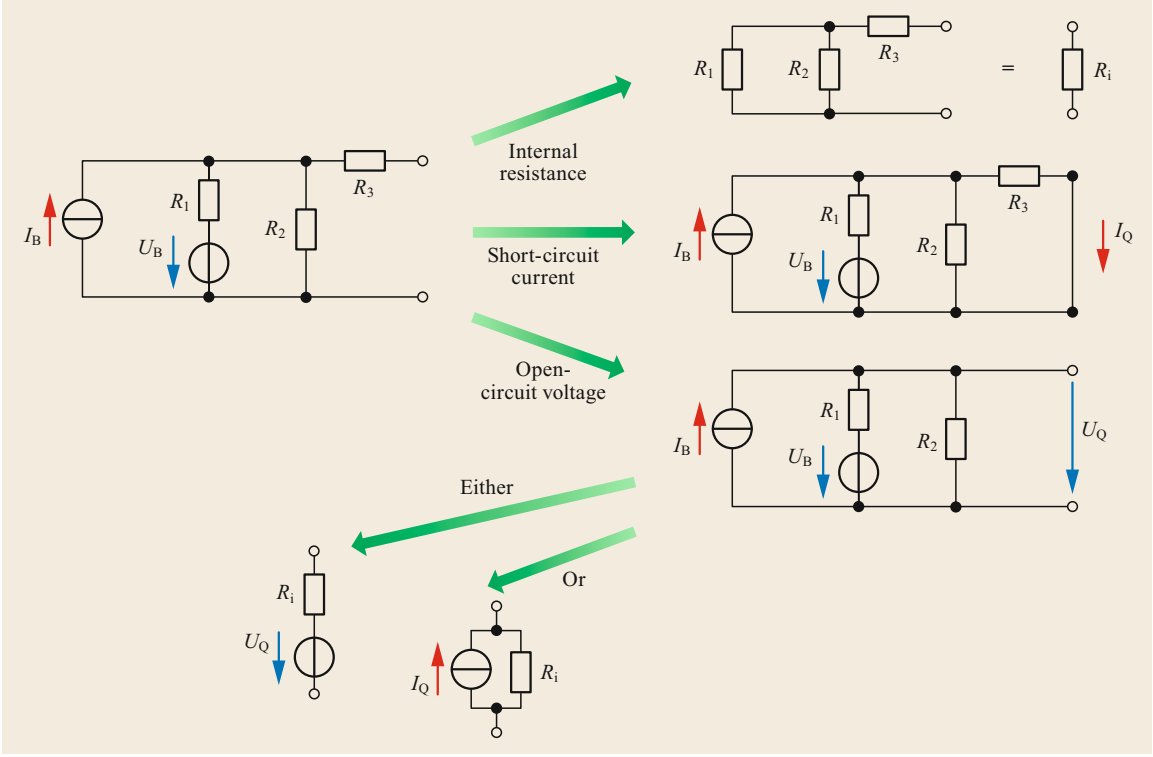

Fig. 26.53 Example for the replacement of a two-terminal network by either a real voltage source or a real current source

part of one mesh only (R_1 and R_2 in Fig. 26.54), the current of the mesh and the current through the component are identical. Clearly, if all the mesh currents are known, the currents through all the components are known as well.

Applying the mesh rule to the complete network is done in two steps. First, the meshes are considered one by one, then in a second step, all voltages from adjacent meshes are added. Hence,

$$(R_1 + R_C + R_2)I_{M1} + R_C I_{M2} = U_Q \qquad (26.89)$$

describes the voltage balance for mesh M_1 in Fig. 26.54. The next step is to write down the equations for all the meshes in such a manner that they may easily be transformed into a matrix equation such as the following one:

$$\begin{pmatrix} R_{11} & R_{12} & \dots \\ R_{21} & R_{22} & \dots \\ \dots & \dots & \dots \end{pmatrix} \cdot \begin{pmatrix} I_{M1} \\ I_{M2} \\ \dots \end{pmatrix} = \mathbf{R} \cdot \begin{pmatrix} I_{M1} \\ I_{M2} \\ \dots \end{pmatrix} = \begin{pmatrix} U_{Q1} \\ U_{Q2} \\ 0 \\ \dots \end{pmatrix}, \qquad (26.90)$$

i.e., the *resistance matrix* $\mathbf{R}$ *times the vector of mesh currents equals the vector of all the source voltages*. The indices in the resistance matrix refer to the meshes of which the resistors are part. Clearly, this preparation requires all voltage sources to appear on the right-hand side of the equations, and that all the mesh currents be written down in the same order in all the equations. Meshes with no voltage source have a 0 on the right. Each diagonal element of the resistance matrix is the sum of all the resistors in a mesh. The off-diagonal elements are the coupling resistors. If a mesh M_x has no common resistor with a different mesh M_y, one has $R_{xy} = 0$.

All elements of the resistance matrix may also be copied directly from the schematic of a network. The diagonal elements are the sums of all the resistances in a mesh. The off-diagonal elements are either zero,

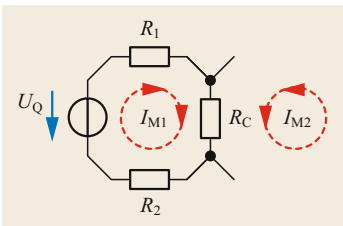

Fig. 26.54 The principle of mesh analysis. First, all the *mesh currents* (I_{M1}, I_{M2}) are computed. Then, the currents through the components are known to be the sums of their mesh currents

or the coupling resistances, or—if the two mesh currents through a resistor are antiparallel—the negative resistance. A check of correctness can then be made by symmetry, i.e., by confirming that $R_{ij} = R_{ji}$.

All mesh currents may now be computed via inversion of the resistance matrix $\mathbf{R}$. Multiplication of (26.90) by $\mathbf{R}^{-1}$ from the left leaves

$$\begin{pmatrix} I_{M1} \\ I_{M2} \\ I_{M3} \\ I_{M4} \\ \dots \end{pmatrix} = \mathbf{R}^{-1} \cdot \begin{pmatrix} U_{Q1} \\ U_{Q2} \\ U_{Q3} \\ 0 \\ \dots \end{pmatrix} ; \qquad (26.91)$$

i.e., all mesh currents can be read directly from the result.

There is, however, one set of networks that cannot be handled by such mesh analysis, viz. all networks with at least one ideal current source. Real current sources are no problem, as they may be replaced by real voltage sources. The method shown next can do so, albeit at the price of not being able to handle ideal voltage sources.

The branch current method, also known as *nodal analysis* or *node-voltage analysis*, reduces the number of equations from $m + k - 1$ to $k - 1$ by automatically incorporating all the mesh equations. Figure 26.55 illustrates the idea. First, the current balance for each node is written down separately. Then, all the resulting equations are put in an order that allows them to be transformed into a matrix equation of the type *conductance matrix times vector of unknown tensions equals vector of given current sources*.

The behavior of a network does not change if all the potentials are augmented by the same, fixed amount. Only potential differences, i.e., voltages, matter. The easiest way to use this freedom is to set one of the potentials to zero (*mass*) and give it the node number zero. For the node shown in Fig. 26.55, the appropriate form to write down the node rule would then be

$$\begin{aligned} & I_1 + I_2 + I_3 + I_Q = 0 \\ \rightarrow & \frac{U_{10} - U_{x0}}{R_1} + \frac{U_{20} - U_{x0}}{R_2} + \frac{U_{30} - U_{x0}}{R_3} + I_Q = 0 \\ \rightarrow & -\frac{1}{R_1} U_{10} - \frac{1}{R_2} U_{20} - \frac{1}{R_3} U_{30} \\ & + \left(\frac{1}{R_1} + \frac{1}{R_2} + \frac{1}{R_3} \right) U_{x0} = I_Q \\ \rightarrow & -G_{x1} U_{10} - G_{x2} U_{20} - G_{x3} U_{30} \\ & + (G_{x1} + G_{x2} + G_{x3})\, U_{x0} = I_Q \, . \end{aligned} \qquad (26.92)$$

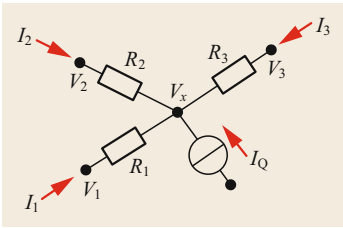

Fig. 26.55 Basic principle of nodal analysis: For each node, the current balance is written down separately. Later, all the equations for all the nodes are combined to form a matrix equation

Here, the indexes of the conductances indicate which nodes they connect; e.g., G_{x1} connects V_x and V_1. All currents entering a node are transformed into potential differences multiplied by the inverse resistances of the components on the branch pointing to the node (second line in (26.92)). Then, all the terms are ordered according to the node numbers. The current sources are moved to the right-hand side of the equation. Finally, for the sake of having easier-to-read formulas, the inverse resistances are replaced by conductances (fourth line in (26.92)). These rearrangements thus result in a form that can be interpreted as being one line of a matrix equation. A closer look at this line

$$\begin{aligned} & (-G_{x1},\ -G_{x2},\ -G_{x3},\ [G_{x1} + G_{x2} + G_{x3}]) \cdot \begin{pmatrix} U_{10} \\ U_{20} \\ U_{30} \\ U_{x0} \end{pmatrix} \\ & = I_Q \end{aligned} \qquad (26.93)$$

again reveals a certain structure of the conductance matrix. The diagonal elements are the sums of all the conductances along the branches connected to the nodes (i.e., $[G_{x1} + G_{x2} + G_{x3}]$ in (26.93)). The off-diagonal elements are the conductances between the nodes, equipped with an extra minus sign. If all but one (i.e., $k - 1$) of the node equations (the ground node gets no equation) are written down in this manner, they can be summarized into the following matrix equation:

$$\begin{aligned} & \begin{pmatrix} G_{11} & G_{12} & \dots & G_{1(k-1)} \\ G_{21} & G_{22} & \dots & G_{2(k-1)} \\ \dots & \dots & \dots & \dots \\ G_{(k-1)1} & G_{(k-1)2} & \dots & G_{(k-1)(k-1)} \end{pmatrix} \cdot \begin{pmatrix} U_{10} \\ U_{20} \\ \dots \\ U_{(k-1)0} \end{pmatrix} \\ & = \begin{pmatrix} I_{Q1} \\ I_{Q2} \\ \dots \\ I_{Q(k-1)} \end{pmatrix} . \end{aligned} \qquad (26.94)$$

Inversion of the conductance matrix then gives then all the voltages relative to the ground potential. Multiplica-

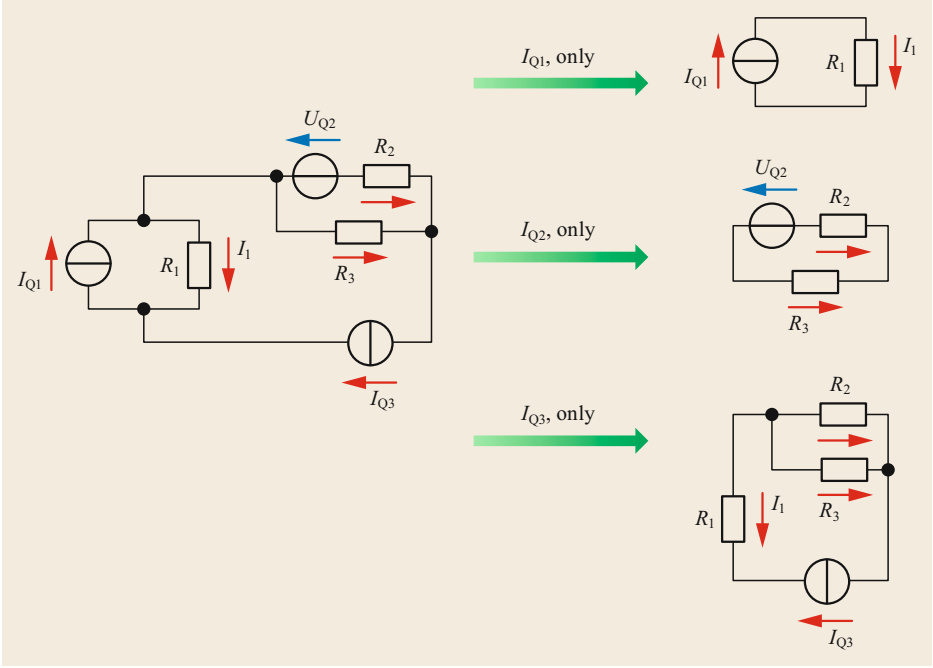

Fig. 26.56 Example for the determination of currents by separating and then adding the contributions from all sources. *Left*: original circuit, *right*: the three circuits used for the determination of the current contributions

tion of (26.94) with $\mathbf{G}^{-1}$ does this, as

$$\begin{pmatrix} U_{10} \\ U_{20} \\ \cdots \\ U_{(k-1)0} \end{pmatrix} = G^{-1} \cdot \begin{pmatrix} I_{Q1} \\ I_{Q2} \\ \cdots \\ 0 \\ 0 \end{pmatrix} \qquad (26.95)$$

shows.

Finally, both nodal analysis and mesh analysis can be combined with a further method, the *superposition of current contributions*. This method is particularly helpful if there are many sources in a network. Figure 26.56 illustrates the principle. For each source, the currents through all the components are calculated separately. For a given component, the total current is then the sum of the currents thus determined. This method is similar to the replacement of two-terminal networks by real sources: an ideal current source not under consideration is replaced by an open switch (no connection), while an ideal voltage source is replaced by a short circuit (connection). In this way, the three sources in the network in Fig. 26.56 yield the three networks shown on the right of this figure. The currents may then be read from the schematics of the networks:

$$\begin{aligned} I(R_1) &= I_{Q1} + 0 \qquad\quad - I_{Q3}\,, \\ I(R_2) &= 0 \quad + \frac{U_{Q2}}{R_2 + R_3} + \frac{I_{Q3}(R_2 \parallel R_3)}{R_2}\,, \\ I(R_3) &= 0 \quad - \frac{U_{Q2}}{R_2 + R_3} + \frac{I_{Q3}(R_2 \parallel R_3)}{R_3}\,. \end{aligned} \qquad (26.96)$$

The current contributions in (26.96) are ordered in the same manner as the networks in Fig. 26.56. The more sources there are, the more drastic the simplifications become.

Table 26.4 presents a comparison of the network analysis algorithms. The compaction of two-terminal networks includes their replacement by real sources. It may be combined with node analysis or mesh analysis. The same holds for the method of current superposition.

Table 26.4 Algorithms for analysis of linear networks

Method	Advantages	Disadvantages
Kirchhoff's rules	Always work	Many equations $(m + k - 1)$
Mesh analysis	Few equations (m)	No ideal current sources
Node analysis	Few equations $(k - 1)$	No ideal voltage sources
Current superposition	Simplified networks	One network computation per source
Two-terminal compaction	Simplified networks	Not always a great help

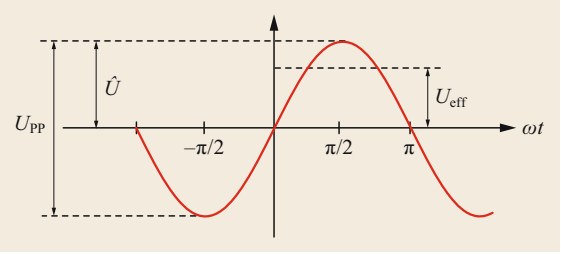

Fig. 26.57 Commonly used variables to describe alternating voltages

26.4.5 Alternating-Current Networks

All the algorithms presented so far may also be applied to alternating-current networks. In this manner, they include analyses of networks with capacitors and inductors. For these applications, the resistances R_i should be replaced by impedances $\underline{Z}_i$ (see below). For simplified calculations, alternating sources should also be represented using complex variables.

There are a variety of representations for alternating currents and voltages. Figure 26.57 shows the most popular ones. Digital oscilloscopes will determine the *peak-to-peak voltage* U_{PP} by subtraction of the smallest value from the largest one. Ideally, this is twice the value of the amplitude $\hat{U}$, known as the factor before the sine function. Books on AC analyses often use the *effective voltage*

$$U_{eff} = \frac{\hat{U}}{\sqrt{2}} , \tag{26.97}$$

because an alternating voltage with $U_{eff} = x\,\mathrm{V}$ will heat up a resistor to exactly the same temperature as a direct-current voltage of $x\,\mathrm{V}$. Many books on AC networks leave out the suffix $_{eff}$, leaving some uncertainty as to whether or not factors of $\sqrt{2}$ have been included. For this reason, in this book, effective voltages are always labeled U_{eff}.

Within AC networks, resistors, inductors, and capacitors are characterized by their impedances:

$$\begin{aligned} \underline{Z}_R &= R \qquad \text{(resistor)} , \\ \underline{Z}_L &= \mathrm{j}\omega L \qquad \text{(inductor)} , \\ \underline{Z}_C &= \frac{1}{\mathrm{j}\omega C} \qquad \text{(capacitor)} , \end{aligned} \tag{26.98}$$

which happen to be either real (R), positive imaginary (L), or because of $1/\mathrm{j} = -\mathrm{j}$ negative imaginary (C). These characteristics form the basis of a rather illuminating way of adding impedances. Each of the components is represented as a vector in one of the complex planes for $\underline{Z}$ or $\underline{Y}$, as shown in Table 26.5. A series connection is then represented by the addition of vectors in the $\underline{Z}$ plane, while a parallel connection is represented by an addition of vectors in the $\underline{Y}$ plane. Figure 26.58 shows the example $\underline{Z} = \underline{Z}_R + \underline{Z}_L + \underline{Z}_C$.

Table 26.5 Impedance vectors for linear components

Component	Resistor	Inductor	Capacitor
Vector in the $\underline{Z}$ plane	$(R, 0)$	$(0, \mathrm{j}\omega L)$	$(0, -\mathrm{j}/(\omega C))$
Vector in the $\underline{Y}$ plane	$(1/R, 0)$	$(0, -\mathrm{j}/(\omega L))$	$(0, \mathrm{j}\omega C)$

Whenever large amounts of energy are to be transported, losses along lines such as those shown in Fig. 26.65 must be minimized. AC currents may produce losses even if no energy is transferred at all. This apparent contradiction results from the fact that, for a component with a 90° angle between current and tension, on average, the energy transfer into the component is exactly balanced by the transfer out of the component. At the same time, the current on the power line is nonzero. For such a component, i.e., one with a 90° angle between current and tension, the current is

$$\begin{aligned} \underline{i} &= \frac{\underline{u}}{\mathrm{j}X} = \frac{\hat{U}}{\mathrm{j}X} \mathrm{e}^{(\omega t - \pi/2)} \\ \rightarrow \quad i &= -\frac{\hat{U}}{X} \cos\left(\omega t - \frac{\pi}{2}\right) , \end{aligned} \tag{26.99}$$

i.e., not zero for most times. Interestingly, the average magnitude of the current

$$\langle |i| \rangle = -\frac{2\hat{U}}{\pi X} \tag{26.100}$$

is exactly as large as the corresponding average for an ohmic resistor of equal magnitude: $\langle |i| \rangle = -2\hat{U}/(\pi R)$. In fact, it turns out that the angle between the voltage and current does not matter at all for the loss in supply lines.

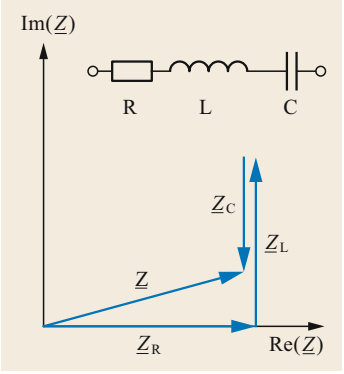

Fig. 26.58 Example of addition of impedances in the $\underline{Z}$ plane, showing the graphical determination of the impedance of an RLC oscillator circuit

Fig. 26.59 Electric cooker. Good ones are equipped with reactive power compensation capacitors (photo: © Oleksandr Delyk/ stock.adobe.com)

The *reactive power* Q is a measure of the power that oscillates back and forth on a power line without ever ending. Hence, only P suits the purpose of a power transmission line. For this reason, electrical energy engineers will try to minimize the reactive power. The method they use is called *reactive power compensation*.

Application Example: Reactive Power Compensation in a Cooker

The heating spiral of an electric cooker has an ohmic resistance of $R = 20\,\Omega$ and an inductance of $L = 30$ mH. It is attached to a 60 Hz network. How can the reactive power be reduced to zero?

Clearly, the only way to compensate the reactive power of the inductance is to add a capacitor, as shown in Fig. 26.60. The task is now to find a value for the capacitance that makes the reactive currents vanish, i.e., to find $\mathrm{Im}(\underline{Y}) = 0$ for

$$\underline{Y}_{\text{including } C} = \frac{1}{R + \mathrm{j}\omega L} + \mathrm{j}\omega C\,.$$

This is achieved by choosing

$$C = \frac{L}{(R^2 + \omega^2 L^2)} = 57\,\mu\mathrm{F}\,.$$

Then, one has

$$\underline{Y}_{\text{including } C} = \mathrm{Re}(\underline{Y}) = \frac{R}{R^2 + \omega^2 L^2}\,.$$

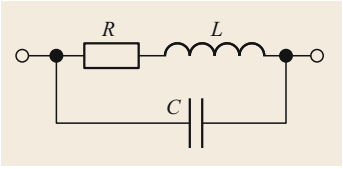

Fig. 26.60 Example of reactive power compensation. A heating resistor R with a parasitic inductance L will have its reactive power compensated by a capacitor of appropriate capacitance C

Now, the reduction of current can be computed. The factor by which the current is reduced is the ratio of the moduli of the acceptances with and without the capacitor:

$$\frac{\hat{I}_{C=0}}{\hat{I}_{\text{including } C}} = \sqrt{\frac{|\underline{Y}_{C=0}|^2}{|\underline{Y}_{\text{including } C}|^2}} = \frac{1}{\sqrt{1 + \frac{\omega^2 L^2}{R^2}}} = 0.87\,,$$

so that the current is reduced by 13%, and there is no price to pay in terms of performance. As long as the losses on the powering network are negligible, the heating power remains unchanged by the capacitor. Otherwise, there may even be a tiny increase of power.

26.4.6 Transformers

The success of AC applications is for exactly one reason: there is an easy way to transform the voltages of AC systems. Figure 26.61 shows that the basic setup of a *transformer* is simple: two coils are wound around a common iron core. Essentially, one of the coils (the *primary coil*) is connected to an alternating voltage. Its alternating current produces a magnetic field that is strengthened and shaped by the iron core. The *secondary coil* is thus exposed to an alternating magnetic

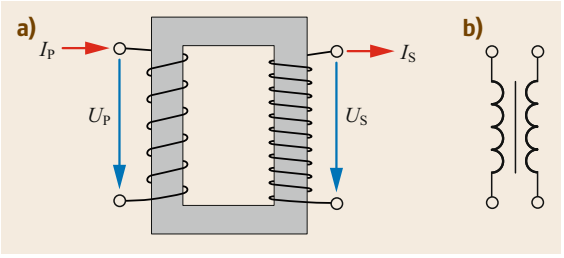

Fig. 26.61a,b A transformer consisting of two coils wound around a common core **(a)** and its schematic symbol **(b)**

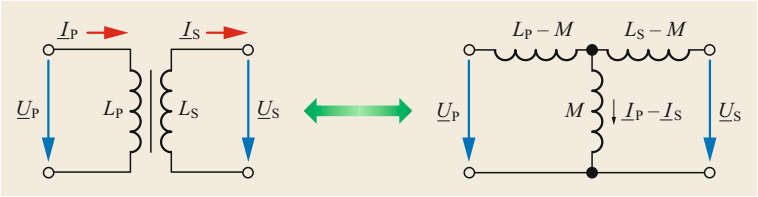

Fig. 26.62 A lossless transformer and a four-terminal network with the same AC behavior

field. Therefore, an alternating voltage will be induced in the secondary coil.

For simplicity, the operation of a transformer is first derived while assuming no losses anywhere. Losses are then introduced in a second step. If the iron core has the same diameter everywhere, each loop carrying the same current I will also produce the same magnetic flux Φ_B:

$$\Phi_B(\text{one loop}) = \Lambda I \,, \tag{26.101}$$

where Λ is some constant. A coil having N loops will then have an inductance

$$L = N^2 \Lambda \,. \tag{26.102}$$

For the setup shown in Fig. 26.61, the magnetic flux will be the sum of the flux Φ_P from the primary coil and that due to the secondary coil, Φ_S:

$$\Phi_B = \Phi_P + \Phi_S = N_P \Lambda I_P + N_S \Lambda I_S \,. \tag{26.103}$$

A change of the magnetic flux will induce a tension $U_{ind} = \pm \mathrm{d}\Phi_B/\mathrm{d}t$ in each loop. The plus sign applies to the primary coil because the reference directions for current and voltage are the same. On the secondary side, they are antiparallel, so the minus sign applies there. The induced voltages are then given by

$$\begin{aligned} U_P &= N_P \Lambda \left(N_P \frac{\mathrm{d}I_P}{\mathrm{d}t} - N_S \frac{\mathrm{d}I_S}{\mathrm{d}t} \right) \,, \\ U_S &= N_S \Lambda \left(N_P \frac{\mathrm{d}I_P}{\mathrm{d}t} - N_S \frac{\mathrm{d}I_S}{\mathrm{d}t} \right) \,, \end{aligned} \tag{26.104}$$

a set of equations that is known as the *transformer equations*. Because the terms in brackets are the same for U_P and U_S, dividing the two equations gives an equally simple and useful result

$$U_S(t) = U_P(t) \frac{N_S}{N_P} \,; \tag{26.105}$$

in plain terms: the ratio of the voltages is determined by the ratio of the number of turns in the coils. The term $N_P N_S \Lambda = \sqrt{L_P L_S}$, which appears in both equations of the system (26.104), is called the *coupling inductance*, M. Using this quantity, the transformer equations can be written in the form

$$\begin{aligned} U_P &= L_P \frac{\mathrm{d}I_P}{\mathrm{d}t} - M \frac{\mathrm{d}I_S}{\mathrm{d}t} \,, \\ U_S &= M \frac{\mathrm{d}I_P}{\mathrm{d}t} - L_S \frac{\mathrm{d}I_S}{\mathrm{d}t} \,. \end{aligned} \tag{26.106}$$

In general, (26.106) are hard to calculate. However, within the framework of complex alternating-current calculus, derivatives may be replaced by factors. Because $\mathrm{d}/\mathrm{d}t \mathrm{e}^{\mathrm{j}\omega t} = \mathrm{j}\omega \mathrm{e}^{\mathrm{j}\omega t}$, the transformer equations simplify to

$$\begin{aligned} \underline{u}_P &= L_P \mathrm{j}\omega \underline{i}_P - M \mathrm{j}\omega \underline{i}_S \,, \\ \underline{u}_S &= M \mathrm{j}\omega \underline{i}_P - L_S \mathrm{j}\omega \underline{i}_S \,. \end{aligned} \tag{26.107}$$

In this way, complex calculus turns a system of differential equations into a system of linear equations.

Most surprisingly, there is a four-terminal network consisting of three inductances which has exactly the same alternating-current behavior. This network is shown in Fig. 26.62. If a two-terminal network with arbitrary impedance $\underline{Z}_S = \underline{u}_S/\underline{i}_S$ is connected to the secondary side of the transformer, its tension and current may be eliminated from the transformer equations, leaving

$$\frac{\underline{i}_P}{\underline{u}_P} = \frac{1}{\mathrm{j}\omega L_P} + \frac{L_S}{L_P} \frac{1}{\underline{Z}_S} \,, \tag{26.108}$$

i.e., a very simple formula for the admittance of the system. Equation (26.108) shows that, seen from the primary side of the transformer, the latter behaves like a parallel connection of the primary inductor and a load with a modified impedance $\underline{Z}_S(L_P/L_S)$. Finally, the current on the secondary side comes out as

$$\underline{i}_S = \frac{N_P}{N_S} \left(\underline{i}_P - \frac{\underline{u}_P}{\mathrm{j}\omega L_P} \right) \,. \tag{26.109}$$

The average power P_P used by a lossless transformer on the primary side is exactly the same amount as the power delivered to the secondary side: $P_S = -P_P$. However, the reactive powers differ.

In literature, $\underline{i}_S = \underline{i}_P(N_P/N_S)$ may be found instead of (26.109) and referred to as describing an

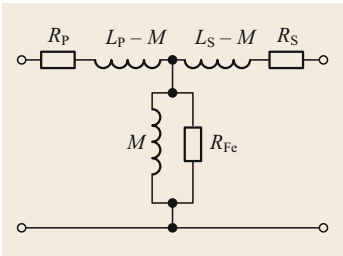

Fig. 26.63 Four-terminal network describing a lossy transformer

ideal transformer. The difference between these two equations results from an additional assumption. The ideal transformer is assumed to have $\mu_r \to \infty$, corresponding to $L_P \to \infty$. If no load is connected to the secondary side, the ideal transformer behaves like an open switch on the primary side, while the lossless transformer behaves like a single inductor with inductance L_P.

A *real transformer* has losses, mainly due to eddy currents and repeated magnetizations in the yoke (iron core), as well as losses in the windings. These can be incorporated into the circuit description as shown in Fig. 26.63. At first glance, it may be irritating that losses within the iron are modeled as a resistor to ground. This resistor should be understood as a feature of the coupling inductor, as it affects both sides of the transformer. Also, as long as the frequency remains unchanged, a suitable value for R_{Fe} can always be found (see also Fig. 26.52). Losses due to stray magnetic fields are usually small compared with the losses just described.

The power that can be transfered by a real transformer is mainly limited by two properties of the iron yoke: remanence and saturation. Both properties become visible if the magnetic field in the iron is plotted as a function of the current in the coil. From Fig. 26.64 one can deduce that an ever-growing current will not produce an equally ever-growing magnetic field. This effect is called *saturation*. It is commonly explained by all of the iron atoms becoming aligned with the field produced by the coil. Saturation has a very disadvantageous consequence, as it produces an almost flat voltage–current characteristic. So, if a transformer is in saturation, a small increase in voltage will provoke a very large additional current. The worst case is then evaporation of the coils. For this reason, transformers are equipped with iron yokes that are large enough to avoid saturation (the larger the yoke, the more atoms to be aligned, and the later saturation will occur).

Remanence describes the fact that a piece of iron remains magnetized even if it is no longer exposed to an external magnetic field. Depending on the direction of the former external field, the remanent field may point in one direction or the other. In physical terms, this

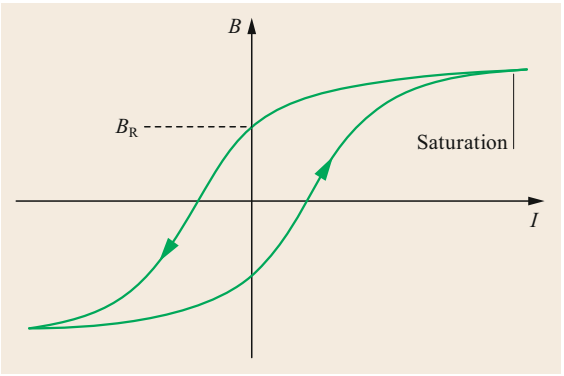

Fig. 26.64 Magnetic field within an iron yoke as a function of the current in the coil around the yoke

means that some of the iron atoms retain their orientation until the external field is strong enough to literally turn them around. This rotation of atoms produces frictional losses in addition to eddy currents. These cannot be avoided, but as in the case of inductors, the eddy currents can be minimized by using stacks of slices of iron whose thicknesses limit the diameter of the eddy currents.

26.4.7 Three-Phase Alternating-Current Systems

Power lines often come in bundles of three, as shown in Fig. 26.65, because three-phase AC systems have been proven to be ideally suited for the transport of large amounts of energy. The backbone of each there-phase AC network is a triplet of power lines whose voltages are shifted by an angle of 120°, as shown in Fig. 26.66. Colloquially, each of the lines is called a *phase*.

The amplitudes of the three phases can be written as

$$\underline{U}_1 = \hat{U}\mathrm{e}^{0}\,, \quad \underline{U}_2 = \hat{U}\mathrm{e}^{\mathrm{j}2\pi/3}\,, \quad \underline{U}_3 = \hat{U}\mathrm{e}^{\mathrm{j}4\pi/3}\,. \tag{26.110}$$

A striking feature of this combination of lines is the fact that the tension between each pair of wires is larger than the tension between each phase and the ground potential. Calculating the instantaneous tension $u_2 - u_1$, for example, gives the tension indicated in red in Fig. 26.67. The corresponding amplitude can be calculated from (26.110). The result

$$\underline{U}_2 - \underline{U}_1 = \hat{U}\left(\mathrm{e}^{\mathrm{j}2\pi/3} - \mathrm{e}^{0}\right) = \sqrt{3}\,\hat{U}\,\mathrm{e}^{\mathrm{j}5\pi/6} \tag{26.111}$$

shows that the tension between each pair of lines is larger than the tension to ground by a factor of $\sqrt{3}$. The

Fig. 26.65 Masts with 2×3 380 kV power line phases in the upper part, and 2×3 20 kV line phases in the lower part. At the top, a lightning conductor can bee seen. (Photo: © okanakdeniz/stock.adobe.com)

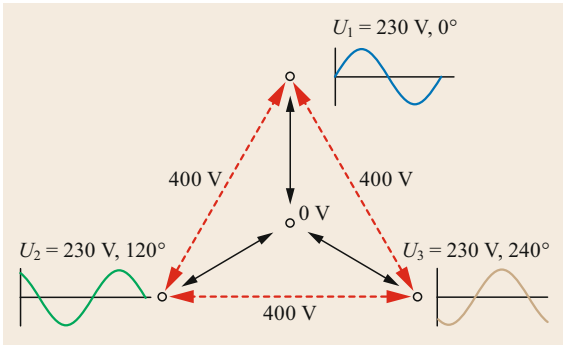

Fig. 26.66 Three power lines forming a three-phase AC network. If each line has an effective tension $V_{\text{eff}} = 230\,\text{V}$, then the effective tension between each pair of lines is $V_{\text{eff}} = 400\,\text{V}$

instantaneous tension is also shifted by an amount of $\omega t = -5\pi/6 = -150°$ relative to $\underline{u}_1$.

This increased tension between two phases can be used in a *triangle network*, as shown on the right in Fig. 26.68. This type of network is particularly popular for high-power devices. Since in a triangle network, there is no connection to ground, the entire energy flow is on the networks with no energy load on the ground. This network is also popular for heating, as the increased tension allows the generation of a given heating power with a reduced current. In this manner, losses on the lines are reduced.

In a home environment, most devices are connected between one of the phases and ground. The typical network of an entire home is therefore rather of the *star* type shown in Fig. 26.68a.

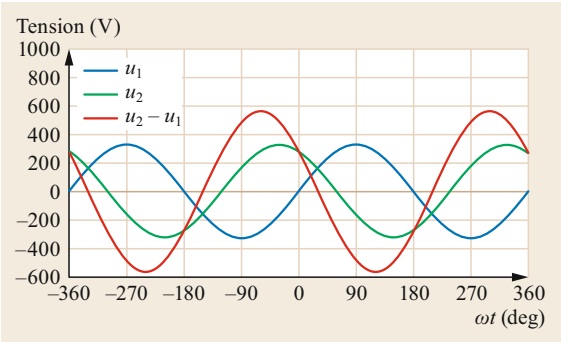

Fig. 26.67 Instantaneous tension between two phases of a three-phase network

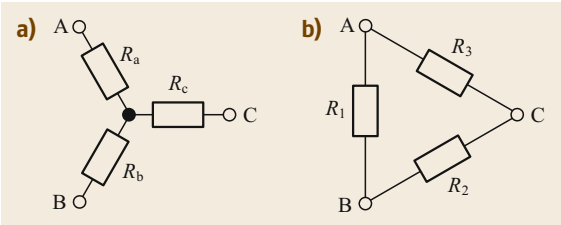

Fig. 26.68a,b Two options to connect three-phase supply lines. The *star* type network **(a)** connects all lines to a ground line, while the *triangle*-type network **(b)** only connects the phases among each other

26.5 Electrical Machines

This section starts with a discussion on the interactions between current loops and magnetic fields, i.e., the Lorentz force and induction. It is shown how these interactions can lead to a conversion of mechanical energy into electrical energy or vice versa. A classification of electrical machines follows, then the features of direct-current machines, asynchronous machines, and synchronous machines.

26.5.1 How Wires Are Forced to Move

Electrical machines use the close relations between moving charges (currents) and magnetic fields. Currents produce magnetic fields, and moving charges are subject to the Lorentz force in magnetic fields. An electrical machine is called a *motor* if it converts electrical energy into mechanical energy, and a *generator* if it converts

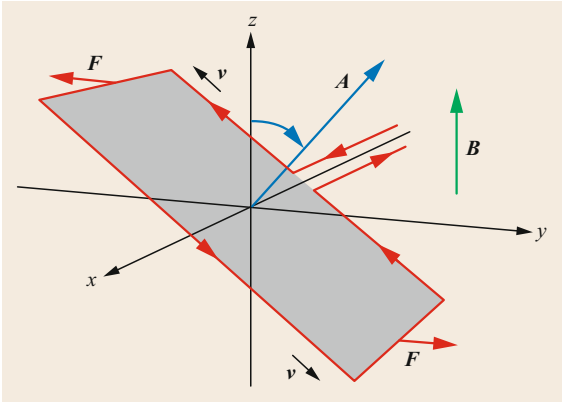

Fig. 26.69 Current loop enclosing an oriented surface $\boldsymbol{A}$ in a magnetic field $\boldsymbol{B}$. Positive charges moving with a velocity $\boldsymbol{v}$, will feel a Lorentz force $\boldsymbol{F}$. This results in a nonzero torque as long as the surface vector is not parallel to the magnetic field

mechanical energy into electric energy. Most electrical machines may be used in either way, i.e. as motors or generators.

The function of electrical machines can be traced back to the behavior of a current loop in a magnetic field, as shown in Fig. 26.69. A rectangular current loop, rotatable around the x axis and placed in a magnetic field $\boldsymbol{B} = (0, 0, B)$ is subject to the Lorentz force. This force is suitably calculated for the four straight elements of the loop, *front*, *back*, *top*, and *bottom*, one by one. If the current loop is made from a wire with a constant diameter, all carriers of charge will move with the same velocity $|\boldsymbol{v}|$. With the magnetic field vector pointing in the z direction, the Lorentz force for any moving charge will point in a direction within the xy-plane. The force on a sample charge ΔQ in the bottom part of the loop will point along the y-axis: $\Delta\boldsymbol{F} = \Delta Q\boldsymbol{v}\times\boldsymbol{B} = (0, \Delta F, 0)$. For a current I traversing the bottom element of length l, summing all the sample charges gives a force $\boldsymbol{F} = (0, BlI, 0)$. The force on the top element of the loop will be $(0, -BlI, 0)$, i.e., equally large, but with the opposite orientation.

The forces on the remaining elements of the loop are of similar size. However, they have little effect, as the loop is mounted such that it can only be rotated around the x-axis. So, the forces can merely *try* to stretch the loop.

The torque $\boldsymbol{M}$ can now be calculated according to $\boldsymbol{M} = \boldsymbol{r}\times\boldsymbol{F}$. It reaches its maximum value when the current loop and force form a right angle. Then, the distance $|\boldsymbol{r}|$ between the charges and the axis of rotation is half as large as the length of the front element of the current loop. Also, because the force itself is proportional to the length of the bottom element, the torque turns out to be proportional to the area enclosed by the loop:

$$\boldsymbol{M} = I\boldsymbol{A}\times\boldsymbol{B}\,. \tag{26.112}$$

The vector on the left of the $\times$ sign is called the *magnetic dipole moment* of the loop

$$\boldsymbol{\mu} = I\boldsymbol{A}\,. \tag{26.113}$$

A more general investigation would show that (26.112) and (26.113) may be used for current loops of arbitrary shape. And

$$\boldsymbol{M} = \boldsymbol{\mu}\times\boldsymbol{B} \tag{26.114}$$

serves as the definition of the magnetic moment $\boldsymbol{\mu}$, because $\boldsymbol{M}$ and $\boldsymbol{B}$ are easily measurable quantities.

If this torque is used to rotate the current loop, Fig. 26.69 shows the most elementary form of an electrical motor—and also of a generator, since there is no action without reaction. If a current in a field forces the angle to change, a change of angle will also force a current to change. So, if a current loop is forced to rotate, the setup shown in Fig. 26.69 represents the most elementary form of a generator. Its function is then governed by the Faraday–Henry law (law of induction, (26.13)), which states that the tension induced in a closed loop, U_{ind}, is determined by the rate of change of the magnetic flux through the surface enclosed by the loop: $\Phi_{\mathrm{B}} = \boldsymbol{B}\cdot\boldsymbol{A}$. In this case,

$$U_{\mathrm{ind}} = \frac{\mathrm{d}\Phi_{\mathrm{B}}}{\mathrm{d}t} = \frac{\mathrm{d}}{\mathrm{d}t}\boldsymbol{B}\cdot\boldsymbol{A} = B\cdot A\frac{\mathrm{d}\cos\theta}{\mathrm{d}t}\,, \tag{26.115}$$

where θ is the angle between the magnetic field $\boldsymbol{B}$ and the surface vector $\boldsymbol{A}$.

As electrical machines transform mechanical energy into electrical energy or vice versa, according to

$$p_{\mathrm{mech}} = -p_{\mathrm{el}}\,, \tag{26.116}$$

the sign in front of the powers determines the direction of the energy transfer. Wherever the sign is positive, energy is used up, while a negative power indicates a gain of energy (see also Fig. 26.43). For the setup shown in Fig. 26.69, the mechanical energy used to rotate the current loop from the xy-plane back into it ($\Delta\theta = 180°$) is the work to be done against the Lorentz force, $\Delta W = -F_y\Delta y$. For a half-turn, summing the forces of both wire elements contributing to the torque gives $W_{180°} = -2BIA$. If one assumes that—by some clever mechanism—the direction of the field is flipped, the same amount of energy will be needed for the next 180°. With power being the energy transfer per unit time, for a frequency f of complete turns, then

$$p_{\mathrm{el}} = -p_{\mathrm{mech}} = 4BAIf \tag{26.117}$$

follows.

The electrical power generated by the above setup can be calculated by assuming that the current induced by the rotation is lead through a resistor R. The rotor is assumed to be forced to have an angle changing according to $\theta(t) = 2\pi ft = \omega t$. The power p_R used by the resistor must be the same as the electrical power generated. According to (26.115), therefore

$$p_{el}(t) = -p_R = -\frac{U_{ind}^2}{R} = -\frac{\omega BA}{R}\sin^2(\omega t)\,, \tag{26.118}$$

which shows that the power rises quadratically with the frequency. The fact that electrical machines can be used to transfer both mechanical energy into electrical energy and vice versa is one of their most outstanding features.

The above formulae assumed a current loop in a constant magnetic field. In this case, the corresponding machine is called a *DC machine* (also called a *commutator machine*). So, DC machines have a constant magnetic field and a *rotor* inside. However, there are also other types of electrical machines, namely *synchronous AC machines* and *asynchronous AC machines*. AC machines use rotating magnetic fields which are produced by coils powered by alternating currents. If the rotor rotates with the same angular velocity as the field, the machine is a synchronous one, otherwise it is called asynchronous.

Figure 26.70 shows a comparison of the efficiencies achieved by synchronous, asynchronous, and direct-current machines. For powers less than 1 kW, machines with permanent magnets have good efficiencies. As the power of the machine increases, permanent magnets no longer offer sufficient field strengths. Therefore, all machines with powers exceeding 10 kW use electromagnets. Induction machines are popular for electric trains. The highest-power machines are synchronous generators in power plants.

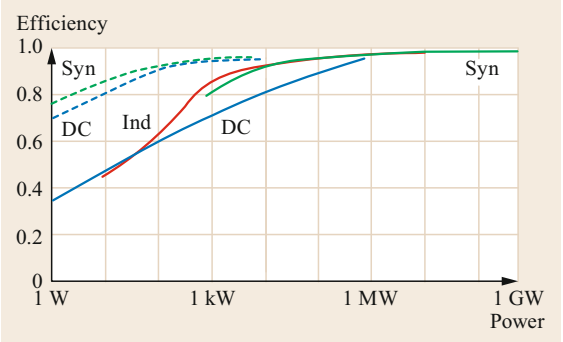

Fig. 26.70 Efficiencies of electrical machines: Syn for synchronous machines, Ind for induction (asynchronous) machines, and DC for direct-current (commutator) machines. *Dashed lines* refer to machines with permanent magnets, while *solid lines* indicate electromagnets

26.5.2 DC Machines

Direct-current motors offer a wide range of frequencies of operation, in no way limited by the frequency of the powering network. This feature guarantees their production in large numbers. In contrast, DC generators can only be found in niches.

Direct-current machines or commutator machines have a stator that delivers a magnetic field which always points in the same direction. If the field is made by permanent magnets, it is even constant. Figure 26.71 shows a typical rotor that may be placed inside a stator of a DC motor. The copper plates seen on the left are connected in pairs. They connect the rotor to the electrical power supply. Each pair of plates is connected to one coil. In Fig. 26.71, the coils are made from copper wires. The copper plates rotate between one (static) pair of *brushes* in such a way that one coil at a time is connected. In this way, the current is forced to *commute* between the coils of the rotor. Accordingly, the ring of copper plates is called a *commutator* and the motor as a whole is referred to as a *commutator machine*. The other metal parts of the rotor are made from ferromagnetic material, thus increasing and guiding the magnetic field. A good quality of these parts requires the metal to be laminated. In this way, eddy currents are minimized. For the following reason, the rotor should fit into the stator as precisely as possible: if μ_r is the relative permeability of the metal, according to Ampère's law, a fraction of $1/\mu_r$ of the magnetic field traversing air will halve the magnetic field strength. For electrical engines, fitting thus refers to accuracies well below 1 mm.

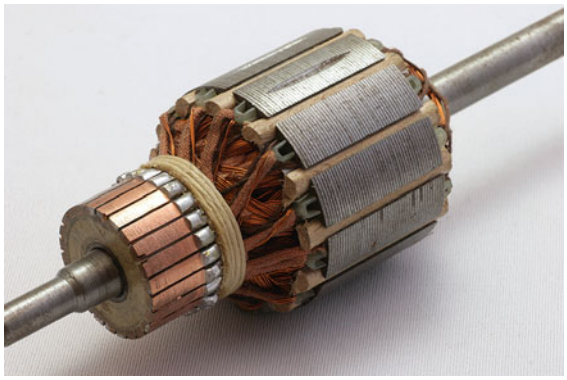

Fig. 26.71 Rotor of a DC machine; the commutator is on the *front left side*; copper wires form the coils. Laminated iron between the coils amplifies the magnetic field (photo by Sebastian Stabinger/CC BY 3.0)

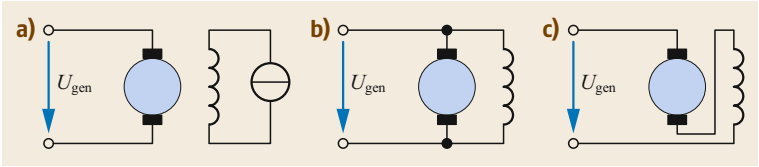

Fig. 26.72a–c Three options for powering the stator magnets of DC engines: **(a)** external; **(b)** parallel; **(c)** series. Case **(a)** includes motors with permanent magnets. U_{gen} is the voltage either generated by the machine or supplied by an external generator if the engine is operated as a motor. The inductances represent the coils of the stator

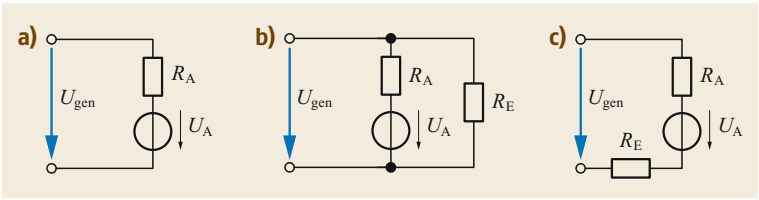

Fig. 26.73a–c Equivalent circuits for the three types of DC machines shown in Fig. 26.72. The inductances are not drawn because they have no influence on the DC behavior. R_A is the resistance of the rotor coil, and R_E that of the stator coil

There are three options to provide the energy to the stator to produce the magnetic field. Figure 26.72 shows that the simplest one (Fig. 26.72a) has a field supplied by an external current source or by permanent magnets. The stator field can also be powered by the same supply as the rotor. Its coil is then connected either in parallel (Fig. 26.72b) or in series (Fig. 26.72c). These three options can be represented by the equivalent circuits shown in Fig. 26.73. For the two options (a) and (b), the torque $M = |\boldsymbol{M}|$ can be calculated for a fixed voltage U_{gen} at different rotation frequencies f by using the relations between the torque and the current in the rotor ($M \approx I$), this current and the tension induced in the rotor coil ($I \approx (U_{gen} - U_A)$), and this tension and the frequency ($f \approx U_A$). As all these relations are linear, thus so is the dependence of the torque. The straight line in the M versus f plane can be fixed at the end points corresponding to the idle speed $f_0 = f(M = 0)$ and the starting torque $M_{start} = M(f = 0)$. The result

$$M = M_{start}\left(1 - \frac{f}{f_0}\right) \quad \text{(DC, parallel)} \qquad (26.119)$$

shows that the torque for this type of machine has a maximum at $f = 0$.

For the motor with the stator coils connected in series (Fig. 26.72c), one has $M \approx I^2$, because increasing the current increases the dipole moment of the rotor as well as the strength of the magnetic field of the stator. The other proportionalities remain as before, giving

$$M = M_{start}\left(1 - \frac{f}{f_0}\right)^2 \quad \text{(DC, series)}\,. \qquad (26.120)$$

Obviously, both types of DC motors have a maximum torque at $f = 0$. They are easy to start.

The rotor field influences the stator field, just as the stator field influences the rotor field. The first effect is wanted, while the second is not. Therefore, stators are usually equipped with *compensation coils* which are connected in series with the rotor. The fields of these coils can almost exactly cancel the field that is imposed on the stator.

Finally, two further points are worth noting. The maximum of the torque goes together with a maximum current through the machine. Therefore, large DC motors need an extra resistor placed in front of the rotor connection. This resistor limits the current while the motor is being started. When DC machines are used as generators, care has to be taken that some stator field is present whenever the rotor is forced to move. If no field is present, nothing will retard the rotor and only destruction will limit its rotational speed.

26.5.3 Asynchronous Machines

All DC engines need brushes, and these are subject to wear and tear. Designers of reliable machines may thus try to avoid the use of brushes altogether. AC machines like the one shown in Fig. 26.74 offer methods to do so. They can be found in electric cars, high-speed trains, and power stations. And their efficiencies are unmatched when powers exceed 10 kW (see Fig. 26.70).

The key idea leading to an asynchronous AC machine is the following: if a static field influences a rotating magnetic dipole, then a rotating field should influence a resting dipole. In fact, it should make it

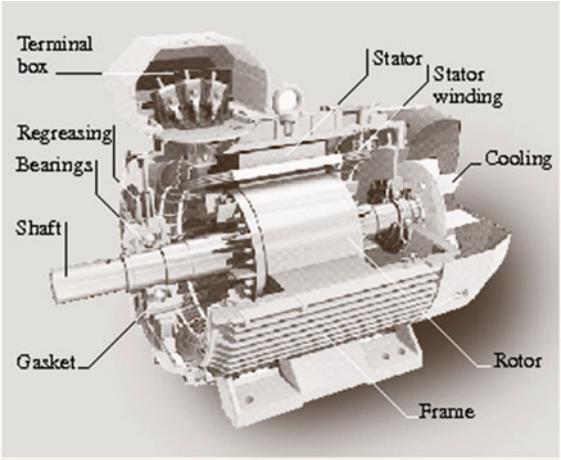

Fig. 26.74 Induction motor (asynchronous machine) (courtesy ABB)

move. Therefore, the key ingredient of an AC machine is a stator that can create a rotating field. Figure 26.75 shows that a three-phase network connected to three coils suffices to achieve this goal. The field will rotate with the same frequency as the AC supply currents.

A current loop placed in such a field will have a tension induced. When the loop is closed, this tension will lead to a current in the loop. The current will produce a magnetic dipole moment, and this will be subject to a torque due to the rotating field from the stator. The net effect is that there is a torque on an element that is not in any way electrically connected to the outside world. The current in the rotor is a result of induction. Therefore, this type of machine is also called an *induction machine*. Clearly, if the speed of the rotor coincides with the rotational speed of the field, there will be neither induction nor any forces. Because the function of the machine relies on the speeds being different, it is called an *asynchronous machine*. No brushes are needed for such a device.

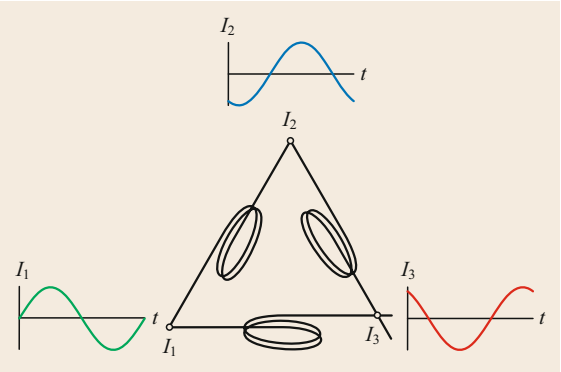

Fig. 26.75 Sketch of three coils in an AC network that produce a rotating magnetic field

As in the case of DC machines, the maximum torque can be achieved by superimposing various current loops with different azimuthal angles around the rotor axis. Joining them makes a metal cage, and such a cage can be found in almost all asynchronous AC machines.

The change of the magnetic flux $\mathrm{d}\Phi_\mathrm{B}/\mathrm{d}t$ only depends on the relative speed between the field and the rotor. The normalized difference of the angular speeds

$$s = \frac{f_\mathrm{field} - f_\mathrm{rotor}}{f_\mathrm{field}} = \frac{\omega_\mathrm{field} - \omega_\mathrm{rotor}}{\omega_\mathrm{field}} \qquad (26.121)$$

is called the *slip*. Therefore, the tension induced in a current loop may be expressed as a function of the slip and the voltage $U_{\mathrm{ind},0}$ which is induced when the rotor is locked (not rotating): $U_\mathrm{ind}(s) = sU_{\mathrm{ind},0}$.

The cage has an ohmic resistance R_A as well as a reactive resistance $L_\mathrm{A}(\omega_\mathrm{field} - \omega_\mathrm{rotor})$, according to the cage inductance L_A. Therefore, the current is related to the induced voltage via

$$U_\mathrm{ind} = \sqrt{R_\mathrm{A}^2 + (\omega_\mathrm{field} - \omega_\mathrm{rotor})^2 L_\mathrm{A}^2}\, I_\mathrm{A} \,. \qquad (26.122)$$

The current may now be expressed as a function of the slip. The result

$$I_\mathrm{A} = \frac{sU_{\mathrm{ind},0}}{\sqrt{R_\mathrm{A}^2 + \omega_\mathrm{field}^2 s^2 L_\mathrm{A}^2}} \qquad (26.123)$$

shows that, the closer the circular frequency of the rotor approaches that of the stator field, the smaller the current becomes.

The relation between the current I_A and the torque is complicated by the fact that the reactive resistance of the cage introduces an angle between I_A and U_ind. If that angle is 90°, the magnetic dipole moment of the rotor is parallel to the field of the stator and the torque is zero. In order to filter out the fraction of the rotor current that does contribute to the torque, I_A has to be multiplied by the cosine of the phase angle $\varphi = \arctan(s\omega_\mathrm{field} L_\mathrm{A}/R)$. According to (26.123), the torque then has the characteristic

$$M \approx \frac{s}{\sqrt{1 + \left(\frac{s\omega_\mathrm{field} L_\mathrm{A}}{R}\right)^2}} \cos\left[\arctan\left(\frac{s\omega_\mathrm{field} L_\mathrm{A}}{R}\right)\right] , \qquad (26.124)$$

which is also shown in Fig. 26.76. The value of the torque at $\omega_\mathrm{rotor} = 0$ is referred to as the *locked rotor torque*. Its nonzero value guarantees an easy start of such engines. The torque increases with the increasing circular frequency of the rotor, reaching a maximum called the *breakdown torque*, and then approaching zero for $\omega_\mathrm{rotor} = \omega_\mathrm{field}$. The *rated torque* (as stated in the

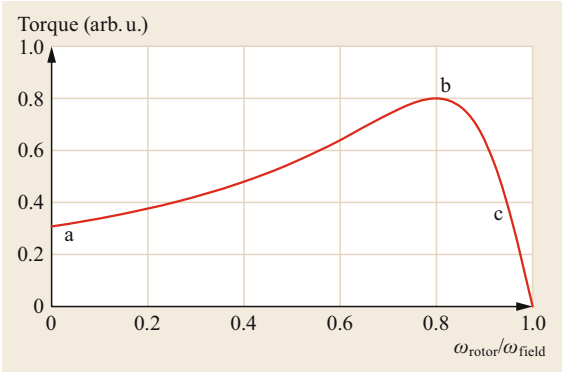

Fig. 26.76 Typical characteristics of the torque of an induction motor according to (26.124) in arbitrary units. Special values are the *locked rotor torque* (a), the *breakdown torque* (b), and the *rated torque* (c), which is about half the breakdown torque

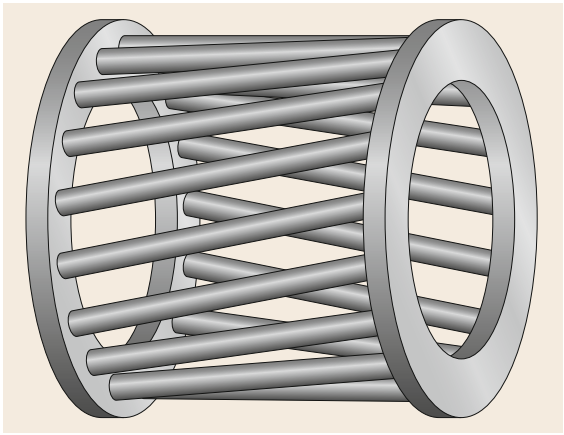

Fig. 26.77 Construction of a squirrel cage rotor: copper or aluminum bars are embedded in laminated iron and short-circuited by rings at the end. Usually, there are more bars than shown here

adverts) of the machine is in some cases half the breakdown torque, and in other cases one-third of it.

As in the case of DC machines, the magnetic field in all the parts has contributions from both the stator and the rotor. According to Lenz's rule, the rotor will always weaken the stator field. When the rotor is locked, the tension induced in the rotor reaches a maximum for a given circular velocity of the stator field. The magnetic field from the current in the rotor then almost suffices to cancel out the field from the stator. When ω_{rotor} approaches ω_{field}, the induced tension approaches zero and the field of the stator is hardly weakened.

Induction motors have excellent efficiencies, and are very reliable and easily maintained. As their torque changes direction when the slip exceeds the value one, they can also serve as electrical brakes to transform kinetic energy back into electrical energy. This makes them the first choice for high-speed trains, trams, and electric cars.

Application Example: Mechanical Construction of a Rotor

The construction of the rotor for an asynchronous machine is shown in Fig. 26.77. Obviously, it does not resemble any other devices which use magnetic fields. There are no windings. Instead, there is a cage embedded in laminated iron (only three slats are drawn in Fig. 26.77). So, the magnetic interaction entirely relies on a single current loop. The currents in the rotor are thus bound to be large. The reason for the absence of windings is the need to have as little inductance as possible in the rotor. According to (26.124), the torque approaches its maximum as the phase angle $\varphi = \arctan(s\omega_{field}L_A/R)$ tends to zero. Therefore, in this case, one loop is better than many loops. A closer look at Fig. 26.77 also reveals that the bars forming the cage are skewed with respect to the rotor's axis. This is a measure to minimize the mechanical oscillations of the cage. The source of these oscillations is the oscillating magnetic attraction of the cage bars by the stator coils. The bars are embedded in laminated iron. The lamination is such that the magnetic field does not traverse the oxide between the sheets. In this manner, the magnetic field strength is maximized while the eddy currents are minimized.

The manufacturing process starts by fixing a bundle of laminated iron (dynamo sheet metal) on an axis. Each of the sheets has a circular shape with notches at the rim. At the end, the bars of the cage have to be placed in the notches. This may be achieved by casting of liquid aluminum or by inserting copper bars (casting copper is difficult). Casting gives more magnetic flux, while copper bars have better conductance.

26.5.4 Synchronous Machines

Some 99% of electric power comes from synchronous generators. In synchronous machines such as that shown in Fig. 26.78, the frequency of the current is a multiple of the angular frequency of the rotor. Therefore, synchronous motors are used when the mechanical speed is to be determined electrically, while synchronous generators are used in the complementary case. For this very reason, the largest electrical engines known, AC generators in power stations, are synchronous ones. Synchronous motors are used in industrial applications and in the French high-speed train *train à grande vitesse* (TGV).

The dipoles rotating in an AC generator need to be powered by a current of almost constant strength. This

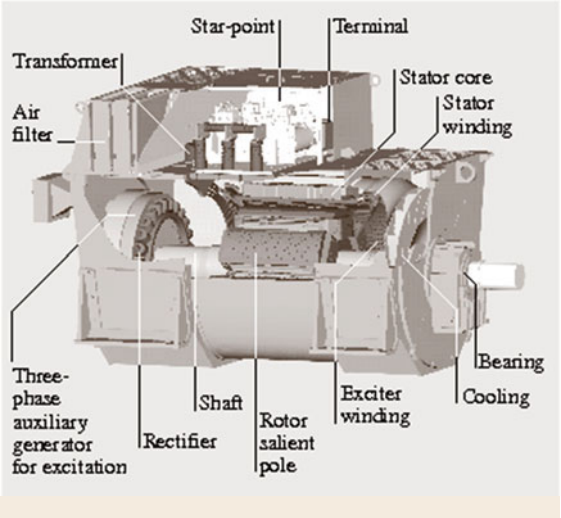

Fig. 26.78 Synchronous generator (courtesy ABB)

can be achieved using mechanical contacts, or by induction. For large machines, the latter is preferred as it causes no frictional losses. The current induced in the rotating coils needs to be rectified by power electronics.

The magnetic flux through a current loop placed next to a rotating dipole oscillates with the dipole's frequency of rotation. An alternating current will thus flow in the loop according to the law of induction. Synchronous generators use this effect by placing windings adjacent to the rotor. The currents through such windings are those delivered by large power stations. Clearly, these windings need to be placed inside laminated iron. In this way, the magnetic flux is maximized and eddy currents are minimized.

The number of dipoles (or pole pairs) of the stator usually equals the number the rotor dipoles. The smaller the angular velocity of the rotor, the larger the number of magnetic poles. In a hydroelectric power station, there may be up to 40 dipoles on the rotor, while generators attached to a steam turbine often have only one dipole. Rotors with two dipoles are found in nuclear power stations due to the mechanical limitations of the materials used. Turbines delivering up to $P = 1.3\,\mathrm{GW}$ of power would simply disintegrate at 3000 rpm (50 Hz current) or even 3600 rpm (60 Hz current). The mechanical stability of the turbine blades is also a limiting factor of the frequency instabilities of supply networks. It is turbines that really need stable frequencies rather than the users of the currents.

The Steering of a Synchronous Generator

In a synchronous generator, the tension and the current and the phase angle between them may be varied during operation. The way this is done is identical for any number of dipoles. For simplicity, a single dipole is assumed in this section. Also, it is assumed that the magnetic fields of the rotor and the stator may simply be added (linear superposition). Usually this is a very good approximation.

The parameter that may be influenced in the most obvious manner is the tension. Suppose there is no load on the coils next to the rotating dipole. Then, the magnetic field in both the rotor and the stator is entirely determined by the rotor. Starting from a dipole coil with no current, the tension induced will rise in proportion to this current until the iron reaches the state of saturation. From then on, the magnetic field and consequently the tension induced in the stator coils rises with a slope which is less steep, 1% of that for small voltages. Such saturation is thus to be avoided under all circumstances.

As soon as there is a load on the generator, the magnetic field acquires a contribution from the stator coils in addition to that from the rotating dipole. The rotor induces a harmonically oscillating tension in the stator coils. It thus acts like an AC voltage source, because both the frequency and magnitude of the voltage are determined by the rotor and not by the stator. As the currents through the stator coils oscillate, they produce an oscillating magnetic field as well. This field will influence the coil as any other coil by introducing an inductance. This situation is sketched in Fig. 26.79. Also shown in the figure is a resistance R to account for the finite conductivity of the wire the stator coil is made of.

According to Fig. 26.79, the tension delivered by one stator coil

$$\underline{U}_{\mathrm{gen}} = \underline{U}_{\mathrm{ind}} - (R + \mathrm{j}\omega L)\underline{I}_{\mathrm{L}} \tag{26.125}$$

contains the *synchronous reactance* $X_{\mathrm{d}} = \omega L$.

The power delivered by one coil can be calculated from (26.125) for a given load impedance as shown in Fig. 26.80. $\underline{Z} = R_{\mathrm{L}} + \mathrm{j}X_{\mathrm{L}}$. The result for the apparent power,

$$\begin{aligned}\underline{S} = \frac{1}{2}\underline{U}_{\mathrm{gen}}\underline{I}_{\mathrm{L}}^{*} &= \frac{1}{2}\hat{U}_{\mathrm{ind}}^{2}\left(\frac{R_{\mathrm{L}} + \mathrm{j}X_{\mathrm{L}}}{(R+R_{\mathrm{L}})^2 + (\omega L + X_{\mathrm{L}})^2}\right) \\ &= U_{\mathrm{ind,eff}}^{2}\left(\frac{R_{\mathrm{L}} + \mathrm{j}X_{\mathrm{L}}}{(R+R_{\mathrm{L}})^2 + (\omega L + X_{\mathrm{L}})^2}\right)\end{aligned} \tag{26.126}$$

can be separated into the power P and the reactive power Q. Neglecting the ohmic resistance of the stator coil, one gets

$$\begin{aligned}P &\approx U_{\mathrm{ind,eff}}^{2}\left(\frac{R_{\mathrm{L}}}{R_{\mathrm{L}}^2 + (X_{\mathrm{d}} + X_{\mathrm{L}})^2}\right) \\ Q &\approx U_{\mathrm{ind,eff}}^{2}\left(\frac{X_{\mathrm{L}}}{R_{\mathrm{L}}^2 + (X_{\mathrm{d}} + X_{\mathrm{L}})^2}\right),\end{aligned} \tag{26.127}$$

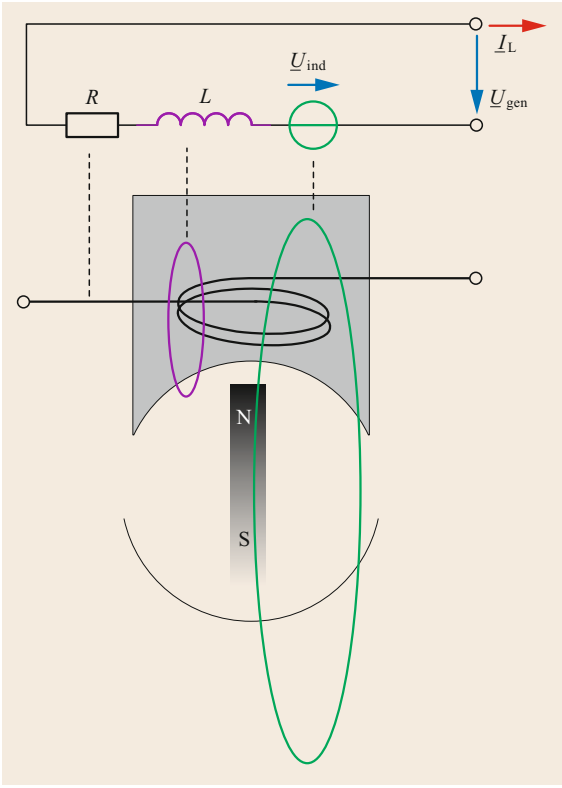

Fig. 26.79 Contributions to the circuit diagram describing one phase of a synchronous generator. The load current is $\underline{I}_L$, while $\underline{U}_{gen}$ is the voltage seen at the terminals

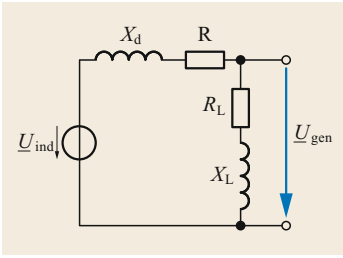

Fig. 26.80 Replacement circuit diagram of the synchronous generator shown in Fig. 26.79 when connected to a load impedance $R_L + X_L$

where, again, $U^2_{ind,eff}$ is a shorthand notation for $\hat{U}^2_{ind}/2$. For a generator with three equally loaded stator coils, the power P calculated by (26.127) is one-third of the mechanical power taken by the generator.

Figure 26.79 shows that the flux through the stator coil reaches a maximum when it is faced by the north pole of the rotor dipole. Then, most of the field lines traverse the stator coil. This situation resembles that shown in Fig. 26.69. Accordingly, the induced voltage depends on the angle θ_P between the dipole and the field of the stator. Because the value of this angle turns out to be crucial for the modes of operation of a synchronous machine, it has been given a name of its own. It is called the *polar wheel angle*.

The field produced by a stator coil is strongest when the current is at its maximum. The polar wheel angle may therefore be regarded as a measure of the delay Δt of the current maximum with respect to the point in time when the dipole field points at the stator coil: $\theta_P = \omega\Delta t$.

The modes of operation of a synchronous machine can now be related to the value of the polar wheel angle as follows:

- $\theta_P = 0$: There are no forces between the rotor and stator. Hence, neither is there any transfer of mechanical power into electric power or vice versa. The machine appears to be idle. It may, however, change the phase angle between the voltage and the current.
- $0 < \theta_P < \pi/2$: The stator field slows down the rotor. In this manner, mechanical energy is transformed into electrical energy. The machine operates as a generator. The larger the polar wheel angle, the larger the torque, and the greater the power transfer.
- $\pi/2 < \theta_P < \pi$: The field of the stator slows down the rotor. However, the slightest disruption will weaken the retarding force. Even the connection of another electrical consumer may be perturbative enough. If the mechanical power input remains unchanged, the angular speed of the rotor will rise in a manner that can no longer be controlled. In the case of a large power input, the result may well be complete destruction of the machine.
- $\theta_P = \pi$: This is the most unstable mode of operation. It corresponds to attempting to balance a compass needle with its north pole pointing downwards somewhere close to the north pole of the Earth.
- $\pi < \theta_P < 3\pi/2$: The machine is in an unstable motor mode.
- $3\pi/2 < \theta_P < 2\pi$: The field of the stator is slightly ahead of the rotor's field. The stator field drags the rotor. The machine thus acts as a motor. A slight additional mechanical load will increase the electromagnetic torque, as required for stable operation.

Power stations are usually run with polar angle values below $\theta_P < 80°$. In this manner, extra electrical loads will not make the machine leave the stable mode of operation.

Although the value of the polar wheel angle is crucial for the machine's operational mode, it is very difficult to measure. Next it will be shown which angle can be measured directly at the terminals of the ma-

chine, and what it means, viz. the angle between the tension and the current, $\varphi_{U_{\text{gen}}} - \varphi_I$.

Comparing the voltages $\underline{U}_{\text{ind}}$ and $\underline{U}_{\text{gen}}$ as shown in Fig. 26.80 gives the phase angle between the two voltages,

$$\varphi_{U_{\text{gen}}} - \varphi_{U_{\text{ind}}} = \arctan\left(\frac{X_{\text{L}}(R+R_{\text{L}}) - R_{\text{L}}(X_{\text{L}}+X_{\text{d}})}{R_{\text{L}}(R_{\text{L}}+R) + X_{\text{L}}(X_{\text{L}}+X_{\text{d}})}\right). \quad (26.128)$$

Usually, the ohmic resistance R of the stator winding can be neglected. The resulting approximation

$$\varphi_{U_{\text{gen}}} - \varphi_{U_{\text{ind}}} \approx \arctan\left(\frac{-R_{\text{L}}X_{\text{d}}}{R_{\text{L}}^2 + X_{\text{L}}(X_{\text{L}}+X_{\text{d}})}\right) \quad (26.129)$$

shows that ohmic loads correspond to small phase angles. Inductive loads give negative values for $\varphi_{U_{\text{gen}}} - \varphi_{U_{\text{ind}}}$, while large capacitive loads ($(X_{\text{L}}+X_{\text{d}}) < 0$) give positive values.

The phase angle $\varphi_{U_{\text{ind}}}$ may also be related to the phase angle of the current. According to Fig. 26.80, one has

$$\varphi_Z = \varphi_{U_{\text{ind}}} - \varphi_I = \arctan\left(\frac{X_{\text{d}}+X_{\text{L}}}{R+R_{\text{L}}}\right). \quad (26.130)$$

The phase angle that can be measured can now be expressed as a function of the impedances of the circuit, because the equation

$$\varphi_{U_{\text{gen}}} - \varphi_I = (\varphi_{U_{\text{gen}}} - \varphi_{U_{\text{ind}}}) + (\varphi_{U_{\text{ind}}} - \varphi_I) \quad (26.131)$$

can be worked out using (26.129) and (26.130).

Powering Three-Phase Alternating-Current Networks

If the stator contains three coils symmetrically placed around the rotor, the tension induced in these coils will have phase angles shifted by 120° with respect to each other. Connecting them in series to form a triangle-type network as sketched in Fig. 26.68 will ensure equal current magnitudes. In this case, the stator produces a rotating $\boldsymbol{B}$ field of almost constant magnitude and angular velocity. These properties are key ingredients for the safe operation of high-power electrical generators. A constant field strength implies a constant torque on the rotor. And a $P = 10^9$ W steam turbine cannot stand anything else.

For the same reason, connecting a power generator to a network requires that the following conditions be met:

- The frequency of the generator must have almost the same value as the network frequency. In fact, it should be slightly higher, as it will be reduced as soon as a load is applied. This can only be achieved by steering the mechanical part of the generator.
- The amplitude of the generator voltage $\hat{U}_{\text{gen}}$ must match the network voltage. This can be achieved by varying the current in and thus field strength of the rotor.
- The phase angle between the generated voltage and the network voltage must be zero.

Once the generator has been connected to the network, the current in the rotor and the load on the stator coils can be increased. Increasing the load current strengthens the stator field, while the latter increases the retarding torque on the rotor. Nevertheless, the frequency of rotation will not change. Instead, because of $\boldsymbol{M} = \boldsymbol{\mu} \times \boldsymbol{B} \rightarrow |\boldsymbol{M}| \approx \sin\theta_{\text{P}}$, the polar wheel angle will increase. The value for the polar angle can be influenced during operation by varying the current that forms the rotor's dipole current: the stronger the dipole, the smaller the polar wheel angle. The polar angle may never approach 90°, because then the machine would become unstable.

State-of-the-art generators have efficiencies beyond 95%. So, the electrical power generated almost equals the mechanical power used. Thus, increasing the mechanical torque will increase the electrical power in almost the same manner as the mechanical power $-P_{\text{electric}} \approx P_{\text{mech}} = M\omega$.

A special feature of synchronous generators appears if the generator is attached to a large network with many power stations. Then, the tension at the terminals of the generator is determined by the network, rather than by the generator. This has a useful practical implication, as can be seen by dividing (26.125) by $\mathrm{j}\omega L$. The result

$$\underline{I}_{\text{L}} = \frac{1}{\mathrm{j}\omega L}\left(\underline{U}_{\text{gen}} - \underline{U}_{\text{ind}}\right) \quad (26.132)$$

shows that the sign of the imaginary part of the current may be chosen by having $\underline{U}_{\text{ind}}$ larger or smaller than the tension fixed by the network, $\underline{U}_{\text{gen}}$. In other words, the sign of the angle between the current and the tension may be chosen by choosing an appropriate rotor current. This characteristic introduces a new application of synchronous generators, i.e., to reduce the reactive power oscillating in supply networks, because their operation can be chosen to be inductive or capacitive. Supplying only reactive power may turn it into a pure *phase shifter*. Phase shifter operation can be achieved by powering the generator with an synchronous motor attached to the same network.

Finally, a sudden change of the electric load current will give a little *kick* to the polar wheel angle. If no countermeasures are imposed, the consequence will be a polar wheel angle oscillating around the value for which the electrical torque matches the mechanical torque. An oscillating polar angle corresponds to a ripple in the rotor's movement. For a gigawatt machine, this is a highly undesirable effect. For this reason, shorted extra windings are placed on the rotor. These extra windings act like a small asynchronous machine. They produce torque if, and only if, there is a mismatch between the stator's frequency and the rotor's frequency. In this way, they damp any oscillations of the polar wheel angle.

When used as motors, synchronous machines are difficult to start, as the operation begins from a not at all synchronous state. Therefore, a synchronous motor attached to an AC network needs an auxiliary starter motor. Electronically steered variable-frequency networks offer an alternative by ramping up the AC frequency. The combination of the motor and the electronic control is called an *electronically controlled motor* and is becoming increasingly popular.

26.6 Energy Storage

In this section, various techniques for storing energy are discussed, including the use of pumped water, double-layer capacitors, lead–acid accumulators, and zinc–air batteries. With hydrogen being a candidate for the storage of large amounts of energy, the production of electricity in a fuel cell will mark the end of this section.

26.6.1 Introductory Remarks

Storing electrical energy is a key challenge for the development of portable devices (smart phones, etc.), electric mobility, and the introduction of renewable sources into power supply chains. Consequently, there is hardly any field of engineering that is as dynamic as this one. Also, it requires cooperation between mechanical and electrical engineers, as well as chemists and physicists. Figure 26.81 shows that a large variety of techniques are presently under investigation, including purely mechanical ones such as spinning wheels (*flywheel energy storage*) or compressed air.

Some storage techniques are directly related to electrical engineering. Double-layer capacitors are particularly suitable for applications in which frequent and

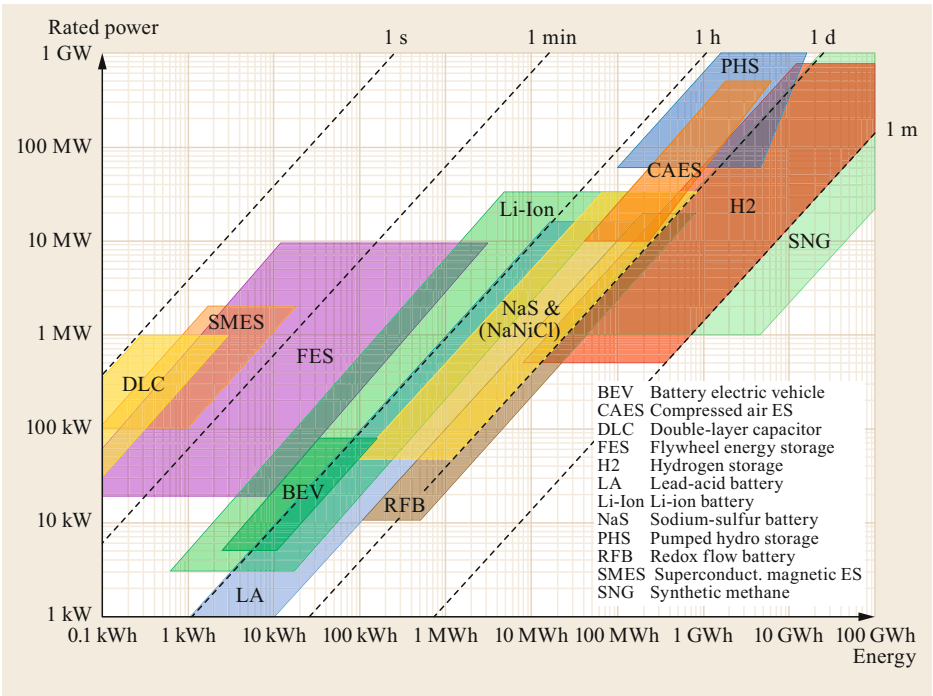

Fig. 26.81 The potential of various storage techniques according to [26.19]. The vertical axis shows the rated power, while the horizontal axis indicates the total amount of energy that may be stored in the future. (Figure by Tom Smolinka, Fraunhofer Institut für solare Energiesysteme)

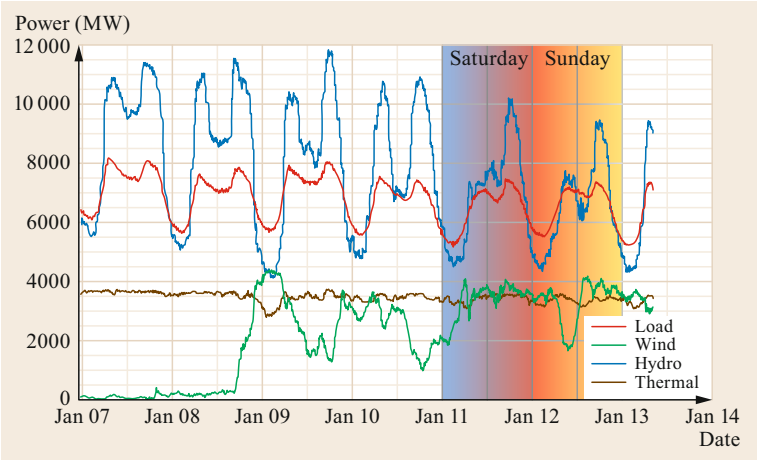

Fig. 26.82 An example of the balance of power being used (*red*) and produced by wind (*green*), water (*blue*), and conventional power houses (brown) (data published by Bonneville Power Administration, www.bpa.gov)

fast charging and discharging is needed. Batteries and their rechargeable variants (accumulators) are the most common devices when mobility is required. Today, almost every car is equipped with a lead acid accumulator (labeled LA in Fig. 26.81).

At the top end of the amount of storable energy, electromechanical techniques such as pumped hydro storage (labeled PHS in Fig. 26.81) or electrochemical techniques can be found. Hydrogen production via steam reforming from hydrocarbons, electrolysis, or thermolysis combined with fuel cells (H2 in Fig. 26.81) has enormous potential. But the cost-effective storage of large amounts of hydrogen is an outstanding problem. A possible solution is to extend hydrogen production by a second step: the synthesis of methane via

$$2H_2 + CO_2 \rightarrow CH_4 + O_2 \qquad (26.133)$$

Methane produced in this manner is easy to store, and the infrastructure already exists. Gas supply networks may thus serve as storage devices for energies in the 100 GWh regime. Unfortunately, at present, the process (26.133) runs at energetic efficiencies near the 1% level. So, the area marked SNG (synthetic methane) in Fig. 26.81 indicates a hope for the future.

26.6.2 Mechanical Storage: Water

This storage technique is both old and up to date. It is old because it consists of components that have been around for more than a century. And it is up to date because, to this day, its capacity is unmatched. Driving supply networks without water turbines is unthinkable, as can be deduced from Fig. 26.82. While power generation by thermal engines needs to be kept constant in time for good efficiency, both the load and contribution of wind turbines suffer from fluctuations with very limited control options. These fluctuations are most easily compensated by changing the contribution from hydro power.

The amount of energy that can be stored by pumping water is limited by the shape of the surface of the Earth and by the number of acres one is willing to dedicate to such energy storage. Figure 26.83 shows a storage plant close to Hohenwarte, Germany. Up to $V = 3 \times 10^6\,\mathrm{m}^3$ of water can be pumped to a height of 304 m. This corresponds to a gain of $\Delta W = mgh \approx 9 \times 10^{12}\,\mathrm{J}$, or $\Delta W = 2.5\,\mathrm{GWh}$. The maximum power of 320 MW can thus be delivered for roughly 7.5 h.

This example shows that such plants are suited to overcome energy shortages in the network that last for periods of several hours. Their commercial use is mainly to deliver power at peak usage times. Discussions are also ongoing concerning the use of such plants as buffers for energy from renewable sources, such as

Fig. 26.83 Energy storage plant near Hohenwarte, Germany. The lake is filled with water if there is more power in the network than is needed. During times of shortage, the water is given back to the River Elbe, which can be seen at the bottom of the image (Photo: Vattenfall)

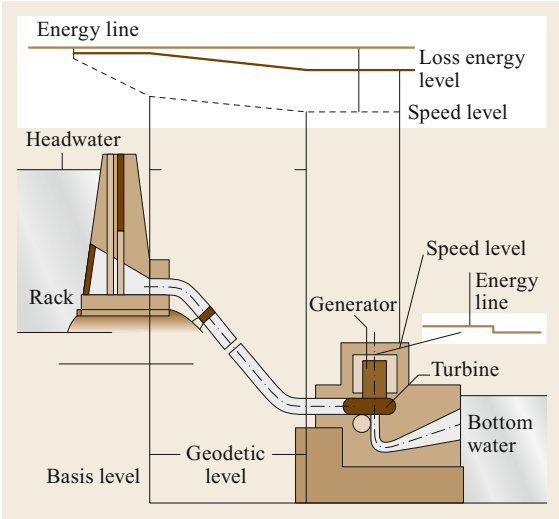

Fig. 26.84 Cross section through a water storage plant

wind energy or energy from solar cells. The time span for the delivery of power would then increase from hours to weeks. The energy to be stored would have to rise by at least three orders of magnitude, meaning that entire valleys in mountainous areas would have to be turned into water storage reservoirs. The limits on the amount of energy stored in this manner are not technical but rather set by the acceptance of the associated environmental impact.

26.6.3 Electric Storage: Supercapacitors

Supercapacitors, also branded as *gold caps*, have energy densities in the range up to 30 Wh per kg. These large values of capacitances are achieved for two reasons. Firstly, their surface area is made extremely large by using active carbon as the electrode material. Secondly, the distance between the positive and negative charge may be shrunk to less than the diameter of a single atom.

Supercapacitors are double-layer capacitors, where a capacity is formed between the anode and a electrolyte, and another between the electrolyte and the cathode. Short circuits are avoided by placing a separator between the electrodes. Ions can pass through this separator.

Figure 26.85 shows the situation at the surface of the cathode if the capacitor is charged. Negative charges (i.e., electrons) find their way right beneath the surface of the cathode. Many of them attract water molecules, as these are electrical dipoles. Some negative charges make positively charged ions (cations) form contacts directly with the surface of the cathode. In this case, they may be loosely bound by van der Waals forces, chemisorption, or simply electrostatics. Often, the positive ions remain surrounded by water molecules, even if adsorbed by the cathode. They are not mobile, but the adsorbing forces are even smaller. The term "adsorption" is used whenever a binding process is limited to taking place at a surface. If the material under the surface is involved, the term "absorption" is used. The plane above the cathode formed by the immobile ions is often referred to as the *outer Helmholtz layer* or the *Stern layer*. It is indicated by a dashed line in Fig. 26.85.

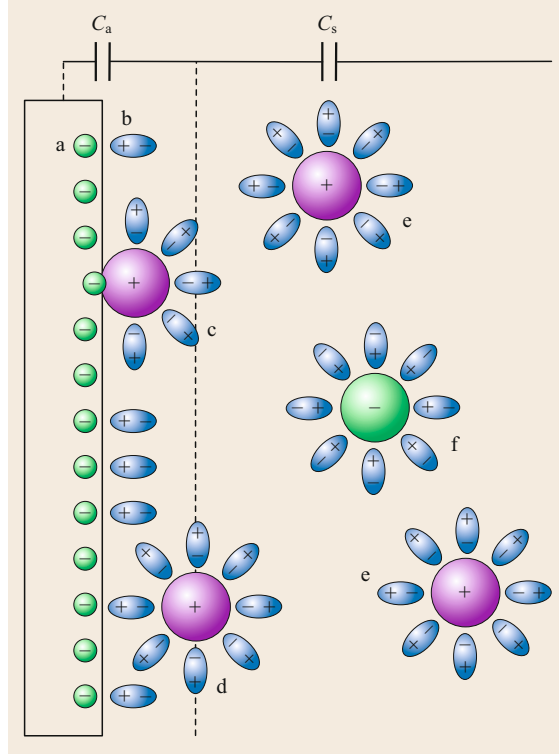

Fig. 26.85a–f Schematic view of the cathode of a supercapacitor. The negative charges **(a)** are directly placed under the surface of the cathode material (carbon). They adsorb water molecules **(b)**, cations **(c)**, and cations surrounded by water molecules **(d)**, thus forming a capacitor C_a. The sum of all these charges is still negative. It forms one electrode of another capacitor C_s with the cations solved in the liquid **(e)**. At large distances, these are balanced by negative ions **(f)**

If all the negative charges were balanced by ion adsorption, one would expect a rather constant value for the capacitance. The similarity to a capacitor with electrons moving on both electrodes seems obvious. In experiments, however, supercapacitors show a strong dependence of the capacitance on the ion concentration, surface charge, and temperature. This can be explained by assuming that only some fraction of the charges on the cathode are neutralized by adsorption of positively

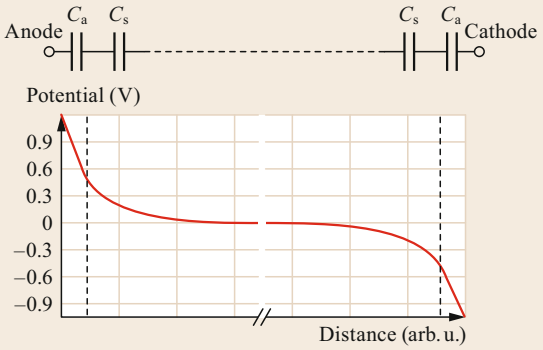

Fig. 26.86 Potential characteristics of a double-layer supercapacitor and the corresponding circuit schematic diagram. The steepest part of the characteristic is between the electrodes and the outer Helmholtz layers (*dashed line*). The shallowing off reveals the effect of diffusion within the liquid

charged ions. Other ions have sufficient thermal kinetic energy to move away from the cathode. So, only at a distance which is much larger than the distance to the outer Helmholtz layer are all the negative charges balanced by cations. The charge imbalance between the outer Helmholtz layer and the liquid far from the cathode will grow the more charge there is on the cathode. This effect is often modeled using a *pseudocapacitor* C_s between the immobile charges and the charges moving about within the solution. Here, the term "pseudocapacitor" refers to the fact that charge is separated (i.e., as in a capacitor), but not strictly, only statistically due to an equilibrium of Brownian motion and electrostatics (i.e., not really like a capacitor). The potential characteristic is sketched in Fig. 26.86, together with the corresponding circuit diagram. The steepest part of the characteristic is in the region where the ions are attached to the electrode's surfaces, either directly or via water bridges. The less steep parts are the result of Brownian motion and electrostatic attraction. Supercapacitors are not to be used for AC applications. Also, with self-discharge times measured in weeks, they cannot replace batteries if a constant supply is needed for years. They are, however, the first choice if large amounts of power are needed for a limited time (see the example from Formula 1 racing below).

Application Example: A Formula 1 Energy Recovery System (ERS)

Formula 1 cars use *energy recovery systems* (ERSs) to increase their energetic efficiency. According to the rules of the sport, such systems are limited to deliver a power of $P_{max} = 120\,\text{kW}$ for at most 33 s. The energy may be stored in supercapacitors, as shown in

Fig. 26.87 Supercapacitors (Photo: Capcomp GmbH)

Fig. 26.87. Each of them has a withstand voltage of 2.7 V, a nominal capacitance of $C = 3\,\text{kF}$, and a weight of 535 g. For the design of the car, it is important to know for how long the energy of one capacitor suffices and the extra weight needed for a given time at the maximum power.

According to (26.46), the energy stored in a single capacitor is $W = 0.5 \times 3000\,\text{F} \times (2.7\,\text{V})^2 \approx 22\,\text{kJ}$. Because $P = W/t$, delivering a constant power of $P = 120\,\text{kW}$ will empty the capacitor after a time

$$t = \frac{W}{P} \approx \frac{22\,\text{kJ}}{120\,\text{kW}} \approx 0.18\,\text{s}\,.$$

This value is quite realistic, because two factors approximately cancel. The huge variation of the values of C due to production uncertainties, usually quoted as $-20\% + 80\%$, allows one to select the best capacitors from large samples (as long as money does not matter). At the same time, the tension at the connections of the capacitor tends to zero as it is emptied, making the last 30% (as a rule of thumb) of the total energy unusable. Thus, to store sufficient energy for 10 s of full ERS power, more than 50 capacitors with a weight of about 30 kg are needed. Achieving the maximum allowed time of 33 s would require an extra weight of roughly 100 kg.

Heating up is a major issue. For an F1 car, one will therefore store the energy in stacks of capacitors connected in series, increasing the voltage and simultaneously reducing the total capacitance according to (26.48). As the power is $P = UI$, such a stack delivers the power with the smallest possible current, thus minimizing losses in wires, connections, etc. The maximum voltage allowed in an ERS is limited to $U = 1\,\text{kV}$.

26.6.4 Electrochemical Storage: Batteries, Accumulators, and Fuel Cells

The basis of all batteries is the *galvanic cell*, in which redox reactions are used to make electrical current flow. In brief: ions transport electrons from one electrode

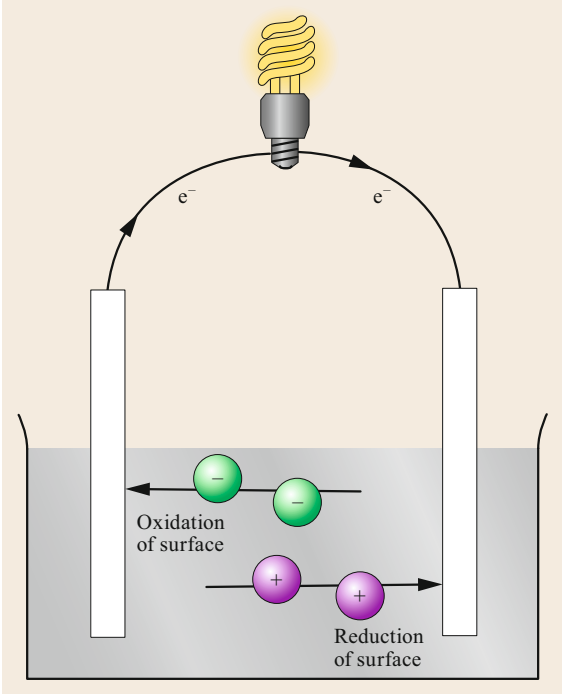

Fig. 26.88 Galvanic cell. In the most general case, there are positive and negative ions in a solution that react with solid bodies. Where the negative ions oxidize, a cathode forms, while the reduction by positive ions makes an anode. When connected, a current flows until the ions are used up

placed in an electrically conducting liquid to another one. If the electrodes are connected by a conductor, as shown in Fig. 26.88, the electrons will find their way to the other electrode. The electrode emitting electrons into the electric circuit is the cathode, while the other one is the anode. The voltage between the electrodes can be calculated in two steps; first the potential of one electrode and the liquid is calculated, then the other. The voltage of the galvanic cell is the difference of both potentials. The potential of an electrode that is reduced by accepting electrons from the liquid is given by a potential V_0 (often called E^0 in books on chemistry) as measured under standard conditions, several constants, and the concentration α of active molecules relative to a concentration of 1 mol/L. For temperatures near 20 °C and normal pressure, it may be calculated as

$$V = V_0 - \frac{0.05916\,\mathrm{V}}{n} \log_{10}\left(\frac{\alpha_{\mathrm{products}}}{\alpha_{\mathrm{reactants}}}\right), \quad (26.134)$$

where n is the number of electrons transferred per molecular reaction. In (26.134), known as the Nernst equation, α is set to 1 mol/L for solid bodies and for water by convention (for details, see [26.20]). The value 0.05916 comes from multiplying various natural constants.

Galvanic cells produce electrical energy, whenever the chemical reactions taking place between the electrodes and the solved substances are exothermic. Most of the energy released by the reaction is then transformed into electrical energy. The rest heats up the cell. There are also cells that use endothermic reactions. They are called *electrolytic cells*. These cells require electrical energy to be used by the cell, so the light bulb in Fig. 26.88 would have to be replaced by some kind of electrical generator. If a cell can be used as both a galvanic cell and an electrolytic cell, it may serve as an *accumulator*.

Lead–Acid Battery

The lead–acid battery is, despite its name, an accumulator, as it can be recharged. It is the workhorse of the automotive world. It offers energy densities of $W/m \approx 30\,\mathrm{Wh/kg}$ and is suited for high currents. It relies on the simultaneous oxidation of lead to form lead sulfate and the reduction of lead oxide, also to form lead sulfate. A fully charged battery has a lead cathode, lead oxide as its anode, and a high concentration of sulfuric acid. A completely discharged battery has both electrodes consisting of lead sulfate and a very low concentration of sulfuric acid.

Before the redox reactions can start, sulfuric acid has to deliver ions according to

$$2\,H_2SO_4 \rightarrow 4\,H^+ + 2\,SO_4^{2-} \quad (26.135)$$

Oxidation of lead produces two electrons according to

$$Pb + SO_4^{2-} \rightarrow PbSO_4 + 2\,e^- \quad \text{(oxidation)} \quad (26.136)$$

thus turning this piece of lead into a *cathode*. Since one atom of lead replaces two hydrogen atoms in H_2SO_4, each lead atom loses two electrons in this reaction ($Pb \rightarrow Pb^{2+}$). At the same time, reduction of lead oxide according to

$$PbO_2 + SO_4^{2-} + 4\,H^+ + 2\,e^- \rightarrow PbSO_4 + 2\,H_2O \quad \text{(reduction)} \quad (26.137)$$

needs exactly those two electrons, thus turning the lead oxide into an *anode*. Because oxygen has a valence of 2, the lead oxide gains two electrons ($Pb^{4+} \rightarrow Pb^{2+}$). If the lead and lead oxide are connected by a wire, electrons will pass through this wire and the current may be

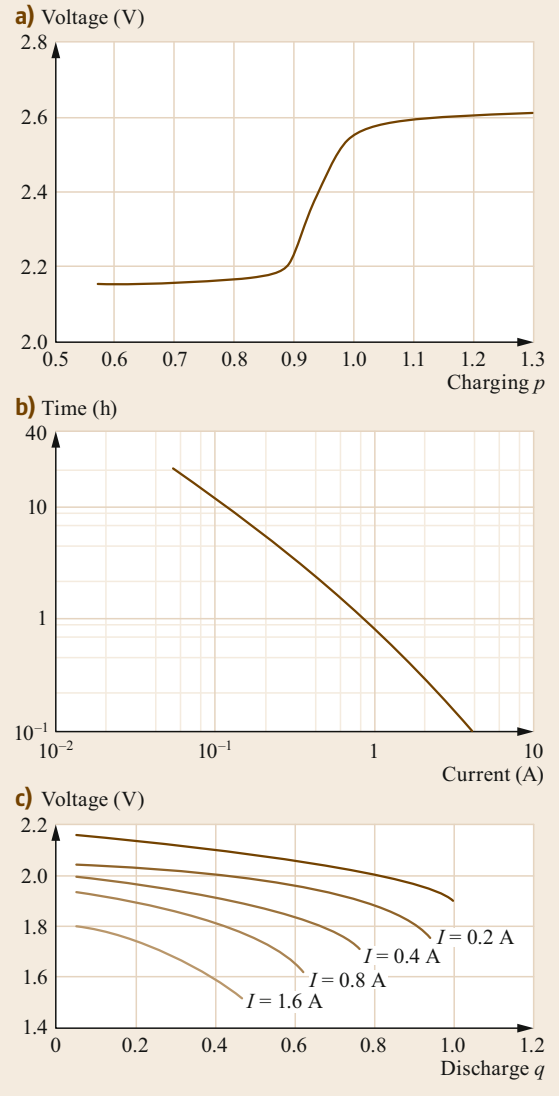

Fig. 26.89a–c Characteristics of lead–acid batteries: **(a)** charge process; **(b)** discharge time of one cell related to discharge current; **(c)** discharge characteristic of a cell at 15 °C

used. If all substances are given in a concentration of 1 mol/L, the log terms in (26.134) vanish, and one gets a cell voltage [26.21] of

$$V_{\text{cell}} = +V_0(\text{reduction}) - V_0(\text{oxidation}) = 1.69\,\text{V} - (-0.36\,\text{V}) = 2.05\,\text{V}\,. \quad (26.138)$$

One may look at the overall reaction

$$\text{Pb} + \text{PbO}_2 + 2\,\text{SO}_4^{2-} + 4\,\text{H}^+ \rightarrow 2\,\text{PbSO}_4 + 2\,\text{H}_2\text{O}$$
$$\text{or} \quad \text{Pb} + \text{PbO}_2 + 2\,\text{H}_2\text{SO}_4 \rightarrow 2\,\text{PbSO}_4 + 2\,\text{H}_2\text{O} \quad (26.139)$$

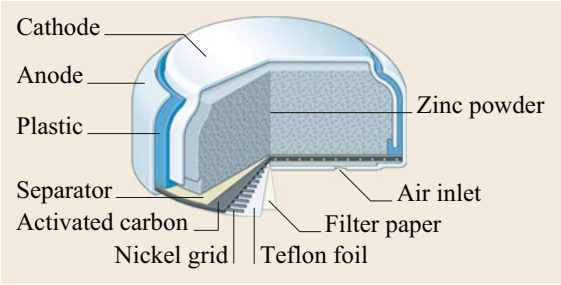

Fig. 26.90 Sketch of a zinc–air battery as used in hearing aids

to determine the voltage for different concentrations

$$V = 2.05\,\text{V} - \frac{0.05916\,\text{V}}{2}\log_{10}\left(\frac{\alpha^2_{\text{PbSO}_4}\alpha^2_{\text{H}_2\text{O}}}{\alpha_{\text{Pb}}\alpha_{\text{PbO}_2}\alpha^2_{\text{H}_2\text{SO}_4}}\right). \quad (26.140)$$

When setting the activities of solids and water to one, the result

$$V = 2.05\,\text{V} - \frac{0.05916\,\text{V}}{2}\log_{10}\left(\frac{1}{\alpha^2_{\text{H}_2\text{SO}_4}}\right) = 2.05\,\text{V} + 0.05916\,\text{V}\log_{10}\left(\alpha_{\text{H}_2\text{SO}_4}\right) \quad (26.141)$$

shows that the voltage depends only on the concentration of the acid. This simple relation offers an easy test of the state of charge. Therefore, the concentration of sulfuric acid is a measure of the charge left in a lead–acid battery. It can be checked by measuring the specific weight of the liquid: the heavier the liquid, the more charged the battery. Commercially available lead–acid accumulators are said to have concentrations up to 6 mol/L, corresponding to a density of roughly 1.34 kg/L.

If the lead–acid accumulator is connected to a generator, the reactions (26.136) and (26.137) are reversed, enhancing the concentration of sulfuric acid and the energy content of the cell. The charging process can be seen in Fig. 26.89. The electrolyte gas starts to appear at above 2.4 V, and charging should be stopped at 2.65 V per cell. During discharging, the minimal voltage should not be below the cut-off of 1.8 V. The usable capacity is a function of the discharge current. Figure 26.89b shows the discharge time as a function of the current for a single cell, on a logarithmic scale. The discharge characteristics of a single cell as a function of the discharge rate with the discharge current as a parameter are presented in Fig. 26.89c. Lead–acid storage batteries are sometimes used as storage devices in the field of electricity supply. Then the battery is used for load leveling, frequency control, provision of instantaneous reserve, or voltage control.

Lead–acid accumulators are rather heavy. A significant weight reduction can be achieved by using

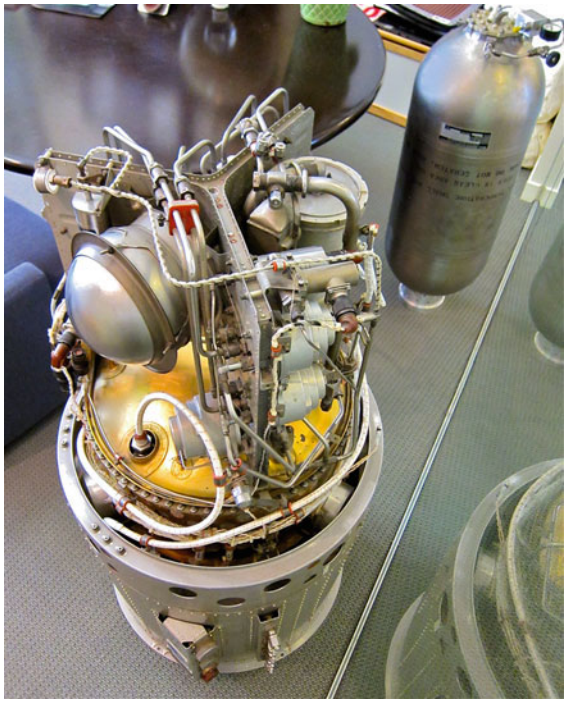

Fig. 26.91 The fuel cell used in the Apollo program (©2011 Steve Jurvetson, flickr.com)

other metals and oxygen in the air. Figure 26.90 shows a widely used variety of this type of battery: the zinc–air battery. It is hoped that, in the near future, lithium–air batteries with a similar construction will achieve very high energy densities.

Fuel Cells

In a fuel cell, chemical energy is transformed into electrical energy by means of a steady material input. The zinc–air battery might also be called a fuel cell, rather than a battery, as its production of electricity stops when the air inlet (Fig. 26.90) is closed. One of the early applications, shown in Fig. 26.91, was electricity generation in the spaceships of the Apollo missions. For an interesting historical overview, see [26.22]. The overall reaction is

$$2\,H_2 + O_2 \rightarrow 2\,H_2O \qquad (26.142)$$

thus producing clean water as a collateral benefit. The two parts forming this reaction can be deduced from Fig. 26.92. They are [26.20]

$$\begin{aligned} &2\,OH^-(\text{sol}) + H_2(\text{gas}) \\ &\quad \rightarrow H_2O(\text{gas}) + H_2O(\text{liq}) + 2\,e^- \quad (\text{cathode}) \\ &2\,H_2O(\text{liq}) + O_2(\text{gas}) + 4\,e^- \\ &\quad \rightarrow 4\,OH^-(\text{sol}) \quad (\text{anode}) \end{aligned} \qquad (26.143)$$

So, the electrolyte has to be a solution with a high concentration of OH^- ions. In the Apollo missions, concentrated potassium hydroxide (KOH) was used at a pressure of 20–40 bar and a temperature of 200 °C. The electrodes were made of porous nickel powder, providing a large surface for catalytic reactions. The tension produced by one cell is then

$$\begin{aligned} V_{\text{cell}} &= V_0(\text{reduction}) - V_0(\text{oxidation}) \\ &= 0.4\,\text{V} - (-0.83\,\text{V}) = 1.23\,\text{V}\,. \end{aligned} \qquad (26.144)$$

With hydrogen being quite difficult to store, a large variety of materials and operating conditions have been tried out during the last decades. An easy-to-read introduction to the more widely used kinds of fuel cells can be found in [26.23].

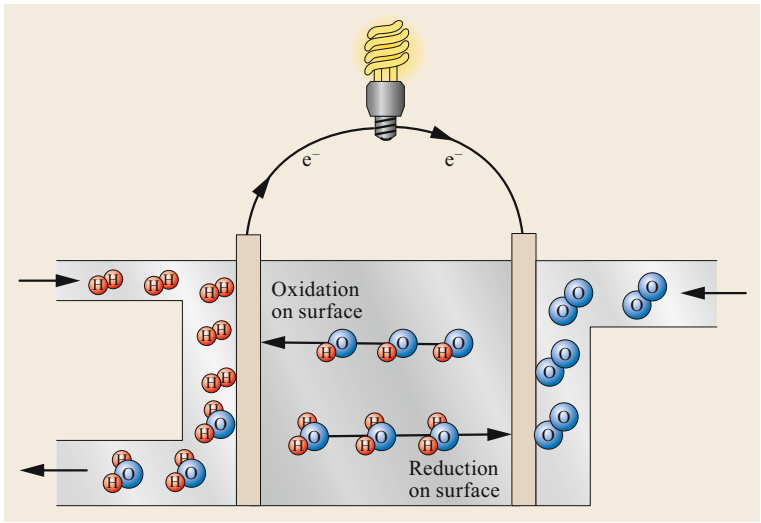

Fig. 26.92 An alkaline fuel cell; at the cathode (*left*), hydroxide ions and hydrogen combine to water. At the anode, oxygen and water form hydroxide ions

References

26.1 A. Einstein: Zur Elektrodynamik bewegter Körper, Ann. Phys. **322**(10), 891 (1905)

26.2 J. Clerk Maxwell: A dynamical theory of the electromagnetic field, Philos. Trans. R. Soc. **155**, 459 (1865)

26.3 M. Poppe: Exclusive hadron production in two-photon reactions, Int. J. Mod. Phys. A **1**(3), 545 (1986)

26.4 R. Van Dyk, P. Ekstrom, H. Dehmelt: Axial, magnetron, cyclotron and spin-cyclotron-beat frequencies measured on single electron almost at rest in free space (geonium), Nature **262**, 776 (1976)

26.5 R.S. Van Dyck Jr., P.B. Schwinberg, H.G. Dehmelt: Precise measurements of axial, magnetron, cyclotron, and spin-cyclotron-beat frequencies on an isolated 1-meV electron, Phys. Rev. Lett. **38**, 310 (1977)

26.6 M. Poppe: *Die Maxwellsche Theorie* (Springer, Heidelberg 2015)

26.7 C.F. Gauss: *Observationes cometae secundi, observatorio Gottingensi factae, adjectis nonnullis adnotationibus circa calculum orbitarum paraboli-carum* (Dieterich'sche Univ.-Buchdruckerei Kaestner, Göttingen 1813)

26.8 M. Faraday: Experimental researches in electricity series XI, Philos. Trans. R. Soc. **128**, 1–40 (1838)

26.9 W.K.H. Panofsky, M. Phillips: *Classic Electricity and Magnetism* (Addison Wesley, Boston 1990)

26.10 R.P. Feynman: *The Feynman Lectures on Physics: The Definitive and Extended Edition*, Vol. 2 (Addison Wesley, Boston 2005)

26.11 P.A. Tipler, G. Mosca: *Physics for Scientists and Engineers*, 6th edn. (Freeman, London 2007)

26.12 P. Drude: *Lehrbuch der Optik* (Hirzel, Leipzig 1906)

26.13 G.S. Ohm: *Die galvanische Kette* (Riemann, Berlin 1827)

26.14 Georgia State University: Hypherphysics, http://hyperphysics.phy-astr.gsu.edu (2016)

26.15 EPCOS AG: Technical library, https://en.tdk.eu/tdk-en/180390/tech-library/publications/capacitors (2016)

26.16 M. Grundmann: *The Physics of Semiconductors*, 3rd edn. (Springer, Heidelberg 2016)

26.17 Intel.com: Standards 22nm-3d-tri-gate-transistors presentation, http://www.intel.com/content/www/us/en/silicon-innovations/standards-22nm-3d-tri-gate-transistors-presentation.html?wapkw=transistor (2016)

26.18 R. Gregorian, G.C. Temes: *Analog MOS Integrated Circuits for Signal Processing* (Wiley, New York 1986)

26.19 Energiespeicher – Forschungsinitiative der Bundesregierung: http://forschung-energiespeicher.info/wind-zu-wasserstoff (2016)

26.20 P.W. Atkins, J. de Paula: *Atkins' Physical Chemistry*, 9th edn. (Wiley, Hoboken 2009)

26.21 S.-C.S. Wang: Advanced secondary batteries and their applications for hybrid and electric vehicles, http://sites.ieee.org/clas-sysc/files/2012/05/Wang-Battery-and-EV.pdf (2011)

26.22 The Smithsonian Institute: Fuel cells, http://americanhistory.si.edu/fuelcells (2016)

26.23 F. Barbir: *PEM Fuel Cells* (Elsevier, Amsterdam 2013)

Martin Poppe

Electrial Engineering and Computer Science
Muenster University of Applied Sciences
Steinfurt, Germany
poppe@fh-muenster.de

Martin Poppe is Professor of Electronics and Prototyping at Muenster University of Applied Sciences. He is a Rhodes Scholar who read Physics at the University of Oxford (DPhil) and worked on experimental quantum electrodynamics at DESY and CERN. The results, published in 1986, are still in use by research collaborations. He is coauthor of several textbooks.

27. Power Generation

Asfaw Beyene, Dwarkadas Kothari, P.M.V. Subbarao

This chapter addresses the process of power generation in eight sections. The principles of energy conversion are discussed in Sect. 27.1, which explains how steam and gas power cycles operate. Internal combustion engines, dual cycles, combined heat and power cycles, integrated gasification and combined cycle plants, and other conversion systems are all described in this section. Fuel cells and magnetohydrodynamic systems are also introduced, and the section concludes with a note on planning and investment. In Sect. 27.2, we discuss primary energy—fuels and their characteristics. Primary energy conversion equipment such as boilers and furnaces are covered in Sect. 27.3. Combustion systems are addressed in Sect. 27.4, together with emissions and environmental control technology. Various types of nuclear reactors and their working principles are elaborated in Sect. 27.5. Renewable energy resources are covered in Sect. 27.6. The chapter also reviews energy storage (Sect. 27.7), and concludes with a discussion of the prospects for power generation in the future (Sect. 27.8).

27.1 **Energy Conversion Principles** 1224
27.1.1 The Steam Power Cycle 1225
27.1.2 Open-Cycle Gas Turbine Power Plants .. 1226
27.1.3 Internal Combustion Engines 1228
27.1.4 Dual Cycle Systems 1228
27.1.5 Combined Heat and Power Generation 1229
27.1.6 Integrated Gasification and Combined Cycle 1231
27.1.7 Other Conversion Systems 1233
27.1.8 Planning and Investment 1235

27.2 **Primary Energy** 1235
27.2.1 The Economics of Fuels 1236

27.3 **Boilers and Furnaces** 1236
27.3.1 Boilers 1236
27.3.2 Furnaces 1243
27.3.3 Furnace Design 1249
27.3.4 Strength Calculations 1252
27.3.5 Heat Transfer Calculations 1253
27.3.6 Flow Resistance 1253
27.4 **Combustion** 1254
27.4.1 Burners 1254
27.4.2 Fluidized-Bed Combustion System 1256
27.4.3 Emissions 1257
27.4.4 Environmental Control Technology 1258

27.5 **Nuclear Power Plants** 1260
27.5.1 Nuclear Reactors 1260
27.5.2 Components of a Nuclear Reactor 1260
27.5.3 Types of Nuclear Reactors 1262

27.6 **Renewable Energy** 1264
27.6.1 Wind Energy 1264
27.6.2 Solar Energy 1265
27.6.3 Geothermal Energy 1266
27.6.4 Wave/Tidal Energy 1267
27.6.5 Biofuels 1268

27.7 **Energy Storage and Distribution** 1268
27.7.1 Pumped Hydropower 1268
27.7.2 Compressed Air Energy Storage 1268
27.7.3 Energy Storage by Flywheels 1269
27.7.4 Electrochemical Energy Storage 1269
27.7.5 Secondary Batteries 1269
27.7.6 Thermal Energy Storage 1269

27.8 **Prospects and Conclusion** 1269

References 1271

Power generation is a thermodynamic process that leads to the generation of electricity through energy conversion. The principles of power generation were discovered in the 1820s by a British scientist, Michael Faraday. Power plants convert the chemical energy in fuels such as coal, natural gas, and petroleum to electrical energy. Other forms of energy that can be converted to electrical energy include nuclear, hydro, wind, solar, tidal, wave, and geothermal. There are also several other less frequently used energy conversion methods that provide electrical energy, such as electrochemical processes in batteries and triboelectric, piezoelectric, thermoelectric, and betavoltaic effects. These methods are conveniently used for special applications such as in control systems. Utility-scale power generation takes place using conversion equipment such as electric generators, batteries, and photovoltaic systems. Among these, electric generators are the most common type

K.-H. Grote, H. Hefazi (Eds.), *Springer Handbook of Mechanical Engineering*, Springer Handbooks,
https://doi.org/10.1007/978-3-030-47035-7_27

of energy conversion equipment. In 2013, 41% of the electricity generated globally came from burning coal and peat, 22% came from burning natural gas, 16% came from hydroelectric sources, and 11% came from nuclear power. Electricity was also generated by burning oil, biomass, and waste, as well as from the wind, from geothermal sources, using solar photovoltaic cells, and using solar thermal systems. Together, the total amount of electricity generated globally in 2013 was 23 322 TWh.

27.1 Energy Conversion Principles

Energy is a useful commodity that allows us to perform many useful tasks such as driving, flying, lifting, cooling, and warming. It can be transported to a different location or object via different media. Energy exists in many *forms*, such as thermal energy, chemical energy, mechanical energy, potential energy, kinetic energy, and nuclear energy. It is a conserved quantity, which means that energy can be transformed from one form to another—a process known as *energy conversion*—but the total amount of energy does not change during the conversion process. Some forms of energy are more useful and appropriate for specific tasks than others; hence the need for conversion.

Electrical energy is a desirable form of energy because it can be generated at one central location in bulk and transmitted economically over long distances. Traditionally, the primary sources of energy have been fossil fuels such as coal (measured in tonnes), oil (measured in barrels), and gas (measured in cubic meters). Due to our ever-increasing energy needs and the exponential growth in the global human population, it is easy to foresee that the Earth's nonreplenishable fuel resources will run out at some point in the not-too-distant future. The combustion of fossil fuels also leads to the emission of CO_2 into the atmosphere, with negative consequences for the environment. This has driven investment in renewable sources of energy generation, such as wind and solar.

Energy is an essential driving force of the economy. The Sun is the main source of energy, as most other sources of energy are derived from it. Figure 27.1 shows that all fossil fuels (oil, gas, and coal) are derived from the Sun through various transformations such as photosynthesis, chemical energy conversion, and fossilization.

The current global average conversion efficiency for coal-fired electricity generation is 34%, and that for gas-fired electricity generation is 37%. Modern coal-fired power plants operate at somewhat higher efficiencies of 43–48%.

Particularly large improvements in the energy conversion efficiencies of lightbulbs—the most common type of *energy conversion device*—have been seen in recent years. Between 2012 and 2014, the energy conversion efficiency of a LED (light-emitting diode) jumped from just over 60 to nearly 100 lm/W, and it is expected to rise to 203 lm/W by 2030. For comparison, compact fluorescent lights offer conversion efficiencies of less than 70 lm/W, and traditional incandescent bulbs have efficiencies that are lower than 18 lm/W. The first LED was priced below $10 in 2013 dropping to $8 by 2014. This implies that the cost of lighting has reduced since 2005, despite the increases in electricity prices that have occurred in many countries since then.

Other examples of energy conversion devices include engines (which convert thermal energy to mechanical work or electricity), air conditioners, and batteries.

Energy conversion is governed by two *laws of thermodynamics*. The first law states that energy is conserved. There are many versions of the second law. The most common version states that the total entropy of an isolated system can only increase over time. In simpler terms, it states that a process in which the sole result is the transfer of heat from a cooler to a hotter body is im-

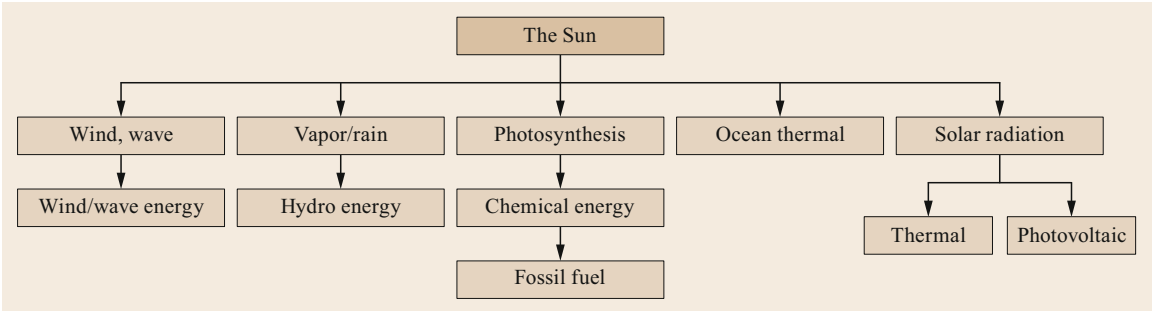

Fig. 27.1 Solar energy system diagram

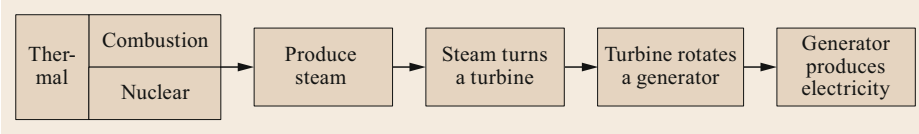

Fig. 27.2 Conversion of thermal energy to power

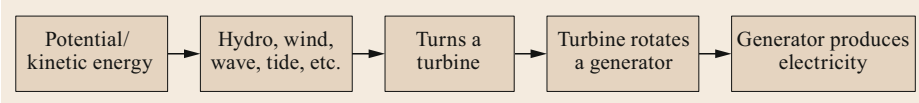

Fig. 27.3 Conversion of kinetic or potential energy to power

possible. Figures 27.2 and 27.3 show energy conversion processes that result in power generation.

Electrical energy is the flow of electric charge. It is a secondary energy source, which means that we get it through the conversion of energy from primary sources such as coal, natural gas, oil, nuclear power, and other natural sources. The energy sources we use to generate electricity can be renewable or nonrenewable, but the electricity itself is neither renewable nor nonrenewable.

27.1.1 The Steam Power Cycle

The Rankine cycle, which is used in a variety of power plants to produce electricity, is the most common thermodynamic process involving indirect combustion. Indirect combustion implies that thermal energy from the combustion gas is used indirectly—it is employed to produce steam, which expands in the steam turbine. In contrast, direct combustion occurs in systems where the exhaust gas is used to transfer energy directly to the turbine, which is the case in a gas turbine engine for example.

The simplest arrangement of a steam power plant is one with no regeneration or reheating, as shown in Fig. 27.4. A simple Rankine cycle consists of four main components: a steam generator, a turbine, a condenser, and a pump. Additional components are sometimes added to enhance cycle performance and to improve efficiency. The Rankine cycle is named after William John Macquorn Rankine (1820–1872), who established it as the fundamental cycle used in steam power plants. In a simple steam power plant that works on a Rankine cycle, heat is added at constant pressure. The efficiency of the Rankine cycle is a function of the temperature of heat rejection and the mean temperature of heat addition. The higher the mean temperature of heat addition, the higher the efficiency. The working fluid in a Rankine cycle is in a closed loop and is constantly reused (although some water must be added to the system due to evaporative losses).

Processes in the Rankine Cycle

There are four processes in the Rankine cycle, each of which changes the state of the working fluid. These states are identified in the T–S (temperature–entropy) diagram shown in Fig. 27.5.

Process 1–2. The working fluid is initially pumped isentropically (i.e., with constant entropy) from low to high pressure by a pump. This pumping requires a power input.

Process 2–3. The high-pressure liquid enters a boiler, where it is heated at constant pressure by an external heat source. The heat sources commonly used for such a power plant are coal, natural gas, and nuclear fuel. The steam is superheated if its temperature is raised above the saturation temperature (the horizontal line during process 2–3 in Fig. 27.5).

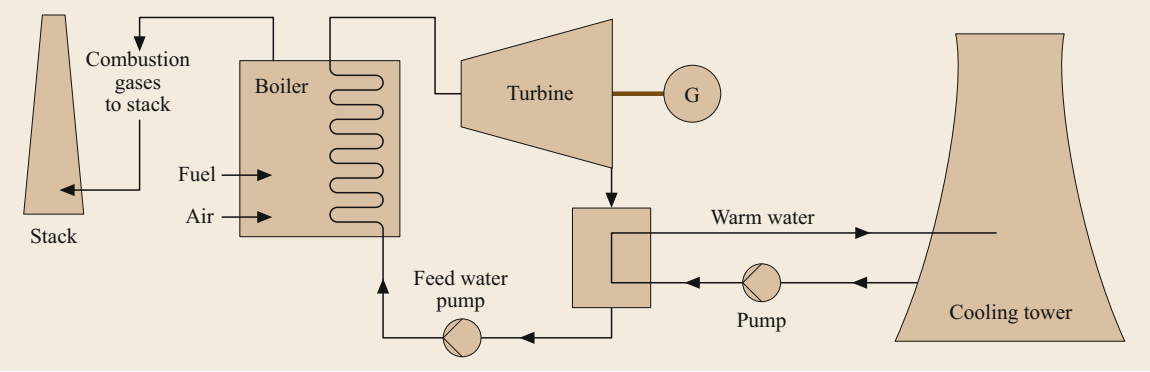

Fig. 27.4 Layout of a simple power plant that uses a Rankine cycle

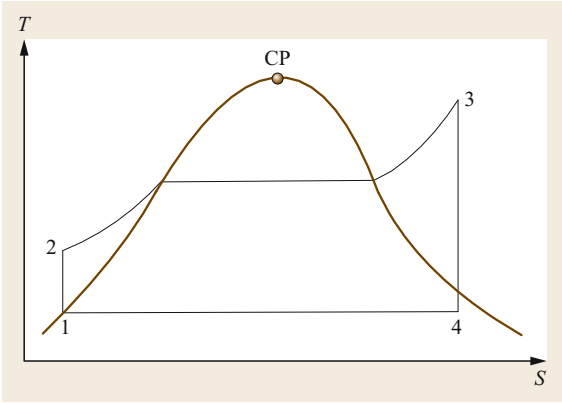

Fig. 27.5 *T–S* diagram of a simple Rankine cycle

Process 3–4. The steam expands in the turbine, generating power; ideally, this expansion should be isentropic. This process decreases the temperature and pressure of the vapor.

Process 4–1. The medium, typically a liquid–vapor mixture, then passes through a condenser, where it is cooled and becomes a saturated liquid. This liquid then reenters the pump and the cycle repeats.

In order to improve coal-fired power plant efficiency and therefore reduce coal consumption and CO_2 emissions, it is widely accepted that the power industry must move from subcritical to supercritical steam cycles. In a supercritical cycle, process 2–3 bypasses the critical point (CP; Fig. 27.5).

A supercritical (SC) efficiency in excess of 45% is reachable with the aid of a SC Rankine steam cycle that includes a reheat and regeneration mode and operates at 250 bar and 540 °C. Today, ultra-supercritical steam (USC) parameters of 345 bar and 700 °C can be realized in steam cycles, resulting in 46% (higher heating value, HHV) efficiency for bituminous coal-fired power plants [27.1] (bitumen is a black viscous mixture of hydrocarbons that exists naturally or is generated as a residue during petroleum distillation).

The challenges of coal-based power generation are primarily environmental; proposed highly efficient technologies target near-zero CO_2 emissions.

Modeling a Rankine Cycle

The work done by pump per kg of water is

$$W_P = h_2 - h_1 \,. \tag{27.1}$$

The energy added to the steam generator is

$$q_1 = h_3 - h_2 \,. \tag{27.2}$$

The work delivered by the turbine is

$$W_T = h_3 - h_4 \,. \tag{27.3}$$

The energy rejected in the condenser is

$$q_{4-1} = h_4 - h_1 \,. \tag{27.4}$$

The thermal efficiency of the Rankine cycle is then given by

$$\eta = \frac{q_1 - q_2}{q_1} = \frac{(h_3 - h_2) - (h_4 - h_1)}{h_3 - h_2} = \frac{(h_3 - h_4) - (h_2 - h_1)}{h_3 - h_2} \,. \tag{27.5}$$

In the above ideal case, the work delivered is higher because of the assumption that the cycle is isentropic. The work done by an actual pump is greater than the work done by the pump in this ideal case.

The thermal efficiency of an actual Rankine cycle is

$$\eta = \frac{(h_3 - h_4') - (h_2' - h_1)}{h_3 - h_2'} \,. \tag{27.6}$$

Enthalpy values are available from steam tables. The performance of an actual turbine or pump is expressed in terms of its isentropic efficiency η_T, which is defined as the ratio of the work actually done by the turbine to the work done by the turbine isentropically,

$$\eta_T = \frac{h_3 - h_4'}{h_3 - h_4} \,. \tag{27.7}$$

The isentropic efficiency of the pump (η_P) is defined as the ratio of the work done by the pump in an isentropic process to the work done by an actual pump,

$$\eta_P = \frac{h_2 - h_1}{h_2' - h_1} \,. \tag{27.8}$$

27.1.2 Open-Cycle Gas Turbine Power Plants

The essential components of a gas turbine power plant are the compressor, the combustion chamber, and the turbine. The air standard cycle of a gas turbine power plant is the Brayton cycle shown in Fig. 27.6. It consists of two reversible adiabatic processes and two constant-pressure processes. Gas turbine plants can be operated in either an open or a closed system configuration. Air standard assumptions include the following: (i) that the working fluid is air that behaves as an ideal gas and is supplied in a closed loop; (ii) that all thermodynamic processes are internally reversible; (iii) that the combustion process is modeled as a heat addition from an external source whereas the exhaust is modeled as a heat rejection that restores the air to its initial state; and (iv) that specific heats are constant and are evalu-

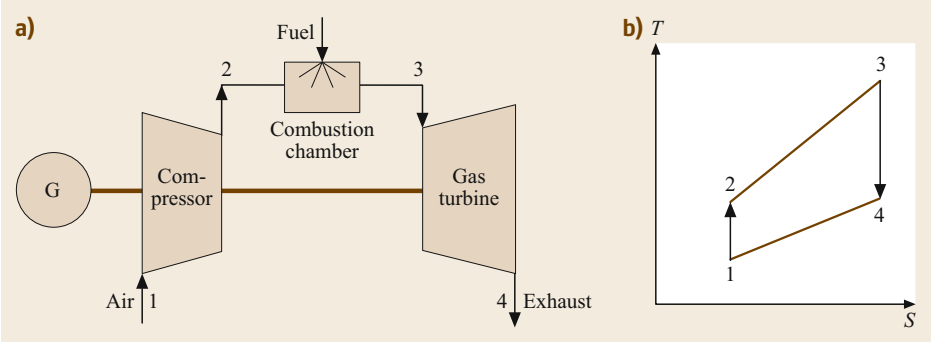

Fig. 27.6a,b Arrangement of an open-cycle gas turbine plant: **(a)** primary components, **(b)** ideal Brayton cycle

ated for an air temperature of 25 °C (this is also known as the *cold air standard assumption*).

Analysis

1–2: Work input

$$w_{\text{comp}} = h_2 - h_1 = c_p(T_2 - T_1)\,. \tag{27.9}$$

2–3: Heat input

$$q_{\text{in}} = h_3 - h_2 = c_p(T_3 - T_2)\,. \tag{27.10}$$

3–4: Work output

$$w_{\text{tur}} = h_3 - h_4 = c_p(T_3 - T_4)\,. \tag{27.11}$$

4–1: Heat rejection

$$q_{\text{out}} = h_4 - h_1 = c_p(T_4 - T_1)\,. \tag{27.12}$$

Isentropic processes

$$\frac{p_2}{p_1} = \left(\frac{v_1}{v_2}\right)^{\gamma} = \left(\frac{T_2}{T_1}\right)^{\frac{\gamma}{\gamma-1}}\,, \tag{27.13}$$

$$\frac{p_3}{p_4} = \left(\frac{v_4}{v_3}\right)^{\gamma} = \left(\frac{T_3}{T_4}\right)^{\frac{\gamma}{\gamma-1}}\,. \tag{27.14}$$

Constant-pressure processes

$$p_3 = p_2 \quad \text{and} \quad p_4 = p_1\,, \tag{27.15}$$

$$r_p = \frac{p_2}{p_1} = \frac{p_3}{p_4} = \left(\frac{v_1}{v_2}\right)^{\gamma} = \left(\frac{v_4}{v_3}\right)^{\gamma}\,,$$

$$[b] \quad = \left(\frac{T_2}{T_1}\right)^{\frac{\gamma}{\gamma-1}} = \left(\frac{T_3}{T_4}\right)^{\frac{\gamma}{\gamma-1}}\,, \tag{27.16}$$

where r_p is the pressure ratio,

$$T_2 = T_1 r_p^{\frac{\gamma-1}{\gamma}} = T_1\rho\,, \tag{27.17}$$

and

$$\rho = r_p^{\frac{\gamma-1}{\gamma}}\,, \tag{27.18}$$

$$T_4 = \frac{T_3}{r_p^{\frac{\gamma-1}{\gamma}}} = \frac{T_3}{\rho}\,, \tag{27.19}$$

$$\eta_{\text{th}} = \frac{w_{\text{net}}}{q_{\text{in}}} = \frac{c_p\left(\frac{T_3}{\rho} - T_1\right)}{c_p(T_3 - \rho, T_1)} = \frac{1}{r_p^{\frac{\gamma}{\gamma-1}}}\,, \tag{27.20}$$

$$\begin{aligned} w_{\text{net}} &= c_p\left[T_3\left(\frac{\rho-1}{\rho}\right) - T_1(\rho-1)\right] \\ &= c_p\left(\frac{\rho-1}{\rho}\right)(T_3 - \rho T_1) \\ &= c_p(\rho-1)\left(\frac{T_3}{\rho} - T_1\right)\,, \end{aligned} \tag{27.21}$$

The thermal efficiency can also be written as

$$\eta_{\text{th}} = \frac{1}{\rho} = \frac{1}{r_p^{\frac{\gamma}{\gamma-1}}}\,, \tag{27.22}$$

For a simple gas turbine cycle, the cycle efficiency is a function of the pressure ratio only. However, the pressure ratio may depend on other factors such as ambient conditions. The gas turbine inlet temperature is an important parameter, as it impacts the cycle efficiency. Modern gas turbine engines can have turbine inlet temperatures that are as high as 1570 K. Research into the closed-cycle steam cooling of turbine blades, protective surface coatings of combustor liners, and new ceramic structural parts of the turbine are expected to lead to higher gas turbine inlet temperatures.

Merits and Demerits of the Brayton Cycle

The Brayton cycle describes the workings of a constant-pressure heat engine such as modern gas turbine engines and air-driven jet engines. Gas turbine engines are compact, which is why they are used in the aircraft industry. They burn a special fuel, making them expensive to operate. The pressure of the exit gases is always just above atmospheric pressure, so full expansion is not achieved. The compressor requires a large power input, leading to

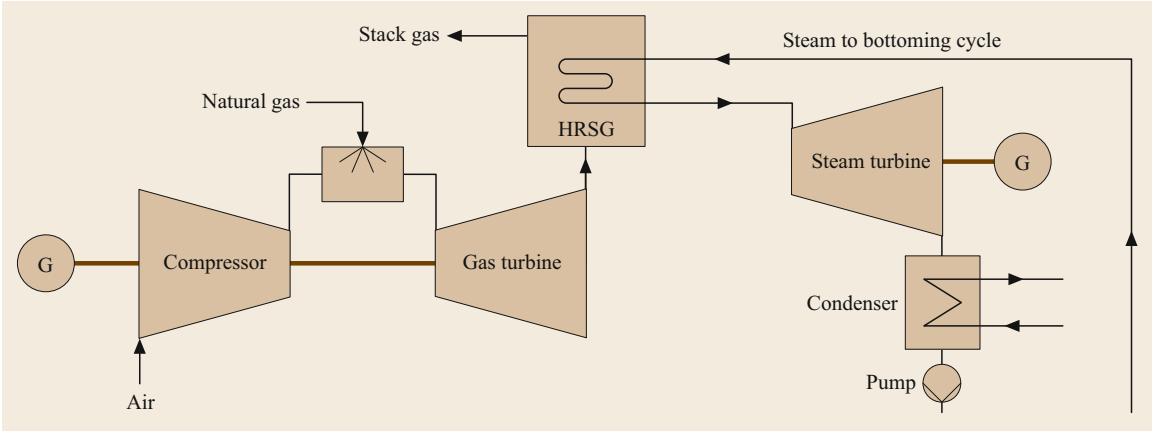

Fig. 27.7 Primary waste heat recovery in a dual cycle system

a high back-work ratio. The Brayton cycle has lower cycle efficiency than the Rankine cycle, mainly due to the high-temperature exhaust loss and its high back-work ratio.

27.1.3 Internal Combustion Engines

A typical internal combustion (IC) engine is the reciprocating engine. Reciprocating engines operate by converting the heat and pressure released during combustion in the cylinder to mechanical energy. The pressure exerted on the piston is converted to vertical (reciprocating) motion of one or more pistons, which is then translated to rotational motion. Reciprocating engines are commonly used for distributed power generation, largely due to their availability and the extensive bank of knowledge regarding these engines that has been accumulated over the decades by the automobile industry. IC engines can run on diesel, gasoline, methane, or natural gas. They contain one or more cylinders in which the fuel is combusted. When it is connected to the shaft of a generator, an IC engine provides the mechanical energy needed to drive the generator to produce electricity. The benefits of using IC engines in power generation include ease of transportation and installation as well as the ability to use them as standby power generation units during emergency outages and periods of peak demand for electricity. However, peak demand is becoming less and less important due to the emergence of large solar photovoltaic (PV) installations, particularly in regions where the peak is due to the need for cooling.

27.1.4 Dual Cycle Systems

A dual cycle system is a combination of two different cycles, normally gas turbine and steam turbine cycles. Combining two different cycles with different working media can be useful because the advantages of one cycle may complement those of the other cycle [27.2]. When two cycles are combined, the cycle operated at the higher temperature is called the *topping cycle*. The waste heat it produces is used in a second process that operates at a lower temperature and is therefore called the *bottoming cycle* [27.3].

The main components of a simple dual cycle power plant that uses both the Brayton and Rankine cycles are shown in Fig. 27.7. The major components present on the steam side of the cycle are a single-pressure heat recovery steam generator (HRSG), a steam turbine, and a water-cooled condenser. The gas side includes a compressor, a combustion chamber, and a gas turbine. The air is compressed by the compressor and then supplied to the combustion chamber. The fuel (natural gas) from the main supply line is compressed by gas compressors and injected into the combustion chamber. The hot gas expands in the gas turbine, producing useful work. The gas is then directed to the HRSG, where it becomes a heat source for producing steam.

Thermodynamic Analysis of a Dual Cycle System

Based on Fig. 27.8, we can determine the net power output of the Brayton cycle as

$$P_{\text{net,B}} = \eta_{\text{B}} \dot{Q}_{\text{in,B}} \,, \tag{27.23}$$

where η_{B} is the Brayton cycle efficiency (typically about 33%).

The rate of heat rejected in the Brayton cycle is

$$\dot{Q}_{\text{out,B}} = (1 - \eta_{\text{B}}) \dot{Q}_{\text{in,B}} \,. \tag{27.24}$$

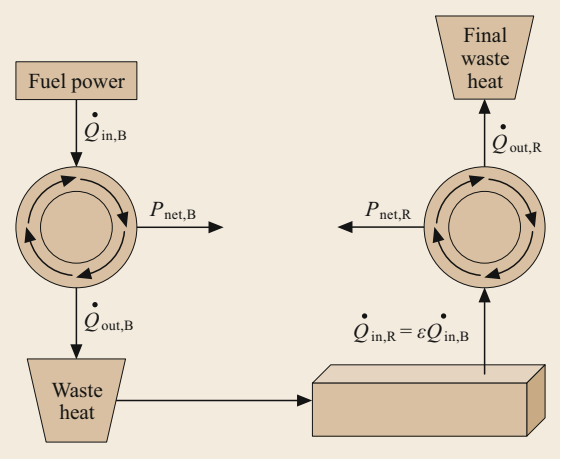

Fig. 27.8 Thermodynamic analysis of a dual cycle system

The rate of heat input to the Rankine cycle is

$$\dot{Q}_{in,R} = \varepsilon \dot{Q}_{out,B} = \varepsilon(1-\eta_B)\dot{Q}_{in,B} \,, \tag{27.25}$$

where ε is the effectiveness.

The net power output of the Rankine cycle is

$$P_{net,R} = \eta_R \dot{Q}_{in,R} = \eta_R \varepsilon(1-\eta_B)\dot{Q}_{in,B} \,, \tag{27.26}$$

where η_R is the Rankine efficiency.

The net power output of the dual cycle system is

$$P_{tot} = P_{net,B} + P_{net,R} \,, \tag{27.27}$$

$$P_{tot} = \eta_B \dot{Q}_{in,B} + \eta_R \varepsilon(1-\eta_B)\dot{Q}_{in,B} \,. \tag{27.28}$$

Overall Efficiency of a Dual Cycle Power Plant

The overall efficiency of a dual cycle power plant is defined as the ratio of the total power output to the heat added to the system, i.e.,

$$\eta_{ov} = \frac{P_{tot}}{\dot{Q}_{in,B}} \,, \tag{27.29}$$

$$\eta_{ov} = \frac{\eta_B \dot{Q}_{in,B} + \eta_R \varepsilon(1-\eta_B)\dot{Q}_{in,B}}{\dot{Q}_{in,B}} \,, \tag{27.30}$$

$$\eta_{ov} = \eta_B + \eta_R \varepsilon(1-\eta_B) \,. \tag{27.31}$$

27.1.5 Combined Heat and Power Generation

A plant that produces both electrical power and process heat simultaneously is called a combined heat and power (CHP) or cogeneration plant. In this scheme, heat rejected in the condenser or through the exhaust is available for reuse in another process. The reuse of otherwise rejected heat makes CHP systems more efficient than conventional non-CHP systems operating under the same conditions. The heat obtained from a cogeneration plant can be used for space heating, drying, to produce hot water or steam, or as a heat source for various industrial processes. Steam turbine, gas turbine, and IC engines can be used in cogeneration systems.

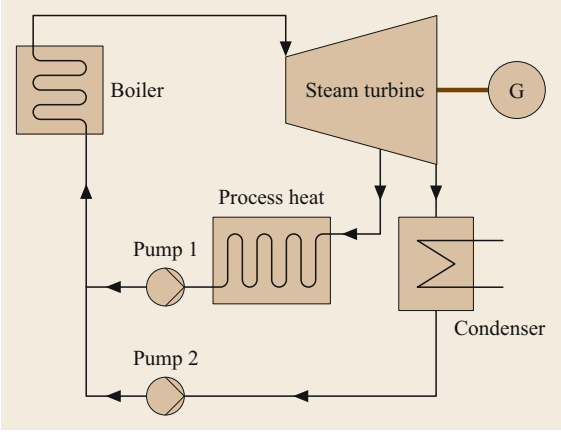

Fig. 27.9 Layout of an extraction condensing turbine

Steam Turbine Cogeneration Systems

In a steam turbine, electricity and heat are the outputs. Heat is generated in boilers by burning a suitable fuel. The steam is sent to the back-pressure extraction turbine, where it is expanded until the design back pressure is reached. The steam drives the steam turbine, which is coupled to electric generators, thus producing electricity. Normally in CHP systems, the required amount of heat is obtained from the liquid–steam mixture after the turbine, from the back-pressure outlet, or from steam extracted at the turbine stage, as depicted in Fig. 27.9. The steam delivers the required thermal energy at the target pressure or temperature (corresponding to the design value, in accord with the available energy).

Gas Turbine Cogeneration Systems

In this design, a combination of gas and steam turbines is installed to convert energy from fuel to mechanical energy in order to drive electric generators.

Figure 27.10 presents the layout of a gas turbine cogeneration system. Hot gases from the gas turbine are used to generate steam for the steam turbine. The thermal energy of the steam from the turbine is used as a heat source. Both the gas turbine and steam turbine produce power by running a generator. The net efficiency of the plant typically exceeds 50%.

IC Engine Cogeneration Systems

CHP systems based on IC engines are also available, and are typically used for relatively small facilities.

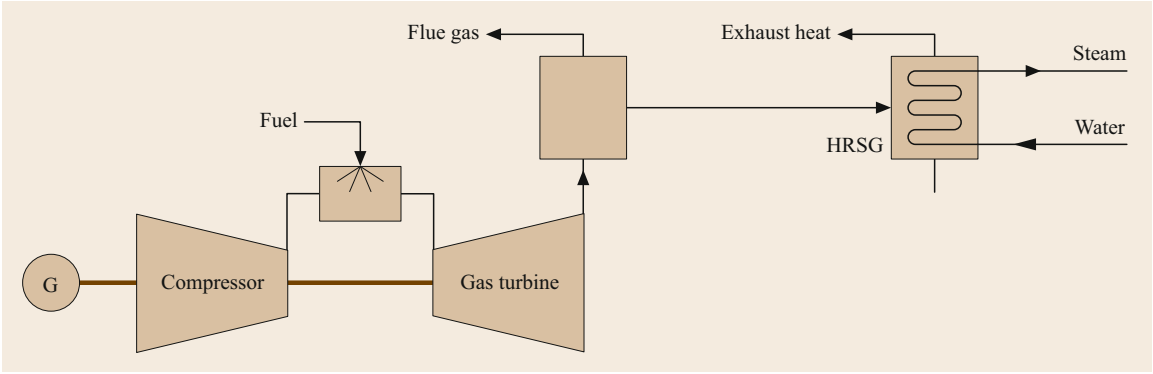

Fig. 27.10 Layout of a gas turbine cogeneration system

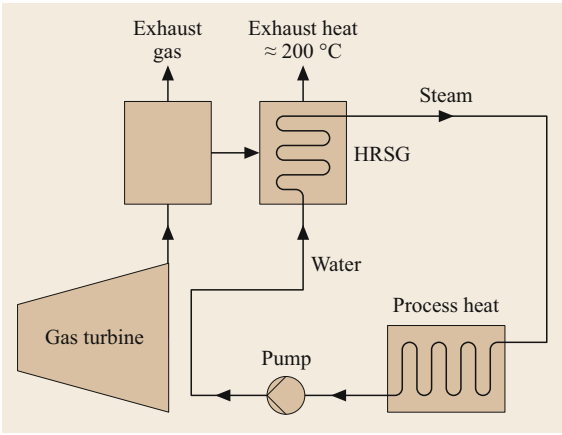

Fig. 27.11 Layout of a gas turbine engine cogeneration system

These small *modular* cogeneration units can generate 20–650 kW and produce hot water. Figure 27.11 presents the layout of an IC engine cogeneration system. The generator converts mechanical work from the engine shaft into electrical energy. Exhaust gases and the engine cooling water are used to supply process heat or heat for space heating or other applications.

Dual Cycle System with Heat Recovery

Figure 27.12 shows the layout of a dual cycle system consisting of a gas-turbine-driven generator package, a heat recovery steam generator that is closely matched to the process steam conditions, and a steam turbine that is matched to the HRSG's output and connected to the generator. The dual cycle system discussed here is different from the one discussed in Sect. 27.1.4. In this case, the exhaust is also used to produce process heat.

The advantages of this design include high thermal efficiency, operating flexibility, and low installation costs.

Gasifier Classification

A wide variety of gasifier designs have been developed for different applications and fuels. The main parameters considered when selecting the optimal gasifier design are typically the temperature, the pressure, and the reacting gases. The types of gasifiers used in combined cycle technology are:

- The entrained flow (downflow) gasifier
- The E-GAS (synthetic methane) entrained flow (upflow) gasifier
- The Shell entrained flow (upflow) gasifier

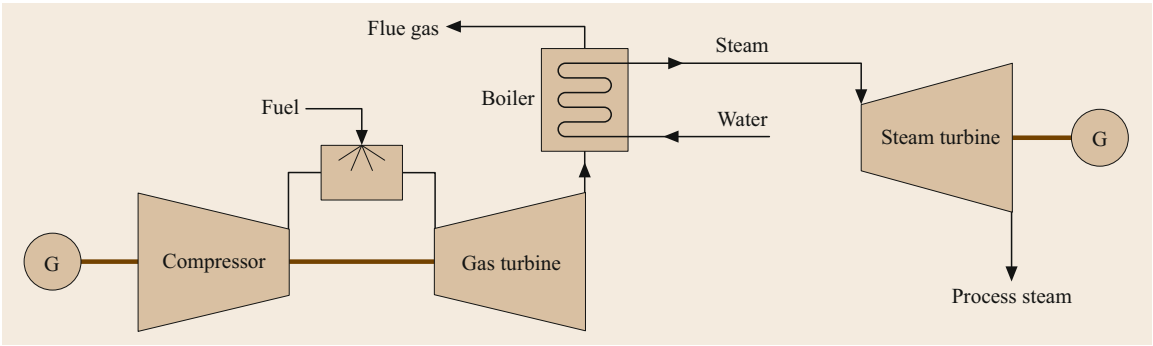

Fig. 27.12 Layout of a dual cycle system

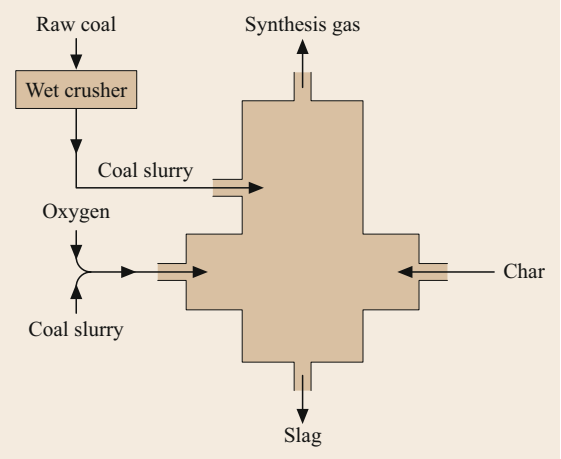

Fig. 27.13 The E-GAS entrained flow system

- The fluidized bed gasifier
- The transport reactor gasifier
- The Lurgi dry ash gasifier
- The British Gas/Lurgi fixed bed gasifier
- The PRENFLO entrained bed gasifier.

Figure 27.13 shows the arrangement of an E-GAS entrained flow gasifier as an example. The gasification reaction occurs in two regions of the gasifier: the primary and secondary regions. The raw feed coal is crushed in a wet crusher to produce slurries which are fed to the gasifier from the bottom portion (the first stage or primary region) of the gasifier. Exothermic gasification/oxidation reactions take place in this region at a temperature of 1300–1400 °C, so great care must be taken over this aspect of the design. This region is normally lined with a special slag-resistant refractory. There are two opposing horizontal burners in a horizontal cylinder in this region. Oxygen is used to gasify the slurry fed to the first stage of the gasifier. 80% of the coal slurry is usually fed into this region; the remaining 20% is injected into the hot raw gas from the first stage.

The second stage contains a vertical cylinder that is perpendicular to the first stage. Endothermic gasification/devolatilization reactions occur in this stage; these reactions reduce the final gas temperature and add some hydrocarbons to the product gas. Char is produced in the second stage. The hot gas leaving the gasifier is cooled in a fire-tube product gas cooler, generating saturated steam that is sent to the steam turbine.

27.1.6 Integrated Gasification and Combined Cycle

Integrated gasification and combined cycle (IGCC) is a promising technology that includes gasification and power generation. A variety of fuels such as bituminous or subbituminous coal, lignite, petroleum coke, heavy oil, and biomass can be used in IGCC. Figure 27.14 shows the layout of an integrated gasification combined cycle scheme. Any grade of coal can be gasified under pressure in the gasifier.

Syngas from the gasifier is cleaned by removing hydrogen sulfide, ammonia, and particulate matter and then mixed with pressurized air from the compressor and fed to the combustion chamber. The hot combustion gas expands through the turbine, producing useful work (i.e., power). The combustion gas exiting from the gas turbine is used to produce steam in the steam generator. The steam drives the steam turbine, which in turn ro-

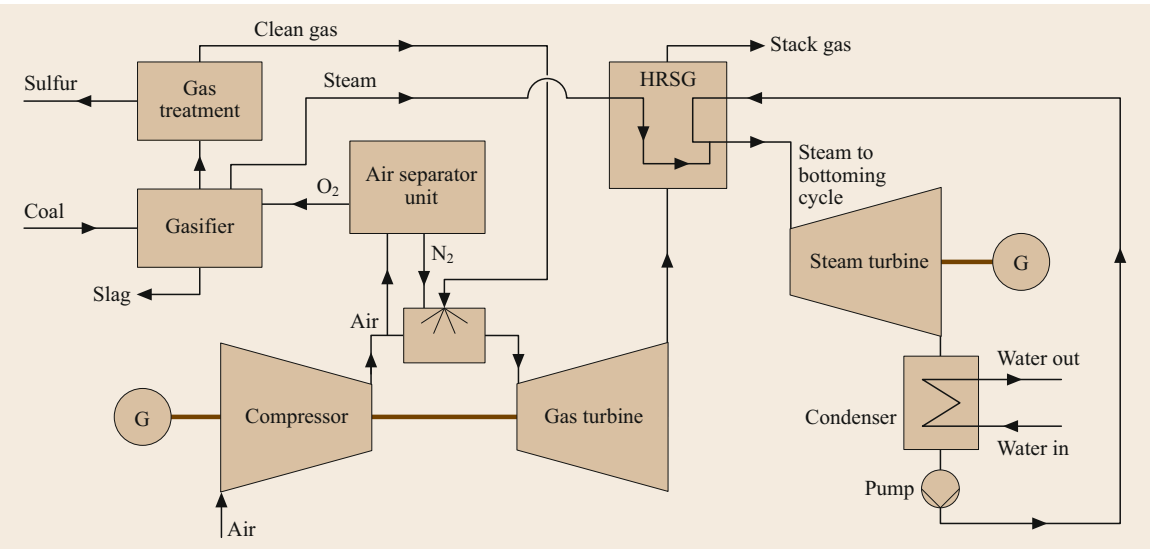

Fig. 27.14 Layout of an integrated gasification and combined cycle power plant

tates the generator to produce power. An air separation unit is also employed in modern IGCC power plants. Nitrogen and oxygen are completely separated in the air separator, and the pure oxygen is then fed into the gasifier. Nitrogen can be used for many other industrial applications that require an inert gas.

IGCC technology makes use of the thermodynamic advantages provided by combining two different cycles: a gas turbine cycle and steam turbine cycle. Cleaning the gas before combustion is more advantageous than flue gas treatment because a much smaller quantity of gas has to be treated. Furthermore, the composition of the coal gas is such that it allows easier purification. The purification process can be extended and can also include the elimination or reduction of exhaust carbon dioxide. Hence, this technology has been proposed as the basis for a coal power plant that has low CO_2 emissions and performs CO_2 capture. Appropriate gasification processes must be selected and it is crucial to integrate and optimize all of the processes involved to enhance the overall efficiency.

Environmental Benefits and Efficiency of Integrated Gasification Combined Cycle Plants

Coal with a high sulfur content can be used in integrated gasification combined cycle (IGCC) plants. The sulfur in the coal is liberated as hydrogen sulfide during the coal gasification process, and capturing hydrogen sulfide is a relatively easy task. In some IGCC plants, the sulfur can be extracted in a form that can be sold commercially. Likewise, the nitrogen in the coal typically forms ammonia during the IGCC process, and this ammonia can be scrubbed from the coal gas by processes that produce fertilizers or other ammonia-based chemicals. If oxygen is used in a coal gasifier instead of air, CO_2 is emitted as a concentrated gas stream. It can be captured more easily and less expensively in this form and then sequestered in various approaches.

The fuel efficiency of an IGCC power plant can be boosted to 50% or more. Proposed technologies that include a fuel cell could potentially achieve even higher efficiencies, likely in the 60% range—nearly double the efficiencies of typical modern coal-fired power plants. Higher efficiencies translate into more cost savings for ratepayers. A more efficient plant also uses less fuel to generate power, meaning that less CO_2 is produced. The flexibility to produce chemicals such as ammonia and hydrogen along with electricity makes IGCC an attractive option for future power plants.

Coal Gasification Reactions

Coal gasification is the chemical reaction of coal, steam, and air or oxygen at high temperatures to produce a mixture of hydrocarbon gases, typically carbon monoxide, carbon dioxide, methane, and hydrogen sulfide.

Coal gasification is the exothermic reaction of coal with oxygen or air to produce CO_2 and water. It is carried out with a limited amount of oxygen, 20–40% of the theoretically required amount for complete combustion. Partial combustion supplies the energy needed to complete the gasification of the coal particles, i.e.,

$$\mathrm{C(s)} + \frac{1}{2}\,\mathrm{O_2} \rightarrow \mathrm{CO} \quad \text{(partial combustion)}$$
$$\Delta H_\mathrm{R} = -1110.5\,\mathrm{MJ/kmol}\,, \tag{27.32}$$

where ΔH_R is the standard heat of reaction at 298 K and atmospheric pressure. This partial combustion reaction is exothermic (i.e., it releases thermal energy). Furthermore, any remaining oxygen rapidly reacts with the CO in the gas phase to produce CO_2, i.e.,

$$\mathrm{CO} + \frac{1}{2}\,\mathrm{O_2} \rightarrow \mathrm{CO_2}$$
$$\Delta H_\mathrm{R} = -283.1\,\mathrm{MJ/kmol}\,. \tag{27.33}$$

The solid carbonaceous material that is not combusted by oxygen reacts endothermically with carbon dioxide, hydrogen, and methane, e.g.,

$$\mathrm{C} + \mathrm{CO_2} \rightarrow 2\,\mathrm{CO}$$
$$\Delta H_\mathrm{R} = +172.0\,\mathrm{MJ/kmol}\,. \tag{27.34}$$

This reaction is called the Boudouard reaction.

In order to control the high temperatures that result from the reactions of C(s) with O_2, and to increase the heating value of the product gas through the production of hydrogen, steam is often added as a reactant, i.e.,

$$\mathrm{C(s)} + \mathrm{H_2O(g)} \rightarrow \mathrm{CO} + \mathrm{H_2}$$
$$\Delta H_\mathrm{R} = +131.4\,\mathrm{MJ/kmol}\,. \tag{27.35}$$

In a coal–steam or oxygen–steam system, the homogeneous water–gas shift reaction

$$\mathrm{CO} + \mathrm{H_2O(g)} \rightarrow \mathrm{CO_2} + \mathrm{H_2}$$
$$\Delta H_\mathrm{R} = -41.0\,\mathrm{MJ/kmol} \tag{27.36}$$

is also important. Hydrogen is added as a reactant in order to increase the quantity of methane. The gas from which the CO_2 is removed is called *synthesis gas*. Synthesis gas can also be used to produce methane or synthetic natural gas (SNG) via

$$\mathrm{CO(g)} + 3\,\mathrm{H_2(g)} \rightarrow \mathrm{CH_4(g)} + \mathrm{H_2O(g)} \tag{27.37}$$
$$2\,\mathrm{CO(g)} + 2\,\mathrm{H_2(g)} \rightarrow \mathrm{CH_4(g)} + \mathrm{CO_2(g)} \tag{27.38}$$

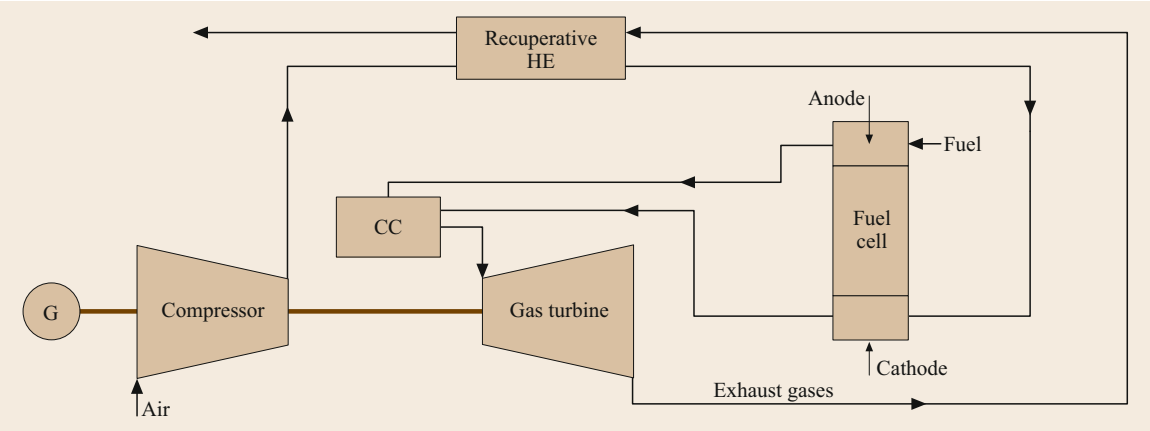

Fig. 27.15 Layout of a regenerative Brayton cycle fuel-cell power system (CC combustion exchanger, HE heat exchanger)

In fuel-rich combustion, the sulfur in the coal is released mainly as hydrogen sulfide (along with a small amount of carbonyl sulfide) and the fuel-bound nitrogen is released as elemental nitrogen, ammonia, and hydrogen cyanide.

In order to capture the sulfur, limestone or dolomite can be fed to the gasifier, i.e.,

$$CaO + H_2S \rightarrow CaS + H_2O \qquad (27.39)$$

27.1.7 Other Conversion Systems

Fuel Cells

A fuel cell is an electrochemical device that converts the chemical energy of a fuel directly into electrical energy. It consists of an electrolyte layer that is in contact with a porous anode and cathode at the sides of the cell. In a typical fuel cell, gaseous fuels are fed continuously to the negative electrode and an oxidant is fed continuously to the positive electrode.

Electrochemical reactions that produce an electric current take place at the electrodes. In general, the oxidation of H_2, CO, CH_4, and higher hydrocarbons in power-producing fuel cells also releases heat, which arises from two sources: the decrease in entropy ΔS caused by the oxidation reaction (during which the number of moles of gases decreases) and the irreversible process that occurs during the operation of the fuel cell. Heat from these two sources must be rejected from the fuel cell in order to maintain the temperature at the desired level. An engine can be added to have a hybrid system which captures the waste heat for power production. For hybridization, the efficiency is the ratio of the sum of the stack electricity and the power generated by the bottoming cycle to the lowest calorific value of the fuel consumed. This can be accomplished using three cycles: the regenerative Brayton cycle, the combined Brayton–Rankine cycle, and the steam-turbine-operated Rankine cycle.

The regenerative Brayton cycle shown in Fig. 27.15 contains a gas turbine compressor for the air flow to the cell. The flow then passes through a countercurrent recuperative heat exchanger to recover heat from the combustion product gases leaving the gas turbine. Next, the air and the fuel streams pass into the cathode and anode compartments of the fuel cell(s). The air and fuel streams that leave the cell(s) enter the combustor, where they mix and the residual fuel burns. The combustion products enter the turbine, expand, and generate additional power. The exhaust gases from the turbine pass through the recuperative exchanger to the stack.

The overall solid oxide fuel-cell reactions are

$$H_2 + \frac{1}{2}O_2 \rightarrow H_2O \qquad \Delta H_{298} = -241\,\mathrm{kJ/mol}\,, \qquad (27.40)$$

$$CO + \frac{1}{2}O_2 \rightarrow CO_2 \qquad \Delta H_{298} = -283\,\mathrm{kJ/mol}\,. \qquad (27.41)$$

The ideal or equilibrium potential (E) for the above overall reactions can be calculated using the Nernst equation,

$$E = E^0 + \frac{RT}{2F}\ln\left(\frac{P_{H_2}P_{O_2}^{\frac{1}{2}}}{P_{H_2O}}\right) \quad \text{and}$$

$$E = E^0 + \frac{RT}{2F}\ln\left(\frac{P_{CO}P_{O_2}^{\frac{1}{2}}}{P_{CO_2}}\right), \qquad (27.42)$$

Fuel cell power output

$$= \text{voltage (cell potential)} \times \text{current (load)}\,. \qquad (27.43)$$

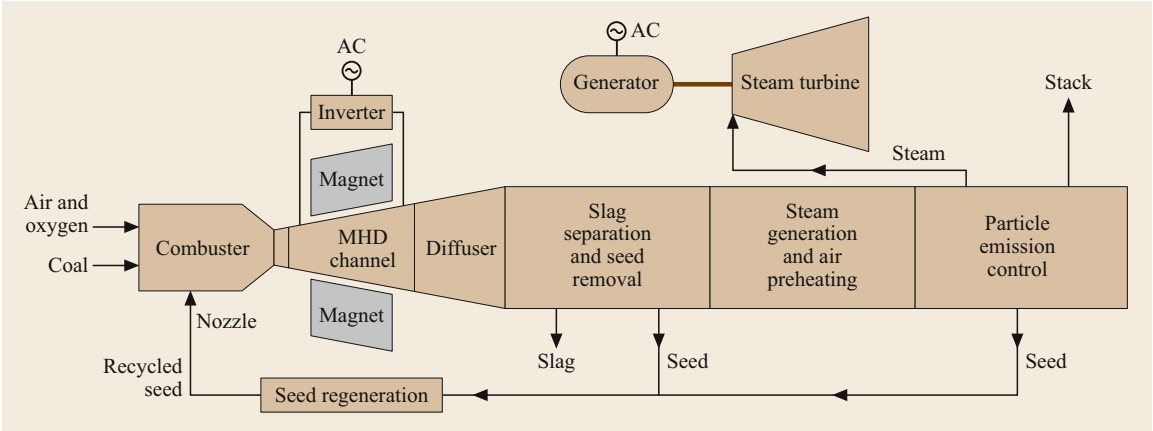

Fig. 27.16 Schematic of a MHD steam power plant

The total power and the total efficiency of the hybrid cycle are calculated as

$$P_{\mathrm{SOFC}} = N_{\mathrm{cell}} P_{\mathrm{cell}} \eta_{\mathrm{DC/AC}} \,, \tag{27.44}$$

$$P_{\mathrm{GT}} = (P_{\mathrm{EXP}} - P_{\mathrm{COMP}}) \eta_{\mathrm{GEN}} \,, \tag{27.45}$$

$$P_{\mathrm{TOTAL}} = P_{\mathrm{SOFC}} + P_{\mathrm{GT}} - P_{\mathrm{AUX}} \,, \tag{27.46}$$

$$\eta_{\mathrm{ele}} = \frac{P_{\mathrm{TOTAL}}}{\sum N_{\mathrm{c}} \mathrm{LHV}_{\mathrm{c}}} \,, \tag{27.47}$$

where P_{SOFC} is the electrical power output from the fuel cell, P_{GT} is the power output from the gas turbine, P_{aux} is the power consumed by the auxiliary units, $\mathrm{LHV_c}$ is the lower heating value, and N_{c} is the number of cells.

Magnetohydrodynamics

The underlying principle of magnetohydrodynamic (MHD) power generation is elegantly simple. An electrically conducting fluid is driven by a primary energy source (e.g., the combustion of coal or any gas) through a magnetic field, which generates an electromotive force within the conductor in accordance with the principle established by Faraday [27.4]. Furthermore, if the conductor is an electrically conducting gas, it will expand, meaning that the MHD system is a heat engine with an expansion process that can drive a gas turbine. However, unlike a conventional gas turbine, which utilizes surface interactions, the MHD system makes use of the change in volume of the gas as it passes through the magnetic field. As such, the MHD generator can be viewed as an electromagnetic turbine, because its output is derived from the electrical interaction between the conducting gas and the magnetic field rather than a direct mechanical interaction. Electrical conduction occurs in a gas that contains free electrons which can be organized into a current by an applied or induced electric field. The free electrons may be injected into the gas or generated internally. Because of the electrostatic forces involved, positively charged ions must also be present to maintain electrical neutrality. Thus, an electrically conducting gas consists of electrons, positively charged ions to balance the electric charge, and neutral atoms or molecules. Such a gas is termed a plasma [27.5].

In MHD generators, the free electrons that can be organized into a current can be obtained by two different methods: thermal and nonequilibrium ionization. In thermal ionization, the plasma is obtained by heating the gas to a sufficiently high temperature until the gas ionizes, releasing electrons. During nonequilibrium ionization, strong electric fields are induced in a manner similar to the mechanism used in gas discharge devices. In either case, energy is transferred from the flowing fluid to the electrical output through the coupling of the electron-containing gas to the ions via electromagnetic forces. The ions are less mobile than the free electrons as they are hindered by collisions with molecules or other ions.

A schematic of a MHD steam power plant is shown in Fig. 27.16. The product gas with high electrical conductivity that is formed by burning the coal in the combustor is mixed with potassium carbonate (termed the *seed*) to increase its conductivity. The ionized gas then flows through a strong magnetic field, which induces an electric field and establishes a potential difference between the walls of the duct. The resulting direct current (DC) is then converted to alternating current (AC) using a solid-state inverter.

After flowing through the magnetic field, the hot gases are used to generate steam and turn a turbine, just as in a conventional plant. As the heat is transferred, slag is removed for disposal and the seed is captured for recycling. One considerable drawback of this scheme is the need to use expensive superconducting magnets that must be cooled to −269 °C (4 K) to generate the

necessary magnetic fields. About 50% efficiency can be achieved if the MHD generator is operated in tandem with a conventional plant.

27.1.8 Planning and Investment

Investment planning for power plants requires a long-term plan which will ensure that costs such as the construction of new power plants or the replacement of existing plants with newer ones in an uncertain economic environment will be covered. Power plants are highly capital intensive. Investment in energy systems and infrastructure (e.g., transportation, availability of fuel, water, communications, and environmental compatibility) must be viewed in the framework of economic growth, savings, and the size and degree of liberalization of capital markets.

Natural gas has several advantages over most other energy resources: it allows high operational flexibility and supply of large supplies to be easily moved to power plants. Also, on a per-kW basis, burning gas produces lower CO_2 emissions than burning oil or coal. Therefore, various studies have revealed that gas is the preferred energy source for new generating capacity.

A power plant should provide a reliable supply of electricity at the lowest cost to the consumer and with minimal environmental impact. The total price we pay for electricity from power plants derives from the capital costs and the operating costs of the plants. The capital costs depend entirely on the investment in the plants, and include interest, depreciation, taxes, insurance, and decommissioning (where applicable). Operating costs include those associated with operation, maintenance, and fuel, and are inversely proportional to the capacity factor. Operating and maintenance costs mainly depend on the type of the plant considered and the fuel used. Maintenance costs may be reduced if the unit is not operating or is operated at a low load.

In 2015, the global investment in energy supplies amounted to US $1.8 trillion, which was 8% lower than the corresponding value for 2014, mainly due to a sharp drop in oil and gas investment. China has become the most important destination for investment in energy supplies, largely due to its high level of investment in its electricity sector.

The global investment in energy efficiency is increasing; it reached US $220 billion in 2015. Oil and gas represent the largest energy investment category, corresponding to 45% of the total global investment. Thus, fossil fuels continue to dominate global energy supplies, but there has been a marked increase in renewable energy supplies. The competition between fossil and renewable resources is expected to continue and is likely to reshape supply-side technologies and suppress unit costs. Supply costs have declined across the energy spectrum, with average cost reductions in 2015 ranging from 3% for onshore wind to 30% for US shale oil and gas. Investment in renewables in 2015—primarily wind, solar PV, and hydropower—was almost US $290 billion. This sharp rise decreased the average carbon intensity (the amount of carbon by weight emitted per unit of energy used) of the power generation from new capacity. Wind and solar investments will have a strong impact on gas-fired generation but less on oil, which is used primarily in transportation. Price variations are mainly due to fluctuations in fuel supplies as well as technology improvements and increased market penetration.

27.2 Primary Energy

Primary energy is that obtained from raw fuels and any other forms of energy received by a system as input(s). Primary energy is transformed to more convenient forms of energy and cleaner fuels. To date, the most important primary energy sources remain carbon-based fossil fuels. Fossil fuels (oil, coal, and natural gas) are said to be nonrenewable because of the long cycle time needed to regenerate stocks of these fuels—they derive from the long-term decomposition of plant and animal matter over millions of years. The Sun is the original source of all such fuel resources because it gradually decomposes fossils into fuels.

Fuels are chemical substances that can be burned (combusted) and thus converted to thermal energy. They mainly consist of carbon and hydrogen, sometimes with small amounts of sulfur or minerals, and may be solid, liquid, or gaseous. Coal and coke are examples of solid fuels, whereas petroleum and natural gas are examples of liquid and gaseous fuels, respectively. Liquid fuels (such as those used in the transportation industry) are easy to handle and transport. Such fuels can be categorized according to their volatility (the ease with which they vaporize). The most volatile fuels are gasoline and kerosene. Less volatile fuels (with a range of viscosities) are used in diesel engines and boilers. Ethanol produced from the fermentation of sugar is another prominent liquid fuel. Petroleum oils are usually a mixture of several liquid fuels.

Gaseous fuels may be a mixture of gases such as methane (CH_4) and ethane (C_2H_6). Gas is a preferred

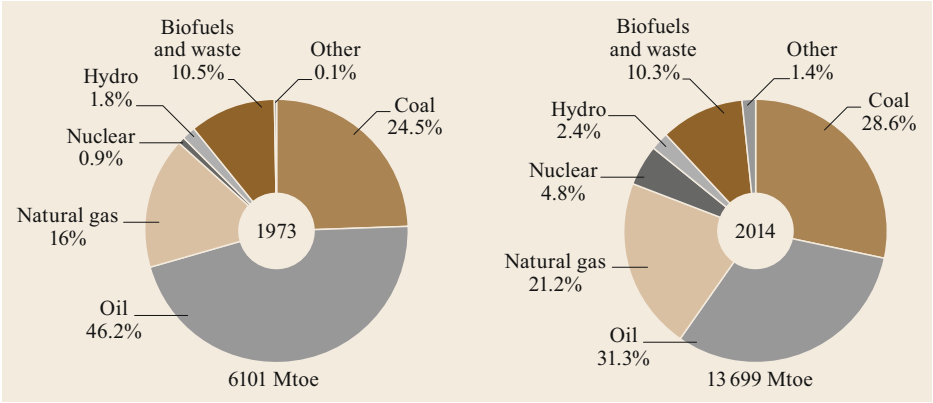

Fig. 27.17 Pie charts showing the total primary energy used globally to produce electricity in 1973 and in 2014 as well the contributions from each primary energy source (including international aviation and international marine bunkers). In these charts, peat and oil shale are aggregated with coal, and the *other* category includes, for example, geothermal, solar, and wind. These energy statistics are from the International Energy Agency (IEA)

fuel, as its combustion has less of an impact on the environment than the burning of other fossil fuels. Gaseous fuels burn more readily and completely than other fuels and are convenient to handle. They are generally odorless and colorless. Because gaseous fuels are in a molecular form, they are easily mixed with the air (as required for combustion) and they oxidize more quickly than solid or liquid fuels.

Fuels that can be used in nuclear reactors as sources of electricity are called nuclear fuels. The energy released during nuclear fission and fusion processes is called nuclear energy. Examples of nuclear fuels include ^{235}U, ^{238}U, and ^{239}Pu. Nuclear energy is discussed later in this chapter.

27.2.1 The Economics of Fuels

Natural gas supplies about 22% of the energy used worldwide, and is used to produce 25% of the electricity generated globally. The natural gas market has grown considerably in recent years due to the availability of shale gas and increasing supplies of liquefied natural gas. Global gas demand is expected to grow by 1.6% per year until 2022, with consumption reaching almost 4000 billion cubic meters (bcm) per year by then, up from 3630 bcm in 2016. The United States remains the world's largest gas consumer and producer. The US is forecast to account for 40% of the world's extra gas production during the five-year period up to 2022, reaching 890 bcm per year, more than a fifth of the global gas output. During this five-year period, the largest increase in gas supplied—up to 45%—is expected to come from the Marcellus fields. China will account for 40% of the projected growth in gas supplies. Between 1971 and 2014, the total primary energy supplied annually around the world more than doubled, and the sources of the gas supplied shifted somewhat (Fig. 27.17).

27.3 Boilers and Furnaces

27.3.1 Boilers

Boiler versus steam generator. Although their definitions are somewhat ambiguous, boilers work at low to medium pressures (7–2000 kPa or 1–290 psi), whereas steam generators operate at pressures above this range. If a boiler operates at pressures above the critical pressure (200 psi or 22 MPa), it is termed a supercritical steam generator.

Oven versus furnace. Traditionally, ovens operate at temperatures below 540 °C (1000 °F), but modern ovens are rated to 760 °C (1400 °F). Furnaces can typically run at temperatures of 1100 °C (2000 °F) or even higher.

A steam generator is one of the main components used in a coal-fired power plant. Its concept, design, and integration into the overall plant considerably influence the costs, operating behavior, and availability of the power plant. The thermal structure of a boiler furnace is shown in Fig. 27.18. In the steam generator, fuel and air are forced into the furnace, where combustion occurs. From there, the fuel gas travels throughout

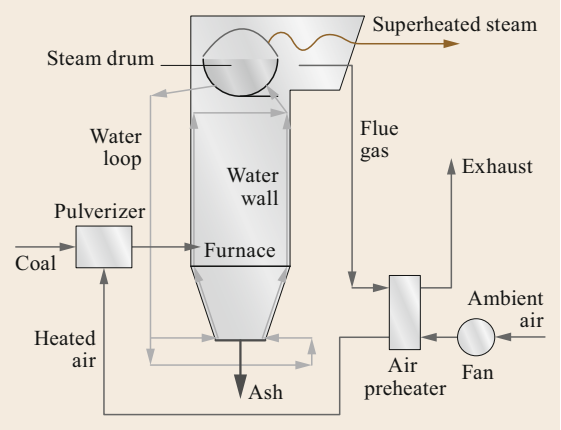

Fig. 27.18 Thermal structure of a boiler furnace

the boiler and the feedwater (the water that enters the boiler) absorbs the heat, eventually absorbing enough energy to vaporize. Boiler makers have developed various designs to maximize the energy extracted from the fuel and transferred to the water.

Preheated water enters the top of the boiler, as shown in Fig. 27.18. The hot water naturally circulates throughout the tubes. The heated water flows back to the steam drum due to buoyancy forces. Steam collects in the drum. Not all of the water is turned to steam, so that water passes through the water loop again and continues to circulate until it changes phase and becomes steam. Meanwhile, the control system monitors the temperature of the steam drum and other parameters to check whether it should keep the burner active or shut it down. Sensors also control the amount of feedwater that enters the boiler.

Types of Boilers

Boilers are categorized based on various factors, such as the furnace position, the type of fuels used, the arrangement of tubes, and circulation characteristics (Fig. 27.19).

Boiler Safety

Safety is a prime consideration when operating a boiler. Operating at pressures above the design pressure is dangerous, so appropriate pressure control inside the steam generator is very important. Although boilers are usually equipped with a pressure relief valve, if the boiler fails to contain the expansion pressure, the steam energy is instantly released to avoid a buildup of pressure.

The concentration of solids in the boiler should be measured, and boiler blowdowns should be performed periodically to keep the boiler within established solid concentration limits. In a blowdown, sediment or scale is blown from the boiler through blowdown valves positioned at the lowest point in the boiler. These valves should be maintained in good working order and must be opened and closed carefully when used.

Boilers should always be brought online slowly, and cold water should never be injected into a hot system, as the resulting sudden change in temperature could warp or rupture the boiler. Because many boilers are fired by natural gas, diesel, or fuel oil, special precautions should be taken to avoid leaks. Boiler operators should ensure that the fuel system—including its valves, lines, and tanks—is operating properly. The low-water cutoff is a very important electrical/mechanical device on a boiler, as it maintains a safe water level. If the water level drops below the minimum required, the boiler could overheat and explode. Therefore, the low-water cutoff should be tested regularly.

To prevent furnace explosions, boiler operators must purge the boiler before igniting the burner. Workers should check the fuel-to-air ratio, the condition of the draft, and the flame to ensure proper operation. Ventilation systems should also be inspected and maintained to make sure that combustion gases do not build up in the boiler room.

Boiler Water Treatment

Efficient boiler performance depends to some degree on the quality of the water. The boiler feedwater must

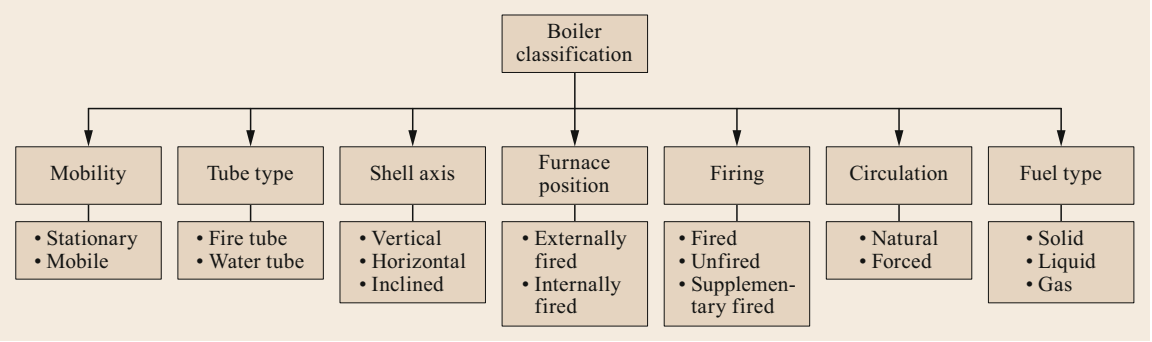

Fig. 27.19 Boiler classification

be treated to prevent excessive fouling of the tubes and heat transfer equipment as well as turbine blade erosion. Common impurities found in untreated water include:

- Dissolved solids (e.g., calcium and magnesium)
- Suspended solids (mineral matter)
- Dissolved gases (oxygen and CO_2)
- Scum-forming substances (carbonate, chlorate, and sulfate).

In the steam boiler industry, high-purity feedwater is required to ensure proper operation of the steam generation system. High-purity feedwater reduces the need for blowdowns, which in turn decreases fuel costs and reduces the costs associated with the boiler chemicals used during blowdowns.

The boiler system loses water through steam and water leaks. Additional water called *make-up water* is therefore added to the boiler to replace these losses. The amount of make-up water used and the level of naturally occurring impurities in the water will determine the type of water treatment required. Boiler systems with fewer leaks require simpler water treatments.

All water contains dissolved minerals. If these minerals are allowed to reach high enough levels in the boiler water, they will form a hard shell on the hot surfaces of the boiler. This hard shell is called *scale*, which is often found on the external surfaces of fire tubes or the internal surfaces of water tubes. Scale insulates the heating surface, thus reducing the ability of fire tubes to transfer heat from the hot combustion gas to the boiler water. Scale can also cause tube rupture and often results in high stack temperatures. Boiler water also contains dissolved gases such as oxygen and carbon dioxide. In the presence of water and metal, these gases can cause corrosion.

A number of processes can be used to treat boiler feedwater, such as chemical treatment/lime softening, dual-media filtration, carbon adsorption, conventional reverse osmosis membranes, and ion-exchange resin polishing. Some methods of pretreating boiler feedwater are discussed below.

Lime Soda Process

Calcium and magnesium salts are removed using lime and soda ash. The chemical reactions involved in this process are

$$\begin{aligned}
Ca(HCO_3)_2 + Ca(OH)_2 &\rightarrow 2\,CaCO_3 + 2\,H_2O \\
MgCl_2 + Ca(OH)_2 &\rightarrow Mg(OH)_2 + CaCl_2 \\
MgSO_4 + Ca(OH)_2 &\rightarrow Mg(OH)_2 + CaSO_4 \\
CaSO_4 + Na_2CO_3 &\rightarrow CaCO_3 + Na_2SO_4 \\
CaCl_2 + Na_2CO_3 &\rightarrow CaCO_3 + 2\,NaCl
\end{aligned}$$

Insoluble components such as calcium carbonate and magnesium hydroxide settle at the bottom.

Deaeration

The feedwater from the condenser contains dissolved gases such as O_2 and CO_2. Oxygen is present at a relatively high partial pressure in feedwater, so a temperature near to the saturation temperature of water is required to disassociate the dissolved oxygen from the water. The removal of oxygen from the feedwater is necessary because the dissolved oxygen (in combination with water) will attack iron, causing corrosion. This reaction occurs in two steps,

$$Fe^{2+} + 2\,OH^- \rightarrow Fe(OH)_2$$

and then

$$\underbrace{4\,Fe(OH)_2}_{\text{Soluble ferrous hydroxide}} + \underbrace{O_2}_{\text{Dissolved oxygen}} + \underbrace{2\,H_2O}_{\text{Water}} \rightarrow \underbrace{4\,Fe(OH)_3}_{\text{Insoluble ferric hydroxide}}$$

A deaerator is an open-type feedwater heater in which steam bled from the turbine is mixed directly with water. As the water temperature increases, the amount of gases dissolved in the water decreases.

Types of Steam Generators

Shell Type. This is a cylindrical boiler with the shell axis perpendicular to the firing floor. Originally, shell-type steam generators included a chamber at the lower end of the shell that contained the combustion appliance. The gases rose vertically through a flue surrounded by a water column. Large-diameter (100 mm) cross tubes were fitted across this flue to help absorb heat from the gases, which were then discharged to the stack. Instead of a vertical flue, more modern shell-type steam generators have one or two banks of small-bore tubes that run horizontally before the gases are discharged. The steam is contained in a hemispherical chamber at the top of the shell.

Vertical boilers are generally used for heat recovery from exhaust gases originating from power generation or marine applications. The gases pass through small-bore vertical tube banks. The same shell may also contain an independently fired section to produce steam when there is no exhaust gas available or when it is insufficient.

A shell-type boiler typically has a much higher water volume than a water tube boiler. Therefore, a shell-type boiler is more robust to load fluctuations or load demands that temporarily exceed the rated boiler capacity.

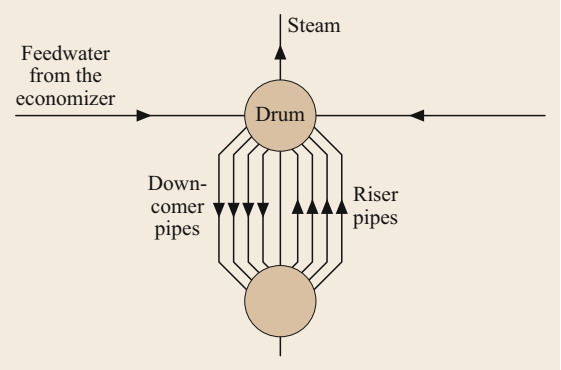

Fig. 27.20 Schematic of a natural circulation water-tube boiler

Shell-type boilers are sometimes referred to as fire-tube boilers because the products of combustion pass through the boiler tubes.

Natural Circulation Boiler. As its name implies, this type of boiler makes use of natural circulation due to the density difference between the fluids in the downcomer and riser. These buoyancy forces result from uneven heating of the water in the boiler. The natural circulation is maintained by the static head difference and natural convection due to the density differential between the mean downcomer density and the mean riser density. The downcomers are located outside the furnace, away from the heat of combustion. They serve as pathways for the downward flow of relatively cool water. Natural circulation has generally been used in boilers at pressures of up to 140 bar. Natural circulation boilers can be classified into vertical-tube and sloped-tube types depending on the positioning of the tubes.

Figure 27.20 shows a schematic of a typical natural circulation waste-heat water-tube boiler with a steam drum and downcomer and riser pipes. Feedwater enters the drum from an economizer. This mixes with the steam–water mixture inside the drum. The downcomers carry the resultant cool water to the bottom of the evaporator tubes, while the external risers carry the water–steam mixture to the steam drum. The heat transfer tubes also act as risers, generating steam.

The circulation ratio is defined as the mass ratio of the steam–water mixture to the steam generated. The natural circulation largely depends upon the heights of the risers and downcomers and the mean density of the fluid. The main feature of natural circulation boilers is an absence of water circulation pumps.

Forced Circulation Boiler. Most modern boilers use forced circulation. When the boiler pressure is very high, the difference in density between the water and the saturated steam decreases, reducing the circulation. Therefore, the difference between the lower drum and the steam drum must be increased to obtain the same output under high-pressure conditions. This can be achieved through forced circulation. The operation of such a boiler is largely similar to that of natural circulation unit, except that a pump is used to circulate water through the risers. The use of pump also means that forced circulation boilers are normally operated at high pressure.

A forced circulation boiler in which water flows sequentially without circulating through its components (economizer, furnace, evaporator, and superheating tubes) is called a *once-through boiler*. These boilers generally operate at high pressure, with feedwater entering at a high subcritical (> 2610.68 psi $= 180$ bar) or supercritical pressure and superheated steam leaving the system at a slightly lower pressure. Once-through boilers are commonly used for supercritical steam generation.

Once-through boilers can be used up to a pressure of more than 30 MPa without requiring any change in process engineering. In these boilers, subcooled water supplied by a feedwater pump at the inlet of the tubes is heated, evaporated, and superheated in long evaporation tubes to produce superheated steam at a prescribed pressure and temperature at the outlet of the tubes.

The main advantage of a once-through boiler is that it does not require circulating pumps or drums. The energy required for circulation is provided by the feed pump. Since the state of the superheated steam at the outlet is determined by the total heat input regardless of the heat flux distribution along the tube at a defined mass flow rate, the once-through boiler is a fairly simple device to use to obtain superheated steam of a prescribed state at any partial load.

In a nuclear plant, a reactor pressure vessel (RPV) contains the nuclear reactor or the fission zone, the coolant, the core shroud, and the reactor core. If the coolant is water (which it usually is), the reactor pressure vessel also includes a pressurized water reactor and a boiling water reactor. The reactor pressure vessel is typically kept at a pressure of about 70 bar (7 MPa). When the temperature reaches approximately 290 °C, the water starts to boil and the resulting saturated steam is produced directly in the reactor pressure vessel. After separating the steam and water in the upper part of the reactor pressure vessel, the steam is routed directly to a turbine driving an alternator. The steam from the turbine is then condensed and fed back into the primary cooling circuit, where it is heated in the fission zone. Since the steam produced in the fission zone is slightly radioactive, mainly due to short-lived activation products, the turbine is housed in the same reinforced building as the reactor.

Parts and Components of a Steam Generator

Superheaters. One of the most important accessories of a boiler is a superheater. The steam that is produced in the boiler and is in direct contact with the hot water is known as saturated steam, which condenses due to the high velocity of the steam inside the turbine. This condensed vapor can erode the turbine blades. A superheater is therefore employed to raise the temperature of the steam above the saturation temperature while keeping the pressure constant. Steam that undergoes this process is referred to as superheated steam. In essence, superheating improves turbine efficiency and hence the lifetime of the turbine and the capacity of the plant by reducing turbine corrosion and steam consumption.

Superheaters can be categorized into three types depending upon the way that the heat is transferred:

- Radiant superheaters
- Convective superheaters
- Combined radiative and convective superheaters.

Convective superheaters are normally called primary superheaters, and are located near the convective zone of the furnace, whereas radiant and combined superheaters are termed secondary superheaters.

Superheater Flow Arrangements. The saturated steam from the drum is sent to a convective superheater and then to a radiant superheater. Steam leaving the radiant superheater is sent to a desuperheater, where clean water is sprayed directly into the steam. The temperature of the steam leaving the pendant superheater should not exceed the rated value.

Also, superheaters often contain multiple superheating stages, such as platen, pendent, horizontal, and radiant superheaters.

Radiant Superheaters. Radiant superheaters receive energy primarily as thermal radiation from the furnace, with little energy originating from convective heat transfer. These superheaters are located at the furnace exit or at the turning section. They absorb more enthalpy at partial loads than the convective type. At lower loads, the flow distribution inside the superheater tubes is less uniform. The radiant superheater outlet temperature decreases with increasing boiler output. At higher loads, the mass flow rate of the combustion gas is high due to the presence of more fuel and air for combustion. The convective heat transfer coefficient increases both inside and outside the tubes. Therefore, more heat is transferred to the steam per unit mass flow rate, and the temperature of the steam increases with the load. Also, the surface area required to transfer a given amount of energy is lower due to the higher log mean temperature difference and higher heat transfer coefficient. Hence, radiant superheaters can be relatively inexpensive despite the better grade of materials required to build them.

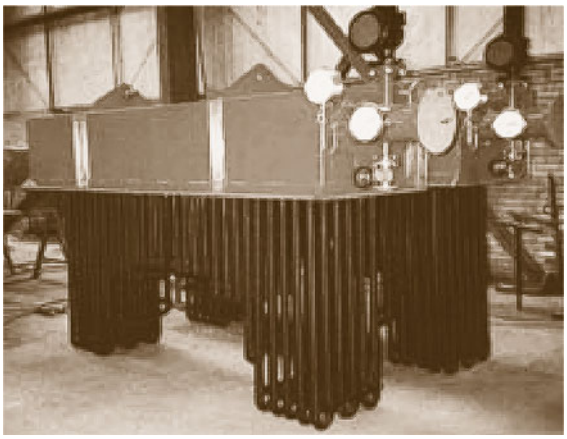

Fig. 27.21 Arrangement of tubes in a pendant superheater

Convective Superheaters. A convective superheater is operated at low gas temperatures that range from 423 to 813 K depending on the degree of superheating required. It is shielded by several rows of screen tubes, so the gas is well mixed and cooled before it encounters the superheater, meaning that the performance of the superheater can be accurately predicted. Due to the low log mean temperature difference and low heat transfer coefficient of a convective superheater, the surface area required is relatively large, which can make convective superheaters more expensive than radiant superheaters.

Pendant Superheaters. Pendant superheaters receive heat through both convection and radiation. They are normally suspended (hence the name), as shown in Fig. 27.21, and are usually located in the crossover duct between the furnace and the back pass.

The outside tube diameter of a pendant superheater is normally 32–51 mm, and the tube thickness is usually 3–7 mm.

Platen Superheaters. These devices consist of flat panels of tubes located in the upper part of the furnace, where the gas temperature is high. The tubes of a platen superheater receive very high levels of radiation and have a heavy dust burden, so great care should be taken when designing platen superheaters. The arrangement of tubes in a platen superheater is shown in Fig. 27.22.

The mass flux of steam in the platen superheater is normally 800–1000 $\mathrm{kg/(m^2\,s)}$. The outer diameter of a platen superheater tube is in the range of 32–42 mm. The number of parallel tubes in a platen is generally 15–35, depending on the design steam velocity.

Fig. 27.22 Arrangement of tubes in a platen superheater

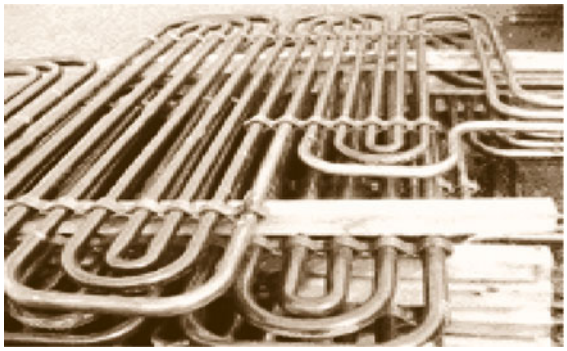

Fig. 27.23 Arrangement of pipes in a convective reheater

Reheaters. The design considerations for reheaters are similar to those for superheaters. The reheater is usually located above the primary or convective superheater in the convective zone of a utility boiler. The arrangement of pipes in a convective reheater is shown in Fig. 27.23. The pressure drop inside the reheater tubes has a significant adverse effect on the efficiency of the turbine, so it should be kept as low as possible. The tube diameter of the reheater is normally 42–60 mm and the overall heat transfer coefficient is 90–110 $W/(m^2 K)$.

Economizers. The feedwater from the first high-pressure heater passes through a heat exchanger and heats up to the saturation temperature at the boiler pressure. This heat exchanger is normally called an economizer. It uses exhaust heat from the stack gases to heat the feedwater to the desired saturation temperature, which decreases the energy that must be fed into the boiler and therefore increases the efficiency and economy of the power plant. The economizer is generally placed between the convective superheater and the air preheater.

An economizer is designed for downward gas flow and upward water flow, and consists of at least 250–300 coils in a single bank with a staggered arrangement. Figure 27.24 depicts the arrangement of coils in an economizer.

Water enters from a low header and flows through horizontal tubes that serve as the heating surface. The tubes are equipped with return bends at their ends to allow for continuous tubing. The upper ends of the tubes connect to outlet headers, which are in turn connected to the boiler drum by means of piping. Modern power plants use steel-tube economizers. The outside diameter of an economizer tube is normally in the range of 25–75 mm, and the tube thickness is 3–5 mm. Providing a large economizer surface area enhances the heat transfer rate.

Feedwater Heaters. Feedwater heaters are used to raise the temperature of the water or to increase the mean temperature of heat addition in the cycle before the water enters the boiler. The feedwater heater utilizes steam extracted from the turbine expansion line for water heating. Feedwater heaters are used in a regenerative feedwater cycle to increase thermal efficiency and thus achieve fuel savings.

Feedwater heaters are normally categorized into two types:

- Open feedwater heaters
- Closed feedwater heaters.

Closed Feedwater Heaters. A closed feedwater heater is typically a shell-and-tube heat exchanger that warms feedwater using steam that may or may not be superheated. Normally, water flows inside the pipe and steam flows on the shell side. A schematic of a closed feedwater heater in a typical steam turbine power plant is shown in Fig. 27.25.

Closed feedwater arrangements are further classified into two types based on the drain release method applied:

- Drain cascaded forward
- Drain cascaded backward.

In the drain cascaded forward type, the drain from the feedwater heater is mixed with the drain from the preceding feedwater heater. The reverse happens in the drain cascaded backward type, as shown in Fig. 27.25. Based on the state of the steam or level of turbine extraction, feedwater heaters can be further classified into high-pressure, intermediate-pressure, and low-pressure feedwater heaters. Modern power plants that employ regeneration normally employ multiple feedwater heaters. There should always be one deaerator along with an open feedwater heater. The purpose

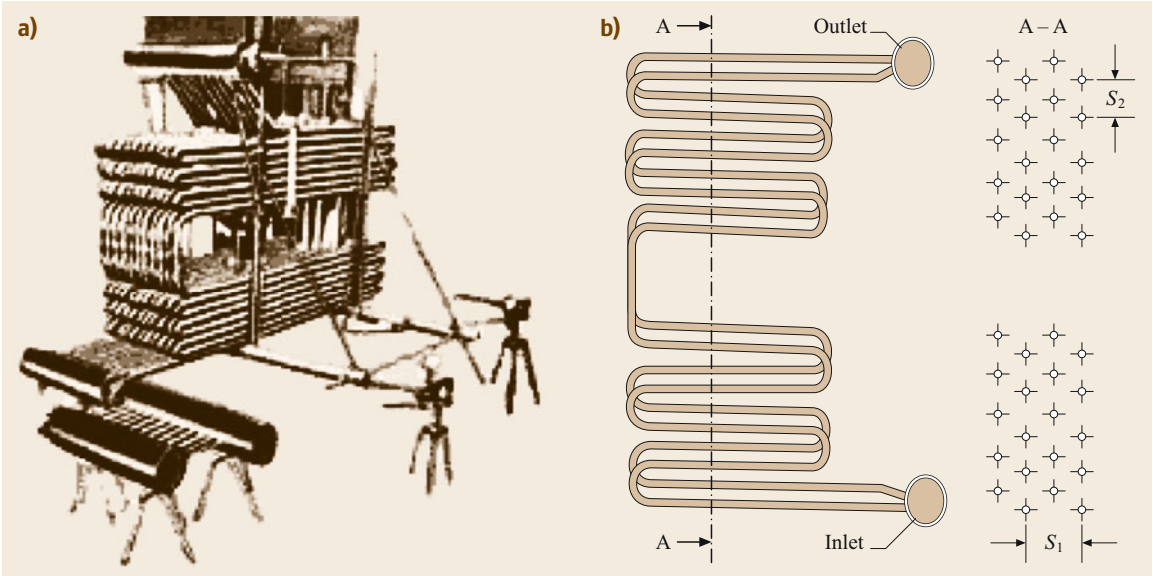

Fig. 27.24a,b Arrangement of coils in an economizer

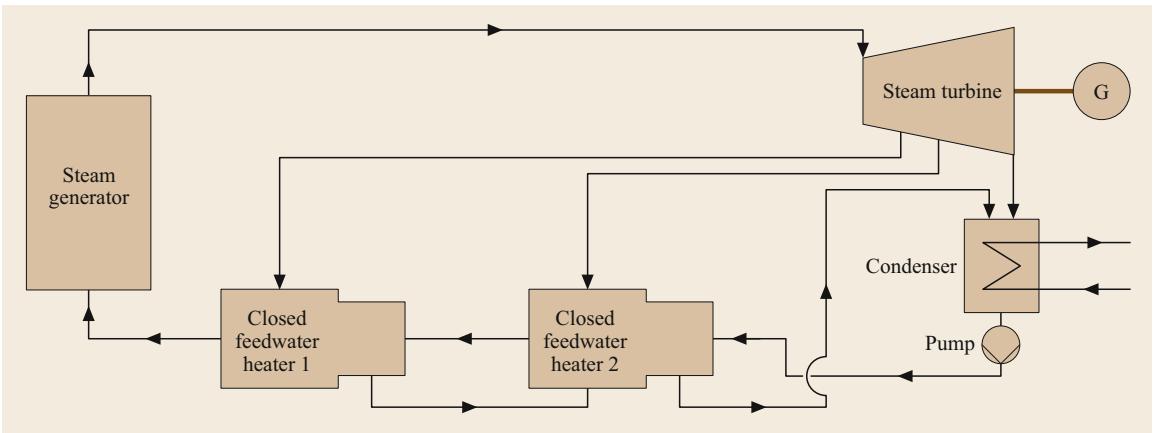

Fig. 27.25 Schematic of a steam turbine regenerative cycle utilizing a closed feedwater heater with drain cascaded backward

of the deaerator is to remove the dissolved oxygen from the system. High-pressure (HP) feedwater heaters utilize steam from the HP turbine and are therefore called high-pressure feedwater heaters. A high-pressure closed feedwater heater has three zones: the desuperheating zone, the condensing zone, and the drain cooling zone. During the design of such a heat exchanger, each zone is considered to be a separate heat exchanger, and the corresponding heat transfer coefficients and pressure drops are evaluated separately. The temperature–duty diagram for a three-zone feedwater heater or high-pressure closed feedwater heater is shown in Fig. 27.26.

Open Feedwater Heaters. In open feedwater heaters, heat transfer takes place through the direct mixing of steam and water. Open feedwater heaters are normally more efficient than closed feedwater heaters. Despite this higher efficiency, closed feedwater is used in most modern power plants because it requires fewer pumps, leading to lower maintenance costs.

Air Preheaters. The temperature of the flue gas leaving the chimney is typically in the range of 280–480 °C, resulting in large energy losses. Air heaters utilize this hot flue gas to preheat the combustion air and boost the combustion efficiency. Since these heaters are gas-

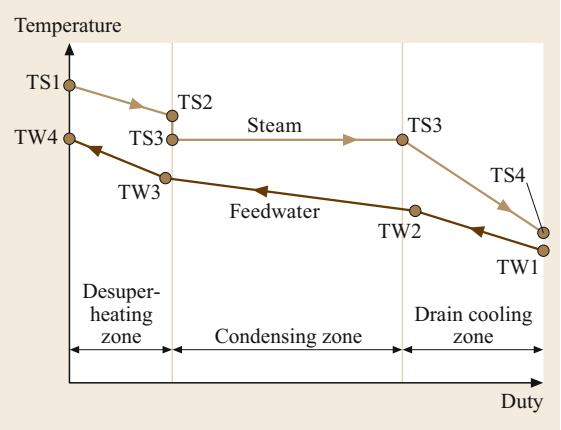

Fig. 27.26 Temperature–duty diagram for a three-zone feedwater heater

to-gas heat exchangers, they have large heat transfer surface areas.

Recuperative or regenerative heaters are used to recover exhaust gas heat. A recuperative air preheater is a shell-and-tube heat exchanger in which hot flue gas flows inside the tubes and air flows on the shell side. Regenerative heat exchangers, also known as rotary preheaters, are counterflow types that consist of a rotor and housing. The rotor is constructed from steel sheets and driven by an electric motor coupled with a worm-gear drive that helps reduce the speed of the rotor to 2–6 rpm. Heat transfer elements on the rotor absorb heat as the rotor rotates through the flue gas side, and this absorbed heat is later released during the rotation through the air section. These heat transfer elements are normally divided into 12–24 sets distributed radially on the rotor.

Rotary preheaters can be categorized into three types based on the number of sections that the rotor passes through: bisector, trisector, and quadsector. Trisector air preheaters are divided into three sections: one for the flue gas, one for the primary section, and one for the secondary section. In the quadsector type, the secondary air section is divided into two sections embracing the primary air section. It is very important to control the leakage of air into the flue gases, as such leakages lead to energy losses in the system. Radial, axial, circumferential, and shaft sealing systems are used to minimize leakages.

Wasted heat is heat released to the atmosphere. Minimizing this waste or reusing it for other purposes is key to maximizing plant economics. One such use of waste heat from power plants is district heating. In this case, steam heated by exhaust heat is distributed through pipelines over a large area. Thus, large industrial or residential neighborhoods can be heated by steam or hot water from a single large central combustion plant. In the summer, space cooling can be provided by using the hot water or steam to run an absorption-type refrigeration plant.

27.3.2 Furnaces

A furnace is an enclosed chamber that is used to heat a working medium such as water. If the furnace is designed to produce steam, it is a steam generator. The capacity of a furnace is determined according to the type of fuel and the firing method employed to promote complete burning of the combustible and suitable disposal of the resulting ash. A furnace can be used to combust solid, liquid, or gaseous fuels.

Ideal Combustion

The generalized ideal combustion equation can be written as

$$\mathrm{C}_X\mathrm{H}_Y\mathrm{S}_Z\mathrm{O}_K + \left(X + \frac{Y}{4} + Z + \frac{K}{2}\right)\mathrm{O}_2 + m\,\mathrm{H_2O} \rightarrow P\,\mathrm{CO_2} + Q\,\mathrm{H_2O} + G\,\mathrm{SO_2} \quad (27.48)$$

Similarly, the generalized combustion equation takes the form

$$\mathrm{C}_X\mathrm{H}_Y\mathrm{S}_Z\mathrm{O}_K + \left(X + \frac{Y}{4} + Z + \frac{K}{2}\right)\mathrm{O}_2 + 3.76\left(X + \frac{Y}{4} + Z + \frac{K}{2}\right)\mathrm{N}_2 + m\,\mathrm{H_2O} \rightarrow P\,\mathrm{CO_2} + Q\,\mathrm{H_2O} + R\,\mathrm{N_2} + G\,\mathrm{SO_2} \quad (27.49)$$

The air–fuel ratio is defined as

$$\frac{A}{F} = \frac{m_{\mathrm{air}}}{m_{\mathrm{f}}}\,. \quad (27.50)$$

Theoretical Dry Air–Fuel Ratio

Adding 1 kmol of oxygen to 3.76 mol of nitrogen generates 4.76 mol of air. The molecular weight of air is therefore

$$\frac{32 + 3.76 \times 28}{4.76} = 28.84\,; \quad (27.51)$$

$$\left(\frac{A}{F}\right)_{\mathrm{TD}} = \frac{m_{\mathrm{air}}}{m_{\mathrm{f}}} = \frac{4.76\left(X + \frac{Y}{4} + Z - \frac{K}{2}\right)28.84}{100}\,. \quad (27.52)$$

Theoretical Wet Air–Fuel Ratio

Since air can be humid, the calculation of the theoretical wet air–fuel ratio depends on the relative humidity,

defined as

$$\phi = \frac{p_{\text{vapor,act}}}{p_{\text{vapor,sat}}} \,. \tag{27.53}$$

The amount of moisture in ambient air is

$$n = \frac{4.76\left(X + \frac{Y}{4} + Z - \frac{K}{2}\right) 28.84 w}{18} \,. \tag{27.54}$$

The theoretical wet air–fuel ratio is then given by

$$\left(\frac{A}{F}\right)_{\text{TW}} = \frac{m_{\text{wet,air}}}{m_{\text{f}}} = \frac{4.76(X + \frac{Y}{4} + Z - \frac{K}{2})(28.84 + w18)}{100} \,. \tag{27.55}$$

Pressure Conditions

Not all boiler furnaces are airtight—especially boilers that burn solid fuels (known as *stokers*). Flue gases may escape into the plant area if the furnace pressure is greater than the atmospheric pressure. Other furnace designs may require draft and furnace pressure control. The furnace pressure is typically controlled using a balance draft system. An induced draft fan is modulated to maintain the furnace at a slightly negative pressure. Furnace pressure measurement and induced fan control is required. The location of the furnace pressure transmitter is important because the pressure is not uniform throughout the furnace. More effective furnace pressure control is possible if combustion airflow rate measurements are available.

Solid Fuel Furnaces

Furnaces that use solid fuels for combustion are normally called solid fuel furnaces. Such fuels include coal, coke, and firewood (wood chips and pellets).

Stokers and Grates. There are various ways to introduce coal into a furnace. Stokers play a vital role in distributing coal into a furnace, and are normally categorized into the following types according to how the coal is introduced into the fire:

- Traveling-grate stokers
- Chain-grate stokers
- Spreader stokers
- Vibrating stokers
- Underfeed stokers.

Traveling-grate stokers have been in use for the past 50 years and are the most popular type of stoker to use to burn coal for boilers. In addition to coal, traveling-grate stokers can handle a wide variety of waste fuels. Underfeed stokers, which push the coal up into the furnace from below the grate, are only used for small plants, and mainly for steam production rather than power generation.

Chain and traveling-grate furnaces have similar characteristics. Coal lumps are fed continuously onto a moving grate or chain. Air is drawn through the grate and through the bed of coal on top. As the coal enters, it is heated by radiation from the refractory. Moisture and volatile matter are released. The chain/grate moves the coal slowly into the region in which ignition is established, and the temperature in the coal bed rises. The carbon gradually burns off, leaving ash that drops off at the end into a receptacle, from which it is removed for disposal. The ash formed may have a carbon content as high as 4–5%.

In the spreader stoker arrangement, a high-speed rotor drops the coal into the furnace over a moving grate to promote fuel distribution.

Pulverized Fuel Furnaces

A boiler furnace consists of a combustion space surrounded by water walls. The principle of combustion in pulverized fuel boilers is that coal ground into a fine powder is mixed with air and transported into a combustion chamber, where it burns with a flame similar to the flame from a liquid or gaseous fuel.

The furnace is designed to burn the fuel efficiently and steadily to ensure the transfer of heat to the working medium. It is also designed to generate a flame with the lowest amount of pollutants. For the furnace to operate properly and safely, it is essential to sustain a controlled furnace exit gas temperature (FEGT).

The combustion gases leave the furnace at a safe temperature that will not cause clinkering to the subsequent heating surface.

A furnace can be characterized geometrically by its linear dimensions: the front width a, the depth b, and the height h_{f}, as shown in Fig. 27.27. The appropriate values of these dimensions depend on the rated fuel consumption and the thermal, physical, and chemical properties of the fuel to be used.

The furnace should be sufficiently high that the flame will not heat the superheater tubes. The minimum furnace depth depends on the capacity of the boiler and the types of fuel burnt.

The width and depth of the furnace are influenced by the arrangement of the burners, the heat release rate per unit furnace area, the power output of each burner, and the flame length. Pulverized furnaces can be classified into two types depending on the condition of the

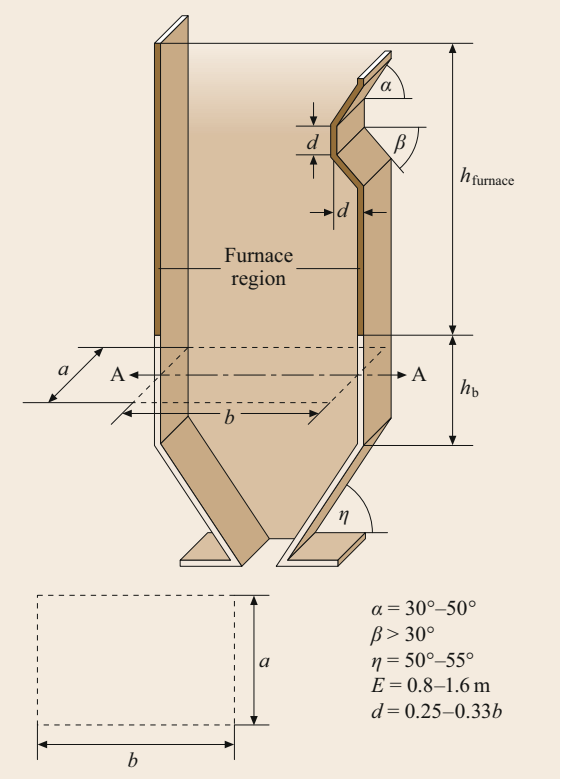

Fig. 27.27 Basic furnace geometry

ash that leaves the bottom of the furnace: dry-bottom and wet-bottom furnaces.

Dry-Bottom Furnaces. Here, a dry bottom means that the boiler has a furnace bottom temperature that is below the melting point of the ash. In this furnace design, ash or slag is removed in the dry state. In the dry-bottom type, ash falling from the boiler furnace is conveyed by a continuously moving scraper chain conveyor to the clinker grinder, which is then conveyed to the slurry sump through sloping trenches with the aid of a high-pressure water jet. The size of the furnace hopper is one of the main influences on the effective removal of dry ash from the furnace. The walls of the hopper are normally inclined at an angle of 48°–60°.

Wet-Bottom Furnaces. In a wet-bottom furnace, the ash is removed wet (i.e., molten). The ash hopper is filled with quenching water; when the ash enters this water, it fractures instantly, crystallizes, and forms pellets (known as slag) that are removed with the aid of a jet pumping system and conveyed to a slurry sump. This type of hopper is known as a water-impounded bottom ash hopper. There are two types of wet-bottom boilers: slag-tap and cyclone boilers. A slag-tap boiler burns pulverized coal and a cyclone boiler burns crushed coal. In each type, the bottom ash is kept in a molten state and tapped off as a liquid. Both boiler types have a solid base with an orifice that can be opened to allow the molten ash that has collected at the base to flow into the ash hopper.

Liquid Fuel Furnaces

Liquid fuels such as gasoline, kerosene, and diesel fuel are used directly for combustion in a liquid fuel furnace. Two major categories of fuel oil are burned: distillate oil and residual oil. Distillate oils such as kerosene and diesel oil are commonly used in domestic and small commercial applications. Residual oil is mainly used by utilities and for large commercial applications.

Special Characteristics. Due to the fine atomization of liquid fuels (e.g., fuel oil has a mean particle size of 20 mm), better combustion is achieved with liquid fuels than solid fuels, meaning that the excess air requirement decreases from 31 to 6% for liquid fuels. Liquid fuels have higher calorific values than solid fuels and occupy less storage space. Liquid fuel furnaces produce almost no ash, and are easy to light up and shut down. They are also more efficient than solid fuel furnaces, and the fuel consumption rate is easy to control in a liquid fuel furnace.

Air Supply

Air is supplied for combustion using either a fan (for forced delivery), a natural draft, or sometimes a combination of both approaches.

Forced Draft Fan. A forced draft fan supplies combustion air and is important because it ensures adequate air–fuel mixing and keeps the flame away from the nozzle. The furnace operates under pressure and flue gases are exhausted by forced draft convection. The airflow rate is typically controlled with air dampers. Some applications use fan speed control.

Induced Draft Fan. An induced draft fan exhausts flue gases from the furnace and draws combustion air into the furnace by ensuring that the furnace operates under negative pressure. Induced draft fans can handle high-temperature gas that may contain corrosive ash.

Balanced Draft. The balanced draft (BD) design uses both forced draft and induced draft fans. This approach is used when the furnace design requires draft and furnace pressure control. BD furnaces are typically operated at a slightly negative pressure, but they

can also operate at a slightly positive pressure. Furnace pressure measurement and induced fan control are required.

Primary Air Fans

In a coal-fired boiler, primary fans are used to supply the air needed to dry the coal and transport it to the boiler. They are usually located before or after the preheater.

Stacks are used to create the pressure differential required to induce the flow of air and flue gas. The draft is the difference between the atmospheric pressure and the static pressure of the combustion gases in a furnace gas passage. In coal-fired power plants, two methods are used to create a draft in the furnace: a natural draft and a mechanical draft.

Natural Draft. In a natural draft scheme (Fig. 27.18), the chimney creates a natural draft due to the temperature difference between the hot gases in the chimney and the cold atmospheric air outside the chimney. The advantages of this method are that it does not require any external power, gases are discharged at a higher elevation (which minimizes the immediate environmental impact of those gases), maintenance costs are low, and capital costs are less than those associated with the implementation of an artificial draft scheme.

The draft or pressure difference produced is given by

$$\Delta p_{\mathrm{nd}} = \pm(\rho_{\mathrm{a}} - \rho_{\mathrm{g}})gH\,, \tag{27.56}$$

where Δp_{nd} is the head of the natural draft (Pa), ρ_{a} is the ambient air density (kg/m^3), ρ_{g} is the gas density in the flue (kg/m^3), and H is the height difference between the beginning and the end of the section (m).

The flue gas density ρ_{g} (kg/m^3) is calculated as

$$\rho_{\mathrm{g}} = \rho_{\mathrm{g}}^{0}\frac{273}{273 + T_{\mathrm{g}}}\,, \tag{27.57}$$

where T_{g} is the gas temperature (°C), ρ_{g} is the gas density in the flue under standard atmospheric conditions (i.e., 1 atm), and

$$\rho_{\mathrm{g}}^{0} = \frac{1 - 0.01A + 1.302\alpha V^{0}}{V_{\mathrm{g}}}\,, \tag{27.58}$$

where α is the excess air ratio in the flue gas, V^0 is the theoretical air requirement per unit weight of fuel (N m^3/kg), V_{g} is the flue gas produced per unit weight of fuel (N m^3/kg $\approx \alpha V^0$), and A is the percentage ash content of the fuel.

The stack assists the fan in overcoming pressure losses and helps to disperse the gas effluent. The flow is limited by the strength of the draft. The pressure variation inside the chimney differs from the variation in atmospheric pressure. The variation in pressure inside the chimney depends on the temperature variation along the chimney, which itself depends on the rate of cooling of the hot gas due to natural convection.

Artificial Draft. In modern power plants, the draft should be flexible enough to meet the needs of fluctuating loads and to be independent of atmospheric conditions. To achieve this, draft fans are needed. The height of the chimney can also be reduced if a fan is used. Three types of fans are used to produce a mechanical draft: forced draft (FD), induced draft (ID), and balanced draft.

Forced Draft. In this system, the blower (forced draft fan) is located at the base of the boiler near the grate. Air is forced into the furnace by the forced fan and the flue gases are forced to chimney through the economizer and air preheater. Since the fan handles cold air, the fan size and the power required are generally relatively small. Also, there is no need for water-cooled bearings because the air handled by the fan is not hot. The pressure is above atmospheric pressure throughout the system, reducing air leakage into the furnace.

Induced Draft. In an induced draft system, a blower (induced draft fan) is placed near or at the base of the chimney. The fan sucks the flue gas from the furnace, creating a partial vacuum inside the furnace. Atmospheric air is therefore induced to flow through the furnace to aid the combustion of the fuel. The flue gases drawn by the fan pass through the chimney and into the atmosphere.

Balanced Draft. In the induced draft system, when the furnace is opened for firing, cold air enters the furnace and dilates the combustion. In the forced draft system, when the furnace is opened for firing, the high-pressure air may cause an abrupt blowout. Hence, the furnace cannot be opened for firing and inspection in either system. The balanced draft scheme, which is a combination of induced draft and forced draft, is used to overcome these difficulties.

Energy Balance of a Furnace/Combustion System

Performance of a Furnace. The following steps are necessary to assess the performance of a furnace:

1. Obtain the fuel analysis
2. Compute the equivalent chemical equation
3. Select the recommended exhaust gas composition

4. Write and balance the combustion equation,

$$\mathrm{C}_X\mathrm{H}_Y\mathrm{S}_Z\mathrm{O}_K + \varepsilon 4.76\left(X + \frac{Y}{4} + Z - \frac{K}{2}\right)$$
$$\text{air} + \text{moisture in air} + \text{ash moisture in fuel}$$
$$\rightarrow P\,\mathrm{CO}_2 + Q\,\mathrm{H}_2\mathrm{O} + R\,\mathrm{SO}_2 + T\,\mathrm{N}_2$$
$$+ U\,\mathrm{O}_2 + V\,\mathrm{CO} + W\,\mathrm{C} + \text{ash}$$

Dry Exhaust Gases.

$$P\,\mathrm{CO}_2 + R\,\mathrm{SO}_2 + T\,\mathrm{N}_2 + U\,\mathrm{O}_2 + V\,\mathrm{CO} \quad \text{(kmol)}\,.$$

1. Carry out first law analysis to calculate the theoretical combustion temperature
2. Calculate the total number of moles of wet exhaust gas for 100 kg of fuel,

$$n_{\text{ex.gas}} = P + Q + R + T + U + V$$

3. $100\,\text{CV of fuel} = n_{\text{ex.gas}} c_{p_{\text{exhaust gas}}} (T_{\text{th}} - T_{\text{atm}})$
4. Calculate the total heat transfer area of the furnace A_{furnace}.

Modeling.

$$\mathrm{C}_X\mathrm{H}_Y\mathrm{S}_Z\mathrm{O}_K + \varepsilon 4.76\left(X + \frac{Y}{4} + Z - \frac{K}{2}\right)$$
$$\text{air} + \text{moisture in air} + \text{ash moisture in fuel}$$
$$\rightarrow P\,\mathrm{CO}_2 + Q\,\mathrm{H}_2\mathrm{O} + R\,\mathrm{SO}_2 + T\,\mathrm{N}_2$$
$$+ U\,\mathrm{O}_2 + V\,\mathrm{CO} + W\,\mathrm{C} + \text{ash}$$

For the dry exhaust gases,

$$P\,\mathrm{CO}_2 + R\,\mathrm{SO}_2 + T\,\mathrm{N}_2 + U\,\mathrm{O}_2 + V\,\mathrm{CO} \quad \text{(kmol)}\,.$$

The volume of gases is directly proportional to the number of moles, i.e.,

$$\text{Volume fraction} = \text{mole fraction}\,.$$

The volume fraction of CO_2 is

$$x_1 = P\frac{100}{P+R+T+U+V}\,.$$

The volume fraction of CO is

$$x_2 = V\frac{100}{P+R+T+U+V}\,.$$

The volume fraction of SO_2 is

$$x_3 = R\frac{100}{P+R+T+U+V}\,.$$

The volume fraction of O_2 is

$$x_4 = U\frac{100}{P+R+T+U+V}\,.$$

The volume fraction of N_2 is

$$x_5 = T\frac{100}{P+R+T+U+V}\,.$$

These are dry gas volume fractions (as presented by devices that measure emissions).

Measurements. The volume flow rate of air and the volume flow rate of the exhaust are obtained from exhaust gas analysis, i.e.,

$$x_1 + x_2 + x_3 + x_4 + x_5 = 100 \text{ or } 1\,.$$

Ultimate Analysis of Coal.

$$n\,\mathrm{C}_X\mathrm{H}_Y\mathrm{S}_Z\mathrm{O}_K + \varepsilon n 4.76\left(X + \frac{Y}{4} + Z - \frac{K}{2}\right)$$
$$\text{air} + \text{moisture in air} + \text{ash and moisture in fuel}$$
$$\rightarrow x_1\,\mathrm{CO}_2 + x_6\,\mathrm{H}_2\mathrm{O} + x_3\,\mathrm{SO}_2 + x_5\,\mathrm{N}_2$$
$$+ x_4\,\mathrm{O}_2 + x_2\,\mathrm{CO} + x_7\,\mathrm{C} + \text{ash}$$

where x_1, x_2, x_3, x_4, and x_5 are dry volume fractions or percentages.

Conserved Species. Carbon, hydrogen, oxygen, nitrogen, and sulfur are conserved during the combustion process.

For the conservation of carbon,

$$nX = x_1 + x_2 + x_7\,.$$

For the conservation of hydrogen,

$$nY = 2x_6\,.$$

For the conservation of oxygen,

$$nK + 2n\varepsilon\left(X + \frac{Y}{4} + Z - \frac{K}{2}\right)$$
$$= 2x_1 + x_2 + 2x_3 + 2x_4 + x_6\,.$$

For the conservation of nitrogen,

$$\varepsilon n 3.76\left(X + \frac{Y}{4} + Z - \frac{K}{2}\right) = x_5\,.$$

For the conservation of sulfur,

$$nZ = x_3\,.$$

By rearranging the terms, we obtain

$$\mathrm{C}_X\mathrm{H}_Y\mathrm{S}_Z\mathrm{O}_K + \varepsilon 4.76\left(X + \frac{Y}{4} + Z - \frac{K}{2}\right)$$
$$\text{air} + \text{moisture in air} + \text{ash moisture in fuel}$$
$$\rightarrow P\,\mathrm{CO}_2 + Q\,\mathrm{H}_2\mathrm{O} + R\,\mathrm{SO}_2 + T\,\mathrm{N}_2$$
$$+ U\,\mathrm{O}_2 + V\,\mathrm{CO} + W\,\mathrm{C} + \text{ash}$$

First Law Analysis of Combustion.

$$\begin{aligned}
&C_X H_Y S_Z O_K + \varepsilon 4.76\left(X + \frac{Y}{4} + Z - \frac{K}{2}\right)\\
&\text{air} + \text{moisture in air} + \text{ash} + \text{moisture in fuel}\\
&\quad \rightarrow P\,CO_2 + Q\,H_2O + R\,SO_2 + T\,N_2\\
&\qquad + U\,O_2 + V\,CO + W\,C + \text{ash}\\
&\sum Q_{CV} + n_{air} h_{f,air} + n_{fuel} h_{f,fuel}\\
&\quad = \sum_{i=1}^{n} n_i h_{f,fluegas,i} + \sum W_{CV}\,. \qquad (27.59)
\end{aligned}$$

The total surface area of the furnace is found via

$$A_{furnace} = \frac{G m_f c_p}{T_{th}^3}\left[\frac{1}{m}\left(\frac{T_{th}}{T_{out}} - 1\right)\right]^{\frac{1}{0.6}}, \qquad (27.60)$$

where G is the furnace quality factor, M is the temperature field coefficient, T_{th} is the theoretical combustion temperature, $A_{furnace}$ is the total surface area of the furnace, and m_f is the mass flow rate of the fuel.

Mathematical Model of Stress. The basic equation for the longitudinal stress σ_1 and hoop stress σ_2 in a vessel of thickness of h, longitudinal radius r_1, and circumferential stress r_2 that is is subjected to a pressure p is

$$\frac{\sigma_1}{r_1} + \frac{\sigma_2}{r_2} = \frac{p}{h}\,. \qquad (27.61)$$

The stresses in the most commonly used shells of revolution can be found by applying this equation and equating the total pressure load to the longitudinal forces that act on a transverse section of the vessel.

Boiler Fuel Consumption and Efficiency Calculation. For any fuel, there is a minimum quantity of oxygen that is required for complete combustion. The amount of air that contains this minimum quantity of oxygen is called the *theoretical air*, which is a measure of the ability of the boiler to transfer heat delivered in the furnace to water and steam.

Sources of Energy Losses in a Steam Generator.

- Heat loss from the furnace surface area
- Unburned carbon loss
- Incomplete combustion loss
- Loss due to hot ash
- Loss due to moisture in the air
- Loss due to moisture in the fuel
- Loss due to combustion-generated moisture
- Dry exhaust gas losses.

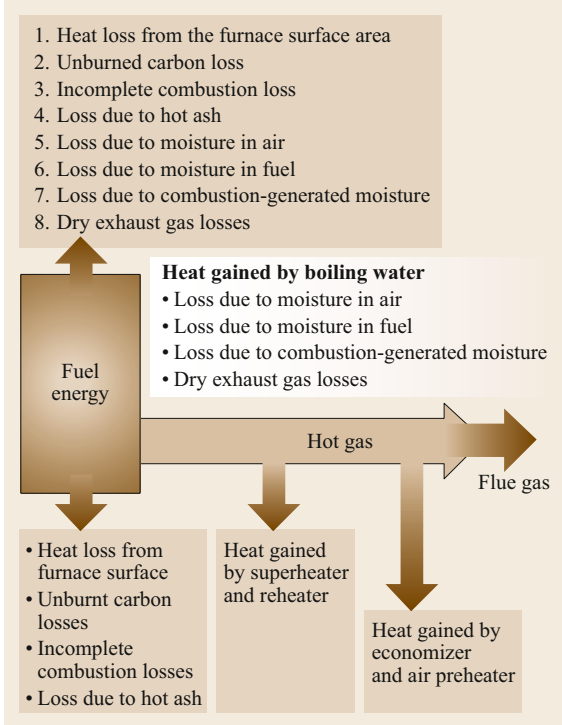

Fig. 27.28 Sankey diagram showing the various energy losses that occur in a steam generator

Figure 27.28 shows a pictorial representation, known as a Sankey diagram, of the various energy losses that occur in a steam generator.

The first law analysis of a steam generator in steady-state steady flow (SSSF) mode in molar form (Fig. 27.29) yields

$$\begin{aligned}
&\sum \dot{Q} + \dot{n}_{air} h_{air} + \dot{n}_{fuel} h_{fuel}\\
&\quad = \sum \dot{n}_{fluegas} h_{fluegas} + \sum \dot{w}\,.
\end{aligned}$$

Dry Exhaust Gas Losses (DEGL). For 100 kg of fuel,

$$\begin{aligned}
Q_{DEGL} &= \Delta n_{fluegas} \Delta h_{fluegas}\,,\\
Q_{DEGL} &= n_{CO_2}\Delta h_{CO_2} + n_{CO}\Delta h_{CO} + n_{O_2}\Delta h_{O_2}\\
&\quad + n_{N_2}\Delta h_{N_2} + n_{SO_2}\Delta h_{SO_2} \quad \text{(kJ)}\,,\\
Q_{DEGL} &= P\Delta h_{CO_2} + R\Delta h_{SO_2} + T\Delta h_{N_2}\\
&\quad + U\Delta h_{O_2} + v\Delta h_{CO} \quad \text{(kJ)}\,.
\end{aligned}$$

Alternative Method of Establishing the Energy Balance. The total number of moles of dry exhaust gas $n_{ex.gas} = P + R + T + U + V$ is given by

$$Q_{DEGL} = n_{ex.gas} c_{p,ex.gas}(T_{ex.gas} - T_{atm})\,.$$

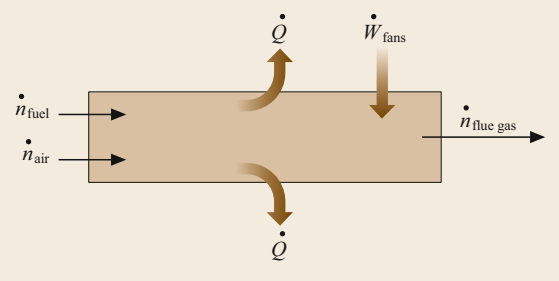

Fig. 27.29 Furnace energy balance

Accurate calculation of the gas enthalpy yields (for any gas)

$$\mathrm{d}h = c_p \mathrm{d}T\,,$$
$$\Delta h = \int_{\text{ambient}}^{\text{SG}_{\text{exit}}} \mathrm{d}h = \int_{T_{\text{amb}}}^{T_{\text{exit}}} c_p(T)\mathrm{d}T\,. \qquad (27.62)$$

Unburnt Carbon Loss (UCL). For 100 kg of fuel, we have

$$Q_{\text{UCL}} = \text{MC} \times W \times \text{calorific value of carbon} \quad (\text{kJ})\,,$$
$$Q_{\text{UCL}} = 12W \times 33\,820\,\text{kJ}\,, \qquad (27.63)$$

where MC is the molecular weight of carbon.

Incomplete Combustion Loss (ICL). For 100 kg of fuel, we have

$$Q_{\text{ICL}} = \text{MCO} \times V \times \text{CV of CO} \quad (\text{kJ})\,,$$
$$Q_{\text{ICL}} = 28V \times 23\,717\,\text{kJ}\,, \qquad (27.64)$$

where MCO is the molecular weight of CO.

Losses Due to Moisture in the Combustion Air (MCAL).

$$Q_{\text{MCAL}} = \varepsilon 4.76\left(X + \frac{Y}{2} + Z - \frac{K}{2}\right) \times 29.9 w c_{\text{steam}}(T_{\text{g}} - 25) \quad (\text{kJ})\,, \qquad (27.65)$$

where w is the absolute or specific humidity (kg of moisture per kg of dry air), c_{steam} is the specific heat of steam at constant pressure (1.88 kJ/(kg K)), and T_{g} is the temperature of the exhaust gas.

Losses Due to Moisture in Fuel and Combustion-Generated Moisture. For 100 kg of fuel, we have

$$Q_{\text{ML}} = (M + 9Y)[2442 + c_{\text{steam}}(T_{\text{g}} - 25)] \quad (\text{kJ})\,, \qquad (27.66)$$

where M is the percentage moisture content in the fuel and Y is the number of combustible hydrogen atoms in the fuel.

Losses Due to Hot Ash or Slag (ASL). For 100 kg of fuel, we have

$$Q_{\text{ASL}} = A c_{p,\text{as}} T_{\text{ash}}\,, \qquad (27.67)$$

where $c_{p,\text{ash}}$ is the specific heat of ash (0.55–0.6 kJ/(kg K)), T_{ash} is the temperature of the ash or slag, and T_{ash} varies from 300 to 800 °C.

Radiation and Unaccounted-For Losses (RUL). The radiation and unaccounted-for losses are relatively small (3–5% of the total losses), and can be estimated using the equation

$$Q_{\text{RCL}} = A_{\text{s}}(h_{\text{s}})(T_{\text{surface}} - T_{\text{amb}}) \quad (\text{kW})\,, \qquad (27.68)$$

where A_{s} is the total surface area (m^2) and h_{s} is the surface heat transfer coefficient.

Steam Generator Performance

Boiler Efficiency. This is a measure of the thermal energy transferred to the working medium—typically water and steam—relative to the total energy obtained from combustion in the boiler. The boiler efficiency may be expressed using either

$$\eta_{\text{boiler}} = \frac{\text{mass flow rate of steam} \times (\text{steam heat} - \text{feedwater heat})}{\text{fuel mass} \times \text{heating value of fuel}}$$

or

$$\eta_{\text{boiler}} = \frac{\text{HHV} - \text{total loss}}{\text{HHV}}\,, \qquad (27.69)$$

where HHV is the higher heating value of the fuel.

27.3.3 Furnace Design

The energy balance within the furnace (i.e., the heat released by combustion must be equal to the heat absorbed by the working medium plus any losses) is utilized during furnace design. The most important thermal characteristics of the furnace in design analysis are the heat release rate per unit cross-sectional area, unit volume, or unit wall area of the burner region as well as the furnace gas temperature.

Heat Release Rate per Unit Volume

The volumetric heat release rate q_{v} depends on various factors, including the characteristics of the ash, the firing method, and the arrangement of the burners, and is

given by

$$q_v = \frac{m_f \mathrm{LHV}}{V_{\mathrm{furnace}}} \quad (\mathrm{kW/m^3}) \,, \tag{27.70}$$

where m_f is the designed fuel consumption rate (kg/s), LHV is the lower heating value of the fuel (kJ/kg), V_f is the volume of the furnace ($a \times b \times h_f$), and h_f is the height of the furnace. The value of q_v depends on the coal type and type of furnace. Selecting the appropriate volumetric flow rate for the heat release rate improves the combustion quality.

Heat Release Rate per Unit Wall Area of the Burner Region

The heat release rate in the burner region is calculated with respect to the water wall in this region. The heat release rate per unit wall area of the furnace q_b depends on the following parameters [27.6]:

- Ash characteristics
- Fuel ignition characteristics
- Firing method
- Arrangement of the burners.

The heat release rate per unit wall area of the burner region can be quantified as

$$q_b = \frac{m_f \mathrm{LHV}}{2(a+b)h_b} \quad (\mathrm{kW/m^2}) \,, \tag{27.71}$$

where a and b are the width and depth of the furnace, respectively, and h_b is the distance between the top edge of the uppermost burner and the lower edge of the lowest burner.

Heat Release Rate per Unit Cross-Sectional Area

The heat release rate per unit cross-sectional area q_f is given by

$$q_f = \frac{m_f \mathrm{LHV}}{A_{\mathrm{furnace}}} \quad (\mathrm{kW/m^2}) \,, \tag{27.72}$$

where A_{furnace} is the cross-sectional area of the furnace in $\mathrm{m^2}$.

Furnace Exit Gas Temperature

The furnace exit gas temperature determines the rate of heat absorption by the radiant heating surface in the furnace and the rate of heat absorption by the convective heating surface of the furnace. The optimum furnace exit gas temperature is in the range 1200–1400 °C.

Example Problem

A test of a model steam generator gives the following data:

- Gas analysis: C: 63.4%, H: 5.7%, O: 16.8%, N: 10%, ash: 8.9%, moisture: 13%
- HHV of coal: 33 318 kJ/kg
- Combustible solid refuse: 7.5%
- Dry exhaust gas analysis: CO_2: 15.4%, CO: 0.5%, O_2: 2.8%, N_2: 81.3%
- Ambient conditions: 50 °C and 100 kPa
- Temperature of the air entering the furnace: 235 °C.

The task is to design a PC (pulverized coal) furnace for a steam generator with a thermal capacity of 1000 MW with the following characteristics:

- Steam generator efficiency: 0.86
- Furnace quality factor: 0.406×10^8
- Temperature field coefficient: $M = 0.405$
- Thermal capacity of the gas: $c_p = 1.17\,\mathrm{kJ/(kg\,K)}$.

A furnace can be characterized geometrically by its linear dimensions—its front width a, depth b, and height h_f (Fig. 27.27)—which are estimated according to the rated fuel consumption and the thermal, physical, and chemical properties of the fuel to be used.

Flow Rate of the Fuel.

$$\begin{aligned} Q_{\mathrm{boiler}} &= m_{\mathrm{coal}} \mathrm{HHV} \eta_{\mathrm{SG}} \\ 1\,000\,000 &= m_{\mathrm{coal}} 33\,318 \eta_{\mathrm{SG}} \\ m_{\mathrm{coal}} &= 34.899\,\mathrm{kg/s} \\ \mathrm{LHV} &= \mathrm{HHV} - \frac{m_{\mathrm{H_2O}}}{\text{kg of fuel}} 2442 \\ \mathrm{LHV} &= 323\,827\,\mathrm{kJ/kg} \,, \end{aligned}$$

where η_{SG} is the efficiency of the steam generator.

Heat Release Rate per Unit Volume (q_v).

$$q_v = \frac{m_f \mathrm{LHV}}{V_f} \quad (\mathrm{kW/m^3}) \,. \tag{27.73}$$

There are high contents of H and O, but these elements occur largely in volatile matter, so the given composition is bituminous. For bituminous coal, q_v takes values in the range 0.14–0.20 $\mathrm{MW/m^3}$ [27.6].

Substituting the appropriate values of q_v, m_f, and LHV from Table 27.1 into (27.73), we obtain the furnace volume

$$V = 7532.05\,\mathrm{m^3} \,.$$

Table 27.1 Typical volumetric heat release values

Coal type	Dry-bottom furnace q_v (MW/m^3)	Wet (slagging) bottom furnace q_v (MW/m^3)		
		Open furnace	Half-open furnace	Slagging pool
Anthracite	0.110–0.140	≤ 0.145	≤ 0.169	0.523–0.598
Semianthracite	0.116–0.163	0.151–0.186	0.163–0.198	0.523–0.698
Bituminous	0.14–0.20	–	–	–
Oil	0.23–0.35	–	–	–
Lignite	0.09–0.15	≤ 0.186	≤ 0.198	0.523–0.640
Gas	0.35	–	–	–

Table 27.2 Upper limits of q_a for tangentially fired furnaces

Boiler capacity (t/h)	Upper limit of q_a (MW/m^2)		
	ST[a] ≤ 1300 °C	ST = 1300 °C	ST ≥ 1300 °C
130	2.13	2.56	2.59
220	2.79	3.37	3.91
420	3.65	4.49	5.12
500	3.91	4.65	5.44
1000	4.42	5.12	6.16
1500	4.77	5.45	6.63

[a] ST is the softening temperature of the ash (°C)

Table 27.3 Lower limit of $h_{furnace}$ (m)

Boiler capacity (t/h)	65–75	130	220	420	670
Anthracite	8	11	13	17	18
Bituminous	7	9	12	14	17

Heat Release Rate per Unit Cross-Sectional Area (q_a).

$$q_a = \frac{m_f \mathrm{LHV}}{A_{CS}} \quad (\mathrm{kW/m^2}) , \tag{27.74}$$

where A_{CS} is the cross-sectional area of the heat exchanger in m^2, as given by

$$A_{CS} = ab = \frac{m_f \mathrm{LHV}}{q_a} \quad (\mathrm{kW/m^2}) . \tag{27.75}$$

Substituting the values of q_a, m_f, and LHV obtained from Table 27.2 into (27.75), we find that the area $ab = 441.46\,\mathrm{m}^2$.

Heat Release Rate per Unit Wall Area of the Burner Region (q_b).

$$q_b = \frac{m_f \mathrm{LHV}}{2(a+b)h_b} \quad (\mathrm{kW/m^2}) . \tag{27.76}$$

Taking the recommended value of the burner region heat release rate h_b to be 1 MW/m^3, we find that

$$2(a+b)h_b = 1129.80\,\mathrm{m}^2 .$$

Based on Tables 27.1 and 27.3, the minimum width $b_{min} = 6\,\mathrm{m}$ was chosen, and $h_{furnace,min} = 11\,\mathrm{m}$.

According to the above constraints, suitable values for a and b are

$$a = 20.62\,\mathrm{m} ,$$
$$b = 21.4\,\mathrm{m} ,$$
$$h_b = \frac{1129.8}{2(21.4+20.62)} = 13.44\,\mathrm{m} .$$

Therefore, the volume of the furnace region (Fig. 27.27) is obtained from

$$V_{furnace} = h_{furnace}ab - \frac{a}{2}(d+d+d\tan\beta+d\tan\alpha)d , \tag{27.77}$$

$$V_{furnace} = h_{furnace}ab - \frac{ad}{2}(2d + d\tan\beta + d\tan\alpha) , \tag{27.78}$$

$$V_{furnace} = h_{furnace}ab - \frac{ad^2}{2}(2 + \tan\beta + \tan\alpha) . \tag{27.79}$$

Substituting the values of a, b, α, β, and $V_{furnace}$ into (27.79) yields

$$h_{furnace} = 19.33\,\mathrm{m} .$$

To find the height of the hopper, we insert the data into

$$h_h = \left(\frac{b-e}{2}\right)\tan\gamma = 14.56\,\mathrm{m} . \tag{27.80}$$

We then calculate the total surface area from the geometry using

$$\begin{aligned} &a(h_f + h_b) + a(h_f + h_b - d - d\tan\alpha - d\tan\beta \\ &+ d\sec\alpha + d\sec\beta) + 2b(h_f + h_b) \\ &- d(d + d + d\tan\alpha + d\tan\beta) + 2\left[\frac{1}{2}h_h(b+e)\right] \\ &+ 2ah_h\,\mathrm{cosec}\,\gamma . \end{aligned} \tag{27.81}$$

Substituting all of these values into (27.81), the surface area of the furnace is calculated to be 3793.98 m^2.

Adiabatic Flame Temperature

Ultimate Analysis.

$$\text{C:}\quad \frac{64.4}{12} = 5.283\,,$$

$$\text{H:}\quad 5.7 - \frac{13}{9} = 4.255\,,$$

$$\text{O:}\quad \frac{16.8}{16} - \left[\left(\frac{8}{9}\right)\left(\frac{13}{16}\right)\right] = 0.327\,,$$

$$\text{N:}\quad \frac{1}{14} = 0.071\,,$$

$$\text{Ash} = 8.9\,,$$

$$\text{Moisture} = \frac{13}{18}\,,$$

$$\mathrm{C}_X\mathrm{H}_Y\mathrm{S}_Z\mathrm{O}_K + \left(X + \frac{Y}{4} + Z - \frac{K}{2}\right)\mathrm{O}_2 \rightarrow 15.4\,\mathrm{CO}_2 + 0.5\,\mathrm{H}_2\mathrm{O} + 2.8\,\mathrm{O}_2 + 81.3\,\mathrm{N}_2 + Z\,\mathrm{H}_2\mathrm{O}$$

For 100 kg of fuel,

$$\mathrm{C}_{5.28}\mathrm{H}_{4.25}\mathrm{O}_{0.327} + 4.76 \times 1.162 \times 6.152\,\text{air} \rightarrow 5.11\,\mathrm{CO}_2 + 0.166\,\mathrm{H}_2\mathrm{O} + 0.933\,\mathrm{O}_2 + 27.1\,\mathrm{N}_2 + 2.13\,\mathrm{H}_2\mathrm{O}$$

$$n_{\text{exit}}\ (\text{moles of exit gases}) = 5.11 + 0.166 + 0.93 + 27.1 + 2.13 = 35.43$$

$$100 \times 33\,318 = 35.43 \times 40 \times (T_{\text{th}} - T_{\text{atm}})$$

$$T_{\text{th}} = 2624\,\text{K}\,.$$

The ash softening temperature is $\geq 1250\,^\circ\text{C}$ and $T_{\text{out}} \leq 1250\,^\circ\text{C}$ (1523 K). With a flow rate of 34.89 kg/s for fuel and 368.68 kg/s for flue gas, we determine that 100 kg of fuel generates 1056.71 kg of exhaust flue gas.

To find T_{out}, we use

$$A_{\text{furnace}} = \frac{G m_{\text{f}} c_p}{T_{\text{th}}^3}\left[\frac{1}{m}\left(\frac{T_{\text{th}}}{T_{\text{out}}} - 1\right)\right]^{\frac{1}{0.6}}\,, \qquad (27.82)$$

where G is the furnace quality factor, M is the temperature field coefficient, T_{th} is the theoretical combustion temperature, A_{furnace} is the total surface area of the furnace, and m_{f} is the mass flow rate of the fuel. Substituting the above values into (27.84), we find that $T_{\text{out}} = 1365.95$ K. Since T_{out} is < 1523 K (the ash softening temperature), the design is safe.

27.3.4 Strength Calculations

Special care must be taken during the design and stress analysis of a steam generator because of the high pressures and temperatures associated with the system.

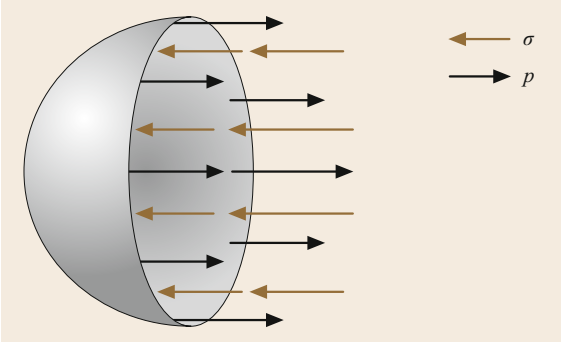

Fig. 27.30 Cross-sectional view of a spherical vessel

Allowable stresses in the pressure vessel depend on the nature of the loading in the pressure vessel and the response to this loading.

Stress can be categorized into:

- Primary stress
- Secondary stress
- Peak stress.

Primary stress is exerted by a mechanical load, and can lead to the mechanical failure of the vessel. An example is the stress produced by the internal pressure, such as that in a steam drum. *Secondary stress* is produced by the mechanical load or thermal expansion. *Peak stress* is stress that is concentrated in highly localized areas at abrupt changes in geometry.

Stress Analysis Methods

Stress analysis can be performed for pressure vessels of different shapes—spheres, cylinders, or ellipses—using analytical or experimental methods.

Spherical Vessel ($r_1 = r_2 = r$). Consider a spherical pressure vessel of radius r and wall thickness h that is subjected to an internal pressure. For reasons of symmetry, all four normal stresses on a small stress element in the wall must be identical. Furthermore, there cannot be any shear stress. The normal stresses σ can be related to the pressure p by inspecting the free-body diagram of the pressure vessel. To simplify this analysis, we split the vessel in half, as illustrated in Fig. 27.30.

The stress around the wall must have a net resultant to balance the internal pressure across the cross-section (Fig. 27.31), so

$$\sigma h 2\pi r = p\pi r^2\,,$$

$$\sigma_1 = \frac{pr}{2h}\,, \qquad (27.83)$$

$$\sigma_2 = \frac{pr}{2h}\,. \qquad (27.84)$$

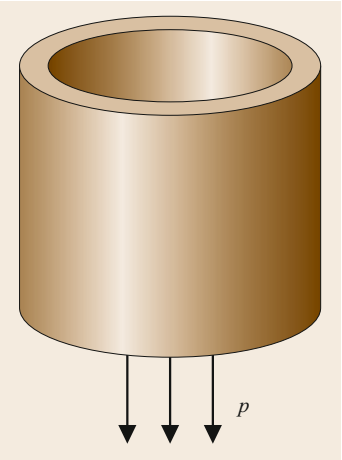

Fig. 27.31 Stress analysis of a cylindrical vessel

Cylindrical Vessel ($r_1 = \infty$, $r_2 = r$).

$$\sigma_1 = \frac{pr}{2h} , \tag{27.85}$$

$$\sigma_2 = \frac{pr}{h} . \tag{27.86}$$

Conical Vessel $r_1 = \infty$, $r_2 = r/\cos\alpha$ (α = Half-Cone Angle).

$$\sigma_1 = \frac{pr}{2h\cos\alpha} , \tag{27.87}$$

$$\sigma_2 = \frac{pr}{h\cos\alpha} . \tag{27.88}$$

Elliptical Vessel.

$$\sigma_1 = \frac{pr_2}{2h} , \tag{27.89}$$

$$\sigma_2 = \frac{p}{h}\left(r_2 - \frac{r_2^2}{2r_1}\right) . \tag{27.90}$$

Design Pressure and Temperature

Generally, the maximum allowable working pressure should not be less than the highest set pressure of any safety valve. The allowable stresses are determined in accordance with the design temperature T, which should not be less than the mean wall metal (through-thickness) temperature expected under the operating conditions for the part considered. The design temperature should be stated by the manufacturer on the drawings of the pressure parts submitted for consideration. Pressure parts are designed in line with the allowable stress S in $\mathrm{N/mm^2}$. The equation used to determine the minimum straight tube thickness is

$$t = \frac{pD_o}{20SE + p} + C , \tag{27.91}$$

where p is the design pressure (bar), t is the minimum thickness (mm), D_o is the outside diameter (mm), S is the allowable stress ($\mathrm{N/mm^2}$), E is the weld efficiency of longitudinally welded tubes (i.e., joints) or ligaments between tube holes or other openings, and C is the corrosion allowance (mm).

27.3.5 Heat Transfer Calculations

Heat Exchangers

Heat exchangers with different flow configurations—parallel flow, counterflow, or crossflow—are generally used.

Heat Transfer Analysis in a Counterflow Heat Exchanger. A counterflow heat exchanger, where the fluid moves in parallel but opposite directions, is shown in Fig. 27.32.

Heat exchanger thermal design involves calculating the surface area required to transfer heat at a given rate for given flow rates and fluid temperatures. The size of the heat exchanger can be obtained from the general heat transfer equation

$$Q = U_o A_o \Delta T_{lm} , \tag{27.92}$$

where A_o is the external heat transfer surface area based on the external diameter of the tube, U_o is the overall heat transfer coefficient based on the external diameter of the tube, and ΔT_{lm} is the log mean temperature difference given by

$$\Delta T_{lm} = \frac{\Delta T_1 - \Delta T_2}{\ln\left(\frac{\Delta T_1}{\Delta T_2}\right)} , \tag{27.93}$$

where $\Delta T_1 = T_{h1} - T_{c2}$ and $\Delta T_2 = T_{h2} - T_{c1}$ for a counterflow heat exchanger.

27.3.6 Flow Resistance

The friction from a flow inside a pipe causes a pressure drop that may occasionally reach unacceptable levels. The pressure drop depends on the friction resistance. Friction resistance values for actual pipes and volume flows may be obtained from special charts that are derived for the pipes or tubes considered. Minor pressure losses due to fittings such as bends, elbows, and valves may be calculated as

$$p_2 = \xi\frac{\rho v^2}{2} , \tag{27.94}$$

or may be expressed as the head

$$h_{loss} = \xi\frac{v^2}{2}g , \tag{27.95}$$

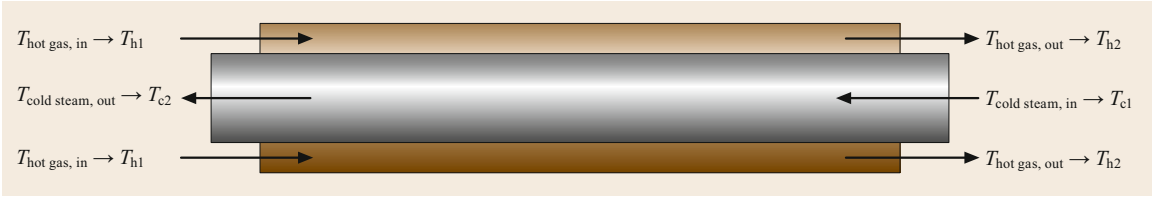

Fig. 27.32 Heat transfer along a counterflow heat exchanger

where ξ is the minor loss coefficient, p_{loss} is the pressure loss (Pa = N/m^2), ρ is the density (kg/m^3), v is the flow velocity (m/s), h_{loss} is the head loss (m), and g is the acceleration due to gravity (m/s^2).

27.4 Combustion

Combustion is a chemical process—an exothermic reaction between a substance (the fuel) and a gas (the oxidizer, usually O_2). The presence of CO implies incomplete combustion, which decreases the combustion efficiency and has well-known environmental disadvantages because of the by-products emitted.

The basic chemical equations for complete combustion are

$$C + O_2 \rightarrow CO_2 \quad (27.96)$$

$$2\,H_2 + O_2 \rightarrow 2\,H_2O \quad (27.97)$$

When the amount of oxygen supplied is insufficient for complete combustion, an incomplete reaction takes place, resulting in the formation of carbon monoxide via

$$2\,C + O_2 \rightarrow 2\,CO \quad (27.98)$$

The most important parameter for estimating the effectiveness of combustion is the combustion efficiency, which depends on various parameters such as the air–fuel ratio, fuel–air mixing, flame temperature, flame shape, fuel residence time, degree of atomization (for liquid fuel), and degree of turbulence.

The theoretical air–fuel ratio required for complete combustion is known as the stoichiometric ratio. However, in practice, not every oxygen molecule comes into contact with a fuel molecule. To ensure complete combustion, some *excess air* is included to ensure that a complete reaction occurs. Turbulence is also employed to enhance the mixing of the fuel and oxygen and hence the combustion efficiency.

27.4.1 Burners

To achieve efficient combustion, the air and fuel must be mixed appropriately. Efficient combustion corresponds to the complete reaction of the fuels in the appropriate air–fuel ratio. An optimal burner design is crucial to achieving high combustion efficiency. Important design parameters for burners include the burning rate, burning velocity, flashback, and quenching diameter. Among these, the main factor that determines the performance of the burner is the combustion velocity, which is defined as the relative velocity of the flame front with respect to the unburned gases propagating perpendicularly to the flame front. We can define several regimes according to the combustion velocity. At the *flashback limit*, the combustion velocity is greater than the flow velocity; at the *blowoff limit*, the combustion velocity is lower than the flow velocity; and the *stable flame* regime is achieved when the combustion velocity is equal to the flow velocity. Blow-off is a phenomenon that takes place when the flow speed is so high that the flame cannot be kept at a fixed location. Flashback happens when the flame returns back into the gas line. These are phenomena that limit the operation of combustion processes. A plot of the fuel flow rate against the airflow rate, as shown in Fig. 27.33, illustrates these regimes. The airflow affects the heat of the flame, and can be controlled by adjusting the slot openings. The amount of air required, the fuel gas produced, and the heat released per unit weight of fuel burnt can be obtained from a stoichiometric calculation of the designed fuel.

Minimum Air Required per Kilogram of Solid or Liquid Fuel Burnt

If a known mass of fuel consists of fractions of carbon, hydrogen, oxygen, and sulfur, then the minimum mass of air required to burn the fuel is calculated as shown below.

For carbon,

$$= \text{mass of carbon (kg)} \times \left(\frac{8}{3\,\text{kg}}\right) \text{of oxygen}\,.$$

For hydrogen,

$$= \text{mass of hydrogen (kg)} \times 8\,\text{kg of oxygen}\,.$$

For sulfur,

$$= \text{mass of sulfur} \times 1\,\text{kg of oxygen}\,.$$

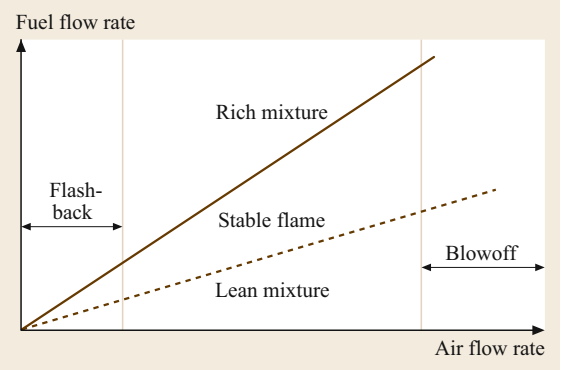

Fig. 27.33 Stability and flammability limits

Therefore, the amount of oxygen required for the complete combustion of 1 kg of fuel is given by

$$\frac{8}{3}\,\mathrm{C} + 8\,\mathrm{H_2} + \mathrm{S} - \mathrm{O_2}$$
$$= \frac{8}{3}\,\mathrm{C} + 8\left(\mathrm{H_2} - \frac{\mathrm{O_2}}{8}\right) + \mathrm{S}\,.$$

Atmospheric air contains 23 wt% oxygen. Therefore, the minimum amount of air required per kilogram of fuel is obtained via

$$\frac{100}{23}\left(\frac{8}{3}\,\mathrm{C} + 8\,\mathrm{H_2} + \mathrm{S} - \mathrm{O_2}\right)$$
$$= 11.6\,\mathrm{C} + 34.8\left(\mathrm{H_2} - \frac{\mathrm{O_2}}{8}\right) + 4.35\,\mathrm{S}\,.$$

This is the theoretical amount of air required. The quantity of air in excess of this theoretical minimum that is actually required for complete combustion of the solid and liquid fuels is the excess air.

Types of Burners

Burners can be categorized in a number of ways: based on the principle of operation (swirl type, parallel, or direct-flow type), fuel (gaseous fuel burners, liquid fuel burners, and solid fuel burners), and geometry (orifice burners, nozzle burners, flat flame burners, and burners with different opening shapes).

Liquid Fuel Burners. Oil is a common liquid fuel. Fuel oil burners can be categorized into:

- Gun-type (atomizing) burners (pressure guns)
- Pot-type (vaporizing) burners
- Rotary-type fuel oil burners.

Burning oil for power production is restricted in some countries and states because of its impact on air quality. When burning oil, the oil is pumped from a storage tank to the burner. Oil burners are designed to increase the contact surface area of the oil with air. To facilitate this, the oil is atomized before entering the combustion chamber. It is difficult to atomize the fuel at ambient temperature, so it has to be heated. This is achieved using single unit heating loops and a centralized heating system. A liquid fuel burner (Fig. 27.34) consists of a fuel supply line with a fuel atomizer, a concentric primary air supply with an air bag, and a secondary air supply with a vane control valve.

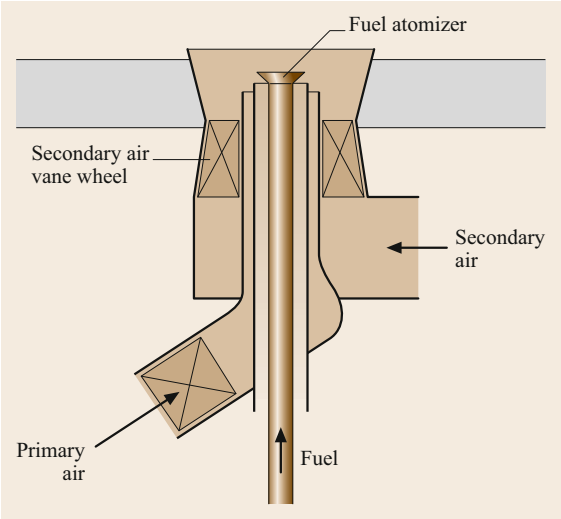

Fig. 27.34 Liquid fuel burner arrangement

Atomized oil is mixed with an appropriate amount of air and transferred to the ignition point in the combustion chamber. To maximize the efficiency of the combustion process, it is essential that the oil–air mixture is well homogenized and has as few pure droplets of fuel oil as possible.

Gun-Type Burners (Pressure Guns). A gun-type burner atomizes the fuel oil by forcing it through a nozzle and spraying it into a gun-like atomic air nozzle. The liquid forms microscopic particles or globules that are well mixed and partially evaporated before being ignited in the combustion chamber. Residential gun-type burners normally require oil pressures of 551–896 kPa, while commercial and industrial burners require oil pressures of 689–2068 kPa. Gun-type burners are very flexible and can be used for a broad range of applications.

Pot-Type Burners. In a pot-type fuel burner, the fuel evaporates into the combustion air. These burners can be subdivided into natural draft burners (see Fig. 27.35), forced draft burners, and sleeve burners. In atmospheric pot-type heaters, gravity causes the oil to flow to the

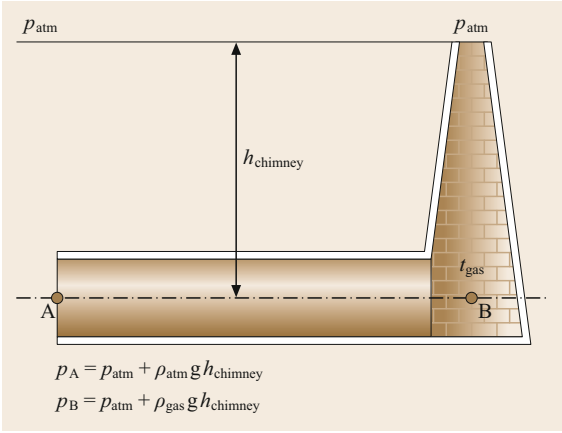

Fig. 27.35 Natural draught produced by a chimney

burner. A natural draft burner relies on the natural draft in the chimney to supply the air. A forced draft burner utilizes a mechanical fan and/or the chimney to obtain its air supply. Perforated sleeve burners are only used in small applications. Pot-type burners are the least expensive type of fuel oil burner and have the lowest operating costs. One disadvantage of a pot-type burner is its limited capacity, which makes it most suitable for smaller applications.

27.4.2 Fluidized-Bed Combustion System

Fluidized-bed combustion (FBC) technology can facilitate efficient solid-fuel combustion. In a typical FBC system, air is injected in an upward direction towards falling soil fuel particles, which causes the solid fuel bed to float and behave like a liquid. The air velocity at which the bed behaves like a fluid is called the fluidization velocity. At this point, the pressure drop across the bed is equal to the weight of the particles per unit cross-section of the bed. There is also an air velocity that imparts turbulent motion, which in turn helps ensure proper mixing of the gas and particles.

Solid coal is crushed in the crusher to the required size (normally a mean particle diameter of around 0.5–12 mm) and fed into the fluidized bed, where it mixes with gas and inert materials and undergoes various reactions such as drying, devolatilization, combustion of volatiles, and combustion of residual tar. During the drying process, all of the moisture present in the coal is removed and the volatile matter is gradually released as the temperature increases. The amount of volatile matter released is proportional to the temperature and inversely proportional to the gas pressure. After the volatile matter has been released it is combusted, and then char burning occurs (depending on the coal type, fluidization system, and char diameter).

FBC leads to a vast improvement in combustion efficiency for fuels with high moisture contents, and is adaptable to a variety of waste-type fuels. The scrubbing action of the bed material on the fuel particles enhances the combustion process by shredding away the CO_2 and char layers that normally form around the particles. FBC reduces the amount of sulfur emitted in the form of SO_x. Limestone is used to precipitate out sulfate during combustion. Fuels other than coal can also be burned in a FBC boiler, and the relatively low combustion temperature (800 °C) applied in FBC boilers has other added benefits as well. FBC at atmospheric pressure can be particularly useful for high-ash coals and/or those with variable characteristics.

Features of Fluidized-Bed Combustion Systems

Emissions from a fluidized-bed combustor are always lower than those from conventional combustion technologies for the following reasons:

- The low combustion temperatures and low excess air within the fluidized bed reduce the formation of NO_x
- The high combustion efficiency results in flue gases that contain low amounts of CO
- Emissions of gases such as SO_x can be abated within the fluidized-bed system by injecting limestone into the bed and ammonia into the vapor space
- Fluidized-bed combustion is an environmentally friendly and proven technology for the disposal of solid wastes and the generation of energy.

Bubbling Fluidized-Bed Combustion

Bubbling beds use a low fluidizing velocity, so the particles are held mainly in a bed with a definable surface (Fig. 27.36). Inert materials are often used to improve the bed stability, together with limestone for SO_2 absorption. In-bed tubes are used to control the bed temperature and generate steam.

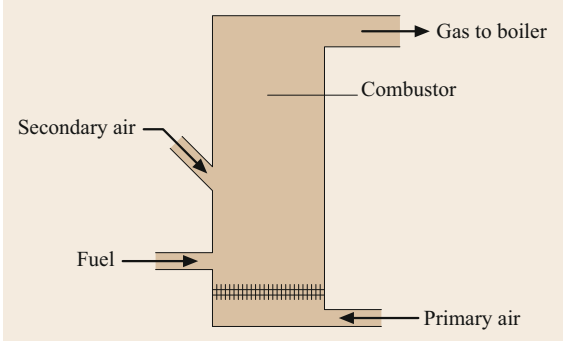

Fig. 27.36 Bubbling fluidized-bed combustion

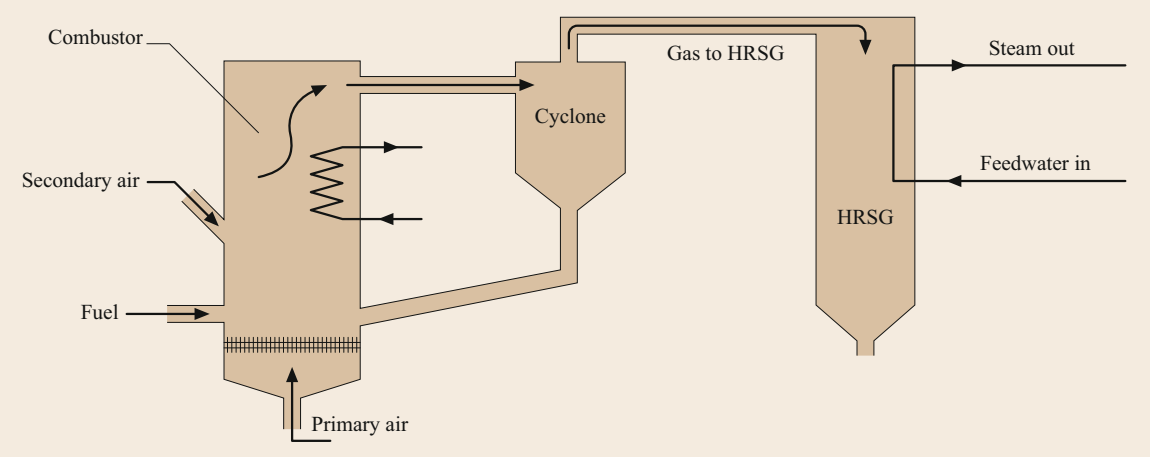

Fig. 27.37 Circulating fluidized-bed combustion

Circulating Fluidized-Bed Combustion

Generally, circulating fluidized-bed combustion is performed with a boiler and a high-temperature cyclone. The gas velocity can be as high as 4–8 m/s. Coarse fluidizing medium and char in the flue gas are collected by the high-temperature cyclone and recycled to the boiler, as shown in Fig. 27.37. Air is introduced into the bed in two regions. About 40–70% of the air, a portion normally called the *primary air*, is injected through the nozzle grate at the bottom of the bed; the remaining air, called the *secondary air*, is injected through nozzles on the side walls of the fluidized bed. The combustion proceeds in two zones: a primary reducing zone in the lower section of the combustor and an oxidizing zone in the upper part of the combustor, where complete combustion is achieved through the use of excess air. This staged combustion at controlled low temperatures effectively suppresses NO_x formation. To increase the thermal efficiency, a preheater for fluidizing air and combustion air and a boiler feedwater heater are installed.

27.4.3 Emissions

The combustion of fuel ultimately leads to the emission of various gases and particulate matter. The amount and chemical components of these emissions depend on the fuel type, the boiler type and size, and the firing method. Different types of emissions are described below.

Particulate Emissions

The particulates present in the stack gases depend primarily on the combustion efficiency and on the amount of ash present in the fuel. All fuels except for natural gas contain some quantity of ash or noncombustible material that forms the majority of these particulates [27.7, 8].

Nitrogen Oxide Emission

The amount of nitrogen oxides (NO_x) present in the stack gas depends on many variables, especially the furnace heat rate level, the temperature, and the excess air. NO_x is one of the main contributors to ozone formation, visibility degradation, and human as well as animal health concerns. Combustion of any fossil fuel generates some NO_x due to the high temperature and availability of oxygen and nitrogen in the air and fuel. Based on how it is formed, NO_x can be subdivided into thermal NO_x and fuel NO_x.

Thermal NO_x

High temperatures (above 1200 °C) can cause the nitrogen and oxygen in the air to dissociate, which can then lead to the formation of so-called thermal NO_x. The formation of thermal NO_x is typically suppressed by reducing the peak and average flame temperatures. Aside from high temperatures, the formation of thermal NO_x is also promoted by long residence times and a high oxygen concentration. Possible reactions leading to the formation of NO_x during combustion include [27.8].

$$N_2 + O \rightarrow NO + N \quad (27.99)$$

$$N + O_2 \rightarrow NO + O \quad (27.100)$$

$$N + OH \rightarrow NO + H \quad (27.101)$$

Fuel NO_x

Fuel NO_x refers to NO_x that is formed by nitrogen in the fuel during combustion. The fuel–air ratio is one of main influences on the formation of fuel NO_x. The conversion of fuel-bound nitrogen to NO_x is strongly dependent on the fuel–air ratio but is relatively independent of the combustion-zone temperature. Fuel NO_x is formed in two ways: through the oxidation of volatile nitrogen and from the char during combustion.

Sulfur Dioxide Emission

SO_2 is an acidic gas formed by the combustion of sulfur in the fuel with oxygen. Dilute sulfuric acid is a major constituent of acid rain—an aqueous solution of sulfurous acid (H_2SO_3) is formed when sulfur dioxide combines with water, and this sulfurous acid can easily oxidize in the atmosphere to form sulfuric acid (H_2SO_4).

27.4.4 Environmental Control Technology

There are many technologies that can be used to control or reduce the emissions of pollutants to the atmosphere. These can be applied before, during, or after combustion.

Particulate Emission Control

Various equipment are used to remove particulate matter from flue gas, including:

- Electrostatic precipitators
- Fabric filters
- Mechanical collectors
- Venturi scrubbers.

Electrostatic Precipitators

When the ash particles present in the flue gas pass through electrostatic precipitators (ESPs) at a certain velocity, they become charged electrically and are attracted towards the collecting plate, which is normally positively charged.

Figure 27.38 shows a schematic of an ESP. The particulate-laden gas, which is normally laden with fly ash, is sent through pipes with negatively charged plates that cause the particles to become negatively charged. The particles are then routed past positively charged plates or grounded plates that attract the newly negatively charged ash particles. The particles stick to the positive plates until they are collected. The air that leaves the plates is therefore stripped of harmful pollutants. Velocity is an important influence on the performance of an electrostatic precipitator: decreasing the velocity allows more time to collect the ash particles.

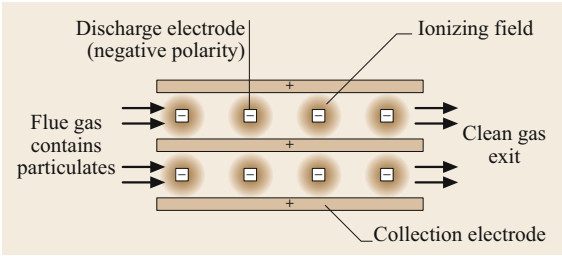

Fig. 27.38 Schematic of an electrostatic precipitator (ESP) viewed from above

Fabric Filters

Fabric filters are used to remove particles from the gas stream. They are made of woven or felted material and generally take the form of a cylindrical bag. Fabric filters are usually operated in the temperature range 120–180 °C. The coal type, plant size, and the boiler type and configuration all influence the choice of whether to use ESP or fabric filtration as the particulate removal technique. The two fundamental parameters to consider when sizing and operating bag houses to collect particulates are the air-to-cloth (A/C) ratio (m/s) and the pressure drop (mm H_2O or Pa). During operation, dust-laden gas flows through the filters, which remove the dust particles from the gas stream.

The following are the key factors in fabric filter performance:

- Flue gas temperature
- Dew point and moisture content
- Particle size distribution
- Chemical composition of the fly ash.

Fabric filters are categorized into three types:

- Pulse jet fabric filters
- Reverse-air fabric filters
- Shake-deflate filters.

Pulse Jet Fabric Filters

Pulse jet fabric filters use high-pressure air to clean the filter bags, and are provided in standard configurations that are capable of treating gas flow rates of up to about 300 000 ACFM (actual cubic feet per minute). Custom-designed units can handle larger flow rates.

Shake–Deflate Filters

This kind of filter collects the dust inside the bags, just as in the reverse-air design. To clean the bags, the top ends are shaken by a driver linkage.

Reverse–Air Fabric Filter

The reverse-air fabric filter is a customized design for utility boilers and industrial applications where large volumes of process gas flow (250 000 ACFM or more) must be cleaned. Such a system consists of 6–24 structural compartments. Typical compartments contain bags that are 20 or 30 cm in diameter and 7.31–11 m long.

Mechanical Collectors

Mechanical dust collectors are often called cyclones. Cyclones are used to remove dust and fibrous material in the first stage of a scrubber or fabric filter system. The arrangement of a cyclone separator is shown in Fig. 27.39. In a cyclone, the centrifugal force created by

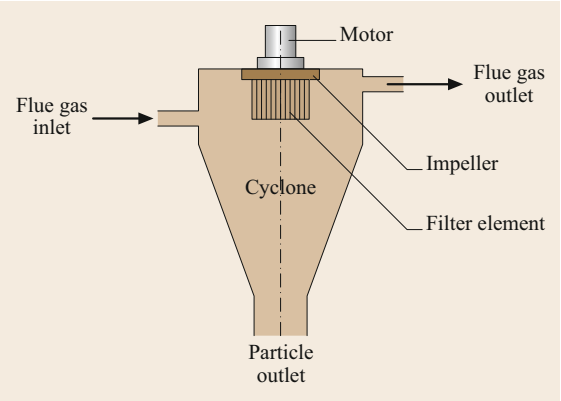

Fig. 27.39 Arrangement of a cyclone

spinning a gas stream is used to separate the particles from the gas. The gas enters the cylinder tangentially in a conventional cyclone and spins in a vortex as it proceeds down the cylinder. The presence of a conic section causes the vortex diameter to decrease until the gas reverses and spins up the center to the outlet pipe or vortex finder. Dust particles are centrifuged toward the wall and collected by inertial impingement.

The collected dust flows down in the gas boundary layer to the cone apex, where it is discharged through an airlock or into a dust hopper serving one cyclone or multiple parallel cyclones.

NO_x Control

It is very important to control the level of NO_x emitted from power plants because the NO_2 in the exhausted gases reacts with sunlight and hydrocarbons to produce photochemical smog and acid rain. The following techniques are used to reduce the level of NO_x formation:

- Low excess air operation
- Off-stoichiometric combustion or modified combustion
- Flue gas recirculation and treatment.

Low Excess Air Operation. In this technique, the total quantity of air used in the combustion process is reduced. By using less oxygen, the amount of NO_x generated is reduced.

Off-Stoichiometric Combustion. This technique involves mixing the fuel and air in such a way that the peak gas temperatures and peak oxygen concentrations are reduced. Advanced low-nitrogen-oxide burners can reduce emissions by up to 30%. These burners can be installed in either new or existing combustion plants. In a low-NO_x burner, the high-temperature zone is very close to the burner compared to a conventional burner, meaning that the pulverized coal is heated very rapidly, which increases the fraction of volatiles and nitrogen released. The recirculation flow near the center of the burner is also important, as returning hot gas creates very high temperatures at this point. Modified flow divider and pulverized fuel nozzle shapes together with optimized air-flow swirl are employed to achieve strong internal recirculation and longer residence times in the NO_x reducing zone, decreasing the amount of unburnt matter. The result is a 50% reduction in unburnt carbon as well as a drop of at least 10% in NO_x production.

Over Fire Air. In the over fire air (OFA) technique, the mixture is kept fuel rich and the combustion process is completed using air injection nozzles. The furnace has a lower zone and a higher zone. OFA systems divert a portion of the combustion air away from the primary combustion zone (i.e., away from the burners) to create a fuel-rich zone in the lower furnace zone, inhibiting conversion to NO. Peak flame temperatures are reduced in gas fired boilers to limit thermal NO_x formation. A flux of air intersects the burner flame in the upper furnace zone, completing the combustion.

Flue Gas Recirculation. A second method involves adding some of the flue gas to the combustion air at the burner in a technique normally termed flue gas recirculation. This increases the weight of the gas that must be heated by the chemical energy in the fuel, thereby reducing the flame temperature.

Flue Gas Treatment

Selective Noncatalytic Reduction Systems. Selective noncatalytic reduction (SNCR) involves the injection of ammonia (NH_3) or urea into the hot gas zone, where reactions leading to the reduction of nitrogen oxides can occur. These reactions are completed within the boiler and no waste products are generated. However, there is a risk of ammonia (NH_3) being emitted into the atmosphere if temperatures are too low. SNCR systems are capable of reducing nitrogen oxide levels by 20–60%. The reactions are

$$4\,NH_3 + 4\,NO + O_2 \rightarrow 4\,N_2 + 6\,H_2O$$
$$4\,NH_3 + 5\,O_2 \rightarrow 4\,NO + 6\,H_2O$$

Flue Gas Desulfurization.

Precombustion Sulfur Control Technologies. Removing the sulfur before burning is a challenging task, but there are a variety of techniques that can be applied to do this, including coal scrubbing and oil desulfurization.

Another removal process involves changing the design of the boiler and installing pressurized fluidized-bed combustors (FBCs) that remove sulfur from the coal during the burning process. Sulfur dioxide can also be removed from coal during combustion in the integrated gasification combined cycle. In this case, coal is gasified under pressure with a mixture of air and steam, and the resulting gas is then burned to produce electricity.

Postcombustion Sulfur Control Technologies. One postcombustion sulfur control method is called flue gas desulfurization (FGD). In FGD, waste gases are scrubbed with a chemical absorbent such as limestone to remove sulfur dioxide. There are many different FGD processes, the main ones being the limestone–gypsum process and the Wellman–Lord regenerative process. In limestone–gypsum FGD, limestone and water are mixed with the flue gases to produce a slurry that absorbs the sulfur dioxide. The slurry is then oxidized to calcium sulfate (gypsum), which can be used as a construction material. FGD technologies can be classified into six main categories: wet scrubbers, spray dry scrubbers, sorbent injection processes, dry scrubbers, regenerable processes, and combined SO_2/NO_x removal processes.

27.5 Nuclear Power Plants

In 1942, Enrico Fermi used uranium to produce the first controlled nuclear chain reaction. In recent decades, due to the depletion of coal and other fossil fuel reserves, nuclear power generation has become increasingly prominent. Nuclear fuels have the potential to release vast amounts of energy from fission reactions. For instance, when one pound of pure uranium (one of the most important nuclear fuels used in nuclear power plants) is bombarded with neutrons, fission reactions take place that cause uranium nuclei to split, releasing neutrons and a tremendous amount of energy—as much as burning 1500 short tons of coal. The amount of energy released in a fission process is calculated using Albert Einstein's famous theory of relativity, which states that

$$E = mc^2 \,, \tag{27.102}$$

where E is the energy in the fissile substance, m is the mass of that substance, and c is the speed of light. Uranium is the main fuel used in nuclear fission reactors to produce energy because it has many useful properties: uranium nuclei can be split by shooting neutrons at them, and this process releases many more neutrons which then split other uranium nuclei, as shown in Fig. 27.40. This phenomenon is known as a chain reaction.

A schematic of a nuclear power plant is shown in Fig. 27.41. The heat released by the nuclear reaction is transported to a heat exchanger via the primary coolant (e.g., CO_2 or water). Steam is then generated in the heat exchanger, which is used in a conventional manner to generate electrical energy by means of a steam turbine. Various types of nuclear reactors are used around the world, such as advanced gas reactors (AGRs), boiling water reactors (BWRs), and heavy-water-moderated reactors.

However, there has been a growing antinuclear sentiment in the world since March 2011, when there was a nuclear accident at the Fukushima Daiichi power plant in Japan. In Germany, antinuclear protests forced the government to promise to close all of its nuclear power plants by 2022. Therefore, the proportion of the electricity generated in Germany that is supplied by nuclear power has dropped from 22.4% in 2010 to 17.7% in 2011 and to 13% in 2016.

27.5.1 Nuclear Reactors

Nuclear reactors are devices that are designed to maintain a chain reaction by ensuring that sufficient neutrons are generated during the fission of heavy nuclei. The chain reaction generates heat, which is mainly used for electricity production. Nuclear reactors are operated in more than 50 countries [27.9].

27.5.2 Components of a Nuclear Reactor

The major components of a nuclear reactor are:

- The fuel core
- The moderator and coolant

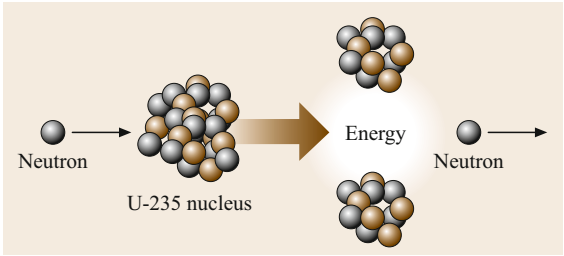

Fig. 27.40 Fission of a uranium-235 nucleus

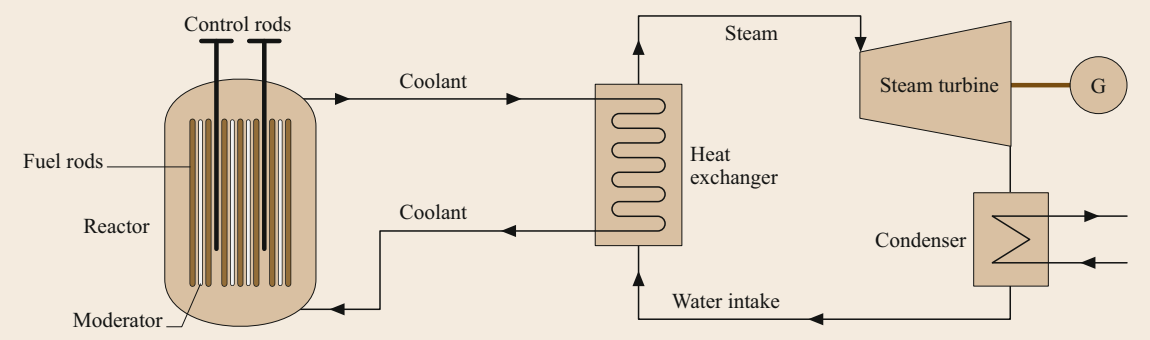

Fig. 27.41 Schematic view of a nuclear power plant

- The control rods
- The reactor vessel.

Fuel Core

The fuel core contains the nuclear fuel and is the part of the reactor where the fission reaction takes place. The nuclear fuel may be either natural or enriched uranium. Natural uranium contains 0.71% fissile ^{235}U and 99.28% fertile ^{238}U and fertile thorium (^{232}Th). Enriched uranium is produced in a gaseous diffusion process and has a ^{235}U content of 2–33%.

The nuclear fuel is generally contained in cylindrical rods surrounded by cladding materials. The fuel-rod cladding materials must be able to maintain the shape of the fuel rod and to sustain the reactor conditions. Materials used for these components include aluminum, magnesium, stainless steel, and graphite.

Moderator and Coolant

The moderator is the substance used in a nuclear reactor to slow down fast neutrons to thermal neutrons, which are much more likely than fast neutrons to induce nuclear fission. Liquid and solid materials with low atomic masses and low neutron capture cross-sections are suitable for this task, such as light water, heavy water, carbon, and beryllium.

The reactor coolant is used to remove heat from the reactor fuel core. Optimal coolant properties include a high specific heat, a high thermal conductivity, and a high boiling point at low pressure. The coolant should also be inexpensive and should have a low power demand for pumping and a high degree of stability in the reactor environment.

Control Rods

Control rods are used to slow down or speed up (i.e., control) a chain reaction. Elements such as boron and cadmium are used in a control rod to absorb fast neutrons and thereby control the chain reaction. An automatic retractable mechanism helps to insert the control rods into the fuel core or withdraw them to slow down or speed up the chain reaction. Types of control rods include shim rods, regulating rods, and safety rods.

Reactor Vessel

The reactor vessel is a tank-like structure that holds the reactor core and other internal components. The walls of the vessel are designed for a high-pressure radiation environment. In most cases, the vessel walls are lined with thick steel slabs to reduce the flow of radiation from the core. Nuclear fission generates large amounts of neutrons and gamma rays, both of which are very harmful, so biological shielding is required around the reactor vessel. This shielding consists of concrete blocks that may be up to 2 m thick.

Various types of nuclear reactors are used in power plants. They may be categorized into three classes:

- *Thermal reactors* use a neutron moderator to slow down or *moderate* fast neutrons by fission, thus increasing the probability that they will produce fission and sustain the chain reaction
- *Fast reactors* sustain the chain reaction without the need for a neutron moderator
- *Subcritical reactors* use an external source of neutrons.

The evolution of nuclear research can be divided into five stages:

- *Generation I* (1950s–1970s): The first nuclear power plants launched for grid-connected commercial generation of electricity. They include pressurized water reactors (PWRs) and boiling water reactors (BWRs).
- *Generation II* (1970s–1980s): light water reactors (boiling, pressurized; still in use) and heavy water reactors are developed
- *Generation III*: advanced designs are developed, including advanced boiling water reactors (ABWRs),

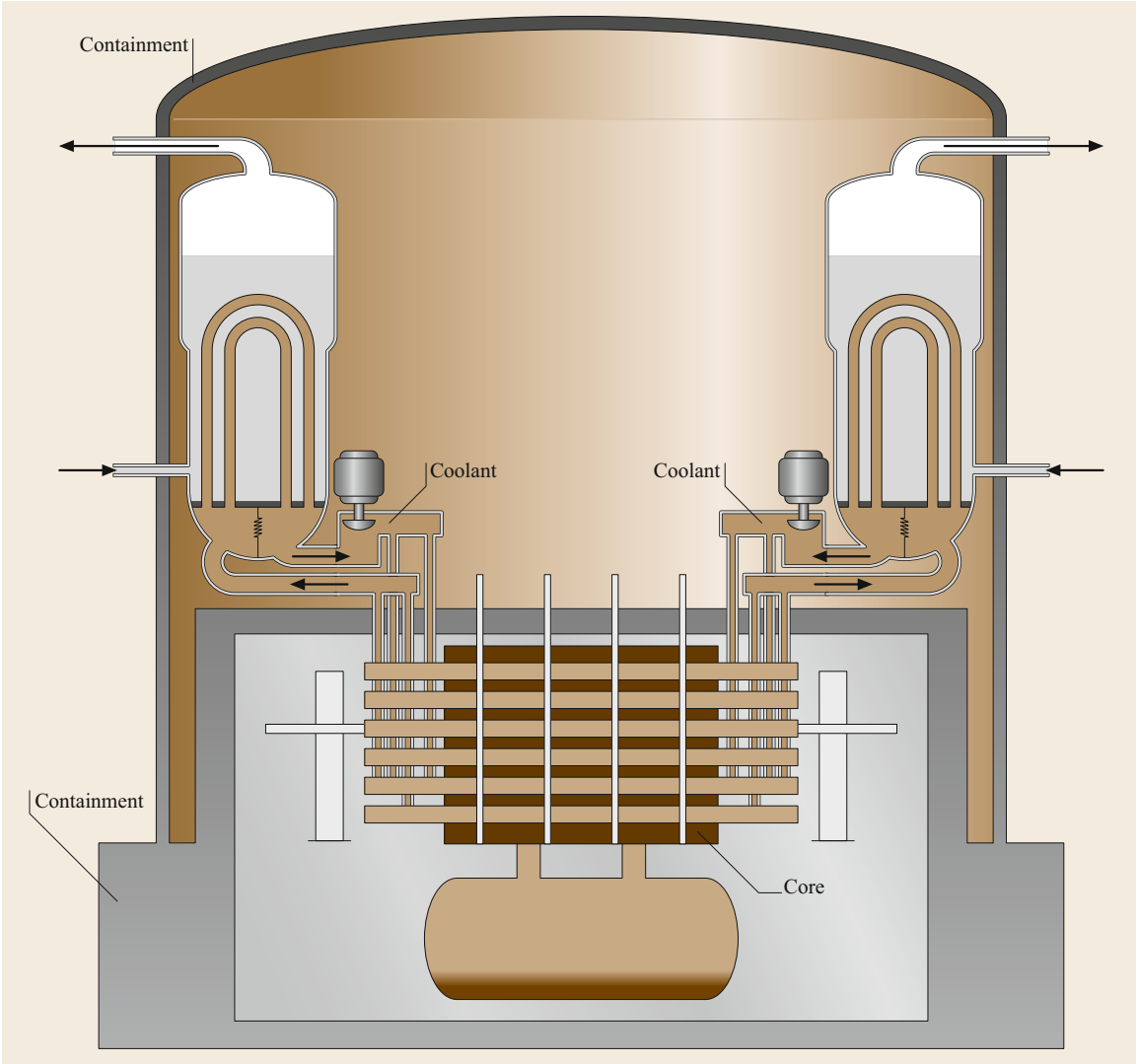

Fig. 27.42 Schematic of the CANDU reactor design used in Canada and India, which utilizes pressurized heavy water as the moderator

advanced pressurized water reactors (APWRs), and passive reactors

- *Generation III+* (used until about 2020, then to be phased out): Russia commissioned the first Gen III+ reactor in August 2016, followed by China in June 2018. Pebble bed reactors and larger passive reactors are developed
- *Generation IV* (conceptual, projected arrival 2030): advantages include improved safety, more economic, minimal waste, and greater public acceptability.

Nuclear power plants are classified according to the type of reactor used.

27.5.3 Types of Nuclear Reactors

Nuclear power plants can be categorized based on the coolant used in the core:

- *Light water reactor*.
- *Graphite-moderated reactor*. Includes the Chernobyl reactor (RBMK) type.
- *Gas-cooled thermal reactor*. An example of a gas-cooled reactor design is the British Magnox reactor type.
- *Heavy water reactor*. These reactors use heavy water, D_2O, as the coolant, which is relatively expensive. An example of a heavy water re-

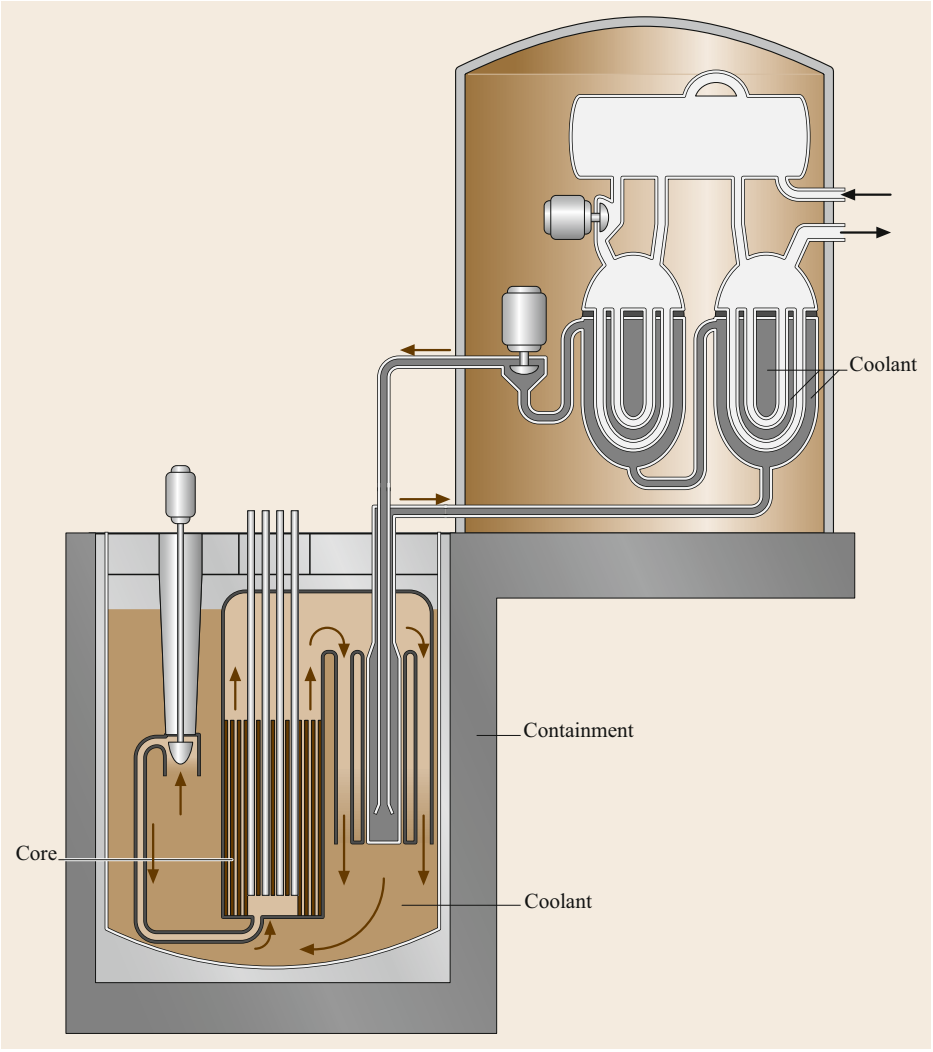

Fig. 27.43 Schematic of a fast breeder reactor

actor design is the Canada Deuterium Uranium (CANDU) reactor type used in Canada and India. A schematic of the CANDU reactor design is shown in Fig. 27.42.

- *Liquid-metal-cooled reactor*. Examples of the coolants used in such reactors include liquid sodium and a liquid lead-bismuth alloy.
- *Molten salt reactor*. Typical examples of the coolant used in these reactors are fluorides of alkali and alkaline earth metals.

Merits and Demerits of Nuclear Power Plants

Merits. A nuclear power plant produces no air pollution and requires only small volumes/masses of fuel; it therefore poses no transportation problems and may be sited close to load centers, regardless of the proximity of nuclear fuel suppliers. However, safety considerations imply that they should be located far from populated areas.

Demerits. Nuclear reactors produce radioactive fuel waste, the disposal of which poses serious environmental hazards. The rate of the nuclear reaction can only be lowered by a small margin, so the load on a nuclear power plant can only be reduced to marginally below its full load value. Because of its relatively high capital costs compared to its running costs, a nuclear plant should be operated continuously as a base load station. Whenever possible, it is preferable to support such a station with a pumped storage scheme. The greatest danger from a fission reactor comes from the potential for coolant loss in an accident. Even when the control rods are quickly lowered as far into the reactor as possible (called a scram operation), fission will continue,

and the afterheat from the reaction may lead to the vaporization and dispersal of radioactive material.

Fast Breeder Reactors

Global uranium resources are quite limited and may not last much more than another 90 years at the present rate of use. However, there is a redeeming feature of the use of uranium in nuclear plants. During the fission of ^{235}U, some of the neutrons are absorbed by the more abundant uranium isotope ^{238}U (enriched uranium contains only about 3% ^{235}U; most of it is ^{238}U), converting it to plutonium (^{239}U), which is also fissile. This plutonium can be extracted from the reactor fuel waste by a fuel reprocessing plant and then used in next-generation reactors known as fast breeder reactors (FBRs), thereby considerably extending the availability of nuclear fuels by several centuries.

Figure 27.43 shows a schematic of an FBR. For successful breeding, the conversion ratio (fissile material generated/fissile material consumed) must be more than unity. This is achieved by performing fission with fast-moving (rather than thermal) neutrons, meaning that no moderator is needed, although the fast neutrons are slowed down slightly by collisions with structural and fuel elements. The energy density per kilogram of fuel is very high, so the core used in an FBR is relatively small. It is therefore necessary for the coolant to have good thermal properties—liquid sodium is a very good candidate. The fuel for an FBR consists of 20% plutonium plus 8% uranium oxide. The coolant, liquid sodium, leaves the reactor at 650 °C and atmospheric pressure. The heat transported in this way is led to a secondary sodium circuit that transfers it to a heat exchanger in order to generate steam at 540 °C.

The release of plutonium—an extremely toxic material—means that environmental regulations are very stringent for an FBR.

27.6 Renewable Energy

Regenerative or renewable energies are energy sources or energy carriers that naturally renew themselves over short timescales (a human lifetime or less). Renewable sources of energy include hydropower, solar, wind, and biomass [27.10, 11].

27.6.1 Wind Energy

Wind is created when the Sun heats the atmosphere. It is an attractive power source because it is plentiful, inexhaustible, nonpolluting, and does not produce any waste heat [27.12]. However, it is also intermittent and variable. Wind turbines are used to convert wind energy into electrical energy. Control equipment that starts the wind turbine whenever the wind speed reaches about 3 m/s (9.8 ft/s) has been developed, as have techniques to generate constant-frequency power with varying wind speeds and consequently varying windmill propeller speeds. Wind power may prove practical for small power needs at isolated sites, but its intermittent nature implies that it should be used in conjunction with other methods of power generation to ensure continuity [27.13]. Wind turbines can be divided into three categories based on size:

- Small generators (0.5–10 kW) for isolated single premises
- Medium generators (10–100 kW) for communities
- Large generators (1.5 MW) for connection to the grid.

Figure 27.44 depicts a wind turbine configuration. The wind power is a measure of the energy available in the wind and is a function of the cube (the third power) of the wind speed. If the wind speed is doubled, the power in the wind increases by a factor of eight, so small differences in wind speed lead to large differences in electric power. This example illustrates that minor differences in wind speed due to either site selection or measurement errors can have a major bearing on the return on investment for a wind turbine.

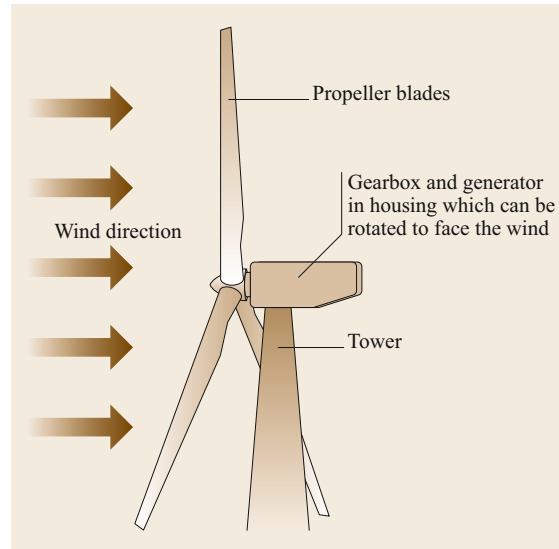

Fig. 27.44 Schematic of a wind turbine

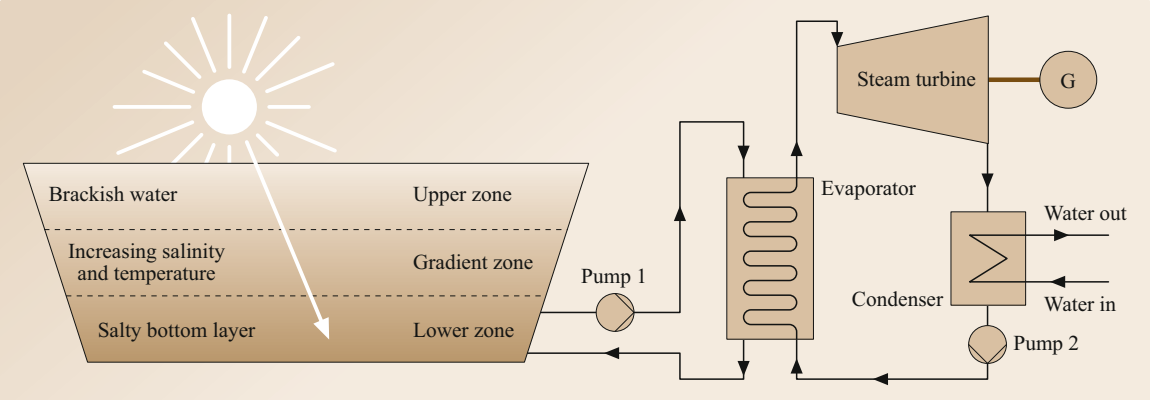

Fig. 27.45 Schematic of a solar pond

The theoretical power in the wind stream is given by

$$P = 0.5\rho AV^3 \quad \text{(W)}\,, \tag{27.103}$$

where ρ is the density of air (1201 g/m^3 at normal temperature and pressure (NTP)), V is the mean air velocity (m/s), and A is the swept area (m^2). The air density varies due to changes in elevation, temperature, and weather fronts. The wind energy market is currently growing due to some recent technical improvements [27.14].

27.6.2 Solar Energy

The Sun acts as an atomic furnace, converting mass into a huge amount of energy according to Einstein's mass–energy relation $E = mc^2$. Every second it converts over 657 million tons of hydrogen into 653 million tons of helium through nuclear fusion; the difference in mass (4 million tons) is discharged into space as energy. The Earth receives only about half a billionth of this energy. The energy radiated from the Sun is tremendous: the Sun radiates the same amount of energy in 15 min that mankind consumes during a whole year.

Solar or Photovoltaic Cells

Solar cells convert light from the Sun to a useful form of energy to generate power. A solar panel is constructed from elemental silicon, which becomes electrically charged when irradiated with sunlight. Sunlight consists of packets of energy called photons; these photons contain various amounts of energy corresponding to the different wavelengths of light. A solar cell is made of a material with well-defined possible energy levels for electrons. When a photon is absorbed by the active material of the solar cell, the energy of the photon is transferred to an electron, which is then excited from a low to a higher energy level. The asymmetric structure of a solar cell ensures that this electron escapes from its normal position, carrying away the extra energy. This electron leaves the cell through a metal contact and produces current in an electrical circuit.

Solar Pond

A solar pond is a relatively low-tech, low-cost approach to harvesting solar energy. It consists of three layers of water with different salt concentrations, as shown in Fig. 27.45. At the top is a low-salt-content layer, and below this is an intermediate layer with a salt gradient. The presence of this salt gradient creates a density gradient that suppresses natural heat exchange from convection in the water, meaning that the bottom layer, which has a high salt content, reaches a temperature of around 90 °C. Thermal energy from the salty bottom layer can be used to generate electricity.

An organic fluid with a low boiling point is usually used to convert this low-grade energy into electricity [27.15]. The hot brine is pumped from the salty bottom layer and sent into the evaporator, where it transfers heat to the organic fluid, and then the brine is pumped back into the salty bottom layer. The vaporized organic fluid at the exit of the evaporator is used to rotate the turbine, generating power.

The exhaust from the turbine is then condensed in the condenser and pumped back to the evaporator, resulting in a closed cycle. The efficiency of the overall system depends entirely on the salinity and purity of the pond, and it is normally quite difficult to maintain optimal salinity and dirt-free conditions.

Solar Chimney

Solar chimney technology is an innovative technique for harnessing energy from the Sun. A solar chimney consists of a glass collector, a wind turbine, an electrical generator, and a chimney. The glass collector is situated

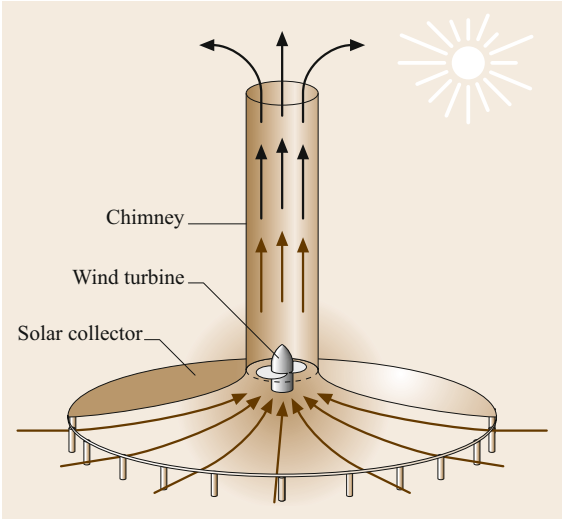

Fig. 27.46 Arrangement of a solar chimney

at the bottom and extends to a height of 2–7 m above the ground, as shown in Fig. 27.46. The chimney, which is 500–1000 m high, is located at the center. The conversion efficiency depends on the chimney height, the collector area, and the intensity of the solar radiation.

The working principle of a solar chimney is quite simple: the air trapped inside the glass collector is heated by the radiation from the Sun and becomes less dense, causing it to ascend the chimney. The rising hot air turns the wind turbine, which generates electricity.

Integrated Solar Combined Cycle Power System

Collecting solar energy using a parabolic trough in a combined cycle leads to high efficiency and low emissions. Figure 27.47 shows the layout of such an integrated solar combined cycle system. The heat from the parabolic trough collector can be utilized directly in the heat-recovery steam generator, in addition to the heat supplied by the gas turbine exhaust. This integration leads to efficient operation, even though solar energy intensity varies according to the weather and the time of day.

Sun-tracking concentrating mirrors called *heliostats* collect the sunlight and concentrate it onto a central receiver located at the top of a high tower, as shown in Fig. 27.48. The receiver converts the reflected solar radiation to thermal energy by heating the air to the temperature required to directly feed the gas turbine.

Other methods of exploiting this energy include endothermic chemical processes or the direct use of thermal energy for process heating. Central receiver technology is a promising alternative method [27.16], as it overcomes the disadvantages of trough technology.

27.6.3 Geothermal Energy

Geothermal energy is thermal energy stored at some depth underground. The heat is produced mainly by the radioactive decay of potassium, thorium, and uranium in the Earth's crust and mantle. It is also produced by friction between continental plates. Geothermal energy can be recovered and used to generate power. The upper 3.3 m (10 ft) of the Earth's surface is at a near-constant temperature (between 10 and 16 °C or 50–60 °F). Geothermal heat pumps can tap into this low-grade energy, which is widely abundant (it covers almost the entire Earth), for space heating or cooling.

The annual global low-grade heat rejection from the Earth averages between 50 and 70 mW/m^2. This is much lower than the solar radiation received annu-

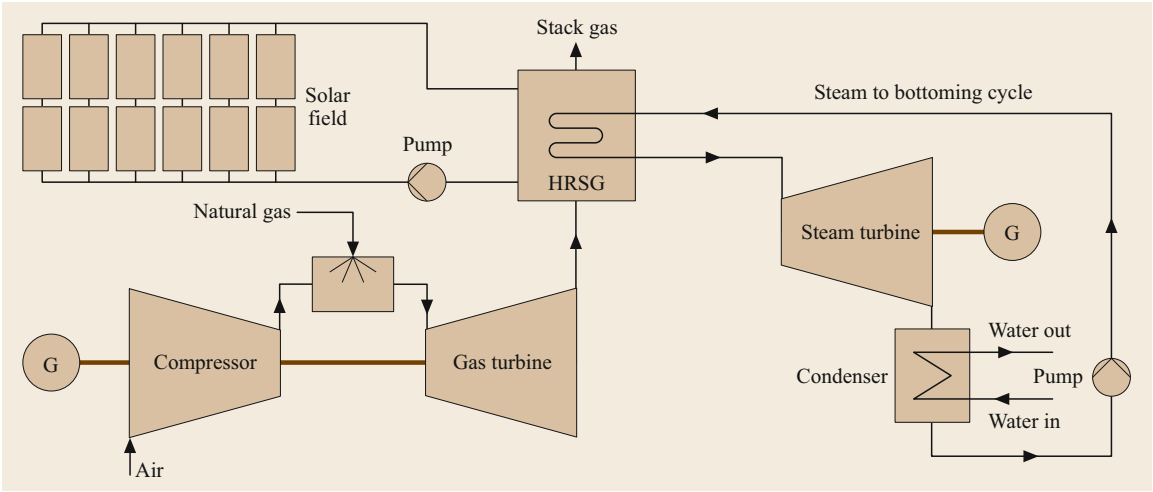

Fig. 27.47 Layout of an integrated solar combined cycle system that uses a solar field

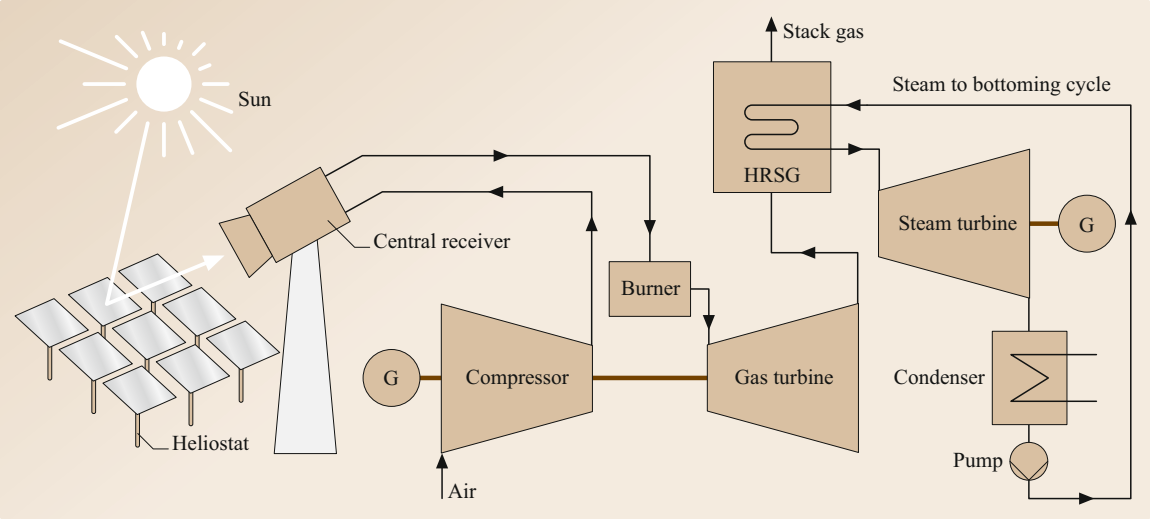

Fig. 27.48 Layout of an integrated solar combined system that uses heliostats

ally by the Earth (342 W/m^2), but it is still significant enough to drive the development of several extraction technologies; in fact, it is estimated to be roughly three times the energy used annually around the world.

The amount of usable energy from geothermal sources varies with depth and the extraction method applied. The quality of a geothermal resource is determined by its temperature. If the temperature and the flow rates are large enough, geothermal energy can be used to generate electricity.

There are three types of geothermal power plants. In *dry steam* operation, the rising steam is simply collected from the ground and funneled directly into a turbine that drives an electric generator. The other two designs are the flash steam and binary cycle designs, which use a mixture of steam and heated water (*wet steam*) extracted from the ground. The United States and China have the largest installed capacities, each totaling over 17 GW. Currently, the Geysers Geothermal Complex located about 121 km north of San Francisco, California, with an installed capacity of 1517 MW and an active production capacity of 900 MW, is the biggest geothermal installation in the world. This complex has 18 power plants.

27.6.4 Wave/Tidal Energy

Ocean waves are generated when solar radiation heats the Earth's surface unevenly, creating surface winds that generate water waves with various frequencies. The lower-frequency waves, called *swell*, propagate out from the storm area with little or no loss of energy until they encounter nearshore surface friction. Thus, swell energy is dissipated only when the swell reaches shallow water, which is why it is said that wave or swell energy is derived from solar energy. But the density of wave energy is orders of magnitude greater than that of solar or wind energy. In fact, if only 0.2% of the energy in the world's ocean waves were to be harnessed, it would supply all of the world's current energy demand as a renewable resource.

Numerous technologies have been proposed for wave energy conversion. However, none of them have been fully tested in the field or survived weather tests, even for just a few cycles. The major challenges involved in developing wave energy technology include a lack of long-term ocean wave measurements nearshore, where refraction effects result in spatially inhomogeneous wave parameters. Sufficient data are needed to identify the optimal location for wave energy conversion. The equation [27.17]

$$E_p = \frac{\rho g^2 H^2 T}{32\pi} \tag{27.104}$$

shows that the wave energy E_p varies with the square of the wave height. For example, a wave with an amplitude of 3 m and a period of 10 s contains 86 kW/m of energy.

Tide energy is distinct from wave energy; it is a form of hydropower that converts the energy obtained from tides into useful forms, mainly electricity. Tidal forces are caused by variations in gravitational attraction exerted on the Earth by celestial bodies; these forces induce currents in the world's oceans [27.18]. The currents manifest as temporary peaks and troughs in the water level that are visible on beaches. The sea

level is raised by onrushing water from the center of the ocean that is pulled by gravitational forces toward shorelines. This happens routinely and consistently because of the cyclic nature of the Moon's orbit around the Earth. Predictable shifts in the Moon's position with respect to the Earth and the Sun also lead to predictable changes in tidal magnitudes. Thus, tides are more predictable than winds and the intensity of solar radiation at the Earth's surface. The world's first large-scale tidal power plant was the Rance Tidal Power Station in France, with a capacity of 240 MW, which opened in 1966. It was the largest tidal power station (in terms of output) until the 254 MW Sihwa Lake Tidal Power Station opened in South Korea in August 2011.

27.6.5 Biofuels

Biofuels are produced by living organisms or from metabolic by-products such as food waste. Since biofuels are generated by photosynthesis, they are also referred to as components or derivatives of solar energy. Biofuels are renewable because they do not introduce new emissions into the environment, in contrast to fossil fuels. For a mixed fuel resource to be considered a biofuel, the fuel must contain over 80% renewable materials. There are many pros and cons of using biofuels as an energy source. The two most common types of biofuels are ethanol and biodiesel, but there are more in the research pipeline, such as algae and microbes. Biofuels that do not compete with food for arable land are of greater interest to society.

Ethanol is an alcohol made by fermenting any biomass high in carbohydrates, and is mostly used as a fuel additive to reduce emissions. Flexible-fuel vehicles that run on mixtures of gasoline and up to 85% ethanol are now available. One form of biofuel is biodiesel, which is typically made by combining methanol with vegetable oil, animal fat, or recycled cooking greases. Biodiesel can be used as an additive to regular diesel or pure in diesel engines.

Another biofuel is methanol, commonly called wood alcohol, which can be obtained from biomass. Methanol is typically produced by gasification, i.e., by vaporizing biomass at elevated temperatures, cleaning the resulting gas, and then passing it through a catalyst that converts it to methanol. Most reformulated gasoline components produced from biomass are used as pollution-reducing agents or additives.

27.7 Energy Storage and Distribution

Storing energy can be very useful in cases where the supply of or demand for energy varies over time. For example, the peak power demand in Europe can rise sharply in the evening, particularly in the winter, when the demand for heating is high. On the other hand, peak demand may occur in the afternoon in tropical and warm climates when the cooling load rises in the summer. Storing the energy available during periods of low demand for use during peak hours could eliminate the need to build new power plants. Storage also reduces operating costs and improves customer satisfaction, which can improve the status of the utility in the international market. Energy storage is commonly used in standalone applications, where it serves as an uninterruptible power supply (UPS) unit.

The most important energy storage technologies are:

- Pumped hydropower
- Compressed energy storage
- Flywheels
- Electrochemical storage devices
- Secondary battery energy storage
- Thermal energy storage devices.

27.7.1 Pumped Hydropower

Pumped hydro facilities consist of two large reservoirs, one located at the base level and the other located at a different elevation. In pumped hydro, surplus power during low demand is utilized to pump the water from the lower reservoir to the upper reservoir, where it can be stored as potential energy. During periods of higher energy demand, water flows back into the lower reservoir, passing through hydraulic turbines that generate electrical power [27.19].

It should noted, however, that the construction costs of pumped hydropower are very high, and its efficiency is fairly low. The combined efficiency of a pumped hydro system is given by

$$\eta_{\text{comb. effic.}} = \frac{\text{Total energy output}}{\text{Total energy input during a charge–discharge cycle}} \,. \quad (27.105)$$

27.7.2 Compressed Air Energy Storage

In this storage method, excess energy is used to compress air and store it in an airtight underground storage

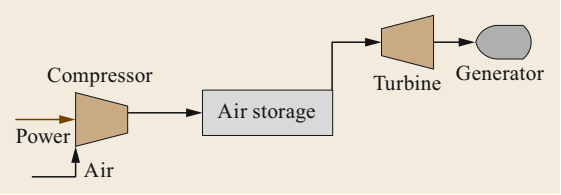

Fig. 27.49 Schematic of a compressed air storage system

cavern. The compressed air is then released during periods of peak demand by expanding the air through an air turbine. Three types of reservoirs can be used to store compressed air: salt caverns, aquifers, and hard rock caverns. When air is compressed for storage, its temperature increases. Assuming a polytropic process, the final temperature is given by

$$T_2 = T_1 \left(\frac{p_2}{p_1}\right)^{\frac{n-1}{n}} , \qquad (27.106)$$

where n is the polytropic index and p_1, T_1 and p_2, T_2 are the pressures and temperatures before and after compression, respectively.

Numerous studies have concluded that compressed air energy storage is competitive with other energy storage systems [27.20]. The layout of a compressed energy storage system is shown in Fig. 27.49. The heat of compression may be retained in the compressed air. This is called adiabatic storage and results in high storage efficiency because more energy is recovered upon the expansion of the compressed air.

27.7.3 Energy Storage by Flywheels

Flywheel energy storage is a promising technology for intermediate energy storage. A flywheel storage system consists of a flywheel that rotates at a very high velocity and an integrated electrical apparatus that can operate as either a motor to turn the flywheel and store energy or a generator to produce electrical power on demand using the energy stored in the flywheel. The use of magnetic bearings and a vacuum chamber helps to reduce energy losses.

In a flywheel, energy is stored in the form of mechanical kinetic energy. The rotating mass stores the energy input so that the rotation can be maintained at a fairly constant rate. There are two main sources of losses when using a flywheel: windage and bearing. The energy stored in a flywheel is given by

$$E_{\mathrm{k,disc}} = \frac{1}{4} M r^2 \omega^2 , \qquad (27.107)$$

where M is the mass of the flywheel and r is the radius of the flywheel. In order to achieve a high energy density, the rotation speed ω must be very high.

27.7.4 Electrochemical Energy Storage

Electrochemical energy storage is another emerging area of technology. Such schemes can be categorized into primary batteries, secondary batteries, and fuel cells. These devices convert stored chemical energy into electrical energy. Primary and secondary batteries utilize the chemicals built into them, whereas fuel cells use chemical energy in the form of a synthetic fuel from an external source [27.21].

27.7.5 Secondary Batteries

Large-scale battery use is almost unfeasible and is limited to battery-powered vehicles and storage for local fluctuating energy sources such as windmills or solar. The most widely used battery is the lead–acid battery, invented by Plante in 1859. The sodium–sulfur battery (200 Wh/kg) and batteries utilizing other combinations of materials are also being developed to obtain more output and storage per unit weight [27.13].

27.7.6 Thermal Energy Storage

Thermal energy storage is ideally suited to applications such as space heating, where a low quantity of heat is required. There are two distinct thermal energy storage mechanisms: sensible heat and latent heat storage. In sensible heat storage, energy is stored as sensible heat by increasing the temperature of the storage medium.

27.8 Prospects and Conclusion

Global energy needs are likely to continue to grow steadily for at least the next few decades. The growth in this energy demand will be curbed somewhat by gains in energy efficiency. Despite considerable uncertainty about exactly how quickly global gross domestic product (GDP) will grow, it seems almost certain that it will rise for at least the next twenty years, leading to a commensurate increase in energy use over that period. It is expected that more than two-thirds of the growth in global energy use will come from developing countries, where economic and population growth are highest.

Population and economic growth are the key drivers of the increase in energy demand. By 2030, the global population is projected to exceed 8.3 billion, meaning that an additional 1.3 billion people (compared to the current population) will be adding to the energy demand. Qualitatively, even if the increase in population is ignored, the economies of many developing countries are expected to grow, which will also add to the energy demand. Developing countries outside the OECD (Organization for Economic Cooperation and Development) will account for over 90% of the population growth up to 2030. Due to rapid industrialization, urbanization, and transportation in non-OECD countries, they will contribute 70% of the global GDP growth and over 90% of the global energy demand growth.

Based on current policies and according to the underlying premise of the World Energy Outlook's Reference Scenario, the world's energy needs will be more than 50% higher in 2030 than today, corresponding to an average annual growth rate of 1.6%. This increase in energy demand is occurring against a backdrop of a turbulent global political climate that threatens energy security as well as environmental concerns resulting from the emission of combustion products. The assumption that fossil fuel reserves are decreasing, the possibility of an unmet but growing energy demand, and scant investment to ensure that energy supplies will be sufficient to meet future energy demands have all muddied the prospects for stable energy supplies. These uncertainties and the concerns about climate change have been reflected in the market as price volatility and instability.

Renewable energy supplies are predicted to grow rapidly (almost fourfold) by 2035, and to supply one-third of the growth in power generation by then. Despite a sharp increase in renewable energy use (solar, wind, and hydro in particular), fossil fuels are expected to remain the dominant source of global energy and to cover 60% of the increase in global energy demand by 2035. Because of the existing supply infrastructure, its relatively low impact on the environment compared to coal and oil, and contributions from US shale gas and liquefication, natural gas will likely dominate the fossil fuel supply market.

The rise in natural gas consumption will contrast with a decline in coal consumption. However, oil demand is expected to increase by almost 20 million barrels per day over the next few decades, particularly in the transportation and industrial sectors of Asia. Oil consumption currently fluctuates at around 93 million barrels per day. This higher rate of use of fossil fuels over the next few decades will mean that carbon emissions are likely to continue to increase, albeit at a checked rate, and that clean coal and liquified gas technologies remain important research topics.

When estimating growth trends, the major uncertainties in the base case assumptions are from global GDP growth, a potential transition to a lower-carbon world due to unforeseen technological solutions, and the prominence of newer and more affordable resources such as shale oil and gas.

Emerging technologies based on renewable energy sources represent a tremendous opportunity to achieve major improvements in energy efficiency and access. Part-load wind energy conversion is still very low, and solar PV barely attains double-digit efficiency in the field, despite claims of much higher efficiencies in labs. Biofuels are still in their infancy. Simply put, continued research into renewable energy is certain to lead to breakthroughs.

Combustion engines still produce a considerable amount of thermal waste. Advanced technologies such as IGCC, ultra-supercritical cycles, cogeneration and combined cycle systems, and advanced gasification molten carbonate fuel cell cycles allow electricity demands to be satisfied and emission levels from power plants to meet air quality standards. Technological advances in integrated gasification combined cycle technologies will permit the exploitation of various kinds of low-grade energy resources such as biomass, low-grade coal, and oil residues, and may improve the reliability and efficiency of energy conversion processes. The development of advanced materials that can withstand elevated temperatures and pressures in gas turbine engines will enhance the thermal efficiency of these cycles. A fraction of a percentage improvement in efficiency can have huge economic and environmental impacts. Using a multicomponent fluid such as an ammonia-water mixture will improve system thermal efficiency.

In conclusion, the prospects for energy are obscured by global conflicts and political developments, population growth, climate change, government policies, resource availability, new research findings, and other unpredictable events that may disturb the supply chain, including the weather. However, to a lesser degree, access to energy impacts global peace, population health and growth, climate change, government policies, and access to resources, among other aspects. Energy and society are incredibly intertwined, and globalization has only added another layer of complexity to this relationship. Energy has become a vital commodity that determines the wellbeing of a society, and only wealthy societies can provide full access to energy supply. This explains why energy—a multidimensional topic that affects all aspects of our lives—has become one of the most studied and researched topics.

References

27.1 I. Seikan: *Steam Power Engineering: Thermal and Hydraulic Design Principles* (Cambridge Univ. Press, Cambridge 1999)

27.2 R. Kehlhofer, R. Bachmann, H. Nielsen, J. Warner: *Combined Cycle Gas and Steam Turbine Power Plant* (PennWell, Tulsa 1999)

27.3 M.S. Briesch, R.L. Bannister, I.S. Diakunchak, A. Huber: A combined cycle designed to achieve greater than 60% efficiency, J. Eng. Gas Turbines Power **117**, 734–741 (1995)

27.4 K.W. Li, A.P. Priddy: *Power Plant System Design* (Wiley, New York 1985)

27.5 D.P.K. Kothari: *Modern Power System Analysis* (McGraw-Hill, New York 2006)

27.6 P. Basu, C. Kefa, L. Jestin: *Boilers and Burners: Design and Theory* (Springer, Heidelberg, Berlin 2000)

27.7 S. Tavoulareas: *Multi pollutant emission control technology options for coal fired power plants*, US Environmental Production Agency Report (EPA, Washington 2005)

27.8 L.E.J. Roberts, P.S. Liss, P.A.H. Saunders: *Power Generation and the Environment* (Oxford Univ. Press, Oxford 1990)

27.9 G. Wills: *Nuclear Power Plant Technology* (Wiley, New York 1967)

27.10 W. Stoecker: *Design of Thermal Systems*, 3rd edn. (McGraw-Hill, New York 2011)

27.11 D.P. Kothari, K.C. Singal, R. Ranjan: *Renewable Energy Sources and Emerging Technologies* (Prentice Hall, New Delhi 2008)

27.12 R.C. Bansal, D.P. Kothari, T.S. Bhatti: On some of the design aspects of wind energy conversion systems, Energy Convers. Manag. **43**, 2175–2187 (2002)

27.13 D.P.K. Kothari, I.J. Nagarth: *Power System Engineering*, 2nd edn. (Tata McGraw-Hill, New Delhi 2007)

27.14 D.W. MacPhee, A. Beyene: Experimental and fluid structure interaction analysis of a morphing wind turbine rotor, Energy **90**(P1), 1055–1065 (2015)

27.15 M. Soda, A. Beyene: Multiphase ultra-low grade thermal energy storage for organic Rankine cycle, Int. J. Energy Res. **40**, 51–60 (2016)

27.16 B. Kelly: Optimization studies for integrated solar combined cycle system. In: *Proc. Solar Forum* (ASME, Washington 2001)

27.17 J.H. Wilson, A. Beyene: California wave energy resource evaluation, J. Coast. Res. **23**(3), 679–690 (2007)

27.18 R.H. Charlier, C.W. Finkl: *Ocean Energy – Tide and Tidal Energy* (Springer, Heidelberg, Berlin 2009)

27.19 R.A. Huggins: *Energy Storage: Fundamentals, Materials and Applications* (Springer, Cham 2015)

27.20 P.G. Hill: *Power Generation: Resources, Hazards Technology, and Costs* (MIT Press, Cambridge 1977)

27.21 W.A. Adams: Electrochemical energy storage systems: A small scale application to isolated communities in the Canadian Arctic, Can. Electr. Eng. J. **4**, 4–10 (1979)

Asfaw Beyene

Mechanical Engineering
San Diego State University
San Diego, USA
abeyene@sdsu.edu

Asfaw Beyene is Professor of Mechanical Engineering and Director of the Renewable Energy and Energy Efficiency Center at San Diego State University (SDSU). He earned his PhD from Warsaw University of Technology. His research integrates computational and experimental techniques to address fundamental and practical issues with energy conversion. He is author of over 120 publications, has received many national and international awards, and is an AMSE Fellow.

Dwarkadas Kothari

School of Electrical Sciences
VIT University
Vellore, India
dkothari@ces.iitd.ac.in

Prof. D.P. Kothari is Vice Chancellor of VIT University (Vellore) and a former Director of IIT Delhi. He is a FNAE, FNASc, SMIEEE, MIEE, FIE (India), and National Khosla Award Winner for lifetime achievements in engineering. He has coauthored 20 books and over 540 research publications, and has guided 28 PhD and 59 masters theses. His research focuses on power and energy system engineering, operation, control, reliability, and optimization.

P.M.V. Subbarao

Mechanical Engineering Department
Indian Institute of Technology
New Delhi, India
pmvs@mech.iitd.ac.in

Dr P.M.V. Subbarao is an Associate Professor of Mechanical Engineering at IIT Delhi. He obtained his PhD in Mechanical Engineering from IIT Kanpur in 1996. He developed ultramicrohydropower plants that are installed in remote rural areas for rural electrification, and a technology for producing biogas-derived bio-CNG to use in automobiles. His current research activities include power generation, renewable energy systems, and micro and pico power-generation systems.

Part G Annex

Part G Annex

28 **General Tables**
Stanley Baksi, Koblenz, Germany

28. General Tables

Stanley Baksi

Often in daily engineering practice, data from various systems and sources need to be merged to develop a product. Not all systems or organizations use the same system to develop their products. The system used may depend on the project requirements, as well as geographical preferences. This chapter provides help for engineers trying to merge or convert data from one system to another. In addition, it provides typical values of some engineering constants used in product development.

References 1285

Table 28.1 Basic dimensions, their symbols, and physical significance

Basic dimension	Symbol	Physical entity
Meter	m	Length
Kilogram	kg	Mass
Second	s	Time
Ampere	A	Electric current
Kelvin	K	Thermodynamic temperature, temperature difference
Mol	mol	Quantity
Candela	cd	Light intensity

Table 28.3 Prefixes for units

Power of ten	Prefix	Symbol
10^{18}	Exa	E
10^{15}	Peta	P
10^{12}	Tera	T
10^{9}	Giga	G
10^{6}	Mega	M
10^{3}	Kilo	k
10^{2}	Hekto	h
10	Deka	da
10^{-1}	Deci	d
10^{-2}	Centi	c
10^{-3}	Milli	m
10^{-6}	Micro	μ
10^{-9}	Nano	n
10^{-12}	Pico	p
10^{-15}	Femto	f
10^{-18}	Atto	a

Table 28.2 Types of units and their explanation

Characteristics of the SI – units derived	Development of symbols for the description of the SI units derived	Example
Units (combined) without special symbols	These symbols are developed by combining the basic units of their constituting elements, for example, units of area, volume, velocity, etc.	m^2, m^3, m/s
Units (combined) with special symbols	–	Newton (N), pascal (Pa), joule (J), watt (W), ohm (Ω)
Units (combined) with mixed symbols	These symbols are developed by combining the specific units of their constituting elements and some basic units of measurement. If necessary, a combination of symbols that describe the properties of the measurement	Newton meter (N m), pascal second (Pa s)

K.-H. Grote, H. Hefazi (Eds.), *Springer Handbook of Mechanical Engineering*, Springer Handbooks,
https://doi.org/10.1007/978-3-030-47035-7_28

Table 28.4 Commonly used units, not defined in the Système International d'Unités (SI) system

Characteristics of units	Example
Generally used units	Liter (L), hour (h), degree (deg, °)
Units with limited use	Electron volt (eV)

Table 28.5 Conversion values to calculate from m-kp-s in the SI system

1 kp ≈ 1 daN	1 at ≈ 1 bar	1 kp m ≈ 1 daJ
1 kp/cm ≈ 1 N/mm	1 PS ≈ 0.75 kW	
1 mm water column ≈ 0.1 mbar	1 kcal ≈ 4.2 kJ	

Table 28.6 Names and abbreviations of English units

atm	Atmosphere
bbl	Barrel
btu	British thermal unit
bu	Bushel
cal	Calorie
cwt	Hundred weight
deg F	Degree Fahrenheit
ft	Foot
gal	Gallon
hp	Horsepower
in	Inch
lb	Pound
lbf	Pound force
lntn	Long ton
mi	Mile
pdl	Poundel
shtn	Short ton
yd	Yard

Table 28.7 Roman counting system

I ≡ 1, V ≡ 5, X ≡ 10, L ≡ 50, C ≡ 100, D ≡ 500, M ≡ 1000					
1	I	10	X	100	C
2	II	20	XX	200	CC
3	III	30	XXX	300	CCC
4	IV	40	XL	400	CD
5	V	50	L	500	D
6	VI	60	LX	600	DC
7	VII	70	LXX	700	DCC
S	VIII	80	LXXX	800	DCCC
9	IX	90	XC	900	CM
The direction of writing is from left to right; the individual values are added to obtain the value. The lesser values always come after the greater values. If otherwise, the lesser values must be subtracted from the greater values.					
V, L, D	Can be written only once				
I, X, C	Can be written up to three times				
Examples					
1496	MCDXCVI				
673	DCLXXIII				
1891	MDCCCXCI				
1981	MCMLXXXI				

Table 28.8 Conversion of important units from the foot-pound-second (fps) system to the SI system [28.1]

	fps (foot-pound-second)	SI (m-kg-s)
Length	1 ft = yd = 12 in	1 ft = 0.3048 m; 1 mi = 1609.34 m
Area	1 ft^2 = 144 in^2	1 ft^2 = 0.092903 m^2
Volume	1 ft^3 = 1728 in^3 = 6.22882 gal (UK) 1 gal (US) = 0.83268 gal (UK)	1 ft^3 = 0.0283169 m^3 1 bu (US) = 35.23931; 1 bbl (US) = 115.6271
Velocity	1 ft/s 1 knot = 1.150785 mi/h = 1.6877 ft/s	1 ft/s = 0.3048 m/s
Acceleration	1 ft/s^2	1 ft/s^2 = 0.3048 m/s^2
Mass	1 lb = cwt/112; 1 shtn = 2000 lb 1 slug = 32.174 lb; 1 lntn = 2240 lb	1 lb = 0.453592 kg 1 slug = 14.5939 kg
Force	1 lbf 1 pdl = 0.031081 lbf	1 lbf = 4.44822 N 1 pdl = 0.138255 N
Work	1 ft lb = 0.323832 cal_{IT} 1 btu = 252 cal_{IT} = 778.21 ft lb	1 ft lb = 1.35582 J 1 btu = 1.05506 kJ
Pressure	1 lb/ft^2 = 6.9444 $\times 10^{-3}$ lb/in^2 1 lb/in^2 = 0.068046 atm 1 atm = 29.92 inHg = 33.90 ft water	1 lb/ft^2 = 47.88 N/m^2 1 lb/in^2 = 6894.76 N/m^2 1 atm = 1.01325 bar
Density	1 lb/ft^3 = 5.78704 $\times 10^{-4}$ lb/in^3 1 lb/gal = 6.22882 lb/ft^3	1 lb/ft^3 = 16.0185 kg/m^3 1 lb/gal = 99.7633 kg/m^3
Temperature	32 °F = 0 °C, 212 °F = 100 °C	1 °F = 0.5556 °C
Power	1 ft lb/s = 1.8182 $\times 10^3$ hp = 1.28505 $\times 10^{-3}$ btu/s	1 ft lb/s = 1.35582 W
Specific heat capacity	1 btu/(lb °F)	1 btu/(lb °F) = 4.1868 kJ/(kg K)
Thermal conductivity	1 btu/(ft h °F)	1 btu/(ft h °F) = 1.7306 W/(m K)
Heat transfer coefficient	1 btu/(ft^2 h °F)	1 btu/(ft^2 h °F) = 5.6778 W/(m^2 K)
Viscosity, kinematic	1 ft^2/s	1 ft^2/s = 0.092903 m^2/s
Viscosity, dynamic	1 lb/(ft s)	1 lb/(ft s) = 1.48816 kg/(m s)

in/s ≡ inch per second; in^2 ≡ square inch; in^3 ≡ cubic inch

Table 28.9 Nomenclature for astronomical prefixes

10^6	Million	Mega	M
10^9	Billion	Giga	G
10^{12}	Trillion	Tera	T
10^{15}	Quadrillion	Peta	P
10^{18}	Quintillion	Exa	E
10^{21}	Sextillion	Zetta	Z
10^{24}	Septillion	Yotta	Y
10^{27}	Octillion	–	–

Table 28.10 Units of space and time [28.2]

Unit[a]	Symbol	Physical relation and technical value	Description through the basic units
Meter	m	Length	–
Second	s	Time	–
Square meter	m^2	Surface	–
Cubic meter	m^3	Volume	–
Meter per second	m/s	Velocity	–
Meter per square second	m/s^2	Acceleration	–
Cubic meter per second	m^3/s	Volume flow	–
Radian	rad	Angle	$1\,\text{rad} = 1\,\text{m/m}$
Steradian	sr	Three-dimensional angle	$1\,\text{sr} = 1\,\text{m}^2/\text{m}^2$
Hertz	Hz	Frequency	$1\,\text{Hz} = 1/\text{s}$
Radian per second	rad/s	Angular velocity	–
Radian per square second	rad/s^2	Angular acceleration	–
Liter	L	Volume	$1\,\text{L} = 10^{-3}\,\text{m}^3$
Degree	°	Angle	$1° = \pi/180\,\text{rad}$
Minute	′	Angle	$1' = \pi/(180 \times 60)\,\text{rad}$
Second	″	Angle	$1'' = \pi/(180 \times 60 \times 60)\,\text{rad}$
Minute	min	Time	$1\,\text{min} = 60\,\text{s}$
Hour	h	Time	$1\,\text{h} = 60\,\text{min} = 3600\,\text{s}$
1 per second	1/s	Frequency	$1/\text{min} = (1/60)\,1/\text{s}$ $1/\text{h} = (1/60)\,1/\text{min} = (1/60)^2\,1/\text{s}$

[a] Both SI and other unit systems (commonly used ones) are presented

Table 28.11 Units commonly used for calculation in mechanics

Unit[a]	Symbol	Physical meaning	Relation to basic units
Kilogram	kg	Mass	–
Kilogram per second	kg/s	Mass flow	–
Kilogram square meter	kg m^2	Mass moment	–
Kilogram per cubic meter	kg/m^3	Density	–
Cubic meter per kilogram	m^3/kg	Specific volume	–
Square meter per second	m^2/s	Kinematic viscosity	–
Newton	N	Force	$1\,\text{N} = 1\,\text{kg m/s}^2$
Pascal	Pa	Pressure	$1\,\text{Pa} = 1\,\text{kg}/(\text{m s}^2)$
Joule	J	Work, energy	$1\,\text{J} = 1\,\text{kg m}^2/\text{s}^2$
Watt	W	Power	$1\,\text{W} = 1\,\text{kg m}^2/\text{s}^3$
Newton meter	N m	Moment	$1\,\text{J} = 1\,\text{N m} = 1\,\text{kg m}^2/\text{s}^2$
Newton per square meter	N/m^2	Pressure	$1\,\text{N/m}^2 = 1\,\text{kg}/(\text{m s}^2)$
Pascal second	Pa s	Dynamic viscosity	$1\,\text{Pa s} = 1\,\text{kg}/(\text{m s})$
Joule per cubic meter	J/m^3	Energy density	$1\,\text{J/m}^3 = 1\,\text{kg}/(\text{m s}^2)$
Ton	t	Mass	$1\,\text{t} = 1000\,\text{kg}$
Gram	g	Mass	$1\,\text{g} = 1/1000\,\text{kg}$

[a] Both SI and other (commonly used) unit systems are presented

Table 28.12 Commonly used units in thermodynamic calculations

Unit[a]	Symbol	Physical relation	Relation to basic units
Kelvin	K	Thermodynamic temperature, temperature potential	–
Square meter per second	m^2/s	Conductivity	–
Joule	J	Heat energy	$1\,J = 1\,kg\,m^2/s^2$
Watt	W	Heat power	$1\,W = 1\,kg\,m^2/s^3$
Joule per kilogram	J/kg	Specific inner energy	$1\,J/kg = 1\,m^2/s^2$
Joule per kelvin	J/K	Heat capacity	$1\,J/K = 1\,m^2/(s^2\,K)$
Joule per kilogram and kelvin	J/(kg K)	Specific heat capacity	$1\,J/(kg\,K) = 1\,m^2/(s^2\,K)$
Watt per square meter	W/m^2	Heat flux density	$1\,W/m^2 = 1\,kg/s^3$
Watt per square meter and kelvin	$W/(m^2\,K)$	Heat transfer coefficient	$1\,W/(m^2\,K) = 1\,kg/(s^3\,K)$
Watt per meter and kelvin	W/(m K)	Heat conductance	$1\,W/(m\,K) = 1\,kg\,m/(s^3\,K)$
Kelvin per watt	K/W	Thermal resistance	$1\,K/W = 1\,K\,s^3/(kg\,m^2)$
Degree Celsius	°C	Temperature	$1\,°C = 1\,K$

[a] Both SI and other (commonly used) unit systems are presented

Table 28.13 Commonly used units in electric current calculations

Unit[a]	Symbol	Physical relation	Relation to basic units
Ampere	A	Electric current	–
Ampere per square meter	A/m^2	Electric current density	–
Ampere per meter	A/m	Electric current distribution	–
Coulomb	C	Electric charge	$1\,C = 1\,A\,s$
Watt	W	Electric power	$1\,W = 1\,kg\,m^2/s^3$
Volt	V	Electric potential	$1\,V = 1\,kg\,m^2/(A\,s^3)$
Farad	F	Electric capacity	$1\,F = 1\,A^2\,s^4/(kg\,m^2)$
Ohm	Ω	Electric resistance	$1\,\Omega = 1\,kg\,m^2/(A^2\,s^3)$
Siemens	S	Electric conductance	$1\,S = 1\,A^2\,s^3/(kg\,m^2)$
Coulomb per square meter	C/m^2	Electric flux density	$1\,C/m^2 = 1\,A\,s/m^2$
Volt per meter	V/m	Electric field intensity	$1\,V/m = 1\,kg\,m^3/(A\,s^3)$
Farad per meter	F/m	Dielectric constant, electric field constant	$1\,F/m = 1\,A^2\,s^4/(kg\,m^3)$
Ohm meter	Ω m	Specific electric resistance	$1\,\Omega\,m = 1\,kg\,m^3/(A^2\,s^3)$
Siemens per meter	S/m	Specific electric conductivity	$1\,S/m = 1\,A^2\,s^3/(kg\,m^3)$

[a] Both SI and other (commonly used) unit systems are presented

Table 28.14 Commonly used units in magnetic calculations

Unit[a]	Symbol	Physical relation	Relation to basic units
Ampere	A	Magnetic potential	–
Ampere per meter	A/m	Magnetic intensity	–
Weber	Wb	Magnetic flux	$1\,Wb = 1\,kg\,m^2/(A\,s^2)$
Tesla	T	Magnetic induction	$1\,T = 1\,kg/(A\,s^2)$
Henry	H	Inductivity, magnetic conductance	$1\,H = 1\,kg\,m^2/(A^2\,s^2)$
Henry per meter	H/m	Permeability, magnetic field constant	$1\,H/m = 1\,kg\,m/(A^2\,s^2)$
1/Henry	1/H	Magnetic resistance	$1/H = 1\,A^2\,s^2/(kg\,m^2)$

[a] Both SI and other (commonly used) unit systems are presented

Table 28.15 Commonly used units in luminosity calculations

Unit[a]	Symbol	Physical relation	Relation to basic units
Candela	cd	Luminosity	–
Candela per square meter	cd/m^2	Light density	–
Lumen	lm	Luminous flux	$1\,lm = 1\,cd\,sr$
Lux	lx	Illumination	$1\,lx = 1\,cd\,sr/m^2$
Lumen second	lm s	Luminous energy	$1\,lm\,s = 1\,cd\,sr\,s$
Lux second	lx s	Exposure	$1\,lx\,s = 1\,cd\,sr\,s/m^2$

[a] Both SI and other (commonly used) unit systems are presented

Table 28.16 Physical constants [28.3]

Gravitational constant	G	$6.672 \times 10^{-11}\,N\,m^2/kg^2$
Acceleration due to gravity	g_n	$9.8067\,m/s^2$
Gas constant	R	$8314.41\,J/(kmol\,K)$
Molar volume	V_m	$22.414\,m^3/kmol$ at 1.01325 bar, 0 °C
Avogadro constant	N_A	$6.0221 \times 10^{26}\,kmol^{-1}$
Loschmidt constant	N_L	$2.6868 \times 10^{25}\,m^{-3}$
Boltzmann constant	k_B	$1.3807 \times 10^{-23}\,J/K$
Electric field constant	ε_0	$8.8542 \times 10^{-12}\,F/m$
Magnetic field constant	μ_0	$1.2566 \times 10^{-6}\,H/m$
Electric charge	e	$1.6022 \times 10^{-19}\,C$
Faraday constant	F	$9.6485 \times 10^{7}\,C/kmol$
Speed of light in vacuum	c	$2.9979 \times 10^{8}\,m/s$
Planck constant	h	$6.626 \times 10^{-34}\,Js$
Wave drag in vacuum	Γ	$376.731\,\Omega$
Stefan–Boltzmann radiation constant	σ	$5.6703 \times 10^{-8}\,W/(m^2\,K^4)$
Planck radiation constants	c_1	$3.741 \times 10^{-16}\,W\,m^2$
	c_2	$1.438 \times 10^{-2}\,m\,K$
Wien constant	K	$2.8978 \times 10^{-3}\,m\,K$
Rydberg constant	R	$1.09737 \times 10^{7}\,m^{-1}$
Static weight of electrons	m_e	$9.109 \times 10^{-31}\,kg$
Radius of an electron	r_e	$2.8178 \times 10^{-15}\,m$
Atomic mass unit	amu	$1.6606 \times 10^{-27}\,kg$

Table 28.17 Basic definitions of nuclear physics

(a) Definitions

Nomenclature	Definition	Unit	Formula	Remarks
Atomic mass	The relative mass of nucleus of ^{12}C is taken as unit weight	amu $= 1.6603 \times 10^{-27}$ kg	amu $= m_{^{12}C}/M_{^{12}C} = 1/N_A$	–
Atomic number	–	–	$N = \frac{m}{N} N_A$	$N = \frac{10^{-3}\,\text{kg}}{226\,\text{kg/kmol}}\, 6.0221 \times 10^{26}\,1/\text{kmol} = 2.665 \times 10^{21}$
Half-life period	Time required for decay of half of the original atomic mass	s, min, d, y	$T_{1/2} = \ln 2/\lambda$	$^{238}_{92}U$: $T_{1/2} = 4.5 \times 10^9$ a, γ and α radiation $^{3}_{1}H$: $T_{1/2} = 2.3$ a, β radiation
Atomic energy	The energy required to move an electron through a voltage of 1 V	Electron volt 1 eV $= 1.6022 \times 10^{-19}$ J	$W = eU$	Nuclear fission of uranium
Mass of electron	Based on Einstein's theory of energy and mass	1 MeV $\approx 1.728 \times 10^{-33}$ g	$m = \frac{E}{c_0^2}$; $m = \frac{m_0}{\sqrt{1-(c/c_0)^2}}$	$m \cong \frac{E}{c_0^2} = \frac{1.6022\times10^{-19}\,\text{J}}{(2.998\times10^8\,\text{m/s})^2} = 1.782 \times 10^{-33}$ g
Absorbed energy	Amount of absorbed radiation energy per unit mass of a material	Gray 1 Gy $= 1$ J/kg	$D = W/m$	–
Equivalent absorption	Measurement of biological radiation effect that is emitted from a γ ray of 10^{-2} Sv and is absorbed in the human body	Sievert 1 Sv $= 1$ J	$H = DQ_F$	X-ray, β, $^{0}_{-1}e$, $^{0}_{+1}e$ radiation Quality factor Q_F Thermal neutrons 3 Alpha radiation 10
Activity	Measurement of intensity of a radioactive ray. Count of decay per unit of time	Bequerel 1 Bq $= 1/s$	–	–
Atomic cross section	Measurement of yield in a nuclear reaction. Virtual cross section of radiating atom	m^2	σ	Fission σ_f Absorption σ_a Scattering σ_s

Explanation of the table entries

$^{A}_{Z}N$: $N =$ mass number of neutron, $Z =$ proton count, $A =$ atomic mass, $N = A - Z$

Fission of uranium:

$$^{235}_{92}U + {}^{1}_{0}n \rightarrow {}^{89}_{36}Kr + {}^{144}_{56}Ba + 3\,{}^{1}_{0}n + 200\,\text{MeV}.$$

Energy emitted by fission of 1 g of uranium:

$$Q = \frac{m}{M} N_A W = \frac{1\,\text{g} \cdot 6.0221 \times 10^{23}\,(1/\text{mol}) \cdot 200\,\text{MeV} \cdot 1.6022 \times 10^{-13}\,\text{W s/MeV}}{235\,\text{g/mol} \cdot 3600\,\text{s/h}} = 22\,810\,\text{kW h}.$$

Isotopes are different types of nucleus of the same chemical elements. Their nuclei have the same proton count but different atomic weights.
For example:

$^{12}_{6}C$, $^{13}_{6}C$, $^{14}_{6}C$ and $^{234}_{92}U$, $^{235}_{92}U$, $^{238}_{92}U$.

Types of radiation:

α: $^{4}_{2}\alpha$ nucleus of helium atom
β: Electrons or positrons
γ: Short wavelength, energy rich penetrative electromagnetic waves, which changes either the nuclear charge or the atomic mass of the radiating nucleus

Neutrons $^{1}_{0}n$, positrons $^{+1}_{0}e$, electrons $^{-1}_{0}e$

Table 28.18 Basic constants of nuclear physics

(b) Constants	
Velocity of light	$c_0 = 2.998 \times 10^8$ m/s
Static weight of electron	$m_{e0} = 9.110 \times 10^{-31}$ kg
Avogadro constant	$N_A = 6.0221 \times 10^{26}$ kmol^{-1}
Static weight of proton	$m_{p0} = 1.6606 \times 10^{-27}$ kg
Electric charge of an electron	$e = 1.6022 \times 10^{-19}$ C
Static weight of neutron	$m_{n0} = 1.675 \times 10^{-27}$ kg

Table 28.19 Basic units for light calculations

Measure	Definition	Unit	Mathematical relation	Remarks
Luminous flux	Amount of rays emanating from a light source in all directions	Lumen (lm)	$\phi = \mathrm{d}Q/\mathrm{d}t$	Light energy emitted per unit time
Light intensity	Intensity of light rays inside the elementary space angle[a]. 1 cd is the radiation emitted by a black body perpendicular to its surface $(1/(6 \times 10^6)\,\mathrm{m}^2)$ at 2042.5 K and 1.0133 bar	Candela (cd) cd = m/sr SI basic units	$I = \mathrm{d}\phi/\mathrm{d}\omega$	Stearin candle ≈ 1 cd Bulb (40 W) ≈ 35 cd
Luminance	Ratio of light emitted at the source to the light received at a particular surface	Lux (lx) lx = lm/m^2	$E = \phi/A = I\omega/A = I/r^2$	Summer sunlight 10^5 lx Living room 10–150 lx Full-moon night 0.2 lx No-moon night 3×10^{-4} lx
Light density	Light intensity per unit of illuminated surface	cd/m^2	–	Full moon 2500 cd/m^2 Candle 7500 cd/m^2 Bulb 2×10^7 cd/m^2 Sun 2.2×10^9 cd/m^2
Light yield	Luminous flux per unit of electric power	lm/W	$\eta = \phi/P$	Tube light 44 lm/W Bulb (1000 W) 19 lm/W Bulb (40 W) 11 lm/W
Light range	Product of luminous flux and the duration of radiation	lm s	$Q = \int \phi \mathrm{d}t$	

[a] The unit steradian (sr) is valid for the space angles. Steradian is the ratio of the surface of a section of a sphere to the square of its radius. If α is the opening angle of a section of a sphere with an area of $A = 2\pi rh$, its height is given by $h = r[1 - \cos(\alpha/2)] = 2r\sin^2(\alpha/4)$. The space angle is defined as $\omega = A/r^2 = 4\pi\sin^2(\alpha/4)$.
Special cases: $\omega = 1$ sr for $\alpha = 4\arcsin(0.5/\sqrt{\pi}) = 65.54°$. For a sphere $\alpha = 360°$ and $\omega = 4\pi$ sr. For $\alpha = 120°$ is $\omega = \pi$ sr

Table 28.20 Important terms in acoustic technology [28.4]

Term	Definition		Mathematical formula	Unit	Remarks
Velocity of sound	Solids	Longitudinal waves in big bodies	$c_L = \sqrt{\frac{2G(1-\upsilon)}{\varsigma(1-2\upsilon)}}$	m/s	1000–5000 m/s
		Transversal waves in big bodies	$c_T = \sqrt{\frac{G}{\varsigma}}$		500–3500 m/s
		Bending waves in bars	$c_D = \sqrt{\frac{E}{\varsigma}}$		Rubber 50 m/s
	Liquids		$c = \sqrt{\frac{\chi}{\varsigma}}$	Water 1485 m/s	
	Gases		$c = \sqrt{xRT}$	Air 331 m/s at 1 bar, 0 °C Hydrogen 1280 m/s at 1 bar, 0 °C	
Transverse vibrational speed of sound	Speed of vibrational part		$u = a_0\omega = 2\pi a_0 f$	m/s	5×10^{-8}–1 m/s
Sound pressure	Static and dynamic pressure in elastic media		p	N/m^2	10^{-2}–10^2 N/m^2 Normal audio waves = 2×10^{-5} N/m^2 Piano = 0.2 N/m^2 Siren = 35 N/m^2
Sound power	Sound energy that passes per unit time through a particular surface area		P	W	1×10^{-12}–1×10^{5} W Audio waves = 1×10^{-12} W Voice ≈ 1×10^{-3} W Siren ≈ 1×10^{3} W
Sound intensity	Sound power per unit area		$I = P/A = p^2/cp$	W/m^2	1×10^{-11}–1×10^{3} W/m^2 Audio waves = 1×10^{-12} W/m^2
Sound level	Logarithmic scale for sound pressure		$L = 10\lg(P/P_0)$ $= 10\lg(I/I_0)$ $= 20\lg(p/p_0)$	Bel B, dB	0–140 dB $P_0 = 1\times10^{-12}$ W $I_0 = 1\times10^{-12}$ W/m^2 $P_0 = 2\times10^{-5}$ N/m^2
Sound volume	Measurement of subjective perception of the sound intensity for the ear		$\Lambda = 10\lg(I/I_0)$	phon	0–130 phon Audio wave 0 phon Entertainment 50 phon Pain level 130 phon
Sound absorption factor	Measurement of loss of sound energy in heat due to friction Indexes a and r indicate absorption and reflection, respectively		$\alpha = (P_a - P_f)/P_f = (p_a^2 - p_r^2)/p_r^2$	1	For 500 Hz Concrete 0.01 Glass 0.03 Foam 0.36
Sound damping	Logarithmic measurement for sound damping by a wall, Index 1 indicates energy before reflection and 2 indicates energy after reflection		$R = 10\lg(I_1/I_2)$	dB	1 mm thick steel plate 29 dB
Acoustic coefficient	Ratio of sound to mechanical power		$\eta = P_{acu}/P_{mech}$	1	See Table 28.21

a_0 Amplitude, A surface area, P power, x isentropic exponent, f frequency, E modulus of elasticity, R gas constant, υ Poisson ratio, G modulus of rigidity, T absolute temperature, ς density, χ compressibility

Table 28.21 Approximated acoustic measures [28.5]

Noise source	$\eta = P_{acu}/P_{mech}$ [a]	Noise source	$\eta = P_{acu}/P_{mech}$
Siren		Diesel engine	
with funnel	$3–7 \times 10^{-1}$	Cylinder at 800 rpm	4.00×10^{-7}
without funnel	1.00×10^{-2}	Cylinder at 3000 rpm	5.00×10^{-6}
Rotating disk with ultrasonic velocity	2.50×10^{-1}	Exhaust with turbocharger	1.00×10^{-4}
Schmidt tube	2.00×10^{-2}	Electromagnetic loudspeaker	5.00×10^{-2}
Ventilator optimal point		Electric motor	
$\Delta p < 2.5$ mbar[a]	1.00×10^{-6}	Special low noise	2.00×10^{-8}
$\Delta p > 2.5$ mbar	$4 \times 10^{-8} \Delta p$	Normal	1.00×10^{-6}
Escape noise		Machines	
Ma < 0.3[a]	$8(1 \times 10^{-6}–1 \times 10^{-5})$ Ma^3	Special class	3.00×10^{-8}
0.4 < Ma < 1.0	1.0×10^{-4} Ma^5	Quiet machines	2.00×10^{-7}
Ma < 2.0	2.00×10^{-3}	Normal	2.00×10^{-7}
		Bad	3.00×10^{-6}
Motor bike 250 cm^3 capacity without damper	1.00×10^{-3}	Airplane propeller 2700 kW in test stand	5.00×10^{-3}
Organ	$1 \times 10^{-3}–1 \times 10^{-2}$	Human voice	5.00×10^{-4}
Small gas turbine		Ship propeller	
Suction	1.00×10^{-4}	Without cavitation	$1 \times 10^{-9}–1 \times 10^{-8}$
Exhaust	1.00×10^{-5}	With cavitation	1.00×10^{-7}
Housing	1.00×10^{-6}		

[a] Δp = compression, P_{acu} = acoustic power, Ma = mach number, P_{mech} = mechanical power

Table 28.22 Periodic table of chemical elements

Period	Group																	
	1	2		3	4	5	6	7	8	9	10	11	12	13	14	15	16	17	18
1	1 H																		2 He
2	3 Li	4 Be												5 B	6 C	7 N	8 O	9 F	10 Ne
3	11 Na	12 Mg												13 Al	14 Si	15 P	16 S	17 Cl	18 Ar
4	19 K	20 Ca		21 Sc	22 Ti	23 V	24 Cr	25 Mn	26 Fe	27 Co	28 Ni	29 Cu	30 Zn	31 Ga	32 Ge	33 As	34 Se	35 Br	36 Kr
5	37 Rb	38 Sr		39 Y	40 Zr	41 Nb	42 Mo	43 Tc	44 Ru	45 Rh	46 Pd	47 Ag	48 Cd	49 In	50 Sn	51 Sb	52 Te	53 I	54 Xe
6	55 Cs	56 Ba	[a]	71 Lu	72 Hf	73 Ta	74 W	75 Re	76 Os	77 Ir	78 Pt	79 Au	80 Hg	81 Tl	82 Pb	83 Bi	84 Po	85 At	86 Rn
7	87 Fr	88 Ra	[b]	103 Lr	104 Rf	105 Db	106 Sg	107 Bh	108 Hs	109 Mt	110 Ds	111 Rg	112 Cn	113 Nh	114 Fl	115 Mc	116 Lv	117 Ts	118 Og
[a] Lantha-noids				57 La	58 Ce	59 Pr	60 Nd	61 Pm	62 Sm	63 Eu	64 Gd	65 Tb	66 Dy	67 Ho	68 Er	69 Tm	70 Yb		
[b] Acti-noids				89 Ac	90 Th	91 Pa	92 U	93 Np	94 Pu	95 Am	96 Cm	97 Bk	98 Cf	99 Es	100 Fm	101 Md	102 No		

Table 28.23 Conversion from dB to pressure or power ratios and vice versa [28.6]

dB	p/p_0	p^2/p_0^2
0	1	1
0.1	1.012	1.023
0.2	1.023	1.047
0.3	1.035	1.072
0.4	1.047	1.096
0.5	1.059	1.122
0.6	1.072	1.148
0.7	1.084	1.175
0.8	1.096	1.202
0.9	1.109	1.23
1.0	1.122	1.259
0	1	1
1	1.122	1.259
2	1.259	1.585
3	1.413	1.995
4	1.585	2.512
5	1.778	3.162
6	1.995	3.981
7	2.239	5.012
8	2.512	6.31
9	2.818	7.943
10	3.162	0.01
0	1	1
10	3.162	10
20	10	10^2
30	31.62	10^3
40	100	10^4
50	316.2	10^5
60	1000	10^6
70	3162	10^7
80	10 000	10^8
90	31 620	10^9
100	100 000	10^{10}

Table 28.24 Important standards and their abbreviations

AGMA	American Gear Manufacturers Association
ANSI	American National Standard Institution
ASTM	American Society for Testing and Materials
API	American Petroleum Institute
BSI	British Standard Institution
CEN	Comité Européen de Normalisation
CENELEC	Comité Européen de Normalisation Electrotechniques
GOST	Government Standard of the former USSR
IEC	International Electrotechnical Commission
ISO	International Organization for Standardization
NF	Normes Françaises
NEN	Netherland Norms
NIST	National Institute of Standards and Technology
ÖNORM	Austrian Norms
SAE	Society of Automotive Engineers
SNV	Swedish Norms
UNI	Unificazione Nazionale Italiana
DIN	Deutsches Institut für Normung

References

28.1 P.F. Dunn: *Measurement and Data Analysis for Engineering and Science*, 3rd edn. (CRC, Boca Raton 2014)

28.2 A.L. Horvath: *Conversion Tables of Units in Science & Engineering* (Palgrave Macmillan, London 1986)

28.3 National Institute of Standards and Technology: The NIST reference on constants, units, and uncertainty, https://physics.nist.gov/cuu/Constants/ (2019)

28.4 J.M. Blatt, V.F. Weisskopf: *Theoretical Nuclear Physics* (Dover, Mineola 2010)

28.5 F. Fahy, D. Thompson (Eds.): *Fundamentals of Sound and Vibration*, 2nd edn. (CRC, Boca Raton 2016)

28.6 International Organization for Standardization: International classification for standards, 7th ed., https://www.iso.org/files/live/sites/isoorg/files/archive/pdf/en/international_classification_for_standards.pdf (2015)

Stanley Baksi

CAE Braking, Active and Passive Safety Systems
ZF Friedrichshafen AG
Koblenz, Germany
stanley.baksi@zf.com

Stanley Baksi received his Doctoral Degree from Otto-von-Guericke University in Bio-mechanical Engineering. He joined TRW Automotive (ZF Friedrichshafen AG) in 2008. He is working as a Six Sigma Black Belt, responsible for implementing the numerical development process in brake development. He is a member of the simulation community for brake squeal and has published numerous papers on brake squeal, stochastics, and optimization in product development and numerical evaluation of product robustness.

Subject Index

3-D surface structure 491

A

a stress cycle 508
ABC analysis 470
abrasion 302, 846, 873
– resistance 332
– resistant cast iron 332
– resisting 332
abrasive waterjet (AWJ) 448
– machining 448
abrasive wear 846
absolutely integrable 18
absorbed natural gas (ANG) 738
acceptor 1184
access time 972
accumulation 887, 889, 922
– pressure 922
accumulator lead acid 1218
accuracy parameter 404
Ackeret–Keller process 104
acoustic
– emission analysis 219
– technology 1283
– testing 217
– vehicle alerting system (AVAS) 998
acousto-ultrasonic interrogation 229
acrylonitrile butadiene rubber (NBR) 587, 612
active safety 1025
actual velocity 1099
additive 313, 315, 736
adhesion 301, 302, 840
adhesive
– bonding 541
– joint 541
adiabatic
– compression 69
– test method 844
adjusted deformation 645
admittance 1182
– of circuit elements 1201
advanced
– boiling water reactor (ABWR) 1261
– driver-assistance system (ADAS) 1002, 1003
– gas reactor (AGR) 1260
– gas-cooled reactor (AGR) 1261
– pressurized water reactor (APWR) 1262
adverse dynamic operation 818
aerodynamic
– characteristics 1109
– force 1098, 1099, 1102
– moment 1098
– stability 1123
aerodynamic center (a.c.) 1124
– location 1124
aerodynamics 1045, 1124
aeroelasticity 1123
aeronautical engineering 1007
aerospace 1006
– and defense (A&D) 1086
– and society 1087
– disciplines 1085, 1088
– emission 1088
– industry 1086
affinity diagram 471
afterburner 1113
age hardening 141
air
– condition 1081
– cycle machine 1081
– fan 1246
– pollution 738
– preheater 1242
– transport system (ATS) 1006, 1088
airborne particulate 845
aircraft 1091
– component nomenclature 1107
– engine 801
– heavier-than-air 1092
– lighter-than-air 1092
– load 1129
– performance 1115
– structure 1134
– turbine 455
– type 1091
airflow 724
airfoil 175
– section geometric parameters 1109
– thickness 1110
air–fuel ratio 1243
airplane 1092, 1102
– axis system 1097
– center of gravity 1123
– component nomenclature 1108
– design 1115
– development of 1009
– lift coefficient 1103
– maintenance check 1136
– nose down (AND) 1124
– pitching moment 1124
– structure 1132
– weight definition 1114
airplane drag 1103
– element 1104
airspeed
– indicator 1100
– sensor 1100
air-supported conveyor 864
alcohol 737
algebraic multiplicity (A.M.) 8
alignment 1061
– measuring system 494
all-terrain (AT) 939
– crane 939
alternate fuel 736
alternating current (AC) 1174, 1234
alternative combustion system 735
aluminum oxide 431
ammonia 88
amorphous solid 132
Ampere–Maxwell law 1172
– in matter 1175, 1179
analysis of
– a surface 488
– combustion 1248
– natural systems 640
analytic function 21
anergy 72
angle of
– internal friction 840
– list 1149
– repose 866
– skew 875

K.-H. Grote, H. Hefazi (Eds.), *Springer Handbook of Mechanical Engineering*, Springer Handbooks,
https://doi.org/10.1007/978-3-030-47035-7

– vanishing stability (AVS) 1148
– wrap 871
angular
– frequency 16
– trolley 933
anisotropy 389
anisotropy coefficient 389
– planar 389
annealing temperature 363
antiphase boundary (APB) 141
antiwear (AW) 310
apron conveyor 882, 886
aquadraw process 399
arched stress field 840
Archimedean screw 894
– pump 895
Archimedes 1145
area reduction 378
– allowable 383
arm of the rolling friction 861, 862
armored face conveyor 884
Arrhenius law 142
arrow diagram 471
artificial friction coefficient 867
assessment list 656
astronomical prefix 1277
asymmetric pressure distribution 861
atmospheric ozone 739
atomic emission spectroscopy (AES) 152
augmented reality (AR) 1042, 1107
ausferrite
– cast iron 330
– spheroidal graphite 330
austempered
– cast iron (ACI) 330
– ductile cast iron (ADI) 257
austenitic cast iron 332
– mechanical properties 332
authorized inspector (AI) 762
autofocus sensor 494
autoignition 734, 735
automated
– driving 999
– guided vehicle (AGV) 953
– miniload system (AMS) 979
– small parts warehouse 979
– storage and retrieval system (AS/RS) 979
automated, connected, electrified, shared/services (ACES) 998
automatic
– coupler 1079
– guided straddle carrier (AGSC) 954
– train control (ATC) 1076
automobile chassis 1002
automotive
– engineering, future of 1020
– industry 1000
– safety 1026
autonomous driving 1026
– function 1029
autonomous vehicle (shuttle) 981
autonomously managed AGV 953
availability 1060
average piston speed 689
Avogadro's law 73
axial
– piston pump 697
– turbine 779, 781
axially moving screw drive 405
axis system 1096
axle 544

B

backhoe loader 946
backpressure 887
backscattered electron (BSE) 156
balanced draft (BD) 1245
ball
– bearing 566
– conveyor 920
– valve 705
ballasted track 1062
ballast-less track 1063
barrel roller bearing 566
barreling 168
base profile 793
baseline gas turbine 808
basic
– dimension 1275
– rating life 572
battery
– electric vehicle (BEV) 1000, 1020
– lead acid 1218
– zinc air 1220
Bauhaus 679
Bauschinger effect 367
beam machining (BM) 452
– electron 454
– laser 452
– plasma 455
beam technology 1092
bearing
– arrangement 574
– damage 576, 577
– dimension 567
– lubrication 583
– material 582
bellow 590
belt
– bucket elevator 878
– carcass construction 872
– carrying capacity 864
– construction 871
– cover 873
– flexure resistance 867
– force 870
– grinding 443
– mistracking 874
– safety factors 872
– sag ratio 871
– speed 866
– strength 872
– surcharge angle 866
– tension 873
– width 866
belt conveyor 834, 864
– resistance 867
benchmarking of car weight 1051
bend test 170
bendability 395
bending 360, 393
– by buckling 393
– moment 546
– resistance 506
– roll 393
– strain 394
Bessel point 481
best practice 664
Bézier polynomial 797
bidirectional tram 1077
bill of materials (BOM) 1035, 1048
bin 832, 837
– shelving 974
binary phase diagram 147
biodegradable oil 313
biodiesel 736
biofuel 1268
bioindustrial design 678
biomass-to-liquid (BTL) 736
bipolar transistor 1187
– active mode 1187
– base 1187
– characteristics 1188
– collector 1187
– emitter 1187

blade design 790
blank holder 396
– pressure 398
blended wing body (BWB) 1089
blind riveting 520
block
– and tackle 849
– coefficient 1142
– stacking 970, 975
body
– in white (BiW) 1038
– plan 1143
body-centered
– cubic (bcc) 134, 235
– tetragonal (bct) 239
bogie
– assembly 1073
– frame 1072
– suspension 1071
– transfer function 1067
boiler 1236
– classification 1237
– efficiency 1249
– furnace 1237
– safety 1237
boiling
– point 65
– water reactor (BWR) 1260, 1261
bolt 523
– dimensioning 532
bolted joint 517
– calculation 524
– design 539
bonding 144
Boolean combination 634
boot 876
boron
– carbide (B_4C) 289
– nitride (BN) 426, 432, 437, 438, 441, 456
bottom dead center (BDC) 403, 406, 684, 716
bottoming cycle 1228
Boudouard reaction 1232
boundary
– friction 300, 840
– layer 295
boundary-layer friction 300
box palette 832
boxer engine 684
box-type casing 876
Bragg grating 231
brainwriting method 640
brake
– power 717
– specific fuel consumption (BSFC) 718
– thermal efficiency 718
– torque 717
braking system 1011
branch current method 1199
branch electric 1195
– compaction 1197
Bravais lattice 133
Brayton cycle 826, 1226
– regenerative 1233
break mean effective pressure (BMEP) 717
breaking force 853, 857
Breguet formula 1119
bridge crane 932
Brinell hardness (BHN) 169, 332
British standard (BS) 758
brittle fracture 169
broaching 427
broaching tool 428
bronze 276
brush 1207
– sorter 922
bucket 876
– conveyor 881
– discharge 877
– elevator 834, 876
– geometry 879
– kinematic 944
– spacing 876
bucket filling 876
– level 876
buckling 169, 402, 505
– bending by 393
– limit 373
bulk
– carrier 1160
– density 842
– material flexure resistance 867, 868
– strength 839
bulk forming 358
– process 372
bulk solid 832, 837, 839
– properties 841
bunker 834, 955
Bureau Veritas (BV) 1140
Burgers vector 137
burner 1254
bursting 402
bush 858
– chain 858
business jet 1109
buttockline 1143
buttress thread 524

C

cable
– car 834
– of power line 1168
cable- and rail-supported belt conveyor system 864
calibrated airspeed (CAS) 1100
calibration 486, 497, 918
caloric properties 90
cam drive unit 708
camber 385
camberline 795
cam-driven pump 726
Canada Deuterium Uranium (CANDU) 1263
CANDU reactor 1261
cantilever shelving 978
capability analysis 474
capacitance 1178
– addition for series or parallel 1178
capacitor 1177
– double layer 1216
– phase shift 1181
– super and gold cap 1216
– type 1178
– whistling 1172
capacity 837
– heat 180
car
– specification 1016
– technical requirements 1020
car development 1015, 1017
– non-engineering 1054
– process (CDP) 1033–1035
carbon
– dioxide 88, 738
– fiber reinforced plastic (CFRP) 224
– monoxide 739, 740
– steel material 771
carburation 722
carburization 209
carcass 871
cardan
– chain 859, 891
– shaft 544
cargo

– capacity 1141
– flow rate 836
Carnot
– cycle 103
– power cycle 103
carousel 978
carrier 834
– chain conveyor 882, 887
casing 876
cast
– alloy 326
– aluminum alloy 334
– copper alloy 335, 336
– iron alloy 328
– low-alloy steel 333
– magnesium alloy 334, 335
– material 326
– metallurgy 144
– zinc alloy 336
cast carbon 333
– steel 333
casting 326
– design 327
– differentiation 326
– machine 340
– of integral components 327
– with moving mold 339
casting material 341
– contraction 351
catalyst three-way 743
catalytic converter 1017
caterpillar drive 891
Cauchy integral
– formula 22
– theorem 22
Cauchy stress 365
Cauchy–Euler equation 11
Cauchy–Riemann equation 21
cause–effect
– diagram 470
– relationship 635
CE marking 474
cell pump 712
Celsius scale 64
cemented carbide 430
central
– chain 879
– wire 849
central-point 729
– injection (CPI) 729
centrifugal
– casting 349
– compressor stage 788
– discharge 877, 878
– seal 593
centripetal turbine stage 787
ceramic 431
– cutting tool 412, 431
– molding 343
ceramics
– nonoxide 289
– refractory 286
certification process 1089
cetane number 736
chain 856
– belt 859, 882
– bucket elevator 879
– conveyor 834, 881
– lock 856
– pitch 856
– polymerization 278
chain link 856
– diameter 857
chain-grate stoker 1244
change
– approval 1053
– in transportation 998
– management 1052
– request 1052
changing of material cohesion 325
channel length modulation 1190
characteristics of test levels 1029
charge 1167
– cycle 683
– elementary 1168
charge-coupled device (CCD) 155, 464, 483
charging infrastructure 1000
Charpy V-notch (CVN) 174, 774
chassis 834
– drive 924
chatter mark 383
chemical vapor deposition (CVD) 144, 211, 311, 429, 461
chemical-mechanical planarization (CMP) 447
chemiluminescent reaction 741
chemisorption 310
chevron crack 381
chip
– formation 410, 439
– shape 415
– type 410
– volume ratio 414
chipless machining 409
chlorofluorocarbon (CFC) 662, 739
chloroprene rubber (CR) 612, 728
chlorosulphonyl polyethylene rubber (CSM) 612
choice of shape 326
choke 894
chute 834, 837, 915
– angle 915
– cross-section 916
– wear 915
circular sawing 429
circulation piston machine 712
circumferential velocity ratio 788
clamping-element connection 562
classification of seals 586
clevis pin 517
climate
– chamber 1047
– stress 1021
climb performance 1103
closed system 70, 93
closed-die forging 374
– force–displacement characteristics 374
clothoid 1061
CNC (computerised numerical control) 436
CO_2 emissions 997, 1020
coal gasification 1232
coal-to-liquid (CTL) 736, 737
coated HSS 430
cobalt 430
Coble creep 172
code français de construction des appareils à pression (CODAP) 769
coefficient
– of friction 299, 301, 556
– of thermal expansion (CTE) 244
cogeneration system 1229
cogging 376
coherency strain 141
cohesion 838
cohesive bulk solid 838
coil
– ignition 731
– primary and secondary 1202
– rope 852
cold
– filter plugging point 736
– splice 872
– upsetting 373
– working 168
cold forging 376
– tool-setup 382
cold-chamber process 347

combined
– Brayton–Rankine cycle 1233
– cycle gas turbine (CCGT) 815
– heat and power (CHP) 108, 1229
combustion 97, 100, 1254, 1257
– cycle 100
– engine 686, 715
combustion chamber (CC) 800, 803, 804, 811, 815, 819, 1233
– gas 821
– low-pressure (LPCC) 815
– mass flow 819
common-rail 726
commutator 1207
compact tension (CT) 177
compacted graphite
– cast iron 331
– iron (CGI) 257
compacted graphite cast iron
– mechanical properties 331
compacted strand 850
comparative vacuum monitoring (CVM) 230
compensation
– coil 1208
– method 483
complementary metal–oxide–semiconductor (CMOS) 155, 1189
complex
– conjugate 19
– function 20
– integration 22
– number 19
component
– characteristic 326
– dimensioning and design 513
– manufacture 328
– safety 513
– strain 504
– strength 511
components and air flow 1082
composite casting 349
composition and hardness 332
compressed
– air energy storage (CAES) 803, 814, 815
– natural gas (CNG) 729, 737
compressibility correction 1101
compression 34
– efficiency 715
– heat pump 108
– ignition engine 734
– pump 705
– refrigeration 107
– spring 617
– test 367
compression-ignited 716
compression-ignition (CI) 744
compression-ignition engine 734
– emissions 744
compressive
– loading 504
– stress 170
compressor 686, 713, 720, 800, 803, 819
– cascade 791
– efficiency 722
– stage 779
compressor blade 790, 794
– design 791
computational fluid dynamics (CFD) 1037, 1046, 1143
computer numerical control (CNC) 436, 485
computer-aided
– design (CAD) 349, 487, 941, 1035, 1143
– manufacturing (CAM) 349
– styling (CAS) 1040, 1100
– tool 1040
concept development 1038, 1039
conception method 640
conceptual design 654
Concorde 1089
concrete sleeper 1063
condensation 124
– chain polymerization 278
conductance
– matrix 1199
– specific 1175
conduction
– band 1183
– by holes 1184
conductor 1176
cone and quartering 838
conformal mapping 22
conformity of geometry 1050
conical seat 705
connecting rod 695
– design 696
– force 691
connection 32
– CMM–CAD 487
– of springs 610
consistent lubricant 316
consolidation pressure 838
constant shear friction model 369
constitutional supercooling 147
constrained motion 52
construction
– catalog 641
– method 638
contact
– angle 874, 875
– geometry 295
– time under pressure 403
contacting seal 585
container 832
– bridge 935
– lifting truck 954
– ship 1141
– stacker 955
continuity equation 1168
continuous
– cast iron 332
– conveying machine 833
– conveyor 834, 863
– cooling transition (CCT) 240
– dressing (CD) 442
continuous casting 340
– process 339
– with stationary mold 339
contour area 296
control
– module, electronic (ECM) 742
– numerical (NC) 436
– system (CS) 728, 811
– unit 728
controllable pitch propeller (CPP) 1157
convection 121
conventional
– coil ignition 731
– transmission electron microscopy (CTEM) 157
conversion of heat 72
conveying
– machinery 830
– route 863
conveyor 868, 920
– belt cover 874
– chain 857, 858
– for general cargo 920
cooker electric 1202
cooled turbine stage 812
cooling 696
coordinate
– measurement 469, 482
– measuring machine (CMM) 487
coordination number (CN) 133
copper 774

core 849
– material 849
corrosion
– cavitation 204
– chemical 207
– contact 192
– crevice 196, 199
– electrochemical 186
– fatigue (CF) 200, 203
– fretting 206
– galvanic 192
– high-temperature 207
– intergranular 193
– microbiologically induced 206
– pitting 196, 198
– resistance 336, 1135
– resistant 771
– selective 193
– stress 219
– testing 212
– uniform 190
corundum (Al_2O_3) 441
cottered joint 565
Coulomb friction model 368
Coulomb's law 1171
counterbalanced truck 950, 951
counterblow hammer 404
coupling switching device 465
cover properties 873
crack
– depth measurement 219, 220
– extension 178
– growth 175
– initiation 175
– mechanism 203
– opening modes 177
crack-growth curve 176
crane 834, 926, 932
crank
– dead center (CDC) 699
– press 403
cranked link plate 859
crankshaft 544, 688, 694, 695
– drive 694
crash
– deformation element 1025
– performance 1021
– scenario 1081
– simulation 1021
crawler track 924
creep 172
– mechanisms 172
– testing 171
crest landing load 1158
Crew Dragon 1093
critical
– bending speed 550
– inclination angle 920
– Mach number 1105
– pitting temperature (CPT) 199, 773
– point (CP) 1226
– radius for nucleation 145
– resolved shear stress (CRSS) 260
– stress intensity 177
– temperature 74
cross-belt sorter 922
crosshead 694, 699
crosswise storage 974
crowned pulley 876
cruise
– Mach number 1119
– performance 1103
crystal
– defect 361
– structure 159
cubic
– boron nitride (CBN) 426, 437, 438, 441, 456
– interstitial lattice 134
cumulative energy demand 354
cup-and-cone fracture 168
curling 393
current 1168
– density 1168
– diffusion 1186
– loop 1206, 1211
– mesh 1197
– superposition 1200
current source
– ideal 1196
– real 1196
cut and chip variable 414
cut-off grinding 446
cutting 409, 410
– edge 412
– fluid 446
– geometry 421
– high-speed 435
– laser 452
– speed 413, 428
cutting force 415, 419, 424
– component 424
cutting tip terminology 414
cutting tool 429, 432
– angle 414
cybersecurity 1033
cycle fatigue 176
cyclic
– process 103
– testing 175
cyclone 1259
cylinder form deviation 492
cylinder-individual fuel injection (CIFI) 723
cylindrical roller bearing 566

D

D'Alembert's principle 52
damage-tolerant approach 176
dangerous good 844
dead mold 338
deadweight (DWT) 1139
dead-zone 380
de-aeration 842
– test 843
Debye temperature 93
deep
– bucket 878, 879
– link chain 859
deep drawing 396
– force 398
– hydromechanical 399, 401
deep-groove thrust ball bearing 567
defect 375, 390
– lattice 132
degree of reaction 782
delivery rate 702
DEM 918
dendritic microstructure 148
density 736
– intrinsic 1185
deoxidized copper (Cu-DHP) 620
depletion region 1185
design
– airspeed 1132
– factor 853
– FMEA 671
– for manufacturability (DFM) 1050
– for the environment (DFE) 629, 669
– guidelines 352, 644, 648
– of experiments 471
– principles 641
– rules for preforms 373
design rule 642
– for tube sheets 769
designing the camberline 795
destructive interference 1155

determinant 5
development, product 631
developments in transportation mobility 999
deviatoric stress tensor 365
diagnosis system for rail vehicles 1061
dialkylbenzenes (DAB) 312
diamond (C) 432, 441
– turning 433
diamond-pyramid hardness (DPH) 169
diamond-pyramid hardness number (DPH) 169
diaphragm 590, 697
– design 697
– metering pump 707
– pump 699
die
– cone angle 380
– failure in forging 375
– upsetting 376
diesel
– fuel 736
– injection 724
– particulate filter (DPF) 745
– pilot natural gas engine 729
diesel engine 101, 102
– for heavy duty 749
diesel-powered passenger vehicle 998
difference measurement 480
differential
– design 645
– interference contrast microscopy (DIC) 155
– scanning calorimetry (DSC) 280
diffuse necking 390
diffuser 811, 814
diffusion 1185
– bonding 144
– factor 790
– vacancy 143
digital mock-up (DMU) 1008, 1035, 1043, 1058, 1089
dihedral angle 1110
dilatometry 181
dimensional
– concept 1035
– measuring interface specification (DMIS) 487
dimensioning principle 504
dimethyl ether (DME) 737
diode 1185
– forward biased 1186
– light-emitting 1187
– photo 1187
– reverse biased 1186
dipole moment magnetic 1206
direct
– current (DC) 346, 450, 462, 1174, 1234
– injection (DI) 718, 724, 735
– measurement 480
– redrawing 397
directional control 1127
disc spring 614, 615
discharge 837
– chute 877
– regime 877
discontinuous
– chip formation 410
– conveying machine 833
– conveyor 834, 863, 923
discrete element
– method (DEM) 942
– modeling (DEM) 918
discursive method 640
dislocation 137, 138, 361
– line energy 138
dispersion strengthening 140, 141
displaced volume 1143
displacement
– drive 900
– pump 686, 697
dissipation
– factor 1182
– work 66
distortion energy theory (DET) 507
distributed force 37
distributor-type
– injection pump 726
– system 732
divergence Mach number 1110
diverter 922
donor 1184
Dorn equation 173
double casing 876
double-acting hammer 404
double-circular arc (DCA) 791, 794
double-deep pallet rack 974
double-flange track wheel 860
double-girder overhead crane 933
down and up-milling 422
downtime 1060
dozer 946
draft 1246
drag 1104
– curve 1103
draw
– bead 399
– bending 393
drawing
– force 398
– of tube 382
– with mandrel 382
drawing machine
– tube 402
– wire 402
dressing 442
drift 479
– velocity 179
drilling 417, 421
– process 417, 419
drive
– and tension station 879
– chain 857
– force 871
– power 899
– pulley 870
– tension 870
– wheel 859
drive-in rack 975
driven wheelset 1070
driverless
– metro 1076
– truck 954
drive-thru rack 975
driving
– dog 892
– force 869
– pulley 870
drop hammer 404
Drude's law 1175
dry
– exhaust gas losses (DEGL) 1248
– friction 580
dry-bottom furnace 1245
dual command operation 981
dual cycle
– power plant 1229
– system 1230
dual-load carrier (DLC) 954
ductile
– failure 176
– to brittle transition temperature (DBTT) 174, 175
ductility 168
dumping 876
durable product 1016
dust
– emission 845

– extinction moisture (DEM) 845, 875
dustiness 845
– classification 845
Dutch roll 1128
duty cycle factor (DCF) 924
dynamic
– pressure 1099
– splice efficiency 872
– storage 972
– strength 509

E

earing 389
early effect 1188
Ebers–Moll model 1188
eccentric screw pump 711, 712
eccentricity 861
economic life cycle 630
economizer 1241
eddy current 224, 1180
– foil sensor 229
edge dislocation 138
effective
– friction coefficient 871
– pressure 717
– stroke rate 403
– work 685
– yield locus (EYL) 838
effectiveness–NTU 768
efficiency 687, 702, 718
– calculation 777, 823
– dynamic 823
– mechanical 702, 718
– of pump 703
– of the battery 1030
– of the reeving system 855
– of the turbine 722
– thermal 718, 803, 806, 825
– total 407
– volumetric 702, 715, 718
efficient manufacture 352
E-GAS entrained flow gasifier 1231
EGR 744
eigenvalue 7
eigenvector 7
elastic
– deformation 166, 549, 1158
– spring 608
– work 403
elastohydrodynamic lubrication (EHD) 567
elastohydrodynamic lubrication (EHL) 308
elastomeric spring 619
electric
– chain hoist 931
– hoist 930
electrical
– conductivity 178, 179
– energy consumption 1032
electrochemical
– energy storage 1269
– grinding (ECG) 448, 456
– machining (ECM) 448, 450
electrochemical-discharge machining (ECDM) 448
electrode 732
electro-discharge
– grinding (EDG) 456
– machining (EDM) 448–450, 1050
electrolytic
– cell 1218
– in-process dressing (ELID) 442
electromagnetic testing 224
electron 1168
– backscatter diffraction (EBSD) 157, 159, 160
– beam machining (EBM) 448, 452, 454, 455
– energy-loss spectroscopy (EELS) 158
– probe microanalysis (EPMA) 158
– scattering 179
– spectroscopy for chemical analysis (ESCA) 159
– speed 1169
electronic control
– module (ECM) 448, 742
– unit (ECU) 728, 1033
electronic ignition 732
electrostatic precipitator (ESP) 904, 1002, 1016, 1258
elementary methods of plasticity 368
elements of a crankshaft 695
elevator 947
emergency shutdown 816
emission 738, 1257
– regulation 739
e-mobility battery safety 1023
empennage 1112
empirical temperature 63
En Masse conveyor 882
enclosed screw conveyor 895
endurance 1120
energy
– change of a system 69
– conversion 1224
– Fermi 1183
– loss of 1201
– mechanical versus electrical 1206
– of charge in an electric field 1173
– overview storage techniques 1214
– recovery system (ERS) 1217
– requirement 665
– sign of 1195
– theorem of mechanics 66
– transfer 66
– volume-specific 688
energy band 1184
– gap 1183
– structure 1185
energy density
– of electric field 1178
– of magnetic field 1179
energy efficiency
– guidelines 670
– operation index (EEOI) 1155
energy storage 1214, 1268
– by pumped water 1215
– gas turbine 815
energy-dispersive x-ray spectrometer (EDX) 157, 195
engine
– failure 1121
– power response 820
– spark ignition 733
– twin-spool 810
– type 716
engineering
– fatigue 175
– stress 166
– system 651
enterprise resource planning (ERP) 978
enthalpy of humid air 111
entrained flow system 1231
entropy 69, 80
entry into service (EIS) 1008, 1089
environmental
– compatibility 1016
– concerns 662
– control technology 1258
– management 328
– safety 643
– SEM (ESEM) 156
environmentally
– assisted cracking (EAC) 200

– friendly transport 1057
equal shape stability 645
equation of
– availability 1060
– reaction 97
equilibrium condition 30
equivalent
– airspeed (EAS) 1100
– conicity 1066
– force 28
– friction coefficient 916
– plastic strain rate 367
ergonomics development 1044
Erichson
– index (IE) 391
– test 391
Ernst and Merchant's force circle 411
erosion 204, 846
erosive wear rate 847
error recognition 673
essential safety requirement (ESR) 760
etch pit 139
ethanol 736
ethylene-propylene diene monomer (EPDM) 587, 612
Euler
– method 12
– turbine equation 779
Euler–Eytelwein equation 855
European
– approval of material (EAM) 761
– Standard (EN) 329
eutectic phase diagram 151
evanescent coupling display device (ECDD) 462, 465
evaporation 125
even-periodic extension 17
excavator 834, 941
exchange variable 70
exciting force 900
– drive 900
exergy 71
exhaust
– emissions 741
– gas recirculation (EGR) 730, 740, 743
– system 1017
– valve 716
expansion turbine 720
expected customer needs 1037
explosive forming machine 402
exposure
– limit 845
– test 845
extension spring end 619
external
– gear 698
– load 1129
extralow interstitial (ELI) 266
extreme pressure (EP) 310, 428
extrinsic property 136
extrusion 359, 376

F

fabric
– filter 1258
– ply conveyor belt 872
fabrication 770
Fabry–Pérot interferometer 464
face
– conveyor 882
– milling 422
face-centered cubic (fcc) 134, 235
factor of throw time 902
Fahrenheit scale 64
failure mode and effects analysis (FMEA) 472, 671, 1050
failure-tree analysis 472
Faraday–Henry law 1171
fast
– breeder reactor (FBR) 1263, 1264
– flow 916
– Fourier transform (FFT) 492
– fracture 176, 510
– reactor 1261
fastener 514
fasteners and connectors 515
fatigue
– analysis 757, 759, 761
– fracture 510
– test 1134
fatty acid methyl ester (FAME) 737
Federal Air Regulations (FAR) 1112, 1117
Federation of European Producers of Abrasives (FEPA) 441
feeder 837, 968
feeding 837
– system 894
feedwater heater 1241, 1242
ferrite number (FN) 773
ferrous material 327
fiber
– Bragg grating 231
– core (FC) 852
fiber-reinforced plastic (FRP) 1076
field
– electric 1169
– electromagnetic types 1175
– inspection, residual 222
– linear superposition of 1170
– magnetic 1169
– of force 1169
field line
– electric 1171
filling 375
– level 702, 836
– station 737
film
– condensation 125
– thickness parameter 297
fine-grain strengthening 140
finger splice 873
finishing operation 354
finite element
– analysis (FEA) 876, 1024, 1037, 1143
– method (FEM) 436
– modeling (FEM) 1037
finite element formulation
– explicit dynamic elasto-plastic 371
– implicit static elastoplastic 371
– rigid-plastic 371
fireclay 286
first law of thermodynamics 66
first-in first-out (FIFO) 975
first-order
– forces of inertia 693
– linear ODE 9
– ODE 8
fixed path method 953
fixing option 657
Fizeau interferometer 464
flange 756
– factor 862
flap 705
– sorter 922
flash 374
– point 736
flashless die forging 376
flat
– bottom rail 1065
– bucket 878, 879
– rolling 384
– seat 705
flat-top chain 882
– conveyor 888

flex-fuel 736
flexible shaft 544
flexure
– resistance 867
– testing 170
flight 882
– conditions 1129
– load factor 1129
– Mach number 1104
– mechanics 1088
– shape 883
– speed 1093, 1102
floor storage 970
flow
– channel 840
– coefficient 782
– curve 367
– function (FF) 838, 839
– gasifier 1231
– nonquadratic 390
– of bulk solid 838
– pattern 837
– properties 837
– rule 367
– stress 366
– through pipes 122
– turning 359
flow condition 365
– von Mises 366
flow forming 387
– process 386
flow table
– test 843
– tester 844
flowability index 840
flue gas desulfurization (FGD) 1260
fluid
– dynamics 1037, 1046
– force 690
– forming 399
– friction 300
– mechanics 68
fluidization 842
– test 842
fluidized-bed combustor (FBC) 1256, 1260
fluorocarbon rubber (FPM) 612
fluoroelastomer (FKM) 587
flux
– magnetic 1203
– of vector field 1170
fly-by-wire technology 1089
flying wing 1090
flywheel 405, 1269
FMEA (failure mode and effects analysis) 671
– form 672
focused ion beam (FIB) 154, 157
foil sensor 229
folding 393
foot-pound-second (fps) system 1277
force 26
– closure joints 523
– Coulomb 1169, 1171
– couple 28
– electrodynamic 1169
– electromotive 1169
– Lorentz 1169, 1171
– on the transmission 691
– resultant 388
– rolling 385
– to limit belt sag 871
– vector 29
forced
– circulation boiler 1239
– convection 122
– draft (FD) 1246
force–displacement curve 378
– for forward rod extrusion 380
forged product failure 375
forging 359, 374, 376
– closed-die 374
– open-die 372, 374
– radial 376
– spread (cross) 376
fork chain 859
forklift truck 834
form
– inspection instrument 491
– milling 426
– of work 67
– tolerance 477
formability of sheet metal 390
form-closure 551
– joint 515
form-fitting drive 859
forming 372, 387
– by casting 350
– limit diagram (FLD) 391
– temperature increase 367
forming machine 402
– energy controlled 403
foundry
– industry 326
– technology 337
Fourier transform infrared spectral analysis 741
Fourier's law 115
four-point probe 219
four-stroke
– cycle 716
– engine 716
fracture
– mechanics 176
– surface 169
– toughness 177
frame 35
– structure 36
free
– bending 393
– flowing bulk solid 838
– forming 372
– round bending 393
free-body diagram 30
freight
– bogie 1072
– transportation 996
– wagon 1074
freshwater (F) 1152
friction 299
– damping 1069
– energy 299
– hill 385
– hoist 849
– law 555
– mechanism 300
– model 368
– model, constant shear 369
– power 299
– state 300
frictional
– connection 555
– resistance 1152
– shaft–hub connection 556
Froude model 1152
fuel 735, 1235
– consumption 1007, 1113, 1120
– mass flow 821
– prices 996
– supply system 724
– system 722
– weight 1113
fuel cell 102, 1220, 1233
– electric vehicle (FCEV) 1031
– power system 1233
– vehicle (FCV) 1020
fuel injection 722, 723
– control system 724, 732
– sequential (SEFI) 723

– system 726
fuel-saving 1016
full mold casting 345
fullering 374
function
– of exponential order 13
– relationship 633
functional
– description 652
– engineering 653
– performance 634
– reliability 643
– structure 654
fundamental
– matrix 11
– solution 646
furnace 1243
– exit gas temperature (FEGT) 1244
fuselage 1112
– cross section 1133
future
– gasoline engine 1004
– of aviation 1005
– project office (FPO) 1008, 1089

G

gallery method 640
galling 381
galvanic cell 1217
gamma-ray testing 229
gantry
– crane 932, 935
– lift 954
gap
– effect 886
– seal 592
gas
– constant 73
– friction 300
– generation spool 800
– metal arc welding (GMAW) 775
– radiation 127
– tungsten arc welding (GTAW) 775
gas turbine 100, 809, 814, 824, 1226, 1229
– combined cycle gas turbine (CCGT) 815
– multispool 809
– process 105, 803
– shutdown 815
– single-spool 818
– startup 815
– thermal efficiency 806
– ultrahigh-efficiency (UHEGT) 809, 824
gas turbine engine 800
– component 800
– power generation 800
– single-spool 801
gases and vapors 73
gasket 585
gasoline
– direct injection (GDI) 723
– engine 746
– fuel 736
gas-to-liquid (GTL) 736
gathering 374, 376
gauging 478
Gaussian elimination 7
Gauss–Jordan elimination 7
Gauss's law
– electric field 1170
– electric field in matter 1175
– magnetic field 1170
gear 593
– geometry 595
– mating 602
– pair 603
– tooth geometry 597
– train 594
– transmission ratio 605
Geiringer equation 370
general
– arrangement (GA) 1008, 1089
– solution process 638
general cargo 832, 949
– storage 972
generator 1206
– load schedule 820
– synchronous 1211, 1212
geometric
– multiplicity (G.M.) 8
– space check 1044
geothermal energy 1266
German
– calibration service (DKD) 497
– In-Depth Accident Study (GIDAS) 1023
Gibbs free energy 145
gland packing 589
glass 285
– ceramics 285
glider performance 1118
gliding 901
global
– aerospace industry 1086
– climate change 662
– energy investment 1235
– loads 1158
glow-discharge optical emission spectroscopy (GDOES) 152
good 832
– load 853
goods-to-man principle 972
governing 728
grab 927, 928
grab-type ship unloader 936
grader 947
grain-boundary sliding 171
graphite
– iron, compacted (CGI) 257
– microstructure 329
gravitational discharge 877, 878
gravity
– die casting 346
– reclaim 837
gravity flow 837
– chute 915
– rack 975
gray cast iron 329
– mechanical properties 330
grease and oil lubrication 576
greenhouse gas (GHG) 662, 997
grinding 439, 448, 456
– defect 443
– electrochemical 456
– electro-discharge 456
– process 440
– with continuous dressing (CD grinding) 442, 443
grinding wheel 441
– conditioning 442
groove radius 854
grooved track wheel 860
gross
– domestic product (GDP) 1269
– tonnage (gt) 1145
group fuel injection 723
guidance navigation and control (GNC) 1088
guided transport mode 1063
guiding obstacle 900
Guillet diagram 244
gust envelope 1131
guy rope 848

H

half mirror 463
half-breadth 1143
halogenation 211
hammer 403, 404
– counterblow 404
hand
– molding 341
– pallet truck 949
handling 837
hang glider 1092
hard
– EHL 309
– machining 436
hardening 366
– strain 362
hardness
– testing 170
– Vickers 169
hardness Rockwell 169
– cone (HRC) 436
hardware crash 1022
hardware-in-the-loop (HIL) 1027, 1047
harmonic 16
hauling capacity 1007
head 755, 876
– dead center (HDC) 699
heading 373
health monitoring 216, 229
heat
– capacity 180
– exchange 127
– exchanger (HE) 763, 1233, 1253
– loss 696
– module 662
– penetration 120
– recovery steam generator (HRSG) 1228
– release rate 1251
– transmission 116, 117
heat transfer 67, 71, 116
– coefficient 116
heat-affected zone (HAZ) 193, 770
heated flame ionization detector (HFID) 741
heating consumption 670
heating, ventilation, air-conditioning, and refrigeration (HVACR) 765
heat-resisting cast steel 334
heavier than air (HTA) 1091
– craft 1092
heavy-duty industrial engine 749
Hecker's test 391
helical
– gearing 597
– screw flight 894
– spring 614
helicopter 1092
Helmholtz layer 1216
Hencky equation 370
hereogeneous nucleation 146
Hertzian contact pressure 504, 861
heterogeneous
– fuel–air mixture 716
– system 148
hexagonal close-packed (hcp) 134, 361
high bay warehouse 979
high pressure (HP) 782, 1242
high-alloy cast steel 333
high-alloyed cast iron 329
high-density polyethylene (HDPE) 234, 279, 667
high-density polyethylene (PE-HD) 621
high-efficiency machining (HEM) 436
higher heating value (HHV) 1226
high-polymer material 337
high-pressure
– combustion chamber (HPCC) 815
– die casting 347
– direct injection (HPDI) 730
– EGR 744, 747
– pump 723
– turbine (HPT) 790, 815
high-speed
– bogie 1073
– machining (HSM) 435
– steel (HSS) 428, 429
high-speed cutting (HSC) 435
– technology 436
high-strength low-alloy (HSLA) 245, 250
high-temperature hydrogen attack (HTHA) 209
high-voltage generation 732
hinge chain 888
histogram 470
hoist 834, 926, 929
– chain 856
– device 834
– winch 834
hoisting
– drive 923
– drum 854, 855
– gear 834
hollow shaft 544
homogeneous
– fuel–air mixture 716
– nucleation 145
– ODE 9
honeycomb rack 977
honeycombing 972
honing 445
hood 876
hopper 837
horizontal
– carousel 978
– tail 1110
hot
– isostatic pressing (HIP) 344, 1135
– vulcanized splice 872
hot-air balloon 1092
hot-chamber process 347
hot-working 168
house of quality 472
HRC (hardness Rockwell cone) 436
hull of vessel 1154
humid air 112
hybrid
– electric vehicle (HEV) 1030
– locomotive 1078
hydraulic
– conveyor 834
– counterpressure deep drawing 399
– drive 697
– elevator 947, 948
– excavator 943
hydrochlorofluorocarbon (HCFC) 662
hydroforming 399
– tube 399, 401
hydrogen attack 209
hydrogen-assisted
– cracking (HAC) 203
– stress corrosion cracking (HASCC) 202
hydrogen-enhanced
– decohesion (HEDE) 203
– localized plasticity (HELP) 203
hydrojoining 561
hydromech process 399
hydropower 1268
hydrostatic
– curve 1150

– pressure 1159
– stress 365
hydrostatics of vessel 1150
hyperelasticity 371
hypoelastic model 371
hysteresis loss 861

I

ideal
– combustion cycle 685
– gas 73, 95
– limiting drawing ratio 397
ideal equivalent plastic strain 372, 378
– rate 372
idealized
– creep curve 172
– wheelset 1066
idler 864
– roll rotating resistance 868
– set 864
IGBT 1193
IGCC plant environmental benefits 1232
ignition 732
– control system 732
– electronic 731
– engine compression 734
– timing 732
ignition system 731
– design 731
imaging microscopy 159
immersed volume 1142
impact 873
– angle 846
– extrusion 376
– testing 174
impedance 1182
– graphical addition 1201
– of circuit elements 1201
– spectroscopy 229
important standard 1285
impression die forging 376
in-car telematics 1039
incomplete
– combustion loss (ICL) 1249
– filling 375
incremental sheet forming 360
indentation
– resistance rolling 867
– rolling resistance 867, 868
independent wire rope core (IWRC) 852
index, Erichson (IE) 391
indicated
– airspeed (IAS) 1100
– efficiency 702
– power 717
indirect
– diesel injection (IDI) 724
– injection (IDI) 735
indium tin oxide (ITO) 465
individual-cylinder pump 727
induced
– air 901
– draft (ID) 446, 1246
inductance 1179
– addition for series or parallel 1179
– coupling 1203
– of torus 1180
inductive guide 977
inductor 1179
– phase shift 1181
industrial
– casting process 334
– truck 949
inertial force 690
– oscillating 691
– rotating 690
ingot casting
– method 339
– process 339
initial
– grasping 385
– value problem (IVP) 8
injected fuel quantity 724
injection 722–724
– duration 724
– pattern 724
– port 723
– pressure 724
– rate shape 724
– system 1004
– throttle body 723
– timing 724
inlet 863, 876
– air temperature 724
in-line control sleeve injection pump 726
inline fuel-injection pump 726
input/output (I/O) 980
inside diameter (ID) 446
inspection
– device 476
– method 497
– planning 469, 497
instantaneous
– flow function 839
– yield locus (IYL) 838
instrument flight rules (IFR) 1091
insulated-gate bipolar transistor (IGBT) 1191
insulator 1176
intake valve 716
integrable square 18
integral casting 326, 353
integrated
– circuit (IC) 289, 1228
– product drawing 476
integrated gasification 1231
– and combined cycle (IGCC) 1231
– combined cycle (IGCC) 1232
intercommunication bellow 1076
interconnectedness of a modern luxury vehicle 1032
intercooler 720
intercooling 715
interdisciplinary development 651
interferometric display 461, 462
– device (IDD) 462
intergranular corrosion testing (IGC) 759
intermediate pressure (IP) 819
internal
– angle of friction 838
– bearing 1072
– combustion engine (ICE) 715
– energy 67, 70
– resultant 36
internal gear 698
– pump 709
International
– Centre for Diffraction Data (ICDD) 153
– Civil Aviation Organization (ICAO) 1096
– System (SI) 1093
international
– building code (IBC) 758
– temperature scale 65
Internet of Things (IoT) 1090
interstitial site 134
intrinsic material property 136
intuitive method 640
inventory turnover rate 972
inversion point 480
inverter 1190
investment casting 344

ion beam 157
– machining (IBM) 448
ion-induced secondary electron (IISE) 157
IPAT equation 671
iron cast 257
iron-carbon phase diagram 235
ironing 359
– process 382
irreducible polynomial 15
– factor 15
irreversibility 69
isentropic efficiency 107
Ishikawa diagram 470
ISO 26262 *Road vehicles* 1033
IT 421, 427
Izod impact test 174

J

Jacobs bogie 1012
Jenike
– flowability classification 840
– shear tester 841
Jenike-type direct shear tester 841
jet
– airplane 1119
– formula 1119
– transport 1109
jib crane 937
joint 515
– compression 559
– diagram 531

K

Kelvin
– scale 64
– wave pattern 1155
key
– connection 552
– technologies 1036
keyed joint 565
Kikuchi band 159
kinematic hardening 367
kinematically admissible velocity field 369
kinematics of cutting 422
king wire 849
Kirchhoff's law 127
knocking combustion 734
Knoop hardness HK 0.1 441
Krueger flap 1111

L

ladder frame 1024
Lagrangian description 68
laminar
– composition 290
– ring 522
landing
– air distance 1122
– conditions 1129
– weight 1114
Lang's lay 850
Lankford parameter 389
Laplace
– equation 21
– transform 13
lapping 446
– process 447
Larson–Miller parameter 174
laser
– flame cutting 453
– flash method 181
– fusion cutting 453
– interferometer 495
– measuring technology 493
– scanner 493
– sublimation cutting 453
– system 454
laser beam (LB) 452
– cutting 452
– machining (LBM) 452
laser cutting (LC) 452
– machining parameter 454
laser-assisted machining (LAM) 456
last-in first-out (LIFO) 970
lateral
– control device 1111
– dynamic motion 1128
– force 691
– resolution 155
lattice
– Bravais 133
– defect 132
– primitive cubic 132
law of mass action (semiconductors) 1185
lay
– angle 849
– direction 849, 851
– length 849
lead acid (LA) 1215
leading edge (LE) 796
leaf
– chain 858
– spring 613
lean NO_x catalyst 745
lean-burn principle 722
left-hand lay 849, 850
lengthwise storage 974
levels of driving automation 1028
lever arm rule 149
Levy–Mises flow rule 367
life cycle 664
– analysis (LCA) 663, 664
– costs (LCC) 1059
– economic 630
– inventory (LCI) 663
– stage 629, 664
– technical 629
lifetime 304
lift
– coefficient 1102
– mast 950
lift/elevator 834
lifter 927
lifting
– chain 857
– hook 926
– magnet 927
– platform 834
– truck 950
lift-to-drag ratio 1103, 1106, 1120
light
– construction 327
– microscopy 154
– water reactor (LWR) 1261
light-emitting diode (LED) 1187, 1224
lighter than air (LTA) 1091
light-off temperature 745
lightweight vehicle design 1002
lime soda process 1238
limit
– gauge 478
– load factor 1129
– of error 479
limiting drawing force 398
line of action 28
linear
– algebra 4
– elastic theory 177
– expansion coefficient 481
– intensity of wear 305

linearly
– dependent 10
– independent 10
link plate 858
lip-type seal 587
liquefaction 843
liquefied
– natural gas (LNG) 730, 736
– petroleum gas (LPG) 736, 950
liquid (viscous) friction 580
liquid fuel 99
– burner 1255
– furnace 1245
liquid–vapor saturation 75
Litz wire 1180
load 504, 756
– attachment device 891
– carrier 832
– chain 857
– coefficient 782
– factor 1129
– handling attachment 853
– securing equipment 832
– spectrum class 854
loaded turbine blade 798
loader 834, 941, 944
loading 756
– bridge 935
– condition 546
– crane 941
– mode 504
– trucks and trains, stacking empty containers, or providing containers for packing and unpacking 955
– unit (LU) 972
localized necking 390
lock bead 399
locking element 540
logical function 634
logistics 830
log-mean temperature difference (LMTD) 767
longitudinal
– cylindrical turning 413
– joint 559
– stability 1151
longitudinal center
– of buoyancy (LCB) 1144
– of flotation (LCF) 1151
– of gravity (LCG) 1149
long-range order (LRO) 132
long-stroke honing 445
longwall mining equipment 884
Lorenz–Pareto analysis 470
loss angle 1182
loss due
– to hot ash or slag (ASL) 1249
– to moisture in the combustion air (MCAL) 1249
lost
– primary shaping tool 340
– wax process 345
lost-foam casting 334
low pressure (LP) 803
low-density polyethylene (LDPE) 279
lower
– heating value (LHV) 718, 1250
– yield stress (LYS) 167
lower-bound method 369
low-floor tram 1069
low-pressure
– combustion chamber (LPCC) 815
– compressor 803
– EGR 744, 747
– system 722, 728
– turbine (LPT) 790, 815
low-pressure permanent mold
– casting 347
– die casting 347
– xcasting 347
low-wing airplane 1110
lubricant 311
lubricating
– grease 316
– oil 312
lubrication 306
– boundary 309
– elastohydrodynamic 308
– fluid film 306
– hydrodynamic 306
– hydrostatic 309
– method 575, 607
– of gear trains 606
– of piston 696
– of piston machine 696
– procedure 382
– state 307
lubricity 736
Lüders strip 391
Ludwik flow curve 390
luffing
– crane 937
– gear 926

M

Mach number 791, 1104
machine 35
– asynchronous 1207, 1208
– commutator 1207
– direct current 1207
– electrical 1205–1207
– induction 1209
– molding 341
– rolling 402
– synchronous 1207, 1210, 1211
– work 683
machining 448, 450
– allowances 327
– beam (BM) 452
– plasma arc (PAM) 448
– spark erosion (SEM) 448
– ultrasonic (USM) 451
magnesium alloy 335
magnetic
– Barkhausen noise 223
– flux inspection 221
– forming machine 402
– particle inspection (MPI) 221, 729
– stray flux 220
– testing 220
magnetohydrodynamics (MHD) 1234
magnox 1261
main
– air pipe (MAP) 1011
– injection 724
– resistance 867
maintenance inspection check 1136
major consolidation
– pressure 839
– stress 839
majority carrier 1185
malleable cast iron 331
– mechanical properties 331
mandrel 382
maneuver
– limit load factor 1130
– load factor 1129
maneuvering envelope 1129, 1130
manikin RAMSIS 1043
man-to-goods principle 972
manufacturer's weight empty (MWE) 1113
manufacturing 325
– cost 419
– process 326, 666

– processes 662
manufacturing-specific design 1050
man-up turret truck 952
maritime transportation 843, 1139
Markov's variational principle 371
martensitic steel 773
mass
– balancing 692
– flow rate 836
– product 1015
mass-produced product 633
material
– characteristics 636
– properties 119, 166
– removal process 409
– standard of pressurized use 771
material-bonded joint 538
materialography 154
materials handling 830
– equipment 834
– system 830
mating gear 595
matrix 4
– diagram 471
– inverse 5
– symmetric 5
– transpose 5
maximum
– contrast 462
– cutting speed 435
– landing weight (MLW) 1114
– lift coefficient 1110
– pressure piston pump 706
– shear theory (MSS) 507
– take-off gross weight (MTOGW) 1114
– zero-fuel weight (MZFW) 1113
Maxwell's equations 1169, 1170, 1174
– in matter 1174
mean
– aerodynamic chord (m.a.c.) 1109
– downtime (MDT) 1060
– effective pressure (MEP) 717
– molar specific heat 80
– piston speed (MPS) 507, 717
– time between failures (MTBF) 1060
measurement deviation 496
measuring
– chain 479
– machine 483
– point 482
– probe system 484
– range 479
– uncertainty 479, 496
mechanical
– abrasion 413
– conveyor 834, 863
– drive 697
– efficiency 687, 718
– guide 977
– properties 336, 1135
– seal 590
– splice 872
medium deep bucket 879
melting point in metals 181
membrane theory 387
meridional velocity ratio 788, 789
mesh
– analysis 1197
– current method 1197
– electric 1195
metacentric height 1149
metal
– cutting 426
– dusting 209
– matrix composite (MMC) 432
– oxide semiconductor (MOS) 1183
– temperature transient 821
metal forming 357
– system 360
metallic materials 179
metal-organic framework (MOF) 738
metering pump 706, 707
methane 737
method 635 640
method of
– joints 35
– sections 35
– undetermined coefficients 10
– variation of parameters 10
methodical approach 638
methyl *t*-butyl ether (MTBE) 742
Meyer hardness 169
mezzanine 974
microanalysis 158
microbiologically induced corrosion (MIC) 206
microcutting 433
– operation 433
– tool 434
microelectromechanical system (MEMS) 461, 462
microfatigue 847
micromirror 462
microscopy 154
– imaging 159
microstructural failure 375
microstructure quantification 160
micro-throw regime 901
microtome 154
microturbine 806
midship area coefficient 1142
milestones 1039
military
– aircraft 1129
– airplane 1130
– specifications (Mil Specs) 1112
– speed definition 1132
Miller cycle 719
milling 421, 426
– process 421, 423
mineral oil 312
minimum
– belt width 866
– control speed 1127
– rope diameter 853
– tensile force 871
minority carrier 1185
misalignment 874
mixed
– discharge 877
– friction 300
– lubrication 311
mixture
– formation 683, 733
– of gas and vapor 109
mobile
– communication network 1032
– crane 939
– rack 977
mobility 1184
– electron 1176
model experiment 640
modeling 1037
moderator 1261
modern vehicle 1032
modes of motion 1128
modular belt 890
– conveyor 889
modulus of elasticity 1158
Mohr semicircle 838
moisture content 842
molding and casting 327
molecular weight of
– carbon (MC) 1249
– CO (MCO) 1249
Mollier diagram 112
molybdenum 430

moment
– of inertia 694
– of the force 28
– rolling 385
– to change the trim by one centimeter (MCTC) 1151
momentum equation 51
Monkman–Grant chart 173
monocrystalline diamond (MCD) 432
monorail 834
morphological box 631, 655
MOS transistor 1189
– 3-D 1189
– active mode 1190
– CMOS 1190
– drain 1189
– NMOS 1189
– PMOS 1189
– source 1189
– threshold voltage 1189
– triode mode 1189
– VDMOS 1193
motion
– resistance 835, 863
– sickness incidence (MSI) 1161
motor
– bogie 1073
– electric 1206
– induction 1208, 1210
– power 870
motorglider 1092
motorized air cycle machine (MAM) 1081
Mukherjee–Bird–Dorn equation 172
multibody simulation (MBS) 943
multi-circular arc (MCA) 791, 794
multicylinder machine 692
multidiaphragm pump 708
multiflex chain 888
multilayer grinding belt 444
multiload carrier (MLC) 954
multipoint open-valve injection (MP-OVI) 729
multisensor technology 484
multistage
– compressor 826
– turbine 787
multistaging 714
multisupport shaft 550
multisystem locomotive 1078
multiwire slicing 447
municipal solid waste (MSW) 667
Muntz metal brass 276

N

Nabarro–Herring creep 172
NAND gate 1190
national building code (NBC) 758
natural
– aspiration 716, 718
– circulation boiler 1239
– convection 124
– fiber core (NFC) 852
– rubber (NR) 612
natural gas (NG) 729, 730, 1232
– combustion 730
– direct injection (NGDI) 730
nautical application 1152
naval architect 1141
n-channel MOS (NMOS) 1189
near-net shaped part 359
near-net-shape production 353
necking 167, 390
needle roller bearing 566
Nernst equation 1218
net
– calorific value 99
– plan 471
– positive suction head (NPSH) 704
net-shaped part 359
network 1194
– algorithms 1200
– star 1205
– three phases 1204
– triangle 1205
– two terminal 1197
network AC 1201
– powering 1213
Neuer Europäischer Fahrzyklus (NEFZ) 1018
neutral plane 384
new car assessment program (NCAP) 1022
New Panamax vessel 1141
nickel (Ni) 430
nickel-alloyed cast iron 332
nickel-based alloy 774
Nippon Kaiji Kyokai (Class NK) 1140
nitriding 211
NLGI classes 321
NO_x emissions 744
NO_x-particulate tradeoff 744
nodal analysis 1199
node
– electric 1195
– electrical equation 1196
noise level 998
noise–vibration–harshness (NVH) 1000
nominal
– area 296
– breaking tensile stress 857
noncontact seal 590
nondestructive
– evaluation (NDE) 215
– inspection (NDI) 215
– testing (NDT) 176, 215, 758
nondispersive infrared (NDIR) 741
non-engineering support 1054
nonlinear dynamic method 809
nonoxide ceramics 289
nonquadratic flow 390
nonrigid airship 1092
non-rotation-resistant 851
normal
– direction (ND) 160
– temperature and pressure (NTP) 1265
not and (NAND) 1190
notch effect 510
notched-bar impact test 174
nozzle 756, 814
nozzle's opening pressure 728
nuclear
– fuel 1236
– power plant 1260, 1261
– reactor 1260
nuclear physics 1281
– constant 1282
number of atoms (NA) 133
numbering system 245
numerical
– control (NC) 436
– method 370

O

oblique flying wing (OFW) 1089
octane number 736
odd-periodic extension 17
off-centered load 875
Ohm's law 179, 1176
Olsen test 391
one-step splice 874
open system 67

open-circuit potential (OCP) 201
open-die forging 372, 374
operating weight empty (OWE) 1114
operation mode of vibratory conveyor 901
optical switching device 462
orange skin 391
ordinary
– differential equation (ODE) 3, 8
– lay 850
organization 1057
orientation 900
– imaging microscopy (OIM) 159
original equipment manufacturer (OEM) 745, 1000, 1016
O-ring 587
orthogonality 16
oscillating inertial force 691
Ostwald ripening 141
Otto engine 101
outer function 675
outlet 863, 877
outside bearing 1072
oval strand 850
over fire air (OFA) 1259
overhead conveyor 834, 890
overlap ratio 296
overlapping splice 873
oxidation 209
– stability 736
oxidative self-heating 844
oxide ceramic 432
oxide-dispersion-strengthened (ODS) 289
oxides of nitrogen 739, 740
ozone 739

P

package freeze 1038
packaging and ergonomics 1042
packing density (PD) 133, 760
palette 832
pallet 887
– jack 949
– rack 974
pan conveyor 882, 886
parallel
– kinematic 944
– wire rope core (PWRC) 852
parallel-lay 850
parasitic drag 1106
parcel 832
Pareto analysis 470
part and component design 1041
partial
– fraction 15
– lubrication 311
particular material appraisal (PMA) 761
particulate 740
– matter (PM) 430, 737
– number (PN) 741
passenger exchange 1058
passivation 196
passive house 667, 669
– estate 669
passive safety 1021, 1022, 1081
paternoster rack 978
payload–range curve 1119
PC diesel engine 745
p-channel MOS (PMOS) 1189
PCI Express 1191
pebble bed reactor (PBMR) 1261
pedestrian
– protection 1038
– safety 1001
– stacker 950, 951
peel grab 929
PEGASUS 1029
Peierls stress 140
pendant superheater 1240
pendulum bucket elevator 880
penetration
– test 843
– tester 844
– testing 226
perfluoroelastomer (FFKM) 587
performance 634
– indicator 972, 1034
– under extreme terrain 1047
periodic
– function 14
– table of chemical elements 1284
peripheral
– component interconnect (PCI) 1191
– milling 422
peristaltic pump 700
permanent mold casting 346
permeability
– of free space 1170
– relative 1175
permittivity
– of free space 1170
– relative 1175, 1177
persistent slip band (PSB) 175
phase boundary
– coherent 141
– incoherent 141
phase shifter 1213
photovoltaic cell 1265
physical
– constant 1280
– principles 479
– simulation 370
– vapor deposition (PVD) 144, 311, 429
physisorption 310
pilot control system 1128
pin 858
– type 516
pinned joint 515
pipe 620
– bend 624
– connection 622
– conveyor 864
– roughness 623
piston 688, 696
– acceleration 690
– engine-propeller 1113
– force 691
– kinematics 689
– pump, single-rotation 710
– ring 696
– speed 689, 717
– travel 689
piston machine 683, 684, 696
– single rotation 709
piston pump 698
– system 702
pitch 858
pitching moment 1128
– diagram 1126
Pitot tube 1100
pitting resistance equivalent numbers (PREN) 199
pivoted bucket 880
plain
– bearing 580
– face milling 425
– roller track wheel 860
planar motion 56
plane
– strain Young's modulus 395
– stress state 365
plane-parallel lapping 446
planetary rotation piston 699, 712
planing 427
planning stage 674

plasma
– arc machining (PAM) 448
– beam machining (PBM) 452, 455
– cutting 455
– spark 733
plastic
– (permanent) strain 364
– chain 889
– strain, total equivalent 367
– top chain 888
plastic deformation 175
– mechanism 361
plasticity 368
plate
– buckling 1154
– heat exchanger (PHE) 765, 775
platen superheater 1240
plating thickness 1159
plena pressure 820
plug-in hybrid electric vehicle (PHEV) 1000, 1020
plunger 697
– piston 697
p–n junction 1185
pneumatic
– and hydraulic conveyor 834
– brake 1080
– braking system 1011
– chain hoist 931
– conveying characteristic (PCC) 914
– conveyor 834, 903
pocket
– bag elevator 881
– conveyor 864
– wheel 860
Poka Yoke method 472
polar
– form 19
– representation 19
– wheel angle 1212
polarization 1174
polyacrylate rubber (ACM) 612
polyaddition 278
polyalphaolefines (PAO) 312
polyamide (PA) 278
polycondensation 278
polycrystalline (PC) 434
– cubic boron nitride (PCBN) 432
– diamond (PCD) 432
polyethylene (PE) 278
– terephthalate (PET) 278, 667
polyethylene terephthalate (PET) 1178
polygon effect 857
polyisobutenes (PIB) 312
polymer 278
polymerization
– chain 278
– condensation chain 278
polymethylmethacrylate (PMMA) 279, 350
polymorphism 134
polyphenylene sulfide (PPS) 278
polypropylene (PP) 278, 621, 1178
polystyrene (PS) 278
polystyrene-butadiene rubber (SBR) 280, 612
polytetrafluoroethylene (PTFE) 278, 306, 712
polytropic 94
– process 713
polyurethane (PUR) 278
polyvinylchloride (PVC) 278, 670
polyvinylidene fluoride (PVDF) 621
poppet valve 719
port injection 723
portable emissions measurement system (PEMS) 742
position tolerance 477
positive displacement
– compressor 686
– pump 686, 697
postheating 770
post-injection 724
postweld heat treatment (PWHT) 770
potassium hydroxide (KOH) 1220
potential
– damage 1024
– drop method 219
– electric 1173
– magnetic 1173
pouch conveyor 864
powder 337, 842
– metallurgical manufacturing 337
– metallurgy (PM) 143, 337, 430
powder diffraction
– file (PDF) 153
– method 153
power 688
– apparent 1182
– brake 717
– compensation of reactive 1202
– consumption 863
– instantaneous inductor, capacitor 1181
– machine 683
– reactive 1182
– requirement 870
– sign of 1177
– spectral density (PSD) 1064
– supply 1268
– turbine 721
power and free
– conveyor 891
– system 894
power generation 802
– gas turbine 818
power-law
– breakdown 173
– creep 173
Prandtl–Reuss equation 371
prechamber 724, 735
precipitate coarsening 141
precipitation strengthening 141
precipitator 1258
precision machining 438
preconsolidation phase 841
predevelopment 1037
– project 1036
prefix for units 1275
preflight check 1136
preform process 374
preheating 770
pre-ignition 734
pre-injection 724
premanufacture 664
press
– eccentric 405
– energy-controlled 404
– force-controlled 403
– hydraulic 407
– knuckle-joint 406
– mechanical 405
– servomotor 406
– stroke-controlled 405
– Vincent 405
press-fit connection 555, 558
pressure
– loss 622, 768
– on piston 690
– vessel 753
– welding 413
Pressure Equipment Directive (PED) 760
pressurized water reactor (PWR) 1261
preventive technique 470
primary
– air fan 1246

– recrystallization 363
– suspension 1071
primary energy 1235
– for electricity 1236
primary shaping 336, 337, 340
– by sintering 338
– tool 338, 339
primitive cubic lattice 132
principal
– radius 387
– value 19
principle
– of transmissibility 28
– of volume constancy 365
prismatic coefficient 1143
problem solving process 638
problem-resolving technique 470
procedure qualification record (PQR) 763
process
– analysis 476
– FMEA 671
– force 942
– limit 373
– monitoring 474
– work 402
process–decision diagram 471
Proctor–Fagerberg
– test 843
– tester 844
product
– assessment matrix 664
– data management (PDM) 1035
– for pressurized use 772
– layout 1040
– life stage 629
– specification 632
– structure and virtual model 1049
– tracking 630
product development 631, 651
– time 1036
product planning 630
– phase 629
production of cast parts 338
profile
– rolling 384
– wire 849
project-specific predevelopment 1038
prompt NO_x 740
propeller efficiency 1118
properties of lubricants 318
prototype and test management 1051
pulley 848
– diameter 874
pump
– power 407
– screw 711
pumped hydro storage (PHS) 1215
pure battery electric vehicle 1030
push conveyor 834
push-back rack 976
pusher 922

Q

quality 469
– control chart (QCC) 473, 474
– factor 1182
– function deployment (QFD) 471
– grade 857
quality management (QM) 469
– system (QMS) 474
– system (QS) 355
quantitative stereology 160
quasi-propulsive coefficient (QPC) 1157
quiet supersonic transport (QueSST) 1092

R

rack 834
– shuttle 834
– stacker 834
– tooth profile 597, 598
racking system 972
radial
– bearing 582
– equilibrium 783
– forging 376
– piston pump 698
– shaft seal 588
– turbine 781
radial-piston pump 726
radiant superheater 1240
radiation and unaccounted-for losses (RUL) 1249
radiographic testing (RT) 179, 228, 273, 763, 803
radioscopy 228
rail
– drive 924
– foot 862
– head 862
– profile 1062
– technology 1009
– track 862
– vehicle 1012
– wheel 861, 862
railway
– organization 1057, 1058
– transportation 1058
ram effect 718
range
– of application 479
– stoichiometry 135
Rankine cycle 1225, 1233
rate of climb (RC) 1117
rated braking strength 873
rate-of-climb equation 1117
reach
– stacker 834, 955
– truck 834, 950, 951
reactance 1182
– synchronous 1211
reactive
– effect of the bulk material 901
– ion etching (RIE) 461
– power 1202
reactivity of bulk material 844
reactor 1261, 1264
– pebble bed (PBMR) 1261
– pressure vessel (RPV) 1239
– pressurized water (PWR) 1261
– RBMK (Chernobyl type) 1261
– vessel 1261
real
– contact area 296
– gas 74, 79
real-world
– driving emission (RDE) 742
– situation 1027
reaming 417
reciprocating
– compressor 713
– machine 684, 688
– pump 697
recovery 362
recrystallization 362
– temperature 363
rectangular chute 916
recuperator 805
– air side (RA) 804
– gas side (RG) 804
recyclability guidelines 670
recycling 327
– option 650
– rate 326

redirection
– factor 893
– resistance 893
– wheel 859
Redlers 882
reduced machining 326
reducing 376
reeving system
– transmission ratio 855
reeving system (block and tackle) 854, 855
reference direction 1194
refractory ceramics 286
refrigeration plant 107
regenerative
– Brayton cycle 1233
– conveyor 870
regression equation by Gauss 482
regulatory test 843
reheater 1241
relative
– humidity 111
– wind 1099
relaxation, stress 173
release
– of hardware 1050
– process 1050
reliability rate 1090
reliability, availability, maintainability and safety (RAMS) 1059
remanence 1204
renewable
– energy 1264
– natural gas (RNG) 737
repeated stress 510
required belt life 873
requirement specification 632
requirements list 653
residual field inspection 222
residual stress 383, 395
– in drawing 385
resin transfer molding (RTM) 1135
resistance
– component 1154
– curve 1155
– internal of source 1197
– matrix 1198
resistance specific 1175
– values for 1176
resistivity 179
resistor 1176
– temperature coefficient 1177
resolution lateral 155
resonance testing 218
response
– amplitude operator (RAO) 1161
– time 479
result hysteresis 479
resultant force 415
retaining element 520
retracting unit 834, 926
reverse redrawing 397
revolutions per minute (rpm) 717
ride-on stacker 951
riffler 838
right-hand lay 849, 850
righting moment 1146
rigid body 26
ring
– lubrication 584
– sorter 922
– spring 612
ring shear
– apparatus 841
– tester 841
Ringfeder clamping 563
risk priority number (RPZ) 672, 673
riveted joint 519
rivetless chain 891
Rockwell hardness 169
roll
– bending 393
– forming 393
– straightening 393
roller 858
– cell pump 712
– conveyor 834, 920
rolling 357, 358, 384
– direction (RD) 160
– force 385
– friction 861
– machine 402
– moment 385, 1099
– thread 386
rolling bearing 566, 569
– damage 576
– lubrication 574
rolling resistance 861, 1010
– coefficient 861
roman counting system 1276
root of unity 20
root-mean-square (rms) 297
rope 850
– calculation 853
– core 849, 850, 852
– diameter 853
– elevator 947
– force 853
– grade 849, 853
– lock 854
– lubrication 850
– termination 854
– wire 849
rope drum 849, 854
– diameter 854
rope-driven trolley 936
rotary
– fuel-injection pump 726
– sample divider 838
– screw pump 710, 711
rotary piston
– machine 698
– pump 697, 708
rotating
– inertial force 690, 692
– masses 690
– sorter 922
rotation 29
rotational resistance 867
rotation-resistant 851
rotor 1207
– mechanical construction of 1210
– speed behavior 821
roughness profile 488
round
– bending 393
– groove 855
– steel link chain 857
– strand 850
roundness deviation 492
round-strand rope 852
row
– echelon form 6
– equivalent 6
– stacking 970
rubber spring 612
rubber-covered belt 864
rubber-cushioned wheel 1069
rule
– Kirchhoff 1195
– mesh 1195, 1196
– node 1195
runaway ignition temperature (RIT) 844
Runge–Kutta method 9, 12
running rope 848
runway friction coefficient 1123
rupture 383
– tearing 390

S

safety
– factors for belt and splice 872
– features 1032
– margin 1060
– value 513
Safety Of Life At Sea (SOLAS) 1140
sample divider 838
sampling
– bulk material 837
– inspection 474
sand casting 334
saturated
– liquid line 76
– vapor line 76
– water 77
saturation 111, 1204, 1211
sawing 428
– variants 428
S-bend 893
scale division value 479
scanning
– Auger electron spectroscopy (SAM) 159
– electron microscopy (SEM) 140, 156
– transmission electron microscopy (STEM) 157
scatter diagram 470
Scharfenberg coupler 1079
scissor grab 929
scooping 876
scrape bucket 859
scraper
– blade 859
– conveyor 834, 882, 884
– flight 884
– reclaimer 882, 884
screw 523
– conveyor 834, 894
– dislocation 137
– drive, axially moving 405
– press 405
– pump 711, 712
– torque 898
screw/bolt selection 537
screw-in joint 530
seakeeping behavior 1161
seal 585
– resistance 861
secant modulus 282
second law of thermodynamics 69
secondary
– electron (SE) 156
– recrystallization 363
– resistance 867
– suspension 1071
secondary ion (SI) 157
– mass spectroscopy (SIMS) 159
second-order
– forces of inertia 692
– linear ODE 9
segmented
– blank holder 399
– chip formation 410
Seiliger process 686
seismic load 758
selection and evaluation 641
selective
– catalytic reduction (SCR) 731, 745
– laser melting (SLM) 350
selective noncatalytic
– reduction (SNCR) 1259
– reduction system 1259
self-centering 874
self-compensating solution 646
self-heating 844
self-protecting solution 647
semiconductor 1167, 1176, 1177, 1183
– doping 1184
– material 1183
– power device 1191
semiinfinite body 118
semi-rotation-resistant 851
sensor technology 1026
separable ODE 8
sequential fuel injection (SEFI) 723
series
– development 1038
– production of vehicles 1036
severity index 392
shaft 544
– connection 554
– diameter 549
shaft–hub connection 551, 555
shaftless screw 895
shape factor 866
shaped-strand rope 852
shapeless material 336
shaping 427
– by casting 353
sharing tasks 645
shear
– forming 387
– modulus 172
– phase 841
– strength 137, 361
– stress 260
– test 841
– theory 507
– turning process 386
sheave 848, 854
– diameter 854
sheet forming
– high-pressure 399, 400
– processes 359, 387
sheet hydroforming 399
shelf racking system 973
shell molding 342
shielded metal arc welding (SMAW) 775
ship
– design 1143
– geometry 1139, 1141
– lines plan 1144
– profile 1142
Shockley equation 1186
short-hole drilling 421
short-range order (SRO) 132
shrink ring 382
shutdown process 817
shuttle
– carrier 954
– system 981
SI
– engine emissions 742
– system 1276
side
– elevation 1143
– force 1099
– impact 1022
– wind 874
sideloader truck 953
sideslip 1127
sign convention 1145
silicon
– carbide (SiC) 289, 441
– drift detector (SDD) 158
– nitride 432
silo 834, 955
simple
– pressure vessel (SPV) 760
– tension test 367
– test tension 367
– truss 34
simulative formability test 391
simulative test formability 391
simultaneous fuel injection 723

single
– degree of freedom system (SDOF) 551
– load carrier (SLC) 954
– rotation piston machine 709
– wheel 1011
single-chain overhead conveyor 891
single-cylinder machine 692
single-flange track wheel 860
single-girder overhead crane 933
single-rotation piston pump 710
single-spool
– gas turbine 804
– power generation gas turbine 802
sink 830
sintering 337
size of ship 1140
skewed idler station 875
skin effect 1180
slab method 368
slat conveyor 882, 888
slewing
– bearing 925
– crane 937
– gear 834, 925
– pillar crane 938
slideway 859
sliding
– chain conveyor 888
– shoe sorter 923
– vane pump 700
sling
– chain 857
– rope 848
slip 873, 1209
– band, persistent (PSB) 175
– line field solution 370
slip-free wheelset 1066
slope
– angle 864
– factor 864
– resistance 867, 869
slow flow 916
soft EHL 309
softening strain 366
solar
– cell 1187, 1265
– chimney 1266
– energy 1265
– field 1266
– pond 1265
soldering 543
solid
– friction 300
– lubricant 311, 316
– lubrication 575
– state of aggregation 338
solid fuel 97
– furnace 1244
solid solution 135
– strengthened cast iron 330
solidification 147
– point 65
solid–liquid interface 147
soluble organic fraction (SOF) 740
solution
– principles 639
– solid 135
sorter 922
source 830
space
– limit payload (SLPL) 1113
– truss 34
– utilization rate 971
spacecraft 1093
– design 1089
spark
– electro-discharge machining (SEDM) 448
– plug design 732
spark ignition (SI) 729
– engine 733
spark-erosion machining (SEM) 140, 448
spark-plug 732
special crash investigation (SCI) 1023
specific
– cutting force 415
– fuel consumption (SFC) 718, 1118
– heat 81, 180
speckle testing 227
spectral analysis 741
speed
– over the ground (SOG) 1152
– through water (STW) 1152
spheroidal graphite cast iron 330
– mechanical properties 330
spindle elevator 947
spinning 360
spiral
– mode 1128
– rope 851, 852
splice 872
splicing 872
split pin 524
spoiler 1111
spontaneous combustion temperature 844
sports utility vehicle (SUV) 1023
spread (cross) forging 376
spreader 935, 954
– stoker 1244
spring 607
– end 617
– loaded valve 705
– material 611
– rate 608
– stack 616
– subjected to bending 613
– system 609
– work 608
springback 395
sprocket wheel 856, 860
spur gear system 605
square
– integrable 18
– matrix 7
squeeze-casting 348
stability 1147
– and crash performance 1024
– buildup 1127
– condition 372
stacking fault energy 141
stage
– configuration 777, 784
– load coefficient 777, 789
– parameters 777, 781
– power 777, 785
– velocity diagram 786
stainless-steel grade 775
standard
– adhesive 542
– atmosphere 1093
– hoist with C-shaped design (Terex MHPS) 931
– strand 849
standards for mechanical testing 178
Starlines 1093
start of production (SOP) 1005, 1036
state of ideal gas 94
static
– balance 1159
– equilibrium 31
– material characteristics 509
– port 1100
– stability 1123
– storage 972

– strength 508, 512
statically
– admissible stress field 369
– determinate 31
– indeterminate 31
statics 26
station availability 1058
stationary rope 848
statistical
– process control (SPC) 472, 852
– research planning 472
stator 1207
– and rotor rows 790
steady-state
– heat conduction 115
– process 67
– steady flow (SSSF) 1248
steam
– generator 1238, 1240, 1248
– power plant 1234
– turbine 1229
steam-turbine-operated Rankine cycle 1233
steel 134, 769
– bodyshell 1075
– casting 333
– cord conveyor belt 872
– gear 605
– link chain 857, 858
– pester 244
steeply inclined transport 876
Stefan–Boltzmann law 126
stepped
– axle 544
– splice 873
stepwise development 633
Stern layer 1216
stiffness of forming press 403
stock keeping unit (SKU) 970
stockpile 834, 837, 884, 963
stoichiometric
– air–fuel ratio 722
– mixture 734
stoichiometry range 135
storage 837
– and racking equipment 834
– and retrieval device 834
– capacity 972
– carousel 834
– equipment 834
– system 955
– utilization 973
straddle carrier 950, 954
strain 504
– bending 394
– coherency 141
– hardening 139, 168, 362
– softening 366
– total 364
strain rate 367, 372
– tensor 364
strand 849
– core 850
– wire 849
streamlined life cycle analysis (SLCA) 664
strength
– calculation 512, 1252
– characteristics 508
– verification 514, 548
stress
– Cauchy 365
– intensity factor 177
– invariant 365
– relaxation 173
– residual 383, 395
– tensor 365
– true 365
stress corrosion 219
– cracking (SCC) 200
stress field 177
– statically admissible 369
stress state
– plane 365
– uniaxial 365
stress-orientated casting design 351
stress-rupture tests 173
stress–strain
– curve 166, 171, 1158
– diagram 509
Stribeck curve 301, 581
strip casting 340
stroke 685
– rate 403
structural
– health monitoring (SHM) 215, 216, 229
– materials distribution 1135
– relationship 636
styling
– concept 1037
– data 1042
– freeze 1038
subcritical reactor 1261
subfunction 633
sublimation curve 90
subsonic
– airplane 1132
– speed range 1104
substance 73
suction
– molding 342
– valve (SV) 699
sulfurization 210
summer saltwater (S) 1152
superabrasive wheel 441
supercharging 719
superconducting quantum interference device (SQUID) 222
supercooled liquid 147
supercritical (SC) 1226
superficial air velocity 843
superfinishing 445
superhard cutting tool 432
superheater 1240
superplasticity 173
supersonic
– compressor blade 795
– diffuser SSD 811
– transport 1090
support 32, 891
– reaction 30
supporting device 863
surface
– area 971
– belt grinding 444
– coating 311
– condition 478
– defect 375, 390
– fatigue 302
– finishing 440
– force 412
– grinding 440
– layer friction 580
– measuring condition 489
– pressure 504, 505, 535
– quality 438
– roughness 449
– texture parameters 489
surface metrology 469, 487
– instrument 488
susceptance 1182
suspension 696, 853
– crane 940
– rope 848
swaging 376
sweepback angle 1109
swept piston volume 685
switch 1064
switching probe system 484
symbols for surface conditions 478
symmetric airplane 1123

synthetic
– coated independent wire rope core (EPIWRC) 852
– fiber core (SFC) 852
– fuel 737
– methane (E-GAS) 1230
– natural gas (SNG) 1215, 1232
– oil 312
system
– energy requirement 666
– FMEA 671
– international (SI) 1093
– relationship 636
systems approach 639

T

table sampler 838
tail arrangement 1112
tailored casting 326
take-off
– field length 1122
– performance 1121
take-up
– device 873
– pulley 874
tally list 470
tantalum carbide (TaC) 430
tapered
– pulley 876
– rail wheel 862
– roller bearing 566
tearing 398
technical
– life cycle 629
– management 1061
– product 638
– reliability 1016
– system 637
technological data 1050
teeth number 856
telescopic arm 955
temperature
– equalization 120
– resistivity coefficient 179
– voltage 1186
tensile
– force distribution 871
– test 166
– testing 166
tensile strength
– of the belt 871
– ultimate (UTS) 167
tension 34
– device 863
– electric 1173
– in three-phase network 1205
tensor
– strain rate 364
– stress 365
terminal, electric 1194, 1195
test
– biaxial stretch 391
– cycle 741
– Hasek 393
– hole expansion 391
– hydraulic bulge 393
– Marciniak 393
– Nakazima 393
– plane torsion 391
– stretch-bend 391
– Swift's cup 391
– torsion 367
– uniaxial tensile 393
– wedge drawing 391
testing 224, 229
– flow chart 1154
– gamma-ray 229
– nondestructive 176, 215
– phase 633
– radiographic 228
– resonance 218
– speckle 227
– thermographic 225
– ultrasonic 217
– visual 226
tetrafluoroethane 89
tetramethyl ammonium hydroxide (TMAH) 465
texture 384
theme concept 1037
thermal
– conductivity 115, 180
– efficiency 718, 803, 806, 825
– energy storage 1269
– engineering 92
– equilibrium 63
– expansion 90, 180, 560
– NO_x 740
– radiation 126
– reactor 1261
– treatment 334
thermodynamic
– equilibrium 145, 148
– process 62
– system 61
thermodynamics 1224
thermographic testing 225
thermometric fixed point 65
thermoplastics 279
thermosetting plastics 338
thickness assessment 223
thixocasting 348
thread 523, 525
– coefficient 534
– rolling 386
three-cylinder
– crankshaft 693
– pump 704
three-force member 32
three-piece bogie 1070, 1071
three-spool high-performance core engine 813
three-way catalyst (TWC) 731
throttle body injection 723
throttle valve 724
through-bolted joint 530
throughput 835, 836
throw number 901
throw-back 899
thrust bearing 582
thyristor 1191
tightening
– factor 532
– torque 535
tilt 875
tilted idler station 875
tilting effect 546
tilt-table sorter 922
time
– flow function 839
– yield locus (TYL) 839
time-of-flight difference 219
time-strain-to-fracture (TSF) 202
time–temperature transition (TTT) 240
time–temperature–precipitation (TTP) 195
timing chain 857
tire drive 924
titanium
– -aluminum nitride (TiAlN) 429, 430
– carbide (TiC) 430, 431
– carbonitride (TiCN) 430
– diboride (TiB_2) 289
– nitride (TiN) 429–431
toggle press 403
tolerance
– frame 478
– specification for lengths 477

tong load handling device 927
tonnes per centimeter (TPC) 1150
tool
– clamping device 433
– construction 374
– wear 426
tooling 433
tool-life equation 418
toothing 596
top
– chain 859
– dead center (TDC) 403, 684, 716
– of rail (TOR) 1064
top-level aircraft requirements (TLAR) 1008, 1089
topping cycle 1228
torque
– current loop 1206
– DC motor 1208
– induction motor 1209, 1210
torsion
– test 171, 367
– testing 170
torsional
– critical speed 551
– load 547
– yield strength 171
total
– equivalent plastic strain 367
– quality management (TQM) 469
– strain 364
total efficiency 703
– hydraulic system 407
toughness 167
tow tractor 834
tower crane 938
toxic material 664
traceability 496
track 859, 891
– bed 1063
– brake 1080
– irregularities 1064
– loader 945
– rope 848
traction sheave 855, 948
traction-type elevator 948
traffic message channel (TMC) 1032
trailing edge (TE) 796
– extension 1111
– flap 1111
train
– brake 1080
– inspection time 1060
– à grande vitesse (TGV) 1059, 1210
– protection 1011
– reliability 1058
– stopping time 1058
– wheel 862
tram wheel 1070
transfer 837
– chute 875
– equipment 834
– function 479
transformer 1202
– equation 1203
– ideal 1204
– real 1204
transient process 68
transistor 1187
transition length 874
translation property 13
transmission 691
– chain 857
– electron microscopy (TEM) 139, 156, 272
– ratio 606
transport
– airplane 1136
– chain 830
transportable moisture limit (TML) 843
transportation 837
– demand 1000
– disk 885
– quality 1058
– technology 998
transportation-related noise 998
transversal direction (TD) 160
transverse
– center of gravity (TCG) 1148
– movement 1150
– pin jointing 515
transverse stability 1146, 1148
– theory 1151
traveling-grate stoker 1244
tree diagram 471
trends in grinding 443
Tresca flow condition 366
TRIAC 1192
triangle strand 850
triangulation sensor 494
triaxial shear tester 841
tribochemical reaction 302, 310
tribological system (TS) 294
– contact geometry 298
– elements of 295
– structure of 294
tribosystem 294
tributaries 634
tricycle landing gear 1113
triode for alternating current (TRIAC) 1192
triple point 65
trolley 891, 950
– conveyor 890
tropical
– freshwater (TF) 1152
– saltwater (T) 1152
trough
– chain conveyor 882
– screw conveyor 899
troughed belt conveyor 864
troughing angle 866
truck 834
true
– airspeed (TAS) 1101
– strain increment 364
– stress 365
– to gauge 857
truss structure 34
tube
– chain conveyor 882, 885
– drawing machine 402
– hydroforming 399, 401
tubular
– chute 916
– product 772
tungsten carbide 430
turbine 722, 800
– blade design 795
– engine-propeller 1113
– equation 779
– inlet temperature 807
– low-pressure (LPT) 803
– mass flow 825
– operation 815
– radial 781
– reheat (RT) 803
– row 779
– stator blade profile 798
turbocharged 716
turbocharger (TC) 745
turbocharging 719
turbocompounding 721
turbofan engine 1113
turbojet engine 1113
turbomachinery 800
– stage 777, 786
turbulence chamber 735
turbulent flow 122

turning 413
turning process 386, 413
turntable 922
turret truck 952, 977
twenty-foot equivalent unit (TEU) 1139
twin turbocharger 721
twin-aisle transport fuselage 1112
twinning 361
twin-spool
– core engine 802
– engine 810
twist
– drill 417
– tendency 850
two-force member 32
two-part catalytic converter 743
two-point contact 1068
two-stage compression process 714
two-step splice 873, 874
two-stroke cycle 716
type of
– boiler 1237
– friction 299
– loading 505
– pipe 624
– toothing 600
– transmission 688

U

U-groove track wheel 860
ultimate tensile
– strength (UTS) 167
– strength/stress (UTS) 167, 250, 1158
ultrahigh-capacity aircraft (UHCA) 1008, 1089
ultrahigh-efficiency gas turbine (UHEGT) 809, 824, 825
ultrasonic (US) 443
– A-scan 217
– far field 217
– machining (USM) 451
– near field 217
– pulse-echo technique 217
– sound field 217
– testing 217
– testing (UT) 763
– transducer 217
– wave 217
ultrasonically assisted grinding 444
ultra-supercritical steam (USC) 1226
ultraviolet (UV) 285
unalloyed cast steel 333
unburned hydrocarbon (UHC) 740
unburnt carbon loss (UCL) 1249
unconfined yield strength 839
unconsolidated bulk density 842
underfeed stoker 1244
unfired pressure vessel (UPV) 769
uniaxial
– shear tester 841
– stress state 365
unified numbering system (UNS) 245
uniform building code (UBC) 758
uninterruptible power supply (UPS) 1268
unit 1275
– injector 727
– pump 726
unit in
– luminosity 1280
– optics 1282
– thermodynamic 1279
universal
– Bauhaus 679
– length gauge 481
unmanned
– aerial vehicle (UAV) 1090
– aircraft system (UAS) 1090
– combat air vehicle (UCAV) 1091
unstable crack 178
upper yield stress (UYS) 167
upper-bound method 369
upright ship stability 1146
upsetting 359, 372
– ratio 372
uptime 402
urbanization 1057
US Space Shuttle 1092
US standard atmosphere 1095
use analysis 676
utility analysis 642

V

vacancy diffusion 143
vacuum
– lifter 927
– molding 344
– monitoring, comparative 230
valence band 1183
valid function 635
valve 705
– timing 719
van carrier 954
vapor 75, 76, 79
– power plant 106
– refrigeration plant 107
variable
– pitch propeller (VPP) 1157
– turbine geometry (VTG) 745
variable-pressure SEM (VPSEM) 156
variational principle, Markov's 371
VDI-guideline 354
vector 4, 27
vehicle
– acceptance 1061
– design process 1088
– nose 1079
– software 1040
– structure 1021
velocity diagram 782
vertical
– carousel 978
– center of gravity (VCG) 1149
– take-off and landing (VTOL) 1007
– transport 876
vertically double-diffused MOS (VDMOS) 1191, 1192
very
– large commercial transport (VLCT) 1008, 1089
– narrow aisle (VNA) 952
vessel stability 1149
V-groove 855
– track wheel 860
vibrating stoker 1244
vibratory conveyor 834, 900
Vickers hardness 169
– number (VHN) 169
Vickers pyramid hardness (VPH) 169
Vincent press 405
vinyl ester resin (VE) 621
virtual
– reality (VR) 1041
– running friction coefficient 862
– styling process 1041
viscosity 318, 736
– group 319
– index (VI) 313
visioplasticity method 370
visual testing 226

visualization of airflow 1046
VNA warehouse 977
volatile organic
– compound (VOC) 739
– fraction (VOF) 741
voltage
– amplitude 1201
– diffusion 1185
– effective 1201
– in three-phase network 1205
– peak to peak 1201
voltage source
– ideal 1196
– real 1196
volume constancy 365
volume-specific energy 688
volumetric
– efficiency 702, 715, 718, 719, 837
– expansion coefficient 90
– flow rate 836
– heat release 1251
von Mises flow condition 366
vortex
– distribution 792
– motion 897
vulcanization 873

W

walking mechanism 924
wall
– liner 842
– yield locus (WYL) 840
wall friction 840
– angle 840
– testing 842
Wankel engine 684
waste gate 720
water
– content 736
– treatment 1237
– vapor 75
waterjet cutting 447
waterjet machining 448
– abrasive (AWJ) 448
waterline 1143
waterplane area 1143
– coefficient 1143
water-tube boiler 1239
Watts linkage 1074
wave
– drag 1106
– resistance 1156
wavelength-dispersive x-ray
– spectrometer (WDX) 157
– spectroscopy (WDX) 159
waviness profile 488
wear 302, 846
– energy density 305
– mechanism 302, 846
– profile 303
– testing 846
– types of cutting tools 412
wear-resistant material 429
weight
– estimate 1149
– loaded valve 705
– management 1051
weld procedure specification (WPS) 763
welded joint 649
welding 542, 770
wet-bottom furnace 1245
wet-bulb temperature 114
wheel 859
– conveyor 920
– flange 861
– loader 945
– profile 1066
wheel–rail
– contact 1067
– interaction 1066
wheelset 1069, 1070
wheel-slide protection (WSP) 1011
whirl-chamber 724
wind
– energy 1264
– guard 876
– load 758
– turbine 1264
wing
– area 1107
– box 1133
– planform parameters 1110
winter
– North Atlantic saltwater (WNA) 1152
– saltwater (W) 1152
wiper bending 393
wire 849
– core (WC) 852
– electro-discharge machining (WEDM) 450
– rope 848, 849
– snap ring 521
– strand core (WSC) 852
– tensile strength 849
wire drawing 358
– machine 402
– process 382
Wöhler curve 510
woodruff key joint 553
work 402, 403
– cycle 683
– hardening 366
– machine 683
working
– chamber 683, 685, 686, 704
– cycle 833
workpiece coordinate system 485
World War I (WWI) 1091
wrap angle 855
wrinkling 383, 390, 402
wrought material 326

X

x-ray
– diffraction (XRD) 152, 280
– fluorescence spectroscopy (XRF) 152
x-ray-exited photoelectron spectroscopy (XPS) 159

Y

Y cycle 944
Y-25 bogie 1072
yard 970
yaw damper 1128
yawing moment 1099
– coefficient 1126
yield
– condition 365
– locus (YL) 838
– point elongation (YPE) 167
– strength 166
Young's modulus
– plane strain 395
Young's modulus 166

Z

zeroth law of thermodynamics 63
zirconium-corundum (ZrO2 with Al2O3) 441
z-kinematic 944
zone in chip formation 411